30TH SYMPOSIUM ON COMPUTER AIDED PROCESS ENGINEERING

PART A

Edited by

SAURO PIERUCCI, FLAVIO MANENTI, GIULIA LUISA BOZZANO AND DAVIDE MANCA

COMPUTER-AIDED CHEMICAL ENGINEERING, 48

ELSEVIER

30TH EUROPEAN SYMPOSIUM ON COMPUTER AIDED PROCESS ENGINEERING

PART A

30TH EUROPEAN SYMPOSIUM ON COMPUTER AIDED PROCESS ENGINEERING

PART A

Edited by

Sauro Pierucci
AIDIC Servizi s.r.l.,
Milano, Italy,
sauro.pierucci@polimi.it

Flavio Manenti
SuPER Team, Sustainable Process Engineering Research
Dipartimento di Chimica, Materiali e Ingegneria Chimica,
Politecnico di Milano, Milano, Italy,
flavio.manenti@polimi.it

Giulia Luisa Bozzano
SuPER Team, Sustainable Process Engineering Research
Dipartimento di Chimica, Materiali e Ingegneria Chimica,
Politecnico di Milano, Milano, Italy,
giulia.bozzano@polimi.it

Davide Manca
PSE-Lab - Process Systems Engineering Laboratory,
Dipartimento di Chimica, Materiali e Ingegneria Chimica,
Politecnico di Milano, Italy,
davide.manca@polimi.it

ELSEVIER

Amsterdam – Boston – Heidelberg – London – New York – Oxford
Paris – San Diego – San Francisco – Singapore – Sydney – Tokyo

Elsevier
Radarweg 29, PO Box 211, 1000 AE Amsterdam, Netherlands
The Boulevard, Langford Lane, Kidlington, Oxford OX5 1GB, UK
50 Hampshire Street, 5th Floor, Cambridge, MA 02139, USA

Notices
Knowledge and best practice in this field are constantly changing. As new research and experience broaden our understanding, changes in research methods, professional practices, or medical treatment may become necessary.

Practitioners and researchers must always rely on their own experience and knowledge in evaluating and using any information, methods, compounds, or experiments described herein. In using such information or methods they should be mindful of their own safety and the safety of others, including parties for whom they have a professional responsibility.

To the fullest extent of the law, neither the Publisher nor the authors, contributors, or editors, assume any liability for any injury and/or damage to persons or property as a matter of products liability, negligence or otherwise, or from any use or operation of any methods, products, instructions, or ideas contained in the material herein.

British Library Cataloguing in Publication Data
A catalogue record for this book is available from the British Library

Library of Congress Cataloging-in-Publication Data
A catalog record for this book is available from the Library of Congress

ISBN (Part A): 978-0-12-823511-9
ISBN (Set) : 978-0-12-823377-1
ISSN: 1570-7946

Publisher: Susan Dennis
Acquisition Editor: Kostas Marinakis
Editorial Project Manager: Lena Sparks
Production Project Manager: Paul Prasad Chandramohan
Designer: Greg Harris

Typeset by SPi Global, India

Contents

Preface

This volume of the Computer-Aided Chemical Engineering series puts together a selection of the contributions presented at the 30th European Symposium on Computer-Aided Process Engineering (ESCAPE), originally scheduled in Milano, Italy, from May 24th to 27th, 2020. Due to Covid-19 contingency, ESCAPE30 has been presented as Virtual Symposium from August 30th to September 2nd, 2020.
This 30th event of the ESCAPE series is a continuation of the conferences under the auspices of the CAPE Working Party of the European Federation of Chemical Engineering (EFCE).

The conference has been organized since 1992, starting with two meetings in 1992 in Denmark and France, and since then having one event annually. Hosting countries to the conference have been Austria (1993, 2018), Ireland (1994), Slovenia (1995, 2016), Greece (1996, 2011), Norway (1997), Belgium (1998), Hungary (1999, 2014), Italy (2000, 2010), Denmark (1992, 2001, 2015), The Netherlands (2002, 2019), Finland (2003, 2013), Portugal (2004), Spain (2005, 2017), Germany (2006), Romania (2007), France (1992, 2008), Poland (2009), and the United Kingdom (2012).
The themes of ESCAPE-30 have been selected after a comprehensive discussion with the CAPE Working Party members and the scientific community. The particular topics within these overarching themes have been formulated to allow researchers from CAPE-related sciences to present their results and exchange valuable knowledge and experience. The themes and topics include:

Theme 1: Modelling and Simulation
Theme Coordinators: Ana Barbosa-Povoa (Spain), David Bogle (UK)
New modelling approaches, Metamodeling, Multi-scale New industrial applications

Theme 2: Synthesis and Design
Theme Coordinators: Antonio Espuna (Spain), Zdravko Kravanja (Slovenia)
Process/Supply chain, Synthesis and design, Advanced materials, Products design, Process intensification, Micro and nano applications. Design for reliability and safety

Theme 3: Process control and operations
Theme Coordinators: Sebastian Engell (Germany), Sigurd Skogestad (Sweden)
Scheduling, operability, Flexibility and optimization under uncertainty, Supply-chains optimization and logistics, Off- and on-line control, Real-time optimization, Nonlinear model predictive control

Theme 4: CAPE in Sustainable Energy Applications
Theme Coordinators: Fabrizio Bezzo (Italy), Francois Marechal (Switzerland)
Heat and power integration, Waste-to-energy applications, Renewable resources in total-site integration, Integration of energy sources & sinks, Reliable dynamic supply & demand

Theme 5: Bioresources, Bioprocesses and Biomedical Systems
Theme Coordinators: Antonis Kokossis (Greece), Stefan Radl (Austria)
Biorefineries, Biomolecular and genetic engineering, Bioreactors applications

Theme 6: Digitalization
Theme Coordinators: Filip Logist (Belgium), Flavio Manenti (Italy)
Cloud application, Digitalization of chemical processes, Industry 4.0

Theme 7: Concepts, Methods and Tools
Theme Coordinators: Xavier Joulia (France), Heinz A. Preisig (Norway)
Advances in numerical methods, Global mixed-integer optimization, Multiobjective optimization, Decision making under uncertainty and risk management, Big data management, methods and tools

Theme 8: Education in CAPE and Knowledge Transfer

Theme Coordinators: Patrizia Perego (Italy), Eric Shaer (France)

Best practices in academia, Continued training in a changing professional practice, Effective selling of high quality CAPE solutions to industry, Knowledge transfer hurdles, Effective exploitation of CAPE tools

ESCAPE-30 attracted 572 contributions from five continents (Europe, Americas, Africa, Asia and Australia). The papers have been reviewed and 345 selected for publication by the International Scientific Committee together with the help of 16 Theme Coordinators. We are deeply thankful for timely and careful reviews by these Scientists, as well as their invaluable help in suggesting lecture speakers..

As Editors of this special volume, we hope that the contributions in this edition of Computer Aided Process Engineering are excellent illustrations of the current state of the art in their respective field.

Sauro Pierucci
AIDIC Servizi srl, Milano

Flavio Manenti
Politecnico di Milano

Giulia Bozzano
Politecnico di Milano

Davide Manca
Politecnico di Milano

Organizing & Scientific Committee

Local National Organizers

Chairboard:	Giorgio VERONESI	(Techint, AIDIC)
	Giulia BOZZANO	(Politecnico di Milano)
	Davide MANCA	(Politecnico di Milano)
Members:	Raffaella DAMERIO	(AIDIC Accounting)
	Manuela LICCIARDELLO	(AIDIC Events)
	Sauro PIERUCCI	(AIDIC Servizi srl)
	Gaia TORNONE	(AIDIC Events)

International Scientific Committee

Chairboard

Sauro Pierucci (Past CAPE Chairman), AIDIC, Italy
David Bogle (EFCE Sc. Vice-President), University College London, United Kingdom
Flavio Manenti (CAPE Chairman), Politecnico di Milano, Italy

Members

Cristhian P. Almeida-Rivera, OPCW, The Netherlands
Olga Arsenyeva, Kharkov Polytechnical Inst., Ukraine
Norbert Asprion, BASF SE, Germany
Roberto Baratti, University of Cagliari, Italy
Ana Paula Barbosa Povoa, Instituto Superior Tecnico, Portugal
Andre Bardow, RWTH Aachen University, Germany
Fabrizio Bezzo, University of Padua, Italy
Lorenz Biegler, Carnegie Mellon University, USA
Giulia Bozzano (CAPE Secretary), Politecnico di Milano, Italy
Xi Chen, Zhejiang University, China
Selen Cremaschi, Auburn University, USA
Vasile Mircea Cristea, Babes-Bolyai University, Romania
Giorgia De Guido, Politecnico di Milano, Italy
Mario Eden, Auburn University, USA
Sebastian Engell, TU Dortmund, Germany
Antonio Espuna, Universitat Politecnica de Catalunya, Spain
Michael Fairweather, University of Leeds, United Kingdom
Miroslav Fikar, Slovak University of Technolog, Slovakia
Rubens Maciel Filho, Unicamp University, Brazil
Ferenc Friedler (EFCE Charity Trustee), Pazmany Peter Catholic University, Hungary
Rafiqul Gani (Past EFCE President), PSE for SPEED, Denmark
Ignacio Grossmann, Carnegie Mellon University, USA
Rene' Hofmann, TU Wien, Austria
Xavier Joulia, University of Toulouse, France
Petro Kapustenko, National Technical University, Ukraine
Anton Kiss, University of Manchester, United Kingdom
Antonis Kokossis, National Technical University of Athens, Greece
Emilia Kondili, University of West Attica, Greece
Andrzej Kraslawski (Past CAPE Chairman), Lappeenranta University of Technology, Finland

Zdravko Kravanja, University of Maribor, Slovenia
Milan Kubicek, Prague Institute of Chemical Technology, Czech Republic
Abderrazak Latifi, University of Lorraine, France
Gregoire Leonard, Universite' de Liege, Belgium
Filip Logist, BASF, Belgium
Davide Manca, Politecnico di Milano, Italy
Seyed Mansouri, Technical University of Denmark, Denmark
Christos Maravelias, Carnegie Mellon University, USA
Francois M.A. Marechal, Ecole Polytechnique Federale de Lausanne Switzerland
Emanuele Martelli, Politecnico di Milano, Italy
Henrique Matos, Universidade de Lisboa, Portugal
Natalia V. Menshutina, Mendeleyev University of Chemical Technology, Russia
Ruth Misener, Imperial College London, United Kingdom
Peter Mizsey, Budapest University, Hungary
Stefania Moioli, Politecnico di Milano, Italy
Ludovic Montastruc, University of Toulouse, France
Iqbal Mujtaba, University of Bradford, United Kingdom
Stavros Papadokonstantakis, Chalmers University of Technology, Sweden
Patrizia Perego, University of Genoa, Italy
Bernhard Peters, Universitè du Luxembourg, Luxembourg
Esfratios Pistikopoulos, Texas A&M University, USA
Igor Plazl, University of Ljubljana, Slovenia
Valentin Plesu, University POLITEHNICA of Bucharest, Romania
Heinz Preisig, Norvegian University, Norway
Luis Puigjaner, Universitat Politecnica de Catalunya, Spain
Stefan Radl, TU Graz, Austria
Esfratios Reklaitis, Purdue University, USA
Francesco Rossi, Purdue University, USA
Jelenka Savkovic-Stevanovic, University of Belgrade, Serbia
Eric Shaer, University of Lorraine, France
Gurkan Sin, Technical University of Denmark, Denmark
Sigurd Skogestad, Norwegian University of Science and Technology, Norway
Jan W. Thullie, Silesian University of Technology, Poland
Stefania Tronci, University of Cagliari, Italy
Anjan K. Tula, Zhejiang Universiity, China
Metin Turkay, Koc University, Turkey
Natasha G. Vaklieva-Bancheva, Bulgarian Academy of Sciences, Bulgaria
Petar Varbanov, Brno University of Technology, Czech Republic
Serafim D. Vlaev, Bulgarian Academy of Sciences, Bulgaria
Siyu Yang, South China University, China
Zhihon Yuan, Tsinghua Universiity, China
Maria Regina Maciel Wolf, Unicamp University, Brazil
Lei Zhang, Dalian University of Technologys, China
Lingyu Zhu, Zhejiang University of Technology, China
Edwin Zondervan, University of Bremen, Germany

Editor Biography

PIERUCCI SAURO

Sauro Pierucci was Full Professor in Chemical Engineering at CMIC Politecnico di Milano, where he graduated in Chemical Engineering in 1969. He retired in 2016.

He was responsible of the course “Chemical Plant” in the faculty of Chemical Engineering at Politecnico di Milano.

His research interests focused on Process System Engineering, Modelling, Online Control and Optimisation of chemical plants (experiences c/o Oxychem (Houston), PolimeriEuropa (France), Erg (Priolo)).
He was Vice President of AIDIC (Italian Association of Chemical Engineering) until 2007 and today covers the office of member of the executive board.
He is responsible of the events organized by AIDIC Servizi srl, held by AIDIC.

He was member of EFCE (European Federation of Chemical Engineering) executive board until 2010.
He has been editor of several international issues as: “Computer Aided Chemical Engineering”, Vol. 8, Elsevier Science, Amsterdam, 2000; “Computers & Chemical Engineering”, Vol. 25, Issue 4-6, Pergamon.2010.
He is editor in chief of Chemical Engineering Transactions Journal, published by AIDIC.
He is author of more than 200 scientific publications.
He was awarded by “the Dieter Behrens Medal” from EFCE, in 2017
Today is President of AIDIC Servizi Srl, a limited company owned by AIDIC.

Sauro Pierucci, Flavio Manenti, Giulia Bozzano, Davide Manca (Eds.)
Proceedings of the 30th European Symposium on Computer Aided Process Engineering (ESCAPE30), May 24-27, 2020, Milano, Italy.
http://dx.doi.org/10.1016/B978-0-12-823377-1.50001-X

Computer-aided Semi-empirical Model of Interphase Mass and Enthalpy Transfer in a Packed Column Distillation Process

Goro Nishimura,[a*] Kunio Kataoka,[a] Hideo Noda,[a] Naoto Ohmura[b]

[a]*Kansai Chemical Engineering Co., Ltd, Minami-nanamatsu-cho, Amagasaki, 660-0053, Japan*
[b]*Dept. Of Chemical Science and Engineering, Kobe University, Rokkodai-cho, Nada, Kobe, 657-8501, Japan*
Nishimura@kce.co.jp

Abstract

The objective of this study is to model the transport phenomena in packed column distillation with the aid of experiment and computer-aided process simulation. The main concept is in that local distillation efficiency *HETP* is considered as the height of control volume for shell balance of mass and enthalpy, so that it becomes possible to bridge between the ideal and real processes. Distillation experiment was conducted under the total-reflux condition. Determination of local *HETP*s was performed by comparing the vertical temperature distribution experimentally observed with the stage-by-stage temperature distribution calculated by computer process simulation. In a manner similar to the analogy analysis of a single-phase boundary layer flow over a flat plate, a semi-empirical model of local similarity between simultaneous interphase mass and enthalpy transfer was successfully built by experiment collaborating with a computer-aided process simulation.

Keywords: mass and enthalpy transfer model, distillation, packed column, similarity

1. Introduction

A packed column distillation proceeds with non-isothermal and counter-diffusional interphase mass transfer accompanied with phase transformation. This complicated mechanism of mass and enthalpy transfer makes not only theoretical but also experimental approaches difficult. Except for the mass transfer model by Bravo *et al.* (1985), there are few investigations analyzing from a viewpoint of transport phenomena. Especially there is no investigation dealing with local variation of mass and enthalpy transfer in packed column distillation. This research deals with a semi-empirical model by making up the mutual defects between the experiment in a real column and the theoretical process simulation based on the equilibrium stage model.

2. Modeling Concept --- Shell Balance and Definition

The concept of modeling is in how to combine the continuous distillation behavior observed in a real packed column with the theoretical stage-by-stage distillation behavior calculated by an equilibrium-stage model in an ideal trayed column. As shown in Figure 1, a cylindrical control volume for shell balance is defined in a packed column. A local *HETP* (Height Equivalent to a Theoretical Plate) obtained at *j*th theoretical stage of process simulation is considered as the *j*th shell height h_{etp} (m) of the real

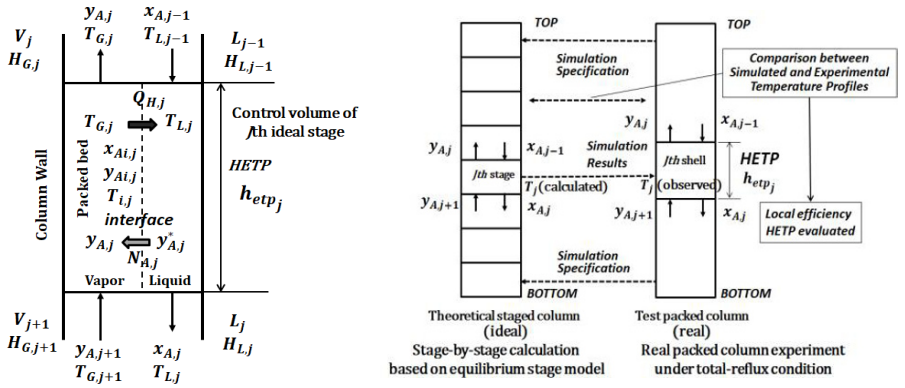

Figure 1 Definition of control volume for shell balance of mass and enthalpy and interrelation of ideal-state stage-by-stage data by computer process simulation with actual experimental data obtained in a real packed column.

differential contacting column. This implies that local distillation efficiency is taken into account in modeling of the real column distillation.

The volumetric mass transfer coefficients $k_{yA}a$, $k_{xA}a$, $K_{yA}a$ $(kmol/m^3s)$ are defined by the molar-flux N_A in the *j*th control volume (y_A, x_A, : vapor- and liquid-phase mole fractions, subscript *A*: component A, *i*: interface, $l.m.$: logarithmic mean):

$$N_{Aj} = V_j y_{Aj} - V_{j+1} y_{Aj\ 1} = \left(k_{yA}a\right)_j \left(y_{Aj,i} - y_{Aj}\right) h_{etp,j}$$
$$= \left(k_{xA}a\right)_j \left(x_{Aj} - x_{Aj,i}\right) h_{etp,j} = \left(K_{yA}a\right)_j \left(y_A^* - y_A\right)_{l.m.} h_{etp,j} \quad (1)$$

Here y_A^* is the bulk concentration of the liquid phase expressed with the units of the gas-phase concentration. Similarly the volumetric enthalpy transfer coefficients $h_G a$, $h_L a$, Ua (W/m^3K) are defined by the enthalpy-flux Q_H equation (T_G , T_L :vapor- and liquid-phase temperature (K) , H_G , H_L : enthalpy $(J/kmol)$, V , L : superficial molar velocity $(kmol/m^2s)$, subscript *G, L*: vapor- and liquid-phase)

$$Q_{Hj} = V_{j\ 1} H_{Gj+1} - V_j H_{Gj} = \left(h_G a\right)_j \left(T_{Gj} - T_{ij}\right) h_{etp,j}$$
$$= \left(h_L a\right)_j \left(T_{ij} - T_{Lj}\right) h_{etp,j} = \left(U\ a\right)\ \left(T_G - T_L\right)_{l.m.} h_{etp\ j} \quad (2)$$

The interrelation between the ideal-state process simulation and the real column experiment is also shown in Fig.1, where *j*th stage of process simulation corresponds to the *j*th shell of a real column.

3. Process Simulation

A convenient process simulator package (PRO/II by Invensys.) serves as a McCabe-Thiele stage-by-stage calculation tool with an assumption of ideal equilibrium stage.

The stage-by-stage process simulation is conducted by the following equations:

(Mass and enthalpy balance set up around *j*th stage under total-reflux distillation)

$$M_{jk} = V_j y_{j,k} + L_j x_{j,k} - V_{j+1} y_{j+1,k} - L_{j-1} x_{j-1,k} = 0 \quad (3)$$

$$E_j = V_j H_{Gj} + L_j H_{Lj} - V_{j+1} H_{Gj+1} - L_{j-1} H_{Lj-1} = 0 \quad (4)$$

(Mass balance and cooling duty of overhead condenser)

$$M_{1k} = L_1 x_{1,k} - V_2 y_{2,k} = 0 \tag{5}$$

$$Q_1 = L_1 H_{1} - V_2 H_{G2} = 0 \tag{6}$$

(Mass balance and heating duty of bottom reboiler)

$$M_{Nk} = V_{Nk} y_{N,k} - L_{N-1} x_{N-1,k} = 0 \tag{7}$$

$$Q_N = V_N H_{GN} - L_{N-1} H_{LN} = 0 \tag{8}$$

(Equilibrium coefficient and vapor-liquid equilibrium condition)

$$K_{j\,k} = p_{k,sat}\left(T_j\right)/P \tag{9}$$

$$S_{j,k} = K_{j,k} x_{j,k} - y_{j,k} = 0 \tag{10}$$

(Mole fraction requirement)

$$_{xj} = \sum_{k=1}^{m} x_{j,k} - 1 = 0 \tag{11}$$

$$_{yj} = \sum_{k=1}^{m} y_{j,k} - 1 = 0 \tag{12}$$

where the NRTL model is used to evaluate activity coefficients and physical properties of vapor and liquid of a binary mixture.

4. Experiment

4.1. Experimental apparatus and operating condition

Figure 2 shows an experimental packed column equipped with three structured packing beds stacked up in series. Those top, central and bottom beds have 1.90 m, 1.90 m, and 1.52 m in height, respectively. The inside diameter of the column is $D_T = 0.1532$ m.

The wire-mesh corrugated structured packing employed has the hydraulic equivalent diameter $d_{eq} = 0.018$ m and the specific surface area $a_p = 490$ m^2/m. In each empty space between the respective packing beds, a funnel-type liquid collector and a channel-type liquid distributor are installed in order to avoid maldistribution of liquid stream. Usually the *HETP* test (Lockett 1998) for practical design of packed columns is conducted under a total-reflux condition.

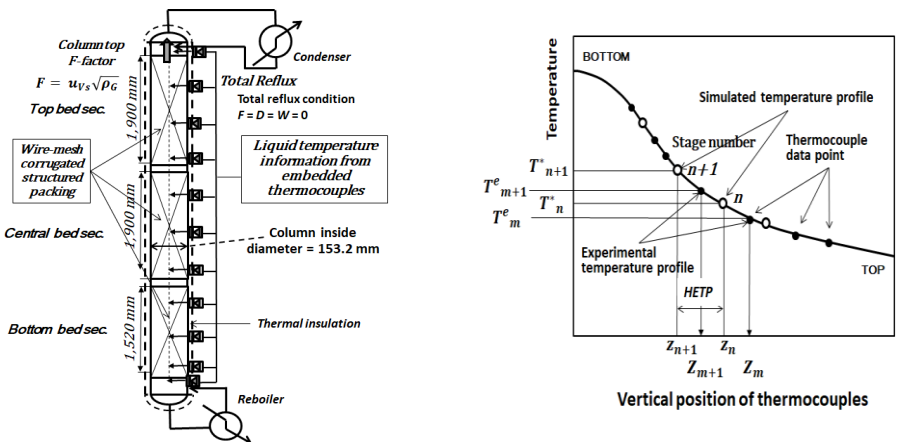

Figure 2 Structured packing column for total-reflux distillation experiment and graphic method for determining local *HETP*s.

In this study, the only total-reflux distillation experiment was conducted to obtain necessary information of performance parameters for a real packed column, which can be used for the specification of computer process simulation. In order to observe a vertical distribution of liquid temperature, 12 sheathed thermocouples were embedded on the centerline of the respective packed beds.

The F-factor $F = u_{Vs}\rho_G^{0.5}$ $(m/s)(kg/m^3)^{0.5}$ based on the superficial vapor velocity u_{Vs} (m/s) is defined at the column top as the control parameter of distillation experiment. Two kinds of binary solutions were tested: methanol-ethanol and methanol-n-butanol. However owing to the page limitation, the only experimental result of methanol-ethanol binary system is reported in this article since the methanol-n-butanol system shows almost the similar tendency of mass and enthalpy transfer. The purpose of this study is to analyze local transfer of mass and enthalpy for future process intensification by a semi-empirical model built with the mutual aid of the computer-aided process simulation and the total-reflux distillation experiment.

*4.2. Determination of local HETP*s

By using the experimental data and condition as the specification of process simulation, the stage-by-stage process simulation based on equilibrium-stage model was performed with a commercial simulator package (`PRO/II by Invensys Systems, Inc.). Assuming the total number of theoretical stages, the process simulation was conducted by a trial-and-error method to obtain a proper required number of theoretical stages until the calculated data became equal to the experimental data within an error limit.

As shown in Fig.2 (right), comparing the calculated liquid temperature T_n^{th} obtained at theoretical stage n with the experimental liquid temperature T_m^{ex} measured by the thermocouple embedded at a vertical position Z_m, a local value of *HETP* can be determined by the following equation:

$$HETP = h_{etp,j} = \frac{T_n^{th} - T_{n+1}^{th}}{T_m^{ex} - T_{m+1}^{ex}} \times (Z_m - Z_{m+1}) \tag{13}$$

4.3. Evaluation of local volumetric coefficient of mass and enthalpy transfer

The following simultaneous equation is obtained applying a mass transfer resistance equation based on two-film theory at arbitrary two positions j and $j+n$, where $1/k_{yA}a$ and $1/k_{xA}a$ are two unknowns to be solved.

$$\frac{1}{(K_{yA}a)_j} = \frac{1}{k_{yA}a} + \frac{m_j}{k_{xA}a} \tag{14}$$

$$\frac{1}{(K_{yA}a)_{j+n}} = \frac{1}{k_{yA}a} + \frac{m_{j+n}}{k_{xA}a} \tag{15}$$

where m is local slope of equilibrium curve and $K_{yA}a$ is local overall volumetric mass transfer coefficient experimentally obtained. Therefore the $k_{yA}a$, $k_{xA}a$ can be obtained as an approximate solution averaged between j and $j+n$. Figure 3 shows local distribution of the molar flux and volumetric mass transfer coefficients $k_{yA}a$, $k_{xA}a$. plotted against the vertical height of packing sections (L_B: total height of packing section). The right side figure suggests the possibility of similarity between the vapor bulk flow in a packed column and the boundary layer flow over a flat plate.

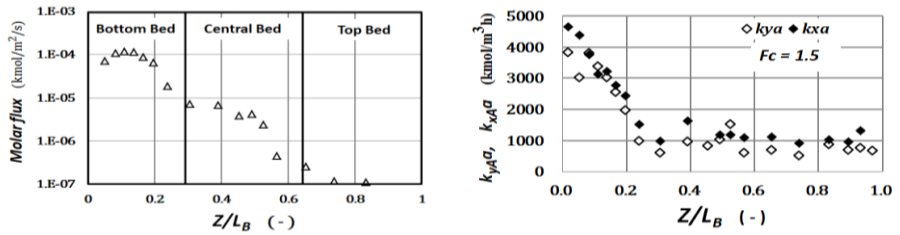

Figure 3 Vertical variation of molar-flux and vapor- and liquid-phase mass transfer coefficients when the column-top F-factor is 1.5 for methanol-ethanol system.

An unavoidable problem has arisen that in the column-top and column-bottom regions, the above elementary equations cannot become consistent to each other owing to almost linear variation of equilibrium curve. In those regions, the film coefficients $k_{yA}a$, $k_{xA}a$ were determined from the slope of the Tie-line $-k_{xA}/k_{yA}$ by assuming that the Tie-line at each stage has a perpendicular intersection with the equilibrium curve.

5. Experimental Results and Similarity Analysis

5.1. Definition of j-factors for volumetric film coefficients

Local variation of mass transfer in Fig.3 (right) resembles the streamwise variation of mass transfer in a boundary layer flow over a flat plate. The superficial vapor velocity is certainly kept almost constant in a packed distillation column. However the only big difference is in that the concentration or temperature changes downstream in the vapor bulk, as distinct from uniform concentration or temperature in the free stream of boundary layer flow. In order to discuss the existence of local similarity between mass and enthalpy transfer, the following j-factors can be defined using local *HETP* h_{etp} :

(vapor-phase) (liquid-phase)

$$j_{DG} = \frac{k_{yA}ah_{etp}}{V} Sc_G^{2/3} \qquad j_{DL} = \frac{k_{xA}ah_{etp}}{L} Sc_L^{2/3} \tag{16}$$

$$j_{HG} = \frac{h_G ah_{etp}}{Cp_G V} Pr_G^{2/3} \qquad j_{HL} = \frac{h_L ah_{etp}}{Cp_L L} Pr_L^{2/3} \tag{17}$$

Therefore in a manner similar to the analogy analysis of single-phase boundary layer flow over a flat plate, the following local length Reynolds numbers are defined based on the superficial relative velocity $u_s = u_{Vs} - u_{Ls}$:

(vapor-phase) (liquid-phase)

$$Re_{zG} = \frac{u_s \rho_G c_G \left(Z/d_{eq}\right)}{a_p \mu_G} \qquad Re_{zL} = \frac{u_s \rho_L c_L \left(Z/d_{eq}\right)}{a_p \mu_L} \tag{18}$$

where Z/d_{eq} indicates local distance from the lowest edge of the bottom bed. The developing-rate parameters c_G and c_L (-) are determined by a trial-and-error method changing them as the control parameter in correlation analysis.

5.2. Similarity analysis between simultaneous interphase transfer of mass and enthalpy

Figures 4 and 5 show the boundary-layer-like plot of j-factors against local length Reynolds numbers. Here F is the F-factor defined at the column top. It has been found that both the j-factors j_{DG}, j_{HG} for mass and enthalpy transfer indicate the same dependency of local length Reynolds numbers. This implies that local similarity exists between mass and enthalpy transfer in the vapor-phase film.

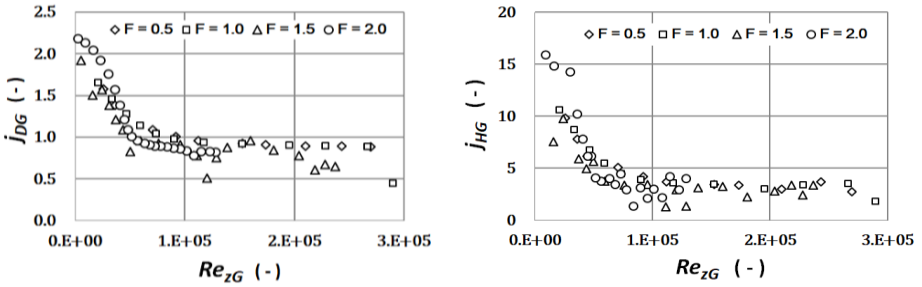

Figure 4 Local vapor-phase j-factors against vapor-phase length Reynolds number.
(c_G = 8.5 when $F = 0.5$, 6.0 when $F = 1.0$, 2.3 when $F = 1.5$, and 1.0 when $F = 2.0$)

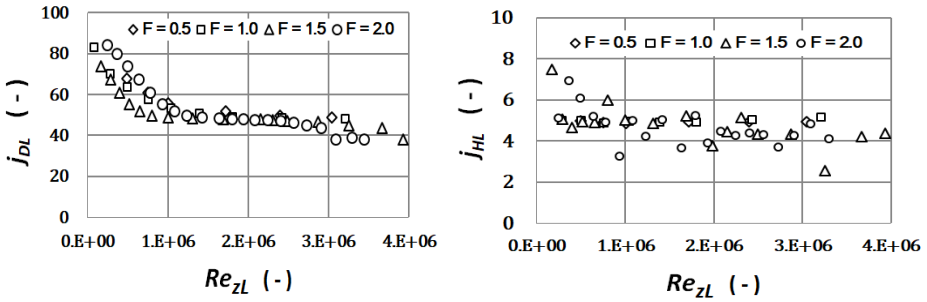

Figure 5 Local liquid-phase j-factors against liquid-phase length Reynolds number.
(c_L = 12.0 when $F = 0.5$, 6.3 when $F = 1.0$, 2.0 when $F = 1.5$, and 1.3 when $F = 2.0$)

The liquid-phase j-factors also indicate similar dependency, but the data points are slightly scattered. At any rate, it has for the first time been demonstrated that the transport phenomena in packed column distillation have local similarity between mass and enthalpy transfer and that the mass and enthalpy transport proceeds accompanied with the streamwise development similar to a boundary layer flow over a flat plate.

6. Conclusions

The local behavior of mass and enthalpy transfer in a structured-packing distillation column has been made clear by proposing a semi-empirical model of transport phenomena. It has been emphasized that the model based on total-reflux distillation experiment cannot be completed without the aid of computer-aided process simulation. It has for the first time been confirmed that the streamwise development of interphase transfer of mass and enthalpy can be correlated by length Reynolds number and that its packed column distillation proceeds downstream with local similarity in a manner similar to the development of a single-phase boundary layer flow over a flat plate.

References

J.L. Bravo, J.A. Rocha, and J.R. Fair, 1985, Mass Transfer in Gauze Packings, *Hydrocarb. Proc.*, 64(1), 91-95

M.J. Lockett, 1998, Easily Predict Structured-Packing HETP, *Chem. Eng. Prog.*, January, 60-66

Sauro Pierucci, Flavio Manenti, Giulia Bozzano, Davide Manca (Eds.)
Proceedings of the 30th European Symposium on Computer Aided Process Engineering (ESCAPE30), May 24-27, 2020, Milano, Italy.
http://dx.doi.org/10.1016/B978-0-12-823377-1.50002-1

Methanol Kinetics from Optimal Dynamic Experiments

Carsten Seidel[a], Achim Kienle[a,b]

[a]*Otto von Guericke University Magdeburg, Universitätsplatz 2, 39106 Magdeburg, Germany*
[b]*Max Planck Institute for Dynamics of Complex Technical Systems, Sandtorstraße 1, 39106 Magdeburg, Germany*
carsten.seidel@ovgu.de

Abstract

Methanol is an essential primary chemical in the chemical industry. Further, there is a growing interest in using methanol also for chemical energy storage. Excess electrical wind or solar energy can be converted to hydrogen and react with CO and CO_2 from bio-gas or waste streams to methanol. Suitable kinetic models are required for designing such processes. Established kinetics need to be extended to account for strongly varying input ratios of H_2, CO, and CO_2 in such applications leading to the need for dynamic process operation. Kinetic models for methanol synthesis accounting for dynamic changes of the catalyst morphology were proposed recently (Seidel et al., 2017). These comprise: a detailed model which relies on elementary reaction steps based on the work of (Vollbrecht, 2007) and a simplified kinetic model where elementary reaction steps are lumped together. Most of the kinetic parameters were determined from steady-state experiments reported by Vollbrecht. As a consequence identifiability was limited. In this contribution, we explore how parameter sensitivity and identifiability can be improved with dynamic experiments using optimal experimental design (OED), i.e., we determine suitable input variations by solving a dynamic optimal control problem. It is shown that for the lumped model, parameter sensitivity and identifiability can be improved. Identifiability is checked quantitatively by bootstrapping (Joshi et al., 2006). Although the sensitivity of the detailed model is also improved, the identifiability of this model has not improved significantly. Hence, it is concluded that additional measurement information is required for the full identifiability of the detailed model.
Keywords: methanol synthesis, optimal experimental design, kinetics

1. Introduction

$$CO + 2H_2 \rightleftharpoons CH_3OH \quad (1)$$

$$CO_2 + 3H_2 \rightleftharpoons CH_3OH + H_2O \quad (2)$$

$$CO_2 + H_2 \rightleftharpoons CO + H_2O \quad (3)$$

Methanol is essential for the chemical industry. It can be used as fuel and starting material for paraffin, olefins, or various organic chemicals like acetic anhydride. It is produced continuously in large amounts from synthesis gas using $Cu/ZnO/Al_2O_3$ catalysts. The reaction network involves three main reactions, i.e. hydrogenation of CO and CO_2 as well as the reverse water-gas shift reaction (RWGS) according to Eq. 1-3. With the upcoming

focus on renewable resources as a basis for energy supply, methanol also becomes a serious option as an energy carrier. Excess wind or solar energy can supply electrolysis for hydrogen, which reacts with CO/CO_2 to methanol for chemical energy storage. In the case of an energy shortfall, methanol can be transformed back into electrical energy. This option results in a more flexible grid and efficient usage of renewable resources. In this case, the methanol reactor will face strongly varying ratios in the feed. The most established kinetics are designed for steady-state operation and are therefore insufficient for these scenarios (Raeuchle et al., 2016). When the dynamic operation of methanol reactors is considered, forced periodic operation becomes an option to improve the process using asymmetrical transient effects (Petkovska et al., 2018). Therefore a detailed and a simplified kinetic model suitable for the dynamic operation were introduced. While the simplified model was identifiable using deterministic global optimization and showed good results for steady-state and dynamic operation, the detailed model was not fully identifiable with the existing data. In this paper, we are using optimal experimental design strategies to improve the identifiability of the detailed model. This approach gives an optimal dynamic control input for the feed for a dynamic experiment that is maximizing the information content and thereby improves the identifiability. As proof of concept, the strategy is also applied to the simplified model.

2. Kinetic Models

2.1. Model Equations

The reaction takes place in an isothermal micro-berty reactor (CSTR). For dynamic operation, accumulation on the catalyst (solid phase) has to be considered. Therefore a set of dynamic equations is formulated, where the left-hand side (LHS) describes the transfer between fluid and solid phase and the right-hand side (RHS) describes the reaction on the catalyst.

$$\left[n^G \cdot I + \mathrm{m}_{kat} q_{sat} p (I - Y) \frac{\partial \Theta}{\partial p} \right] \frac{dy}{dt} = \dot{n}_0 \left(y_0 - y \right) + m_{kat} (I - Y) \nu r \tag{4}$$

2.2. Simplified Model

The recently developed kinetics describe the reactions Eq. (1-3) using lumped reactions (Seidel et al., 2017). Three different surface centers are assumed and will be denoted by $\theta^{\square}$ for oxidized centers, θ^{*} for reduced centers, and $\theta^{\otimes}$ for hydrogen. All equations are summarized in Table 1.

The Arrhenius-equation describes the temperature dependence of the rate constants with six additional parameters (k_i & E_A). The equilibrium constants K_{P1}-K_{P3} are taken from (Vollbrecht, 2007). The unknown parameters were estimated by using deterministic global optimization and steady-state experimental data (Seidel et al., 2017). To explain transient effects, as seen in (Choi et al., 2001; Muhler et al., 1994; Nakamura et al., 2003; Peter et al., 2012) after feed changes, we considered a conversion of reduced to oxidized centers and vice versa which is described by the following dynamic equation:

$$\frac{d\phi}{dt} = k_1^+ \left(y_{H_2} (1 - \phi) - \frac{1}{K_1} y_{H_2O} \phi \right) + k_2^+ \left(y_{CO} (1 - \phi) - \frac{1}{K_2} y_{CO_2} \phi \right) \tag{5}$$

The two unknown parameters k_1^+ and k_2^+ are fitted to dynamic experiments.

2.3. Detailed Model

The model is based on the elementary reaction steps behind Eq. 1-3 with one rate determining step each (Seidel et al., 2017; Vollbrecht, 2007). The temperature dependence and the equilibrium constants are the same as for the lumped model. The corresponding equations are summarized in Table 1. Parameter estimation for this model was done by Bert Vollbrecht with gradient-based methods with non-satisfying results, which is probably caused by a non-convex problem with multiple minima. Even a deterministic global optimization did not converge for the steady-state experiments. This indicates that different parameters were not structurally identifiable for the existing experimental data.

Table 1: Reaction rates and surface coverage equations of both kinetic models

Eq.	Simplified model	Detailed model
r_{CO}	$(1-\phi)k_1 p_{CO} p_{H_2}^2 \left(1-\frac{1}{K_{P1}}\frac{p_{CH_3OH}}{p_{CO}p_{H_2}}\right)\theta^{\bigcirc}\theta^{\otimes}$	$(1-\phi)k_1\left(p_{CO}p_{H_2}^2-\frac{p_{CH_3OH}}{K_{P1}}\right)\theta^{\bigcirc}\theta^{\otimes}$
r_{CO_2}	$\phi^2 k_2 p_{CO_2} p_{H_2}^2\left(1-\frac{1}{K_{P2}}\frac{p_{CH_3OH}p_{H_2O}}{p_{CO_2}p_{H_2}^3}\right)\theta^{*2}\theta^{\otimes 4}$	$\phi^2 k_2\left(p_{CO_2}p_{H_2}-\frac{1}{K_{P2}}\frac{p_{CH_3OH}p_{H_2O}}{p_{H_2}^2}\right)\theta^{*2}\theta^{\bigcirc}$
r_{RWGS}	$\phi(1-\phi)^{-1}k_3 p_{CO_2}\left(1-\frac{1}{K_{P3}}\frac{p_{CO}p_{H_2O}}{p_{CO_2}p_{H_2}}\right)\theta^{*}\theta^{\bigcirc}$	$\phi(1-\phi)^{-1}k_3\left(p_{CO_2}-\frac{1}{K_{P3}}\frac{p_{CO}p_{H_2O}}{p_{CO_2}p_{H_2}}\right)\theta^{*}\theta^{\bigcirc}$
$\theta^{\otimes}$	$\left(1+\sqrt{K_{H_2}p_{H_2}}\right)^{-1}$	$\left(1+\beta_7\sqrt{p_{H_2}}\right)^{-1}$
$\theta^{\bigcirc}$	$\left(\begin{array}{l}1+K_{CO}p_{CO}+K^{\bigcirc}_{CH_3OH}p_{CH_3OH}\\+K^{\bigcirc}_{CO}p_{CO}\end{array}\right)^{-1}$	$\left(\begin{array}{l}1+\beta_8 p_{CO}+\beta_9 p_{H_2}^{3/2}p_{CO}+\beta_{10}p_{CH_3OH}\\+\beta_{11}p_{CO_2}\end{array}\right)^{-1}$
θ^{*}	$\left(\begin{array}{l}1+\frac{K_{H_2O}K_O}{K_{H_2}}\frac{p_{H_2O}}{p_{H_2}}+K_{CO_2}p_{CO_2}\\+K^{*}_{CH_3OH}p_{CH_3OH}+K_{H_2O}p_{H_2O}\end{array}\right)^{-1}$	$\left(\begin{array}{l}1+\beta_{13}\frac{p_{H_2O}}{p_{H_2}}+\beta_{16}\frac{p_{CH_3OH}}{p_{H_2}^{1/2}}+\beta_{14}p_{CH_3OH}\\+\beta_{15}\frac{p_{H_2O}}{p_{H_2}^{1/2}}+\beta_{12}p_{H_2O}\end{array}\right)^{-1}$

3. Optimal Experimental Design

To design an optimal experiment, we consider an objective which maximizes the information content and also minimizes the correlation between the parameters. In the present paper, we choose the E^*-criterion that minimizes the ratio of biggest and smallest eigenvalue of the Fisher-Information-Matrix (FIM) (Pronzalo and Walter, 1997).

$$obj = \min\left(\frac{\lambda_{max}}{\lambda_{min}}\right) \tag{6}$$

By minimizing this objective, we find an optimal control input that maximizes the sensitivity S for unknown parameters p of the functions f (Eq. (4-5)). For dynamic experiments, the sensitivity function is also time-dependent and has to be evaluated at every time point.

$$\dot{S} = \frac{df}{dx} S + \frac{df}{dp} \tag{7}$$

The overall sensitivity is calculated by evaluating the sensitivity of every time-point and is then used to calculate the FIM or respectively, the inverse, which is the covariance matrix. An experiment with high sensitivities raises the information content and therefore minimizes the correlation between the unknown parameters, resulting in more precise parameter estimation.

Available inputs for the optimal control are steps in concentration of CO, CO_2, H_2, temperature, and variable time between each step. The number of steps for the experiment is fixed because, after a certain amount of steps, repetitions occur. The following outputs can be measured: methanol, CO, CO_2, and H_2. They are therefore considered for the sensitivities. Additionally, we are assuming that ϕ from Eq. 5 is also measurable. For each model, the parameter estimation can be divided into three sub-problems that reduce the number of simultaneously estimated parameters (Seidel et al., 2017). For the optimization problem, we used a genetic algorithm (MATLAB) with a population size of 1000 and 30 generations. The result of this optimization is applied as the starting point for a second optimization with *fmincon* to check for nearby optima.

$$FIM = \begin{bmatrix} S(t_k) \\ S(t_{k+1}) \\ \vdots \\ S(t_{k+n}) \end{bmatrix}^T C_{y_t}^{-1} \begin{bmatrix} S(t_k) \\ S(t_{k+1}) \\ \vdots \\ S(t_{k+n}) \end{bmatrix} \tag{8}$$

4. Parameter Estimation

To evaluate the optimal experimental design, bootstrapping (1000 runs) is applied (Joshi et al., 2006). The standard approach relies on steady state experiments from (Vollbrecht, 2007), which are perturbed with some normal distributed measurement noise ($\sigma = 0.01$) After identification the noisy measurements translate in parameter distributions as indicated in the blue bars in Figure 1 & 2.

For the optimal experimental design, artifical experimental data were generated with the optimal controls from Section 3 and the same measurement noise as above. Parameter distributions obtained after identification are illustrated in red in Figure 1 & 2. The given values for the artificial dynamic experiments are marked as black lines in both figures. We are minimizing the residuals of CH_3OH, CO, CO_2, H_2 at the output, and additionally ϕ by using a Maximum-log-Likelihood estimator (Myung, 2003).

$$\min L = -\left(\log\sigma + \frac{1}{2}\log 2\pi - \frac{1}{2N\sigma^2} \sum_{i=1}^{N_k} \sum_{k=1}^{N} \left(y_i^M(t_k) - y_i^{EXP}(t_k) \right)^2 \right) \tag{9}$$

For the simplified and the detailed model, the parameter estimation is divided into three sub-problems. The first sub-problem takes all parameters for the CO-hydrogenation into account. These results are used for the other sub-problems, considering the parameters

for the CO_2-hydrogenation and the RWGS. In the case of the simplified model, the first sub-problem contains five unknown parameters, the second seven, and for the third four with a total number of 16 unknown parameters. The detailed model is also separated in three sub-problems considering six, nine and three unknown parameters for the first, second, and third sub-problem with a total number of 18 unknown parameters.

5. Results

For the simplified model, the standard design results in parameter distributions that are giving rise to different locally optimal parameter sets, as can be seen in Figure 1. Additionally, E_{A,CO_2}, K_{H_2}, $K^{\square}_{CH_3OH}$, and k_2 seem to be not identifiable using the standard design. Applying the OED, the parameter sets are showing definite improvement. The parameter distribution corresponds, as shown in Figure 1, with the used reference

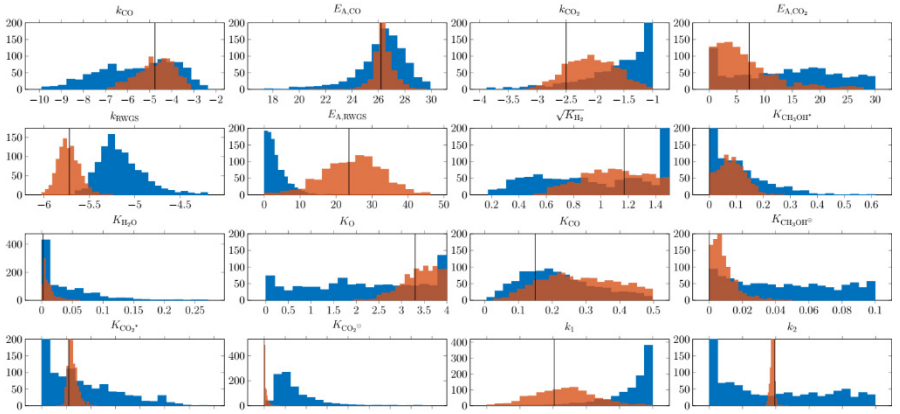

Figure 1: Parameter distribution simple model with OED (red), Standard design (blue) and reference value (black).

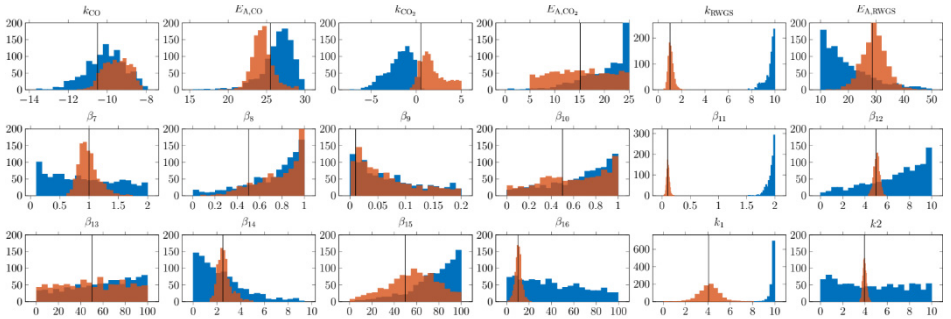

Figure 2: Parameter distribution detailed model with OED (red), Standard design (blue) and reference value (black).

parameter set, and the confidence intervals are 42.6% smaller compared to the standard design. The detailed kinetic model is, however, not completely identifiable with the standard design, which is pictured in the corresponding parameter distributions. For the majority of the parameters, the standard design results in distributions on the upper or lower bounds or in a uniform distribution of the allowed parameter region, as shown in Figure 2. When applying the OED, an apparent enhancement of the parameter distribution is noticeable. Ten parameters become identifiable with distinct distribution around the

reference parameter set. The parameters β_4, β_8, β_{10}, and β_{13} are still not identifiable with given measurement information. Nevertheless, the average confidence intervals for the detailed model is 21.2% smaller than the standard design.

6. Conclusion

The proposed optimal experimental design strategy was implemented, and the effectiveness is shown for the simplified model. The parameter sensitivity can be increased and confidence intervals decreased. Various parameters of the detailed model are, however, not identifiable. Additional measurement information like intermediates on the catalyst or adsorption constants under reaction conditions may improve the identifiability of the model. Besides, the shown method only uses local sensitivities and the linear approximation of the nonlinear model. So global sensitivity strategies (McRae et al., 1982) and derivation of the covariance matrix directly from the nonlinear model, like the sigma point method (Mangold et al., 2009), could improve the results and will be the object of future work.

Acknowledgements

Gefördert durch die Deutsche Forschungsgemeinschaft (DFG) – SPP2080 "Katalysatoren und Reaktoren unter dynamischen Betriebsbedingungen für die Energiespeicherung und -wandlung" - KL 417/6-1. Financial support by the German Research Foundation (DFG) is gratefully acknowledged through the priorty program SPP 2080 under the grant KL 417/6-1.

References

Y. Choi, K. Futagami, T. Fujitani, J. Nakamura, 2001. The difference in the active sites for CO2 and CO hydrogenations on Cu/ZnO-based methanol synthesis catalysts. Catal. Letters 73, 27–31.

M. Joshi, A. Seidel-Morgenstern, A. Kremling, 2006. Exploiting the bootstrap method for quantifying parameter confidence intervals in dynamical systems. Metab. Eng.

M. Mangold, R. Schenkendorf, A. Kremling, 2009. Optimal experimental design with the sigma point method. IET Syst. Biol. 3, 10–23.

G.J., McRae, J.W. Tilden, J.H. Seinfeld, 1982. Global sensitivity analysis-a computational implementation of the Fourier Amplitude Sensitivity Test (FAST). Comput. Chem. Eng.

M. Muhler, E. Törnqvist, L.P. Nielsen, B.S. Clausen, H. Topsøe, 1994. On the role of adsorbed atomic oxygen and CO2 in copper based methanol synthesis catalysts. Catal. Letters 25, 1–10.

I.J. Myung, 2003. Tutorial on maximum likelihood estimation. J. Math. Psychol.

J. Nakamura, Y. Choi, T. Fujitani, 2003. On the issue of the active site and the role of ZnO in Cu/ZnO methanol synthesis catalysts. Top. Catal. 22, 277–285.

M. Peter, M.B. Fichtl, H. Ruland, S. Kaluza, M. Muhler, O. Hinrichsen, 2012. Detailed kinetic modeling of methanol synthesis over a ternary copper catalyst. Chem. Eng. J. 203, 480–491.

M. Petkovska, D. Nikolić, A. Seidel-Morgenstern, 2018. Nonlinear Frequency Response Method for Evaluating Forced Periodic Operations of Chemical Reactors. Isr. J. Chem.

L. Pronzalo, E. Walter, 1997. Identification of parametric models from experimental data, Springer, Berlin

K. Raeuchle, L. Plass, H.-J. Wernicke, M. Bertau, M., 2016. Methanol for Renewable Energy Storage and Utilization. Energy Technol. 4, 193–200.

C. Seidel, A. Jörke, B. Vollbrecht, A. Seidel-Morgenstern, A. Kienle, 2017. Kinetic Modeling of Methanol Synthesis from Renewable Resources. Chem. Eng. Sci. 175, 130–138.

B. Vollbrecht, 2007. Zur Kinetik der Methanolsynthese an einem technischen Cu/ZnO/Al2O3-Katalysator. Otto-von-Guericke-Universität Magdeburg.

Sauro Pierucci, Flavio Manenti, Giulia Bozzano, Davide Manca (Eds.)
Proceedings of the 30th European Symposium on Computer Aided Process Engineering (ESCAPE30), May 24-27, 2020, Milano, Italy.
http://dx.doi.org/10.1016/B978-0-12-823377-1.50003-3

Rigorous Modelling and Simulation of the Mass transfer on the Trays of a Pilot Scale Distillation column

Mayra Margarita May-Vázquez, [a] Fernando Israel Gómez-Castro, [a,*] Mario Alberto Rodríguez-Ángeles [b]

[a] *Departamento de Ingeniería Química, División de Ciencias Naturales y Exactas, Campus Guanajuato, Universidad de Guanajuato, Noria Alta S/N, Col. Noria Alta, Guanajuato, Guanajuato, 36050, México, fgomez@ugto.mx*
[b] *Departamento de Ingeniería en Plásticos, Universidad Politécnica de Juventino Rosas, Calle Hidalgo 102, Comunidad de Valencia, Santa Cruz de Juventino Rosas, Guanajuato, 38253, México.*

Abstract

Distillation is a well-known separation process, which takes advantage on the differences on the relative volatilities of the components of a given mixture. Separation occurs on either trayed or packed towers, where simultaneous mass and heat transfer occurs. One of the mathematical models used to represent the phenomena occurring in distillation is the rate-based model. Opposite to the equilibrium model, the rate-based model avoids the use of efficiencies and computes mass and heat transfer rates. One of the most important requirements of the rate-based model is an adequate mass transfer model, whose structure depends on the kind of mixture and the trays/packing geometry.
In this work, a mass transfer model is proposed for the sieve trays on a pilot scale batch distillation column. In this column, a mixture of 50 mol% methanol and 50 mol% ethanol is separated. The column used in this work has four trays, a total condenser and a pot. The operation regime of the column is bubbling. The whole rate-based model of the column is solved using Matlab R2013a, and the composition and temperature profiles are obtained. The results indicate that rate-based model with the proposed mass transfer model has a mean decrease of 7% in the error for the compositions, in comparison with previously reported approaches.
Keywords: batch distillation, rate-based modelling, mass transfer model.

1. Introduction

Distillation is among the most important operations for the separation and purification of multicomponent mixtures in the chemical industry. This process is based on the differences on relative volatilities and boiling points between the components. Distillation can be done either in a continuous operational regime or a discontinuous regime (batch distillation). Batch processes are commonly used in pharmaceutical, food, and specialized products as alcoholic beverages, essential oils, perfume, pharmaceutic and petroleum products (Lucet et al., 1992). The advantages of batch distillation over a continuous distillation relies on its capacity to produce many different products.
Two models are commonly used to represent the phenomena occurring during distillation: the equilibrium model and nonequilibrium (rate-based) model. The first one assumes that phase equilibrium occurs in all the stages of the column, making use of efficiencies to predict the deviation from the actual performance of the column; the

second one avoids the use of efficiencies, instead, it involves calculations for the mass transfer rates between the phases. Rate-based model consist of material and energy balances for each phase, models for mass and energy transfer rates across the interface, and equilibrium relations for the interface compositions. An important requirement of the rate-based model is an adequate mass transfer model, which is related with the kind of mixture and the trays/packing geometry. Trays are used to contact the liquid and vapor phase and through these the mass transfer takes place. Trays are widely used in distillation columns because they are easy to design and have a relatively low cost. Correlations of mass transfer coefficients for a wide variety of contacting devices have been published in the literature. The mass transfer coefficients depend on properties such as viscosity and diffusivity, as well as on operating and design parameters such as flowrates and column diameter, tray or packing type and so on. Khrishnamurthy and Taylor (1985) published a mathematical model for nonequilibrium stages in multicomponent separation processes. The model includes the mass balance of each component in each phase, the heat balances, the mass transfer rate, energy transfer equations and the equilibrium equations at the interface. Gorak et al. (1991) found that the compositions predicted by the nonequilibrium model are closer to the experimental data than those predicted by an equilibrium model. Kooijman and Taylor (1995) presented a nonequilibrium model for the dynamic simulation of distillation columns. Nada et al. (2009) presented two models (equilibrium and nonequilibrium) to study the dynamic behavior of multicomponent azeotropic system in a batch column with bubble-cap trays. Taylor y Krishna (1993) used a model in which they consider the bubbling and jet regime for a sieve tray in a distillation column.

The batch column involves a time-dependent process, therefore requires differential equations for the molar and energy balances and algebraic equations for all other relationships; i.e. a differential-algebraic (DAE) system. There are methods for solve the DAE system: solver than employ backwards differentiation formulas (BDF) and one-step implicit methods (such as Runge-Kutta methods). In this work, a pilot-scale batch distillation column is modelled through a rate-based approach. A mass transfer model is proposed for the sieve trays on the column. The mass transfer model is incorporated to the rate-based model, and the whole set of equations is solved using a specialized software (Matlab R2013a).

2. Methodology

The present work concerns on the rigorous modelling and simulation of the mass transfer on the trays of a pilot scale distillation column using the rate-based model. The methodology can be divided in four stages: (i) experimental, (ii) simulation in Aspen Plus V8.8, (iii) development of the mass transfer model, and (iv) solution of the obtained system of equations (DAE), using Matlab R2013a.

The experimental work was performed in a batch distillation column with four sieve trays, a pot and a total condenser. Figure 1 shows a diagram of the column. The batch system separates a methanol/ethanol, mixture, with an initial composition of 50% mol of methanol. Initial charge of the mixture is 0.172 kmol. The operation is stopped at 80 minutes, with constant thermal duty of 500 W. Samples were taken in each stage and analyzed in a gas chromatographer.

The simulation in Aspen Plus V8.8 was performed to obtain preliminary values of the mass and heat transfer rates. Methodology for this simulation has been already reported in a previous work (May-Vázquez et al., 2019). These constant mass transfer rates are included in a first version of the rate-based model, which will be labeled as Model 1.

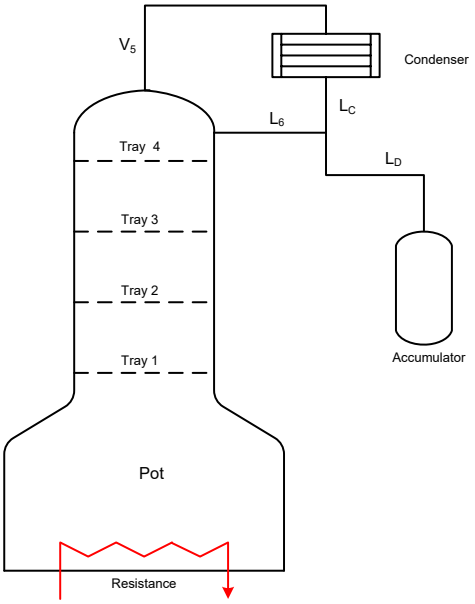

Figure 1.- Simplified representation of the batch column.

The proposed mass transfer model is based on the one reported by Locket (Taylor and Krishna, 1993), which considers a free bubbling regime and a spray regime. The first one is divided in jetting zone and free bubbling zone. In the second zone a distribution of bubble size is usually obtained. This model assumes a bimodal bubble size distribution (large and small bubbles). During the experimental work it was observed that the column operates in bubbling regime, with only one size of bubble. The Locket model is thus adapted for the system under study. The mass transfer model for the batch column is presented next.

The average molar fluxes:

$$N = c_t^V \beta^V K_{OV} \left(\Omega^V\right)^{-1} Q_I \left(y_{1E} - y_1^*\right) \tag{1}$$

Where c_t^V is mixture molar density of the vapor [mol/m^3], β^V is the bootstrap coefficient for the vapor, y_{iE} is the mol fraction on the component *i* in the vapor entering the tray and y_1^* is the mole fraction of the vapor in equilibrium with the bulk liquid.

The function Ω^V is defined as:

$$\Omega^V = \left(-N_{OV}\right) / \left(\exp\left(-N_{OV}\right) - 1\right) \tag{2}$$

The departure from equilibrium in the bubbles is given by:

$$Q_I = \exp\left(-N_{OV}\right) \tag{3}$$

The overall number of transfer units is:

$$N_{OV} = K_{OV} a' t \tag{4}$$

Overall mass transfer coefficient:

$$\frac{1}{K_{OV}} = \frac{1}{k^V} + \frac{c_t^V}{c_t^L}\frac{K_1}{k^L} \tag{5}$$

The mass transfer coefficient for the liquid phase:

$$k^L = 2\left(D^L \Big/ \left(\pi d \Big/ U\right)\right)^{1/2} \tag{6}$$

The vapor phase mass transfer coefficient

$$k^V = -\ln(1-F)/(a't) \tag{7}$$

The fractional approach to equilibrium in the bubbles

$$F = 1 - \frac{6}{\pi^2}\sum_{n=1}^{\infty}\frac{1}{n^2}\exp\left\{-n^2\pi^2 Fo\right\} \tag{8}$$

The Fourier number for the bubbles

$$Fo = 4D^V t \Big/ d^2 \tag{9}$$

Where d is the bubble diameter [m], a´ is the interfacial area per unit of volume of vapor in the bubbles, t is the residence time, K_1 is the equilibrium ratio, D^V is the vapor-phase Maxwell-Stefan diffusivity, D^L is the liquid-phase Maxwell-Stefan diffusivity and c_t^L is mixture molar density of the liquid. Hereby, the rate-based model including equations (1)-(9) for the calculation of the mass transfer rates will be labeled as Model 2.

The whole rate-based model of the pilot scale distillation column was reported by May-Vazquez et al. (2019). The solution of the model for the batch column requires initial values for all the time-dependent variables. The initial values required for the solution were computed by solving the model under total reflux for 10 minutes. With the initial values obtained, the simulation of the distillation column with the rate-based model was carried out. The rate-based model is codified and solved in Matlab R2013a, aiming to obtain the composition and temperature profiles. The simulation time was 80 minutes.

3. Results

In this section, the obtained experimental data is compared with the data predicted by the developed rate-based model. Table 1 shows the component mass transfer rates, the positive sign indicates that the transfer is from vapor to liquid. In the case of Model 2, the reported mass transfer rates are for t = 80 min.

The mass transfer rate equations were included in the rate-based model, the numerical method used to solve the system of differential and algebraic equations was Runge-Kutta with constant step size of 0.001.

Table 2.-Mass transfer rates (kmol/s)

	Mass transfer rate – Model 1		**Mass transfer rate – Model 2**	
Tray	Methanol	Ethanol	Methanol	Ethanol
4	-6.36E-08	5.69E-08	-6.47E-09	6.84E-09
3	-4.94E-08	3.98E-07	-5.48E-09	5.78E-08
2	-2.97E-08	2.67E-08	-3.91E-09	4.13E-09
1	-1.93E-08	1.74E-08	-1.73E-09	1.83E-09

The composition profiles obtained are presented in Figures 2 and 3.

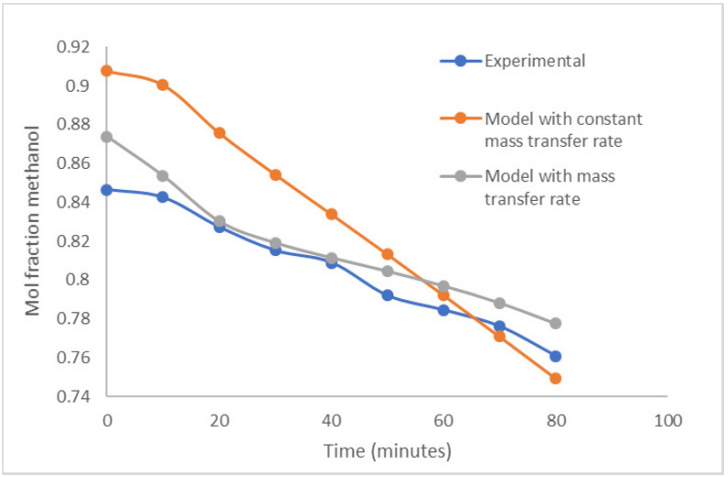

Figure 2.- Variation with time for liquid composition of methanol in the tray 1

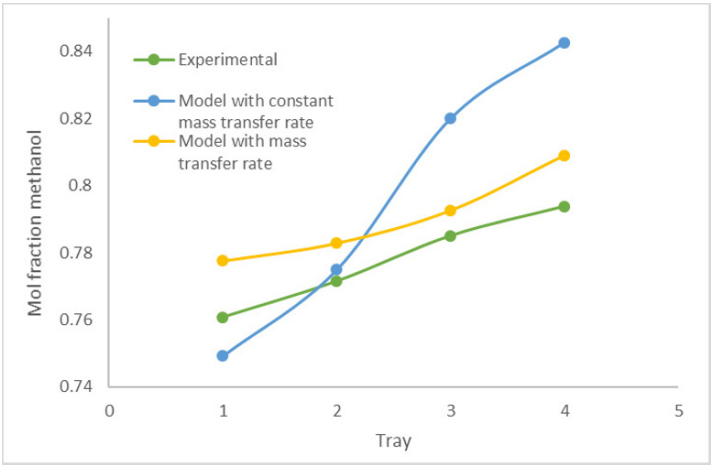

Figure 3.- Liquid composition profiles for methanol at 80 minutes.

Figure 2 shows the variation with time of the experimental and computed liquid composition of methanol in the tray 1. Methanol composition in tray 1 decreases as time

progresses since it is the light component, thus, it is expected to concentrate in the distillate. Figure 2 shows a good agreement between the experimental data and the results predicted by Model 2. In the case of Model 1, the composition of methanol decreases more rapidly because the mass transfer rate is higher compared to that obtained with Model 2. The deviations between the experimental data Model 2 were ±1.41%.

Figure 3 shows a comparison between the experimental and simulation results for methanol in the final time. For Model 2, the average error is 1.64%. Figure 3 shows a good agreement between the experimental results and Model 2. The composition of methanol in the liquid phase increases in each tray since it is the lightest component.

4. Conclusions

The mass transfer rate is an important variable in the rate-based model. The most important variables in the mass transfer model are the diameter of the bubble and the bubble rising velocities. The lower the bubble rising velocity, the smaller the mass transfer rate is, and less variation in the compositions of methanol is obtained.

The proposed mass transfer rate model, which originates Model 2, allows a best fit with experimental data than Model 1. The mass transfer model predicts higher mass transfer rates than Aspen Plus, making use of the experimental information to compute the mass transfer rates.

Acknowledgements

The authors acknowledge the financial support provided by Universidad de Guanajuato and CONACYT, through the scholarship granted to M.M. May-Vázquez.

References

A. G. Gorak, G. Wozny, L. Jeromin, 1991, Industrial application of the rate-based approach for multicomponent distillation simulation. Proceedings of the 4th World Congress in Chemical Engineering.

H. A. Kooijman, R. A. Taylor, 1995, A nonequilibrium model for dynamic simulation of tray distillation columns, AIChE Journal, 41, 8, 1852-1863.

R. Krishnamurthy, R. Taylor, 1985, A nonequilibrium stage model of multicomponent separation processes. Part II: comparison with experiment, AIChE Journal, 31, 3, 456-465.

M. Lucet, A. Charamel, G. Guido, A. Chapuis, J. Loreau, 1992, Role of batch processing in the chemical process industry, Batch Processing Systems Engineering: Fundamentals and Applications for Chemical Engineering, 143, 43-48.

M.M. May-Vázquez, F.I. Gómez-Castro, M.A. Rodríguez-Ángeles, 2019, Rate-based modelling and simulation of pilot scale distillation column, Computer Aided Chemical Engineering, 46, 625-630.

B. Nada, K. Neran, S. Ibrahim, 2009, Rate-based model in bubble-cup batch distillation column, Engineering and Technology Journal, 27, 14, 2566-2583.

R. Tarikh, T. Fadilatul, N. Siti, A. Ali, 2019, Study of packed sieve tray column in ethanol purification using distillation process, Malaysian Journal of Fundamental and Applied Sciences, 15, 1, 69-74.

R. Taylor, R. Krishna, 1993, Multicomponent mass transfer, Wiley-Interscience.

Sauro Pierucci, Flavio Manenti, Giulia Bozzano, Davide Manca (Eds.)
Proceedings of the 30th European Symposium on Computer Aided Process Engineering (ESCAPE30), May 24-27, 2020, Milano, Italy.
http://dx.doi.org/10.1016/B978-0-12-823377-1.50004-5

Development of a Virtual Environment for the Rigorous Design and Optimization of Shell-and-tube heat Exchangers

Oscar Daniel Lara-Montaño [a] , Fernando Israel Gómez-Castro [a,*] , Claudia Gutiérrez-Antonio [b]

[a] *Departamento de Ingeniería Química, División de Ciencias Naturales y Exactas, Campus Guanajuato, Universidad de Guanajuato, Noria Alta S/N, Col. Noria Alta, Guanajuato, Guanajuato, 36050, México, fgomez@ugto.mx*
[b] *Facultad de Química, Universidad Autónoma de Querétaro, Av. Cerro de las Campanas s/n, Col. Las Campanas, Querétaro, Querétaro, 76010, México*

Abstract

Heat exchangers are one of the auxiliary equipment in industry, being the shell-and-tube heat exchangers (STHE) the most used. The design procedure of a heat exchanger is an iterative process, which is greatly affected by the designer experience; in spite of this, the designer can't know if the optimum design has been selected. Existing design methods involve solving a non-linear model with multiple decision variables. Therefore, it is convenient to use an optimization algorithm to select the best design. In order to solve this kind of optimization problems, meta-heuristic algorithms are the most promissory approach, which have exploration and exploitation capabilities. In this work, a virtual environment is created for the design and optimization of STHE, using the Kern and the Bell-Delaware methods, which are easily integrated with meta-heuristic algorithms. The STHE models and the optimization algorithms were coded in Python, supporting the particle swarm optimization and gray wolf optimization algorithms. Three constrains are always active, but the user can establish new ones easily if necessary. The default objective function is the total annual cost, but this can be also modified by the user.

Keywords: heat exchangers, meta-heuristic optimization, virtual environment.

1. Introduction

Shell-and-tube heat exchangers (STHE) are the most widely thermal equipment used in industry, and they provide a large heat exchange area in a small volume. Furthermore, they can be constructed using a wide range of materials to resist various kinds of fluids. Kern as well as Bell-Delaware methods are the most common strategies to design STHE. Kern method considers a single stream that advances in a zigzag flow pattern through the shell of the heat exchanger. On the other hand, Bell-Delaware method uses five factors to correct the shell-side heat transfer coefficient, and provide more accurate predictions of the actual thermal and hydraulic performance in shell-side as well as pressure drop calculations, since it takes into account leakage and bypass effects. Regard the optimization of STHE, there are plenty of works in which the main objective is to optimize thermal equipment using deterministic technics (Ponce-Ortega et al., 2006; Ravagnani and Caballero, 2007) or metaheuristic algorithms (Ponce ortega et al., 2009; Patel and Rao, 2010). The optimization of STHE represents a challenge due to the nonlinearity, nonconvexity and the presence of continuous and discrete variables in the

mathematical model. Usually, a single tool is employed to perform the optimization of STHE; however, the availability of several optimization strategies in a toolbox could be useful to analyze the pros and cons of each one of them. Therefore, in this work, a computational tool to optimize STHE using metaheuristic algorithms is developed. The virtual environment uses Kern method and the Bell-Delaware method, while Particle Swarm Optimization (PSO) and Gray Wolf Optimization (GWO) methods are implemented in this first version.

2. Shell-and-tube heat exchanger models

The common equations of STHE models are the energy balances, the design equation, the mean logarithmic temperature differences. Each methodology are described next.

2.1. Shell-side calculations

2.1.1. Kern's method

The shell-side convective heat transfer coefficient, $h_{s,id}$, is computed with Equation (1). Re_s is the shell-side Reynolds number, Pr_s is the Prandtl number, k_f is the thermal conductivity of the shell-side fluid, j_h is the heat transfer factor, obtained from Sinnott (2005). μ_s is the fluid viscosity at mean temperature and μ_w is the fluid viscosity at wall temperature, this variable is calculated iteratively.

$$h_{s,id} = \frac{k_f}{d_e} j_h Re_s Pr_s^{\frac{1}{3}} \left(\frac{\mu_s}{\mu_w}\right)^{0.14} \tag{1}$$

For the equivalent diameter, d_e, either equations (2) or (3) are used, depending on the tube layout. Equation (2) is used for square layout, while equation (3) is for triangular layout. d_o is the outer tube diameter and p_t is the tube pitch.

$$d_e = \frac{1.27}{d_o}(p_t^2 - 0.785 d_o^2) \tag{2}$$

$$d_e = \frac{1.1}{d_o}(p_t^2 - 0.917 d_o^2) \tag{3}$$

Shell-side pressure drop, ΔP_s, is calculated using equation (4). ρ_s is the shell-side fluid density at mean temperature, v_s is the fluid velocity, L is the tube length, D_s is the shell diameter, B is the baffles spacing, D_e is the equivalent shell diameter, and f_s is the shell-side friction factor, which is calculated according to $f_s = 1.44 Re_s^{-0.15}$, for $Re_s \leq 40{,}000$ (Peters and Timmerhaus, 1994). Full Kern model can be obtained from Sinnott (2005).

$$\Delta P_s = \frac{\rho_s v_s^2}{2} \frac{L}{B} \frac{D_s}{D_e} f_s \tag{4}$$

2.1.2. Bell-Delaware's method

Equation (1) is used to calculate an ideal shell-side convective heat transfer coefficient. In Bell-Delaware method, this value is modified using five correction factors (equation (5)), where J_c is the correction factor for baffle configuration, J_l is the correction factor

due to the baffle leakage effect, J_b is the correction factor for bundle and pass partition bypass streams, J_s is the correction factor for larger baffle spacing at the inlet and outlet sections, and J_r is a correction factor for adverse temperature gradient in laminar flow (Shah & Sekulić, 2003).

$$h_s = h_{s,id} J_c J_l J_b J_s J_r \tag{5}$$

Shell-side pressure drop has three components, (i) pressure drop in the central section, (ii) pressure drop in the window area, and (iii) pressure drop at the inlet and outlet sections. Further details for thermal and hydraulic calculations for shell side using the Bell-Delaware method can be obtained from Shah and Sekulić (2003).

2.2. Tube-side calculations

For Kern's and Bell Delaware methodologies, thermal and hydraulic calculations are made using the following correlations. Where h_t is the tube-side convective heat transfer coefficient, k_t is the thermal conductivity of the tube-side fluid, f_t is the friction factor in tube side, d_i is the inner diameter of tubes, Re_t and Pr_s are the Reynolds and Prandtl number in tube-side, respectively. To calculate the tube-side convective heat transfer coefficient, equation (6) is used if $Re_t < 2300$, (7) if $2300 \leq Re_t \leq 10{,}000$, and (8) if $Re_t > 10{,}000$.

$$h_t = \frac{k_t}{d_i} 1.86 \left(\frac{Re_t Pr_t d_i}{L} \right)^{1/3} \tag{6}$$

$$h_t = \frac{k_t}{d_i} \left(\frac{\frac{f_t}{2} Re_t Pr_t}{1.07 + 12.7 \left(\frac{f_t}{2} \right)^{0.5} \left(Pr_t^{\frac{2}{3}} - 1 \right)} \right) \tag{7}$$

$$h_t = \frac{k_t}{d_i} 1.86 \left(\frac{Re_t Pr_t d_i}{L} \right)^{1/3} \tag{8}$$

3. Optimization algorithms

3.1. Particle Swarm Optimization

Particle Swarm Optimization (PSO), developed by Kennedy and Eberhart (1995), is inspired in the movement of a school of fishes or a flock of birds. It only uses two main equations:

$$\boldsymbol{v_i^{t+1}} = \boldsymbol{v_i^t} + \alpha r_1 (\boldsymbol{g^*} - \boldsymbol{x_i^t}) + \beta r_2 (\boldsymbol{x_i^*} - \boldsymbol{x_i^t}) \tag{9}$$

$$\boldsymbol{x_i^{t+1}} = \boldsymbol{x_i^t} + \boldsymbol{v_i^{t+1}} \tag{10}$$

where $\boldsymbol{x_i^t}$ and $\boldsymbol{v_i^t}$ indicate position and velocity of particle i at iteration t, respectively. $\boldsymbol{g^*}$ is the best solution found so far by all particles, $\boldsymbol{x_i^*}$ is the best individual position and parameter α and β are set equal to 2.0. Equation (9) is used to calculate velocity for each particle and equation (10) is used to update the particle position. Finally, r_1 and r_2 are random parameters which are computed on each iteration.

3.2. Gray Wolf Optimization

Gray Wolf Optimization (GWO) algorithm, proposed by Mirjalili et al. (2014), emulates the hunting behavior and hierarchy of a wolf pack. The highest level in hierarchy is the alpha wolf, is the one who takes important decisions. The second level in hierarchy are beta grey wolves, which are subordinates that help the alpha one in decision making. Lowest level in hierarchy correspond to omega wolves; they must submit to all other levels. Other wolves who are not alpha, beta or omega, are delta. Delta wolves can be scouts, hunters, elders and caretakers, and they submit to alpha and beta wolves. This metaheuristic algorithm has three main phases (i) tracking, chasing and approaching to the prey (objective), (ii) pursuing, encircling and harassing the prey until stops moving, (iii) attack the prey.

4. Heat exchanger optimization system

The computational tool to optimize STHE, using metaheuristic algorithms, employs Python as codification environment. In the current version the user can choose between Kern's and Bell-Delaware methodologies, and also the optimization method, either PSO or GWO algorithms; the total annual cost is the objective function.

If Kern method is selected, the decision variables are shell diameter (D_s); outer tube diameter (d_o); tube layout (TL), square or triangular; number of tube passes (N_p), 1, 2 and 4; baffle spacing (B_s); diameter of tube bundle (D_{otl}); and diametrical clearance of shell to baffle (d_{sb}). For the Bell-Delaware method, the design variables are D_s; d_o; tube pitch (P_t, which can be either $1.25d_o$ or $1.5d_o$); TL ($30^o, 45^o$ or 90^o); number of passes (N_p, 1, 2 or 4); percentage baffle cut (B_c, 25%, 30%, 40% or 45%); baffle spacing at center (L_{bc}), defined from $0.2D_s$ to $0.55D_s$; baffle spacing at the inlet and outlet ($L_{bi} = L_{bo}$), defined from L_{bc} to $1.6L_{bc}$; d_{tb}, in the range $0.01D_s$ to $0.1D_s$; and diametrical clearance of tube to baffle (d_{tb}), in the range $0.01d_o$ to $0.1d_o$.

Figure 1 shows how this tool is designed. MainProgram is the run file, which allows the user to select the STHE model, metaheuristic algorithm and some parameters of the algorithm, such as population size, number of iterations, number of runs and design variable boundaries. MainProgram calls an optimization algorithm that links to the STHE design model. Both, Kern and Bell-Delaware methods are interconnected with a code that calculates the thermal convection coefficient in tube side (ThermalCoefConvTub). If Bell-Delaware model is selected the Geometry package is used to calculate geometrical parameters. Then, important variables for cost estimation are exported to CostCalculation to get the objective function value, this is the sum of operation and fixed cost. When the stop criterium is satisfied the STHE optimum design is showed.

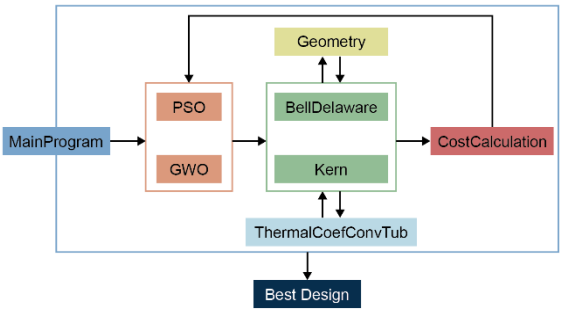

Figure 1. Design of STHE optimization tool.

Four constrains are applied: pressure drop in tube-side and shell side must be less or equal to a maximum pressure drop, fluid velocity in tubes must be between 1 m/s and 3 m/s, and the ratio between STHE length and shell diameter must be less or equal to 15. If one or more constrains are not satisfied a penalty value is applied to the objective function value.

5. Case studies

Case studies are taken from Taborek (1983); physical properties and process information is given in Table 1. For cost calculations interest rate of 5% per year is assumed; expected lifetime for STHE is 20 years; electricity cost is 0.1$/kWh; 5000 operational hours per year are used; and pump efficiency is 0.85. All codification was implemented in Python. 30 experiments were made to have enough information for a statistical analysis with 50 individuals and 50 iterations.

Table 1. Physical properties and process information for case studies.

	Case study 1		Case study 2	
	Tube side	Shell side	Tube side	Shell side
Fluid	Cooling water	Naphtha	Heavy gas oil	Crude oil
Flow rate (kg/m^3)	30	2.7	29.36	102.12
Inlet fluid temperature (°C)	33	114	319	209
Outlet fluid temperature (°C)	37.2	40	269	226
Density of fluid (kg/m^3)	1000	656	678	723
Heat capacity (kJ/kg-k)	4.187	2.646	3.161	2.679
Viscosity (Pa-s)	0.00071	0.00037	0.00032	0.00049
Thermal conductivity (W/m-K)	0.63	0.11	0.089	0.1
Fouling resistance (m^2K/W)	0.0004	0.0002	0.0006	0.0006
Allowed pressure drop (Pa)	70,000	70,000	10,000	10,000
Material	Stainless steel	Carbon steel	Carbon steel	Carbon steel

6. Results

Table 2 summarizes the optimal design variables found for both case studies. It is important to notice that Table 2 only shows the results for the best (optimal) heat exchanger designs using the different combinations of design and optimization methods.

Table 2. Optimized STHE for using both design methods and optimization algorithms.

Parameter	Case study 1				Case study 2			
	Bell-Delaware		Kern		Bell-Delaware		Kern	
	PSO	GWO	PSO	GWO	PSO	GWO	PSO	GWO
Shell diameter (m)	0.3024	0.3024	0.3141	0.3148	0.5816	0.5806	1.0	1.0
Outer tube diameter (m)	0.01587	0.01587	0.015	0.015	0.01587	0.01587	0.015	0.015
Number of tubes	144	144	216	217	319	320	2762	2762
Area (m^2)	32.56	32.56	25.96	26.029	138.75	138.81	150.92	150.92
Length (m)	4.53	4.53	2.55	2.54	8.72	8.70	1.159	1.59
Operation cost (USD/year)	160.51	160.51	263.34	257.76	589.67	590.51	3430.25	3430.25
Fixed cost (USD/year)	3865.99	3806.01	3262.45	3275.97	9597.72	9600.51	10162.02	10162.02
Total annual cost (USD/year)	3966.50	3966.53	3525.80	3525.73	10187.40	10191.03	13592.27	13592.27

In a more detailed analysis, for case study 1 both optimization algorithms reach the same optimal solution. However, after 30 experiments the average total annual cost and standard deviation are 4,234.35 USD/year and 431.09 USD/year for PSO, and 4,074.93 USD/year and 52.15 USD/year for GWO, respectively. Therefore, GWO has a better performance for this problem and it is more likely to avoid local optima. When Kern's

method is used, both optimization method has very similar statistical results. Average value for standard deviation are 3,535.72 USD/year and 16.64 USD/year for PSO, and 3,536.14 USD/year and 18.72 USD/year for GWO. It can be inferred that it is easier to have reproducibility between simulations when Kern method is used; this is because the model is simpler, contains less design variables, and less non-linear equations. Optimal designs calculated with Kern method have a lower cost than with Bell-Delaware. Nevertheless, results obtained with the Bell-Delaware method are expected to be more approximate to the actual performance of the exchanger.

The optimal STHE for case study 2 is larger than the first case. Considering Bell Delaware model, a better optimal design is calculated when PSO is used. The average total annual cost and standard deviation for PSO is 10,590.14 USD/year and 481.11 USD/year, while for GWO these values are 10,274.19 USD/year and 248.05 USD/year. In this case, the design calculates using Kern model is more expensive. For both PSO and GWO the minimum total annual cost is 13,592.07 USD/year. Nevertheless, an important difference occurs with standard deviation, having a value of 224.09 USD/year for PSO and 0.05 USD/year for GWO. This demonstrates that for all of 30 experiments GWO reached practically the same minimum value.

7. Conclusions

A tool for the optimization of STHE considering two models and two meta-heuristic approaches has been proposed. The design tool successfully optimizes STHE with no phase transition. Considering 30 experiments, both optimization methods calculates at least one design with the same minimum total annual cost value. GWO algorithm has a better ability to avoid local minima, this can be inferred by looking at the lower standard deviation compared to PSO algorithm. Although the user can choose between PSO and GWO, it is recommended to use GWO because of its better overall performance.

References

A.C. Caputo, P.M. Pelagagge, P. Salini, P, 2008, Heat exchanger design based on economic optimisation, Applied Thermal Engineering, 28, 10, 1151-1159.

J. Kennedy, R. Eberhart, 1995, Particle swarm optimization, Proceedings of ICNN'95 - International Conference on Neural Networks, 4, 1942-1948.

S. Mirjalili, S.M. Mirjalili, A. Lewis, 1995, Grey wolf optimizer, Advances in Engineering Software, 69, 46-61.

V.K. Patel, R.V. Rao, 2010, Design optimization of shell-and-tube heat exchanger using particle swarm optimization technique, Applied Thermal Engineering, 30, 11, 1417-1425.

M. Peters, K. Timmerhaus, 1994, Plant design and economic for chemical engineers. Mc Graw Hill.

J.M. Ponce-Ortega, M. Serna-González, L.I. Salcedo-Estrada, A. Jiménez-Gutiérrez, 2006, Minimum-investment design of multiple shell and tube heat exchangers using a MINLP formulation. Chemical Engineering Research and Design, 84, 10, 905-910.

J.M. Ponce-Ortega, M. Serna-González, A. Jiménez-Gutiérrez, 2009, Use of genetic algorithms for the optimal design of shell-and-tube heat exchangers. Applied Thermal Engineering, 29, 2, 203-209.

M.A.S.S. Ravagnani, J.A. Caballero, 2007, A MINLP model for the rigorous design of shell and tube heat exchangers using the TEMA standards. Chemical Engineering Research and Design, 85, 10, 1423-1435.

R.K. Shah, D.P. Sekulić, 2003, Fundamentals of heat exchanger design, Wiley.

R.K. Sinnott, 2005, Chemical Engineering Design, volume 6, 4th edition, Coulson & Richardson's Chemical Engineering Series, Elsevier.

J. Taborek, 1983, Shell-and-tube heat exchangers: single-phase flow, in "Heat exchanger design handbook" (Ed. G.F. Hewitt), Belleg House, 3.3.3.1-3.3.11.5.

Sauro Pierucci, Flavio Manenti, Giulia Bozzano, Davide Manca (Eds.)
Proceedings of the 30th European Symposium on Computer Aided Process Engineering (ESCAPE30), May 24-27, 2020, Milano, Italy.
http://dx.doi.org/10.1016/B978-0-12-823377-1.50005-7

A Multiscale Modelling Approach for the Design of new Polymer Materials

Alain Dequidt,[a] Sébastien Garruchet,[b] Benoit Latour,[b] Nicolas Martzel,[b] Ronald Blaak,[a] Etienne Munch,[b] Nicolas Seeboth,[b] Patrice Malfreyt[a]

[a]*Université Clermont Auvergne, CNRS, SIGMA Clermont, Institut de Chimie de Clermont-Ferrand, 63000 Clermont-Ferrand, France*
[b]*Manufacture Française des Pneumatiques Michelin, 23, place des Carmes, 63040 Clermont-Ferrand, France*
Patrice.Malfreyt@uca.fr

Abstract

We report examples of industrial interests for which only multi-scale simulations are able to provide bridges between consecutive scales. We focus here on the transfer of information between the atomic and mesoscopic scales. We treat the impact of the architecture of the polymer chains and the nature of the surface. We also investigate the phenomena of crystallization under shear and complete by a study of the deformation of an elastomer network.

Keywords: multiscale modelling, mesoscopic simulation, coarse-grain models, mechanical properties, polymer materials.

1. Introduction

Simulations have become an essential tool for analyzing, interpreting experimental data and generating new experiments. We can even imagine that in the near future (less than ten years) no experiment will be carried out without having launched before a simulation. It is now established that the improvement of the desired properties and of the performance of a material requires investigating the relationship between its structure at the atomic or molecular length and their macroscopic properties. However, the ability to perform molecular simulations of polymer materials over length scales that are relevant to experiments represents a grand challenge. Indeed, when studying polymer composite materials, polymers at the surface, we need to consider structures from the length scale of a single chemical bond (≈1 Å) to the persistence length (≈10 Å) to the coil radius (≈100 Å). The second factor that may control the practicality of the simulation is the time scales involved in the polymeric materials that can reach times of microsecond and beyond (full relaxation of the polymer chains, crystallisation).

One solution to simulate these time and length scales consists of reducing the degrees of freedom by coarsening the model. Each interaction center (called bead) may represent then few atoms or several monomers (see Figure 1). Numerous coarse-graining approaches have been developed in the past to conserve chemical information at the mesoscopic length scales. The idea behind our coarse-grained (CG) approach is to map atomistic configurations onto a coarser (Maurel et al., 2012; Maurel et al., 2015a, Maurel et al. 2015b; Kempfer et al., 2019a, Kempfer et al., 2019b, Kempfer et al., 2019c) configuration. We propose here to show the performance of the multi-scale approach for

a quantitative prediction of thermodynamic and mechanical properties of different polymer materials.

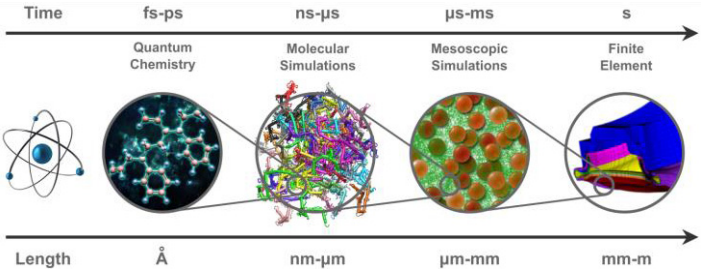

Figure 1: Different types of length and time scales associated with the methods of simulations from the quantum to macroscopic scales.

2. Coarse-grain simulations of polymer materials

2.1. Development of coarse grain (CG) models

We use the Statistical Trajectory Matching (STM) to develop the CG models. The reference trajectories are obtained from atomistic simulations from which the positions of the coarse-grains are determined. With the STM method, we use a degree of coarse-graining of 1 indicating that a grain corresponds to 1 monomer. This size of grain allows to reproduce both the structural properties of chains in the melt and the melt density. We are currently working for increasing the degree of coarse-graining to simulate larger systems on millisecond scales. The reader is redirected to the following papers [1-6] to have a comprehensive description of the STM method.

2.2. Effects of molecular structure on mechanical properties

Molecular structure of polymer materials is tightly correlated to their rheology and mechanical properties. Yet, molecular time-scales are very different from observable mechanical phenomena making it hard to link one with the other. Several models attempt to do so, and it is still a challenge for molecular modeling to develop tools to predict mechanical of polymer materials up to macroscopic timescales. This is partly due to the explicit simulation of molecular motions and partly to time limits from computational power. The recent development of coarse-grain models allowed to overcome such limits. By reducing the complexity of the system while keeping a correct representation of polymer molecules, they gave access to time-scale up to the microseconds for polymeric systems. It is likely that fine tuned molecular model will be able to give quantitative prediction of material properties. For example, recent models of CG *cis*-1,4-polybutadiene (cPB) are able to reproduce molecular structure in agreement with experimental results (for example for cis-polybutadiene $\rho^{exp} = 0.90\ g/cm^3$; $\rho^{sim} = 0.90\ g/cm^3$, $\frac{R_{ee}^{exp}}{M} = 0.76\ A^2 \frac{mol}{g}$, $\frac{R_{ee}^{sim}}{M} = 0.7\ A^2 \frac{mol}{g}$) (Pearson et al., 2014). From stress auto-correlation up to the micro-second, plateau modulus is still overestimated with high coarse-graining ($G^{exp} = 0.76\ MPa$, $G^{sim} = 1.12\ MPa$) (Maurel et al., 2012) as dynamics is difficult to reproduce and entanglements are lost. Nevertheless, it is already possible to see effects of molecular structure on rheological properties [8]. While it is not

possible to simulate true polymeric structures with long enough molecules, we now try to see molecular effects of branching on mechanical properties and compare it with analytical models in order to validate our explicit simulation models. Our recent results show that G(t) decays slower for the star than for the linear polymer in line with recent experiments and simulations (Liu et al., 2018).

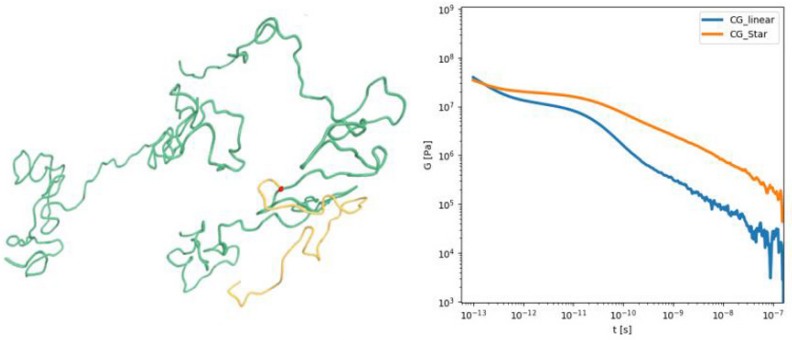

Figure 2 **:** Shear-modulus for linear (blue) and star polymers (orange) cis-1,4- polybutadiene polymer melts obtained from CG simulations.

2.3. Effects of free and grafted chains under shear

We show results of this methodology applied to polymers between confining surfaces that are grafted. We employ the model for cPB in contact with a cuprous oxide layer that was recently derived. The confining surfaces are represented by four layers of coarse-grained beads. For simplicity, we have assumed that each bead in the top layers of either surface can act as a grafting site for exactly one polymer. The grafting locations are selected randomly for a given grafting density. The grafted polymers themselves are short spacers of 5 beads and are attached at the other end to the middle of a normal polymer to create a ``Y"-like structure. In the current formulation the beads and bonds in grafted, attached, and free polymers are all identical to the *cis*-1,4-polybutadiene model. The separation between the two surfaces is chosen such that the density and pressure in the middle of the system, where there are just free polymers, are corresponding to the bulk value.

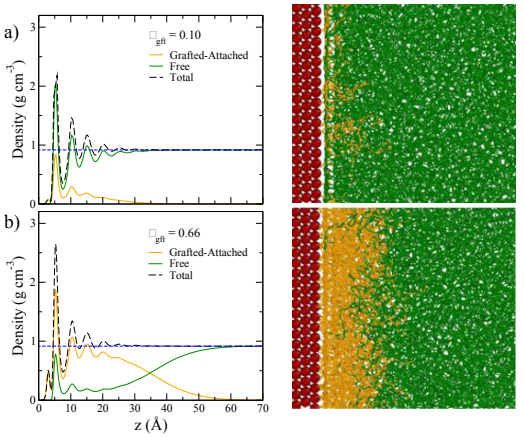

Figure 3 : Monomer density profiles for free and grafted polymers at (a) low (ϕ = 0.1 nm^{-2}) and (b) (ϕ=0.66 nm^{-2}) high grafting densities and corresponding representative snapshots. The blue

dashed line corresponds to the bulk density ρ =0.92 g/cm^3. The average position of the top layer of surface beads is found at z=0. The red, yellow, and green spheres correspond to surface, grafted, and free polymers.

Figure 3 shows two snapshots at low and high grafting densities for relative short polymers consisting of 41 beads (one bead corresponds to four united atoms). The grafting densities ϕ = 0.1 and 0.66 molecules/nm^2 correspond to the polymer chains to be grafted respectively at 7% and 45% of the available sites. The monomer density profiles show the characteristic oscillations of surface induced ordering. The slight sub-peak close to the surface is due to the short bond length between the grafted and the surface beads. The larger grafting density causes an effective thicker brush and expels the free polymers from the surface and ultimately from the brush. In future work, we will explore the behavior of this and similar systems when exposed to shear.

2.4. Strain-induced of polymers

A commonly used model to simulate the crystallization process of polymers as well as their properties, is the coarse-grained model for poly(vinyl alcohol) (PVA) that was introduced by Meyer and Müller-Plathe (2001). It takes the form of a simple bead-spring model, where individual grains represent single PVA-monomers rather than united atoms. The connectivity within polymers is modeled by means of a harmonic potential and the steric interaction is represented by a Lennard-Jones 9-6 potential. The angle and torsion potentials found in a united atom representation of this system, have been replaced by a single tabulated angle potential. In order to study the effects of strain on polymer systems, we have simulated a system of 2700 polymer chains with a length of 100 beads of this type at a pressure P*=8 in reduced units. An equilibrated melt configuration at T*=1 (reduced units) is quenched to T*=0.2 at the constant cooling rate $10^{-6}/\tau$, which is slow enough to avoid the glass and results in semi-crystalline order. Configurations from different temperatures during this process are subjected to a constant true strain-rate $10^{-5}/\tau$, under constant lateral pressure. Figure 4 shows two snapshots for the lowest temperature, one before and one after the maximum strain ε=1.59. Bonds in the polymers are color coded according to the local nematic order parameter N, which is the largest eigenvalue of the tensor $Q_{\alpha\beta} = \Sigma\ 3/2\ b_{\alpha\beta}\text{-}1/2\delta_{\alpha\beta}$ in terms of the unit-vectors **b** associated to them. The average is taken over all bonds in proximity, i.e., within a distance 1.1σ The probability distribution functions P(N) of the local nematic order for different strains ε are shown in Figure 5 and indicate that the strain enhances the alignment in weakly ordered regions. Counterintuitively in some of the strongly ordered regions (N > 0.98) it will be somewhat lowered in favour of the range 0.6 <N <0.98, an effect that appears to be associated with those regions whose alignment direction differs significantly from the strain direction. Finally, the cooling to extremely low temperature not only results in alignment of the polymers, but also in some short range positional order as can be observed in the sub-structure in the PDF at zero-strain.

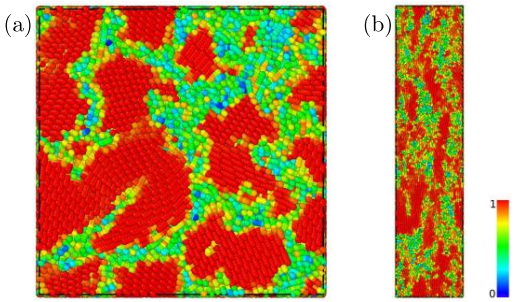

Figure 4: Snapshots representing the local nematic order parameter (a) before (ε=0) and (b) after ((ε=1.59) applying strain. Each sphere represents a bond in the polymer and the color coding corresponds to its local nematic order parameter N.

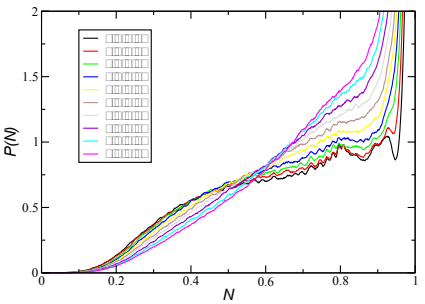

Figure 5: Probability distributions of the local nematic order parameter N at various strains ε

2.5. Molecular elastomer networks under high deformation

Resistance to fracture is a key property of materials in many practical applications. The optimization of the breaking strain and energy is thus a concern for the industry, in particular in elastomers (cross-linked polymers). In a cross-linked polymer under high deformation, the force felt by each chain depends on the local configuration of the network (chain length, entanglements, orientation of the neighboring chains...). The rupture of a chain is all the more likely that it is submitted to a great tension. During a rupture, the stress supported by the broken chain is distributed to its neighbors, whose stress increases and which may break in turn. In the end, this avalanche of ruptures leads to the rupture of the sample. To study the behavior of elastomer networks, we chose to develop a numerical model to simulate polymers at the scale of the cross-linked network. Our approach differs from previous analytical models (Wu, 1993) concerning network rupture by using a coarse grained model and method (based on Elastic Network Models (Rubinstein, 2002) with parameters estimated from quantum mechanics, dissipative particle dynamics and experimental data). In practice, in our simulations, the topological constraints (cross-links, entanglements…) are represented by a network of beads connected together by polymer chains with distributed lengths. To produce these systems, we adopt a specific network generation approach (Hansen, 2015) which takes into account polymer properties (Kuhn length, density) and network characteristics (cross-link density). We are able to measure the local stress distribution during the simulation. We

show that stress is indeed distributed. Under strain, the stress distribution is not only shifted, but also broadened. The most remarkable element is that, under stretch, localized parts of the sample are under pressure, with a positive stress value along the stretch axis, while the average negative stress is of course negative. Rupture behavior will be obviously affected by this heterogeneity. Regions with high or low absolute stress value should correspond respectively to breaking zones and zones helping to relax constraint.

3. Conclusion

A multi-scale stratgey approach was used to link the atomistic and mesoscopic scales. The aim is to maintain a realistic chemical representation of the microstructure and to simulate the polymer materials at longer time scales. We have discussed the effects of the molecular structure on the mechanical properties, the impact of the grafting on the resulting rheological properties on the brush and of the shear on the crystallization process. We complete this paper by the simulation of molecular elastomer networks und high deformation.

Acknowledgments

This work was performed in SimatLab, a joint public-private laboratory dedicated to the modeling of polymer materials. This laboratory is supported by Michelin, Clermont Auvergne University (UCA), SIGMA Clermont and CNRS. It is a pleasure to thank F. Goujon, G. Clavier, J. S. Canchaya, J. Devémy, G. Munoz, H. Nagaraj.

References

D. E. Hanson, 2015, A new paradigm for the molecular basis of rubber elasticity, Contemp. Phys., 56, 319-337.

K. Kempfer, J. Devemy, A. Dequidt, M. Couty, P. Malfreyt, 2019a, Atomistic descriptions of the cis-1,4-polybutadiene/silica Interfaces, ACS Appl. Polym. Mater., 1, 969-981.

K. Kempfer, J. Devemy, A. Dequidt, M. Couty, P. Malfreyt, 2019b, Development of coarse-grained models for polymers by trajectory matching, ACS Omega, 4, 5955-5967.

K. Kempfer, J. Devemy, A. Dequidt, M. Couty, P. Malfreyt, 2019c, Realistic coarse-grain model of cis-1,4-polybutadiene: from chemistry to rheology, Macromolecules, 52, 2736-2747.

L. Liu, W. K den Otter, W. J. Briels, 2018, Coarse-grained Simulations of three-armed star polymer melts and comparison with linear chains, J. Phys. Chem. B, 122, 10210-10218.

G. Maurel; B. Schnell; F. Goujon; M. Couty; P. Malfreyt, 2012, Multiscale modeling approach toward the prediction of viscoelastic properties of polymers, J. Chem. Theory Comput., 8, 4570-4579.

G. Maurel; F. Goujon; B. Schnell, P. Malfreyt, 2015a, Prediction of structural and thermomechanical properties of polymers from multiscale simulations, RSC Adv., 5, 14065-14073.

G. Maurel; F. Goujon; B. Schnell, P. Malfreyt, 2015b, Multiscale modeling of the polymer−silica surface interaction: from atomistic to mesoscopic simulations, J. Phys. Chem. C., 119, 4817-4826.

H. Meyer and F. Müller-Plathe, 2001 Formation of chain-folded structures in supercooled polymer melts, J. Chem. Phys., 115, 7807.

D. S. Pearson, L. J. Fetters, W. Graessley, G. Ver Strate, E. von Meerwall, 2014, Viscosity and self-diffusion coefficient of hydrogenated polybutadiene, Macromolecules, 27, 711-719.

M. Rubinstein, 2002, Elasticity of polymer networks, Macromolecules, 35, 6670-6686.

P. D. Wu, 1993, On improved network models for rubber elasticity and their applications to orientation hardening in glassy polymers, J. Mech. Phys. Solids, 427-456.

Sauro Pierucci, Flavio Manenti, Giulia Bozzano, Davide Manca (Eds.)
Proceedings of the 30th European Symposium on Computer Aided Process Engineering
(ESCAPE30), May 24-27, 2020, Milano, Italy.
http://dx.doi.org/10.1016/B978-0-12-823377-1.50006-9

Structured and Unstructured (Hybrid) Modeling in Precision Medicine

Linas Mockus, Gintaras V. Reklaitis, Yuehwern Yih

Purdue University, 610 Purdue Mall, West Lafayette, IN, 47907, USA
lmockus@purdue.edu

Abstract

One of the key objectives in precision medicine is to determine the right dose for the individual patient at the right time so that the desired therapeutic effect is achieved. The focus of this work is on modeling of pharmacokinetic/ pharmacodynamic data to facilitate the achievement of this goal. One novelty of our approach is to use structured models, such as physiologically-based compartment models and un-structured models, such as artificial neural networks or Gaussian Processes in a hierarchical fashion. The reason for using a hierarchical structure is that there are available well-established empirical compartmental and mechanistic physiologically based models, which do not explicitly account for various predictive covariates such as co-administered drugs or different laboratory measurements such as total protein, blood urea nitrogen, or urine output. Thus, we extend the structured models with the second hierarchical layer of an un-structured model and utilize the unstructured model to capture the effects of those covariates. Secondly, we employ Bayesian inference which allows direct quantification of uncertainty in the model predictions. Thirdly, utilization of Bayesian inference for the un-structured models (specifically Bayesian neural networks) allows the determination of important predictive covariates such as serum creatinine, blood urea nitrogen, or urine output.

Keywords: Pharmacokinetics, pharmacodynamics, Bayesian statistics, Artificial Intelligence.

1. Introduction

There is a plethora of literature on modeling of the drug kinetics in the human body, but the published models are typically structured (Colin, et al., 2019) with predictive covariates such as postmenstrual age, weight and serum creatinine. The literature on purely unstructured models is sparse (Roy, Dabbagh, Nguyen, & Hildgen, 2006), while the use of hierarchical approaches has not been reported. In this work we demonstrate the effectiveness of the hierarchical approach using the data from 2000 patients from Children's Hospital of Wisconsin. The data is imperfect – it has a large volume of missing vancomycin intermittent IVs. Moreover, for most patients there was a single concentration measurement at the trough per administration. The Bayesian framework allowed us to train the one-compartmental model combined with Bayesian neural networks models and Gaussian Process models for clearance and volume of distribution on data from patients for whom we have several concentration measurements. The predictive covariates were age, weight, height, gender, and serum creatinine. The results are encouraging – model predictions and actual measurements agree quite well. While these results must be viewed as only a proof of concept, they do suggest that such models can indeed help physicians to establish the right dose in a systematic way, accounting for different lab measurements, replacing the traditional approach in which the dosage is

determined only based on weight and vancomycin half-life (the predominant practice). We expect that the proposed hybrid model may aid physician in prescribing the right dose at the right time as well as in facilitating Bayesian adaptive phase I/II trials. The problem with current trials is that the "applied dose" is controlled, rather than the achieved "exposure". One can imagine that with a "day one pharmacokinetic (PK) Profile" of a "low" dose, we could train a reasonable model to select a dose that would deliver the desired area under the curve for that specific patient. The achieved exposure would then be confirmed, and further dosing continued. The process is safe for the patient and further supports testing clinical hypotheses around how the actual exposure relates to pharmacodynamics (PD). In addition, our hypothesis is that establishing importance of various lab measurements will help to focus on those that are indicative for that particular disease.

2. Materials and Methods

In this work we use the data from 2000 vancomycin patients from Children's Hospital of Wisconsin. However, the data has a large volume of missing vancomycin intermittent IVs. Moreover, for most patients there was a single concentration measurement at the trough point per administration. In addition, age, height, weight were not recorded consistently nor were serum creatinine levels. There were approximately 100 patients that had several concentration measurements at the trough for the same administration as well as that had consistent records for age, weight, height, gender, and serum creatinine. We selected 20 patients at random to demonstrate the proposed approach. The predictive covariates were age, weight, height, gender, and serum creatinine.

The statistical analysis was performed using R (R: A Language and Environment for Statistical Computing, 2009) and Markov Chain Monte Carlo software Stan (StanDevelopmentTeam, 2019) by employing Extreme Science and Engineering Discovery Environment (XSEDE) (Towns, et al., 2014) environment. It was assumed that pharmacokinetics is defined by a one compartmental model (Buelga, del Mar Fernandez de Gatta, Herrera, Dominguez-Gil, & García, 2005).

3. Hierarchical modeling of structured and un-structured models

We assume that the structured pharmacokinetics/pharmacodynamics model is defined by a system of differential algebraic equations (DAE):

$$\tilde{y} = f\left(x(t), \theta\right)$$

$$\frac{dx}{dt} = g\left(x(t), \theta\right)$$

$$h\left(x(t), \theta\right) = 0$$

$$x(0) = x_0$$

In this model, $\tilde{y}$ is the predicted value for an experimental observation, while f is a function relating the state variables $\boldsymbol{x}(t)$ to the predicted value. $\boldsymbol{\theta}$ represents the vector of unknown parameters. The vectors of DAEs that define the predictive model are $\boldsymbol{g}$ and $\boldsymbol{h}$, respectively. The vector of initial conditions is given by $\boldsymbol{x}_o$. Assuming an exponential error, the relationship between the experimental observation (y) and its associated predictive value is established by $\ln(y) = \ln(\tilde{y}) + \varepsilon$ where ε is observation error. The exponential error model is more appropriate for PK data since it is always positive. For

one compartmental PK models, for example, $\boldsymbol{\theta}$ consists of the clearance (CL) and the volume distribution (V_d).
In purely structured models V_d is often assumed to be a simple function of weight and CL as a simple function of creatinine clearance, using the Cockcroft and Gault equation which itself is a function of sex, age, weight, and serum creatinine (Buelga, del Mar Fernandez de Gatta, Herrera, Dominguez-Gil, & García, 2005; Cockroft & Gault, 1976). However, in practice there is a plethora of additional lab measurements collected, such as total protein, albumin, blood urea nitrogen (BUN), and urine output. In general, not all these lab measurements are included in the PK model. We propose to consider relevant lab measurements by extending the purely structured PK model with unstructured machine learning (ML) models (neural network, Gaussian Process, random forest etc.) for each or for at least some of the PK/PD parameters.

3.1. Neural network model

The architecture of neural network used in this work is depicted in Figure 1. A network consists of a layer of input units (which correspond to each line), one or more hidden layers with tanh activation function, and output unit (which corresponds to some PK parameter). Each hidden layer is connected to the preceeding hidden layer. The output is connected to the last hidden layer. Each unit in the hidden layers and output have a bias added to its input. The key difference between Bayesian Neural Networks (BNN) and traditional neural networks is that a probability distribution is associated with each weight and bias as opposed to the single point value used in conventional NNs. This allows estimating the uncertainty in the value of the output.

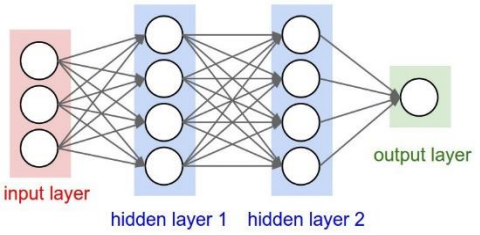

$$v_i^l = \tanh\left(u_i^l\right), u_i^l = b_i^l + \sum_k w_{ki}^{l-1,l} v_k^{l-1}, l = 1,\ldots,\#OfHiddenLayers$$

$$v^{Out} = b^{Out} + \sum_k w_k^{H,Out} v_k^H$$

Figure 1. The architecture of BNN

Here b_i^l is the bias for i[th] unit in hidden layer l, b^{Out} is the bias for output unit, $w_{ki}^{l-1,l}$ is the weight from k[th] unit in hidden layer l-1 to i[th] unit in hidden layer l, $w_k^{H,Out}$ is the weight from k[th] unit in the last hidden layer H to output unit, v_k^l is the value of the k[th] hidden unit, v_k^H is the value of the k[th] unit in the last hidden layer, v^{Out} is the value of the output unit (the value of PK parameter such as CL), and u_i^l is the value of the input to the i[th] hidden unit. The input layer may be interpreted as layer zero, i.e. v_k^0 is the value of the k[th] input (covariate). $w_{ki}^{0,1}$ corresponds to the weight from the k[th] unit in

input layer to the i[th] unit in first hidden layer. The BNN model for the clearance parameter may be expressed as CL~ $P\left(v^{Out}\right)$ where $P\left(v^{Out}\right)$ is a posterior of v^{Out}

In the case of Bayesian Neural Networks (BNN), the weights and biases have associated probability distributions (Neal, 1996). BNN model allows establishing the importance of critical covariates by using automatic relevance determination (ARD) (Husmeier, 1999) which is integral to BNN. The determination of important covariates allows the physician to concentrate on lab measurements relevant to specific disease.

3.2. Gaussian process model

The alternative to a neural network is the Gaussian Process (Rasmussen & Williams, 2006) which is another machine learning technique. The latent variable Gaussian Process model for the clearance parameter can be expressed as $CL \sim MVN\left(0, K\left(x \mid \theta\right)\right)$, where K is the kernel of the Gaussian Process, θ is the vector of parameters of kernel K, and MVN indicates a multivariate normal distribution. In this work we have used the squared exponential kernel with two parameters.

4. Results

We compared the predictions of these various models:

- **One compartmental PK model** with clearance and volume of distribution parameters specific to each patient. Such a model does not account for the change in clearance or volume of distribution that occur during treatment (i.e. renal function change or amount of liquid in the body)
- **Hybrid one compartmental PK model** with clearance represented as a BNN with one hidden layer and 10 nodes in the hidden layer with age, weight, height, gender, and serum creatinine as covariates.
- **Hybrid one compartmental PK model** with clearance represented as GP and the volume of distribution specific to each patient. This model does not account for change in weight and height in growing infants or the amount of liquid in the body.

The model predictions are summarized in Figure 2. It can be easily observed that the predictions enhanced with the Gaussian Process match the measured concentration more accurately since almost all blue lines cross the ideal line in red and uncertainty in estimates is lowest. The uncertainty (measured as a width of the 90% CR) is high because some patients have only few concentration observations at the trough. Uncertainty in the BNN estimates is similar to the predictions of the structural model.

The importance of covariates is summarized in Figure 2. If the weights of covariates are close to zero, then those covariates may be excluded from the model. In this case all covariates are important since 50% CR for all covariates are of comparable magnitude. The Bedside Schwartz equation confirms that height and serum creatinine are important for pediatric and adolescent patients (Schwartz & Work, 2009). The Cockcroft and Gault equation (Cockroft & Gault, 1976) confirms the importance of age, weight, and serum creatinine.

XSEDE environment allowed to parallelize training (or parameter estimation) of BNN and Gaussian Process (GP) models. For this dataset the training time was slightly less than 1 hour for the GP model and close to 15 minutes for the BNN model. Please note that it is possible to optimize parallelization to reduce training time significantly by exploring various approximations of Gaussian Process. Convergence was assessed visually as well as with R-hat statistics provided is stan (StanDevelopmentTeam, 2019).

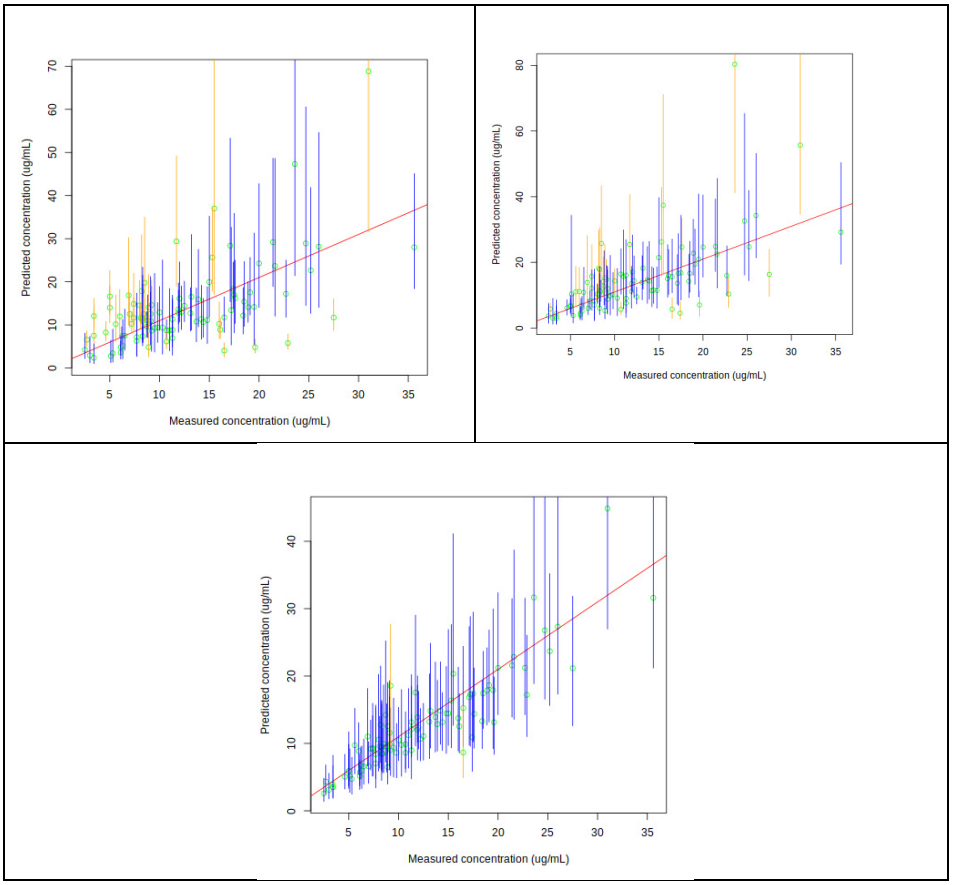

Figure 2. Predicted concentration for structured PK model (left panel), hybrid PK model where clearance parameter is represented as BNN (right panel), and the PK model where clearance parameter is represented as Gaussian Process (bottom panel). The green circles indicated the median of predicted concentration while the blue vertical lines indicate the 90% Credible Region (CR) of posterior distribution of predicted concentration. Vertical orange lines indicate where measured concentration is not within CR.

Table 1. Importance of covariates as determined by BNN

Covariate	50% CR of covariate for BNN
Weight	0.99
Serum creatinine	4.11
Age	2.76
Height	0.8
Sex	2.7

5. Conclusions

In this work we demonstrate the effectiveness of the hierarchical approach using the data from 2000 patients from Children's Hospital of Wisconsin. The data is not ideal – it has a large volume of missing vancomycin intermittent IVs. Moreover, for most patients there was single concentration measurement at the trough per administration. The Bayesian framework allowed us to train the one-compartmental model combined with Bayesian

neural networks models and Gaussian Process models for clearance and volume of distribution on data from patients for which there were several concentration measurements available (20 patients). The predictive covariates were age, weight, height, gender, and serum creatinine. The results are encouraging – model predictions and actual measurements agree quite well. While these results must be viewed as only a proof of concept, they do suggest that such models can indeed help physicians to establish the right dose in a systematic way, accounting for different lab measurements, replacing the traditional approach in which the dosage is determined only based on weight and vancomycin half-life (the predominant practice). We also hypothesize that establishing the importance of various lab measurements will help to focus on those that are indicative for the disease.

We plan to validate those preliminary results on a large Cerner Heath Facts dataset (https://business.okstate.edu/chsi/cerner-health-facts.html). Instead of maintaining the volume of the distribution to be specific for each patient we are planning to have an non-structured model for volume of distribution to allow for changes in liquids content as well changes in weight and height for rapidly growing infants. Additional covariate to include would be urine output.

Acknowledgement

This work used the Extreme Science and Engineering Discovery Environment (XSEDE), which is supported by National Science Foundation grant number ACI-1548562, and is supported, in part, by the College of Engineering at Purdue University. We also would like to thank the Children's Hospital of Wisconsin for providing access to the dataset.

References

Buelga, D., del Mar Fernandez de Gatta, M., Herrera, E., Dominguez-Gil, A., & García, M. (2005). Population pharmacokinetic analysis of vancomycin in patients with hematological malignancies. *Antimicrob Agents Chemothe, 49*(12), 4934-41.

Cockroft, D., & Gault, M. (1976). Prediction of creatinine clearance from serum creatinine. *Nephron, 16*(1), 31-41.

Colin, P., Allegaert, K., Thomson, A., Touw, D., Dolton, M., Hoog, M., . . . Eleveld, D. (2019). Vancomycin Pharmacokinetics Throughout Life: Results from a Pooled Population Analysis and Evaluation of Current Dosing Recommendations. *Clinical Pharmacokinetics*.

Husmeier, D. (1999). Automatic Relevance Determination (ARD). In *Neural Networks for Conditional Probability Estimation.* London: Springer.

Neal, R. M. (1996). *Bayesian Learning for Neural Networks.* Springer.

(2009). *R: A Language and Environment for Statistical Computing.* Manual, R Foundation for Statistical Computing, Vienna, Austria.

Rasmussen, C., & Williams, C. (2006). *Gaussian Processes for Machine Learning.* Boston: MIT Press.

Roy, J., Dabbagh, N., Nguyen, A., & Hildgen, P. (2006). Application of an artificial neural network (ANN) for the monitoring of vancomycin IV in the intensive care unit. *Clinical Pharmacology & Therapeutics, 79*(2).

Schwartz, G., & Work, D. (2009). Measurement and estimation of GFR in children and adolescents. *Clin J Am Soc Nephrol, 4*(11), 1832-43.

StanDevelopmentTeam. (2019). CmdStan: the command-line interface to Stan. Retrieved from http://mc-stan.org/

Towns, J., Cockerill, T., Dahan, M., Foster, I., Gaither, K., Grimshaw, A., . . . Wilkins-Diehr, N. (2014). XSEDE: Accelerating Scientific Discovery. *Computing in Science & Engineering, 16*(5), 62-74.

Sauro Pierucci, Flavio Manenti, Giulia Bozzano, Davide Manca (Eds.)
Proceedings of the 30th European Symposium on Computer Aided Process Engineering (ESCAPE30), May 24-27, 2020, Milano, Italy.
http://dx.doi.org/10.1016/B978-0-12-823377-1.50007-0

A Two Carriers Reactor Configuration for Packed Bed Chemical-Looping for Power Generation

Erasmo Mancusi, Piero Bareschino, Annunziata Forgione, Francesco Pepe

Dipartimento d'Ingegneria, Università degli Studi del Sannio, Piazza Roma 21, Benevento, 82100, Italia

erasmo.mancusi@unisannio.it

Abstract

This work presents the model of a Chemical Looping Combustion fixed bed reactors network for CH_4 combustion. The network is made of couples of reactors arranged in series, the first one filled with a Cu-based oxygen carrier, already active at low temperature, while the second reactor exploits an Ni-based OC, which allows the achievement of high temperatures. The model developed will allow to evaluate the performances of the proposed reactor system in terms of both generated thermal power and flow and composition of gaseous current in output. The proposed two-stage CLC is shown to be able to reach same performances in terms of outlet gas temperature of a single carrier/single bed configuration while exposing each oxygen carrier to a narrower cyclic temperature increase.

Keywords: Chemical looping Combustion, CO_2 Capture, Two stages CLC, Packed Bed.

1. Introduction

The need for Carbon Capture (CC) from power plants has been thoroughly debated In the recent Paris Conference of the Parties (Rogelj *et al.* 2016). Within the framework of CC, several methods have been extensively studied. Although post-combustion capture seems to be well advanced in terms of maturity, pre-combustion capture using chemical looping processes retains an attractive thermodynamic potential for reducing energy penalty. Chemical Looping Combustion (CLC) is a two-step combustion technology for power generation that allows the inherent separation of CO_2, thus reducing the inherent penalties of the separation processes. In CLC, fuel and oxygen are not mixed but contacted via an intermediate, a metal oxide (oxygen carrier OC) able of being alternately oxidized and reduced. In this way, direct contact between fuel and combustion air is avoided and an N_2-free, CO_2 rich stream is produced (Adanez *et al.* 2012).

Generally, air is pressurized from ambient conditions up to 20-30 bar and a temperature of approximately 450-500°C is reached for the fed gas. To achieve a high electricity efficiency the flue gas for turbine system need to be produced at 1200°C (Hammers *et al.* 2015), so that the OC must withstand cyclic temperature jumps in order of ~700 °C, which puts its chemical and mechanical stability at great risk (Adanez *et al.* 2012). A strategy to reduce such danger could be to carry out the process in Two Stages-CLC (TS-CLC), so to avoid cyclical large thermal variations in a single stage. This goal can be pursued by pairing reactors in series (Hamers *et al*, 2015). The first reactor is responsible for first temperature rise, demanding that the oxygen carrier should be reactive at low temperature (e.g. copper-based materials), while the second bed is

responsible for the remaining temperature rise, and thus the OC should be able to withstand higher temperatures. To circumvent the problem of maximum temperature achievable Hammers *et al*. (2015) and Kooiman *et al.* (2015) have proposed a TS-CLC using the pair Cu/Mn in the first case and Cu/Ni in the second one. In both cases the syngas is used as fuel. Differently from syngas methane is a reliable and an abundantly available energy source occurring in nature but the methane reduction is endothermic and therefore an accurate heat management strategy occurs (Diglio *et al* 2017a).
In this work the model of a CLC fixed bed reactor network for CH_4 combustion with a TS-CLC is numerically investigated. The network consists of two reactors arranged in series. The first reactor is filled with a Cu-based carrier, this metal has shown high reaction rates even at low temperature and, in addition, is cheaper than other carriers. The second reactor exploits an Ni-based OC, which allows the achievement of high temperatures even if used in low percentages (Adanez *et al.* 2012). The proposed model will allow to optimize and evaluate the performances of suggested reactor system in terms of developed thermal power and of the flow and composition of the gaseous current in output. It will be shown that this TS-CLC is a good alternative to the single bed configuration.

2. Kinetic scheme and mathematical model

The reaction kinetic model for Cu/CuO (Abad *et al*. 2007) and Ni/NiO (Iliuta *et al*. 2010) carriers on γ-Al_2O_3 is summarized in Table 1.

Table 1 – Kinetic scheme adopted.

Reaction	ΔH^0, kJ·mol^{-1}	
Oxidation Stage		
$2Cu + O_2 \rightarrow 2CuO$	-296	R1
$2Ni + O_2 \rightarrow 2NiO$	-479	R2
Reduction Stage		
$4CuO + CH_4 \rightarrow 4Cu + O_2 + H_2O$	-209	R3
$CH_4 + 2NiO \leftrightarrow 2Ni + CO_2 + 2H_2$	161	R4
$H_2 + NiO \leftrightarrow Ni + H_2O$	-2	R5
$CO + NiO \leftrightarrow Ni + CO_2$	-43	R6
$CH_4 + NiO \leftrightarrow Ni + CO + 2H_2$	203	R7
$CH_4 + H_2O \overset{Ni}{\leftrightarrow} CO + 3H_2$	206	R8
$CH_4 + CO_2 \overset{Ni}{\leftrightarrow} 2CO + 2H_2$	247	R9
$CO + H_2O \overset{Ni}{\leftrightarrow} CO_2 + H_2$	-41	R10

Two main stages can be individuated during the CLC, namely Oxidation (OS), and Reduction (RS) stage. Over the OS air is fed to the TS-reactors and Cu (R1) and Ni (R2) oxidation in the first and second reactor occurs. When the second reactor is fully oxidized fed is switched to CH_4 and RS stage occurs. During RS the CuO is reduced to Cu (R3) in the first reactor while in the second reactor NiO reduction (R4-R7) occurs simultaneously to CH_4 reforming reactions. The kinetic expressions of reaction rate R1

and R3 are reported in Diglio *et al*. (2018a), while for R2 and R4-R10 see Diglio *et al.* (2017b, c).

To describe axial concentration and temperature profiles in TS-CLC reactors, a 1D pseudo-homogenous packed-bed model was used. The absence of radial concentration and temperature gradients, as well as the lack of both interphase and intra-particle concentration and temperature gradient has been validated and more details can be found for Cu OC in Diglio *et al* (2018a) and Ni OC in Diglio *et al.* (2017b). The model equations for both carriers are reported in Eqs. (1)-(4). TS-CLC is a periodically forced reactor (Altimari *et al*., 2012) and when it is simulated the exit temperature and concentrations from the first reactor coincide with the inlet valued of the second reactor.

$$\varepsilon_g \frac{\partial c_i}{\partial t} + u_{sg} \frac{\partial c_i}{\partial z} = \varepsilon_g \frac{\partial}{\partial z}\left(D_{ax} \frac{\partial c_i}{\partial z} \right) - r_i \rho_{OC} \tag{1}$$

$$\frac{dX_k}{dt} = \sigma \frac{r_k}{C_{0k}} \tag{2}$$

$$\left[\varepsilon_g cp_g \rho_g + \left(1-\varepsilon_g\right) cp_s \rho_{oc} \right] \frac{\partial T}{\partial t} + u_{sg} cp_g \rho_g \frac{\partial T}{\partial z} = \varepsilon_g \frac{\partial}{\partial z}\left(\lambda_{eff} \frac{\partial T}{\partial z} \right) + \rho_{OC} \sum_j \left(r_{Rj} \Delta H_{Rj} \right) \tag{3}$$

$$\frac{dP}{dz} = \frac{150 \mu_g \left(1-\varepsilon_g\right)^2}{d_p^2 \varepsilon_g^3} u_{sg} + \frac{1.75\left(1-\varepsilon_g\right)\rho_g}{d_p \varepsilon_g^3} u_{sg}^2 \tag{4}$$

Mass balance Eq. (1) has to be defined for each species, then *i* is the gas species (CH_4, H_2, CO_2, H_2O, CO, O_2, N_2), *k* is the solid species (Ni, Cu). *C* is the gas concentration in $mol \cdot m^{-3}$, C_{0k} is the initial concentration of solid species in the carrier, *T* is the temperature in K, X is the solid conversion, *P* is the pressure in Pa, *z* is the axial variable in m, *t* is the time in s, ε_g is the bed void fraction, u_{sg} is the gas superficial velocity in $m \cdot s^{-1}$, D_{ax} is the axial dispersion, ρ_{oc} and ρ_g are the density of oxygen carrier and gas, respectively, in $kg \cdot m^{-3}$, c_{pg} is the gas heat capacity in $J \cdot kg^{-1} \cdot K^{-1}$, λ_{eff} is the effective thermal conductivity in $W \cdot m^{-1} \cdot K^{-1}$, d_p is the particle diameter in m, ΔH is the reaction enthalpy in $kJ \cdot mol^{-1}$. The mathematical model Eqs. (1)-(4) is completed by the following set of boundary condition:

$$\frac{\partial c_i(0,t)}{\partial t} = \frac{u_{sg}}{\varepsilon_g D_{ax}} \left(c_i(0,t) - c_{i,in} \right), \frac{\partial c_i(L,t)}{\partial t} = 0 \tag{5}$$

$$\frac{\partial T(0,t)}{\partial t} = \frac{u_{sg} c_{pg} \rho_g}{\varepsilon_g \lambda_{eff}} \left(T(0,t) - T_{in} \right), \frac{\partial T(L,t)}{\partial t} = 0 \tag{6}$$

$$P(0,t) = P_{in} \tag{7}$$

The rates of consumption or formation of gas r_i solid, r_k species in $mol \cdot kg_{oc}^{-1} \cdot s^{-1}$ are determined according to the reaction scheme reported in Tab.1 by summing up the reaction rates of that species in all the reactions Rj (j=1,…,10). The numerical model was solved using the commercial software package Comsol Multiphysics®. Reactor length, *L*, for each reactor of the series was discretized with 500 nodes and it was

carefully checked that further refinements of the spatial discretization did not produce any appreciable changes in the computed concentration and temperature profiles (Diglio *et al.*, 2018b).

3. Results and discussion Measurement units, numbers

In the proposed system the air is pressurized from ambient conditions up to 30 bar, a temperature of 500°C is obtained. The main idea behind the TS-CLC process is essentially that the heat developed during each stage in the first of the reactors should be transferred to the second so that from this it is possible, with fewer carriers than in the single stage, to achieve the desired temperature increase. In this way the burden of temperature variation is split between the two reactors instead of just one.
Two packed bed of same length are operated in series and the operating conditions, reactor and catalyst data used in the simulations are reported in Table 2.

Table 2 – Parameters used in the simulations

Parameter	Value
P_{in}, MPa	3.0
T_{in}, °C	520
L_{Cu}=L_{Ni}, m	1.0
d_r, m	0.65
$w_{act,Cu}$	0.12
$w_{act,Ni}$	0.1
$\rho_g v_{g,os}$, kg·m^{-2}·s^{-1}	2
$\rho_g v_{g,hr}$, kg·m^{-2}·s^{-1}	2
$\rho_g v_{g,ps}$, kg·m^{-2}·s^{-1}	4
$\rho_g v_{g,rs}$, kg·m^{-2}·s^{-1}	2/15

The TS-CLC process can be seen as a five stages sequence, namely: (I) reduction of carriers (RS): during this stage CH_4 is fed; (II) purge (PS): to avoid the formation of a potentially explosive mixture a purge stage is mandatory in industrial operation; (III) oxidation of carrier (OS): during this stage air if fed to the reactor and the oxidation of the carrier occurs generating heat at high temperature; (IV) heat removal (HR): at the end of OS the most of the heat produced is trapped inside the reactor and all the OC is in the oxidize form thus air is fed to the reactor in order to obtain a high temperature gas stream for subsequent power generation; (V) purge (PS): before to switch again the feed to CH_4 and restart the cycle. Then, the TS-CLC includes RS-PS-OS-HR-PS that cyclically follows each other in a fixed bed reactor. The length of each stage was not fixed a priori, but a controller automatically sets it. To clearly explain the adopted switching strategy, Figure 1 reports monitored outlet temperature (a) and gas concentrations (b) during a CLC cycle starting from RS. It can be inferred from Figure 1: i) the controller dictates the switch between RS and PS when CH_4 concentration at the second reactor outlet reaches about 90% its inlet value in order to fully reduce the OC in the reactor, ii) the subsequent PS length has been chosen equal to 15% of previous RS. iii) the switch between OS and HR is dictated when O_2 concentration at the reactor outlet reached 95% of its inlet value in order to fully oxidize the carrier in the reactor, iv) the subsequent HR is continued until outlet gas temperature drops below 1150°C in order to feed a gas stream at approximately constant temperature to a downstream unit, v) a quick purge is provided before switching to RS. The overall period of a CLC cycle is of 940 s and for the adopted gas flow rates and the percentage

of the active phase the time length of OS is very similar to those of RS (~210 s), the HR stage has a time length of 460 s and both PS stages have a time length of 25 s. Moreover, as it is possible to observe in Fig.1, the time required to oxidize and/or reduce the first of the two reactors is the same as that required to complete the oxidation and/or reduction in the second reactor.

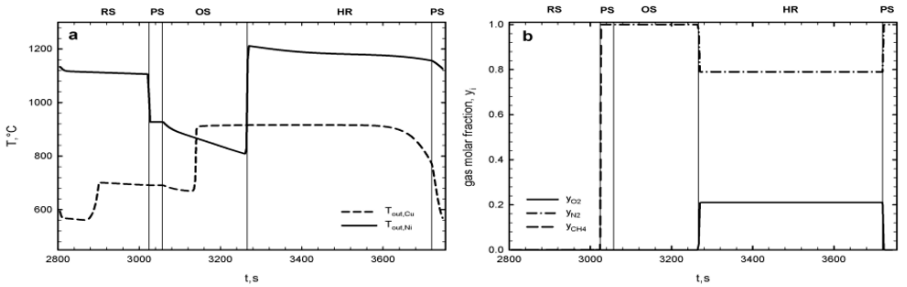

Figure 1 – Outlet temperature (a) and gas molar fractions during a CLC cycle

To gain insight about the TS-CLC process the spatial temperature profiles are depicted in Figure-2. During the RS (Fig.2a) in the first reactor the exothermic Cu reduction occurs (R3) while in the second the process of Ni reduction is strongly endothermic (R4-R10), therefore the temperature at the end of the RS is higher than the initial one in the first reactor while it decreases in the second. When both the carriers are oxidized (Fig.2b) two distinct temperature plateaus are observed, i.e. 970 °C and 1200°C for first and second reactor respectively. HR is extended until outlet gas temperature drops below 1150 °C.

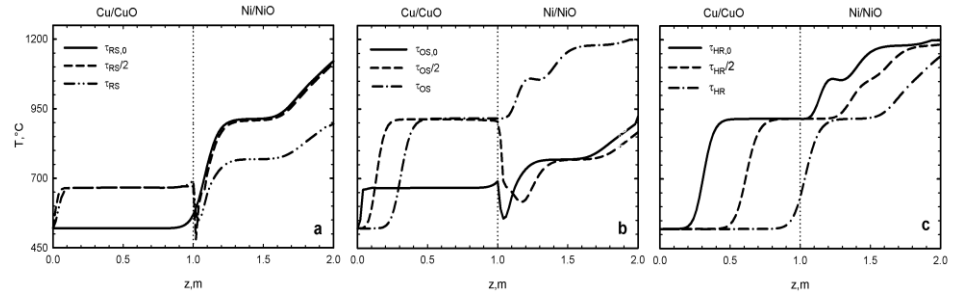

Figure-2 Spatial temperature profiles at several time instants during RS (a), OS (b) and HR (c)

Finally, the outlet gas temperatures at the outlet of first and second reactor are reported for several CLC cycles in Figure 3. It is possible to see that the temperature increase of 700°C between inlet and outlet, is equally split between the two oxygen carrier.

4. Conclusions

In this work, it has been demonstrated that a TS-CLC system based on Cu and Ni OC can guarantee a cyclical temperature variation of ~700 °C by evenly dividing it between two oxygen carriers. The TS-CLC system has two concurrent advantages: it is possible to reach higher outlet gas temperature than those achievable using only copper or to reduce the amount of carrier needed when only Ni is used. These results encourage a future detailed analysis of the costs of this process and a comparison with the most common CLCs.

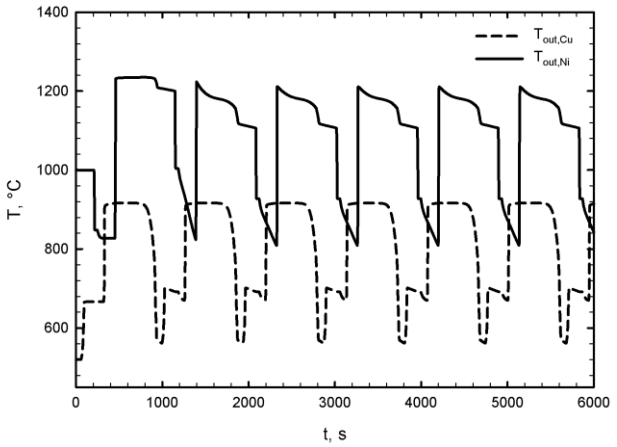

Figure 3 – Outlet gas temperature during multiple CLC cycles.

References

A. Abad, J. Adànez, F. Garcìa-Labiano, L.F. de Diego, P. Gayàn , J. Celaya , 2007,Mapping the range of operational conditions for Cu-, Fe-, and Ni-based oxygen carriers in chemical-looping combustion, Chem. Eng. Sci. 62, 533-54.

A. Adànez, F. Abad, P. Garcia-Labiano, L. Gayan, L. De Diego, 2012, Progress in chemical looping combustion and reforming technologies, Progress in Energy and Combustion Science 38, 2, 215–282.

P. Altimari, E. Mancusi, L. Russo, S. Crescitelli, 2012, Temperature wave-trains of periodically forced networks of catalytic reactors, AIChE J. 58 (3), 899-913.

G. Diglio, P. Bareschino, E. Mancusi, F. Pepe, 2017a, Numerical Assessment of the Effects of Carbon Deposition and Oxidation on Chemical Looping Combustion in a Packed-bed Reactor, Chem. Eng. Sci. 160, 86-96.

G. Diglio, P. Bareschino, E. Mancusi, F. Pepe, 2017b, Novel quasi-autothermal hydrogen production process in a fixed-bed using a chemical looping approach: A numerical study, International Journal of Hydrogen Energy, 42, 22, 15010-15023.

G. Diglio, P. Bareschino, R. Solimene, E. Mancusi, F. Pepe, P. Salatino, 2017c, Numerical simulation of hydrogen production by chemical looping reforming in a dual fluidized bed reactor, Powder Technol., 316, 614–627

G. Diglio, P. Bareschino, E. Mancusi, F. Pepe, 2018a, Techno-Economic Evaluation of a Small-Scale Power Generation Unit Based on a Chemical Looping Combustion Process in Fixed Bed Reactor Network, Industrial and Engineering Chemistry Research, 57, 33, 11299-11311.

G. Diglio, P. Bareschino, E. Mancusi, F. Pepe, F. Montagnaro, D.P. Hanak, V. Manovic, 2018b, Feasibility of CaO/CuO/NiO sorption-enhanced steam methane reforming integrated with solid-oxide fuel cell for near-zero-CO_2 emissions cogeneration system, Appl. Energy, 13, 241.

H.P. Hamers, M.C. Romano, V. Spallina, P. Chiesa, F. Gallucci, M. van Sint Annaland, 2015,Energy Analysis of Two Stage Packed-Bed Chemical Looping Combustion Configurations for Integrated Gasification Combined Cycles, Energy, 85, 489.

I. Iliuta, R. Tahoces, G. Patience, 2010, Chemical-looping combustion process: Kinetics and mathematical modeling, AIChE J., 56, 1063–1079.

R. F. Kooiman, H.P. Hamers, F. Gallucci, M. Van Sint Annaland, 2015, Experimental Demonstration of Two-Stage Packed Bed Chemical-Looping Combustion Using Syngas with CuO/Al_2O_3 and $NiO/CaAl_2O_4$ as Oxygen Carriers, Ind. Eng. Chem. Res, 54, 7, 2001-2011.

J. Rogelj, M. Den Elzen, N., Hohne, T. Fransen, H. Fekete, H. Winkler, R. Schaeffler, F. Shar, K. Riahi, M. Meinshausen, 2016, Paris Agreement Climate Proposal Need a Boost to Keep Warming Weel below 2 C. Nature , 534(7609), 631.

Sauro Pierucci, Flavio Manenti, Giulia Bozzano, Davide Manca (Eds.)
Proceedings of the 30th European Symposium on Computer Aided Process Engineering (ESCAPE30), May 24-27, 2020, Milano, Italy.
http://dx.doi.org/10.1016/B978-0-12-823377-1.50008-2

Modeling of Liquid-Liquid Phase Transfer Catalysis: Process Intensification via Integration of Process Systems Engineering and Computational Chemistry

Abhimanyu Pudi, Adam P. Karcz, Vahid Shadravan, Martin P. Andersson, Seyed Soheil Mansouri*

Department of Chemical and Biochemical Engineering, Technical University of Denmark, Søltofts Plads 229, Kgs. Lyngby, DK-2800, Denmark
seso@kt.dtu.dk

Abstract

Phase transfer catalysis is an important intensified extraction-reaction process and a powerful tool applied in a vast array of chemical synthesis applications. This technique allows for reactions that are generally not feasible through conventional synthesis routes via the introduction of a heterogeneous transfer catalyst that can carry a reactant species across two immiscible phases. These biphasic conditions enable novel synthesis routes, higher yields, and faster reactions, while also facilitating the separation of certain species. The economic viability and successful large-scale implementation of such processes are heavily contingent on the design and modelling of the systems under consideration. Although a few attempts have been made to create case-specific and generic models for phase transfer catalysis, they suffer from the lack of modelling considerations or thermodynamic model parameters. These limitations restrict the solution space to design new phase transfer catalysis-based processes. In the present work, an integrated and multiscale modelling framework is presented to overcome such limitations for liquid-liquid phase transfer catalysis. The proposed framework requires little to no experimental data and employs different tools at different scales of time and space to model nearly any liquid-liquid phase transfer catalytic system. The objective of this work is to apply this framework towards the process of H_2S recovery and conversion from an aqueous alkanolamine solution to value-added products as a means to improve process economics and sustainability, particularly in offshore oil and gas platforms. The framework is validated by comparing the preliminary results with known experimental behaviour. The final results are expected to contribute towards further developing a generic, systematic framework for biphasic reaction-separation processes.

Keywords: Phase transfer catalysis, multiscale modelling, resource recovery.

1. Introduction

Advances in computing have greatly revolutionized science and engineering. Coupled with massive progress in fundamental chemical physics theory, mathematics, and computer science, they have contributed to the constant evolution in the fields of chemistry and chemical engineering, essentially giving rise to the disciplines of computational chemistry and process systems engineering (PSE), respectively. These two disciplines play a major role in providing new understanding and development of computational procedures for the simulation, design, and operation of systems ranging

from atoms and molecules to industrial-scale and enterprise-wide processes—an enormous span of scales of space and time that form the chemical supply chain. Despite being part of the same overarching field, chemistry and chemical engineering have generally remained two distinct areas working at different scales with partial overlap; while computational chemistry focuses on the small scale, PSE focuses on the intermediate and large scales. However, over the past two decades, it has become increasingly clear that the modelling, design and development of new and innovative reaction and separation processes requires going below the scale of unit operations—the holy ground of traditional process engineering—towards the underlying molecules, clusters and their behavior that make up the functions/tasks carried out by the unit operations (Babi et al., 2016). This trend of moving beyond traditional chemical engineering has emerged because the concept of unit operations, although useful and easy to understand, inherently restricts the solution space to a limited number of well-known and ready-made solutions (Freund and Sundmacher, 2008).

To overcome these limitations, engineers and industrial researchers have been working on novel equipment and techniques that could potentially transform our concept of chemical plants and lead to compact, safe, energy-efficient, and environment-friendly sustainable processes (Stankiewicz and Moulijn, 2000). These developments share a common theme: process intensification. In this regard, bridging computational chemistry and PSE to achieve process intensification could qualitatively change the way chemical products and processes are designed.

Phase transfer catalysis (PTC) is one such case of process intensification that could hugely benefit from a multiscale outlook. In liquid-liquid (L-L) PTC, the reactions take place in heterogeneous two-phase systems (organic-aqueous) with negligible mutual solubility of the phases. The catalyst, located in the aqueous phase, acts as a source of lipophilic cations and continuously introduces the reacting anionic species in the form of lipophilic ion pairs into the organic phase. However, the downside of PTC is the need to quantify exacting reaction conditions and parameters that are difficult to uncover and, in some cases, are counterintuitive. Although there has been some progress in terms of mathematical modeling of PTC systems (Anantpinijwatna et al., 2016), availability of accurate thermodynamic parameters still proves a major limitation as the chemical domain in the group contribution methods is inherently limited to the portion of the chemical design space for which every binary interaction parameter is available.

2. Modelling Framework

Anantpinijwatna et al. (2016) presented a systematic procedure for modelling biphasic systems that is based on the model generation method of Cameron and Gani (2011). The procedure serves to reduce the complexity of the modelling problem by breaking it into a series of sub-problems. A schematic of the various steps in the procedure can be seen in Figure 1.

The heart of a successful PTC modelling framework lies in the methods and/or tools used to describe the system in the three modules shown in Figure 1 since the methods used to calculate the molecular and mixture properties largely determine the breadth, accuracy and performance of the framework. The present work employs sequential multiscale modelling by using different tools for different scales of time and space to model and predict the behaviour of the PTC system. Although modules 2 and 3 remain largely the

same as defined in Anantpinijwatna et al. (2016), the methods used in module 1 make the framework much more generic in terms of its application. The integration of quantum chemical calculations into a process modelling framework greatly expands the envelope of chemical species that can be modelled at a high level of accuracy. A more thorough description of the framework can be found in Pudi (2019).

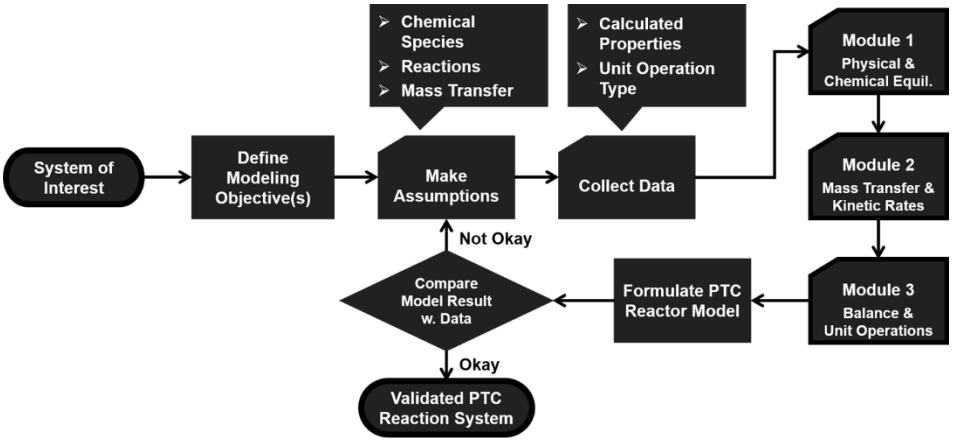

Figure 1 Generic Modelling Procedure for Biphasic Reaction Systems. Adapted from Anantpinijwatna et al. (2016)

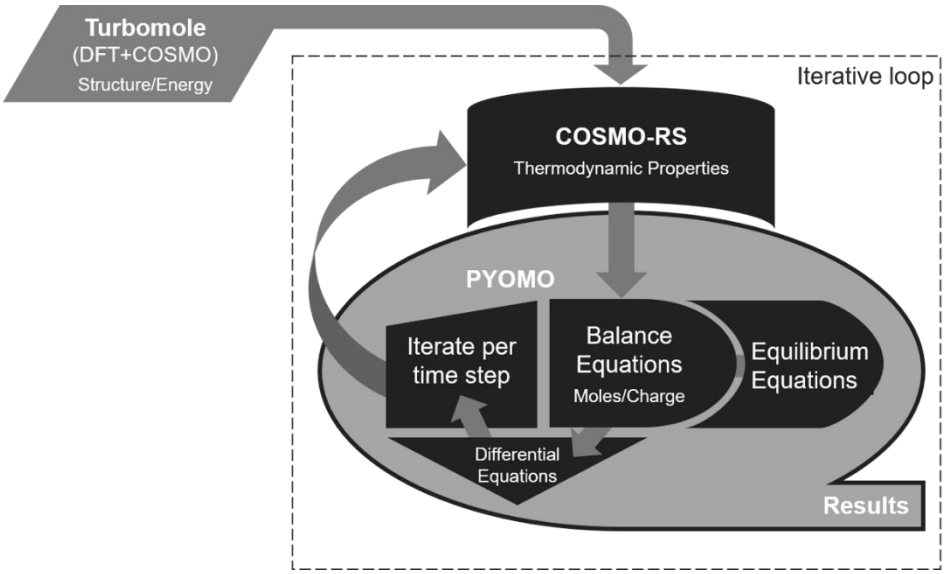

Figure 2 Solution Algorithm for the Proposed Framework

The algorithm is illustrated in Figure 2. With Python as the high-level interface, three different tools are employed at three different levels of space and time as follows:

- Molecular/electronic level: Turbomole
- Transport and reaction thermodynamics level: COSMOtherm

- Reactor level: Pyomo.

For each species in the system, geometric optimization calculations are performed in Turbomole to obtain their ground-state and gas-phase energies and screening charge density profiles. These are then transferred to COSMOtherm to obtain partition coefficients, activity coefficients, and chemical equilibrium constants, which are all parameters for the PTC model. These parameters are then input in Pyomo where the equations for equilibria, kinetics, and balances are solved to model the system behaviour.

3. Application and Validation

Hydrogen sulfide is a highly toxic chemical that is found as an impurity or an inhibitor in many petrochemical, chemical and biochemical processes. In fact, it is classified as a hazardous industrial waste. Environmental and/or process constraints often require the removal of this compound to trace amounts. This is usually accomplished by capturing H_2S and later oxidizing it to elemental sulfur, a process generally referred to as sulfur recovery. Recovered elemental sulfur is produced primarily during the processing of natural gas and crude petroleum. Due to the depletion of sweet oil and gas reserves around the world, players in the O&G industry are increasingly looking toward sour fields to meet our energy needs. In the past 2-3 decades, sulfur production has consistently outpaced the demand leading to the large stockpiles of block sulfur *waste* in several countries around the world. At a time when the world is striving to achieve a zero-waste and circular economy, sulfur disposal poses a serious barrier to such a transition. Therefore, it is vital to develop a viable alternative to the practice of converting H_2S to elemental sulfur.

L-L PTC offers one such alternative by converting H_2S to value-added products. Since alkanolamine-based processes are widely used for the removal of acid gases from gaseous streams, it is assumed that the capture of H_2S from a gas phase to a liquid phase uses a 30 % solution of methyldiethanolamine (MDEA). Traditional approach for the next step is the use of a stripping column to separate H_2S and regenerate MDEA; MDEA is then sent back to the absorber while H_2S is directed towards further process steps to convert it to elemental sulfur. However, the regeneration step requires high operational costs. In order to overcome the drawbacks of this process, PTC is explored as the cornerstone for the capture and utilization of H_2S. One major advantage of this route is the ability to target a wide variety of products, instead of only elemental sulfur or inorganic sulfates. Using L-L PTC in a continuous stirred tank reactor, the H_2S-rich aqueous phase is put in contact with an organic phase (here toluene) containing benzyl chloride (BC) to produce benzyl mercaptan (BM) in the presence of a PT catalyst such as tetrabutylammonium bromide (QBr). The objective is to model the complex interlinked phenomena—multiple reactions in each phase and partitioning of various species between the phases—occurring in such a system. The reactions presumed to occur in this biphasic system are given below.

Organic Phase:

$$QSH + BC \rightleftharpoons QCl + BM \tag{1}$$

Aqueous Phase:

$$2H_2O \rightleftharpoons H_3O^+ + OH^- \tag{2}$$

$$MDEAH^+ + H_2O \rightleftharpoons MDEA + H_3O^+ \quad (3)$$

$$H_2S + H_2O \rightleftharpoons HS^- + H_3O^+ \quad (4)$$

$$HS^- + H_2O \rightleftharpoons S^{2-} + H_3O^+ \quad (5)$$

$$QBr + HS^- \rightleftharpoons QSH + Br^- \quad (6)$$

$$\mathrm{QCl + HS^- \rightleftharpoons QSH + Cl^-} \quad (7)$$

$$\mathrm{HBr + H_2O \rightleftharpoons Br^- + H_3O^+} \quad (8)$$

$$HCl + H_2O \rightleftharpoons Cl^- + H_3O^+ \quad (9)$$

$$QBr \rightleftharpoons Q^+ + Br^- \quad (10)$$

$$QCl \rightleftharpoons Q^+ + Cl^- \quad (11)$$

The PT catalysts, QBr & QCl, react with the inorganic sulfide anion in the aqueous phase to produce the active catalyst species, QSH. These active catalysts species partition into the organic phase transporting the hydrosulfide ion to participate in the nucleophilic substitution reactions with BC. A few of the reactor specifications are taken from the experimental data reported by Singh et al. (2016). Preliminary findings from the application of the modelling framework to this case are presented below.

3.1. Phase Partitioning

From the phase equilibrium calculations in COSMOtherm, affinities of each species in the system to each of the two phases can be understood. To this end, the partition coefficient values of a few important components calculated in the first iteration of the implicit solution method are listed in Table 1.

Table 1 Partition Behaviour Characteristics

Chemical Species	Partition Coefficient	Preferential Phase
H_2O	0.06	Aqueous
Toluene	1104.57	Organic
BM	1040.48	Organic
BC	912.15	Organic
QSH	100.86	Organic
QBr	26.82	Organic
QCl	24.31	Organic
MDEA	0.44	Aqueous
HS^-	0	Aqueous

A partition coefficient greater than 1 implies a relatively higher affinity towards the organic phase, while a value less than 1 implies a relatively higher affinity towards the aqueous phase. In this context, the reported values are consistent with and explain the experimental behaviour observed by Singh et al. (2016). The main reactant and product in the organic phase reaction, benzyl chloride and benzyl mercaptan, are heavily partitioned into the organic phase. This provides for a cleaner product separation in the downstream purification processes. The three catalyst species (QSH, QBr, and QCl) mildly prefer the organic phase. Among the three, the active catalyst form of QSH exhibits about four times higher affinity to the organic phase than the two inactive catalyst species. This enables the preferential partition of the necessary active form into the organic phase to undergo the reaction to form the required product BM.

3.2. General Performance

The first iteration found a 23 % conversion of benzyl chloride to benzyl mercaptan. Although the final rate of conversion is expected to be high, it is worth noting that the value from the first iteration matches the first data point obtained by Singh et al. (2016) in the first 5-10 minutes of the experiment. This shows that the current version of the modelling framework does indeed work and is headed in the right direction.

4. Conclusions

A rigorous multiscale modelling framework to describe the behaviour of a phase transfer catalysis system is presented. The framework incorporates a series of computational tools covering different scales of time and space in a sequential/dynamic modelling approach. The current implementation offers great advantages over the previously developed modelling framework reported in Anantpinijwatna et al. (2016). Due to the incorporation of quantum chemical and continuum solvation methods, the limitation due to the unavailability of accurate thermodynamic model parameters has been overcome in the present work. Further work is expected to fully develop the tool integration in the framework.

References

A. Anantpinijwatna, M. Sales-Cruz, S. H. Kim, J. P. O'Connell, and R. Gani, 2016, A systematic modelling framework for phase transfer catalyst systems, Chem. Eng. Res. Des., 116, 407-422

D. K. Babi, M. Sales-Cruz, and R. Gani, 2016, Fundamentals of Process Intensification: A Process Systems Engineering View, In: Segovia-Hernández J., Bonilla-Petriciolet A. (eds) Process Intensification in Chemical Engineering, Springer, Cham, Switzerland, 7-33

I. T. Cameron and R. Gani, 2011, Product and Process Modelling: A Case Study Approach, Elsevier, Amsterdam, Netherlands

H. Freund and K. Sundmacher, 2008, Towards a methodology for the systematic analysis and design of efficient chemical processes. Part 1. From unit operations to elementary process functions, Chem. Eng. Process., 47, 12, 2051-2060

A. Pudi, 2019, From Molecule to Process: Multiscale Modeling of Liquid-Liquid Phase Transfer Catalysis, M.Sc. Thesis, Technical University of Denmark, retrieved from https://findit.dtu.dk/en/catalog/2452812532

G. Singh, P. G. Nakade, D. Chetia, P. Jha, U. Mondal, S. Kumari, and S. Sen, 2016, Kinetics and mechanism of phase transfer catalyzed synthesis of aromatic thioethers by H_2S-rich methyldiethanolamine, J. Ind. Eng. Chem., 37, 190-197

A. I. Stankiewicz and J. A. Moulijn, 2000, Process Intensification: Transforming chemical engineering, Chem. Eng. Prog., 96, 22-23

Sauro Pierucci, Flavio Manenti, Giulia Bozzano, Davide Manca (Eds.)
Proceedings of the 30th European Symposium on Computer Aided Process Engineering (ESCAPE30), May 24-27, 2020, Milano, Italy.
http://dx.doi.org/10.1016/B978-0-12-823377-1.50009-4

Investment Planning in Personalised Medicine

Despoina Moschou[a], Maria M. Papathanasiou[a], Matthew Lakelin[b], Nilay Shah[a]

[a]*Dept. of Chemical Engineering, Centre for Process Systems Engineering (CPSE), Imperial College London SW7 2AZ, London, U.K*

[b]*TrakCel Limited, 10/11 Raleigh Walk, Cardiff, CF10 4LN UK*

maria.papathanasiou11@imperial.ac.uk

Abstract

Personalised cancer therapies are gaining increasing attention due to their demonstrated clinical potential. Nonetheless, such patient-centric, 1:1 business models encompass significant manufacturing and distribution challenges that are directly associated with the patient schedule. In this work we focus on the development and solution of a mixed-integer optimisation problem to suggest cost-efficient candidate networks that guarantee responsiveness and successful delivery of the therapy. The developed model is tested under two demand scenarios, incorporating economies of scale elements.

Keywords: mixed integer programming, personalised medicine, optimisation, supply chain

1. Introduction

Personalised medicine is dedicated to the discovery, manufacturing and delivery of patient-specific therapy protocols that can more effectively target autoimmune diseases and malignancies related to patient-specific mutations, such as cancer. Chimeric Antigen Receptor (CAR) T cell therapy is one of the latest personalised therapies developed and approved in in the United States (Novartis, 2018), Europe (European Medicines Agency, 2018), Australia (Lymphoma Australia, 2018) and Japan (Biomedica, 2019). These use recombinant receptors for antigens that can make T lymphocytes tumour-specific. Through genetic modification, T cells are engineered to express the CAR receptor that redirects their specificity and function, enabling them to recognize and destroy cancer cells (Sadelain, Brentjens, Rivière, & Park, 2015). This individualized, emerging immunotherapy has shown promising results particularly in the treatment of B-cell lymphoma (Jackson, Rafiq, & Brentjens, 2016; Maude et al., 2018; Neelapu et al., 2017) and has encouraged further clinical research.

The delivery of gene-modified T cells is different from that of the traditional off-the-shelf medicines. CAR-T cell therapy is a dynamic treatment process that requires collaboration and effective communication between several parties (healthcare providers, cancer treatment centres, manufacturing facilities) (Novartis, 2017). Currently, this innovative therapy is provided through a service model, developed based on the requirements for allogeneic Blood and Marrow Transplantation (BMT)(NHS, 2018). The analogy between these two treatments lies in the pairing of one cell donor with one patient (Foley & Whitaker, 2012). The different stages of the treatment's delivery are illustrated in Figure 1. Currently, the end-to-end process comprises 7 steps, namely: leukapheresis (extraction of T cells from patient's blood stream), cryopreservation, manufacturing, quality control and cryopreservation, thawing and

administration. It should be underlined that cryopreservation is a step highly dependent on the individual manufacturer models. Therefore, there may be processes where the patient T cell sample is transferred fresh (at -80ºC). Following administration, patients are monitored short-term for side effects and long term for possible disease relapse.

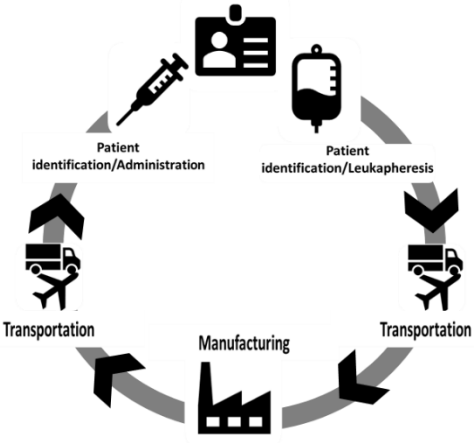

Figure 1 Different stages of CAR-T cell therapy delivery

The successful operation of such a supply chain model requires the orchestration of multiple components (Shah, 2004). In a typical supply chain model in the pharmaceutical industry there are usually established warehouses/distribution centres in place, responsible for the storage and distribution of the manufactured drug to the retailers. By contrast, in the case of CAR T cells, cells are transported directly from the clinical site to the manufacturing locations and back to the hospital, thus imposing additional constraints with respect to storage, activity coordination and sample tracking. Considering the uniqueness of the therapy's delivery, the supply chain of gene modified T-cells can be identified as a service starting and finishing with a specific patient (Wei Teng, Foley, O'Neill, & Hicks, 2014). CAR T cell therapy can be characterised as one-on-one autologous treatment (1:1 model) as cells are harvested form a single patient, manipulated and then returned to the same patient. Similar to classical pharmaceuticals, even more so in the case of CAR T cells, systematic decision making in the design and planning of supply chain networks can significantly reduce risk of failure and increase efficiency. In this framework, here we present for the first time the design of a comprehensive Mixed Integer Linear (MILP) model to allow decision-making in CAR T cell supply chain.

2. The model

2.1. Case under study

In this work we consider today's CAR T cell supply chain network (Figure 2), comprising 3 main nodes: (a) leukapheresis site, (b) manufacturing facility and (c) hospital. Often, the leukapheresis site and the hospital are either co-located or close to one another in the same city. Here, we consider the United Kingdom (UK) as the geographical area of interest and we develop two cases for 200 and 500 patients annually. The patient population is distributed in time based on a separate algorithm, considering the daily capacity of the leukapheresis centers.

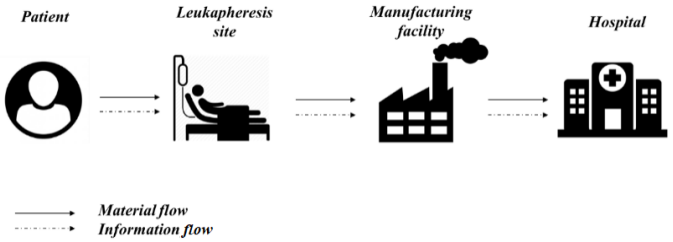

Figure 2 Classical CAR T cell supply chain network

2.2. Mathematical formulation

The optimisation problem described in the previous section is formulated as a mixed-integer linear programming (MILP) model, and the general formulation is presented in Table 1.

Table 1 Mixed Integer Linear Problem (MILP) formulation developed to solve the supply chain optimisation scenarios generated for the network as shown in Figure 2.

Index	Mathematical Formulation	Description
Objective function		
(1)	$TCO = C_{manufacturing} + C_{quality} + C_{apheresis} + C_{transportation} + C_{capital}$	Total Network Cost
OR (2)	$ART = \left(\sum_p T_{transport} + T_{manufacturing} + T_{leukap\ heresis}\right)/_{NP}$	Average Return Time of Therapy
Constraints		
(3)	$Y1_{l,m} \le E1_m \ \forall m,l, Y4_{m,h} \le E1_m \ \forall m,h, \sum_m E1_m \le 2,$ $Y2_{p,l,m,k,t} \le Y1_{l,m} \ \forall p,l,m,k,t, \ Y3_{p,m,h,k,t} \le Y4_{m,h} \ \forall p,m,h,k,t$	Network/Transportation
(4)	$XTA_{p,l,t} = \sum_m \sum_k XTAM_{p,l,m,k,t+TL} \ \forall p,l,m,k,t, XTAM_{p,l,m,k,t} = XTM_{p,l,m,k,t+TDEL_k},$ $\sum_l \sum_k XTM_{p,l,m,k,t} = \sum_h \sum_k XTMH_{p,m,h,k,t+TM+TQC} \ \forall p,m,t,$ $XTMH_{p,m,h,k,t} = XTHI_{p,m,h,k,t+TDEL_k}, \sum_m \sum_k XTHI_{p,m,h,k,t} = XTHO_{p,h,t+TH}$	Sequencing/ Scheduling
(5)	$\sum_p XTA_{p,l,t} = \sum_p \sum_m \sum_k XTAM_{p,l,m,k,t+TL} \ \forall l,t,$ $\sum_p \sum_l \sum_k XTM_{p,l,m,k,t} = \sum_p \sum_h \sum_k XTMH_{p,m,h,k,t+TM+TQC} \ \forall m,t, \sum_m \sum_k XTHI_{p,m,h,k,t} = XTHO_{p,h,t+TH}$	Sample Balances
(6)	$\sum_p \sum_l \sum_k XTM_{p,l,m,k,t} \le MMCAP_m - \sum_p \sum_l \sum_k \sum_t^{t-TM} XTM_{p,l,m,k,t} \ \forall m,t,$ $\sum_p \sum_m \sum_k XTHI_{p,m,h,k,t} \le MHCAP_h - \sum_p \sum_m \sum_k \sum_t^{t-TH} XTHI_{p,m,h,k,t} \ \forall h,t$	Capacity Constraints

Two functions are selected as candidate minimisation objectives; namely the total cost (Eq. (1)) and the average network response time, reflecting the urgency of the treatment (Eq. (2)). The total network cost is associated with the capital, fixed operational (leukapheresis and in-house quality control expenses), manufacturing and transportation cost (Eq. (1)). The responsiveness of the network is measured through the average lead time for the production and delivery of a therapy, which is the sum of the time a treatment spends at every stage of the supply chain. For the cost minimisation scenarios, an upper bound on the response time is introduced ($ART \le U$, where U corresponds to the maximum time allowed before the therapy is be administered to the patient). A set of network and transportation constraints (Eq. (3)), ensures that only feasible connections are established inside the supply chain network. As regulatory authorities require manufacturers of biological medicinal products to conduct costly cooperabilities studies for the introduction of new manufacturing facilities, an upper bound constraint is introduced to prevent the establishment of more than two production sites. Sequencing constraints and material balances (Eq. (4)-(5)) at each supply chain node impose the correct sequence of events inside the supply chain for every treatment. Finally, capacity constraints on the treatment centres and the manufacturing sites (Eq. (6)) enforce upper bound limitations on the scheduling of therapies.

2.3. Model input

Here we consider 6 candidate locations for the manufacturing facilities with different annual capacities. Based on current standard practice, the choice of leukapheresis sites and hospitals is not entirely under the manufacturers' control and is tightly associated to regulations and reimbursement procedures. Therefore, in this case the latter are treated as inputs for the model formulation and the locations are depicted in Table 2. For the transportation of the therapies between the supply chain nodes two shipment options are considered (1-day and 2-day delivery). In addition, given the complex nature of the leukapheresis and administration procedures, we impose a daily demand equal to 10 patients for the leukapheresis sites and 5 patients for the hospitals.

Table 2 Model fixed and candidate location inputs for leukapheresis sites, manufacturing facilities and administration sites.

Leukapheresis site (fixed input)		Manufacturing facility (candidate locations)		Administration site (hospital) (fixed input)	
Geographical Location	**Capacity (patients/day)**	**Geographical Location**	**Capacity (patients/year)**	**Geographical Location**	**Capacity (patients/day)**
London	10	Stevenage	200	London	5
Glasgow	10	Glasgow	1500	Glasgow	5
Manchester	10	Berlin	500	Manchester	5
Birmingham	10	Belgium	200	Birmingham	5
		Pennsylvania	1500		
		Virginia	500		

3. Results and discussion

The optimisation algorithm presented above was modelled using the GAMS modelling system coupled with the CPLEX 12.9 solver. The optimal manufacturing facilities for each scenario and demand pattern are presented in Table 3. In general, the optimiser selected the establishment of manufacturing sites with annual production capacity higher than the demand of the scenario under investigation. This is attributed to the randomness of the demand distribution, a common characteristic of CAR T cell therapies. Higher production capacities ensure that enough production lines are available to serve patients in periods with high demand density. In addition, the proximity to the market influenced the solutions of the cost minimisation scenarios, as production sites located closer to the United Kingdom where selected, contributing to lower transportation costs.

Table 3 Model fixed and candidate location inputs for leukapheresis sites, manufacturing facilities and administration sites.

	Minimisation of ART	**Minimisation of Total Cost with no time constraints**	**Minimisation of Total Cost with time constraints (ART<20)**	**Minimisation of Total Cost with time constraints (ART<21)**	**Annual patient population**
Optima Manufacturing facilities	Stevenage, Virginia	Berlin	Berlin	Berlin	200
	Glasgow, Berlin	Glasgow	Glasgow	Glasgow	500

The economic performance of each network can be evaluated through the achievable average cost per therapy. Figure 2, shows that the cost significantly decreased with an increase in patient demand. The high demand scenarios presented reduced operational costs, due to higher manufacturing capacity utilisation. In addition, there is a clear cost trade-off between the supply chain responsiveness and economies of scale. Strict time constraints resulted in higher infrastructure and transportation costs, decreasing the profit gap per therapy. Finally, the capital costs are identified as the major cost contributor in the production of CAR-T cell therapies, while transportation costs only correspond to ~ 2% of the total therapy cost (Table 4).

Figure 2 Average cost per therapy for 200 and 500 patients annual demand for 4 different scenarios.

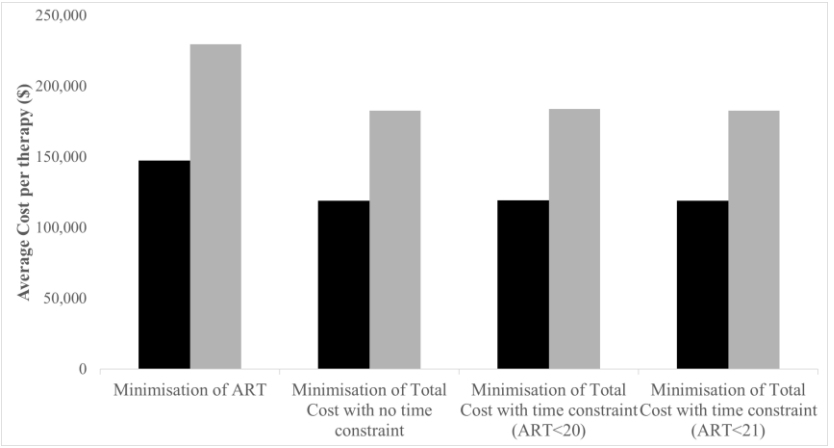

Table 4 Therapy cost breakdown for 200 and 500 patients annual demand for 4 scenarios.

	Minimisation of ART	Minimisation of Total Cost with no time constraints	Minimisation of Total Cost with time constraints (ART<20)	Minimisation of Total Cost with time constraints (ART<21)	Annual patient population
% Transport	2.07%	1.37%	1.99%	1.37%	200
% CAPEX/OPEX manufacturing	97.93%	98.63%	98.01%	98.63%	
% Transport	3.20%	0.97%	1.40%	0.97%	500
% CAPEX/OPEX manufacturing	96.80%	99.03%	98.60%	99.03%	

4. Conclusions

A complete optimisation algorithm able to design agile and cost-effective CAR T cell supply chain networks was developed. The case study on cost-time trade off at different demand patterns, revealed that the supply chain becomes more profitable as the number of patients receiving the treatment increases. The demand distribution uncertainty and the limiting production capacity were identified as the major supply chain bottlenecks, that lead to increased network costs. The current work considered the traditional supply

chain model for delivering personalised cancer treatments. Future work will focus on novel network structures that introduce intermediate storage points and could possible increase the flexibility and efficiency of the current network.

Acknowledgements

Funding from the UK Engineering & Physical Sciences Research Council (EPSRC) for the Future Targeted Healthcare Manufacturing Hub hosted at University College London with UK university partners is gratefully acknowledged (Grant Reference: EP/P006485/1). Financial and in-kind support from the consortium of industrial users and sector organisations is also acknowledged.

References

Biomedica, O. (2019). Oxford Biomedica notes the Japanese approval of Kymriah® (tisagenlecleucel), the first CAR-T cell therapy authorised in Asia | OxfordBiomedica.

European Medicines Agency. (2018). First two CAR-T cell medicines recommended for approval in the European Union | European Medicines Agency.

Foley, L., & Whitaker, M. (2012). Concise Review: Cell Therapies: The Route to Widespread Adoption. *STEM CELLS Translational Medicine*. https://doi.org/10.5966/sctm.2011-0009

Jackson, H. J., Rafiq, S., & Brentjens, R. J. (2016). Driving CAR T-cells forward. *Nature Reviews Clinical Oncology*, *13*(6), 370–383. https://doi.org/10.1038/nrclinonc.2016.36

Lymphoma Australia. (2018). CAR-T cell therapy.

Maude, S. L., Laetsch, T. W., Buechner, J., Rives, S., Boyer, M., Bittencourt, H., … Grupp, S. A. (2018). Tisagenlecleucel in Children and Young Adults with B-Cell Lymphoblastic Leukemia. *New England Journal of Medicine*, *378*(5), 439–448. https://doi.org/10.1056/NEJMoa1709866

Neelapu, S. S., Locke, F. L., Bartlett, N. L., Lekakis, L. J., Miklos, D. B., Jacobson, C. A., … Go, W. Y. (2017). Axicabtagene Ciloleucel CAR T-Cell Therapy in Refractory Large B-Cell Lymphoma. *New England Journal of Medicine*, *377*(26), NEJMoa1707447. https://doi.org/10.1056/NEJMoa1707447

NHS. (2018). Axicabtagene Ciloleucel Chimeric Antigen Receptor T Cell (CAR T) Therapy for the treatment of adult patients with relapsed or refractory large B-cell lymphoma. *Nature Reviews Clinical Oncology*. https://doi.org/10.1038/nrclinonc.2017.148

Novartis. (2017). Starting Your Patients on Kymriah. *Novartis*.

Novartis. (2018). Kymriah® (tisagenlecleucel), first-in-class CAR-T therapy from Novartis, receives second FDA approval to treat appropriate r/r patients with large B-cell lymphoma. Retrieved July 24, 2018, from https://www.novartis.com/news/media-releases/kymriahr-tisagenlecleucel-first-class-car-t-therapy-from-novartis-receives-second-fda-approval-treat-appropriate-rr-patients-large-b-cell-lymphoma

Sadelain, M., Brentjens, R., Rivière, I., & Park, J. (2015). CD19 CAR Therapy for Acute Lymphoblastic Leukemia. *American Society of Clinical Oncology Educational Book*, *35*, e360–e363. https://doi.org/10.14694/EdBook_AM.2015.35.e360

Shah, N. (2004). Pharmaceutical supply chains: Key issues and strategies for optimisation. In *Computers and Chemical Engineering* (Vol. 28, pp. 929–941). Pergamon. https://doi.org/10.1016/j.compchemeng.2003.09.022

Wei Teng, C., Foley, L., O'Neill, P., & Hicks, C. (2014). An analysis of supply chain strategies in the regenerative medicine industry - Implications for future development. In *International Journal of Production Economics*. https://doi.org/10.1016/j.ijpe.2013.06.006

Sauro Pierucci, Flavio Manenti, Giulia Bozzano, Davide Manca (Eds.)
Proceedings of the 30th European Symposium on Computer Aided Process Engineering
(ESCAPE30), May 24-27, 2020, Milano, Italy.
http://dx.doi.org/10.1016/B978-0-12-823377-1.50010-0

A Stochastic Modelling Approach to Describe the Effect of Drying Heterogeneity in the Lyophilisation of Pharmaceutical Vaccines

Gabriele Bano,[a,b] Riccardo De-Luca,[b] Emanuele Tomba,[c] Fabrizio Bezzo,[b] Massimiliano Barolo[b*]

[a] *GSK, Ware, United Kingdom*
[b] *CAPE-Lab, Department of Industrial Engineering, University of Padova, Italy*
[c] *GSK, Siena, Italy*
max.barolo@unipd.it

Abstract

In sterile drug product and vaccine manufacturing, reducing the duration of the primary drying stage of a lyophilisation cycle is pivotal to streamline process development and optimise commercial plant operation. Mathematical models can be used to assist this optimisation exercise. However, the models currently available in the literature usually neglect the effect of intra-lot drying heterogeneity in the optimization framework. In this study, we provide a description of drying heterogeneity using a deterministic model that mimics the behavior of a single vial, while treating the most impacting model parameter as a stochastic quantity. The novelty of the proposed approach lies in the description of drying heterogeneity using a single additional parameter, without further complicating the single-vial model structure. The prediction fidelity of the proposed model is assessed with experimental data obtained in an industrial equipment. Results show a robust prediction fidelity of the model in describing the effect of intra-lot drying heterogeneity on the process key performance indicators (KPIs).
Keywords: freeze-drying, lyophilisation, vaccines, quality by design.

1. Introduction

Freeze-drying is widely used in the biopharmaceutical industry to increase the shelf life of temperature-sensitive products (e.g., vaccines) that are processed in aqueous solution. The process first involves freezing the initial product, typically placed inside vials, then water removal by direct sublimation at low temperature and low pressure (*primary drying*). The residual water bounded to the product matrix is desorbed at higher temperature (*secondary drying*). Primary drying is the most energy-intensive and time-consuming process step (Liu *et al*., 2008), and minimising its duration is crucial to reduce the overall process duration and energy requirement. However, primary drying protocols must respect hard constraints on both product temperature, which cannot exceed the collapse temperature of the product, and total sublimation rate, which cannot exceed the maximum capacity of the duct connecting the drying chamber with the condenser (to avoid choked flow). Different mathematical models have been proposed in the literature over the years, which could be used for primary drying optimisation (Pikal, 1985; Velardi and Barresi, 2008). These models describe the relevant heat and mass transfer mechanisms involved in ice sublimation and can be exploited to determine the optimal profiles of the manipulated variables (chamber pressure and shelf temperature) that

minimise the drying time. Different attempts have also been made to embed in these models the intra-lot drying heterogeneity by describing the differences in heat and mass transfer mechanisms between vials placed at different locations inside the drying chamber, or accounting for parameter uncertainty (Barresi *et al*., 2010; Scutellà *et al*., 2018). These approaches typically result in a higher number of parameters to be estimated from experimental data, or in an amplification of the uncertainty in the model predictions due to parameter correlation. In this study, we propose a modelling framework that describes drying heterogeneity as stochastic uncertainty on the model parameter with the highest influence on the process KPIs. The proposed model is identified and its predictions verified through experiments conducted in an industrial lab-scale equipment.

2. Materials and methods

The experiments presented in this study were performed with a 5% w/w sucrose solution, processed in a VirTis Genesis 25EL freeze-dryer (SP Scientific, Stone Ridge, NY, USA); one full shelf out of a total of five was loaded for a total of 476 non-siliconized 3 mL vials filled with 0.6 mL of solution; the freezing step before primary drying was carried out at a freezing rate of –1 °C/min down to –50 °C. The condenser temperature was kept at –85 °C during the entire freeze-drying cycle. Product temperature measurements were obtained by placing thermocouple probes (T type, copper constantan wire, AWG 24) inside 12 different vials placed in different zones of the chamber. The software used for process simulation is gPROMS Model Builder v. 5.1 (Process Systems Enterprise, 2019).

3. Single-vial model

The proposed model has been derived from the model by Velardi and Barresi (2008) by introducing a dynamic energy balance to describe the time-varying system heat capacity.

3.1. Mass transfer

Since no radial gradients of temperature and ice composition during sublimation are assumed, the length of the frozen layer decreases along the axial direction, until the end of sublimation, according to Eq. (1):

$$\frac{\mathrm{d}L_f}{\mathrm{d}t} = -\frac{1}{\rho_f - \rho_d} J_w \tag{1}$$

where L_f [m] is the length of the frozen layer, ρ_f [kg m^{-3}] is the density of the frozen layer, ρ_d [kg m^{-3}] is the density of the dried layer and J_w [kg m^{-2} s^{-1}] is the sublimation flux. The sublimation flux is proportional to a driving force given by the difference between the water partial pressure at the sublimation interface $p_{w,in}$ [Pa] and the water partial pressure in the chamber $p_{w,c}$ [Pa] according to Eq. (2):

$$J_w = \frac{1}{R_p}\left(p_{w,in} - p_{w,c}\right) \tag{2}$$

where R_p [m s^{-1}] is the mass transfer resistance for the water flow. R_p depends on the length of the dried layer L_d [m] according to the experimentally verified empirical expression (Pikal, 1985):

$$R_p = R_0 + \frac{R_1 L_d}{1 + R_2 L_d} \tag{3}$$

with R_0 [m s^{-1}], R_1 [s^{-1}] and R_2 [m^{-1}] model parameters to be estimated from experimental data.

3.2. Heat transfer

The mechanisms through which heat is supplied to each vial inside the drying chamber are conduction and radiation. The dynamic energy balance for a single vial is given by:

$$\rho_f c_{p,f} A_v \frac{\mathrm{d}(L_f T_p)}{\mathrm{d}t} = Q_w + Q_r + Q_s - \Delta H_{sub} J_w A_v \tag{4}$$

where $c_{p,f}$ [J kg^{-1} K^{-1}] is the specific heat capacity of the frozen product, A_v [m^2] is the cross sectional area of the vial (assumed constant), T_p [K] is the temperature of the product (assumed constant along the axial direction) and ΔH_{sub} [J kg^{-1}] is the heat of sublimation. $\dot{Q}_w$ [J s^{-1}] is the heat rate supplied by the chamber walls through radiation; $\dot{Q}_r$ [W] is the radiant heat rate supplied by the rails along which vials are placed on the shelves; $\dot{Q}_s$ [J s^{-1}] is the heat rate supplied by the shelf upon which the vial is placed (lower shelf) and by the shelf placed on top of the vial (upper shelf) and involves both radiation and conduction mechanisms. The radiation from chamber walls is modelled according to a simplified expression of the Stefan-Boltzmann equation:

$$\dot{Q}_w = a_1 \sigma_{SB} \left(\bar{T}_w^4 - {T_p}^4 \right) \tag{5}$$

where σ_{SB} [W m^{-2} K^{-4}] is the Stefan-Boltzmann constant, $\bar{T}_w$ [K] is the mean temperature of the chamber walls and a_1[m^2] is an equipment-dependent parameter to be estimated from experimental data. Similarly, the radiant heat rate from the rails is modelled as:

$$Q_r = a_2 \sigma_{SB} \left(\bar{T}_r^4 - {T_p}^4 \right) \tag{6}$$

where $\bar{T}_r$ is the mean temperature of the rails and a_2 [m^2] is an equipment-dependent parameter that needs to be estimated from experimental data.

The heat rate supplied by the lower and upper shelves involves both conduction and radiation mechanisms. Mathematically, $\dot{Q}_s$ can be described as:

$$Q_s = Q_{sv} + Q_{sr} = (K_v + K_r) A_v \left(T_{shelf} - T_p \right) \tag{7}$$

with $\dot{Q}_{sv}$ [J s^{-1}] = heat rate supplied by conduction; $\dot{Q}_{sr}$ [J s^{-1}] = heat rate supplied by radiation and T_{shelf} [K] = shelf temperature. The conductive heat transfer coefficient K_v [W m^{-2} K^{-1}] depends on the total chamber pressure P_c [Pa] according to the experimentally verified empirical expression (Pikal, 1985):

$$K_v = C_1 + \frac{C_2 P_c}{1 + C_3 P_c} \tag{8}$$

where C_1 [W m^{-2} K^{-1}], C_2 [W m^{-2} K^{-1} Pa^{-1}] and C_3 [Pa^{-1}] are parameters to be estimated from experimental data. The effective radiation heat transfer coefficient K_r [W m^{-2} K^{-1}] can be derived according to a simplified Stefan-Boltzmann expression:

$$K_r = a_3 \sigma_{SB} (T_{shelf} + T_p)(T_{shelf}^2 + {T_p}^2) \tag{9}$$

with a_3 [-] an equipment-dependent parameter to be estimated from experimental data.

4. Effect of drying heterogeneity: multi-vial stochastic model

Describing the evolution of the partial pressure dynamics $p_{w,c}(t)$ is key to obtain an accurate description of the sublimation driving force, according to Eq. (2). A simple expression that can be used to this purpose is the one proposed by Scutellà *et al*. (2018):

$$\frac{\mathrm{d}p_{w,c}}{\mathrm{d}t} = \frac{R_g \bar{T}_w}{V_c M_w}\left(\dot{m}_s^{tot} - \dot{m}_{cd}\right) \tag{10}$$

where R_g [J mol^{-1} K^{-1}] is the gas law constant, V_c [m^3] is the chamber volume, M_w [kg kmol^{-1}] is the molecular weight of water, $\dot{m}_s^{tot}$ [kg s^{-1}] is the total sublimation flow and $\dot{m}_{cd}$[kg s^{-1}] is the water vapor rate removed by the condenser. $\dot{m}_{cd}$ can be modelled as (Trelea *et al*., 2015):

$$\dot{m}_{cd} = \frac{1}{\alpha\, \bar{T}_{cd}} \log \frac{(P_c - p_{w,cd})}{(P_c - p_{w,c})} \tag{11}$$

with $\bar{T}_{cd}$ = mean temperature of the condenser; $p_{w,cd}$ = water vapor partial pressure at the condenser interface and α [s kg^{-1} K^{-1}] = equipment-dependent parameter to be estimated from experimental data. The total sublimation flow can be derived as the sum of all the contributions from the different vials placed inside the drying chamber:

$$\dot{m}_s^{tot} = \sum_{n=1}^{N_v} \dot{m}_s^{(n)} = \frac{\pi d_v^2}{4} \sum_{n=1}^{N_v} J_w^{(n)} \tag{12}$$

with d_v [m] = vial diameter and N_v [-] = number of vials inside the drying chamber.

Vials placed at different positions on the shelf are exposed to different levels of radiation, meaning that the single sublimation rates $\dot{m}_s^{(n)}$ differ between vials of the same batch. In order to describe this intra-lot drying heterogeneity, we carried out the following sequential modelling activities:

1) global sensitivity analysis (GSA) to understand the effect of model parameters on the two process KPIs (product temperature and sublimation flow);
2) stochastic description of the parameter with the highest influence towards the process KPIs (with a given probabilistic distribution);
3) description of the total mass flow $\dot{m}_s^{tot}$ in Eq. (4) by sampling N_v samples from the distribution of the stochastic parameter using Monte-Carlo techniques;
4) model calibration using historical experimental data of product temperature and water vapor partial pressure.

We used Sobol's GSA (Saltelli *et al*., 2008) to carry out the first step. The analysis was carried out by implementing 1100 scenarios that span the entire parameter domain to consider batch heterogeneity. The lower and upper bounds for the model parameters considered in the GSA are reported in Table 1. The analysis was performed at fixed values of shelf temperature (250.15 K) and chamber pressure (10 Pa). Dynamic sensitivities were collected every 10 min over a time horizon of 500 min. The dynamic profiles of the total sensitivity indices for all the model parameters with respect to product temperature (KPI) are shown in Fig. 1. Similar profiles were obtained for the other KPI (sublimation flow) and are not reported here for brevity.

Table 1. Model parameters and their lower and upper bounds used for global sensitivity analysis (uniform distributions).

Parameter	Bounds	Units
R_1	$[1 \times 10^8, 9 \times 10^8]$	[s^{-1}]
R_2	$[1 \times 10^2, 1 \times 10^4]$	[m^{-1}]
A	[1000, 3000]	[s kg^{-1} K^{-1}]
C_1	[0, 10]	[W m^{-2} K^{-1}]
C_2	[0, 2]	[W m^{-2} K^{-1} Pa^{-1}]
C_3	[0, 2]	[Pa^{-1}]
a_1	$[1\times 10^{-5}, 9 \times 10^{-5}]$	[m^2]

Figure 1. Dynamic profiles of the global sensitivity indices for all model parameters.

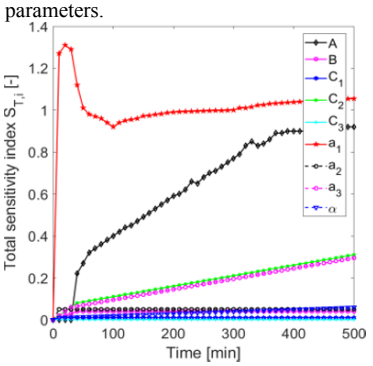

The results of GSA suggested three key considerations: (*i*) the parameter with the highest sensitivity towards the process KPIs is a_1, i.e. the parameter describing the effect of thermal radiation from the chamber walls; (*ii*) three parameters (a_2, R_2, C_3) have negligible impact on the process KPIs, and therefore can be set to their nominal values and do not need to be included in the model calibration activity; (*iii*) all the remaining parameters $(C_2, a_3, \sigma_{a_1}, \alpha)$ significantly affect at least one KPI; therefore, their values must be accurately estimated to guarantee a good model prediction fidelity.

Table 2. Estimated values for the model parameters together with their confidence intervals and *t*-values.

Parameter	Units	Value	95% CI	t-value
C_1	[W m^{-2} K^{-1}]	2.825	$\pm$ 0.112	39.70
C_2	[W m^{-2} K^{-1} Pa^{-1}]	0.215	$\pm$ 0.09	31.20
$\bar{a}_1$	[m^2]	7.625×10^{-5}	$\pm$ 8.213×10^{-7}	25.12
σ_{a_1}	[m^2]	1.545×10^{-5}	$\pm$ 9.416×10^{-7}	12.36
a_3	[-]	2.723×10^{-6}	$\pm$ 1.014×10^{-7}	4.12
R_1	[s^{-1}]	3.288×10^8	$\pm$ 8.935×10^6	68.12
α	[Pa s kg^{-1} K^{-1}]	2580	$\pm$ 15	11.30
			Reference t-value (95%)	**1.645**

Based on these results, step #2 was carried out on the parameter a_1. We used a normal distribution for a_1 with mean $\bar{a}_1$ and standard deviation σ_{a_1}, i.e. $a_1 \sim N(\bar{a}_1, \sigma_{a_1})$. Both $\bar{a}_1$ and σ_{a_1} were treated as parameters to be estimated from experimental data.
Model calibration (step #4) was carried out using a maximum likelihood estimator and experimental data of product temperature and water vapor partial pressure from historical runs performed in the same equipment with the same formulation. The resulting optimal parameter estimates, together with their uncertainty statistics, are reported in Table 2.
Model validation (step #4) was obtained by carrying out a new experiment and by comparing model predictions with the experimental observations. Fig.2a shows the dynamic profiles of the control variables (shelf temperature and chamber pressure) used in this experiment. The good agreement between the model predictions and the experimental data (see Fig.2b, c) confirms the ability of the proposed approach in describing both the contributions of the single vials to the total sublimation flow (Eq.11) and the maximum product temperature within the batch.

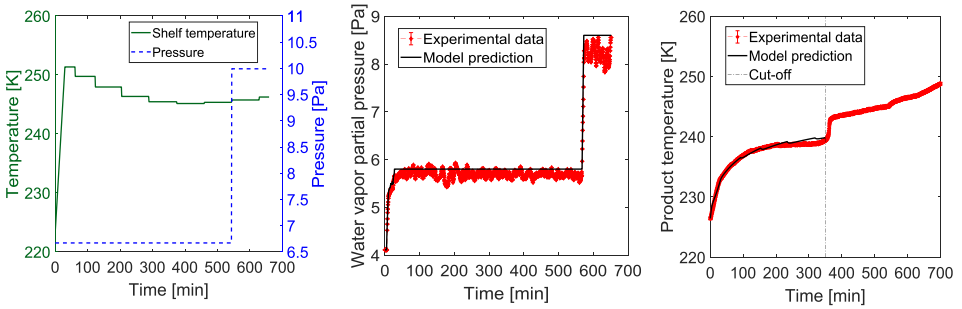

Figure 2. (a) Dynamic profiles of the control variables used during the validation experimental run. (b) Predicted trajectory for the water vapor partial pressure (black line) Vs experimental data (red dots). (c) Predicted trajectory for the maximum product temperature (black line) Vs experimental data (red dots).

5. Conclusions

In this study, we developed a stochastic modelling framework to describe the primary drying stage of a lyophilisation cycle by considering intra-lot heterogeneity. We showed that the proposed model formulation allows obtaining an accurate description of those KPIs (maximum product temperature and sublimation flow) for which hard constraints must be satisfied. Further work will focus on applying the proposed modelling framework to different pieces of equipment/formulated products.

Acknowledgments

This study was conducted under a cooperative research and development agreement between University of Padova and GlaxoSmithKline Biologicals SA. GSK co-funded this study in the framework of the University of Padova project "Uni-Impresa 2017 – DIGI-LIO – Towards digitalization of the pharmaceutical industry: generation of data with high information content for industrial freeze-drying process optimization". Gabriele Bano and Emanuele Tomba are employees of the GSK group of companies. Riccardo De-Luca, Fabrizio Bezzo and Massimiliano Barolo report no financial conflict of interest.

References

Barresi, A. A.; Pisano, R.; Rasetto, V.; Fissore, D. (2010) Model-based monitoring and control of industrial freeze-drying processes: effect of batch nonuniformity. *Drying Technol.*, **28**, 577-590.

Liu, Y.; Zhao, Y.; Feng, X. (2008) Exergy analysis for a freeze-drying process. *Appl. Therm. Eng*. **28**, 675 – 690.

Pikal, M. J. (1985). Use of laboratory data in freeze drying process design: heat and mass transfer coefficients and the computer simulation of freeze drying. *PDA J. Pharm. Sci. Technol.*, **39**, 115-139.

Process Systems Enterprise Ltd. (2019) gPROMS Model Builder v 5.1; Process Systems Enterprise Ltd: London, UK

Saltelli, A.; Ratto, M.; Andres, T.; Campolongo, F.; Cariboni, J.; Gatelli, D.; Saisana, M.; Tarantola, S. (2008) Global Sensitivity Analysis: The Primer; Wiley: Hoboken, NJ, USA.

Scutellà, B., Trelea, I. C., Bourlés, E., Fonseca, F., Passot, S. (2018). Use of a multi-vial mathematical model to design freeze-drying cycles for pharmaceuticals at known risk of failure. In *IDS 2018. 21st International Drying Symposium Proceedings* (pp. 315-322). Editorial Universitat Politècnica de València.

Trelea, I.-C.; Fonseca, F.; Passot, S.; Flick, D. (2015). A binary gas transport model improves the prediction of mass transfer in freeze drying. *Drying Technol.*, **33**, 1849-1858.

Velardi, S. A.; Barresi, A. A. (2008). Development of simplified models for the freeze-drying process and investigation of the optimal operating conditions. *Chem. Eng. Res. Des.*, **86**, 9-22.

Sauro Pierucci, Flavio Manenti, Giulia Bozzano, Davide Manca (Eds.)
Proceedings of the 30th European Symposium on Computer Aided Process Engineering (ESCAPE30), May 24-27, 2020, Milano, Italy.
http://dx.doi.org/10.1016/B978-0-12-823377-1.50011-2

CFD Simulation of Film and Rivulet Flows on Microstructured Surfaces

R. Bertling[a] , M. Hack[b], I. Ausner[b], M. Wehrli[b], E.Y. Kenig[a*]

[a] *Paderborn University, Chair of Fluid Process Engineering, Pohlweg 55, 33098 Paderborn, Germany*
[b]*Sulzer Chemtech AG, Neuwiesenstrasse 15, 8401 Winterthur, Switzerland*
eugeny.kenig@upb.de

Abstract

The flow of liquid-gas systems on surfaces of corrugated sheet packings was studied numerically and experimentally. In simulations the concept of "effective contact angles" was used to take surface microstructures into account. With this approach, resolving the microstructure geometries by the numerical grid can be avoided, which significantly reduces the numerical effort. Several combinations of liquid systems and surface structures were investigated under various liquid flow rates. Generally, the approach showed good capability to reproduce the different flow morphologies found in the experiments and to predict the flow behavior for different flow rates.

Keywords: CFD, Microstructure, Contact angle, Structured packings

1. Introduction

Corrugated sheet packings are the most common type of structured packings widely used in separation columns. Since the interfacial area is a key parameter affecting the column efficiency, the surface of corrugated sheet packings is usually microstructured to enhance liquid spreading. For most commercial packings, different types of microstructure are available.

In this work, a pyramidal structure used by Sulzer Chemtech AG was investigated. Since the size of microstructures is typically smaller than the size of packing channels by factors of up to 20, it is hardly possible to numerically resolve the microstructure of the packing surface simultaneously with the packing geometry in CFD simulations. Therefore, the concept of the so-called "effective contact angle", which is applied as a boundary condition on a smooth packing wall, has become established in the modeling of the surface wetting behavior and several studies reported significant influence of the effective contact angle on the liquid flow behavior in structured packings (e.g., Sebastia-Saez et al., 2015, Singh et al., 2018). However, to find the "correct" effective contact angle that would represent the effects of a given microstructure on a certain liquid flow is not at all easy and a consistent database or a methodology for reasonable selection of an effective contact angle for each microstructure–fluid combination is not yet available. Therefore, the aim of this study is to provide a method to find proper effective contact angles for realistic consideration of the microstructure within the modeling of structured packings.

The commercial software ANSYS Fluent was applied, with the volume-of-fluid method used for the capturing of the free phase interface. Validation experiments for the investigation of the wetting behavior of microstructured plates were carried out at Sulzer Chemtech AG.

The value of the effective contact angle in the simulations was selected from the best fit of experimental results obtained for one fixed flow rate and one plate inclination angle of 30° to the vertical. Both flow rate and plate inclination angle were then varied to examine the predictivity of this approach. The most relevant physical liquid properties influencing the liquid flow are surface tension, viscosity and density. Furthermore, process parameters, especially the specific liquid flow rate, affect the liquid flow topology. The studied systems were water, ethanol and a mixture of water and triethyleneglycol (TEG). They were investigated under varied flow rates. These systems cover a broad range with respect to both surface tension and viscosity. The following cases were investigated experimentally and numerically:

- Surface structure: pyramidal grooving, smooth
- Liquid system: water, water/TEG mixture, ethanol
- Liquid loads:
  - water: 4.5 m^3/m^2h, 15m^3/m^2h, 45m^3/m^2h
  - water & TEG: 4.5 m^3/m^2,15m^3/m^2h, 45m^3/m^2h
  - ethanol: 4.5m^3/m^2h, 7.5m^3/m^2h, 15m^3/m^2h
- Plate inclination: 0° and 30° inclination to vertical

2. Experiments on inclined plates

A method which had already been successfully used by Sulzer Chemtech to evaluate the wetting performance of structured surfaces in lab-scale investigations served as a basis to characterize the liquid flow behavior. The test setup shown in Fig. 1 is applied to investigate microstructured packing sheets, while mesoscale packing features, such as sheet corrugations or contact points, are not included. In this setup, a free liquid jet leaves the vertically oriented pipe and hits the plate covered by a microstructured sheet. Originally, the plate had an inclination of 30° to the vertical. For the investigations on the vertically oriented plate, the relative orientation of the pipe remained the same, e.g. a pipe inclination of 30° to the vertical. The flow morphology and the wetted area on the sheet were evaluated optically using the open source software ImageJ.

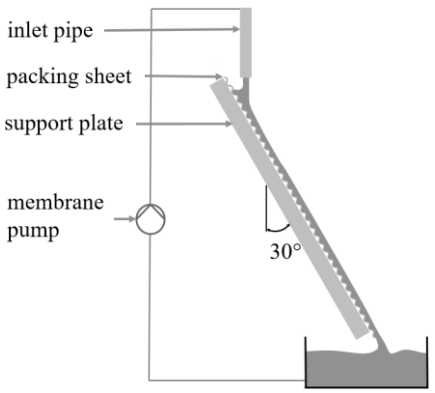

Figure 1: Experimental setup

The measured properties of the liquids are summarized in Table 1:

Table 1: Measured fluid properties at 20°C (literature values are marked with an asterics)

system	**surface tension/ mN/m**	**density/ kg/m³**	**viscosity / mPas**	**contact angle with smooth steel**
water	50.4	993	1.0	42° - 62°
ethanol	23.4	824.2	0.27	not measurable
water & TEG	38.7	1021.2	8.6	26°- 48°
air*	-	1.2	0.0179	-

Since a dye is used for increasing the contrast between liquid and background, this had an influence on the liquid properties, especially on the surface tension; hence the values somewhat differ from literature values. The surface tension was measured using a bubble tensiometer with a bubble formation time of five seconds. The contact angle on a smooth steel surface was measured optically on static droplets. This method bears some uncertainties; hence, a certain range is given for the contact angles. For the CFD simulations, the material data were set in accordance with Table 1.

3. CFD-Modeling

3.1. Governing equations

CFD simulations were performed with the software ANSYS Fluent (version 19.1). Both phases were assumed as incompressible and isothermal. The equations for continuity and momentum applied for both phases are as follows:

$$\nabla \cdot \boldsymbol{u} = 0 \tag{1}$$

$$\frac{\partial}{\partial t}(\rho \boldsymbol{u}) + \nabla \cdot (\rho \boldsymbol{u}\boldsymbol{u}) = -\nabla p + \rho \boldsymbol{g} + \eta \Delta \boldsymbol{u} + \boldsymbol{f}_\sigma \tag{2}$$

where $\boldsymbol{u}$ is velocity vector, t is time, ρ is density, η is dynamic viscosity, p is pressure; $\boldsymbol{g}$ is gravity and $\boldsymbol{f}_\sigma$ is a source term governing surface tension. The interface movement was captured by the volume of fluid (VOF) method (Hirt and Nichols, 1981), with the following transport equation for the liquid-phase volume fraction α:

$$\frac{\partial \alpha}{\partial t} + \boldsymbol{u} \cdot \nabla \alpha = 0 \tag{3}$$

The liquid-phase properties were calculated by

$$\Phi = \alpha \Phi_L + (1-\alpha)\Phi_G \text{ with } \Phi = \rho, \eta \tag{4}$$

For the consideration of the surface tension σ, the continuum surface force (CSF) model (Brackbill et al., 1992) was applied to determine $\boldsymbol{f}_\sigma$:

$$\boldsymbol{f}_\sigma = \sigma \kappa \boldsymbol{n} \text{ with } \boldsymbol{n} = \nabla \alpha \text{ and } \kappa = -\nabla \cdot \frac{\boldsymbol{n}}{|\boldsymbol{n}|} \tag{5}$$

The contact angle γ is considered in the calculation of the surface force term via the surface normal vector in the cells adjacent to the walls:

$$\boldsymbol{n} = \boldsymbol{n}_{wall} \cos\gamma + \boldsymbol{t}_{wall} \sin\gamma \tag{6}$$

Where $\boldsymbol{n}_{wall}$ is the unit normal vector of the wall and $\boldsymbol{t}_{wall}$ is the corresponding unit tangential vector.

3.2 Boundary conditions and implementation

The discretization scheme used for Eq. 3 was the "Geo-Reconstruct" scheme available in ANSYS Fluent, which is based on the PLIC (piece wise linear interface construction) algorithm. The computational domain with the specified boundary conditions is displayed in Fig. 2. The initial conditions were zero values of liquid volume fraction (no liquid inside the domain) and velocity magnitude as well as ambient pressure.

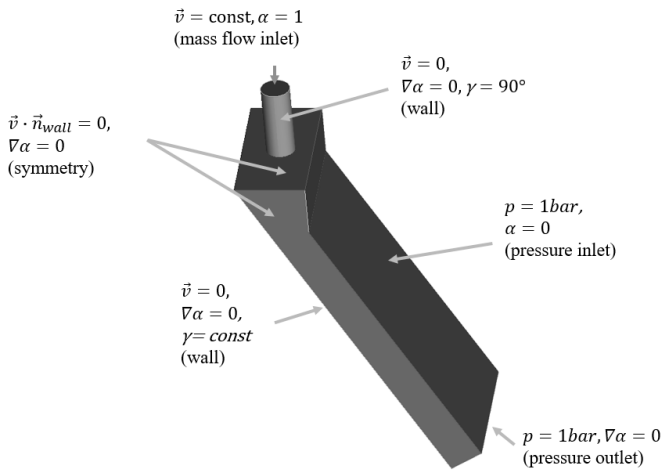

Figure 2: Computational domain and boundary conditions

3.3. Meshing

The meshes used in this work were generated using the "bloc structured" meshing function in ANSYS ICEM 19.1. As recommended for the VOF framework by ANSYS Fluent, exclusively hexahedral cells were used. The resolution was increased towards the bottom wall, in order to accurately resolve the phase interface near the triple line and velocity gradients normal to the wall. The cell growth rate in this direction was 1.1 (geometrical stretching), starting with a cell height of 20µm for water and the water-TEG mixture. This was equivalent to approximately 30 cells over the film thickness, depending on the liquid system and the simulated flow rate. For the simulation of ethanol, the cell size near the wall had to be decreased in order to resolve the film near the triple line where

the solid, liquid, and gas phase are in contact properly. The first cell height was set to 10µm for this case.

4. Results

The introduced method showed good capability in predicting the flow behavior both qualitatively (see Fig. 3 and 4) and quantitatively (see Table 2).

Table 2: overview results

System	γ	u_L / m³/m²h	A_{sim} /A_{exp}
Water	32°	15	+19%
		45	-17%
Water & TEG	35°	15	+10%
		45	+3%
Ethanol	20°	4.5	-24%
		7.5	+3%
		15	+3%

For the lowest flow rate of 4.5m³/m²h droplet formation was observed in the experiments directly at the end of the pipe. This could not be reproduced by the simulations which, contrary to the experiments, showed a stable jet flow leaving the pipe. The problem also appeared for water as a working fluid with the same flow rate. The ethanol flow on grooved plates could be captured well (Fig. 3). Generally, the model had a slight tendency to overestimate the effect of the liquid flow rate on the wetted surface area, e.g. the wetted area in the simulations grew more significantly than in the experiments when a higher flow rate was applied. The contact angles that are specified in Table 2 were derived in a series of simulations, in which the contact angle was varied to find the best fit between simulations and experiments at a liquid flow rate u_L of 15m³/m²h. The ratio of the simulated wetted area A_{sim} and the wetted area measured in the experiments A_{exp} served to evaluate the agreement, while A_{exp} was calculated from processing photographs using the open source software ImageJ. In the process of searching for the contact angle that reproduces the flow morphology the best, it became clear that the flow morphology was strongly sensitive to the changes in the effective contact angle, especially for the water-TEG-mixture.

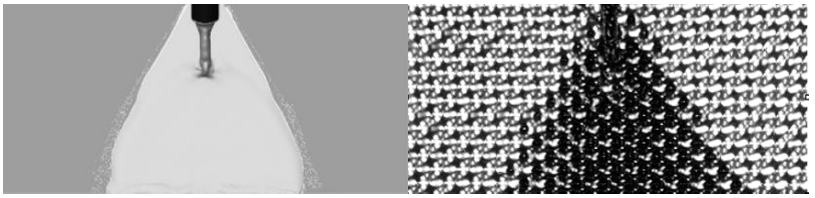

Figure 3: Simulated results (left) and experimental results (right) for ethanol flow on grooved plate with u_L=7.5m³/m²h and γ=20°

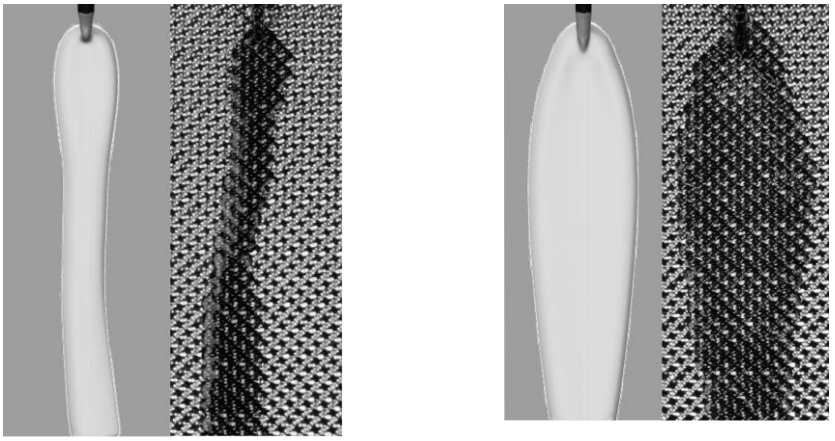

Figure 4: Water-TEG mixture on a grooved plate: $u_L = 15m^3/m^2h$ (left), $u_L = 45m^3/m^2h$ (right) with γ=35°

5. Conclusions

A new method to find effective contact angles that realistically reproduce the effects of common microstructures on rivulet and film flow was proposed. The methods novelty lies in the combination of experiments on non-corrugated, microstructured plates with CFD methods, which removes disturbing factors in evaluating how well a certain contact angle reproduces the effect of the investigated microstructures. The studies showed that the solutions are very sensitive to the effective contact angle variation, which underlines the importance of a proper choice of this parameter. Generally, the proposed method is capable of reasonably reproducing and predicting the flow morphology. Future work will focus on the application of the newly derived contact angles to packing structures.

References

J.U. Brackbill, D.B. Khote, C. Zemach, 1992, A continuum method for modelling surface tension, J. Comput. Phys. 100, 335–354.

C.W. Hirt, B.D. Nichols, 1981, Volume of fluid method for the dynamics of free boundaries, J. Comput. Phys. 39, 201–225.

D. Sebastia-Saez, S. Gu, P. Ranganathan, K. Papadikis, 2015, Meso-scale CFD study of the pressure drop, liquid hold-up, interfacial area and mass transfer in structured packing materials, Int. J. Greenh. Gas Control 42, 388–399.

R.K. Singh, J.E. Galvin, X. Sun, 2018, Multiphase flow studies for microscale hydrodynamics in the structured packed column, Chem. Eng. J. 353, 949–963.

Sauro Pierucci, Flavio Manenti, Giulia Bozzano, Davide Manca (Eds.)
Proceedings of the 30th European Symposium on Computer Aided Process Engineering (ESCAPE30), May 24-27, 2020, Milano, Italy.
http://dx.doi.org/10.1016/B978-0-12-823377-1.50012-4

Energy Reduction Potential in Natural Gas Processing through Heat and Process Integration

Mohamed Berchiche [a,b], Salah Belaadi [a], Grégoire Leonard [b]

[a] *Université des Sciences et de la Technologie Houari Boumediene, Laboratory of Reaction Engineering, FGMGP, BP32 El-Alia 16000, Algeria,*
[b] *Université de Liège, Department of Chemical Engineering, B6a Sart-Tilman, 4000 Liège, Belgium,*
mea.berchiche@doct.uliege.be

Abstract

Despite the advantages of Natural Gas (NG) over other fossil fuels, natural gas supply chain is still impacted by a high energy demand and a negative impact on the environment as a result. This work investigates the potential of reducing energy penalty of natural gas sweetening processes through energy integration with upstream compression units and the use of Organic Rankine Cycle as a bottoming technology.

The integration was studied over a range of inlet CO_2 content and admission pressure varying between 4 to 10% and 30 to 50 bar respectively. Results of heat integration showed an ample reduction in heating requirements ranging from 40 to 100%. Furthermore, the integration of an optimized ORC as a second recovery tool yielded in a net power output equivalent to 30% to 190% of the required pumping power and a reduction of cooling load ranging from and 4 to 16% respectively.

Keywords: Natural gas sweetening, Heat and process integration, ORC.

1. Introduction

Natural gas has the lowest CO_2 emissions rate per energy unit among fossil fuels; it is expected to play a significant role as a bridge fuel toward complete decarbonization of the global energy supply (BP Energy Outlook, 2016). Consequently, its demand is forecasted to witness a total increase of 60% by 2035 (Costello, 2017). Natural gas supply chain, however, is an energy intensive sector characterized by an important amount of waste heat which not only weights on the efficiency of the process and its profitability margin but also contributes to greenhouse gas emissions. Moreover, 50% of the remaining NG reserves are sour (i.e. containing more than 2% mole CO_2 or 4 ppmv of H_2S) implying the inevitable implementation of an additional sweetening step and further increasing the energy penalty (Brugers et al., 2011).

Several technologies were developed for NG sweetening purposes among which amine based absorption remains the most used. Despite its maturity and wide deployment, this technology is impacted by its high energy demand. Several improvement routes have been proposed in the literature, such as the development of new solvents with reduced regeneration requirement and the optimization of plant operating parameters using process simulation tools (Leonard et al., 2011 and Nuchitprasittichai et al. 2013).

In this regard, energy integration along with the use of low temperature waste heat recovery technologies, such as Organic Rankine Cycle (ORC), Heat pumps (HP) or

Absorption Chillers (AbC) can play a significant role in cutting emissions and alleviating the impact of this energy intensive process.

Because of the multiple advantages it presents, such as efficiency, simple layout and moderate operating conditions, the use of ORC as a waste heat recovery tool from energy intensive processes is receiving increasing interest. For instance, Yu et al. (2016) developed a systematic approach using waste heat composite curve for the optimization of the design of ORC as a tool of multiple-source waste heat recovery from refineries. In the context of CO_2 capture from natural gas supply chain, several studies focused on the energy integration of CO_2 capture with natural gas liquefaction and regasification processes. Abdulkareem et al. (2012) investigated the integration of several waste heat sources from the NG liquefaction process into a CO_2 capture and sequestration unit. They found that a 23% reduction in cooling loads could be achieved as a result of an improved heat integration and waste heat utilization. Zhao et al. (2016) integrated a two-stage ORC to recover cold energy from a regasification unit coupled with a CO_2 capture process.

In this paper, we have developed a two-steps approach to investigate the potential of energy integration in the context of upstream natural gas processing, first through the integration of waste heat and second, with the use of ORC as a bottoming technology.

Upstream natural gas compression is a crucial step to insure a constant pressure at the inlet of the processing unit. The exhaust of the compression process is therefore a non-intermittent source of waste heat that can potentially be integrated in the processing unit. In this work, we have assessed the direct use of high-temperature compression waste heat to satisfy the demand of the sweetening process and the integration of ORC as a secondary recovery tool to harness the low temperature waste heat.

2. Methodology

Process simulation tool Aspen Hysys V9 was used to simulate both processes, i.e. the amine based CO_2 capture and the natural gas driven turbo-compression. A feed of 5 MMSCM/Day of raw NG at different reservoir pressures (30, 40 and 50 bar) was considered in this study. CO_2 molar content in the feed was ranged between 3 to 10% whereas CO_2 content of the sweet gas outlet was set at the limit requested by pipeline transport constraint, i.e. 2%. The captured CO_2 is then compressed up to 200 bar.

The MDEA/DEA based acid gas sweetening unit was simulated using an equilibrium approach and Li-Mather thermodynamic model whereas the compression and turbine systems where simulated using Peng-Robinson equation of state. Sweetening and turbo-compression models were validated against plant and manufacturer data respectively.

For the NG sweetening unit, the predicted CO_2 content and temperature profiles in absorber and regeneration columns showed a deviation of less than 4% from plant data whereas, for the turbo-compression unit, the model presented a deviation of less than 2% from the overall efficiency and exhaust flow specified by the manufacturer.

The available exhaust waste energy depends on the pressure ratio of the compression unit. Consequently, three scenarios were investigated, P30, P50 and P60, referring respectively to inlet pressures of 30, 40 and 50 bar upstream the compression unit. The adequate turbine type was used for each scenario and a waste heat recovery unit (WHRU) was used to recover energy from the exhaust gas to the heating oil loop. A cold temperature limit of 140 °C was set as a technical constraint on the heating oil side

to prevent Sulphur condensation in the exhaust gas. The remaining energy required to satisfy the solvent regeneration was provided by an external source.

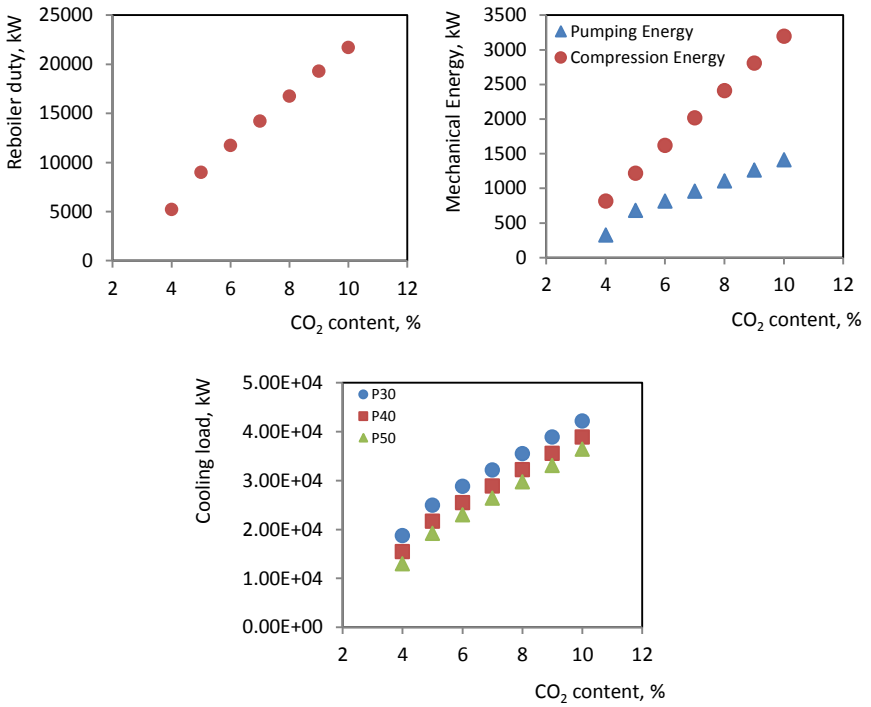

Figure 1 Energy demand of the process for different CO_2 molar fraction in the feed NG, a) Reboiler thermal energy, b) Mechanical energy, c) Cooling load

Low temperature waste heat from both processes (NG compression and CO_2 capture) was recovered by a set of heat exchangers and was used to power the ORC. The minimum temperature approach was fixed at 5 °C except for the WHRU where due to the restriction on pressure drop a minimum approach of 10 °C was chosen.

An ORC with a simple layout and R600 as a working fluid was used for recovering low grade waste heat. The optimal working conditions of the ORC, i.e. temperature, pressure and heating oil flow rate, corresponding to a maximal net power generation, were identified for each scenario by linking Aspen Hysys to Matlab and using Matlab's prebuilt optimization abilities.

In order to reduce computing time, the heat recovery network was solved separately for maximum outlet temperature versus heating oil flow rate. The resulting relationship was used as a constraint to the ORC optimization problem reducing thereby the number of variables and eliminating the necessity of solving both processes (heat recovery network and ORC) simultaneously.

3. Heat integration

Reboiler energy, pumping energy and cooling loads of the process were calculated for an inlet CO_2 molar content ranging from 4 to 10%. Figures 1a and 1b depict the regeneration energy and the mechanical shaft power demand of the sweetening process

for the indicated range of CO_2 content in raw NG. With increasing CO_2 content, the amine flow rate required to achieve CO_2 specification increases which results in a subsequent increase in reboiler and pumping energy and cooling loads.

Also, the increase in CO_2 content in the raw NG will increase the amount of captured CO_2 and result in an increase of compression energy. Figure 1c shows the total cooling loads of both compression and sweetening processes for different inlet pressures 30, 40 and 50 bar and a CO_2 content ranging from 4 to 10%. The lower the reservoir pressure, the higher the compression duty and thus the higher the cooling loads. On the other side, with less CO_2 in the raw natural gas, the cooling duty decreases due to a lower release of absorption heat in the amine loop.

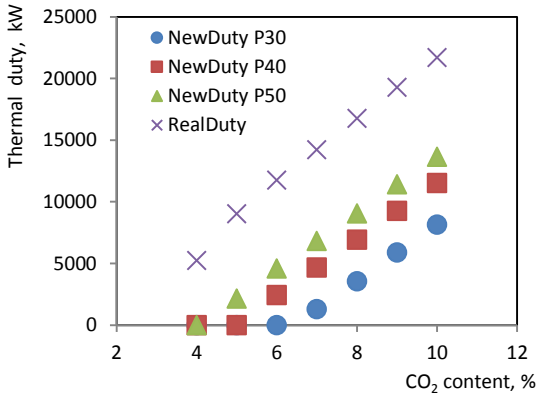

Figure 2 Reboiler thermal energy before and after integration for three inlet pressures 30, 40 and 50 bar

As explained in the previous section, waste heat from the compression units was used to supply the solvent regeneration reboiler. Figure 2 shows the reboiler duty before integration and the new reboiler duty after integration. For natural gas feed at low CO_2 content and at low inlet pressure the available waste energy is as high as the reboiler duty. We have found that it is therefore possible to cover all the regeneration energy from the waste heat sources.

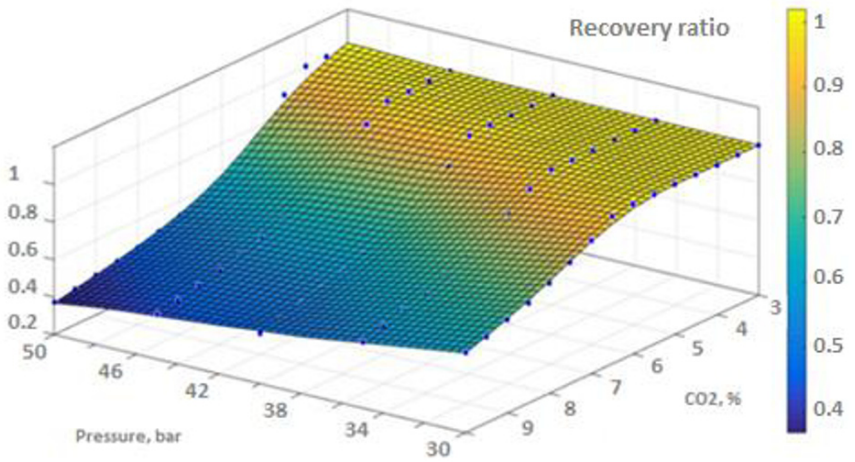

Figure 3 Ratio of recovered energy to the initial reboiler energy for different CO_2 contents and inlet pressures

As shown in figure 3, the potential of heat integration depends on both inlet pressure and CO_2 content and varies from 40 to 100%. Higher integration potential is met at lower CO_2 contents (less heat is required by the sweetening process) and lower inlet pressures (more heat is available from the NG compression step).

4. Secondary heat recovery

The use of Organic Rankine Cycle as a second recovery technology was investigated at the different scenarios of inlet pressure and CO_2 content discussed earlier. For each scenario, the optimal recovery temperature and working pressure yielding the highest energy output were identified. R600 was used as working fluid in this study as it was reported to demonstrate low global warming potential and high energy efficiency (Darvish et al. 2015).

The use of Organic Rankine Cycle presented a double advantage by harnessing a fraction of the waste heat into useful electricity and reducing the overall cooling load of the background process. Figures 4a and 4b show respectively the reduction in cooling load and the amount of maximal electricity output for three inlet pressures 30, 40 and 50 bar and for a CO_2 content ranging from 4 to 10%. The average efficiency of the Organic Rankine Cycle applied for the three inlet pressure scenarios P30, P40, and P50 was found to be 14%, 10%, and 9% respectively.

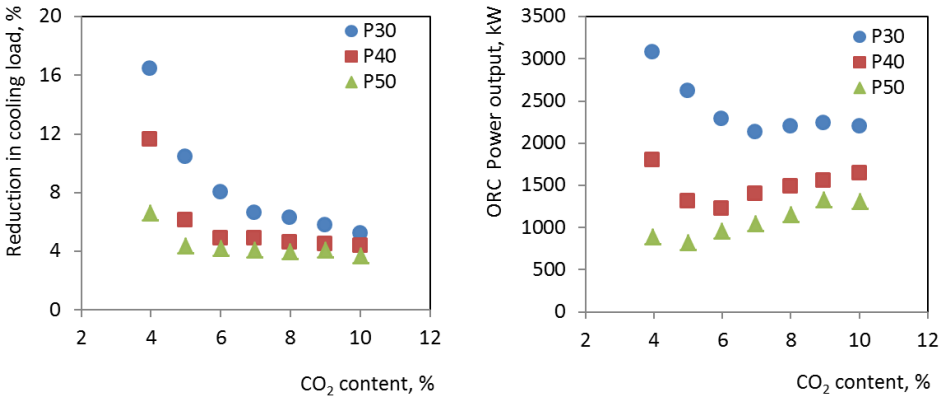

Figure 4 a) Reduction in cooling requirements for different CO_2 molar contents and inlet pressures, b) Energy optimal ORC energy output for different CO_2 contents and inlet pressures

The electricity output of the ORC is the contribution of the quantity of the available waste heat as well as its quality. Consequently, high energy output at low CO_2 contents is explained by the low energy demand of the capture process allowing more high-temperature waste heat to be recovered by the ORC whereas the slight increase of energy output at high CO_2 contents is due to the quantity of low-temperature waste heat available from the capture process.

5. Conclusion

Energy and process integration of amine based natural gas sweetening unit with upstream compression with ORC as a bottoming technology was investigated in this

study. The potential of the integration was estimated for different compression ratios and CO_2 content scenarios.

The available waste heat from the compression units is a reliable source that showed an important potential for alleviating the energy demand of the natural gas sweetening process. The recovered waste heat varied from 40 up to 100% of the energy required for solvent regeneration. Maximal integration potential was found at low CO_2 content and high compression requirements where the available waste heat is high and the regeneration energy is low.

On another hand, the use of ORC as a second recovery technology allowed to further increase the energy efficiency of the process by using low temperature and fatal waste heat for power production. The energy output was found to vary from 30 to 190% of the required pumping power with a reduction in cooling loads of the process ranging from 4 to 16%.

References

Alabdulkarem A., Hwang H., Radermacher R., 2012, Energy consumption reduction in CO_2 capturing and sequestration of an LNG plant through process integration and waste heat utilization, International Journal of Greenhouse Gas Control, 10:215–228

BP Energy Outlook, 2016, BP p.l.c, London, United Kingdom,

Burgers1W., Northropb P., Kheshgic H., Valenciad J., 2011, Worldwide development potential for sour gas, Energy Procedia , 4:2178–2184

Costello K., 2017, Why natural gas has an uncertain future, The Electricity Journal, 30:18-22

Darvish K., Ehyaei A., Atabi F., Rosen M., 2015, Selection of optimum working fluid for organic rankine cycles by exergy and exergy-economic analyses, sustainability, 7:15362-15383

Leonard G., Heyen G., 2011, Modeling post-combustion CO_2 capture with amine solvents, Computer Aided Chemical Engineering, 29: 1768-1772

Nuchitprasittichai A., Cremaschi S., 2013, Optimization of CO_2 capture process with aqueous amines, a comparison of two SO approaches, Industrial and Engineering chemistry research, 52, 10236−10243

Yu H., Feng X., Wang Y., Biegler L., Eason J., 2016, A systematic method to customize an efficient organic Rankine cycle to recover waste heat in refineries, Applied Energy, 179:302–315

Zhao H., Dong H., Tang J., Cai. J., 2016, Cold energy utilization of liquefied NG for capturing carbon dioxide in the flue gas from the magnesite processing industry, Energy, 105:45-56

Sauro Pierucci, Flavio Manenti, Giulia Bozzano, Davide Manca (Eds.)
Proceedings of the 30th European Symposium on Computer Aided Process Engineering (ESCAPE30), May 24-27, 2020, Milano, Italy.
http://dx.doi.org/10.1016/B978-0-12-823377-1.50013-6

An adaptive data-driven modelling and optimization framework for complex chemical process design

Thomas Savage,[a] Hector Fernando Almeida-Trasvina,[a] Ehecatl Antonio del Río-Chanona,[b] Robin Smith,[a] Dongda Zhang[a,b]

[a]*Centre for Process Integration, University of Manchester, The Mill, Sackville Street, Manchester, M1 3AL, UK.*

[b]*Centre for Process Systems Engineering, Imperial College London, South Kensington Campus, London SW7 2AZ, UK.*

dongda.zhang@manchester.ac.uk

Abstract

Current advances in computer-aided chemical process design and synthesis take advantage of surrogate modelling and superstructure optimization techniques. Conventionally, this is completed by using first-principle physical models or data-driven models to replace the original rigorous models for optimization and selection of a specific unit operation. Despite its achievements, this strategy is inefficient when dealing with complex process flowsheets such as utility and refrigeration systems where a large number of unit operations are heavily connected by recycling streams. To address this problem, an integrated data-driven modelling and optimization framework is proposed in this work. The framework first constructs a hybrid machine learning based surrogate model to automatically reduce the system dimensionality and capture the nonlinearity of the underlying chemical process. Then, an efficient optimization algorithm, in specific, evolutionary algorithm, is embedded to identify the optimal solution of this surrogate model. Quality and accuracy of the estimated optimal solution is finally validated against the rigorous process model. Through an iterative approach, optimal operating conditions for the entire process flowsheet are efficiently identified. Furthermore, the novel CryoMan Cascade cycle system for large scale liquefied natural gas manufacturing is used as the case study. This framework is demonstrated to be superior regarding time-efficiency, solution quality, and flexibility over the rigorous model based optimization approach.

Keywords: large-scale chemical process, surrogate modelling, dimensionality reduction, Gaussian processes, artificial neural network.

1. Introduction

Developing disruptive digital technology to enable the design and operation of cost-effective and energy-efficient manufacturing systems is one of the grand research themes under the context of the 4th Industrial Revolution. Given the large amount of data accumulated from process industries, building data-driven models to enable rapid decision-making is of critical importance in order to guarantee the process performance and safety (Bhosekar and Ierapetritou, 2018). This directly triggers the development and application of surrogate modelling technology in the current industry and research community (McBride and Sundmacher, 2019).

Specific to the chemical industry, rigorous process models derived from mass and energy balances allow for accurate determination of states of a system, and can be directly constructed using multiple computer-aided software packages such as Aspen (Bhosekar

and Ierapetritou, 2018; Zhang *et al.*, 2018) However, due to their complexity, the computational time to evaluate a rigorous model can be relatively large (e.g. potentially weeks to months), hence limiting their applications for process control and optimization (del Rio-Chanona *et al.*, 2018; McBride and Sundmacher, 2019). As a result, surrogate models have been adopted to replace rigorous models and help with identifying optimal operating conditions.

However, at present, surrogate models are predominantly used to replace single unit operations (Henao and Maravelias, 2011; Quirante, Javaloyes and Caballero, 2015), whilst their applicability in terms of substituting more complex systems such as entire process flowsheets has not been well explored. Therefore, in this study, different cutting-edge surrogate models are tested to simulate and optimize a novel liquefied natural gas (LNG) refrigeration cycle, with their performance thoroughly compared against the optimal solution identified through the rigorous model. The structure of this paper is organized as follows. Section 2 introduces the LNG production process. The approach to optimize the rigorous model and the associated primary challenges are also explained. Section 3 details the construction and optimization of different surrogate models. Section 4 summarizes the results of these surrogate models and compares them with the rigorous model's verification. A thorough discussion regarding the advantages of combining Gaussian processes and partial least squares for large scale complex chemical process simulation and optimization is presented in the Results and Discussion section.

2. Introduction to the CryoMan Cycle

Commercial scale production of LNG involves the use of large, complex and energy-intensive refrigeration cycles. The costs associated with the energy for refrigerant compression (shaft work energy) dominate the overall operating costs of the LNG plant. The CryoMan Cascade cycle recently developed by (Almeida-Trasvina and Smith, 2018) (shown in Fig. 1(a)) is a novel refrigeration configuration that can save significant energy demand in shaft work compared to current commercial processes. In this process, within the precooling cycle, a 'heavy' mixed refrigerant provides cooling in a series of two multi-stream heat exchangers (MSHEs); three stages are employed for refrigerant compression. In the liquefaction cycle, the 'light' mixed refrigerant is first fed into a liquid-vapour separator. The resulting outlet streams are partially mixed with each other to create the two refrigerant streams that provide cooling in a series of two MSHEs. Refrigerant compression is also carried out in three compression stages. In both precooling and liquefaction cycles, a pump after the second compression stage pumps any condensed refrigerant to the compressor discharge pressure.

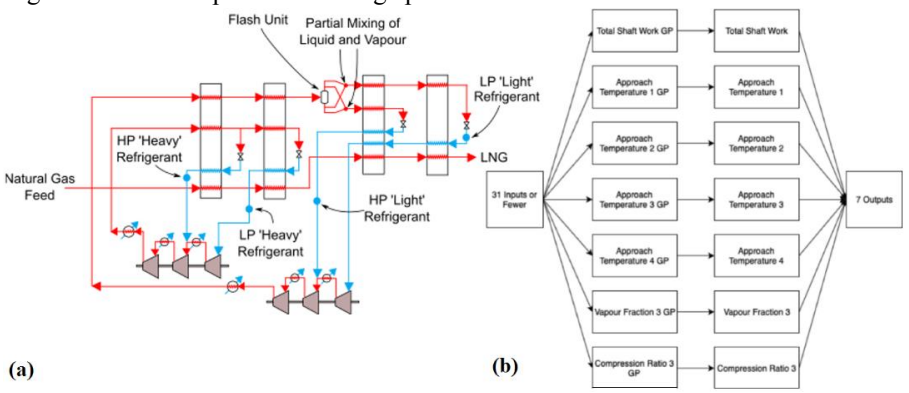

Figure 1: The CryoMan Cascade cycle (a), and its KPLS based surrogate model (b).

The rigorous model of the CryoMan Cascade cycle was implemented in Aspen HYSYS v8.2 and subsequently linked to MATLAB. This resulted in a callable function taking 31 inputs and producing 20 outputs. The inputs include the refrigerant mass flowrates, refrigerant compositions, discharge pressure, refrigerant evaporating pressures, MSHE outlet temperatures, compression ratios and refrigerant split fractions (where applicable) for both precooling and liquefaction cycles. The outputs from the process are eight values of shaft work demand, four MSHE approach temperatures, vapour fractions of four streams (to assess wetness at inlet of compressors), and four compression ratios.

The optimization problem for the rigorous model is defined as follows:

$$\min_{\varphi} \left(\sum_{i=1}^{N} W_1 \right) / m_{LNG}$$

$$\textit{s.t.}\ \Delta T_{min} \geq 2°\text{C};\ \ P_{rat} \leq 3.5;\ \ \sum_{j=1}^{m} x_j = 1\,,\ x_j \in X^{MR};\ \ VF^{ref} = 1;\ \ \varphi_{lb} \leq \varphi \leq \varphi_{ub}$$

where the specific shaft work, defined as the sum of the individual shaft works W_i divided by the mass flow rate of LNG m_{LNG}, is the objective function to be minimized. The 31 inputs to the rigorous model are represented by φ with the set of inputs having corresponding upper and lower bounds φ_{ub} and φ_{lb}, respectively. Constraints include minimum approach temperatures for MSHEs ΔT_{min}, maximum compression ratios P_{rat} to discourage mechanical damage to compressors, valid molar compositions represented by x_j, and no wetness within compressors by constraining vapour fractions at the inlet of compressors VF^{ref} to zero. An evolutionary algorithm (EA) is first employed for the optimization of the rigorous model. The way on which constraints are dealt with in stochastic optimization is by applying penalties to invalid solutions. Successive Quadratic Programming (SQP) is next used to identify a local optimal solution around the best candidate resulting from the stochastic optimization.

3. Developing Surrogate Models

Directly optimizing the rigorous model is time consuming (over 17 hours per run), whilst the real-time decision-making of a commercial LNG plant is often around once per 4 hours. Therefore, surrogate models are used to resolve this challenge. Different from using surrogate models to substitute a unit operation, building a surrogate model to replace an entire process flowsheet is more challenging due to the high nonlinearity of the underlying process and high dimensionality of the involved design variables. To guarantee success, several surrogate model structures were proposed and their performance was thoroughly compared in this work. Furthermore, taking advantage of both supervised (dealing with nonlinearity) and unsupervised (dealing with dimensionality reduction) machine learning techniques is another strategy proposed in this work, as this may greatly simplify the process complexity for surrogate model construction and meanwhile obtain high quality optimal solutions.

3.1. Artificial Neural Network based surrogate models

To consider the nonlinearity of this highly interconnected process flowsheet, different structures of artificial neural networks (ANN) based surrogate models are constructed. These include: (1) a single ANN directly simulating the entire process (31 inputs and 20 outputs); (2) an ANN framework comprising 2 independent ANNs, one simulating the 8 shaft works, 4 compression ratios and 4 vapour fractions given the 31 inputs, and the other simulating the 4 temperature differences given the same inputs; (3) an ANN framework comprising 5 separate ANNs, one simulating the 8 shaft works, 4 compression ratios and 4 vapour fractions, and the other 4 each of which only simulating a specific

temperature difference. The reasoning behind designing different ANN model structures is thoroughly discussed in the Results and Discussion section.

3.2. Kriging Partial Least Squares based surrogate model

In the method described by (Bouhlel *et al.*, 2016) to integrate partial least squares (PLS) into Gaussian Processes (GPs), PLS is performed in the data and the PLS weights (projected spaces of inputs and outputs) are used to construct a lower dimensional covariance matrix over which a GP model is constructed. By reducing the model dimensionality it allows for easier determination of the minimum log-likelihood resulting in a lower computational time cost, and more accurate mapping of between the input space and the output space. This integrated modelling strategy (embedding PLS into GP), namely KPLS, is adopted in this research to complete the construction of the GP based surrogate model superstructure. 7 GP models are constructed in this work to account for the 7 most important outputs. The structure of this model is shown in Fig. 1(b).

3.3. Data generation and selection

Three different datasets were generated with differing qualities and time costs in order to create the surrogate models: *Dataset 1:* 5000 random data points. Data points in this dataset were generated randomly within 10 minutes. Despite the negligible time cost, this dataset consists of mostly invalid solutions due to the nonlinearity and complexity of the LNG production process; *Dataset 2:* 500 refined data points. The input bounds were slightly more constricted to result in an increased proportion of valid solutions; *Dataset 3:* 350 high-quality data points. This dataset consists completely of valid solutions and was created by discarding invalid solutions. Despite the high accuracy, it takes 50 minutes to generate this dataset, thus the time cost is much higher than Dataset 1.

As the accuracy of a surrogate model heavily relies on the data quality, Dataset 1 was found incapable of constructing an accurate surrogate model. However, having a large size of data is also a prerequisite to build an accurate surrogate model, thus purely using Dataset 3 (*i.e.* only using feasible points) is not enough. Hence, Datasets 2 and 3 were combined (well mixed) to provide global representation of the rigorous model as well maintain a relatively large proportion of valid solutions. For a highly nonlinear system with 31 inputs and 20 outputs, 850 data points is not necessarily large. The ratio between feasible and infeasible data points in the combined dataset is approximate 3:1. Although extra high-quality data can be generated, the overall surrogate model construction time will be increased, diminishing its advantage over the rigorous model.

A specifically designed evolutionary algorithm was employed to optimize the surrogate models, taking advantage of tournament selection and single point crossover. A mutation rate of 3% and selection percentage of 98% were used over a population size of 100. The optimization scheme was chosen to run for 500 generations. Moreover, a linear penalty is implemented in order to guide the optimization initially towards a valid solution space. Finally, the ANN based surrogate models were implemented using PyTorch 1.2.0 and the KPLS based surrogate models were implemented using the SMT toolbox by (Bouhlel *et al.*, 2019), both within Python 3.7.3 on a Windows 10 operating system. Total construction of the KPLS models takes on average 2 minutes using 850 data points, and that for the ANN based surrogate models takes approximately 5 minutes.

4. Results, Discussion and Conclusions

4.1. Results of ANN based surrogate model frameworks

As shown in Fig. 2, after validation with the rigorous model, it is found that although the single ANN model can well predict total shaft work and vapour fractions, its predicted

MSHE approach temperatures (*i.e.* temperature constraints) are infeasible and greatly deviate from the rigorous model's verification result. The single large ANN is here unable to capture the nonlinearity of the process, and its accuracy is verified to be low. A straightforward improvement to the single ANN surrogate model is to split this large ANN into a two separate ANNs to deal with the nonlinear temperature constraints. In other words, a surrogate model framework can be built to include two independent ANNs, one only predicting the four highly nonlinear MSHE approach temperatures and the other estimating the remaining 16 outputs. Breaking a surrogate model up into a series of parallel sub-models may increase accuracy in capturing specific nonlinearities that are particularly prominent in a complex process flowsheet. Hence, a second surrogate model framework is constructed to further separate the MSHE approach temperature ANN into four separate ANNs, each predicting an individual approach temperature. This will allow the overall surrogate model to gain better accuracy still with regards to the individual approach temperatures, and ensure that a prediction made using the surrogate model remains feasible when validated with the rigorous model.

Indeed, through verification, the second framework (consisting of 5 ANNs) successfully meets all the constraints, hence resulting in feasible solutions (Fig. 2). Nonetheless, the optimal total shaft work identified in the third surrogate model is 160 MW, much higher than the optimal solution (144 MW) identified using the rigorous model. Hence, the surrogate model is still not efficient in terms of process optimization. Overall, the results from the three ANN based surrogate models suggest that due to the high nonlinearity and dimensionality of the underlying process and limited amount of data, it may not be ideal to use ANNs to construct surrogate models to simulate a whole process flowsheet.

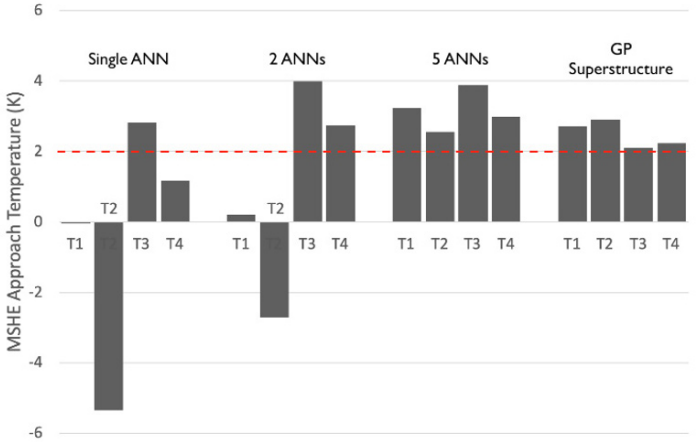

Figure 2: Plot of validated approach temperatures for 4 different surrogate model structures. Infeasible MSHE approach temperatures have values below the dotted red line.

4.2. Results of the KPLS superstructure model

Due to the system having a relatively large number of inputs and outputs, unsupervised learning techniques are adopted to reduce the dimension of the solution space (i.e. reducing the impact of the curse of dimensionality) for the construction and optimization of surrogate models. In addition, after assessing the rigorous optimization problem described in Section 2, it was observed that there exists no constraint on individual shaft works within the refrigeration cycle, thus using the summation of individual shaft works (*i.e.* total shaft work, one output) to substitute for the 8 individual shaft works (8 outputs) can potentially simplify the surrogate model construction. If the individual shaft works

did need to be accessed after gaining a solution from the surrogate model with a reduced output such as this, the solution can be directly entered into the rigorous model to gain the relevant process information. Likewise, it was also observed from the ANN based surrogate models that the majority of data regarding 3 out of the 4 vapour fractions and 3 out of the 4 shaft works exist in feasible solution space all the time (*i.e.* redundant constraints). Due to this fact, it is decided to neglect to model these outputs in the first place to further reduce the dimension of the outputs. From Fig. 2, it is seen that the KPLS superstructure model (consisting of 7 GPs) satisfies all the practical constraints. Furthermore, its predicted total shaft work is verified to be accurate (147.4 MW verified by the Aspen model), and is comparable to the optimal result obtained using the rigorous optimization (144.4 MW). In addition, individual shaft works are found to be feasible after verification. Most importantly, the full time to train and optimize this surrogate model only takes around 10 minutes (*i.e.* 2 minutes for model construction and 8 minutes for stochastic optimization) as opposed to 17 hours spent when optimizing the rigorous model. This directly demonstrates the superiority and practical advantages of using the integrated KPLS modelling strategy for the optimization and real-time decision-making of high dimensional complex chemical systems (e.g. entire process flowsheet).

5. Conclusions

To conclude, Gaussian processes and artificial neural networks can be used as building blocks to construct efficient surrogate models to represent highly nonlinear systems such as an entire chemical process flowsheet. However, selection of surrogate model structure, fidelity of available data, and amount of data can greatly affect the accuracy and efficiency of surrogate models. Moreover, unsupervised learning techniques can also be taken advantage of to reduce the high dimensionality encountered in large scale processes simulation. Through the use of data-driven models and efficient stochastic optimization algorithms, it is possible to greatly reduce the computational time cost and meanwhile identify a high quality optimal solution for the operation of large scale systems.

References

Almeida-Trasvina, F. and Smith, R. (2018) 'Design and Optimisation of Novel Cascade Refrigeration Cycles for LNG Production', *Comput. Aided Chem. Eng.*, pp. 621–626.

Bhosekar, A. and Ierapetritou, M. (2018) 'Advances in surrogate based modeling, feasibility analysis, and optimization: A review', *Comput. Chem. Eng.*, 108, pp. 250–267.

Bouhlel, M. A. et al. (2016) 'Improving kriging surrogates of high-dimensional design models by Partial Least Squares dimension reduction', *Struct. Multidiscipl. Optim.*, 53(5), pp. 935–952.

Bouhlel, M. A. et al. (2019) 'A Python surrogate modeling framework with derivatives', *Advances in Engineering Software*, 135, p. 102662.

Henao, C. A. and Maravelias, C. T. (2011) 'Surrogate-based superstructure optimization framework', *AIChE J.*, 57(5), pp. 1216–1232.

McBride, K. and Sundmacher, K. (2019) 'Overview of Surrogate Modeling in Chemical Process Engineering', *Chemie Ingenieur Technik*, 91(3), pp. 228–239.

Quirante, N., Javaloyes, J. and Caballero, J. A. (2015) 'Rigorous design of distillation columns using surrogate models based on Kriging interpolation', *AIChE J.*, 61(7), pp. 2169–2187.

del Rio-Chanona, E. A. et al. (2018) 'Deep learning-Based surrogate modeling and optimization for microalgal biofuel production and photobioreactor design', *AIChE J.*, p. aic.16473.

Zhang, D. et al. (2018) 'Life cycle assessments of bio-based sustainable polylimonene carbonate production processes', *Sustain. Prod. Consum.*, 14, pp. 152–160.

Sauro Pierucci, Flavio Manenti, Giulia Bozzano, Davide Manca (Eds.)
Proceedings of the 30th European Symposium on Computer Aided Process Engineering (ESCAPE30), May 24-27, 2020, Milano, Italy.
http://dx.doi.org/10.1016/B978-0-12-823377-1.50014-8

Modelling and Optimisation of Middle Vessel Batch Distillation

Elena Cătălina Udrea, Romuald Győrgy, Costin Sorin Bîldea

University Politehnica of Bucharest, Department of Chemical and Biochemical Engineering, Gh. Polizu street, no. 1-7, Bucharest, 011061, Romania

sorin.bildea@upb.ro

Abstract

This contribution demonstrates that middle vessel batch distillation can be conveniently studied using commercial process engineering software such as Aspen Plus and Aspen Dynamics. A steady-state model is initially developed in Aspen Plus, in order to obtain the starting point for the batch operation – total reflux operation. The model is exported to Aspen Dynamics as flow-driven or pressure-driven simulations. After the relevant controllers are added, the dynamic simulation model predicts the evolution of products composition. The optimal operation strategy can be easily found (for example, the setpoints of temperature and flow controllers which achieve the required product purities, while minimizing the energy requirements). This approach has significant advantages: rigorous distillation models including mass and energy balances; tray hydraulics calculations; temperature-dependent physical properties available from an extensive library; built-in models for other process units and control elements; robust numerical algorithms, including dynamic optimization.

Keywords: Middle vessel, batch distillation, control structure, dynamic optimisation.

1. Introduction

Batch distillation is extensively used in laboratory and chemical, pharmaceutical, biochemical and polymers industries. It is often preferred to continuous distillation because it provides a unitary solution and different separations can be performed in the same equipment by simply changing the operating conditions. Middle vessel batch distillation (MVBD) is a special configuration in which the mixture to be distilled is fed into a vessel placed between the rectifying section and the stripping section of a batch distillation column. During operation of a MVBD, the low- and high-boiling components are removed as distillate and bottoms products, respectively. At the end, the components with intermediate boiling points are found in the middle vessel. For ternary separations, this configuration is better compared with conventional batch distillation, having shorter operating time, lower energy requirements and higher product purities (Luyben, 2015, Li et al., 2018).

Various experimental and theoretical studies highlight the advantages of this configuration. Over time, MVBD processes have been developed for special scenarios, such as multi-component distillation (Wittgens et al., 1996), extractive distillation (Warter et al., 2000; Espinosa, 2002) and reactive distillation (Carmona et al., 2006; Arellano-Garcia et al., 2008). Many researchers have studied and contributed with improvements to the process by performing simulation and dynamic optimisation (Gruetzmann et al., 2008; Leipold et al., 2009; Rao et al., 2012; Luyben, 2015; Zhu et al., 2016).

2. Problem formulation

Mathematical models of middle vessel batch processes are useful for design and optimal operation studies. They include mass and energy balance equations, together with equilibrium relationships. This leads to a system of differential and algebraic equations which can be solved using general purpose software. However, reliable thermodynamic models for computation of physical properties (such as heat of vaporization, vapor pressure, density, viscosity, etc.) and access to a database with the parameters of the thermodynamic models are needed. Moreover, during the integration of the dynamic model the phase equilibria (vapor-liquid, liquid-liquid, or vapor-liquid-liquid) equations must be repeatedly solved by robust numerical methods. For all these reasons, the programming effort is significant, and the speed of execution is quite low.

The modelling approach suggested here makes use of available process simulation software such as Aspen Plus and Aspen Dynamics. In this way, new and efficient MVBD processes can be developed by process engineers faster, with reduced effort, and without requiring advanced modelling or programming skills. This approach has significant advantages: rigorous distillation models including mass and energy balances; tray hydraulics calculations; temperature-dependent physical properties readily available from an extensive library; built-in models for other process units and control elements; robust numerical algorithms, including dynamic optimization.

3. Development of the Aspen Dynamics model

This section considers the separation of an equimolar ethanol / 1-propanol / 1-butanol mixture in a laboratory-scale unit. The required purities are 0.95 (mole fractions). The upper (rectifying) and lower (stripping) sections house 20 and 10 theoretical stages, respectively. Including the condenser, middle vessel and reboiler, the total number of stages is 33. The column diameter is 5 cm. The reboiler duty is limited to 3 kW. The middle vessel, distillate and bottoms collectors have 10 L each. The initial amount subjected to distillation is 134.5 moles (8.1 kg), which are fed into the middle vessel. Note that this is different from the approach taken by Luyben (2015), who considered that the mixture to be separated is initially at the bottom of the column. When operation begins, the liquid flows from the middle vessel towards the bottom of the column. Once enough liquid accumulates, the heating is started, vapour flows upwards, condenses, and returns as reflux. After a certain time, a stationary state is achieved – the total reflux operation. Our goal is to get a dynamic simulation model having the initial state as close to total reflux operation as possible. Thus, a steady state simulation is built in Aspen Plus (Figure 1, left). The feed flow rate is small (0.02 mol/min) and is distributed between the top (high purity ethanol), middle (ethanol / 1-propanol / 1-butanol, equimolar) and bottom (high purity 1-butanol) products. The reboiler duty is set to 1 kW, and the reflux ratio is very high (R = 375). This simulation is used to check that the hydrodynamic conditions are feasible, i.e. there is no flooding or weeping. Then, an Aspen Dynamics flowsheet is exported, including level controllers for the sumps of the upper and lower sections (not shown in Figure 1). After initialization of the dynamic simulation, the feed is cut off and no products are withdrawn. Finally, valves VE and VB are open, to empty the distillate and bottoms collectors, and the product streams (ETOH, PROH and BUOH) are simply deleted (Figure 1, right). The operation starts by increasing the lower reflux (L_i). The liquid level at the bottom of the lower section increases, and the bottoms product W is withdrawn. Fixing the operating variables to Q_{reb} = 1.2 kW, L_b = 1.5 mol/min, L_i = 2.5 mol/min (0.15 kmol/h), after 5 hours of operation the purities of the products are

$z_{EtOH,B2}$=0.926, $z_{PrOH,B1}$=0.585, $z_{BuOH,B3}$=0.925. Products of higher purity are obtained after adding temperature controllers for the upper and lower sections (Figure 1, left). Figure 2 presents the evolution of amounts of collected products and their purities, while a summary of the results for the initial operating conditions is shown in Table 1.

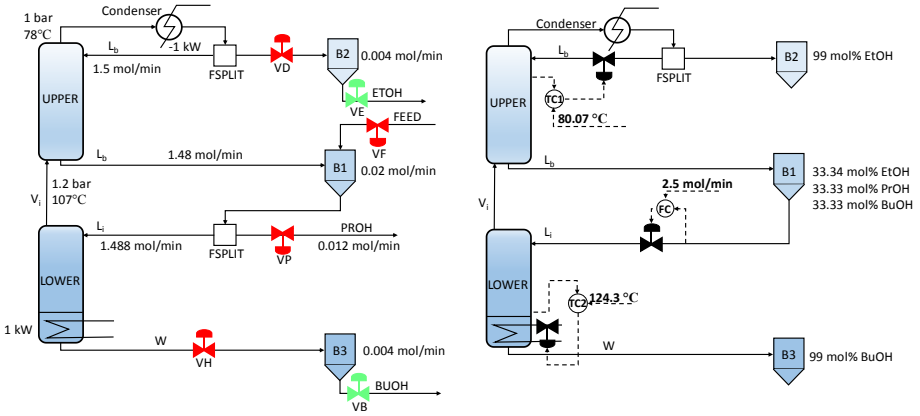

Figure 1. Steady state simulation (left); Dynamic simulation (right)

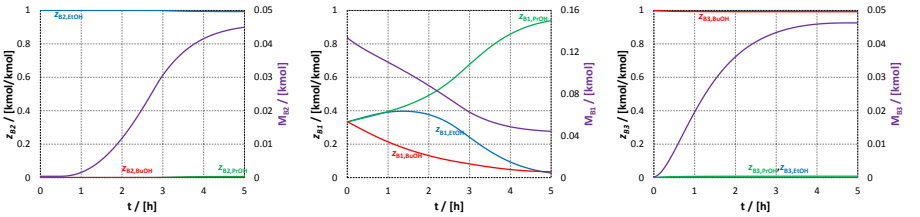

Figure 2. Simulation results (base case) showing the change of composition and holdup in the distillate vessel (left), middle vessel (center), and bottom vessel (right)

Table 1. Comparison between the values of the decision variables before and after the optimization

Variables	Base-case	Optimization	Dynamic optimization
TC1.Gain / [%/%]	1	0.1	4.63
TC1.Integral_time / [min]	20	16.46	19.88
TC1.SP / [°C]	80.07	82.5	81.79
TC2.Gain / [%/%]	1	5	2.81
TC2.Integral_time / [min]	20	40	19.97
TC2.SP / [°C]	124.3	124.5	115.15
Purities (top / middle / bottom)	0.99 / 0.94 / 0.99	0.95 / 0.95 / 0.95	0.95 / 0.95 / 0.95
Reflux (lower) / [mol/min]	2.5	2.6	Varying
Energy requirement / [kWh]	7.58	4.26	4.07

4. Process optimization

The base-case operating conditions lead to distillate and bottoms product with purities exceeding the specifications. To bring the unnecessarily high energy requirements down, a minimisation problem is formulated, with the cumulative reboiler duty as the objective function. The decision variables are the settings of the temperature controllers (setpoint,

gain, integral time) and lower section reflux. The problem is completed by the constraints specifying that, at the end of distillation, the purities should exceed 0.95. The optimisation problem is solved using the facilities offered by Aspen Dynamics. As expected, the purity constraints are active and, compared with the initial case, the energy requirement is significantly reduced from 7.58 kWh to 4.26 kWh (Table 1).

Then, a dynamic optimisation is performed, with the lower reflux as the control variable, which is discretized into a 16-intervals piecewise constant function. The solution shows further decrease of the energy requirements (4.07 kWh) and of the batch time (4 h). Figure 3 presents the collected products and their purities, while the cumulative reboiler duty and the change of the control variable are shown in Figure 4. It should be noted that, during the entire process, the maximum heating duty does not exceed 2.5 kW.

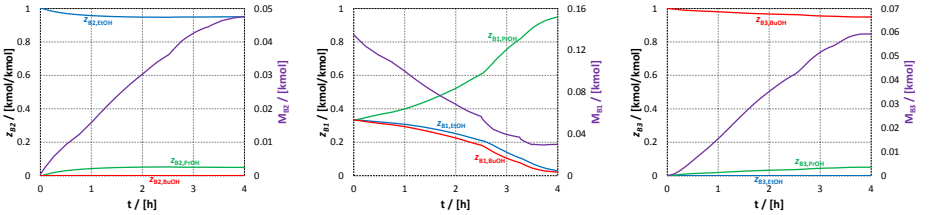

Figure 3. Simulation results (dynamic optimization) showing the change of composition and holdup in the distillate vessel (left), middle vessel (center), and bottom vessel (right)

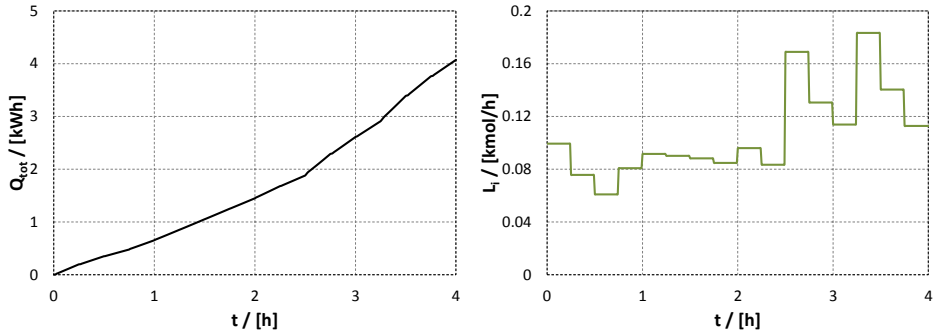

Figure 4. Results of the optimization study: total amount of heat (Q_{tot}, left side) and optimal reflux rate policy for the lower column (L_i, right side)

5. Complex operating sequence – separation of a quaternary mixture

This section describes the development of a model for separating 100 kmol of an equimolar methanol / ethanol / 1-propanol / 1-butanol mixture by MVBD. The required product purity is 0.99. The upper and lower sections have 20 and 30 theoretical trays, respectively. Methanol and ethanol are obtained as distillates, 1-butanol as bottoms. At the end of distillation, 1-propanol will be found in the middle vessel.

Figure 5 shows the process setup. The dynamic simulation is constructed as explained previously. However, the control structure is more complex, the products purities being controlled by concentration–temperature cascade loops.

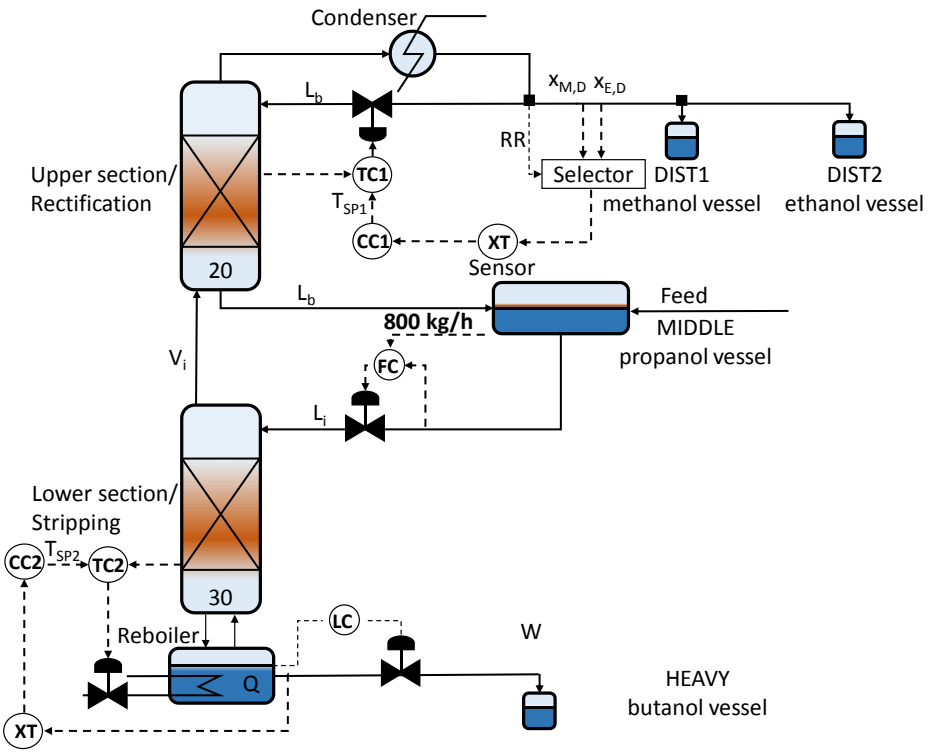

Figure 5. Middle vessel batch column for distillation of 4-components mixture

After the dynamic simulation reaches total reflux operating conditions, the lower section reflux rate is increased. At the bottom, high purity n-butanol is obtained. In the beginning, the methanol-rich distillate is collected in DIST1 vessel. As distillation proceeds, the lightest component (methanol) is depleted from the middle vessel. Consequently, it becomes increasingly difficult to achieve high-purity methanol product, and the required reflux ratio increases. When the reflux ratio becomes excessively high (200), the concentration sensor XT switches from measuring the ethanol concentration (the impurity in the methanol product) to measuring the n-propanol concentration (the impurity in the ethanol product), and the distillate is collected in the DIST2 vessel. The process stops when the n-propanol mole fraction in the middle vessel reaches the specification. It should be noted that this rather complex operating procedure can be reliably implemented by means of Aspen Dynamics "tasks":

```
Task etanol
   Runs Once When BLOCKS("B1").sf("LB") > 0.995 AND time >= 1
   Ramp (BLOCKS("B2").sf("ETOH"), 1, 0.1);
   BLOCKS("B11").SelSig : 2;
End
```

The amount of product collected in each vessel and their purities are shown in Figure 6. Throughout the process, methanol and n-butanol are obtained with the required purity (0.99 mole). At the end of the process, the n-propanol product also satisfies the specifications. However, the ethanol purity is only 0.95, due to impurification with

methanol during the product switching. In order to improve the purity of the ethanol product, an off-cut vessel can be introduced.

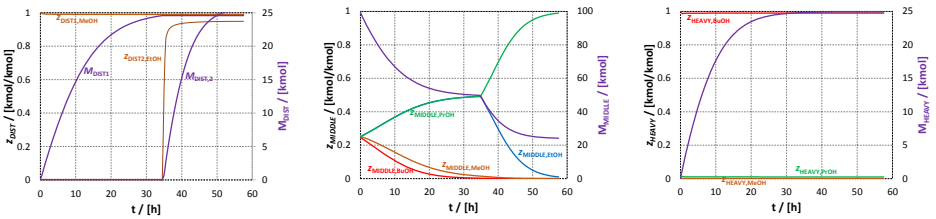

Figure 6. Simulation results (four-component mixture) showing the change of composition and holdup in the distillate vessel (left), middle vessel (centre), and bottom vessel (right)

6. Conclusions

Middle vessel batch distillation can be conveniently studied using commercial process engineering software such as Aspen Plus and Aspen Dynamics. In this way, models including rigorous physical properties, tray hydraulics, process control can be easily developed and solved using robust numerical algorithms. Such models are useful for simulating the behaviour of existing columns, designing new columns, or optimizing complex operating policies.

Acknowledgement

The financial support of the European Commission through the European Regional Development Fund and of the Romanian state budget, under the grant agreement 155/25.11.2016 (Project POC P-37-449, acronym ASPiRE) is gratefully acknowledged.

References

H. Arellano-Garcia, I. Carmona, G. Wozny, 2008, A new operation mode for reactive batch distillation in middle-vessel columns: Start-up and operation, Computers and Chemical Engineering, 32, 161-169.

J. Espinosa, 2002, On the Integration of Reaction and Separation in a Batch Extractive Distillation Column with a Middle Vessel, Industrial and Engineering Chemistry Research, 41, 3657-3668.

S. Gruetzmann, G. Fieg, 2008, Startup Operation of Middle-Vessel Batch Distillation Column: Modelling and Simulation, Industrial and Engineering Chemistry Research, 47, 813-824.

M. Leipold, S. Gruetzmann, G. Fieg, 2009, An evolutionary approach or multi-objective dynamic opimization applied to middle vessel batch distillation, Computers and Chemical Engineering, 33, 857-870.

X. Li, T. Zhao, Y. Wang, Y. Wang, Z. Zhu, 2018, Operational design and improvement of conventional batch distillation and middle-vessel batch distillation, Brazilian Journal of Chemical Engineering, 35, 2, 769-784.

W. L. Luyben, 2015, Aspen Dynamics simulation of a middle-vessel batch distillation process, Journal of Process Control, 33, 49-59.

C. S. Rao, K. Barik, 2012, Modeling, Simulation and Control of Middle Vessel Batch Distillation Column, Procedia Engineering, 38, 2383-2397.

M. Warter, J. Stichlmair, 2000, Batch Distillation of Azeotropic Mixtures in a Column with a Middle Vessel, European Symposium on Computer Aided Process Engineering, 10, 691-696.

B. Wittgens, B. Litto, E. Sørensen, S. Skogestad, 1996, Total reflux operation of multivessel batch distillation, Computers and Chemical Engineering, 20, 1041-1046

Z. Zhu, X. Li, Y. Cao, X. Liu, Y. Wang, 2016, Design and Control of a Middle Vessel Batch Distillation Process for Separating the Methyl Formate/Methanol/Water Ternary System, Industrial and Engineering Chemistry Research, 55, 10, 2760-2768.

Sauro Pierucci, Flavio Manenti, Giulia Bozzano, Davide Manca (Eds.)
Proceedings of the 30th European Symposium on Computer Aided Process Engineering (ESCAPE30), May 24-27, 2020, Milano, Italy.
http://dx.doi.org/10.1016/B978-0-12-823377-1.50015-X

Investigation of Heat Transfer Enhancement in a Microchannel Heat Sink with the Aid of Internal Fins: A Metamodel Approach

Vahid Hosseinpour, Mohammed Kazemeini *

Department of Chemical and Petroluem Engineering, Sharif University of Technology, Tehran, Iran
kazemini@sharif.edu

Abstract

Heat transfer enhancement with microchannel tools has been increased in recent year. In this study effect of geometric parameters as well as Reynolds number have been studied with experimental design approach. A metamodel was generated in this study for pressure drop and average Nusselt number passed all statistical tests. Order of an individual effect upon a response has been evaluated and interaction effects have been determined. Numerical results indicated that heat transfer increased significantly with inserting pyramidal micro fins.

Keywords: Metamodeling, Finned Microchannel Heat Sink (FMCHS), Experimental Design, Heat Transfer Enhancement Introduction

Heat transfer handling has a crucial role in the performance of engineering devices. Recently, miniaturized engineering devices such as micropumps (Liu et.al, 2018), microvalves(Huang et. Al, 2016), microsensors (Maegaard et. al, 2018) and high-performance electronic devices with a small size containing additional integrated circuits have been increasingly developed (Leela et. al, 2015). Accordingly, micro-size heat transfer devices have been favoured which opened new avenues for engineers to working on design and development of new micro heat sink systems (Kandlikar et.al, 2005, Naphon, et.al 2018). A higher heat transfer coefficient, a small inventory of coolant fluid and a large surface to volume ratio, are the most common excellence of Microchannel Heat Sink (MCHS) devices over conventional version of heat sink systems (Whitesides, 2006). However, several parameters affected the performance of these micro-scale devices including; the specific rate of heat dissipation, flow rate, pressure drop of coolant, fluid temperature rise, and the fluid inlet to surface temperature ought to be considered in microchannel designs.
Concerning the high capability of MCHS in heat transfer, various researches have been done for finding the proper design of microchannel and investigation of flow characteristics in these devices. Design, optimization and improvement for double layer microchannel heat sink performed by Wang et.al., (2015). In these studies, several parameters simultaneously optimized while minimization of thermal resistance chosen as an objective function. Lee et al. (2006) predicted the thermal behaviour of single-phase flow in a rectangular microchannel while correlating results with those of conventional sized channel. These results were validated through experimental data obtained in a microchannel with width ranging from 194 to 534 μm and depth range of five times of

width in each case. Through investigation of heat transfer and fluid flow characteristics in MCHS, Philips (1987) developed a formulation for designing microchannel geometry. In this study microchannel with pyramid micro fins thoroughly investigated with statistical concepts. To verify effects of geometric parameters of pyramid fin on thermal performance of microchannel heat sink experimental design approach was used. Finally, a metamodel was developed for Nusselt number and pressure drop prediction as geometric parameter and Reynolds number.

1. Numerical Model

To save computation time only on channel of heat sink was modeled and simulated with the CFD technique. Dimension of single microchannel and computation domain presented in the figure 1 and Table 1. Geometrical parameters of micro-fins survived in this study was described as follows; ratio of cross-section of fins to microchannel width, $\left(\alpha = \frac{d_f}{W_c}\right)$, the ratio of fin height to the height of the microchannel $\left(\beta = \frac{h_f}{H_c}\right)$, and fins spacing (Sf) indicating the center to center distance of two adjacent fins.

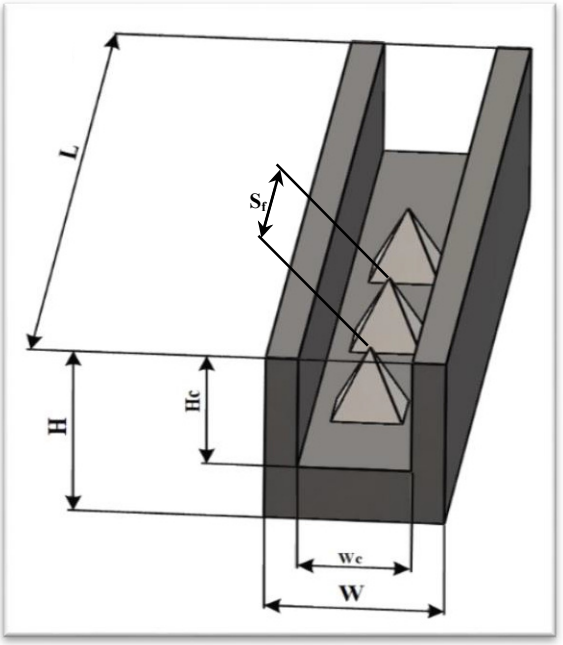

Figure 1) Schematic diagram of Computational domain

To solve governing equations some assumptions were accounted for. These included; steady state, laminar and no slipping flow, incompressible Newtonian fluid, uniform heat flux at the bottom wall, insignificant radiation, hydraulic and thermally fully developed flow; constant and varied thermos-physical properties for solid and fluid section;

respectively, and no gravity. Governing equation (continuity, momentum and energy balance) solved with the Finite Element Method with the tools of the in-house coding.

Table 1. Geometric parameters of computational domain and microchannel utilized in this study

Parameter	**value**
W	0.800 (mm)
H	0.800 (mm)
L	30 (mm)
W_c	0.325 (mm)
H_c	0.650 (mm)
$\boldsymbol{\alpha}$	0.3-0.9
$\boldsymbol{\beta}$	0.0.3-0.9
S_f	0.5-2 (mm)
L_{int}	$3W_c$

2. Experimental Design

To evaluate fined microchannel heat sink performance, an experimental design approach was used. Central composite design at 5 levels was utilized to generate design points. Range of parameters displayed in table 2.

Table 2. Levels for input parameters used in the simulation of experiment in actual and coded values used in this research

Parameter	**Description**	**Unit**	**Level**				
			$-\boldsymbol{\alpha}(-\mathbf{2})$	**-1**	**0**	**+1**	$+\boldsymbol{\alpha}(+\mathbf{2})$
$A:\alpha$	$\frac{d_f}{W_c}$		0.3	0.45	0.6	0.75	0.9
$B:\beta$	$\frac{h_f}{H_c}$		0.3	0.45	0.6	0.75	0.9
$C:S_f$	adjacent fin's distance	(μm)	500	875	1250	1625	2000
$D:Re$	Reynold number		180	345	510	675	840

3. Developing a metamodel

Generated quadratic equations for prediction of Nusselt number and pressure drop for pyramidal FMCHS were presented in Eqs. (1) and (2). Power Box-Cox transformation with 0.32 for the pressure response and natural logarithm transforms for the average Nusselt number was performed.

$$(\Delta p)^{0.32} = 23.36 + 1.08A + 2.07B - 0.69C + 3.89D + 0.51AB + 0.22AD - 0.29BC + 0.45BD - 0.12CD + 0.2B^2 + 0.11C^2 - 0.36D^2 \quad (1)$$

$$\ln(Nu) = 3.13 + 0.054A + 0.070B - 0.058C + 0.12D + 0.025AB - 0.013AC - 0.021BC + 0.015C^2 - 0.024D^2 \quad (2)$$

ANOVA table for the two responses presented in the table 3. Parameter in this table revealed that developed models passed statistical tests and these models. P-valuer less than 0.05 indicated models fits data properly. Adjusted R^2 and predicted R^2 were in less than 0.2 differential. This fact also confirmed that, the statistical tests passed properly.

Table 3. The ANOVA results for responses for pyramidal-FMCHS

Source	Sum of Square	DF	Mean Square	F-Value	$p-$ value probability $> F$
ΔP					
Model	520.53	12	43.38	913.35	<0.00001
Residual	0.81	17	0.047		
R^2=0.9985, Adj- R^2=0.9974, Pred- R^2=0.9930, Adequate Precision= 128.82					
$\overline{Nu}$					
Model	0.64	9	0.071	168.41	<0.00001
Residual	0.008403	20	0.0004202		
R^2=0.9870, Adj- R^2=0.9811, Pred- R^2=0.9580, Adequate Precision= 57.098					

Equation (1) demonstrated that the Reynold number had the most significant effect on the pressure drop. Fin height ranked second in terms of importance and fin base diameter came third. Fin spacing had the least (and adverse) effect upon the pressure drop across the microchannel with pyramid micro-fins. The insignificant AC and A2 terms were removed from the quadratic equation.

According to equation (2), AD, BD, CD, A2, and B2 terms were determined to be trivial in the model regarding the design space and they were removed from the model. Water velocity had the greatest effect upon the average Nusselt number.

4. Overall Performance

The relationship between the thermal resistance and the Reynolds number is depicted in figure 2. In general, thermal resistances dropped with the enhancement of the Reynolds number due to improvement in the heat transfer coefficient. This Figure indicated that pyramid fins geometries enhanced the thermal performance of the considered microchannel. For a Reynolds number of 840, the thermal resistance of the plain microchannel was about 65% higher than that of the microchannel with pyramid micro-fins.

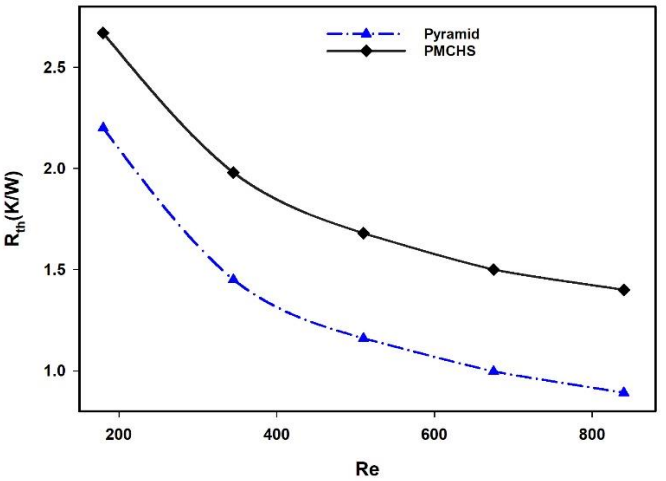

Figure 2. Comparison of pyramid fins microchannel with plain microchannel

Effect of micro-fins on convection heat transfer in microchannel heat sinks was examined by relative Nusselt number illustrated in figure 3. As shown, Nu0 stands for the average Nusselt number of PMCHS selected as the base case, for microchannel with pyramid fins, the relative average Nusselt number was greater than 1 implying that inserting micro-fins enhanced convection heat transfer due to increased heat transfer area as well as interruption in flow field. This behavior was considered as a typical characteristic of a microchannel. Moreover, this Figure emphasized that, the relative Nusselt number (Nu/Nu_0) increased through enhancement of the Re_{in} due to the fluid disturbance as a consequence of rising in flow velocity.

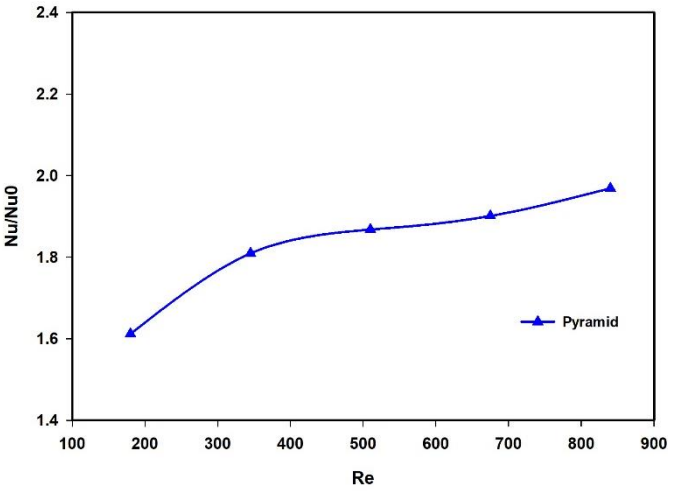

Figure 3. average Nusselt number for pyramid micro fins

5. Conclusion

In this research, inserting pyramid micro-fins onto microchannel were thoroughly investigated. To evaluate effects of geometric parameters as well as Reynolds number upon the performance of Finned Microchannel Heat Sinks, experimental approach was utilized. With the aid of the DOE software, a metamodel was generated for the pressure drop and average Nusselt number predictions. This metamodel passed all statistical tests that confirmed such model fitted data properly. These types of models might be used in the optimization of such microchannel greatly saving in computation time. Another benefit of the developed model is to determine the affect of parameters upon a selected response. Moreover, synergism of interaction of parameters for a particular response may also be determined.

References

B. Liu, Z. Zhang, J. Yang, J. Yang, D. Li, A rotary ferrofluidic vane micropump with C shape baffle, Sensors Actuators, B Chem. 263 (2018) 452–458.

B. bo Huang, M. jie Yin, A.P. Zhang, X. song Ye, On-chip microfabrication of thermally controllable PNIPAAm microvalves by using optical maskless stereolithography, Sensors Actuators, A Phys. 247 (2016) 397–402.

K. Maegaard, E. Garcia-Robledo, N.P. Revsbech, Microsensor for simultaneous measurement of H_2 and H_2S, Sensors Actuators, B Chem. 259 (2018) 560–564.

V. Leela Vinodhan, K.S. Rajan, Fine-tuning width and aspect ratio of an improved microchannel heat sink for energy-efficient thermal management, Energy Convers. Manag. 105 (2015) 986–994.

S. Kandlikar, S. Garimella, D. Li, S. Colin, M. King, Heat transfer and fluid flow in minichannels and microchannels, Elsevier, 2005.

P. Naphon, L. Nakharintr, S. Wiriyasart, Continuous nanofluids jet impingement heat transfer and flow in a micro-channel heat sink, Int. J. Heat Mass Transf. 126 (2018) 924–932.

G.M. Whitesides, The origins and the future of microfluidics, Nature. 442 (2006) 368–373.

C. Leng, X.D. Wang, T.H. Wang, An improved design of double-layered microchannel heat sink with truncated top channels, Appl. Therm. Eng. 79 (2015) 54–62.

P.S. Lee, S. V. Garimella, Thermally developing flow and heat transfer in rectangular microchannels of different aspect ratios, Int. J. Heat Mass Transf. 49 (2006) 3060–3067.

R.J. Phillips, Forced-convection, liquid-cooled, microchannel heat sinks, Massachusetts Institute of Technology, 1987.

Sauro Pierucci, Flavio Manenti, Giulia Bozzano, Davide Manca (Eds.)
Proceedings of the 30th European Symposium on Computer Aided Process Engineering (ESCAPE30), May 24-27, 2020, Milano, Italy.
http://dx.doi.org/10.1016/B978-0-12-823377-1.50016-1

Optimization of RFCC Process Considering Particle Deposition Model

Hyungtae Cho[a], Kwang Cheol Oh[a], Jiheon Lee[b], Seokyoung Hong[b], Junghwan Kim[a,*]

[a]*Green Materials & Processes Group, Korea Institute of Industrial Technology, 55 Jongga-ro, Jung-gu, Ulsan 44413, Republic of Korea*
[b]*Department of Chemical and Biomolecular Engineering, Yonsei University, 50 Yonsei-ro, Seodaemun-gu, Seoul, 03722, Republic of Korea*
kjh31@kitech.re.kr

Abstract

Formation of particle deposit in the reactor cyclone of the commercial residue fluidized catalytic cracking (RFCC) process is one of the major problems causing serious catalyst carryover into the fractionators and process shutdown. This problem has been considered as an unavoidable issue in sustainable operations and required an accurate forecasting model. The particle deposition model in the cyclone dipleg of RFCC process is developed considering both of mathematical particle deposit factors and actual operating data. The model for particle deposition was researched in the viewpoint of transport phenomenon of particle. Verification of the model is conducted with actual plant data using parameter estimation method. Optimization model of RFCC process is developed by combining particle deposition model and cracking reaction model to find optimal operating conditions. The optimal operating conditions are found by selection of reaction temperature, catalyst/oil ratio and feed rate, to minimize particle deposit thickness. As a result, the operating cycle time is increased from 31 to 47 months (52%) by the decreasing particle deposition rate and the productivity of gasoline is increased at about 46% by increasing RFCC operation period.

Keywords: Residue Fluidized Catalytic Cracking (RFCC), particle deposit, modeling and optimization

1. Introduction

A residue fluid catalytic cracking (RFCC), typical heavy oil upgrading (HOU) process, is a key process in refinery industry (Pinheiro, 2011). In this process, the residue from atmospheric distillation towers are converted into highly valuable light hydrocarbons such as gasoline and naphtha (Song, 2010). The RFCC unit is in the Ulsan Complex of SK energy, Korea. The unit has operated with atmospheric residue feed rates at ca. 58,000 BPSD (Kim, 2012). An RFCC process is composed of a reactor, and a regenerator. The cracking reaction occurs in the riser, and the product gas and catalysts are separated in a reactor cyclone. The riser is 60 m long; the upper section is 35 m long with a diameter of 1.6 m ID, and the lower section is 25 m long with a diameter of 1.0 m ID. The particle deposit, i.e. coking, has been commonly observed in the RFCC reactor as a black deposit on the surface of the cyclone barrels, reactor dome, and walls. It is also quite common for the deposit to form stalactites from the plenum chamber or dome steam rings. The deposit is often deposited on the cyclone barrels. Coking within the cyclones can be potentially very troublesome since any coke spalls going down into the dipleg could restrict catalyst

flow or jam the flapper valve. Either situation reduces cyclone efficiency and can increase catalyst losses from the reactor. Also, the formation of deposit in the reactor cyclone dipleg incurs serious catalyst carryover in the fractionators and process shutdown (Kim, 2012).

In this study, Particle deposition on the wall of cyclone dipleg in a RFCC reactor is modeled. The different mechanisms of particle transport to the wall are considered, i.e., Brownian motion and turbulent diffusion. A boundary condition that accounts for the probability of particle sticking to the wall is suggested. An analytical solution for deposition of small Brownian particles is obtained. The model parameters are estimated: (1) the particle–wall sticking probability, (2) the shear removal constant parameter, (3) the shear removal exponent parameter. Also, developed particle deposit forecasting model and tuned cracking reaction model are combined in this optimization model. And its results of optimization are compared and discussed

2. Particle deposition model in the dipleg

The particle deposit forecasting model is considered the deposition from a turbulent steady-state flow of a particulate suspension on the wall of a cyclone dipleg in RFCC reactor. And the model is developed considering a dilute flow where particle–particle collisions and a particle effect on a fluid flow can be neglected over the entire computational domain. For accuracy, this model is adopted a poly-dispersed particulate system.

The deposition velocity of the dipleg, calculated as the fluxes caused by particle diffusion and advection, is

$$V_{deposit} = -(D_{Br} + D_{PT})\frac{dc}{dy} + cV_p^y \tag{1}$$

where D_{Br} is the Brownian particle diffusivity and D_{PT} is the particle turbulent diffusivity, c is the particle concentration by volume, y is the coordinate determining particle distance from the wall and V_p^y is the particle drift velocity caused by turbophoresis and the other forces affecting particle motion in the direction, normal to the wall (Brennen,2005).

2.1. Determination of critical particle diameter

The forces that act on a particle attached to the wall of dipleg are considered for determining a critical particle size. Figure 1 shows a diagram illustrating forces acting on a particle attached to the wall surface. The force balance of the maximum static liquid bridge force, F_{Liquid}, and the sum of the drag force, F_{Drag}, and gravity force, F_g is calculated for estimating of the order of magnitude of the critical particle diameter.

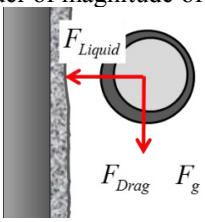

Figure 1. Diagram illustrating forces acting on a particle

2.2. The particle deposition model

The particle deposition flux, i.e. the deposition velocity, can be calculated by the product of the particle transport to the wall and the sticking probability. Though the concentration gradient in the wall vicinity is zero the chaotically moving particles reach the wall being transported by different mechanisms such as Brownian and turbulence.

First, the particles are involved into Brownian motion; that is, particles chaotically move due to multiple collisions with fluid molecules. The particle deposition flux caused by the Brownian motion is:

$$q_{Bi} = p_i \; m(d_i) \; N_i \; v_{dBi} \tag{2}$$

where p_i is the particle–wall sticking probability of the ith size fraction particle with the wall $m(d_i)$ is mass of ith size fraction, N_i is concentration of ith size fraction, v_{dBi} the most probable velocity directed to the wall.

As we already mentioned, small particles follow the fluid in fluctuation motion caused by turbulence. The deposition rate due to turbulence fluctuations is calculated based on the particle velocity at the time it touches the wall:

$$q_{Ti} = p_i \; m(d_i) \; N_i \; v_{dTi} \tag{3}$$

The total mass deposition flux of the ith size fraction particles is:

$$q_i = q_{Bi} + q_{Ti} = p_i \; m(d_i) \; N_i \; [v_{dBi} + v_{dTi}] \tag{4}$$

As a reasonable approximation for modelling such a complex system we assume that the particle–wall sticking probability is constant: that is, $p_i = p$.

The total deposition mass flux is:

$$q_\Sigma = \sum_{i=1}^{i_{cr}} q_i = p \; \sum_{i=1}^{i_{cr}} m_i \; N_i \; [v_{dBi} + v_{dTi}] \tag{5}$$

where i_{cr} is the size fraction number corresponding to the critical particle size d_{cr} that is a tuning parameter of our model.

According to Eskin et. Al. (2011) their experiments showed that increasing the Couette device rotation speed (i.e., the shear rate at the wall) leads to a reduction of the deposit mass. To account for the shear removal effect, the total depositing particle flux should be reduced as follows:

$$q_a = q_\Sigma - q_{SR} \tag{6}$$

The deposit thickness data of the commercial RFCC process is needed to identify the model parameters. The model parameters, included those for the shear removal model, are: (1) the particle–wall sticking probability, p; (2) the shear removal constant parameter, α_r; (3) the shear removal exponent parameter, n. For conducting calculation, every variable is collected from commercial RFCC process data. The particle size distribution (PSD) is adopted for robust simulation of the particle deposition. Also, fluid velocity and particle concentration are obtained from CPFD simulation result.

In Figure 6 a system boundary is presented. For accuracy of simulation, the system boundary is divided 4 zones and 6 blocks as height.

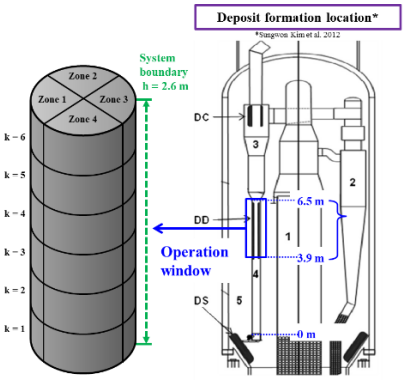

Figure 2. System boundary of particle deposit model

3. Results and discussion

3.1. Parameter estimation results

The deposit thickness data (thickness of the particle deposit at the different process operation times) were fitted to the simulation results upon identification of the following model parameters: (1) the particle–wall sticking probability, p= 0.023; (2) the shear removal constant parameter, α_r= 0.009; (3) the shear removal exponent parameter, n= 0.557.

Figure 3 shows the parameter estimation results and presents deposit thickness versus time at each zone of cyclone dipleg. As shown in Figure 3 (b), the two deposit thickness data (Plant data) points are also presented. One can see that agreement between the calculated and the plant data is good in this case

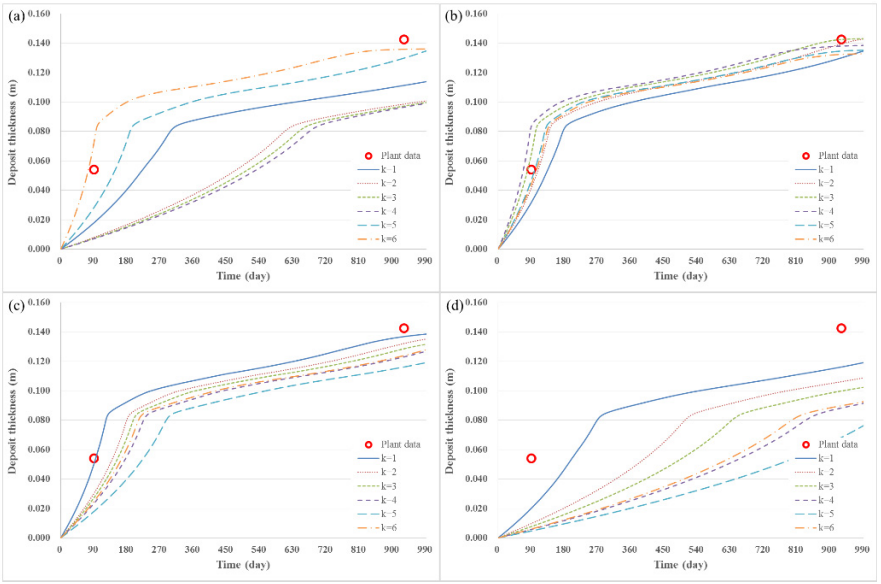

Figure 3. Parameter estimation results for deposit thickness versus time: (a) zone 1, (b) zone 2, (c) zone 3, (d) zone 4.

3.2. Optimization Results

The reaction model is assumed that the Residue is cracked into the most desired gasoline, and Cl-C4 gas and coke. One objective function is selected for the study. It is to minimize the deposit thickness at the certain operation day by using three decision variables: 1) the reaction temperature, 2) the catalyst oil ratio, 3) the feed flow rate, i.e. capacity of residue.

Optimization model is solved with constraints to search the optimum values of reaction parameters. In doing this, the reaction model and the particle deposit thickness is calculated again by using optimum values predicted by GA as shown in Table 1.

Table 1. Optimization results

Optimum operation conditions		
Temperature, $\boldsymbol{T_f}$ (℃)	Catalyst oil ratio, C/O	Feed rate, M_{feed} (BPSD)
505.429	8.981	72851.121
Reaction model result		
	Original operation conditions	Optimized operation conditions
Conversion	0.891	0.936

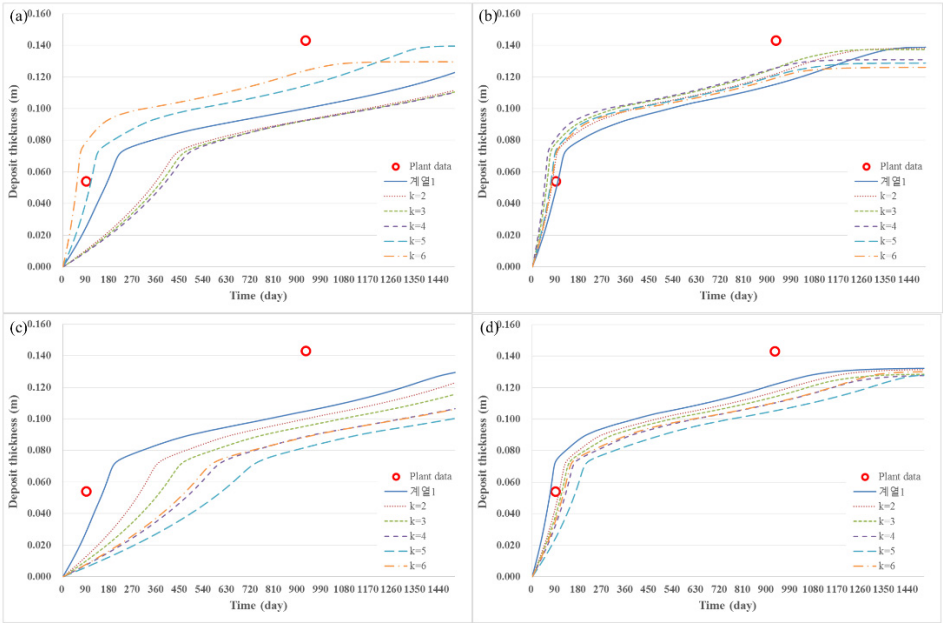

Figure 4. Minimized deposit thickness versus time: (a) zone 1, (b) zone 2, (c) zone 3, (d) zone 4.

Figure 4 shows the deposit thickness versus time at each zone of cyclone dipleg. And the maximum deposit thickness data (plant data) points is also presented. As shown in Figure 4 (b), the deposit thickness of optimized data is clearly lower than the plant data. The

deposit thickness value of 0.126 cm that is lower than the values of experimental measurements, 0.146 cm in commercial RFCC process. Also, the operation period of optimized RFCC process is increased from 990 to more than 1400 days.

4. Conclusion

This study is developed the particle deposition model validated with real plant data and the optimization model including particle deposit effect. As a result, we found the optimal operating conditions, selection of reaction temperature, catalyst oil ratio and feed rate, to minimize particle deposit thickness. It has also demonstrated that feed conversion rate, amount of gasoline production and amount of C1-C4 production is increased about 4.5%, 3.5% and 79.2%, respectively. The operating cycle time expanded from 990 to 1400 years by the decreasing particle deposit rate. The proposed model is expected to benefit refinery industries by enabling them to determine optimal decision variables related to particle deposit formation.

References

Pinheiro, C. I., Fernandes, J. L., Domingues, L., Chambel, A. J., Graça, I., Oliveira, N. M., Cerqueira, H. S. & Ribeiro, F. R. (2011) Fluid Catalytic Cracking (FCC) Process Modeling, Simulation, and Control, Industrial & Engineering Chemistry Research, 51(1), 1–29.

Song, J., Sun, G., Chao, Z., Wei, Y. & Shi, M. (2010) Gas flow behavior and residence time distribution in a FCC disengager vessel with different coupling configurations between two-stage separators. Powder Technology, 201(3), 258-265.

Kim, S. W., Lee, J. W., Kim, C. J., Koh, J. S., Kim, G. R., & Choi, S. (2012). Characteristics of deposits formed in cyclones in commercial RFCC reactor. Industrial & Engineering Chemistry Research, 51(30), 10238-10246.

Kim, S. W., Lee, J. W., Koh, J. S., Kim, G. R., Choi, S., & Yoo, I. S. (2012). Formation and characterization of deposits in cyclone dipleg of a commercial residue fluid catalytic cracking reactor. Industrial & Engineering Chemistry Research, 51(43), 14279-14288.

Brennen, C. E. (2005) Fundamentals of multiphase flow. Cambridge university press

Guha, A. (2008). Transport and deposition of particles in turbulent and laminar flow. Annu. Rev. Fluid Mech., 40, 311-341.

Eskin, D., Ratulowski, J., Akbarzadeh, K., & Pan, S. (2011). Modelling asphaltene deposition in turbulent pipeline flows. The Canadian Journal of Chemical Engineering, 89(3), 421-441.

Eskin, D., Ratulowski, J., & Akbarzadeh, K. (2011). Modeling of particle deposition in a vertical turbulent pipe flow at a reduced probability of particle sticking to the wall. Chemical engineering science, 66(20), 4561-4572.

Cho, H., Kim, J., Park, C., Lee, K., Kim, M., & Moon, I. (2017). Uneven distribution of particle flow in RFCC reactor riser. Powder technology, 312, 113-123.

Cho, H., Cha, B., Kim, S., Ryu, J., Kim, J., & Moon, I. (2013). Numerical analysis for particle deposit formation in reactor cyclone of residue fluidized catalytic cracking. Industrial & Engineering Chemistry Research, 52(22), 7252-7258.

Sauro Pierucci, Flavio Manenti, Giulia Bozzano, Davide Manca (Eds.)
Proceedings of the 30th European Symposium on Computer Aided Process Engineering (ESCAPE30), May 24-27, 2020, Milano, Italy.
http://dx.doi.org/10.1016/B978-0-12-823377-1.50017-3

Dimethyl Carbonate Production by Urea Transesterification, Process Simulation and Environmental Assessment

Laurent Astruc, José Miranda, Ivonne Rodriguez Donis, Claire Vialle, Caroline Sablayrolles

Laboratoire de Chimie Agro-industrielle, Université de Toulouse, INRA, INPT, Toulouse, France

laurent.astruc@toulouse-inp.fr

Abstract

Evaluation of the environmental sustainability to synthesize dimethyl carbonate (DMC) from the urea transesterification with methanol is carried out by using Life Cycle Assessment (LCA) methodology for the first time. Foreground data for LCA analysis are supplied by simulation results using ProSimPlus®. The LCA is modelled with SimaPro, and Ecoinvent database provides background data. LCA results show that the urea production has the main impact in 10/11 impact categories whereas the ionizing radiation is mainly influenced by downstream separation. Finally, the urea route shows better results than the oxidative carbonylation of methanol.

Keywords: Life Cycle Assessment (LCA), urea route, DMC, ProSimPlus, Process design

1. Introduction

DMC is a highly attractive chemical that is considered as a green chemical with applications in pharmaceutics, coatings or battery electrolytes. DMC biodegrades readily in the atmosphere, and is non-toxic and noncorrosive to metal. Several studies have demonstrated that the synthesis of DMC via the methanolysis reaction with urea involves two-step reaction including methyl carbamate (MC) as the first intermediate product according to the following mechanism (Huang et al., 2015):

(R1) $NH_2CONH_2(Urea) + CH_3OH \overset{K_1}{\leftrightarrow} NH_2COOCH_3(MC) + NH_3$

(R2) $NH_2COOCH_3 + CH_3OH \overset{K_2}{\leftrightarrow} CH_3OCOOCH_3(DMC) + NH_3$

(R3) $CH_3NHCOOCH_3 + CH_3OCOOCH_3 \overset{K_3}{\leftrightarrow} NH_2COOCH_3(NMMC) + CH_3OH + CO_2$

MC is produced by reaction R1 with high yield even in the absence of catalyst. However, the conversion of MC into DMC by adding methanol requires the use of a solid catalyst at high temperature and pressure achieving a DMC yield up to 54% (Huang et al., 2015). Besides, the DMC yield is affected by a third side reaction with MC to form N-methyl,methyl-carbonate (NMMC). Kongpanna et al. (2015) carried out the simulation of the urea route process with ASPEN PLUS software including reactions R1 and R2 from CO_2 and ammonia as chemical feedstock. The commercial oxidative carbonylation of methanol (ENI Process) was selected as the base case design producing about $4x10^3$ kg/h of DMC with 0.998 of purity. They concluded that ethylene carbonate route is the most promising alternative. Nevertheless, they also highlighted that the energy consumption of the urea route process could be drastically reduced through process

intensification and change of the operating conditions. Monteiro et al. (2009) compared the ethylene carbonate transesterification with the urea route including a reactive distillation (RD) column to produce DMC and using sustainability metrics in two domains gate to gate and cradle to gate. Simulation of the urea route process was carried out with HYSYS to produce about $13.5x10^3$ kg/h of DMC in a RD column but omitting reaction R3. The ethylene carbonate transesterification showed better material and energy index as well as ecoefficiency. Later, Wang et al. (2010) developed a non-equilibrium model to simulate the RD column to synthetize DMC but also neglecting reaction R3. Experiments were carried out in a bench scale RD column and they were in good agreement with simulation results. Vazquez et al. (2018) run simulations with ASPEN Plus software including a RD column for synthetizing DMC considering the whole three reactions. Urea and methanol were the initial raw materials for a manufacturing production capacity of $74x10^3$ t/y of DMC. The authors concluded that urea route process is an environmental friendly alternative without any environmental assessment. According to our knowledge, not much rigorous multicriteria methods as life cycle assessment (LCA) have been used for the sustainability evaluations of the urea route. This work focuses on the assessment of the environmental performance of the urea transesterification pathway in the light of LCA. The entire process with RD column is simulated using ProSimPlus® and the results from the mass and energy balance are used as foreground data for LCA. The main goal is to investigate this promising pathway from an environmental point of view and to highlight hotspots. To our knowledge, this work is the first to assess environmental performance of this DMC production alternative using LCA from cradle to gate.

2. Process simulation

2.1. Physicochemical properties and thermodynamic analysis

Simulation of the entire flowsheet requires the knowledge of the properties of the involved pure compounds as well as the thermodynamic information about the phase's equilibrium and the equilibrium constant or kinetic of the reactions. Group contribution methods is a suitable solution when experimental values are missing even for the computation of the variation of the Gibbs energy of the reactions ($\Delta_r G$) from the standard formation enthalpy and the standard absolute entropy of pure compounds.

2.1.1. Physicochemical properties database

Required physicochemical properties for the process simulation including CO_2, ammonia, urea, methanol and DMC are available in DIPPR database. MC and NMMC are missing. Many experimental data are available in NIST webBook for MC. However, NMMC has been scarcely studied and even the boiling point was hard to find. Hence, all required properties were computed from group contribution methods available in ProSimPlus®.

2.1.2. Equilibrium reactions

Since urea decomposes easily to MC and ammonia at temperature higher than 400K (Huang et al., 2015), in this work we use the kinetic model proposed by Zhao et al. (2012), where the Arrhenius parameters were computed from batch experiments without catalyst in the temperature range 403 – 433K. The Arrhenius frequency factor ($L.mol^{-1}.s^{-1}$) and the activation energy (kJ/mol) is $1.20x10^6$ and 84.7, respectively. Kongpanna et al. (2015) and Vazquez et al. (2018) obtained a model for K_1 and K_2 vs temperature by fitting predicted values of the ($\Delta_r G$) at different temperatures using the Benson method in gas state (Poiling et al. 2001). This strategy seems not to be suitable because the reactions take place into the liquid phase. Similar to Monteiro et al. (2009), we use the kinetic model proposed by Wang et al. (2007) for reaction R2 based on experimental kinetic data

with the solid ZnO catalyst at temperatures between 423 – 473K. For the forward R2, the Arrhenius frequency factor ($g^{-1}.L.mol^{-1}.s^{-1}$) and the activation energy (kJ/mol) are $1.10x10^3$ and 101, respectively, while for the reverse reaction, the respective values are $1.464x10^{-3}$ and 49. Most of kinetic studies of the reaction R2 (Huang et al., 2015) have shown that there is an optimal residence time between 5 - 10 hours at temperature of 443 – 453K. The average yield of DMC is between 35-55% whereas NMMC yield varies from 2 to 12% depending on the catalyst. Vázquez et al. (2018) underlined that this residence time is unreachable in a real RD column. Hence, we also keep the assumption that the equilibrium is reached in the every reactive plate. An equilibrium constant K_2 model was fitted from the kinetic model proposed by Zhao et al. (2012):

$$K = 158.5 - 1.7027 * T + 0.0068 * T^2 - 1.10^{-5} * T^3 + 8.10^{-9} * T^4 \quad (1)$$

Similar to Vázquez et al. (2018), the extension of reaction R3 was set at 4% of MC yield.

2.1.3. Vapor – liquid equilibrium

The DMC synthesis process involves seven compounds: ammonia, CO_2, urea, methanol, MC, DMC and NMMC. The maximum reaction temperature at normal pressure is limited by the boiling point of methanol (337.66K) and DMC (363.45K). The plug reactor for carrying out R1 and the RD column works at high pressure because the optimal reaction temperature exceeds 363.45K. Similar to previous works, the non-ideality in the liquid phase was only considered in the simulation study. There is a minimum boiling azeotrope methanol – DMC that boils at 337.35K with a methanol molar fraction of 0.85. The increasing of the pressure up to 16 atm allows increasing of the methanol purity up to 0.9625. Wilson thermodynamic model was chosen using the binary interaction parameters available in Wang et al. (2007). Binary ideal mixtures were set when missing binary parameters because the boiling temperature difference is higher than 30°C.

2.2. Process simulation results

Gate to gate domain process is simulated using ProSimPlus®. Figures 1.(a) and (b) display the final optimal flowsheet for the MC production in a plug reactor, the RD column to synthetize the DMC and the NMMC and the subsequent downstream process to produce DMC at 0.998 of mass fraction. The optimal conditions to reach 100% of conversion in the plug reactor are set. A sensitivity analysis was carried out to determine the optimal pressure for the RD column and the distillation columns of the downstream section (see Figure 1. (b)) where the heat duty, the total number of trays and the position of the feeds were set as key operating variables. The SPEC facility in ProSimPlus® software was used to optimize the reflux ratio satisfying the required purity constraints of each distillation column. The simulated process is similar to those proposed by Vázquez et al. (2018) but making some significant modifications. In the first section, the ammonia is separated with a distillation column instead of a flash separation. In the second section, the bottom product of RD column is recycled to the RD column. The DMC is separated from the methanol with only one distillation column at P =16 atm with a recovery yield of 99.88%. The conversion from MC to DMC in the RD column reached 94.7%.

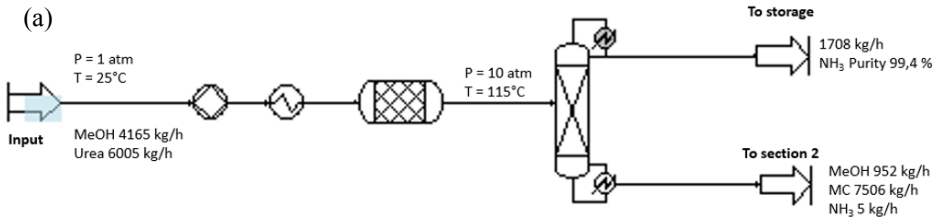

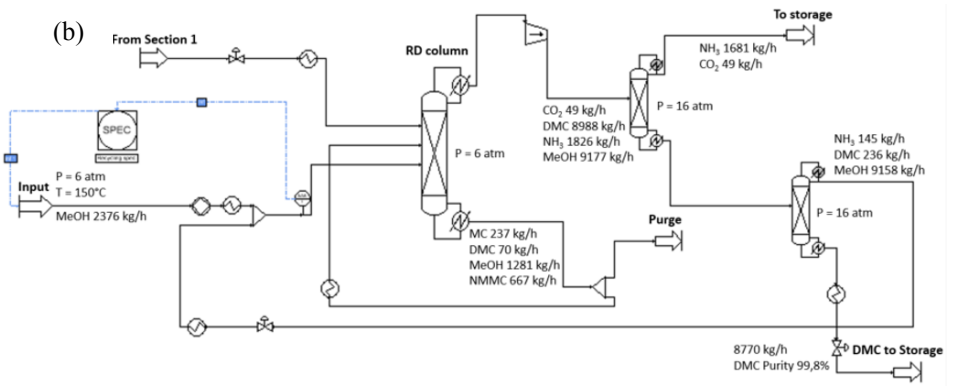

Figure 1. (a) Section 1: MC production and separation from the urea methanolysis (b) Section 2: DMC synthesis in the RD column and two distillation columns for DMC purification.

3. Environmental Assessment

The life cycle assessment (LCA) study is carried out in accordance with the ISO 14040/44 methodology (ISO, 2006a/b). SimaPro v8.5.0.0 Developer is used for the LCA modeling.

3.1. Goal and scope of the study

The system studied is described in the previous part about the process. The main goal of the study is to assess environmental performance of an emerging process of DMC production. The functional unit is the production of 1kg of DMC with a purity > 99% (molar). Hotspot analysis is performed to understand which part of the process has the higher impact and to identify opportunities of improvement. This study is conducted from cradle (raw material) to gate (DMC production). The geographical scope considers that the DMC production stems from a company located in France. The temporal scope considers the short-term horizon. The system boundaries comprise infrastructure and functioning: raw materials (extraction and production), utilities (production and use), process unit operations, transport, wastes end of life and avoided impacts link to co-products. The process tree is presented Figure 2.

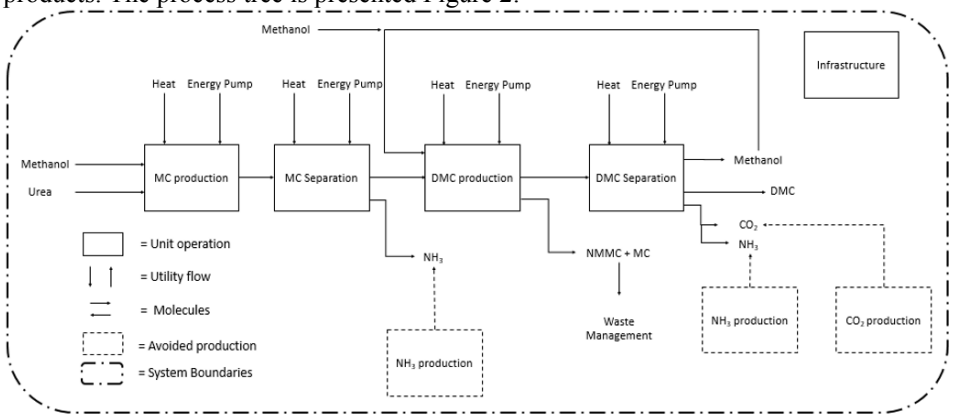

Figure 2. Process tree of DMC production

3.2. Life cycle inventory

Foreground inventory data come from process simulation. Infrastructures are taken into account according to Althaus et al. (2007) recommendations. Direct emissions are

calculated according to Hischier et al. (2005) recommendations. Background data are provided by Ecoinvent v3.4, Cut-Off database.

3.3. Life cycle impact assessment (LCIA)

ReCiPe Midpoint (H) 2016 v1.13 impact assessment method is chosen to calculate the following environmental impacts: Climate change, Ozone depletion, Particulate matter formation, Photochemical oxidant formation, Terrestrial acidification, Marine eutrophication, Freshwater eutrophication, Fossil depletion, Metal depletion, Water depletion (EC, 2013). The impact category Ionizing radiation is added because of the use of nuclear energy in the French electricity mix.

3.4. Results and interpretation

Over the entire life cycle, "MC production" is the mayor contributor to 10 categories out of 11 (Figure 3a), mostly due to the production and supplying of Urea (Figure 3b). The second hotspot is linked to "DMC separation" accounting for 50% of the category Ionizing radiation, due to electricity consumption. Infrastructure contributes to "Freshwater eutrophication" and "Metal depletion" because of the water, steel and copper consumption. Ammonia recovered permits to avoid from 12% to 46% depending on the category considered. It underlines the importance of recovering this gas during the process. The first clear improvement opportunity raised by this hotspot analysis is the urea production, which is mainly due to required ammonia. Ammonia is produced by a reaction of nitrogen from the atmosphere with hydrogen. This hydrogen currently produced from fossil fuel could be replaced by bio-based hydrogen or hydrogen produced from water electrolysis (Ni et al., 2006). Process simulation permits to face two LCA challenges: life cycle inventory collection and scaling up of an emerging process. The comparison of our emerging process with Eni process was performed. Eni process life cycle inventory is based on Garcia-Herrero et al. (2016). The results show that our emerging urea process has lower impact for 9 categories out of 11. Two co-products, carbon dioxide and ammonia, are considered as avoided production (avoided production of liquid under pressure). NMMC and MC contained in the purge are considered as wastes (incineration).

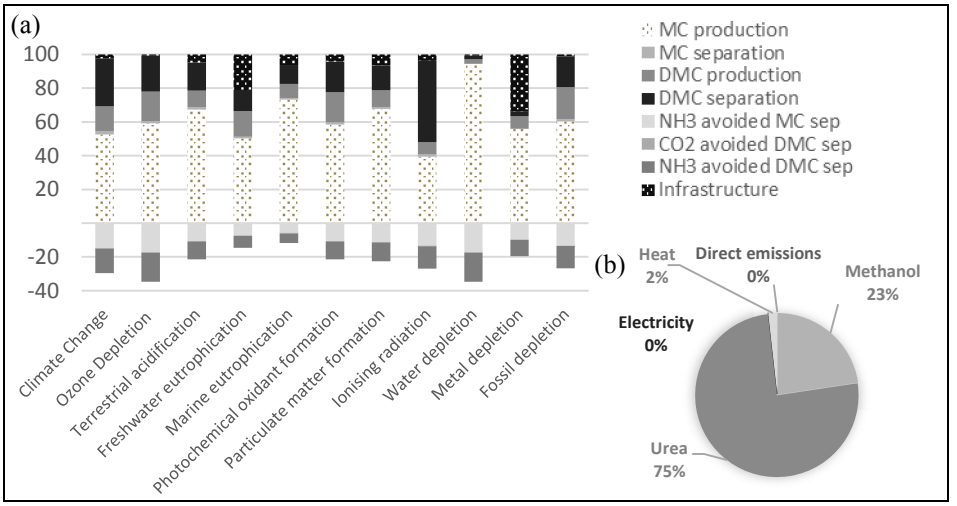

Figure 3. Environmental impacts from cradle to gate (a) Relative contributions to the corresponding impact categories of the different stages of the life cycle (b) Contribution of each foreground data to the climate change of "MC Production"

4. Conclusion

The environmental sustainability of the urea route for producing DMC has been evaluated and compared with the oxidative carbonylation of methanol (Eni process). Mass and energy balances of process are calculated by ProSimPlus simulations by considering the urea and methanol as chemical feedstock. A good conversion of 94.7% of MC is reached in the RD column. However, more experimental work have to be done for the NMMC side reaction to obtain a more realistic effect over the MC selectivity. The distillation columns are optimized to produce DMC at 0.998 of mass purity. The urea route to produce DMC appears as a promising alternative with improvement opportunities. The environmental assessment show better results than currently most used processes in Europe. The main issue in this synthesis pathway is the urea production and supply. Solutions can be proposed and further work can study these opportunities to show their environmental assets. Coupling process simulation with life cycle assessment has allowed us to face two LCA challenges, the scale up in LCA and the life cycle inventory collection.

Acknowledgments

The financial support allocated to this project by the French Ministry of Higher Education and Research (MESR) is gratefully acknowledged.

References

H.-J. Alhtaus, R. Hischier, M. Osses, A. Primas, S. Hellwag, N. Jungbluth, M. Chudacoff, 2007, Life Cycle Inventories of Chemicals, EcoInvent report No. 8

EC 2013, “Commission Recommendation of 9 April 2013 on the Use of Common Methods to Measure and Communicate the Life Cycle Environmental Performance of Products and Organisation”

I. Garcia-Herrero, R.M. Cuéllar-Franca, V.M. Enríquez-Gutiérrez, M. Alvare-Guerra, A. Irabien, A. Azapagic, Environmental Assessment of Dimethyl Carbonate Production: Comparison of a Novel Electrosynthesis Route Utilizing CO_2 with a Commercial Oxidative Carbonylation Process, ACS Sustainable Chemistry & Engineering, 4, 4, 2088-2097

R. Hischier, S. Hellweg, C. Capello, A. Primas, Establishing Life Cycle Inventories of Chemicals Based on Differing Data Availability, The Int Journal of Life Cycle Assessment, 10, 1, 59,67

S. Huang, B. Yan, S. Wang, X. Ma, Recent advances in dialkyl carbonates synthesis and applications, Chem. Soc. Rev., 2015, 44, 3079-3116

ISO, 2006a/b, ISO 14040/14044: Environmental Management – Life Cycle Assessment – Principles and framework / Requirements and Guidelines.

P. Kongpanna, V. Pavarajan, R. Gani, S. Assabumrungrat, 2015, Techno-economic evaluation of different CO2-based processes for dimethyl carbonate production, Chem. Engineering Research and Design, 93, 496-510

J.G.M-S. Monteiro, O. De Querioz Fernandes Araújo, J.L. De Medeiros, 2009, Sustainability metrics for eco-technologies assessment, Part II. Life cycle analysis, Clean Technologies and Environmental Policy, 11, 4, 459-472

M. Ni, D.Y.C Leung, M.K.H Leung, K. Sumathy, 2006, An overview of hydrogen production from biomass, Fuel Processing Technology, 87, 5, 461-472

B.E Poiling, J.M. Prausnitz, J.P O'Connel, 2001, The properties of liquid gases and liquids. Fifth edition. McGraw_Hill. Chapter 3, pages 3.14 - 3.50.

D. Vázquez, J. Javaloyes-Antón, J.D. Medrano-García, R. Ruiz-Femenia, J.A Cabellero, 2018, Dimethyl Carbonate Production Process from Urea and Methanol, Computer Aided Chemical Engineering, 43

F. Wang, J. Li, W. Zhao, F. Xiao, W. Wei, Y. Sun, 2007, Modeling of the Catalytic Distillation Process for the Synthesis of Dimethyl Carbonate by Urea Methanolysis Method, Industrial & Engineering Chemistry Research, 46, 26, 8972 -8979

W. Zhao, B. Han, N. Zhao, F. Xiao, W. Wei, 2012, Macro kinetics for synthesis of dimethyl carbonate from urea and methanol on Zn-containing catalyst, J Cent South Univ, 19, 1, 85-92

Sauro Pierucci, Flavio Manenti, Giulia Bozzano, Davide Manca (Eds.)
Proceedings of the 30th European Symposium on Computer Aided Process Engineering
(ESCAPE30), May 24-27, 2020, Milano, Italy.
http://dx.doi.org/10.1016/B978-0-12-823377-1.50018-5

Modeling and Study of Hydrodynamic flow within the Preneutralizer Reactor using CFD Approach

S. Elmisaoui[a,b], L. Khamar[a,c], S. Benjelloun[a], M. Khamar[b], J.M. Ghidaglia[a,d]

[a] *MSDA Modeling, simulation, and Data Analysis, Mohammed VI Polytechnic University, Benguerir, Morocco*

[b] *LGCE, Laboratoire du génie civil et environnement, Mohamed V University, Rabat, Morocco*

[c] *LIPIM, Laboratoire d'ingéneirie des procédés, informatique et mathématiques, ENSA-Khouribga, Sultan Moulay Slimane University, Khouribga, Morocco*

[d] *CMLA Centre des mathématiques et leurs applications, ENS Cachan, Paris Saclay University, Paris, France*

Safae.elmisaoui@um6p.ma

Abstract

Mathematical modelling and numerical simulations are widely used in the petrochemical industries for operator training, design, and process optimization. However, there is a lack of rigorous numerical modelling and simulations in the phosphate fertilizer industry. There exist many challenges in the production systems of phosphate fertilizers including (i) multiphase flows in the system involving liquids, solids or gases, (ii) particles with different size distributions, and (iii) dynamic variations in the physical properties including rheology and thermodynamic behavior.

In the current study, using well-established techniques from computational fluid dynamics, we develop a model for the numerical simulation of multiphase flows in a conditioner operation unit used in the phosphate fertilizers facilities. The proposed model deals with the first step in the process, consisting on the preneutralizer, and it uses the Reynolds-averaged Navier-Stokes equations for modeling turbulent flow in the system. The preneutralization consist on a partial reaction between ammonia and phosphoric acid. Numerical results are presented for several scenarios and we particularly show the importance of the baffles on eliminating vortices, and also their effect on the different hydrodynamic performance criteria. This approach can be used to describe the behavior of reaction systems within this type of industrial plants and the analysis of the other sub-process of the fertilizer plant is an ongoing work.

Keywords: CFD; numerical simulation; multiphase flow; turbulence; vortex.

1. Introduction

Industrial manufacturing has relied on batch operation units mainly due to regulatory requirements (Driss Z. et al., 2012). However, the use of continuous processes and unit operations would provide a high flexibility in production capacity. Stirred tank reactors are encountered operation units in matter processing as in food, pharmaceutical, and chemical industries. Various research works (Khamar L et al., 2016) have been conducted in order to provide interesting information allowing to understand the complexity of the flow behavior in stirred tank reactors. This work uses CFD simulations of a chemical reactor characterized by a non-standard design in terms of the different characteristic dimension ratios of the vessel, and the shape. The stirred reactor is used in fertilizers manufacturing process as a preneutralization operation unit allowing to produce a chemical slurry with specific physicochemical characteristics and under special operating conditions.The main goal of this paper is to study the multiphase flow and mixing within the preneutralizer; and evaluate the effect of baffling on its hydrodynamic which should improve agitation performance and chemical species mixing.

2. Conceptual model of the preneutralizer reactor

2.1. CAD model and computational approach

Using a computational fluid dynamics (CFD) software package, we had defined the computational domain equipped with four baffles spaced uniformly around the preneutralizer periphery as shown in Figure 1. The mixing system is a pitched blade turbine (Figure 1.B) with inclined blade impellers. The CAD file is developed for the total reactor (Figure 1.A), and in order to study

the hydrodynamic flow behaviour, we had activated only the part that will be full of the mixture (Figure 1.C). On the other hand, two CAD models are developed: baffled and unbaffled cases.

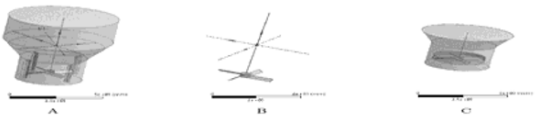

Figure 1: A: Preneutralizer geometry, B: Agitator Pitched blade turbine, C: Simulated fluid using MRF

For the study and the simulation of the agitation mechanism within the targeted equipment using CFD, the preneutralization reactor was conceptually split by two separate and adjacent zones (Figure 1.C):

- A rotor defined by a rotating zone which surrounds the agitator;
- A stator as the stable and steady zone of the rest of the preneutralizer.

Hence, in this Multiple Referential Frame (MRF) approach, the flow domain is split in two parts. The first one is around the agitator that is simulated in a rotating frame with the stirrer and the equations are solved taking into consideration a Coriolis term. For the rest of the domain, the equations are solved in the fixed frame (T. Ian, et al.,2018 and Hadane A. et al., 2019). This approach is an approximate one but it has the advantage of involving stationary calculations (fixed mesh) and therefore faster simulation time.

2.2. Domain meshing

A mesh was generated to discretize the domain into small control volumes, where the governing equations (continuity and momentum) where be approximated by numerical schemes. Figure 2 represent the tetrahedral mesh grids for the unbaffled and baffled preneutralizers. It contains near to 287 843 cells for the first case and 389 772 cells for the second. As for the CFD model, grid dependence tests were carried out to choose the appropriate grid geometry for wich the grid density does not influence the simulation results.

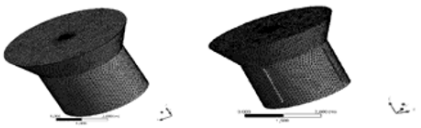

Figure 2: Meshing of the preneutralizer fluid domain (Mesh of the unbaffled preneutralizer (left), Mesh of the baffled preneutralizer (right))

3. Mathematical model and calculation setup

In the current study, we have considered that the multiphase flow behaves like an incompressible Newtonian viscous flow, and the system is isothermal.

3.1. Operational inputs of the preneutralizer

Some parameters are crucial for calculating and simulating mixing in the preneutralizer, which we summarize in the following table:

Table 1: Preneutraliser's operating parameters

Parameter	Value
Ammonia acid density (kg/m^3)	0.6894
Phosphoric acid density (kg/m^3)	1272.64
Ammonium acid viscosity (kg/m. s)	1.015 e^{-5}
Phosphoric acid viscosity (kg/m. s)	0.0203
Rotational speed of the agitator (rpm)	68

3.2. Turbulence model

The aim of turbulence modelling is to predict the physical behaviour of the turbulent flow generated in the system. A modelling method used should ensure accuracy, simplicity and computational

efficiency (Dagadu C. P. K., 2015). In order to study the flow behaviour and the mixing quality in the preneutralizer, the chosen model is based on Reynolds Averaged Navier Stokes Equations (RANS). This model is indeed adapted for the majority of industrial problems. For turbulence modelling, the K-ε RNG model is used. It is a model where the smallest eddies are first resolved in the inertial range and then represented in terms of the next smallest eddies (Ansys. Inc., Canonsburg, 2011). More details on setting the solver for simulating the preneutralizer are given in the following table 2:

Table 2: Solver setup for the hydrodynamic flow in the preneutralizer

Turbulence model	K-ε
Fluids in the stirred vessel (Preneutralizer)	Phosphoric Acid & Ammonia
Boundary conditions	Rotation MRF (68 rpm) Liquid level - free surface
Discretization - pressure	PRESTO!
Discretization - momentum	Second order upwind
Discretization	Species transport approach
Discretization-turbulent kinetic energy	Second order upwind
Discretization-turbulent dissipation rate	Second order upwind

3.3. Governing equations

The CFD software allow us to model the mixing and transport of chemical species by solving conservation equations describing convection, diffusion, and reaction sources for each component species. Multiple simultaneous chemical reactions can be modelled, with reactions occurring in the bulk phase (volumetric reactions) and/or on wall or particle surfaces. For this study we will use the transport species equation coupled to Navier Stokes equations and Turbulence equations:

(1) Mass conservation equation

$$\frac{\partial \rho}{\partial t} + \nabla.(\rho.\vec{v}) = S_m \tag{1}$$

The equation (1) is the general form of the mass conservation one and is valid for incompressible as well as compressible flows. The source S_m is the mass added to the continuous phase.

(2) Momentum conservation equation (Three-dimensional system)

$$\frac{\partial \rho.\vec{v}}{\partial t} + \nabla.(\rho.\vec{v}.\vec{v}) = -\nabla p + \nabla(\bar{\bar{\tau}}) + \rho\vec{g} + \vec{F} \tag{2}$$

With p is the static pressure, $\bar{\bar{\tau}}$ is the stress tensor, $\rho\vec{g}$ and $\vec{F}$ are respectively the gravitational body force and external body forces. For the turbulence model, as we had mentioned in section 3.2, the useful one is RNG K-ε, we have two equations to solve:

(3) Turbulent kinetic energy equation

$$\frac{\partial(\rho k)}{\partial t} + \frac{\partial(\rho.k.u_i)}{\partial x_i} = \frac{\partial}{x_j}[(\mu + \frac{\mu_t}{\sigma_k})\frac{\partial k}{\partial x_j}] + P_k - \rho.\varepsilon \tag{3}$$

(4) Turbulent dissipation equation

$$\frac{\partial(\rho\varepsilon)}{\partial t} + \frac{\partial(\rho.\varepsilon.u_i)}{\partial x_i} = \frac{\partial}{x_j}[(\mu + \frac{\mu_t}{\sigma_\varepsilon})\frac{\partial \varepsilon}{\partial x_j}] + C_{1\varepsilon}\frac{\varepsilon}{k}P_k - C^*_{2\varepsilon}\rho\frac{\varepsilon^2}{k} \tag{4}$$

Where $C^*_{\varepsilon\varepsilon} = C_{2\varepsilon} + C_v\frac{\eta^3(1-\frac{\eta}{\eta_0})}{1+\beta\eta^3}$ and $\eta = \frac{Sk}{\varepsilon}$, with S is the modulus of the mean rate of strain tensor.

(5) Transport equations: A prediction of the local mass fraction of each species (H_3PO_4 or H_2SO_4), through the solution of a convection-diffusion equation for the i_{th} species. This conservation equation takes the following general form:

$$\frac{\partial(\rho Y_i)}{\partial t} + \nabla.(\rho \vec{v} Y_i) = -\nabla.\overline{J_i} + R_i + S_i \quad (5)$$

Where R_i is the net rate of production by chemical reaction and S_i is the rate of creation by addition from the dispersed phase if it exists. For this stage of the study we don't take into account the reaction between the defined species. So, we have:

$$\frac{\partial(\rho Y_{H_3PO_4})}{\partial t} + \nabla.(\rho \vec{v} Y_{H_3PO_4}) = -\nabla.\overline{J_{H_3PO_4}} \quad (6)$$

$$\frac{\partial(\rho Y_{H_2SO_4})}{\partial t} + \nabla.(\rho \vec{v} Y_{H_2SO_4}) = -\nabla.\overline{J_{H_2SO_4}} \quad (7)$$

$$\overline{J_i} = -(\rho.D_{i,m} + \frac{\mu_t}{Sc})\nabla Y_i$$

With $D_{i,m}$ is the diffusion coefficient for species *i* in the mixture, μ_t the turbulent viscosity, and Sc_t is the turbulent Schmidt number.

(6) The seventh equation is the Energy equation, for this study we suppose that we have an isothermal system, so this one doesn't make part of the system to solve.

3.4. Boundary conditions

It is imperative to provide information on the flow at different boundaries of the flow domain. In this study, we have considered that the liquid level surface (The top of the geometry) is a symmetry surface, which mean that the free surface is assumed to be flat. This is generally the good assumption for stirred vessels with at least three baffles (Khamar et al. 2016). The agitator is divided in two parts, the first one is in the fixed reference frame and the second part is in the rotating reference frame.

4. CFD calculations and Simulation results

The CFD calculations and simulation are carried out for two cases. The first one is for the baffled preneutralizer with the characteristics mentioned before. The second case is for an unbaffled one, in order to evaluate the effect of baffles on the vortex formation.

4.1. Flow regime

Turbulence represents an important phenomenon that characterize the flow according to the value of Reynolds number (Ansys. Inc., Canonsburg, 2011). For this study Re = 3.8 10^7 which implies that the flow regime induced by the stirred is turbulent.

4.2 Type of flow induced by mechanical agitator

The analysis of the shape of the current's lines developed within the preneutralizer fluid sheath in the two studied cases (Figure 3) shows that the fluid is ejected from the blades of the agitator turbine towards the walls of the vessel and is divided into two parts. Thus, giving two loops of recirculation which develop, one below.

Consequently, it can be directly concluded that this stirrer ensures a radial flow of the mixture within the preneutralizer (Roustan M. 1997). Through a projection of the three-dimensional current lines on the longitudinal plane, we note the existence of two loops (Figure 3). A smaller one underneath the agitator turbine and relatively larger one that develops above the blades.

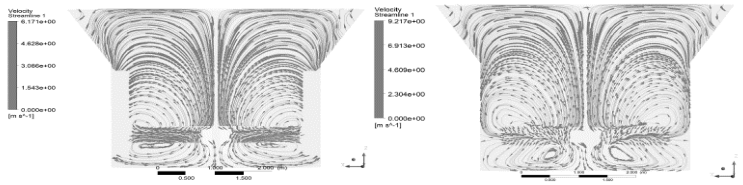

Figure 3: Streamlines inside the unbaffled (left) and baffled (right) preneutralizer

4.3 Balance of the torques exerted on the agitator

For a speed of rotation of 68 rpm, the main results from the CFD simulation are given in the following tables:

Table 3: Details of consumed power for unbaffled and baffled preneutralizer

Designation	Unbaffled (N.m)	Baffled (N.m)
Agitator	14501	27342.1102
Shaft in the static zone	0.0119	0.0186
Shaft in the MRF zone	0.0002	0.0159
Total	14501.0121	27342.1202

4.4 Power calculated using CFD

The general formula for the power is given by (Mununga L.,2003):

$$P = 2\pi NC \tag{8}$$

With N: number of rotations per minute (Hz), and C: the torque (N.m). For a speed of 68 rpm, the power calculated using the CFD are given in table 4:

Table 4: Details of consumed power for unbaffled and baffled preneutralizer

Designation	Unbaffled (N.m)	Baffled (N.m)
Agitator	103.2084	194.1232
Shaft in the static zone	$8.5230e^{-5}$	$1e^{-4}$
Shaft in the MRF zone	$1.0889e^{-6}$	0.0113
Total	103.2084	194.4661

4.5 Number of power N_p

This parameter is dimensionless, and it's based on the hydraulic power calculated before Eq. (8), using the following formula (Mununga L.,2003):

$$N_P = \frac{P}{\rho N^3 D^5} \tag{9}$$

The results of obtained using the CFD post processing tools gives a value of $N_{p\_unbf} = 0.2948$ for the unbaffled preneutralizer and $N_{p\_bf} = 0.5559$ for the baffled one. This values are similar with what is existing in the literature (Mununga L.,2003):

4.6 Pumping rate Q_p

The pumping rate is the volume flow rate of fluid that passes through the agitator turbine. Indeed, the stirrer rotating in the tank can be considered as a pump. This flow is also called the agitator pumping capacity noted Q_p From the results of the simulation $Q_{p\_unbf} = 79.72$ m^3/s, and for the baffled preneutralizer the flow is $Q_{p\_bf} = 85.97$ m^3/s.

4.7 Number of pumping N_q

It is the dimensionless formula of the pumping rate of an agitator. It depends essentially on the type of impellers and the hydrodynamic flow regime and it is given by the following expression:

$$N_q = \frac{Q_p}{ND^3} \tag{10}$$

With Q_p is the pumping flow (m^3/s) and N is the rotation speed of the stirrer (rad/s), D is the turbine diameter. The results are $N_{q\_unbf} = 0.51$ and for the baffled one $N_{q\_bf} = 0.54$.

4.8 Vortex detection

The results presented in Figure 4 shows the vortex form in the preneutralizer using the Q-criterion parameter (G. Guyot, 2014), that define the vortex as a connected fluid region with a positive second invariant. This criterion also adds a secondary condition on the pressure, requiring it to be lower than ambient pressure in the vortex.

Figure 4 : Vortex inside the baffled and unbaffled preneutralizer

The Q represents the local balance between shear strain rate and vorticity magnitude, defining vortices as areas where the vorticity magnitude is greater than the magnitude of rate-of-strain. So, these results validate the baffles effect on the vortex appearance inside stirred vessels. For the baffled case baffles inhibit the vortex formation, which increase the mixing performance. On the other hand, the deformation of the free surface in the unbaffled preneutralizer make mixing operation more difficult and less efficient.

Conclusion

In this work, a modelling study and CFD calculations of a turbulent multiphase flow carried out for a mechanically agitated industrial reactor. It is a preneutralizer, with a specific geometry, used in the phosphate fertilizer industries. The effect of baffle's presence on the hydrodynamic performances and the vortex appearance inside the preneutralizer was studied. We have found that the baffles have a significant effect on the power consumption, they represent barriers to the flow which required the double of the normally consumed power.

The high Reynolds number resulted from the simulation proves the right choice of RANS (k-ϵ) turbulence regime to model the system. Two recirculation loops are formed for the studied cases that confirm the radial flow generated by Pitched Blade turbine as known in the literature (Roustan M. 1997). Also, our calculation results affirm that baffles effectively break up the vortex generally observed in unbaffled preneutralizer. The developed CFD model is useful to understand the flow behaviour, and in identifying the key parameters that affect directly the process effectiveness.

References

Driss Z., Karray S., Chtourou W., et al. 2012, a study of mixing structure in stirred tanks equipped with multiple four-blade Rushton impellers. Archive of Mechanical Engineering, vol. 59, no 1, p. 53-72.

Khamar L. et Samrane K. 2016, the use of the CFD for the hydrodynamic flow diagnostic and study in a Phosphoric Acid Reactor. Proceedia Engineering, vol. 138, p. 369-377.

T. Ian et J. Changying. 2018, a Study of the Mixing Performance of Different Impeller Designs in Stirred Vessels Using Computational Fluid Dynamics. Designs, vol. 2, no 1, p. 10.

Handane A., Khamar L., Benjelloun S., et al. 2019, hydrodynamic study of a phosphate flotation cell by CFD approach. Chemical Engineering and Processing-Process Intensification, vol. 135, p. 190-203.

Dagadu C. P. K., Stegowski Z, Sogbye, B. J. A. Y., et al. 2015, mixing analysis in a stirred tank using computational fluid dynamics. Journal of Applied Mathematics and Physics, vol. 3, no 06, p. 637.

Fluent ansys 14.0 user's guide, 2011. Ansys. Inc., Canonsburg, PA.

Mununga L., Hourigan K., et Thompson M. 2003, numerical study of the effect of blade size on pumping effectiveness of a paddle impeller in an unbaffled mixing vessel. In: Third International Conference

G. Guyot, A. Pittion R.and A. Archer. 2014, a free surface vortex modelling with a 3D CFD comparison between an experimental case and a numerical one.

Roustan Michel. 1997, agitation et mélange : caractéristiques des mobiles d'agitation. Techniques de l'ingénieur. Génie des procédés, vol. 4, no J3802, p. J3802. 1-J3802. 10.

Sauro Pierucci, Flavio Manenti, Giulia Bozzano, Davide Manca (Eds.)
Proceedings of the 30th European Symposium on Computer Aided Process Engineering (ESCAPE30), May 24-27, 2020, Milano, Italy.
http://dx.doi.org/10.1016/B978-0-12-823377-1.50019-7

Modelling and Optimization of a Multi-regional Hydrogen Supply System: a Case Study of China

Tianxiao Li,[a]Pei Liu,[*] Zheng Li

Department of Energy and Power Engineering, Tsinghua University, Beijing, 100084, China

liu_pei@tsinghua.edu.cn

Abstract

Hydrogen is likely to be widely used in the future due to its great potential to reduce carbon emissions. Planning and operation of a hydrogen supply system with multiple generation and transmission technologies, multiple consumers, and large infrastructure among regions are challenging tasks. Seasonal fluctuation of generation and demand would further make the problem more complex. In this paper, a long-period, multi-region and monthly-scale optimization model is developed, and China is taken as a case study. The optimal planning and operation strategy of China's hydrogen supply system before 2050 could be obtained by minimizing the overall system cost. Two scenarios are provided describing coal-based and power-based generation pathways. The overall costs in the power-based pathway is 2.4 times than the coal-based pathway due to higher cost of power. If zero carbon emissions are required, the economic balance point of two pathways would be when CCS cost is 525 yuan/tCO2. Furthermore, system planning is quite different in two pathways. Generation capacity would concentrate more in North China in the coal-based pathway, and nationwide pipeline networks are required in the power-based pathway.

Keywords: Hydrogen, Modelling, Optimization, Planning, China.

1. Introduction

Hydrogen is considered as a sustainable, clean and low-carbon energy carrier, and would have an important role in global low-carbon development. If hydrogen is widely used, a hydrogen energy supply system will be required in the future.

Planning and operation of a hydrogen supply system would be challenging. Firstly, multiple generation resources, transmission technologies, infrastructure and end-consumer in multi-regions are integrated in the supply system. Secondly, hydrogen generation and demand would fluctuate hourly and monthly, when hydrogen is generated from renewable resources. Thirdly, energy infrastructure requires large quantity of investment and a long construction period, which makes it difficult to maintain a high usage rate and secure economic return.

The planning of a hydrogen system in a long period has been studies in many studies, considering multi-regions and multiple resources. A linear programming model was developed to design the hydrogen delivery system for transportation demand towards 2040 in South Korea (2012). Almansoori, A. and A. Betancourt-Torcat (2016) developed a 16-region Mixed Integer Linear Programming (MILP) model and obtained the optimal layout of the generation capacity, storage facility and pipelines of hydrogen in Germany. Geographical Information System (GIS) method was also applied to develop planning models solving spatial issues (Baufume et al., 2013).

The planning of hydrogen supply systems could be further improved in two aspects. Firstly, intertemporal factors are not considered in most planning models, where monthly fluctuation of hydrogen demand and generation from renewable resources have great impacts on system layout. Li et al. (2019a) reviewed planning models for hydrogen systems and pointed out that integrating intertemporal factors into long-period planning would improve the planning outcome. Secondly, fossil-based hydrogen generation is neglected in most studies, which could be low-carbon when integrating carbon capture and storage technology. The difference between power-based and fossil-based pathway has not been pointed out.

In this paper, a long-period, multi-regional and monthly mathematical model of a hydrogen supply system is developed, and China is taken as a case study. China is facing duel challenges of more energy and low carbon. On the one hand, it is estimated that China's total energy demand would keep increase at an average rate of 1.5 % towards 2040 (BP, 2019). On the other hand, policy targets are set that non-fossil energy consumption would account for 50 % in 2050 (Commission, 2016). Hydrogen Industrial Technology Innovation Alliance of China (2019) made a positive estimation that hydrogen would account 10 % in final use in 2050 in China. The location of energy resources varies huge across the country, and renewable resources varies greatly within a year, which make planning and operation of China's hydrogen supply system more complicated. Therefore, in this model, monthly fluctuation of demand and power-based generation are described regionally. Two scenarios are set up to analyze the difference between power-based and coal-based generation pathway, assuming that hydrogen will account for 10 % in final consumption in 2050. This paper is organized as follows. In Section two, the methodology and scenario set are illustrated. In Section three, results are presented and discussed. In Section four, main conclusions are summarized.

2. Methodology and scenarios

2.1. Modelling framework

China Regional Hydrogen Supply System Optimization Model (CRHSSOM) includes 30 regions in China, and the planning period covers from 2019 to 2050. The input of CRHSSOM includes geographical data, cost data, technology choice as well as assumptions of economic growth, intensity decrease and hydrogen shares. The output includes monthly and regional hydrogen demand, and the optimal layout of the hydrogen supply system.

Hydrogen can be generated from eight resources in CRHSSOM, namely coal, natural gas, hydropower, nuclear power, onshore wind power, offshore wind power, solar power, and grid power, which describes generation without self-owned power plants. Hydrogen can be transmitted by pipeline and road, or stored in storage facility, to meet hydrogen demand.

CRHSSOM comprises of two parts, namely demand forecast and system planning. The demand forecast part generates monthly hydrogen demand, based on assumptions of economic growth, intensity decrease and hydrogen shares. The system planning part obtains the optimal layout of the hydrogen supply system applying the superstructure modelling method.

2.2. Mathematical model

The Mixed Integer Liner Programming (MILP) is applied to describe the hydrogen supply system. The input parameters are hydrogen demand, which is generated first, resources, transportation distance, geographical location and the cost in the supply chain. Yearly hydrogen generation capacity, pipeline transmission capacity and storage

capacity are design variables. Monthly hydrogen generation, transmission and storage are operational variables. Equality constraints describe the monthly supply-demand balance in each region. Inequality constraints comprise of resources limitation, geographical limitation and infrastructure limitation. Objective function indicates the overall supply cost in a long period. The notation is listed below, and subscripts $e, r(rr), t, m$ represent generation technologies, regions, year and month, respectively.

2.2.1. Demand forecast and equality constraints

Hydrogen demand is forecast in each region and each month, as shown in Eq.(1). Monthly fluctuation of demand in each region refers to fluctuations of natural gas (Li et al., 2019b). Total hydrogen supply comprises of domestic production, net import from other regions, and net reduction of storage, as shown in Eq.(2).

$$D_{r,t,m} = GDP_{r,t} \times ID_{r,t} \times HS_{r,t} \times MF_{r,m} \tag{1}$$

$$D_{r,t,m} = \sum_{e} ge_{e,r,t,m} + \sum_{rr} (tp_{rr,r,t,m} - tp_{r,rr,t,m} + tr_{rr,r,t,m} - tr_{r,rr,t,m}) + (bs_{r,t,m} - es_{r,t,m}) \tag{2}$$

2.2.2. Inequality constraints

Resources limitation indicates that hydrogen generation could not exceed its resources, as shown in Eq.(3). Yearly renewable resources come from a power system planning model of China, considering the expansion capability of power plants (Chen et al., 2019). Monthly renewable resources are generated from historical data in 2018, describing seasonal power generation fluctuation of hydropower, wind power and solar power (Statistic, 2019). Hydrogen generation capacity, pipeline capacity and storage capacity would limit hydrogen generation, transmission and storage, as shown in Eq.(4) – Eq.(6). Geographical limitation indicates that hydrogen could be transmitted only between adjacent regions, as shown in Eq.(7) – Eq.(8). Binary variables $b_{r,rr}$ are applied to describe the location of two regions. It would equal to 1, if two regions are adjacent, otherwise it would be 0.

$$R_{e,r,t,m} \geq ge_{e,r,t,m} \tag{3}$$

$$ge_{e,r,t,m} \leq \sum_{t \leq t0} ing_{e,r,t} / 12 \tag{4}$$

$$tp_{r,rr,t0,m} \leq \sum_{t \leq t0} inp_{r,rr,t} / 12 \tag{5}$$

$$es_{r,t,m} \leq \sum_{t \leq t0} ins_{r,t} \tag{6}$$

$$-L \times b_{r,rr} \leq tp_{r,rr,t,m} \leq L \times b_{r,rr} \tag{7}$$

$$(b_{r,rr} - 1) \times L \leq trt_{r,rr,t,m} \tag{8}$$

Table 1 Parameters

Symbol	Meaning and unit	Symbol	Meaning and unit
$DP_{r,rr}$	Distance by pipeline *km*	FC_e	Carbon factor *tCO2/t or bcm*
$DR_{r,rr}$	Distance by road *km*	$GF_{e,t}$	Fuel use *bcm/t or bcm or kwh*
$D_{r,t,m}$	Demand *bcm*	CTX	Transmission cost *yuan/(bcm*km)*
$GDP_{r,t}$	GDP *yuan*	$CG_{e,t}$	Generation capacity cost *yuan/(bcm/y)*
$ID_{r,t}$	Intensity *bce/yuan*	CP_t	Pipeline investment cost *yuan/km*
$HS_{r,t}$	Hydrogen share *%*	CS_t	Storage facility cost *yuan/bcm*
$MF_{r,m}$	Monthly factor	$CF_{e,r,t}$	Fuel cost *yuan/ton or bcm or kwh*
$R_{e,r,t,m}$	Resources limitation	DIS	Discount rate
CC_t	Carbon cost *yuan/t*		

Table 2 Variables

Symbol	Meaning and unit	Symbol	Meaning and unit
$ge_{e,r,t,m}$	Generation *bcm*	$ins_{r,t}$	Storage investment *bcm*
$tp_{r,rr,t,m}$	Pipeline transmission *bcm*	tct_t	Total transmission cost *yuan*
$tr_{r,rr,t,m}$	Road transmission *bcm*	tci_t	Total investment cost *yuan*
$bs_{r,t,m}$	Store at 1st *bcm*	tcf_t	Total fuel cost *yuan*
$es_{r,t,m}$	Store at 30th *bcm*	tcc_t	Total carbon cost *yuan*
$ing_{e,r,t}$	Generation investment *bcm/y*	c	Overall cost *yuan*
$inp_{r,rr,t}$	Pipe investment *bcm/y*		

2.2.3. Objective function

The objective function describes the overall costs during a long period, including transmission cost, infrastructure investment cost, fuel cost and carbon cost, and the overall costs could be calculated using a discount rate, as shown in Eq.(9) – Eq.(13).

$$c = \sum_t ((tct_t + tci_t + tcf_t + tcc_t) / (1 + DIS)^{t-2019}) \tag{9}$$

$$tct_t = \sum_{r,rr,m} (tp_{r,rr,t,m} \times DR_{r,rr} \times CTP + tr_{r,rr,t,m} \times DR_{r,rr} \times CTR) \tag{10}$$

$$tcf_t = \sum_{e,r,m} ge_{e,r,t,m} \times GF_{e,t} \times CF_{e,r,t} \tag{11}$$

$$tci_t = \sum_{e,r} ing_{e,r,t} \times CG_{e,t} + \sum_{r,rr} inp_{r,rr,t} \times DR_{r,rr} \times CP_t + \sum_r ins_{r,t} \times CS_t \tag{12}$$

$$tcc_t = \sum_{e,r,m} ge_{e,r,t,m} \times GF_{e,t} \times FC_e \times CC_t \tag{13}$$

2.3. Scenarios

Basic assumptions are set in Table 3, and hydrogen would account for 10 % in total energy demand in 2050. Two scenarios are set, which are coal-based scenario and power-based scenario, by setting zero carbon price and high carbon price respectively.

3. Results and discussion

3.1. Costs

The overall costs and composition are shown in Figure 1. Over costs in the power-based scenario would be 2.4 times that of the coal-based scenario, and the fuel cost is the main reason. In the coal-based scenario, accumulated carbon emissions would be 28.88 bt, which indicates that the coal-based pathway would be more economic, if average cost of carbon capture and storage is less than 525 yuan/tCO_2.

3.2. Generation capacity

Generation technology would have great impacts on generation capacity distribution. Results show that generation capacity would concentrate more in North China, where coal resources are abundant, and coal is cheaper, whist it would concentrate more in Southwest and Northwest China, where renewable resources are abundant in the power-based scenario, as shown in Figure 2.

3.3. Pipelines and storage facility

National pipeline networks are required in the power-based scenario as shown in Fig.3, and would be helpful to manage monthly fluctuation. Therefore, total storage capacity would be required less, which is 26.6 bcm in 2050. On the country, pipelines networks are required mainly in North China, as shown in Fig.4, whilst other regions manage monthly fluctuation using their own storage facilities. In view of that, more storage capacity would be required in the coal-based scenario, which is 35.0 bcm in 2050.

Table 3 Basic assumptions

Year	2020	2030	2040	2050
GDP growth rate *%*	6.54	4.56	2.67	1.03
Energy intensity *tec/10^4 yuan*	0.493	0.350	0.253	0.188
Total energy demand *btce*	4.99	6.05	6.16	5.45
Hydrogen share *%*	0.3	3.3	6.3	10.0
Hydrogen demand *Mtce*	14.96	199.54	387.95	544.60

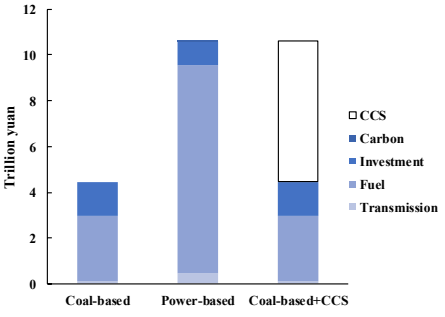

Figure 1 Overall costs and composition

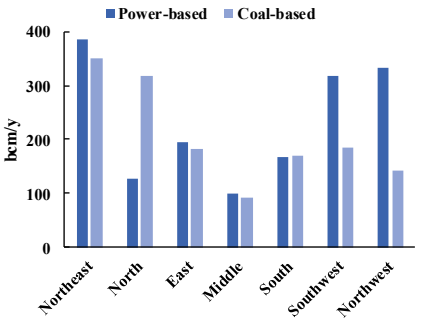

Figure 2 Generation capacity distribution

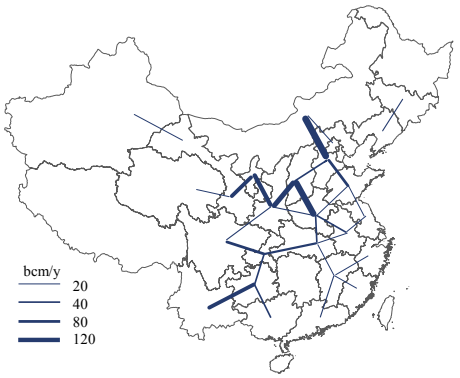

Figure 3 Pipelines in the power-based scenario

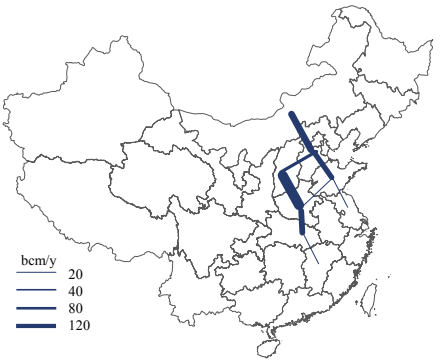

Figure 4 Pipelines in the coal-based scenario

4. Conclusions

In this study, China Regional Hydrogen Supply System Optimization Model is developed, and two scenarios are designed describing coal-based and power-based pathways. The overall costs in the power-based pathway are 2.4 times that of coal-based mainly due to fuel cost. The economic balance point of two pathways is when CCS cost is 525 yuan/tCO2. In the coal-based pathway, generation capacity concentrates more in North China, and pipelines are required mainly in North China. More storage capacity is required because of self-sufficiency in most regions. In the power-based pathway, nationwide pipelines are required, and less storage capacity is required.

Acknowledgement

The authors gratefully acknowledge the support by The National Key Research and Development of China (2018YFB0604301), National Natural Science Foundation of China (71690245) and the Phase Ⅲ Collaboration between BP and Tsinghua University.

References

Almansoori, A., Betancourt-Torcat, A., 2016. Design of optimization model for a hydrogen supply chain under emission constraints - A case study of Germany. Energy 111, 414-429.
Baufume, S., Grueger, F., Grube, T., Krieg, D., Linssen, J., Weber, M., Hake, J.-F., Stolten, D., 2013. GIS-based scenario calculations for a nationwide German hydrogen pipeline infrastructure. International Journal of Hydrogen Energy 38, 3813-3829.
BP, 2019. BP Energy Outlook 2019 edition.
Chen, S.Y., Liu, P., Li, Z., 2019. Multi-regional power generation expansion planning with air pollutants emission constraints. Renewable & Sustainable Energy Reviews 112, 382-394.
Hydrogen Industrial Technology Innovation Alliance of China, 2019. China's hydrogen energy and fuel cell industry.
National Development and Reform Commission, 2016. Strategies on energy production and consumption (2016-2030).
Gim, B., Boo, K.J., Cho, S.M., 2012. A transportation model approach for constructing the cost effective central hydrogen supply system in Korea. International Journal of Hydrogen Energy 37, 1162-1172.
Li, L., Manier, H., Manier, M.-A., 2019a. Hydrogen supply chain network design: An optimization-oriented review. Renewable & Sustainable Energy Reviews 103, 342-360.
Li, T., Liu, P., Li, Z., 2019b. Modelling and optimization of a natural gas supply system at a transient stage: a case study of China. BMC Energy 1, 5.
National Bureau of Statistic, 2019. Monthly power generation in 2018.

Sauro Pierucci, Flavio Manenti, Giulia Bozzano, Davide Manca (Eds.)
Proceedings of the 30th European Symposium on Computer Aided Process Engineering (ESCAPE30), May 24-27, 2020, Milano, Italy.
http://dx.doi.org/10.1016/B978-0-12-823377-1.50020-3

A Hybrid Modelling Approach to Developing Digital Twins of an Ultra-supercritical Steam Turbine Control Stage

Jianxi Yu, Pei Liu,* Zheng Li
Department of Energy and Power Engineering, Tsinghua University, Beijing, 100084, China
liu_pei@tsinghua.edu.cn

Abstract

Modelling for digital twins is a key technology in smart power plants. A control stage is a key component for pressure and flow control in steam turbines of power plants. Its modelling and simulation for digital twins are important measures for steam turbine operation diagnosis and optimization. However, sequential operation modes of valves in a control stage result in dramatic changes in thermal and mechanical behaviours of the control stage, and modelling the change in behaviours still remains a challenge due to lack of measurements. In this paper, a hybrid modelling method based on the first-principle mechanism and actual operation data is proposed. Inlet flow of a control stage are obtained by calculating flow coefficient at the full range of sequential operation of valves. Then, characteristic functions of a control stage are obtained using the first-principle mechanism. In order to verify the reliability of the proposed method, a control stage of an ultra-supercritical steam turbine with typical sequential valves operation mode is modelled and simulated. Results show that the average value of the simulation relative error is less than 1%, which proves that the method has high simulation accuracy and reliability and lays a foundation for application of digital twins in smart power plants.

Keywords: Control stage; Sequential valve; First-principle mechanism; Digital twins

1. Introduction

Digital twins based on industrial big data plays an increasingly important role in industries with the advancement of information technology. It is a combination of physical principle and data science, which provides us precise and comprehensive guidance in design, operation and maintenance of manufactures (Tao et al., 2019). In power generation domain, digital twins are a key technology of smart power plant with operation diagnosis, optimization and smart control (Hua et al., 2019). Therefore, the development of power plant modelling and simulation for digital twins is very significant for promotion of smart power plants.

A control stage is one of the key components of a steam turbine worth further studying in a higher integration target of renewable power. A steam turbine is one of the main units of thermal power plant, the main components of which comprise valves, stages, pipes, heat exchangers and condensers. Its thermal characteristics have a critical impact on the overall cycle of power generation. Besides, the power output of a steam turbine need to be adjusted quickly due to continuous integration of renewable energy (Li and Wang J., 2018). A control stage is a key component which determines the power output of steam turbine. Therefore, quantitative study of its actual operating characteristics is significant for the performance monitoring and optimization of power plant. However, it still remains

a challenge to establish the model of control stage based on digital twins due to sequential operation modes of valves and lack of measurement data. The sequential operation modes result in dramatic changes in thermal and mechanical behaviours of the control stage, which is difficult to quantity the changes with insufficient measurement data.

There are many studies which focus on steam turbine models for digital twins, however, lacking models of control stages of ultra-supercritical steam turbines which conform to physical mechanisms. Yu et al. (2019) developed a control stage model of a subcritical steam turbine rely on operation data, and simulation of digital twins was obtained through this model. Zhong (2014) established models of main components of a supercritical steam turbine using operation data, then obtaining simulation results of digital twins for online monitoring. The internal physical process of control stage was neglected and summarized into a quadratic function in this study, which cannot reflect the physical mechanisms of the control stage. Zhu (2015) established a modified model of the control stage of a supercritical steam turbine in Ebsilon software, which derived a linear function for simulation of digital twins. But the influence of valve opening degree on power output was neglected, which overshadowed the utility of the model. Zheng Y. (2018) established a big data model of thermal power plants for operation optimization based on pure data method, which lacked component models and cannot reflect actual operating characteristics. Despite these studies, a model of the control stage of ultra-supercritical steam turbines which can quantify its actual operating characteristics is rather lacking.

In this paper，a hybrid modelling method based on first-principle mechanism and actual operation data for digital twins is proposed. The paper is organized as follows. Modelling methodology is illustrated in Section 2. A case study and results are presented in Section 3. Some conclusions are summarized in Section 4.

2. Methodology

2.1. Flow calculation of sequential valves

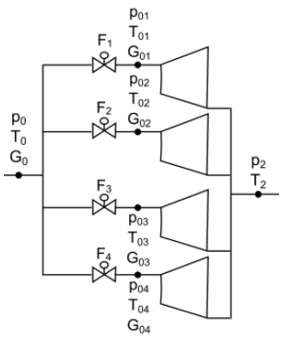

Figure 1 Overall structure with data illustration of a control stage system

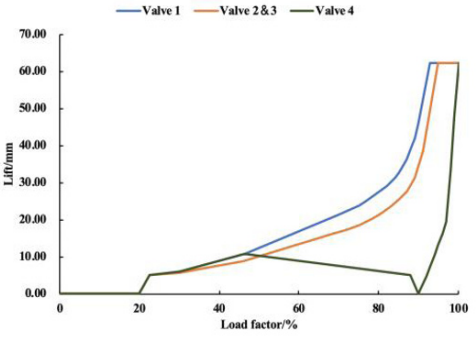

Figure 2 Typical operation curves of sequential valves of ultra-supercritical steam turbines

Four high-pressure control valves are in front of a control stage which operate at certain modes. Figure 1 illustrates the control stage system consisting of four valves, four groups of nozzles and moving blades. Figure 2 shows typical operation curves of the four valves at sequential valve mode. The sequential valves are opened and closed in a certain order, regulating the flow and pressure in front of a control stage.

It's difficult to obtain the flow of sequential valves due to lack of measurement data. The main steam is separated through the four valves and then enter into corresponding group of nozzles. The only flow data we can get from measurement is the main steam. Although there are various formulas to calculate the theoretical flow of valves, flow characteristics

of valves are required to obtain the actual flow. However, the flow characteristics of sequential valves are not available through experiment. So a calculation method rely on operation data is necessary.

We calculate the theoretical flow of the sequential valve on the analogy of nozzles, as shown in Eq.(1)- Eq.(3) (Xiao et al., 2008), where p_0 and p_{0i} is the inlet and outlet pressure of valve i, respectively. v_0 is the inlet specific volume. A_{Vi} is the opening area of valve i. ε_{cr} is the critical pressure ratio of steam flow.

$$G_{0i,t} = 0.648\beta_i A_{Vi}\sqrt{\frac{p_0}{v_0}} \tag{1}$$

$$\beta_i = \sqrt{1-\left(\frac{\varepsilon_{Vi}-\varepsilon_{cr}}{1-\varepsilon_{cr}}\right)^2} \tag{2}$$

$$\varepsilon_{Vi} = \frac{p_{0i}}{p_0} \tag{3}$$

After calculating the theoretical flow of each valve, it is also necessary to obtain flow coefficient to match the actual flow. Flow coefficient of valves are determined by lift of valve core and fluid state (Wang Y. and Zheng Z., 2018). Since the structure of sequential valves are identical, and the influence of lift of valve core on flow is already contained in the opening area A_{Vi} in Eq.(1). Besides, the valves have the same inlet steam state under the same working condition. Therefore, we regard flow coefficient of each valve under the same conditions as equal. Then we can calculate the actual flow of each valve using Eq.(4)-Eq.(5), where G_0 is the measurement flow of main steam.

$$\mu = \frac{G_0}{\sum_i G_{0i,t}} \tag{4}$$

$$G_{0i} = \mu G_{0i,t} \tag{5}$$

2.2. First principles models of mechanisms

2.2.1. Flow characteristics model

For common stages, Flugel formula can be used to quantify the mathematical relationship between pressure and flow (Cao., 1991). Zhong (2014) derived flow capacity coefficient φ and reduced flow G' from flugel formula, which are used in the model of common stages. As for control stages, the definitions of φ and G' for each group of nozzles are shown in Eq.(6)-Eq.(7), where T_{0i} is the outlet temperature of valve i, p_2 is the outlet pressure of control stage.

$$\varphi_i = \frac{G_{0i}\sqrt{T_{0i}}}{\sqrt{p_{0i}^2 - p_2^2}} \tag{6}$$

$$G_i^{'} = \frac{G_{0i}\sqrt{T_{0i}}}{p_{0i}} \tag{7}$$

Flow characteristics of control stages change as the opening degree of sequential valves change. We can obtain the change of characteristics through quantifying the relationship between flow capacity coefficient and reduced flow. Further more, the characteristics of each group of nozzles interact with each other due to the shared moving blades of control stages. Therefore, the first-principle mechanisms of flow model of control stages are reduced flow of all nozzles.

2.2.2. Efficiency characteristics model

The main loss of control stages occurred in the moving blades, which is the characteristics of efficiency model. Moving blades reduced enthalpy rise can reflect the efficiency characteristics of control stages, and the definitions are shown in Eq(8) -Eq.(10) (Yu et al., 2019), where h_2 is outlet enthalpy of control stages, h_{1i} is inlet enthalpy of moving blades.

$$\Delta h_b^{'} = \frac{\Delta h_b}{\varepsilon} \tag{8}$$

$$\Delta h_b = \sum_i \frac{G_{0i}}{G_0}\left(h_2 - h_{1i}\right) \tag{9}$$

$$\varepsilon = \frac{p_2}{p_0} \tag{10}$$

Reduced flow is one of the dominant factor which determines efficiency of common stages (Zhu., 2015). For control stages, the efficiency is determined by all groups of nozzles and moving blades. So the first-principle mechanisms of efficiency model of control stages are reduced flow of all nozzles.

2.3. Characteristic functions of first principles models

We figure out characteristic functions which are the quantitative relationship between characteristics and the first-principle mechanisms using actual operation data. The form of characteristic functions of flow and efficiency model are shown in Eq.(11) - Eq.(12) according to the analysis in section 2.2. Then the parameters of the characteristic functions are calibrated from the actual operation data.

$$\varphi_i = a_{i0} + a_{i1}G_1^{'} + a_{i2}G_2^{'} + a_{i3}G_3^{'} + a_{i4}G_4^{'} \tag{11}$$

$$\Delta h_b^{'} = b_0 + b_1G_1^{'} + b_2G_2^{'} + b_3G_3^{'} + b_4G_4^{'} \tag{12}$$

3. Case study

A control stage of an ultra-supercritical steam turbine is chosen to establish the model using the method proposed in this paper. One week of operation data are used for modelling and another week for simulation.

3.1. Modelling results

3.1.1. Flow model

A group of nozzles and moving blades are considered as one stage. The flow characteristics are obtained through Eq(11) and operation data, which are listed in Table 1. The R-Square of all functions exceeds 0.9, which proves high correlation of characteristics and the first-principle mechanisms. It also demonstrates the rationality of the method to some extent.

Table 1 Characteristic functions of flow model

Function	R^2
$\varphi_1 = -251.72 + 1.2556G_1' + 1.1219G_2' - 0.6833G_3' + 0.4394G_4'$	0.9236
$\varphi_2 = -255.13 - 0.0625G_1' + 2.5242G_2' - 0.7823G_3' + 0.3940G_4'$	0.9908
$\varphi_3 = -265.97 - 0.0723G_1' + 1.1711G_2' + 0.5995G_3' + 0.4041G_4'$	0.9904
$\varphi_4 = -97.718 + 0.0151G_1' + 0.5541G_2' - 0.4710G_3' + 1.5938G_4'$	0.9970

3.1.2. Efficiency model

We have to treat all the nozzles and moving blades as a whole when it comes to efficiency characteristic since the outlet temperature of corresponding moving blades of each group of nozzles is different. The four steam streams are blended after the control stage and reach the same post-stage temperature. However, we cannot calculate the individual outlet temperatures by the post-stage temperature. Besides, what we need to focus on is not the efficiency of each group of nozzles and moving blades, but the whole.

Table 2 Characteristic functions of efficiency model

Function	R^2
$\Delta h_b' = -78.96 + 0.2035G_1' - 0.0902G_2' + 0.0520G_3' - 0.0471G_4'$	0.6707

Therefore, the efficiency characteristic of the control stage is summarized as a function obtained through Eq(12) and operation data, which is shown in Table 2. The R-Square has a certain decline compared with flow characteristic functions. Since the loss in control stages is hard to quantify precisely. It decreases the correlation of efficiency characteristic and the first-principle mechanisms. But we can see that its correlation can still be acceptable for simulation in Section 3.2.

3.2. Simulation results

The data of another week are used for simulation in order to verify the models. The post-stage pressure p_2 and temperature T_2 are calculated through the two models and then compared with the actual measurement data.

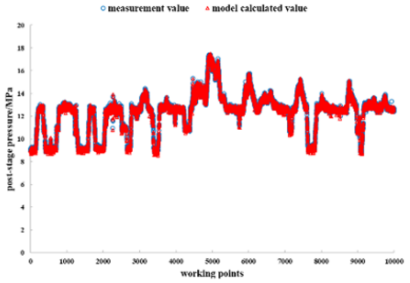

Figure 3 Comparison of measured values and simulated values of p_2

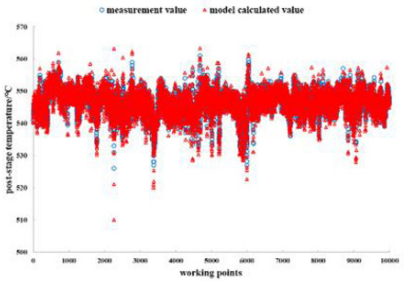

Figure 4 Comparison of measured values and simulated values of T_2

Results shown in Figure 3 and Figure 4 demonstrate that the simulated values match the actual measurement values under 10000 working points which cover full working range of the steam turbine. So digital twins models reflecting actual operating characteristics of the control stage are developed. The average value of relative error of post-stage pressure and temperature simulation is 0.53% and 0.20% respectively. It proves accuracy of the models and validity of the method, which lays a foundation for applications in smart power plants.

4. Conclusions

A hybrid modelling approach based on first-principle mechanism and operation data to the ultra-supercritical steam turbine control stage is developed in this paper. The flow characteristic of control stage is flow capacity coefficient and the efficient characteristic is moving blades reduced enthalpy rise. And the first-principle mechanisms of both characteristics are reduced flow of all nozzles. Results show that the hybrid approach can establish the models of control stage for digital twins effectively, and represent the change of operating characteristics. The average relative error of simulation is less than 1%, which proves accuracy and validity of the approach.

Acknowledgement

The authors gratefully acknowledge the support by The National Key Research and Development of China (2018YFB0604301) and the Phase Ⅲ Collaboration between BP and Tsinghua University.

References

Tao F., Qi Q.L., Wang L.H., Nee A.Y.C., 2019, Digital Twins and Cyber–Physical Systems toward Smart Manufacturing and Industry 4.0: Correlation and Comparison, Engineering, 5, 4, 653-661

Hua Z.G., Guo R., Cui X., Wang Y., 2019, Discussion and Study on Technical Route of Smart Thermal Power Plant, Thermal Power Generation, 10, 8-14

Li D.C., Wang J.H., 2018, Study of supercritical power plant integration with high temperature thermal energy storage for flexible operation, Journal of Energy Storage, 20, 140-152.

Yu J.X., Liu P., Liu S.J., Li Z., 2019, Modeling of Variable Conditions of Steam Turbine Control Stage Based on Operation Data, Journal of Chinese Society of Power Engineering, 39, 7, 541-547

Zhong X.B., 2014, The Research of High Precision Model Used for On-line Monitoring of Thermal System of Thermal Power Units, Thesis, Tsinghua University, Beijing, China

Zhu H.L., 2015, The Research of Modeling, Monitoring and Optimizing for Thermal System of Thermal Power Plant Based on Ebsilon, Thesis, Tsinghua University, Beijing, China

Zheng Y., 2018, Operation Optimization of In-service Thermal Power Plants Based on Big Data Modeling, Thesis, Tsinghua University, Beijing, China

Xiao Z.H., Sheng W., Xia Y., 2008, Turbine Equipment and System, China Electric Power Press, 13-15 (in Chinese)

Wang Y.D., Zheng Z.J., 2018, Experimental and Numerical Research on Influence of Spool Stroke on Flow Characteristics of Angle Seat Valve, Chinese Hydraulics and Pneumatics, 327, 11, 46-51

Cao Z.Q., 1991, Turbine Variable Working Condition Characteristics, Water Power Press, 36-38 (in Chinese)

Sauro Pierucci, Flavio Manenti, Giulia Bozzano, Davide Manca (Eds.)
Proceedings of the 30th European Symposium on Computer Aided Process Engineering (ESCAPE30), May 24-27, 2020, Milano, Italy.
http://dx.doi.org/10.1016/B978-0-12-823377-1.50021-5

Stochastic Analyses on Relative Viscosity of Water-in-oil Emulsions

Ana M. Sousa,* Maria J. Pereira, Henrique A. Matos

[a]*CERENA, Instituto Superior Técnico, Universidade de Lisboa, 1049-001 Lisboa, Portugal*
ana.margarida.sousa@tecnico.ulisboa.pt

Abstract

Have not only water-in-oil emulsions been a ubiquitous flow assurance challenge in oilfield operations, but also future perspectives suggest its increasing importance. In fact, as oil reserves are becoming depleted, the crude oil is becoming heavier, and the quantity of produced water is increasing. Understanding water-in-oil emulsions behaviour is crucial to design or to optimize production, transportation and refining.
This work provides a new approach to estimate water-in-oil emulsions viscosities given a certain crude oil viscosity value, since literature does not provide empirical correlations with excellent accuracy, especially for higher water fractions. Moreover, with this proposed methodology, the uncertainty metrics can be obtained by a statistical function, which best fits to the data histogram. This yields a valuable tool for matching of data to models. Stochastic analyses were developed using @RISK software and MATLAB programming. The proposed method suggests a solution for estimating the water-in-oil emulsion viscosity, which has been widely regarded as a major challenge.
Keywords: Water-in-oil emulsions (W/O), relative viscosity, waxy crude oils

1. Introduction

In a typical oil field, it is unusual to produce solely crude oil, since the presence of solids and water is frequent. This amount of water and solids, also named as Basic Sediment and Water (BSW), can cause several operational problems. Consequently, the measures to evaluate these problems need to be assessed.
The produced water can flow as 'free water' or as an 'emulsion'. At almost all the stages, emulsions can be encountered, namely in production, transportation, storage, and processing. This work will focus on the ability to describe emulsions rheological behaviour during the production phase. Through wellbores and pumps, crude oil and co-produced water are mixed, due to the high shear forces that occur. Knowing the amount of water in oil emulsions is essential to design the equipment, and to control and improve the operation.
Emulsions rheological properties and stability are dependent on the droplet size distribution, the volume fraction, the chemical composition which affects the continuous and dispersed viscosities, the shear rate, and the thermodynamic perturbations (Rønningsen 1995).
Depending on the crude oil properties and the range of operating conditions (Sousa et al. 2019b), different hydrodynamic behaviours can be found in an oil and water multiphase flow system. Although a considerable effort has been undertaken to generalize liquid-liquid models, there are not yet universal empirical correlations applicable for all types of crude oils. Fluid's global viscosity increases as emulsions are formed, attaining higher effective viscosities than the continuous oil phase. Due to the

importance of knowing the fluid characteristics to design the production and process equipment, there are several methods to estimate the fluid relevant physical properties. Nevertheless, there is not an empirical correlation able to accurately predict the emulsion viscosity for each crude oil, still. It is important to highlight these methods for emulsion viscosity estimation not only face major challenges to provide vaguely accurate values, given emulsions' properties significantly sensitive nature, but also cannot offer insights about the uncertainty of such values.

This work provides a new approach to estimate water-in-oil emulsions viscosity, given a value for the crude oil viscosity. Moreover, the uncertainty metrics were also assessed, and it was obtained by the statistical function associated with the best fitting to the histogram data. The proposed method suggests a solution for such issue, which has been widely regarded as a significant hindrance from the industry point of view. One way to integrate a myriad of factors that influence the behaviour of emulsions into the computer-aided models is using a statistical approach. The research methodology to simulate emulsions viscosities encompassed the following steps:

i. Performing experimental tests to measure the waxy crude oil viscosity, as a function of temperature;
ii. Evaluating the accuracy of empirical correlations used to calculate the emulsions viscosities against the experimental data, gathered from literature;
iii. Developing a statistical approach to characterize the emulsions relative viscosities, in order to overcome the limitations found in the existent methods;
iv. Performing stochastic analyses to evaluate the uncertainties.

2. Experimental methods

To determine the waxy crude oil viscosity, as a function of temperature, a set of experiments were performed using a Brookfield (DV-II+ Pro) viscometer, and a cryostat to guarantee the desired temperature. The experimental apparatus is presented in Figure 1. Viscosimetry tests were performed under ASTM D4402 guidelines.

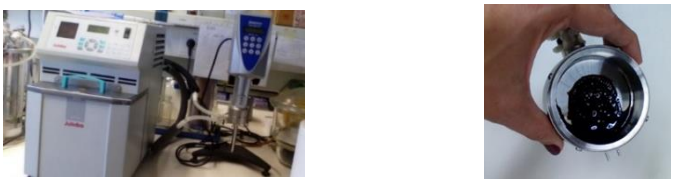

Figure 1 – Cryostat and Viscometer (left), and waxy crude oil sample (right).

The viscosity rapidly decreases with the temperature, until it reaches the Wax Appearance Temperature (WAT), as presented in Figure 2. For higher temperatures, the viscosity will be less affected by the temperature, and the wax crystals will be dissolved in the fluid.

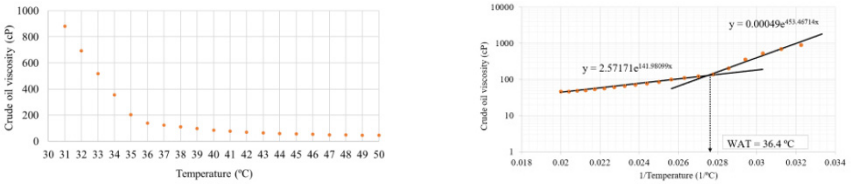

Figure 2 – Waxy crude oil viscosity as a function of temperature

The determination of the Wax Appearance Temperature resulted from intersecting two straight lines, adjusted to the attained test points, over a logarithmic scale. Eq. (1) enables to estimate the viscosity (cP) for this waxy crude oil, as a function of temperature (ºC), for this specific crude oil:

$$\mu_{oil} = \begin{matrix} 0.00049e^{453.46714\ \frac{1}{T})} & if\ T \leq WAT \\ 2.57171e^{141.98099\ \frac{1}{T})} & if\ T > WAT \end{matrix} \quad (1)$$

3. Theoretical methods

Due to the importance of knowing the fluid characteristics to design the equipment, there are several methods to estimate the viscosity of the emulsion. Since 1906, the effective viscosity of a mixture of two immiscible liquid phases has been intensively discussed. This section will present the methods available in Aspen HYSYS, which is a software that enables modelling the upstream and downstream processes and has a worldwide crude oil database (Sousa et al. 2019a) which supports modelling the problem, even if the specific crude oil physical properties are unknown. The predefined method to estimate the emulsion viscosity is defined by Eq. (2):

$$\mu_{emulsion} = \begin{matrix} \mu_{oil} \cdot e^{3.6(1-\phi_{oil})} & if\ \phi_{water} < 0.5 \\ \mu_{water} \cdot \left[1 + 2.5\phi_{oil}\left(\frac{\mu_{oil} + 0.4\mu_{water}}{\mu_{oil} + \mu_{water}}\right)\right] & if\ \phi_{water} > 0.7 \end{matrix} \quad (2)$$

Where $\mu_{emulsion}$ is the emulsion viscosity, μ_{oil} and μ_{water} are the oil and water viscosity, respectively, ϕ_{oil} is the oil fraction (1-ϕ_{water}), and ϕ_{water} is the water fraction.

Brinkman method can be selected in the Aspen HYSYS pipe segment (Brinkman 1952), and it is defined by Eq. (3):

$$\mu_{emulsion} = \begin{cases} \mu_{oil} \cdot (1 - \phi_{water})^{-2.5} & if\ W/O\ emulsion \\ \mu_{water} \cdot \phi_{water}^{-2.5} & if\ O/W\ emulsion \end{cases} \quad (3)$$

Guth and Simha method (Guth and Simha 1936) can also be chosen in the Aspen HYSYS pipe segment, and it is described by Eq. (4):

$$\mu_{emulsion} = \begin{cases} \mu_{oil} \cdot (1 + 2.5\phi_{water} + 14.1\phi_{water}^2) & if\ W/O\ emulsion \\ \mu_{water} \cdot (1 + 2.5\phi_{oil} + 14.1\phi_{oil}^2) & if\ O/W\ emulsion \end{cases} \quad (4)$$

Levinton and Leighton method (Leviton and Leighton 1936) is another option, and it is expressed by Eq. (5):

$$\mu_{emulsion} = \begin{cases} \mu_{oil} \cdot e^{\left[2.5\left(\frac{0.4\mu_{oil} + \mu_{water}}{\mu_{oil} + \mu_{water}}\right)\left(\phi_{water} + \phi_{water}^{\frac{5}{3}} + \phi_{water}^{\frac{11}{3}}\right)\right]} & if\ W/O\ emulsion \\ \mu_{water} \cdot e^{\left[2.5\left(\frac{0.4\mu_{water} + \mu_{oil}}{\mu_{oil} + \mu_{water}}\right)\left(\phi_{oil} + \phi_{oil}^{\frac{5}{3}} + \phi_{oil}^{\frac{11}{3}}\right)\right]} & if\ O/W\ emulsion \end{cases} \quad (5)$$

For all these methods, Aspen HYSYS assumes that the inversion point occurs for a water fraction of 50 %. At that moment, when water-in-oil changes to oil-in-water, or vice-versa, the model will predict the highest viscosity.

These empirical correlations were analysed against experimental data gathered from the literature (Oliveira et al. 2018). The main conclusion was that in general, these equations could describe the rheological behaviour for lower water fractions (below 20 %). However, they show disagreements with the experimental data, especially when the water fraction increases, near the phase inversion.

The general polynomial method, expressed by Eq. (6), fulfils the need of specifying a correlation that fits the experimental data.

$$\mu_{emulsion} = \begin{cases} \mu_{oil} \cdot (1 + \beta_1 \phi_{water} + \beta_2 \phi_{water}^2 + \beta_3 \phi_{water}^3) & if\ W/O\ emulsion \\ \mu_{water} \cdot (1 + \beta_1 \phi_{oil} + \beta_2 \phi_{oil}^2 + \beta_3 \phi_{oil}^3) & if\ O/W\ emulsion \end{cases} \quad (6)$$

This model enables to tune β_1, β_2, and β_3 parameters, as well as to define where the inversion phase occurs, for each emulsion. The parameters were obtained by fitting the function to the emulsion viscosities data. The main advantage of this method is the possibility of finding individual equations for each crude oil samples, which better resembles the emulsion rheological behaviour, rather than the other pre-settled methods. On the contrary, the main setback is that experimental tests are required to model the fluid dynamics.

All these methods describe the emulsion viscosity as a function of the continuous phase viscosity. For a water-in-oil emulsion, the relative viscosity is defined by Eq. (7):

$$\mu_{relative} = \frac{\mu_{emulsion}}{\mu_{oil}} \quad (7)$$

4. Results

4.1. Statistical analyses to characterize the emulsion relative viscosity

To overcome the limitation of fitting the parameters for each crude oil, a statistical analysis was performed upon available data for Brazilian crude oils. Experimental data was gathered from a set of 126 crude oil samples (Oliveira et al. 2018), and the relative viscosities of the water-in-oil emulsions are available for 10 %, 30 %, 50 % and 70 % water fractions, and for 4 ºC, 30 ºC and 50 ºC, for a shear rate equals to $50\ s^{-1}$. To perform this statistical approach, Newtonian behaviour was assumed.

Using the @RISK software a set of pre-defined statistical distributions were fitted to the relative viscosity experimentally determined, and the Akaike Information Criterion (AIC) estimator was used to compare the relative quality of the statistical models. The probability density function chosen (with the minimum global AIC value) was the Gumbel distribution, also known as Extreme Value distribution, which is defined by a location parameter (α), and a shape parameter (β). This probability density function is defined by the Eq. (8):

$$f(x) = \frac{1}{\beta}\left[\frac{1}{e^{\left[\frac{x-\alpha}{\beta} + \exp\left(-\frac{x-\alpha}{\beta}\right)\right]}}\right] \quad (8)$$

The cumulative distribution function is determined by the Eq. (9):

$$F(x) = \frac{1}{e^{\exp(-z)}} \quad (9)$$

To exemplify how the Gumbel distribution was fitted to relative viscosity for T = 50 ºC and ∅ = 50 %, Figure 3 shows the probability density function and the cumulative distribution function.

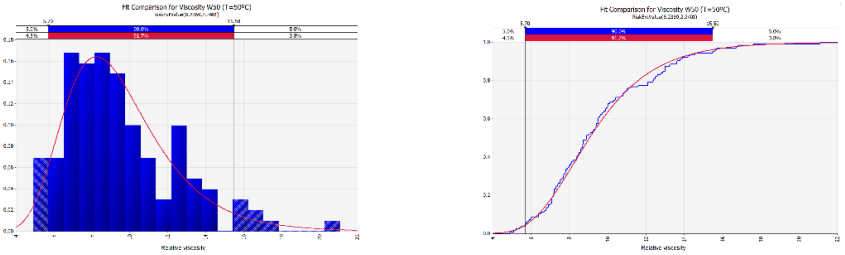

Figure 3 – Fitting Gumbel distribution to relative viscosity for T = 50 ºC and ∅ = 50 %

Table 1 presents the location and shape parameters determined for the Gumbel probability density function.

Table 1 – Location and shape parameters for Gumbel probability density function

	Location parameters (a)			Shape parameters (b)		
	T = 4 ºC	T = 30 ºC	T = 50 ºC	T = 4 ºC	T = 30 ºC	T = 50 ºC
Ø=10 %	1.28235	1.24124	1.26947	0.18255	0.13486	0.13412
Ø=30 %	2.36553	2.46371	2.56775	0.62618	0.49967	0.4801
Ø=50 %	5.4988	7.8153	8.2369	2.3179	2.561	2.2401
Ø=70 %	12.6202	23.134	27.458	7.812	13.417	14.626

These parameters were plotted on two 3D graphs, and then two polynomial surfaces were fitted, applying the Eq. (10):

$$sf(T,\emptyset) = p_{00} + p_{10}\cdot\emptyset + p_{01}\cdot\emptyset + p_{20}\cdot T^2 + p_{11}\cdot T\cdot\emptyset + p_{02}\cdot\emptyset^2 + p_{21}\cdot T^2\cdot\emptyset + p_{12}\cdot T\cdot\emptyset^2 + p_{03}\cdot\emptyset^3 \quad (10)$$

The fitted coefficients for the location and shape values, from Gumbel density function, are presented in Table 2.

Table 2 – Fitted coefficients for Gumbel distribution

Polynomial parameters	Location	Shape	Polynomial parameters	Location	Shape
p00	-1.244	-1.376	p02	-0.01077	-0.009001
p10	-0.005888	-0.04223	p21	-6.99E-05	-5.61E-05
p01	0.3509	0.2475	p12	0.0001631	5.88E-05
p20	0.001427	0.001333	p03	0.0001178	9.83E-05
p11	-0.004152	-0.0002101			

The fitted surfaces are presented in Figure 4.

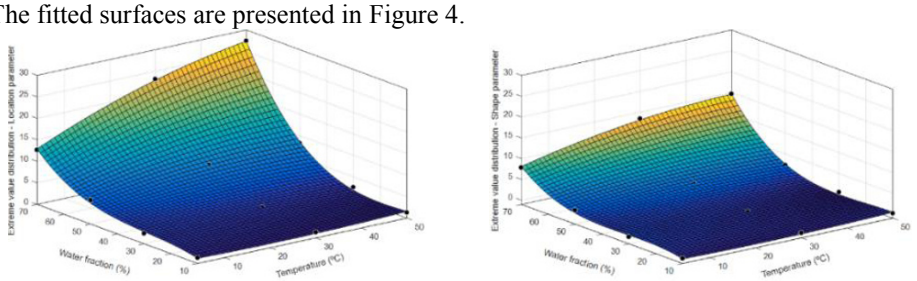

Figure 4 – Gumbel distribution. Location parameter (left) and shape parameter (right)

4.2. Monte Carlo Simulation applied to a case study

Monte Carlo simulation is a process that repeats an experiment many times and generates a large amount of randomized data in order to better describe the system. Such random data is gathered, organized and analysed to allow understanding the likelihood of an occurrence. Software @RISK was used to perform the Monte Carlo simulations. The results allow transforming analyses by considering probabilities, leaving the single point estimative to histograms.

A case study was simulated using the Monte Carlo approach to determine emulsions viscosities and their uncertainties for different well depths. Figure 5 represents the temperature density functions used as input, and the simulation results applied to the Eq. (3), after using the Gumbel distribution shown in Figure 4.

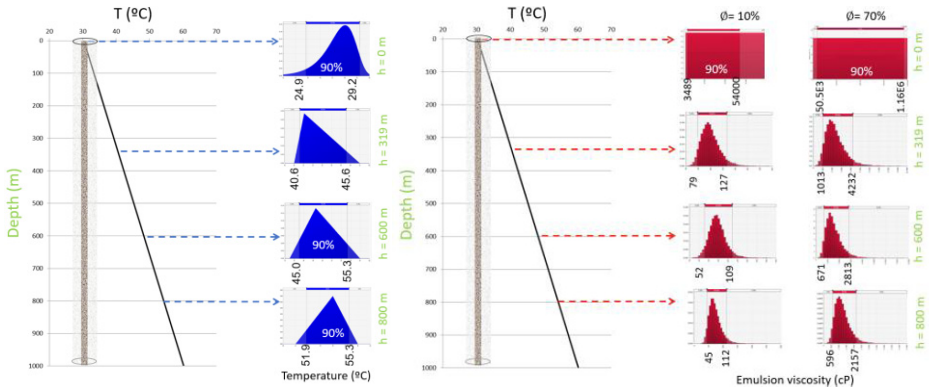

Figure 5 – Temperature distribution functions (left). Emulsion viscosities results for 10 000 Monte Carlo iterations (right), for different depths

5. Conclusions

It has been observed that W/O emulsions viscosity increases with the water fraction until reaching the inversion point. The herein proposed methodology allowed estimating emulsions viscosities, at temperatures ranging from 4 until 50 ºC and water fractions between 10 and 70 %, for Brazilian crude oils. Using Monte Carlo simulations, it was possible to estimate the expected uncertainties on the emulsion viscosity, by incorporating the uncertainty on the temperature profile and the relative viscosity.

The major accomplishment of this work is the ability to predict the rheological behaviour of emulsions, not only for modelling processes but also for inside-wells equipment design. Matching the experimental data with computer-aided models is essential to accurately forecast the fluid properties. The employed statistical methodology can be applied in several other matters for assessing and validating models to data, making it a valuable tool for computer aided engineering.

Acknowledgements

The authors would like to acknowledge F.C.T., I.P. support through the PhD grant number SFRH/BD/131005/2017.

References

H. Brinkman, 1952, The viscosity of concentrated suspensions and solutions, The Journal of Chemical Physics, 20, 4, 571. DOI: 10.1063/1.1700493

V. Guth, R. Simha, 1936, Kolloid Zeitschrift, 74, 3, 266-275. DOI: 10.1007/BF01455734

A. Leviton, A. Leighton, 1936, Viscosity relationships in emulsions containing milk fat, Journal of Physical Chemistry, 40, 1, 71-80. DOI: 10.1021/j150370a010

M. Oliveira, L. Miranda, A. Carvalho, D. Miranda, 2018, Viscosity of Water-in-Oil Emulsions from Different API Gravity Brazilian Crude Oils, Energy & Fuels, 32, 3, 2749–2759. DOI: 10.1021/acs.energyfuels.7b02808

H. Rønningsen, 1995, Correlations for predicting Viscosity of W/O-Emulsions based on North Sea Crude Oils, SPE, SPE 28968, 1-7. DOI: 10.2118/28968-MS

A. Sousa, H. Matos, M. Pereira, 2019a, Modelling Paraffin Wax Deposition Using Aspen HYSYS and MATLAB, 29th European Symposium on Computer Aided Process Engineering, 46, 973-978. DOI: 10.1016/B978-0-12-818634-3.50163-6

A. Sousa, H. Matos, L. Guerreiro, 2019b, Wax deposition mechanisms and the effect of emulsions and carbon dioxide injection on wax deposition: Critical review, Petroleum. DOI: 10.1016/j.petlm.2019.09.004

Sauro Pierucci, Flavio Manenti, Giulia Bozzano, Davide Manca (Eds.)
Proceedings of the 30th European Symposium on Computer Aided Process Engineering (ESCAPE30), May 24-27, 2020, Milano, Italy.
http://dx.doi.org/10.1016/B978-0-12-823377-1.50022-7

Efficient Data-based Methodology for Model enhancement and Flowsheet analyses for Continuous Pharmaceutical Manufacturing

Pooja Bhalode[a], Nirupaplava Metta[a], Yingjie Chen[b], Marianthi Ierapetritou[b*]

[a]*Department of Chemical and Biochemical Engineering, Rutgers University, 98 Brett Road, Piscataway, New Jersey, 08854, USA*
[b]*Department of Chemical and Biomolecular Engineering, University of Delaware, 150 Academy Street, Newark, Delaware, 19716, USA*
mgi@udel.edu

Abstract

Accurate process predictability and efficient flowsheet analysis has been the focus of research in pharmaceutical manufacturing. Currently available mechanistic models, being unable to account for all complex powder variabilities, need to be improved for accurate digital twin framework of the manufacturing plant. In this work, we propose a novel methodology of integrated plant data for model enhancement. These enhanced models are applied for flowsheet analyses focusing on design space identification. Surrogate-based feasibility analysis is implemented using artificial neural network with adaptive sampling techniques. This strategy is demonstrated for a direct compaction line capturing realistic scenarios observed in the manufacturing plant.

Keywords: Pharmaceutical, Surrogate, Feasibility, Hybrid modeling, Industry 4.0

1. Introduction

Research efforts driven by FDA's Quality-by-design (QbD) initiative has led to development of detailed predictive models of continuous pharmaceutical manufacturing lines. These studies mainly focus on process flowsheet simulation using a combination of mechanistic and empirical models to demonstrate dynamic effects of process and material parameters on critical quality attributes, with tracking of powder material properties (Boukouvala et al. 2011; Wang et al. 2017). However, these models are not able to capture all observed process variabilities due to the inherent hard-to-predict nature of pharmaceutical powder materials. In this study, we aim to address these limitations by employing a data-based methodology for model enhancement focusing on inclusion of process data collected under Industry 4.0 framework. Developed process flowsheets models are applied for data-based system analyses. This study focuses on feasibility analysis to address the goal of identification of the design space of a process. In this analysis, a feasibility function which characterizes the maximum constraint violation, is evaluated. For a process with design variables d and uncertain parameters θ, the J constraints that represent feasible operation can be expressed as $g_j(d,\theta) \leq 0$. Following this, the feasibility function is defined as shown in Eq (1).

$$\psi(d,\theta) = \max_{j \in J} g_j(d,\theta) \tag{1}$$

Since the constraints in the process models are not always available in closed form or are computationally expensive to evaluate, surrogate-based feasibility analysis methodology

is implemented wherein a computationally efficient surrogate model is used to represent the feasibility function. The following sections focus on describing Industry 4.0 dataflow and methodology for model enhancement, followed by feasibility studies using the enhanced models. Concluding remarks are provided in Section 6.

2. Industry 4.0 Dataflow

Recent interest in application of Internet of Things (IoT) (Liao et al. 2017) aimed at developing an integrated data collection, storage, and knowledge extraction framework for efficient and effective manufacturing. This framework for pharmaceutical industry is illustrated in Figure 1, wherein the overall manufacturing plant data is stored to be used for predictive modelling. Data acquisition starts from the bottom up where all data are being generated. Data from Process Analytical Tools (PAT) and sensors are collected and sent to different prediction tools and OPC servers, whereas the raw data from the continuous pilot plant are sent to control software. To facilitate overall data storage and integration, data from these sources are sent to a local historian and then to a cloud storage infrastructure for ease of accessibility for predictive digital twin models. Material calibration and experimental data is stored using standardized data structures within cloud-based electronic laboratory notebooks (ELNs) for efficient data integration with the overall plant and extraction to modelling and simulation platforms.

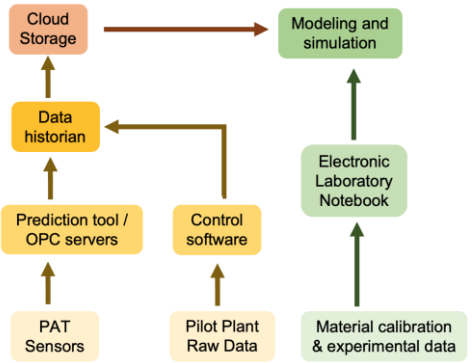

Figure 1: Data flow within Industry 4.0 framework for continuous pharmaceutical manufacturing

3. Methodology for Model Enhancement

In this section, the methodology for model enhancement based on the Industry 4.0 framework is presented. With this framework, process model outputs and actual plant data can be compared and analyzed to identify if a significant residual exists, indicating a potential departure between the model and the plant. The following sub-sections entail different methods for model enhancement with process data.

3.1. Identification and correction of process-model mismatch

A typical cause of departure can be attributed to the parameters used in the model (namely parametric mismatch). It is important to identify a suitable set of parameters that can appropriately describe the system. Using Industry 4.0 data framework, different parameter estimation methods including least squares fitting and Kalman filtering (Zhang 1997) can be applied to obtain a set of physically suitable parameters. Kravaris et al. (2013) identifies global optimization-based algorithms for parameter estimations under measurement uncertainty, and Wang et al. (2018) introduces a Bayesian approach for data from different scales. In certain situations, if the best set of parameters still does not yield

good model predictability, structural mismatches exist within the model, meaning that the functional forms within the model are not suitable to describe the actual system. For identification of structural mismatches, principal component analysis and correlation methods like partial correlation and mutual information are implemented (Badwe et al. 2009; Chen et al. 2013; Meneghetti et al. 2014). These methods can qualitatively determine the sources of structural mismatch. After identifying the source of mismatch, model selection and discriminations methods like posterior probability study and Akaike Information Criterion can be used to identify the most probable model (Wu et al. 2011; Wang et al. 2018).

3.2. Non-Parametric or Surrogate modeling

The non-parametric or surrogate model development method is implemented if the desired model predictability is not achieved after addressing process-model mismatch or when the cost of mismatch identification and correction is high. Non-parametric modeling includes developing an efficient surrogate based on input-output datasets. Kriging model, Artificial Neural Networks, and related methods are often used in developing the surrogate (Rogers et al. 2013). Datasets availed from the Industry 4.0 framework are applied to develop the computationally efficient surrogate models which captures the overall process without inclusion of mechanistic information.

3.3. Hybrid Modeling

Hybrid modeling approach focuses on capturing the mechanistic information along with data-driven surrogate models. The essence is to combine *a priori* knowledge like conservation and kinetic laws with nonparametric models built using process data (Stosch et al. 2014). Proposed hybrid structures can be broadly categorized as parallel and serial structure. For parallel structure, inputs are fed into both the mechanistic part and data-driven part of the model, and the model outputs are combined by superposition, multiplication, or weighting. This structure is often used to correct for errors of the original model. For serial structure, inputs are fed into the mechanistic and data-driven models in a sequential way, meaning that the output of the first part of the model serves as an input to the next, and the final outputs can be combined with appropriate weighting. The serial structure is prevalent when mechanism of the original model is not well-understood (Stosch et al. 2014). By integrating the mechanistic and data-driven models, the overall predictability of the model can be increased, and the enhanced model can then be integrated into flowsheet to conduct further flowsheet analyses.

4. Surrogate-based Feasibility Analysis

This section focuses on surrogate based feasibility analysis methodology where, an inexpensive feed-forward ANN model combined with Bayesian regularization (Burden and Winkler 2008) for network training is explained. The number of hidden neurons is determined in an initial model selection, minimizing the sum of squared errors between target and prediction data. In the model improvement stage, adaptive sampling is used to choose additional samples for improving the ANN model. In this work, a modified expected improvement function (EI_{feas}) proposed by Boukouvala and Ierapetritou (2012) as given in Eq. (2) is used to implement the adaptive sampling strategy.

$$EI_{feas}(x) = s\phi\left(\frac{-y}{s}\right) = s\frac{1}{\sqrt{2\pi}}e^{-0.5\frac{y^2}{s^2}} \tag{2}$$

where, y and s are the surrogate model predictor and standard error of the prediction at x respectively. Maximization of EI_{feas} identifies sample points close to the feasible region boundary or in the region of high prediction uncertainty. Thus, as samples are added, the surrogate model accuracy is improved focusing on identification of feasible region. In this work, the variance s^2 of ANN model predictor y at a sample point x is estimated using a statistical technique known as jack-knifing (Eason and Cremaschi 2014) wherein, sample set is divided into K disjoint sample sets. K neural networks are built for the sets and variance of prediction s^2 is estimated using Eq (3).

$$s^2(x) = \frac{1}{K}\sum_{k=1}^{K}\left(U_k(x) - \sum_{k=1}^{K}\frac{U_k(x)}{K}\right)^2 \tag{3}$$

Figure 2 illustrates the algorithm for implementation of the ANN based feasibility analysis methodology. This methodology is tested on Continuous Direct Compaction (CDC) process explained by (Wang et al. 2017), where the uncertain parameters used for the problem and their bounds are tabulated in Table 1. The constraints for the problem that define the feasible region is given in Table 2.

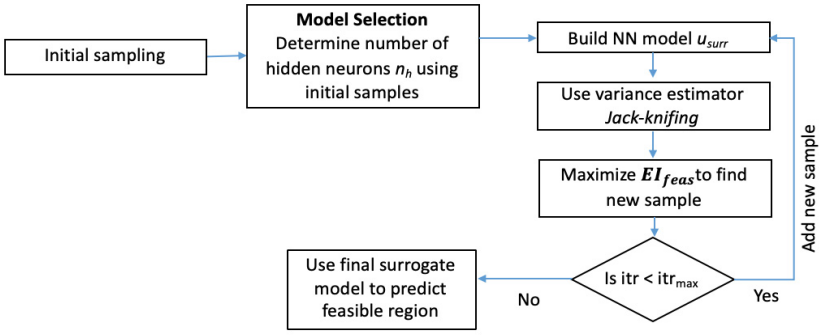

Figure 2: Algorithm for ANN based feasibility analysis methodology

Table 1: Variable bounds for CDC process feasibility case study

Factors	Units	Nominal	LB	UB
API flowrate	kg/h	3	2.85	3.15
Excipient flowrate	kg/h	26.7	25.36	28.03
Mill impeller speed	rpm	1120	1064	1176
Blender blade speed	rpm	250	237.5	262.5
Fill depth	m	0.01	0.0095	0.0105
Thickness	m	0.0025	0.002375	0.002625

Overall, the ANN based feasibility analysis is applied to the six-dimensional problem with 20 inequality constraints. 2^6 Latin Hypercube samples are used in the initial model selection phase. Using the initial samples, number of hidden neurons are varied. 8 hidden neurons yield the least sum of squared errors between predicted and target feasibility function values. 500 samples are iteratively added using the adaptive sampling strategy. Since this is a high dimensional problem, the feasible region is represented using a matrix of contour plots of feasibility function values as shown in Figure 3. For each contour plot, only two factors are varied, and the remaining two factors are set at nominal values. The feasible region boundary predicted by the final ANN model is represented using a red

line. Feasible region boundary from the original process model is also plotted using red dashed line. Good agreement between the original and predicted feasible regions is observed.

Table 2: Constraints for the CDC process feasibility case study

Unit operation	Variable	Units	Limits based on % nominal value
Blender	Mean residence time	s	+/- 20%
	Delay time	s	
	Mass hold SS	kg	
	Mean bulk, true density	kg/m^3	
	Mean d10, d50, d90	µm	
Comill	Mean d10, d50, d90	µm	+/-20%
	Mean bulk, true density	kg/m^3	
	Mean residence time	s	
	Mass holdup SS	kg	
Tablet Press	Concentration	%	+/-5%
	Weight	kg	+/-10%
	Hardness	kp	
	Main compression pressure	MPa	
	Pre compression pressure	MPa	

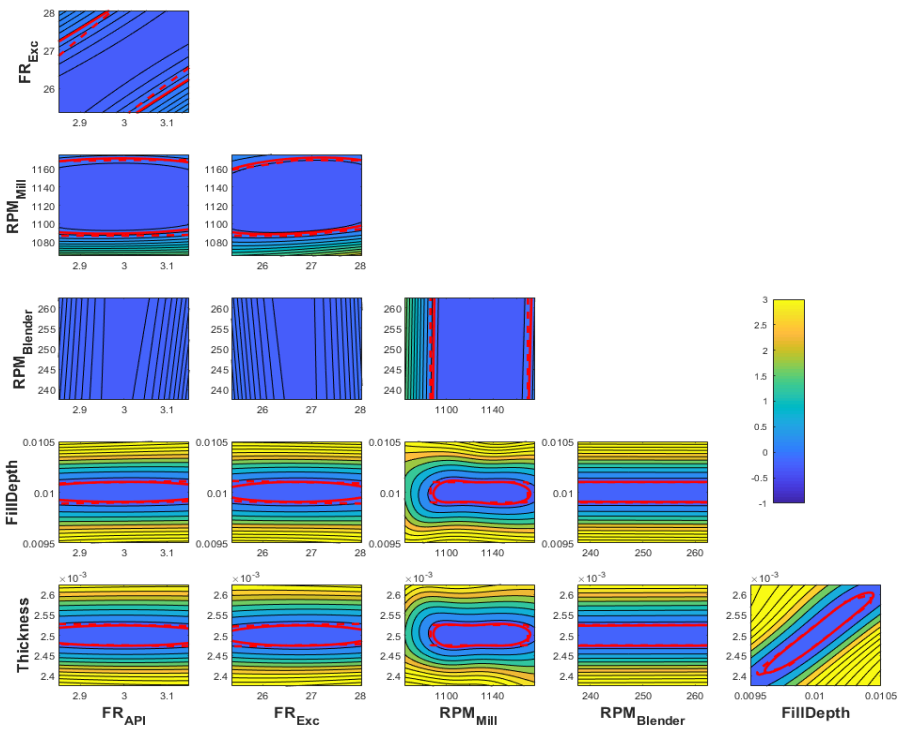

Figure 3: Matrix of feasibility function contour plots representing the feasible region of the continuous direct compaction process (Feasible region boundary from the original model and predicted by the ANN model are represented as red dashed lines and red solid lines respectively)

5. Conclusions

We propose an integrated methodology for data-based model enhancement using Industry 4.0 framework for surrogate-based feasibility analysis. Pilot plant and laboratory data collected from Industry 4.0 framework is applied for enhancement of mechanistic models. The enhanced flowsheets are proposed to be applied for feasibility analysis on a continuous direct compaction line. A good agreement between the actual and the predicted feasible regions is observed. For future work, we aim to extend the methodology to other continuous manufacturing lines with the inclusion of process dynamics.

Acknowledgement

The authors would like to acknowledge funding from U.S. Food and Drug Administration (FDA) through grant 1U01FD006487-01.

References

Badwe AS, Gudi RD, Patwardhan RS, Shah SL, Patwardhan SC. Detection of model-plant mismatch in MPC applications. Journal of Process Control. 2009;19:1305–13.

Boukouvala F, Ierapetritou MG. Feasibility analysis of black-box processes using an adaptive sampling Kriging-based method. Computers & Chemical Engineering. Pergamon; 2012 Jan 10;36:358–68.

Boukouvala F, Ramachandran R, Vanarase A, Muzzio FJ, Ierapetritou MG. Computer Aided Design and Analysis of Continuous Pharmaceutical Manufacturing Processes. Computer Aided Chemical Engineering. 2011;29:216–20.

Burden FR, Winkler D. Bayesian Regularization of Neural Networks. Methods in Molecular Biology. 2008;458:25–44.

Chen G, Xie L, Zeng J, Chu J, Gu Y. Detecting Model–Plant Mismatch of Nonlinear Multivariate Systems Using Mutual Information. Journal of Quality Technology. American Chemical Society; 2013 Jan 22.

Eason J, Cremaschi S. Adaptive sequential sampling for surrogate model generation with artificial neural networks. Computers & Chemical Engineering. Pergamon; 2014 Sep 4;68:220–32.

Kravaris C, Hahn J, Chu Y. Advances and selected recent developments in state and parameter estimation. Computers & Chemical Engineering. Pergamon; 2013 Apr 5;51:111–23.

Liao Y, Deschamps F, de Freitas Rocha Loures E, Ramos LFP. Past, present and future of Industry 4.0 - a systematic literature review and research agenda proposal. International Journal of Production Research. Taylor & Francis; 2017 Mar 28.

Meneghetti N, Facco P, Bezzo F, Barolo M. A Methodology to Diagnose Process/Model Mismatch in First-Principles Models. Ind Eng Chem Res. 2014;53(36):14002–13.

Rogers AJ, Hashemi A, Ierapetritou MG. Modeling of Particulate Processes for the Continuous Manufacture of Solid-Based Pharmaceutical Dosage Forms. Processes. 2013;1(2):67–127.

Stosch von M, Oliveria R, Peres J, de Azevedo SF. Hybrid semi-parametric modeling in process systems engineering: Past, present and future. Computers & Chemical Engineering. Pergamon; 2014 Jan 10;60:86–101.

Wang Y, Biegler LT, Patel M, Wassick J. Parameters estimation and model discrimination for solid-liquid reactions in batch processes. Chemical Engineering Science. Pergamon; 2018 Sep 21;187:455–69.

Wang Z, Escotet-espinoza MS, Ierapetritou MG. Process Analysis and optimization of continuous pharmaceutical manufacturing using flowsheet models. Computers and Chemical Engineering. Elsevier Ltd; 2017 Feb 21;107:77–91.

Wu S, McAuley KB, Harris TJ. Selection of simplified models: I. Analysis of model- selection criteria using mean- squared error. The Canadian Journal of Chemical Engineering. 2011 Feb;89:148–58.

Zhang Z. Parameter estimation techniques: a tutorial with application to conic fitting. Image and Vision Computing. Elsevier; 1997 Jan 1;15(1):59–76.

Sauro Pierucci, Flavio Manenti, Giulia Bozzano, Davide Manca (Eds.)
Proceedings of the 30th European Symposium on Computer Aided Process Engineering (ESCAPE30), May 24-27, 2020, Milano, Italy.
http://dx.doi.org/10.1016/B978-0-12-823377-1.50023-9

Artificial Neural Network to capture the Dynamics of a Dividing Wall Column

Eduardo Sánchez-Ramírez[a], Juan Gabriel Segovia-Hernández[a],
Esteban A. Hernández-Vargas[b,c]

[a] *Chemical Engineering Department, Universidad de Guanajuato, Noria Alta s/n, Guanajuato, Gto., 36050, México*

[b] *Instituto de Matematicas, UNAM, Unidad Juriquilla, Blvd. Juriquilla 3001, Juriquilla, Queretaro ,C.P. 76230, México*

[c] *Frankfurt Institute for Advanced Studies, Ruth-Moufang-Strae 1, 60438, Frankfurt am Main, Germany*

eduardo.sanchez@ugto.mx; esteban@im.unam.mx

Abstract

The forecasting ability of Artificial Neural Network (ANN) has made it received a widespread application in the field of engineering, biology, energy, and finance. One of the main advantages of ANN is its ability to capture complex dynamics, in fact, ANNs can approximate non-linear input-output relationships to any degree of accuracy in an iterative manner. Despite the forecasting ability of ANN, its application for the downstream process is still fragmented. This study applies an artificial neural network to model the dynamics of a dividing wall column that separates an effluent coming from fermentation producing acetone, butanol, and ethanol (ABE) for spark-ignition purposes. Considering the dynamic of the diving column simulated in Aspen Plus Dynamics, a 4-10-3 multi-layer perceptron with back-propagation algorithm was enough to reproduce the dynamics reported by the simulator. Two kind of dynamic studies were performed, an open-loop and closed-loop analysis. Four disturbances for six different percentages were applied in the open-loop policy; and three set point changes in the closed-loop policy. To ensure the reproducibility of the results, a dynamic simulation in Aspen Dynamics was performed. Results from the validated models show that the predicted versus actual values were bounded. Different input scenarios were evaluated promptly where the manipulated variables presented peaks in their values, and the result was relatively good. Between the two scenarios, the open-loop test, and closed-loop test, the closed-loop test showed a lower error percentage than the open-loop test. The largest error percentage values were close to 0.9%, however, the majority of errors were between 0.1 and 0.4%.

Keywords: Artificial Neural Network, Downstream process, ABE purification.

1. Introduction

The reproduction by simulation of chemical processes is associated with the reproduction of models; in such a way that the quality and reliability of said reproduction depends on the quality and certainty of the process model. Although the reproduction of these types of processes with variations in time can take a considerable period of. An interesting methodology to address complex models is that input and output data can be approximated as black boxes, with the main objective of obtaining reliable predictions. The problem then lies now in the quality of data with which the black box must be built. Artificial neural networks (ANN's) are a technique that can meet those requirements. The

basic feedforward network is shown in Figure 1. The data enters the network at the input nodes, the data is propagated through the network through the hidden layers towards the output layer. Although ANNs have a relatively rudimentary structure, several studies conclude that any continuous and non-linear function can be successfully reproduced by an ANN (Cybenko 1989). One of the main advantages of using ANNs is the ability to initially use information to model complex systems, and predict results in a robust manner, since they can approximate non-linear input-output relationships of any degree of accuracy in an iterative manner (Safa and Samarasinghe 2011). Despite the great forecasting skills of the ANNs, their application to predict the behavior of separation processes is quite limited. One reason is the number of equations involved in the modeling of this kind of process, for example, considering that for each equilibrium stage and each component C, the total of MESH (mass and energy balance, thermodynamic equilibria, and purity constraint) equation solved are 2C +3. In addition, if the equations are modeling with variation in time the complexity increase. In the same way, the use of ANNs for more complex distillation systems has not been reported. That is, as far as the authors' knowledge is concerned, no work has been reported in which ANNs are used to model the dynamic behavior of intensified separation systems such as dividing wall columns (DWC). The interest of such intensified alternatives is the advantages that they represent over the conventional option regarding energy requirements and cost savings. In addition, due to the extra complexity it represents, no work has been reported that involves the handling of mixtures with high complexity relative to thermodynamic modeling. With this in mind, the aim of this work is to use an ANN to model and forecasting the dynamic behavior of a dividing wall column for the separation of a mixture composed of Acetone-Butanol-Ethanol and Water from a fermentation process. The modeling process was performed in two scenarios, *i)* modeling the dynamic behavior of the process under an open-loop analysis, *ii)* modeling the dynamic behavior of the process under a closed-loop analysis. The input data were obtained by means of Aspen Dynamics under both open-loop and closed-loop policy.

2. Case Study

Errico et al. (2017) presented a methodology to generate intensified alternatives to separate butanol from ABE fermentation. For the development of this methodology, they start from a hybrid design that considers a liquid-liquid extraction column and conventional distillation columns. Errico et al. (2017) apply a methodology to generate different intensified alternatives based on DWC. All the generated alternatives were evaluated and optimized by means of a robust optimization algorithm, differential evolution with tabu list (DETL), evaluating the total annual cost and the eco-indicator 99 as economic and environmental performance indices. As a result of their research, it was obtained several hybrid designs. Among those designs, the scheme in Figure 1 is considered as a case study. This scheme was initially simulated in Aspen Plus considering the NRTL-HOC as a thermodynamic model to describe phase equilibrium. The feedstream considered a mixture of Acetone, Butanol, Ethanol, and water in a proportion of 0.3018, 0.1695, 0.0073 and 0.5214 % wt respectively. Furthermore, the simulation was exported from Aspen Plus to Aspen Dynamics to obtain the dynamic behavior in both open-loop and closed-loop policy. The data from the dynamic simulation was used for being used as input data in the ANN.

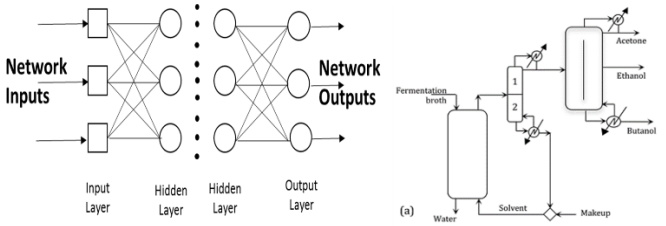

Figure 1. General topology of an ANN and DWC considered a case study

3. Methodology

3.1 Data Generation

The data to train the NNs were based on data using simulations for two cases, open-loop and close-loop policy in Aspen Dynamics. Regarding the open-loop, to generate the input data a step change of 5% every 5 hours in the manipulated variable was performed in a single manipulated variable until it reaches +20% of the nominal value. After that step change of -5% every 5 hours until reach again the nominal state, the other manipulated variables were kept as constant. The same procedure applied to the other variables in such a way that it was applied 3 different disturbances in 6 different percentages of the nominal point. Each manipulated variable was chosen according to each product stream, i.e., when a component was purified in the top of a distillation column, the manipulated variable was the reflux ratio; however, if the component purified remained in the distillation column as a bottom product, the manipulated variable was the reboiler heat duty, and so on. As output data, it was considered the composition profiles of all interest components obtained jointly the disturbances in Aspen Dynamics. Regarding the closed-loop test, the input data were obtained as follows. A setpoint change was implemented in the composition of each component of interest (Acetone-Butanol-Ethanol), in this way three changes of set points were performed and tuned at the same time. The analysis was based on the operation of a proportional-integral controller (PI). Because we considered PI controllers, the proportional gain (K_c) and the reset times (τ_i) were tuned up for each scheme studied here; in addition, we compared the dynamic performance by using the integral of the absolute error (IAE) criterion. To control the composition of distillate and funds, an LV structure was selected. As output data in this test, it was considered the composition profiles obtained. Once all input-output data was obtained, a 4-10-3 multi-layer perceptron with back-propagation algorithm was enough to reproduce the dynamics reported by the simulator.

3.2 Neural Network procedures

This subsection presents the procedures to establish the ANNs. The basic elements of the artificial neuron are: *i)* A set of synapses, or connecting links, each of which is characterized by weight or strength of its own. Specifically, a signal x_j at the input of synapse j connected to neuron k is multiplied by the synaptic weight w_{kj}. The first subscript in w_{kj} refers to the neuron in question, and the second subscript refers to the synapse's input end to which the weight refers. *ii)* An adder for summing the input signals, weighted by the respective synaptic strengths of the neuron; the operations described here constitute a linear combiner. *iii)* An activation function for limiting the amplitude of the neuron's output to the closed unit interval [0,1], or, alternatively, [-1,1]. However, there are exceptions like the linear activation function which covers the open range $(-\infty, \infty)$. A neuron can be mathematically described by the following equations:

$$u_k = \sum_{j=1}^{m} w_{kj} x_j \quad \text{and} \quad u_k = \sum_{j=1}^{m} w_{kj} x_j \qquad (1)$$

where $x_1, x_2, \ldots, x_m$ are the input signals; $w_{k1}, w_{k2}, \ldots, w_{km}$ are the respective synaptic weights of the neuron k. u_k is the linear combiner's output due to the input signals. b_k is the bias. $\varphi()$ is the activation function. y_k is the neuron's output signal. The use of bias b_k has the effect of applying an affine transformation to the linear combiner's output u_k as shown by

$$v_k = u_k + b_k \qquad (2)$$

where v_k is the induced local field or activation potential. The activation function considered in this work is the logistic function:

$$\varphi(v) = 1 \Big/ 1 + e^{-av} \qquad (3)$$

where a is the slope parameter of the logistic function. Note that the previous equation ranges from zero to one in a strictly increasing fashion and exhibits a graceful balance between linear and nonlinear behaviors. The Feedforward Network (FFN) used in this work is the Multilayer Perceptron (MLP) which consists of full connected consecutive layers of neurons that can be classified as input, hidden and output layers. The input layer contains independent variables that are connected to the hidden layer for processing. Each of the hidden layers contains neurons with logistic activation functions. These are responsible for the nonlinear mapping between the network's inputs and outputs. The output layer, which in this work is composed of neurons with linear activation functions, finishes the prediction or the classification process and presents the results with a small estimation error. The Matlab neural networks toolbox allows the use of multiple network architectures. Each one of the NARX networks was constructed by means of the feedforward neural network's command of the Matlab toolbox *Feedforwardnet Toolbox:feedforward net(hiddenSizes,trainFcn)*. This command creates a MLP with hidden layers. The hiddenSizes parameter is a row vector whose k_{th} element represents the number of neurons that compose the k_{th} hidden layer. Thus, the *hiddenSizes* vector length is the number of hidden layers composing the MLP. The parameter trainFcn defines the training algorithm for the new MLP. The algorithm backpropagation was considered in this work.

4. Results

4.1. Open-loop input data

Once the step changes in the manipulable variables were implemented, the variation of all of them in time was obtained. Despite all manipulated variables and all components were also monitored, Figure 2 A) shows only the variation of the reboiler duty over time, which together with the variation of the reflux ratio and the flow of the lateral current, were used as input data for the ANN. The composition profile of butanol in Figure 2 was used as output data together with the composition profiles of acetone and ethanol. With that input-output data, the neural network was trained. Both stages are shown in Figure 2. Regarding the closed-loop test, once the data for proportional gain (K_c) and the reset times (τ_i) were tuned with the minimum IAE. The values of the manipulated variables and the resulting composition profiles associated with those values of K_c and τ_i were considered as input-output data for training the ANN. Again, despite all variables were

disturbed and the three components were studied, Figure 2 B) shows only the input and output data for Reboiler Heat duty and Butanol. According to Table 1, both AAN were able to reproduce the entire dynamic of the process with relatively good accuracy. Between both test, open-loop, and closed-loop, the ANN showed better accuracy to predict the complexity of the model under the presence of a PI controller. The K_c, τ_i and IAE values for all loops were 140/150/0.0677, 100/100/0.0183, 45/50/0.611 for acetone, butanol, and ethanol respectively.

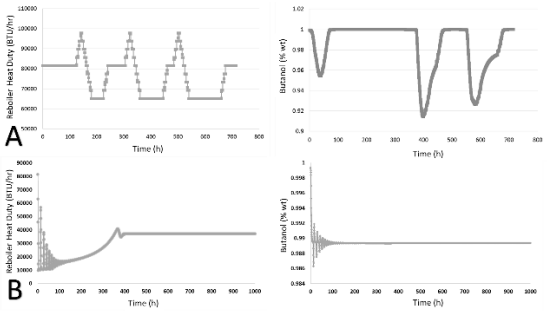

Figure 2. Input and output data Input and output data of the ANN in the open-loop test (A) and closed-loop policy (B).

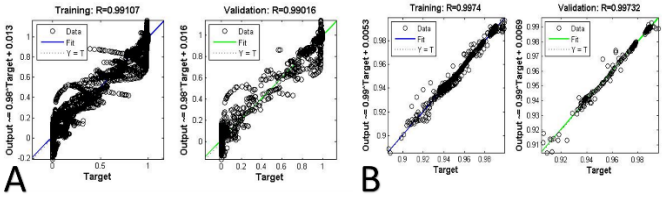

Figure 3. Training and validation data fit process for the open-loop test (A) and closed-loop policy (B).

Table 1. Data Validation for open-loop policy

INPUT			**OUTPUT (%wt)**		
			ANN	**Aspen Dynamics**	**% Error**
Time (h)	0.1	**Acetona**	0.9643	0.997	3.39106
Reb Duty (cal/s)	60413.5	**Butanol**	1.072	0.9992	6.79104
Reflux ratio (lb/lb)	24.3128	**Etanol**	0.9837	0.9864	0.27447
Side stream flow (lb/s)	0.724				
Time (h)	0.3	**Acetona**	0.8645	0.997	15.3268
Reb Duty (cal/s)	87014.5	**Butanol**	0.7313	0.9959	36.1821
Reflux ratio (lb/lb)	36.2144	**Etanol**	1.0488	0.9841	6.16895
Side stream flow (lb/s)	0.724				

Additionally, the computational time for reproducing in ANN was quite low (few seconds) in comparison with that in Aspen Dynamics (10-20 minutes). The values of the

manipulated variables and the resulting composition profiles associated with those values of K_c and τ_i were considered as input-output data for training the ANN. Figure 2-3 shows the input and output data. According to Table 2, both AAN were able to reproduce the entire dynamic of the process with relatively good accuracy. Between both test, open-loop, and closed-loop, the ANN showed better accuracy to predict the complexity of the model under the presence of a PI controller. The K_c, τ_i and IAE values for all loops were 140/150/0.0677, 100/100/0.0183, 45/50/0.611 for acetone, butanol, and ethanol respectively. Additionally, the computational time for reproducing in ANN was quite low (few seconds) in comparison with that in Aspen Dynamics (10-20 minutes).

Table 2. Data Validation for closed-loop policy

INPUT			OUTPUT		
			Aspen Dynamics	ANN	% Error
Time (h)	3.6	ACETONE	0.995598	0.9889	0.672761496
Reflux ratio (lb/lb)	0	ETHANOL	0.959805	0.9686	0.916331963
Side stream flow (lb/s)	0	BUTANOL	0.992269	0.9902	0.208512006
Reb Duty (cal/s)	10555.8				
Time (h)	30	ACETONE	0.988805	0.9912	0.242211558
Reflux ratio (lb/lb)	0.617515	ETHANOL	0.970426	0.9724	0.203415819
Side stream flow (lb/s)	0.668623	BUTANOL	0.99086	0.9925	0.165512787
Reb Duty (cal/s)	11162				

5. Conclusions

Through de use of a 4-10-3 multi-layer perceptron with the back-propagation algorithm it was possible to reproduce the entire dynamic of a complex process to separate a highly nonideal mixture. The ANN showed the potential to reproduce the dynamic behavior of the process under two different test, an open-loop, and a closed-loop test. Between both tests, the ANN showed a minor error reproducing the closed-loop test in comparison with the open-loop test. Taking advantages of the capacities of ANN such as relative easy applications, computing time, and inferring on unseen data numerical convergence; it is possible to perform many studies considering the robustness, non-linearity, and complexity of the model involved in a divided wall column: controllability analysis, dynamic optimization, and model reduction for planning and scheduling works considering the application of the entire model of these complex schemes.

References

Cybenko, G., 1989, Approximation by Superpositions of a Sigmoidal Function. Mathematics of Control. Signals and Systems, 2, pp. 303-314.

Safa, M., & Samarasinghe, S.,2011,. Determination and modelling of energy consumption in wheat production using neural networks: “A case study in Canterbury province, New Zealand”. Energy, 36(8), 5140-5147.

Errico, M., Sanchez-Ramirez, E., Quiroz-Ramìrez, J. J., Rong, B. G., & Segovia-Hernandez, J. G., 2017,. Multiobjective optimal acetone–butanol–ethanol separation systems using liquid–liquid extraction-assisted Divided Wall columns. Industrial & Engineering Chemistry Research, 56(40), 11575-11583.

Sauro Pierucci, Flavio Manenti, Giulia Bozzano, Davide Manca (Eds.)
Proceedings of the 30th European Symposium on Computer Aided Process Engineering (ESCAPE30), May 24-27, 2020, Milano, Italy.
http://dx.doi.org/10.1016/B978-0-12-823377-1.50024-0

An Optimal Design of Expansion-contraction Microchannel Based on Blockage Analysis

Lin Wang*, De Yan, Shuzhi Song, Jiarui Liu

Department of Control Science and Engineering, *Inner Mongolia University of Technology*, *Huhhot*, *010080*, *China*
lwang@imut.edu.cn

Abstract

Microchannel blockage is a common problem in microreactor applications. The principle of inertial aggregation in microchannel is used to analyze the formation of secondary flow and the wall effect of blockage. A heterogeneous microchannel structure combined with expansion and contraction is designed to achieve separation of blockage and solution. Finally, the designed microchannel is compared with the straight tube microchannel which has the same volume by CFD simulations, and the blockage distribution in the microchannel of the expansion-contraction structure is 340% larger than that of the straight tube structure, and the blockages are effectively collected in a predetermined separation position.

Keywords: Expansion and contraction structure, Blockage, Inertial Aggregation, Secondary Flow, Microchannel

1. Introduction

The microchannel reactor has the advantage of large surface volume ratio, fast mass and heat transfer and high safety (Luo et al., 2014). The size of the microreactor is between 10~1000 microns, and the microfluidics in the microchannel are more sensitive to the increasing intermolecular forces (Zhao et al., 2015). Moreover, microchannel is difficult to transport solid materials due to its structural characteristics. If there are solid impurities or solid particles formed by the reaction in the microchannel, the microchannels are prone to be blocked since the intermolecular forces cause the microparticle molecules to aggregate and adhere to the wall of the microchannel, thus, which interrupts production. At the same time, the manufacturing process of microchannels needs to be carried out in a clean room due to the rigorous production conditions of microreactors, which satisfies high requirements for solutions and reactants. Therefore, once a blockage occurs in the microchannel, the entire microreactor is scrapped, and the replacement cost is increased. Hence, it's necessary to study a method that can eliminate the solid-state blocking particles in microchannels.

Bayer et al. (2000) proposed a continuous radiation polymerization method using a micro premixer, which mentions that poor mixing conditions resulted in reactor clogging. Blockage could also be observed in the microfluidic-based systems of solid aggregation and precipitation, which ultimately leads to the blockage of the microchannels (Dressaire and Sauret, 2016). The accumulation of fouling of the microchannel surface is also led to the blockage formation and the progressively reduction of the flow rate until the entire microchannel cross-section is blocked in one or more areas. The deposition and aggregation growth are dominated by the interaction

between particle-particle as well as particle-surface attraction/rejection forces and hydrodynamic forces, which depends on the flow state (Sicignano et al. 2018). Jespers et al. (2018) studied the fluid contact area of a microchannel disperser in the presence of a blockage. In order to prevent large blockage from appearing in the microchannels, the structure of the microchannel is optimized from the initial stage of the formation of blocking particles, i.e. the particles are still in the micro-nano stage. In the study, the stresses of the particles are analyzed, then the principle of inertial aggregation is used in the new designed structure to separate the blocking particles from the liquid phase flow for the purpose of filtering and separating the blocking body. Finally, the separation efficiency is compared by using CFD simulations.

2. Inertial aggregation and separation of particles in microchannels

2.1. Inertial aggregation

When a fluid with uniformly dispersed fine particles flows into a straight pipe at a low Re number of laminar flows, the particles are stably aggregated and move at a concentric annular position from the center of the pipe after a sufficiently long flow distance. This is inertial aggregation. In the experiments study of Segre and Silberberg (1961), the particles move at a concentric circular ring position, which is 0.6 times the distance from the center of the microchannel. The particle aggregation position is shown in Figure 1.

2.2. Dean secondary flow

When the fluid flows at a laminar flow in the straight channel, the fluid close to the channel wall is subjected to the frictional force of the channel wall, then hindering its movements and the fluid velocity near the channel wall is the lowest. Eventually, the velocity of the fluid is presented in a parabolic distribution, as shown in Figure 2 (Huang et al., 2011). The shear force gradient is generated along with this parabolic flow velocity distribution, which produces shear-induced lift force that pushes the particles suspended in the fluid toward the channel wall.

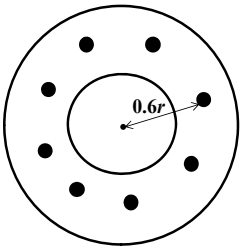

Figure 1 Particle aggregation location

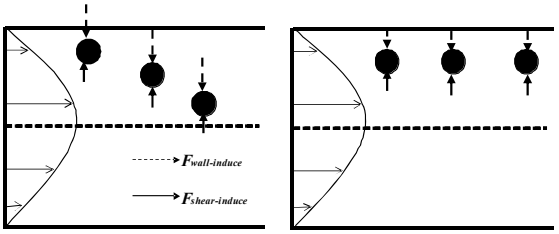

Figure 2 Schematic diagram of particle inertial focusing flow in linear micro-channel

However, when the particles move closer enough to the channel wall, the wall-induced lift force pushes the particles away from the channel wall i.e. wall effect (Zhang et al. 2018).

Furthermore, according to the fluid mass conservation equation, a pair of counter-rotating and symmetrical vortices is formed in a direction perpendicular to the flow of the fluid, respectively located at the upper and lower portions of the channel cross-section, i.e. Dean vortices. Therefore, the flowing particles are simultaneously subjected to the inertia lift and the Dean drag force in the curved channel, the relative magnitude of these two forces determines the flow situation of particles in the curved channel.

The expression of inertial lift is as follows：

$$F_L = \frac{\mu^2}{\rho} \mathrm{Re}_P^2 \, f_c(\mathrm{Re}_c, x_c) = \frac{\rho U_m^2 a^4}{D_h^2} f_c(\mathrm{Re}_c, x_c) \tag{1}$$

Where, Re_c and Re_p are the channel Reynold number and the blocking body Reynolds number, respectively. ρ is the fluid density, μ is the fluid viscosity, Um is the maximum flow velocity in microchannel, a is the diameter of the blocking body, D_h is the channel hydraulic diameter, f_c is the lift coefficient. When the blocking body is in the equilibrium position, f_c=0, and $f_c \approx 0.5$ at the center of the fluid flow line (Zhang et al. 2018). In this paper, it is assumed that the blocking body is generated from the center of the microchannel, that is f_c is taken as 0.5.

The Dean drag force satisfies the Eq. (2):

$$F_D \sim \rho U_m^2 a D_h^2 / r \tag{2}$$

Where, r is the radius of curvature of the curved channel. The scale of R_f is defined as the ratio of inertial lift to Dean drag force：

$$R_f = \frac{F_L}{F_D} \sim \frac{1}{\delta} (\frac{a}{D_h})^3 f_c(\mathrm{Re}_c, x_c) \tag{3}$$

Where, δ is the curvature ratio ($\delta = D_h/2r$). The radius of curvature is calculated by taking the arc of the midpoint of the opposite side for a square microchannel. If $R_f \geq 1$, the particles is pushed to the equilibrium position, and the flow of the fluid is dominated by the inertial lift. If $R_f < 1$, the particles is pushed toward the center of the streamline and the fluid is dominated by the Dean drag force, which leads to disorder of the particles. The microchannel where the blocking body is easy to be precipitated is designed to move the sedimentation position away from the center of the microchannel, instead of causing it to exit the microchannel with the fluid by using the secondary flow and the structure characteristic. When the diameter of the blocking body a is a constant, D_h is dominated by the characteristics of the channel. According to the Eq. (3), $R_f \geq 1$ is hoped.

3. Structure optimization of the microchannel

3.1. Structure of the microchannel

Based on above analysis, A microchannel with an expanding and contracting alternating structure is designed for the separation and elimination of the blocking body. In this configuration, the fluid flows from the contraction part to the expanded channel with a wide cross-section. The two structural microchannels are then alternately linked. When the fluid flows to the interface between the expansion unit and the contraction part, the secondary eddy current is formed at the top corner of the expanded structure due to the

sudden enlargement of the cross-section of the microchannel. The vortex diagram in the structure is shown in Figure 3.

3.2. Parameters of the microchannel

The blocking body is subjected to the upward combined force, which will cause the body to deviate from the original motion trajectory and aggregate toward the walls of the microchannel. Meanwhile, the parameters of an expansion-contraction structure are calculated by combining with the inertial lift and Dean drag force. Its structure parameters are shown in Figure 3.

The optimized microchannel structure can be calculated based on the block size (4 μm) and the inlet channel size. The optimization problem is:

$$\begin{aligned} &\max_{W_e, L_e} \quad R_f \\ &\text{s.t.} \quad \Delta P < \Delta P^{\max} \\ &\qquad W_c = W_1;\ L_c = L_1 \\ &\qquad 0.6W_e > W_c \end{aligned} \tag{4}$$

In the study, $\Delta P^{\max}=0.25\times10^4$ Pa, W_1 = 40 μm and L_1 = 100 μm are assumed, and the expansion structures adopt the cube structure, that is $W_e = L_e$. Therefore, there is only one optimal variable (W_e) in Eq. (4), the steepest gradient descent method is used to solve the optimization problem. The results are: W_e = 187 μm, $R_f^{\max}$ =3.1, the flow rate is 1.39 m/s. Simulations are performed by using CFD with W_e = 200 μm for the convenience of computation.

4. Results and Discussions

The simulation is solved by Fluent, in which the expansion-contraction structure is composed of 3 expansion units and 4 contraction units. The results are compared with straight microchannel which has the equal volume and length. The design parameters are shown in Table 1. The simulation parameters are shown in Table 2. The model is shown in Figure 4(a) and the straight microchannel is shown in Figure 4(b).

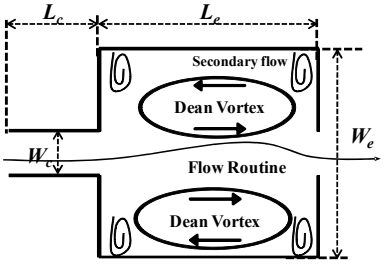

Figure.3 Vortex in the expansion structure

Table 1 Micro-channel model parameters

Type	Inner diameter (mm)	Volume (mm^3)	Length (mm)	Cross section (mm^2)
Straight channel	0.157	0.025	1	2.4649×10^{-2}
expansion-contraction channel	0.04/0.2	0.025	1	1.6×10^{-3}

Table 2 Simulation parameters in CFD

Model	Inlet velocity	Turbulent energy	Turbulent ratio	Wall
DPM	1.39m/s	0.1	0.1	escape

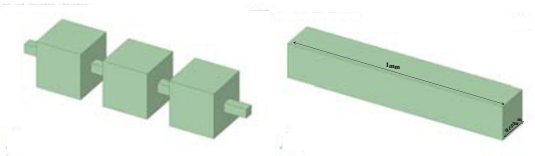

(a) (b)

Figure 4 Expansion-contraction microchannel and straight tube microchannel

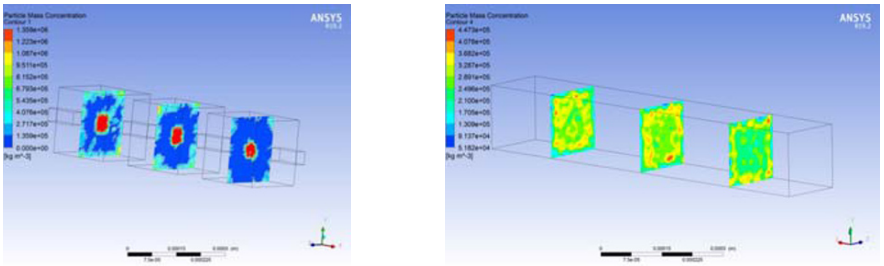

(a) (b)

Figure.5 Location of YZ plane particle aggregation in (a) the expansion-contraction microchannel, (b) the straight microchannel

Figure 5(a) and Figgure 5(b) are the distribution of the concentration of the blocking body in the axial and longitudinal sections of the microchannel with two structures, respectively. From Figure 5(a), it can be seen that the effect of Dean secondary flow is apparent from the concentration profile of the blocking body in the microchannel with the expansion -contraction structure. The blocking body particles at the inlet are uniformly dispersed in the solution, but the focusing of the blocking body is clearly achieved when it reaches the extended structure. Meanwhile, the effect of two symmetrical Dean secondary vortex flow is shown clearly in the corner. From Figure 5(b), the concentration of the blocking body in the microchannel is represented as a green area, and the aggregation effect on the blocking body is not obvious. The simulation results verify the previous analysis that the use of straight microchannels requires a longer axial length to achieve the inertial aggregation of the blocking body.

Figure 6 is the histograms of the concentration distribution of the blocking body in the microchannel with the expansion-contraction structure and the straight microchannel respectively. It is shown that there are more low-density regions of the concentration distribution of the blocking body in the expansion-contraction microchannel. Compared with 25% ratio of the low-blocking density area of the straight microchannel, the proportion of the new designed microchannel with 85% ratio is increased by 340% in the low density area. That is to say, the larger the low-density area of the blocking body, the better the separation effect of the blocking body, which shows the optimal design of microchannel can effectively realize the separation of the blocking bodies.

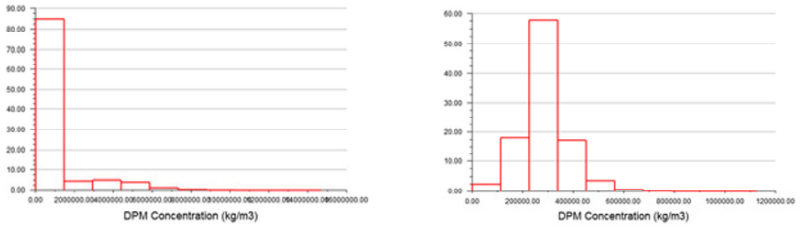

Figure 6 Histogram of blockage concentration distribution of the expansion-contraction microchannel (left) and straight microchannel (right)

5. Conclusions

A new method concerning the exclusion of blocking particles is introduced based on inertial aggregation principle and Dean secondary flow. By using the superposition of the inertial lift and Dean drag force, a microchannel with expansion-contraction structure is designed to achieve the aggregation separation and elimination of the blocking particles. By conducting the CFD simulation experiments, the new designed microchannel with expansion-contraction structure has a good performance of separating the blocking particles and can collect them at the top corners of the microchannel which are favourable for separation compared with the ordinary straight microchannel under the same conditions including particles and inlet velocity. The separation performance of the new designed microchannel is increased by about 340% compared to the ordinary straight one since the particles are concentrated at the four apex angles of the microchannel. The next work is to further optimize the expansion-contraction structure to achieve the shortest axial length for the particles separation.

References

T. Bayer, D. Pysall, O. Wachsen. 2000, Micro mixing effects in continuous radical polymerization. IMRET 3: Proceedings of the Third International Conference on Microreaction Technology, 165-170.

E. Dressaire, A. Sauret, 2016, Clogging of microfluidic systems, Soft Matter, 13(1): 37-48.

W. Huang, H. Zhang, T. Xu, 2011, Separation of blood plasma by inertial focusing using microfluidic chips (in Chinese). Chinese Sci Bull (Chinese Ver), 56: 1711–1719.

S. Jespers, S. Deridder, G. Desmet, 2018, A microfluidic distributor combining minimal volume, minimal dispersion and minimal sensitivity to clogging, J Chromatography A, 1537, 75-82.

G. Luo, K. Wang, J. Xu, Y. Wang, Y. Lv, 2014, Advances in research of microstructured chemical process (in Chinese), Scientia Sinica Chimica (Chinese Ver), 44(9), 1404-1412.

G. Segre, A. Sillberberg. Radial particle displacements in Poiseuille flow of suspensions[J]. Nature, 1961, 189 (4760): 209-210.

L. Sicignano, G. Tomaiuolo, A. Perazzo, 2018, The effect of shear flow on microreactor clogging, Chemical Engineering Journal, 341, 639-647.

B. Zhang, B. Yang, S. Yang, M. Su, G. He, X. Guo, H. Jin, 2018, Deposition behavior of barium sulfate in microchannel reactors (in Chinese), CIESC Journal (Chinese Ver), 69(4): 1461-1468.

S. Zhao, L. Bai, Y. Fu, Y. Jin, Y. Cheng, 2015, Fundamental research and applications of droplet-based microreactor (in Chinese), Chemical Industry and Engineering Progress (Chinese Ver), 34(3), 593-616.

Sauro Pierucci, Flavio Manenti, Giulia Bozzano, Davide Manca (Eds.)
Proceedings of the 30th European Symposium on Computer Aided Process Engineering
(ESCAPE30), May 24-27, 2020, Milano, Italy.
http://dx.doi.org/10.1016/B978-0-12-823377-1.50025-2

Comparative Study of Surrogate Modelling Techniques Applied to Three Different Chemical Processes

Ramón Mur, Ismael Díaz, Manuel Rodríguez

Departamento de Ingeniería Industrial y del Medio Ambiente, ETSI Industriales, Universidad Politécnica de Madrid, Calle de José Gutiérrez Abascal, 2, 28006 Madrid

r.mur@alumnos.upm.es

Abstract

In this paper, a comparative study of surrogate modelling techniques applied to chemical processes of different complexity is presented. The surrogate modelling techniques considered in this work are support vector regressions (SVR), Kriging and artificial neural networks (ANN). The surrogates were obtained by fitting to process data obtained from rigorous flowsheeting simulations previously developed in Aspen Plus v10. The processing schemes to be surrogated were (in order of decreasing complexity):1) the separation of aromatics-aliphatics mixtures by liquid-liquid extraction using ionic liquids as novel and more sustainable solvents, 2) the toluene hydrodealkylation process and 3) a simple distillation of organic solvents. Besides, in the first process (aromatics-aliphatics separation), advanced predictive thermodynamic models based on quantum chemical calculations (COSMO-SAC) were considered, allowing for the prediction of fluid phase equilibria properties of mixtures containing ionic liquids. In addition, the robustness of the surrogate techniques was assessed by adding a random noise contribution to the variables sampled. Thus, the paper is organized as follows: in section 1 an introduction to the surrogate modelling techniques is presented along with a short description of the chemical processes modelled in Aspen Plus. Afterwards, section 2 includes the methodology detailing the computational approach presented. The main results obtained in the study are presented in section 3 and the final the conclusions summarized in section 4.

Keywords: Surrogate Modelling, Process Modelling

1. Introduction

1.1. Surrogate modeling techniques

There are many advanced surrogate modelling libraries available for the scientific/engineering community, ready to be used in the fields of engineering for optimization, parametric analysis, etc. Three of the most widely employed are support vector regression (SVR), Kriging interpolation and artificial neural networks (ANN); which have been considered in this work to test their performance for the modelling of chemical processes.

1.1.1. Support vector regression

SVR surrogates are represented as the weighted sum of basis functions added to a constant term. A general form of SVR surrogate is given in Eq. (1).

$$\hat{f}(X) = \mu + \sum_{i=1}^{n} w^i \psi(X, X^i) \quad (1)$$

Assuming a simple basis function $\psi = X$, the surrogate can be written as per Eq. (2).

$$\hat{f}(X) = \mu + w^T X \quad (2)$$

The unknown parameters μ and w in the model are obtained by solving an optimization problem (Cortes et al (1995)).

1.1.2. Kriging

Kriging is based on the idea that a surrogate can be represented as a realization of a stochastic process. Kriging is a two-step process. First, the regression function f(x) is constructed on the basis of Generalized Least Squares (GLS) regression. Then, a stochastic Gaussian process that represents the uncertainty about the mean of Y (x) with expected value zero is constructed based on the residuals (Z(x)).

$$Y(x) = f(x) + Z(x) \quad (3)$$

Where f(x) is a regression function and Z(x) is a Gaussian process with mean 0, variance θ^2 and a correlation matrix Ψ. Depending on the form of the regression function f(x), Kriging has different prefixes. Simple Kriging assumes the regression function to be a known constant. On the other hand, Ordinary Kriging assumes an unknown constant regression function (f(x) = a). In general, Universal Kriging assumes amultivariate polynomial regression function:

$$f(x) = \sum_{i=1}^{p} \alpha_i b_i(x) \quad (4)$$

Given p the number of candidate functions, $b_i(x)$ the base functions and α_i the coefficients determined by regression. Further details can be found at (Krige et al (1960)).

1.2. Artificial Neural Networks (ANN)

The structure of ANN typically consists of three distinct layers: the input layer, the hidden layer(s), and the output layer. The connections of neurons across layers represent the transmission of information between neurons. A typical ANN with three layers and one single output neuron has the following form:

$$\hat{y} = \hat{f}(X) = \sum_{j=1}^{J} w_j f\left(\sum_{i=1}^{k} v_{ij} f(x_i) + \alpha_j\right) + \beta \quad (5)$$

Where X is an k-dimensional vector with $\{x_1, x_2, \ldots, x_k\}$ as its elements, f is the transfer function, v_{ij} is the weight on the connection between the i^{th} input neuron and j^{th} hidden neuron, α_j is the bias in j^{th} hidden neuron, w_j is the weight on connection between j^{th} hidden neuron and the output neuron, J is the total number of hidden neurons, and β is the bias of the output neuron. The weights and biases can be determined by the training procedure minimizing the training error (McCulloch et al (1943)).

1.3. Benchmark chemical processes

1.3.1. Aromatic-Aliphatic separation from low aromatic content naphta using ionic liquids

The liquid-liquid extraction process to separate aromatic components from a naphta stream using ionic liquids as solvents is studied in the present work as shown in Figure 1. For this purpose, an Aspen Plus flowsheet was developed based on the work of (de Riva et al (2016)). In this process, the naphtha entering the process (S-NAP-IN) contacts the extraction solvent stream (S7-IL) in a liquid-liquid extraction column (EXT). The raffinate (S-AL+N2) of this operation is the aliphatic product while the extract (S-AR+IL, rich in aromatic components) enters the intermediate stripper (STRIP) where the remaining aliphatic components are separated by an inert gas (N2) (S2) and exit the process in stream S-AL. After this gas stripping, the gas and the aliphatic hydrocarbons are separated in column SEP. The aromatic-rich stream (S1-IL) and the ionic liquid are separated in a vacuum distillation vessel (FLASH) after being conditioned (HEAT1). The aromatic components obtained in this vessel (S1-AR) are conditioned (HEAT2, PUMP1) before leaving the process as product (S3-AR). The regenerated ionic liquid (S3-IL) is recirculated as extraction solvent (S4-IL) to the extraction column (EXT-DIST), after being conditioned (HEAT1, HEAT3, PUMP2).

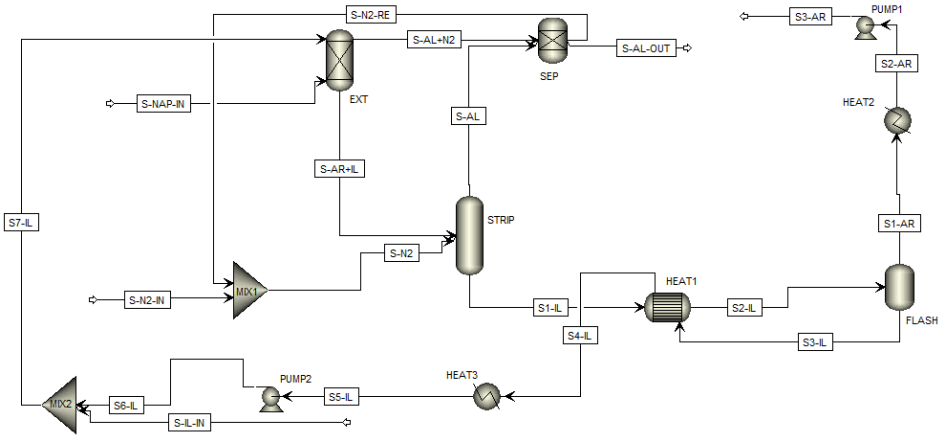

Figure 1: Aromatic-aliphatic separation from low aromatic content naphta using ionic liquids

The following process variables have been sampled (input of the model):

- Theoretical number of stages of the liquid-liquid extraction column (EXT): 2-30.
- Molar solvent to feed ratio of the liquid-liquid extraction column (EXT): 1-4.
- Recovery temperature of the ionic liquid (FLASH): 130-230ºC.
- Nitrogen mass flow input into the stripper column (STRIP): 40-80 ton/h.

The final output variable to be regressed is the total mass fraction of aromatics (sum of all aromatics compound) in the product stream.

1.3.2. Toluene Hydrodealkylation

The purpose of this process is to produce benzene from toluene rich streams using H_2 as reagent, see Figure 2.The toluene entering the process (S1-TO-IN) contacts the recovery toluene (S3-TOL) as well as the hydrogen entering the process (S-H2-IN) contacts the recovery hydrogen (S3-H2). These streams after being conditioned (HEAT1) enter the reactor (REACT) where the hydrodealkylation reaction occurs. Afterwards, methane and hydrogen are separated from the S2-TO-BE stream by flash separators (FLASH1

and FLASH2) and then toluene and benzene are also separated using distillation columns (COL1 and COL2). Hydrogen and toluene are finally recycled to the process.

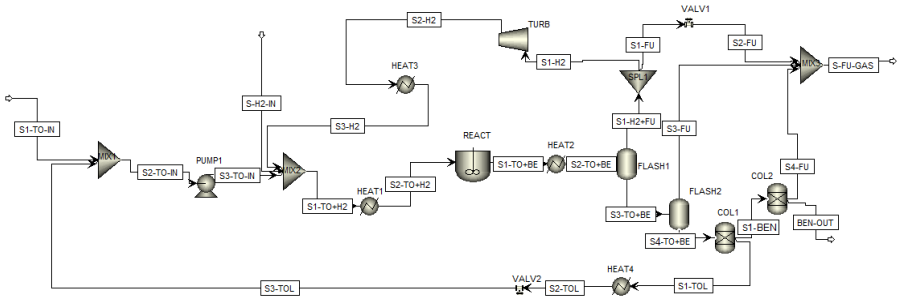

Figure 2: Toluene hydrodealkylation process

The following main chemical reaction has been assumed, and the kinetic equation and parameters adopted from (Dimian et al (2014)):

$$H_2 + C_6H_5CH_3 \rightarrow C_6H_6 + CH_4$$

The following process variables have been sampled (input of the model):

- Volume of the reactor (REACT): 0.8-200 m^3.
- Temperature of the reactor (REACT): 550-850ºC.
- Pressure of the reactor (REACT): 3-240 bar.
- Fraction of recovered toluene after the first distillation column (COL1): 0.2-0.95.

The final output variable to be regressed is the mass fraction of benzene in the product.

1.3.3. Distillation of organic solvents

A solvent mixture of acetone, methanol and water enters the first distillation column (COL1) along with a water stream and the acetone is separated as depicted in figure 3. Then, the bottom stream (S-WA-MET) enters the second distillation column (COL2) where methanol and water are separated; the process scheme is shown in Fig 3.

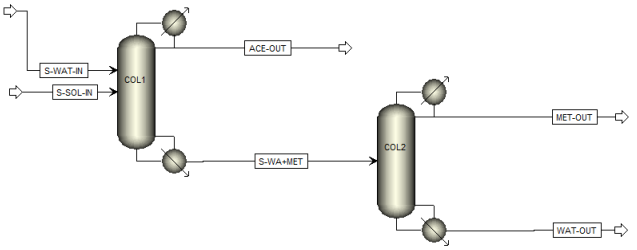

Figure 3: Distillation of organic solvents

The following process variables have been sampled (input of the model):

- Number of theoretical stages at the first column (COL1): 5-40.
- Number of theoretical stages at the second column (COL2): 5-40.
- Molar reflux ratio at the first column (COL1): 1-10.
- Molar reflux ratio at the second column (COL2): 1-10.

The final output variable to be regressed is the acetone mass fraction in the product.

2. Methodology

The methodology followed in this work can be split into three steps: the development of a communicating interface for sampling; the sampling and data preprocessing; and the fitting of the surrogate models. The first step is needed to call the variables values on the Aspen Plus models from MATLAB (COM interface), which is the main coding platform where the preprocessing and fitting steps are carried out. Both the input (before the execution of the process simulator) and the output variables (resulting from the Aspen Plus execution) were normalized to fit the [0,1] range. Data sampling was repeated 150 times using the LHS method adding a random noise value (low noise was considered to be$\eta \approx N(0,0.1)$ and large noise $\eta \approx N(0,0.2)$). The ranges of the input variables sampled are shortlisted for each process in sections 1.3.1 to 1.3.3. Then, data regression is carried out using different toolboxes available in MATLAB. Data fitting for Support Vector Regression and Artificial Neural Networks were performed using the built-in Statistics and Machine Learning and the Deep Learning toolboxes, whereas Kriging regressions were conducted using the ooDace toolbox developed by (Couckuyt et al (2014)) also available for MATLAB. The workstation used for the calculations was a computer with a 3.40GHz Intel Core i7-6700 CPU and 16 GB of RAM under Windows 10.

3. Results

In order to evaluate the performance of each surrogate modelling technique, the data sampling, noise addition (small or large) and regression process was repeated 25 times for each surrogate technique over each individual process in order to compute the average mean squared error (MSE) and the std deviation (the average and std deviation of the 25 surrogate models developed). Figures 4 to 6 show the average values and standard deviation for the three different processes studied in this work. The average and std deviation of the MSE values obtained have been normalized by dividing by the values obtained for SVR with large noise (deemed as the reference value).

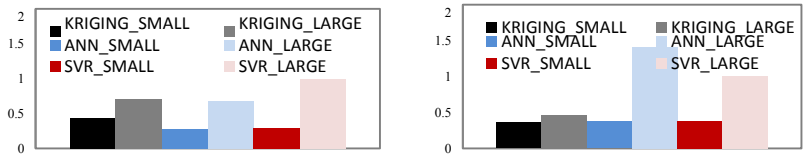

Figure 4: Average (a) and std deviation (b) of the MSE (aromatics-aliphatics separation).

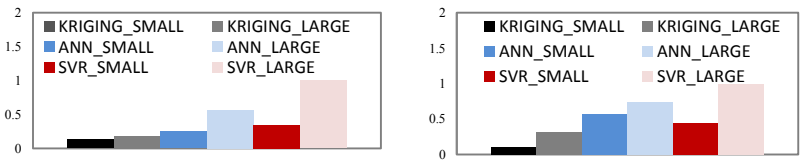

Figure 5: Average (a) and std deviation (b) of the MSE (toluene hydrodealkylation)

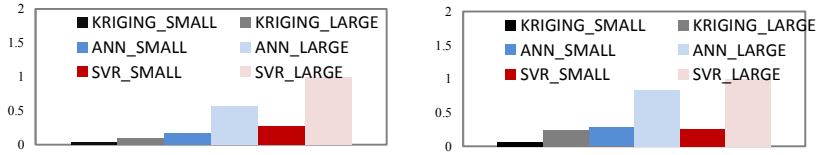

Figure 6: Average (a) and standard deviation (b) of the MSE (distillation of organic solvents).

Figure 4 shows that for the more complex process involving liquid-liquid extraction of aromatics-aliphatics mixtures with ionic liquids, the smaller MSE average value are obtained by ANN (SVR show similar performance), whereas the largest MSE standard deviation is also obtained by ANN (SVR show also similar values). In the other two processes (Figures 5 and 6, toluene hydrodealkylation and distillation of organic solvents), Kriging regression have shown to be the more accurate technique (lowest average deviations obtained) and the less sensitive to data changes (lowest standard deviation in the set of 25 regressions carried out). As it can be also seen in the previous figures, the imposed noise applied to the variables during the sampling step clearly influences the final deviation of the fitted models. It agrees with the fact that the more dispersed the sampled data to fit, more deviations are expected between the final surrogates fitted. However, the discussion presented herein is quite limited and is only valid in the restricted scope of this work. A broader study considering a larger pool of chemical processes, different variable nature (temperature, pressure, compositions, flows…) and different surrogate modelling parametrizations is under development at this moment which is expected to shed more light on the discussion presented herein.

4. Conclusions

In this work, a systematic study of surrogate modelling techniques (SVR, Kriging and ANN) applied to different chemical processes has been carried out. The performance of these techniques has been evaluated in the presence of imposed noise during variable sampling. Results show that for the more complex process model (aromatics-aliphatics separation), ANN and SVR have achieved the lowest MSE value. On the contrary, for the less complex processes (solvent distillation and toluene hydrodealkylation), Kriging regression was the most promising technique. However, a wider study is needed to obtain less case dependent results and deeper insights about the suitability of the different surrogate modelling techniques currently available.

Acknowledgements

The authors are grateful to the Com. de Madrid (project P2018/EMT-4348 SUSTEC) for financial support.

References

Cortes, C., & Vapnik, V. (1995). Support-vector networks. Machine learning, 20(3), 273-297.

Couckuyt I, Dhaene T, Demeester P (2014). OoDACE toolbox: A flexible object-oriented kriging implementation. J Mach Learn Res,15,3183–3186.

De Riva, J., Ferro, V. R., Moreno, D., Diaz, I., & Palomar, J. (2016). Aspen Plus supported conceptual design of the aromatic–aliphatic separation from low aromatic content naphtha using 4-methyl-N-butylpyridinium tetrafluoroborate ionic liquid. Fuel processing technology, 146, 29-38.

Dimian, A. C., Bildea, C. S., & Kiss, A. A. (2014). Integrated design and simulation of chemical processes (Vol. 13). Elsevier.

Krige, D. G. (1960). On the departure of ore value distributions from the lognormal model in South African gold mines. Journal of the Southern African Institute of Mining and Metallurgy, 61(4), 231-244.

McCulloch, W. S., & Pitts, W. (1943). A logical calculus of the ideas immanent in nervous activity. The bulletin of mathematical biophysics, 5(4), 115-133.

Sauro Pierucci, Flavio Manenti, Giulia Bozzano, Davide Manca (Eds.)
Proceedings of the 30th European Symposium on Computer Aided Process Engineering (ESCAPE30), May 24-27, 2020, Milano, Italy.
http://dx.doi.org/10.1016/B978-0-12-823377-1.50026-4

A Non-Autonomous Relativistic Frame of Reference for Unit Operation Design

Andres Carranza-Abaid,* Jana P. Jakobsen

Norwegian University of Science and Technology (NTNU), Department of Chemical Engineering, 7491, Trondheim, Norway
andres.c.abaid@ntnu.no

Abstract

This contribution presents an efficient systematic algorithm for unit operation design that uses a newly developed non–autonomous relativistic frame of reference (NARF). The NARF is aimed towards the conceptual design of unit operations that require solving systems of ordinary differential equations (ODE) where the system volume is unknown. The improved NARF algorithm was tested and compared against the classical modelling method that utilizes the Eulerian reference frame (ERF). To assess and validate the qualities of the NARF, a gas-liquid contactor was modelled using both frames of reference. The results show that the NARF significantly outperforms the computational speed of the ERF up to 1 order of magnitude, all of this, without compromising the accuracy of the results of the unit operation. The NARF can become invaluable in the conceptual design and optimization in computational chemical engineering.
Keywords: Modelling, Process Design, Multiphase Reactors, Absorption, CO_2

1. Introduction

The conceptual design and optimization of chemical processes has become a must in the later decades because of the ever-increasing economic competitive standards. Therefore, the optimization of chemical plants design has become common task in chemical engineering. Nevertheless, the optimization of a chemical process is a complex and computationally intensive problem that may require long periods of time to complete if the calculations are too extensive. This problem arises because unit operations are commonly designed using the ERF, that although useful, it jeopardizes the computational speed due to its iterative algorithm. The improved algorithm using NARF was conceived by making an analogy with the Galilean relativity principle: “if the laws of nature are valid in one frame of reference, they must be valid on a different frame of reference”.

2. Modelling

2.1. Eulerian Reference Frame

In order to model a unit operation, the Lagrangian and Eulerian frames of reference are usually utilized. The last one being the most used because it is computationally more efficient (Jakobsen, 2008). In most 1-D problems, unit operations can be described in the ERF as an autonomous system of *c* ODEs. When using this reference frame, the modelled system is considered as a physical entity and the obtained solution describes how the dependent variables change within it. The ODE system has the following general form:

$$\frac{d}{d\theta}\left(\underline{\beta}(\theta)\right) = \underline{f}\left(\underline{\beta}(\theta), \underline{\mu}\right) \tag{1}$$

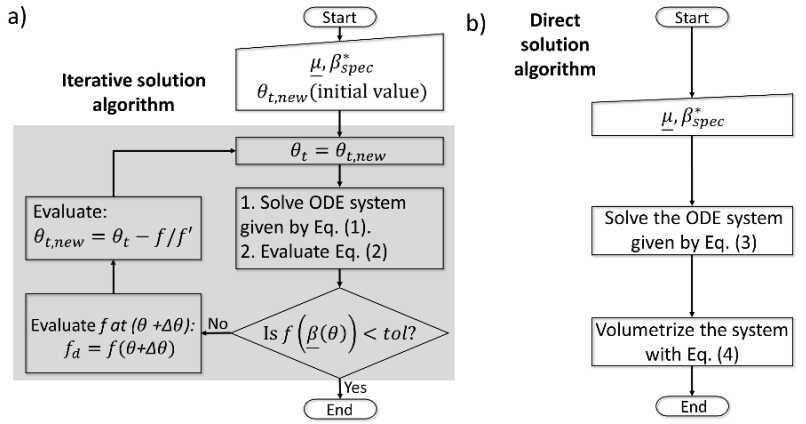

Figure 1: Algorithm to design a unit operation using a) Eulerian frame of reference and b) Non- Autonomous Relativistic Frame of Reference.

Where θ is the control volume (we refer to this variable as volume throughout the paper, but it can be time as well), $\underline{\beta}$ is the vector of state variables (mass or energy flow velocities), $\underline{\mu}$ is the vector of parameters. If a variable has a line _ underneath, it indicates that the variable is a vector, otherwise it is a scalar. Eq. (1) is said to be autonomous because it is not an explicit function of the independent variable (θ). A unit operation design problem fixes a design specification at a specific position (i.e. the outlet). Thus, a discrepancy function between the actual calculated value of the design variable Eq. (1) and the design specification must be set. This discrepancy function has the form:

$$f\left(\underline{\beta}(\theta)\right) = \beta^*(\theta) - \beta^*_{spec} \tag{2}$$

Where the superscript * indicates that it is the specified state variable and the subscript *spec* means that it is the fixed or specified variable in the problem. To solve a problem with the abovementioned characteristics, the procedure depicted in Figure 1a must be executed. Although this modelling approach has been used extensively, the procedure is computationally expensive because the ODE given by Eq. (1) must be solved as many times as necessary until Eq. (2) is satisfied (Figure 1a). Furthermore, a unit operation can be designed if and only if the solution of the state variables satisfies $\underline{\beta} \in \mathbb{R}$; hence, unit operation design implicitly assumes that the solution is within physical boundaries.

2.2. Non-Autonomous Relativistic Frame of Reference

Considering the main assumption of unit operation design: that the solution is within the real numbers ($\underline{\beta} \in \mathbb{R}$), it is possible to transform the ODE system from being autonomous to non-autonomous by deriving the conservation equations in terms of the design specification variable. This is done by performing a differentiation on the design specification conservation equation and substituting the result into all the remaining conservation equations of the ERF. The final non-autonomous ODE system has the form:

$$\frac{d}{d\beta^*}\left(\underline{\beta}^r\left(\beta^*\right)\right) = \underline{f}\left(\underline{\beta}^r\left(\beta^*\right), \underline{\mu}\right) \tag{3}$$

$$\frac{d\theta}{d\beta^*} = f\left(\underline{\beta}^r\left(\beta^*\right), \underline{\mu}\right) \tag{4}$$

Where the superscript *r* indicates a reduced vector that includes all the state variables except the design specification variable. Eq. (3) demonstrates that it is possible to determine the values of the state variables in an "spaceless" form before knowing the spatial dimensions of the system. Therefore, the solution given by Eq. (3) is a geometrical reduction of the solution given by the ERF. Even though Eq. (3) solves all the conservation equations, the unit operation volume has yet to be calculated. In order to transform the solution from the "spaceless" form to a solution with actual spatial dimensions, Eq. (4) must be used as a volumetrizing function to determine the required volume of the unit operation. A summary of the algorithm to design a unit operation in the NARF is illustrated in Figure 1b. It must be noted that a model based on the NARF describes how the non-design specification state variables behave with respect to the design specification variable (Eq. (3)) and how much volume is needed (Eq. (4)) to go from an initial state to a final state of the design specification variable.

2.3. Example Model

As an example, a design calculation of an amine-based CO_2 gas-liquid contactor has been performed in order to illustrate the equivalence between both frames of reference and to quantify the computational advantages that the NARF possess. The model of the CO_2 absorber is a boundary value problem (BVP) and was solved in Matlab 2018b with the bvp4 in-built function. The following assumptions were done:

- steady state and plug flow hydrodynamic regime
- four components are considered (CO_2, MEA, H_2O and N_2) and only CO_2 and H_2O go through a phase change. The mass transfer is assumed to go from the vapor to the liquid phase
- the two-film theory describes the mass and energy transfer
- the gas-phase mass transfer resistance is negligible
- the absorber is considered adiabatic and isobaric
- the kinetics are described by a second order irreversible enhancement factor model

2.3.1. Eulerian Conservation Equations

The conservation equations in the ERF are discretized in terms of the system volume. This method of developing the equations has been extensively discussed in the literature (Gabrielsen et al., 2007). The resulting equations that raise from this approach have the general form of Eq. (1), and for the current example the ODE system is described by:

$$\frac{d\underline{\beta}}{d\theta} = -\underline{\mathrm{r}} \tag{5}$$

Where $\underline{\mathrm{r}}$ is the rate of property transfer that can be either a mass or energy flow transfer rate. An absorber is usually a countercurrent unit operation, hence, there are two groups of boundary conditions. The first group describes the material and energy flows of the inlet vapor phase at the bottom of the absorber while the second group accounts for the material and energy flows of the liquid phase at the top of the absorber. The B.C. are:

$$\underline{\beta_v} = \underline{\beta_{v,0}} \quad at \quad \theta = 0 \ (Top) \qquad\qquad \underline{\beta_l} = \underline{\beta_{l,1}} \quad at \quad \theta = \theta_t \ (Bottom) \tag{6}$$

The subscripts indicate: *v* applies for the property flows in the vapor phase, *l* for the property flows in the liquid phase, *t* is the total volume of the system, *0* stipulates that the B.C. is at the bottom of the absorber while *1* shows that it is at the top of the absorber. It

is clear from Eq. (6) that the B.C. of the system are the spatial boundaries of the absorber. In order to obtain the total volume of the unit operation, Eqs. (5) and (6) are to be solved along with a discrepancy function with the form of Eq. (2) where the value of the CO_2 molar flow at the top β_{v,CO_2} must be equal to the design specification β^*_{spec}.

2.3.2. Non-Autonomous Relativistic Conservation Equations

The conservation equations in the NARF are derived using the CO_2 molar flow as the independent variable. It is possible to do so because the boundaries are specified in the design problem, therefore the CO_2 molar flow will change from the CO_2 molar flow in the inlet stream to the specified CO_2 molar flow in the outlet stream. The following equations are obtained by following the procedure described in section 2.2:

$$\frac{d\underline{\underline{\beta^r}}}{d\beta^*} = \frac{\underline{\underline{r^r}}}{r^*} \tag{7}$$

$$\frac{d\theta}{d\beta^*} = -r^* \tag{8}$$

The B.C. of the ODE system given by Eq. (7) is numerically the same as the ones used in the ERF. Except for the fact that the B.C. for the CO_2 molar flow cannot be used because they are being utilized as the boundaries of the independent variable. Therefore, there is one less B.C. in the vapor phase in the NARF. The B.C. are:

$$\underline{\beta_v} = \underline{\beta_{v,0}} \quad at \quad \beta^* = \beta^*_0 \left(Initial\ state\right) \qquad \underline{\beta_l} = \underline{\beta_{l,1}} \quad at \quad \beta^* = \beta^*_{spec} \left(Final\ state\right) \tag{9}$$

Following the algorithm in Figure 1b, Eqs. (7) and (9) must be evaluated first, and after the solution is obtained, Eq. (8) can be evaluated. The B.C. for Eq. (8) are:

$$\theta = 0 \quad at \quad \beta^* = \beta^*_0 \left(Initial\ state\right) \qquad \theta = \theta_t \quad at \quad \beta^* = \beta^*_{spec} \left(Final\ state\right) \tag{10}$$

The volumetrizing function Eq. (8) along with the B.C. (Eq. (10)) must be solved to calculate the volume of the absorber. Eq. 8) is analogous to the performance equation for reactors developed by Levenspiel (2003); but Eq. (8) is not limited mass balances as the original equation.

2.3.3. Complementary Equations

The equations presented in this section apply for both frames of reference. The material balances source term is:

$$r_i^m = \frac{x_i \rho_l E k_{i,l} a}{\bar{M}_l H_i} \left(y_i - y_i^{eq}\right) \tag{11}$$

Where r^m is the mass transfer rate of component *i*, ρ_l is the liquid density, *E* is the enhancement factor, k_l is the mass transfer coefficient of the component *i* in the liquid phase, a is the ratio between the effective interfacial area and the gas-liquid contactor volume, $\bar{M}_l$ is the average molar fraction, *H* is the thermodynamic factor that relates the distribution of the component *i* between the vapor and the liquid phase, y_i is the molar fraction of component *i* in the vapor phase and the superscript ^{eq} indicates the equilibrium vapor composition of the liquid phase. The mass transfer coefficients and the effective interfacial area are calculated with Onda's correlation for random packings. For H_2O, the value of the enhancement factor is equal to 1, the equilibrium composition is given by

Raoult's law and the H_2O thermodynamic factor was estimated in Aspen Plus to be 0.117. The physical properties, the equilibrium composition of CO_2 and the enhancement factor are calculated using the SOFT model proposed by (Luo et al., 2014). The source term in the energy balance equations is calculated by:

$$\underline{r^E} = h_h \left(T_v - T_l \right) \tag{12}$$

Where $\underline{r^E}$ is energy transfer rate for both phases, h_h is the overall heat transfer coefficient, T_v is the bulk temperature of the vapor phase and T_l is the bulk temperature of the liquid phase. The heat capacities of the vapor and the liquid phase are estimated to be 30.1 and 85.1 kJ/kmol K respectively. The heat of phase change for CO_2 is 88,000 kJ/kmol (Gabrielsen et al., 2005) and 44,000 kJ/kmol for H_2O. The overall heat transfer coefficient was estimated using the Chilton-Colburn analogy and is considered constant and equal to 25.3 kJ/s m^2 K.

3. Results and Discussion

The problem statement of the study case is: Design an absorber that removes 90% of CO_2 from a flue gas (1 kmol/s) containing a 10/90% mol CO_2/N_2 mixture at 40 °C and 105 kPa with a solvent containing 30% wt. MEA, 70% wt. H_2O at 40 °C. The absorber packing is Mellapak 250Y and the superficial vapor velocity is set to be 1.5 m/s at the bottom. The design variables are the loading α (mol CO_2/mol MEA) at the solvent input and the molar liquid to gas ratio (LG) between the solvent and the flue gas. Note that the design specification is the outlet CO_2 mole flow given by the 90% reduction requirement and the volume is the unknown variable.

A set of 10,000 simulations were performed to show the equivalence between both frames of reference. The design variables values used were among the following ranges α = (0.05-0.24) and LG = (4.0-8.0). The tolerance for the discrepancy function in the ERF was set to 10^{-5}. The profiles of the state variables with respect to the volume were compared in each one of the simulations by calculating the relative deviation between both frames of reference. The maximum, minimum and average deviations of the profiles of the CO_2 molar flow in the vapor phase, H_2O molar flow in the liquid phase, the energy flow in the liquid phase are presented in Table 1. In the last column of Table 1, the relative deviation the total volume of the absorber is also shown. As seen in Table 1 the NARF modelling scheme always gives the same results as the ERF; where the negligible differences are of numerical nature. This agrees with the principle of the Galilean invariance: all frames of reference are related to one another by a mathematical transformation.

Table 1. Relative deviation of the results of representative state variables between both frames of reference

Relative Deviation / 10^6	$\beta_{v,CO2}$	$\beta_{l,H2O}$	$\beta_{l,E}$	θ_t
Min	-1.5	-7.1	-0.5	-2.7
Max	0.7	7.4	4.2	1.2
Average	-0.1	-0.6	0.5	-0.2

The algorithmic and computational advantages of the NARF are shown in Figure 2. It compares the relative computational speed between both reference frameworks at different tolerances for convergence for the iteration loop described in Figure 1a. A total of 1,000 simulations were performed in each one of the runs. Figure 2 shows that as the ERF becomes more exact, the computational advantage of NARF increases. It is seen that this behavior is proportional to the amount of iterations that the ERF must perform in order to reach the desired design specification. Consequently, the NARF is more accurate than the ERF for unit operation design and, additionally, takes less time to solve.

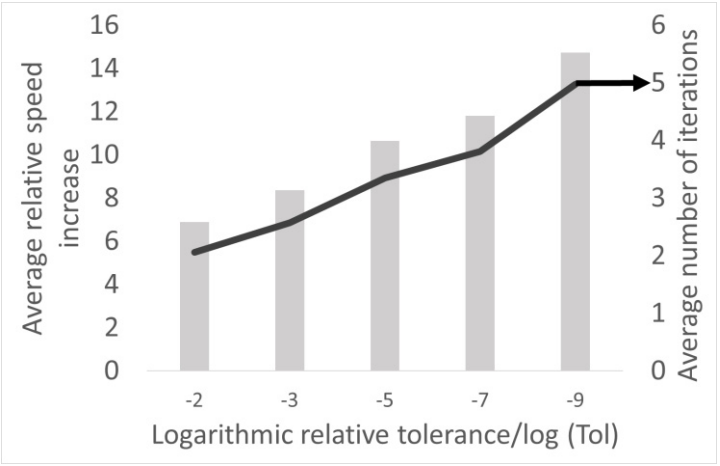

Figure 2: Computational comparison between both frames of reference. Left axis: how many times is the NARF compared to the ERF. Right axis: Average number of iterations.

4. Conclusions

An efficient algorithm for unit operation design calculations based on new non-autonomous relativistic reference frame was developed, numerically validated and tested on an example case of CO_2 absorption. The NARF unit operation design algorithm is faster and is even more accurate than using an algorithm developed in the ERF. This shows that this frame of reference can substitute the classical Eulerian frame of reference in the conceptual design of unit operation equipment. This frame of reference will be especially advantageous in the development of computationally demanding optimization and mapping frameworks for chemical engineering processes.

References

Gabrielsen, J, Svendsen H.F., Michelsen, M.L., Stenby E.H., Kontogeorgis, G.M., 2007, Experimental Validation of a Rate-Based Model for CO_2 capture using AMP solution, Chemical Engineering Science, 62, 2397-2413.

Jakobsen, H., 2008, Chemical Reactor Modeling Multiphase Reactive Flows, 2nd ed., McGraw-Hill, England, Chapters 1-2.

Levenspiel, O., Chemical Reaction Engineering, 3rd ed., John Wiley & Sons, Chapters 23-24.

Luo X., Hartono A., Hussain, S., Svendsen H., 2015, Mass transfer and kinetics of carbon dioxide absorption into loaded aqueous Monoethanolamine solutions, Chemical Engineering Science, 123, 57-59.

Tobiesen, F.A., Svendsen H.F., 2007, Experimental Validation of a Rigorous Absorber Model for CO_2 Postcombustion Capture, AIChE Journal, 53, 4, 846-865.

Sauro Pierucci, Flavio Manenti, Giulia Bozzano, Davide Manca (Eds.)
Proceedings of the 30th European Symposium on Computer Aided Process Engineering (ESCAPE30), May 24-27, 2020, Milano, Italy.
http://dx.doi.org/10.1016/B978-0-12-823377-1.50027-6

Evaluating the Transient Operation of PCC for fast Response gas Turbines in a Future Low-carbon Energy System

Mathew Dennis Wilkes, Solomon Brown*
Department of Chemical and Biological Engineering, University of Sheffield, Sheffield, S1 3JD, United Kingdom
s.f.brown@sheffield.ac.uk

Abstract

Dispatchable power generators with fast ramping capabilities are essential to combat the intermittency issues of renewable energy, and to ensure system security and flexibility. Quick starting gas turbines accompanied with post-combustion carbon capture utilisation and storage (CCUS), can play a vital role in decarbonising the energy sector.
To analyse the transient behaviour of post-combustion capture (PCC), a dynamic rate-based model is developed in gPROMS® gCCS 1.1.0. The aim of this paper is to simulate the flexible operation of a PCC plant attached to a small-scale (<50MW) open-cycle gas turbine (OCGT) power station. Model validation is carried out against a dynamic pilot-scale study, then scaled up to match the typical flue gas output from a modern gas turbine. Data from the Balancing Mechanism Reporting Service (BMRS) and industrial suppliers is used to assess transient nature of OCGT power generation. It is found that keeping utility streams constant causes a decrease in capture plant efficiency during the constant flowrate phases; however, the rapid transitioning between loads is beneficial as the time averaged capture rate remains above 90% capture.

Keywords: CO_2 capture, Dynamic Modelling, Post-Combustion Capture, Chemical Absorption, Flexible Operation

1. Introduction

It is internationally understood that the targets set to combat climate change cannot be achieved without Carbon Capture, Utilisation and Storage (CCUS). It is vital in developing a low-carbon electricity system, as well as decarbonising heavy polluting industries such as cement and steel production (Global CCS Institute, 2018). Energy systems with near-100% renewable power are feasible; however, a high penetration of intermittent renewables leads to realistic constraints on electricity grids with significant operational challenges (Heuberger & Mac Dowell, 2018).
For system security and flexibility, gas turbines are desirable due to their low greenhouse gas emissions (compared to other fossil sources), operational flexibility, reliability, fast ramping rates and short lead times (Parsons Brinckerhoff, 2014). With the role small-scale decentralised energy could play in decarbonising the electricity sector, the number of quick-response gas turbines is expected to increase (Heuberger & Mac Dowell, 2018). To have a low-carbon electricity system these generators will require CO_2 capture, and this paper focuses on post-combustion capture (PCC). The most commonly used and researched PCC technology is amine-based chemical absorption, with 30 wt. % monoethanolamine (MEA) the benchmark solvent (Oko, et al., 2017).
To ensure security of electricity supply, understanding the operational flexibility of fossil power generation coupled with PCC is essential. Several studies have tackled this issue

experimentally and using dynamic models (Bui, et al., 2014). However, the focus in the literature has been on large scale system (>300MWe). To the author's knowledge, there are no examples in the literature for the flexible operation of PCC for small scale power generators (<50MWe), which has been highlighted as a key challenge by Bui et al. (2018a) due to economies of scale. The aim of this paper is to develop, validate and analyse a dynamic model of CO_2 absorption using the benchmark MEA solvent, for a small-scale quick response open-cycle gas turbine (OCGT) plant. The capture model is built in the equation-oriented systems modelling tool - gPROMS® gCCS 1.1.0 by Process Systems Enterprise Limited. Data from the Balancing Mechanism Reporting Service (BMRS) is used to assess the transient nature of OCGT power plants.

2. Model Development

2.1. Capture Plant

The complex reaction kinetics and the interaction between integrated system parts is difficult to accurately assess through steady-state modelling. Bui et al. (2014) reviewed dynamic modelling and optimisation of PCC CO_2 absorption using amine solvents, and rate-based models are more capable of handling transient operating scenarios. Figure 1 shows the model topology of a conventional amine-absorption process. The cooled exhaust gases enter the absorption column, with the 'lean' solvent flowing in a counter current direction. After absorbing the CO_2 the 'rich' solvent passes through a cross heat-exchanger before entering a stripping column. A reboiler maintains the elevated stripper temperature required for solvent regeneration and the condenser ensures a pure CO_2 stream (Bui, et al., 2014).

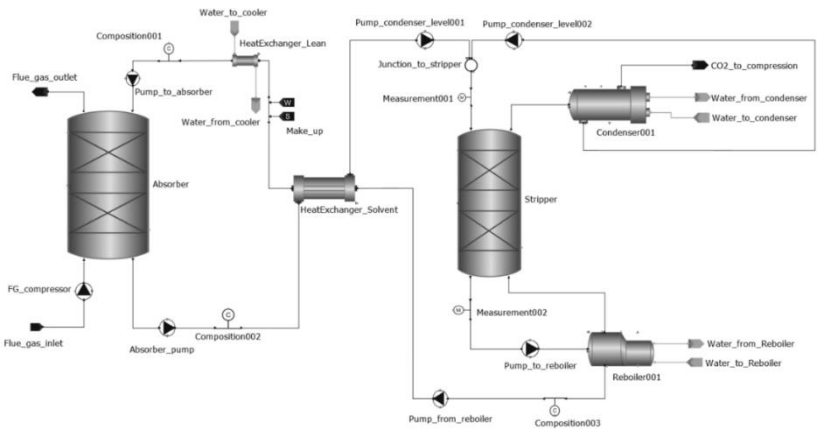

Figure 1: Model topology of the CO_2 absorption process, built in gPROMS® gCCS 1.1.0.

For absorption/desorption units, gCCS uses a rate-based approach where the multi-component mass and heat transfer is described through two-film theory. Each column is represented by a cascade of non-equilibrium stages, with the following assumptions:

- one-dimensional (axially distributed)
- reactions are treated implicitly and only occur in the bulk-liquid phase
- chemical equilibrium in the entire liquid phase
- phase equilibrium is assumed at the vapour-liquid interface
- negligible solvent degradation

Each column uses the Billet & Schultes pressure drop correlation and the Onda mass transfer correlation. The thermophysical properties are described through the Statistical Associating Fluid Theory (SAFT) properties package called gSAFT-VR (PSE, 2016).

2.1.1. Capture Plant Model Validation

Although a large number of pilot plant data is openly available, the number of dynamic operating data sets is limited. Currently only a small number of studies have validated dynamic models against dynamic pilot plant data (Bui, et al., 2018b). Tait et al. (2016) performed five different dynamic capture plant scenarios: startup, shutdown, capture plant decoupling, reboiler decoupling, and frequency reponse. A summary of the baseload operating conditions are shown in Table 1. The capture plant uses 30.16 wt.% MEA, and the flue gas is representative of a gas turbine (GT) with 4.27 vol.% CO_2.

Table 1: Baseload operating conditions from Tait et al. (2016)

Process Parameter		**Value**
Absorber	Packing material	Sulzer Mellapak 250.X
	Packing height (m)	6.92
	Packing diamater (mm)	158.00
Stripper	Packing material	Sulzer Mellapak 500.X
	Packing height (m)	5.00
	Packing diameter (mm)	350.00
Flue gas flowrate (Nm^3/h)		120.50
Flue gas temperature (°C)		46.14
Flue gas CO_2 concentration (vol.%)		4.27
Solvent flowrate (L/h)		344.40
Solvent temperature into absorber (°C)		40.05
Solvent temperature into stripper (°C)		104.07
L/G ratio (L/m^3)		2.86
Steam flowrate to reboiler (kg/h)		19.50
Steam pressure (bar)		4.00
Desorber pressure (bar)		1.80

For this study the shutdown procedure is used for dynamic validation. The flue gas and solvent flowrates are simultaneously decreased over 16 minutes to 40% baseload, then

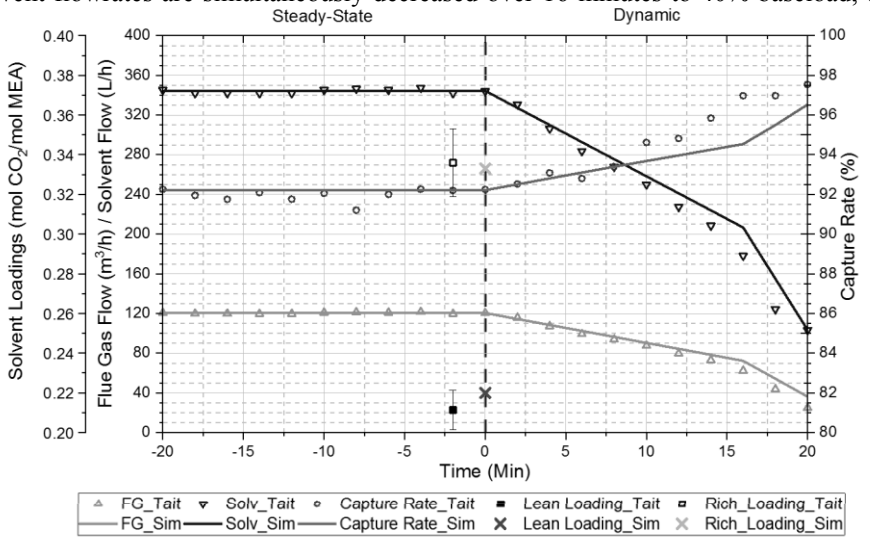

Figure 2: Model validation against steady-state and dynamic plant data from Tait et al. (2016)

further decreased to 30% baseload over the next 4 minutes. Figure 2 shows a comparison of the first 40 minutes of the shutdown procedure.

During steady-state operation the rich- and lean-loadings are 0.22 and 0.33 mol CO_2/mol MEA respectively, which are within the errors indicated by Tait et al. (2016). The average experiemental capture rate in the steady-state section is 92.28%, the predicted capture rate is 92.21%. Therefore, the model accurately simulates steady-state operation. In the capture plant shutdown experiment the steam flowrate to the reboiler is decreased to 0 kg/h between 0-10 minutes, however, due to model constraints this could not be included. This accounts for the small deviation in the capture rate during the dynamic operation, which has an increased gradient between 10-16 minutes, and showed a maximum deviation of 3.3% at 16 minutes.

2.2. Flexible Gas Turbine Operation

Data from the Balancing Mechanism Reporting Service (BMRS) and industrial suppliers is used to simulate the transient operation of an open-cycle gas turbine (OCGT) plant. BMRS is an open access electricity market databank providing data on the demand, generation and transmission of electricity in Great Britain (GB). The typical operating times and load changes follow a 30 minute time interval, based off the balancing and settlement period in GB (ELEXON, 2019). OCGT generation typically only comes on the system during periods of high strain, during the colder winter months in December, January and February. Figure 3 shows the time and load of OCGT's in January over the last 3 years in GB. The key points from the data set:

- over a 240 hour period an OCGT plant will start-up and shutdown on average five times
- typically coming on between 15:00-20:00
- used to deliver peak daily demand, which also have the highest peaks in the evening.
- the sporadic and inconsistent behaviour makes planning PCC operation difficult.

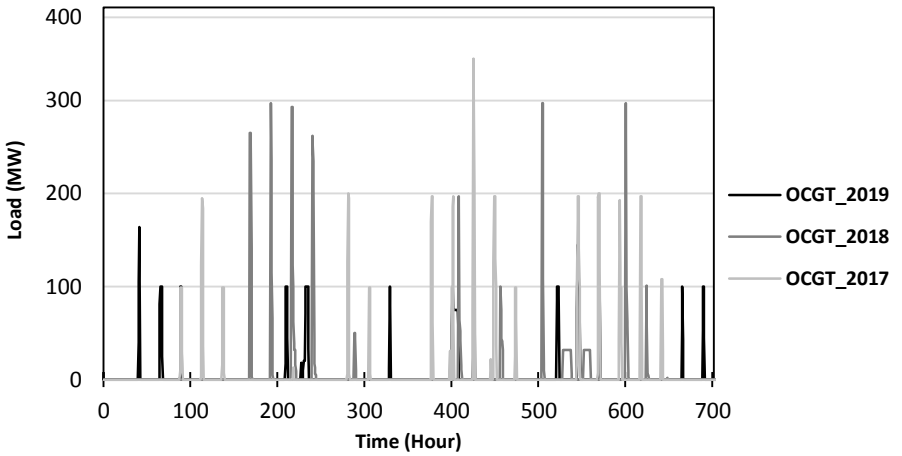

Figure 3: OCGT operation for 700 hours, data sourced from BMRS

This study uses the Siemens SGT-400 as an example modern gas turbine, the 11 MW version produces 33.80 kg/s of exhaust mass flow with low NO_X (≤25 ppm). The rated power output in open-cycle power generation is 10.40 MWe, and can be used for range of onshore and offshore applications (Siemens, 2019). For a typical OCGT power station, the average ramp rate is between 8-12% maximum load per minute, and the hot and cold start-up times are 5-11 minutes (Agora Energiewende, 2017).

Assuming the exhaust temperature can be reduced to a suitable inlet absorber temperature through a pinch analysis, the model is then scaled up to handle 33.80 kg/s of flue gas, and equipment sizes are scaled to maintain key process parameters highlighted in Table 1. The capture plant initially starts when the GT is at full load, the start-up procedure is not investigated in this study, and the shutdown time is 8 minutes. Initially, the capture plant is operated at full load (GT output = 10.40 MWe) for 1 hour, before progressing through two ramping cycle at 70% and 50% load. This study assumes a ramp rate of 10% full load per minute, therefore, the SGT-400 can increase or decrease power at 1.04 MWe/Minute. Flowrate changes follow the 30-minute balancing and settlement period in GB. The flue gas flowrate is assumed to be directly affected by load, i.e. 70% load correlates to 70% flowrate. The concentration of each emission is assumed to be constant, in reality power ramping effects the level of incomplete combustion, and thus the formation of CO and unburnt hydrocarbons, which will affect the capture plant. However, this is beyond the scope of this study.

3. Results

The flue gas flowrate entering the absorber column at maximum gas turbine load is 33.80 kg/s and the solvent flowrate is 83.04 L/s, consistent with the L/G ratio in Tait et al. (2016). Figure 4 shows the calculated capture rate is initially 92.48%, comparable to the 92.28% in Tait et al. (2016). The capture rate decreases to 90.37% over the initial hour due to the constant steam/water supply to the reboiler, condenser and lean solvent heat exchanger. This decrease during full load operation is also exhibited in the validation simulation, however, due to the smaller flowrates and column geometries it is not as substantial. Keeping the utility streams constant causes an increase in lean-loading, therefore, as more CO_2 is entrained in the solvent, less CO_2 can be removed from the flue gas. The increase in loadings was a result of the fraction of CO_2 released during the stripping process decreasing by 25%. The gas inlet and liquid outlet stripper temperatures decreased by 9°C and 2°C respectively, over the simulation prior to shut down; therefore, further work is required to analyse this decrease in recovery rate.

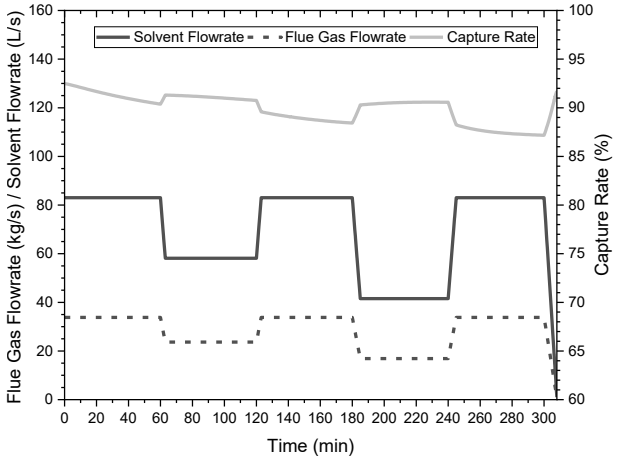

Figure 4: Flexible commercial scale post-combustion capture plant operation

Ramping to 70% load, the inlet absorber gas flowrate decreases to 23.66 kg/s in 3 minutes,during which the capture rate increases to 91.30%. Interestingly, once the flowrate is returned to full load the capture rate continues the original trajectory, going from 90.75 to 89.58%.

This pattern is also shown in the second ramping cycle at 50% load. Over both the cycles the capture plant efficiency drops 5.30%. If the plant was to have continuous operation this loss of efficiency would be alarming. However, when operating in the more dynamic future energy system, it is likely that gas-PCC systems will only be operating for short periods of time and the efficiency drop is less severe. The time-averaged capture rate including the shutdown procedure is 90.02%.

4. Conclusion

The fast ramping capabilities of modern gas turbines can be used as dispatchable generation, and accompanied with CCUS they can play a vital role in decarbonising the energy sector. This paper presents the steady-state and dynamic validation of a rate-based CO_2 absorption model, using the benchmark 30 wt.% MEA process. The process is scaled to capture CO_2 from the flue gas of a 10.40 MWe gas turbine in open cycle configuration. Capture plant operation during two ramping cycles, at 70% and 50% full load, shows the rapid load transitioning assists in maintaining a time-averaged capture rate above 90%. Therefore, while employing the right operating strategy for gas-PCC the time-averaged capture rate can be maintained without being a barrier to flexible operation. Future work should focus on optimising process parameters to minimise the energy penalty related to the desorption step, during various dynamic operating scenarios.

Acknowledgements

This work is funded by the Engineering and Physical Sciences Research Council (EPSRC) Centre for Doctoral Training in Carbon Capture and Storage and Cleaner Fossil Energy (EP/L016362/1), and Drax Group Plc.

References

Agora Energiewende, 2017. *Flexibility in thermal power plants ,* Berlin: Agora Energiewende.
Bui, M. et al., 2018a. Carbon capture and storage (CCS): the way forward. *Energy & Environmental Science,* 11(5), pp. 1062-1176.
Bui, M. et al., 2014. Dynamic modelling and optimisation of flexible operation in post-combustion CO2 capture plants—A review. *Computers & Chemical Engineering,* Volume 61, pp. 245-265.
Bui, M., Tait, P., Lucquiaud, M. & Mac Dowell, N., 2018b. Dynamic operation and modelling of amine-based CO2 capture at pilot scale. *International Journal of Greenhouse Gas Control,* Volume 79, pp. 134-153.
ELEXON, 2019. *Balancing Mechanism Reporting Service (BMRS).* [Online]
Available at: https://www.bmreports.com
[Accessed 1 November 2019].
Global CCS Institute, 2018. *The Global Status of CCS - 2018,* Melbourne: Global CCS Institute.
Heuberger, C. F. & Mac Dowell, N., 2018. Real-World Challenges with a Rapid Transition to 100% Renewable Power System. *Joule,* 2(3), pp. 367-370.
Oko, E., Wang, M. & Joel, A. S., 2017. Current status and future development of solvent-based carbon capture. *International Journal of Coal Science & Technology,* Volume 4, pp. 5-14.
Parsons Brinckerhoff, 2014. *Technical Assessment of the Operation of Coal & Gas Fired Plants,* London: Department of Energy and Climate Change.
PSE, 2016. *gCCS Documentation,* London: Process Systems Enterprise Limited.
Siemens, 2019. *Gas Turbine Portfolio Brochure,* Munich: Siemens.
Tait, P. et al., 2016. A pilot-scale study of dynamic response scenarios for the flexible operation of post-combustion CO2 capture. *International Journal of Greenhouse Gas Control,* 48(2), pp. 216-233.

Sauro Pierucci, Flavio Manenti, Giulia Bozzano, Davide Manca (Eds.)
Proceedings of the 30th European Symposium on Computer Aided Process Engineering (ESCAPE30), May 24-27, 2020, Milano, Italy.
http://dx.doi.org/10.1016/B978-0-12-823377-1.50028-8

Increasing Power System Flexibility to Integrate High Share of Renewable Energy

Siyuan Chen, Pei Liu*, Zheng Li

State Key Lab of Power Systems, Department of Energy and Power Engineering, Tsinghua-BP Clean Energy Center, Tsinghua University, 100084 Beijing, China
liu_pei@tsinghua.edu.cn

Abstract

The variability and intermittency of renewable energy brings about technical challenges for its integration. In order to integrate high share of renewable energy, more flexibility is needed in the power system. Among all the flexibility options, taking customer-sited energy storage systems as demand response could be a promising measure addressing both grid needs and customer needs. In order to analyse the effect of customer-sited energy storage systems on renewable energy integration, an integrated power generation and customer-sited energy storage systems expansion planning model is proposed in this paper. The expansion and operation of energy storage systems are based on the objective of reducing total power generation costs. Sichuan province in China is taken as a case study due to its abundant renewable energy resources and increasing renewable energy share in the power system. The results indicate that: 1) demand response provided by customer-sited energy storage could partially replace coal power plants to provide flexibility for integrating high share of renewable energy into power system; 2) The utilization scale of renewable energy could be increased and CO_2 emissions could be reduced significantly. In order to encourage the deployment of customer-sited energy storage systems, more policy support for energy storage technology and electricity market mechanism improvement are needed to enhance the development of customer-sited energy storage systems.

Keywords: Renewable energy integration, Customer-sited energy storage, Modelling and optimization, Power generation expansion planning

1. Introduction

Renewable energy is expected to be the fastest growing source of energy, contributing half of the growth in global energy supplies and becoming the largest source of power by 2040 (BP, 2019). However, renewable energy output is highly dependent on weather conditions, which means it is variable and non-dispatchable. More flexibility is needed in the power system to balance the fluctuation of renewable energy in parallel with higher share of renewable energy. There are a range of measures to increase the power system flexibility including flexible power generation, demand side management, grid ancillary services, energy storage, power-to-gas and vehicle-to-grid (Lund et al., 2015). Among these measures, energy storage technologies have recently drawn much attention as a promising flexibility provider due to the technical maturity and decreasing costs (Hadjipaschalis et al., 2009). Existing researches mainly focus on using energy storage to provide flexibility on the supply side. However, if an energy storage system is located along the point of generation, its operation is tied to this individual facility and the potential utility is severely limited. Moreover, energy storage on the supply side

will not change the power load profile. High capacity of power distribution networks and facilities are still needed in order to balance the peak load of consumers, while they remain idle in the rest of time. One way to manage power load profile is by demand response, which means customers shift their power demand among time periods in one day. However, the change of electricity usage pattern may cause discomfort for customers (Parrish et al., 2019). Using customer-sited energy storage systems as demand response could be a promising measure addressing both grid needs and customer needs. Peak load could be reduced without changing customers' usage pattern. Furthermore, the flexibility level that customer-sited energy storage can provide is higher than conventional demand response.

Wang et al. (2018) designed a user-side energy storage system and analyzed the effect on the grid side and user side. The simulation results demonstrate that power quality of the users is improved whilst reactive compensation is realized on the grid side in the presence of user-side energy storage. Hu et al. (2016) developed a scheduling model for customer-sited energy storage system, capturing the dynamics and operational constraints. A rolling-horizon approach is applied to optimize the schedule and assess the economics of energy storage system. They found that using customer-sited energy storage system to support only one or two of the services may not yield a positive profit based on current costs. Telaretti et al. (2015) proposed a charging strategy for customer-sited energy storage in presence of hourly electricity prices, aiming to maximize the profit for storage owners. A heuristic approach is applied to determine the optimal schedule of energy storage system regardless of the customer load profile.

Major concerns of existing literatures are to determine the optimal charging and discharging behavior of customer-sited energy storage system to maximize the profit. However, the resulting schedule of energy storage system may not be totally consistent with the grid needs. This inconsistency limits the potential effects of customer-sited energy storage on renewable energy integration and total social cost reduction. It is essential to consider the expansion and operation strategy of customer-sited energy storage systems from the perspective of whole society so that appropriate market mechanisms could be designed for customer-sited energy storage systems. In order to address this issue, we extended our previous power generation expansion planning model (Chen et al., 2019) to an integrated power generation and customer-sited energy storage systems expansion planning model. The expansion and operation of energy storage systems are based on the objective of reducing total power generation costs. The model is applied to the case study of Sichuan province in China, which has abundant renewable energy resources and increasing renewable energy share in the power system, to evaluate the effect of installing customer-sited energy storage facilities as demand response on the integration of renewable energy into power system.

2. Methodology

2.1. Model description

The integrated power generation and customer-sited energy storage systems expansion planning model proposed in this paper aims to optimize both long-term planning and short-term scheduling of power system. The optimal type, size, construction time and scheduling of both power generation units and customer-sited energy storage systems are obtained with this model. Five types of power generation technologies are included in this model: Pulverized Coal (PC) power plants, Natural Gas Combined Cycle (NGCC) power plants, Hydro (HD) power plants, Wind (WD) power plants and Solar Photovoltaic (PV) power plants. All power generation technologies are set a lifetime

and assumed to be decommissioned at the end of their lifetime. The optimal development path is then calculated based on the objective function, which is to minimize the total system cost of power sector in the planning horizon. In order to reflect the fluctuation of variable renewable energy, the model takes hourly power balance into account to determine operational variables such as hourly power output of different power generation technologies. In this model, demand response is assumed to be implemented by installing customer-sited energy storage facilities without changing customers' usage patterns.

2.2. Mathematical formulation

Four sets, t, g, f and s stand for time, power generation technology type, fuel type, and time slice respectively. Parameters are expressed by upper-case characters and Greek alphabet whilst variables are expressed by lower-case characters.

2.2.1. Objective function

The objective function of this model is to minimize the total system cost of the power sector from 2018 to 2050. The total system cost comprises capital expenditure, operation and maintenance cost, fuel cost, start-up and shut-down cost. Eq. (1) shows the objective functions whilst all five parts of costs are listed in Eq. (2) - Eq. (5). Capital expenditure for power generation units are amortized equally to each year during the entire lifetime. Operation and maintenance costs equal the installed capacity multiplied by annual unit O&M cost. Fuel costs are the product of fuel prices and fuel consumption. Start-up costs equal unit start-up cost multiplying start-up capacity.

$$atc = \sum_{t=2018}^{2050} \frac{tinv_t + tom_t + tfc_t + tssc_t}{(1+I)^{t-2018}} \tag{1}$$

$$tinv_t = \sum_g inv_{t,g} = \sum_{t'=t-TLT_g+1}^{t} \left(CAP_{t',g} \cdot nb_{t',g} \cdot \frac{I \cdot (1+I)^{-1}}{1-(1+I)^{-TLT_g}} \right) \tag{2}$$

$$tom_t = \sum_g om_{t,g} = \sum_g OM_{t,g} \cdot ic_{t,g} \tag{3}$$

$$tfc_t = \sum_f FP_{f,t} \cdot \sum_{g,s} fd_{f,t,g,s} \tag{4}$$

$$tssc_t = \sum_{g,s} SSC_{t,g} \cdot (su_{t,g,s} + st_{t,g,s}) \tag{5}$$

2.2.2. Operational constraints

The power balance constraints ensure that power load in each time slice is satisfied by the sum of power generation from all types of generation units as shown in Eq. (6).

$$load_{t,s} = \sum_g pgs_{t,g,s} \tag{6}$$

In terms of renewable energy, power output is limited by capacity factor constraints which relate to the climate and weather. Renewable energy power generation in each time slice should not exceed the upper limit of capacity factor, as presented in Eq. (7).

$$pgs_{t,g,s} \le CF_{g,s} \cdot ic_{t,g} \quad g \in \{HD, WD, PV\} \tag{7}$$

For thermal power plants, unit commitment constraints are included to represent the status of operation, start-up, shut-down and reserve in Eq. (8) - (10).

$$ic_{t,g} = or_{t,g,s} + rs_{t,g,s} \quad g \in \{PC, NGCC\} \tag{8}$$

$$or_{t,g,s+1} = or_{t,g,s} + su_{t,g,s+1} - sd_{t,g,s+1} \quad g \in \{PC, NGCC\} \tag{9}$$

$$rs_{t,g,s+1} = rs_{t,g,s} + sd_{t,g,s+1} - su_{t,g,s+1} \quad g \in \{PC, NGCC\} \tag{10}$$

Thermal power plants can only operate in a specific load factor range, limited by the load factor constraints. Besides, the fuel consumption rate of thermal power plants is strongly influenced by the load factor. More fuel would be needed to generate electricity in off-design working conditions. Piecewise linearization method is used to reflect this relationship as shown in Eq. (11) - (12).

$$LFMIN^{i}_{g,s} \cdot or_{t,g,s} - M(1-x_i) \le pgs_{t,g,s} \le LFMAX^{i}_{g,s} \cdot or_{t,g,s} + M(1-x_i) \quad g \in \{PC, NGCC\} \tag{11}$$

$$pgs_{t,g,s} \cdot FCR^{i}_{f,t,g} - M(1-x_i) \le fd_{f,t,g,s} \le pgs_{t,g,s} \cdot FCR^{i}_{f,t,g} + M(1-x_i) \quad g \in \{PC, NGCC\} \tag{12}$$

Electricity consumption behavior is assumed to remain unchanged. Then, power load of the power grid is equal to the fixed power demand plus the power charged to customers' storage facilities minus the power discharged from customers' storage facilities as presented in Eq. (13). The storage balance constraints in Eq. (14) show that electricity storage level in each time slice equals the storage level in the previous time slice plus power charged minus power discharged in the current time slice.

$$load_{t,s} = PD_{t,s} + charge_{t,s} - discharge_{t,s} \tag{13}$$

$$storage_{t,s+1} = storage_{t,s} + charge_{t,s+1} \cdot \eta_{charge} - discharge_{t,s+1} / \eta_{discharge} \tag{14}$$

2.2.3. Investment constraints

Eq. (15) expresses the installed capacity of power generation units. The capacity of energy storage facilities is presented in Eq. (16).

$$ic_{t,g} = \sum_{t'=t-TLT_g+1}^{t} nb_{t',g} \tag{15}$$

$$ices_{t} = \sum_{t'=t-TLT_{es}+1}^{t} nbes_{t'} \tag{16}$$

Due to the limited renewable energy resources, an upper bound for the installed capacity of renewable energy is set in Eq. (17). Eq. (18) shows the policy targets for the development of renewable energy.

$$ic_{t,g} \le RL_g \quad g \in \{HD, WD, PV\} \tag{17}$$

$$ic_{t,g} \ge PT_{t,g} \quad g \in \{HD, WD, PV\} \tag{18}$$

3. Case study

The proposed model is implemented in General Algebraic Modelling System (GAMS) and solved using the CPLEX solver. It is applied in a case study for power generation expansion planning in Sichuan Province of China. Input parameters, including existing installed capacity, future power demand, techno-economic parameters of technologies, renewable energy resources endowment and capacity factor, power transmission limits, losses and costs are imported from previous work (Chen et al., 2019).

3.1. Scenario setting

Two scenarios are set in this case study. The first scenario is named as "Baseline Scenario". Power load curve is input as a fixed parameter to be satisfied in this scenario. The second scenario is named as "Demand Response Scenario". In this scenario, power load curve is relaxed to a variable and can be adjusted by demand response with customer-sited energy storage facilities.

3.2. Results and discussion

In "Baseline Scenario", the flexibility in the power system is provided by coal power plants with more frequent ramping processes as well as start-up and shut-down actions. More ramping processes mean that coal power plants are running at off-design conditions more often, which has lower efficiency and more emissions. In "Demand Response Scenario", demand response can provide flexibility for the power system from the demand side and reduce the need for flexible operation of coal power plants. Figure 1 shows the load dispatch profile of a winter day in 2050 in the two scenarios. It can be noticed that coal power plants are running flexibly in "Baseline Scenario". At noon time when the sunlight is strong, coal power plants have to run at low load to absorb PV power output. At about 19:00 – 20:00 when the power load is high whilst the PV power output is nearly zero, coal power plants have to ramp up to high load for peak regulation. In "Demand Response Scenario", peak load at 19:00 – 20:00 is shifted to low load time period (0:00 – 8:00) and noon time by demand response. After that, coal power plants can run at stable load at all times.

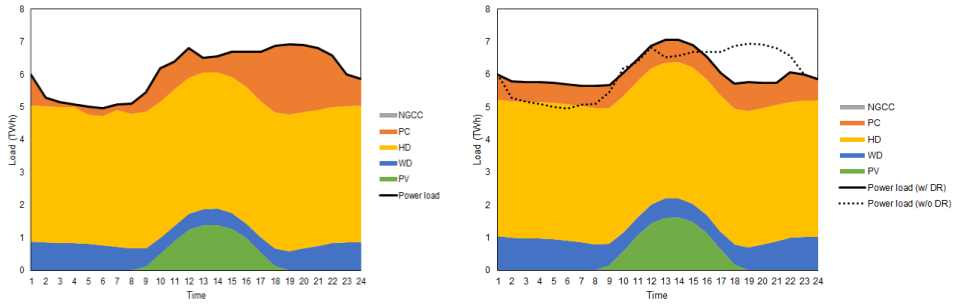

(a) Baseline Scenario (b) Demand Response Scenario

Figure 1. Load dispatch profile of a winter day in 2050

As the power load is adjusted in consistent with the renewable energy power output, more variable renewable energy could be integrated into the power system whilst fewer coal power plants are needed for peak regulation. The comparison of installed capacity between the two scenarios is presented in Figure 2. In "Demand Response Scenario", wind and PV power plants increase by 5 GW and 4 GW respectively whilst coal power plants decrease by 15 GW by the year 2050 compared with "Baseline Scenario". Overall, demand response increases the utilization of renewable energy and reduces coal power generation simultaneously. The effect of these benefits is the significant CO_2 emission reduction. In "Demand Response Scenario", total CO_2 emissions in the planning horizon are reduced by 422 Mt compared with "Baseline Scenario".

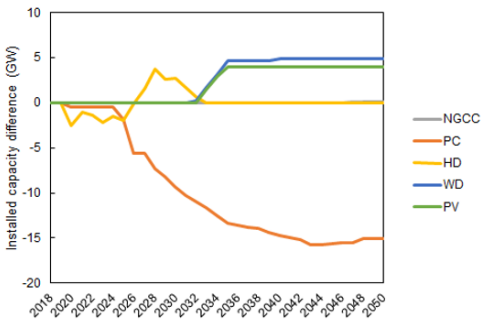

Figure 2. Installed capacity difference between the two scenarios

Despite the benefits that demand response brings about, it will also incur additional costs. In "Demand Response Scenario", 47.4 GW of energy storage capacity is needed by 2050 for demand response. It is noteworthy that power generation cost is reduced by 45 billion RMB whilst the additional storage cost is 117 billion RMB. Therefore, the benefits of demand response mentioned above are at the expense of the increased total cost (72 billion RMB). In order to encourage the installation of customer-sited energy storage facilities, policy-makers should enhance policy support for energy storage technology to promote technological innovation and cost reduction. Electricity market mechanism should also be improved to make it profitable for customers.

4. Conclusions

This paper analyses the effect of using customer-sited energy storage as demand response on integrating high share of renewable energy into power system. The results show that demand response provided by customer-sited energy storage increases the utilization of renewable energy, reduces the flexibility need for coal power generation and realizes significant CO_2 emissions reduction. In order to enhance the development of customer-sited energy storage systems, storage costs need further reduction with technology improvement and policy support. Electricity market mechanism needs to be improved to add more incentives for customer-sited energy storage systems, such as real-time pricing and two-part electricity tariff.

Acknowledgement

The authors gratefully acknowledge the support by The National Key Research and Development of China (2018YFB0604301) and the Phase Ⅲ Collaboration between BP and Tsinghua University.

References

B. Parrish, R. Gross, P. Heptonstall, 2019. On demand: Can demand response live up to expectations in managing electricity systems?. Energy Research & Social Science, 51: 107-118.

BP Group, 2019. BP Energy Outlook 2019, BP p.l.c., London, United Kondom.

E. Telaretti, E.R. Sanseverino, M. Ippolito, S. Favuzza, G. Zizzo, 2015. A novel operating strategy for customer-side energy storages in presence of dynamic electricity prices. Intelligent Industrial Systems, 1(3): 233-244.

I. Hadjipaschalis, A. Poullikkas, V. Efthimiou, 2009. Overview of current and future energy storage technologies for electric power applications. Renewable and Sustainable Energy Reviews, 13(6-7):1513-1522.

P.D. Lund, J. Lindgren, J. Mikkola, J. Salpakari, 2015. Review of energy system flexibility measures to enable high levels of variable renewable electricity. Renewable and Sustainable Energy Reviews, 45:785-807.

Q. Wang, Y. Zhang, Z. Yun, X. Wang, D. Zhang, D. Bian, 2018. Research on Battery Energy Storage System Based on User Side. IOP Conference Series: Earth and Environmental Science. IOP Publishing, 108(5): 052122.

S. Chen, P. Liu, Z. Li, 2019. Multi-regional power generation expansion planning with air pollutants emission constraints. Renewable and Sustainable Energy Reviews, 112: 382-394.

W. Hu, P. Wang, H. B. Gooi, 2016. Assessing the economics of customer-sited multi-use energy storage. 2016 IEEE Region 10 Conference (TENCON). IEEE, 651-654.

Sauro Pierucci, Flavio Manenti, Giulia Bozzano, Davide Manca (Eds.)
Proceedings of the 30th European Symposium on Computer Aided Process Engineering (ESCAPE30), May 24-27, 2020, Milano, Italy.
http://dx.doi.org/10.1016/B978-0-12-823377-1.50029-X

A Discrete Modeling Approach for Excess Gibbs-energy Models Combined with Molecular Sampling

Christoph Mayer,* Thomas Wallek
Institute of Chemical Engineering and Environmental Technology, Graz University of Technology, Inffeldgasse 25C, 8010 Graz, Austria
cmayer@tugraz.at

Abstract

In this work, a modeling approach using the discrete states of molecules in an equilibrium lattice is introduced. The discrete states are considered in terms of probabilities to describe condensed phase mixtures. The molecules themselves are modeled with a dice-like geometry, providing the opportunity for up to six different energetic interaction sites per molecule. A link to real molecules is created by combining the model with a molecular sampling algorithm which determines the energetic interaction parameters for molecule clusters through a force field model. The comparison of model results with experimental data for the systems acetone – methanol and acetone – n-heptane shows that the deviations are comparable in magnitude to those of the UNIFAC model.

Keywords: chemical thermodynamics, lattice system, discrete modeling, UNIFAC

1. Introduction

Thermodynamic models for fluid phase equilibria calculations, such as equations of state and activity coefficients, are being challenged by the need to describe complex molecules. Especially systems with strong interactions which show large deviations from ideal mixture behavior are increasingly difficult to describe using conventional modeling approaches.

In this context, previous papers proposed ‘discrete modeling’ as a novel approach to incorporate a more detailed molecular picture into thermodynamics from scratch. The approach is characterized by the rigorous use of Shannon information equivalently to thermodynamic entropy (Pfleger et al., 2015; Wallek et al., 2016) and can be categorized among classical local-composition models and the more complex cluster variation method.

A previous application of discrete Markov-chains to thermodynamic modeling of two-dimensional lattices describing solid solutions, as developed by Vinograd and Perchuk (1996), was modified and extended from a flat lattice towards a three-dimensional, Ising-type model. The initial step of this model was the description of spherical molecules which are characterized by a uniform energetic interaction across the surface (Wallek et al., 2018).

In this paper, the molecules are modeled with a dice-like geometry, allowing there to be up to six different interaction sites per molecule, aiming at describing isomers and more complex molecules. This approach is combined with a molecular sampling algorithm to establish a link to real molecules. This link enables the possibility to compare the model based on this abstract molecule representation to both established models such as

UNIFAC and experimental data. This was impossible for prior stages of the model development where comparisons were limited to Monte-Carlo simulations of lattice systems and thus marks an important milestone for the approach.

Figure 1: Sequential lattice construction: neighborhood into which a new molecule is inserted.

2. Discrete modeling of dice-like molecules

In this work, molecules are modeled as dice in a simple cubic lattice. This means that at the current stage of model development all molecules are assumed to be of similar size and have up to six different energetic interaction sites positioned in a dice-like structure. Every molecule thus has 24 different orientations.

Each molecule interacts only with its nearest neighbors in the lattice. Further, each site interacts only with the closest site of the nearest neighbor. For a binary mixture, this results in 12 different interaction sites which can form 78 distinct pairwise interactions. The parameters which are the model input are the global composition of the mixture and a temperature-dependent interaction energy for each of the possible pairs of sites.

2.1. Sequential lattice construction

The basis of this work is an approach for two-dimensional solid solutions developed by Vinograd and Perchuk (1996). It was developed to create phase diagrams for crystals and works with uniform molecules, which have only one interaction property along the entire surface. The fundamental feature of this approach is a sequential construction of the lattice in equilibrium. Each molecule is placed into a partial neighborhood of previously inserted molecules. An example of one of these neighborhoods is given in Figure 1. Such an insertion process is only dependent on its particular neighborhood. This insertion of a molecule with a specific orientation into a neighborhood is described using conditional probabilities. The entropy and internal energy of a system are expressed using these conditional probabilities.

A previous work (Wallek et al., 2018) extended this approach to three-dimensional systems. This work focusses on dice-like binary mixtures and the combination of this approach with molecular sampling. The novelty of describing binary mixtures with dice-like components unlocks the desired determination of excess properties. This means that significant progress compared to previous works on this modeling methodology has been achieved.

2.2. Constrained optimization

The goal of the approach is to calculate the thermodynamic equilibrium state of the system of abstract, dice-like, molecule representations. This is achieved via a constrained minimization of the Helmholtz free energy, a.

$$a = u - T\,s \tag{1}$$

The free energy can be expressed using the internal energy, *u,* and the entropy, s, which is demonstrated in Eq. (1).

2.2.1. Constraints

The optimization is subject to constraints. These are based on the law of total probabilities or can be viewed as marginal probabilities. The constraints are formed by the sum of cluster probabilities over every possible state for all but one molecule. This sum must be equal to the global composition of the remaining molecule species divided by the number of possible orientations. The interpretation of a cluster probability is the probability of occurrence in the equilibrium lattice of a cluster of molecules each being in specific states concerning component and orientation. After consideration of symmetries, the number of constraints is reduced to 12.

2.2.2. Correlations between cluster of different sizes

The variables for the minimization are the probabilities of molecule pairs. Other equations are formulated with the neighborhood and insertion probabilities of the sequential construction step. These probabilities combined represent a larger cluster. A correlation between the larger cluster and the pairs of molecules is thus necessary. The used approach is chosen for its simplicity and equation size and connects the neighboring molecules to the newly inserted molecule via one-dimensional chains.

2.2.3. Internal energy

The internal energy of the system is expressed using the conditional probabilities of the insertion process. It is defined as the sum over all possible neighborhoods, *n*, of the probability of each neighborhood times the sum over all possible insertions, *m*, of the conditional insertion probability times the respective interaction energy, ε.

$$u = \sum_{j=1}^{n} p_j \cdot \sum_{i=1}^{m} p_{i|j} \cdot \varepsilon_{ij} \tag{2}$$

Eq. (2) expresses the internal energy as a function of the neighborhood probabilities and the insertion probabilities. Three new contact pairs are created per insertion step. By applying the constraints as well as the correlations between the different cluster sizes, the equation for the internal energy can be reduced to three times the sum of all pair probabilities multiplied by their respective interaction energy.

2.2.4. Entropy

The entropy is expressed using the neighborhood and insertion probabilities.

$$s = -R\left[\ln(24) + \sum_{j=1}^{n} p_j \cdot \sum_{i=1}^{m} p_{i|j} \cdot \ln\left(p_{i|j}\right)\right] \tag{3}$$

The particular way in which the entropy is formulated in Eq. (3) can also be interpreted as treating each orientation of the dice-like molecules as individual components. The constraints of the system then link every set of 24 components back to each respective molecule. In terms of entropy, this method for looking at the system contains too much information. Therefore it has to be corrected with ln(24) to account for the fact that there is in fact only one molecule behind these 24 pseudo-components.

3. Molecular sampling

The model based on dice-like molecules needs the interaction energy of every possible configuration as one of the inputs. These are specific to each pairing of components and provide the interface for linking the abstract model to real molecules. One possible strategy for this is a molecular sampling algorithm. Small molecular clusters, i.e., pairs of molecules, are formed and their potential interaction energy is subsequently evaluated.

The OPLS-AA force field, developed by Jorgensen et al. (1996), is chosen for the interaction energy calculations. It is well known and broadly accepted for potential energy calculations in the liquid phase. Since the focus of the model is to calculate the excess Gibbs-energy, only the intermolecular energy of the OPLS-AA force field is important. The intramolecular part is omitted.

The sampling procedure places each pair of molecules in specific rotations next to each other and reduces the distance until the smallest distance between the closest surfaces reaches a specific value. This procedure is similar to the sampling algorithm used by Sweere and Fraaije (2015). In their work, they have used different distances between molecules to better represent some mixture properties like a coordination number of ten. For the example systems presented in this work the distance between the molecules is reduced until the van der Waals surfaces are touching.

To establish a link between dice and molecules, the molecules are rotated in 90° steps until all 24 members of the cube symmetry group are sampled for each molecule in the cluster. From the point of view of contacting surfaces in a pair cluster of dice-like molecules, the sampling of all cube rotations leads to more than the 78 needed pairwise interactions for the current model formulation. Therefore, the mean of all combinations which lead to the same contact site pairing is calculated and used as resulting interaction energy.

The starting orientation of the molecules inside the dice-like model framework has an effect on how well components are represented by their dice counterpart. For the systems discussed in the results section, the orientation of acetone is such that the oxygen atom is pointing towards a corner of the dice. Heptane is placed on one of the room diagonals of the dice. The methanol molecule is oriented such that the hydroxy group is pointing at a face of the dice.

4. Results

Two systems are discussed to show the results of this modeling approach. The model is compared to experimental data, the (original) UNIFAC model (Fredenslund et al., 1975) as a representative state-of-the-art approach, and Monte-Carlo simulations. The Monte-Carlo simulations are performed using dice-like molecules in a regular lattice with the same interaction parameters as the model. They converge towards the real solution of these model assumptions and can be used to show the deviation of other model assumptions, for instance the sequential construction and the constraints which are part of the system of equations.

Figure 2 shows the excess Gibbs-energy of a mixture of acetone and methanol at a constant temperature of 323.15 K. The graph is plotted over the composition of acetone. The experimental data, as the base for comparison, are taken from Gmehling and Onken (2005) in the form of a Redlich-Kister polynomial.

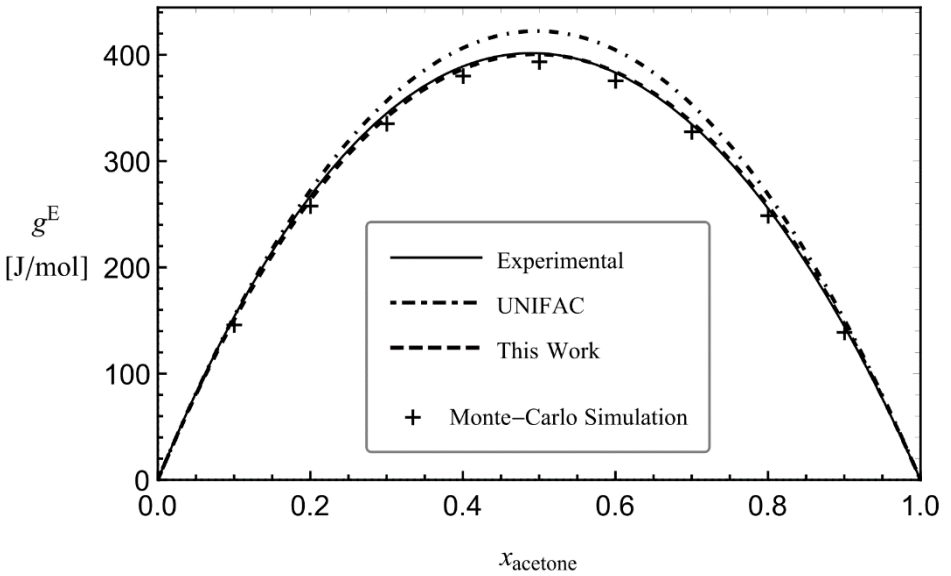

Figure 2: Excess Gibbs-energy over acetone composition for a mixture of acetone and methanol. Comparison between experimental data (Gmehling and Onken, 2005), UNIFAC (Fredenslund et al., 1975), Monte-Carlo simulations and this work.

The model presented in this work is slightly below the experimental data up to an acetone composition of 0.5 and slightly above for larger acetone amounts. The model shows in general a good agreement with the experimental data. Compared to the Monte-Carlo simulation of the dice-like molecules, the model displays a small positive deviation. The UNIFAC model, however, demonstrates a noticeably larger deviation from the experimental data for this case.

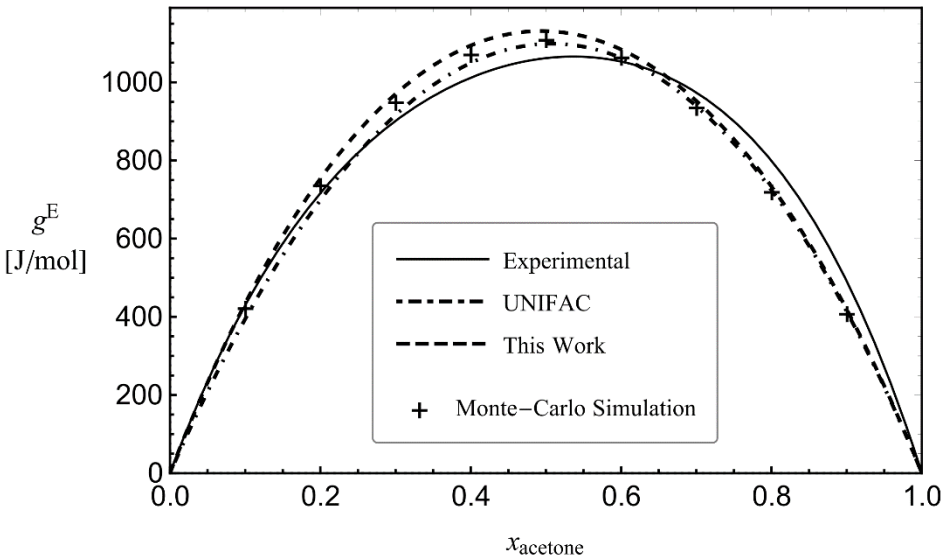

Figure 3: Excess Gibbs-energy over acetone composition for a mixture of acetone and n-heptane. Comparison between experimental data (Krenzer, 1985), UNIFAC (Fredenslund et al., 1975), Monte-Carlo simulations and this work.

The system acetone and n-heptane, given in Figure 3 at a temperature of 298.15 K, experiences slightly larger deviations compared to the previous one. This can be explained by the fact that n-heptane is, because of its elongated form, not as well described by a dice-like shape as methanol. Nevertheless, the magnitude of the deviation to the experimental data gathered from Krenzer (1985) is still comparable to the UNIFAC model. Again the model slightly overestimates the Monte-Carlo simulation data.

5. Conclusions

First results of the combination of the discrete modeling approach and molecular sampling show that small molecules, especially acetone and methanol, can be well described using dice-like molecules in a regular simple cubic lattice. For the example systems acetone – methanol and acetone – n-heptane it is shown that the deviations from experimental data are similar in magnitude to the UNIFAC model. In contrast to the simple cubic lattice with a coordination number of six, the UNIFAC model uses a coordination number of ten and the molecules are not restricted by a lattice.

The effect of the molecule orientation inside the dice and the link to the sampling algorithm are subject to further investigation. The results of this work show that discrete modeling approach is a promising basis for further investigation and development towards an activity coefficient model.

References

A. Fredenslund, R. L. Jones, J. M. Prausnitz, (1975), Group- contribution estimation of activity coefficients in nonideal liquid mixtures, AIChE J., vol. 21, no. 6, 1086–1099

J. Gmehling, U. Onken, (2005), Vapor-Liquid Equilibrium Data Collection, Dechema Chemistry Data Series, Vol. I, Part 2g

W.L. Jorgensen, D.S. Maxwell, J. Tirado-Rives, (1996), Development and testing of the OPLS all-atom force field on conformational energetics and properties of organic liquids, J. Am. Chem. Soc. 118, 11225–11236

G.M. Kontogeorgis, G.K. Folas, (2010), Thermodynamic models for industrial applications, From Classical and Advanced Mixing Rules to Association Theories

L. Krenzer, (1985), [in German] Untersuchungen zur Beeinflussung der Exzessenthalpie, der freien Exzessenthalpie und der Exzessentropie von binären Mischungen mit polaren Komponenten durch die Moleküleigenschaften, PhD thesis, Technische Hochschule Darmstadt

M. Pfleger, T. Wallek, A. Pfennig, (2015), Discrete modeling: Thermodynamics based on Shannon entropy and discrete states of molecules, Ind. Eng. Chem. Res. 54, 4643–4654

A.J.M. Sweere, J.G.E.M. Fraaije, (2015), Force-Field Based Quasi-Chemical Method for Rapid Evaluation of Binary Phase Diagrams, J. Phys. Chem. B. 119, 14200–14209

V.L. Vinograd, L.L. Perchuk, (1996), Informational models for the configurational entropy of regular solid solutions: flat lattices, J. Phys. Chem. 100, 15972–15985

T. Wallek, M. Pfleger, A. Pfennig, (2016), Discrete Modeling of Lattice Systems: The Concept of Shannon Entropy Applied to Strongly Interacting Systems, Ind. Eng. Chem. Res. 55, 2483–2492

T. Wallek, C. Mayer, A. Pfennig, (2018) , Discrete Modeling Approach as a Basis of Excess Gibbs-Energy Models for Chemical Engineering Applications, Ind. Eng. Chem. Res. 57, 1294–1306

Sauro Pierucci, Flavio Manenti, Giulia Bozzano, Davide Manca (Eds.)
Proceedings of the 30th European Symposium on Computer Aided Process Engineering (ESCAPE30), May 24-27, 2020, Milano, Italy.
http://dx.doi.org/10.1016/B978-0-12-823377-1.50030-6

Reliable Modelling of Twin-screw Extruders by Integrating the Backflow Cell Methodology into a Mechanistic Model

Maximilian Cegla, Sebastian Engell

TU Dortmund University, Biochemical and Chemical Engineering, Process Dynamics and Operations Group, Emil-Figge-Straße 70, 44227, Dortmund ,Germany

maximilian.cegla@tu-dortmund.de

Abstract

Process modelling for twin-screw extruders is important for the optimal design, control and understanding of these machines. Existing models are often describing the residence time distribution (RTD) of the melt based on experimental data without the usage of further process knowledge. These completely data driven methods are unreliable for more advanced extrusion processes as a strong coupling between many internal states exists, which may not be reflected in the measurements. Therefore the use of a mechanistic model is beneficial to be able to address all important effects simultaneously. The standard mechanistic model describes the RTD as a series of continuous stirred tank reactors. However, this approximation is not capable of describing tailing effects that can occur when elements that promote distributive mixing are present. These effects can be described by the backflow cell model (BCM). Within the BCM the unidirectional flow is divided into an upstream flow and downstream flow with a fixed flow ratio for a series of tanks. This model can be in cooperated into the CSTR model, exploiting the similarities of the structure of the two models. In this work, the combination of the two methods is presented and applied to different screw geometries.

Keywords: Extrusion, Reactive Extrusion, Twin-Screw Extrusion, Backflow cell model, Residence Time Distribution

1. Introduction

Twin-screw extruders provide high mixing efficiency, high specific energy inputs and the ability to process solids and highly viscous material. Consequently, they are interesting for various industries such as the pharmaceutical and the chemical industry for blending, reacting and compounding purposes. The agile operation of these extruders creates a need for dynamic models that are capable of describing start-up, shut down, and product changeovers. Furthermore these models can be used for the optimization of screw setup and operating conditions. Pioneering work for the modeling of twin-screw extruders has been performed by Todd 1975. Todd approximated the residence time distribution with the help of an axial dispersion model. Based on the works of Todd, Vergnes 1998 presented a first twin-screw extruder model that describes the flow within the extruder and approximates the geometry as two C-shaped chambers. Further development led to a successful application of this model to the reactive extrusion of caprolactone by Poulesquen in 2001. A drawback of this method is the missing flexibility that results from the fact that the model relies on two nested iterative

loops to converge the melt temperature and the conversion, and it is only usable at steady state. Choulak 2004 suggested a first dynamic model for the reactive extrusion of caprolactone that is based upon the approximation by a cascade of continuous stirred tank reactors (CSTR). The number of CSTRs as well as the internal flows were determined by parameter estimation on experimental data and therefore are not suitable for predictions. Eitzlmayr 2014 suggested a mechanistic twin-screw extruder model that describes the extruder as series of finite ideally mixed volumes that captures the dynamics of the extrusion process while maintain predictive capabilities. In this work, the model of Eitzlmayr is extended to account for the tailing effects in the RTD that were already reported by Todd in 1975. In the following sections the general modeling of twin-screw extruders is described, the investigated mixing elements and the BCM are presented, and a model extension is proposed and demonstrated for several typical screw geometries.

2. General

2.1. Twin-Screw Extrusion modeling

The mass-transport effects within a co-rotating twin screw extruder can be condensed to two simultaneously occurring effects. First, a flow that is being generated by conveying elements in the direction of the die or of the feed, depending on the screw geometry. The second effect is a pressure driven flow that transports the material into the direction of the die due to pressure differences. The pressure buildup within the extruder is realized by so called left handed or restrictive screw elements that convey material in the direction of the feeding port.

To describe the dynamics over the extruder length, the extruder can be discretized in finite volume elements as presented by Eitzlmayr 2016. These elements are connected by internal conveying and pressure driven flows as shown in Figure 1.

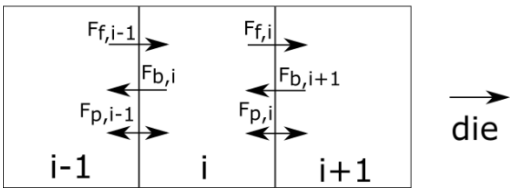

Figure 1: Schematic representation of the finite volumes and the internal flows.

The mass balance of each finite volume can be formulated in terms of the conveying flows F_f, F_b and the pressure flow F_p as:

$$\frac{df_i}{dt}V_i = F_{f,i-1} + F_{b,i+1} + F_{p,i} - F_{f,i} - F_{b,i} - F_{p,i} \qquad (1)$$

With the screw volume V_i and the filling ratio f_i. Pressure can only build up in completely filled volumes. The flow contributions can be calculated as follows:

$$F_{f,i} = K_f \cdot n \cdot D^3 \qquad F_{b,i} = K_{fb} \cdot n \cdot D^3 \qquad F_{p,i} = K_p \cdot \frac{D^4}{\eta} \cdot \frac{\Delta p}{\Delta x} \qquad (2),(3),(4)$$

With the speed of rotation of the screw n, the screw diameter D, the viscosity η and the pressure p. K_f and K_b describe the overall conveying capacity of a screw element in opposite directions, therefore classically only one of the values is nonzero depending on the geometry of the given element. K_p is factor that describes the pressure drop over an element. These factors are determined either experimentally as suggested by Kohlgrüber

2008 or mathematically by a rigorous modelling based on a two plate model in cylindrical coordinates as suggested by Vergnes 1996. Similar to Equation 4 the balances for heat, mass of species, pressure can be set up to take into account effects of temperature, dissipation, reaction as well as changing physical properties of the melt. By the nature of this model the RTD is described by a series of CSTRs with a small contribution of pressure induced backflow. This is reported to be a good accordance to literature for the classical conveying elements which can be described well by a cascade of 5 CSTRs (Poulesquen 2002b). However the model is not suitable for the description of distributive mixing. To describe this effect, the assumption of a uniform conveying capacity is relaxed in the following sections to take into account contributions in forward and backward direction in analogy to the BCM. This model describes a CSTR cascade with an additional countercurrent backflow.

2.2. Backflow cell model

Classically RTDs are described by a combination of ideal reactors, plug flow reactors and CSTRs. The BCM describes a series of CSTRs with a backflow countercurrent to the main flow direction. Mathematically the BCM was first described by Roemer in 1967. Figure 2 shows the graphical representation of the BCM and the comparison with figure 1 shows the obvious analogies. The BCM is defined by the number of cells N and the backflow ratio σ_B that is defined as: $\sigma_B = Q_B / Q$ (5)

Paux 2000 investigated different RTD models for extrusion applications and reports that the model describes processes accurately where the mixing is caused primarily by splashing and large eddies. Compared to other models such as the axial dispersion model, the double BCM, or an arithmetic progression the prediction error is comparable.

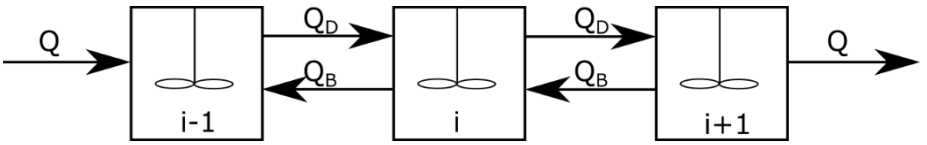

Figure 2: Graphical representation of the backflow cell model.

2.3. Investigated Screw Elements

Screw setups of twin-screw extruders consist of forward conveying elements, backward conveying elements and mixing elements. Forward conveying elements are used for material transport towards the die whereas backward conveying elements are used to generate a pressurized zone with completely filled elements. Mixing elements are used to achieve a maximum of distributive mixing with the minimal energy input. This distributive mixing has a significant impact on the RTD. Tooth mixing blocks (ZME), screw mixing elements (SME), turbine mixing elements (TME) and kneading blocks (KB) are shown in figure 2 and are investigated in the following section.

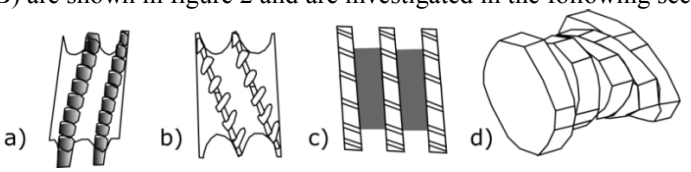

Figure 3: Sketches of the investigated screw elements. a) ZME b) SME c) TME d) KB

Tooth mixing elements are left handed elements with slots through the flight that provide a frequent flow division. Screw mixing elements are standard forward conveying elements with reverse conveying gaps milled into the profile. These gaps ensure a constant flow against the main conveying direction. Turbine mixing elements consists of rings with turbine blades which can have different orientations. Those elements have no pitch and are followed by empty sleeves and that have no conveying capacity. In this work only left handed TMEs are considered. Kneading blocks are typically multiple double flighted discs without pitch with a certain length of each disc staggered by a certain angle. Depending on the staggering angle they act as forward conveying elements with positive staggering angles or vice versa. Todd 1998 gives a broad overview of the advantages and application areas of the investigated screw types.

3. Method and Results

The goal of the presented method is the description of the effects of mixing elements on the RTD. The RTDs are characterized by a tailing of the distribution which the BCM can describe well. As the BCM and the existing extruder models show structural similarities, the results of the RTD model can be added to the existing extruder model. This is performed by the relaxation of the uniform conveying capacity to consider flows in both directions in the conveying parameters.

To validate this method, it was tested on experimental RTD data taken from Brouwer 2002 and Poulesquen 2003. These authors captured the contribution to the RTD of the special screw elements using a tracer method. This data was being normalized, nondimensionalized, and transformed into 100 equidistant data points. The theoretical RTD is calculated with the BCM as presented by Roemer 1967. The numbers of cells is calculated as the ratio of the measured length to the fixed discretization length of 1cm. The summed quadratic deviation of the calculated and experimental data is being minimized by optimizing the backflow ratio for the objective function

$$\min_{\sigma_B} \sum (E_{M,\exp}(\tau) - E_{M,theo}(\tau))^2 \tag{6}$$

The solution for the optimization problem is obtained with the MATLAB solver fmincon. The results are presented in table 1. For all screw elements but TMEs and kneading blocks with 30° staggering angle this method shows improvements compared to the classical CSTR cascade model. The results for the screw mixing elements show a perfect description with the backflow cell model at a backflow ratio of 0.684. The physical explanations for this result are the gaps within the elements that provide a frequent backflow and favor distributive mixing. In contrast, applying the method to the TME is not beneficial as the calculated optimum is a zero backflow ratio. The overall error is higher than for any other screw element. Potentially the influence of the empty sleeves after each TME element is not negligible and causes a very narrow RTD. In order to compensate this effect, one would have to increase the number of cells. This shows a significant reduction in the overall error but is not applicable in practice due to a uniform discretization length in the existing extruder model . The application of the BCM to the ZME shows a minor improvement with a small backflow. This is caused by the teeth that are not perfectly sealing. The optimum for kneading blocks with negative staggering angle is found at a backflow of about 0.456 and 0.497, respectively. It is possible to reduce the overall error compared to the representation as CSTR cascade to 1/4. It is not possible to generalize the results for positive and negative staggering angles as he kneading block with +60° staggering angle benefits from the backflow whereas the +30° block does not. For kneading blocks in general, the error decreases

similar to the TME with an increasing number of cells because of a narrower RTD. A drawback of increasing the number of cells is the insufficient description of the tailing after 1.5 mean residence times as shown in figure 4. Moreover the presented method shows advantages over other methods for the description of RTDs for kneading blocks. Poulesquen 2003 reported the RTD of kneading blocks as a single CSTR with an unspecified delay time. The determination of this delay time is very inconvenient as experimental RTD measurements have to be carried out for different processing conditions. Consequently the proposed method is beneficial as it provides predictive capabilities such as the description of the mean residence time.

Table 1: Results of the optimization for the different screw elements for N=10. The experimental data was taken from Brouwer 2002[a] and Poulesquen 2003[b]. The total error is the summation for all 100 equidistant data points.

Screw Element	σ_B [-]	Error BCM [-]	Error CSTR Cascade [-]
SME[a]	0.684	0.074	4.521
TME[a]	0	3.848	3.848
ZME[a]	0.040	0.364	0.391
+60°KB[b]	0.247	2.856	4.837
+30°KB[b]	0	2.521	2.521
-30°KB[b]	0.497	1.580	6.263
-60°KB[b]	0.456	1.475	6.078

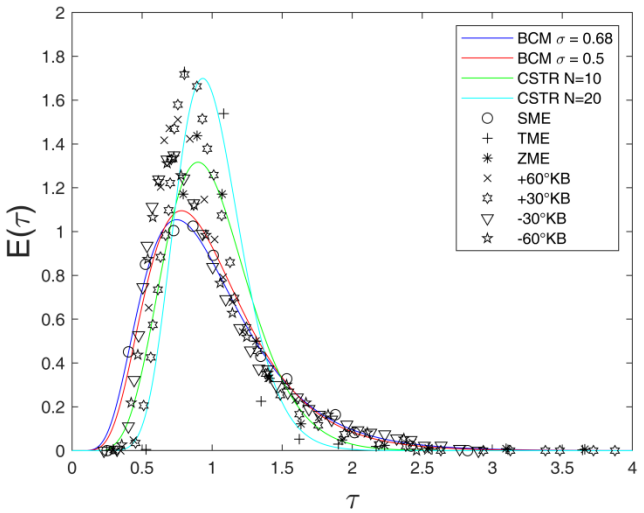

Figure 4: Comparison of the experimental RTD data with the BCM with 10 cells and with the series of CSTRs with 10 and 20 cells.

To apply the results to the existing extruder model, adapted conveying capacities K_f' and K_b' have to be calculated. No further structural changes within the model are necessary. The adapted screw parameters can be calculated as follows:

$$\sigma_B = \frac{K_b'}{K_f} \qquad K_f' = K_f - K_b' \qquad (7),(8)$$

4. Conclusion

In this work we presented incorporate the backflow cell model into a mechanistic extruder model to describe the effects of distributive mixing. By the application of the BCM, it is possible to improve the representation of the RTD and especially to reproduce the occurring tailing effects. Various types of mixing elements were investigated. Hereby it is possible to combine the information on the shape of the screw elements with the calculated backflow ratio to draw conclusions on the mixing efficiency. The results of the optimization of the backflow ratio show a sufficiently accurate description of the RTD especially considering the very limited number of fitted parameters. The obtained results can be directly used in an existing extruder model by simply modifying the forward and backward conveying capacities. With the help of the more complex mechanistic model it is possible to address the influence of changing processing parameters such as local filling ratios and melt temperatures within the extruder sections on the resulting residence time. This improves the prediction quality for RTDs over a broad range of operating conditions and can reduce or completely replace experimental investigations on the RTD during process development. In the future, the results of this work will be applied to the simulation and optimization of reactive extrusion processes. This makes the optimization of entire screw configuration with various screw geometries for complex processes possible, thus transforming the decision making process from being based upon expert knowledge to model-based science.

Acknowledgements

This was performed with funding from the European Union's Horizon 2020 research and innovation programme under grant agreement No 820716 (SPIRE project SIMPLIFY).

References

T.Brouwer et al., 2002, Flow Characteristics of Screws and Special Mixing Enhancers in a Co-rotating Twin Screw Extruder, Intern. Polymer Processing, Volume 17, Issue 1, pp. 26-32

S.Choulak et al., 2004, Generic Dynamic Model for Simulation Control Reactive Extrusion, Industrial Engineering Chemical Research, Volume 43, Issue 23, pp. 7373-7382

A. Eitzlmayr et al., 2014, Mechanistic modeling of modular co-rotating twin-screw extruders, International Journal of Pharmaceutics, Volume 474, Issues 1-2, pp. 157-176

Kohlgrüber et al., 2008, Co-Rotating Twin-Screw Extruders – Fundamentals,Technology and Applications, Carl Hanser Verlag, Munich

A.Poulesquen, 2003, A Study of Residence Time Distribution in Co-Rotatintg Twin-Screw Extruders. Part II: Experimental Validation, Polymer Engineering and Science, Volume 43, Issue 12, pp. 1849-1862

A.Poulesquen et al., 2001, Polymerization of Caprolatone in a Twin Screw Extruder, International Polymer Processing, Volume 16, Issue 1, pp. 31-38

J.P. Puaux et al., 2000, Residence time distribution in a corotating twin-screw extruder, Chemical Engineering Science, Volume 55, Issue 9, pp. 1641-1651

M. Roemer et al., 1967, Transient response and moments analysis of backflow cell model for flow systems with longitudinal mixing, Industrial and Engineering Chemistry Fundamentals, Volume 6, Issue 1, pp. 120-129

D.B. Todd, 1975, Residence time distribution in twin- screw extruders, Polymer Engineering Science,Volume 15 , Issue 6, pp. 437-443

D.B. Todd, 1998, Plastics Compounding, Carl Hanser Verlag, Munich

B.Vergnes et al., 1998, A Global Computer Software for Polymer Flows in Corotating Twin Screw Extruders, Polymer. Engineering Science, Volume 38, Issue 11, pp. 1781-1792

Sauro Pierucci, Flavio Manenti, Giulia Bozzano, Davide Manca (Eds.)
Proceedings of the 30th European Symposium on Computer Aided Process Engineering (ESCAPE30), May 24-27, 2020, Milano, Italy.
http://dx.doi.org/10.1016/B978-0-12-823377-1.50031-8

Comparison of two Meta-Heuristics for the Bi-Objective Flexible Job Shop Scheduling Problem with Sequence Dependent Setup Times

João Sacramento[a] , João Pedrosa[a], Nelson Chibeles-Martins[b] *, Tânia Pinto-Varela[a]

[a]*Centro Estudos Gestão, Instituto Superior Tecnico, Universidade Lisboa, Lisboa, Portugal*

[b]*Centro de Matemática e Aplicações and Departamento de Matemática, Faculdade de Ciências e Tecnologia, UNL, 2829-516 Caparica, Portugal*

npm@fct.unl.pt

Abstract

The increasingly competitivity in the plastic container market is driving companies toward a greater focus on efficiency, and mass production customisation, which triggers the increase of productivity by implementing more efficient and faster IT solutions. This work is based on a Portuguese case study, to develop a scheduling model considering the specific characteristics of this type of facilities and increase its competitiveness. To this end, two different approaches, the Tabu Search and Genetic Algorithm, were developed to solve a flexible job shop scheduling problem under a make-to-order production strategy. Each approach was validated using the case study, and the model's applicability were testes trough five instances. The results have shown that Tabu Search has a better efficacy and the Genetic Algorithm shows better efficiency.

Keywords: Flexible Job Shop Problem, Tabu Search, Genetic Algorithm, Metaheuristics, Multi-objective

1. Introduction

Nowadays, the industrial sector faces a new challenge. The traditional tactics used to increase productivity are outdated and companies are looking for new factors that may lead to improvement. Considering the fourth industrial revolution, Industry 4.0, more detailed and deep problem characterization is necessary. The speed of sharing information to and from the facility is crucial. The real-time information availability is required to support the decision making. To satisfy this challenge an agile and fast solution approach, with the aim of increasing flexibility and get competitive leverage is necessary. Therefore companies are becoming highly invested in developing customized information systems to manage, plan and schedule its manufacturing processes.

Despite some research has already been made using exact approaches, the FJSP's complexity and intractability usually lead to high computational times when these kind of algorithms are applied. On the other hand, meta-heuristics go towards the fourth revolution concepts, with lower computational burdens, being the Tabu Search (TS) and Generic Algorithm (GA), two of the most promising alternatives. Therefore the authors opted for focusing their efforts on the proposed Metaheuristics approaches.

Some of the work developed using a mono-objective TS were developed by Dell'Amico and Trubian (1993) with an algorithm that solve the classical Job-Shop Scheduling Problem (JSSP) makespan minimization. However, several authors, like Brandimarte (1993), Dauzère-pérès and Paulli (1997), Mastrolilli and Gambardella (2000), C. Scrich, V. Armentano (2004), and Abdelmaguid (2015) developed TS to solve the Flexible Job-Shop Scheduling Problem (FJSSP) in regards to makespan minimization, except C. Scrich, V. Armentano (2004) whom proposed to minimize tardiness. More recently the authors Saidi-Mehrabad and Fattahi (2007) and Shen et al. (2018) considered the sequence dependent setup times case of the FJSSP. GA approaches have also been applied to Scheduling problems. Pezzella et al. (2008) proposed several improvements to the generic GA in order to make them more efficient solving SP.
However, some research has been done concerning multi-objective approaches. Jia and Hu (2014) developed a TS procedure based on path relinking to solve a multi-objective FJSSP considering the minimization of the makespan, total workload and maximum workload, using the Pareto approach. Li et al. (2010) proposed a hybrid TS based algorithm to solve the multi-objective FJSSP with the three criteria chosen being makespan, total workload and maximum workload. Murata and Ishibuchi (1995) proposed a framework for GA with a weighted sum using randomly specified weights for each selection. It was already applied to several multi-objective optimization problems but never to a FJSSP. Morinaga et al. (2014) solved a FJSSP with MTO policy using a GA to minimize tardiness and setup-worker load. It was used a classic weighted sum approach to deal with the bi-objective problem.
The proposed work explores two multi-objective approach, a Genetic and a Tabu Search algorithm to define the production scheduling considering the tardiness and makespan minimization, as objective functions. The facility follows a make-to-order strategy, with sequence dependent setup time. To illustrate the methodologies applicability and its performance, not only a real case study is explored, but also, five more instances.
This work is based on the same case studied in Chibeles-Martins et al. (2017).

2. Modelling Characterization

Multi-objective Genetic Algorithm - BObGA
A new multi-objective genetic algorithm is developed based on the classical algorithm proposed by the authors Murata and Ishibuchi in (1995) extending it with the integration of randomly weights for each selection of the best chromosomes. To take into account the mitigation of customers' service level impact, the tardiness has a higher importance than the makespan. This is achieved by introducing a new parameter defining a lower bound that controls the minimum weight that is applied to the tardiness. Finally, the BObGA uses a hill climbing heuristic introduced by Greiner (1992) to perform a local search. The BObGA algorithm pseudocode is shown in Figure 1.

Multi-objective Tabu Search Algorithm - BObTS
The Tabu Search proposed algorithm is based on Shen et al. in (2018) extended to explore a Lexicographic Multi-objective approach, considering the tardiness minimization, with highest priority and the makespan minimization as a second priority objective. It uses the neighborhood structure developed on the aforementioned work but is adapted to be applicable in a multi-objective perspective by assigning different importance levels to objective functions according to the stage the algorithm is in. A diversification strategy is employed to avoid a premature stop at local minima. The BObTS algorithm pseudocode is presented in Figure 2.

```
Algorithm: Bi-Objective Genetic Algorithm
begin
    Initialize parameters;
    Evaluate population;
    while Generations number not reached do
        Select the best-fit individuals for reproduction;
        Apply crossover;
        Apply mutation;
        Apply local search;
        Evaluate population;
```

Figure 1–Bi-objective Genetic algorithm pseudocode – BobGA

```
Algorithm: Bi-Objective Tabu Search
begin
    Initialize parameters;
    Evaluate initial solution;
    while Tardiness not null or maximum iterations not reached do
        Generate neighborhood;
        Evaluate neighbors;
        Select neighbor;
        Update tabu list;
    while Maximum iterations not null do
        Generate neighborhood;
        Evaluate neighbors;
        Select neighbor;
        Update tabu list;
```

Figure 2 – Bi-objective Tabu Seach pseudocode – BObTS.

3. Instances Characterization

The case study (CS) is based on a mould industry production of plastics containers. The plastic containers are characterized by a bottom and a cover, produced using an injection moulding process. The process requires different changeovers, based on the product sequence production, each one with different setup time associated. The production process requires mainly three tasks. However, each product manufacture follows a different path, triggering different setup times. Nevertheless, all machines are able to produce all the products. For confidential reasons detailed production process information is omitted. Beyond the case study implementation, five instances with increase complexity were explored over the two approaches. In Table 1 is shown instances' characterization with the respective number of orders, the produced quantity, due date and number of machines.

Table 1 – Instances characterization.

Instances	#orders	Quantity (units)	Average due date (minutes)	# Machines
CS	40	8888	40	8
1	70	2162	1765	8
2	30	9797	853	8
3	40	5000	880	8
4	40	8888	1765	7
5	100	7189	2091	8

4. Results

BObGA and BObTS algorithms were executed for the six instances on a PC with an Intel Core i7-6700HQ, 2.60GHz, 8 GB RAM. A detailed characterization of the results obtained are shown in Table 2, and its graphic representation in Figure 3 and Figure 4.

Table 2 – BObGA and BObTS performance results.

	Instance	(Order x Machine)	Tardiness		Makespan	CPU Time
			% Optimal values	Average (min)	Average (min)	Average (seconds)
Genetic Algorithm	CS	40 x 8	84%	8.6	1,510.2	27.7
	1	70 x 8	98%	0.2	1,160.1	143.1
	2	30 x 8	86%	19,4	1,018.2	17.1
	3	40 x 8	48%	46	1,040.3	32.1
	4	40 x 7	48%	130.3	1,950	34.9
	5	100 x 8	0%	718.4	2,892.5	364.3
Tabu Search	CS	40 x 8	100%	0	1,349.5	267
	1	70 x 8	100%	0	994.4	300
	2	30 x 8	100%	0	887.3	301
	3	40 x 8	87%	4	931.3	304
	4	40 x 7	0%	395	1,833.3	303
	5	100 x 8	0%	425.5	2,910.4	663

The BObTS reaches the optimum value for the tardiness objective function (which is zero value) in all iteration, in the Instances: CS, 1 and 2. In third Instance 87% of iterations reached the optimal value, followed by instances 4 and 5, with a non-optimum, justified by the decreased number of machines or the increase number of orders. The BObGA shown a decrease number of optimal solutions for the tardiness, as the complexity increases, with Instance 5, reaching only non-optimum solution. However, considering the case study, BObTS showed a 100% of optimum solutions for the Tardiness vs the 84% for the BObGA (Table 2). As is shown in Figure 4, the BObGA is more efficient, being less time consuming than BObTS. However, BObTS denotes a higher efficacy (Figure 3).

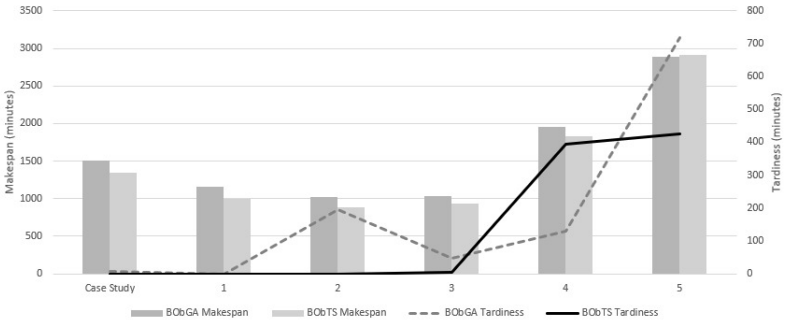

Figure 3 – BObGA and BObTS non dominated solution characterization

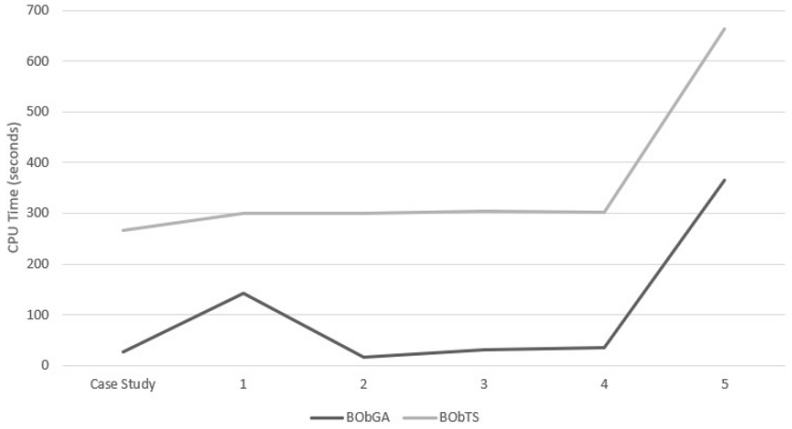

Figure 4 – BObGA and BObTS computational performance.

5. Conclusion

Nowadays, industry is triggered to increase its efficiency and productivity by developing tools to support decision making processes in real time. To overcome this challenge the authors propose two Meta-heuristic multi-objective algorithms (BObGA and BObTS) to explore the scheduling of a flexible job shop facility with product sequence setups. Both Meta-heuristics considered the tardiness and makespan minimization as objective functions. The MObGA explored the randomly weighted sum, while the MObTS a lexicographic approach. The Algorithm applicability and its performance comparison were made over a real case study, followed by five instances with increased complexity, to stress the algorithms. As the results showed, BObTS algorithm outperformed the BObGA in almost all cases, reaching better objective functions values denoting a higher efficacy. However, BObGA is less time consuming showing a higher efficiency. Nevertheless, further work should be done, exploring other production strategies and stressing the algorithm with tighter due dates.

Acknowledgements

The authors gratefully acknowledge the support of the Portuguese National Science Foundation through Portugal 2020 project POCI-01-0145-FEDER-016418 by UE/FEDER through the program COMPETE2020. This work was partially supported by

the Fundação para a Ciência e a Tecnologia (Portuguese Foundation for Science and Technology) through the project UIDB/00297/2020 (Centro de Matemática e Aplicações).

References

T. F. Abdelmaguid, 2015, A neighborhood search function for flexible job shop scheduling with separable sequence-dependent setup times. Applied Mathematics and Computation, 260, 188–203. https://doi.org/10.1016/J.AMC.2015.03.059

P. Brandimarte, 1993, Routing and scheduling in a flexible job shop by tabu search. Annals of Operations Research, 41(3), 157–183. http://doi.org/10.1007/BF02023073

N. Chibeles-Martins, A. Marques, and T. Pinto-Varela, 2017, A Bi-objective two step Simulated Annealing Algorithm for Production Scheduling. Computer Aided Chemical Engineering, 40, 1351–1356. https://doi.org/10.1016/B978-0-444-63965-3.50227-0

C. R. Scrich, V. A. Armentano and M. Laguna, 2004, Tardiness minimization in a Flexible job shop/: A tabu search approach, Journal of Intelligent Manufacturing, 15, pp. 103–115, http://dx.doi.org/10.1023/B:JIMS.0000010078.30713.e9

S. Dauzère-Pérès and J. Paulli, 1997, An integrated approach for modeling and solving the general multiprocessor job-shop scheduling problem using tabu search. Annals of Operations Research, 70(0), 281–306. https://doi.org/10.1023/A:1018930406487

M. Dell'Amico and M. Trubian, 1993, Applying tabu search to the job-shop scheduling problem. Annals of Operations Research, 41(3), 231-252.

R. Greiner, 1992, Probabilistic Hill-Climbing: Theory and Applications. Proceedings of the Ninth Canadian Conference on Artificial Intelligence.

S. Jia and Z. Hu, 2014, Path-relinking Tabu search for the multi-objective flexible job shop scheduling problem', Computers and Operation Research. Elsevier, 47, pp. 11–26. DOI: 10.1016/j.cor.2014.01.010

J.-Q. Li, Q.-K. Pan and Y.-C. Liang, 2010, An effective hybrid tabu search algorithm for multi-objective flexible job- shop scheduling problems, Computers & Industrial Engineering, 59(4), pp. 647–662. https://doi.org/10.1016/j.cie.2010.07.014

M. Mastrolilli and L. M. Gambardella, 2000, Effective neighbourhood functions for the flexible job shop problem. Journal of Scheduling, 3(1), 3–20.

Y. Morinaga, M. Nagao and M. Sano, 2014, Optimization of flexible job-shop scheduling with weighted tardiness and setup-worker load balance in make-to-order manufacturing. In Joint 7th International Conference on Soft Computing and Intelligent Systems (SCIS) and 15th International Symposium on Advanced Intelligent Systems (ISIS) (pp. 87–94). https://doi.org/10.1109/SCIS-ISIS.2014.7044681

T. Murata and H. Ishibuchi, 1995, MOGA: Multi-objective genetic algorithms. In Proceedings of 1995 IEEE International Conference on Evolutionary Computation (Vol. 1, pp. 289-). https://doi.org/10.1109/ICEC.1995.489161

F. Pezzella, G. Morganti and G. Ciaschetti, 2008, A genetic algorithm for the Flexible Job-shop Scheduling Problem. Computers and Operations Research, 35(10), 3202–3212. https://doi.org/10.1016/j.cor.2007.02.014.

M. Saidi-Mehrabad and P. Fattahi, 2007, Flexible job shop scheduling with tabu search algorithms. The International Journal of Advanced Manufacturing Technology, 32(5), 563–570. https://doi.org/10.1007/s00170-005-0375-4.

L. Shen, S. Dauzère-Pérès and J. S. Neufeld, 2018, Solving the flexible job shop scheduling problem with sequence-dependent setup times, European Journal of Operational Research, 265(2), 503-516. DOI: 10.1016/j.ejor.2017.08.021

Sauro Pierucci, Flavio Manenti, Giulia Bozzano, Davide Manca (Eds.)
Proceedings of the 30th European Symposium on Computer Aided Process Engineering (ESCAPE30), May 24-27, 2020, Milano, Italy.
http://dx.doi.org/10.1016/B978-0-12-823377-1.50032-X

Simulation of the Crystallization Process based on Cellular Automata --- Snowflake Formation from Pure Water System

Jianmin Liu,[a] Jindong Dai,[a] Chengyu Han,[a] Junkai Zhang,[a] Jiali Ai,[a] Chi Zhai,[b] Xiaolin Liu[a]*, Wei Sun[a]*

[a]*College of Chemical Engineering, Beijing University of Chemical Technology, North Third Ring Road 15, Chaoyang District, Beijing, 100029, China*
[b]*Faculty of chemical engineering, Kunming University of Science and Technology, Kunming 650500, China*
liuxl@mail.buct.edu.cn
sunwei@mail.buct.edu.cn

Abstract

Crystallization is an important unit operation process in chemical industry production. Generally, there are a variety of morphology in most crystals and different crystal morphology varies greatly in physicochemical properties. As different crystal morphology may be obtained by changing its ambient conditions surrounding the crystal. In previous studies, the research for crystallization are usually conducted by experiments, which could be very time-consuming and resource-intensive. A cellular automata, CA, is a method by simulating the interaction among subsystems to obtain the description of the patterned system behavior. CA not only provides a description of the physical properties of the material but can also predict changes on the micro-level. Using the cellular automaton to simulate the crystallization process will be more efficient in terms of both time and computation load. In this paper, the crystallization process is simulated by the method of cellular automata. By changing the model parameters, the effects of the parameters on the crystal morphology are studied.

Keywords: crystallization, cellular automaton, simulation, morphology

1. Introduction

The crystallization process includes nucleation and crystal growth (Jungblut and Dellago, 2016). As the growth center of crystal, nucleus is composed of a set of regularly arranged particles, and exists stably in liquid phase. In the process of crystal growth, different crystal morphology of a substance can be generated under different conditions, such as temperature, saturation, solvent, seed crystals added, and the pH of solution. Furthermore, different crystal morphology varies greatly in physicochemical properties, exhibiting different thermodynamic and mechanical properties, such as particle size distribution, melting point, stability and habit. Suitable crystal morphology can improve the quality of products. (Wang et al., 2002). Therefore, it is promising to research on controlling the conditions to get effective crystal morphology.

Generally, the crystallization process is studied by experiments (Thompson et al., 2004). However, experiment study requires significant input of time and resource. With the development of computer technology, this situation can be improved through computer simulation.

According to classical diffusion theory, crystallization is achieved by the diffusion of solute molecules from the bulk of solution to the crystalline surface, the surface reaction in which the solute molecules are embedded in the crystal lattice, and the heat transfer of crystallization from crystalline surface to the bulk of solution.

Partial differential equation (PDE), as a commonly used mathematical tool, can be applied to describe crystallization process, which is established based on the mechanism theories of transfers. However, solving process of PDE is very time consuming and requires certain proficiency in professional software or programing.

In simulation practice, PDE is usually solved by dividing the solution area into subsets through methods, such as finite element or finite difference. And the subsets are related to adjacent regions through the law of diffusion. If the crystalline region is divided into grids, the crystal growth process can be regarded as the mass and heat transfer among adjacent grids, resulting in changes in the state of grids. Thus, from the system point of view, crystallization process can be also considered as a self-assembled complex system.

Cellular automata (CA) is a method to obtain the pattern of system behavior by simulating the interaction among subsystems. Through research on CA, S. Wolfram (Wolfram, 2002) thought that CA is suitable for simulating the self-assembled complex system, such as crystallization process. Then, the simulation of crystallization process by CA has attracted great attention of researchers (Mourachov, 1997).

In 2015, K. Libbrecht used CA model to research the effect of surface diffusion parameters on the columnar crystalline morphology of water (Libbrecht, 2015). However, the influence of density distribution parameters and the increment in three-dimensional spatial on the crystal morphology was not discussed. In this work, CA method is applied to simulate the crystallization of water into snowflake of different shapes. At the same time, the influence of the parameters on the crystal morphology was discussed by changing the parameters of crystal.

2. CA simulation: snowflake formation as an example

2.1. Basic hypothesis and Parameter setting

It is assumed that the system is pure water system with constant temperature and no impurities. The ideal process of water crystallizing into snowflakes was simulated without considering stirring, the influence of the outside environment of the wall and the crystal dissolution. Since the water molecules are arranged according to the rules of the hexagonal system (Figure. 1), the cell space is set to a regular hexagonal grid. Snowflakes are made by copying and shifting this structure (Nakaya, 1954).

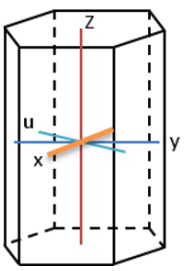

Figure. 1 The structure of hexagonal crystal system.

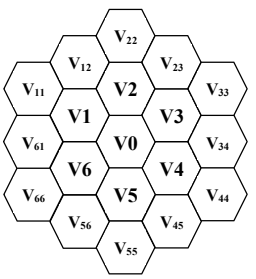

Figure. 2 The range of cellular neighbors.

The simulated region is *R*, that is, the distance from the most central cell to the outermost cell is *R* cells. There is a state value *S* for each cell. *S* is a number greater than

0, represented in grayscale. When the cell state $S \geq 1$, the cell is in the crystalline state and the color is white. When the cell state $S < 1$, the cell is in the uncrystallized state and is represented by different grey scales. In the initial state, $S = 1$ is set as the initial state of the cell at the most central point of the cell space. The growth and final shape of snowflakes are influenced by two parameters. One is the initial density distribution α, and the initial state of the cell is set to $S = \alpha$, except for the central cell. And the other one is the cellular capture of water at a three-dimensional level, called β. The neighborhood scope is shown in Figure. 2. The change of cellular state is influenced by its neighbors.

2.2. CA evolution rules

Based on the cellular automata method, all cells states are recognized simultaneously. When the state of cell is crystalline, that is, when its value is greater than or equal to 1, the state of cell remains unchanged at the next moment. The calculation of S at the next moment is shown in (1). And it can also be applied to the condition where the central cell is uncrystallized and there are no crystalline cells in either of the first and second circles.

$$S_{V0}^{t+1} = S_{V0}^{t} + \beta \tag{1}$$

When the cell state is not crystallized and the crystal cell exists in the two surrounding circles, this situation can be divided into three cases, in the first two cases, formula (2) is used to calculate the next value, and in the last case, formula (3) is used.

$$S_{V0}^{t+1} = S_{V0}^{t} + \beta + (V1 + V2 + V3 + V4 + V5 + V6)/12 \tag{2}$$

$$S_{V0}^{t+1} = 0.5 * S_{V0}^{t} + (V1 + V2 + V3 + V4 + V5 + V6)/12 \tag{3}$$

In the first case, crystallized cells only exist in the first cycle. It is worth noting that the values of cells in the crystalline state and the values of cells around the crystalline cell are represented by 0 when formula (2) is used.

In the second case, crystals both exist in the first and second cycles. Besides the rule in the previous paragraph, it is only necessary to add judgment on the cells in the second cycle and identify the crystalline cells in the second cycle. Then, the values of cells adjacent to the crystallized cells of second cycle are also regarded as 0 during calculation.

In the third case, if there is no crystalline cell in the first cycle but there are crystalline cells in the second cycle, formula (3) will be used to calculate the next value of central cell and the regulation is same as the second case.

It can be seen that the principle in the process of formulating rules is as follows. The crystallized cell is relatively stable, and its value is not affected by around cells in horizontal plane. Uncrystallized cells around crystalline cells tend to crystallize faster, and if there are no crystalline cells around the uncrystallized cell, its value will be contributed to cells closer to crystalline cells.

3. Results and discussion

The following image is set to $R = 200$ and the computer operation stops until the crystal grows to the boundary or iterates 10,000 times. The number of iterations for each crystal is below the figures.

3.1. The effect of changing the initial state value on snowflake

Under the condition of $\beta = 0$, the influence of α on crystal habit is studied by setting the value of α to 0.2, 0.4, 0.5 and 0.6.

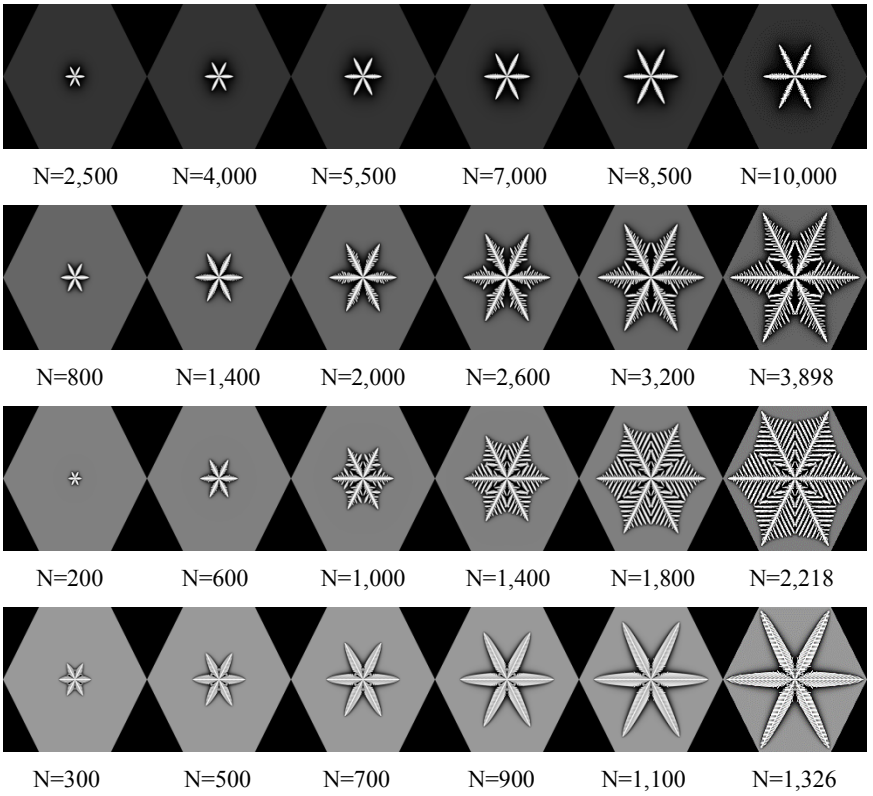

Figure. 3 Snowflake growth under different α conditions. Each row represents the process of snowflake growth under a set of parameters. *N* is the number of iterations. Different rows represent different α values. From top to next time, take 0.2/0.4/0.5/0.6.

These are a series of pictures of snowflake growth as shown in Figure. 3, and the last picture is the final state of the iteration. When α is 0.2, that is, the initial density distribution is 0.2, the calculation can still be iterated for 10,000 times before reaching the boundary, but when α is 0.4, the calculation is iterated for 3,898 times before reaching the boundary, and when α is 0.6, it is only iterated for 1,326 times before ending. With the increasing of α, the crystallization rate gets faster and faster and the branches appear earlier. Diffusion limits the growth as the crystal becomes larger, and eventually this causes branches to form. The two branches continued to grow outward after contacting and then stopped. When $\alpha = 0.4$, branches first meet at about 1/3 of the center of the dendrite. During the whole process of growing snowflakes, the growth rate of crystal branches is the fastest. When $\alpha = 0.5$, branches meet about 1/5 away from the center of the dendrite. When $\alpha = 0.6$, branches meet about 1/12 away from the center of the dendrites (Figure. 4). The voids in the central area are reduced and the structure is more compact. Six dendrites grow simultaneously and are identical in shape due to symmetry. The growth morphology of the branches on the dendrites became more regular and uniform gradually. In other words, the density distribution has an effect on the growth rate of the crystal and the location of the main branches. The greater the

density distribution, the closer the branches meet to the center. The structure of the whole snowflake becomes tighter as the density distribution increases.

Figure. 4 From left to right α is 0.4/0.5/0.6, the growth state of the dendrites and branches.

Schematic diagram of crystal growth process of snowflake under set parameters β is an increment in three dimensions. The presence of β makes the snowflakes denser and the gaps between the branches smaller. Next, β is used to reflect the influence on crystallization habit.

3.2. The effect of changing the three-dimensional space increment on snowflake

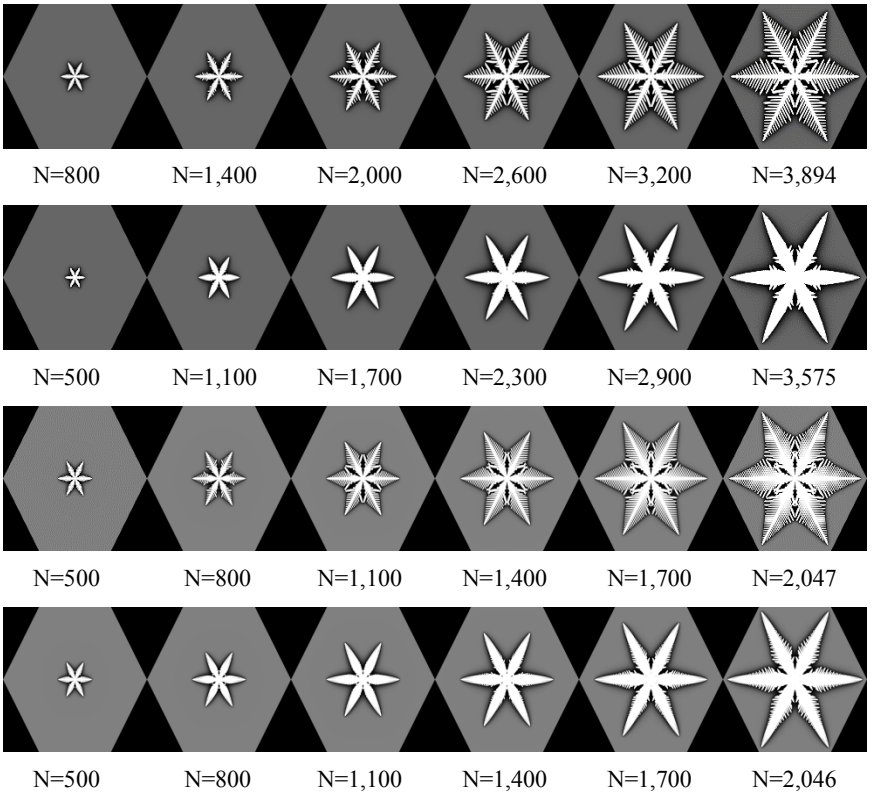

Figure. 5 Snowflakes grow under different conditions. Each row represents the snowflake's growth under a set of parameters. *N* is the number of iterations. The first two lines represent the case where α is 0.4 and β is 0.0005/0.002. The last two lines indicate the case where α is 0.5 and β is 0.001/0.002.

The effect of β on the rate of crystal growth is particularly significant because β is added directly to the cell value at each iteration. In order to study the influence of β on water crystal habit, the value of β was made smaller to observe the change of crystal

morphology. When α is 0.4 and 0.5, two groups of pictures reflect the effect of β as shown in Figure. 5. When α is constant and the value of β is within consideration in this work, the change of β has less impact on the number of iterations, but the shape of the snowflakes is different significantly.

The presence of β makes the dendrite grow more robust, and the overall snowflake morphology tends to be more central, that is, the dendrite is closer to the length rather than the flake. The central area of a snowflake is less void and more compact. The branches have been reduced because the addition of β has increased the number of dendrites. Increased moisture content in the air has an effect on snowflake thickness. Its effect is on the upper and lower surfaces of the entire crystal. However, if the influence of the thickness of the crystal is not considered, it is equivalent to the growth only in the horizontal direction.

The overall complexity of the dendritic pattern increases with increasing supersaturation as well as with increasing crystal size. Libbrecht has reported that the growth is simple six-branch shape at the lower supersaturations, slenderer, often hollow columns at intermediate supersaturations, and firm crystals at higher supersaturations (Libbrecht, 2005). The shape of simulated crystal conforms to this situation.

4. Conclusion

In this work, CA method is used to simulate the process of snow crystal, and the effects of density distribution and three-dimensional spatial increment on snowflake are discussed. The effects on crystallization rate, dendrite and branch growth are studied. The model provides a basis for systematic studies with morphology substances. It can be concluded that it is a potential way to control the crystal growth process in order to obtain the effective crystal morphology and increase its yield. This method can also be applied to the systematic study of other substances with complex crystal morphology, which can be the starting point for controlling the growth process of crystals to increase the crystal yield with desired morphology in the future.

Acknowledgments

This work was supported by National Natural Science Foundation of China No. 21878012 and No. 21576015.

References

S. Jungblut, C. Dellago, 2016, Pathways to self-organization: Crystallization via nucleation and growth. The European Physical Journal E, 39(8): 77.

K. Libbrecht, 2015, Incorporating Surface Diffusion into a Cellular Automata Model of Ice Growth from Water Vapor.

S. Wolfram, 2002, A New Kind of Science.

J. Wang, X. Huang, B. Liu, 2002, Research progress in predicting the habit of organic molecular crystals. Journal of Synthetic Crystals, 31(3): 218-223.

U. Nakaya, 1954, Snow crystals: Natural and Artificial.

C. Thompson, M. Davies, C. Roberts, 2004, The effects of additives on the growth and morphology of paracetamol (acetaminophen) crystals. International Journal of Pharmaceutics, 280(1-2): 137-150.

S. Mourachov, 1997, Cellular automata simulation of the phenomenon of multiple crystallization. Computational Materials Science, 7(4): 384-388.

K. Libbrecht, 2005, The physics of snow crystals. Reports on progress in physics, 68(4): 855-895.

Sauro Pierucci, Flavio Manenti, Giulia Bozzano, Davide Manca (Eds.)
Proceedings of the 30th European Symposium on Computer Aided Process Engineering (ESCAPE30), May 24-27, 2020, Milano, Italy.
http://dx.doi.org/10.1016/B978-0-12-823377-1.50033-1

A Thermo-Economic Analysis Method for Combined Cycle Power Plants under Flexible Operation Modes

Senjing Qin,[a] Pei Liu,[a,*] Zheng Li[a]

Department of Energy and Power Engineering, Tsinghua University, Beijing, 100084, China
liu_pei@tsinghua.edu.cn

Abstract

Gas steam combined cycle power plants have been playing an important role in peak shaving of a power grid. The increasingly complexity of power demand and power supply structure puts forward higher requirements for flexible operation, which is characterized by frequent load changes and start-stop operation. Under such circumstances, obtaining an optimal operation strategy becomes essential for profitability of combine cycle power plants. In this paper, a thermodynamic model comprising key functional modules of a combined cycle power plant and its overall cycle process are presented. An economic analysis method based on heat consumption rate is proposed. The proposed model is applied in a combined cycle power plant in China, and quantitative impacts of flexible operation on maintenance cost are discussed. Results show that the model can reflect the thermal economy of the power plant under variable environmental conditions. The economic analysis shows that there are significant economic differences between different flexible operation cases.

Keywords: Combined Cycle Power Plant, Thermo-Economic Analysis, Flexible Operation

1. Introduction

Gas steam combined cycle (GTCC) power plants perceives the advantages of high cycle efficiency and clean emissions. Also, due to its feature of very short-time start-up and load-change operations, GTCC have been playing an important role in peak shaving and demand respond of electricity grid. Recently, the availability of renewable energy and complex power demand have placed greater requirements on grid stability. Accordingly, GTCC faces a more arduous task of peak shaving and flexible operation. The economy of GTCC is highly sensitive to fuel cost, also frequent load changes will affect the service life of components, determining maintenance and replacement costs. It is essential to establish a thermo-economic analysis method applicable to GTCC under flexible operation modes.

Many studies have been done using different analysis methods to investigate the cost and economy of GTCC. Based on exergy analysis, the thermal economics model and cost equation of GTCC are established, and the exergy cost of each component of the system is calculated (Li et al., 2015). Considering the multiple benefits of the economy and environment, multi-objective optimization was carried out using three objective functions, concerned with exergy efficiency, total cost rate and CO_2 emission (Avval et al., 2011). Moreover, intelligent search techniques such as genetic algorithm was applied to find the

Pareto Frontier of exergy efficiency and total cost rate of GTCC, and best values of design parameters were presented (Ahmadi et al., 2011).
However, the existing research mainly focus on GTCC operating under design mode and aim at finding the best design values of cycle parameters. There are few studies focused on economy of an established GTCC under different flexible operation modes. Also the analysis of operation and maintenance cost related to drastic load changes is still lacking. In response to these research gaps, this paper proposes a thermal-economic analysis method, which is based on a thermal dynamic GTCC model. In terms of fuel cost, this paper calculates fuel consumptions under various operating conditions with different power output and environmental conditions. In terms of maintenance cost, this paper quantitatively describes the impact of start-stop and load-change operations by investigating equivalent operation hours. Moreover, a GTCC power plant in China is taken as a case study to verify the applicability of the method.

2. Methodology

2.1. Thermal dynamic model of GTCC

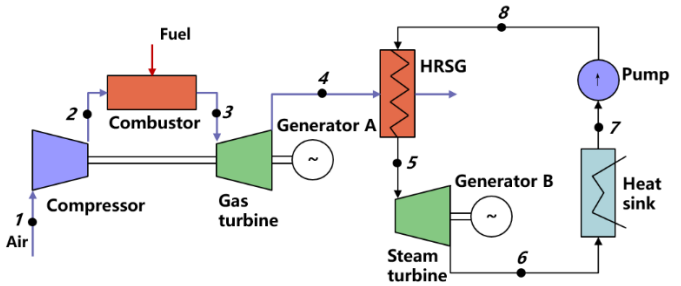

Figure 1 Schematic of GTCC

Figure 1 illustrates a gas steam combined cycle with a non-additionally heat recover steam generator (HRSG). In this study, thermo-dynamic models of gas turbine, steam turbine and HRSG are established, and parameters of gas and steam function as connections among each component model.
A typical gas turbine consists of a compressor, a combustor and a turbine. For compressor, parameters that characterizes its performance under off-mode operation are relative reduced pressure ratio $\dot{\pi_C}$ and relative reduced efficiency $\dot{\eta_C}$, which are affected by relative reduced flow rate $\dot{M_{red}}$ and relative reduced speed $\dot{n_C}$. Empirical formula as Eq. (1) - Eq.(5). can be constructed based on compressor characteristic diagrams (Zhang et al., 2011). The two empirical parameters p and m can be obtained from Figure 2 and Figure 3.

$$\dot{\pi_C} = c_1 \cdot \dot{M_{red}}^2 + c_2 \cdot \dot{M_{red}} + c_3 \tag{1}$$

$$\dot{\eta_C} = [1 - c_4(1 - \dot{\pi_c})^2] \cdot \left(\frac{\dot{n_{red}}}{\dot{M_{red}}}\right) \cdot \left[2 - \left(\frac{\dot{n_C}}{\dot{M_{red}}}\right)\right] \tag{2}$$

$$c_1 = \frac{\dot{n_C}}{p\left(1 - \frac{m}{\dot{n_C}}\right) + \dot{n_C}(\dot{n_C} - m)^2} \tag{3}$$

$$c_2 = \frac{\left(p - 2mn_C^{\cdot 2}\right)}{p\left(1 - \frac{m}{n_C^{\cdot}}\right) + n_C^{\cdot}(n_C^{\cdot} - m)^2} \tag{4}$$

$$c_3 = \frac{-\left(pmn_C^{\cdot} - m^2 n_C^{\cdot 3}\right)}{p\left(1 - \frac{m}{n_C^{\cdot}}\right) + n_C^{\cdot}(n_C^{\cdot} - m)^2} \tag{5}$$

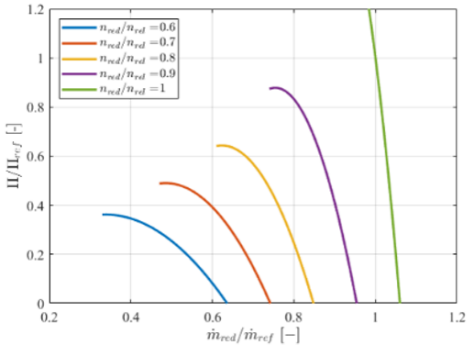

Figure 2 Compressor characteristic diagrams related to $\pi_C^{\cdot}$

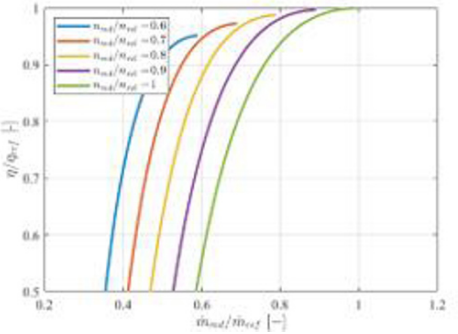

Figure 3 Compressor characteristic diagrams related to $\eta_C^{\cdot}$

The gas temperature at combustor outlet follows the energy balance equation Eq.(6). For turbine, the mathematical relationship between pressure and flow can be quantified by Flugel formula Eq.(7). Net power output of gas turbine is shown in Eq.(8).

$$\begin{aligned} &m_{fuel} * \left[c_{p,fuel} * \left(T_{fuel} - T_{ref}\right) + LHV\right] + m_{air} * c_{p,air} * \left(T_2 - T_{ref}\right) \\ &= m_t * c_t * \left(T_3 - T_{ref}\right) \end{aligned} \tag{6}$$

$$\frac{M_t}{(M_t)_0} = \sqrt{\frac{p_3^{\,2} - p_4^{\,2}}{(p_3^{\,2} - p_4^{\,2})_0}} * \sqrt{\frac{(T_3)_0}{T_3}} \tag{7}$$

$$P_{GT} = M_{air} \cdot c_{p,air} \cdot (T_2 - T_1) + M_t \cdot c_t \cdot (T_4 - T_3) \tag{8}$$

The steam turbine in GTCC usually operates under sliding pressure mode. The characteristics of it under off-mode operation also follow Flugel formula Eq.(7).Variables in the formula represent the state of superheated steam.

2.2. Operation and maintenance cost related to start-stop operation and load change

This study applied equivalent operating hours (EOH) to describe the life expenditure of gas turbine. And there exists a threshold of EOH for maintenance and replacement of parts. Start-stop operation and load change can be expressed quantitatively by adding additional EOH. Eq.(9) shows the calculation of EOH, where AOH represents actual stable operating hours. And A represents a correction coefficient, which shows the amount of actual stable operating hours equivalent to a normal Start-stop operation. The value of A is determined by the ratio of the thermal stress applied to the high-temperature components during start-stop operation to the thermal stress during stable operation.

The influence of load change is essentially similar to start-stop operation, so we can use Eq.(10) to describe the equivalent number of Start-stop during a period of time comprising j Start-stop operation and n load-change operation. LC is a correction

coefficient indicating the amount of equivalent number of start-stop operation of a single load-change operation. Fig 4 shows the value of LC as a function of percentage change in load and rate of load change, which is suggested by Mao (2010).

$$EOH = (AOH + A \times E) \times F \tag{9}$$

$$E = j + \sum_{i=1}^{n} (LC)_i \tag{10}$$

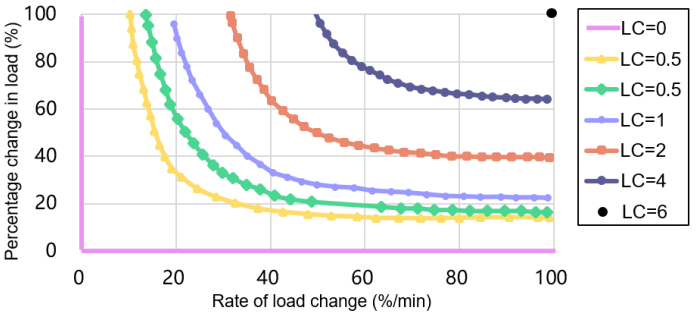

Figure 4 Value of LC as a function of percentage change in load and rate of load change

3. Case study

A GTCC power plant in China is chosen to carry out case study using the method proposed. The power plant consists of a 9E gas turbine, a non-additionally HRSG and a steam turbine. Values of operation parameters under design mode are listed in Table 1.

Table 1 Values of operation parameters under design mode of selected GTCC

Parameters of gas turbine	Value	Unit	Parameters of steam turbine	Value	Unit
power output	125.9	MW	power output	61.61	MW
speed	3000	rpm	HP steam pressure	62	bar
pressure ratio	12.3	-	HP steam temperature	519	℃
air/fuel inlet temperature	15	℃	HP steam flow rate	51.56	kg/s
air/fuel inlet pressure	1.013	bar	LP steam pressure	6.5	bar
mass flow of air	402.8	kg/s	LP steam temperature	259	℃
mass flow of fuel	8.3	kg/s	LP steam flow rate	8.72	kg/s
			back pressure	0.07	bar

3.1. Gas turbine simulation

This study takes power output, environment pressure and environment temperature as the input to figure out the fuel consumption. Then we select 1400 sets of measurement data for simulation, and the result is shown as Fig 5. Average relative error of simulation is 1.7%, and it demonstrate the accuracy of the model.

3.2. Steam turbine simulation

The HRSG produces high-pressure steam and low-pressure steam simultaneously. The high-pressure steam enters steam turbine at inlet directly, whilst the low-pressure steam enters at the middle of steam turbine and expands at remaining stages. Therefore, this study divides the steam turbine into high-pressure section and low-pressure section.

Simulation of the model is carried out with 2000 sets of operating data. Fig 6 shows the results and average relative error of simulation is 0.8%.

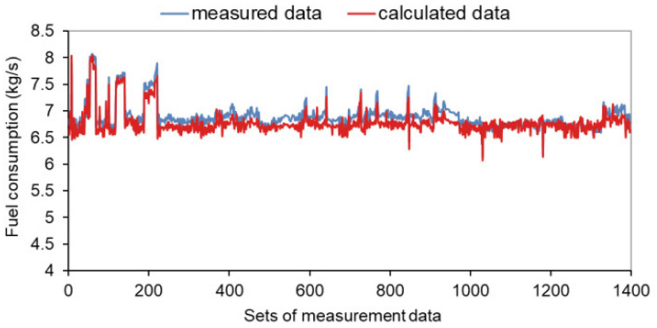

Figure 5 Comparison of measured values and calculated values of gas turbine fuel consumption

Figure 6 Comparison of measured values and calculated values of steam turbine power output

3.3. Operation and maintenance cost calculation

This study designs three scenarios with different load curve, as is shown in Fig 7. The most important factors that distinguish the three scenarios are the number and severity of start-stop operations and load changes. Scenario A reproduces the actual load curve of a given day of the GTCC power plant in China. The gas turbine starts and stops daily for the purpose of peak shaving. Scenario B shows that the gas turbine only starts and stops once a week, and the rest of the time it operates at continuous constant load. Scenario C indicates frequent start-stop operation and load change. The time range is one week and the output range of gas turbine under stable operation is between 80MW and 125.9MW. The AOH of the three scenarios are controlled as 95.08h, and the power generation is controlled as 11.1GW·h.

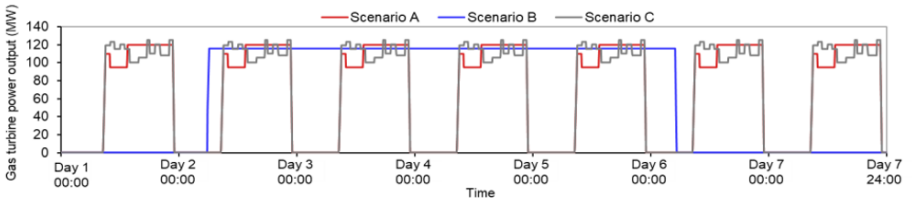

Figure 7 Different load curves of three scenarios

Table 2 displays the results of calculation. Compared to Scenario A, a constant-load operation strategy like scenario B will extend the service life of components to 2.06 times. However, frequent load change like scenario C will shorten the service life by 0.6%.

In general, the EOH threshold of components such as combustion chamber flame tube is 24,000h (Mao et al., 2010). This study supposes that a single maintenance and replacement cost is 26,000 EUR and the interest rate is 15%. Compared to scenario A, a constant-load operation strategy like scenario B can save 24.75% of the replacement and maintenance cost, whilst frequent load change like scenario C will increase 0.3% of the replacement and maintenance cost.

Table 2 Calculation results of three scenarios

	scenario A	scenario B	scenario C
EOH (h)	238.93	116	240.47
number of start-stop operations	7	1	7
number of load-change operations	14	0	70
service life (a)	1.93	3.97	1.91
discounted maintenance and replacement cost (EUR)	19,853	14,928	19,909

4. Conclusions

A thermo-economy analysis method based on thermo-dynamic GTCC model is proposed in this paper. Off-mode modeling is carried out for key components such as gas turbine and steam turbine. The simulation results indicate that average relative error of thermo-dynamic gas turbine model is 1.7%, and the average relative error of steam turbine model is 0.8%. This paper also applies equivalent running hours to quantify the cost of start-stop and load-change operations. Three scenarios with different load curves are studied. Results show that there are significant economic differences between different flexible operation scenarios. These differences are reflected in the huge difference in service life of equipment, which affects the maintenance and replacement costs.

Acknowledgement

The authors gratefully acknowledge the Phase Ⅲ Collaboration between BP and Tsinghua University.

References

Li Y., Chen J.H.,2015, Thermoeconomic Analysis of Conbined Cycle Power Plants by Structure Theory, Thesis, Zhejiang University, Zhejiang, China. https://kns.cnki.net/KCMS/detail/detail.aspx?dbcode=CMFD&dbname=CMFD201501&filename=1015539697.nh&v=MzEwNjJDVVI3cWZadWRuRmlublVyckxWRjI2RzdhN0Y5ZkZxSkViUElSOGVYMUx1eFlTN0RoMVQzcVRyV00xRnI= (in Chinese)

Zhang N., Cai R,.2002,Analytical solutions and typical characteristics of part-load performances of single shaft gas turbine and its cogeneration, Energy Conversion and Management, 43, 1323-1337

Avval H.B., Ahmadi P., Ghaffarizadeh A.R., et al., 2011,Thermo-economic-environmental Multiobjective Optimization of a Gas Turbine Power Plant with Preheater using Evolutionary Algorithm, International Journal of Energy Research, 35, 5, 389-403

Ahmadi P, Dincer I, Rosen M.A., 2011, Exergy, exergoeconomic and environmental analyses and evolutionary algorithm based multi-objective optimization of combined cycle power plants. Energy, 36, 10, 5886-5898

Mao D., Zhu Y.S., 2010, Maintenance Concept Analysis of Mitsubishi M701F Gas Turbine, Gas Turbine Technology, 3, 57-61 (in Chinese)

Sauro Pierucci, Flavio Manenti, Giulia Bozzano, Davide Manca (Eds.)
Proceedings of the 30th European Symposium on Computer Aided Process Engineering (ESCAPE30), May 24-27, 2020, Milano, Italy.
http://dx.doi.org/10.1016/B978-0-12-823377-1.50034-3

Two-phase Flow Modelling and Simulation of Gas Purification Column

Lívia Gyurik, Attila Egedy, Tamás Varga, Zsolt Ulbert

Department of process engineering, University of Pannonia, H-8200 Veszprém, Hungary

gyurikl@fmt.uni-pannon.hu

Abstract

In the technologies where harmful organic solvents are used it is necessary to purify the waste gases in order to ensure the protection of environment and the fulfillment of environment protecting laws. A wide-spread solution is to adsorb the undesired components on a porous fixed bed but it saturates during the operation and should be regularly regenerated resulting in an economic loss. One of the solutions to improve the process is the use of a moving bed equipment, where the regenerated particles are continuously fed to the adsorber and the saturated particles are transferred toward the regenerator providing this way a continuous operation. The objective of our research is to model and simulate the gas-solid two-phase flow using the immersed boundary method and calculate the particle movement and the adsorption process for the individual adsorber particles applying the principles of discrete element method. The surface of particles is discretized and the component transport to the surface element and the degree of saturation of surface element is calculated by a first-order adsorption kinetics. The calculation method is demonstrated on a single particle. The two-dimensional compressible Euler equations are discretized and solved by the second-order accurate TVD-MacCormack method to effectively handle the oscillations arising in the vicinity of steep spatial fronts. Furthermore, considering the physical bases of compressible gas flow, we used non-reflecting numerical boundary condition at the outflow boundary of calculation domain.

Keywords: adsorption, immersed boundary method, discrete element method, TVD-MacCormack, non-reflecting boundary condition

1. Introduction

Harmful organic solvents are used in many chemical technologies. For example, chlorinated hydrocarbons are applied during the swelling of ion-exchange resins (Kumagai et al., 2018) or gas emissions during the pyrolysis (Veksha et al., 2018). Waste gas purification is necessary for all related technologies since environment protection and sustainability are highly desired as well as decreasing the emission of greenhouse gases. A wide-spread solution of gas purification is to adsorb the undesired components on a porous fixed bed. The main operational characteristic of these units is that the fixed bed saturates during its operation and should be regularly regenerated. Improving the operational characteristic often two columns are used, while one of them operates in adsorption mode, the other one can be regenerated. Another approach is to use a moving bed equipment, where the regenerated particles are continuously fed into the adsorption column and the outgoing saturated particles are transferred into the regenerator

equipment. This type of construction seems more effective, however it is challenging to control the two-phase flow inside both the adsorption and regenerator column, even more if temperature change plays an important role as in case of CO_2 capture technologies (Mondino et al., 2019). Both adsorber constructions can be investigated using models developed in the last decades in the research area of modeling gas-solid two-phase flows. However, they have to be completed with the model equations describing the component transport to the surface of adsorber particles and the diffusion toward the inside of particle.

One of the modeling approaches in modeling gas-solid two-phase flows is the direct numerical simulation (DNS) (Deen et al., 2014) which is basically coupled with the discrete particle treatment. In DNS models the Navier-Stokes equations are derived by the usual point variables and the fluid flow between the particles is fully resolved. Several DNS methods have been proposed by the authors. In the case of immersed boundary method the goal is to solve Navier-Stokes equations inside the complex calculation domain between the particles without using boundary-fitted or unstructured meshes. The flow equations are solved on a structured mesh over the entire calculation domain. The particles are virtually defined inside the flow by adding Lagrangian points on their surfaces. Then additional forcing terms are added to the Navier-Stokes equations to mimic the no slip boundary condition on these surface points. In this way a local force density is introduced to modify the flow field that realizes the particle boundaries. The motion of the particles calculated by the total surface force and torque evaluated on the surface of particles by one of the forcing approaches like direct forcing or feedback forcing (Fadlun et al., 2000). To describe the contacts between solid particles the discrete element method can be used.

The coupled application of immersed boundary method and discrete element method makes it possible to examine the gas purification process in detail. Modeling and simulation of gas-solid two-phase flow including the calculation of discrete particle motion and gas adsorption provides insight to the physical and chemical processes. By applying numerical investigation more information is available about the processes which take place in the equipment than measuring the properties of the waste gas only at the outlet. The aim of our research is to estimate the separation efficiency and the optimal operating parameters regarding both the adsorbent particles and the gas inflow. For this reason in our model the 2D Euler equation is completed with the mass balance equation of harmful organic gas component and the differential equation describing the adsorption process for the individual adsorbent particles. The applied model and simulation method can greatly help the process intensification and the tuning of operating parameters due to the better understanding of the detailed processes inside the gas purification column.

2. Model development and numerical solution

A two-dimensional flow model is set to model the compressible gas flow in the gas purification column shaped as a rectangular channel (Figure 1a). The inlet boundary is located at the bottom of left sidewall while the outflow boundary defined at the top of the column.

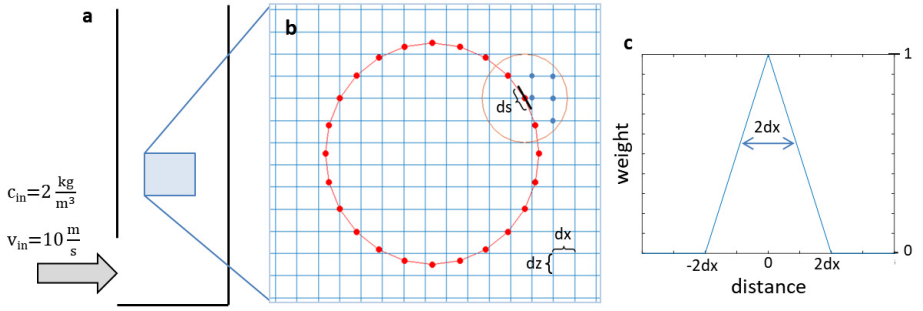

Figure 1. a) Geometry of the purification column. Inlet gas velocity is 10 m/s, concentration of the harmful gas component is 2 kg/m^3. b) Immersed boundary, Eulerian and Lagrangian grid points with grid sizes dx, dz and ds respectively. c) Distance-based weight function for the extrapolation

The two-dimensional flow model consist of the continuity equation for the non-harmful gas components, the mass balance equation for the harmful gas component which is to be adsorbed, the two momentum and the energy balances:

$$\frac{\partial \rho_g}{\partial t} + \frac{\partial\left(\frac{m}{\rho}\cdot\rho_g\right)}{\partial x} + \frac{\partial\left(\frac{n}{\rho}\cdot\rho_g\right)}{\partial z} = 0 \tag{1}$$

$$\frac{\partial c}{\partial t} + \frac{\partial\left(\frac{m}{\rho}\cdot c\right)}{\partial x} + \frac{\partial\left(\frac{n}{\rho}\cdot c\right)}{\partial z} = \mathrm{R} \tag{2}$$

$$\frac{\partial m}{\partial t} + \frac{\partial\left(\frac{m^2}{\rho}+p\right)}{\partial x} + \frac{\partial\left(\frac{n\cdot m}{\rho}\right)}{\partial z} = F_x \tag{3}$$

$$\frac{\partial n}{\partial t} + \frac{\partial\left(\frac{m\cdot n}{\rho}\right)}{\partial x} + \frac{\partial\left(\frac{n^2}{\rho}+p\right)}{\partial z} = F_z \tag{4}$$

$$\frac{\partial \rho E}{\partial t} + \frac{\partial\left(\frac{m}{\rho}\cdot(\rho E+p)\right)}{\partial x} + \frac{\partial\left(\frac{n}{\rho}\cdot(\rho E+p)\right)}{\partial z} = 0 \tag{5}$$

where ρ_g is the mass density of the mix of non-harmful gas components, c is the component mass density of the harmful gas component, ρ is the total mass density ($\rho=\rho_g+c$). m and n are the components of the mass velocity vector in x and z direction. R is the loss term describing the mass flow rate of harmful gas component to be adsorbed, p is the pressure (calculated according to the ideal gas law), F_x and F_z are the force densities introduced according to the immersed boundary method and ρE is the sum of the inner and kinetic energy.

The adsorption of harmful gas component is calculated for the individual adsorber particles. The surface of particles is discretized and the component transport to the surface element (c_S) and the degree of saturation of related particle volume element is calculated by the following first-order adsorption kinetics (Eq(6)).

$$\frac{\partial c_s}{\partial t} = k \cdot ds \cdot (c - c_0) \tag{6}$$

where c_s [kg/m^3] is the harmful gas component concentration in the particle volume element, k [m$^{-2}\cdot$ s^{-1}] is the mass transfer coefficient, ds [m^2] is the area of surface element, c [kg/m^3] is the mass density of the harmful gas component in the gas phase and c_0 [kg/m^3] is the equilibrium mass density of harmful components on the solid surface, which is calculated as $c_0=bc_s$ (Bird et al., 2002), where b is a constant.

Eq(6) supposes the development of a homogeneous concentration profile in the individual particle volume element of the adsorber particle after the component transport to the surface element.

The source term R in Eq(2) is calculated by Eq(7). For a given grid point of gas phase it is the sum of component rates that absorbed through the surface elements (n) located in the vicinity of calculation cell i,j.

$$R_{i,j} = -\sum_{n=1}^{n=N} k \cdot ds \cdot \left(c_{i,j} - c_{0,n}\right) \tag{7}$$

Eqs (1)-(5) are solved by the TVD-MacCormack second order accurate scheme (Yee, 1989) in order to get physically admissible solutions. In this scheme the two steps MacCormack's scheme is completed with a third step by introducing a dissipation term to avoid any unphysical oscillation in the vicinity of strong gradients in the numerical solution. At the outflow boundary, taking into account of the physical bases of compressible gas flow, non-reflecting numerical boundary condition is applied. The application of non-reflecting boundary condition at outflow boundary instead of constant physical boundaries prevents reflections of the unsteady compression and expansion waves back into the calculation domain. In our simulation study a generalized method of non-reflecting outflow boundary condition specification, developed by (Thompson, 1990) is applied. All the calculations are carried out in a self-developed program in MATLAB environment.

In order to calculate the flow field around the adsorber particle and the interaction between solid particle and gas-phase the immersed boundary method is used. The flow equations are solved on a structured and stationary mesh over the entire calculation domain and the solid adsorbent particles occur with a virtual boundary (Figure 1b). As the flow field around the particle is fully resolved, the size of the calculation grid should be approximately one order of magnitude smaller than the size of the particles, which is set in our simulation to 2 mm in diameter like a usual activated carbon adsorber particle. Lagrangian points (red dots in Figure 1b) are defined equidistantly around the particle. The distance (ds) is tuned to the Eulerian grid size and equal to 0.0002 m. Extrapolating between the two grid point locations are carried out by a distance-based weight function (Figure 1c), in our case a simple triangle function.

The calculation algorithm takes all the Lagrangian grid points of virtual particle and looks for the Eulerian grid points in a certain distance limit. In Figure 1b the orange colored circle shows the distance limit and the blue dots are the Eulerian grid points that influence the given Lagrangian grid point. The degree of influence of Eulerian grid points is a function of their distance to the Lagrangian grid point. The gas flow is forced to bypass the virtual solid body by the application of direct forcing method in which an extra force density terms are added to the momentum Eqs (3) and (4). The extra term balances the momentum equation such a way that the modified flow field realizes the particle boundary.

3. Results and discussion

The dynamic model given by Eqs (1)-(5) was solved by TVD-MacCormack scheme using non-reflecting outlet boundary condition. The inlet harmful gas component concentration was set to 2 kg/m^3. The non-harmful gas was considered as air. The inlet gas velocity was set to 10 m/s. The mass transfer coefficient k and constant b in the equations were equal to 1x10^8 m^{-2}·s^{-1} and 1.1. The time step of numerical solution was determined in each iteration step according to the Courant-Friedrich-Lewy criteria, and was changing around 2x10^{-7} s. At simulation time 5x10^{-3} s the velocity field of the gas phase around the particle is shown in Figure 2a and the concentration field of harmful gas component show in Figure 2b. The concentration of harmful gas component in the particle volume elements around the particle is shown in Figure 2c giving a picture of the saturation state of the particle surface. The saturation state around the particle shows a distribution due to the dynamically changing concentration values of those gas phase elements which interact the surface of adsorber particle. Figure 2d shows the dynamic change of saturation at six highlighted surface points. It can be seen that surface points located at the different points of the particle surface are saturated by different velocity depending on the concentration of interacting gas-phase elements.

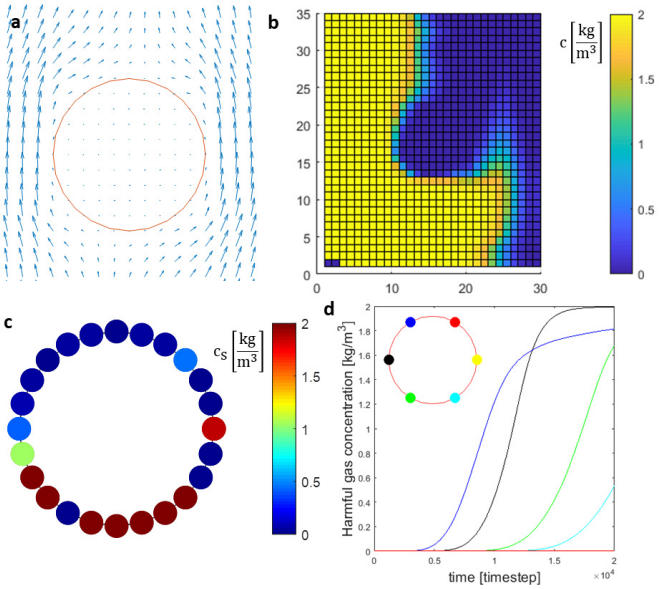

Figure 2. a) Velocity field of the gas phase around the particle. b) Concentration field of the gas phase around the particle. c) Degree of saturation around the adsorbent particle after 2x10^4 timesteps. d) Saturation curves at specific surface points of the adsorber particle.

As it is seen from the simulation results the model is able to calculate the saturation curves of particle surface points and can provide information about the necessary residence time of particles in the purification column at given operating parameters and this way it can help in the optimal design of column.

4. Conclusions

Adsorption process is modeled for a single particle by a first order adsorption kinetics with the fully resolved dynamic gas flow around the particle. The gas flow around the

motionless adsorber particle is modeled by immersed boundary method, and the gas-solid interaction is calculated regarding the velocity field and the harmful component adsorption. The adsorber material is considered a layer on the carrier particle in our case, in which the diffusion is fast, therefore homogenous concentration field is assumed. However, the main achievement of this study is to calculate the saturation state of the adsorber layer resolved for the small segments of particle surface. This knowledge helps to define the overall saturation time of particle more accurately, and could also help in other process development issues.

Motion and collision of particles is not calculated in the current work, however the next step in improving our detailed model is to populate the gas purification column with more particles, which can interact with the gas flow and each other. Using our extended model it will be possible to simulate the whole purification column and the operating parameters can be designed more efficiently.

Acknowledgment

We would like to express our acknowledgement for the financial support of Széchenyi 2020 under the GINOP-2.2.1-15-2017-00059, MOL Group and Peregrinatio I. Foundation.

References

Bird, R.B., Stewart, W.E., Lightfoot, E.N., 2002. Transport phenomena, 2nd, Wiley international ed ed. J. Wiley, New York.

Deen, N.G., Peters, E.A.J.F., Padding, J.T., Kuipers, J.A.M., 2014. Review of direct numerical simulation of fluid–particle mass, momentum and heat transfer in dense gas–solid flows. Chem. Eng. Sci. 116, 710–724. https://doi.org/10.1016/j.ces.2014.05.039

Fadlun, E., Verzicco, R., Orlandi, P., Mohd-Yusof, J., 2000. Combined Immersed-Boundary Finite-Difference Methods for Three-Dimensional Complex Flow Simulations. J. Comput. Phys. 161, 35–60. https://doi.org/10.1006/jcph.2000.6484

Kumagai, S., Lu, J., Fukushima, Y., Ohno, H., Kameda, T., Yoshioka, T., 2018. Diagnosing chlorine industrial metabolism by evaluating the potential of chlorine recovery from polyvinyl chloride wastes—A case study in Japan. Resour. Conserv. Recycl. 133, 354–361. https://doi.org/10.1016/j.resconrec.2017.07.007

Mondino, G., Grande, C., Blom, R., Nord, L.O., 2019. Moving bed temperature swing adsorption for CO2 capture from a natural gas combined cycle power plant. Int. J. Greenh. Gas Control 85, 58–70. https://doi.org/10.1016/j.ijggc.2019.03.021

Thompson, K.W., 1990. Time-dependent boundary conditions for hyperbolic systems, II. J. Comput. Phys. 89, 439–461. https://doi.org/10.1016/0021-9991(90)90152-Q

Veksha, A., Giannis, A., Oh, W., Chang, V., Lisak, G., 2018. Upgrading of non-condensable pyrolysis gas from mixed plastics through catalytic decomposition and dechlorination. Fuel Process. Technol. 170, 13–20. https://doi.org/10.1016/j.fuproc.2017.10.019

Yee, H.C., 1989. A class of high resolution explicit and implicit shock-capturing methods. NASA Technical Memorandum 101088

Sauro Pierucci, Flavio Manenti, Giulia Bozzano, Davide Manca (Eds.)
Proceedings of the 30th European Symposium on Computer Aided Process Engineering (ESCAPE30), May 24-27, 2020, Milano, Italy.
http://dx.doi.org/10.1016/B978-0-12-823377-1.50035-5

Parameters Influencing the Rate-based Simulation of CO_2 Removal units by Potassium Taurate Solvent

Stefania Moioli[a,*], Minh T. Ho[b], Laura A. Pellegrini[a], Dianne E. Wiley[b]

[a]*GASP, Group of Advanced Separation Processes and GAS Processing, Dipartimento di Chimica, Materiali e Ingegneria Chimica "Giulio Natta", Politecnico di Milano, Piazza Leonardo da Vinci 32, I-20133 Milano, Italy*
[b]*The University of Sydney, School of Chemical and Biomolecular Engineering, 2006 Australia*
stefania.moioli@polimi.it

Abstract

CCS (Carbon Capture & Storage) is being widely considered for reducing the emissions of greenhouse gases to the atmosphere and is already industrially applied by use of chemical absorption with aqueous amines, as MonoEthanolAmine (MEA). This solvent is well performing, though being characterized by several drawbacks as high regeneration energy requirements, corrosion and toxicity.
The excessive use of toxic solvents is environmentally detrimental and recognized as an unstable practice. In the efforts to address the issues of sustainability established in the 2030 Agenda for Sustainable Development, also the carbon dioxide absorption process is being studied and one key point is the employment of more environmentally friendly solutions.
Aqueous amino acid salt solutions have been considered in the last years a viable alternative to traditional solvents for carbon dioxide removal. Moreover, some of them, such as the potassium taurate solvent, are characterized by precipitation at specific conditions during absorption, thus providing further advantages in terms of potential reduction in energy requirement to the process and/or costs.
For any system, a validated process and thermodynamic model and simulation is one essential tool used by process engineers to assist with a thorough evaluation of different process options and designs. Choice of model parameters is fundamental to the accurate and reliable representation of the process. This work focuses on the analysis of the parameters influencing the rate-based simulation of the carbon dioxide removal section of a 500 MW coal-fired power plant. Results confirm that for the considered system the mass transfer coefficient is strongly influenced by the viscosity of the solvent and the diffusivity of CO_2 in the aqueous solution. The results also show that different values of the film discretization can lead to differences in the required solvent flowrate.

Keywords: CO_2 removal; rate-based simulation; potassium taurate solvent; physical properties, film discretization.

1. Introduction

The application of Carbon Capture & Storage (CCS) technology, that can significantly reduce the emissions of CO_2 produced in electricity generation and in industrial processes, is getting more and more attention.
The mostly employed method of removing CO_2 from industrial gaseous streams is chemical absorption (Kohl and Nielsen, 1997; Rochelle, 2009), with aqueous solutions

of MonoEthanolAmine (MEA) being the benchmark solvent. Though being well performing, this solvent is corrosive and toxic and for its regeneration high energy consumption (Moioli and Pellegrini, 2019) is needed.
For this reason different types of amine solvents started to be considered (Moioli and Pellegrini, 2015, 2016; Rochelle et al., 2011) and, recently, with the aim of achieving the goals of the 2030 Agenda for Sustainable Development, innovative solvents, with environmentally friendly characteristics, are being studied (Lerche, 2012; Majchrowicz, 2014; Sanchez-Fernandez, 2013).
Among these, some amino acids (as taurine (Lerche, 2012)) in aqueous solution favor CO_2 absorption by forming a precipitate at high CO_2 loadings (Kumar et al., 2003a; Kumar et al., 2003b; Sanchez Fernandez et al., 2013) and may favor a reduction of the steam to be employed for the reboiler of the regeneration section (the most energy demanding section of the plant) by variations of pH of the solution (Moioli et al., 2019c). Compared to the MEA solvent, in addition, they are much less corrosive (Ahn et al., 2010) and with lower enthalpy of reaction (Brouwer et al., 2009).

1.1. The considered process

The process taken into account in this work employs an aqueous solution of potassium taurate (4M KOH, 4M taurine) for removing 90% of CO_2 from a flue gas stream of a 500 MW coal-fired power plant, before emitting it to the atmosphere (Moioli et al., 2019a).
The flue gas has a flowrate of 19.60 kmol/s and a molar fraction (y) of CO_2 equal to 0.13, in the range of the ones typical of flue gas from coal generation. Water (y = 0.07), N_2 (y = 0.75) and O_2 (y = 0.05) are the other main components. The stream is available at atmospheric pressure and 40°C.
The process scheme, with also some possible alternative configurations for energy saving, is described in (Ho et al., 2019).

1.2. Rate-based simulation

For the rate-based simulation of the process, the commercial software ASPEN Plus® V9 has been employed. Because some species are not present by default in the database, the tool has been customized by adding these species and by developing a thermodynamic model with good agreement with the experimental vapor-liquid-solid equilibrium data (Moioli et al., 2018).
The physical properties such as density and viscosity of the solvent and the diffusivity of carbon dioxide in the liquid phase are variables used for the estimation of the mass transfer coefficient, which in rate-based calculations is employed for the evaluation of mass transfer on each stage of the column.
In order to understand the impact that the values used for these variables have on the estimation of the amount of carbon dioxide absorbed, a sensitivity analysis has been carried out, by estimating the mass transfer coefficient and the terms composing it.
The mass transfer resistance is taken into account through a film, which is present both for the vapor phase and for the liquid phase. In the liquid film, reactions occur, therefore a further influence on mass transfer is obtained. In ASPEN Plus® the reacting film can be modeled by choosing “filmrxn” or “discrxn” as options: according to the first one, the film is divided into two segments, while according to the second one, the number of segments for discretization of the film can be chosen by the user.
The number of segments in which subdividing the film is important for the description of the mass transfer in that region. A high number of segments can guarantee a more rigorous analysis, though requiring high computational times, while a low number of segments may lead to differences in results.

2. Methodology

This work focuses on both the study of the influence of the physical properties on the mass transfer coefficient and on the choice of the film discretization in simulation.
As for the former, the analysis has been focused on the variation of density and viscosity and of diffusivity of carbon dioxide in a range of possible values occurring for the potassium taurate process. The expression of mass transfer coefficient from the correlation by Onda (AspenTech, 2016) has been considered for the calculation.
The number of segments in which the film must be subdivided has been determined by performing several simulations with different number of discretization points of the absorption column. The column is characterized by the same height and the same diameter and is fed with a sour gas stream and a solvent with lean loading equal to 0.27, as considered in previous works on this topic (Moioli et al., 2019b). No liquid-solid separator is considered. The obtained outputs have been considered for the analysis.

3. Results and discussion

3.1. Influence of the physical properties on the mass transfer coefficient

The results are reported in terms of relative sensitivity, defined as the ratio of the difference of the considered output variable, for instance the mass transfer coefficient, and the difference of the input variable (*i.e.* the density, the viscosity or the diffusivity of CO_2). A low value of this ratio indicates that the output variable is not significantly influenced by variations in the input variable, while high values of the relative sensitivity mean that the value of the input variable should be chosen carefully, since it strongly influences the value of the output variable.
Figure 1a) shows that the value of density of the liquid phase has not a significant influence on the mass transfer coefficient. On the right axis of the same figure also the Schmidt number is reported, being the variable that shows the highest difference between the value of density at 1000 kg/m^3 and 2000 kg/m^3. However, the variation is low, in the range of order of magnitude of 10^{-5}.

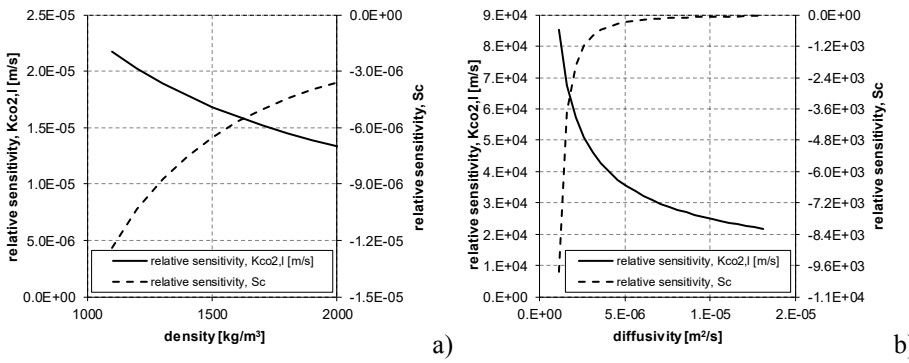

Figure 1. Relative sensitivity of mass transfer coefficient (left axis) and of Schmidt number (right axis) for different values of a) density of the solvent and b) diffusivity of carbon dioxide in the solvent.

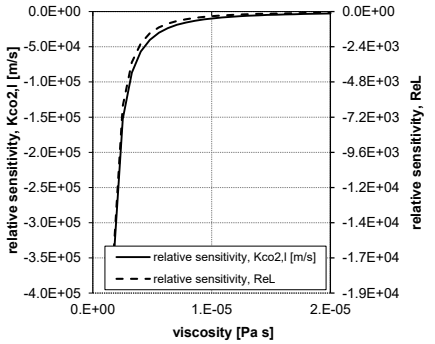

Figure 2. Relative sensitivity of mass transfer coefficient (left axis) and of Reynolds number (right axis) for different values of viscosity of the solvent.

The viscosity of the aqueous solution and the diffusivity of carbon dioxide in the solvent, on the contrary, exerts a high influence on the estimation of the mass transfer coefficient. In particular, a relative sensitivity of the viscosity of the liquid phase on the Reynolds number of order of magnitude of 10^4 is obtained, which contributes in the evaluation of a relative sensitivity for the mass transfer coefficient resulting in the order of magnitude of 10^5 (Figure 2).

As for the diffusivity of carbon dioxide in the solvent, the Schmidt number is reported in Figure 1b) because one of the parameter most influenced by the variation of the input variable considered. The relative sensitivity results in the order of magnitude of 10^4 both for the Schmidt number and for the overall mass transfer coefficient.

The proper description of these properties is therefore fundamental for obtaining a good representation of the process. For the considered system, the values of density and viscosity of the potassium taurate solution estimated in ASPEN Plus® have been compared with the available experimental data (Kumar et al., 2001; Wei et al., 2014). The density of the lean solvent is within 10 % of the experimental data. As resulting from the analysis carried out in this work, this variation in density does not exert a significant influence on the description of mass transfer. As for viscosity, the values calculated by ASPEN Plus® have been considered as representing with good approximation the experimental data.

Data of loaded solutions are not available for the potassium taurate solvent, so the description of these two properties may be further improved if additional experimental data becomes available.

The diffusion coefficient of carbon dioxide is calculated by means of the Wilke-Chang correlation, in ASPEN Plus® considering water as solvent. The results have been compared with the values estimated by Wei et al. (Wei et al., 2014) using a correlation of diffusivity of N_2O as a function of viscosity of the potassium taurate solvent, resulting within the range of those obtained by Wei et al. (Wei et al., 2014).

3.2. Choice of the film discretization

As can be seen from Figure 3a), the addition of two discretization points to the default values results in an increase in the amount of carbon dioxide present in the purified gas of 5%. The amount of carbon dioxide reacted also influences the temperature along the column, in particular at the top, where variations up to about 1.5 K have been obtained, though not shown here for reasons of limiting space.

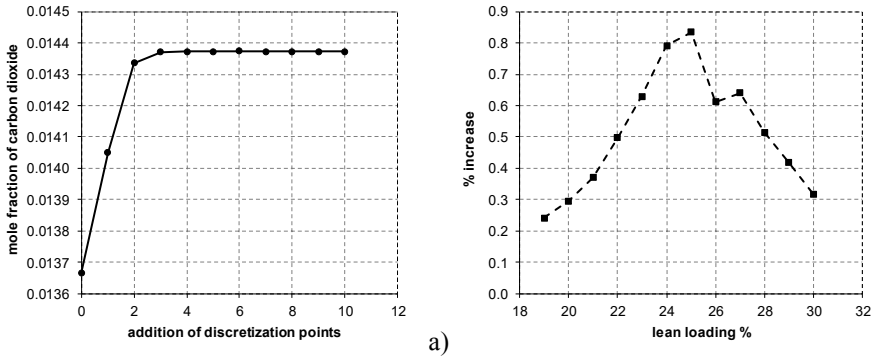

Figure 3. a) Mole fraction of carbon dioxide in the purified flue gas for simulation of the absorption column with different numbers of discretization points for the film; b) % variation in the amount of solvent flowrate calculated with "filmrxn" and with "discrxn" with addition of 3 discretization points for removing 90% of carbon dioxide for different lean loadings.

When the number of added segments is higher than 8, no changes in the results are obtained. However, no significant changes are also obtained when adding three points for discretization, with the result that the time for the calculation is significantly reduced. Since the variation between adding three points and adding eight points can be considered not remarkable and about half computational time is required, the "discrxn" option with the addition of three points has been considered for the simulations.
The discretization ratio, *i.e.* the ratio of the extension of each segments of the film to the following one, has been found not affecting significantly the results of the simulation, therefore the default values have been maintained.
The choice of the film discretization has an influence on the results obtained from the simulation of the process, with all the other parameters and variables set equal for the two simulations. In detail, Figure 3b) shows results obtained in estimating the solvent flowrate needed for removing 90% of carbon dioxide for different lean loadings when the option "filmrxn" is considered or when simulations are performed with the option "discrxn" with addition of 3 segments. Depending on the considered lean loading, a maximum percentage increase in the solvent flowrate of 0.83 % is obtained. This difference in the circulating flowrate has an influence also on the required reboiler duty, to which it is strongly related.

4. Conclusions

This paper has analyzed the influence that different values of density and viscosity of the solvent and diffusivity of CO_2 in the solvent can have on the estimation of the mass transfer coefficient. It has also taken into account the variation of results related to the choice of how to discretize the film.
Results confirm the need of an accurate representation of properties, in particular the viscosity of the solvent and the diffusivity of CO_2 in the liquid phase. Experimental data of CO_2 loaded solutions would help in achieving higher accuracy in their description and thus in the estimation of mass transfer. Moreover, the option "discrxn" with addition of three segments results the best choice for film discretization.

References

S. Ahn, H.-J. Song, J.-W. Park, J.H. Lee, I.Y. Lee, K.-R. Jang, 2010, Characterization of metal corrosion by aqueous amino acid salts for the capture of CO_2, Korean Journal of Chemical Engineering 27, 1576-1580.

AspenTech, 2016, ASPEN Plus® Guidelines. AspenTech, Burlington, MA.

J.P. Brouwer, P.H.M. Feron, N.A.M. ten Asbroek, 2009, Amino-acid salts for CO_2 capture from flue gases.

M.H. Ho, E.G.C. Conde, S. Moioli, D.E. Wiley, 2019, The effect of different process configurations on the performance and cost of potassium taurate solvent absorption, International Journal of Greenhouse Gas Control 81, 1-10.

A.L. Kohl, R. Nielsen, 1997, Gas Purification, 5th ed. Gulf Publishing Company, Book Division, Houston, Texas, USA.

P.S. Kumar, J.A. Hogendoorn, P.H.M. Feron, G.F. Versteeg, 2001, Density, viscosity, solubility, and diffusivity of N_2O in aqueous amino acid salt solutions, Journal of Chemical and Engineering Data 46, 1357-1361.

P.S. Kumar, J.A. Hogendoorn, P.H.M. Feron, G.F. Versteeg, 2003a, Equilibrium solubility of CO_2 in aqueous potassium taurate solutions: Part 1. Crystallization in carbon dioxide loaded aqueous salt solutions of amino acids, Industrial & Engineering Chemistry Research 42, 2832-2840.

P.S. Kumar, J.A. Hogendoorn, S.J. Timmer, P.H.M. Feron, G.F. Versteeg, 2003b, Equilibrium solubility of CO_2 in aqueous potassium taurate solutions: Part 2. Experimental VLE data and model, Industrial & Engineering Chemistry Research 42, 2841-2852.

B.M. Lerche, 2012, CO_2 Capture from Flue gas using Amino acid salt solutions. Technical University of Denmark, Lyngby, Denmark.

M.E. Majchrowicz, 2014, Amino Acid Salt Solutions for Carbon Dioxide Capture. University of Twente, Twente, The Netherlands.

S. Moioli, M.H. Ho, L.A. Pellegrini, D.E. Wiley, 2019a, Application of Absorption by Potassium Taurate Solutions to Post-Combustion CO_2 Removal from Flue Gases with Different Compositions and Flowrates, Chemical Engineering Transactions 74, 823-828.

S. Moioli, M.H. Ho, D.E. Wiley, L.A. Pellegrini, 2018, Thermodynamic Modeling of the System of CO_2 and Potassium Taurate Solution for Simulation of the Process of Carbon Dioxide Removal, Chemical Engineering Research and Design 136, 834-845.

S. Moioli, M.H. Ho, D.E. Wiley, L.A. Pellegrini, 2019b, Assessment of carbon dioxide capture by precipitating potassium taurate solvent, International Journal of Greenhouse Gas Control 87, 159-169.

S. Moioli, L.A. Pellegrini, 2015, Physical properties of PZ solution used as a solvent for CO_2 removal, Chemical Engineering Research and Design 93, 720-726.

S. Moioli, L.A. Pellegrini, 2016, Modeling the methyldiethanolamine-piperazine scrubbing system for CO_2 removal: Thermodynamic analysis, Frontiers of Chemical Science and Engineering 10, 162-175.

S. Moioli, L.A. Pellegrini, 2019, Operating the CO_2 absorption plant in a post-combustion unit in flexible mode for cost reduction, Chemical Engineering Research and Design 147, 604-614.

S. Moioli, L.A. Pellegrini, M.T. Ho, D.E. Wiley, 2019c, A comparison between amino acid based solvent and traditional amine solvent processes for CO_2 removal, Chemical Engineering Research and Design 146, 509-517.

G. Rochelle, E. Chen, S. Freeman, D. Van Wagener, Q. Xu, A. Voice, 2011, Aqueous piperazine as the new standard for CO_2 capture technology, Chemical Engineering Journal 171, 725-733.

G.T. Rochelle, 2009, Amine Scrubbing for CO_2 Capture, Science 325, 1652-1654.

E. Sanchez-Fernandez, 2013, Novel Process Designs to Improve the Efficiency of Postombustion Carbon Dioxide Capture. Technische Universiteit Delft, Delft, The Netherlands.

E. Sanchez Fernandez, K. Heffernan, L.V. van der Ham, M.J.G. Linders, E. Eggink, F.N.H. Schrama, D.W.F. Brilman, E.L.V. Goetheer, T.J.H. Vlugt, 2013, Conceptual Design of a Novel CO_2 Capture Process Based on Precipitating Amino Acid Solvents, Industrial & Engineering Chemistry Research 52, 12223-12235.

C.C. Wei, G. Puxty, P. Feron, 2014, Amino acid salts for CO_2 capture at flue gas temperatures, Chemical Engineering Science 107, 218-226.

Sauro Pierucci, Flavio Manenti, Giulia Bozzano, Davide Manca (Eds.)
Proceedings of the 30th European Symposium on Computer Aided Process Engineering (ESCAPE30), May 24-27, 2020, Milano, Italy.
http://dx.doi.org/10.1016/B978-0-12-823377-1.50036-7

Innovative Hybrid Energy System for stable Power and Heat Supply in offshore oil & gas Installation (HES-OFF): System Design and Grid Stability

Luca Riboldi[a*], Erick F. Alves[b], Marcin Pilarczyk[a], Elisabetta Tedeschi[b], Lars O. Nord[a]

[a]*Department of Energy and Process Engineering, Norwegian University of Science and Technology-NTNU, Trondheim 7491, Norway*
[b]*Department of Electric Power Engineering, Norwegian University of Science and Technology-NTNU, Trondheim 7034, Norway*
luca.riboldi@ntnu.no

Abstract

This paper presents an innovative hybrid energy system for stable power and heat supply in offshore oil & gas installations (HES-OFF). The hybrid concept integrates offshore wind power with gas turbines and a H_2 energy storage solution based on proton exchange membrane fuel cells and electrolysers. The objectives are: 1) improve the environmental performance of offshore installations by maximizing the exploitation of offshore wind and partially decarbonizing the gas turbines by co-feeding H_2; 2) minimize the negative effects that wind power variability has on the electrical grid frequency stability. This study presents a first assessment of the HES-OFF concept performance using an offshore platform in the North Sea as case study. The results show that the HES-OFF concept: 1) cuts CO_2 emissions up to 40 % when compared to the reference case but requires large H_2 storage capacity to fully exploit wind power throughout the year; 2) allows higher wind power penetration without infringing on the grid frequency requirements.

Keywords: offshore energy, hybrid system, energy storage, system design, grid stability.

1. Introduction

Due to the long-term character of the energy transition and the many technical limitations to replace fossil fuels with renewable energy sources (RESs), hybrid energy systems (HESs) with energy storage (ES) can be affordable alternatives. The choice of the HES configuration and its specification depends on the availability of RESs and the general purpose of the system. Optimum design can be achieved through comprehensive analyses and optimisation of layouts and the size of system components. Offshore oil and gas (O&G) production is likely to increase in the near future and thus its related CO_2 emissions. In Norway, the petroleum sector is the main contributor to greenhouse gas emissions, making up 27 % of the total emissions in 2018 (Statistics Norway, 2018). Several options to reduce the carbon footprint of the O&G sector have been investigated (Riboldi and Nord, 2017), including the electrification of offshore facilities (Riboldi et al., 2019). The utilization of RESs is a very promising opportunity, though there are challenges for their efficient exploitation offshore. This article presents the concept of an innovative hybrid energy system for stable power and heat supply in offshore oil & gas installation (HES-OFF), which considers wind energy along with H_2 ES using a proton exchange membrane (PEM) fuel cell (FC) and electrolyser (EL) system.

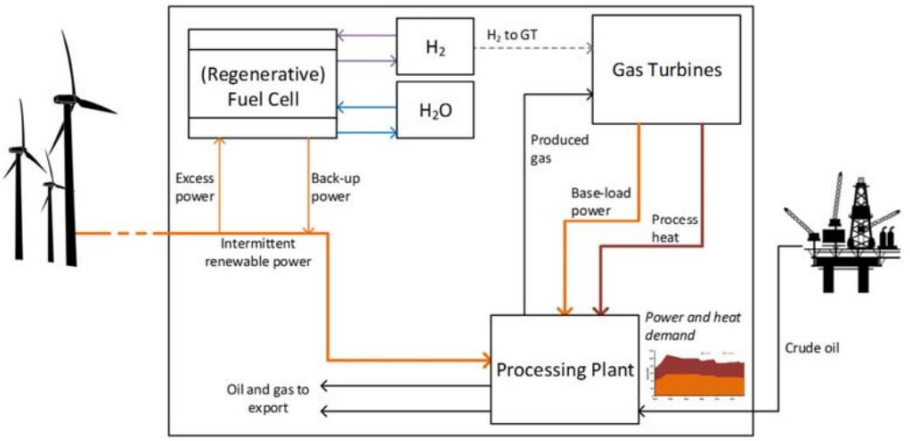

Figure 1. Schematic of the HES-OFF system proposed.

2. The HES-OFF hybrid concept

The HES-OFF concept consists of a HES integrating an offshore wind farm, stacks of PEM FC and EL for ES and back-up power supply, and a gas turbine (GT). The ES is further integrated with the GT, where the possibility to co-feed H_2 is envisioned. Fig. 1 depicts the HES-OFF system layout.

Within this energy system, the GT operation meets the process heat demand and supplies base-load power to a processing plant. Wind turbines (WTs) provide the remaining load. The FC and EL stacks smooth out the intermittent wind power output by: 1) storing excess power in the form of gaseous H_2 when production is larger than demand; 2) providing back-up power on the contrary. This HES is expected to reduce CO_2 emissions from an offshore facility due to: 1) enhanced exploitation of RESs; 2) clean fuel to GTs; 3) improved operational strategy of the GTs.

3. Modelling framework

Two main areas of the modelling activity are distinguished, namely (1) process components and (2) offshore grid modelling. The general intention is to pre-screen the feasibility of the HES-OFF concept and to assess the potential reduction of CO_2 emissions.

3.1. Process components

The HES-OFF process components are modelled in MATLAB and are presented below.

GTs: Two types of gas turbines are considered for the study, namely a GE LM2500+G4 (rated power 32.2 MW) and a GE LM6000 PF (rated power 41.9 MW). To simulate the GTs, two data-defined models are used. Those are based on performance curves retrieved from tabulated data and assess the effect of changing working conditions as well as off-design operation. The models were validated against the Thermoflow library (Thermoflow Inc, 2016). The performance of the LM2500+G4 model was further checked against real operational data by Riboldi and Nord (2018), showing good agreement, and used in previous publications (e.g., Riboldi and Nord, 2017).

FCs&ELs stacks: The models used in this study are based on zero-dimensional, static models of PEM FC and EL stacks, which describe the electrical domain of cells. The FC stack model is based on Spiegel (2008), improved and tuned according to Dicks et al.

(2018). The EL stack model is based on Zhang et al. (2012) with further improvements based on Millet (2015). The output of the model is the overall performance of the FC and EL stacks as a function of load expressed in MJ/kgH_2 and kgH_2/MJ, respectively. The obtained results reflect the state-of-the-art for high capacity PEM systems on the market. **WT:** The conversion of wind speed into power was simulated through the power curve of the Hywind Scotland WT (Nielsen, 2018). The wind speed distribution throughout a year was based on the measurements from a platform in the North Sea made available by the Norwegian Meteorological Institute (reported in Korpås et al., 2012).

3.2. Offshore grid

A surrogate model of the electrical grid (Alves et al., 2019) was developed in Simulink. It evaluates frequency dynamics using Eq. (1):

$$\dot{\omega} = \frac{P_a - k_d \omega^2}{2H_{GT}\omega} \tag{1}$$

$$P_a = P_{GT} + P_{FC} + P_{WT} - P_{EL} - P_{LD} \tag{2}$$

where ω is the frequency in per unit[1] (pu), the model state and output; P_a is the net accelerating power in pu and the model input; H_{GT} and k_d are model parameters, defined as the equivalent inertia constant in s and the equivalent damping constant of the plant in pu/pu. Base values are: $\omega_b = 2.\pi.60$ rad/s; $P_b = 44.7$ MW.

P_a is defined by Eq. (2) where P_{GT}, P_{FC}, P_{WT}, P_{EL}, P_{LD} are respectively the power in pu of GT, FC, WT, EL and loads. The model from Eq. (1) is extended to include PID controllers for the GT, FC and EL (Alves et al., 2019 and Sanchez et al., 2017). Those keep the grid frequency at its rated value. The choice of controller parameters follows the magnitude optimum criteria as outlined by Papadopoulos (2015).

4. Results

The developed methodology was tested on a case study: an offshore facility in the North Sea, for which an estimation of the energy requirements throughout its lifetime was made available by the operator (18 years). To ease the analysis, the power and heat supply demand was discretized: 1) Peak (2 years): 43.6 MW electrical power, 14.0 MW heat power; 2) Mid-life (4 years): 35.2 MW electrical, 11.0 MW heat; 3) Tail (12 years): 32.9 MW electrical, 8.0 MW heat.

4.1. Long-term system design

The long-term analysis sizes the components of the HES by: 1) ensuring that power and heat demand is always met; 2) maximizing the reduction of CO_2 emissions; 3) removing one GT; 4) avoiding waste of wind power.

The discretized lifetime energy demand of the offshore installation is considered, where each year is simulated with an hourly resolution. Table 1 reports the input parameters varied to define a design.

The storage strategy adopted ensures a net-zero balance of H_2 at the end of the year and the storage size is determined by the largest variation in the storage level. At first the design is tested over one year without ES.

[1] per unit (ou) is a system for expressing values in terms of a reference or base quantity.

Table 1. Input parameters for the long-term system design

INPUT PARAMETERS	
GT type	GE LM2500 or LM6000
Max. GT load	95 %
Min. GT load	40 %
Max. H_2 in GT	20 % vol.
Wind turbine	Hywind Scotland
Wind farm size (MW)	12-18-24

Table 2. Input parameters for the short-term grid stability analysis

INPUT PARAMETERS	
H_{GT}	1.85s for LM2500 1.8s for LM6000
k_d	7 pu/pu
GT PID controller	Kp = 3.8, Ki=1.6, Kd=0, Td=100
EL / FC PID controllers	Kp = 0, Ki=0, Kd=6, Td=50

In case of a net deficit of power (typical of peak years), the strategy: 1) evaluates total H_2 needed; 2) when possible, increases GT load and uses extra power to produce H_2; 3) stops when reaching a maximum storage level; 4) stops when reaching overall H_2 needed. In case of a net surplus of power (typical of tail years), the strategy: 1) evaluates total H_2 produced due to surplus power; 2) when possible, decreases GT load and use fuel cells to produce power; 3) when the level of H_2 storage reaches a maximum, uses H_2 in the GT; 4) if some H_2 is still unused, sends H_2 to GT. Table 3 and
Table 4 shows results obtained for the small and large GTs, respectively.

The designs of the HES-OFF concept reduce CO_2 emissions both compared to the reference case (only GT) and to the basic integration of wind power (GT+WIND). The lowest cumulative CO_2 emissions are obtained by the HES-OFF designs based on the small GT (LM2500). However, those are also characterized by extremely large (possibly unfeasible) sizes of the H_2 storage and fail to remove one GT. Conversely, the HES-OFF design based on the large GT obtain a more limited CO_2 emission reduction but with more acceptable sizes of the H_2 storage and with a single GT.

The size of the H_2 storage is given in kg of H_2 as the storage technology is not specified. Cryogenic option has been ruled out because of the significant energy requirements. H_2 storage in gaseous form has been considered as more appropriate for this application. The very large volumes connected with this option would require a storage on the seabed. Some technologies have been qualitatively investigated such as the utilization of gas balloons (Pimm et al., 2014), gas pipes and underground formations (Kruck et al., 2013). Additional analyses are planned to identify the most promising option.

Table 3. Output results of the HES-OFF concept based on the LM2500 GT

INPUTS		**Only GT**	**GT + WIND**			**HES-OFF**		
GT type		LM2500	LM2500	LM2500	LM2500	LM2500	LM2500	LM2500
No. GT		2	2	2	2	2	2	2
Max. GT load	%	90 %	90 %	90 %	90 %	95 %	95 %	95 %
Min. GT load	%	40 %	40 %	40 %	40 %	40 %	40 %	40 %
Wind farm size	MW	-	12	18	24	12	18	24
OUTPUTS								
Size H_2 storage	kg	-	-	-	-	175334	81605	71062
Size EL stacks	MW	-	-	-	-	6	6	6
Size FC stacks	MW	-	-	-	-	4	4	4
CO_2 emissions	Mt	3.51	2.71	2.42	2.25	2.50	2.27	2.09
Max. frequency	Hz	60.00	60.15	60.23	60.31	60.12	60.19	60.25
Min. frequency	Hz	59.22	59.02	58.91	58.79	59.13	59.04	58.95
Max. dP/dt GT	%/s	1.52	1.88	2.11	2.33	1.68	1.86	2.03

Table 4. Output results of the HES-OFF concept based on the LM6000 GT

INPUTS		**Only GT**	**GT + WIND**			**HES-OFF**		
GT type		LM6000	LM6000	LM6000	LM6000	LM6000	LM6000	LM6000
No. GT		2	2	2	2	1	1	1
Max. GT load	%	90 %	90 %	90 %	90 %	95 %	95 %	95 %
Min. GT load	%	40 %	40 %	40 %	40 %	40 %	40 %	40 %
Wind farm size	MW	-	12	18	24	12	18	24
OUTPUTS								
Size H_2 storage	kg	-	-	-	-	10010	8014	11824
Size EL stacks	MW	-	-	-	-	4.0	4.0	6.6
Size FC stacks	MW	-	-	-	-	1.1	1.1	1.1
CO_2 emissions	Mt	2.92						
Max. frequency	Hz	60.00	60.15	60.23	60.31	60.14	60.22	60.30
Min. frequency	Hz	59.21	59.02	58.90	58.78	59.06	58.92	58.75
Max. dP/dt GT	%/s	1.05	1.30	1.46	1.61	2.49	2.88	3.32

4.2. Short-term grid stability analysis

This step verifies if each proposed design of the long-term analysis: 1) is stable from the frequency stability perspective (Kundur et al., 2004); 2) complies with industry requirements (IEC, 2015) for frequency deviations (± 2%) during normal operation conditions; 3) complies with technical specifications of GT ramp rates.

For that, it simulates the offshore grid model presented in section 3.2. Inputs are obtained as following: 1) P_{GT}, P_{FC}, and P_{EL} are results from the long-term analysis of the process model and are assumed as constants; 2) P_{WT} and P_{LD} are results from analyses of 1-year long datasets of wind speeds and loads sampled every minute and are assumed as variables. These datasets are stored in an NTNU repository and are not publicly available. To reduce total simulation time, two synthetic time series reflect the worst-case scenarios of operation during the offshore platform lifetime. Those are 3-minutes long and contain the most sharp and common positive and negative variations of P_{WT} and P_{LD}. Parameters for the short-term grid stability analysis are reported in Table 2.

The bottom part of Table 3 and

Table 4 presents the obtained results. Note that as the wind farm size increases: 1) the frequency deviations increase and, in the extreme cases (24 MW wind farm), the minimum frequency limit (58.8 Hz) is always violated, except for the LM2500 HES-OFF concept; 2) the rate of change of power (*dP/dt*) of the GT increases, which translates into increased actuation of the governor and consequently additional wear and tear. The HES-OFF concept contributes to decrease frequency deviations and GT ramp rates. Note that, in the LM6000 HES-OFF concept with 24 MW wind farm, the minimum frequency limit can be respected if the FC increases to 1.6 MW. This shows the importance of considering grid requirements in the design phase of a HES.

5. Conclusions

The HES-OFF concept was presented and tested on a case study. Six configurations were assessed using two GTs of different rated power. Long- and short-term analyses verified the HES potential to reduce CO_2 emissions and to provide a stable offshore grid. The HES-OFF concept demonstrated the ability to reduce the cumulative CO_2 emissions of an O&G platform not only compared to a reference case using only GTs but also compared to a concept integrating GTs and WTs without ES. The designs based on the

small GT return the highest CO_2 emission reductions (between 29 % and 40 % depending on the wind farm size) but are unable to remove one of the GTs and involve very large H_2 storage capacity. Conversely, the designs based on the large GT return lower CO_2 emission reductions (between 16 % and 24 % depending on the wind farm size) but use a single GT and more limited H_2 storage capacity. It is also shown that the addition of ES helps reducing the frequency variations in the offshore grid. The minimum frequency specification is generally met by the HES-OFF solutions but at 24 MW wind capacity for the large GT. However, an increase in the FC stack size would allow the frequency to be within the required limits. Not least, GTs ramp rates are reduced as well, with potential advantages in terms of decreased wear, tear and maintenance requirements. Further work in this ongoing research project envisions the development of more complex models, optimization of the HES and validation by means of hardware-in-the-loop simulation.

References

E. Alves, S. Sanchez, D. Brandao, E. Tedeschi, 2019, Smart load management with energy storage for power quality enhancement in wind-powered oil and gas applications, Energies, 12, 1-15.

A.L. Dicks, D.A.J. Rand, 2018, Fuel Cell Systems Explained, Wiley&Sons

IEC 61892, 2015, Mobile and fixed offshore units - Electrical installations, 3.0. ed, IEC, Geneva, Switzerland.

M. Korpås, L. Warland, W. He, J. O. G. Tande, 2012, A case-study on offshore wind power supply to oil and gas rigs, Energy Procedia, 24, 18–26.

O. Kruck, F. Crotogino, R. Prelicz, T. Rudolph, 2013, Overview on all known underground storage technologies for hydrogen, HyUnder, Deliverable 3.1.

P. Kundur, J. Paserba, V. Ajjarapu, G. Andersson, A. Bose, C. Canizares, N. Hatziargyriou, D. Hill, A. Stankovic, C. Taylor, T. Van Cutsen, V. Vittal, 2004 Definition and classification of power system stability, IEEE Transactions on Power Systems 19, 1387–1401.

P. Millet, 2015, PEM Water Electrolysis, in book: Hydrogen Production by Electrolysis, ed. Agata Dodula-Jopek, Wiley-WCH Verlag, Weinheim.

F. G. Nielsen, 2018, Hywind – From idea to world's first wind farm based upon floaters. Available at: https://bit.ly/2QYQIGM

K.G. Papadopoulos, 2015, PID controller tuning using the magnitude optimum criterion. Springer International Publishing, Cham.

A. J. Pimm, S. D. Garvey, M. de Jong, 2014, Design and testing of Energy Bags for underwater compressed air energy storage, Energy, 66:496–508.

L. Riboldi, L. O. Nord, 2017, Concepts for lifetime efficient supply of power and heat to offshore installations in the North Sea, Energy Convers Manag, 148:860–75.

L. Riboldi, L. O. Nord, 2017, Lifetime Assessment of Combined Cycles for Cogeneration of Power and Heat in Offshore Oil and Gas Installations. Energies, 10:744.

L. Riboldi, L. O. Nord, 2018, Offshore Power Plants Integrating a Wind Farm: Design Optimisation and Techno-Economic Assessment Based on Surrogate Modelling. Processes.

L. Riboldi, S. Völler, M. Korpås, L. O. Nord, 2019, An Integrated Assessment of the Environmental and Economic Impact of Offshore Oil Platform Electrification. Energies, 12.

S. Sanchez, E. Tedeschi, J. Silva, M. Jafar, A. Marichalar, 2017, Smart load management of water injection systems in offshore oil and gas platforms integrating wind power, IET Renewable Power Generation 11, 1153–1162.

C. Spiegel, 2008, PEM Fuel Cell Modeling and Simulation Using Matlab, Academic Press.

Statistics Norway, 2018, Table 1: Emissions to air of greenhouse gases, Available at: https://www.ssb.no/en/natur-og-miljo/statistikker/klimagassn

Thermoflow Inc., 2016, Thermoflex Version 26.0, Fayville, MA, USA.

H. Zhang, S. Su, G. Lin, J. Chen, 2012, Efficiency Calculation and Configuration Design of a PEM Electrolyzer System for Hydrogen Production, International Journal of Electrochemical Science, 7, 4143-4157.

Sauro Pierucci, Flavio Manenti, Giulia Bozzano, Davide Manca (Eds.)
Proceedings of the 30th European Symposium on Computer Aided Process Engineering (ESCAPE30), May 24-27, 2020, Milano, Italy.
http://dx.doi.org/10.1016/B978-0-12-823377-1.50037-9

Nonlinear Prediction Model of Blast Furnace Operation Status

Pourya Azadi[a,*], Saeid Ahangari Minaabad[a], Hauke Bartusch[b], Rainer Klock[c], Sebastian Engell[a]

[a]*Process Dynamics and Operations Group, Department of Biochemical and Chemical Engineering, TU Dortmund, Emil Figge Straße 70, 44227 Dortmund, Germany*
[b]*Process Optimisation Iron and Steel Making Department, VDEh-Betriebsforschunginstitut GmbH, Sohnstraße 65, 40237 Düsseldorf, Germany*
[c]*thyssenkrupp Steel Europe AG, Kaiser-Wilhelm-Straße 100, 47166 Duisburg, Germany*
pourya.azadi@tu-dortmund.de

Abstract

The operation status of a process in the steel industry is mainly defined by three aspects, efficiency, productivity and safety. It provides guidance for the operators to make decisions on their future actions. The abrasive process environment inside a blast furnace (BF) makes it demanding to analyse the operation status by direct internal measurements. The blast furnace gas utilization factor (ETACO) is an essential indicator of the process efficiency. Besides efficiency, productivity and safety can, to some extent, be derived from the pressure drop (DP) and the top gas temperature (TG). This paper presents a nonlinear autoregressive network with exogenous inputs (NARX) model for the simultaneous multistep ahead prediction of ETACO, DP and TG, based upon a new set of fast and slow dynamic input attributes. Validation results using real industrial plant measurements show that this approach not only enables monitoring of the current operation status but also provides prediction capability by including the slow dynamics of the blast furnace into the model.

Keywords: Blast furnace operation status, NARX model, Multistep ahead prediction

1. Introduction

The ironmaking blast furnace (BF) is a very energy-intensive metallurgical process and the prime route for steel production, from which about 70% of the world's steel consumption is produced (Geerdes et al., 2015). The BF system receives coke and ore solid raw material along with hot blast air and continuously produces hot metal as the main product, as well as top gas and slag as the by-products. The performance of a BF is commonly characterized by its efficiency, productivity and safety. Currently, the BF industry is very focused on energy-saving and environmental-friendly operation. Productivity is a function of fuel efficiency and the amount of available gas in the process (Seetharaman, 2013). The complex physical and chemical phenomena inside the BF, with nonlinearly interconnected process variables in three dimensions, make the application of dynamic first-principle models demanding. Alternatively, in recent years, data-based modelling and prediction algorithms have shown great potential and been used more often for representing the BF process with less effort than the first-principle models. High temperatures and the corrosive internal environment of the blast furnace make continuous direct internal measurements impossible and hence the operation status must be monitored via the conditions at the boundaries (Saxén et al., 2013). The gas utilization factor, defined as the ratio of the carbon dioxide and carbon monoxide

concentration of the BF top gas, is an essential indicator of the process efficiency. In (Li et al., 2018) and (Zhang et al., 2018), the authors established a soft sensing scheme to predict the gas utilization ratio based on hot blast flowrate, temperature and pressure, as well as top gas pressure and permeability index input attributes. However, there are several shortcomings in these works. Firstly, the gas utilization ratio is additionally dependent on the physical, chemical and metallurgical properties of the solid feedstock (Geerdes et al., 2015). However, these attributes have not been considered in the development of the models. As explained below, in order to ensure the productivity and safety of the BF operation by control strategies, the model prediction should also incorporate pressure drop and top gas temperature (Geerdes et al., 2015). In (Zhang et al., 2016), a nonlinear autoregressive and moving average (NARMA) model was developed to predict the BF operation status. However, this model does not consider exogenous inputs and therefore cannot be used to determine future actions.

In this work, we propose a new set of exogenous input variables and develop a nonlinear autoregressive with exogenous input (NARX) model for the multistep prediction of the BF efficiency, productivity and safety. The paper is structured as follows. First, the process is described in more detail. Then, the selection of the input variables based on the process knowledge and the data pre-processing are explained. The structural parameters of the NARX model are discussed, followed by a discussion on the multistep prediction results of the outputs of interest. Finally, an outlook on future research is given.

2. Process description

The overview of a blast furnace with its basic terminology is related to Figure 1. The internal part of a blast furnace is divided into five major zones: the throat, the stack, the belly, the bosh and the hearth. A blast furnace is a counter-current gas-solid reactor where the ascending gas reacts with the descending solid bed, producing hot metal as the main product. The coke and iron-ore bearing burden (lump ore, sinter and pellets) along with flux materials are fed from the top until the BF is filled with alternating layers of coke and ore at the level of the stockline at the bottom of the throat. Compressed hot blast air (1000 – 1300 °C) containing oxygen, nitrogen and moisture, along with additional enriching pure oxygen and pulverized coal is blown into the furnace via the tuyeres. The hot blast oxidizes all carbon-based materials (coke and coal) in the raceways and produces the reducing agent, gaseous carbon monoxide (CO) and hydrogen (H_2) with a flame temperature of 1900 – 2300 °C. The gas ascends through the furnace while heating up the materials, melting the iron ore and conducting chemical reactions. This gas leaves the top of the BF at around 100 °C after 6 – 10 seconds. On the other hand, the iron-ore is first heated up to about 600 °C at the top of the furnace until the indirect reduction reactions, Eqs. (1) and (2), start in the stack.

$$FeO_x + CO \rightarrow FeO_{x-1} + CO_2 \tag{1}$$

$$FeO_x + H_2 \rightarrow FeO_{x-1} + H_2O \tag{2}$$

The reduced iron-ore materials descend further to the belly and bosh regions at the softening/melting temperature of 1000 – 1100 °C. At this stage, the molten wustite (FeO) undergoes the cyclic reactions, Eqs. (3) and (4), to produce the molten iron.

$$FeO + CO \rightarrow Fe + CO_2 \quad \text{(Direct reduction reaction)} \tag{3}$$

$$CO_2 + C \rightarrow 2CO \quad \text{(Boudouard reaction)} \tag{4}$$

Afterwards, the liquid iron and slag, which is mainly formed from the burden gangue materials (CaO, MgO, Al_2O_3 and SiO_2) and the coke ash, drip through the active coke and accumulate in the voids between the inactive coke particles (deadman) in the hearth. The hot metal is cast via the taphole at a temperature around 1500 °C. The residence time of the solid is around 6 – 10 hours. More detailed information can be found in (Geerdes et al., 2015).

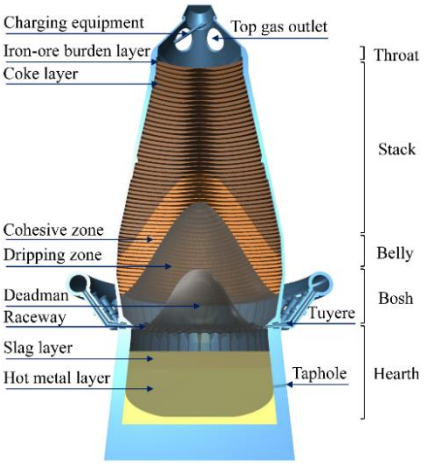

Figure 1: Overall sketch of a blast furnace

3. Analysis of the process variables

In this section, an overview of the input and output variables of the model is given.

3.1. Model outputs

The BF operation status can be monitored through the gas utilization factor (ETACO), the pressure drop (DP), and the top gas temperature (TG). Eq. (5) gives the definition of the gas utilization factor:

$$\eta_{CO} = \frac{CO_2}{CO+CO_2} \tag{5}$$

where CO_2 and CO stand for the concentration of carbon dioxide and carbon monoxide in the top gas. This factor reflects the amount of indirect and direct reduction reactions of the iron oxide and ranges between 0.45 – 0.52. The higher the value of ETACO is, the more efficient the BF operation is, which indicates that the oxygen is removed from the ore using less coke and coal (Geerdes et al., 2015). Another significant aspect of the operation status is productivity. The BF productivity can be assessed through the maximum pressure drop and the top gas temperature. Operating the BF above the maximum DP (1.4 – 1.7 bar) results in decayed burden descent and hence decreased productivity (Geerdes et al., 2015). Furthermore, since the BF is a gas-solid reactor, the productivity increases when more gas is produced at the tuyeres. The more oxygen is injected through the tuyeres, the more gasification takes place in the raceways, resulting in higher productivity. However, too much oxygen injection results in higher temperatures at the raceways. All reactions shift to the lower furnace regions and the wall, resulting in higher heat loss and delayed indirect reduction reaction. This leads to a lowered top temperature. If the top gas temperature becomes too low (less than 100 °C), the effective volume of the furnace, the bed permeability for the gas and liquid flows and thus the productivity decrease (Geerdes et al., 2015). In addition, the drying of the burden materials is prolonged and the BF process becomes more sensitive to wet and low-quality raw materials, rising the risk of process instabilities such as hanging and slipping of the burden (irregular burden descent) and channelling (a direct gas tunnel from the tuyeres to the BF top). In the worst case, the risk extends to a chilled hearth where the connection between tuyeres and hearth is lost and the outflows of the produced hot metal and slag are ceased (Schwalbe et al., 2015; Geerdes et al., 2015). This event can be identified in top gas temperatures falling below 80 °C (Seetharaman, 2013). Based on these insights, ETACO, DP and TG are considered as the model outputs for monitoring the BF operation status.

3.2. Model inputs

The proposed set of input variables are listed in Table 1. The hot blast is the origin of the produced gas at the tuyere level of the furnace. Its parameters affect the reaction conditions. Due to the very short residence time of the gas, changes in the hot blast variables can be directly detected in the top gas. More oxygen in the raceways results in more gasification. Then, not only a large amount of heat is released, but also more gaseous reducing agents are produced, promoting the reduction reactions, which can be identified through the gas utilization rate and the top gas temperature. The blast moisture reacts with the available carbon in front of the tuyeres and produces H_2. Part of the oxygen in the iron-ore is removed by H_2. Therefore, varying the hot blast moisture changes the portion of the reduction reactions between CO and H_2, which is reflected in the gas utilization factor. The gas flow distribution depends on the blast volume and the bed permeability. The bed permeability is an essential characteristic in the BF process. It is influenced by fine particles and the reduction disintegration (RDI) feature of the sinter. Generally, FeO, SiO_2 and MgO make the burden more resistant, and CaO and Al_2O_3 more prone to RDI. The changes in RDI also affect the pressure drop and the gas utilization factor. The top pressure is an independent control variable in the process that is regulated by the annular gap elements of the exhaust system. It influences the gas velocity and the pressure drop, the intensity of the chemical reactions and, thus, the gas utilization factor. The sinter materials contain less oxygen than pellets to be removed. Thus, the effect that the amounts of sinter and pellet have on ETACO should also be incorporated into the model. For further details see (Geerdes et al., 2015).

Table 1: Input variables

Variable name	Symbol	Unit
Blast volume	VB	m^3/h
Blast temperature	TB	°C
Top pressure	PG	bar
Oxygen enrichment	OE	m^3/h
Coal injection	PCI	m^3/h
Blast moisture	MB	g/m^3
Burden depth	BD	m
Coke reactivity index	CRI	-
Coke mass flow	Coke	t/min
Sinter mass flow	Sinter	t/min
Pellet mass flow	Pellet	t/min
CaO mass flow	CaO	t/min
MgO mass flow	MgO	t/min
Al_2O_3 mass flow	Al2O3	t/min
SiO_2 mass flow	SiO2	t/min
FeO mass flow	FeO	t/min
Permeability index	PI	-

A principal component analysis (PCA) is used to support the choice of the input

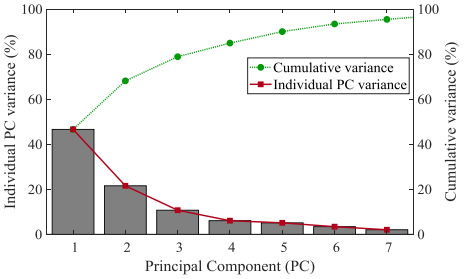

Figure 2: PCA scree plot

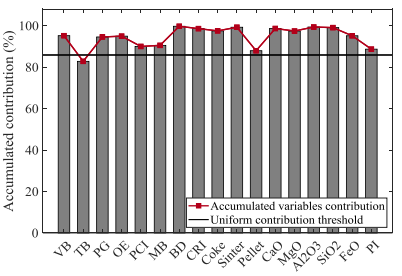

Figure 3: Variables contribution to all 7 PCs

variables. As Figure 2 reveals, 95% of the major variations in the input variables are incorporated by 7 principal components. The accumulated contribution of all input variables, except the blast temperature (TB), to all 7 principal components, as shown in Figure 3, is above the uniform contribution threshold, approving the importance of the variables influencing TG, DP and ETACO. As a result, the set of input attributes is finalized with 16 variables, excluding the blast temperature: VB, PG, OE, PCI, MB, BD, CRI, Coke, Sinter, Pellet, CaO, MgO, Al2O3, SiO2, FeO and PI. This is also motivated by the fact that, in practice, this variable is highly correlated (more than 0.8) with the pulverized coal injection which is an input variable.

4. Multistep ahead prediction of operation status

In this work, a nonlinear autoregressive model with exogenous inputs (NARX) is used to represent the nonlinear relation between the input and output variables. NARX is a feedforward neural network-based model with external memory. Such a model can mathematically be stated as follows:

$$y(t) = f(y(t-1),\ldots,y(t-d_y),u(t),u(t-1),\ldots,u(t-d_u)) \tag{6}$$

where y represents the output vector and u is the set of exogenous inputs. The blast variables, due to the gas residence time being shorter than the sampling time (1 minute), are considered to have no time delay with respect to the output variables. A time delay of 5 minutes is chosen for the slow dynamic (solid phase) variables based on the influence of burden loading on the output variables. The output autoregressive order and the number of hidden layers of the embedded network (p) are chosen based on the Bayes Information Criterion (BIC), defined in Eq. (7), with SSR and T as the sum of squared regression and number of data points:

$$BIC(p) = \ln\left(\frac{SSR(p)}{T}\right) + (p+1)\frac{\ln T}{T} \tag{7}$$

The first term penalizes the error of the model, while the second term penalizes the complexity of the network. The parameters with the minimum BIC value are chosen for the network. Table 2 summarizes the BIC analysis.

The dataset for the model with 400000 samples was obtained from plant measurements of the large-scale blast furnace 2 Schwelgern in thyssenkrupp Steel Europe with the working volume of about 4800 m^3. In our study, 98% of the samples were used for training and cross-validation and the rest for testing. One-step ahead prediction based training was carried out. Figure 4 depicts the free-running forward simulation results of the multistep ahead prediction (MSAP) of the BF operation status, over a horizon of 3 hours, using the proposed input variables. The quality of the predictions over such a long horizon in comparison with the test

Table 2: Bayes information criterion analysis

Autoregressive order	Hidden layers	Hidden neuron per layer	BIC	R^2
1	3	30	6.6500	0.9509
15	**5**	**30**	**6.6355**	**0.9623**
30	6	30	6.6361	0.9689
60	6	30	6.6457	0.9696

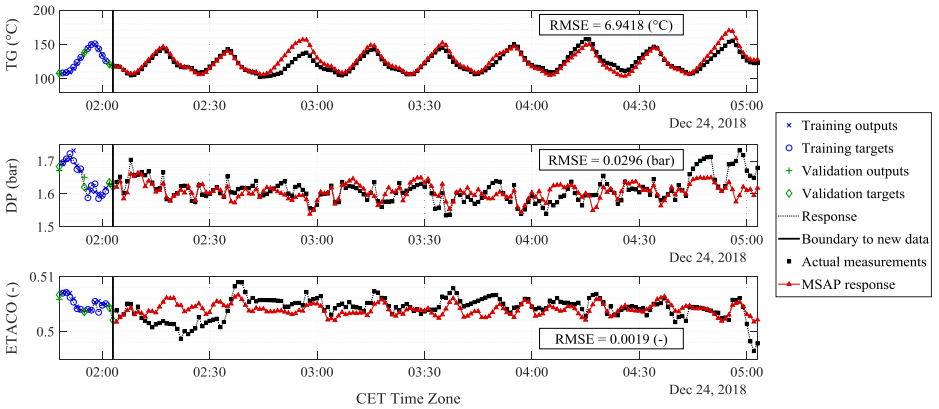

Figure 4: Multistep ahead prediction of BF operation status – validation results (TG: top gas temperature; DP: pressure drop; ETACO: gas utilization factor)

dataset demonstrates the reliable prediction of the operation status when using the proposed input attributes. Despite the influence of unknown disturbances, the root mean squared errors (RMSE) of the predictions are small (se**e figure 4**) so the model can be used in a model-based control scheme.

5. Conclusions and outlook

A nonlinear data-based prediction model of blast furnace operation status with a set of carefully selected exogenous inputs has been developed and validated by real plant measurements. The validation results show that the model is able to predict the main trend of the BF operation status under the stable working condition over a long prediction horizon. In the future, we plan to apply the model to compute control strategies for optimal decision-making on the future input variables to the process.

Acknowledgement

The project leading to this publication has received funding from the Bundesministerium für Wirtschaft und Energie under the grant agreement number 03ET1524B. The responsibility for the content of this publication lies solely with the authors.

References

M. Geerdes, R. Chaigneau, I. Kurunov, O. Lingiardi, J. Ricketts. 2015. Modern blast furnace ironmaking: an introduction. Amsterdam, NL: IOS Press BV.

Y. Li, S. Zhang, Y. Yin, J. Zhang, W. Xiao. 2018. A soft sensing scheme of gas utilization ratio prediction for blast furnace via improved extreme learning machine. Neural Process. Lett 1-23.

H. Saxén, C. Gao, Z. Gao. 2013. Data-driven time-discrete models for dynamic prediction of the hot metal silicon content in the blast furnace - a review. IEEE Trans. Ind. Informat. 9 (4): 2213 - 2225.

R. Schwalbe, R. Klock, U. Janhsen, P. Schmöle, M. Peters. 2015. Influence of intentionally deteriorated coke properties on performance of blast furnace 2 schwelgern. METEC & 2nd ESTAD.

S. Seetharaman. 2013. Treatise on Process Metallurgy, Volume 3: Industrial Processes. Oxford, UK: Elsevier.

L. Zhang, C. Hua, J. Li, X. Guan. 2016. Operation Status Prediction Based on Top Gas System Analysis for Blast Furnace. IEEE Trans. Control Syst. Technol. 25 (1): 262-269.

S. Zhang, H. Jiang, Y. Yin, W. Xiao, B. Zhao. 2018. The prediction of the gas utilization ratio based on TS fuzzy neural network and particle swarm optimization. Sensors 18 (2): 625.

Sauro Pierucci, Flavio Manenti, Giulia Bozzano, Davide Manca (Eds.)
Proceedings of the 30th European Symposium on Computer Aided Process Engineering (ESCAPE30), May 24-27, 2020, Milano, Italy.
http://dx.doi.org/10.1016/B978-0-12-823377-1.50038-0

CFD Simulation of a Solid-Liquid Counter-Current Screw Extractor

Annemarie Lehr,[a*] Gábor Janiga,[a] Andreas Seidel-Morgenstern,[a,b] Dominique Thévenin[a]

[a]*Otto von Guericke University Magdeburg, Universitätsplatz 2, 39106 Magdeburg, Germany*
[b]*Max Planck Institute for Dynamics of Complex Technical Systems, Sandtorstraße 1, 39106 Magdeburg, Germany*
annemarie.lehr@ovgu.de

Abstract

More efficient processes to obtain artemisinin from *Artemisia annua* leaves via a solid-liquid extraction process are desirable, since artemisinin is increasingly needed as anti-malaria drug. As a substitute for conventional batch extraction technology, continuously operated counter-current processes are highly attractive for that purpose. To get first a better understanding of the hydrodynamics controlling the extraction, a multiphase 3D computational fluid dynamics (CFD) simulation model has been developed in the present project. It relies on the Volume of Fluid (VoF) model, leading to a purely Eulerian description of the flow. Using VoF, the distribution of the different phases within the screw extractor can be obtained. When varying the two inlet flow rates, different residence times for the liquid and the solid phases are obtained. This is particularly important, since the residence time is the most important process parameter to adjust. Currently, the predicted residence times for the liquid solvent amount to only one third of the experimentally determined values. However, accurate measurements are difficult, the assessment of residence times is different in the experiments and in the simulations, and the numerical model does not consider mass exchange processes between the phases yet. In spite of this discrepancy, a very good qualitative agreement is obtained, and these first results can be used to support the development of a compartment model, able to capture later both hydrodynamic and mass exchange processes with short computational times.

Keywords: CFD, fluid dynamics, mass exchange, screw extractor, VOF

1. Introduction

Counter-current extraction processes are widely used in the food industry, where they are applied, for example, in the solid-liquid extraction of beet sugar or rapeseed oil. With this method, higher final concentrations of the target substance in the solvent can be obtained compared to the direct current method. Additionally, the yield of the extraction process can be increased. This leads in the pharmaceutical industry to a growing interest in continuously operated counter-current processes. High yields are required for the extraction of plant substances from natural materials, used further for the preparation of drugs (Lack, 1985). Following this concept, the Max Planck Institute (MPI) Magdeburg has developed a continuous process based on a solid-liquid counter-current screw extraction to gain artemisinin from *Artemisia annua* leaves. Derivatives of artemisinin (e.g., artesunate) are increasingly used as efficient anti-malaria drugs (Gilmore et al., 2014). According to the World Malaria Report 2018, 219 million people worldwide were

infected with malaria in 2017. About 435,000 people died as a result of malaria infection, of which 61 % were children under 5 years (World Health Organisation, 2018). These facts demonstrate the importance of efficient extraction of artemisinin, which would allow a higher treatment rate thanks to a decrease in production costs. For this aim an appropriate solvent is necessary. For this particular separation problem, toluene is a promising substance (Lapkin et al., 2010, Gilmore et al., 2014). However, this organic solvent is highly explosive and requires a lot of safety procedures. Experimental counter-current extraction studies have just started in our group. Here, the use of CFD in preliminary studies is an advantage and can contribute to a better understanding of the process. The implemented counter-current screw extractor at the MPI Magdeburg represents a combination of screw extractor and extruder. The complexity of the system is very high as it involves a multiphase (solid-liquid) flow with a free surface, and rotating components. A detailed overview of the state of the art regarding CFD for modelling positive displacement screw machines is provided by Kovacevic et al. (2016), who focus on the importance of capturing the leakage gaps on the grid. Bahadar et al. (2013) performed a CFD simulation of a screw expeller for performance analysis regarding massive Jatropha biomass in connection with oil extraction. Lübke and Wünsch (2012) dealt with free-surface flows of highly viscous liquids in single screw extruders, using a combination of an Euler-Euler approach with the Volume of Fluid method.

In this work, a 3D investigation relying on the industrial CFD software package StarCCM+ has been performed in order to represent the extraction process. Due to the high complexity of this configuration, mass exchange processes and reactions between the natural material and the solvent are first neglected. The results are compared with experimental data using water as a solvent. In addition, the results are currently used to derive and parameterize a compartment model. Ultimately, this model will be used to optimize solvent choice and extraction process.

2. Methods and Implementation

The geometry used for the preliminary simulations corresponds to the original pilot plant of the screw extruder. This has a length of 321 mm, smaller than the production extraction device now used for all experiments at MPI Magdeburg, with a length of 640 mm. As all other dimensions are identical, a first analysis of the flow behaviour can be obtained more rapidly with the smaller geometry, imported as a CAD file (Figure 1). Since only the screw shall rotate, the domain has been separated into a rotating and a stationary domain. The employed mesh was created with a polyhedral mesher, with a base size of Δx = 8 mm.

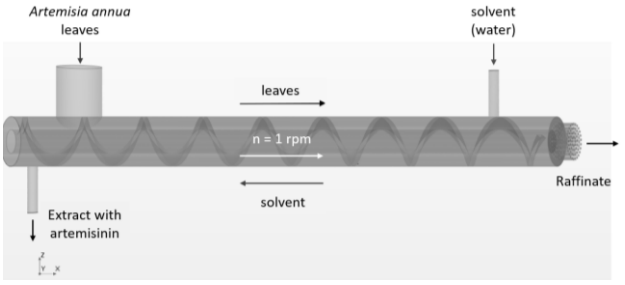

Figure 1: Geometry of the horizontal screw extruder, where the introduced leaves are transported in axial direction by the screw, while the solvent flows in counter-current direction due to a perforated disc at the outlet of the raffinate. This corresponds to the experimental procedure. The length of the geometry amounts to l = 321 mm and the diameter has a value of d = 29.7 mm.

Refinements at the interface between the domains were implemented to accurately capture the occurring leakage flows. A total number of roughly 1 million finite-volume cells were generated. For the considered flow, a Reynolds number of 26 can be computed, so that the flow is laminar. The flow simulation is based on a purely Eulerian approach. In addition, the VoF model has been activated to track the boundary of the two involved phases. As the complexity of the process is very high (three phases: gaseous, liquid, and solid), with additional rotation of the screw, separate CFD simulations have been performed. First simulations consider a free-surface flow between solvent and air, neglecting the solid phase; this simulation shall deliver information regarding the steady-state position of the liquid surface. A second simulation set was performed to investigate an extruder filled with liquid, neglecting the gas and the solid phase; this simulation is used to get first estimates concerning residence times and deliver information for fitting a compartment model.

2.1. Two-Phase Flow: Liquid – Gas

Since the gas phase is not significantly influenced by the low-speed liquid and screw, it can be regarded as incompressible. In order to capture the free surface between the liquid and the gaseous phase, the VoF model is suitable. For the simulation, the default material properties of water and air provided by the employed software (StarCCM+) at room temperature have been used. At the start of the simulation the screw extruder is filled with water by 60 % in volume. This corresponds to the initial filling degree with solid matter in the experiments. Starting screw rotation at a speed of n = 1 rpm, water is continuously injected into the system with a volumetric flow-rate of $\dot{V}$= 1 L/h, again mimicking the experimental procedure. The time step of this unsteady simulation was set constant to Δt = 0.01 s; this small value was necessary to get a stable free surface.

2.2. Two-Phase Flow: Liquid – Highly Viscous Phase

As the numerical simulation of a solid phase is very complex, the water-soaked *Artemisia annua* leaves have been represented in an approximate manner as a Newtonian fluid with a very high viscosity of η = 1,000 Pa·s, chosen after viscosity measurements of the raffinate using an available rotational rheometer (Kinexus pro+, Malvern). Since mass exchange processes between the phases are not considered yet, the effects of density and viscosity differences on the residence time of the liquid phase will be analysed instead by setting constant, linear profiles of these quantities in the device. In addition, the values of the injected liquid volumetric flow-rate and of the rotational speed of the screw have been varied in order to quantify the corresponding changes in residence time and compare these numerical predictions with experimental data. Finally, the residence time of the solvent toluene has been compared with that obtained for water, keeping all other conditions identical. This will help preparing corresponding modifications of the experimental studies.

3. Results and Discussion

3.1. Two-Phase Flow: Liquid – Gas

Figure 2 illustrates the distribution of the water and air phases along a vertical cross-section of the extractor (*y*-*z* plane). This result is obtained by VoF after a process time of 120 s, which corresponds to two complete revolutions of the screw and could be obtained with a computational time of four days using 6 cores. This state corresponds visually to near steady state.

Figure 3 shows the evolution with time of the air/water interface. It corresponds to a volume fraction of $0 \leq \alpha_{water} \leq 1$, which extends over one to three control volumes in the present simulations. Due to the slow rotation of the screw, the interface is found to remain stable even when the screw crosses it. With time, a movement of the interface starting from a horizontal state, is observed as expected (Figure 3), due to the conveying of the screw in axial direction. At steady-state, the height of the interface increases continuously over the length of the reactor from left to right in axial direction *x* (with $x = 0$ at the left side, where the outlet of the extract is located). Its position can be approximated by $z = -0.044x^2 + 0.036x + 0.001$.

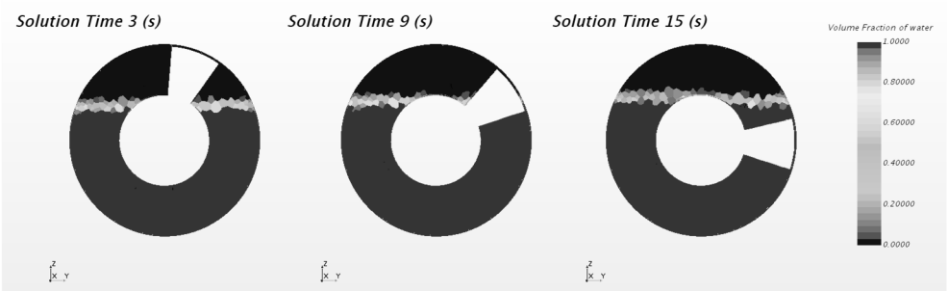

Figure 2: Distribution of the phases water (bottom) and air (upper) along a vertical cross-section (*y*-*z* plane) during the passage of the screw (white) through the interface (from air into water).

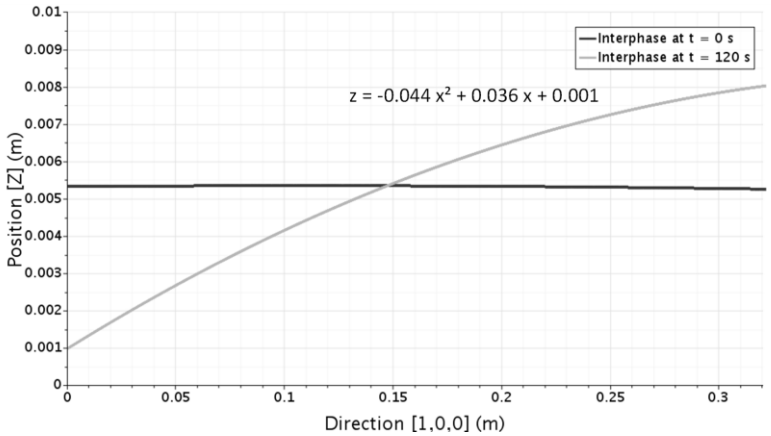

Figure 3: Height curve of the interface between water and air caused by the conveying of the screw in axial direction at the solution times $t = 0$ s (initial) and $t = 120$ s (steady-state). The value $z = 0$ corresponds to the axis of the extractor.

3.2. Two-Phase Flow: Liquid – Highly Viscous Phase

Implementing a fixed linear density difference between the left and right end of the plant for the highly viscous phase varying from $\Delta\rho$ = 140 to 420 kg/m³ leads with increasing values to a decrease of the residence time of water from τ = 3.78 min to τ = 3.05 min (Figure 4). For comparison, the residence time of water in the extractor without any density difference using the value corresponding to the dry leaves, leads to a higher value of τ = 4.5 min. This must be compared to the experimental residence time, estimated as 10.7 min. In addition, the implemented viscosity difference for the highly viscous phase, which leads to a linear decrease of the viscosity value from η = 1,000 Pa·s at the left end of the screw to a value of η = 100 Pa·s at its right end, results in an increase of the residence time from 3.15 min to 3.42 min. To analyse the most relevant quantities for the process, a constant viscosity of η = 1,000 Pa·s and a density difference of $\Delta\rho$ = 340 kg/m³ were set. Keeping these conditions but doubling the volumetric flow-rate of water injected into the extractor, a halving of the residence time from 3.15 min to 1.53 min is observed in the CFD (Figure 5), as expected, since water is then the dominant phase. Hence, it is shown that the residence time can be tuned to a desired value by setting in an appropriate manner the water flow-rate entering the extractor. Comparing the numerical residence times for changing volumetric flow-rates with experimental values determined at the MPI Magdeburg (Figure 5), a good qualitative agreement can be observed despite quantitative differences by a factor 3.5. The residence times increase exponentially for smaller volumetric flow-rates. In contrast, changing the rotational speed from n = 1 to 1.5 rpm (increase by 50 %) has only a minor influence on the numerical residence times. This also corroborates experimental observations. Switching now the liquid phase from water to toluene as solvent by changing the corresponding density and viscosity values while keeping all other parameters identical, the residence time increases slightly from 3.15 min to 3.31 min. This must be kept in mind when planning the modifications of the experimental set-up.

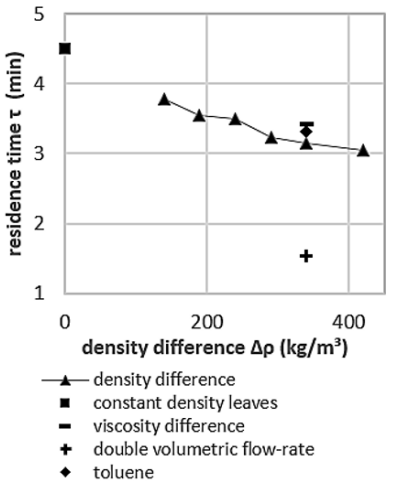

Figure 4: Change in residence time of the solvent predicted by numerical simulation when varying different flow quantities with density differences for the highly viscous phase ranging from $\Delta\rho$ = 140 to 420 kg/m³.

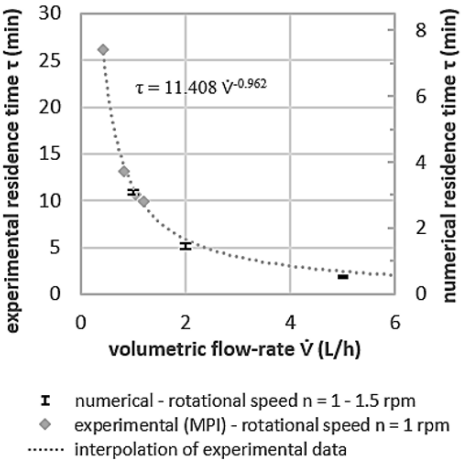

Figure 5: Comparison between numerical and experimental (MPI Magdeburg) residence times of water (in min) as a function of the volumetric flow-rate injected into the extractor and of the rotational speed of the screw.

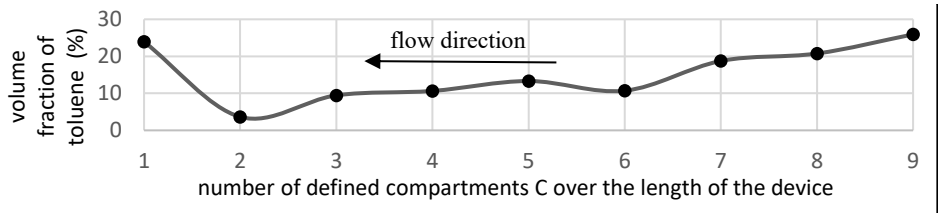

Figure 6: Volume fraction of toluene in defined compartments (C), C1-outlet, C9-inlet

The obtained numerical results show lower residence times compared to the experimental observations of 10 min. The predicted residence times are shorter by a factor 3.5. Apart from the smaller length of the used geometry compared to the experiments (factor 2), at least three reasons can be proposed to explain this discrepancy: 1) Currently, all mass exchange processes between the phases are neglected; 2) The numerical model contains simplifications, e.g. concerning material properties; 3) The residence time is measured in the simulations by tracking the first appearance of solvent at the outlet, while a different protocol based on a pulse injection is used in the experiments.

4. Conclusions and Outlook

A 3D multiphase CFD model for a counter-current extraction process has been developed. This model has been used to investigate the effect of different quantities. For instance, the rotational speed of the screw is not significant for small values, while the injected volumetric flow-rate of the solvent can be modified to set a desired value of the residence time. Both findings corroborate well with experimental observations, even if quantitative differences by a factor 3.5 are still found, due to the different lengths of the reactors but also to limited model and measurement accuracy. This will be further refined in on-going studies. The developed CFD approach is currently used to parametrize a compartment model for toluene with a view toward process optimization. As a first step, the volume fractions of toluene in manually-defined compartments have been obtained on the basis of pressure (Figure 6) where a decrease from inlet to outlet can be observed, which is in qualitative agreement with the expectations for this system. Additionally, mass exchange processes between the different phases will be implemented in the solver in the future.

References

A. Bahadar, M.B. Khan, T. Mehran, 2013, Design and development of an efficient screw press expeller for oil expression from Jatropha Curcas seeds, 2013, Industrial & Engineering Chemistry Research, 52, 5, 2123-2129

K. Gilmore, D. Kopetzki, J. W. Lee, Z. Horvath, D. T. McQuade, A. Seidel-Morgenstern, P. H. Seeberger, 2014, Continuous synthesis of artemisinin-derived medicines, Chemical Communications, 50, 12652-12655

A. Kovacevic, S. Rane, N. Stosic, 2016, Computational fluid dynamics in rotary positive displacement screw machines, 16th International Symposium in Transport Phenomena and Dynamics of Rotating Machinery, Honolulu, United States, hal-01879361

E. A. Lack, 1985, Kriterien zur Auslegung von Anlagen für die Hochdruckextraktion von Naturstoffen, PhD Thesis, Graz, Austria

A. A. Lapkin, M. Peters, L. Greiner, S. Chemat, K. Leonhard, M. A. Liauw, W. Leitner, 2010, Screening of new solvents for artemisinin extraction process using *ab initio* methodology, Green Chemistry, 12, 2, 241-251

M. Lübke, O. Wünsch, 2012, Two-Phase Flow in Single Screw Extruders, Proceedings in Applied Mathematics and Mechanics, 12, 1, 509-510

World Health Organisation, 2018, World Malaria Report (accessed on: November 08, 2019)

Sauro Pierucci, Flavio Manenti, Giulia Bozzano, Davide Manca (Eds.)
Proceedings of the 30th European Symposium on Computer Aided Process Engineering (ESCAPE30), May 24-27, 2020, Milano, Italy.
http://dx.doi.org/10.1016/B978-0-12-823377-1.50039-2

Optimum Utilization of *Jatropha* Seedcake Considering the Energy, Water and Food Nexus

Mohammad Alherbawi,[a] Ahmed AlNouss,[a] Gordon Mckay,[a] Tareq Al-Ansari [a,b*]

[a] *Division of Sustainable Development, College of Science and Engineering, Hamad Bin Khalifa University, Qatar Foundation, Doha, Qatar.*

[b] *Division of Engineering Management of Decision Sciences, College of Science and Engineering, Hamad Bin Khalifa University, Qatar Foundation, Doha, Qatar.*

talansari@hbku.edu.qa

Abstract

Biofuel production has attracted significant attention from researchers and policymakers as a carbon-neutral source of energy. However, corresponding intensive land and water requirements have hindered the advancement of the biofuel industry. Consequently, second-generation biofuels from non-edible biomass have been promoted as suitable alternatives. In this context, the *Jatropha curcas* has proved to be a promising feedstock for various types of biofuels due to its competences over other oil-bearing crops, and its suitability to grow in non-arable lands with minimal water and energy requirements. In addition to utilising *Jatropha* oil as a source of energy, *Jatropha* seedcake has been used to produce energy and food-related products. Although, there are several processing pathways of seedcake which have been investigated, there are no conclusions on the optimum overall pathway. Meanwhile, the Energy-Water-Food (EWF) Nexus approach has recently become an important tool to ensure efficient and optimum management of the three vital resources by considering the inter-dependencies amongst them. It can also guide decision making in terms of identifying optimal processing and utilisation pathways. Therefore, this study presents an analysis of different production routes, and defines the optimum utilisation of *Jatropha* seedcake, by ensuring that the highest possible net energy, water and food are achieved. Required data are obtained via Aspen Plus' simulation of potential processes, while MATLAB is used to develop the mathematical optimisation model. The model produced 77 different solutions, with gasification being the dominant pathway in most of the given solutions, followed by livestock feed and fertilizers production.

Keywords: *Jatropha*, Biofuels, Seedcake, EWF Nexus, Optimisation.

1. Introduction

Biofuel production has been widely investigated throughout the past two decades to mitigate the carbon emissions and to combat global warming. Various energy crops have been tested for biofuel production worldwide. However, the widely used feedstock such as sunflower and corn oils have been criticized for being used as a source of energy at the expense of food, land and water resources. Since then, vast efforts have been directed towards a second generation of feedstock represented in non-edible biomass, where *Jatropha curcas* has been selected because of its properties compared to various other energy crops. *Jatropha*, a non-food competing crop can tolerate difficult soil conditions and is able grow in non-arable and arid lands (Tomar et al., 2014). In addition, *Jatropha* is well known for its minimal demand of water and energy. Not

only its oil can be converted to biofuel, but also the fruit residues of *Jatropha* such as the seedcake can be transformed into multiple energy and food-related products as presented in Figure 1. Furthermore, *Jatropha* seedcake can be processed into livestock feed as it contains approximately 60 % of crude protein (Islam et al., 2011). However, it must be detoxified first to decompose its toxic phorbol esters content (Makkar, 2016). *Jatropha* seedcake contains up to 4.44 % nitrogen, 2.09 % phosphorus and 1.68 % potassium which makes it a good candidate to be used as a fertilizer (Islam et al., 2011). Several studies have highlighted the attractive multiple uses of *Jatropha* fruit residues in energy and food production. Yet, no conclusions are drawn on the optimum utilization of these residues. In terms of managing resources, the energy, water and food (EWF) Nexus concept has been used to promote efficient management of the three vital resources considering the inter-dependencies amongst them (AlNouss et al., 2019). It can also serve as a decision-making methodology to identify the synergies and trade-offs amongst different process pathways and product utilization options. Using an EWF Nexus approach, this article investigates the optimum processing routes of *Jatropha* seedcake to produce energy and food-related products.

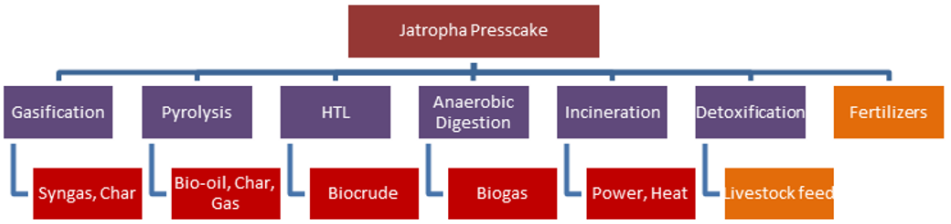

Figure 1: *Jatropha* seedcake processing routes into energy and food-related products.

2. Methodology

The net energy, water and food$_{(eq)}$ outputs of different processing pathways of seedcake is assessed from cradle to gate. For the cultivation and pre-processing stages, the required data are dependent on literature reports. Whereas, at processing level, Aspen Plus (V.9) is used to simulate all processes, except for the production of fertilisers, as it is assumed that the seedcake can be utilised directly as a fertiliser without further processing. The data obtained is then used to run an optimisation mathematical model using MATLAB (R2016b) to determine the optimum processing routes. All models are developed based on the assumptions of steady state and isothermal processes. In this study, 10,000 hectares of *Jatropha* plantations considered at a (3x3m) spacing, which is assumed to yield 100,000 tonnes of *Jatropha* fruits per year. The seedcake accounts for 40 wt.% of the whole-fruit (Singh et al., 2008) and 32 % of its net heating value (Jourabchi et al., 2014). Seedcake is defined based on its proximate and elemental analyses reported earlier (Ramírez et al., 2019).

2.1. Flowsheets Development

Gasification: The *Jatropha* seedcake is initially converted into conventional components using an "Ryield" reactor associated with a calculator block (AlNouss et al., 2018). The ash is then separated using solid separator before introducing the stream into the gasifier. The Cl_2, S and N_2 compounds are first converted completely to HCl, H_2S and NH_3 in a stoichiometric reactor and removed from the inlet stream to the gasifier. Steam is used as a gasifying agent at a steam to biomass ratio of 0.75. While the process is conducted in "RGibbs" reactor at 850 °C and 1 atm. The heat of the gasifier is provided by means of external combustion for a small portion of the carbon.

Pyrolysis: The seedcake is decomposed at 500 °C in "RGibbs" block into pre-defined conventional components. The stream is then introduced into a cyclone unit for solid

removal, while the gas stream is cooled down to separate the low boiling-point components to yield bio-oil and syngas products. Besides, the solid stream is further processed into a solid separator, yielding an ash-free biochar (Elkhalifa et al., 2019).

Hydrothermal liquefaction (HTL): The seedcake is initially decomposed into conventional components using a calculator block. The stream is then fed into the main reactor following the removal of ash. A hot and pressurized water is pumped to create a slurry with the presence of sodium hydroxide catalyst. The reaction is conducted at 300 °C and 150 bars using "RGibbs" reactor. Besides, predicted product are defined with reference to earlier reports (Pedersen et al., 2017).

Anaerobic digestion (AD): The process is simulated with reference to literature published models (Salman et al., 2017). The seedcake is converted into conventional components in an "RYield" block based on specific defined yields. The stream is then introduced into a solid separator to remove the solid digestate, while the gaseous stream is further processed into "RStoic" reactor, in which all carbon content is converted into methane and carbon dioxide.

Incineration: The model is simulated as a combined cycle process. Whereby, the seedcake is initially converted into conventional components using a calculator block connected to an "RYield" reactor. In addition, the ash content is removed using a solid separator. The flow is then introduced along with air into an "RStoic" block representing a combustion chamber, in which the process stichometry is defined, yielding a mixture of gases at 8 bar that pass through a gas turbine to generate power. Furthermore, a turbine is used to generate power out of the high-pressure stream generated from the excess heat of the effluent gases.

Detoxification: The model is developed based on the experimental work of Diwani et al. (2011). The process aims at degrading the toxic content of phorbol ester in seedcake, which is assumed to account for 0.29 wt.% (Gogoi et al., 2014). Sodium bicarbonate solution is added to seedcake in an "RGibbs" reactor, then the seedcake is separated and sent to an "RYield" reactor for thermal treatment at a temperature level of 120 °C. The defined yield assumes that all phorbol ester content has been degraded.

2.2. EWF Quantification

The net energy, water and food of the different investigated systems are assessed throughout the process lifecycle including cultivation, transportation, extraction and processing. At pre-processing stages, the EWF inputs are allocated over the *Jatropha* fruit parts based on their calorific values. The energy requirements for cultivation, transportation and extraction are adapted from studies reported by Neto et al. (2018), Han et al. (2013) and Ju et al. (2010) respectively. While the processing energy requirement are estimated by the Aspen Plus simulations. For net water analysis, an average watering value of 1200 mm/year is considered to ensure an optimum seed production (Tomar et al., 2014). Whereas, Aspen Plus estimates the water requirement for processing and cooling, as well as the process' water generation.

Furthermore, the plantation and processing of *Jatropha* do not consume or generate food directly, as it is a non-edible fruit. However, the land used to grow *Jatropha* could have been used at the expense of growing food crops. The area of the land used is converted into a food equivalent (food-$_{eq}$) quantity. For conversion purpose, "cereals" were used as reference crops, as they account for nearly 80 % of global food supply (Markussen and Østergård, 2013). One hectare of land can yield up to 2.25 tonnes of cereals (Roser and Ritchie, 2018), therefore a hectare of land is converted intoa quantity of 2.25 tonnes of food$_{(eq)}$. Besides, the food-related products such as fertilizers and livestock feed are also converted into food$_{(eq)}$ quantity. For fertilizers, the conversion is conducted based on seedcake's nitrogen content (wt.%) versus N-fertilizer requirement to grow cereals (Ladha et al., 2016). While the livestock feed is converted into food$_{(eq)}$ quantity in the form of meat instead of crops. For this purpose, beef is selected as a reference meat, whereby the conversation is conducted based on the seedcake's protein content (wt.%) versus protein requirement to raise cows (kg/kg) (Mekonnen and Hoekstra, 2010).

2.3. Optimization

A mathematical model to define the optimum processing routes for *Jatropha* seedcake is developed as presented in Table 1. The model aims at maximizing the net energy, water and food outputs. All seedcake shall be processed; therefore, the sum of all technologies' share shall be equal to 100 %. The Genetic Algorithm process of MATLAB is used for the optimization. The constants of the objective functions are obtained from simulations, calculations and literature reports as explained in section 2.2.

Table 1: Mathematical formulation of the optimization problem.

Objective functions	**Definitions**
$Z_E = (\sum_{i=1}^{7} E_i\ X_i)$	Z_E: net energy outcome.
	E_i: Net energy generated from process (i).
$Z_W = (\sum_{i=1}^{7} W_i\ X_i)$	X_i: Share of process (i).
	Z_W: net water outcome.
$Z_F = (\sum_{i=1}^{7} F_i\ X_i)$	W_i: Net water generated from process (i).
	Z_F: net food$_{(eq)}$ outcome.
	F_i: Net food$_{(eq)}$ generated from process (i).
Constraints	
$\sum_{i=1}^{7} X_i = 1$	All seedcake must be utilized.
$X_i \geq 0$	Positivity condition.

3. Results and Discussion

3.1. Processes Outputs

The different investigated processing pathways have yielded significant quantities of energy and food-related products. The energy products are in the form of direct power generation, gaseous fuels such as syngas and biogas, liquid fuels like bio-oil/biocrude or solid fuels like biochar. The food-related products including fertilizers and livestock feed are produced in almost a similar quantity as the feed flow (seedcake). The different processes outputs are illustrated in Figure 2.

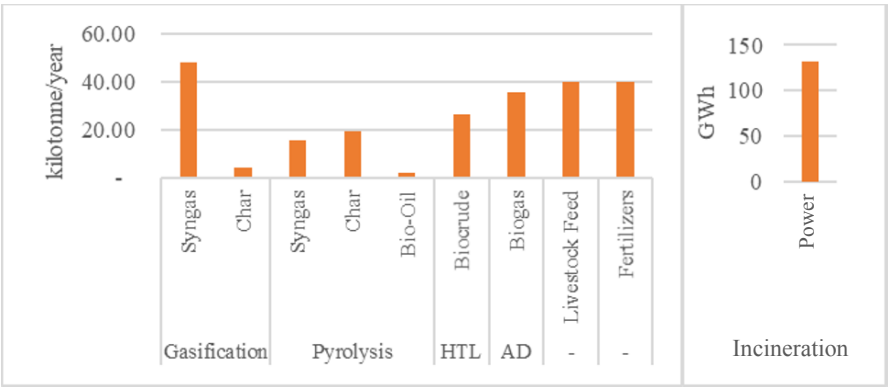

Figure 2: Main products distribution of *Jatropha* processing.

3.2. Net Energy, Water and Food Outputs

The net EWF evaluation of the *Jatropha* seedcake processing pathways is illustrated in Figure 3. The most energy-intensive stage throughout the lifecycle of all products is the cultivation, which is a common stage amongst them. All energy producing pathways are energy efficient with high energy return. Overall, the gasification process is the most energy

efficient pathway. Besides, all the processing pathways are water-consuming, with insignificant water generation. Moreover, pyrolysis is the most water consuming pathway, while incineration is the most water generating process. Amongst all energy producing pathways, anaerobic digestion is the least water consuming as no system cooling is required. Obviously, the $food_{(eq)}$ consumption for all pathways is equal, since it accounts for the land use only. Whereas, livestock feed and fertilizers production are the only $food_{(eq)}$ producing pathways, with livestock being the highest food producing in terms of quantity.

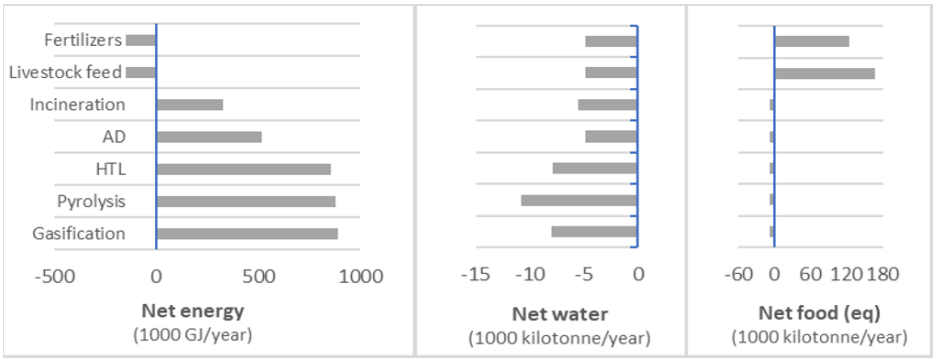

Figure 3: Net value of energy, water and $food_{(eq)}$ outputs for different pathways.

3.3. Optimum Technology

The MATLAB optimization model predicted 77 optimum solutions. The optimum technology share (%) with their corresponding outputs are presented in Figures 4 and 5 respectively. Since the variations in net water values are not great amongst all pathways, it is noticeable that the model conducted a trade-off mainly between both, the net energy and $food_{(eq)}$. The main suggested pathways are gasification followed by livestock feed and fertilizers production.

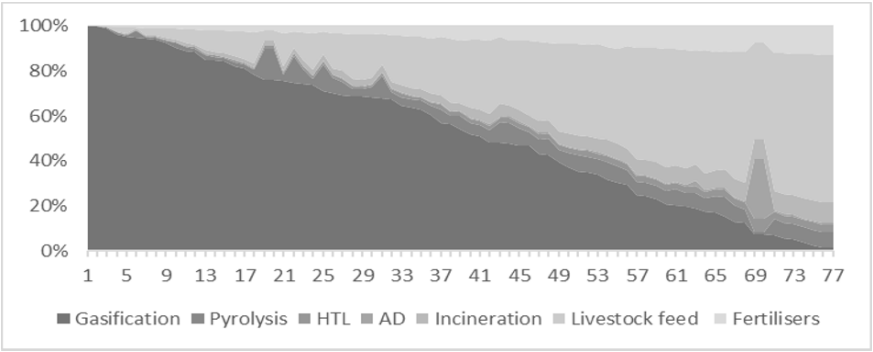

Figure 4: Optimum technology share (%) for *Jatropha* seedcake utilization.

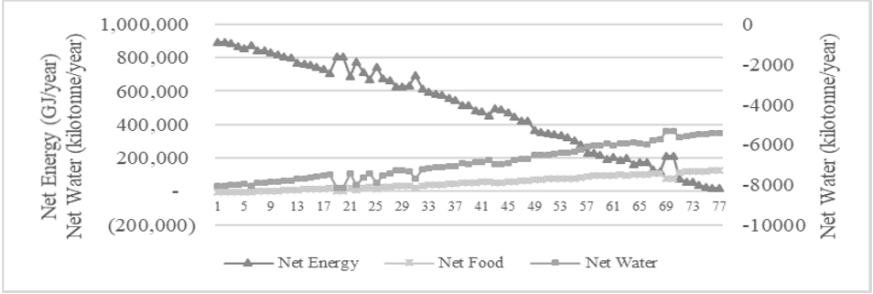

Figure 5: Optimum net energy, water and $food_{(eq)}$ of seedcake processing pathways.

4. Conclusions

Jatropha curcas proved to be a good source for both, energy and food-related production, though, it is still a water-consuming biomass as indicated throughout the various analyses in this study. Seven processing routes of *Jatropha* seedcake were investigated to identify the optimum amongst them in the light of the energy, water and food (EWF) Nexus. The optimisation model yielded 77 different solutions, with gasification being the dominant pathway in most of the given solutions, followed by livestock feed and fertilizers production.

References

A. K. M. A. Islam, Z. Yaakob & N. Anuar, 2011, Jatropha: A multipurpose plant with considerable potential for the tropics. *Scientific Research and Essays*, *6*(13), 2597–2605.

A. AlNouss, G. Mckay & T. Al-ansari, 2018, Optimum Utilization of Biomass for the Production of Power and Fuels using Gasification. In *28th European Symposium on Computer Aided Process Engineering* (Vol. 43, pp. 1481–1486). Elsevier Masson SAS.

A. AlNouss, S. Namany, G. McKay, and T. Al-Ansari, 2019, Applying a Sustainability Metric in Energy, Water and Food Nexus Applications; A Biomass Utilization Case Study to Improve Investment Decisions, Computer Aided Chemical Engineering, 46, 205-10.

C. A. Salman, S. Schwede, E. Thorin & J. Yan, 2017, Predictive Modelling and Simulation of Integrated Pyrolysis and Anaerobic Digestion Process. *Energy Procedia*, *105*, 850–857.

H. P. S. Makkar, 2016, State-of-the-art on detoxification of Jatropha curcas products aimed for use as animal and fish feed: A review. *Animal Feed Science and Technology*, *222*, 87–99.

J. Han, A. Elgowainy, H. Cai & M. Q. Wang, 2013, Life-cycle analysis of bio-based aviation fuels. *Bioresource Technology*, *150*, 447–456.

J. K. Ladha, A. Tirol-Padre, C. K. Reddy, K. G. Cassman, S. Verma, D. S. Powlson, H. Pathak, 2016, Global nitrogen budgets in cereals: A 50-year assessment for maize, rice, and wheat production systems. *Scientific Reports*, *6*, 19355.

L. P. Ju & B. Chen, 2010, Embodied energy and emergy evaluation of a typical biodiesel production chain in China. *Ecological Modelling*, *222*(2011), 2385–2392.

M. M. Mekonnen & A. Y. Hoekstra, 2010, *The green, blue and grey water footprint of farm animals and animal products*.

M. Roser & H. Ritchie, 2018, Yields and Land Use in Agriculture. *Our World In Data*.

M. V. Markussen & H. Østergård, 2013, Energy Analysis of the Danish Food Production System: Food-EROI and Fossil Fuel Dependency. *Energies*, *6*, 4170–4186.

N. S. Tomar, M. A. Ahanger & R. M. Agarwal, 2014, Jatropha curcas: An Overview. In P. Ahmad & M. R. Wani (Eds.), *Physiological Mechanisms and Adaptation Strategies in Plants Under Changing Environment: Volume 2* (pp. 361–383). New York, NY: Springer New York.

O. Neto, A. Santos, M. V. Folegatti, B. P. Lena, A. V. Diotto, J. P. Francisco & T. L. Romanelli, 2018, Energy analysis of Jatropha curcas under irrigation and rainfed at the Southeast Brazilian humid subtropical. *CIGR Journal*, *20*(3), 116–126.

R. Gogoi, U. K. Niyogi & A. K. Tyagi, 2014, Reduction of phorbol ester content in jatropha cake using high energy gamma radiation. *Journal of Radiation Research and Applied Sciences*, *7*(3), 305–309.

R. N. Singh, D. K. Vyas, N. S. L. Srivastava & M. Narra, 2008, SPRERI experience on holistic approach to utilize all parts of Jatropha curcas fruit for energy. *Renewable Energy*, *33*(8), 1868–1873.

S. A. Jourabchi, S. Gan & H. K. Ng, 2014, Pyrolysis of Jatropha curcas pressed cake for bio-oil production in a fixed-bed system. *Energy Conversion and Management*, *78*, 518–526.

S. Elkhalifa, A. AlNouss, T. Al-Ansari, H. R. Mackey, P. Parthasarathy & G. Mckay, 2019, Simulation of Food Waste Pyrolysis for the Production of Biochar: A Qatar Case Study. In *29th European Symposium on Computer Aided Process Engineering* (Vol. 46, pp. 901–906). Elsevier.

T. H. Pedersen, C. U. Jensen, L. Sandström & L. A. Rosendahl, 2017, Full characterization of compounds obtained from fractional distillation and upgrading of a HTL biocrude. *Applied Energy*, *202*, 408–419.

V. Ramírez, J. Martí-Herrero, M. Romero & D. Rivadeneira, 2019, Energy use of Jatropha oil extraction wastes: Pellets from biochar and Jatropha shell blends. *Journal of Cleaner Production*, *215*, 1095–1102.

Sauro Pierucci, Flavio Manenti, Giulia Bozzano, Davide Manca (Eds.)
Proceedings of the 30th European Symposium on Computer Aided Process Engineering (ESCAPE30), May 24-27, 2020, Milano, Italy.
http://dx.doi.org/10.1016/B978-0-12-823377-1.50040-9

Potential Integrated Pathways for Jet Biofuel Production from Whole Fruit of *Jatropha*

Mohammad Alherbawi,[a] Tareq Al-Ansari,[a,b] Gordon Mckay [a*]

[a] *Division of Sustainable Development, College of Science and Engineering, Hamad Bin Khalifa University, Qatar Foundation, Doha, Qatar.*

[b] *Division of Engineering Management of Decision Sciences, College of Science and Engineering, Hamad Bin Khalifa University, Qatar Foundation, Doha, Qatar.*

gmckay@hbku.edu.qa

Abstract

Civil Aviation is responsible for nearly 5 % of total radiative forcing of climate and 2.5 % of annual global CO_2 emissions, while the demand on Jet fuel is rising rapidly. As such, Jet Biofuel (JBF) has been recognised by the aviation industry as the best option to mitigate its carbon footprint. In this regard, *Jatropha curcas* has proved to be a promising biomass for JBF production due to its unique competences over other energy crops. Not only can its oil be converted into high performance fuels, but also its fruit residues are considered a valuable source for multiple energy carriers. However, *Jatropha* is not yet fully utilized in the Jet Biofuel industry. Therefore, this study presents three novel integrated systems that utilize all parts of the *Jatropha* fruit to produce JBF. These systems integrate the conventional hydroprocess along with one of three thermochemical processes including gasification, pyrolysis and hydrothermal liquefaction. Aspen Plus® is used to develop the systems and investigate the optimum amongst them based on Jet Biofuel yield. All the three systems resulted in significant increments in the JBF yield. While, the hydroprocess-gasification system demonstrated promising results; whereby, 65 wt.% of the *Jatropha* whole-fruit is converted into green liquid fuels with 57 % Jet Biofuel selectivity. The results indicate over a 90 % increment in JBF yield as compared to the utilization of *Jatropha* oil alone in the best reported scenarios.

Keywords: *Jatropha*, Jet Biofuel, Hydroprocess, Fischer-Tropsch, Gasification, Pyrolysis, Hydrothermal liquefaction.

1. Introduction

Civil aviation contributes to nearly 2.5 % of global carbon emissions, which is predicted to double in the coming three decades (ICAO, 2016). Meanwhile, Jet Biofuel (JBF) produced from renewable resources has been intensively investigated and proved to be a promising technology to mitigate the carbon footprint of aviation sector. As airplanes depend exclusively on liquid fuels as compared to road transportation, the shifting of the refining process towards maximizing JBF becomes a favorable practice (Anand et al., 2016).

Currently, four main JBF production pathways have been certified, including Oil to Jet (OTJ) by the conventional hydroprocess, Gas to Jet (GTJ) by gasification of biomass followed by Fischer-Tropsch technology, Alcohol to Jet (ATJ) by bio-alcohol upgrading

and Sugar to Jet (STJ) by the catalytic upgrading of sugar (Gutiérrez-Antonio et al., 2017). Though, the hydroprocess is still identified as the most cost-effective pathway (de Jong et al., 2015).

Since the feedstock price accounts for up to 75 % of JBF net cost (de Jong et al., 2015), great efforts have been paid to identify the best feedstock in terms of cost and sustainability. In this context, *Jatropha curcas* is considered a promising feedstock due to its high competences as compared to other oil-bearing crops. Several demonstration and commercial flights have already been operated using different blending ratios of *Jatropha* JBF (Wang and Tao, 2016). The JBF industry has been greatly developed in a relatively short time, yet, it is still facing great challenges related to the availability of sufficient feedstock to fulfill future JBF demands, as well as offering biofuels with competitive prices as compared to conventional Jet-A fuels.

Amongst the various attempts to lower JBF production costs, Zech et al. (2018) reported that a 30 % cost reduction can be achieved by running the process in diesel-mode rather than jet-mode; as diesel has a higher market value. While, Gutiérrez-Antonio et al. (2016) integrated the heat among the process subsystems to reduce the energy consumption. In addition, Wang (2016) has utilized the *Jatropha* fruit's shells and seedcake for power generation and bio-oil production respectively to enhance the process' efficiency. Although previous attempts have managed to lower the production cost, but the yield of JBF is not enhanced or even dropped. Meanwhile, experimental studies reported a maximum JBF selectivity of around 70 % (YaJie et al., 2017), which corresponds to less than 20 wt.% of the *Jatropha* fruit.

Although the *Jatropha* fruit residues have been earlier converted into multiple energy carriers, no reports were found in literature on the utilization of these residues directly in JBF production, to the knowledge of the authors. As such, this study investigates three novel integrated systems to utilize all parts of the *Jatropha* fruit including its oil, shells and seedcake for JBF production. The proposed systems integrate the conventional hydroprocess technology along with one of three thermochemical processes including gasification, pyrolysis and hydrothermal liquefaction. The optimum utilization of *Jatropha* residues is believed to be a key factor to enhance the JBF yield, and therefore lower its production cost. The integrated systems are simulated in Aspen Plus to investigate the potential JBF yields and to identify the highest-yielding system amongst them.

2. Methodology

Aspen Plus (V.9) is used to develop the proposed integrated systems based on the assumptions of steady state and isothermal processes. A plant feed capacity of 100 tonne/hour is considered. Besides, *Jatropha* fruit feed is assumed to split into (30 wt.%) oil, (35 wt.%) shells and (35 wt.%) seedcake upon the deshelling and extraction processes (Singh et al., 2008). The *Jatropha* oil is defined based on its triglycerides' content (Chen et al., 2014), while the shells and seedcake are defined based on their proximate and elemental analysis (Ramírez et al., 2019). All nitrogen and sulphur contents are assumed to be converted into NH_3 and H_2S respectively, while char is assumed to be composed of carbon only. The *Jatropha* oil is processed by the conventional hydroprocess, while the residues are processed by three different thermochemical processes before introducing the resulting oils into the hydroprocessing reactors. All the three systems are optimized for the highest liquid fuels production and highest JBF selectivity. The simplified process flow diagrams are presented in Figure 1.

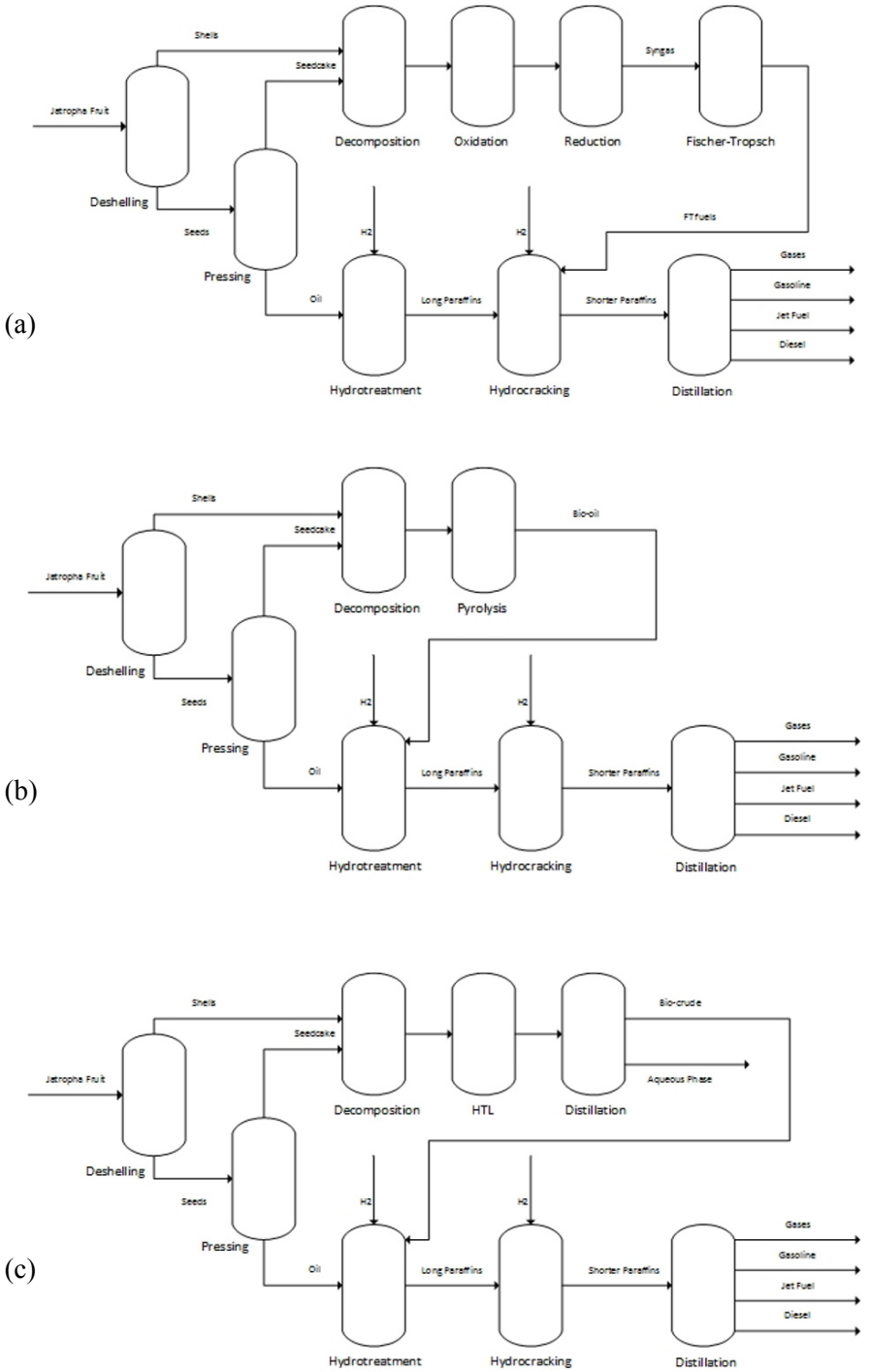

Figure 1: Process flow diagrams of integrated systems of (a) Gasification and hydroprocess, (b) Pyrolysis and hydroprocess and (c) HTL and hydroprocess.

2.1. Hydroprocess

In the hydroprocess model, the triglycerides of *Jatropha* oil are broken down into saturated fatty acids and propane in a hydrogenation reactor. The oxygen content of fatty acids is then removed in a deoxygenation reactor, yielding long-chain paraffins (C15-C18) along with H_2O, CO and CO_2. The former two steps are conducted in an "RGibbs" block at 300 °C and 45 bars. The long paraffins are transferred into a hydrocracking and isomerizing reactor to obtain paraffins with carbon chain lengths that correspond to kerosene (C8-C16). The cracking step is performed in an "RYield" block at 350 °C and 80 bars, whereby, all paraffins of chain lengths (C1-C20) are defined. The flow is then directed to a distillation column.

2.2. Gasification and Fischer-Tropsch

The *Jatropha* shells and seedcake are initially dried in "RYield" block at 120°C, in which the proximate analysis is modified by setting the moisture content to zero. A calculator block is used to convert the non-conventional components of *Jatropha* residues into their corresponding conventional compounds (Alnouss et al., 2018). Consecutively, the flow is introduced into oxidation and reduction reactors, while all related chemical equations are defined. Produced syngas is introduced into a Fischer-Tropsch (FT) reactor, where potential products are predicted based on the Anderson-Schulz-Flory (ASF) distribution (Al-Yaeeshi et al., 2019). The FT process is conducted at 250 °C and 25 bars. The produced FT fuels are finally introduced into the hydrocracking and isomerising reactor.

2.3. Pyrolysis

Similar to gasification model, the *Jatropha* residues are initially dried and decomposed into conventional compounds before being introduced into the pyrolysis reactor at 400 °C. The possible products are defined according to the study reported by Murata et al. (2012). Solids and gases are separated before introducing the bio-oil into the hydrotreatment reactor.

2.4. Hydrothermal Liquefaction

The *Jatropha* residues are initially converted into conventional compounds using a calculator block. The HTL process does not require a drying step, but rather pumping a hot and pressurized water to decompose the *Jatropha* residues with the presence of alkaline catalyst. The main reaction is conducted using an "RGibbs" reactor at 300 °C and 150 bars. Predicted products are adapted from earlier studies (Pedersen et al., 2017). Ash is removed using a solid separator, while the aqueous phase is separated from the bio-crude in a distillation column. The biocrude is then introduced into the hydrotreatment reactor.

3. Results and Discussions

The simulation results indicated a significant increment in liquid fuel yields for all the proposed integrated systems. The gasification-hydroprocess pathway has shown the best overall yield. Whereby, nearly 65 wt.% of the *Jatropha* whole-fruit is converted into liquid fuels, which represents double the initial oil content of the fruit. Nevertheless, 12 wt.% of the fruit is converted into useful gaseous fuel that can be directly used for power generation. The yields of the integrated systems as compared to the hydroprocess alone are illustrated in Figure 2. The increment in the fuel yield may contribute to enhancing the sustainability of *Jatropha* fruit and saving land, water and energy.

Besides, the selectivity of different liquid fuels is illustrated in Figure 3. A jet fuel selectivity of around 60% has been achieved for all processes. Whereas, the best JBF yield has also been achieved via the gasification-hydroprocess integrated system, where nearly 37 wt.% of the fruit has been converted into JBF, which represents over a 90% increment in JBF yield as compared to processing the oil alone in the conventional hydroprocess.

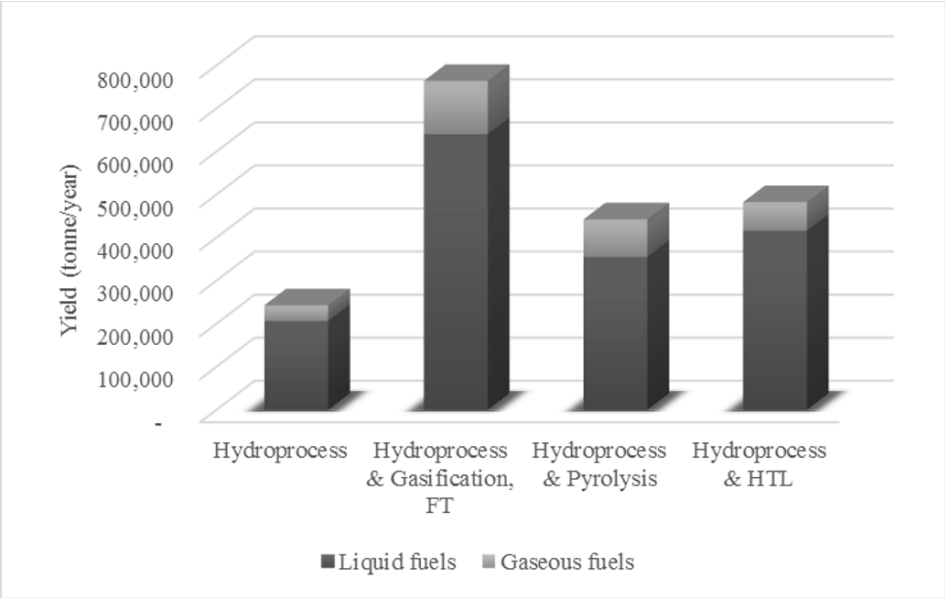

Figure 2: Yields of Integrated systems as compared to the hydroprocess alone.

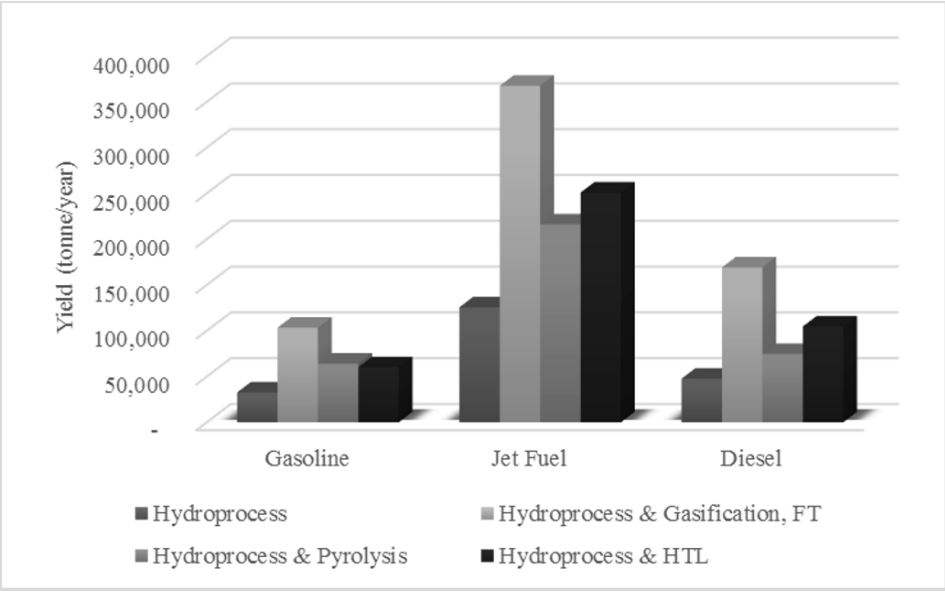

Figure 3: Liquid products 'distribution for the proposed integrated systems.

4. Conclusion

The optimum utilization of all parts of *Jatropha* fruit has been proved to be a key factor in enhancing the feedstock sustainability. In this study, three novel integrated systems have been investigated with the goal of boosting the JBF yield. The systems integrated the conventional hydroprocess with one of three thermochemical processes including gasification, pyrolysis

and hydrothermal liquefaction. 65 wt.% of *Jatropha* whole-fruit is converted into green liquid fuels with 57 % Jet Biofuel selectivity. The results indicated over a 90 % increment in JBF yield as compared to the utilization of *Jatropha* oil alone.

References

A. Alnouss, G. Mckay & T. Al-ansari, 2018, Optimum Utilization of Biomass for the Production of Power and Fuels using Gasification. In *28th European Symposium on Computer Aided Process Engineering* (Vol. 43, pp. 1481–1486). Elsevier Masson SAS.

A. Al-Yaeeshi, A. AlNouss, G. McKay & T. Al-Ansari, 2019, A Model based analysis in applying Anderson–Schulz–Flory (ASF) equation with CO2 Utilisation on the Fischer Tropsch Gas-to-liquid Process. In A. A. Kiss, E. Zondervan, R. Lakerveld, & L. B. T.-C. A. C. E. Özkan (Eds.), *29 European Symposium on Computer Aided Process Engineering* (Vol. 46, pp. 397–402). Elsevier.

C. Gutiérrez-Antonio, F. I. Gómez-Castro, A. G. Romero-Izquierdo & S. Hernández, 2016, Energy integration of a hydrotreating process for the production of biojet fuel. In Z. Kravanja & M. B. T.-C. A. C. E. Bogataj (Eds.), *26 European Symposium on Computer Aided Process Engineering* (Vol. 38, pp. 127–132). Elsevier.

C. Gutiérrez-Antonio, F. I. Gómez-Castro, J. A. de Lira-Flores & S. Hernández, 2017, A review on the production processes of renewable jet fuel. *Renewable and Sustainable Energy Reviews*, *79*, 709–729.

H. Chen, Q. Wang, X. Zhang & L. Wang, 2014, Hydroconversion of Jatropha oil to alternative fuel over hierarchical ZSM-5. *Industrial & Engineering Chemistry Research*, *53*(51), 19916–19924.

H. YaJie, C. YuBao, L. Qiang, Z. ShaoPeng, H. BenYong & D. JunChen, 2017, Preparation of biological aviation kerosene from Jatropha curcas oil by one-step hydrogenation with Pt/SAPO-11 as catalyst. *China Oils and Fats*, *42*(6), 110–114.

ICAO, 2016, *On Board a Sustainable Future: 2016 Environmental Report*.

K. Murata, Y. Liu, M. Inaba & I. Takahara, 2012, Catalytic fast pyrolysis of jatropha wastes. *Journal of Analytical and Applied Pyrolysis*, *94*, 75–82.

K. M. Zech, S. Dietrich, M. Reichmuth, W. Weindorf & F. Müller-Langer, 2018, Techno-economic assessment of a renewable bio-jet-fuel production using power-to-gas. *Applied Energy*, *231*, 997–1006.

M. Anand, S. A. Farooqui, R. Kumar, R. Joshi, R. Kumar, M.G. Sibi & A. K. Sinha, 2016, Optimizing renewable oil hydrocracking conditions for aviation bio-kerosene production. *Fuel Processing Technology*, *151*, 50–58.

R. N. Singh, D. K. Vyas, N. S. L. Srivastava & M. Narra, 2008, SPRERI experience on holistic approach to utilize all parts of Jatropha curcas fruit for energy. *Renewable Energy*, *33*(8), 1868–1873.

S. de Jong, R. Hoefnagels, A. Faaij, R. Slade, R. Mawhood & M. Junginger, 2015, The feasibility of short-term production strategies for renewable jet fuels - a comprehensive techno-economic comparison. *Biofuels, Bioproducts and Biorefining*, *9*(6), 778–800.

T. H. Pedersen, C. U. Jensen, L. Sandström & L. A. Rosendahl, 2017, Full characterization of compounds obtained from fractional distillation and upgrading of a HTL biocrude. *Applied Energy*, *202*, 408–419.

V. Ramírez, J. Martí-Herrero, M. Romero & D. Rivadeneira, 2019, Energy use of Jatropha oil extraction wastes: Pellets from biochar and Jatropha shell blends. *Journal of Cleaner Production*, *215*, 1095–1102.

W. C. Wang, 2016, Techno-economic analysis of a bio-refinery process for producing Hydro-processed Renewable Jet fuel from Jatropha. *Renewable Energy*, *95*, 63–73.

W. C. Wang & L. Tao, 2016, Bio-jet fuel conversion technologies. *Renewable and Sustainable Energy Reviews*, *53*, 801–822.

Sauro Pierucci, Flavio Manenti, Giulia Bozzano, Davide Manca (Eds.)
Proceedings of the 30th European Symposium on Computer Aided Process Engineering (ESCAPE30), May 24-27, 2020, Milano, Italy.
http://dx.doi.org/10.1016/B978-0-12-823377-1.50041-0

Environmental Impacts of the Future German Energy System from Integrated Energy Systems Optimization and Life Cycle Assessment

C. Reinert[a], S. Deutz[a], H. Minten[a], L. Dörpinghaus[a], S. von Pfingsten[a], N. Baumgärtner[a], and A. Bardow[a,b,*]

[a] *Institute of Technical Thermodynamics, RWTH Aachen University, Aachen, Germany*
[b] *Institute of Energy and Climate Research IEK-10, Jülich Research Center, Jülich, Germany*
andre.bardow@ltt.rwth-aachen.de

Abstract

Climate change mitigation requires a fundamental transition of our energy systems to reduce greenhouse gas (GHG) emissions. At the same time, ambitions to reduce GHG emissions should not shift burdens to other environmental impacts. Environmental impacts of technologies can be evaluated holistically using Life Cycle Assessment (LCA). Classical LCA is static and relies on historic process data. In contrast, dynamic LCA incorporates future changes in production processes and therefore allows for a consistent assessment of future environmental impacts. In this work, we develop a dynamic LCA model for the German energy transition. For this purpose, we combine LCA with energy systems optimization. We model the German electricity, heat, and transport sectors. For a given GHG target, the model designs the cost-optimal transition of the energy system. Environmental impacts are evaluated using dynamic LCA based on global energy scenarios. Compared to static LCA, dynamic LCA shows a 75 % higher impact in agricultural land occupation and smaller impacts in 15 out of 18 impact categories, demonstrating the need for the consistent assessment by dynamic LCA.

Keywords: Dynamic LCA, Supply chain analysis, Synthesis optimization, Energy transition, Background changes

1. Introduction

The significant reductions in greenhouse gas (GHG) emissions needed to mitigate climate change require a fundamental transition of our energy systems. This energy transition is expected to increase sector coupling and fluctuating renewable electricity supply. We therefore need sector-coupled optimization models of energy systems that account for renewable electricity supply while achieving the GHG emission targets.
However, the ambition to reduce GHG emissions should not shift burdens to other environmental impacts. To achieve an environmentally sustainable design, the planning of energy systems should therefore consider environmental impacts beyond GHG emissions. Such a holistic assessment of environmental impacts is enabled by Life Cycle Assessment (LCA). LCA has therefore been combined with energy systems optimization for the electricity sector in Germany (Rauner and Budzinski 2017), the energy system in Switzerland (Volkart et al. 2017), and the US electricity sector (Algunaibet and Guillén-Gosálbez 2019).

The available methods for the design and environmental assessment of national energy systems currently face one major issue: the studies use static Life Cycle Inventories (LCI's) for the environmental assessment. As a result, improvements in energy systems are not reflected for newly installed infrastructure produced in other countries. Because such changes in the background affect environmental impacts of the energy transition (Mendoza Beltran et al. 2018), it is necessary to include global developments in national long-term assessments, leading to a dynamic LCA approach (García-Gusano et al. 2016). Global energy models already integrate dynamic LCA: future impacts of global, low-carbon electricity system scenarios are examined by Pehl et al. (2017) and Luderer et al. (2019). The global, multi-sectoral energy transition is optimized by updating LCI's model endogenously by Volkart et al. (2018); however, endogenous LCI updating is not applicable for national studies.

In this work, we present a national energy model that uses dynamic LCA to integrate global developments for the electricity sector. Using Germany as an example, we present a fully sector-coupled energy systems optimization for the years 2016-2050 based on dynamic LCA and global electricity transition scenarios. In section 2.1, we briefly describe the optimization model SecMOD. In section 2.2, we dynamize electricity processes in Life Cycle Inventories using a regionalized energy transition scenario. In section 3, the resulting dynamic LCA database is integrated in SecMOD. We then compare the economic and environmental results of the energy optimization to using the static database.

2. Dynamization of the optimization model SecMOD

First, we present our optimization model SecMOD, a national energy model combining optimization and LCA. In section 2.2, SecMOD is expanded by dynamic LCA (Figure 1).

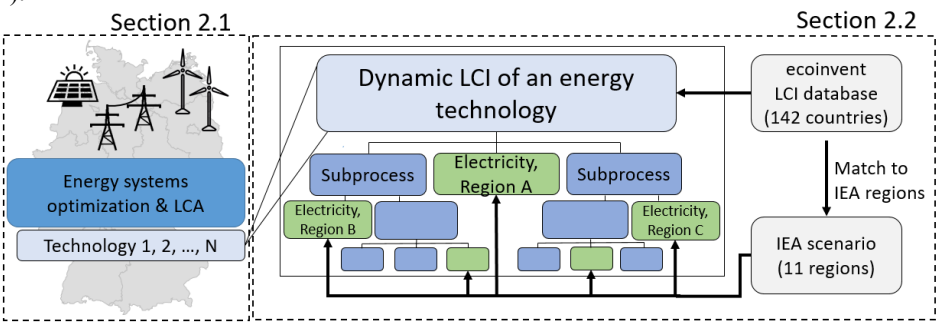

Figure 1: Optimization of an energy system using dynamic LCA using the SecMOD model (section 2.1). The electricity-related background processes of the Life Cycle Inventories (LCI's) are modified using a multiregional scenario (section 2.2).

2.1. SecMOD: Combined energy systems optimization and Life Cycle Assessment

SecMOD (Baumgärtner et al. 2020) is an optimization model of the sectors electricity, heat (household and industrial), and private transport in Germany. The linear model optimizes a least-cost transition pathway to a low-carbon economy for the years 2016 – 2050. The existing capacity of the starting year 2016 is modeled to represent the actual technology mix in Germany. The model consists of 18 geographic zones (as defined by the German Energy Agency) which are interconnected by a grid following the DC load-

flow approach (Egerer 2016). For each zone, the mass and energy balances are solved for each time step.

We simultaneously optimize the design and the operation of the energy system, using an aggregated time series (Bahl et al. 2018) of 60 time steps. The GHG emissions resulting from the operation of the energy system are constrained to achieve a GHG emission reduction of 85% in year 2050. Existing infrastructure is extended by infrastructure investments to meet the electricity, heat and transport demands at each time step (Baumgärtner et al. 2020). Subsequent to the optimization, we perform a complete LCA study to evaluate the energy system in 18 environmental categories, as proposed in the ReCiPe 2008 method (Goedkoop et al. 2009). Environmental impacts for the energy system are based on the LCI database ecoinvent 3.5 APOS (Wernet et al. 2016).

2.2. Dynamization of LCA database

The ecoinvent database relies on static data and thus does not consider improvements in the background systems of the newly installed infrastructure. To improve the assessment of energy technologies in future energy systems, we present a method to incorporate long-term energy scenarios in national energy systems optimization. Since electricity processes contribute by up to 70 % to the global warming impact (GWI) of the considered technologies, we focus on the electricity sector. Based on a multiregional energy scenario, we modify the ecoinvent 3.5 database by updating the electricity processes in the background to generate dynamic Life Cycle Inventories for all investment periods. The dynamic LCI's are then included in the SecMOD optimization for transition pathways of the electricity, heat, and transportation sectors in Germany.

As scenario for regionalized technology mixes from year 2014 to 2050, we select the "2 °C sustainable development scenario" (IEA scenario) (International Energy Agency 2017). The scenario provides the annual electricity generation by technology for 11 world regions and is used here to modify the Life Cycle Inventories of all technologies in SecMOD.

Similarly to Mendoza Beltran et al. (2018), we use Brightway 2 (Mutel 2017) to identify the background processes of the LCI's and modify the electricity processes according to the IEA scenario. First, electricity processes are identified in all LCI's used in SecMOD and classified by region. Second, all ecoinvent regions (comprising 142 countries) are matched to the 11 regions of the IEA scenario. The region matching is a necessary step for dynamization; however, the matching also causes some loss of spatial detail. For each region, a new electricity market mix is defined for every considered future year, corresponding to the electricity mix of the IEA. The new regional market mixes generate electricity by various technologies. The Life Cycle Inventories of the electricity generation technologies depend on the region of electricity generation – if no matching region is found, we use a dataset from the nearest geographic region. Some LCI's do not exist in ecoinvent and were added based on literature data: carbon capture and storage (Volkart, 2013), wave power plants (Thomson et al. 2011), hydroelectric power stations (Douglas et al. 2008), and concentrated solar power plants (Mendoza Beltran et al. 2018). For each investment period, we generate a dynamic LCI, updating the electricity processes in the LCI with the regional market mix from the IEA scenario.

In summary, we modify the ecoinvent 3.5 database based on the IEA scenario, updating the electricity mix for all investment periods to generate dynamic LCI's. In section 3, the LCI's are employed in the SecMOD optimization.

3. Results: Optimal energy transition from SecMOD using static and dynamic LCA

In the following, we compare the SecMOD optimization using static and dynamic LCI's. The functional unit of our assessment is the total energy supply for Germany, comprising all technologies and their operation to satisfy the electricity, heat, and private transport demands in one year. We compare the total annualized costs and the environmental impact during the transition to a low-carbon economy.
Figure 2 shows the total annualized costs for the design and operation of the energy system during the transition pathway (left: static, right: dynamic). The cost difference between both transitions pathways does not exceed 1.2 % of the total annualized costs.

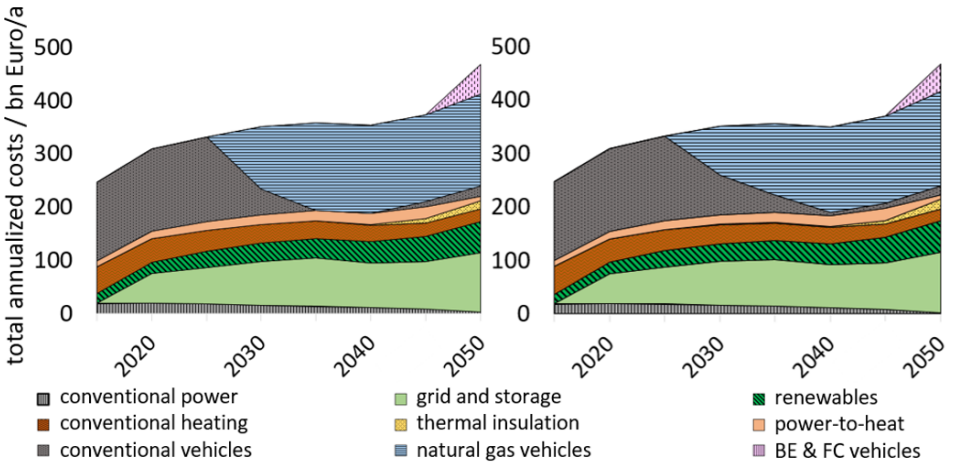

Figure 2: Comparison of total annualized costs: optimization using static LCA (left) and dynamic LCA (right). BE & FC vehicles: battery electric and fuel cell vehicles.

However, the choice of technology is affected by the dynamic LCA database most strongly for transportation: in year 2050 the optimization using dynamic LCA leads to higher shares of natural gas vehicles and lower shares of conventional and battery electric vehicles (Figure 3, left). The share of power-to-heat and thermal insulation is higher in the static case. These changes can be attributed to electricity background processes, which vary and thus change per technology; the change in GHG emission intensity leads to a shift in technology preference. As a result, the total annualized costs in year 2050 vary by up to 15 % for the different technologies.

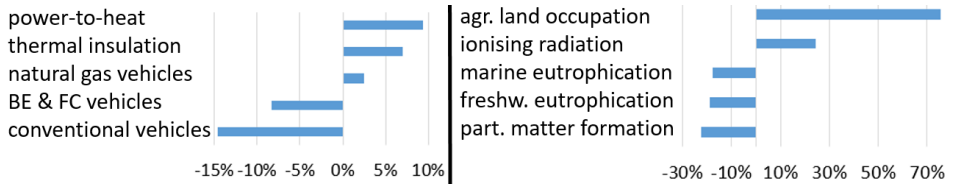

Figure 3: Largest changes in technology-specific cost (left) and environmental impacts (right) in the dynamic assessment of year 2050 compared to the static case. BE & FC vehicles: battery electric and fuel cell vehicles.

Additionally, dynamic LCA changes the results of the environmental evaluation of the energy system: in the dynamic case, we find higher impacts for ionizing radiation (24 %) and agricultural land occupation (75 %) compared to the static case in year 2050 (Figure 3, right). The higher impact in agricultural land occupation compared to the static assessment is caused by the globally increasing use of biomass. All other impacts (15 out of 18) are smaller in the dynamic assessment of year 2050.

4. Conclusions

In this work, we present a long-term energy systems optimization model. We assess the resulting energy system using dynamic LCA instead of the typically used static LCA. A comparison between integrating static and dynamic LCI data shows differences both in the optimal transition pathway and in the environmental assessment. The total cost of the static and the dynamic pathway are almost the same, however, the total annualized costs for specific technologies differ by up to 15 %. In the dynamic LCA for year 2050, 15 out of 18 impact categories are smaller compared to the static case. However, the impact of agricultural land occupation is higher in dynamic LCA, due to the globally increasing share of biomass in the electricity mix.
In conclusion, we show that fundamental trends and costs of the German energy system are predicted with sufficient accuracy even with static LCA. However, dynamic LCA is necessary to consider individual technology developments. Further, the dynamic assessment leads to fundamentally different results for some environmental impacts.

Acknowledgements

This study was funded by the Ministry of Economics, Innovation, Digitalization and Energy of North-Rhine Westphalia (Grant number: EFO 0001G). The support is gratefully acknowledged.

References

Algunaibet, I. M.; Guillén-Gosálbez, G. (2019): Life cycle burden-shifting in energy systems designed to minimize greenhouse gas emissions: novel analytical method and application to the United States. *Journal of Cleaner Production* (229), pp. 886–901.

Bahl, B.; Söhler, T.; Hennen, M.; Bardow, A. (2018): Typical periods for two-stage synthesis by time-series aggregation with bounded error in objective function. *Front. Energy Res.* (5), 35.

Baumgärtner, N.; Deutz, S.; Reinert, C.; Nolzen, N.; Küpper, E.; Hennen, M. et al. (2020): Life-cycle assessment of sector-coupled national energy systems: environmental impacts of future electricity, heat & transportation in Germany. In preparation.

Douglas, C. A.; Harrison, G. P.; Chick, J. P. (2008): Life cycle assessment of the seagen marine current turbine. *Proceedings of the IMechE* 222 (1), pp. 1–12.

Egerer, J. (2016): Open source electricity model for Germany (ELMOD-DE). Data Documentation. DIW Berlin, German Institute for Economic Research (83). Available online at https://www.diw.de, checked on 11/27/2019.

García-Gusano, D.; Martín-Gamboa, M.; Iribarren, D.; Dufour, J. (2016): Prospective Analysis of Life-Cycle Indicators through Endogenous Integration into a National Power Generation Model. *Resources* 5 (4), 39.

Goedkoop, M.; Heijungs, R.; Huijbregts, M.; Schryver, A.; Struijs, J.; Zelm, R. (2009): ReCiPE 2008. A life cycle impact assessment method which comprises harmonised category indicators at the midpoint and the endpoint level. Available online at http://www.lcia-recipe.net, checked on 11/27/2019.

International Energy Agency (2017): Energy technology perspectives 2017. Catalysing energy technology transformations. Edited by OECD/IEA.

Luderer, G.; Pehl, M.; Arvesen, A.; Gibon, T.; Bodirsky, B. L.; Boer, H. Sytze de et al. (2019): Environmental co-benefits and adverse side-effects of alternative power sector decarbonization strategies. *Nature communications* 10 (1), 5229.

Mendoza Beltran, A.; Cox, B.; Mutel, C.; Vuuren, D. P.; Font Vivanco, D.; Deetman, S. et al. (2018): When the background matters. Using scenarios from integrated assessment models in prospective life cycle assessment. *Journal of Industrial Ecology* 7 (6), pp. 1-16.

Mutel, C. (2017): Brightway: An open source framework for life cycle assessment. *The Journal of Open Source Software* 2 (12), 236.

Pehl, M.; Arvesen, A.; Humpenöder, F.; Popp, A.; Hertwich, E. G.; Luderer, G. (2017): Understanding future emissions from low-carbon power systems by integration of life-cycle assessment and integrated energy modelling. *Nat Energy* 2 (12), pp. 939–945.

Rauner, S.; Budzinski, M. (2017): Holistic energy system modeling combining multi-objective optimization and life cycle assessment. *Environ. Res. Lett.* 12 (12), 124005.

Thomson, R. C.; Harrison, G. P.; Chick, J. P. (2011): Full life cycle assessment of a wave energy converter. In : IET Conference on Renewable Power Generation. IET, pp. 63–68.

Volkart, K.; Mutel, C. L.; Panos, E. (2018): Integrating life cycle assessment and energy system modelling. Methodology and application to the world energy scenarios. *Sustainable Production and Consumption* 16, pp. 121–133.

Volkart, K.; Weidmann, N.; Bauer, C.; Hirschberg, S. (2017): Multi-criteria decision analysis of energy system transformation pathways. A case study for Switzerland. *Energy Policy* 106, pp. 155–168.

Wernet, G.; Bauer, C.; Steubing, B.; Reinhard, J.; Moreno-Ruiz, E.; and Weidema, B. (2016): The ecoinvent database version 3 (part I): overview and methodology. *The International Journal of Life Cycle Assessment* (21 (9)), pp. 1218-1230.

Sauro Pierucci, Flavio Manenti, Giulia Bozzano, Davide Manca (Eds.)
Proceedings of the 30th European Symposium on Computer Aided Process Engineering (ESCAPE30), May 24-27, 2020, Milano, Italy.
http://dx.doi.org/10.1016/B978-0-12-823377-1.50042-2

A General Dynamic Model of a Complete Milk Pasteuriser Unit Subject to Fouling

Mengjia Zhu, Federico Lozano Santamaria, Sandro Macchietto

Department of Chemical Engineering, Imperial College London South Kensington Campus, London SW7 2AZ, UK

Abstract

Heat treatment of milk for hygiene and preservation is carried out in energy integrated pasteurisers units which include several plate heat exchangers (PHEs), a holding tube and ancillary piping. Fouling reduces energy efficiency and cleanings generate downtime and wastes. No detailed dynamic models are currently available of full heating-cleaning cycles for an overall unit. Using a first principle modelling approach, a 2D dynamic thermal model, coupled with semi-mechanistic fouling and cleaning in place (CIP) models, is developed for the whole pasteurisation process, and used to test various heating-cleaning cycles. The model generality and flexibility are demonstrated for high temperature short time (HTST) and ultra-high temperature (UHT) treatments. The whole unit thermal model is validated against experimental data for a HTST process, with excellent agreement. Fouling evolution, distribution and impact are assessed for both processes. A UHT heating-cleaning cycle simulation enables quantifying the amounts of cleaning agent and waste water produced. The new model is suitable for control, optimisation of heating and cleaning strategies, and waste reduction studies.

Keywords: food processing, pasteurisation, plate heat exchanger, milk fouling, dynamic modelling.

1. Introduction and background

Heat treatments eliminate pathogenic microorganisms in raw milk for safety and extended shelf life. A typical pasteuriser unit (Figure 1) includes a preheater (regenerator), a main heater, a cooler, using plate heat exchangers (PHEs), as well as a holding tube, and ancillary pipework (Wang, et al., 2007). Fouling leads to economic (e.g. energy use, downtime for cleaning) and environmental problems (e.g. cleaning water and chemicals use, waste treatment). Fouling mitigation treatments (Müller-Steinhagen, et al., 2011), mostly focus on a qualitative analysis. Experimentation is time-consuming and costly, and results are often difficult to extrapolate to other conditions. In spite of much modelling research over many years (e.g. Georgiadis et al. 1998a, 1998b), no current model can comprehensively and accurately (1) capture the main thermal and hydraulic behaviours of fluids within the PHEs; (2) reflect the interactions among different sections of the pasteuriser; (3) predict deposit severity, location and composition during heating and cleaning; (4) optimize the overall operation of a full pasteuriser. Here we present a general model for the whole pasteuriser with all these features, and demonstrate it for high temperature short time (HTST) and ultra-high temperature (UHT) milk treatments. The thermal model of the whole unit is validated vs. experimental data for a HTST process. The evolution and impact of fouling are then assessed for both HTST & UHT.

Finally, a UHT full heating-cleaning cycle simulation calculates the amount of cleaning agent and rinsing water required, as well as the cleaning time needed and cycle time.

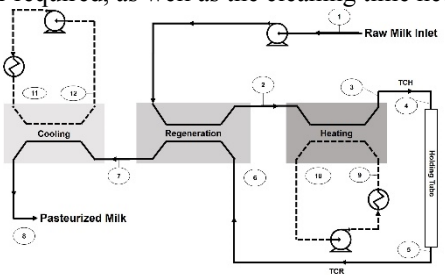

Figure 1. Schematic diagram of a pasteuriser unit (reproduced from Gutierrez et al *(2014)*).

2. Pasteurisation system modelling

The structure of the overall pasteuriser model and sub-models involved (Figure 2) includes heating, regeneration and cooling PHEs, a non-isothermal holding tube and two non-isothermal tubular connections (TCH & TCR). Initial conditions, equipment data and configurations are specified in the main unit model, and passed to the section models for PHEs and tubes, enabling continuity of fluid and temperature among sections. The thermal model in each section (PHE or tube) is coupled with fouling and CIP models.

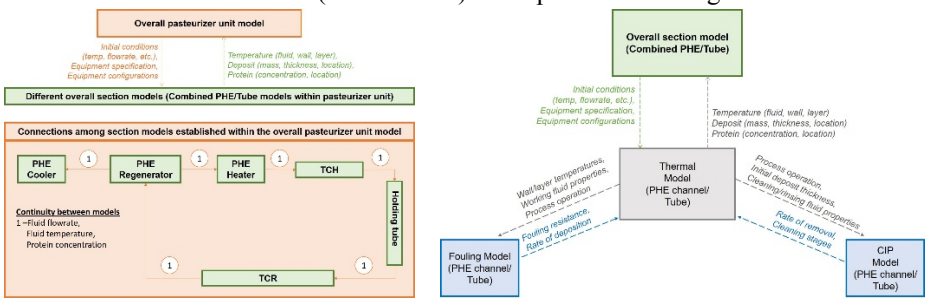

Figure 2. Overall model of the pasteuriser (left) and model components in each section (right).

The PHE dynamic model is modified from those proposed by (Guan & Macchietto, 2018) for single channel and (Sharma & Macchietto, 2019a). Here, each internal PHE channel is delimited by the two side half-plates, the end channels by a half (internal) plate and a full (end) plate. Any desired PHE arrangement is then assembled as a collection of individual channels (Figure 3), using a hierarchal model building design which sets the appropriate boundary conditions. For the two end plates, adiabatic condition is assumed. All models are implemented in gPROMS (PSE, 2018). The holding tube "holds" the heated milk at a desired temperature for a specified time. For skimmed milk, the requirement is to hold milk for at least 15 seconds at or above 72 ℃ in a HTST process, and for 2 to 5 seconds at 135-140℃ in a UHT process (FDA, 2018). The thermo-hydraulic tube model used, adapted from (Diaz-Bejarano, et al., 2016) consists of working fluid, deposit layer, and tube wall domains connected via suitable boundary conditions. Previous holding tube models in milk pasteurisation either assumed isothermal condition or a constant temperature drop based on experimental data (Grijspeerdt, et al., 2004) (Aguiar & Gut, 2014) (Gutierrez, et al., 2014). Here, non-isothermal condition was used, with an average external heat flux determined from experimental data, assuming convective heat transfer to air around uninsulated holding tube and tubular connections. Reaction mechanisms in milk fouling were discussed in Sharma and Macchietto (2019b).

For HTST processes, protein fouling (type A) is the dominant fouling type; while for UHT process, both protein and mineral fouling (type B) are known to occur in different temperature ranges (Khaldi et al., 2015). Only type A fouling was used, so the calculated

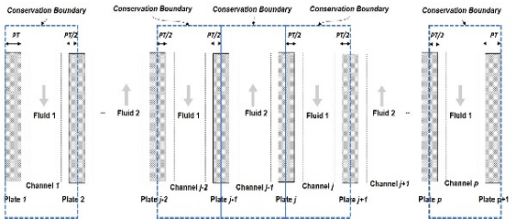

Figure 3. Schematic illustration for PHE channel modelling.

deposit mass is expected to be lower than the experimental one in UHT process. The fouling model of Georgiadis and Macchietto (2000), Sharma and Macchietto (2019a) was adopted with minor modifications. Two β-lg reaction schemes are considered: fouling due to (1) aggregated protein (Dep_A) and (2) unfolded protein (Dep_U) deposition (Figure 4). Here, N, U and A represent the native, unfolded and aggregated β-lg protein, respectively. Reactions of $N \rightarrow U$ and $U \rightarrow A$ occur in both bulk fluid as well as the thermal boundary layer. Fouling can occur anywhere in the pasteuriser unit and its severity is temperature dependent. The fouling model is coupled with the thermal model of both PHE channel and tube (Figure 2). In the combined models, all equations in the thermal and fouling models are solved simultaneously, using a standard DAE solver in gPROMS (PSE, 2018).

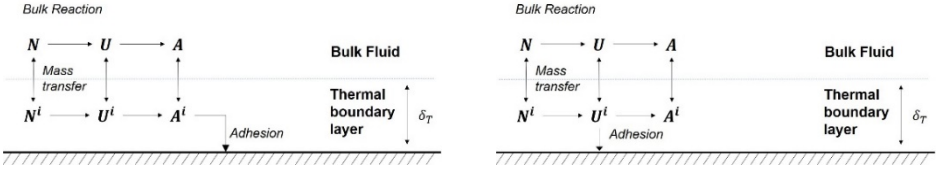

Figure 4. β-lg reaction schemes with fouling due to aggregated protein (Dep_A) and unfolded protein (Dep_u) (adapted from Georgiadis and Macchietto (2000)).

3. Validation of full pasteurisation unit model

A well-documented steady state experimental case for a HTST process was simulated (Gut and Pinto, 2004; Gutierrez, Diniz and Gut, 2014). The heating, regeneration and cooling PHEs consists of 12, 20 and 8 channels, respectively, each with a single-inlet-multiple-pass configuration. Details of experimental apparatus and experimental conditions, at steady-state, for a thermal test with water as both heating/cooling and process fluid are given in the references. The water physical properties, assumed constant within each section at average conditions, estimated from correlations based on the NIST database (Linstrom and Mallard, no date) are detailed in Zhu, 2019. The average external heat flux in the tubes was estimated to be 467 W/m^2 (Zhu, 2019). The key experimental and calculated temperatures in the entire pasteuriser (Figure 5 left.) show excellent agreement. The simulated temperature profiles of the working fluid in different PHE channels within the heating section (Figure 5 right) are very plausible, although no experimental data were available. This validation test confirms that the thermal model of the whole integrated pasteuriser unit matches well the experimental results.

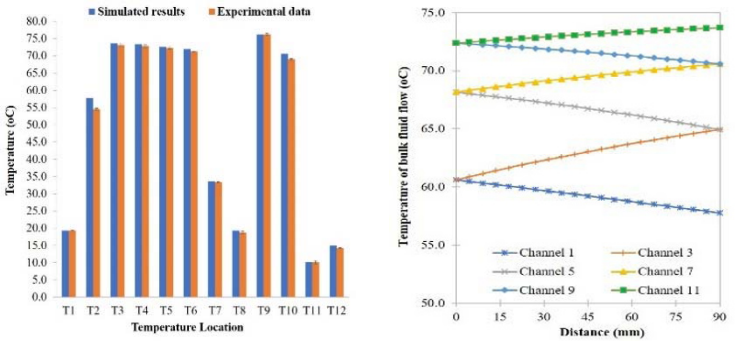

Figure 5. Thermal model validation: Key calculated and experimental temperatures - Exp. Data from Aguiar and Gut *(2014)* – left. Temperature profiles of the working fluid (water) within the heating section - right.

4. Operation and cleaning cycles - full pasteurisation unit

A fouling simulation for the HTST process, with the same experimental conditions used for thermal model validation, shows that fouling is not significant for the first 2.1 days. As a result, a heating-cleaning cycle of the complete pasteuriser unit was studied for the UHT process. As no experimental data on configuration or measured performance of a unit was available in literature, a realistic case was defined based on a typical UHT process (Tetra-Pak, 2015) (FDA, 2018). The PHE plate geometry is adopted from Georgiadis and Macchietto (2000). The heating, regeneration and cooling PHEs, all of single-inlet-multiple-pass configuration, have 12, 8 and 12 channels. The holding, TCH and TCR tubes have lengths of 1.0, 0.42, 1.06 m, internal diameter 40, 30, 30 mm and outer diameter 44, 33 and 33 mm, respectively. Milk, heating water and cooling water enter at 4, 140 and 4 ℃. The milk physical properties (Fernández-Martín, 1972; Kessler, 2002; Minim et al., 2002) are detailed in Zhu, 2019. The Dep_U fouling mechanism was used, with β = 15.1 , as estimated for the PHE heating section in previous studies (Zhu, 2019).

The two-stage CIP model of Bird and Fryer (1992), detailed in Sharma and Macchietto (2019b), is used for cleaning, however applied to the whole system, in a CIP procedure with Heating, cleaning and rinsing phases (Figure 6). Heating is terminated when the total deposit mass in any of the sections reaches a certain critical mass. A 3 minutes Rinsing phase follows, where it is assumed that no heat transfer and deposit removal occur. The Cleaning phase then starts, using the above cleaning model. Process-side fluid properties are switched from milk to cleaning solution in both the thermal and fouling models, the latter causing deposit removal. The Cleaning phase stops when the mass left on each plate in any PHE is less than 0.1 g., followed by a final Rinsing phase. Multiple fouling-cleaning cycles can be implemented back to back using this model.

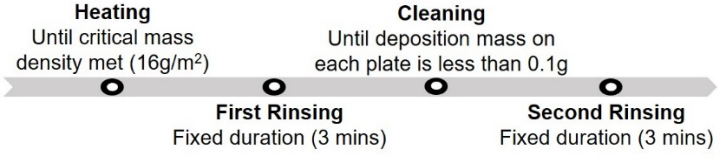

Figure 6. Heating-CIP operation cycle.

The predicted deposit mass over time in the heating PHE and the holding tube are shown in Figure 7. Relative to HTST, much more severe fouling is found in the main PHE heater

for the UHT process. The switch from heating to first Rising is triggered by the deposit mass in the main heating PHE. No significant deposit is observed in most of the regeneration PHE channels, although there is deposit in some of them, and the cooling PHE. For numerical reasons, a small initial deposit thickness (1.0E-7 m) was applied to all tubes, while zero initial deposit thickness was set for PHEs. This explains the rapid initial jump of the deposition mass in the holding tube. Cleaning starts before significant drop in the exit milk temperature of the main PHE heater occurs. Considering the overall interactions between the sections of the pasteuriser unit, fouling effects in one section have limited impact on the overall processing temperature. This suggests that a less stringent global stopping criteria could be used for heating phase termination. With the cleaning lasting about 30 minutes, the total cycle time is rather short. The CIP requires 404 Kg of Cleaning fluid (caustic solution) and 85.3kg of wastewater (both circulated at a rate of 0.237 Kg/s).

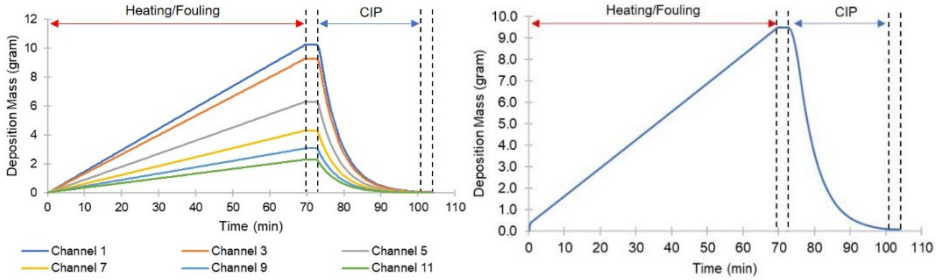

Figure 7. UHT Pasteuriser - Deposit mass during Heating-CIP cycle in the heating PHE (left) and holding tube (right).

5. Conclusions and perspectives

This work extended to a full pasteuriser the 2D distributed model developed by Guan & Macchietto (2018) and Sharma & Macchietto (2019) respectively for a single PHE channel and a PHE. This model is general, modular and versatile. Its predictions have been validated with good agreement against available experimental results. Fouling is considered in all the pasteurisers elements, reflecting configuration and operating conditions. Coupling fouling and cleaning models enables the simulation of heating-cleaning cycles for the whole unit, based on user-defined procedures and phase switching conditions. The model may be used to optimize of the overall operation, considering complex trade-offs between energy for heating, use of cleaning agents and rinsing water for CIP, downtime due to cleaning and cycle length (hence throughput and productivity). It could also be used to optimise continuous and sequential control strategies, and provide diagnostic information. There is scope for further validation of all models, in particular the prediction of local deposit growth/removal and its distribution over time. Only protein fouling was considered here. Further work and validation are also needed to improve the kinetic models, to better link process performance to the inlet milk properties.

References

Aguiar, H. F. & Gut, J. A. W., 2014. Continuous HTST pasteurization of liquid foods with plate heat exchangers: Mathematical modeling and experimental validation using a time-temperature integrator. *Journal of Food Engineering,* 123, 78-86.

Bird, M. R. & Fryer, P. J., 1992. An analytical model for cleaning of food process plant. *Food Engineering in a computer climate. ICHEME Symposium Series,* Issue 126, 325–330.

Diaz-Bejarano, E., Coletti, F. & Macchietto, S., 2016. A new dynamic model of crude oil fouling deposits and its application to the simulation of fouling-cleaning cycles. *AIChE Journal,* 62(1), 90-107.

FDA, 2018. *CFR - Code of Federal Regulations Title 21.* https://www.accessdata.fda.gov/scripts/cdrh/cfdocs/cfcfr/CFRSearch.cfm?fr=1240.61 [Accessed 9 9 2019].

Fernández-Martín, F., 1972. Influence of temperature and composition on some physical properties of milk and milk concentrates. II. Viscosity. *Journal of Dairy Research,* 39(1), 75–82.

Georgiadis, M. C. & Macchietto, S., 2000. Dynamic modelling and simulation of plate heat exchangers under milk fouling. *Chemical Engineering Science,* 55(9), 1605–1619.

Georgiadis, M.C. Rotstein, G.E. Macchietto, S., 1998a. Modelling and simulation of complex plate heat exchanger arrangements under milk fouling. *Computers and Chemical Engineering*, 22 (SUPPL.1), 331-338

Georgiadis, M.C. Rotstein, G.E. Macchietto, S., 1998b. Optimal design and operation of heat exchangers under milk fouling. *AIChE Journal*, 44(9), 2099-2111.

Grijspeerdt, K., Mortier, L., De Block, J. & Van Renterghem, R., 2004. Applications of modelling to optimise ultra high temperature milk heat exchangers with respect to fouling. *Food Control,* 15(2), 117–130.

Guan, S. & Macchietto, S., 2018. A novel dynamic model of Plate Heat Exchangers subject to fouling. Computer-Aided Chemical Engineering Vol. 43 Part B, 1679-1684, Elsevier, Amsterdam.

Gutierrez, C. G. C. C., Diniz, G. N. & Gut, J. A. W., 2014. Dynamic simulation of a plate pasteuriser unit: Mathematical modeling and experimental validation. *J. Food Eng.,* 131, 124-134.

Gut, J. A. W. & Pinto, J. M., 2004. Optimal configuration design for plate heat exchangers. *International Journal of Heat and Mass Transfer,* 47(22), 4833–4848.

Kessler, H. G., 2002. *Food and bio process engineering: dairy technology.* 5th ed. Munich, Germany: Verlag A. Kessler.

Khaldi, M., Blanpain-Avet, P., Guérin, R., Ronse, G., Bouvier, L., André, C., Bornaz, S., Croguennec, T., Jeantet, R., Delaplace, G., 2015. Effect of calcium content and flow regime on whey protein fouling and cleaning in a plate heat exchanger. *J. Food Eng.* 147, 68–78.

Linstrom, W. G. & Mallard, P. J. eds., (no date), *NIST Chemistry WebBook, NIST Standard Reference Database Number 69.* Gaithersburg MD, 20899: National Institute of Standards and Technology.

Minim, L. A., Coimbra, J. S. R., Minim, V. P. R. & Telis-Romero, J., 2002. Influence of Temperature and Water and Fat Contents on the Thermophysical Properties of Milk. *Journal of Chemical & Engineering Data,* 47(6), 1488–1491.

Müller-Steinhagen, H., Malayeri, M. R. & Watkinson, A. P., 2011. Heat exchanger fouling: Mitigation and cleaning strategies. *Heat Transfer Engineering,* 32(3-4), 189–196.

PSE, 2018. *gPROMS,* s.l.: Process System Enterprise Limited.

Sharma, A. & Macchietto, S., 2019a. Fouling and cleaning of Plate Heat Exchangers for Milk Pasteurisation: a moving boundary model. Computer Aided Chemical Engineering 46, Part B, 1483-1488, Elsevier, Amsterdam.

Sharma, A. & Macchietto, S., 2019b. Fouling and cleaning of Plate Heat Exchangers for Milk Pasteurisation: Dairy Application. Heat Exchangers Foulingand Cleaning – XIII, Warsaw, Poland, 2-7 June 2019.

Tetra-Pak, 2015. *Dairy Processing Handbook.* [Online].

Wang, L., Sundén, B. & Manglik, R., 2007. *Plate heat exchangers : design, applications and performance.* s.l.:WIT Press.

Zhu, M., 2019. *A general dynamic model of a complete milk pasteuriser unit subject to fouling,* Imperial College London.

Sauro Pierucci, Flavio Manenti, Giulia Bozzano, Davide Manca (Eds.)
Proceedings of the 30th European Symposium on Computer Aided Process Engineering (ESCAPE30), May 24-27, 2020, Milano, Italy.
http://dx.doi.org/10.1016/B978-0-12-823377-1.50043-4

A Nonsmooth Approach to Multicontaminant Mass and Water Integration

Caroline J. Nielsen[a,*], Paul I. Barton[a]

[a]*Massachusetts Institute of Technology, 77 Massachusetts Ave., Cambridge, MA, USA*
cjn1994@mit.edu

Abstract

This work presents a novel approach for process integration that accounts for the presence of multiple contaminants in fixed-load water integration problems and mass exchange networks with a single solvent source. Existing approaches to the multicontaminant problem are either unable to solve for contaminant concentrations or use superstructures that grow rapidly with problem size and require solving nonconvex mixed-integer programs. To address these limitations, we have extended previous work on solving single contaminant problems using the generalized nonsmooth integration operator. By assuming mass transfer relations and scaling the concentrations according to the limiting contaminant, we can directly apply a nonsmooth integration operator to solve the mass integration problem. The result is a simple nonsmooth system of two equations for each mass exchange system regardless of the system size that can be used to solve for any selection of unknowns including contaminant concentrations.

Keywords: Water Integration, Mass Integration, Multicontaminant, Nonsmooth

1. Introduction

There are significant incentives to reduce the use of water and other materials in chemical processes including resource scarcity and regulations on waste discharge. Process integration methods have been widely proposed and utilized to address this challenge by minimizing resource use through optimal reuse, beginning with heat recovery problems (Linnhoff and Flower, 1978) which were later extended to the recovery of materials in mass exchange networks (El-Halwagi and Manousiouthakis, 1989) and fixed-load water networks (Wang and Smith, 1994). However, the body of work on solving the heat integration problem cannot be directly generalized to mass and water integration in real systems where multiple components or contaminants are present. In these systems, contaminant transfer cannot occur independently, so considering each component independently will underestimate the required external utilities and provide infeasible results. Therefore, it is necessary to develop methods to consider multiple contaminants simultaneously to improve the usefulness and accuracy of process integration approaches.

As summarized in the review of Khor et al. (2014), the existing approaches to solving multicontaminant process integration problems primarily use complex heuristics or superstructures to solve the network design problem by including multicomponent mass transfer relations in each mass exchange unit. However, superstructure approaches typically scale exponentially with the number of mass or water streams in the problem and also require solving potentially nonconvex mixed-integer nonlinear programs. To reduce problem size and intractability, alternative approaches have been presented that use heuristics or solve the resource targeting problem, which determines the minimum external mass or water utilities without the network design step. These approaches scale

the contaminant concentrations for each operation to account for simultaneous mass transfer and then use the scaled concentrations with classical pinch analysis methods such as graphical pinch analysis or the transshipment formulation (Wang and Smith, 1994; Alva-Argáez et al., 1999). Although these methods can significantly reduce the size of the problem, they also require the construction of concentration intervals through nonsmooth mappings that prevents them from solving for unknown concentrations in the system or being embedded in process optimization problems.

In this work, we present an alternative approach to solving the resource targeting problem for multiple contaminants and a single fresh solvent source. We extend our previous work on the nonsmooth integration operator, which is able to solve the general targeting problem using a system of two nonsmooth equations per integrated resource regardless of system size (Nielsen and Barton, 2019). We adapt the concentration-scaling approach for the nonsmooth integration operator whose unique structure makes it ideal for incorporating the nonsmooth mappings. Our new approach retains the compact scaling of the integration operator and is also able to solve for any unknown process variable, including contaminant concentrations, making it a good candidate for solving large-scale integration and process optimization problems.

2. Problem Statement

This work considers a specific instance of the general integration problem. For each resource n in a set T with a set of resource sources, SR_n, and a set of sinks, SK_n, the general integration problem seeks to determine the system specifications, either resource targets or process variables, at which minimal feasible resource use and waste production occur. Mathematically, this problem can be represented by a system of equations describing a process model, $\mathbf{h}$, and a set of embedded optimization problems that minimize the fresh loads of each resource and are parametric in the process variables, $\boldsymbol{x}$, as outlined below:

$$\begin{aligned} \mathbf{0} &= \mathbf{h}(\boldsymbol{x}, \boldsymbol{y}_1, \ldots, \boldsymbol{y}_{|T|}) \\ \{\boldsymbol{y}_n\} &= \left.\begin{array}{l} \arg\min_{\boldsymbol{y}_n} R_{SR,n}(\boldsymbol{x}) \\ \text{s.t. Resource balance holds and transfer is feasible} \end{array}\right\} \forall n \in T, \end{aligned} \tag{1}$$

where, for each resource type, $\boldsymbol{y}_n = (R_{SR,n}\,;\, r_{SK,n})$, where $R_{SR,n}$ is the fresh resource supply and $r_{SK,n}$ is the waste resource flow. The feasibility of resource transfer between the sources and sinks for each resource is limited by their qualities $Q_i^{\text{in,out}}$ and $q_j^{\text{in,out}}$, respectively, which change with resource transfer at a rate determined by their constant states, $S_{i,n}$ or $s_{j,n}$. In the general integration problem, we assume that the qualities are linearly related to the resource transfer by the state and that the transfer of each resource is independently limited at a pinch point based on enforced or driving force limitations.

Here we consider an instance of the general integration problem in which we wish to determine the minimum solvent requirement to remove multiple contaminants from a set of rich streams. A commonly addressed problem of this type is the fixed-load water integration problem, which considers process units with constant water flow rates as rich streams for mass integration. The minimum feasible fresh water supply for removing the contaminant loads from the process units is then determined as a single lean stream in the

mass integration problem. In this problem type, the resource quantities are contaminant mass load flow rates, the states are the solvent mass flow rates, and the qualities are the concentrations of contaminants scaled to a chosen reference stream using equilibrium relations. For this analysis, we assume that the external mass loads for each contaminant are zero and a single solvent stream is available for contaminant removal.

In this problem type, the feasibility of the contaminant transfers to the solvent cannot be independently considered using pinch analysis because contaminant transfer between streams occurs simultaneously. Considering each component independently will underestimate the required external utilities and provide infeasible results. Therefore, traditional approaches to solving the embedded optimization problems in Eq. (1) must be adapted to account for the dependent mass transfer of the contaminants. In the following section, we present one such adaptation for the nonsmooth integration operator.

3. Nonsmooth Approach

The nonsmooth integration operator is a system of two equations per resource to express the solutions to the minimization problems in Eq. (1). The first equation is an overall resource balance, and the second is a pinch point balance which enforces the resource balance to be nonnegative at each quality value for feasibility and zero at one pinch quality for optimality. Neglecting the index n for clarity, the nonsmooth integration operator for a given resource is:

$$0 = \sum_{i \in SR} S_i (Q_i^{in} - Q_i^{out}) - \sum_{j \in SK} s_j (q_j^{out} - q_j^{in}) + R_{SR} - r_{SK} \tag{2}$$

$$0 = \min_{p \in P} \{RBP_{SK}^p - RBP_{SR}^p\} + r_{SK} \tag{3}$$

Where P is the finite index set of pinch point candidates and

$$RBP_{SR}^p := \sum_{i \in SR} S_i [\max\{0, Q^p - Q_i^{out}\} - \max\{0, Q^p - Q_i^{in}\} - \max\{0, Q^{\min} - Q^p\} + \max\{0, Q^p - Q^{\max}\}], \quad \forall p \in P,$$

$$RBP_{SK}^p := \sum_{j \in SK} s_j [\max\{0, (Q^p - \Delta Q_{\min}) - q_j^{in}\} - \max\{0, (Q^p - \Delta Q_{\min}) - q_j^{out}\} + \max\{0, (Q^p - \Delta Q_{\min}) - q^{\max}\} - \max\{0, q^{\min} - (Q^p - \Delta Q_{\min})\}], \quad \forall p \in P,$$

where $\Delta Q_{\min}$ is the minimum feasible quality difference at which resource transfer can occur and the source qualities at the potential pinch points are

$$Q^p = \begin{cases} Q_i^{in}, & \forall p = i \in SR, \\ q_j^{in} + \Delta Q_{min}, & \forall p = j \in SK,\ q_j^{in} \neq 0. \end{cases}$$

$Q^{min,max}$ and $q^{min,max}$ are the minimum and maximum qualities across the sources or sinks, respectively, and the max terms containing these variables create nonphysical extensions to the cumulative resource quantities, which ensure the difference between the source and sink resource balances is always defined.

To solve the general integration problem, one nonsmooth operator is constructed for each resource, and these are combined with a process model to form a system of nonsmooth equations. In addition to retaining the same size regardless of the number of sources and sinks in the system, one of the advantages of the generalized nonsmooth integration operator is that it can be directly applied to any pinch-constrained resource as long as the resource states and qualities are correctly defined, even if they are nonsmooth functions of other process variables. This property allows us to easily incorporate elements of previous scaling approaches to solve the multicontaminant problem presented above.

Wang and Smith (1994) first proposed the scaling approach for the fixed-load water integration problem which was later extended by Alva-Argáez et al. (1999). These approaches assume a mass transfer relation between contaminants in a given operation and use this relation to determine both the limiting contaminant for the operation and the transfer of the other contaminants in the limiting case. The adjusted concentrations for the limiting case describe a pinch-constrained integration problem that can be solved using pinch analysis methods. Note that for these scaled concentrations to fully describe the mass integration problem, the system must have a single, uncontaminated, lean solvent stream for mass removal. Otherwise, the lean stream concentrations must also be adjusted to the limiting case based on the rich streams present in the same concentration interval. While these scalings are a good candidate for nonsmooth approaches, they are beyond the scope of this paper and remain a subject of future work.

This paper considers the case of fixed mass load distribution in which the contaminant load transferred for any contaminant c in the set C in the rich stream i to the fresh solvent stream is proportional to its inlet concentration. However, in theory, this approach can be extended to any functional mass transfer relation and can even vary between operations. For the case of a fixed mass load distribution, Alva-Argáez et al. (1999) show that the concentration scaling in an outlet rich stream with relative use RU_i is

$$\overline{C}_{c,i}^{out} = RU_i C_{c,i}^{in}, \quad RU_i = \min_{c \in C} \left(\frac{C_{c,i}^{out}}{C_{c,i}^{in}} \right). \tag{4}$$

These equations assume that the unscaled concentrations $C_{c,i}$ have already been transformed to their equilibrium values in the lean solvent streams as required for the single contaminant problem. In this formulation, the inlet concentrations remain unscaled, so to maintain the overall contaminant mass load balances, the rich stream flow rates must also be scaled according to

$$\overline{G}_{c,i} = \frac{C_{c,i}^{in} - C_{c,i}^{out}}{C_{c,i}^{in} - \overline{C}_{c,i}^{out}} G_i. \tag{5}$$

To solve the multicontaminant integration problem, the scaled outlet concentrations and solvent flow rates are selected as the source outlet qualities and states, respectively, and the source inlet qualities and sink properties take their unscaled values. Using this scaling, any contaminant can be selected equivalently as the reference contaminant. Since the problem is now pinch constrained, the nonsmooth integration operator in Eqs. (2) and (3) can be applied directly to solve for a selection of unknowns. Because the equation system is already nonsmooth, the rich stream concentrations can be selected as unknowns even though they are the arguments of nonsmooth functions in Eqs. (4) and (5). To solve the nonsmooth system, we use a semismooth Newton method implemented in MATLAB. Generalized derivative elements are automatically calculated from LD-derivatives using a vector forward mode of automatic differentiation developed by Khan and Barton (2015).

4. Example

To demonstrate the ability of our method to solve for both water targets and concentration limits in multicontaminant systems, we consider a fixed-load water integration problem with three contaminants and three water-using operations. The data for this problem is adapted from Alva-Argáez et al. (1999). The concentration and flow rate values for the contaminant-rich operations are given in Table 1. We assume this data is already transformed to the equilibrium values in the water lean stream, that the single lean water stream is supplied free of any contaminants, and that there are no additional external mass sources or sinks. We also assume that contaminants are transferred to the water stream according to a fixed mass load distribution.

Table 1: Data for the example problem, adapted from Alva-Argáez et al. (1999).

Operation	Contaminant	$C_{c,i}^{in}$ (ppm)	$C_{c,i}^{out}$ (ppm)	$\overline{C}_{c,i}^{out}$ (ppm)	RU_i
Operation 1	HC	1	0	0	0
G_1 = 45 t/h	H_2S	400	0	0	0
	SALT	35	0	0	0
Operation 2	HC	90	30	30	0.33
G_2 = 34 t/h	H_2S	1200	600	400	0.5
	SALT	90	54	30	0.6
Operation 3	HC	220	120	4.6	0.55
G_3 = 56 t/h	H_2S	45	20	0.95	0.45
	SALT	9500	200	200	0.02

We applied the nonsmooth approach as described above for two selections of unknowns, using HC as the reference contaminant. For the first case, we solved the typical integration problem to find the water target for known rich stream data. Table 1 gives the reuse factors and scaled outlet concentrations for this case. Solving this problem gave a minimum fresh water flow rate of 47.8 t/h and an outlet HC concentration of 160.6 ppm. The outlet concentrations of the other contaminants can be determined from these results through mass balances. Figure 1 shows the resulting pinch plots for both the scaled and unscaled HC concentrations. These results demonstrate that in the multicontaminant case, limiting resource transfer may not result in a pinch point for any single contaminant. In the second case, we demonstrate the ability of our approach to solve for rich stream concentrations

by determining the limiting inlet HC concentration in Operation 2 required to reduce the fresh water consumption to 45 t/h. We calculated the new concentration limit to be 73 ppm which gives an outlet HC concentration in the water stream of 158.9 ppm.

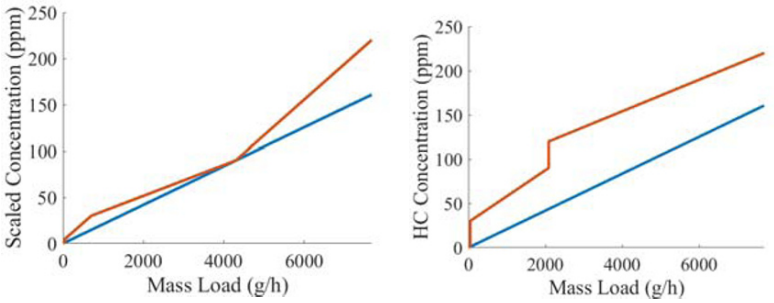

Figure 1: Pinch plots for the example problem with unknown water flow rate. The red curves shown the rich streams for each operation and the blue are the lean water streams. Left shows the scaled HC concentrations and right the unscaled.

5. Conclusions

This paper represents a new approach to solving the multicontaminant mass integration problem to determine the minimum feasible flow rate for a single pure solvent stream. This approach adapts known scaling methods based on the limiting contaminant to be used with the nonsmooth integration operator. The resulting formulation solves a system of two nonsmooth equations per independent set of contaminants regardless of system size. We present a fixed-load water-integration problem to demonstrate the success of this approach for solving for both unknown water flow rates and contaminant concentrations. In future work, we plan to extend our approach to include multiple lean streams with varying inlet contaminant concentrations and to adapt the results to the fixed-flow rate water integration problem. Compared to existing methods, our formulation both significantly reduces the problem complexity and retains the ability to solve for unknown concentrations in the system or be embedded in process optimization problems, making it an ideal candidate for solving large-scale multicontaminant problems.

Acknowledgements

We are grateful to the OCP Group financial support and to the Université Mohammed VI Polytechique - MIT Research Program for supporting and facilitating this collaboration.

References

A. Alva-Argáez, A. Vallaintos, A. Kokossis, 1999. A multi-contaminant transhipment model for mass exchange networks and wastewater minimisation problems. Computers and Chemical Engineering 23, 1439-1453.

M. M. El-Halwagi, V. Manousiouthakis, 1989. Synthesis of Mass Exchange Networks. AIChE Journal 35 (8), 1233–1244.

K. A. Khan, P. I. Barton, 2015. A vector forward mode of automatic differentiation for generalized derivative evaluation. Optimization Methods and Software 30 (6), 1185–1212.

C. S. Khor, B. Chachuat, N. Shah, 2014. Optimization of Water Network Synthesis for Single-Site and Continuous Processes: Milestones, Challenges, and Future Directions. Industrial & Engineering Chemistry Research 53. 10257-10275.

B. Linnhoff, J. R. Flower, 1978. Synthesis of heat exchanger networks: I. Systematic generation of energy optimal networks. AIChE Journal 24 (4), 633–642.

C. J. Nielsen, P. I. Barton, 2019. A Generalized, Nonsmooth Operator for Process Integration. Computer Aided Chemical Engineering 46, 385-390.

Y. P. Wang, R. Smith, 1994. Wastewater Minimisation. Chemical Engineering Science 49 (7), 981-1006.

Sauro Pierucci, Flavio Manenti, Giulia Bozzano, Davide Manca (Eds.)
Proceedings of the 30th European Symposium on Computer Aided Process Engineering (ESCAPE30), May 24-27, 2020, Milano, Italy.
http://dx.doi.org/10.1016/B978-0-12-823377-1.50044-6

Systematic Generation of a Robust Compartment Model for Counter-current Spray Dryers

Borja Hernández[ab], Mark A. Pinto[a], Mariano Martín[b].

[a]*Procter and Gamble R&D, Newcastle upon Tyne NE12 9TS, United Kingdom.*
[b]*Chemical Engineering Department, University of Salamanca,37008 Salamanca, Spain.*
hernandezblazquez.bh@pg.com

Abstract

This work presents a novel methodology using machine learning techniques to generate a robust compartment model for unit operations that process particulate materials. The methodology is based on generating a multi-level model from multiple CFD simulations. The reduced-order model comprises flexible phenomenological compartments that modify their size, fluxes and momentum properties according to the different operating conditions of the unit. Each compartment is represented by a set of equivalent CSTR reactors that are used to reproduce the residence time distribution (RTD) for the entire compartment. In each of the CSTR reactor, mass and population balances for continuous and discrete phases are performed along with calculations addressing physical properties and phase momentum. The methodology has been developed for the complete operating space of a counter-current spray dryer. It is able to reproduce the mean residence time and average volume fraction of each compartment with an average error of 21% in the contact region and 11% at the bottom of the counter-current dryer.
Keywords: CFD based compartment model, Population balances, model reduction, robust modelling, multiphase flows.

1. Introduction

Multiphase particulate processes have been traditionally modelled using detailed methods such as CFD-DPM (Computational Fluid Dynamics coupled with Discrete Particle Dynamics) or DEM (Discrete Element Method). Besides helping to understand the mass and energy fluxes in the unit, they provide details of (1) the dispersion of momentum and (2) the spatial variation of phase properties for the continuous and discrete phases (Bezzo et al. 2003). However, CFD-DPM and DEM methods involve a high computational cost; they are not recommended for process optimization and design, or when a complex process phenomenon is considered (Tajsoleiman et al. 2019). In this context, the use of tools that combine CFD and process system engineering (PSE) approaches have shown to provide a significant benefit, without missing the spatial distribution of the phases within a unit. One of the most relevant approaches in this area was introduced by Bezzo et al. (2003). A hybrid CFD-compartment framework was developed, with both models connected by a 2-way coupling approach. This hybrid method was able to reproduce the fluxes with accuracy, with the properties of this flow highly dependent on the procedure used to construct the compartment model. If turbulent dispersion is to be reproduced, zoning is controlled by Damköler and Peclet numbers (Le Moullec et al. 2010); if kinetics is governing, the number of compartments needs to be high enough to capture the speed of the kinetics (Yang et al. 2019). The use of this method has been applied beyond single-phase fluid CFD simulations to multiphase and particulate processes. For example, a DEM-compartment method was developed for modelling particle dispersion and RTD in

a particle mixer (Portillo et al. 2007). In this case the number of compartments was homogeneously distributed through the system. However, if more complex cases are to be studied, a phenomenological distribution of the compartments is critical in terms of computational cost and accuracy (Freireich et al. 2011). Freireich et al. (2011) presented a methodology based on (1) characterizing a region where there is a predominating phenomenon and (2) generating a compartment model within each region that is able to reproduce the RTD of the particles. The RTD of each bin of the population balance was introduced by generating two new variables for the 1st and 2nd moments of the RTD, with the 2nd moment of the RTD fitted to an exponential function. The method accurately reproduced the RTD for a mixer-coater under fixed operating conditions. Similarly, Tajsoleiman et al. (2019) recently proposed an automatic method for identifying such regions within CFD codes. However, in all the previous cases, the methods were always studied under a single fixed operating condition. Changes in the size and distributions of the zones, fluxes and momentum as a function of the operating conditions have not been considered. It is necessary to generate a new compartment model every time a change in the operation conditions modifies the distribution of the system's properties (Jourdan et al. 2019). Thus, the aim of this work is to propose a novel methodology for generating a robust compartment model that will be able to reproduce the change in the size of the zones, the particle fluxes and RTD under different operating conditions without the need of repeating CFD or DEM simulations every case. Furthermore, a physics-based approach based on the equivalent number of CSTRs is proposed for reproducing the 2nd moment of the RTD within each phenomenological region. For the demonstration of this methodology a counter-current spray dryer is used.

2. Methodology for robust compartment model generation based on CFD-DPM simulations.

Figure 1 shows the methodology for generating a robust compartment model based on CFD-DPM simulations. It consists of two parts. In the first part, mass balance models for continuous and discrete phases are generated based on monodisperse distributions. In the second part, the characteristic parameters of the discrete phase are determined. Some of the dimensionless groups used for computing the momentum balances and the fluxes are dependent on a single particle diameter, and it is necessary to identify the characteristic diameter (For example, Sauter or mean) of the PSD that is used in each group.

2.1. Description of the stages.

The generation of the models in the first stage is carried out following the procedure presented in Figure 1. In the following paragraphs, the systematic methodology is presented using the case of an industrial counter-current spray dryer:

- The first stage of the process is the generation of a design of experiments (DOX) for studying the mass fluxes with monodispersed particles. A fast-flexible filling method is selected since fouling in the walls is introduced as a discrete variable and the method ensures non duplicity for the remaining continuous variables studied. The DOX is built with a statistical software. In the current case, JMP ® was used to define 20 experiments.
- In the second stage, the experiments are run in a CFD software such as ANSYS® Fluent. The CFD-DPM model used for running the virtual experiments is based on the methodology previously presented by Hernández et al. (2018). This methodology has been extended by validating particle dispersion for different particle sizes, air fluxes and injection characteristics. For each experiment, the

spray dryer is divided into the following phenomenological zones based on differences in the momentum behavior of the particles: injection, elutriates, falling region with concentrated particles, center of the dryer and bottom cone, see left part of Figure 1. Since the RTD and fluxes of particles can also change within each of the zones, each phenomenological zone is also internally analyzed to obtain the fluxes and momentum of air and particles. After obtaining this information, the experiments are evaluated together against each zone. A minimum number is needed to generate the reduced order models. For example, only 2 of the initial experiments resulted in elutriated particles so more we needed to model the fluxes in this zone. It is assumed that the number of representative experiments must be at least one half of the original size.

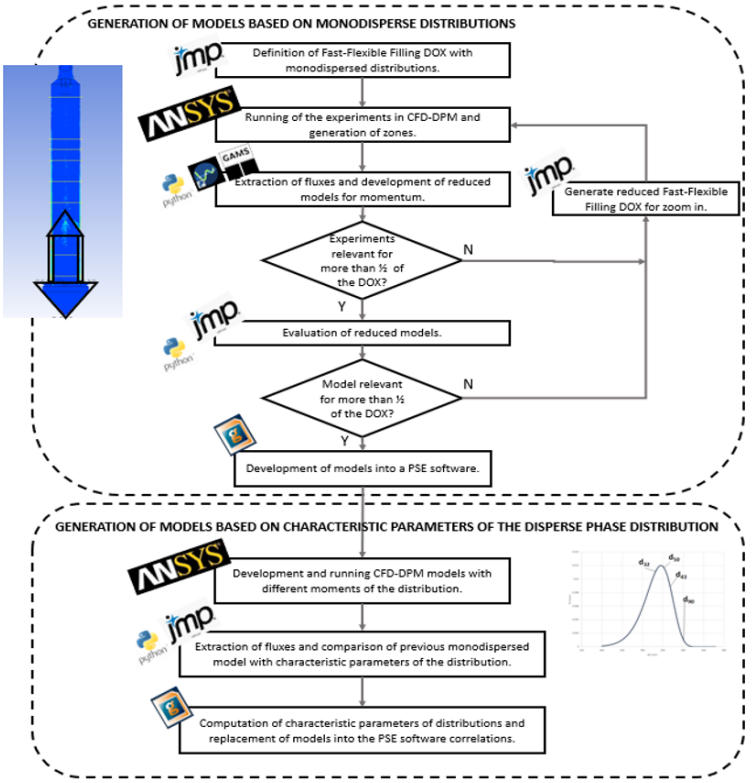

Figure 1. Methodology for the generation of a robust compartment model for multiphase flows based on CFD fluxes.

- In the third stage, reduced models are generated from the fluxes extracted from the CFD simulations. If the data needs post-processing, a data science software such as Python ®TM can be used. The models generated should preferably be based on dimensionless groups as this facilitates scale-up and application to units with similar geometry. For determining the dimensionless groups that are needed and the model to be applied for calculate the momentum in each compartment, machine learning techniques such as Bayesian Information Criteria (BIC) minimization are used. In simple cases BIC minimization can be performed with software such as Alamo (Cozad et al. 2014). In most complex cases where the correlation is included within other models, the terms and parameters are determined by developing the BIC minimization problem in an

optimization software as GAMS ® and optimizing with a suitable solver as BARON.

- Once the reduced models are developed for the size of the zones, fluxes of air and particles, momentum and number of equivalent CSTR in each of the zones, the results are validated with the CFD model. If there are enough valid experiments for obtaining the reduced order models and if the models are representative enough of the complete space of operating conditions, the model can be applied to the zone. Otherwise, a new DOX is generated and the new experiments are added to the previous ones. In the current case we assumed that the new DOX needs to have at least half of the experiments of the original DOX.
- The last stage using the monodisperse experiments is the implementation of the reduced order models into a process modeling software. In this work gProms ® is used. The compartment model is structured using a multi-level approach as presented in Figure 2. The first layer contains the phenomenological zones and the core model for computing the size of such zones and the number of equivalent reactors within each of them. In the second layer, the equivalent number of CSTR tanks are modelled. They are modeled with an internal by-pass in case the CSTR equivalent is less than one. The maximum number of tanks is also limited by the accuracy of the model of the momentum in each region. Each tank contains the general mass and energy balances for the air and the population balances for the particles. In order to address the individual phenomena such as drying, lower levels are defined within each CSTR. In this study, the models in the third level are the continuous and discrete phase property models and the momentum model.

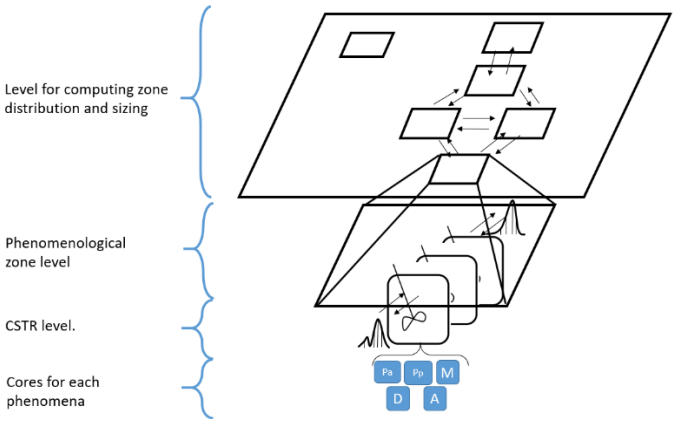

Figure 2. Structure of the compartment model.

Since different PSDs are processed within the unit, the second part of the work focuses on identifying the characteristic diameter of the PSD for properties that depend on particle size. For example, the airflow dynamics are affected by the Stokes number of the particle since it produces a drag on it. This Stokes number can be computed with a characteristic Sauter mean or mass mean diameter.

- The first stage of this part focuses on performing a comparative analysis where four PSDs with (1) different Sauter and similar mass mean and (2) with different mass mean a similar Sauter mean are run in Ansys ® Fluent.
- The second stage involves the extraction of the zone characteristics, fluxes, and momentum properties and performing a comparative analysis for each of them in order to identify the one that governs each property.

- The final stage is the modification of the models in the process modeling tool to make use of the characteristic numbers based on the simulated PSD. For example, to make the Stokes number as function of the characteristic diameter that govern the property for the one that this number is used.

3. Results

In this section the results obtained from the compartment model are presented. To validate the results, the mean residence times predicted, the volume fraction in the most relevant region (the region with falling particles near the wall), and the RTD curves are used. For computing the cumulative error in the RTD of the particles, the differences between the mass fraction predicted by the compartment model, w_{comp}, and the mass fraction predicted by the CFD-DPM model, $w_{CFD-DPM}$, are approximated as presented in Eq. (1) for intervals of 0.5 s.

$$\varepsilon = \sqrt{\sum (w_{comp} - w_{CFD-DPM})^2} \qquad \text{Eq. (1)}$$

3.1. Results for monodispersed particles.

In the case of monodispersed particles, the average volume fraction in the falling region and one example of the RTD curves is provided in Figure 3. The average error in the prediction of the volume fraction and mean residence times is 26% and the case with highest error has an average volume fraction 48% lower than the one obtained from CFD. However, evaluating the error of the cumulative RTD, an average 21% of the mass fraction is missed before the cone (a maximum of 65% is missed) and an average of 11% (maximum of 17%) is missed when the recovered mass is evaluated at the bottom of the dryer. From these results, it is determined that the main source of error is due to the mean residence time. That error is especially significant at the beginning of the introduction of the particles as also observed by Portillo et al. (2007). Here, the dispersion of the flux is much smaller than in the cone, where the particles spent more time (up to 90% of the total residence time) and have much higher dispersion.

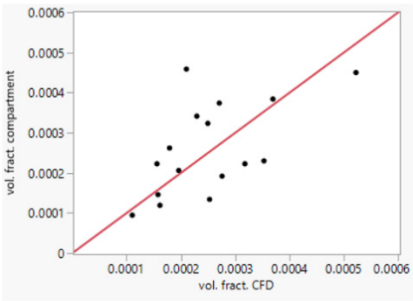

Figure 3 (a)

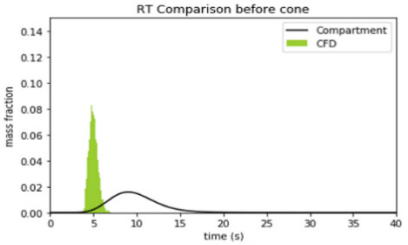

Figure 3 (b)

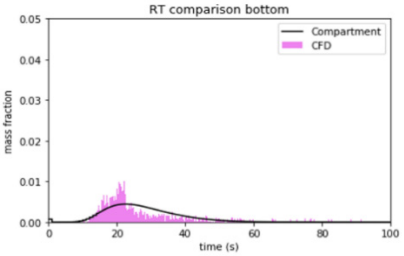

Figure 3 (c)

Figure 3. (a) Parity plot of the volume predicted for different monodispersed injection experiments, (b) RTD comparison before the cone and (c) at the bottom of the dryer.

3.2. Results for particles distribution.

In this second part, the results for the concentration of particles and the RTD curves have been studied. Since different sizes are considered, the cumulative error computed by Eq. (1) is averaged between them, with values up to 21% of mass lost and an average missed mass of 18.5% before the bottom cone. At the bottom of the dryer the maximum mass not captured is 9% and the average error is 8.4%. This lower error is obtained because the particle size bins are not captured individually, but as group. Thus, the use of monodisperse particles proves more reliable for validation.

4. Conclusions

In the current work a novel methodology for generating a robust compartment model for multiphase unit operations is developed. The methodology, using machine learning approaches, focused on generating different phenomenological zones that are flexible and that compute the fluxes and momentum for the entire range of operating conditions. This eliminates the need of generating a new CFD-type model for each new operating condition. The method has been applied to modelling an industrial counter current spray dryer. Particle concentration and momentum have been used to validate this methodology. The results show that errors of up to 48% are obtained for the prediction of the mean residence time. A large part of this error is generated due to lack of accuracy in determining the mean residence time. The substitution of the Navier-Stokes equations in the CFD-DPM model by correlations of dimensionless numbers does not allow the accurate reproduction of the mean residence time in the zones where such particles spend very low residence times. However, the methodology shows better results when the residence time and dispersions are higher, for example in the bottom cone of the spray dryer.

References

F. Bezzo, S. Macchietto, C. Pantelides, 2004, General hybrid multizonal/CFD approach for bioreactor modeling. AIChE Journal. 49,8, 2133-2148.

A. Cozad, N.V. Sahinidis, D.C. Miller, 2014, Learning surrogate models for simulation-based optimization. AIChE J. 60 (6), 2211-2227.

B. Freireich, J. Li, Lister, J. C. Wassgren, 2011, Incorporating particle flow information from discrete element simulations in population balance models of mixer-coaters. Chemical Engineering Science, 66, 3592-3604.

B. Hernández, B. Fraser, L. Martín de Juan, M. Martín, 2018 Computational Fluid Dynamics (CFD) Modeling of Swirling Flows in Industrial Counter-Current Spray-Drying Towers under Fouling Conditions. Ind. Eng. Chem. Res. 57, 35, 11988-12002.

N. Jourdan, T. Neveux, O. Potier, M. Kanniche, J. Wicks, I. Nopens, U. Rehman, Y. Le Moullec, 2019, Compartmental Modelling in chemical engineering: A critical review. Chemical Engineering Science 210, 115196.

Y. Le Moullec, C. Gentric, O. Potier, J.P. Leclec, 2010, Comparison of systemic, compartmental and CFD modelling approaches: Application to the simulation of a biological reactor of wastewater treatment. Chemical Engineering Science, 65, 1, 343-350.

Portillo, P.M. Muzzio, F.J. Ierapetritou, M.G, 2007, Hybrid DEM-Compartment Modeling Approach for Granular Mixing. AIChE Journal, 53, 1, 119-128.

Tajsoleiman, T. Spann, R. Bach, C. Gernaey, K.V. Huusom,J.K. Krühne, U, 2019, A CFD based automatic method for compartment model development. Computers and Chemical Engineering, 123, 236-245.

Yang, S. Kiang, S. Farzan, P. Ierapetritou, M.G., 2019, Optimization of Reaction Selectivity using CFD-Based Compartmental Modeling and Surrogate-Based Optimization. Processes, 7(1), 9.

Sauro Pierucci, Flavio Manenti, Giulia Bozzano, Davide Manca (Eds.)
Proceedings of the 30th European Symposium on Computer Aided Process Engineering (ESCAPE30), May 24-27, 2020, Milano, Italy.
http://dx.doi.org/10.1016/B978-0-12-823377-1.50045-8

Multiobjective Dynamic Optimization of Slow Freezing Processes for Human Induced Pluripotent Stem Cells by Modeling Intracontainer Condition

Yusuke Hayashi[a,*], Ikki Horiguchi[b], Masahiro Kino-oka[b], Hirokazu Sugiyama[a]

[a]*Department of Chemical System Engineering, The University of Tokyo, 7-3-1, Hongo, Bunkyo-ku, 113-8656, Tokyo, Japan*

[b]*Department of Biotechnology, Osaka University, 2-1, Yamadaoka, Suita, 565-0871, Osaka, Japan*

y-hayashi@pse.t.u-tokyo.ac.jp

Abstract

This work presents multiobjective and dynamic optimization of temperature profile for the slow freezing of human induced pluripotent stem (hiPS) cells. A single-cell model was developed that can quantify (i) temperature distribution in a container that causes intracontainer conditional variation, (ii) cell volume change through transmembrane water transport, (iii) intracellular ice formation during freezing, and (iv) cell survival rate after thawing. The phenomena (i) to (iii) were described by white-box (ODE/PDE) models. The phenomenon (iv) was statistically modeled, for which experiments using hiPS cells provided the necessary parameter values. The overall hybrid model can produce cell survival rate and required freezing time as the quality and the productivity objectives, respectively. Multiobjective dynamic optimization was performed on the freezer temperature profile. Among the Pareto optimal solutions, a specific profile was identified that maximized the joint objective of quality and productivity.

Keywords: Regenerative medicine, Cells, Cryopreservation, Hybrid modeling, Numerical simulation

1. Introduction

Human induced pluripotent stem (hiPS) cells are one of the most promising sources of regenerative medicine products. Along with the successful clinical studies, e.g., Parkinson's disease (Morizane, 2019) and spinal cord injuries (Goulão et al., 2016), the demand of hiPS cells is increasing. It is now an urgent task to establish cell freezing process that is necessary for the supply chain with storage and transportation.

As the technique of cell freezing, slow freezing is considered more appropriate for commercial production than vitrification because of scalability, simplicity in operation, and no direct contact with liquid nitrogen. On the other hand, attention needs to be paid to various process conditions that can have significant influence on process performance. Xu et al. (2014) investigated the choice of cryoprotective agent, and observed the consequential influence on cell survival rate. Li et al. (2018) measured the influence of temperature profile on intracellular ice crystals of hiPS cells after freezing. Most recently, we published a single-cell model that defined the estimated cell quality and productivity as a function of the process conditions, e.g., temperature profile of the freezer (Hayashi et al., 2020). However, rigorous temperature optimization was yet to be performed.

In this work, we present multiobjective and dynamic optimization of temperature profile in the slow freezing of hiPS cells. The basis here is the single-cell model that can account for intracontainer temperature distribution. On top of the mechanistic models on heat transfer, transmembrane water transfer, and crystallization of water inside the cell, we developed a statistical model to estimate cell survival rate after thawing. Freeze/thaw experiments using hiPS cells provided the required parameter values. The overall hybrid model was applied for dynamic optimization of temperature profile using quality and productivity objectives.

2. Experimental Methods

hiPS cells in a container, namely vial, with a cryoprotective agent were cooled in a direct-contact freezer at a determined cooling rate. The side of the vial contacted the duralumin freezer plate. The initial temperature of all elements was 277 K and the freezing process was completed when the center temperature of the vial was 193 K. The frozen cells were stored in liquid nitrogen. In order to investigate the cell survival rate, the frozen cells were thawed at 310 K in water. The living cells were counted by trypan blue extrusion test with an automated cell counter before/after freezing-thawing. The cell survival rate was derived by calculating the rate of the number of living cells before/after freezing-thawing.

3. Single-cell Model

Figure 1 shows the structure of the developed model. The mechanistic part consists of the models on heat transfer, mass transfer, and crystallization, which produces the cell volume change and the ice crystal volume. The statistical part, which was newly added in this work, relates these two parameters further with the cell survival rate. The overall model produces the quality and productivity indicators given the process conditions. The modeling concept was based on so-called two-factor hypothesis by Mazur et al. (1972). They investigated the slow freezing of animal cells, and determined the cell volume change by dehydration and the intracellular ice formation as the major cause of damage.

3.1. Heat Transfer Model

Considering conduction as the primary mode of heat transfer in a vial, we adopted the following equation to calculate the temperature profile inside a vial:

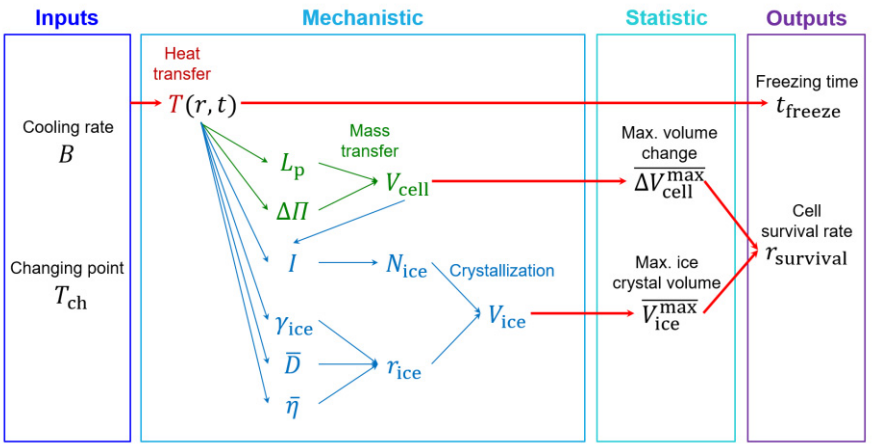

Figure 1. Overview of the developed model.

$$\frac{\partial T}{\partial t} = \alpha\left(\frac{\partial^2 T}{\partial r^2} + \frac{1}{r}\frac{\partial T}{\partial r}\right) \tag{1}$$

where T [K] is the temperature, t [s] is the time, α [m^2 s^{-1}] is the thermal diffusion coefficient, and r [m] is the radial distance from the center of a vial. The position of the solid–liquid interface from the vial center, δ [m], can be calculated as follows:

$$\frac{\rho_{\mathrm{ice}}\Delta H_{\mathrm{f}}}{M_{\mathrm{ice}}}\frac{\mathrm{d}\delta}{\mathrm{d}t} = k_{\mathrm{ice}}\left(\frac{\partial T}{\partial r}\right)_{r=\delta} - k_{\mathrm{w}}\left(\frac{\partial T}{\partial r}\right)_{r=\delta+\mathrm{d}\delta} \tag{2}$$

where ρ [kg m^{-3}] is the density, ΔH_{f} [J mol^{-1}] is the molar heat of fusion of ice, M [kg mol^{-1}] is the molar mass, k [J s^{-1} m^{-1} K^{-1}] is the thermal conductivity, and the subscripts of w and ice represent water and ice. The required time for completing the freezing, t_{freeze} [min], was defined as the productivity indicator:

$$t_{\mathrm{freeze}} = t|_{T(0,t)=193\ \mathrm{K}} \tag{3}$$

3.2. Mass Transfer Model

Transmembrane mass transport of water by the osmotic pressure difference was modeled using the following equations (Xu et al., 2014):

$$\frac{\mathrm{d}V_{\mathrm{cell}}}{\mathrm{d}t} = \frac{L_{\mathrm{p}}A_{\mathrm{cell}}RT}{v_{\mathrm{w}}}\left[\frac{\Delta H_{\mathrm{f}}}{R}\left(\frac{1}{T_0}-\frac{1}{T}\right) - \ln\left\{\frac{V_{\mathrm{w}}}{V_{\mathrm{w}} + v_{\mathrm{w}}\left(\mu_{\mathrm{s}}n_{\mathrm{s}} + n_{\mathrm{cpa}}\right)}\right\}\right] \tag{4}$$

$$\frac{\mathrm{d}n_{\mathrm{cpa}}}{\mathrm{d}t} = \frac{(C_{\mathrm{ex}} + C_{\mathrm{in}})(1-\sigma)}{2}\frac{\mathrm{d}V_{\mathrm{cell}}}{\mathrm{d}t} + A_{\mathrm{cell}}P_{\mathrm{cpa}}(C_{\mathrm{ex}} - C_{\mathrm{in}}) \tag{5}$$

where V [m^3] is the volume, L_{p} [m s^{-1} Pa^{-1}] is the water permeability, A [m^2] is the surface area, R [J mol^{-1} K^{-1}] is the gas constant, v [m^3 mol^{-1}] is the partial molar volume, μ [–] is the dissociation constant, n [mol] is the molar amount, C [mol m^{-3}] is the cryoprotective agent concentration, σ [–] is the reflection coefficient, and P_{cpa} [m s^{-1}] is the cryoprotective agent permeability. The subscripts of cell, 0, s, cpa, in, and ex represent cell, reference, salt, cryoprotective agent, intracellular, and extracellular, respectively. Normalized maximum cell volume change, $\overline{\Delta V_{\mathrm{cell}}^{\max}}$ [–], was defined as follows:

$$\overline{\Delta V_{\mathrm{cell}}^{\max}} = \max\left\{\frac{\left|V_{\mathrm{cell}}^{\mathrm{fin}}(r) - V_{\mathrm{cell}}^{\mathrm{init}}\right|}{V_{\mathrm{cell}}^{\mathrm{init}}}\right\} \tag{6}$$

where the superscripts init and fin represent the initial and final state of freezing, respectively.

3.3. Crystallization Model

The radius of an intracellular ice crystal was defined using the following equation (Karlsson et al., 1994):

$$r_{\mathrm{ice},i} = \begin{cases} 0 & (0 \le N_{\mathrm{ice}} < 1) \\ \sqrt{\int_{\tau_i}^{t} \gamma_{\mathrm{ice}}^2 \bar{D}\,dt} & (N_{\mathrm{ice}} \ge 1) \end{cases} \tag{7}$$

where r_{ice} [m] is the radius of an ice crystal, N_{ice} [–] is the number of intracellular ice crystals, γ_{ice} [–] is the non-dimensional ice crystal growth parameter, τ [s] is the starting

time of ice crystal formation, and $\overline{D}$ [m^2 s^{-1}] is the average water diffusion coefficient. The total volume of intracellular ice crystals $V_{\mathrm{ice}}(r)$ [m^3] can be calculated using the following equation:

$$V_{\mathrm{ice}}(r) = \sum_{i=1}^{N_{\mathrm{ice}}} \frac{4}{3}\pi r_{\mathrm{ice},i}^3 \tag{8}$$

Normalized maximum ice crystal volume, $\overline{V_{\mathrm{ice}}^{\mathrm{max}}}$ [–], was defined as follows:

$$\overline{V_{\mathrm{ice}}^{\mathrm{max}}} = \max\left\{\frac{V_{\mathrm{ice}}^{\mathrm{fin}}(r)}{V_{\mathrm{cell}}^{\mathrm{fin}}(r)}\right\} \tag{9}$$

3.4. Cell Survival Rate Model

As the output of the model, the cell survival rate after thawing, r_{survival} [–], was defined as follows:

$$r_{\mathrm{survival}} = \omega_1\left(\overline{\Delta V_{\mathrm{cell}}^{\mathrm{max}}}\right)^2 + \omega_2\overline{\Delta V_{\mathrm{cell}}^{\mathrm{max}}} + \omega_3(\overline{V_{\mathrm{ice}}^{\mathrm{max}}})^2 + \omega_4\overline{V_{\mathrm{ice}}^{\mathrm{max}}} + \omega_5 \tag{10}$$

where ω_1 [–] to ω_5 [–], are the fitting coefficients to the experimental results. The experiments presented in Chapter 2 provided the necessary values.

4. Results and Discussion

4.1. Freeze/thaw Experiments Using Constant Cooling Rates

The circles in Figure 2 show the results of freeze/thaw experiments using constant cooling rates. The highest cell survival rate was observed at B = 1.0 K min^{-1}. This result can be explained by the two-factor hypothesis advocated by Mazur et al. (1972). In the range of $B \leq 0.50$ K min^{-1}, the survival rate decreased because the value of $\overline{\Delta V_{\mathrm{cell}}^{\mathrm{max}}}$ increased along with the decrease of B. In contrast, in the range of $B \geq 3.0$ K min^{-1}, the value of $\overline{V_{\mathrm{ice}}^{\mathrm{max}}}$ increased with the increase of B, which decreased the cell survival rate. The solid line in Figure 2 shows the fitted curve for the experimental results. The coefficient of determination was 0.83. The curve was used in the succeeding dynamic optimization.

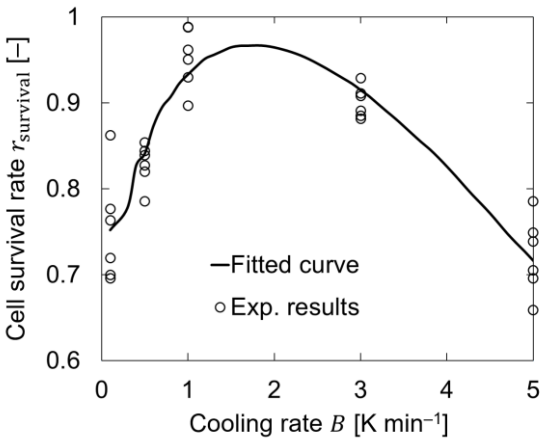

Figure 2. Experimental results of the cell survival rate after thawing and fitted curve for the experimental results.

4.2. Dynamic Optimization of Freezer Temperature Profile

With assuming two-stage temperature profile, multiobjective and dynamic optimization was performed on the first cooling rate, the changing point of the temperature, and the second cooling rate. The optimization problem was formulated as shown in Eq. (11):

$$\min S_{\text{total}}\{r_{\text{survival}}(B_1, T_1^{\text{ch}}, B_2), t_{\text{freeze}}(B_1, T_1^{\text{ch}}, B_2)\} \tag{11}$$

subject to

$$\begin{aligned} B_1 &\in \{0.50, 1.0, 1.5, 2.0, 2.5, 3.0, 3.5, 4.0, 4.5, 5.0\} \\ T_1^{\text{ch}} &\in \{-5.0, -10, -15, \ldots, -65, -70, -75\} \\ B_2 &\in \{0.50, 1.0, 1.5, 2.0, 2.5, 3.0, 3.5, 4.0, 4.5, 5.0\} \end{aligned}$$

where B_1 [K min^{-1}] is the first cooling rate, T_1^{ch} [℃] is the changing point of the freezer temperature, B_2 [K min^{-1}] is the second cooling rate. The joint objective function, S_{total}, [–] was defined as follows:

$$S_{\text{total}} = \left(\frac{1 - r_{\text{survival}}}{1 - r_{\text{survival}}^{\text{min}}}\right) + \left(\frac{t_{\text{freeze}}}{t_{\text{freeze}}^{\text{max}}}\right) \tag{12}$$

where $r_{\text{survival}}^{\text{min}}$ [–] is the minimum cell survival rate in the all considered temperature profiles, and $t_{\text{freeze}}^{\text{max}}$ [min] is the maximum required freezing time in the all considered temperature profiles.

Figure 3(a) shows the relationship between the calculated survival rate and the required freezing time for 1,360 different temperature profiles considered. Large difference is observed even at the same required time depending on the profile. A trade-off between the quality and the productivity can be seen from the increase of the survival rate along with the increase of the required time. The red dot in Figure 3(a) represents the optimal solution to the problem in Eq. (11). The solution is $(B_1, T_1^{\text{ch}}, B_2) = (2.0, -45, 5.0)$. Figure 3(b) shows the temperature profile of this optimal solution. This profile can reduce the damage due to both dehydration and intracellular ice formation, and at the same time, achieve short freezing time. The profile can be appropriate for practical use.

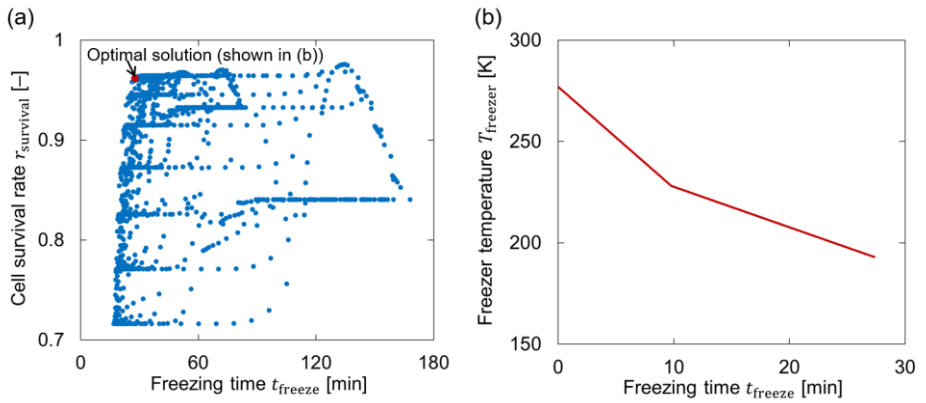

Figure 3. (a) Relationship between the cell survival rate and the required freezing time for each temperature profile, (b) Optimal temperature profile obtained by Figure 3(a) for both the cell quality and the productivity.

Runge-Kutta/Crank-Nicolson methods were used for solving the ODEs/PDEs, and the algorithm was implemented in Python 3.7. The total CPU time for the results in Figure 3 was ca.10 h using Intel® Xeon® Platinum 8160T CPU @ 2.1 GHz with 512 GB RAM.

5. Conclusions and Outlook

We presented multiobjective and dynamic optimization of slow freezing processes for hiPS cells considering an intracontainer condition. A single-cell model was developed by integrating models describing temperature profile, cell volume change, intracellular ice formation, and cell survival rate. The developed model can produce the survival rate and the required freezing time as the quality and the productivity objectives, respectively. We applied the model to evaluate 1,360 different temperature profiles. The optimal temperature profile for both the cell quality and the productivity was obtained, which is suitable for practical application. In an ongoing work, we are conducting freeze/thaw experiments to validate the obtained optimal profile, and also investigating the impact of the choice of cryoprotective agent on the results. In the field of computer aided process engineering, regenerative medicine related researches are becoming increasingly relevant, e.g., Győrgy et al. (2017) and Wang et al. (2018). More model- and simulation-based researches in this area are encouraged to move away from empirical approaches in product and process development.

Acknowledgements

This study was supported by the Japan Agency for Medical Research and Development (No. P14006) and the Japan Society for the Promotion of Science (No. 17H04964). We thank Mr. Yuki Uno in Osaka University for the support in experiment.

References

M. Goulão, A. C. Lepore, 2016. iPS cell transplantation for traumatic spinal cord injury. Curr. Stem Cell Res. Ther. 11, 321-328.

R. Győrgy, M. E. Klontzasb, M. Kostoglouc, N. Panoskaltsisd, A. Mantalarisb, M. C. Georgiadisa, 2017. A Population Balance Model for Stem Cell Differentiation Bioprocesses. Comput. Aided Chem. Eng. 40, 2761-2766.

Y. Hayashi, I. Horiguchi, M. Kino-oka, H. Sugiyama, 2020. Slow freezing process design for human induced pluripotent stem cells by modeling intracontainer variation. Comput. Chem. Eng. 132, 106597.

J. O. M. Karlsson, E. G. Cravalho, M. Toner, 1994. A model of diffusion-limited ice growth inside biological cells during freezing. J. Appl. Phys. 75, 4442‑4455.

R. Li, G. Yu, S. Azarin, A. Hubel, 2018. Freezing Responses in DMSO-Based Cryopreservation of Human iPS Cells: Aggregates vs. Single Cells. Tissue Eng. Part C Methods 24, 289–299.

P. Mazur, S. P. Leibo, E. H. Y. Chu, 1972. A two-factor hypothesis of freezing injury: Evidence from Chinese hamster tissue-culture cells. Exp. Cell Res. 71, 345–355.

A. Morizane, 2019. Cell therapy for Parkinson's disease with induced pluripotent stem cells. Rinsho Shinkeigaku 59, 119–124.

X. Wang, Q. Kong, M. M. Papathanasiou, N. Shah, 2018. Precision healthcare supply chain design through multi-objective stochastic programming. Comput. Aided Chem. Eng. 44, 2137-2142.

Y. Xu, L. Zhang, J. Xu, Y. Wei, X. Xu, 2014. Membrane permeability of the human pluripotent stem cells to Me2SO, glycerol and 1,2-propanediol. Arch. Biochem. Biophys. 550–551, 67–76.

Sauro Pierucci, Flavio Manenti, Giulia Bozzano, Davide Manca (Eds.)
Proceedings of the 30th European Symposium on Computer Aided Process Engineering (ESCAPE30), May 24-27, 2020, Milano, Italy.
http://dx.doi.org/10.1016/B978-0-12-823377-1.50046-X

Optimal Design of a Non-isothermal Hybrid Catalyst Pellet based on POD-DEIM Reduced-order Methodology

Katarzyna Bizon[a*], Gaetano Continillo[b]

[a]*Faculty of Chemical Engineering and Technology, Cracow University of Technology, ul. Warszawska 24, 31-155 Kraków, Poland*
[b]*Dipartimento di Ingegneria, Università degli Studi del Sannio, Piazza Roma 21, 82100 Benevento, Italy*
katarzyna.bizon@pk.edu.pl

Abstract

The problem of the optimal design of a catalyst pellet occupied by different types of active sites was formalized and solved for a non-isothermal system of two consecutive chemical reactions. The maximization of the desired product yield was tackled with model-order reduction techniques. *Proper Orthogonal Decomposition* (POD) and *Discrete Empirical Interpolation Method* (DEIM) were employed to reduce the catalyst pellet balance equations that need to be resolved to evaluate the objective function. It was demonstrated that the pellet performance may be significantly improved by choosing proper fractions of two types of catalytic active centers. Moreover, application of the model-order reduction procedure permitted to solve the problem with a minimal numerical effort without affecting significantly the accuracy.

Keywords: hybrid catalyst pellet, process integration, model-order reduction, POD.

1. Introduction

Hybrid catalyst pellets, also referred as to multifunctional catalyst pellets, enable to integrate different functionalities, including different types of catalytic active centers or catalyst and adsorbent on a single particle level (Grünewald and Agar, 2004). In contrast to the chemical processes carried out in multifunctional reactors integrating different functionalities on an apparatus level, mass transport by diffusion in hybrid pellets takes place over much smaller distances, and this may improve the product yield.
While the optimization of the distribution of a single type of catalytic active centers was examined extensively in the past (Morbidelli et al., 2001), there are very little reports dealing with optimal distribution of two or more functionalities within the pellet. In a previous study (Bizon and Continillo, 2019a) concerning isothermal catalyst pellets integrating two types of active centers, it was demonstrated that optimal distribution of the catalysts within the pellet may lead to a substantial increase of the product yield.
In this study, the analysis of the yield maximization is extended to a non-isothermal catalyst pellet integrating two types of catalytic active sites. The case of two consecutive reversible chemical reactions is investigated. To keep the computational costs low, the optimization algorithm is coupled with *Proper Orthogonal Decomposition* (POD) and a Galerkin projection method (Holmes et al., 1996) employed for the order reduction of the model of a single catalyst pellet. Moreover, since when modelling a non-isothermal hybrid catalyst pellet, the computational efficiency of the standard POD method may fall down, due to the presence of a highly nonlinear Arrhenius term, to reduce the com-

putational burden the POD approach was additionally combined with a *Discrete Empirical Interpolation Method* (DEIM) (Chaturantabut and Sorensen, 2010).

2. Mathematical model and computational methods

2.1. Mathematical model of a single non-isothermal catalyst pellet

Let us consider a system of two reversible first-order chemical reactions:

$$\mathrm{A} \underset{k_{-1}}{\overset{k_1}{\rightleftarrows}} \mathrm{B} \underset{k_{-2}}{\overset{k_2}{\rightleftarrows}} \mathrm{C} \tag{1}$$

taking place in a non-isothermal spherical catalyst pellet of radius R_p including two types of active centers. Steady-state mass and energy balance in the pellet are written as:

$$\frac{d^2\beta_\mathrm{A}}{d\zeta^2} + \frac{2}{\zeta}\frac{d\beta_\mathrm{A}}{d\zeta} - \Phi_1^2 f_1 \frac{\hat{r}_1}{\hat{r}_{1,ref}} = 0 \tag{2a}$$

$$\frac{d^2\beta_\mathrm{B}}{d\zeta^2} + \frac{2}{\zeta}\frac{d\beta_\mathrm{B}}{d\zeta} + \Phi_1^2 f_1 \frac{\hat{r}_1}{\hat{r}_{1,ref}} - \Phi_2^2 f_2 \frac{\hat{r}_2}{\hat{r}_{2,ref}} = 0 \tag{2b}$$

$$\frac{d^2\theta}{d\zeta^2} + \frac{2}{\zeta}\frac{d\theta}{d\zeta} + \Phi_1^2 \delta_1 f_1 \frac{\hat{r}_1}{\hat{r}_{1,ref}} + \Phi_2^2 \delta_2 f_2 \frac{\hat{r}_2}{\hat{r}_{2,ref}} = 0 \tag{2c}$$

where:

$$\beta_\mathrm{A} = C_\mathrm{A}/C_{ref}\,,\ \beta_\mathrm{B} = C_\mathrm{B}/C_{ref}\,,\ \theta = \frac{T}{T_{ref}},\ \zeta = r/R_p \in [0,1] \tag{3a}$$

$$\hat{r}_1 = k_{01}\exp\left(-\frac{\gamma_1}{\theta}\right)\left(\beta_\mathrm{A} - \frac{1}{K_{p1}}\beta_\mathrm{B}\right),\ \hat{r}_2 = k_{02}\exp\left(-\frac{\gamma_2}{\theta}\right)\left(\beta_\mathrm{B} - \frac{1}{K_{p2}}\beta_\mathrm{C}\right),\ \gamma_j = \frac{E_j}{RT_{ref}} \tag{3b}$$

$$\hat{r}_{j,ref} = k_{0j}\exp(-\gamma_j)\left(1 + \frac{1}{K_{pj}(T_{ref})}\right),\ \Phi_j^2 = \frac{R_p^2 \hat{r}_{j,ref}}{D_{eff}},\ \delta_j = \frac{D_{eff}\left(-\Delta h_j\right)C_{ref}}{\lambda_{eff}T_{ref}},\ j = 1, 2 \tag{3c}$$

whereas f_1 and $f_2 = 1 - f_1$ are the volume fractions of the pellet occupied by active sites catalyzing, respectively, the first and the second step of the process given by Eq. (1). The boundary conditions associated with Eq. (2) are:

$$\left.\frac{d\beta_i}{d\zeta}\right|_{\zeta=0} = 0,\quad \left.\frac{d\beta_i}{d\zeta}\right|_{\zeta=1} = \mathrm{Bi}_m\left(\beta_{i,bulk} - \beta_i(1)\right),\ i = \mathrm{A, B}\ \text{ where }\ \mathrm{Bi}_m = \frac{k_m R_p}{D_{eff}} \tag{4a}$$

$$\left.\frac{d\theta}{d\zeta}\right|_{\zeta=0} = 0,\quad \left.\frac{d\theta}{d\zeta}\right|_{\zeta=1} = \mathrm{Bi}_q\left(\theta_{bulk} - \theta(1)\right)\ \text{ where }\ \mathrm{Bi}_q = \frac{\alpha_q R_p}{\lambda_{eff}} \tag{4b}$$

More detailed description of the model, including its formulation and definition of state variables and parameters, can be found in Bizon et al. (2019b), where the intensification

of catalytic processes through pellet structuring is investigated by means of parameter continuation of steady-state properties of a bifunctional catalyst pellet.

2.2. Formulation of the optimization problem

Assuming for simplicity that each type of catalytic active centers is distributed uniformly along the pellet radius, and that C is the desired product, the optimization problem consists in finding the value of f_1 and $f_2 = 1 - f_1$ that maximizes the yield of C with respect to reactant A (Morbidelli et al., 2001; Bizon and Continillo, 2019a):

$$Y_{\mathrm{CA}} = \frac{3\int_0^1 f_2 k_{02} \exp\left(-\gamma_2/\theta\right)\left(\beta_{\mathrm{B}} - \beta_{\mathrm{C}}/K_{p2}\right)\zeta^2 d\zeta}{k_{01}\exp\left(-\gamma_1/\theta_{bulk}\right)\left(\beta_{\mathrm{A},bulk} - \beta_{\mathrm{B},bulk}/K_{p1}(T_{bulk})\right)} \quad \text{where } 0 \le f_1, f_2 \le 1 \tag{5}$$

2.3. Model-order reduction techniques

Evaluation of the cost function (Eq. (5)) requires the numerical resolution of Eq. (2) at every iteration of the optimization algorithm. To keep the computational expenses at a reasonable level, the reduced-order modelling technique based on POD (Holmes et al., 1996) was employed to reduce the number of equations resulting from the discretization of the model equations. In the second step, the POD approach was additionally combined with DEIM (Chaturantabut and Sorensen, 2010), that permits to further increase the computational efficiency in case of occurrence of nonlinearities in the equations.

Let us consider the following system of N algebraic equations, referred to as *full-order model* (FOM), resulting from the discretization of spatial derivatives in Eq. (2) in N discrete nodes distributed uniformly along the particle radius:

$$\mathbf{A}\mathbf{y} + \mathbf{G}(\mathbf{y}) = 0 \tag{6}$$

Employing the method of POD that consists in the resolution of the eigenvalue problem:

$$\mathbf{C}\boldsymbol{\Phi} = \boldsymbol{\Lambda}\boldsymbol{\Phi} \quad \text{where} \quad \mathbf{C} = \frac{1}{M}\mathbf{Y}\mathbf{Y}^T \tag{7}$$

the state variable vector, $\mathbf{y}$, can be represented in a truncated form as a linear combination of modal coefficients, $\mathbf{c}_K$, and K leading POD modes, that is $\boldsymbol{\Phi}_K = \left[\phi_1, \phi_2, \ldots, \phi_K\right] \in \mathbb{R}^{N\times K}$, $K << N$. Symbol $\mathbf{Y}$ in Eq. (7) denotes a matrix of the model solutions obtained for M values of a selected parameter. Introduction of the truncated state variable into Eq. (6) followed by the Galerkin projection onto the POD basis, $\boldsymbol{\Phi}_K$, yields the following *reduced-order model* (ROM) consisting of K algebraic equations:

$$\boldsymbol{\Phi}_K^T\mathbf{A}\boldsymbol{\Phi}_K\mathbf{c}_K + \boldsymbol{\Phi}_K^T\mathbf{G}(\boldsymbol{\Phi}_K\mathbf{c}_K) = 0 \quad \text{where} \quad \mathbf{y} \approx \boldsymbol{\Phi}_K\mathbf{c}_K \tag{8}$$

When dealing with strongly nonlinear algebraic equations the reduction of the number of equations from N to K usually does not result in computational savings since the value of the nonlinear term $\mathbf{G}$ in Eq. (8) still depends on the full set of variables of the FOM. Computational costs related to the evaluation of the nonlinear terms can be decreased by applying DEIM. DEIM permits to determine a relatively small number of grid nodes optimally distributed along the domain, in correspondence of which the model nonlinearities are evaluated. Following the procedure described in (Chaturantabut and Sorensen, 2010; Bizon, 2017), Eq. (8) can be recast as follows:

$$\mathbf{\Phi}_K^T \mathbf{A} \mathbf{\Phi}_K \mathbf{c}_K + \mathbf{\Phi}_K^T \mathbf{\Psi}_J (\mathbf{P}^T \mathbf{\Psi}_J)^{-1} \mathbf{G}(\mathbf{P}^T \mathbf{\Phi}_K \mathbf{c}_K) = 0 \tag{9}$$

where $\mathbf{\Psi}_J = [\psi_1, \psi_2, \ldots, \psi_J] \in \mathbb{R}^{N \times J}$ is the POD basis determined from Eq. (7) based on the snapshots of the nonlinear term, whereas $\mathbf{P} = [e_{p_1}, \ldots, e_{p_J}] \in \mathbb{R}^{N \times J}$, $J << N$ is a matrix of interpolation indices, that is the grid nodes at which the nonlinear terms are evaluated, with $e_{p_i} = [0, \ldots, 0, 1, 0, \ldots, 0] \in \mathbb{R}^{N \times J}$ being the p_i^{th} column of the identity matrix $\mathbf{I} \in \mathbb{R}^{N \times N}$. The interpolation indices can be determined using the algorithm presented in (Chaturantabut and Sorensen, 2010; Bizon, 2017).

3. Results and discussion

Table 1 reports the main parameters of the model employed in the numerical simulations. The values of dimensionless concentrations and temperature of the bulk gas were set, respectively, to $\beta_{bulk,\mathrm{A}} = 1$, $\beta_{bulk,\mathrm{B}} = 0$ and $\theta = 1$. To construct the FOM, the derivatives in Eq. (2) were approximated by finite differences at $N = 51$ discrete nodes. Both the POD modes and DEIM indices were calculated from FOM solutions obtained for 25 random values of f_1.

Table 1. Main model parameters used in the numerical simulations.

Parameter	Value	Parameter	Value
D_{eff}	10^{-6} m^2·s^{-1}	k_m	0.03 m·s^{-1}
$E_1 = E_2$	$6 \cdot 10^4$ kJ·kmol^{-1}	k_m	0.03 m·s^{-1}
Δh_1	$-7 \cdot 10^4$ kJ·kmol^{-1}	k_q	0.02 kW·m^{-2}·K^{-1}
Δh_2	$-5 \cdot 10^4$ kJ·kmol^{-1}	R_p	$2.5 \cdot 10^{-3}$ m
$k_{01} = k_{02}$	10^7 s^{-1}	λ_{eff}	10^{-4} kW·m^{-1}·K^{-1}

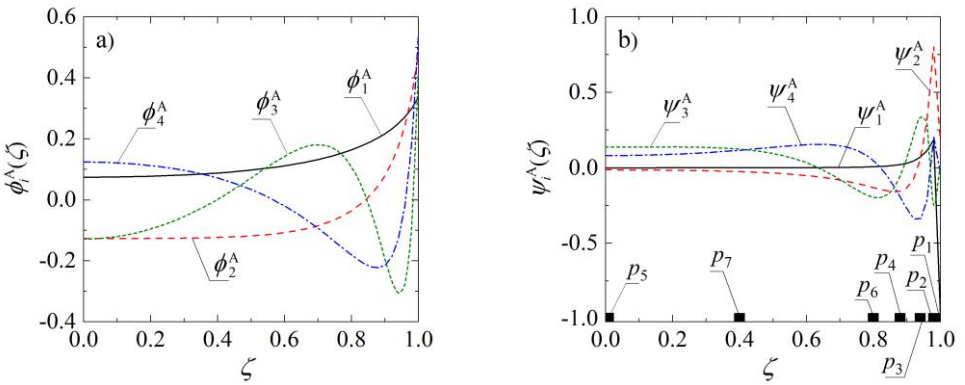

Figure 1. Leading POD modes of the concentration of A, β_{A} (a) and nonlinear term present in mass balance of component A together with first 7 interpolation indices (b).

Figure 1 shows leading POD modes of β_{A} (ϕ_i^{A}, Fig. 1a) and of the nonlinear term present in the component A mass balance (ψ_i^{A}, Fig. 1b), together with location of the first

J =7 interpolation indices (marked with ■). The non-smooth character of ψ_i^{A} close to $\zeta = 1$ results from the incorporation of the boundary conditions in **G**. Higher density of DEIM indices is observed in the outer part of the pellet, characterized by larger variations of the state variables.

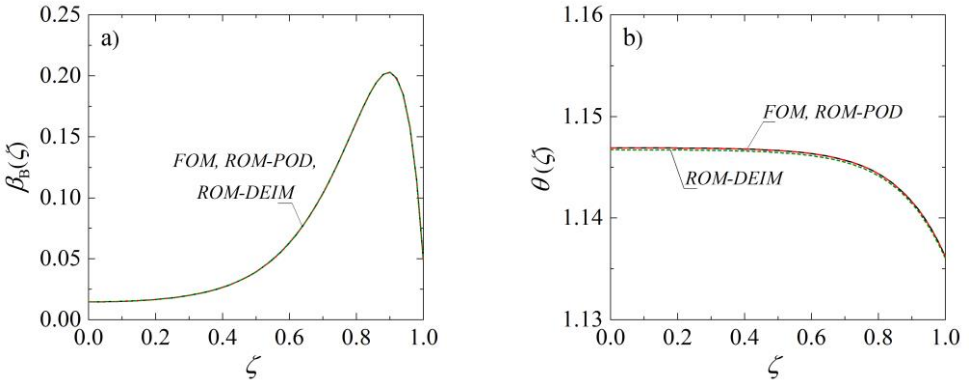

Figure 2. Intraparticle concentration of intermediate product B, β_{B} (a) and temperature, θ (b) obtained for $f_1 = f_2 = 0.5$ using FOM, ROM-POD (K = 7) and ROM-DEIM (K = 7 and J = 7).

Representative solutions obtained using full-order (FOM) and reduced-order models (ROM) are presented in Fig. 2. It can be observed that employing K = 7 POD modes gives a very accurate approximation, when compared with the FOM solution, both for concentration (Fig. 2a) and temperature (Fig. 2b). Actually, the three profiles are virtually indistinguishable. A slight discrepancy between FOM and ROM temperature profiles is encountered when coupling the POD approach with DEIM and the nonlinear term evaluated at only J = 7 points of the domain (curve denoted with ROM-DEIM in Fig. 2b). It must be emphasized here that the number of POD modes, K, does not have to be necessarily equal to the number of DEIM indices, J, however in this case such a combination resulted to perform best. The ROM-POD model constructed using 7 modes to approximate each state variable resulted to be about 6.2 faster than FOM, whereas ROM-DEIM with K = 7 and J = 7 was about 6.8 faster than FOM.

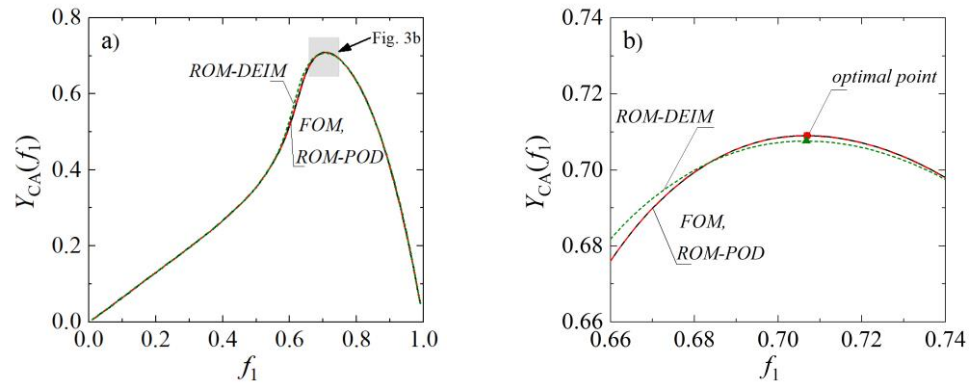

Figure 3. Values of the yield of C with respect to reactant A, Y_{CA}, obtained using FOM, ROM-POD (K = 7) and ROM-DEIM (K = 7and J = 7) and positioning of the optimum.

Figure 3 shows the values of Y_{CA} determined for varying value of f_1 with the aid of FOM, ROM-POD and ROM-DEIM, together with the positioning of the optimum (Fig. 3b) determined using the interior-point algorithm coupled with FOM and ROM. Both ROMs approximate the objective function and the optimum very accurately. To better visualize the great accuracy of ROMs, representative results of the optimization are reported in Table 2, where FOM is to be regarded as the reference solution.

Table 2. Comparison of the optimal solutions obtained using FOM, ROM-POD and ROM-DEIM.

Model	FOM	ROM-POD $K = 7$	ROM-POD $K = 8$	ROM-DEIM $K = 7, J = 7$	ROM-DEIM $K = 8, J = 8$
f_1	0.70701	0.70696	0.70698	0.70679	0.70842
f_2	0.29299	0.29304	0.29302	0.29321	0.29158
Y_{CA}	0.70899	0.70897	0.70902	0.70762	0.70739

4. Conclusions

The resolution of the optimization problem consisting in the maximization of the product yield demonstrates that properly selected fractions of different types of catalytic active centers may significantly increase the catalyst pellet performance. The proposed computational methodology based on reduced-order modelling gives considerable computational savings without affecting significantly the solution accuracy. For demonstrative reasons it was assumed that both catalysts are uniformly distributed in the entire pellet volume, however, the methodology can be easily adapted for determination of the optimal non-uniform intraparticle distribution of the catalytic active sites.

Acknowledgements

The research was partly financed by the Polish National Science Centre, project number 2017/26/D/ST8/00509.

References

K. Bizon, 2017, Assessment of a POD Method for Dynamical Analysis of a Catalyst Pellet with Simultaneous Chemical Reaction, Adsorption and Diffusion: Uniform Temperature Case, Computers & Chemical Engineering, 97, 259-270.

K. Bizon, G. Continillo, 2019a, Determination of the Optimal Distribution of Active Centers in a Multifunctional Catalyst Pellet Using Global Searching Combined with Reduced-order Modeling Approach, Computer Aided Chemical Engineering, 46, 1015-1020.

K. Bizon, K. Skrzypek-Markiewicz, D. Pędzich, N. Reczek, 2019b, Intensification of catalytic processes through the pellet structuring: steady-state properties of a bifunctional catalyst pellet applied to generic chemical reactions and the direct synthesis of DME, Catalysts, 9 (12), 1020.

S. Chaturantabut, D.C. Sorensen, Nonlinear Model Reduction via Discrete Empirical Interpolation, SIAM Journal of Scentific Computing, 32, 5, 2737–2764.

M. Grünewald, D.V. Agar, 2004, Enhanced Catalyst Performance Using Integrated Structured Functionalites, Chemical Engineering Science, 59, 22-23, 5519-5526.

P. Holmes, J.L. Lumley, G. Berkooz, 1996. Turbulence, Coherent Structures, Dynamical Systems and Symmetry, Cambridge University Press, Cambridge, UK.

M. Morbidelli, A. Gavriilidis, A. Varma, 2001, Catalyst Design. Optimal Distribution of Catalyst, Pellets, Reactors, and Membranes, Cambridge University Press, UK.

Sauro Pierucci, Flavio Manenti, Giulia Bozzano, Davide Manca (Eds.)
Proceedings of the 30th European Symposium on Computer Aided Process Engineering (ESCAPE30), May 24-27, 2020, Milano, Italy.
http://dx.doi.org/10.1016/B978-0-12-823377-1.50047-1

Cyclopentane Purification from Multicomponent Azeotropic Mixtures

Nuchteera I.,[a] Thirasak P.,[b] Chavagorn M., [c] Thanyalak C.,[a] Kitipat S.[a]

[a,]*Chulalongkorn University, The Petroleum and Petrochemical College, Bangkok 10330, Thailand*
[b]*Thaioil Public Company Limited, Chonburi 20230, Thailand*
[c]*Sak Chaisidhi Company Limited, Rayong 21150, Thailand*
Kitipat.S@chula.ac.th

Abstract

The distillation technique plays a key role in a separation and purification of multicomponent mixtures. Several alternative designs using conventional distillation for purifying cyclopentane with high purity have been done using Pro/II Process Engineering Software. Using conventional distillation process for purifying cyclopentane from close boiling point mixture is uneconomic and impractical. The distillation technique is also applied in the cyclopentane production. However feed mixture contains multicomponent of hydrocarbons including cyclopentane and 2, 2-dimethylbutane forming azeotrope. Only 80-85%wt cyclopentane purity can be achieved from the conventional distillation. Therefore, a widely used technology, extractive distillation is applied for purifying cyclopentane with 95%wt purity. High-purity cyclopentane gains higher benefit from a larger cyclopentane market.

Keywords: distillation, azeotropic and close boiling point mixture, extractive distillation

1. Introduction

Distillation is a purification technique based on a separation of different volatility or boiling point of the components. In practice we often deal with system of the nonideal mixtures and azeotropic behavior. One kind of azeotropic mixtures is a close boiling point mixture, having the same vapor and liquid composition at a specific temperature and pressure. Then the proper selection of a separation technology depends on the physical or chemical properties between components in the mixtures. Due to the azeotropic properties, a conventional distillation technology cannot be applied to achieve high purity because it requires a large number of trays, which is an economic inefficiency. Several techniques have been developed to eliminate the azeotrope to get higher product purity such as the pressure-swing distillation, azeotropic distillation and extractive distillation (Luyben and Chien, 2010).

The simplest technique for the cyclopentane production is fractionating a light naphtha fraction and natural gas liquid by using the conventional distillation. Due to a presence of an azeotrope within the mixtures or feeds like naphtha fraction, a cyclopentane purity could be achieved only 80-85%wt (Lavanya et al, 2007). Therefore, other feeds and technologies were invented. A high cyclopentane purity can be obtained by processing a feed of partially pyrolysis gasoline using conventional distillation and selective hydrogenation unit (Kanne et al, 1997). Dicyclopentadiene can be used as a feedstock

processing through the distillation and hydrotreating unit to produce high cyclopentane purity (Halsey, 2003).

2. Separation and purification processes

This work focuses on distillation, which is a widely used techniques in the chemical and petroleum industries. Distillation principle is operated based on the differences in volatility between mixtures. The higher volatility substances or the lighter molecules are vaporized to the top of column. The vapor molecules are then condensed at the condenser. The condensed liquid is drawn from column as distillate called overhead product. While lower volatility substances or heavier molecules are drawn from the bottom of column as a bottom product (Wankat, 2013). Relative volatility plays a key parameter in the separation process. The relative volatility is a parameter to measure the volatility of components in a liquid mixture. The relative volatility (α_{AB}) can be expressed as shown in following equation (1):

$$\alpha_{AB} = \frac{y_A / x_A}{y_B / x_B} \tag{1}$$

Where x_A and y_A are the molar fractions of the most volatile, having high purity in the top product in the liquid and vapor phase, respectively. While x_B and y_B are the molar fractions of the least volatile substance, having high purity in the bottom product in the liquid and vapor phase, respectively. For their meaning, if the relative volatility (α) equals to one, the separation of the mixtures would be impossible. Conversely, the separation becomes possible for mixtures with relative volatility greater than one (Doherty and Malone, 2001).

In practice, we often deal with the nonideal, azeotropic or close boiling point mixtures. Azeotropic phenomenon or close boiling point mixtures occurs at the same vapor and liquid compositions (Gmehling and Kleiber, 2014). And their relative volatility equals to one. The formation of close boiling point mixtures of this work is the mixtures of cyclopentane and 2, 2-dimethylbutane. The difference in boiling point between cyclopentane and 2, 2-dimethylbutane is less than 1 degree Celsius. Then close boiling point mixtures limit purity of the products. Only 80-85%wt purity of cyclopentane and 15-20%wt purity of 2, 2-dimethylbutane obtained via conventional distillation.

The data used in this work are acquired from hydrocarbon feed (HC-FEED) stream from the solvent plant in Thailand. HC-FEED contains more than 10 components of hydrocarbon. HC-FEED is fed into the complex distillation column (T1) with total 80 trays and weight reflux ratio of 21. By product from the process is withdrawn as overhead product from the top of column T1. Cyclopentane rich stream is then sent to the second column (T2) for purifying with 80-85%wt along with 15-20%wt purity of 2, 2-dimethylbutane as bottom product from column T2. The top product stream of column T2 is recycled to column T1 to improve concentration of cyclopentane in the system. Process simulation by Pro/II Process Engineering Software has been applied for the cyclopentane purifying process as shown in Figure 1.

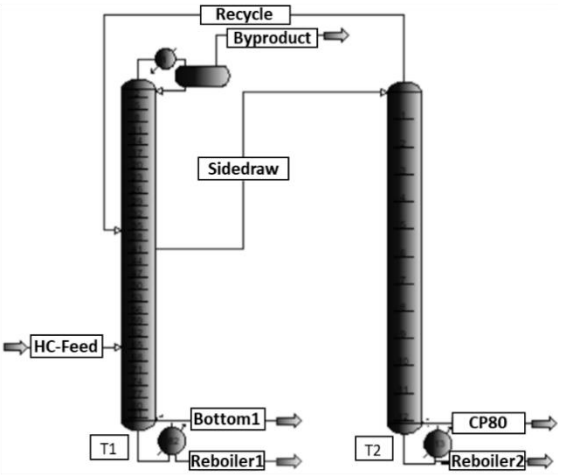

Figure 1: Base-case cyclopentane purifying process by Pro II simulation program

3. Sensitivity analysis

95%wt purity of cyclopentane can be obtained by retrofitting the base-case distillation columns giving 80-85%wt purity cyclopentane. The sensitivity analysis in ProII program was applied to increase cyclopentane purity by modifying base-case process as shown in the Figure 1 into many alternative designs with 95%wt cyclopentane purity. First alternative design was done by decreasing from 12 to 5% yield of cyclopentane from the bottom of column T2, to very low amount as shown in Figure 2. Side-draw tray position from column T1 was moved from trays number 40 to 24 as shown in Figure 3. This helps increase separation ability of cyclopentane at column T1. Then it helps decrease the loss of cyclopentane at column T1. Higher cyclopentane content in the side draw stream from column T1 is sent to further purify at column T2. Moreover weight reflux ratio of column T1 was increased from 21 up to 36.5 as shown in Figure 4. The increase of reflux ratio in column T1 helps reduce loss of cyclopentane to bottom of column T1 and increase by-product content in the overhead stream of column T1. From these conditions, only less than 10 trays was added to the column T1. However, only 35%wt recovery of cyclopentane at the bottom of column T2 was obtained.

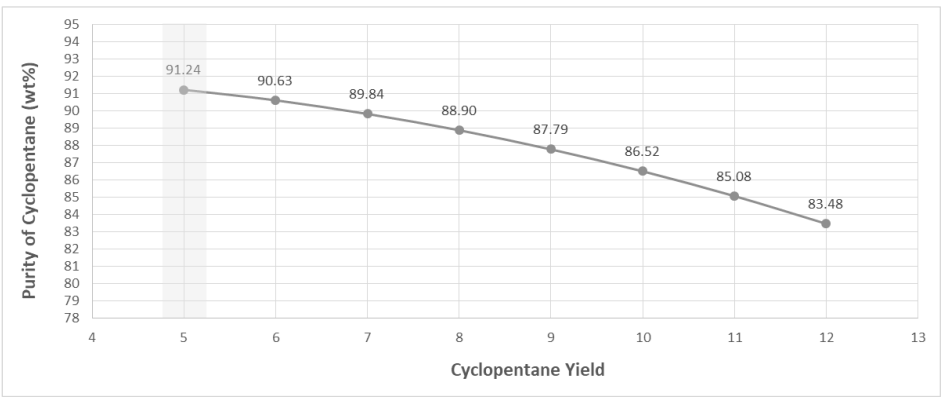

Figure 2: Sensitivity analysis on production yield of cyclopentane

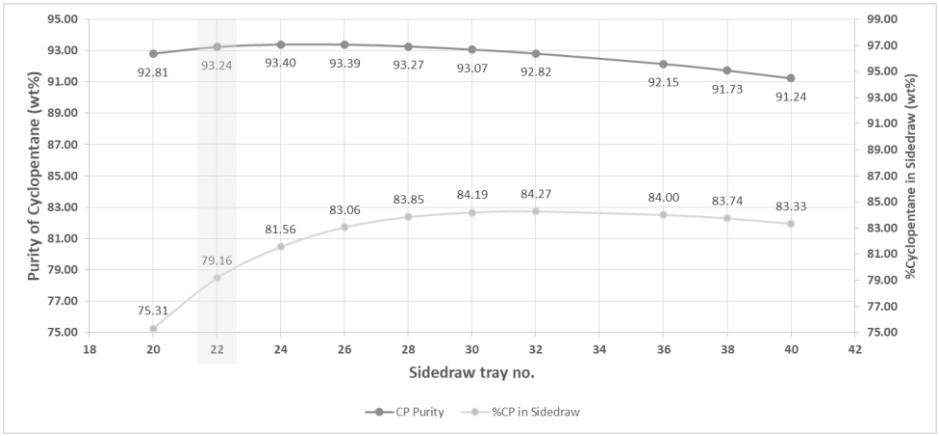

Figure 3: Sensitivity analysis on side draw tray position

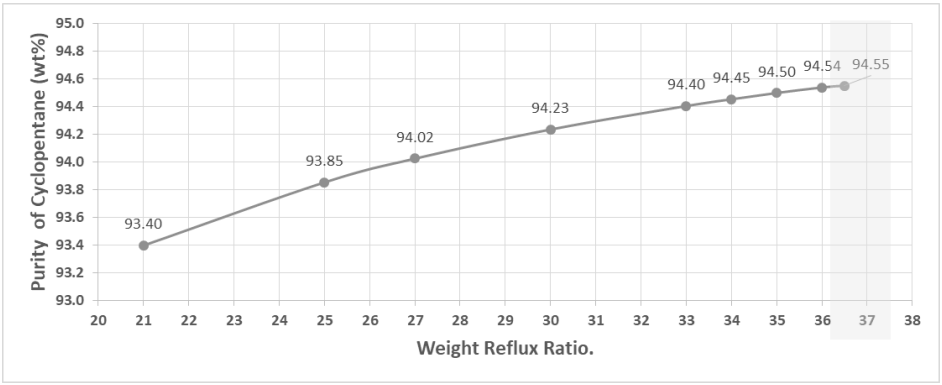

Figure 4: Sensitivity analysis on weight reflux ratio at column T1

For second alternative design, total trays at column T1 are increased about twice of base-case ones as shown in Figure 5. Side-draw tray position at column T1 was moved from trays number 40 to 24. Weight reflux ratio was changed from 21 to 29 to reduce loss of cyclopentane in both distillate and bottom streams at column T1. All of process modifications enhance separation ability of cyclopentane in column T1. Moreover, high purity of by product could be obtained at distillate stream. Higher cyclopentane content will be sent to purify in the column T2. Moreover, flow of cyclopentane was also reduced some amount to meet higher cyclopentane purity. Then 70%wt recovery of cyclopentane at the bottom of column T2 was obtained. Besides higher tray numbers and weight reflux ratio, more column modification of column was also required. From these two alternative designs using base-case distillation column is impractical and uneconomical. Therefore other alternative technology and design, like extractive distillation, becomes more concerns.

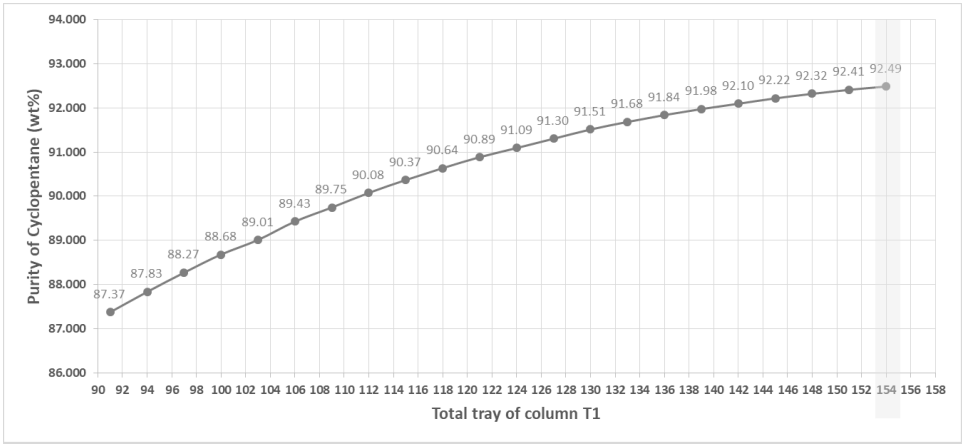

Figure 5: Sensitivity analysis on total tray required

4. Extractive distillation

Extractive distillation is an effective separation technique for azeotrope mixtures or close boiling point mixture. A polar solvent, entrainer or separating agent with high boiling point is added to interact with the components in the azeotropic or close-boiling mixtures. The solvent changes the relative volatility of the component to be separated. This work is focused on the simulation of extractive distillation for purifying cyclopentane with 95%wt purity, which based on the extractive distillation process from a publication (Lehuan Wu et al, 2018). In the publication, the extractive distillation simulation from Aspen 9.0 program was applied to simulate a cyclopentane and 2, 2-dimethylbutane separation process using solvent DMF. In this work, solvent NMP has been used as a solvent for purifying cyclopentane with 95%wt purity in column simulated by Pro/II Process Engineering Software as shown in Figure 6.

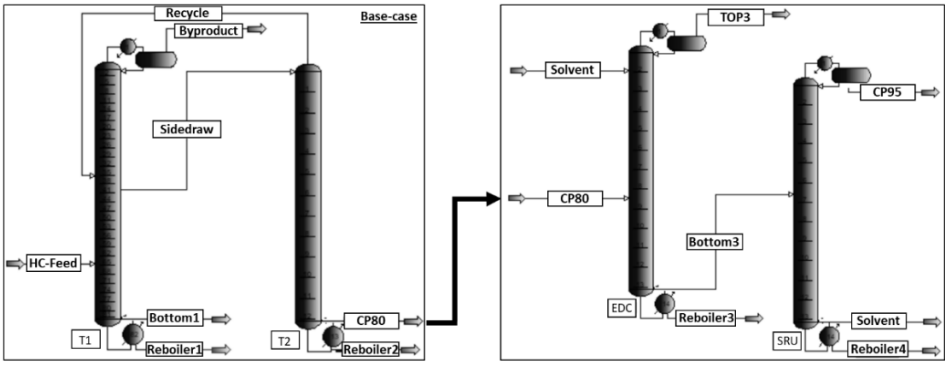

Figure 6: Extractive column (EDC) and recovery unit (SRU) added to base-case process

The bottom product stream containing 80-85%wt (CP80) along with 15-20%wt 2, 2-dimethylbutane from column T2 of the base-case distillation has been used as the close boiling point mixture feed stream in the extractive distillation simulation. The solvent NMP is used and fed to the top section to be the liquid phase in all stages of the extractive distillation column (EDC). While the close boiling point mixture is fed into the middle section of the EDC column. Once the mixture is distilled, solvent NMP will come out

with high concentrated cyclopentane at the bottom of EDC column. Mixture of solvent NMP and cyclopentane is then separated apart from each other at a solvent recovery unit (SRU). 95%wt of cyclopentane and 100%wt of solvent NMP are withdrawn at column SRU as the distillate and bottom product, respectively. And 70%wt recovery of cyclopentane at the top of the solvent recovery unit (SRU) was obtained as shown in Figure 6.

5. Conclusions

Base-case distillation models for separating extremely nonideal azeotropic mixture have been generated via Pro/II Process Engineering Software. Simulation results show large numbers of trays and reflux required. It can be concluded that it is impractical and uneconomical for purifying the close boiling mixture by base-case distillation column. While extractive distillation technology can reduce 30% and 25% of total condenser and reboiler duty, respectively. Moreover, only two additional small columns are needed in the extractive distillation process. Therefore, extractive distillation is the most promising techniques for separating and purifying of the azeotropic and close boiling mixture.

Acknowledgments

This work was funding supported by the 30th Years PPC 30 Scholarships of The Petroleum and Petrochemical College (PPC) and Pro/II Process Engineering Software was supported by Thai Oil Public Company Limited. Authors also thank Damrong Taksanont from Thai Oil Public Company Limited and Supanan Suppawatin from Sak Chaisidhi Company Limited to promote the cooperation between academic and industry.

References

W. L. Luyben, I- Lung Chien, 2010, Design and Control of Distillation Systems for Separating Azeotropes, John Wiley & Sons, Ltd., ISBN:9780470448625

M. Lavanya, M. N. S., and B. Sairam, K. Balu, 2007, Petroleum Science and Technology. Effect of Solvents for the Production of Cyclopentane by Extractive Distillation Taylor & Francis: 12

U. Kanne, F. J. H., B. Dürkheim; T. Krug, Worms, all of Germany Production of cyclopentane and/or cyclopentene from partially hydrogenated pyrolysis gasoline, BASF Aktiengesellschaft, Ludwigshafen, Germany

Richard B. Halsey, H., TX (US) (1998). METHOD OF PRODUCING PURIFIED CYCLOPENTANE. US, Equitar Chemicals, LP, Houston, TX (US).

P. C. Wankat, 2013, Separation process engineering : includes mass transfer analysis, PEARSON Education, Inc., 3rd edition

M. F. Doherty and M. F. Malone, 2001, Conceptual Design of Distillation Systems, McGraw-Hill Science/Engineering/Math, Chemical Engineering Series

J. Gmehling, M. Kleiber, 2014, Chapter 2 - Vapor–Liquid Equilibrium and Physical Properties for Distillation, Distillation: Fundamentals and Principles, Pages 45-95

Z. Lei , C. Li and B. Chen, 2003, Extractive Distillation: A Review. Separation and Purification Reviews - SEP PURIF REV. 32. 121-213. 10.1081/SPM-120026627

K. Anton, 2013, Distillation | Extractive Distillation. 10.1016/B978-0-12-409547-2.05949-7

L. Wu, L. W., Y. Liu∗, X. Guo, Y. Hu, R. Cao,X. Pu, X. Wang, 2018, "Conceptual design for the extractive distillation of cyclopentane and neohexane using a mixture of N,N-dimethyl formamide and ionic liquid as the solvent." Elsevier-Chemical Engineering Research and Design: 197-208.

Sauro Pierucci, Flavio Manenti, Giulia Bozzano, Davide Manca (Eds.)
Proceedings of the 30th European Symposium on Computer Aided Process Engineering (ESCAPE30), May 24-27, 2020, Milano, Italy.
http://dx.doi.org/10.1016/B978-0-12-823377-1.50048-3

Rigorous Simulation and Optimization of a Plant-wide Glycerol Carbonate (GC) Production Process

Bor-Yih Yu* and Wei-Jen Chen

Department of Chemical and Materials Engineering, Chang Gung University No. 259, Wenhua 1st Road, Guishan District, Taoyuan City, 333, Taiwan
boryihyu@mail.cgu.edu.tw

Abstract

The spurring increase in bio-diesel production produces a large amount of glycerol as side product, which causes its over-supply. Hence, converting glycerol (GLY) into other value added chemicals would be a promising solution. In this work, the design and optimization of a plant-wide glycerol carbonate (GC) production processes of GLY and dimethyl carbonate (DMC) is firstly proposed, which is consisted of a reactive distillation section and an extractive distillation-based separation section. The research scope includes regressing the thermodynamic parameters suitable for representing both vapour-liquid and liquid-liquid equilibrium, correcting the kinetic parameters, developing process flowsheets, and optimization.

Keywords: glycerol, glycerol carbonate, process design, optimization, reactive distillation

1. Introduction

The production of bio-diesel has been spurred in the recent years, in order to fight against the oil depletion and global warming. Yet large amount of glycerol (GLY) is also generated as the side product in accompany with bio-diesel. Hence, how to convert glycerol into the other value-added chemicals has attracted wide attention. Among the various GLY utilization routes, a very promising one is to convert it into glycerol carbonate (GC). Holding favorable properties such as low volatility, low toxicity, high bio-degradability and good reactivity, GC finds its uses as solvents, adhesives, chemical intermediate, monomers of polymers and so on.

The process studied in this work is the transesterification reaction between GLY and DMC to produce GC. Considering the difficult handling of using homoogeneous catalyst such as the need of separation from the product, the possibility of equipment corrosion, catalyst deactivation and so on, heterogeneous catalyst is used in the process design. To this end, the kinetic parameters proposed from Singh et al. (2014), in which the performance of zinc/lanthanum mixed-oxide (Zn4La1) catalyst was evaluated for temperature from 120 to 140 ˚C and DMC excess ratio from 2 to 6. According to this contribution, there are two reactions included in this process. The main reaction is to react GLY with DMC to become GC and MeOH. This is a reversible reaction, indicated by the following eq. (1) and (2). The side reaction is that GC dissociates into glycidol (GLC) and CO_2 under higher temperature, as indicated by the following eq. (3).

$$\mathrm{GLY} + \mathrm{DMC} \xrightarrow{r_1} \mathrm{GC} + 2\mathrm{MeOH} \quad (1)$$

$$\mathrm{GC} + 2\mathrm{MeOH} \xrightarrow{r_2} \mathrm{GLY} + \mathrm{DMC} \quad (2)$$

$$\mathrm{GC} \xrightarrow{r_3} \mathrm{GLC} + \mathrm{CO_2} \quad (3)$$

The main contribution of this work is to develop the plant-wide process for GC production based on reactive distillation. The proposed process is then optimized, and the limitations for operation are summarized. This paper will provide another baseline for further studies, especially in scale-up, control, operation and economical evaluation.

2. Overview of this work

In this work, simulations were performed in Aspen Plus V10. NRTL is selected as the thermodynamic model in simulation. There are seven components included in this work, which are glycerol (GLY), dimethyl carbonate (DMC), methanol (MeOH), glycidol (GLC), glycerol carbonate (GC), carbon dioxide (CO2) and aniline (ANI). The Aspen built-in binary parameters are used if they exist. Otherwise, they are estimated by UNIFAC. Note that the binary pairs in between DMC, GLY, MeOH, and GC were regressed based on the liquid-liquid equilibrium data found in the paper by Esteban et al. (2014), and the vapour-liquid equilibrium data from NIST. The regressed parameters are listed in Table 1.

Table 1. Re-regressed binary interaction parameters in between the selected components

Comp i	Comp j	Temp. Unit	a_{ij}	a_{ji}	b_{ij}	b_{ji}	c_{ij}
GLY	MEOH	C	-0.89448	0.200844	162.205	259.384	0.3
GLY	DMC	C	-2.04183	-0.75795	1300.07	1063.04	0.2
GLY	GC	C	0	0	980.274	-402.219	0.3
DMC	MEOH	C	-1.22636	-1.19606	563.468	669.367	0.1
DMC	GC	C	0	0	143.475	-127.974	0.2
MEOH	GC	C	0	0	58.5085	1638.81	0.3

The reaction kinetic is referenced from Singh et al. (2014), which is a power-law model. The kinetic parameters are re-regressed to reach a better fit of reaction conversion and GC selectivity. The rate equations are listed in eq. (4) to (6).

$$r_1 = 2.29 \times 10^{15} \exp\left(\frac{-138719}{RT}\right) X_{DMC} X_{GLY} \quad (4)$$

$$r_2 = 1.04 \times 10^{7} \exp\left(\frac{-77500}{RT}\right) X_{GC} X_{MeOH}{}^2 \quad (5)$$

$$r_3 = 2.72 \times 10^{9} \exp\left(\frac{-115346}{RT}\right) X_{GC} \quad (6)$$

In the optimization part, the objective function was to minimize total annual cost (TAC), which was calculated as the following eq. (7). Correlation provided by Luyben was used to calculate the capital and operating cost (Luyben , 2011), with the assumption of 3-year payback period and 8000 hours of annually operation. In eq. (7) the correction term on the GC production rate (in kg/year) is included, in which GC_{optim} represents the GC production rate in the final optimal case, GC_i means the GC production rate in any other case. GC_{cost} is the price of GC, which is assumed to be 2.4 USD/kg. With this expression, the difference of GC production rate comparing with the optimal case is quantified as a correction term in TAC.

$$\mathrm{TAC(kUSD/yr)} = \frac{\mathrm{Capital\,Cost}}{\mathrm{Payback\,Period}} + \mathrm{Operating\,Cost} + (\mathrm{GC_{optim}} - \mathrm{GC_i}) \times \mathrm{GC_{cost}} \quad (7)$$

3. Process Design and Optimization

One intuition when mentioning reactive distillation technique is that, whether the stoichiometric ratio of DMC to GLY (ER=1) can be used to achieve the targeted (99% in this work) in a single reactive distillation column. However, it may not be feasible in this process, and the reason is two-fold. Firstly, if ER=1 is used for reactive distillation, the bottom stream will be high-purity GC. But GC holds a very high normal boiling point, which makes the bottom temperature unfavourably high. If this is the case, then electricity (or other higher grade heat sources) must be used at the column bottom. Secondly, a very high column temperature may lead to more GC decomposition, which is also undesired.

One solution to this condition is to operate the reactive distillation column under vacuumed condition in order to let HPS usable. However, this means that the reaction would be operated at a relatively lower temperature region. As Singh et al.'s kinetic data is used in this work, we would keep the reaction temperature in between 120 to 140 ˚C.at which the interested operating temperature is in between 120 to 140 Hence we consider this aspect outside the scope of this paper. The possibility of a vacuumed distillation column was not ruled out, but would be discussed if there is a more suitable kinetic data in the future.

In this work, we analysed the case which also uses excess of DMC in the reactive distillation process. The optimized flowsheet with ER=2 is illustrated in Figure 1, with the details of optimization addressed later.

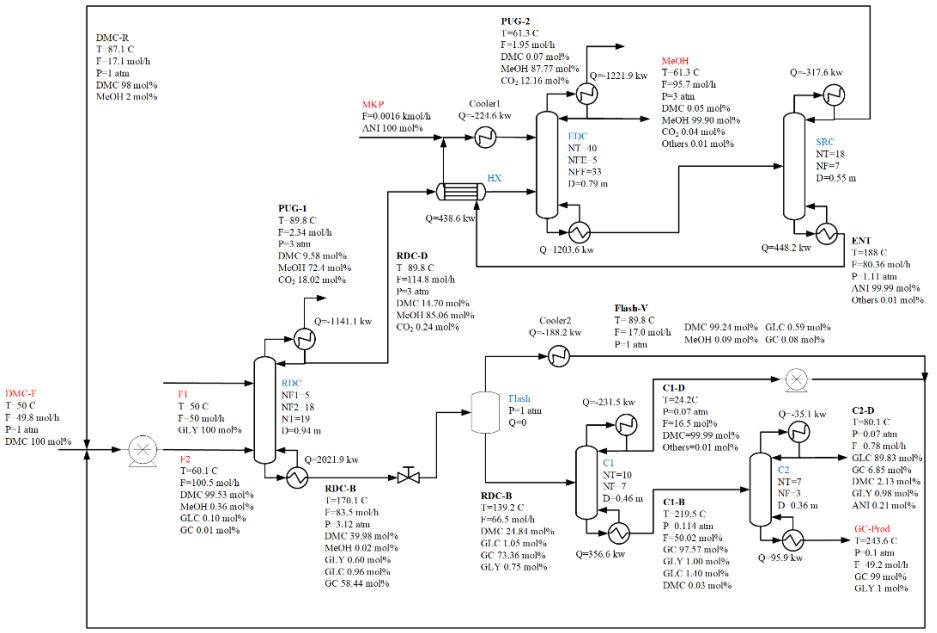

Figure 1. The optimal flowsheet of the RD process.

Firstly, the GLY feed enters at the upper section (5th tray), and the combined DMC stream enters at the lower section (18th tray) into a reactive distillation column (RDC). The reactive section is in between these two feed locations, in which each tray packed with 50% volume of the solid catalyst. The catalyst holdup is calculated by the following equation:

$$\text{holdup} = \frac{\pi D^2}{4} \times WH \times 0.9 \times 0.5 \times \rho_{cat} \quad (8)$$

Where D is the column diameter in meter; WH is the weir height which is set to be 0.1016 meter (4-inch), and ρ_{cat} is the catalyst density (1000 kg/m^3). A downcomer area of 10% is also assumed. The calculated holdup is in unit of kg catalyst.

From RDC, a near-azeotropic DMC/MeOH mixture is obtained at the top, while the bottom stream contains the generated GC, the remaining DMC, the unreacted GLY and the slight amount of side product GLC. Besides, as slight amount of CO_2 is formed by GC dissociation, a partial vapour-liquid condenser is equipped in this column, setting 2% vapour purged from the column. The optimal column pressure is 3 atm, with 0.0068 atm pressure drop per tray. The bottom stream from RDC is then depressed to 1 atm, and is flashed. The flash liquid is sent to downstream columns, C1 and C2, for GC recovery. The flash vapour stream contains very high purity of DMC, so it is condensed to become saturated liquid, combined with the C1 distillate, and is then recycled to RDC. The purity for the final GC product is set at 99 mol%, and other specifications for the units in the processes can be found in Figure 1. In order to let the high pressure steam usable (254 ˚C) as the reboiler heat source, both C1 and C2 are operated under 0.07 atm. The pressure drop of these two vacuumed columns are set at 0.005 atm per stage.

On the other side, the distillate from the RDC is sent to the extractive distillation section to separate DMC and MeOH, which uses ANI as an entrainer. The design concept is similar to that in Yu et al's previous work (Yu et al., 2018). The entrainer to feed molar ratio is set to be 0.7 in this case. The DMC purity from the SRC top is set at 98 mol%, which is determined from optimization, and is going to be discussed in more detail in the following.

The proposed RD process is also optimized by sequential iterative method to minimize TAC. Due to the text size, only the most influential variables are discussed here. These variables are the pressure of the reactive distillation column (P_{RDC}), excess ratio (ER) and the DMC purity from the extractive distillation section. Figure 2(a) shows the TAC change of the optimal cases with varying ER under P=3 atm, while Figure 2(b) and 2(c) records the temperature profiles and the reaction profiles of these cases. It is found that the TAC continues to drop with decreasing ER, which means that the reduction in separation cost dominates. From the temperature profile, it is observed that the bottom temperature becomes higher with decreasing ER. The corresponding bottom temperature is 156.3 ˚C for ER=2.5, and 170.0 ˚C for ER=2. Under these cases, the MPS should be used as the heat sources in the RDC reboiler. On the opposite, the bottom temperature is 149.6 ˚C for ER=3, in which the low pressure steam (LPS, 6 bar, 160 ˚C) may still be used. Although it requires a lower grade of heating source, the cost saving do not make up for the higher cost resulted from the increased system loading in the ER=3 case comparing with those lower ER cases.

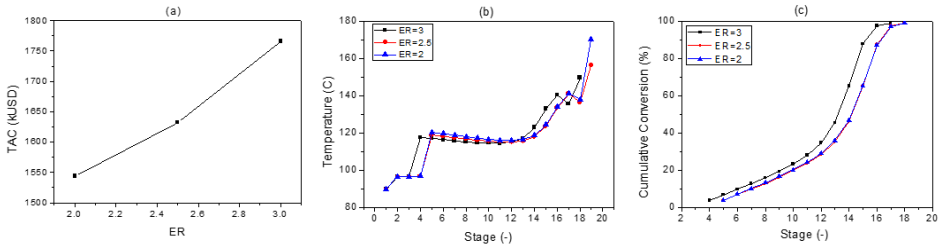

Figure 2. Optimization Results under P_{RDC}=3 atm and varying ER. (a) TAC; (b) Reaction temperature; (c) Reaction conversion profile in RDC.

Figure 3(a) shows the TAC variation of the optimal cases with different P_{RDC} under ER=2, while Figure 3(b) and 3(c) recorded the temperature profile and the reaction profile of these cases, respectively. From these figures, it is observed that TAC becomes lower as P_{RDC} decreases, although greater P_{RDC} leads to higher column temperature which benefits the reaction rate. This represents again the fact that the system loading plays a dominant role in this process. The large drop at P_{RDC}=3 atm in Figure 3(a) is because the cheaper MPS can be used in RDC reboiler. While in P_{RDC}=3.25 and 3.5 atm cases, HPS is needed. Also, it is clear that the number of reaction trays becomes larger as P_{RDC} decreases. From Figure 7(b) it is noted that under P_{RDC}=2.5 atm, the temperature in the reactive section mostly lies below 115 ˚C, with the lowest tray temperature at 111.7 ˚C. Hence, we do not consider this case as the optimal one, as the temperature is too far away from the lowest validated value (120 ˚C). For the case at P_{RDC}=3 atm and 3.25 atm, it is also observed that at some of the reactive trays have temperature lower than 120 ˚C. The lowest tray temperature at P_{RDC}=3 atm case is around 116 ˚C, and in P_{RDC}=3.25 atm case it is 117.6 ˚C. For the P_{RDC}=3.5 atm case, almost all the tray temperature lies in the range between 120 to 140 ˚C, with the lowest temperature at 119.7 ˚C. But when considering the highest temperature on the reactive section, they are 141.3 ˚C, 142.5 ˚C and 143.6 ˚C for P_{RDC}=3, 3.25 and 3.5 atm, respectively. In the 3 atm case, only one tray exceeds 140 ˚C, while two trays exceed this limit for the 3.25 and 3.5 atm cases. Because high reaction temperature leads to greater GC decomposition, here we consider exceeding the temperature upper limit to be more undesired. Hence, the P_{RDC}=3 atm case would be viewed as the optimal one, as it shows a reasonable length of reactive section in RDC as well as a low TAC.

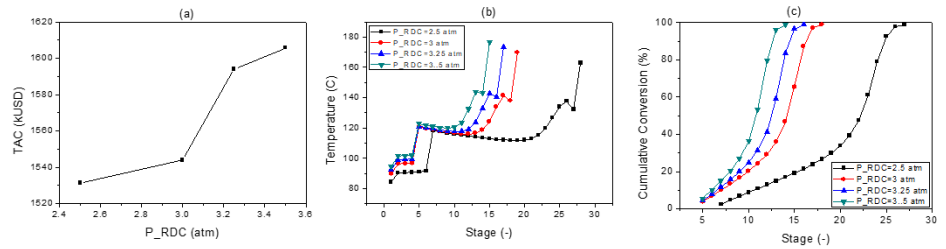

Figure 3. Optimization Results under ER=2 and varying P_{RDC}. (a) TAC; (b) Reaction temperature; (c) Reaction conversion profile in RDC.

The test results on how the DMC purity from SRC distillate affects the performance are illustrated in Figure 4. Previously, we found that the case operating at P=3 bar and

ER=2 is the best case. Here, the analysis starts from this case, varying the DMC purity from 0.995 down to 0.96. From Figure 4(a) it is observe that the DMC purity slightly affects the TAC for this case, and the optimal point is at 0.98. However, the difference is very small. The reason is due to the fact that the recycled DMC from the extractive distillation accounts only for less than 20% of the total flowrate in the combined feed. Even if the small variation, the trade-off caused by different DMC purity can be discovered. Based on this fact, the optimal cases under different P, ER, and DMC purity are compared, and the results are shown in Figure 9(b) and 9(c). From this figure, it is observed that in all cases, DMC purity at 98mol% has a slightly better economic performance comparing with the 99.5 mol% case.

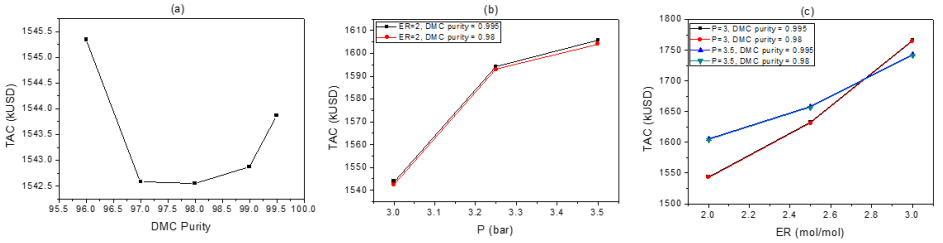

Figure 4. TAC comparison under DMC purity=99.5 and 98 mol%. (a) Optimized TAC comparison; (b) TAC comparison at ER=2 and different P_{RDC}; (c) TAC comparison at P_{RDC}=3 and 3.5 bar under varying ER.

4. Conclusions

In this work, two plant-wide processes to produce GC based on reactive distillation and extractive distillation were rigorously simulated and optimized. The investigation started from regressing the binary interaction parameter sets in the GLY/DMC/MeOH/GC quaternary system. The regressed parameters can be used to represent both the vapour-liquid equilibrium, and also the LLE equilibrium under different temperatures. Besides, the reaction kinetics parameters were also re-regressed to better fit the experimental data. Then, the process was rigorously simulated, and then optimized by sequential iterative method to minimize TAC. The variation of TAC caused by three important variables (P_{EDC}, ER and DMC purity) were clearly illustrated. Note that the process was designed at ER=2 in this work. From the viewpoint of adopting reactive distillation, we suggest that the future kinetic research focus more on the reaction performance at a lower temperature, and also for a larger temperature range. This would lead to another possible improvement in the operation of the RD process.

References

J. Esteban, M. Ladero, L. Molinero, F. Garcia-Ochoa, 2014, Liquid-liquid equilibria for the ternary systems DMC-methanol-glycerol, DMC-glycerol carbonate-glycerol and the quaternary system DMC-methanol-glycerol carbonate-glycerol at catalytic reacting temperatures, Chem Eng Res Des, 92 (12), 2797-2805.

W. L. Luyben, 2011, Principles and Case Studies of Simultaneous Design, Chap. 5. Wiley: New York.

D. Singh, B. Reddy, A. Ganesh, S. Mahajani, 2014, Zinc/Lanthanum Mixed-Oxide Catalyst for the Synthesis of Glycerol Carbonate by Transesterification of Glycerol, Ind Eng Chem Res, 53 (49), 18786-18795.

B. Y. Yu, M. K. Chen; I. L. Chien, 2018, Assessment on CO2 Utilization through Rigorous Simulation: Converting CO2 to Dimethyl Carbonate, Ind Eng Chem Res, 57 (2), 639-652.

Sauro Pierucci, Flavio Manenti, Giulia Bozzano, Davide Manca (Eds.)
Proceedings of the 30th European Symposium on Computer Aided Process Engineering (ESCAPE30), May 24-27, 2020, Milano, Italy.
http://dx.doi.org/10.1016/B978-0-12-823377-1.50049-5

CFD-based Design Optimization of Air Quenching Equipment to Enhance the Cooling Effect

Jiwon Roh,[a,b] Hyungtae Cho,[a] Yeongryeol Choi, [a] Hyundo Park, [a] Il Moon,[b] Junghwan Kim[a,*]

[a]*Korea Institute of Industrial Technology, 55 Jongga-ro, Jung-gu, Ulsan 44413, Republic of Korea*
[b]*Yonsei University, 50 Yonsei-ro, Seodaemun-gu, Seoul 03722, Republic of Korea*
kjh31@kitech.re.kr

Abstract

To improve the productivity and quality of industrial products, it is necessary to improve the cooling effect of the air quenching equipment. To optimize the design of the air quenching device, case studies involving numerical analyses using the computational fluid dynamics (CFD) technique were performed. The reliability of the CFD model was validated by comparing the product temperature results obtained using the CFD model with the experimental results obtained using an actual commercial equipment to cool an aluminum alloy product weighing 36 kg. It was observed that the main variables influencing the cooling effect of the air quenching equipment included the distance between air inlet and the product, air velocity at the inlet, and inlet design. A smaller distance between the inlet and the product corresponded to a better cooling effect. The air velocity at the inlet was dependent on the inlet design and flow rate of the air, and the cooling effect varied with the inlet design. When the products at a temperature of 535 °C were cooled for 1200 s, the average temperatures of the cooled products were 190 °C and 117 °C in the cases involving air quenching equipment with a non-optimized and optimized inlet design, respectively. Thus, the optimization of the inlet design could lead to a higher cooling effect, with a temperature reduction of 73 °C. It is expected that the findings of this work can be used to design air quenching equipment with an excellent cooling effect.

Keywords: CFD, air quenching, air cooling, numerical analysis, design optimization, cooling effect.

1. Introduction

Quenching is a crucial part of the heat treatment process of hardening in metals. Alloys are subjected to the quenching process to convert the pearlite grain structure, which is soft and unsuitable for practical uses, into a considerably harder form known as martensite. Previous studies employed different types of simulation techniques to produce high-quality alloys via the quenching process. Xiao et al. (2010) studied the heat transfer during the water quenching process of aluminum alloys, and Yang et al. (2013) performed a finite element method (FEM)-based investigation of the residual stress distribution on the surface of a metal after quenching. Based on the cooling rate required for each alloy type, different types of heat media, such as air, water, and oil, can be used. However, when using a liquid heat medium such as water or oil, it is difficult to remove the generated by-products or liquid waste during the quenching process. Furthermore, it is difficult to ensure a uniform residual stress distribution on the alloy surface. Consequently, the use

of air quenching, which is a relatively environmentally friendly technique, has recently become popular in the industry. Although the cooling rate of air quenching is lower than that of other quenching techniques, this technique allows the realization of an advanced heat treatment, and the products can be cooled uniformly without the generation of any additional by-products or waste.

Despite the usefulness of this technique, no existing study has reported on the improvement of the cooling efficiency of air quenching equipment by analyzing the cooling stream inside the device and changing the inlet design of the air flowing from the blower. To allow a wider implementation of air quenching in the industry, the objective of this study was to enhance the cooling effect of the air quenching equipment via design optimization using CFD techniques. The inlet design parameters influencing the cooling efficiency were identified by performing case studies, and the design optimization was carried out accordingly.

2. CFD Simulation

The model setup and simulation analysis were performed using the commercial software Star CCM+. Each case required approximately one hour of computation time.

2.1. Numerical analysis procedure

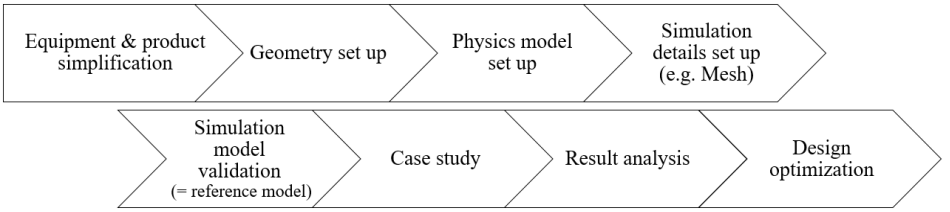

Figure 1. CFD simulation set up and numerical analysis procedure

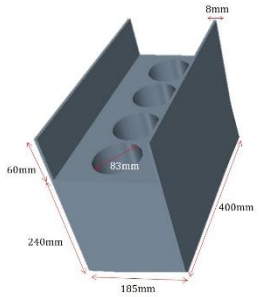

Figure 2. Product geometry

Table 1. Equipment properties

Set up region	Specific heat capacity	Density
Tray	25.10 J/mol·K (25℃)	7.324 g/cm^3
Conveyor	27.23 J/mol·K (25℃)	7.850 g/cm^3

Table 2. Product properties

Set up region	Specific heat capacity	Density
Product	24.14 J/mol·K (25℃)	2.701 g/cm^3

The model setup and numerical analysis procedure for the design optimization using a CFD simulation is shown in Figure 1. Similar to the actual device and product, a model simplification is required to design a shape suitable for the CFD analysis. However, the characteristic parts of the shape, such as the wings and corners, should be the same as those in the actual device to accurately reflect the flow distribution in the CFD analysis. In addition, the physical information and mass of the device and the product should be the same to ensure that the heat capacity is the same in both cases. In this study, a product model with a mass of 34 kg and composed of the same aluminum alloy as the actual product is simplified, as shown in Figure 2. The physics model is required to be established carefully, and the governing equations used in this work are described in detail in Section 2.2. Among the simulation details, the post-processing settings must be set appropriately for displaying the research results; in addition, it is important to suitably set

the shape type and number of meshes to perform accurate calculations and obtain accurate results. The validation of the simulation model is shown in Figure 3. By analyzing the quenching results for each inlet design through a case study, the most optimum design was identified, and the design parameters for the optimized design were determined.

2.2. CFD modeling equations

The CFD simulations were performed based on the Navier–Stokes equation. The heat transfer method involved a thermal analysis of a high temperature model, with a temperature of more than 500 ℃; however, only conduction and convection were considered and the radiation phenomenon was ignored to improve the convergence of the result data and reduce the calculation cost. The flow used in the simulation was evaluated using the k-epsilon turbulence model.

2.3. Equipment geometry

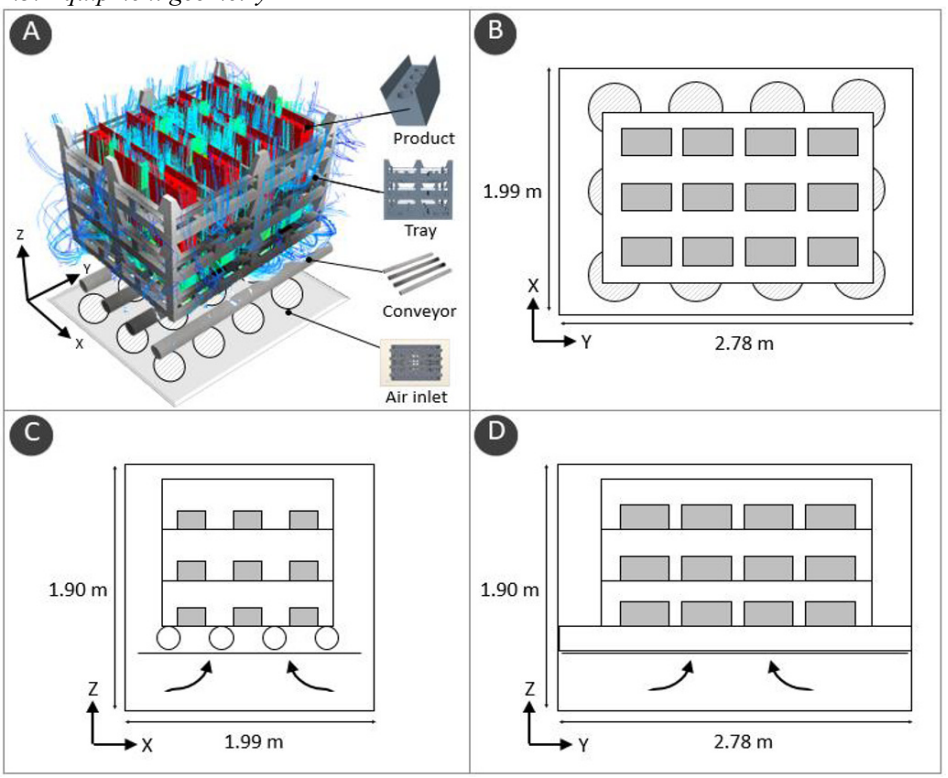

Figure 3. (A) Geometry model of the equipment in the CFD simulation. (B) Side view; (C) front view; and (D) top view of the equipment

The geometry of the simulation model used in this study is shown in Figure 3. Figure 3 (A) shows the overall geometry. Air is supplied from the lower air inlet, and the conveyor is located in the upper area adjacent to the air inlet. The total number of layers is 3. A total of 36 products are considered, and the tray of each layer above the conveyor has 12 products. The product placement and other internal geometry parameters of the equipment are shown in Figures (B), (C), and (D) using the orthogonal coordinate system represented in Figure (A).

2.4. Simulation conditions

The boundary conditions of the CFD simulation can be defined as follows. The external air enters through the air inlet located at the bottom of the device, cools 12 products per

layer on the tray, and is later vented through the top air outlet. The product and tray are heated to 535 ℃ in the furnace and supplied to the equipment by the conveyor. In this study, the heat exchange in the equipment for only one cycle of cooling was considered.

Table 3. Summary of simulation conditions

Domain	Value
Air inlet speed [m/s]	9.037
Air inlet temperature [℃]	80
Gravity [m/s^2]	-9.81

2.5. Inlet design

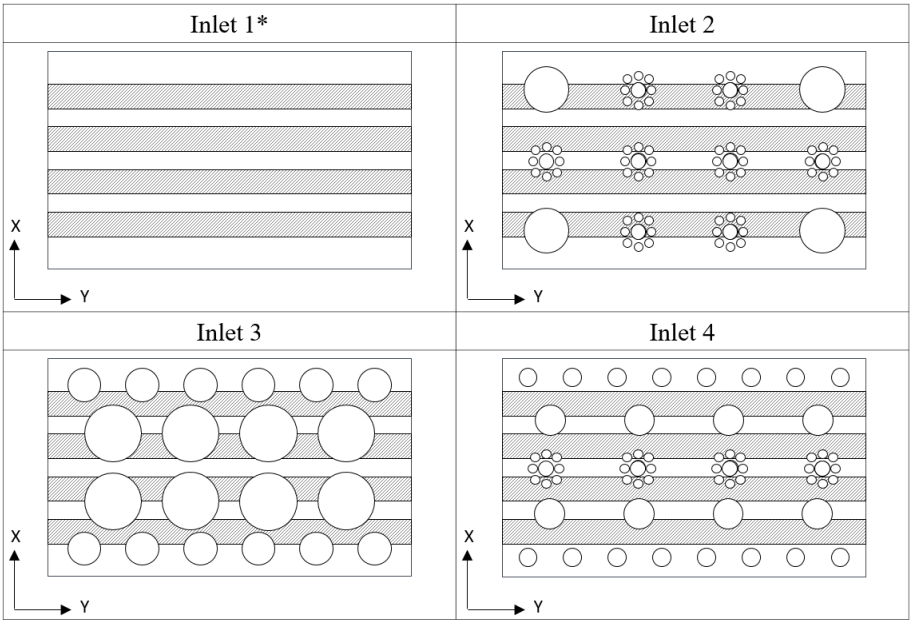

Figure 4. Inlet design

The inlet design used in the simulation is shown in Figure 4. The four long rectangles in Figure 4 represent the conveyor, and the circles represent the inlet. When air enters the equipment using the same number of blowers, a larger size of the inlet and more number of inlets correspond to a lower airspeed per unit through the inlet. Furthermore, the conveyor acts as a type of baffle that changes the flow distribution upon contact, and thus it is important to distribute the inlets to ensure that the flow does not change around the conveyor position. To investigate the effect of the inlet design on the cooling effect, the reference model (inlet 1) is compared with inlets 2, 3, and 4 without setting up a detailed inlet.

3. Model validation

The simulation results for the reference model, that is, inlet 1 indicated that the cooling rates of the product, as obtained using the model and the actual experimental equipment were nearly equivalent with a value of -4.9628 ℃ / s

4. Results and discussion

The results of the CFD case studies corresponding to the inlet design are presented in Table 5. After 1200 s, inlets 1 and 2 exhibited a temperature difference of more than two times.

Figure 5. Average temperature of the products with different quenching times

Inlet	Average temperature for quenching time of 600 s	Average temperature for quenching time of 1200 s
1	329.91	215.47
2	182.13	99.30
3	221.23	130.90
4	202.86	130.96

Figure 6 shows the average temperature for different quenching times. The results indicated that an excellent cooling effect occurs when a separate inlet exists.

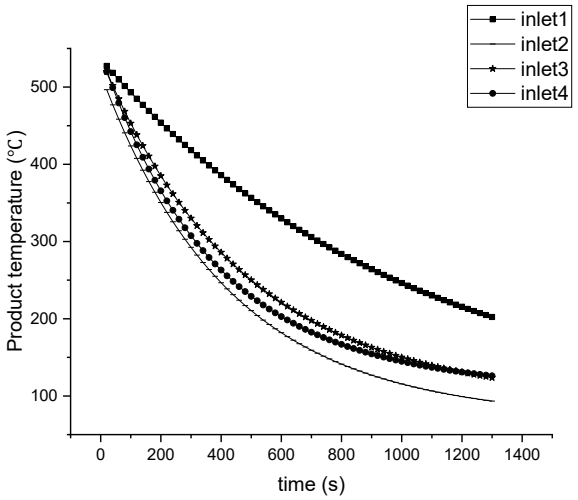

Figure 6. Comparison of average temperature of the products for different quenching times and inlet designs

The flows of inlets 1 and 2, which exhibited a notable difference in the cooling, were compared, as shown in Figure 7, to identify the cause of the difference. As shown in Figure 7 (A), the products located on the outside of the inlet 1 case experienced only a few cooling streams and a low flow rate, resulting in a relatively small cooling. However, the flow distribution of the inlet 2 case involved several cooling streams passing around the product and the flow rate was high, leading to a high cooling effect, as shown in Figure 7 (B). As shown in Figure 7 (C), the flow rate of the upper layer was approximately 30 m/s, which is relatively low compared to the flow rate of 40–60 m/s observed in Figure (D). Consequently, the cooling effect of the quenching equipment with inlet 1 was not satisfactory, since the cooling flow disappeared after impacting the wall and efficient cooling was not performed. As shown in Figure 7 (D), the upper part involved a flow faster than 40 m/s, which passed the product at a high speed, thereby generating an excellent cooling effect. In the case of inlet 2, the air passing through the inlet hit the conveyor and was evenly distributed, thereby effectively cooling the first-floor products. Rapid flows through the small-sized inlets often moved to the top without disappearing.

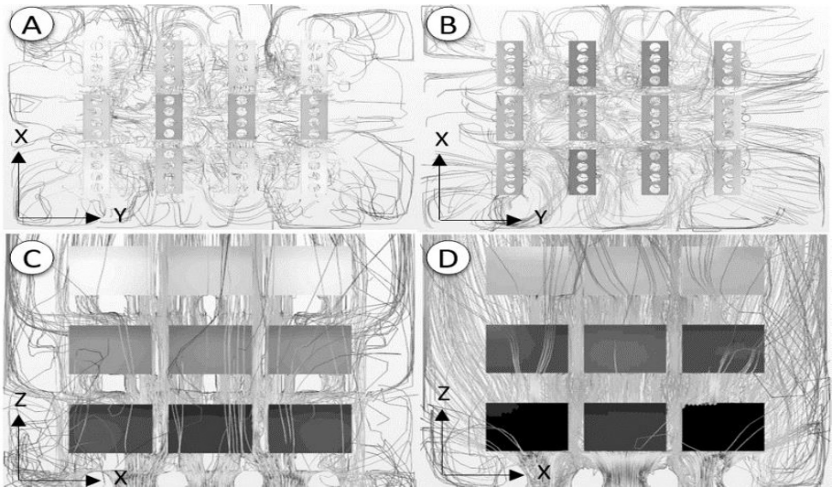

Figure 7. Flow distribution in the air quenching equipment. Top view for (A) inlet 1 and (B) inlet 2. Front view for (C) inlet 1 and (D) inlet 2

5. Conclusions

In this study, four case studies were investigated using CFD to increase the cooling effect of the air quenching equipment. The results indicated that the cooling effect of the different inlet designs was significantly different from that of the reference model. To enable the application of the findings in the actual industry, design optimization was performed in terms of the design optimization parameters. The flow of inlet 2, which led to the best cooling effect, was analyzed, and the following two factors were noted to increase the cooling effect.

(1) If the flow through the air inlet hits the conveyor and is evenly distributed, the cooling effect of the first-floor products is improved. Therefore, it is more desirable to place the inlet close to the conveyor to ensure that it can be directly cooled.

(2) The cooling rate is higher when the air inlet is smaller. Consequently, a smaller air inlet is more desirable, as it can improve the cooling of the products located in the upper layer of the third floor of the tray.

In future studies, the layout and size for the inlet can be numerically formulated for the optimization. The optimized inlet design will be applied directly to the equipment.

References

B. Xiao, Q. Wang, P. Jadhav, K. Li, 2010, An experimental study of heat transfer in aluminum castings during water quenching, Journal of Materials Processing Technology, Volume 210, Issue 14, Pages 2023-20281

X. Yang, J. Zhu, Z. Nong, Z. Lai, D. He, 2013, FEM simulation of quenching process in A357 aluminum alloy cylindrical bars and reduction of quench residual stress through cold stretching process, Computational Materials Science, Volume 69, Pages 396-413

L.Huiping, Z. Guoqun, N. Shanting, H. Chuanzhen, FEM simulation of quenching process and experimental verification of simulation results, Materials Science and Enginering: A, Volumes 452–453, Pages 705-714

Sauro Pierucci, Flavio Manenti, Giulia Bozzano, Davide Manca (Eds.)
Proceedings of the 30th European Symposium on Computer Aided Process Engineering (ESCAPE30), May 24-27, 2020, Milano, Italy.
http://dx.doi.org/10.1016/B978-0-12-823377-1.50050-1

Integration of Computational Chemistry and Artificial Intelligence for Multi-scale Modeling of Bioprocesses

Nima Nazemzadeh, Laura Wind Sillesen, Rasmus Fjordbak Nielsen, Mark Nicholas Jones, Krist V. Gernaey, Martin P. Andersson, Seyed Soheil Mansouri*

Process and Systems Engineering Centre, Department of Chemical and Biochemical Engineering, Technical University of Denmark, Building 229, 2800, Lyngby, Denmark

Seso@kt.dtu.dk

Abstract

Bio-based manufacturing is playing an increasingly important role. Flocculation is an important step in bio-manufacturing, and in water, wastewater treatment and the food industry. Flocculation is a multi-scale process with phenomena that span from the nano-scale all the way beyond the microscale. The control and monitoring of such a process is a difficult task due to the lack of knowledge towards modeling the process across the scales. The intention of this work is to develop a hybrid systematic model-based framework, which integrates the computational methods in chemistry and stochastic modeling approaches for monitoring and control of the flocculation process above microscale. The framework therefore utilizes a hybrid model structure. Since industry resorts to either manual control or no control at all for flocculation, it is aimed to reduce the time required for manual control and to avoid unnecessary product losses and unwanted process variations during the operation.

Keywords: Flocculation, Hybrid Modeling, Computational Chemistry, Artificial Intelligence

1. Introduction

Separation of particles from a suspension in a liquid can be studied in different research areas and applications. The removal of particles from suspensions can be facilitated by flocculation in a stirred reactor [1], since the velocity gradient in the system brings the particles close enough to each other to collide and make an aggregate [1].

Figure 1 represents a schematic figure of shear induced flocculation with polymers as surfactant. Flocculation is a process where two or more particles of the dispersed phase collide and cluster as an aggregate. This process consists of different phenomena including aggregation/agglomeration, fragmentation, breakage and erosion. The mathematical modeling of flocculation, leads to employing a population balance model (PBM) [2] similar to other applications of modeling particle processes. In this work, flocculation dynamics are simulated with a basic form of a PBM represented in Eq. (1). The first and third terms in Eq. 1 account for the generation of flocs of size class *i* due to the aggregation of smaller size aggregates and fragmentation of larger size aggregates respectively, while the second term represents the destruction of such aggregates due to

the fragmentation, and the remaining terms stand for the destruction of flocs considering breakage and erosion [2].

$$\frac{dN_i}{dt} = \sum_{\substack{j,k \\ v_{i-1} \le (v_j + v_k) \le v_{i+1}}}^{j \ge k} (1 - \frac{1}{2}\delta_{j,k})\eta_i \alpha_{j,k} \beta_{j,k} N_j N_k - N_i \sum_k \alpha_{i,k} \beta_{i,k} N_k + \sum_k \gamma_{j,i} S_j N_j - S_i N_i \quad (1)$$

Where N_i is the number of flocs in size class i, v_i stands for the volume of a size class i. $\delta_{j,k}$ is the delta-dirac function in order to avoid considering the collisions twice, η is a proportional coefficient that shows how the generated floc size should be assigned to the size classes of the model, while α is the collision efficiency and β is the kernel corresponding to aggregation. S is the breakage kernel and γ is the breakage distribution function that determines the fraction of daughter particles in each size class. The subscripts j and k represent the size classes collide. This PBM is implemented with the python based package TensorFlow in a hybrid framework [3].

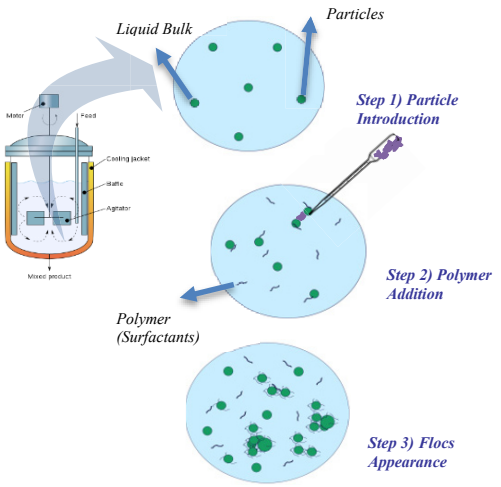

Figure 1: Schematic overview of a flocculation in three sequential steps

2. Hybrid Framework

The aim of this study is to develop a hybrid framework that uses computational methods in chemistry as the first-principles model and a data driven method as the black box element to train the model to find the best fitting flocculation kinetics for the PBM presented previously. Figure 2 represents the overview of this hybrid framework. The model of the process can be represented through the use of constitutive equations and balance equations. The variable u is a vector of input variables including the particle size distribution and process variables from the sensor measurements, while x is the vector of state variables retrieved from density functional theory (DFT) calculations, and together

with the process variables the interfacial tension (IFT) between the particles is determined. The machine learning algorithm receives the constitutive variables and the input variables, in order to train the neural network and to predict the kinetic rates of the population balance model (y; vector of output variables). The output variables are used to update the constitutive equation. Then the particle size distribution during the operation is predicted by the model during the operation of the process and it is compared with the experimental results to validate the model.

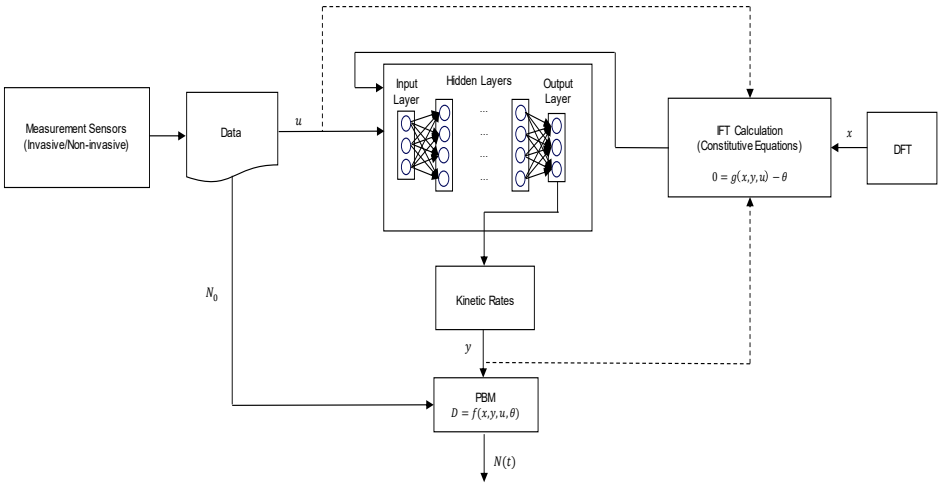

Figure 2: General overview of the hybrid framework

The framework uses computational quantum chemistry as the means to provide a more precise phenomenological understanding of the process. The first-principles model employs DFT calculations to carry out a geometry optimization on the molecules in the system by Turbomole®. Afterwards, possible conformers of these molecules are determined by using COSMOconfX® with BP-TZVPD-FINE basis set. Then, the conformers are introduced in COSMOthermX® to generate the σ surfaces profiles (COSMO surfaces). The σ surface shows the screening charge density, σ, on the molecule surface [4]. The σ surface is then used to calculate the interfacial tension between the particles in the system. The interfacial tension between particles has to be calculated for a solid-liquid interface, which is developed based on the liquid-liquid model of this property in Andersson et al. [4].

The data-driven model is composed of a neural network, which is utilized to find the best kinetics of agglomeration and breakage for the flocculation process. The framework is structured such that the data collected from the first-principles model is used to determine the parameters required for the kinetics of the process. In order to provide the machine learning algorithm with the process variables and floc properties, an experimental setup is prepared. The experimental setup consists of an optical scanning device (oCelloscope by ParticleTech ApS) and an in-line pH measurement for the suspension and an impeller with velocity data transmission. The deep learning algorithm uses the data from the first-principles model (at non-observable scale) and the measurements at microscale to find the best fitting expression governing the system. The proposed framework in this study includes an array of technologies at different technology readiness level (TRL) from fundamental research in nano-scale (low TRL) to using advanced optical measurements

(high TRL). Thereby, this facilitates the industry to use a systematic design framework for such complex processes towards industrial implementation. An optimal or near optimal solution will be the outcome of the framework. For instance, by using such framework the polymer usage for flocculation can be optimized during the operation, which is one of the important variables that industry can hardly optimize it in lack of an efficient control and monitoring strategy.

3. Experimental Procedure

A thorough literature study has been carried out to determine the most important parameters for flocculation processes. Among different process variables, pH and velocity gradient induced by the impeller are studied in this work. A design of experiments (DoE) is carried out using the Sobol method [5]. The DoE analysis is carried out for the two variables pH and the shear induced in the range of 2-8 and 50-500 s^{-1}, respectively [6,7]. The Sobol method applies a quasi-random sequences over the parameter space. This will allow to re-use the measurements when conducting more physical experiments with additional process parameters and to use the same sample set for the computational model by applying Monte Carlo based statistical analysis. In this way a cyber-physical setup for the automation of experiments in future research work will be prepared.

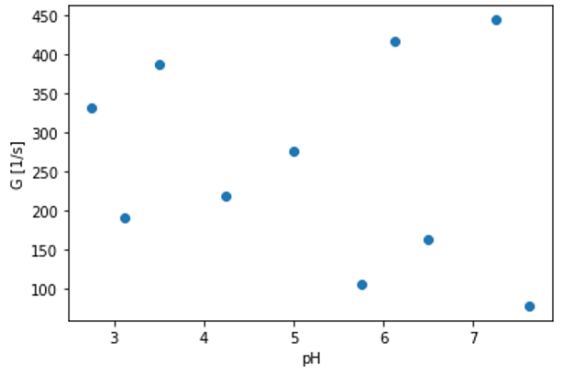

Figure 3: Sampling points for the Sobol method for pH and induced shear

Silica nanoparticles (7631-86-9, size range 0.5-10 μm, Sigma Aldrich) were used as received. 5 M hydrochloric acid and 5 M sodium hydroxide solutions were prepared and used for pH adjustment. The experimental procedure was carried out using the image analysis device (oCelloscope by ParticleTech ApS) and the reactor setup (by Applikon biotechnology) was used for pH measurement and an impeller velocity control system. The sample was agitated by ultrasonication (UP200S Ultrasonic Processor by Hielscher).

A silica suspension was prepared with demineralized water (0.02% wt/wt), 200 mL were ultrasonicated for 5 minutes at an amplitude of 60%, and then transferred to the reactor, which has an impeller to provide shear and a pH probe for measurement. The pH was adjusted and a sample taken (t=0). The samples were taken with a syringe and transferred to a well in a titer plate. Images were made from the silica solution every 5 min. over a 30 min. time span.

4. Case study and results

The application of the hybrid framework is highlighted with a simple binary suspension of silica particles in water. The experimental setup discussed in the previous section is applied to generate the data required for the flocculation of these particles. The particle size distribution of silica in water is plotted every 5 min for 30 min of process operation. Figure 4 illustrates the size distribution of the silica particles at $pH = 2.25$ and an impeller velocity of $N = 200\ rpm$. It can be seen that the mean value of the equivalent diameter is decreased within the first 10 min. Then the mean diameter of the particles starts to increase.

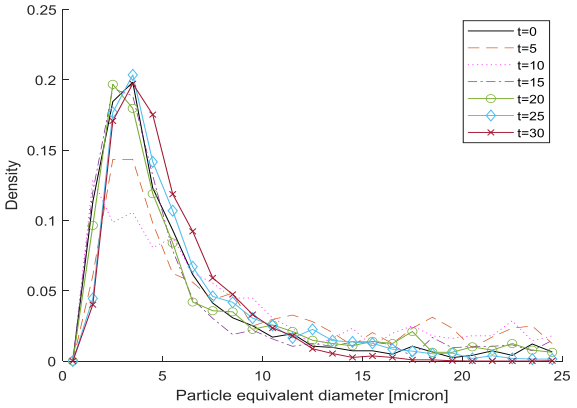

Figure 4: Silica size distribution for $pH = 2.25$, $N\ (impeller\ velocity) = 200\ rpm$, $t = [0.30]\ min$

The optimized geometry of the components in the system shall be introduced to the IFT calculation routines in the framework. In order to determine the state variables, it is aimed in this study to use DFT calculation for geometry optimization of the molecules present in the system. Hence, a pentamer of polyacrylamide is built in Avogadro® and a geometry optimization is carried out in Turbomole® by using DFT calculations.

Table 1: Sigma surfaces of polyacrylamide conformers

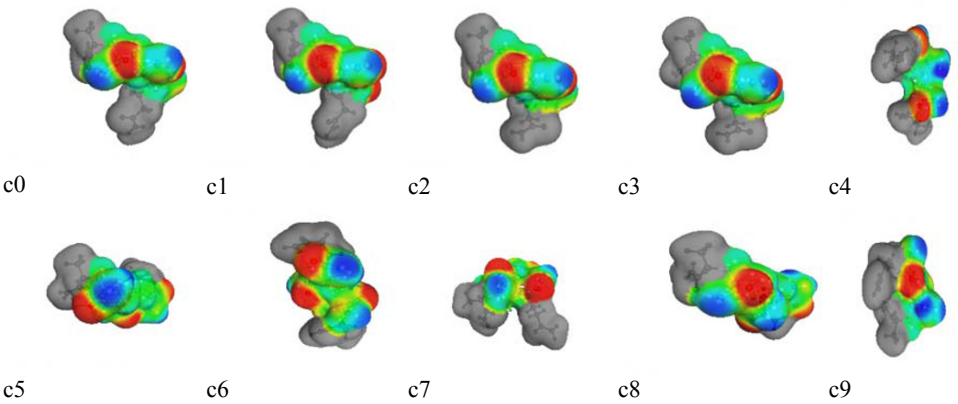

A conformer search is conducted for all possible conformers of this polymer in COSMOconfX® by using BP-TZVPD-FINE basis set. Subsequently, the conformers of the molecule are provided in COSMOthermX® in order to simulate the polymer and to generate the σ surfaces for each conformer. For all of the conformers, it is considered that the weight fraction of the two edges of the molecule is zero. It is an approximation of a larger polymer chain, where the edge effects will be minimal and the ends of of the model molecule will not be included. A pentamer has been chosen for the simulation of the polymer in order to avoid a too large effect of the edges in further calculations. All determined conformers are illustrated in Table 1.

5. Conclusions and future developments

In this work it is shown that a silica particles suspension in water can be observed with the oCelloscope and its image analysis algorithms. A fine segmentation is performed on this system. Hence, most of the silica particles in the sample can be identified by the segmentation algorithm and the process of silica flocculation can be monitored above microscale by the experimental setup. In order to have a phenomenological understanding of the process in nano-scale (i.e. non-observable state) a DFT calculation is carried out to determine all possible conformers of a polyacrylamide molecule. It can clearly be seen from the conformer presented in Table 1 that each conformer has different sigma surfaces. Therefore, the interaction of silica particles will be different with each possible conformer. In the next step of this study it is intended to determine the sigma surface for silica particles and calculate the solid-liquid interfacial tension between the silica and polyacrylamide molecules. Moreover, the population balance model of flocculation is under implementation as a hybrid model combining first-principles with process data driven neural networks.

Acknowledgement

We would like to thank Novozymes A/S, ParticleTech ApS and Greater Copenhagen Food Innovation (CPH_FOOD) for co-financing this research and also for their support during this project.

References

[1] J.C. Flesch, P.T. Spicer, S.E. Pratsinis, Laminar and turbulent shear-induced flocculation of fractal aggregates, AIChE J. 45 (1999) 1114–1124.

[2] Z. Li, P. Lu, D. Zhang, F. Song, Simulation of Floc Size Distribution in Flocculation of Activated Sludge Using Population Balance Model with Modified Expressions for the Aggregation and Breakage, Math. Probl. Eng. 2019 (2019) 1–10.

[3] F. Nielsen, Rasmus, K. V. Gernaey, S.S. Mansouri, Hybrid machine learning assisted modeling framework forparticle processes, Comput. Chem. Eng. (2019) (Submitted).

[4] M.P. Andersson, M. V. Bennetzen, A. Klamt, S.L.S. Stipp, First-principles prediction of liquid/liquid interfacial tension, J. Chem. Theory Comput. 10 (2014) 3401–3408.

[5] M. Cavazzuti, Optimiization Methods: From Theory to Design Scientific and Technological Aspects in Mechanics, Springer, 2013.

[6] J. Rubio, J.A. Kitchener, The mechanism of adsorption of poly(ethylene oxide) flocculant on silica, J. Colloid Interface Sci. 57 (1976) 132–142.

[7] J. Gregory, S. Barany, Adsorption and flocculation by polymers and polymer mixtures, Adv. Colloid Interface Sci. 169 (2011) 1–12.

Sauro Pierucci, Flavio Manenti, Giulia Bozzano, Davide Manca (Eds.)
Proceedings of the 30th European Symposium on Computer Aided Process Engineering (ESCAPE30), May 24-27, 2020, Milano, Italy.
http://dx.doi.org/10.1016/B978-0-12-823377-1.50051-3

Performance Enhancement of Acid Gas Cleaning Units in the Natural Gas Processing via Design Modification

Umer Zahid *, Amr Al-Amri

Department of Chemical Engineering, King Fahd University of Petroleum and Minerals, Dhahran, 34464, Saudi Arabia

uzahid@kfupm.edu.sa

Abstract

Acid gas cleaning is one of the natural gas processing steps where the acid gases are removed to satisfy the quality of the sweet gas. Conventionally, this is achieved by processing the sour gas through an acid gas removal (AGR) unit to produce the desired sweet gas, while concentrating the H_2S gas in the acid gas enrichment (AGE) unit. In this study, a novel acid gas cleaning design has been proposed that can significantly reduce the energy requirement while maintaining all the streams design specifications. The proposed design recommends to first produce acid gas with the required purity and then producing the sweet gas in another AGR unit. The results show that the proposed design requires 22 % lower operational energy compared to the base design.

Keywords: Acid gas removal, energy efficiency, economic analysis, amines.

1. Introduction

Natural gas goes through a series of processing units where various impurities are removed to meet the desired product specification. Removal of acid gases from the natural gas is known as gas sweetening which is a critical process. Acid gases if not removed may cause corrosion in the pipeline, formation of SOx after the fuel combustion and a decrease in the fuel heating value. In addition, H_2S is an extremely toxic gas, hence, the sales gas must not contain more than 16 ppmv of H_2S. There are several methods that can be used to clean the natural gas from acid content. The selection among various methods rely on factors such as concentrations of H_2S and CO_2 in the feed gas, the required product specifications, feed flowrate, and feed gas pressure and temperature (Kidnay et al., 2011). Chemical absorption using amines is the recommended process for the treatment of natural gas at high pressure containing high acid gas content with the requirement of sweet gas to contain very low acid gas concentration. Various efforts have been reported in the literature to improve the performance of AGR plants by different methodologies. Abotaleb et al., (Abotaleb et al., 2018) studied the impact of selective amine application with different additives concentrations on the energy consumption. They reported that based on the acid loading, an addition of piprazine (PZ) to MDEA can increase the absorption and reduce the circulation rate leading to an enhanced performance. Nejat et al., (Nejat et al., 2018) studied the impact of blending a chemical amine solvent with the physical solvent on the energy requirement. They reported an energy savings of 30 – 42 % when using MDEA with a physical solvent such as Sulfinol compared to the chemical amine system. The acid gases separated in the AGR unit are sent to the sulfur recovery unit (SRU). The most common sulfur recovery process in the oil and gas industry is Claus

process which can achieve more than 95 % recovery of elemental sulfur. However, the quality of the acid gas feed stream to SRU is critical for its efficient operation. For a straight-through Claus process, the minimum H_2S amount in the acid gas stream should be at least 30 % for an effective operation (Weiland and Khanmamedov, 2010). This becomes an issue especially with high CO_2 content natural gas because a single absorber cannot meet the desired H_2S concentration in the acid gas stream. Hence, the use of acid gas enrichment (AGE) unit is typically employed for increasing the H_2S concentration to enhance the Claus plant performance. The purpose of the AGE unit is to maximize the CO_2 slip in the reject gas stream while minimizing the H_2S loss from the system. The novel contribution of this study is the design development of an integrated acid gas cleaning unit which considers the downstream quality requirements of both the sweet gas and acid gas streams with reduced energy requirements compared to the conventional design.

2. Process Details

2.1. Basis and Assumptions

The simulation models in this study have been developed using a commercial process simulator Aspen HYSYS V.9. Acid gas removal – Chemical solvent fluid package has been used in this study, which is suitable for the amine systems (Dyment and Watanasiri, 2015). The feed specifications used in this study with CO_2 to H_2S ratio of 3.95. The sweet gas HHV must be maintained above 930 BTU/SCF and the hydrogen sulfide content must be below 1 grain/100 SCF or 16 ppmv (Russell et al., 2004).

2.2. Existing Design

Acid gas cleaning for the sour gas with CO_2 to H_2S ratio of more than 2 takes place in two amine units arranged in series (Rufford et al., 2012) namely AGR and AGE, respectively. Since, the CO_2/H_2S ratio of sour feed gas is almost 4, the base case design consists of AGR and AGE units as shown in figure 1. The base case design employs MDEA solvent in both the AGR and AGE units. AGR unit has a lean amine (MDEA) circulation rate of 4,633 USGPM to sweeten the sour gas. Approximately 457.6 MMSCFD of sweet gas with a HHV of 950 BTU/SCF containing 6.8 ppmv of hydrogen sulfide content leaves at the top of the AGR absorber. The rich amine leaving at the bottom of the AGR absorber is flashed in a drum where the flash gas at a flow rate of 2 MMSCFD with HHV of 538 BTU/SCF and H_2S content of 68 ppmv is produced which is sent to the tail gas thermal oxidizer. The rich amine from the AGR absorber is sent to the AGR regenerator where 45 MMSCFD of acid gas containing 23 % of H_2S content is produced at the top. Since the H_2S in the acid gas stream is very dilute, it is sent to the AGE unit. The acid gas from AGR unit enters the bottom of AGE contactor where it contacts the lean MDEA with circulation rate of 3,810 USGPM. Since MDEA selectively removes the hydrogen sulfide, the overhead product of the AGE absorber is the waste gas which contain minimal amount of H_2S. Waste gas mainly containing CO_2 with a flowrate of 19.14 MMSCFD with 104 ppmv of H_2S leaves at the top of the AGE absorber and is fed to thermal oxidizer. Unlike the design of AGR unit, AGE unit is not equipped with flash drum after the absorber due to the low hydrocarbon content. The rich amine from the bottom of the absorber is sent to the AGE regenerator, where 24 MMSCFD of acid gas with 43 mol% H_2S content is produced at the top of the column. The key parameters of the base case model have been validated against the GPSA guidelines to ensure the accuracy of the model results as shown in Table 1. The key material balance results are shown in Table 2.

Table 1: Comparison of base case parameters with GPSA guidelines

Operating Parameters	Normal Range (MDEA)	AGR (MDEA)	AGE (MDEA)
Acid Gas Pickup Ratio (SCF/gal)	3 – 7.5	6.5	4.4
Lean Amine Residual Acid Gas (mol/mol amine)	0.005 – 0.01	0.006	0.005
Re-boiler Heat Duty Ratio (Btu/gal)	800 - 1200	935	916

2.3. Proposed Design

In this study, a novel design has been proposed that can potentially reduce the overall energy consumption of the AGR and AGE units. The idea of the proposed design is to first produce acid gas stream with a desired H_2S content instead of the sweet gas. The off-spec sweet gas is then treated in another AGR unit to produce the desired quality sweet gas. Therefore, this alternative design consists of two AGR units in series, the first unit will produce the acid gas stream while the second AGR unit will produce the sweet gas with the desired specifications. Similar to the base case design, MDEA has been used to analyze the process performance for the proposed design. Figure 2 shows the process flow diagram for the proposed design. The sour gas is counter contacted with the lean MDEA in the first AGR absorber, where the low HHV sweet gas leaves at the top of the column while the rich amine leaves at the bottom of the contactor and is flashed in a flash drum. The rich amine after exchanging heat with the lean amine is fed to the regenerator, where acid gas stream containing 34 mol % H_2S content is produced at the top of the column. The off-spec sweet gas produced at the top of the first AGR absorber has a CO_2 content of more than 5 mol% which reduces the HHV of the sweet gas compared to the desired value of 930 BTU/SCF. Therefore, this off-spec sweet gas is sent to the second AGR unit where more CO_2 is removed to meet the desired purity. MDEA is employed in the second AGR unit with the circulation rate of 2470 USGPM. The off-spec sweet gas and the lean MDEA contacts in the second AGR absorber, where sweet gas with HHV of 949 BTU/SCF containing 1 PPMV H_2S content is produced at the top of the column. The rich amine leaves at the bottom of the absorber and is flashed to release the hydrocarbons. The combined flashed stream with a HHV of 779 BTU/SCF and H_2S content of 42 ppmv is sent to the thermal oxidizer. The rich amine stream after flashing exchanges heat with the lean amine and is sent to the regenerator. The regenerator produces a waste gas stream at the top of the column while the lean amine leaves at the bottom.

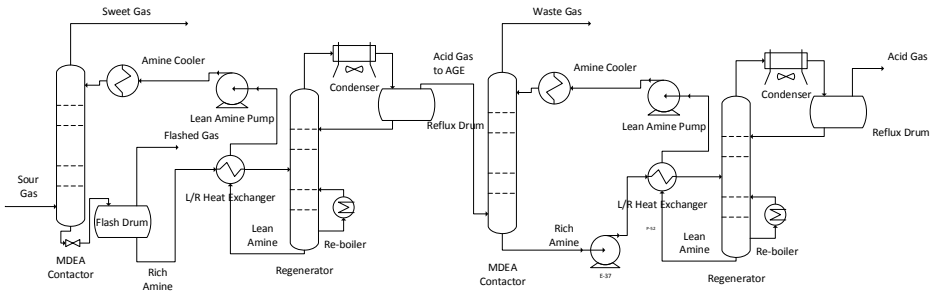

Figure 1. Process flow diagram for base case design

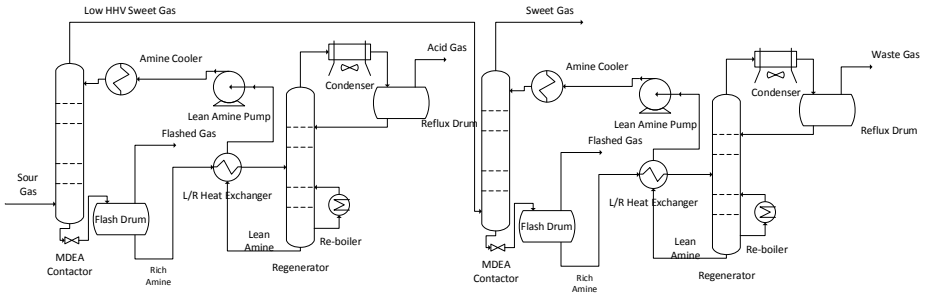

Figure 2. Process flow diagram for the proposed design

Table 2: Stream specifications for the conventional and proposed designs

	Feed	Conventional Design			Proposed Design		
		Sweet Gas	Acid Gas	Waste Gas	Sweet Gas	Acid Gas	Waste Gas
Temperature (°C)	37.8	47.4	47.6	41.2	48.9	60.7	62.9
Pressure (bar)	63.1	61	2	1.8	59.6	2.3	2.3
Composition (mol. fr.)							
H_2O	0.001	0.003	0.055	0.037	0.003	0.093	0.103
Nitrogen	0.060	0.065	0.000	0.000	0.065	0.000	0.000
CO_2	0.082	0.020	0.512	0.958	0.021	0.558	0.890
H_2S	0.021	0.000	0.431	0.000	0.000	0.345	0.001
Methane	0.802	0.874	0.000	0.002	0.873	0.001	0.003
Ethane	0.028	0.031	0.000	0.000	0.031	0.000	0.000
Others	0.007	0.007	0.003	0.002	0.007	0.003	0.003

3. Results

3.1 Energy Analysis

Energy analysis has been performed in order to identify the most energy consuming units in the gas cleaning plant. The main utilities of amine acid gas cleaning systems are power (electricity), cooling agent (cooling water) and heating agent (MP/LP stream). A high amount of steam is required in the reboiler for the regeneration of rich amine. The results show that the base case design requires a total of 274.7 MW energy in comparison to the proposed design which consumes 208.8 MW of the total energy. The proposed design requires 22 % less energy than the base case design mainly because of the reduction in the steam and cooling water usage. The base case design has a high steam consumption because the major amount of acid gas is first stripped in the AGR unit and then the same acid gas goes through the AGE unit. The cooling load in the proposed design could be reduced because of the decreased lean amine circulation rates in both the AGR units. Figure 3 shows the main utilities consumption for the base case and the proposed design. The results show that the proposed design requires 23.3 % less steam compared to the base case. Similarly, the cooling water consumption reduced by 25.5 % for the proposed

design in comparison to the base case design. However, the electricity consumption increased slightly in the case of the proposed design. The consumption of utilities shown in figure 3 have been translated into the cost as shown in figure 4.

3.2 Economic Analysis

Economic analysis has been performed to study the impact of new design on the overall cost of the process. The computation of process economics follows the estimation of capital expenditures (CAPEX) and operating expenditures (OPEX) to calculate the total annual cost (TAC). The gas processing cost (GPC) is then calculated by dividing the TAC and the annual plant sweet gas production. The plant life and investment interest rate are assumed to be 30 years and 10 % respectively for the both cases. Annual plant availability also known as stream factor has been assumed as 95 %.

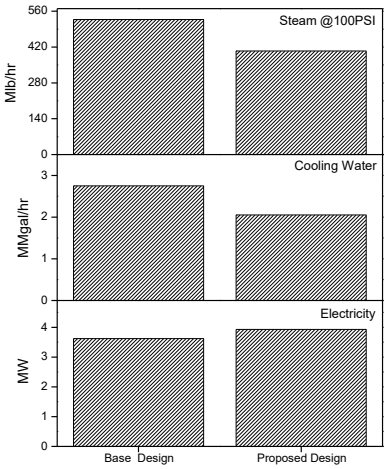

Figure 3. Utilities requirement for the base case and the proposed design

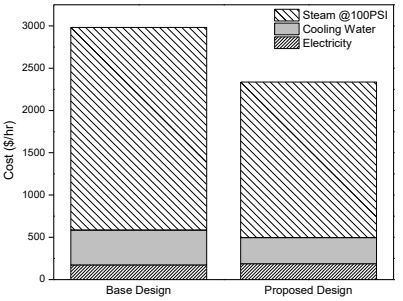

Figure 4. Utilities cost for the base case and the proposed design

The results show that the main contributor to the CAPEX is the cost of the towers. The total equipment cost for the base case and the proposed design is calculated as M$ 54.9 and M$ 47.4 respectively. The lower equipment cost for the proposed design is mainly because of the lower amine circulation rate and reboiler duties compared to the base case design. Figure 5 shows the annualized capital cost for the two designs. The results show that the proposed design requires 20 % less variable operating and maintenance cost (VOM) annually compared to the base case as shown in figure 6. The utilities for the proposed design cost around 21.4 % less compared to the base case design. The huge utility savings for the proposed design comes mainly from the reduced steam requirement. The results show that the amine makeup cost for the two designs is almost the same. The TAC for the base case and proposed design comes out to be M$ 39.2 and M$ 31.9 respectively. The results show that the gas processing cost for the proposed design is $ 201.8 per MMSCF which translates into the cost reduction of around 18.5 % compared to the base case.

4. Conclusion

A novel acid gas cleaning system for the natural gas with high CO_2 content has been proposed in this work that can potentially reduce the energy requirement and gas processing cost compared to the conventional design. The proposed design employs two AGR units for the acid gas cleaning instead of a typical AGR-AGE setup while maintaining the specifications for the sweet gas, acid gas, waste gas and amine unit flashed gas. The new design consumes 22 % less energy compared to the base case because of the reduced amine circulation flow leading to a decrease in reboiler duties. The study compared the two designs in terms of energy and economics to ascertain the process improvement. The results show that the proposed design requires 18.6 % lower total annual cost compared to the base case. In order to have a fair comparison, MDEA has been employed for both the designs in this study.

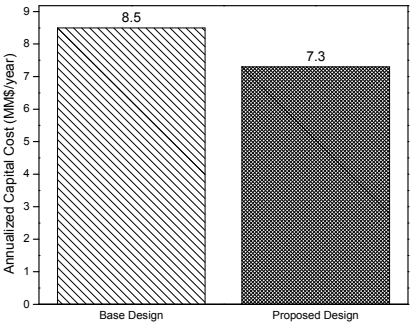

Figure 5. Annualized capital cost for the base case and the proposed design

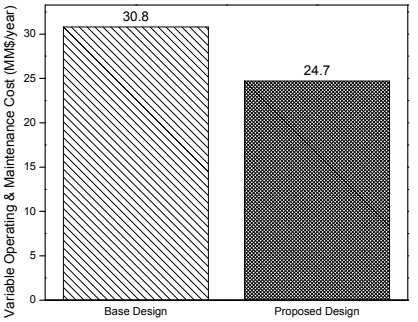

Figure 6. Variable operating and maintenance cost for the base case and the proposed design

Acknowledgment: The authors would like to acknowledge financial support from King Fahd University of Petroleum & Minerals (KFUPM).

References

Abotaleb, A., El-Naas, M.H., Amhamed, A., 2018. Enhancing gas loading and reducing energy consumption in acid gas removal systems: A simulation study based on real NGL plant data. J. Nat. Gas Sci. Eng. 55, 565–574.

Dyment, J., Watanasiri, S., 2015. Acid gas cleaning using DEPG physical solvents: validation with experimental and plant data. USA Aspen Technol. Inc.

Kidnay, A.J., Parrish, W.R., D.G.M, 2011. Fundamentals of natural gas processing 218.

Nejat, T., Movasati, A., Wood, D.A., Ghanbarabadi, H., 2018. Simulated exergy and energy performance comparison of physical–chemical and chemical solvents in a sour gas treatment plant. Chem. Eng. Res. Des. 133, 40–54.

Rufford, T.E., Smart, S., Watson, G.C.Y., Graham, B.F., Boxall, J., Da Costa, J.C.D., May, E.F., 2012. The removal of CO2 and N2 from natural gas: A review of conventional and emerging process technologies. J. Pet. Sci. Eng. 94, 123–154.

Russell, F.G., Adler, S., Albaugh, L.R., Aldana, G.J., 2004. GPSA Engineering Data Book. Gas Process. Suppliers Assoc. 821.

Weiland, R.H., Khanmamedov, T.K., 2010. Acid Gas Enrichment Flow Sheet Selection. Sulphur, Sept.

Sauro Pierucci, Flavio Manenti, Giulia Bozzano, Davide Manca (Eds.)
Proceedings of the 30th European Symposium on Computer Aided Process Engineering (ESCAPE30), May 24-27, 2020, Milano, Italy.
http://dx.doi.org/10.1016/B978-0-12-823377-1.50052-5

Profitability Increase of a Formaldehyde Plant

Catarina G. Braz[a], J. Rocha[b], R. Alvim[b], Henrique A. Matos[a*]

[a]*Centro de Recursos Naturais e Ambiente, Instituto Superior Técnico, Universidade de Lisboa, Av. Rovisco Pais 1, 1049-001 Lisboa, Portugal*
[b]*EuroResinas – Indútrias Químicas S.A., Plataforma Industrial de Sines – Lote Industrial I, 7520-064 Sines, Portugal*
henrimatos@tecnico.ulisboa.pt

Abstract

This work aimed at the development of a model of an industrial formaldehyde production plant, to identify the process variables that will have the most impact in the improvement of the process efficiency and the increase of its profitability. The model of the process was developed and implemented in *gPROMS® Modelbuilder 5.1.1,* and the system analysed. From the scenarios tested, it was possible to conclude that smaller production costs are obtained for lower operation regimes and when higher oxidation reactor inlet temperatures and methanol concentrations are used.

Keywords: Formaldehyde, Industrial data, Process Modelling, Dynamic Simulation

1. Introduction

The increase of energy costs and the stringent environmental regulations observed in the last years has proved to be a great challenge to chemical industries that try to maintain their product quality and secure their profit and market share. Process modelling and optimisation becomes a powerful tool, using mathematical models based on the chemical and physical phenomena that allow to have a better understanding of the systems and help to make better decisions. Optimal operating conditions and modifications in the plant design can be implemented to improve efficiency, reduce waste and increase the profitability.

The aim of this work was the development of a process model of the above described industrial formaldehyde production unit, and identify the process variables that will have the most impact in the enhancement of the process efficiency and the increase of its profitability. It is the first time that a study on a formaldehyde production unit includes the effects of the deactivation of the catalyst, which, as the results suggest, will have a major impact on the overall plant profitability throughout its lifetime.

Formaldehyde is produced in large amounts due to its broad application as a raw material in industrial and end-use products in more than 50 industrial segments. The *Formox* process is one of the main formaldehyde production processes, in which formaldehyde is obtained by partial oxidation of methanol on an iron-molybdenum catalyst, according to reaction (1).

$$CH_3OH + 1/2O_2 \rightarrow CH_2O + H_2O \quad (1)$$

In the industrial unit subjected to study and presented Figure 1, there are two independent lines producing formaldehyde, which join at the bottom of the absorption column T-1. System 1 is used as an example throughout the description of the process.

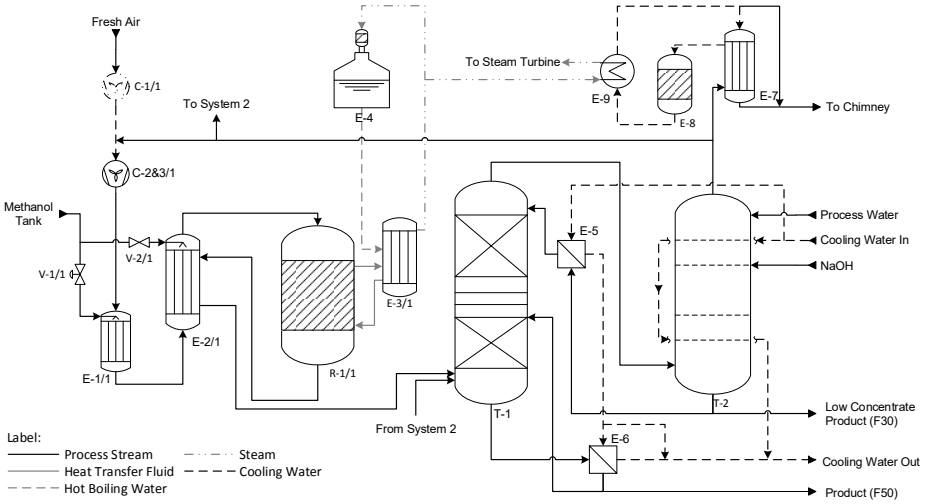

Figure 1 – Scheme of the industrial formaldehyde production process.

Methanol is fed to the formaldehyde plant and is divided into two lines, where the mainline goes into the pre-vaporiser E-1/1, while the second one goes into the vaporiser E-2/1. This division is controlled by the remote-controlled valve V-1/1 and the manual valve V-2/1.

Fresh air is introduced in the processing system, through the pressurisation fan C-1/1 and mixed with the recycled gas coming from the absorption column T-2. The recycling rate is determined by the oxygen content of the gas stream after the recirculation fans C-2&3/1, which must be close to 11 %. During normal operation, approximately one-third of the total gas flow is fresh air. The gas from the recirculation fans is heated by compression in C-2&3/1 and mixed with methanol at the top of the pre-vaporiser E-1/1. In the vaporiser E-2/1, the gas from E-1/1 is further heated by the hot outlet gas coming from reactor R-1/1.

The air-methanol mixture leaving the vaporiser E-2/1 enters at the top of the multitubular reactor with a fixed bed of iron-molybdenum oxide (R-1/1) with a methanol concentration between 8.4 and 8.6 %. . The shell side is filled with boiling heat transfer fluid (HTF) to remove the heat of reaction.

HTF vapours condensate later in the HTF condenser E-3/1 by evaporating bolling feed water (BFW), coming from the BFW tank E-4, into saturated steam at 21 barg, which is later superheated in E-9 to be used in a steam turbine and produce electricity.

In the oxidation reactor R-1/1, the gas mixture reacts into formaldehyde and water and cool down in the vaporiser E-2/1 before entering the absorption column T-1.

In the absorption system, columns T-1 and T-2 remove the formaldehyde from the gas stream to produce aqueous solutions with concentrations of about 55 (F50) and 35 wt % (F30), collected at the bottom of column T-1 and column T-2, respectively. Recirculation from the column T-2 is used to achieve the required flow of liquid. In column T-2, a

caustic solution is added at the top to promote absorption, especially at this stage, where the concentration of formaldehyde in the gas is very low.

Finally, the tail gases from the absorption column T-2 are split up between the recirculation fans C-2&3/1, and the Emission Control System (ECS). In the ECS, the process gas is pre-heated in E-7 before reacting in the catalytic reactor E-8, where all organic compounds suffer total oxidation over a catalytic bed. The gases leave reactor E-8 and are cooled down in the steam superheater E-9 before heading to the pre-heater E-7 and afterwards to the plant chimney.

2. Model development and assumptions

The methanol oxidation reactor was described as a pseudo-homogeneous plug-flow reactor model and the kinetic and deactivation parameters estimated in Braz et al. (2017) and Braz et al. (2019). Afterwards, a rate-based model of the absorption columns was developed, that took into account the chemical reactions occurring in the liquid phase and the thermodynamic non-idealities, described in Braz et al. (2018). These models were later revised and validated in Braz (2019), and implemented together with the models of the remaining process units, to analyse the entire production system. Physical properties were obtained using *Aspen Plus V8.8* through the Thermo CAPE-OPEN Standard properties system with the Formaldehyde-Methanol-Water Data Package. In order to simulate the formaldehyde production process, some simplifications and assumptions had to be employed:

- **Operation regime**

The simulation of the different operation scenarios was accomplished, assuming that only one of the formaldehyde production lines is functioning and that the results are the same for the other production line. The formaldehyde production unit operates during the year in four main methanol inlet flowrates, defined here as operation regimes and presented in Table 1. Regime 1 is the maximum methanol capacity (MMC) of one production line, meaning that the maximum methanol capacity of the entire industrial unit is two times Regime 1.

Table 1 – Definition of the four main operation regimes implemented at the formaldehyde industrial unit and their terminology.

Name	% of MMC
Regime 1	100
Regime 2	92
Regime 3	85
Regime 4	66

- **Oxygen and methanol concentrations**

The control of the oxygen content in the methanol oxidation reactor R-1/1 is achieved by regulating the flow of recycle gas to the recirculation fans C-2&3/1, while the normal flow of methanol is calculated as the volumetric percentage of the total gas entering reactor R-1/1. During the process simulation, the operation regime was defined, the

methanol concentration fixed to 8.9 and the flowrate of the mixture of fresh air and recycled gas calculated. The fraction of fresh air inserted into the system was then calculated by fixing the concentration of oxygen in the gas mixture at 11 %. At oxygen concentrations above 13 %, there is a risk of explosion due to pressure surge, and at too low concentrations (< 9.5 %), there is a risk of damaging the catalyst because of the reduction and volatilisation of the active centres, according to Andersson et al. (2016).

- **Cost of the production of 1 t of formaldehyde**

The cost of the production of one ton of formaldehyde (C_{CH_2O}) is calculated considering the cost of the catalyst purchase (C_{cat}). After each simulation, the total amount of methanol and electricity consumed (M_{CH_3OH} , C_{MWh}), and the formaldehyde and electricity produced (M_{CH_2O} , P_{MWh}) during the catalyst lifetime were calculated, and the cost of the production of one ton of formaldehyde was determined by equation (2).

$$C_{CH_2O}(€/t_{CH_2O}) = \frac{M_{CH_3OH} \times Price_{CH_3OH} + (C_{MWh} - P_{MWh}) \times Price_{MWh} + C_{cat}}{M_{CH_2O}} \quad (2)$$

3. Process analysis

A sensitivity analysis of several operating variables was carried out to the industrial formaldehyde production plant for three main operating variables: Process operation regime; Opening of valve V-1/1; Methanol concentration. The effect of these operating variables was observed in four process key performance indicators (KPIs): Lifetime of the catalyst; Formaldehyde production capacity; Superheated steam production; Cost of production of 1 ton of formaldehyde.

Each simulation was carried out throughout time until the catalyst had to be replaced. It was defined that the catalyst reached its end of life when the molar yield of the process was less than 80 %.

3.1. Process operation regime

The first operating variable studied was the operation regime. The four main regimes implemented at the industrial plant were tested, and the results presented in Table 2.

Table 2 – Analysis of the effect of the operation regime in the performance indicators.

	Catalyst lifetime (days)	CH_2O Prod. Variation (%)	Steam Prod. Variation (%)	CH_2O Cost Variation (%)
Regime 1	297	NA	NA	NA
Regime 2	331	3.5	3.9	-0.49
Regime 3	372	7.0	7.8	-0.94
Regime 4	525	18.2	20.9	-2.45

NA – Not applicable (base case)

Table 2 shows that the operation regime will have a significant influence on the catalyst lifetime. If operating on the lowest regime, the catalyst lifetime will increase by 77 %

compared with the highest regime. Moreover, although the operation in higher regimes will increase the methanol conversion and the production of steam in the HTF condenser, the selectivity of the reactions to formaldehyde will decrease, increasing the amount of methanol necessary to produce 1 t of formaldehyde. The result is that the cost of the production of formaldehyde is lower for the lowest operation regime. This is because, according to Andersson et al. (2016), about 94 % of the cost of the formaldehyde comes from the methanol consumed.

Assuming that with the two formaldehyde production lines operating at the same time, the unitary production costs will not increase, with both lines working at Regime 4, the same amount formaldehyde produced during the catalyst lifetime running in one line at Regime 1, would be achieved in 218 days with savings of about 329 k€.

3.2. Opening of valve V-1/1

Later, the effect of the opening of the valve V-1/1 to increase the ratio of fresh methanol flowing to the methanol pre-vaporiser E-1/1 was studied. Opening valve V-1/1 will raise the inlet temperature of reactor R-1/1 and increase the amount of HTF vaporising inside the oxidation reactor.

During the model simulations, it was considered that the opening of valve V-1/1 (%) is equal to the percentage of fresh methanol flowing to pre-vaporiser E-1/1. For the initial simulation, a valve opening of 60 % was implemented, followed by openings of 10 % until valve V-1/1 was completely open. The results presented in Table 3 show that the lifetime of the catalyst is not significantly affected, and an increase in the total formaldehyde and steam produced is observed, decreasing the final production cost of formaldehyde.

Table 3 – Analysis of the effect of valve V-1/1 opening (VO) for Operation Regime 1.

VO (%)	Catalyst lifetime (days)	CH_2O Prod. Variation (%)	Steam Prod. Variation (%)	CH_2O Cost Variation (%)
60	297	NA	NA	NA
70	297	0.17	4.1	-0.10
80	297	0.34	8.2	-0.20
90	298	0.51	12.3	-0.30
100	298	0.69	16.5	-0.40

NA – Not applicable (base case)

3.3. Methanol concentration

The effect of the methanol concentration on the process KPIs was studied by increasing the reactor R-1/1 inlet methanol volumetric concentration until the maximum limit was reached before it could damage the catalyst [112]. The increase of methanol concentration was achieved by decreasing the recycling fraction of the process gas coming from Column T-2, meaning that more gas was directed to the Emission Control System (ECS) for the combustion of the hydrocarbons, and the production of superheated steam.

Table 4 shows that, although the production of formaldehyde decreases with the increase of methanol concentration, the cost of production continually decreases. The main

contributor to the fall of the production cost is the reduction of the expenses with electricity because less gas is being introduced into the reactor. Secondly, the catalyst is operating for fewer days, reducing the total consumption of methanol. And finally, the production of steam also increases, reaching a maximum value at a methanol concentration between 10.1 and 10.5 %.

Table 4 – Analysis of the effect of the reactor R-1/1 inlet methanol concentration at Operation Regime 1.

Met %	Catalyst lifetime (days)	CH_2O Prod. Variation (%)	Steam Prod. Variation (%)	CH_2O Cost Variation (%)
8.9	297	NA	NA	NA
9.3	297	0.01	1.37	-0.30
9.7	296	-0.15	2.49	-0.60
10.1	294	-0.84	3.02	-0.92
10.5	291	-2.07	2.97	-1.25

4. Conclusions

In this work, a dynamic model of an industrial formaldehyde production unit was developed, and the effect of several process variables analysed. From the analysis of the formaldehyde production process, some recommendations aroused. Methanol accounts for about 94 % of the formaldehyde production cost; therefore, all operating changes that reduce the consumption of fresh methanol will have the highest impact on the operation costs. In this work, it is showed that lower operation regimes would increase the lifetime of the catalyst and the total amount of formaldehyde produced compared with the highest one. Moreover, the inlet methanol concentration on the oxidation reactor R-1/x should be increased by reducing column T-2 exhaust gas recirculation fraction, and finally, the opening of valve V-1/x will increase the production of steam without compromising the production of formaldehyde, nor the lifetime of the catalyst.

Acknowledgements

The authors greatly acknowledge EuroResinas and FCT support through the project UID/ECI/04028/2013 and the PhD grant number PD/BDE/113539/2015.

References

A. Andersson, J. Holmberg, R. Häggblad, 2016, Process Improvements in Methanol Oxidation to Formaldehyde: Application and Catalyst Development. Topics in Catalysis, 59, 17–18, 1589–1599.

C.G. Braz et al., 2018, Model of a Formaldehyde Absorption System Based on Industrial Data. In *Computer Aided Chemical Engineering*. Elsevier, pp. 25–30.

C.G. Braz et al., 2019, Model of an Industrial Multitubular Reactor for Methanol to Formaldehyde Oxidation in the Presence of Catalyst Deactivation. Chemical Engineering Science, 195, 347–355.

C.G. Braz et al., 2017, Model of an Industrial Reactor for Formaldehyde Production with Catalyst Deactivation. In *Computer Aided Chemical Engineering*. pp. 121–126.

C.G. Braz, 2019, Profitability Increase of a Formaldehyde Production Plant, PhD Thesis.

Sauro Pierucci, Flavio Manenti, Giulia Bozzano, Davide Manca (Eds.)
Proceedings of the 30th European Symposium on Computer Aided Process Engineering (ESCAPE30), May 24-27, 2020, Milano, Italy.
http://dx.doi.org/10.1016/B978-0-12-823377-1.50053-7

Automatic Improved Hybrid Scheduling and Worker-task Allocation Method Applied to Multi-purpose Production Plants

Raul Calvo Serrano,[a*] Matteo Luigi Abaecherli,[b] Ruben Jungius,[c] Thomas Kreuzer,[b] Gonzalo Guillen Gosalbez,[a]

[a]*ICB Institute of Chemical and Bioengineering, ETH Zürich, Vladimir-Prelog-Weg 1, 8093 Zürich, Switzerland*
[b]*Pharma Biotec & Nutrition, Lonza AG, Rottenstrasse 6, 3930 Visp, Switzerland*
[c]*Ecole polytechnique federale de Lausanne, Station 7, 1015 Lausanne, Switzerland*

raulc@ethz.ch

Abstract

Contract Development and Manufacturing Organisations (CDMOs) are becoming a key element in the pharma and fine chemical industries during the development and production of precursor components. Most CDMOs provide their services to several companies, having to operate and organise several production lines simultaneously, complying with specific production and product requirements for each customer. Under this scenario, the operation of CDMOs depends on market changes as well as customer and product regulations, these conditioning the definition and optimization of operational plans, and in turn, hindering the definition clear routines for workers. Ultimately, the difficulties may cause planning inconsistencies, generating production delays or disruptions. For that purpose, here we present a novel methodology able to automate the scheduling and worker-task allocation for several simultaneous production lines. This is done through the sequential application of specifically designed scheduling and allocation optimization models, first identifying the optimal periodic production plan and then finding the optimal transition from current to optimal operation conditions. This approach has been applied to a real industrial process with several simultaneous production lines, successfully identifying periodic production strategies and optimal transition and worker-task allocation plans for the different lines. Overall, the proposed tool presents a first step towards the automatic integrated optimisation of production planning in fine chemical and pharmaceutical multi-purpose production plants.
Keywords: Scheduling, Allocation, Python, Optimisation, Multi-purpose process

1. Introduction

The Pharmaceutical and fine chemical industries have long relied on Contract Development and Manufacturing Organizations (CDMOs) to carry out the scale-up of synthesis processes as well as the production of some key products, ranging from early precursors to final products ready for encapsulation or tableting. This tendency has increased in both popularity and volume in the last years, with big companies exclusively relying on CDMOs for their bulk production (Miller, 2017). In turn, this model of production exerts substantial pressure on CDMOs, which have to supervise simultaneously several production lines for different products and customers. Furthermore, these CDMOs need to accommodate all the customers' requirements in their

production processes, the tightness of which make disruptions in one or more production lines critical. In order to address these disruptions, CDMOs need to rely on agile strategies for adapting and planning their operational strategies. The common practice nowadays is to solve the planning problem manually by a panel of experts, a task that is highly time consuming and cannot guarantee the optimality of the solutions found. In this work we present a novel methodology to identify potentially optimal process and operating plans and apply it to a real industrial problem. Our approach is based on the sequential optimization of several scheduling and allocation optimization models, while accounting for technical and workers availability constraints. The core optimization models here considered are based on the work by (Castro et al., 2003), but have been modified to consider several simultaneous production lines and handle both the design of the full production schedule and the rescheduling of tasks to cope with disruptions.

2. Methodology

The presented methodology is divided in two stages: first, the calculation of the optimal operational plan, and second, the rescheduling of operations and the corresponding worker-task allocation. Figure 1 provides a graphical summary of the presented methodology, describing the information required and models solved in each of the two stages.

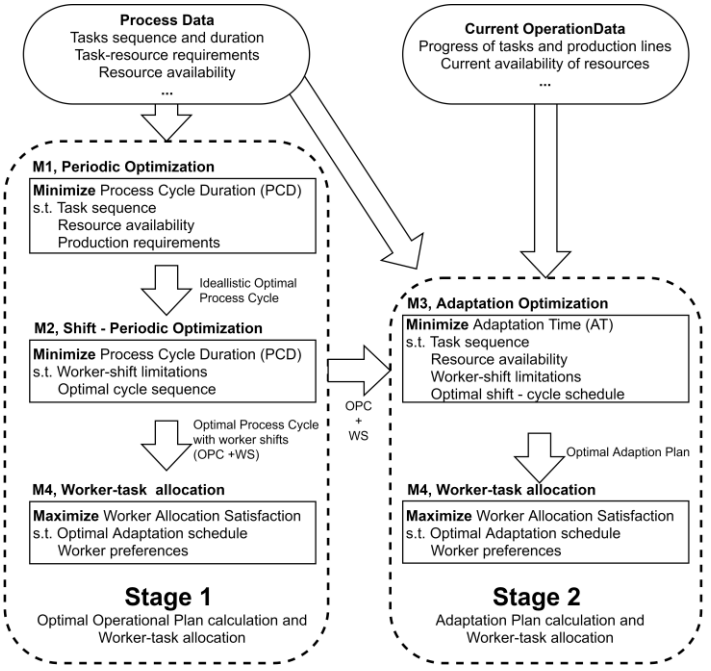

Figure 1, graphical representation of the proposed methodology, describing for the two considered calculation stages, the different data requirements and a general description of the models, broadly defining the respective objective functions and constraints considered in each model.

2.1. Stage 1: Optimal Operational Plan calculation and Worker-task allocation

The first stage of the proposed methodology aims to identify the optimal operational plan for the different production lines considered, providing the ideal plan to be followed assuming normal behaviour of the production process without disturbances or

disruptions. The models we use here are based on the on the continuous-time resource-task network periodic scheduling approach presented by Castro et al., (2003), on which some significant modifications have been applied to better characterize the processes present in CDMO companies. In particular, the starting, progress and ending at a given time t of task i are characterized by three binary variables y^S_{it}, y^P_{it} and y^E_{it}, these taking a value of 1 if task i starts, is taking place or ends, respectively, at a time reference point t, and taking a value of 0 otherwise. These three new variables modify most of the formulation of the original problem, with Eqs. (1) to (8) below representing the most significant modifications.

$$\sum_t y^S_{it} \geq 1, \forall i \quad (1)$$

$$\sum_t y^E_{it} \geq 1, \forall i \quad (2)$$

$$\sum_t y^S_{it} - y^E_{it} = 0, \forall i \quad (3)$$

$$y^S_{it} \leq \sum_{t'=t+1}^{|t|} y^E_{it'}, \forall i \quad (4)$$

$$y^E_{it} \leq \sum_{t'=1}^{t-1} y^S_{it'}, \forall i \quad (5)$$

$$y^P_{it} = \sum_{t'=1}^{t} y^S_{it'} - \sum_{t'=1}^{t} y^E_{it'}, \forall i, t \quad (6)$$

$$\tau_{t'} - \tau_t \geq \delta_i - M\left(2 - y^S_{it} - y^E_{it'} + \sum_{t''=t}^{t'-1}\left(1 - y^P_{it''}\right)\right), \forall i, t, t' \big| |t| \geq t' \geq t \quad (7)$$

$$R_{rt} - R_{r\,t-1} = \sum_i \mu^S_{ir} y^S_{it} + \mu^E_{ir} y^E_{it}, \forall r, t > 1 \quad (8)$$

Eqs. (1) to (6) characterise the starting, progress and ending binary variables. For example, Eq. (6) calculated the difference between the amount of times a task has started and ended prior to a particular reference time, obtaining as a result whether a task is taken place at that time. Eq. (7) characterises the reference time values τ_t from the continuous-time approach, to that end using the previously defined binary variables and the task durations δ_i. Eq. (8) represents the balance of resources between two consecutive time reference points, calculating the change of each resource r using the amounts generated or consumed either at the start (μ^S_{ir}) or end (μ^E_{ir}) of a particular task. Among other equations, the balance of resources is particularly critical for the correct definition of the models in the proposed methodology, with resource availability being a major limitation on the scheduling of tasks (e.g. workers are here modelled as a resource required to carry out manual tasks). Furthermore, the sequence of tasks (i.e. in which order or priority should tasks be carried out) is here enforced through the use of resources. This approach provides a direct and systematic approach to define complex task sequences (i.e. recipes), enhancing the automation of the presented models. The presented eight equations represent the core of the scheduling optimization models in the proposed methodology, with each of these models presenting a different variation on the general scheduling optimization model in order to achieve their individual objectives. Model M1is used first to identify the "idealistic optimal process operation", disregarding restrictions on the scheduling of manual tasks derived from the worker-shifts. To this end, this model aims to identify the minimum possible Production Cycle Duration using a periodic scheduling optimization approach. In this approach, since the specific time values are calculated variables in the model (τ_t), it is fundamental to define the amount of time reference points t that ensures the feasibility of the problem and leads to a model of reasonable size. In this case, the amount of time reference points used has been defined as twice the minimum required to achieve a feasible solution. In order to include the effects of the worker-shifts into the general scheduling, model M2 aims to adapt the solution found from model M1, again minimising the Process Cycle Duration while enforcing manual tasks to be completed by the available amount of workers in no more than one shift. To

this end, model M2 only considers constraints directly related with the timing of the manual tasks (e.g. Eq. (7)) and their interaction with the worker-shifts. In addition, model M2 fixes the starting, processing and ending task binary variables (i.e. y^{S}_{it}, y^{P}_{it} and y^{E}_{it}) from the solution of M1, only modifying the reference time values τ_t. The operational plan obtained in model M2 is then used in the worker-allocation model M4, which uses binary variables x_{iwt} that take a value of 1 if worker w is allocated to task i at reference time t. These variables are used to determine the allocation that minimises the maximum workload among the workers.

2.2. Stage 2: Adaptation Plan calculation and Worker-task allocation

The second stage of the proposed methodology aims to identify the task schedule that minimises the time required to transition from a set of initial operation conditions to an optimal production plan operation (i.e. adaptation time). This, in turn, is aimed to minimise the disruption caused by process irregularities, which are assumed to be more frequent than major changes in the process, thus making the application of this second stage more frequent than the first. Unlike the previous stage, this schedule optimisation is done in a single model M3, which aims to minimise the adaptation time again using Eqs. (1) to (8) as the core of the model, also considering the limitations imposed by the worker-shifts in the scheduling of manual tasks. Furthermore, this model uses the starting, processing and ending task binary variables values from the optimal schedule obtained in the first stage (i.e. $y^{CS}_{it_2}$, $y^{CP}_{it_2}$ and $y^{CE}_{it_2}$) and a binary variable (z_{t_2}) in order to identify the optimal operational time reference point (t_2) to which transition, as enforced by Eqs. (9) to (12).

$$y^{S}_{i|t|} = \sum_{t_2} z_{t_2} y^{CS}_{it_2}, \forall i \quad (9)$$

$$y^{E}_{i|t|} = \sum_{t_2} z_{t_2} y^{CE}_{it_2}, \forall i \quad (10)$$

$$y^{P}_{i|t|} = \sum_{t_2} z_{t_2} y^{CP}_{it_2}, \forall i \quad (11)$$

$$\sum_{t_2} z_{t_2} = 1 \quad (12)$$

The particular amount of time reference points $|t|$ used in model M3 is the same as in model M1 ($|t_2|$), as it has been considered sufficient to cover most potential current production scenarios regardless of the level of their similarity with any of the optimal production plan reference points. As in the previous stage, the worker-task allocation model M4 is then used on the adaptation schedule from model M3, obtaining particular schedules for each one of the individual workers. Altogether, all the models included in the proposed methodology present Mixed Integer Linear Programming (MILP) structures. Furthermore, the presented methodology can be easily automated, as the only information required is generally fundamental process information generally measured and recorded (e.g. task durations, resource consumption and availability, current progress of the production lines …).

3. Case Study

The methodology here presented was developed in collaboration with LONZA AG Pharma, Biotech & Nutrition. In particular, our approach was applied to two production lines (L1 and L2) consisting of 6 (E1 to E6) and 11 (E7 to E17) equipment units, respectively, in total considering 114 tasks, 29 of which are manual tasks require one or more workers to be completed.

4. Results

The models here presented (M1 to M4) were implemented in PYOMO (Hart et al., 2012) and solved interfacing with the solver GLPK 4.65 (Sottinen, 2009), using an Intel Core i5-4570 3.20 GHz computer. Model M1 contains 2400 continuous and 5600 binary variables, and 54000 equations. A computation time limit of 24 CPU-hours was set for the models in the first stage of the methodology (i.e. models M1, M2 and M4). This time was sufficient to identify a potentially optimal feasible solution (i.e. optimality gap of 20%), although longer calculation times or more effective commercial solvers may reach better solutions. On the other hand, only 2 CPU-hour was more than enough for the models in the second stage (i.e. models M3 and M4) to reach optimal solutions. Figure 2a presents the resulting Gantt chart, indicating the distribution of automatic and manual tasks and which of these are bottlenecks of the process. Figure 2b provides the corresponding worker-task allocation schedule of the considered production lines.

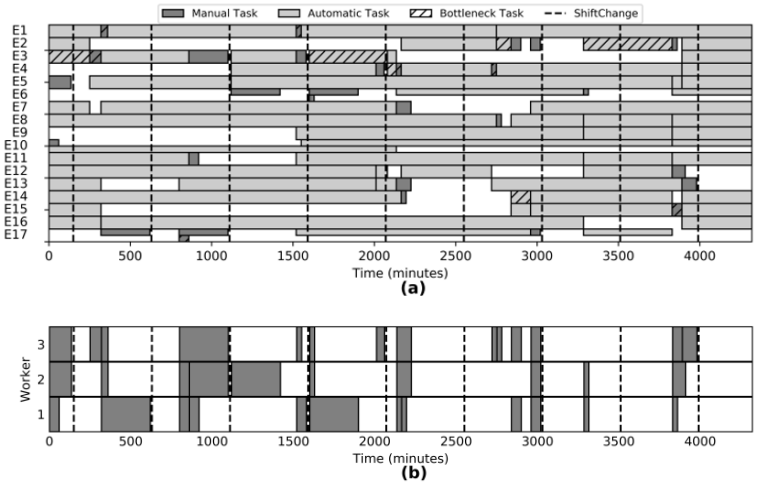

Figure 2, (a) Schedule structure of the operating cycle and (b) corresponding worker-task allocation schedule obtained in the first stage of the methodology.

The optimal production cycle schedule obtained presents manual tasks fairly distributed across the calculated 9 shifts, with all shifts having at least one manual task. This indicates that the schedule of the process is mostly determined by the limitations imposed by the worker-shifts and the availability of workers. At the same time, the obtained schedule hints that faster process cycles could be achieved, as most tasks are being carried out longer than their minimum required durations, with only a few automatic and manual tasks acting as bottlenecks. The obtained operation schedule was then used to determine the adaptation schedule using the second stage in the methodology. In this case, both models M3 and M4 reached global optimality, providing the adaptation and worker schedule presented in Figure 3.

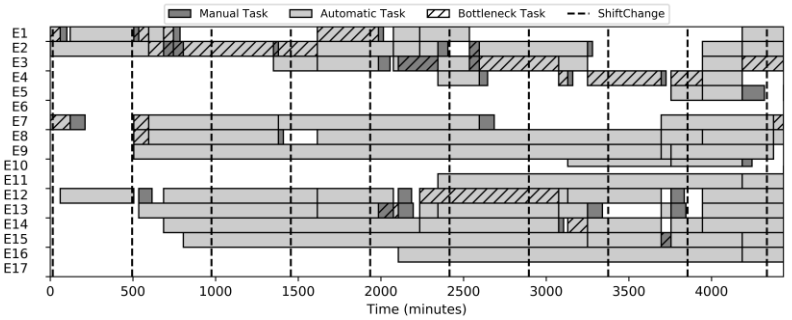

Figure 3, Schedule structure of the obtained adaptation in the second stage of the methodology.

The adaptation schedule obtained significantly contrast with the production cycle schedule, as the former presents significantly more tasks acting as bottlenecks, with one or more tasks being a bottleneck of their respective production line at almost all times. This, in turn, confirms the global optimality of the obtained adaptation schedule, as there are no clear windows for improvement in the schedule.

5. Conclusions

This work presents a methodology that aims to facilitate the planning and management of Contract Development and Manufacturing Organizations (CDMOs), enabling the automatic long and short term scheduling of specific tasks and workers. To that end, the methodology is divided into two stages, with the first stage sequentially solving three optimization models to identify the optimal production cycle and the corresponding worker-task allocation. The second stage encompasses two optimization models that aim to minimize the impact of production irregularities by identifying the schedule that minimizes the adaptation time to optimal process conditions, also identifying the corresponding worker-task allocation. This methodology has been applied to a real process involving two production lines and 114 different tasks. The methodology's first stage was only able to identify a feasible solution with potential for further optimization. In contrast, the second stage was able to identify the optimal adaptation schedule and corresponding worker-task allocation. Overall, the presented methodology has been able to automatically generate feasible and potentially optimal operational planning schedules and their corresponding worker schedules. These results highlight how scheduling approaches specifically designed for particular processes may significantly reduce the time and resources spent in the design of production and work organization, also supporting the transition to a more automated production industry.

References

Castro, P.M., Barbosa-Póvoa, A.P., Matos, H.A., 2003. Optimal periodic scheduling of batch plants using RTN-based discrete and continuous-time formulations: A case study approach. Ind. Eng. Chem. Res. 42, 3346–3360. https://doi.org/10.1021/ie0203781

Hart, W.E., Laird, C., Watson, J.-P., Woodruff, D.L., 2012. Pyomo – Optimization Modeling in Python. Springer Optim. Its Appl. 67, 13–28. https://doi.org/10.1007/978-1-4614-3226-5

Miller, J., 2017. Contract manufacturing through the years. BioPharm Int. 30, 12–13.

Sottinen, T., 2009. operatins research with GNU Linear Programming Kit.

Sauro Pierucci, Flavio Manenti, Giulia Bozzano, Davide Manca (Eds.)
Proceedings of the 30th European Symposium on Computer Aided Process Engineering (ESCAPE30), May 24-27, 2020, Milano, Italy.
http://dx.doi.org/10.1016/B978-0-12-823377-1.50054-9

Efficient Amine-based Carbon Capture in a Power-to-Jet process under varying Renewable Electricity supply

Mahmoud Mostafa,[a*] Christopher Varela,[a] Elvis Ahmetović,[b] Edwin Zondervan,[a]
[a]*University of Bremen, Leobener Straße 6, 28359 Bremen, Germany*
[b]*University of Tuzla, Faculty of Technology, Univerzitetska 8, 75000 Tuzla, Bosnia and Herzegovina*
mmostafa@uni-bremen.de

Abstract
To comply with the outcomes of the Climate Change Conference in Paris (COP 21), the ever-growing greenhouse gas (GHG) emissions has to be drastically reduced. With the soaring growth rates of GHG emissions in the aviation sector, the need for a near zero-net greenhouse emission alternative is essential. The novel concept of the Power-to-Jet pathway directly utilizes renewable electricity, carbon dioxide and water to synthesize a sustainable kerosene fuel that chemically resembles the one produced from fossil sources, having 'Drop-in' capability allowing the use and distribution within existing architectures. In the Power-to-Jet process, hydrogen is produced via water electrolysis. Captured CO_2 (from rich point sources) then reacts with hydrogen to produce the intermediate methanol, before being upgraded to the final synthetic jet fuel along with by-products (Schmidt et al., 2012). With fluctuating electricity inputs due to the variability in photovoltaic and wind power generation, the process units within the Power-to-Jet process have to be adjusted at each time-instant to satisfy the production constraints. To find the best operating strategy for these fluctuating conditions, dynamic models are needed. In this work, we will propose a model that describes the dynamic behaviour of the carbon capture section in the Power-to-Jet process. Several dynamic scenarios can be introduced for the carbon capture rate by altering the lean solvent concentration, flue gas flow rates and re-boiler duty. The dynamic information obtained from the simulations (such as: Open loop gain, time constants and dead time) can be used to device an appropriate control scheme under varying electricity inputs, while satisfying all operational constraints.

Keywords: Dynamic, Carbon Capture, Amine, Aspen, Renewables

1. Introduction
According to the International Air Transport Association (IATA), more than 3.8 billion passengers and 54.9 Mt of goods (worth around 5.5 trillion US dollars) were transported by air in 2016. By producing around 781 Mt of CO_2 in 2015, the aviation sector is responsible for 2 % of the world's total anthropogenic emissions of carbon dioxide. With new technologies emerging from electric vehicles to hydrogen-powered buses, airplane engines will still run on high quality paraffinic fuel for quite some time in the future increasing the total share of emissions. Synthetic kerosene is considered a promising answer to the every growing aviation demand, being carbon neutral is an essential aspect in complying with the strict environmental regulations.

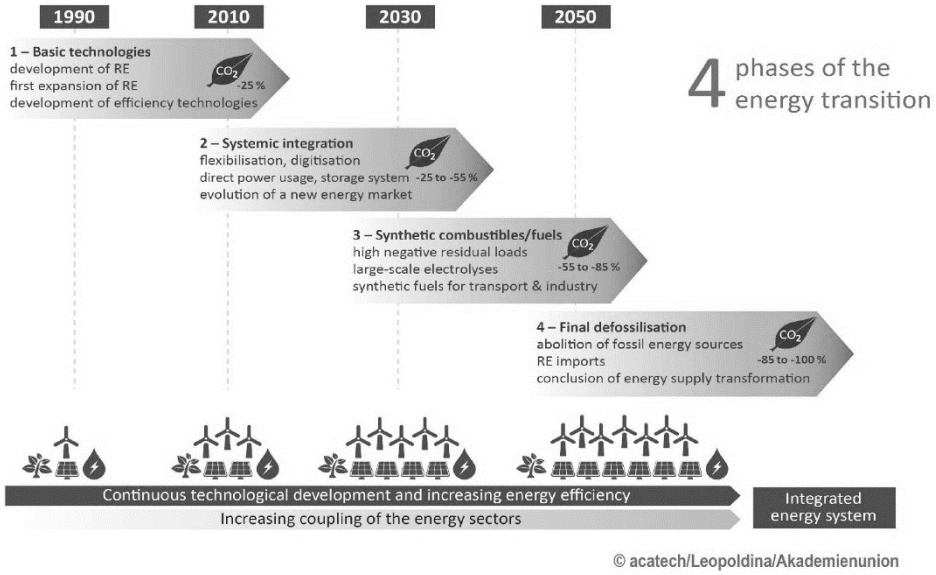

Figure 1 - Timeline of the four-energy transition phases (Acatech, 2018)

Photovoltaic, wind and biomass technologies have matured and built over the last 30 years, decreasing the costs strongly. As shown in Figure 1, we are currently ending the systemic integration phase and entering a phase of utilizing renewable electricity. A serious challenge we face currently is the volatile behavior of supply of renewable energy, where there are periods during which large amounts of electricity aren't utilized due to short-term storage and load management (Acatech, 2018). The Power-to-Jet pathway enables us to convert this unutilized intermittent production into valuable aviation kerosene.

The process is divided into 4 main stages namely: carbon capture (CC) and electrolysis stage that provide the raw materials. The raw materials then react to produce the intermediate product methanol. Methanol is subsequently converted into olefins (mixture of ethylene and propylene) by passing it over a zeolite catalyst, oligomerized/isomerized and finally hydro-treated to achieve the final synthetic fuel (Schmidt et al., 2018). This fuel has advantageous chemical and physical properties as compared to the fossil-based kerosene. It also complies with the ASTM-D7566 standard and offers a far superior environmental performance with overall GHG emissions of 1 g CO_2 per MJ of final fuel (German Environment Agency, 2016). This research will focus on the CC stage simulation using Aspen Plus for the steady-state model and Aspen Plus Dynamics for the dynamic analysis. The feedstock for the model is the flue gas of a refinery (Raffinerie Heide located north of Germany) with a concentration of 15.36 wt % CO_2. Post-combustion scrubbing using the base monoethanolamine (MEA) is the most suitable technology, with a technology readiness level of nine. This technology can be easily integrated into an existing infrastructure of a plant with minimal modifications. MEA high reactivity with CO_2 makes it the most studied solvent, but with this high reactivity, large amounts of steam are required in the desorber stage to regenerate the gas. Dynamic scenarios will be investigated with a specific control strategy ensuring a stable operation for the various units.

2. Model description

2.1. Steady-state rate-based model

The flow sheet of an amine based CO_2 capture process consists of a packed absorber unit where countercurrent contact of the incoming flue gas with an amine solution occurs. The structured packing 250Y FLEXIPAC are considered in this study with HETP of 315 mm. The flue gas rich in CO_2 enters the absorber at the bottom with a flow rate of 325,130 kg/hr while the lean amine solvent is introduced at the third equilibrium stage with a flow rate of 958,371 kg/hr (L/G 2.9). The treated flue gas is then washed in a water-wash section (accounting for two equilibrium stages) to remove any entrained valuable solvent droplets and to meet any environmental regulations concerning the solvent emission. MEA solution of 30 % by weight is chosen to reduce the energy requirement of the solvent regeneration. The rich solvent stream leaves at the bottom of the absorber and is sent to a stripper where the reverse of what happened in the absorber occurs. Before entering the stripper, the stream absorbs some of the heat in the lean solvent exiting the stripper and heading towards the absorber in the closed loop recycle. In the stripper, the rich amine is introduced at the top and the CO_2 is released by the upward flowing steam generated by the reboiler. The exiting stream passes through a condenser and all of the condensed liquid is returned to the top of the stripper as reflux stream. The uncondensed stream is mainly CO_2 with 98.95 % purity, which will be later on delivered to the methanol reactor. The absorber and stripper are both modeled using the Aspen RadFrac model unit, the Unsymmetric Electrolyte NRTL property method is adopted which uses the Redlich-Kwong equation of state for vapour phase properties. All reactions in the absorber and stripper units are assumed to be in equilibrium except those of CO_2 with OH^- and CO_2 with MEA. The chemistry of EQU consists of the following equilibrium reactions (Agbonghae et al., 2014):

$$MEAH^+ + H_2O \longleftrightarrow MEA + H_3O^+ \quad (1)$$

$$MEACOO^- + H_2O \longleftrightarrow MEA + HCO_3^- \quad (2)$$

$$2H_2O \longleftrightarrow H_3O^+ + OH^- \quad (3)$$

$$CO_2 + 2H_2O \longleftrightarrow HCO_3^- + H_3O^+ \quad (4)$$

$$HCO_3^- + H_2O \longleftrightarrow CO_3^{2-} + H_3O^+ \quad (5)$$

The reaction models of the Absorber/Stripper consist of the instantaneous reactions (1), (3), (5) and the following finite rate reactions governed by the power law:

$$CO_2 + OH^- \longrightarrow HCO_3^- \quad (6)$$

$$HCO_3^- \longrightarrow CO_2 + OH^- \quad (7)$$

$$MEA + CO_2 + H_2O \longrightarrow MEACOO^- + H_3O^+ \quad (8)$$

$$MEACOO^- + H_3O^+ \longrightarrow MEA + CO_2 + H_2O \quad (9)$$

The column diameters were designed based on 70 % of the flood point velocity and a capture rate of 90 % was adopted, as it's a commonly used basis for amine-based capture design in open literature. Reboiler duty was adjusted to achieve the desired CO_2 loading. The value of 0.19 was maintained for the lean loading stream while the rich

MEA stream had a loading ratio of 0.43. The specific reboiler duty achieved was 3.9 MJ/ton CO_2.

2.2. Dynamic equilibrium-based model

After converging the steady-state model in Aspen Plus, additional data (such as the vessel geometry e.g. sump volume and heat transfer data) is required to export the model into Aspen Plus Dynamics. The flow-driven dynamic mode was selected and the equilibrium equations had to be split into forward and backward reactions to export the model. Once the model is exported, controllers are added to the desired units. In our model, we focus on the behaviour of the absorber/stripper unit. The goal is to smoothly run the process by keeping the controlled variable within the specified limits. The controllers were assigned default tuning-parameters, which proved inefficient when tested.

2.3. Controller tuning

An open-loop dynamic run was implemented; first, the process was run for 2 hours before ramping down the flue gas flow rate by 50 %. The process then stabilizes before ramping up again 50 %. The controller has no feedback from the process, and the scenario caused a deviation in the parameters from the set point as shown in figure 2. The pressure and temperature both take one hour to stabilize to a new steady state condition.

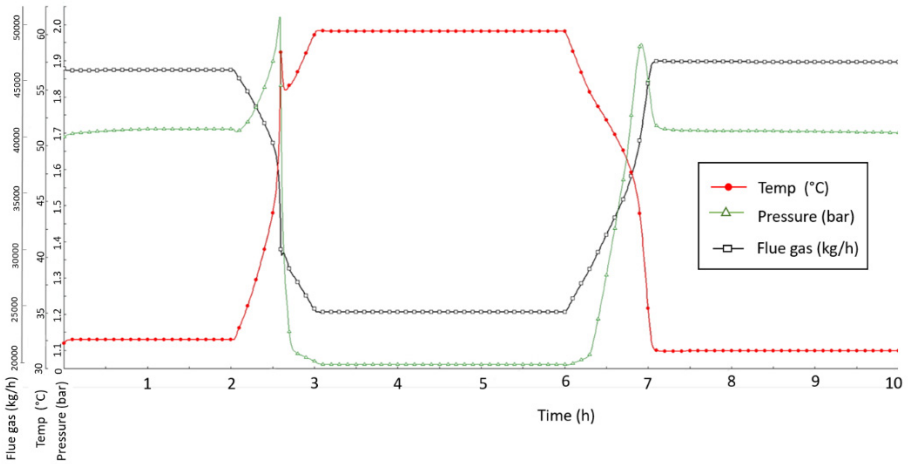

Figure 2 – open-loop simulation for a ramp down/up of the flue gas flow rate for 10 hours

Aspen Plus Dynamics tuning tool, was used to tune the controllers. The controller is tuned handling both set-point and load disturbances by causing 5 % step up on the process output range. The open loop steady-state gain, dead-time and time constant are estimated and the values are used to calculate the tuning parameters using Ziegler-Nichols method, giving approximate values of gain and integral time for each PI controller. Table 1 shows the tuning results from 2 different tests indicating the effect of the sump volume on the dead-time and time constant.

Table 1 - Tuning parameters for 2 different sump heights (P=Pressure controller, LC= Level controller, TC= Temperature controller, L= sump level height)

	Absorber				*Stripper*		
L = 1m	Gain %	Dead time min	Time constant min		Gain %	Dead time min	Time constant min
P	-6.1	0.6	2.44	P	-0.6	0.058	0.599
LC	-9.15	23.16	13.86	LC	-9.22	5.86	5.95
				TC	0.33	0.60	0.5058
L = 2m							
P	-6.18	0.6	2.49				
LC	-9.24	30.05	18.36				

The height of the sump was increased by one meter to analyze the effect on the tuning parameters, the dead time increase by 6.89 minutes while the time constant increased by 4.5 minutes.

3. Results

A disturbance was introduced to the dynamic model representing the worst-case scenario to test the flexibility of the process. The model was allowed to run at initial conditions to ensure steady-state operation, and then a ramp up of 50 % was implemented to the flue gas flow rate for a duration of 1 hour. The temperature and pressure were stabilized in a matter of a few minutes. A more severe disturbance of ramp down 50 % in 5 minutes was introduced at the 7th hour and a small disturbance was caused that also lasted for a few minutes before stabilizing back to the set-point conditions. The capture rate was maintained at 90 %.

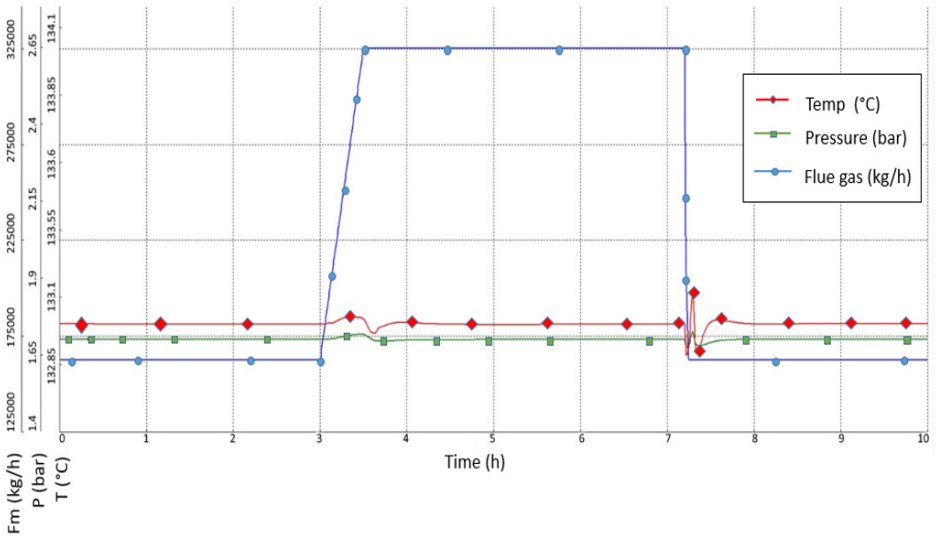

Figure 3 - Dynamic behaviour to disturbances in the flue gas flow-rate showing the stability in the temperature and pressure of the column

4. Conclusion

Utilising renewable energy to produce synthetic combustibles will be an important element in achieving the carbon reduction objectives. Dynamic models help us in studying the effect of various controlled and uncontrolled disturbances on the operation of the carbon capture plant, to be able to implement a control strategy and apply and necessary improvements to the design. It was noticed that the sump volume has an effect on the dead time, time constants and steady-state gain meaning that a reasonable sump volume has to be calculated for each plant. The controllers were tuned using an open loop test and a dead time of 23.16 minutes was noticed in the level controller for the absorber (sump height of 1 m). Sudden and abrupt disturbances are introduced in 1 hour and in 5 mins to study the effect on the pressure and temperature of the column and the results proved flexibility of the capture process. Further tuning tests are required in closed loop with alternative control strategies that covers the whole plant, to successfully maintain the process parameters at the desired set points while flexibility adjusting to the change in inputs such as flue gas flow rates.

Acknowledgements

The authors are grateful to the German Federal Ministry of Economic Affairs and Energy for funding the KEROSyN100 project (funding code 03EIV051A).

References

Chikukwa, A., Enaasen, N., Kvamsdal, H. M., & Hillestad, M. (2012). Dynamic Modeling of Post-combustion CO_2 Capture Using Amines - A Review. *6th Trondheim Conference on CO_2 Capture, Transport and Storage, 23*, 82-91. doi:10.1016/j.egypro.2012.06.063

Jung, H., Im, D., Kim, S. H., & Lee, J. H. (2018). Dynamic Modeling and Analysis of Amine-based Carbon Capture Systems. *Ifac Papersonline*, 51(18), 91-96. doi:10.1016/j.ifacol.2018.09.263

Schmidt, P., Batteiger, V., Roth, A., Weindorf, W., & Raksha, T. (2018). Power-to-Liquids as Renewable Fuel Option for Aviation: A Review. *Chemie Ingenieur Technik, 90*(1-2), 127-140. doi:10.1002/cite.201700129

Cames, M. (2019, February 12). The global decarbonization challenge and aviation within it: Where are we now, where are we going ? Lecture presented at Aviation Decarbonization Forum in Canada, Montréal.

Coupling the different energy sectors − options for the next phase of the energy transition. (2018, August). Retrieved from https://www.acatech.de/wp-content/uploads/2017/11/ESYS_Summary_Position_Paper_Coupling_the_energy_sectors-1.pdf.

Aspen Technology, Inc. Rate-based model of the CO_2 capture process by MEA using Aspen Plus. Burlington (USA);2012.

Zhang, Y.; Chen, C.-C. Modeling CO2 Absorption and Desorption by Aqueous Monoethanolamine Solution with Aspen Rate-Based Model. Energy Procedia 2013, 37, 1584−1596.

Agbonghae, E. O.; Hughes, K. J.; Ingham, D. B.; Ma, L.; Pourkashanian, M. Optimal Process Design of Commercial-Scale Amine-Based CO2 Capture Plants. Ind. Eng. Chem. Res. 2014, 53 (38), 14815−14829.

Sauro Pierucci, Flavio Manenti, Giulia Bozzano, Davide Manca (Eds.)
Proceedings of the 30th European Symposium on Computer Aided Process Engineering (ESCAPE30), May 24-27, 2020, Milano, Italy.
http://dx.doi.org/10.1016/B978-0-12-823377-1.50055-0

Analysis and Optimization of Carbon Supply Chains Integrated to a Power to Gas Plant in Italy

Grazia Leonzio,[a*] Edwin Zondervan[b]

[a]*Department of Industrial and Information Engineering and Economics, University of L'Aquila, Via Giovanni Gronchi 18, 67100 L'Aquila, Italy*

[b]*Laboratory of Process Systems Engineering, Department of Production Engineering, Universität Bremen, Leobener Str. 6, 28359 Bremen, Germany*

grazia.leonzio@graduate.univaq.it

Abstract

Italy should solve the problem related to carbon dioxide emissions for the next years and carbon supply chains can be a strategic solution. In this research work, mixed integer linear programming models are developed for carbon capture, utilization and storage supply chains in Italy with multiple storage sites (saline aquifers) while one main utilization section, producing methane via power to gas, is considered. Currently, there are no carbon supply chains integrated to a power to gas system. The systems under investigation are designed and optimized minimizing the total costs. A supply chain with the offshore Adriatic sea as storage site is the best solution: a lower value of methane production cost (19.1 €/MWh) and incomes (carbon tax of 80 €/t and economic incentives of 260 €/MWh) are required as compared to the other cases. The total costs of this supply chain are of 7.34·104 million €/y, while 16.1 Mt/y of methane are produced.

Keywords: carbon supply chain, mathematical model, optimization, reduction of carbon dioxide

1. Introduction

Globally, carbon dioxide emissions increased over the last years amounting to 33.1 Gt with a concentration of 395 ppm in 2018 (IEA, 2019; Goel et al., 2015). Emissions lead to a climate change and an increase of global average temperature. Different countries in the world agreed to reduce carbon dioxide emissions of 40% by 2030 and of 80% by 2050, compared to the level of 1990 (IPCC, 2013). Italy must decrease carbon dioxide emissions to a value of 275 Mt by 2030, considering that in the 2016 they were 352 Mt (Gracceva et al., 2017). To this aim, carbon supply chains, as carbon capture utilization and storage (CCUS), carbon capture and utilization (CCU) and carbon capture and storage (CCS) technologies have an important and strategic role. In these systems, carbon dioxide is captured at the source site, transported generally via pipeline, and then stored and/or utilized according to the specific case (Hasan et al., 2015). In addition to methanol, formic acid, dimethyl ether, methyl formate, ethylene glycol, acetic acid and other compounds, are considered. Also, carbon dioxide can be valorized and used in the utilization section to produce methane, through the Sabatier reaction (Vooradi et al., 2018; Schiebahn et al., 2015). In this case, hydrogen can be provided by water electrolysis, as in a common power to gas process, exploiting renewable energies (Leonzio, 2017). Studies where a power to gas system is used in the utilization section of a carbon supply chain are rarely considered: they are mainly focused on the production of other compounds (Leonzio et al., 2019a,b;

Hasan et al., 2015). On the other hand, the technical potential for wind and solar power generation, at the base of power to gas processes, as well as the potential application of power to gas systems in Italy are assessed in several studies (Hoefnagels, 2011; Guandalini et al., 2017). This encourages the study of a carbon supply chain integrated to a power to gas system as a possible solution to reduce carbon dioxide emissions in Italy, satisfying at the same time the national methane demand. This research work wants to overcome this gap. Mixed integer linear programming (MILP) models are developed for different CCUS supply chains with different storage sites (mainly saline aquifers), with the same utilization site, producing methane. These systems are compared in terms of topology, costs and required economic incentives to find the best scenario. A comparison with a CCU supply chain is also analyzed.

2. Mathematical model of carbon supply chains

2.1. Problem statement

For the formulation of the mathematical model, a number of realistic and simplified assumptions are made. Intrinsic assumptions are the following: i) capture plants and carbon dioxide sources are located at the same place; ii) one source node can be connected to only one capture node in the storage and utilization section; iii) carbon dioxide is transported via pipeline; iv) the hydrogen required for the Sabatier reaction is provided by a PEM electrolyzer using renewable energy power, but a portion of electricity from the network is any case present (Matzen and Demirel, 2016); v) the network structure is designed for steady state conditions over a period of 25 years; vi) methane production is constant over time, due to the stationary conditions and it is sent to the gas grid; vii) methane is sold a stable price set by the market. Moreover, some information (i.e. locations, costs, capture materials/technologies, carbon dioxide compositions, etc.) is provided about carbon dioxide sources, capture and compression technologies, carbon dioxide transportation, utilization and storage sites. The model can be used to find the best connection between each element inside the supply chain, the amount of considered carbon dioxide and produced methane through the minimization of the total costs, setting a target for emissions reduction: economic and environmental are both considered for the optimization.

2.2. CCUS supply chain model

The considered model, like others developed by us, is based on the work of Hasan et al. (2015). More details (the expressions of equations) of the CCUS supply chain model can be found in our recent work (Leonzio et al 2019a). In these sections, we shortly describe the main features of this model, that can be widely applied in other similar problems.

2.2.1. Sets

As in the most of carbon supply chains, each element inside the considered supply chains is defined by a set: carbon dioxide sources are defined by *"i"*, capture technologies are defined by *"j"*, geological storage and utilization site by *"k"*.

2.2.2. Parameters and variables

Some parameters are considered for the developed mathematical model and these are related to the minimum target of carbon dioxide reduction (Gracceva et al., 2017), to carbon dioxide emissions from each source i (Green, 2014), to flue gas flow rate from source i calculated by carbon dioxide composition (Zhang et al., 2018), to the lowest and highest carbon dioxide composition processed by the capture technology j (Zhang et al., 2018), to the maximum storage capacity (Moia et al., 2012). As in our previous work, binary and continuous variables are introduced to define the selected storage site ($X_{i,j,k}$),

the selected capture technology ($Y_{i,j,k}$), the amount of carbon dioxide that is stored ($FR_{i,j,k}$) and sent to the utilization ($MR_{i,j,k}$) for methane production.

2.2.3. Constraints and equations

The same constraints set in the model presented in Leonzio et al. (2019a) are considered (regarding the selection of capture technologies and storage site based on one to one coupling, maximum storage capacity that can not be exceed, minimum target for emissions reduction that should be achieved, purity on carbon dioxide that should be ensured and glover linearization). However, the constraint for the national demand of methane, that should be satisfied, equal to 46.5 Mt/y (Alverà et al., 2017), is not considered because, the amount of captured carbon dioxide is not sufficient to produce methane at this rate. Equations are defined to express the capture and compression costs (Hasan et al., 2014), carbon dioxide transportation costs (Knoope et al., 2013), carbon dioxide storage costs (Hendriks, 1994). The methane production cost through a power to gas system including also the electrolysis process is of 300 €/MWh, due to the high cost of electricity (Ma et al., 2018; Reichert, 2012).

2.2.4. Objective function

As in our models, the objective function of the developed mathematical model contains the total costs of the supply chain that are the sum of carbon dioxide capture and compression costs, carbon dioxide transportation costs, carbon dioxide storage costs and methane production costs. The objective function is minimized to design an optimal system.

2.3. Case study

Italy must reduce carbon dioxide emissions to 275 $MtCO_2$ by 2030 (Gracceva et al., 2017). To suggest a solution for this objective, CO_2 source, utilization and storage sites are defined in the supply chain. Ten Italian regions, those with higher emissions, are selected as sources: Puglia (68.64 $MtCO_2$/y), Lombardy (46.8 $MtCO_2$/y), Sicily (41.53 $MtCO_2$/y), Lazio (28.16 $MtCO_2$/y), Sardinia (26.4 $MtCO_2$/y), Veneto (22.5 $MtCO_2$/y), Emilia Romagna (21.82 $MtCO_2$/y), Piedmont (19.71 $MtCO_2$/y), Liguria (17.6 $MtCO_2$/y), Tuscany (16.9 $MtCO_2$/y) (Green, 2014). The nodes for the system are located at the capital cities of each region. Seven carbon dioxide storage sites with a defined storage capacity, as saline aquifers, are selected: Malossa San Bartolomeo, Pesaro sea, offshore Adriatic sea, Cornelia, offshore Marche, offshore Calabria ionic sea, Sulcis area (Moia et al., 2012). Verbania is chosen as the utilization site, with an infinite capacity, replacing an existing biogas plant and supposing that in the next future solar energy will be available (Colbertaldo et al., 2018). Monoethanolamine (MEA) and ionic liquid absorption, membrane, pressure swing adsorption (PSA) and vacuum swing adsorption (VSA) are the capture technologies available inside the supply chain.

3. Results and discussion

The AIMMS software (Version 4.3) is used to solve MILP models with CPLEX 12.7.1 as selected solver. The computer processor is 2.5 GHz while the memory is 4 GB. For the different CCUS supply chains, MILP models are made of 711 variables (50 integer) and 684 constraints. The solutions are found in some seconds and with a maximum of 100 iterations. For the CCU supply chain, the MILP model is composed by 460 variables (50 integer) and 482 constraints. The problem is solved in 1.69 s with 142 iterations.

The topologies of different carbon supply chains, connecting sources and utilization sites, obtained by the optimization, are shown in figure 1. For each system, a specific capture technology is selected to achieve the minimum target of carbon dioxide reduction of 77

$MtCO_2$. Table 1 shows the economic analysis: total costs, methane yields, set carbon tax and economic incentives, net methane production costs are presented for each considered supply chain. Then, carbon tax and economic incentives are required to have a profitable system (Di Costanzo, 2017). By comparing the different case studies, it is evident that the CCUS supply chain with the offshore Adriatic sea as storage site has a lower value of economic incentives and production cost (lower than the selling price of 25 €/MWh (ec.europe.eu)), compared to other case studies. For this scenario, the methane production cost is 19.1 €/MWh while the economic incentives are 260 €/MWh. Considering economic incentives and carbon tax, the net total costs of supply chain is, instead, of 59.69 €/tCO_2 captured, comparable with other studies (Zhang et al., 2018). The CCU supply chain, producing only methane, is not a profitable solution because, with the highest economic incentives of 260 €/MWh, a high methane production cost is obtained.

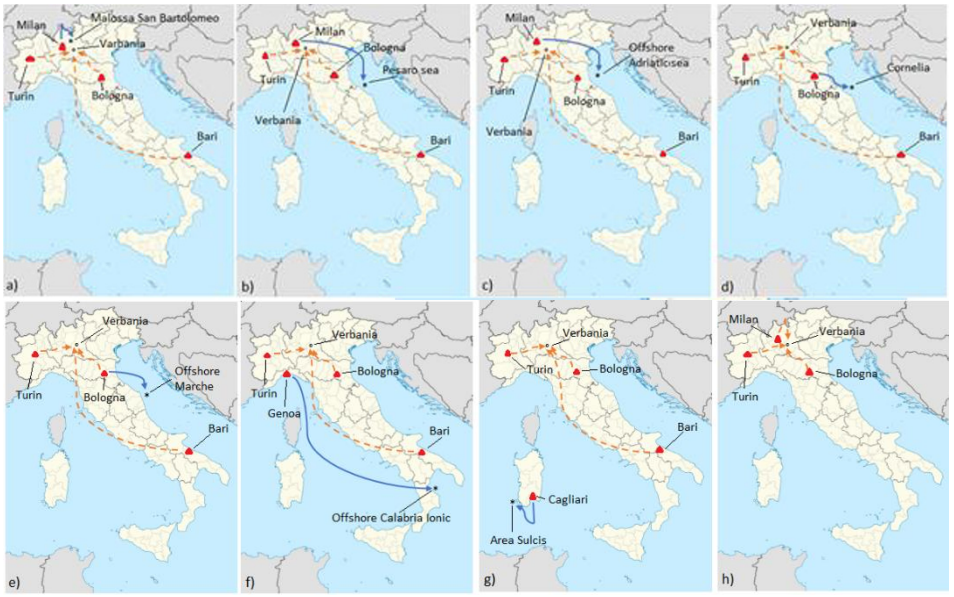

Figure 1 Results of carbon supply chains: a) CCUS supply chain with Malossa San Bartolomeo as storage site; b) CCUS supply chain with Pesaro sea as storage site; c) CCUS supply chain with Offshore Adriatic sea as storage site; d) CCUS supply chain with Cornelia as storage site; e) CCUS supply chain with offshore Marche as storage site; f) CCUS supply chain with offshore Calabria Ionic as storage site; g) CCUS with Area Sulcis as storage site; h) CCU supply chain. (Legend: ▲ CO_2 source; * CO_2 storage site; ° CO_2 utilization site, – – CO_2 transportation from a source to the utilization site, ——— CO_2 transportation from a source to the storage site)

For all scenarios, the methane production cost including hydrogen production via electrolysis has the highest contribution to the total costs. The designed system allows to reduce methane importation. Currently the Italian methane production is 3.9 Mt/y (yearbook.enerdata.net), and to satisfy a methane demand of 46.5 Mt/y, 43 Mt/y of methane should be imported. With the proposed best system, producing 16.1 Mt/y of methane, it is possible to reduce the methane importation to 26.9 Mt/y.

Table 1 Economic results of the analyzed carbon supply chains

Storage site	Total costs (million€/year)	Methane yield (Mt/y)	Carbon tax (€/t)	Economic incentives (€/MWh)	net Methane production costs (€/MWh)
Malossa San Bartomeo	$10.17 \cdot 10^4$	22.5	80	260	23.4
Pesaro sea	$11.09 \cdot 10^4$	24.5	80	260	24.6
Offshore Adriatic sea	$7.34 \cdot 10^4$	16.1	80	260	19.1
Cornelia	$11.32 \cdot 10^4$	25.1	80	260	24.4
Offshore Marche	$10.07 \cdot 10^4$	22.2	80	260	24.1
Offshore Calabria Ionic	$12.15 \cdot 10^4$	26.5	80	270	19.4
Area sulcis	$12.51 \cdot 10^4$	27.8	80	270	15.2
-	$12.88 \cdot 10^4$	28	80	270	21.8

4. Conclusions

In this research, mathematical models for CCUS and CCU supply chains integrated to a power to gas system are compared and developed to solve CO_2 emission problem in Italy. Carbon dioxide is used to produce methane and in the literature no similar work have been considered before. Mainly, CCUS supply chains with different storage sites and a CCU supply chain are compared in terms of topology,costs and required economic incentives. The CCUS system with the offshore Adriatic sea as storage site provides the best case, due to a lower methane production cost and required incentives, that are needed to have a profitable process. Without considering economic incentives before, the total costs of the best framework is of $7.34 \cdot 10^4$ million €/y producing 16.1 Mt/y of methane, at a production cost of 19 €/MWh when a proper level of incomes are considered (carbon tax of 80 €/t and economic incentives of 260 €/MWh). The national import of methane is in this way reduced significantly. In addition, it result that the storage is important inside the carbon supply chain, to have the most economically profitable solution, with a fixed carbon dioxide reduction rate. Only utilization is not sufficient to achieve the target set by the environmental policies at an advantage cost and this motivats the support of carbon storage.

References

1. M. Alverà, 2017, Snam Rete Gas Ten-year network development plan of the natural gas transmission network 2017-2026, Document prepared by Snam Rete Gas S.p.A. In compliance with the D.L. 93 of 11 June 2011 and subsequent amendments and additions.
2. P. Colbertaldo, G. Guandalini, S. Campanari, S., 2018. Modelling the integrated power and transport energy system: The role of power-to-gas and hydrogen in long-term scenarios for Italy, Energy 154, 592-601.
3. F. Di Costanzo, 2017. Analisi energetica ed economica di un sistema "Power to gas" con produzione biologica di metano. [Laurea magistrale], Università di Bologna, Corso di Studio in Ingegneria energetica [LM-DM270], Documento full-text non disponibile.
4. F. Gracceva, E. De Luca, A. Fidanza, P. Del Nero, L.G. Giuffrida, B. Felici, C. Pona, A. Zini, 2017, Analisi trimestrale del sistema energetico italiano. Report 1/2017. ISSN 2531-4750.
5.Green, 2014, https://www.google.de/search?q=percentuale+emissioni+co2+regioni+italiane&source=lnms&tbm=isch&sa=X&ved=0ahUKEwi22_WKvtHeAhVJFywKHaQTACUQ_AUIDigB&biw=1366&bih=608#imgrc=_Q4uMiUoDub58M:

6. C. Goel, H. Bhunia, P.K. Bajpai, 2015. Development of nitrogen enriched nanostructured carbon adsorbents for CO2 capture. J. Environ. Manag. 162, 20-29.
7. G. Guandalini, M. Robinius, T. Grube, S. Campanari, D. Stolten, 2017. Long-term power-to-gas potential from wind and solar power: A country analysis for Italy, International Journal of Hydrogen Energy, 42, 13389-13406.
8. M.M.F. Hasan, L.E. First, F. Boukouvala, C.A. Floudas, 2015, A multi-scale framework for CO2 capture, utilization, and sequestration: CCUS and CCU, Computers and Chemical Engineering 81, 2–21.
9. M.M.F. Hasan, F. Boukouvala, E.L. First, C.A. Floudas, (2014). Nationwide. regional. and statewide CO2 capture. utilization. and sequestration supply chain network optimization. Ind Eng Chem Res 53. (18). 7489–7506.
10. C.A. Hendriks. Carbon Dioxide Removal from coal-Fired power plant. In department of science. technology. and society. Utrecht University. 1994: Utrecht. Netherlands.
12. R. Hoefnagels, M. Junginger, C. Panzer, G. Resch, A. Held, 2011, Reshaping project e long term potentials and costs of RES-Part I: potentials. diffusion and technological learning. [Online]. Available: www.reshaping-res-policy.eu [Accessed 09 March 2017].
12. https://ec.€europa.eu/€eurostat/statistics-explained/index.php?title=File:Gas_prices_for_non-household_consumers,_second_half_2017_(EUR_per_kWh).png#filehistory
13. https://yearbook.enerdata.net/natural-gas/world-natural-gas-production-statistics.html
14. IEA (International Energy Agency), 2019. Global energy & CO2 status report. https://www.iea.org/geco/emissions/.
15. IPCC, 2013. Climate Change 2013: the Physical Science Basis. Technical Report. Intergovernmental Panel on Climate Change.
16. M.M.J. Knoope, A. Ramrez, A.P.C. Faaij, 2013. A state of the art review of techno-economic model predicting the costs of CO2 pipeline transport. Int. J. Greenh. Gas Control 16. 241-270.
17. G. Leonzio, 2017, Design and feasibility analysis of a Power-to-Gas plant in Germany, Journal of Cleaner Production, 162, 609-623.
18. G. Leonzio, P.U. Foscolo, E. Zondervan, 2019a, Sustainable utilization and storage of carbon dioxide: Analysis and design of an innovative supply chain, Computer and Chemical Engineering, 131, 106569.
19. G. Leonzio, D. Bogle, P.U. Foscolo, E. Zondervan, 2019b, Optimization of CCUS supply chains in the UK: a strategic role for emissions reduction, Chemical Engineering Research and Desing, under review.
20. J. Ma, Q. Li, M. Kühn, N. Nakaten, 2018, Power-to-gas based subsurface energy storage: A review, Renewable and Sustainable Energy Reviews 97, 478–496.
21. M. Matzen, Y. Demirel, 2016, Methanol and dimethyl ether from renewable hydrogen and carbon dioxide: alternatve fuels production and life cycle assessment, Journal of Cleaner Production, 139, 1068-1077.
22. F. Moia, S. Fais, F. Pisanu, G. Sardu, P. Casero, R. Guandalini, G. Agate, S. Beretta, F. Cappelletti, F. Colucci, 2012. La fattibilità dello stoccaggio geologico della CO2 negli acquiferi salini profondi nell'onshore e offshore italiano, 1º Congresso dell'Ordine dei Geologi di Basilicata,"Ricerca, Sviluppo ed Utilizzo delle Fonti Fossili: Il Ruolo del Geologo", Potenza, 30 Novembre - 2 Dicembre 2012.
23. F. Reichert, 2012, Wind-to-Gas-to-Money? Economics and Perspectives of the Power-to-Gas Technology. Aalborg University Department of Development and Planning MSc (Eng) Sustainable Energy Planning and Management. master thesis.
24. R. Vooradi, M.O. Bertrana, R. Frauzema, S.B. Anne, R. Gani, 2018. Sustainable chemical processing and energy-carbon dioxide management: Review of challenges and opportunities, Chemical Engineering Research and Design, 131, 440-464.
25. S. Schiebahn, T. Grube, M. Robinius, V. Tietze, B. Kumar, D. Stolten, 2015. Power to gas: Technological overview, systems analysis and economic assessment for a case study in Germany, International Journal of Hydrogen Energy, 40, 4285-4294.
26. S. Zhang, L. Liua, L. Zhang, Y. Zhuang, J. Du, 2018. An optimization model for carbon capture utilization and storage supply chain: A case study in Northeastern China, Applied Energy 231, 194–206.

Sauro Pierucci, Flavio Manenti, Giulia Bozzano, Davide Manca (Eds.)
Proceedings of the 30th European Symposium on Computer Aided Process Engineering (ESCAPE30), May 24-27, 2020, Milano, Italy.
http://dx.doi.org/10.1016/B978-0-12-823377-1.50056-2

Effect of Selective Size Extraction of Microalgae from a Photobioreactor

Ergys Pahija[a], Chi-Wai Hui[b,*], John M. Woodley[a], Gürkan Sin[a]

[a]*Process and Systems Engineering Research Center (PROSYS), Department of Chemical and Biochemical Engineering, Technical University of Denmark, 2800 Kgs. Lyngby, Denmark*
[b]*Department of Chemical and Biological Engineering, The Hong Kong University of Science and Technology, Clear Water Bay, Hong Kong SAR*
kehui@ust.hk

Abstract

A good understanding of population dynamics can give relevant insights and process understanding to improve the production of microalgae. To this end, population balance modelling (PBM) can be used to study population dynamics that can provide information such as the size distribution of cells. This detail can then be used to comprehend whether and how certain process strategies are beneficial to the population growth. The objective of this work is to understand how different cell removal strategies can affect the production of microalgae, using a model-based approach.

Keywords: microalgae, harvesting, population dynamics, population balance.

1. Introduction

A good understanding of microalgae dynamics can be particularly beneficial to improve the efficiency of the production process. Several models of microalgae growth can be found in the literature (Lee et al., 2015). Likewise, models for harvesting cells have been considered to reduce the costs of the process (Salim et al., 2013; Lee et al., 2018). Among others, the PBM can give relevant information about biological systems, and unicellular organisms in particular (Pahija et al., 2019b). Looking at these two processes separately is relevant to develop an essential strategy in their design and select the best operating conditions.

A possible scenario for a microalgae production plant consists of a production or biomass growth unit, where microalgae grow in a photobioreactor (PBR), and a harvesting unit, where the microalgae are collected. Part of the solution flows from the PBR to a sedimentation tank, where cells tend to settle on the bottom as sludge and from there to a downstream process (e.g., extraction, recovery, and isolation of valuable products from inside the cells). Although this paper focuses on the growth unit, future works should consider the integration of all units operating in the process to maximise the production of microalgae.

Microalgae size and internal composition are affected by environmental conditions and are dependent upon which stage of the life cycle the cell is located (Morimura, 1959).

The aim of this work is to apply a population balance model (PBM) to simulate the growth and show the effect of extracting a specific size distribution of cells from the PBR. Several examples will be used to illustrate the impact and importance of the size distribution in this process. In particular, we will demonstrate how extracting a specific

size of microalgae from the bioreactor will affect the overall performance and yield of cells. The effects on the harvesting unit will be taken into account in future studies.

2. Methodology

The PBM is used to simulate the population dynamics of microalgae inside the PBR. The population balance is solved using a discretization method and it appears as shown in Equation (1).

$$N_i^{j+1} = N_i^j + \Delta t \left[-\frac{G_i}{\Delta L_i} S_i N_i^j + \frac{G_{i-1}}{\Delta L_{i-1}} S_{i-1} N_{i-1}^j \right] - S_i N_i^j \Delta t + \sum_{k=L_{cr}}^{L_{\max}} \left(X S_k b_{ki} N_k^j \Delta t \right) \quad (1)$$

Where N_i^j is the number of particles in the size interval i at time j, G_i is the growth rate of interval i, S_i is the size-specific division rate and X is the number of daughter cells. b_{ki} is the probability for particles of size k to divide into particles of size i. Finally, Δt and ΔL_i are the time and size interval i, respectively. In case the size discretization is uniform, then it can be assumed that $\Delta L = \Delta L_i$. In this first example, b_{ki} is taken as equal to 1 for the first size interval ($i = 1$) and equal to 0 for all other size intervals ($i \neq 1$). It is assumed that the new-born cells are generated in the first interval and division starts only after the size of microalgae is larger than 5 μm. The equation was solved following the methodology proposed by Pahija et al. (2019b), and the growth and division rates are a function of temperature and light intensity. The PBM was implemented and solved in MATLAB and is used to evaluate different extraction strategies. Although this paper proposes only simulations, all initial conditions shown in the results below are taken from experimental data. The measurements of the number density of cells and their size distribution were conducted as explained by Pahija et al. (2019a).

Three strategies are considered in order to demonstrate the importance of size distribution in the production of microalgae:

- Removal from a perfectly mixed PBR
- Removal from a perfectly mixed PBR including the stationary phase
- Removal of a selected size of cells from the PBR

3. Results

3.1. Extraction from a perfectly mixed PBR

This first basic application consists of the continuous removal of microalgae cells from a perfectly mixed PBR. Figure 2 shows the change in cell population in case different flowrates are removed from the PBR. The size distribution of particles is not affected by the removal of microalgae. The volumetric removal rate can be addressed as a fraction of the total population collected. Let's assume a PBR containing 300,000 L of microalgae solution. A specific flowrate is then removed from the reactor and sent to the harvesting unit. The volume of the solution inside the PBR is assumed constant and we suppose that BG11 ($NaNO_3$, K_2HPO_4, $MgSO_4 \cdot 7H_2O$, $CaCl_2 \cdot 2H_2O$, Citric Acid$\cdot H_2O$, Ferric Ammonium Citrate, $Na_2EDTA \cdot 2H_2O$, Na_2CO_3, Trace Metal Solution, Sodium

Thiosulfate Pentahydrate) is used as a medium, being the initial condition taken from experimental data.

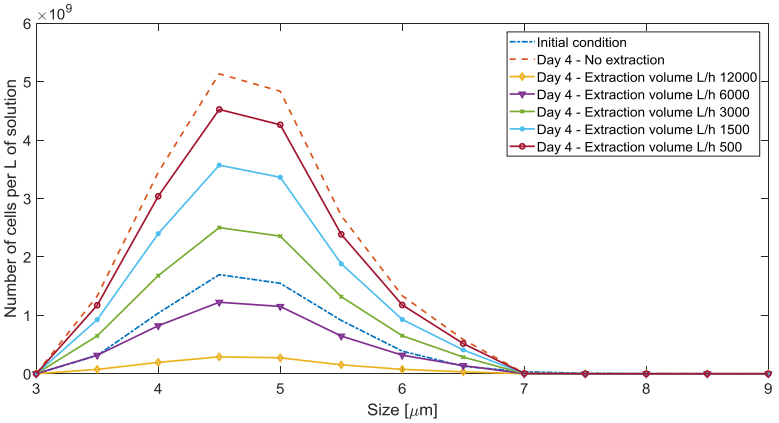

Figure 1 Effects on microalgae population by cell removal at different flowrates from the PBR.

Figure 1 and Figure 2 depict that there is a value of flowrate that allows the population to slightly increase, even when cells are removed. Intuitively, a decision should be taken according to the given process objectives. In this case, our goal is to maximise the production of microalgae. Removing 12,000 L/h of solution from the PBR can provide a good production rate for a small amount of time, while after two to three days, the production is reduced considerately. The reason is that the population growth of microalgae is not as fast as the removal rate, resulting in a reduction in the overall population inside the PBR. Reducing the flowrate to 500 L/h has a much lower impact on the population inside the reactor, but only a small mass of microalgae is collected. Figure 2 indicates that there is an optimal flowrate to guarantee the maximum production of microalgae in a certain period. From the proposed graph, in order to maximize the production, we need to make a trade-off between collected cells and population growth in the reactor.

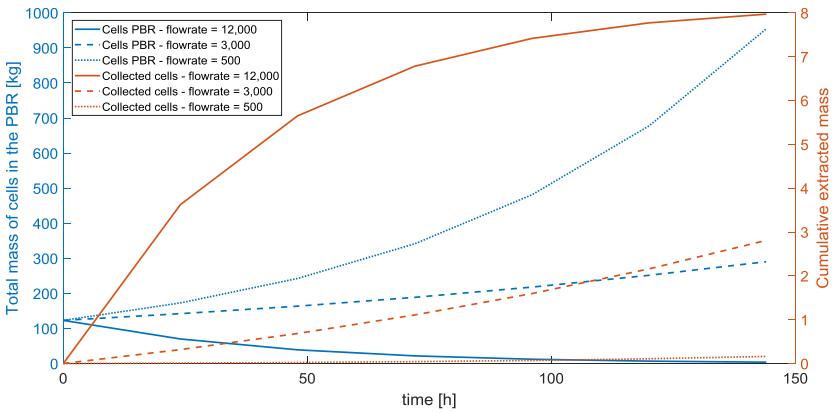

Figure 2 Effect of different flowrates on the total mass of microalgae collected and the total mass of cells inside the PBR.

Figure 2 shows the increase in the concentration of cells with time. In this case, the mass of cells in 144 hours is equal to almost 900 kg of cells; the value is not a dry

weight, according to literature the water content depends on the cell species, composition, and may vary according to the conditions can be higher than 90 %, as described by Kanda and Li (2011).

3.2. Considerations on the stationary phase

However, it is common to work with a higher concentration of microalgae in order to collect more biomass. Therefore, a possible approach could consist of reaching the stationary phase to have a higher biomass concentration. Nevertheless, the composition of cells in the stationary phase must be in line with the production requirements; the environmental condition should allow the achievement of high microalgae concentration and the health condition of the population should be monitored. If all these requirements are met, maintaining the population in the stationary phase would be beneficial in terms of biomass production.

In the case of limited nutrients concentration (0.5 BG11) in continuous production of microalgae, if the removal rate of cells from a PBR of 300 m^3 of solution is limited to 500 L/h, the stationary phase would be reached after several days.

Figure 3 represents an extension of Figure 2. Here more appropriate values of removal flowrates are selected, and the simulation is extended for a relevant period in order to see the effect of the cumulative biomass removed and how the population inside the PBR responds. The maximum number of cells in the reactor is related to the concentration of nutrients and, as shown below, the maximum biomass concentration inside the selected reactor, and the proposed conditions. It is now particularly evident that there is an optimal removal rate, and it would beat the value that causes the cumulative removal of biomass to increase fastest. The increase in cumulative biomass collected becomes linear after the stationary phase is reached.

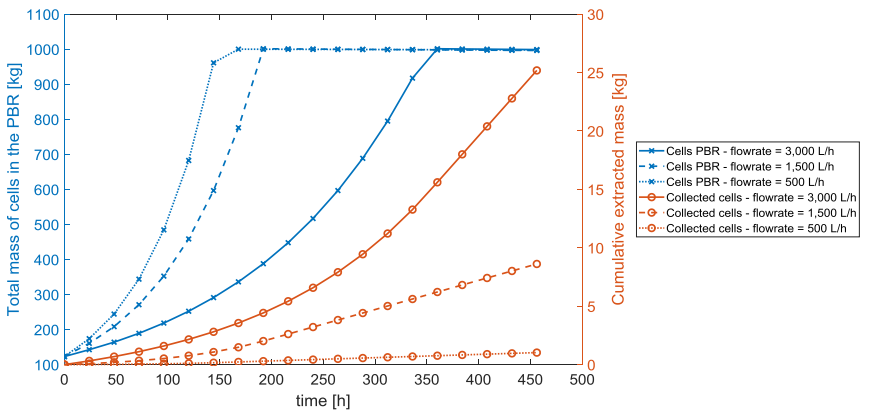

Figure 3 Effect of different flowrates for 20 consecutive days of production, considering the stationary phase.

The specific growth rates and division rates are considered equal to zero when the population becomes higher than the set limit (stationary phase). In case no cells are removed from the PBR, the number of cells remains constant. After reaching the removal, the population stops growing, while removal of the solution is in progress. As shown in Figure 4, the case with a higher extraction rate reaches the limit later than the other cases. The reason the maximum concentration remains constant is that the stationary phase is generally long, and we assume that all the medium removed from the reactor is instantly recirculated while eventual losses of the volume are reintroduced by using deionized water. If these assumptions are respected, the maximum population

would approximately maintain the same value. Notice that Figure 4 the axes are adjusted to focus on the differences in the stationary phase.

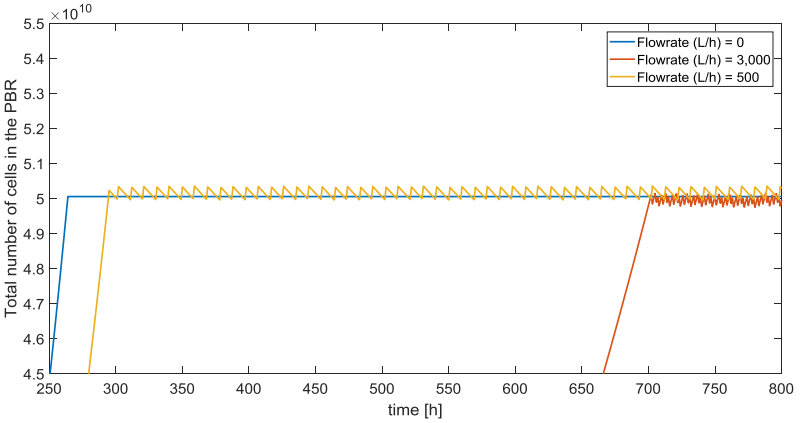

Figure 4 Stationary phase with a continuous collection of cells.

3.3. Extraction of a selected size of cells

Finally, the extraction of a specific size of microalgae is now proposed. Let us suppose that an ideal harvesting system is used to collect microalgae and that it is able to collect 100 % of a defined size range of cells. This test would allow to better visualize the population dynamics in case a specific size is continuously removed from the system.

As a case study, the growth of microalgae at 30°C and 600 lumens is considered. The medium is BG11. The time interval is equal to 0.5 h while the size interval is fixed to 0.5 µm.

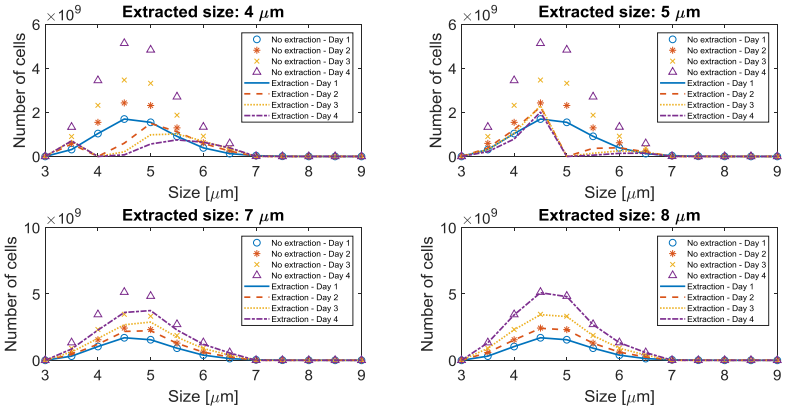

Figure 5 Growth of microalgae in case a specific size of microalgae is continuously extracted from the PBR.

Figure 5 shows the effect of extracting a different size of microalgae. The number of cells per litre of solution is affected by the size range of removed cells. Looking at the four graphs, it is clear that extracting small cells affects the population more than extracting larger sizes. This is because we assume new-born cells are generated in the first interval, and the division starts only after the size of microalgae is larger than 5 µm. Therefore, removing smaller cells would reduce the overall younger population, that can grow to the mature phase. Furthermore, this demonstrates the importance of cells in the range 5-8 µm, where the majority of divisions occur. Removal of cells larger than 7.5

μm can be considered as negligible for the simulation because of the low number of cells, and the resulting dynamics with be very similar to the one without any extraction. An additional consideration can also be made with respect to the model. Looking at the figure with size 4 μm removal, it is noticeable that the concentration of cells of size 4.5 μm in day 2 is not zero. This is due to the fact that in this case, we are not assuming the Courant–Friedrichs–Lewy condition to be equal to unity when trying to solve the population balance model. Consequently, we have a residual number of cells remaining in the interval but, because of microalgae growth, the number of cells in the interval is reduced at each time step.

4. Conclusions and future work

The results show the effect of microalgae size distribution in a photobioreactor. Several case studies have been simulated in this work. In particular, the first case has demonstrated how removing more cells than those obtained from the population growth, the concentration of cells drops. Similarly, a case study by including the stationary phase shows that an optimal extraction flowrate should be calculated. Following, the example of specific size removal of cells indicates it can strongly affect the dynamics, and it is a function of the size distribution. This work is a simulation-based work and although the results give some relevant information on the possibility of size-specific microalgae removal. The simulation results provided some relevant information on the population dynamics and process performance, which will be tested using experimental investigations for improving the microalgae production process.

The achieved results are relevant in the case a specific size of microalgae wants to be concentrated inside the photobioreactor. This allows a higher concentration of cells in a specific stage of the life-cycle, and it can be further correlated to the concentration of desired substances inside the cells. However, the proposed work could also be applied to other biological and non-biological reactors when a specific internal coordinate (size of cells or particles) wants to be achieved.

References

E. Lee, M. Jalalizadeh, and Q. Zhang, 2015, Growth kinetic models for microalgae cultivation: A review, Algal Research, 12, 497–512.

P. Y. Lee, E. Pahija, Y. Z. Liang, K. P. Yeoh, and C. W. Hui, 2018, Population Balance Equation Applied to Microalgae Harvesting, Computer Aided Chemical Engineering, 43, 1299–1304.

Y. Morimura, 1959, Synchronous Culture of Chlorella, Plant and Cell Physiology, 1, 49–62.

E. Pahija, and C.W. Hui, 2019a, A systematic study on the effects of dynamic environments on microalgae concentration, Algal Research, 42, 101599.

E. Pahija, P. Y. Lee, and C. W. Hui, 2019b, A Revision of Population Balance Equation Applied to Microalgae with Birth, Growth, and Death, Process Integr. Optim. Sustain., 3, 1, 125–141.

S. Salim, L. Gilissen, A. Rinzema, M. H. Vermuë, and R. H. Wijffels, 2013, Modeling microalgal flocculation and sedimentation, Bioresour. Technol., 144, 602–607.

H. Kanda, and P. Li, 2011, Simple extraction method of green crude from natural blue-green microalgae by dimethyl ether, Fuel, 90(3), 1264-1266.

Sauro Pierucci, Flavio Manenti, Giulia Bozzano, Davide Manca (Eds.)
Proceedings of the 30th European Symposium on Computer Aided Process Engineering (ESCAPE30), May 24-27, 2020, Milano, Italy.
http://dx.doi.org/10.1016/B978-0-12-823377-1.50057-4

Numerical Modelling for Environmental Impact Assessment of Sediment Dispersion in Port Areas

Stefania Magrì[a*], Patrizia De Gaetano[a], Alessandra Feola[b], Iolanda Lisi[b], Andrea Salmeri[b], Francesco Venti[b], Andrea Pedroncini[c]

[a]*ARPAL - Agenzia Regionale per la Protezione Ambiente Liguria, Via Bombrini 8, 16149 Genova, Italy*
[b]*ISPRA - Istituto Superiore per la Protezione e la Ricerca Ambientale, Loc. Brondolo, 30015 Chioggia, Italy*
[c]*ISPRA - Istituto Superiore per la Protezione e la Ricerca Ambientale, Via Brancati 48, 00144 Roma, Italy*
[d]*DHI Italia, Via Bombrini 11, 16149 Genova, Italy*

stefania.magri@arpal.gov.it

Abstract

In port areas, sediments resuspension can be critical for the presence of contaminants (such as metals from industrial effluents), which may be dispersed to unpolluted areas under different hydrodynamics forces. In the framework of the interregional project SE.D.RI.PORT (SEdimenti, Dragaggi e RIschi PORTuali) project, the Institute for Environmental Protection and Research (ISPRA) and Regional Agency for Environmental Protection–Liguria (ARPAL) have implemented a numerical model to simulate the sediment plume dynamics for bed levelling operation in the pilot area of La Spezia harbour (Italy). The area is characterized by a diffused pollution and subjected, since the 90s, to different dredging and reclamation activities, as well as monitoring and environmental characterization, providing data for the model. According to sectors references, different modelling tools has been applied to characterize the area interested by sediment plume dynamics, in term of significant variations of suspended sediment concentration (SSC) and sediment deposition rates (DEP). Model results are presented by means of synthetic maps showing the meaningful effects of operations at different water depths and at different key sites in order to support the dredging project and the environmental monitoring planning and optimization.

Keywords: Dredging and bed levelling, environmental assessment, mathematical modelling, port areas, sediment dispersion.

1. Introduction

The removal of sediments from the bottom of harbours is often necessary to maintain or increase the depth of navigation channels or berthing areas, thus ensuring the functionality of the port. The increase of suspended solid concentration due to resuspended bottom sediments can determine negative environmental effects both on the abiotic and biotic marine ecosystem, as reported by Wilber & Clark (2001), Erftemeijer et al. (2012). In coastal marine systems at high level of anthropization, like harbours, sediments represents a sink and a source for contaminants, and resuspension can contribute to propagate pollution even in clean areas (e.g. PIANC, 2006; Lisi et al., 2017 e 2019; CEDA/IADC, 2018). Most dredged material in ports are rich in fine

sediments and often contain many anthropogenic substances, some of which have a toxic character: heavy metals, tributyltin (TBT), polycyclic aromatic hydrocarbons (PAHs), polychlorinated biphenyls (PCBs), pesticides and biocides whose effects on health are multiple (carcinogenic, mutagenic, toxic for reproduction) and attempts have been made to define protocols to determine the dangerousness of contaminated sediments (Garbolino et al., 2014). The problem of metal contamination in marine sediments have recently lead to proposed techniques for environmentally friendly strategies for removal, such as bioleaching (Fonti et al., 2013) or nano-based products site-remediation (De Gisi et al., 2017).
For projects that involve the handling of sediments, a detailed Environmental Impact Assessment (EIA, Directive 2014/52/UE) should be carried out to determine the potential environmental impacts, evaluate technical alternatives and design appropriate mitigation, management and monitoring measures. Recently, in absence of local legislation, guidelines for the use of numerical modelling to support environmental studies have been published (Lisi et al., 2017).
The present paper describes an application of the Integrated Modelling Approach for simulating Sediment Dispersion (IMAforSED) proposed by Lisi et al. (2017, 2019) and of the Dredging Environmental Assessment Module (Dr-EAM) proposed by Feola et al. (2015, 2016), specifically developed by ISPRA as supporting tools for dredging activities. The approach is applied to bed levelling operations with grab dredger planned for 2019 in the harbour basin in La Spezia, Italy. Bed levelling is a technique consisting in removal of sediments from an area and their consequential re-disposal in an adjacent area. The main objective of the work is to test the replicability of the methodology to a sea bed levelling activity and capture the spatial (vertical and horizontal) and temporal variability of the modelled SSC and DEP levels by means of maps showing statistical measures usable for decision support and environmental management.

2. Material and Methods

2.1. The study area

La Spezia harbour basin, located in Liguria region (Italy) covers an area of about 16 km^2, bounded to the south-east by a breakwater, of about 2.8 km. The basin is connected to the open sea by two entrances about 400 m and 200 m wide. The enclosed bay is influenced by the runoff of several small rivers, characterized by seasonal and discontinuous discharges, as well as civil and industrial discharges, in particular by the Enel thermoelectric power plant. The heavy industrial, military, commercial and anthropic activities have caused terrestrial as well as marine widespread contamination. Since 2006 many sectors of the harbour area have been dredged for environmental reclamation and depth maintenance.

2.2. Integrated Modelling Approach

An Integrated Modelling Approach for simulating Sediment Dispersion (IMAforSED), developed by ISPRA (Lisi et al., 2017; 2019) has been applied to provide a characterization of the area interested by sediment passive plume dynamics, in term of significant variations of suspended sediment concentration (SSC) and sediment deposition rates (DEP). Basically, the IMAforSED consists in the implementation in series of three numerical modules, hereinafter referred to as the hydrodynamic module, source term module and transport module. Finally an Environmental Assessment Module (Dr-EAM) is implemented, to synthesize numerical results and to make them usable for decision support. Available data (e.g. ARPAL and ISPRA seabed sediment

characterization and environmental monitoring of dredging activities in the area) have been used to feed the numerical models implemented in the proposed methodology.

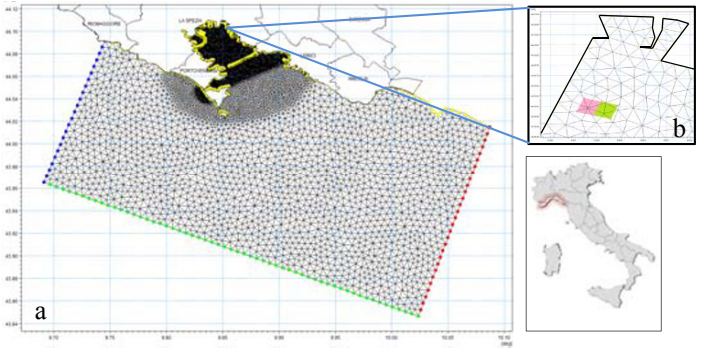

Figure 1. a) Model domain and b) location of the area object of the bed levelling activity (left area for removal and right area for deposition)

2.2.1. Hydrodynamic Module (HM)

The characteristics of La Spezia harbour have suggested the application of a three-dimensional hydrodynamic model. The three-dimensional finite volume MIKE 3 Flow Model FM (DHI, 2019) was used to model the stratified flow field and to obtain hydrodynamic parameters at a high-resolution scale for a full reference year. The model uses a three-dimensional, Reynolds averaged, Navier-Stokes equations for solving the full non-linear equations of continuity and conservation of momentum. On-field data from monitoring activities were used to calibrate the coefficient that parametrizes vertical dispersion. A flexible mesh with maximum horizontal resolution of 50 m was chosen to properly describe the complex geometry and dynamics of the site (Figure 1). An hybrid vertical discretization system (σ and z) was used to account for the stratification effects. An entire reference year of climatic conditions was used, and, in particular, 2015 was chosen. At the open boundaries, reanalysis from the 3D model of the Mediterranean sea, available through the Copernicus Service (Marine Environment Monitoring Service, marine.copernicus.eu), were applied. For the tidal component of water level and current, data from the OSU Tidal Prediction Software (OTPS) were used. Wind forcing from the meteorological model MOLOCH, developed and run at the Meteo Hydrological Functional Centre for Civil Protection (CFMI-PC) in ARPAL, was introduced. While runoff of the several small rivers, characterized by seasonal and discontinuous discharges, were not considered, the input from the thermoelectric power plant was introduced as input of warmer water, with a constant flow of 15 m^3/s and an exceeding temperature of 5 °C. Also, Magra river freshwater input, obtained from the hydrological model DRiFt, also developed at the CFMI-PC in ARPAL, was considered in the domain.

2.2.2. Definition of the source for levelling operations

The simulation of the plume evolution requires the definition of the potential dredging source and the sediment loss rate in the "near-field" area, related to the equipment and operational techniques, as well as operational cycle of the specific case study.

The sediment source, as flux of fine sediment released during operations, is defined taking into account: dredged volume, percentage of sediments fine fraction (d_{50}<63 μm) and sediment spill related to the used operational technique. Based on information provided by La Spezia Port Authority (AdSP MLO) and on the available sediment characterization data (ISPRA - ARPAL, 2016), a suspended sediments flux rate of 18

kg/s was estimated, for a source term representative of bed leveling operation with grab dredge, considering different spill coefficient for the removal (σ_{dr}=0.1) and the disposal (σ_{ds}=0.75) operational phases (Table 1). These spill coefficients were settled according to a specific sensitivity analysis.

Table 1. Detail of bed levelling activities

Total volume to be removed (m^3)	4,000	Operational technique	grab dredge
Daily production (m^3/d)	800	Spill coefficient for removal	σ_{dr}=0.1
Operations time (days)	5	Spill coefficient for disposal	σ_{ds}=0.75
Operations time (hs/d)	16	Release depth	Bottom layer

2.2.3. Transport Module (TM)

The application of the sediment transport and deposition model is applied to a series of 51 independent consecutive dredging scenarios, covering the entire reference year, and thus the action of different seasonal conditions. The Mud Transport module (MIKE 3 MT) was used, decoupled from the hydrodynamic module, to simulate transport and deposition of the fine sediments, as suggested in ISPRA Guidelines (Lisi et al., 2017), considering the two different sediment fractions d_{50}=32 µm, and d_{50}=16 µm. Each scenario represents the whole bed levelling activity, covering 5 days operations and 2 days to take into account the deposition of all the suspended sediment.

2.2.4. Dr-EAM Module

Dr-EAM tools, specifically developed by ISPRA to provide maps that synthesize the modeling results of sediment dispersion for long-term modeling scenarios (Feola et al., 2015; 2016), was applied. In order to compare numerical results, obtained within the local model domain (Figure 2A), a regular grid (step 160 m, Figure 2B) was used to synthetize results of both hydrodynamics and Mud Transport simulations. For each regular grid element (Figure 2E), time series of the current speed, SSC, and DEP output parameter were extracted from corresponding elements (Figure 2C) and statistically analyzed. In particular, statistics were calculated for specific layers: the bottom layer, the surface layer and two layers (sub and intermediate) in between. Maps of different statistical parameters (mean, max) were produced for specific periods (i.e. seasonal and annual mean).

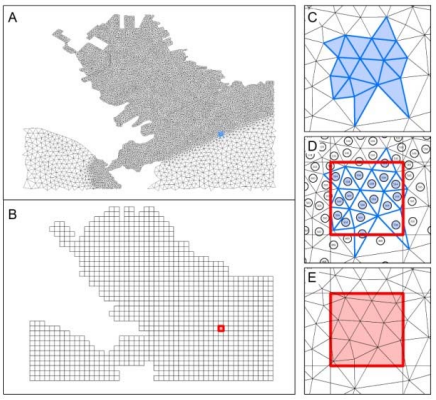

Figure 2. A) Mesh of the model domain; B) regular grid for result synthesis. Association between mesh elements and model results within (C) through centroids (D) to a specific regular grid element (E)

3. Results and Discussion

The output maps obtained from the model show that the considered activity show a limited influence area. In particular, as shown Figure 3, in the area within 500 metres of the dredging area, SSC shows mean values below 3 mg/L while maximum values do not exceed 11 mg/L. The maximum values of DEP, which near the dredging/ levelling area have recorded mean values higher than 10,000 g/m^2, decrease rapidly in the first 500 meters (average values of about 3,500 g/m^2 and maximum values of about 5,600 g/m^2). Within 1,000 m of the dredging area, the mean and maximum values are less than 6 and 10 g/m^2 respectively. Significant variations for SSC > 1 mg/ L and DEP > 1 g/m^2 are confined within 500- 1,000 meters from the source.

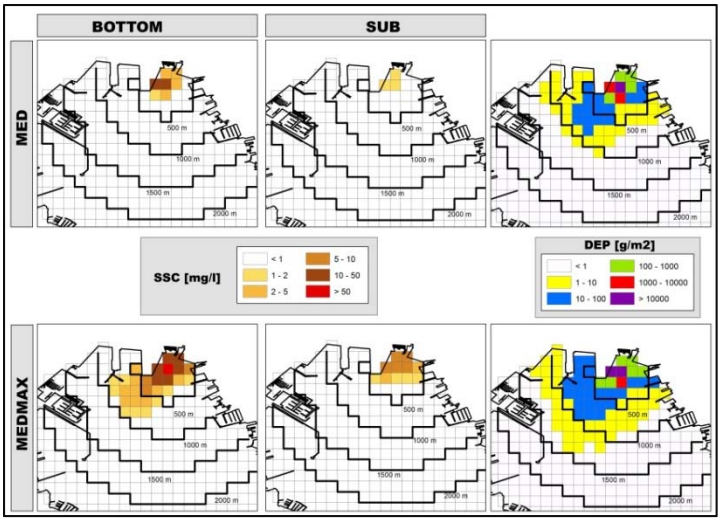

Figure 3. Distribution of the mean values, and mean of the maximum values of SSC in the deepest levels and DEP in reference to the distance from the dredging/levelling area (step 500 m)

Table 2. Mean and maximums annual values of SSC (modeled for bottom, sub and intermediate layers) and DEP calculated at regular distance from the intervention area

		SSC [mg/L]						DEP [g/m2]	
		bottom		sub		intermediate		bottom	
distance [m]	N	mean	max	mean	max	mean	max	mean	max
0-500	24	2.9	10.9	0.4	2.6	0.2	1.3	3544.6	5601.2
500-1000	48	0.1	0.8	0.0	0.2	0.0	0.2	5.5	9.8
1000-1500	69	0.0	0.1	0.0	0.1	0.0	0.0	0.4	0.9
1500-2000	83	0.0	0.0	0.0	0.0	0.0	0.0	0.1	0.2
2000-3000	207	0.0	0.0	0.0	0.0	0.0	0.0	0.0	0.1
>3000	666	0.0	0.0	0.0	0.0	0.0	0.0	0.0	0.0

4. Conclusions

This work proposes an application of the Integrated Modelling Approach for simulating Sediment Dispersion (IMAforSED) reported in Lisi et al. (2017, 2019) and of the Dredging Environmental Assessment Module (Dr-EAM) reported in Feola et al. (2015, 2016) and specifically developed by ISPRA as supporting tools to dredging activities. The approach was tested on bed levelling operations with grab dredger, to characterize the sediment plume dynamics and the areas interested by significant variations of suspended sediment concentration (SSC) and sediment deposition rates (DEP). Results of the present work has shown that the proposed methodology can be easily applied to any area and to different activities of sediment displacement, where information of the specific technology used is known. In addition, maps comparing results for different climatic conditions can show the ability of the applied methodological approach to support the management of dredging project (e.g. selection of the appropriate operating windows in relation to the presence of different sensitive receptors) and the environmental monitoring planning (e.g. sampling station location and frequency).

References

CEDA/IADC, 2018. Dredging for Sustainable Infrastructure. CEDA/IADC, The Hague, The Netherlands. Revision no. 1021 logged at 2017-10-05 13:35

DHI, 2019. MIKE 21 & MIKE 3 Flow Model FM, Hydrodynamic and Transport Module – Scientific documentation. Release 2019

Erftemeijer P.L.A., Riegl B., Hoeksema B.W., Todd P.A., 2012. Environmental impacts of dredging and other sediment disturbances on corals: a review. Mar.Pollut.Bull.64 (9),1737-65

Feola A., Lisi I., Venti F., Salmeri A., Pedroncini A., Romano E., 2015. A methodological modelling approach to assess the potential environmental impacts of dredging activities. In Proc. Of CEDA. Dredging Days, Innovative Dredging Solutions for Ports, Rotterdam

Feola A., Lisi I., Salmeri A., Venti F., Pedroncini A., Romano E., 2016. Platform of integrated tools to support environmental studies and management of dredging activities, J. Env. Manag. 166

Fonti V., Dell'Anno A., Beolchini F., 2013, Mutualistic interactions during bioleaching of marine contaminated sediment, Chemical Engineering Transactions, 32, 979-984 DOI:10.3303/CET1332164

Lisi I., Feola A., Bruschi A., Di Risio M., Pedroncini A., Pasquali D. & Romano E., 2017. La modellistica matematica nella valutazione degli aspetti fisici legati alla movimentazione dei sedimenti in aree marino-costiere. Manuali e Linee Guida ISPRA, 169/2017, pp.144

Garbolino E., Aqua J.L., Abriak N.E., 2014, Applicability of h14 protocol for sediments in order to consider their valorization: limits and benefits, Chemical Engineering Transactions, 36, 631-636 DOI: 10.3303/CET1436106

Lisi I., Feola A., Bruschi A., Pedroncini A., Pasquali D., Di Risio M., 2019(b). Mathematical modeling framework of physical effects induced by sediments handling operations in marine and coastal areas. J. Mar. Sci. Eng., 7, 149

PIANC, Permanent International Association of Navigation Congresses, 2006. Environmental risk assessment of dredging and disposal operations. Report of Working Group 10 of the Environmental Commission. pp.40

De Gisi S., Minetto D., Lofrano G., Libralato G., Conte B., Todaro F., Notarnicola M., 2017, Nano-scale Zero Valent Iron (nZVI) treatment of marine sediments slightly polluted by heavy metals, Chemical Engineering Transactions, 60, 139-144 DOI: 10.3303/CET1760024

Wilber DH., Clarke DG., 2001. Biological Effects of Suspended Sediments: A Review of Suspended Sediment Impacts on Fish and Shellfish with Relation to Dredging Activities in Estuaries. North American Journal of Fisheries Management 21(4). 855-875

Sauro Pierucci, Flavio Manenti, Giulia Bozzano, Davide Manca (Eds.)
Proceedings of the 30th European Symposium on Computer Aided Process Engineering (ESCAPE30), May 24-27, 2020, Milano, Italy.
http://dx.doi.org/10.1016/B978-0-12-823377-1.50058-6

An Efficient Hybridization of Gaussian Processes and Clustering for Electricity Price Forecasting

Aaron S. Yeardley, Diarmid Roberts, Robert Milton, Solomon F. Brown*

Department of Chemical and Biological Engineering, University of Sheffield, Sheffield, S1 3JD, United Kingdom
s.f.brown@sheffield.ac.uk

Abstract

Electricity retailers and power generators have an increasing potential to profit from selling and purchasing electricity as wholesale electricity prices are encouraged to be introduced to both industrial and domestic customers. Hence, this paper focuses on developing an efficient method to aid decision-makers in forecasting the hourly price of electricity 4 weeks ahead. The method developed in this paper uses an approach to hybridize Gaussian Process (GP) regression with clustering to improve the predictive capabilities in electricity price forecasting. By first clustering all the input data and introducing a cluster number as a new input variable, the GP is conditioned to aid predictive process through data similarity.

This proposed method has been successfully applied to real electricity price data from the United Kingdom, comparing the predictive quality of the novel method (GPc1) to that of an original GP and that of a method which pre-clusters and filters the data for numerous GPs (GPc2). By comparing the predictive price distributions to the observed prices in the month of December 2018, it was found that clustering improves the predicted mean values of a GP while the mean predictive quality of GPc1 and GPc2 are of equal standing. Therefore, the number of outliers at 2 STD's were compared, showing GPc1 to have a predicted distribution with uncertainty that covers more of the true electricity prices than that of GPc2. In conclusion, the novel method provides the decision-maker with greater reliability so that the true electricity prices will be within the confidence limits predicted.

Keywords: Gaussian Process, hierarchical clustering, hybridization, forecasting, electricity prices.

1. Introduction

Increasingly, the rollout of intermittent renewable power sources with zero marginal cost of generation is resulting in a more dynamic electricity supply price curve. Coupled with variation in demand, this has the potential to increase the volatility of wholesale electricity prices. Within the existing electricity market structures, all of the proposed approaches to dealing with intermittency – storage, demand-side response and spatial interconnection - may be encouraged by exposing all customers, from domestic to industrial, to these variations. Hence accurate price forecasting will be of the utmost importance in the coming years.

Attempts to construct bottom-up models for electricity price based on predictions of demand and supply price curve at a given time run into difficulties due to the non-transparency of constraints in the system (Staffell and Green, 2016) and high levels of residual variance are associated with this approach (Pape *et al.*, 2016). There is, therefore, a role for statistical models in improving predictions of the electricity price. A common choice of a statistical model is the Gaussian process (GP) (Milton *et al.*, 2019), which is

computationally efficient and the use of it for regression (Zanella *et al.*, 2019) has been proven to be effective for electricity price forecasting (Kou *et al.*, 2015; Mori and Nakano, 2015). The flexibility of GPs allows the clustering of the inputs to be directly incorporated into the prediction of the output, so combining GPs with clustering techniques allows them to learn from data points of similar nature. In this work, we introduce a hybrid method which uses clustering to improve the predictive capabilities of a GP by first applying a hierarchical clustering technique and using this to condition a single GP. The cluster number becomes an additional input variable that aids the GP learning process through data similarity.

This new hybridization method is then compared to a GP without the hybridization with clustering and to a known method by Mori and Nakano (2015) which applies individual GPs to each cluster of inputs. The comparison is achieved through an analysis of electricity price forecasting using real data from the United Kingdom (NordPool) which is split at a specific date to give two datasets, a past and a future, providing results which show the forecasting capabilities of each GP method. The forecasted results of each GP are then compared to the true observed prices proving that the proposed method can be used by power generators and electricity retailers for electricity price forecasting while considering the uncertainties of the proposed predictions.

2. Method

2.1. Clustering

In clustering processes, a set of vectors is divided into subsets based on a proximity measure. In the present work, five potential predictors of electricity price at the UK national level are taken as input variables; electricity demand, CCGT generation, coal generation, wind generation and solar generation (BMReports).

For each day, the hourly profiles of each predictor were normalized to the maximum observed value, then concatenated. Hierarchical clustering was then performed on the 5×24 D vectors, as this approach makes no prior assumption regarding the number of clusters. The Ward algorithm was used to judge the intercluster distance (SciPy.org). The second derivative of the merge distance plot was used to judge the emergence of genuine clusters (Hees). By this measure, the data set was judged to contain 5 clusters (see). The centroids of the corresponding 5 clusters are shown in Fugure 1. It is worth noting that the price input vectors contain several outliers, which is why the normalized profile is highly compressed (coordinates 1 to 24).

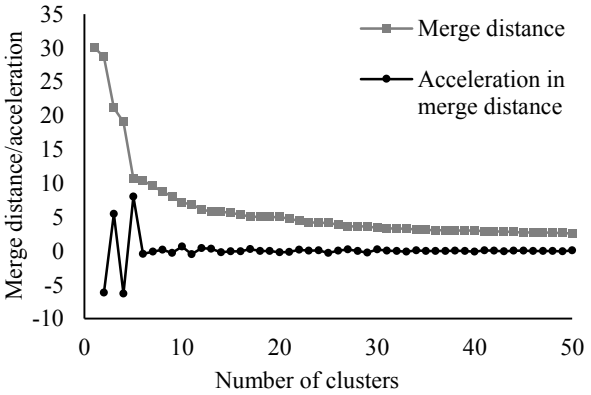

Figure 1: An elbow plot showing the merge distance and acceleration for the last 50 cluster merges.

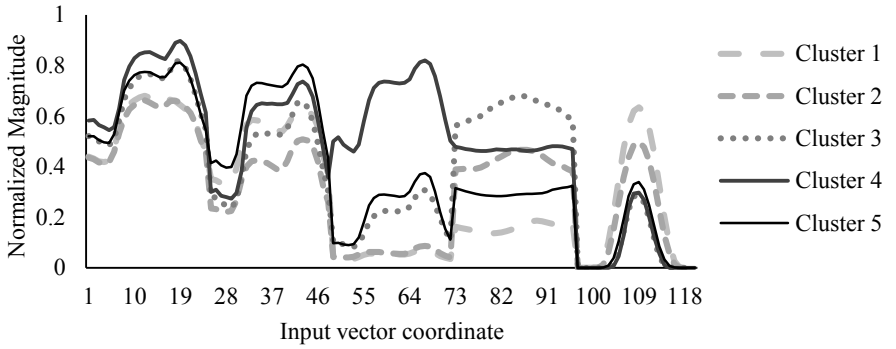

Figure 2: Centroids for the five clusters identified in the 5 x 24D predictor vector set.

2.2. Gaussian Process Regression

The use of GPs for regression begins with standard Bayesian conditioning of Gaussian priors to derive a predictive process. This creates a GP which takes a $(1 \times d)$ row vector of input variables $\boldsymbol{x}$ and returns a Gaussian random variable through calculations using the predictive equations

$$y(\boldsymbol{x}) \sim \mathcal{N}\left[\bar{f}(\boldsymbol{x}), \Sigma_y + {\sigma_e}^2\right] \tag{1}$$

where

$$\bar{f}(\boldsymbol{x}) \coloneqq k(\boldsymbol{x}, \mathbf{X})(k(\mathbf{X}, \mathbf{X}) + {\sigma_e}^2\mathbf{I})^{-1}\boldsymbol{y} \tag{2}$$

$$\Sigma_y = k(\boldsymbol{x}, \boldsymbol{x}) - k(\boldsymbol{x}, \mathbf{X})(k(\mathbf{X}, \mathbf{X}) + {\sigma_e}^2\mathbf{I})^{-1}k(\mathbf{X}, \boldsymbol{x}) \tag{3}$$

The mean $\bar{f}(\boldsymbol{x})$ and variance Σ_y is learnt using n amounts of training data $\boldsymbol{y} = f(\mathbf{X}) + e$. Standard Bayesian inference has been used to express the mean prediction in terms of the $(n \times 1)$ observed responses $\boldsymbol{y}$ to $(n \times d)$ training inputs $\mathbf{X}$. In this work, the observed responses $\boldsymbol{y}$ are the electricity price at a given time from the 01/02/2017 to the 30/11/2018 corresponding to the training inputs $\mathbf{X}$. The predictions are then made using Eq. (1), the predictive equation, which takes test data from December 2018, allowing comparisons to the true electricity prices for that timeframe. At the heart of these equations lies the kernel function k which expresses the correlation between the responses to the input variables. Exclusively, this work uses the automatic relevance determination (ARD) kernel (Wipf and Nagarajan, 2009):

$$k(\boldsymbol{x}', \boldsymbol{x}) \coloneqq {\sigma_f}^2 exp\left(-\frac{(\boldsymbol{x} - \boldsymbol{x}')\boldsymbol{\Lambda}^{-2}(\boldsymbol{x} - \boldsymbol{x}')^{\mathrm{T}}}{2}\right) \tag{4}$$

where $\boldsymbol{\Lambda}$ is a $(d \times d)$ diagonal positive definite lengthscale matrix. This choice can be entirely justified from the assumption that the similarity function $k(\boldsymbol{x}', \boldsymbol{x})$ is differentiable at $\boldsymbol{x}' = \boldsymbol{x}$, together with the assumption that the output is normal. The learning from the training data requires optimizing $d + 2$ hyperparameters, constituting of $\boldsymbol{\Lambda}$, σ_f, and σ_e, through the optimization of the marginal likelihood $p[\boldsymbol{y}|\mathbf{X}]$ using the ROMCOMMA software library (Milton and Brown, 2019).

2.3. Hybridization Method

On a given day, we wish to predict the hourly electricity price for 4 weeks ahead given the input variables. We apply a novel method, combining the clustering technique in Section 2.1 with the GP in Section 2.2 to create a hybridized method (GPc1).

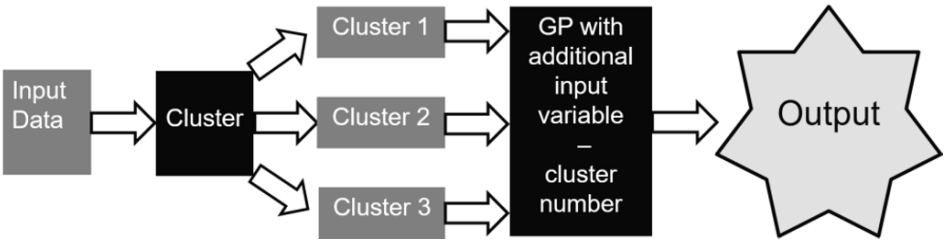

Figure 3: A flowchart showing the methodology for the hybridization of clustering and GPs.

Figure 3 describes the methodology for predicting the electricity profile as the input data for both training and testing are put through the clustering method creating clusters of data which are similar. The cluster number then becomes an additional input variable (along with the time, date, day of the week, price 4 weeks previously, electricity demand and electricity generation from various types) used in the GP for both the training data and the test data.

3. Results

In this section, the methodology developed above is applied to the December 2018 electricity price test data with direct comparison to a GP without hybridization and a method which uses clustering to create individual GPs as developed by Mori and Nakano (2015) (GPc2).

The forecasted results for three full weeks in December can be seen in Figure 4 for each method. In each sub-figure, the black dots show the true electricity price every hour from 00:00 on the 03rd of December to 23:00 on the 23rd of December. Within these time-dependent graphs, the Gaussian Process' predictive distributions can be seen by the mean centre grey line and the 95 % confidence intervals that bound the line. Throughout the three weeks, it can be seen that all three methods have difficulties predicting the extremely high and low electricity prices. The predictions using GPc2, shown in Figure 4 (c), has a distribution that varies closest to the true prices almost capturing the extremely high price on the 4th of December at 17:00. However, the predicted uncertainty in GPc2 tends to be smaller in comparison to the GPc1 and so more of the true prices are captured within the predicted distribution of the third novel method, shown in Figure 4 (b). Table 1 presents the correlation coefficient r^2, the root mean squared error (RMSE) and the outliers at 2 STD's for each of the methods for the December 2018 predictions. The introduction of clustering has improved the predictive quality of an original GP as shown by an increase in the r^2 and a decrease in the RMSE. Furthermore, the two values are very similar for GPc1 and GPc2 showing the mean predictions are equal in quality with respect to the nearness to the observed electricity price. Given that a major advantage of GPs is that they produce uncertainty in the predictions allowing the decision-maker to further understand the range of values that the electricity price could be instead of the singular mean predicted value. Therefore, the outliers at 2 STD's is a preferred diagnostic for this type of predictive model as it measures the number of true values outside of the predictive distribution. As can be seen, Table 1 shows the third method, GPc1, produces the lowest amount of outliers at just 2.55 %. Therefore, this method of forecasting allows the decision-maker to reliably estimate the degree of uncertainty in the electricity price efficiently, trusting that the true price is within the predicted distribution.

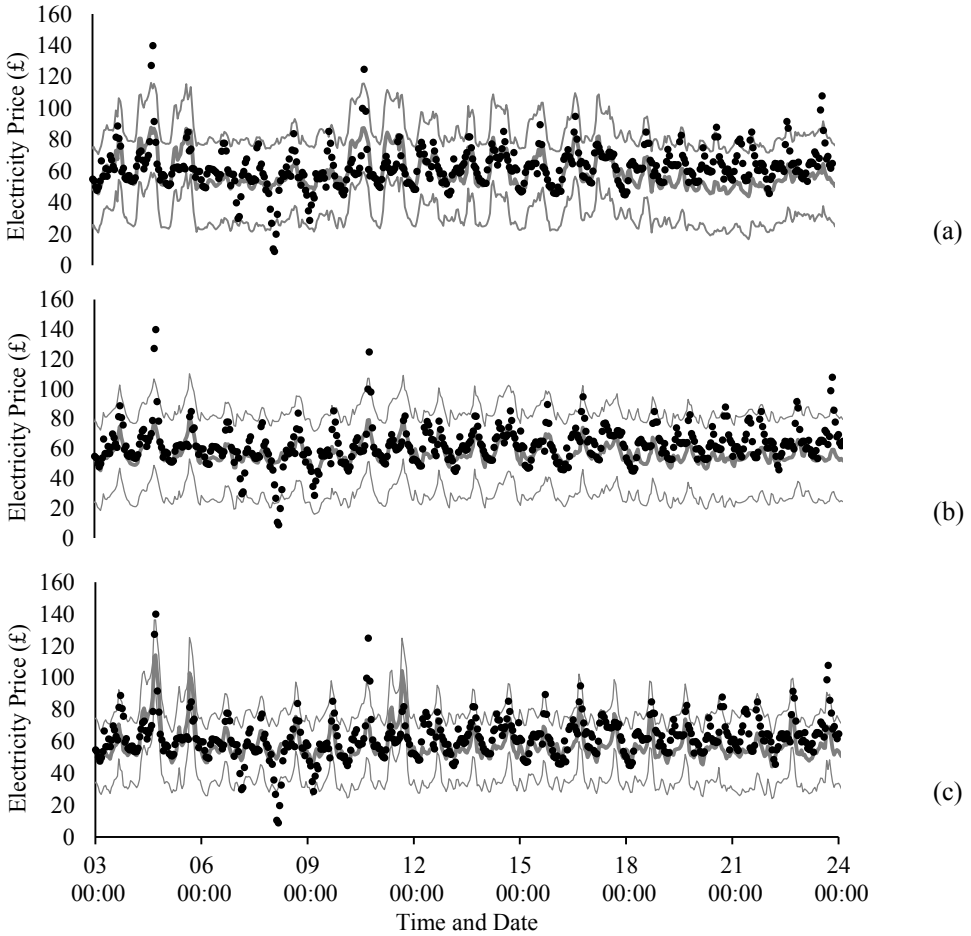

Figure 4: Forecasted electricity price distribution and true electricity price for 3 weeks in December from the 3rd to the 24th using (a) a GP without hybridization, (b) GPc1, and (c) GPc2.

Table 1: The diagnostic results for testing the three methods with electricity price data from December 2018.

Method	r^2	RMSE	Outliers at 2 STD's
GP without hybridization	0.216	0.904	3.90 %
GPc1	0.358	0.840	2.55 %
GPc2	0.405	0.833	3.90 %

4. Conclusion

In this work, a novel hybridization method was produced to effectively forecast the hourly price of electricity for 4 weeks ahead. The method used hierarchical clustering to create an extra input variable for a GP regression model. This extra input variable gives the GP additional information on the electricity data due to data similarity.

The method was applied to real wholesale electricity price data for the United Kingdom from 2017 to 2018 using the month of December 2018 as test data allowing a comparison to the capabilities of the novel forecasting method to an independent GP and to individual GPs produced for each cluster number. In conclusion, the results found that introducing clustering to a GP improves the mean predictive quality for electricity price forecasting,

with both clustering methods being equal with respect to the nearness of the predicted price to the observed price. However, GPs have the advantage of producing a predicted distribution which includes the uncertainty in the predictions. Hence, this gives electricity retailers and power generators more insight into the forecasted price. Therefore, the outliers at 2 STD's were an important diagnostic which discovered the novel hybridization method produces a predicted distribution which covers the most observed values compared to the other two methods.

Overall, the method is proven to be reliable, giving the decision-maker greater confidence when compared to other prediction methods so that the true price will be within the 95 % confidence interval predicted by the GP. However, this work does have limitations as some of the input variables do need to be forecasted, such as the electricity demand and the electricity generated by various types. Although the national grid does provide forecasted demand profiles, further work will need to be dedicated to understanding the importance of each of the input variables and how errors in the forecasted input variables may affect the forecasted electricity price in this method. Additionally, comparing the relative computational efficiency of the two hybridization methods in an attempt to understand how the data size, dimensionality and number of clusters scale with the efficiency would further benefit the development of this technique.

References

BMReports (no date) *Balancing Mechanism Reporting Service (BMRS)*. Available at: https://www.bmreports.com/bmrs/?q=help/about-us.

Hees, J. (no date) *SciPy Hierarchical Clustering and Dendrogram Tutorial*. Available at: https://joernhees.de/blog/2015/08/26/scipy-hierarchical-clustering-and-dendrogram-tutorial/.

Kou, P. *et al.* (2015) 'Probabilistic electricity price forecasting with variational heteroscedastic Gaussian process and active learning', *Energy Conversion and Management*. Elsevier Ltd, 89, pp. 298–308. doi: 10.1016/j.enconman.2014.10.003.

Milton, R. A. and Brown, S. F. (2019) 'ROMCOMMA'. Available at: https://github.com/C-O-M-M-A/rom-comma.

Milton, R., Bugryniec, P. and Brown, S. (2019) 'Parameter Estimation for Thermal Runaway of Li-ion cells: a Gaussian Process approach', *Computer Aided Chemical Engineering*. Edited by A. A. Kiss et al. Elsevier (Computer Aided Chemical Engineering), 46, pp. 775–780. doi: https://doi.org/10.1016/B978-0-12-818634-3.50130-2.

Mori, H. and Nakano, K. (2015) 'Development of advanced Gaussian Process for LMP forecasting', *2015 18th International Conference on Intelligent System Application to Power Systems, ISAP 2015*. IEEE, pp. 1–6. doi: 10.1109/ISAP.2015.7325553.

NordPool (no date) *Historical Market Data*. Available at: https://www.nordpoolgroup.com/historical-market-data/.

Pape, C., Hagemann, S. and Weber, C. (2016) 'Are fundamentals enough? Explaining price variations in the German day-ahead and intraday power market', *Energy Economics*. Elsevier B.V., 54, pp. 376–387. doi: 10.1016/j.eneco.2015.12.013.

SciPy.org (no date) 'Clustering package (scipy.cluster)'. Available at: https://docs.scipy.org/doc/scipy/reference/cluster.html.

Staffell, I. and Green, R. (2016) 'Is There Still Merit in the Merit Order Stack? The Impact of Dynamic Constraints on Optimal Plant Mix', *IEEE Transactions on Power Systems*. IEEE, 31(1), pp. 43–53. doi: 10.1109/TPWRS.2015.2407613.

Wipf, D. and Nagarajan, S. (2009) 'A new view of automatic relevance determination', in *Advances in Neural Information Processing Systems 20 - Proceedings of the 2007 Conference*.

Zanella, L. *et al.* (2019) 'Real-time determination of optimal switching times for a H2 production process with CO2 capture using Gaussian Process Regression models', *Computer Aided Chemical Engineering*. Elsevier, 46, pp. 1219–1224. doi: 10.1016/B978-0-12-818634-3.50204-6.

Sauro Pierucci, Flavio Manenti, Giulia Bozzano, Davide Manca (Eds.)
Proceedings of the 30th European Symposium on Computer Aided Process Engineering (ESCAPE30), May 24-27, 2020, Milano, Italy.
http://dx.doi.org/10.1016/B978-0-12-823377-1.50059-8

CFD Analysis of the Use of Desert Sand as Thermal Energy Storage Medium in a Solar Powered Fluidised Bed Harvesting Unit

Mustapha Hamdan[a], Daniel Sebastia-Saez[a], Malak Hamdan[c], Harvey Arellano-Garcia[a,b*]

[a]*Dep. of Chemical and Process Eng.,University of Surrey, Guildford, GU2 7XH, UK*
[b]*LS Prozess- und Anlagentechnik, Brandenburgische Technische Universität Cottbus-Senftenberg, D-03046 Cottbus, Germany*
[c]*The Claude Littner Business School, University of West London, TW8 9GA, UK*
h.arellano-garcia@surrey.ac.uk)

Abstract

This work presents an Euler-Euler hydrodynamic and heat transfer numerical analysis of the multiphase flow involving desert sand and a continuous gas phase in a compact-size fluidised bed. The latter is part of a novel conceptual solar power design intended for domestic use. Desert sand is a highly available and unused resource with suitable thermal properties to be employed as thermal energy storage medium. It also allows for high working temperatures owing to its high resistance to agglomeration. Computational Fluid Dynamics simulations are used here to assess the heat transfer between desert sand and several proposed working fluids (including air, argon, nitrogen and carbon dioxide) to justify the design in terms of equipment dimensions and suitability of the materials used. The results show that the device can provide up to 1,031 kW when using carbon dioxide as the heat transfer fluid.

Keywords: sensible heat storage, desert sand, fluidised bed, solar energy, carbon dioxide utilization.

1. Introduction

Concentrated solar power (CSP) is a promising energy capture technology that uses optical devices to concentrate the power of the sun on to a surface and in turn generates power by means of a thermal-to-electric conversion unit (Zhang et al., 2011). Each year 885 million TWh of solar power reaches the earth surface, however, less than 0.002% of primary energy is consumed by humans (IEA, 2011). The International Energy Agency suggest that approximately 11.3% of the global electricity demand could be met by Concentrated Solar Power (CSP) by 2050 (Pramanik et al., 2017). However, the U.S. Department of Energy released a target for concentrated solar power (CSP) cycles to be more than 50% efficient by 2030 to reduce the levelized cost of energy (LCOE) to 5¢/kWh (SETO, 2018).

Concentrated solar power technology which integrates Thermal Energy Storage (TES) materials is seen as the way forward to solving the current problem of solar energy discontinuity. Thermal energy storage materials have the ability to store heat and thus enable power production in the absence of sunlight, at night or in poor weather

conditions (Fernández et al., 2014). An example of TES material used currently to store energy is a binary molten salt mixture of 60 wt% $NaNO_3$ 40 wt% KNO_3(solar salt) which can currently store energy for up to 15 hours (Today, 2011). However, molten salts present a significant problem in that their use results in a high levelized cost of energy. The use of molten salts as TES materials carries with it high maintenance and operation costs due to a number of reasons: 1) highly corrosive and thus requiring expensive containment materials; 2) Molten salt must be kept heated at approximately 200°C to prevent freezing, thus, solidifying in pipes; 3) high viscosity has a negative impact of pump performance adding to LCOE. Molten salts are also costly materials and have an outlet receiver temperature below 600°C which limits the thermal-to-electric efficiency of the power cycle (Kearney et al., 2003). To overcome the current limitations of CSP technologies, it is necessary to select an alternative TES material as well as a new receiver design improving LCOE and profitability of these plants (Almendros et al., 2018).

Current CSP plants employ conventional receiver technologies that use gas or liquid continuous phase TES or HTF fluid which flow through pipes. However, temperature limitations, corrosion and costly maintenance of conventional TES materials result in high LCOE. This has led researchers to alternative TES material and CSP receiver systems. Such systems being researched include high-temperature particle receivers which use air as the HTF (Clifford et al., 2016). The natural abundance of desert sand is an interesting option for thermal energy storage especially in regions such as the GCC. There are several benefits using desert sand: 1) desert sand is a costless local material which is a key factor to reduce the LCOE of CSP systems (Schlipf et al., 2015); 2) it is a highly stable material, and therefore requires significantly cheaper containment units; 3) the sand is stable above 1000°C, resulting in higher thermal-to-electric efficiency (Ma et al., 2014).

In this study, computational fluid dynamics (CFD) will be used to model the gas/sand two-phase fluid flow in a fluidised bed system. This study will look at maximising the rate of heat transfer from sand to HTF by addressing the following. Selecting the optimum fluidising agent (HTF), based on achieving high heat transfer rates - a comparison between various fluidising agents - Air, Carbon dioxide, Argon, Nitrogen (similar densities to air and most abundant) will be performed in this work. Optimising and identifying the parameters related to the fluidised bed system. Varying the mass flowrate of the HTF to fluidise the particulate material (sand) in the fluidised bed. Air will be used to choose optimum flowrate since all other HTF's selected have similar densities to air. It should be noted that a large difference in HTF density would mean the requirement of a large difference in velocity to produce same mass flowrates for each HTF being tested – a large velocity difference would have a major impact on the fluidisation. Selecting the optimum HTF based on maximum heat transfer values between sand and the HTF.

2. Method

The conceptual design proposed in this work is depicted in Figure 1, where the flow of materials and basic equipment are shown. Figure 2 shows a schematic of the device and preliminary biphasic solid-gas flow results obtained with CFD. The thermal energy storage media (Desert sand) stores the energy from the sun gathered by means of the CSP receiver. The heat exchange between the particulate material and the working fluid (air, carbon dioxide, argon and nitrogen) would take place in the fluidised bed, which constitutes the numerical domain. Finally, the energy stored in the working fluid would

be used to produce power in the energy harvesting unit. Further numerical results will be obtained to establish a comparison, in terms of hydrodynamics and heat exchange performance of the use of natural desert sand and a cost assessment to determine the best option for the gas used as the working fluid.

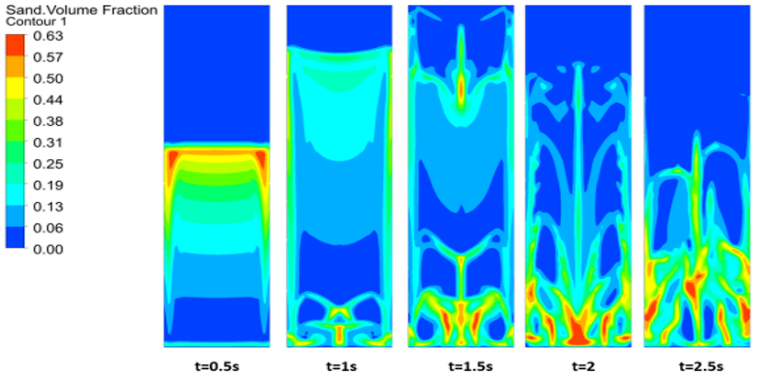

Figure 1. Schematic detail of the geometry and the solid-gas flow obtained using CFD.

The gases air, argon, nitrogen and carbon dioxide were analysed for their heat transfer characteristics to identify the optimum HTF. The four gases were selected as they are abundant in air and have similar densities. Air was used to determine the optimum velocity and thus mass flow rate. The mass flow rate was used to analyse the gases for their heat transfer performance. All the selected gases have a similar density to air, and therefore, the velocity of the gas at inlet was adjusted to keep a constant mass flowrate.

The selected velocity of air was used as a benchmark to achieve greater homogenisation of the two phases, thus reducing the variation of the flow of sand and the outlet temperatures.

This can be observed from the mass flow rate equation below.

$$\dot{m} = \rho \cdot v \cdot A \qquad \text{(Eq. 1)}$$

Where ρ is the density v is the velocity and A is the gas inlet area.

The equation used to calculate the heat transfer from the sand to the HTF is show bellow.

$$Q = \dot{m} \cdot C_P \cdot \Delta T \qquad \text{(Eq. 2)}$$

Where $\dot{m}$ is the mass flow rate, C_P is the specific heat capacity and ΔT is the change in temperature of the gas.

3. Computational Fluid Dynamics model

The Euler-Euler model is selected to treat both phases as interpenetrating continua, introducing the concept of volume fraction α (Sivier et al., 1993). The model includes an additional transport equation for the volume fraction, the value of which varies between 0 (primary phase) and 1 (secondary phase). A computational cell with a value of the volume fraction equal to 1 means, thus, that is entirely occupied by the secondary phase. Therefore, if the volume fraction in a particular computational cell is 0, that means it entirely occupied by the primary phase. Any cell with a volume fraction

between 0 and 1 forms the interface. The software solves, thus, n conservation equations, which correspond to the n phases present in the model. The continuity equation for thei^{th} phase is given by

$$\frac{\partial}{\partial t}(\alpha_i \rho_i) + \nabla \cdot (\alpha_i \rho_i \vec{v}_i) = \sum_{j=1}^{n} (\dot{m}_{ij} - \dot{m}_{ji}) + S_i, \quad \text{(Eq. 3)}$$

where the term $\dot{m}_{ij}$ and $\dot{m}_{ji}$ account for the interphase mass transfer, and S_i is an additional mass source term that can be used to introduce the creation/consumption rate of a given species due to the existence of a chemical reaction. However, since no chemical reaction is taking place S_i is assumed zero.

The equation of the conversation of momentum for the i^{th} phase reads

$$\frac{\partial}{\partial t}(\alpha_i \rho_i \vec{v}_i) + \nabla \cdot (\alpha_i \rho_i \vec{v}_i \vec{v}_i) = -\alpha_i \nabla p + \nabla \cdot \bar{\bar{\tau}}_i + \alpha_i \rho_i \vec{g}_i + \sum_{j=1}^{n-1} \vec{R}_{ij}, \quad \text{(Eq. 4)}$$

where $\bar{\bar{\tau}}_i$ is the stress-strain tensor, and $\vec{R}_{ij}$ account for any other interaction between the phases. Drag interaction was accounted for by selecting the Syamlal-O'brien model and Gunn model was selected for the heat transfer between the two phases.

4. Results and discussion

The gas mass flow rate passing through the bed was therefore, modified to observe its effect on the fluidisation process, and to optimise the heat capacity of the gas at outlet conditions. The three superficial gas velocities used were v_g = 1.5, 1.75 and 2 m·s^{-1}, which was over five to seven times more than the minimum velocity for fluidisation. The velocities correspond to air mass flow rates of $\dot{m}_g$ = 0.92, 1.07, and 1.23 kg·s^{-1} per meter depth of the device, respectively, at T_g = 300 K. These three simulations have the same initial height of the packed bed h_{bed}=0.4 m. Figure 2a shows plots of the solid volume fraction for the different air inlet velocities after a flow time t_{flow}= 10 s. The effect of the gas mass flow rate on the solid distribution within the vessel is clearly shown in Figure 2a, where the greatest value of the mass flow rate gives rise to smaller accumulations of solids along the high of the vessel. The plot also shows greater average values, and therefore, greater accumulations for a mass flow rate of 0.92 kg·s^{-1} and a less homogenous sand distribution. Figure 2b shows the air velocity profiles along the height of the device, their average value increasing with the air mass flow rate at inlet conditions as expected. The greatest effect of the inlet mass flow rate is observed in the amount of particulate material distributed along the height of the bed, with a mass flow rate of $\dot{m}_g$=1.23 kg·s^{-1} causing the sand to occupy almost the entirety of the space available. In terms of hydrodynamics therefore, the ideal range of values for the mass flow rate lie between 1.07 and 1.23 kg·s^{-1}.

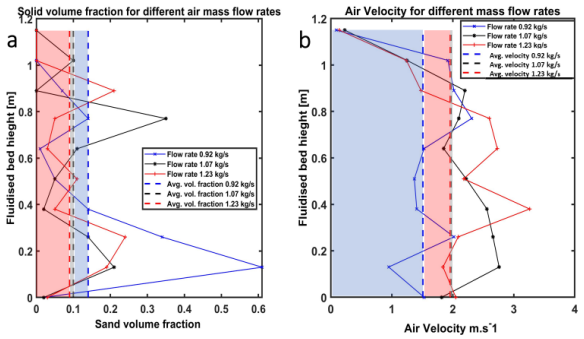

Figure 2. Solid volume fraction along the height of the vessel for all flow rates at flow time t_{flow}=10 s (a), the gas phase velocity (b).

Figure 3a indicates that increasing the mass flow rate will slightly decrease the outlet temperature. However, the slightly higher temperature of the lowest mass flow rate is not large enough to produce a higher power output. The power output of the device is defined as the change in enthalpy of the gas stream, which is calculated as the product between the mass flow rate, the specific capacity and the change in temperature between inlet and outlet conditions. Considering the results presented in Figure 3a, one can conclude that the reason for a greater heat capacity in the gas stream is primarily due to the flow rate and the ability of the fluidised bed to effectively transfer heat between the desert sand and the gas phase. This indicates that the proposed fluidised bed can greatly homogenise the two phases allowing the gas phase to have a stable uniform high outlet temperature. As a comparison, Figure 3b shows the transient behaviour of the power output at a constant gas mass flow rate of 1.07 kg·s^{-1} per meter depth using different gases. Carbon dioxide is the most favourable case, with a maximum power output of 1031 kW found after pseudo-steady fluidisation conditions unfold at flow time t_{flow}=2 s. In this instance, with all of the four gases tested matching closely the temperature of the particulate material when exiting the device, and with the gas mass flow rate having been kept constant, the key to obtaining more usable power at outlet conditions lies in the specific heat capacity of the gas phases employed to retrieve the heat stored in the sand. The greatest power output corresponds, therefore, to carbon dioxide, which has a specific heat capacity of C_p=1.24 kJ·kg·K at T_g=1073.15 K, greater than that of nitrogen (C_p=1.16 kJ·kg·K), air (C_p=1.14 kJ·kg·K) and argon (C_p=0.9 kJ·kg·K).

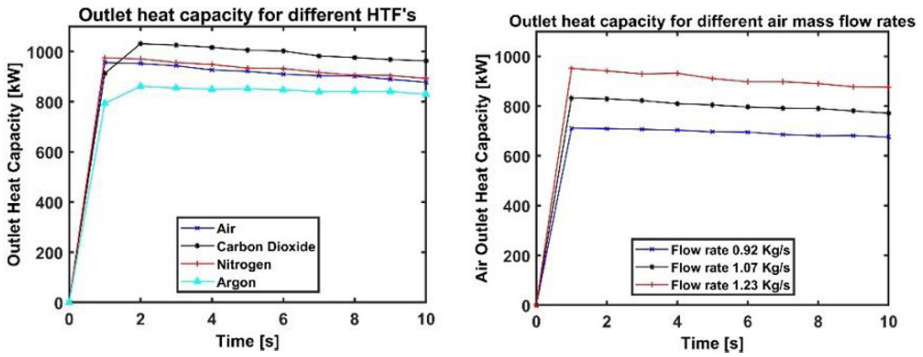

Figure 3. Heat capacity of the gas streams at outlet conditions (Left plot). Effect of different working fluids for the same gas mass flow rate (1.07 Kg/s) (right plot).

5. Conclusions

Desert sand as a particulate material offers high interface area, combined with its capability to withstand temperatures of up to 1000°C without undergoing agglomeration and subsequent degradation, makes it an attractive option to be used in thermal systems. Moreover, desert sand is highly abundant in GCC countries and has suitable thermal properties, which add to its potential as a heat storage medium. With the gas phase attaining the same temperature throughout the vessel regardless of the gas used, the better results must correspond to the gas with the highest specific heat capacity (C_p) provided the mass flow rate is kept constant. This is confirmed in Figure 3, where the highest enthalpy change corresponds to carbon dioxide, followed by nitrogen, air, and argon. From the results included in Figure 3 one can conclude that the present fluidised bed can deliver an increase in enthalpy of air at ≈1000 kW, with carbon dioxide offering the best results. The results herein prove the feasibility of desert sand as a suitable material for energy storage, with effective energy transfer towards a working fluid.

References

H.L. Zhang, J. Baeyens, J. Degreve, G. Caceres, 2013, Concentrated solar power plants: Review and design methodology, Renewable and Sustainable Energy Reviews 22:466-481.

IEA (International Energy Agency), Solar Energy Perspectives; 2011.

S. Pramanik and R.V. Ravikrishna, 2017, A review of concentrated solar power hybrid technologies. Applied Thermal Engineering 127, 602–637.

Solar Energy Technologies Office Funding Opportunity Announcement Supporting Research 2018.

A.G. Fernández, S. Ushak, H. Galleguillos, F.J. Pérez, 2014, Development of new molten salts with LiNO3 and Ca(NO3)2 for energy storage in CSP plants, Applied Energy, 119: 131-140.

C. Today, SENER and Torresol Energy win U.S. CSP Today awards, Renew Energy Focus 2011.

Kearney, D., Herrmann, U., Nava, P., Kelly, B., Mahoney, R., Pacheco, J., Cable, R., Potrovitza, N., Blake, D., Price, H., 2003, Assessment of a molten salt heat transfer fluid in a parabolic trough solar field. J. Solar Energy Eng. 125 (2), 170–176.

J.A. Almendros-Ibáñeza, M. Fernández-Torrijos, M. Díaz-Heras, J.F. Belmonte, C. Sobrino, 2018, A review of solar thermal energy storage in beds of particles: Packed and fluidized beds, Solar Energy.

Clifford K. Ho, 2016, A review of high-temperature particle receivers for concentrating solar power, Applied Thermal Engineering 109, 958–969.

D. Schlipf, P. Schicktanz, H. Maier, G. Schneider, 2015, Using sand and other small grained materials as heat storage medium in a packed bed HTTESS. Energy Procedia 69:1029–1038.

Z. Ma, M. Mehos, G. Glatzmaier. B. B. Sakadjian, 2015, Development of a Concentrating Solar Power System Using Fluidized-bed Technology for Thermal Energy Conversion and Solid Particles for Thermal Energy Storage. Energy Procedia 69, 1349 – 1359.

S. Sivier, E. Loth, J. Baum, and R. Löhner, 1993, Eulerian-Eulerian and Eulerian-Lagrangian methods in two phase flow. Editor: Napolitano M., Sabetta F. (eds) Thirteenth International Conference on Numerical Methods in Fluid Dynamics. Lecture Notes in Physics, 414, 473-477.

Sauro Pierucci, Flavio Manenti, Giulia Bozzano, Davide Manca (Eds.)
Proceedings of the 30th European Symposium on Computer Aided Process Engineering (ESCAPE30), May 24-27, 2020, Milano, Italy.
http://dx.doi.org/10.1016/B978-0-12-823377-1.50060-4

Model of Spray-Drying for Encapsulation of Natural Extracts

Andrea Bassani,[a] * Francesco Rossi,[b] Cecilia Fiorentini,[a] Guillermo D. Garrido,[a] Gintaras V. R. Reklaitis,[b] Irene Bonadies,[c] Giorgia Spigno[a]

[a]*Università Cattolica del Sacro Cuore, Department for Sustainbale Food Process (DiSTAS), Via Emilia Parmense 84, 29122 Piacenza, Italy*
[b]*Purdue University, Forney Hall of Chemical Engineering, 480 Stadium Mall Drive, West Lafayette, IN 47907, United States.*
[c]*Italian National Research Council CNR, Institute for Polymers, Composites and Biomaterials (IPCB-CNR), Via Campi Flegrei 34, Comprensorio "A. Olivetti", 80078 Pozzuoli (NA), Italy*
andrea.bassani@unicatt.it

Abstract

Spray drying unit operation is generally used for separating and drying a solid that cannot be mechanically dried because cannot be exposed to high-temperature atmospheres for long periods. For this reason, spray dryers are related to heat-sensitive products like food or drugs but can be also used for natural extract encapsulation in order to increase their thermal stability. In this work, this last aspect was investigated and a model of co-current spray-drying, was developed and validated. This model is based on mass, energy and momentum balances and take into account of the distribution of the particle size. An experimental campaign was performed using a laboratory scale spray dryer (Büchi Mini Spray Dryer B-290, Switzerland) to validate the model. Maltodextrin and cyclodextrin were used as carrier to encapsulate grape skin and citrus extracts respectively. Different tests were done varying the operating condition of the spray dryer like the inlet air temperature (from 120°C to 180°C) and the mass ratio between carrier and natural extract. Simulation results and experimental data showed a good agreement in terms of mass yield and outlet temperature, while the outlet moisture content show slightly difference e needs to be further investigated.

Keywords: Natural extract, Encapsulation, Spray dryer, Model.

1. Introduction

Spray drying is a technology that has been widely used since '50s in food industry for its economic convenience, flexibility and ease of use. This technology can be also used for coating very small drops of liquid or gas to form microcapsules with an external thin layer of solid (wall material) made from natural polymers (e.g. carbohydrates, proteins, fibers and gums) and the core material inside. In the case of natural extracts, typically containing bioactive compounds material, microencapsulation can give protection from oxidation, light and temperature and, at the same time, a controlled release (Gharsallaoui et al., 2007). For instance, spray-drying encapsulation could be applied to increase thermal stability of natural extracts in order to include them into (bio)plastic film before extrusion (Bassani et al., 2019). The most used technique is the encapsulation of target molecules using polysaccharides like (starch, cellulose, cyclodextrins, pectin and maltodextrin). Encapsulation spray drying process consists of three basic steps: fluid power preparation,

homogenization and atomization in the drying chamber. The compounds to be encapsulated should be homogenized together with the material that surround them and then the mixture has to be sent to the spray-drier and atomized through a nozzle. The water is evaporated through the contact of the atomized material with the hot air. The particles obtained have a spherical morphology and a uniform distribution of sizes. However, a limitation of the use of spray-drying is due to the type of coating material, which must necessarily be soluble and so the choice of the coating material is a critical step in the process of encapsulation because it must ensure the stability and the quality of the final product. Another important parameter is also the inlet air temperature, which could deteriorate the encapsulated compound (Georgetti et al., 2008). The aim of this work is to develop and validate a suitable model of co-current spray-drying for natural extract encapsulation with particular reference to grape skin (Spigno et al., 2007) and citrus extract (Bassani et al., 2019). As first, experimental data was collected using a laboratory scale spray dryer and different operating condition was tested. Then the spray dryer model was developed including mass, energy and momentum balances and taking into account of the distribution of the particle size. Finally, the model simulation and the experimental results were compared.

2. Material and Methods

In this section, materials and methods concerning the experimental campaign and the model development are briefly described.

2.1. Natural extract extraction procedure

The extracts used in this study were made with Barbera grapes skin, kindly provided by different wineries from Piemonte (North Italy), while the citrus extracts are a commercial type one. For this reason, only Barbera grape skin needs an extraction procedure. The extraction was made using ethanol-water (60:40 v/v) as solvent with 1:8 (w/v) solid-to-solvent ratio at 60°C (Amendola et al., 2010).

2.2. Production of natural extract encapsulated powders trough Spray-dryer

Spray Drying process was performed with a laboratory scale spray dryer (Büchi Mini Spray Dryer B-290, Switzerland), with a 0.0007 m diameter of the nozzle. The height of the spray is equal to 0.45 m while the diameter is equal to 0.16 m. Compressed and pure air was used to disperse the liquid in fine droplets which was subsequently dried. Samples were introduced into the main chamber through a peristaltic pump. Drying air flow rate was 35 m^3/h, while the its temperature varied from 120 °C to 180 °C. The feed flow rate was 4 ml/min, for each experimental trials. One disadvantage of this laboratory spray dryer is related to the angle of exit of the particles from the nozzle (assumed to be equal to 55°). Indeed, during the process, some particles end up against the wall of the spray dryer and so there is a reduction of the global mass yield of the process. For this reason, the following useful index has been defined in order to evaluate the overall yield:

$$Recovery\ yield\ (\%) = \frac{weight\ of\ the\ dried\ powder\ (g)}{Theoretical\ total\ solids\ of\ the\ feed\ (g)} \quad (1)$$

As already mentioned, maltodextrin and cyclodextrin were used as a carrier for grape skin and citrus extracts respectively. Maltodextrin, with dextrose equivalent (DE) value equal to 12, was used in three series of experiments with grape skin extracts. The first tests were done at different inlet air temperatures (120 – 150 – 180 °C) and at a constant molar ratio (dextrose equivalent/ gallic acid equivalent = DE/GAE) equal 2.5. The second tests were done at constant inlet air temperature (150°C) with different DE/GAE (0.3 - 0.6 - 1.3 - 2.5). The third tests were equal to the previous one with the only variation of the inlet air

temperature (120°C). On the other hand, cyclodextrin (CD) was used just for one test, which operating condition is: inlet air temperature equal to 120°C, cyclodextrin to citrus extract ratio (CD/CIT, w/w) equal to 0.750 and 97.8% of initial humidity.

2.3. Analysis

Several analysis needs to be done in order to properly characterize both the original and the encapsulated extract. However, for this first study, only the total phenols and the moisture content were evaluated.

2.3.1. Total phenols content (TPC)

Total phenols content were determined with Folin-Ciocalteu assay and with direct reading of the absorbance at 280 nm (Vadivel et al., 2017). In both methods, total phenols were expressed as Gallic Acid Equivalents (GAE) by means of calibration curves with a Gallic acid standard.

2.3.2. Moisture content

The moisture content of the powders was determined weighing 5 g of powders in a pre-weighed ceramic crucible and dried at 105 ± 2 °C for 24 h.

2.4. Spray dying model

In this section, the model equations and the assumption made are shown. Only the main equation and parameters are presented, with the necessary modification, while the clear and in-deep description of the whole set of equations is given by Truong et al (2005).

2.4.1. Momentum balance equation

The droplet trajectory are described by equation (2) and (3), which represent axial and radial trajectory respectively, while the tangential one is neglected due to the mechanical characteristic of the spray dryer. v_p and v_a represent the velocity (m/s) of the particles and air, respectively. The axial distance from the atomizer is h (m).

$$\frac{dv_{px}}{dh} = \frac{\left[\left(1-\frac{\rho_a}{\rho_p}\right)g - \frac{\frac{3}{4}\rho_a C_D v_R\left(v_{px}-v_{ax}\right)}{\rho_p d_p}\right]}{v_{px}} \tag{2}$$

$$\frac{dv_{pr}}{dh} = \frac{\left[-\frac{\frac{3}{4}\rho_a C_D v_R\left(v_{px}-v_{ax}\right)}{\rho_p d_p}\right]}{v_{px}} \tag{3}$$

Here ρ is the density (kg/m3), d_p is the droplet diameter (m), v_r is the relative velocity between the droplet and the air, and C_D is the drag coefficient.

2.4.2. Mass balance equation

The unsteady-state mass balance for the droplet can be stated as follows:

$$\frac{dm_p}{dh} = -\frac{\xi A_p K_p}{v_{px}}(P_{sv} - P_{vb}) \tag{4}$$

$$\frac{dY_b}{dh} = \sum_{droplets} \frac{\left(-\frac{dm_p}{dh}\right) n_{droplets}}{G} \tag{5}$$

Where m_p is the mass of the particle or droplet (kg), ξ is the relative drying rate (evaluated as reported by Truong et al (2005)), A_p is the droplet surface area (m^2), Kp is the mass-

transfer coefficient (kg/(m*s*Pa), p_{vs} is the partial pressure of the surface of the droplet (Pa) and p_{vb} is the partial pressure of water vapour in the bulk air (Pa). For equation (5), Y is the gas humidity on dry basis, G is the mass flow rate of the dry air (kg/s), and $n_{droplets}$ is the flow rate of droplets (number of particle/s)

2.4.3. Energy balance equation

The unsteady-state heat balance for the droplet or particle is:

$$\frac{dT_p}{dh} = \frac{A_p H\left(T_g - T_p\right) + \left(-\frac{dm_p}{dh}\right)\Delta H_{ev}}{m_p c_{p_{mix}} v_{px}} \tag{6}$$

$$\frac{dT_g}{dh} = \sum_{droplets} \frac{A_p H\left(T_p - T_g\right) n_{droplets}}{G_{tot} m_p c_{p_{air}} v_{px}} - \frac{U_{glob} D_{spray} \pi \left(T_g - T_{amb}\right)}{G_{tot} c_{p_{air}}} \tag{7}$$

where, Tp and Tg are the particle and gas temperature [K] respectively, H is the heat convection coefficient (W/(m^2*K)), ΔH_{ev} is the latent heat of water evaporation (J/kg) (Green and Perry, 2003), cp_{mix} is the specific heat capacity of the droplet that is a mixture of water, natural extract and maltodextrin or ciclodextrin. As assumption, cp_{mix} was consider as constant and equal to 4186 (J/(kg*K)). Concerning equation (7), G_{tot} is the total gas flow rate (kg/s), Cp_{air} is the air specific heat, U_{glob} is the global heat transfer coefficient and was assumed equal to 22.2 (W/(m^2*K)), T_{amb} is the ambient temperature, assumed constant and equal to 25°C, and D_{spray} is the diameter of the spray dryer.

2.4.4. Equilibrium moisture content through sorption isotherm

For the relative drying rate (ξ) evaluation it is necessary to evaluate the equilibrium moisture content of the solid. The equilibrium moisture content is a function of the relative humidity of the gas, the temperature of the gas and the nature of the solid and the liquid. The variation of the equilibrium moisture content with relative humidity at a constant temperature is called a sorption isotherm. Sorption isotherms can be correlated by using equations such as the one proposed by Ozmen and Langrish (2003).

$$X_{eq} = Aexp\left(-BTln\left(\frac{1}{\psi}\right)\right) \tag{8}$$

where X_{eq} is the equilibrium moisture content on a dry basis, T is the temperature of the gas (K), and ψ is the relative humidity of the gas. A and B are empirical constants with units and in this study A and B were evaluated as a function of the mass fraction of maltodextrin or cyclodestrix into the dry particle (ω):

$$A = 0.03315\exp(2.92745\omega) \quad B = -0.00127786\ln(\omega) - 0.00168899 \tag{9}$$

2.4.5. Droplet size distribution

In this study, the size of the droplets are assumed to follow a log-normal distribution. To define the mean value to be include into log-normal distribution, different equations are available for prediction of droplet size for sprays from two-fluid nozzles. The following one, reported by Green and Perry (2003), was chosen:

$$d_{50} = K_t \rho_a^{-0.325} \left(\frac{m_L}{m_L U_L + m_a U_a}\right)^{0.55} \tag{10}$$

Where d_{50} is the mass median droplet size, K_t is an empirical value equal to 0.008, m_l and m_a are the liquid feed rate and the atomization gas rate respectively, while U_l and U_a are

liquid velocity and atomization gas velocity respectively. Knowing d_{50} it is possible to evaluate the mean value of log-normal distribution.

3. Results and Discussions

As first, Barbera extract had a total polyphenol content of 7.44 ± 0.55 GAE/L at 280nm, while with Folin-Ciocalteau assay, the result was 14.61 ± 0.65 GAE/L. this results are obtained through a calibration curve and are important in order to properly evaluate the inlet ratio DE/GAE previously defined. Table 1 shows the principal experimental and simulated results as function of the inlet air temperature and DE/GAE molar ration. The experimental results are reported with the related standard deviation value.

Table 1 Experimental and Simulation results of grape skin natural extract encapsulation

T_{air_in} (°C)	DE/GAE	Recovery (%)		T_{air_out} (°C)		Moisture (%)	
		exp	*sim*	*exp*	*sim*	*exp*	*sim*
120	2.5	80.4 ± 2.58	78.52	66 ± 1	71.79	3.48 ± 0.13	6.63
150	2.5	81.7 ± 0.65	78.52	83 ± 2	86.91	3.65 ± 0.23	5.01
180	2.5	80.5 ± 0.50	78.52	97 ± 1	101.17	3.78 ± 0.19	3.85
150	1.3	80.77 ± 8.19	80.71	83 ± 0	86.32	4.17± 0.23	4.73
150	0.6	83.96 ± 5.58	81.51	83 ± 0	86.15	5.35± 0.14	5.19
150	0.3	78.57 ± 9.75	82.05	83 ± 0	86.10	7.66± 0.23	7.11
120	1.3	81.36 ± 3.25	80.71	66 ± 0	71.14	5.43 ± 0.32	5.75
120	0.6	83.45 ± 7.09	81.51	66 ± 0	70.96	5.96 ± 0.26	5.76
120	0.3	80.24 ± 0.73	89.94	66 ± 0	70.89	7.58 ± 0.12	7.00

A good agreement between experimental and simulated data can be highlighted, especially regarding the percentage of the mass recovered and the outlet air temperature. At the same time, there are still slightly discrepancies regarding the outlet moisture content. For this reason, further development the model, for instance removing one of the hypotheses made, and further experimental tests will be necessary. The model was also validated by the residence time of the particles in the spray dryer and by the final distribution of the particles (Figure 1). Indeed, according to the technical manual of the spray dryer, the average residence time of the particles in the spray dryer and in the subsequent cyclone is about 1.0 second, while the average residence time evaluated by the model for spray dryer only is about 0.85 seconds. Concerning the final distribution,

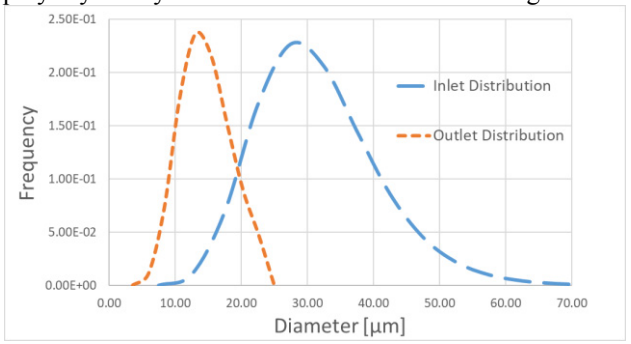

Figure 1 Size distribution of the inlet and outlet particle

Figure 1 reports the initial particle distribution and the final particle distribution. It can be noted that the final distribution is still log-normal and the highest diameter never exceeds the value of about 25 µm. This is in perfect agreement with the technical manual of the

spray dryer where it is reported that the final particles have a size between 1 and 25 μm. Moreover, this model was also validated trough the simulation of the citrus extract encapsulation with cyclodextrine. Table 2 shows a good agreement between simulation experimental data. It is important to underline the fact that the commercial citrus extract was solubilized in 0.5% (w/v) solution of NaOH.

Table 2 Experimental and Simulation results of citrus natural extract encapsulation

T_{air_in} (°C)	CD/CIT	Recovery (%)		T_{air_out} (°C)		Moisture (%)	
		exp	*sim*	*exp*	*sim*	*exp*	*sim*
120	0.750	82.34 ± 0.93	89.7	64 ± 0	69.99	5.38 ± 0.03	6.11

4. Conclusions

Spray dryer technology is found to be suitable for natural extracts encapsulation with, with different carriers, such as maltodextrins or cyclodextrins. In this work, a model for natural extract encapsulation was developed and validated at different temperatures and at different ratios between natural extract and carrier. The results show a good agreement in terms of process yield and outlet temperature, while there are still slightly differences in the outlet moisture prediction. For this reason, an in-deep investigation needs to done both in terms of model and in terms of experimental data collection. Moreover, an optimization of the process could be done to obtain, for instance, the inlet temperature or the ratio between carrier and natural extract related to the highest recovery yield.

Acknowledgments

This research was financially European Union's Horizon 2020 Research and Innovation programme under grant agreement No 792261 (NewPack project).

References

D. Amendola, D. M. De Faveri, G. Spigno, 2010, Grape marc phenolics: Extraction kinetics, quality and stability of extracts, Journal of Food Engineering, 97(3), 384-392.

A. Bassani, S. Montes, E. Jubete, J. Palenzuela, A. P. Sanjuan, G. Spigno, 2019, Incorporation of Waste Orange Peels Extracts into PLA Films, Chemical Engineering Transactions, 74, 1063-1068

S. R. Georgetti, R. Casagrande, C. R. F. Souza, W. P. Oliveira, M. J. V. Fonseca, 2008, Spray drying of the soybean extract: effects on chemical properties and antioxidant activity, LWT-Food Science and Technology, 41(8), 1521-1527.

A. Gharsallaoui, G. Roudaut, O. Chambin, A. Voilley, R. Saurel, 2007, Applications of spray-drying in microencapsulation of food ingredients: An overview, Food research international, 40(9), 1107-1121

D. W. Green, R. H. Perry, 2003, Perry's Chemical Engineers' Handbook, 8Th edition.

L. T. A. G. Ozmen, T. A. G. Langrish, 2003, A study of the limitations to spray dryer outlet performance, Drying technology, 21(5), 895-917.

G. Spigno, L. Tramelli, D. M. De Faveri, 2007, Effects of extraction time, temperature and solvent on concentration and antioxidant activity of grape marc phenolics, Journal of food engineering, 81(1), 200-208.

V. Truong, B. R. Bhandari, T. Howes, 2005, Optimization of co-current spray drying process of sugar-rich foods. Part I—Moisture and glass transition temperature profile during drying, Journal of Food Engineering, 71(1), 55-65.

V. Vadivel, A. Moncalvo, R. Dordoni, G. Spigno, 2017, Effects of an acid/alkaline treatment on the release of antioxidants and cellulose from different agro-food wastes, Waste Management, 64, 305-314.

Sauro Pierucci, Flavio Manenti, Giulia Bozzano, Davide Manca (Eds.)
Proceedings of the 30th European Symposium on Computer Aided Process Engineering (ESCAPE30), May 24-27, 2020, Milano, Italy.
http://dx.doi.org/10.1016/B978-0-12-823377-1.50061-6

Modelling and Simulation of Low Pressure Carburizing Furnaces

Fatima Matamoros[a,b,*], Pierre-Alexandre Glaude[a], Roda Bounaceur[a], Hubert Monnier[b], Abderrazak M. Latifi[a]

[a]*Laboratoire Réactions et Génie des Procédés, CNRS-ENISC, Université de Lorraine, Nancy, France*
[b] *Institut National de Recherche et de Sécurité, Vandoeuvre-lès-Nancy, France*
fatima.matamoros-marin@univ-lorraine.fr

Abstract

In this paper, modelling of a low pressure carburizing furnace is developed. Acetylene is chosen as the reactive gas and its pyrolysis, described by a detailed kinetic mechanism is studied in a perfectly stirred tank reactor. Special attention is paid to the fluid-solid interactions; adsorption is described using a Langmuir approach and a first order surface reaction in acetylene is assumed. The diffusion of carbon in the steel is modelled by means of Fick's second law and solved numerically using a finite volume method. All the simulations are performed using MATLAB environment. The numerical results provide the composition of the gas phase in the reactor as well as the spatio-temporal carbon profile in the steel, and are consistent with the experimental observations.

Keywords: Modelling, simulation, carburizing, PAH.

1. Introduction

Low pressure carburizing is a thermochemical process that aims to harden the surface of metals by increasing their carbon concentration. This is done by supplying a carburizing gas in a furnace containing non-treated steel. The process is conducted at pressures far below atmospheric pressure and temperatures within the range of 900°C to 1050°C (Buchholz et al., 2010). At such temperatures however, there is pyrolysis of the reactive gas and this leads to the production of toxic compounds in the form of polycyclic aromatic hydrocarbons (PAHs). This group of organic molecules is harmful to human health and some are considered carcinogenic. The current operating procedure used in carburizing consists of a discontinuous feed of hydrocarbons. Boost stages, where carburizing gas is fed into the reactor and surface reaction takes place, are followed by diffusion stages, where an inert gas is fed into the reactor and only the diffusion of carbon into the metal takes place. The operating conditions (temperature, boost and diffusion times…) are generally determined by trial and error with the sole objective of satisfying the desired carbon profile in the steel. However, the production of toxic compounds is a major issue which has not been extensively investigated, and deserves to be addressed. A mathematical modelling of the different stages of carburizing and a subsequent optimization are therefore necessary to determine the operating conditions that not only guarantee the carbon content in the metal but also minimize the production of PAHs.
The aim of the present work is to propose a modelling of low pressure carburizing process in its entirety. A detailed gas phase mechanism of the pyrolysis of acetylene is coupled to a surface reaction and diffusion model and the numerical modelling of these different stages is described. The results of simulations using the software MATLAB are presented.

2. Model description

Low pressure carburizing process (LPC) consists of three main phenomena, presented in Figure 1. The carburizing gas, in this case acetylene, undergoes pyrolysis and simultaneous external transfer to the surface of the metal where it is adsorbed and decomposes into solid carbon. The latter then joins the crystalline lattice of iron and diffuses into the depth of the steel. Each phenomenon is described as follows.

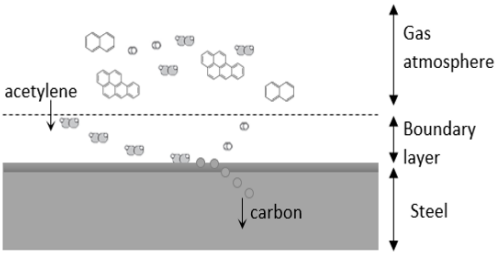

Figure 1: Phenomena occurring during LPC

2.1 Gas phase mechanism of the pyrolysis of acetylene

The mechanism describing the pyrolysis of acetylene selected for this study is the one proposed by Bensabath (2017). It was chosen because it considers the formation of the sixteen PAHs that the U.S. Environmental Protection Agency (EPA) labeled as priority pollutant PAH compounds. The mechanism consists of 1255 reactions and 363 species and some modifications were deemed necessary. First, a reduction of the mechanism carried out to lower its computational cost in view of the optimization; then, the coupling of a soot model to the homogenous reactions. Indeed, it is a consensus in the literature that PAHs are precursors to soot and therefore a soot model would allow to more correctly determine PAH production.

2.1.1. Reduction of the kinetic mechanism

The reduction was carried out with the workbench of the software Chemkin Pro by implementing a skeletal mechanism reduction. This type of reduction consists in eliminating unimportant reactions and species. The skeletal methods used are the Directed Relation Graph with Error Propagation method (DRGEP) and the Full Species Sensitivity Analysis method (FSSA). The description of these methods is not presented in this paper but can be found in Pepiot et al. (2005). The target species and the relative and absolute tolerances R and A respectively used to compute the error E (Eq.(1)) were the required inputs. Target species are the species that the skeletal mechanism should reproduce the most accurately possible when compared to the master mechanism and are represented in our case by the 16 U.S EPA PAHs. For each set *j* of operating conditions, error E for target species *i* is:

$$E_i = \frac{\left| x_{i,master} - x_{i,skeletal} \right|}{R_i \times \left| x_{i,master} \right| + A_i} \tag{1}$$

where *x* are molar fractions, *i* represents a target species and *j* a set of operating conditions. Error E determines whether a skeletal mechanism is acceptable. If it is lower than 1 for all *j* and *i*, then the skeletal mechanism is considered satisfactory, otherwise it is not, and another skeletal mechanism is determined. The tolerances were chosen accordingly for each target species in order to obtain the smallest skeletal mechanism possible. The ranges of conditions in which the skeletal mechanism had to be valid were set as [880-1100] °C for temperature and [300-8000] Pa for pressure. The skeletal mechanism obtained consists of 139 species and 444 reactions with the methods applied.

2.1.2. Soot model

The method of moments (MOM) with interpolative closure presented by Frenklach (2002) was deemed the best option to study particle evolution of soot in our case. This choice is based on the low computational cost of MOM compared to other methods as well as the nature of its outputs, i.e. global properties such as the total number of particles, average diameter, etc. Other methods provide more detailed results like the density of each particle class of soot (N_i in Eq. (2)) but this results in a higher computational cost. In our case however, global properties are sufficient because the focus is not on soot itself but its impact on PAHs. The MOM focuses on the determination of the moments of the particle size distribution function (PSDF). The knowledge of all the moments would allow to determine the PSDF itself but only the first few moments are calculated because they are the ones that can be physically interpreted, e.g. the 0th order moment is the total number of particles and the 1st order moment is the total mass of the particles. The rth moment and its derivative are defined as:

$$M_r = \sum_{i=1}^{\infty} m_i^r N_i \tag{2}$$

$$\frac{dM_r}{dt} = \sum_{i=1}^{\infty} m_i{}^r \frac{dN_i}{dt} = \left(\sum_{i=1}^{\infty} m_i{}^r \frac{dN_i}{dt} \right)_{nuc} + \left(\sum_{i=1}^{\infty} m_i{}^r \frac{dN_i}{dt} \right)_{coa} + \left(\sum_{i=1}^{\infty} m_i{}^r \frac{dN_i}{dt} \right)_{sur} \tag{3}$$

where N_i is the number density and m_i is the mass of particles of class (size) i. In order to determine the time evolution of each moment, different phenomena are considered: nucleation, coagulation and surface growth of soot. For each particle class, population balances are developed considering each phenomenon separately. By multiplying by m_i^r and doing the summation for all particle classes, a source term for each phenomenon in terms of moments can be established. The derivative of moment r can then be written as the summation of the source terms (Eq. (3)) (Frenklach, 2002).

2.1.3 Mass balance on gaseous phase species

The mass balance for gas species k in a continuously stirred tank reactor can be written as:

$$\rho V \frac{dY_k}{dt} = \dot{m}_{in}(Y_{kin} - Y_k) + Vr_k W_k + V_P s_k W_k - Y_k(\dot{m}_{surf} + \dot{m}_{soot}) \tag{4}$$

where ρ is the mass density of the mixture, V is the volume of the reactor, Y_k is the mass fraction of species k, Y_{kin} is the inlet mass fraction of species k, $\dot{m}_{in}$ is the inlet mass flowrate, r_k and s_k are the molar production rates per unit volume of species k by gas-phase reactions and the heterogeneous reaction respectively, W_k is the molar weight of species k, V_P is the volume of the steel and $\dot{m}_{surf}$ and $\dot{m}_{soot}$ are the total mass production rates of gaseous species by the surface reaction and by soot nucleation respectively. Production of gas species by the surface reaction (s_k and $\dot{m}_{surf}$) are determined from the surface reaction rate, which is developed in the following sections.

2.2 External mass transfer

The film theory is used to model the external mass transfer of acetylene to the surface of the steel. A mass balance on acetylene leads to Eq.(5) and by considering only the flux due to molecular diffusion, Eq.(6) is obtained. At the boundary in contact with the gas

phase, (z=0), the concentration of acetylene is taken equal to the acetylene concentration in the reactor. At the boundary in contact with the steel, (z=δ) the flux is assumed equal to the acetylene that is consumed by the heterogeneous reaction per unit area $\dot{m}_{C2H2}$.

$$\frac{\partial[C_2H_2]}{\partial t} + \frac{\partial F_{C_2H_2}}{\partial z} = 0 \tag{5}$$

$$\frac{\partial[C_2H_2]}{\partial t} = D_{C_2H_2}\frac{\partial^2[C_2H_2]}{\partial z^2} \tag{6}$$

$$[C_2H_2]\big|_{z=0} = [C_2H_2]_{PSTR} \tag{7}$$

$$-D_{C_2H_2}\frac{\partial[C_2H_2]}{\partial z}\bigg|_{z=\delta} = \dot{m}_{C_2H_2} \tag{8}$$

where $[C_2H_2]$ and $[C_2H_2]_{PSTR}$ are the acetylene concentration in the reactor and the film respectively, F_{C2H2} is the acetylene flowrate per unit area in the film and D_{C2H2} is the diffusion coefficient of acetylene in the mixture.

2.3 Adsorption and surface reaction

Once the acetylene in the gas phase reaches the surface of the solid, it will adsorb and react. Ryzhov et al. (2004) describe its decomposition on the surface of iron as an adsorption phenomenon followed by dissociation with simultaneous chemisorption of the products. Surface reaction is considered irreversible, leading to solid carbon and gaseous hydrogen. This is illustrated by Eq.(9) and (10), where S represents a surface adsorption site. Adsorption, desorption and surface reaction rates are then readily deduced.

$$C_2H_{2(g)} + S \longleftrightarrow C_2H_2* \tag{9}$$

$$C_2H_2* + S \longrightarrow 2C* + H_{2(g)} \tag{10}$$

$$r_{ads} = k_{ads}[C_2H_{2(g)}][S] \tag{11}$$

$$r_{des} = k_{des}[C_2H_2*] \tag{12}$$

$$r_{surf} = k_{surf}[C_2H_2*][S] \tag{13}$$

where k_{ads}, k_{des} and k_{surf} are the kinetic constants of adsorption, desorption and surface reaction, $[C_2H_{2(g)}]$ is the concentration of acetylene in the gas phase at the surface of steel and $[C_2H_2*]$ and $[S]$ are the concentrations of adsorbed acetylene and unoccupied sites at the surface of the steel. By analogy with catalytic reactions, a Langmuir-Hinshelwood-Hougen-Watson methodology is adopted to study the phenomena involved at the surface. One rate limiting step is assumed, in our case this corresponds to the chemical reaction, Eq.(10), and the other step, Eq. (9), is considered at equilibrium. This means that the

adsorption rate is taken equal to the desorption rate. The Langmuir constant and fractional surface coverages are defined and conservation of surface sites is applied to determine the surface reaction volumetric rate.

$$r_{surf} = k_{surf} K_{eq} C_{tot}^2 \left(\frac{1-\theta_C}{1+K_{eq}\left[C_2H_2\right]} \right)^2 \left[C_2H_2\right] \tag{14}$$

where K_{eq} is the Langmuir constant, C_{tot} is the total quantity of surface sites in a monolayer per unit volume and θ_C is the fractional surface coverages of carbon. Its value is deduced from the concentration of carbon at the surface of the steel; the assumption is made that any carbon atom at the surface of the steel occupies a free site.

2.4 Carbon diffusion

The diffusion of the carbon resulting from the surface reaction is modelled by means of Fick's second law in one dimension (Eq.15). Only the diffusion of carbon is considered. At the upper boundary ($x=x_0$), the flow of carbon that diffuses from the surface is supposed equal to the amount of carbon produced by the heterogeneous reaction per unit area, $\dot{m}_C$ (Eq.16). At the lower boundary ($x=x_L$) a null flux is imposed (Eq.17). Here C denotes the concentration of carbon in the steel and D is the diffusion coefficient of the carbon in austenite.

$$\frac{\partial C}{\partial t} = \frac{\partial^2 DC}{\partial x^2} \tag{15}$$

$$-D\frac{\partial C}{\partial x}\bigg|_{x=x_0} = \dot{m}_C \tag{16}$$

$$-D\frac{\partial C}{\partial x}\bigg|_{x=x_L} = 0 \tag{17}$$

3. Simulation results

The process model was implemented and solved within MATLAB environment. Only nucleation and coagulation are considered for the soot model and nucleation is taken to be the dimerization of two pyrene molecules. Fick's second law and the boundary conditions are discretized using a finite volume method. Operating temperature, number of cycles, boost and diffusion times, the dimensions of the steel and the diffusion coefficient of carbon in steel are chosen as in the studies by Zajusz et al. (2014) and Kula et al. (2005). There remain however some unknown parameters in the model that are needed to perform the simulations, i.e. K_{eq}, C_{tot} and k_{surf}. The order of magnitude of C_{tot} was determined from the maximum solubility of carbon in austenite at 920 °C and the values of K_{eq} and k_{surf} were chosen in a way to obtain the same orders of magnitude in the results as Zajusz et al. (2014).

Table 1: PAH, soot production and carbon introduced in the steel at T= 920 °C

Total PAH production	Total soot production	Carbon introduced in the steel
4 .2 . 10^{-1} g	1.3 . 10^{-6} g	3.5 10^{-3} g

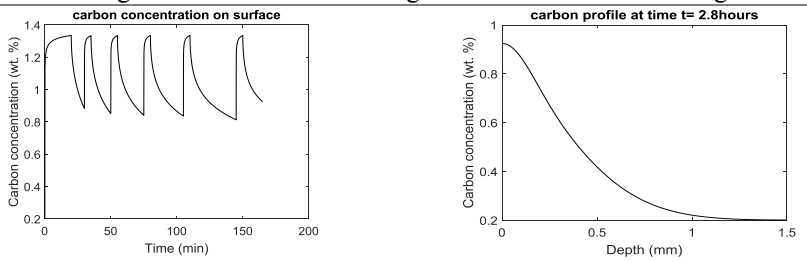

Figure 2: Results from the simulation at T= 920 °C after 6 cycles

Some of the values that will be used for experimental validation such as soot production and the quantity of carbon introduced in the steel are presented in

Table 1. The composition of the gas phase is determined during each cycle and the total mass of PAH that is produced during the process is deduced. The results of carbon profiles are presented in Figure 2 and show that the predictions of the model developed are consistent with the experimental observations. However, some parameters are still to be measured or deduced from the experimental measurements in order to improve the predictions and validate the model. The latter will then be used to optimize the design and operation of the carburizing furnace.

4. Conclusions

In this paper, modelling of low pressure carburizing furnace has been developed and simulated in the MATLAB environment. The model reproduces the correct tendencies and it represents a first step in the optimization objective. The upcoming tasks will focus on the determination of the unknown parameters as well as a refinement of the model. Indeed, the Langmuir isotherm equation assumes equilibrium between the acetylene in the gas phase and the acetylene adsorbed in the solid and it is a starting point for modelling. However, non-equilibrium between the phases will have to be considered before attempting to validate the model from experimental data.

References

D. Buchholz, R.U. Khan, S. Bajohr, R. Reimert, 2010,Computational fluid dynamics modelling of acetylene pyrolysis for vacuum carburizing of steel, Ind. Eng. Chem. Res. 49, 1130-1137.

M. Frenklach, 2002, Method of moments with interpolative closure, Chemical Engineering Science, 57, 2229-2239

M. Zajusz, K. Tkacz-Smiech, M. Danielewski, 2014, Modelling of vacuum pulse carburizing of steel, Surface & Coatings Technology, 258, 646–651.

N. M. Ryzhov, A. E. Smirnov, R.S Fakhurtdinov, L.M Mulyakaev, V.I Gromov, 2004, Special features of vacuum carburizing of heat-resistant steel in acetylene, Metal Science and Heat Treatment, Vol. 46, Nos. 5-6, 230-235.

P. Kula, R. Pietrasik, K. Dybowski, 2005, Vacuum carburizing-process optimization, Journal of Materials Processing Technology 164–165, 876–881

P. Pepiot, H. Pitsch, 2005, Systematic reduction of large chemical mechanisms, 4th Joint Meeting of the US Sections of the Combustion Institute. Vol. 2123

T. Bensabath, 2017, Approche préventive pour une réduction des Hydrocarbures Aromatiques Polycycliques (HAP) dans les fours à pyrolyse, PhD thesis, Université de Loraine, France.

Sauro Pierucci, Flavio Manenti, Giulia Bozzano, Davide Manca (Eds.)
Proceedings of the 30th European Symposium on Computer Aided Process Engineering (ESCAPE30), May 24-27, 2020, Milano, Italy.
http://dx.doi.org/10.1016/B978-0-12-823377-1.50062-8

Thermodynamic Analysis of Different Methanation Reactors for Biogas Upgrading

Sayed Ebrahim Hashemi[a], Kristian M. Lien[a], Sondre K. Schnell[b], Bjørn Austbø[a,*]

[a]*Department of Energy and Process Engineering, Norwegian University of Science and Technology (NTNU), NO-7491, Trondheim, Norway.*
[b]*Department of Materials Science and Engineering, Norwegian University of Science and Technology (NTNU), NO-7491, Trondheim, Norway.*
bjorn.austbo@ntnu.no

Abstract

Biomethane production from biogas can be increased by methanation of carbon dioxide with hydrogen through the Sabatier reaction. In this work, the performance of the methanation process is investigated under isothermal and adiabatic conditions for different temperature and pressure levels. The processes were modelled assuming equilibrium conditions, minimizing the Gibbs free energy. The results indicate that the exergy of heat removed from the process, and thereby the integration potential, increases with increasing temperature. The internal irreversibility is smaller and the heat integration potential larger for adiabatic reactors than for isothermal reactors.

Keywords: Biogas upgrading, Sabatier reaction, Exergy analysis, Process integration

1. Introduction

The global share of renewable energy in the transportation sector is limited to 3.3 % (REN21, 2019). High quality biomethane in liquid form, with characteristics similar to liquefied natural gas (LNG), is considered to be one alternative to fossil fuels. However, production of LBM requires upgrading biogas whereby undesired contaminants (mainly CO_2) are removed, increasing the CH_4 content of the final product. In conventional approaches, biogas is upgraded through gas separation technologies such as absorption, adsorption, and membrane separation (Kadam and Panwar, 2017). One drawback of conventional biogas upgrading technologies is that the removed CO_2, typically 25−55 mol% of the biogas (Kadam and Panwar, 2017), is emitted to the atmosphere.

Recently, application of the Sabatier reaction for biogas upgrading has gained attention (Witte et al., 2018). Here, CO_2 in the raw biogas reacts with H_2 in order to increase the CH_4 content in the final product. Depending on the CO_2 content in the raw biogas, the biomethane production can increase up to 80 % compared to common biogas upgrading technologies (Witte et al., 2018). As a Power-to-Gas concept, biomethane can be used as an energy carrier for intermittent energy sources, with hydrogen produced from excess electricity (Wang et al., 2018).

The Sabatier reaction is a catalytic reaction that is a linear combination of the CO methanation reaction (Eq. (1)) and the reverse water gas shift reaction (Eq. (2)) (Witte et al., 2018):

$$CO + 3H_2 \rightleftharpoons CH_4 + H_2O \qquad \Delta h^0_{298\,K} = -206.3 \text{ kJ/mol} \tag{1}$$

$$CO_2 + H_2 \rightleftharpoons CO + H_2O \qquad \Delta h^0_{298\,K} = +41.2 \text{ kJ/mol} \tag{2}$$

The Sabatier reaction is typically carried out under either isothermal or adiabatic conditions. Gao et al. (2012) conducted a detailed thermodynamic equilibrium analysis for carbon oxides methanation under isothermal conditions through minimization of Gibbs free energy, reporting results in good accordance with experimental data. Jürgensen et al. (2015) considered biogas methanation through the Sabatier reaction under equilibrium and isothermal conditions. They observed that the starting temperature for carbon formation increased with increasing pressure. Moreover, they demonstrated that the CO_2 conversion was highly influenced by the CH_4 content of biogas at pressure levels below 8 bar.
The design of isothermal reactors for the Sabatier reaction is complex and costly. Hence, a series of adiabatic reactors with intercooling is often used in practice (Walspurger et al., 2014). Since heat will be available at different temperature levels for isothermal and adiabatic conditions, the heat integration potential will also be different.
This study aims to evaluate the performance of methanation reactors for biogas upgrading running under isothermal and adiabatic conditions. In addition, potential use of available heat from the reactors is examined through exergy analysis.

2. Methodology

2.1. Model description

Process configurations for isothermal and adiabatic reactors are illustrated in Figure 1. Under isothermal conditions (Figure 1 (a)), the biogas methanation takes place in a single stage reactor at constant temperature, assuming that heat is removed at the reactor temperature. Under adiabatic conditions (Figure 1 (b)), a series of reactors with intercooling is used, and heat will be removed at higher temperature than for the isothermal case. The number of reactors was chosen such that the composition of the final product stream was the same for both designs.

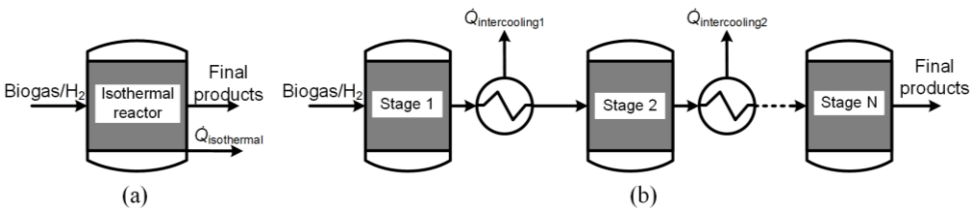

Figure 1. Methanation process configuration for (a) Single stage isothermal reactor (b) Series of adiabatic reactors with intercooling

In this study, it was assumed that equilibrium was reached in all the reactors. The two models were simulated for different temperatures and pressures with Aspen HYSYS® V9.0, using Gibbs reactors and Soave-Redlich-Kwong (SRK) equation of state. The advantage of using Gibbs reactors is that the final equilibrium composition is determined in accordance with the minimum Gibbs energy of the system without considering the equilibrium constants of the involving reactions. However, the Gibbs reactors do not provide information regarding kinetics or size of the reactors. The pressure drops within reactors and intercoolers were assumed negligible.
In order to make a reasonable comparison between isothermal and adiabatic conditions, it was assumed that the temperature after each intercooler was equal to the temperature of the feed stream, except for the last reactor, where the inlet temperature was manipulated in order to obtain the same final product as for the isothermal reactor.
The temperature of the isothermal reactor was assumed to be 10 °C above the feed stream temperature (Wang et al., 2018). The feed stream contained biogas (a mixture of

60 mol% CH_4 and 40 mol% CO_2) with a molar flow rate of 1 kmol/h, and H_2 with a flow rate four times as large the flow rate of CO_2 (stoichiometric ratio).
First, the performance of the Sabatier reaction was examined in terms of CO_2 conversion (Eq. (3)) and CH_4 yield (Eq. (4)), comparing the single stage isothermal reactor with the first stage of the adiabatic reactors:

$$X_{CO_2} = \frac{\dot{n}_{CO_2,in} - \dot{n}_{CO_2,out}}{\dot{n}_{CO_2,in}}, \tag{3}$$

$$Y_{CH_4} = \frac{\dot{n}_{CH_4,out} - \dot{n}_{CH_4,in}}{\dot{n}_{CO_2,in}}. \tag{4}$$

Here, $\dot{n}$ denotes the molar flow rate.
Second, potential use of available heat from the methanation reactors was assessed through exergy analysis, comparing the single stage isothermal reactor and the complete series of adiabatic reactors with intercooling. The exergy of material streams was calculated in accordance with the methodology described by Kotas (2012), implemented as in the work by Hashemi et al. (2019). At steady state operation, the irreversibility rate within the system can be expressed as

$$\dot{I} = \dot{E}_{x,in} - \dot{E}_{x,out} + \dot{E}_x^Q, \tag{5}$$

where $\dot{E}_{x,in}$ and $\dot{E}_{x,out}$ denotes the exergy of inlet and outlet material streams, respectively. The exergy of heat is given as

$$\dot{E}_x^Q = \dot{Q} \cdot (1 - \frac{T_0}{T}), \tag{6}$$

where $\dot{Q}$ is the amount of heat supplied (negative if removed), T_0 the ambient temperature (assumed to be 25 °C) and T the temperature at which the heat is transferred. For the intercoolers, the exergy of the heat removed is equal to the difference in exergy for the inlet and outlet material streams.
Unlike the internal irreversibilities within the methanation reactors, the exergy of the heat produced in the reactors can potentially be utilized. However, if the generated heat is not utilized, the total exergy loss in the system can be expressed as

$$\dot{E}_x^{loss} = \dot{I} - \dot{E}_x^Q \tag{7}$$

In the present study, the use of availabe heat was investigated only for temperatures at which the methanation reaction occurres.

3. Results and discussion

3.1. Isothermal vs. adiabatic (conversion performance)

Figure 2 illustrates the effects of temperature and pressure on CO_2 conversion and CH_4 yield for the isothermal reactor and the first stage of the adiabatic reactors. The CO_2 conversion is higher for the isothermal reactor than for the first stage of the adiabatic reactors. The CO_2 conversion decreases with increasing temperature, and is higher at higher pressure.
As can be seen from Figure 2, an increase in temperature reduces the CH_4 yield, while the CH_4 yield increases at higher pressure under both isothermal and adiabatic conditions. The changes in CO_2 conversion and CH_4 yield with temperature and pressure are smaller for the first stage of the adiabatic reactors than for the isothermal reactor.
The results demonstrate that optimal CO_2 conversion and CH_4 yield are obtained at lower temperature and higher pressure, which is in accordance with Le Chatelier's principle.

While the Sabatier reacion is limited by the chemical equilibrium at high temperature, it is limited by reaction kinetics at low temperature (depending on the type and quantity of the catalyst) (Wang et al., 2018). Hence, an operating temperature below 200 °C is not favorable. Moreover, the optimal operating pressure for the Sabatier reaction depends on the application of the produced CH_4 and a trade-off between extra compression work and improvements in the CO_2 conversion.

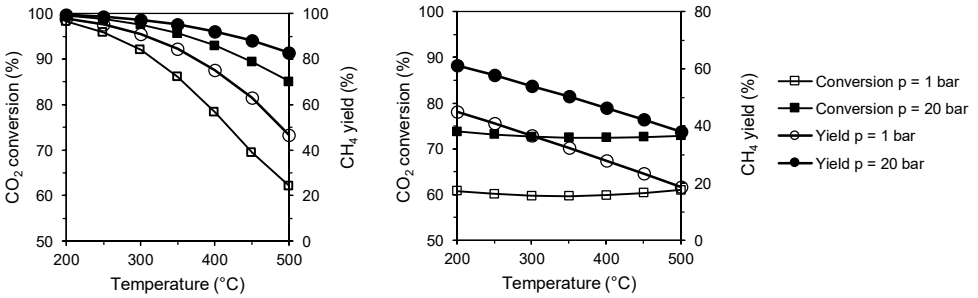

Figure 2. CO_2 conversion and CH_4 yield as functions of temperature and pressure within isothermal reactor (left) and the first stage of adiabatic reactors (right)

3.2. Isothermal vs. adiabatic (potential use of available heat)

Figure 3 demonstrates the effects of temperature and pressure on the amount of heat supplied to the isothermal reactor. The negative values illustrate exothermic reactions, where heat is removed from the reactor. The amount of heat supplied to the single stage isothermal reactor and the series of adiabatic reactors is equal since the feed and product streams are identical. The higher the pressure, the larger the heat removal from the reactor. As can be seen from Figure 3, increasing the inlet temperature reduces the heat generated within the reactor until the point at which the reaction becomes endothermic. This means that the reverse water gas shift reaction (Eq. (2)) dominates the overall reaction, producing more CO and less CH_4.

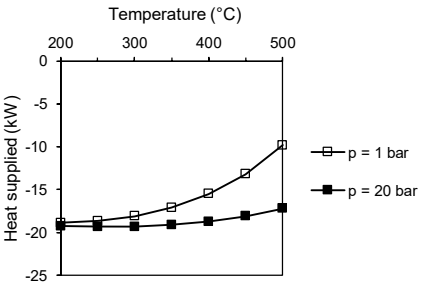

Figure 3. Heat supplied for isothermal reactor

The number of stages required under adiabatic conditions (see Figure 1 (b)) is indicated in Figure 4. The number of required stages increases with increasing feed stream temperature, while it reduces with increasing pressure.

Results from the exergy analysis for the two reactor models are given in Table 1. Since the inlet and outlet streams are the same, the total exergy loss is the same for both rector models if the heat from the processes is not utilized. However, under adiabatic conditions, the internal irreversibility rate is smaller and the exergy content of the heat is higher (due to higher temperature). Moreover, operating the methanation reactors at lower pressure and higher temperature results in lower exergy loss within the reactors. The maximum exergy

of heat at fixed pressure is achieved at lower temperature for the methanation reactors running under adiabatic conditions.

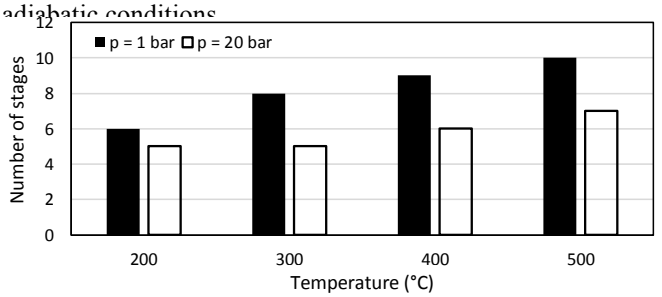

Figure 4. Required stages for adiabatic conditions as a function of temperature and pressure

As can be noticed, favourable pressure and temperature for higher CH_4 yield contradicts the reduction in the irreversibilities within the reactors. Hence, for system level process integration, the CH_4 yield must be weighed against the irreversibilities when determining the operating temperature and pressure.

Table 1 demonstrates that running the Sabatier reaction within the series of adiabatic reactors leads to the larger amounts of exergy of heat and lower irreversibilities within reactors at given temperature and pressure. This suggests that a series of adiabatic reactors could provide improved process integration potential compared to an isothermal reactor.

Table 1. Results from the exergy analysis for isothermal and adiabatic reactors

Isothermal								
	p = 1 bar				p = 20 bar			
Temp. *(°C)*	$\dot{n}_{CH_4,out}$ (kg/h)	$\dot{I}$ (kWh/kg CH_4)	$\dot{E}_x^Q$ (kWh/kg CH_4)	$\dot{E}_x^{loss}$ (kWh/kg CH_4)	$\dot{n}_{CH_4,out}$ (kg/h)	$\dot{I}$ (kWh/kg CH_4)	$\dot{E}_x^Q$ (kWh/kg CH_4)	$\dot{E}_x^{loss}$ (kWh/kg CH_4)
200	15.9	0.28	-0.45	0.73	16.0	0.38	-0.46	0.84
300	15.5	0.16	-0.56	0.72	15.9	0.26	-0.59	0.84
400	14.5	0.09	-0.58	0.66	15.5	0.17	-0.67	0.84
500	12.6	0.05	-0.43	0.47	14.9	0.11	-0.69	0.80
Adiabatic								
200	15.9	0.16	-0.57	0.73	16.0	0.21	-0.63	0.84
300	15.5	0.10	-0.62	0.72	15.9	0.15	-0.69	0.84
400	14.5	0.06	-0.60	0.66	15.5	0.11	-0.73	0.84
500	12.6	0.04	-0.43	0.47	14.9	0.08	-0.72	0.80

In order to complete the present analysis with respect to the potential use of available heat, consideration of reaction kinetics is essential, as the performance of the reactor is highly dependent on the catalyst and operating temperature.

From a practical point of view, the application of the Sabatier reaction for biogas upgrading depends on the availability of hydrogen, because the production of hydrogen is a major cost driving factor. Besides, the temperature and pressure within the reactors influence the amount of unreacted hydrogen. In this sense, operating with less hydrogen than the stoichiometric amount and operating the series of adiabatic reactors, which improves the usable exergy of heat, might benefit the economy of the overall process. However, further studies must be conducted to determine the appropriate ratio between H_2 and CO_2.

4. Conclusions

Biogas upgrading through the Sabatier reaction was examined for a single stage isothermal reactor and a series of adiabatic reactors with intercooling, with respect to conversion of CO_2 to CH_4 and the potential use of available heat from the reactors. The reactor models were simulated in Aspen HYSYS® V9.0 using Gibbs reactors. The use of available heat was evaluated by exergy analysis.

The results indicate that the performance of the single stage isothermal reactor is better than the first stage of adiabatic reactors in terms of CH_4 yield. In order to achieve the isothermal performance, a series of adiabatic reactor with intercooling is required.

On the one hand, operating the methanation reactors at higher pressure and lower temperature leads to greater CO_2 conversion and CH_4 yield. On the other hand, the total exergy loss decreases with decreasing pressure and increasing temperature. The number of adiabatic reactors required to reach the same product conditions as for the isothermal reactor increases with increasing temperature and decreasing pressure. Ideally, the internal irreversibilities would be minimized and the heat integration potential maximized if the Sabatier reaction was carried out in stages at gradually reducing temperature, keeping the process close to equilibrium all the way. The heat integration potential must, however, be balanced against reaction kinetics and equipment size.

Acknowledgments

Financial support from the Norwegian University of Science and Technology (NTNU) through the strategic research program ENERSENSE is greatly acknowledged.

References

J. Gao, Y. Wang, Y. Ping, D. Hu, G. Xu, F. Gu, F. Su, 2012, A thermodynamic analysis of methanation reactions of carbon oxides for the production of synthetic natural gas, RSC Advances, 2, 6, 2358-2368.

S.E. Hashemi, K.M. Lien, S.K. Schnell, B. Austbø, 2019, Optimization of an Absorption-Based Biogas Upgrading and Liquefaction Process, Chemical Engineering Transactions, 76, 697-702.

R. Kadam, N.L. Panwar, 2017, Recent advancement in biogas enrichment and its applications, Renewable and Sustainable Energy Reviews, 73, 892-903.

T.J. Kotas, 2012, The Exergy Method of Thermal Plant Analysis, Exergon Publishing Company, London, UK.

L. Jürgensen, E.A. Ehimen, J. Born, J.B. Holm-Nielsen, 2015, Dynamic biogas upgrading based on the Sabatier process: Thermodynamic and dynamic process simulation, Bioresource Technology, 178, 323-329.

REN21, 2019, Renewables 2019 Global Status Report, Renewables Energy Policy Network for 21st Century, accessed 14.11.2019.

S. Walspurger, G.D. Elzinga, J.W. Dijkstra, M. Sarić, W.G. Haije, 2014, Sorption enhanced methanation for substitute natural gas production: Experimental results and thermodynamic considerations, Chemical Engineering Journal, 242, 379-386.

L. Wang, M. Pérez-Fortes, H. Madi, S. Diethelm, J.V. Herle, F. Maréchal, 2018, Optimal design of solid-oxide electrolyzer based power-to-methane systems: A comprehensive comparison between steam electrolysis and co-electrolysis, Applied Energy, 211, 1060-1079.

J. Witte, J. Settino, S.M.A. Biollaz, T.J. Schildhauer, 2018, Direct catalytic methanation of biogas – Part I: New insights into biomethane production using rate-based modelling and detailed process analysis, Energy Conversion and Management, 171, 750-768.

Sauro Pierucci, Flavio Manenti, Giulia Bozzano, Davide Manca (Eds.)
Proceedings of the 30th European Symposium on Computer Aided Process Engineering (ESCAPE30), May 24-27, 2020, Milano, Italy.
http://dx.doi.org/10.1016/B978-0-12-823377-1.50063-X

Optimisation of Energy Consumption in a Medium-scale Reverse Osmosis Brackish Water Desalination Plant

Alanood A. Alsarayreh [a], M. A. Al-Obaidi [b], A. M. Al-Hroub [c], R. Patel [a], I. M. Mujtaba [a]

[a] *Department of Chemical of Engineering, Faculty of Engineering and Informatics. University of Bradford.Bradford, West Yorkshire, BD7 1DP, UK*
[b] *Middle Technical University, Technical Institute of Baquba, Dayala – Iraq*
[c] *Senior Chemical Engineer, Energy and Water Directorate, Arab Potash Company, Jordan*
I.M.Mujtaba@bradford.ac.uk

Abstract

The Reverse Osmosis (RO) process has been universally employed for the production of potable water from brackish water resources. However, the RO process still operates at an elevated level of an energy consumption, in kWh per m^3 of product water, due to the use of high-pressure pumps. In this study, an earlier steady-state operation model developed by the same authors for a medium-scale RO brackish water desalination system of Arab Potash Company (APC) (Jordan) is embedded within an optimisation framework. Typically, the optimisation problem is expressed as a Nonlinear Programming problem to attain the lowest specific energy consumption (objective function), as well as optimising the decision variables of operating flow rate and pressure for a given feed concentration and temperature. Moreover, the optimisation problem has been associated with upper and lower limits of decision variables as characterised by the membrane manufacturer. Also, to quantify the high-standards of filtration process, feasible constraints of the pressure loss along the x-axis of membrane length and upper and lower bound of feed flow rate of each membrane are considered. Interestingly, detailed optimisation results have conceived the optimal operating conditions that have the potential to gain net energy saving of RO system by 35%, whilst fulfilling the need for producing high-quality water. This research has economically upgraded the RO system of APC with a substantial improvement of process performance.

Keywords: Brackish water desalination; Arab Potash Company; Reverse Osmosis process; Optimisation; Energy consumption.

1. Introduction

Fresh water is becoming rare in some regions of the world that associated with progressive people worldwide demands due to increase of population growth and change of their lifestyle. Therefore, several desalination processes were invented. In this regard, the desalination of brackish water offers a feasible solution to tackle the water shortage.

Membrane technology has been used very effectively to produce fresh water from different resources of water (Tsiourtis, 2001). Specifically, RO process is a pressure-

driven process and considered as one of the commercially attractive membrane technology available for desalting brackish and seawater (Peñate and García-Rodríguez, 2012). The RO membrane has the ability to differentiate and selectively separate salts and water based on the operating conditions such as feed salinity, applied pressure, flow rate and temperature (Tsiourtis 2001). Simple design of RO process and high quality of water produced are the main reasons why it is widely accepted throughout the world compared to, for example, thermal desalination processes. However, the RO process consumes a considerable amount of energy that needs to be reduced considerably. Therefore, several studies have been carried out to minimise the specific energy consumption or the production cost, which in turn make this process more affordable. In this regard, the optimisation of the RO system has been successfully used to mitigate the energy consumption. For this, the RO process market has seen a steady increase due to a primitive advancement in RO operation that is associated with a lower energy consumption and reduced fresh water production cost (Shenvi et al., 2015). Some comments on the most successful research are reported below.

Zhu et al. (2008) minimised the energy consumption of RO membrane process via constraining the thermodynamic cross flow and feed or permeate flow rate. Results showed that lowering of osmotic pressure would limit the energy consumption The optimisation of energy consumption of two-pass RO seawater desalination unit and a single pass membrane desalination unit, by considering the goal of product recovery and salt rejection, was investigated by Zhu et al. (2009). This in turn affirmed the optimal operational conditions to lowering the energy consumption. Their studies showed that the two-pass process performs better than the single-pass RO one. Bartman et al. (2010) used an energy optimisation methodology of multiple RO system variables to estimate the optimal operating conditions that minimise the specific energy consumption. The results showed that increasing water recovery would lower the energy consumption with reduced salt rejection. Li (2010) implemented a constrained nonlinear optimisation to minimise the total energy consumption of single-stage, two-stage, and single-stage RO modules with an energy recovery device (ERD). The results showed that the two-stage module is better than one stage based on specific energy consumption and water recovery. To the best of the authors' knowledge, the lowering of the total energy consumption of RO system of APC via optimisation cannot be found in the open literature. Therefore, the current research attempts to optimise the decision variables of feed pressure and flow rate for a considered feed concentration 1098.62 ppm and temperature 25 °C to explore the lowest energy consumption.

2. Plant description and feed characteristics

Figure 1 shows the layout of BWRO (Brackish Water Reverse Osmosis) for the APC plant (with capacity 1200 m^3/day and conductivity 1983.06 µs/cm). It consists of two passes with permeate and retentate reprocessing designs. The 1st pass comprises two stages with pressure vessels design (4:2). However, the 2nd pass holds two stages with pressure vessel design (2:1:1) as a sequence. The permeate of 1st pass is fed to the 2nd pass for further processing. The high-concentration stream of the 1st pass is sent to drain. However, the low-concentration streams of the 2nd pass are collected to constitute the high-quality water (salinity 2 ppm). The high-concentration stream of 2nd pass is reprocessed back to the raw feed water of the 1st pass. The feed characteristics of RO plant are 1098.62 ppm, 74 m^3/h, 25 °C, and 9.22 atm of feed water salinity, flow rate, temperature, and pressure, respectively. Table 1 gives the specification of RO module.

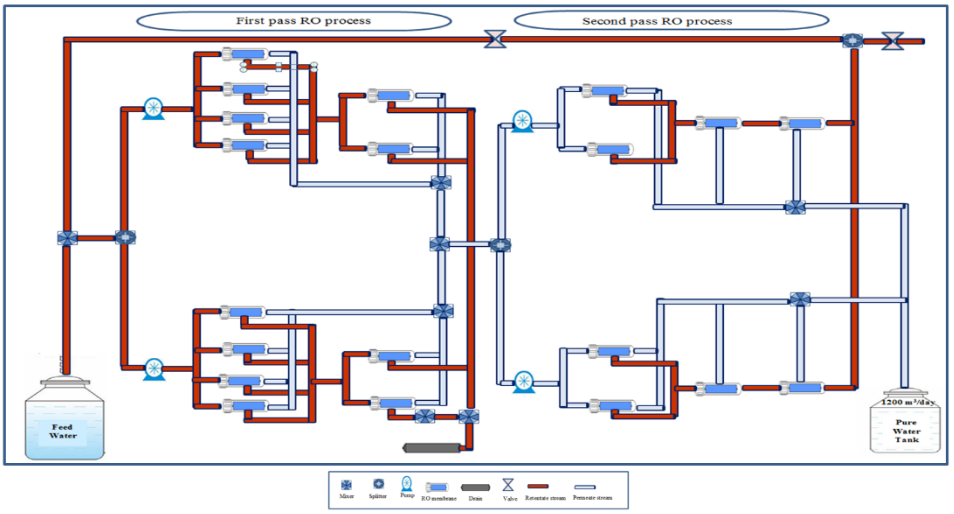

Figure1. Layout of BWRO desalination plant of APC (Adapted from Al-Obaidi et al., 2018)

Table 1. Specifications of Ro module of APC plant.

Parameter	Value
Membrane provider, brand and configuration	Toray Membrane USA Inc, TMG20D-400, spiral wound
Membrane area A (m²)	37.2
Water permeability constant (A_w)(m/atm s) at 25 °C	9.6203×10^{-7}
Salt permeability constant (B_s) (m/s) at 25 °C	1.61277×10^{-7}
Pump efficiency (η)	85%
Max. operating pressure (atm)	40.464
Max. operating temperature (°C)	45
Salt rejection (%)	99.5
Max. and Min. feed flow rate (m³/s)	0.001-0.005

3. Modelling of RO system of APC

Al-Obaidi et al. (2018) established a steady-state operation model for a medium-scale BWRO desalination system of APC. The detailed model was validated against actual data collected from the APC and then used to study the plant performance with operating conditions variation. However, this model is modified by including energy consumption correlations as shown in Table A.1 of Appendix. A.

4. Simulation of RO system of APC plant

The simulation of the specified RO plant is achieved under the base operating conditions and using the gPROMS suites. The performance indicators results are given in Table 2.

5. Optimisation of the RO system of APC plant

5.1 Problem construction

The main goal of this section is to optimise the RO system of APC, i.e., to target the objective function of minimising the specific energy consumption by forecasting the best-operating conditions (optimal values) of the process which include feed flow rate and feed operating pressure at fixed temperature and concentration. Therefore, the model of RO system is incorporated in a single optimization framework as a Non-Linear Programming (NLP) Problem with consideration of varying operating conditions within upper and lower limits which recommended by the module's manufacturer. The fixed feed water characteristics of 988.93 ppm and 25 °C of feed water salinity and temperature respectively, are considered.

5.2 Mathematical optimisation problem

Given: Feed water conditions, RO module specifications.
Optimise: The optimisation variables of feed pressure, and flow rate.
Minimise: The total energy consumption of RO system.
Subject to: Equality and inequality constraints of process model and limits of optimisation variables, respectively.
Hence, the optimisation problem is mathematically fashioned as;

$$\underset{Q_{f(plant)}, P_{p(plant)},}{\text{Min}} \quad E_{consumption}$$

Subject to: Equality constraints: RO process model
Inequality constraints:

a) lower and upper limits of feed flow rate of RO system

$$(29.04\ \text{m}^3/\text{h}) \quad {Q_{f(plant)}}^{L} \leq Q_{f(plant)} \leq {Q_{f(plant)}}^{U} \ (154.48\ \text{m}^3/\text{h})$$

$$(5\ \text{atm}) \quad {P_{f(plant)}}^{L} \leq P_{f(plant)} \leq {P_{f(plant)}}^{U} \ (20\ \text{atm})$$

b) lower and upper limits of feed flow rate of each membrane module

$$(3.63\ \text{m}^3/\text{h}) \quad {Q_{f(membrane)}}^{L} \leq Q_{f(membrane)} \leq {Q_{f(membrane)}}^{U} \ (19.31\ \text{m}^3/\text{h})$$

5.3 Optimisation results

Table 2 displays the simulation values as the base case (not optimised) of the RO process at given feed operating (salinity and temperature). Also, the optimisation results including the performance indicators are presented in Table 2. The ratio of energy-saving of RO system is accounted by subtraction of simulated and optimised values. It can be clearly seen that the optimisation framework has entailed a gain of energy saving of 35% based on the optimum feed flow rate of 0.0171 m³/s and pressure of 7.5743 atm. Moreover, there is a considerable enhancement of water recovery (12.8 %), which contributes to improving the produced water concentration by 15.6 %. Furthermore, the produced water flow rate is enhanced by 130 % whilst at the same time reducing the retentate flow rate by 50%.

Table 2. Simulation and optimisation results at base case operating conditions (988.93 ppm and 25 °C).

Feed conditions			Optimised feed conditions	
Parameter	Value	Unit	Parameter	Value
Plant feed pressure	9.2202	atm	Optimal operating pressure	7.5743
Plant feed flow rate	0.0235	m^3/s	Optimal feed flow rate	0.0171
Feed operating salinity	988.93	ppm	Feed operating salinity	988.93
Feed operating temperature	25	°C	Feed operating temperature	25
Simulation results			Optimised results	
Plant water recovery	57.205	%	Plant water recovery	64.545
Plant salt rejection	99.797	%	Plant salt rejection	99.922
Produced water flow rate	0.0135	m^3/s	Produced water flow rate	0.03105
Produced water concentration	2.0052	ppm	Produced water concentration	1.7345
Retentate flow rate	0.0032	m^3/s	Retentate flow rate	0.0016
Specific energy consumption	0.9977	kWh/m^3	Specific energy consumption	0.6478
Energy-saving = 35%				

6 Conclusions

In this research, a single optimisation framework was developed to mitigate the total energy consumption of a medium-scale RO brackish water desalination system of APC. This is basically carried out within allowed operational limits of the operating conditions to maintain a safe process. In general, the manipulation of control variables via optimization has a positive influence on reducing the energy consumption by 35% when compared with the original simulation value of consumed energy. Also, the product water salinity has been enhanced by 15.6% to fulfill the requirements of high-quality water.

References

Al-Obaidi M.A., Alsarayreh A.A., Al-Hroub A.M., Alsadaie S., Mujtaba I.M., 2018. Performance analysis of a medium-sized industrial reverse osmosis brackish water desalination plant. Desalination, 443, 272-284.

Bartman A.R., Zhu A., Christofides P.D., Cohen Y., 2010. Minimizing energy consumption in reverse osmosis membrane desalination using optimization-based control. Journal of Process Control, 20 (10), 1261-1269.

Li M., 2010. Minimization of energy in reverse osmosis water desalination using constrained nonlinear optimization. Industrial & Engineering Chemistry Research, 49(4), 1822-1831.

Peñate B., García-Rodríguez L., 2012. Current trends and future prospects in the design of seawater reverse osmosis desalination technology. Desalination, 284, 1-8.

Shenvi S.S., Isloor A.M., Ismail A.F., 2015. A review on RO membrane technology: Developments and challenges. Desalination, 368, 10-26.

Tsiourtis N.X., 2001. Desalination and the environment. Desalination, 141(3), 223-236.

Zhu A., Christofides P.D., Cohen Y., 2008. Effect of thermodynamic restriction on energy cost optimization of RO membrane water desalination. Industrial and Engineering Chemistry Research, 48(13), 6010-6021.

Zhu A., Christofides P.D., Cohen, Y., 2009. Minimization of energy consumption for a two-pass membrane desalination: effect of energy recovery, membrane rejection and retentate recycling. Journal of Membrane Science, 339(1-2), 126-137.

APPENDIX A

Table. A.1. Mathematical model of RO system of APC

No.	Model equation	Specifications
1	$Q_p = A_{w(T)}\, NDP_{fb}\, A_m$	Total water flux (m³/s)
2	$A_{w(T)} = A_{w(25\,C)}\, TCF_p\, F_f$	Water permeability constant at 25 °C (m/s atm)
3	$TCF_p = \exp[0.0343\,(T-25)] \quad < 25\,°C$ $TCF_p = \exp[0.0307\,(T-25)] \quad > 25\,°C$	Temperature correction factor of permeate
4	$NDP_{fb} = P_{fb} - P_p - \pi_b + \pi_p$	The driving pressure (atm)
5	$P_{fb} = P_f - \frac{\Delta P_{drop,E}}{2}$	The feed brine pressure (atm)
6	$\Delta P_{drop,E} = \frac{9.8692x10^{-6}\, A^*\rho_b\, {U_b}^2\, L}{2d_h\, Re_b^n}$	The pressure drop along the membrane element (atm)
7	$\pi_b = 0.7994\, C_b\,[1+0.003\,(T-25)]$ $\pi_p = 0.7994\, C_p\,[1+0.003\,(T-25)]$	The bulk and permeate osmotic pressure (atm)
8	$C_b = \frac{C_f + C_r}{2}$	The bulk salinity (kg/m³)
9	$Q_s = B_{s(T)}(C_w - C_p)$	The solute flux through the membrane (kg/m² s)
10	$B_{s(T)} = B_{s(25\,C)}\, TCF_s$	The solute transport parameter at operating temperature (m/s)
11	$C_w = C_p + \left(\frac{C_f + C_r}{2} - C_p\right) exp\left(\frac{Q_p/A_m}{k}\right)$	The concentration at the membrane surface (kg/m³)
12	$k = 0.664\, k_{dc}\, Re_b^{0.5}\, Sc^{0.33}\, \left(\frac{D_b}{d_h}\right)\left(\frac{2d_h}{L_f}\right)^{0.5}$	Mass transfer coefficient (dimensionless)
13	$Sc = \frac{\mu_b}{\rho_b D_b}$	Schmidt number (dimensionless)
14	$\mathrm{Re} = \frac{\rho\, d_e J_w}{\mu}$	Reynolds number (dimensionless)
15	$Rec = \frac{Q_p}{Q_f} = \frac{(C_r - C_f)}{(C_r - C_p)}$	Total recovery (dimensionless)
16	$Rej = \frac{C_f - C_p}{C_f}$	Observed rejection (dimensionless)
17	$J_w = \frac{B_{s(T)}\, Rej_{real}}{(1-Rej)}$	The water flux (m/s)
18	$C_p = \frac{C_f}{Rec}\,[1-(1-Rec)]^{(1-Rej)}$	The average permeate salinity at the permeate channel (kg/m³)
19	$C_r = C_f\,[1-Rec]^{-Rej}$	The average retentate salinity at the permeate channel (kg/m³)
20	$E1 = \frac{Pf(in)_{(plant)}*101325*Qf_{(Raw\ water)}}{\frac{Qp_{(plant)}*\varepsilon\, punp}{36x10^5}} + \frac{Pf_{(Block\,3)}*101325*Qf_{(Block\,3)}}{\frac{Qp_{(plant)}*\varepsilon\, punp}{36x10^5}}$	The total plant energy consumption (kWh/m³)

Sauro Pierucci, Flavio Manenti, Giulia Bozzano, Davide Manca (Eds.)
Proceedings of the 30th European Symposium on Computer Aided Process Engineering (ESCAPE30), May 24-27, 2020, Milano, Italy.
http://dx.doi.org/10.1016/B978-0-12-823377-1.50064-1

Minimisation of Energy Consumption via Optimisation of a Simple Hybrid System of Multi Effect Distillation and Permeate Reprocessing Reverse Osmosis Processes for Seawater Desalination

O. M. A. Al-hotmani [a], M. A. Al-Obaidi [b], Y. M. John [a], R. Patel [a], F. Manenti [c], I. M. Mujtaba [a],*

[a] *Department of Chemical Engineering, Faculty of Engineering and Informatics. University of Bradford. Bradford, West Yorkshire BD7 1DP, UK*
[b] *Middle Technical University, Technical Institute of Baquba, Baquba, Dayala - Iraq*
[c] *Chemical Engineering Department, Politecnico di Milano, Milan, Italy*
I.M.Mujtaba@bradford.ac.uk

Abstract

Multi Effect Distillation (MED) and Reverse Osmosis (RO) processes have been expansively explored for fresh water production from seawater resources. Interestingly, the performance indicators including energy consumption of different proposed arrangements of hybrid system of MED and RO processes have been analysed in a previous study by the same authors. This in turn has explored the feasibility of a simple design of permeate reprocessing RO process and MED process of hybrid system that corresponding the lowest energy consumption compared to other experienced arrangements of hybrid system. However, this design still operated at a significantly high level of energy utilisation measured in kWh per m^3 of produced water. In this research, the lowest possible energy consumption of the chosen hybrid system is investigated via the embedment of an optimisation framework in the same author's previous operation model for the same design. Occasionally, the optimisation problem is framed as a Nonlinear Programming problem to locate the optimal control variables of the associated RO process within their upper and lower limits to achieve the main objective function. This in turn has resulted in mitigating the total energy utilisation of the hybrid system with satisfying a constraint of high-quality produced water.

Keywords: Seawater desalination, Multi Effect Distillation + Reverse Osmosis hybrid system, Permeate processing design of RO, Optimisation, Energy Consumption.

1. Introduction

Due to a continuous growth for water demand in warm areas, seawater desalination technologies have seen a surge in popularity.in providing potable water. In this regard, the MED and RO systems have been nominated as the favorable thermal and membrane processes respectively, due to their stability, high quality and product capacity. Specifically, MED process can produce salt free water from very poor seawater. Moreover, RO process has been utilised for different kinds of water including seawater, brackish water and wastewater with strong potential. Therefore, the integration of MED with a variety of industrial processes such as concentrated solar power cogeneration

scheme and RO process has been investigated by some new studies (Cipollina et al., 2017; Filippini et al., 2018). Recently, Filippini et al. (2018) compared the performance of several designs of hybrid system of MED + retentate reprocessing design of RO process via a detailed model developed by the same authors. The performance or effectiveness of the hybrid system was assessed and quietly generated an improved performance compared to individual processes of multi effect distillation - thermal vacuum compressor (MED_TVC) and RO. This is followed by a novel design of a simple hybrid system of permeate reprocessing RO process integrated with MED_TVC process suggested by Al-hotmani et al. (2019). The performance metrics of this design have been compared against other proposed designs of hybrid systems of MED process and retentate reprocessing RO process of Filippini et al. (2018). This in turn has affirmed the suitability of the simple hybrid MED_TVC+ permeate reprocessing design of RO process as a superior layout. Specifically, it is concluded that this layout has attained the lowest energy consumption measured in kWh per m^3 of fresh water when compared to other configurations of hybrid systems. de Boer (2014) confirmed that both the RO and MED processes are the most energy demanding filtration processes because of the use of high-pressure pump and steam generator, respectively. However, it is believed that there is still scope to reduce the total consumption energy of the chosen hybrid design of MED_TVC and permeate reprocessing RO process proposed by Al-hotmani et al. (2019). Therefore, this work intends to solve the problem using the model developed by the same authors for this layout with an optimisation framework. This is specifically targeted at the lowest energy consumption (objective function) at an optimum control variables of the related RO process. Moreover, the optimisation has respected the upper and lower limits of the control variables with training a practical constraint of high-quality produced water.

2. Description of the simple hybrid system and feed characteristics

Figure 1 shows the projected design of a permeate reprocessing RO process integrated with MED_TVC process in a simple hybrid system. The MED system usually contains TVC section as an external steam provider, which in turn give advantages of upgrading the total energy of MED system. In this respect, the feed water is split into two parts to simultaneously feed the RO process and MED process (simple layout). The design of the RO process comprises a high pressure pump and three blocks of twenty, fifteen, and eight pressure vessels joined in parallel with 8 spiral wound modules, made by Toray, and connected in series. Of high importance is the flow rate of feed for all blocks and each module which is restricted to the acceptable limits of feed flow rate specified by the manufacturer. The high-concentration stream of the 1st block is directed to the 2nd block for advanced filtration. However, the 3rd block is used to further polish off the joined permeate streams of 1st and 2nd blocks. In this regard, the 3rd block operates at approximately similar operating pressure of the 1st block using an ERD system of 80% efficiency. This in turn would upgrade the quality of low-salinity water produced from 3rd block. Occasionally, the existence of ERD in the RO system would decrease the total energy consumption compared to RO systems without ERD. The features of produced water including its salinity and quantity are characterised by the combination of product streams of RO process and MED process. Moreover, the retentates of both MED and RO systems are blended to form the main disposed stream. The RO membrane measurements and its lower and upper constraints, water and solute transport

coefficients, and the allowed control variables are given in Table 1. Also, the design parameters of Multi Effect Distillation process are presented in Table 1.

Table 1. Design and technical parameters of RO and MED_TVC processes with the operating conditions

	Parameter	Unit	Value
RO Process	Membrane supplier and brand	(-)	Toray membrane, TM820M-400/ SWRO
	Module configuration	(-)	Spiral wound
	Maximum pressure	(atm)	81.91
	Maximum and minimum feed flow rate	(m^3/s)	0.00536 – 0.001
	Maximum temperature	(°C)	45
	Membrane area (A_m)	(m^2)	37.2
	A_w and B_s NaCl at 25 °C	(m/s atm) and (m/s)	3.1591×10^{-7} and 1.74934×10^{-8}
	η_{pump}, $\eta_{Booster\ pump}$ and η_{ERD}	(-)	85%, 85% and 80%
MED Process	Number of stages	(-)	10
	External steam temperature / flow rate / pressure	(°C / kg/s / kPa)	70 / 8 / 1300
	Brine temperature / salinity	(°C / ppm)	40 / 6000

Operating conditions		
Parameter	Unit	Value
Feed pressure of RO process	(atm)	50
Feed flow rate of RO process	(m^3/s)	0.058
Seawater salinity	(ppm)	39000
Seawater temperature	(°C)	25

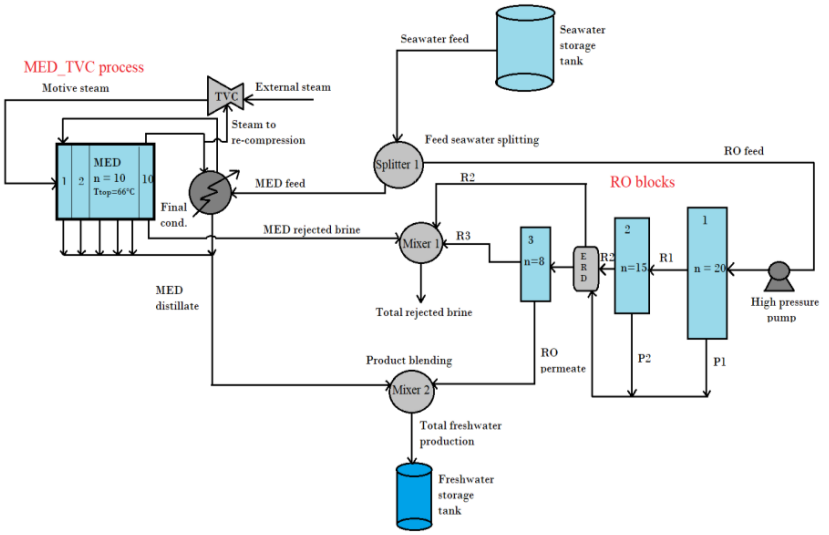

Figure 1. Simple hybrid MED_TVC and permeate reprocessing RO processes (Al-hotmani et al., 2019)

3. Modelling of the hybrid system

Al-hotmani et al. (2019) modified the model developed by Filippini et al. (2018) by incorporating a detailed set of model equations to investigate the performance indicators of permeate reprocessing RO process of the hybrid MED_TVC+RO processes.

The detailed model is included in Table 3 (APPENDIX A). The nonlinear algebraic equations of the hybrid model of MED_TVC+RO processes are tabulated in a compact form $f(x, u, v) = 0$.

4. Simulation of the hybrid system

Al-hotmani et al. (2019) simulated the hybrid system shown in Fig. 1 under the control variables of both processes (shown in Table 1). This in turn has obtained the performance results as shown in Table 2.

5. Optimisation of the hybrid system

This section aims to optimise the hybrid system shown in Fig. 1 in such a way as to minimise the total energy consumption (objective function) measured in kWh per m³ of the produced water by predicting the best control variables of the RO process. Therefore, the model established by Al-hotmani et al. (2019) is embedded in a single optimisation framework as a Non-Linear Programming (NLP) Problem using the gPROMS suites to allow the operating conditions to vary within the upper and lower limits constrained by the manufacturer as reported in Table 1 and one constraint of fresh water concentration less than 100 ppm. The seawater characteristics including salinity and temperature have been taken same as what has been considered by Al-hotmani et al. (2019) of 39000 ppm and 25 °C, respectively.

a) Single objective optimisation problem

Given: Seawater feed conditions, MED_TVC design specifications, RO design specifications (Table 1).

Optimisation variables:

Operating conditions of RO process (pressure, feed flow rate, and temperature)

Minimise: Total energy consumption of the hybrid system of MED+RO processes

Subject to:

Equality (MED_TVC + RO hybrid system model of Al-hotmani et al., 2019)

Inequality constraints (linear limits of optimisation variables)

Therefore, the mathematical description of the optimisation problem is formulated as;

$$\underset{F_b, P_b, T_b}{Min} \quad E_{consumption}$$

Subject to: Equality constraints: Hybrid system model: $f(x, u, v) = 0$

Inequality constraints of Block 1 of the RO process:

(0.02 m³/s) $F_b{}^L \leq F_b \leq F_b{}^U$ (0.1072 m³/s); (40 atm) $P_b{}^L \leq P_b \leq P_b{}^U$ (81.91 atm);

(20 ºC) $T_b^L \leq T_b \leq T_b^U$ (45 ºC)

Inequality constraints of each single membrane in the RO process:

(0.001 m³/s) $F_{b(membrane)}{}^L \leq F_{b(membrane)} \leq F_{b(membrane)}{}^U$ (0.00536 m³/s);

(40 atm) $P_b(membrane)^L \leq P_{b(membrane)} \leq P_{b(membrane)}{}^U$ (81.91atm);

(20 ºC) $T_{b(membrane)}^L \leq T_{b(membrane)} \leq T_{b(membrane)}^U$ (45 ºC)

End-point constrain: $C_{p_{Hybrid\ system}} \leq 100$ ppm

U and L are the upper and lower limits of the optimisation variables provided by the manufacturer (Table 1).

b) Optimisation results

Table 2 shows the optimisation results including the total energy consumption of the hybrid system at specified seawater concentration and temperature. In this regard, the simulation results (base case, not optimised) are also presented in Table 2. Both simulation and optimisation are compared to account the ration of energy saving. Interestingly, Table 2 shows a noticeable energy saving of 25.14% as a result of optimising the control variables of the RO process. This is basically associated with optimal values of 81.915 atm, 0.1072 m³/s, and 38.85 °C of pressure, flow rate, and temperature, respectively.

The total flow rate of fresh water of the RO process has been significantly increased from 0.0216 m^3/s to 0.06726 m^3/s (increase around 212%) which expresses an improvement of water flux. This has entirely enhanced the total fresh water flow rate of the hybrid system from base case of 0.08994 m^3/s to 0.1355 m^3/s (increase around 51%), which contributes to the decrease in energy consumption. Interestingly, increasing the feed pressure with its allowed value of the Toray membrane at an elevated temperature showed a positive contribution on the water recovery compared to the base case. Moreover, the salt concentration in the fresh water of the hybrid system has also significantly improved from 10.88 ppm to 6.13 ppm. This is already attributed to a considerable increase happened in the water recovery of the RO process.

Table 2. Simulation and optimisation results of the hybrid system and relevant processes

Parameter					Unit			Simulation results	Optimisation results
Total energy consumption (hybrid system)					(kWh/m^3)			14.296	10.702
Specific energy consumption (RO process)					(kWh/m^3)			2.622	3.301
Specific energy consumption (MED process)					(kWh/m^3)			17.988	17.988
%Water recovery% (RO process)					(-)			37.26	62.744
%Salt rejection (RO process)					(-)			99.965	99.994
Fresh water flow rate (RO process)					(m^3/s)			0.0216	0.06726
Salt concentration of the fresh water (RO process)					(ppm)			13.67	2.20
Fresh water flow rate (hybrid system)					(m^3/s)			0.08994	0.1355
Salt concentration of the fresh water (hybrid system)					(ppm)			10.88	6.13
Optimal values	Flow rate	(m^3/s)	0.1072	Pressure	(atm)	81.915	Temp.	(°C)	38.85
Energy saving = 25.14%									

6. Conclusions

A single objective problem optimisation methodology of the hybrid system of MED+RO processes was developed and introduced a reliable increase in the operating pressure, flow rate and temperature of the RO process compared to the base case of not optimised operating conditions presented by Al-hotmani et al. (2019). This in turn has confirmed the capacity of reducing the total energy consumption of the hybrid system by 25%. The noticed reduction in energy consumption is ascribed to a greater portion of high-quality produced water that meets the demands of generating high quantity of fresh water.

References

Al-hotmani O.M.A., Al-Obaidi M.A., Patel R., Mujtaba I.M., 2019. Performance analysis of a hybrid system of multi effect distillation and permeate reprocessing reverse osmosis processes for seawater desalination. Desalination, 470, 114066.

Cipollina A., Agnello M., Piacentino A., Tamburini A., Ortega B., Palenzuela P., Alarcon D., Micale G., 2017. A dynamic model for MED-TVC transient operation. Desalination, 413, 234–257

de Boer R., 2014. Vital Membrane Processes, in: de Boer, R. (Ed.), From Milk By-Products to Milk Ingredients: Upgrading the Cycle. John Wiley and Sons, Hoboken, 141–167. https://doi.org/10.1002/9781118598634.ch6

Filippini G., Al-Obaidi M.A., Manenti F., Mujtaba I.M., 2018. Performance analysis of hybrid system of multi effect distillation and reverse osmosis for seawater desalination via modeling and simulation. Desalination, 448, 21–35. Y. Brown, Year, Article or Chapter Title, etc.

APPENDIX A

Table 3. Model equation of MED process and RO process (Al-hotmani et.at. 2018)

No	Title / MED process	Unit	Equation
1	Temperature drop among effects first attempt	(°C)	$\Delta T = \frac{T1-Tb}{n-1}$ or $\Delta T = \frac{Ts-Tb}{n}$
2	Mean temperature in the plant	(°C)	$T_{mean} = \frac{T1+Tb}{2}$
3	Mean salinity	(ppm)	$x_{mean} = \frac{xf+xb}{2}$
4	Fraction of flashed distillate	(-)	$\propto = \frac{cp(T_{mean}, x_{mean})\Delta T}{\lambda(T_{mean})}$
5	Fraction of total distillate boiled in each evaporator	(-)	$\beta = \frac{\alpha[xb(1-\alpha)^n - xf]}{(xb-xf)[1-(1-\alpha)^n]}$
6	Heat load in i-th effect	(kJ/s)	$Qi = D_{boiled,i-1}\lambda(Tv_{i-1})$
7	Sensible heat used in first effect	(kJ/kg)	$Q_{sensible} = Mf\int_{t1}^{T1} cp(T1,x1)dT$
8	Feed flowrate	(kJ/s)	$Mf = \frac{Ms\ \lambda(Ts)}{Q_{sensible}+Q_{latent}}$
9	Latent heat in first effect	(kJ/s)	$Q_{latent} = D1\lambda(Tv1)$
10	Rejected brine flowrate	(kg/s)	$Mb = Mf - Md$
11	Feed flow rate	(kg/s)	$Mf = Md\frac{xb-xf}{xb}$
12	Total distillate produced in i-th effect	(kg/s)	$D_i = D_{boiled,i} + D_{flash,i}$
13	Brine rejected in the i-th effect	(kg/s)	$B_i = B_{i-1} - D_i$
14	Mean salinity in the plant	(ppm)	$x_i = \frac{x_{i-1}B_{i-1}}{B_i}$
15	Feed temperature in first effect	(°C)	$t1 = tn + (n-1)\Delta t$
16	Temperature of the vapour phase in i-th effect	(°C)	$Tv = T - BPE(T,x)$
17	Driving force for heat exchange in i-th pre-heater	(°C)	$\Delta t_{\log,i} = \frac{\Delta t}{\log(\frac{Tv_i - t_{i+1}}{Tv_i - t_i})}$
18	Gained Output Ratio	(-)	$GOR = \frac{Md}{Ms}$
19	Specific total area	(m^2 s/kg)	$Atot_s = \frac{Atot}{Md}$
20	Specific seawater intake	(-)	$Mw_s = \frac{Mw}{Md}$
No	Title / RO process	Unit	Equation
1	Material balance	(m^3/s)	$Q_{f(plant)} = Q_{r(plant)} + Q_{p(plant)}$
2	Mass balance	(ppm)	$Q_{f(plant)}\,C_{f(plant)} = Q_{r(plant)}\,C_{r(plant)} + Q_{p(plant)}\,C_{p(plant)}$
3	Retentate concentration	(ppm)	$C_{r(plant)} = \frac{(C_{r(Block\,2)}Q_{r(Block\,2)})+(C_{r(Block\,3)}Q_{r(Block\,3)})}{Q_{r(plant)}}$
4	Water recovery	(-)	$Rec_{(plant)} = \frac{Q_{p(plant)}}{Q_{f(plant)}}\,x100$
5	Solute rejection	(-)	$Rej_{(plant)} = \frac{C_{f(plant)} - C_{p(plant)}}{C_{f(plant)}}\,x100$
6	Energy consumption	(kWh/m^3)	$E_{s,RO} = \left\{\frac{[(P_{f(plant)}\,x101325)\ Q_{f(plant)}]}{\frac{\eta pump\ Q_{p(plant)}}{3600000}}\right\} - \frac{(P_{r(block2)}\,x101325)\,Q_{f(block3)}\,\eta_{ERD}}{\frac{Q_{p(plant)}}{3600000}}$

Sauro Pierucci, Flavio Manenti, Giulia Bozzano, Davide Manca (Eds.)
Proceedings of the 30th European Symposium on Computer Aided Process Engineering (ESCAPE30), May 24-27, 2020, Milano, Italy.
http://dx.doi.org/10.1016/B978-0-12-823377-1.50065-3

Modelling and Performance Evaluation of Humidification-Dehumidification Desalination Plant with Column Packing of Various Textures

Damson Kaunga, Raj Patel, Iqbal Mujtaba*

Department of Chemical Engineering, Faculty of Engineering and Informatics. University of Bradford. Bradford, West Yorkshire BD7 1DP, UK
I.M.Mujtaba@bradford.ac.uk

Abstract

In this study a detailed mechanistic model for the packed column of the humidification-dehumidification (DHD) desalination plant was developed. This model was derived by considering an individual raschig ring with porous wall within a column as control volume then used to establish the relationship of vapor transfer rate to temperature and moisture gradients. gPROMS software was used to simulate the model with second order centered finite difference as discretization method and the results compared with those from literature. It was found that the maximum vapor transfer rate corresponds with coarse-textured media at volumetric moisture content of 0.05 m^3/m^3. While the volumetric moisture content was highly influential to the isothermal vapor diffusivity which had maximum value of 1.17 x 10^{-5} cm^2/s it had negligible influence to the thermal vapor diffusivity that was relatively low at 4.3 x 10^{-8} cm^2/s for the entire range.

Keywords: Desalination, Humidification, Moisture, Diffusivity, Porous.

1. Introduction

Demand for fresh water has been increasing in many parts of the world. This has been caused by various factors including rapid growth of population, industrialization, urbanization and climate change. On the other hand, sea water or underground saline water is abundantly available in most areas where fresh water shortage persists. As demand for fresh water keeps on increasing; desalination of saline water is inevitable. A process of Humidification-Dehumidification (HDH) desalination, using solar energy is viewed by many researchers as a promising technique for small capacity fresh water production plants. The advantages of this technique over others are the ability to operate at low temperature, utilization of solar energy and the use of low level technology to operate the process (Kang, et al., 2015).

Numerous researchers (Zubair, et al., 2018) and (Kang, et al., 2015) have investigated influential factors on improving the performance and efficiency of the HDH systems. Nafey, et al (2004) investigated the effect of system configuration and air-water flow orientation on system productivity. They compared four different systems which were; air heated, water heated, air heated-water heated open loop and air heated-water heated closed loop systems. They found that the air heated-water heated closed loop system as the most effective with the highest productivity. Their findings coincided with those of Yamali & Solmus (2008) who noticed a 15% decrease of system productivity when a double-pass solar air heater for heating the air was not used.

Although considerable research has been devoted to the influential factors on HDH desalination processes, less attention has been paid to the influence of packing materials' texture on rate of evaporation in the humidifier column. Research has shown that porous media of different textures influences differently the evaporation rates (Moroi, et al., 2004) and (Brutin & Starov, 2018). Therefore, the purpose of this study is to develop and simulate a mechanistic model of the HDH desalination system. The refined model is then used to investigate performance of the system, particularly, the influence of packing materials' texture on rate of humidification in the column.

2. Description of model

2.1. Flow configuration

The flow configuration considered in this work is typical of humidifier columns of HDH plants. As shown in Figure 1, a bed of height (L) is formed by packing porous Raschig rings of random orientation in a cylindrical column of diameter (D). Saline water enters the column at the top with the flat velocity profile, flows through the packing of rings and leaves the column at the bottom while the air flows in the opposite direction. Figure 1 also shows an individual ring with internal diameter (d_i), external diameter (d_o) and porosity (e). If the saline water stream is hotter than air, then a simultaneous flow of heat and water vapor (q_v) will occur across the porous wall of the ring with thickness (t). Finally, the flowing heat and water vapor will heat and humidify the dry air passing inside the ring.

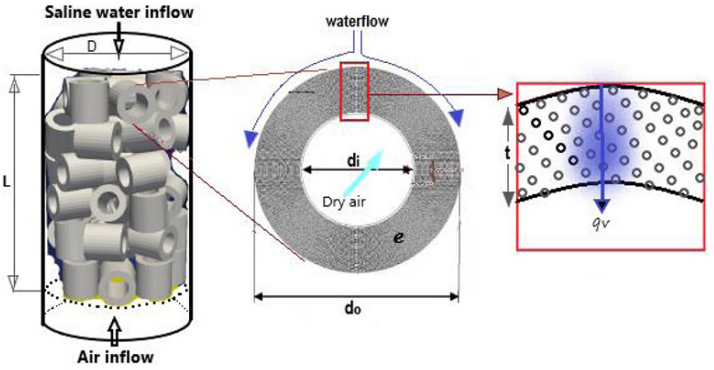

Figure 1: Flow configuration in the humidifiers' column of the HDH plant

2.2. Vapor transfer model

The water vapor diffusion can be described using a modified Fick's law, applied to porous media (Nassar & Horton, 1997) and (Philip & De Vries, 1957)

$$q_v = -D\alpha v \vartheta \nabla \rho \qquad (1)$$

Where q_v is a mass flux of vapor in porous media (kg/m^{2}s), D a molecular diffusivity of water vapor in air (m^2/s), α a tortuosity factor allowing for the extra path length (dimensionless) and v the mass-flow factor introduced to allow for the mass flow of vapor arising from the difference in boundary conditions governing the convective movement of vapor and air components. ϑ is the volumetric air content of the medium (m^3 of air/m^3) and ρ is the density of water vapor (kg/m^3).

Vapor flux is a function of two components which are temperature gradient and moisture gradient. Therefore, equation 1 can be modified to describe water vapor movement due

to both components in unsaturated, non-isothermal porous material. This is achieved by introducing the thermodynamic relationship as suggested by Edlefsen & Anderson (1943)

$$\rho = \rho_0 h = \rho_0 \exp\left({}^{\Psi g}/_{RT}\right) \quad (2)$$

In which ρ_0 is the density of saturated water vapour (kg/m^3), h the relative humidity, g the acceleration due to gravity (m/s^2), R the gas constant of water vapour (J/kg.K) and Ψ the water pressure (m) in thermodynamic equilibrium with water in the medium. This pressure depends on volumetric moisture content θ (m^3/m^3) and temperature T.

From equation 2 the following can be deduced:

$$\nabla\rho = h\nabla\rho_0 + \rho_0\nabla h \quad (3)$$

By differentiating wrt temperature and volumetric moisture content we obtain

$$\frac{\partial\rho}{\partial T} = h\frac{\partial\rho_0}{\partial T} + \rho_0\frac{\partial h}{\partial T} \quad (4)$$

$$\frac{\partial\rho}{\partial\theta} = h\frac{\partial\rho_0}{\partial\theta} + \rho_0\frac{\partial h}{\partial\theta} \quad (5)$$

Since ρ_0 is a function of T only while h is a function of θ only (Philip & De Vries, 1957) then

$${}^{\partial h}/_{\partial T} = 0 \ \ and \ \ {}^{\partial\rho_0}/_{\partial\theta} = 0$$

Equation 3 therefore becomes

$$\nabla\rho = h\frac{d\rho_0}{dT}\nabla T + \rho_0\frac{dh}{d\theta}\nabla\theta \quad (6)$$

Equation 2 can also be used to evaluate ${}^{dh}/_{d\theta}$ in equation 6 to obtain

$$\nabla\rho = h\frac{d\rho_0}{dT}\nabla T + \frac{g\rho}{RT}\frac{d\Psi}{d\theta}\nabla\theta \quad (7)$$

Substituting equation 7 in equation 1 we obtain an equation of the form

$$q_v\frac{p}{\rho_w} = -D_{Tv}\nabla T - D_{\theta v}\nabla\theta \quad (8)$$

whereby, ρ_w is the density of liquid water and p the partial pressure of water vapor

Equation 8 describe vapor transfer under combined moisture and temperature gradients in porous materials. From this equation two coefficients which are thermal vapor diffusivity (D_{Tv}) and isothermal vapor diffusivity ($D_{\theta v}$) are defined as

$$D_{Tv} = D\alpha v\vartheta h\frac{d\rho_0}{dT} \quad (9)$$

$$D_{\theta v} = \frac{D\alpha v\vartheta g\rho}{\rho_w RT}\frac{d\Psi}{d\theta} \quad (10)$$

Using the moisture retention function as proposed by Campbell (1974), the derivative of the Ψ in equation 10 is given as

$$\frac{d\Psi}{d\theta} = \frac{-\lambda\Psi_e}{\theta_s}\left(\frac{\theta}{\theta_s}\right)^{-(\lambda+1)} \quad (11)$$

where θ_s is a saturated volumetric water content; λ and Ψ_e are dimensionless fitting parameters.

The developed model equations were simulated using a general PROcess Modelling System (gPROMs) software for an entire tube length L and Diameter D with the assumptions that, the porous media are rigid, unsaturated and inert materials, the transfer of mass and energy occurs in one-dimension only i.e across porous wall and solute movement doesn't interfere with vapor transfer. During simulation, the discretisation

method used was a second order Centered Finite Difference Method (CFDM). Simulation results are shown in Figures 2 and 3.

Parameter	Value	Unit	Parameter	Value	Unit
D	2.93E-5	m^2/s	p	12350	Pascal
α	0.67		h	0.6	
ν	1		θ_s	0.2	m^3/m^3
ϑ	0.349	m^3/m^3	Ψ_e	-1	m
ρ_w	1000	kg/m^3	λ	0.25	

Table 1**:** Parameters used in simulation

3. Results and discussion

A water vapor transfer rate in porous wall of Raschig ring (packed in humidifier's column) was investigated using mechanistic models developed in this study. Specifically, we have analyzed the influence of volumetric moisture content on both isothermal coefficient of vapor diffusivity and vapor flowrate.

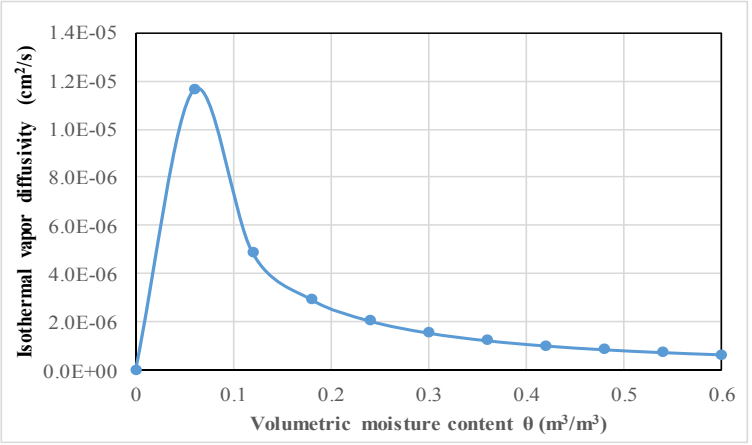

Figure 2: The influence of volumetric moisture content on Isothermal vapor diffusivity

As shown in Figure 2, the isothermal coefficient of vapor diffusivity increases initially with increasing moisture content within a porous media until a peak value (maximum point) was obtained; then a further increase in moisture content resulted into decrease of the vapor diffusivity coefficient. This maximum value occurred at moisture content of 0.05 m^3/m^3. On the other hand, the thermal vapor diffusivity was 4.3 x 10^{-8} cm^2/s and constant for the entire range of moisture content.

This finding is similar to the results demonstrated by Nassar & Horton (1997) and those of Philip & De Vries (1957) who also studied the effect of texture on the point of maximum transfer rate. From their findings it is interesting to note, that, maximum point occurs at low moisture content in coarse-textured media, while in fine-textured media it occurs at relatively high moisture contents.

The influence of moisture content on vapor transfer (resulted by both temperature and moisture gradients) is shown in Figure 3. There is a clear resemblance in trend between Figures 2 and 3 which supports the observation of many other investigators (Hadley & Eisenstadt, 1955), (Srikiatden & Roberts, 2007) and (Baker, et al., 2009) that, moisture transfer under temperature gradients is relatively small in both dry and wet media compared to transfer under moisture gradients. It can also be noted that for non-porous media (such as glass raschig rings), diffusion of vapor across the wall as well as moisture content are absolutely negligible because the pore sizes are extremely small. Under such circumstances the dominant process is convective mass transfer of water vapor at the water-air interface, whereby, the description of such process is beyond the scope of the current study.

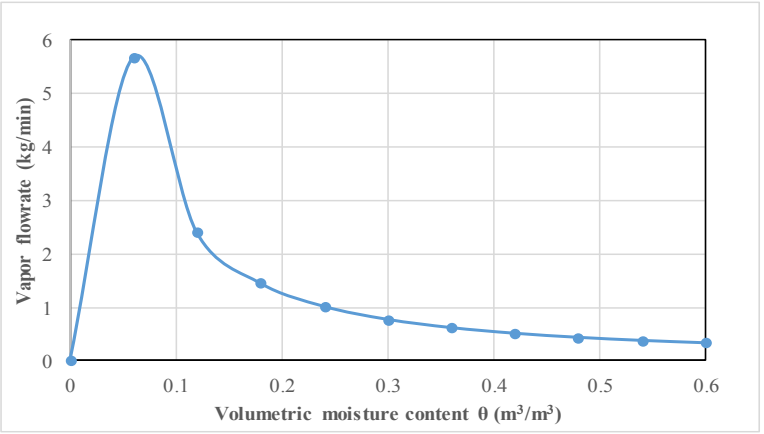

Figure 3: The influence of volumetric moisture content on Vapor flowrate

In general, the findings of this study are of particular importance in improving the performance of the humidification-dehumidification desalination process. Previous studies (Nematollahi, et al., 2013) and (Adel, 2011) has attempted to model this process using black box models, whereby, only relationship of the input and output properties are given without providing analysis of such problems as the heat and mass transfer within the packed column. This study has provided a plausible model and explanation of the classical mechanisms of vapor diffusion within porous packing under the influence of temperature gradient and moisture gradient. On the other hand, these findings can be useful in choosing appropriately the packing of an optimum texture, that could enhance optimum performance of the HDH system by improving the rate of evaporation within its column.

In order to improve the prediction accuracy of the proposed model, future research should address the contribution of convective vapor transfer taking place at the air-water interface on the outer surface of the ring; to the total vapor transfer. Moreover, it has been suggested by Nassar & Horton (1997) that for salt concentrated solution like saline water, there is flow of solute in unsaturated, non-isothermal porous material driven by moisture content, solute concentration and temperature gradients. Future research should therefore focus on investigating at what extend the flow of solute influences the vapor transfers within the media and hence for the entire humidification process within a column.

4. Conclusion

In this study we have developed a simulation model for vapor transfer within a packed column (humidifier) of the HDH system. This model was used to investigate the influence of moisture content on the rate of vapor transfer. In general, it was shown that the driving forces for vapor diffusion within a porous packing of the column are the temperature gradient and moisture gradient and two coefficients of vapor diffusivity were deduced. These were thermal vapor diffusivity and isothermal vapor diffusivity.

The volumetric moisture content was found to be highly influential to the isothermal vapor diffusivity that had maximum value of $1.17 \times 10^{-5} cm^2/s$ as well as to the total vapor flow rate. On the other hand, it had negligible influence to the thermal vapor diffusivity that was relatively low at 4.3×10^{-8} cm^2/s for the entire range. The maximum vapor transfer rate was corresponding with volumetric moisture content of 0.05 m^3/m^3. It is hoped that the findings of this study will enable designers to choose appropriately the packing of an optimum texture that could enhance optimum performance of the HDH system.

References

Adel, A. D., 2011. Pioneer Solar Water Desalination System: Experimental Testing and Numerical Simulation. *Energy Science and Technology,* 1(1), pp. 33-48.

Baker, P., Galbraith, G. & McLean, C., 2009. Temperature gradient effects on moisture transport in porous building materials. *Building Serv. Eng. Res. Technol,* 30(1), p. 37–48.

Brutin, D. & Starov, V., 2018. Recent advances in droplet wetting and evaporation. *Chem Soc Rev,* Volume 47, pp. 558--585.

Campbell, G., 1974. A simple method for determining unsaturated conductivity from moisture retention data. *Soil Science,* 117(6), pp. 311-314.

Edlefsen, N. & Anderson, A., 1943. The thermodynamics of soil moisture. *Hilgardia,* Volume 16, pp. 231-299.

Hadley, W. & Eisenstadt, R., 1955. Thermally actuated moisture migration in granular media. *Trans. Amer. Geophys. Union,* Volume 36, pp. 615-623.

Kang, H. et al., 2015. Performance of a 3-stage regenerative desalination system based on humidification-dehumidification process. *Applied Thermal Engineering,* Volume 90, pp. 182-192.

Moroi, Y., Rusdi, M. & Kubo, I., 2004. Difference in Surface Properties between Insoluble Monolayer and Adsorbed Film from Kinetics of Water Evaporation and BAM Image. *J. Phys. Chem. B,* Volume 108, pp. 6351-6358.

Nafey, A., Fath, H., El-Helaby, S. & Soliman, A., 2004. Solar desalination using humidification dehumidification processes. Part I. A numerical investigation. *Energy Conversion and Management,* Volume 45, p. 1243–1261.

Nassar, I. & Horton, R., 1997. Heat, Water, and Solute Transfer in Unsaturated Porous Media: I – Theory Development and Transport Coefficient Evaluation. *Transport in Porous Media,* Volume 27, p. 17–38.

Nematollahi, F., Rahimi, A. & Gheinani, T., 2013. Experimental and theoretical energy and exergy analysis for a solar desalination system. *Desalination,* 317(317), p. 23–31.

Philip, J. & De Vries, D., 1957. Moisture Movement in Porous Materials under Temperature Gradients. *Transactions, American Geophysical Union,* 38(2), pp. 222-232.

Srikiatden, J. & Roberts, . J., 2007. Moisture Transfer in Solid Food Materials. *International Journal of Food Properties,* Volume 10, p. 739–777.

Yamali, C. & Solmus, I., 2008. A solar desalination system using humidification–dehumidification process: experimental study and comparison with the theoretical results. *Desalination,* Volume 220, p. 538–551.

Zubair, S., Antar, M., Elmutasim, S. & Lawal, D., 2018. Performance evaluation of humidification-dehumidification (HDH) desalination systems with and without heat recovery options: An experimental and theoretical investigation. *Desalination,* p. 161–175.

Sauro Pierucci, Flavio Manenti, Giulia Bozzano, Davide Manca (Eds.)
Proceedings of the 30th European Symposium on Computer Aided Process Engineering (ESCAPE30), May 24-27, 2020, Milano, Italy.
http://dx.doi.org/10.1016/B978-0-12-823377-1.50066-5

Application Domain Discovery of Thermodynamic Models by Mixture of Experts Learning

Omar Péter Hamadi[a], Tamás Varga[a], János Abonyi[a,b]

[a]*Department of Process Engineering, University of Pannonia, Egyetem str. 10, Veszrpém H-8200, Hungary*
[b]*MTA-PE Lendület Complex System Monitoring Research Group, Egyetem str. 10, Veszrpém H-8200, Hungary*
hamadio@fmt.uni-pannon.hu

Abstract

The proper selection of thermodynamic models (TM) is a starting point for an accurate process simulation. It can occur in a process simulation that the proper thermodynamic model changes with the operating conditions. Therefore, the application domains for all appropriate models have to be determined and the models have to be used respectively to the domains. In this work, six TMs are investigated in case of hydrogen solubility in several n-paraffin, olefins and aromatic compounds. In petroleum industry, the most commonly used TMs are the Soave-Redlich-Kwong EOS, and the Peng-Robinson EOS. The Zudkevitch Joffee, Chao Seader and Grayson Streed models are recommended to use in case of high hydrogen content. As the first step to determine the application domains, several measurements were collected from literature, and the solubility of hydrogen was estimated with the abovementioned TMs. Based on the prediction error, a mixture of experts-based expectation maximization (EM) algorithm was used to explore the optimal combination of a set of TMs through the corresponding application domains. As multivariate Gaussian distributions with zero covariance represent the mixture-of experts, the resulted axis-parallel clusters can be easily visualized as a set of univariate normal distributions determining the suggested application regions. The results illustrate that the developed Gaussian mixture model not only significantly improves the prediction performance of the TMs, but the extracted information also supports the systematic development of the models.

Keywords: hydrogen solubility, fluid packages, Gaussian mixture model

1. Introduction

To calculate the hydrogen solubility in different mixtures even in pure components is a challenging mission. However in many processes (e.g. hydrocracking) the concentration of hydrogen in the liquid phase plays a very important role. The solubility of hydrogen is mainly depend on pressure and temperature, therefore with calculating the optimal amount of dissolved hydrogen and the softening operating conditions can help to reduce the operating cost of the process.

One way to calculate the amount of dissolved hydrogen is the application of the appropriate thermodynamic model (TM), but the proper selection of TMs is a recurrent problem in process simulations. According to the *Aspen HYSYS Property Package Selection Assistant*, there are four possible packages to calculate the properties of hydrocarbons in case of non-vacuum conditions, these are: SRK, Peng-Robinson (PR), Chao-Seader (CS), and Grayson-Streed (GS).

The conditions of applicability of the recommended and an extra (Zudkevitch-Joffee (ZJ)) property packages are summarized in Table 1. Three of these models were developed to calculate the properties of systems with high hydrogen content, these are: ZJ (Zudkevitch and Joffe 1970) CS (Chao and Seader 1961) and GS (Torres, de Hemptinne, and Machin 2013).

Table 1 Conditions of applicability of the TMs recommended by *Aspen HYSYS Property Package Selection Assistant*

		CS	GS	PR	SRK	ZJ
T [K]		255 to 533	255 to 698	> 2	> 130	-
p [bar]		<100	<200	<1,000	<350	>10
For all hydrocarbons (except CH_4)		$0.5<T_R<1.3$ $P_{mixture}$ <0.8	$0.5<T_R<1.3$ $P_{mixture}$ <0.8	-	-	-
If CH_4 or H_2 is present:	*-molal average T_r*	< 0.93	< 0.93	-	-	-
	CH_4 mole fraction	<0.3	<0.3	-	-	-
	-mole fraction dissolved gases	<0.2	<0.2	-	-	-
Predicting K values for:	*-Paraffinic or olefinic mixtures, liquid phase aromatic mole fraction:*	< 0.5	< 0.5	-	-	-
	-Aromatic mixtures, liquid phase aromatic mole fraction:	> 0.5	> 0.5	-	-	

According to Table 1, different models are recommended to use based on the operating conditions. However, there are several domains where multiple models are suitable for modeling, and there is no pure measure to compare their goodness based on the "selection guideline". For example, every model is suitable in temperature range between 255 and 533 K and pressure range between 10 and 100 bar.

In addition not all models can be compared to each other, rather a pairwise analysis is possible (CS and GS, PR and SRK have similar characterization). Based on these considerations, one can conclude that the provided framework for the selection of proper TM is not straightforward (at least in case of predicting the hydrogen solubility), despite to the fact, that selecting the appropriate model is the first task for describing successfully the physical properties (Carlson 1996). Moreover, the available decision trees for the selection of TMs lead to several cases, when multiple models can be used (Al-Matar 2015).

The application of the proper model is not the only way to improve the prediction: if there are multiple candidates, one can take the advantage of all models and combine them into a mixture model. There are several techniques to combine multiple models e.g.: simple weighted average of the predictions of individual models or the mixture of experts approach, where the weights are the function of the feature space (Yuksel, Wilson, and Gader 2012).

As we would like to explore the application domains of the TMs, we designed a Gaussian mixture of experts model that combines the TMs, in which the products of univariate Gaussian functions representing the optimal regions of the models. The proposed generative model can be easily visualized with the distribution of the planned applications, so the developed tool highlights how the available sets of TMs should be combined for a given set of applications. According to our knowledge, this is the first work discussing how the trained Gaussian mixture of expert approach can be utilized for the determination of application domains of TMs.

In this work, we compared the aforementioned TMs calculation obtained by Aspen HYSYS to measurement data (634) from literature (Tsuji et al. 2014; Young 1981). The collected measurements consist of data on the solubility of H_2 in paraffins, olefins and aromatic compounds. The results illustrate that the developed Gaussian mixture model gives excellent prediction performance, and the proposed visualization provides interpretable information about how TMs should be applied for specific applications.

2. Gaussian mixture of thermodynamic models

The key idea of the proposed approach is that the distribution of the validation data used to represent the planned prediction tasks is approximated by a Gaussian mixture of the available TMs. In the studied specific problem the N pairs of validation data is represented as $\{(\boldsymbol{x}_k, y_k)\}_{k=1}^{N}$, where y_k is the measured hydrogen solubility and $\boldsymbol{x_k}$ denotes the explanatory variables including molecular descriptors like the carbon number (C_n) and the number of the hydrogen atoms (H_n) and the operating conditions of the experiments (pressure and temperature). The set of the predictions of the available TMs are also represented as paired samples $\left\{\left(\boldsymbol{x}_k, \hat{y}_{k,j}\right)_{j=1}^{n}\right\}_{k=1}^{N}$ where $\hat{y}_{k,j}$ is the k^{th} predicted hydrogen solubility by the j^{th} thermodynamic model, hence the k^{th} prediction error of the j^{th} TM can be calculated as $e_{k,j} = (y_k - \hat{y}_{k,j})^2$. The identification of the model is formulated as a clustering problem in which the prediction error is used to measure the distance of the models and the validation data. The clustering is based on the Expectation Maximization algorithm that minimizes the sum of the weighted squared distances: $J = \sum_{j=1}^{n}\sum_{k=1}^{N}\left(u_{j,k}\right)^m D^2\left(\boldsymbol{x}_k, y_k, \eta_j\right)$, where η_j represents the parameters of the j^{th} cluster including the j^{th} TM. The proposed clustering algorithm can be interpreted in a probabilistic framework, the distance is inversely proportional to the $p\left(\boldsymbol{x}_k, y_k|\eta_j\right)$ probability that the $\boldsymbol{x}_k$ data point belongs to the i^{th} cluster,

$$\frac{1}{D^2\left(\boldsymbol{x}_k, y_k, \eta_j\right)} = \alpha_j \frac{1}{\sqrt{2\pi\sigma_{j,l}^2}} e^{\left(-\frac{e_{k,j}^2}{2\sigma_{j,l}^2}\right)} \frac{1}{\sqrt{2\pi\left|\Sigma_j\right|}} e^{\left(-\frac{1}{2}\cdot(\boldsymbol{x}_i - \boldsymbol{v}_j)^T\cdot\Sigma_j^{-1}(\boldsymbol{x}_i - \boldsymbol{v}_j)\right)} \tag{1}$$

The first α_j term represents the a priori probability of the cluster, while second is the distance between the k^{th} data point and the j^{th} model. The third term defines the distance between the cluster prototype and the data in the feature space of the variables describing the applicability domain of the models represented by the mean and the covariance matrices calculated as:

$$\boldsymbol{v}_j = \frac{\sum_i\left(u_{j,k}\right)^m \boldsymbol{x}_i}{\sum_i\left(u_{j,k}\right)^m}, \Sigma_j = \frac{\sum_i\left(u_{j,k}\right)^m (\boldsymbol{x}_i - \boldsymbol{v}_j)^T(\boldsymbol{x}_i - \boldsymbol{v}_j)}{\sum_i\left(u_{j,k}\right)^m}, \alpha_j = \frac{\sum_i\left(u_{j,k}\right)^m}{N} \tag{2}$$

the $u_{j,k}$ weights are updated in every iteration.

$$u_{j,k} = \frac{1}{\sum_{l=1}^{n}\left(D^2\left(\boldsymbol{x}_k, y_k, \eta_j\right)/D^2\left(\boldsymbol{x}_k, y_k, \eta_l\right)\right)^{2/(m-1)}}, \forall j, k \tag{3}$$

The Alternating Optimization (AO) of these clusters is identical to the Expectation Maximization (EM) (maximum likelihood estimation) identification of the mixture of these Gaussian models when the fuzzy weighting exponent $m = 2$.

3. Application domains of thermodynamic models

To investigate the goodness of the TMs, 634 solubility data from literature was collected. The data set contains of H_2 solubility in paraffinic (458), olefinic (49), and aromatic (127) compounds with carbon range between 1-16, 2-8 ,6-13, temperature range between 90.5-623 K, 123.15-436.15 K , 208.15-621.75 K and pressure range between 7.08-784.5 bar, 20.3-304 bar, and 20.3-507 bar respectively. In Figure 1 every data point is marked according to the smallest prediction error.

In paraffinic compounds all models are required to predict the H_2 solubility, but it can be noted, that different models dominate different, but well specified domains. However, in case of olefinic and aromatic compounds the usage of ZJ model is not recommended at all, and the application domains distributed lightly. There are a few but coupled measurements for olefinic compounds, hence it is hard to make proper conclusions. The only thing is clear that the CS GS and PR are the dominant models and the application domains mainly distributed along the carbon number and the temperature. The PR is the best approach to reproduce the measurements in aromatic compounds, but in case of lower pressure and carbon number mainly the SRK performs better.

The selection of the proper model is really challenging based on Figure 1. To determine well defined application domains, Gaussian mixture model was used. As the TMs are treated like black box models, the application domains are investigated along arbitrary chosen variables. The selection of pressure and temperature as variables is natural, but for identifying different molecule types and size, carbon number (C_n) and the number of the hydrogen atoms (H_n) in the molecules was applied.

The mean square errors for 10-fold cross-validation based training are presented in Figure 2. Despite that the linear mixed model is not suitable to determine the application domains, it is a good benchmark to compare the prediction errors. The Gaussian mixed model has better performance than the individual models, but slightly worse than the linear combination. Based on the mean square errors, the developed mixed model is a reasonable choice to investigate the application domains of the TMs.

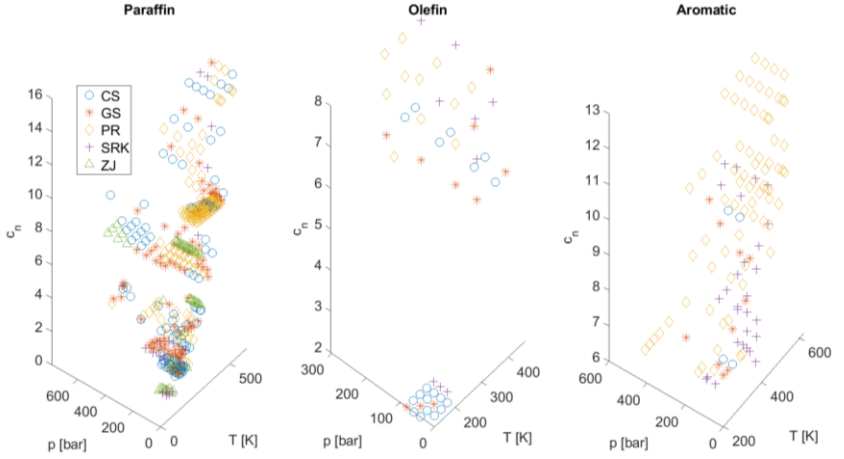

Figure 1 Different markers represents the TMs which obtained with the smallest prediction error at each investigation condition.

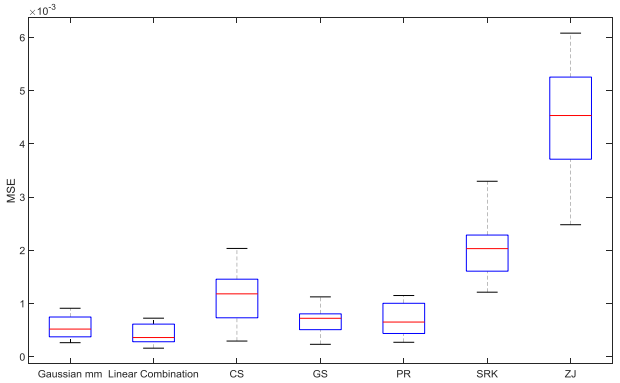

Figure 2 The mean square error of individual TMs and mixture models

In Figure 3 the distribution of the data along the variables is presented as histograms, and the calculated application domains are presented as Gaussian distributions. The multivariate distribution used by the algorithm can be obtained with multiplying the individual distributions. The height of curves represents the "probability of being appropriate" for the TMs at a specified modeling condition, moreover this height is proportion to the weights of the TMs in the mixed model. The conclusions which can be made based on Figure 3 can be divided into two main groups:

1) The ones which are confirm or at least not disprove the fluid package selection guideline:
   - PR has the widest application domain, and dominates most of the domains of investigated variables.
   - ZJ is recommended only in case of light hydrocarbons and extremely low temperature, but as the solubility exists in liquid phase and the light hydrocarbons have low dew point, these statements can be coupled.
   - The performance of CS and GS are nearly the same, but in higher temperatures GS predicts better.
2) The others which are disprove some of the statements of Table 1:
   - From those models which were developed for calculate properties in high H_2 content, only the ZJ dominates a wide range of domain.
   - The CS performs best at extremely high pressure outside the recommended application range, but it can be the result of the lack of data in this domain.
   - The performance of SRK is far worst then the performance of PR.

4. Conclusion

We developed a tool to explore the optimal combination of a set of thermodynamic models for a set of planned applications or validation data but it should be mentioned, that the well distributed the data is in the planned application domain, the better the exploration is. The visualization of the proposed Gaussian mixture of expert model with the distribution of the data along the variables determines the suggested application domains of TMs. The application domains of five TMs were investigated based on the hydrogen solubility in paraffinic, olefinic, and aromatic compounds. The results illustrate that the developed method not only explores how the models should be combined or under which operating conditions should be used. Next to this the resulted model gives significantly better prediction performance than the TMs which can be a good starting point of the kinetic model development of hydrocracking.

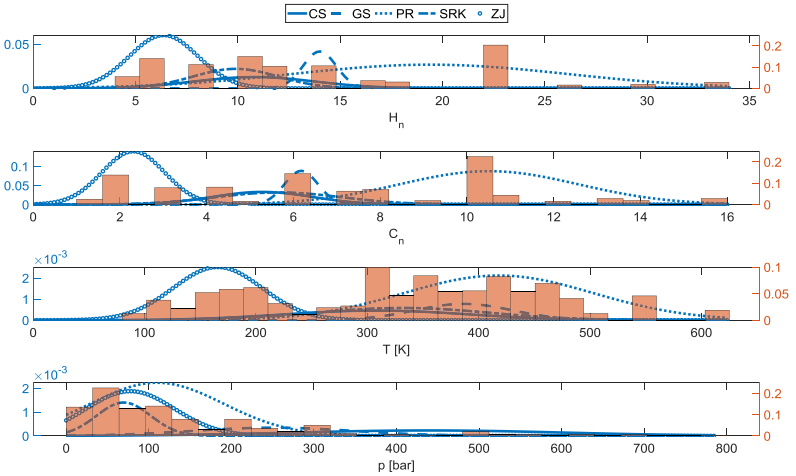

Figure 3 The proposed application domains of TMs and the distribution of the data set along the variables

Acknowledgment

We acknowledge the financial support of Széchenyi 2020 under the GINOP-2.3.2-15-2016-00053. Tamás Varga's contribution to this paper was supported by the Janos Bolyai Research Scholarship of the Hungarian Academy of Sciences.

References

Al-Matar, Ali. 2015. 'Selecting Fluid Packages (Thermodynamic Model) for HYSYS/ Aspen Plus/ ChemCAD Process Simulators'. Unpublished. https://doi.org/10.13140/RG.2.1.3461.4487.

Carlson, Eric. 1996. 'Don't Gamble with Physical Properties for Simulations'. *Chemical Engineering Progress* 92: 35–46.

Chao, K. C., and J. D. Seader. 1961. 'A General Correlation of Vapor-Liquid Equilibria in Hydrocarbon Mixtures'. *AIChE Journal* 7 (4): 598–605. https://doi.org/10.1002/aic.690070414.

Torres, R., J.-C. de Hemptinne, and I. Machin. 2013. 'Improving the Modeling of Hydrogen Solubility in Heavy Oil Cuts Using an Augmented Grayson Streed (AGS) Approach'. *Oil & Gas Science and Technology – Revue d'IFP Energies Nouvelles* 68 (2): 217–33. https://doi.org/10.2516/ogst/2012061.

Tsuji, Tomoya, Koh-hei Ohya, Taka-aki Hoshina, Toshihiko Hiaki, Koji Maeda, Hidetoshi Kuramochi, and Masahiro Osako. 2014. 'Hydrogen Solubility in Triolein, and Propane Solubility in Oleic Acid for Second Generation BDF Synthesis by Use of Hydrodeoxygenation Reaction'. *Fluid Phase Equilibria* 362 (January): 383–88. https://doi.org/10.1016/j.fluid.2013.11.006.

Young, Colin Leslie, ed. 1981. Hydrogen and Deuterium. 1st ed. Solubility Data Series, v. 5-6. Oxford ; New York: Pergamon Press.

Yuksel, S. E., J. N. Wilson, and P. D. Gader. 2012. 'Twenty Years of Mixture of Experts'. *IEEE Transactions on Neural Networks and Learning Systems* 23 (8): 1177–93. https://doi.org/10.1109/TNNLS.2012.2200299.

Zudkevitch, David, and Joseph Joffe. 1970. 'Correlation and Prediction of Vapor-Liquid Equilibria with the Redlich-Kwong Equation of State'. *AIChE Journal* 16 (1): 112–19. https://doi.org/10.1002/aic.690160122.

Sauro Pierucci, Flavio Manenti, Giulia Bozzano, Davide Manca (Eds.)
Proceedings of the 30th European Symposium on Computer Aided Process Engineering (ESCAPE30), May 24-27, 2020, Milano, Italy.
http://dx.doi.org/10.1016/B978-0-12-823377-1.50067-7

Kinetics Study on Removal of Cadmium from Wastewater

Haya Alyasi, Hamish R. Mackey, Gordon McKay

Division of Sustainable Development, College of Science and Engineering, Hamad Bin Khalifa University, Qatar Foundation, Qatar
gmckay@hbku.edu.qa

Abstract

Cadmium is a toxic heavy metal prevalent in the industry that frequently enters waterways through industrial effluents and stormwater runoff, posing a threat to the environment and human health. Strict water quality guidelines of 5 μg/L exist in the United States and European Union and adsorption provides an ideal treatment technology for reducing cadmium to these levels. This study utilizes nanochitosan, a natural polymer derived from seafood shell waste, as an effective cadmium adsorbent. The kinetics are studied through experimental batch tests and common kinetic models are examined to identify which is the most suitable for predicting the cadmium-nanochitosan adsorption rates by comparing the sum of the square errors and the correlation coefficient. The process is then optimized to minimize the contact time in a two-stage batch absorber system. It has been found that the Elovich kinetic model was the most suitable, followed closely by the pseudo-second-order kinetic model. The Elovich kinetic model is utilized to determine the minimum contact time necessary for a two-stage process at various initial and target cadmium concentrations with different adsorbent masses through optimization. A significant reduction in volume was found with the two-stage batch absorber compared to a one-stage process, which was accentuated when low discharge concentrations such as regulatory limits needed to be met.

Keywords: cadmium removal, contact time minimization, equilibrium and kinetic studies, nanochitosan adsorbent.

1. Introduction

Water contamination is a major concern globally because of its impact on human and environmental health and wellness. The degradation of water quality may be attributed to causes such as industrialization, farming practices, rapid urbanization, and global population growth, among other issues. Cadmium is one of the most troublesome water pollutants due to its widespread use in industry and high toxicity. The binding of cadmium with cystein-metallothionein inside the human liver leads to the development of hepatotoxicity (Jaishankar et al., 2014; Valko et al., 2016). Therefore, efficient methods for its removal are necessary.

Chitosan is a prominent, deacetylated biopolymer of chitin. On the surface, there are –OH and $–NH_2$ functional groups. The existence of these groups allows for many modifications. The usage of chitosan in heavy metal elimination from wastewater is widespread. This research utilizes nanochitosan as an active cadmium adsorbent, an organic polymer produced from seafood shell waste (Pal & Pal, 2017). Nanochitosan is

an effective adsorbent for cadmium removal from water. Based on our isotherm study from our previous work (Alyasi et al., 2020), the uptake capacity of nanochitosan was 219 mg Cd/g, which is higher than most of other adsorbents studied for cadmium removal reported in the literature. This previous study used the optimization of a two stage adsorber based on adsorbent mass distribution using the isotherm data to reduce the quantity of adsorbent required to treat cadmium polluted water. Therefore, the focus of this study is on an alternate space based (time) optimization using adsorption kinetic data to minimize the total treatment time and reactor volume.

Equilibrium study outcomes are described and kinetics are investigated by laboratory batch tests and multiple kinetic designs to determine which is most appropriate for predicting adsorption rates of cadmium through nanochitosan by making comparisons between the sum of the square of the errors and the correlation coefficient. The process design is then optimized in order to reduce the contact time in a staging batch absorber process.

2. Methods and methodology

Nanochitosan was synthesized from chitosan flake purchased from Sigma-Aldrich Ltd. The synthesizing method has been explained previously (Anand et al., 2017). Analar grade cadmium nitrate was provided by Sigma-Aldrich and all solutions were made up using deionized water. A sequence of cadmium solutions with concentrations of 0.50–10.0 mmol/L was used to test equilibrium isotherms. The pH and temperature were maintained at 5.50 ± 0.05 and 22 ± 1 °C, respectively. Next, 0.50 g nanochitosan was mixed with 100 mL of aqueous Cd (II) solution by means of capped 125 mL HDPE flasks with a temperature-controlled water bath shaker at 200 rpm for 24 h. This contact period allows the adsorbent and cadmium solution to reach equilibrium.

The kinetic evaluations for Cd (II) adsorption on nanochitosan were achieved by mixing different masses of a specimen in 1.7 L of Cd (II) solution of different concentrations for 6 hours in a baffled agitated batch absorber. The impeller rate was set at 400 rpm, the temperature was maintained at 22 ± 1 ºC and the pH at 5.50 ± 0.05. The details of the absorber vessel are described in preceding work (Alyasi et al., 2019).

3. Results and discussion

Analysis of the kinetic data showed that the Elovich model is the best-fit kinetic model by means of two statistical error analyses (SSE and R^2) as presented in Table 1.

Table 1: Kinetic parameters for pseudo-first order (PFO), pseudo-second order (PSO) and Elovich kinetic models.

Kinetic Parameters	PFO	Kinetic Parameters	PSO	Kinetic Parameters	Elovich
k_1 (min^{-1})	0.003	k_2 (kg/g·min)	0.016	β (mmol/g.min)	3.618
q_e (mmol/g)	1.554	q_e (mmol/g)	1.472	α (g/mmol)	0.118
R^2	0.961	R^2	0.991	R^2	0.998
SSE	0.655	SSE	0.067	SSE	0. 027

Kinetic data has been utilized to determine the minimum contact time necessary for a two-stage process at various initial and target cadmium concentration (Ho & McKay, 1999). An optimization model has been developed to determine the minimum contact time needed to remove the cadmium from water based on Elovich, "best-fit kinetic model", to assist in the process treatment plant design. A significant reduction in the required adsorption time was found with the optimization process for a multi-stage batch adsorber compared to a one-stage process, which was greatly accentuated when low discharge concentrations such as regulatory limits needed to be met.

As the Elovich model is ideally suited to the kinetic data due to a lower SSE of 0.027 in comparison with two other models, the lowest contact time for a two-stage mechanism has been determined at various initial concentrations of cadmium and adsorbent mass (Ho & McKay, 1999). In order to identify the lowest possible contact time required to remove cadmium from water, a best fit kinetics model based on Elovich has been designed to help with the wastewater treatment procedure design. With the optimized method for a dual-stage batch absorber, the necessary adsorption period was significantly reduced in contrast to a one-stage system. It was significantly highlighted if low levels of discharge, such as controlling limitations, were to be achieved.

For the cadmium adsorption, a combination of the time required in both phases will attain the lowest possible cumulative contact time. The operating time at each phase can be calculated with a mass balance calculation and the kinetic parameter. Generally, the mass balance gives:

$$V(C_{n-1} - C_n) = m(q_n - q_0) \tag{1}$$

where V is the volume, C is the pollutant concentration, m is the mass of adsorbent and q is the adsorbent capacity. Subscript n and $n-1$ refer to the stage and 0 to the initial condition. The Elovich kinetic model can be written as:

$$q_t = \frac{1}{\beta}\ln(\alpha\beta) + \frac{1}{\beta}\ln t \tag{2}$$

where α is the initial rate of sorption and β is the activation energy in the context of chemisorption and the degree of surface coverage.

By combining these two equations, the mass balance equation becomes:

$$C_n = C_{n-1} - \frac{m}{V}\left(\frac{1}{\beta_n}\ln(\alpha_n\beta_n) + \frac{1}{\beta_n}\ln t_n\right) \tag{3}$$

where β and α are expressed as a function of C_o for metal ion removal onto the sorbent as follows:

$$\beta = x_\beta C_0^2 + x_\beta C_0 + x_\beta \quad (4)$$

$$\alpha = x_\alpha C_0^2 + x_\alpha C_0 + x_\alpha \quad (5)$$

In this study, nanochitosan was examined to determine the lowest possible contact times for 90%, 95% and 99% of cadmium removal using a two-stage batch method. For the simulation of contact period, cadmium doses of 1, 1.5 and 3 mmol/L were used for adsorbent mass 1.7 and 3.4 g.

Substituting Equations (5) and (4) into Equation (3) are used to calculate the total contact time for any removal percentage. The optimum contact time for the process can was then determined by setting t_1 and calculating the necessary t_2 to meet the required removal percentage using the solver optimisation function in Microsoft Excel. The final optimum was determined by plotting the time required for stage 1, stage 2 and total time. The results are shown in Figures 1 and 2.

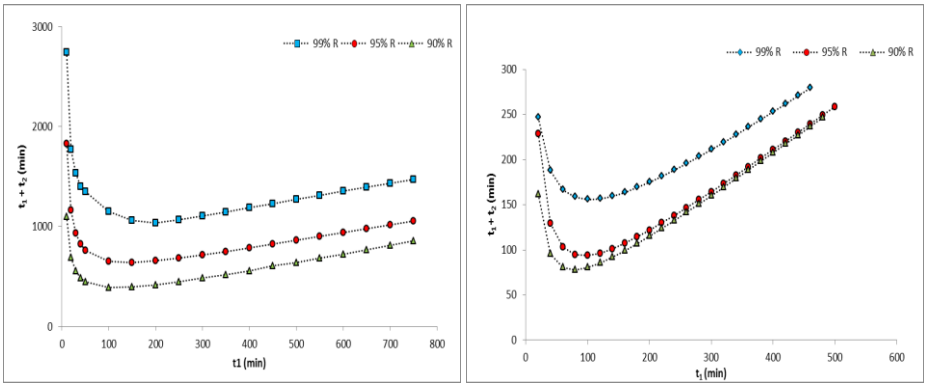

Figure 1: Minimum contact time for various percentage removal at the intial metal ion concentration 3 mmol/L and a) adsorbent mass = 1.7g b) adsorbent mass = 3.4g.

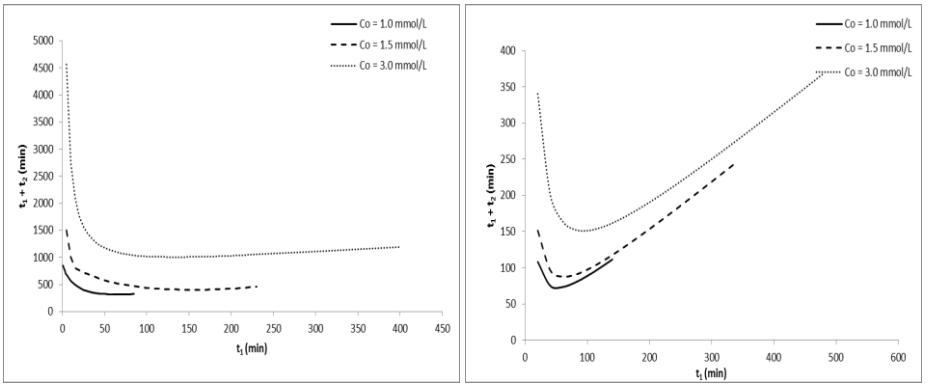

Figure 2:The total time optimisation at different initial concentrations of metal ion at removal 99% and a) adsorbent mass = 1.7g b) adsorbent mass = 3.4g.

Figure 1 shows the minimum contact time for different percentage removal at initial ion concentration 3.0 mmol/L and adsorbent mass 1.7 and 3.4 g. The optimum contact time for different removal percentage is lower for larger amount of adsorbent. For mass adsorbent 3.4 g, the minimum contact time to achieve 90% removal is 80.8 min while the minimum contact time to achieve the same removal percentage for adsorbent mass 1.7 g is 387.0 min. A large mass adsorbent provides more active site for metal ions to attach hence shorter contact time is needed.

The results from Figure 2a show that the contact time for initial concentrations 1.0 and 1.5 mmol/L is lower than initial metal ion concentration 3.0 mmol/L. This is due to the fact that at higher metal ion concentration, the adsorbent active sites are more limited and longer contact time is needed. To overcome the problem, more adsorbent mass can be used to reduce the contact time by providing more sites for the reaction. In Figure 2b, the minimum contact time for 1.0, 1.5 and 3.0 mmol/L were reduced from 312.5, 402.5 and 1031.8 min to 73.3, 90.3 and 151.2 min respectively by increasing the mass of adsorbent from 1.7 to 3.4 g.

Table 2 summarize the results obtained by using two stage batch system to achieve 90, 95 and 99% removal at different metal ion initial concentrations and adsorbent mass = 1.7g.

Table 2: Calculated minimum contact times to achieve 99%, 95% and 90% cadmium removal for different initial concentrations and 1.7g of adsorbent.

C_o (mmol L^{-1})	Minimum contact time (min) one stage absorber	Minimum contact time (min) two stage absorber		
	T	Stage 1 t_1	Stage 2 t_2	T (t_1+t_2)
99% removal				
1	676.3	65.0	247.5	312.5
1.5	1609.5	155.0	247.5	402.5
3	4118.1	200.0	831.8	1031.8
95% removal				
1	520.4	60.0	149.9	209.8
1.5	1193.9	125.0	137.7	262.7
3	2967.5	150.0	490.3	640.3
90% removal				
1	374.3	50.0	86.3	136.3
1.5	821.4	80.0	90.1	170.1
3	1969.2	100.0	287.0	387.0

The results show that the contact time for stage 1 is shorter than contact time for stage 2 due to the higher activation and strong bonding. In stage 1, high initial concentration and availability of active site speed up the reaction. Therefore, a shorter contact time is needed. In stage 2, the initial concentration of metal ion has been reduced from C_0 to C_1 and the active sites available for the ions exchange have been limited. Hence, a longer contact time is needed. Figure 1 and 2 also show that the optimum point is much more defined for larger mass and lower initial concentration.

4. Conclusion

The Elovich kinetic model was observed to be the most effective and accurate kinetic model for cadmium removal using nanochitosan. Therefore, a method for optimizing the contact times required to remove cadmium from wastewater based on an Elovich kinetic model has been designed to help developing a process system in a two-stage batch adsorber system. The optimum time in stage 1 was significantly less than stage 2 and showed a strong optimal point (more sensitive design) for systems operated at larger adsorbent masses and lower pollutant concentrations. The two-stage batch absorber showed a large decrease in volume compared to a one-stage process that has been enhanced when low release levels such as regulatory limits had to be fulfilled.

Acknowledgment

One of the authors (HA) wishes to thank the Qatar National Leadership Program of the Qatar National Research Foundation for a scholarship award.

References

Alyasi, H., Mackey, H.R., Loganathan K., & McKay, G. (2020) Adsorbent minimisation in a two-stage batch adsorber for cadmium removal. *J. Ind. Eng. Chem.* 81, 153-160. doi: 10.1016/j.jiec.2019.09.003.

Alyasi, H., Mackey, H. R., & McKay, G. (2019). Removal of cadmium from waters by adsorption using nanochitosan. *Energy & Environment*, 0958305X19876191. doi: 10.1177/0958305X19876191

Anand, S., Hadi, P., Hui, C.-W., Ansari, T. A., & McKay, G. (2017). Optimisation of the Removal of Arsenate from Water using Nanochitosan. *Des. Water Treat.*, 1-9. doi: 10.5004/dwt.2017.20561

Ho, Y. S., & McKay, G. (1999). Pseudo-second order model for sorption processes. *Process Biochem, 34*, 451-465.

Jaishankar, M., Tseten, T., Anbalagan, N., Mathew, B. B., & Beeregowda, K. N. (2014). Toxicity, mechanism and health effects of some heavy metals. *Interdisciplinary toxicology, 7*(2), 60-72. doi: 10.2478/intox-2014-0009

Pal, P., & Pal, A. (2017). Modifications of Chitosan for Cadmium Removal: A Short Review. *Journal of Polymer Materials, 34*(1), 331-341.

Valko, M., Jomova, K., Rhodes, C. J., Kuča, K., & Musílek, K. (2016). Redox- and non-redox-metal-induced formation of free radicals and their role in human disease. *Archives of Toxicology, 90*(1), 1-37. doi: 10.1007/s00204-015-1579-5

Sauro Pierucci, Flavio Manenti, Giulia Bozzano, Davide Manca (Eds.)
Proceedings of the 30th European Symposium on Computer Aided Process Engineering (ESCAPE30), May 24-27, 2020, Milano, Italy.
http://dx.doi.org/10.1016/B978-0-12-823377-1.50068-9

Cost-Effective Processes of Solar District Heating System Based on Optimal Artificial Neural Network

Mohamed Hany Abokersh,[a] Manel Vallès,[a] Laureano Jiménez,[b] Dieter Boer,[a]
[a]*Departament d'Enginyeria Mecànica, Universitat Rovira i Virgili, Av. Països Catalans 26, 43007 Tarragona, Spain*
[b]*Departament d'Enginyeria Química, Universitat Rovira i Virgili, Av. Països Catalans 26, 43007 Tarragona, Spain*
Dieter.boer@urv.cat

Abstract
Aligning with the EU 2030 climate and energy package to achieve a share of at least 27% of renewable energies, and to improve the energy efficiency by at least 27%, the future solar district heating systems (SDHS) may enable the transition to a complete renewable society. Even though this promising tendency of the SDHS, a range of potential barriers are obstructing the wide deployment of SDHS and promoting high variation in quantifying the SDHS benefits over its lifetime. In this context, the optimization approaches are a viable option for determining the optimal structure, sizing, and operation of the SDHS. However, Meta-heuristics optimization models are computationally very expensive and have many limitations regarding the optimization process. Aligning with these challenges, this work tends to develop a robust Artificial Neural Network model based on Bayesian Optimization to solve the computational obstacle associated with heuristics optimization models for SDHS.
Keywords: Solar District Heating, Cost-effective, TRNSYS, Artificial Neural Network, Bayesian Optimization.

1. Introduction
One goal of the European Union "2030 Agenda for Sustainable Development" (European Commission, 2012) is the transition to a more efficient, and sustainable energy future that will include high shares of renewable energy in the global energy mix with major intention to cut 80% of the green emission. A promising pathway towards this vision lies in the adoption of solar district heating systems (SDHS). SDHS are placed in proximity to the energy end-use sector they serve, hence, minimizing energy transmission losses and incorporating locally available energy resources. Moreover, they typically incorporate multiple energy carriers and renewable and other efficient technologies that convert, store and deliver energy in the form of heating, cooling, and electricity or as other energy carriers (e.g., hydrogen) (Di Somma et al., 2015), which allows them to increase operational flexibility. Overall, SDHS delivers a series of economic, environmental, and technical benefits, as discussed in (Akorede et al., 2010). However, the vast quantity of combinations of available devices into a SDHS and the specific subsidies require a systematic analysis and evaluation method (Yang et al., 2015), making modeling and optimization approaches a viable option for determining the optimal structure, sizing and operation of SDHS.
During the design phase of a SDHS, several questions are answered by a quantitative analysis, which is usually performed with specific software simulation tools. However, the complexity of the system increases rapidly with the increment in the design variables. The coupling between the stochastic energy production and the energy consumption

determined by the system properties makes the influences of single elements hard to estimate without the appropriate tools. In this respect, software simulation tools (TRNSYS, Modelica, EnergyPlus, etc.) offer the possibility to achieve a high level of rationalization and transparency, enabling users to make informed choices. However, in order to produce accurate results, the level of abstraction of the system description must be accurately chosen. For instance, the system parametrization must cover all relevant variables, and the resolution of the weather data used must be relevant. Thus, a significant amount of time is required for completing a simulation with the use of a detailed (e.g., first principles) model, which we will call a fine model.

This computational obstacle of SDHS simulation may be overcome by supercomputers, cloud computing, or metamodeling. Supercomputers are expensive if not managed efficiently to avoid downtime. Cloud computing is presumably a cheaper alternative. Still, if the design team wishes to perform sensitivity analysis to identify relevant inputs or interaction effects, such analysis easily requires thousands of simulations to cover the design space sufficiently. This is likely to take hours or days – even with access to cloud computers (Yang, 2011). In this work we aim to create a fast-robust machine learning technique based on an artificial neural network (ANN) to predict the performance of the SDHS with diverse outputs. This will be a bridge to introduce the disciplines of Meta-heuristics optimization in SDHS simulation models.

2. Methodology Framework

The robust machine learning framework of this study includes three sequential steps. First, a set of SDHS cases were created and simulated in TRNSYS with different decision variables for the sizing and operation of the equipment, resulting in a simulation generated database. The hyperparameters of the ANN, such as the number of hidden layers, the number of neurons per hidden layer, the activation function, etc. are often set via rules of thumb or trial and error. However, suitable hyperparameters depend on the system considered and generally cannot be determined beforehand. For this propose, the Bayesian optimization is employed to find a suitable set of hyperparameters for the prediction of the ANNs. Once the robust optimal design of the ANN is achieved, in the third step, the simulations generated data are used to train and validate the robust ANN-based model for predicting the performance of the SDHS instead of using a software simulation tool (TRNSYS).

2.1. SDHS Model in TRNSYS

The SDHS is designed to fulfill energy demands for space heating (SH) and domestic hot water (DHW) in a residential sector. Usually, these systems are designed to supply district heating for more than 100 apartments with a solar fraction of approximately 50%. The main components of the SDHS simulation model, as shown in Figure 1, are the thermal solar collector, the seasonal storage tank (SST), and the DHW storage tank (DHWT). The solar collector transfers the heat gained from the solar radiation to the storage tanks, which is then supplied to the customer on demand. The mismatching between the energy supply and demand in the daily and seasonal bases is balanced through the storage tanks. Auxiliary natural gas heaters are installed to back up the required heat demand in case the solar heating system failed to cover it. The SST based on water storage tank facilitates long-term storage of thermal energy used to cover the SH demand during the winter season with solar energy stored during a summer period. The long-term storage implies relatively large dimensions for the SST, which favors slow charging and discharging processes. On the other hand, the

DHWT is a short-term independent storage tank which is used to cover the daily DHW service at a temperature of 60ºC. The proposed simulation model follows the models previously developed by Tulus et al. (Tulus et al., 2016).

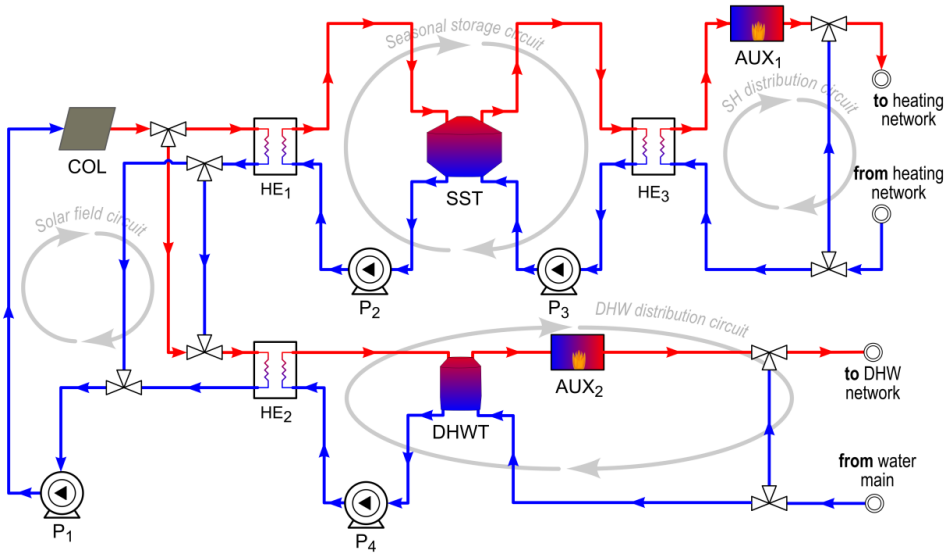

Figure 1: Process flow diagram of the SDHS simulated in TRNSYS 18

2.2. Robust ANN model approach

The robust surrogate model building process has been divided into two main steps; the model setting selection and the model convergence testing. In the first step (Step A), this study emphasizes on the model settings and its relative hyperparameters through using the Bayesian optimization approach at different training set sizes. In the second step (Step B), the convergence of the ANN model is assessed through testing the develop a surrogate model based on the optimal model settings under a wide range of training set to define the optimal sample size.

3. Results and discussion

The results of the model setting and its convergence with various training sets are summarized in this section. First, the results of Bayesian optimization are analyzed for three primary training set to define the optimal setting model. Then, the ANN performance is tested under various training sets to identify the optimal sample size with consideration for the computational model expenses.

3.1. Model Setting

The solution of Bayesian optimization is given by an interactive parallel coordinate plot to identify suitable hyperparameters settings for the reduced number of configurations in step B (see.Figure 2). The plot shows the top 20% ranked optimal solutions results comprising 500 ANN model settings where each line represents one of these optimal solutions along with the achieved coefficient of variation ($\boldsymbol{C.V}$) values. The table below the interactive parallel coordinate plots shows the optimal metamodel setting that achieves the highest accuracy at step (A) training sets. In case of no agreement for selecting a certain optimal setting at different sample sizes, the histogram attached to each interactive parallel coordinate column is utilized to propose the most frequently setting at each hyperparameter. The hyperparameters, including the training function, number of

layers, layer function, hidden function, and momentum mean at each training set, have the same optimal setting at different training sets, whereas the number of neurons and learning rate change at each training set. As observed from the histogram, most of the optimal results setting for the learning rate are set in a range below 0.01. Thus, the learning rate is set to 0.001 for the convergence stage (step B) to sustain the training set converge. On the other hand, the number of neurons with the size of 3, 14, and 20 are set for the convergence stage (Step B) since its optimal value is different for the training set size 64, 256, and 1024. A summary of the selected settings in the convergence stage (step B) is shown in the below table in Figure 2, where the nominated settings are highlighted.

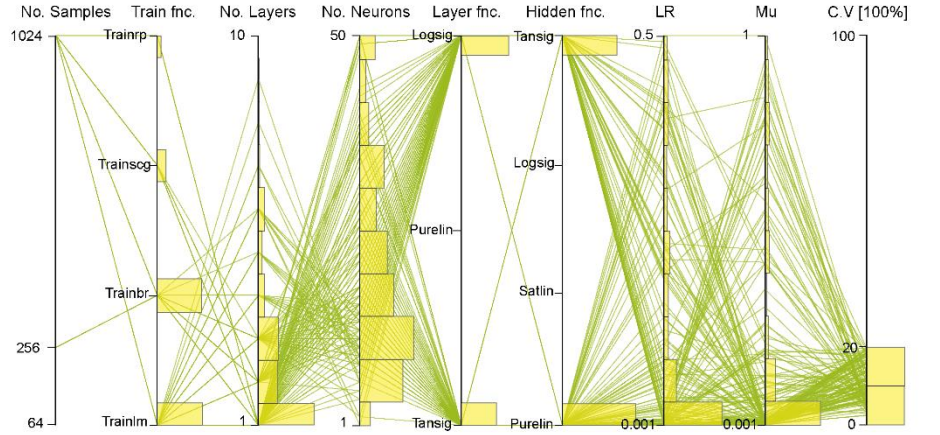

Optimal Hyperpar.	64	Trainbr	3	3	Logsig	Purelin	0.042	0.004	49.7%
	256	Trainbr	3	14	Logsig	Purelin	0.004	0.836	9.42%
	1024	Trainbr	3	20	Tansig	Purelin	0.001	0.004	2.49%

Figure 2: interactive parallel coordinate plot combined with histograms are utilized to identify the optimal hypermeters setting for the ANN model in step A. The plot shows the top 20% ranked ANN model settings. The table below shows the optimal hyperparameters

Following the interactive parallel coordinate plot, a box plot (see. Figure 3) is built to show the performance of the three-training sets (64, 256, and 1024) based on the $C.V$ rank under the optimal selected hyperparameters with considering for three neurons sizes comprising 3, 14, and 20 in comparison to the default settings.

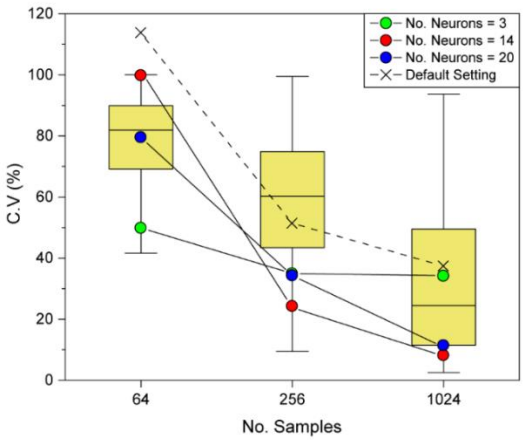

Figure 3: Box plot for the output in step A including the ANN model performance under the optimal and default settings

The box plot is characterized by the central mark and the upper and lower quartiles, which correspond to the box edge and show other optimal solutions. While the minimum and maximum optimal values are indicated at the whiskers. On the plot, the lined circles at each sample size show the results under optimal settings at a different number of neurons, whereas the cross symbols represent the results at the default settings. In general, the default setting does not yield to build accurate ANN models that approve the importance hyperparameters tuning. Moreover, fixing the number of neurons at 14 provides the most accurate results with a $C.V$ value of 24.1% and 9.2% for the 256 and 1024 training set, respectively.

3.2. Model Setting

In step B, we test the performance of the selected optimal hyperparameters at various training sizes in order to choose the most accurate ANN model with consideration for its efficiency in terms of the computational cost, as shown in Figure 4.

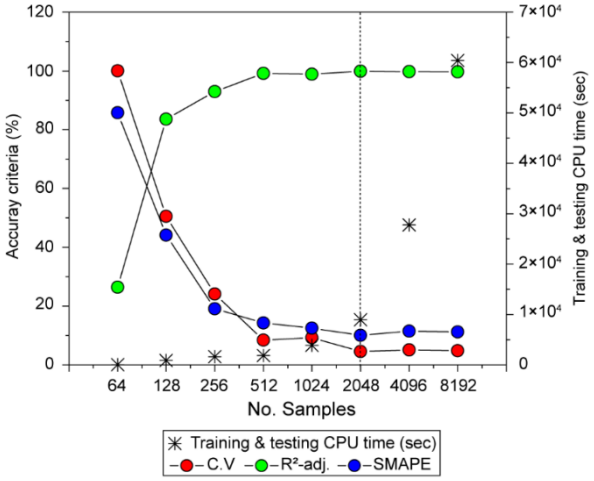

Figure 4: Convergence of accuracy criteria at various training size with consideration for its relative computational cost

In terms of the convergence, three accuracy criteria comprising the adjusted R-squared (R^2-adj), $C.V$, and Symmetric mean absolute percentage error (SMAPE) are utilized to evaluate the performance of the ANN model. The results show that the R^2-adj is a misleading criterion since most of the sample sizes excess 97%. Therefore, using $C.V$ and SMAPE can be more efficient to measure the ANN model accuracy. Increasing the sample size has a clear tendency to improve the ANN model accuracy where the highest accurate value of 4.5% and 10% was indicated in a sample size of 2048 for the $C.V$ and SMAPE criterion, respectively.

In terms of the ANN model computational cost, an exponential behavior is indicated by increasing the sample size where the CPU time at 8192 sample size is 6×10^4 sec. Comprising the model accuracy with its efficiency simultaneously, the sample size 2048 provides the highest accuracy at an affordable computational time of 8.9×10^3 sec using an Intel® Xeon® E5-2620 v4 2.10 GHz processor with 32.0 GB RAM.

4. Conclusion

Following the high computational expenses obstacles associated with the SDHS simulation, this study proposes a complete framework based on a robust ANN model to

solve this computational obstacle. a summary of the robust ANN model key findings is the following:

- Relate to the ANN model settings, the hyperparameters comprising the number of hidden layers at 3, the number of neurons at 14, training function at Bayesian regularization, layer function at logsig, hidden function at purelin, learning rate at 0.001 and Momentum mean at 0.004 show the highest accurate ANN model at various training set size.
- Relate to the ANN model convergence at different training set sizes, the sample size of 2048 shows the highest accurate model prediction, where the $C.V$ criterion does not get below 4.5% for all model outputs at an affordable computational time of 8.9×10^3 sec.

In general, the proposed robust surrogate model built based on the two-model steps offers a sufficient approach for the construction of fast metamodels to overcome the computational barrier related to design space exploration, design optimization, and sensitivity analysis of heuristics optimization models.

Acknowledgment

The authors would like to acknowledge financial support from the Spanish Ministry of Economy and Competitiveness (RTI2018-093849-B-C33 (MCIU/AEI/FEDER, UE) and CTQ2016-77968 (MINECO/FEDER)) and to thank the Catalan Government for the quality accreditation given to their research group (2017 SGR 1409). This project has received funding from the European Union's Horizon 2020 research and innovation programme under the Marie Skłodowska-Curie grant agreement No. 713679 and from the Universitat Rovira i Virgili (URV).

References

Akorede, M.F., Hizam, H., Pouresmaeil, E., 2010. Distributed energy resources and benefits to the environment. Renew. Sustain. Energy Rev. 14, 724–734. https://doi.org/10.1016/j.rser.2009.10.025

Di Somma, M., Yan, B., Bianco, N., Graditi, G., Luh, P.B., Mongibello, L., Naso, V., 2015. Operation optimization of a distributed energy system considering energy costs and exergy efficiency. Energy Convers. Manag. 103, 739–751. https://doi.org/10.1016/j.enconman.2015.07.009

European Commission, 2012. Energy: Roadmap 2050, European Commissioner for Energy. https://doi.org/10.2833/10759

Klein, S.A. et al., 2004. TRNSYS Version. 18, Solar Energy Laboratory, University of Wisconsin-Madison, Website: <http://sel.me.wisc.edu/ trnsys>.

Tulus, V., Boer, D., Cabeza, L.F., Jiménez, L., Guillén-Gosálbez, G., 2016. Enhanced thermal energy supply via central solar heating plants with seasonal storage: A multi-objective optimization approach. Appl. Energy 181, 549–561. https://doi.org/10.1016/j.apenergy.2016.08.037

Yang, J., 2011. Convergence and uncertainty analyses in Monte-Carlo based sensitivity analysis. Environ. Model. Softw. 26, 444–457. https://doi.org/10.1016/j.envsoft.2010.10.007

Yang, Y., Zhang, S., Xiao, Y., 2015. Optimal design of distributed energy resource systems coupled withenergy distribution networks. Energy 85, 433–448. https://doi.org/10.1016/j.energy.2015.03.101

Sauro Pierucci, Flavio Manenti, Giulia Bozzano, Davide Manca (Eds.)
Proceedings of the 30th European Symposium on Computer Aided Process Engineering (ESCAPE30), May 24-27, 2020, Milano, Italy.
http://dx.doi.org/10.1016/B978-0-12-823377-1.50069-0

Packed-bed and Microchannel Reactors for the Reactive Capture of CO_2 within Power-to-Methane (P2M) Context: A Comparison

Santiago Ortiz [a], Camilo Rengifo [b], Martha Cobo [c], Manuel Figueredo [d,*]

[a] *Master in Process Design and Management. Faculty of Engineering, Universidad de La Sabana, Km. 7 Autopista Norte, Bogotá, Colombia.*

[b] *Department of Mathematics, Physics and Statistics. Faculty of Engineering, Universidad de La Sabana, Km. 7 Autopista Norte, Bogotá, Colombia.*

[a, c, d] *Energy, Materials, and Environment Laboratory. Department of Chemical Engineering, Universidad de La Sabana, Km. 7 Autopista Norte, Bogotá, Colombia.*
manuel.figueredo@unisabana.edu.co

Abstract

Carbon capture and utilization technologies have recently boomed as strategies to decrease carbon dioxide (CO_2) emissions, in which methanation (via-Sabatier process) seems to be a prominent pathway. However, CO_2 methanation involves technical challenges to be overcome, such as heat removal and high intermittency during the operation. This study assesses the operation of a packed-bed and a microreactor in the Synthetic Natural Gas (SNG) production through computational fluid dynamics modeling. The data compilation from simulations and further analysis provides valuable information about hot spots formation and CO_2 conversion under established dimensional specifications and cooling conditions. From the above configurations, microreactor configuration was the best option to control the hot spot formation without leaving aside the SNG production.

Keywords: Methanation, Microreactor, Packed–bed reactor; Hot spot formation, Computational Fluid Dynamics.

1. Introduction

Carbon Capture and Utilization (CCU) technologies such as Power-to-methane (P2M) have brought advantages to overcome the environmental issues by reducing greenhouse gas emissions. Accordingly, P2M aims to capture carbon dioxide (CO_2) and transform it into methane (CH_4) to produce Synthetic Natural Gas (SNG) by catalytic methanation (Ghaib and Ben-Fares, 2018). However, CO_2 methanation exhibits a highly exothermic nature that triggers the hot spots formation inside the reactor and, therefore, contributes to catalyst deactivation. Moreover, appropriate heat management is challenging owing to the operation intermittency that catalytic methanation units must deal under the P2M context. Consequently, maintaining the operating temperature within an ideal range without leaving aside the CH_4 production presents a technological trial (Sun et al., 2017). Several studies have tackled this technical challenge considering aspects in the reactor design (Schlereth and Hinrichsen, 2014) or by proposing optimal control strategies (Bremer and Sundmacher, 2019). In most of the cases, packed bed reactors (PBRs) have been selected as the catalytic-reaction system. Nonetheless, some alternative reaction technologies have also been proposed so far, such as microchannel reactors (Engelbrecht et al., 2017). These reactors may afford large heat- and mass-transfer rates that ease heat removal from the system due to high interfacial surface areas and short diffusion paths

(Némethné-Sóvágó and Benke, 2014). Hence, improving CCU technologies is necessary to make alternatives suchlike P2M more competitive within the electricity and fuel markets. However, their improvement will be barely accomplished without a deeper understanding of the process fundamentals. This research aims to compare the operation of a microchannel and average PBR employed for CO_2 methanation through Computational Fluid Dynamics (CFD). This study focuses on analyzing the thermal performance of both reactors owing to the importance that this matter represents within the P2M context.

2. Model formulation

2.1. Methanation reactions and kinetics

During CO_2-methanation there are multiple reactions involved. Nevertheless, for simulation, modeling purposes and available information about kinetics, only the Sabatier reaction is considered:

$$\boldsymbol{CO_2 + 4H_2 \Leftrightarrow CH_4 + 2H_2O} \quad ; \quad \Delta H_R^{298K} = -164.9\ kJ\ mol^{-1}.$$

Methanation reactions are thermodynamically favored at lower temperatures. Therefore, more active and thermally fewer sensitive catalysts should be employed. Consequently, with the purpose of including a state-of-the-art methanation catalyst, this research, employs the model proposed by Koschany et al. (2016) for Ni/SiO_2. It relies on a Langmuir-Hinshelwood-Hougen-Watson (LHHW) type rate equation and it is parametrized for the Sabatier reaction:

$$r_{Sab}^{intrinsic} = k\, p_{H_2}^{0.5} p_{CO_2}^{0.5} \left(1 - \frac{p_{CH_4} p_{H_2O}^{2}}{p_{CO_2} p_{H_2}^{4} \mathrm{K}_{eq}}\right) / DEN^2\,, \tag{1}$$

$$DEN = 1 + K_{OH} \frac{p_{H_2O}}{p_{H_2}^{0.5}} + K_{H_2} p_{H_2}^{0.5} + K_{mix} p_{CO_2}^{0.5}\,, \tag{2}$$

where $p_{\propto}$ accounts for the species partial pressure, k refers to the catalytic rate coefficient, and K_{eq} denotes the temperature dependent equilibrium constant, Eq.(1). Further, DEN is a dimensionless parameter determined by correlations of the adsorption constants (K_x), Eq.(2). For a detailed description about Ni/SiO_2 kinetic parametrization refers to Koschany et al. (2016).

2.2. Reaction systems

2.2.1. Packed-bed reactor

Regarding PBR, this study considers the simulation of one single tube part of an entire tube-bundle pilot-scale reactor employed in the methanation process. These reactors are composed by heat exchangers and reacting tubes of relatively small diameters (i.e., 1 - 5 cm) and lengths (i.e., 0.3 - 10 m) (El Sibai et al., 2015). Bremer et al. (2019) evaluated some control strategies for CO_2−methanation in PBRs, aiming to avoid distinct hot spots formation. Therefore, this study harnesses some of the reactor parameters applied in that research (close reactor dimensions, cooling and feed conditions).

2.2.2. Microreactor

A 2-D geometry of a single micro-channel was used for the CFD simulations. All micro-channels were assumed to be identical. They were established as follows: height = 190μm and length = 5cm. The microchannel model is composed of a free-fluid region together with a porous catalytic washcoat layer of 40 μm, as exemplified by Engelbrecht et al. (2017). The latter implies the coupling and computation of two sets of PDEs referring to mass-, heat- and momentum- transport in each domain.

2.3. Governing transport phenomena

Both reactors envisage a porous domain of catalytic nature, leading the reactive source to be exclusively considered within each porous region. Subsequently, governing equations through porous media concerning mass-, heat- and momentum- transport are supposed to be stationary and pseudo-homogeneous, Eqs.(3-6):

$$\frac{\mu}{\Phi}\boldsymbol{u} = \vec{\nabla}\cdot\left[-PI + \frac{\mu}{\varepsilon_p}(\nabla\boldsymbol{u} + (\nabla\boldsymbol{u})^T)\right] - \frac{\rho\varepsilon_p C_f}{\sqrt{\Phi}}\boldsymbol{u}|\boldsymbol{u}| \ , \tag{3}$$

$$\vec{\nabla}\cdot(\varepsilon_p\rho\boldsymbol{u}) = 0 \ , \tag{4}$$

$$\frac{\partial\rho_\propto}{\partial t} = -\boldsymbol{u}\cdot\vec{\nabla}\rho_\propto + D_\propto^{eff}(\nabla^2\rho_\propto) + (1-\varepsilon)M_\propto v_{\propto_{Sab}} r_{Sab}^{eff} \ , \tag{5}$$

$$(\rho C_p)^{eff}\frac{\partial T}{\partial t} = -\sum_\propto (\rho_\propto C_{p_\propto})\boldsymbol{u}\cdot\vec{\nabla}T + \lambda^{eff}(\nabla^2 T) - (1-\varepsilon)(\Delta_R H_{Sab})r_{Sab}^{eff} \ . \tag{6}$$

Momentum transport was modeled with the Brinkman-Forchheimer extended Darcy equation, Eqs.(3-4); where μ denotes the dynamic viscosity, $\boldsymbol{u}$ the fluid velocity, ρ the fluid's density ($\rho_\propto$ for single component density), P the total pressure, Φ the porous permeability, ε_p the bed porosity, and C_f the dimensionless friction coefficient as a function of ε_p. Likewise, mass- and heat- transfer are computed through Eq.(5) and Eq.(6), respectively. These models include mass ($D_\propto^{eff}$) and heat (λ^{eff}) dispersion effective coefficients as well as temperature-dependent thermo-physical properties obtained by polynomial correlations referred to as NASA format. Further, the resistance effects in the solid and void regions of the catalyst are quantified through an effectiveness factor (η):

$$r_{Sab}^{eff} = \eta\, r_{Sab}^{intrinsic} \ . \tag{7}$$

This factor exclusively contemplates intraparticle (internal) temperature-dependent diffusion resistances, and its calculation procedure was proposed by Kiewidt and Thöming (2015). Finally, flow through the free channel (fluid region) within the microreactor is described by the stationary, incompressible Navier-Stokes equations:

$$\rho(\boldsymbol{u}\cdot\nabla)\boldsymbol{u} = -\nabla\cdot[-pI + \mu(\nabla\boldsymbol{u})] \ , \tag{8}$$

$$\nabla\cdot\boldsymbol{u} = 0 \ . \tag{9}$$

Herein, the gradient operator $\vec{\nabla}$ accounts for the vector $\frac{\partial}{\partial x}\hat{\imath} + \frac{\partial}{\partial z}\hat{\jmath}$, which provides a two (2) dimensional notation for the model spatial distribution.

3. Computational and simulation aspects

The commercial software COMSOL Multiphysics® was employed to couple and solve the reacting-flow model for each case. 3D simulations no longer reflected different results from 2D simulations, so all the simulations were performed over 2D symmetric domains to reduce computational effort. Furthermore, grid independence was achieved above fine grids for both 2D geometries. PBR and microreactor meshes consist of 101966 and 79318 free-triangular elements, respectively. In addition, methanation simulations were developed in both cases by feeding a stoichiometric gas mixture of H_2/CO_2 (ratio of 4:1) at 400 K and 5 bar. These operating conditions have been found to be favorable for the SNG production and process profitability (Ghaib and Ben-Fares, 2018). Lastly, each porous media is assumed to be loaded with spherical particles of catalyst Ni/SiO_2.

4. Results and discussion

This section presents the CFD modeling results of both PBR and microreactor used for CO_2 methanation, together with the appropriate comparative discussion. The reactor axial (relative) position z was normalized with respect to the total length L. Besides, the CO_2 is given by Eq.(10), where ρ_{CO_2} is the CO_2 mass concentration, g/m^3.

$$X_{CO_2} = \frac{\rho_{CO_2}|_{in} - \sum \rho_{CO_2}|_{z/L=1}}{\rho_{CO_2}|_{in}}. \quad (10)$$

4.1. Effect of coolant temperature on CO_2 conversion

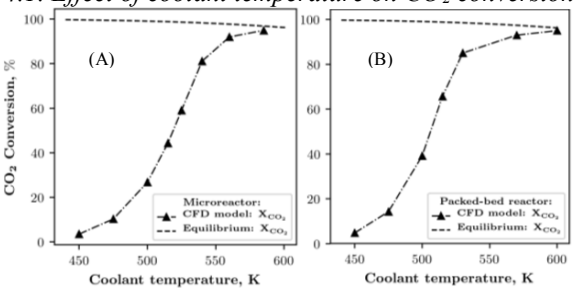

Figure 1. Effect of the CJ temperature on CO_2 conversion for microreactor (A) and PBR (B).

As a point of reference, the maximum achievable conversion, based on a thermodynamic analysis, was carried out in AspenPlus™. This evaluation was developed at 5 bar, at the coolant temperature. The Peng-Robinson package was used to model the gas mixture. Figure 1 shows that regardless the reaction exothermic nature (thermodynamically limited at higher temperatures), the higher the temperature of the Cooling Jacket (CJ), the higher the CO_2 conversion. Therefore, at low temperatures (< 500 K), the Ni/SiO_2 is not active enough to convert more than 45 % of reagent into SNG in any of the reactors with such dimensions and catalytic features. Still, an increment on the jacket temperature chemically activates the system until it is thermodynamically limited. Nevertheless, unlike the microreactor, in the PBR, higher coolant temperatures are required to achieve conversions close to equilibrium.

4.2. Effect of coolant temperature on Hot spot formation

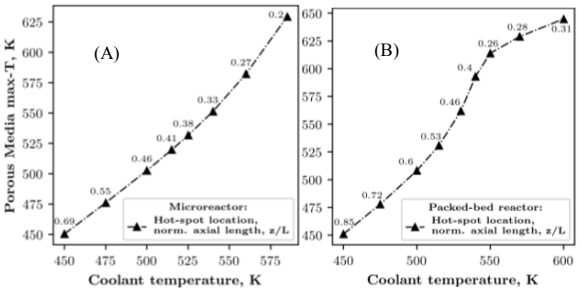

Figure 2: Effect of the CJ temperature on the hot spot max-T (with location) for microreactor (A) and PBR (B).

As a result of the chemical activation caused by temperature increment in the CJ, the formation of hot spots is also triggered. Figure 2 presents the temperature of the hottest spots inside each reactor. This analysis was performed over the axial coordinate (symmetric plane for the PBR) and along the porous-fluid media interface (referring to the microreactor). The rise of the coolant temperature has not only a direct impact on the max-temperature reached by the system (hot spot), but also its axial location. Each marker-text indicates the axial position (normalized, z/L) where the hot spot max-T occurs. The location of the hot spot approaches the reactor entrance as the coolant temperature increases ascribed to speeded activation effects resulting from heat-transfer from wall in each case. In other words, the residence time required to attain a precise conversion becomes shorter. Otherwise, when comparing both reactors, the hot spots temperature within the PBR (Figure 2A) exceeds

the microreactor (Figure 2B), despite the wall temperature is the same. At first glance, this disparity should represent an improvement in reaction kinetics within the PBR. However, the space-times required to reach certain conversions in this reactor are "delayed". This affair may be better understood by inspecting the effectiveness factor as discussed in the following section.

4.3. Study case comparison

4.3.1. Hot spot formation

A heterogeneous catalytic system is susceptible to the wall temperature when it comes to an exothermic reaction since hot spots are unavoidable. Figure 3 depicts the isothermal contours of both microreactor and PBR when CJ operates at 588K. It can be appreciated that even though the max-T reached in both cases differ by about 15 degrees, the

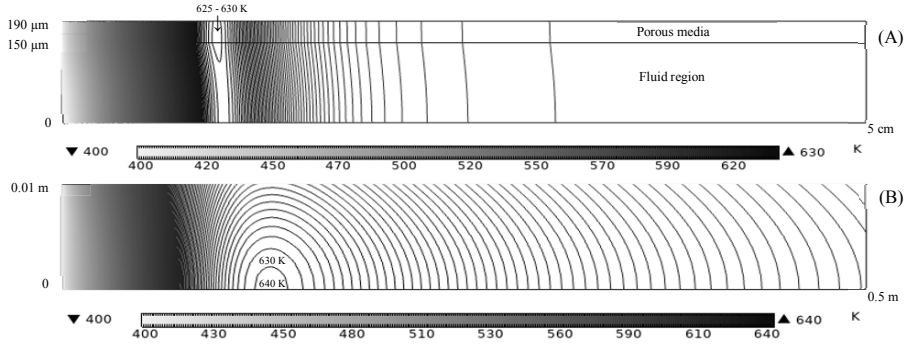

Figure 3: Isothermal contours of microreactor (A) and PBR (B), with a stochiometric gas feed (H_2:CO_2, 4:1) at 400 K, 5 bar, and a constant wall temperature of 588 K.

thermally affected area is greater within the PBR. It means that the energy dispersion in the packed-bed suffers a higher transfer resistance than in the microreactor due to reactor dimensions, leading energy removal to be less efficient. Therefore, the radial temperature profile is no longer negligible in the PBR. Besides, the role of the free-fluid region is also relevant within the microreactor owing to the provision of a convective energy dispersion, which decreases the energy accumulation in a specific location inside this reactor. Moreover, note that within the later, this accumulation of energy is mainly located at the porous media. Unlike the PBR, where the energy is concentrated at the furthest site from the wall (the symmetric plane).

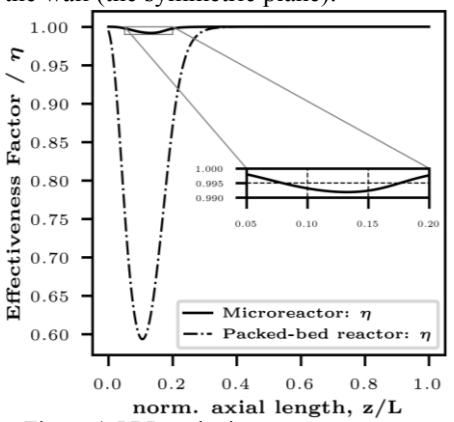

Figure 4. PBR and microreactor: Effectiveness factor (η) comparison.

4.3.2. Effectiveness factor involvement

The solid-fluid interaction in heterogeneous processes is associated with transfer resistances at catalyst level, which can be accounted through the Effectiveness Factor (EF). Figure 4 compares the PBR and microreactor EFs from the study case in section 4.3.1. In both cases, it is shown that the formation of the hot spot concurs with the lowest EF. Notwithstanding, the hot spot presence implies a catalytic rate peak regardless of a drop in the EF, pointing that, there is a thermal effect prevailing over other factors (transfer-resistances, heat removal, and the EF itself). The EF reached higher

values in the microreactor because catalyst particle size was about 330 times smaller (0.002 m / 6 μm) than in PBR, which causes an almost negligible effect on the transport-resistances (catalyst internal diffusion). Therefore, regardless the formation of more extensive hot spots in the PBR, said reactor had longer residence time than microreactors.

5. Conclusions and Outlook

This work compares the operation (under the criteria of hot spots formation) of a microreactor and PBR to produce SNG from H_2 and CO_2 by CFD modeling. This approach represents a sharp insight to better understand the integration between the transport processes and the intrinsic chemistry of CO_2 methanation. Simulations showed the direct relation between cooling jacket temperature and hot spots formation (max-T and its location). Indeed, the exemplified microreactor allows both more efficient heat removal and conversions closer to the equilibrium. On the other hand, PBR must be operated under stricter cooling strategies to avoid larger hot spots, while affecting the SNG production. Efficient heat-removal strategies are key point on the CO_2 methanation to maintain a suitable balance between kinetic and thermodynamic limitations, as well as a techno-economic feasibility that warrants the operability of the process. Moreover, results showed the relevance of involving the EF calculation as it becomes substantial to determine the effective reaction rate within the system. Lastly, this study represents a first step analysis in the search for a suitable reactor technology. However, additional variables should be incorporated into the sensibility evaluation to boost methanation systems with P2M applications.

References

J. Bremer and K. Sundmacher, 2019. Operation range extension via hot-spot control for catalytic CO_2 methanation reactors. Reaction Chemistry and Engineering, 4(6), 1019–1037.

A. El Sibai, L. Rihko-Struckmann and K. Sundmacher, 2015. Synthetic Methane from CO_2: Dynamic Optimization of the Sabatier Process for Power-to-Gas Applications. Computer Aided Chemical Engineering (Vol. 37).

N. Engelbrecht, S. Chiuta, R. C. Everson, H. W. J. P. Neomagus and D. G. Bessarabov, 2017. Experimentation and CFD modelling of a microchannel reactor for carbon dioxide methanation. Chemical Engineering Journal, 313, 847–857.

K. Ghaib and F.-Z. Ben-Fares, 2018. Power-to-Methane: A state-of-the-art review. Renewable and Sustainable Energy Reviews, 81(June 2017), 433–446.

L. Kiewidt and J. Thöming, 2015. Predicting optimal temperature profiles in single-stage fixed-bed reactors for CO_2-methanation. Chemical Engineering Science, 132, 59–71.

F. Koschany, D. Schlereth and O. Hinrichsen, 2016. On the kinetics of the methanation of carbon dioxide on coprecipitated NiAl(O)<inf>x</inf>. Applied Catalysis B: Environmental, 181, 504–516.

J. Némethné-Sóvágó and M. Benke, 2014. Microreactors: a new concept for chemical synthesis and technological feasibility. Materials Science and Engineering, 39(2), 89–101.

D. Schlereth and O. Hinrichsen, 2014. A fixed-bed reactor modeling study on the methanation of CO_2. Chemical Engineering Research and Design, 92(4), 702–712.

D. Sun, F. M. Khan and D. S. A. Simakov, 2017. Heat removal and catalyst deactivation in a Sabatier reactor for chemical fixation of CO_2 : Simulation-based analysis. Chemical Engineering Journal, 329, 165–177.

Sauro Pierucci, Flavio Manenti, Giulia Bozzano, Davide Manca (Eds.)
Proceedings of the 30th European Symposium on Computer Aided Process Engineering (ESCAPE30), May 24-27, 2020, Milano, Italy.
http://dx.doi.org/10.1016/B978-0-12-823377-1.50070-7

Design and Eco-techno-economic Analyses of SOFC /Gas Turbine Hybrid Systems Accounting for Long-Term Degradation

Haoxiang Lai,[a] Nor Farida Harun,[b] David Tucker,[b] and Thomas A. Adams II[a*]

[a] *McMaster University, Department of Chemical Engineering, Hamilton, ON, Canada*
[b] *US Department of Energy, National Energy Technology Laboratory, Morgantown, WV, USA*
tadams@mcmaster.ca

Abstract

Solid oxide fuel cells (SOFCs) are a promising next-generation technology for power production from fossil fuels. Because they convert chemical energy into electricity electrochemically, they are generally more efficient than combustion-based power plants due to the thermodynamic limitations of combustion cycles, and accordingly, have lower carbon intensities. However, one of the major drawbacks of SOFCs is that they degrade over time, and the degradation rate varies with different operating conditions. When operated in constant power mode (the most common way of baseload power production), the degradation rate is fast such that the lifetime of the SOFC stack is around one tenth of that when in constant voltage mode (in which the power output from SOFC stack decreases). To achieve baseload power production and a long lifetime simultaneously, one potential solution is to integrate SOFC stack (operated in constant voltage mode) with a gas turbine (GT) in a SOFC/GT hybrid system. As the SOFC stack degrades, the power produced from GT increases over time by using the increasing heating value of the unspent fuel from the SOFC exhaust. We performed an eco-technoeconomic analysis (eTEA) of the SOFC/GT concept with degradation in comparison with the SOFC standalone system. The results of model simulations showed that, with certain operating conditions, the SOFC/GT hybrid system was around 36% more efficient than the SOFC standalone system, and also had about 18 times longer lifetime. On a 550 MW scale and 30-year-lifetime, SOFC/GT hybrid system can reduce the levelized cost of electricity (LCOE) by around 80 % as well as CO_2 emission by around 27 %, compared to the SOFC standalone system. The results show that SOFC/GT hybrids are a promising near-term approach because existing SOFC technology can be used directly while both avoiding short cell lifetimes and still getting near-baseload performance.

Keywords: Solid oxide fuel cell, SOFC/GT hybrid, eco-technoeconomic analysis

1. Introduction

Solid oxide fuel cells (SOFCs) produce power electrochemically, which is more efficient than conventional combustion-based power production processes such as coal power plants (Adams et al., 2013). By using coal-based syngas (a mixture of mainly CO and H_2) as a fuel source, SOFCs generate electricity through electrochemical reactions shown in Figure 1. However, one of the main drawbacks of SOFCs (and SOFC stacks) is that they can degrade over time in a variety of ways, including accruing damage to

the anode, cathode, interconnects, and other cell or stack components. SOFCs are most

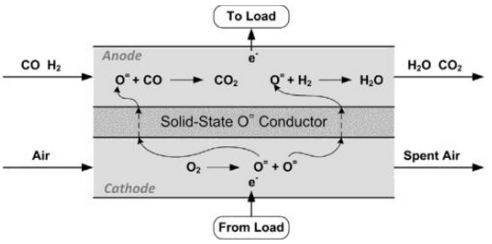

Figure 1. Simple schematic of a SOFC. Reproduced from (Nease and Adams, 2014).

commonly used in constant power mode, in which the fuel flow rate and current density are increased over time to counteract the degradation effects and yield a constant power output. However, higher flow rates cause the degradation rates to grow even faster, resulting in a lifetime potentially as short as 1.5 years (Tucker et al., 2014).

Recent research has found that by operating in constant voltage mode, along with some other operating strategies, SOFC lifetime can greatly increase to as long as 13-14 years (Tucker et al., 2014). However, the power produced decays over time, and in fact, the fuel utilization (the percentage of fuel oxidized in the anode) decays as well. This means that the anode exhaust has a large and increasingly unused heating value. The solution is to use this anode exhaust as a fuel for a gas turbine (GT), creating the SOFC/GT hybrid system (Tucker et al., 2012). The system is designed such that as the SOFC decays in power production while operating in constant voltage mode, the GT turbine increases in power production over time as the anode exhaust heating value increases. The efficiency of the GT changes during its life as well depending on the anode exhaust conditions. The net effect is that the total system power decays slowly over time, and is suitable for baseload grid-power generation in the long term. It is also more efficient than a standalone GT system.

In this work, we present an eco-technoeconomic analysis (eTEA) of the SOFC/GT concept with degradation considered. Dynamic Matlab Simulink models of the SOFC which considers degradation effects were coupled with Aspen Plus steady-state models of the balance of plant in a pseudo-steady approach. This enables the simulation of the gradual degradation of the plant over a 14 year lifetime. This simulation was used to compute key performance indicators like levelized cost of electricity, greenhouse gas emissions, efficiency, and dynamic performance curves for power, current, voltage, fuel utilization, etc. These are used in turn to quantify the trade-offs between standalone SOFC, standalone GT, and SOFC/GT hybrid systems on a power production scale of 550 MW for a lifetime of 30 years.

2. Methodology

The proposed SOFC standalone system consists of two main components: a SOFC stack with a post combustor, and an upstream syngas production and clean-up process (Figure 2). The upstream syngas process provides clean syngas as the fuel source to the SOFC anode, and it includes a coal gasifier (producing syngas from coal), an air separation unit (providing oxygen for the gasifier), scrubber (removing HCl from syngas), water-gas shift reactor (converting CO and H_2O to CO_2 and H_2, also converting COS and H_2O to CO_2 and H_2S), and a Selexol process (a solvent-based H_2S removal process). The

SOFC is operated at near atmospheric pressure, and so cathode air is provided through a blower and then preheated by the gas exhaust from the post-combustion. Similarly, the

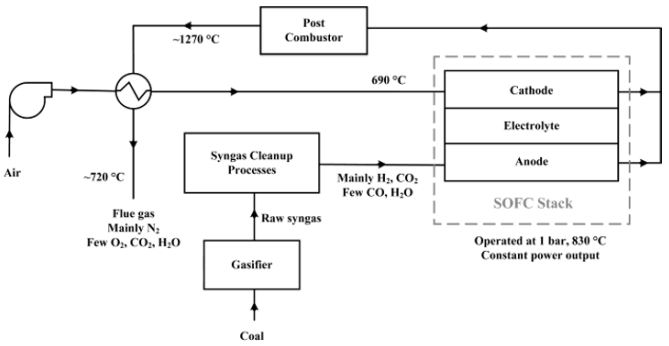

Figure 2. Process flow diagram of SOFC standalone system.

proposed SOFC/GT hybrid system consists of three main components: a SOFC stack with a post combustor, upstream syngas production and clean-up process, and a gas turbine (including a compressor and a recuperator) (Figure 3). The SOFC stack section and the upstream syngas process are the same as in the SOFC standalone system, except that the SOFC stack is operated at 4 bar. The hybrid system also has cold air bypass streams to control the cathode inlet temperature and the gas turbine inlet temperature. In these two proposed systems, models of SOFC stack and post combustor were developed in Matlab Simulink R2017a in a prior work (Zaccaria et al., 2016), and were coupled with steady-state models of the balance-of-the-plant developed in Aspen Plus V10. Because the time scale of degradation is slow, a pseudo-steady-state approach with a weekly time step was used. The models were connected through Aspen Simulation Workbook (add-in application in Microsoft Excel) and macro scripts developed in Microsoft Excel VBA (Visual Basic for Applications). The dynamic model in Simulink considers the spatial degradation over the axial length of the cells over time based on factors such as fuel composition, fuel rate, humidity, utilization, current, voltage, and other factors. The Aspen Plus models were developed using the Peng-Robinson equation of state (EOS) with the Boston-Mathias modification (PR-BM) with a few exceptions: the NBC/NRC steam tables were used for pure water streams, the Electrolyte-NRTL method with Henry coefficients and electrolyte chemistry specification obtained from the AP065 databank was used for streams consisting of mostly CO_2 and H_2O near the critical point, and the Redlich-Kwong-Soave EOS with predictive Holderbraum mixing rules was used for streams consisting of mostly CO_2 and H_2O below the critical point. Since the heating value of the gas turbine inlet stream increased over time as the fuel cells degraded, a gas turbine efficiency curve was considered in the model which accounts for off-design turbine operating conditions. This curve uses propritary data from the turbine manufacturer (Siemens) for the selected turbine (SGT6-9000HL) and so cannot be released for intellectual property reasons.

3. Results and Discussions

The simulation results of the SOFC standalone system are shown in Figure 4. Figure 4 (a) shows the dynamic performance of the SOFC stack. The power production and fuel

utilization were kept as 550 MW and 80 %, respectively. The voltage dropped from the initial condition of around 0.8 V, and the current density increased from 0.5 A/cm^2. The average temperature of the SOFC stack was maintained at around 830 °C. With the

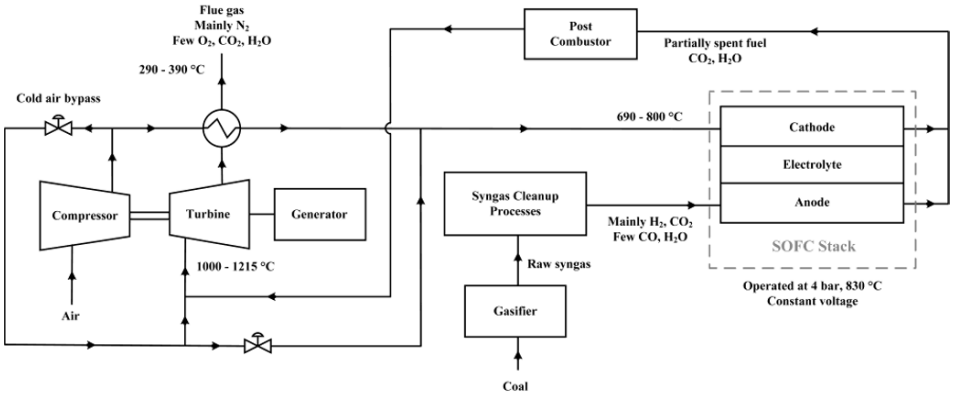

Figure 3. Process flow diagram of SOFC/GT hybrid system.

above operating conditions, the lifetime of the SOFC in the standalone system was around 3132 hours (which is around 19 weeks) before catastrophic breakage was predicted. Figure 4 (b) shows the replacement of SOFC stack every 19 weeks throughout the lifetime of 30 years. The SOFC stack efficiency was defined as the power output from the SOFC stack over the low heating value (LHV) of the portion of the fuel that was consumed by the SOFC stack. The net efficiency was calculated as the net power produced by the system over the LHV of the coal entering the system. The efficiency dropped as SOFC degraded because the stack produced the same amount of power by consuming an increasing amount of fuel. The SOFC standalone plant has a high value of waste heat (flue gas stream in Figure 2) that can be used in a steam bottoming cycle for extra power production, which would alternatively increase the net efficiency of the system. Such combined cycles were not considered in this work.

The dynamic performance of the SOFC stack in the hybrid system can be seen in Figure 5 (a). The SOFC stack was operated in constant voltage mode so that the lifetime of the SOFC stack increased. Although the simulation predicted that catastrophic SOFC breakdown would not occur until about 14 years of use, a practical regular replacement time of 351 weeks (or 6.7 years or 58968 hours) was selected because at this point, the fuel utilization dropped to 25 % from 80 % at the beginning of life. The power output from the SOFC stack decreased to 150 MW which is around 37.5 % of its initial capacity (400 MW) as the fuel utilization dropped to 25 %. Accordingly, the current density dropped from 0.5 A/cm^2 to around 0.19 A/cm^2. Further optimization studies would be needed to determine an optimal replacement time of the SOFC stack in the hybrid system. The spatial average temperature of the stack was regulated at 830 °C. Figure 5 (b) shows that the power load shifted from the SOFC stack to the GT as the SOFCs degraded, so that the net power was essentially constant at 550 MW. The GT was designed such that its maximum power capacity would be reached at the end of the lifetime of 351 weeks. As such, the GT efficiency increased over time as the GT operation gradually moves closer to peak design performance. The net efficiency of the whole system decreased gradually over time since the power load was being shifted from a more efficient component SOFC stack to the less efficient GT. Similar to the

standalone system, the waste heat could also be captured and used for extra power production in a steam cycle, but this was not considered in this analysis. However, the quality, temperature, and exergetic value of the waste heat in the hybrid system is lower than that of the standalone system.

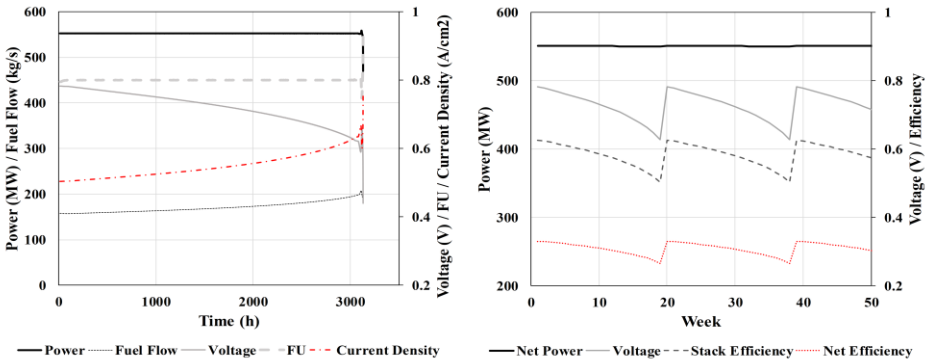

Figure 4. System performance curves of (a) the SOFC stack in SOFC standalone plant and (b) the SOFC standalone plant.

Table 1 summarizes the key parameters for the eco-technoeconomic comparison between the SOFC standalone plant and the SOFC/GT hybrid plant. The costs of the plants were estimated based on literature (Adams et al., 2017; James et al., 2019). SOFC stacks were purchased and replaced in a cycle of 19 weeks for SOFC standalone plant, and in a cycle of 351 weeks for SOFC/GT hybrid plant over the 30-year-lifetime. The first year capital cost of SOFC standalone plant was higher than SOFC/GT hybrid plant, because three SOFC stacks with a capacity of 550 MW were needed in the standalone plant while only one stack with a capacity of 400 MW was needed in the hybrid plant. The SOFC/GT hybrid plant has higher efficiency, lower costs, and lower greenhouse gas emission than the SOFC standalone plant over the 30-year-lifetime. The levelized cost of electricity (LCOE) of SOFC/GT hybrid plant was computed as \$85/MWh, which is around 20 % of the LCOE of SOFC standalone plant. The CO_2 emissions of the hybrid plant was calculated as 493 kg/MWh, which is around 27 % lower than that of the standalone plant.

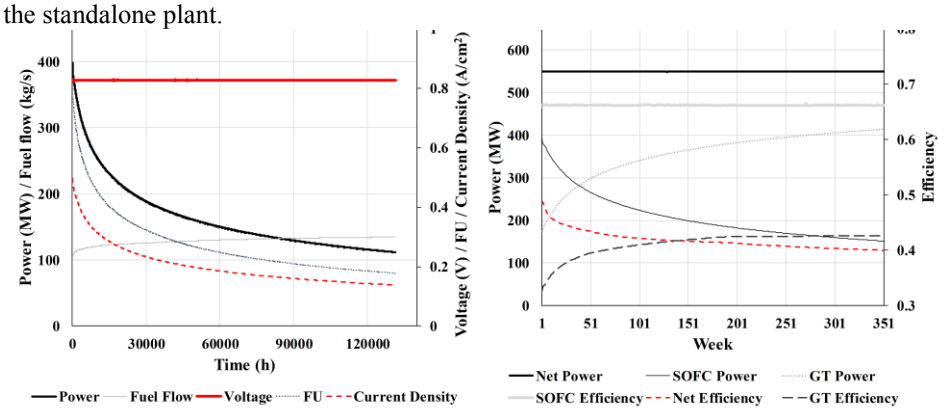

Figure 5. System performance curves of (a) the SOFC stack in SOFC/GT hybrid plant and (b) the SOFC/GT hybrid plant.

Table 1. Key performance indicators of SOFC standalone plant and SOFC/GT hybrid plant.

	SOFC Standalone Plant	SOFC/GT Hybrid Plant
SOFC Stack Efficiency (LHV)	57.9 %	66.2 %
Overall Plant Efficiency (LHV)	30.7 %	41.8 %
First year Capital Cost ($ Million)	$7,216	$4,129
Average Annual SOFC Replacement Cost ($ Million)	$3,048	$109
Annual Material, Operating and Maintenance Cost ($ Million)	$421	$398
LCOE ($/MWh)	$426	$85
CO_2 Emission (kg/MWh)	673	493

4. Conclusion

The proposed SOFC standalone plant and SOFC/GT hybrid plant were modelled and simulated with a pseudo-steady-state approach. By utilizing the simulation results, the eco-technoeconomic analysis showed that the SOFC/GT hybrid plant is more efficient with less cost compared to SOFC standalone plant. The overall plant efficiency of the hybrid plant was found to be 41.8 % which was around 36 % more efficient than the standalone plant. The hybrid plant had an LCOE of $85/MWh, and was around 80 % lower than the LCOE of the standalone plant. The CO_2 emission from the hybrid plant was also 27 % lower compared to the standalone plant. Therefore, the SOFC/GT hybrid was found to be a promising near-term approach for baseload power production in comparison with SOFC standalone system. Alternative designs with steam cycles will be analysed and included in future work.

References

T. A. Adams, L. Hoseinzade, P. B. Madabhushi, and I. J. Okeke. "Comparison of CO2 capture approaches for fossil-based power generation: review and meta-study." Processes 5, no. 3 (2017): 44.

T. A. Adams, J. Nease, D. Tucker, and P. I. Barton, “Energy Conversion with Solid Oxide Fuel Cell Systems: A Review of Concepts and Outlooks for the Short- and Long-Term,” Ind. Eng. Chem. Res., vol. 52, no. 9, pp. 3089–3111, Mar. 2013.

R. James, A. Zoelle, D. Keairns, M. Turner, M. Woods, and N. Kuehn, “Cost and Performance Baseline for Fossil Energy Plants Volume 1: Bituminous Coal and Natural Gas to Electricity”, Sept. 2019. NETL-PUB-22638

J. Nease and T. A. Adams, “Coal-fuelled systems for peaking power with 100% CO2 capture through integration of solid oxide fuel cells with compressed air energy storage,” J. Power Sources, vol. 251, pp. 92–107, Apr. 2014.

D. Tucker, M. Abreu-Sepulveda, and N. F. Harun, “SOFC Lifetime Assessment in Gas Turbine Hybrid Power Systems,” J. Fuel Cell Sci. Technol., vol. 11, no. 5, pp. 051008-051008-7, Aug. 2014.

D. Tucker, J. VanOsdol, E. Liese, L. Lawson, S. Zitney, R. Gemmen, J. C. Ford, and C. Haynes, "Evaluation of methods for thermal management in a coal-based SOFC turbine hybrid through numerical simulation." Journal of Fuel Cell Science and Technology 9, no. 4 (2012): 041004.

V. Zaccaria, D. Tucker, and A. Traverso, “A distributed real-time model of degradation in a solid oxide fuel cell, part I: Model characterization,” J. Power Sources, vol. 311, pp. 175–181, Apr. 2016.

Sauro Pierucci, Flavio Manenti, Giulia Bozzano, Davide Manca (Eds.)
Proceedings of the 30th European Symposium on Computer Aided Process Engineering (ESCAPE30), May 24-27, 2020, Milano, Italy.
http://dx.doi.org/10.1016/B978-0-12-823377-1.50071-9

Analysis of the Effect of the Ceramic Membrane Module Based on Ebsilon Software on Water Recovery of Flue Gas from Coal-fired Power Plants

Chao Jiang, Chenhui Jia, Pei Liu, Zheng Li

State Key Lab of Power Systems, Department of Energy and Power Engineering, Tsinghua University, Beijing 100084, China
liu_pei@tsinghua.edu.cn

Abstract

In this paper, the mechanism of flue gas desulfurization and membrane module water recycling was studied, based on Ebsilon software modeling of the thermal system of coal-fired power plant unit, under different operation conditions on the basis of this study membrane module set mode for water recycling effect, the results show that the membrane module placed in front of the desulfurization tower can effectively reduce the temperature of flue gas, recover heat and reduce the water consumption in the desulfurization process; the membrane module placed behind the desulfurization tower, it can recover the desulfurization process of flue gas absorption of water effective. The results provide support and guidance for the practical application of flue gas moisture recovery in coal-fired power plants.

Keywords: water recovery, Ebsilon software, setting mode

1. Introduction

Coal-fired power generation is China's main source of electricity. By the end of 2017, China's total installed capacity of power generation was 1.77 billion kilowatts, of which 0.98 billion kilowatts were coal-fired, accounting for 55.2 %. Coal-fired power generation uses and consumes a lot of water. In 2017, China's water consumption for coal-fired power generation was 5.187 billion m^3, accounting for 17.7 % of the country's industrial water consumption. The uneven distribution of water resources in China and the reverse spatial distribution of water resources and fossil energy lead to the prominent contradiction between regional supply and demand of water resources in China. Therefore, it is of great significance for coal-fired power plants to save water consumption.

According to the different functions of water in each subsystem or equipment, the water system of the coal-fired power plant can be roughly divided into 7 subsystems (Li,2011). For the air-cooled coal-fired power plant, the water consumption of the desulfurization system accounts for 38.40 %, which is the main water consumption point of this power plant. At present, more than 90 % of coal-fired power plants in China adopt the limestone-gypsum wet desulfurization process. The main water consumption of the system includes Gas and liquid water carried away by flue gas in desulfurization tower; Free water and crystal water contained in the reaction product gypsum; Discharge of desulfurization wastewater.

Table 1 shows the water consumption of the desulfurization system of a 2×300 MW coal-fired power plant as an example.

Table 1 The water consumption of the desulfurization system of a 2×300MW coal-fired power plant

Consumption	Water Consumption（t/h）	Proportion（%）
Evaporated Water	106.16	90.80
Liquid Water in Flue Gas	0.15	0.13
Free Water in Gypsum	2.02	1.73
Crystal Water in Gypsum	4.24	3.62
Desulfurization Waste Water	4.35	3.72

Table 1 shows that the gaseous water taken away by the flue gas after the absorption tower, namely the evaporation loss, accounts for 90.80 % of the system's water consumption and it is the most important water consumption point in the desulfurization process. The flue gas will contain trace sulfuric acid vapor, so that the flue gas dew point temperature increases, contact with the heating surface will condense and form sulfuric acid solution corrosion heating surface. On the other hand, desulfurization wastewater contains a lot of waste liquid of chloride and fluoride. To maintain the material balance of the slurry circulation system of the desulfurization unit, prevent the desulfurization equipment from being corroded and ensure the quality of gypsum. Therefore, recovery and effective treatment of water in the flue gas of coal-fired power plants is necessary. (Ma et al.,2017).

The main methods of recovering water vapor from flue gas are condensation, drying and composite membrane. The condensation method separates water from flue gas by lowering the temperature of flue gas below the dew point temperature (Xiong et al.,2017). The absorption method is based on the water vapor pressure difference between the flue gas and the desiccant solution as the driving force (Wang et al.,2016). The principle of composite membrane is to separate water and gas by driving differential pressure and using mixed gas components to have different adsorption capacity and permeation rate to water vapor on the membrane surface.

Compared with the other two methods, the composite membrane method can recycle the moisture in the flue gas with higher efficiency and quality (Gao et al.,2019). This project will mainly adopt the composite membrane method to research the moisture recovery of flue gas.

2. Methodology

2.1. Water absorption mechanism of desulfurization tower

There are many kinds of desulphurization processes. The most widely used process is selected in this research. The basic process flow is as in Figure 1.

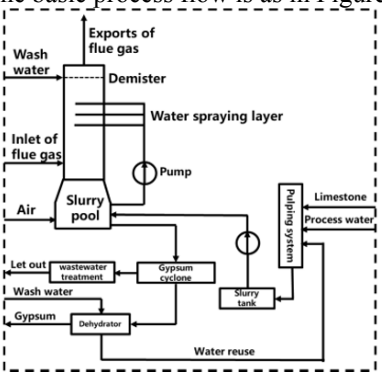

Figure 1 Schematic diagram of limestone - gypsum desulphurization system

The flue gas enters the lower part of the desulfurization absorption column under the action of the booster fan after being dusted by the dust collector. In the rising process, it comes into full contact with the falling limestone slurry sprayed by the spray. SO_2 in the flue gas is absorbed by the slurry and falls into the slurry pool at the bottom of the column. This is a complex process of heat and mass transfer accompanied by chemical reactions. This project mainly simulates the evaporation of water accompanying the heat transfer process, so the following assumptions are made:

(a) the flue gas passes through the absorber quickly, and the reaction process between flue gas and slurry is adiabatic.

(b) the heat transfer process in the tower is rapid and complete;

(c) the kinetic energy of flue gas inlet and outlet are ignored;

(d) the heat change of slurry entering and leaving the tower was ignored.

At this time, the thermal process of the hot flue gas in the absorption tower is similar to adiabatic humidification process, the enthalpy value of the flue gas in the tower is unchanged, the moisture content increases continuously, and it is saturated when it leaves the tower, given by Eq. (1)

$$hi = ho \tag{1}$$

Where h_i and h_o are the specific enthalpy of the flue gas inlet and outlet absorption towers respectively.

Therefore, the enthalpy value can be obtained from the state parameters of the flue gas entering the tower, and then other state parameters such as temperature and moisture content of the flue gas can be obtained. The calculation steps are shown in Figure 2.

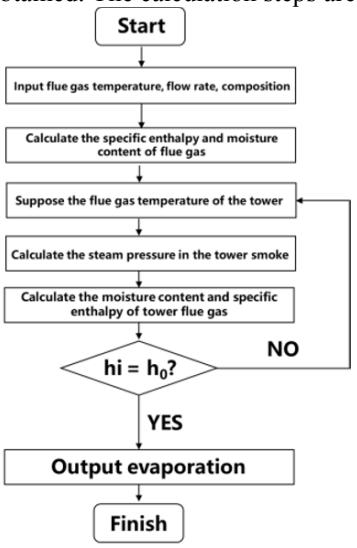

Figure 2 Calculation diagram of evaporation water in the desulfurization process

This model is used to analyze the characteristics of the process of flue gas desulfurization and water absorption, and to simulate and compare the results under different conditions such as flue gas inlet temperature and flue gas flow, as shown in Figure 3.

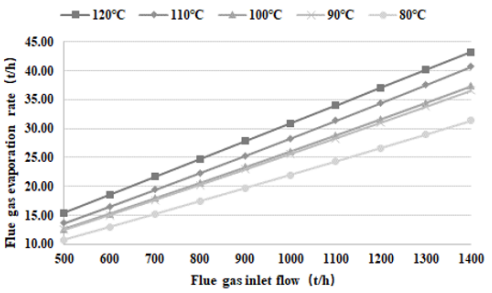

Figure 3 The variation of evaporation water with flue gas flow and inlet temperature in the desulfurization process

The results show that the desulfurization process of evaporation of water with the flue gas flow rate increases, the flue gas flow rate, water evaporation increases with flue gas inlet temperature increased significantly, therefore in flue gas desulfurization absorption tower set before the membrane module was carried out on the water and flue gas waste heat recovery is necessary, it can reduce the consumption of water in the desulfurization process.

2.2. Ceramic membrane module

The membrane module used in the water recovery system of coal-fired units are a ceramic composite membrane, and the ceramic membrane bundle is arranged in a cross row, and perpendicular to the flue gas flow direction, with cooling water inside. The ceramic-composite film is highly selective. When the smoke flows through the surface of the ceramic film, the water vapor condenses and condenses into water on the ceramic film wall. Under the action of the vapor pressure difference, the condensate water in the ceramic film enters the ceramic film tube, and nitrogen, sulfur dioxide, and other substances are blocked outside the film tube. The latent heat released by the condensation of steam and the sensible heat released by the flue gas is carried away by the cooling water to complete the process of mass transfer and heat transfer.

According to the flue gas water recovery system, the relevant research team（Gao et al.,2019）used the established membrane module mechanism model to analyze the water recovery and recovery rate under different flue gas flow, flue gas temperature, and other conditions, and the conclusions were as follows:

With the increase of flue gas flow in a certain range, the water recovery volume increases, but the water recovery efficiency decreases. When the flue gas flow exceeds a certain value, all the membrane tubes in the membrane assembly are close to full load, and the water recovery tends to be stable. As the temperature of the flue gas increases, the temperature difference between the flue gas and the condensed water increases, the heat exchange is enhanced, and more water vapor in the flue gas condenses into water and is recycled, so the amount of water recycling increases and the recovery rate increases. The influence of temperature on water recovery decreases with the increase of flue gas flow.

3. Analysis results and discussion

According to this unit 6 typical design conditions, Ebsilon software was used to model the thermal system of a 330MW coal-fired unit. The main component characteristics and leading factors of the system were determined by the dominant factor method, and the main component models of heat exchanger, pipeline, steam turbine unit and water

pump were established respectively, and the overall variable condition simulation was realized, as shown in Figure 4.

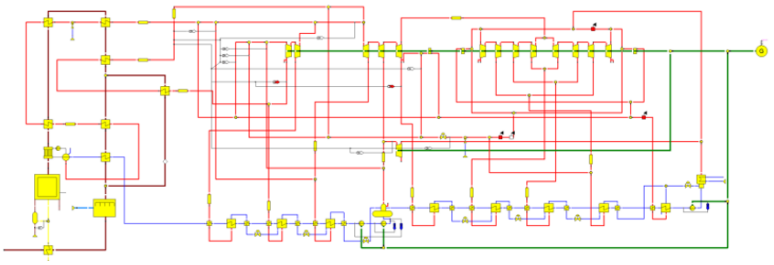

Figure 4 The thermal system of a 330MW coal-fired unit based on Ebsilon software

The simulation results were compared with the design values, and the average error of each measurement point was less than 1 %. The simulation results of the model were accurate. Through this model, the physical parameters of flue gas in the tail flue can be obtained under the actual operating conditions, and then the water recovery effect can be simulated and evaluated under different Settings of the membrane components.

Under different working conditions, the setting mode of the membrane module was used to simulate the water recovery effect in the flue gas. The setting mode of the membrane module was as follows: (a) No membrane module; (b) Set membrane module only in the flue in front of the desulfurization tower; (c) Set membrane module only in the flue behind the desulfurization tower; (d) Set membrane modules in the flue both in front of and behind the desulfurization tower, as shown in Figure 5, and results are shown in Figure6.

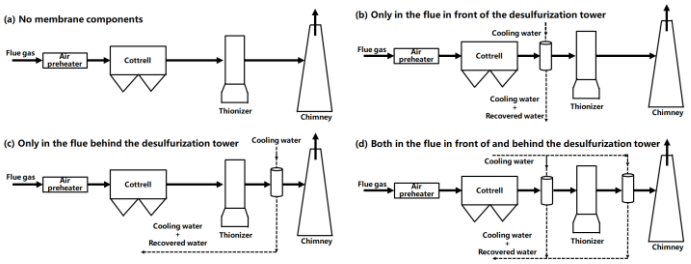

Figure 5 Four types of membrane module settings

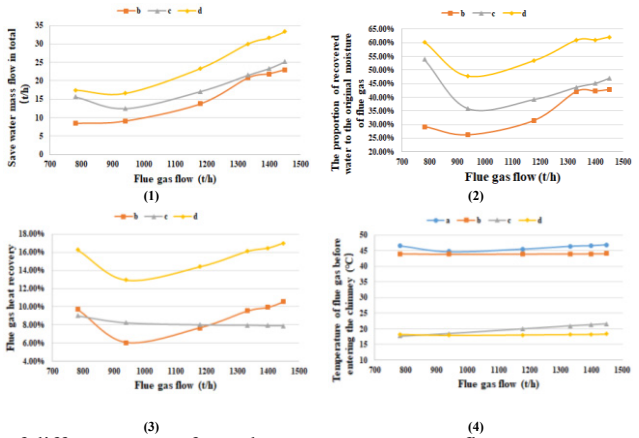

Figure 6 Effects of different types of membrane components on flue gas water recovery and heat recovery

As shown in Figure 6, although the water recovered by placing the membrane module before the desulfurization tower is not as much as that after the desulfurization tower, it can greatly reduce the temperature of flue gas entering the desulfurization tower, thus reducing the absorption of flue gas during the desulfurization process. After placing the membrane assembly in the desulfurization tower, more moisture can be recovered from the flue gas and the temperature of the flue gas outlet can be reduced. In addition, the membrane module is set in front of the desulfurized tower and behind the desulfurized tower to maximize the water recovery and heat recovery in the flue gas. Therefore, it is necessary to set up the membrane assembly before and after the desulfurization tower in the actual operation of the coal-fired power plant.

4. Conclusions

This work based on the existing water recovery technology on the basis of investigation and the key parts of the mechanism analysis and modeling, and combined with the actual situation of coal-fired power plants, coal-fired units were built based on Ebsilon software system and combustion system of variable working condition model, analysis of membrane module in all operating conditions, and the effects of different settings of flue gas water recycling. The results provide support and guidance for the practical application of membrane modules in the recovery of flue gas water in coal-fired power plants.

Acknowledgment

The authors gratefully acknowledge the support by The National Key Research and Development of China (2018YFB0604301) and the Phase Ⅲ Collaboration between BP and Tsinghua University.

References

Li, Y., 2011. Water Consumption Calculation Model and Water-saving Analysis of Thermal Power Plant（in Chinese）, Master's degree dissertation, Tsinghua University, 17-21.

Ma, S., Chai, J., Jiao, K., Ma, L., Zhu, S., Wu, K., 2017. Environmental influence and countermeasures for high humidity flue gas discharging from power plants, Renew. Sustain. Energy Rev. 73, 225-235.

Xiong, Y., Tan, H., Wang, Y., Xu, W., Mikulcic, H., Duic, N., 2017. Pilot-scale study on water and latent heat recovery from flue gas using fluorine plastic heat exchangers, J. Clean. Prod. 161, 1416-1422.

Wang, Z., Zhang, X., Li, Z., 2016. Evaluation of a flue gas driven open absorption system for heat and water recovery from fossil flue boilers, Energy Convers. Manag. 128, 57-65.

Gao, D., Li, Z., Zhang, H., Chen, H., Cheng, C., Liang, K., 2019. Moisture and latent heat recovery from flue gas by nonporous organic membranes, J. Clean. Prod. 225, 1065-1078.

Gao, D., Li, Z., Zhang, H., Chen, H., Wang, L., Liu, H., 2019. The investigation of desulphurization and water recovery from flue gas using a ceramic composite membrane, Int J Energy Res., 43,1747 – 1759.

Sauro Pierucci, Flavio Manenti, Giulia Bozzano, Davide Manca (Eds.)
Proceedings of the 30th European Symposium on Computer Aided Process Engineering (ESCAPE30), May 24-27, 2020, Milano, Italy.
http://dx.doi.org/10.1016/B978-0-12-823377-1.50072-0

Multi-objective Optimization under Uncertainty of Novel CHPC Process

Daniele Previtali[a], Francesco Rossi[b], Gintaras Reklaitis[b], Flavio Manenti*[a]

[a] *Politecnico di Milano, Dipartimento di Chimica, Materiali e Ingegneria Chimica "G.Natta", Piazza Leonardo da Vinci 32, 20133 Milano, Italy*

[b] *Purdue University, Forney Hall of Chemical Engineering, 480 Stadium Mall Drive, West Lafayette, IN 47907-2100, United States*

flavio.manenti@polimi.it

Abstract

Combined Heat and Power (CHP) and biomethane upgrading plants are the two main processes that use biogas in Europe. The first converts biogas into electric energy and heat while the second consist of the purification of methane, via removal of other components, and its injection into the national natural gas distribution grid. They both are considered to be green technologies but the overall carbon balance is positive for both processes. Use of biogas as raw material in chemical synthesis allows to fix carbon in the chemical molecule and avoid its release as carbon dioxide. This is the basic idea of Combined Heat Power and Chemical plants (CHPC). Starting from biogas, CHPC produces methanol, a valuable and important building block for industrial chemistry. In this work we optimized the entire process by using multiple objective functions (economics and environmental) and considering the uncertainty of the feed composition. The results of mono-objective optimization show that the CHPC plant can be economically feasible with a net consumption of CO_2. Multiple objective optimization identified the operating conditions in which payback time is reasonable and CO_2 balance negative. Optimization under uncertainty allowed to design a more flexible and realistic process which can accommodate the variations in inlet biogas composition.

Keywords: biogas, CHPC, optimization, process simulation.

1. Introduction

Biogas is a mixture of methane (CH_4) and carbon dioxide (CO_2), produced by anaerobic digestion of organic matter (sewage, manure, organic/agricultural waste, etc.). It is considered a renewable energy source with zero carbon emissions. Biogas is usually used as fuel in Combined Heat and Power (CHP) plant to produce heat and electricity or is upgraded to bio-methane, via removal of CO_2 and other impurities, which then can be injected into the natural gas distribution grid. In Europe, the electrical energy production from biogas increased from 4,778 MWe in 2011 to 10,532 MWe in 2017, while the biomethane production rose from 752 GWh in 2011 to 19,352 GWh in 2017 (EBA, 2018). Although these two technologies for energy production (thermal and/or electrical) may be considered green since the organic matter comes from fixed atmospheric CO_2, the overall carbon emissions are not zero, if all of the processing steps needed to produce feedstocks, biogas and its use are taken into account. The impact of CHP can be improved (Hijazi et al., 2016) but it is important also to evaluate alternative uses of biogas, which

can lead to no carbon emissions like the novel concept of the Combined Heat, Power and Chemical (CHPC) plant (Previtali et al., 2018). A CHPC plant converts biogas into bio-methanol (MeOH) such that at least part of the carbon of the biogas feedstock is not released back into the atmosphere as CO_2. Methanol is a widely used chemical with an annual world production of about 100 Mt [Alvarado, 2016], which is used as solvent and building-block to produce other chemicals, like dimethyl ether, acetic acid and formaldehyde. This chemical conversion process takes place in two principal unit operations, namely a reformer and a methanol synthesis reactor, the first of which converts biogas into syngas while the second transforms syngas into methanol. Compared to most conventional biogas conversion processes, CHPC plants offer lower environmental impact and generate a valuable chemical. Therefore, it is important to investigate the optimal design, optimal operating conditions and flexibility of this novel type of chemical process. The principal sources of uncertainty, considered in this analysis, will consist of the variations in the biogas feedstock composition. This aspect is extremely important due to the intrinsic variations of biogas composition which result from different biomass feedstocks and processing time (Herout et al., 2011). In this work we developed C++ models of each process unit (compressors, membranes, heat exchangers, reformers, plug flow reactors, etc.) and combined these models into a simulation which represent the entire CHPC process. The C++ implementation enables the efficient execution of the stochastic optimization computations. The model is validated by comparing results with PRO/II®, a well-recognized process simulation software by AVEVA (former Schneider Electric). Finally, using stochastic optimization and uncertainty quantification techniques, we establish robust optimal operating conditions and assess the degree of flexibility, offered by this new chemical process. All the optimization tasks are carried out using both conventional economic optimization and multi-objective optimization methods, which allows us to consider both economic and environmental impact indicators.

2. Materials and Methods

The CHCP process which converts biogas to methanol, is shown in Figure 1.

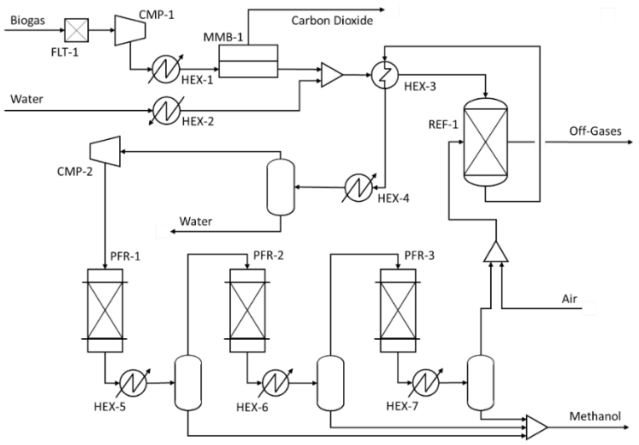

Figure 1. Process scheme of CHPC process

Biogas fed to the CHPC plant and is compressed up to about 15 bar by compressor CMP-1. We assumed that the only components in biogas are CH_4 (60%), H_2S (200ppm) and CO_2 (the remaining, about 40%); in other words, methane and carbon dioxide are the main components while although H_2S composition is small it cannot be neglected due to its important poisoning effects on reformer and methanol catalysts. The FLT-1 unit is an activated carbon filter for H_2S removal. This kind of guard bed is able to remove also other impurities (ammonia, siloxane…) but in this study its sizing is directly determined by the H_2S concentration and flowrate. Heat exchanger HEX-1 cools the purified biogas before processing in the membrane MMB-1. The biogas is partially upgraded to increase the methane fraction, since too high of a CO_2 content causes the production of a syngas with a low methanol module number which, in the PFRs, facilitates the reverse Water Gas Shift (rWGS) reaction favouring production of CO and H_2O instead of methanol (Bozzano, 2016). Steam is added before heat exchanger HEX-3 where the mixture is preheated recovering heat from the products of the reformer REF-1. The reformer is simulated as an equilibrium reactor since products can be considered to exit at the thermodynamic equilibria. Hot produced syngas is sent to the preheater HEX-3 to recover part of the sensible heat and then to the condenser HEX-4 where water is removed. Syngas is sent to compressor CMP-2 which increases the pressure up to 40 bar. The outlet of the third reactor is mixed with air (5% of oxygen in excess) and burned to provide heat for REF-1. The combustion can be considered to occur at the equilibria; a Gibbs reactor simulates the hot side of the reformer REF-1. The heat duty produced by combustion of off-gases sustains the reforming reactions. The CHPC process was modelled using C++ code. The Object-Oriented Programming (OOP) paradigm allows implementation of a general framework which is able to model several plant configurations. Each equipment is coded as a class with a standardized structure. Inputs and outputs are divided as Model Parameters, Manipulated Variables and State Variables. Model Parameters are the design variables associated with each equipment, such as the internal diameter of heat exchanger tubes, volume of a PFR, area of membranes, thermal coefficients of building materials. The manipulated Variables are operating conditions and parameters that can be adjust for the equipment its design like flowrate of heat exchanger coolant or heating medium, power of compressor or temperature, pressure, composition and flowrate of feed streams. Redlich-Kwong-Soave equation of state is the thermodynamic model implemented (Soave, 1972). The binary parameters for each compound were extracted from the PRO/II® 10.0 database. Functions for estimation of liquid and vapor properties such as the density, specific heat capacity, vaporization enthalpy, vapor liquid equilibria, thermal conductivity and viscosity, are available in PRO/II® 10.0 and online from the NIST database. Usually all these properties are described by complicated functions and, since they are called numerous times during each iteration, they can lead to high computational time. Use of simplified correlations, usually a second-degree function, facilitates computational efficiency. Re-regression and code cleanness are mandatory steps to keep the program execution as fast as possible; this is particularly important for the Thermopackage class which is the most frequently called class during the execution of the entire program. BzzMath library (Buzzi-Ferraris, 2012) routines were used to solve Non-Linear Systems, Differential Algebraic Equations, Ordinary and Differential Equations and to conduct the minimizations. The final software, called BigSQRT, was tested comparing the technical results with the those obtained with PRO/II®. Guthrie's method was used to estimate capital costs (Guthrie, 1969, Guthrie et al, 1974). Capital expenses (CAPEX) are estimated considering three main parameters: equipment type, characteristic dimension (power for pumps, area for heat exchanger…), operating pressure and material of construction. The life-time of the plant is 10 years according with

Turton (Turton et al., 2012). Operating expenses (OPEX) considered include cooling water, electricity, steam, catalysts and maintenance. The environmental footprint is calculated considering the impact due to equipment construction (steel production, manufacturing, welding…) as well as that one due to consumables such as (steam, electricity, heat, catalysts…). The Carbon footprint, or global warming according with IPCC, was the only indicator considered (IPCC, 2013), implementation of more complex models like ReCiPe or ILCD was considered overly complex and unnecessary for this work. Environmental data and impacts for secondary data were extracted from Ecoinvent 3.1 database. The CHPC process was optimized with respect to two different criteria: a mono-objective and a multi-objective. Mono-objective optimization minimizes an economic function (payback time), an environmental function (carbon footprint) or both, using a traditional economic function in which CO_2 emissions are weighted by a carbon tax. The Multi-objective optimization is based on using the utopian point method instead of the more traditional one based on a Pareto-curve. The latter method produces a series of points, a curve (grey line in Figure 2), in which the improvement of one criterion (payback time) causes the deterioration of the other (carbon footprint). This method is not an actual optimization since does not produce an optimal point, rather several optimal points. Moreover, the computational effort is high due to the high number of points that must be calculated.

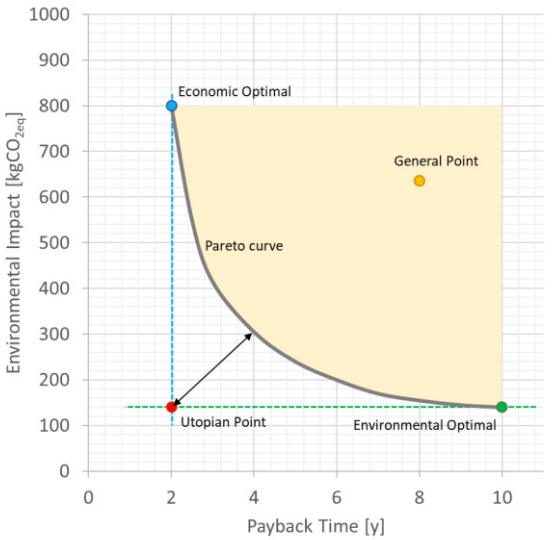

Figure 2. Scheme of multi-objective optimization based on the utopian point method

Multi-objective optimization based on the utopian point method allows faster optimization and leads to a single solution. The utopian point (red point) is defined by the optimal results of each mono-objective optimization (green and blue points), the result of multi-objective optimization is the point on the pareto curve at which the distance z is minimum. Optimization was done also considering uncertainty on inlet biogas composition, an annual variation of methane (55 – 65 %vol), carbon dioxide (33 – 43 %vol) and hydrogen sulphide (150 – 300 ppm) was assumed. Traditional mono-objective optimization was run also with PRO/II® in order to compare the robustness and the speed of the two optimization approaches.

3. Results and Discussion

Thermodynamic properties of pure components were found to be equal to those calculated with PRO/II® (average difference lower than 1%) while for mixtures the average error is slightly higher but acceptable (lower than 5%). Other calculated properties like dew/bubble point temperature and pressure can be considered equal (average difference lower than 2%). Simulation of single unit like heat exchanger, flash, compressor, equilibrium and plug flow reactor, H_2S filter and membrane gives similar results. Calculated duties, outlet compositions, flowrates, temperatures and pressures have an average error lower than 5%. Relative errors of composition can be higher for some components, up to 50% – 70%, but in those limited cases the difference is due to substances with a very low concentration, which means that the error can be considered negligible. BigSQRT is about 10 times faster than PRO/II®, the average computational time of 1 iteration is 0.2 sec compared to 2.2 sec for the latter. Optimizations were run varying several parameters: power of compressors CMP-1 and CMP2, area of heat exchangers HEX-1, HEX-2, HEX-3, HEX-4, HEX-5, HEX-6, HEX-7, temperature of equilibrium reactor REF-1, length of PFRs PFR-1, PFR-2, PFR-3, area of membrane MMB-1, volume of filter FLT-1. Robustness of BigSQRT is higher than PRO/II®, starting from the same initial conditions the first one can reach better terminal points. Optimized results obtained with BigSQRT were verified by using the calculated optimal parameters as input to PRO/II®.

Table 1. Results of different optimization

Optimization function	CAPEX [M$]	OPEX [M$/y]	Payback [y]	Net Present Value [M$]	CO_2 emissions [tonCO_{2eq}/y]
Economic	4.78	0.59	6.06	2.22	7,195
Environmental	4.33	0.35	9.96	-0.47	5,507
Eco – Environmental	4.65	0.92	10.85	-0.78	7,142
Eco – Environmental (MultiObjective)	4.61	0.51	6.81	1.78	6,636

Economic optimization results in a payback time of 6.06 years; while minimizing the overall CO_2 emissions (without considering the stored carbon dioxide as methanol) the carbon footprint can be decreased up to 24% but with a payback time of 10 years (Table 1). An initial eco-economical optimization was done considering a carbon tax of 70€ per tons of CO_2 but this kind of optimization may give misleading results since the result is strictly dependent on the selected value of the carbon tax. The Eco-Environmental optimization using multi-objective function was performed setting 6.06 years of payback and 5,507 tonCO_{2eq}/y as utopian point. The multi-objective optimization shows that the operating parameters can be optimized to obtain a good balance between environmental impact and economics. Considering uncertainty, both payback time and CO_2 emissions increase to 7.74 years and 7,812 tonCO_{2eq}/y respectively. Variations in biogas composition cause higher CAPEX and OPEX, the first is due to the need to oversize the design of some equipment like H_2S filter, membrane, reactors and compressors while, higher OPEX are mainly caused by a higher consumption of catalysts and higher pressure in the methanol synthesis section. Although these results seem worse that those obtained without considering uncertainty, the latter cannot be considered reliable since they are

based on the assumption that biogas composition is always the same. Using a different inlet biogas composition of (CH_4 56%, H_2S 230ppm and remaining CO_2) and the operating parameters obtained with the optimization without uncertainty, the methanol production decreases and so the resulting payback time to 8,93 years, while with operating parameters optimized considering uncertainty the payback time increase only to 8.18 years. This is due to the plant design which in the first case is optimized for only one biogas composition, namely the average value. Variations in feed composition cannot be considered negligible since they lead to important differences in process design that can only be evaluated with optimization under uncertainty.

4. Conclusions

Optimization of processes that use bio-feedstock as raw material can be challenging because traditional methods can lead to misleading results. The CHPC is a novel process which converts biogas into methanol. In this work we developed a software tool for optimizing the design of the CHPC process in order to minimize environmental impact and payback time. Several methods were considered, the results of the optimization under uncertainty showed that the results can be significantly influenced by variations of biogas composition. Payback times and environmental impacts that are too optimistic could be obtained if optimization under uncertainty is not performed. The CHPC process does offer a promising payback time and its carbon footprint, under some conditions, may be negative. Future work will be focussed on improvements to the stochastic optimization.

References

Alvarado M., (2016). The changing face of the global methanol industry, HIS Chemical Bulletin (Issue 3, pp. 10-11)

Bozzano G., Manenti F., (2016), Efficient methanol synthesis: Perspectives, technologies and optimization strategies, Progress in Energy and Combustion Science, 56, 71-105.

Buzzi-Ferraris G, Manenti F. BzzMath: Library Overview and Recent Advances in Numerical Methods. vol. 30. Elsevier B.V.; 2012. doi:10.1016/b978-0-444-59520-1.50121-4.

EBA Annual Statistical Report (2018), European Biogas Association

Previtali D., Vita A., Bassani A., Italiano C., Furtado Amaral A., Pirola C., Pino L., Palella A., Manenti F., (2018). Methanol Synthesis: a Distributed Production Concept Based on Biogas Plants, Chemical Engineering Transactions, 65, 409-414.

Guthrie K.M., 1969, Capital cost estimating, Chemical Engineering, 76, 114-142

Guthrie, K.M. Eds., 1974, Process Plant Estimating, Evaluation and Control, Craffsman Book Company, Solana Beach, USA

Herout, M., Malaťák, J., Kučera, L., & Dlabaja, T. (2011). Biogas composition depending on the type of plant biomass used. Research in Agricultural Engineering, 57(4), 137-143.

Hijazi O., Munro S., Zerhusen B., Effenberger M. (2016). Review of life cycle assessment for biogas production in Europe Renewable and Sustainable Energy Reviews (Vol. 54, pp. 1291–1300)

IPCC. Climate Change 2013 2013. http://www.climatechange2013.org/

Rossi, F., Manenti, F., Buzzi-Ferraris, G., & Reklaitis, G. (2017). Stochastic NMPC/DRTO of Batch Operations: Batch-to-Batch Dynamic Identification of the Optimal Description of Model Uncertainty. In Computer Aided Chemical Engineering (Vol. 40, pp. 2251-2256). Elsevier.

Soave, G., (1972) Equilibrium constants from a modified Redlich-Kwong equation of state, Chemical Engineering Science, (Vol. 27, pp. 1197-)

Turton R, Bailie RC, Whiting WB, Shaeiwitz JA. (2012) Analysis, Synthesis, and Design of Chemical Processes. Fourth Edi. Pearson Education, Inc.

Sauro Pierucci, Flavio Manenti, Giulia Bozzano, Davide Manca (Eds.)
Proceedings of the 30th European Symposium on Computer Aided Process Engineering (ESCAPE30), May 24-27, 2020, Milano, Italy.
http://dx.doi.org/10.1016/B978-0-12-823377-1.50073-2

Multi-objective Dynamic Optimisation of Ampicillin Batch Crystallisation

Antonios Dafnomilis[a], Samir Diab[b], Alistair D. Rodman[b], Andreas G. Boudouvis,[a] Dimitrios I. Gerogiorgis[b*]

[a] *School of Chemical Engineering, National Technical University of Athens, Athens 15780, Greece*
[b] *Institute for Materials and Processes (IMP), School of Engineering, University of Edinburgh, The Kings Buildings, Edinburgh, EH9 3FB, United Kingdom*
D.Gerogiorgis@ed.ac.uk

Abstract

Ampicillin is a key β-lactam antibiotic listed as a World Health Organisation (WHO) *Essential Medicine*. Crystallisation is a unit operation of paramount importance in pharmaceutical manufacturing, whose design and operation are essential in controlling process yield and important product quality attributes, such as mean product crystal size (MCS) and size distribution width. A published model for the solubility of ampicillin as a function of pH as well as growth and nucleation kinetics is used towards the simulation and optimisation of its batch crystallisation. This study performs multi-objective dynamic optimisation of the batch crystallisation of ampicillin to establish optimal pH trajectories for different production objectives, including maximising the mean crystal size whilst minimising the size distribution width subject to various yield constraints. Trade-offs between different product quality attributes are thus quantified, visualised and discussed.

Keywords: Multi-objective dynamic optimisation; batch crystallisation; ampicillin.

1. Introduction

Ampicillin is a broad-spectrum, semi-synthetic β-lactam antibiotic, used to treat various bacterial infections such as urinary and respiratory tract infections, being one of the ten most consumed antibiotics worldwide (Hamed et al., 2015). The β-lactam family of antibiotics are typically delivered orally and hence crystallisation is an essential unit operation in the production of these drugs, including ampicillin. The design and optimisation of crystallisation processes for efficient antibiotic production is important for its lean and agile manufacturing. The final size, shape and form of crystalline products are essential in pharmaceutical manufacturing as these product quality attributes influence downstream operations as well as the bioavailability of the crystalline product. Significant efforts in the development of batch crystallisation processes for their design and control have furthered pharmaceutical crystallisation significantly (Gao et al., 2017). Process modelling and optimisation studies performed before laborious, expensive experimental campaigns can elucidate optimal batch crystallisation manipulations (e.g. temperature, pH, antisolvent dosing) profiles, thus allowing for significant R&D time and cost savings.

The batch crystallisation of ampicillin via pH manipulation has been demonstrated in the literature, including a model with detailed kinetics and solubility behaviour as a function of pH (Encarnación-Gómez et al., 2016). Dynamic optimisation of pH-profiles for ampicillin batch crystallisation may establish improved operating policies for improved

process performances vs. straightforward linear pH variations demonstrated in the literature thus far. This study implements the described ampicillin batch crystallisation model for dynamic optimisation of pH manipulation profiles to optimise product quality attributes subject to different operational and performance constraints. First, the published dynamic model for batch crystallisation is described in detail. The formulation of a dynamic optimisation problem with pH as the manipulated variable is described, with different case studies corresponding to experimental demonstrations. Optimisation results for different considered cases are presented in detail, followed by a critical comparison regarding trade-offs between process performance and key product quality attributes.

2. Batch Crystallisation Model

The ampicillin batch crystallisation model describes the antibiotic's aqueous solubility vs. pH, nucleation and growth kinetics and population and mass balance equations, the simultaneous solution of which describes the crystallisation process (Encarnación-Gómez et al., 2016). It is assumed that all considered processes are isothermal at T = 25 °C, crystallisation is only induced via pH-variation and that pH variation in mixtures are instantaneous upon the implemented manipulation. The solubility of ampicillin as a function of pH is described using the extended Pitzer model (de Pessôa Filho et al., 2008) in Eqs. 1–2, where constants ε, σ, pK_{A1} and pK_{A2} are taken from the literature (Encarnación-Gómez et al., 2016), k_B = Boltzmann constant, N_A = Avogadro number, ρ = ampicillin density and the isoelectric point (pI) and its corresponding solubility (S(pI)) are regressed in previous work (Dafnomilis et al., 2019)

$$\log\frac{S(pH)}{S(pI)} = pI - pH + \log\left[\frac{1+10^{pH-\mathrm{p}K_{A1}}}{1+10^{pI-\mathrm{p}K_{A1}}}\right] + \log\left[\frac{1+10^{pH-\mathrm{p}K_{A2}}}{1+10^{pI-\mathrm{p}K_{A2}}}\right] + \frac{2}{\ln 10}\lambda[S(pI) - S(pH)] \quad (1)$$

$$\lambda = \frac{2\pi\sigma^3 N_A \rho}{3}\left(1 - \frac{\varepsilon}{k_B T}\right) \quad (2)$$

Crystallisation kinetics are described by Eqs. 3–7, where J = overall nucleation rate, G =linear growth rate, M = suspension density, SS = supersaturation (all of which are a function of time, t), and parameters k_B, B_0, b, s, k_G and g are found in the literature (Encarnación-Gómez et al., 2016). The population balance in a batch crystalliser is described by Eq. 8, where n = the population density function, L = characteristic crystal length (assuming linear 1D growth), complimented by the boundary (Eq. 9) and initial (Eq. 10) conditions, corresponding to the population density of nuclei at t and that of seeds (n_0), respectively. The solute mass balance across the liquid and solid phases is described by Eq. 11, where the ampicillin concentration, [Amp], removed from solution via crystallisation and contributes to the suspension density (M).

$$G(t) = k_G\,(SS(t) - 1)^g \quad (3)$$

$$J(t) = B_1(t) + B_2(t) \quad (4)$$

$$B_1(t) = k_{B1}\exp\left(-\frac{B_0}{\ln(SS(t)^2)}\right) \quad (5)$$

$$B_2(t) = k_{B2}\,M(t)^b\,(SS(t) - 1)^s \quad (6)$$

$$SS(t) = \frac{[Amp](t)}{S(t)} \quad (7)$$

$$\frac{\partial n(t,L)}{\partial t} = -\frac{\partial\left(G(t)n(t,L)\right)}{\partial L} \quad (8)$$

$$n(t,0) = \frac{J(t)}{G(t)} \quad (9)$$

$$n(0,L) = n_0 \quad (10)$$

$$\frac{\mathrm{d}[Amp]}{\mathrm{d}t} = -\frac{\mathrm{d}M}{\mathrm{d}t} \quad (11)$$

3. Dynamic Optimisation Problem Formulation

This study considers the dynamic optimisation of the batch seeded crystallisation of ampicillin by manipulation of the pH trajectory over the batch duration. Generally, large Mean Crystal Sizes (*MCS*) and narrow size distributions (i.e., low *STD* or *CV*) are desired. Here, we maximise *MCS* while minimising *STD* by considering the objective function as a weighted sum of *MCS* and *STD* (Eq. 12), with associated weights W_{STD} and W_{MCS}. Imposed constraints on the problem are defined as follows. The first constraint (Eq. 13) ensures sufficient supersaturation at the beginning of the batch. The second constraint (Eq. 14) ensures the pH is not too low (causing ampicillin degradation) or high (forming undesirable non-trihydrate ampicillin polymorphs); ampicillin has limited chemical stability at pH ≤ 5, below which degradation products are formed, and undesired non-trihydrate polymorphs are formed at pH > 8 (Bezerra et al., 2018). The third constraint (Eq. 15) ensures that a minimum of a target amount of ampicillin is crystallised from solution at the end of the batch duration, t_f. The fourth constraint (Eq. 16) ensures sufficient *SS* is maintained. We consider W_{STD} = 1.0, W_{MCS} = 1.5 and the number of equispaced time discretisation intervals in the time domain, N = 30. The number of state variable collocation points, K_x = 3, and the initialisation pH profile is constant $pH(t) = 7$, unless stated otherwise in Section 4; the effects of varying W_i on the objective function and values of N have been considered and analysed previously (Dafnomilis et al., 2019).

$$\min_{pH(t),t_f} f(x, t_f) = W_{STD}STD - W_{MCS}MCS \tag{12}$$

$$7 \leq pH(t_0) \tag{13}$$

$$5.5 \leq pH(t) \leq 8.0 \tag{14}$$

$$[Amp](t_f) \leq [Amp]_{target} \tag{15}$$

$$1 < SS(t) \tag{16}$$

The optimisation problem is solved using orthogonal collocation on finite elements via the DynOpt package in MATLAB (Čižniar et al., 2005), which has been used in previous work for the optimisation of biochemical process control trajectories (Rodman and Gerogiorgis, 2019). We compare dynamic optimisation results for different cases of seed loading. Table 1 summarises parameters considered for each case, corresponding to three (experimentally demonstrated already) seeded ampicillin crystallisation cases. The target crystallisation yields are comparable with experiments (Encarnación-Gómez et al., 2016).

Table 1: Dynamic optimisation problem cases considered.

Case	1	2	3
Seeding (wt%)	1.8	3.0	15.0
$[Amp](t_f)$ (g kg^{-1})	{6.8, 8.0}	{6.8, 8.0}	{6.9, 9.0}
Yield (%)	{39.8, 29.2}	{39.8, 29.2}	{46.4, 52.1}
t_f (min)	250	350	1,500

4. Results and Discussion

Optimal *pH*, nucleation, growth, *SS* and *MCS* profiles for different cases and yields are shown in Fig. 1. For lower crystallisation yields, the general pH manipulation is a drop near the beginning of the batch, followed by an increase and then a drop towards the end; this results in high *SS* at the start, followed by a decrease and then an increase towards the end. The initial high *SS* promotes nucleation; the subsequent lower supersaturation allows nuclei to grow to attain high *MCS* as per the defined objective function. The final increase in *SS* allows further nucleation to increase the yield to meet the target yield. This

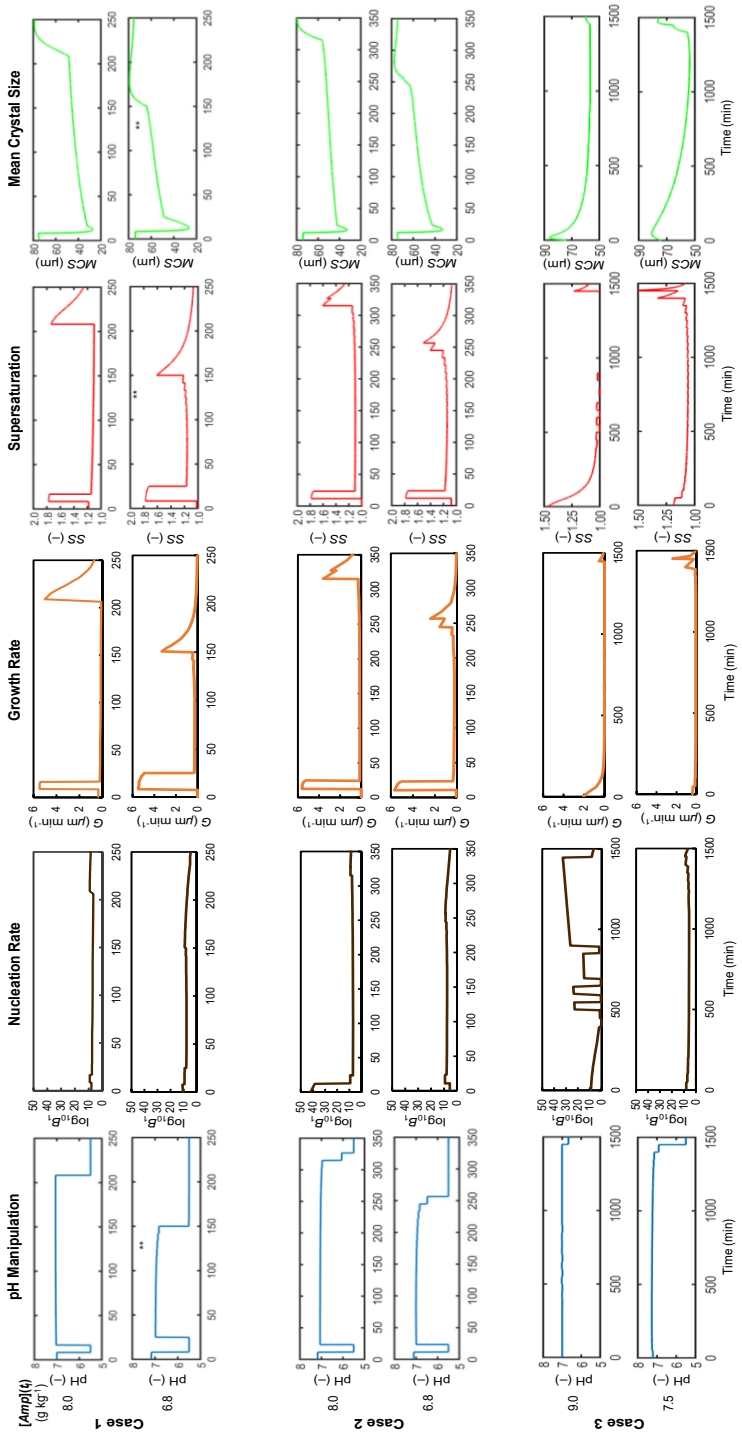

Figure 1: Optimal trajectories for all cases; $N = 30$; $K_x = 3$; initialised at $pH(t) = 7$.

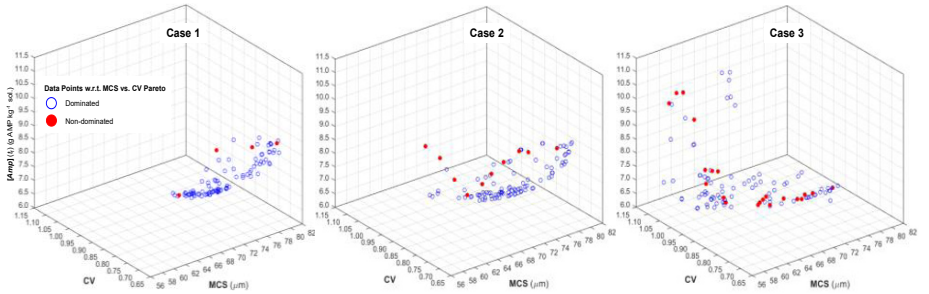

Figure 2: 3D Pareto front of the multiobjective dynamic optimisation problem (all cases).

results in *MCS* profiles which drop at the start (as nuclei form, the average *MCS* decreases) followed by an increase (due to growth dominating). As the target crystallisation yield is increased, the resulting optimal profiles change. The final decrease in pH in order to enhance the yield occurs earlier; this is due to the need to crystallise more nuclei in order to meet the target yield. As a consequence, *MCS* profiles begin to gradually decrease due to the formation of nuclei, although are approximately the same as for lower yields. Lower W_{MCS} values result in similar forms of pH manipulation and state trajectories, with more drastic pH drops resulting in more nucleation, and thus lower final *MCS* values, as *MCS* is given less importance in the objective function (Dafnomilis et al., 2019). As the seed loading is increased, the pH drop towards the end of the batch duration is observed later. For higher seed loading; the yield is enhanced as fewer nuclei are needed to meet the target yield. In all cases, a pH drop is only implemented towards the end of the batch duration, as growth is more important than generating new nuclei.

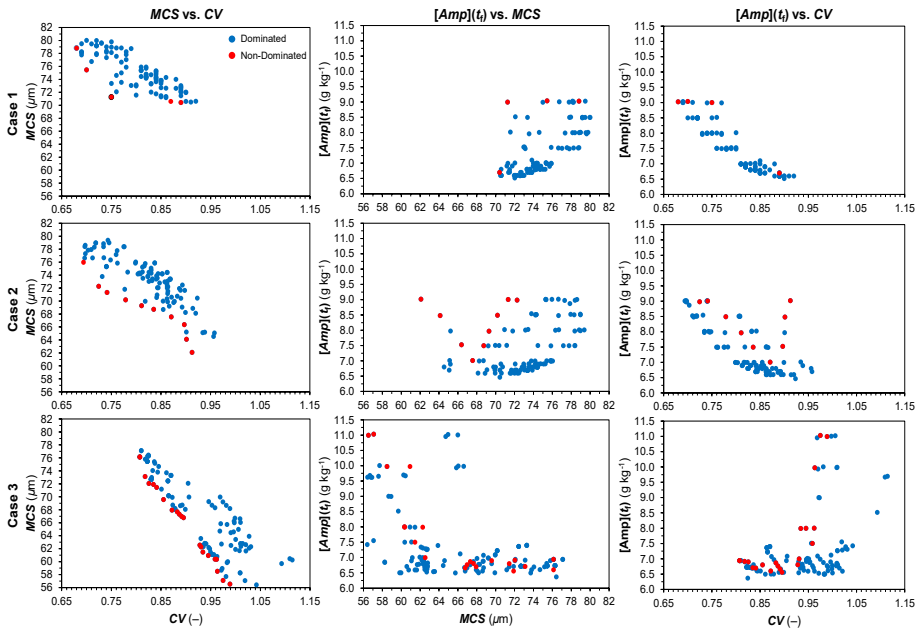

Figure 3: 2D Pareto front projections of the dynamic optimisation problem.

Pareto fronts of $[Amp](t_f)$ vs. *MCS* and *CV* are shown in Figs. 2 and 3 to quantify and visualise production trade-offs. For lower seed loadings, the attained *MCS* and *CV* are higher and lower, respectively, than for higher loading. For Case 3, there is not as evident

a trade-off between yield and *MCS* or *CV*. Investigating the effect of intermediate seed loadings and dynamic seeding policies will further elucidate process improvements. While experimental values of *CV* for different seeded cases are not provided in the literature (Encarnación-Gómez et al., 2016), computed *MCS* values attained via dynamic optimisation of pH profiles in this study are higher than reported values, illustrating the benefit of the implemented framework for batch crystallisation process improvements.

5. Conclusions

This study implemented dynamic optimisation for the batch crystallisation of ampicillin via pH control. The dynamic batch crystallisation model encompasses ampicillin solubility behaviour as a function of pH, growth and nucleation kinetics as a function of crystallisation pH, population balances (using the method of moments to reduce their complexity) and solute mass balances. The optimal pH manipulation trajectory varies with target crystallisation yield and considered seed loading. Optimal pH profiles are such that high supersaturation is generated at the start of the batch run in order to meet the target crystallisation yield followed by lower supersaturation to promote growth and minimise the size distribution width. Illustrations of Pareto fronts of target yield vs. product quality attributes (*MCS* and *CV*) show evident trade-offs between the crystallisation performance and desired product size distribution properties. Future work will consider seed loading as a dynamic control variable to further optimise dynamic control profiles to meet different production specifications of ampicillin production.

Acknowledgements

The authors acknowledge the support of the Engineering and Physical Sciences Research Council (EPSRC)/IAA, the Japan Society for the Promotion of Science, the Great Britain Sasakawa and Nagai Foundations and the Royal Academy of Engineering (RAEng). We are grateful for recent support by the Erasmus+ Student/Teaching Exchange Programme (A.D., A.B., D.G.) and a completed Eric Birse Charitable Trust PhD Fellowship (A.R.).

References

I.M. Bezerra, L.C. Moreira, O. Chiavone-Filho and S. Mattedi, 2018, Effect of different variables in the solubility of ampicillin and corresponding solid phase, *Fluid Phase Equilib.*, 459, 18–29.

M. Čižniar, M. Fikar and M.A. Latifi, 2005, MATLAB Dynamic optimisation code DynOpt. User's guide, *KIRP FCHPT STU Bratislava*.

A.D. Dafnomilis, S. Diab, A.D. Rodman, A.G. Boudouvis and D.I. Gerogiorgis, 2019, Multi-objective dynamic optimization of ampicillin crystallization: sensitivity analysis of attainable performance vs. product quality constraints, *Ind. Eng. Chem. Res.*, 58, 40, 18756–18771.

L.G. Encarnación-Gómez, A.S. Bommarius and R.W. Rousseau, 2016, Crystallization kinetics of ampicillin using online monitoring tools and robust parameter estimation, *Ind. Eng. Chem. Res.*, 55, 7, 2153–2162.

Z. Gao, S. Rohani, J. Gong and J. Wang, 2017, Recent developments in the crystallization process: toward the pharmaceutical industry, *Engineering*, 3, 3, 343–353.

R.B. Hamed, J.R. Gomez-Castellanos, L. Henry, C. Ducho, M.A. McDonough and C.J. Schofield, 2013, The enzymes of β-lactam biosynthesis, *Nat. Prod. Rep.*, 30, 1, 21–107.

P.A. de Pessôa Filho and G. Maurer, 2008, An extension of the Pitzer equation for the excess Gibbs energy of aqueous electrolyte to polyelectrolyte solutions, *Fluid Phase Equilib.*, 269, 25–35.

A.D. Rodman and D.I. Gerogiorgis, 2019, An investigation of initialisation strategies for dynamic temperature optimisation in beer fermentation, *Comput. Chem. Eng.*, 124, 43–61.

Sauro Pierucci, Flavio Manenti, Giulia Bozzano, Davide Manca (Eds.)
Proceedings of the 30th European Symposium on Computer Aided Process Engineering (ESCAPE30), May 24-27, 2020, Milano, Italy.
http://dx.doi.org/10.1016/B978-0-12-823377-1.50074-4

Reliability Estimation for Sensor Networks in Chemical Plants using Monte Carlo Methods

José Hernández[a] ,Carolina Salto[b], Gabriela Minetti[b], Mercedes Carnero[a], Mabel Sánchez[c]

[a] *Grupo de Optimización Facultad de Ingeniería – Universidad Nacional de Río Cuarto*
[b]*Lab. de Investigación en Sistemas Inteligentes-Universidad Nacional de La Pampa*
[c]*Universidad Nacional del Sur (UNS-CONICET), (8000) Bahía Blanca, Argentina*
jlh@ing.unrc.edu.ar

Abstract

The aim of this work is to analyze and determine an efficient and flexible resolution methodology to address the design of a minimum cost instrument network subject to restrictions over a set of key variables. In this sense, a Monte Carlo Simulation method is proposes to evaluate the reliability of the network defined as the probability of continuing to observe the keys variables when the instruments fails according to a given failure model. This is a powerful technique to model this stochastic behavior of systems and components. The optimization engine chosen is a heuristic, Simulated Annealing, which has shown to have a good performance for this kind of problems. Industrial examples of increasing complexity are provided to show the efficiency of the algorithms.

Keywords: sensor network, combinatorial optimization, reliability, metaheuristics.

1. Introduction

In a chemical plant, having a knowledge of the process state at any time is absolutely crucial with impact on aspects such as economic, control, energy efficiency or safety. In other words, the monitoring of the plant must be guaranteed. The information is collected by sensors distributed throughout the plant, responsible for measuring and transmitting the values of magnitudes such as flows, temperature, humidity, pressure, etc. The set of devices used in the measurement is called the sensor network (SN, Sensor Network). The SN design systematically made by formulating an optimization problem called Sensor Network Design Problem (SNDP), which is a discrete optimization problem. The design of sensor networks in process plants can be stated in a general way as a strategy whose objective is to reach a certain degree of estimability for a set of key process variables, while a certain quality is required on these estimates. In general, the number of variables that are involved in these problems for a real work scenario is quite large and the formulation can be more or less complex depending on the performance criteria and the restrictions set imposed on it. The optimal design of instrumentation networks in chemical plants involves two fundamental aspects. The first one is associated to the different formulations in terms of performance functions to optimize, and restrictions imposed. The second aspect is related to the choice of the resolution methodology. Although exact methods have been presented for this purpose, (Zhang and Chmielewski, 2017), there is today a more or less generalized consensus that the methods encompassed within metaheuristic techniques are the ones that provide the possibility to solve problems more real that can involve hundreds of variables while offering greater flexibility and shorter computation times, (Carnero et al., 2018, He et al., 2014).

The aim of this work is to analyze and determine an efficient and flexible resolution methodology to address the design of a minimum cost instrument network subject to restrictions over a set of key variables.
In literature, there can be found works that have addressed the problem of sensor network design where the reliability associated with the instrument system to be installed is considered as a fundamental performance criterion. Kotecha et.al (2008), proposed an explicit Mixed Integer Nonlinear Programming (MINLP) optimization framework, based on cut sets, for the design of sensor network which maximizes the network reliability for the non redundant case, in linear systems.
This means that the number of sensors is known in advance, which simplifies the optimization problem to be solved and allows to express and calculate in relatively simple way the reliability associated with the sensor network. On the other hand, Wang et al, (2007) show a procedure for the design of a sensor network that uses the graph theory and takes the reliability objective and cost constraint into account for small instances.
In the case of designing more general sensor networks that involve the observability of only a set of variables, in a redundant instrumentation system, the calculation of the reliability associated with any variable implies determining all possible ways of estimate it, a task that becomes impracticable as the number of variables grows.
This work proposes to use a Monte Carlo Simulation method, MS, to evaluate the reliability of the network defined as the probability of continuing to observe the keys variables when the instruments faults according to a given failure model. This is a powerful technique to model this stochastic behavior of systems and components. The optimization engine chosen is a trajectory heuristic, Simulated Annealing, SA.
The rest of this article is organized as follows. In Section 2 the SNDP is described. Section 3 introduces and explains the approach proposed in this work. Section 4 refers to the experimental analysis and the methodology used. Then, a study and analysis of the results obtained are presented. Finally, the main conclusions and future lines of research are drawn in Section 5.

2. Problem Formulation

The SNDP is summarized as a discrete optimization problem of finding the minimum cost network that satisfies estimability, precision and reliability constraints. Formally, an SNDP solution has to satisfy these constraints for a set of key variable estimates, as stated by Eq(1), where $\mathbf{q}$ is an n-dimensional vector of binary variables such that $q_i = 1$ if variable i is measured, and $q_i = 0$ otherwise, $\mathbf{c}^{\mathrm{T}}$ is the cost vector; $\hat{\sigma}_k$ is the estimate standard deviation of the k-th variable contained in S_σ after a data reconciliation procedure is applied, and E_l stands for the degree of estimability of the l-th variable included in S_E Furthermore, S_σ , S_R and S_E are the set of key process variables with requirements in precision, reliability and ability to be estimated, respectively.

$$
\begin{aligned}
\min \quad & \mathbf{c}^{\mathsf{T}}\mathbf{q} \\
\text{s.t.} \quad & \\
& \hat{\sigma}_k(\mathbf{q}) \le \sigma_k^*(\mathbf{q}) \qquad \forall\, k \in S_\sigma \\
& R_i(t,\mathbf{q}) \ge R_i^*(t,\mathbf{q}) \quad \forall\, i \in S_R \\
& E_l(\mathbf{q}) \ge 1 \qquad \forall\, l \in S_E \\
& \mathbf{q} \in \{0,1\}^n
\end{aligned}
\tag{1}
$$

Precision and estimation constraints are evaluated using a matrix-oriented data reconciliation algorithm.

2.1. Exact reliability computation

To determine the reliability associated to each variable, two cases must be considered according to whether or not the variable is measured directly. If a variable is measure, then its reliability simply coincides with the reliability of the instrument with which it is measured. Otherwise, it is necessary to know all the possible alternatives of calculating through the balance equations where this variable appears.

Kotecha et al. (2007) proposed an expression that uses the concept of cut sets for evaluation of reliability. It is possible to demonstrate that, given a process flowsheet, all the ways of estimating a variable correspond to the determination of the set, C^i of all possible cut sets where such variable appears. If $\#C^i$ is the cardinal of the C^i set, then the reliability associated with the i-th variable is given by:

$$R_i(t,\mathbf{q}) = q_i R_i(t) + (1-q_i)\sum_{k=1}^{\#C^i}\left(\prod_{\substack{j\in C_k^i \\ j\neq i}} R_j(t)\right) \qquad \text{con} \quad i=1:n \tag{2}$$

If the sensor network is a minimum sensors one, then each unmeasured variable belongs to a single cut set, where the rest of the intervening variables are measured and the $\#C^i$ is equal to one. However, in the case of general sensor networks, where observability is required on a set of key variables and redundancy that ensures a certain level of reliability on them, $\#C^i$ constitutes a true bottleneck for the calculation of this expression. The number of cut sets where the considered variable appears grows exponentially with the increase in the size of the problem. For this reason this methodology is only applicable to plants with a small number of variables and balance equations.

2.2. Simulation approach to evaluate the variable relialibity

As it is known evaluation of reliability in engineering systems of different types is a complex task that presents, for example, the difficulties above mentioned. For this reason, other alternative estimation methods appear, such as MS methods. In this context, let $R_i(t,\mathbf{q})$ the probability of random event A defined as:

A = {continue observing at the time t the ith key variable included in S_R, when the implemented instrumentation network fails according to a given model}.

If a model for the fault associated with each installed instrument is available, then the occurrence of event A can be computed simulation a number of tests, N, enough large, so that relative frequency of occurrence of A, f_A, differs of $R_i(t,\mathbf{q})$ an arbitrarily small number ε . The above can be expressed in terms of the probability, Pr, as follows:

$$\Pr\left(\left|f_A - R_i(t,\mathbf{q})\right| \le \varepsilon\right) \ge 1-\delta \quad \textit{then} \quad N \ge \frac{1}{4}\left(\frac{1}{\delta\varepsilon^2}\right) \tag{2}$$

Where δ is a confidence level. Although the number of trials necessary to achieve adequate convergence must be large with its consequently high computation time, this technique can be applied to any type of process system.

3. Hybrid Simulated Annealing Algorithm

In this section, a brief description of SA and its variants is introduced. After that, the Hybrid Simulated Annealing, HSA, to optimize the cost instrumentation in chemical plants is explained and how the SA variants are adapted the HSA.

3.1. Simulated Annealing Algorithm

SA is a well-studied trajectory-based metaheuristic used to address discrete and, to a lesser extent, continuous optimization problems. The SA algorithm simulates the energy changes in a system subjected to a cooling process until it converges to an equilibrium state, where the physical material states correspond to problem solutions, the energy of a state to cost of a solution, and the temperature to a control parameter. At the beginning SA accepts solutions with high cost values under a certain probability in order to explore the search space and to escape from local optima. During the annealing process this probability decreases according to temperature cooling; intensifying the search and reducing the exploration in order to exploit a restricted area of a search space. SA evolves by a sequence of transitions between states and these transitions are generated by transition probabilities. Consequently, SA can be mathematically modeled by Markov chains, where a sequence of chains is generated by a transition probability, which is calculated involving the current temperature. Most of the search components of SA are fixed in function of the problem to be solved. Consequently, the search space, cost (evaluation) function, perturbation operator, and local search are directly related to the problem. The main search components, which are variable during the process, are the initial temperature, $T^{0,}$ the temperature through their annealing schedules, and the Markov chain length, *MCL*, (Talbi, 2009). The most known cooling process in the literature are proportional, exponential and logarithmic schemes. Furthermore, a random schedule is considered (Bermúdez, et al., 2019). *MCL*, the number of required transitions to reach the equilibrium state at each temperature can be either static or adaptive. At the first case, it is calculated before the search starts.

3.2. Hybrid Simulated Annealing Algorithm for SNDP

In Hernández et al. (2019) an adapted and hybridized SA algorithm to solve the SNDP in chemical plants has been proposed. SA works as main heuristic with a subordinated ad-hoc local search, inspired in Tabu Search with strategic oscillation technique, SOTS, giving rise to the Hybrid Simulated Annealing (HSA_SOTS) algorithm. The hybridization in HSA_SOTS is applied in two levels: in the first one to generate an initial solution, and in the second level to improve the solution during the annealing process.

The perturbation scheme of the current solution is carried out through a certain swapping number of measured variables to unmeasured ones and vice versa in order to generate a candidate solution $\mathbf{q}_2$ from $\mathbf{q}_0$. Furthermore, the temperature is updated using the geometric criterion (Du and Swamy, 2016).

4. Experiments and results

In this section, two examples of increasing size are presented for stationary state process plants which are represented by lineal equations. However, the proposed methodology is applicable even when balances by components or non-linear systems are considered. Case 1 corresponds to a simplified hydrodealkylation plant, HAD, which due to its reduced dimension, it allows to implement not only a method for exact calculus of key variables reliability but also a simulation method based. Process graph is constituted by 8 nodes and 14 edges. Case 2 corresponds to the flowsheet of a Steam Metering Network plant, SMN, which has been wildly used in literature as an example of medium size. It consists of 28 flows and 11 equations of mass balance

The standard deviation of flow meters is 2%, 2.5%, of the corresponding true flow rates for case studies 1and 2, respectively.

In all cases, it is considered that for a proposed instrumentation system, reliability of each variable is evaluated to time t=2 years.

Furthermore, it is estimated that the time of life of each sensor is modeled with a Weibull distribution, whose instant rate of failure is constant and it has a medium time up to the specific failure for each sensor μ_i. Table1 shows the complexity of the set of constraints imposed for Case Studies 1 and 2.

The interested readers can gain access to the file containing information about the case studies, from https://www.ing.unrc.edu.ar/archivos/sndp_cases.doc. In this file, process flowsheet, purchase cost, precision and μ_i data for the set of sensors are available.

Table 1: Constraints for case studies

Case Study	Constraints
1	$E_l \geq 1$ for streams 3 4 8 10 12 $R(t)_4^* = 0.8$ $R(t)_8^* = 0.8$ $R(t)_{10}^* = 0.8$ $\sigma_3^* = 0.7$ $\sigma_8^* = 0.15$ $\sigma_{12}^* = 0.40$
2	$E_l \geq 1$ for streams 2 4 8 12 17 21 23 25 27 28 $R(t)_8^* = 0.7$ $R(t)_{12}^* = 0.65$ $R(t)_{23}^* = 0.8$ $R(t)_{27}^* = 0.80$ $\hat{\sigma}_4^* = 2.2$ $\sigma_8^* = 3.28$ $\sigma_{12}^* = 1.54$ $\sigma_{27}^* = 1.41$ $\sigma_{28}^* = 1.44$

The set of parameters used to carry out the optimization with HSA_SOTS, as well as the simulation experiments, are shown in Table 2. Because of the stochastic nature of the algorithms, 30 independent runs of each instance were performed to gather meaningful experimental data.

Table 2: Parameter setting

Parameter	HAS_SOTS	Parameter	MS
T^0	900	N	25000
CL	30	ε	0.01
PSO	0.005	δ	0.01

Tables 3 and 4 reports the best attained solutions for the case studies. These are expressed in terms of the set of measured variables, the standard deviation of their estimates after the data reconciliation procedure is done, the reliability obtained and the total instrumentation cost. For comparative purposes, it should be noted that the cost is expressed in units of generic cost, CU. In addition, the reliability evaluated using an exact method is shown for the first design analyzed. In this smaller instance, it can be seen that the value reached by MS estimates $R_i(t)$ with an error of less than 0.3%.

Table 3: Optimization Results for Case 1

Best Solution	Standard deviation	Reliability Exact Method	Reliability Simulation Method	Cost [CU]
1,2,4,5,7-11,13	$\sigma_3 = 0.32$ $\sigma_8 = 0.136$ $\sigma_{12} = 0.238$	$R(t)_4 = 0.8150$ $R(t)_8 = 0.8150$ $R(t)_{10} = 0.8150$	$R(t)_4 = 0.8115$ $R(t)_8 = 0.8129$ $R(t)_{10} = 0.8115$	623222

Table 4: Optimization results for Case 2

Best Solution	Standard deviation	Reliability	Cost [U]
1 2 4-7 9-11 13 16 17 19-24 26-28	$\sigma_4 = 2,06$ $\sigma_8 = 1,5$ $\sigma_{12} = 0.09$ $\sigma_{27} = 1.2$ $\sigma_{28} = 1.44$	$R(t)_8 = 0.7421$ $R(t)_{12} = 0.6921$ $R(t)_{23} = 0.8369$ $R(t)_{27} = 0.8723$	1086.10

The design analyzed in case 2 has a high specification degree. Consequently the best solution found involves placing a set of 22 instruments. The variance of the reliability estimation is also calculated. The maximum value obtained is 4.10^{-5} for $R(t)_{27}$.

5. Conclusions

This work presents an analysis on the behavior of two particular simulations technique for the SNDP resolution. The first, HSA_SOTS a simulation optimization technique is performed for search the optimum solutions to SNDP problem which is formulated as a combinatorial optimization problem and includes the selection and determination of the number of process variables that must be measured to achieve the specific state of knowledge about the plant. The second, MS, a mechanism for the simulation of a failure scenarios, is used with the aim of evaluating the key variables reliability. Besides, the variance of the estimator is also returned, which is a measure of the quality of the estimate reached. MS is analyzed and discussed, as well as their performance in two industrials example of increasing size and complexity. The simulation results for the reliability calculation are coincident with the one obtained when an exact method is applied for the small size instance. In the second design analyzed, a high precision reliability estimation was obtained. The simulation tool proposed is a flexible and scalable one to solve other formulations of SNDP. However, for large plants with high reliability restrictions, generating samples of failure scenarios that lead to the non-observability of a key variable can result in a very large number of trials with the consequent increase in computational effort. This suggests, in these cases, the need to parallelize the proposed tool.

References

Bermudez C., Salto C., Minetti G. 2019, “Solving the Multi-Period Water Distribution Network Design Problem with a Hybrid Simulated Anealling”. In: Pesado P., Aciti C. (eds) Computer Science – CACIC 2018. CACIC 2018. Communications in Computer and Information Science, vol 995. Springer, Cham.

Carnero, M., Hernández, J.L., Sánchez, M. 2018, “Optimal sensor location in chemical plants using the estimation of distribution algorithms”. Ind. & Eng. Chem. Res. doi.org/10.1021/acs.iecr.8b01680.

Du Ke-Lin, Swamy M. N. S. (Ed), Search and Optimization by Metaheuristics, Techniques and Algorithms Inspired by Nature, Springer International Publishing, Switzerland (2016)

He, Y.J., Ma, Z.F. 2014, “Optimal Design of Linear Sensor Networks for Process Plants: A Multi-Objective Ant Colony Optimization Approach”. Chemometrics and Intelligent Laboratory Systems, 135, 37-47, 2014.

Hernandez J., Salto C., Minetti G., Carnero M., Sanchez M.C., Hybrid Simulated Annealing for Optimal Cost Instrumentation in Chemical Plants, Chemical Engineering Transactions, 74, 709-714 (2019)

Kotecha PR, Bhushan M, Gudi RD. 2007, Constrained programming based robust sensor network design. Ind. Eng. Chem. Res.; 46, 5985-99.

Kotecha PR, Bhushan M, Gudi RD. 2007, Constrained programming based robust sensor network design. Ind. Eng. Chem. Res.; 46, 5985-99.

Kotecha, P., Bhushan, M., Gudi, R., Keshari, M. 2008, “A duality based framework for Integrating reliability and precision for sensor network design”. Journal of Process Control, 18(2):189 – 201.

Talbi E. G., 2009, Metaheuristics: From Design to Implementation, Wiley.

Xu Wang, Gang Rong, Jianlie Li. “A New Approach To Design Reliable General Sensor Network on the Basis of Graph Theory”. Ind. Eng. Chem. Res., 46, 2520-2525, 2007.

Zhang, Jin and Donald J. Chmielewski, 2017 “Profit-based Sensor Network Design using the Generalized Benders Decomposition.” American Control Conference, (ACC) 3894-3899.

Sauro Pierucci, Flavio Manenti, Giulia Bozzano, Davide Manca (Eds.)
Proceedings of the 30th European Symposium on Computer Aided Process Engineering (ESCAPE30), May 24-27, 2020, Milano, Italy.
http://dx.doi.org/10.1016/B978-0-12-823377-1.50075-6

Low Temperature Applications for CO_2 Capture in Hydrogen Production

Donghoi Kim,[a] David Berstad,[b] Rahul Anantharaman,[b] Julian Straus,[b] Thijs A. Peters,[c] Truls Gundersen[a*]

[a]*Department of Energy and Process Engineering, Norwegian University of Science and Technology (NTNU), Trondheim 7491, Norway*
[b]*SINTEF Energy Research, Trondheim 7465, Norway*
[c]*SINTEF Industry, Oslo 0314, Norway*
Truls.gundersen@ntnu.no

Abstract

The recent development of the protonic membrane reformer (PMR) technology allows an energy efficient hydrogen production from natural gas. To liquefy and separate CO_2 from the retentate gas of the PMR, various low temperature processes are modelled and compared. The optimization results indicate that the single mixed refrigerant based process gives the smallest power consumption and fewest number of units. The cascade and the self-liquefaction processes can be considered as alternatives when the retentate gas is rich and lean in CO_2 respectively.

Keywords: Low temperature separation, CO_2 capture, hydrogen production, CO_2 liquefaction.

1. Introduction

Due to the increasing demand for clean fuels, hydrogen has been considered a promising energy carrier since it does not emit CO_2 after combustion. However, current hydrogen production relies on fossil fuels (98% of world H_2 production), thus emitting a large amount of carbon dioxide (IEA, 2019). Nevertheless, in the short/mid-term perspective, fossil fuel based hydrogen production is expected to increase before the transition to environmentally friendly hydrogen production like water electrolysis using renewable energy sources is completed (Voldsund et al., 2016). Thus, it is essential to develop efficient CO_2 capture processes for hydrocarbon based H_2 production.

Natural gas is the main fossil fuel to produce hydrogen, accounting for over 70% of total production (IEA, 2019). Such a hydrocarbon mixture is transformed into hydrogen and carbon dioxide by steam reforming (SR) and water gas shift (WGS). Then, CO_2 and other impurities are removed from the shifted syngas to produce pure hydrogen. Thus, the hydrogen production system consists of multiple sub-processes. As an alternative, SR and WGS stages can be replaced by the protonic membrane reformer (PMR) technology (Malerød-Fjeld et al., 2017). The PMR acts as a combined reactor and separator, where natural gas and electricity are consumed to produce a CO_2 rich stream with impurities and electrochemically compressed pure hydrogen separated through the membrane. The net endothermic chemical reaction is balanced with the heat evolved from the galvanic operation of the membrane reformer, resulting in higher overall energy efficiency compared to conventional hydrogen production processes. Therefore, the PMR system can be an attractive technology for efficient hydrocarbon based H_2 production.

The retentate gas from the PMR has a relatively high fraction of CO_2, which makes cryogenic separation technologies promising options to achieve a high CO_2 capture rate with reasonable energy consumption (Berstad et al., 2013a) and cost (Berstad et al., 2014). Applicable cryogenic CO_2 separation processes are flashing-based and external refrigeration-based. Thus, this paper suggests various types of cryogenic processes that are applied to the PMR based hydrogen production system. This work also performs a comparative evaluation of the cryogenic processes by conducting optimization work based on thermodynamic efficiency. Besides, the results from sensitivity analysis with different compositions of the retentate gas are analyzed to evaluate the operational flexibility of the CO_2 separation processes.

2. Background

After dehydration, the retentate gas from the PMR typically contains CO_2, CO, CH_4, and H_2 (Malerød-Fjeld et al., 2017). For the separation of carbon dioxide from a PMR based H_2 production system, the retentate gas can be compressed and cooled to sub-ambient temperatures using compressors and external refrigeration. Then, a part of CO_2 can be condensed to liquid phase and removed by a phase separator. During this process, the pressure and temperature of the retentate gas at the inlet of the phase separator decide the performance of CO_2 separation such as CO_2 capture rate and CO_2 mole fraction in the liquid CO_2.

Figure 1 shows the performance of such a CO_2 separation system with the dehyrated retentate gas having around 55 mol% CO_2 as obtained at a hydrogen recovery factor (HRF) of near 91%. As seen in Figure 1, the CO_2 capture rate (CCR) increases with higher pressures and lower temperatures. In this case, however, energy consumption for the CO_2 capture system will also be larger due to the increased compression and refrigeration duties. In addition, higher pressure levels result in lower CO_2 mole fraction in the liquid CO_2, which is not ideal for CO_2 transport and storage. Although lowering the temperature is beneficial to have higher CCR and CO_2 mole fraction for a given pressure, the lower bound of the temperature level is limited by CO_2 freezing temperature. Therefore, optimal pressure and temperature levels of the retentate gas are required to have an energy efficient CO_2 separation system for the PMR, while achieving high CCR and CO_2 mole fraction in the captured CO_2.

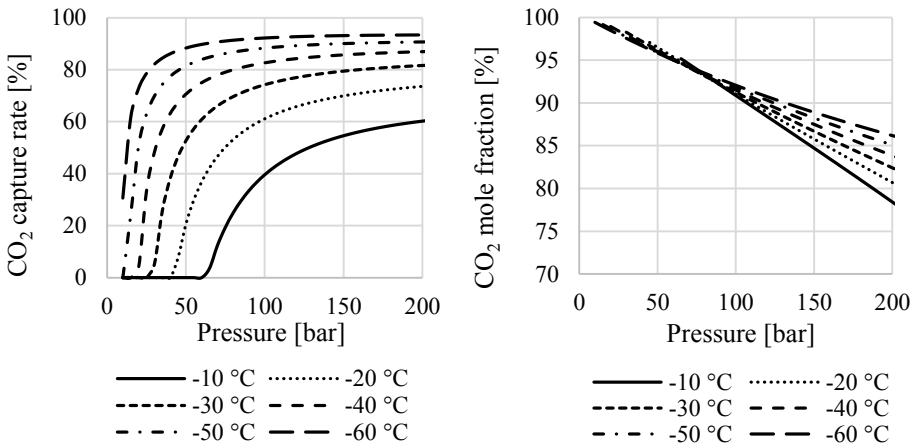

Figure 1. CO_2 capture rate (left) and CO_2 mole fraction in liquefied CO_2 (right) versus the retentate gas pressure with varying temperature at phase separator inlet.

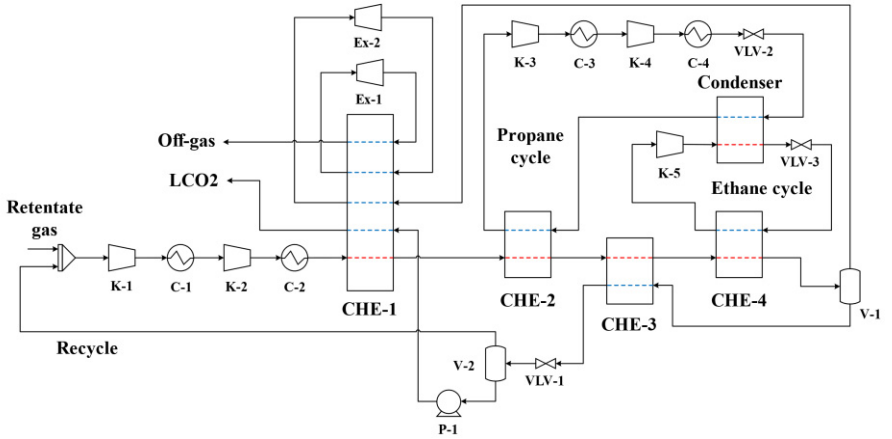

Figure 2. Cascade CO_2 liquefaction system (Berstad et al., 2013b).

3. CO_2 liquefaction processes

This CO_2 capture system is varying depending on the selection of refrigeration process. Berstad et al. (2013b) suggested a cascade type of CO_2 liquefaction process using pure component refrigerants such as propane and ethane. As shown in Figure 2, the retentate gas is pressurized through multi-stage compression and cooled mainly by the propane and ethane refrigeration cycles. Then, the retentate gas is separated into a CO_2 rich liquid stream and an H_2 rich vapor stream by phase separator V-1. The liquid stream gives the cold duty to heat exchanger CHE-3 to reduce the load of the external refrigeration cycles. The warmed liquid is then throttled to remove impurities through a flash gas. This flash gas is recycled for further purification. The purified CO_2 rich liquid is pumped to high pressure before it delivers cold duty for heat exchanger CHE-1.

The H_2 rich vapor stream from phase separator V-1 also precools the retentate gas from the compressors. The warmed H_2 rich vapor from CHE-1 can still supply refrigeration duty for heat exchanger CHE-1 by being depressurized through two gas expanders, which produce low temperature streams. The power produced from the expanders is also an extra benefit to reduce the total power consumption of this liquefaction process. The H_2 rich stream depressurized to the operating pressure of the PMR through the expanders (Off-gas) is then returned to the membrane reformer to maximize the overall HRF.

The cascade system using two pure component refrigerants can be replaced by a single mixed refrigerant (SMR) process, thus having a simpler configuration as seen in Figure 3. Compared to the cascade system, the CO_2 rich liquid from phase separator V-1 in the SMR based process is used not for liquefaction but precooling of the compressed retentate gas. Therefore, only one gas expander is required to supply enough cold duty to heat exchanger CHE-1, reducing the capital cost of this system.

The CO_2 liquefaction and separation can be performed without any external refrigerants as seen in Figure 4. A part of the refrigeration duty of this self-liquefaction system is produced by Joule-Thomson (JT) throttling of the CO_2 rich liquid stream and the H_2 rich vapor from phase separator V-1. Besides, this process heavily relies on the two gas expanders in order to generate sufficient amounts of refrigeration for the system.

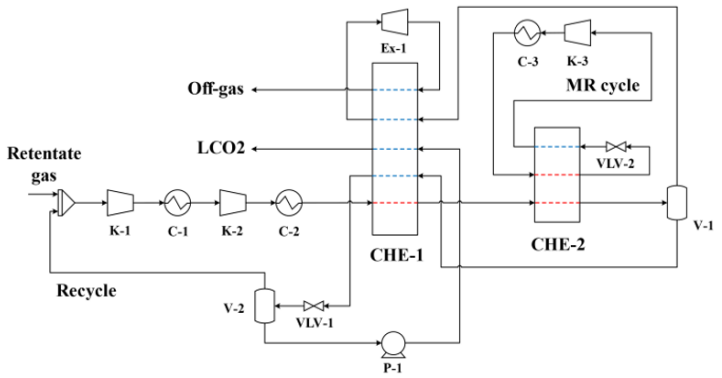

Figure 3. Single mixed refrigerant (SMR) CO_2 liquefaction system.

However, the retentate gas has to be compressed to very high pressure in order to have a large enough refrigeration from JT throttling and gas expanders, requiring a larger number of compression stages. Moreover, this high pressure feed gas results in low CO_2 fraction in the captured CO_2. Thus, the self-liquefaction process uses an additional phase separation for the partially condensed retentate gas from the precooling heat exchanger (CHE-1) in order to increase the purity of the captured CO_2.

4. Design basis and optimization

The three CO_2 liquefaction processes were simulated in Aspen HYSYS. The retentate gas from the PMR was assumed to be dehydrated. For case studies, the composition of the retentate gas was varied from CO_2 lean to CO_2 rich gas (Table 1) in order to evaluate the efficiency changes of the processes. These cases represent an HRF of 79.3, 91.4, and 97.8, respectively. Other design specifications are listed in Table 2. Optimization of the systems was also conducted by a particle swarm optimization algorithm in Matlab, connected to Aspen HYSYS. The objective function is minimizing specific power consumption for 1kg of liquid CO_2 (LCO2) production. Outlet pressure levels of compressors, expanders, and JT valves were set as variables. Outlet temperature levels of heat exchangers were also varied. The molar flow rates and compositions were also variables for the cascade and the SMR process. The mixed refrigerant of the SMR process is composed of CH_4, C_2H_6, C_3H_8, and C_4H_{10}.

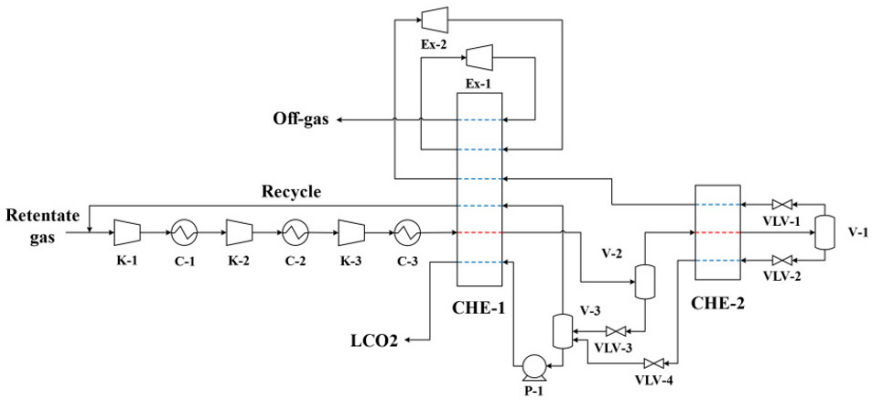

Figure 4. Self-liquefaction system for CO_2 liquefaction.

Table 1. Dehydrated PMR retentate composition (Malerød-Fjeld et al., 2017).

Component	Mole fraction [-]		
	CO_2 lean case	Base case	CO_2 rich case
Methane	0.0082	0.0012	0.0000
Carbon monoxide	0.2369	0.2072	0.1028
Carbon dioxide	0.3321	0.5491	0.8200
Hydrogen	0.4228	0.2425	0.0772

The minimum temperature difference of heat exchangers and minimum superheating of compressor inlet were set to 3 K. In order to avoid solid formation, the temperature of all the streams was constrained to be 3 K warmer than its CO_2 freezing temperature. Higher than 95 mol% of CO_2 and lower than 0.5 vol% of CO in the liquefied CO_2 were product specifications (Harkin et al., 2017), also satisfying 70, 85, and 95 % of CO_2 capture rate for CO_2 lean, base, and CO_2 rich cases respectively.

5. Results

The optimization results in Table 3 indicate that the SMR process is the most energy efficient process to liquefy CO_2 from the base case retentate gas. The cascade system only requires a marginally larger energy consumption compared to the SMR process since the two gas expanders allow a smaller overall temperature difference in the precooling part (CHE-1), indicating better heat integration. However, the cascade system has larger temperature differences in heat exchangers operating at low temperatures than the SMR process, resulting in larger entropy generation and reduced overall thermodynamic efficiency. The composition of the mixed refrigerant in the SMR system can be manipulated to have a better temperature match with the retentate gas. The self-liquefaction system shows the largest power consumption due to its inherent low efficiency, requiring a considerable increase in the retentate gas pressure level and thus compression work. However, the high pressure feed gas results in a warmer operating temperature for CO_2 separation, thus a larger temperature margin to CO_2 freeze-out.

When the feed gas is lean in CO_2, the cascade process consumes slightly less power than the SMR process. Due to the increased impurities, the retentate gas has to be flashed more. This results in a larger amount of flash gases, which is more favorable for CO_2 liquefaction systems having two gas expanders to produce refrigeration duty and work. However, the self-liquefaction process will also have significantly increased recycle stream and compression work, thus giving the largest power consumption. For the CO_2 rich case, the SMR process has noticeably smaller power consumption than the cascade system because of less impurities in the feed gas and flash gases in the processes, resulting in a reduced influence of the expanders on the process efficiency.

Table 2. Simulation conditions and assumptions.

Property	Value	Unit	Property	Value	Unit
Feed temperature	25	°C	Equation of state	PR	-
Feed pressure	10	bar	Δp in heat exchangers	2% of p_{in}	-
Feed flow rate	200	kmol/h	Compressor efficiency*	80	%
Off-gas pressure	25	bar	Pump efficiency*	75	%
LCO2 pressure	150	bar	Expander efficiency *	85	%

*Isentropic efficiency

Table 3. Specific power consumption with the temperature and pressure levels at the first phase separator (V-1).

Process	Cascade			SMR			Self-liquefaction		
	Power	T	p	Power	T	p	Power	T	p
	MJ/kgCO_2	°C	bar	MJ/kgCO_2	°C	bar	MJ/kgCO_2	°C	bar
CO_2 lean	0.781	-55.6	68.5	0.786	-55.6	64.7	0.993	-46.9	169.2
base	0.460	-55.2	64.6	0.455	-55.5	56.1	0.555	-45.8	160.4
CO_2 rich	0.337	-54.0	50.3	0.316	-54.7	40.3	0.470	-40.0	125.4

6. Conclusions

In this paper, different low temperature processes for CO_2 liquefaction and separation from a membrane retentate gas were compared. Considering the overall efficiency with changes in CO_2 fraction of the feed gas, the SMR process gives the highest energy efficiency. This process also has the smallest number of units compared to other processes, which may give a smaller capital cost than other systems. When the feed gas is lean in CO_2, the cascade process will be an alternative option to the SMR system. The self-liquefaction process can be considered if the feed gas is rich in CO_2 and no external refrigerant is accessible. Thus, proper process selection for CO_2 liquefaction will depend on the feed gas conditions and other design criteria such as cost.

Acknowledgements

This publication has been produced within the CLIMIT-KPN MACH-2 project (294629) with support from the NCCS Centre, performed under the Norwegian research program Centres for Environment-friendly Energy Research (FME). The authors acknowledge the following partners for their contributions: Aker Solutions, ANSALDO Energia, CoorsTek Membrane Sciences, Equinor, EMGS, Gassco, KROHNE, Larvik Shipping, Norcem, Norwegian Oil and Gas, Quad Geometrics, Shell, TOTAL, and the Research Council of Norway (257579).

References

International Energy Agency (IEA), 2019, The future of hydrogen. Available from https://www.iea.org/hydrogen2019/.

M. Voldsund, K. Jordal, R. Anantharaman, 2016, Hydrogen production with CO_2 capture, International Journal of Hydrogen Energy, 41, 9, 4969-4992.

H. Malerød-Fjeld, D. Clark, I, Yuste-Tirados, R. Zanón, D. Catalán-Martinez, D. Beeaff, S.H. Morejudo, P.K. Vestre, T. Norby, R. Haugsrud, J.M. Serra, C. Kjølseth, 2017, Thermo-electrochemical production of compressed hydrogen from methane with near-zero energy loss, Nature Energy, 2, 12, 923-931.

D. Berstad, R. Anantharaman, P. Nekså, 2013a, Low-temperature CO2 capture technologies – Applications and potential, International Journal of Refrigeration, 36, 5, 1403-1416.

D. Berstad, R. Anantharaman, P. Nekså, 2013b, Low-temperature CCS from an IGCC Power Plant and Comparison with Physical Solvents, Energy Procedia, 37, 2204-2211.

D. Berstad, S. Roussanaly, G. Skaugen, R. Anantharaman, P. Nekså, K. Jordal, 2014, Energy and Cost Evaluation of A Low-temperature CO2 Capture Unit for IGCC plants, Energy Procedia, 63, 2031-2036.

T. Harkin, I. Filby, H. Sick, D. Manderson, R. Ashton, 2017, Development of a CO2 Specification for a CCS Hub Network, Energy Procedia, 114, 6708-6720.

Sauro Pierucci, Flavio Manenti, Giulia Bozzano, Davide Manca (Eds.)
Proceedings of the 30th European Symposium on Computer Aided Process Engineering (ESCAPE30), May 24-27, 2020, Milano, Italy.
http://dx.doi.org/10.1016/B978-0-12-823377-1.50076-8

Development and Application of Simulation-based Methods for Engineering Optimization Under Uncertainty

Atli Freyr Magnússon, Resul Al, Gürkan Sin

Process and Systems Engineering Center (PROSYS), Department of Chemical and Biochemical Engineering, Technical University of Denmark, Building 227, 2800 Kgs, Lyngby, Denmark

Abstract

This study presents a methodology that combines Monte Carlo methods for uncertainty propagation along with modern stochastic programming methods for optimization of chemical engineering process models. The aim is to integrate uncertainty information of model parameters directly into optimization workflow. Successful implementation will give statistically strong optimum designs that do not require the use of safety factors that could compromise the cost competitiveness of the process design. Assuming that uncertainty behaves as random disturbances, Monte Carlo sampling techniques of model parameters uncertainty are used to quantify disturbances effects in model output. The resulting information is then used in a surrogate assisted optimization approach designed specifically for stochastic simulations. The surrogate methods used are the developed Stochastic Kriging methods along with a novel infill criterion. This work will also include an Artificial Neural Network alternative approach. The methodology is applied to two distillation flowsheets built in *Aspen Plus*. Both proposed methods showcase superior results to a traditional SQP in a case study. Stochastic Kriging approach showcases superior results when optimizing a two-column distillation loop of a DIPE + IPA + 2MEt system, showcasing three times lower cost evaluation compared to other methods while respecting propagation of uncertainty. This work demonstrates the applicability of simulation-based optimization for engineering designs under uncertainty.
Keywords: Kriging, optimization, uncertainty, process simulators, artificial neural networks

1. Introduction

Process optimization is an important tool in chemical engineering to ensure that process designs remain cost competitive while upholding specifications. Many mathematical programming techniques exist and are applied in process optimization. Process optimization is usually performed on a deterministic model where the selected model parameters are put in place with no assumed disturbances. In reality most model parameters in process models are subject to varying degrees of uncertainty. Variety of studies have showcased that uncertainties in model parameters can have great impact on reliability and sensitivity of the model as well as the propagation of uncertainties in the model outputs (Frutiger et al. (2017)). While optimization under uncertainty has been performed in bioprocess design by Morales-Rodriguez et al. (2012), the prospect remains a challenge and is rarely conducted in chemical engineering practice. One

possible reason is the lack of a concise and reliable methodology that engineers can apply directly to their process models.

Recently Wang and Ierapetritou (2018) developed a novel robust method of optimizing stochastic simulations using a surrogate assisted optimization method (SAO). SAO are attractive to chemical engineering research field due being a global and derivative free optimization solver that are highly efficient for time consuming simulations making them prime candidates when applied directly to process simulators like SimSci PRO\II or Aspen Plus. This method uses a Stochastic Kriging meta-model developed by Ankenman et al. (2010) to assist in exploiting and exploring the design space. Their newly developed Feasibility-enhanced Expected Improvement (FEI) infill criterion is used to select new input points to improve meta-model accuracy iteratively until the computational budget runs out and the optimum is reported. In this study a Monte Carlo based methodology is presented on optimizing process design variables while integrating the effects of model parameter uncertainties during the optimization workflow. The methods are showcased by applying them on a case studies developed in the commercial process simulation software Aspen Plus. The Stochastic Kriging approach is considered along with an Artificial Neural Network (ANN) approach, whose performances will be compared along with a Sequential Quadratic Programming (SQP) optimization algorithm built into the Aspen Plus software.

2. Surrogate Assisted Optimization

Surrogate Assisted Optimization (SAO) methods are best utilized in computationally intensive tasks. The basis of all SAO methods is to create a simple meta-model to capture input-output correlations of a complex model. These meta-models are mathematically well defined and easy to compute so they can be used to exploit and explore the input space.

Meta-models are not always reliable and can have significant errors if not enough data exists in areas of interest. To improve reliability more data is supplied to the meta-model where the optimum point is likely to be located. Promising candidates are identified using an infill criterion or acquisition function which use meta-model predictions as the input. Thus, SAO methods are an iterative sequence where a meta-model accuracy is continuously improved in areas of interest via rigorous simulations of new infill points generated by the acquisition function. A common acquisition function that provides a decent balance between exploring and exploiting is the Expected Improvement (EI) method by Jones (1998).

2.1. Stochastic Kriging approach

Wang and Ierapetritou (2018) coupled their novel Feasibility-enhanced Expected Improvement (FEI) to a Stochastic Kriging (SK) meta-model for optimization which will be referred to as SK-FEI. SK was developed by Ankenman et al. (2010) and is an extension of ordinary Kriging which are popular meta-models in SAO methods. SK attempts to account for randomness by incorporating an intrinsic noise factor based on the measured variance of model outputs. For run *j* the SK model predicts a following output

$$y_j = \alpha_0 + M(\mathbf{x}) + \grave{o}_j \tag{1}$$

Where α_0 is a constant capturing the surface trend, *M* is a Gaussian process with mean 0 and variance modelled using spatial correlation functions of already visited input points and $\grave{o}_j$ is a random noise of observation j estimated using measured variances.

FEI is an extension of the traditional EI approach. The modifications are done to make the algorithm more efficient at solving optimization problems that have imposed non-linear constraints which are the most common types of problem in process optimization. This was accomplished by including a feasibility factor that actively tries improving knowledge of the feasible region i.e. where the non-linear constraints are met. Furthermore, randomness of a stochastic simulation is accounted for by assuming that process variance can be explained by a numerical function $\sigma^2 = V(\mathbf{x})$ which are fitted using another meta-model and by reducing focus on areas with large predicted $V(\mathbf{x})$. For further details the reader is referred to the Wang and Ierapetritou (2018) original paper.

2.2. Artificial Neural Network approach

This work will also attempt to introduce a SAO approach using ANN. This is to provide alternatives to SK which are known to cause computational issues as amount of data grows due to inversion of a correlation matrix. ANN are known to be exceptional at function fitting and interests in this technology is rapidly growing. ANN is constructed like a biological brain system where information from the input is fed forward through neurons in hidden layers in order to produce an output

Traditional EI family of methods do not work with ANN meta-models as they require an increased error approximation in unexplored regions which is provided by Kriging models but not ANN. In order to solve optimization problems under uncertainty the assumption that process variance can be described by a function $V(\mathbf{x})$ is repeated. Two ANN models are then fitted to each stochastic output, one predicts the mean value and one predicts the variance. These models are then coupled to an extension to the classic Probability of Improvement (PI) for non-linear constraints used by Carpio et al. (2018) which is as follows

$$cPI(\mathbf{x}) = PI(\mathbf{x}) \prod_{i=1}^{m} PC_i \mathbf{x} \tag{2}$$

Where $PI(\mathbf{x})$ is the probability that x is an improvement in the objective function for an already established $\mathbf{x}_{min}$ and $PC_i(\mathbf{x})$ is the probability that x upholds the constraint for output *i*. This approach will be further referred to as ANN-cPI.

3. Monte Carlo based optimization strategy

Current proposal of optimization under uncertainty only works if the process can be treated as a stochastic simulation. This can be achieved using a Monte Carlo based method of uncertainty analysis. The Monte Carlo method recommended by Sin et al. (2009) can be summarized in four steps

1. Define input parameters and distribution
2. Sample from defined distribution using a random number generator
3. Perform the simulations with the generated samples
4. Statistical analysis and interpretation of the results

Monte Carlo simulations provide information of mean and measured variance which can then be used to generate SK and ANN models for optimization. If a commercial process simulator is used to build the model it is recommended to follow the procedure of Jones et al. (2019) who utilized Monte Carlo simulations to perform uncertainty and sensitivity analysis on a *PRO\II* simulation using Component Object Model (COM) interface that allows communication between process simulators and numerical

software. Before optimization starts it is important to decide on how to distribute the computational budget. Currently one must decide on initial sample size (*N*) in which to create a working initial meta-model, number of Monte Carlo Simulations (*m*) per sample point xi and number of iterations (*n*) in which the acquisition function is to generate new sample points. The total computational budget i.e. number of times the objective and constraint functions are evaluated respectively then becomes

$$M = (N + n)m \tag{3}$$

This computational budget is used to determine the stopping criterion of the optimization workflow as randomization factors prevent the use of any reliable convergence criterion. The optimization workflow is then:

1. **Initial Sampling** Generate *N* number of initial samples. To improve the reliability of the meta-model the initial samples should be randomized and space-filling thus the recommended approach is to use Latin Hypercube Sampling (LHS).
2. **Monte Carlo Simulations** Sample point x_i is sampled *m* times in the original model or process simulations to get mean and variance for each sample point.
3. **Dataset evaluation** The results of the Monte Carlo Simulations are used to identify the current strongest sample point subject to minimizing the objective function and constraints. To account for uncertainty, one should factor in the measured standard deviation as well. Example for this work is to use confidence intervals for measured mean values.

$$y_{min,f} = min(y_f(\mathbf{x}) + \frac{z}{\sqrt{m}} s_f(\mathbf{x})) \quad x \in \chi \tag{4}$$

   Where *s* is measured standard deviation from Monte Carlo simulations, subscripts *f* and *g* denote objective and constraint values respectively and *z* is the standard score used in statistics. For this work *z* was set to 1.96 in both cases. χ is the set of all previously visited sample points ensuring that reported optimum has been rigorously simulated.
4. **Computational budget check** If total number of simulations has exceeded *M* then the optimization is terminated and result of step 3 is reported as the optimum. Else Step 5 is executed.
5. **Fit Surrogate model** Using the measured means and standard deviations from Monte Carlo simulations a surrogate model is fit to the outputs of the objective function and constraint functions to predict stochastic responses of unvisited **x**.
6. **Maximize infill** Depending on the surrogate model either cPI or FEI acquisition functions should be maximized to generate the next sample point $\mathbf{x}_{infill}$ Since cPI and FEI are deterministic functions one should set up a traditional global solver. This work saw good success using a Particle Swarm Optimization (PSO) algorithm. The generated $\mathbf{x}_{infill}$ is then sent to step 2.

4. Case Studies

The applications of the current strategy are demonstrated on a case study. A distillation network separating DiIsoPropyl-Ether (DIPE) and IsoPropyl Alcohol (IPA) using a pressure swing and a 2-MethoxyEthanol (2MEt) as a solvent.

The process model is developed in the process simulator *Aspen Plus* v10. *MATLAB* 2018b is used to generate the Monte Carlo samples and run the optimization algorithm. *MATLAB* and *Aspen Plus* are interconnected using COM interface, SK models are built using the ooDACE toolbox (Couckuyt et al. (2014)) and ANN models are trained using *MATLAB* Neural Network toolbox. For comparison purposes, the models are also solved deterministically i.e. neglecting uncertainty using Aspen's built in optimizer which by default uses an SQP approach.

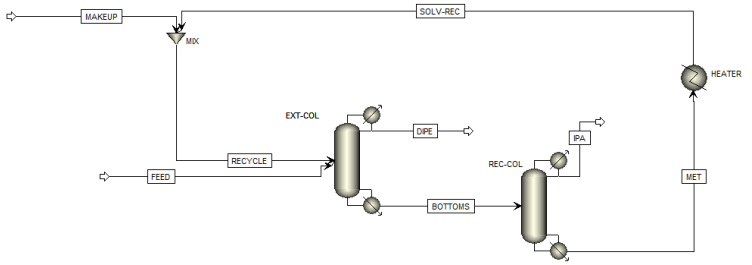

Figure 1:Aspen Plus flowsheet of the extractive distillation process

The flowsheet is depicted in figure 1. This process entails a pressure swing distillation with a solvent of 2MEt to break the azeotrope of DIPE and IPA. The feed consists of 100 *kmol/h* of 25 mol% IPA and 75 mol% DIPE at 1.42 bar and 55 °C. The primary column consists of 67 theoretical stages with the feed entering on stage 56 and the 2MEt solvent enters at stage 29. The primary column produces pure DIPE in the distillate, while the bottoms is sent to a secondary recovery column to recover the solvent for recycle as well as pure IPA.

The goal is to optimize the operational parameters *distillate rate* and *reflux ratio* of the two columns in the flowsheet in order to drive operating costs down while keeping DIPE and IPA purity over 95% on a mass basis. The operating costs associated with the process is the energy requirements of the two columns as well as the solvent makeup required. To that end the following formula is adopted for cost estimation

$$C = 180V_{2MEt} + 0.048\sum Q_H + 0.0013\sum \| Q_C \| \tag{5}$$

Where V_{2MEt} is the volume flow of the solvent in *L/h* while Q_H and Q_C are the heat duties of the reboilers and condenser respectively. Uncertainties in the process model stem from the thermodynamic method used. For this work NRTL method is used. The parameters of NRTL are based on regression of experimental data. Correlation control in the sampling step is used by utilizing the multivariate normal distribution (Kotz et al. (2005)). For comparison purposes both SK-FEI and ANN-cPI will be provided the same computational budget of *(N, m, n) = (40,100,100)*. This simulation is adapted from works of Burger and Schwarz (2018) whose paper will provide all simulation details and input uncertainties of the NRTL parameters. The optimization results are shown in table 1. In terms of constraints, no algorithm violated the non-linear constraints imposed on the problem. However, SQP results are on the constraint boundary of 95% mass fraction of DIPE. Uncertainty analysis concluded that the product purities are not sensitive to uncertainties of the NRTL parameters for the selected operating parameters. These results could be cause for alarm, nonetheless. ANN-cPI and SK-FEI are both well within the non-linear constraints with no risks of not fulfilling product specifications.

Table 1: Reported optimum design variables and results

	SQP	SK-FEI	ANN-cPI
Extractive Column Distillate Rate ($kmol/h$)	81.71	79.76	80.27
Recovery Column Distillate Rate ($kmol/h$)	18.29	20.44	20.36
Extractive Column Reflux Ratio	1.78	1.78	3.34
Recovery Column Reflux Ratio	3.14	2.34	1.32
Cost Evaluation (USD/h)	10447.97 ± 2.68	3045.42 ± 2.94	9319.99 ± 4.14
DIPE Mass Fraction	0.950	0.964	0.960
IPA Mass Fraction	0.953	0.988	0.960

Cost wise SK-FEI showcases the best performance, tripling the cost efficiency compared to the design proposed by the ANN-cPI algorithm. This is likely due to ANN-cPI lacks proper balance between exploiting and exploring for a global optimization and needs further development before it can be reliably applied to optimize process models under uncertainty.

5. Conclusions

This study presented an optimization strategy for engineering system subject to model uncertainties using Monte Carlo simulation approaches combined with new novel methods in stochastic programming. The methodology was applied to a case study developed in *Aspen Plus* process simulator to minimize the cost of running a distillation method of a DIPE-IPA-2MEtsystem subject to product specifications. Two SAO approaches were considered, both methods show superior results to a traditional SQP algorithm while accounting for the uncertainty effects in the workflow. The proposed ANN method is an attempt to provide alternatives to Kriging based methods, but direct comparison showcases it to be underdeveloped, more research is required to improve robustness. This study showcases that the SK-FEI approach can reliably solve optimization problems in a commercial process simulator under uncertainty.

References

B. Ankenman, B. L. Nelson, J. Staum,2010. Stochastic Kriging for Simulation Metamodeling. Operations Research 58 (2), 371–382.

L. Burger, C. Schwarz,2018. Sensitivity of process design to phase equilibrium uncertainty: Study of the isopropanol + DIPE + 2-methoxyethanol system. Fluid Phase Equilibria 458, 234–242.

R. R. Carpio, R. C. Giordano, A. R. Secchi, oct 2018. Enhanced surrogate assisted framework for constrained global optimization of expensive black-box functions. Computers & Chemical Engineering 118, 91–102.

I. Couckuyt, T. Dhaene, P. Demeester, 10 2014. ooDACE toolbox: A flexible object-oriented kriging implementation. Journal of Machine Learning Research 15, 3183–3186.

J. Frutiger, I. Bell, J. P. O'Connell, K. Kroenlein, J. Abildskov, G. Sin, 2017. Uncertainty assessment of equations of state with application to an organic Rankine cycle. Molecular Physics 115 (9-12), 1225–1244.

D. Jones, 1998. Efficient global optimization of expensive black-box functions. Journal of Global Optimization 13 (4).

M. N. Jones, J. Frutiger, N. G. Ince, G. Sin, 2019. The Monte Carlo driven and machine learning enhanced process simulator. Computers & Chemical Engineering 125, 324–338.

S. Kotz, N. Balakrishnan, N. L. Johnson, 2005. Continuous Multivariate Distributions, Models and Applications: Second Edition. Vol. 1. John Wiley and Sons Inc.

R. Morales-Rodriguez, A. S. Meyer, K. V. Gernaey, G. Sin, 2012. A framework for model-based optimization of bioprocesses under uncertainty: Lignocellulosic ethanol production case. Computers & Chemical Engineering 42, 115–129.

G. Sin, K. V. Gernaey, A. E. Lantz, 2009. Good modeling practice for PAT applications: Propagation of input uncertainty and sensitivity analysis. Biotechnology Progress 25 (4), 1043–1053.

Z. Wang, M. Ierapetritou, oct 2018. Constrained optimization of black-box stochastic systems using a novel feasibility enhanced Kriging-based method. Computers & Chemical Engineering 118, 210–22

Sauro Pierucci, Flavio Manenti, Giulia Bozzano, Davide Manca (Eds.)
Proceedings of the 30th European Symposium on Computer Aided Process Engineering (ESCAPE30), May 24-27, 2020, Milano, Italy.
http://dx.doi.org/10.1016/B978-0-12-823377-1.50077-X

An Application of Computer Vision for Optimal Sensor Placement in Drop Printing

Andrew J. Radcliffe,* Gintaras V. Reklaitis

Purdue University, Forney Hall of Chemical Engineering, 480 Stadium Mall Drive, West Lafayette, IN 47907-2100, United States
aradcli@purdue.edu

Abstract

The use of imaging technologies in the process industries has the potential to provide state, dynamic, statistical or modal information that cannot otherwise be obtained from systems which limit or invalidate the use of physical property and spectroscopic measurement methods for real-time acquisition. To extract the desired information, computer vision techniques can be used to reduce the high-dimensional image data to the salient features, which can then be employed for modelling, optimization, and control purposes. This work applies such an approach to determine the optimal placement of a high-resolution camera for online quantification of drops printed in a slurry-based additive manufacturing process for pharmaceuticals. Systematic selection requires a model of drop instability, which, due to stochastic effects introduced by particles, must be based on real data with sufficient temporal discretization to capture the event dynamics. Thus, high-speed imaging was utilized to generate representative videos, and computer vision algorithms were employed to automate extraction of the coupled temporal evolution of object shape and position, and to detect and recognize breakup and coalescence events. The resultant data were subsequently employed to determine the image sensor and fiber-optic placements that maximize measurement information acquired by online acquisition system. Results are presented for drop printing slurries at 15 distinct ink formulations – spanning several particle size distributions and particle loadings – which are comprised of a set of 250,000 images.

Keywords: add three to five keywords here, separated with a comma.

1. Introduction

Drop printing serves as an important component of widely varied manufacturing processes, encompassing examples from semi-conductors, pharmaceuticals and biomaterials – essentially, anywhere precision deposition of material is required. In such applications, drops serve as the source of a critical chemical component themselves, or as a liquid binder, the patterning of which on the substrate enables creation of two-/three-dimensional structures. Consequently, in order to control the drop formation/deposition, online monitoring of the generated drops is desirable; this would be best achieved by high-speed imaging due to the small timescales involved, but economic and practical considerations encourage the use of a normal camera to capture one image of each emergent drop. In this context, placement of the online imaging system in relation to the printing nozzle determines what can be extracted and inferred from the resultant images, thus, it is important to optimize the arrangement of the camera, flashbulb & fiber-optic sensor (camera trigger) so as to maximize the information about each drop.

Previously work by colleagues (Hirshfield et al. 2015) designed a system for online image acquisition that considered the optics, using the system geometry to select lens and camera *y*-axis placements that maximize the depth of field for objects emerging from the nozzle; this incorporated an actuation system based on a fiber-optic sensor positioned at the same *z*-height as the center of the imaged area. The position of these two components will be selected by the user; for well-behaved inks (i.e. ideal fluids), a trial and error approach can affect a suitable measurement, with errors as low as 0.33% (Hirshfield et al. 2015). However, for cases in which printing exhibits non-ideal effects – multiple satellite droplets, variability in trajectory, non-deterministic events (breakup, coalescence) – the captured images can be quite different (Figure 1, Inset #1, 2, 3), despite apparent uniformity of drop volume at the eventual point of deposition. Consequently, it becomes difficult to even arrive at a satisfactory result, or to be convinced that such a placement captures the maximum amount of information.

In the pharmaceutical manufacturing process considered here, the printed drops contain the active drug compound, thus, the images obtained by the online acquisition system enable model-based estimates of the product content; maximizing the information contained in the captured images through optimization of component placement with respect to drop formation phenomena reduces uncertainty in the model structures and in the product content predictions. This work focuses on non-Brownian particle inks, which motivate the use of a data-driven approach due to the substantial non-idealities involved– high particle loading, distributed particle size, non-spherical shape. High-speed imaging of drop printing across a range of operating conditions and ink formulations is used to record the dynamics from the incipience of flow to the eventual stabilization of the drop(s) after detachment. Then, computer vision algorithms are applied to each image sequence to extract the total lifetime of each drop: dynamic evolution of position and shape; non-deterministic events and spatiotemporal location thereof; parent-child relations with other drop(s). With this information, particle-driven effects on detachment, trajectory and events can thus be accounted for.

2. Problem Description

2.1. Components of Online Image Acquisition System

In order to formulate the problem, one must first define the geometry and adjustable components of the online imaging system. From the previous work, camera and lens are fixed, thus leaving the position of the camera and fiber-optic sensor as the only variables. The camera is to be placed at some *z*-position below the nozzle orifice so as to capture a single image for each drop; the fiber-optic sensor consists of a light beam, which when interrupted by the drop triggers the acquisition of the image. The high-resolution camera captures an area with dimensions H, W, which is effectively constant due to the fixed distance between the lens and drop paths. The high-speed camera captures a substantially larger actual area; with the actual sizes and known conversion factors (real length per pixel), the potential positions of the area captured by the online camera can be superimposed onto the images from the high-speed videos, as shown in Figure 1.

2.2. Feasible camera, fiber-optic sensor placements

Given the geometry (Figure 1) thus defined, and the total imaged area from the high-speed sequences, one can then define the set of feasible camera positions as $\mathbf{Z} = \{\boldsymbol{\zeta} \; \forall \; z_{Box,L} \mid z_{Box,L} = (z_{nozzle} + H), \dots, z_{limit}\}$, in which a single camera position encompasses the set of points: $\boldsymbol{\zeta} = \{z_{Box,L} - j \mid j = 1, \dots, H\}$. As the area imaged by the online camera covers 90% of the *x*-axis, the problem can justifiably be simplified by

fixing the camera box *x*-position at the centerline. Feasible positions of the fiber-optic sensor for each $\boldsymbol{\zeta}$ are constrained to be $z_{FbOp} \leq z_{Box,L}$, though, given the configuration in which interruption of the fiber-optic signal is exactly coincident with the camera trigger, one can further limit the feasible points to $z_{FbOp} \in \boldsymbol{\zeta}$, as image acquisition, triggered at some position outside the camera box is readily identifiable as leading to suboptimal results. The former, more lenient constraint could be used if one considers adding a time delay between the fiber-optic signal interrupt and image acquisition.

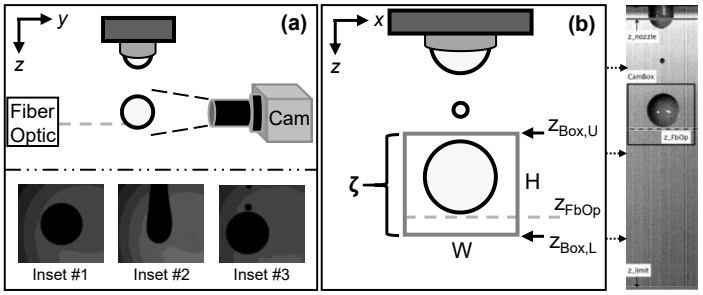

Figure 1. (a): Side-view of online image acquisition setup. (b): Scene as observed by camera

2.3. Objective function

With the feasible sensor placements defined, consider the following scenario in which a drop is printed: mechanical actuator induces pressure wave, fluid is emitted from the nozzle, and after thinning of the liquid thread, one or more drops detach; thereafter, these drops deform, and potentially undergo breakup or coalescence. Let us assume that the operating conditions and ink formulation are such that per actuation event, one large drop ("primary drop") is formed, with the possibility of one or more smaller drops ("satellites"). The system can acquire one image per actuation event, given limitations on the flashbulb frequency and online camera, and the volume of fluid deposited will be estimated using an object detection and segmentation algorithm (Radcliffe & Reklaitis, 2019) to extract the diameter for each object, $\boldsymbol{D}(\boldsymbol{z})$, which, assuming axial symmetry, is used to compute: $V_{Drop} = (\pi/4) \int D(z)^2 dz$. For the purposes of online process monitoring in the pharmaceutical manufacturing process, as accurate as possible estimate of drop volume is desired; as illustrated by Figure 1, there is considerable uncertainty as to whether the acquired image contains representative information of the deposited volume (e.g. Inset #2, 3), due to differing detachment phenomena, and the potential for satellite drops. Thus, the optimal camera placement and fiber-optic sensor position are the $\boldsymbol{\zeta}, z_{FbOp}$ that maximize the observed drop volume – either across a range of conditions (if $\boldsymbol{\zeta}, z_{FbOp}$ are to be fixed henceforth), or, for each operating condition/ink formulation, provided the flexibility exists to make automatic adjustments in response to process changes. Noting that the volume computed from the image is proportional to the area, the objective function can be defined based on the area of the object(s) of interest inside the box, normalized to the total area of said object(s), evaluated at the instant of image acquisition – that is, the point at which the lowermost drop interrupts the fiber-optic signal. If only the primary drop is considered, the object function can be defined as the sum across *p* sequences, as shown in Eq. (1):

$$f(\boldsymbol{\zeta}, z_{FbOp}) = \sum\nolimits_p \left(\frac{A_{obj,in}}{A_{obj}} \right)_p \tag{1}$$

In which the total area of the object, A_{obj}, is defined as in Eq. (2):

$$A_{obj} = \int_{z_L}^{z_U} D(z)dz = \sum_j D(z_j)\Delta z\,, \qquad \{\forall j : z_j \in ID_{Primary}\} \tag{2}$$

wherein the limits on the integral are the respective lower/upper boundaries of the primary object. The area of the object inside the camera box, $A_{obj,in}$, is evaluated analogously, with the limits on the integral such that only the area contained within $\boldsymbol{\zeta}$ contributes, illustrated in Figure 2; the index set is then: $\{\forall j : z_j \in ID_{Primary} \cap z_j \in \boldsymbol{\zeta}\}$.

This serves as a reasonable approximation for cases in which the primary drop is much larger than the satellite drops. However, given the detailed information, one can more rigorously re-define the objective function for multiple drops (Figure 2) as the sum of areas of all objects inside the camera box, normalized by the total areas of all objects both inside/outside, as shown in Eq (3):

$$F(\boldsymbol{\zeta}, z_{FbOp}) = \sum\nolimits_p \left(\frac{\sum_{\widetilde{ID(p)}} A_{obj,in,ID}}{\sum_{\widetilde{ID(p)}} A_{obj,ID}}\right)_p \tag{3}$$

With the object-specific event information extracted by the computer vision algorithms, one is able to make an important distinction in terms of the objects and their eventual fates: Eq.(3) should be evaluated for all objects that do not merge with the nozzle, thus, $\widetilde{ID}$ is the subset of all object identities, ID, that satisfy this condition. The reasoning for this is straightforward: through the objects detach, they do not actually contribute to the deposited volume, hence, they should be excluded from the set of objects over which the multi-drop objective function is evaluated. A further note on the definition of what precisely constitutes an object – $A_{obj,in,ID}$ or $A_{obj,ID}$ – is warranted. Consider a case in which the camera box is positioned as close to the nozzle as possible: when the fluid filament begins to form, it then extends into the box, and may perhaps trigger image acquisition before the drop detaches. If the area in the camera box were simply the apparent area, this would result in objective functions that favour being close to the nozzle – as perhaps more volume is extended from the nozzle than actually forms a drop. This problem can be elegantly dealt with utilizing the object-specific events construction inherent to the CV algorithms, therefore enabling one to evaluate the objective function for all dynamically instantiated objects active at a given spatiotemporal point, while excluding persistent objects (i.e. fluid attached to nozzle). This enables consideration of the full range of possible $\boldsymbol{\zeta}'s$ without the need to artificially set an upper bound so as to exclude contributions from the nozzle-attached filament. The convenience of the object-oriented perspective is that it permits us to specify in the objective function the high-level criterion that "valid" area within the camera box must belong to a free liquid fragment (nozzle-attached filament can be present, but its contribution is always zero), and to easily re-define subsets of objects to evaluate Eq. (3).

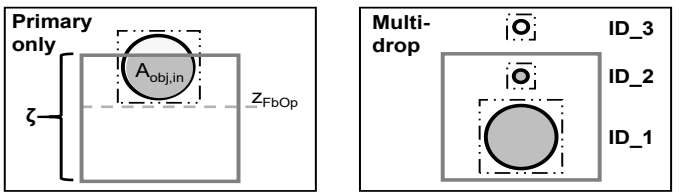

Figure 2. Illustration of contributions to objective function: area inside and total areas

2.4. Solution Method

From the definitions of the objective functions, it can be readily inferred that a gradient-based method may not be preferable. As one expects that a range of $\boldsymbol{\zeta}, z_{FbOp}$ are likely to yield quite similar objective function values, a derivative free method is selected; the classic formulation of the particle swarm optimization algorithm, using 50 particles and 150 generations is used to obtain solutions. An additional advantage for the problems posed here is due to the shape of the objective function (obtained by exhaustive evaluations for p sequences at one set of operating conditions), which resembles a plateau with very steep slopes along the boundary where z_{FbOp} is very near to $z_{Box,L} + H$. Intuitively, this must be the case: as one allows more of the drop area to enter the imaged box, the function changes rapidly.

3. Results: Primary drop, Multi-drop, Primary drop + Interaction partners

The solution to the optimization problem yields a set $\boldsymbol{\zeta}$, parameterized by $z_{Box,L}$, which comprises the camera box positions and a z_{FbOp} which constitutes the location of the fiber-optic sensor. Results are presented in this section for the cases involving only the primary drop, multiple drops, and a third case that takes further advantage of the vent information which pertains to the parent-child relations of the objects. In this third case, the primary object and its interaction partners form a subset of the objects, therefore, by replacing $\widetilde{ID}$, one can evaluate the respective objective function (Eq.(3) directly.

The solutions obtained indicate that when only the primary drop is considered in the objective function, multiple optimal solutions exist, as shown in Figure 3 by the light gray dots, at which points $(\boldsymbol{\zeta}, z_{FbOp})$ the objective function is essentially equal. Including the extra drops in the objective function – multi-drop form, $F(\boldsymbol{\zeta}, z_{FbOp})$ – has a dramatic effect (black dots, Figure 3), in that solutions are then essentially limited to one location which has strong dependence on the satellite drop trajectories. In the third case (dark gray dots, Figure 3), which considers all the events and drop-drop interactions, but limited to the perspective of the primary drop and its interaction partners; the optimal placements are nearly equal – around z_{FbOp} ≈400, which corresponds to a physical distance approximately 4 drop diameters from the nozzle, essentially in the middle of the potential placements.

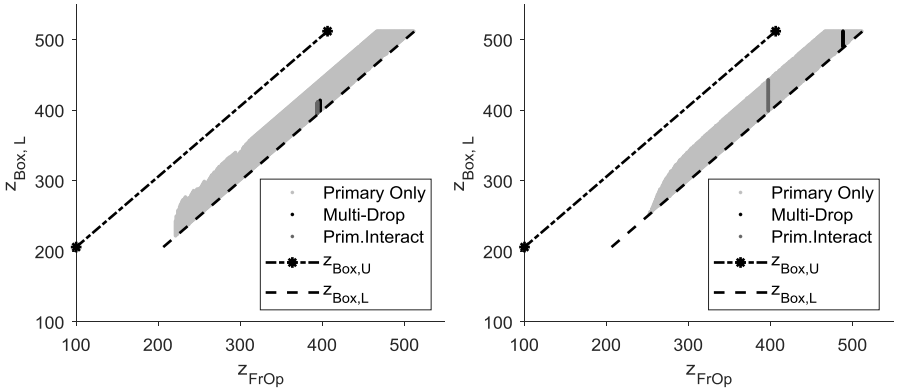

Figure 3. Optimal solutions for each objective. Left: μ-APAP, Φ=0.22; Right: sf-APAP, Φ=0.28

Closer inspect of the primary-only objective function evaluated on all points in the feasible region indicates larger gain as one moves away from the nozzle orifice, but, from

≈225 onward, the gain levels off rapidly with respect to camera placement, akin to a plateau. With respect to fiber-optic placement, generally the closer it is to the upper limit of the camera box, the lower the objective function value – which fits with intuition.

4. Discussion

The difference in the placements for the primary-only and multi-drop objective function fits with intuition – for a single object, there should be many camera/sensor placements that enable one to capture the entire volume of the primary drop across all the sequences at a given condition. Coincidentally, this is why it is easy to select by trial and error a camera/sensor position capable of capturing the whole deposited volume when the fluid properties yield a single drop per actuation event. On the other hand, the placement for the primary+interaction and full multi-drop cases yield very specific regions which are respectively far from many of the points that are potential optima for the primary drop. There are only a few possible $\boldsymbol{\zeta}, z_{FbOp}$ that maximize the objective function; this results from the variability in the spatiotemporal events (particularly those that involve the primary drop) which lead to satellite drop formation. Comparison of the two conditions shown in Figure 3 indicates a significant difference in the placements between them for the multi-drop case; in the μ-APAP set, the placement is nearly the same as the primary+interaction, whereas in the sf-APAP set, the multi-drop placement is notably farther from the nozzle, and from the primary + interaction. This is due to the difference in the volumes of the satellite drops, as their contribution is proportionate – μ-APAP generally produced smaller satellites, but sf-APAP yielded larger satellites whose volume more significant, hence the shift to a position which was able to achieve approximately 1% greater imaged volume by their inclusion.

5. Conclusion

The optimization problem posed here becomes particularly important when one expects to have multiple droplets which undergo breakup or coalescence, as exemplified by the severely restricted regions which contain optima obtained for the primary+ and multi-drop cases. As these images provide a critical process measurement, minimizing uncertainty at the point of acquisition improves predictions from any models that subsequently make use of this information. Though trial and error enables one to guess the conditions when only the primary drop is considered, the treatment presented here demonstrates that some information would inherently be missing. What enables us to approach this problem despite the marked stochastic effects is the use of a data-driven approach which utilizes computer vision to extract object-specific and event type information, from a large number of images – 250,000+ - for real data obtained by high-speed imaging. This provides clear guidance on placements for the complex (multiple drops) scenarios regularly encountered when working with non-ideal inks.

References

L. Hirshfield, E. Icten, A. Giridhar, Z.K. Nagy, G.V. Reklaitis, 2015, “Real-Time Process Management Strategy for Dropwise Additive Manufacturing of Pharmaceutical Products”, J. Pharm. Innov., 10, 2, 140-155

A.J. Radcliffe, G.V. Reklaitis, 2019, “Dynamic Object Tracking, Event Detectino and Recognition for High-speed Imaging of Drop Formation Phenomena”, Intl. J. Comput. Vis. (in review at time of submission)

Sauro Pierucci, Flavio Manenti, Giulia Bozzano, Davide Manca (Eds.)
Proceedings of the 30th European Symposium on Computer Aided Process Engineering (ESCAPE30), May 24-27, 2020, Milano, Italy.
http://dx.doi.org/10.1016/B978-0-12-823377-1.50078-1

Livestock Production Planning with Batch-lines in the Agriculture Industry

Brenno C. Menezes,[a,*] Jeffrey D. Kelly,[b] Tareq Al-Ansari[a,c]

[a]*Division of Engineering Management and Decision Sciences, College of Science and Engineering, Hamad Bin Khalifa University, Qatar Foundation, Doha, Qatar*

[b]*Industrial Algorithms Ltd., 15 St. Andrews Road, Toronto M1P 4C3, Canada*

[c]*Division of Sustainable Development, College of Science and Engineering, Hamad Bin Khalifa University, Qatar Foundation, Doha, Qatar*

bmenezes@hbku.edu.qa

Abstract

With the expansion of the global population coupled with the improving quality of life in developing countries, an increasing demand of food for humans and feed for livestock are expected. Therefore, global pressures and food security issues encourage research, development and deployment of alternatives to improve the performance of the production of livestock and crops in the agriculture industry. Considering such environment, we propose a production planning optimization to be applied in livestock growth (of fish, poultry, pork, cattle, etc.) that considers the necessary feed (ration, vitamins, etc.) and number of animals (from the hatchery) to be placed into appropriate spaces (cages) or facilities (farms) for their proper growth. In the proposed livestock planning model, the placed animals are grown considering the assigned unit-places as batch-processes with limited capacity and variate time-of-growing of the livestock batches. For complex animals such as gallinaceous, swine, caprine and bovine (cattle) species, they are separated by gender to reduce the competition for feed and have comparable time-of-growth (within a range) among the live entities. The results show the batch-lines (batch-processes in lines) of production per gender and time-of-growth to be sequenced and assigned to maintain stable feed amounts in number of individuals and weights to the food processing plant.

Keywords: Livestock planning, Batch process, Feed-to-food, Agriculture industry.

1. Introduction

The increase in the costs of feed inputs and more expensive management of livestock and crops along with higher demands of food outputs and reducing farming resources have been pushing a move in academia and industry in the recent years in researching, developing and deploying novel apparatus and operations in the agriculture field. The expected outcome from this so-called precise farming aims to a) increase the reliability of farming decisions and operations (Anbuselvan et al., 2014); b) reduce inputs such as raw materials, assigned spaces and low-skilled labor; and c) improve livestock and crop yields and qualities. The multidisciplinary expertise in both fundamental and applied sciences for advanced operations in agricultural systems counts on pervasive sensing and actuation, automated decisions, advanced analytics, autonomous machinery and embedded computer control (Muangprathub et al., 2019) as the elements for smart manufacturing and high-performance logistics in this field.

In such context, considering accurate engineering management by the utilization of decision sciences in the agriculture industry (an automated decision element), a livestock production planning is proposed for the growth of fish, poultry, pork, goat, cattle, etc., whereby the number of male and female to be placed in spaces (cages) or facilities (farms) for the proper animal growth is addressed using batch-processes. The needs of separation by gender is more prominent in complex animals as gallinaceous, swine, caprine and bovine species to reduce the male and female competition among the live entities in the assigned spaces. In such model, although the average time of the life growth of each specie is well-known, two issues that conduce to the spread of the time-of-growing of the animals in different assigned places are acknowledged. The fundamental one is to circumvent congestion during the livestock slaughter or harvesting procedures that would drive to infeasible management of the animals in the slaughtering houses during the pre-slaughter handling (immobilization), stunning (to render the animal unconscious) and slaughtering per se. Such over handling may also cause mismanagement in the additional stages of separation of the animal parts and their packing and stocking in the industrial processing plants. The secondary matter to distribute the time-of-growth of the animals, considered as a virtuous side effect of the primary one, is to reduce the impact of the genetics differences. Within the same caged, assigned or placed group-to-grow, there are animals requiring lower time-of-growing (when compared to the average time to grow) and are those that demand longer time before the slaughtering or butchery assignment and further packing, freeze-stocking and selling to the market.

2. Problem statement

Batch-processes with a variate time-of-growing for the animal batches are proposed in the livestock planning model to determine the sequence and amounts of the types (per time-of-growing) of batch-processes in-line to be processed (the batch-lines) in the plant. Availability of the cages or free-range spaces to grow is controlled in the pool of cages. The network in Figure 1 shows a unitary livestock production system constructed in the unit-operation-port-state superstructure (UOPSS) from Kelly (2005) and its objects are defined as: a) unit-operations m for sources and sinks (◇), tanks or inventories (Δ), batch-processes (☐) and continuous-processes (⊠) and b) the connectivity involving arrows (→), inlet-port-states i (○) and outlet-port-states j (⊗). Unit-operations and arrows have binary y and continuous x variables and the ports as process yields or qualities.

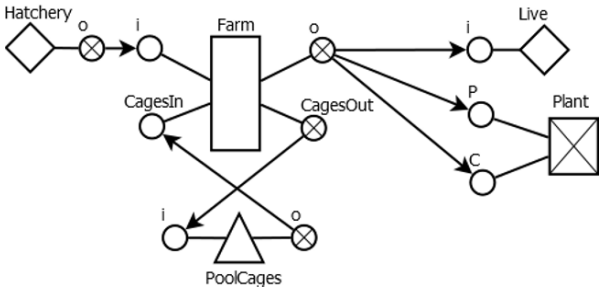

Figure 1. Unitary livestock production system.

Brunaud et al. (2020) demonstrate that the UOPSS formulation is computational superior to STN (Kondili et al., 1993; Shah et al., 1993) and RTN (Pantelides, 1994) in complex scheduling cases tested from the chemical production industry using batch processes,

reducing large-scale problems from quarter of hours to seconds. See Kelly and Menezes (2019) for more details on the UOPSS and other large-scale examples.

3. Mathematical formulation

In the mixed-integer linear (MILP) problem (*P*), the objective function (1) maximizes the outputs of the livestock production $x_{j,i,t}$ (to the plant and as live entities) by discounting the feed costs of the animal batches with inventory or holdup $xh_{m,t}$ ($m \in M_{Farm}$). The semi-continuous constraints of the unit-operations m for the plant are controlled by $x^L_{m,t}\, y_{m,t} \le x_{m,t} \le x^U_{m,t}\, y_{m,t}$. For the batch-process farm, $xh_{m,t}$ is taken when the unit-operation m starts up ($zu_{m,t}$= 1) considering the respective bounds ($xh^L_{m,t}\, zsu_{m,t} \le xh_{m,t} \le xh^u_{m,t}\, zsu_{m,t}$). The arrows or connecting-flows from out- to in-port-states, are bounded as $x^L_{j,i,t}\, y_{j,i,t} \le x_{j,i,t} \le x^U_{j,i,t}\, y_{j,i,t}$. In Eqs. (2) to (9), $j \in J_{up}$ and $i \in I_{do}$ represent, respectively, up and downstream ports of other unit-operations. For $x \in \mathbb{R}^+$, $y \in \{0,1\}$ and $zsu_{m,t} \in [0,1]$:

$$(P)\ \ Min\ Z = \sum_t \left[\sum_{ji \in JI_{Plant}} \left(pr_P\, x_{j,i_p,t} + pr_C\, x_{j,i_p,t} \right) + \sum_{ji \in JI_{Live}} pr_L\, x_{j,i,t} - \sum_{m \in M_{Farm}} c_F\, xh_{m,t} \right] \qquad s.t. \tag{1}$$

$$\frac{1}{x^U_{m,t}} \sum_{j \in J_{up}} x_{j,i,t} \le y_{m,t} \le \frac{1}{x^L_{m,t}} \sum_{j \in J_{up}} x_{j,i,t} \quad \forall\, (i,m) \in (M_{Live}, M_{Plant})\,, t \tag{2}$$

$$\frac{1}{x^U_{m,t}} \sum_{i \in I_{do}} x_{j,i,t} \le y_{m,t} \le \frac{1}{x^L_{m,t}} \sum_{i \in I_{do}} x_{j,i,t} \quad \forall\, (m,j) \in M_{Hatchry}, t \tag{3}$$

$$\sum_{tt<t} r_{j,tt}\, xh_{m,t} \ge \sum_{i \in I_{do}} x_{j,i,t} \quad \forall\, (m,j) \in M_{Farm}, t \tag{4}$$

$$\frac{1}{r^U_{i,t}} \sum_{j \in J_{up}} x_{j,i,t} \le x_{m,t} \le \frac{1}{r^L_{i,t}} \sum_{j \in J_{up}} x_{j,i,t} \quad \forall\, (i,m) \in (M_{Live}, M_{Plant})\,, t \tag{5}$$

$$\frac{1}{r^U_{j,t}} \sum_{i \in I_{do}} x_{j,i,t} \le x_{m,t} \le \frac{1}{r^L_{j,t}} \sum_{i \in I_{do}} x_{j,i,t} \quad \forall\, (m,j) \in M_{Hatchry}, t \tag{6}$$

$$\frac{1}{r^U_{i,t}} \sum_{j \in J_{up}} x_{j,i,t} \le xh_{m,t} \le \frac{1}{r^L_{i,t}} \sum_{j \in J_{up}} x_{j,i,t} \quad \forall\, (m,j) \in M_{Farm}\,, t \tag{7}$$

$$\frac{1}{r^U_{j,t}} \sum_{i \in I_{do}} x_{j,i,t} \le xh_{m,t} \le \frac{1}{r^L_{j,t}} \sum_{i \in I_{do}} x_{j,i,t} \quad \forall\, (m,j) \in M_{Farm}, t \tag{8}$$

$$xh_{m,t} = xh_{m,t-1} + \sum_{j' \in J_{up}} x_{j',i,t} - \sum_{i' \in I_{do}} x_{j,i',t} \ \forall\, (i,m,j) \in M_{Cages}, t \tag{9}$$

$$y_{m',t} + y_{m,t} \leq y_{j,i,t} \;\; \forall\,(m', j, i, m), t \tag{10}$$

$$\sum_{tt<t} zsu_{m',tt} + y_{m,t} \leq y_{j,i,t} \;\; \forall\,(m', j, i, m), t \tag{11}$$

Equations (2) and (3) represent, respectively, the sum of the arrows leaving from the out-port-states j (or splitters) and arriving in the in-port-states i (or mixers) and their summation must be between the bounds of the unit-operation m connected to them. These constraints can be considered semi-continuous constraints for the summation of the flows in- and out- of a port connected to a unit-operation or more specifically to the setup or binary variable of the unit-operation. The production from the farm are controlled by Eq. (4) with the proposition of considering them as a batch-process with a decaying plot $r_{j,tt}$. Equations (5) to (8) consider bounds on yields, both inverse ($r_{i,t}^{L}$ and $r_{i,t}^{U}$) in the in-port-states i and direct ($r_{j,t}^{L}$ and $r_{j,t}^{U}$) in the out-port-states j, since the unit-operations m can have more than one stream arriving in or leaving from their connected ports. Equations (7) and (8) are related to yields of the batch-process, when occurs the starts up, i.e, $zsu_{m,t} = 1$, its holdup $xh_{m,t}$ is taken at this moment to start the animal creation.

The quantity balance of the inventory or holdup for unit-operations of tanks is defined in Eq. (9) and manages the availability of the cages. Equations (10) and (11) are the structural transition constraints to facilitate the setup $y_{m,t}$ or startup $zsu_{m,t}$ of different unit-operations interconnected by out-port-states j and in-port-states i. If the setup of unit-operations m and m' are true in Eq. (10), then the setup variable $y_{j,i,t}$ of the arrow stream between them are implicitly turned-on. In Eq. (11), the setup variable of m' is replaced by the summation of the startups as the farm cages are treated as batch-processes. These logic valid cuts reduce the tree search in branch-and-bound methods. Other constraints to model the run-length or uptime of the batch-processes and the sequence-dependency can be found in Kelly and Zyngier (2007).

4. Results

The livestock planning model in Figure 2 applied for a gallinaceous species is constructed considering the male growing from 16 to 20-months and the female from 13 to 17-months. The optimization for the proposed MILP in Figure 2 for 52-weeks as time-horizon with 1-week time-step gives 20,959 K USD of profit for the planning growth. The problem is solved in 45 seconds with GUROBI 9.0 and > 3600 seconds with CPLEX 12.10 both at 1.0% of MILP relaxation gap using an Intel Core i7 machine at 3.4 GHz (8 threads) with 64 GB of RAM. There are 16,888 constraints (4,613 equality) for 5,895 continuous variables and 4,704 binary variables with 5,986 degrees-of-freedom in the problem (variables minus equality constraints).

The Gantt chart in Figure 3 shows the startups of the animal growth in cages considering the different types of time-of-growing batches for male (16 to 20-months) and female (13 to 17-months). The different types of batch-processes representing the male and female types of cages can be started up continuously or in-line since the batch is initialized by using the available resource cages (of any type of time-of-growing or gender) taken from the PoolCages inventories.

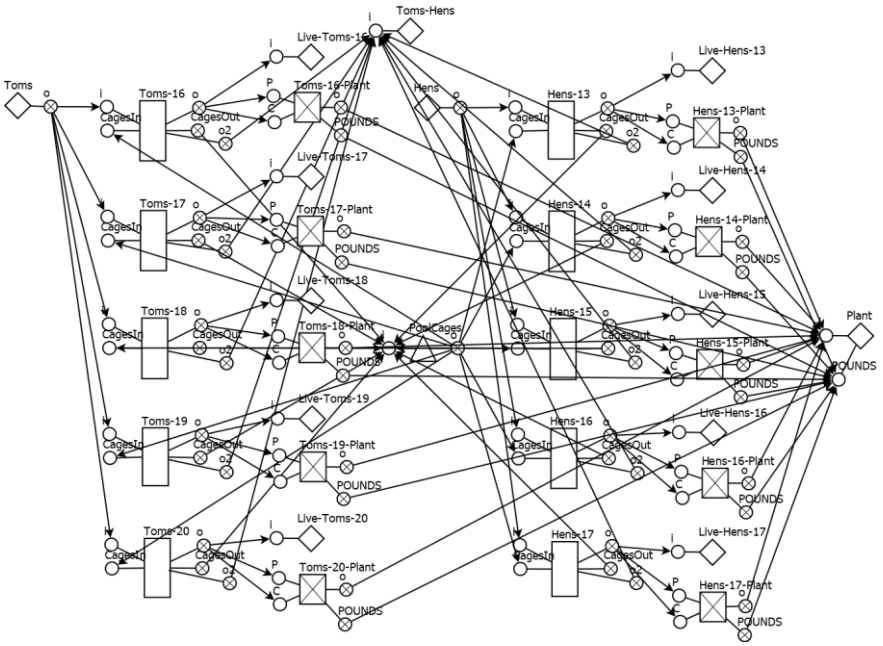

Figure 2. Livestock production planning considering variate time-of-growing of male (toms) and female (hens) cages.

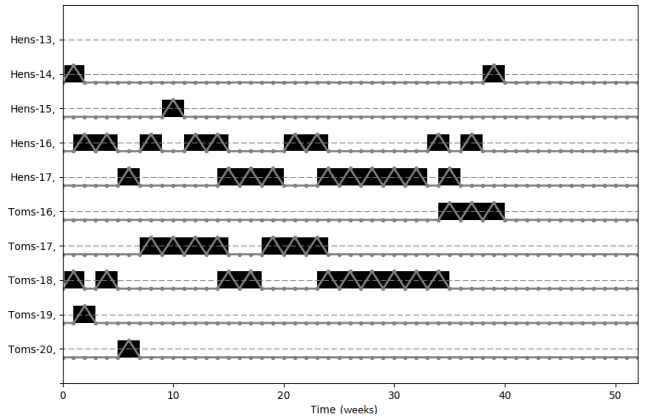

Figure 3. Startups of the male and female procreation cages considering the variate time-of-growing batches.

The Gantt chart in Figure 4 shows the PoolCages object that represents the inventory of cages to start the livestock production. The inventory upper bound is two cages ready for the procreation to be initialized per week. The formulation uses inventories to control the resources of cages in the out-port-states of the PoolCages inventory for the batch startups (see Figure 2 the PoolCages object). It may be considered as the capacity of workers or machinery limits to be modeled in a problem.

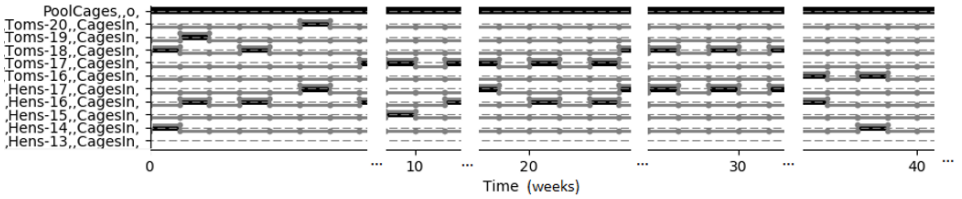

Figure 4. PoolCages release of the male and female cages and time-of-growing batches.

5. Conclusions

The livestock planning approach using batch-lines to manage animal procreation is an effective tool to improve overall gains and avoid mismanagement in the agriculture industry. When planning the livestock growth by distributing its time-of-growing in the different cages, the uncertainties and bottlenecks related to the production (from the management/processing) and from the hatchery (incubator or breeding locations), are reduced or mitigated. The high-performance management of livestock demonstrated in this work is mandatory to face higher demands of food outputs and reducing farming resources as well as in the global competitiveness of the new industrial efficiency age.

References

S. Anbuselvan, S. Arunkumar, G. Guhan, K. Muruganantham, T. Rajesh, 2014, Optimization of Productivity in Agro Industries Using Reliability Centered Maintenance, International Journal of Technology and Engineering System, 6 (2), 203-208.

B. Brunaud, S. Amaran, S. Bury, J. Wassick, I.E. Grossmann, 2020, Batch Scheduling with Quality-Based Changeovers, Computer and Chemical Engineering, Computers and Chemical Engineering, 132, 106617.

J.D. Kelly, 2005, The Unit-Operation-Stock Superstructure (UOSS) and the Quantity-Logic-Quality Paradigm (QLQP) for Production Scheduling in The Process Industries, In Multidisciplinary International Scheduling Conference Proceedings: New York, United States, 327-333.

J. D. Kelly, D. Zyngier, 2007, An Improved MILP Modeling of Sequence-Dependent Switchovers for Discrete-Time Scheduling Problems, Industrial and Engineering Chemistry Research., 46, 4964-4973.

J.D. Kelly, B.C. Menezes, 2019, Industrial Modeling and Programming Language (IMPL) for Off- and On-Line Optimization and Estimation Applications. In: Fathi M., Khakifirooz M., Pardalos P. (eds) Optimization in Large Scale Problems. Springer Optimization and Its Applications, 152, 75-96.

E. Kondili, C.C. Pantelides, R.W.H. Sargent, 1993, A General Algorithm for Short-Term Scheduling Of Batch Operations – I MILP Formulation, Computers and Chemical Engineering, 17, 211-227.

J. Muangprathub, N. Boonnam, S. Kajornkasirat, N. Lekbangpong, A. Wanichsombat, P. Nillaor, 2019, IoT and Agriculture Data Analysis for Smart Farm, Computers and Electronics in Agriculture, 156, 467-474.

N. Shah, C.C. Pantelides, R.W.H. Sargent, 1993, A General Algorithm for Short-Term Scheduling of Batch Operations – II. Computational Issues. Computers and Chemical Engineering, 17, 229-244.

C.C. Pantelides. Unified Frameworks for the Optimal Process Planning and Scheduling. Proceedings on the Second Conference on Foundations of Computer Aided Operations. 1994, 253-274.

Sauro Pierucci, Flavio Manenti, Giulia Bozzano, Davide Manca (Eds.)
Proceedings of the 30th European Symposium on Computer Aided Process Engineering (ESCAPE30), May 24-27, 2020, Milano, Italy.
http://dx.doi.org/10.1016/B978-0-12-823377-1.50079-3

Ethanol Reforming: Setting up Performance Target

Shahid H Ansari, Baraka C Sempuga, Xinying Liu

Institut of Development of Energy for African Sustainability, University of South Africa, Private Bag X6, Florida, 0710, Johannesburg, South Africa
liux@unisa.ac.za

Abstract

Process Synthesis techniques and Attainable region principles were used to determine the target of ethanol reforming to hydrogen from a material, energy and work balance point of view. From a material balance point of view, 100% hydrogen efficiency, defined as the fraction of hydrogen in the feed that is converted into the desired product (H_2), can be achieved by partial oxidation at the ratio of ethanol to oxygen of 1 : 1.5, producing H_2 and CO_2. However, the process releases a significant amount of energy and work potential, which might not be economically recovered especially for small scale applications. Co-feeding water is one of the ways to recover this energy by producing more H_2. We, therefore, look at the ultimate energy target for the process, which is considered to be at the point where ΔH across the process is zero. In order to achieve this water and oxygen must be fed to the process at ratios of 1:1.77 and 1: 0.62 respectively. This increases H_2 production by 59%. However, the process will still have a significant amount of work potential indicated by the negative change in Gibbs free energy across the process. When work balance target of $\Delta G = 0$ was considered, we can show that the hydrogen production can be increased up to 87%. However, the process will require heat to be supplied. If a low cost heat source is available, such as solar or waste heat from other processes, then a maximum of 187% selectivity of H_2 based on ethanol can be achieved. For a fully energy integrated process, at $\Delta G = 0$ the process does not require high quality heat for it to proceed. Therefore, at this point any source of heat at a temperature high enough to enable heat flow at any point in the process will be sufficient to drive the process. We consider this to be the ultimate target for ethanol reforming, which not only enables to conserve the chemical potential of ethanol but also provides an opportunity to store additional external energy in the form of H_2. The feasibility of these targets were validated by Aspen Plus simulation.

Keywords: Ethanol autothermal reforming, Process Target, Gibbs free energy minimization, Hydrogen production, Tail gas

1. Introduction

Hydrogen fuel cell technologies has big potential to be used in vehicle or portable power plants as a clean energy supply solution. But there are challenges in its implementation such that currently most of the hydrogen is produced from fossil fuel such as natural gas or coal, which are not renewable, while the hydrogen produced from water electrolysis by using renewable power is still expensive. Furthermore, if hydrogen is produced from a big hydrogen plant, it still needs to be transported to the user end and stored at the user end, which raised concerns of its safety. It would be a good option to study the potential of using liquid fuel, which are easy to be stored and transported as a feed stock for on-

site hydrogen production in vehicle or hydrogen filling station (Di Marcoberardino 2017). Among various ethanol to hydrogen processes studied, ethanol autothermal reforming, which is a combination of the exothermic ethanol partial oxidation process and endothermic ethanol steam reforming process, is most suited for mobile application as it doesn't require external heat load (Hou 2015). Furthermore, ethanol water mixture can be used in the autothermal reforming process, thus the high energy cost paid to remove all water in the ethanol production by distillation and zeolite adsorption can be saved (Deluga 2004).

To achieve thermal neutral, for every mol of ethanol, 1.78 mole of water and 0.61 mole of Oxygen is needed (Graschinsky 2012), to produce 4.78 mole of hydrogen. But there is still a significant amount of work as indicated by the negative change in the free energy across the process. To utilize this work, a work balanced target at $\Delta G = 0$ was considered and analyzed by targeting techniques.

2. Method

The targeting technique employs three basic tools namely the mass, energy and work (entropy) balance to determine a feasible region from which a design target for the process can be set. It starts by first identifying the major components of the process and ignores the components in smaller quantities and the impurities. This is done to simply the analysis while extracting the essential information that does not require the details, which will be included at a later stage of design. The major components that were considered here are C_2H_6O, H_2, CO_2, H_2O, CO, CH_4, O_2. From these components, we can derive the following independent material balances using the method by (Yin, 2010)

$$\begin{aligned} &C_2H_6O + 0.5O_2 \Rightarrow 3H_2 + 2CO \ldots\ldots\ldots\ldots E_1 \\ &CO_2 + H_2 \Rightarrow CO + H_2O \ldots\ldots\ldots\ldots\ldots\ldots E_2 \\ &CH_4 + 2O_2 \Rightarrow CO_2 + 2H_2O \ldots\ldots\ldots\ldots\ldots E_3 \\ &H_2 + 0.5O_2 \Rightarrow H_2O \ldots\ldots\ldots\ldots\ldots\ldots\ldots E_4 \end{aligned} \qquad (1)$$

Note that these are not necessarily the actual reactions occurring in the process, they are simply material balances representing all achievable outcome from the process. Each component can then be written in terms of extent as $N_i = \sum_{i,j} v_{ij} E_j$.

The constraints set by the energy and work balances are also included. These are expressed as follows:

$$\begin{aligned} \Delta H_P &= \sum_i N_i \Delta \hat{H}_i(T_O) \\ \Delta G_P &= \sum_i N_i \Delta \hat{G}_i(T_O) \end{aligned} \qquad (2)$$

ΔHp represents the net energy requirement of the process and ΔG_P is the change in the Gibbs free energy and represents the work requirement (or work potential) of the process.

In other words, ΔG_P represents the portion of the energy equivalent to mechanical work that must be supplied (positive) or removed (negative) from the process.

3. Results and Discussion

It can be shown that the process has four degrees of freedom representing four possible targets that can be set simultaneously. In order to explore these targets, we used a linear programming approach to determine the feasible regions. Two cases are considered namely $\Delta Hp = 0$ for an energy neutral process and $\Delta Gp = 0$ for a work neutral process. Figure 1 shows the feasible regions obtained by plotting the oxygen fed to the process versus the hydrogen production at $\Delta Hp = 0$ per mole of ethanol fed. The negative number of moles indicates that the component is a feed while the positive number indicates that the component is a product. The feasible region is considered to be where H_2, CO_2, CO, CH_4 are products and O_2 is feed. H_2O is allowed to be either feed or products. It is clear from Figure 1 that the maximum H_2 production occurs at zero CH_4 and CO produced. At this point $\Delta Gp < 0$, this means that the process should proceed with less effort. It also means that the process has the potential to do work, which can be recovered by applying an appropriate process configuration. Therefore, the ultimate H_2 production target for an autothermal ethanol reformer is about 4.77 per mole of ethanol.

$$C_2H_6O + 1.77H_2O + 0.62O_2 \Rightarrow 4.77H_2 + 2CO_2 \quad \Delta G = -195\ \text{kJ};\ \Delta H = 0\ \text{kJ} \quad (3)$$

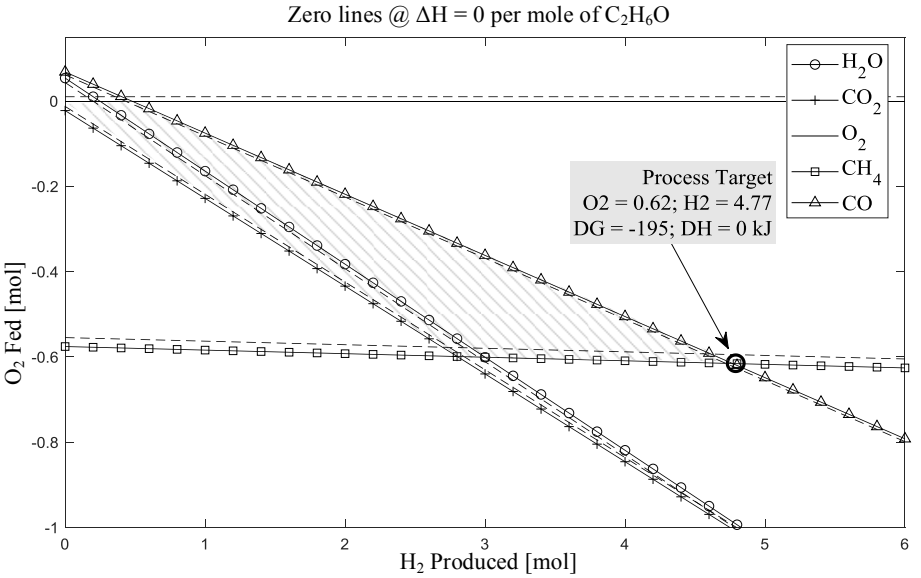

Figure 1: Feasible region for an energy neutral ethanol reforming process. The solid lines are the boundaries indicating zero moles of the components. The dashed lines indicate the side where the components are net products. The ultimate hydrogen production target is 4.77 moles per mole of C_2H_6O.

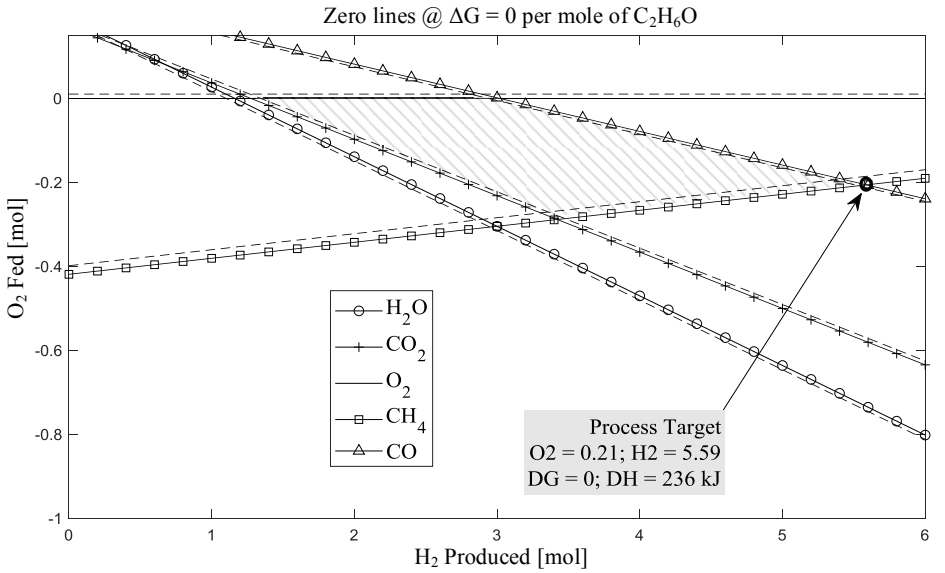

Figure 2: Feasible region for a work neutral ethanol reforming process. The solid lines are the boundaries indicating zero moles of the components. The dashed lines indicate the side where the components are net products. The ultimate hydrogen production target is 5.59 moles per mole of C_2H_6O

Figure 2 shows the feasible region for a work neutral process ($\Delta G_p = 0$). The maximum hydrogen production also occurs at zero CH_4 and CO produced. However, at this point $\Delta H_p > 0$. This means that energy in the form of heat must be supplied to the process from an external source. The significance of a work neutral process is that the chemical potential of the feed material is fully conserved when they are converted into products (Sempuga and Yao, 2017). Consequently, the energy that must be supplied can be in the form of heat and can be at any temperature that enables the flow of energy from an external source to the process, not necessarily higher than the actual reforming temperature. This target represents the limit of performance for any ethanol reforming process contrary to what is considered to be the limit set by an auto thermal reformer (Graschinsky 2012). The H_2 production target at this limit is 5.59 per mole of ethanol.

$$C_2H_6O + 2.59H_2O + 0.21O_2 \Rightarrow 5.59H_2 + 2CO_2 \quad \Delta G = 0 \text{ kJ}; \ \Delta H = 236 \text{ kJ} \quad (4)$$

This target provides a means for improving the hydrogen production of an auto thermal reformer by up to 17%, if a source of low cost energy is available, which is likely the case in the actually application environmental such as in the vehicle. For a fully energy integrated process, at $\Delta G = 0$ the process does not require high quality heat for it to proceed. Therefore, at this point any source of heat at a temperature high enough to enable heat flow at any point in the process will be sufficient to drive the process. For example, one of the efficient ways of supplying the energy to the process is by generating steam using any heat source at low temperature but high enough to produce the steam (above 100°C at 1atm) and feed the steam that carries the required amount of energy into the process.

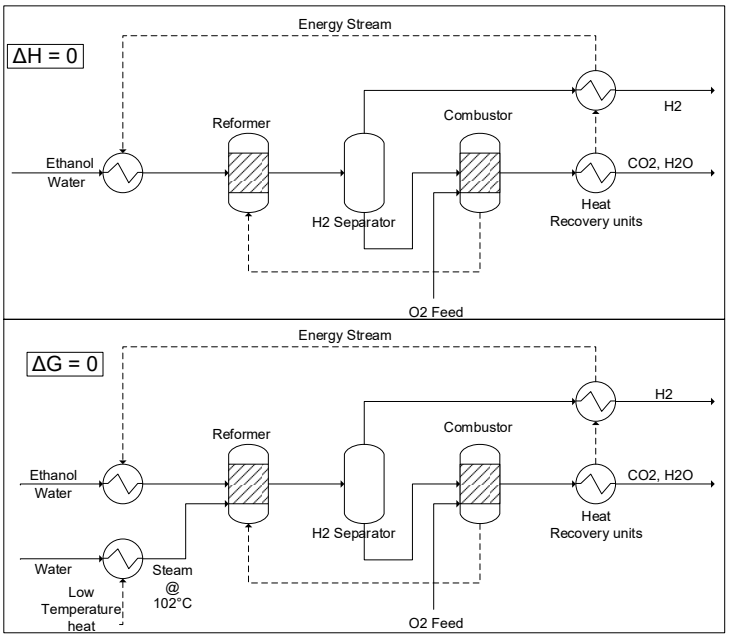

Figure 3: Flow diagram for the Aspen Plus simulations at $\Delta H = 0$ and $\Delta G = 0$

Simulations in Aspen Plus ® were conducted to explore how the targets in (3) and (4) can be achieved. The flow sheets are shown in figure 3. The main assumptions taken in the simulation are: 1) the reforming reaction reaches equilibrium and therefore an equilibrium reactor (RGibbs) was used to simulate the reaction. 2) Pure H_2 can be recovered from the product stream at the reactor temperature therefore; a perfect separator was used to selectively remove H_2 from the other products. The latter assumption is possible in a membrane reactor, which can separate out H_2 during the reaction.

For the $\Delta H = 0$ process, the feed stream containing ethanol and water is pre-heated and fed to membrane reactor. The temperature in the reactor is set to between 500°C and 1000°C. The membrane process, which selectively removes H_2 from the reactor, is simulated by multistage equilibrium reactors with hydrogen separation between stages. The energy required in the reformers is supplied by burning the tail gas from the reformer after H_2 has be separated out. For this purpose, a stoichiometric reactor (Rstoic) was used. The combustion is assumed to occur at the same temperature as the reactor. Heat integration is done between the feed stream and the product streams from the combustor. A temperature approach of 10°C is considered in the heat integration process.

The flowsheet of the $\Delta G = 0$ process is the same as that of $\Delta H = 0$ except for the additional steam generated from an external source of energy and fed to the reactor. The stream brings in the additional energy required to reach the target H_2 at $\Delta G = 0$. In the current simulation it assumed that external heat is available to generate steam and 102°C and 1bar from a stream of liquid water at 25°C.

The simulation results show that for the $\Delta H = 0$ process the H_2 production target of 4.77/mole of ethanol at an oxygen to ethanol ratio of 0.62 : 1 can be achieved over the temperature range 500 - 1000°C. The water to ethanol feed ratio varies depending on the reaction temperature, the minimum feed ratio 4.40 : 1 occurs at 700°C. If we consider recycling the water, then the net water to ethanol feed ratio is constant over the temperature range and is 1.77 : 1; this is the same as the target water feed ratio in (3).

The simulation results for the $\Delta G = 0$ process show that the H_2 production target of 5.59/mole of ethanol at an oxygen to ethanol ratio of 0.21 : 1 can be achieved over the temperature range 500 - 1000°C. The water to ethanol feed ratio also varies depending on the reaction temperature, the minimum feed ratio 9.01 : 1 occurs at 620°C. If we consider recycling the water, then the net water to ethanol feed ratio is constant over the temperature range and is 2.59 : 1; this is the same as the target water feed ratio in (4).

4. Conclusions

By conducting work balance target analysis, we found that hydrogen production of the ethanol to hydrogen process can be increased up to 87% compared to ethanol partial oxidation process and 17% more compared to the target of the energy neutral process, with less oxygen required and more water tolerated in the feed. Although external heat is needed, a low cost heat can be utilized in a fully energy integrated process operated at $\Delta G = 0$. We consider this to be the ultimate target for ethanol reforming, which not only enables to conserve the chemical potential of ethanol but also provides an opportunity to store additional external energy in the form of H_2.

Acknowledgement

The authors would like to acknowledge the University of South Africa (UNISA) and the financial support from National Research Foundation (NRF) with grant numbers 95983 and 113648.

References

G a Deluga, J R Salge, L D Schmide, X E Verykios, 2004, Reneable hydrogen from ethanol by autothermal reforming, Sciences, 303, 993-997

C Graschinsky, P Giunta, N Amadeo, M Laborde, 2012, Thermodynamic analysis of hydrogen production by autothermal reforming of ethanol, International Journal of Hydrogn Energy, 37 (13), 10118-10124

T Hou, S Zhang, Y Chen, D Wang, 2015, W Cai, Hydrogn production from ethanol reforming: Catalysts and reaction mechanism, Reneable and Sustainable Energy Reviews, 44, 132-148

G Di Marcoberardino, M Binotti, G Manzolini, J L Viviente, A Arratibel, L Roses, F Gallucci, 2017, Achievements of European projects on membrane reactor for hydrogen production, Journla of Cleaner Production, 161, 1442-1450

B C Sempuga and Y Yao, 2017, CO_2 hydrogenation from a process synthesis perspective: Setting up process targets', Journal of CO_2 Utilization, 20, 34–42.

Yin, F., 2010, A simple method for finding independent reactions, Chemical Engineering Communications, 83 (1), 117–127.

Sauro Pierucci, Flavio Manenti, Giulia Bozzano, Davide Manca (Eds.)
Proceedings of the 30th European Symposium on Computer Aided Process Engineering (ESCAPE30), May 24-27, 2020, Milano, Italy.
http://dx.doi.org/10.1016/B978-0-12-823377-1.50080-X

Thermodynamic Framework for Cryogenic Carbon Capture

Laura A. Pellegrini,[a*] Giorgia De Guido,[a] Stefania Ingrosso[b]

[a]*Dipartimento di Chimica, Materiali e Ingegneria Chimica "G. Natta", Politecnico di Milano, Piazza Leonardo da Vinci 32, I-20133 Milan, Italy*
[b]*SAIPEM S.p.A., via Martiri di Cefalonia 67, I-20097 San Donato Milanese (MI), Italy*
laura.pellegrini@polimi.it

Abstract

Carbon dioxide capture and storage (CCS) is an important option for climate change mitigation and it has been extensively analysed in recent years to face the climate challenge. A portion of the emitted CO_2 comes from fossil fuel power plants. Several post-combustion technologies are available for separating CO_2 from the flue gases produced by the combustion of fossil fuels. In recent years, low-temperature/cryogenic technologies have been investigated for this purpose, which rely on the fact that CO_2 can be separated out of flue gas by freezing it out. As a consequence, when dealing with the design of this type of processes, it is of paramount importance to be able to satisfactorily predict the thermodynamic phase behaviour of the system of interest, which involves equilibrium conditions also in the presence of solid CO_2.

The classical approach for phase equilibria calculations involving a solid phase is based on the equality of components' fugacities in the different phases and on the use of an expression for the fugacity of the freezing component in the solid phase that can be derived by relating it to its fugacity in the vapor phase following a proper thermodynamic cycle. This work compares the predictions for solid-vapor equilibria (SVE) conditions of a flue gas mixture that are obtained using such a classical approach with those obtained using the RGibbs calculation block available in the Aspen Plus® process simulator. The latter one enables SVE calculations by minimizing the Gibbs energy. The obtained results are useful for determining suitable operating conditions for the separation process, depending on the desired level of CO_2 recovery to be achieved.

Keywords: CO_2, carbon capture, solid-vapor equilibria, cryogenic gas separation, flue gas

1. Introduction

Climate change represents a serious challenge the world has to face today. At the 21st Conference held in Paris in 2015, Parties in the United Nations Framework Convention on Climate Change reached an agreement to combat this issue and to accelerate and intensify the actions and investments needed for a sustainable low carbon future. In this context, CCS techniques have been extensively studied in recent years as a mitigation option for reducing anthropogenic CO_2 emissions into the atmosphere.
Different technologies are currently available for CO_2 removal from flue gases, including chemical (De Guido et al., 2018) and physical absorption, adsorption (Gutierrez-Ortega et al., 2017), permeation through membranes (Leimbrink et al., 2015) and low-temperature or commonly referred to as "cryogenic" separation. Recently, a great attention has been devoted to cryogenic separation methods for application not

only to natural gas purification (De Guido et al., 2015) and biogas upgrading (Pellegrini et al., 2017), but also to nitrogen rejection (De Guido et al., 2019) and CO_2 capture from flue gas. When this last application is considered, the separation process aims at reducing the flue gas temperature from ambient to a low temperature range at which CO_2 freezes out and can be removed from the main gas stream in a solid phase. The advantages of this technology can be summarized as follows: liquid CO_2 is directly produced, thus making it relatively easy to be stored or to be used for Enhanced Oil Recovery; the use of solvents is avoided (Sipöcz et al., 2013). Certainly, a major disadvantage consists in the large amount of energy required for refrigeration. However, literature works have proved that the use of low-temperature technologies for natural gas purification becomes less energy demanding at CO_2 concentrations higher than 8-9 mol% (Langè et al., 2015).

Clodic et al. (Clodic et al., 2005) proposed a cryogenic technology for CO_2 separation from the flue gases for a conventional pulverized coal-fired power boiler, which is based on CO_2 frosting (anti-sublimation) and defrosting at atmospheric pressure in a low-temperature evaporator. Baxter et al. (Baxter et al., 2009) proposed the CCC^{TM} (Cryogenic CO_2 Capture^{TM}) technology, which uses a phase change (*i.e.*, desublimation) to separate CO_2 from exhaust or process gases. Tuinier et al. (Tuinier et al., 2010) developed a novel post-combustion CO_2 capture process concept, based on cryogenic CO_2 freeze-out in dynamically operated packed beds. Song et al. (Song et al., 2012) developed a novel cryogenic CO_2 capture system based on the use of Stirling coolers, which is able to condense and separate CO_2 from flue gas according to differences in condensation and desublimation.

The increased interest in this type of processes requires a proper tool to be available for the correct prediction of phase equilibria also involving the solid phase. In this work, a method based on a classical approach is presented and results are compared with those found in the literature and the ones that can be obtained using a tool available in a commercial process simulator. These results are exploited to establish the suitable operating conditions for CO_2 separation from flue gas by a cryogenic separation method.

2. Methods

2.1. Proposed thermodynamic approach for SVE calculations

In this work, a classical approach has been used (it will be referred to as "proposed approach" in the following) to solve a two-phase solid-vapor equilibrium (SVE) problem for a flue gas mixture having the following composition: 14.0 mol% CO_2, 83.0 mol% N_2, and 3.0 mol% O_2. Since the number and type of phases present at equilibrium are not known *a-priori*, the choice of studying SVE conditions for the system of interest has to be considered as an assumption based on the type of components the system consists of. The SVE problem has been solved assigning the pressure and recovery of CO_2 with the aim of plotting the equilibrium temperature curve as a function of pressure for each recovery level. In particular, three values have been chosen for that (*i.e.*, 90 %, 95 % and 99 %) for comparison of the results obtained in this work with those presented in the literature (Baxter et al., 2009).

The recovery of CO_2 in the solid phase (*REC*) is calculated according to Eq. (1):

$$REC = \frac{S \cdot x_{CO_2}^{S}}{F \cdot z_{CO_2}} = \frac{S}{F \cdot z_{CO_2}} \tag{1}$$

In Eq. (1), $x_{CO_2}^S$, which denotes the molar fraction of CO_2 in the solid phase, has been set equal to one since the solid phase is assumed to consist of pure CO_2. Moreover, in Eq. (1) *F* and *S* denote the molar flow rates, respectively, of the feed stream and of the solid phase, and z_{CO_2} refers to the molar fraction of CO_2 in the feed stream (*i.e.*, 0.14). By combining Eq. (1) with the material balances on the species involved in the investigated system, it is possible to get the composition of the vapor phase at equilibrium for each case study (*i.e.*, each pair of pressure and CO_2 recovery). The SVE calculation is based on the equality of fugacity of each *i*-th component in the two considered phases (*i.e.*, solid and vapor), and Eq. (2) holds:

$$\hat{f}_i^S(T,P,\underline{x}^S) = \hat{f}_i^V(T,P,\underline{x}^V) \tag{2}$$

Since CO_2 is the only species to be present in both phases at equilibrium, Eq. (2) can be rewritten, according to the classical method, as Eq. (3), where $\phi_{CO_2}^V$ is the fugacity coefficient of pure CO_2 in the vapor phase evaluated at the sublimation pressure, $P_{CO_2}^{subl}$, and equilibrium temperature, *T*, and $\hat{\phi}_{CO_2}^V$ is the fugacity coefficient of CO_2 in the vapor mixture evaluated at the equilibrium temperature, at the given pressure, *P*, of the system and composition.

$$\phi_{CO_2}^V(T,P_{CO_2}^{subl}(T))\cdot P_{CO_2}^{subl}(T)\cdot\exp\left(\frac{v_{CO_2}^S\cdot(P-P_{CO_2}^{subl}(T))}{RT}\right) = P\cdot x_{CO_2}^V\cdot\hat{\phi}_{CO_2}^V(T,P,\underline{x}^V) \tag{3}$$

The two fugacity coefficients in Eq. (3) have been calculated using the Peng-Robinson Equation of State (Peng and Robinson, 1976). As for the binary interaction parameters, the values have been taken from the Aspen Hysys® V9.0 database (AspenTech, 2016a). Therefore, Eq. (3) can be solved in the unknown temperature, at given pressure and CO_2 recovery. The solid molar volume, $v_{CO_2}^S$, in the Poynting correction term has been assumed to be constant and equal to 0.0282 m^3/kmol. As for the sublimation pressure, $P_{CO_2}^{subl}$, it has been computed using the expression proposed by Jensen et al. (Jensen et al., 2015) and reported in Eq. (4), where $P_{CO_2}^{subl}$ is in Pa and *T* in K.

$$P_{CO_2}^{subl}(T) = \exp\left(57.52-\frac{3992.84}{T}-4.9003\cdot\ln(T)+2.415\cdot10^{-15}T^6+\frac{8125.6}{T^2}\right) \tag{4}$$

2.2. Thermodynamic approach available in the process simulator

The RGibbs reactor is the only calculation block available in Aspen Plus® V9.0 (AspenTech, 2016b) that is able to solve a system involving phase equilibria also in the presence of a solid phase (Schach et al., 2011). It uses Gibbs energy minimization techniques, instead of methods based on the equality of fugacities of each component in each phase. The system is considered at equilibrium when the distribution of the components corresponds to the minimum of the Gibbs energy (subject to atom balance constraints). According to the literature from Aspen Technology, this method can be used for any number of phases and components and always yields stable solutions. Since the RGibbs cannot handle phase equilibria between solid and fluid phases of a component directly (*e.g.*, CO_2-dry ice equilibria), it is necessary to identify the solid component as a different one. The Peng-Robinson Equation of State (Peng and

Robinson, 1976) has been used as property method and the values of the standard solid heat of formation and of the standard solid Gibbs free energy of formation have been specified.

3. Results and discussion

Before solving the SVE problem investigated in this work with the proposed approach, the reliability of Eq. (4) in predicting the CO_2 sublimation pressure has been checked. Results are shown in the parity plot in Fig. 1. They suggest a good agreement between calculated and experimental values (Fernández-Fassnacht and Del Río, 1984; Levenson, 1974), with an average absolute deviation of 23.6 %.

Fig. 2 illustrates the results obtained using the proposed approach (dashed line), which are compared with those obtained using the RGibbs tool available in Aspen Plus® V9.0 (dotted lines) and with those available in the literature (Baxter et al., 2009) (solid line). In Fig. 2, the symbols refer to the points of the curves where each approach registers a maximum. The proposed approach is about 2 degrees more conservative in correspondence of the value of pressure where the maximum is found in the literature and is in good agreement with the results obtained using the RGibbs tool.

As a general result, it is possible to state that, for achieving a higher recovery at a given pressure, it is necessary to operate the process at a lower temperature. Moreover, the maximum trend the curves in Fig. 2 exhibit suggests that, if a certain CO_2 recovery is desired, the process can be operated at a higher temperature at increasing pressure and viceversa for pressures up to the labelled maximum point. Beyond the labelled points in Fig. 2, higher pressures and lower temperatures are required to achieve the same CO_2 recovery in the solid phase, both of which would make the CO_2 separation process more energy-intensive. Therefore, for each curve in Fig. 2, the portion up to the labelled point is the one corresponding to the operating conditions of interest for the process, which aims at separating CO_2 from a flue gas mixture by desublimation.

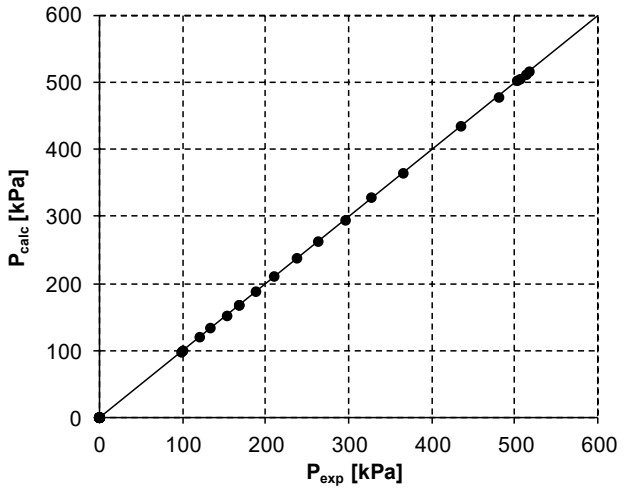

Figure 1. Parity plot for CO_2 sublimation pressure. Experimental data have been taken from the literature (Fernández-Fassnacht and Del Río, 1984; Levenson, 1974) and cover the temperature range 69.7-216.6 K; calculated values have been obtained using Eq. (4).

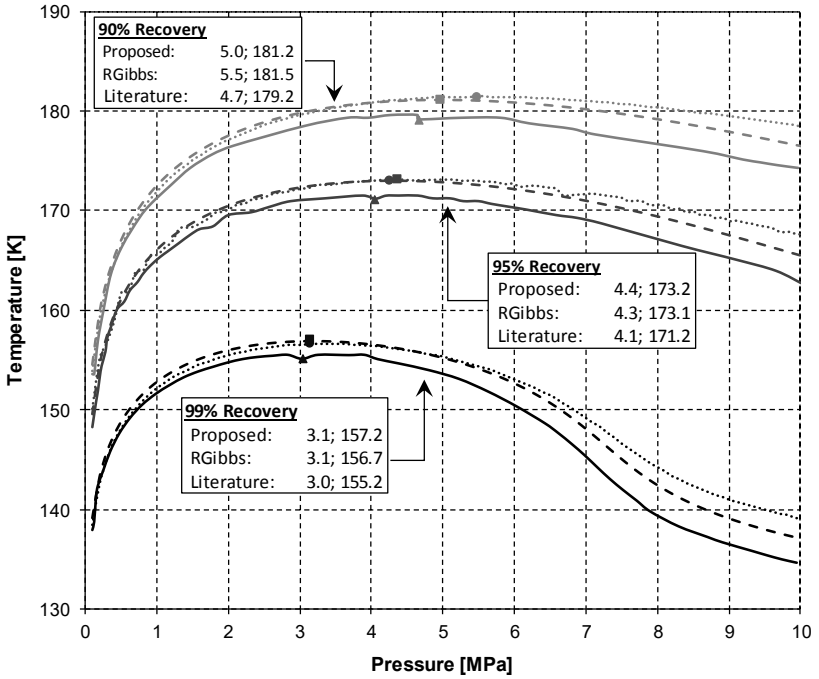

Figure 2. SVE temperatures as a function of pressure at assigned recovery of CO_2 in the solid phase. Comparison between the results obtained using: the proposed approach (dashed line), the RGibbs tool of Aspen Plus® V9.0 (AspenTech, 2016b) (dotted line), and the ones presented in the literature (Baxter et al., 2009) (solid line). The different colors refer to different CO_2 recovery values: 90 % (light grey); 95 % (grey); 99 % (black). For each curve, the symbols (square: proposed approach; circle: RGibbs; triangle: literature) refer to the values in the text box that correspond to the pressure at which each approach registers the maximum temperature.

4. Conclusions

Low-temperature or cryogenic technologies for CO_2 capture from flue gases have received great attention in the last years to cope with the disadvantages of conventionally adopted technologies mainly based on absorption. Since these novel separation methods are operated at conditions where CO_2 freezes out, it is important to have a tool capable of satisfactorily predicting phase equilibria in the presence of a solid phase, which is not always taken into account in phase equilibria calculations. This is important for a correct process design.

In this work, a calculation method is proposed for this purpose and the obtained results are compared with those of a calculation block available in a commercial process simulator, based on a different approach. The good agreement suggests that the proposed method can be used to design the CO_2 separation process.

In particular, for achieving 99 % recovery of CO_2 in the solid phase, temperatures of about 140 K have to be reached at atmospheric pressure or higher temperatures (up to about 155 K) at increasing pressures up to about 3 MPa. Above this pressure value, due to the maximum trend exhibited by the temperature-pressure curve at fixed CO_2 recovery, the process should be operated at lower temperatures, which is disadvantageous since this makes it more energy-intensive.

For an improved analysis, an advanced phase equilibria calculation method has been developed in the framework of a joint project between the GASP group of Politecnico di Milano and Saipem S.p.A. and implemented in the "SLVEcalc" tool. The advanced model takes into account the phase stability analysis (Gupta, 1990) for the identification of the type of phases present at equilibrium and will be the subject of a future work.

References

AspenTech, 2016a. Aspen Hysys®. AspenTech, Burlington (MA), United States.
AspenTech, 2016b. Aspen Plus®. AspenTech, Burlington (MA), United States.
L. Baxter, A. Baxter, S. Burt, 2009. Cryogenic CO_2 capture as a cost-effective CO_2 capture process, International Pittsburgh Coal Conference, Pittsburgh, USA.
D. Clodic, R. El Hitti, M. Younes, A. Bill, F. Casier, 2005. CO_2 capture by anti-sublimation Thermo-economic process evaluation, 4th Annual Conference on Carbon Capture and Sequestration. National Energy Technology Laboratory Alexandria (VA) USA, pp. 2-5.
G. De Guido, M. Compagnoni, L.A. Pellegrini, I. Rossetti, 2018. Mature versus emerging technologies for CO_2 capture in power plants: Key open issues in post-combustion amine scrubbing and in chemical looping combustion. Frontiers of Chemical Science and Engineering 12, 315-325.
G. De Guido, S. Langè, L.A. Pellegrini, 2015. Refrigeration cycles in low-temperature distillation processes for the purification of natural gas. Journal of Natural Gas Science and Engineering 27, 887-900.
G. De Guido, F. Messinetti, E. Spatolisano, 2019. Cryogenic nitrogen rejection schemes: analysis of their tolerance to CO_2. Industrial & Engineering Chemistry Research 58, 17475-17488.
E. Fernández-Fassnacht, F. Del Río, 1984. The vapour pressure of CO_2 from 194 to 243 K. The Journal of Chemical Thermodynamics 16, 469-474.
A.K. Gupta, 1990. Steady state simulation of chemical processes. Chemical and Petroleum Engineering, University of Calgary.
A. Gutierrez-Ortega, J. Menacho, R. Gonzalez-Olmos, R. Nomen, J. Sempere, 2017. Numerical simulation of fixed bed for CO_2 capture in a fossil fuel emission points by Pressure Swing Adsorption system, Computer Aided Chemical Engineering. Elsevier, pp. 415-420.
M.J. Jensen, C.S. Russell, D. Bergeson, C.D. Hoeger, D.J. Frankman, C.S. Bence, L.L. Baxter, 2015. Prediction and validation of external cooling loop cryogenic carbon capture (CCC-ECL) for full-scale coal-fired power plant retrofit. International Journal of Greenhouse Gas Control 42, 200-212.
S. Langè, L.A. Pellegrini, P. Vergani, M. Lo Savio, 2015. Energy and Economic Analysis of a New Low-Temperature Distillation Process for the Upgrading of High-CO_2 Content Natural Gas Streams. Industrial & Engineering Chemistry Research 54, 9770-9782.
M. Leimbrink, A.-K. Kunze, D. Hellmann, A. Górak, M. Skiborowski, 2015. Conceptual Design of Post-Combustion CO_2 Capture Processes-Packed Columns and Membrane Technologies, Computer Aided Chemical Engineering. Elsevier, pp. 1223-1228.
L. Levenson, 1974. Sublimation rates and vapor pressure of H_2O, CO_2, N_2O and Xe. Journal of Chemical & Engineering Data 19, 107-110.
L.A. Pellegrini, G. De Guido, S. Langé, 2017. Biogas to liquefied biomethane via cryogenic upgrading technologies. Renewable Energy 124, 75-83.
D.-Y. Peng, D.B. Robinson, 1976. A new two-constant equation of state. Industrial & Engineering Chemistry Fundamentals 15, 59-64.
M.-O. Schach, B. Oyarzún, H. Schramm, R. Schneider, J.-U. Repke, 2011. Feasibility study of CO_2 capture by anti-sublimation. Energy Procedia 4, 1403-1410.
N. Sipöcz, A. Hernandez-Nogales, M.A. Gonzalez-Salazar, R. Shisler, V. Lissianski, 2013. Low temperature CO_2 capture for near-term applications. Energy Procedia 37, 1228-1238.
C.-F. Song, Y. Kitamura, S.-H. Li, K. Ogasawara, 2012. Design of a cryogenic CO_2 capture system based on Stirling coolers. International Journal of Greenhouse Gas Control 7, 107-114.
M. Tuinier, M. van Sint Annaland, G.J. Kramer, J. Kuipers, 2010. Cryogenic CO_2 capture using dynamically operated packed beds. Chemical Engineering Science 65, 114-119.

Sauro Pierucci, Flavio Manenti, Giulia Bozzano, Davide Manca (Eds.)
Proceedings of the 30th European Symposium on Computer Aided Process Engineering (ESCAPE30), May 24-27, 2020, Milano, Italy.
http://dx.doi.org/10.1016/B978-0-12-823377-1.50081-1

Investigation of a Hybrid Approach to Find all Solutions of Nonlinear Equation Systems

Saskia Bublitz*, Erik Esche, Jens-Uwe Repke

Technische Universität Berlin, Chair of Process Dynamics and Operation, Str. del 17. Juni 135, 10623 Berlin, Germany

saskia.bublitz@tu-berlin.de

Abstract

We examine a novel procedure to solve nonlinear systems without manual initialization and apply it on the model of a Methanol-Water distillation process. The approach starts with a reduction of user-defined variable bounds by a box reduction procedure based on interval arithmetic. Secondly, the narrowed search space is sampled to finally start a numerical solver from the most promising initial points. For our tested example, we could find a solution with MATLAB's fsolve function and the TNC solver from the python package SciPy.

Keywords: box reduction, interval arithmetic, sampling, multi-start

1. Motivation

Numerically solving nonlinear systems, as they frequently appear in chemical process models, is still quite challenging. While local solvers combined with line search or trust region methods as described by Deuflhard (2011) work well on Lipschitz-continuous solution spaces, there is still no generally applicable procedure in place to find good initial values for them. Global optimization methods, such as described by Floudas (2000), adequately find all solutions of small systems for a given set of function terms. Nevertheless, they are *a priori* not applicable to all types of systems and especially large systems of equations. Constraint propagation methods based on expression trees or directed graphs as detailed in Moore et. al. (2009) are designed to find all solutions of a problem but are computationally intractable for large systems (Schnepper & Stadtherr, 1996). Therefore, we suggest a hybrid approach consisting of box reduction, sampling, and multi-start that tries to avoid the individual flaws of these methods.

2. Solution Approach: Box Reduction and Multi-start

The initial bounds of iteration variables from a process model span a certain multi-dimensional solution space called a *box*. Box volumes of large equation systems are mostly enormous in case tight variable bounds are not at hand. Besides, they often contain singular points that cause failure of derivative-based solvers. Hence, we develop a box reduction algorithm that lowers the initial volume down to tighter solution enclosures by interval bisection and removes singular points by interval nesting. This may result in multiple multi-dimensional boxes as possible solution space.

On the reduced box(es), a Hammersley low-discrepancy sequence is applied to generate pseudo-random sample points. Nevertheless, the point-density (number of points per box volume) in reduced boxes of large systems can still be relatively low.

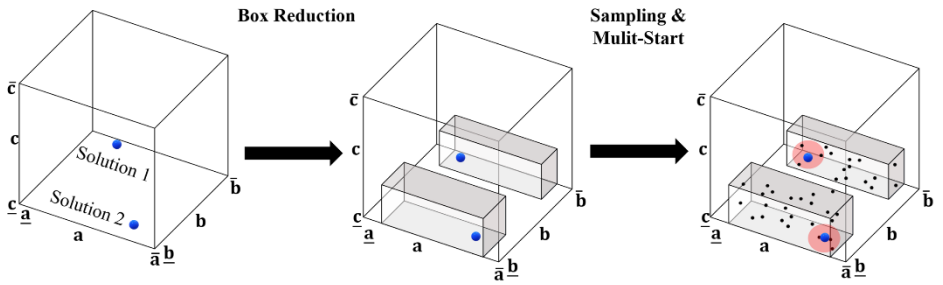

Figure 1. Hybrid approach sketched for a three-dimensional system with two actual solutions.

Hence, the chance that the majority of points does not converge in finite time is still quite high. This makes a direct multi-start very inefficient. Therefore, the residual of the nonlinear equation system at each sample point is tested before a numerical equation solver is only applied on a predefined number of promising candidate points, i.e., those with the lowest residuals. The Newton-type solvers applied are MATLAB's fsolve function (MATLAB, 2019) and TNC from the python package SciPy (Jones et. al. 2001). Both box reduction and multi-start procedure are parallelized using the python package multiprocessing (McKerns, 2011).

The box reduction algorithm tries to reduce an interval x in functions of the form:

$$f(x,y) = 0 \tag{1}$$

with y being intervals of other variables that stay constant in one reduction step. Eq. (1) is reformulated into an x-dependent part $g(x,y)$ and an x-independent part $b(y)$:

$$g(x,y) = b(y) \tag{2}$$

The algorithm matches the interval $g(x,y)$ as tightly as possible to the interval $b(y)$. The interval functions are evaluated by interval arithmetic. Here, the python package mmpath (Johannsson, 2013) is employed for these operations. In the linear case with a constant interval or scalar a:

$$g(x,y) = a(y) \cdot x = b(y), \tag{3}$$

the Gauss-Seidl Operator Γ (Montanher et. al., 2017) is applied to calculate the reduced interval $x^{(1)}$ from the initial $x^{(0)}$:

$$x^{(1)} = \Gamma\left(b, a, x^{(0)}\right) = b \backslash a \cap x^{(0)} \tag{4}$$

Three cases for $b \backslash a \cap x^{(0)}$ can occur:

1. $x^{(1)} = \emptyset$: no solution (the user has to reconsider the initial bounds of x)
2. $x^{(1)} \subseteq x^{(0)} \wedge x^{(1)} = \{x_1^{(1)}, x_2^{(1)}\}$: two reduced intervals (branching)
3. $x^{(1)} \subseteq x^{(0)}$: one interval

In case the intersection is empty, there cannot be a solution in $x^{(0)}$. Branching occurs when a contains positive and negative values ($\underline{a} < 0 < \bar{a}$). Referring to general interval arithmetic, a division of b by a results in an unbounded interval and information is lost

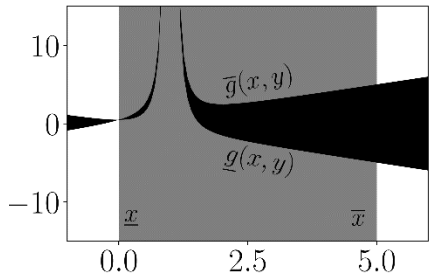

I) Evaluated functional extension in x

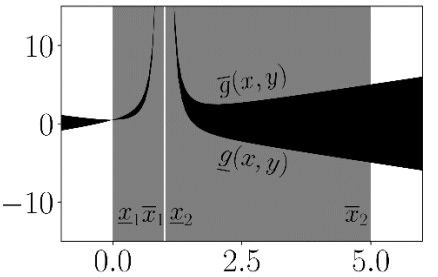

II) Removal of discontinuities

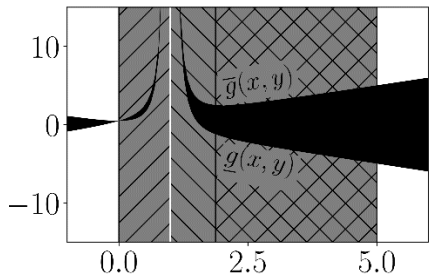

III) Detection of monotonously increasing (/), decreasing (\), and non-monotone sections (X)

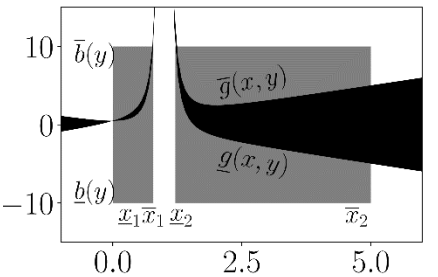

IV) Reduction of x by b

Figure 2. Scheme of INES applied on a function g(x, y) for an initial interval $x = [0, 5]$ and a right-hand side interval $b = [-10, 10]$.

about maximum negative values and minimum positive values. The Gauss-Seidl Operator retains these bounds by bisecting the interval into a negative interval bounded from above and a positive interval bounded from below. In the third case, the initial interval is reduced or remains constant, if it is already a subset of $b \backslash a$.

Intervals in nonlinear functions are reduced by our three-step interval nesting procedure (INES). First, the discontinuous functions terms $g(x, y)$ are divided into continuous parts by bisection at the discontinuity. The procedure stops as soon as the width of the interval around the discontinuity is below a pre-defined tolerance or bisection lasts too long.

All continuous, non-monotone functions are sorted into increasing, decreasing, and apparently non-monotone sections. Through interval bisection and nesting the sub-intervals are checked regarding their first derivatives of $g(x, y)$ being ≥ 0 (monotonously increasing) or ≤ 0 (monotonously decreasing). The non-monotone intervals are further processed until the remaining interval width is below a pre-defined tolerance or the latter cannot be reduced in case of apparently non-monotone intervals. They occur whenever the derivative includes positive and negative values at certain points within x.

In the last step, INES intersects all monotone, continuous functions with $b(y)$. Two cases exist: one solution interval or no solution. If a solution exists, the algorithm proceeds with bisecting x to find a tighter enclosure $g(x, y)$ for $b(y)$. If $b(y)$ contains $g(x, y)$ no reduction of x is possible. All remaining, apparently non-monotone and discontinuous

intervals are separated into subintervals, for which $g(x,y)$ is directly evaluated and checked for intersections with $b(y)$.

Figure 2 shows the stepwise reduction with INES for the function:

$$g(x,y) = y \cdot x + \frac{0.5}{(1-x)^2} = b(y) \tag{5}$$

with initial bounds $x = [0,5]$ and $y = [-1,1]$. The interval x is reduced to the sub-intervals $[0, 0.785]$ and $[1.2, 5]$.

In multi-dimensional systems, the box reduction algorithm is applied on all iteration variables separately. The algorithm reduces each variable's bounds by analysing all equations it appears in. Once this is completed for all variables the procedure is repeated on the reduced set of boxes. The algorithm terminates, when the intervals cannot be further reduced or the maximum number of iteration steps is reached. Since the key task of the box reduction algorithm is to remove discontinuities and to find better solution enclosures, and not the solution itself, we choose the maximum number of iteration steps to be 10 at most. Whenever interval branching occurs, the resulting boxes are iterated independently.

The success of the k-th box reduction of an n-dimensional system is measured by the dimensionless hypercubic length $l^{(k)}$:

$$l^{(k)} = \sqrt[n]{\prod_{i=1}^{n} \frac{\sum_{j=1}^{m_i} w(x_{i,j}^{(k)})}{w(x_i^{(0)})}}\,, \tag{6}$$

wherein $w(x_{ji}^{(k)})$ is the width of the j-th interval that results from branching $x_i^{(0)}$. The quantity ranges from 0 (solution(s) found) to 1 (no reduction). All solved variables $(\sum_{j=1}^{m_i} w(x_{i,j}^{(k)}) = 0)$ are removed from the box.

3. Case Study

3.1. Process Model

The presented hybrid approach is tested on a steady-state model for a methanol-water-distillation column consisting of ten equilibrium trays, a total condenser, and a partial reboiler. The model has been implemented in MOSAICmodeling (Esche et. al., 2016).

3.2. Initialization of Variable Bounds

Our hybrid approach requires some carefully chosen initial bounds based on the range of validity of the process model. Otherwise interval branching can occur. If k intervals decompose each into two sub intervals, the number of boxes n grows by 2^k. This increases the processing time greatly. Besides, interval bounds cannot be reduced at all occasionally if other variable bounds are chosen too loose.

Since the mixture is zeotropic minimum and maximum values of pure component data is used to initialize the bounds of stream enthalpies, tray temperatures and pressures.

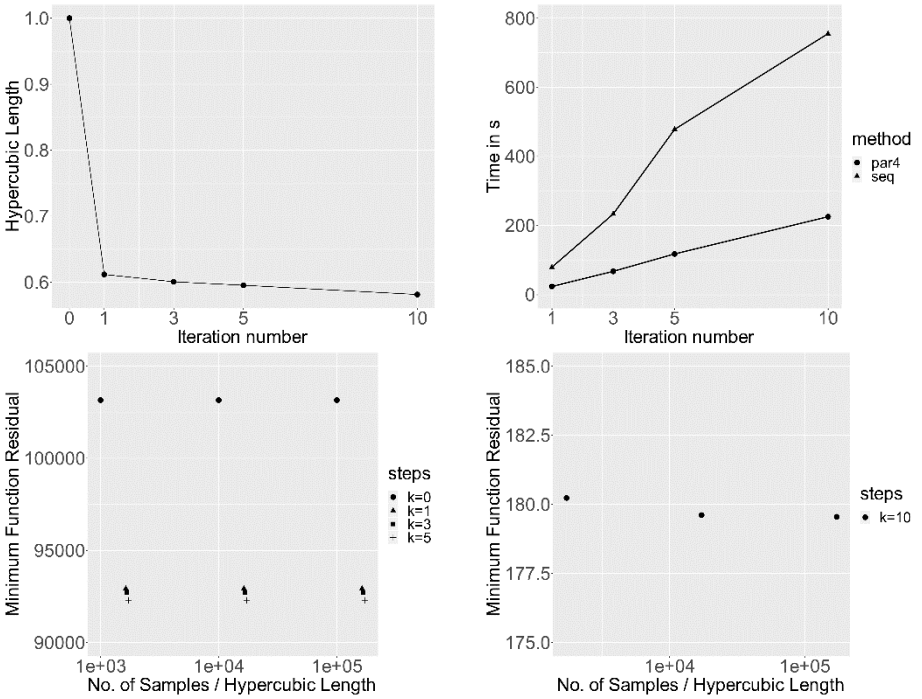

Figure 3. Results of the box reduction (top) and sampling (bottom)

Flowrates range from zero to the user-specified feed flow rate, for the bottom and distillate stream. Upper bounds for the internal streams are roughly overestimated by the user-specified reflux ratio. Their lower bounds equal 0. The initial intervals of the mole fractions range from 0 to 1.

3.3. Analysis

After initialization, 1, 3, 5, or 10 reduction steps were performed and the corresponding hypercubic lengths of the reduced boxes were computed as given in Fig. 3. The method works efficiently for the first iteration step and after that stagnates as shown. Since the purpose is to remove discontinuities and reduce bounds rather than solving the system, higher number of reduction steps are not tested. Within 10 reduction steps no branching occurs. Through parallelization of the procedure CPU time is greatly decreased as shown here for using 4 processors (par4) instead of one (seq).

For the initial box (k=0) and each reduced box 1.0E3, 1.0E4 and 1.0E5 samples are generated. As can be seen from Fig. 3 no great reduction in function residuals can be achieved if the number of samples is increased in the constant box volumes. Hence, only the five samples with the lowest residual out of 1.0E3 generated samples for the different box volumes are passed to Newton-type solvers. The function residuals of the samples after 10 box reduction steps decrease by almost 3 orders of magnitude in comparison to the other cases (Fig. 3, bottom right).

The function tolerance of the solvers was set to 1.0E-7 and the maximum iteration number to 10^5. Tab. 1 shows the results of both solvers for all tested box reduction steps.

Table 1 Results from Multi-Start procedure

Box reduction steps	Number of converged samples out of the 5 best for	
	MATLAB	TNC
0	0	0
1	0	0
3	0	1
5	0	1
10	1	3

4. Conclusions & Outlook

A solution to the investigated Methanol-Water distillation column is successfully found by the hybrid approach presented in this contribution without passing any initial guess to the problem highlighting the capabilities compared to usual solution based on manually obtained initial guesses. In future research we will apply this method on more challenging problems such as separation processes of multicomponent and / or azeotropic mixtures and full process models with recycle streams. Through tests on the presented process model and further unit operations such as a flash, a heat exchanger and a reactor three bottlenecks were identified that can further improve the performance of this approach. Firstly, the equation formulation has a great influence on the box reduction efficiency and reformulations should hence be investigated. Secondly, complex values should be filtered the same way as discontinuities. Currently, the box reduction algorithm lets variable intervals unchanged whenever complex values occur. Finally, the test results show that the procedure greatly under- and overestimates bounds for fugacity coefficients by conventional interval arithmetic due to interval dependency (Moore, 2009). This problem can be solved by applying INES on the righthand side of Eq. (2) as well to identify its monotonous continuous y intervals and to determine tighter bounds for $b(y)$.

References

C.A. Floudas, 2000, Deterministic Global Optimization, Springer-Science-Business Media
C.A. Schnepper, M.A. Stadtherr, 1996, Robust Process Simulation using Interval Methods, Computers & Chemical Engineering, 20, 2, 187-199
E. Esche, C. Hoffmann, M. Ilner, D. Müller, S. Fillinger, G. Tolksdorf, H. Bonart, G. Wozny, J.-U. Repke, 2016, MOSAIC, Chemie Ingenieur Technik,89, 5, 1522-2640
E. Jones, T. Oliphant, P. Petersion & others, 2001, SciPy: Open Source Scientific Tools for Python
F. Johansson, 2013, mpmath: a Python library for arbitary-precision floating-point arithmetic, version: 1.1.0., http://mpmath.org/
M. M. McKerns, L. Strand, T. Sullivan, A. Fang, M. A. G. Aivazis, 2011, Building a framework for predictve science, version: 0.70, Proceedings of 10th Pyhton in Science Conference, 67-78
MATLAB, 2019, The MathWorks Inc., version 7.10.0 (2019b)
P. Deuflhard, 2011, Newton Methods for Nonlinear Problems, Springer
R. E. Moore, R. Baker Kearfott, M.J. Cloud, 2009, Introduction to Interval Analysis, SIAM, 7-40
T. Montanher, F. Domes, H. Schichl, A. Neumaier, 2017, Using interval unions to solve linear systems of equations with uncertainties, BIT Numerical Mathematics, 57, 3, 901-926

Sauro Pierucci, Flavio Manenti, Giulia Bozzano, Davide Manca (Eds.)
Proceedings of the 30th European Symposium on Computer Aided Process Engineering (ESCAPE30), May 24-27, 2020, Milano, Italy.
http://dx.doi.org/10.1016/B978-0-12-823377-1.50082-3

Fast and Accurate Simulation of Simulated Moving Bed Chromatographic Processes with Linear Adsorption Isotherms

Rojiar Pishkari,[b,*] and Achim Kienle[a,b]

[a] *Max Planck Institute for Dynamics of Complex Technical Systems, Sandtorstrasse 1, 39106 Magdeburg, Germany*

[b] *Otto von Guericke University Magdeburg, Universitätplatz 2, 39106 Magdeburg*
Pishkari@mpi-magdeburg.mpg.de

Abstract

In this paper, we propose a new fast and accurate simulation method for highly efficient chromatographic columns with linear adsorption isotherms. The method is based on an analytical solution of the underlying partial differential equations using the method of characteristics, which describes the propagation of selected concentration values. The method is exact. The discretization of the concentrations is only used for the representation of the solution and the evaluation of the coupling conditions between the different columns. Application is demonstrated for binary 4-zone and ternary 8-zone SMB processes with center-cut separation. It is shown, that the computational effort can be reduced by more than factor 100 compared to the popular discrete cell model.

Keywords: Simulated moving bed chromatography, simulation, method of characteristics, cell model.

1. Introduction

Simulated moving bed (SMB) processes are an advanced technology for continuous chromatographic separations (Schmidt Traub et al., 2012). The main advantage is an increased productivity and a reduced solvent consumption compared to conventional batch processes. A standard configuration for a binary separation process is shown in Figure 1a. It consists of four chromatographic columns representing the four zones of the process. They are connected to a ring. The component with the higher affinity to the solid phase located in the columns is obtained at the extract, while the component with the lower affinity to the solid phase, i.e. the higher affinity to the fluid phase, is obtained at the raffinate. The counter-current flow of the solid phase which is essential for continuous operation is simulated by cyclic switching of the in- and outlets in direction of fluid flow or by switching the columns in the opposite direction.

In practice, besides binary separation processes, often ternary separation problems play an important role in isolating an intermediate adsorbing component from a complex mixture. This type of process is also termed as a center-cut separation. For center-cut separation problems various options are available including a cascade of two binary separation processes, as well as eight or nine zone SMB processes (Nicolaos et al., 2001, Kessler et al., 2006). Focus in this contribution, is on an eight zone process with raffinate recycle as illustrated in Figure 1b. It is worth noting that with this configuration a fraction of pure intermediate B can be obtained in the extract 2 flow, but not all three product

flows can be obtained as pure components (Nicolaos et al., 2001). For example, the raffinate 2 product may also contain some amount of component B.

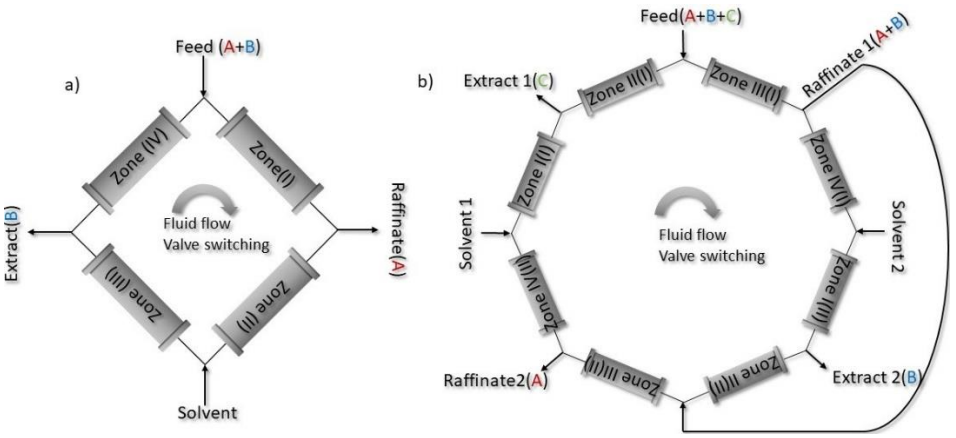

Figure 1. Schematic illustration of SMB system. (a) 4-zone SMB. (b) 8-zone SMB.

The conceptual process design of SMB processes is based on the true moving bed analogon using triangle theory (Migliorini et al., 1998) or standing wave theory (Ma et al., 1997). Numerical simulation of the simulated moving bed process can be applied to further optimize the separation. For this purpose, some discretization using well known finite difference, finite volume, or finite element schemes can be used. Due to the presence of steep concentration fronts this may require a large number of grid points leading to a considerable computational effort, in particular, when a large number of simulations is required, for example during optimization. For this purpose, we propose an alternative approach based on an analytical solution which is possible for linear adsorption isotherms using the method of characteristics.

In 1995, an analytical solution for binary SMB process was proposed by (Zhong et al., 1995) using a set of algebraic equation to calculate the concentration profiles assuming linear adsorption isotherm and highly efficient columns. Although the present approach is based on the same principles it is more flexible, much easier to implement and is therefore readily extended to more complex process configurations like the ternary center-cut separation considered in this paper.

2. Model description

The model of the SMB plants shown in Figure 1 consists of the models of the chromatographic columns, the material balances of the in- and outlet ports and the switching conditions. The chromatographic columns can be described by the well-known equilibrium dispersion model.

$$\varepsilon \frac{\partial c_i}{\partial t} + (1-\varepsilon)\frac{\partial q_i}{\partial t} + \varepsilon v \frac{\partial c_i}{\partial z} = D_{ax}\varepsilon \frac{\partial^2 c_i}{\partial z^2} \tag{1}$$

Therein, ε is the volume fraction of the fluid phase, v the interstitial velocity and D_{ax} an apparent dispersion coefficient, which lumps together all effects contributing to band broadening. Moreover, c_i is the concentration of component 'i' in the fluid phase and q_i

the corresponding concentration in the solid phase. Since the model assumes thermodynamic equilibrium between both phases, q_i is directly related to the fluid phase composition by the adsorption isotherm. In the following focus is on linear isotherms according to

$$q_i = H_i c_i \tag{2}$$

with Henry coefficient H_i.

For highly efficient columns, axial dispersion can be neglected in a first step, leading to a system of first order partial differential equations.

$$\frac{\partial c_i}{\partial t} + \frac{(1-\varepsilon)}{\varepsilon}\frac{\partial q_i}{\partial t} + v\frac{\partial c_i}{\partial z} = 0 \tag{3}$$

Together with the adsorption isotherm Eq. (2), this represents a set of linear decoupled transport equations, where every concentration value of component 'i' is transported with the corresponding constant characteristic velocity.

$$w_i = \frac{dz}{dt} = \frac{v}{(1+\frac{1-\varepsilon}{\varepsilon}H_i)} \tag{4}$$

3. Analytical solution

For simulating the SMB processes shown in Figure 1, the analytical solution which is obtained from Eq. (4) is implemented in discrete form, i.e. the initial profile of each component in each column is discretized and put into a matrix form according to

$$\begin{bmatrix} concentration\ value\ 1 & concentration\ value\ 2 & \dots & concentration\ value\ n \\ position\ value\ 1 & position\ value\ 2 & \dots & position\ value\ n \end{bmatrix} \tag{5}$$

In the multicomponent case, the corresponding concentration profiles are put together in a multi-dimensional tensor form and the positions for each component are calculated using its specific propagation velocity.
In the remainder, 100 spatial grid points are used for this purpose. Further, time is also discretized. In particular, 100 time steps per switching interval are used in this study. For the calculation of the concentration profiles in the next time step, first, new positions are calculated for the concentration values in Eq. (5) using Eq. (4) according to:

$$new\ position = old\ position + w_i dt \tag{6}$$

Afterwards, the concentration vector is rearranged. Concentration values with positions beyond the actual column length are removed, and the remaining values are shifted to the right. Then node balances at the entrance of the columns are evaluated and resulting values are propagated into the column to fill the gaps in the concentration vector from the left. For this purpose, it is important to calculate at which exact intermediate time point the concentration values have left the previous column, which is again simply done by application of Eq. (4) according to:

$$intermediate\ time\ point = old\ time\ point + (column\ length - old\ position)/w_i \tag{7}$$

Corresponding node balances are evaluated at this time point and the propagation into the subsequent column for the remaining time of this interval is determined. In this way, the solution is exact. Discretization is done only for the graphical representation of the solution. Accuracy is not affected.

4. Numerical solution (cell model)

For comparison with the analytical approach, a simple numerical solution is applied using the popular cell model. This corresponds to a 1st order finite volume discretization of Eq. (3) on an equidistant grid assuming piecewise constant profiles. From the physical point of view, the continuous column is replaced by a discrete series of stirred tanks. The material balance of component 'i' at cell 'j' is then

$$V_{cell}\frac{d}{dt}(\varepsilon c_i + (1-\varepsilon)H_i c_i) = q(c_{i,j-1} - c_{i,j}) \tag{8}$$

with the cell volume $V_{cell} = \frac{V_{col}}{n}$ and the volumetric flow rate $q = \varepsilon A_{col} v$. Therein, n is the number of cells per column.

The resulting system of ordinary differential equations is solved numerically in MATLAB using the integrator ode45. For this purpose, node balances are directly included in the material balances of the corresponding cells.

5. Results

In this section, application is demonstrated for the binary and the ternary processes presented in Figure 1. Model parameters and column properties used in this simulation study are given in Table 1.

Table 1. Model parameters and column properties

Parameter	(4-zone SMB)	(8-zone SMB)
Number of the column	4	8
Column dimensions	100[mm]	100[mm]
Column porosity	0.75	0.75
Henry constant A	5	1.1
Henry constant B	7.5	1.7
Henry constant C	-	2.5
Switching time	100[s]	654[s]
Feed concentration A	2 [gr/L]	2 [gr/L]
Feed concentration B	3 [gr/L]	3 [gr/L]
Feed concentration C	-	4 [gr/L]

Table 2. Dimensionless flow rates

4-zone SMB			
m_I	m_{II}	m_{III}	m_{IV}
7.5	4.5	7.7	5.0
8-zone SMB			
$m_{I(1)}$	$m_{II(1)}$	$m_{III(1)}$	$m_{IV(1)}$
2.55	1.57	2.19	0.86
$m_{I(2)}$	$m_{II(2)}$	$m_{III(2)}$	$m_{IV(2)}$
1.82	1.22	2.55	1.01

Optimal operating conditions for the binary true moving bed analogon to Figure 1a follows in the linear case directly from the Henry coefficients of the two components using triangle theory (Migliorini et al., 1998). To account for numerical dispersion in the discrete model and prevent breakthrough, some safety margins were introduced. The operating conditions for the ternary process in Figure 1b were taken from (Kessler et al.,

2006) Operating conditions in terms of m-values are given in Table 2. These m-values are related to the fluid flow rate and the switching time in the following way.

$$m_k = \frac{Q_k T_{sw} - \varepsilon V_{col}}{(1-\varepsilon) V_{col}} \tag{9}$$

Figure 2 shows the internal concentration profiles during start up at the end of each cycle for the binary and the ternary SMB processes shown in Figure 1. The left diagrams show the numerical solution using the cell model.

To achieve steeps fronts as predicted by the equilibrium model a large number of 1,000 cells per column is required. The right column shows the corresponding solution using the analytical approach described above. The arrows at the bottom of each of the diagrams indicate the positions of the in- and outlet streams as indicated in Figure 1. 'F' stands for feed, 'R' for raffinate and 'E' for extract. The numerical and analytical solutions in Figure 2 show good agreement. Minor differences are due to the numerical dispersion introduced by the cell model in the left diagrams. It could be reduced by a further increase of the number of grid points or by using some more advanced discretization of the underlying partial differential equations as briefly mentioned above.

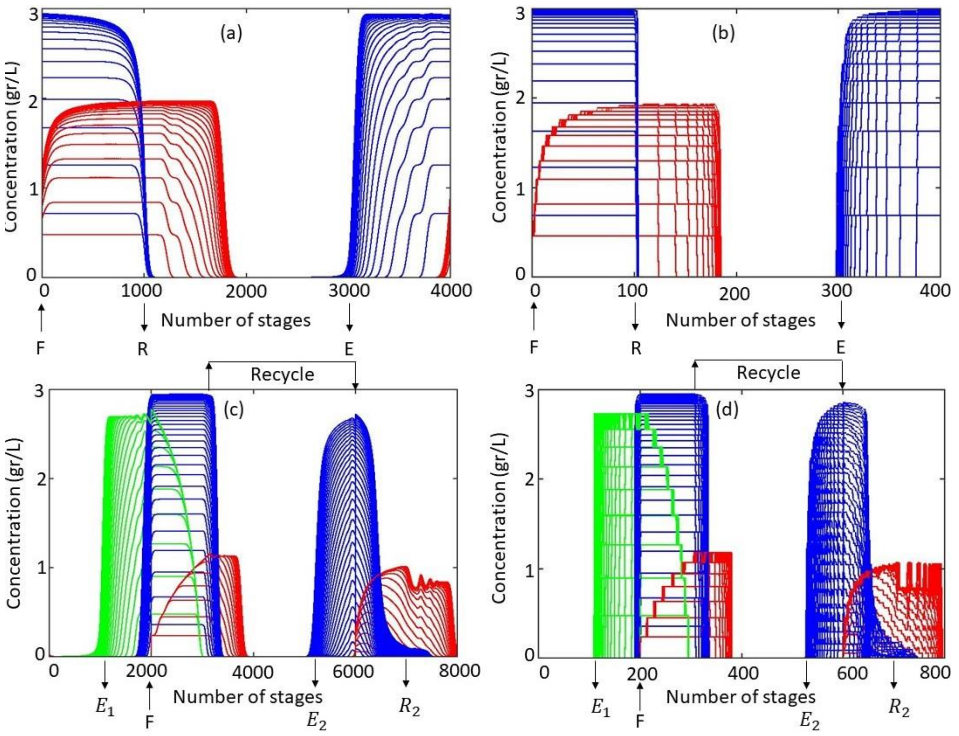

Figure 2. Internal concentration profiles of (a) Binary mixture inside 4-zone SMB using cell model with 1000 grid points (b) Binary mixture inside 4-zone SMB using analytical model. (c) Ternary mixture inside 8-zone SMB using cell model with 1000 grid points (d) Ternary mixture inside 8-zone SMB using analytical model.

Corresponding computation times are shown in Table 3, the analytical model is about 400 times faster than the cell model in the 4-zone SMB simulation and 800 times faster in the 8-zone SMB simulation. It is worth noting, the computational time of the numerical solution is further increasing drastically if an implicit integration scheme like ode 15s in MATLAB is used.

Table 3. Computational times for 4- and 8-zone configuration using cell and analytical model

Model	**Cell model**		**Analytical model**
No of grid points	100	1,000	-
4-zone SMB	2.80 (s)	167.34 (s)	0.34 (s)
8-zone SMB	10.00 (s)	689.46 (s)	0.77 (s)

6. Conclusion

In this paper, a fast and accurate method for the simulation of chromatographic columns with linear adsorption isotherms using the ideal equilibrium model was presented. It is most suitable for highly efficient chromatographic columns with negligible axial dispersion and steep concentration fronts. It outperforms standard approaches based on the popular cell model.

An application was demonstrated for binary and ternary SMB processes with center-cut separations. However, the method can be easily applied to other process configurations and will be used in the future for rigorous optimization and evaluation of alternative process schemes for ternary center-cut separations.

References

A. Nicolaos, M. Laurence, P. Gotteland, R.M. Nicoud, M. Bailly, 2001, Application of the equilibrium theory to ternary moving bed configurations (4+4, 5+4, 8 and 9 zones) II. Langmuir case. Journal of Chromatography A. 908(1-2): p. 87-109.

C. Migliorini, M. Mazzotti, M. Morbidelli, 1998, Continuous chromatographic separation through simulated moving beds under linear and nonlinear conditions. Journal of Chromatography A, 827, 161–173.

G. Zhong, G. Guiochon, 1996, Analytical Solution for the linear ideal model of simulated moving bed chromatography. Chemical Engineering Science. 51, 4307–4319.

H. Schmidt-Traub, M. Schulte, and A. Seidel-Morgenstern, 2012, Preparative chromatography, 2nd completely revised and enlarged edition.

L.C. Keßler, A. Seidel-Morgenstern, 2006, Theoretical study of multicomponent continuous countercurrent chromatography based on connected 4-zone units. Journal of ChromatographyA, 1126, 323–337.

Z. Ma, N.-H. L. Wang, 1997, Standing wave analysis of smb chromatography: linear systems, AIChE 20 J. 43, 2488-2508.

Sauro Pierucci, Flavio Manenti, Giulia Bozzano, Davide Manca (Eds.)
Proceedings of the 30th European Symposium on Computer Aided Process Engineering (ESCAPE30), May 24-27, 2020, Milano, Italy.
http://dx.doi.org/10.1016/B978-0-12-823377-1.50083-5

Efficient Parameterization of a Surrogate Model of Molecular Interactions in Crystals

David H. Bowskill,[a] Isaac J. Sugden,[a] Neil George,[b] Adam Keates,[b] Jennifer Webb,[b] Constantinos C. Pantelides,[a] Claire S. Adjiman[a*]

[a]*Department of Chemical Engineering, Centre for Process Systems Engineering, Imperial College London, London, SW7 2AZ, United Kingdom*
[b]*Process Studies Group, Syngenta, Jealott's Hill International Research Centre, Bracknell, Berkshire, RG42 6EY, United Kingdom*
c.adjiman@imperial.ac.uk

Abstract

We propose a surrogate model for lattice energy that allows the accurate prediction of the crystal structures formed by a given molecule and their relative stability ranking. The model is derived from a combination of isolated-molecule quantum mechanical calculations and a relatively small number of more expensive solid-state DFT-D computations. The surrogate model provides an effective mechanism for refining the crystal structure landscape predicted by current Crystal Structure Prediction methodologies. Applied to the agrochemical Chlorothalonil, the approach is shown to be highly accurate whilst reducing the computational costs by approximately a factor of 20 compared to refinement of all structures using solid-state DFT.

Keywords: Crystal Structure Prediction, Parameter Estimation, DFT-D

1. Introduction

The material properties of crystalline solid materials are dependent on both the molecular compound and the arrangement of molecules in a 3-dimensional lattice. This is especially important due to the prevalence of polymorphism, whereby different stable structures may be observed depending on crystallization temperature, pressure and composition. Furthermore, kinetic barriers can result in the synthesis of metastable polymorphs (Bernstein, et al., 1999). There are well-recorded cases where failure to identify the most stable polymorph of a substance during product development has led to major operational disasters when a more stable form has appeared during production (Bauer, et al., 2001). Understanding the crystallization behaviour and relative stability of the polymorphs of an active ingredient is therefore critical for the pharmaceutical and agrochemical industries, where many products involve crystalline solids.

Crystal Structure Prediction aims to predict all possible polymorphs of a compound given only the molecular connectivity diagram as input. Observable crystal structures of a given compound are assumed to be local minima at, or close to, the global minimum in the Gibbs free energy of the crystal. For practical reasons, this is often approximated as low-lying minima in the lattice energy, U^{latt} (Day, 2011). Thus, the output of a CSP investigation is a list of crystal structures ranked in order of increasing U^{latt}. These putative structures can be compared to known polymorphs to assess the risk of more stable, as yet unsynthesized, polymorphs appearing, or to rationalize observed polymorphic behaviour (Price, et al., 2016).

One current approach to modelling crystalline energies makes use of hybrid *ab initio*/empirical models. These combine tailor-made potentials (derived from quantum mechanical calculations on isolated molecules) for the intramolecular and electrostatic contributions to the lattice energy, with transferable empirical potentials for the remaining contributions, in particular those arising from repulsive/dispersive interactions. Such empirical potentials have previously been derived using training sets containing experimental data of many diverse compounds (Gatsiou, et al., 2018; Pyzer-Knapp, et al., 2016). However, the transferable component can often lack the accuracy required for CSP to be effective. An alternative is to derive a tailor-made force field (TMFF) of all interactions for the particular system of interest using the results of solid-state DFT-D calculations (Neumann, 2008). However, whilst accurate, this approach requires a large number of computationally very expensive solid-state DFT-D calculations.

Here we seek to achieve the accuracy of solid-state DFT-D at a fraction of the cost. This is achieved by deriving a surrogate lattice energy model from a small number of DFT-D calculations. The surrogate model can then be used to refine and re-rank the large sets of structures typically generated by existing CSP methodologies. The proposed methodology is presented in Section 2 of this paper. Section 3 illustrates its application to predicting the polymorphs of Chlorothalonil, a polymorphic agrochemical.

2. Methodology

2.1. Surrogate lattice energy model

Our surrogate lattice energy model is of the form:

$$U^{latt}(\boldsymbol{\theta}, \boldsymbol{p}) = \Delta U^{intra}(\boldsymbol{\theta}) + U^{elec}(\boldsymbol{\theta}) + U^{resid}(\boldsymbol{\theta}, \boldsymbol{p}) \tag{1}$$

where $\boldsymbol{\theta}$ represents the crystal structure in terms of the lattice lengths and angles of the unit cell, and positions of all atoms in the asymmetric unit. The first two terms on the right-hand side represent the contributions of intramolecular and intermolecular electrostatic interactions; as in well-established CSP methodologies, those are derived from quantum mechanical calculations on isolated molecules (Pantelides, et al., 2014). The last, "residual", term attempts to capture all the effects, such as dispersive/repulsive interactions and induction, that are not already accounted for by the first two terms. This last term includes a set of parameters $\boldsymbol{p}$ that can be adjusted to match the predictions of a more accurate but computationally much more expensive model such as DFT-D.

In principle, there are many possible algebraic forms for the residual term, including some based on standard machine learning methodologies, such as artificial neural networks. For the purposes of this paper, we choose one that is based on the standard Buckingham potential for repulsive/dispersive interactions:

$$U^{resid}(\boldsymbol{\theta}, \boldsymbol{p}) \equiv \sum_{ij} A_{ij} \exp\left(-r_{ij} \middle/ B_{ij}\right) - \frac{C_{ij}}{r_{ij}^{\,6}} \tag{2}$$

where the parameters $\boldsymbol{p} \equiv \{A_{ij}, B_{ij}, C_{ij}\}$ describe the interactions between atoms i and j, and $r_{ij}(\boldsymbol{\theta})$ is the corresponding interatomic distance in the crystal lattice.

2.2. Deriving the surrogate lattice energy model

The proposed methodology is intended to be applied as a final refinement step to a crystal structure landscape determined by standard CSP techniques. This landscape consists of a minimum lattice energy structure and all other structures identified within, typically, 5-

20 kJ/mol above the minimum. Overall, this may involve several hundreds or thousands of structures.

As illustrated in Figure 1, our methodology selects a small subset of *NS* structures out of the *N* structures in the initial landscape (Step 1). The lattice energy of each of these *NS* structures is then minimized using an accurate solid-state DFT-D model (Step 2). The lattice energies and crystal geometries determined at Step 2 are then used to estimate the surrogate model parameters $\boldsymbol{p}$ (Step 3). Finally, the surrogate model is used to re-optimize the energy/geometry of all *N* structures in the original landscape (Step 4), which results in the final crystal structure landscape.

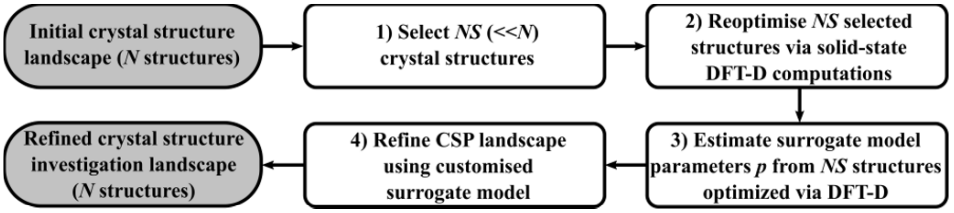

Figure 1: Flowchart of proposed methodology

2.3. Estimation of surrogate model parameters

The accurate DFT-D calculations applied at Step 2 to each selected crystal structure s generate the minimized lattice energy U_s^{ref}, and the corresponding crystal structure geometry in terms of the unit cell lattice parameters $\boldsymbol{l}_s^{ref}$, and the relative fractional coordinate positions $\boldsymbol{\delta x}_s^{ref}$ for all atomic sites within the asymmetric unit. These "reference" data are collectively denoted as $\boldsymbol{a}_s^{ref}$.

At Step 3, the parameters $\boldsymbol{p}$ are adjusted so that the corresponding *NS* crystal structures properties $\boldsymbol{a}_s$ derived via lattice energy minimization using the surrogate model match as closely as possible the reference data $\boldsymbol{a}_s^{ref}$. This is achieved via the solution of a weighted nonlinear least squares optimization problem:

$$\min_{\boldsymbol{p}\in[\boldsymbol{p}^L,\boldsymbol{p}^U]} \sum_{s=1}^{NS} \| \boldsymbol{a}_s(\boldsymbol{p}) - \boldsymbol{a}_s^{ref} \|^2 \tag{3}$$

where $\boldsymbol{p}^L$ and $\boldsymbol{p}^U$ denote lower and upper bounds on the parameters $\boldsymbol{p}$, and $\|.\|$ denotes a weighted square norm. The weights are selected so that the objective function measures the *relative* deviations in U_s and $\boldsymbol{l}_s$, and the *absolute* deviations in $\boldsymbol{\delta x}_s$, and also scales with the number of elements in each of the vectors $\boldsymbol{l}_s$ and $\boldsymbol{\delta x}_s$.

2.4. Numerical considerations

The parameter estimation problem is a bilevel optimization problem since the vector $\boldsymbol{a}(\boldsymbol{p})$ at a given $\boldsymbol{p}$ needs to be determined by minimization of the lattice energy (cf. Eq. (1)). Thus, each evaluation of the objective function in Eq. (3) requires *NS* minimizations.

The parameter estimation problem is solved for each initial parameter vector using a specialized unconstrained nonlinear residual least squares solver, nl2sol (Dennis Jr, et al., 1981). A smooth penalty function is included in the objective function to constrain allowable parameter values between $\boldsymbol{p}^L$ and $\boldsymbol{p}^U$, and line searches are also constrained to keep the parameter values within these bounds. The gradients of the objective function are obtained using second-order centered finite differences.

Over the space of parameter values, the objective function is non-convex, exhibits discontinuities and its evaluation is subject to numerical instabilities due to the complexity of the lattice energy minimization code used. Due to these characteristics, a multistart global optimization approach is employed, whereby multiple initial parameter vectors $\boldsymbol{p}^{[0]}$ lying between $\boldsymbol{p}^{L}$ and $\boldsymbol{p}^{U}$ are generated using low-discrepancy Sobol' sequences (Bratley & Fox, 1988). A distributed computing implementation has been developed so that optimizations from different starting points can be run simultaneously. The set of parameters $\boldsymbol{p}$ resulting in the lowest objective function value among all runs is selected and used to refine the crystal structure landscape in Step 4 of the methodology.

3. Application to Chlorothalonil

To test the effectiveness of the proposed approach, we carry out a case study on the agrochemical fungicide Chlorothalonil (m-$C_6(CN)_2Cl_4$). There are currently two experimentally identified polymorphs with one molecule in the asymmetric unit (Z'=1): Form I, the most stable known polymorph at ambient conditions, and Form II, a metastable form which is stabilized at higher temperatures through structural disorder.

An initial CSP investigation is carried out in Z'=1 space using the CSP methodology presented by Pantelides, et al. (2014) and related publications. It is assumed that the intramolecular energy contributions are negligible, and the molecule's conformation is fixed to its gas-phase conformation, as calculated via an isolated-molecule quantum mechanical calculation. The latter also allows the determination of point charges located at atomic sites that are used to describe intermolecular electrostatic interactions. Intermolecular repulsive/dispersive interactions are described via an empirical potential of the form given by Eq. (2) with transferable parameters (Gatsiou, et al., 2018).

This initial CSP study results in a ranked set of candidate structures. The 92 structures identified with lattice energies within 8 kJ/mol of the global minimum are shown in Figure 2 (left). They include the experimentally known Forms I & II, with energetic rankings of 6th and 60th, respectively. However, five structures are predicted to be lower in energy, and thus more stable, than either of the experimental forms. This suggests that a more stable crystal, yet unidentified, form may exist, something which, in practice, could have serious technical and financial implications.

On the other hand, as the energy difference between Form I and the global minimum structure is small (0.72 kJ/mol), the use of more accurate DFT-D calculations could well lead to a different conclusion. However, applying DFT-D calculations directly to all structures in the landscape would be prohibitively expensive. Instead, we apply the methodology described in Section 2. At Step 1, we select NS=5 structures out of the 92 structures in the landscape, as indicated by the blue circles in Figure 2 (left). The selection is performed randomly, except that, in order to test the robustness of the methodology, the lowest-energy structures and the two experimental forms are excluded.

At Step 2, each of these 5 structures is optimized using DFT-D calculations, using a large basis set and a tight convergence tolerance. These are particularly expensive calculations, taking between 5,000 to 15,000 CPU h per structure.

Step 3 derives the surrogate lattice energy model by determining the parameters in the residual term U^{resid} (cf. Eq. (2)) that describe the interactions between Carbon, Nitrogen, and Chlorine atoms. Here we decide to fix B_{ij} at the values used by the empirical potential (Gatsiou, et al., 2018) employed in the initial CSP study, and refit all A_{ij} and C_{ij}

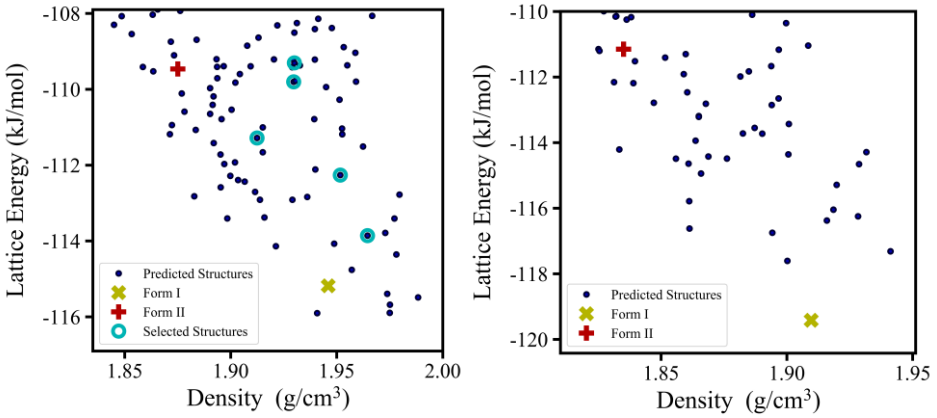

Figure 2: Lattice energy landscape for Chlorothalonil using transferable parameters (left), and using customized parameters (right). Each point corresponds to the energy and density of a predicted structure. Experimental Forms I & II are marked with crosses on the plots. The five structures randomly selected for refinement using solid-state DFT-D are also highlighted.

parameters. This includes the explicit fitting of all cross-interactions, resulting in a total of 12 parameters. The parameter estimation makes use of the reference data determined at Step 2, comprising 5 lattice energy values and 225 data points relating to crystal structure geometry. The estimation is repeated using 1,000 different sets of initial guesses generated via Sobol' sequences, with each such calculation taking between 1 and 2 hours on a single computer core. The parameter values leading to the lowest value of the objective function computed via Eq. (3) are incorporated in the surrogate model. Compared to the original transferable potential parameters (Gatsiou, et al., 2018), they reduce the geometric deviation ($RMSD_{15}$) from the DFT-D data by approximately 45%, and the absolute mean deviation in energy from 1.61 kJ/mol to 0.57 kJ/mol.

Finally, in Step 4, we minimize the lattice energy of all 92 structures in the original crystal structure landscape using the surrogate model. This takes approximately 1 CPU h, and results in the landscape shown in Figure 2 (right). Form I & II of Chlorothalonil are now ranked as 1st and 44th on the landscape, respectively, indicating a clear improvement in the model's prediction in line with known experimental information. Moreover, Form I is predicted to be 1.8 kJ/mol more stable than the second most stable predicted structure. From a practical perspective, this provides a much higher degree of confidence that the most stable crystal structure has already been identified experimentally, while reducing the overall computational cost of refining the landscape by approximately 94% compared to refinement of the whole landscape using solid-state DFT-D.

4. Concluding remarks

The mathematical form of the surrogate lattice energy model proposed in this paper is, in fact, identical to that of the hybrid *ab initio*/empirical models used in many current CSP methodologies. This is a deliberate choice as the current approaches have proven quite successful in identifying all putative solid forms, and in producing reasonable predictions of their geometries. Their main deficiency is in predicting the correct relative energetic ranking of these forms. This is something that more accurate techniques based on solid-state DFT-D computations are capable of correcting. However, the application of these computations to landscapes involving large numbers of structures is prohibitively

expensive, especially in the case of the more complex molecules of interest to the pharmaceutical industry.

The novel aspect of our proposed methodology is in the way in which the parameters in the term described by Eq. (2) are obtained. Current methodologies attempt to derive a generally applicable ("transferable") potential for each type of pairwise atom-atom by fitting the parameters to a number of experimental data. Notwithstanding the obvious attractions of transferability, this approach suffers from a number of deficiencies, e.g. the relative lack of experimentally-measured energetic data such as sublimation energies, the difficulty of accurately relating the latter to theoretically predicted lattice energies, and, ultimately, the fact that experimental data from completely different systems may not be particularly relevant to the system that is currently under investigation. In contrast, our approach derives a customized parameterization for the system of interest using high-accuracy data from DFT-D computations. Unlike techniques that derive tailor-made force fields (TMFF) entirely from such computations, the number of the latter is kept to a minimum by the fact that the first two terms of the proposed surrogate model (cf. Eq. (1)) already capture a significant part of the lattice energy while being derived from much cheaper isolated-molecule quantum mechanical calculations.

Acknowledgements

The authors gratefully acknowledge funding from the United Kingdom's Engineering and Physical Sciences Research Council (EPSRC) (EP/M507878/1), and Syngenta. We are also grateful for access to computational resources from the High-Performance Computing Cluster at Imperial College London.

References

J. Bauer, S. Spanton, R. Henry, J. Quick, W. Dziki, W. Porter, J. Morris, 2001, Ritonavir: an extraordinary example of conformational polymorphism, *Pharmaceutical research,* 18, 6, 859-866

J. Bernstien, R. J. Davey, J.-O. Henck, 1999, Concomitant Polymorphs, *Angewandte Chemie International Edition,* 38, 23, 3440-3461

P. Bratley, B. L. Fox, 1988, Algorithm 659: Implementing Sobol's quasirandom sequence generator, *ACM Transactions on Mathematical Software (TOMS),* 14, 1, 88-100

G. M. Day, 2011, Current approaches to predicting molecular organic crystal structures, *Crystallography Reviews,* 17, 1, 3-52

J. E. Dennis Jr, D. M. Gay, R. E. Welsch,1981, Algorithm 573: NL2SOL—an adaptive nonlinear least-squares algorithm [E4], *ACM Transactions on Mathematical Software (TOMS),* 7 3, 369-383

C.-A. Gatsiou, C. S. Adjiman, C. C. Pantelides, 2018, Repulsion-dispersion parameters for the modelling of organic molecular crystals containing N, O, S and Cl, *Faraday discussions,* 211, 297-323

M. A. Neumann, 2008, Tailor-made force fields for crystal-structure prediction, *The Journal of Physical Chemistry B*, 112, 32, 9810-9829

C. C. Pantelides, C. S. Adjiman, A. V. Kazantsev, 2014, General computational algorithms for ab initio crystal structure prediction for organic molecules, *Prediction and Calculation of Crystal Structures,* Springer, 25-58

S. L. Price, D. E. Braun, S. M. Reutzel-Edens, 2016, Can computed crystal energy landscapes help understand pharmaceutical solids?, *Chemical Communications,* 52, 44, 7065-7077

E. O. Pyzer-Knapp, H. P. G. Thompson, G. M. Day, 2016, An optimized intermolecular force field for hydrogen-bonded organic molecular crystals using atomic multipole electrostatics, *Acta Crystallographica Section B: Structural Science, Crystal Engineering and Materials*, 72, 4, 477-487

Sauro Pierucci, Flavio Manenti, Giulia Bozzano, Davide Manca (Eds.)
Proceedings of the 30th European Symposium on Computer Aided Process Engineering (ESCAPE30), May 24-27, 2020, Milano, Italy.
http://dx.doi.org/10.1016/B978-0-12-823377-1.50084-7

Computational Fluid Dynamics Simulation of CO_2 Methanation in a Fixed-bed Profile Reactor

Steffen Flaischlen[a,b,*], Jan Martin[a,b], Bjarne Kreitz[a,b], Thomas Turek[a,b,]
Gregor D. Wehinger[a,b]

[a]*Institute of Chemical and Electrochemical Process Engineering, Clausthal University of Technology, Leibnizstr. 17, 38678 Clausthal-Zellerfeld, Germany*
[b]*Research Center Energy Storage Technologies (EST), Clausthal University of Technology, Am Stollen 19A, 38640 Goslar, Germany*
flaischlen@icvt.tu-clausthal

Abstract

In this contribution, we present a detailed three-dimensional computational fluid dynamics (CFD) model of a fixed-bed reactor processing the catalytic CO_2 methanation reaction. Due to the small tube-to-particle-diameter ratio, particle-resolved CFD simulations are carried out, since they can locally account for transport phenomena, i.e. momentum, heat, and mass transfer. In addition to the interstitial flow simulation, three-dimensional diffusion plus reaction is modelled inside the catalytic pellets. The comparison in terms of axial temperature with a one-dimensional model shows the discrepancy between the models. Additional CFD simulations with different pellet shapes show that the shape has little influence on the heat transfer in these slender fixed-bed arrangements. Experimental results of axial concentration profiles will further validate the CFD model.

Keywords: Methanation, Computational Fluid Dynamics (CFD), Particle-resolved CFD, Fixed-bed reactors

1. Introduction

In the context of the energy transition to renewable energies, energy storage is a key stone. The surplus energy can be used for the electrolysis of water into hydrogen and oxygen. However, the storage of hydrogen is challenging due to reactivity, diffusivity and corrosion. This is why the hydrogen obtained is further converted into methane with carbon dioxide in the methanation process. The advantage is the storage and use of the existing natural gas infrastructure, since methane is the key component. For the catalytic methanation of CO_2, fixed-bed reactors are typically used in which the particles are coated or impregnated with the active catalytic component, e.g. nickel, ruthenium and palladium. Due to the exothermic reaction, the use of small tube diameters is necessary to increase the cooling surface area. Another process engineering aspect is to maintain a low pressure drop. While small particle diameters lead to higher pressure drops, the methanation reaction is realized in fixed-bed reactors with a small tube-to-particle diameter ratio D/d_p. The simplest catalyst particle geometry is the sphere, but over the years, various complex geometries have been developed to increase the surface area and to reduce the pressure drop. For the prediction of the reaction process, the use of computer-aided models is the state of the art. For the development of more comprehensive models, a better understanding of the underlying kinetics is important. In addition, the effect of model assumptions and uncertainties should be quantified wherever possible. Since the porosity

in fixed-bed reactors with small D/d_p is highly local dependent, the assumption of a plug flow behavior is not very precise. Therefore, particle-resolved computational fluid dynamic (CFD) simulations are used, where every particle in the bed is described with the three dimensional discretization (Jurtz et al. 2019). To get a better insight into the process occurring in the bed, axial temperature and concentration profiles are measured in a special reactor setup. The obtained detailed experimental data allow a critical validation of the detailed CFD model.

2. Methods

2.1. Experimental Setup of the Profile Reactor

The profile reactor is a special research reactor developed and distributed by REACNOSTICS GmbH (Hamburg, Germany), which enables the user to obtain axial temperature and concentration profiles. A capillary is inserted in the center of the bed. This is an advantage over traditional fixed-bed reactors in which only data can be obtained before and after the bed. The capillary can be used in two ways. First, it is possible to place a thermocouple inside. The temperature sensor is in contact with the gas flowing through the reactor through a small opening in one position. In the second mode, a small portion of the gas in the reactor is sucked through the capillary for concentration measurement by gas chromatography. Both temperature and concentration measurement can be carried out simultaneously. The bed is positioned on a movable carriage, which changes the position of the small capillary hole. With one movement of the carriage, it is possible to perform the measurement at different axial positions of the fixed bed. The bed is located in a heated isothermal zone. The experimental setup of the profile reactor is shown in Figure 1 (A).

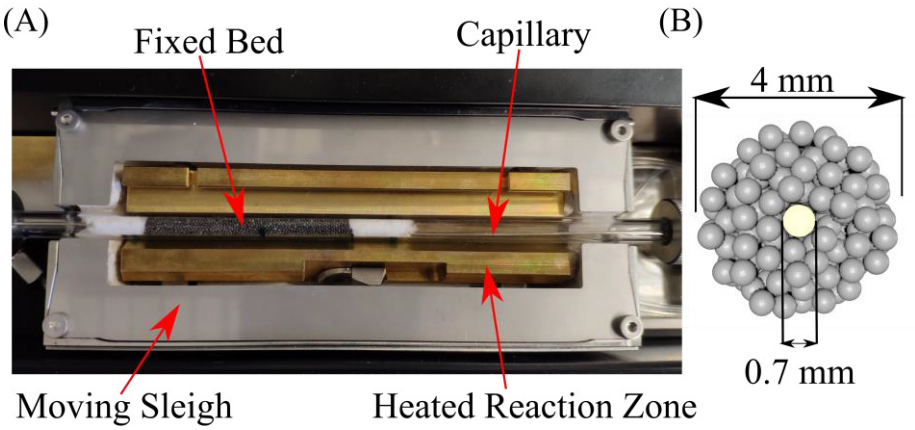

Figure 1: (A) Parts of the profile reactor (B) Dimensions of the fixed-bed.

The fixed bed in the heating zone has a length up to 60 mm, a tube diameter $D = 4$ mm, the capillary diameter $d_c = 0.7$ mm, and the particle diameter $d_p = 0.5$ mm (Figure 1 (B)). The resulting tube-to-particle diameter is $D/d_p < 10$, where particle resolved CFD simulations should be applied.

2.2. Numerical Setup for synthetic fixed-beds

Before applying fixed-bed CFD simulations, it is necessary to obtain an input geometry. Different methods are known, but the most common are the Discrete Element Method (DEM) and the Rigid Body Approach (RBA). In this contribution, the RBA is used with the open source video animation software Blender. Boccardo et al. (2014) first published this approach of using RBA for the synthetic generation of fixed-beds. The results of Flaischlen and Wehinger (2019) showed the advantages of RBA over the classical DEM, especially for non-spherical pellets and in terms of simulation time. The beds consisted of 1000 to 1500 particles and required some hours for packing generation. In the case of the profile reactor, the total number of particles for a bed height of 60 mm is about 6,000. While the simulation time scales with the number of particles, more precisely the number of particle contacts, the simulation time is very high. Therefore, a smaller number of particles is used for the model development. This leads to shorter bed generation times and faster CFD simulations as the number of mesh cells also increases with the number of particles.

2.3. Numerical Setup for CFD Simulations

The complexity of the CFD simulations is increased stepwise. In a first step, only heat transfer investigations are carried out in which no chemical reaction is taken into account. Nitrogen flows through the reactor and the wall temperature is set to a constant value. The particles are described with a solid model and a fixed thermal conductivity in the range of a typical porous Ni catalyst. The boundary conditions for the heat transfer simulation are summarized in Tab. 1.

Tab. 1: Boundary conditions of CFD simulations for heat transfer studies.

	Heat Transfer	*Methanation*	
Velocity Inlet /m s^{-1}	0.3421	0.3421	
Inlet Temperature /°C	25	281.85	
Wall Temperature /°C	250	281.85	
Capillary Wall Temperature	*Adiabatic*	*Adiabatic*	
Solid Thermal Conductivity /W m^{-1} K^{-1}	0.3	0.3	
Pellet Diameter /mm	0.6	0.524	
Number of Pellets	450	450	
Bed Height /mm	6.184	6.184	
Mole Fraction	$N_2 = 1$	$H_2 = 0.8, CO_2 = 0.1$	
Pellet Dimensions	*Spheres*	*Cylinders*	*Rings*
Diameter /mm	0.6	0.524	0.524
Height /mm	–	0.524	0.524
Inner Diameter /mm	–	–	0.210

In the next step, the methanation reaction is included in the CFD pellet model. The reaction kinetics from Koschany et al. (2016) describe the CO_2 methanation with a Langmuir-Hinshelwood-Hougon-Watson approach. Due to the small pore size of the porous catalyst, convection is assumed to be negligible and hence only diffusion is the transport mechanism inside the catalyst pellets. In the CFD simulations, only the values for temperature and mole fractions are exchanged via an internal table across the gas-solid interface. This guarantees that no momentum is transferred into the particle region and hence, the velocity inside the pellets is exactly zero. This is similar to the method of co-simulations described in Wehinger et al. (2017) with the advantage that all models are contained in only one CFD simulation.

3. Results

3.1. Porosity and Velocity Profile

As already mentioned, wall effects have a large influence on heat and mass transfer in small $\boldsymbol{D}/\boldsymbol{d}_p$ fixed-bed arrangements. The capillary has additional wall effect leads to an even severe situation. This can be shown with the centroid representation, where the midpoint of every spherical particle is projected to the *x*-*y* plane (Figure 2 (A)).

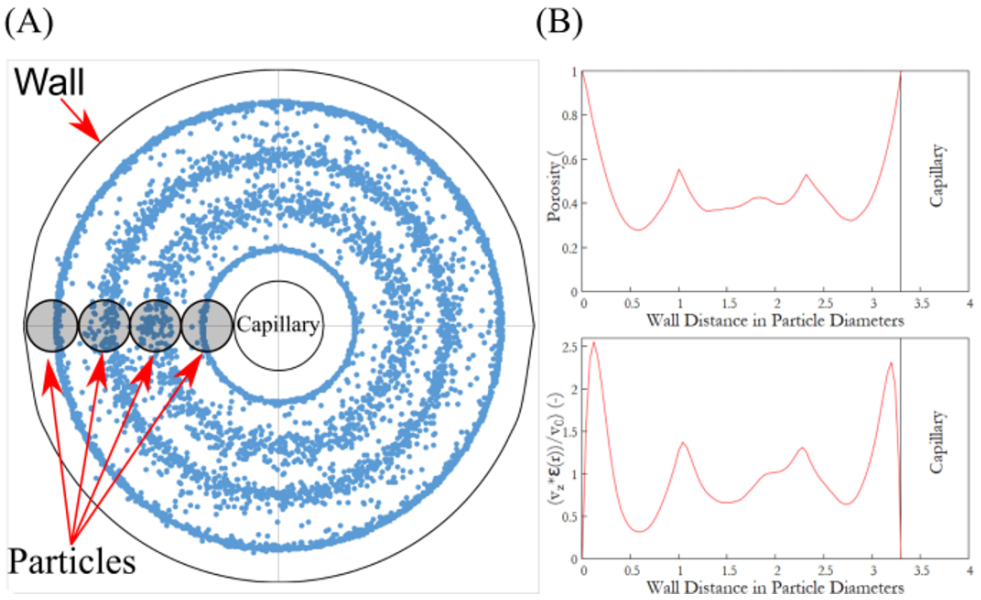

Figure 2: CFD results. (A) Centroid representation of spherical particles in the profile reactor. (B) Radial porosity and normalized velocity profile. Volume flow is $4.167 \cdot 10^{-6}$ m³ s^{-1}.

The centroids are grouped in concentric circles with a clear structure. This is in contrast to a random distribution of the particles in the bed. The bed structure can also be represented by the radial porosity profile, where the porosity is averaged in the axial and azimuth direction (Figure 2 (B) top). The shape of the curve is almost mirrored at the wall distance of approx. 1.7. Irregularities are due to the convex shape of the capillary. Taking the flow simulation into account, it can be seen that the radial velocity profile follows the porosity profile. The velocity peak close to the wall is larger, since the cross section at this position is larger than at the capillary. The results show the difference to other models where the flow is modeled under the plug flow assumption.

3.2. Heat Transfer

The first step of the heat transfer CFD simulations is to compare the performance of different particle shapes, i.e. spheres, cylinders, and rings. The results for the simulation with the boundary conditions from Tab. 1 are shown in Figure 3. It can be observed that the particle shape has only little influence on the heat transfer in the fixed bed. Nevertheless, heat transfer from the wall to the fluid is intensified with particles inserted in comparison to the empty tube.

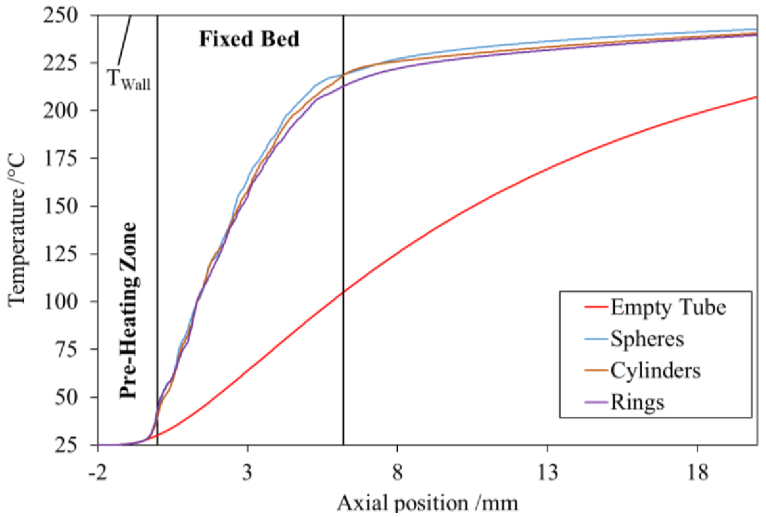

Figure 3: Comparison of heat transfer simulations for different particle shapes.

Figure 4 shows the axial temperature profile of the 3D particle-resolved CFD model and a 1D heterogeneous model. The increase of temperature of the 1D model is much steeper and the wall temperature is reached at the end of the bed. The difference between the two models can be attributed to the strong wall channeling effects and hence to a reduced radial mixing, which is not accounted for in the 1D model.

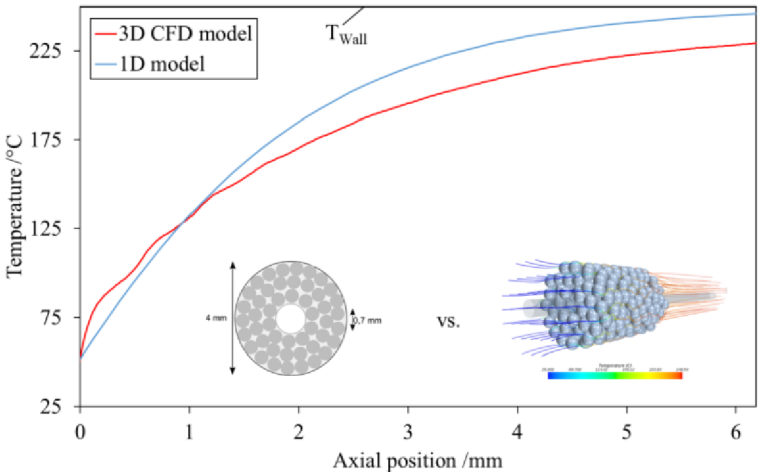

Figure 4: Comparison of the heat transfer in a fixed-bed between one-dimensional and three-dimensional models

3.3. Methanation of CO_2

Figure 5 shows a fixed-bed reactor consisting of rings under catalytic reaction conditions. The results show the conversion of carbon dioxide and hydrogen into methane. The largest mole fractions occurring inside the rings which are close to the capillary (Figure 5 (A)). The velocity inside the porous catalyst pellets is zero (Figure 5 (B)).

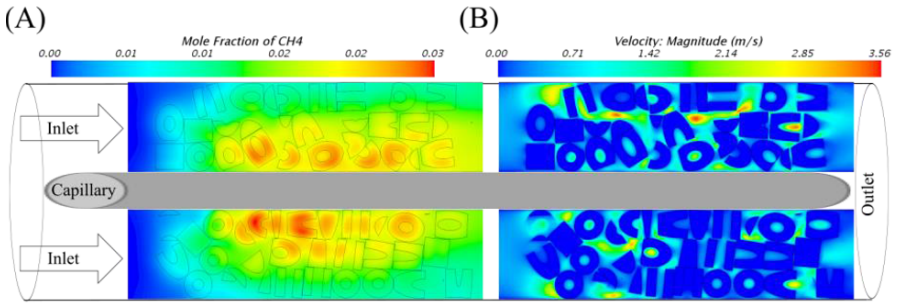

Figure 5: (A) Methanation reaction in the profile reactor with ring particle shape (B) Velocity in the reactor and the pellets.

This shows the complex interplay between local kinetics and local transport phenomena. In the next step, we compare quantitatively axial experimental concentration profiles with the CFD model.

4. Conclusion

This study shows clearly that the profile reactor is highly influenced by wall effects, both at the reactor wall and at the capillary, which makes it necessary to apply particle-resolved CFD simulations. The comparison between the detailed CFD model and the 1D heterogeneous model for heat transfer shows a significant difference in the axial temperature profile. With the particle-resolved CFD simulation approach, different particle shapes can be studied. The reaction model of Koschany et al. (2016) can be included in the simulation and preliminary results show a locally varying conversion of CO_2 and H_2 into CH_4. With a fully validated CFD model, the reactor performance can be improved by analyzing the simulation results, which have a nearly unlimited level of detail.

References

Boccardo, G., Del Plato, L., Marchisio, D., Augier, F., Haroun, Y., Ferre, D., & Icardi, M. (2014, June). Pore-scale simulation of fluid flow in packed-bed reactors via rigid-body simulations and CFD. In *Conference proceedings. SINTEF-NTNU*.

Flaischlen, S., & Wehinger, G. D. (2019). Synthetic Packed-Bed Generation for CFD Simulations: Blender vs. STAR-CCM+. *ChemEngineering*, *3*(2), 52.

Jurtz, N., Kraume, M., & Wehinger, G. D. (2019). Advances in fixed-bed reactor modeling using particle-resolved computational fluid dynamics (CFD). *Reviews in Chemical Engineering*, *35*(2), 139-190.

Koschany, F., Schlereth, D., & Hinrichsen, O. (2016). On the kinetics of the methanation of carbon dioxide on coprecipitated NiAl (O) x. *Applied Catalysis B: Environmental*, *181*, 504-516.

Wehinger, G. D., Klippel, F., & Kraume, M. (2017). Modeling pore processes for particle-resolved CFD simulations of catalytic fixed-bed reactors. *Computers & Chemical Engineering*, *101*, 11-22.

Sauro Pierucci, Flavio Manenti, Giulia Bozzano, Davide Manca (Eds.)
Proceedings of the 30th European Symposium on Computer Aided Process Engineering (ESCAPE30), May 24-27, 2020, Milano, Italy.
http://dx.doi.org/10.1016/B978-0-12-823377-1.50085-9

Data-Driven Approach for Predictive Modeling of By-Product Formation in Methanol Synthesis

Tibor Svitnic[a], Nga T. Q. Do[a*], Timm Schuhmann[b], Thomas Renner[a], Stéphane Haag[a], Evrim Örs[a,*]

[a] *AIR LIQUIDE Forschung und Entwicklung GmbH, Frankfurt Innovation Campus, Gwinnerstrasse 27-33, Frankfurt am Main, Germany*

[b] *AIR LIQUIDE Global E&C Solutions Germany GmbH, Olof-Palme-Strasse 35,60439, Frankfurt am Main, Germany*
ngathiquynh.do@airliquide.com; evrim.oers@airliquide.com

Abstract

In this work, the application of a novel data-driven approach for predictive modeling of by-product formation in methanol (MeOH) synthesis is demonstrated. Due to the number of by-products present in MeOH synthesis, building reliable first-principles models for each by-product is very complex and time consuming. The total by-products of MeOH synthesis are classified into 5 main groups, namely alcohols, esters, ketones, ethers and paraffins, where alcohol and ester groups are usually predominant. In the data preparation phase, a collection of more than 900 experimental points for each individual from test campaigns conducted at a pilot plant was preprocessed using Python™. This cleaned dataset was used for model development in proprietary software JMP® via neural networks, where special care was taken to ensure a representative training vs. test set distribution, avoidance of overfitting, as well as the physical interpretability of data-driven models. The resulting predictive models have a very good generalization behavior covering the wide range of operating conditions, e.g. the alcohol predictive model has an R^2 value of 0.96, and 66.4% of experimental data points are predicted with ±15% accuracy. While a further refinement of the model can be possible through physical considerations, the integration of the model within the MeOH process design workflow is recommended. Moreover, the approach can be extended to other chemical processes.

Keywords: By-products, Methanol, Neural Networks, Predictive Modeling.

1. Introduction

To understand, design and optimize a chemical process, an engineer conventionally uses physical modelling, however practical limitations caused by high computational effort and time can be associated with this first-principles approach. Moreover the designer may not have the complete knowledge of physico-chemical relationship of input-output variables in the system. On the other side, with the rise of artificial intelligence and machine learning techniques in chemical engineering (Venkatasubramanian, 2019), data-driven modeling approach gains increasing interest. McBride and Sundmacher (2019) summarize the various computational methodologies and applications of data-driven approach in different disciplines of chemical engineering. While reduction of model complexity, faster solutions and easier deployment options constitute the primary advantages of data-driven modeling, an integrated approach with process know-how is required for developing reliable applications with this approach. As mentioned by

Asprion et al. (2019), there is growing effort for the corresponding hybrid modeling within chemical and process engineering community.

As for the industrial aspect, digital transformation is a key driver for businesses in all sectors, including process industry (Les Echos, 2019). While the deployment of digital tools primarily targets to achieve operational excellence, the corresponding applications range from plant economic performance monitoring and predictive asset maintenance, to advanced process control and real time optimization (OSIsoft, 2019). Prior work on catalyst deactivation (Örs et al., 2018) and ash fusion behavior prediction (Sasi et al., 2018) demonstrate the potential of data-driven methodologies in H_2/Syngas production. Regarding the further development of novel digital solutions for process industry (especially based on artificial intelligence), collaboration projects with academia represent a strong enhancer for business (chemie.de, 2019).

Methanol (MeOH) is one of the value molecules for convenient energy carrier and for chemical storage. Nowadays, MeOH is synthesized from syngas generated from several carbon-containing feedstocks including natural gas and coal. The reactors are imbedded with $Cu/ZnO/Al_2O_3$ catalyst and operated usually from 50 to 100 bar and 200-300 °C (Bozzano et al., 2016). In the context of energy transition and global warming, an efficient and flexible MeOH process to additionally deal with unconventional gas i.e. stranded gas, biomass syngas, unused syngas capacities and CO_2 rich gases are required. The efforts in this regards can be seen in several works and projects (i3upgrade, 2017), (Haag et al, 2019), (Do et al., 2019). The variety of syngas precursor, resulting in diversity of reactor inlet compositions compared to conventional design, can be challenging for not only reactor design but also for the separation section. Therefore, the ability to predict catalyst performance (Bonilla, 2017) and by-product formation are key for designing new technologies and offering commercial guarantees.

Considering the high number of by-products in methanol synthesis loop, it is a challenge to build first-principles models for each component. The total by-products of MeOH synthesis can be classified into 5 main categories based on similar functional groups in each molecule, namely alcohols, esters, ketones, ethers and paraffins, where the alcohol group is usually predominant. There is effort in literature to build up models for major by-products nonetheless they are limited in prediction due to the narrow range of experimental data and different reactor systems (Wu et al., 2017). In this work, we demonstrate the predictive model of individual by-products group and total by-products in MeOH synthesis depending on the operating conditions following a data-driven approach. While the current design of the methanol distillation unit is able to meet required methanol grade, an integrated implementation of the by-product model with first-principles model may lead to further improvement.

2. Computational Methodology

2.1. Data collection and preparation

The methodology applied for the development of a data-driven model for the by-products formation consists of several steps. First, the measured data of the by-products formation was consolidated into one dataset. This covers different test campaigns carried out at the methanol synthesis pilot plant in the last 10 years, and is finally comprised of ca. 900 data points for each of the by-product groups. The detail of the pilot plant can be referred in the work of Do et al. (2019). The collected data points represent only the water cooled reactor unit at the pilot unit. The measured compositions for individual by-products were

grouped into 5 categories based on their similar chemical characteristics (Figure 1). The dataset was cleaned to only include points satisfying the mass balance closure criterion.

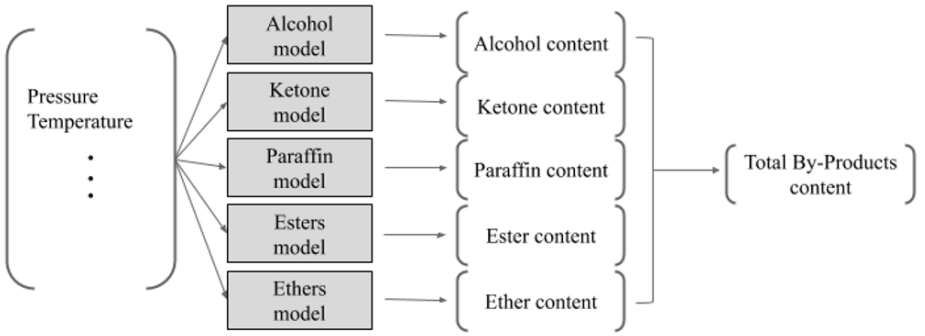

Figure 1: Schematic representation of modeling input and output variables

From the set of all measured process variables, a subset of relevant features were selected as model input. This selection step requires process know-how and technical understanding, considering not only the pilot plant of concern, but also applicability at commercial scale. The selected model input includes process variables such as temperature, pressure, etc. (Figure 1). Furthermore, since the model input and target variables are of significantly different order of magnitude, a normalization procedure was implemented to avoid potential problems in model development such as transfer function saturation and non-homogeneous weight and bias values (Sasi et al., 2018).

2.2. Model development

The cleaned and scaled data was randomly split into training and blind test sets, where 70% of the data was used for model training and the remaining 30% to evaluate the predictive capabilities of the developed model on data points that the model has never seen before. The statistical representability of both sets was checked by comparing the means, standard deviations and visually inspecting the histograms of all model variables. To ensure a systematic and reusable computational workflow, the consolidated dataset was imported into Python™ where the abovementioned steps were implemented.

Following input selection and training/test set distribution, the data was imported into JMP® for model development. The selected model structure in JMP® was neural networks with 1 hidden layer. For each by-product group, several models were built based on the training dataset following the K-fold cross-validation feature with k=5, and compared based on their performance metrics, namely R^2 and RMSE. After a thorough screening, the number of nodes was determined by reaching the best model performance while keeping model complexity as low as possible. Additionally, to integrate the model selection phase with physical interpretability, sensitivity analyses were carried out. This helped to prevent potential overfitting via eliminating models which show a physically unexplainable response (such as unsmooth and/or with several local extrema). That is, even though a model structure was observed to yield better results based on performance metrics, it was disregarded if its sensitivity analysis showed poor response.

After careful execution of all these steps of computational methodology, a final set of models for each by-product group was selected and combined into a total by-product prediction model as shown in Figure 1.

3. Results and Discussion

In this part, the modeling results of the two most dominant by-product groups (alcohols and esters), will be illustrated, as well as the total by-products. Table 1 shows selected computational performance metrics, R^2 and NRMSE (normalized root mean squared error). Note that the NRMSE is calculated via dividing the RMSE by the overall range of the corresponding variable. The comparable values among training, test and all data points indicate the appropriate data splitting and statistical representativeness of the training and test data distribution. Also note that no training and test metrics are tabulated for the total by-product model, since it was not constructed following the model development steps and is a post-processed summation of prediction results based on individual by-product models. It can be concluded that the models have not undergone overfitting and the generalization capability is good for the whole set of data points.

Table 1: Performance metrics of the developed by-product formation models

	Alcohol Model		**Ester Model**		**Total By-Product Model**	
Dataset	NRMSE (%)	R^2 (%)	NRMSE (%)	R^2 (%)	NRMSE (%)	R^2 (%)
Training	3.04	95.82	1.61	95.81	-	-
Testing	2.87	96.34	1.59	96.35	-	-
All Data Points	2.99	95.98	1.61	95.97	1.86	97.44

3.1. Prediction of Selected Individual Groups: Alcohols and Esters

The prediction of both alcohol and ester formation showed best performance for a 4-node neural network structure. Figure 2 shows the parity plot of the measured and predicted values after normalization for alcohols (a) and esters (b). The results indicate that 66.4% and 70.0% of all the predicted points for alcohols and esters respectively fall within 15% deviation interval (dashed lines in Figure 2). The performance metrics shown in Table 1 are calculated based on alcohol and ester model results illustrated in Figure 2. For instance the R^2 value of 95.82 refers to the accuracy of alcohol model considering the training dataset, i.e. the data points depicted with circles in Figure 2.a.

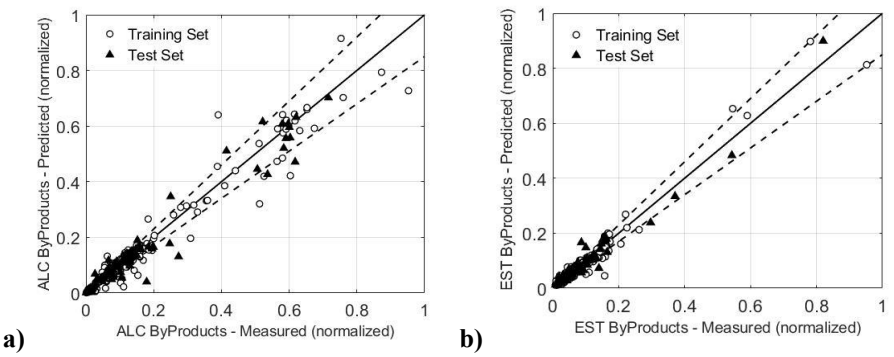

Figure 2: Normalized parity plot of alcohol (a) and ester (b) by-product models, dashed lines indicate 15% deviation from perfect prediction

In order to ensure physical interpretability of the developed models, sensitivity analyses of the finally selected alcohol model prediction showed smooth response (Figure 3). Note that for each single sensitivity plot, only one variable was altered and all others were kept constant at their mean values. At this condition, the sensitivity analysis indicates a proportional relationship of higher alcohol by-product formation with the temperature. This agrees with the process know-how and literature (Wu et al., 2017). Similarly, the decrease of higher alcohol formation (i.e. C_2+) at higher pressure can be ascribed to better carbon efficiency favoring the main product. This analysis denotes the importance of optimal operating conditions in order to reduce the forming of higher alcohols.

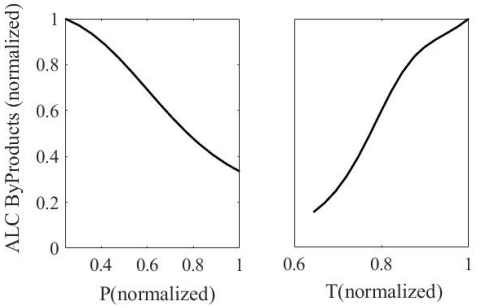

Figure 3: Sensitivity analyses of the alcohol by-product model (P = pressure, T = temperature)

3.2. Total By-Products Model

The total by-product model is the sum of all individual groups and 80.2% of the predicted data points fall within the 15% deviation interval (dashed line in Figure 4). The accuracy of the total by-products model approaches the values of alcohols and esters group model, which is logical since their quantities dominate the whole by-products spectrum. Similar to Figure 2, the performance metrics for total by-products shown in Table 1 are calculated based on prediction results depicted in Figure 4.

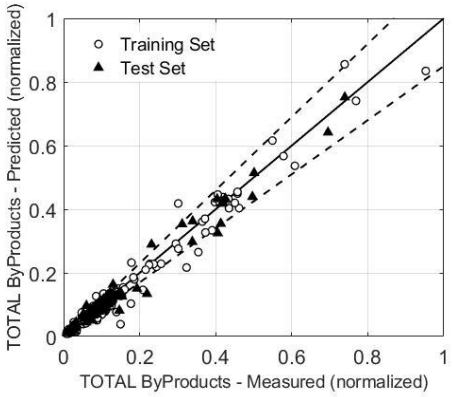

Figure 4: Total by-product model parity plot, dashed lines indicate 15% deviation

4. Conclusion and Outlook

In this work, the application of a data-driven approach for the development of a predictive model of by-product formation in MeOH synthesis process is demonstrated. Two

representative groups and total by-product models have been shown. It is observed that the resulting predictive models have a very good generalization behavior covering the wide range of operating conditions. The sensitivity analysis shows the dependency of by-products formation based on input variables allowing physical interpretability. This data-driven approach is promising for every process in which data can be exploited but is too complex to construct a first-principles model. The main challenges are the need of collecting sufficiently large and reliable data to develop the model. Finally, model update, validation and improvement for different scenarios are key to increase the reliability of the model and to adapt it for further applications.

References

N. Asprion, R. Böttcher, R. Pack, M. Stavrou, J. Höller, J. Schwientek, M. Bortz, 2019, Gray-box Modeling for the Optimization of Chemical Processes, Chem. Ing. Tech. 91(3): 305–313.

A. Bonilla, 2017, Catalyst Deactivation Estimation in Methanol Synthesis and Medium Temperature Shift Processes, M.Sc. thesis, Process Dynamics and Operations Group, TU Dortmund, Germany.

G. Bozzano, F. Manenti, 2016, Efficient methanol synthesis: perspectives, technologies and optimization strategies, Prog. Energy Combust. Sci. 56: 71–105.

Chemie.de, 2019, 17 Mio. EUR für die künstliche Intelligenz in Prozessindustrie, https://www.chemie.de/news/1162875/17-mio-eur-fuer-die-kuenstliche-intelligenz-in-der-prozessindustrie.html?pk_campaign=ca0259&WT.mc_id=ca0259

N. T. Q. Do, S. Haag, V. Gronemann, T. Schuhmann, T. Oelmann, M. Gorny, H. Schwarz, S. Werner, S. J. Reitmeier, S. Gebert, A. Reitzmann, 2019, Layer Management for Methanol Process, DGMK Circular Economy - A Fresh View on Petrochemistry, ISBN 978-3-941721-98-2.

Les Echos, 2019, eCAC40: chez Air Liquide, Le numérique a changé d'échelle, https://business.lesechos.fr/directions-generales/strategie/transformation/ 0602026569459-ecac40-chez-air-liquide-le-numerique-a-change-d-echelle-332389.php

S. Haag, F. Castillo-Welter, T. Schuhmann, B. A. Williams, T. Oelmann, A. Günther, M. Gorny, 2019, How to Convert CO_2 to Green Methanol. Oil and Gas Magazine, 46 edition, Issue 2.

i3upgrade, 2017, Integrated and intelligent upgrade of carbon sources through hydrogen addition for the steel industry, https://www.i3upgrade.eu/

K. McBride, K. Sundmacher, 2019, Overview of Surrogate Modeling in Chemical Process Engineering, Chem. Ing. Tech., 91(3): 228-239.

E. Örs, R. Schmidt, M. Mighani, K. Dabhadkar, K. Ingale, N. Sahinidis, 2018, Data Science Applied to the Monitoring of Catalyst Deactivation, Presentation at SFGP Big Data and Process Engineering Thematic Day, Paris (available on demand).

OSIsoft, 2019, How Air Liquide leverages on PI technologies to optimize its operations - SIO.Optim program, Presentation at PI World Conference, San Francisco, https://www.osisoft.com/presentations/how-air-liquide-leverages-on-pi-technologies-to-optimize-its-operations---sio-optim-program/

T. Sasi, M. Mighani, E. Örs, R. Tawani, M. Gräbner, 2018, Prediction of ash fusion behavior from coal ash composition for entrained-flow gasification, Fuel Processing Technology, 176: 64-75.

V. Venkatasubramanian, 2019, The promise of artificial intelligence in chemical engineering: Is it here, finally?, AIChE J.; 65(2):466–78.

Z. Wu, M. Qin, Y. Liu, H. L. Fang, 2017, Prediction of Major Impurities during MeOH Synthesis over a $Cu/ZnO/Al_2O_3$ Catalyst, Ind. Eng. Chem. Res., 56, 49: 14430-14436.

Sauro Pierucci, Flavio Manenti, Giulia Bozzano, Davide Manca (Eds.)
Proceedings of the 30th European Symposium on Computer Aided Process Engineering (ESCAPE30), May 24-27, 2020, Milano, Italy.
http://dx.doi.org/10.1016/B978-0-12-823377-1.50086-0

Modeling of The Solid Oxide Fuel Cell Considering H2 and CO Electrochemical Reactions

Jia-Lin Kang[a*], Chien-Chien Wang[b], Po-Hsun Chang[b], David Shan-Hill Wong[b], Shi-Shang Jang[b], Chun-Hsiu Wang[c]

[a] *Department of Chemical and Material Engineering, National Yunlin,University of Science and Technology, Yunlin, 64002, Taiwan, ROC*

[b] *Department of Chemical Engineering, National Tsing Hua University, Hsinchu,30013, Taiwan, ROC*

[c] *Green Energy & System Integration Research & Development Department, China Steel Corporation, Kaohsiung 81233, Taiwan, ROC*

jlkang@yuntech.edu.tw

Abstract

this study presented a competitive electrochemical mechanism of the hydrogen and carbon monoxide to describe the real electrochemical reactions in SOFC. The SOFC models employed the competitive electrochemical mechanism was validated with a variety of fuels as the feedstocks, such as methane, mixing gas of H2 and CO, blast furnace gas (BFG), and coke oven gas (COG), via pilot-scale SOFC modules of 1 kW and 50 kW. The models were implemented on Aspen Custom Modeler platform to simulate steady-state results. Further, the SOFC of the 50 kW pilot simulation considering the whole pilot process including pre-reformers, heat exchangers, and fuel recycling. The results showed the SOFC employed the competitive electrochemical mechanism has the better performances of the power generation and voltage predictions regardless of the what fuel used in SOFC of the 1 kW scale, compared to the SOFC only employed hydrogen electrochemical mechanism. The mean voltage error of the SOFC with the competitive electrochemical mechanism using various fuels was 1.52%. the minimum error was 0.73% using COG as the feedstock. The validation of the SOFC model of the 50 kW scale showed that only a 5% error with the experiment in steady-state and 6.91% error in transition.

Keywords: solid oxide fuel cell, electrochemical reaction, pilot-scale validation, Aspen simulation

1. Introduction

Most Solid Oxide Fuel Cell (SOFC) studies (Aguiar et al., 2004; Debenedetti and Vayenas, 1983; Nikooyeh et al., 2007; Stiller et al., 2005) employed only the hydrogen electrochemical reaction to predict power generation regardless of the fuel resources used, which contains methane and carbon monoxide. However, in fact, the pure CO or the CO produced by CH4 can directly conduct electrochemical reactions to generate power. Especially when the SOFC scales up, the CO electrochemical reaction becomes more significant. Suwanwarangkul (Suwanwarangkul et al., 2006) established a 2D-SOFC model for syngas (H2, H2O, CO, and CO2). The model could demonstrate the effects of the electrochemical reaction of using hydrogen and carbon monoxide. The result

suggested that CO should be considered as a useful fuel for SOFCs. Andersson(Andersson et al., 2013) also stated that both CO and H2 were considered as electrochemical reactants within the anode. They also found that the activation polarization for the electrochemical reaction with hydrogen as a reactant and the one with carbon monoxide as reactant did not correspond to the same current density. Hence, the authors suggested that these two electrochemical reactions should be treated as two individual ones in parallel current density. As the above two studies mentioned, the use of CO as the electrochemical reactants was necessary. However, regarding an electrochemical reaction of the SOFC considering H2 and CO as reactants, there were few studies discussed. Furthermore, how to determine the voltages of these two electrochemical reactions is a big issue if considering H2 and CO electrochemical reactions in a SOFC. Thus, the purpose of this study was to present a competitive electrochemical mechanism of the H2 and CO to describe the real electrochemical reactions in SOFC. The SOFC models employed the competitive electrochemical mechanism was validated with a variety of fuels as the feedstocks, such as methane, mixing gas of H2 and CO, blast furnace gas (BFG), and coke oven gas (COG), via pilot-scale SOFC modules of 1 kW and 50 kW.

2. Modeling of SOFC

The developed SOFC model in this study was based on a cell of the SOFC, which was modified from Aguiar et al. (2004). Figure 1 shows the structure of a SOFC cell.

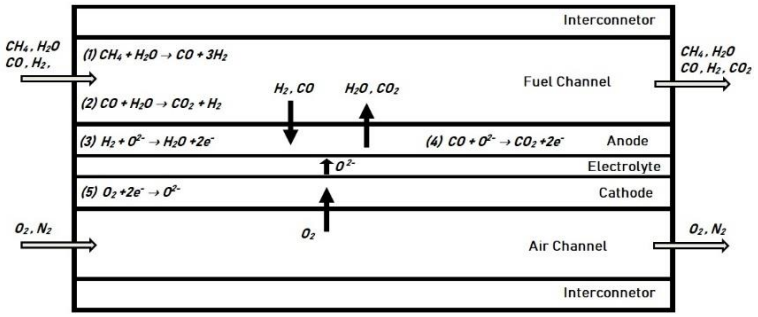

Figure 1 Schematic of SOFC Structure

2.1. Chemical Reactions

Table 1 shows the reactions considered in the SOFC model. The use of methane as a fuel is accompanied by the methane steam reforming reaction (MSRR) and a water gas shift reaction (WGSR). Carbon monoxide (CO) and hydrogen (H_2) are produced as elements of power generation during the reaction. The reaction rate of the MSRR(Aguiar et al., 2004) was shown as following:

$$r_{MSRR} = k_{\mathrm{MSRR}} p_{CH_4} e^{-\frac{E_a}{RT}} \quad (1)$$

where k_{MSRR} represents the reaction rate constant of MSRR; p_{CH_4} represents the partial pressure of methane; Ea represents the activation energy; R represents the ideal gas coefficient. The activation energy of Ea = 82 kJ mol^{-1} and the reaction rate constant of k_{MSRR} = 4274 mol s^{-1} m^{-2} bar^{-1}, has been adopted.

The reaction rate of the WGSR(Haberman and Young, 2004) is expressed in the below:

$$r_{WGS} = k_{0,\mathrm{WGSR}} \times e^{-\frac{E_a}{RT}} \times p_{CO} \left(1 - \frac{p_{CO_2} p_{H_2} / p_{CO} p_{H_2O}}{K_{eq,WGSR}}\right) \quad (2)$$

$$K_{eq,WGSR} = e^{(-0.2935Z^3 + 0.6351Z^2 + 4.1788Z + 0.3169)} \quad (3)$$

$$Z = \frac{1000}{T} - 1 \quad (4)$$

where k_{WGSR} represents the reaction rate constant of the WGSR; $K_{eq,WGSR}$ represents the equilibrium reaction rate constant of the WGSR; p_i represent partial pressure of the i spices. The activation energy, Ea is 103.191 kJ mol^{-1} and the reaction rate constant, k_{MSRR} is 1.71×10^8 mol s^{-1} m^{-3} bar^{-1} . The reaction rates of the overall oxidation reactions of hydrogen, R_v and carbon monoxide, R_{vii} are shown as following:

$$R_v = \frac{j_{H_2}}{2F} \quad (5)$$

$$R_{vii} = \frac{j_{CO}}{2F} \quad (6)$$

where j_{H_2} and j_{CO} are the current used by hydrogen and carbon monoxide, respectively; F represents Faraday constant. The reaction rate of the Oxygen reduction reaction, R_{iv}:

$$R_{iv} = \frac{j_{H_2}+j_{CO}}{2F} \quad (7)$$

Table 1 Chemical Reactions of SOFC

Reaction	Mechanism	Standard reaction heat
(i) Methane steam reforming reaction	$CH_4 + H_2O \Leftrightarrow CO + 3H_2$	ΔH° = 205.81 kJ/mol
(ii) Water gas-shift reaction	$\mathrm{CO} + H_2O \Leftrightarrow CO_2 + H_2$	ΔH° = -41.16 kJ/mol
(iii) Hydrogen oxidation reaction at (+)	$H_2 + O^{2-} \rightarrow H_2O + 2e^-$	
(iv) Oxygen reduction reaction at (-)	$\frac{1}{2}O_2 + 2e^- \rightarrow O^{2-}$	
(v) Overall hydrogen oxidation in a cell	$H_2 + \frac{1}{2}O_2 \rightarrow H_2O$	ΔH° = -241.82 kJ/mol
(iv) Carbon monoxide oxidation reaction at (+)	$\mathrm{CO} + O^{2-} \rightarrow CO_2 + 2e^-$	
(vii) Overall carbon monoxide reaction in a cell	$\mathrm{CO} + \frac{1}{2}O_2 \rightarrow CO_2$	ΔH° = -282.98 kJ/mol

2.2. Electrochemical reaction

The open-circuit potential of the H2 and CO are shown as follows:

$$U^{OCP}_{H_2/O_2} = U^0_{H_2/O_2} - \frac{\Re T}{2F} ln\left(\frac{p_{H_2O}}{p_{H_2} p_{O_2}^{1/2}}\right) \quad (8)$$

$$U^{OCP}_{CO/O_2} = U^0_{CO/O_2} - \frac{\Re T}{2F} ln\left(\frac{p_{CO_2}}{p_{CO} p_{O_2}^{1/2}}\right) \quad (9)$$

where U^{OCP} represents open-circuit potential; $U^0_{H_2}$ and U^0_{CO} represents H2 and CO reduction potentials at standard conditions; $\Re$ represents the ideal gas constant; T represents the temperature of SOFC; F represents Faraday constant; p_{i} represent the partial pressure of i spices. The output voltage, U of the SOFC is shown as below:

$$U = U^{OCP}_{H_2/O_2} - \left(\eta_{Ohm} + \eta_{conc,anode,H_2} + \eta_{conc,cathode} + \eta_{act,anode,H_2} + \eta_{act,cathode}\right)$$
$$= U^{OCP}_{CO/O_2} - \left(\eta_{Ohm} + \eta_{conc,anode,CO} + \eta_{conc,cathode} + \eta_{act,anode,CO} + \eta_{act,cathode}\right) \quad (10)$$

where η_{Ohm} represents Ohmic loss; η_{conc} represents the concentration overvoltage loss at anode and cathode; η_{act} represents the active overvoltage loss at anode and cathode. Ohmic loss, η_{Ohm} is estimated by the following equations:

$$\eta_{Ohm} = jR_{Ohm} \quad (11)$$

$$R_{Ohm} = \frac{\tau_{anode}}{\sigma_{anode}} + \frac{\tau_{electrolyte}}{\sigma_{electrolyte}} + \frac{\tau_{cathode}}{\sigma_{cathode}} + R_i \quad (12)$$

where j represents the current density; R_{Ohm} represents Ohmic resistance; τ_i represent the thickness of i layer in SOFC; σ_i represent the conductivity of i layer; R_i represents Interconnect resistance. The concentration overvoltage losses of the anode and cathode are shown as below:

$$\eta_{conc,anode,H_2} = \frac{\Re T}{2F} ln\left(\frac{p_{H_2O,TPB} p_{H_2,f}}{p_{H_2O,f} p_{H_2,TPB}}\right) \quad (13)$$

$$\eta_{conc,anode,CO} = \frac{\Re T}{2F} ln\left(\frac{p_{CO_2,TPB} p_{CO,f}}{p_{CO_2,f} p_{CO,TPB}}\right) \quad (14)$$

$$\eta_{conc,cathode} = \frac{\Re T}{4F} \ln\left(\frac{p_{O_2,a}}{p_{O_2,TPB}}\right) \quad (15)$$

where $p_{i,TPB}$ represent the partial pressures of i specie at three-phase boundaries. The partial pressures at three-phase boundaries are calculated as follows:

$$p_{H_2,TPB} = p_{H_2,f} - \frac{\Re T \tau_{anode}}{2F D_{eff,anode}} j \quad (16)$$

$$p_{CO,TPB} = p_{CO,f} - \frac{\Re T \tau_{anode}}{2F D_{eff,anode}} j \quad (17)$$

$$p_{H_2O,TPB} = p_{H_2O,f} + \frac{\Re T \tau_{anode}}{2F D_{eff,anode}} j \quad (18)$$

$$p_{CO_2,TPB} = p_{CO_2,f} + \frac{\Re T \tau_{anode}}{2F D_{eff,anode}} j \quad (19)$$

$$p_{O_2,TPB} = P - (P - p_{O_2,a}) exp\left(\frac{\Re T \tau_{cathode}}{4F D_{eff,cathode} P} j\right) \quad (20)$$

where $D_{eff,i}$ represent the effective diffusivities of i species. In this study, $D_{eff,i}$ were assumed as constants evaluating at 1073K of the temperature of SOFC. The active overvoltage loss, η_{act} at the anode and cathode can be expressed as follows:

$$j_{0,electrode} = \frac{\Re T}{nF} k_{electrode} exp(\frac{E_{electrode}}{\Re T}) \quad (21)$$

$$j_{H_2} = j_{0,anode,H_2}\left[\frac{p_{H_2,TPB}}{p_{H_2,f}} exp\left(\frac{\alpha nF}{\Re T}\eta_{act,electrode}\right) - \frac{p_{H_2O,TPB}}{p_{H_2O,f}} exp\left(-\frac{(1-\alpha)nF}{\Re T}\eta_{act,electrode}\right)\right] \quad (22)$$

$$j_{CO} = j_{0,anode,CO}\left[\frac{p_{CO,TPB}}{p_{CO,f}} exp\left(\frac{\alpha nF}{\Re T}\eta_{act,electrode}\right) - \frac{p_{CO_2,TPB}}{p_{CO_2,f}} exp\left(-\frac{(1-\alpha)nF}{\Re T}\eta_{act,electrode}\right)\right] \quad (23)$$

$$j = j_{H_2} + j_{CO}$$

$$j = j_{0,cathode}\left[exp\left(\frac{\alpha nF}{\Re T}\eta_{act,cathode}\right) - exp\left(-\frac{(1-\alpha)nF}{\Re T}\eta_{act,cathode}\right)\right] \quad (24)$$

where $k_{electrode}$ represents Electrode reaction constant; $E_{electrode}$ represents Electrode activation energy; n represents the number of electrons; α represents the Transfer coefficient.

2.3. A Cell Specification and Material Properties

The Material Properties of Electrons were obtained from Aguiar et al. (2004). The specification of a cell of the SOFC is shown in Table 2.

Table 2 Specification of SOFC

Specification	Value
Cell Length, L	0.15 m
Cell Width, W	0.12 m
Cell height, H	0.12 m
Channel height, h_f 、h_a,	0.001 m
Anode thickness, τ_{anode}	10^{-6} m
Cathode thickness, $\tau_{cathode}$	10^{-6} m
Electrolyte thickness, $\tau_{electrolyte}$	$150*10^{-6}$ m
Interconnect thickness, τ_I	$150*10^{-6}$ m

The SOFC models of 1 kW and 50kW scales were implemented on Aspen Custom Modeler platform. The SOFC of the 50 kW pilot simulation considering the whole pilot process, including pre-reformers, heat exchangers, and fuel recycling.

3. Results and Discussions

3.1. Adjusting and Validation of 1 kW SOFC model

The experimental data of the 1 kW SOFC were obtained from China Steel Corporation (CSC). Figure 2 shows the agreements between the experimental data from various fuel sources and predictions from the competitive H2+CO electrochemical mechanism and the single H2 electrochemical mechanism, using H2 + CO as a fuel source and BFG. As Figure 2(a) shows, the SOFC model using the single H2 electrochemical

mechanism underestimated the output voltage, while the SOFC model using the competitive electrochemical mechanism significantly corrected the predicted performance with experimental voltage data. The average error of using the single H2 electrochemical mechanism and using the competitive electrochemical mechanism was 2.63% and 0.98 %, respectively. In Figure 2(b), the SOFC model using the competitive electrochemical mechanism obtained much more accuracy of the prediction than the model using the single H2 electrochemical mechanism. The average errors of the single and competitive electrochemical mechanisms were 5.78% and 1.60%, respectively. As Figure 2(c) shows, the average error of the voltage can be improved from 2.12% to 0.73%. Hence, using the competitive H2+CO electrochemical mechanism can obtain more accuracy of the output voltage of the SOFC with various fuel sources.

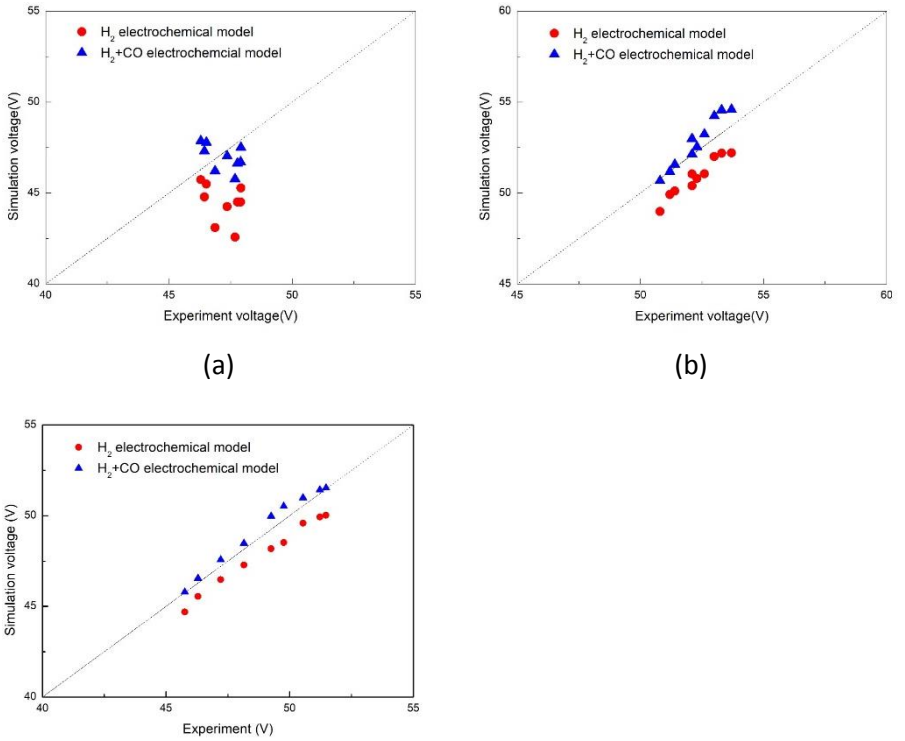

Figure 2 Cell Voltage Agreement between Experiments and Predictions using (a)H2+CO, (b) BFG, and (c) COG as the feeding fuel in Steady State

3.2. Steady State Validation of 50 kW SOFC Plant Test

The real plant data of the 50 kW SOFC were also obtained from CSC. The fuel source was CH4. The fuel source would go through a pre-former to product a certain amount of H2 and CO with a part of CH4, and then going into the 50 kW SOFC to generate electricity. Figure 3 shows the voltage agreement between experiments and predictions of the 50 kW SOFC. As the figure shows, the SOFC model can predict the output voltage in the 50 kW pilot-scale SOFC system. The average error of the voltage was 4.61%.

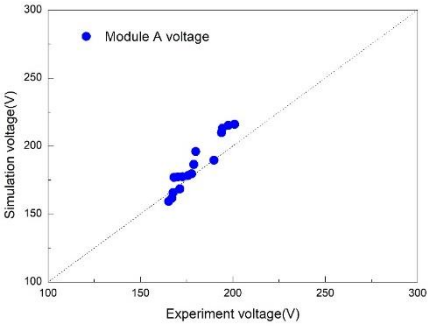

Figure 3 Cell Voltage Agreement between Experiments and Predictions in Steady State

4. Conclusions

In the study, we presented a competitive electrochemical mechanism of the H2 and CO to correct the prediction of the output voltage of SOFCs. The results showed the SOFC employed the competitive electrochemical mechanism has the better performances of the power generation and voltage predictions regardless of the what fuel used in SOFC of the 1 kW scale, compared to the SOFC only employed the single hydrogen electrochemical mechanism. The mean voltage error of the SOFC with the competitive electrochemical mechanism using various fuels was 1.52%. the minimum error was 0.73% using COG as the feedstock. The validation of the SOFC model of the 50 kW scale showed that only a 5% error with the experiment in steady-state and 6.91% error in transition.

References

Aguiar, P., Adjiman, C., & Brandon, N. P. (2004). Anode-supported intermediate temperature direct internal reforming solid oxide fuel cell. I: model-based steady-state performance. *Journal of Power Sources, 138*(1-2), 120-136.

Andersson, M., Yuan, J., & Sundén, B. (2013). SOFC modeling considering hydrogen and carbon monoxide as electrochemical reactants. *Journal of Power Sources, 232*, 42-54.

Debenedetti, P., & Vayenas, C. (1983). Steady-state analysis of high temperature fuel cells. *Chemical Engineering Science, 38*(11), 1817-1829.

Haberman, B., & Young, J. (2004). Three-dimensional simulation of chemically reacting gas flows in the porous support structure of an integrated-planar solid oxide fuel cell. *International Journal of Heat and Mass Transfer, 47*(17-18), 3617-3629.

Nikooyeh, K., Jeje, A. A., & Hill, J. M. (2007). 3D modeling of anode-supported planar SOFC with internal reforming of methane. *Journal of Power Sources, 171*(2), 601-609.

Stiller, C., Thorud, B., Seljebø, S., Mathisen, Ø., Karoliussen, H., & Bolland, O. (2005). Finite-volume modeling and hybrid-cycle performance of planar and tubular solid oxide fuel cells. *Journal of Power Sources, 141*(2), 227-240.

Suwanwarangkul, R., Croiset, E., Entchev, E., Charojrochkul, S., Pritzker, M., Fowler, M., . . . Mahaudom, H. (2006). Experimental and modeling study of solid oxide fuel cell operating with syngas fuel. *Journal of Power Sources, 161*(1), 308-322.

Sauro Pierucci, Flavio Manenti, Giulia Bozzano, Davide Manca (Eds.)
Proceedings of the 30th European Symposium on Computer Aided Process Engineering (ESCAPE30), May 24-27, 2020, Milano, Italy.
http://dx.doi.org/10.1016/B978-0-12-823377-1.50087-2

Design Optimization of C3MR Natural Gas Liquefaction Process

Pavan Kumar Veldandi , Sunjay Kurian

Connected Products, Industrial Operations Group, Cognizant Technology Solutions, Hyderabad-500008,India
Pavan.veldandi@cognizant.com

Abstract

Liquefied Natural Gas plants are energy intensive processes. In order to reduce their energy consumption, optimization is an often-sought step in process design. But it is less common for real existing plants. This is especially laborious for plant operators when they need to work with design simulation software in conjunction myriad of other tools to evaluate equipment adequacy for new HMB or use a dynamic simulation software in steady state mode with an optimizer linked.

The novelty of this paper is to showcase how intuitive open modelling with right specifications and in-built optimizers can be the right tool for both Process Designs as well as for re-optimizing/debottlenecking for real plants. This study uses AVEVA SimCentral Simulation Platform to develop the optimized design and real plant model within same simulation.

The process design was created with specifications that reflect the process design objectives and then optimized for compressor power by varying refrigerant compositions and compression pressure. This becomes the basis for the real plant studies like similar optimization for a changed natural gas feed. This is where real plant operators can save efforts by working with a steady state pressure solved network simulation which obeys the equipment limitations. Since this is a steady state simulation the transient to steady state is not a concern, hence time/effort is saved when operators can simplify the simulation by simply swapping detailed controls for simple specifications in open modelling environment.

Keywords: C3MR Process, Energy Optimization, Mixed Refrigerant Composition

1. Introduction

Natural Gas Liquefaction plants are energy intensive processes. With growing demand of Liquefied Natural Gas (LNG), it is important to review the simulation solutions available to process designers and operators to find optimized solutions.

Several studies discuss about optimization different aspects of LNG process design and operation. Among studies in design optimization, it is important to note that Abbas et al. [1] studied the design optimization of LNG mixed-refrigerant processes to conclude that the most effective operation optimisation objective function is the minimisation of the major operating cost, being compressor power. The other flavour of optimization studies is like the energy and cost optimization done by M Wang et al. [2] which considered a minimization of the CAPEX and OPEX. This paper reviews existing optimization studies and suggests the combined use of flexible specifications, multiple modes and optimizers to help process designers and operators.

When process designers begin design simulations, they use a sequential modular based simulator which forces design to detail refrigerant flowrate which is often an unknown. This unknown then becomes part of an optimization objective. The process design should focus on objectives like liquefaction temperature and should allow the refrigerant flowrate to be calculated based on heat balance. This was achieved with ease in AVEVA SimCentral Simulation Platform Process (design) mode. With the simulation with true process objectives, designers can run the optimization for compression power as an objective as suggested by Abbas Ali et al. [1]. As this design becomes a real plant, there is a common need for operators to optimize for changed natural gas feeds based on changing market conditions. This is where the same Process mode simulation was be updated to FluidFlow (steady state pressure solve network) mode which will reflect real plants. The key here is that simulation gets set to equipment sizes that were calculated in design. The complexity with detailed controls can be mimics with specifications like liquefaction product temperature can be specified / maintained by letting the expansion valve position be calculated by simulation. With all appropriate controls mimicked correctly and equipment sizes set, operators can identify new optimums for compression power by varying mixed refrigerant compositions and compressor outlet pressure. Husnil et al.(2014)[3] proposed a new Control structure synthesis for operational optimization of mixed refrigerant processes.

2. Process Description

Figure 1 shows the propane pre-cooled C3MR NG liquefaction process. Propane pre-cooling refrigeration process is not modelled as part of this study, it is assumed that natural gas is precooled and available at -36.3°C. The natural gas is pre-cooled and subcooled to -160°C with two rigorously modelled spiral wound exchangers that exchange heat with mixed refrigerant (MR). The MR cycle is compressed in two compressor stages with an intercooler and an aftercooler. The after cooler outlet (2-phase) is separated as MRV (mixed refrigerant vapor) and MRL (mixed refrigerant liquid) before entering the spiral wound exchangers and then back. The design objectives of simulation model are given in Table 1.

Table 1. Process objectives

Natural gas liquefaction objectives			
Feed Pressure (bar)	61.70	Composition (fraction)	
Feed Temperature (°C)	-32.70	Nitrogen	0.05
Product Temperature (°C)	-160.00	Methane	0.87
		Ethane	0.05
		Propane	0.02

3. Process (design) simulation and optimization

Table 2 gives the specifications/flowsheet equations that help to set up the design simulation with design target objectives and calculate unknowns on the refrigeration/compression system:

The natural gas cooler and subcooling unit are modelled with spiral wound heat exchangers with discretization of heat transfer by splitting (5 times) the heat transfer across the tube lengths. These spiral wound heat exchangers are set with area and heat transfer coefficient. With above updates, the simulation can be solved with an initial mixed refrigerant composition. See Figure 1 for a preview of simulation.

*T*able 2. Setting simulation with process design objectives

Variable	Changes done	Justification
Mixed refrigerant flow	Flow is commonly specified in sequential solve simulator, but it is made calculated here.	Flow is best identified based on heat balance
Cryogenic exchanger outlet i.e. mixed refrigerant to compressor suction drum	Vapor fraction set to above dew point.	Dew point specification will avoid liquid in compressor suction drum.
Liquefied Natural Gas to storage - target temperature	Product temperature is generally a calculated variable, but it set as specified here to 160 C.	Natural gas heat balance to calculate required refrigerant flow.
Expansion valve pressure drop	Pressure drop is made calculated.	Liquefied natural gas target temperature should calculated expansion valve pressure drop.
Compression ratio per stage.	Flowsheet equation setting both stages with equal compression ratio.	Compression system is defined by desired outlet pressure.
Mixed refrigerant N2 composition	N2 composition set as calculated. Total refrigerant composition is summed to 1 with a flowsheet equation.	Specified composition of C1, C2 and C3 should defined N2 composition.

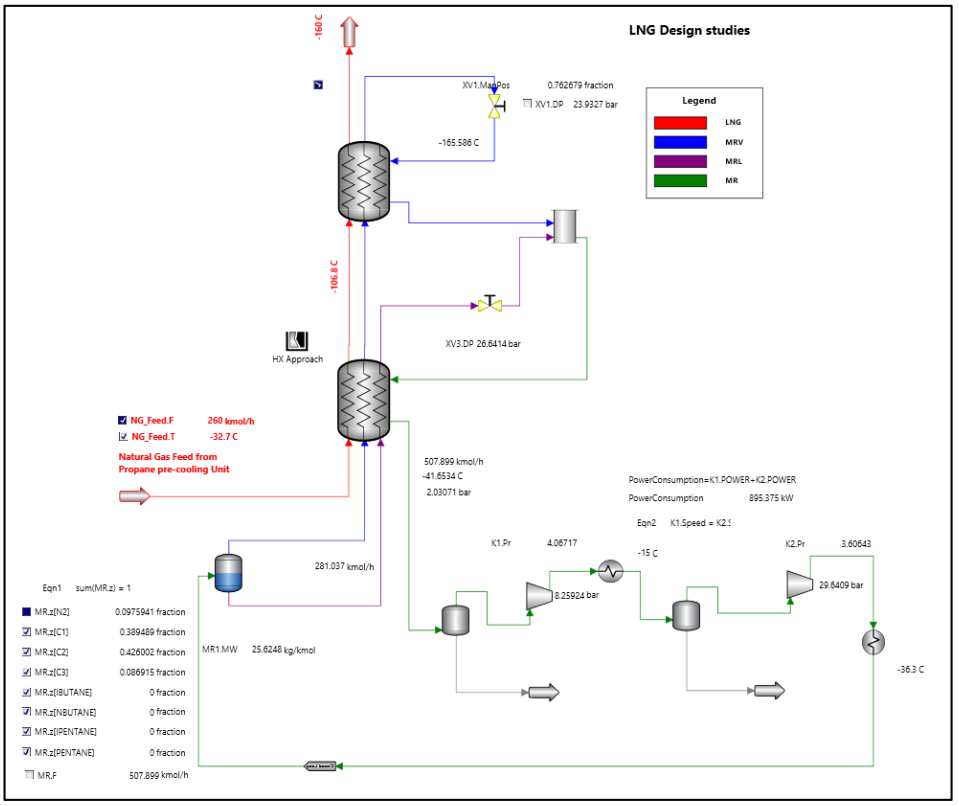

Figure 1. Simulation for propane precooled C3MR Natural Gas liquefaction Process

Table 3. Summary of design optimization of mixed refrigerant composition and compression outlet pressure

	Optimization setting	**Bounds**	**Base**	**Optimized**
Composition (fraction)				
Nitrogen	Dependent	0-100%	0.10	0.08
Methane	Independent	0-100%	0.40	0.39
Ethane	Independent	0-100%	0.30	0.40
Propane	Independent	0-100%	0.20	0.13
Compressor 2nd stage outlet pressure (bar)	Independent	0-100%	62.10	33.67
Compression power consumption (kW)	Objective function		1351	1044
Mixed Refrigerant flow (kmol/h)	Dependent	Positive values	397	474
Compression suction drum vapor fraction	Dependent	Above dew point	1	1

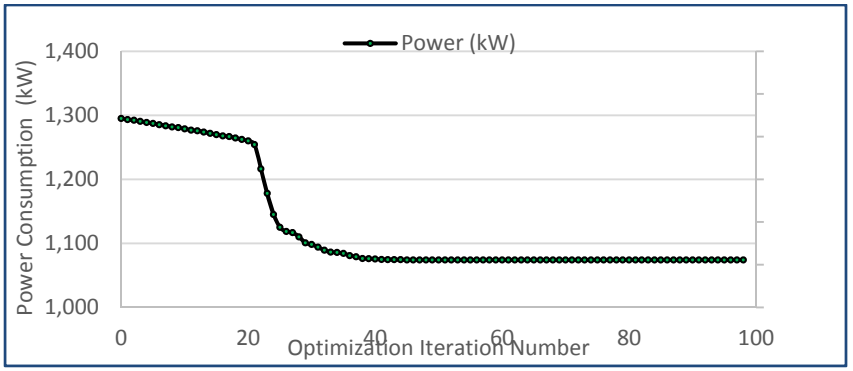

Figure 2. Design optimization iteration path

The optimization achieved a 22% reduction in power consumption as shown in Figure2.

Table 4. Simplifying detailed controls

Variable	**Changes done**	**Justification**
Natural gas flow	Natural flow is specified instead of pressure	Flow is expected to maintained by product flow control valve.
Compressor outlet pressure	Both stages speed is set to be same with a flowsheet equation assuming that it run by same rotor.	Controlling compressor in simulation can done via speed/outlet pressure.
Liquefied natural gas temperature to storage – target temperature	Liquefied natural gas temperature is assumed to be maintained by letting simulation calculate expansion valve position.	Natural gas heat balance to calculate required refrigerant flow.
Mixed refrigerant drum separation level	Level in drum is specified instead of position of the mixed refrigerant liquid expansion valve.	Level in drum is assumed to be maintained by control that maintains the mixed refrigerant liquid expansion valve.

Table 5. Natural gas feed changes in pressure solve network

Natural Gas			**Mixed Refrigerant**		
	Design	Feed Changed		Design	Feed Changed
Feed Pressure (bar)	61.70	61.84	Power Consumption (kW)	1044.22	1038.85
Feed Temperature (°C)	-32.70	-32.70	Mixed Refrigerant flowrate (kmol/h)	473.97	470.70
Product Temperature (°C)	-160.00	-160.00			
Composition (fraction)			Composition (fraction)		
Nitrogen	0.05	0.06	Nitrogen	0.08	0.08
Methane	0.87	0.80	Methane	0.39	0.39
Ethane	0.05	0.10	Ethane	0.40	0.40
Propane	0.02	0.03	Propane	0.13	0.13
i-Butane	0.00	0.01			
n-Butane	0.00	0.01			
i-Pentane	0.00	0.00			
n-Pentane	0.00	0.00			

4. Real plant (pressure solved network) optimization

Real plant can be modelled with steady state pressure solve network called Fluid Flow mode.

The above design Process (design) simulation was switched to Fluid Flow mode (steady state pressure solve network) with the design equipment sizes. This is generally when operator can now use the same process design simulation for his operational needs.

Since FluidFlow is a pressure solve network with steady state, detailed controls were replaced with specifications to simplify the real plant simulation as given in Table 4.

Table 6: Summary of real plant optimization of mixed refrigerant composition and compression speed

	Optimization setting	**Bounds**	**Base**	**Optimized**
Composition (fraction)				
Nitrogen	Dependent	0-100%	0.08	0.10
Methane	Independent	0-50%	0.39	0.39
Ethane	Independent	0-50%	0.40	0.43
Propane	Independent	0-50%	0.13	0.09
Compressor 2nd stage outlet pressure (bar)	Dependent		33.87	29.64
Compressor speed (rpm)	Independent	3000 - 4200 rpm	3600.00	3582.15
Power Consumption (kW)	Objective function		1039	895
Mixed Refrigerant flow (kmol/h)	Dependent	Positive values	471	508
Compression suction drum vapor fraction	Dependent	Above dew point	1	1

4.1. Natural Gas Composition change case study

The fluid flow mode model has been tested for fidelity by varying the Natural Gas feed composition as shown in Table 5Now with "Feed Changed" case as the starting point in fluid flow mode, the optimization problem has been run again to yield below results given in Table 6.

The optimization achieved a 14% reduction in power consumption as shown in Figure 3.

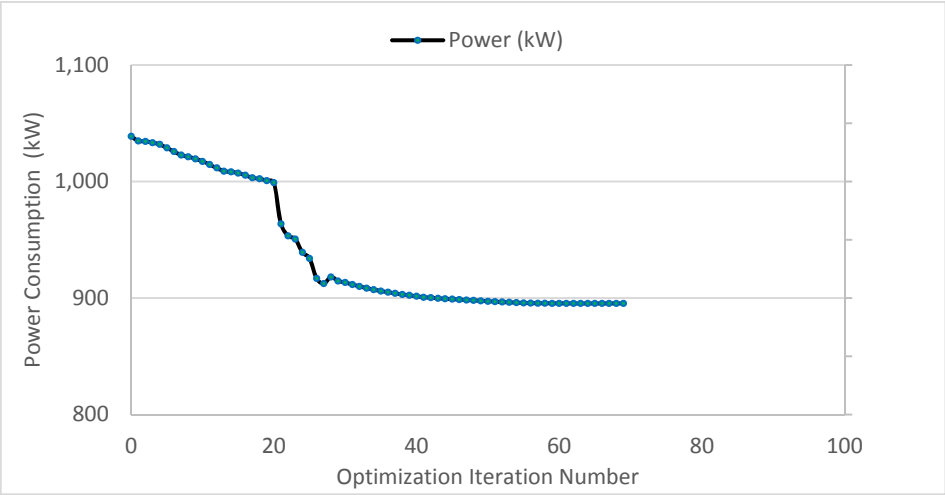

Figure 3. Real optimization iteration path

5. Conclusion

In this work the C3MR Natural Gas liquefaction process has been modeled using Aveva SimCentral Simulation platform for process design as well as operations. The design simulation was successfully set to work with process objectives instead of unknowns of refrigeration cycle. Now the compressor power consumption is minimized by optimizing mixed refrigerant composition and compressor outlet pressure. It is found that the compressor power can be reduced by 22% for design. Further this simulation was successfully moved to a simplified (no controls) pressure driven network steady state simulation. Operators can now use this simulation to identify optimized solutions for changes in natural gas feed composition. In this case the optimizer reduced the compressor power consumption by 14%.

References

1. Hatcher, Prue & Khalilpour, Kaveh & Abbas, Ali. (2012). Optimization of LNG mixed refrigerant process considering operation and design objectives. Computers & Chemical Engineering. 41. 123–133. 10.1016/j.compchemeng.2012.03.005.
2. Mengyu Wang, Rajab Khalilpour, Ali Abbas (2014). Thermodynamic and economic optimization of LNG mixed refrigerant processes.
3. Yuli Amalia Husnil Moonyong Lee,(2014), Control structure synthesis for operational optimization of mixed refrigerant processes for liquefied natural gas plant, Vol 60, No. 7 2428- 2441. 10.1002/aic.14430

Sauro Pierucci, Flavio Manenti, Giulia Bozzano, Davide Manca (Eds.)
Proceedings of the 30th European Symposium on Computer Aided Process Engineering (ESCAPE30), May 24-27, 2020, Milano, Italy.
http://dx.doi.org/10.1016/B978-0-12-823377-1.50088-4

A Practical Application of Simulation-based Surrogate Modeling for Prereformer Reactor

Robin Schmidt, Amélie Chattot, Amal Bouchrit, Moein Mighani, Evrim Örs*

AIR LIQUIDE Forschung und Entwicklung GmbH, Frankfurt Innovation Campus, Gwinnerstrasse 27-33, Frankfurt am Main, Germany
evrim.oers@airliquide.com

Abstract

In this work, a practical example of surrogate modeling in process engineering is demonstrated in the field of hydrogen production: Modeling of a prereformer reactor. The main motivation is to show the potential of this approach for performance increase of simulations in process design and operation optimization. In a first step, sample points were generated following a computational design of experiments procedure. A prereformer reactor model was built in Aspen Plus®, and corresponding simulation results were collected based on the sample points. The resulting dataset, i.e. sample points and simulation outputs, were used for surrogate model development for the reactor outlet temperature and concentrations, via built-in artificial neural networks (ANN) feature of JMP®. It was observed that resulting surrogate models, with a single layer ANN of 100 hidden nodes, satisfied the expected accuracy limits, e.g. the outlet temperature was predicted with an RMSE of less than 0.04 °C. The predictive behavior of the models was also examined via a blind test set, and the speedup in computation was shown. While this study constitutes a successful proof-of-concept, further improvements are possible via e.g. customization of model development, employment of adaptive sampling methodology.

Keywords: Surrogate, Data-Driven, Neural Networks, Prereformer, Hydrogen

1. Introduction

In engineering practice, one uses physical modeling approach to understand, design and optimize a process. Nonetheless, this first-principles approach can be limited requiring a substantial computational effort and time, and the physico-chemical relationship of input-output variables may not always be accessible to the designer. On the other hand, data-driven modeling approach, i.e. a mapping of input and output variables, gains increasing interest in chemical engineering with the rise of artificial intelligence and machine learning techniques (Venkatasubramanian, 2019). Various applications of this approach employing different computational methodologies can be found in multiple disciplines of chemical engineering, where simulation-based surrogate modeling constitutes a key branch (McBride and Sundmacher, 2019), (Nentwich and Engell, 2019). Along with its advantageous aspects such as reducing the model complexity and allowing faster solutions and deployment options, surrogate modeling also requires an integrated approach with process know-how for developing reliable applications. The corresponding hybrid modeling is therefore being addressed more and more by the academic chemical and process engineering community (Asprion et al., 2019).

From an industrial perspective, digitalization is becoming more and more an integral part of business in all sectors, including process industry (Les Echos, 2019). The digital solutions usually target to achieve operational excellence, where the applications primarily consist of plant economic performance monitoring, predictive asset maintenance, real time optimization (OSIsoft, 2019) and advanced process control. Prior work on catalyst deactivation modeling (Schmidt et al., 2017) and ash fusion behavior prediction (Sasi et al., 2018) are exemplary in H_2/Syngas production field. It is also notable that collaboration projects with academia constitute a key driver for business in exploiting the increasing digitalization trend, especially regarding development of novel AI-based solutions for process industry (chemie.de, 2019).

In this work, focusing on the extension of abovementioned activities with faster and accurate modeling strategies, we conduct a proof-of-concept study concentrating on one unit operation, namely a prereformer reactor as a key component of H_2/Syngas production plants offered and operated by Air Liquide. We describe an approach to illustrate the employment of surrogate models as an enabler for faster computation of first-principles models. Moreover, their integration with optimization procedures can significantly reduce the computational effort in process design and operation. Finally, allowing an explicit mathematical formula, surrogate models based on process simulator results may lead to easily deployable solutions.

2. Prereformer Reactor Simulation

To illustrate the potential of surrogate modeling, an industrial prereformer reactor was selected. From process aspect, a prereformer is frequently used in H_2/Syngas production plants and targets to convert heavy hydrocarbons (C2+) into methane irreversibly. This allows a better heat utilization in the plant by achieving higher preheating temperature for natural gas (NG) as feedstock. Furthermore, it enables the processing of heavy feedstock's, such as naphtha, refinery off-gases, via preventing coke deposition on the subsequent reforming catalyst.

In this work, carbon formation and heavy hydrocarbons were neglected for demonstration purpose and the dry inlet gas is considered a NG containing CO and CO_2 (e.g. originating from refinery-off gas). With these assumptions, only steam methane reforming (SMR) and water gas shift (WGS) reactions are required to describe chemical conversion:

$$\mathrm{SMR:}\ \mathrm{CH_4 + H_2O \leftrightarrow CO + 3\,H_2} \qquad \Delta H = 206.2\ \mathrm{kJ/mol} \tag{1}$$

$$\mathrm{WGS:}\ \mathrm{CO + H_2O \leftrightarrow H_2 + CO_2} \qquad \Delta H = -41.2\ \mathrm{kJ/mol} \tag{2}$$

The amount of reaction can be expressed by the reaction extent ξ_{SMR} and ξ_{WGS} in mol/h.

The steam-to-carbon ratio *S/C*, which is a parameter varied independent from the dry inlet gas composition to determine the steam amount, is defined as:

$$S/C = x_{\mathrm{H_2O}} / x_{\mathrm{CH_4}} \tag{3}$$

with the mole fraction of methane $x_{\mathrm{CH_4}}$ and steam $x_{\mathrm{H_2O}}$. Based on the dry gas composition and steam-to-carbon ratio *S/C*, wet compositions are calculated:

$$x_{\mathrm{i}} = x_{\mathrm{i,dry}} / (1 + x_{\mathrm{CH_4,dry}} \cdot S/C) \tag{4}$$

Other parameters describing the process are the inlet temperature T_{in}, inlet pressure p_{in}, the pressure drop over the reactor Δp and the approach temperatures for the two reactions $T_{ap,SMR}$ and $T_{ap,WGS}$. Due to the fact that we use an adiabatic reactor the molar flow rate has no influence on the resulting outlet temperature, pressure or gas compositions, hence the total inlet flow was set at 100 mol/h.

The outlet of the prereformer is fully described if we predict the T_{out}, p_{out} and flow rates of all components. A possible solution strategy is to predict the outlet temperature and the two extents of reaction, ξ_{SMR} and ξ_{WGS}.

The outlet flow rates of all components are then calculated using ξ_j:

$$\dot{n}_{i,out} = \dot{n}_{i,in} + \sum_j \nu_{i,j} \cdot \xi_j \tag{5}$$

with the stoichiometric number ν, and the indices *j* for reactions and *i* for components.

The outlet pressure is calculated directly from the inputs as:

$$p_{out} = p_{in} + \Delta p \tag{6}$$

Based on these conditions, a prereformer simulation in Aspen V9 using Peng-Robinson equation of state was built as a data generator for the surrogate model development.

3. Computational Methodology

3.1. Data Generation using Design of Experiments

For this application, a training dataset with 100,000 sample points was generated. To construct the design of experiments (DoE), input variables were divided into two groups and their ranges were determined considering wide operating conditions as follows:

i) Dry gas composition: x_{CH_4} [0.44, 0.98], x_{CO} [0.00, 0.12], x_{H_2} [0.00, 0.12], x_{CO_2} [0.00, 0.12], x_{N_2} [0.00, 0.20]

ii) Process conditions: T_{in} [350, 600] °C, p_{in} [10, 50] barg, Δp [0, 5] bar, $T_{ap,SMR}$ [-50, 50] °C, $T_{ap,WGS}$ [-50, 50] °C, *S/C* [1, 3]

For both of these variable groups, a separate design was created using JMP 14 software and the two sets were combined. A space filling latin hypercube design with 25,000 runs was generated for the process conditions ii), which was followed by 10,000 runs using a space filling mixture design for the dry gas composition i). Consequently 100,000 data points were created by random combinations of both variable groups.

The test set consists of 10,000 points. Data generation differs slightly from the training set, conducted this time in Matlab. For the dry gas compositions, a grid sampling using 0.5 % steps was implemented. Among the resulting 397,169 possible gas mixtures, 10,000 points were randomly selected. As for the operating variables, we randomly selected 10,000 points within the variable ranges. Finally both groups were combined.

The simulation results were calculated in Aspen and stored in Excel. After accounting for the convergence of Aspen, the training and test sets contained 99,982 and 9,993 data points, respectively. While both sets cover the same range for model input variables, their statistical representativeness was ensured by randomness.

3.2. Model Development

The selected model structure in JMP 14 was artificial neural networks (ANN) with one hidden layer, where the K-fold cross validation method was employed with k=4. As a preliminary investigation, the model training was conducted using 25, 50 and 100 nodes, and resulting RMSE values were observed. In addition to RMSE, the model robustness was also monitored via observing the fraction of predicted outcomes within a specified error range. All three target variables, i.e. the outlet temperature and the two extents of reaction, were modeled using all input variables following a multi-input single-output (MISO) structure. It is notable that, thanks to the prediction of the extents of reaction, the mass balance around the reactor is ensured to be closed.

4. Results and Discussion

As mentioned earlier, in order to have a full description of the prereformer reactor outlet, the outlet temperature, and the two extents of reaction for SMR and WGS are to be predicted. However, in this section, the reactor outlet concentrations are presented to allow a more tangible interpretation of the results, since the extents are relatively harder to be interpreted as they are intermediate variables by nature.

4.1. Model Selection

In this part, modeling results illustrating both accuracy and robustness are tabulated. Table 1 focuses on the model accuracy with RMSE values. It can be seen that the training accuracy is significantly improved with increasing number of nodes, therefore the 100-nodes model is chosen for further investigation. It is observed that RMSE values for test set are also comparable with the training results, showing a good predictive behavior. Considering test set, the largest error is in H_2 concentration prediction with 0.0056 %-points, which can be considered as an acceptable deviation for a practical application.

Table 1: Model accuracy - RMSE values for outlet temperature and compositions

Number of nodes	T_{out} (° C)	CH4 (pp)	CO (pp)	CO2 (pp)	H2 (pp)	H2O (pp)	N2 (pp)
25 (Train)	0.0867	0.0034	0.0036	0.0037	0.0080	0.0065	0.0003
50 (Train)	0.0463	0.0016	0.0017	0.0016	0.0035	0.0028	0.0001
100 (Train)	0.0326	0.0014	0.0010	0.0010	0.0029	0.0023	0.0001
100 (Test)	0.0345	0.0027	0.0010	0.0015	0.0056	0.0042	0.0001

Table 2 concentrates on the robustness of the selected 100-node model, tabulating the fraction of data points predicted within a specific error range. For instance, the temperature is predicted for 99.90 % of the test dataset with an error less than 0.3 °C. The most significant error is observed in H_2 (as in Table 1), which can be explained by the error propagation of ξ_{SMR} on the amount of H_2 produced (i.e. $\nu_{H_2} = 3$ for SMR reaction).

Table 2**:** Model robustness - Fraction of data points within specified error range

	Outlet Temperature		x_{CO}		x_{H2}	
Criteria	**< 0.3 K**	**< 0.1 K**	**< 0.02 pp**	**< 0.01 pp**	**< 0.02 pp**	**< 0.01 pp**
100 (Train)	99.97	98.07	100.00	99.97	99.89	98.79
100 (Test)	99.90	98.17	100.00	99.99	99.86	98.82

4.2. Modeling Results : Outlet Temperature and Concentrations

In this section, first the residual plot of the outlet temperature model based on the selected 100-node ANN is depicted, both for training (Figure 1.a) and test sets (Figure 1.b). It can be seen that the residual distribution has no systematic dependency, and that the predictive capability of the outlet temperature model is very good.

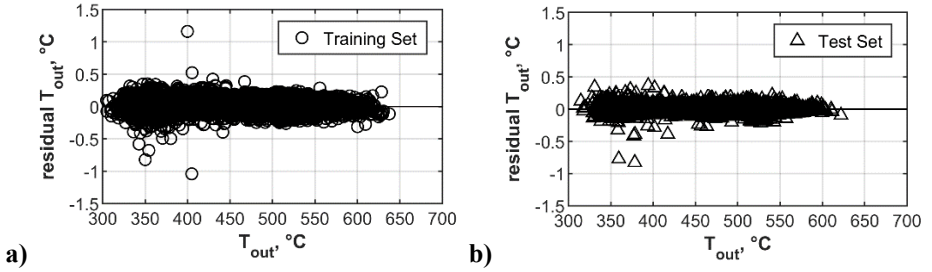

Figure 1: Residual values for outlet temperature - training (a) and test set (b)

Figure 2 shows the residual plot for x_{CO}^{out} values as a representative outlet concentration. Similar to outlet temperature, it can be seen that the prediction capability of the x_{CO}^{out} model is good, with no systematic deviation.

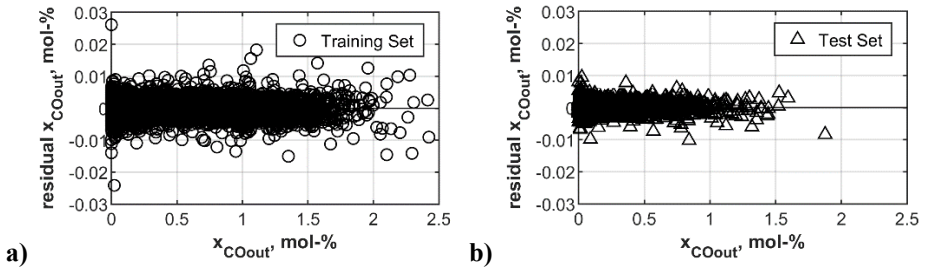

Figure 2: Residual values for x_{CO}^{out} - training (a) and test set (b)

Although a good overall prediction capability is achieved and the closing of mass balance is ensured, one deficit of the current model is that the predicted CO outlet concentration can be negative. This has been observed for 0.11 % of data points in the test set.

4.3. Computing Time

Based on the computing time measurements throughout this study, a comparable call in Aspen (avoiding the communication overhead) for a bunch of 100 simulations takes 0.54 seconds, whereas a function call based on a non-optimal implementation of the resulting 100-nodes ANN in Matlab takes 0.00014 seconds on average. It can be concluded with this preliminary investigation that a speed-up of ca. 40 was reached.

5. Conclusion and Outlook

In this work we showed a practical application of surrogate modeling for a prereformer reactor, based on the results of an Aspen Plus flowsheet simulation. Three ANN models with single layer were developed to predict the target variables, i.e. the outlet temperature and the extents of the two reactions, namely SMR and WGS. This modeling strategy enabled to fully describe the reactor outlet conditions including gas compositions with a high accuracy and less computing time. The work showed the potential of surrogate modeling to achieve improved performance for process simulations in design and operation optimization problems. Further improvements to increase model quality are possible via e.g. customization of model development, and adaptive sampling methodology. It is also anticipated to use other machine learning methods, e.g. Kriging, as well as to extend the modeled unit operations and to combine them for efficient deployment of applications, such as data reconciliation, and real-time optimization.

References

N. Asprion, R. Böttcher, R. Pack, M. Stavrou, J. Höller, J. Schwientek, M. Bortz, 2019, Gray-box Modeling for the Optimization of Chemical Processes, Chem. Ing. Tech.. 91(3): 305–313.

Chemie.de, 2019, 17 Mio. EUR für die künstliche Intelligenz in Prozessindustrie, https://www.chemie.de/news/1162875/17-mio-eur-fuer-die-kuenstliche-intelligenz-in-der-prozessindustrie.html?pk_campaign=ca0259&WT.mc_id=ca0259

Les Echos, 2019, eCAC40: chez Air Liquide, Le numérique a changé d'échelle, https://business.lesechos.fr/directions-generales/strategie/transformation/0602026569459-ecac40-chez-air-liquide-le-numerique-a-change-d-echelle-332389.php

K. McBride, K. Sundmacher, 2019, Overview of Surrogate Modeling in Chemical Process Engineering, Chem. Ing. Tech., 91(3): 228-239.

C. Nentwich, S. Engell, 2019, Surrogate modeling of phase equilibrium calculations using adaptive sampling, Computers and Chemical Engineering, pp. 204-217.

OSIsoft, 2019, How Air Liquide leverages on PI technologies to optimize its operations - SIO.Optim program, Presentation at PI World Conference, San Francisco, https://www.osisoft.com/presentations/how-air-liquide-leverages-on-pi-technologies-to-optimize-its-operations---sio-optim-program/

R. Schmidt, E. Örs, A. Chattot, 2017, Prediction of Catalyst Lifetime: Example MT-Shift Reactor, Presentation at 50. Jahrestreffen Deutscher Katalytiker, Weimar (available on demand).

T. Sasi, M. Mighani, E. Örs, R. Tawani, M. Gräbner, 2018, Prediction of ash fusion behavior from coal ash composition for entrained-flow gasification, Fuel Processing Technology, 176: 64-75.

V. Venkatasubramanian, 2019, The promise of artificial intelligence in chemical engineering: Is it here, finally?, AIChE J., 65(2):466–78.

Sauro Pierucci, Flavio Manenti, Giulia Bozzano, Davide Manca (Eds.)
Proceedings of the 30th European Symposium on Computer Aided Process Engineering (ESCAPE30), May 24-27, 2020, Milano, Italy.
http://dx.doi.org/10.1016/B978-0-12-823377-1.50089-6

Development of a Microkinetic Model for the CO_2 Methanation with an Automated Reaction Mechanism Generator

Bjarne Kreitz[a,b,*], Gregor D. Wehinger[a], C. Franklin Goldsmith[b], Thomas Turek[a]

[a] *Institute of Chemical and Electrochemical Engineering, Clausthal University of Technology, Leibnizstr. 17, 38678 Clausthal-Zellerfeld, Germany*
[b] *School of Engineering, Brown University, 184 Hope Street, RI 02912 Providence, USA*
kreitz@icvt.tu-clausthal.de

Abstract

The automated reaction mechanism generator (RMG) is used to investigate the methanation of CO_2 on the Ni(111) and Ni(211) surface. Linear scaling relations are applied for the thermochemistry of the adsorbates, which are compared to state-of-the-art electronic structure calculations and show a reasonable predictability. RMG discovers nearly the same amount of species and reactions for both facets. However, a reaction path analysis in a reactor simulation shows that the reaction pathways on both surfaces differ significantly, which is caused by the difference in the binding energy of the adsorbates. Reactor simulations reveal a lower methane production rate compared to experiments obtained in a Berty reactor with a Ni/Al_2O_3 catalyst, which is a result of a high surface coverage with CO^* and demands, therefore, the inclusion of a coverage dependent heat of formation of the adsorbates.

Keywords: Methanation, Microkinetic modeling, Rate-based algorithm

1. Introduction

The hydrogenation of carbon dioxide with hydrogen to methane in the Power-to-Gas process is a crucial method to tackle the requirements of long-term energy storage and the production of sustainable natural gas (Götz et al., 2016). The knowledge of the kinetics of all elementary steps of the methanation mechanism, the microkinetics, is the key to develop more active catalysts and to describe the transient operation of the reactor, which is caused by the volatile feed supply. Simulation studies have shown that drastic variations in the hot-spot temperature and productivity are possible during dynamic operation (Kreitz et al., 2019a).

However, the theoretical construction of a microkinetic model from scratch is a long process, requiring substantial computational resources to determine binding energies and to elucidate the pathway with the lowest energy barrier on a crystal facet. An alternative approach is the automated reaction mechanism generation (Gao et al., 2016). This is a promising method for the fast creation of microkinetic models by relying on databases and parameter estimation methods (Gao et al., 2016). RMG has extensively and successfully been used for the development of gas-phase mechanisms. In the work of Goldsmith and West (2017), a functionality for heterogeneously catalyzed reactions was added to RMG, which is denoted as RMG-Cat. This extension to heterogeneous systems is based on scaling relations for the thermochemistry of the adsorbates and the

reaction rate expressions (Mazeau et al. 2019). Goldsmith and West (2107) showed that RMG-Cat could rediscover a mechanism for dry reforming of methane as predicted by sophisticated experiments.

In this study, we use RMG-Cat to determine the mechanism of the CO_2 methanation for the Ni(111) and Ni(211) surface, which are discussed as the active facets for the methanation reaction (Andersson et al., 2008). The microkinetics are evaluated in a Berty reactor model and compared to experimental results.

2. Methods

RMG-Cat determines the mechanism based on reaction libraries and the estimation of thermodynamic properties of the adsorbates (Goldsmith and West, 2017). Specific rules for the evaluation of reaction rates are assigned to the reaction families, such as Brønsted-Evans-Polanyi (BEP) relations, for the determination of activation energies. Thermodynamic properties of the adsorbates depend on the metal surface and are therefore computed with linear scaling relations (Abild-Pedersen et al., 2007). The thermochemistry of unknown species can be automatically estimated by the method proposed by Goldsmith (2012), which enables the algorithm to consider all possible reactions and intermediates. For the generation of a mechanism, it is necessary to specify the temperature T, pressure p, active surface area a, the surface site density Γ the initial mole fractions of the educts x^0 and binding energies for C, H, and O for linear scaling relations. Moreover, it is necessary to specify starting species for the core mechanism. RMG-Cat estimates all possible reactions between the core species and evaluates the rates in a batch reactor simulation. If a generated species exceeds a certain threshold, this species is included in the core mechanism along with the reaction through which it is formed. Other species and reactions are discarded and stored in an edge mechanism. With the new species in the core, RMG-Cat starts over again and predicts new reactions and species. This loop breaks when a previously defined termination criterion, e.g. reaction time or conversion (X) of a reactant, is reached. Table 1 shows the input parameters for RMG-Cat, which are used for the generation of the microkinetic model.

Table 1: Parameters used for the generation of the methanation mechanism for both Ni facets with RMG-Cat.

Parameter	Value
T / K	573
p / bar	1
Γ / mol cm^{-2}	$2.9 \cdot 10^{-9}$
$x^0_{H_2}$ / –	0.8
$x^0_{CO_2}$ / –	0.2
X_{CO_2} / –	0.8
a / m^{-1}	$1 \cdot 10^5$

Density functional theory (DFT) calculations for the adsorbates on the Ni surface are calculated with the Vienna ab-initio Simulation Package (Kresse, Furthmüller, 1996a, Kresse, Furthmüller, 1996b) in the Atomic Simulation Environment using plane-wave

pseudopotentials. The single-point energy for the Ni(111) [Ni(211)] surface is computed for a p(3x3) [p(1x3)] supercell with 4 [12] layers of Ni atoms where the 2 [6] top layers are relaxed together with the adsorbate with a cut-off energy of 400 eV and the usage of the RPBE exchange-correlation functional. The Brillouin zone is sampled with a (3x3x1) [(4x3x1)] Monkhorst-Pack mesh and the structure is relaxed until all forces are below 0.02 eV A^{-1}. Thermodynamic properties for the adsorbates are calculated based on the harmonic oscillator approximation. Further details can be found in the work of Blondal et al. (2019). The model generation is assisted by steady-state and transient methanation experiments carried out in a Berty reactor with an 11 wt.-% Ni/Al_2O_3 catalyst. For details on the setup, refer to previous work (Kreitz et al., 2019b). Generated microkinetics are evaluated in a reactor model of the Berty reactor, which is implemented in Cantera and based on the governing equations of an isothermal continuously stirred tank reactor (CSTR).

3. Results and Discussion

Binding energies obtained from the DFT calculations in Table 2 are in good agreement with literature values (Catapan et al., 2012, Blaylock et al., 2009). The binding energies of H and O remain merely unchanged by the facet, but carbon binds stronger to the Ni catalyst in the 4-fold hollow site on the (211) surface. Additional DFT calculations for various adsorbates on the (111) surface are performed to determine if the linear scaling relations work accordingly. For the (211) facet, additional adsorbates are computed based on literature values (Andersen et al., 2017, Medford et al., 2014).

Table 2: Zero-point corrected binding energies for C, O, and H on Ni(111) and Ni(211) with adsorption position in brackets and referenced according to Blondal et al. (2019).

	Ni(111)	Ni(211)
C	- 6.44 eV (hcp)	- 7.33eV (4f)
H	- 2.76 eV (fcc)	- 2.76 eV (bridge)
O	- 4.70 eV (fcc)	- 4.88 eV (bridge)

Thermodynamic properties of the adsorbate are scaled from a Pt(111) and a Pt(211) database with the binding energies from Table 2. The Pt(111) database is based on the work of Blondal et al. (2019), while the Pt(211) database is created from the work of Medford et al. (2014) and Andersen et al. (2017). The results of the linear scaling predictions are displayed in Figure 1 in the form of a parity plot for the standard heat of formation ($\Delta_f H$) of the adsorbates.

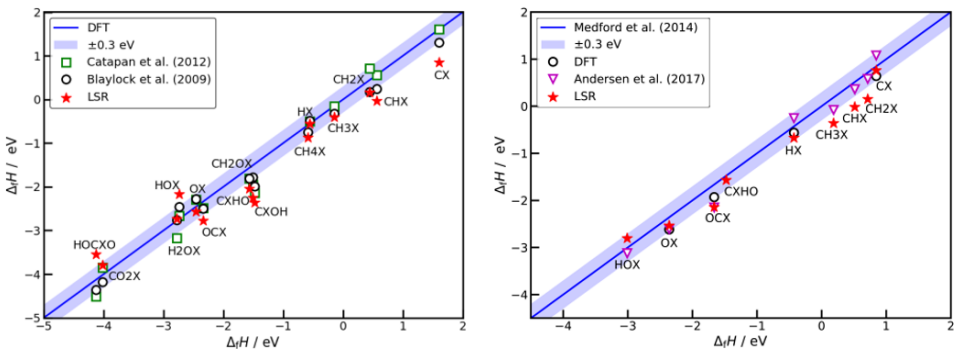

Figure 1: Parity plot of the standard heat of formation of the adsorbates predicted by linear scaling relations for Ni(111) and Ni(211) and the values calculated from the DFT calculations.

The scaling based on the (111) surface is relatively accurate, with a mean absolute error (MAE) of 0.41 eV to the heat of formation from the DFT calculation and 0.22 eV to the values from Blaylock et al. (2009). Values from Blaylock et al. (2009) and Catapan et al. (2012) are also depicted to illustrate that there is also a distinct difference between the DFT calculations, which is caused by the different pseudopotentials and exchange-correlation functionals. For the thermochemistry of the (211) surface, the values from Medford et al. (2014) are arbitrarily chosen as the reference, which results in a MAE of 0.33 eV. In conclusion, RMG-Cat can accurately estimate the thermochemistry of the adsorbates of the investigated Ni facets.

For the conditions mentioned in Table 1, RMG-Cat discovers 28 [27] species and 47 [38] reactions for the Ni(111) [Ni(211)] facet. The model generation takes approx. 2 min on an Intel i7-8565U processor. In the edge mechanism, RMG-Cat stores an additional 55 species and 76 reactions. The mechanism contains 15 [15] reactions from a library for steam reforming on Ni from Delgado et al. (2015) and the rest of the reactions is determined from reaction families such as dissociation (7 [8]) , van-der-Waals adsorption (5 [5]), and abstraction reactions (18 [11]). Two [one] reactions are discovered from a newly implemented family for the dissociation of a molecule in the "beta" position, which considers the formation of COH^* from CO^* since it is discussed as the rate-limiting step by Andersson et al. (2008), with BEP parameters from Sutton and Vlachos (2015). The generated microkinetic model is evaluated with a model of the Berty reactor. Figure 2 shows a reaction path analysis of this model when tracking carbon.

Ni(111)

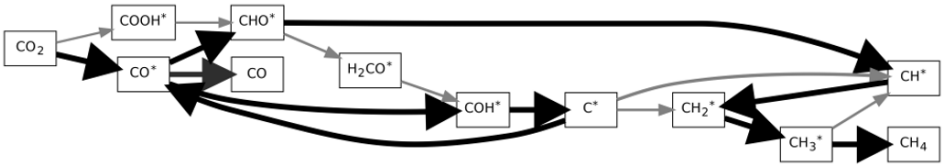

Ni(211)

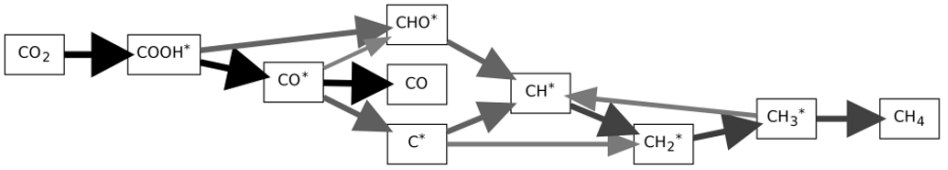

Figure 2: Reaction path analysis for the steady-state CO_2 methanation on the Ni(111) (upper) and Ni(211) (lower) surface. The thickness of the arrow illustrates the reaction rate. The reaction path analysis is conducted with a model of the Berty reactor in Cantera. *Conditions: T=400 °C, p=5* bar*,* m_{cat}*=0.3* g*,* a_{cat}*=10* $m^2\ g^{-1}$*,* V*=299* $mL_N\ min^{-1}$*,* V_R=88 mL.

On the Ni(111) facet CO_2 adsorbs via a dissociative adsorption and CO^* is further hydrogenated to CHO^* and COH^*. The unassisted dissociation of CO^* to surface carbon does not proceed with a sufficient rate at these conditions. It is interesting to note that COH^* decomposes to C^*, which is then again oxidized to CO^*. Carbon monoxide also desorbs in significant amounts from the surface, which is contradictory to the experiment because the Ni/Al_2O_3 catalyst shows a high selectivity towards methane. The dominant pathway at these conditions passes over CHO^*, which undergoes an O^* abstraction reaction. The methylene species is further hydrogenated to methane. A carboxyl route ($COOH^*$) contributes only to a small extent to the overall rate on the (111) surface. However, CO_2 adsorbs with the assistance of hydrogen on Ni(211) and

forms $COOH^*$, which dissociates to OH^* and CO^*. On the (211) surface, CO^* dissociates to C^*, because of a reduced activation energy for the dissociation by the stepped surface. Figure 3 (a) compares the methane yield from steady-state experiments to the simulation results, obtained from a model of the Berty reactor with the generated microkinetics, and the corresponding equilibrium yield.

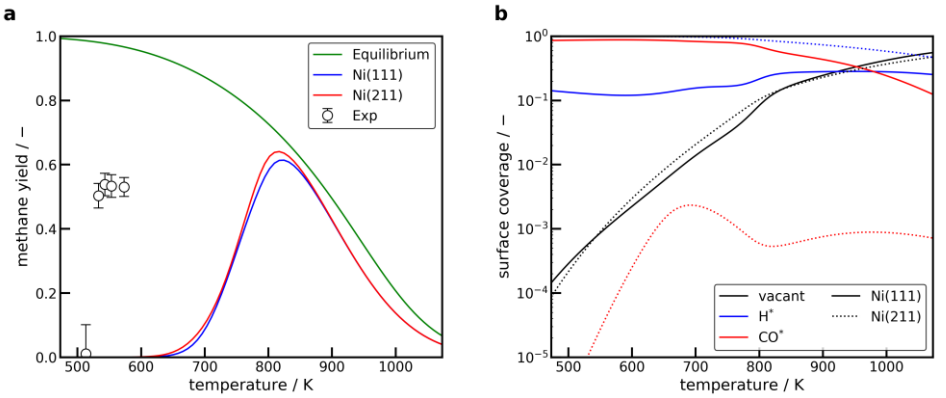

Figure 3: (a) Comparison of the steady-state results from the Berty reactor simulations with the generated microkinetic models for the two surfaces and experimental data from an 11 wt.-% Ni/Al_2O_3 catalyst. (b) Simulated steady-state surface coverages of the most abundant adsorbates. *Conditions:* $p=5$ bar, $m_{cat}=0.3$ g, $a_{cat}=10$ m^2 g^{-1}, $V=299$ mL_N min^{-1}, $V_R=88$ mL, *Feed:* $x_{CO_2}=13.81$ %, $x_{H_2}=55.25$ %, $x_{He}=7.69$ %, $x_{Ar}=23.2$ %.

At a temperature of 573 K, a methane yield of 53 % is measured in the experiment. The microkinetic model, however, shows a low yield, with a methane production only at temperatures above 650 K. At lower temperatures, the most abundant adsorbate on the (111) facet is CO^*, which prohibits H_2 from adsorbing. This results in an extremely low reaction rate and the hydrogen deficiency leads to a formation of CO, as shown in the reaction path analysis. At high temperatures, does the CO^* coverage decrease, which allows the H^* concentration to increase, resulting in a high methane formation rate. An H^* covered (211) surface is predicted due to an estimated lower CO^* binding energy. This surface needs further investigation because of the sparsely populated thermochemical database. The comparison to the calculated equilibrium composition shows that the predicted methane yield does not exceed the thermodynamic limit, which indicates a thermodynamic consistent microkinetic model. For the improvement of the microkinetics, it is necessary to include coverage effects, e.g. coverage dependent heat of formation of the adsorbates, to increase the low-temperature reaction rates (Lausche et al., 2013).

Conclusions

It was shown that generating a microkinetic model for the CO_2 methanation with RMG-Cat is possible and results in a mechanism, which is in good agreement with mechanisms discussed in the literature. The usage of the generated microkinetics in a model of the Berty reactor results in a low CH_4 formation rate. Analysis of the results reveals that the surface is mostly covered by one species (CO^*, H^*) at low temperatures. Consequently, coverage effects need to be considered to bridge the gap between experiments and simulation. In future work, sensitivity analysis will be applied to the generated mechanism to explore the most important elementary reactions, for which rate parameters can then be refined based on transition-state theory calculations.

Acknowledgments

Bjarne Kreitz gratefully acknowledges financial support from the German academic exchange service (DAAD) for a research stay at Brown University in the group of Franklin Goldsmith.

References

F. Abild-Pedersen; J. Greeley, F. Studt, J. Rossmeisl, T. R. Munter, P. G. Moses, E. Skúlason, T. Bligaard, J. K. Nørskov, 2007, Scaling properties of adsorption energies for hydrogen-containing molecules on transition-metal surfaces, Phys. Rev. Lett., 99, 1, 16105

M. Andersen, C. P. Plaisance, K. Reuter, 2017, Assessment of mean-field microkinetic models for CO methanation on stepped metal surfaces using accelerated kinetic Monte Carlo, J. Chem. Phys., 147, 15, 152705

M. P. Andersson, F. Abild-Pedersen, I. N. Remediakis, T. Bligaard, G. Jones, J. Engæk, O. Lytken, S. Horch, J. H. Nielsen, J. Sehested, J. R. Rostrup-Nielsen, J. K. Nørskov, I. Chorkendorff, (2008), Structure sensitivity of the methanation reaction: H_2-induced CO dissociation on nickel surfaces, J. Catal., 255, 6-19

D. W. Blaylock, T. Ogura, W. H. Green, G. J. O. Beran, 2009, Computational Investigation of Thermochemistry and Kinetics of Steam Methane Reforming on Ni(111) under Realistic Conditions, J. Phys. Chem. C, 113, 12, 4898–4908

K. Blondal, J. Jelic, E. Mazeau, F. Studt, R. H. West, C. F. Goldsmith, 2019, Computer-Generated Kinetics for Coupled Heterogeneous/Homogeneous Systems: A Case Study in Catalytic Combustion of Methane on Platinum, Ind. Eng. Chem. Res., 58, 38, 17682–17691

R. C. Catapan, A. A. M. Oliveira, Y. Chen, D. G. Vlachos, 2012, DFT Study of the Water–Gas Shift Reaction and Coke Formation on Ni(111) and Ni(211) Surfaces, J. Phys. Chem. C, 116, 38, 20281–20291

K. Delgado, L. Maier, S. Tischer, A. Zellner, H. Stotz, O. Deutschmann, 2015, Surface Reaction Kinetics of Steam- and CO_2-Reforming as Well as Oxidation of Methane over Nickel-Based Catalysts, Catalysts, 5, 2, 871–904

W. C. Gao, J. W. Allen, W. H. Green, R. H. West, 2016, Reaction Mechanism Generator: Automatic construction of chemical kinetic mechanisms, Comput. Phys. Commun., 203, 212–225

C. F. Goldsmith, 2012, Estimating the Thermochemistry of Adsorbates Based Upon Gas-Phase Properties, Top. Catal., 55, 5-6, 366–375

C. F. Goldsmith, R. H. West, 2017, Automatic Generation of Microkinetic Mechanisms for Heterogeneous Catalysis, J. Phys. Chem. C, 121, 18, 9970–9981

M. Götz, J. Lefebvre, F. Mörs, A. McDaniel Koch, F. Graf, S. Bajohr, R. Reimert, T. Kolb, 2016, Renewable Power-to-Gas: A technological and economic review. Renew. Energy, 85, 1371–1390

A. C. Lausche, A. J. Medford, T. S. Khan, Y. Xu, T. Bligaard, F. Abild-Pedersen, J. K. Nørskov, F. Studt, 2013, On the effect of coverage-dependent adsorbate-adsorbate interactions for the CO methanation on transition metal surfaces, J. Catal., 307, 275-282

E. Mazeau, P. Satupte, K. Blondal, C. F. Goldsmith, R. H. West, 2019, Catalytic Partial Oxidation of Methane Using Linear Scaling Relationships and Sensitivity Analysis in RMG, submitted to ChemSystemsChem

A. J. Medford, A. C. Lausche, F. Abild-Pedersen, B. Temel, N. C. Schjødt, J K. Nørskov, F. Studt, 2014, Activity and Selectivity Trends in Synthesis Gas Conversion to Higher Alcohols, Top. Catal., 57, 1-4, 135–142

B. Kreitz, G. D. Wehinger, T. Turek, 2019a, Dynamic simulation of the CO_2 methanation in a micro-structured fixed-bed reactor, Chem. Eng. Sci., 195, 541-552

B. Kreitz, J. Friedland, R. Güttel, G. D. Wehinger, T. Turek, 2019b, Dynamic Methanation of CO_2 - Effect of Concentration Forcing, Chem. Ing. Tech., 166, 4, 276

G. Kresse, J. Furthmüller, 1996a, Efficient iterative schemes for ab initio total-energy calculations using a plane-wave basis set, Phys. Rev. B: Condens. Matter, 54, 16, 11169–11186

G. Kresse, J. Furthmüller, 1996b, Efficiency of ab-initio total energy calculations for metals and semiconductors using a plane-wave basis set. Comput. Mater. Sci., 6, 1, 15–50

J. E. Sutton, D. G. Vlachos, 2015, Ethanol Activation on Closed-Packed Surfaces, Ind. Eng. Chem. Res., 54, 16, 4213–4225

Sauro Pierucci, Flavio Manenti, Giulia Bozzano, Davide Manca (Eds.)
Proceedings of the 30th European Symposium on Computer Aided Process Engineering (ESCAPE30), May 24-27, 2020, Milano, Italy.
http://dx.doi.org/10.1016/B978-0-12-823377-1.50090-2

Custom-made Temporomandibular Joint Mechanical Simulation: Different Fixation Pattern

Anita G. Mazzocco,[a*] André L. Jardini,[b] Elifas L. Nunes,[c] Rubens Maciel Filho[a,b]

[a]*University of Campinas (Unicamp), Campinas, ZP: 13083-852, SP, Brazil* [b]*National Institute of Biofabrication (INCT BIOFABRIS), Campinas, ZP: 13083-852, SP, Brazil*
[c]*Medical School, São Paulo State University (Unesp), Botucatu, ZP: 18618-687, SP, Brazil*
anitagaia.mazzocco@gmail.com

Abstract

Nowadays Computed Aided Design (CAD) and additive manufacture technologies are widely used in orthopedic field. These technologies allow to build anatomic 3D model in CAD software from tomographic data and then to fabricate a replacement device matching patient specific anatomy. Temporomandibular joint (TMJ) is small size joint and its replacement surgery is complicated and requires specialized surgeons. Thus CAD allows surgery planning and custom-made TMJ prosthesis developing. This study shows a pre-operative step that is to simulate physiological mechanical loading of TMJ replacement device in Ansys software with the purpose of testing device mechanical resistance and verifying osseointegration. Correct fitting is the primary stability which is necessary for osseointegration process to take place and so replacement device gain long-term stability. Therefore different pattern of screw fixation are tested and the effect in terms of strain and stress generated is evaluated to predict post-implant mechanical behaviour.

Keywords: temporomandibular joint, custom-made, computer aided design, mechanical simulation, Ansys.

1. Introduction

Medical imaging was used initially for diagnostic purposes, nowadays with the advent of Computer Aided Design (CAD) technology and 3d printing, the health care is revolutionizing. Thus, Computed Tomography (CT) and Magnetic Resonance Imaging (MRI) provide detailed anatomic images to be processed with CAD software to create a three-dimensional computational model. This model allows surgeons to see patient anatomy in more concrete way and to plan and simulate surgery, not only in virtual view but also on physical 3d printed model (Altobelli et al. 1993; Liu et al., 2006). In orthopedics field, additive manufacturing provides customized surgical instrument, intraoperative guidance and custom-made implant production (Eltorai et al., 2015). Temporomandibular Joint (TMJ) is characterized by complex kinematics, small dimensions and difficult surgery that needs specialized surgeon. Thus, CAD and 3D printing technologies can be considered a relevant approach to investigate better replacement solutions. TMJ replacement device is developed to mimics TMJ in function and form, so it has to be able to withstand bite loading, imitate joint kinematics, be biocompatible and be osseointegrated in surrounding anatomical structure. To

osseointegration occur, primary stability is necessary, so correct fitting during surgery is a requisite for long-term stability. This study aims to analyze the effect on mechanical behavior of TMJ custom-made prosthesis, manufactured from tomographic data, of five different pattern of screw fixation, by Finite Element Analysis (FEA).

2. Materials and methods

FEA is performed using Ansys Workbench (Swanson Analysis, Canonsburg, PA, USA), TMJ mandible model is constructed by CT-data and TMJ condylar prosthesis is created by SolidWorks (Dassault Systèmes, SolidWorks Corporation) and Magics (Materialise, Belgium). Mandible finite element model is composed by linear tetrahedral elements and condylar prosthesis by linear hexagonal element. Whole model is formed by 40030 nodes and 187931 elements. Mandible is modeled as cortical bone characterized by isotropic and linear elastic material (Hsu et al. 2011) with 13 GPa elastic modulus and 0.3 Poisson ratio. TMJ condylar replacement device is implanted on the right mandibular ramus. Since we want to simulate a prosthesis manufactured with 3d printing, the material used is a titanium alloy (Ti6Al4V) and properties derived from mechanical characterization of Ti6Al4V ELI produced by DMLS (Direct Metal Laser Sintering) technology (Longhitano et al. 2018). Thus, condylar prosthesis properties are 110 GPa of elastic modulus and 0.3 Poisson ratio. Fixation system is composed by five cylindrical screw of 2.7 mm diameter, made with commercial Ti6Al4V ELI (120 GPa elastic modulus and 0.3 Poisson ratio).

2.1. Muscular force and boundary conditions

FEA realizes a static structural analysis of TMJ replacement system subjected to bite loading to calculate mechanical response in terms of stress and strain produced. Thus, bite loading is simulated applying muscular force of six masticatory muscle on virtual model. The model is fully constrained at condyle extremities and vertical movement, along z axis, is blocked at incisors (Huang et al. 2015). Screw contact is modeled as bonded to simulate bi-cortical locking fixation system and bone-implant contact as frictional with a friction coefficient of 0.3 (Shirazi-Adl et al., 1993). Muscular forces magnitude and directions are shown in Table 1 and they derive from validated model (Korioth and Hannam 1994; Huang et al. 2015). In this study unilateral bite on Right Molar (RMOL) and Left Molar (LMOL) is simulated blocking the movement respectively on right and left molar. Figure 1.A shows whole finite element model and the number of screw positions. The different fixation pattern tested are the following: Pattern 1) 1, 2, 5, 9, 10; Pattern 2) 1, 2, 4, 7, 10; Pattern 3) 1, 3, 6, 9, 10; Pattern 4) 2, 3, 4, 7, 10; Pattern 5) 1, 2, 3, 7, 10.

Table 1. Muscular Forces. The following values refer to forces applied to right mandibular ramus; the corresponding forces on left are obtained by inverting x-direction forces.

	RMOL			LMOL		
	Fx	Fy	Fz	Fx	Fy	Fz
Superficial Masseter	-28.38	-57.44	121.32	-23.65	-47.87	101.10
Deep Masseter	-32.08	21.03	44.53	-26.73	17.53	37.11
Medial Pterygoid	71.36	-54.62	116.14	50.97	-39.02	82.96
Anterior Temporal	-17.19	-5.07	113.96	-13.65	-4.03	90.54
Middle Temporal	-13.94	31.55	52.81	-14.16	32.03	53.61
Posterior Temporal	-9.28	38.14	21.14	-6.13	25.21	13.98

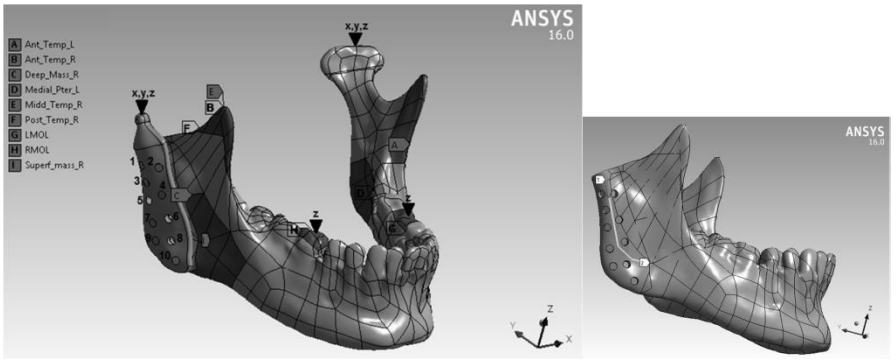

Figure 1. A) Finite Element Model with muscular forces and boundary conditions; and screw position number. B) Control line: Ansys collects strain variations on this control line from 1 to 2.

3. Result and discussion

The aim of this study is to analyze how different positions of fixation screws influence mechanical behavior of TMJ replacement subjected to right and left unilateral bite. Thus, results collected in Ansys are equivalent Von Mises stress on TMJ condylar prosthesis and distribution of minimum principal elastic strain on mandibular bone. According to previous studies (Van Loon et al. 1998; Huang et al. 2015; Mazzocco et al. 2019), unilateral bites are more critical loading cases than bilateral bite. Unilateral bite causes an overloading on contralateral side, also called balancing side, of about two times clenching side. Results of equivalent stress calculated on TMJ condylar prosthesis shows that maximum stress in LMOL case are about four times greater than maximum stress in RMOL (Fig. 2-3), moreover, distribution of strain collected in LMOL is almost twice the RMOL (Fig. 3-4). Distribution of stress on prosthesis in all cases simulated does not reach material yield stress (Ackland et al., 2015) and presents that maximum occurs at first screw holes: in RMOL, stress is concentrated on positions number 1-5, instead in LMOL simulation it is concentrated on position screws 1-3. Both in RMOL and LMOL cases, Pattern 1 generates the minor loading of 42.5 MPa and 182.7 MPa, respectively. The major loading in case of bite on working side (RMOL) is found with Pattern 3, instead in case of bite on balancing side (LMOL) Pattern 4 produces major stress.

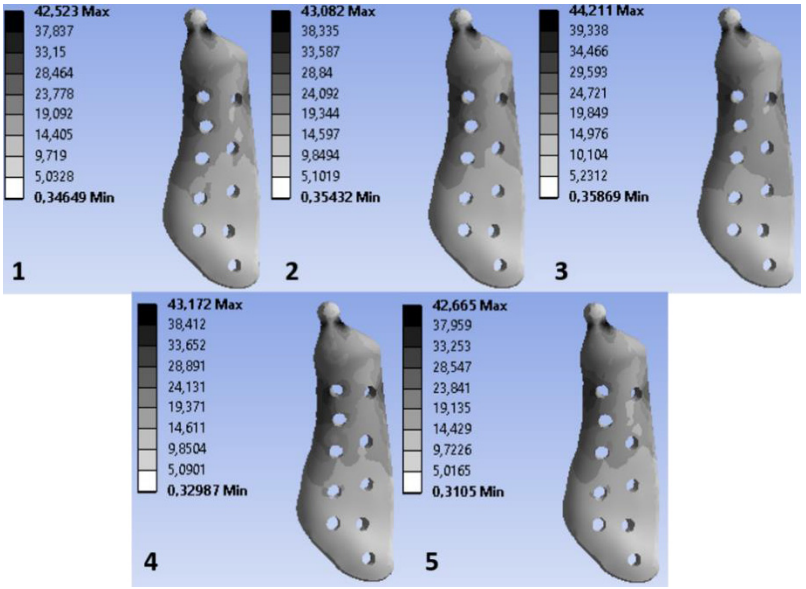

Figure 2. Equivalent Von Mises Stress [MPa] on TMJ condylar prosthesis in RMOL simulation.

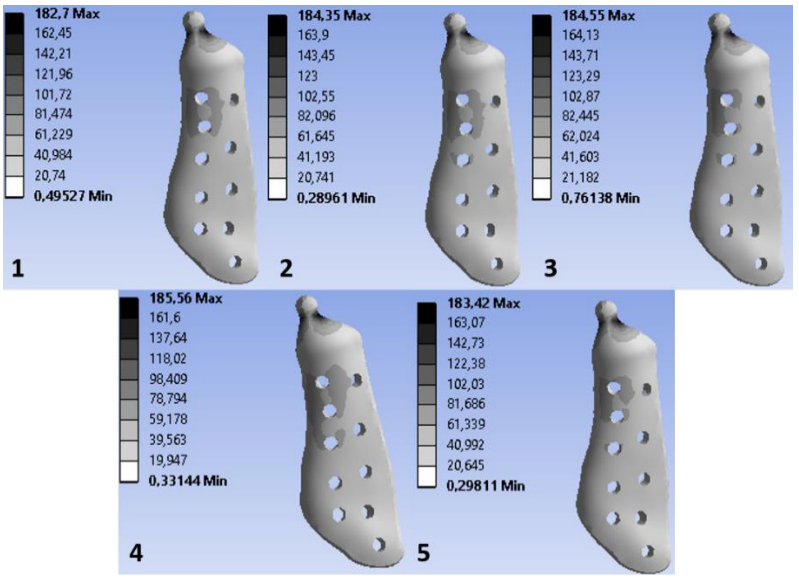

Figure 3. Equivalent Von Mises Stress [MPa] on TMJ condylar prosthesis in LMOL simulation.

Distribution of Minimum Principal Elastic Strain in case of RMOL (Fig. 4) on mandibular bone in contact with prosthesis shows that closest to condyle resection Pattern 1, Pattern 2 and Pattern 3 present the smallest strain peak of 1.1e-4 mm/mm. These patterns are characterized by initial screws fixed on positions 1 and 2. Pattern 3 produces two strain peaks of 1.95e-4 and 1.6e-4 mm/mm caused by screws 1 and 3; Pattern 4 (without any screw in position 1) presents major initial strain of 2.3e-4 mm/mm. In Pattern 3 and Pattern 5, the strain increase at 10 mm from point 1 of control line is caused by screw number 6 and 7 without any screw fixed in position 4 or 5. Unlike RMOL, Figure 4 shows maximum strain occurring at 10 mm on control line of

4e-4 mm/mm. This maximum is reached by Pattern 3 and Pattern 5, probably due to the absence of screw in position 4, 5. Similarly to RMOL, Pattern 4 produces the largest strain of 2.7e-4 mm/mm closest to condyle resection.

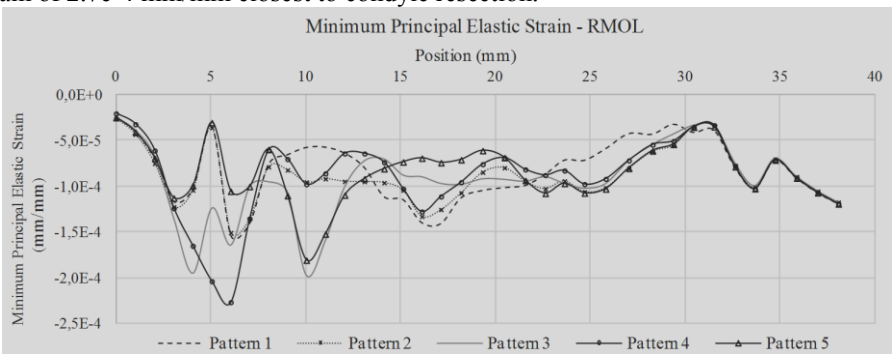

Figure 4. Minimum Principal Elastic Strain collected on control line in RMOL simulation.

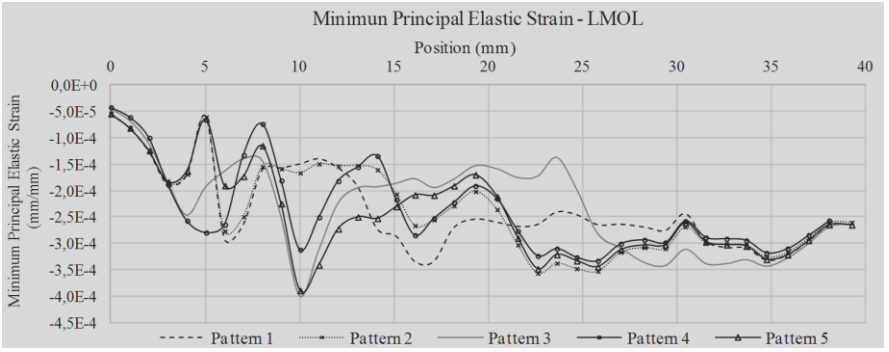

Figure 5. Minimum Principal Elastic Strain collected on control line in LMOL simulation.

4. Conclusion

Literature of FEA of TMJ fixation screw offers the following findings: minimum of three staggered screws provides stable fixation and good strain distribution (Hsu et al., 2011), and maximum stresses occurred at the first screw hole closest to condyle resection (Kashi et al., 2010). According to results collected, this study reveals that to solve overload problem on the first screw it should require to insert a screw laterally to the first one than inferiorly and that staggered distribution of screw is preferable because it distributes strain along bone. Thus, considering that TMJ prosthesis does not run any failure risk and therefore focusing on strain distribution, Pattern 2 can be considered biomechanically the best. Moreover, Roberts theory (Roberts et al., 2004) of bone remodeling explains that dynamic loading included within 0.2–2.5e-3 mm/mm produces bone remodeling and if strain peaks are lowest than 0.2e-3 mm/mm bone undergoes atrophy and if strain peaks exceed 2.5e-3 mm/mm it undergoes bone hypertrophy. Considering that mastication cycle by which TMJ is physiologically loaded, is a combination of bilateral and unilateral bite and that LMOL result are included in remodeling range, it might be considered that in this study TMJ replacement with fixation Pattern 2 should undergo osseointegration in mandibular bone.

This FEA result shows how CAD technology is considered revolutionizing the medical field because it allows planning a customized surgery decreasing the risk of TMJ replacement failure and optimizing the surgery time.

References

Altobelli, D. E., Kikinis, R., Mulliken, J. B., Cline, H., Lorensen, W., Jolesz, F. (1993), *Computer-Assisted Three-Dimensional Planning in Craniofacial Surgery*. Plastic and Reconstructive Surgery, 92 (4): 576–77.

Eltorai, A. E., Nguyen, E., Daniels, A. H. (2015), *Three-Dimensional Printing in Orthopedic Surgery.* Orthopedics, 38 (11): 684–87, DOI: https://doi.org/10.3928/01477447-20151016-

Hsu, J. T., Huang, H. L., Tsai, M. T., Fuh, L. J., Tu, M. G. (2011), *Effect of Screw Fixation on Temporomandibular Joint Condylar Prosthesis.* J Oral Maxillofac Surg, 69 (5): 1320–28. DOI: https://doi.org/10.1016/j.joms.2010.05.074.

Huang, H. L., Su, K. C., Fuh, L. J., Chen, M. Y., Wu, J., Tsai, M. T., Hsu, J. T. (2015). *Biomechanical Analysis of a Temporomandibular Joint Condylar Prosthesis during Various Clenching Tasks.* J Craniomaxillofac Surg, 43 (7): 1194–1201. DOI: https://doi.org/10.1016/j.jcms.2015.04.016.

Kashi, A., Chowdhury, A. R., Saha, S. (2010) *Finite element analysis of a TMJ implant,* J Dent Res, 89(3): p. 241-5.

Korioth, T. W., Hannam, A. G., (1994). *Deformation of the Human Mandible during Simulated Tooth Clenching.* J Dent Res 73 (1): 56–66. DOI: https://doi.org/10.1177/00220345940730010801.

Liu, Q., Leu, M. C., Schmitt, S. M., (2006) *Rapid Prototyping in Dentistry: Technology and Application.* The International Journal of Advanced Manufacturing Technology 29 (3): 317–35. DOI: https://doi.org/10.1007/s00170-005-2523-2.

Longhitano, G. A., Larosa, M. A., Jardini, A. L., de Carvalho Zavaglia, C. A., Filippini Ierardi, M. C., (2018) *Correlation between Microstructures and Mechanical Properties under Tensile and Compression Tests of Heat-Treated Ti-6Al–4V ELI Alloy Produced by Additive Manufacturing for Biomedical Applications.* Journal of Materials Processing Technology 252: 202–10. DOI: https://doi.org/10.1016/j.jmatprotec.2017.09.022.

Loon, J. P., Otten, V. E., Falkenstrom, C. H., de Bont, L. G., Verkerke, G. J. (1998) *Loading of a Unilateral Temporomandibular Joint Prosthesis: A Three-Dimensional Mathematical Study.* J Dent Res 77 (11): 1939–47. DOI:https://doi.org/10.1177/00220345980770111201.

Mazzocco, A. G., Jardini, A. L., Nunes, E. L., Maciel Filho, R. (2019) *Custom-Made Temporomandibular Joint Prosthesis: Computer Aided Modeling and Finite Elements Analysis.* Chemical Engineering Transactions. DOI: https://doi.org/http://dx.doi.org/10.3303/CET1974249.

Roberts, W. E., Huja, S., Roberts, J. A., (2004) *Bone modeling: biomechanics, molecular mechanisms, and clinical perspectives*, Seminars in Orthodontics, 10, 2, 123-161.

Shirazi-Adl, A., Dammak, M., Paiement G. (1993) *Experimental Determination of Friction Characteristics at the Trabecular Bone/Porous-Coated Metal Interface in Cementless Implants*. J Biomed Mater Res 27 (2): 167–75. DOI:https://doi.org/10.1002/jbm.820270205.

Sauro Pierucci, Flavio Manenti, Giulia Bozzano, Davide Manca (Eds.)
Proceedings of the 30th European Symposium on Computer Aided Process Engineering (ESCAPE30), May 24-27, 2020, Milano, Italy.
http://dx.doi.org/10.1016/B978-0-12-823377-1.50091-4

Cluster Analysis of Crude Oils based on Physicochemical Properties

Andre Sancho,[a,b] Jorge C. Ribeiro,[b] Marco S. Reis,[c] Fernando G. Martins[a*]

[a]*LEPABE, Chemical Engineering Dpt., Faculty of Eng.University of Porto, Portugal*

[b]*Petrogal SA, Laboratory of Matosinhos Refinery, Rua Belchior Robles, 4452-852 Leça da Palmeira, Matosinhos*

[c]*CIEPQPF, Department of Chemical Engineering, University of Coimbra, Rua Sílvio Lima, 3030-790 Coimbra, Portugal*

fgm@fe.up.pt

Abstract

The physicochemical properties of the crude oils can vary significantly, depending on their sources. While cheaper crude oils are desirable, the selection and blending operations should also take into consideration the potential operational problems on the downstream processing units. Cluster analysis is a data science technique that groups observations based on their similarity. By clustering crude oils based on their properties, it is expected that observations within a cluster will present similar behavior in the refining process. In this work, a data set from Galp's refineries containing 418 observations, with 9 properties, from 38 different sources was used. K-means clustering was applied after preprocessing and good results were obtained by selecting both 3 and 8 clusters, with only 0.7% and 3.7%, respectively, being placed in different clusters than the one with the highest family representation. This method also identified some observations with abnormal properties such as iron content. These results show the potential of grouping crudes based on their properties and the capability of finding potential outliers. This work allows the refineries to know how similar different sources are, potentially improving the task of formulating crude oil blends.

Keywords: crude oil; cluster analysis; k-means

1. Introduction

Crude oils are composed mostly by different organic components, containing also metals, sulfur, nitrogen and oxygen (Silva et al., 2011). The amount of each component in crude oil varies, depending on the crude geographic source and on the petroleum reservoir itself, causing crude oils to have physicochemical properties within a wide range of values. It is of economic interest to process cheaper crude oils, but these contain more impurities, which can cause operational problems on the downstream processing units.

With the increasing amount of data available in the industry, the use of data science techniques to extract additional knowledge is becoming popular (Hassani and Silva, 2018). Cluster analysis is an unsupervised method that groups information in clusters, where a cluster is a group of observations that are similar to each other and dissimilar to those in other clusters. By grouping crude oils based on their physicochemical properties using cluster analysis, it is expected that crude oils within a cluster will present similar behavior during the refining process.

2. Background

Crude oils are typically characterized based on their API gravity and sulfur content. Lighter crude oils tend to produce products with high added value, but are generally more expensive, while heavier crudes tend to be cheaper, but have more impurities. Depending on the amount of sulfur content, a crude can be considered "sweet" or "sour", with the latter requiring more intense treatment in the refining process. More recently, advanced characterization techniques such as near-infrared spectroscopy (Falla et al., 2006), nuclear magnetic resonance spectroscopy (Masili et al., 2012) and gas chromatography (El Nady et al., 2014) have also been used to successfully determine physicochemical properties of crude oils.

Cluster Analysis is used in a wide range of fields, including the chemical industry. However, applying cluster analysis to crude oils has been done scarcely, and usually confined to the use of techniques such as dendogram (Onojake et al., 2015) and swarm particle clustering (Ferreira et al., 2017) to compare against the typical crude classification based on the density.

3. Methods

The data set used in the present work was composed by the crudes processed in Matosinhos and Sines refineries of Galp in the last years, containing 418 observations from 38 different crude oils sources (here designated by families), and with the following measured properties: API; sulfur content; pour point; acidity; CCR content; nickel content; vanadium content; iron content; vanadium-nickel ratio. The data set was firstly preprocessed using the following techniques:

- For "less than" entries, the inequality values were assumed;
- For "more than" entries, the values were replaced using the mean based on observations of the crude oils from the same family that have higher values. If there are no higher values, the inequality values were assumed;
- Zero values were replaced by the lower detection limits;
- A mean value imputation technique was applied to missing values using the crude oils from the same family.

While the purpose of cluster analysis is to group observations in different groups, which implies that they have different properties from each other, outliers can worsen the results of centroid based clustering by shifting the kernel of the clusters in order to be accommodated. Typical outlier detection tools such as box plot with standard deviations, while good for univariate problems, are not adequate for multivariate data. Thus, the Mahalanobis (1936) distance was applied for this purpose as a multivariate metric that also takes into account the correlation between properties. The last preprocessing technique implemented was standardization by z-scores.

Cluster analysis was performed using the k-means clustering method (Lloyd, 1982), available in the scikit-learn library for *python*, and the silhouette score (Rousseeuw, 1987) was used as the internal validation metric to determine the best number of clusters for both low and high discrimination.

While the clusters are determined by k-means, typically, it is of interest to visualize graphically the results. This however is a challenging task for high dimensional data, and

while it is always possible to do pairwise plots, each alone cannot show all the variables' interactions. So, a data reduction technique to project this high dimensional data to 2D was needed. For this, the uniform manifold approximation and projection, UMAP, (McInnes et al., 2018) technique was chosen and applied.

4. Results

4.1. Outlier Detection

Figure 1 shows the violin plot of the data set, and presents the cutoff point determined by the Mahalanobis distance. 10 observations were considered outliers and excluded from the data set.

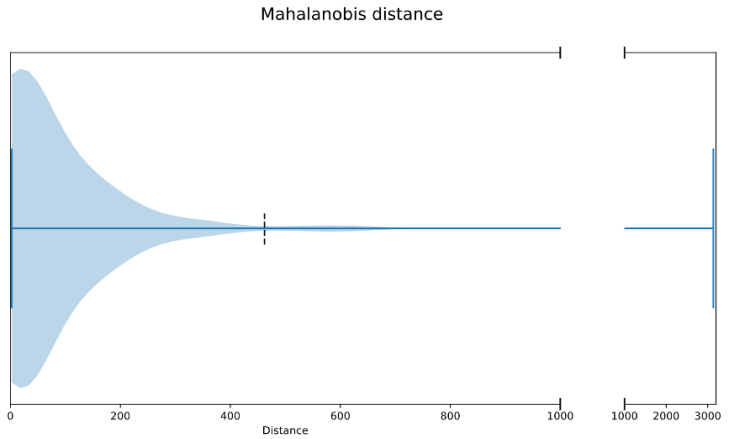

Figure 1: Mahalanobis distance for the crude oils data.

4.2. Cluster Analysis

The optimal number of clusters was selected based on the mean silhouette value, giving high values for 3 and 8 clusters. Thus, these were the selected number of clusters, corresponding to a low and high discriminant power.

The crude oils distributions for 3 and 8 clusters were analyzed by families and are shown on Table 1 and Table 2, respectively. It was verified that only 0.7% and 3.7%, for 3 and 8 clusters, respectively, were placed in different clusters than the one where it is found the highest representation of observations from the same crude oil family. As an example, the crude oil family XU (Table 1), composed by 14 different observations, had all but one of its observations allocated to cluster A for the 3 clusters case.

To visualize the high dimensional data, UMAP was applied to the data set and as a post-processing step, the observations were colored based on the clustering results. Figure 2 and Figure 3 show the data projection for 3 and 8 clusters, respectively, where the different crude oils cluster are displayed by the datapoint shape.

Table 1: Crude oil distribution (3 clusters).

A	187	B	132	C	89
CQ	58	BQ	3	CE	1
FC	4	CL	34	CF	3
GU	16	EV	2	DD	42
JF	65	FS	1	EF	3
NV	1	HU	1	GE	1
OV	24	MG	1	HF	1
XU	13	OI	33	IM	2
ZC	5	RJ	1	IV	2
ZS	1	RX	49	LU	1
		SE	2	ON	1
		SW	1	RF	4
		UV	1	SW	1
		XJ	3	UM	7
				XU	1
				YC	19

Table 2: Crude oil distribution (8 clusters).

A	77	B	65	C	108	D	26	E	86	F	29	G	8	H	9
CQ	58	CL	33	BQ	3	FC	4	JF	63	DD	2	CE	1	CL	1
JF	1	EV	1	CF	3	GU	16	OV	23	EF	3	UM	7	EV	1
ON	1	OI	31	DD	40	NV	1			HF	1			JF	1
RJ	1			FS	1	ZC	5			IV	1			OI	2
SW	1			GE	1					RF	3			OV	1
XU	14			HU	1					YC	19			RF	1
ZS	1			IM	2									RX	2
				IV	1										
				LU	1										
				MG	1										
				RX	47										
				SE	2										
				SW	1										
				UV	1										
				XJ	3										

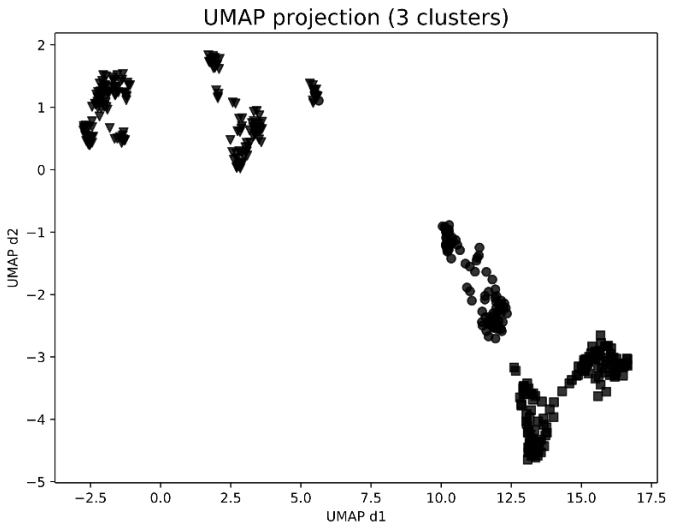

Figure 2: UMAP projection (3 clusters).

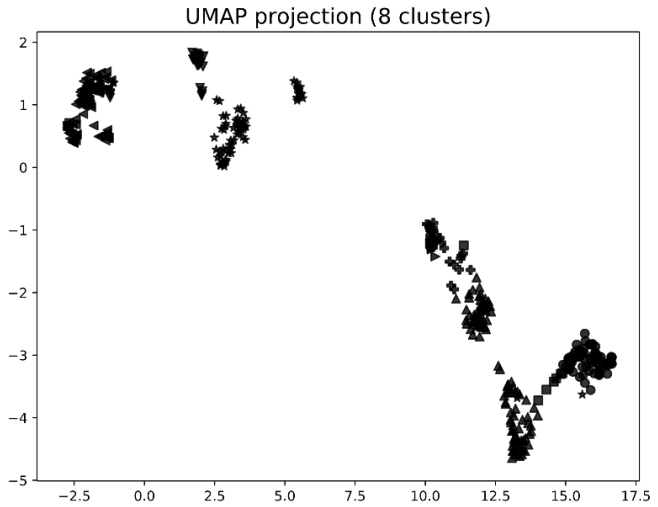

Figure 3: UMAP projection (8 clusters).

5. Discussion

The results show that the crude oils properties data is highly clusterable, and that, with few exceptions, crude oils from the same family are clustered together. After a closer look into the observations placed on different clusters, it was noted that they have some abnormal properties, when compared to the rest of the family members.

When comparing the crude families in both 3 and 8 clusters, it was found that the 8 clusters are primarily subclusters of the former. This behavior is beneficial and helps to further understand the relationships between clusters.

In the case of 8 clusters, one of them was composed solely by observations with abnormally higher amounts of iron when compared to the rest of their families. This is shown in Figure 4, for crude of the family RX.

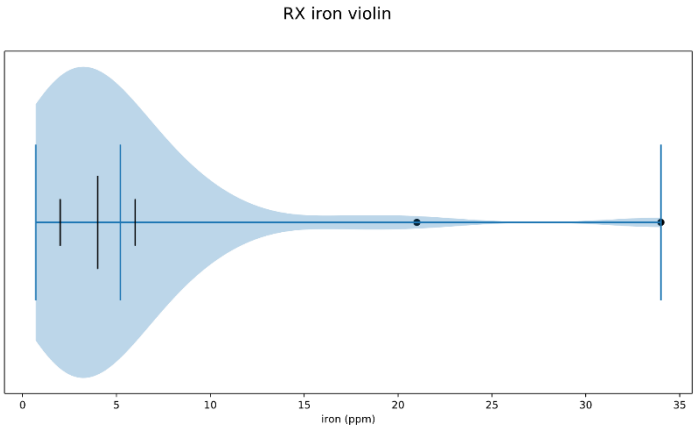

Figure 4: Violin plot for the RX crude family.

6. Conclusions

These findings demonstrate the potential of grouping crude oils based on their physicochemical properties. The k-means method gave good results for 3 and 8 clusters, with most of the observations of each family being allocated to the same cluster. It was also shown the capability of detecting crude oils with abnormal properties. The 8 clusters correspond to a further subdivision of the crude oils groups for 3 clusters, with one cluster being composed by observations with rather abnormal properties.

The information about the clusters can be very usefully in the plant management, namely: i) to improve the refining operations, where operating conditions and challenges can be associated to each cluster; ii) to predict the behavior of a crude oil that is being processed the first time and; iii) to help in the decision-making of the crude oils to be processed, by formulating a blend that will fall in a desired cluster or to prevent the blending of certain crude oils that are allocated to incompatible clusters.

References

Silva, S. L., Silva, A. M., Ribeiro, J. C., Martins, F. G., Da Silva, F. A., & Silva, C. M. (2011). Chromatographic and spectroscopic analysis of heavy crude oil mixtures with emphasis in nuclear magnetic resonance spectroscopy: A review. Analytica Chimica Acta, 707(1-2), 18-37.

Hassani, H., & Silva, E. S. (2018). Big Data: a big opportunity for the petroleum and petrochemical industry. OPEC Energy Review, 42(1), 74-89.

Falla, F. S., Larini, C., Le Roux, G. A. C., Quina, F. H., Moro, L. F. L., & Nascimento, C. A. O. D. (2006). Characterization of crude petroleum by NIR. *Journal of petroleum science and engineering*, *51*(1-2), 127-137.

Masili, A., Puligheddu, S., Sassu, L., Scano, P., & Lai, A. (2012). Prediction of physical–chemical properties of crude oils by 1H NMR analysis of neat samples and chemometrics. *Magnetic Resonance in Chemistry*, *50*(11), 729-738.

El Nady, M. M., Harb, F. M., & Mohamed, N. S. (2014). Biomarker characteristics of crude oils from Ashrafi and GH oilfields in the Gulf of Suez, Egypt: An implication to source input and paleoenvironmental assessments. *Egyptian Journal of Petroleum*, *23*(4), 455-459.

Onojake, M. C., Abrakasa, S., & Osuji, L. C. (2015). Chemometric representation of molecular marker data of some Niger Delta crude oils. *Egyptian Journal of Petroleum*, *24*(2), 139-143.

Ferreira, F., Ciodaro, T., de Seixas, J. M., Xavier, G., & Torres, A. (2017). Clustering Crude Oil Samples Using Swarm Intelligence. XIII Brazilian Congress on Computational Intelligence.

Mahalanobis, P. C. (1936). On the generalized distance in statistics. *Proceedings of the National Institute of Sciences (Calcutta)*, 2:49-55.

Lloyd, S. (1982). Least squares quantization in PCM. IEEE transactions on information theory, 28(2), 129-137.

Rousseeuw, P. J. (1987). Silhouettes: a graphical aid to the interpretation and validation of cluster analysis. Journal of computational and applied mathematics, 20, 53-65.

McInnes, L., Healy, J., & Melville, J. (2018). Umap: Uniform manifold approximation and projection for dimension reduction. *arXiv preprint arXiv:1802.03426*.

Sauro Pierucci, Flavio Manenti, Giulia Bozzano, Davide Manca (Eds.)
Proceedings of the 30th European Symposium on Computer Aided Process Engineering (ESCAPE30), May 24-27, 2020, Milano, Italy.
http://dx.doi.org/10.1016/B978-0-12-823377-1.50092-6

Optimization and Control of a Rainwater Detention and Harvesting Tank

Qiao Yan Soh,* Edward O'Dwyer, Salvador Acha, Nilay Shah

Center for Process Systems Engineering, Department of Chemical Engineering, Imperial College London, London SW7 2AZ, UK
qiaoyan.soh13@imperial.ac.uk

Abstract

Decentralized rainwater detention tanks are usually implemented as a method for reducing rainfall runoff volumes entering centralized reservoirs and treatment plants, but these systems also provide the opportunity for harvesting and locally treating rainwater such that local demand for potable water can be reduced. Here we evaluate the effectiveness of real time control strategies in a detention and harvesting system as a primary step towards future-proofing existing urban drainage infrastructure against increased rainfall loads. The implementation of control strategies has allowed for a four-fold increase in harvested water yield and shows promise in reducing the tank capacities necessary in handling high rainfall intensities.

Keywords: Real-time Control, Rainwater harvesting, Urban Water Management

1. Introduction

Stormwater management systems play a crucial part in maintaining sanitation and livability in an urban environment by efficiently removing excess water from population centers. However, once the infrastructure for these systems has been built, these stormwater management strategies have remained largely unchanged and modifications typically relied on increasing the physical capacities of the system. Spatial constraints faced in well-established cities have spurred researchers to look to alternative methods for improving existing stormwater management infrastructure, resulting in a steady increase in literature in recent years focusing on real-time control (RTC) methods applied to urban water systems.

RTC methods in application to urban drainage systems have been around since the 1960s [2], but only in the last decade after rapid developments in control strategies have RTC methods become more feasible to implement in practice. Exploiting reduced costs in sophisticated sensor and communication systems that are now available, Bartos et al., 2018 developed a platform for more autonomous management of water systems in cities [1]. This has been implemented in a 4 km^2 watershed in Ann Arbor, Michigan by Wong et al. 2018 for flood mitigation and flow reduction purposes [6]. Rohrer and Armitage, 2017 have also used stormwater detention ponds in Cape Town, South Africa to demonstrate the rainwater harvesting potential of these systems, and the potential of RTC strategies in improving water yield without significant impacts to the flood mitigation performance [4]. A comprehensive review on the use of Model Predictive Control (MPC) strategies on urban drainage systems was presented by Lund et al., 2018, discussing the strategies and challenges faced by researchers in developing MPC systems into mature technology for this use case, highlighting the rate of innovation from cross-disciplinary teams over the globe [3].

This paper presents a comparative analysis of rule-based and proportional controllers in achieving improved system performances in terms of maximizing rainwater harvested and minimizing stress in a stormwater detention and harvesting tank. The system and a case study are presented in Section 2.1, where a base configuration is used to determine the impact of the control strategies outlined in Section 2.2. The results are discussed in Section 3, with further work and conclusions discussed in Section 4.

2. Methods

2.1. Tank system set up and working principles

The system explored in this paper is a three-tank water harvesting and detention system, shown in Figure 1. Rainwater enters the system through a first tank that acts as a separation filter, directing flow towards either the detention or the harvesting tanks. Water is held within the detention tank to ensure that rainfall runoff is efficiently collected but also discharged into the public drain network at a suitable rate. The harvesting tank is used to collect cleaner water that can be used to satisfy non-potable water demands in the residential estate. To reduce sedimentation and pollutants, water can only be directed into the harvesting tank 10 minutes after the start of the rain event.

This demand is satisfied through a pumped treatment system from the harvesting tank source, allowing improved water use efficiency in the urban environment as well as reducing costs associated with purchasing potable water. However, the local water demand is not necessary in achieving a representative study of the effects of implementing control strategies, and henceforth the harvesting tank will be treated as a collection tank.

The water tank is modelled using equations of motion derived from mass balances for each individual tank. Explicitly, the state dynamic equations for each tank j with area A_j and water levels H_j, follow Equations (1-3) where Q_k is the flowrate between the tanks through orifice or weir k.

$$A_s \frac{dH_s}{dt} = Q_{in}(t) - Q_1(t) - Q_2(t) - Q_3(t) \tag{1}$$

$$A_d \frac{dH_d}{dt} = Q_1(t) + Q_3(t) - Q_{out}(t) \tag{2}$$

$$A_h \frac{dH_h}{dt} = Q_2(t) \tag{3}$$

The discharge rate at each tank can be modelled as an orifice or a weir, introducing nonlinearities into the model. For a small, sharp edged orifice with an area a and a rectangular weir of length L, these can be derived from Bernoulli's principle[6] to follow Equations (4) and (5) respectively for a water level H above the orifice opening or weir height. The additional parameters are the discharge coefficient C_d, and gravitational constant g.

$$Q_{orifice}(t) = C_d\, a \sqrt{2gH(t)} \tag{4}$$

$$Q_{weir}(t) = \frac{2}{3} C_d\, L \sqrt{2g}\, H(t)^{\frac{3}{2}} \tag{5}$$

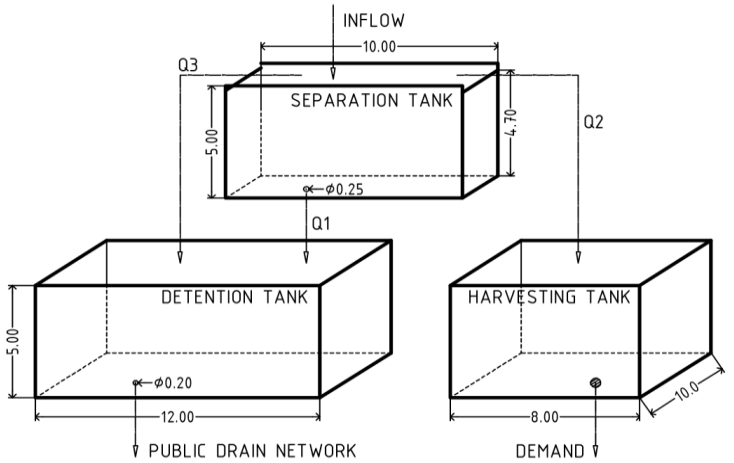

Figure 1: Tank schematic with parameter values used in the base configuration

2.1.1. Case Study

A base configuration was developed such that the constraints and fill rules are satisfied in a passive, uncontrolled system, and is used to evaluate the impact of each control strategy implementation. This can also be used as a simulation framework for determining a suitable strategy for the purposes of retrofitting an existing tank. In this configuration, $Q_1(t)$ and $Q_{out}(t)$ are modelled as small orifices, and $Q_2(t)$ and $Q_3(t)$ are weirs, and the parameter values used are as shown in Figure 1.

In developing suitable tank configurations for evaluation, the maximum depth allowable is defined to be 5 m. The case study area is based on a residential estate of 4.53 ha, and a detention tank servicing the entire estate would require a volume of 1250 m^3 with an allowable public drain discharge rate of 1.34 m^3/s.

2.2. Implemented Control Strategies

The passive, uncontrolled tank response was first determined to provide a baseline for evaluating the control strategies. In this section, the simulations consider the implementation of a control valve located at the orifice between the separation and detention tanks, adjusting $Q_1(t)$ only.

2.2.1. Rule-based Controller

The rule-based controllers implemented acts to open or close the valve based on the value of one or more monitored parameters. More specifically, these are the time elapsed since the start of the rain event, and tank water levels. The first strategy monitors the elapsed time such that cleaner runoff can be collected into the harvesting tank as soon as possible, where the valve leading to the detention tank is closed when harvesting can start taking place. The second strategy opens the same valve when the water level in the separation tank is close to capacity to prevent surface overflows.

A tuned rule-based controller for the base configuration was also implemented, monitoring time elapsed to ensure cleaner harvested water, as well as the harvesting tank water levels such that water can be discharged into the detention tank as quickly as possible once the harvesting tank is full.

2.2.2. Proportional Controller

The proportional controller adjusts the flowrate by changing the orifice area, calculated as a function of an error signal $\varepsilon(t)$, which is measured as the difference between the

observed and desired ("set point") tank levels [5]. The desired system behavior over the course of a rainfall event can be represented by a setpoint profile, $H_{sp}(t)$ and the control action $u(t)$ follows Equation (6), with proportional gain K.

$$u(t) = K \times \varepsilon(t) = K(H(t) - H_{sp}(t)) \quad (6)$$

The controller gain K is designed such that the orifice is fully open when the tank level exceeds a user-specified tank level. The separation tank set point profile $H_{sp}(t)$ implemented is a rectangular function that always minimizes the water level, except after the first 10 minutes of the event for a period sufficiently long for the harvesting tank to fill up completely. During this period, the water level is set just below the harvesting outlet height to ensure that there is no system overflow, as the controller action would result in a steady state offset above the new desired set point level.

2.3. Optimal Strategy

An idealized benchmark was developed to determine the most optimal performance achievable by the system. For the rainfall profile outlined above, an optimal strategy for a tank with the same volume configuration was determined for comparison purposes with the assumption that the flow rate between each tank can be fully controlled, such that these are only dependent on the volume of water available in the source tank. This was formulated as an LP problem and solved with GAMS [8]. The optimization objective was to maximize the amount of rainwater harvested, whilst maintaining a balance between minimizing the amount of water discharged into the public drain network and minimizing the use of the separation and detention tank volumes such that the system is able to handle a second rainfall event. Under this problem formulation, the optimal strategy can maximize the flow rates between each tank to the value allowable to enhance the system performance in each of the desired goals, outlined in the next section.

2.4. Rainfall input

The existing stormwater detention tanks are designed using a 10-year design storm with an average intensity of 193 mm/h. The Modified Rational Method assumes that the inflow hydrograph with the highest peak intensity is an event with a duration equal to the time of concentration of the catchment, which is the maximum time required for water to flow to the outlet from the furthest point in the catchment. Hence, in this study we seek to utilize the rainfall profile used in designing the systems, which corresponds to a 10-minute event with a peak inflow rate of 2.24 m^3/s.

3. Results

3.1. Key Performance Indicators

There are four key quantitative measures used to evaluate the system performance under the influence of each control strategy:

- Water harvesting potential, indicated by total amount of rainfall collected in the harvesting tank
- Risk of surface pooling, characterized by the ratio of the time-averaged water level in the separation tank after the rainfall event, and the maximum separation tank height.
- Tank size reduction, represented by the unused separation and detention tank capacities in the base configuration
- Public drain network integration, as indicated by the maximum public drain discharge rate.

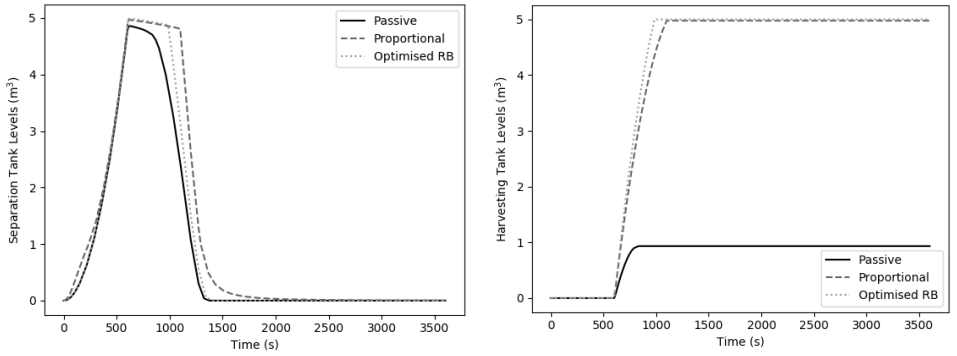

(a) (b)

Figure 2: Simulation results for the passive system baseline and optimized controlled systems for (a) Separation tank levels and (b) Harvesting tank levels.

3.2. Results and discussion

The response of the system and the impacts of the rule-based and proportional control strategies were evaluated for the 10-minute high intensity storm, over the course of an hour by which it would reach system steady state. Figure 2 shows the simulation results for the rule-based and proportional controllers in comparison to the equivalent passive system. The ideal separation tank performance should always minimize the water level but hold the water level close to the harvesting orifice when this element is desired.

To increase the harvested yield, both the rule-based and P-control approaches were designed to maintain a high separation tank water level to ensure that the water height was near the harvesting outlet. This in turn would tend to increase the pooling risk relative to the passive approach. This could be improved through optimizing the tank configuration for each control strategy. By virtue of requiring less water to pass through the detention tank route with a higher amount of water harvested, the tank capacity required to deal with a high intensity storm can be significantly lowered when there is a higher degree of control over the flow of water within the system.

Figure 3 shows the performance of each single-event control strategy with a control valve implemented at the primary separation to detention tank outlet only. The harvested yields are significantly increased in all the control strategies implemented, with the lowest performing control strategy demonstrating a 4.35-fold increase in the harvested yield.

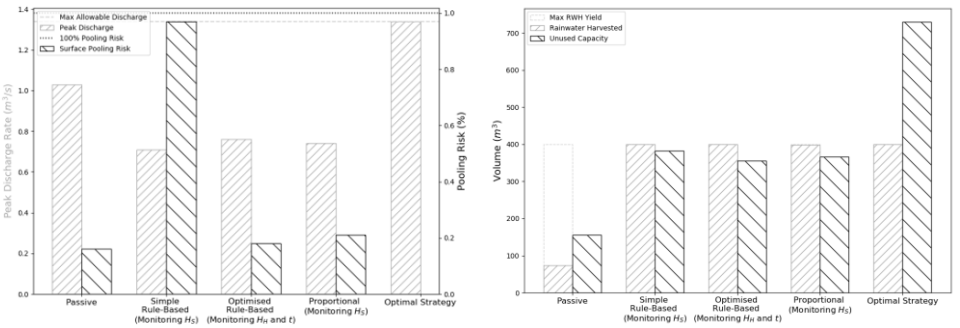

(a) (b)

Figure 3: Results of implemented control strategies in achieving desired KPIs of (a) Minimizing discharge rates and pooling risk and (b) Maximizing unused capacities and harvested water yield

Under the optimal strategy the controller utilizes the peak allowable discharge such that the system can maximize the amount of rainwater harvested, whilst draining the separation tank to achieve negligible pooling risk and high unused capacity in the separation and detention tanks.

4. Conclusion

The simulations show significant improvements to the stormwater management system in all the performance measures, demonstrating that simple retrofitting of actuators and controllers within a tank allows it to be more adaptable to change. However, for the implementations to be effective, expertise in the systems operations may be required in order to achieve an optimized controller with a suitable set point profile.

In cases where the tank configuration can be altered and further optimized, the system has the potential to handle much higher intensity rainstorms with the same volume capacity. However, further analyses should be taken to evaluate such an operation strategy on the downstream public drain network.

This study serves as a primary step towards future-proofing existing urban drainage infrastructure. The full potential of utilizing control strategies in this context can be realized with further work focusing on the system response towards longer, more extreme events and optimizing the control strategies in consideration of water demand profiles. A significant area of study could look at the potential of reducing the required tank volume using a virtual tank and combining the detention and harvesting tanks.

Acknowledgement

This research is supported by the Singapore Ministry of National Development and the National Research Foundation, Prime Minister's Office under the Land and Liveability National Innovation Challenge (L2 NIC) Research Programme (L2 NIC Award No. L2NICTDF1-2017-3). Any opinions, findings, and conclusions or recommendations expressed in this material are those of the author(s) and do not reflect the views of the Singapore Ministry of National Development and National Research Foundation, Prime Minister's Office, Singapore.

References

[1] Bartos, M., Wong, B., & Kerkez, B. (2018). Open storm: A complete framework for sensing and control of urban watersheds. Environmental Science: Water Research and Technology, 4(3), 346–358. https://doi.org/10.1039/c7ew00374a

[2] García, L., Barreiro-gomez, J., Escobar, E., Téllez, D., Quijano, N., & Ocampo-martinez, C. (2015). Modeling and real-time control of urban drainage systems: A review. 85, 120–132. https://doi.org/10.1016/j.advwatres.2015.08.007

[3] Lund, N. S. V., Falk, A. K. V., Borup, M., Madsen, H., & Steen Mikkelsen, P. (2018). Model predictive control of urban drainage systems: A review and perspective towards smart real-time water management. Critical Reviews in Environmental Science and Technology, 48(3), 279–339. https://doi.org/10.1080/10643389.2018.1455484

[4] Rohrer, A. R., & Armitage, N. P. (2017). Improving the viability of stormwater harvesting through rudimentary real time control. Water (Switzerland), 9(6). https://doi.org/10.3390/w9060371

[5] Ogunnaike, B.A. and Ray, W.H., 1994. Process dynamics, modeling, and control (Vol. 1). New York: Oxford University Press.

[6] Streeter, Victor L., Bedford, K. W, and Wylie, E. Benjamin. Fluid Mechanics. 9th ed. Boston: McGraw-Hill, 1998. Print.

[7] Wong, B. P., & Kerkez, B. (2018). Real- Time Control of Urban Headwater Catchments Through Linear Feedback: Performance, Analysis, and Site Selection. Water Resources Research, 54(10), 7309–7330. https://doi.org/10.1029/2018WR02265

[8] GAMS Development Corporation. General Algebraic Modeling System (GAMS) Release 27.1.0, Fairfax, VA, USA, 2019.

Sauro Pierucci, Flavio Manenti, Giulia Bozzano, Davide Manca (Eds.)
Proceedings of the 30th European Symposium on Computer Aided Process Engineering (ESCAPE30), May 24-27, 2020, Milano, Italy.
http://dx.doi.org/10.1016/B978-0-12-823377-1.50093-8

Modelling and Simulation of Methanol Production and Conversion into Various Chemical Intermediates and Products

Letitia Petrescu*, Stefan-Cristian Galusnyak, Dora-Andreea Chisalita,

Calin-Cristian Cormos

Babes-Bolyai University, Faculty of Chemistry and Chemical Engineering, Arany Janos 11, Postal code: RO-400028, Cluj-Napoca, Romania
letitiapetrescu@chem.ubbcluj.ro

Abstract

The present work is focused on process modeling and simulation of methanol production and conversion into various chemical intermediates and final products. Methanol synthesis is achieved by chemical reaction between CO_2 and H_2, this method being considered an important method for carbon dioxide valorization. The main advantages of this route are the reduction of greenhouse gas emissions and production of one valuable chemical, methanol. A productivity of 500 kmols/h of methanol was set in the present study. Methanol is furthermore converted into useful intermediates and products such as: *1)* acetic acid, *2)* dimethyl carbonate (DMC), *3)* formalin *4)* dimethyl ether (DME) *5)* biodiesel and *6)* methyl tert-butil ether (MTBE). The proposed design models were validated using data from the scientific literature. Purities higher than 99% for methanol and methanol derived products were achieved in all cases. The designs under investigation are compared from technical and environmental point of view leading to the conclusion that biodiesel and MTBE productions are the most convenient routes for methanol valorization.

Keywords: Methanol production; Methanol valorisation; CO_2 valorisation; Process design; Environmental evaluation.

1. Introduction

Nowadays methanol is considered to be an essential chemical for our society. It has applications in two important sectors: chemical industry and transportation sector. Each day, nearly 200,000 tons of methanol are used as raw-material for the production of various chemicals or as a transportation fuel. On one hand, in the chemical industry, formaldehyde, methyl tert-butil ether (MTBE), acetic acid, dimethyl ether (DME), TAME (tert-amyl methyl ether), biodiesel, DMT (dimethyl terephthalate), MMA (methyl metacrylate), dimethyl carbonate (DMC) are relevant products derived from methanol (Simões et al., 2013). On the other hand, methanol is considered to be a low-emission fuel. The NO_x emissions from methanol are approximately 45% of those from conventional fuels while the SO_x emissions are approximately 8% of those from conventional fuels per unit energy. The emissions reductions are due to the fact that methanol results in lower emissions during the combustion phase (IMO, 2016).

Methanol demand is continuously increasing due to its multiple ways of valorisation, the demand increase is supposed to expand more in the future (Jarvis and Samsatli, 2018). Methanol can be produced using several technologies and feed stocks (e.g. natural gas, coal and biomass) (Dalena et al., 2018). Most of the methanol produced industrially today is derived from syngas, a gaseous mixture of CO and H_2, most of it being produced from natural gas (Simões et al., 2013). Natural gas is converted to syngas using steam in the well-known reforming technology. Furthermore, syngas reacts over a $CuO/ZnO/Al_2O_3$ catalyst at 250-300°C and 10 MPa to produce methanol and water (Jarvis and Samsatli, 2018).

In recent years, several research groups and studies have considered methanol synthesis through CO_2 hydrogenation (Jarvis and Samsatli, 2018), the process belonging to the carbon dioxide utilization (CCU) topic. According to Dalena and co-authors methanol production from CO_2 offers at least two significant advantages: i) the overcoming of CO_2 sequestration and ii) mitigation of greenhouse gas effect through an efficient CO_2 recycling (Dalena et al, 2018). Figure 1 presents a simplified flow-diagram of methanol synthesis and methanol derived products considered in the present study. The novelty of the work consists on the comparison of various routes for methanol valorisation this comparison being based on technical and environmental key performance indicators.

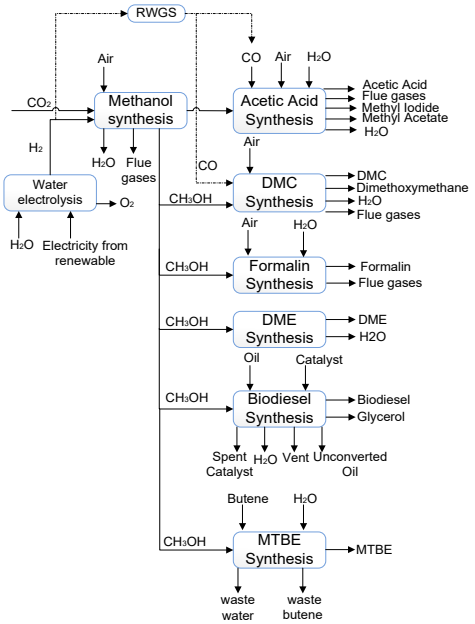

Figure 1. Conceptual configuration of methanol synthesis and conversion into various chemicals

2. Plants configurations & models assumptions

The cases investigated in the present paper are presented in Table 1.

Table 1. Case studies description

Name	Description
Case 1	Methanol production from CO_2 and H_2 coupled with Acetic Acid production
Case 2	Methanol production from CO_2 and H_2 coupled with DMC production
Case 3	Methanol production from CO_2 and H_2 coupled with formalin production
Case 4	Methanol production from CO_2 and H_2 coupled with DME production
Case 5	Methanol production from CO_2 and H_2 coupled with biodiesel production
Case 6	Methanol production from CO_2 and H_2 coupled with MTBE production

Each case under investigation can be divided in two sections. The first section is a common section and refers to the methanol production process, described in detail in the next paragraphs. The second section is not common any more, being different in terms of raw - materials, units operations and reactions involved for each case under investigation (see Table 2). Figure 2 presents the methanol production process from CO_2 and H_2.

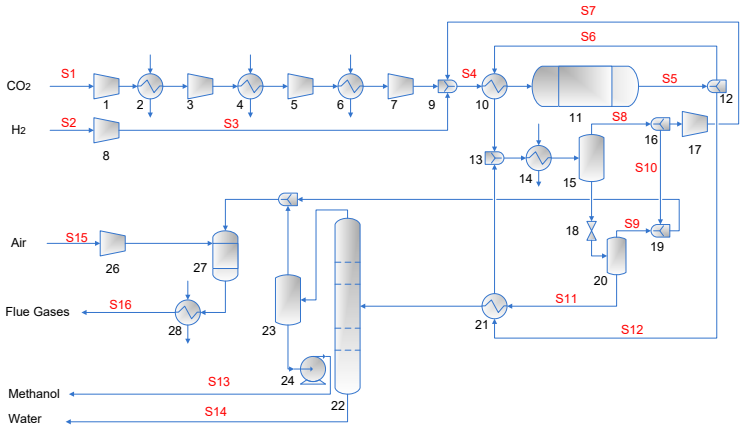

Figure 2. Process flow diagram for methanol production

The CO_2 feed, S1, is compressed to 78 atm, through a four-stage compressor with intermediate cooling. The H_2 feed stream, S2, is compressed also up to 78 atm using a compressor (Unit 8). The raw-materials streams are mixed with recycled stream (S7), heated up in heat exchanger (Unit 10) and sent to the plug flow rector, Unit 11, where the following reactions occur at 210˚C:

$$CO_2 + 3H_2 \rightarrow CH_3OH + H_2O \quad (1)$$

$$CO_2 + H_2 \rightarrow CO + H_2O \quad (2)$$

The output stream of the reactor is divided into two streams: S6 is used to heat the reactor feed through the heat exchanger (Unit 10) and Stream 12 is used to preheat the column feed through the heat exchanger (Unit 21). After this thermal integration, the streams are mixed and cooled to 35˚C in Unit 14. The liquid and gaseous phases are separated in the flash (Unit 15). Part of the gas stream from Unit 15 is compressed and recycled to the reactor. After a second gas-liquid separation in Unit 20, S11 stream containing methanol and water; the mass concentration of methanol being 63%, was obtained. This mixture is preheated in the heat exchanger (Unit 21) using the heat of the residual gas reactor. Then, the stream is fed to the distillation column (Unit 22). Liquid methanol is produced in S13 (wt. methanol 99.80%) (Prez-Fortes et al., 2016).

Table 2. Evaluated case studies and main design assumptions

	Modeling and simulation details and main design assumptions
Case1	*Raw-materials*: methanol, H_2, CO_2, water; *Main product*: Acetic Acid; *By-products*: wastewater, Methyl Iodide, Methyl Acetate, Flue gases; *Thermodynamic package used*: SRK; *Units operations*: 3 reactors, 2 distillation columns, 5 separators, 6 compressors, 6 pumps, 11 HE, 6 mixers, 4 dividers

Case 1(cont.)	*Reactions involved*: $CH_3OH + CO \rightarrow CH_3COOH$ (3) $CH_3COOH + CH_3OH \rightarrow CH_3COOCH_3 + 2H_2O$ (4) $CO + H_2O \rightarrow CO_2 + H_2$ (5) *Assumptions*: reactor thermal mode adiabatic, reactor pressure 30 atm; off-gas treatment column 35 stages, methanol recovery 96%; acetic acid purification column 50 stages, RR 3.54; pumps efficiencies 80%; compressors efficiencies 75%; HE min ΔT 10˚C.
Case 2	*Raw-materials*: methanol, H_2, CO_2, air; *Main product*: DMC; *By-products*: dimethoxymethane, Water, Flue gases; *Thermodynamic package used*: PSRK; *Units operations*: 3 reactors, 3 distillation columns, 5 separators, 4 compressors, 3 pumps, 4 HE, 5 mixers, 1 divider *Reactions involved*: $CO_2 + H_2 \rightarrow CO + H_2O$ (6) $4CH_3COOH + 2CO + O_2 \rightarrow 2C_3H_6O_3 + 2H_2O$ (7) $4CH_3COOH + 2CO \rightarrow 2C_3H_8O_2 + O_2$ (8) *Assumptions*: reactor thermal mode-isothermal, reactor pressure 20 atm; methanol recovery column 30 stages, methanol recovery 99%; DMC purification column 45 stages; pumps efficiencies 80%; compressors efficiencies 75%; HE min ΔT 10˚C.
Case 3	*Raw-materials*: methanol, air, water; *Main product*: formaldehyde; *By-products*: off gases *Thermodynamic package used*: SRK; *Units operations*: 1 reactor, 2 pumps, 4 HE, 2 mixers, 1 compressor, 1 absorber, 1 distillation column *Reactions involved*: $CH_3OH + \frac{1}{2}O_2 \rightarrow CH_2O + H_2O$ (9) $CH_3OH \rightarrow CH_2O + H_2$ (10) *Assumptions*: reactor thermal mode isothermal, reactor pressure 1.83 atm; absorber 20 stages; formaldehyde separation column 20 stages; pumps efficiencies 80%; compressors efficiencies 75%; HE min ΔT 10˚C.
Case 4	*Raw-materials*: methanol; *Main product*: DME; *By-products*: wastewater; *Thermodynamic package used*: SRK; *Units operations*: 1 reactor, 1 pump, 4 HE, 1 valve, 2 distillation columns *Reaction involved*: $2CH_3OH \rightarrow C_2H_6O + H_2O$ (11) *Assumptions*: reactor thermal mode isothermal, reactor pressure 14.5 atm; DME separation column 24 stages, RR 0.35, bottom product temperature 153˚C; pumps efficiencies 80%; compressors efficiencies 75%; HE min ΔT 10˚C.
Case 5	*Raw-materials*: methanol, oil, catalyst (NaOH), water, H_3PO_4; *Main product*: biodiesel; *By-products*: glycerol, vent, unconverted oil, Na_3PO_4; *Thermodynamic package used*: SRK; *Units operations*: 2 reactors, 4 mixers, 4 pumps, 2 HE, 3 distillation columns, 1 extractor *Reactions involved*: $C_{57}H_{104}O_6 + CH_3OH \leftrightarrow C_{39}H_{72}O_5 + C_{19}H_{36}O_2$ (12) $C_{39}H_{72}O_5 + CH_3OH \leftrightarrow C_{21}H_{40}O_4 + C_{19}H_{36}O_2$ (13) $C_{21}H_{40}O_4 + CH_3OH \leftrightarrow C_3H_8O_3 + C_{19}H_{36}O_2$ (14) $3NaOH + H_3PO_4 \rightarrow Na_3PO_4 + 3H_2O$ (15) *Assumptions*: biodiesel reactor thermal mode-isothermal (60˚C); catalyst neutralization reactor thermal mode - isothermal (60˚C); extractor stages 4; biodiesel distillation column
Case 5	10 stages, RR 4, bottom product temperature 382˚C; glycerol distillation column RR 2, bottom product temperature 112˚C; pumps efficiencies 80%; compressors efficiencies 75%; HE min ΔT 10˚C.

Case 6	*Raw-materials*: methanol, butylene, water; *Main product*: MTBE; *By-products*: wastewater, waste butylene; *Thermodynamic package used*: SRK; *Units operations*: 1 reactor, 1 absorber, 2 distillation columns, 2 mixers, 3 pumps, 2 valves, 1HE *Reaction involved*: $CH_3OH + C_4H_8 \rightarrow C_5H_{12}O$ (16) *Assumptions*: reactor mode isothermal (130˚C) reactor pressure 30 atm; MTBE column 72 stages; RR 1.62; methanol absorber 5 stages; methanol separation column 42 stages, RR 3.44; pumps efficiencies 80%; compressors efficiencies 75%, HE min ΔT 10˚C.

HE - heat exchanger, RR - reflux ratio, SRK - Soave Redlich Kwong, PSRK – Predictive Soave Redlich Kwong

3. Results and discussions

All evaluated cases were modelled, simulated and validated (Turton et al., 2008) using ChemCAD process simulation software. The validation differences between the literature results and those obtained from the simulations were below 2%. Once the models were validated they were scaled-up to the same quantity of methanol used (e.g. 500 kmols/h). The mass and energy balances from the simulation were used to calculate technical and environmental indicators. For environmental impact Waste Reduction (WAR) Algorithm, developed by US EPA, was applied (EPA, 2019). The WAR methodology is not a complete LCA tool since it is focused only on the manufacturing aspect without considering the upstream (i.e. raw-materials supply chain) and downstream processes. The technical indicators obtained are summarized in Table 3. Electricity to run the machineries was considered under electricity consumption.

Table 3. Technical comparison between investigated cases

Parameter	Unit	Case 1	Case 2	Case 3	Case 4	Case 5	Case 6
Methanol used	t/h	16	16	16	16	16	16
Product Name	-	AceticAcid	DMC	Formalin	DME	Biodiesel	MTBE
Product Rate	t/h	25.52	18.06	37.35	11.46	143.48	36.31
Product Purity	%	100	99.58	32.38	99.44	99.99	99.92
El.consumption	kW_e	6,056.65	6,630.74	6,878.66	5,822.59	5,859.21	5,907.90

It can be noticed from Table 3 that starting from the same quantity of methanol different quantities of products are obtained. The highest quantities of products are obtained in Case 5 followed by Case 3. Purities of methanol derived products are higher than 99%, except Case 3. Formalin obtained in Case 3 represents a diluted solution of formaldehyde (wt. 32.38%). Another issue with Case 3 is the fact that it has the highest electricity consumption among all cases under investigation. Methanol conversion into biodiesel (Case 5) and MTBE (Case 6) seem to be more profitable compared to other cases due to high quantity of products obtained, high purities and low energy consumption. The environmental indicators obtained are reported in Table 4. Those indicators consider: the inputs and the outputs streams from the chemical process as well as from the energy generation process related to the chemical process and the toxicity of the substances involved. Considering the indicators reported in Table 4, the most environmentally friendly designs are Case 2 and Case 4 having the lowest emissions to air, water and soil. For instance, for Case 2, six of nine impact indicators (i.e. AP, ATP, TTP, ODP, HTPE. HTPI) have the lowest values in the above mentioned scenario. On the other hand Case 2 and Case 4 are not so advantageous from a technical point of view (see Table 3). Even if the purities of the products obtained are high, their flow-rates are relatively low (e.g. 18.06 tons/h in Case 2 and 11.46 tons/h in Case 4). Case 5 and Case 6 have a medium environmental impact and good technical performance.

Table 4. Environmental comparison between investigated cases

Parameter	Units	Case 1	Case 2	Case 3	Case 4	Case 5	Case 6
GWP	PEI/h	12.4	6.74	5.95	8.00	5.25	36.2
AP	PEI/h	130	143	148	125	126	127
PCOP	PEI/h	5,510	1370	38,300	2,840	14,800	8,210
ATP	PEI/h	180	11.8	206	6.35	86.40	27
TTP	PEI/h	44,000	623	5,890	214	5,950	4,640
ODP * 10^5	PEI/h	4.43	4.85	5.03	4.26	4.28	4.32
HTPE	PEI/h	315	0.59	3,200	0.29	1800	51.5
HTPI	PEI/h	44,000	623	5,890	214	5,950	4,640
Total Impact	PEI/h	94,200	2,780	53,600	3,410	28,700	17,700

GWP - Global Warming Potential, AP - Acidification Potential, PCOP - Photochemical Oxidation Potential, ATP - Aquatic Toxicity Potential, TTP - Terrestrial Toxicity Potential, HTPE - Human Toxicity Potential by Exposure, HTPI - Human Toxicity Potential by Ingestion, ODP - Ozone Depletion Potential, PEI - Potential Environmental Impact

4. Conclusions

The present paper evaluates methanol production from CO_2 and H_2 and its conversion into various chemicals. Technical and environmental indicators were calculated and compared for the evaluated cases. A quantity of 143.48 t/h of biodiesel with a purity of 99.44% and 36.31 t/h of MTBE with a purity of 99.92% were obtained starting from 16 t/h of methanol. These two products have a medium environmental impact, lower than the environmental impact of methanol transformation into acetic acid or formalin (e.g. 28,700 PEI/h in biodiesel production and 17,700 PEI/h for MTBE vs. 94,200 PEI/h for acetic acid and 53,600 PEI/h for formalin) but higher than the impact of methanol conversion into DMC and DME. Even if DMC and DME processes are more environmental friendly they are not so convenient from technical point of view. The technical and environmental evaluations lead to the conclusion that methanol conversion into biodiesel and MTBE are the most convenient solutions from technical and environmental point of view.

Acknowledgement

This work was supported by CONVERGE Project, European Union's Horizon 2020 research and innovation programme under grant agreement No. 818135.

References

F. Dalena, A. Senatore, M. Basile, S. Knani, A. Basile, A. Iulianelli, 2018. Advances in Methanol Production and Utilization, with Particular Emphasis toward Hydrogen Generation via Membrane Reactor Technology, Membranes 8, 98, 1-27

IMO, 2016. Methanol as marine fuel: Environmental benefits, technology readiness, and economic feasibility. http://www.imo.org (las accessed January 2020)

EPA, 2019. https://www.epa.gov/chemical-research (last accessed November 2019)

S. M. Jarvis, S. Samsatli, 2018. Technologies and infrastructures underpinning future CO_2 value chains: A comprehensive review and comparative analysis, Renewable and Sustainable Energy Reviews, 85, 46-68

M. Prez-Fortes, J. Schoneberger, A. Boulamanti, E. Tzimas, 2016. Methanol synthesis using captured CO_2 as raw material :Techno-economic and environmental assessment, Applied Energy, 161, 718-732

É. Simőes, Van-Dal, C. Bouallou, 2013. Design and simulation of a methanol production plant from CO_2 hydrogenation, Journal of Cleaner Production 57, 38-45.

R. Turton, R.C. Bailie, W.B. Whiting, A. Shaeiwitz, 2008. Analysis, Syinthesis, and Design of Chemical Processes, Perason Education.

Sauro Pierucci, Flavio Manenti, Giulia Bozzano, Davide Manca (Eds.)
Proceedings of the 30th European Symposium on Computer Aided Process Engineering (ESCAPE30), May 24-27, 2020, Milano, Italy.
http://dx.doi.org/10.1016/B978-0-12-823377-1.50094-X

Evaluating the Existing Protocol for LNG Bunkering Operations

Aruna Coimbatore Meenakshi Sundaram, Iftekhar Abubakar Karimi

Department of Chemical & Biomolecular Engineering, National University of Singapore, 4 Engineerign Drive 4, 117585, Singapore

Abstract

IMO 2020, a regulation mandated by the International Maritime Organization, demands an 80% reduction in NOx emissions and limits Sulphur to 1000 ppm in fuels used for maritime transportation. This forces the need for a cleaner and sustainable fuel for the ocean-going ships to reduce the emissions generated by the conventional Heavy Fuel Oil (HFO). Liquefied Natural Gas (LNG) turns out to be a promising and long-term solution that complies with the new set of emission standards, but the technology to use LNG for ships is still underdeveloped. The cryogenic nature of LNG demands a special infrastructure and protocol for LNG bunkering operations. However, the procedures suggested in the literature seem to be mere concepts/ideas proposed without detailed quantitative evaluation. In this study, a comprehensive evaluation of the existing LNG bunkering protocol was conducted using a Unisim Dynamic Simulation (DS) model of the LNG bunkering system. The major pitfalls identified in the current protocol are a) the time taken for inerting and purging processes, b) GHG emissions (methane/CO2) released from frequent inerting and purging operations, c) high cost of inerting gas and d) improper pressure management resulting in increased Boil-Off Gas (BOG) generation. These shortcomings will have a major impact on the safety and operating cost of an LNG bunkering system, especially for busy bunkering ports/facilities.

Keywords: LNG, Bunkering, Marine Fuel, IMO 2020

Introduction

Heavy Fuel Oil (HFO), the traditionally used bunker fuel for maritime transportation is accompanied with significant amount of Sulphur and particulate matter emissions. To reduce the emissions from these ocean-going ships, the International Maritime Organization (IMO) enforced a new regulation, IMO2020 from 1st January 2020 (Seas, 2008). This forced many shipping companies and regulatory bodies to come up with a solution that can comply with the new set of standards. Several alternatives such as the use of (a) HFO with a scrubber, (b) Marine Diesel Oil (MDO) with lower Sulphur content and (c) an alternative fuel like Liquefied Natural Gas (LNG) were suggested. Critical evaluation of these alternatives showed that the scrubber installation cost and the scrubbed waste disposal are problematic for HFO and the cost of producing low Sulphur MDO is very high. On the other hand, LNG (primarily methane) is the cheapest low-carbon intensive fossil fuel available today and hence turned out to be the most promising and long-term solution (Danish Maritime Authority, 2012).

Unlike HFO, LNG is stored and transported in heavily vacuum-insulated large tanks under cryogenic conditions (about 1.2 atm and 113 K) (Han and Lim, 2012). Thus, LNG demands special treatments and procedures during transfer. Hence, developing a reliable

and safe bunkering procedure is essential for global standardization of LNG transfer operations. The process of transferring LNG from one vessel to another as a marine fuel is termed as LNG bunkering and can be performed in any of three modes: Truck-to-Ship (TTS), Shore-to-Ship (PTS) or Ship-to-Ship (STS), based on the location of the bunkering facility and the volume of fuel to be transferred (DNV GL, 2017).

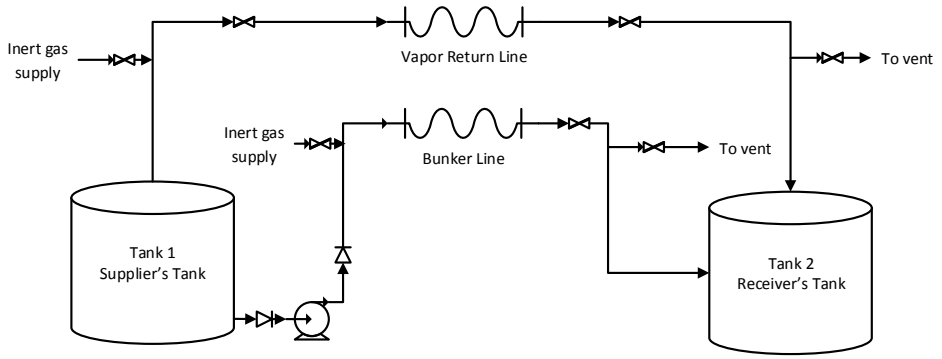

Figure 1: LNG Bunkering System

American Bureau of Shipping (ABS, 2014) suggested a protocol for LNG bunkering operations. According to this protocol, a bunkering system consists of two LNG tanks on the supplier and receiver end irrespective of the mode of transfer (shown in Figure 1). The process begins by connecting the two LNG tanks with a flexible, cryogenic bunker hose. The first step is *Pre-Inerting* (shown in Figure 2) where the moisture/air in the hose is removed using an inert gas like nitrogen to bring the air vol% below the flammability limits of methane (5-15 vol%). Once the hose has been inerted with nitrogen, a small amount of LNG is used to purge/flush out the nitrogen in the hose to avoid nitrogen contamination in the receiver's LNG tank. This *Purging* process will also ensure that the hose is cooled down to LNG temperature without causing mechanical stress or fractures in the bunkering hose. On completion of purging, *Filling* commences wherein the actual transfer of LNG from the supplier to the receiver tank takes place. Once the required filling level has been achieved, the valves leading to the supplier LNG tank is closed while the valve going to the receiver's tank is opened and closed multiple times until the LNG in the hose is pressurized and forced towards the receiver's tank, to ensure complete *Draining* of LNG from the hose. Before disconnecting the hose, the traces of methane vapors left in the hose is removed by *Post-Inerting* using nitrogen. This completes the LNG bunkering process and the hose is disconnected.

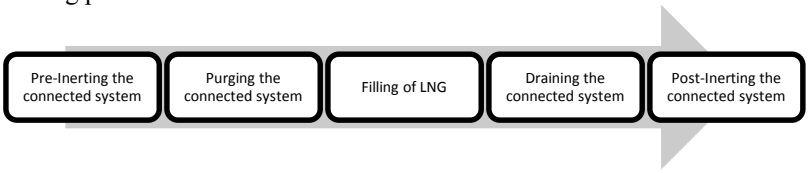

Figure 2: Step-by-Step LNG Bunkering Procedure

Despite the insulation, heat ingress into the LNG tanks are unavoidable, and it causes LNG to vaporize. These LNG vapors called Boil-Off Gas (BOG) occupies more volume than LNG itself causing an increase in tank operating pressure. In some systems, the use of a Vapor Return Line (VRL) (Figure 1), additional flexible cryogenic hose identical to

a bunker hose that connects the vapor outlets of the two tanks was suggested to maintain a constant pressure difference between the two tanks by allowing bidirectional flow of vapors from one vessel to the other.

Though the protocol describes the complete step-by-step process, it lacks several technical and operational details such as the time taken for each step, the source of nitrogen used for inerting, the amount of methane or LNG vapors emitted during the inerting and purging operations and the applicability of the suggested protocol to various modes of bunkering. Literature show that many industrial experts and shipping companies are focused on the construction of LNG fueled ships (Danish Maritime Authority, 2012) and the safety issues in handling LNG (EMSA, 2017) (Vandebroek and Berghmans, 2012). But least attention has been given to the development of LNG bunkering procedure. Thus, in this paper a quantitative evaluation of the suggested LNG bunkering protocol will be presented using a dynamic simulation model.

Methodology

The cryogenic and flammable nature of LNG does not allow for experimentation. Thus, a simulation model for the LNG Bunkering system was developed using a well-known process simulator, Unisim®. The Unisim Dynamic Simulation (DS) uses a pressure flow solver to compute the system dynamics as a function of time. The DS model was constructed using the bunkering system outline provided in Figure 1 with a Peng-Robinson fluid package.

Table 1: Bunkering System Parameters (DNV-GL, 2014)

Parameters	**Truck-to-Ship**	**Shore-to-Ship**	**Ship-to-Ship**
Tank 1 Volume (m^3)	1500	4000	7500
Tank 2 Volume (m^3)	500	1500	3000
Tank 1 Pressure (barg)	2.8	2.8	2.8
Tank 2 Pressure (barg)	5.8	5.8	5.8
Tank 1 Temperature (˚C)	-147	-147	-147
Tank 2 Temperature (˚C)	-134.5	-134.5	-134.5
Tank 1 Level (%)	90	90	90
Tank 2 Level (%)	20	20	20
Pipe length (in)	4	8	10
VRL length (in)	2	4	4
Transfer rate (m^3/s)	75	200	400

The most important component in the DS model for LNG bunkering process is the simulation of an LNG tank. Though these process simulators have an inbuilt tank module, they do not allow providing separate heat leak rates for the tank wall, roof and top. On the contrary, these heat leaks are the major reason for the vaporization of LNG resulting in BOG generation and tank pressurization. Hence to compute the BOG generation rate accurately, a corrected LNG tank model suggested by (Khan et al., 2019) was employed.

For the system parameters such as flowrate, tank size, hose size etc., literature provides a range of values suitable for each mode of bunkering. Hence an arbitrary value in the

suggested range was chosen for this study (see Table 1) to develop the DS model for all three modes of bunkering with and without the presence of VRL.

Following the model development, a step-by-step bunkering process was carried out using an Event Scheduler available in Unisim DS. The Event Scheduler treats each bunkering step as an event and enables us to provide a set of instructions/actions to be performed for each event along with a set of conditions to mark the end of that event. Once the condition(s) is(are) satisfied, the event scheduler switches the simulation from one event to another by executing the set of actions provided. For example, a reduction in air vol% from 100% to less than 3% in the bunkering hose indicate the completion of pre-inerting and commencement of purging process. After providing necessary conditions and actions for all the steps, the entire sequence of events was executed at once to compute the time taken for each step. The same procedure was followed for all the three modes of bunkering (both with and without VRL).

Results & Discussion

In this study, the missing information in the existing LNG bunkering protocol were computed using the developed DS model. Firstly, the time taken for each mode of transfer was computed (shown in Table 2). Though in literature the use of VRL was suggested, they failed to consider the additional inerting and purging required for the VRL. Here, the bunkering time computed in the presence of a VRL is indicated by the numbers within the parentheses in Table 2. Thus, from table 2 we conclude that the inerting and purging processes contribute to the maximum % of the total bunkering time.

Table 2: LNG Bunkering Timeline (min)

Steps	**Truck-to-Ship**	**Shore-to-Ship**	**Ship-to-Ship**
Pre-inerting	8 (14)	14 (29)	19 (39)
Purging	7 (12)	12 (21)	16 (29)
Filling	62 (259)	70 (292)	75 (292)
Draining	29 (26)	48 (43)	81 (54)
Post-Inerting	8 (14)	14 (29)	19 (39)
Total Time (min)	114 (325)	158 (414)	210 (453)

Secondly, the nitrogen source for inerting was not mentioned in the current protocol. From the DS model, the nitrogen requirement for inerting was computed to be approximately 7.5 kg, 18 kg and 28 kg for TTS, PTS and STS respectively without VRL and 12 kg, 27 kg and 42 kg with VRL for one bunkering process. While the cost of nitrogen is directly proportional to the amount of nitrogen required, the current protocol will suffer from high inerting cost in the absence of a nitrogen generation unit. On the other hand, installing a nitrogen generation unit will increase both the capital and operating cost. Thus, in either case inerting processes will increase the operating cost of LNG bunkering system.

Another important issue to be addressed is the methane emissions. Though the use of LNG can eliminate the Sulphur and NOx emissions, the current protocol emits significant amount of methane during the purging and inerting processes. The amount of methane

emitted per bunkering process was computed to be 11 kg, 28 kg and 52 kg for TTS, PTS and STS respectively without VRL and 15 kg, 40 kg and 80 kg with VRL. Published literature does not indicate the presence of any Incineration Unit (IU) that can convert the methane vapors to CO_2 before releasing to the atmosphere. In the absence of an IU, direct release of methane to the atmosphere can worsen the situation as methane is a more potent greenhouse gas (GHG) compared to CO_2. An IU installation in the bunkering port will still result in carbon emissions to the atmosphere.

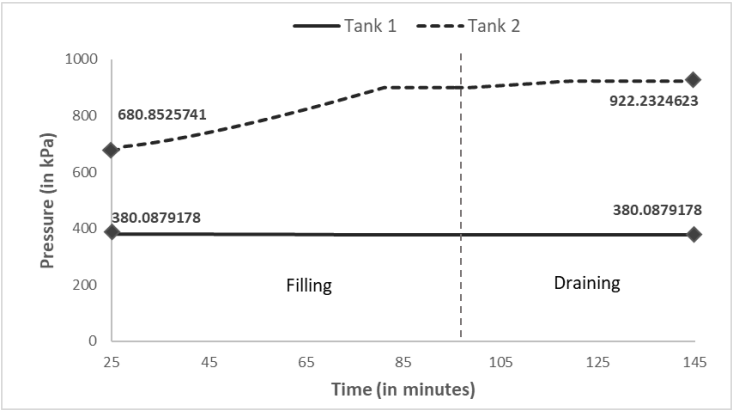

Figure 3: PTS Bunkering Vessel Pressure Profiles Without VRL

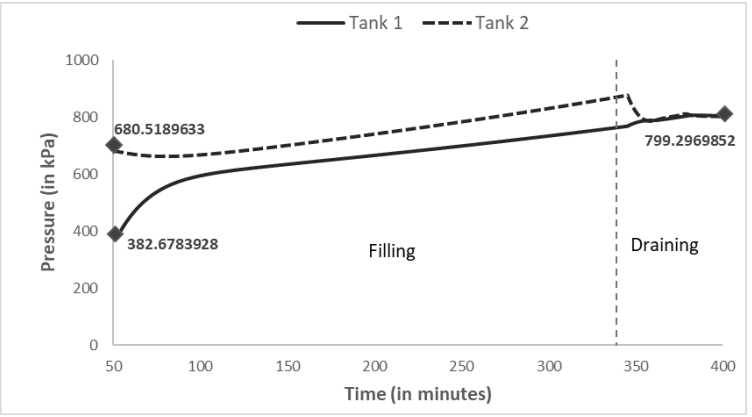

Figure 4: PTS Bunkering Vessel Pressure Profiles With VRL

BOG generation from LNG tanks will also result in methane emissions in the absence of an IU. Further, improper planning and management of LNG delivery can result in significant amount of BOG generation and tank pressurization. Figure 3 and Figure 4 show the tank pressure profiles obtained during filling and draining stages of a Shore-to-Ship LNG bunkering system with both the absence and presence of VRL respectively. The dotted and continuous lines represent the pressure profiles of receiver and supplier tank respectively. The tank relief valve pressure was set to 1000 kPa for both the tanks in the DS model. The event scheduler condition was programmed to stop the filling process if the pressure in either tanks exceeded 900 kPa to ensure safe operation. In the absence of a VRL, it was noted that the pressure difference between the two tanks increased continuously due to excess BOG generation (shown in Figure 4). As a result,

the filling was stopped by the scheduler when the receiver vessel liquid % reached 35% tank level in all three modes. On the other hand, in the presence of a VRL, 85% filling level was achieved by maintaining a constant pressure difference (shown in Figure 5) between the two tanks allowing the excess BOG to flow from one vessel to the other through VRL ensuring a smooth transfer process. During the draining process, the pressure of the two vessels almost became equal for a system with VRL (after t=342 min in Figure 5). Clearly, the presence of a VRL is mandatory to maintain a constant pressure difference between the two tanks and manage the BOG generated during the bunkering operation.

In brief, the evaluation of the existing bunkering protocol informs us that the current protocol has been proposed without much quantitative analysis on the time, cost, BOG generation and emissions. The several shortcomings associated with the current protocol, as discussed above, will definitely affect the operational safety of a bunkering port and inhibit the standardization of the procedure for worldwide operation.

Conclusion

The step-by-step LNG bunkering procedure suggested by ABS was simulated using Unisim Dynamic Simulation. The simulation results concluded that the inerting and purging operations waste a lot of material and are also time consuming. Additionally, purging operations release LNG vapors to the atmosphere which leads to loss of LNG/methane which is 2600 times more potent than carbon dioxide as a GHG. Further, in the absence of a VRL, a large pressure difference was observed between the two tanks directly impacting the filling rate and preventing the system from attaining the required filling level. Thus, the presence of VRL is mandatory to maintain a constant pressure difference between the two tanks to enable smooth transfer process. But, this in turn will result in increased time, cost and emissions as the inerting and purging process are performed for both bunkering and vapor return line. The effect of these issues will be manifold for busy bunkering ports which receive around 200-300 ships per day, as the cost, emissions, and time taken are directly proportional to the number of bunkering operations conducted at a facility. Undoubtedly, a better LNG bunkering system that is operationally safe, economically viable and environment-friendly must be designed in the future for worldwide standardization of LNG bunkering procedure.

References

ABS, 2014, LNG Bunkering: Technical and Operational Advisory 68.
Danish Maritime Authority, 2012, North European LNG Infrastructure Project- A feasibilty study for an LNG filling station infrastructure and test of recommendations.
DNV-GL, 2014, Liquefied Natural Gas (LNG) Bunkering Study.
DNV GL, 2017, Gas as a Marine Fuel.
EMSA, 2017, Guidance on LNG Bunkering to Port Authorities and Administration.
Han, C., Lim, Y., 2012, LNG Processing: From Liquefaction to Storage, Comput. Aided Chem. Eng. 31, 99–106.
Khan, M.S., Effendy, S., Karimi, I.A., Wazwaz, A., 2019, Improving design and operation at LNG regasification terminals through a corrected storage tank model. Appl. Therm. Eng. 149, 344–353.
Seas, N., 2008, Maritime Gas Fuel Logistics, Transportation.
Vandebroek, L., Berghmans, J., 2012, Safety aspects of the use of LNG for marine propulsion. Procedia Eng. 45, 21–26.

Sauro Pierucci, Flavio Manenti, Giulia Bozzano, Davide Manca (Eds.)
Proceedings of the 30th European Symposium on Computer Aided Process Engineering (ESCAPE30), May 24-27, 2020, Milano, Italy.
http://dx.doi.org/10.1016/B978-0-12-823377-1.50095-1

A Recycle Model of Spent Liquor in Pre-treatment of Lignocellulosic Biomass

Franco Mangone*, Soledad Gutiérrez

Chemical and Process Systems Engineering Group – Chemical Engineering Institute - Engineering School – Universidad de la República, Julio Herrera y Reissig 565, PC 11300, Montevideo, Uruguay

Abstract

The pre-treatment of lignocellulosic biomass to produce valuable products is one of the key steps of the process, due to the high costs involved. In most typical methods, biomass is treated with a water solution of either mineral or organic acids, caustic soda or organic solvents. The high costs associated with supply of these chemicals and energy requirements make the pre-treatment step a bottleneck in the development of cost-effective bioprocesses. In order to save water, chemicals and energy, a strategy that decouples liquid and solid residence time is proposed. A sequential re-use strategy of the spent liquor has been proposed recently by many authors, independently. It consists in retaining part of the liquor for the subsequent batch, instead of utilizing a fresh liquid mixture. This causes the conditions in every batch cycle to be different, which is a hindrance to effective overall process integration, because it is difficult to include such operation in a general process flowsheet. However, we observe that after several batches have occurred, cycles reach a stationary condition in the sense that initial and final conditions do not change. The presented model describes the behaviour of the cyclic re-use of spent liquor as a function of decision variables such as *removed spent liquor (r)* and *cycle time (t_c)*. For a series of first order reactions, it will be shown that the cyclic condition can be obtained analytically without needing to simulate every preceding stage.

Keywords: sequential, batch, re-use, pre-treatment, biorefinery.

1. Introduction

Pre-treatment of lignocellulosic biomass is a key step in preparation for its conversion to valuable products. Several alternatives exist for this purpose. Some examples are dilute acid pre-treatment, organosolv, steam explosion, and water-solvent fractionation (Davis et al., 2018). The main drawback associated with these processes are their high energy and chemicals related costs – most of them operate at high temperatures and pressures, and some need the addition of solvents or water which incur in additional costs.

In order to develop cost-effective processes, alternatives or enhancements to these technologies need to be proposed. Recently, the strategy of re-utilizing part of the spent liquor from one batch as solvent for the next one has been proposed by different authors (Chen et al. 2018, Park et al. 2018, Vergara et al. 2019). This strategy generates both energy and chemical savings, because the amount of fresh reposition liquid required for each batch (including solvents) is reduced, while also retaining some of the energy from the spent liquor in the form of higher temperatures. Also, more concentrated solutions of valuable sugars released from lignocellulosic biomass are obtained, thus reducing the downstream handling costs (concentration steps).

However, a framework for the design and integration of these kind of batch recycle strategies has not yet been developed, as suggested in the revised literature. The present work will focus on a case-study which will serve as a basis for the development of such framework.

2. Kinetic Model

A diluted acid pretreatment was selected for the case-study. In this process, lignocellulosic biomass is submerged in a diluted sulfuric acid solution, and then heated to temperatures higher than 100°C. Because of this, a fraction of cellulose, hemicelluloses, and acid-soluble lignin are hydrolyzed. The remaining solid is washed and then usually undergoes a hydrolysis step, while the spent liquor can be treated to remove lignin, converting it into a sugar-rich solution.

The hydrolysis of both cellulose and hemicelluloses yields a plethora of 5 and 6 carbon sugars. Oligomer formation is neglected, as suggested by various authors (Aguilar et al., 2002; Guerra-Rodríguez et al. 2012). Also, 5 and 6-carbon sugars will be modeled as xylose and glucose, respectively. Taking this into account, the following kinetic model can be used to represent the system (Aguilar et al., 2002):

$$Gn \xrightarrow{k_1} G \xrightarrow{k_2} Gd$$

$$Xn \xrightarrow{k_3} X \xrightarrow{k_4} Xd$$

Where *Gn*, *G*, and *Gd* represent glucan, glucose and glucose decomposition products, respectively; similarly, *Xn*, *X*, and *Xd* represent xylan, xylose and xylose decomposition products. The main decomposition products of glucose and xylose are hydroximethylfurfural (HMF) and furfural.

This set of chemical reactions occurring in a batch reactor yield a set of ordinary differential equations, whose solution represents the evolution in time of the species present in the broth. The solution is of the form:

$$C_{Gn} = C_{Gn,0}.e^{-k_1 t} \tag{1}$$

$$C_G = C_{G,0}.e^{-k_2 t} + C_{Gn,0}.\frac{k_1}{k_2 - k_1}(e^{-k_1 t} - e^{-k_2 t}) \tag{2}$$

$$C_{Gd} = C_{Gd,0} + C_{G,0}.(1 - e^{-k_2 t}) + C_{Gn,0}.\frac{k_1.k_2}{k_2 - k_1}\left(\frac{1 - e^{-k_1 t}}{k_1} - \frac{1 - e^{-k_2 t}}{k_2}\right) \tag{3}$$

$$C_{Xn} = C_{Xn,0}.e^{-k_3 t} \tag{4}$$

$$C_X = C_{X,0}.e^{-k_3 t} + C_{Xn,0}.\frac{k_3}{k_4 - k_3}(e^{-k_3 t} - e^{-k_4 t}) \tag{5}$$

$$C_{Xd} = C_{Xd,0} + C_{X,0}.(1 - e^{-k_3 t}) + C_{Xn,0}.\frac{k_3.k_4}{k_4 - k_3}\left(\frac{1 - e^{-k_3 t}}{k_3} - \frac{1 - e^{-k_4 t}}{k_4}\right) \tag{6}$$

Where C_j represents the concentration of species j at time t, and $C_{j,0}$ is the concentration of said species at the start of the cycle. For simplicity, it can be observed that every equation can be written in the following form:

$$C_i = \sum_j C_{j,0} \cdot a_{i,j}(t) \tag{7}$$

Where $a_{i,j}(t)$ is a coefficient that is a function of t.

3. Cyclic behavior

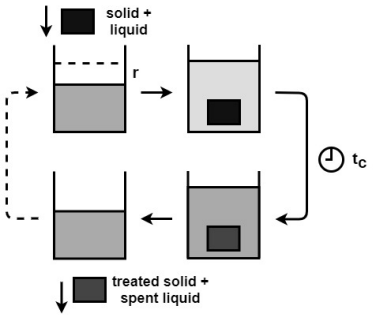

Figure 1– Operation diagram for the reutilization process.

Once the evolution during a single cycle has been deduced, the next step is to model the transition to one cycle to the next. It is assumed that any change is performed instantly, although a time evolution could also be formulated. Figure 1 shows schematically how the cyclic operation works.

The operations that take place between cycles correspond to the removal of the treated solid, alongside a portion r of the total volume of liquid. Then, a new solid is loaded, and enough reposition liquid is added to ensure that the initial liquid volume is the same as in the last cycle. This causes the initial concentration of polymers (glucan, xylan) to be the same for every cycle, since they are contained in the solid. The calculation of polymer concentration is detailed in Aguilar et al., 2002. At the same time, the concentration of monomers and decomposition products will experiment a dilution process, since this species are not added with the reposition. Thus, the process could be described as follows:

$$C_{Gn,0}{}^{k+1} = C_{Gn,in} \tag{8}$$

$$C_{G,0}{}^{k+1} = r.C_{G,f}{}^{k} \tag{9}$$

$$C_{Gd,0}{}^{k+1} = r.C_{Gd,f}{}^{k} \tag{10}$$

$$C_{Xn,0}{}^{k+1} = C_{Xn,in} \tag{11}$$

$$C_{X,0}{}^{k+1} = r.C_{X,f}{}^{k} \tag{12}$$

$$C_{Xd,0}{}^{k+1} = r.C_{Xd,f}{}^{k} \tag{13}$$

Where the supraindex k represents the cycle number. This set of equations will be denominated *handling functions.* This sequential operation is expected to reach a stationary condition after several cycles. An intuitive approach to understand this is that as the solution concentrates from cycle to cycle, the liquor removal step will remove more and more dissolved species (because of high concentrations); thus, at some point, the removed material will be equal to the generated species during the reaction step. Furthermore, it is assumed that after a large time t has passed, the concentrations will reach a "stationary condition", in the sense that the initial and final conditions for subsequent batches will be the same. One way to formulate that observation is by imposing the following:

$$C_{j,f}{}^{k+1} = C_{j,f}{}^{k} = C_{j,f}{}^{\infty} \tag{14}$$

Which states that the concentration at the end of cycles k and k+1 must be the same for a given species j. With Eq. 14, it is possible to find the initial and final concentrations for the stationary condition mentioned earlier, which will be called the *invariant cycle* (IC). This IC will have an *invariant initial condition* (IIC), and an *invariant final condition* (IFC).

The analytical procedure for the IC condition is rather straightforward:

1. Take the final condition for cycle k, for any given species j.
2. Apply the *handling functions* described in equations 8 to 13. A new initial condition will be obtained.
3. Apply the time evolution described by equations 1 to 6. A new final condition will be obtained.
4. Impose the condition described in equation 14. Operate to find and expression for $C_{j,f}{}^{\infty}$, the IFCs.
5. Find the IICs by applying the *handling functions* again, to the values found in the previous point.

This results in the expressions shown below:

$$C_{Gn,f}{}^{\infty} = C_{Gn,in}.a_{Gn,Gn} \tag{15}$$

$$C_{G,f}{}^{\infty} = \frac{C_{Gn,in}.a_{G,Gn}}{1 - r.a_{G,G}} \tag{16}$$

$$C_{Gd,f}{}^{\infty} = \frac{C_{Gn,in}.a_{Gd,Gn} + r.C_{G,f}{}^{\infty}.a_{Gd,G}}{1 - r.a_{Gd,Gd}} \tag{17}$$

$$C_{Xn,f}{}^{\infty} = C_{Xn,in}.a_{Xn,Xn} \tag{18}$$

$$C_{X,f}{}^{\infty} = \frac{C_{Xn,in}.a_{X,Xn}}{1 - r.a_{X,X}} \tag{19}$$

$$C_{Xd,f}{}^{\infty} = \frac{C_{Xn,in}.a_{Xd,Xn} + r.C_{X,f}{}^{\infty}.a_{Xd,X}}{1 - r.a_{Xd,Xd}} \tag{20}$$

These values are shown in Figure 2 as dashed lines, plotted alongside a simulation of several cycles of operation. The obtained expressions are an accurate representation of the initial and final conditions of the invariant cycle.

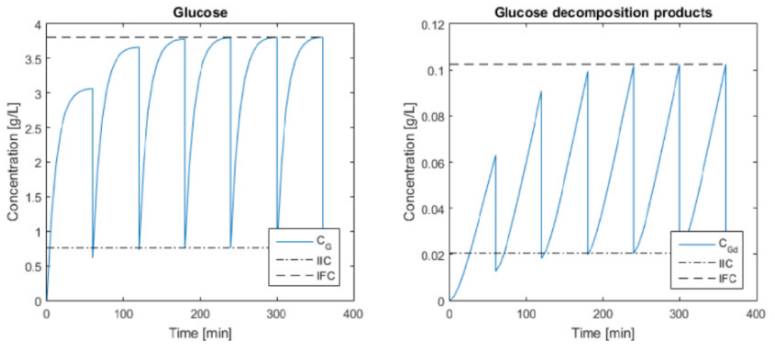

Figure 2 – Stationary condition reached after a few cycles for glucose and its decomposition products.

3.1. Inspecting the solution

Upon inspection, the expressions obtained in equations 15 to 20 do not depend on the initial conditions of the system. That is, given two different initial conditions, eventually the exact same IC will be reached. Importantly then, what determines the IC is not the selected initial condition, but rather the operative parameters governing the cyclic behavior, such as the cycle time t_c. Figure 3 shows this principle in action, where two different initial conditions are chosen for the glucose decomposition products.

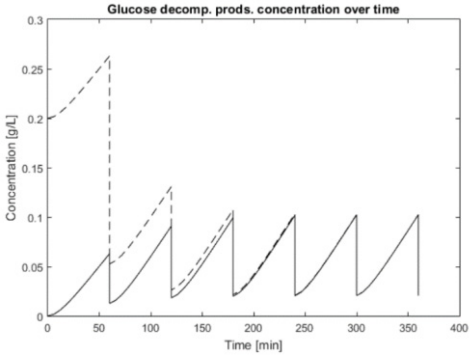

Figure 3 – Two different initial conditions reaching the same IC for glucose decomposition products.

4. Invariant-cycle-oriented design

In practice, the first few cycles will resemble a continuous reactor startup, since subsequent cycles will have different initial conditions. But after enough time, the IC condition will be *the only* operative condition. Thus, the IC is what should be incorporated for equipment and process design, utilizing the results from equations 15 to 20. However, the advantages of this approach are not immediately obvious.

In the presented system, operating with this reutilization strategy allows for reduction of liquid reposition costs, and heating utilities. Also, the concentrated spent liquor could be

utilized for fermentation purposes after adequate treatment. Usually, this liquid must be concentrated prior to further usage - and because of the reutilization scheme, the liquid will naturally be more concentrated even before being treated. This means that lower concentration utilities will be needed, which in turn means lower overall costs.

All the previously mentioned points, however, are not independent from the selected downstream process. Integration is key for the design of the reutilization strategy. In this sense, having explicit, analytical expressions for the IC (Eq. 15 to 20) could allow for optimization opportunities, by manipulating decision variables such as the cycle time t_c, the reposition factor r, or the solid to liquid ratio. As an example, higher values of r cause the initial concentrations to resemble the reposition concentrations more strongly. Taking it to an extreme, when $r = 1$, then the initial concentrations of the IC will be *exactly* the ones from the reposition. This is in fact the case of standard batch operation, where no liquor is reutilized from cycle to cycle.

5. Conclusions and future work

IC conditions could potentially appear in various operation types, the obvious example being the cyclic batch operations. Other examples could include more complex cyclic operations (for instance, Sequential Batch Reactors in the context of wastewater treatment), as well as integration of discrete and continuous flows. This work presents a first approach to a simple case, to illustrate how the methodology works.

Nevertheless, cases may and will arise in which analytical solutions are not attainable, and at that point, a deeper understanding of the IC phenomenon will be needed. It is in this regard that further developments need to be made. Questions such as existence of the IC, or its unicity should be addressed. This has deep implications, connecting to the stability of the solutions and how it interacts with the sequential operation.

Lastly, algorithms may be developed where analytical solutions are not possible, to allow for process integration even in complex operation schemes.

References

R. Aguilar, J.A. Ramirez, G. Garrote, M. Vázquez, 2002, “Kinetic dtudy of the acid hydrolysisof sugar cane bagasse”, Journal of Food Engineering, 55, 309-318.

X. Chen, E. Kuhn, N. Nagle, R. Nelson, L. Tao, N. Crawford, M. Tucker, 2018, “Recycling of Dilute Deacetylation Black Liquor to Enable Efficient Recovery and Reuse of Spent Chemicals and Biomass Pretreatment Waste”, Frontiers in Energy Research.

R. Davis, N. Grundl, L. Tao, M. J. Biddy, E.C.D. Tan, G.T. Beckham, D. Humbird, D.N. Thompson, M.S. Roni, 2018, “Process Design and Economics for the Conversion of Lignocellulosic Biomass to Hydrocarbon Fuels and Coproducts: 2018 Biochemical Design Case Update”.

E. Guerra-Rodriguez, O. M. Portilla-Rivera, L. Jarquín-Enríquez, J. A. Ramírez, Manuel Vázquez, 2012, “Acid hydrolisis of wheat straw: A kinetic study”, Biomass and Bioenergy, 36, 346-355.

Y.C. Park, T.H. Kim, J.S. Kim, 2018, “Flow-Through Pretreatment of Corn Stover by Recycling Organosolv to Reduce Waste Solvent”, Energies, 11.

P. Vergara, F. García-Ochoa, M. Lardero, S. Gutiérrez, J.C. Villar, 2019, “Liquor re-use strategy in lignocellulosic biomass fractionation with ethanol-water mixtures”, Bioresource Technology, 280, 396-403.

Sauro Pierucci, Flavio Manenti, Giulia Bozzano, Davide Manca (Eds.)
Proceedings of the 30th European Symposium on Computer Aided Process Engineering (ESCAPE30), May 24-27, 2020, Milano, Italy.
http://dx.doi.org/10.1016/B978-0-12-823377-1.50096-3

Promo – a Multi-disciplinary Process Modelling Suite

Heinz A Preisig

Dept of Chemical Engineering, Norwegian University of Science and Technology, Trondheim, Norway

Heinz.Preisig@chemeng.ntnu.no

Abstract

Multi-disciplinary, multi-scale simulations are in demand as computing becomes increasingly available and the different disciplines' problem solutions become mature and broadly applicable. Material modelling has taken a lead in the subject and ProMo is one of the possible solutions to the still very intrinsic problem of supporting the process of sketching a process as a topology to an integrated solution solving multi-faceted problems that require bits and pieces from various knowledge domains. ProMo coupled with the open platform of MoDeNa provide an integrated solutions.

Keywords: simulation, ontology, computational engineering

1. Concepts

Modelling of chemical/biological processes is intrinsically a multi-scale, and not at least, a multi-disciplinary task. It incorporates the macroscopic scale of the process, the intrinsic smaller elements that make up the process, the description of the process-enabling control layer and not at least the description of all the materials in that make up the process and are being processed. Often one requires a finer granular model for individual processes where it is necessary to include a minimal level of detail to capture the larger-scale behaviour. Capturing the behaviour of the involved materials is nearly always a major challenge. It is either macroscopic models of generic nature fitted to experimental data or increasingly the option of using molecular modelling or related techniques, such as reported by Klamt (2018) to estimate the physical properties of the involved materials. Mixtures represent one of the main challenges. Experimental data are either difficult to obtain or very expensive to generate.

Multi-scale modelling and consequent simulation are seen as a difficult subject. It requires input from several disciplines' information that requires several specialists. The Framework 7 MoDeNa project (MoDeNa 2016) is a nice demonstration where polyurethane foam was modelled from quantum to mechanical properties. The project used quantum chemistry to model the chemical reactions and molecular modelling for physical properties of the polymer system and the gas phase. On top came several layers of mesoscopic models that yield beyond other things the viscosity for the combined evolving polymer and gas bubbles. At last, computational fluid mechanics reconstructed the growth of the foam in a cylinder that corresponded to the standardised laboratory experiments. The whole is followed by a mechanical analysis, which again stretches the length scales from the molecular level to the mesoscopic structures to the macroscopic mechanical properties of the foam product. The project demonstrates the multi-scale, multi-disciplinary aspect of such a process nicely.

Several of the large companies have established multi-disciplinary modelling groups who have the task to meet these challenges. ProMo is one possible answer as it is the multi-disciplinary aspect that is approached in ProMo: models to be built on the foundation of discipline-specific ontologies.

The ProMo environment grew out of an earlier development, which started in the mid 1980ties with the modelling of life support systems for NASA and eventually resulted in a software package we called Modeller, currently maintained by Mobatec BV (NL). ProMo is ontology-based and enabling the integration of different disciplines' models generically.

2. Approach

ProMo is a pure mathematical modelling tool, which consists of several components that support three classes of users: The first class makes it possible for the expert to capture the domain-specific knowledge in the form of mathematical equations. The second class of users utilises the captured knowledge by using the defined entity models as standard building blocks. The third using the final product to explore the issues defined for the associated case.

2.1. The Expert

The overall philosophy is to build models from principle components, entity models, which describes the conceptional basic units in the discipline.

In physics, depending on the scale, this may be a model for an electron, an atom or a molecule if one requires molecular information or it may be a unit cell if one describes a continuous material. It is the purpose of the model that determines on what level to model and to what level of detail, thus the fundamental granularity of the models to be constructed using the entity models captured in the respective ontology.

The process starts with generating a tree of what later is linked mathematical model ontologies. It reflects the structure of the disciplines. In physics, the tree on the top level typically reflects the fact that one conceptionally distinguishes between continuum models and particulate models. Within the continuum, one has the two classes of phases, namely fluids and solids and fluids split into liquids and gases, for example. On how to structure this tree is up to the experts but may also be taken from the European Material Modelling Council's EMMO, which stands for European Material Modelling Ontology. The EMMO is an attempt to standardise primarily the language, which is used to describe models. Thus defines a taxonometry/syntax that serve the purpose of establishing in the next step the mathematical entity models.

2.2. The Translator

In the broadest sense, a translator is a person who translates a given problem into a solver for the given case. Previously, we would use the term "modeller", though this would also include the expert's activity, namely the definition of the entity models.

2.2.1. Topology

The translator is building the application process model by composing the topology of the process model using the canvas of a graphical tool. The graphical language is purposely kept simple leaning on to the representation introduced in the past (Elve & Preisig 2017). The process begins by utilising the entity models taken from ProMo's initial model library. Each of these entity models is equipped with the graphical symbol.

The translator can choose from whatever ontologies are being made available to him. For example, there is an ontology for physical processes, an ontology that captures the physical property computations based on energy functions constructed from equations of states. An ontology capturing controllers provides the means to construct process models with controllers. An ontology that captures the ecology-related measures or techno-economical measures provides the means to add performance measures. Ontologies may also provide the information of linking in external programs that solve a particular problem, such as molecular dynamics codes, or computational fluid dynamics code.
The constructed topology can be saved either in pieces or as a whole to establish a composite model, which though is stored as an extension to the initial entity model library.

2.2.2. Case
This block building process is followed by an instantiation procedure, where constants and initial conditions are equipped with numerical values and assumptions can be introduced, allowing for the simplification of the build unit model. The initialisation section may also add order-of-magnitude assumptions requiring a model reduction in order to maintain a proper unit model.

2.2.3. Cases of Cases
The so-constructed unit model can then be placed into the extended entity model library where it awaits further use in an even more complex model. The building process is thus recursive, including all disciplines at all times.

2.2.4. Task Factory
The last element in the sequence is the generation of the actual code, a process that is done fully automatically except for instantiating the numerical solver. Here one may choose between different alternatives but also the settings of the parameters controlling the performance of the numerical solver. This approach is applicable if one solves essentially a set of equations that are properly instantiated and structured.

If the model includes the use of external programs, then two things need to happen. The first is the above, namely the parts that are to be solved as sets of equations must be coupled with an appropriate numerical solver, which applies to each cluster of equations. Key is that the tasks are not independent. They have built-in sections that are devoted to the interaction with the other tasks. The overall problem is then represented as a workflow. It is executed in what is currently called an Open System Platform or an Orchestrator, of which the MoDeNa (2016) and the Symphony (Ashibon et al 2015) are examples.

2.3. The User
The term "digital twin" is lately used for a simulation of a specified system. One may project the idea into the "digital twin" that it is meant to behave the same way as the modelled system, where "behave" relates to input/output behaviour: if I tickle it on this point, it does respond in a particular way, kind of thought.

If one allows for "tuning knops" allowing for changing the behaviour and allows for modifying the quantities that relate to defining the operating conditions, then the "digital twin" is to replace the real-world object with a virtual, computational experiment. Driving force to establish a "digital twin" is costs, ability to cover a wide range of operating conditions, experimentation with design parameters, consequently quite

obviously also optimisation an many other attractive possibilities to "play" with the system.

One of the objectives of ProMo is to produce stand-alone digital twins, thus allowing to use it in isolation, out in the plant, or without a network, thereby avoiding all issues about protecting data and other commercial interests.

3. The Challenges

The project has to respond to many challenges. Not at least a social one: anything new is different, and anything different is not what people know. Indeed, this also applies to the theoretical background required to get a complete insight into the definition of patterns that are generic enough to capture the multi-disciplinary, and consequently multi scientific language, problems. It requires a high level of abstraction, while for the users, the interfaces must be simple, self-explainable, nice to look at and not at least functional.

Interoperability of the different parts is a key technical issue. The developments in the Web-based community is moving fast and generates increasingly more facilities to raise the level of abstraction to improve interoperability. Technologies like the semantic network, REST and other efforts move towards a more structured approach to the problem. To mention one of the currently hot issues is to collect data from a distributed set of databases, each of which has a different structure though with related contents.

ProMo implements model reduction technology, thereby removing the effects of some typical assumptions, like order-of-magnitude assumptions often in their core being time-scale assumptions. Pressure dynamics being event-dynamic requires rather sophisticated splitting of the process topology into two (Pujan & Preisig 2020), a slow one for the mass & energy dynamics and one for the pressure/velocity distribution of the fluids in the plant. Othe assumptions lead to overdetermined equation systems because it introduces an algebraic relation between fundamental state variables, therefore requiring a reduction of the state space. A common assumption of the latter type is a constant volume assumption for a multi-phase control volume.

A specific challenge is the design of the input language for the input language. The introduction of explicit naming of the dimensions and associating them with index sets, provided an elegant and efficient solution that certainly is a compromise to the intrinsic, domain-specific terminologies and symbolisms.

3.1. Workflows

When approaching multi-scale modelling and simulation problems, it becomes necessary to enable the use of external programs. It is common that different disciplines generate their own solutions, and it is certainly not productive to re-invent the wheel by mapping the equations into the ontology, define simulation cases and solve them using a numerical solver. Instead, one needs to enable the construction of a workflow, which logically couples different computing activities together. The cited MoDeNa project is an illustrative example. In the ontology, external solutions appear as input/output functions with well-defined interfaces to the calling and receiving code. ProMo represents and handles interfaces such that they are mapped into a data model ontology, which in turn can be used to generate automatically the code pieces that realise the interfaces. The MoDeNa orchestrator, an Open System Platform, executes the workflow using the defined logics, models and external solvers. Obviously, to execute a

workflow, one must have access to the required external codes, which for commercial tools implies having licences for their use.

4. Architecture

ProMo utilises existing ontologies. Specifically the EMMO, European Material Modelling Ontology, is used to describe the physical parts. It introduces the nomenclature, taxonometry of the physics world seen from the material modelling side. ProMo is though not limited to EMMO, but currently also used control in order to enable the simulation of plants. We plan to extend this in the near future to the techno-economic domain, life-cycle analysis and other relevant subject. Figure 1 shows the current arrangements.

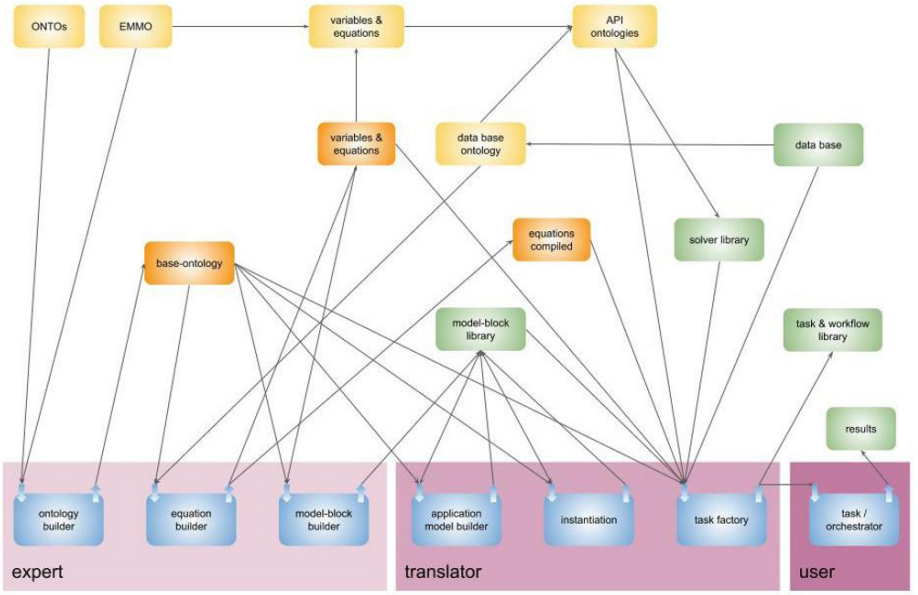

Figure 1: ProMo's components and functionalities

The yellowish boxes are OWL-based ontologies generated and maintained by Protege or from the software using python's "owlready" package. The variable/equations ontology is the core object of interest. It represents a super bipartite graph of variables and equations, where the "super" indicates that a variable may be computed by more then one expression. The latter requirement becomes obvious if one thinks of issues like computing the chemical potential for different phases. The task builder uses a type of reasoner, as they are termed in the internet-related jargon. The reasoner is tailored to process super bipartite graphs. ProMo's equation editor insists of building the equation system systematically, as reported earlier (Preisig 2010), which addresses also very important the indexing issue. The process is preceded by defining the index sets and the object required to capture the topology, thus the incidence matrices. In the equation editor, one starts with defining the constants, the initial conditions of the state equations. One then follows the scheme of defining the integrals of the differential states, followed by the differential balances. Those are defined by giving the flows and the kinetics, latter representing the internal change, of the balance equations. Finally one requires to

close the loop and define the material properties and geometry. The material properties is of particular interest. We favour the idea to use the canonical energy surfaces and the configuration space as defined in the contact geometry theory (Arnold 1989). The specific models for the materials, including mixtures then come in as equation of states and properties are canonical derivatives.

5. Conclusions

ProMo as the principle modelling tool combined with the MoDeNa's composer develop into a powerful tool to model a wide range of processes. The ontology-based approach yields a compact and effective representation of multi-disciplinary model components, which in the continuation can be utilised to build recursively more an more complex models. Equation systems are constructed systematically satisfying stringent consistency conditions resulting in a lower-triagonal multi-bipartite graph, which allows for systematic handling in the task and workflow builder. Particularly, it should be noticed, that a given equation only appears once in contrast to what the standard approach is in block-based modelling tools, both on chemical engineering but also in other domains.

The future looks bright: we have the algebra to generate reduced-order models thereby implementing time-scale and other order-of-magnitude assumptions systematically. This then removes all a priori checks on the equations usually done, like degree of freedom and differential index. Scale integration has no real limits beyond not being able to compute it. ProMo allows to do derivations in the sense that starting with generic equations like the conservation of fundamental extensive quantities, one can generate simplified models through the implementation of assumptions and constraints combined with model reduction. The technology can be extended to include the development of solution algorithms. Here the feature of automatic compilation in any target language is a key.

6. References

Arnold, V I, **1989**, Contact geometry: The geometrical method of Gibbs's thermodynamics, in Proc. Gibbs Symp (new Haven, CT), 163-179

Elve, A T & Preisig, H A, **2017**, Graph-based mathematical modelling – concepts, FOCAPO/CPC

Hashibon, A.; Rasp, T.; Franklin, N.; Tziakos, I.; Pinte, D.; Dadvand, P.; Roig, C.; Mattila, K.; Puurtinen, T.; Hiltunen, K.; Roman-Perez, G.; Garcia, G.; Adler, J. 2015 Common universal data structures (CUDS) and vocabulary in the SimPhoNy integrated framework , INTOP, Workshop of the European Multi-Scale Modelling Cluster EUMMC - Interoperability in MultiscaleModelling of Nano-Enabled Materials, 3, **2015**, Jyväskylä/Finland

Klamt, A. **2018** The COSMO and COSMO-RS solvation models WIREs Comp Mol Sci, 8,

1-11 MoDeNa, **2016,** http://modena.units.it, accessed 11/2019

H.A. Preisig, **2014**, A Graph Approach to Representing the Pressure Distribution in Complex Plants, Comput. Aided Chem. Eng., 33, 865-870

Preisig, H A **2010**, Constructing and maintaining proper process models. Comp & Chem Eng 34(9) 1543-1555

Pujan, R & Preisig, Heinz A, **2020**, Systematic modelling of flow and pressure distribution in a complex tank, Comp Aided Chem Eng, this volume

Sauro Pierucci, Flavio Manenti, Giulia Bozzano, Davide Manca (Eds.)
Proceedings of the 30th European Symposium on Computer Aided Process Engineering (ESCAPE30), May 24-27, 2020, Milano, Italy.
http://dx.doi.org/10.1016/B978-0-12-823377-1.50097-5

Performance Evaluation of Solid Oxide Fuel Cell Coupling to Biogas Tri-reforming with Installation of Hydrogen-Selective Membrane Separator

Saebea D.[a,b*],Soisuwan S.[a,b],Patcharavorachot Y.[c]

[a]*Department of Chemical Engineering, Faculty of Engineering, Burapha University, Chonburi 20131, Thailand*
[b]*Reasearch Unit of Developing technology and Innovation of Alternative Energy for Industries, Burapha University, Chonburi 20131, Thailand*
[c]*Department of Chemical Engineering, Faculty of Engineering, King Mongkut's Institute of Technology Ladkrabang, Bangkok 10520, Thailand*

Abstract

Due to high CO_2 composition in biogas, hydrogen concentration produced from the biogas reforming process is low, which has negative effect on the SOFC efficiency. Therefore, aims of this study are to improve and analyze the performance of solid oxide fuel cell (SOFC) integrated with hydrogen production from tri-reforming process of biogas coupling to hydrogen-selective membrane separator. The simulation results show that the increase of pressure increases the hydrogen separation in Pd/Ag membrane separator. The Pd/Ag membrane separator can separate hydrogen of 47.5 %, at 8 bar. When comparing the integrated system of SOFC and biogas tri-reforming without/with installing hydrogen-selective membrane separator, the efficiency of system with coupling to hydrogen-selective membrane separator is higher than that without coupling to hydrogen-selective membrane separator about 13-14.7 %.

Keywords: Solid oxide fuel cell; Hydrogen-selective membrane separator; Tri-reforming process; Biogas

1. Introduction

Solid oxide fuel cell (SOFC) is interesting device for electricity generation of large scale. It is operated at high temperatures. It has high electrical efficiency, fuel flexibility, and high efficiency system from using high-grade heat of exhaust (Saebea et al., 2018), compared to other types of fuel cell. Hydrogen as fuel is required for SOFC operation to product the electricity via the electrochemical reaction. Generally, hydrogen is mainly produced from fossil resources, i.e., steam reforming of natural gas, fraction of petroleum refining process, and coal gasification (Cruz et al., 2018). To reduce the environmental problem and enhance energy security, the utilization of sustainable and environment-friendly resources to substitute fossil resources has been concerned. Biogas has been considerably received attention because it can be produced through anaerobic digestion from different feedstocks such as seeds, crop residues, woody crops, and agricultural wastes (Ithnin and Hashim, 2019).

There are various reforming processes of hydrocarbon production. The main compositions of raw biogas are methane (40-70%) and carbon dioxide (30-60 %) (Gao et al., 2018). Thus, the biogas can produce hydrogen via the dry reforming in order not to separate CO_2 and to utilize CO_2 as main composition of biogas. However, the dry

reforming is also strongly endothermic reaction and lower hydrogen yield than the steam reforming. To overcome these problems, the tri-reforming is interesting for hydrogen production derived from biogas due to including advantages of steam reforming, partial oxidation, and dry reforming.

Many researchers have been focused on the instillation of increased purified hydrogen process in the SOFC system. The instillation of hydrogen purification process can be improved the SOFC performance. There are various technologies of hydrogen purification. Pd/Ag membrane separator shows an interesting technology for hydrogen purification due to its large solubility of hydrogen over a wide temperature range (Sharma et al., 2017). The installation of Pd/Ag membrane separator after biogas tri-reforming can increase the hydrogen concentration in syngas. However, the suitability of installation of membrane separator for the combined system of SOFC and tri-reforming should be studied. This work aims to study the combined system between SOFC and biogas tri-reforming with/without installing Pd/Ag membrane separator. The effect of pressure on the membrane separation and SOFC electrical efficiency is firstly investigated. Then, the performance of biogas-fuelled SOFC systems with and without installing Pd/Ag membrane separator is compared.

2. Process description

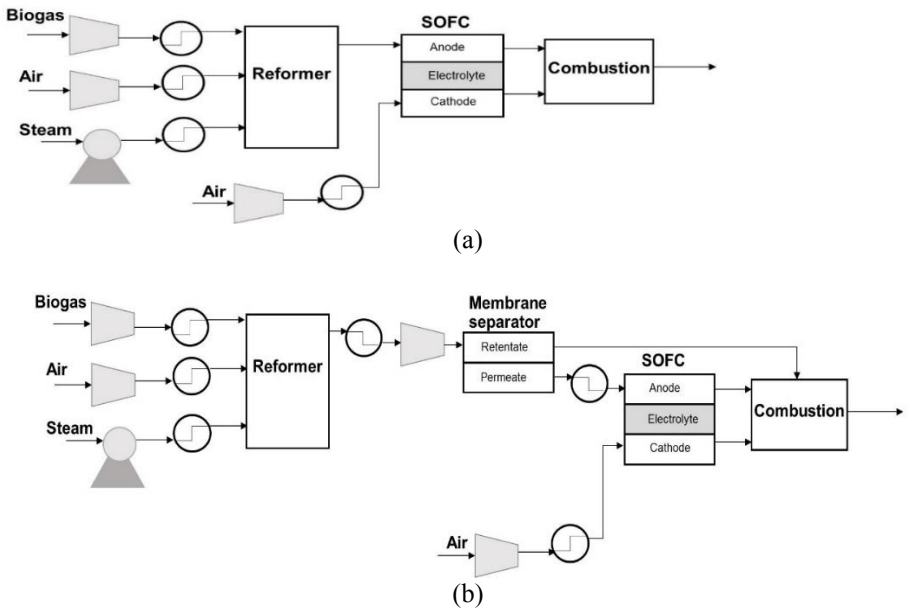

Figure 1: Schematic diagram of the integrated system (a) without and (b) with coupling to hydrogen-selective membrane separator.

The treated biogas is considered as feedstock. Biogas contains 60 %CH_4 and 40 %CO_2. Figure 1(a) shows the integrated systems between SOFC and reformer without coupling to hydrogen-selective membrane separator. From Figure 1(a), the biogas and air are compressed while water is pumped. They are heated at 873 K and fed to the mixer. In tri-reforming process, the syngas is produced from conversion of biogas with steam reforming, partial oxidation, and dry reforming reactions. The reactions of biogas tri-

reforming were reported by Saebea et al. (2019). Then, the syngas is heated and introduced to the fuel channel of SOFC. Meanwhile the compressed air is heated and sent to SOFC at the air channel. The electricity is produced from SOFC via the electrochemical reaction. Figure 1(b) shows the retrofitted system with adding the hydrogen-selective membrane separator between the tri-reforming unit and SOFC. In the integrated systems between SOFC and reformer with coupling to hydrogen-selective membrane separator, the temperature of syngas from reformer is decreased at the suitable condition of hydrogen-selective membrane separator. It is fed to the retentate side of the membrane separator. H_2 from the retentate side permeates through membrane to the permeate side. Subsequently, H_2 from the permeate side is compressed and heated at the operating temperature of SOFC. The exhausted gas from the retentate side of the membrane separator is sent to the combustor.

2.1 *SOFC model*

SOFC can produce the electrical power via the electrochemical reaction. In the cathode side, oxygen ion is produced from the reduction reaction. Oxygen ion diffuses from the cathode to the anode through electrolyze and reacts with hydrogen via the oxidation reaction. Consequently, the electrons are produced and flows to external circuit. This is the generation of the electricity. The SOFC electrical power can be calculated as follows:

$$P_{\text{sofc}} = V \times I \tag{1}$$

where I is the current density and V is the operating voltage. The operating voltage can be evaluated from the reversible voltage (Eq. (2)) subtracted by three main internal voltage losses, i.e., ohmic overpotential (η_{ohmic}), activation overpotentials (η_{act}), and concentration overpotentials (η_{conc}), as shown in Eqs.(3)-(5).

$$E^{\text{OCV}} = E^{0} - \frac{RT}{2F}\ln\left(\frac{P_{\text{H}_2\text{O}}}{P_{\text{H}_2} P_{\text{O}_2}^{0.5}}\right) \tag{2}$$

$$\eta_{\text{ohm}} = iR_{\text{ohm}} \tag{3}$$

$$\eta_{\text{act}} = \frac{RT}{F}\sinh^{-1}\left(\frac{i}{2i_{0,\text{a}}}\right) + \frac{RT}{F}\sinh^{-1}\left(\frac{i}{2i_{0,\text{c}}}\right) \tag{4}$$

$$\eta_{\text{conc,anode}} = \frac{RT}{2F}\ln\left(\frac{p_{\text{H}_2\text{O,TPB}} p_{\text{H}_2,\text{f}}}{p_{\text{H}_2\text{O,f}} p_{\text{H}_2,\text{TPB}}}\right) + \frac{RT}{4F}\ln\left(\frac{p_{\text{O}_2,\text{a}}}{p_{\text{O}_2,\text{TPB}}}\right) \tag{5}$$

where $p_{\text{i,}}$ is the partial pressure of H_2, H_2O and O_2 at air and fuel channels; $p_{\text{i,TPB}}$ is the partial pressure of gases at triple phase boundary; R_{ohm} is the internal electrical resistance; $i_{0,\text{a}}$ and $i_{0,\text{c}}$ are the exchange current density pre-exponential factors of the anode and cathode respectively. The electrochemical parameters can refer from Saebea et al. (2018).

2.2 *Hydrogen-selective membrane separator model*

Pd/Ag composite membrane is used as hydrogen-selective membrane in separator. H_2 flux is the amount of H_2 diffusing through membrane as follows:

$$J_{H_2} = P_i \cdot \frac{A}{L} \cdot \left(\left(\mathrm{P_r} \cdot X_{\mathrm{H_2,r(ave)}} \right) - \left(P_\mathrm{p} \cdot X_{\mathrm{H_2,p}} \right) \right) \tag{6}$$

Gas flux is function of the membrane permeability (Pi), the membrane thickness (L), and the gas concentration. P_r and P_p are pressure at retentate side and permeate side, respectively. $X_{\mathrm{i,r(ave)}}$ is average mole fraction of species i at the feed side. $X_{\mathrm{i,p}}$ is mole fraction of species i at the permeate side. The membrane permeability depends on the temperature can be explained by Arrhenius equation.

$$X_{\mathrm{i,r(ave)}} = Q_0 \exp\left(\frac{-Ea}{RT} \right) \tag{7}$$

Q_0 is pre-exponential factor; and Ea is the activation energy for permeation. Q_0 and Ea are 2.06×10^{-8} mol/m.s.$Pa^{0.5}$ and Ea = 2.59×10^{3} kJ/mol, respectively (Faizal et al, 2015). SOFC electrical efficiency (η_{el}) and the thermal efficiency (η_{th}) are calculated by using the following expression;

$$\text{SOFC electrical efficiency} = \frac{P_{\mathrm{sofc}}}{\dot{n}_{\mathrm{H_2}} LHV_{\mathrm{H_2}} + \dot{n}_{\mathrm{CO}} LHV_{\mathrm{CO}} + \dot{n}_{\mathrm{CH_4}} LHV_{\mathrm{CH_4}}} \tag{8}$$

$$\text{Thermal efficiency} = \frac{Q_{\mathrm{rec}} - Q_{\mathrm{use}}}{\dot{n}_{\mathrm{i}} LHV_{\mathrm{i}}} \tag{9}$$

where $\dot{n}_{\mathrm{i}}$ is the molar flow rate of species i at inlet; LHV_i is the lower heating value; Q_{use} is the overall thermal energy consumption in the system; and Q_{rec} is the thermal energy obtained from the combustion referring to 100 ºC.

3. Results and discussion

3.1. Effect of pressure on hydrogen-selective membrane separator

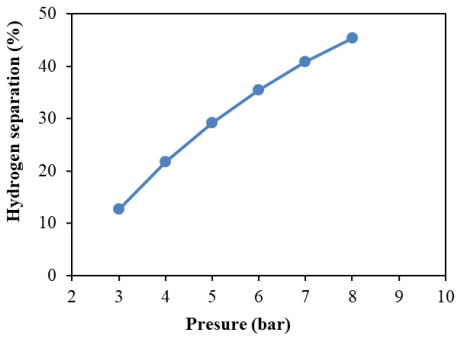

Figure 2: Effect of operating pressure on hydrogen separation.

The operating pressure of system has a direct effect on the retentane pressure of hydrogen-selective membrane separator. Figure 2 shows the effect of various retentate pressures in the range of 3-8 bar on the percentage of hydrogen separation, at 623 K. The membrane area and thickness are specified at 5,200 m^2 and 200 μm, respectively. From Figure 2, it indicates that the separation of hydrogen from syngas increases with increasing the retentane pressure. At pressure of 8 bar, Pd/ Ag membrane separator can separate hydrogen of 47.5 %. This can be explained that the increase of retentate pressure results in enhancing the difference of pressure between retentate and permeate sides, leading to the rise of driving force of hydrogen flux and diffusing hydrogen through membrane.

3.2. Comparison of systems without/with H2 selective-membrane separator

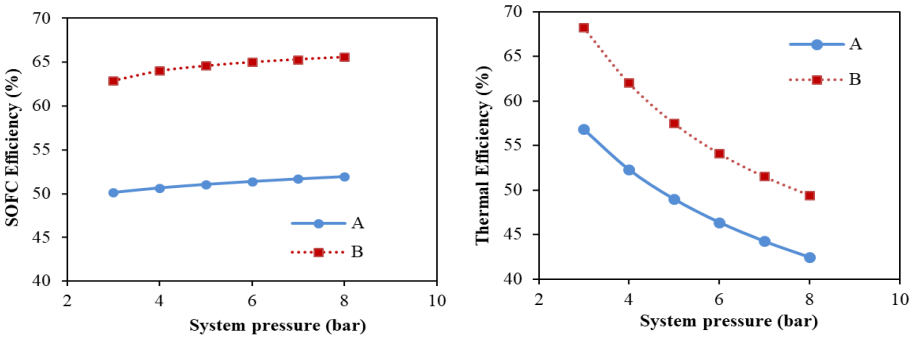

(a) (b)

Figure 3: Comparison of the integrated system of SOFC and tri-reforming without coupling to hydrogen-selective membrane separator (System A) and that with coupling to hydrogen-selective membrane separator (System B) at various operating pressures (a) SOFC efficiency and (b) thermal efficiency.

The integrated systems of SOFC and tri-reforming without or with coupling to hydrogen-selective membrane separator at various operating pressures in the range of 3 to 8 bar are compared. The biogas tri-reforming process and SOFC of both systems are operated at the same condition. SOFC was operated at the fuel utilization of 75 %, air ratio of 8.5, and temperature 1073 K. For the system with hydrogen-selective membrane separator, the membrane was fixed at area of 5,500 m^2 and temperature of 623 K. Figure 3(a) indicates the SOFC with coupling to hydrogen-selective membrane separator can increase the SOFC efficiency about 13-14.7 %, compared with system without coupling to hydrogen-selective membrane separator. This is because the fuel fed to SOFC in system with coupling to hydrogen-selective membrane separator has rather high hydrogen purity. The increase of hydrogen concentration in the gas input to SOFC results in the enhancement of SOFC power density. The increment of system pressure has a more effect on the increase of efficiency of system with coupling to hydrogen-selective membrane separator than that without coupling to hydrogen-selective membrane separator, as shown in Figure 3(a). It can be explained that the increasing in the operating pressure has a positive effect on both membrane separator and SOFC. Meanwhile, the increase of pressure has a minor influence on SOFC efficiency under operation at high pressure. From 3(b), the thermal efficiency of both systems reduces with incresing pressure. When

comparing both systems, the thermal efficiency of system coupling to Pd/Ag membrane separator is higher than that without coupling to Pd/Ag membrane separator.

4. Conclusions

In this work, the integrated system SOFC and biogas tri-reforming without/with coupling to Pd/Ag membrane separator were investigated and compared. The hydrogen permeability of Pd/Ag membrane separator at various pressures was firstly studied. The increase of retentate pressure enhances the hydrogen permeability of Pd/Ag membrane separator specified membrane area of 5,200 m^2 and 200 μm. At pressure of 8 bar, the hydrogen permeability is highest of 47.5 %. Moreover, the SOFC efficiency of the integrated system of SOFC and biogas tri-reforming without/with coupling Pd/Ag membrane separator increases whereas thermal efficiency of both systems reduces with increasing the pressure. When comparing the both systems, the electrical and thermal efficiencies of the integrated system with coupling to the Pd/Ag membrane separator are higher than that without coupling to the Pd/Ag membrane separator.

Acknowledgments

Support from the Thailand Research Fund and the Office of the Higher Education Commission (MRG6280043) and Burapha University is gratefully acknowledged.

References

P. L. Cruz, Z. Navas-Anguita, D. Iribarren, J. Dufour, 2018, Exergy analysis of hydrogen production via biogas dry reforming. International Journal of Hydrogen Energy, 43, 1168-11695.

H. M. Faizal. Y. Kawasaki, T. Yokomori, T. Ueda, 2015, Experimental and theoretical investigation on hydrogen permeation with flat sheet Pd/Ag membrane for hydrogen mixture with various inlet H_2 mole fractions and species. Separation and Purification Technology, 149, 208–215.

N. H. C. Ithnin, H. Hashim, 2019. Predictive modelling for biogas generation from palm oil mill effluent (POME). Chemical Engineering transaction, 72, 313-318.

Y. Gao, J. Jiang, Y. Meng, F. Yan, A. Aihemaiti, 2018, A review of recent developments in hydrogen production via biogas dry reforming. Energy Conversion and Management, 171, 133-135.

D. Saebea, S. Authayanun, Y. Patcharavorachot, N. Chatrattanawet, A. Arpornwichanop, 2018, Electrochemical performance assessment of lowtemperature solid oxide fuel cell with YSZ-based and SDC-based electrolytes. International Journal of Hydrogen Energy, 43, 921-931.

D. Saebea, S. Authayanun, A. Arpornwichanop, 2019, Process simulation of bio-dimethyl ether synthesis from tri-reforming of biogas: CO_2 utilization. Energy, 175, 36-45.

D. Saebea, S. Authayanun, Y. Patcharavorachot, A. Arpornwichanop, 2018, Performance evaluation of biogas-fed solid oxide fuel cell system coupling with CO_2-selective membrane separator. Chemical Engineering transaction, 70, 1963-1968.

R. Sharma, A. Kumar, R. K. Upadhyay, 2017, Performance comparison of methanol steam reforming integrated to Pd/Ag membrane: Membrane reformer vs. membrane separator. Separation and Purification Technology, 183, 194–203.

Sauro Pierucci, Flavio Manenti, Giulia Bozzano, Davide Manca (Eds.)
Proceedings of the 30th European Symposium on Computer Aided Process Engineering (ESCAPE30), May 24-27, 2020, Milano, Italy.
http://dx.doi.org/10.1016/B978-0-12-823377-1.50098-7

A Grain-Scale Study of Swelling Composite Porous Media Made of Fibres and Particles

Tommaso Santagata[a], Roberto Solimene[b]*, Gilberto Aprea[c], Piero Salatino[a]

[a]*Dipartimento di Ingegneria Chimica, dei Materiali e della Produzione Industriale, Università degli Studi di Napoli Federico II, P.le Tecchio, Napoli, Italy*
[b]*Istituto di Ricerche sulla Combustione, Consiglio Nazionale delle Ricerche, P.le Tecchio, Napoli, Italy*
[c]*Fater S.p.A., Via Alessandro Volta, 10, Pescara, Italy*
solimene@irc.cnr.it

Abstract

A numerical study based on the discrete element method (DEM) is presented for the characterization of morphological properties of absorbent hygiene products (AHP) relevant to their performance. The model was developed in YADE, an open source software focused on DEM. The simulations reproduce the samples as they were granular beds. The code allows an easily tuning of relevant numerical and physical parameters. A series of preliminary estimations has been necessary to faithfully represent a realistic AHP sample. The results of the DEM computational experiments have been compared to the values obtained from physical experiments reported in literature.

Keywords: porous media, swelling, absorbent hygiene products, SAP, DEM.

1. Introduction

In the field of absorbent porous media, a high demand for accurate and reliable measurements strongly drives the scientific community to take the knowledge further. Many permeable objects show a change in their domain sizes while fluids pass across them. This phenomenon can affect clay soils used in agricultural or urban activities (Aksu et al., 2015), wood and other materials employed as building material (Karoglou et al., 2005), absorbent hygiene products (AHPs) such as diapers and pads (DeVane et al., 2016; Diersch et al., 2010; Diersch et al., 2011), foods (Datta, 2007) or printer paper (Masoodi and Pillai, 2010). Among them all, an improvement in the characterization and prediction of AHPs' properties might immediately result in a considerable upgrading in daily living conditions for many people.

The latest AHPs are made of two components: the cellulose fibre matrix (fluff), which acts as a carrier material for the liquid, and the super absorbent polymer (SAP) particles, which is the absorbent and swelling material. SAP is a partially cross-linked polyelectrolyte, which can retain the water through the solvation of the free end-parts of the polymer chains. While the polymers chains absorb water molecules, the particle of SAP swells up to reach the size where the equilibrium of internal and external forces (cross-links forces and interphase polymer–solvent forces, respectively) is guaranteed. SAP particles change their stiffness during the process, passing from the sugar-like hardness of the dry state to a gel softness at a high liquid uptake (Zohuriaan-Mehr and Kabiri, 2008).

A good prediction of the performances of these products is essential to avoid gel-blocking and loss of liquid, due to too high or too low SAP amount, respectively (Buchholz and

Graham, 1997). Numerical simulations of absorbent pads may effectively speed up the design of AHPs, reducing the number of tests conducted on these materials. Since a representation of the fluid in a realistic pore scale would not be affordable because of the high computational costs, several simplified models were born in the last decades, to represent the fluid intrusion inside the porous material (Diersch et al., 2011). One of the coarsest methods is to consider the whole sample as a single porous block, considering spatial averaged properties in the whole domain. For instance, the porosity and the permeability are evaluated from the local liquid uptake of the material in each point of the domain. However, to resolve the mass and momentum balances of the liquid, the constitutive equations of the materials need to be determined through the experiments, which significantly increase the modelling effort (Diersch et al., 2010).
Although the analysis of porous materials at the pore scale must be avoided for large domains, the study of a representative elementary volume (REV) (Bear, 1988) at this scale may considerably increment the knowledge on the investigated sample. In this study we performed several simulations at the REV scale with the discrete element method (DEM) (Cundall and Strack, 1979) to obtain the constitutive equation of the higher scales' method. The exploited technique allows to literally assemble the sample by adding the constituents of the composite material. To have a realistic representation of the physical sample, many parameters at the REV scale need to be defined, such as the sizes and the shape of the particles.

2. Model description

The model developed here is a DEM model in which the two phases, SAP particles and fluff, are treated as two interacting granular phases. While the SAP phase is actually a granular phase, the same cannot be said for the fluff phase, which is composed by a very intricated fibrous net. Then, it is necessary to consider a granular phase, whose bulk properties resemble those of the fluff.
Heyden (2000) has studied the mechanical properties of fluff exploited in AHP products through numerical simulations in which a periodic cubic domain made of cellulose fibres is studied. Many parameters have been investigated, such as the fibres bulk density or the interactions between the fibres, and the results are shown in terms of stiffness and Poisson's ratio of the ensemble. Among the long list of results obtained by Heyden (2000), in the present model the properties of the fluff phase considered are reported in Table 1.
The stiffness of the SAP particles decreases with the liquid uptake (Zohuriaan-Mehr and Kabiri, 2008). While a dry SAP particle is conventionally represented as a sugar-like granule, and so it is quite hard, during the water absorption the mechanical properties change, and they become softer and softer. In the work of Sweijen et al. (2017a), the mechanical properties of SAP particles were related to the liquid uptake as shown in the following equation:

$$E = 2\left(1+\nu\right)G = 2\left(1+\nu\right)\frac{\beta}{Q^{\frac{1}{3}}} \tag{1}$$

where G is the shear modulus, ν is the Poisson's ratio, Q is the liquid uptake, expressed as mass of liquid absorbed per mass of polymer, and β is related to the shear modulus at the maximum swelling extent and it depends on the specific polymer. The Poisson's ratio used here is ν_{SAP}=0.5, typical of non-deformable materials.

Table 1 Values extracted from Heyden (2000) and exploited in the present work.

Cell size (mm)	Number of fibres per cell	Cross section area of the fibre (μm^2)	Porosity	Interactions among fibres
1	250	250	0.96	1

The liquid uptake of SAP particles was modelled in the time domain by means of a constant swelling rate of the absorbent material. In order to dynamically represent the liquid uptake, Sweijen et al. (2017b) developed a model in terms of radial coordinates adopting a water diffusion coefficient inside the SAP particles of D=10^{-3}–10^{-4} cm^2/min. In the present study, however, a higher value of the diffusion is requested, to speed up the simulations. In order to reduce the forces exerted on particles due to a so fast swelling, a high damping factor on contact force components is implemented. Being the interaction of the granular phases during the SAP swelling a quasi-static phenomenon, this artifice brings stability to the simulation, without compromising the quality of model outcomes. For more information regarding the usage of the damping factor in DEM simulations, the reader is referred to the website of the YADE software, where a large bibliography is quoted (Šmilauer and Chareyre, 2015).

3. General scheme of the simulations

Two assemblies of particles of two different sizes are generated in a parallelepiped domain. The size of the cross-section area is the characteristic length of the REV considered. The height of the box is much longer than the characteristic length, to generate two assemblies of non-overlapping particles, avoiding many numerical issues. The number of the spheres are calculated to have a determined basis weight of the two granular phases.

The particles fall driven by gravity and they deposit at the bottom of the domain. Once the unbalanced force of the particles ensemble is below 0.001 (Šmilauer and Chareyre, 2015), the deposition is considered completed and the result is an uncompressed granular material, with SAP particles and fluff pseudo-particles well-mixed. At this point, a plate with no thickness is generated above the particles.

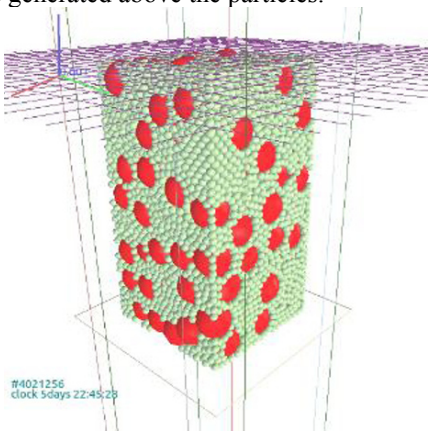

Figure 1 A generic simulated sample. The green (lightest) particles are the fluff pseudo-particles, the red (darkest) ones are the SAP particles.

While it moves downwards, it compresses the granular bed below. The compression is calculated as the ratio between the sum of the forces acting on the plate and the cross-section area of the domain. At the desired value of compression, the plate stops and the initial thickness and porosity of the sample are registered.
At the end of the compression, the SAP particles are allowed to swell, in a very controlled way. During the swelling of the SAP particles, the size of the whole sample is blocked by the domain walls and the plate above the granular bed, as shown in Figure 2. The volumetric growth of the particles increases the sum of the forces exerted on the plate above, and so the compression value of the sample. The considered swelling step conventionally corresponds to a liquid uptake of 1 g/g. Then, the plate slowly moves upwards to relax the sample and to bring back the compression value to the desired value. Therefore, the plate stops and a new swelling step starts with the same procedure. The algorithm goes on until the maximum liquid uptake of SAP particles is obtained. For each absorption level, the porosity and the thickness of the granular bed are registered. The results are shown in plots comparing these two quantities with the uptake of the liquid by SAP particles (Santagata et al.; 2019).

4. Preliminary simulations on fluff pseudo-particles

Before simulating realistic materials, we performed a convergence analysis on the size of the sample and of the fluff pseudo-particles and a sensitivity analysis on Young's modulus of the fluff pseudo-particles. Heyden (2010) reported that varying the bulk density, and so the porosity, for a given value of the interaction between fibres, has an effect on Young's modulus of the sample. Considering the void space between the granules (η), the porosity of the fluff pseudo-particles must be lower than the desired value (ε_{eq}=0.96-0.92, Table 1). With η=0.36 as the void fraction of a face-centred cubic structure, the fluff pseudo-particle intrinsic porosity was set at ε_f=0.9.
The results of the preliminary evaluations are summarized in Table 2. The size of the fluff grains and of the domain (REV) guarantees an error below 10 % respect to the ideal case (infinitesimal grains and infinitive domain, respectively). No relevant differences were observed varying the Young's modulus around the value reported by Heyden (2010).

5. Simulation of realistic absorbent layers

Once all model parameters are defined, the simulation results can be compared with the experimental values, to validate the model against the experiments. Some previously analysed absorbent pads were considered as a benchmark (Santagata et al.; 2019).

Table 2 Parameters obtained from the preliminary simulations.

Fluff pseudo-particle porosity	Fluff pseudo-particle radius (µm)	Young's modulus (kPa)	Domain (REV) size (mm)
0.9	100	200	4

Table 3 Properties of the different composite materials considered as a benchmark.

Label	Basis weight	SFR	Initial thickness	Initial porosity
1	502 g/m^2	0.67	3.31 mm	0.886
2	569 g/m^2	0.89	3.72 mm	0.889
3	669 g/m^2	1.22	4.22 mm	0.888
4	803 g/m^2	1.67	4.22 mm	0.868

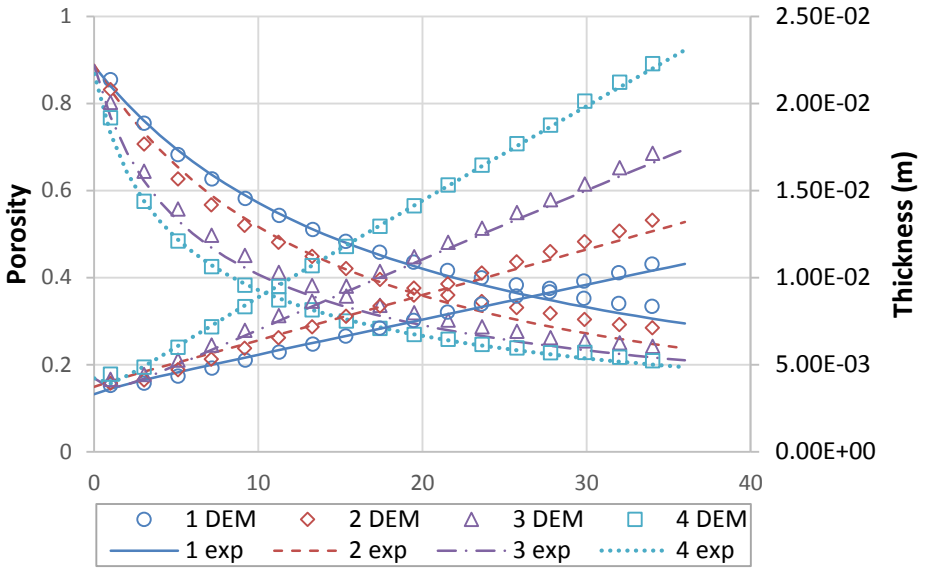

Figure 2 Porosity and thickness values from DEM and lab experiments. The properties of the investigated samples are listed in Table 3.

In Figure 2 the variables porosity and thickness are plotted against the liquid uptake of SAP particles. The basis weights and the initial thickness and porosity of these composite materials are reported in Table 3. The results of simulations carried out on the investigated samples show an excellent agreement with the experimental results, as shown in Figure 2. For each of the three samples, both the thickness and the porosity trends with the increasing liquid uptake are well predicted.

6. Conclusions

A DEM model of absorption in swelling porous media relevant to absorbent hygiene products is presented. The sample is described as a granular bed of two different granular matters: the super absorbent polymer (SAP) particles and the fluff pseudo-particles. Only uniform distributions are considered, for each phase. The water absorption of SAP particle is simulated increasing the size and decreasing the elastic modulus of the grains. The fluff pseudo-particles do not change in size or in mechanical properties during the absorption of liquid. The compression of the simulated samples is imposed and mimics the conventional body weight on absorbent products. The porosity and the thickness of the swollen samples are evaluated against the liquid uptake.

The parameters needed for DEM modelling were taken from both literature and preliminary simulations. A sensibility analysis on the size and the stiffness of the fluff pseudo-particles has been done. The size of the domain considered and the estimation of the REV have been evaluated as well.

The model has been validated against experimental results. The investigated samples have different compositions of SAP and fluff and express different changes in porosity and thickness. For all the four investigated samples, a remarkable agreement between the experiments and the DEM results is achieved. Further estimations and comparisons on

many more samples are required to confirm the predictability of the model. Altogether, the model developed in the present study has the potential to effectively predict the volume averaged properties of porous swelling media and may lead to a deeper knowledge of morphological modifications occurring in similarly soft and swelling materials.

References

I. Aksu, E. Bazilevskaya, Z.T. Karpyn,.2015, Swelling of clay minerals in unconsolidated porous media and its impact on permeability, GeoResJ., 7, 1–13

J. Bear, Dynamics of fluids in porous media, 1988, Dover Publications, Inc., Mineola, NY

R.H. Brooks, A.T. Corey, 1966, Properties of porous media affecting fluid flow, J. Irrig. Drain. Div., 92, 2, 61–90

F.L. Buchholz, A.T. Graham, 1997, Modern superabsorbent polymer technology, Wiley-VCH, Boca Raton, FL

P.A Cundall, O.D.L. Strack, 1979, A discrete numerical model for granular assemblies, Geotechnique, 29, 1, 47–65

A.K. Datta, 2007, Porous media approaches to studying simultaneous heat and mass transfer in food processes. I: Problem formulations, J. Food Eng., 80, 1, 80–95

R.H. DeVane, 2016, The Procter and Gamble Company: Current State and Future Needs in Materials Modeling, Materials Research for Manufacturing, Springer series in Material Science, 224, 303–328

H.-J.G. Diersch, V. Clausnitzer, V. Myrnyy, R. Rosati, M. Schmidt, H. Beruda, B.J.. Ehrnsperger, R. Virgilio, 2010, Modeling Unsaturated Flow in Absorbent Swelling Porous Media: Part 1. Theory, Transp. Porous Media, 83, 3, 437–464

H.-J.G. Diersch, V. Clausnitzer, V. Myrnyy, R. Rosati, M. Schmidt, H. Beruda, B.J.. Ehrnsperger, R. Virgilio, 2011, Modeling Unsaturated Flow in Absorbent Swelling Porous Media: Part 2. Numerical Simulation, Transp. Porous Media, 86, 3, 753–776

M.T. Van Genuchten, 1980, A closed form equation for predicting the hydraulic conductivity of unsaturated soils, Soil. Sci. Soc. Am. J., 44, 892–898

S. Heyden, 2000, Network modelling for the evaluation of mechanical properties of cellulose fibre fluff, Lund University

M. Karoglou, A. Moropoulou, A. Giakoumaki, M.K. Krokida, 2005, Capillary rise kinetics of some building materials, J. Colloid Interface Sci., 284, 1, 260–264

R. Masoodi, K.M. Pillai, 2010, Darcy's law-based model for wicking in paper-like swelling porous media, AIChE J., 56, 9, 2257–2267

T. Santagata, R. Solimene, G. Aprea, P. Salatino, Modelling and experimental characterization of unsaturated flow in absorbent and swelling porous media – Part 2: Material characterization, *submitted to Chem Eng J.*

V. Šmilauer, B. Chareyre, 2015, DEM Formulation, Yade Documentation 2nd ed.

T. Sweijen, B. Chareyre, S.M. Hassanizadeh, N.K. Karadimitriou, 2017a, Grain scale modelling of swelling granular materials; application to super absorbent polymers, Powder Technol., 318, 411-422

T. Sweijen, C.J. van Duijin, S.M. Hassanizadeh, 2017b, A model for diffusion of water into a swelling particle with a free boundary: Application to a super absorbent polymer particle, Chem. Eng. Sci., 172, 407–413

M.J. Zohuriaan-Mehr, K. Kabiri, 2008, Superabsorbent polymer materials: a review, Iran. Polym. J., 17, 6,451–477

Sauro Pierucci, Flavio Manenti, Giulia Bozzano, Davide Manca (Eds.)
Proceedings of the 30th European Symposium on Computer Aided Process Engineering (ESCAPE30), May 24-27, 2020, Milano, Italy.
http://dx.doi.org/10.1016/B978-0-12-823377-1.50099-9

Assessing the Sensitivity of Technical Performance of three Ethanol Production Processes based on the Fermentation of Steel Manufacturing Offgas, Syngas and a 3:1 Mixture Between H_2 and CO_2

Eduardo Almeida Benalcázar [a,b], Henk Noorman[b,c], Rubens Maciel Filho[a], John Posada[b]

[a] *Department of Product and Process Development, Faculty of Chemical Engineering, State University of Campinas, Av. Albert Einstein 500, 13083-852, Campinas – SP, Brazil.*
[b] *Department of Biotechnology, Faculty of Applied Sciences, Delft University of Technology, Van der Maasweg 9, 2629 HZ, Delft, the Netherlands.*
[c] *DSM Biotechnology Center, A. Fleminglaan 1, 2613 AX, Delft, the Netherlands.*

Abstract

This study assesses the sensitivity of the technical, environmental and economic performance of three ethanol production process based on the fermentation of three gas mixtures: i) CO-rich flue gas from steel manufacturing, ii) biomass-based syngas with a H_2/CO ratio of 2 and iii) a 3:1 combination between H_2 and CO_2. The sensitivity analysis is based on stochastic bioreactor simulations constructed by randomly generated combinations of eight parameters that command the fermentation process i.e., temperature, pressure, gas feed dilution with an inert components, ethanol concentration, height of the liquid column, mass transfer coefficients, superficial gas velocity and, acetic acid co-production.

The sensitivity analysis identified that the bioreactor technical performance is highly sensitive to variations on pressure, liquid column height and the mass transfer coefficients. The pressure mainly improves mass transfer and consequently ethanol productivity whereas liquid column height improves the gas residence time and consequently the efficiency in the gas utilization. The trend was common for the three gas supply options. The results suggested that in order to produce an optimal bioreactor design, there are options to optimize the productivity and the gas utilization simultaneously.

The results from the sensitivity analysis may help guiding a subsequent multi-objective process optimization study.

Keywords: ethanol, syngas fermentation, sensitivity analysis, stochastic simulation.

1. Introduction

Prevention of global warming is currently pushing global policy-making towards the reduction of CO_2 emissions, which are mostly derived from the combustion of fossil fuels (Boden et al., 2013). Lignocellulosic biomass is seen as an alternative sources of fuels and chemicals that during their life cycle may result in lower carbon emissions (Liu et al., 2017). These feedstocks are abundant and renewable and can be thermochemically converted into gas mixtures containing mainly CO, H_2, CO_2 (Heidenreich and Foscolo,

2015; Matsakas et al., 2017). The gas is commonly referred as syngas and can be used as feedstock for fermentations (Kundiyana et al., 2010).
Only limited details about the industrial process performance have been made public. What has been reported is that microbial selectivity for ethanol falls around 95 % and that gas utilization overpasses 90 % (Simpson, 2018); additionally, it is argued that the exist an energy surplus generated from the based fermentation of syngas (Handler et al., 2016). Moreover, the claims that ethanol concentration in the fermentation media could be held above 50 g/L and overhead pressure should not overpass 3 atm (Li et al., 2017; Trevethick et al., n.d.) have been patented.
In consequence, a mathematical model was developed and reported elsewhere [Almeida, forthcoming] to simulate ethanol production in a bubble column bioreactor fed by CO, H_2 and CO_2 mixtures. That model is used to quantify the sensitivity of the bioreactor technical performance to certain parameters that command the fermentation step. The assessment is applied to three different gas feed compositions.

2. Methodology

2.1. Process configurations

The three process configurations which have been considered in this study differ on the gas production processes: CO-rich BOF offgas from the steel-manufacturing process; *ii)* a 3:1 mixture between H_2 and CO_2, and *iii)* syngas with a H_2/CO ratio of 2.
The fermentation process consists on a bubble column bioreactor fed by the gas mixture. The ethanol produced inside the fermentor is at all times given two possible exit routes *i.e. i)* pre-concentrated along the offgas, where it is subsequently condensed and recovered from by flash separation, and *ii)* along a liquid broth outflow. Acetic acid, also exits the bioreactor along the liquid outflow. The alcohol is distilled out of the two streams by atmospheric distillation and finally dehydrated. The unconsumed gas is here treated as waste and combusted before being released into the atmosphere, as proposed by Handler et al, 2016 (Handler et al., 2016).

2.2. Simulation of the fermentation processes

The simulation of the bioreactor uses a model previously presented elsewhere [Almeida, forthcoming]; therefore, only the basic structure of such model is introduced here.

2.2.1. Simulation of the fermentations of BOF offgas and the H_2/CO_2 mixture

The fermentation model for these two cases is formed by *i)* a black-box model of the main reactions carried out by acetogenic bacteria and *ii)* a mass transfer model of the large bubble column bioreactor. The stoichiometry of the microbial metabolic reaction is constructed by the combination of the catabolic and anabolic reactions.
Ethanol and acetic acid are the products of catabolism, thermodynamically powered by the uptake of the electron donors, CO and H_2. Cells are produced during anabolism. The Gibbs free energy harvested from the electron donors (CO and H_2) during catabolism powers cells. The uptake of CO and H_2 are assumed to follow hyperbolic kinetics. The maximum uptake rate of the electron donors is estimated using thermodynamics (Heijnen, 2013).
Mass transfer in the bioreactor is simulated assuming the process operates in continuous mode at steady-state (Heijnen and van't Riet, 1984; van't Riet and Tramper, 1991). Mass transfer is driven by the energy input provided by the gas sparging [42]. A system of non-linear equations formed by the mass balances is solved by a constrained optimization of the volumetric ethanol productivity (R_{et}).

2.2.2. Simulation of the fermentation of biomass-derived syngas

Since the black-box model of microbial reactions is only able to simulate the consumption of either CO or H_2, the simulation of biomass-derived syngas (BDS) consumption is done indirectly adding the mass and energy streams contributions from CO fermentation (the BOF offgas case) and H_2/CO_2 fermentation cases. The H_2/CO ratio in syngas is assumed to be 2.

2.3. Process assessment and performance indicators

The ethanol production processes are evaluated from the perspective of the bioreactor technical performance through the ethanol volumetric productivity (R_{et}) and gas utilization (U_S), defined as the percent change on the gas molar flow rate of electron donors across the fermentor.

2.4. Stochastic simulation of the bioreactor

The operation of the bioreactor is simulated under 5000 randomly generated combinations of eight input parameters, which are considered to command the bioreactor performance *i.e., i)* process temperature (T), *ii)* top reactor pressure (p_t), *iii)* gas feed dilution (f_{Dil}), *iv)* maximum ethanol concentration (C_{et}^{max}), *v)* liquid column height (h_L), *vi)* mass transfer coefficient factor (f_{k_La}), *vii)* acetic acid production factor (f_{Ac^-}) and *viii)* the pressure-corrected superficial gas velocity (v_{sG}^c). See Table 1.

Table 1 Maximum and minimum values used the input parameters in the stochastic bioreactor simulation

Input parameter	T **[°C]**	p_t **[atm]**	f_{Dil} **[%vol.]**	C_{et}^{max} **[g/L]**	h_L **[m]**	f_{k_La} **[-]**	f_{Ac^-} **[%]**	v_{sG}^c **[m/s]**
Minimum value	27	0.5	0	30	8	0.5	0	0.07
Maximum value	67	3.5	45	120	64	2.0	0.15	0.14

2.5. Sensitivity analysis

The sensitivity of bioreactor and overall process performance indicators (or output parameters - OP) is evaluated using standardized regression coefficients since it offers "a good approximation to a global sensitivity with affordable computational demand" (Morales-Rodriguez et al., 2012), and allows establishing a hierarchical classification of the model IP's according to the level of impact on a determined OP. This method implies that process performance has a linear relation with each input parameter (IP). The reliability of the regression coefficients is evaluated using coefficients of determination (R^2).

3. Results and discussion

3.1. Distribution trends in the performance indicators

The distribution of the bioreactor performance indicators corroborates previous observations suggesting that the fermentation of H_2-rich gases may lead to higher productivity and gas utilization than the fermentation of CO-rich gases (Noorman and Heijnen, 2017) (Almeida et al., forthcoming) (see Figure 1). The observation is sustained on the fact that H_2 mass transfer to the liquid is faster than CO transfer; since mass transfer is linearly related for bioreactor productivity, then a higher mass transfer rate means higher productivity. Similarly, a higher productivity means than the gas consumption inside the bioreactor is more efficient, and therefore, gas utilization is higher.

Since BDS fermentation is simulated using the respective contributions of CO and H_2/CO_2 fermentations, then it is reasonable that bioreactor performance lies between the

performances obtained for BOF offgas and H_2/CO_2 fermentations. In addition, as the H_2/CO ratio in the syngas is 2, then the performance of the syngas fermentor falls closer to that of the H_2/CO_2 fermentor than to the CO fermentor.
By comparing bioreactor performances with other study (Almeida et al., forthcoming) there is a high probability that gas utilization may be improved far more than bioreactor productivity. This observation is based on the fact that while the median gas utilization

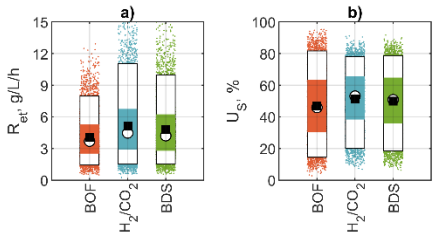

Figure 1 Boxplots summarizing the distribution of a) ethanol productivity and b) gas utilization. On the boxplots: the colored vertical rectangles represent the extension of the 25th and 75th percentiles; the white vertical rectangles represent the extension of the 5th and 95th percentiles; the small colored dots represent the outliers; the white circles represent the median values; and the black square boxes represent the mean values.

values are 45 and 53 % for CO and H_2/CO_2 fermentations, respectively, the median ethanol productivities are 3.7 and 4.5 g/h/L for CO and H_2/CO_2 fermentations, respectively. However, this observation does not necessarily suggest that productivity cannot be further increased, as there is a 25 % probability (see 25th and 75th percentiles in Figure 1) that R_{et} may increase to 5.3, 6.8 and 6.2 g/L/h for BOF offgas, H_2/CO_2 and BDS fermentations, respectively. In addition, there is a 5 % probability (see 5th and 95th percentiles in Figure 1) that R_{et} may be further improved to 8, 11 and 10 g/L/h for the same three gas supply options. That would be an improvement between 2 and 2.5 times from a previous report (Almeida et al., forthcoming).
Similarly, gas utilization in the bioreactor could be as high as 63, 66 and 65 % for BOF offgas, H_2/CO_2 and BDS fermentations, respectively with a 25 % probability. Gas utilization could climb to 82, 78 and 79 % for the same gas supply options with a 5 % probability. It is therefore, more probable that the BOF offgas fermentation case has a better gas utilization than the fermentation of H_2-rich gases.
In addition, although it may be encouraging to see that gas utilization could surpass 90 % as previously reported by LanzaTech, such achievement is highly unlikely with the proposed bioreactor configuration as there is only a 5 % probability that U_S may increase beyond 80 % (see Figure 1).

3.2. Sensitivity analysis by the standardized regression coefficients

Table 2 shows the standardized regression coefficients (β_{IP_i}) of ethanol volumetric productivity and gas utilization in the bioreactor. The value of R^2 is also included in Table 2 to show which OP's had an acceptable linear relation with all the IP's.
The relation between R_{et} and U_S and all the IP's is acceptably linear for the three gas supply cases. Remarkably, the IP's hierarchical classification is also common for these two OP's in three gas supply cases. Considering that the sign of the β_{IP_i} indicates whether the influence of each IP on one OP is positive or negative, R_{et} may be largely improved by p_t and the f_{k_La} and in a lower level of influence by the v_{sG}^c. On the other hand, the most detrimental IP for R_{et} is the gas feed dilution. According to [Almeida, forthcoming],

these four IP's are deeply related to the rate of mass transfer in the bioreactor. f_{k_La} and v^c_{sG} determine the value of the mass transfer coefficients while p_t and f_{Dil} determine the value of the partial pressures of the electron donors in the gas phase and therefore their saturation concentrations in the liquid phase and thus, their driving forces for mass transfer. While increases in p_t will widen the mass transfer driving force, increases in dilution will shrink the driving force.

Table 2 Standardized regression coefficients (β_{IP_i}) relating the model outputs with each input parameter

OP	Gas supply case	IP								R^2
		T	p_t	f_{Dil}	C^{max}_{et}	h_L	f_{k_La}	f_{Ac^-}	v^c_{sG}	
R_{et}	BOF	0.13	0.57	-0.36	0.02	0.14	0.54	-0.06	0.32	0.90
	H_2/CO_2	0.07	0.61	-0.43	0.00	0.07	0.45	-0.05	0.28	0.86
	BDS	0.09	0.60	-0.41	0.00	0.09	0.48	-0.05	0.29	0.88
U_S	BOF	0.18	-0.05	0.01	0.01	0.77	0.55	0.00	-0.13	0.95
	H_2/CO_2	0.11	0.15	-0.04	0.01	0.77	0.54	0.00	-0.13	0.92
	BDS	0.14	0.08	-0.02	0.01	0.78	0.55	0.00	-0.13	0.95

Gas utilization, in turn may be mostly improved by h_L, f_{k_La} and T, while v^c_{sG} will be slightly detrimental. The sensitivity of U_S to h_L is remarkably high as the β_{IP_i} is the closest to one, the maximum possible value. This relation is due to the fact that as the liquid column height increases, so does the residence time of the gas inside the bioreactor. On the other hand, v^c_{sG} offers the opposite effect: as the gas velocity through the bioreactor increases, the residence time decreases. In addition, the influence of f_{k_La} and T over U_S could be regarded as a side effect of their positive influence over R_{et}, which means that the mass transfer increases, the gas consumption is more efficient.

The influence of ethanol concentration over R_{et} and U_S is negligible according the estimated β_{IP_i}; the lack of mathematical connection between this IP and the two specified OP's (Almeida et al., forthcoming) might be the cause of this negligible influence of C^{max}_{et} over bioreactor performance. Thus, regarding the fact that possible inhibition by ethanol is not considered by the electron uptake kinetic expressions in the black-box model of microbial reactions, the negligible influence of C^{max}_{et} might be somewhat underestimated. The similarity between the sensitivities for the three gas supply cases is caused by the fact that the operation of the bioreactor does not differ significantly when either CO or H_2 are the electron donors (Almeida et al., forthcoming). However, the intensity of such sensitivities differ between the three cases. For example, BOF offgas fermentation R_{et} is the most benefited indicator when the mass transfer coefficient factor increases. Similarly, due to the inhibition of CO at high partial pressures, the bioreactor pressure has a negative effect over gas consumption in the BOF offgas case while pressure is mostly beneficial for the fermentation of H_2-rich gases.

4. Conclusions

The present study showed that ethanol volumetric productivity could be as high as 8, 11 and 10 g/L/h for the fermentation of BOF offgas, H_2/CO_2 and biomass-derived syngas, respectively. This increase may be achieved by a combination of high mass transfer coefficients, high top bioreactor pressure and large gas flow rates across the bioreactor.

These three IP's improve mass transfer rates and therefore ethanol productivity. In addition, the dilution of the gas feed is to be avoided since it has the most negative effect over productivity. The IP's that increase the productivity also have a positive impact on gas utilization. However, gas utilization may be mainly improved by tall bioreactors where the residence times are higher.

References

Boden, T., Andres, R., Marland, G., 2013. Global, Regional, and National Fossil-Fuel CO2 Emissions (1751 - 2010) (V. 2013). https://doi.org/10.3334/CDIAC/00001_V2013

Handler, R.M., Shonnard, D.R., Griffing, E.M., Lai, A., Palou-Rivera, I., 2016. Life Cycle Assessments of Ethanol Production via Gas Fermentation: Anticipated Greenhouse Gas Emissions for Cellulosic and Waste Gas Feedstocks. Industrial & Engineering Chemistry Research 55, 3253–3261. https://doi.org/10.1021/acs.iecr.5b03215

Heidenreich, S., Foscolo, P.U., 2015. New concepts in biomass gasification. Progress in Energy and Combustion Science 46, 72–95. https://doi.org/10.1016/j.pecs.2014.06.002

Heijnen, J., 2013. A thermodynamic approach to predict black box model parameters for microbial growth, in: Biothermodynamics. EPFL Press, Switzerland.

Heijnen, J.J., van't Riet, K., 1984. Mass transfer, mixing and heat transfer phenomena in low viscosity bubble column reactors. The Chemical Engineering Journal 28, B21–B42. https://doi.org/10.1016/0300-9467(84)85025-X

Kundiyana, D.K., Huhnke, R.L., Wilkins, M.R., 2010. Syngas fermentation in a 100-L pilot scale fermentor: Design and process considerations. Journal of Bioscience and Bioengineering 109, 492–498. https://doi.org/10.1016/j.jbiosc.2009.10.022

Li, X., Cossey, B.J., Trevethick, S.R., 2017. Fermentation Of Gaseous Substrates. US 9,617,509 B2.

Liu, W., Zhang, Z., Xie, X., Yu, Z., von Gadow, K., Xu, J., Zhao, S., Yang, Y., 2017. Analysis of the Global Warming Potential of Biogenic CO2 Emission in Life Cycle Assessments. Scientific Reports 7. https://doi.org/10.1038/srep39857

Matsakas, L., Gao, Q., Jansson, S., Rova, U., Christakopoulos, P., 2017. Green conversion of municipal solid wastes into fuels and chemicals. Electronic Journal of Biotechnology 26, 69–83. https://doi.org/10.1016/j.ejbt.2017.01.004

Morales-Rodriguez, R., Meyer, A.S., Gernaey, K.V., Sin, G., 2012. A framework for model-based optimization of bioprocesses under uncertainty: Lignocellulosic ethanol production case. Computers & Chemical Engineering 42, 115–129. https://doi.org/10.1016/j.compchemeng.2011.12.004

Noorman, H.J., Heijnen, J.J., 2017. Biochemical engineering's grand adventure. Chemical Engineering Science 170, 677–693. https://doi.org/10.1016/j.ces.2016.12.065

Simpson, S.D., 2018. CCU-Now: fuels and chemicals from Waste.

Trevethick, S.R., Bromley, J.C., Waters, G.W., Kopke, M., Tran, L., Jensen, R.O., n.d. Multi-stage Bioreactor Processes. US 9834792 B2.

van't Riet, K., Tramper, J., 1991. Basic bioreactor design. M. Dekker, New York.

Sauro Pierucci, Flavio Manenti, Giulia Bozzano, Davide Manca (Eds.)
Proceedings of the 30th European Symposium on Computer Aided Process Engineering (ESCAPE30), May 24-27, 2020, Milano, Italy.
http://dx.doi.org/10.1016/B978-0-12-823377-1.50100-2

Techno-economic and Environmental Assessment of Electrofuels: a Case Study of Gasoline Production using a PEM Electrolyser

Diego Freire Ordóñez [a,*], Gonzalo Guillén-Gosálbez [b]

[a] *Department of Chemical Engineering, Imperial College London, South Kensington, London, SW7 2AZ, UK*

[b] *Institute for Chemical and Bioengineering, Department of Chemistry and Applied Biosciences, ETH Zürich, Vladimir-Prelog-Weg 1, 8093, Zürich, Switzerland*
dmf15@ic.ac.uk

Abstract

This work assesses, technically, economically and environmentally, the production of a liquid electrofuel, with the potential to replace conventional petrol. A conceptual design of a Power-to-Liquids process, which considers wind electricity and captured CO_2, was taken as a starting point for developing a process model in the commercial software Aspen Plus. The flowsheet includes water electrolysis, and the reverse water-gas shift (rWGS), Fischer-Tropsch (FT) and hydrocracking (HC) processes. The environmental impact assessment (EIA) of the process was conducted by means of the SimaPro 8 software, following a cradle-to-gate scope and the ReCiPe 2016 LCA damage model. The economic analysis was carried out in Aspen Process Economic Analyzer, after including the quoted costs for the electrolyser and reactors. We found that under current market conditions, the production cost of the electrofuel is higher than that of petrol in the UK for 2018 (10.03 USD/GGE and 1.71 USD/gal, respectively). However, the produced fuel shows better environmental performance than conventional gasoline in all three categories at the endpoint level (Human health, Ecosystems and Resources), which should become a major driver for its widespread adoption.

Keywords: Electrofuel production, Techno-economic assessment, Environmental Impact assessment, Sensitivity analysis, Uncertainty analysis

1. Introduction

Transportation is known as one as the most demanding consumers of energy in Europe and around the world. Nowadays, most of the fuels utilised for transportation are produced from fossil feedstocks. This makes this sector one of the main contributors to global warming, being responsible at present for more than 20% of the emissions of greenhouse gases (Brynolf *et al.*, 2018). In this context, electrofuels based on CO_2 have gained increasing significance during the last years. An electrofuel can be defined as a carbon-based fuel, ideally neutral concerning greenhouse gas emissions, that is obtained from carbon dioxide and water, employing renewable electricity as the primary source of energy (Ridjan *et al.*, 2016; Brynolf *et al.*, 2018). Hence, these fuels are regarded as a viable alternative to address climate change and energy security of supply (Schemme *et al.*, 2017), while contributing to overcome the problems associated with the intermittency of renewable sources.

In this work, we propose an integrated approach to evaluate techno-economically and environmentally a production process to obtain liquid fuel with similar properties to that of conventional petrol. The methodology followed through this case study provides a solid base that can be replicated to assess and compare the integral performance of other Power-to-Liquid (PtL) and Power-to-Gas (PtG) processes.

2. Methodology

2.1. Model description

A simulation model was run in Aspen Plus, based on a previous conceptual process design (König *et al.*, 2015), which is illustrated in Fig. 1.

2.1.1. Hydrogen Production

Wind power is utilised to produce hydrogen through water electrolysis. A PEM (Polymer Exchange Membrane) electrolyser was simulated based on a previous study (Michailos *et al.*, 2019), and incorporated in the original flowsheet. This type of electrolyser was considered due to its maturity (high TRL) and current market availability (Schmidt *et al.*, 2017).

2.1.2. Carbon dioxide capture

Post-combustion capture of carbon dioxide from flue gas streams was considered as main carbon source. The capturing process was not simulated, but rather its environmental impacts were retrieved from a previous study (Iribarren *et al.*, 2013).

2.1.3. Syngas Production

The reduction of carbon dioxide (CO_2) to carbon monoxide (CO) is achieved through the reverse water-gas shift reaction (rWGS):

$$CO_2 + H_2 \leftrightarrow CO + H_2O \qquad \Delta H = 41.2\,\text{kJ/mol} \tag{1}$$

For this study, it was considered a nickel-based catalyst, with Al_2O_3 as base support material (Frazier *et al.*, 2015)

2.1.4. Fischer-Tropsch (FT) synthesis

The FT process comprises a set of polymerisation chemical reactions through which liquid hydrocarbons can be obtained from syngas. In this study, a cobalt-based catalyst (Jungbluth *et al.*, 2007) was employed since it is widely used in FT industrial applications. The products of the Fischer-Tropsch synthesis are FT gases and FT waxes.

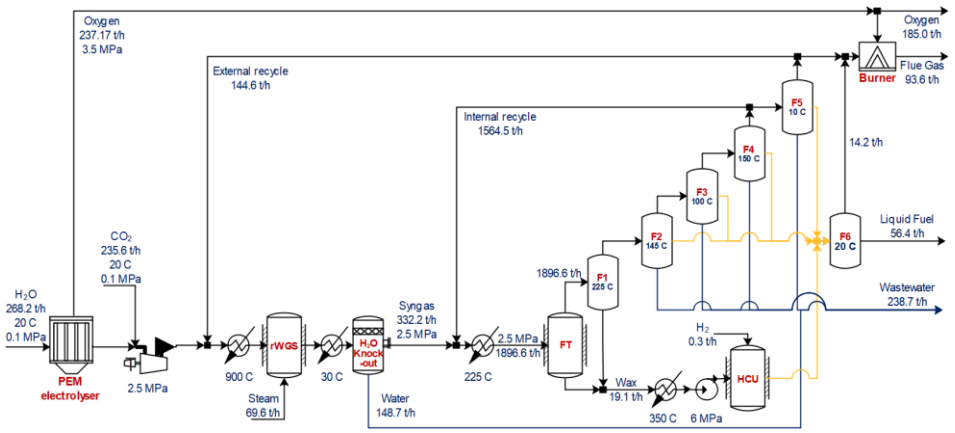

Figure 1. Process flowsheet

2.1.5. Hydrocracking Process

Hydrocracking is a catalytic cracking method supported by high partial hydrogen pressure by which hydrocarbon chains are rearranged and broken, and hydrogen is added to aromatics and olefins to produce naphthenes and alkanes (Viswanathan, 2017). A platinum-based catalyst (Calemma *et al.*, 2010) was considered because of high hydrogenation/dehydrogenation activity for heavy hydrocarbon cracking.

2.1.6. Separation and upgrading of products

The FT gas and the product from hydrocracking are separated in flash drums, thereby exploiting the different volatilities of the products (Fig. 1)

2.2. Economic Analysis

The CAPEX and OPEX of the flowsheet were estimated using the results from Aspen Process Economic Analyzer, after including the quoted costs for the electrolyser and reactors. The latter were obtained by applying Eq. (2), with information retrieved from several sources (Albrecht *et al.*, 2017; Dimitriou *et al.*, 2015; Hoseinzade and Adams, 2019; Keith *et al.*, 2018; Michailos *et al.*, 2019; Posdziech *et al.*, 2019; Wind Power Offshore, 2018). All costs, including raw materials, utilities, products and equipment, were updated to 2018, except for the PEM electrolyser that was projected for 2020. Two main scenarios were analysed; one considering the wind power cost for the electrolyser to be free and the other with a cost of 0.0744 USD/kWh, which was the reported cost in the UK for 2018.

$$\mathrm{PC} = \mathrm{PC}_{\mathrm{ref}} \cdot \left(\frac{S}{S_{\mathrm{ref}}} \right)^{D} \cdot \left(\frac{\mathrm{CEPCI}_{2018}}{\mathrm{CEPCI}_{\mathrm{ref}}} \right) \quad (2)$$

Each case study was also evaluated with and without heat integration, which was regarded through energy targeting in the composite curves of the process. Finally, a sensitivity analysis was performed on the main CAPEX and OPEX variables along with a Monte Carlo-based uncertainty analysis. For the latter, a normal distribution with a standard deviation of 20% was assumed for the uncertain parameters. Both analyses were applied to the case study in which a non-zero cost of electricity was evaluated.

2.3. Environmental Impact Assessment (EIA)

In general terms, an Environmental Impact Assessment (EIA) is a standard methodology to evaluate and mitigate the negative consequences caused by a project on its operation area and surroundings.

In this study, an EIA was conducted based on a cradle-to-gate approach and the life cycle impact model ReCiPe 2016, through the commercial software SimaPro. In addition, an uncertainty analysis was performed through a Monte Carlo Assessment. The life cycle assessment of the PEM electrolyser was not included in this analysis since its construction is considered to have negligible influence compared to the electrolysis process itself (Bareiß *et al.*, 2019). The inventory data were retrieved from the previous simulation.

3. Results and Discussion

The results of the annualised costs and the net production costs for this case study are shown in Fig. 2 and Fig. 3. It can be seen that the estimated net production cost (NPC) of the electrofuel, assuming a zero-cost for the electricity from wind power, is 2.84 USD/GGE without heat integration and 2.58 USD/GGE after applying heat integration through pinch analysis.

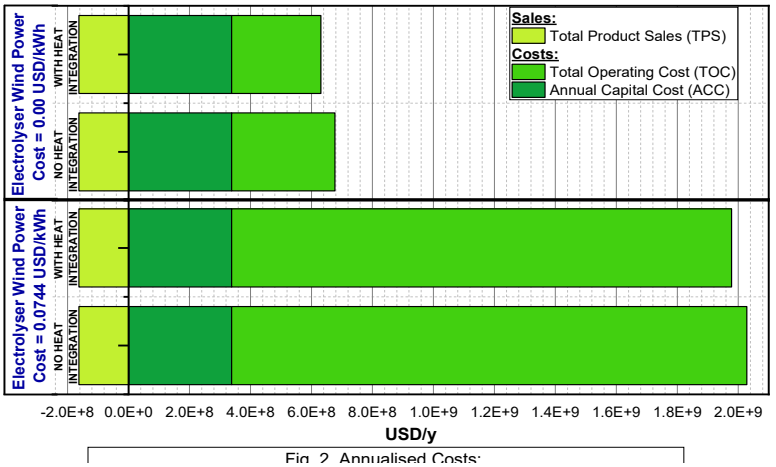

Fig. 2. Annualised Costs; Wind Power Cost for the electrolyser: 0.00 USD/kWh and 0.0744 USD/kWh

On the other hand, when including the actual cost of the electricity from wind power, the NPC is 10.28 USD/GGE without heat integration and 10.03 USD/GGE after heat integration. In all cases, the results show that the production cost of the electrofuel is higher than that of the conventional petrol in the UK, which is approximately 1.71 USD/gal (Open Government License v3.0, 2018).

As expected, it can be seen from the sensitivity analysis (Fig. 4) that the operating costs have more influence than the capital costs on the net production cost of the fuel, especially the costs of the electricity from wind power as and CO_2, and the revenue from a potential sale of oxygen. Therefore, these three variables were considered for the uncertainty estimation through the Monte Carlo simulation, whose results showed a minimum NPC of 4.53 USD/GGE and a maximum NPC of 14.91 USD/GGE.

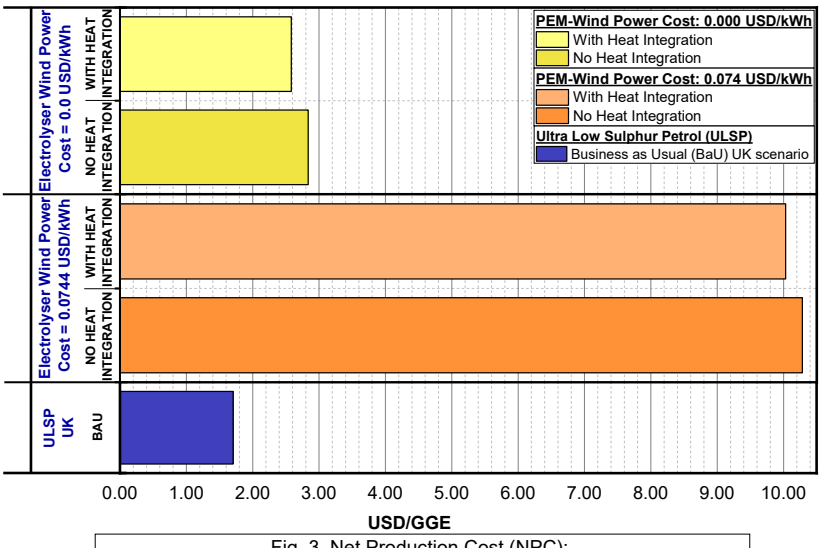

Fig. 3. Net Production Cost (NPC); Wind Power Cost for the electrolyser: 0.00 USD/kWh and 0.0744 USD/kWh

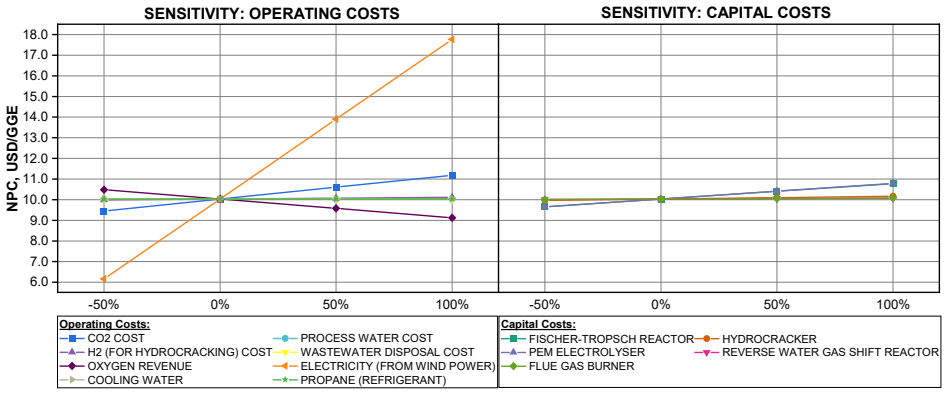

Fig. 4. Sensitivity analysis of cost parameters on the NPC; Wind Power Cost: 0.0744 USD/kWh

From the life cycle inventory (LCI) analysis at the endpoint level (Fig. 5), it can be observed that the environmental performance of the electrofuel is better than that of conventional petrol, in all three categories. However, there is high uncertainty in the results of the electrofuel since most inputs for the analysis come from the simulation of a conceptual design rather than from measurements from operating processes.

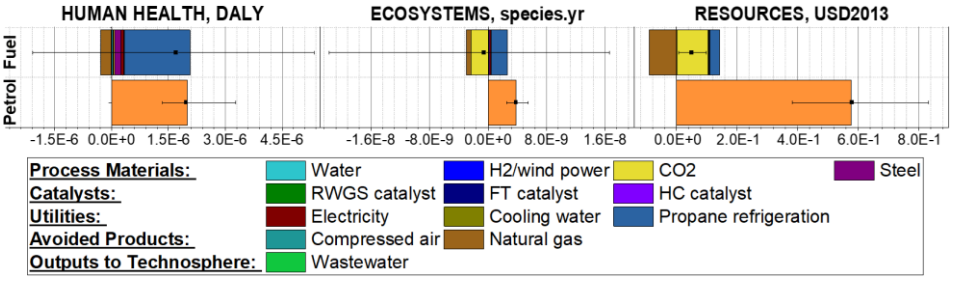

Fig. 5. ReCiPe 2016 LCI analysis at the endpoint level including absolute uncertainties

4. Conclusion

Here we carried out an economic and environmental assessment of an electrofuel using process simulation, LCA and uncertainty analysis. Under the actual market conditions, the production of the electrofuel based on the studied process would not be economically viable since its net production cost would be around 10.03 USD/GGE while the production cost of gasoline in the UK is currently around 1.71 USD/gal. However, it can be noted the potential benefits of the produced fuel from an environmental point of view. According to the results of the ReCiPe 2016 LCI analysis at the endpoint level, it can be concluded that the obtained electrofuel would have lower environmental impact compared to conventional petrol in all three categories of the analysis (Human health, Ecosystems, and Resources). This is particularly clear in the "Resources" category, for which there would be approximately 90% less impact in comparison to gasoline.

Hence, as the renewable electricity and carbon capture costs are expected to fall, and taxes on CO_2 emissions are anticipated to be applied in the coming years, the production of electrofuels may be regarded as a promising alternative to decarbonise the transportation sector.

References

F. Albrecht, D. König, N. Baucks and R.-U. Dietrich (2017), "A standardized methodology for the techno-economic evaluation of alternative fuels – A case study", *Fuel*, Vol. 194, pp. 511–526.

K. Bareiß, C. de La Rua, M. Möckl and T. Hamacher (2019), "Life cycle assessment of hydrogen from proton exchange membrane water electrolysis in future energy systems", *Applied Energy*, Vol. 237, pp. 862–872.

S. Brynolf, M. Taljegard, M. Grahn and J. Hansson (2018), "Electrofuels for the transport sector. A review of production costs", *Renewable and Sustainable Energy Reviews*, Vol. 81, pp. 1887–1905.

V. Calemma, C. Gambaro, W. Parker, R. Carbone, R. Giardino and P. Scorletti (2010), "Middle distillates from hydrocracking of FT waxes: Composition, characteristics and emission properties", *Catalysis Today*, Vol. 149 No. 1-2, pp. 40–46.

I. Dimitriou, P. García-Gutiérrez, R. Elder, R. Cuéllar-Franca, A. Azapagic and R. Allen (2015), "Carbon dioxide utilisation for production of transport fuels. Process and economic analysis", *Energy & Environmental Science*, Vol. 8 No. 6, pp. 1775–1789.

R. Frazier, E. Jin and A. Kumar (2015), "Life Cycle Assessment of Biochar versus Metal Catalysts Used in Syngas Cleaning", *Energies*, Vol. 8 No. 1, pp. 621–644.

L. Hoseinzade and T. Adams (2019), "Techno-economic and environmental analyses of a novel, sustainable process for production of liquid fuels using helium heat transfer", *Applied Energy*, Vol. 236, pp. 850–866.

D. Iribarren, F. Petrakopoulou and J. Dufour (2013), "Environmental and thermodynamic evaluation of CO2 capture, transport and storage with and without enhanced resource recovery", *Energy*, Vol. 50, pp. 477–485.

N. Jungbluth, R. Frischknecht, Faist Emmenegger, M., Steiner, R. and M. Tuchschmid (2007), "Life Cycle Assessment of BTL-fuel production: Inventory Analysis. Deliverable: D 5.2.7.".

D. Keith, G. Holmes, D. St. Angelo and K. Heidel (2018), "A Process for Capturing CO2 from the Atmosphere", *Joule*, Vol. 2 No. 8, pp. 1573–1594.

D. König, M. Freiberg, R.-U. Dietrich and A. Wörner (2015), "Techno-economic study of the storage of fluctuating renewable energy in liquid hydrocarbons", *Fuel*, Vol. 159, pp. 289–297.

S. Michailos, S. McCord, V. Sick, G. Stokes and P. Styring (2019), "Dimethyl ether synthesis via captured CO2 hydrogenation within the power to liquids concept. A techno-economic assessment", *Energy Conversion and Management*, Vol. 184, pp. 262–276.

Open Government License v3.0 (2018), "Weekly road fuel prices. Statistical data set", available at: https://www.gov.uk/government/statistical-data-sets/oil-and-petroleum-products-weekly-statistics (accessed 2 August 2019).

O. Posdziech, K. Schwarze and J. Brabandt (2019), "Efficient hydrogen production for industry and electricity storage via high-temperature electrolysis", *International Journal of Hydrogen Energy*, Vol. 44 No. 35, pp. 19089–19101.

I. Ridjan, B. Mathiesen and D. Connolly (2016), "Terminology used for renewable liquid and gaseous fuels based on the conversion of electricity. a review", *Journal of Cleaner Production*, Vol. 112, pp. 3709–3720.

S. Schemme, R. Samsun, R. Peters and D. Stolten (2017), "Power-to-fuel as a key to sustainable transport systems – An analysis of diesel fuels produced from CO2 and renewable electricity", *Fuel*, Vol. 205, pp. 198–221.

O. Schmidt, A. Gambhir, I. Staffell, A. Hawkes, J. Nelson and S. Few (2017), "Future cost and performance of water electrolysis: An expert elicitation study", *International Journal of Hydrogen Energy*, Vol. 42 No. 52, pp. 30470–30492.

B. Viswanathan (2017), *Energy sources: Fundamentals of chemical conversion processes and applications*, Elsevier, Amsterdam, Boston.

Wind Power Offshore (2018), "UK offshore capped at €63/MWh for next auction", available at: https://www.windpoweroffshore.com/article/1519177/uk-offshore-capped-%E2%82%AC63-mwh-next-auction (accessed 15 June 2019).

Sauro Pierucci, Flavio Manenti, Giulia Bozzano, Davide Manca (Eds.)
Proceedings of the 30th European Symposium on Computer Aided Process Engineering (ESCAPE30), May 24-27, 2020, Milano, Italy.
http://dx.doi.org/10.1016/B978-0-12-823377-1.50101-4

Dynamic Simulation of Chemical Looping Combustion in Packed Bed Reactors

Vlad C. Sandu, Calin C. Cormos, Ana-Maria Cormos*

Babes-Bolyai University, Faculty of Chemistry and Chemical Engineering, Arany Janos 11, Postal code: RO-400028, Cluj-Napoca, Romania
cani@chem.ubbcluj.ro

Abstract

Chemical looping combustion (CLC) is a promising energy conversion technology for fossil fuel combustion with inherent carbon dioxide separation and minimum energy and cost penalties for CO_2 capture. Designing and setting the optimum operating conditions for the CLC reactors are important steps to be taken before implementing the process on an industrial scale. In this work, a dynamic mathematical model has been developed to simulate packed bed reactors used in a methane-based chemical looping combustion process with iron-based oxygen carrier. The air and fuel reactor models were interconnected with the models describing the purge steps of the process to highlight the dynamic behaviour of the entire process. The developed model was used to predict (in space and time): gas flow profile, gas composition distribution, behaviour of oxygen carrier and temperature profiles inside the air and fuel reactors. The simulation results of the 1D model had been compared with the experimental data published in the literature. The model developed is able to describe the process very accurately, for a wide range of gas flow rates. Increasing the flowrate by 20% of the base value lead to a shorter time in which the process achieved stationarity by approximately 300 s (for oxidation step). During the reduction step, the reaction rate decreases very fast at a solid conversion above 85%.

Keywords: Flexible energy conversion systems, Carbon Capture and Storage (CCS), Chemical looping combustion, Packed bed reactors, Dynamic modelling and simulation.

1. Introduction

There are numerous methods for reducing greenhouse gas emissions (mainly CO_2) into the atmosphere, such as decreasing the global energy consumption by increasing the efficiency of energy consumption, or turning to alternative energy sources (wind or solar energy). However, since most of the world's electric energy comes from fossil fuel-based power plants, which produce a large amount of CO_2, carbon capture and storage (CCS) technologies seem to be a viable solution, with the potential to reduce CO_2 emissions by 90%.

Chemical looping combustion (CLC) is a promising energy conversion technology for fossil fuel combustion with inherent carbon dioxide separation and minimum energy losses. In CLC, oxygen is brought into contact with the fuel through an oxygen carrier (OC) material, a metal oxide that can alternately be oxidized and reduced. An interconnected fluidized bed system has often been used (Chisalita and Cormos 2018). The main drawbacks of the concept for fluidized reactors are related to the transport of the OC (Adanez et al., 2012). In a recent work, Noorman et al. (2011) proposed a

reactor concept based on packed bed reactor technology, in which the solids are stationary and are alternately exposed to reducing and oxidizing conditions via periodic switching of the gas feed streams. The advantages of reactor concepts based on packed bed reactor technology are that the separation of gas and particles is intrinsically avoided, the reactor design can be much more compact, and they allow for better utilization of the OC. A purge step can be used in between the oxidation and reduction steps in order to avoid formation of explosive mixtures and to provide a better use of the heat produced during oxidation (usually an exothermic process) in reduction step (usually endothermic).

Setting the optimum operating conditions for the CLC reactors are important steps to be taken before implementing the process on an industrial scale. In this work, a dynamic mathematical model was developed in MATLAB/Simulink to simulate a packed bed reactor used in alternating steps for a methane-based CLC process with an iron-based OC. The steps studied in a full cycle were reduction of oxygen carrier, purge, OC oxidation of oxygen carrier, purge. A graphical representation of the dynamic CLC reactor is presented Figure 1. Although a single reactor was considered, it will be referred to as a fuel reactor during the reduction step and air reactor during the oxidation step.

The OC considered was activated ilmenite, an iron/titan oxide. Furthermore, this work assumed only iron-based OC, with the simplified oxidation and reduction reactions presented in Eqs. (1-3). The ferric component was Fe_2O_3, while the ferrous one was represented by FeO.

Initially, methane gas enters fuel reactor, filled with the iron-based OC, where Eq. 1 takes place. After the oxygen from the carrier is exhausted, the inflow of methane is stopped and a purge step takes place with a CO_2 stream to remove the unreacted methane. Subsequently, a stream of air enters the air reactor during the regeneration step, in which the oxidation reaction (Eq. 2) takes place. Finally, after the iron-based OC is regenerated, another purge step with CO_2 is required to clear the unreacted oxygen and provide a better use of the heat produced during oxidation.

$$4Fe_2O_3 + CH_4 \rightarrow 8FeO + CO_2 + 2H_2O \quad (1)$$

$$4FeO + O_2 \rightarrow 2Fe_2O_3 \quad (2)$$

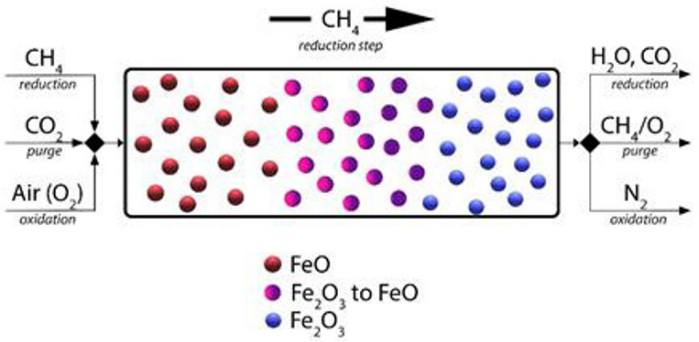

Figure 1. Process diagram during the reduction step, when CH_4 reacts with Fe_2O_3 leaving behind inactive FeO.

2. Model development

This paper is evaluating the dynamic simulation of methane-based CLC with an iron-based OC in a packed bed reactor running in alternating combustion/regeneration steps. The mass and energy balance equations for the packed bed reactor, together with the equations that describe the kinetics model and heat transfer processes were implemented in MATLAB/Simulink. After development, the air and fuel reactor models were interconnected with models describing the purge steps of the process to highlight the dynamic behaviour of the entire process.

2.1. Reactor model parameters and assumptions

The following assumptions are defined for the reactor mathematical model:

1) The solid (iron-based OC) is stationary;
2) Plug flow model for gas phase velocity profile;
3) Non-porous solid particles of spherical shape and uniform initial radius;
4) Reaction takes place inside the solid pellet.

Process and model parameters are presented in Table 1:

Table 1. Reactor model parameters used in the dynamic CLC reactor model

Parameter	Value	Parameter	Value
Reactor length, m	0.93	Solid mass, kg	3
Reactor diameter, m	0.035	O_2 concentration, kmol m^{-3}	0.003
Particle diameter, m	0.002	CH_4 concentration, kmol m^{-3}	0.016
Work pressure, atm	1.2	Air density, kg m^{-3}	0.4841
Temperature, K	873÷1073	CH_4 density, kg m^{-3}	0.263
Air flow rate, L min^{-1}	40	CH_4 flow rate, L min^{-1}	200

2.2. Reactor model equations

The reactor is mathematically represented by the following set of equations:

a) Total mass balance for the fuel and air reactor:

$$\frac{\partial m_s}{\partial t} = w_p \cdot nM_{O_2} \tag{3}$$

$$\frac{\partial F_g}{\partial t} = -w_g \cdot \frac{\partial F_g}{\partial z} + w_p \cdot \frac{w_g \cdot nM_{O_2}}{dz} \tag{4}$$

b) Component mass balance for the fuel and air reactor:

$$\frac{\partial m_{FeO}}{\partial t} = w_p \cdot nM_{FeO} \tag{5}$$

$$\frac{\partial m_{Fe_2O_3}}{\partial t} = w_p \cdot nM_{Fe_2O_3} \tag{6}$$

$$\frac{\partial F_{O_2}}{\partial t} = -w_g \cdot \frac{\partial F_{O_2}}{\partial z} + w_p \cdot \frac{w_g \cdot nM_{O_2}}{dz} \quad (7)$$

$$\frac{\partial F_{CH_4}}{\partial t} = -w_g \cdot \frac{\partial F_{CH_4}}{\partial z} + w_p \cdot \frac{w_g \cdot nM_{CH_4}}{dz} \quad (8)$$

$$\frac{\partial F_{CO_2}}{\partial t} = -w_g \cdot \frac{\partial F_{CO_2}}{\partial z} + w_p \cdot \frac{w_g \cdot nM_{CO_2}}{dz} \quad (9)$$

$$\frac{\partial F_{H_2O}}{\partial t} = -w_g \cdot \frac{\partial F_{H_2O}}{\partial z} + w_p \cdot \frac{w_g \cdot nM_{H_2O}}{dz} \quad (10)$$

where w_g was gas velocity, w_p was process velocity, m_i, F_i, M_i and n_i were mass, mass flow rate, molar mass and stoichiometric coefficient of component i, respectively. Eqs. (5, 6) took place in both reactors, Eq. (7) took place in the air reactor, while Eqs. (8-10) described the component mass balances for the fuel reactor.

2.3. Reactor model kinetics

A mixed kinetic model was used to describe the CLC process, accounting for both homogeneous and heterogeneous models. The model assumed a uniform initial solid particle radius and that the reaction took place inside the pellet, based on the shrinking core model (Abad et al., 2011). As the process velocity was directly proportional to the reaction rate and the mass transfer resistance in the gas film and diffusion inside the pellet were not considered, the reaction rate for the oxidation reaction was:

$$\frac{dn_{Fe_2O_3}}{dt} = 2.776 \cdot e^{\frac{-3.067121 0^3}{T}} \cdot m_{FeO}{}^{\frac{2}{3}} \cdot m_p{}^{\frac{1}{3}} \cdot C_{O_2} \quad (11)$$

and for the reduction reaction:

$$\frac{dn_{FeO}}{dt} = 8.957 \cdot 10^4 \cdot e^{\frac{-1.626171 0^4}{T}} \cdot m_{Fe_2O_3}{}^{\frac{2}{3}} \cdot m_p{}^{\frac{1}{3}} \cdot C_{CH_4} \quad (12)$$

where $mFeO$ and mFe_2O_3 represented the masses for iron (II) and (III) oxide respectively, C_{CO2} and C_{CH4} were the concentrations for oxygen and methane.

3. Results and discussions

Figure 2 shows the breakthrough curves for O_2 during oxidation and for CH_4 and CO_2 during reduction. Using different flow rate values for each gas, breakthrough times were close, with around 1000 s for the oxidation step and 1500 s for the reduction step, in accordance with literature (Gallucci et al. 2015, Zhang et al., 2018). Figure 3 shows three full cycles, highlighting the dynamic nature of the CLC reactor with alternating operation of the fuel and air reactors. Figure 4 presents the consumption of the solid reactants in time for the oxidation (Left) and reduction (Right) steps at different axial positions inside the reactor. Figure 5 presents the temperature variation in time for the solid during the oxidation step. The temperature increased by around 250 K, in line with literature (Gallucci et al. 2015).

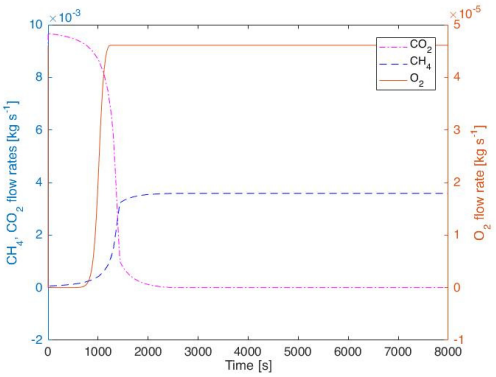

Figure 2. Flow rate profiles for CH_4, CO_2 in fuel reactor and for O_2 in air reactor.

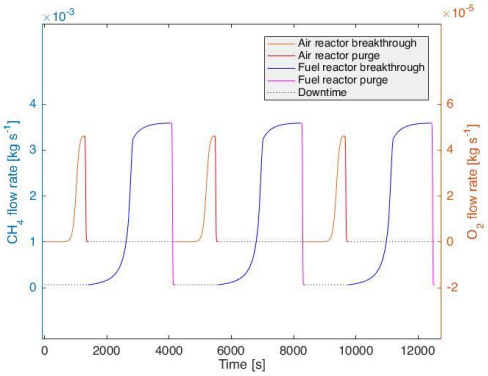

Figure 3. CH_4 and O_2 flow rates during three full cycles for the CLC reactor.

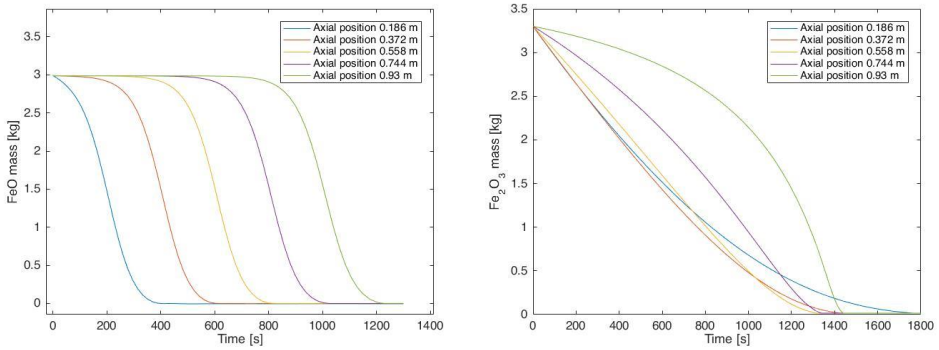

Figure 4. FeO mass (Left) and Fe_2O_3 mass (Right) as functions of time at different axial positions in the reactor during oxidation and reduction, respectively.

Finally (Figure 6), a sensitivity analysis was done for flow rate during the oxidation step, studying the time necessary for the system to reach a steady state. Increasing the flow rate by 20% led to less time required for the system to stabilize (83% of the initial time), while decreasing flow rate by 20% yielded a longer time for the system to reach stationarity (125% of initial time).

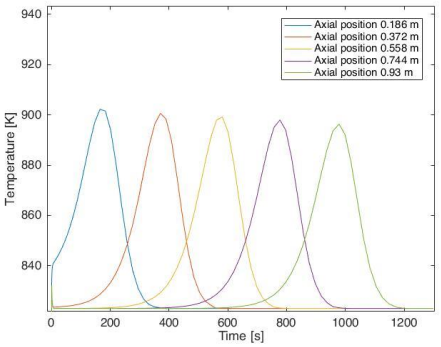

Figure 5. Temperature of the solid (FeO) during oxidation step at three different axial.

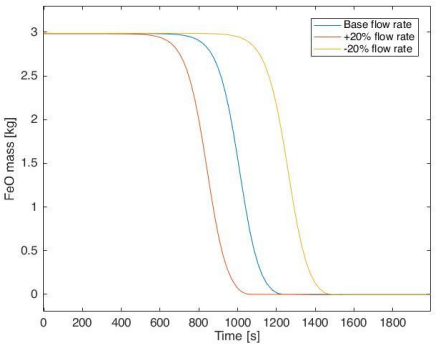

Figure 6. - FeO mass profiles during oxidation step for different flow rates

4. Conclusions

A mathematical model for a packed bed reactor used alternately in a methane-based CLC process with iron-based OC was developed. The developed model was used to predict (in space and time) the gas flow profile, velocity distribution, gas composition distribution, behaviour of OC and temperature profiles inside the air and fuel reactors. The MATLAB/Simulink model predictions were in line with published literature data. Changes to the oxygen flowrate had a high impact over the total time required to reach the complete conversion of the solid. A flow rate increase of the air stream by 20% showed the system reached a stationary state in less time by 200 seconds, while the decrease by 20% in air flow rate determined a longer time to reach steady state by 300 seconds.

References

A. Abad, J. Adánez, A. Cuadrat, F. García-Labiano, P. Gayán, L.F. de Diego, 2011, Kinetics of redox reactions of ilmenite for chemical-looping combustion, Chem. Eng. Sci., 66, 4, 689–702.

J. Adanez, A. Abad, F. Garcia-Labiano, P. Gayan, L.F. De Diego, 2012, Progress in chemical-looping combustion and reforming technologies, Prog. Energy Combust. Sci., 38, 2, 215–282.

D.A. Chisalita, A.M. Cormos, 2018, Dynamic simulation of fluidized bed chemical looping combustion process with iron based oxygen carrier, Fuel, 214, October 2017, 436–445.

F. Gallucci, H.P. Hamers, M. van Zanten, M. van Sint Annaland, 2015, Experimental demonstration of chemical-looping combustion of syngas in packed bed reactors with ilmenite, Chem. Eng. J., 274, 156–168.

S. Noorman, F. Gallucci, M. Van Sint Annaland, J.A.M. Kuipers, 2011, Experimental investigation of chemical-looping combustion in packed beds: A parametric study, Ind. Eng. Chem. Res., 50, 4, 1968–1980.

J.M. Parker, 2014, CFD model for the simulation of chemical looping combustion, Powder Technol., 265, 47–53.

H. Zhang, X. Liu, H. Hong, H. Jin, 2018, Characteristics of a 10kW honeycomb reactor for natural gas fueled chemical-looping combustion, Appl. Energ., 213, 285-292.

Sauro Pierucci, Flavio Manenti, Giulia Bozzano, Davide Manca (Eds.)
Proceedings of the 30th European Symposium on Computer Aided Process Engineering (ESCAPE30), May 24-27, 2020, Milano, Italy.
http://dx.doi.org/10.1016/B978-0-12-823377-1.50102-6

Life Cycle Analysis of Phenol - Formaldehyde Resins Substituted with Lignin

Olivia A. Perederic[a], Aikaterini Mountraki[b], Electra Papadopoulou[c], John M. Woodley[a], Georgios M. Kontogeorgis[a]*

[a]*Department of Chemical and Biochemical Engineering, Technical University of Denmark, DK-2800 Kgs. Lyngby, Denmark*
[b]*Department of Engineering, Aarhus Univeristy, DK-8200 Aarhus, Denmark*
[c]*CHIMAR HELLAS SA, GR-57001, Thermi-Thessaloniki, Greece*

Abstract

Phenol-formaldehyde (PF) resins are widely used in wood-based applications by reason of their heat and water resistance, high mechanical strength and chemical stability. Challenges regarding the environmental impact of petroleum-based resources lead to an increased interest of developing new resins where components such as phenol are replaced with renewable materials. This work evaluates the environmental impact of phenol-formaldehyde resins using an organosolv lignin as phenol replacement. Two life cycle analysis (LCA) boundaries (i.e. Cradle-to-Gate, Gate-to-Gate) are studied for PF resin having different substitution levels of phenol: 0%, 40% and 100%. The LC Soft (ICAS) is used for the LCA, which provides information regarding the carbon footprint (CF), fifteen environmental impact categories (e.g.: soil, water, air, human toxicity) and the life cycle inventory (LCI) contribution. The results show improvements for all environmental impact categories for the lignin substituted resins compared to PF resin, confirming the significant role of lignin. Moreover, the impact of the raw materials (Cradle-to-Gate) is significantly higher than the impact of the production process (Gate-to-Gate).
Keywords: PF resin, LPF resin, LCA, LCI

1. Introduction

The PF resins are considerably used for the production of wood-based panels as they provide water resistance, mechanical strength, chemical and thermal stability (1). The PF resins are produced from the reaction of phenol and formaldehyde under alkaline conditions. Phenol is mainly produced by petroleum, yet the environmental impact of products can be reduced when replacing the fossil-based compounds with renewable ones. Under this current trend, new alternatives, which are capable to maintain the original properties of the product, are investigated. One alternative to PF resins is the lignin-PF resins, where phenol is replaced by lignin in different amounts. Lignin is a natural wood component, which proves to be a very good additive for different polymers and adhesives (2,3). Lignin can be sourced from different biomass pretreatment processes (i.e. thermal, kraft, organosolv). The advantage of organosolv lignin is that the process has lower environmental impact compared to other pulping processes (e.g. no waste streams are generated in organosolv process, while liquid waste stream and gaseous releases result from the kraft process), and the lignin product can be obtained in higher purity and with better properties (e.g.: low molecular weight, smaller particle with better dispersity, higher reactivity, etc.) compared to the lignin resulted from other processes(4). Advanced processes for lignin extraction, such as ionic liquids extraction (5), deep

eutectic solvent mixtures or other type of solvents (6) can have better extraction performances, but issues like solvent recovery and cost, together with lignin characteristics might be a limiting condition of using these methods at the industrial scale. LCA studies show that the use of kraft lignin as phenolic substitute for PF resins has better environmental profile (7). However, the use of organosolv lignin is not thoroughly studied in the literature. The aim of this work is to evaluate the environmental impact of the resin production process when phenol is replaced by an organosolv lignin.

2. Methodology

2.1. Goal, scope definition, function, and functional unit

This work is a comparative LCA study among different productions of resins. The aim is to evaluate the environmental impact of the production process, of the raw materials, and of the composition of the resins when phenol is replaced by lignin. The production is postulated to be part of a real-life lignocellulosic biorefinery, the CIMV biorefinery (Compagnie Industrielle de la Matière Végétale) (8,9). It is experimentally verified that CIMV lignin can successfully substitute phenol for the production of PF resins, while maintaining the properties of the final product (10). It is postulated that the production of all resins is at an industrial level. The resin production process consists of two main process sections: reaction and cooling. The process output is 32.2 t/h of resin. The function of the study is the synthesis and cooling of the product. The selected functional unit (FU) of the product is 1 kg of resin (solution), which is representative for industrial scale production. The LC Soft (ICAS) (11) is used for the LCA, which provides information regarding the carbon footprint (CF), the LCI contribution, and fifteen environmental impact categories.

2.2. System description and boundaries

Two case studies with different LCA boundaries are evaluated: (A) Gate-to-Gate, considering only the impact of the resin production process, and (B) Cradle-to-Gate, considering also the impact of the production of raw materials, without taking into account the impact of transportation. Three different ratios for the substitution of phenol by lignin are studied for each case study: 100% phenol-formaldehyde (PF), 60% phenol 40% lignin-formaldehyde (LPF), and 100% lignin-formaldehyde (LF). The assessment of cradle-to-grave is a challenge, since there are different applications of the final product and not enough data is available for the product after the production stage. A representation of the system boundary for the selected case studies is showed in Figure 1.

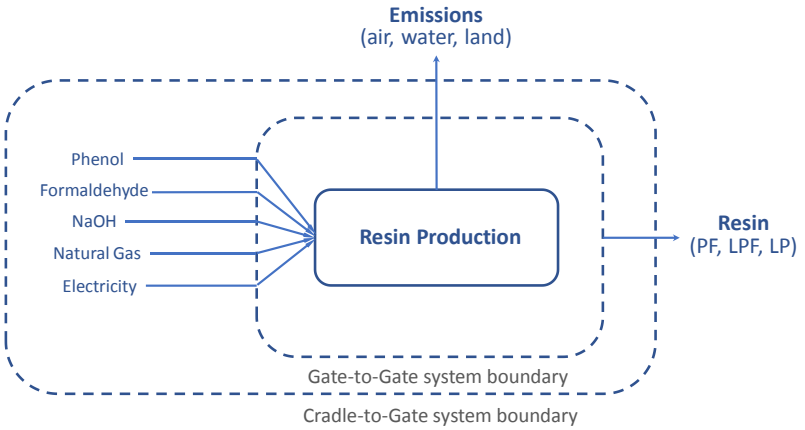

Figure 1. System boundary with Input and Output streams for the two case studies.

The reaction section for the resin production consists in mixing the raw materials in a batch reactor (12,13). The reaction takes place at 1 atm and 90 °C for a period of 8 hours. Then, the product is cooled down at 25 °C with cooling water (Ts=15 °C, Tt=22 °C). The heating is provided by low pressure steam (p=4 bar). The raw materials are: phenol 95% wt. solution, formaldehyde 37% wt. solution, sodium hydroxide (NaOH) 50% wt. solution, and organosolv lignin with 5% water content. The three different resins use the materials in following ratios:

- *PF resin*: lignin:phenol=0:1 (wt.); formaldehyde: phenol = 2.25:1 (mol fr.); formaldehyde:NaOH = 6.3:1 (mol fr.), phenol (95% wt.) flowrate = 11773 kg/h;
- *LPF resin*: lignin:phenol=2:3 (wt.); formaldehyde:phenol=3.75:1 (mol fr.); formaldehyde:NaOH= 6.3:1 (mol fr.), lignin (5% wt. humidity) flowrate = 5121 kg/h;
- *LF resin*: lignin:phenol=1:0 (wt.); formaldehyde:lignin=2.25:1 (wt. fr.), formaldehyde:NaOH = 4.7:1 (wt. fr.); lignin (5% wt. humidity) flowrate =12803 kg/h.

2.3. Data collection

The data for the analysis comes from the industry, simulation results of the industrial process, the literature, and the LC soft.

- *Industrial and simulation data*: this data provides the main information regarding process mass and energy balance (i.e. stream and equipment data,) which accounts for stream and equipment table data in LC Soft. The data is provided by Chimar (14) and Mountraki et al. (12) for PF resin. The stream data for LPF and LF resin is calculated from PF resin data, based on mass ratio substitution of phenol with lignin, while the equipment data (Table 1) is assumed to be the same for all the three resins.
- *Literature data*: emissions of the industrial process, that were not taken into account within the process simulation and could not be provided from the industry, were collected from the work of Wilson (2010) (15). The emission data used for the analysis is presented in Table 2.
- *LC Soft database*: provides all the data for chemicals and utilities used in the LC models. The data from LC Soft comes from various databases and literature.
- *Data excluded from the study*: raw materials transportation; miscellaneous materials; resources for equipment, facilities, infrastructure, support activities and personnel (materials, waste, and utilities).

The environmental impact assessment is performed with LC Soft from ICAS (11). The analysis provides information regarding carbon footprint (CF) and 15 impact categories regarding soil, water, air, and human toxicity, as well as LCI contribution. The data for each of the case studies, as implemented in LC Soft, is presented in Table 1, regarding the equipment data, and in Table 2, regarding the emission data. The emission data is adapted from Wilson (2010) (15) by considering the phenol emissions for the lignin resin (LPF) proportional with the amount of phenol available in the resin. No phenol emissions are considered for LF resin. It is assumed that the organosolv lignin has no emissions and that it is produced from wheat straw.

Table 1. Process and equipment data used for LCA for 1 kg of resin[a].

Type of unit	Duty, kW	Activity	Energy source
Emissions control[b]	0.09	Electric usage	Electricity, at grid
Process electricity[b]	0.22	Electric usage	Electricity, natural gas, at power plant
Reactor	0.21	Heating	Natural gas, combusted in industrial equipment
Heat Exchanger	0.20	Cooling	Chilled water, engine-driven chiller using natural gas

[a] Same equipment data is used for all three resins and for all case studies.
[b] Data adapted from (15)

Table 2. Plant emissions to air as undefined source for 1 kg of resin[a]

Resin	PF	LPF[b]	LF[b]
VOC[c], kg	2.89E-05	2.89E-05	2.89E-05
Formaldehyde (HAP), kg	6.69E-06	6.69E-06	6.69E-06
Phenol (HAP), kg	2.04E-06	1.22E-06	0.00E+00
Particulate, kg	2.31E-06	2.31E-06	2.31E-06

[a] Values adapted from Wilson (2010) (15)
[b] LPF resin considers 60% of the phenol emission from FP production; LF has zero phenol emissions
[c] The volatile organic compounds (VOC) are defined/assumed as benzene emissions.

3. Results and discussion

Table 3 presents the carbon footprint of the production process of the three resins. Since it is considered that all three resins have the same utility consumption, the carbon foot print of their process is similar, and it is the same for both case studies. The total carbon footprint for the production of 1 kg of resin is 0.072 g CO_2.

Table 3. Carbon footprint results for the resins production process.

Type of unit	Carbon Footprint (CO_2 eq.)
Emission control	0
Process electricity	1.81e-05
Reactor	2.02e-02
Heat Exchanger	5.22e-02
Total	7.24e-02

The environmental impact is evaluated through several indicators that cover different areas such as environmental effects (e.g. GWP, PCOP), human toxicity (e.g. HTPI, HTPE aquatic and terrestrial ecotoxicity effects and which importance is treated equally in this work. The complete list of indicators and the results for the two case studies are presented in Table 4. The results from the two case studies show the importance of a complete analysis of a process, and the impact of the raw materials. The environmental impact of the resin production (case A Gate-to-Gate) contribution is only 1% within the lifecycle of the product (case B Cradle-to-Gate), an exception is given by the global warming potential (GWP), where the production accounts for 2% for PF resin, and 3% for LPF and LF resins within the product lifecycle. In case study B (Cradle-to-Gate), the results for all three resins show significant improvements in all environmental impact indicators for the lignin-based resins. LPF resin show an improved performance for all indicators compared to PF resin, while LF resin shows the best performance across all environmental impact indicators. The LPF resin shows an average drop of 11% in all the impact categories when compared to PF resin. The highest drop is estimated for the aquatic potential (AP, H^+ eq.) indicator (19%), while the lowest value drop is estimated for the non-renewable resources (MJ eq) (8.5%). When comparing the results for LF resin to those of PF resin, the average drop over all the environmental indicators is 25%. The best performances are achieved for the AP indicator (i.e. 42% lower values), while the smallest variation is estimated for the non-renewable resources (i.e. 18%). The results show potential of future improvement if the energetic requirements for the processing of the raw materials and the resins can be provided by renewable resources.

The LCI contribution comprises of a list of 190 chemicals, where the top contributors are represented by CO_2 emissions in the air, which results from different parts of the product

life cycle, and fuel emissions (e.g. natural gas, oil) in the ground. The complete LCI results can be provided upon request.

Table 4. Environmental impact generated for the production of 1 kg of resin.

Indicator [a]	**Unit**	**Case study A** Gate-to-Gate			**Case study B** Cradle-to-Gate		
		PF	**LPF**	**LF**	**PF**	**LPF**	**LF**
HTPI	1/LD50	2.12E-05	2.12E-05	2.12E-05	3.85E-03	3.51E-03	3.10E-03
HTPE	1/TWA	3.83E-07	3.83E-07	3.83E-07	6.17E-05	5.56E-05	4.83E-05
ATP	$1/LC_{50}$	1.32E-05	1.32E-05	1.32E-05	2.00E-03	1.79E-03	1.54E-03
GWP	CO_2 eq	7.24E-02	7.24E-02	7.24E-02	3.13E+00	2.69E+00	2.18E+00
ODP	CFC-11 eq	7.26E-12	7.26E-12	7.26E-12	1.03E-09	9.16E-10	7.77E-10
PCOP	C_2H_2 eq.	4.07E-05	4.07E-05	4.07E-05	5.31E-03	4.66E-03	3.88E-03
AP	H^+ eq	3.45E-03	3.45E-03	3.45E-03	6.48E-01	5.23E-01	3.75E-01
HTC	kg benzen eq	4.93E-05	4.93E-05	4.93E-05	6.86E-03	6.07E-03	5.13E-03
HTNC	kg toluen eq	1.23E+00	1.23E+00	1.23E+00	1.78E+02	1.58E+02	1.34E+02
ET	kg 2,4-D eq	3.06E-03	3.06E-03	3.06E-03	4.44E-01	3.94E-01	3.36E-01
Non-renewable, fossil	MJ eq	3.37E-01	3.37E-01	3.37E-01	6.47E+01	5.92E+01	5.28E+01
Photochemical Ozone Formation	kg NMVOC eq	1.79E-06	1.79E-06	1.79E-06	3.14E-04	2.85E-04	2.51E-04
Marine eutrophication	kg N eq	1.16E-05	1.16E-05	1.16E-05	1.32E-03	1.13E-03	9.06E-04
Terrestrial eutrophication	molc N eq	1.30E-04	1.30E-04	1.30E-04	1.48E-02	1.27E-02	1.02E-02
Particulate matter	kg PM2.5 eq	1.19E-06	1.19E-06	1.19E-06	2.00E-04	1.81E-04	1.59E-04

[a] HTPI – human toxicity potential by ingestion, HTPE – human toxicity by exposure, ATP – aquatic toxicity potential, GWP – global warming potential, ODP - ozone depletion potential, PCOP – photochemical oxidation potential, AP – acidification potential, HTC – human toxicity carcinogenic, HTNC - human toxicity non-carcinogenic, ET - fresh water ecotoxicity.

4. Conclusion

This work is a comparative LCA study among different resins productions in order to provide an overview of the impact of different factors (e.g. raw materials, resin composition) in the production of the phenol-aldehyde resins. The paper highlights the importance of replacing fossil fuels derived materials with ones derived from renewable sources. The life cycle analysis is performed for the production of three different phenol substitution ratios by an organosolv lignin (0% as PF, 40% as LPF, and 100% as LF) for two different system boundaries (case study A: Gate-to-Gate and case study B: Cradle-to-Gate). The results show that the impact of the raw materials is significantly higher than the impact of the production process. The LPF and LF resins presented lower values for all the environmental impact indicators compared to the PF resin, showing that the organosolv lignin has a positive impact in replacing the phenol within this type of resins. Further studies should include a detailed evaluation of the process parameters at industrial

level for the three resins together with the impact of using renewable resources in other areas of the process (e.g. utilities, fuels, transportation, etc.).

Acknowledgments

This work has received funding from European Union's Horizon 2020 research and innovation programme under Marie Skłodowska-Curie RISE action, grant agreement No 778332, project RENESENG II.

References

1. W. Qiao, S. Li, F. Xu. Preparation and Characterization of a Phenol-formaldehyde Resin Adhesive Obtained from Bio-ethanol Production Residue. Polym Polym Compos. 2016;24(2):99–105.
2. V. Mimini, E. Sykacek, S.N.A. Hashim, J. Holzweber, H. Hettegger, K. Fackler, A. Potthast, N. Mundigler, T. Rosenau. Compatibility of Kraft Lignin, Organosolv Lignin and Lignosulfonate with PLA in 3D Printing. J Wood Chem Technol. 2019;39(1):14–30.
3. J. Lima García, G. Pans, C. Phanopoulos. Use of lignin in polyurethane-based structural wood adhesives. J Adhes. 2018;94(10):814–28.
4. J. Banoub, G.H Delmas Jr., N. Joly, G. Mackenzie, N. Cachet, B. Benjelloun- Mlayah, M. Delmas. A critique on the structural analysis of lignins and application of novel tandem mass spectrometric strategies to determine lignin sequencing. Journal of Mass Spectrometry, 2015; 50(1), pp.5-48.
5. X. Zhu, C. Peng, H. Chen, Q. Chen, Z.K. Zhao, Q. Zheng Q, H. Xie. Opportunities of Ionic Liquids for Lignin Utilization from Biorefinery. ChemistrySelect. 2018;3(27):7945–62.
6. D. Tian, R.P. Chandra, J.S. Lee, C. Lu, J.N. Saddler. A comparison of various lignin-extraction methods to enhance the accessibility and ease of enzymatic hydrolysis of the cellulosic component of steam-pretreated poplar. Biotechnol Biofuels. 2017;10(1):1–10.
7. E. Bernier, C. Lavigne, P.Y. Robidoux. Life cycle assessment of kraft lignin for polymer applications. Int J Life Cycle Assess. 2013;18(2):520–8.
8. J. Snelders, E. Dornez, B. Benjelloun-Mlayah, W.J.J. Huijgen, P.J. de Wild, R.J.A. Gosselink, J. Gerritsma, C.M. Courtin. Biorefining of wheat straw using an acetic and formic acid based organosolv fractionation process. Bioresour Technol. 2014;156:275–82
9. COMPAGNIE INDUSTRIELLE DE LA MATIERE VEGETAL (CIMV) [Internet]. Available from: www.cimv.fr/
10. N. Tachon, B. Benjelloun-Mlayah, M. Delmas. Organosolv wheat straw lignin as a phenol substitute for green phenolic resins. BioResources, 2016;11(3), 5797-5815.
11. S. Kalakul, P. Malakul, K. Siemanond, R. Gani. Integration of life cycle assessment software with tools for economic and sustainability analyses and process simulation for sustainable process design. J Clean Prod. 2014;71:98–109.
12. A. Mountraki, K. Pyrgakis, A. Nikolakopoulos, B. Benjelloun-Mlayah, A. Kokosis. D5.5: Process Designs and Flowsheet Models: CIMV and the BIOCORE pilots; 2013, report no: D5.5 FP7-241566.
13. B. Pang, S. Yang, W. Fang, T.Q. Yuan, D.S. Argyropoulos, R.C. Sun. Structure-property relationships for technical lignins for the production of lignin-phenol-formaldehyde resins. Ind Crops Prod. 2017;108:316-326.
14. Chimar Hellas [Internet]. Available from: www.chimarhellas.com
15. J.B. Wilson. Life-cycle inventory of formaldehyde-based resins used in wood composites in terms of resources, emissions, energy and carbon. Wood Fiber Sci. 2010;42(SUPPL. 1):125–43.

Sauro Pierucci, Flavio Manenti, Giulia Bozzano, Davide Manca (Eds.)
Proceedings of the 30th European Symposium on Computer Aided Process Engineering (ESCAPE30), May 24-27, 2020, Milano, Italy.
http://dx.doi.org/10.1016/B978-0-12-823377-1.50103-8

Transport Model of Fluids Injected in a Landfill Polluted with Lindane Wastes

David Lorenzo[a*], Aurora Sanots[a], Carmen M. Domínguez[a], Joaquín Guadaño[b], Jorge Gómez[b], Jesús Fernández[c]

[a] *Chemical Engineering and Materials Department. Universidad Complutense de Madrid. Spain*
[b]*EMGRISA, Empresa Para la Gestión de Residuos Industriales, S.A., Madrid, Spain.*[c]*Department of Rural Development and sustainability, Government of Aragon, Spain.*
dlorenzo@ucm.es

Abstract

Dense non-aqueous phase liquids (DNAPLs) are ubiquitous environmental problem causing contamination of soil and groundwater. The remediation strategies, such us in situ chemical oxidation (ISCO), need a good preliminary characterization of injected chemicals transport within the subsoil in order to select an adequate injection-extraction strategy and calculate both the chemical dosage and the contact time required.

In this work, the flow was studied in a polluted site located in Sabiñanigo (Spain) where a DNAPL generated by lindane production process was dumped as production waste. The flow was studied using a tracer step experiment injecting a constant flow rate of tap water with bromide. Analysis of the groundwater samples composition of tracer with time obtained was accomplished at several monitoring wells being used to propose a transport model, which was implemented in gPROMS. The experimental data were used to fit a dispersion coefficient to depend on the velocity of the fluid. The transport model was validated with a second step tracer experiment, carried out at lower flowrate. Besides, the transport model obtained has been used to predict the oxidant (persulfate) concentration profiles from the injection point, considering different flow rates in an ISCO treatment.

Keywords: Landfill, Tracer step experiment, Advection-Dispersion model, Anisotropy, ISCO.

1. Introduction

Many industrial activities have produced the emission and spills of dangerous substances that greatly impact the quality of soil and particularly groundwater. This is the case of Sabiñanigo, Spain, where a factory synthesized lindane (with insecticidal properties), generating a high amount of solid and liquid wastes of a mixture of isomers of hexachlorocyclohexane (HCH) (Vijgen et al., 2011). These mixtures were dumped in a non-controlled way at Sardas landfill. The liquid waste has formed a Dense Non-Aqueous Phase Liquid (DNAPL) composed by 30 different chlorinated organic compounds (COCs). This phase has progressively migrated through the subsurface (density-driven) reaching high depths and polluting the soil and groundwater (Santos et al., 2018).

The most suitable remediation strategies are those based on in situ treatments, such us: Enhanced Surfactant Product Recovery (ESPR), with the injection of a surfactant solution to facilitate the DNAPL extraction (Wu et al., 2016); in situ chemical oxidation (ISCO), injecting an oxidant (persulfate for instance) to abate the COCs (Santos et al., 2017), or

the simultaneous injection of a surfactant with an oxidant (S-ISCO) (Dahal et al., 2016). All these technologies need a good preliminary characterization of injected chemicals transport within the subsoil in order to select an adequate injection-extraction strategy.

For small-scale injection points, the local flow can be influenced by the nature of the dispersion of the solute, such as its anisotropy. However, the transport of the injected substances is frequently described only by an isotropic advective flow (plug flow). Nevertheless, dispersion, as well as anisotropy, can have a remarkable contribution to the transport of the injected chemicals (Vasco et al., 2018). To characterize more accurately the transport of the injected fluids in the subsurface, the use of tracers, such us bromide, has been applied (Aggelopoulos and Tsakiroglou, 2007). Bromide as a conservative tracer has been used in this work to study the flow of the injected fluid proposing and validating a transport model. Besides, the model was used to predict the oxidant (persulfate) concentration profiles from the injection point, considering different flow rates in an ISCO treatment.

2. Experimental

Two step tracer experiments have been carried out using bromide in a test cell built ad hoc in the alluvium of the Sardas landfill. The bromide concentration at several monitoring wells was measured to obtain profiles vs. time. The first experiment (STE-1) was used to propose the transport model and the second (STE-2), which was carried out 1 month after the STE-1, was employed to validate it.

A tracer aqueous solution of bromide of 120 mg/L was injected (zero time) through flexible PVC 1-inch hose (Tiger Flex) by using an electric transfer pump. In STE-1 a flow rate of 3.9 m3/h of the tracer aqueous solution was delivered at the well PS14B at a depth of 14.5 m (thus, in the gravel-sand layer) during 5.1 h. In STE-2, a flow rate of 0.6 m^3/h of the tracer solution was injected at the same well and depth (PS14B, 14.5 m) but during 8.33 h. The cell test built can be conceptualized by the scheme shown in Figure 1. Monitoring wells PS14, PS14C, and PS14D were periodically sampled at a depth of 14.5 m in both step tracer experiments with a Mini-Typhoon® DTW 40ft12V electric. After purging, a volume of about 200 mL was sampled and bromide concentration was measured, using an ionic chromatograph (Metrohm 761 Compact IC) with anionic chemical suppression coupled with a conductivity detector.

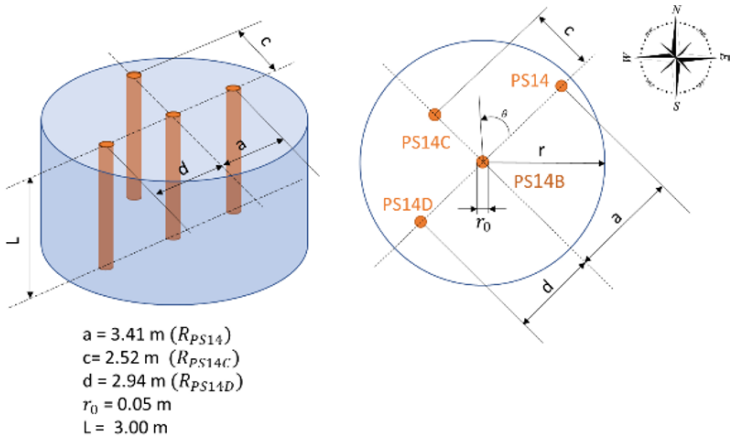

Figure 1. Scheme of the cell test.

3. Results and discussion.

The bromide concentration profiles measured in PS14, PS14C and PS14D wells are given in Figure 2. As can be seen, a rise in the bromide concentration is noted in all the wells shortly after the tracer injection began. Bromide ions were first detected in PS14C, then in PS14D and finally in PS14, accordingly with the distance between the wells and the injection point (Figure 1). If the advective flow was the only contribution to the bromide transport in the alluvium, a step for bromide concentration should be obtained at each monitoring well (show as solid line in Figure 2a, and calculated using Eq. (1)) at the corresponding time. However, the response of the tracer measured with time at each well suggests that the flow in the alluvial groundwater during the injection cannot be described only by advection, but dispersion of the fluid injected should be also considered.

$$t_{PF} = \frac{\pi L \varepsilon_L R_{well}^2}{Q_{inj}} \tag{1}$$

Since the plug flow model from the injection point has been ruled out, the Advection-Dispersion Model has been tested with STE-1 data. This model explains the transport of a conservative solute in the subsurface by the advection-dispersion equation shown in Eq. (2) (Aggelopoulos and Tsakiroglou, 2007).

$$\frac{\partial C_j}{\partial t} + \nabla \cdot \left(u_i C_j \right) = \nabla \cdot \left(D_T \cdot \nabla C_j \right) \tag{2}$$

where u_i is the interstitial velocity, D_T is the dispersion coefficient tensor, and C_j is the concentration of the compound j.

To solve the Eq. (2) the following assumptions have been used: i) The axial dispersion has been considered negligible because the gravel–sand layer is confined between two low-permeability layers; ii) The liquid flow has been assumed as a steady incompressible flow of a liquid with a constant density. As the injected fluid is non-compressible, the interstitial velocity at any distance in the length (r) from PS14 to the corresponding well in the direction θ can be calculated as:

$$\mathrm{u_i}\left(r, \theta_{well}\right) = \frac{\mathrm{u_0}\left(\theta_{well}\right) r_0}{r} = \frac{Q a_{well}}{r} \tag{3}$$

where r is the radial distance in length from PS14B to the well and $u_0(\theta_{well})$, the interstitial velocity at the wall of the injection point (r_0) in the direction from PS14B to the well (θ). The possibility of anisotropy in the injected fluid flow having a different direction θ relative to the injection point has been considered in Eq.(3) . Furthermore, as $u_o(\theta_{well})$

depends linearly on the flow rate Q, $u_i(r,\theta_{well})$ can be expressed as a function of a defined parameter a_{well}, as given in Eq. (3).Taking into account these assumptions, the tracer mass balance shown in Eq. (2) can be simplified to Eq. (4).

$$-\frac{Q a_{well} dC_{Br}}{r dr} + D_T(r) \left[\left(\frac{d^2 C_{Br}}{dr^2} \right) + \frac{1}{r} \frac{dC_{Br}}{dr} \right] = \frac{dC_{Br}}{dt} \tag{4}$$

The boundary and initial conditions used to solve Eq.(2) are the following:

$$C_{Br} = 0 \therefore t = 0, r > r_0 \; ; \; C_{Br} = C_{Br,inj} \therefore t \geq 0, r = r_0 \; ; \; \frac{dC_{Br}}{dt} = 0 \therefore t \geq 0, r = R \qquad (5)$$

The dispersion radial coefficient $D_T(r)$ has been described in the literature as a function of the interstitial velocity, according to Eq. (6) (Gunn, 1987). The effective diffusivity D_{eff} of the solute in the subsurface corresponds to the molecular diffusion Dm (7.26. 10^{-6} m^2/h for bromide) of the solute corrected by the porosity and tortuosity of the porous media. Therefore, a negligible contribution of D_{eff} was expected in Eq. (6).

$$D_T(r) = D u_{i,well}(r) + D_{eff} \qquad (6)$$

The problem was compounded by non-linear and partial equations, which were solved using DASOLV algorithm available in gPROMS. To estimate the coefficients D, and a_{well}, the bromide concentration (C_{Br}) vs. time obtained at each well during the tracer step experiment STE-1 (Figure 4) have been fitted to the model in Eqs. (4) to (6) using a gPROMS tool.The estimated values for STE-1 are summarized in Table 1. Predicted values have been plotted as dashed lines in Figure 2.

Table 1. Parameter estimated of Eqs. (4) to (6) to the experimental C_{Br} in Figure 2.

Well	a'$_{well}$ ± CI[a], m^{-1}	Standard Deviation	D[b] ± CI[a], m	Standard Deviation	SQR, m^2
PS14	0.162 ± 4.0·10^{-4}	1.8·10^{-4}	12.29 ± 0.018	0.0087	43.93
PS14D	0.244 ± 6.2·10^{-4}	2.7·10^{-4}			
PS14C	0.427 ± 1.3·10^{-4}	5.5·10^{-4}			
[a] Confidence interval at 95%. [b]Deff estimated= 10-5 m2/h.					

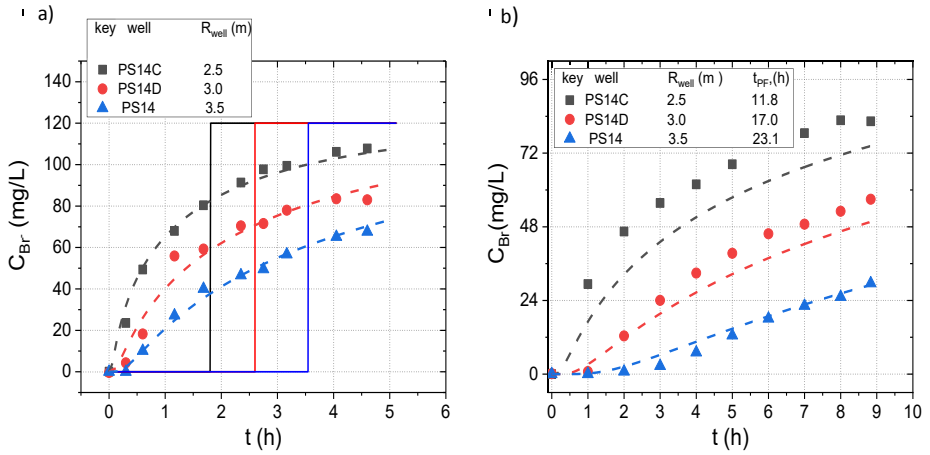

Figure 2. Bromide concentration measured at each monitoring well during the tracer step experiment a) STE-1 Q=3.9 m^3/h and b) STE-2. Q=0.5 m^3/h using $C_{Br,0}$ =120 mg/L. Symbols depict the experimental values. Dashed lines depict the bromide concentration using Eqs. (4) to (6) and parameters in Table 1. Continuous lines depict the simulated bromide concentration profiles with time in Eq. (1) (effective porosity of the soil 0.12).

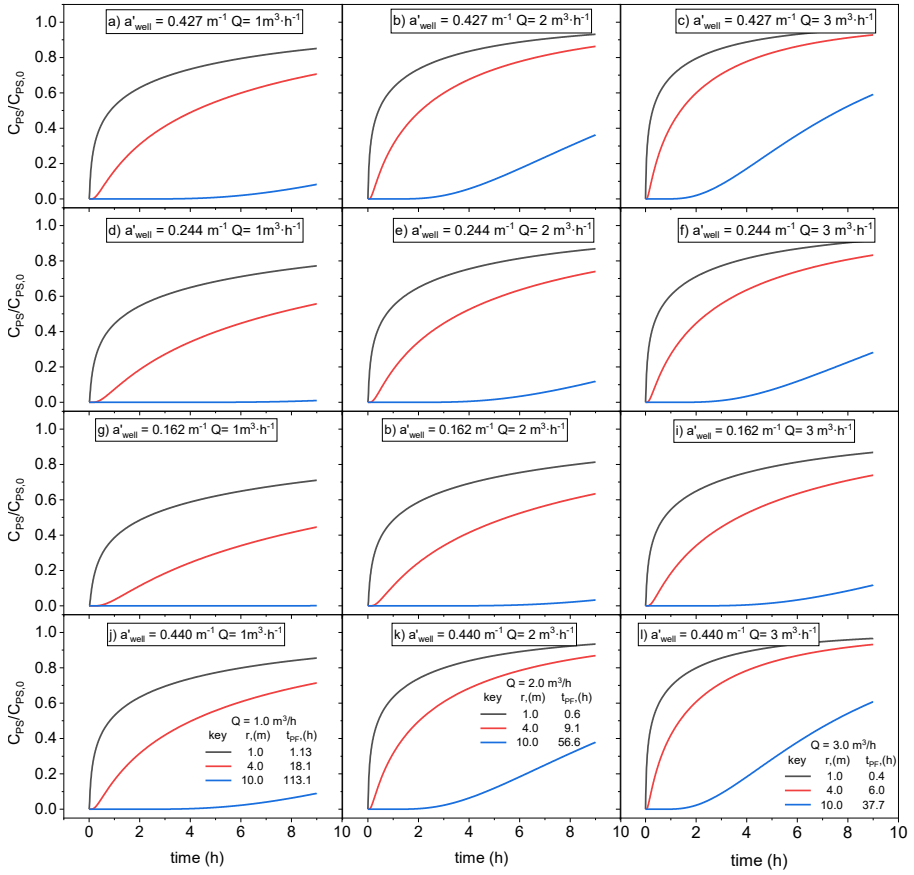

Figure 3. Simulated values of persulfate concentration ratios ($C_{PS}/C_{PS,0}$) using Eqs. (4) to (6) at different injection flow rates, Q. Porosity ε_L=0.12. The legend also indicates the required time for $C_{PS}/C_{PS,0}=1$ calculated with Eq. (7) in only advective flow, named as t_{FP}.

The model proposed in Eqs. (4) to (6) and the parameters summarized in Table 4 were used to predict the bromide concentration profiles in STE-2 bromide was injected at Q=0.6 m^3/h in PS14B during 8.3 h. The values predicted by the model are in good agreement with the experimental data in both experiments (STE-1, Figure 2a and STE-2, Figure 2b) .Moreover, The advection-dispersion has been used to predict the radial profiles of the oxidant injected in PS14B during the injection period in an ISCO treatment using Persulfate (PS). In Figure 2, the dimensionless profiles of persulfate ($C_{PS}/C_{PS,0}$) vs. time has been predicted at several injection flows rates and at several distances from the injection point (PS14B) As can be seen, a high dispersion of the injected persulfate is predicted. These profiles could be compared with those expected considering only advective flow (from Eq. (1), named as t_{PF}) have been included in the legend of Figure 2. If only advective flow were used to interpret the persulfate profiles obtained in an oxidant injection event, erroneous conclusion would be obtained.

4. Conclusions

Upon analyzing the tracer profiles at the three monitoring wells located around the injection point, it was found that the injected flow exhibited no isotropy in any direction from the injection point. A model that includes the advective and dispersive components, as well as the anisotropy of the flow, has been developed to describe the transport of the injected substances. The dispersion coefficient obtained depended linearly on the interstitial velocity. For the directions considered from the injection point, the model developed can be used to predict the concentration of the injected substances with time at other flow rates. The advection-dispersion model obtained was used to predict the oxidant profiles during the injection event in an ISCO application.

Acknowledgments

The authors acknowledge the financial support from the Comunidad Autonoma de Madrid, project CARESOIL (S2018/EMT-4317) and from the Spanish Ministry of Economy, Industry and Competitiveness, projects CTM2016-77151-C2-1-R.

References

C.A Aggelopoulos, C.D. Tsakiroglou, 2007, The longitudinal dispersion coefficient of soils as related to the variability of local permeability, Water Air Soil Poll.,185, 223-237.

G. Dahal, J. Holcomb, D. Socci, 2016, Surfactant-Oxidant Co-Application for Soil and Groundwater Remediation, Rem. J. Environ. Cleanup Costs Tech. Techni. 26, 101-108.

D.J. Gunn, 1987, Axial and radial dispersion in fixed beds, Chem.Eng. Sci. 42, 363-373.

A. Santos, J. Fernandez, J. Guadano, D. Lorenzo, A. Romero, 2018, Chlorinated organic compounds in liquid wastes (DNAPL) from lindane production dumped in landfills in Sabinanigo (Spain), Environ. Poll. 242, 1616-1624.

A. Santos, J. Fernandez, L. Perez, S. Rodriguez, C. Dominguez., M. Lominchar, D. Lorenzo, A. Romero, 2017, Abatement of chlorinated compounds in groundwater contaminated by HCH wastes using ISCO with alkali activated persulfate, Sci. Total Environ., 615, 1070-1077.

D.W. Vasco, S.R. Pride, C. Zahasky, S. M. Benson, 2018, Calculating Trajectories Associated with Solute Transport in a Heterogeneous Medium, Wat. Resources Res.54, 6890-6908.

B. Wu, H. Y. Li, X.M. Du, L. R. Zhong, B. Yang, P. Du, Q.B. Gu, F. S. Li, 2016, Correlation between DNAPL distribution area and dissolved concentration in surfactant enhanced aquifer remediation effluent: A two-dimensional flow cell study, Chemosphere 144, 2142-2149.

Sauro Pierucci, Flavio Manenti, Giulia Bozzano, Davide Manca (Eds.)
Proceedings of the 30th European Symposium on Computer Aided Process Engineering (ESCAPE30), May 24-27, 2020, Milano, Italy.
http://dx.doi.org/10.1016/B978-0-12-823377-1.50104-X

Modeling and Optimization for Short-term Scheduling of Plastic Bag Plants

Myrian Santos-Torres[a,b]*, J. Alberto Bandoni[b], M. Susana Moreno[b]

[a]*Escuela Superior Politécnica del Litoral, ESPOL, Facultad de Ciencias Naturales y Matemáticas, Campus Gustavo Galindo, km 30.5 Vía Perimetral, P.O. BOX 09-01-5863,Guayaquil, Ecuador.*

[b]*Planta Piloto de Ingeniería Química - PLAPIQUI (Universidad Nacional del Sur-CONICET), Camino La Carrindanga km 7, 8000 Bahía Blanca, Argentina*
mgsantos@espol.edu.ec

Abstract

This work presents a mixed-integer nonlinear programming (MINLP) formulation for the short-term scheduling of a multistage multiproduct batch facility producing different types of plastic bags. Given a number of customer orders that must be satisfied at specific due dates, the proposed model is able to determine the optimal assignment of orders to units and the sequence of orders on each unit at every processing stage. In contrast to previous works, it allows calculating both the processing rate of each equipment and the processing time of each product as a function of the bag's parameters. Also, the number and diameter of film rolls obtained in the extrusion step as well as the product quality are accounted for in the model. Two alternative performance criteria are used. The first minimizes the delay in the delivery (tardiness) of all orders in the scheduling horizon while the second minimizes the total time required for processing all the orders (makespan). The model efficiency has been evaluated using real data from a plant located in the city of Guayaquil, Ecuador. The results demonstrate the improvements obtained with the proposed model when compared to the actual situation in the company.

Keywords: short-term scheduling, optimization, MINLP model, batch plant, plastic bag.

1. Introduction

Plastic bags are everyday objects that facilitate people's lifestyle. In industry, innumerable types of bags are made according to their purpose, for example, to transport goods, keep fresh food for a certain time, protect products from harmful pollutants, etc. Therefore, plastic bags are versatile products that, despite environmental concerns due to their slow biodegradability, are still in demand.

High- and low-density polyethylene and linear low-density polyethylene are the polymers mostly used in the production of plastic bags. Here, the most important operation in the process is the film blowing to obtain the plastic film in the extruder. This process is followed by the printing, converting, and packaging stages (Gopura and Jayawardene, 2009). In the converting stage, there are units that perform varied tasks such as cutting, drilling, and sealing.

Generally, polyethylene bags are manufactured in batch facilities with multiple stages each having several units running in parallel. In this kind of industry, several production orders can be processed in the same unit at each stage of the process so the plant manager must decide where, when, and how to process them in order to avoid delays in delivering the products to the customers. Given the combinatorial nature of this problem, the best

way to solve it is to use optimization-based computational tools that allow the short-term scheduling of the process operations, increasing both the productivity and profitability as well as the level of service offered to the customers.

In literature, there are few papers specifically dedicated to plastic bag production plants. Leung (2009) proposed an MINLP model to optimize the production scheduling at a plastics compounding plant considering only the extrusion stage and incorporating product quality constraints into the formulation. Then, Gopura and Jayawardene (2009) developed a simulation model to improve the production time in the plastic bag manufacturing process. Nevertheless, there are many mathematical modeling proposals for the treatment of short-term scheduling problems in similar plants. Méndez et al. (2000) posed a continuous-time MILP model for the short-term scheduling of single-stage batch plant with parallel units. They considered multiple product orders with different due-dates and accounted for sequence-dependent setups. The assignment and sequencing decisions were handled separately. Later, Gupta and Karimi (2003) improved this model by considering a multistage problem and using two-index discrete decision variables allowing to achieve a reduction in the number of binary and solve industrial-size problems in reasonable times. A. Merchan et al (2016) proposed four different discrete-time MIP models for production scheduling problems in multistage facilities.

Considering previous contributions, in this work an MINLP model is proposed for the short-term scheduling of a multistage batch plant that produces different types of plastic bags. The formulation determines, in an optimal way, the sequencing of the production orders of plastic bags and their assignment to units in different stages of the process, as well as the processing rate of each unit and processing time of each order considering product quality constraints.

2. Problem Definition

Figure 1 shows a generalized scheme of the plastic bag production plant consisting of S processing stages (i.e. extrusion, printing, and converting stages), where I customer orders must be processed in U production units over a specified scheduling horizon H. At each processing stage s, there is a number of units U_s, and each unit u processes a certain set I_u of production orders. Since the plant produces both printed and unprinted bags, there are orders that do not go through all the processing stages. For this reason, a subset I_s is defined which indicates the orders i that are processed in stage s.

Figure 1. General process scheme of a plastic bag production plant.

Each order i specifies the product (i.e., a type of bag) to be manufactured according to the specifications requested by customers where the $m \in M_i$, raw materials and $a \in A_i$ additives are indicated and, if it is a bag printed, the $k \in K_i$ types of printing inks used. In addition, the length Lb_i, width Ab_i, and thickness Eb_i of a bag, the width Ar_i and thickness Er_i of a film roll, the number of bags Nb_i, and the percentages of raw materials PM_{mi} and additives PA_{ai} used in each order i are problem data. For each order i, several parameters are defined: the weight of a bag Qb_i as the product between the volume (Lb_i x Ab_i x Eb_i) and the density De_i, the weight of one meter of film roll Qm_i as the product between the area (Ar_i x Er_i) and the density De_i, and the total extruded weight QT_i as the product between the weight of the bag Qb_i and the total number of bags Nb_i requested by the customer.

The quantity of raw material of an order MP_{mi} is defined as the product between the percentage of raw materials PM_{mi} and the total extruded weight QT_i; while the quantity

of additives of an order AD_{ai} is determined by the product between the percentage of additives PA_{ai} and the total extruded weight QT_i. All orders must be delivered in a given deadline dd_i, usually 7 days.

The basic data for the processing units are the maximum production capacity CAP_u, the change time of a film roll TCr_u, and the maximum permissible weight of a roll $PTMAX$ obtained in the first processing stage s_1 (extrusion).

The main assumptions for these types of problem are summarized below:

1. There are a fixed number of units in each processing stage that operate in parallel.
2. The processing units at each stage are not identical, as they vary by brand, model, serial number and year of manufacture, type of raw material (extrusion), number of colors (printing) and type of bag (conversion).
3. A unit cannot process more than one order at a time and an order cannot be processed by more than one unit at the same time.
4. There are no restrictions on resources, labor or materials during the orders production.
5. Unlimited intermediate storage is available after each processing stage.

The main goal of the problem is to find the detailed program of the plant operations that determines: (1) the assignment of orders to a specific unit in each processing stage, (2) the processing sequence of orders in each unit available, (3) the production time of a bag, (4) the processing rate of an order in each unit, (5) the start and end times of processing each order in all stages, (6) the number, (7) diameter and (8) weight of each film roll in the extrusion stage, (9) the quality indexes, and (10) the energy consumption in the plant.

3. Mathematical formulation

The optimization model for the short-term scheduling of the plastic bag production process can be represented mathematically through: (a) binary variables associated to the assignment of orders to units, W_{iu}, and to the sequencing of orders in a stage, X_{ijs}, and an integer variable related to the number of film rolls for each order i, Nr_i; (b) a set of different operational constraints in terms of continuous and discrete variables and, (c) two objective functions that consist in minimizing either the delay in the delivery of all orders, TD, or the makespan, MK. For space reasons, only some problem constraints are presented, mostly those nonlinear due to the multiplication between variables, for example, Tb_{ius} by Pr_{ius}.

$$Tb_{ius}\, Pr_{ius} = (1 + DEX) Lb_i\, W_{iu} \qquad \forall i \in I_s, \forall u \in U_s, s = 1 \tag{1}$$

$$Tb_{ius}\, Pr_{ius} = Filh_i\, Lb_i\, W_{iu} \qquad \forall i \in I_s, \forall u \in U_s, s = 2 \tag{2}$$

$$Tb_{ius}\, Pr_{ius} = Lb_i\, W_{iu} \qquad \forall i \in I_s, \forall u \in U_s, s = 3 \tag{3}$$

$$TT_{ius} = Tb_{ius}\, Nb_i \qquad \forall i \in I_s, \forall u \in U_s, \forall s \in S \tag{4}$$

$$Qp_{iu} = Pr_{ius}\, Qm_i \qquad \forall i \in I_s, \forall u \in U_s, \forall s \in S \tag{5}$$

$$Qr_i = \frac{\pi\, Ar_i}{4}\left(Dr_i^2 - DEM^2\right) De_i \qquad \forall i \in I_s, s = 1 \tag{6}$$

$$Qr_i \leq PTMAX \qquad \forall i \in I \tag{7}$$

$$QT_i = Qr_i\, Nr_i \qquad \forall i \in I \tag{8}$$

$$TTC_{iu} = Nr_i\, TCr_u \qquad \forall i \in I_u, u \in U \tag{9}$$

$$MVR_{iu} = 28.8 + 0.0857Nt_u - 0.0812(Qp_{iu}\,60) \quad \forall i \in I_1, u \in U_1 \tag{10}$$

$$IMP_{iu} = 14.5 - 0.012Nt_u + 0.0150(Qp_{iu}\,60) \quad \forall i \in I_1, u \in U_1 \tag{11}$$

$$D_i \geq TS_{is} + \sum_{u \in U_s}(TT_{ius} + TTC_{iu}) \quad dd_i \quad \forall i \in I_s \tag{12}$$

$$MK \geq TF_{is} \quad \forall i \in I_s, s = 3 \tag{13}$$

$$MinTD = \sum_i D_i \tag{14}$$

$$MinMK \tag{15}$$

Eqs. (1), (2) and (3) calculate the time required to process a bag of the order i in a unit u at each stage s in terms of the length of the bag and the processing rate of the order in the unit at that stage. The parameter DEX in Eq. (1) represents the waste percentage in the extrusion stage and $Filb_i$ in Eq. (2) denotes the bag printing factor. Eq. (4) specifies the total time for processing the order i in unit u TT_{ius} based on the time Tb_{ius} and the required number of bags Nb_i. Eq. (5) determines the production capacity of order i in unit u Qp_{iu} based on the processing rate and the weight of one meter of film roll, Qm_i.

Eq. (6) calculates the weight of a film roll of order i Qr_i made in the first stage in terms of the volume of the cylindrical roll and the density of the material to be processed. In this expression, Dr_i is the diameter of the film roll of order i and DEM is the diameter of the reel bobbin. Since each extruder u can handle a maximum roll diameter, the variable Qr_i can be constrained to be lower than an upper limit $PTMAX$ as stated in Eq. (7). The number of film rolls Nr_i is obtained in Eq. (8) while the total time for changing all the rolls of order i in unit u TTC_{iu} is determined in Eq. (9), where TCr_u is the change time of a film roll in unit u.

Eqs. (10) and (11) introduce the quality constraints. In case of plastic bags, there are two main quality control measures known as melt volumetric flow rate MVR and impact dart test IMP. These measurements depend on processing rate of the extruder Pr_{ius} and the screw rotating speed N_u, which in turn affect the production time of the orders.

In Eq. (12) the tardiness of order i D_i is calculated as the positive difference between the actual completion time of an order i and its deadline for delivery while in Eq. (13) the makespan MK is defined as the total time required for the completion of a series of orders. Eqs. (14) and (15) establish the objective functions of this problem which are the total tardiness TD (commonly used as an optimization criterion for a production scheduling, defined as the sum of the delay of all orders) and the makespan MK.

The remaining constraints used in this problem are mentioned below:

1. Assignment of orders to units at each stage
2. Each unit can process only one order first.
3. Each order i can have at most one direct preceding order j.
4. Each order i can have at most one successive direct order j.
5. Sequencing of consecutive orders in the same unit at each stage.
6. Relationship between start times of an order in consecutive stages.
7. Relationship between start times of consecutive orders in the same stage.
8. Relationship between restrictions 1 and 3 mentioned above.
9. Determination of the final execution time of orders at each stage.

4. Case Study: Results

The results of a real case study of a plastic bag plant in Ecuador are presented below. This plant operates 24 hours per day during 7 days a week with two daily shifts of 12 h each. Table 1 shows the main data required by the model for this particular case.

Table 1. Data for the case study

Order	Nb_i	dd_i (min)	Lb_i (m)	Qm_i (kg)	Ar_i (m)	$Filb_i$	De_i (kg/m^3)
i_1	125,000	10,080	1.8288	0.016	0.8128	0	1,900.28
i_2	100,000	10,080	1.8288	0.016	0.8128	0	1,900.28
i_3	50,000	10,080	1.3462	0.05	0.9652	0.96	1,845.97
i_4	50,000	10,080	1.3462	0.05	0.9652	0	1,845.97
i_5	50,000	10,080	1.2319	0.072	1.0287	0	1,845.97
i_6	50,000	10,080	1.3462	0.05	0.9652	0.96	1,845.97
i_7	250,000	10,080	0.254	0.048	0.8128	0.94	1,845.97
i_8	250,000	10,080	0.254	0.048	0.8128	0.94	1,845.97
i_9	400,000	10,080	0.5334	0.028	0.9652	0.48	1,900.28
i_{10}	200,000	10,080	0.5715	0.046	0.9525	0.44	1,900.28

Other required data are: (i) the waste percentage in the extrusion, DEX = 5%, (ii) the diameter of the bobbin DEM = 0.1 m, (iii) maximum weight allowed in each extruder, $PTMAX$ = 180 kg, (iv) the change time of a film roll in each unit TCr_u= 0.3 - 3 min.
The processing of orders in different stages is as follows: (a) Stage 1: orders 1 and 2 can be processed in units 6 and 7; orders 3 to 6 in units 1, 2, 3 and 5; orders 7 and 8 in units 2, 3 and 5; and orders 9 and 10 in unit 4; (b) Stage 2: orders 3 and 6 in units 9 and 10; orders 7 and 8 in units 8 to 10; orders 9 and 10 in unit 8; (c) Stage 3: orders 1 and 2 in units 19 and 20; orders 3 and 6 in units 11 to 14; orders 4 and 5 in units 11 to 15; orders 7 and 8 in units 16 and 17; and orders 9 and 10 in unit 18.

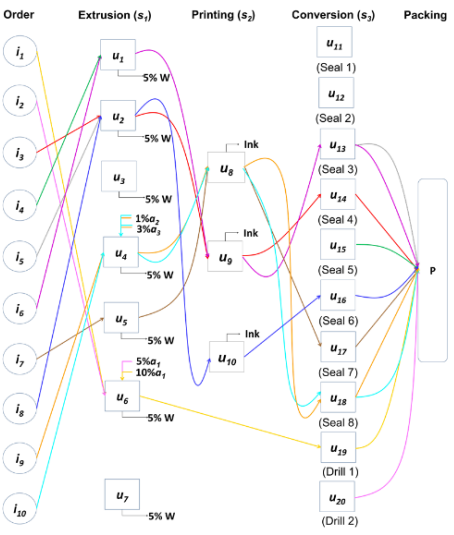

Figure 2. Optimal assignment of orders to units, tardiness minimization.

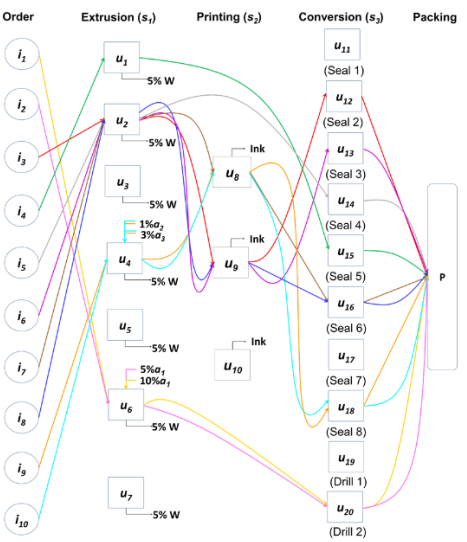

Figure 3. Optimal assignment of orders to units, makespan minimization.

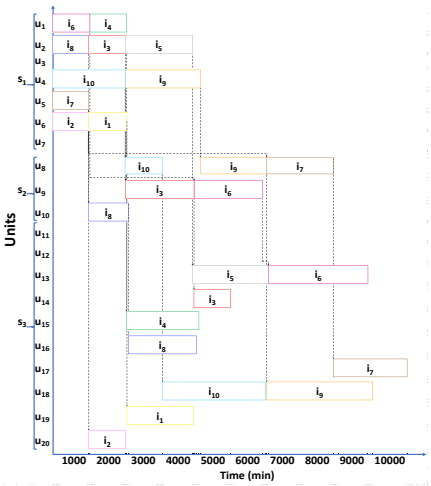

Figure 4. Gantt chart obtained minimizing tardiness.

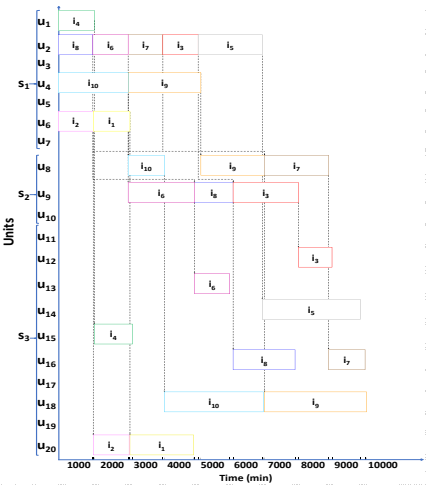

Figure 5. Gantt chart obtained minimizing makespan.

The model was implemented in GAMS 24.1.3 and solved using BARON code for both objectives. The formulation involves 777 continuous and 220 binary variables in 1,511 constraints. The optimal solution $TD = 0$ min was obtained in 1016 s for minimizing the tardiness and $MK = 9{,}829$ min was obtained in 543 s for the makespan in an Intel (R) Core (TM) i7-6,500CPU. Figs. 2 and 3 show the processing path of the different production orders for the minimization of tardiness and makespan, respectively. Figs. 4 and 5 present the Gantt charts of these optimal solutions, showing the sequencing and assignment of each order to a unit at each processing stage. In addition, it is observed that all orders are delivered on time during a horizon of one week, but when minimizing makespan only 13 units are used and the solution is obtained in less CPU time than tardiness.

5. Conclusions

An MINLP model was presented for optimizing the short-term scheduling of a plastic bag plant located in Ecuador. The model captures the main operational considerations of this type of plant while verifying restrictions on unit and product quality. The results obtained by the model were compared with the actual data from the plant for the case study where some orders were delivered late. By using the model solution with zero tardiness can be obtained. Therefore, the model is a tool that allows improving the plant scheduling activity and minimizing the production times.

References

1. Gopura, R.A.C.R; Jayawardane T.S.S, (2009) “A Study on a Poly-Bag Manufacturing System Preliminary Analysis and Simulation”. DOI: 10.1109/ICIINFS.2009.5429802, 4, 1-5.
2. Gupta, S; Karimi I.A. An Improved MILP Formulation for Scheduling Multiproduct, Multistage Batch Plants. Ind. Eng. Chem. Res. 2003, 42, 2365-2380.
3. Leung, Michelle, (2009). “Production Scheduling Optimization of a Plastics Compounding Plant with Quality Constraints”. Master's Thesis. Chemical Engineering Department. Waterloo University, Ontario, Canada, 32-44.
4. Mendez, C.A.; Henning, G.P.; Cerdá, J. Optimal Scheduling of Batch Plants Satisfying Multiple Product Orders with Different Due Dates. Computers and Chemical Engineering, 2000, 24, 2223–2245.
5. Merchan, Andres et al; (2016) “Discrete-Time MIP Methods for Production Scheduling in Multistage Facilities”. Computer Aided Process Engineering. Elsevier, DOI: 10.1016/B978-0-444-63428-3.50065-5.

Sauro Pierucci, Flavio Manenti, Giulia Bozzano, Davide Manca (Eds.)
Proceedings of the 30th European Symposium on Computer Aided Process Engineering (ESCAPE30), May 24-27, 2020, Milano, Italy.
http://dx.doi.org/10.1016/B978-0-12-823377-1.50105-1

Analysis of an Industrial Adsorption Process based on Ammonia Chemisorption: Modeling and Simulation

Cristian Cardenas[a,b,*], Stéphanie Marsteau[b], Léa Sigot[a], Cécile Vallières[a], Abderrazak M. Latifi[a]

[a]*Laboratoire Réactions et Génie des Procédés, CNRS-ENSIC, Université de Lorraine, Nancy, France*
[b]*Insitut National de Recherche et de Sécurité, Vandoeuvre-Lès-Nancy, France*
cristian-geovanny.cardenas-sarabia@univ-lorraine.fr

Abstract

In this study, a one-dimensional first principles model was developed to simulate an ammonia adsorption process. It is described by the mass balance equations, thermodynamic and transport properties. In order to build the adsorption process model, we started with experimental measurements of adsorption isotherms of ammonia on a doped activated carbon. A procedure was developed in order to assess the estimability of the unknown parameters involved in the Sips adsorption isotherm model. The estimable parameters were identified from the experimental data of ammonia adsorption equilibrium at 288, 303 and 313 K. The values of the parameters considered as non-estimable are fixed from one of our previous studies. In addition, we used experimental breakthrough curves to predict the kinetics of adsorption. The mass transfer coefficient K_{LDF} and axial dispersion coefficient D_{ax} were identified from the experimental breakthrough curves for different gas flow rates. The adsorption model was implemented and solved within COMSOL Multiphysics. The predicted model results using the fitted parameters exhibit a good agreement with the experimental measurements.

Keywords: Air purification boxes, ammonia adsorption, experimental analysis, modeling, simulation.

1. Introduction

Gaseous ammonia emission is one of the major concerns in composting or methanization organic waste facilities. Ammonia causes chronic respiratory diseases such as asthma, chronic bronchitis to workers when occupational exposure is too high. The French labour authorities (Courtois and Cadou, 2016) have set an occupational exposure limit for ammonia at 10 ppm. Mechanic machines used in composting and methanization plants often operate in an atmosphere where the ambient ammonia concentration is above this limit value. The cabins of these machines are then equipped with purification boxes to limit driver exposure. The boxes are composed of two separation phases in series. A filter that separates solid particles and/or aerosols and a doped activated carbon bed that removes ammonia by adsorption. The objective of the present paper is to analyze and model the adsorption process of ammonia. The model developed is a first principles model considering all the phenomena involved in the process. More specifically, it consists of momentum and mass balance equations, along with relations for the prediction of adsorption isotherms and kinetics.

2. Ammonia adsorption isotherms

For the adsorption process model development, experimental adsorption isotherms of ammonia on a doped activated carbon in a temperature range of 288–313 K at ammonia concentrations up to 1600 ppm were determined with a thermo-gravimetric analyzer from Setaram Instrumentation (SETSYS TAG). The ammonia adsorption capacity was thus evaluated from the mass gained by the sample at various ammonia concentrations. The whole experiences represent thirty equilibrium adsorption measurements.

2.1. Adsorption isotherms

In order to accurately describe the ammonia adsorption phenomenon on the doped activated carbon, the well-known Sips' adsorption model was used. This semi-empirical equation considers the interactions between the adsorbate molecules and the adsorbing surface with a heterogeneity factor, and is written as (Bedel, 2017):

$$q_e = \frac{q_m (bc)^{\frac{1}{s}}}{1+(bc)^{\frac{1}{s}}} \tag{1}$$

with the maximum amount adsorbed:

$$q_m = q_{m0} \exp\left[\chi\left(1-\frac{T}{T_0}\right)\right] \tag{2}$$

equilibrium constant:

$$b = b_0 \exp\left[\frac{Q}{R\,T_0}\left(\frac{T_0}{T}-1\right)\right] \tag{3}$$

and heterogeneity factors:

$$\frac{1}{s} = \frac{1}{s_0} + \alpha\left(1-\frac{T}{T_0}\right) \tag{4}$$

where α, χ are constants, q_{m0} is the maximum amount adsorbed at the reference temperature (mol.kg^{-1}), b_0 is the equilibrium constant at the reference temperature (m^3.mol^{-1}), s_0 the Sips heterogeneity factor at the reference temperature, T and T_0 are the operation and reference temperatures respectively (K), Q is the adsorption heat (J.mol^{-1}), and R is the ideal gas constant (J.mol^{-1}K^{-1}).

The isotherm equation (Eq.1) involves therefore six unknown parameters that should be deduced from experimental measurements.

2.2. Global parameter estimability analysis and identification

A preliminary step in the development of a reliable mathematical model, before the problem of parameter identification, is to evaluate the structural identifiability and estimability of the model parameters. The objective is to determine the most estimable parameters from the available measurements and possibly to design appropriate experiments to determine the less estimable ones.

The estimability algorithm used in this work is the same as the one developed by Yao et al. (2003) and used in Lei et al. (2013) and Bedel et al. (2017). The main difference here is that the sensitivity coefficient matrix is based on global sensitivities (Saltelli et al., 2006) rather than local ones. Moreover, the choice of the estimability threshold value which defines the limit between estimable and non-estimatable parameters, is still arbitrary and depends on the studied process. In this work, it is set equal to 0.04 as in Yao et al. (2003) and gives a good idea about the actual sensitivity of the isotherm models to

the unknown parameters. However, it should be noted that there are more advanced and sophisticated methods in the literature (Eghtesadi and McAuley, 2014).

2.2.1. Parameters estimability analysis results

The estimability analysis algorithm using the orthogonalization algorithm described by (Yao et al. 2003) was applied to the ammonia adsorption models on doped activated carbon and led to the following estimability order : $b_0 > \chi > Q/RT_0 > q_{m0} > s_0 > \alpha$. It is noteworthy that the last parameter α is non estimable based on the available experimental measurements. Therefore, its value was taken from one of our previous studies and set equal to **0.17** (Bedel, 2017).

2.2.2. Parameters identification

The five most estimable parameters are then identified from the available experimental measurements using the COMSOL optimizer. The results are presented in Table 1 as well as the 95% confidence intevals (CI) and the correlation matrix. The accuracy of the parameters is consistent with the values reported in the literature works.

Table 1. Values of the identified parameters for the Sips model

			Correlation matrix				
θ	Value	95% CI	q_{m0}	b_0	s_0	Q/RT_0	χ
q_{m0}	2.83	±0.23	1				
b_0	152.39	±48.53	-0.85	1			
s_0	1.69	±0.26	-0.58	0.21	1		
Q/RT_0	8.72	±5.77	0.75	-0.82	-0.29	1	
χ	1.58	±1.24	-0.74	0.70	0.24	-0.92	1

Figure 1 compares the predictions of Sips model to the adsorption equilibrium measurements.

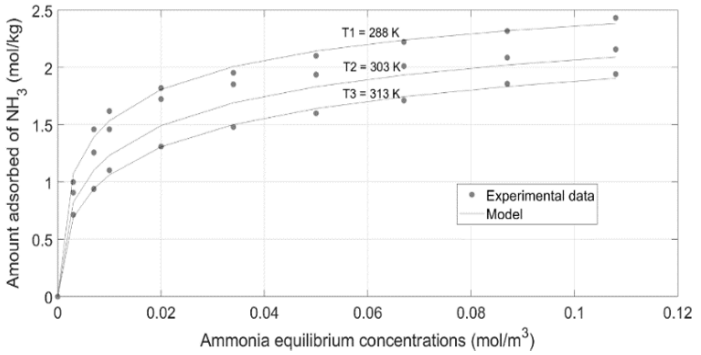

Figure 1. Comparison of Sips prediction model and experimental isotherms

The comparison exhibits a good agreement in the range of temperature and ammonia concentrations considered. The identified Sips isotherm will be used later in the modeling of the adsorption process.

3. Ammonia process experimental rig

In this section, the dynamic adsorption of ammonia in a packed column with doped activated carbon particles is studied experimentally.

3.1. Experimental set-up

The ammonia adsorption experimental set-up is presented in Figure 2. The studied gas is realized by mixing compressed dry air and bottles of pure ammonia by the use of two calibrated mass flowmeters. A small column is used to mix NH_3 and air before entering the adsorption column. The height and diameter of the column are 40 cm and 32 cm respectively. The doped activated carbon particles used without any pre-treatment. Temperature, pressure and humidity sensors are placed upstream and downstream of the adsorption column. A calibrated PID sensor is used to measure the ammonia concentration at the column exit. All the sensors are connected to an acquisition module.

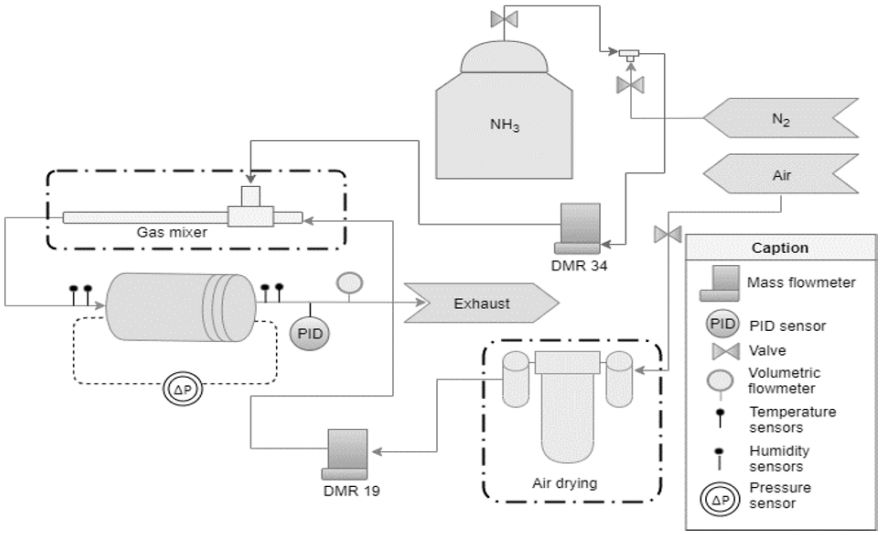

Figure 2. The ammonia adsorption experimental set-up

3.2. Experimental procedure

The adsorption column is filled with 22 g of doped activated carbon particles. The air from air network is dried in a silica gel column before entering the adsorption column. The adsorption column is kept under dry air until the column stabilizes in temperature (23°C) and a relative humidity (5%). A mixture of 1000 ppm NH_3 and air is then produced and fed the adsorption column. Three experiments were carried out at 6.9, 4.3 and 2.2 $L.min^{-1}$. Each experiment was repeated three times to check the reproducibility of the results.

4. Ammonia adsorption process modeling

In this section, the objective is to develop a mathematical model that accurately predicts the experimental measurements.

4.1. Model assumptions

The process model developed is based on the following assumptions: the gaseous mixture obeys the ideal gas law; the pressure drop is neglected, only ammonia is adsorbed; the resistance of mass transfer in the gas phase is negligible and the kinetics of mass transfer within a particle is approximated by the linear driving force (LDF) model; the gas phase is in equilibrium with the adsorbent; the adsorbent is considered as a homogeneous phase; the column temperature as well as the physical properties of the adsorbent are assumed to be constant.

4.2. Model Equations

The model developed is a one-dimensional first principles model. It is described by the mass balance equations, thermodynamic and transport properties. The mass balance for ammonia can be written as:

$$\frac{\partial c}{\partial t} - D_{ax}\frac{\partial^2 c}{\partial z^2} + \frac{\partial (vc)}{\partial z} = -\frac{1-\varepsilon_b}{\varepsilon_b}\frac{\partial q}{\partial t} \tag{5}$$

where c and q are the gas phase and the adsorbed phase concentrations of the adsorbate respectively (mol.m^{-3}), v is the interstitial velocity (m.s^{-1}) and D_{ax} is the axial dispersion coefficient (m^2.s^{-1}), ε_b is the bed void fraction.

The kinetics of mass transfer is approximated by the LDF equation as:

$$\frac{\partial q}{\partial t} = K_{LDF}\left(q_e - q\right) \tag{6}$$

where K_{LDF} is the overall mass transfer coefficient (s^{-1}) and q_e is the amount of adsorbed component at equilibrium (mol.m^{-3}).

The initial conditions of the variables are given as:

- For $0 \le z \le L$, $t = 0$: $c = 0$, $q = 0$,

and the boundary conditions are expressed as:

- For $t > 0$, $z = 0$: $c = c_{in}$, $q = 0$ and z =L: $\partial c/\partial z = 0$.

The values of the model constants are given in Table 2.

Table 2. Model constants

Parameter	Value	Unit
Solid density, ρ_p	2044.7	kg.m^{-3}
Bed density, ρ_b	675.4	kg.m^{-3}
Bed porosity, ε_b	0.67	-

The only parameters whose values are not determined are the axial dispersion coefficient D_{ax} and the material transfer kinetics K_{LDF}. These two parameters will be identified from experimental breakthrough curves.

4.3. Results and discussion

The adsorption model was implemented and solved within COMSOL Multiphysics. The identified values of K_{LDF} and D_{ax} are presented in Table 3.

Table 3. Identified values of the parameters of the ammonia adsorption process

v, (m.s^{-1})	K_{LDF}, (s^{-1})	D_{ax}, (m^2.s^{-1})
0.19	5.98E-04	0.0083
0.12	5.38E-04	0.0077
0.06	3.90E-04	0.0059

Their magnitudes are consistent with the values determined in similar operating conditions in literature (Knox et al, 2016). The predicted model results using the fitted parameters exhibit a good agreement with the experimental data (Figure 3).

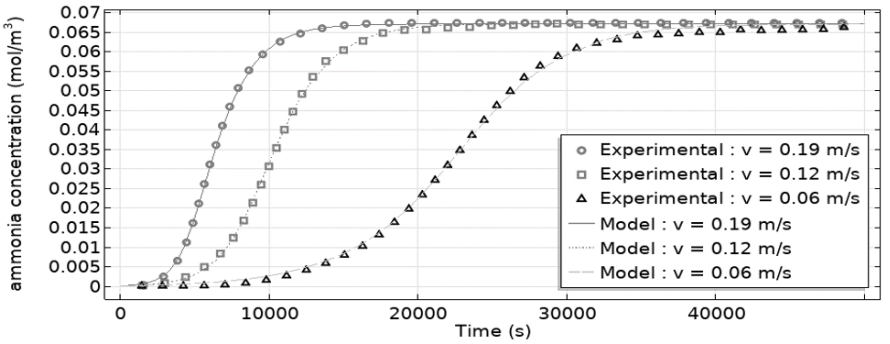

Figure 3. Comparison of predicted NH_3 breakthrough curves with experimental data

This agreement points out the accuracy of the model predictions. The resulting identified model will be further used in optimal design and operation of the ammonia adsorption process.

5. Conclusions

A procedure was developed in order to assess the estimability of the unknown parameters involved in the Sips adsorption isotherm model of ammonia on a doped activated carbon. The estimable parameters were identified from the equilibrium experimental data at 288, 303 and 313 K. The values of the parameters considered as non-estimable are fixed from literature or previous studies. A one-dimensional model was developed to simulate a column used for ammonia adsorption. The model predictions computed using the fitted parameters were in good agreement compared to the experimental measurements. This work demonstrated that it was possible to estimate the axial dispersion coefficient and the mass transfer coefficient from experimental breakthrough curves using a one-dimensional model.

References

S. Bedel, C. Vallières, M. A. Latifi, 2017, Parameters estimability analysis and identification for adsorption equilibrium models of carbon dioxide, Adsorption, 23(2-3), 373-380.

B. Courtois, S. Cadou, 2016, Valeurs limites d'exposition professionnelle aux agents chimiques en France, Institut National de Recherche et de Sécurité, ED 984, 14.

Z. Eghtesadi, K. B. McAuley, 2014, Mean square error-based method for parameter ranking and selection to obtain accurate predictions at specified operating conditions, Industrial & Engineering Chemistry Research, 53(14), 6033-6046.

J. C. Knox, A. D. Ebner, M. D LeVan, R. F. Coker, J. A. Ritter, 2016, Limitations of breakthrough curve analysis in fixed-bed adsorption, Industrial & engineering chemistry research, 55(16), 4734-4748.

M. Lei, C. Vallières, G. Grévillot, M. A. Latifi, 2013, Thermal swing adsorption process for carbon dioxide capture and recovery: modeling, simulation, parameters estimability, and identification, Industrial & Engineering Chemistry Research, 52(22), 7526-7533.

B. F. Lund, B. A. Foss, 2008, Parameter ranking by orthogonalization-Applied to nonlinear mechanistic models. Automatica, 44(1), 278-281.

A. Saltelli, M. Ratto, S. Tarantola, F Campolongo, E. Commission, 2006, Sensitivity analysis practices: Strategies for model-based inference, Reliability Engineering & System Safety, 91(10-11), 1109-1125.

K. Z. Yao, B. M. Shaw, B. Kou, K. B. McAuley, D. W. Bacon, 2003, Modeling ethylene/butene copolymerization with multi-site catalysts: parameter estimability and experimental design, Polymer Reaction Engineering, 11(3), 563-588.

Sauro Pierucci, Flavio Manenti, Giulia Bozzano, Davide Manca (Eds.)
Proceedings of the 30th European Symposium on Computer Aided Process Engineering (ESCAPE30), May 24-27, 2020, Milano, Italy.
http://dx.doi.org/10.1016/B978-0-12-823377-1.50106-3

Propagation of Parametric Uncertainty in a Conceptually Designed Bioethanol Production Process

Dilara B. Yıldız,[a] Nihat A. Sayar[a*]

Marmara University, Faculty of Engineering, Department of Bioengineering, Göztepe Campus, 34722, Kadikoy, Istanbul, Turkey

alpagu.sayar@marmara.edu.tr

Abstract

Understanding the propagation of parametric uncertainty in model-based computer simulations of conceptually designed bioprocesses and their metamodels is a critical step in improving the utilization and usefulness of such models. Generally, the number of design and operational parameters to be identified, calculated or assumed is very high. However, uncertainty analyses of these parameters usually focus on a selected few. The aim of this paper is to analyse the effect of increasing the number of uncertain parameters on the uncertainty of the metrics of interest acquired from the simulations and metamodels generated to relate these metrics to the uncertain parameters. The results indicate that overall uncertainty in simulated process metrics stabilises after a certain number of uncertain parameters is reached regardless of the characteristics of parametric uncertainty. However, metamodeling options such as sampling method, number of samples used, and type of metamodels used have direct effects on how the overall uncertainty can be represented by these metamodels. A demonstrative analysis is offered on a bioethanol production process model as a case study. In conclusion, the findings in this paper highlight the importance of the workflow followed in generating metamodels of bioprocess simulations under uncertainty.

Keywords: Parametric uncertainty, Kriging, bioethanol production

1. Introduction

Model-based simulations of conceptually designed bioprocesses are important tools esp. during the early techno-economic evaluation of process alternatives. The designs are generally implemented in specialized software such as SuperPro Designer or Aspen Plus. The number of design and operational parameters to be specified in such implementations of industrially relevant bioprocesses is in the order of several hundred. In the early stages of design and development, the values of most of these parameters can only be assumed. Only a critical few are obtained experimentally or calculated as development targets. Nevertheless, there is considerable uncertainty associated with the values used in the early simulations. Therefore, uncertainty analysis regarding these techno-economic parameters can be considered an important tool. Efficient workflows to facilitate such analyses have been developed (Morales-Rodriguez et al., 2012). However, in most examples of uncertainty analysis, only a selected few uncertain parameters are examined. Hence, it is important to understand the effects of increasing the number of uncertain parameters on the propagation of uncertainty into simulated process metrics (Bernardo, 2016).

Uncertainty analysis workflow involves the characterization and quantification of parametric uncertainty by probability density functions (pdfs) for the uncertain parameters followed by sampling from these distributions and propagating the uncertainty into process metrics by simulating the samples. Depending on the number of uncertain parameters involved and sampling preferences (such as sampling type and number of samples), the resulting number of simulations to be performed can be high and computationally expensive. Therefore, it may be practically preferable to generate metamodels, which describe the behavior of the simulated process metrics in the design space created by the selected uncertain parameters, to be used in subsequent tasks like optimization under uncertainty. Consequently, it is also important to understand the relationship between the uncertainty analysis workflow and subsequent metamodeling.
It is the aim of this paper to analyze the effects of the number of uncertain parameters selected as well as uncertainty analysis workflow and metamodeling preferences such as types of pdfs used to characterize parametric uncertainty, type of sampling, number of samples used and type of metamodels on the propagation of parametric uncertainty into uncertainty in simulated process metrics and their metamodels. The analysis is demonstrated on a case study involving the production of second-generation bioethanol from a lignocellulosic feedstock (hazelnut husk).

2. Propagation of uncertainty

2.1. Lignocellulosic bioethanol production process

In a previously proposed process model, hazelnut husk was used as the lignocellulosic feedstock for a bioethanol production process (Sayar et al., 2019). Figure 1 shows the process flow diagram of this process, where hazelnut husk is steam-pretreated in a reaction vessel and cooled down before a lignocellulolytic enzyme mixture is fed into the hydrolysis vessel. The hydrolysate is then used for fermentation. Crude fermentation product (including bioethanol) is filtered through microfiltration and this filtrate is then distilled for final product recovery. Over 500 design and operational parameters were specified and 15 of these are selected for analysis in this paper.

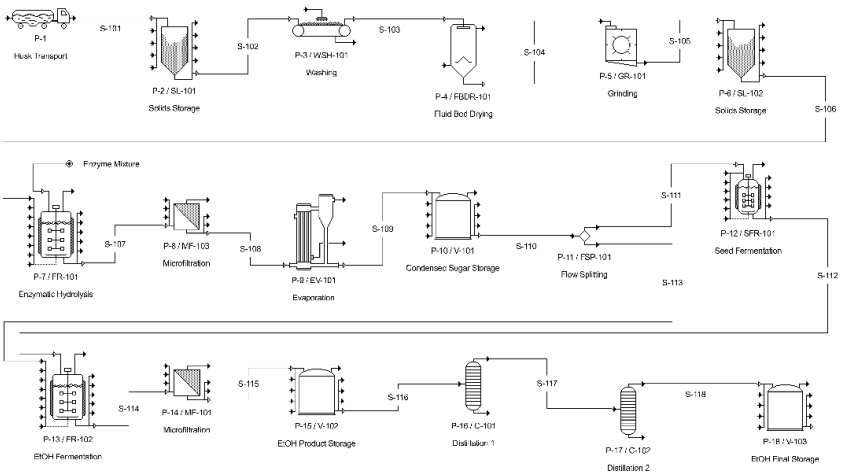

Figure 1: Simplified process flow diagram of bioethanol production process

2.2. Propagation of uncertainty into simulated process metrics

Propagation of parametric uncertainty into simulated process metrics entails the steps of uncertainty analysis. The first step is the characterization of parametric uncertainty in the selected uncertain parameters. Ideally, each uncertain parameter should be described by an appropriate pdf. In this paper, uniform and normal distributions were used as examples similar to that has been suggested by Gargalo et al. (2016). Table 1 provides the 15 selected parameters and their distribution parameters for both cases.

Table 1: Selected uncertain parameters and their uncertainty characterization

	Parameter	Uniform Distribution		Normal Distribution	
		Min Value	Max Value	Mean	Std Dev.
1	Throughput	180000	360000	270000	30000
2	Selling price	1	1.5	1.25	0.075
3	Enzyme loading	1/1000	2.5/1000	0.00175	0.0005
4	Cellulose-Glucose conversion	0.75	0.99	0.87	0.035
5	Hemicellulose–xylose conversion	0.75	0.99	0.87	0.035
6	Glucose-EtOH conversion	0.75	0.96	0.855	0.03
7	Xylose-EtOH conversion	0.75	0.96	0.855	0.03
8	Enzyme price	1	3	2	0.255
9	Peptone price	1	3	2	0.255
10	Yeast ext. price	1	3	2	0.255
11	Steam price	3	5	4	0.355
12	Electricity price	0.07	0.09	0.08	0.0058
13	Water price	0.1	0.03	0.2	0.015
14	Hazelnut husk price	0	0.005	0.0025	0.000125
15	Labor	15	30	22.5	2.25

At fifteen steps, the effect of increasing the number of uncertain parameters (from 1 to 15) was analyzed by performing Monte Carlo simulations of important process metrics (unit cost -UC- and net present value -NPV-). Sampling from the distributions were performed using Halton (HS), Sobol (SS), and Latin hypercube sampling (LHS) methods (Garud et al., 2018). With each sampling method, three sets with 25, 100, and 250 samples were generated. UC and NPV were simulated for each set using SuperPro Designer platform. Each step was repeated 30 times to represent the stochastic nature of the sampling methods. Resulting UC and NPV values (30 values for each case) were fitted to a normal distribution characterized by a mean and a standard deviation. The standard deviation obtained was considered as the measure of uncertainty in the simulated process metric. Figure 2 shows the change in the standard deviation of process metrics as a function of increasing number of uncertain parameters (NUP) for 100-sample cases.

Overall, propagation of parametric uncertainty into the selected process metrics seems to stabilize after a certain NUP is reached in all cases; although critical NUP differs for UC and NPV depending on the type of distribution used. However, these results support the hypothesis that overall metric uncertainty can be approximated by analyzing the propagation of uncertainty from a few selected uncertain parameters. Previous works on biorefineries show similar effects of parametric uncertainty on economic process metrics such as NPV and EBITDA (Chaeli et al., 2014). The results from 25 and 250 sample cases reinforce this finding (data not shown). The effect of the type of distribution used is clear from Figure 2. This means that it's an important task to identify the appropriate distribution for each selected parameter.

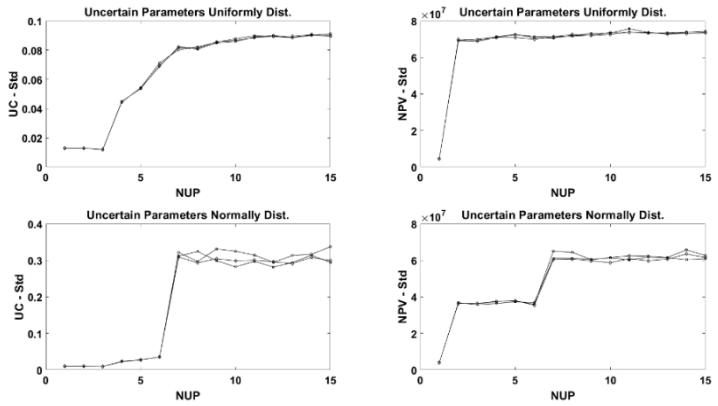

Figure 2: Propagation of parametric uncertainty as a function of NUP (HS: circle; SS: square; LHS: diamond)

2.3. Metamodeling under uncertainty

Simpler surrogate models are often used to represent computationally expensive simulations in modeling, feasibility analysis, and optimization (Bhosekar and Ierapetritou, 2018). Amongst the commonly used types of metamodels are conventional low-order polynomial models and Gaussian process-based Kriging (Kleijnen, 2017). It is important to evaluate how different types of metamodels perform under parametric uncertainty. In order to perform such an evaluation, each set of simulations detailed in the previous section were used to train metamodels using i) low-order polynomial models (LOP - quadratic), and ii) Kriging. Each resulting case is identified by its NUP (1-15), type of distribution used (Uniform, Normal), sampling method (HS, SS, LHS), number of samples (25, 100, 250), and metamodel type (LOP, Kriging).

The resulting metamodels were tested against one of 15 separate validation datasets (depending on the NUP involved). Many measures of goodness-of-fit such as root mean square error or mean absolute error (MAE) can be used for this evaluation. MAE between the simulated validation dataset values and metamodel predictions was used for the following analyses.

Each boxplot in Figure 3 illustrates a case as described above and summarizes the evaluation of 30 metamodels (one metamodel generated per repetition to represent the stochastic nature of sampling) generated under the stated preferences. Gaussian process-based Kriging can be seen to perform much better compared to conventional low-order polynomial models (LOP). It is also observed that for the Kriging models, the overall variability of model goodness-of-fit is similar for 10 and 15 uncertain parameter cases compared to 5 uncertain parameter case where variability is much lower. If these results are considered together with Figure 2 (bottom row), it can be argued that the elevated variability in model goodness-of-fit for higher NUP is due to propagated parametric uncertainty rather than the inadequacy of the models. Findings are very similar for both process metrics (UC and NPV). The analysis shown is for normally distributed uncertain parameters, sampled using LHS with 100 samples. Other cases support these general findings (data not shown).

Figure 4 shows the comparison of sampling methods for a selected case (normally distributed uncertain parameters, 100-sample sets, modelled by Kriging). In this case, HS seems to give the best results overall. The differences are qualitatively the same for both process metrics although slightly more pronounced for NPV. The difference

between the sampling methods diminishes for increased NUP. Results in other cases do not correlate exactly with this case. The most significant commonality is the fact that increased NUP seems to reduce the difference between sampling methods. The combined effect of sampling method and number of samples should be considered.

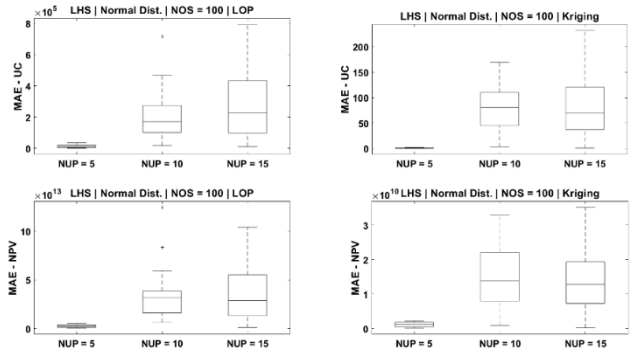

Figure 3: Effect of NUP on the propagation of metric uncertainty into metamodels

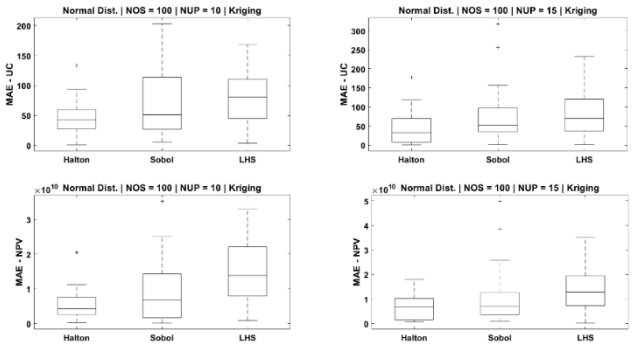

Figure 4: Effect of sampling method on the propagation of metric uncertainty into metamodels

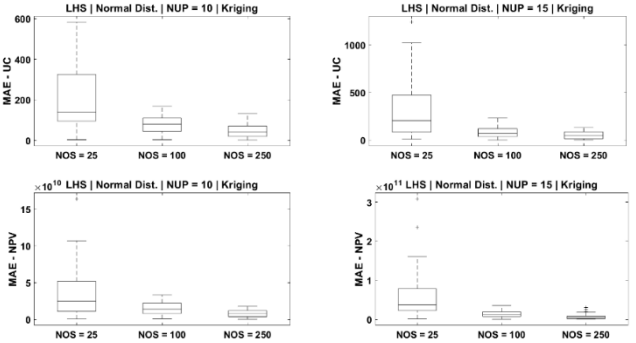

Figure 5: Effect of number of samples on the propagation of metric uncertainty into metamodels

Figure 5 illustrates the effect of number of samples on the goodness-of-fit of the generated metamodels. Clearly, the higher the number of samples the higher the accuracy of the resulting models is. However, increased NOS means additional computational burden. So, there is a trade-off between acceptable model accuracy and computational burden. The analysis summarized in Figure 5 helps to quantify that trade-off. Very similar results were obtained in the other cases not depicted here.

3. Conclusions

The increase in the overall metric uncertainty of the simulated process metrics of a conceptually designed bioprocess stops after a certain the number of uncertain design and operational parameters is reached. Therefore, it is an acceptable strategy to limit the focus of uncertainty analysis to a selected few uncertain parameters. However, the type of probability distribution selected to characterize the parametric uncertainty seems to be a critical factor. Hence, attention must be paid to select the appropriate pdf.
Gaussian-process based Kriging performs better for metamodeling under uncertainty compared to conventional low-order polynomials. The accuracy of the metamodels depend on number of samples used much more than sampling method.

Acknowledgements

This work was supported by The Scientific and Technological Research Council of Turkey (TUBITAK) by the project 217M526.

References

F. P. Bernardo, 2016, Model analysis and optimization under uncertainty using highly efficient integration techniques, in: Z. Kravanja and M. Bogataj (Eds.), ESCAPE 26, European Symposium on Computer Aided Process Engineering. Elsevier, Portoroz (Slovenia), pp. 2151-2156.

A. Bhosekar, M. Ierapetritou, 2018, Advances in surrogate based modeling, feasibility analysis, and optimization: A review, Computers and Chemical Engineering, 108, 250-267.

P. Cheali, A. Quaglia, K. V. Gernaey, G. Sin, 2014, Effect of market price uncertainties on the deisgn of optimal biorefinery systems – A systematic approach, Industrial & Engineering Chemistry Research, 53, 6021-6032.

C. L. Gargalo, P. Cheali, J. A. Posada, K. V. Gernaey, G. Sin, 2016, Economic risk assessment of early stage designs for glycerol valorization in bioreninery concepts, Industrial & Engineering Chemistry Research, 55, 6801-6814.

S. S. Garud, I. A. Karimi, G. P. E. Brownbridge, M. Kraft, 2018, Evaluating smart sampling for constructing multidimensional surrogate models, Computers and Chemical Engineering, 108, 276-288.

J. P. C. Kleijnen, 2017, Regression and Kriging metamodels with their experimental designs in simulation: A review, European Journal of Operational Research, 256, 1-16.

R. Morlaes-Rodrigues, A. S. Meyer, K. V. Gernaey, G. Sin, 2012, A framework for model-based optimization of bioprocesses under uncertainty: Lignocellulosic ethanol production case, Computers and Chemical Engineering, 42, 115-129.

N. A. Sayar, O. Pinar, D. Kazan, A. A. Sayar, 2019, Bioethanol production from Turkish hazelnut husk process design and economic evaluation, Waste and Biomass Valorization, 10(4), 909-923.

Sauro Pierucci, Flavio Manenti, Giulia Bozzano, Davide Manca (Eds.)
Proceedings of the 30th European Symposium on Computer Aided Process Engineering
(ESCAPE30), May 24-27, 2020, Milano, Italy.
http://dx.doi.org/10.1016/B978-0-12-823377-1.50107-5

New set of Graphical Axes for Grassroots Design of Heat Exchanger Networks for Chemical Engineering Applications

Dina Kamel [a*], Mamdouh Gadalla [b], Fatma Ashour[c]

[a] *British University in Egypt, 11837, Cairo, Egypt.*
[b] *Port Said University, Port Said, Egypt.*
[c] *Cairo University, Giza, Egypt.*
Dina.ahmed@bue.edu.eg

Abstract

This paper presents a graphical technique for optimum design of heat exchanger networks (HENs) by applying the pinch analysis rules. The new contribution of this graphical approach is to include the driving force of temperatures and their variations throughout the design in the graphical representations. This would allow the consideration of both heat transfer area and energy during the design/analysis. The graphical approach is applied on a case study of low temperature distillation process.

Keywords: Pinch analysis, Heat exchanger network, Graphical approach, Driving force.

1. Introduction

The HEN is a group of heat exchangers connected for the maximization of heat integration in chemical plants by using the heating duties of process sources to heat the cold streams and on the same time the hot streams are being cooled, this process integration will reduce the use of external utilities for heating and cooling and consequently reduce the overall operating cost.

Several methods and approaches are present in literature for the design of heat exchanger networks. Klemeš et al. (2018) reviewed in their work the new directions of implementation of pinch technology through the previous years in different engineering applications, based on that study they suggested possible direction of development in each field.

Heat integration using pinch analysis is an organized method for designing of efficient thermal processes. It helps in the calculation of the minimum energy requirements and maximum possible heat integration by detecting any thermodynamic bottleneck, or the pinch point for heat integration (Alwi, et al., 2010). According to pinch analysis principles, transferring heat through the pinch temperatures will require more energy than the minimum required energy. Linnhoff and Hindmarsh (1983) provided the important steps to decrease the energy necessities. The minimum energy required (targets) for heating and cooling were either determined by the composite curves; graphically (Smith, 2005), or numerically by problem table algorithm (Linnhoff, et al., 1978).

Liu et al. (2013) applied the principle of mass and heat integration for introducing a systematic simultaneous technique for the design of mass and heat exchanger networks.

Anastasovski (2014) established a new methodology for designing HENs; this methodology combined both problem table algorithm and pinch design method. The

methodology worked on dividing the problem to several enthalpy intervals; each interval is determined from the breaking points at composite curves. Liu et al. (2018) presented in their work a MINLP model for simultaneous integrated design for HENs and cooling

Zubairu et al. (2015) indicated that the composite curves, which were initially introduced by Hohmann (1971) as a graphical tool for identifying the energy targets along with the pinch temperatures, have been widely used and is considered as an incomparable method.

The new contribution of this graphical approach is that it provides a visual representation for each heat exchanger, position of inefficiencies, and temperature driving forces in each exchanger, to overcome any mistakes in the design, Moreover the new approach provides simple and applicable insights for efficient design with respect to the heat exchanger area.

2. Temperature- driving force (TDF) graphical approach

This graphical technique follows and applies the principles of pinch analysis. This graphical technique describes the heat recovery through employing two axes of temperatures. For a given heat exchanger, the driving force across each end are plotted on the Y-axis against the corresponding cold stream temperature on the X-axis as presented in Figure (1).

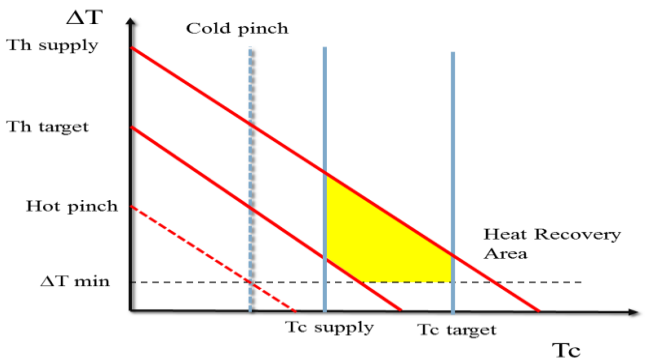

Figure (1): Key lines in the graphical representation

Figure (1) represents the driving forces in heat exchanger against the cold streams temperature that flow through these exchangers. At any given point in this graph both driving force across an exchanger; the corresponding cold temperatures can be identified. The basic characteristics of the new approach are as follows:

A given cold stream is represented as a vertical straight line at the value of the cold temperature on the X-axis, while the hot stream line is plotted as an inclined straight line that starts from the value of Th =ΔT on the Y- coordinate (Tc=zero) and ends at the value of Th= Tc on the X-coordinate (ΔT=zero) as shown Figure (1).

ΔT_{min} is represented as horizontal line starting at $\Delta T=\Delta T_{min}$.

The shaded area in Figure (1) represents the heat recovery area; the site of heat integration between the hot stream and the cold stream supply and target temperatures.

Each exchanger is plotted as a straight line (assuming constant heat capacities). The exchanger starts at the hot end driving force and ends at the cold end driving force.

The graph is divided into 5 regions according to the pinch analysis principals as shown in Figure (2):

- Region (1): exchangers matches integrate heat between hot streams below the pinch with cold streams below the pinch.
- Region (2): exchangers matches integrate heat between hot streams above the pinch with cold streams below the pinch
- Region (3): exchanger matches integrate heat between hot streams above the pinch with cold streams above the pinch
- Region (4): exchangers matches integrate heat between hot streams below the **ΔTmin line**
- Region (5): exchangers matches integrate heat below ΔT=0, thermodynamically infeasible.

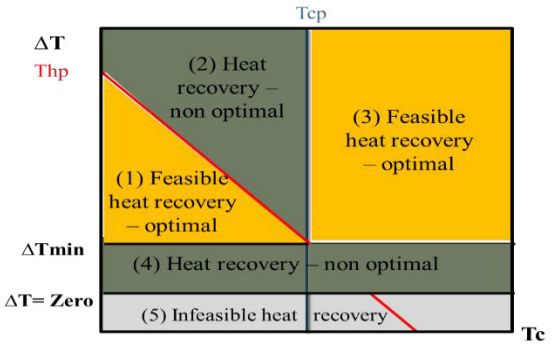

Figure (2): Feasible regions for heat integration

3. Graphical design of new HENs

As presented above in the literature, the pinch technology–based design methods were applied to design HENs according to energy matches and to then calculate the heat transfer area for the final heat exchanger network. In several design practices, the heat transfer area is a key issue in reaching an optimum design. The new TDF graphical method considers the temperature driving forces while designing HENs to obtain relatively optimum network with respect to energy targets, area and cost.

3.1 Procedure for graphical design

1. The design of the network is divided into 2 sections; above and below the pinch.

2. Above the pinch:

The first step is to determine the starting point for the 1st heat exchanger above the pinch, in general cases it exists at (T_{ht} , T_{cs}). In certain cases, the hot target temperature value is less than the hot pinch temperature value, so the starting point should be at the hot pinch temperature. Similarly, if the T_{cs} value is less than the T_{cp} value, start at the cold pinch temperature. For proper heat exchanger network design, heat integration should be fulfilled above the pinch by selecting the best exchanger matches.

3. Below the pinch:

The steps are similar to the design above the pinch except that the starting point for the 1st heat exchanger is at (T_{hs} , T_{ct}).

The principals of heat integration are applied to recover heat from hot streams graphically.

4. For the complete heat exchanger network design both algorithms are merged.

4. Case study: Low – temperature distillation process

The design of heat exchanger networks for low temperature applications is very challenging; it is very difficult to meet the minimum temperature difference while not crossing the pinch temperatures.

The minimum hot and cold utility requirements are 1.84 MW and 1.84 MW, respectively. The hot pinch temperature = -19ºC and the cold pinch temperature = -24ºC, assuming a minimum temperature difference of 5ºC.

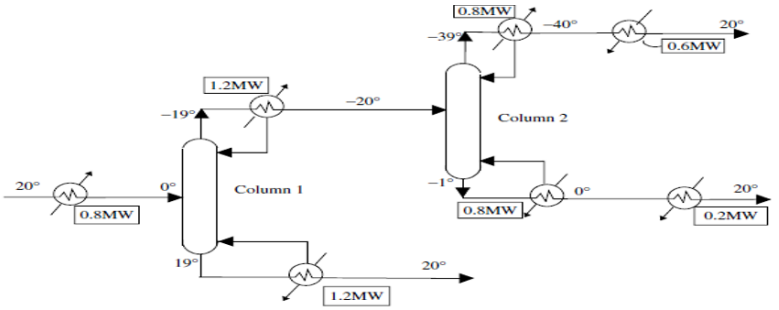

Figure (3): A low temperature distillation process (Smith, 2005)

The process has three hot streams and four cold streams, their temperatures and heat capacities are presented in Figure (3).

4.1 Graphical design of HEN

The first step in the graphical design of any HEN is plotting all the available hot and cold streams using the supply and target temperatures, and then representing graphically the key lines; hot pinch temperature line, cold pinch temperature line and ΔT_{min} line. At this point the design of the HEN is divided into two problems; above the pinch and below the pinch.

4.1.1 Graphical design below the pinch

Exchanger E1 is plotted in Figure (4) between the hot stream H2 and the cold stream C3, the starting point of this exchanger is at the intersection between the hot pinch line at -19ºC and the cold pinch line at -24ºC. The hot stream is only cooled from -19ºC till -19.13ºC, this minor change is due to the relatively high slope value as it nearly equal -1; at which the line concise with the hot stream. External cooling is used for cooling the *u*nsatisfied hot streams.

4.1.2 Graphical design above the pinch

As presented in Figure (5), Exchanger E2 is plotted between H1 and C3, this exchanger will neither satisfy the hot stream nor satisfy the cold stream as it will intersect the ΔT_{min} line first, and here it come the advantage of this method even though through duty calculations the available duty of the hot stream can completely satisfy C3 to reach its target temperature at 20ºC, this will lead to unfeasible design the minimum difference will be less than zero.

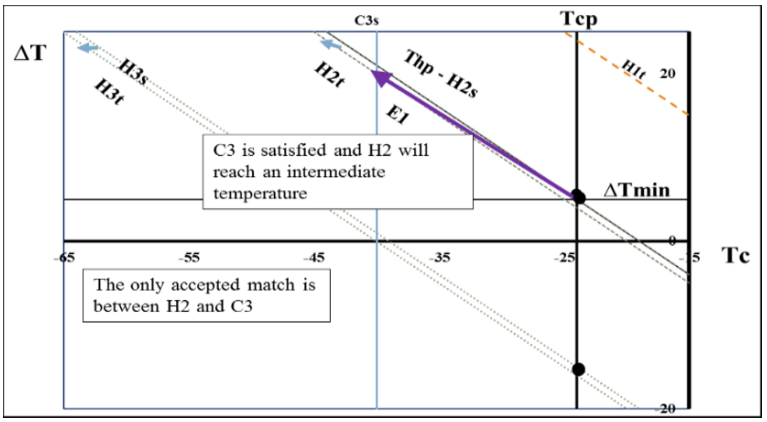

Figure (4): HEN design below the pinch

Similarly, Exchanger E3 is plotted between H1 and C2, the hot stream is completely satisfied, while the cold stream will reach an intermediate temperature of -0.315ºC. External heating is required for heating the unsatisfied cold streams.

Figure (6) present a grid diagram of the HEN

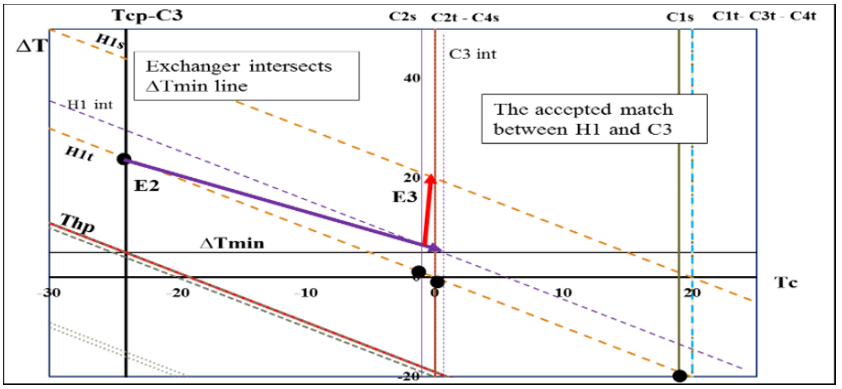

Figure (5): HEN design above the pinch

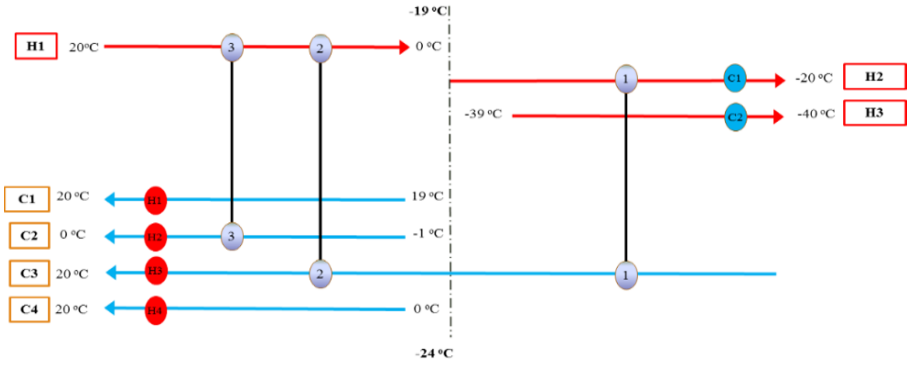

Figure (6): Grid diagram for HEN

The above design has been compared by a design generated by Aspen energy analyzer (V. 7.3) discussed above the disadvantages of the second design are: Exchanger 1 is crossing the pinch temperature, The design does not reach the hot and cold utility target requirements, and The design has more units which affects the total cost of the HEN.

Its only advantage that it has lower area of heat transfer, and even this advantage has minimum or zero effect as the total cost of the graphical approach design is lower than the total cost of the energy analyzer design by 7.9 %; this difference is due to the fact that the second design consumes more external utilities and has one more unit.

5. Conclusion

A new graphical approach was presented, which follows completely the pinch analysis principals.

The main merits of this approach are: its simplicity as each heat exchanger in the HEN can be represented by a straight line. Both the length and the slope of each exchanger line has a significant physical meaning. Other advantages are the visibility of the feasible regions for the heat integration.

The TDF approach provides a complete and systematic procedure for the grassroots design of HENs, the new approach is characterized by several advantaged, including: visual identification of the temperature driving force for each exchanger to avoid the presence of network pinch, visual and easy identification of possible and excluded matches regarding the driving force, visual and easy identification of optimum matches with respect to the area; as the exchanger approaches ΔT_{min} line, its area increases. Visualization in design especially for low temperature applications.

References

B. Zubairu, B. Highina and B. Gutti, "Minimizing hot and cold utility requirements for vegetable oil refinery plant using pinch Analysis," International journal of scientific engineering and technology, vol. 4, no. 5, pp. 298-301, 2015.
J. Klemeš, P. Varbanov, T. Walmsley and X. Jia, "New directions in the implementation of Pinch Methodology (PM)," Renewable and Sustainable Energy Reviews, vol. 98, pp. 439-468, 2018.
B. Linnhoff and E. Hindmarsh, "The pinch design method for heat exchanger networks," Chemical engineering science, vol. 38, no. 5, p. 745–763, 1983.
S. Alwi and Z. Manan, "STEP—A new graphical tool for simultaneous targeting and design of a heat exchanger network," chemical engineering journal, vol. 162, no. 1, pp. 106-121, 2010.
R. Smith, Chemical process design and integration, England: John Whiley & Sons Ltd, 2005.
B. Linnhoff and J. Flower, "Synthesis of heat exchanger networks: I. Systematic generation of energy optimal networks," Alche, vol. 24, no. 4, pp. 633-642, 1978.
A. Anastasovski, "Enthalpy Table Algorithm for design of Heat Exchanger Network as optimal solution in Pinch technology," Applied thermal engineering, vol. 73, no. 1, pp. 1113-1128, 2014.
F. Liu, J. Ma, X. Feng and Y. Wang, "Simultaneous integrated design for heat exchanger network and cooling water system," Applied Thermal Engineering, vol. 128, pp. 1510-1519, 2018.
E. Hohman, "Optimum networks of heat exchange," Ph.D. thesis ; University of Southern California, USA, 1971.
Aspen HYSYS, V7.3,Aspen technology inc, USA: University program, 2011.

Sauro Pierucci, Flavio Manenti, Giulia Bozzano, Davide Manca (Eds.)
Proceedings of the 30th European Symposium on Computer Aided Process Engineering
(ESCAPE30), May 24-27, 2020, Milano, Italy.
http://dx.doi.org/10.1016/B978-0-12-823377-1.50108-7

A Novel Process for Dimethyl Ether Synthesis Using Inter-Stage Ceramic Membrane for Water Removal

Abdulrahman A. Al-Rabiah

Department of Chemical Engineering, College of Engineering, King Saud University, P. O. Box 800 , Riyadh 11421, Saudi Arabia

arabiah@ksu.edu.sa

Abstract

Dimethyl ether has received great interest since it is considered as an environmentally-friendly chemical and can be utilized in a wide range of applications. DME is mainly used as aerosol propellant and intermediate in oil industry. It is also used as clean fuel in power generation and diesel engines. DME is produced directly from synthesis gas and indirectly via methanol dehydration over commercial γ-Al_2O_3 pellets. The methanol dehydration process has a low conversion which is limited by the thermodynamic equilibrium leading to a large recycle stream and size equipment. In addition, the presence of water in the feed with methanol reduces the equilibrium conversion that can be attained. An inter-stage membrane for water removal can overcome the thermodynamic limitations related to the conventional process.

In this study, two adiabatic reactor stages with inter-stage hydrophilic ceramic membrane for water removal were considered for the synthesis of DME via methanol dehydration. A commercial conventional process was simulated using Aspen-Plus ™ for an annual plant capacity of 50,000 metric tons and a 99.5 wt. % purity of DME product. A modified process for DME synthesis using water-selective alumina-silica composite membrane was developed and simulated. A parametric study was conducted to show the effect of inlet temperature on the reactor conversion which can be increased to 93 % using the inter-stage membrane. The high temperature reactor effluent was used to preheat methanol feed. The modified process shows potentials to reduce both energy and equipment size which leads to a lower process cost for DME production.

Keywords: dimethyl ether, process synthesis, membrane, simulation.

1. Introduction

Dimethyl ether is an alternative clean fuel that can be used in diesel engines for electric power generation, and in domestic applications such as heating. DME is used primarily as an aerosol propellant (Turton et al., 2013). It can be produced from many sources, including natural gas, crude oil, coal and biomass. DME is produced directly from synthesis gas or indirectly via methanol dehydration. Most of the industrial DME processes are based on methanol dehydration over γ-alumina catalyst.

In commercial DME production from methanol, the conversion is thermodynamically limited to about 82 %, leading to large recycle of non-converted methanol. There are many attempts to use new technologies to improve the DME process. Most of suggested schemes are hindered by the limited conversion of methanol which requires costly downstream processing (Azizi et al., 2014). For example, Luyben (2017) investigated the

use of a vaporizer, a cooled tubular reactor and an economizer in a conventional methanol dehydration process. The methanol conversion in the reactor under these operating conditions was increased only by 1.1 %. The increase in conversion results in a 12.8 % decrease in methanol recycle which shows the dominant effect of conversion on methanol recycle.

Membrane reactor has been suggested to enhance the conversion of methanol by removing water during the reaction. The ceramic membrane reactor was recently proposed to improve the performance of DME synthesis via dehydration of methanol (Lee, 2006). However, the conversion, when using the membrane reactor was improved by 6.2 % compared to the industrial reactor (Farsi, 2011).

In this study, an inter-stage membrane will be investigated to remove water between two reactor stages. There are many materials that can be used for water removal. Ceramics and polymers are the two main materials that are used for water separation. Currently, polymeric membranes are dominant in water treatment. However, their drawbacks, such as poor stability, easy fouling and short lifetime, are limiting their applications (He, 2019). Hydrophilic membranes such as zeolite, silica and alumina are suitable for water removal from organic mixtures at high temperatures. Lee et al. (2006) studied the separation of water from methanol and DME using alumina-silica composite membrane which provides high water selectivity.

The objective of this study is to determine the effects of using an inter-stage hydrophilic ceramic membrane on the conventional DME process. A hydrophilic ceramic (alumina-silica) membrane for water removal is proposed in this study to develop an intensified process for DME synthesis. A comparison with the conventional process will be illustrated.

2. Conventional Process

The synthesis of DME is via the catalytic dehydration of methanol over γ-alumina. The reaction is exothermic and reversible as shown:

$$2CH_3OH \leftrightarrow CH_3OCH_3 + H_2O \qquad \Delta H^0_{298K} = -23.5\,kJ/mol \tag{1}$$

The reaction rate of the gas phase methanol dehydration, on a commercial γ-alumina catalyst, was precisely described by the following kinetic model (Berčič and Levec, 1993):

$$-r_m = \frac{k_s K_M^2 \left(C_M^2 - \frac{C_D C_W}{K_{eq}}\right)}{\left(1+2\sqrt{K_M C_M} + K_W C_W\right)^4} \tag{2}$$

$$k_s = 5.35 \times 10^{13} e^{\frac{-17280}{T}} \quad , \quad kmol/(kg.h) \tag{3}$$

$$K_M = 5.39 \times 10^{-4} e^{\frac{8487}{T}} \quad , \quad m^3/kmol \tag{4}$$

$$K_W = 8.47 \times 10^{-2} e^{\frac{5070}{T}} \quad , \quad m^3/kmol \tag{5}$$

The equilibrium constant K_{eq} is calculated (by Aspen Plus) from Gibbs free energies.

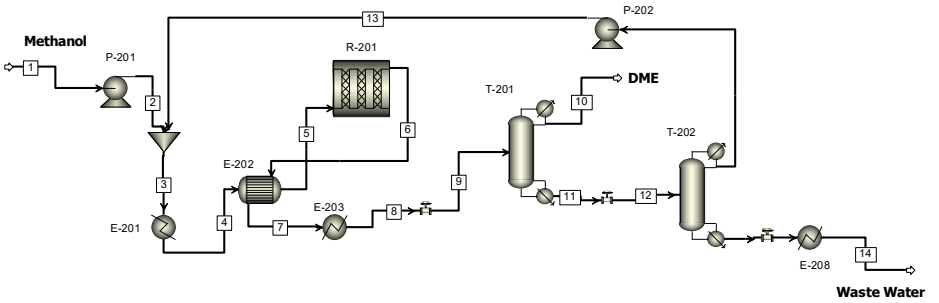

Figure 1. Dimethyl Ether Conventional Process Flow Diagram

The conventional industrial flowsheet based on DuPont process (Turton et al., 2013) is shown in Figure 1. The conventional process was rigorously simulated by Aspen Plus using UNIFAC thermodynamics model. The plant annual capacity is 50,000 tons of 99.5 wt. % DME product. The dehydration of methanol is a vapor-phase reaction conducted in an adiabatic reactor. The LHHW (Langmuir-Hinshelwood Hougen-Watson) kinetic model described in Eq. (2) was used to simulate the reactor and determine the conversion of methanol and the effluent yield. Figure 1 shows the base-case design that represents the industrial process. The liquid fresh methanol and recycle stream are first vaporized in E-201 and then preheated in a feed-effluent heat exchanger, E-202, before entering the reactor operating at 14.7 bar. The reactor effluent is then cooled in a cooler, E-203, and fed to the first distillation column operating at 10.3 bar (cooling water is used in the condenser), which produces a DME as distillate. The bottoms stream is separated in the second distillation column, which produces a water bottoms and a methanol distillate for recycle back to the feed vaporizer. The streams data calculated by Aspen Plus are shown in Table 1. The temperature profile and mole compositions of methanol and DME are shown in Figure 2. The calculated conversion of methanol is about % 81.8 which is in a good agreement with the industrial conversion using adiabatic fixed bed reactor. The maximum conversion is attained at an adiabatic temperature of 371.2 °C.

Table 1. Streams Data of Dimethyl Ether Conventional Process

Stream Number	**1**	**2**	**3**	**4**	**5**	**6**	**7**
Temperature (°C)	25.00	25.40	46.10	154.00	250.00	371.23	288.34
Pressure (bar)	1.10	15.50	15.50	15.10	14.70	13.90	13.80
Vapor Fraction	0.00	0.00	0.00	1.00	1.00	1.00	1.00
Mass Flows (t/h)	9.22	9.22	11.31	11.31	11.31	11.31	11.31
Mole Flows (kmol/h)	262.20	262.20	321.23	321.23	321.23	321.23	321.23
Component flowrates (kmol/h)							
DME	0.00	0.00	1.40	1.40	1.40	130.67	130.67
METHANOL	259.70	259.70	316.03	316.03	316.03	57.48	57.48
WATER	2.50	2.50	3.80	3.80	3.80	133.07	133.07
Stream Number	**8**	**9**	**10**	**11**	**12**	**13**	**14**
Temperature (°C)	100.00	90.53	45.75	152.98	140.02	120.72	50.00
Pressure (bar)	13.40	10.40	10.30	10.50	7.40	15.50	1.20
Vapor Fraction	0.16	0.22	0.00	0.00	0.04	0.00	0.00
Mass Flows (t/h)	11.31	11.31	6.58	4.72	4.72	2.09	2.64
Mole Flows (kmol/h)	321.23	321.22	129.80	191.42	191.42	59.03	132.39
Component flowrates (kmol/h)							
DME	130.67	130.67	129.27	1.40	1.40	1.40	0.00
METHANOL	57.48	57.48	0.53	56.95	56.95	56.33	0.62
WATER	133.07	133.07	0.00	133.07	133.07	1.30	131.77

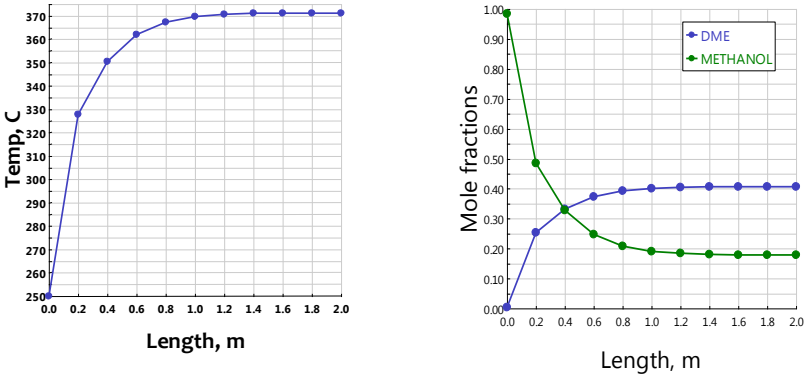

Figure 2. Temperature Profile and Mole Fractions of Methanol and DME along the Adiabatic Reactor Length

3. Membrane for Water Removal

A hydrophilic ceramic membrane is very suitable and selective for water removal from organic mixtures. Lee et al. (2006) developed a selective alumina-silica composite membrane for water removal from methanol and DME. The water-selective alumina-silica composite membrane is permeable to water with a permeability of 1.1440×10^{-7} mol m^{-2} s Pa^{-1} at a temperature of 250 °C. The water/methanol and water/DME selectivities are 8.4 and 62.9, respectively. Eq. 6 is used to calculate the membrane flux:

$$Q_i = \pi_i (P_i - P_i^m) \tag{6}$$

Where π_i, P_i and P_i^m are the membrane permeance, partial pressure at feed and partial pressure at permeant of component *i*, respectively. The water vapor which is generated via methanol dehydration in the first reactor stage is removed from the effluent before sending methanol and DME to the second reactor stage.

4. Modified Process

Figure 3 shows the flowsheet of modified process for DME production. The plant capacity and product purity of modified process are kept identical to the conventional process. The changes from the conventional process include the use of two identical reactor stages and an inter-stage alumina-silica composite membrane. The two fixed bed reactors are operated adiabatically using γ-alumina catalyst with an inlet feed temperature of 240 °C to the first stage reactor and 250 °C to the second stage reactor. Water is removed through the ceramic membrane which is located between the two reactor stages. Water (stream 9) is used to preheat the methanol feed (stream 3). The methanol feed is further preheated to 153 °C using the effluent of the first reactor stage (stream 6) which is cooled to 250 °C. Two additional heat exchangers (E201 and E202) are required to replace the preheater for heat integration. The methanol conversion of modified process was increased to 93 % which is improved by 13.7 % compared to the conventional industrial reactor. Table 2 shows the streams data of the modified process. A comparison between the modified process and the conventional process is shown in Table 3. There are significant improvements on the conventional process when the inter-stage membrane

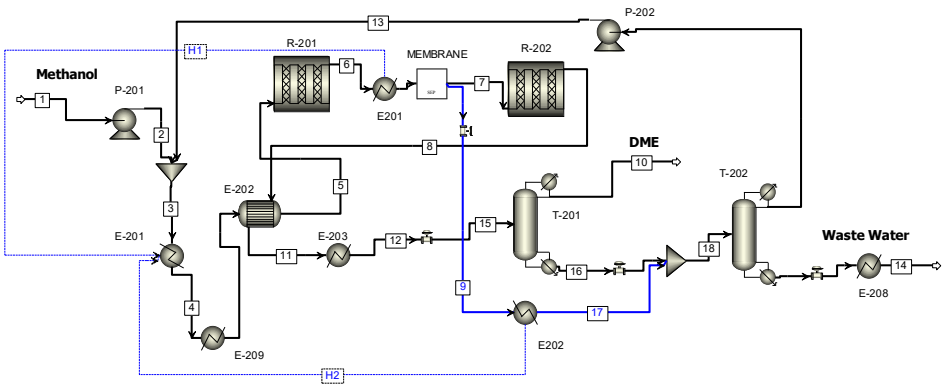

Figure 3. Dimethyl Ether Modified Process Flow Diagram

is used. The conversion of methanol was increased while the recycle was decreased. The major decrease is on the reboiler duty of first column (T-201) since water was separated via the membrane unit and then sent to the second column (T-202) for further purification. The effect of inlet temperature was investigated. The amount of unconverted methanol which is separated with water and unconverted methanol which exits the second reactor stage were calculated to optimize the inlet temperature, as shown in Figure 4. The highest conversion can be attained at feed temperature between 240 °C and 245 °C.

5. Conclusions

The industrial process for production DME was improved significantly when using an inter-stage hydrophilic alumina-silica membrane for water removal. The conversion was increased to 93 % with a decrease of about 59.7 % in methanol recycle stream. The process was heat integrated by preheating methanol feed using the two reactors effluents and the separated water in the membrane unit. The total hot and cold utilities were considerably decreased to 60.3 % and 69.5 %, respectively. The results proved that DME synthesis in the suggested inter-stage ceramic membrane is feasible and promising.

Table 2. Streams Data of Dimethyl Ether Modified Process

Stream Number	**1**	**2**	**3**	**4**	**5**	**6**	**7**
Temperature (°C)	25.00	25.40	28.50	153.28	240.00	361.20	250.00
Pressure (bar)	1.10	15.50	15.50	15.10	14.70	13.90	13.80
Vapor Fraction	0.00	0.00	0.00	0.55	1.00	1.00	1.00
Mass Flows (t/h)	9.22	9.22	10.09	10.09	10.09	10.09	7.45
Mole Flows (kmol/h)	262.20	262.20	286.01	286.01	286.01	286.01	160.36
Component flowrates (kmol/h)							
DME	0.00	0.00	3.26	3.26	3.26	117.32	115.47
METHANOL	259.70	259.70	278.95	278.95	278.95	50.82	44.78
WATER	2.50	2.50	3.81	3.81	3.81	117.87	0.12
Stream Number	**8**	**9**	**10**	**11**	**12**	**13**	**14**
Temperature (°C)	272.60	239.83	45.62	162.66	100.00	58.86	50.00
Pressure (bar)	13.00	3.10	10.30	12.90	12.80	15.50	1.20
Vapor Fraction	1.00	1.00	0.00	1.00	0.91	0.00	0.00
Mass Flows (t/h)	7.45	2.65	6.59	7.45	7.45	0.87	2.63
Mole Flows (kmol/h)	160.36	125.65	129.80	160.36	160.36	23.81	132.39
Component flowrates (kmol/h)							
DME	131.08	1.85	129.68	131.08	131.08	3.26	0.00
METHANOL	13.54	6.04	0.13	13.54	13.54	19.25	0.21
WATER	15.73	117.75	0.00	15.73	15.73	1.31	132.18

Table 3. Comparison of Conventional Process with Modified Process

Cases	Conventional Process	Modified Process	Comparison %
Methanol conversion %	81.8	93.0	+13.7
Methanol recycle, kmol/h	59.03	23.81	-59.7
Condenser duty of T-201, cal/s	217,197	213,162	-1.86
Reboiler duty of T-201, cal/s	167,118	2568	-98.46
Condenser duty of T-202, cal/s	344,221	164,847	- 52.1
Reboiler duty of T-202, cal/s	338,579	215,472	-36.4
Recycle pump (P-202) , hp	2.94	1.69	-42.5
Total heating utilities, cal/s	1,520,000	603,100	-60.3
Total cooling utilities, cal/s	2,206,000	671,900	-69.5

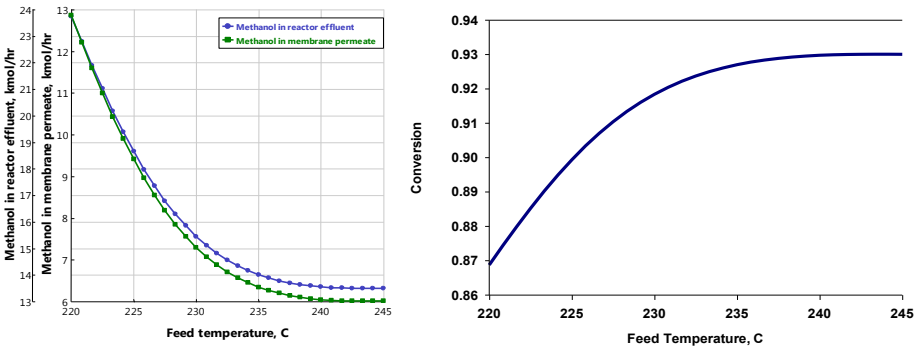

Figure 4. The Effect of Feed Temperature on Methanol Outlet Flowrates and Conversion

References

Azizi Z., Rezaeimanesh M., Tohidian T., Rahimpour M., 2014, Dimethyl ether: A review of technologies and production challenges, Chemical Engineering and Processing: Process Intensification, 82, 150-172.

Berčič G., Levec J., 1993, Catalytic Dehydration of Methanol to Dimethyl Ether. Kinetic Investigation and Reactor Simulation, Ind. Eng. Chem. Res.,32, 2478-2484.

Farsi M., Jahanmiri A., 2011, Enhancement of DME Production in an Optimized Membrane Isothermal Fixed-Bed Reactor, International Journal of Chemical Reactor Engineering, 9, 1-18.

He Z., Lyu Z., Gu Q., Zhang L., Wang J., 2019, Ceramic-based membranes for water and wastewater treatment, Colloids and Surfaces A, 578, 1-19.

Lee K., Youn M., Sea B., 2006, Preparation of hydrophilic ceramic membranes for a dehydration membrane reactor, Desalination, 191, 296-302.

Luyben W., 2017, Improving the conventional reactor/separation/recycle DME process, Computers and Chemical Engineering, 106, 17-22.

Turton R., Bailie R., Whiting W., Shaeiwitz J., Bhattacharyya D., 2013, Analysis, Synthesis, and Design of Chemical Processes, 4th edition, Prentice Hall, USA.

Sauro Pierucci, Flavio Manenti, Giulia Bozzano, Davide Manca (Eds.)
Proceedings of the 30th European Symposium on Computer Aided Process Engineering
(ESCAPE30), May 24-27, 2020, Milano, Italy.
http://dx.doi.org/10.1016/B978-0-12-823377-1.50109-9

Computer-aided Solvent Mixture Design for the Crystallisation and Isolation of Mefenamic Acid

Suela Jonuzaj,[a] Oliver L. Watson,[a] Sara Ottoboni,[b] Chris J. Price,[b] Jan Sefcik,[b] Amparo Galindo,[a] George Jackson,[a] Claire S. Adjiman[a,*]

[a]*Centre for Process Systems Engineering, Department of Chemical Engineering, Imperial College London, SW7 2AZ, UK*
[b]*Department of Chemical and Process Engineering, University of Strathclyde, G1 1XQ, Glasgow, UK*
c.adjiman@imperial.ac.uk

Abstract

We present a systematic computer-aided methodology for the integrated design of solvent blends used in the purification (i.e., crystallisation and isolation) of pharmaceutical compounds. In particular, we investigate the design of optimal solvent mixtures for combined cooling and antisolvent crystallisation, taking into account interlinked design decisions across both crystallisation and isolation (washing) stages. Within the proposed approach, the optimal solvents, antisolvents, the best mixture composition and the optimal process temperatures are determined simultaneously. Furthermore, comprehensive design specifications for both crystallisation and isolation units, such as the miscibility of crystallisation and wash solvents, their environmental impact, and health and safety metrics, are investigated. The design method is applied to identifying potential high-performance solvent blends for the purification of mefenamic acid, while removing an impurity, chlorobenzoic acid, from the system.

Keywords: Crystallisation, isolation, CAM^{b}D, solvent blends, mefenamic acid.

1. Introduction

The importance of solvents in the manufacturing of pharmaceutical products has long been established and their presence is essential in many steps of the process, spanning synthesis, separation/purification and product formulation. Of particular interest are purification processes, where the extensive use of solvents in different process units can affect process efficiency, cost/environmental/safety performance, and final product quality. A comprehensive study on the green manufacturing of pharmaceuticals by Jiménez-González et al. (2011) and a life cycle assessment of pharmaceutical products by Ott et al. (2014) have shown that the choice of solvents is one of the key drivers to improving the sustainability of the manufacturing process. Currently, several pharmaceutical companies are using in-house solvent selection guides and workflows that have been developed based on heuristic approaches. Despite these tools, the development and manufacturing of a new medicine continues to require time-consuming and costly experimental investigations if a wide range of options is to be explored. Thus, more streamlined and systematic methods and workflows are required to enable the rapid exploration of numerous design options and to enhance innovation (Brown et al., 2018).

Computer-aided mixture/blend design (CAM^{b}D) (Gani, 2004) is a promising approach for identifying suitable solvent blends that meet predefined target properties and optimise a given performance measure. CAM^{b}D has often been used in the design of optimal

solvent mixtures for crystallisation processes (Austin et al., 2016; Jonuzaj et al., 2016, 2018; Karunanithi, et al., 2006; Watson et al., 2019) in order to facilitate and improve the production of pharmaceuticals. Karunanithi et al. (2006) proposed a decomposition-based approach for the design of binary solvent and/or antisolvent mixtures used in the crystallisation of active pharmaceutical ingredients (APIs), where smaller molecular and mixture design subproblems were posed and solved. The design of solvent mixtures for crystallisation was also studied by Austin et al. (2016), where the mixture design problem with a fixed number of ingredients was decomposed into molecular and mole fraction optimisation formulations. Jonuzaj et al. (2016, 2018) presented a general CAM^{b}D formulation for the selection and design of solvent mixtures for separation processes, in which the number of ingredients in the blend, the identities of solvents and their mole fractions are optimised at the same time.

To date, most solvent mixture design approaches have been applied to optimise a single purification process unit with fixed operating conditions. Selecting optimal solvents for a specific unit (e.g., crystallisation), without consideration for the overall process, may impact negatively on the effectiveness of subsequent purification steps (e.g., washing), and thus deteriorate the efficiency of the overall process. Furthermore, by operating at fixed process conditions, such as temperature, the entire design space of possibilities is not fully explored. The latter issue has been addressed in the recent work by Watson et al. (2019) who proposed a solvent mixture design formulation for the coupled cooling and antisolvent crystallisation, with variable process temperature. In this work, we extend the approach and present a comprehensive methodology for the design of solvent mixtures that includes both the crystallisation and the isolation of pharmaceutical compounds. In our new integrated formulation, optimal mixtures of crystallisation solvents and antisolvents, their compositions, and the optimal process temperatures are determined simultaneously. To ensure the overall purification process is effective, mixture property constraints (such as the miscibility of crystallisation and washing solvent mixtures) are enforced for both crystallisation and isolation stages. The methodology is applied to the design of solvent blends for the purification of mefenamic acid (MA), with the aim to minimise solvent consumption, while ensuring a high crystal yield of MA is achieved, and avoiding the crystallisation of a given impurity (chlorobenzoic acid (CBA)). In addition, the crystallisation solvents are selected subject to health-and-safety constraints that are included within the optimisation formulation, and they are screened for miscibility with a wash solvent at optimal values of the composition.

2. Solvent mixture design for crystallisation and isolation processes

2.1. Problem definition

The proposed CAM^{b}D problem involves a comprehensive formulation for the design of optimal solvent mixtures for the cooling/antisolvent crystallisation and washing processes of pharmaceutical compounds. Mixtures of N_c components are designed and consist of an active pharmaceutical ingredient (API), a solid impurity, a crystallisation solvent and antisolvent pair, and a wash solvent. In order to develop the mathematical formulation, we define the sets $I = \{1, \dots, N_c - 1\}$ and $\tilde{I} = \{1, \dots, N_c\}$ for all components in the crystallisation and washing blends, respectively. The first two elements of sets I and $\tilde{I}$ consist of the API and its impurity (denoted by subset JJ), while the rest of the elements, denoted by subsets II and $\widetilde{II}$, represent the solvent molecules ($I = JJ \cup II$; $\tilde{I} = JJ \cup \widetilde{II}$). The set $S = \{1, \dots, N_s\}$ defines the lists of chemical compounds from which the optimal

solvents are to be chosen. The crystallisation process consists of initial/heated (in) and final/cooled (f) states, denoted by the set $St = \{\text{in}, \text{f}\}$.

2.2. MINLP formulation of the integrated CAM^{b}D problem

The integrated formulation of the CAM^{b}D problem consists of an objective function (f) to be optimised, general constrains ($g, \tilde{g}$) that hold regardless of the discrete choices, and conditional constraints ($h, \tilde{h}$) that depend on the logic decisions (e.g., solvent identity), and are formulated using the big-M approach (Jonuzaj et at., 2016), as shown below:

$$
\begin{aligned}
&\min_{x,p,y} \quad f(x,p) \\
&\text{s.t.} \quad g_t(x,p) \le 0, \;\; t \in St \\
&\qquad \tilde{g}(x,p) \le 0 \\
&\qquad h_{i,s,t}(x,p) \le M_{i,s,t}\big(1 - y_{i,s}\big), i \in I \;\; ; s \in S; \;\; t \in St \\
&\qquad \tilde{h}_{i,s}(x,p) \le \widetilde{M}_{i,s}\big(1 - y_{i,s}\big), i \in \tilde{I} \;\; ; s \in S \\
&\qquad Ay \le a \\
&\qquad x \in [x^L, x^U] \subset \mathbb{R}^{N_c}; \; p \in [p^L, p^U] \subset \mathbb{R}^{m_p}; \; y \in \{0,1\}^q
\end{aligned}
\qquad (P)
$$

where x is a vector of mole fractions for the components in the crystallisation and wash blends, p is a vector of other continuous variables and y is a binary variable for assigning solvents from the set S to the solvent components in the mixture. The constraints g and h describe the initial/final states of the coupled cooling-antisolvent crystallisation, whereas $\tilde{g}$ and $\tilde{h}$ functions correspond to the washing process at ambient conditions.

3. Case study: solvent mixture design for purifying mefenamic acid

3.1. Problem description

Mefenamic acid (MA) is a nonsteroidal anti-inflammatory drug with analgesic properties. Its low solubility in common solvents requires identifying suitable solvents and solvent mixtures for the efficient purification of the drug. Specifically, we identify optimal solvent mixtures for the cooling and antisolvent crystallisation of MA with the objective to minimise solvent consumption (χ_s in (g solvents/g MA crystals)), while achieving high crystal yield of the API and avoiding crystallisation of CBA, an impurity. Here, the crystal yield of MA is set to be greater than or equal to a user-specified lower bound of 90 % (i.e., $\acute{Y}_{\text{MA}} \ge 90$ %), whereas the crystal yield of CBA is set to zero (i.e., $\acute{Y}_{\text{CBA}} = 0$). The initial amounts of MA and CBA in the crystallisation blend are set to be $n_{MA,\text{in}}$= 1 mol and $n_{CBA,\text{in}}$= 0.2 mol, respectively. Solvent use is bounded by a (heuristic) lower value of 3.5 (g total solvent/g MA crystals) to ensure that adequate amounts of solvents are present to facilitate processing. The optimal crystallisation blend at final (cooled) conditions goes through a filtration and washing (isolation) process. The solvent & antisolvent mixture present in the cake after filtration needs to be miscible with the wash solvent, so that the crystallisation solvents and the impurity are removed successfully from the system (Ottoboni, 2018). In this case study, n-heptane is chosen as the wash solvent and the miscibility of each crystallisation solvent with n-heptane is tested. It is noted that MA has very low solubility in n-heptane around ambient conditions ensuring that the solid API is not dissolved in the wash solvent. The optimal crystallisation solvents/antisolvents are selected from a list of 69 candidates. The design specifications and the main model equations (i.e., relations for calculating solvent consumption and crystal yields; solid-liquid equilibrium equation for calculating the solubilities of MA and CBA in the solvent mixtures; and the miscibility function to ensure that there is no phase split between the different pairs of solvent, antisolvent and wash solvent) are presented in Table 1. The

liquid-phase activity coefficients, denoted by γ, are calculated with the UNIFAC model (Fredenslund et al., 1975). Superscript ^{i,j} indicates the binary mixture of components i and j considered, at the ratio of mole fractions found in the multicomponent mixture.

Table 1: Main problem equations and design specifications. See Table 2 and text for symbols.

Description	**Main model equations and design specifications**
Solvent use; crystal yield	$\chi_s \left[\frac{\text{g solvents}}{\text{g MA crystals}}\right] = \frac{\sum_{ii} m_{ii}}{m_{MA,\text{in}} - m_{MA,\text{f}}}$; $\acute{Y}_{jj} = \frac{n_{jj,\text{in}} - n_{jj,\text{f}}}{n_{jj,\text{in}}}$
Solubility; miscibility	$\ln x_{jj,t} + \ln \gamma_{jj,t} = \frac{\Delta H_{fus,jj}}{R}\left[\frac{1}{T_{m,jj}} - \frac{1}{T_t}\right]$; $\frac{\partial \ln \gamma_{i,t}^{i,j}}{\partial x_{i,t}^{i,j}} + \frac{1}{x_{i,t}^{i,j}} \geq 0$
Components in the mixture	1 API (MA), 1 impurity (CBA), 2 crystallisation solvents (s_1, s_2) and 1 wash solvent (s_w)
Fixed components in the blend	MA, CBA, s_w (n-heptane)
Designed solvents in the blend	s_1, s_2
Problem size	32,048 eqns.; 29,334 continuous and 360 discrete vars.

3.2. Results and discussion

The integrated formulation is implemented and solved in GAMS version 28.2.0, using SBB, a local branch & bound MINLP solver. The integrated MINLP model for the crystallisation and washing of MA can be found at *doi.org/10.5281/zenodo.3628753* and the results obtained are summarized in Table 2.

Table 2: Optimal solutions obtained when solving the integrated formulation of the case study. Fixed mixture ingredients (MA, CBA, s_w) and optimal solvents (s_1, s_2); solvent use (χ_s); % crystal yields of MA and CBA (% $\acute{Y}_{jj}$); composition ($x_{i,t}$) & mass ($m_{i,t}$) of mixture ingredients, and initial (T_{in}) & final (T_{f}) temperatures in the crystallisation unit; composition ($\tilde{x}_i$) and mass ($\tilde{m}_i$) of mixture ingredients in the wash solvent, after washing.

Components (i)	Crystallisation							Washing	
	χ_s (g/g)	% $\acute{Y}_{jj}$	$x_{i,\text{in}}$	$x_{i,\text{f}}$	$m_{i,\text{in}}$ (g)	$m_{i,\text{f}}$ (g)	T_{in} (K) T_{f} (K)	$\tilde{x}_i$	$\tilde{m}_i$ (g)
API: MA	3.5	97.2	0.108	0.003	241	7	380	0.001	0.02
Impurity: CBA		0	0.021	0.024	31	31	290	0.006	0.10
s_1: n-methylpyrrollidone			0.523	0.584	479	479		0.139	1.48
s_2: o-xylene			0.348	0.389	342	342		0.092	1.05
s_w: n-heptane								0.762	8.21
API: MA	3.5	94.5	0.073	0.004	241	13	364	0.001	0.06
Impurity: CBA		0	0.015	0.016	31	31	292	0.004	0.14
s_1: DMAC			0.401	0.431	477	477		0.113	2.18
s_2: formic acid			0.511	0.549	321	321		0.143	1.46
s_w: n-heptane								0.739	16.4
API: MA	3.5	90.0	0.119	0.011	241	24	362	0.002	0.06
Impurity: CBA		0	0.024	0.023	31	31	290	0.005	0.08
s_1: pyridine			0.663	0.642	440	440		0.142	1.18
s_2: 2,2,4-trimethylpentane			0.194	0.324	186	320		0.072	0.86
s_w: n-heptane								0.779	8.21

A ranked list of 10 optimal solutions is generated by including integer cuts in the MINLP formulation. The optimal value of solvent consumption obtained in all cases is at the

lower bound. Three of the optimal solutions obtained are presented in Table 2. These solutions show large variations in the crystal yields and in the solvent blends used, demonstrating the benefits of the proposed approach, where many design decisions are optimised simultaneously. In the first two solutions, MA is crystallised by a cooling process (starting at 380 K or 364 K) and there is no addition of solvent between the initial and final states of the crystallisation. In the third solution a high crystal yield and a low solvent consumption are achieved by the combination of cooling and antisolvent crystallisation, where MA crystals are produced by increasing the amount of antisolvent, 2,2,4-trimethylpentane and reducing the process temperature from 362 K. Thanks to the constraints imposed in this model, the crystallisation solvent blends obtained with the integrated model are in a single liquid phase in both initial and final crystallisation stages, and both solvents used are miscible with n-heptane in the washing unit. In a non-integrated approach (without considering washing), several optimal blends obtained consist of solvents acetic acid and 1,2-propanediol, which are immiscible with n-heptane at the washing stage. Hence, the use of models that consider the purification process in an integrated fashion is essential to achieve a feasible design.

The list of optimal blends generated includes solvents that have high environmental and health impact, such as n-methylpyrrolidone, o-xylene & pyridine. To ensure that safe solvents are chosen, we extend the approach to use the GSK solvent selection guide (Henderson et al., 2011) and include constrains on the flammability, health and environmental impacts, and reactivity of each solvent in the optimisation model. A set of optimal blends is obtained with a multiobjective optimisation (MOO) formulation, where solvent use is minimised whereas the GSK safety indicator values are maximised. The set of Pareto optimum solutions given in Figure 1 is obtained using the ϵ-constrained method, in which solvent consumption is optimised and the safety indicators are constrained by a given lower bound. The generated Pareto set consists of blends with different solvents and compositions. As shown in Figure 1, there are several solutions that yield the same low solvent consumption but very different safety indicators. However, a safety indicator greater than 6 can only be achieved with a significant increase in solvent use. Thus, MOO provides a useful tool to make better design decisions, in conjunction with other key aspects related to solvent selection, such as stability of solid form and crystal morphology, that ensure downstream process feasibility.

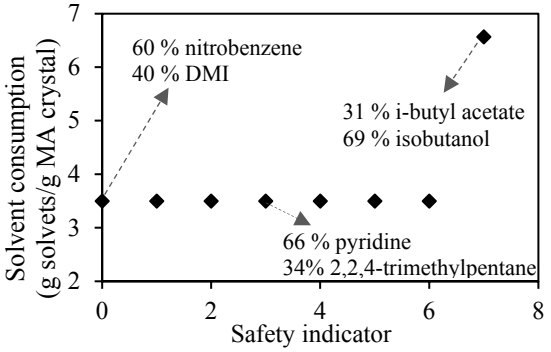

Figure 1: Pareto optimal solutions when solving the integrated crystallisation and washing process. Minimum solvent consumption for different safety indicator values.

4. Conclusions

In this work, a systematic methodology for the design of optimal solvent mixtures for integrated purification processes of pharmaceuticals has been presented. Within the proposed approach, the simultaneous optimisation of crystallisation and washing steps was explored, where optimal solvent mixtures were identified for the combined cooling and antisolvent crystallisation and their interaction with the wash solvent was

investigated. The model was applied to the selection of optimal solvent mixtures for the purification of mefenamic acid. A range of design options were obtained, achieving both low solvent use and high crystal yield, while limiting impurities in the crystallisation. Further, the use of a comprehensive framework has been shown to lead to a wide range of more promising design options. This highlights the necessity of developing integrated approaches to solvent design for purification over sequential solvent selection workflows. Future work will focus on optimising the identity of the wash solvent and the overall crystal yield and solvent consumption across both purification stages, while taking into account critical factors such as the solid form stability and crystal morphology.

Acknowledgments: The authors gratefully acknowledge financial support from the EPSRC and the Future Continuous Manufacturing and Advanced Crystallisation Research Hub (Grant Ref: EP/P006965/1) for funding this work. The Molecular Systems Engineering Group also appreciated support from the EPSRC (grants GR/T17595, GR/N35991, EP/E016340, EP/J014958 and a Doctoral Prize to S.J.).

Data statement: Data underlying this article can be accessed and used under the Creative Commons Attribution license on Zenodo at *doi.org/10.5281/zenodo.3628753*.

References

N.D. Austin, A.P. Samudra, N.V. Sahinidis, D.W. Trahan, 2016. Mixture design using derivative-free optimization in the space of individual component properties. AIChE Journal 62, 1514-30.

C.J. Brown, T. McGlone, S. Yerdele, V. Srirambhatla, F. Mabbott, R. Gurung, M.L. Briuglia, B. Ahmed, H. Polyzois, J. McGinty, F. Perciballi, 2018. Enabling precision manufacturing of active pharmaceutical ingredients: workflow for seeded cooling continuous crystallisations. Molecular Systems Design & Engineering 3, 518-549.

A. Fredenslund, R.L. Jones, J.M. Prausnitz, 1975. Group-contribution estimation of activity coefficients in nonideal liquid mixtures. AIChE Journal 21, 1086–1099.

R. Gani, 2004. Chemical product design: challenges and opportunities. Computers & Chemical Engineering 28, 2441-2457.

R.K. Henderson, C. Jiménez-González, D.J.C. Constable, S.R. Alston, G.G.A. Inglis, G. Fisher, J. Sherwood, S.P. Binksa, A.D. Curzons, 2011. Expanding GSK's solvent selection guide - embedding sustainability into solvent selection starting at medicinal chemistry. Green Chemistry 13, 854-862.

C. Jimenez-Gonzalez, P. Poechlauer, Q.B. Broxterman, B-S. Yang, D. am Ende, J. Baird, C. Bertsch, R.E. Hannah, P. Dell'Orco, H. Noorman, S. Yee, R. Reintjens, A. Wells, V. Massonneau, J. Manley. 2011. Key green engineering research areas for sustainable manufacturing: A perspective from pharmaceutical and fine chemicals manufacturers. Organic Process Research & Development 15, 900-911.

S. Jonuzaj, P.T. Akula, P. Kleniati, C.S. Adjiman, 2016. The formulation of optimal mixtures with generalized disjunctive programming: A solvent design case study. AIChE Journal 62, 1616-33.

S. Jonuzaj, A. Gupta, C.S. Adjiman, 2018. The design of optimal mixtures from atom groups using generalized disjunctive programming. Computers & Chemical Engineering 116, 401-421.

AT. Karunanithi, L.E.K. Achenie, R. Gani, 2006. A computer-aided molecular design framework for crystallization solvent design. Chemical Engineering Science 61, 1247-60.

D. Ott, D. Kralisch, I. Denčić, V. Hessel, Y. Laribi, P. Perrichon, C. Berguerand, L. Kiwi-Minsker, P. Loeb, 2014. Life cycle analysis within pharmaceutical process optimization and intensification: Case study of an API production. ChemSusChem 7, 3521-3533.

S. Ottoboni, 2018. Developing strategies and equipment for continuous isolation of active pharmaceutical ingredients (APIs) by filtration, washing and drying. PhD Thesis, Chemical and Process Engineering, University of Strathclyde.

O.L. Watson, A. Galindo, G. Jackson, C.S. Adjiman, 2019. Computer-aided design of solvent blends for the cooling and anti-solvent crystallisation of ibuprofen. Computer Aided Chemical Engineering 46, 949-954.

Sauro Pierucci, Flavio Manenti, Giulia Bozzano, Davide Manca (Eds.)
Proceedings of the 30th European Symposium on Computer Aided Process Engineering (ESCAPE30), May 24-27, 2020, Milano, Italy.
http://dx.doi.org/10.1016/B978-0-12-823377-1.50110-5

Direct DME Synthesis from Syngas: a Technoeconomic Model-based Investigation

Andrea Bernardi[a,b], Yuchu Chen[b], David Chadwick[b] , Benoît Chachuat[a,b,*]

[a]*Centre for Process Systems Engineering, Imperial College London, SW7 2AZ, UK*
[a]*Department of Chemical Engineering, Imperial College London, SW7 2AZ, UK*
b.chachuat@imperial.ac.uk

Abstract

Dymethyl ether (DME) is of industrial interest since it is used as a precursor in many other chemical processes and it can be used as fuel in diesel engines. Nowadays, the main route to produce DME is a two-step process in which a methanol dehydration unit is connected to a methanol synthesis plant (indirect synthesis). Combining methanol synthesis and dehydration in a single reactor (direct synthesis) has attracted significant attention in recent years as it offers a theoretically higher syngas conversion per pass but leads to a more challenging downstream separation. The main contribution of this paper is a model-based comparison between an indirect DME process and two direct DME processes: a standard reactor/separation/recycle process and a once-through configuration where the unreacted syngas is used to co-produce electricity. The key-performance indicators in our analysis are the break-even price of DME, the carbon efficiency, and the energy return on energy invested. The results suggest that indirect and direct DME synthesis have similar performances both in economic terms, and in carbon and energy efficiencies terms.

Keywords: DME, process simulation, techno-economic analysis, carbon efficiency, energy efficiency

1. Introduction

Dimethyl ether (DME) is an important precursor for a large number of chemicals, including light olefins, acetic acid, and methyl acetate. It is also an interesting fuel alternative due to its high cetane number—which makes it ideal for diesel engines—and its similar vapor pressure as LPG—which makes it compatible with existing infrastructure for fuel transportation and storage. The traditional method of DME synthesis in the chemical industry is the indirect synthesis, a two-step process whereby syngas is first converted to methanol and the methanol is then dehydrated to DME in a separate reactor. The equilibrium limitation of methanol synthesis in the first step calls for large recycle loops in order to achieve high syngas conversion. Nevertheless, the indirect synthesis has the advantage of a well-developed catalytic system and the fact that DME has a much lower boiling point than water and methanol, so their separation is easy (Azizi et al., 2014).

The combination of methanol synthesis and methanol dehydration in a single reactor has generated a lot interest over the past decades. The main advantage of this direct synthesis is that methanol is consumed in the same reactor where it is produced, therefore shifting the equilibrium towards higher syngas conversion (Ng et al., 1999). Significant research has been devoted to the development of suitable catalysts for direct

DME synthesis (Sun et al., 2014), with a focus on catalyst stability and reactor technology (Mondal and Yadav, 2019). But there has been comparatively little research conducted on the techno-economic assessment of direct DME synthesis in a plantwide manner. The low boiling point of DME makes its separation from the unreacted syngas challenging, which may have a large impact on the overall process performance in turn. Other process configurations have been suggested for direct DME synthesis. In the once-through configuration for instance, the unreacted syngas is used to generate electricity, which may lower the capital and operating costs as a compressor is no longer needed for recycling the syngas (Narvaez et al., 2019). Trippe et al. (2013) compared direct DME synthesis and FT synthesis, using syngas from biomass gasification. However, in their study the DME reactor is followed by a gasoline-synthesis reactor without intermediate purification of the DME since they were interested in comparing gas-to-liquid technologies. They furthermore used equilibrium models (Gibbs reactor) of the DME and FT reactors to conduct the assessment. Hankin and Shah (2017) compared methanol and DME syntheses (both direct and indirect) using CO_2 and H_2 as feedstock focusing on the energy efficiency. They considered different layouts, including electrocatalytic cells (SOECs) and a separate water-gas-shift reactor prior to the reactor in order to adjust the $CO:CO_2:H_2$ ratio for each conversion technology, and they also used equilibrium models in their assessment. Detailed process simulations for indirect DME synthesis has also been carried out for process intensification purposes: Luyben (2017) proposed an optimized version of the conventional reactor/separation/recycle DME process, which compares favorably to intensified configurations, such as the DME process based on a reactive dividing-wall column developed by Kiss and David (2012).

The main purpose of this paper is to conduct a comparative assessment of direct and indirect DME synthesis from syngas, by accounting for different H_2:CO feed ratios. The methodology applied for the assessment is described in the next section, followed by results and discussions, before concluding the paper.

2. Methodology

In Figure 1 the block flow diagrams of the different processes considered in this paper are presented. The indirect DME synthesis (i-DME) is a two step process, in which methanol synthesis and methanol dehydration occur in two separate reactors. In the direct synthesis (d-DME) the DME is produced from syngas in a single reactor using a bi-functional catalyst. Since the compressors to recycle the syngas contribute a significant part of the capital and operational expenditures, a once-through configuration (d-DME-OT) is also analyzed whereby the unreacted syngas is burned to produce electricity.

The analysis is conducted on the basis of a plant producing 100,000 tonnes of DME a year (273 kmol/h) at 99.5% purity. The influence of the syngas composition is analyzed by simulating each process for three different H_2:CO inlet ratios (1, 1.5 and 2), with the molar fractions of CO_2, H_2O and N_2 kept constant at 0.03, 0.01 and 0.01 in all the scenarios. The syngas feed stream is assumed to be available at 25°C and 25 bar, and its flowrate is adjusted in order to meet the productivity requirements. Three key-performance indicators (KPIs) are used to assess and compare the DME production processes. The *break-even price* (BEP) indicator represents the lowest DME selling price for the process to remain economically feasible, here considering a process life-

time of 30 years and the price scenario of Europe 2018. The *carbon efficiency* (CE) indicator accounts for the fraction of carbon from the syngas that ends up in the DME. Lastly, the *energy return on energy investment* (EROEI) is the amount of energy in the products divided by the amount of energy provided to the process, considering chemical, thermal and electrical energy all together.

Process flowsheets for methanol synthesis and methanol dehydration (i-DME), and for direct DME synthesis with and without recycle of the unreacted syngas are simulated in Aspen HYSYS®. Heat integration is performed for all the process alternatives using Aspen Energy Analyzer to minimize the external heating and cooling utilities requirement. The techno-economic KPIs are computed using the information provided by the process simulator, which relies on mass and energy balances, thermodynamic properties and reaction kinetics. Specifically, the kinetic rate expressions are taken from the work of Van-Dal and Bouallou (2013), and Bercic and Levec (1993) for methanol and DME synthesis, respectively. In the following the three processes are described in more details.

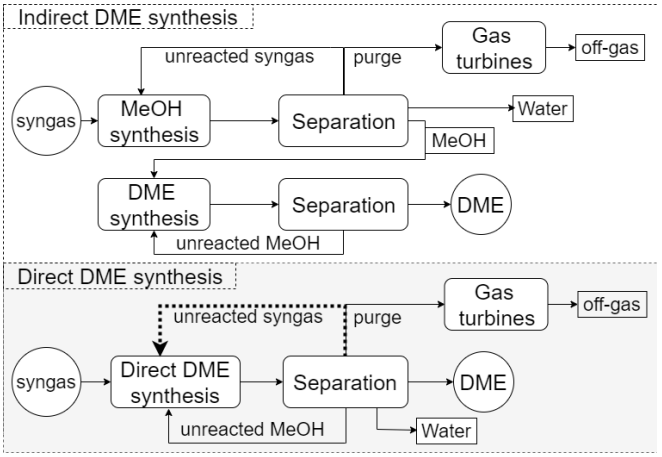

Figure 1: Block flow diagrams for the indirect (top), and direct DME process (bottom). In the direct DME synthesis the unreacted syngas (dotted line) is either recycled back to the reactor or used for electricity production.

Indirect DME synthesis. The i-DME plant is based on the work of Luyben (2010) for methanol synthesis and Luyben (2017) for methanol dehydration. The operating pressure of the methanol reactor is set to 75 bar, which is the upper bound for the kinetic model used, and the temperature is set to 250°C. The unreacted syngas is separated from the liquid products (methanol and water) using two consecutive flashes operating at different pressures. A distillation column then separates the methanol from the water. A small (2%) fraction of the unconverted syngas is purged and burned to produce electricity, while the rest is recycled back to the reactor. The electricity production unit is simulated as a syngas-fired gas turbine integrated with a steam turbine. The gas turbine cycle consists in a compressor to pressurize the air at 15 bar, a combustion chamber, and an expander. The hot flue-gas are then used to produce additional electricity with a Rankine cycle. The operating variable such as the pressure of the combustion chamber, and the parameters as the compressors and turbines efficiencies are taken from Narvaez et al. (2019). The methanol is fed at 250 °C to the DME reactor where it is dehydrated at 12 bar. The reactor is cooled to keep the internal temperature

lower than 400 °C to avoid catalyst deactivation, and the outlet stream exits at 360°C. Two distillation columns are used to separate the products. DME is extracted from the top of the first column at the required purity, while methanol is separated from the water in the second column and recycled to the reactor. Since water is the only impurity present in the recycle stream, a purge stream is not necessary.

Direct dimethyl ether synthesis. In the direct DME process the syngas is fed to an isothermal reactor operated at 55 bar and 260°C. The outlet stream is a mixture containing the unreacted syngas, DME, methanol and water. Off the possible downstream separation strategies investigated we only report the one we found the most promising. The outlet stream is cooled to 35 °C and sent to a flash separator. The flashed gas contains most of the DME and is fed to an absorption column where a mixture of water and methanol is used as the absorbing agent. The gas stream leaving the absorption column has most of the unreacted syngas with traces of DME. In the d-DME configuration a small (2%) fraction is used to produce electricity while the rest is recycled to the reactor. In the d-DME-OT process all the unreacted syngas is burned to produce electricity with a combined gas and steam turbine. DME, methanol and water exit the absorption column in the liquid stream and are fed to a mixed distillation sequence. The first column separates water and methanol from the DME and gaseous impurities. Water and methanol are in part recycled to the absorption column and in part fed to a second distillation column for their separation. The top stream of the first column is fed to a third column operated at 10 bar where DME is obtained from the bottom at the required purity. A small (3%) fraction of DME is lost from the top of the column in order to maintain a temperature above -20°C in the condenser.

3. Results and discussion

The process simulation results are summarized in Figure 2 and Table 1. A first observation is that the H_2:CO ratio of the syngas has a very large effect on the carbon efficiency and to a lower extent on the economic performances and the energy efficiency. We also note that d-DME-OT is always a net producer of electricity while the other two processes either consume or produce electricity depending on the syngas composition.

Table 1: Syngas consumption and net electricity production for d-DME, d-DME-OT and i-DME, for the three syngas compositions considered.

H_2:CO	Syngas consumption [kmol/h]			Electricity production [MW]		
[-]	d-DME	d-DME-OT	i-DME	d-DME	d-DME-OT	i-DME
1.0	2060	2070	2390	2.1	6.5	16.0
1.5	1890	2450	1900	-1.6	19.0	2.4
2.0	1830	2690	1800	-1.5	28.0	-1.7

Economic performance. We start by noting that for a syngas with H_2:CO equal 1.5 and 2 the three processes present a similar economic performance. When the syngas has a lower hydrogen content the direct synthesis becomes significantly cheaper than the indirect process, because the latter requires a high recycle rate and a high excess of fresh syngas in the methanol synthesis section to meet the productivity requirements. An advantage of d-DME-OT is that it requires 2.5 to 4 times less cooling water than the

other alternatives. It is interesting to note that at H_2:CO = 1 the once-through configuration has almost the same syngas consumption as the direct DME synthesis with recycle, which is due to the high CO conversion per pass (80%). We also note that, regardless of the high recycle rate in the indirect synthesis, the process is a net electricity producer since the purge is rich in CO and can therefore produce a large amount of electricity. The base case assumes an electricity price of 0.06 $/kWh, in addition an optimistic scenario with electricity price of 0.15 $/kWh, and a pessimistic scenario where no electricity is sold are represented. The processes that produce electricity benefit from an high electricity price and in particular the once-through configuration performs better for all the syngas compositions considered when the electricity price is 0.15 $/kWh. Finally, the direct DME synthesis with recycle is the least sensitive to both the electricity price and the syngas composition.

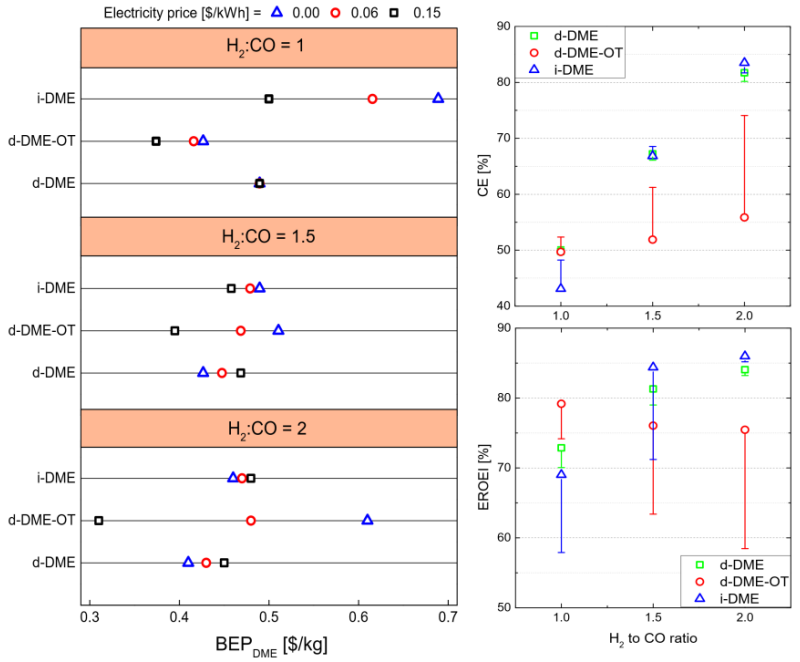

Figure 2: Comparison between d-DME, d-DME-OT and i-DME processes in terms of break-even price (left), carbon efficiency (top right), and energy efficiency (bottom right)

Carbon conversion efficiency. The d-DME-OT process has a low carbon efficiency, around 50% at H_2:CO=1 and increasing only slightly thereafter. The d-DME and i-DME processes also have a low CE between 40-50% at H_2:CO = 1 but show a significant increase thereafter, reaching a value of about 80% at H_2:CO = 2. The electricity produced/consumed by each process can be included in the CE by substracting/summing the carbon emission related to the production of the same amount of electricity, for instance from using natural gas. The whiskers in the plot represents the CE obtained considering a value of 380 kg-CO_2-eq/MWh for electricity produced from natural gas in a combined cycle (Turconi et al., 2013).

Energy efficiency. The three processes show a similar EROEI with an efficiency ranging between 75% and 85%. The bars represent the contribution of the produced electricity to the EROEI value. If the chemical energy of the DME (based on the LHV)

is considered the only output of the system the i-DME for H_2:CO = 1 and the d-DME-OT for H_2:CO = 2 share the lowest EROEI value of about 60%, while the d-DME process is less affected and its efficiency remains in the range of 70-85%.

4. Conclusions

This paper has presented a systematic, model-based comparison between different DME production technologies. Our results show that the production of DME via direct synthesis presents a similar performance to the indirect synthesis both in economic terms and in carbon and energy efficiencies terms. The indirect synthesis performs worse than the direct synthesis if a H_2 lean syngas is used. It is also worth noting that the once-through configuration may be the best alternative from an economic point of view when the selling price for the electricity is high, but it has the lowest carbon efficiency and therefore the highest CO_2 emissions. Our current investigations aim at completing the sustainability assessment by looking at additional environmental impacts and including the syngas production step in the analysis.

Acknowledgements: This paper is based upon work supported by the Engineering and Physical Sciences Research Council (EPSRC) under Grant EP/P016650/1 “Flexible routes to liquid fuels from CO_2 by advanced catalysis and engineering”.

References

Z. Azizi, M. Rezaeimanesh, T. Tohidian, M. R. Rahimpour, 2014. Dimethyl ether: A review of technologies and production challenges. Chemical Engineering and Processing: Process Intensification 82, 150–172.

G. Bercic, J. Levec, 1993. Catalytic dehydration of methanol to dimethyl ether – Kinetic investigation and reactor simulation. Industrial & Engineering Chemistry Research 32 (11), 2478–2484.

A. Hankin, N. Shah, 2017. Process exploration and assessment for the production of methanol and dimethyl ether from carbon dioxide and water. Sustainable Energy & Fuels 1 (7), 1541–1556.

A. A. Kiss, J.-P. S. David, 2012. Innovative dimethyl ether synthesis in a reactive dividing-wall column. Computers & Chemical Engineering 38, 74–81.

W. L. Luyben, 2010. Design and control of a methanol reactor/column process. Industrial & Engineering Chemistry Research 49 (13), 6150–6163.

W. L. Luyben, 2017. Improving the conventional reactor/separation/recycle dme process. Computers & Chemical Engineering 106, 17–22.

U. Mondal, G. D. Yadav, 2019. Perspective of dimethyl ether as fuel: Part ii- analysis of reactor systems and industrial processes. Journal of CO_2 Utilization (32), 321–338.

A. Narvaez, D. Chadwick, L. Kershenbaum, 2019. Performance of small-medium scale polygeneration systems for dimethyl ether and power production. Energy 188, 116058.

K. L. Ng, D. Chadwick, B. Toseland, 1999. Kinetics and modelling of dimethyl ether synthesis from synthesis gas. Chemical Engineering Science 54 (15-16), 3587–3592.

J. Sun, G. Yang, Y. Yoneyama, N. Tsubaki, 2014. Catalysis chemistry of dimethyl ether synthesis. ACS Catalysis 4 (10), 3346–3356.

F. Trippe, M. Fröhling, F. Schultmann, R. Stahl, E. Henrich, A. Dalai, 2013. Comprehensive techno-economic assessment of dimethyl ether (DME) synthesis and Fischer–Tropsch synthesis as alternative process steps within biomass-to-liquid production. Fuel Processing Technology 106, 577–586.

R. Turconi, A. Boldrin, T. Astrup, 2013. Life cycle assessment (lca) of electricity generation technologies: Overview, comparability and limitations. Renewable and sustainable energy reviews 28, 555–565.

E. S. Van-Dal, C. Bouallou, 2013. Design and simulation of a methanol production plant from CO2 hydrogenation. Journal of Cleaner Production 57, 38–45.

Sauro Pierucci, Flavio Manenti, Giulia Bozzano, Davide Manca (Eds.)
Proceedings of the 30th European Symposium on Computer Aided Process Engineering (ESCAPE30), May 24-27, 2020, Milano, Italy.
http://dx.doi.org/10.1016/B978-0-12-823377-1.50111-7

Microbial Pb(II) Precipitation: Kinetic Modelling of Pb(II) Removal and Microbial Growth

Carla Hörstmann, Hendrik G. Brink*, Evans M.N. Chirwa
Department of Chemical Engineering, Faculty of Engineering, Built Environment and Information Technology, University of Pretoria, Pretoria, South Africa
deon.brink@up.ac.za

Abstract

The study aimed to propose a preliminary kinetic model for Pb(II) bioremoval by an industrially obtained microbial consortium. The consortium has previously been shown to be extremely effective at precipitating Pb(II) from solution. For data generation, 100 mL batch reactors were set up anaerobically and spiked with either 80 ppm Pb(II) or 500 ppm Pb(II). Each of the concentrations contained either Standard LB broth or Simulated LB broth; Simulated LB broth contained double the amount of nutrients (yeast extract and tryptone) as Standard LB broth. Four datasets where thus used with notation, 80LB, 80Sim, 500LB and 500Sim. The study focused on the initial 33 h of experimentation with all four conditions. It was observed that most of the Pb(II) were removed within the first 3 h (± 50%) in all the reactors, in the absence of visual changes, followed by a slower rate of Pb(II) removal and dark precipitation forming. The Pb(II) removal was found to be independent of the amount of the microbial growth rate or nutrients present. A two-phase exponential decay model was proposed with rapid Pb(II) removal linked to an adsorption mechanism within the initial 3 h, followed by a slower Pb(II) precipitation mechanism. Microbial growth was found to be dependent on the concentration of Pb(II), nitrates, and available nutrients in the system. Growth in the samples in all the samples was modelled in one phase, namely a nitrate dependent exponential growth phase, modelled using Monod type kinetics. The nitrate dependent exponential growth phase was constructed using the Monod kinetic model in conjunction with a non-competitive Pb(II)-inhibition Michaelis–Menten term. The same maximum specific growth rate (28.2 d^{-1}) and Pb(II)-inhibition constant were determined for all fermentation conditions. These results suggest a detoxification mechanism via adsorption of Pb(II) onto biomass present in order to initiate growth, followed by the biological precipitation of the adsorbed Pb(II). The study presents the first model for microbial Pb(II) precipitation and provides a basis for the design of a continuous reaction setup required for future industrial application.

Keywords: Bioremediation, kinetic model, lead, anaerobic.

1. Introduction

Lead is a widely distributed and mobilized toxic heavy metal that accumulates in living organisms as well as the environment. The estimated maximum safe concentration of lead in drinking water is 0.01 ppm and the limit for causing serious harm to aquatic life is 0.0058 ppm (Duruibe et al., 2007). The major health effects are identified to be neurological, cardiovascular, renal, immunological, haematological, reproductive, and developmental (Substances Agency for toxic and disease registry, 2019). The recovery and not just removal of Pb(II) is of importance due to the continuing demand for and limited supply of raw lead reserves. It is estimated that there is roughly 17 years supply

of lead available worldwide with an annual global consumption rate of about 5 million t/a (International Lead Association, 2019) and only a total of 83.3 x 10^6 t of reserve remaining (Statista, 2019).

Background on anaerobic respiration is required for this study as it is conducted with viable microbial biomass under anaerobic conditions. Anaerobic respiration is a metabolic process, during which microbes transfer electrons to terminal electron acceptors. It is essential when the bacteria require the removal of residual electrons to maintain the internal redox balance in the cell. Compounds such as nitrate or metals have been used in the past as electron acceptors for oxidizing NAD(P)H to NAD(P)+ (Kim et al, 2016).

The current research team have conducted various studies on Pb(II) removal using the same industrially obtained microbial consortia used in this specific study under anaerobic conditions. The bioremoval of Pb(II) has been demonstrated for the microbial consortium under investigation, with a dark grey precipitate observed when cultivated using Luria Bertani broth as growth substrate (Brink et al., 2018). The precipitate was identified as mostly PbS and a fractional amount of elemental Pb (Brink et al., 2019). No kinetic study has however been conducted on the mechanisms responsible and Pb(II) removal from solution and consequent precipitation by this consortium. The purpose of the study was to determine the effects of substrate levels and Pb(II) concentration on the kinetics of the microbial consortium.

2. Materials and Methods

2.1. Materials

The experiments were conducted anaerobically with 100 mL serum bottles. A lead stock solution was prepared using $Pb(NO_3)_2$ (Merck, Kennelworth, NJ). A rich growth media, standard Miller Luria Bertani Broth (Sigma Aldrich, St Louis, MO) was used, made to a final concentration of 25 mg/L or simulated LB broth which consists out of double the amount of nutrients and less NaCl. Metabolic activity (MA_{550}) measurements were conducted with 3-(4,5-dimethylthiazol-2-yl)-2,5-diphenyl tetrazolium bromide (MTT) and dimethyl sulfoxide (DMSO) at a wavelength of 550 nm (Sigma Aldrich, St Louis, MO). The nitrate levels were tested using nitrate testing kits (Merck, Darmstadt, Germany) and measured photometrically using the Spectroquant Nova 600 (Merck, Darmstadt, Germany).

2.2. Microbial culture

The Pb(II) resistant microbial consortium was collected from a borehole at an automotive-battery recycling plant in Gauteng, South Africa. The inoculum was prepared by adding 1 g of Pb(II) contaminated soil to a mixture of LB (Luria Bertani) broth and 80 ppm Pb(II) in a 100 mL serum bottle, which was then incubated anaerobically for 24 hours at 32 °C at a speed of 120 rpm. Glycerol was added to a final ratio of 20% v/v and stored at -77 °C cryogenically. The preculture was then prepared from the stored inoculum. It was prepared by inoculating one loop of stock culture to 100 mL anaerobic serum bottles containing LB broth spiked with either 80 ppm Pb(II) or 500 ppm Pb(II) depending on the subsequent experiment. The serum bottles were purged with nitrogen gas for 3 min and sealed to maintain anaerobic conditions, then incubated at 30°C and 120 rpm for a period of 3 days before inoculation of the experiments took place.

2.3. Experimental

The Pb(II) stock solution and simulated or standard LB broth were prepared and autoclaved separately, after which it was cooled to room temperature. The Pb(II) stock

solution was added to the standard or simulated LB broth in a biological safety cabinet under sterile conditions. The serum bottles were inoculated with an inoculation loop from the abovementioned preculture. The batch reactors were purged with nitrogen gas for 3 min, sealed with a rubber stopper and clamped with a metal cap to ensure anaerobic conditions. The batch reactors were placed in a shaker incubator at a speed of 120 rpm and 35 °C for a period of 33 h. The experiments were conducted in triplicate.

2.4. Sampling

Samples were taken for a period of 33 h, every 3 h at 3h, 6h, 9h, 24h, 27h, 30h, 33h. The sealed serum bottles were shaken thoroughly before sampling. A hypodermic needle and sterile syringe were used to pierce the rubber stopper.

2.5. Analysis

The metabolic activity measurements are performed immediately after sampling. The metabolic activity of bacterial cells was quantified using MTT (Wang et al., 2010). Two sets of analyses were performed, one with biomass and the other without. The samples were filtered with 25 mm nylon syringe filters with 0.45 μm pores (Anatech), to represent the sample without biomass. The rest of the analysis was conducted by diluting the sample (with or without biomass) and adding the MTT solution and finally incubated for one hour at 35 °C. The samples were then dissolved in DMSO after incubation. The absorbance at 550 nm on a V spectrophotometer was measured and recorded as an indication of metabolic activity.

The residual aqueous Pb(II) was measured using an atomic absorption spectrometer (Perkin Elmer AAnalyst 400, Waltham, Massachusetts), with a Pb Lumina hollow cathode lamp. The supernatants of the samples stored at 5 °C were used, to avoid causing blockages on the instrument.

The samples used for nitrate testing were stored and measured at a later stage using nitrate testing kits (Merck, Darmstadt, Germany). The nitrate ions react with a form of benzoic acid in sulfuric acid to form a red nitro solution that is measured photometrically using the Spectroquant Nova 600 (Merck, Darmstadt, Germany).

3. Results and Discussion

3.1. Overall discussion

It was observed from the results that the most of the Pb(II) (approximately 50 %) was removed within the first 3 h. The rapid removal was then followed by a slower more gradual decrease. Metabolic activity lagged within the first 6 h, after which a dramatic increase in growth was observed. It was subsequently observed that the increase of growth was coupled with a sharp decrease in nitrate levels in all the reactors. From these findings, it was hypothesised that Pb(II) removal was not dependent on the amount of nutrients present. Growth may, however, are dependent on the initial rapid removal of Pb(II) as an initial detoxification mechanism to initialise growth.

3.2. Pb(II) Removal

Pb(II) removal in all the reactors followed a clear trend, with initial rapid Pb(II) removal followed by a slow gradual rate of removal. The Monod equation was proposed as appropriate model, with a few adjustments (Roestorff and Chirwa, 2018):

$$-\frac{\mathrm{dPb(II)}}{\mathrm{dt}} = \frac{\mathrm{k_m Pb(II)}}{\mathrm{Pb(II)} + \mathrm{K_c}} \cdot \mu \quad (1)$$

Which reduces to the first order rate expression (equation 2) for $K_c \gg Pb(II)$

$$-\frac{dPb(II)}{dt} = \frac{k_m}{K_C} Pb(II) \cdot \mu \quad (2)$$

It was observed that Pb(II) removal is not dependent on growth at any time in the system and that an adsorption mechanism might be responsible for rapid and slow Pb(II) removal. A global differential equation was proposed. The constant parameters τ and ϕ incorporated the fraction of Pb(II)-removal by each phase as well as the growth contribution to the mechanism.

$$-\frac{dPb(II)}{dt} = \tau\left(\frac{k_m}{K_c} Pb(II)\right)_{rapid} + \phi\left(\frac{k_m}{K_c} Pb(II)\right)_{slow} \quad (3)$$

The differential equation was solved and simplified with two constants α_{rapid} or α_{slow} equal to k_m/K_c for each phase, respectively.

$$Pb(II) = \tau \cdot \Delta Pb(II) e^{-\alpha_{rapid} \cdot t} + \phi \cdot \Delta Pb(II) e^{-\alpha_{slow} \cdot t} + c \quad (4)$$

The model was fitted on Aquasim (Reichert, 1994) to produce the following results for both the short and extended experiments.

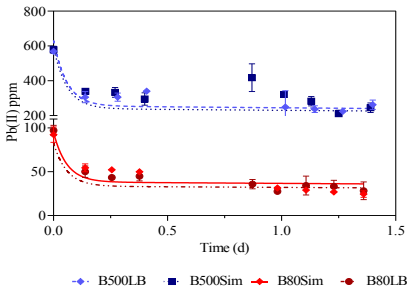

Figure 1: *Pb(II) concentration measurements with time, with the fitted kinetic model.*

Table 1: *Parameter estimation for Pb(II) removal*

Reactor	τ	α_{rapid} (d^{-1})	ϕ	α_{slow} (d^{-1})	c	R^2
B500Sim&LB B80Sim&LB	0.596	17.4	0.404	0.0436	0	0.966

3.3. Growth

It was observed that initial growth was directly dependent on the amount of nitrate available, while the concentration of aqeous Pb(II) had an inhibitory effect on growth. The differential mathematical relationship identified for the growth model (equation 5) was that of specific growth and non-competitive Pb inhibition (Birgin and Preisig, 2018) and was related to the rate of nitrate reduction $\left(\frac{dN}{dt}\right)$.

$$\frac{dX}{dt} = \mu_{apparent} X = \frac{\mu}{1+\frac{Pb(II)}{K_i}} X = \frac{\mu_{max}\left(\frac{N-N_{critical}}{k_s+(N-N_{critical})}\right)}{1+\frac{Pb(II)}{K_i}} X = Y_{XN}\frac{dN}{d_t} \quad (5)$$

With $N_{critical}$ the critical amount of Nitrate needed in the system, μ_{max} the maximum specific growth rate (d^{-1}) and k_s the half-velocity constant. The constant K_i refers to the estimated inhibition constant due to Pb(II). Y_{XN} is the yield of biomass versus nitrates measured over time. The model was only proposed for the first day, as it was observed that an apparent second phase of growth appeared in samples containing double nutrients (B500Sim and B80Sim), but further investigations should be conducted into this hypothesis. The proposed growth models are presented in Figure 4, followed by the necessary parameter estimation in Table 4.

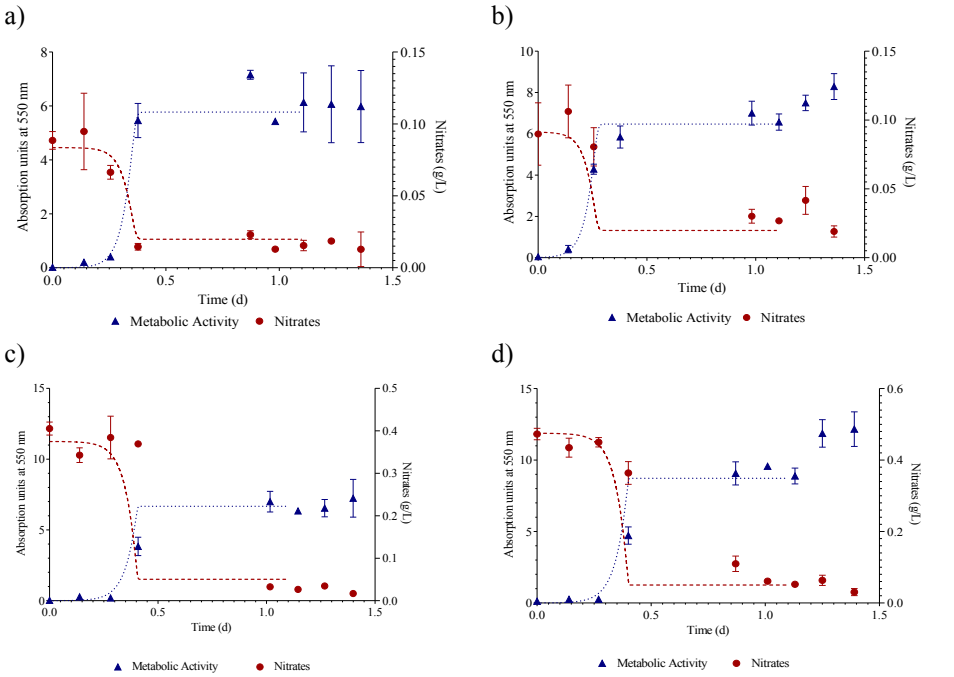

Figure 4: *a) B80LB, b) B80Sim, c) B500LB and d) B500Sim growth and nitrates with time.*

Table 4: *Estimated Nitrate dependent growth parameters.*

Reactor Type	μ_{max}	k_s	Y_{XN}	K_i	R^2
B500Sim&LB	28.2	0.01	0.0487	498.8	0.966
B80Sim&LB			0.0110		

It was observed in the data gathered above that the μ_{max} values were equal for all the reactors (28.2 d^{-1}). The biomass to nitrate yields was equal for both the 80 ppm (0.011) samples and the 500 ppm (0.049) samples respectively. The k_s and K_i constants were equal for all experiments, indicating non-competitive inhibition.

4. Conclusions

The amount of nutrients available does not promote Pb(II) bioremoval. The results indicate an adsorption mechanism for the initial rapid removal of available Pb(II) before precipitation. An anaerobic respiratory denitrification mechanism is suggested during the first phase of exponential growth when NO_{3-} is used as an alternative electron sink for oxidising NAD(P)H to NAD(P)+ to produce cellular energy by the microorganism. It is known from previous studies conducted by this team that the precipitate consists of mostly PbS and a small amount of Pb0 (which is higher in samples containing more Pb(II). It can be hypothesised that sulphur is released during denitrification with the enzyme nitrate reductase from cysteine and methionine present in the substrate during the first stage of growth, which in turns binds with Pb(II) to form PbS. When the nitrates are depleted and the second stage of growth might be initiated in the samples containing simulated LB broth, the remainder of available Pb(II) is used as an alternative electron sink for further anaerobic respiration to produce Pb0.
A kinetic model has been proposed for microbial Pb(II) removal and further studies should be conducted into applying this knowledge to develop a design for industrial application. The validation of the model will first be established by comparing the current model to more data gathered through experimentation. Further design and research can then be conducted into continuous industrial application.

References

Birgen C, Preisig HA, 2018, Dynamic Modeling of Butanol Production from Lignocellulosic Sugars. Comput Aided Chem Eng 43:1547–1552. doi: 10.1016/B978-0-444-64235-6.50270-9
Brink HG, Hörstmann C, Peens J, 2019, Microbial Pb(II)-precipitation: the influence of oxygen on Pb(II)-removal from aqueous environment and the resulting precipitate identity. Int J Environ Sci Technol. doi: 10.1007/s13762-019-02502-4
Brink HG, Mahlangu Z, 2018, Microbial Lead(II) precipitation: the influence of growth substrate, Chemical Engineering Transactions, 64, doi: 10.3303/CET1864074
Duruibe J O, Ogwuegbu M O C and Egwurugwu J N, 2007, Heavy metal pollution and human biotoxic effects, International Journal Physical Sciences, 2(5), 112–118. doi: 10.1016/j.proenv.2011.09.146.
International Lead Association, 2019, ILA - International Lead Association, 1–4.
Statista, 2019, Lead reserves worldwide as of 2018, by country (in million metric tons), 1–5.
Kim C, Ainala S K, Oh Y, Jeon B, Park S and Kim J R, 2016, Metabolic Flux Change in Klebsiella pneumoniae L17 by Anaerobic Respiration in Microbial Fuel Cell, 260, 250–260. doi: 10.1007/s12257-015-0777-6.
Reichert P, AQUASIM - A tool for simulation and data analysis of aquatic systems, Water Science Technology, 30(2), 21-30, 1994. http://wst.iwaponline.com/content/30/2/21(open access)
Roestorff M M and Chirwa E M N, 2018, Comparison of the Performance of Chlorococcum Ellipsoideum and Tetradesmus Obliquus as a Carbon Source for Reduction of Cr (VI) with Bacteria, Chemical Engineering Transactions, 70(VI), 463–468, doi: 10.3303/CET1870078.
Substances Agency for toxic and disease registry, 2019, Toxicological Profile for Lead.
Wang H, Cheng H, Wang F, Wei D and Wang X, 2010, An improved 3-(4,5-dimethylthiazol-2-yl)-2,5-diphenyl tetrazolium bromide (MTT) reduction assay for evaluating the viability of Escherichia coli cells, Journal of Microbiological Methods, 82(3), 330–333, doi: 10.1016/j.mimet.2010.06.014.

Sauro Pierucci, Flavio Manenti, Giulia Bozzano, Davide Manca (Eds.)
Proceedings of the 30th European Symposium on Computer Aided Process Engineering (ESCAPE30), May 24-27, 2020, Milano, Italy.
http://dx.doi.org/10.1016/B978-0-12-823377-1.50112-9

Optimization of a Cyclone Reactor for Biomass Hydropyrolysis through Global Sensitivity Analysis and Stochastic Optimization

Yris Gonzalez[a], Wilfredo Angulo[a], Dany De Cecchis[a], María Lucena[b], Santiago D. Salas[a]*

[a] *Escuela Superior Politécnica del Litoral, ESPOL, Facultad de Ciencias Naturales y Matemáticas, Campus Gustavo Galindo Km 30.5 Vía Perimetral, Guayaquil, Ecuador.*

[b] *Departamento de Ingeniería Química. Universidad Nacional Politécnica Antonio José de Sucre. Av. Corpahuaico con Av. La Salle. UNEXPO, Barquisimeto - 3001. Venezuela. sdsalas@espol.edu.ec*

Abstract

This study investigates the use of global sensitivity analysis combined with stochastic optimization for improving the conversion of biomass in an inverted cyclone reactor. A validated mathematical model of the process permits to develop a model-centric framework that analyzes the most important process variables and design parameters, for later selecting the combination that achieves the highest biomass conversion rate.

The implemented global sensitivity analysis, which is a variation of the Sobol method, permits to identify the most influential variables in biomass conversion. Thereafter, the important process variables of the system are optimized respecting inequality and equality constraints towards the maximization of the conversion, providing an improved reactor setup. The proposed framework has the potential of evaluating different biomass conversion models that aim to transform biomass into value-added chemicals through different objective functions.

Keywords: Biomass hydropyrolysis, global sensitivity analysis, evolutionary optimization.

1. Introduction

Several processes have been proposed to produce fuels from lignocellulosic biomass. Hydropyrolysis is one of the most promising paths. This process characterizes by the rapid thermal degradation of organic material, under high heating rates in a hydrogen environment. The rapid heating decomposes the large molecules of biomass into smaller ones, which are released into the form of volatile compounds. The volatiles are then quickly cooled back producing biofuel. The key to maximize valuable biofuels is a short residence time for the volatiles (usually a few seconds), to prevent secondary cracking reactions (*Resend F.,* 2016).

In hydropyrolysis, the use of inverted cyclone reactors provides the advantage of short residence times and high efficiency in the separation of the solid, as well as that the feed does not require to be preheated to the high temperature demanded by the reaction. In a previous study, the simulation model of an inverted cyclone reactor for flash hydropyrolysis of biomass was developed from mass and energy balances, combined with the kinetics and fluid dynamics. The performance analysis applied to the model evaluated the conversion effect of two process variables while the other variables remained constant (*Galiasso et al.*, 2014).

In this work, a validated mathematical model permits to develop a framework that analyzes the most influential process variables and design parameters for later finding the process setting that achieve the highest conversion of the system. In this sense, initially the important variables are selected using a global sensitivity analysis based on the Sobol method (*Salas et al.,* 2017, 2019). Then, these important variables are optimized using a stochastic optimization algorithm based on evolutionary principles seeking to maximize the biomass conversion.

2. Background

2.1. System Description

The potential reactors for hydropyrolysis are a riser cyclone or a downer cyclone. They are transport reactors that could work satisfactorily for the thermal cracking of biomass. In both types of reactors, the residence time could be from a few to several seconds because the separation takes additional time. In this context, the inverted cyclone reactor appears to be ideal for carrying out these ultrafast chemical reactions coupled with separation (*Galiasso et al.*, 2011).

In the inverted cyclone reactor portrayed in Figure 1a, a solid at high temperature combined with biomass feed, which is mixed with hydrogen, moves spirally downflow inside the reactor. This fluid experiences a brief gas-solid contact at the inlet. Then, it is separated by centrifugal forces while it moves down the reactor in the so-called Zone 1. In the lower part of the cylindrical section, the gas and micro-particles disengage from the solid and move up spirally around the central pipe to leave the reactor, referred as the Zone 2. At the top, they are carried down again inside the internal pipe to leave by the side, identified as Zone 3. The zones location is depicted in Figure 1b.

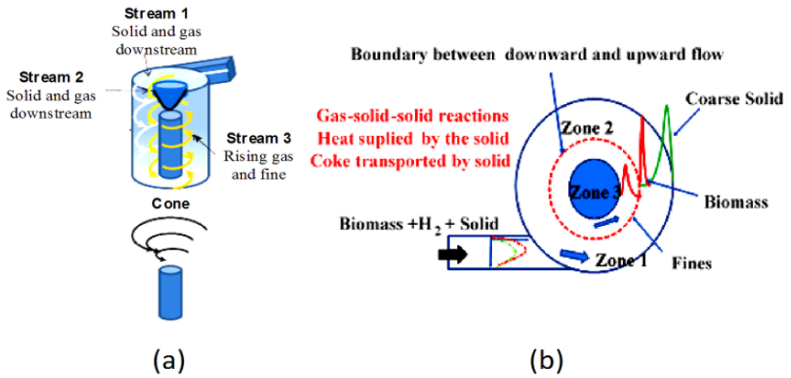

Figure 1. Schematic illustrating the trajectory of the three streams inside the reactor (a), and a view inside of the reactor from the top of the transversal cylindrical section (b).

2.2. Nonlinear model

The nonlinear model of the system was reported only for the Zone 1 of the reactor because in this region takes place the highest conversion (*Galiasso et al.*, 2014). The model is described by the gas phase mass balance of the reactive system; the mass balance of the solid phase (biomass); the energy balances for the gas phase and solid phase, which equations are, respectively,

$$\frac{dM_j}{dL_1} = \sum_{i=1}^{z} r_{ij(\tau_{g1})} \frac{a_{t1}}{\frac{\dot{m}_s}{0.45\rho_s} + v_{o_1}} \tag{1}$$

$$\frac{dM_{Bio}}{dL_1} = \sum_{i=1}^{z} -r_{1Bio(T_{g1})} \frac{a_{t1}}{\frac{\dot{m}_s}{0.45\rho_s} + v_{o_1}} \tag{2}$$

$$\frac{dT_{g_1}}{dL_1} = \frac{Ua\left(T_S - T_{g_1}\right) + \sum_{i=1}^{q} r_{ij}\left[-\Delta H_{Rx_{ij}}\left(T_{g_1}\right)\right] \frac{a_{t1}}{\frac{\dot{m}_s}{0.45\rho_s} + v_{o_1}}}{\sum_{j=i}^{n} M_j C_{p\left(T_{g_1}\right)_j}} \tag{3}$$

$$\frac{dT_S}{dL_1} = -\frac{Ua\left(T_S - T_{g_1}\right)}{M_S C_{ps(T_S)}} \tag{4}$$

where M_j is the flow rate of the compound j, L_1 is the reactor spire length, a_{t1} is the cross-section area where solid-free gas stream in Zone 1, Tg is the solid-free gas phase temperature, $\Delta H_{Rx_{ij}}$ is the heat of reaction i for compound j, Ts is the solid phase temperature, U is the overall heat transfer coefficient, a is the heat exchange area per unit reactor length, and C_{pj} is the heat capacity of compound j. For a detailed model description and definition of variables and constants, please refer to *Galiasso et al*. (2014).

2.3. A global sensitivity analysis

A global sensitivity analysis (GSA) shows the importance of input variables along with an output of interest. A widely used variance-based GSA method is the Sobol method. A more computationally efficient Sobol approach is introduced by *Wu et al.* (2012). Here, the considered samples are augmented by averaging the evaluated points. In this study, the utilized approach is the one proposed by *Salas et al.* (2019), which is a robust computational implementation of the Sobol method. For more details about Sobol's GSA methods please refer to *Salas et al.* (2017, 2019) and *Fesanghary et al.* (2009).

The GSA algorithm calculates the first-order and the total sensitivity indices of all the input variables. The implemented GSA algorithm is shown in Figure 2. For this approach, it is defined that n_p is the number of input variables $\boldsymbol{z} = (z_1, \ldots, z_{np})$, or parameters considered by the GSA, of a function $G = g(\boldsymbol{z})$. Three matrices are considered for sampling, resampling, and reposition. Finally, for each variable z_n, it is obtained $\hat{S}_n$ and $\hat{S}_{T\,n}$ as the first-order and the total sensitivity indices, respectively. The first-order index $\hat{S}_n$ indicates its sensitivity depending on the individual contribution of the variance whenever changing z_n in the function G. While the total index $\hat{S}_{T\,n}$ incorporates the effect of all other variables when excluding the variable z_n. The indices $\hat{S}_n$ and $\hat{S}_{T\,n}$ can be compared to evaluate whether a model is additive or not. Non-additive models hold the characteristic $\hat{S}_j < \hat{S}_{Tj}$, while additive models $\hat{S}_j = \hat{S}_{Tj}$. Additive models are those in which no interactions between evaluated parameters occur.

In this study, the GSA is performed analyzing the reactor conversion. The evaluated input variables, reported in Table 1, are those related to the process variables and the design parameters of the reactor.

The range of variation of these input variables has an uncertainty index of 5% from its average value reported in *Galiasso et al*. (2014). The length of the reactor spire was estimated from the validated model, and it shows that the highest conversion is reached almost at three meters, suggesting that three reactor zones are not required to evaluate the maximum biomass conversion.

Input: Given $np, nd \in \mathbb{R}$, $\overline{\mathbf{z}} \in \mathbb{R}^{np}$, γ, $G = g(\mathbf{z})$.
Output: $\hat{S}_n$, and $\hat{S}_{T\,n}$, with $n = 1, \ldots, np$.
Initialization:
Let generate $nd \times np$ matrices $M1$, $M2$ and $M3$ with rows varying randomly $\overline{\mathbf{z}} \pm \gamma\%$
Sampling & Resampling:
for $d \leftarrow 1$ **to** nd **do**
  $Y_d \leftarrow g(M1_{d,:})$ { $M1_{d,:}$ is the d-th row of matrix $M1$.}
  if (Y_d is not a feasible value) **then**
    while (Y_d is not a feasible value) **do**
      Use the first not used row r, to make $Y_r \leftarrow g(M3_{r,:})$
    end while
    $M1_{d,:} \leftarrow M3_{r,:}$
  end if

  $Y_{R\,d} \leftarrow g(M2_{d,:})$
  if ($Y_{R\,d}$ is not a feasible value) **then**
    while ($Y_{R\,d}$ is not a feasible value) **do**
      Use the first not used row r, to make $Y_{R\,d} \leftarrow g(M3_{r,:})$
    end while
    $M1_{d,:} \leftarrow M3_{r,:}$
  end if
end for

Output varying the input variables:
$\hat{f}_0 \leftarrow (\text{mean}(Y) + \text{mean}(Y_R))/2$
for $n \leftarrow 1$ **to** np **do**
  $N \leftarrow M2$; $[N]_{:,n} \leftarrow [M1]_{:,n}$
  $NT \leftarrow M1$; $[NT]_{:,n} \leftarrow [M2]_{:,n}$
  for $d \leftarrow 1$ to nd **do**
    $Y_{P\,d,n} \leftarrow g([N]_{d,:})$
    if ($Y_{P\,d,n}$ is not a feasible value) **then**
      $Y_{P\,d,n} \leftarrow \hat{f}_0$
    end if
    $Y_{RP\,d,n} \leftarrow g([NT]_{d,:})$
    if ($Y_{RP\,d,n}$ is not a feasible value) **then**
      $Y_{RP\,d,n} \leftarrow \hat{f}_0$
    end if
  end for
end for

Individual & global variances
$\widehat{V} = \sum_{d=1}^{nd}(Y_d^2 + Y_{R\,d}^2)/(2\,nd) - \hat{f}_0^2$
$\Gamma_P^2 \leftarrow \sum_{d=1}^{nd}(Y_d\,Y_{R\,d} + Y_{P\,d,:}\,Y_{RP\,d,:})/(2\,nd)$
$\widehat{V}_P = (Y_P^T\,Y + Y_{RP}^T\,Y_R)/(2\,nd) - \Gamma_P^2$
$\widehat{V}_{-P} = (Y_{RP}^T\,Y + Y_P^T\,Y_R)/(2\,nd) - \Gamma_P^2$
$\hat{S} = \widehat{V}_P./\widehat{V}$ {Where ./ is the element-wise division}
$\hat{S}_T = 1 - \widehat{V}_{-P}./\widehat{V}$

Figure 2. GSA algorithm to calculate, in one run, the first-order and the total sensitivity indices for all the input variables.

Table 1. The range of values for the input variables of the uniflow reactor.

Input Variables	Description	Unit	Range
H2Bi	Hydrogen/Biomass Relation	--	0.1 to 0.5
P	Pressure	MPa	0.1E-06 to 0.2E-06
Ts	Solid Temperature	K	880 to 1000
Tg	Gas Temperature	K	600 to 700
mso	Solid Flow	kg/s	0.02 to 0.03
*D*1	External Cylinder Diameter	m	0.0486 to 0.054
*D*2	Internal Cylinder Diameter	m	0.031 to 0.042
L	Reactor Spire Length	m	1 to 6

2.4. Stochastic Evolutionary Optimization

The evolutionary heuristic referenced as the differential evolution (DE) algorithm is employed for the optimization of the sensitive input variables (*Storn & Price*, 1997). The DE has demonstrated proficiency when it is compared with other heuristic algorithms (*Salas et al.*, 2017). It involves the evolution of a population of solutions by applying mutation, crossover, and selection as operators. The initial population follows a uniform distribution over the solution domain. Each solution vector resembles a target vector during a generation. For each target vector, the mutation operator generates a new vector by adding a weighted difference between two population vectors. These three vectors are selected randomly and must differ from the target. A scaling factor β controls the amplification of the differential variation between the second and the third randomly chosen vectors. In the crossover, a uniform arrangement builds trial vectors from values

replicated from two different vectors. Finally, the vector which maximizes the objective function is the target for the next generation.
In this work, a crossover rate of 0.70 was selected, and β was randomly chosen between [0.2, 0.8]. A total of 25 generations with a population size of 20 generated sufficient simulations. The method runs 30 times to verify its consistency.

3. Results

From the GSA applied to the model, it is assessed the relative importance of each model variable. It is found that some input variables are rather insensitive. Thus, a simpler optimization problem can be formulated when the insensitive input variables are maintained constant. This model is then used to optimize the biomass conversion of the reactor. The results for the GSA are shown in Figure 3. The black horizontally striped bars on the left are the first-order sensitivity indices. The grey vertically striped bars on the right are the total sensitivity indices. Considering the first-order sensitivity index, four input variables affect significantly the conversion of the reactor. They are *Ts*, *Tg*, *mso*, and *D*1. On the other hand, it is observed from the total sensitivity index that all the parameters have some effect on its cooperation respecting the others. Although, similarly to the first-order indices, they show the same pattern of importance in terms of the reactor conversion.

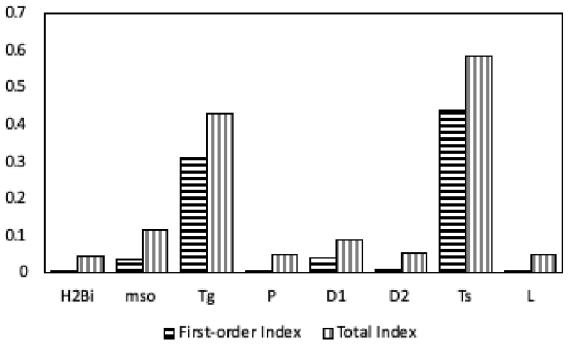

Figure 3. First-order sensitivity indices, black horizontally striped bars on the right; and total sensitivity indices, grey vertically striped bars on the left, for each of the input variables considered in the reactor conversion.

Therefore, *Ts*, *Tg*, *mso*, *D*1 were the decision variables considered in the optimization problem. These variables are reported in Table 2. The base case and optimal case for biomass conversion are depicted as a function of the spire length in Figure 4. The plot shows an improvement, and it suggests that it is possible to reach the highest conversion with certain operating conditions with less spire length. Additionally, from the 30 optimal set of values, the set with the lowest *Tg* was selected among all others for reducing the heat demand of the feed.

Table 2. The values of the input variables for the base and optimal cases.

Case	***mso***	***Tg***	***D1***	***Ts***
Base	0.025	650	0.0513	940
Optimal	0.030	669	0.0527	995

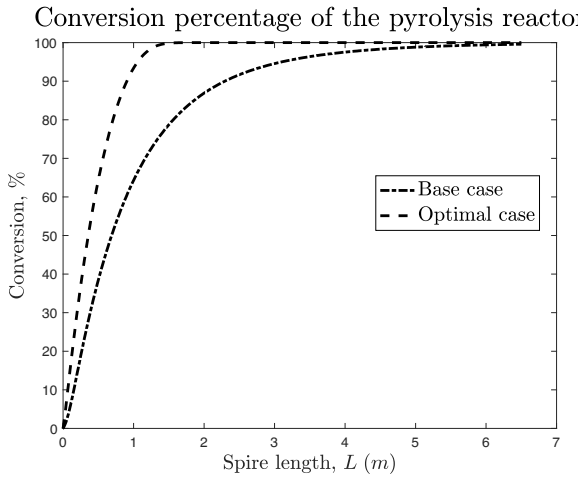

Figure 4. Conversion rate between the base case and the optimal case vs. the reactor spire length.

4. Conclusions

The global sensitivity analysis, in contrast with the previous evaluations; allows identifying new variables that affect significantly the conversion of the reactor. The main input variables that have a significant influence on the reactor conversion are, in priority order, the solid and gas temperature, solid mass, and external diameter. The optimization allows to reach an improvement of about one-third from the base case conversion. The obtained results highlight that the biomass hydropyrolysis is conditioned by its solid carrier, the gas phase and by the reactor geometry. The developed framework could be a potential tool for the study of other types of biomass and other objective functions.

References

Fesanghary M, Damangir E, Soleimani I. 2009. Design optimization of shell and tube heat exchangers using global sensitivity analysis and harmony search algorithm. *Applied Thermal Engineering*. 29, 1026-1031.

Galiasso R, Gonzalez Y, Lucena M. 2014. New inverted cyclone reactor for flash hydropyrolysis. *Catalyst Today*. 220, 186-197.

Galiasso, R., Freitez J., González, Y. y Rodríguez, J. 2011. Pyrolysis of cracked gasoline into olefins: I. design and construction of a cold model for circulating type reactor. *Ind. Eng. Chem. Res.* 50 (5), 2726-2735.

Resende F. 2016. Recent advances on fast hydropyrolysis of biomass. *Catalysis Today*. 269, Pages 148-155.

Salas, S. D., Brandão, A. L., Soares, J. B., & Romagnoli, J. A. 2019. Data-Driven Estimation of Significant Kinetic Parameters Applied to the Synthesis of Polyolefins. *Processes*. 7(5), 309.

Salas, S. D., Chebeir, J., Tronci, S., Baratti, R., & Romagnoli, J. A. 2018. Real-Time Nonlinear State Estimation in Polymerization Reactors for Smart Manufacturing. *In Computer Aided Chemical Engineering* (Vol. 43, pp. 1207-1212). *Elsevier*.

Salas, S. D., Geraili, A., & Romagnoli, J. A..2017. Optimization of renewable energy businesses under operational level uncertainties through extensive sensitivity analysis and stochastic global optimization. *Ind. Eng. Chem. Res.* 56(12), 3360-3372.

Storn, R., & Price, K..1997. Differential evolution–a simple and efficient heuristic for global optimization over continuous spaces. *Journal of Global Optimization*. 11(4), 341-359.

Wu, Q. L.; Cournede, P. H.; Mathieu, A. 2012. An efficient computational method for global sensitivity analysis and its application to tree growth modelling. *Reliability Engineering and System Safety*. 107, 35−43.

Sauro Pierucci, Flavio Manenti, Giulia Bozzano, Davide Manca (Eds.)
Proceedings of the 30th European Symposium on Computer Aided Process Engineering (ESCAPE30), May 24-27, 2020, Milano, Italy.
http://dx.doi.org/10.1016/B978-0-12-823377-1.50113-0

Dynamic Modeling for PHB Production Based on Linear MFA and Measurements from Batch Fermentation

Adriana C. Torres Ospina, Carlos A. M. Riascos*

Institute of Biotechnology, Universidad Nacional de Colombia, Av. Carrera 30 No. 45-03, Bogota 111321, Colombia
camartinezri@unal.edu.co

Abstract

Mathematical models of fermentative processes allow to predict their behaviour, both in steady state and in dynamic conditions, so they are a key tool in the improvement of these processes. The objective of this work is to develop a mathematical model that simulates the growth and production of polyhidroxybutirate (PHB) in a hyper-producing *Burkholderia cepacia* strain, considering metabolic changes that occur between the phases of feast & famine, and that allows the process optimization. To achieve this objective, it was necessary: i) to analyse the behaviour of the strain in batch fermentation, ii) to characterize the metabolism of the strain by linear metabolic flux analysis (MFA), iii) to adjust semi-empirical models for each phase, and iv) to validate the model with new experimental data. Results show that metabolic fluxes undergo significant changes during the batch process: metabolic pathways are adjusted to lead carbon, in a greater extent, towards growth in the feast phase, and towards PHB production in the famine phase. Fed batch fermentation for model validation employs pulses for adding carbon and nitrogen sources, separately. Feeding allows to extend the feast phase and obtain higher biomass concentrations. The developed model will allow to analyse new operational options and increase process productivity by mathematical programming. In other way, the proposed methodology, that considers results of MFA for model formulation, is a novel strategy to improve modelling.

Keywords: *B. cepacia*, linear MFA, feast & famine,

1. Introduction

Metabolic pathways involved in PHAs metabolism are complex and depend on the selected microorganism. Additionally, metabolic analysis for PHAs production must include reactions for polymer synthesis and hydrolysis, granules formation, as well as the connection of these pathways with central and peripheral ones (Fernández, 2012).

Vegetable oils have been studied as an alternative to traditional carbon sources, specifically for PHAs production at commercial scale. An advantage of using fatty acids is the higher yield, compared with sugars (Riascos et al., 2013), and as a complex carbon source, it is metabolized through several metabolic pathways. Experimental yields (Suriyamongkol et al., 2007) obtained for butiric acid (0.65-0.98 kg/kg) and glucose (0.32-0.48 kg/kg) confirm the advantage suggested from metabolic analysis.

A novel strategy to improve the prediction of mathematical models on fermentative processes is to include metabolic issues in the models. An example of applying metabolic information in modeling was presented by Nandong et al. (2008) who

formulated a model for alcoholic fermentation; it relates specific rates for growing and production with metabolic fluxes, obtaining improvements in the prediction.

2. Methodology

The inclusion of information from MFA in the mathematical model of fermentative processes requires to connect extra- with intra-cellular information. Extra-cellular information allows to identify the stages that take place in the process, while intra-cellular information will show how the metabolism operates in each stage.

2.1. Behaviour Analysis of the Strain

Batch fermentations were performed to analyse the behaviour of the strain. These fermentations allow to identify the stages of the process and to define characteristic time instants for each stage. Measurements of viable cells as colony-forming units by mL (CFUs/mL) were key for this analysis. Batch fermentations were developed at the best conditions identified in a previous work: 20 g/L of fatty acids, 2.5 g/L of ammonium as nitrogen source, 2 vvm of air supply, pH = 6.5 (Mendez, 2016).

2.2. Metabolism Characterization

The metabolism was characterized by linear MFA and the measurement of specific rates for growth, PHB and CO_2 production, and carbon source consumption. Specific rates were useful to propose the phenomena that we must include in the model and as measured fluxes to solve the MFA without including cofactor balances (Gombert and Nielsen, 2013). The stoichiometric matrix for the metabolic analysis was based on genome of the parental strain *B. cenocepacia J2315* (Fang et al., 2011), and an analysis of biomass generation to create a stoichiometric equation.

2.3. Model Fitting and Validation

The fitting was developed by a cyclic procedure starting with a simple model, and then, adding mathematical elements to include observed phenomena and to improve the fitting. The differential equation system was solved by the ODE23 function, and parameters were estimated by minimizing residuals on concentrations with a genetic algorithm (GA function), both in MatLab programming environment. Data from long-time fermentation was employed for model fitting; whereas, data from fed-batch fermentation was employed for validation.

2.4. Specific Rates Estimation

Rates for biomass, product and fatty acids were estimated based on their definition, i.e. $\mu_P = dP/dt * 1/X$. Measurements of concentrations were performed in the following way: dry weight for total biomass, liquid chromatography (Aminex HPX-87H column) for PHB, and gas chromatography (Agilent 6890, with DB 23 column) for fatty acids, whereas the quantification of CO_2 rates employed measurements of CO_2 concentration and air supply, as well as the estimation of air molar volume (Torres, 2019).

3. Results and Analysis

3.1. Extra- and Intra-cellular Characterization

From the behaviour analysis, it was observed that in long-time batch fermentation the process goes through a short lag stage (0-4 h), an exponential growing stage (4-14 h), a stationary stage (14-54 h), and a death stage (54-96 h). With that observation 12, 24, 48 and 96 h were selected as characteristic instants of the main stages. Figure 1 shows the profile obtained for the CFU, and Table 1 shows the specific rates for the characteristic instants.

For the MFA, a stoichiometric matrix considering 59 reactions and 55 intracellular metabolites was built, and the measurement of four specific rates (Table 1) allowed to quantify the metabolic fluxes in the characteristic instants (Figure 2).

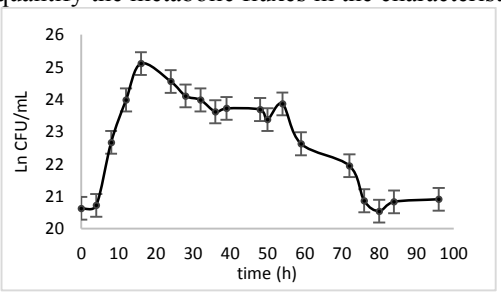

Figure 1. CFU profile in batch fermentation.

Table 1. Specific rates (g/g X h).

Time (h)	μ_X	μ_P	μ_S	μ_{CO2}
12	1.18	0.18	0.598	0.097
24	0.48	0.21	0.186	0.081
48	0.04	0.26	0.058	0.085
96	0.00	0.12	0.039	0.070

The rates of metabolic reactions at each instant evidence that fluxes in β-oxidation, depolymerisation, and tricarboxylic acid (TCA) pathways achieve their maxima values during the exponential growing stage (t = 12 h) which is consistent with a higher biomass production; in contrast, reactions of gluconeogenesis, phosphate pentoses, phaA (acetyl-coA generation as ending step of β-oxidation), and succinate production in TCA run at their highest values but in the inverse direction. This metabolic behaviour is due to the sugar unavailability and the necessity of generating biomass precursors. In the stationary stage (t = 24 h) it is observed that those reactions keep the direction but the rates are significantly reduced. Finally, at the end of the stationary stage (t = 48 h) and at the death stage (t = 96 h) most fluxes are almost zero. The MFA results confirm that the metabolism experiment strong changes during a batch process: at the beginning, with well-balanced carbon and nitrogen sources, the carbon is mainly driven to biomass production (87 %); whereas, during the stationary phase, with a reduced C/N ratio, the fraction of carbon driven to biomass goes from 70 % (t = 24 h) to 14 % (t = 48 h). It confirms that process goes from a feast phase to a famine phase.

3.2. Model Formulation and Fitting

The model considers that biomass is formed by two components: residual biomass (with the metabolic capacities) and the polymer. The initial formulation included limitations on growing and production by carbon source (*Sc*), carbon consumption for growing and production, and nitrogen consumption for growing and maintenance. The fitting of the initial model was non-satisfactory and it was observed that it is impossible to adjust simultaneously the behaviour at the starting and at the ending of the batch fermentation, confirming that a feast & famine approach is necessary.

$$\mu_X = \mu_{X\max} * \left(\frac{Sc}{K_{ScX} + Sc} \right)$$

$$\mu_P = \mu_{P\max} * \left(\frac{Sc}{K_{ScP} + Sc} \right)$$

Initial Model

$$\mu_{Sc} = -\left\lfloor \frac{1}{Y_{X/Sc}} * \mu_X \right\rfloor - \left\lfloor \frac{1}{Y_{P/Sc}} * \mu_P \right\rfloor$$

$$\mu_{Sn} = -\frac{1}{Y_{X/Sn}} * \mu_X - m_n$$

For the next cycle in the fitting procedure, a feast & famine approach was included (*CN chang*). It improved the fitting but an overestimation of the production in the beginning

of the famine phase was observed (results not shown). Because of that, a term to consider adaptation (*Tadapt*) on the production period was included, and finally, limitation on growing by nitrogen was added. The fitting of the model is in Figure 3 and its parameters in Table 2.

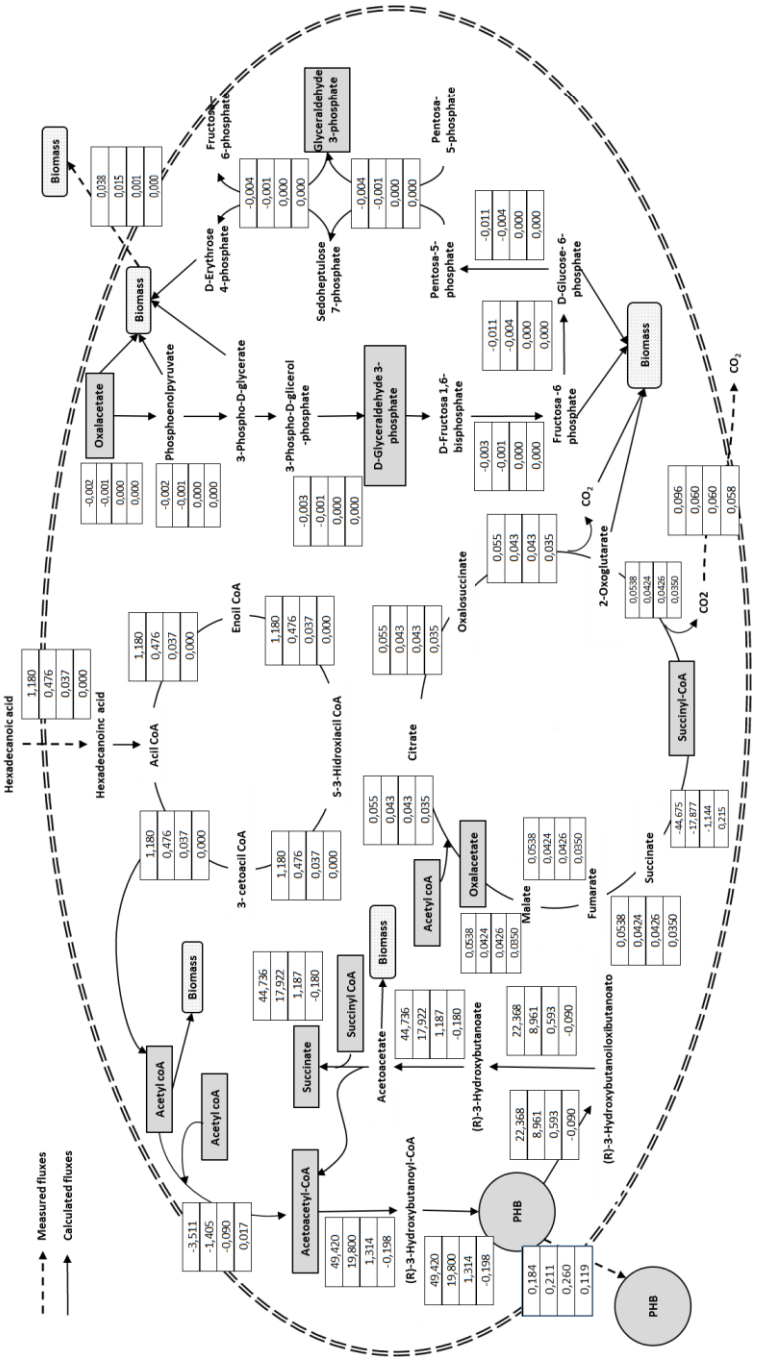

Figure 2. Metabolic network with quantified fluxes (mmol/mmol X h).

A key observation is that the transition from feast to famine was identified as happening at *Tchang* = 12.9 h, which strongly coincide with the end of the exponential stage. The carbon/nitrogen rate for this transition was 5.9 g/g and this value was selected as the mathematical criteria for switching between the models; additionally, the time for total adaptation of the metabolism (T_{adap}) was estimated as 14 h. The final model is as follows:

$$if \quad C/N > C/N_{chang} \begin{cases} \mu_X = \mu_{X\max} * \left(\frac{Sc}{K_{ScX} + Sc}\right) * \left(\frac{Sn}{K_{SnX} + Sn}\right) \\ \mu_P = \mu_{P\max} * \left(\frac{Sc}{K_{ScP} + Sc}\right) \end{cases} \quad \text{Feast Phase}$$

$$if \quad C/N = C/N_{chang} \qquad t_{chang} = t \quad \text{Phase Change}$$

$$if \quad C/N < C/N_{chang} \begin{cases} \mu_X = \mu_{X\max 2} * \left(\frac{Sc}{K_{ScX2} + Sc}\right) * \left(\frac{Sn}{K_{SnX2} + Sn}\right) \\ if \ t < t_{chang} + t_{adap} \quad \mu_P = \mu_{P\max 2} * \left(\frac{Sc}{K_{ScP2} + Sc}\right) * \left(\frac{t - t_{chang}}{t_{adap}}\right)^{\alpha} \\ if \ t > t_{chang} + t_{adap} \quad \mu_P = \mu_{P\max 2} * \left(\frac{Sc}{K_{ScP2} + Sc}\right) \end{cases} \quad \text{Famine Phase}$$

$$\mu_{Sc} = -\left[\frac{1}{Y_{X/Sc}} * \mu_X\right] - \left[\frac{1}{Y_{P/Sc}} * \mu_P\right] \quad \text{Both Phases}$$

$$\mu_{Sn} = -\frac{1}{Y_{X/Sn}} * \mu_X + m_n$$

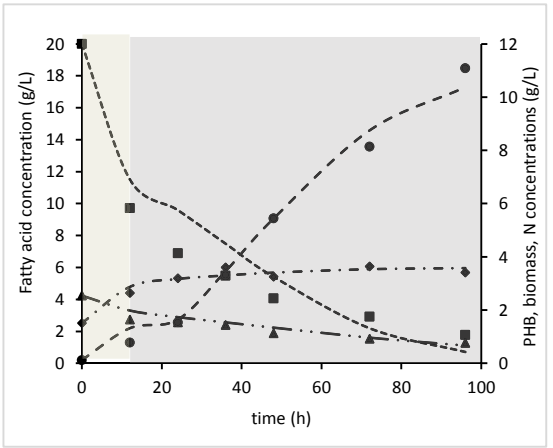

Figure 3. Fitting of final model (in-silico). ■ fatty acid (….) , ▲ ammonium (-..-), ● PHB (---), ♦ biomass (-.-.).

Table 2. Parameters of final model.

Parameter	unit	value
$\mu_{X\max}$	h^{-1}	0.059
K_{ScX}	g/L	4.68
K_{SnX}	g/L	0.048
$\mu_{P\max}$	h^{-1}	0.093
K_{ScP}	g/L	12.85
K_{SnX2}	g/L	3.998
C/N_{chang}	g/g	5.9
$\mu_{X\max 2}$	h^{-1}	0.040
$\mu_{P\max 2}$	h^{-1}	0.10
t_{adap}	h	14
$Y_{P/Sc}$	g PHB/g Sc	1.37
$Y_{X/Sc}$	g X/g Sc	0.18
$Y_{X/Sn}$	g X/g Sn	2.97
K_{ScP2}	g/L	6.50
K_{ScX2}	g/L	63.40
m_n	g Sn/g X h	0.005

3.3. Model Validation

A fed-batch fermentation with independent pulses of fatty acids and a 50 g/L ammonium solution was employed for model validation. Magnitude and time location of pulses were defined to extend the feast phase to 24 hours and increase biomass

concentration to 5,8 g/L (residual Biomass). Measured and predicted concentrations are shown in Figure 4. It can be seen that the model generates a very good prediction for carbon (R^2 0,96) and nitrogen (R^2 0,94), while for biomass (R^2 0,94) and PHB (R^2 0,99) the prediction is satisfactory with overestimations at the end of the process.

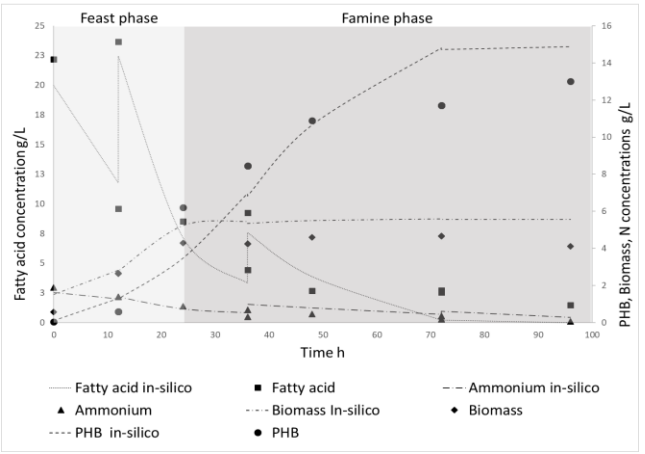

Figure 4. Profiles for model validation and optimization.

4. Conclusions

The strong change in the fraction of carbon driven to biomass production confirms that the metabolism experiments structural modifications; these modifications are consistent with a process with feast and famine phases. The C/N ratio is the key operational condition to move from feast to famine phase. The incorporation of an adaptation time during the change of phase generates an improving in the fitting, confirming that this change is not instantaneous. The satisfactory fitting for a fed-batch fermentation supports that the model is phenomenologically right.

References

K. Fang, H. Zhao, C. Sun, C.M.C. Lam, S. Chang, K. Zhang, J. Wang, 2011, Exploring the metabolic network of the epidemic pathogen *Burkholderia cenocepacia J2315* via genome-scale reconstruction. BMC Systems Biology, 5, 1, 83.

I. Fernández, 2012, Estudio del metabolismo de polihidroxialcanoatos en *Pseudomona putida*: implicaciones fisiológicas y aplicaciones en el desarrollo de bioplásticos funcionalizados. Ph.D. Thesis, Universidad Complutense de Madrid, España.

A.K. Gombert, J. Nielsen, 2003, Quantification of Metabolic Fluxes, Encyclopedia of Life Sciences, McMillan Publishers Ltda.

D.A. Méndez, 2016, Modelamiento matemático y optimización del proceso de producción de Polihidroxialcanoatos empleando la bacteria *Burkholderia cepacia B27* a partir de ácidos grasos, M.Sc. Thesis, Universidad Nacional de Colombia, Bogotá, Colombia.

J. Nandong, Y. Samyudia, M. Tadé, 2008, Multi-scale Framework for Modeling and Control of Fermentation Processes, IFAC Proceedings, 41, 2, 9673-9678.

C.A.M. Riascos, A.K. Gombert, L.F. Silva, M.K Taciro, J.G.C. Gomez, G.A.C. LeRoux, 2013, Metabolic pathways analysis in PHAs production by *Pseudomonas* with ^{13}C-labeling experiments, Computers Aided Chem. Eng., 32, 121-126.

P. Suriyamongkol, R. Weselake, S. Narine, M. Moloney, S. Sahah, Biotechnological approaches for the production of polyhydroxyalkanoates in microorganisms and plants: A Review, Biotechnological Advances, 25, 2 148-175.

A.C. Torres, 2019, Formulación de un modelo metabólicamente estructurado para optimizar la producción de Polihidroxialcanoatos (PHA) a partir de *Burkholderia cepacia*.Ph.D. Thesis, Universidad Nacional de Colombia, Bogotá, Colombia.

Sauro Pierucci, Flavio Manenti, Giulia Bozzano, Davide Manca (Eds.)
Proceedings of the 30th European Symposium on Computer Aided Process Engineering (ESCAPE30), May 24-27, 2020, Milano, Italy.
http://dx.doi.org/10.1016/B978-0-12-823377-1.50114-2

A Methodological Design Framework for Hybrid "Power-to-Methane" and "Power-to-Hydrogen" Supply Chains: application to Occitania Region, France

Eduardo Carrera Guilarte, Catherine Azzaro-Pantel

Laboratoire de Génie Chimique, Université Toulouse, CNRS, INPT, UPS, Toulouse, France
eduardo.carreraguilarte@toulouse-inp.fr

Abstract

This work presents a methodological design framework for hybrid Hydrogen and Methane Supply Chains (HMSC). The optimization approach of De-León Almaraz et al. (2012) has been extended to meet simultaneous demands for hydrogen and methane. The overall objective is to model and optimize HMSC in order to provide effective support for the study of deployment scenarios. The methodological framework is based on a multi-period mono-objective optimization formulation of the linear programming type in mixed variables (MILP). It is implemented in the GAMS environment and solved by using CPLEX 12. The objective to be minimized is the Total Annual Cost (TAC) of the HMSC over the entire period studied. The optimization variables involve the number and size of both production and storage units, the number of tanker truck and the flows of imported/exported hydrogen from one grid to another. The methodology is applied to the case study of Occitania (France). The costs of hydrogen and methane were obtained from the optimization strategy. The results show that hydrogen could be used as fuel for Fuel Cell Electric Vehicles (FCEV). However, synthetic methane could not be competitive without carbon tax implementation.
Keywords: Power-to-Gas, Hydrogen, Methane, MILP, Gams

1. Introduction

One response to the threat of climate change is to develop energy systems based on renewable energies (RES). However, the intermittent nature of renewable energy production remains a potential barrier to its increased penetration into the electricity mix. To meet this challenge, Power-to Gas systems (PtG) represent a promising alternative to valorize the overproduction of renewable electricity (mainly solar and wind) by transforming it into gas for different uses and, consequently, an option to decarbonize sectors such as transport and heat generation (Ademe, 2018). The scientific objective of this work is to develop a methodological framework for the deployment and design of PtG systems, involving the hybridization of hydrogen and methane supply chains: PtG implies the conversion of Power-to-Hydrogen, which can be subsequently used as an energy carrier or as a reactant for further compounds, i.e. methane. A CO_2 methanation reactor is considered here for producing synthetic methane due to the additional environmental benefit of the CO_2 reuse . It must be highlighted that if modelling and optimization of hydrogen supply chains started to gain some attention roughly ten years ago (the work developed in Almansoori and Shah (2009) can be viewed as a starting point), there is a lack of network modelling approaches considering their integration with

other networks (Samsatli and Samsatli, 2019). Both pathways are therefore explored in this study, considering hydrogen both as an intermediate product to produce methane and as a final product for several market segments (industry, transport, buildings): via a methanation step, hydrogen can be converted with CO_2 to produce synthetic methane and water (Sabatier Reaction), which facilitates the use of the existing gas network (E&E consultant et al., 2014; Götz et al., 2016). Such process conversions have a typical efficiency of 65–75% for Power-to-Hydrogen (electrolysis) and 75% for hydrogen to methane (HHV) (Götz et al., 2016). This paper is divided into five sections following this introduction: section 2 presents the problem formulation; section 3 highlights the key points involved in the optimization model. The case study is the core of section 4 and some typical results are discussed in section 5. Finally, conclusions and possible future research directions are proposed in section 6.

2. Problem formulation

The contribution of this work is the development of a comprehensive optimization model, that can simultaneously determine the design and operation of hydrogen and methane value chains mainly based on renewable energies such that the Total Annual Cost (TAC) of the whole network is minimized. The problem formulation is based on the guidelines proposed by De-León Almaraz et al. (2012) for hydrogen network modelling with the following assumptions:

- The territory to be studied is divided into a set of grids.
- In each grid, production, transport and storage plants of hydrogen and methane can be installed.
- Two demands need to be satisfied, respectively for hydrogen and methane, only through Power-to-Gas systems.
- There is limited availability of primary energy and CO_2 sources.
- Transport may exist only between grids.
- A multi-period formulation is involved.

The decision variables considered are the following ones:

- Number, size, capacity, production rate and location of hydrogen and methane production and storage units.
- Number of transport units and flow of hydrogen transported between grids.
- Specification of the sources and quantity of electricity and CO_2 consumed.

So as to:

- Minimize TAC.

3. Model description

The methodological framework is based on Mixed Integer Liner Programming (MILP). The formulation aims to satisfy the demands of both energy vectors “i” (in this case, hydrogen and methane), considering the potentialities of each grid “g”. The availability of energy source “e” and CO_2 “c”, production type “p”, storage option “s”, transport option “l”, for each period “t” are taken into account. The model involves a steady-state balance of mass/energy and possibilities of import of primary resources. The fundamental constraint is the resource balance, which considers all possible flows of each resource into or out of each zone (import, export, transportation). The model is solved through CPLEX 12, by using the GAMS environment, in an Intel Xeon E3-1505MV6, 3.00 GHz computer with 32 GB RAM. The superstructure of the HMSC is shown in Figure 1. Only the key points are discussed below.

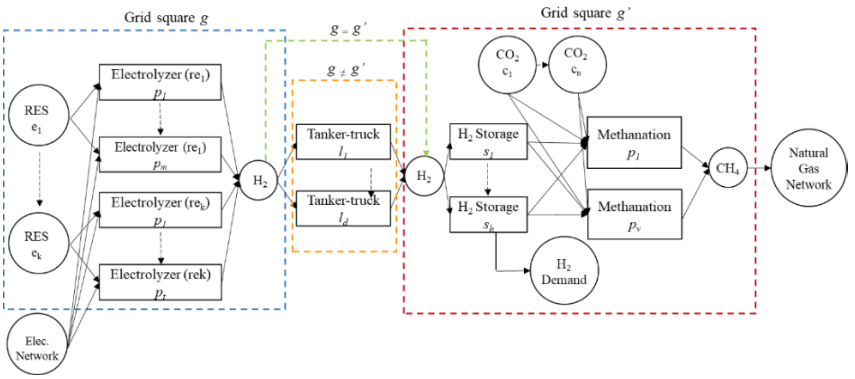

Figure 1. Superstructure of the multi-period HMSC model

3.1. Methanation facility capital cost

The methanation facility capital cost ($MFCC_t$, €/year) (see Eq. (1)) involves the Capital Cost for the installation of a methane plant ($MPCC_{pijt}$, €) as well as the Number of Facilities installed in each period (MIP_{pijgt}, year^{-1}).

$$MFCC_t = \sum_{pijg} MPCC_{pijt} MIP_{pijgt} \quad \forall t \tag{1}$$

3.2. Methanation facility operational cost

Methanation facility operational cost ($MFOC_t$, €/year) is determined in Eq. (2), taking into account the operational and maintenance cost ($MMOC_{pij}$, €/kg-CH_4), the production rate of methane (MPR_{pigt}, kg-CH_4/year) and CO_2 cost (CO_2SC_t, €/year).

$$MFOC_t = \sum_{pijg} MMOC_{pij} MPR_{pigt} + CO_2SC_t \quad \forall t \tag{2}$$

3.3. CO_2 source constraint

The CO_2 available amount (CO_{2cgt}, kg-CO_2) to produce methane is calculated in Eq. (3), considering the availability of CO_2 sources on the territory (CO_2A_{cgt}, kg-CO_2/year), the imported CO_2 ($IPCO_2S_{cgt}$, kg-CO_2/year) and the consumed CO_2 during methane production ($SSF\sum_{pji}\delta_{cpj}MPR_{pijgt}$). In the last term, the amount of CO_2 needed to produce 1 kg of methane (δ_{cpj}, kg-CO_2/kg-CH_4) and a safety stock factor (SSF = 5%) for storing a small inventory of CO_2 are involved.

$$CO_{2cgt} = CO_2A_{cgt} + IPCO_2S_{cgt} - SSF\sum_{pji}\delta_{cpj}MPR_{pijgt} \forall c,t,g; g \neq g' \tag{3}$$

3.4. CO_2 cost

The CO_2 cost (see Eq. (4)) depends on the total CO_2 consumption and the cost of each CO_2 source (UCO_2C_{ct} , €/kgCO_2) and is expressed as follows:

$$CO_2SC_t = \sum_{cg} UCO_2C_{ct} \times \left(IPCO_2S_{cgt} + \sum_{pji} \delta_{cpj} MPR_{pijgt} \right) \quad \forall t \tag{4}$$

3.5. Total annual cost

The Total Annual Cost (TAC_t , €/year, Eq. (5)) takes into account the investment ($MFCC_t$) and operating costs ($MFOC_t$) for methane production. A discount cost of hydrogen production ($HTAC_t$) is calculated according to (De-León Almaraz et al. (2012)) (with discount rate (r)) :

$$TAC_t = \left(\frac{MFCC_t + MFOC_t + HTAC_t}{(1+r)^t} \right) \forall t \tag{5}$$

3.6. Objective function

The objective function to be minimized is expressed by Eq. (6) in which *TACtotal* represents the total cost of the HMSC over the entire period studied.

$$TACtotal = \sum_t TAC_t \tag{6}$$

3.7. Levelized Cost of Energy (LCOE)

Finally, the Levelized Cost of Energy ($LCOE_i$, €/MWh) is calculated in Eq. (7) for hydrogen and methane demands (E_{it} , MWh/year).

$$LCOE_i = \frac{\sum_t \frac{TAC_{it}}{(1+r)^t}}{\sum_t \frac{E_{it}}{(1+r)^t}} \quad \forall i \tag{7}$$

4. Case study

The Occitania region in the south of France that aims to become the first positive energy region in Europe by 2050 is taken as a case study. The territory is divided into 36 grids that correspond to the districts of this region. An average inter-district distance has been considered for transport purpose. Three renewable energy sources have been identified, that are solar, wind and hydro-power. Hydrogen is produced in the form of gas and cryogenic storage is assumed for hydrogen with gaseous transportation by tanker trucks. Synthetic methane is assumed to be produced from hydrogen in a catalytic methanation process (Collet et al., 2017; Götz et al., 2016). Medium sized electrolysers and catalyst reactors are taken into account. CO_2 sources stem from methanisation and gasification processes. Hydrogen demand was determined based on the expected use of fuel cell electric vehicles (FCEVs). The demand for renewable

methane has been estimated from the scenarios developed by Ademe and Occitania Region (Ademe, 2018; E&E consultant et al., 2014). A three-year period is used in time discretization. The cost of electricity varies according to the source, which is a key parameter in the resulting cost of hydrogen.

5. Results and discussion

The optimal values of the decision variables and the associated costs that define the configuration of the future HMSC are shown in Table 1. This network uses tanker trucks to deliver H_2 to storage facilities. A decrease in the use of transport between grids is also observed as new hydrogen plants are installed. A high investment cost is due to the HMSC deployment in the first period. Although the involved costs progressively decrease until 2050, the LCOE of methane is yet too high to be competitive compared to natural gas cost of 45 €/MWh (ADEME, 2018). The LCOE of hydrogen reaches less than 130 €/MWh, which could be an interesting option for the transport sector (Hydrogen Europe, 2018). The HMSC configuration in 2050 can be visualised in Figure 2. The main source of electricity used is wind energy followed by solar energy. Yet, a part of the electricity is satisfied through electricity imported from the national electricity network (71.6% nuclear basis) in order to minimize costs. The main characteristics and computational effort of the solution found for the optimization model are summarized in Table 2.

Table 1. Optimization results of the hydrogen and methane supply chain

Year	2035	2038	2041	2044	2047	2050
H_2 Demand (GWh-H_2 per year)	38	54	70	86	102	117
CH_4 Demand (GWh-CH_4 per year)	98	235	438	783	1,237	1,845
Number of hydrogen production facilities	5	5	7	11	15	21
Number of hydrogen storage facilities	10	14	17	21	31	44
Number of methane production facilities	7	7	7	7	7	7
Number of transport units	9	8	5	2	2	3
TAC (M€/year)	87.69	13.38	18.24	26.42	34.62	40.45
CH_4 LCOE (€/MWh)			158			
H_2 LCOE (€/MWh)			112			
Objective function: TACtotal (M€)			**220.82**			

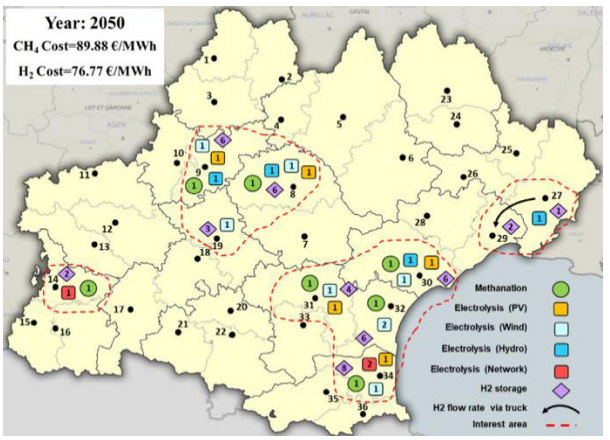

Figure 2. Network structure of hydrogen and methane supply chain distributed via tanker trucks in Occitania region

Table 2. Computational results for the optimization

Continuous variables	Binary Variables	Constraints	CPU (s)	GAP
44,684	23,328	338,462	5400	0.006

6. Conclusion and perspectives

In this paper, a general methodology for the design and deployment of a hybrid hydrogen and methane supply chain was developed and used for a base case study devoted to the Occitania region in France. The unit cost of hydrogen was obtained from the optimization strategy, using different parameters, for example the price of electricity. The results show that with electricity prices close to 31 €/MWh, FCEVs and synthetic methane could play an important role as energy vectors, even if their evolution will depend on the policy implemented, such as carbon tax.

The approach and results presented in this paper are useful for policy-makers as they provide insights and recommendations as to what technologies should be accelerated (hydrogen, synthetic methane) and where subsidies and other policy instruments should be applied to make the deployment of these supply chains viable. A more exhaustive methodological framework could be achieved by carrying out a multi-objective optimization, taking into account performance indicators (e.g. exergy and thermoeconomic costs) and environmental impacts (i.e. Global Warming Potential).

References

ADEME. (2018). Un mix de gaz 100 % renouvelable en 2050 ? Paris, France.

Almansoori, A., & Shah, N. (2009). Design and operation of a future hydrogen supply chain: Multi-period model. International Journal of Hydrogen Energy, 34(19), 7883–7897. https://doi.org/10.1016/j.ijhydene.2009.07.109

Collet, P., Flottes, E., Favre, A., Raynal, L., Pierre, H., Capela, S., & Peregrina, C. (2017). Techno-economic and Life Cycle Assessment of methane production via biogas upgrading and power to gas technology. Applied Energy, 192, 282–295. https://doi.org/10.1016/j.apenergy.2016.08.181

De-León Almaraz, S., Azzaro-Pantel, C., Montastruc, L., Pibouleau, L., & Senties, O. B. (2012). Design of a hydrogen supply chain using multiobjective optimisation. Computer Aided Chemical Engineering, 30, 292–296. https://doi.org/10.1016/B978-0-444-59519-5.50059-9

E&E consultant, HESPUL, & Solagro. (2014). Etude portant sur l'hydrogène et la méthanation comme procédé de valorisation de l'électricité excédentaire. Paris, France.

Götz, M., Lefebvre, J., Mörs, F., McDaniel Koch, A., Graf, F., Bajohr, S., Kolb, T. (2016). Renewable Power-to-Gas: A technological and economic review. Renewable Energy, 85, 1371–1390. https://doi.org/10.1016/j.renene.2015.07.066

Hydrogen Europe. (2018). Hydrogen, enabling a zero emission Europe.Brussels, Belgium

Samsatli, S., Samsatli, N. J. The role of renewable hydrogen and inter-seasonal storage in decarbonising heat – Comprehensive optimisation of future renewable energy value chains, Applied Energy, Volumes 233–234, 2019, Pages 854-893, ISSN 0306-2619, https://doi.org/10.1016/j.apenergy.2018.09.159.

30TH SYMPOSIUM ON COMPUTER AIDED PROCESS ENGINEERING

PART B

Edited by

SAURO PIERUCCI, FLAVIO MANENTI, GIULIA LUISA BOZZANO AND DAVIDE MANCA

COMPUTER-AIDED CHEMICAL ENGINEERING, 48

ELSEVIER

30TH EUROPEAN SYMPOSIUM ON COMPUTER AIDED PROCESS ENGINEERING

PART B

30TH EUROPEAN SYMPOSIUM ON COMPUTER AIDED PROCESS ENGINEERING

PART B

Edited by

Sauro Pierucci
AIDIC Servizi s.r.l.,
Milano, Italy,
sauro.pierucci@polimi.it

Flavio Manenti
SuPER Team, Sustainable Process Engineering Research
Dipartimento di Chimica, Materiali e Ingegneria Chimica,
Politecnico di Milano, Milano, Italy,
flavio.manenti@polimi.it

Giulia Luisa Bozzano
SuPER Team, Sustainable Process Engineering Research
Dipartimento di Chimica, Materiali e Ingegneria Chimica,
Politecnico di Milano, Milano, Italy,
giulia.bozzano@polimi.it

Davide Manca
PSE-Lab - Process Systems Engineering Laboratory,
Dipartimento di Chimica, Materiali e Ingegneria Chimica,
Politecnico di Milano, Italy,
davide.manca@polimi.it

ELSEVIER

Amsterdam – Boston – Heidelberg – London – New York – Oxford
Paris – San Diego – San Francisco – Singapore – Sydney – Tokyo

Elsevier
Radarweg 29, PO Box 211, 1000 AE Amsterdam, Netherlands
The Boulevard, Langford Lane, Kidlington, Oxford OX5 1GB, UK
50 Hampshire Street, 5th Floor, Cambridge, MA 02139, USA

Notices
Knowledge and best practice in this field are constantly changing. As new research and experience broaden our understanding, changes in research methods, professional practices, or medical treatment may become necessary.

Practitioners and researchers must always rely on their own experience and knowledge in evaluating and using any information, methods, compounds, or experiments described herein. In using such information or methods they should be mindful of their own safety and the safety of others, including parties for whom they have a professional responsibility.

To the fullest extent of the law, neither the Publisher nor the authors, contributors, or editors, assume any liability for any injury and/or damage to persons or property as a matter of products liability, negligence or otherwise, or from any use or operation of any methods, products, instructions, or ideas contained in the material herein.

British Library Cataloguing in Publication Data
A catalogue record for this book is available from the British Library

Library of Congress Cataloging-in-Publication Data
A catalog record for this book is available from the Library of Congress

ISBN (Part B): 978-0-12-823512-6
ISBN (Set) : 978-0-12-823377-1
ISSN: 1570-7946

Publisher: Susan Dennis
Acquisition Editor: Kostas Marinakis
Editorial Project Manager: Lena Sparks
Production Project Manager: Paul Prasad Chandramohan
Designer: Greg Harris

Typeset by SPi Global, India

Contents

Sauro Pierucci, Flavio Manenti, Giulia Bozzano, Davide Manca (Eds.)
Proceedings of the 30th European Symposium on Computer Aided Process Engineering (ESCAPE30), May 24-27, 2020, Milano, Italy.
http://dx.doi.org/10.1016/B978-0-12-823377-1.50115-4

A Two-stage Stochastic Programming Model to Determine the Optimal Screening Strategy for Colorectal Cancer

David Young, Selen Cremaschi*

Department of Chemical Engineering, Auburn University, Auburn, AL 36849, USA
Szc0113@Auburn.edu

Abstract

Screening for colorectal cancer (CRC) is an effective way to drastically reduce the impact of the disease or prevent it altogether. This paper presents a stochastic mathematical programming model to determine the optimal screening strategy for CRC of a given population. The objective of the model is to maximize the expected quality adjusted life years an individual would gain by following the optimum screening strategy. The model incorporates the uncertainty of CRC progression through the use of the time taken to progress to the various stages of the disease. The data to model the uncertainty of the progression of CRC within an individual was obtained from a continuous time simulation. The solution of the stochastic programming model for the average-risk male population yielded an expected gain of 0.2384 quality-adjusted life years with three colonoscopies.

Keywords: Colorectal cancer, stochastic programming, cancer screening

1. Introduction

According to the World Health Organization, colorectal cancer (CRC) was the 3rd most common, as well as the 2nd most deadly, form of cancer in the world in 2018 (World Health Organization, 2019). The lethality of CRC increases drastically as the disease spreads throughout the entire body, with the 5-years survival rate of the diagnosis at the most advanced cancer stage being 14 %, whereas diagnosis at the less advanced stages average to a 5-year survival rate of 80 % (National Cancer Institute, 2019). There is also a significant economic burden due to CRC. It has been estimated that CRC related costs will be 17 billion USD for the US alone in 2020 (Mariotto et al., 2011). Therefore, early detection of CRC can drastically reduce both the lethality and the economic burden of the disease. The process of testing asymptomatic individuals for the presence of CRC, or its precursor adenomas, is known as screening.

When screening for CRC, there are a number of possible test types to use, each with their own advantages and drawbacks. These tests can be placed into two main categories, visual and stool-based tests. The visual tests, e.g., colonoscopy, sigmoidoscopy or computed tomographic colonography, are generally more accurate than the stool based tests, but considered to be more of a burden on the patient (Issa and Noureddine, 2017). The stool based tests, e.g., FIT, gFOBT or MT-sDNA, are less accurate but less burdensome (Issa and Noureddine, 2017). Four components define a screening strategy: screening (1) starting age (2) test type(s), (3) frequency, and (4) ending age. The current screening strategy suggestions for the US are presented in a report by the US Preventative Services Task Force (USPSTF) and were determined through a combination of expert opinions and simulation evaluations (Bibbins-Domingo et al., 2016).

The ideal outcome for screening is to identify the precursors of CRC to prevent CRC from developing in the first place. The most common pathway for the development of CRC is known as the adenoma-carcinoma sequence (Loeve et al., 2004). This pathway, depicted in Figure 1, begins with a healthy individual developing a precancerous lesion known as an adenoma. As the adenoma grows, the likelihood of it transitioning into a cancerous state increases with the adenoma's size. However, it has been observed that some cases of CRC occur with no visible adenomas present (Soetikno et al., 2008), which is represented by the pathway from a flat adenoma to a cancerous state in Figure 1. It should also be noted that not all adenomas proceed to a cancerous state within an individual's life. Although the general progression of CRC is known, the exact transition rates are not known with certainty.

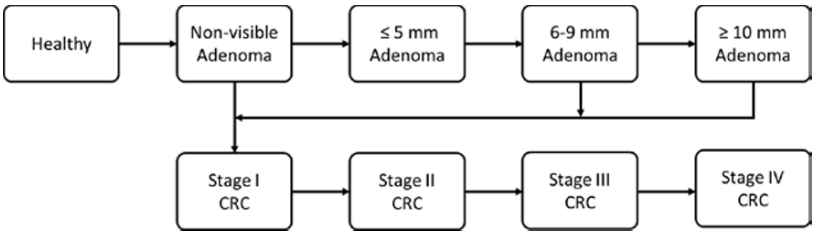

Figure 1 Adenoma-carcinoma sequence

Numerous studies have been conducted to evaluate various screening strategies for CRC. To account for the uncertain nature of CRC progression, researchers turn to the use of microsimulations. Microsimulations are models used to study the population level trends of an applied policy through the simulation of a large number of unique entities and applying the same policy across the population (Orcutt, 1957). When used for evaluating screening strategies for CRC, microsimulations treat the strategies as the policies applied to the population with each individual demonstrating a different progression of CRC. Cost-effectiveness metric is a common approach to compare screening strategies for a given population. The metric measures the total cost for gaining an additional quality adjusted life year for a population, where a quality adjusted life year (QALY) is a discounted measure of quality of life based on an individual's health state. For example, in a recent study, Haug *et al.* (2016) investigated the cost effectiveness of a hypothetical screening test and FOBT. The hypothetical test had a higher sensitivity for detecting CRC but could not detect adenomas. It was found that the hypothetical test was not cost effective compared to FOBT. The study concluded that new tests should be able to detect the presence of adenomas to be considered an effective screening test. However, it is computationally prohibitive to analyze all potential screening strategies using simulation-based what-if analysis. The most extensive of the cost-effectiveness studies (Knudsen et al., 2016) evaluated around only 11 % of the potential screening strategies defined by the range of starting and ending ages as well as the range of the screening frequency. Therefore, there is no guarantee that the strategies deemed the best are the optimal, or near optimal, screening strategies.

This paper introduces a mathematical programming model to determine the optimal screening strategy for CRC using a two-stage stochastic programming (TSSP) model. The goal of the TSSP is to determine a screening strategy that maximizes the expected QALY gained by a population. As a case study, we utilize data generated by a microsimulation model to construct our uncertain distributions for the TSSP, and evaluate the effect of number of screenings in an individual's lifetime on the optimal screening strategy.

2. Problem statement and formulation

The objective of the TSSP model is to maximize the expected value of the total quality adjusted life years (QALY) gained from screening, by identifying which screening test type and at what age a screening test should occur for a given population. The identified screening strategy, $\boldsymbol{X}$, is the first-stage decisions of the model, with the resulting life span from screening, $\boldsymbol{Y}$, representing the fixed recourse actions for the TSSP. The uncertain parameter sets of the model, $\boldsymbol{\theta}$ and τ, represent the ages at which CRC progresses to the next state and the ages of death from both non-CRC and CRC sources. The different potential sources of death are described through set $\boldsymbol{D}$. Health states are defined with set $\boldsymbol{H}$, where each element corresponds to a health state in Figure 1. The scenarios in which the uncertainties are realized represent individuals within a population. The scenarios are generated through sampling from distributions that describe at what age the individual progresses to the next health state. These ages are then converted into a $|\boldsymbol{H}|\text{x}|\boldsymbol{A}|$ or $|\boldsymbol{D}|\text{x}|\boldsymbol{A}|$ matrix of binary values to describe the progression through the various health states or death states for that scenario, respectively.

The deterministic equivalent of the two-stage stochastic program, which is a mixed integer linear programming model, is given in Figure 2, along with the corresponding nomenclature. The value for expected QALY gained is calculated in Eqn. (1), in which the difference from the health states for the screened, $\boldsymbol{Y}$, and unscreened, $\boldsymbol{\theta}$, lifetime of an individual are weighted according to the health state specific utility factor, C_h, with a disutility, $Dis_{h,t}$, of the screen tests performed on the individual. The effects of the screening decisions, $\boldsymbol{X}$, are enforced through fixed recourse actions, Eqns. (2)-(18), modifying an individual's lifetime given the health state they are in at the time a screening action is taken. The state an individual is screened is determined through Eqns. (2)-(4). The screening result, $\boldsymbol{\nu}$, for the first test performed is enforced through the product of the screening decision and the unscreened lifetime health matrix, $\boldsymbol{\theta}$, in Eqn. (2). Subsequent screening results are enforced through Eqn. (3), with the additional term disallowing positive screens, $\boldsymbol{\nu=1}$, for cases in which the first screening test returned a positive result for a health state other than healthy. Eqn. (4) allows the screening results to only identify one health state per screening of previously healthy individuals. The ages at or after which a positive result is obtained for a screening test are tracked through Eqns. (5)-(10). Eqns. (5) and (6) track the results from the first screening test, identifying if the individual has a screening test that detected a health state other than healthy at or prior to the specified age. Eqns. (7) and (8) provide a lower bound for the results of the subsequent screening tests with an additional term to disallow multiple positive screens, with an upper bound for the screening results enforced in Eqns. (9) and (10). The ages at which an individual is no longer living, $\boldsymbol{\xi}$, is evaluated through Eqns. (11)-(13), where Eqns. (11) and (12) set the lower bounds for the ages of death from various sources, and Eqn. (13) sets the upper bound on $\boldsymbol{\xi}$ at a given age. Finally, the individuals' new lifetimes are constructed through Eqns. (14)-(18), where Eqn. (14) tracks the health state of healthy for the individual, allowing the individual to return to healthy state if a positive screening test occurs while the individual is within the adenoma health state. Eqn. (15) corresponds to the health states of adenoma and undetected CRC stages, in which once the state is detected via screening, the individual is no longer within that state and shifts to healthy or clinically detected CRC states, respectively. Eqn. (16) enforces the states associated with clinically detected CRC, where if an individual has a positive screening result within an undetected CRC stage, that individual then has the state set to clinical stages disallowing the further progression of CRC. The ages at which the health state is at death is tracked via Eqn. (17),

and Eqn. (18) requires the individual to be at only one health state at each given age. Eqn. (19) allows only one screening test type per year. The ordering of the screening tests is enforced through Eqn. (20), requiring the second screening test to occur at an age after the first test, etc. Finally, Eqns. (21)-(29) are implemented to introduce variables, $\boldsymbol{\eta}$, $\boldsymbol{\omega}$, and $\boldsymbol{\varphi}$ to linearize the nonlinear relationships of the "and" binary operator. The variable $\boldsymbol{\eta}$ introduced through Eqns. (21)–(23) are used to remove the multiplication of binary variables ν and $\boldsymbol{\psi}$ through exact linearization. Similarly, ω and φ are introduced in Eqns. (24)-(26) and (27)-(29) to remove the multiplication of ξ by ψ and η by ξ via exact linearization respectively.

Objective Function

Max: Expected quality adjusted life years gained

$$\mathrm{E(QALYG)} = \sum_{s\in S} P(s) \sum_{h\in H}\left[\sum_{a\in A} C_h\left(Y_{h,a,s} - \theta_{h,a,s}\right) - \sum_{t\in T} Dis_{h,t}\left(\sum_{z\in Z} \nu_{h,z,s}\right)\right] \quad (1)$$

Subject to

Screening results

$$\nu_{h,1,s} = \sum_{t\in T}\sum_{a\in A} \theta_{h,a,s} X_{t,a,1} \qquad \forall h \in \{1,2,\ldots,6\}, \forall s \in \boldsymbol{S} \quad (2)$$

$$\nu_{h,z,s} \geq \sum_{t\in T}\sum_{a\in A} \theta_{h,a,s} X_{t,a,z} - \sum_{j=1}^{z}\sum_{k=2}^{6} \nu_{k,j,s} \qquad \forall h \in \{1,2,\ldots,6\}, \forall s \in \boldsymbol{S}, \forall z \in \boldsymbol{Z} | z \geq 2 \quad (3)$$

$$\sum_{h\in H} \nu_{h,z,s} \leq 1 - \sum_{j=1}^{z}\sum_{k=2}^{6} \nu_{k,j,s} \qquad \forall s \in \boldsymbol{S}, \forall z \in \boldsymbol{Z} | z \geq 2 \quad (4)$$

$$\psi_{20,1,s} = \sum_{h=2}^{6} \theta_{h,20,s} \sum_{t\in T} X_{t,20,1} \qquad \forall s \in \boldsymbol{S} \quad (5)$$

$$\psi_{a,1,s} = \psi_{a-1,1,s} + \sum_{h=2}^{6} \theta_{h,a,s} \sum_{t\in T} X_{t,a,1} \qquad \forall a \in \boldsymbol{A} | a > 20, \forall s \in \boldsymbol{S} \quad (6)$$

$$\psi_{20,z,s} \geq \sum_{h=2}^{6} \theta_{h,20,s} \sum_{t\in T} X_{t,20,z} - \sum_{j=1}^{z} \psi_{a,j,s} \qquad \forall s \in \boldsymbol{S}, \forall z \in \boldsymbol{Z} | z > 1 \quad (7)$$

$$\psi_{a,z,s} \geq \psi_{a-1,z,s} + \sum_{h=2}^{6} \theta_{h,a,s} \sum_{t\in T} X_{t,a,z} - \sum_{j=1}^{z} \psi_{a,j,s} \qquad \forall a \in \boldsymbol{A} | a > 20, \forall z \in \boldsymbol{Z} | z > 1, \forall s \in \boldsymbol{S} \quad (8)$$

$$\psi_{20,z,s} \leq \sum_{h=2}^{6} \theta_{h,20,s} \sum_{t\in T} X_{t,20,z} \qquad \forall s \in \boldsymbol{S}, \forall z \in \boldsymbol{Z} | z > 1 \quad (9)$$

$$\psi_{a,z,s} \leq \psi_{a-1,z,s} + \sum_{h=2}^{6} \theta_{h,a,s} \sum_{t\in T} X_{t,a,z} \qquad \forall a \in \boldsymbol{A} | a > 20, \forall z \in \boldsymbol{Z} | z > 1, \forall s \in \boldsymbol{S} \quad (10)$$

Screened Lifetime

$$\xi_{a,s} \geq \tau_{1,a,s} \qquad \forall a \in \boldsymbol{A}, \forall s \in \boldsymbol{S} \quad (11)$$

$$\xi_{a,s} \geq \tau_{d,a,s} \sum_{z\in Z} \nu_{h,z,s} \qquad \forall a \in \boldsymbol{A}, \forall s \in \boldsymbol{S}, (h,d) \in \{(\mathbf{3},\mathbf{2}),(\mathbf{4},\mathbf{3}),(\mathbf{5},\mathbf{4}),(\mathbf{6},\mathbf{5})\} \quad (12)$$

$$\xi_{a,s} \leq \tau_{1,a,s} + \sum_{(h,d)\in\{(3,2),(4,3),(5,4),(6,5)\}} \tau_{d,a,s} \sum_{z\in Z} \nu_{h,z,s} \qquad \forall a \in \boldsymbol{A}, \forall s \in \boldsymbol{S} \quad (13)$$

$$Y_{1,a,s} \leq \theta_{1,a,s}\left(1 - \xi_{a,s}\right) + \sum_{z\in Z} \eta_{2,a,z,s} - \phi_{2,a,z,s} \quad \forall a \in \boldsymbol{A}, \forall s \in \boldsymbol{S} \quad (14)$$

$$Y_{h,a,s} \leq \theta_{h,a,s}\left(1 - \xi_{a,s} + \sum_{z\in Z} \omega_{a,z,s} - \psi_{a,z,s}\right) \qquad h \in \{2,3,4,5,6\}, \forall a \in \boldsymbol{A}, \forall s \in \boldsymbol{S} \quad (15)$$

$$Y_{h,a,s} \leq \theta_{h,a,s}\left(1 - \xi_{a,s}\right) + \sum_{z\in Z} \theta_{h,a,s}\left(\omega_{a,z,s} - \psi_{a,z,s}\right) + \eta_{h-4,a,z,s} - \phi_{h-4,a,z,s} \qquad h \in \{7,8,9,10\}, \forall a \in \boldsymbol{A}, \forall s \in \boldsymbol{S} \quad (16)$$

$$Y_{11,a,s} \geq \xi_{a,s} \qquad \forall a \in \boldsymbol{A}, \forall s \in \boldsymbol{S} \quad (17)$$

$$\sum_{h\in H} Y_{h,a,s} \leq 1 \qquad \forall a \in \boldsymbol{A}, \forall s \in \boldsymbol{S} \quad (18)$$

Screening restrictions

$$\sum_{a\in A}\sum_{t\in T} X_{t,a,z} \leq 1 \qquad \forall z \in \boldsymbol{Z} \quad (19)$$

$$\sum_{t\in T} X_{t,a,z} \leq \sum_{t\in T}\sum_{b\in\{20,\ldots,a\}} X_{t,b,z} \qquad \forall a \in \boldsymbol{A}, \forall z \in \boldsymbol{Z} | z > 1 \quad (20)$$

Linearization constraints

$$\eta_{h,a,z,s} \leq \nu_{h,z,s} \qquad \forall h \in \{1,2,\ldots,6\}, \forall a \in \boldsymbol{A}, \forall z \in \boldsymbol{Z}, \forall s \in \boldsymbol{S} \quad (21)$$

$$\eta_{h,a,z,s} \leq \psi_{a,z,s} \qquad \forall h \in \{1,2,\ldots,6\}, \forall a \in \boldsymbol{A}, \forall z \in \boldsymbol{Z}, \forall s \in \boldsymbol{S} \quad (22)$$

$$\eta_{h,a,z,s} \geq \nu_{h,z,s} + \psi_{a,z,s} - 1 \qquad \forall h \in \{1,2,\ldots,6\}, \forall a \in \boldsymbol{A}, \forall z \in \boldsymbol{Z}, \forall s \in \boldsymbol{S} \quad (23)$$

$$\omega_{a,z,s} \leq \xi_{a,s} \qquad \forall a \in \boldsymbol{A}, \forall z \in \boldsymbol{Z}, \forall s \in \boldsymbol{S} \quad (24)$$

$$\omega_{a,z,s} \leq \psi_{a,z,s} \qquad \forall a \in \boldsymbol{A}, \forall z \in \boldsymbol{Z}, \forall s \in \boldsymbol{S} \quad (25)$$

$$\omega_{a,z,s} \geq \psi_{a,z,s} + \xi_{a,s} - 1 \qquad \forall a \in \boldsymbol{A}, \forall z \in \boldsymbol{Z}, \forall s \in \boldsymbol{S} \quad (26)$$

$$\phi_{h,a,z,s} \leq \eta_{h,a,z,s} \qquad \forall h \in \boldsymbol{H}, \forall a \in \boldsymbol{A}, \forall z \in \boldsymbol{Z}, \forall s \in \boldsymbol{S} \quad (27)$$

$$\phi_{h,a,z,s} \leq \xi_{a,i} \qquad \forall h \in \boldsymbol{H}, \forall a \in \boldsymbol{A}, \forall z \in \boldsymbol{Z}, \forall s \in \boldsymbol{S} \quad (28)$$

$$\phi_{h,a,z,s} \geq \eta_{h,a,z,s} + \xi_{a,s} - 1 \qquad \forall h \in \boldsymbol{H}, \forall a \in \boldsymbol{A}, \forall z \in \boldsymbol{Z}, \forall s \in \boldsymbol{S} \quad (29)$$

Nomenclature

Sets

$t \in \boldsymbol{T}$ = Set of all screening test types

$d \in \boldsymbol{D}$ = Set of all potential death sources

$a, b \in \boldsymbol{A}$ = Set of all ages

$h, k \in \boldsymbol{H}$ = Set of all health states

$s \in \boldsymbol{S}$ = Set of scenarios/individuals

$j, z \in \boldsymbol{Z}$ = Set of possible screening tests

Known Parameters

$\boldsymbol{C_h}$: Health utility factor of health state h

$\boldsymbol{Dis_{h,t}}$: Disutility factor of test t on health state h

Uncertain Parameters

$$\boldsymbol{\theta_{h,a,s}} = \begin{cases} 1 & \text{if scenario } s \text{ is naturally at health state } h \text{ at age } a \\ 0 & \text{otherwise} \end{cases}$$

$$\boldsymbol{\tau_{d,a,s}} = \begin{cases} 1 & \text{if scenario } s \text{ naturally dies at age } a \text{ from death source } d \\ 0 & \text{otherwise} \end{cases}$$

Binary Variables

$$\boldsymbol{X_{t,a,z}} = \begin{cases} 1 & \text{if screening test } t \text{ is chosen at age } a \text{ for test number } z \\ 0 & \text{otherwise} \end{cases}$$

$$\boldsymbol{Y_{h,a,s}} = \begin{cases} 1 & \text{if scenario } s \text{ is at health state } h \text{ at age } a \text{ by screening} \\ 0 & \text{otherwise} \end{cases}$$

$$\boldsymbol{\xi_{a,s}} = \begin{cases} 1 & \text{if scenario } s \text{ is decseaded at age } a \text{ after screening} \\ 0 & \text{otherwise} \end{cases}$$

$$\boldsymbol{\psi_{a,z,s}} = \begin{cases} 1 & \text{if scenario } s \text{ receives a positive screen from screen } z \text{ at or before age } a \\ 0 & \text{otherwise} \end{cases}$$

$$\boldsymbol{\nu_{h,z,s}} = \begin{cases} 1 & \text{if scenario } s \text{ is detected at health state } h \text{ by screen } z \\ 0 & \text{otherwise} \end{cases}$$

$$\boldsymbol{\eta_{h,a,z,s}} = \begin{cases} 1 & \text{if scenario } s \text{ receives a positive screen by screen } z \text{ at health state } h \text{ at or before age } a \\ 0 & \text{otherwise} \end{cases}$$

$$\boldsymbol{\omega_{a,z,s}} = \begin{cases} 1 & \text{if scenario } s \text{ receives a positive screen by screen } z \text{ and is deceased at or before age } a \\ 0 & \text{otherwise} \end{cases}$$

$$\boldsymbol{\phi_{h,a,z,s}} = \begin{cases} 1 & \text{if scenario } s \text{ receives a positive screen by screen } z \text{ at health state } h \text{ and is deceased at or before age } a \\ 0 & \text{otherwise} \end{cases}$$

Figure 2 TSSP formulation of determining screening decisions for detecting CRC

3. Case study

We use the TSSP formulation of the CRC screening planning problem applied to data generated from a CRC microsimulation based on the CRC-SPIN model (Rutter and Savarino, 2010) from the US's Nation Institute of Health's cancer modeling consortium, CISNET. The uncertain distributions for constructing θ and τ were created by fitting distributions for the ages at which different health states were reached using the

microsimulation to generate 40 million individuals. This case study aims to understand the effect of the maximum number of screens within an individual's lifetime when incorporating data from a microsimulation for uncertain parameters. For this study, we only consider a single test type, colonoscopy. Additionally, we assume that the accuracy of the test is 100%, and individuals are perfectly compliant. The screening window is set to ages 20 to 100. The model is constructed and solved within Pyomo 5.6.6.

3.1. Maximum screens within a lifetime

The TSSP model requires that the maximum number of screens within a lifetime, $|\mathbf{Z}|$, to be specified. The maximum allotted screens were raised from one to five screens to evaluate its impact on the optimum solution and the model's computational complexity. The same 100 scenarios were used for all five cases, and the model was solved using an Intel® Xeon® 20-core 2.30 GHz processor with CPLEX 12.6.3.0. Table 1 presents the optimal solution, the corresponding objective function value, model size and solution time based on the maximum number of possible screens, $|\boldsymbol{Z}|$. As the value of $|\boldsymbol{Z}|$ increases, the ages of screening expand to later years, as the largest gain in life years can be attributed to the individuals who develop CRC early on in life. This trend can be seen through the expected QALY gained, in which the incremental gain decreases as the value of $|\boldsymbol{Z}|$ increases. As can be seen from Table 1, the number of constraints and variables increases linearly with the increase in the maximum number of screens, which is expected. The solution time grows exponentially with the increase in the maximum number of screens.

Table 1 TSSP model results for an increasing number of total screening tests in a lifetime

$\|\mathbf{Z}\|$	Age(s) to screen	E(QALYG)	Variables	Constraints	Solution time (s)
1	48	0.1438	292,781	713,902	4.09
2	44,72	0.2384	488,362	1,290,284	15.20
3	44,72,91	0.2386	683,944	1,866,666	52.89
4	44,72,91	0.2386	879,524	2,443,048	111.45
5	44,72,91	0.2386	1,075,105	3,019,430	251.77

Given the 100 scenarios, we observe diminishing returns in the benefits of allowing additional screenings. There is a 66 % increase in the expected QALY gained when the maximum number of screens, $|\boldsymbol{Z}|$, is increased from one to two. However, when increasing the maximum number of screens from two to three there is a less than 0.1 % increase in QALY gained, with no gain for increasing the maximum number of allowable screens any further. With a single screening, the optimum age is 48. However, the age for the first screening is lower for more than one screening. With the ability to screen more times within a life, the optimal strategy can allow for an early screening to maximize the life gain for individuals that develop cancer early on in their life. With the inclusion of a third screening, the first two ages for screening remain the same for the case of two screens. This behavior explains the small increase in the expected QALY gained, allowing for the prevention of the cases of CRC for the older population, which only provides a marginal benefit from a quality of life standpoint.

4. Conclusions and future recommendations

This paper presented a TSSP model to determine the optimal screening strategy for colorectal cancer within a population. The uncertainty in the TSSP is the progression of CRC. The model was solved for a range of the maximum number of screens within an individual's lifetime. As the number of maximum screens increased, the model size only

had a linear increase while the solution time encountered an exponential growth. The optimum solutions for each number of maximum allotted screens showed diminishing returns with the increase in the total number of maximum screens. This behaviour is expected to be seen, as for the majority of the population, who never develop colorectal cancer, screening is a burden on life rather than providing a benefit. Additionally, as more were allowed, screens late in life were recommended, though the gain in quality of life was minimal.

In the formulation of the model, many simplifying assumptions have been made which will lead to the determined screening strategies to not translate well to clinical settings. As future work, the model will rectify the assumptions of perfect compliance and perfect test accuracy through the incorporation of uncertainty for both screening test adherence and test accuracy. The result of a test will become uncertain and depend on the health state of the individual at the time of screening, the test type chosen, and the individual themselves, and the uncertainty for test adherence will depend both on the individual and the test type chosen.

References

Bibbins-Domingo, K., Grossman, D.C., Curry, S.J., Davidson, K.W., Epling, J.W., Garc\'\ia, F.A.R., Gillman, M.W., Harper, D.M., Kemper, A.R., Krist, A.H., others, 2016. Screening for colorectal cancer: US Preventive Services Task Force recommendation statement. Jama 315, 2564–2575.

Haug, U., Knudsen, A.B., Lansdorp-vogelaar, I., Kuntz, K.M., Baden-wuerttemberg, C.R., Cancer, G., Hospital, M.G., 2016. Development of new non-invasive tests for colorectal cancer screening: The relevance of information on adenoma detection 136, 2864–2874. https://doi.org/10.1002/ijc.29343.Development

Issa, I.A., Noureddine, M., 2017. Colorectal cancer screening/: An updated review of the available options 23, 5086–5096. https://doi.org/10.3748/wjg.v23.i28.5086

Knudsen, A.B., Zauber, A.G., Rutter, C.M., Naber, S.K., Doria-Rose, V.P., Pabiniak, C., Johanson, C., Fischer, S.E., Lansdorp-Vogelaar, I., Kuntz, K.M., 2016. Estimation of Benefits, Burden, and Harms of Colorectal Cancer Screening Strategies: Modeling Study for the US Preventive Services Task Force. JAMA 315, 2595–2609. https://doi.org/10.1001/jama.2016.6828

Loeve, F., Boer, R., Zauber, A.G., Van Ballegooijen, M., Van Oortmarssen, G.J., Winawer, S.J., Habbema, J.D.F., 2004. NATIONAL POLYP STUDY DATA/: EVIDENCE FOR REGRESSION OF, International Journal of Cancer. https://doi.org/10.1002/ijc.20277

Mariotto, A.B., Robin Yabroff, K., Shao, Y., Feuer, E.J., Brown, M.L., 2011. Projections of the cost of cancer care in the United States: 2010-2020. J. Natl. Cancer Inst. 103, 117–128. https://doi.org/10.1093/jnci/djq495

National Cancer Institute, 2019. Cancer Intervention and Surveillance Modeling Network (CISNET) [WWW Document]. URL https://cisnet.cancer.gov/ (accessed 2.27.19).

Orcutt, G.H., 1957. A new type of socio-economic system. Rev. Econ. Stat. 116–123.

Rutter, C.M., Savarino, J.E., 2010. An evidence-based microsimulation model for colorectal cancer: Validation and application. Cancer Epidemiol. Biomarkers Prev. 19, 1992–2002. https://doi.org/10.1158/1055-9965.EPI-09-0954

Soetikno, R.M., Kaltenbach, T., Rouse, R. V, Park, W., Maheshwari, A., Sato, T., Matsui, S., Friedland, S., 2008. Prevalence of Nonpolypoid (Flat and Depressed) Colorectal Neoplasms in Asymptomatic and Symptomatic Adults. JAMA 299, 1027–1035. https://doi.org/10.1001/jama.299.9.1027

World Heath Organization, 2019. Cancer [WWW Document]. URL https://www.who.int/news-room/fact-sheets/detail/cancer (accessed 2.27.19)

Sauro Pierucci, Flavio Manenti, Giulia Bozzano, Davide Manca (Eds.)
Proceedings of the 30th European Symposium on Computer Aided Process Engineering (ESCAPE30), May 24-27, 2020, Milano, Italy.
http://dx.doi.org/10.1016/B978-0-12-823377-1.50116-6

Beyond OPOSPM: A Corrected Maximum Entropy Weibull Distribution for Solving Population Balances

Menwer Attarakih[a], Hans-Joerg Bart[b]

[a]*The University of Jordan, School of Engineering, Department of Chemical Engineering, 11942 Amman, Jordan*
[b]*Chair of Separation Sciences and Technology, The University of Kaiserslautern, 67653 Kaiserslautern, Germany*
m.attarakih@ju.edu.jo

Abstract

The Population Balance Equation is a transport equation which accommodates the evolution of particle size distribution due to convection, nucleation, growth, breakage and coagulation in space-time with no general analytical solution. As a reduced model, OPOSPM is a two-moment model for solving this equation and finds its way in modelling real chemical engineering equipment ranging from pilot extraction columns to annular centrifugal extractors with no fundamental principle to predict the full-size distribution. To overcome this problem, we decoded the underlying distribution that is consistent with the two moments of OPOSPM by maximizing the Shannon entropy. The analytical form of this distribution is found to be a Weibull distribution. This distribution is evolved by the two moments of OPOSPM which may move faster or slower than the exact solution. To correct the prior Weibull distribution, we minimized the relative entropy as represented by the Kullback-Leibler divergence (KLD) with Weibull distribution as the most uncommitted prior probability distribution. The posterior distribution, viewed as a correction to the prior Weibull distribution, is found by expanding the minimum KLD solution using a set of orthogonal Legendre polynomials. This sequence of continuous approximations is found to converge exponentially to the exact solution in the sense of RMSE, KLD and mean properties.

Keywords: OPOSPM, Maximum Entropy, Kullback-Leibler Divergence, Weibull.

1. Introduction

Physical and engineering sciences which are discrete either at the micro or macroscopic levels are of great theoretical and practical applications. The evolution of these systems is governed by a Boltzmann-like equation which is coined as the population balance equation (Ramkrishna and Singh, 2014). The PBE is known to admit analytical solution only for a few cases with restricted forms of interaction kernels. As a special case of the discrete sectional quadrature method of moments (SQMOM) (Attarakih et al., 2009), the reduced two-equation model OPOSPM (One Primary and One Secondary Particle Method) for solving the PBE finds its way in modelling real chemical engineering equipment ranging from pilot extraction columns to annular centrifugal extractors used to recover spent nuclear fuels and online monitoring and analysis of the multiphase flow behaviour in industrial and chemical engineering equipment (Wardle, 2013, Mickler et al., 2014, Attarakih et al., 2019, Schaefer et al., 2019). In spite of this, OPOSPM like other moment methods, fails to predict the full-size distribution which is vital for online

control purposes (Mickler et al., 2014) and to evaluate the particle fluxes at zero particle size in cases such as droplet evaporation. To overcome this problem, we used the Shannon maximum entropy method to decoded the underlying distribution, which is consistent with the two moments of OPOSPM, namely the total number and volume concentrations of the particulate system. The analytical form of this distribution is found to be the well-known Weibull distribution. Generally speaking, this distribution needs further corrections for complicated shapes of the evolving number concentration function in space and time. To accomplish this, the KLD is minimized to extract the OPOSPM corrected functional.

2. Solution of the PBE using the corrected Weibull distribution method

In one dimensional particle property space the PBE which takes into account particle growth (rate G), breakage (frequency Γ) and coagulation frequency (ω) is written as:

$$\frac{\partial f(x,\mathbf{r},t)}{\partial t}+\nabla\cdot(\langle u\rangle f(x,\mathbf{r},t))+\frac{\partial(G(x,S)f(x,\mathbf{r},t))}{\partial x}=R\{f\} \tag{1}$$

$$\begin{aligned} R\{f\} &= -\Gamma f(x,\mathbf{r},t)+\int_x^\infty \upsilon(x')\Gamma(x',S)\beta(x,x')f(x',\mathbf{r},t)dx' \\ &- f(x,\mathbf{r},t)\int_0^\infty \omega(x,y)f(y,\mathbf{r},t)dy+\frac{1}{2}\int_0^\infty \omega(x,y)f(y,\mathbf{r},t)f(x-y,\mathbf{r},t)dy \end{aligned} \tag{2}$$

where $f(x,\mathbf{r},t)$ is the number density concentration as function of particle size (x), physical space vector ($\mathbf{r}$), time (t) and $\langle u\rangle$ is the mean particle velocity vector in physical space which is function of particle size and other continuous environment variables S. During growth the particles undergo relatively slow process relative to the instantaneous breakage with daughter particle distribution $\beta(x,x')$ and mean particle number $\upsilon(x')$, while the binary coagulation frequency is $\omega(x,y,S)$ between particle of sizes x and y.

2.1. OPOSPM: A reduced population balance model

The OPOSPM transport model consists of two equations one for the dispersed particulate phase volume concentration (α) and the total number concentration (N). The transport equation for (α) is derived from Eqs(1) and (2) by mathematically representing the number density function by a single Dirac delta function centered at particle volume $v(d_{30})$: $f=N\delta(x-v(d_{30}))$, and by multiplying Eqs.(1) and (2) by x and integrating both sides with respect to x from 0 to ∞ one gets (Attarakih et al., 2013):

$$\frac{\partial\alpha}{\partial t}+\nabla\cdot(\langle u\rangle\alpha)=G(d_{30},S)N \tag{3}$$

On the other hand, the number concentration transport equation is derived by setting: $f=N\delta(x-v(d_{30}))$ and integrating both sides of Eqs.(5) and (6) with respect to x from 0 to ∞ to get:

$$\frac{\partial N}{\partial t}+\nabla\cdot(\langle u\rangle N)=(\upsilon(d_{30})-1)\Gamma(d_{30},S)N-\frac{1}{2}\omega(d_{30},d_{30},S)N^2 \tag{4}$$

The source term in Eq.(3) takes into account particle growth while that in Eq.(4) accounts for the net total number produced by particle breakage and coagulation. It is clear that the particle breakage is linear in N while particle coagulation is a second-order process in terms of N. Both breakage and coagulation frequencies are functions of d_{30}.

2.2. Derivation of OPOSPM-Weibull distribution using the MaxEnt Method

The OPOSPM loses the particle density concentration because of averaging (f) over the particle property space where the reconstruction of (f) in simple or complex physical space domains is by no means trivial (Gzyl and Tagliani, 2010). In theoretical physics literature, this problem is usually encountered and is known as the moment problem which is faced by the uniqueness of distribution reconstruction. To overcome the uniqueness problem, the maximum entropy method is used to reconstruct a continuous number concentration function constrained by the OPOSPM transported moments (α and N). By maximizing the Shannon entropy, one gets a distribution that is statistically most likely to occur (Gzyl and Tagliani, 2010). The result is a solution of constrained convex NLP which is given by the following optimal functional:

$$f(x,\mathbf{r},t) = p(x)\exp\left(\lambda_0(\mathbf{r},t) + \lambda_3(\mathbf{r},t)x^3\right) \tag{5}$$

In Eq.(5) λ is a vector of Lagrange multipliers that are derived by matching the moments of Eq.(5) to those found from OPOSPM model; namely, α and N. The preexponential $p(x)$ is particle property space coordinate transformation to satisfy left regulatory condition $f(0) = 0$. Based on the derived analytical forms of λ_0 and λ_3, we found that the normalized f^* is a Weibull distribution with shape parameter equals to 3 (due to conservation of mass), scale parameter d_{30} (mean mass particle diameter) and zero location parameter. The particle property space transformation $p(x)$ is found to be $p(x) = x^2$ which is related to the transformation of dimensionless particle volume to dimensionless particle diameter.

2.3. Correction of OPOSPM-Weibull distribution using the KLD

Following the standard nomenclature of entropy information theory, the OPOSPM-Weibull distribution is called prior distribution. To correct this distribution, we minimized the relative entropy as represented by the Kullback-Leibler divergence (KLD) (Tanaka and Toda, 2012) with Weibull distribution as the most uncommitted probability distribution with respect to the unknown information:

$$f(x,\mathbf{r},t) = f^*(x,\mathbf{r},t)\exp\left[\sum_{n=0}^{N-1}\gamma_n(\mathbf{r},t)\varphi_n(\zeta(x))\right] \tag{6}$$

In this equation φ_n is the n^{th} degree Legendre polynomial and $\zeta(x)$ is a linear transformation to convert actual grid points to the domain of $\varphi_n \in (-1,1)$. The expansion coefficients (γ_n) are derived in closed analytical form following the same lines of Attarakih et al. (2019) that allowed us to derive the expansion coefficients in a closed form using the Gauss-Legendre integration quadrature to sample the number concentration function. This pointwise sampling using the orthogonal collocation method results in a set of N-PDEs when applied to the system of equations (1) and (2). In this way we provide a moment consistent solution to the PBE and minimize the lost information contained in the number density function due to the averaging process with respect to particle phase space.

3. Results and discussion

Since particle coagulation is the most complicated source term in the PBE, we concentrated on two coagulation mechanisms; namely, Brownian motion and turbulent diffusion. Therefore, the corrected OPOSPM-Weibull distribution method is validated through comparison to well-known analytical solutions. These solutions depend on the

binary collision coagulation frequency (ω) which may occur through variety of mechanisms which include Brownian motion, turbulent diffusion and laminar shear. The Brownian motion and turbulent diffusion are the two popular mechanisms (Hidy and Brock, 1970) that are frequently used. In Brownian coagulation, ω depends on the volumes of the two colliding particles when one particle is in the continuum regime:

$$\omega(x,x') = \omega_0 (x + x')(x^{-1} + x'^{-1}) \tag{7}$$

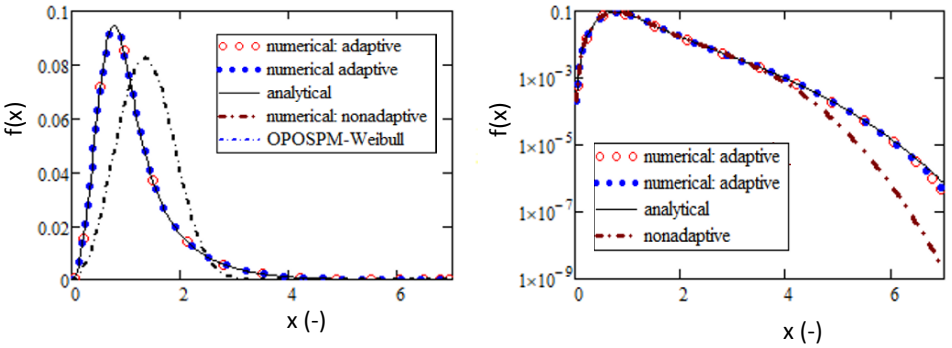

Figure (1): Comparison between the analytical solution (Gelbard and Seinfeld, 1978) and the predicted one by the OPOSPM-Weibull corrected method using 15 Gauss-Legendre nodes for the coagulation equation with Golovin kernel and first-order removal rate in a batch stirred vessels. τ = 2, θ = 0.45 (first order particle removal frequency), a = 0, b = 7 (limits of integration).

As an interesting case, we consider the Brownian coagulation with Knudsen number less than 0.1 where ω is approximately constant. If the initial population of the coagulating particles in a closed homogeneous space follows a Weibull distribution, then the maximized Shannon entropy constrained by OPOSPM moments is a Weibull distribution coinciding exactly with the analytical solution (Gelbard & Seinfeld) and spreading as a function of time with mean size and dispersion proportional to the mean mass particle diameter (d_{30}) and $(d_{30})^2$ respectively. In case of coagulation resulting from turbulent diffusion, the Golovin kernel is used which is proportional to the volumes of the colliding particles. The Weibull distribution for this case, with first order removal rate of particles, is evolved by the exact moments of OPOSPM which is found to move faster than the exact solution as shown in Figure (1) (Left). Therefore, a corrected Weibull distribution is used based on Eq.(6) in which the expansion coefficients were calculated based on the evolution of $f(x_i,t)$,i = 0, 1, ..N-1 as function of time. The index of coagulation for this case is ≈ 90 percent which is defined as $I = 1 - m_0(t)/m_0(0)$. As time ODE solver, the AdamsBDF (Adams method with backward differentiation formulas) was used. It is clear that the corrected OPOSPM-Weibull distribution is artificially delayed by adding more exponential terms to recover the missed information due to using only two particle population moments (α and N) included in $f^*(x,t)$. For this case 15 sampling points, placed at the roots of Legendre polynomials, were found enough to predict the exact solution with root mean square error equals to 1.916×10^{-4}. (refer to Figure (2) (Right). The distribution of the expansion coefficients which appears in Eq.(6) (γ_n, n =1,2 …N-1) was found concentrated in the interval $x \in (0, 2)$ near the sharp part of the exact distribution. On the right hand part of Figure (1), we zoomed in the tail of the distribution where particles of small concentration were underpredicted using 15 nodes of Gauss-Legendre fixed quadrature

to integrate Eq.(2). This error is removed by using an independent adaptive integration quadrature (background grid) as shown in Figure (1) (Right) or by increasing the number of sampling points. The cost of computation in terms of the CPU time needed for integration of Eq.(2) using an adaptive quadrature is approximately 10 times that needed as compared to a nonadaptive Gauss-Legendre quadrature using 15 nodes.

Table (1): Comparison between adaptive and nonadaptive integration of Eq.(2) in the PBE to predict the first six low-order moments of the particle size distribution ($N = 15$ nodes, $\tau = 2$).

	Analytical	Integration	Integration	Relative error	
r	m_e	m_n: adaptive	m_n: nonadaptive	Adaptive	nonadaptive
0	0.108746	0.108938	0.110175	0.00176	0.01314
1	0.125471	0.125666	0.125854	0.00156	0.00305
2	0.196859	0.196924	0.192368	0.00033	0.02281
3	0.406493	0.405846	0.37809	0.00159	0.06988
4	1.051971	1.047919	0.9082	0.00385	0.13667
5	3.236571	3.215298	2.534925	0.00657	0.21679

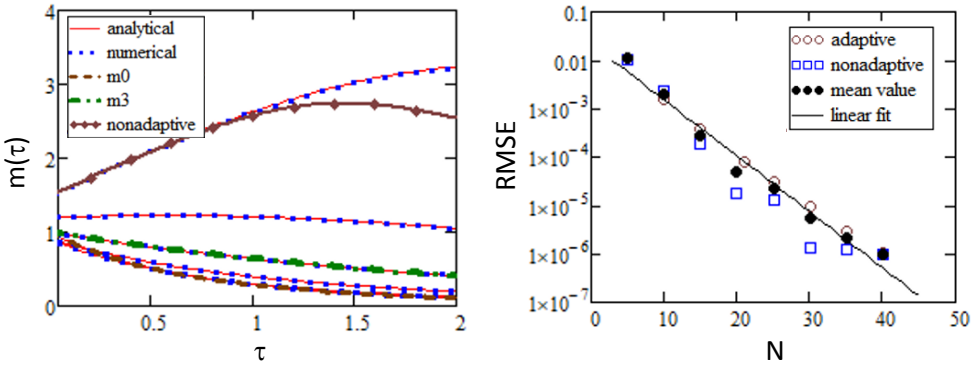

Figure (2): (Left) Comparison between predicted and calculated analytical first six low-order moments for the coagulation equation with first order removal. (Right): Effect of number of Gauss-Legendre nodes on the RMSE as compared with the analytical solution.

Concerning the calculated particle integral properties, and as shown in Figure (2) (Left), the predicted first low-order moments as compared to those calculated from the exact solution (Gelbard and Seinfeld, 1978) are indistinguishable. However, the 6th order moment deviates considerably from the exact one because of the error in the integration of the source term (Eq.(2)) due to using a nonadaptive integration quadrature. This effect of using nonadaptive and adaptive quadrature is shown in clearly in Table (1). This table compares the analytical and numerical moments for the PBE with coagulation source term using $N = 15$ and $\tau = 2$. Again, the error of integration is almost removed when switching to an adaptive integration quadrature with the same number of nodes (15 nodes). The convergence of the corrected OPOSPM-Weibull distribution method, as measured by the RMSE, is shown in Figure (2) (Right) based on fixed and adaptive integration quadrature. The regular convergence of the method based on the adaptive integration scheme of Eq.(2) for the coagulation part is due to fixing the source term integration error. On the other hand, the RMSE as function of number of integration

nodes for the case of a nonadaptive scheme exhibits an irregular convergence behaviour. This is due to the combined effects of truncation error from the corrected OPOSPM-Weibull method and the nonadaptive integration schemes. The speed of convergence follows an exponential decay with a number constant $n_b \approx 4.0$. This means that the RMSE decreases to more than 99 percent of its initial value using $4n_b$ nodes.

4. Summary and Conclusions

It is proved that the MaxEnt distribution constrained by the OPOSPM moments is a Weibull distribution with shape parameter equals to three and scale parameter as d_{30}. This coincides with the exact solution for the case of Brownian coagulation with Knudsen number less than 0.1 and Weibull distribution as an initial condition. For general coagulation mechanism, OPOSPM-Weibull distribution needs to be corrected to account for lost information (shape) due to particle phase space averaging. To correct the prior OPOSPM-Weibull distribution, we minimized the relative entropy as represented by the Kullback-Leibler divergence with OPOSPM-Weibull distribution as the most uncommitted prior probability distribution. The posterior distribution, viewed as a correction to the prior OPOSPM-Weibull distribution, is found by expanding the KLD minimum solution using a set of orthogonal Legendre polynomials. As a test case with known analytical solution, the turbulent particle coagulation with first-order removal of particles is studied. The sequence of continuous approximations to the exact solution is found to converge exponentially in the sense of the RMSE, on the pointwise (in the sense of Kullback-Leibler divergence) and mean (weak convergence) levels. As a main conclusion, the OPOSPM-Weibull distribution as well as its corrected version are proved to be general methods to solve the PBE irrespective of the coagulation mechanism or any other active ones such as particle growth and breakage.

References

M.Attarakih, H.-J. Bart and M. Abu-Khader, 2019, On the solution of the population balance equation: From global to local constrained maximum entropy method. Chem. Eng. Sci., 2019, 115168.

M. Attarakih, M., Abu-Khader and H.-J. Bart, 2013, Modelling and Dynamic Analysis of an RDC Extraction Column using OPOSPM. Chem. Eng. Sci., 91, 180-196.

M. Attarakih, C. Drumm snd H.-J. Bart, 2009, Solution of the population balance equation using the sectional quadrature method of moments(SQMOM). Chem. Eng. Sci., 64, 742--752.

F. Gelbard and J. H. Seinfeld, 1978, Numerical solution of the dynamic equation for particulate systems. J. Comput. Phys., 28, 357-375.

H. Gzyl and A. Tagliani, 2010, Stieltjes moment problem and fractional moments, Applied Mathematics and Computation, 216, 3307–3318.

G. M. Hidy and J. R. Brock, 1970, The Dynamics of Aerocolloidal Systems, Pergamon Press, Oxford, England.

M. Mickler, H. B. Jildeh and H. J. Bart, 2014, Online monitoring, simulation and prediction of multiphase flows. Can. J. Chem. Eng., 92, 307–317.

D. Ramkrishna and M. R. Singh, 2014, Population Balance Modeling: Current Status and Future Prospects, Annu. Rev. Chem. Biomol. Eng., 5, 123-146.

J. Schaefer, M. W. Hlawitschka, M. Attarakih and H.-J. Bart, 2019, Experimental investigation of local bubble properties: Comparison to the sectional quadrature method of moments. AIChE J., e16694.

K. Tanaka and A. A. Toda, 2012, Discrete approximations of continuous distributions by maximum entropy. Economics Letters, 118, 445-450.

K. E. Wardle and H. G. Weller, 2013, Hybrid multiphase CFD Solver for coupled dispersed/segregated flows in liquid-liquid extraction. Int. J. Chem. Eng., 2013, 1-14.

Sauro Pierucci, Flavio Manenti, Giulia Bozzano, Davide Manca (Eds.)
Proceedings of the 30th European Symposium on Computer Aided Process Engineering (ESCAPE30), May 24-27, 2020, Milano, Italy.
http://dx.doi.org/10.1016/B978-0-12-823377-1.50117-8

The Effect of Age on the Delivery of Intravenous Anesthesia: a Physiologically-based Modeling Approach to Pediatric Patients

Daniel Salis, Adriana Savoca, Davide Manca

PSE-Lab, Process Systems Engineering Laboratory
Dipartimento di Chimica, Materiali e Ingegneria Chimica "Giulio Natta"
Politecnico di Milano
Piazza Leonardo da Vinci 32, 20133 Milano, Italy

Abstract

Selection of optimal dosing in anesthesia is a complex task because of the inter-individual variability in patients' response. In this context, computer-aided modelling can be a powerful tool to assess the impact of anatomical and physiological differences among patients and simulate different administration protocols. *In silico* simulations via pharmacokinetic (PK) and pharmacodynamic (PD) models allow investigating the concentration profiles and the resulting effects of drugs in patients. A physiologically-based (PB) approach to pharmacokinetic modeling is thus required to account for the influence of both anatomical and physiological features. We focus on the administration of propofol to patients from 1 to 19 years old and propose new correlations for the estimation of volumes of organs and tissues in these patients. The adapted PBPK model is then combined with a specific PD model, to predict the hypnotic effects of propofol in pediatric patients. The proposed model can thus be used for simulation, training, and control applications.

Keywords: physiologically-based pharmacokinetic model; anesthesia; propofol; bispectral index; pharmacodynamic model.

1. Introduction

From birth to adulthood, several anatomical, physiological, and biochemical changes occur in the human body. Most of them are simply related to its natural growth with increasing age while others to the progressive development and modification of the biochemical environment. These continuous changes affect drugs transport mechanisms in the body and thus, their pharmacodynamic effects on patients. For this reason, pediatric patients often require dosing modifications compared to adults. The changes that the body undergoes during child development make the physiological modeling of pediatric patients' rather challenging. However, a physiologically-based (PB) approach allows suitably describing the relation between the dose and the concentration of drugs, *i.e.* the pharmacokinetic (PK) profile, within the body of this patients' category. The PBPK model can then be combined to a pharmacodynamic (PD) model to simulate and predict the drug effect. This paper focuses on propofol, an intravenous (IV) anesthetic, whose administration is rather challenging because of its narrow therapeutic window. Although some general guidelines on propofol dosing exist, anesthesiologists rely heavily on their experience and habits to select the dose for induction (*i.e.* loss of consciousness produced with general anesthesia) in pediatric patients. The scientific literature proposes several

basic three-compartment PK models for those patients. However, these models are neither anatomically- nor physiologically-based and, since they were identified from different groups of patients characterized by variable ages and body features, they show remarkable variability in predictions. This can easily generate confusion and ambiguity among clinicians. In this context, the introduction of a PBPK-PD model, specifically developed for pediatric patients in the 1-19 y age range, can help anesthesiologists. Indeed, computer-aided modeling and simulation is a suitable tool to identify ranges of optimal dosing and individualize clinical treatments, with the goal of making the whole procedure safer. In this work, we adapt a PBPK model previously developed for adult patients and combine it with a suitable PD model to predict the impact of age on propofol hypnotic effects.

2. Methods

2.1. Adaptation of the model to the anatomical differences of pediatric patients

The easiest and earliest change of the body with age that one can observe is related to its dimensions. Indeed, while growing up, a child increases the dimensions (weight) of their tissues, *e.g.*, bones, muscles, fat, and skin, but also of some organs *e.g.*, brain, heart, and liver. Other relevant changes are related to physiological aspects (*e.g.*, pH, immature enzymes, and membranes permeability) that influence the absorption, distribution, metabolism, and elimination of drugs in the body. To account for the differences among pediatric and adult patients, some parameters of the reference PBPK model of this work (Abbiati et al., 2016), *i.e.* the volume of organs and tissues and blood flowrates, were adapted. Specific correlations were identified with experimental data of cardiac output, blood volume, and organs and tissues weights of pediatric patients via either linear or nonlinear regressions. Gender-specific correlations were derived whenever gender-specific data were available.

To describe the cardiac output, we tested a set of correlations depending on total body weight (TBW) and age. Similarly, we tested the functional dependency of blood volume from age, TBW, and body surface area (BSA). The weights of organs and tissues were correlated either linearly or exponentially with age. An exception to this methodology was made for the adipose tissue weight. In this case, in agreement with the data trend, the age range was divided into subgroups, which allowed evaluating specific correlations.

2.2. Physiologically-based pharmacokinetic-pharmacodynamic modelling

The reference PBPK model presented by Abbiati et al. (2016) for IV drugs consists of five interconnected compartments (*i.e.* Plasma (P), Liver (L), Poorly perfused Tissues (PT), Highly perfused Organs (HO), and Gastro-Intestinal Circulatory System (GICS)) and was adapted to propofol by considering both hepatic (H) and extra-hepatic (K, kidneys and T, tissues) routes of metabolism and elimination. The dynamic profile of the drug concentration C_i within each compartment can be obtained by solving a system of five ordinary differential equations (ODEs) (Eqs. (1-5)) that consist of the drug material balances over those compartments, complemented by suitable initial conditions. In our model, compartment volumes V_i were estimated from the weights of organs and tissues as discussed in Section 2.1. Similarly, blood flowrates Q_{HA} (HA, hepatic artery), Q_{HV} (HV, hepatic vein), Q_{PV} (PV, portal vein), and Q_K (K, kidneys) were calculated as a fraction of cardiac output. Conversely, the fraction R of drug bound to plasma proteins was kept unchanged compared to adult patients (Brines et al., 1941). The remaining 7

parameters, *i.e.* drug transfer coefficients k and hepatic and renal efficiencies to calculate hepatic and renal clearances CL were identified by means of a nonlinear regression respect to experimental PK data of pediatric patients from Kataria et al. (1994) (age range 3-11 y). The prediction of the PBPK model was then validated with additional experimental PK data from the same study.

$$\frac{dC_P(t)}{dt} = -C_P(t)\left(k_{P-PT}(1-R) + k_{P-HO}(1-R) + \frac{Q_{HA}}{V_P} + \frac{Q_{PV}}{V_P} \right) + C_P(t)k_{PT-P}\frac{V_{PT}}{V_P} + C_L(t)\frac{Q_{HV}}{V_P} +$$

$$+C_{HO}(t)k_{HO-P}\frac{V_{HO}}{V_P} - C_P(t)(1-R)k_{E,P} - C_P(t)\frac{CL_K}{V_P} + \frac{IV(t)}{V_P} \quad (1)$$

$$\frac{dC_L(t)}{dt} = -C_L(t)\left(\frac{Q_{HV}}{V_L} + \frac{CL_H}{V_L} \right) + C_P(t)\frac{Q_{HA}}{V_L} + C_{GICS}(t)\frac{Q_{PV}}{V_L} \quad (2)$$

$$\frac{dC_{PT}(t)}{dt} = -C_{PT}(t)\left(k_{PT-P} + k_{E,T} \right) + C_P(t)k_{P-PT}(1-R)\frac{V_P}{V_{PT}} \quad (3)$$

$$\frac{dC_{HO}(t)}{dt} = -C_{HO}(t)k_{HO-P} + C_P(t)k_{P-HO}(1-R)\frac{V_P}{V_{HO}} \quad (4)$$

$$\frac{dC_{GICS}(t)}{dt} = -C_{GICS}(t)\frac{Q_{PV}}{V_{GICS}} + C_P(t)\frac{Q_{PV}}{V_{GICS}} \quad (5)$$

In order to model the pharmacological effect of propofol, the PBPK model was linked to a PD model by introducing an effect-site compartment. This extra compartment represents the propofol site of action, which embodies specific receptors located in the brain. Eq. (6) models the effect-site compartment by means of a first-order transport mechanism, governed by a kinetic constant k_{e0} (Sheiner et al., 1979). This approach allowed accounting for the delay between the time course of the pharmacological effect and the dynamics of plasma concentration. We adopted the modified sigmoid E_{max} equation (Eq. (7)) as PD model, in line with Rigouzzo et al. (2010) formulation. The drug PD effect consists in the bispectral index (BIS), a statistically-based empirically-derived parameter, which is obtained from the re-elaboration of electroencephalographic tracing (Kaul and Barthi, 2002). BIS baseline (*i.e.* E_0 in Eq. (7)) is usually around 95-100, while recommended BIS range for depth of anesthesia is 40-60 (Singh, 1999) also in pediatric patients.

$$\frac{dC_e}{dt} = k_{e0}C_P - k_{e0}C_e \quad (6)$$

$$E = E_0 - (E_0 - E_{\max})\frac{C_e^{\gamma}}{(EC_{50}^{\gamma} + C_e^{\gamma})} \quad (7)$$

Parameter E_{max} in Eq. (7) was fixed at 0, as this is the minimum value that BIS can reach in clinical practice. The PD parameters ɣ (*aka* Hill parameter) and EC_{50} (concentration corresponding to 50% of E_{max}) were identified by means of a nonlinear regression procedure with BIS experimental data from Coppens et al. (2011). Additional data from the same study were used for validation of the combined PBPK-PD model.

3. Results and Discussion

3.1. Estimation of the individualized parameters

For the sake of space, we only show 4 representative correlations derived for the pediatric population. The rest of the proposed correlations are available in Salis (2019). Figure 1 reports the trends of cardiac output, blood volume, and brain and kidneys weights as a

function of age, with the aim of showing the effect of growth stage on the anatomy of pediatric patients. While in some cases gender differences manifest from young age (see C panel), in other cases they are more evident after puberty (see A, B, D panels). When the trend of the data showed a constant increase across the age range, a linear correlation was implemented (*e.g.*, D panel). Differently, when adult values were reached around 11-12 y (*e.g.*, C panel) an exponential correlation was the preferred one. With respect to cardiac output, the correlation with age rather than TBW improved data fitting. Interestingly, no gender-differences were evident for patients younger than 7 y old. A correlation depending on BSA provided the highest R^2 value (0.97) to estimate the blood volume.

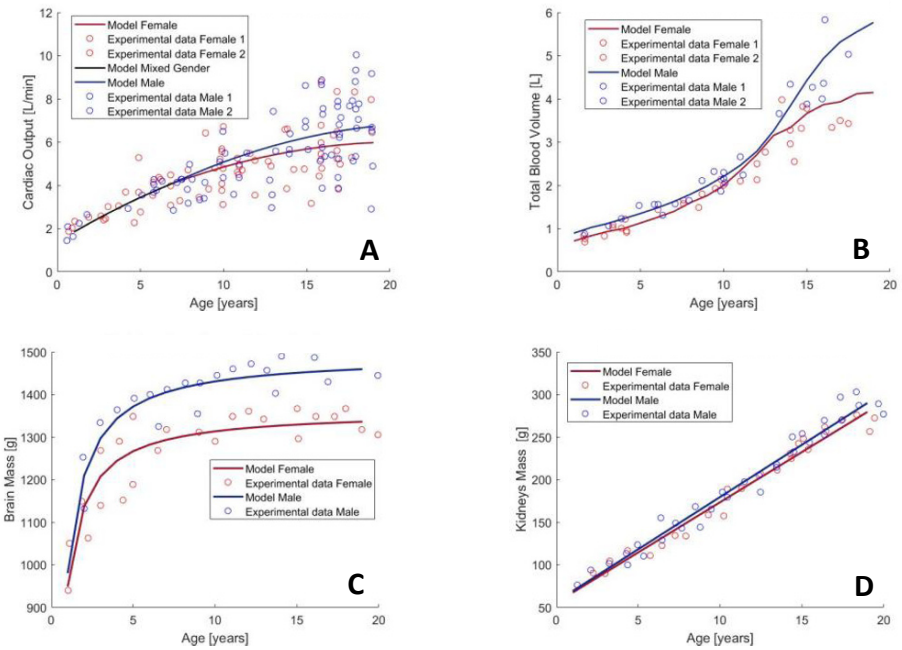

Figure 1 – Estimated (continuous line) vs measured (circles) values of cardiac output (A), blood volume (B), brain mass (C), and kidneys mass (D) of pediatric patients. Data from Valentin (2002), Brines et al., (1941), and Williams (1994). Blue refers to males, red to females.

3.2. Validation of the PBPK-PD model

Figure 2 (top panel) compares the predicted and measured concentration values of 3 representative patients studied by Kataria et al. (1994). The prediction capability of the model was acceptable in most patients, independently of the administration protocols. Despite the lack of experimental data on the very sharp peaks due to the quick re-distribution of propofol after the initial bolus, the simulated profile is consistent with the administered dose. The prediction capability of the model is quantified by evaluating the median absolute prediction error (MDAPE) between the model and the experimental data. The MDAPE for the three patients presented in Figure 2 (top panel) are respectively 16.78, 19.76, and 8.25%. Figure 2 (bottom panel) shows the predicted and observed BIS profiles for three patients (studied by Coppens et al., 2011). The combined PBPK-PD model shows a rather satisfactory prediction capability. It is worth mentioning that intra-operative BIS values are often affected by drug-independent disturbances that produce

model deviations (*e.g.*, see the observed BIS increase in A panel after approximately 2 min). The model prediction capability is additionally assessed by evaluating MDAPE, which for the three patients is 17.94, 24.0, and 20.32% respectively.

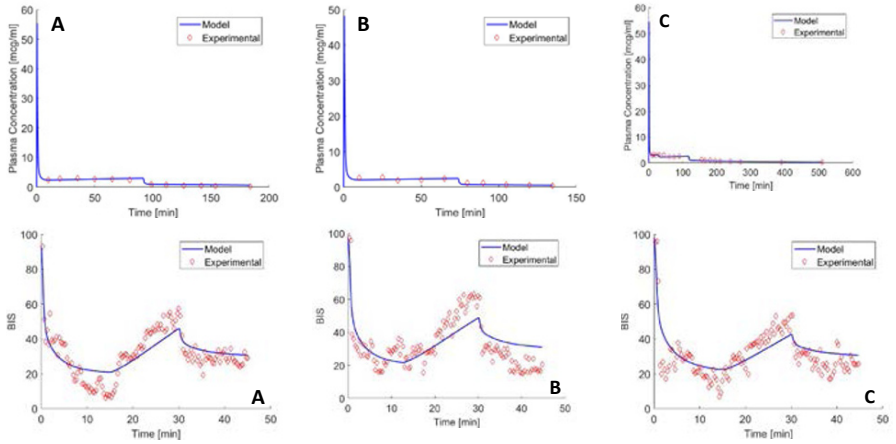

Figure 2 – (Top panel) Validation of the PBPK model with PK data of three patients administered with single (A and B) and double (C) propofol infusions. (Bottom panel) Validation of the PD response in terms of BIS simulated by the PBPK-PD model.

Figure 3 shows the comparison between the predicted concentration via PBPK and the classical three-compartment PK model of Kataria against data of two pediatric patients from a different study (Marsh et al., 1991). It is worth noticing that the early concentration dynamics is not well-described by the classical three-compartment model, as it does not display any concentration peaks.

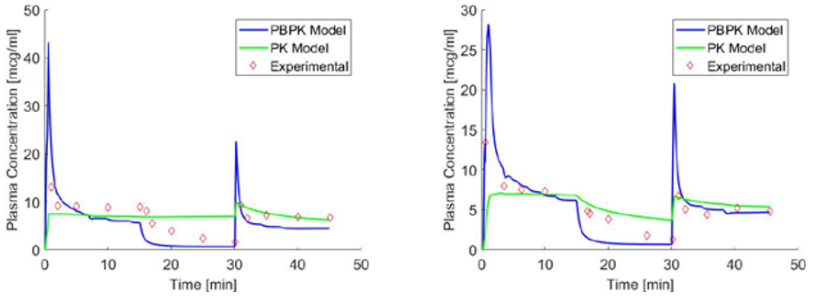

Figure 3 – Comparison of PBPK (blue continuous line) and classical PK (green continuous line) simulations with measured concentrations (red diamonds) of two pediatric patients from Marsh et al. (1991). As a result, in case of model-predictive control applications, the PBPK model can provide a more conservative control action. In addition, close plasma peaks prediction is particularly important to prevent adverse effects. In this dataset, the PBPK model overestimates the drug elimination, thus the metabolism and elimination description should be improved in future work.

4. Conclusions

The proposed PBPK model showed an acceptable predictive capability, with superior performance than the commonly used Kataria's PK model. We deem that the anatomical and physiological foundations are an important element to enhance the understanding and adoption by clinicians. The combined PBPK-PD model showed a satisfactory level of prediction of BIS data, with poor forecasts often caused by intra-operative disturbances. *In silico* simulations can enhance the understanding of patients' variability in the response to anesthetic drugs and improve clinical practice. Control applications of the developed PBPK-PD model are even more interesting. Specifically, the model can be implemented in target-controlled infusion (TCI) pumps (*i.e.* only the PBPK component) or closed-loop model predictive controllers of anesthesia (*i.e.* the full PBPK-PD model). In the first case, a target concentration is assigned by the anesthetist to the TCI device, and the model-based algorithm calculates the corresponding infusion rate. In the second case, a BIS setpoint is implemented and the model-predictive controller optimizes the propofol administration basing on actual BIS and the optimal predicted trajectory of patient's BIS, achieved by smooth and safe changes of propofol infusion rates, while maintaining the desired target value against external disturbances.

References

Abbiati RA, Lamberti G, Grassi M, Trotta F, Manca D, 2016, Definition and validation of a patient-individualized physiologically-based pharmacokinetic model. Comput. Chem .Eng. 84, 394-408.

Brines JK, Gibson JG, Kunkel P, 1941, The blood volume in normal infants and children. The J. Pediatrics 18, 447-57.

Coppens MJ, Eleveld DJ, Proost JH, et al., 2011, An evaluation of using population pharmacokinetic models to estimate pharmacodynamic parameters for propofol and bispectral index in children. JASA 115, 83-93.

Kataria B, Sudha A, Nicodemus HF, et al., 1994, The Pharmacokinetics of Propofol in Children Using Three Different Data Analysis Approaches. JASA 80 (1), 104-22.

Kaul H, Bharti N, 2002, Monitoring Depth of Anaesthesia. Indian J.Anaesth. 46, 323-32.

Marsh B, White M, Morton N, Kenny GNC, 1991, Pharmacokinetic model driven infusion of propofol in children. Br. J. Anaesth. 67, 41-48.

Rigouzzo A, Servin F, Constant I, 2010, Pharmacokinetic-Pharmacodynamic Modeling of Propofol in Children. JASA 113(2), 343-52.

Salis D, 2019,. Physiologically based pharmacokinetic-pharmacodynamic modelling for anesthesia in children (Master's thesis, Politecnico di Milano, Milan, Italy).

Sheiner LB, Stanski DR, Vozeh S, et al., 2019, Simultaneous modeling of pharmacokinetics and pharmacodynamics: Application to d-tubocurarine. Clin. Pharma. Therapeutics 25(3), 358-71.

Singh H, 1999, Bispectral index (BIS) monitoring during propofol-induced sedation and anaesthesia. Eur. J. Anaesthesiol. 16(1), 31-6.

Valentin J, 2002, Basic anatomical and physiological data for use in radiological protection: reference values: ICRP Publication 89. Annals of the ICRP, 32, 1-277.

Williams LR, 1994, Reference values for total blood volume and cardiac output in humans. In: Oak Ridge National Lab., TN (United States).

Sauro Pierucci, Flavio Manenti, Giulia Bozzano, Davide Manca (Eds.)
Proceedings of the 30th European Symposium on Computer Aided Process Engineering (ESCAPE30), May 24-27, 2020, Milano, Italy.
http://dx.doi.org/10.1016/B978-0-12-823377-1.50118-X

Physiologically-Based Pharmacokinetic and Pharmacodynamic Modeling of Unfractionated Heparin to Predict Activated Clotting Time

Filippo Regorda[a], Emiliano Vigoni[a], Giuseppe Pesenti[a], Marina Pieri[b], Alessandro Belletti[b], Davide Manca[a,*]
[a]*PSE-Lab, Process Systems Engineering Laboratory, Dipartimento di Chimica, Materiali e Ingegneria Chimica "Giulio Natta", Politecnico di Milano, Piazza Leonardo da Vinci 32, 20133 Milano, Italy*
[b]*Department of Anesthesia and Intensive Care, IRCCS San Raffaele Scientific Institute, Via Olgettina 60, 20132 Milano, Italy*
davide.manca@polimi.it

Abstract

Monitoring the coagulation time and regulating the administration of unfractionated heparin (UFH) during cardiopulmonary bypass (CPB) are challenging activities. The manuscript focuses on the development of a mathematical model to predict the activated clotting time (ACT) during CPB following an intravenous administration of heparin.
The overall mathematical tool features a physiologically-based pharmacokinetic (PBPK) model and a pharmacodynamic (PD) model. The PBPK model describes the human circulatory system and employs correlations from the literature to estimate its physiological parameters from individual characteristics (*i.e.* age, sex, race, weight, height, serum creatinine, and hematocrit) to yield a prediction of heparin plasma concentration as a function of time. The PD model predicts the ACT as a function of heparin concentration thanks to several differential equations that describe the coagulation cascade. The combined PBPK/PD model produces, for each patient, an individualized prediction of the resulting ACT dynamics, using either a population or an individualized approach. The model can be used to help monitoring the ACT trend during CPB and to optimize heparin administration in order to reach and maintain the therapeutic goal of 480 s.

Keywords: Heparin, ACT, Pharmacokinetics, Pharmacodynamics, Mathematical model.

1. Introduction

Heparin is the most widely used anticoagulant drug. Unfractionated heparin is administered intravenously for the prevention and treatment of thrombosis, especially in cardiac surgery. During this kind of operations, plasma concentration of heparin and the consequent effect on patient's body are difficult to control. The activated clotting time (ACT) is a widely used indicator capable of describing this anticoagulant effect during cardiopulmonary bypass (CPB) and involves the intrinsic coagulation cascade. It can be obtained through a quick bedside test that measures the time needed for the blood to clot after the addition of an activator. The established ACT clinical target during cardiac surgeries is 480 s. The present work considers as a case study the intravenous administration of UFH during CPB operations. During this type of surgical interventions, patients are connected to an external heart-lung machine, whose goal is to reproduce the vitals of heart and lungs. UFH is administered to patients to prevent the activation of the

hemostatic process within the artificial circuit. Despite its widespread use, the pharmacokinetic and pharmacodynamic properties of heparin appear poorly understood. Consistently, only few models of heparin pharmacology are available in the literature. Most of these focus exclusively on the pharmacokinetics (PK), *e.g.*, (Jia *et al.*, 2015), or on the pharmacodynamics (Kogan *et al.*, 2001; Zhu, 2007). Furthermore, Delavenne (2017) developed a population-based PK/PD model, which adjusts the predicted ACT according to the measured anti-Xa activity, *i.e.* one of the enzymes of the coagulation cascade. However, these PK models are not physiologically-based and do not account for patients' characteristics such as the degree of renal function, whereas the PD models, with the exception of the one by Kogan *et al.* and Zhu, do not describe the complete coagulation cascade. We present a combined mathematical model featuring an individualized PBPK model and a PD one. The overall model is able to estimate heparin concentration in the human body to predict the ACT during CPB.

2. Methods

The experimental data used to validate the model were collected from San Raffaele hospital in Milan, after Ethical Committee approval and with patients' written consent. The data collection included sex (17 males and 6 females), age (36-77 y), height (160-190 cm), weight (46-115 kg), serum creatinine (0.63-1.46 mg/dL), hematocrit (31.9-54.9 %), antithrombin (ATIII, 65-109 %) and body surface area (BSA, 1.45-2.43 m^2) of a heterogeneous population of 23 *naïve* patients, *i.e.* without any clinical complications nor any kind of pre-operatory treatment. Furthermore, the data comprised the trend of ACT during CPB. Each patient received an initial bolus of heparin equal to 300 IU/kg. During the operation, they were connected to the extra-corporeal circuit (ECC), which contained a priming volume in the 750-1,600 mL range, containing 3,000-5,000 IU of heparin. Additional boluses in the 1,500-10,000 IU range were administered during the operation to maintain ACT at or above the 480 s target. UFH is a heterogeneous molecule with a wide range of molecular weights (5,000 to 30,000 Da, 20,000 Da on average). We describe heparin through its average molecular weight of 20,000 Da. Since the administered heparin remains confined within the intravascular area, the model takes into account the circulatory system as its distribution volume. Heparin is eliminated from the body through two pathways: (i) a metabolic process due to the aggregation of heparin to receptors of endothelial cells and macrophages, and (ii) an excretion one via renal filtration. The PBPK model features a total of three compartments, (i) RCS stands for the fraction of plasma contained within the kidneys, (ii) CS representing the human circulatory system (Pesenti *et al.*, 2019), and (iii) ECC that accounts for the extra-corporeal circuit.

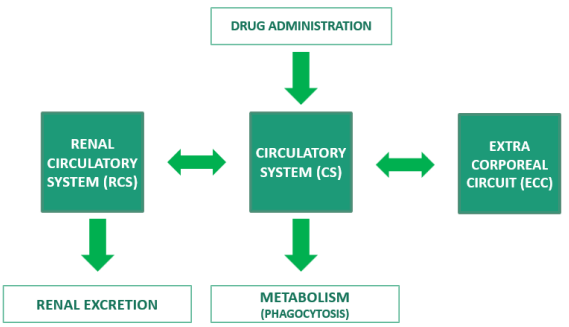

Figure 1 – Compartments of the PBPK model.

The model consists of three ordinary differential equations (ODEs), which describe the material balances of heparin in each compartment.

$$\frac{dC_{CS}}{dt} = \frac{\dot{m}_{bolus}}{V_{CS}} + \frac{(Q_{CS\leftrightarrow RCS}C_{RCS})}{V_{CS}} - \frac{(Q_{CS\leftrightarrow RCS}C_{CS})}{V_{CS}} + \frac{(Q_{CPB}C_{ECC})}{V_{CS}} - \frac{(Q_{CPB}C_{CS})}{V_{CS}} - K_{met}C_{CS} \quad (1)$$

$$\frac{dC_{RCS}}{dt} = \frac{(Q_{CS\leftrightarrow RCS}C_{CS})}{V_{RCS}} - \frac{(Q_{CS\leftrightarrow RCS}C_{RCS})}{V_{RCS}} - \frac{(GFRC_{RCS}(1-R))}{V_{RCS}} \quad (2)$$

$$\frac{dC_{ECC}}{dt} = \frac{(Q_{CPB}C_{CS})}{V_{ECC}} - \frac{(Q_{CPB}C_{ECC})}{V_{ECC}} \quad (3)$$

C_{CS}, C_{RCS}, and C_{ECC} are the concentrations of heparin (IU/mL) in the CS, RCS and ECC compartments. $\dot{m}_{bolus}$ is the flowrate of administered heparin (IU/min), R is the fraction of heparin bound to blood proteins (equal to 0.95), Q_{CPB} is the volumetric flow (mL/min) of the ECC priming volume. $Q_{CS\leftrightarrow RCS}$ and Q_{GFR} are the volumetric flowrates (mL/min) that represent, respectively, the plasma flow that reaches the kidneys and the glomerular filtration rate (GFR). They are estimated as a function of sex, age, serum creatinine, BSA, and hematocrit (Pesenti *et al.*, 2019). V_{CS}, V_{RCS}, and V_{ECC} are the volumes (mL) of plasma in the corresponding compartments. The CS and RCS volumes are evaluated as the 98% and 2% of the total blood volume, which is individualized according to patients' height and weight (Nadler *et al.*, 1962). Finally, the kinetic constant of the phagocytosis reaction rate, K_{met}, is evaluated through a nonlinear regression of PK data extracted from Olsson (1963). The initial concentration of heparin in each compartment is zero. The PD model implements the description of the intrinsic coagulation cascade published by Kogan *et al.* (2001) and Zhu (2007). Their models describe the whole reaction cascade with a Michaelis-Menten kinetics and employ second order kinetics for the inhibitory reactions, without considering the presence of heparin. UFH can reversibly bind to ATIII, which strengthens the coagulation cascade inhibitory activity. This reversible interaction causes an ACT increase. The heparin-antithrombin complex interacts with several coagulation factors. Since factors II_a and X_a are the most important during the hemostatic process, we consider only the interaction between the complex and these factors. Thus, the ODEs system developed by Kogan and Zhu is complemented with three additional reactions, which describe the interactions between heparin-antithrombin and factors II_a and X_a.

$$He + ATIII \rightarrow He\_ATIII \quad (4)$$

$$He\_ATIII + II_a \rightarrow II_a\_ATIII + He \quad (5)$$

$$He\_ATIII + X_a \rightarrow X_a\_ATIII + He \quad (6)$$

Assuming that during the incubation period (60 s) the reactions affecting the activation phase are negligible, the initial concentrations of the model are equal to the initial concentrations (μmol/L) of each factor and inhibitor taken from Kogan *et al.* (2001) and Zhu (2007). Because of the lack of data on the individual factor concentrations (but for ATIII), we assumed these values constant for all the patients. ACT is evaluated as the 30% of the conversion of fibrinogen (factor I_a) plus the incubation time (Eq. 7).

$$ACT = 60 + t|_{\chi=0.3} \quad (7)$$

The kinetic constant related to the interaction between the heparin-ATIII complex and factor II_a, due to the lack of experimental data, is evaluated through a nonlinear regression. In particular, it is evaluated both through an individualized approach, which minimizes the sum of squared errors between experimental values of ACT and the simulated ones of a single patient, and through a population approach that uses 8 patients for the identification procedure and 15 patients for the validation one.

$$\min_{K_5^{ind/pop}} SSE = \min_{K_5^{ind/pop}} \frac{1}{N_p}\sum_{i=1}^{N_p}\left(\frac{1}{N_i^{exp}}\sum_{j=1}^{N_i^{exp}}\left(\frac{ACT_{ij}^{exp}-ACT_{ij}^{sim}}{ACT_{ij}^{exp}}\right)^2\right) \quad (8)$$

N_p is the number of patients, N_i^{exp} is the number of single patients' experimental values of ACT, ACT_{ij}^{exp} and ACT_{ij}^{sim} are, respectively, the experimental and simulated ACT values. The value of the population constant is 5.6 [µmol/L/min], while the individualized one is specific for each patient and covers a range of 2.4-33.5 [µmol/L/min].
The overall PBPK/PD model is completely individualized, since it grounds on the patients' clinical data. If one uses the individualized value of the kinetic constant related to Eq. 5, K_5, for the simulation, the ACT trend is obtained only *a posteriori* since it requires all the available experimental values of ACT during CPB. Vice versa, if one adopts the population value of K_5 for the simulation, it is possible to forecast the ACT trend *a priori*, although at the cost of reducing the prediction's precision. Therefore, we also proposed an adaptive model, which, starting from the population ACT model, can adapt its ACT prediction in real time by receiving as input the individualized experimental ACT measurements of patients undergoing CPB.

3. Results

For sake of space, we are presenting the results of the combined PBPK/PD model for only one patient, while the results of the adaptive algorithm refer to an outlier to show the progressive improvement of adapting the ACT predictions with the individualized on-line measurements during CPB. Figure 2 (panel a) shows the heparin plasma concentration in each compartment. The green line describes the heparin concentration in the circulatory system. Following the administration of the first heparin bolus (at 20 min), which depends on the weight of the patient, a first peak can be observed. The subsequent linear decrease is due to the metabolic and the excretion mechanisms. The most appreciable decrease in heparin concentration occurs when the patient is connected to ECC (at 44 min). Thus, the mixing of the priming volume within the CS and RCS compartments results in a significant dilution of blood, with a consequent decrease of heparin concentration. Finally, we observe again the linear decrease for the reasons previously cited.

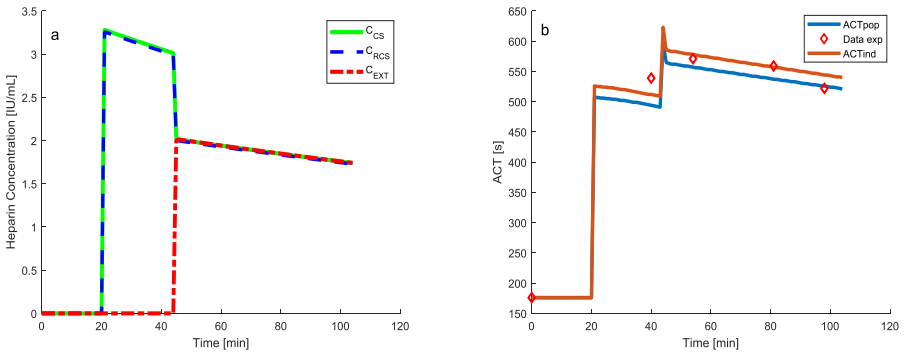

Figure 2 – (a) Heparin plasma concentration dynamics in each compartment. (b) Pharmacodynamic population/individual ACT dynamics during CPB.

The dashed blue line stands for heparin concentration in RCS. It is very close to the green line because the exchanged flow between RCS and CS is very high. Finally, the red line represents the heparin concentration trend in ECC. The initial concentration of heparin in

this compartment is equal to 0 [IU/mL]. Afterwards, with the connection of ECC to the patient's plasma, the ECC heparin concentration increases due to the mixing and then linearly decreases according to the renal and hepatic elimination pathways. Figure 2 (panel b) shows the ACT dynamics adopting the population value of K_5 (blue line) and its individualized value (red line). It is worth observing that the two trends are similar, with SSE values equal to 0.0018 and 0.0008, respectively. Although both of them are completely individualized, since they are based on the patient's clinical data, the difference between the two curves is that the one obtained with the population approach is completely predictive and less precise. Conversely, the one obtained with the individualized approach simulates more precisely the patient's ACT trend, but it calls for the whole set of individual experimental data, which is available only at the end of the CPB procedure.

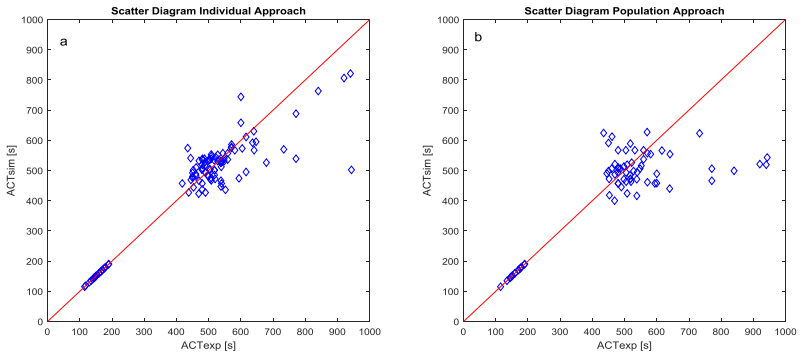

Figure 3 – Parity plots obtained with the (a) individual and (b) approach.

Figure 3 shows the model-simulated vs measured ACT values related to the individualized approach (panel a) and population approach (panel b). It is worth noticing that the individualized approach produces a significant improvement of the correlation between the experimental and simulated values of ACT. This is substantiated by the SSE values that are 0.0101 for the individualized approach and 0.0291 for the population one.

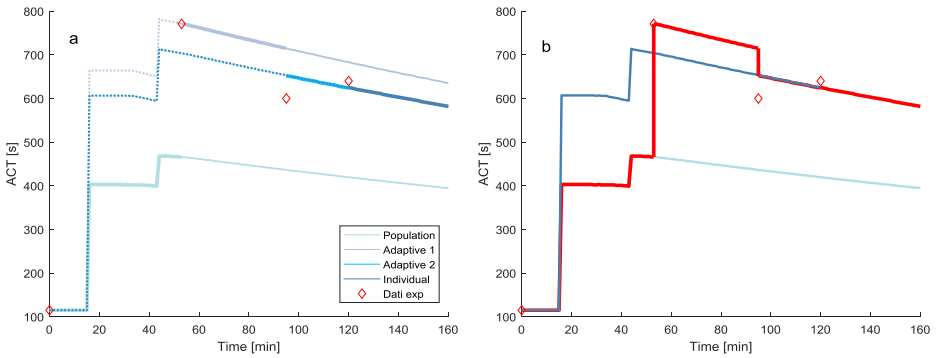

Figure 4 – Adaptive individualized approach to the PBPK-PD modeling.

Figure 4 (panel a) shows the dynamics of the ACT as a function of the different values of the kinetic constant K_5, which are obtained through different regressions carried out each time a new experimental value of ACT becomes available.

At the beginning (at 0 min), the basal value of ACT is known. Thus, we can simulate the *Population* curve using the population value of K_5. When a new experimental value of

ACT is available (at 53 min) we can simulate the ACT trend again taking into account the basal value and the new experimental value, obtaining a new prediction of ACT, *i.e. Adaptive 1* curve. This prediction replaces the former *Population* curve as the best current prediction, as it is based on a more individualized value of K_5, obtained via a nonlinear regression based on the two experimental ACT values. Then, the curve *Adaptive 2* is obtained by using the third experimental ACT value and the two previous measurements to regress the next adaptive value of K_5. Following this methodology, the curve *Individual* is obtained considering all the experimental ACT values available, yielding an individualized simulation of the ACT trend based on an individualized value of K_5. In Figure 4 (panel a), each curve is composed of (i) a continuous thick part, representing the best current prediction of ACT between two ACT measurements, (ii) a thin continuous part, which stands for the fragment of curve which is not considered once a new experimental ACT value is available, and (iii) a dotted part that represents the retrospective reconstruction of the past ACT trend. Despite the predictive uncertainty of each curve, the dynamic application of the model allows predicting the progress of the operation through the graphic display of the probable ACT trend. Figure 4 (panel b) shows the detail of the marching adaptive procedure of the ACT trend (red line), *i.e.* the connection between useful parts of each simulate curve, that moves from the population prediction (light blue line) to the individualized one (dark blue line).

4. Conclusions

Despite the existence in literature of a few models capable of describing heparin pharmacokinetics and pharmacodynamics, to our knowledge our model is the first one that combines the heparin concentration predictions from a PBPK model and a fully-mechanistic PD model of the intrinsic coagulation cascade. Indeed, it can be used as a fully individualized predictive tool. In fact, thanks to the patient's clinical data, it can describe the trend of the coagulation time. Using the population approach, we implemented a predictive model that achieves a rather acceptable precision. In addition, using the individualized approach, we obtained an even more precise model that can be used *a posteriori*. Finally, thanks to an adaptive identification algorithm, it is possible to predict the future ACT trends during CPB, and forecast, in real time, the ACT trend, according to the dynamic measurement of ACT experimental values.

References

Delavenne, X., et al., 2017. Pharmacokinetic/pharmacodynamic model for unfractionated heparin dosing during cardiopulmonary bypass. Br J Anaesth 118(5), 705-712.

Jia, Z., et al., 2015. Pharmacokinetic model of unfractionated heparin during and after cardiopulmonary bypass in cardiac surgery. J Transl Med 13, 45.

Kogan, A.E., Kardakov, D.V., Khanin, M.A., 2001. Analysis of the activated partial thromboplastin time test using mathematical modeling. Thromb Res 101(4), 299-310.

Nadler, S.B., Hidalgo, J.U., Bloch, T., 1962. Prediction of blood volume in normal human adults. Surgery 51(2), 224-232.

Olsson, P., Lagergren, H., Ek, S., 1963. The elimination from plasma of intravenous heparin. An experimental study on dogs and humans. Acta Med Scand 173, 619-630.

Pesenti, G., Savoca, A., Manca, D., 2019. Optimal dose administration of renally excreted drugs, Computer Aided Chemical Engineering. Elsevier, pp. 547-552.

Zhu, D., 2007. Mathematical modeling of blood coagulation cascade: kinetics of intrinsic and extrinsic pathways in normal and deficient conditions. Blood Coagul Fibrinolysis 18(7), 637-646.

Sauro Pierucci, Flavio Manenti, Giulia Bozzano, Davide Manca (Eds.)
Proceedings of the 30th European Symposium on Computer Aided Process Engineering (ESCAPE30), May 24-27, 2020, Milano, Italy.
http://dx.doi.org/10.1016/B978-0-12-823377-1.50119-1

Application of a Pharmacokinetic Model to Inform the Optimal Dose for Individualized Drug Administration

Giuseppe Pesenti[a], Marco Foppoli[b], Adriana Savoca[a], Davide Manca[a]*

[a]*PSE-Lab, Process Systems Engineering Laboratory, Dipartimento di Chimica, Materiali e Ingegneria Chimica "Giulio Natta", Politecnico di Milano, Piazza Leonardo da Vinci 32, 20133 Milano, Italy*
[b]*Unit of Lymphoid Malignancies, Division of Onco-Hematological Medicine, Department of Onco-Hematology, IRCCS San Raffaele Scientific Institute, Via Olgettina 60, 20132 Milano, Italy*
davide.manca@polimi.it

Abstract

Dose selection is critical in clinical settings and standard dosing protocols are not suitable for every patient, due to the significant degree of inter- and intra-individual variability of their pharmacokinetic response. Pharmacokinetic models can be used as clinical support tools to suggest individualized, optimal dosages according to each patient's characteristics. We consider the case study of high-dose methotrexate administration for the application of a physiologically-based pharmacokinetic model, with the goal of obtaining model-informed dosages that we also compare with the standard dosing protocol. The results demonstrate the feasibility of this approach, the potential benefits of improved individualized dosages, and the importance of establishing rational and well-defined administration targets.

Keywords: Optimal dosage, Personalized medicine, Model informed precision dosing, Pharmacokinetics, Methotrexate.

1. Introduction

Drug administration requires considering the individual characteristics of patients and dose selection becomes especially critical in clinical settings, as the pharmacokinetic response of hospitalized and ill patients presents a significant degree of inter- and intra-individual variability. Standard dosage guidelines and protocols are usually developed for average healthy subjects and therefore might be not suitable for clinical patients.
Pharmacokinetic models are mathematical tools that can be applied to suggest optimized dosages according to individual characteristics such as body weight, height, age, sex and degree of renal function (Pesenti et al., 2019a), within the context of personalized medicine and model-informed precision dosing.
This manuscript focuses on methotrexate (MTX) administration as a suitable case study to demonstrate the application of pharmacokinetic models. MTX is administered intravenously (IV) at high doses (HDMTX) to treat malignant tumors such as primary central nervous system lymphoma (PCNSL). HDMTX administration is characterized by a very large inter- and intra-individual variability of its pharmacokinetics, and dosages are usually administered as predetermined amounts per m^2 of body surface area (BSA), *i.e.* a function of body weight and height. They therefore exhibit a limited degree of dose adjustment, and appear to inadequately account for the individual degree of renal

function. Furthermore, the literature reports that dose-finding studies in PCNSL are lacking and that there is no clear consensus regarding HDMTX optimal dosages (Joerger et al., 2012a). We therefore implemented and applied a physiologically-based pharmacokinetic model for HDMTX to this case study, to obtain model-informed optimal dosages for different targets and compare them with the clinical dosing protocols.

2. Methods

The minimal physiologically-based pharmacokinetic (PBPK) model for intravenous (IV) HDMTX developed in Pesenti et al. (2019b) was applied to this case study. This pharmacokinetic model was developed and validated using an experimental dataset of 89 Chinese patients with PCNSL (Mei et al., 2018).

The model explicitly accounts for the distribution, metabolism, and excretion of MTX within plasma, interstitial fluid (ISF), and intracellular fluid (ICF), as shown in Figure 1.

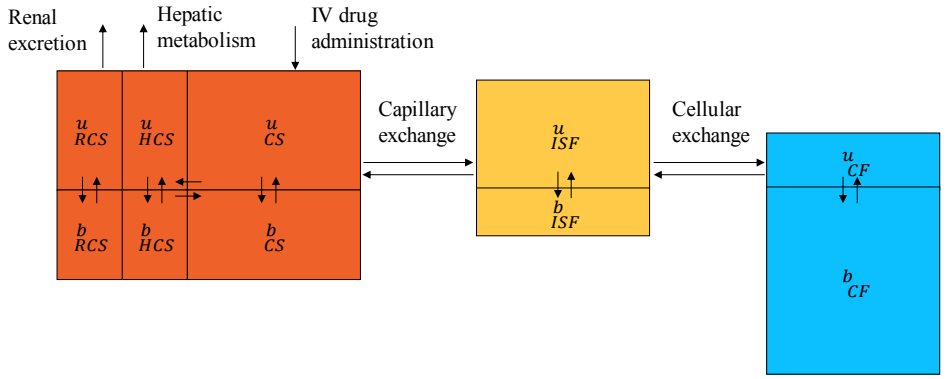

Figure 1 – Main processes and exchanges described by the minimal PBPK model (Pesenti et al., 2019b).

The model describes plasma with three compartments, *i.e.* the renal and hepatic circulatory systems (RCS and HCS), and the remaining overall circulatory system (CS), whereas the ISF and ICF compartments lump the interstitial and intracellular fluid of the entire human body. In each compartment, the concentration of the drug is considered homogeneous. The mathematical description is substantiated by five ordinary differential equations, describing the dynamics of the drug material balances within the five compartments (Eqs. 1-5).

$$\frac{dm_{CS}}{dt} = \dot{m}_{IV} - Q_{RCS}c_{CS} + Q_{RCS}c_{RCS} - Q_{HCS}c_{CS} + Q_{HCS}c_{HCS} + \\ -K_{CS\to ISF}c^{u}_{CS} + K_{ISF\to CS}c^{u}_{ISF} \quad (1)$$

$$\frac{dm_{RCS}}{dt} = Q_{RCS}c_{CS} - Q_{RCS}c_{RCS} - \dot{m}^{renal}_{filtration} - \dot{m}^{renal}_{secretion} + \dot{m}^{renal}_{reabsorption} \quad (2)$$

$$\frac{dm_{HCS}}{dt} = Q_{HCS}c_{CS} - Q_{HCS}c_{HCS} - \dot{m}^{hepatic}_{elimination} \quad (3)$$

$$\frac{dm_{ISF}}{dt} = K_{CS\to ISF}c^{u}_{CS} - K_{ISF\to CS}c^{u}_{ISF} - \dot{m}_{ISF\to ICF} + \dot{m}_{ICF\to ISF} \quad (4)$$

$$\frac{dm_{ICF}}{dt} = \dot{m}_{ISF\to ICF} - \dot{m}_{ICF\to ISF} \quad (5)$$

MTX is characterized by a reversible binding with plasma proteins both in plasma and in ISF compartments, and with cellular enzymes within ICF. The MTX bound fractions are estimated as $f^b_{plasma} = 0.42$, $f^b_{ISF} = 0.28$, $f^b_{ICF} = 0.90$ as in Pesenti et al. (2019b). In all model compartments, therefore, Eqs. (1-5) use the *b* and *u* superscripts to refer to bound and unbound concentrations respectively. Following its IV administration to the CS compartment ($\dot{m}_{IV}$, in mg/min), MTX is distributed via blood circulation to all body tissues and organs, where the unbound fraction is exchanged at the capillary level mainly by simple diffusion according to the capillary exchange parameters $K_{CS \rightarrow ISF}$ and $K_{ISF \rightarrow CS}$ (in mL/min). In addition, $\dot{m}_{ISF \rightarrow ICF}$ and $\dot{m}_{ICF \rightarrow ISF}$ (Eqs. (4-5), in mg/min) represent the active-transport MTX exchanges at the cellular level, that is modelled via a Michaelis-Menten kinetics as a function of c^u_{ISF} and c^u_{ICF} (Pesenti et al., 2019b).

Q_{RCS} and Q_{HCS} represent the plasma flows (in mL/min) that reach the kidneys, where MTX undergoes renal filtration, secretion and reabsorption, and the liver, where it is metabolized and secreted into the bile. While the model considers all these elimination pathways (for further details, see Pesenti et al. (2019b)), we focus on renal filtration (Eq. 6), which accounts for approximately 90% of elimination following IV HDMTX administration and is therefore the most important MTX elimination pathway.

$$\dot{m}_{filtration} = Q_{GFR} c^u_{RCS} \tag{6}$$

Q_{GFR} is the glomerular filtration rate (GFR, in mL/min), *i.e.* the plasma flow that is filtered by the kidneys, and is individualized as a function of the patient's body weight, height, gender, age, and plasma creatinine (Ma et al., 2006). Similarly, the compartment volumes, the volumetric plasma flows, and the other model parameters are estimated considering the patient's characteristics such as body weight, height, gender, and hematocrit, as in Pesenti et al. (2019b). Four constants, related to the capillary and cellular exchanges, were identified with a population PK approach through a nonlinear regression against an experimental dataset (Mei et al., 2018).

3. Results and discussion

The minimal PBPK model was applied to investigate HDMTX pharmacokinetics by simulating MTX administration to virtual patients defined with average characteristics, *i.e.* male, 57 years old, 168 cm high, with 38.1 % hematocrit. Since body weight and GFR are key determinants of MTX pharmacokinetics, we investigated their effect by defining three/five different virtual patients and changing their body weight and GFR within the ranges found in the experimental dataset, *i.e.* 50-100 kg (for a fixed 120 mL/min GFR value) and 50-250 mL/min (for a fixed 68 kg weight). We considered the IV administration of a standard MTX dose for PCNSL, *i.e.* 500 mg/m^2 over 15 min followed by 3000 mg/m^2 over 3 h (Joerger et al., 2012a). Assuming an average 68 kg weight, the total 3500 mg/m^2 corresponds to 6203 mg.

Fig. 2 shows the simulated MTX plasma concentration profiles over 48 h with the fixed MTX 6203 mg dose and shows the effect of body weight (panels a-b) and GFR (panels c-d). MTX concentrations higher than 1 μmol/L after 48 h are widely considered a threshold for MTX toxicity (Joerger et al., 2012b) and the simulated profiles can also be evaluated to assess the associated toxicity.

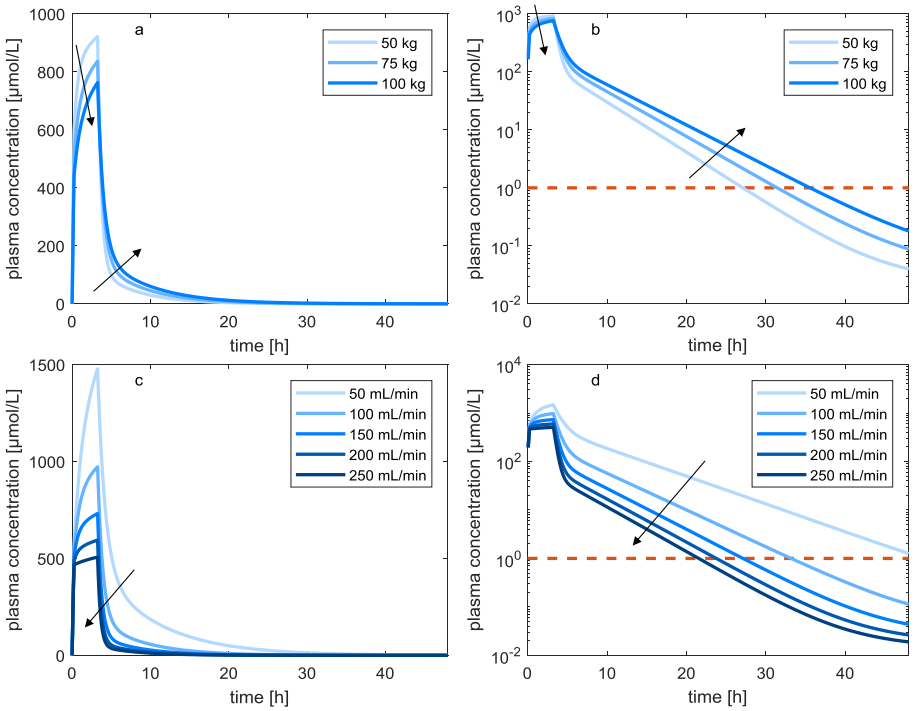

Figure 2 – Simulated MTX plasma concentrations for different virtual patients as a function of their body weight (top panels) and GFR (bottom panels), in both linear and logarithmic coordinates. In panels b and d, the dashed red line represents a toxicity threshold concentration after 48 h (Joerger et al., 2012b).

Higher body weights correspond to lower concentration peaks, which occur at the end of the infusion, since the same dose distributes in a larger volume. However, larger volumes would also require a higher volumetric clearance, whereas the fixed GFR determines a slower elimination following the peak. This can be seen as an inversion in the trend of the three lines after about 5 h from the infusion start.

According to model simulations, these two effects almost compensate each other, leading to values of the area under the curve (AUC) that only slightly increase with body weight in the 50-100 kg range, ranging from 3565 to 3578 µmol/L·h. The effect of GFR, which represents the degree of renal function, is more evident in panels 2c-d. Higher GFRs lead to both lower concentration peaks, and faster elimination dynamics. The AUC correspondingly decreases from 7929 µmol/L·h in case of 50 mL/min GFR, to 1926 µmol/L·h in case of 250 mL/min.

Our pharmacokinetic model was then applied to determine MTX optimal dosages that reach a given target. While the efficacy of MTX is mainly evaluated as the overall survival of the patients and MTX concentration targets are usually not defined, Joerger et al. (2012b) found that an MTX AUC of 1000-1100 µmol/L·h may be associated to improved clinical outcomes. They also reported a 24 h MTX concentration equal to 4-5 µmol/L as a suitable surrogate for the same AUC target. We simulated MTX infusions according to the standard PCNSL dosing protocol, *i.e.* up to 500 mg/m^2 during the first 15 min, and the remaining dose over 3 h. For each target, we identified the optimal dosage for the same virtual reference patient, at varying values of body weight and GFR, normalized over the patient's BSA/1.73 m^2.

Figure 3a shows the standard MTX dosing protocol for PCNSL (Joerger et al., 2012a), *i.e.* a 3500 mg/m^2 dose as a function of the individual BSA, which is administered to patients with a 60 mL/min minimum GFR. Figures 3b-c display the optimal dosages that, according to the model, lead to an AUC of 1050 µmol/L·h and a 24 h concentration of 4.5 µmol/L, respectively.

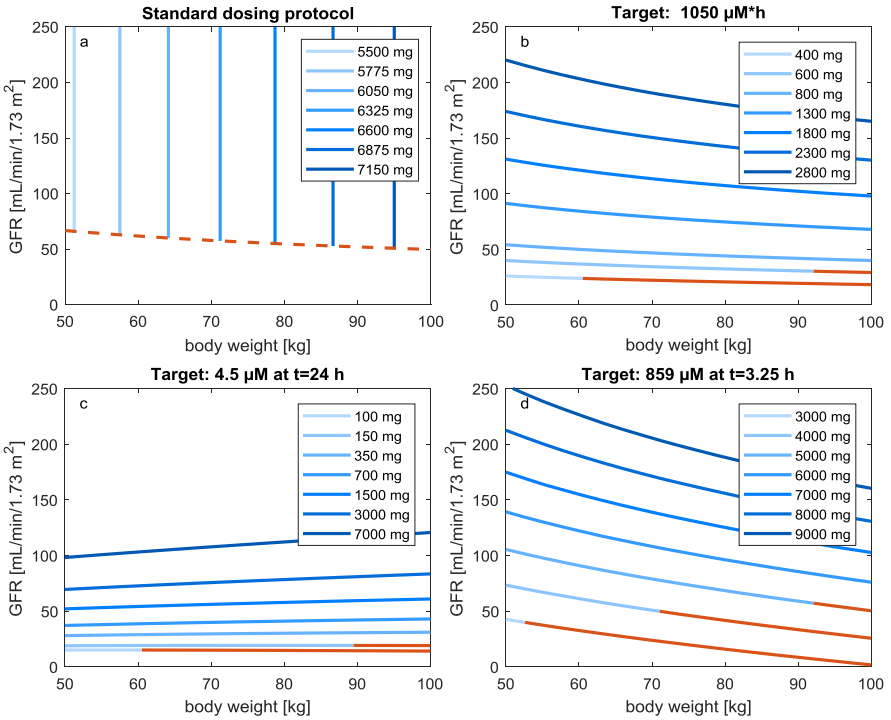

Figure 3 – MTX dosages as a function of body weight and BSA-weighted GFR. The standard dosing protocol for PCNSL from Joerger et al. (2012a) (a) is compared with model-suggested dosages corresponding to different targets (b-d). The bottom dashed red curve in panel a represents the GFR minimum threshold for administration, equal to 60 mL/min. In panels b-d, the red parts of the curves refer to dosages that lead to concentrations higher than 1 µmol/L after 48 h, which are associated to MTX toxicity (Joerger et al., 2012b).

We investigated as an additional target a concentration of 859 µmol/L at the end of the infusion (Fig. 3d), which corresponds to the model-simulated peak concentration following the administration of the standard 3500 mg/m^2 to a reference virtual patient with 68 kg body weight and 120 mL/min GFR.

As discussed earlier, the model describes a weak dependence of AUC from body weight, and thus the optimal dosages to reach the target AUC present little changes with body weight (Fig. 3b). In Figure 3d, suggested dosages show a weight-dependence similar to the standard dosing protocol, *i.e.* for a given GFR both the administered and the model-informed doses increase of about 2000 mg. Conversely, optimal dosages to reach the 24 h concentration target (Fig. 3c) suggest an inverse relation with weight. In case of renal function, all model-informed doses present a significant increase with GFR, consistently with renal filtration being the most important MTX elimination pathway. Unlike these, however, the standard protocol does not account for the individual degree of renal function, since dosages are only adjusted according to BSA, if the GFR is above 60 mL/min.

The optimal dosages determined via our PK model differ from the standard protocol considering both the doses (especially in case of AUC target), and the trends as a function of individual body weight and GFR. While the reliability of the optimal dosages depends on the accuracy of the model simulations and should be subject to further studies and improvements, we believe that these results confirm that current MTX dosing protocols can be optimized in an individualized manner to achieve improved outcomes, in agreement with Abrey (2010).

4. Conclusions

Pharmacokinetic models are mathematical tools that can be applied as clinical support tools to suggest individualized, optimal drug dosages to reach desired targets. We applied a pharmacokinetic model of HDMTX for patients with PCNSL to demonstrate its usability, which allows comparing our model-informed dosages with the standard dosing protocol. The results prove the feasibility and potential benefits of this approach, and suggest, in agreement with the literature, that current MTX dosing protocols should be improved and optimized according to the patient's characteristics.
Finally, we believe that the difference among the obtained optimal dosages for different clinical targets underlines the importance of the administration targets, and shows again that pharmacokinetic models can guide their rational definition (Pesenti et al., 2019b), while simultaneously considering toxicity thresholds and other constraints.

References

Abrey, L. E. (2010). Hematology: Individualized methotrexate dosing in primary CNS lymphoma. Nature Reviews Clinical Oncology 7(6): 306.

Joerger, M., Ferreri, A. J. M., Krähenbühl, S., Schellens, J. H. M., Cerny, T., Zucca, E., Huitema, A. D. R. (2012a). Dosing algorithm to target a predefined AUC in patients with primary central nervous system lymphoma receiving high dose methotrexate. British Journal of Clinical Pharmacology 73(2): 240-247.

Joerger, M., Huitema, A. D. R., Illerhaus, G., Ferreri, A. J. M. (2012b). Rational administration schedule for high-dose methotrexate in patients with primary central nervous system lymphoma. Leukemia & Lymphoma 53(10): 1867-1875.

Ma, Y. C.., Zuo, L., Chen, J. H., Luo, Q., Yu, X. Q., Li, Y., Xu, J. S., Huang, S. M., Wang, L. N., Huang, W., Wang, M., Xu, G. B., Wang, H. Y. (2006). Modified Glomerular Filtration Rate Estimating Equation for Chinese Patients with Chronic Kidney Disease. Journal of the American Society of Nephrology. 17 (10):2937-2944.

Mei, S., Li, X., Jiang, X., Yu, K., Lin, S., Zhao, Z. (2018). Population Pharmacokinetics of High-Dose Methotrexate in Patients With Primary Central Nervous System Lymphoma. Journal of Pharmaceutical Sciences 107 (5):1454-1460.

Pesenti, G., Foppoli, M., Manca, D. (2019b). Development of a minimal physiologically-based pharmacokinetic model for high dose methotrexate. Submitted to Journal of Pharmacokinetics and Pharmacodynamics.

Pesenti, G., Savoca, A., Manca, D. (2019a). Optimal dose administration of renally excreted drugs. Computer Aided Chemical Engineering. 46: 547-552.

Sauro Pierucci, Flavio Manenti, Giulia Bozzano, Davide Manca (Eds.)
Proceedings of the 30th European Symposium on Computer Aided Process Engineering (ESCAPE30), May 24-27, 2020, Milano, Italy.
http://dx.doi.org/10.1016/B978-0-12-823377-1.50120-8

Energy-efficient Solvent Properties for the Post-combustion Carbon Dioxide Capture

He Jin, Pei Liu*, Zheng Li

State Key Lab of Power Systems, International Joint Laboratory on Low Carbon Clean Energy, Innovation, Department of Energy and Power Engineering, Tsinghua University, Beijing, 100084, China
liu_pei@tsinghua.edu.cn

Abstract

Heat consumption is a major concern for the development of the post-combustion CO_2 capture in thermal power plants. In this work, a mathematical model is implemented to minimize the heat duty for a conventional post-combustion CO_2 capture process. An explicit three-parameter vapor-liquid equilibrium (VLE) model is developed. In the VLE model, the solvent is characterized by the absorption heat, indexes for cyclic capacity and absorption capacity. The configuration of these properties is based on typical commercially available solvents. The minimal heat consumption of the optimal solvent is 2.44 MJ/kmol CO_2, which is 70 percent of the conventional MEA solvent. Besides, the match relationship between the absorption heat and lean solvent loading is investigated from the view of balance between absorption and regeneration processes.
Keywords: post-combustion CO_2 capture, modeling and simulation, solvent properties

1. Introduction

Post-combustion CO_2 capture is regarded as a most feasible approach to be configured with coal-fired power plants. However, the major limit for the technology is the high energy consumption for the conventional solvent regeneration, which leads to about ten percentage points penalty for net efficiency (Goto et al, 2013).

Improving solvent properties to be more energy-efficient in carbon capture process has become a focus in recent years. Li et al. proposed a simple VLE approach to optimize a conceptual solvent by using 2-amino-2-methyl-1-propanol (AMP) and N-methyl-diethanolamine (MDEA) aqueous solution (Li et al, 2016). The result showed that the conceptual solvent can reduce 34 percent of total equivalent work comparing to MEA solvent. Kim et al. pointed that the cyclic capacity, absorption performance and reaction heat should be considered simultaneously to minimize the energy demand (Kim et al, 2016). It was because that the impact of different properties on heat duty were interactive. The minimum achievable regeneration heat requirement in a typical process configuration was estimated to be 2.3~2.5 GJ/t CO_2 and the optimal reaction heat was in the range of 60~70 kJ/mol CO_2. Lee et al. developed a semi-empirical method to model CO_2 vapor-liquid equilibrium and absorption rate in a ternary amine solvent (Lee et al, 2019) and provided a new sight for identifying cost effective blended amine solvents in a traditional CO_2 capture process. Ahmad et al. took advantage of a computer aided molecular design technique for developing alternative solvents to replace conventional absorbents (Ahmad et al, 2018). By using the energy-efficient solvent, energy savings can be achieved up to 31.4% compared to the conventional MEA aqueous solvent.

This paper develops a simplified model to obtain an optimal conceptual solvent that owns a minimal heat consumption in a conventional post-combustion CO_2 capture process. An

explicit three-parameter vapor-liquid equilibrium model is introduced. The solvent properties are characterized by the absorption heat, cyclic capacity and absorption capacity. The effect of the absorption heat on the heat duty is investigated. The match relationship between the absorption heat and lean solvent loading is also discussed from a view of balancing absorption and regeneration process.

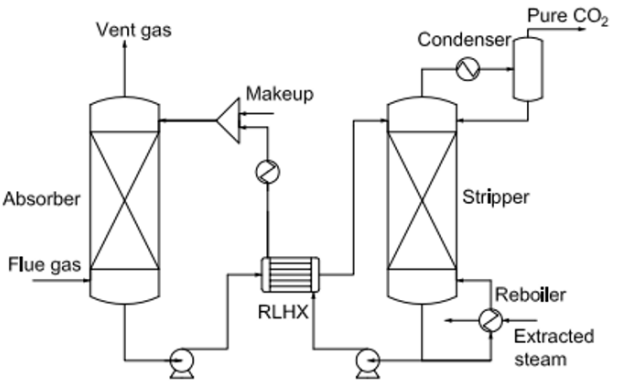

Figure 1. Configuration of a conventional post-combustion CO2 capture process

2. Model development

A typical configuration of a post-combustion CO_2 capture system applied in this study is shown in Figure 1. The flue gas is introduced to the bottom of the absorber and contacts with the countercurrent lean solvent. The CO_2 in the flue gas is absorbed and clean vent gas flows from the top of the column. Through the preheating process in the rich/lean heat exchanger (RLHX), the rich solvent enters the top of the stripper. The CO_2 in the rich solvent is desorbed by the steam generated from the bottom reboiler. The reboiler is heated by extracted steam from the stream cycle. The lean solvent flows from the reboiler to the RLHX to form a closed loop. The CO_2 stream in a high purity is obtained through a condenser. The key to describe the process is modeling the absorbing/striping process in the column, solvent vapor-liquid equilibrium (VLE) properties and heat consumptions.

2.1. Balance equations

The dominant control equations in the absorber and stripper column are balance equations, including mass, component and energy balances, which are listed as follows:

$$0 = \frac{\partial \dot{n}_{tot}^{L}}{\partial z} + \sum_i N_i \tag{1}$$

$$0 = -\frac{\partial \dot{n}_{tot}^{V}}{\partial z} - \sum_i N_i \tag{2}$$

$$0 = \frac{\partial \dot{n}_{i}^{L}}{\partial z} + N_i \tag{3}$$

$$0 = -\frac{\partial \dot{n}_{i}^{V}}{\partial z} - N_i \tag{4}$$

$$0 = C_p^L \dot{n}_{tot}^{L} \frac{\partial T}{\partial z} + N_{CO_2} \Delta H_{abs} + N_{H_2O} \Delta H_{vap} \tag{5}$$

where the subscripts i represents components H_2O and CO_2, L and V denote liquid and vapor phases respectively, $\dot{n}$ is the flow rate, N is mass transfer rate per unit height, T is temperature, C_p is the specific heat capacity, ΔH_{abs} and ΔH_{vap} stand for the absorption heat of CO_2 and vaporization heat of H_2O respectively.

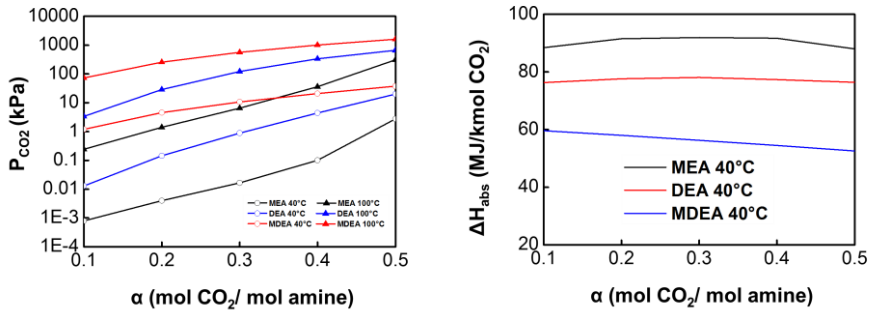

(a) (b)

Figure 2. The vapor-liquid equilibrium (a) and heat absorption (b) of typical solvents

2.2. Vapor-liquid equilibrium (VLE) model for solvents

The vapor-liquid equilibrium is essential to present solvent properties that affect the performance of a CO_2 capture process. The VLE reflects the absorption heat, cyclic capacity and absorption capacity for an absorbent. The absorption heat can be obtained by Gibbs-Helmholtz equation as Eq. (6) shows, where $P^*_{CO_2}$ denotes equilibrium pressure of CO_2. A parameter $\Delta\alpha$ is defined in Eq. (7), referring the form of Eq. (6), which is the index to present the cyclic capacity in this work. The curves of VLE and absorption heat of typical amines are depicted in Figure 2. According to the data, the absorption heat ΔH_{abs} can be treated as a constant and $\ln P^*_{CO_2}$ is assumed as a linear function of carbon loading α. Then $\ln P^*_{CO_2}$ is integrated to $\Delta\alpha$ and $\frac{1}{T}$ and a three-parameter ($\Delta H_{abs}, \Delta\alpha, \alpha_0$) model can be derived, as Eq. (8) shows. The parameter α_0 is an integral constant which stands for the absorption capacity of a solvent. Thus, the Eq. (8) is an explicit equation for the three main properties. The values of ΔH_{abs}, $\Delta\alpha$ and α_0 for typical commercially available solvents are listed in Table 1, including primary amine (MEA), secondary amine (DEA), tertiary amine (MDEA) and sterically hindered amine (AMP).

$$\Delta H_{abs} = -R\frac{\partial\left(\ln P^*_{CO_2}\right)}{\partial\left(\frac{1}{T}\right)} \tag{6}$$

$$\Delta\alpha = \frac{\partial\alpha}{\partial\left(\frac{1}{T}\right)} \tag{7}$$

$$\ln P^*_{CO_2} = \frac{\Delta H_{abs}}{R\Delta\alpha}(\alpha - \alpha_0) - \frac{\Delta H_{abs}}{RT} \tag{8}$$

Table 1. Values of ΔH_{abs}, $\Delta\alpha$ and α_0 for typical solvents

	Unit	MEA	DEA	MDEA	TEA	AMP
ΔH_{abs}	MJ/kmol CO_2	90.7	79.6	63.3	50.6	55.1
$\Delta\alpha$	(kmol CO_2*K)/mol amine	0.69	0.66	0.97	0.93	0.62
α_0	mol CO_2/mol amine	-1.68	-1.80	-3.10	-3.36	-1.75

2.3. Heat consumptions

In the carbon capture process, the total heat demand q contains three parts: the sensible heat q_{sen}, the vaporization heat q_{vap} and absorption heat q_{abs}.

$$q = q_{sen} + q_{vap} + q_{abs} \tag{9}$$

$$q_{sen} = C^L_p(T_{reb} - T_{RLHX})\dot{n}^L_{tot}/\Delta\dot{n}^V_{CO_2} \tag{10}$$

$$q_{vap} = \Delta\dot{n}^V_{H_2O} \cdot \Delta H_{vap}/\Delta\dot{n}^V_{CO_2} \tag{11}$$

$q_{abs} = \Delta H_{abs}$ (12) where $\Delta \dot{n}^{V}_{CO_2}$ is captured CO_2 flow rate, $\Delta \dot{n}^{V}_{H_2O}$ is stripped H_2O flow rate. In this work, a conceptual solvent with heat consumption minimum can be derived through solving an optimization problem. The structure of the optimization problem is presented in Table 2. In addition, the boundary conditions for ΔH_{abs}, $\Delta\alpha$ and α_0 refer to the data listed in Table 1.

Table 2. The structure of optimization problem for conceptual solvents

Objective function	Optimization variables	Main constraints for the process
Min q	ΔH_{abs}, $\Delta\alpha$ and α_0 α	$\Delta T = 5\ K, P_{ABS} = 100\ kPa,$ $P_{RLHX} = P_{STR} = 200\ kPa, \eta = 90\%$

3. Results and discussions

The optimization results of conceptual solvents are listed in Table 3. The minimum for total heat demands in the typical carbon capture process is 2.44 MJ/kg CO_2. Comparing with 3.5 MJ/kg CO_2 for the conventional MEA solvent, the optimal solvent can reduce 30 percent of the heat consumption. Table 4 shows the impact of the increase of each property on absorption and regeneration. From this qualitative analysis, it can be noted that the raise of absorption heat ΔH_{abs} promotes the regeneration process but resists absorption process. The raise of cyclic capacity $\Delta\alpha$ and absorption capacity α_0 promotes the absorption process but resists regeneration process. Due to the opposite effect on absorption and regeneration, the values of properties may achieve to an optimal point that balances both the absorption and regeneration.

Table 3. The optimization results of conceptual solvents

	q	ΔH_{abs}	$\Delta\alpha$	α_0	α
Unit	MJ/kg CO_2	MJ/kmol CO_2	(kmol CO_2*K)/mol amine	mol CO_2/mol amine	mol CO_2/mol amine
Values	2.44	61.1	0.97	-3.26	0

Table 4. Effect of the increase of each property on the absorption and regeneration

	ΔH_{abs}	$\Delta\alpha$	α_0
Absorption	-	+	+
Regeneration	+	-	-

where '+' stands for promotion, '-' stands for inhibition.

3.1. Impact of the absorption heat on the heat duty

Keeping the cyclic capacity, absorption capacity and lean solvent loading the same as the optimal solvent, the effect of heat absorption on the heat duty is displayed in Figure 3(a). The total heat reaches a minimum as the heat absorption increases, which is a balance result between sensible and vaporization heat. A higher heat absorption results in a higher CO_2 equilibrium pressure, so the absorption process is repressed. The adverse influence is characterized by the decrease of the cyclic loading as shown in Figure 3(b). Therefore, a higher lean solvent flow rate is required to capture the same amount of CO_2 as the heat absorption raises as shown in Figure 3(c). The increase in circulating rate leads to the increase of sensible heat. On the contrary, the higher CO_2 equilibrium pressure is, the easier for CO_2 to be stripped. As displayed in Figure 3(d), the temperature in reboiler decreases monotonically with the increase of absorption heat, which lowers the

vaporization heat. In addition, the temperature of hot rich solvent is higher than the bubble point so a part of CO_2 is pre-stripped in the RLHX.

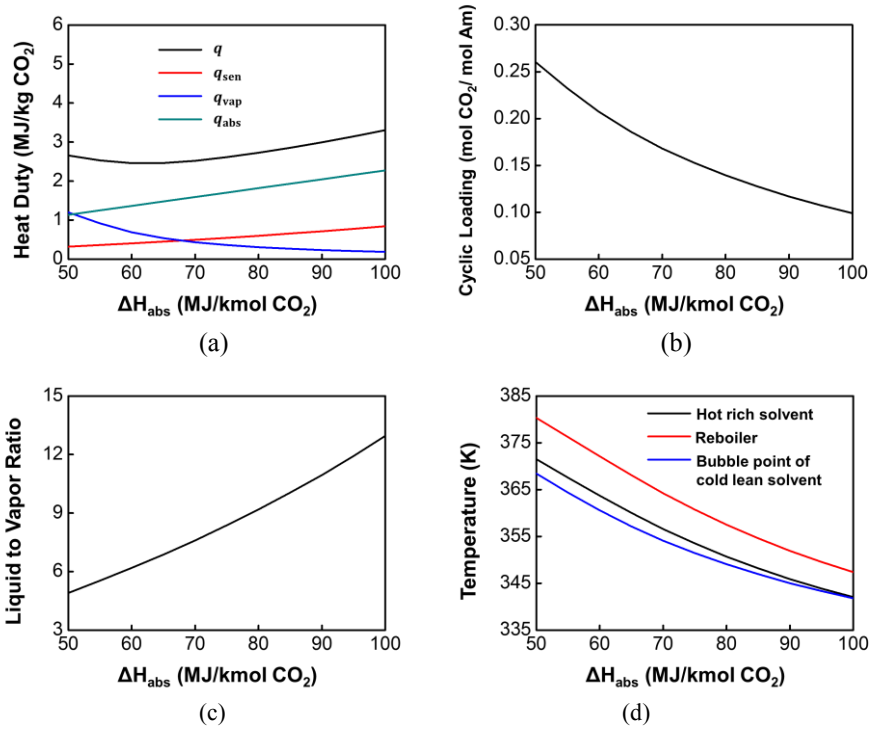

Figure 3. Effect of the absorption heat on the heat duty (a), cyclic loading (b), liquid to vapor ratio (c) and temperature in the regeneration side (d)

3.2. The match relationship between the absorption heat and lean solvent loading

In order to minimize the energy consumption, operational parameters should match the circulating solvents with different properties. In this study, the operational parameter is specifically lean solvent loading α. Keeping the cyclic capacity and absorption capacity the same, Figure 4 displays the effect of lean solvent loading on the heat requirement under different absorption heat. It is noteworthy that the total heat consumption is reduced at first then increased as lean carbon loading raises. The total heat consumption achieves to a minimum value as a result of mutual effect between the sensible heat and vaporization heat. The sensible heat raises with the lean solvent loading, as a higher lean loading results in a higher demand for the lean solvent flow rate to achieve the given CO_2 capture rate. Meanwhile, the vaporization heat decreases obviously with the lean solvent loading because a lower amount of stripping steam is required to reach a higher loading in the regeneration part. Comparing the solvents with different absorption heat, a lower absorption heat leads to a higher optimal lean solvent loading. The phenomenon can be explained by the opposite effect on absorption and regeneration. The increase of absorption heat and lean solvent both enhances absorption and inhibits regeneration. As the absorption heat raises, the increment of sensible heat is lower than the reduction of vaporization heat. In order to reach a new balance between absorption and regeneration, optimal lean solvent tend to move to an opposite direction to offset the effect.

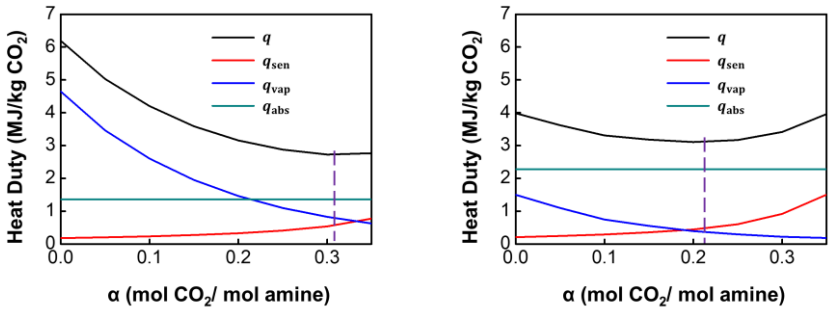

(a) $\Delta H_{abs} = 60\ MJ/kmol\ CO_2$ (b) $\Delta H_{abs} = 90\ MJ/kmol\ CO_2$

Figure 4. The effect of the lean solvent loading on the heat requirement for solvents with different absorption heat.

4. Conclusions

This paper develops a model for deriving a conceptual solvent with minimum of heat consumption in the post-combustion CO_2 capture process. A simplified three-parameter vapor-liquid equilibrium model is implemented. In the VLE model, solvent properties are characterized by the absorption heat, cyclic capacity and absorption capacity. The minimum of heat consumption is 2.44 MJ/kg CO_2, which is 70% of conventional MEA solvent. The increase of absorption heat raises sensible heat but reduces vaporization heat so the minimal heat consumption is a result of balancing between the absorption and regeneration process. In addition, to minimize heat duty, lean solvent loading is required to the match with the absorption heat. The optimal lean solvent loading is determined by offsetting the impact of changes in the absorption heat on the absorption and regeneration process.

Acknowledgments

The authors gratefully acknowledge the support by The National Key Research and Development of China (2016YFE0102500, 2018YFB0604301), Shanxi Key Research and Development Program (201603D312001), National Natural Science Foundation of China (71690245), and the Phase Ⅲ Collaboration between BP and Tsinghua University.

References

Ahmad, M. Z., Hashim, H., Mustaffa, A. A., Maarof, H., & Yunus, N. A., 2018, Design of energy efficient reactive solvents for post combustion CO2 capture using computer aided approach. Journal of cleaner production, 176, 704-715.

Goto, K., Yogo, K., Higashii, T., 2013, A review of efficiency penalty in a coal-fired power plant with post-combustion CO2 capture. Applied Energy, 111, 710-720.

Kim, H., Lee, K. S., 2016, Design guidance for an energy-thrift absorption process for carbon capture: Analysis of thermal energy consumption for a conventional process configuration. International Journal of Greenhouse Gas Control, 47, 291-302.

Lee, J., Kim, J., Kim, H., 2019, A new modeling approach for a CO2 capture process based on a blended amine solvent. Journal of Natural Gas Science and Engineering, 61, 206-214.

Li, Z., Chen, S., Hopkinson, D., Luebke, D., 2016. Verification of a solvent optimization approach for postcombustion CO2 capture using commercial alkanolamines. International Journal of Greenhouse Gas Control, 44, 59-65.

Sauro Pierucci, Flavio Manenti, Giulia Bozzano, Davide Manca (Eds.)
Proceedings of the 30th European Symposium on Computer Aided Process Engineering
(ESCAPE30), May 24-27, 2020, Milano, Italy.
http://dx.doi.org/10.1016/B978-0-12-823377-1.50121-X

The Role of Process Engineering in the Digital Transformation

Norbert Jung

AVEVA, Germany

Norbert.jung@aveva.com

Abstract

The process engineering discipline has been largely excluded from Digital Transformation trends. The objective of this presentation is to provide an overview of the obstacles to Digital Transformation for the process discipline and explain how these can be overcome. A special emphasis will be given on the role of the process simulation tool (white box modelling) as a catalyst for transformational change.

The presentation will examine several challenges specific to process engineering:

1) Process simulators are divided into single-purpose point solutions. Separate models may be created for process design, control strategy design, operator training simulation, performance monitoring and online optimization.

2) Process simulators are typically poorly integrated into engineering workflows beyond the process world, and if so, with a single directional information flow.

3) Legacy process simulators are overloaded with niche features and functions only usable by experts.

4) The potential benefits of Artificial Intelligence and Machine Learning for process engineering are not widely understood.

Industry stakeholders see the Digital Twin as the most important building block for Digital Transformation of the process industries. While legacy simulators are well-suited to accurately simulate processes, their decades-old architectures mean they are not ideal to serve the entire plant lifecycle and support the Digital Transformation. We will use the AVEVA SimCentral Simulation Platform[4] as an example of how the identified obstacles can be overcome with a next generation process simulator. Case examples from leading companies will be outlined.

Keywords: Process Simulation, Digital Transformation, Unified Engineering.

1. The Role of Process Engineering in the Digital Transformation

While Digital Transformation hits every corner of industry, the process engineering discipline has been largely excluded from this trend so far. PwC foresee that for process licensors / EPCs, data driven digital services can displace process technology as a differentiator[1].

2. An Industry in Need of Change

Never have the stakes been higher for companies when it comes to making improvements to their engineering work processes to maximize ROI on Capital Projects. Productivity has not developed in decades – the average Capital Project schedule lags by 20 months and goes over budget by 80%[5]. While the cost of engineering and design typically amounts to just 10% of the overall project cost, the work being carried out here heavily influences what happens in procurement and construction. The leading cause of rework in project execution is design errors and omissions, and according to research, they contribute to over 5.4% of the total construction cost[6]. Engineering errors alone make up 14.2% of the total contract value[7].

3. A New Approach for Unified Engineering

Companies' are beginning to make progress on their digitalization journey, finding the right applications for digital transformation and seeing increasingly better returns on their investment. While the age-old market environment challenges (such as supply and demand, cost and price) haven't gone away, competitive pressures are making the digital transformation opportunity more pressing than ever.

Many have already started to leverage the latest data-centric technology and work processes for their workforce to collaborate and take control of their data, reducing the risk for errors, delays and increased project cost throughout the asset lifecycle. This phase of the digitalization journey is what we call EPC 4.0.

To reduce the number of iterations in FEED, process engineers must work concurrently with other disciplines. All information must be stored and exchanged as data to ensure there is always clear visibility of progress across the entire project. Unified Engineering manages and drives positive change within an organization to ensure risk is minimized during the early project phase right up to the Digital Twin deliverable to the Owner.

Unified Engineering breaks down the silos between process and engineering design and ensures each discipline has ownership of their data and the reassurance that it is always correct. Early FEED is a highly iterative process but with Unified Engineering data is entered only once. The simulation data created in FEED is readily available for use in Detailed Design, increasing efficiency across projects. Procurement errors and delays are avoided, and rework caused by poor quality deliverables is eliminated.

Unified Engineering is not just about collecting simulation data into a database. It is about empowering people to take full control, to manage the data effectively. Even when big changes have been made, Unified Engineering ensures they can be easily validated.

4. Lifecycle Simulation Supports Unified Engineering

According to DECHEMA, one major obstacle for digital transformation is the division of process simulators into single-purpose point solutions. Today, separate models may be

created – often in different tools – for process design, control strategy design, operator training simulation, performance monitoring and online optimization. This drives up the total cost of modelling to a degree than can become prohibitively expensive. One single model should be able to cover the entire plant lifecycle from idea to operations[2].

4.1 Problems with Legacy Simulators

Process simulators are irreplaceable tools for every process engineer. Since the nineteen seventies, process simulators have found widespread adoption within operating companies in oil & gas, refining and chemical industries, as well as the engineering companies and equipment manufacturers that service these industries. The tools available in the market today have incrementally improved over the years to provide more features and functionality. However, they trace their origins to legacy architectures, operating systems and aftermarket user interfaces, which create inherent limitations:

- They cannot support the full plant lifecycle as they are limited by their single-purpose architecture such as steady state process simulation, dynamic simulation, optimization, or flow network analysis for which they were originally designed.

- Extending their functionality can be performed by a very small number of software developers with chemical engineering knowledge, software programming skills, and/or knowledge of that particular specialized program.

- They are often based on decades old programming code that cannot leverage the more recent technological developments within the software industry.

The next generation of workers also expects a modern, scalable and easy to use solution with technology they now take for granted – high speed internet access, mobile devices, touch screens and virtual reality. New concepts like the Industrial Internet of Things (IIoT), Industry 4.0, and Artificial Intelligence have created greater opportunities with a new next generation platform that provides a "Digital Twin" of the plant through the process lifecycle that cannot be provided with today's tools.

4.2 Lifecycle Simulation

Lifecycle Simulation means that one process model is extended throughout the entire lifecycle of the plant, from concept through to operations. This requires a process design mode, a fluid flow/rating mode and a dynamic mode, in combination with the ability to toggle back and forth between modes. Optimization may be provided to any mode. Table 1 describes each phase of the project lifecycle, and how a maturing Digital Twin develops and provides benefits for each phase.

Lifecycle Phase	Model	Benefits
Conceptual Engineering	The Digital Twin of a process plant is "first born"	• Fast evaluation of design alternatives due to continuously solved and flexible specifications
		• A native Cloud application that protects IP to reduce IT costs • Open modeling for first-of-a-kind processes and equipment
Front End Engineering and Design (FEED)	The Digital Twin grows to represent all plant process equipment	• One product with one learning curve for multiple applications, such as process, process utilities, and relief and flare • Integrated Asset Modeling of interacting but separate systems, such as, an oil field gathering and topsides processing, or the process and its flare system • Automated population of the Unified Engineering database • Automated creation of FEED engineering deliverables • Multi-user collaboration of a single simulation
Detailed Engineering	Simulation-Driven Engineering: The Digital Twin grows to also represent the mechanical design and the control strategy	• Other disciplines, such as Controls, Mechanical, Piping, all contribute to the Unified Engineering database • Simulation takes information from the engineering database to test the Digital Twin continuously as it is designed • Process engineering trends towards new agile software engineering practices with a test-driven development now made possible because of the existence of the Digital Twin
Startup and Commissioning	The Digital Twin is used for Operator Training and Controls Checkout	• The actual DCS logic can be integrated to the Digital Twin • Operators are trained without a separate operator training simulator investment
Operations	The Digital Twin is a master simulation model for process improvement, equipment monitoring, optimization, and more	• One master Digital Twin model can be spawned to many applications, such as, training, equipment monitoring, and real-time optimization to reduce the sustainment costs associated with separate point solutions • No longer need to maintain several process simulation models for a plant—design model, operator training simulator (OTS) model, unit performance monitoring and real-time optimization (RTO)

4.3 Agile Process Design

In another engineering discipline, software engineering, work practices have changed significantly over the last 15 years. Previous software development followed a "waterfall" process of design specifications, component development, integration, in a sequential process with exit stage gates similar to the process engineering lifecycle stages. Now, software engineers embrace a new work process known as agile software development with test-driven development at its core.

Agile development plans small amounts of work with continuous integrated testing to reduce development cost while eliminating surprises at the end of the project. But, as plants are made of steel and concrete it is not easy to test a process design until it is procured, constructed, and started, at which time it is too late. Accordingly, engineering companies have numerous design reviews and use simulation as appropriate in dedicated studies to ensure design.

Next generation simulation software must allow process facilities engineering to move towards agile software development concepts using the Digital Twin during the design of the process plant. This First Born Digital Twin during design provides an opportunity to test new design and to continuously check inconsistencies at minimum cost.

For example, a process engineer of the future needs to design the emergency depressuring system for an offshore system. The engineer specifies a dynamic simulation from the engineering database. The valve Cv, and equipment volumes are taken from the engineering database. The engineer confirms the valve Cvs, that the depressuring time meets requirements, and that the temperatures are not too cold for the metallurgy. The emergency controls are integrated so that the volume between isolation valves is used for the calculation. Instead of doing this one time, the test is automated to confirm that the design continues to be adequate as the plant is further designed. Future changes to vessel size, control size, valve Cv will create a warning to the engineer. This depressuring test is one of hundreds of similar design tests necessary to prove the plant can start, operate, and shutdown properly given its feedstock, equipment design, and control design, as specified by the owner operator, and process, mechanical, and control engineers.

5. Conclusions

It used to be claimed that in order to cut cost and reduce project risks during the design and construction phase of major capital projects, you had to ensure that the plant design was completed 'right first time'. To eradicate iterations and rework in design and get it right from the outset, you would need to ensure that everyone in project execution was equipped with the latest and most accurate information. Although the 'right first time' approach is an attractive vision, the realities of a complex capital project present far too many obstacles. Reducing the risk of engineering and design errors is therefore an essential factor in lowering project cost and minimising the risk for overruns and delays.

To minimize the risk of cost overruns and delays, companies need an integrated, data-centric solution to manage all engineering information in one place. This enables engineers from all disciplines to collaborate effectively, detect and identify changes as soon as they occur and compare and update them efficiently. Organizations who rapidly

and accurately communicate change in the FEED and detailed design phase will be the most effective during procurement and construction to capitalize on project execution.

Unified Engineering enables companies to leverage their EPC 4.0 strategy with data-centric collaboration on a global scale, digitally through one platform, so the entire process can be traced, tracked, and linked – from FEED engineering and detailed design, all the way up to day-to-day operations and maintenance of your asset.

Lifecycle process simulation has been a vision for process simulation providers and their customers for a long time. Today's simulators cannot leverage the rapid developments occurring in the software industry due to legacy architecture. The next generation Unified Lifecycle Simulation platform SimCentral Simulation Platform, by AVEVA is a brand new offering in the market. Being built from the ground up, it offers many advantages as this paper has outlined.

References

[1]Digital business models in plant engineering and construction in an international comparison, A benchmarking study of PwC and VDMA, May 2019 (link)

[2]DECHEMA Whitepaper Digitalisierung in der Chemieindustrie, September 2016 (link)

[3]DECHEMA Tutzingen Thesen 2018 (link in english)

[4]AVEVA SimCentral Simulation Platform (link)

[5]Optimise your engineering and design processes to boost collaboration and reduce project costs and delays; Sabharwal, A., Taylor, M.

[6]Unified Engineering: A new proposition to break down the silos between FEED and Detailed Design to minimize risk and maximize return on Capital Investment; Taylor, M.

[7]Building a Digital Twin of Your Process Plant with Unified Lifecycle Simulation; Jung, N., Depew, C.

Sauro Pierucci, Flavio Manenti, Giulia Bozzano, Davide Manca (Eds.)
Proceedings of the 30th European Symposium on Computer Aided Process Engineering (ESCAPE30), May 24-27, 2020, Milano, Italy.
http://dx.doi.org/10.1016/B978-0-12-823377-1.50122-1

A Mixed Integer Nonlinear Approach for the Automated Superstructure Generation Problem

Luca Mencarelli,* Alexandre Pagot

IFP Energies nouvelles, Rond-point de l'échangeur de Solaize, 69360 Solaize, France

luca.mencarelli.home@gmail.com

Abstract

We describe a new mixed integer nonlinear programming approach for the automated superstructure generation problem in process synthesis engineering, whose target consists in defining and optimizing the superstructure, i.e., the union of all the alternative structures, of a given chemical process cluster. We develop a mixed integer nonlinear formulation for the problem in order to define the links between the chemical units and we implement it with respect to the integrated process of catalytic reforming and light naphtha isomerization in petroleum refinery. The formulation is based on the definition of a graph, whose nodes are the chemical units and whose arcs represent the links between units. The chemical processes are then replaced by their corresponding surrogate models, which represent a systematic way to mathematically represent the input/output relationships of the given processes.

Keywords: Mixed Integer Nonlinear Programming, Superstructure, Surrogate modelling.

1. Introduction

Superstructure generation and optimization constitutes an emerging topic in Process System Engineering (PSE) (see Chen and Grossmann (2017)). The superstructure of a given chemical process is defined as the set of all possible alternative process structures. Generally, a superstructure is manually defined and then optimize, see, e.g., Duchêne et al. (2019) where a superstructure-based optimization methodology is proposed for the integrated process of catalytic reforming and light naphtha isomerization. However, when the superstructure is manually defined, several feasible or even optimal structures may be not encoded in superstructure representation: automated superstructure procedures can cope with this drawback. Automated superstructure approaches consider computational procedures in order to algorithmically define and optimize the superstructure. For a detailed survey about superstructure generation methodologies we refer the interested reader to Mencarelli et al. (2019).

2. Mixed integer nonlinear formulations

In this section, we introduce our mixed integer nonlinear programming (MINLP) formulations for the automated superstructure generation problem. A superstructure is represented by a graph $G(N,A)$ whose nodes represent units and edges represent links between units. We present two formulations: in the first one, nodes are splitters or

process units, while, in the second one, there are no more nodes for splitters, which are substituted by cut-points.

2.1. With splitters nodes

Sets. Let L be the set of splitter branches and J be the set components in the superstructure. F and P represent the set of feed and products, respectively. We indicate with S the set of splitters. U is the set of process units and C is the set of process unit configuration.

Binary variables. Each arc is represented by a binary variable equal to 1 if the arc belongs to $G(N,A)$. a_{fu} indicate feed/unit arcs (f in F, u in U), a_{fn} feed/node arcs (f in F, n in N), a_{fnl} node/unit arcs (f in F, n in N, l in L), a_{n1n2l} node/node arcs (n_1,n_2 in N, l in L), a_{un} unit/node arcs (u in U, n in N), a_{upl} unit/product arcs (u in U, p in P, l in L), and a_{npl} node/product arcs (n in N, p in P, l in L),. Let v_{ns} and w_{uc} be two binary variables such that $v_{ns}=1$ if there is splitter s in S in node n in N and $w_{uc}=1$ if the process unit u in U is in configuration c in C, respectively.

Continuous variables. Each component flow is represented by a (non-negative) continuous variable Q_j. The superscripts *in* and *out* indicate inflow and outflow, respectively, while the subscripts have the same meaning as for the arc variables. Q_{uj} is the total inflow per component j in J per unit u in U, Q_{nj} is the total inflow per node n in N, and Q_{pj} is the total inflow per product p in P. V_{uc} indicates the vector of process variables per configuration c in C of process unit u in U.

Constraints. The total inflow for process unit, node, and product are given by:

$$Q_{nj}^{in} = \sum_{u\in U} Q_{unj} + \sum_{f\in F} Q_{fnj} + \sum_{n_1\in N}\sum_{l\in L} Q_{n_1nlj} \qquad \forall n\in N, \forall j\in J \tag{1}$$

$$Q_{uj}^{in} = \sum_{f\in F} Q_{fuj} + \sum_{n\in N}\sum_{l\in L} Q_{nulj} \qquad \forall u\in U, \forall j\in J \tag{2}$$

$$Q_{nj}^{in} = \sum_{u\in U} Q_{upj} + \sum_{n\in N}\sum_{l\in L} Q_{nplj} \qquad \forall p\in P, \forall j\in J \tag{3}$$

Let i_{slj} be the outflow fraction per splitter s in S, branch l in L, and component j in J. The splitter outflow Q_{nlj}^{out} is such that the following big-M constraints hold:

$$Q_{nlj}^{out} \le i_{slj} Q_{nj}^{in} + M(1-v_{ns}) \qquad \forall n\in N, \forall j\in J, \forall l\in L \tag{4}$$

$$Q_{nlj}^{out} \ge i_{slj} Q_{nj}^{in} - M(1-v_{ns}) \qquad \forall n\in N, \forall j\in J, \forall l\in L \tag{5}$$

$$Q_{nlj}^{out} \le M \sum_{s \in S} v_{ns} \qquad \forall n \in N, \forall j \in J, \forall l \in L \tag{6}$$

$$Q_{nj}^{out} = \sum_{u \in U} Q_{nulj} + \sum_{p \in P} Q_{nplj} + \sum_{n_1 \in N} Q_{n_1 plj} \qquad \forall n \in N, \forall j \in J, \forall l \in L \tag{7}$$

Constraints (4)-(6) force splitter outflow to be equal to splitter inflow multiplied by the corresponding outflow fraction. Equation (7) is the material balance constraint between arc output and outflow. Let R_{ucj} be the surrogate model for all components but two of configuration c in C in process unit u in U.

$$Q_{uj}^{out} \le R_{ucj}(Q_{ucj}^{in}, V_{uc}) + M(1 - w_{uc}) \qquad \forall u \in U, \forall j \in J \tag{8}$$

$$Q_{uj}^{out} \ge R_{ucj}(Q_{ucj}^{in}, V_{uc}) - M(1 - w_{uc}) \qquad \forall u \in U, \forall j \in J \tag{9}$$

$$Q_{uj}^{out} \le M \sum_{c \in C} w_{uc} \qquad \forall u \in U, \forall j \in J \tag{10}$$

$$Q_{uj}^{out} = \sum_{n \in N} Q_{unj} + \sum_{p \in P} Q_{upj} + \sum_{u_1 \in U} Q_{uu_1 j} \qquad \forall u \in U, \forall j \in J \tag{11}$$

We retrieve the values of the two (not modelled) components by mean of carbon/hydrogen molar balance constraints (see Duchêne et al. (2019)). Moreover, we consider also the following arc constraints:

$$a_{nnl} = 0 \qquad \forall n \in N, \forall l \in L \tag{12}$$

$$\sum_{p \in P} a_{up} + \sum_{n \in N} a_{un} \le 1 \qquad \forall u \in U \tag{13}$$

$$\sum_{u \in U} a_{nu} + \sum_{n_1 \in N} a_{nn_1 l} + \sum_{p \in P} a_{npl} \le 1 \qquad \forall n \in N, \forall l \in L \tag{14}$$

$$\sum_{n \in N} a_{fn} + \sum_{u \in U} a_{fu} = 1 \qquad \forall f \in F \tag{15}$$

$$\sum_{u \in U} a_{up} + \sum_{n \in N} \sum_{l \in L} a_{npl} \le 1 \qquad \forall p \in P \tag{16}$$

$$\sum_{l \in L} (a_{n_2 n_1 l} + a_{n_1 n_2 l}) \leq 1 \qquad \forall n_1 n_2 \in N \tag{17}$$

Constraint (12) prevents node loops in *G(N,A)*. Equations (13)-(14) constraint each arc from unit and node, respectively, to appear at most one time in *G(N,A)*, while constraints (15)-(16) force arcs from feed and product, respectively, to appear exactly one time in *G(N,A)*. Eq. (17) is the constraint selection for the node/node arcs.

Finally, we model splitter selection per node and configuration selection per process unit, respectively, as follows:

$$\sum_{s \in S} v_{ns} = 1 \qquad \forall n \in N \tag{18}$$

$$\sum_{c \in C} w_{uc} = 1 \qquad \forall u \in U \tag{19}$$

Several additional constraints can also be enforced for process output quality (see Duchêne et al. (2019)).

Objective function. We maximize the net (hourly) profit given by the difference between input naphtha costs and output earnings (see Duchêne et al. (2019)).

2.2. With cut-points

Instead of modelling explicitly the splitters, we define "common cuts" for splitter, feeds and products, by means of a binary matrix D_{lj} whose columns sum up to 1. The flows can be split in "common cuts" by applying the previous matrix to the flows. For instance, for unit/unit flows we have

$$Q_{u_1 u_2 lj} = D_{lj} Q_{u_1 u_2 j} \qquad \forall u_1, u_2 \in U, \forall l \in L, \forall j \in J \tag{20}$$

Then, we select the routing of each common cut for each process, feed, and product by summing the previous common cut flows.

Moreover, several types of constraints are implemented:

- selection constraints: there should be at exactly one destination per feed split, one destination per nodes split:

$$\sum_{u \in U} a_{ful} + \sum_{p \in P} a_{fpl} = 1 \qquad \forall f \in F, \forall l \in L \tag{21}$$

$$\sum_{u_2 \in U} a_{fuu_2 l} + \sum_{p \in P} a_{upl} \leq 1 \qquad \forall u \in U, \forall l \in L \tag{22}$$

respectively, and at least one surrogate model configuration per process (see Eq. (19));

- arc rates constraints: the flow is equal to 0 if the corresponding arc does not belong to *G(N,A)* (see Eq. (10));
- material balance constraints: flow conservation between process unit inlet and outlet flows (see Eq. (11));
- product quality constraints: minimum level of RON and maximum level of benzene for the gasoline (see Duchêne et al. (2019)).

Moreover, constraint (12) is removed. We introduce also the concept of "cut-point": there is a cut-point if the difference of consecutive values of the binary decision variables for arc activation/deactivation is equal to 1. We have as many types of cut-point as arc types. We can consider the splitter costs in the economic objective function by considering a penalty for the cut-point.

The next step consists in considering continuous splitters by introducing additional continuous variables:

- b_{u1u2l} for the flow ratio between process units u_1, u_2 in U per branch l in L,
- b_{ful} for the flow ratio between feed f in F and unit u in U per branch l in L, and
- b_{upl} for the flow ratio between units u in U and product p in P per branch l in L.

For each continuous variable, we add a bunch of constraints in order to guarantee the corresponding value is 0 if the arc is not activated. For instance, for process units we have

$$b_{u_1 u_2 l} \leq a_{u_1 u_2 l} \qquad \forall u_1, u_2 \in U, \forall l \in L \tag{23}$$

Analogous constraints are considered for arcs between feeds and nodes, and nodes and products. Constraints (21)-(22) are replaced by

$$\sum_{u \in U} a_{ful} + \sum_{p \in P} a_{fpl} \leq \max\_arc \qquad \forall f \in F, \forall l \in L \tag{24}$$

$$\sum_{u_2 \in U} a_{uu_2 l} + \sum_{p \in P} a_{upl} \leq \max\_arc \qquad \forall u \in U, \forall l \in L \tag{25}$$

where max_*arc* is the maximum number of arcs among which a flow can be split.

Our superstructure generation methodology is hence articulated in two main steps: (i) find a first feasible solution with continuous splitter and high value for cut points penalty, and (ii) solve the problem by varying the number of cut point with low penalty.

3. Numerical Results

We consider the integrated process of catalytic reforming and light naphtha isomerization with aromatic extraction to obtain high octane gasoline with low level of benzene (for complete information about processes and instances, see Duchêne et al. (2019)). We set max_*arc* := 2 and *M := 600*.

The codes are implemented in GAMS 25.1.2 running BARON 18.5.8 on a Dell machine equipped with an Intel(R) Xeon(R) E5-1620 v3 CPU @ 3.50GHz with 16.00 GB RAM mounting Windows 7 Professional Operating System. For the Manual superstructure, allowed arc and splits have been bounded to represent the superstructure considered in previous works (see Duchêne et al. (2019)).

Table 1: Numerical results

Model type	Objective function	CPU time
Manual superstructure	42.41	1,060 seconds (*)
Formulation without cut-points variation	42.41	3,600 seconds (**)
Formulation with cut-points variation	42.21	2,581 seconds (***)

(*) optimality satisfied, optimal solution found after 19 seconds
(**) maximum time, optimal solution found after 17 seconds
(***) maximum time per iteration = 600 seconds

4. Conclusion

In this paper, we have proposed a novel automated superstructure methodology in order to (i) retrieve the best process structure, and (ii) determine the best operating conditions for the process. We have applied our method to the catalytic reforming and light naphtha isomerization integrated process. We obtain promising preliminary results: results obtained with our methodology based on cut-point variation provide similar results that direct optimization but provides objective function sensitivity to number of cut points.

References

Q. Chen, I. Grossmann, 2017, Recent developments and challenges in optimization-based process synthesis, Annual Review of Chemical and Biomolecular Engineering 8, 249–283.

P. Duchêne, L. Mencarelli, A. Pagot, 2019, Optimization approaches to the integrated system of catalytic reforming and isomerization processes in petroleum refinery, Tech. rep., IFP Energies nouvelles, Solaize, France.

L. Mencarelli, Q. Chen, A. Pagot, I. Grossmann, 2019, A review on superstructure optimization approaches in process system engineering, Tech. rep., IFP Energies nouvelles, Solaize, France, and Department of Chemical Engineering, Carnegie Mellon University, Pittsburgh.

Sauro Pierucci, Flavio Manenti, Giulia Bozzano, Davide Manca (Eds.)
Proceedings of the 30th European Symposium on Computer Aided Process Engineering (ESCAPE30), May 24-27, 2020, Milano, Italy.
http://dx.doi.org/10.1016/B978-0-12-823377-1.50123-3

Rational Design of Ion Exchange Simulated Moving Bed Processes

Marcus Fechtner[a,*], Achim Kienle[a,b]

[a]*Otto-von-Guericke-Universität Magdeburg, Chair for Automation and Modelling, Universitätsplatz 2, 39106 Magdeburg, Germany*
[b]*Max Planck Institute for Dynamics of Complex Technical Systems,Process Synthesis and Process Dynamics, Sandtorstraße 1, 39106 Magdeburg, Germany*
fechtner@ovgu.de

Abstract

Triangle theory, a powerful tool for the rational design of simulated moving bed processes, was developed by the group of Morbidelli, see (Migliorini et al., 1998) and references therein. In this paper, we extend this theory to classical ion exchange processes by applying the generalized approach of Migliorini et al. (2000). Results are verified by simulations of the related true moving bed process. For this purpose, our numerical approach for single column processes introduced in (Fechtner and Kienle, 2017) is extended to these types of processes while preserving all its advantages.

Keywords: triangle theory, ion exchange, true moving bed, simulated moving bed.

1. Introduction

Chromatographic ion exchange is an important class of separation processes applied in biotechnology and the pharmaceutical industry for the separation of amino acids and proteins, for example. Simulated moving bed (SMB) processes represent a powerful technology for continuous chromatographic separations. Triangle theory as introduced by Migliorini et al. (1998) can be used for the rational design of SMB processes. The theory is based on an idealized mathematical model that allows an analytical solution using the method of characteristics (MOC) for certain types of explicit adsorption isotherms including linear and Langmuir isotherms (Mazzotti et al., 1997). In the present contribution the theory is extended to stoichiometric ion exchange, which is also referred to as classical ion exchange (CIE) if a constant solution normality is assumed. Sorption is described by

Table 1: Process and simulation parameters.

parameter	value	description
$L[m]$	0.5	column length
$L_j[m]$	0.125	section length
$A[m^2]$	0.2	cross sectional area
$N_z[-]$	800	spatial grid points
$v_s[m/s]$	0.1	interstitial velocity
$\varepsilon[-]$	0.5	void fraction
$q_{tot}[mol/l]$	2.0	exchanger capacity
$c_{tot}[mol/l]$	1.0	solution normality
$K_{13}[-]$	8.0	equilibrium constant
$K_{23}[-]$	1.143	equilibrium constant
$\mu_1[-]$	2	stoichiometric factor
$\mu_2[-]$	1	stoichiometric factor
$\mu_3[-]$	1	stoichiometric factor
$c_1^{feed}[mol/l]$	0.3	feed of component 1
$c_1^{feed}[mol/l]$	0.4	feed of component 2

implicit isotherms resulting from the corresponding mass cation laws. Therefore, an analytical approach is not possible anymore. Using the theoretical results for a single column (Fechtner and Kienle, 2017, 2019) and following the ideas presented by by Migliorini et al. (2000), a corresponding semi-analytical approach is proposed. The approach allows to determine the total separation in the space of the design parameters. Results are validated by rigorous numerical solution of the full blown model. Further, they are shown to be superior to a simplified approach, where the ion exchange equilibrium is fitted with a Langmuir isotherm, and which is frequently applied in practice. Finally, use of the solution normality as additional design parameter is discussed.

2. Triangle theory

2.1. Ideal Model and CIE

The design procedure for the SMB first introduced by Migliorini et al. (1998) is based on the analytical solution of an ideal true moving bed (TMB) model

$$\frac{\partial}{\partial t}(c_{i,j} + Fq_{i,j}) + Fu_s \frac{\partial}{\partial z}(m_j c_{i,j} - q_{i,j}) = \mathbf{0} \tag{1}$$

using the MOC in case of Riemann problems, i.e. piece-wise constant initial conditions $\mathbf{c}_j(0, z) = \mathbf{c}_j^{init}$ and boundary conditions $\mathbf{c}_j(t, 0) = \mathbf{c}_j^{feed}$ as well as $\mathbf{q}_j(t, 1) = \mathbf{q}^{feed}$ (Rhee et al., 1989). Note, the process is initially equilibrated and the thermodynamic equilibrium between the fluid phase with c and the solid phase with q represented by some isotherm $\mathbf{q}(\mathbf{c})$ holds, i.e. $\mathbf{q}_j(0, z) = \mathbf{q}_j(\mathbf{c}_j)$. Variable $t = t^* u_s / L$ and $z = z^* / L_j$ denote dimensionless time and space coordinates, respectively. The parameter F denotes the phase ratio and $m_j = u_j / Fu_s$ denotes the dimensionless flowrate ratio in section j. Eq. (1) is used to describe a true counter current continuous process divided into 4 sections for the separation of two components. A detailed representation of the process can be found in (Storti et al., 1993). The following conditions for a complete separation of components '1' and '2' have to be satisfied

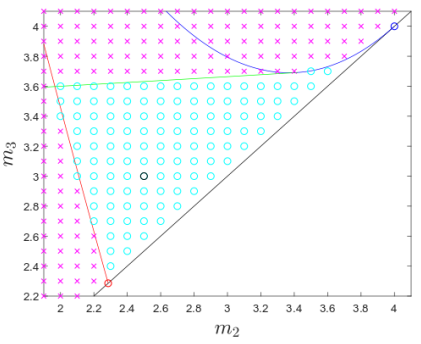

Figure 1: TMB triangle showing predicted region of complete separation. Circles indicate complete separation and crosses incomplete separation. Steady states obtained from dynamical simulation.

$$\begin{aligned} &\text{Section 1: } m_1 \geq \frac{q_{1,1}}{c_{1,1}},\ m_1 \geq \frac{q_{2,1}}{c_{2,1}},\ \text{Section 2: } \frac{q_{2,2}}{c_{2,2}} \leq m_2 \leq \frac{q_{1,2}}{c_{1,2}}, \\ &\text{Section 3: } \frac{q_{2,3}}{c_{2,3}} \leq m_3 \leq \frac{q_{1,3}}{c_{1,3}},\ \text{Section 4: } m_4 \leq \frac{q_{1,4}}{c_{1,4}},\ m_4 \leq \frac{q_{2,4}}{c_{2,4}}. \end{aligned} \tag{2}$$

The quasi-linear PDE system in Eq. (1) in conjunction with the Riemann conditions can be solved apriori (Rhee et al., 1989) using the MOC. In short, a solution is composed of simple waves and shock waves for both components (Rhee et al., 1989; Smoller, 1994).

The velocities of these waves is related to the m_j values in Eq. (3) by (Migliorini et al., 2000)

$$\lambda_{k,j} = \frac{Fu_s(m_j - \lambda_k)}{1 + F\lambda_k},\ \tilde{s}_{k,j} = \frac{Fu_s(m_j - s_k)}{1 + Fs_k},\ k = 1,2,\ j = 1,...,4, \tag{3}$$

where λ_k are the eigenvalues of the Jacobian $\partial\mathbf{q}/\partial\mathbf{c}$ and s_k follows from the jump conditions (Smoller, 1994) and is defined by $s_k = \Delta q_i / \Delta c_i$ for both components.

In this work, the CIE is used to define the thermodynamic equilibrium, thus the following implicit isotherm is used (Helfferich and Klein, 1970)

$$\begin{aligned} K_{i3} &= \left(\frac{q_i}{c_i}\right)^{\mu_i}\left(\frac{c_3}{q_3}\right)^{\mu_3} = const,\ i = 1,2, \\ c_3 &= \mu_3\left(c_{tot} - \frac{c_1}{\mu_1} - \frac{c_2}{\mu_2}\right),\ q_3 = \mu_3\left(q_{tot} - \frac{q_1}{\mu_1} - \frac{q_2}{\mu_2}\right). \end{aligned} \tag{4}$$

Therein, μ_i denotes the reciprocal of the ionic charge and K_{i3} the equilibrium constant of component i. The index '3' refers to the component that is used to keep the solution normality constant. Using the general approach of Migliorini et al. (1998) described by Migliorini et al. (2000), Eqs. (4) can be used to obtain constraints on every m_j such that complete separation of components '1' and '2' can be achieved.

2.2. Results

Assuming complete regeneration in sections 1 and 4, we obtain for m_1 and m_4 the following bounds

$$m_1 \geq \left.\frac{dq_1(c_1)}{dc_1}\right|_{c_1=0} = \left(K_{13}\frac{q_{tot}}{c_{tot}}\right)^{\frac{\mu_3}{\mu_1}},\ -\frac{1}{F} \leq m_4 \leq \frac{q_2(c_2^{\text{å}})}{c_2^{\text{å}}}. \tag{5}$$

Note, any differential terms are obtained through implicit differentiation of Eq. (4). The required value of $c_2^{\text{å}}$ is obtained from an overall mass balance for component '2' and total regeneration in Section 4

$$(m_3 - m_2)c_2^{feed} = \left(m_3 - K_{23}^{\frac{1}{\mu_2}}\left(\frac{q_{tot} - q_2(c_2^{\text{å}})}{c_{tot} - c_2^{\text{å}}}\right)^{\frac{\mu_3}{\mu_2}}\right)c_2^{\text{å}} \tag{6}$$

for given values of m_2 and m_3. The value of $q_2(c_2^{\text{å}})$ is obtained by solving Eq. (4) for $c_1 = 0$. Assuming the variables m_1 and m_4 to satisfy Eq. (5), complete separation depends only on the choice of m_2 and m_3. Therefore, a corresponding region of complete separation can be projected into the m_2, m_3-plane, see the triangular shaped set in Fig. 1. The bounds of the triangular-like set are obtained by following Migliorini et al. (2000). The black line is simply defined by $m_3 = m_2$. The red and blue lines in Fig. 1 follow from

$$m_3 = \frac{q_1}{c_1^{feed}} + m_2\left(1 - \frac{c_1}{c_1^{feed}}\right),$$

$$\text{red line: } m_2(c_1) = \left.\frac{\partial q_2}{\partial c_2}\right|_{c_2=0} = \left.\frac{q_2}{c_2}\right|_{c_2=0} = K_{23}^{\frac{1}{\mu_2}}\left(\frac{q_{tot} - q_1/\mu_1}{c_{tot} - c_1/\mu_1}\right)^{\frac{\mu_3}{\mu_2}}, \tag{7}$$

$$\text{blue line: } m_2(c_1) = \left.\frac{\partial q_1}{\partial c_1}\right|_{c_2=0} = K_{13}^{\frac{1}{\mu_1}}\left(\frac{q_{tot} - q_1/\mu_1}{c_{tot} - c_1/\mu_1}\right)^{\frac{\mu_1+\mu_3}{\mu_1}}\left(\frac{c_{tot} - c_1/\mu_1^2}{q_{tot} - q_1/\mu_1^2}\right),$$

where c_1 is used for parametrization. Finally, calculation of the green line in Fig. 1 is required, which is more involved. The parameters of our example, see Tab. 1, are chosen such that they define a purely competitive adsorption without selectivity reversal and with favorable pure component isotherms. These assumptions allow to conclude that completely separated components define a solution in the concentration phase space that is composed of the four states $(0,0)$, $(c_1^0,0)$, (c_1^*,c_2^*), and $(0,c_2^0)$ (Storti et al., 1993; Migliorini et al., 2000). These states are connected by two shocks and two simple waves. In particular, $(c_1^0,0)$ and (c_1^*,c_2^*) are connected by a 1-simple wave, therefore they lie on the same integral curve Γ_1 corresponding to eigenvalue λ_1. In case of the green line, c_2^0 is the running parameter and the variables c_1^0, c_1^*, c_2^*, m_2, and m_3 are unknown. Their values are obtained by solving the following set of equations

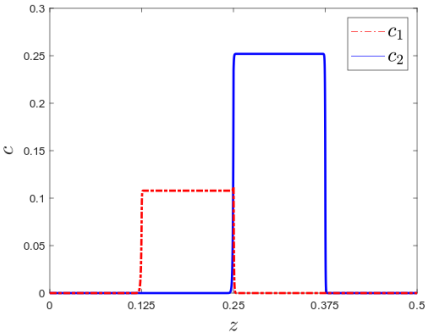

Figure 2: Steady state concentration profile for $m_2 = 2.5$ and $m_3 = 3.0$ (indicated by black circle) obtained through dynamical simulation.

$$m_2 = \frac{q_1^0/c_1^{feed}(c_2^{feed} - c_2^0) + q_2^0}{c_1^0/c_1^{feed}(c_2^{feed} - c_2^0) + c_2^0}, \quad m_3 = \frac{q_1^0 - m_2 c_1^0}{c_1^{feed}} + m_2, \tag{8a}$$

$$0 = \frac{q_1^*}{c_1^*} - m_3, \quad 0 = q_2^* - q_2^0 - m_3(c_2^* - c_2^0), \tag{8b}$$

$$\tilde{c}_1^0 = \int_{c_2^*}^{c_2^0} \frac{q_1}{q_2}\frac{\mu_2}{\mu_1}\frac{q_2/c_2 - \lambda_1}{q_1/c_1 - \lambda_1} dc_2 + c_1^*, \tag{8c}$$

where q_1^0 and q_2^0 are obtained by solving Eq. (4) for $c_2 = 0$ and $c_1 = 0$, respectively.

Similarly, $\mathbf{q}^*$ is obtained by solving Eq. (4) for $\mathbf{c}^*$. Note, equations in (8a) are easily solved for m_2 and m_3. However, they require some initial guess for c_1^0. Subsequently, equations in (8b) are solved for c_1^*, c_2^*. Finally, Eq. (8c) is used to obtain a $\tilde{c}_1^0$ that lies on the same integral curve Γ_1 as c_1^* does. Thus, the set of equations in Eq. (8) has to be

solved iteratively until $|\tilde{c}_1^0 - c_1^0| < \varepsilon$ for some small $\varepsilon << 1$. The triangle-like set in Fig. 1 is verified by performing numerical simulations of the TMB (1) for different combinations (m_2, m_3). For this purpose, the numerical approach for a single column presented in (Fechtner and Kienle, 2017) was extended to solve also the continuous true counter-current model (1) without requiring a Jacobian. Since the same soprtion isotherm is applied as in (Fechtner and Kienle, 2017), the differential index (Unger et al., 1995) is one. Hence, standard solvers to efficiently solve the corresponding DAE system, for example trough method of lines (Schiesser, 1991), can be used providing the same advantages. Additionally, the Riemann set-up easily allows to obtain consistent initial conditions by solving Eq. (4) for piece-wise constant initial values just once. A particular simulation with $(m_2 = 2.5, m_3 = 3.0)$ is shown in Fig. 2. It clearly shows the complete separation of the target components as predicted by the Triangle-theory.

3. Simplified approach using Langmuir isotherms

One of the most popular sorption isotherms is the so-called Langmuir isotherm

$$q_i = \frac{a_i c_i}{1 + \sum_j b_j c_j} \tag{9}$$

Beside the flexibility to reproduce many sorption mechanisms (Guiochon et al., 2006), it provides many mathematical features that simplify an analysis, in particular related to equilibrium theory (Rhee et al., 1989) and therefore also for the triangle theory (Mazzotti et al., 1997). If Eq. (9) is fitted to Eq. (4), the corresponding sets of complete separation predicted by the two different models can be compared. Fig. 3 shows that the Langmuir-related triangular-like shape is a subset of one related to the CIE. There is a distinct difference particularly close to the optimal operating point, i.e. the intersection of the red and green lines. Hence, a design based on Langmuir isotherm can lead to suboptimal operating conditions. The results presented in Section 2, allow also an investigation of the effect of the solution normality c_{tot}, which can be used as a process design parameter. For this purpose, three scenarios with different but fixed solution normalities are considered. Further, the values of c_{tot} do not lie within a reversal zone (Fechtner and Kienle, 2019), i.e. $c_{tot} \notin [7,8]/49\ mol/l$. The corresponding triangular-shaped sets can be seen in Fig. 4. From this figure it is clear that, at least in the range of these cases, c_{tot} differences have only a minor effect on the shape of the three sets. However, there is a significant change in the position of these sets in the m_2, m_3-plane. Thus, completely different regions for the sets of complete separation are available through variation of c_{tot}

.

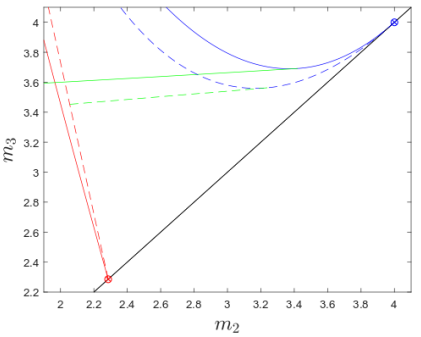

Figure 3: Comparison of predicted TMB triangles using CIE (solid lines) and Langmuir (dashed lines), respectively. Parameters: $a_1 = 4.0,\ b_1 = 0.413,\ a_2 = 2.286,\ b_2 = 0.095$

4. Conclusion

In this paper, the triangle theory was applied to the classical ion exchange, which allows the rational design of ion exchange simulated moving bed processes. This can also be done also by using the Langmuir isotherm, which however is shown to lead to regions of suboptimal process conditions. In a first step, the potential of the solution normality as additional design parameter was investigated. It provides a greater flexibility for the choice of (m_2, m_3) values, which then can be used to accommodate other process aspects in order to increase the performance. Further, the efficient numerical approach for implicit adsorption isotherms presented in Fechtner and Kienle (2017) was successfully extended to TMB processes.

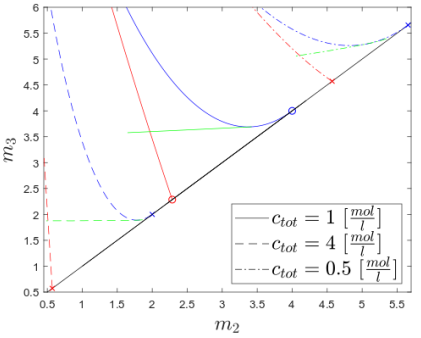

Figure 4: Effect of different but constant solution normality on the predicted TMB triangle. All three cases $c_{tot} = 1$ (solid lines), $c_{tot} = 4$ (dashed lines), and $c_{tot} = 0.5$ (dashdot lines) without selectivity reversal.

Acknowledgments
The financial support of the International Max Planck Research School for Advanced Methods in Process and Systems Engineering - IMPRS ProEng is greatly acknowledged. The research was also supported by the center of dynamic systems (CDS), funded by the EU-programme ERDF (European Regional Development Fund).

References

M. Fechtner, A. Kienle, 2017, Efficient simulation and equilibrium theory for adsorption processes with implicit adsorption isotherms – mass action equilibria, Chem. Eng. Sci., 171, 471-480

M. Fechtner, A. Kienle, 2019, Equilibrium theory of ion exchange chromatography with variable solution normality and steric hindrance, Chem. Eng. Sci., 199, 508-527

G. Guiochon, A. Felinger, D. G. Shirazi, A. M. Katti, 2006, Fundamentals of Preparative and Nonlinear Chromatography, Elsevier Academic Press, San Diego , 2

F. G. Helfferich, G. Klein, 1970, Multicomponent Chromatography Theory of Interference, M. Dekker, New York, 1

M. Mazzotti, G. Storti, M. Morbidelli, 1997, Optimal operation of simulated moving bed units for nonlinearchromatographic separations, J. Chrom. A, 769, 3-24

C. Migliorini, M. Mazzotti, M. Morbidelli, 1998, Continuous chromatographic separation through simulated moving beds under linear and nonlinear conditions, J. Chrom. A, 827, 161-173

C. Migliorini, M. Mazzotti, M. Morbidelli, 2000, Robust design of countercurrent adsorption separation processes: 5. nonconstant selectivity, AIChE J., 46, 1384-1399

H.-K. Rhee, R. Aris, N. R. Amundson, 1989, First-Order Partial Differential Equations: Volume II – Theory and Application of Hyperbolic Systems of Quasilinear Equations, Prentice Hall, New Jersey, 1

W. E. Schiesser, 1991, The Numerical Method of Lines Integration of Partial Differential Equations, Academic Press, San Diego, 1

J. Smoller, 1994, Shock Waves and Reaction–Diffusion Equations, Springer, New York, 2

G. Storti, M. Mazzotti, M. Morbidelli, 1993, Robust design of binary countercurrent adsorption separation processes, AIChE J., 39, 1825-1842

J. Unger, A. Kröner, W. Marquardt, 1995, Structural analysis of differential-algebraic equation systems: Theory and applications, Comp. & Chem. Eng., 19, 867-882

Sauro Pierucci, Flavio Manenti, Giulia Bozzano, Davide Manca (Eds.)
Proceedings of the 30th European Symposium on Computer Aided Process Engineering (ESCAPE30), May 24-27, 2020, Milano, Italy.
http://dx.doi.org/10.1016/B978-0-12-823377-1.50124-5

Optimal use of Process Streams as Working Fluids in Work and Heat Exchange Networks (WHENs)

Haoshui Yu[a,b], Chao Fu[c], Truls Gundersen[a*], Emre Gençer[b]

[a]*Department of Energy and Process Engineering, Norwegian University of Science and Technology, Kolbjoern Hejes v. 1A, NO-7491 Trondheim, Norway*
[b]*MIT Energy Initiative, Massachusetts Institute of Technology, 77 Massachusetts Avenue, Cambridge, MA 02139, United States*
[c]*SINTEF Energy Research, Kolbjoern Hejes vei 1.B, NO-7491 Trondheim, Norway*
truls.gundersen@ntnu.no

Abstract

Design of Heat Exchanger Networks (HENs) has been widely studied and applied since it can significantly reduce energy consumption in the process industries. However, pressure effects are ignored in HENs. To consider temperature and pressure simultaneously, Work and Heat Exchange Networks (WHENs) emerge as a new research topic in Process Systems Engineering. Even in cases where the supply and target pressures of the process streams are the same, the HENs problem can benefit from being expanded to a WHENs problem. In this paper, a methodology to extend the Heat Exchange Networks (HENs) problem to a Work and Heat Exchange Networks (WHENs) problem is proposed with the objective of improving energy/exergy efficiency of process plants. A case study illustrates the profitability of manipulating the pressure of streams that in the original problem definition are constant pressure streams. The exergy consumption is reduced by 29.92% in the case study.

Keywords: Heat Exchanger Network, Work and Heat Exchange Network, Working Fluids, Process Streams

1. Introduction

Heat Integration has been a successful field of Process Synthesis in reducing specific energy consumption in the process industries. Both Pinch Analysis pioneered in the 1970s and extended to a design methodology in the 1980s (Linnhoff and Hindmarsh, 1983), and Mathematical Programming formulations (Cerda and Westerberg, 1983), developed in the 1980s, have been used to design and optimize Heat Exchanger Networks (HENs). While significant savings have been achieved in thermal energy by using these methodologies, mechanical energy is also an important element in the energy system for most process industries. Similar to heat exchange for increasing or decreasing the temperature of process streams, compression and expansion are used to manipulate the pressure of process streams. As a result, the design task of Work Exchange Networks (WENs) was introduced (Huang and Fan, 1996) for savings in mechanical energy by work recovery. Both direct (flow work) and indirect (shaft work) exchange have been studied. Since pressure manipulations (compression/expansion) affect the temperatures of process streams, HENs and WENs should be designed simultaneously. Heating from compression and cooling from expansion may have a considerable impact on the heat recovery problem. Similarly, heat integration affects the temperatures of process streams and thus the work consumed/produced in pressure

change. As a result, a new research field referred to as Work and Heat Exchange Networks (WHENs) has emerged during the last decade (Yu et al., 2019a). For this design problem, process streams have a specified supply and target state (temperature and pressure), and the objective is to develop a network of heat exchange equipment (heat exchangers, heaters and cooler) and pressure manipulators (compressors, pumps, expanders and valves) in such a way that a selected Key Performance Indicator (e.g. Energy/Exergy Efficiency or Total Annualized Cost) is optimized. Some early works (Fu and Gundersen, 2016b; Zhuang et al., 2018; Yu et al., 2019b) have demonstrated the potential of WHENs to significantly improve the energy situation in process plants beyond what can be obtained by HENs. Even in cases where the supply and target pressures of the process streams are the same, the HENs problem can benefit from being expanded to a WHENs problem. This is typically the case when the hot and cold composite curves do not match well and where pressure manipulations may bring the curves closer together to increase heat recovery. While this could be achieved by heat engines and heat pumps (Colmenares and Seider, 1987), a more direct and economic solution would be to manipulate the pressure of the process streams rather than using external working fluids. One example based on using the WHENs methodology is the novel sensible heat pump scheme (Fu and Gundersen, 2016c), where a stream with equal supply and target pressure is used as working fluid for a reversed Brayton cycle. Both compression and expansion are correctly placed above and below Pinch, respectively. In effect, process streams temporarily act as working fluids, i.e. they are compressed/expanded in such a way that their target pressures (equal to their supply pressures) are satisfied. The idea behind the sensible heat pump can also be applied to heat engines, where a process stream can be used as working fluid to generate power. One such power cycle is the open Organic Rankine Cycle (ORC) (Yu et al., 2017), where process streams act as working fluids. Thus, WHENs represent a generalization of industrial heat engines and heat pumps. For sub-ambient applications, pressure manipulation of process streams may replace external refrigeration cycles.

2. Problem statement and methodology

As stated above, it is quite common that composite curves do not match well, i.e. they open up considerably above and/or below Pinch. This means significant exergy losses from heat transfer. If, in addition, there is considerable heat surplus (below Pinch) or heat deficit (above Pinch), opportunities for work generation or heat pumping are lost. In such cases, regardless of the configuration of the heat exchanger network, the energy efficiency of the system is not satisfactory. To further improve the efficiency of the system, one can change the shape of the hot/cold composite curves, which means manipulation of the process streams beyond heat exchange. Pressure manipulation of process streams is an alternative scheme. As shown in Figure 1 (stream data in Table 1), the composite curves of the system do not match well. The temperature difference between the hot and cold composite curves below Pinch is very large. The exergy destruction is therefore large no matter how the heat exchanger network is designed.

Thus, to improve the energy efficiency of the system, one would like to extend the HEN synthesis problem to a corresponding WHEN problem. As shown in Figure 2, the pressure of process streams can be manipulated to enhance the match between the hot and the cold composite curves. In HENs, a process stream often passes through several heat exchangers to reach the target temperature. If the pressure of process streams is manipulated by a compressor, an expander, a pump, or a valve, as shown in Figure 2, the energy efficiency of the system can be improved. The maximum energy efficiency

depends on the intermediate pressure level P_{int}, as indicated in Figure 2. In this study, we would like to determine the optimal pressure operator and the intermediate pressure to achieve the maximum energy/exergy efficiency of the system.

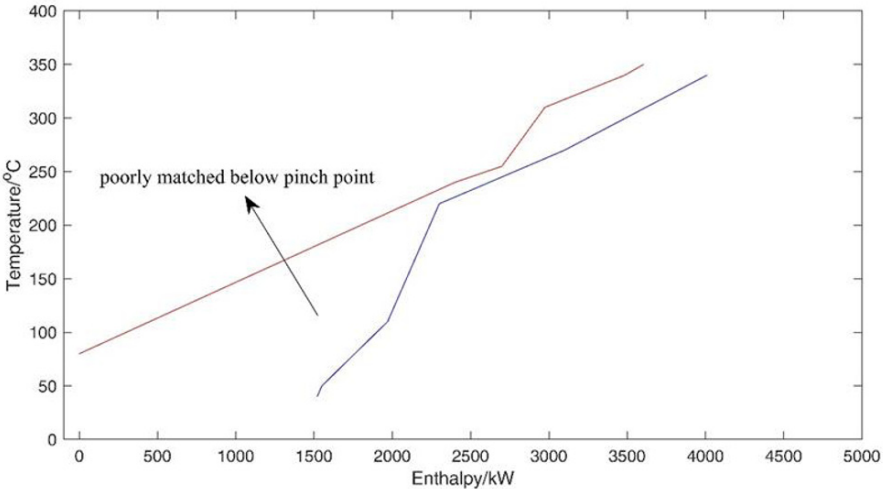

Figure 1. Example of poorly matched composite curves

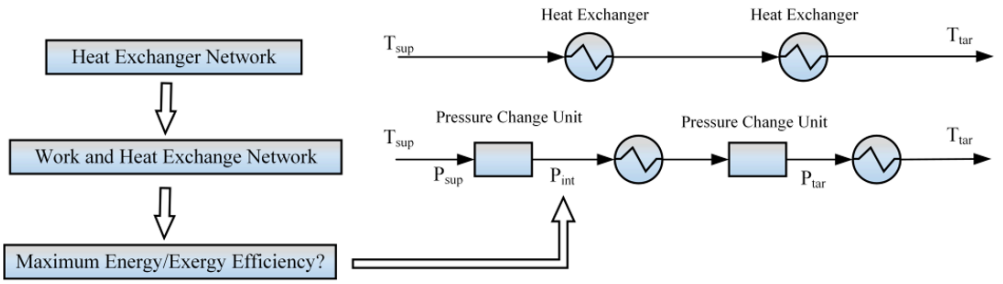

Figure 2. The HEN problem extended to a WHEN problem

Based on the shape of the composite curves, the pressure manipulator of one of the process streams should first be selected. If the first pressure changing unit is a turbine or a valve, the second pressure changing unit should be a compressor or a pump, and vice versa. In this study, to determine the near-optimal intermediate pressure, a simulation of the different intermediate pressures is performed in Aspen HYSYS. With different intermediate pressures, the hot and cold composite curves and the energy target of the system can be determined using heat integration methods. Finally, the optimal pressure changing units and the optimal intermediate pressure can be determined. Once the pressure manipulators and optimal intermediate pressure are determined, the final heat exchanger network can be synthesized based on conventional heat exchanger network synthesis technologies or models.

Since both work and heat are involved when pressure changing units are introduced to the system, exergy consumption of the system is chosen as the indicator of energy efficiency. Following Fu and Gundersen (2016a), the Carnot factor is adopted as the coefficient to calculate the exergy of thermal energy, however, this is an optimistic estimation assuming reversible operations. The coefficient can easily be changed depending on the process and the application.

3. Case study

In this section, an example is chosen to illustrate the advantage of extending HENs to WHENs. The process stream data are listed in Table 1 and the corresponding hot and cold composite curves are shown in Figure 1. It should be noticed that the composite curves are poorly matched below the Pinch, which indicates a large heat transfer irreversibility below the Pinch.

Table 1. Process stream data for the case study

Stream	Supply temperature (°C)	Target temperature (°C)	FCp (kW/°C)	Duty (kW)
H1	350	310	12	480
H2	340	240	5	500
H3	255	80	15	2625
C1	220	340	13	1560
C2	50	110	4	240
C3	40	270	3	690

When the problem is solved as a conventional heat integration problem, the corresponding minimum hot and cold utility loads are 405 kW and 1520 kW with a minimum heat recovery approach temperature of 10°C. The Pinch corresponds to 255°C for hot streams and 245°C for cold streams. In this case study, the hot and cold utilities are assumed to be supplied at 400°C and 15°C respectively. The reference temperature for exergy is chosen to be 15°C, which means the exergy content of cold utility is zero. As a result, the minimum exergy consumption of the system is 231.6 kW.

To improve the energy efficiency of the system, attention should be paid to the below Pinch part of the problem. If the pressure of a process stream below Pinch is changed, a better energy system could be expected. A process stream with appropriate thermodynamic properties should be chosen as the stream for pressure manipulation. In this case study, we assume that C2 is n-Hexane at the pressure of 3.13 bar (slightly above the saturation pressure at 110°C). The reason for this assumption is to guarantee C2 in liquid phase in the entire temperature range of 50°C to 110°C. The stream could have been other substances as long as they can act as working fluid for a heat engine in the relevant temperature range.

There is excess amount of heat below Pinch, thus the manipulation of a cold stream should be able to convert excess heat into power. Therefore, the first pressure manipulator should be a pump and the second one should be a turbine. Since the critical pressure of n-Hexane is 30.32 bar, the upper bound for the intermediate pressure is set to 30 bar in this study. The lower bound for the intermediate pressure is set to 8 bar.

The results under different intermediate pressures are illustrated in Figure 3, where the total exergy consumption, net power output and hot utility consumption are presented. It is clear that the net power output increases with the intermediate pressure. However, the variation in hot utility consumption is more complex. Hot utility consumption is constant when the intermediate pressure is less than 18 bar, which means that the pressure manipulation of C2 has no effect above the Pinch as long as the intermediate pressure is below 18 bar. When the intermediate pressure is larger than 18 bar, the hot utility consumption increases first and then decreases. With the increase in intermediate pressure, the evaporation temperature of C2 increases and the available heat above the evaporation temperature decreases. As a result, a new Pinch occurs in the system and the original Pinch is no longer a bottleneck of the system. More hot utility is required in such cases. However, when the intermediate pressure increases towards the critical

pressure, hot utility consumption tends to decrease. This phenomenon can be explained as follows: With the increase of intermediate pressure, the evaporation heat decreases considerably, and C2 does not require as much heating load from hot process streams as in the low intermediate pressure situation. Therefore, the total exergy consumption of the system decreases at first, and it increases with the intermediate pressure in the range between 18 bar and 25 bar, while it finally decreases with intermediate pressure above 25 bar. The optimal intermediate pressure is thus 18 bar. When the intermediate pressure is less than 18 bar, the hot utility is 405 kW and pressure manipulation of process stream C2 has no effect on the heat integration above the original Pinch.

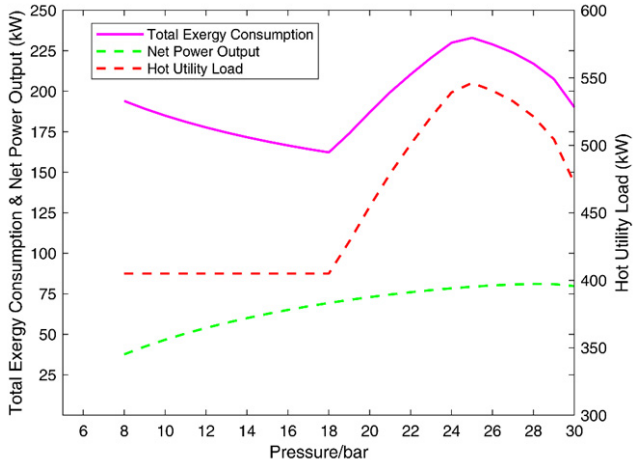

Figure 3. System performance with variation of the intermediate pressure

The optimal results indicate that C2 is pumped to 18 bar first, and then the hot streams in the system heat C2 to a saturated vapor state before entering a turbine. C2 is expanded to the original pressure 3.13 bar and generates 69.3 kW electricity (net power output). After expansion, C2 becomes a hot stream to be cooled to 110°C. In this process, the identity (hot/cold) of C2 changes.

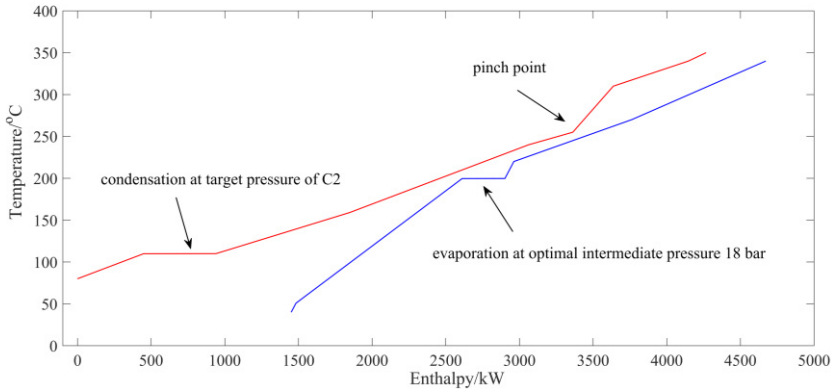

Figure 4. Hot and cold composite curves with the intermediate pressure at 18 bar

Figure 4 illustrates the composite curves under optimal conditions. Compared with the original composite curves shown in Figure1, a much better match between the curves is achieved. In the original HEN, the minimum exergy consumption is 231.6 kW, while

the exergy consumption can reach 162.3 kW with one pressure changing stream. The exergy consumption is reduced by 29.92%. This case study shows the potential benefit of extending HENs to WHENs, even in cases where all the process streams are at constant pressure in the process.

4. Conclusions

In this paper, the Heat Exchanger Networks (HEN) problem is extended to a Work and Heat Exchange Network (WHEN) problem for cases where the hot and cold composite curves do not match well. Pressure manipulation of a process stream with the same supply and target pressure can improve the exergy efficiency of the whole system. The pressure changing units and the near-optimal intermediate pressure can be determined based on simulation and sensitivity analysis. A case study shows the potential advantage of extending the HEN to a WHEN problem. In this specific case study, the manipulation of a single process stream results in an open Organic Rankine Cycle (ORC). This also reveals that the integration of heat engines and heat pumps with HENs can be solved from the perspective of WHENs. A more systematic investigation on heat engines, heat pumps and refrigeration cycles will be performed in future work.

Acknowledgments

This publication has been funded by HighEFF—Centre for an Energy Efficient and Competitive Industry for the Future. The authors gratefully acknowledge the financial support from the Research Council of Norway and user partners of HighEFF, an 8-year Research Centre under the FME-scheme (Centre for Environment-friendly Energy Research, 257632).

References

J. Cerda, A. W. Westerberg, 1983, Synthesizing heat exchanger networks having restricted stream/stream matches using transportation problem formulations, Chemical Engineering Science, 38, 1723-1740.

T. R. Colmenares, W. D. Seider, 1987, Heat and power integration of chemical processes, AIChE Journal, 33, 898-915.

C. Fu, T. Gundersen, 2016a, Correct integration of compressors and expanders in above ambient heat exchanger networks, Energy, 116, Part 2, 1282-1293.

C. Fu, T. Gundersen, 2016b, Heat and work integration: Fundamental insights and applications to carbon dioxide capture processes, Energy Conversion and Management, 121, 36-48.

C. Fu, T. Gundersen, 2016c, A novel sensible heat pump scheme for industrial heat recovery, Industrial & Engineering Chemistry Research, 55, 967-977.

Y. L Huang, L. T. Fan, 1996, Analysis of a work exchanger network, Industrial & Engineering Chemistry Research, 35, 3528-3538.

B. Linnhoff, E. Hindmarsh, 1983, The pinch design method for heat exchanger networks, Chemical Engineering Science, 38, 745-763.

H. Yu, J.Eason, L. T. Biegler, X. Feng, 2017, Process integration and superstructure optimization of Organic Rankine Cycles (ORCs) with heat exchanger network synthesis, Computers & Chemical Engineering, 107, 257-270.

H. Yu, C. Fu, M. Vikse, T. Gundersen, 2019a, Work and heat integration – A new field in process synthesis and process systems engineering, AIChE Journal, 65(7):e16477.

H. Yu, C. Fu, M. Vikse, C. He, T. Gundersen, 2019b, Identifying optimal thermodynamic paths in work and heat exchange network synthesis, AIChE Journal, 65, 549-561.

Y. Zhuang, L. Zhang, L. Liu, Q. Meng, J. Du, 2018, Simultaneous Synthesis of WHEN based on Superstructure Modelling Considering Thermodynamic and Economic Factors, Computer Aided Chemical Engineering, 44, 1033-1038.

Sauro Pierucci, Flavio Manenti, Giulia Bozzano, Davide Manca (Eds.)
Proceedings of the 30th European Symposium on Computer Aided Process Engineering (ESCAPE30), May 24-27, 2020, Milano, Italy.
http://dx.doi.org/10.1016/B978-0-12-823377-1.50125-7

Computer Aided Molecular Design of Green Solvents for the Hydroformylation of Long-Chain Olefines

Tobias Keßler[a,*], Christian Kunde[a], Steffen Linke[b], Kevin McBride[c], Kai Sundmacher[b,c] and Achim Kienle[a,d,*]

[a]*Otto-von-Guericke University Magdeburg, Chair for Automation/Modelling, Universitätsplatz 2, 39106 Magdeburg*
[b]*Otto-von-Guericke University Magdeburg, Chair for Process Systems Engineering, Universitätsplatz 2, 39106 Magdeburg*
[c]*Max-Planck-Institute for Dynamics of Complex Technical Systems, Process Systems Engineering Group, Sandtorstr. 1, 39106 Magdeburg*
[d]*Max-Planck-Institute for Dynamics of Complex Technical Systems, Process Synthesis and Dynamics Group, Sandtorstr. 1, 39106 Magdeburg*
tobias.kessler@ovgu.de; achim.kienle@ovgu.de

Abstract

A hydroformylation process of long-chain olefines is investigated. In an attempt to replace an established, toxic solvent used in this process, a computer aided molecular design approach based on group contribution methods is used to predict the solvent properties, as well as the liquid-liquid equilibrium of the mixture and environment, health and safety (EHS) criteria. Generating chemically feasible solvent candidates with the desired properties requires the solution of combinatorially complex mixed-integer nonlinear programs. First results of the approach are presented and discussed.

Keywords: MINLP, CAM(x)D, Green Chemistry, EHS Criteria, Group Contribution Methods

1. Introduction

The concept of “Green Chemistry” has gained an evergrowing interest over the last years. The focus of chemical engineers shifted from a mainly economical view on the process efficiency to a view on process efficiency with an awareness for the ecological impact. Solvents are a class of chemicals that are widely used in the chemical industry to dilute or extract other chemical species. Some well-established and frequently used solvents are toxic, for example dimethylformamide (DMF). Due to the many ways by which humans and the environment may be exposed to toxic solvents, they pose a potential health risk and should, therefore, be replaced by safer and ecologically benign alternatives.

The case study considered in this work is the hydroformylation of n-decene. For the economic efficiency of the process a high space-time yield of the catalyzed reaction needs to be achieved and the rhodium based catalyst needs to be recovered. To meet these requirements a thermomorphic multiphase system (TMS) (Schäfer et al., 2012) consisting of the polar solvent DMF and the non-polar solvent dodecane is employed. The TMS is homogeneous at reaction conditions to allow for good contact between the

reactants and the catalyst, and biphasic at lower temperatures to allow for catalyst recycling.
In an attempt to replace the developmentally toxic solvent DMF by a safer and ecologically more benign alternative, a screening method was recently employed and two promising alternatives for DMF were identified (McBride et al., 2018). In a further study by the authors, a process optimization for those two alternatives was conducted and one of them delivered promising results (Keßler et al., 2019). Screening methods are, by design, only able to find alternatives already contained in the considered databases. In contrast to that, this work also aims at identifying new ecologically benign solvent candidates not yet included in the databases. To achieve this, a hierarchical computer aided molecular design approach based on group contribution methods is used.

2. Computer Aided Molecular Design

Computer Aided Molecular and Mixture Design problems are complex mixed-integer non-linear programs (MINLP) of the following form:

$$
\begin{aligned}
\min_{n,x} \quad & J(n,p,q), \\
\text{s.t.} \quad & s_1(n) \le 0, \\
& s_2(n) = 0, \\
& p = f(n), \\
& q = g(x,n,p), \\
& h_1(p,q,n) \le 0, \\
& h_2(p,q,n) = 0, \\
& p_k^L \le p_k \le p_k^U, \\
& n_d^L \le n_d \le n_d^U, \\
& q_j^L \le q_j \le q_j^U, \\
& \sum_i x_i = 1,
\end{aligned}
\tag{1}
$$

where $\boldsymbol{s}$ are structural feasibility constraints, p and q are estimated molecule/mixture properties, and $\boldsymbol{h}$ are thermodynamic/physical property constraints. Upper and lower bounds are denoted by L and U, respectively. Each of the constraint types will be discussed in the following.

2.1. Structural Feasibility Constraints

Structural feasibility constraints are needed to ensure that the molecule obtained by a combination of predefined atom groups is chemically feasible. A list of the groups used in this work can be found in Table 1. The constraints used in this work are based on the works of Sahinidis et al. (2003) and Churi and Achenie (1996), namely:
The number of single and double bonds must be even. There must be a sufficient number of transition groups, having single and double bonds, to connect groups with only one bond type.
The number of bonds must at least equal the number of groups minus one and the number of bonds cannot exceed that of a complete graph in which all groups are connected.

The octet rule: Each groups valency is satisfied with a covalent bond. Note, that even if the valencies of the groups are satisfied, the bond types need to be checked in order to guarantee consistency.

Table 1: Groups in group set *i*. s denotes a free single bond valence, d denotes a free double bond valence, r denotes a free cyclic bond valence and AC denotes an aromatic C.

Main groups							
sCH3	ssCH2	dCH2	sssCH	sdCH	ssssC	ssdC	ddC
Aromatic groups							
rrACH	rrACs	rrACCH3	rrACCH2s	rrACCHss	rrACCHd	rrACNH2	
Functional groups							
sCH3CO	sCH2COs	CH=Os	sCH3COO	sCH2COOs	sOCH3	sOCH2s	sOCHss
sOCHd	sCH2NH2	ssCHNH2	dCHNH2	sCH2NHs	sCH2CN	sCOOH	sCH2NO2
ssCHNO2	dCHNO2						

Two adjacent groups may not be linked by more than one bond. This ensures that there are no double or triple bonds, which are formulated explicitly in the groups, i. e. C (valence: 4) can either be: ssCss, dCss, dCd, where s are single and d are double bonds. Each active group gets an index by consecutive numbering, allowing for a mapping of the connections of each group to other groups. Each group needs to be connected to at least one group with a lower index. Though the mapping may not be unique, this makes sure that only one connected molecule is obtained.

2.2. Property Estimation

Pure species properties: To estimate the properties of a structurally feasible molecule, so called group contribution methods are employed. In their simplest form, these methods assume that each of the groups in the molecule contributes a specific value to a specific property p,

$$p = \sum_i n_i c_i, \tag{2}$$

Where n_i is the number of occurrences of group i and c_i is the contribution of group i to property p. There exist numerous group contribution methods for various molecule properties. In this work, the group contribution method by Marrero and Gani (2001) is used to estimate the boiling point T_b, as well as the heat of vaporization H_v of the generated molecule. Furthermore, to obtain a greener solvent candidate, the toxicity of the new molecule is measured by the oral rat LD_{50} and the permissible exposure limit PEL, calculated using the group contribution method by Hukkerikar et al. (2012). As an approximation of the thermodynamic properties of the solvent candidate, the Hansen solubility parameter (HSP) is determined using the group contribution method by Panayiotou (2008).

Mixture properties: The liquid-liquid equilibrium (LLE) of the mixture is defined as

$$\boldsymbol{\gamma}^{\mathrm{I}}\mathbf{x}^{\mathrm{I}} = \boldsymbol{\gamma}^{\mathrm{II}}\mathbf{x}^{\mathrm{II}}, \tag{3}$$

where $\boldsymbol{\gamma}$ is the activity coefficient and $\mathbf{x}$ is the composition of phases I and II. One of the most well known group contribution methods to model the non-ideal phase behavior in the activity coefficient is modified UNIFAC (Dortmund) (called UNIFAC in the remainder of this manuscript) (Weidlich and Gmehling, 1987). Group contribution

methods are not able to sufficiently capture the behavior of large molecules (Struebing, 2011). In the hydroformylation process a rhodium-biphephos catalyst complex is used. Therefore, the catalyst distribution of the process during the phase separation cannot be modeled using UNIFAC. However, as the catalyst distribution has a high impact on the overall process cost (Keßler et al., 2019) the phase behavior of the mixture needs to be described during the generation of the new solvent candidate. To achieve this, COSMO-based methods are employed.

COSMO-RS is a quantum chemistry based method for the prediction of chemical potentials. The main idea is that each species has a characteristic charge density (the so-called σ-Profile). Those charge densities can be used to predict how the species will interact (Klamt et al., 2010). The σ-profiles can be calculated using commercial software packages. Additionally, there exists a group contribution method to calculate them (Liu et al., 2019). In our approach, the σ-profiles of the already known species of the mixture (decene, dodecane, undecanal, biphephos) are calculated a priori, while the σ-profile of the new molecule is estimated using the aforementioned group contribution method. Lin and Sandler (2002) proposed an activity coefficient model named COSMO-SAC (segment activity coefficients) based on σ-profiles,

$$\ln \gamma_{j/S} = \sum_m p_j(\sigma_m) \cdot \left[\ln \Gamma_S(\sigma_m) - \ln \Gamma_j(\sigma_m) \right] + \ln \gamma_{j/S}^{\mathrm{SG}}, \tag{4}$$

where index j denotes the pure species and index S the mixture, $\gamma_{j/S}$ is the activity coefficient of species j in mixture S, $p_j(\sigma_m)$ is the charge density p of species j on segment σ_m, $\boldsymbol{\Gamma}$ are the segment activity coefficients and $\gamma_{j/S}^{SG}$ is the Stavermann-Guggenheim combinatorial term. The segment activity coefficients $\boldsymbol{\Gamma}$ are defined as

$$\ln \Gamma_k(\sigma_m) = -\ln\left(\sum_n p_k(\sigma_n) \Gamma_k(\sigma_n) \exp\left(\frac{-\Delta W(\sigma_m, \sigma_n)}{\mathrm{R}T} \right) \right), k \in \{j, S\}, \tag{5}$$

where $\mathrm{R} = 0.001987$ kcal/(mol · K) is the ideal gas constant and $\Delta W(\sigma_m, \sigma_n)$ is the energy required to obtain a (σ_m, σ_n) pair. This energy is called exchange energy, it is defined as

$$\Delta W(\sigma_m, \sigma_n) = \frac{\alpha}{2}(\sigma_m + \sigma_n)^2 + c_{\mathrm{hb}} \max(0, \sigma_{\mathrm{acc}} - \sigma_{\mathrm{hb}}) \cdot \min(0, \sigma_{\mathrm{don}} + \sigma_{\mathrm{hb}}). \tag{6}$$

Here, σ_{don} is the smaller and σ_{acc} is the larger value of σ_m and σ_n, c_{hb} is a constant for hydrogen bonding interaction, σ_{hb} is a hydrogen bonding cutoff value and α is the misfit energy.

2.3. Constraints

The solvent we are looking for is meant for a specific process, therefore some specific property constraints are necessary. The boiling point is constrained to $T_{\mathrm{b}} \in [350, 600]$ K, because the product of the process reacts to an unwanted side product at higher temperatures. Ideally, the new solvent has the same characteristics as DMF regarding the affinity to the catalyst and the reactant after the phase split. Therefore, as a pre-screening step to reduce the search space, the HSP is constrained to values close to the HSP value of DMF, $\delta_0 \in [24, 25.6] \sqrt{\mathrm{MPa}}$.

Furthermore, to guarantee that the solver does not select the trivial solution of Eq. (3), the phase compositions are constrained to $x_1^{\mathrm{I}} \in [0.7648, 0.9671]$, $x_2^{\mathrm{II}} \geq 0.3$, following a

prior optimization study (Keßler et al., 2019). Here, component 1 is the new polar solvent candidate and component 2 is the fixed non-polar solvent dodecane. In addition to the property constraints some complexity constraints are necessary, because GC methods only yield poor approximations if the molecules are too complex (Struebing, 2011). The number of groups is constrained to $\sum_i n_i \in [2,7]$, the number of main groups is constrained to 2 for cyclic molecules, the number of aromatic groups allowing side chains is constrained to 1, the number of chain-ending groups is constrained to 4 for acyclic and 1 for cyclic molecules, the number of non-chain-ending groups is constrained to 3 for acyclic and to 1 for monocyclic molecules.

2.4. Hierarchical Decomposition

The problem is decomposed into two relatively easy to solve subproblems. In the first step, the objective is to generate a molecule with a low boiling point, a high PEL and a high LD_{50},

$$\min_n J_1 = T_\mathrm{b} - 20PEL - 50LD_{50}, \tag{7}$$

20 molecules are generated. Note, that the problem is a representative of a multi-objective optimization (MOO) problem. However, for this study we have chosen fixed weights.

In the second step, COSMO-SAC is solved for each of the 20 candidates with the objective to optimize the catalyst distribution between the phases,

$$\max_x J_2 = x_\mathrm{cat}^\mathrm{I} - x_\mathrm{cat}^\mathrm{II}, \tag{8}$$

where the existence of two phases is enforced through the constraint mentioned above. The optimizations are implemented as MINLPs and solved using the GAMS 26.1.0 framework with deterministic global optimization software BARON 18.11.12., Cplex 12.8.0 is used as an LP/MIP subsolver and CONOPT 4.09 is utilized as an NLP subsolver. The calculations are carried out on a Linux PC with 3.40 GHz Intel Core i7-6700 CPU and 16 GB memory. During the hierarchical optimization, the optimization time for the solution of COSMO-SAC is constrained to 9000 s.

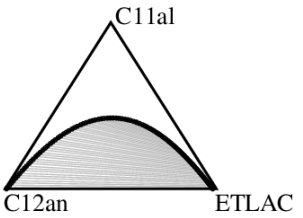

Figure 1: Phase equilibrium for ethyl lactate (ETLAC), calculated using COSMO-SAC.

2.5. Results

The solution of the first subproblem yields 20 solvent candidates. In the second subproblem, all except 6 candidates were eliminated based on the results of the COSMO-SAC calculations. For the eliminated candidates, the solver was not able to find feasible equilibrium compositions within the maximum allowable computation time. For all remaining solvent candidates, the applied models predict that the requirements on the boiling temperature, EHS criteria, and phase behavior are fulfilled. For one exemplary remaining candidate, ethyl lactate (ETLAC), the phase diagram calculated with COSMO-SAC is depicted in Figure 1.

3. Conclusion

In this work, we presented a systematic solvent and mixture design approach for identification of feasible solvent candidates for the hydroformylation of long-chain

olefines. In our hierarchical approach, the molecule candidates are designed using group contribution methods. After suitable solvent candidates are chosen with a rough approximation of their thermodynamic behavior, a subsequent optimization with quantum chemical based methods is conducted to identify the best suitable candidates. The approach yields feasible green solvent candidates. Further investigation of the candidates is necessary to account for model prediction errors and additional process constraints. Future work will also account for process design to determine the green solvent with the best process performance. Furthermore, the MOO (Eq. (7)) will be investigated more thoroughly.

Acknowledgement: Gefördert durch die Deutsche Forschungsgemeinschaft (DFG) - TRR 63 "Integrierte chemische Prozesse in flüssigen Mehrphasensystemen" (Teilprojekt B9) - 56091768.

References

N. Churi, L. E. K. Achenie, 1996. Novel mathematical programming model for computer aided molecular design. Ind. Eng. Chem. Res. 35, 3788–3794.

A. S. Hukkerikar, S. Kalakul, B. Sarup, D. M. Young, G. Sin, R. Gani, 2012. Estimation of Environment-Related Properties of Chemicals for Design of Sustainable Processes: Development of Group-Contribution+ (GC+) Property Models and Uncertainty Analysis. J. Chem. Inf. Model 52, 2823-2839.

T. Keßler, C. Kunde, S. Linke, K. McBride, K. Sundmacher, A. Kienle, 2019. Systematic Selection of Green Solvents and Process Optimization for the Hydroformylation of Long-Chain Olefines. Processes, 7, 882.

A. Klamt, F. Eckert, W. Arlt, 2010. COSMO-RS: An alternative to simulation for calculating thermodynamic properties of liquid mixtures. Annu. Rev. Chem. Biomol. Eng. 1, 101–122.

S.-T. Lin, S. I. Sandler, 2002. A priori phase equilibrium prediction from a segment contribution solvation model. Ind. Eng. Chem. Res. 41 (5), 899-913.

Q. Liu, L. Zhang, L. Liu, J. Du, Q. Meng, R. Gani, 2019. Computer-aided reaction solvent design based on transition state theory and COSMO-SAC. Chemical Engineering Science 202, 300-317.

J. Marrero, R. Gani, 2001. Group-contribution based estimation of pure component properties. Fluid Ph. Equilibria, 183-208.

K. McBride, S. Linke, S. Xu, K. Sundmacher, 2018. PSE 2018, San Diego, USA. Ch. Computer Aided Design of Green Thermomorphic Solvent Systems for Homogeneous Catalyst Recovery, pp. 1783-1788.

N. V. Sahinidis, M. Tawarmalani, M. Yu, 2003. Design of alternative refrigerants via global optimization. AIChE J 49 (7), 1761–1775.

E. Schäfer, Y. Brunsch, G. Sadowski, A. Behr, 2012. Hydroformylation of 1-Dodecene in the Thermomorphic Solvent System Dimethylformamide/Decane. Phase Behavior-Reaction Performance-Catalyst Recycling. Ind. Eng. Chem. Res. 51, 10296-10306.

E. Stefanis, C. Panayiotou, 2008. Prediction of Hansen solubility parameters with a new group-contribution method. Int. J. Thermophys. 29 (2), 568-585.

H. Struebing, 2011. Identifying optimal solvents for reactions using quantum mechanics and computer-aided molecular design. Ph.D. thesis, Imperial College London.

U. Weidlich, J. Gmehling, 1987. A modified UNIFAC model. 1. Prediction of VLE, h^E and γ^∞. Ind. Eng. Chem. Res. 26 (7), 1372-1381.

Sauro Pierucci, Flavio Manenti, Giulia Bozzano, Davide Manca (Eds.)
Proceedings of the 30th European Symposium on Computer Aided Process Engineering (ESCAPE30), May 24-27, 2020, Milano, Italy.
http://dx.doi.org/10.1016/B978-0-12-823377-1.50126-9

Integration of Design and Operation Using Dynamic Perturbation and Chance Constraints with Unscented Transform

Christian Hoffmann, Joris Weigert, Erik Esche[a], Jens-Uwe Repke

Technische Universität Berlin, Process Dynamics and Operations Group, Straße des 17. Juni 135, 10623 Berlin, Germany
c.hoffmann@tu-berlin.de

Abstract

Process design is performed based on experience, heuristics, or simulation and optimization using mathematical models. However, many of these approaches focus on the steady-state design and only a few publications consider process operability under variability. In this contribution, we use a fully discretized dynamic model in combination with an optimal economic NMPC for process design. Fluctuations in the feed are modeled by an amplitude-modulated pseudo-random binary sequence to gain as much information as possible. Parametric uncertainty is accounted for by using the unscented transform approach for chance constraints. This framework enables simultaneous optimization under uncertainty. We successfully apply this framework to the process design of a simplified Williams-Otto process.

Keywords: Integration of Design and Operation, Economic NMPC, Unscented Transform, Optimization under Uncertainty, Chance-constrained Optimization

1. Introduction

Process design is a fundamental aspect of process systems engineering. An optimal design reduces both investment and operating costs and at best also increases separation efficiency and product purity. Conventionally, process design and control design are performed sequentially or as an iterative process (Seider et al., 2017) in which design decisions are made based on economic or other soft criteria for steady-state. Afterward, the design is fixed and the control structure is set up. However, this approach may lead to dynamic constraint violations, hinder robust performance, or simply reduce the controllability of a process during plant operation (Malcolm et al., 2007). Currently, there is a growing desire to perform these two subsequent tasks simultaneously (Seider et al., 2017).

Three approaches to solving optimization problems regarding the integration of design and operation (IDOP) have been suggested and their advantages and disadvantages have been discussed (Ricardez-Sandoval et al., 2009): (1) controllability index-based approaches, (2) robust approaches, and (3) dynamic optimization approaches.

In a previous contribution (Hoffmann et al., 2019), we suggested using the objective function of an economic nonlinear model-predictive controller (eNMPC) (Diehl et al., 2011), to account for the connection of economics and variability. In this work, we will extend our framework to incorporate parametric uncertainty. We will also elaborate on our strategy to account for dynamic disturbances.

In the next section, we describe our IDOP-eNMPC framework in more detail by discussing the methodology to account for dynamic fluctuations/variability and

parametric uncertainty using amplitude-modulated pseudo-random binary sequences and the unscented transform of chance constraints. Afterward, we present a case study of a simplified Williams-Otto process to show the performance of the framework.

2. Theoretical Background

In the proposed framework, the dynamic optimization problem is turned into an NLP using orthogonal collocation on finite elements. Under these conditions, the optimization problem is

$$\begin{aligned} &\min_{u,d} f \\ &\text{s.t. } g(x,u,v,\theta,\xi,d) = 0 \\ &\quad h(x,u,v,\theta,\xi,d) \leq 0 \end{aligned} \tag{1}$$

where x is the state vector, u is the vector of manipulated variables, v represents dynamic disturbances, d represents the design vector, θ and ξ are the vectors of certain and uncertain model parameters. In addition, g are the algebraic constraints of the discretized dynamic process model and h are inequality constraints.

2.1. Dynamic disturbances

As we want to design a process, which is able to reject external disturbances, we have to represent these external disturbances by some method. In the past, several publications assumed sine signals whereas we use an amplitude-modulated pseudo-random binary sequence (APRBS) to generate our disturbance signal. These sequences are typically used for system identification (Nelles, 2001) and represent a signal that varies over the whole amplitude range. For this reason, they are more suitable for nonlinear systems compared to conventional pseudo-random binary sequences (PRBS). In this work, external disturbances in feed flows are represented by an APRBS (see Figure 5).

2.2. Introduction of uncertainty using chance constraints via the unscented transform

Another challenge in design is parametric uncertainty, e.g., in thermodynamic or kinetic models. Several approaches to consider uncertainty have been suggested, e.g., stochastic programming, probabilistic programming, and fuzzy mathematical programming (Sahinidis, 2004). In this contribution, we use chance-constrained optimization, i.e., we set a probability level α to which an inequality constraint must hold. The probability is computed by using the unscented transform (UT) of the inequality constraint, originally proposed by Julier and Uhlmann (2004). Here, the probability density function (PDF) of the prior variables, i.e., the uncertain parameters, is approximated via several sigma points (index *sp*). These sigma points propagate the prior distribution through the model to approximate the PDF of the inequality constraint. The idea of the UT is sketched below. Figure 1 shows the assumed prior PDF of an uncertain parameter. This prior PDF is approximated by sigma points whose number and location depend on the applied method. The equation system is formulated for all sigma points simultaneously. The expected value of the inequality constraint μ_h and its variance σ_h^2 are obtained by assuming a normal distribution and by weighting the specific realizations of the inequality constraints accordingly:

$$\mu_h = \sum_{sp} W_{sp} h_{sp} \tag{2}$$

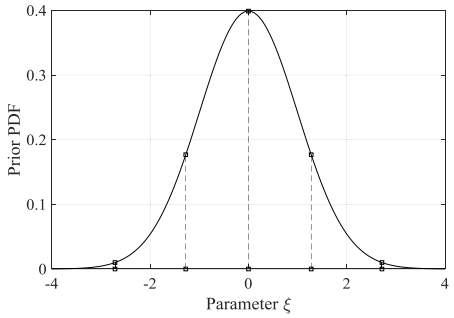

Figure 1: Prior PDF and sigma points with mean = 0 and standard deviation = 1.

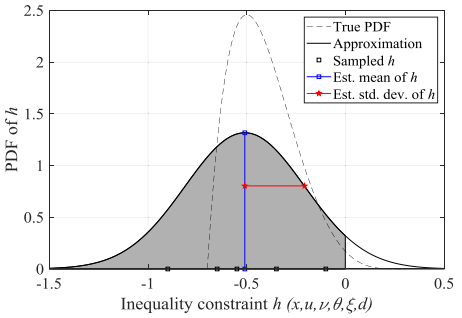

Figure 2: True and approximated PDF of an inequality constraint h.

$$\sigma_h^2 = \sum_{sp} W_{sp}\left(h_{sp} - \mu_h\right)^2 \tag{3}$$

This is illustrated in Figure 2, in which the gray area represents the probability that an inequality constraint holds. The true distribution, however, might be different, as shown in dashed lines in Figure 2. Hence, the assumption of a normal distribution does not necessarily have to hold and must be verified afterward.

Recently, Maußner and Freund (2018) compared several UT methods. They found the UT by Lévesque (2006) to yield a reasonable approximation and a weak dependence on the tuning parameters. Hence, we apply the Lévesque method in this framework and solve the following chance-constrained optimization problem in which we minimize the expected value of the objective function while ensuring that the inequality constraint holds to a probability level α:

$$\begin{aligned} &\min_{u,d} E[f] \\ &\text{s.t. } g\left(x,u,v,\theta,\xi_{sp},d\right) = 0 \\ &\quad Pr\ \{h(x,u,v,\theta,\xi,d) \le 0\} \ge \alpha \end{aligned} \tag{4}$$

2.3. Stability

Stability is considered by a strict formulation of the terminal cost of the eNMPC problem. In this case, all differential states at the end of the horizon must be equal to their initial states, i.e. the process must be able to return to the initial state in spite of the disturbances:

$$x(t = t_{\text{end}}) = x(t = 0) \tag{5}$$

3. Algorithmic procedure and implementation

Based on the presented theoretic aspects, we develop an algorithmic framework presented in Figure 3. The dynamic model is initialized, preferably at steady-state. The process is then optimized based on steady-state assumptions by setting all derivatives of the Lagrange polynomials in the collocation approach to zero. Afterward, one may obtain an optimal steady-state design under uncertainty by using the UT method. In the next step, the derivatives of the Lagrange polynomials are assigned their non-zero values and dynamic disturbances are introduced via APRBS. This way, we obtain the design under variability with or without uncertainty. Finally, the results are verified by obtaining the true PDF of the inequality constraints via Monte-Carlo sampling. Note that the steady-

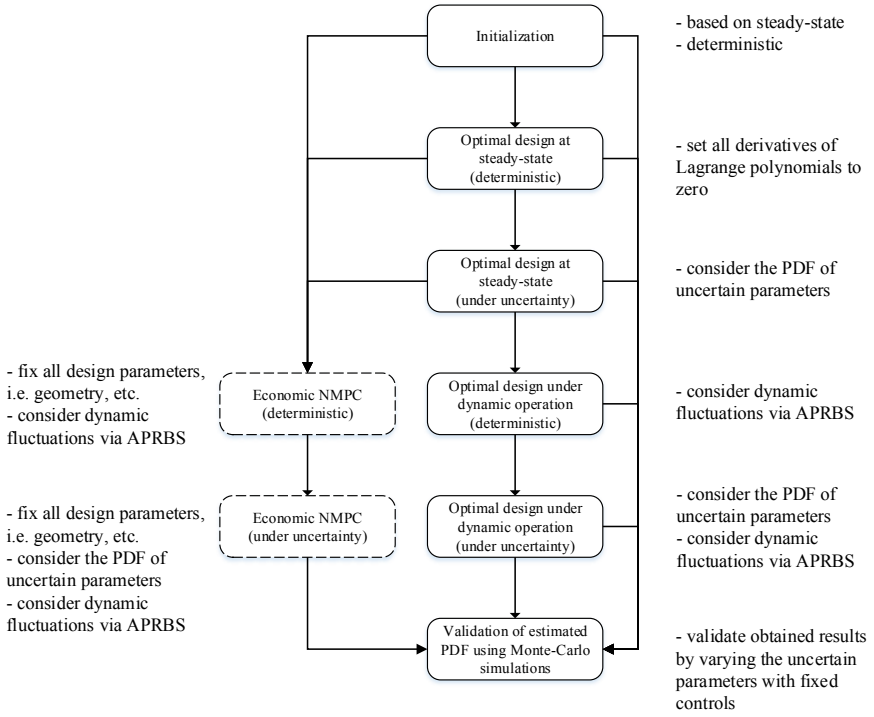

Figure 3: Algorithmic framework.

state optimizations are not necessary but optional. An advantageous side-effect of this model formulation is the ability to fix certain model parts to obtain a simpler problem, e.g. if design variables are fixed an optimal control problem is solved (dashed). This framework has been implemented in AMPL (Fourer et al., 2002), the optimization problems are solved with IPOPT (Wächter and Biegler, 2005). The process model is generated with MOSAICmodeling (Esche et al., 2017).

4. Case Study

The simplified Williams-Otto process (Williams and Otto, 1960) is shown schematically in Figure 4 and is chosen as a case study for the proposed method. The reactor is a continuously-stirred tank reactor (CSTR). Decanter, Distillation column, and recycle are expressed via component balances and splitting factors. Due to space limitations, we do not present the model here, but it can be found in (Hoffmann et al., 2019). Contrary to Hoffmann et al. (2019), we no longer assume the reactor level to remain constant to allow for more flexibility during operation. The manipulated variables of this process are the temperatures of streams 1, 2 and 3, and the reactor outlet. They are constant over a finite element and their change

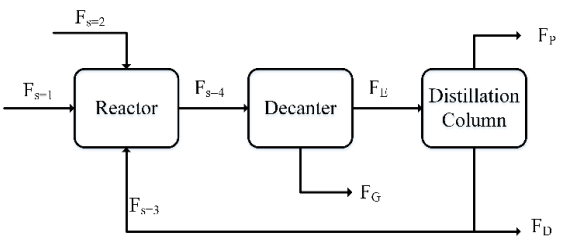

Figure 4: Scheme of the simplified Williams-Otto process.

from one finite element to the next is bounded. The design variables are the height and the diameter of the reactor and we maximize the net present value of the process. In addition, the reactor temperature shall remain below an upper bound:

$$h = T_R - T_R^{UB} \leq 0. \tag{6}$$

This inequality is transformed into a chance constraint (see Equation (4)). In our framework, we assume both feed streams 1 and 2 vary by ±5 % of their nominal values and introduce these fluctuations via APRBS as shown in Figure 5. The uncertain parameter is the activation energy of the first of three reactions, which is assumed to have a standard deviation of 3 %. We carried out process design for this system at steady-state (with and without uncertainty) and for dynamic (with and without uncertainty) but will limit ourselves to the comparison of the dynamic cases herein.

5. Results and Discussions

The IDOP is first solved deterministically. The inequality for the reactor temperature is considered as shown in Equation (6). This yields a reactor volume of 9.5 m^3 and a net present value of 2.55 Mio. $. The results obtained under probabilistic conditions are shown in Figure 6. We see that (i) the net present value of the process has been decisively reduced in case uncertainty is introduced, and (ii) the reactor volume increases with an increasing probability level. In addition, contrary to the steady-state results for which every probability level was feasible, the process was not feasible for probability levels above 60 % under dynamic conditions. This demonstrates that dynamic fluctuations have a decisive impact on process design and that a pure steady-state analysis may not suffice to obtain sufficient disturbance rejection.

Referring to Figure 3, the last step of the framework is the validation of the actual probability distribution via Monte-Carlo sampling. In this case, 300 samples were taken for fixed manipulated variables. The results are shown in Figure 7 and demonstrate that the assumption of a normal distribution was justified in this case. However, this must always be validated and the results will depend on the nonlinearity of the process model, the magnitude of the standard deviations of the prior PDF, and presumably the number of uncertain parameters.

6. Conclusion and Outlook

In this contribution, our approach for integrating design and operation into a simultaneous optimization framework was extended to consider uncertain parameters by applying the unscented transform method. This makes it possible to approximate the probability density function of the inequality constraints and the expected value of the objective function without sequentially sampling over sigma points. Moreover, we elaborated on our methodology of introducing dynamic disturbances by using amplitude-modulated pseudo-random binary sequences. These cover a wider range of frequencies compared to a single sine signal. We successfully demonstrated this methodology for a case study: The design changes notably when considering dynamic fluctuations and

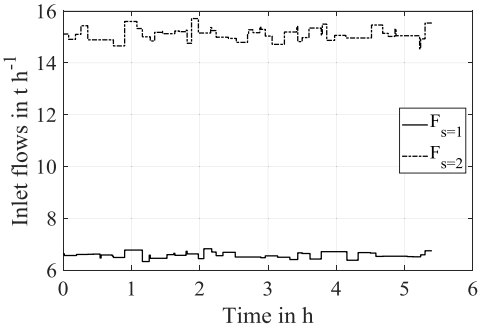

Figure 5: Feed fluctuations within ±5% of nominal feed flow using two APRBS.

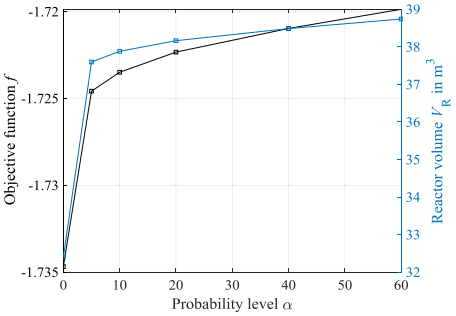

Figure 6: Objective function and reactor volume over the probability level for the chance constraint.

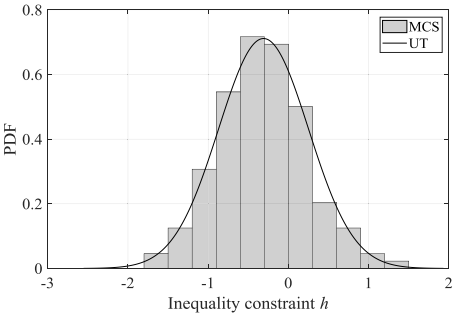

Figure 7: PDF of the inequality constraint obtained by 300 Monte-Carlo samples (MCS) and UT; probability level α = 60 %.

uncertainty. For high probability levels, no feasible solution could be obtained, i.e. the process design would have to be changed, e.g. by adding additional units. In the future, we will combine this approach with a less restrictive formulation for stability and apply this framework to larger process models.

References

M. Diehl, R. Amrit, J.B. Rawlings, 2011, A Lyapunov Function for Economic Optimizing Model Predictive Control, IEEE Transactions on Automatic Control, 56, 3, 703–707.

E. Esche, C. Hoffmann, M. Illner, D. Müller, S. Fillinger, G. Tolksdorf, H. Bonart, G. Wozny, J.-U. Repke, 2017, MOSAIC - Enabling Large-Scale Equation-Based Flow Sheet Optimization, Chemie Ingenieur Technik, 89, 5, 620–635.

R. Fourer, D.M. Gay, B.W. Kernighan, 2002, Ampl: A Modeling Language for Mathematical Programming, Duxbury Thomson.

C. Hoffmann, E. Esche, J.-U. Repke, 2019, Integration of Design and Control Based on Large-Scale NLP Formulations and An Optimal Economic NMPCs, Proceedings of the 9th International Conference on Foundations of Computer-Aided Process Design, Computer Aided Chemical Engineering, Elsevier, 125–130.

S.J. Julier, J.K. Uhlmann, 2004, Unscented Filtering and Nonlinear Estimation, Proc. IEEE, 92, 3, 401–422.

J.-F. Lévesque, 2006, Second-Order Simplex Sigma Points for Nonlinear Estimation, AIAA Guidance, Navigation, and Control Conference and Exhibit, 6093.

A. Malcolm, J. Polan, L. Zhang, B.A. Ogunnaike, A.A. Linninger, 2007, Integrating systems design and control using dynamic flexibility analysis, AIChE Journal, 53, 8, 2048–2061.

J. Maußner, H. Freund, 2018, Optimization under uncertainty in chemical engineering: Comparative evaluation of unscented transformation methods and cubature rules, Chemical Engineering Science, 183, 329–345.

O. Nelles, 2001, Nonlinear system identification, Springer.

L.A. Ricardez-Sandoval, H.M. Budman, P.L. Douglas, 2009, Integration of design and control for chemical processes: A review of the literature and some recent results, Annual Reviews in Control, 33, 2, 158–171.

N.V. Sahinidis, 2004, Optimization under uncertainty: state-of-the-art and opportunities, Computers & Chemical Engineering, 28, 6-7, 971–983.

W.D. Seider, D.R. Lewin, J.D. Seader, S. Widagdo, R. Gani, K.M. Ng, 2017, Product and process design principles, Wiley.

A. Wächter, L.T. Biegler, 2005, On the implementation of an interior-point filter line-search algorithm for large-scale nonlinear programming, Mathematical Programming, 106, 1, 25–57.

T.J. Williams, R.E. Otto, 1960, A generalized chemical processing model for the investigation of computer control, Transactions of the American Institute of Electrical Engineers, Part I: Communication and Electronics, 79, 5, 458–473.

Sauro Pierucci, Flavio Manenti, Giulia Bozzano, Davide Manca (Eds.)
Proceedings of the 30th European Symposium on Computer Aided Process Engineering (ESCAPE30), May 24-27, 2020, Milano, Italy.
http://dx.doi.org/10.1016/B978-0-12-823377-1.50127-0

Modelling of Organophilic and Hydrophilic Pervaporations for Separation of Ethyl Acetate – water Mixture

Andras Jozsef Toth,[*,a] Eniko Haaz,[a] Reka Ladanyi,[a] Botond Szilagyi,[a] Daniel Fozer,[a] Asmaa Selim,[a,b] Tibor Nagy,[a] Peter Mizsey,[a,c]

[a]*Department of Chemical and Environmental Process Engineering, Műegyetem rkp. 3., Budapest, 1111, Hungary*
[b]*Chemical Engineering Department, National Research Centre, 33 El Buhouth Street, 12622 Cairo, Egypt*
[c]*Department of Fine Chemicals and Environmental Technology, Egyetemváros C/1 108., Miskolc, 3515, Hungary*
ajtoth@envproceng.eu

Abstract

Pervaporation is a separation method that is considered as green technology because of its low energy consumption. The mechanism of component separation in a liquid mixture by pervaporation is complex but it can be explained with the solution-diffusion mechanism. The work is motivated by an industrial separation problem, that is, ethyl acetate removal from aqueous mixture. To complete this goal hybrid organophilic/hydrophilic pervaporation of ethyl acetate/water mixture through commercially available Sulzer PERVAP™ 4060 and 1510 membranes are investigated to obtain information about the removal of ethyl acetate. Our experimental data are evaluated with the pervaporation model of our improvement (Valentínyi et al., 2013) and it is found that the model can be applied also for both cases. The hybrid separation process is rigorously modelled in professional flowsheet environment, and optimized with the dynamic programming optimization method. The objective function is product purity of 99.0, 99.5 m/m% in water and ethyl acetate content and the total annual cost is also determined. It can be determined, this hybrid separation should be become the alternative of distillation if the energy prices are too high.

Keywords: organophilic and hydrophilic pervaporation, flowsheet environment, model optimization, ethyl acetate removal

1. Introduction

Pervaporation (PV) is a chemical unit operation where the liquid mixture to be separated is vaporized at low pressure on the downstream/permeate side of the membranes and the separation of the mixtures takes place by preferential sorption and diffusion of the desired component through the membrane (Valentínyi et al., 2013). A solution to achieve the difference in the partial pressures is to maintain a low vapour pressure using a vacuum pump on the permeate side (Van Baelen et al., 2005). Pervaporation shows good features such as special separation effect, no-extra material addition and energy-saving which are difficult to obtain by other conventional methods (Szabados et al., 2018). Depending on

the permeating component two main areas of pervaporation can be identified: hydrophilic (HPV) and organophilic pervaporation (OPV) (Heintz and Stephan, 1994a, b).

The aim of this work is to examine the ethyl acetate (EtAc) - water separation with pervaporation. The organophilic-hydrophilic pervaporation process is modelled and optimized for the separation of a binary mixture. EtAc forms heteroazeotrope with water (Gmehling et al., 1978), therefore this mixture cannot be separated with conventional distillation (Waltermann et al., 2017). Basically, the problem and the aims must be defined, that is, 5 m/m% ethyl acetate–water mixture with a feed flow of 1000 kg/h should be separated. The product purity of 99.0 and 99.5 m/m% should be achieved both for water and ethyl acetate.

2. Material and methods

Modelling of pervaporation has the following main steps (Toth et al., 2015):

1. System identification,
2. Model parameters estimation for pervaporation model,
3. Model verification/validation and
4. Optimization.

For the modelling of pervaporation, our model is selected and applied (Haaz and Toth, 2018). The parameters of the model are determined on the basis of experiments using the parameter estimation process (Valentínyi et al., 2013). The pervaporation model with the determined parameters is verified with the comparison of measured and modelled data (Toth, 2019). If the model is verified, which is, the model parameters are accurate, it can be applied for rigorous modelling in the professional flowsheeting environment (ChemCAD). In this step, the accuracy of calibrated model is checked with defined objective function (OF) that shows the sum of deviations of the modelled and measured data. (J means partial flux in Eq. (1)).

$$OF = \sum_{i=1}^{n} \left(\frac{J_{i,measured} - J_{i,modelled}}{J_{i,measured}} \right)^2 \tag{1}$$

The validation of the pervaporation model takes also place in the flowsheeting environment. At first, the simulator program must be run with experimental data and if the results are suitable, the optimization process can be carried out. In this case, the membrane transfer area (A) is determined and changed for the sake of the minimum Total Annual Cost (TAC).

The composite PDMS (Sulzer PERVAP™ 4060) membrane is applied in organophilic experiments. The hydrophilic pervaporation is carried out with Sulzer PERVAP™ 1510 composite PVA membrane. The experimental set up is a P-28 membrane unit from CM-Celfa Membrantechnik AG (see Figure 1). The flat sheet membrane with 28 cm^2 effective area (A) is placed on a sintered disc separating the feed and the permeate sides. The volume of the feed tank is 500 ml. The concentration of the feed is considered to be constant. Cross-flow circulation velocity is kept at a permanent value of ~182 l/h.

The vacuum on the permeate side is maintained with a VACUUMBRAND PC2003 VARIO vacuum pump and kept at 6 Torr (8 mbar). The isotherm conditions are assured with a thermostat. The permeate is collected in two traps connected in series and cooled with liquid nitrogen to prevent loss of the permeate. The EtAc concentration of the feed (F), retentate (R) and permeate (P) are measured with Shimadzu GC2010Plus+AOC-20 autosampler gas chromatograph with a CP-SIL-5CB column connected to a flame

ionization detector, EGB HS 600 headspace apparatus is used for sample preparation. The water content is measured with Hanna HI 904 coulometric Karl Fischer titrator (Haaz and Toth, 2018).

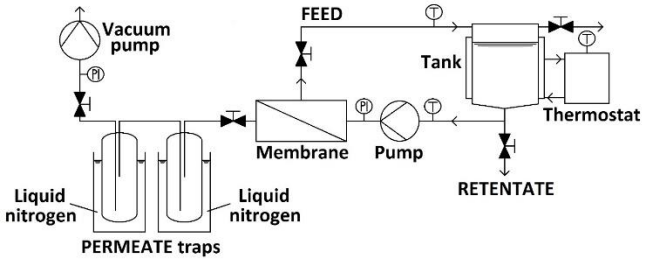

Figure 1. Schematic figure of CM-Celfa P-28 pervaporation unit (Haaz and Toth, 2018)

The pervaporation experiments are carried out at different temperatures (40; 50; 60°C) and feed ethyl acetate concentrations (OPV: 0.5; 1; 3 and 5 m/m% and HPV: 97; 98; 98.5; 99 m/m%) to investigate the temperature and concentration dependence of the pervaporation process.

In our modelling work, the methodology of Valentínyi et al. (2013) is selected. The model has been tested on several case studies and proved to be a good one for the description of pervaporation for engineering applications and design. The basic equation of the model introduces Eq. (2).

$$J_i = \frac{1}{1+\{[\bar{D}_i \cdot exp(B \cdot x_{i1})]/(Q_0 \cdot p_{i0} \cdot \bar{\gamma}_i)\}} \cdot \frac{[\bar{D}_i \cdot exp(B \cdot x_{i1})]}{\bar{\gamma}_i} \cdot \left(\frac{p_{i1} - p_{i3}}{p_{i0}}\right) \qquad i = (1, \ldots, k) \qquad (2)$$

The model is an improvement of Rautenbach's work (Rautenbach et al., 1990) and the improvements consider the concentration dependencies of the transport coefficient and the temperature dependencies of the pervaporation process. These improvements enable the accurate modelling of the pervaporation both for organophilic and hydrophilic ones (Lovasz et al., 2007).

The modelling of separation of binary ethyl acetate - water mixture consists of four main steps as follows in the simulator program (Toth et al., 2015):

1. Organophilic separation: this first step is to be designed that the permeate of the feed is enriched in the organic compound so that it enters the region where the hydrophilic pervaporation can be applied with success. The other design parameter is that in the retentate (water) there has to be practically no organic liquid since this flow will be discharged.

2. Liquid-liquid phase separator: the permeate of the organophilic pervaporation is separated into two phases: organic-rich and water-rich phases, if there is limited solubility. The aqueous phase is recycled to the feed of the first step. (If there were no limited solubility, this step can be omitted.)

3. Hydrophilic pervaporation: the organic-rich phase is fed into the hydrophilic pervaporation. The retentate of the hydrophilic unit is called the 'Ethyl acetate (organic) product', the concentrated ethyl acetate.

4. The retentate of the organophilic pervaporation and the permeate of the hydrophilic one are mixed with each other. This stream is the 'Water product' and this will be discharged.

Figure 2 shows the novel hybrid separation system.

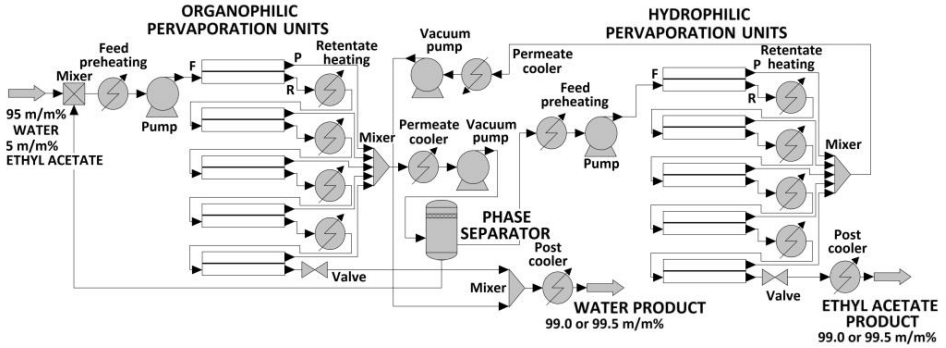

Figure 2. Flowsheet of ethyl acetate – water mixture separation with organophilic and hydrophilic pervaporation systems

3. Results and discussion

A comparison of the measured and calculated partial fluxes are presented in Figure 3 and Figure 4.

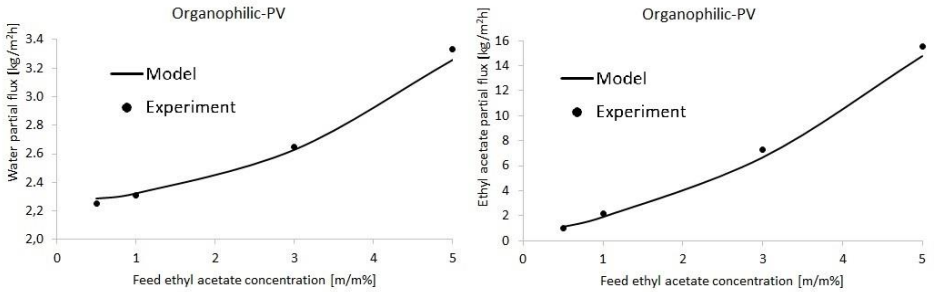

Figure 3. Measured partial fluxes of ethyl acetate and water compared to fluxes calculated with pervaporation model in a function of feed ethyl acetate concentration with PERVAP™ 4060 organophilic membrane at 60°C

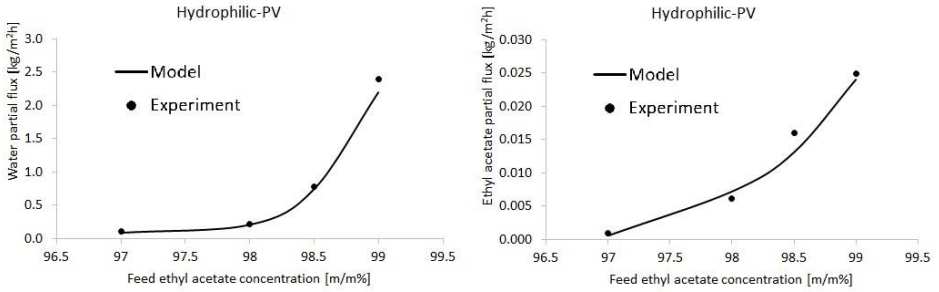

Figure 4. Measured partial fluxes of ethyl acetate and water compared to fluxes calculated with pervaporation model in a function of feed ethyl acetate concentration with PERVAP™ 1510 hydrophilic membrane at 60°C

The minimized objective functions are shown in Table 1.

Table 1 Objective functions resulted by pervaporation model

OF	Water	Ethyl acetate
Organophilic-PV	0.001	0.055
Hydrophilic-PV	0.021	0.245

Generally, it can be concluded that the pervaporation model with the concentration dependency of the transport coefficient fit for the pervaporation experiments in a wide concentration range of the feed flow, particularly in the case of water fluxes. Table 2 shows the necessary total membrane surface areas in the function of product purities.

Table 2 Effective membrane surface areas

Total A	EtAc product EtAc	Water product Water
[m^2]	[m/m%]	[m/m%]
20	99.0	99.0
27	99.0	99.5
38	99.5	99.0
52	99.5	99.5

The conceptual design of an industrial process takes a small part of the project costs but offers a huge cost reduction opportunity for the whole project (Dimian, 2003). Investment costs are calculated according to the cost correlations of Douglas (1988) with the current M&S index. Heat exchangers and the low-temperature cooling apparatus for the permeates are also calculated (Toth et al., 2015). Membrane area-price function is determined on industrial data and used for the calculation of the capital costs of membrane modules (Koczka, 2009). Investment costs of the pervaporation depend on many parameters, e.g.: effective membrane area, the volume of the streams and purity of the products. 8000 annual continuous working hours are selected for the calculation of the operating cost. In this work, 2.5 years are taken as membrane depreciation time, because membranes should be generally replaced in approximately every 2-5 years (Haaz and Toth, 2018). 10-year amortization of capital cost is assumed for the total cost estimation. Table 3 shows the cost elements of hybrid organophilic-hydrophilic pervaporation system in the case of 52 m^2 membrane area.

Table 3 Main cost elements of hybrid ethyl acetate-water pervaporation system

10 years amortization	Investment cost	Operating cost	Total cost
	1000 USD/year	1000 USD/year	1000 USD/year
Phase separator	3	8	11
Permeate cooling	17	97	113
Heat exchangers	9	110	119
Membrane modules	197	41	238
Total	225	256	481

4. Conclusions

The experiments and simulations suggest that the pervaporation is able to remove the ethyl acetate from an aqueous mixture. Organophilic and hydrophilic pervaporations are modelled with our verified and adequate model in professional flowsheeting environment that enables verified rigorous modelling, optimization and cost estimation. The results show that the capital cost of the pervaporation unit is the highest part of the total annual cost.

Acknowledgments

This publication was supported by the János Bolyai Research Scholarship of the Hungarian Academy of Sciences, ÚNKP-19-4-BME-416 New National Excellence Program of the Ministry for Innovation and Technology, OTKA 112699, 128543 and 131586. This research was supported by the European Union and the Hungarian State, co-financed by the European Regional Development Fund in the framework of the GINOP-2.3.4-15-2016-00004 project, aimed to promote the cooperation between the higher education and the industry. The research reported in this paper has been supported by the National Research, Development and Innovation Fund (TUDFO/51757/2019-ITM, Thematic Excellence Program).

References

A. C. Dimian, 2003, Integrated Design and Simulation of Chemical Processes, Elsevier Science, Amsterdam, The Netherlands.
J. M. Douglas, 1988, Conceptual design of chemical processes, McGraw-Hill, New York.
J. Gmehling, U. Onken, J. R. Rarey-Nies, 1978, Vapor-liquid equilibrium data collection, Dechema, Virginia.
A. Heintz, W. Stephan, 1994a, A generalized solution-diffusion model of the pervaporation process through composite membranes Part I. Prediction of mixture solubilities in the dense active layer using the UNIQUAC model, J Membrane Sci 89, 1-2, 143-151.
A. Heintz, W. Stephan, 1994b, A generalized solution-diffusion model of the pervaporation process through composite membranes Part II. Concentration polarization, coupled diffusion and the influence of the porous support layer, J Membrane Sci 89, 1-2, 153-169.
E. Haaz, A. J. Toth, 2018, Methanol dehydration with pervaporation: Experiments and modelling, Sep Purif Technol 205, 121-129.
K. Koczka, 2009, Environmental conscious design and industrial application of separation processes, PhD Thesis, BME, Budapest.
A. Lovasz, P. Mizsey, Z. Fonyo, 2007, Methodology for parameter estimation of modelling of pervaporation in flowsheeting environment, Chem Eng J 133, 219-227.
R. Rautenbach, C. Herion, U. Meyer-Blumentoth, 1990, Pervaporation membrane separation processes, Membrane Science and Technology Series 1, 181-191.
E. Szabados, A. Jobbagy, A. J. Toth, P. Mizsey, G. Tardy, C. Pulgarin, S. Giannakis, E. Takacs, L. Wojnarovits, M. Mako, Z. Trocsanyi, A. Tungler, 2018, Complex Treatment for the Disposal and Utilization of Process Wastewaters of the Pharmaceutical Industry, Period Polytech Chem Eng 62, 76-90.
A. J. Toth, 2019, Comprehensive evaluation and comparison of advanced separation methods on the separation of ethyl acetate-ethanol-water highly non-ideal mixture, Sep Purif Technol 224, 490-508.
A. J. Toth, A. Andre, E. Haaz, P. Mizsey, 2015, New horizon for the membrane separation: Combination of organophilic and hydrophilic pervaporations, Sep Purif Technol, 156, 2, 432–443.
N. Valentínyi, E. Cséfalvay, P. Mizsey, 2013, Modelling of pervaporation: Parameter estimation and model development, Chem Eng Res Des 91, 1, 174-183.
D. Van Baelen, B. Van der Bruggen, K. Van den Dungen, J. Degreve, C. Vandecasteele, 2005, Pervaporation of water–alcohol mixtures and acetic acid–water mixtures, Chem Eng Sci 60, 1583-1590.
T. Waltermann, D. Münchrath, M. Skiborowski, 2017, Efficient optimization-based design of energy-intensified azeotropic distillation processes, Comput Aided Chem Eng 40, 1045-1050.

Sauro Pierucci, Flavio Manenti, Giulia Bozzano, Davide Manca (Eds.)
Proceedings of the 30th European Symposium on Computer Aided Process Engineering (ESCAPE30), May 24-27, 2020, Milano, Italy.
http://dx.doi.org/10.1016/B978-0-12-823377-1.50128-2

Superstructure Optimization for the Design of a Desalination Plant to Tackle the Water Scarcity in Texas (USA)

Marcello Di Martino[a,b,c], Styliani Avraamidou[b], Efstratios Pistikopoulos[a,b*]

[a]*Artie McFerrin Department of Chemical Engineering, Texas A&M University*
[b]*Texas A&M Energy Institute, Texas A&M University*
[c]*RWTH Aachen University*
stratos@tamu.edu

Abstract

Depleting water sources, as well as a growing population, together with the threats of climate change, emphasize the necessity of novel water sources for municipal use, as well as for energy generation. Desalination processes could play a key role in tackling these challenges since treating sea water, industrial wastewater or brackish water for reuse becomes possible. Consequently, this work focusses on the analysis and optimization of various reverse osmosis desalination systems through superstructure optimization for the development of optimal designs of desalination plants, to address the energy-water nexus.

The superstructure model and its optimization could be valuable for the evaluation of the best possible design and operation of a desalination system for a given input framework (energy and water) to meet set restrictions on output water specifications and energy or environmental goals. Additionally, the applicability of the developed superstructure model is illustrated through the case study of the design of a new desalination plant in South Central Texas.

Since the superstructure framework is formulated as a mixed-integer programming problem, the model can be optimized for varying scenarios, resulting in a plethora of optimal solutions for decision makers, including different desalination plant designs depending on the distinct input water characteristics, output restrictions and goals.

Keywords: Desalination, Optimization, Superstructure, Reverse Osmosis

1. Introduction

Water scarcity is a severe challenge, especially for arid and semi-arid regions such as Texas (USA), California (USA) and Baja California (Mexico) or the Middle Eastern Region. With a growing population, both water and energy demands are increasing. Since water is traditionally used as a coolant in energy production plants the water consumption further rises. Consequently, water and energy production are linked to each other, which in turn means that these challenges need to be solved by a Water-Energy Nexus approach (Allen et al. 2019, Gabriel et al. 2016).
Further, existing water supplies, like groundwater aquifer storage systems, are depleting globally (Y. Wada et al. 2010). Additionally, climate change is expected to make water shortages worse: The Inter-governmental Panel on Climate Change (IPCC) projected that up to two billion people worldwide could be facing water shortages by 2050 (R. C. Kundis, 2010). Therefore, to cope with these severe challenges, novel water sources are needed. Desalination processes could play a key role in tackling these challenges since

treating sea water, surface water, industrial wastewater or brackish water for reuse becomes possible.

So far, there have been a variety of distinct optimization analyses concerning reverse osmosis desalination systems addressing the energy-water nexus: Vakilifard et al. (2018) review optimization models concerning the energy-water nexus in water supply systems and identify knowledge gaps, as well as suggest future works. Among other things, a general lack of holistic water-energy nexus optimization approaches and a lack of optimization frameworks considering environmental impacts of solution strategies were identified. To address the energy-water nexus, Li (2018) minimizes the specific energy consumption of a hybrid membrane process consisting of reverse osmosis for desalination and pressure retarded osmosis for power generation. A systematic procedure for the optimization of the benefits of the water-energy nexus on the basis of a surplus on energy has been determined by Gabriel et al. (2016). Further, Tsolas et al. (2018) make use of water-energy nexus diagrams to identify a nexus for optimal resource generation and utilization.
These works focus on key parts and challenges of reverse osmosis desalination processes to address the interconnectivity of energy and water resources.

To our knowledge a holistic energy-water nexus approach optimizing the water and energy sources, as well as the membrane system, together with the operating conditions of the process, in an attempt to meet the local water demands for varying output water applications, has not yet been investigated.
Various desalination alternatives have been modeled and simulated permitting and facilitating superstructure optimization. The superstructure is formulated as a mathematical model, which has the form of a mixed-integer programming problem. The developed model can then be optimized for distinct scenarios resulting in a plethora of optimal solutions for decision makers, enabling a framework methodology, for the techno-economic and feasibility analysis of desalination plants. Hence, the elaborated approach can be used for reliable and fast screening of reverse osmosis plant designs prior to detailed plant modeling.

2. Reverse Osmosis Desalination Process Superstructure

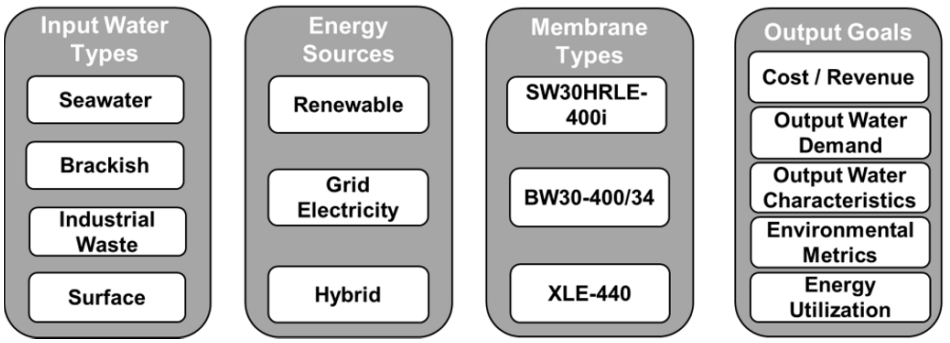

Figure 1: Overview of the reverse osmosis desalination process superstructure considerations.

The design of a reverse osmosis desalination process is addressed holistically in terms of the input water types, the energy sources (like grid electricity or renewable energies), the

membrane types, as well as the process operation and parameters, for various output goals, not only maximizing revenue or minimizing cost, but also satisfying a given water demand for different output water characteristics (like municipal, irrigation, livestock or power plant usage), while environmental metrics can be considered. The framework is modifiable for any given region around the world, by adjusting restrictions concerning water and energy availability, emphasizing the framework methodology nature of the implemented approach. An overview of the general considerations for the superstructure can be found in Figure 1. The visualized framework is subsequently translated into a mathematical model, which has the form of a MINLP problem.

A schematic representation of a one-stage reverse osmosis process, together with the variables describing it are illustrated in Figure 2. A feed stream is pressurized so that a separation of the saline feed (Q_f, C_f, P_f) into a diluted permeate (Q_p, C_p, P_p) and a concentrated retentate (Q_r, C_r, P_r) can be achieved in the reverse osmosis membrane module.

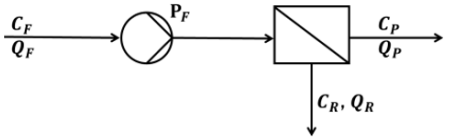

Figure 2: Schematic representation of the desalination separation step.

Membrane modeling is classically used to calculate the necessary pressurization of the feed streams, for a certain permeate concentration quality (or vice versa), since the pressurization is the main energy cost driver of the desalination system (A. Zhu et al. 2009).

To determine the properties of a desalination stage the following equations (1) to (5) are utilized:

$$SEC_{pump} = \frac{Q_f \cdot \Delta P}{\eta_{pump} \cdot Q_p} \tag{1}$$

$$\Delta P = P_f - P_p \tag{2}$$

$$Q_f = Q_p + Q_r \tag{3}$$

$$Q_f \cdot C_f = Q_p \cdot C_p + Q_r \cdot C_r \tag{4}$$

$$C_p = f\left(C_f, \Delta P, A, WR, Q_p\right) = x_1 \cdot \frac{Q_p}{A} + x_2 \cdot \frac{Q_p}{Q_f} + x_3 \cdot \Delta P \tag{5}$$

The energy consumption of the pump (see Equation 1) is mainly dependent on the transmembrane pressure (ΔP), as well as on the ratio of feed (Q_f) to permeate volume flow (Q_p). The transmembrane pressure (see Equation 2) is defined by the difference of the pressurized feed (P_f) and the permeate pressure (P_p). Further, a total mass balance, as well as a component mass balance are necessary to characterize the process stage (Equations 3 and 4).

The permeate concentration correlation (Equation 5) is based on a surrogate model, which in turn is a multivariate linear regression of normalized data. This data has been generated with the membrane supplier simulation tool WAVE from DOW Chemical for varying

feed concentrations (C_f), membrane surface areas (A), output permeate flows and water recoveries ($WR = Q_p/Q_f$). To improve the accuracy of the surrogate model the parameters $x_i, \forall i = 1, \dots, 3$, change with the feed concentration, water recovery and water flux ($J_v = Q_p/A$). With the help of the multivariate-linear surrogate model, the high-fidelity membrane model is replaced, resulting in a model with reduced overall complexity, that requires reduced computational effort when embedded in an optimization problem.
Subsequently, either the permeate or the retentate flow (Q_r) can be redefined as the feed flow of a successive stage (dependent on the concentration). The optimization model has $DOF = w \cdot (4 \cdot n + 1)$ degrees of freedom, dependent on the number of stages n and available water sources w. The design variables include the feed flow ($Q_{f,1,j}$), the number of parallel flows ($m_{i,j}$), the surface area ($A_{i,j}$), the water recovery ($WR_{i,j}$), the transmembrane pressure ($\Delta P_{i,j}$), as well as the number of stages n_j, for stages $i = 1, \dots, n_j$ and for each water source $j = 1, \dots, w$.

3. Case Study

To illustrate the potential and functionality of the superstructure model the following case study is analysed. The design of a desalination plant which uses aquifer water ($C_f = 1500 mg/L$ and $Q_{f,1} \leq 35000 m^3/d$) and a minimal water utilization restriction of $WR \geq 57\%$, for South Central Texas, defined as region L by the Texas Water Development Board, is the focus of this scenario.
Firstly, the design of the desalination plant is determined, when only grid electricity is used. Secondly, the same optimization is performed, but now only solar and wind energy are available as energy supply sources. Then, the water utilization is maximized by maximizing the water recovery for a given feed flow restriction. With these solutions a Pareto Front for minimizing operational costs and maximizing the water recovery is determined.

In the first two optimization problems, the reverse osmosis operational process costs are minimized, which consist primarily of energy costs (A. Ghobeity, A. Mitsos 2014). Therefore, only energy costs together with concentrated brine disposal costs and membrane costs are considered as cost constituents of operational costs, to ensure that a membrane budget, as well as disposal limitations can be considered.
The energy costs are calculated based on the specific energy consumption of the pump, as well as an energy recovery device, which enables the usage of, for the separation not viable, high residual retentate pressures of respective stages to increase the overall process efficiency. Subsequently, the determined energy consumption is multiplied with an energy cost factor dependent on the energy source. The brine disposal costs are dependent on the feed concentration of the system, as well as the ratio of the retentate volume flow to the permeate volume flow. The disposal costs are scaled with a brine cost factor dependent on the water source. Further, the membrane costs summarize the purchase price of the selected membranes, as well as the pressure vessels with regard to an assumed membrane lifetime and the overall permeate water output. This results in operational costs in terms of $\$/m^3$ permeate.
The energy cost factor for grid electricity ($22.4\$/MWh$) is obtained from averaging the day-ahead market price from ERCOT (Electric Reliability Council of Texas). The price for using solar and wind energy results from an energy superstructure optimization for minimizing investment and operational costs of a set of renewable energy sources for

constant power output. The power output is then varied over a specific range resulting in a constant slope of $29.84\$/MWh$ for solar and wind energy.
The results of the optimization are summarized in Table 1, as well as in Figure 4. In both cases, a three-stage process results in minimal operational costs. Although the energy price rises by 33%, the operational costs only increase by 11%. This is possible, because of lower pressures for each stage and a higher number of parallel flows for stages two and three. Consequently, the energy cost, as well as the membrane cost increase only slightly, to offset the higher energy price, resulting in a lower than expected operational cost increase.

Table 1: Top: Results of the design optimization with grid electricity; Bottom: Results of the design optimization with solar and wind energy (with batteries).

Grid Electricity, Cost: 22.4 $/MWh							
Stage	Q_f [m³/d]	C_f [mg/L]	P [mg/L]	WR [%]	C_p [mg/L]	C_r [mg/L]	m_i [-]
1	**26961**	**1500**	**21.13**	**55.58**	**35.92**	**3332**	**5**
2	**11975**	**3332**	**20.93**	**60.98**	**45.84**	**9997**	**3**
3	**3954**	**9997**	**22.85**	**70.0**	**199.94**	**32858**	**2**
Renewable Energy, Cost: 29.84 $/MWh							
Stage	Q_f [m³/d]	C_f [mg/L]	P [mg/L]	WR [%]	C_p [mg/L]	C_r [mg/L]	m_i [-]
1	**25499**	**1500**	**18.11**	**50.63**	**39.81**	**2997**	**5**
2	**12589**	**2997**	**19.03**	**69.90**	**46.75**	**9848**	**4**
3	**3790**	**9848**	**18.39**	**69.99**	**192.78**	**32373**	**3**

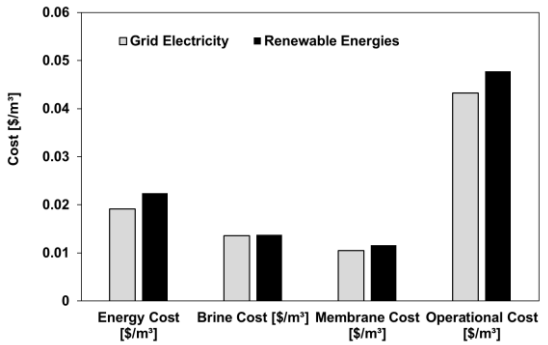

Figure 3: Comparison of operational cost constituents from the design optimization results, grid electricity and renewable energies.

Additionally, the energy consumption of the system using only renewable energies is minimized, for varying water recovery restrictions. This results in the Pareto Fronts summarized in Figure 4, for the operational costs (left), as well as cost constituents of these (right) versus the water recovery. Because of the nearly linear brine disposal cost decline ($-0.0034\$/(m^3 \cdot \%)$, $R^2 = 0.99$) and only marginally energy cost rise (for a water recovery of 88% to 98%, by 18%) with an increasing water recovery, decline the overall operational cost until a water recovery of 98%. If the water recovery needs to be

further increased the energy cost increase significantly to offset the brine disposal savings. Consequently, the operational cost rise. In contrast, the membrane costs do not follow a specific trend as indicated by the dotted line in Figure 4.

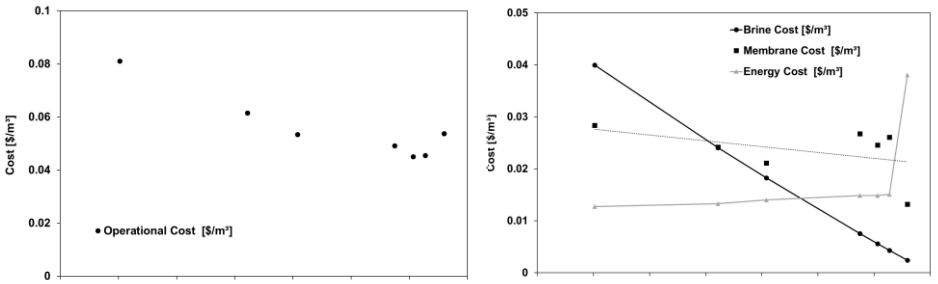

Figure 4: Pareto front minimizing energy and maximizing water recovery, Left: Operational cost dependent on water recovery; Right: Operational cost constituents dependent on water recovery.

4. Conclusion

With the newly developed framework methodology for the superstructure optimization of desalination plants, it is possible to assess desalination alternatives and analyse the impact of changing supply systems, e.g. like the energy source. Therefore, the analysis of various possible scenarios is enabled and facilitated. Further, the elaborated approach can be used for a reliable and fast screening of reverse osmosis plant designs, prior to detailed plant modelling, to advise decision makers, which desalination alternatives are worth further exploring and which not.

References

R. C. Allen, Y. Nie, S. Avraamidou, E. N. Pistikopoulos, 2019, Infrastructure Planning and Operational Scheduling for Power Generating Systems: An Energy-Water Nexus Approach, Computer Aided Chemical Engineering, 47, 233-238.
K. J. Gabriel, M. M. El-Halwagi, P. Linke, 2016, Optimization across water-energy nexus for integrating heat, power and water for industrial processes coupled with hybrid thermal-membrane desalination, Industrial & Engineering Chemistry Research, 55, 12, 3442–3466.
A. M. A. Ghobeity, A. Mitsos, 2014, Optimal design and operation of desalination systems: new challenges and recent advances, Current Opinion in Chemical Engineering, 6, 61-68.
R. C. Kundis, 2010, Water Supply, Desalination, Climate Change, and Energy Policy Symposium: Critical Intersections for Energy & Water Law: Exploring New Challenges and Opportunities, Pacific McGeorge Global Business & Development Law Journal 2, 2, 225–255.
M. Li, 2018, Optimization of multi-stage hybrid RO-PRO membrane processes at the water-energy nexus, Chemical Engineering Research and Design, 137, 1-9.
S. D. Tsolas, M.N. Karim, M. M. F. Hasan, 2018, Optimization of water-energy nexus: A network representation-based graphical approach, Applied Energy, 224, 230-250.
N. Vakilifard et al., 2018, The role of water-energy nexus in optimising water supply systems - Review of techniques and approaches, Renewable and Sustainable Energy Reviews, 82, Part1, 1424-1432.
Y. Wada et al., 2010, Global depletion of groundwater resources, Geophysical Research Letters, 37, 20.
A. Zhu, P. D. Christofides, Y. Cohen, 2009, Energy Consumption Optimization of RO Membrane Desalination Subject to Feed Salinity Fluctuation, Ind. Eng. Chem. Res., 48, 21, 9581–9589.

Sauro Pierucci, Flavio Manenti, Giulia Bozzano, Davide Manca (Eds.)
Proceedings of the 30th European Symposium on Computer Aided Process Engineering (ESCAPE30), May 24-27, 2020, Milano, Italy.
http://dx.doi.org/10.1016/B978-0-12-823377-1.50129-4

Optimal Design of a Multi-Product Polycrystalline Silicon Facility

César Ramírez-Márquez[a], Edgar Martín-Hernández[b], Mariano Martín[b], Juan Gabriel Segovia-Hernández[a]

[a]*Universidad de Guanajuato, Campus Guanajuato, División de Ciencias Naturales y Exactas, Departamento de Ingeniería Química, Noria Alta S/N, 20256, Guanajuato Gto., México*

[b]*University of Salamanca, Department of Chemical Engineering. Pza. Caídos 1-5, 37008 Salamanca, Spain.*

Abstract

The silicon industry is a source of different types of products, including materials for the implementation of renewable energy systems, with a comparatively lower environmental impact than conventional fossil energy sources, and high added value by-products. In this context, the exploitation of the different by-products generated in the production of polycrystalline silicon (polysilicon) offers opportunities to increase the economic efficiency of the polycrystalline silicon production processes. In this work, a silicon based refinery is conceptually designed, estimating the optimal operating conditions by using surrogate models for the major units involved. Although the main product is polysilicon, there are different products that could be generated in the process increasing its profitability, such as tetraethoxysilane (at different purities). Likewise, series of chlorosilanes with high added value, including SiH_4, SiH_2Cl_2, and SiH_3Cl, can also be produced. Additionally, an economic evaluation of the facility is carried out to determine its economic feasibility. The results show that the refinery produces tetraethoxysilane and chlorosilanes in addition to the production of polysilicon. The proposed design reduces the cost for polycrystalline silicon to 6.86 $/kg, below the commercial price estimated at 10 $/kg. Therefore, the refinery is not only capable to meet the market share requirements but that the generation of different high added value by-products increases the plant profit compared with the net income earned by a traditional polysilicon mono-product plants.

Keywords: Multi-Product, Polycrystalline Silicon, Economic Evaluation.

1. Introduction

In recent years, the polycrystalline silicon photovoltaic (PV) industry has grown vividly, developing a truly global supply chain. In the past 10 years, polycrystalline silicon based solar panels represent more than 90% of photovoltaic production, accounting more than 95% of production in 2018 (Mints, 2018). This development has been induced by the increase in the demand of photovoltaic (PV) energy, as well as by the technical progress in the performance of PV cells, and the improvement in the manufacturing processes of polycrystalline silicon, allowing drastic cost reductions in PV modules cost. However, the polysilicon production costs can be further improved valorizing the by-products generated in the process, which otherwise would be considered as waste.

In the case of the polycrystalline silicon industry, the main by-product of polycrystalline silicon manufacturing is tetrachlorosilane, which currently is fed back into the production cycle. Tetrachlorosilane can also be extracted and post-processed to obtain added value products. However, the processing tetrachlorosilane to obtain high added value by-products can be integrated with the main polycrystalline silicon production process, avoiding the need to dispose of waste streams and increasing the economic and environmental efficiencies of the process.

The statement above has been demonstrated by the polycrystalline silicon company Wacker™, who integrated the production of pyrogenic silica from tetrachlorosilane to the polycrystalline silicon process in different facilities, such as Charleston in the USA, and Burghausen and Nuenchritz in Germany (Rubber & Plastics News Report, 2016). Pyrogenic silica is a valuable product used as a filler in silicone elastomers and as an archeology control additive in paints, adhesives, and unsaturated polyester resins (Rubber & Plastics News Report, 2016). However, pyrogenic silica is not the only product that can be generated from tetrachlorosilane.

In the present work develops a superstructure for the selection of the portfolio of products from quartz including the production tetraethoxysilane (TEOS), which is the most prominent derivative of the family of silicon compounds. Tetraethoxysilane is mainly used in the manufacture of chemical and heat resistant coatings, organic silicon solvents, and precision casting adhesives. Additionally, the production of a series of chlorosilanes with high added value (silane, dichlorosilane and monochlorosilane) is also considered from trichlorosilane.

2. Methodology

To design a polycrystalline silicon process with an analogous production capacity to current polycrystalline silicon production companies as Wacker Co., an average production capacity of the plant of 15,000 annual metric tons of polycrystalline silicon is considered (Rubber & Plastics News Report, 2016). The polycrystalline silicon production process expand the one proposed by Ramírez-Márquez et al., (2019). In this work, the conceptual design of the process, named as Hybrid Process, is presented. The Hybrid Process is the result of a strategic combination of the stages of the Siemens and the Union Carbide process. The Hybrid Process is extended using a couple of reactive distillation columns for the production of high added value products such as: TEOS 98.5, TEOS 99.0, TEOS 99.5, silane, dichlorosilane and monochlorosilane. The process diagram for Multi-Product Polycrystalline Silicon Facility that was used in the present work is showed in Figure 1.

2.1 Modelling approach

The model for the superstructure is developed based on mass and energy balances, thermodynamics, experimental data and rules of thumb for basic units and surrogate models for major ones such as reactors and distillation columns. The process starts with the carboreduction process of quartz. The raw materials used are silica in form of quartz (SiO_2) and carbon (C). These raw materials are stored in storage tanks, to be further blended in a mixer, and fed into the carboreduction reactor. The storage tanks and mixers have been modeled through material balances. The model for the carboreduction reactor is based on the work reported by Wai and Hutchison (1989), computing the products distribution for a C/SiO_2 feeding molar ratio of 2:1, a total pressure of 1 atm, and a temperature range of 2500-3500 K. To achieve the production capacity of typical

industrial plants, in the present work a feed of 150 kmol/h of SiO_2 and 300 kmol/h of C is considered. Based on that work, correlations are developed to estimate the distribution of the products obtained at the reactor (mol fraction) as a function of the reaction temperature (K).

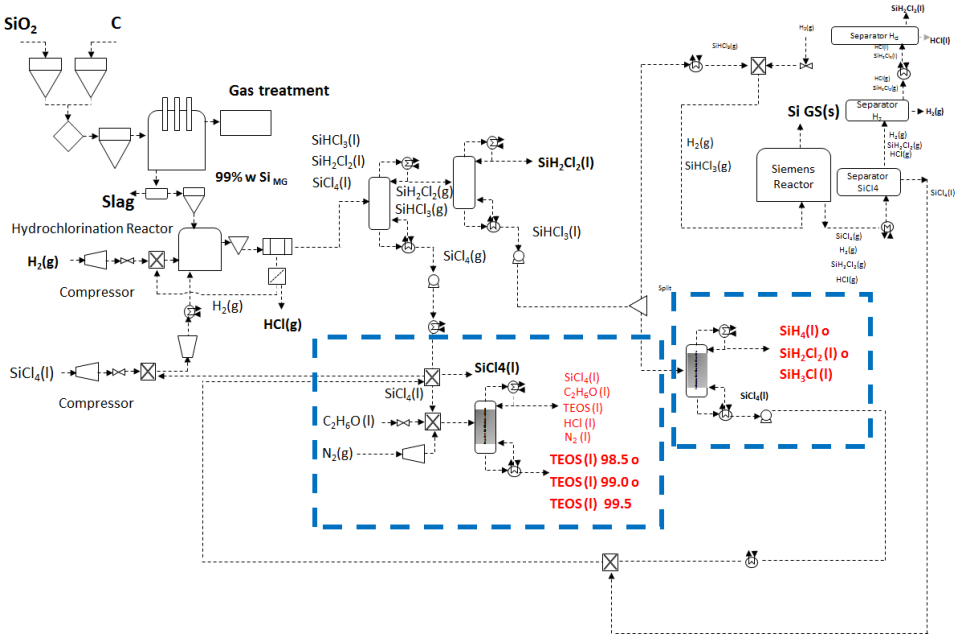

Figure 1. Flowsheet of the Multi-Product Polycrystalline Silicon Facility.

In the hydrochlorination reactor, $SiCl_4$ is hydrogenated in the presence of Si_{MG}. To model this equipment, the minimization for the Gibbs free energy for the system $SiCl_4$−H_2−Si_{MG} is used, based on the work by Ding, et al., (2014). For convenience, the reaction system $SiCl_4$−H_2−Si_{MG} was treated as ideal, and the following variables ranges were studied: temperature (T), 573−873 K; pressure (P), 1−20 atm; y molar feeding ratio (Rel) $H_2/SiCl_4$, 1-5 evaluating the yield to each product as a function of them. Then the surrogate models are developed to estimate the composition as a function of the operating conditions.

The condensation step was modelled based on material and energy balances considering complete separation of the effluent in a gas phase stream and the liquid phase stream. For the separation of the chlorosilanes two convectional distillation columns are used. The rigorous modeling and sizing of the columns was performed using the Aspen Plus software, based on a previous work (Ramírez-Márquez et al., 2019). By varying the feeding and the degrees of freedom as the reflux ratio, surfaces of response are obtained to estimate the energy involved in the reboiler, at the condense and their operating temperatures. The variables evaluated were the feeding molar ratio $SiCl_4$-(SiH_2Cl_2-$SiHCl_3$), within the range from 1 to 2.1698 for the first column; the SiH_2Cl_2-$SiHCl_3$ molar ratio, for a range from 2.99 to 7.5678 for the second column; and reflux ratio from 10 to 80 for the first column and from 60 to 90 for the second column.

For waste streams of $SiCl_4$, remnants of the first column at the bottom, process intensification adding a reactive distillation (RD) column is suggested to produce TEOS

(at different purities 98.5-99.0 or 99.5). Sánchez-Ramírez et al. (2018) showed that the reactive distillation has a better performance than the conventional system regarding TAC values. The variables were evaluated in the following ranges: feeding molar ratio $SiCl_4$- C_2H_5OH values from 1 to 100 for the TEOS reactive column. Also, in the second distillation column at the bottom, a stream of pure trichlorosilane is obtained. That stream is divided into a splitter to feed the Siemens reactors or the reactive distillation columns for the disproportion of trichlorosilane to obtain silane, dichlorosilane or monochlorosilane (each one at 99.0 purity), as proposed by Ramírez Márquez et al. (2016). The trichlorosilane feed was varied in a range of 1 to 10 kmol/h.
The deposition of polycrystalline silicon was modeled according to the work presented by Del Coso and Luque, (2008). In this work, the kinetics of the deposition for polycrystalline silicon in the traditional Siemens reactor are provided. They present analytic solutions for the deposition process, based on the approach of splitting the second-order reaction rate into two systems of first-order reaction rate. The growth rate, deposition efficiency, and power-loss dependence on the gas velocity, the mixture of gas composition, the reactor pressure, and the surface temperature have been analyzed, providing information regarding the deposition velocity and the polycrystalline silicon production rate. The variables analyzed were the polysilicon growth rate, the deposition efficiency and the system temperature. The model defined was solved with the data reported by Del Coso and Luque, (2008) for a temperature range from 1372 to 1500 K.

2.2 Solution procedure

The process was formulated as a nonlinear programming (NLP) problem. The model consists of 3,014 equations and 3,716 variables, which are solved to optimize the operating conditions of the Multi-Product Polycrystalline Silicon facility, using a profit objective function, Eq. 1. Hence, the main variables of decision are: the temperature of the thermal carboreduction reactor; the temperature, pressure, and $H_2/SiCl_4$ feeding molar ratio of the hydrochlorination reactor, the feeding ratio and the reflux ratio of each distillation column, for the reactive columns the feeding ratio, and the operating temperature of the Siemens Reactor.
The objective function, Eq. 1, aims to maximize the process total profit, considering not only the production of the main product (polysilicon), but also the income from by-products (chlorosilanes), deducting the manufacturing cost.

$$\text{OF)}\ \max z = S_{polycrystalline\ silico} + p\,SP - b\,RM - c\,E \quad (1)$$

where, b is the unit cost of each raw material RM; c is the cost of each utility E; d MO is the labour cost; p is the price of each by-product SP, and $S_{polycrystalline\ silicon}$ is profit from the sale of the polycrystalline silicon.
Also, a detailed economic evaluation based on the procedure proposed by Turton et al. (2012) has been carried out, estimating the equipment cost, production cost, maintenance, administration and manpower. The NLP problem was solved using a multistart initialization approach with CONOPT as the preferred solver.

3. Results

The results shown in Table 1 summarize the economic parameters of the process. It can be seen how with an adequate arrangement of the operation conditions of each unit, the production of tetraethoxysilane and chlorosilanes, the raw material consumption, and the services consumption, it is possible to reduce the cost for polycrystalline silicon to 6.86 $/kg, below the commercial price estimated at 10 $/kg. Besides, the comparison

was made with the model without the addition of high value-added products, and the price of polycrystalline silicon in this context is 8.93 $/kg (higher than the price by adding high value-added products). Also, the byproducts cost are: 1.5 $/kg for TEOS 98.5; 2.5 $/kg for TEOS 99.0; 3.75 $/kg for TEOS 99.5; 88.44 $/kg for SiH_4; 3.0 $/kg for SiH_3Cl; and 3.67 $/kg for SiH_2Cl_2. Despite being able to choose from a wide range of high value-added products such as: TEOS 98.5, TEOS 99.0, TEOS 99.5, silane, dichlorosilane and monochlorosilane, in the optimization it can be seen that solution choose the components of greater economic value for its production, as is the case of polycrystalline silicon, silane and TEOS 99.5. The objective function maximizes the profit of the Multi-Product Polycrystalline Silicon Facility, giving a maximum profit in the process of 113.57 M$/y, and presents some particularities. For example, for a large production of silicon, the hydrochlorination reactor temperature is 573 K using a $H_2/SiCl_4$ molar ratio of 2.17. However, despite the low energy requirement of the reactor, high production costs of $SiHCl_3$ are obtained due to the use of considerable amounts of $SiCl_4$. It should be also noted that the process requires a high energy consumption in the distillation columns due to the high values of the reflux ratios. This guarantees a high polycrystalline silicon production capacity although the operating cost is high it also respects an adequate production of high value-added products such as TEOS and chlorosilanes, which makes the process of production of polycrystalline silicon much more profitable. The investment cost of the Multi-Product Polycrystalline Silicon Facility results in 85.93 $M. It can be seen that the distillation columns (conventional or reactive) are the most expensive units, followed by the Siemens reactor and the thermal carboreduction reactor. Only these equipment represent more than 75% of the total cost of the process. Figure 2 shows the consumption of each one of the utilities and raw materials for the objective function evaluated, showing that the maximum profit in a Multi-Product Polycrystalline Silicon Facility.

Table 1. Profit [M$/y], Operating costs [M$/y], kg of polycrystalline silicon/h, kg of TEOS, and kg of silane of the objective function.

Profit [M$/y]	113.57
Operating costs [M$/y]	10.10
kg of polycrystalline silicon/h	1800.50
kg of TEOS (99.5 of purity)/h	632.84
kg of SiH_4/h	42.68
Price of Polycrystalline Silicon $/kg	6.86
Price of TEOS 99.5 $/kg	3.75
Price of SiH_4 $/kg	88.44

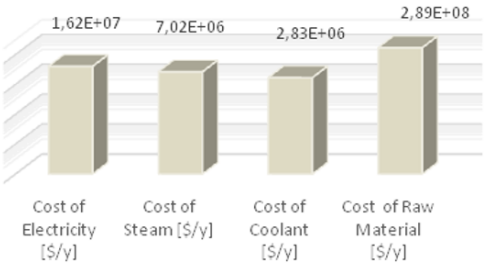

Figure 2. Utilities and raw materials for the Multi-Product Polycrystalline Silicon Facility.

4. Conclusions

In this work a superstructure optimization approach is used for the selection of the portfolio of products within a Multi-Product Polycrystalline Silicon Facility. Surrogate models for major units allow selecting the yield and operating conditions. The proposed process is able to meet the same production of polysilicon than current tradition polysilicon facilities at a lower production cost since the benefits obtained from selling the high added value by-products obtained increase the profit of the facility. The complete process, and therefore the operating conditions of each unit of the process were optimized under the objective of the maximization profit of the process. The optimal operating conditions of the facility that guarantee a lower energetic consumption, meeting with the required production of polycrystalline silicon require the production of high valuable by-products (TEOS 98.5, TEOS 99.0, TEOS 99.5, SiH_4, SiH_3Cl and SiH_2Cl_2), which aid in the economic sustainability of the process. The results after operating expenses, and considering the sale of polycrystalline silicon and the byproducts of the process, are an operational cost of 10 M$/y. The investment for the process is 85.93M$. Obtaining a competitive production cost for polycrystalline silicon of 6.86 $/kg, below the commercial price estimated at 10 $/kg, and the byproducts cost are: 1.5 $/kg for TEOS 98.5; 2.5 $/kg for TEOS 99.0; 3.75 $/kg for TEOS 99.5; 88.44 $/kg for SiH_4; 3.0 $/kg for SiH_3Cl; and 3.67 $/kg for SiH_2Cl_2.

References

E. Sánchez-Ramírez, C. Ramírez-Márquez, J. J. Quiroz-Ramírez, G. Contreras-Zarazúa, J. G. Segovia-Hernández, & J. A. Cervantes-Jauregui, 2018. Reactive Distillation Column Design for Tetraethoxysilane (TEOS) Production: Economic and Environmental Aspects. Industrial & Engineering Chemistry Research, 57(14), 5024-5034.

C. Ramírez-Márquez, E. Sánchez-Ramírez, J. J. Quiroz-Ramírez, F. I. Gómez-Castro, N. Ramírez-Corona, J. A. Cervantes-Jauregui, & J. G. Segovia-Hernández, 2016. Dynamic behavior of a multi-tasking reactive distillation column for production of silane, dichlorosilane and monochlorosilane. Chemical Engineering and Processing: Process Intensification, 108, 125-138.

Rubber & Plastics News Report, 2016. Wacker to build silica plant in Tenn. https://www.rubbernews.com/article/20161214/NEWS/161219980/wacker-to-build-silica-plant-intenn.

C. Ramírez-Márquez, G. Contreras-Zarazúa, M. Martín, & J. G. Segovia-Hernández, 2019. Safety, Economic, and Environmental Optimization Applied to Three Processes for the Production of Solar-Grade Silicon. ACS Sustainable Chemistry & Engineering, 7(5), 5355-5366.

G. Del Coso, C. Del Canizo, & A. Luque, 2008. Chemical vapor deposition model of polysilicon in a trichlorosilane and hydrogen system. Journal of the Electrochemical Society, 155(6).

W. J. Ding, J. M. Yan, & W. D. Xiao, 2014. Hydrogenation of silicon tetrachloride in the presence of silicon: thermodynamic and experimental investigation. Industrial & Engineering Chemistry Research, 53(27).

C. M. Wai & S. G. Hutchison, 1989. Free energy minimization calculation of complex chemical equilibria: Reduction of silicon dioxide with carbon at high temperature. Journal of Chemical Education, 66 (7), 546.

P. Mints, 2018. Photovoltaic Manufacturer Capacity, Shipments, Price & Revenues 2017/2018. SPV Market Research.

Sauro Pierucci, Flavio Manenti, Giulia Bozzano, Davide Manca (Eds.)
Proceedings of the 30th European Symposium on Computer Aided Process Engineering (ESCAPE30), May 24-27, 2020, Milano, Italy.
http://dx.doi.org/10.1016/B978-0-12-823377-1.50130-0

Synthesis and Optimization of a Furfural Production Process. A case Study of Mexico Considering Different Lignocellulosic Feedstocks

Gabriel Contreras-Zarazúa[a], Mariano Martin- Martin[b], Eduardo Sanchez-Ramirez[a], Juan Gabriel Segovia-Hernandez[a]

[a]*Department of Chemical Engineering University of Guanajuato, Noria Alta S/N,36000, Guanajuato,Gto., Mexico.*
[b]*Department of Chemical Engineering, University of Salamanca, Plz. Caídos 1-5, 37008, Salamanca,Spain.*
gsegovia@ugto.mx

Abstract

In this work the design, synthesis and optimization of a furfural production plant, considering the most abundant and common lignocellulosic wastes of Mexico is proposed. For the process, different pretreatment technologies and different purification process including intensified schemes are considered giving a total of 32 possible process alternatives. The pretreatment technologies are the dilute acid (DA) and ammonia fiber explosion (AFEX) respectively, for the separation zone we considered an azeotropic distillation process, a thermally coupled scheme distillation, a dividing wall column and one liquid- liquid extraction process. A two-stage procedure is used to determine the best process per biomass type. First, the processes are modelled in Aspen plus. Next, the best option per biomass is optimized using the differential evolution with tabu list in order to minimize the total annual cost and the environmental impact. The prescreening results indicate that the dilute acid pretreatment and the thermally coupled distillation provide the lowest cost and environmental impact for furfural production for all the raw materials. The optimization results indicate that a biorefinery with wheat straw as raw material is the best option to produce furfural due to its low cost and environmental impact which are 13 M$/yr and 4,536,512 eco-points/year respectively.

Keywords: Furfural, Process Design, Multi-Objective Optimization, Process Intensification, Biorefinery

1. Introduction

Every year in Mexico the agricultural activities generate approximately 640 billion tons of lignocellulosic residues. However, only 5% of these wastes are used. This small percentage is used as food for livestock, compost or burned as fuel mainly, while the rest is incinerated at the harvest sites, which provokes several environmental problems. The lignocellulosic residues can be used to produce high-added value biochemicals. The use of waste has several advantages with respect to other biomasses. The two most important are that these residues do not compete with food avoiding ethical problems and the second reason is because these wastes are cheap. Furfural had been listed by The National Renewable Energy Laboratory (NREL) of the United States as one of the most important biochemicals produced from lignocellulosic residues due to its wide

range of applications as fungicides, extractant for lubricant oils and its ability to compete with chemicals derived from petroleum (Marcotillio, 2011).

Traditionally Furfural has been synthesized by the acid hydrolysis and dehydration of hemicellulose fraction contained inside biomass. For this reason, raw materials with high content of hemicellulose are considered better raw materials. In this work is proposed the synthesis, design and optimization of furfural production processes considering the four most abundant agricultural residues of Mexico. The synthesis phase considers two different pretreatment options and four different process separation schemes including two intensified alternatives in order to generate the most energetic efficient process resulting in 32 possible designs. The best process scheme for each raw material was optimized using the differential evolution with tabu list. Two different indexes, which are the total annual cost (TAC) and eco-indicator 99 (EI99) have been used as performances criteria in order to determinate which are the best raw materials, and which is the best process structure for a furfural plant located at Mexico.

2. Methodology

The selection of raw materials is realized according to the four most abundant agricultural wastes generated in Mexico per year (SIAP, 2019), which are corn stover, wheat straw, sorghum bagasse and sugar cane bagasse. The furfural plants were designed considering a typical size production of 1000 kg/hr furfural (Marcotullio, 2011). We considered that the biomass is formed by cellulose, hemicellulose and lignin the most abundant fractions. An average for these three main fractions composition obtained from different works was used in order to consider the biomass variability.

The design and simulations of the processes were carried out using the software ASPEN PLUS®.The thermodynamic model used at the simulations is Non-random two-liquids coupled with the Hayden-O´Connell (NTRL-HOC) equation of state in order to predict the formation of two liquid phases characteristics of processes with organic compounds and water. The processes are divided in three sections, pretreatment, reaction and purification. For the pretreatment zone, to release of pentoses, two pretreatments have been considered. These pretreatments are the dilute acid with hot water (DA) and the ammonia fiber explosion (AFEX). During the DA pretreatment, the biomass is mixed with a dilute solution of acid in medium-high temperatures around 150-220°C and pressures of 4.75- 23.15 bar. One of the most common acid used is sulfuric acid. The main objective of this process is the solubilization of hemicellulose fractions and the reduction in the crystallinity of cellulose. During the AFEX pretreatment the biomass is exposed with ammonia at high pressure conditions (13.7-20.68 bar) and moderate temperatures (60-160°C) during residence times of 5 min in order to break the fibers inside biomass and release the sugars. Then the biomass is treated with enzymes to hydrolysate the chains of polysaccharides and convert them into monomers like glucose or xylose. Both pretreatments were simulated according with the methodology proposed by Conde-Mejia et al., (2012).

For reaction zone where the furfural is produced, the aqueous solution rich in pentoses produced during the pretreatment stage is introduced into a CSTR reactor with thermal conditions of 190°C and 13.14 atm. Sulfuric acid is fed to the catalyzed the reactor, the concentration of the acid inside the reactor needs to be 0.1M. Under these conditions the conversion of pentoses to furfural is 53%wt, which, represents an efficiency of 82.82% with respect to the theoretical value. A scheme of the reactor and a more detail about the conditions are reported by Zeitsch, (2000).

Different processes have been considered for the purification stage in order to reduce the energy consumption and determinate which is the best option to purify the furfural. The processes are Convectional azeotropic distillation (Quaker oats), which is the typical process used to purify the furfural. In order to reduce energy costs and consumption and improve the thermodynamic efficiency two intensified schemes have been considered: a thermally coupled scheme (TCC) and a divided wall column scheme (DWC). Finally, a liquid-liquid extraction coupled with distillation has also been considered (ED). The distillation schemes were designed in order to get a purity of furfural of 99.2% by mass, that is the minimum purity required to use the furfural in the production of fuels and polymers. The design parameters used for simulating were taken from the previous work,Contreras-Zarazúa et al., (2019). Figure 1 shows the superstructure diagram, which contains all the process alternatives considered in this work. Due to the magnitude of the problem a two-step procedure was used to solve the superstructure. In this case only the best process flowsheet with the less total annual cost and environmental impact for each raw material. These processes are selected to be optimized within Aspen Plus using the differential evolution algorithm with tabu list, which was programed in Visual basic inside EXCEL.

The Total annual cost (TAC) was chosen as a parameter to evaluate the processes economics and this metric was calculated using Guthrie method, the parameters for the equipment's were taken from Turton et al. (2008). We assume steel stainless steel as the construction material for all the equipment, and payback period of 10 years. The trays type sieve are selected with spacing between trays of 2 ft are considered. 8500 hours of yearly operation for each configuration were defined cooling water, heating and electricity are considered has operating cost. **The Eco-indicator** (EI99) was the index used to evaluate the environmental impact of biorefineries, it is a lifecycle method that evaluates different categories (steel, electricity, and vapor) where individual scores are assigned depending of amount of water used, emission produced during the operation of the plant among others.

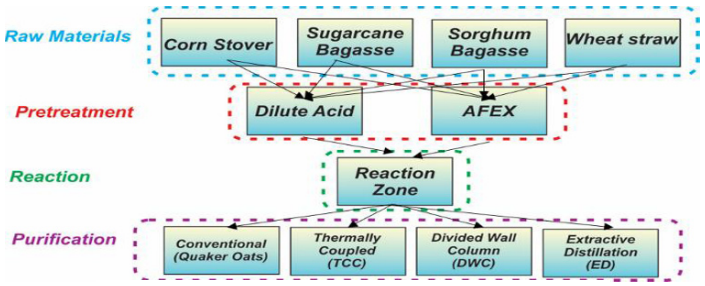

Figure 1. Superstructure for furfural production.

The Differential Evolution with Tabu List Algorithm proposed by Sharma and Rangaiah 2010 has been used at this work. The parameters required by DETL algorithm are the following: Population size (NP): 120 individuals, Generations Number (GenMax): 834, Tabu List size (TLS): 60 individuals, Tabu Radius (TR): 0.01, Crossover fractions (Cr): 0.8, Mutation fractions (F): 0.3. These values were determined through a previous tuning process of the algorithm. The implementation of the multi-objective optimization strategy involved a hybrid platform, which linked Aspen Plus™ and Microsoft Excel™ . The decision variables for each reactive distillation configuration are reported in Table 1. Finally, the multi-objective optimization problem can be expressed mathematically as in Eq. (1) and Eq. (2):

$$\min \quad Z = \{TAC; EI99\} \tag{1}$$

$$\text{Subject to:} \quad \begin{matrix} y_{i,PC} \geq x_{i,PC} \\ w_{i,FC} \geq u_{i,FC} \end{matrix} \tag{2}$$

The objective function is constraint to fulfill the purity and the mass flowrate vectors for the components in the mixture. For example, the values of the purities for the components obtained during the optimization process $y_{i,PC}$ must be either greater or equal to the specified values of purities for the component $x_{i,PC}$. Furthermore, the mass flowrates obtained $w_{i,PC}$ must also be either greater or equal to the specified values of the mass flowrate $u_{i,PC}$.

Table 1. Desion variables and optimization results for fufural production biorefineries.

Decision variables	Discrete variables	Continuous variables
Amount of raw material (kg/hr)	---	X
Number of stages extraction column, E1	X	---
Number of stages columns,	X	---
Feed stage, columns	X	---
Steam flowrate reaction zone (kg/hr)	---	X
Pressure steam in the reaction zone (atm)	---	X
Discharge pressure in AFEX pretreatment (atm)	---	X
Pressure reactor AFEX pretreatment (atm)	---	X
Entrainer mass flow (kg/hr)	---	X
Interlinking flow (kg/hr)	---	X
Reflux ratios	---	X
Heat duties equiments	---	X
Diameter columns	---	X

Finally, it is important to mention that this methodology is not exclusive for this process and it can be applied to different raw materials, chemical products and regions of Mexico and the world. Only data of conversion, pretreatment conditions or product specifications are required to apply this methodology to other raw materials and products.

3. Results

In this section are the prescreening results of 32 possible biorefineries are showed. Figure 2 shows a comparison of the TAC for all alternatives, the EI99 follows the same tendency that cost, due to the environmental impact depends strongly of utilities the electricity used for pumping cooling water, and the steam to provide energy to the process. The results indicate that biorefineries with AFEX pretreatment have higher energy consumption than biorefineries with DA. The AFEX pretreatment needs the compression and purification of ammonia which increases considerably the cost. The DA only requires the addition of sulfuric acid, which is a cheaper alternative, for this reason the AFEX alternatives are considerably more expensive. In the case of processes separations, the Extractive liquid -liquid processes are expensive compared with the Quaker Oats, TCC and DWC options. These results are due to the need for solvents since it involves additional energy consumption, environmental impact and solvent

recovery/separation units. In Figure 2 the TCC and DWC processes have similar cost with respect to the conventional Quaker Oats processes, because these alternatives does not have important energy savings, which is reflected on the total annual cost and eco-indicator. The large amounts of water inside the processes avoiding the elimination remixing phenomena, which is the main cause of inefficiency in distillation columns on DWC and TCC processes. However, the DA TCC has the lowest energy for all the raw materials. For this reason, DA pretreatment with the thermally coupled processes are considered as the best option because they show the lowest total annual cost and environmental impact.

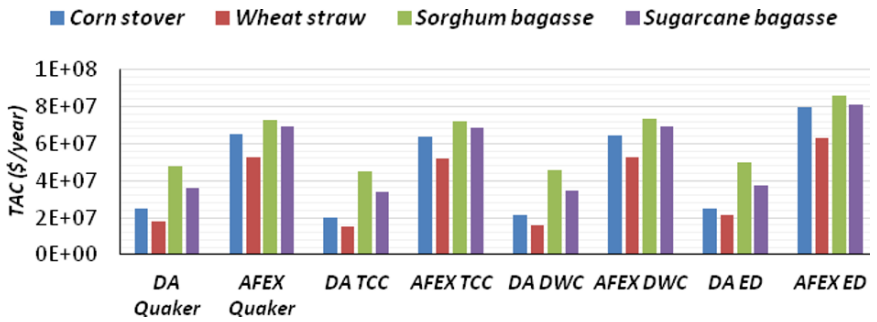

Figure 2. Total anal cost for all the alternatives.

In the Figure 3a the Pareto front of the DA using a thermally coupled column to process wheat straw is shown as a representative case, while in Figure 3 b are showed all the pareto fronts are presented. Note that in Figure 3 the designs obtained with the process optimization method converges to a single point, this point is called utopia point. This point represents the solution that has the best equilibrium for both objectives. Based on the results and considering only the total annual cost and the environmental impact as criteria, wheat straw is the best raw material to produce furfural. In contrast, sugarcane and corn stover are noticeably more abundant in Mexico, which can represent an advantage when supplying raw material to the process, however this process have higher TAC and EI99.

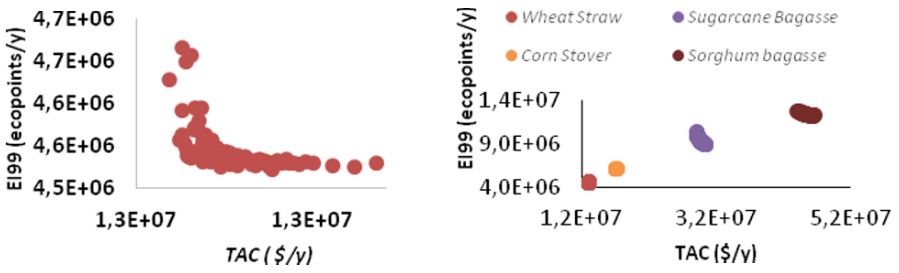

a) b)

Figure 3. Pareto Fronts for DA coupled with TCC separation.

A scheme of the optimal process selected is presented in the Figure 4 that correspond DA pretreatment coped with a thermally coupled distillation. Some design parameter for wheat straw and corn stover processes as a representative case are showed in Table 2 using DA and TCC. Note, that the amount of biomass and water required in the wheat

process is fewer than corn stover process which explain the lowest cost an environmental impact.

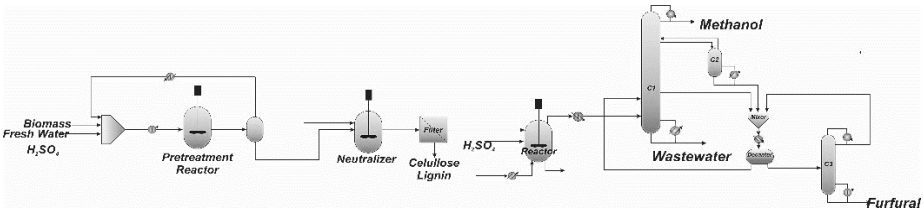

Figure 4. Scheme of the process selected.

Table 2.Representative parameter for bio refineries with wheat straw and corn stover.

Decision variables	Wheat straw	Corn Stover
Amount of raw material (kg/hr)	12213	15981
Amount of water (kg/hr)	10843.9	13680
Energy consumption (kW)	24,681	33,716
Total Annual cost ($/y)	13,092,504	17,122,917
Eco.indicator 99 (Eco-points/y)	4,536,512	6,130,272

4. Conclusions

This work has performed the synthesis, design and optimization of furfural production plants, considering different lignocellulosic wastes produced in Mexico. A two-stage procedure of synthesis and optimization is used to select the process alternative. Based on results of prescribing and optimization phases, we considered that a biorefinery to produce furfural with wheat straw as raw material is the best option based on lowest cost and eco indicators which correspond to values of 13M$/yr and 4,536,512 eco-points/year respectively.

Acknolwledgements

Authors acknowledge JCYL SA026G18 and CONACYT

References

Conde-Mejia, C., Jimenez-Gutierrez, A., & El-Halwagi, M., (2012). A comparison of pretreatment methods for bioethanol production from lignocellulosic materials. Process Safety and Environmental Protection, 90(3), 189-202.

Contreras-Zarazúa, G., Sánchez-Ramírez, E., Vázquez-Castillo, J. A., Ponce-Ortega, J. M., Errico, M., Kiss, A. A., & Segovia-Hernández, J. G. (2019). Inherently safer design and optimization of intensified separation processes for furfural production. Industrial & Engineering Chemistry Research, 58(15), 6105-6120.

http://infosiap.siap.gob.mx/gobmx/datosAbiertos.php accesed 10-June-2019

Marcotullio, G., (2011). The chemistry and technology of furfural production in modern lignocellulose-feedstock biorefineries.

Rangaiah, G. P. (2010). Stochastic global optimization: techniques and applications in chemical engineering. World Scientific.

Turton, R., Bailie, R. C., Whiting, W. B., & Shaeiwitz, J. A. (2008). Analysis, synthesis and design of chemical processes. Pearson Education.

Zeitsch, K. J. (2000). The chemistry and technology of furfural and its many by-products (Vol. 13). Elsevier.

Sauro Pierucci, Flavio Manenti, Giulia Bozzano, Davide Manca (Eds.)
Proceedings of the 30th European Symposium on Computer Aided Process Engineering (ESCAPE30), May 24-27, 2020, Milano, Italy.
http://dx.doi.org/10.1016/B978-0-12-823377-1.50131-2

Heat Exchanger Network Retrofit for Processes with Multiple Operating Cases: a Metaheuristic Approach

Jan A. Stampfli,[a,b,*] Donald G. Olsen,[a] Beat Wellig,[a] René Hofmann[b,c]

[a]*Lucerne University of Applied Sciences and Arts, Competence Center Thermal Energy Systems and Process Engineering, Technikumstrasse 21, 6048 Horw, Switzerland*
[b]*Vienna University of Technology, Institute for Energy Systems and Thermodynamics, Getreidemarkt 9/BA, 1060 Vienna, Austria*
[c]*AIT Austrian Institute of Technology GmbH, Center for Energy, Sustainable Thermal Energy Systems, Giefinggasse 2, 1210 Vienna, Austria*
jan.stampfli@hslu.ch

Abstract

An essential method to improve industrial energy efficiency is through the retrofitting of existing heat exchanger networks. This method presents a difficult challenge that is often compounded by the need to handle multiple operating cases behavior as well. Most research has been tackling retrofitting of such processes by deterministic mathematical approaches. With the increase in size and complexity, however, metaheuristic algorithms provide advantages in the search for the global optimum due to their exhaustive exploration of the search space. Hence, this research provides a two-level metaheuristic approach for the retrofit of processes with multiple operating cases. The retrofit problem is decomposed into a master and slave problem, whereby a genetic algorithm optimizes the network topology, and a differential evolution algorithm optimizes continuous variables such as the heat loads of heat exchangers. The developed algorithm has been successfully applied to a case study from literature with results showing that the incorporation of the suggested modifications can halve the total annual cost of the process.

Keywords: heat exchanger network (HEN), retrofit, multiple operating cases, genetic algorithm, differential evolution

1. Introduction

Energy optimization of industrial processes is an essential aspect of the general goal of improving energy efficiency worldwide. A key approach to help reach this goal is to use process integration techniques that focus on the network of heat exchangers (HEXs) used extensively in industry. A large portion of these process integration projects involves the retrofitting of existing industrial plants. However, industrial processes also exhibit multiple operating cases (MOCs) over time such as in the pharmaceutical, chemical, food, and beverage industries. Methods to help optimize MOCs design for the retrofit case are needed. To date, most research has focused on each challenge individually. Both are commonly solved as optimization problems using mathematical programming (MP). The MP approach can also be used to optimize for the retrofit case subject to MOCs behavior. The resulting mixed-integer nonlinear programming (MINLP) problem formulation can be solved using either deterministic or metaheuristic algorithms. Common deterministic methods that address retrofit MOCs design are the reverse matching approach (Kang and

Liu, 2014) and the reduced superstructure synthesis (Isafiade, 2018). However, the search for the global optimum is hampered by the increase in problem size and complexity, in particular by the implementation of mixers (bypassing and admixing). Metaheuristic algorithms are capable of a broader exploration of the search space owing to their ability to escape local optima by generating a random new solution. Aguitoni et al. (2018), in particular, showed the applicability of a metaheuristic for heat exchanger network (HEN) synthesis.

The specific contribution of this research to literature is to use a metaheuristic approach for the retrofit MOCs design. Thereby a two-level optimization approach is used based on a genetic algorithm (GA) for topology optimization and a differential evolution (DE) algorithm for continuous optimization.

2. Methodology

2.1. Heat Exchanger Network Retrofit of Processes with Multiple Operating Cases

In processes with multiple operating cases, the mass flows, specific heat capacity, supply, and target temperatures change over the course of the production period. To ensure a feasible HEN for each operating case, bypassing as well as admixing around key HEXs is often needed. There are basically five distinct operations to modify the existing HEN design which are often combined together: (1) re-piping of a HEX, (2) re-sequencing of a HEX, (3) modifying the area of a HEX, (4) adding bypasses or admixers to a HEX, and (5) incorporating a new HEX into the design. In practice, the cost to modify the area may differ between HEXs. Therefore, it is necessary to have different cost factors for each HEX. Fig. 1 shows the associated superstructure model of the retrofitting of MOCs design. In each enthalpy stage *k*, every hot process stream *i* can be matched with every cold process stream *j* and utility matches are possible (utility optimization). To ensure the energy balance of every process stream is balanced, utilities are also placed at the streams end. Each HEX can be bypassed (shown in stage 2) or admixed (shown in stage 1).

2.2. Metaheuristic approach

The metaheuristic approach uses an evolutionary concept of survival of the fittest. Thereby, a population of solutions (chromosomes) is initialized. In each generation, evolutionary operations (selection, crossover, and mutation) are applied. During the evolution, *n* best solutions are stored in a list, which is updated as soon as a better solution is found. As a result, several near-optimal solutions are determined, which can be compared in terms of practicability for detail engineering. The MINLP problem is decomposed into a master and slave problem (two-level optimization). To solve the master problem (modification of the HEN topology) a GA, and to solve the slave problem (modification of heat loads, bypassing, and admixing of fractions) a DE algorithm is used.

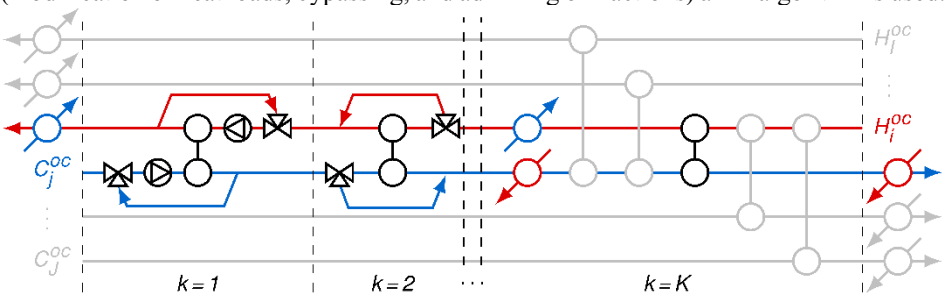

Figure 1: Superstructure for retrofit of MOCs design (*i*: hot process streams, *j*: cold process streams, *k*: enthalpy stages, *oc*: operating cases)

The algorithm is implemented in Python 3.7 using by using the Distributed Evolutionary Algorithms in Python (DEAP) library (Fortin et al. 2012). Experiments are run on a 2.8 GHz Intel i7 computer with 16 GB RAM.

2.2.1. Master Problem: Topology Optimization by Genetic Algorithm

A GA is used to optimize integer variables of the topology (HEX matches as well as the existence of bypassing or admixing). Thereby, the exchanger address matrix (EAM) represents individual solutions (chromosomes). Among others, Rezaei and Shafiei (2009) have used this approach. For the selection of a new chromosome, tournament selection is performed. Thereby, the fittest among n randomly chosen chromosome is selected. For evaluation of the fitness of each chromosome, the DE algorithm (described in section 2.2.2) solves the slave problem. With the probability of crossover P_C, selected parents mate to generate new children using the one-point crossover operation. By the probability of mutation P_M, genes (vector which, e.g., represents matches of a HEX to a process stream) in a chromosome are mutated based on a uniform distribution.

2.2.2. Slave Problem: Continuous Optimization by Differential Evolution

The DE algorithm initializes individuals consisting of continuous optimization variables (heat loads and split fractions for bypassing and admixing). The standard algorithm is configured as *DE/rand/1/bin*. This means that individuals for mutation are selected randomly, only one difference for perturbation (F_P: perturbation factor) is considered, and a binomial crossover is performed. Further, a stopping criterion is implemented, which terminates the DE evolution if no improvement in fitness after n generations is achieved.

2.2.3. Fitness Function and Constraints

For evaluation of the population, the fitness (maximization) is given by the inverse of the total annual cost (TAC) composed of yearly utility cost and annualized retrofit cost for area extensions, splits, re-piping, bypasses, admixers, and new HEXs:

$$fitness = \frac{1}{TAC} \tag{1}$$

In order to ensure thermodynamically feasible solutions, some constraints must be defined. First, the energy balance for all process streams i, j is fulfilled in each OC by:

$$\sum_k \sum_j \dot{Q}_{i,j,k}^{oc} \leq CP_i^{oc} (T_S^{oc} - T_T^{oc}) \qquad \forall i \tag{2}$$

$$\sum_k \sum_i \dot{Q}_{i,j,k}^{oc} \leq CP_j^{oc} (T_T^{oc} - T_S^{oc}) \qquad \forall j \tag{3}$$

Thereby, the sum of all heat loads matched with the actual process stream

Table 1: Stream data of OC 1 (4,664 h/y)

#	T_S (°C)	T_T (°C)	CP (kW/K)
H_1	280	50	50
H_2	210	100	70
C_1	30	190	40
C_2	150	280	60

For all streams: h = 0.1 kW/(m^{2}K)

Table 2: Stream data of OC 2 (3,336 h/y)

#	T_S (°C)	T_T (°C)	CP (kW/K)
H_1	290	80	60
H_2	180	110	50
C_1	160	300	40
C_2	70	130	60

For all streams: h = 0.1 kW/(m^{2}K)

In order to ensure practicality, the number of splits (corresponds to the sum of *Match*) per stage k and process stream is limited by

$$\sum_j Match_{i,j,k}^{oc} + 1 \le MaxSplits \qquad \forall i,k,oc \qquad (6)$$

$$\sum_i Match_{i,j,k}^{oc} + 1 \le MaxSplits \qquad \forall j,k,oc \qquad (7)$$

whereby *MaxSplit* is a user-defined parameter. All constraints are implemented using quadratic penalty functions described by

$$penalty = \Delta(X_{opt} - X_{viol})^2. \qquad (8)$$

This penalty function is applied to the fitness of each infeasible chromosome. X_{viol} describes the violation of the constraints (distance to the feasible region). X_{opt} describes the optimal value of X_{viol}. The weight ” ensures that an infeasible solution is always larger than a feasible solution.

3. Illustrative Case Study

The introduced methodology is applied to a case study first introduced by Jones (1991). Stream data for the two operating cases (OCs) are shown in Tab. 1 and Tab. 2. Tab. 3 provides utility and cost data.

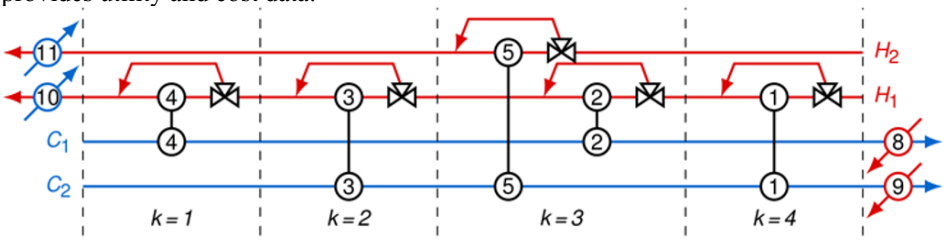

Figure 2: Existent HEN design

Table 3: Optimization parameters

Alg.	Pop. size	P_C	P_M	F_P	Max. iterations
GA	50	0.9	0.1	-	50
DE	100	0.9	-	0.5	200

Table. 4: Utility and cost data

Utility stream	T_s (°C)	T_T (°C)	h (kW/m²/K)	c_{UT} (CHF/MWh)
Steam (HU)	350	349	6	80
Cooling water (CU)	10	11	2	8

Cost for area extension of existing HEX (CHF): $1{,}474A_{ext}^{0.63}$; Cost for new HEX (CHF): $18{,}920+1{,}474A^{0.63}$; Split, bypassing, admixing, and re-piping cost per changed stream (CHF): 4,000; Plant lifetime: $n = 5$ y; Interest rate: $i = 10\%$

Tab. 4 includes optimization parameters of for the algorithm. Fig. 2 shows the actual MOCs design established by Pinch Analysis. The investment cost of the existent plant is depreciated, and thus resulting in TAC of 2,295,000 CHF/y.

4. Results and Discussion

Depending on the size of the EAM, it can be defined how many new HEX can be integrated during the retrofit process. For the actual case study, it was decided to have the possibility to integrate two new HEX (6 and 7). In Fig. 3, the resulting HENs for the best and the 2nd best solution are shown. Thereby, it can be seen that only existent HEXs are re-piped, re-sequenced, and extended but no new HEXs, splits, bypasses, or admixers are incorporated. A comparison of heat loads and corresponding areas of the retrofitted networks, as well as the existing design, is shown in Tab. 5. The TAC for the best solution amounts to 1,038,000 CHF/y, which is composed of 538,000 CHF investment cost and 896,000 CHF/y yearly operating cost. For the 2nd best solution, TAC accumulates to 1,046,000 CHF/y consisting of 555,000 CHF investment cost and 900,000 CHF/y yearly operating cost. It is imperative to notice that due to the assumption of constant re-piping cost, it cannot be clearly determined which of these solutions would be favorable to implement in practice. Nevertheless, compared to the existing design, a reduction of TAC of around 55 % can be achieved. For both solutions, substantial modifications to the HEN are needed.

Table 5: Comparison of heat loads and installed area of existent design with optimized solutions

	Existing design			Best solution			2nd best solution		
HEX	$\dot{Q}_{OC1}$ (kW)	$\dot{Q}_{OC2}$ (kW)	A (m²)	$\dot{Q}_{OC1}$ (kW)	$\dot{Q}_{OC2}$ (kW)	A (m²)	$\dot{Q}_{OC1}$ (kW)	$\dot{Q}_{OC2}$ (kW)	A (m²)
1	3,500	0	1,726	2,803	3,500	1,726	6,400	5,080	4,222
2	0	3,800	1,546	-	-	-	-	-	-
3	0	100	13	-	-	-	-	-	-
4	5,800	0	2,414	6,400	5,070	4,022	4,143	100	7,107
5	1,500	3,500	1,594	4,096	100	7,264	2,741	3,500	1,594
8	600	1,800	708	0	530	708	0	520	708
9	2,800	0	505	901	0	505	916	0	505
10	2,200	8,700	262	1,004	7,430	736	958	7,420	735
11	6,200	0	313	4,897	0	485	4,959	0	490

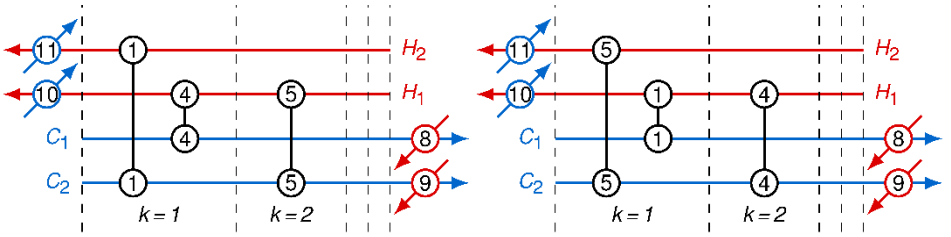

Figure 3: Optimized HEN design for the best solution (left) and 2nd best solution (right)

5. Conclusions

The presented approach introduces metaheuristic algorithms to the retrofitting of MOCs HEN designs. The method has been successfully applied to the case study. However, due to the assumption of fixed costs for splitting, re-piping, bypassing, and admixing, it cannot be clearly stated which solution is most beneficial to implement in practice. Therefore, these costs should be refined by making them dependent on plant layout, mass flow, and pressure drop. Using an evolutionary-based algorithm for topology optimization leads to substantially different solutions compared to the existing design. It should be investigated whether algorithms based on neighborhood structures (e.g., simulated annealing or variable neighborhood search) would be more appropriate to use. Such algorithms apply retrofit modifications such as re-piping and re-sequencing as neighborhood moves on the existing design.

Acknowledgments

This research project is financially supported by the Swiss Innovation Agency Innosuisse and is part of the Swiss Competence Center for Energy Research – Efficiency of Industrial Processes SCCER EIP. Further support is provided by the Lucerne University of Applied Sciences and Arts, Switzerland.

References

A.J. Isafiade, 2018, Retrofitting Multi-Period Heat Exchanger Networks using the Reduced Superstructure Synthesis Approach, Chemical Engineering Transactions, 70, 133-138.

E. Rezaei, S. Shafiei, 2009, Heat exchanger networks retrofit by coupling genetic algorithm with NLP and ILP methods, Computers and Chemical Engineering, 33, 1451-1459.

F.-A. Fortin, F.-M. De Rainville, M.-A. Gardner, M. Parizeau, C. Gagné, 2012, DEAP : Evolutionary algorithms made easy, Journal of Machine Learning Research, 13, 2171-2175.

L. Kang, Y. Liu, 2014, Retrofit of Heat Exchanger Networks for Multiperiod Operations by Matching Heat Transfer Areas in Reverse Order, Industrial & Engineering Chemistry Research, 53(12), 4792-4804.

M.C. Aguitoni, L.V. Pavão, P.H. Siqueira, L. Jiménez, M.A.S.S. Ravagnani, 2018, Heat exchanger network synthesis using genetic algorithm and differential evolution, Computers and Chemical Engineering, 117, 82-96.

P.S. Jones, 1991, Targeting and design for heat exchanger networks under multiple base case operation, PhD Thesis, University of Manchester Institute of Science and Technology, Manchester, United Kingdom of Great Britain and Northern Ireland.

Sauro Pierucci, Flavio Manenti, Giulia Bozzano, Davide Manca (Eds.)
Proceedings of the 30th European Symposium on Computer Aided Process Engineering (ESCAPE30), May 24-27, 2020, Milano, Italy.
http://dx.doi.org/10.1016/B978-0-12-823377-1.50132-4

Sustainable Process Synthesis, Design and Innovation of Bio-succinic Acid Production

Rofice Dickson[a,b], Enrico Mancini[a], Nipun Garg[a], Jay Liu[b], Manuel Pinelo[a], Seyed Soheil Mansouri[a,*]

[a]*Department of Chemical and Biochemical Engineering, Technical University of Denmark, Søltofts Plads, Building 229, DK- 2800 Kongens Lyngby, Denmark*

[b]*Department of Chemical Engineering, Pukyong National University, Busan, 48513, Korea*

seso@kt.dtu.dk

Abstract

Over the last decades, bio-succinic acid from renewable resources has gained significant attention as a precursor molecule for the synthesis of an array of other chemicals. The goal of this study is to obtain a novel process alternative for bio-succinic acid production, which is optimal and realistic in terms of process economics, implementation as well as environmental sustainability. Thereby, a hierarchical approach consisting of 3 stages: synthesis, design (& analysis) and innovation is used. In stage 1, a comprehensive superstructure is developed to systematically find the optimal processing route to produce bio-succinic acid. The proposed superstructure contains multiple process alternatives including different types of feedstock, pretreatment steps, fermentation technologies, and separation technologies all at acceptable technology readiness level (TRL). Based on the superstructure, a mixed-integer linear model was formulated. Once an optimal processing route is identified, then in stage 2, the selected process flowsheet is designed and analysed in detail. The primary goal at this stage is to identify process hotspots which enables to set design targets for further improvements. The identified process bottlenecks are then used in the 3rd stage where a phenomena-based synthesis methodology is applied, generating non-trade off and more sustainable process alternatives for producing bio-succinic acid.

Keywords: Process synthesis, Process intensification, Sustainable solutions, Succinic acid

1. Introduction

Succinic acid is an important precursor for producing more than 30 commercially valuable products in pharmaceutical, food, and agriculture industries. Succinic acid is largely produced from petroleum feedstock. However, technological advances in biorefinery have facilitated its production from renewable feedstock. Bio-succinic (bio-SA) acid is reported by both the European Commission (EC-DGE, 2015) and the U.S. Department of Energy (Werpy and Petersen, 2004) one of the top growing products within bio-based market, which is projected to reach 7 – 10 billion USD per year. Despite its numerous applications and growing market, bio-SA production is still at its fancy and not economically lucrative compared with that from petroleum.

It has been estimated that bio-SA leads to greenhouse gas saving of 4.5 – 5 kg per kg of succinic acid when compared to petrochemical based succinic acid (Hermann et al., 2007). However, bio-SA is not cost competitive with its petrochemical rival, mainly due to its high production cost. Purification of succinic acid from the fermentation broth is

estimated to account 60 – 70% of the total production costs, while only 20 – 25% of the costs can be allocated to the upstream process including biomass pretreatment and fermentation process, and only 10 – 15% to the purchase of the feedstock itself (Morales et al., 2016). Therefore, bio-SA can only be a viable replacement for petroleum derived succinic acid if upstream and downstream technologies can lower the production cost by increasing the product yield and selectivity in former while lowering the purification cost in latter.

The necessity of major technological improvements to lower production cost makes the bio-SA process design, a complex combinatorial optimization problem. For instance, bio-SA can be produced from different feedstock including 1st (sugar/starch), 2nd (lignocellulose) and 3rd (aquatic biomass) generation. Different feedstock sources require different pretreatments, which in turn decides the formation of fermentation process inhibitors. To achieve high yield and selectivity of succinic acid, fermenter design and its operating condition, selection of appropriate microorganism and buffer are crucial decision variables that will decide the downstream purification. The potential technological decision variables in bio-SA purification include: centrifugation or microfiltration for cell separation, evaporation, solvent extraction, activated carbon, ultrafiltration, precipitation, ion exchange, reactive extraction, bipolar membrane, electrodialysis, direct crystallization and nanofiltration for succinic acid separation. Combining all process alternatives from feedstock selection to downstream processing makes the bio-SA production process very complicated in order to find best flowsheet for large-scale production taking into account technology readiness level (TRL) of these various technologies. Therefore, the goal of this study is to determine best (innovative and intensified) flowsheet for bio-SA production using 3 stage approach (Babi et al., 2015; Garg et al., 2019; Mansouri et al., 2013), as shown in Fig.1 with an aim that the resulting solution is the closest towards large scale implementation.

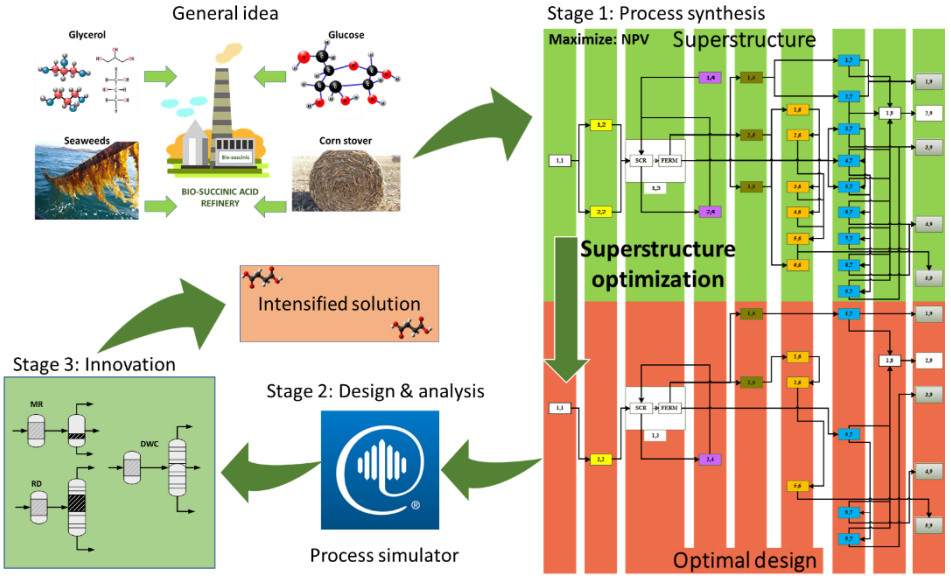

Figure 1. Methodology for determining innovative and intensified process design of bio-SA.

2. Methodology

The central theme of the proposed methodology is to increase the search space in stage 1 to find the base case flowsheet. Since the output from stage 1 comprises of single flowsheet, thus, search space is reduced in stage 2. The base case flowsheet is then rigorously simulated and analysed to determine improvement targets, leading to search space expansion using phenomena-based methodology in stage 3. Here feasibilities rules are used to reduce the search space to generate non-trade off solutions that are better than the base case as well as fulfils all desired improvement targets set in stage 2.

2.1. Stage 1: Synthesis

Objective: To identify an optimal processing route of bio-succinic acid among numerous process alternatives.

In stage 1, a superstructure is developed to systematically finding the optimal processing route to produce bio-SA, as shown in Fig.2. The proposed superstructure contains multiple process alternatives including different types of feedstock, different pretreatment steps, different fermentation technologies, and different separation technologies. The novelty of the proposed process synthesis superstructure features comprehensive network of 34 process alternatives with technology readiness level of 5–9 as the basis for optimal design identification. This is to ensure that the resulting solution from superstructure optimization is appealing from an implementation point of view. As indicated in Fig.2, bio-SA can be produced using glucose and glycerol (1st generation biomass), corn stover (2nd generation biomass), and *Saccharina japonica* (3rd generation biomass). It is assumed that glycerol is obtained from biodiesel and bioethanol industries, whereas glucose is obtained from 1st generation biomass. For effective utilization of biomass in fermentation, five pretreatment technologies are included in the superstructure: acid thermal hydrolysis of corn stover, deacetylation followed by acid thermal hydrolysis, alkaline (sodium hydroxide) hydrolysis, acid thermal hydrolysis of *Saccharina japonica*, and hot water wash hydrolysis. Once biomass is pretreated, it is processed using enzymatic hydrolysis in the presence of cellulase enzyme. The fermentation (production) of sugars can be carried out in batch or fed-batch fermenter in the presence of different microorganism and buffers. Nine fermentation technologies are included in the superstructure, which correspond to different titer (g/l), yield (g/g), and productivity (g/l/h) of succinic acid. After fermentation, cell mass can be removed using microfiltration or centrifuge. The broth can be then concentred either before or after isolation of succinic acid using evaporation or vacuum distillation. The colour impurities and protein can be removed from broth using activated carbon or nanofiltration. Isolation can be defined as recovering succinic acid from its salt. Since isolation is energy intensive, six processing alternatives namely electrodialysis, direct crystallization, reactive extraction, ion exchange column, reactive crystallization, and membrane technology (combination of ultra- and nano-filtration) are included in the superstructure. The isolated succinic acid is then purified using solvents, (such as methanol) or crystallization, and finally dried to remove moisture to desired purity.

To determine optimal flowsheet of bio-SA with purity of at least 99 wt.%, a techno-economic mixed-integer linear model (MILP) is formulated. The production target of succinic acid is set to 30 kt/y based on the capacity of main producers of bio-SA (Cavani et al., 2016). The objective function (*OBJ*) for the model is defined as

$$OBJ = S^{PROD} - C^{RAW} - C^{C} - C^{U}, \quad (1)$$

where S^{PROD} is revenue from the sales of succinic acid, C^{RAW} is raw material cost, C^{C} is chemical cost, and C^{U} is utilities cost.

2.2. Stage 2: Design and analysis

Objective: To conduct detailed design and analysis in order to identify process hotspots and set design targets.

Once an optimal route (base case) is identified, then in stage 2, the selected flowsheet is designed rigorously in PRO/II using the UNIQUAC thermodynamic method for modelling liquid–vapour and liquid–liquid equilibria of strongly non-ideal solution (Garg et al., 2019). The mass and energy balances are then utilized to carry out analysis in terms of process economics and environmental impact. The primary goal at this stage is to identify process hot-spots which enables to set new targets for further improvements to be achieved in innovation stage.

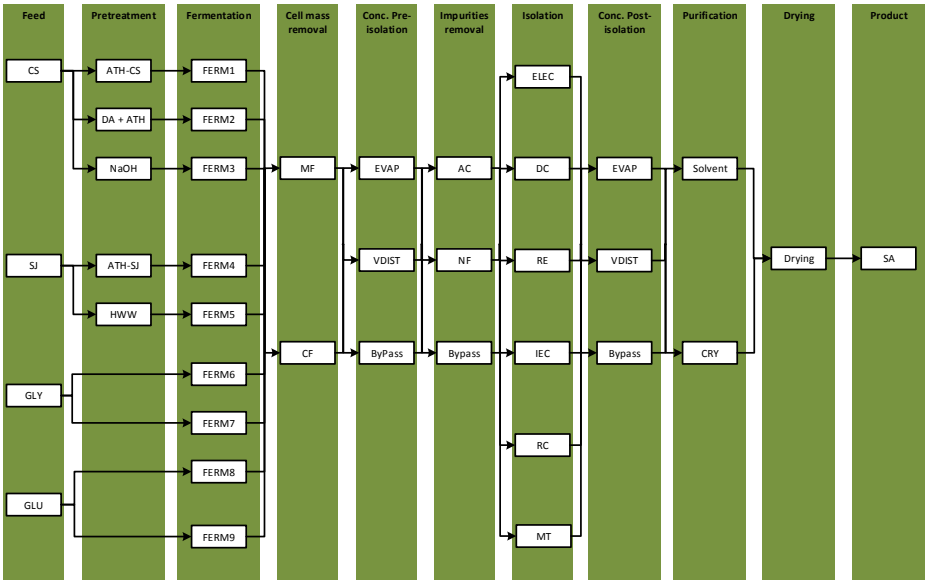

Nomenclature: CS = Corn stover; SJ = Saccharina japonica; GLY = Glycerol; GLU = Glucose; ATH-CS = Acid thermal hydrolysis of CS; DA + ATH = Deacetylation followed by ATH; ATH-SJ = Acid thermal hydrolysis of SJ; HWW = Hot water wash; FERM = Fermentation; MF = Microfiltration; CF = Centrifuge; AC = Activated carbon; NF = Nano-filtration; EVAP = Evaporation; VDIST = Vacuum distillation; ELEC = Electrodialysis; DC = Direct crystallization; RE = Reactive extraction; IEC = Ion exchange column (chromatography); RC = Reactive crystallization; MT = Membrane technology; CRY = Crystallization; SA = succinic acid

Figure 2. Superstructure for bio-SA production.

2.3. Stage 3: Innovation

Objective: To generate more sustainable and intensified (multi-functional) alternatives using phenomena-based synthesis method (Babi et al., 2015). In other words, flowsheets that meet both design specification of base case and improvement targets both economically and environmentally are considered non-trade off and more sustainable solutions.

In stage 3, the base case is translated into a task-based flowsheet; and later to phenomena-based flowsheet to identify an initial list of phenomena building blocks leading to increased search space. Since all the combination in phenomena building blocks are not feasible due to thermodynamic infeasibilities, the search space is then reduced by identifying feasible flowsheet alternatives that match the design specification of the base case as well as improvement targets determined in pervious stage.

3. Results and discussion

A hybrid approach consisting of 3 stages: synthesis, design (& analysis) and innovation is used to determine sustainable process design of bio-SA (Babi et al., 2015; Garg et al., 2019). As shown in Fig.3, the optimal flowsheet consists of a glucose as a feed, fermenter, centrifuge for broth clarification, distillation to concentrate the broth and remove unwanted organic acids and alcohols, followed by carbon treatment for removal of soluble solids causing colour and then finally crystallization and drying to get pure crystals of succinic acid. The solution is computed in 2.56 s and objective function value correspond to USD 48.61 million.

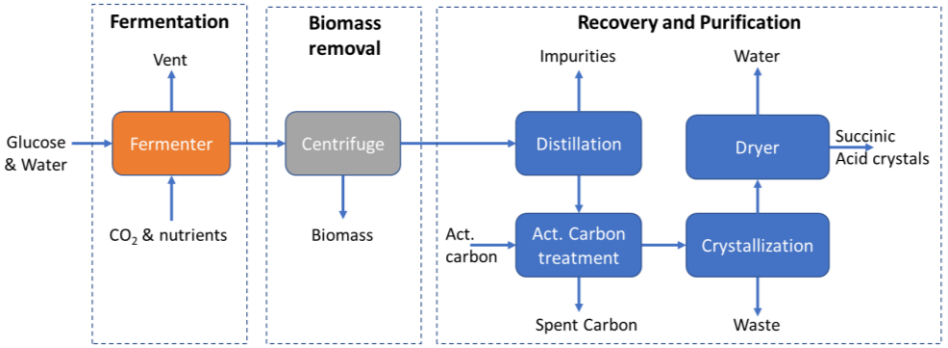

Figure 3. Optimal flowsheet in stage 1.

The optimal flowsheet is then simulated in PRO/II and process analysis is performed. Results indicate that the process requires heating and cooling loads of 20.3 and 19.1 MW, respectively, and yields 30 kt/y of succinic acid with purity greater than 99 wt.%. The sustainability analysis indicates loss of product and raw material in open path (in-out streams) containing crystallizer. The economic analysis shows high utility costs related to unit-op in open path i.e. reboiler of distillation column. As expected, the LCA analysis confirms with the high carbon footprint for reboiler of the distillation column.

Based on process analysis results, high energy consumption leading to high utility costs, loss of product and raw material, and high carbon footprint in distillation column are identified as process hotspots that are translated into design targets (reverse of hotspots). These design targets should be achieved in innovation stage to generate intensified sustainable flowsheet. Three intensified flowsheets are determined that satisfy base case constraints as well as design targets. In alternative 1, membrane bioreactor is considered as intensified flowsheet, in which reaction synthesis and separation take place simultaneously. In other words, the reaction product is removed continuously while cell remain in the fermenter, leading to increased cell concentration, thus, high product yield. In alternative 2, membrane crystallizer is considered as an intensified flowsheet, combining crystallization and separation of crystals from liquid phase. Whereas, alternative 3 is a combination of previous intensified flowsheet i.e., both membrane bioreactor and membrane crystallizer. Results of three alternative intensified flowsheets can be seen from radar plot depicted in Fig.4. The base case design is at the boundary while the more sustainable alternatives are all within the boundary, indicating that these intensified alternatives are non-trade off alternatives. It can be seen that process economics and environmental performance of alternative 3 is superior compared to base case and remaining intensified alternatives. Likewise, compared to base case, the number of required unit operation are decreased from 6 to 4 in alternative 3.

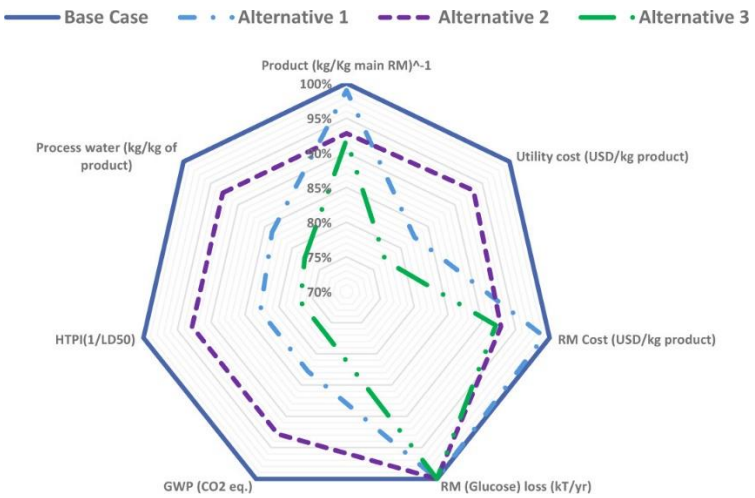

Figure 4. Economic, sustainability and LCA improvements relative to the base case design (HTPI: Human toxicity potential by ingestion, GWP: Global warming potential).

4. Conclusion

A hybrid approach comprising of 3 layers: synthesis, design (& analysis) and innovation is used to find non-trade off, more sustainable and intensified solutions to produce bio-SA. Results revealed that superstructure-based approach is useful to find novel processing route. However, if superstructure-based approach is combined with process intensification methodology remarkable improvement can be achieved. In this work, intensified flowsheet (alternative 3) compared to base case have achieved about 22% reduction in utility cost and 23% improvements in terms of environmental performance.

References

Babi, D.K., Holtbruegge, J., Lutze, P., Gorak, A., Woodley, J.M., Gani, R., 2015. Sustainable process synthesis-intensification. Comput. Chem. Eng. 81, 218–244. https://doi.org/10.1016/j.compchemeng.2015.04.030

Cavani, F., Albonetti, S., Basile, F., Gandini, A., 2016. Chemicals and Fuels from Bio-Based Building Blocks. John Wiley & Sons.

EC-DGE, 2015. From the Sugar Platform to biofuels and biochemicals, E4Tech, RE - CORD (Consorzio per la Ricerca e la Dimostrazione sulle Energie Rinnovabili), Wageningen University and Research Center. https://doi.org/contract No. ENER/C2/423-2012/SI2.673791

Garg, N., Woodley, J.M., Gani, R., Kontogeorgis, G.M., 2019. Sustainable solutions by integrating process synthesis-intensification. Comput. Chem. Eng. 126, 499–519. https://doi.org/10.1016/j.compchemeng.2019.04.030

Hermann, B.G., Blok, K., Patel, M.K., 2007. Producing Bio-Based Bulk Chemicals Using Industrial Biotechnology Saves Energy and Combats Climate Change. Environ. Sci. Technol. 7915–7921. https://doi.org/10.1021/es062559q

Mansouri, S.S., Ismail, M.I., Babi, D.K., Simasatitkul, L., Huusom, J.K., Gani, R., 2013. Systematic sustainable process design and analysis of biodiesel processes. Processes 1, 167–202. https://doi.org/10.3390/pr1020167

Morales, M., Ataman, M., Badr, S., Linster, S., Kourlimpinis, I., Papadokonstantakis, S., Hatzimanikatis, V., Hungerbühler, K., 2016. Sustainability assessment of succinic acid production technologies from biomass using metabolic engineering. Energy Environ. Sci. 9, 2794–2805. https://doi.org/10.1039/c6ee00634e

Werpy, T., Petersen, G., 2004. Top Value Added Chemicals from Biomass Volume I — Results of Screening for Potential Candidates from Sugars and Synthesis Gas Top Value Added Chemicals From Biomass Volume I : Results of Screening for Potential Candidates. https://doi.org/10.2172/15008859

Sauro Pierucci, Flavio Manenti, Giulia Bozzano, Davide Manca (Eds.)
Proceedings of the 30th European Symposium on Computer Aided Process Engineering (ESCAPE30), May 24-27, 2020, Milano, Italy.
http://dx.doi.org/10.1016/B978-0-12-823377-1.50133-6

Optimal Design of Macroalgae-based Integrated Biorefinery: Economic and Environmental Perspective

Rofice Dickson[a], Jun-Hyung Ryu[b], Jay Liu[a,*]

[a]*Department of Chemical Engineering, Pukyong National University, Busan, 48513, Korea*

[b]*Department of Energy Engineering, Dongguk University, Gyeongju Campus, Gyeongju, 38066, Korea*

jaylie@pknu.ac.kr

Abstract

With the rapid depletion of fossil fuels and increasing environmental issues, viable alternatives are crucially needed to create a more sustainable and balanced energy infrastructure. Macroalgae have recently gained attention as a possible feedstock for biorefinery because of their high content of carbohydrates, proteins, and vitamins. To date, no commercial macroalgae-based biorefinery exists. Identifying efficient and environmentally friendly biorefining process is challenging due to many processing alternatives. Therefore, the aim of this study is to determine optimal design of macroalgae-based biorefinery employing a superstructure-based approach. Seventeen alternative processing technologies at acceptable technology readiness level are included in the superstructure to determine an optimal and realistic processing route by maximizing the net present value in the most environmentally beneficial manner. The results indicated that biofuel production from macroalgae is economically viable, at minimum ethanol selling price of USD 1.18/gal. Furthermore, the optimal design has achieved a 90% reduction in CO_2 emissions. Sensitivity analysis indicated that the purchasing price of macroalgae and selling price of heavier alcohols are the most sensitive parameters to process economics.

Keywords: Superstructure optimization, Process synthesis, Process integration, Macroalgae, Biofuel

1. Introduction

The current pace of utilizing petroleum resources is causing ecosystem damages. Global warming is a serious environmental issue, common to all mankind. Carbon dioxide emissions (CEs) from burning fossil fuel are thought of as one major contribution to global warming. To mitigate climate change impacts, highly efficient biorefineries utilizing sustainable biomass must be developed in order to replace fossil-based energy infrastructure.

Macroalgae (seaweed) have been considered as more sustainable biomass compared to agricultural crops since they do not compete for land and freshwater (Dickson and Liu, 2019). In particular, they are not quite used as food source on a global scale, which minimizes the impact on price related to the food versus fuel debate for terrestrial crops. Brown seaweed, *Saacharina japonica* (SJ) are fast-growing, high photosynthetically efficient aquatic plants (Brigljević et al., 2019). From an industrial point of view, numerous researchers have conducted techno-economic assessments of SJ and concluded

that it is an excellent feedstock for producing biofuels owing to high carbohydrates contents, lack of lignin, and extensively available feedstock (Fasahati and Liu, 2015; Dickson et al., 2018). Therefore, the present study utilizes SJ as a feedstock for producing biofuels and value-added chemicals using the volatile fatty acid platform (VFAP).

In the VFAP, all non-lignin components of seaweed including carbohydrates, protein, and lipids are converted into volatile fatty acids (VFAs) consisting of acetic acid, propionic acid, and butyric acid through partial anaerobic digestion. VFAs can be then hydrogenated to produce mixed alcohols (MAs) consisting of ethanol, propanol, and butanol. Both VFAs and MAs have numerous applications in industries such as chemical, food, and pharmaceutical, and transportation sector, respectively. Pham et al. (2012) demonstrated that high product yields ranging from 0.31–0.41 g/g dry feed can be achieved through VFAP. Despite numerous application and promising yields, the effective and economically viable separation of VFAs is a key bottleneck to industrial scale application of VFAP owing to close boiling point of water and acetic acid (Dickson and Fasahati, 2019). Furthermore, determination of effective separation system for VFAs requires systematically evaluation of various alternative pathways, which make it complex combinatorial decision-making problem. Regarding environmental sustainability, anaerobic fermentation of biomass produces massive CO_2. It is reported that medium-sized biorefinery, processing 2–3.5 Mt/y sugarcane produces 110–193 kt/y of CEs during fermentation (Bonfim-Rocha et al., 2018), which requires process integration techniques to utilize CEs in order to improve environmental performance.

Based on the presented challenges, the aims of the present study are to determine the optimal pathway for the VFAP and to utilize all waste streams including CEs, wastewater, and undigested biomass from the processing to value-added chemicals through process integration techniques.

2. Methodology

To determine the optimal and sustainable processing route for the VFAP, superstructure-based approach is used. The major decision variables include technology selection for the VFAP and CO_2 utilization; the mass flow rate of each species in every stream; the heat and power consumption of each piece of equipment; the capital and the operating cost required for economic evaluation; and all emissions required for environmental evaluation.

2.1. Superstructure development

The superstructure is developed to systematically find the optimal processing route of VFAP, as shown in Fig.1. The proposed superstructure contains 7 processing intervals, each embedded with multiple process alternatives. The novelty of the superstructure features a comprehensive network of 17 process alternatives with technology readiness level of 5–9 as the basis for optimal design identification.

The biorefinery process starts with the anaerobic digestion of SJ. Anaerobic digestion consists of four stages; and in order to produce VFAs, partial anaerobic digestion is carried out using inhibitor such as iodoform, which eliminates methanogenesis step. The operating conditions for anaerobic digestion are 13 wt.% solid loading; a retention time of 120 h; an inhibitor loading of 30 ppm; a digestion temperature of 35 °C, and a yield of 0.35 g VFA/g of dry feed. After anaerobic fermentation, the outlet stream from the digester consists of solid, liquid, and gaseous products, which is sent to the purification section. In the purification section, gaseous- and solid- products are separated from the liquid products. Liquid products consisting of VFAs are sent to VFA extraction section,

in which two alternative technologies are considered: classical dehydration and hybrid dehydration. The main equipment of the classical dehydration contains an extraction column, a rectification column, a stripping column, and a decanter. The hybrid process involves the combination of membranes and the classical dehydration process. The main goal in VFA extraction section is to concentrate VFAs from 5 wt.% to 95 wt.%. Once the VFAs are concentrated, they can be hydrogenated in the mixed alcohols synthesis section to produce mixed alcohols consisting of ethanol, propanol, and butanol.

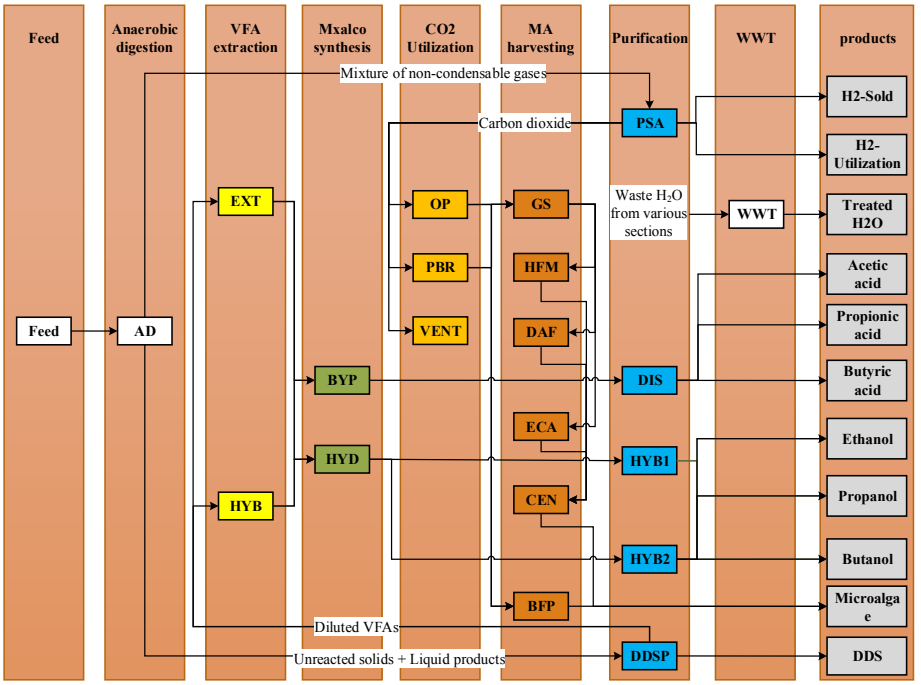

Nomenclature: AD = Anaerobic digestion; EXT = Extraction followed by distillation; HYB = Membranes followed by extraction and distillation; BYP = Bypass; HYD = Hydrogenation; OP = Microalgae cultivation in open ponds; PBR = Microalgae cultivation in photo-bioreactor; VENT = Venting CO_2 to atmosphere; GS = Gravity settler; HFM = Hollow filter membranes; DAF = Diffused air flocculation; ECA = Electrocoagulation; CEN = Centrifuge; BFP = Belt filter press; PSA = Pressure swing distillation; DIS = VFAs purification via distillation; HYB1 = MAs purification via pervaporation followed by distillation; HYB2 = MAs purification via molecular sieves followed by distillation; DDSP = Dry distillery solid purification;

Figure 1. The superstructure of biorefinery for producing biofuels and chemicals from *Saccharina Japonica*.

Alternative, hydrogenation can be bypassed and concentrated VFAs are separated into pure compounds. Mixed alcohols and mixed acids will be produced as the main products of biorefinery in the former (hydrogenation) and latter (bypass), respectively. If the latter is selected as an optimal decision, an upper limit of utilizing 30 wt.% of the VFAs is set for mixed acids production, because the main objective of the biorefinery is to produce biofuels. In CO_2 utilization section, the key objective is to convert CO_2 into microalgae either in open ponds or photobioreactor. If the production of microalgae is not economically favorable then the CO_2 is vented to the environment by paying a carbon tax of USD 20/t. For microalgae harvesting and dewatering, six process alternatives are included in microalgae harvesting section. The microalgae can be harvested in gravity settler, which can be dewatered either by hollow filter membranes, diffused air flocculation, or electrocoagulation followed by centrifugation. Alternatively, a belt filter press can be implemented at the outlet stream of gravity settler. The operating data and

equipment costs considered for microalgae production are based on the work of (Davis et al., 2016). In purification section, separation of non-condensable gases, VFAs, MAs, and dry distillery solid (DDS) take place in pressure swing adsorption, distillation columns, pervaporation or molecular sieves followed by distillation, and centrifuge and dryer, respectively. A complete wastewater network consisting of anaerobic digestion, aerobic digestion, and reverse osmosis is included in the superstructure that treats polluted water from various processing stages back to the process.

2.2. Mathematical formulation and objective function

The optimal processing route of integrated biorefinery is determined by formulating mixed-integer non-linear model (MINLP), and its solution is computed using DICOPT solver. The model contained 7,476 continuous variables, in which 1,680 variables are nonlinear, 22 variables are binary, and the remaining variables are linear, and 6,517 equality and inequality constraints. The objective function for the model is the net present value that should be maximized and is defined as

$$NPV = \sum_{n=0}^{20} \frac{NCF_n}{(1+r)^n}, \tag{1}$$

where NCF_n is non-discounted cash flow for the year n, and r is the discount rate.

3. Results and discussion

The proposed process synthesis superstructure was implemented in GAMS (29.1.0) to find optimal processing route for VFAP and CEs utilization. The chemical composition (wt.%) of the SJ species reported by Roesijadi et al. (2010) was used in the present study. An upper limit of 400 kt/yr (dry basis) is set on the SJ supply.

The optimal flowsheet is an integrated biorefinery producing both mixed acids, mixed alcohols, and microalgae production, as shown in Fig.2. The optimal pathway consists of anaerobic digestion, extraction followed by distillation, partial bypass and hydrogenation, hydrogen purification via pressure swing adsorption, the distillation of mixed acids, the dehydration of mixed alcohols using molecular sieves followed by distillation, DDS purification, wastewater treatment. In the integrated design, 30 wt.% of the concentrated VFAs are utilized to produce mixed acids, whereas the remaining VFAs are utilized to produce mixed alcohols. For CO_2 utilization, the optimal pathway consists of cultivation in open ponds, harvesting by gravity settler, and dewatering by hollow filtration membranes followed by centrifuge.

Flowrate summary balance results indicate that the biorefinery utilizes 400 kt/y biomass. It produces 19 Mgal/yr mixed alcohols and 17 Mgal/yr mixed acids as main products and 0.98 kt/yr hydrogen, 111.8 kt/yr DDS, and 28.17 microalgae as byproducts. Integration of microalgae process with biorefinery utilized 90% of CO_2 emissions from processing.

Techno-economic results indicate that the minimum ethanol selling price and the net present value of optimal design are USD 1.18/gal and USD 44 million, respectively. The total capital investment of biorefinery is calculated to be USD 215 million, where 69% is consumed by the VFA section and the remaining 31% by microalgae section. The total cost of manufacturing is calculated to be USD 102.93 million/y, where VFA section accounts for 89% and reaming 11% to microalgae section.

The freshwater requirement of the VFA process is calculated to be 6.26 gal/gal of alcohols and acids. About 73% of the overall water makeup is due to water evaporation in the

cooling tower. The water requirement of microalgae section is 157.7 t/h owing to the evaporation of water from the pond surfaces.

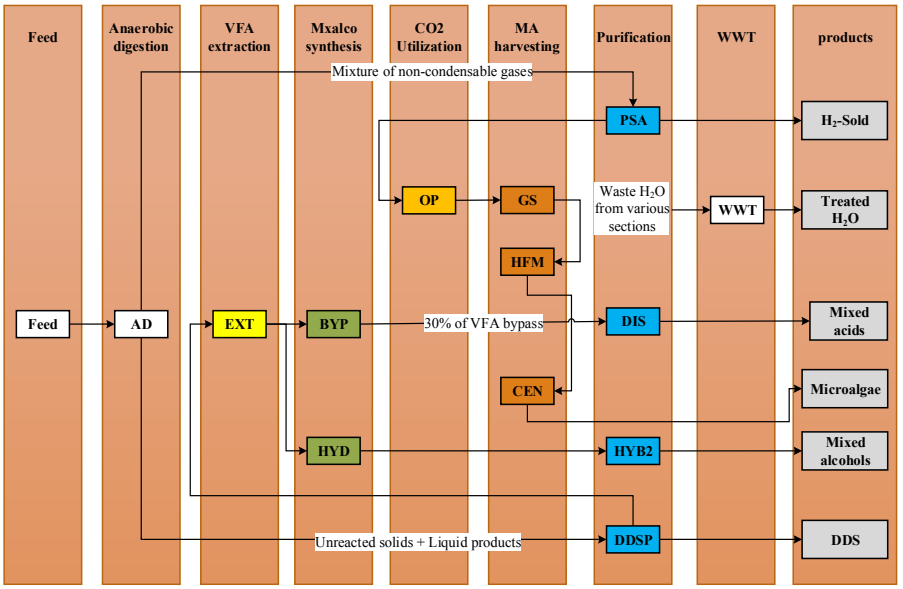

Figure 2. Optimal biorefinery structure.

3.1. Sensitivity analysis

The optimization model also performs sensitivity analysis to evaluate the major bottlenecks to the process economics. The results indicate that fixed capital investment, the seaweed price, and the internal rate of return (IRR) are the most important parameters for determining the economic viability of a biorefinery. Therefore, to ensure the economic viability of a seaweed-based biorefinery, efficient farming is necessary to increase the seaweed productivity.

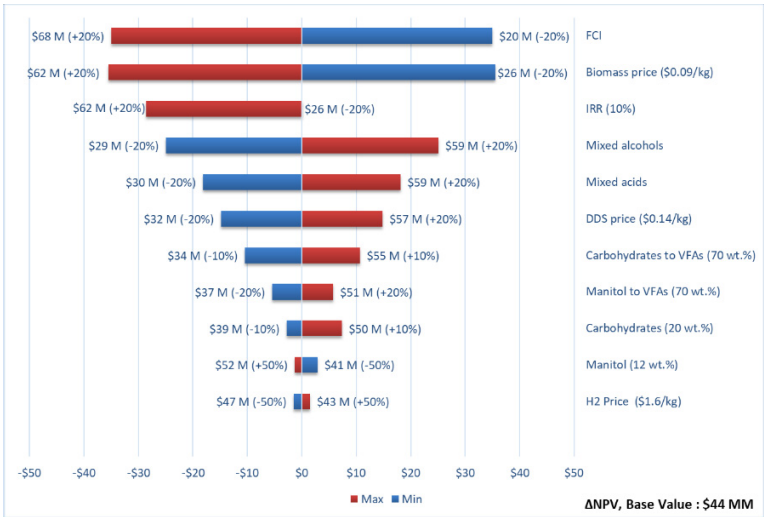

Figure 3. Sensitivity analysis of biorefinery parameter.

4. Conclusion

An optimization-based superstructure for macroalgae-based integrated biorefinery is proposed that determines optimal topology based on net present value as well reduces CO_2 emissions from the processing. A techno-economic assessment indicated that the production of biofuels and value-added chemicals results in a minimum ethanol selling price of $1.18/gal. An environmental assessment indicated that the optimal design is an environmentally friendly process because it utilizes 90% of CEs produced by biorefinery processing.

Acknowledgement

This research was supported through the Basic Science Research Program of the National Research Foundation of Korea (NRF) funded by the Ministry of Science and ICT (2017R1A2B4004500).

Reference

Bonfim-Rocha, L., Gimenes, M.L., Bernardo de Faria, S.H., Silva, R.O., Esteller, L.J., 2018. Multi-objective design of a new sustainable scenario for bio-methanol production in Brazil. J. Clean. Prod. 187, 1043–1056. https://doi.org/10.1016/j.jclepro.2018.03.267

Brigljević, B., Liu, J.J., Lim, H., 2019. Comprehensive feasibility assessment of a poly-generation process integrating fast pyrolysis of S. japonica and the Rankine cycle. Appl. Energy 254, 113704. https://doi.org/10.1016/j.apenergy.2019.113704

Davis, R., Markham, J., Kinchin, C., Grundl, N., Tan, E.C.D., Humbird, D., 2016. Process Design and Economics for the Production of Algal Biomass: Algal Biomass Production in Open Pond Systems and Processing Through Dewatering for Downstream Conversion. Natl. Renew. Energy Lab. 128. https://doi.org/10.2172/1239893

Dickson, R., Fasahati, P., 2019. Optimal design for integrated macroalgae-based biorefinery via mixed alcohol synthesis, in: 29th European Symposium on Computer Aided Process Engineering. Elsevier Masson SAS, pp. 253–258. https://doi.org/10.1016/B978-0-12-818634-3.50043-6

Dickson, R., Liu, J., 2019. Optimization of seaweed-based biorefinery with zero carbon emissions potential, in: 29th European Symposium on Computer Aided Process Engineering. Elsevier Masson SAS, pp. 247–252. https://doi.org/10.1016/B978-0-12-818634-3.50042-4

Dickson, R., Ryu, J.-H., Liu, J.J., 2018. Optimal plant design for integrated biorefinery producing bioethanol and protein from Saccharina japonica: A superstructure-based approach. Energy 164. https://doi.org/10.1016/j.energy.2018.09.007

Fasahati, P., Liu, J.J., 2015. Impact of volatile fatty acid recovery on economics of ethanol production from brown algae via mixed alcohol synthesis. Chem. Eng. Res. Des. 98, 107–122. https://doi.org/10.1016/j.cherd.2015.04.013

Roesijadi, G., Jones, S.B., Zhu, Y., 2010. Macroalgae as a Biomass Feedstock: A Preliminary Analysis, Pacific Northwest National Lab.(PNNL). https://doi.org/10.2172/1006310

Sauro Pierucci, Flavio Manenti, Giulia Bozzano, Davide Manca (Eds.)
Proceedings of the 30th European Symposium on Computer Aided Process Engineering (ESCAPE30), May 24-27, 2020, Milano, Italy.
http://dx.doi.org/10.1016/B978-0-12-823377-1.50134-8

Integrating Superstructure Optimization under Uncertainty and Optimal Experimental Design in early Stage Process Development

Stefanie Kaiser, Sebastian Engell

TU Dortmund University, Chemical and Biochemical Engineering, Process Dynamics and Operations Group, Emil-Figge-Straße 70, 44227 Dortmund, stefanie2.kaiser@tu-dortmund.de

Abstract

We present an iterative methodology that combines superstructure optimization, sensitivity analysis, and optimal design of experiments. In the early design phase, usually no accurate models for use in superstructure optimization are available, and the uncertainties of the models can influence the structure of the optimal design. The accuracy of the models is gradually increased by experimental investigations. In order to reduce the time and effort needed for process development, the experiments should focus on the most influencing parameters with respect to the design decisions. After one or few process structures have been fixed, further experiments will then lead to quantitatively accurate predictions. The methodology is applied to the case study of the hydroaminomethylation of decene.

Keywords: Early stage process design, superstructure optimization, model refinement, optimal experimental design

1. Introduction

Early stage process design is a crucial phase in the development of new processes in the chemical industry, because it largely determines the final investment and production costs. On the other hand, in this phase decisions have to be taken based on limited knowledge and uncertain data. Due to shorter product cycles, the pressure to reduce the development time is increasing. Therefore, fast, efficient, and risk aware process development strategies are needed. The known methodologies for process synthesis can be divided into two categories – hierarchical or knowledge-based methods (Douglas, 1985) and optimization-based methods (Grossmann et al., 1999). In the process industries, knowledge-based methods are still common. However, they generally fall short in terms of finding synergies between the different unit operations and innovative process layouts, because the choice of the process structure and the unit operations, laboratory experiments, and process optimization are performed consecutively. The work of different groups on different unit operations is combined at a very late stage of process development, which can lead to suboptimal decisions, avoidable cost, time delays, and re-work in later stages. Optimization-based methods have become popular in academia (Kuhlmann & Skiborowski, 2016) but they usually require good process models. Since the process models are uncertain in an early design phase, superstructure optimization under uncertainties has been proposed by Steimel & Engell (2015) and Steimel & Engell (2016). To overcome these issues, a holistic approach is proposed in this work that bridges between the planning and design of laboratory experiments and superstructure

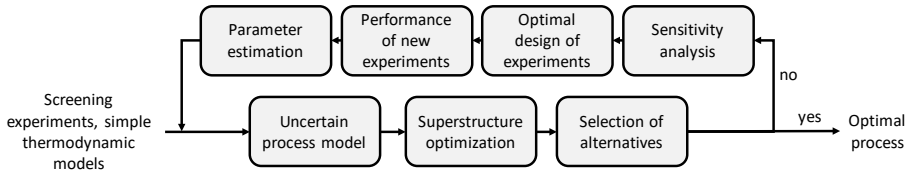

Figure 1: Schematic representation of the approach for integrated process development.

optimization under uncertainty. Promising process designs are optimized with respect to the production costs using superstructure optimization for early stage models with large uncertainties. The impact of the uncertain parameters is analyzed via a local sensitivity analysis. The computed sensitivities are then used as weights in an optimal design of experiments to perform experiments which provide most information. The methodology is applied to a case study from the Berlin-Dortmund-Magdeburg Collaborative Research Center InPROMT, a homogenously catalyzed hydroaminomethylation process.

2. Methodology

The starting point of the design process is that coarse models of all process units under consideration are available, typically based on screening experiments and simple thermodynamic models. Moreover, confidence intervals for the uncertain model parameters must be known. The subsequent iterative cycle of the choice of unit operations, laboratory experiments, and process optimization is depicted in Figure 1.

The models with uncertainties are used for a superstructure optimization under uncertainty, and thereafter a sensitivity analysis with respect to the uncertain parameters is performed. Optimal design of experiments is used to design experiments that target the most cost-influencing parameters. After performing the targeted experiments, improved models are fitted, and the procedure is repeated until one design is found to be superior over all other designs. This work focuses on the superstructure optimization, the sensitivity analysis, and the optimal design of experiments, which are explained in the following subsections.

2.1. Superstructure optimization under uncertainties

In superstructure optimization under uncertainties, first, a set of process alternatives is generated. Secondly, models of the process units in the superstructure are set up. The optimal configuration can then be determined by solving the following optimization problem (Steimel & Engell, 2015):

$$\begin{aligned} &\min_{x_\omega, y} Z = G(y) + \sum_{\omega=1}^{\Omega} \pi_\omega F_\omega(x_\omega, y) \\ \text{s.t. } &h(x_\omega, y) = 0 \\ &g(x_\omega, y) \leq 0 \\ &x_\omega \in X_\omega, y \in \{0,1\} \end{aligned} \tag{1}$$

Usually binary and continuous decisions are involved. Thus the optimization problems typically results in mixed integer nonlinear programs (MINLP (Chen & Grossmann, 2017)). The objective function is composed of a part $G(y)$ describing the costs taking the first-stage decision and a part $\sum_{\omega=1}^{\Omega} \pi_\omega F_\omega(x_\omega, y)$ describing the expected cost of the second stage decision via weighting and summation of the costs of Ω discrete scenarios F_ω. It is minimized subject to the equality constraints $h(x_\omega, y)$, given by physical relations such as mass and energy balances, kinetics, and thermodynamics. Process specifications and equipment limits are modeled by the inequality constraints $g(x_\omega, y)$. Nonlinearities

introduced by e.g. the reaction kinetics often result in nonconvex problems and therefore global optimization techniques, such as evolutionary algorithms are required.
In this work, the superstructure optimization platform FSOpt is used, which was developed by (Steimel & Engell, 2015). In FSOpt, a two stage optimization is performed, where decisions that cannot be adapted to the realization of the uncertainty are fixed but operational parameters are assumed to be adapted to the future realization of the uncertainty and therefore act as recourse variables. Internally, a memetic algorithm is employed (Urselmann et al., 2011). Discrete decisions (e.g., binary decisions as selection or omission of a process unit), are optimized by an evolutionary algorithm while continuous variables are handled by a gradient-based solver.

2.2. Sensitivity analysis

A sensitivity analysis is used to identify the most cost-influencing parameters among the uncertain parameters. For sensitivity analysis a sampling is needed. Latin hypercube sampling (LHS) was chosen in this work, because it covers the complete space with a comparably small number of samples. A linear regression is performed that correlates the n uncertain parameters x_i to the regressed objective value $\hat{Z}_j$:

$$\hat{Z}_j = \beta_0 + \sum_{i=1}^{n} \beta_i x_i. \tag{2}$$

The intercept β_0 and the regression coefficients β_i are determined via least squares. In order to make the regression coefficients comparable they are standardized with zero mean and a standard deviation of one. The Standardized Regression Coefficients SRC are computed as:

$$SRC_j = \frac{\beta_j \hat{s}_i}{\hat{s}}, \qquad \text{with } \hat{s} = \left[\sum_j^N \frac{(Z_j - \bar{Z})^2}{N-1}\right]^{1/2} \text{ and } \hat{s}_i = \left[\sum_j^N \frac{(x_i - \bar{x})^2}{N-1}\right]^{1/2}, \tag{3}$$

where N is the number of samples. The SRCs are independent on the regessor x_j. Therefore, they can be used to compare the impact of the uncertain model parameters. A large SRC means that the corresponding parameter has a large impact on the objective.

2.3. Optimal design of experiments

New experiments are designed such that the most influencing parameters found by the sensitivity analysis can be estimated more precisely. The methodology described by Franceschini & Macchietto (2008) is applied and in addition to the standard approach, the parameters are weighted with the previously computed SRC. Improving the parameter precision is mathematically equivalent to decreasing a measure of the parameter variance-covariance matrix $\boldsymbol{V}$, which is computed as

$$\boldsymbol{V}(\hat{\boldsymbol{\theta}}, \boldsymbol{\phi}) = \left[\sum_r^{n_{resp}} \sum_s^{n_{resp}} \tilde{\sigma}_{rs} \boldsymbol{Q_r^T} \cdot \boldsymbol{SRC} \cdot \boldsymbol{Q_s}\right]^{-1}, \tag{4}$$

with the number of responses n_{resp} and a diagonal matrix containing the previously computed SRCs $\boldsymbol{SRC}$. $\boldsymbol{Q_r}$ is the dynamic sensitivity matrix that contains the sensitivities of the expected model outputs $\hat{\boldsymbol{y}}$ with respect to the parameters $\boldsymbol{\theta}$ at all sampling times. Here, a D-optimal design is chosen that minimizes the determinant of the variance-covariance matrix $\boldsymbol{V}$ by variation of the experimental conditions and the sampling times.

3. Case study – Hydroaminomethylation of 1-Dodecene

The proposed approach is applied to the homogeneous catalysed hydroaminomethylation of 1-decene. The catalyst is rhodium that has been preformed with a sulphoxantphos ligand. To recover the expensive catalyst, the usage of a thermomorphic solvent system (TMS) with the solvents methanol and dodecane as proposed by Huxoll et al. (2019) is used. The reaction medium is miscible at reaction temperature, and after cooling it splits

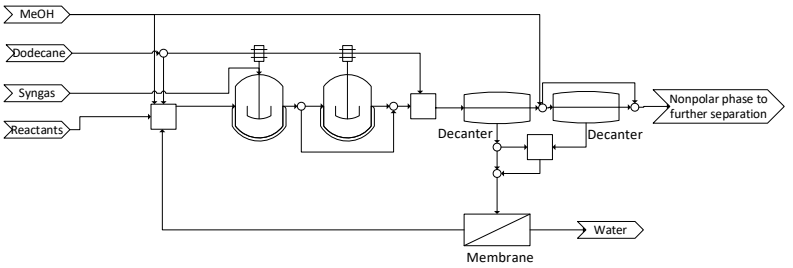

Figure 2: Superstrucure of the hydroaminomethylation process.

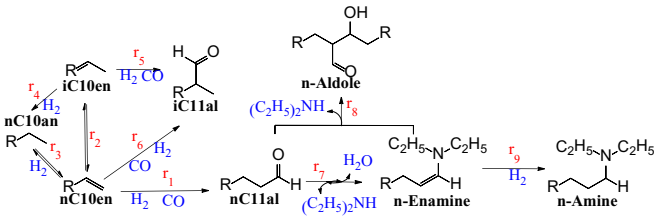

Figure 3: Reaction network of the hydroaminomethylation.

in two phases. The catalyst and the polar solvent methanol can be recycled and the unpolar solvent, the product, and the remaining reactants can be purified further. This purification stage is not considered in this work. The water that is formed during the reaction is separated via a membrane from the recycle stream. The process superstructure considering reactors, decanters, and a membrane is depicted in Figure 2.

3.1. Process model

For the modeling of the reactor the reaction kinetics are needed. The hydroaminomethylation is a combination of a hydroformulation step and a subsequent reductive amination. The reaction kinetics of the hydroformulation as described by Hentschel et al. (2015) and of the reductive amination as proposed by Kirschtowski et al. (2019) are combined. The reaction network is depicted in Figure 3. All parameters were fitted to experimental data of the hydroaminomethylation in a solvent system consisting of methanol and dodecane.

Thermodynamic models are needed to compute the gas solubilities in the reaction medium and the phase separation in the decanter. The solubilities of hydrogen (H_2) and carbon dioxide (CO_2) are approximated by the solubilities in pure solvent and calculated with the equation of state PC-SAFT. Since the PC-SAFT models are not suitable for optimization (Nentwich & Engell, 2019), neural networks were trained to the calculated H_2 and CO_2 concentrations with respect to the temperature, the partial pressures, and the solvent composition. The liquid-liquid equilibrium in the decanter is modeled with the g^E-Model UNIFAC-DO. A neural network was trained to fit the distribution coefficients $K_i = \frac{x_1}{x_{FEED}}$. The membrane is described by a constant retention for each component i, defined as $R_i = 1 - \frac{w_{i,Perm}}{w_{i,Feed}}$, with w_i as the weight fraction in the permeate and in the feed respectively, and a constant area specific permeate flow. The production cost per ton of product is the objective function. It is composed of the costs of the raw materials, the investment costs and the utility costs. The costs for the solvents are not considered, because it is assumed that the solvents can be recovered in the downstream processing.

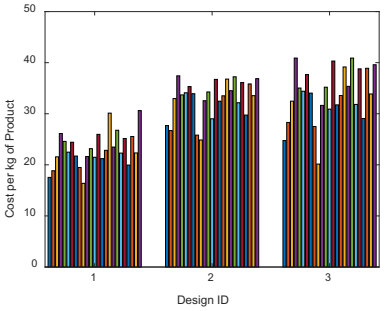

Figure 4: Costs for the three best designs.

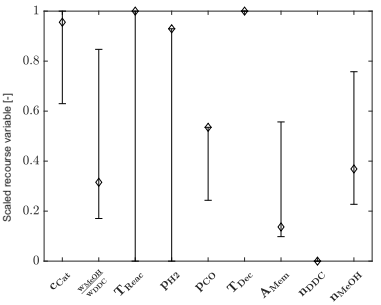

Figure 5: Recourse variables scaled with respect to their bounds.

3.2. Optimization results

In this work, we only consider the kinetic parameters as uncertain. Other parameters such as the distribution coefficients and the membrane retentions that are also uncertain and influence the production costs will be considered in future work. For 18 uncertain parameters (9 pre-exponential factors k_i and 9 activation energies E_A) discrete realizations were considered, giving rise to 25 different scenarios. In Figure 4, the costs for the three best designs that are structurally different are shown for these 25 scenarios. It can be seen that design one is superior to the others. However, the costs vary a lot and the equipment size still has to be chosen. Therefore, a model improvement is necessary. For the best design, two reactors and two decanters are used and the nonpolar solvent is fed between the reactors and the decanters. Depending on the realizations of the uncertainties, the operating conditions are adjusted as shown in Figure 5.

3.3. Sensitivity analysis and design of a new experiment

For the best design, the SRCs are computed and presented in Figure 6. It can be seen that the reaction rate constant k_3 has the largest impact on the production costs due to the large confidence interval, followed by the parameters $k_1$and E_{A1}.

An optimal design of experiments, weighted by the SRCs, was performed as described in section 2.3. The decision variables were the sampling times, the temperature, the partial pressures of H_2 and CO, and the solvent composition. The optimal experimental conditions are shown in Table 1 and were found to be independent of the initial values. The optimal sampling times are after 40, 44, 62, 161 and 166 minutes. It is predicted that by performing this experiment the confidence intervals of the most influencing parameters k_3 and k_1 will be reduced by 35% and 14% respectively.

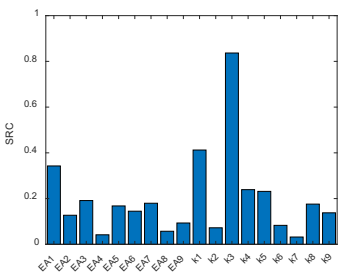

Figure 6: SRCs for the kinetic parameters.

Table 1: Optimized conditions for the next kinetic experiment.

	Temperature [K]	Pressure [bar]	Catalyst concentration [mol/mol]	Gas composition (CO: $\mathbf{H_2}$) [mol/mol]	Solvent composition (MeOH:DDC) [kg/kg]
Optimal value	386	37.76	0.0001	0.2	7.19

4. Conclusion and Outlook

We presented a systematic methodology for early phase process development. By combining superstructure optimization under uncertainty, sensitivity analysis, and optimal design of experiments, the experimental work is focussed on determining the most influencing parameters and thus the time for process development can be reduced. The designed experiments will be conducted in the future to continue with the iterative cycle. The approach will also be applied to uncertainties in thermodynamic models and other models of other process units.

Acknowledgement

Gefördert durch die Deutsche Forschungsgemeinschaft (DFG) - TRR 63 "Integrierte chemische Prozesse in flüssigen Mehrphasensystemen" (Teilprojekt D1) – 56091768.
Funded by the Deutsche Forschungsgemeinschaft (DFG) - TRR 63 "Integrated Chemical Processes in Liquid Multiphase Systems" (subproject D1) - 56091768.

References

Chen, Q., & Grossmann, I. E. (2017). Recent Developments and Challenges in Optimization-Based Process Synthesis. *Annu. Rev. Chem. Biomol. Eng.*, *8*(1), 249–283.

Douglas, J. M. (1985). A hierarchical decision procedure for process synthesis. *AIChE J.*, *31*(3), 353–362.

Franceschini, G., & Macchietto, S. (2008). Model-based design of experiments for parameter precision: State of the art. *Chem. Eng. Sci.*, *63*(19), 4846–4872.

Grossmann, I. E., Caballero, J. A., & Yeomans, H. (1999). Mathematical programming approaches to the synthesis of chemical process systems. *Korean J. Chem. Eng.*, *16*(4), 407–426.

Hentschel, B., Kiedorf, G., Gerlach, M., Hamel, C., Seidel-Morgenstern, A., Freund, H., & Sundmacher, K. (2015). Model-based identification and experimental validation of the optimal reaction route for the hydroformylation of 1-dodecene. *Ind. Eng. Chem. Res.*, *54*(6), 1755–1765.

Huxoll, F., Bianga, J., Vogt, D., & Sadowski, G. (2019). Model-based Solvent Screening for a Reductive Amination. *ECCE12*.

Kirschtowski, S., Kadar, C., Seidel-Morgenstern, A., & Hamel, C. (2019). Reductive amination in different solvent systems: reaction network analysis and kinetics. *ECCE12*.

Kuhlmann, H., & Skiborowski, M. (2016). *Synthesis of Intensified Processes from a Superstructure of Phenomena Building Blocks*.

Nentwich, C., & Engell, S. (2019). Surrogate modeling of phase equilibrium calculations using adaptive sampling. *Comput. Chem. Eng.*, 204–217.

Steimel, J., & Engell, S. (2015). Conceptual design and optimization of chemical processes under uncertainty by two-stage programming. *Comput. Chem. Eng.*, *81*, 200–217.

Steimel, J., & Engell, S. (2016). Optimization-based support for process design under uncertainty: A case study. *AIChE J.*, *62*(9), 3404–3419.

Urselmann, M., Barkmann, S., Sand, G., & Engell, S. (2011). Optimization-based design of reactive distillation columns using a memetic algorithm. *Comput. Chem. Eng.*, *35*(5), 787–805.

Sauro Pierucci, Flavio Manenti, Giulia Bozzano, Davide Manca (Eds.)
Proceedings of the 30th European Symposium on Computer Aided Process Engineering (ESCAPE30), May 24-27, 2020, Milano, Italy.
http://dx.doi.org/10.1016/B978-0-12-823377-1.50135-X

A Thermodynamic Approach for Simultaneous Solvent and Process Design of Continuous Reactive Crystallization with Recycling

Nethrue Pramuditha Mendis,[a] Jiayuan Wang,[b] Richard Lakerveld[a,*]

[a]*Department of Chemical and Biological Engineering, The Hong Kong University of Science and Technology, Clear Water Bay, Hong Kong S.A.R.*
[b]*School of Chemical Engineering, Zhejiang University of Technology, Hang Zhou 310014, China.*
r.lakerveld@ust.hk

Abstract

Solvent selection for continuous reactive crystallization processes with downstream separation of reactants and solvents for recycling is challenging due to the influence of the solvent type on various equilibria that occur within such process and their close interaction with operating conditions. Therefore, computational tools are needed to support decision making. In this work, a simultaneous solvent and process optimization framework for continuous reactive crystallization processes with recycling is presented. The PC-SAFT equation of state is used as the unified thermodynamic framework, which is combined with continuous mapping to make the resulting optimization problem computationally tractable. The approach is demonstrated for a continuous synthesis and purification process of the active pharmaceutical ingredient dalfampridine.

Keywords: reactive crystallization, pharmaceuticals, solvent design, process design, PC-SAFT

1. Introduction

Separation and purification of active pharmaceutical ingredients (APIs) are carried out extensively through solution crystallization in the pharmaceutical industry. Solvents are the medium for solution crystallization processes and have a substantial impact on the process performance and on aspects related to safety, health, and environment. However, solvent selection is generally complicated by the large number of available solvent types and their mixtures and different process performance criteria. Traditional methods based on heuristics may not lead to an optimal trade-off. Furthermore, important progress on the prediction of solvent properties from thermodynamic models has been achieved. Therefore, there is a need to replace solvent selection heuristics with mathematical optimization-based approaches. Due to the strong interconnection between the solvent choice and process operating conditions, those two design problems need to be solved simultaneously to identify the optimal solvent mixture. Such optimization-based solvent selection approaches have been developed for stand-alone crystallizers (Karunanithi et al., 2006). However, solvent recycling may be important for reducing the solvent waste and aligns well with the pharmaceutical industry's current trend towards continuous manufacturing. Therefore, solvent separation needs to be considered as well. Wang and Lakerveld (2018a, 2018b) developed a solvent selection framework for continuous antisolvent crystallization with solvent recycling based on the PC-SAFT equation of state (Gross and Sadowski, 2001), where solvent selection,

crystallization and downstream separation were all treated in an integrated manner. Supersaturation is the driving force for crystallization, which can be generated through a reaction. Reactive crystallization is complicated by the necessity to consider reaction equilibria and the potential to form multiple solid phases. Recycling of reactants and solvents is likely to be important for optimal performance. However, optimization-based solvent selection methods for reactive crystallization processes (with or without recycle structures) have not been developed yet.

The objective of this work is to develop a simultaneous solvent and process optimization framework for continuous reactive crystallization processes with recycling. The PC-SAFT equation of state (Gross and Sadowski, 2001) is used as the unified thermodynamic model to predict reaction, solid-liquid, and, vapor-liquid equilibria. The continuous mapping method (Stavrou et al., 2014) is adopted to convert the original MINLP problem into a computationally tractable NLP problem.

2. Approach

The proposed approach involves a process model with a unified thermodynamic model and optimization. The synthesis and crystallization of dalfampridine, a potassium channel blocker API for treatment of multiple sclerosis, from isonicotinamide is used to illustrate the approach.

2.1. Synthesis Reaction

Dalfampridine can be synthesized via the Hofmann rearrangement of isonicotinamide (sub), where an isonicotinamide solution reacts with an alkaline aqueous solution of NaOCl at 45-80 ℃ (Rane and Sharma, 1994) as follows:

$$Sub + NaOCl(io_1) + 2NaOH(io_2) = API + NaCl(io_3) + Na_2CO_3(io_4) + H_2O(w) \quad (1)$$

The use of an inert organic co-solvent (sol), typically sulfolane (Rane and Sharma, 1994), is preferred to minimize side reactions and to dissolve the substrate.

2.2. Process Configuration

The process consists of a continuous crystallizer followed by a flash drum, which enables the recycling of reactants and solvents (see Figure 1). The substrate (in solid form), a pure make-up solvent stream, and the recycled solvent stream are mixed before being fed to the crystallizer. In the crystallizer, the fully dissolved substrate is mixed with an alkaline aqueous solution of NaOCl. The API is synthesized in the crystallizer and will crystallize immediately due to its low solubility in the reaction medium. Note that the solubility of the substrate in the reaction medium should be sufficiently high to avoid its crystallization. The API crystals are separated by a filter, and the mother liquor is sent to the flash drum, where the mother liquor (consisting of reactants) is concentrated and partially recycled. The flash drum is considered a single vapor-liquid equilibrium stage. The main purpose is to enable recycling of the reactant, but the possibility of solvent recycling is also included by considering an additional recycle from the top of the flash drum, which may contain a substantial amount of solvents that can be suitable for recycling.

2.3. Thermodynamic Modeling

The PC-SAFT equation of state describes the Helmholtz free energy of a mixture, which is the starting point to calculate all thermodynamic properties in this type of processes such as fugacity coefficients, activity coefficients, and residual enthalpies (Gross and Sadowski, 2001). In this work, a pure substance is characterized by five parameters described in detail by Gross and Sadowski (2002), which consider dispersive and associative interactions. Ionic interactions are not explicitly considered, and both the

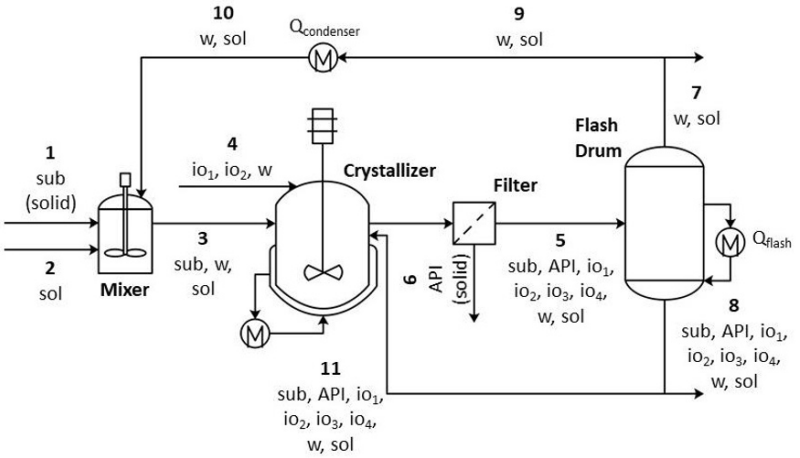

Figure 1: Process configuration

substrate and the API are assumed to be neutral due to the presence of a strong base (NaOH) in the reaction medium.

Solubility data are typically used for parameterization of compounds that are solid at room temperature, which includes many APIs. Due to insufficient solubility data, the PC-SAFT pure component parameters of isonicotinamide and dalfampridine (Table 1) are determined by fitting their activity coefficients in a selected set of solvents, which are calculated using the Pharma Mod. UNIFAC group contribution-based activity coefficient model (Diedrichs and Gmehling, 2011). The pure component parameters for water were obtained from the literature (Gross and Sadowski, 2002). The synthesis reaction is modeled as an equilibrium reaction using activities (a), according to:

$$\prod_i a_i^{\nu_i} = K_{eq} \tag{2}$$

where i and ν stand for compounds and their stoichiometric coefficients in Eq. (1), respectively. The experimental system described in Rane and Sharma (1994) is used to determine the reaction equilibrium constant (K_{eq}=4.13×10^5 at 80 °C). Activities are approximated with mole fractions for the ionic compounds. Crystal formation in the crystallizer is modeled by assuming solid-liquid equilibrium, described by:

$$x^{sol}\gamma^{sol} = \exp\left[\frac{\Delta H_f^m}{R}\left(\frac{1}{T_m}-\frac{1}{T}\right)\right], \tag{3}$$

where x^{sol} and γ^{sol} are the mole fraction solubility and the activity coefficient of the solute, respectively. ΔH_f^m and T_m are the enthalpy of fusion (22.6 kJ/mol for isonicotinamide (Li et al., 2016); 20.07 kJ/mol for dalfampridine (Chen et al., 2017)) and the solid melting temperature (428.5 K for isonicotinamide (Li et al., 2016); 432.2 K for dalfampridine (Chen et al., 2017)).

The downstream separation in the flash drum is modeled as a vapor-liquid equilibrium using fugacity coefficients in liquid and vapor phases.

Table 1: PC-SAFT parameters for the substrate and the API

Component	m	σ (Å)	ε/k (K)	ε^{AB}/k (K)	κ^{AB}	*Association Scheme*
Isonicotinamide	5.45	2.41	160.86	1807.86	0.010	2/2
Dalfampridine	6.30	2.87	131.29	2027.81	0.010	2/2

The total molar enthalpy of a given stream is determined as the sum of ideal and residual contributions, where the latter is directly calculated from PC-SAFT. The ideal contribution to the total enthalpy is linked with the PC-SAFT pure component parameters of the compounds of a mixture using a quantitative structure-property relationship (QSPR), which is described elsewhere in detail (Stavrou et al., 2014). The process model (assuming steady-state conditions) is completed by material balances (over the mixer, crystallizer and filter, and flash separator) and enthalpy balances (over the flash separator and the condenser), which are omitted here for brevity. Only the solvent and water are considered for enthalpy calculations.

Reaction equilibrium is assumed within the crystallizer, and the crystal formation is calculated by assuming solid-liquid equilibrium at the crystallizer outlet. The vapor-liquid equilibrium in the flash drum is modeled assuming that the vapor phase consists of solvent and water only. Several inequality constraints are imposed to enforce a practically feasible process. In particular, the substrate should be fully dissolved when entering and leaving the crystallizer, which leads to the following constraints:

$$x_{sub,3} \le x_{sub,3}^{sol},\ x_{sub,5} \le x_{sub,5}^{sol},\ x_{sub,11} \le x_{sub,11}^{sol}. \tag{4}$$

Furthermore, it is assumed that all the ionic compounds are fully dissolved in all streams in which they are present. The following constraint is applied to avoid an impractically small liquid fraction of the material in the bottom of the flash drum:

$$x_{liquid,8} \ge 0.7. \tag{5}$$

The following constraint on the crystallizer size is applied to avoid that the reactant recycle stream would become excessively large:

$$(F_5 + F_6)\tau \le V, \tag{6}$$

where F stands for stream flow rates, τ is the residence time (set as 1 h), and V is the reactor volume (set as 10 m^3). Finally, the solvent parameter space, y, was constrained to the PC-SAFT parameters from a solvent database, adopted from Wang and Lakerveld (2018a), using a convex hull.

2.4. Optimization Problem

The objective function represents the total production cost normalized by the product (i.e., API) flow rate, which is minimized to determine the optimal solvent parameters, y, and operating conditions, x, for the process, as follows:

$$\min_{x,y} J = \frac{c_{sol}F_2(x,y) + c_{cw}Q_{condenser}(x,y) + c_{steam}\dfrac{Q_{flash}(x,y)}{eff}}{F_6(x,y)}$$
$$s.t.\quad \text{process model}$$
$$\text{thermodynamic model} \tag{7}$$
$$\text{Constraints (4)-(6) and convex hull constraint for y}$$

where Q stands for heat flow rates. The parameters c_{sol} (7.94 USD/L), c_{cw} (2.07×10^{-7} USD/kJ), and, c_{steam} (2.24×10^{-5} USD/kJ) represent the costs for solvent, cooling water, and steam, respectively. The average solvent and utility costs are estimated from Lab Alley (www.laballey.com), and the U.S. Energy Information Administration (https://www.eia.gov), respectively. An efficiency factor (*eff*) of 0.8 was used to account for losses during steam generation and distribution. The substrate flow rate, F_1, is fixed at 1 mol/s, and NaOCl and NaOH are fed at stoichiometric ratios. The water flow rate in Stream 2 is fixed at 30 mol/s to ensure full dissolution of NaOCl and NaOH. The crystallizer and flash pressures are atmospheric and the mixer and crystallizer

temperatures are set to room temperature (25 °C) and 70 °C (which falls within the temperature range reported in the literature for dalfampridine synthesis (Rane and Sharma, 1994)), respectively. The solvent type, make-up solvent flow rate, flash temperature, and two split fractions are the free variables. The resulting MINLP is solved with the continuous mapping method (Stavrou et al., 2014).

3. Results

The use of the continuous mapping method allowed for a tractable optimization problem, which is otherwise computationally prohibitive in its original MINLP form. By relaxing the PC-SAFT pure component parameters and solving the resulting NLP using the GAMS/CONOPT solver, a hypothetical optimal solvent had been identified before it was mapped on to the solvent database using Taylor expansion to identify a real solvent. The real solvent identified in this case was 2-propanol, which was verified for its miscibility with water. Miscibility with water is essential to avoid any liquid-liquid phase separation in the crystallizer, which is undesirable. The optimal operating conditions (see Table 2) were determined by solving an NLP with fixed solvent PC-SAFT parameters for 2-propanol, which correspond to an objective function value of 0.0582 USD/mol.

The solvent for a reactive crystallization process in general needs to have a higher solubility for the substrate and a lower solubility for the API to enable efficient crystallization-based separation of the API. Furthermore, the solvent should favor the forward reaction and allow for easy recovery in a flash drum from the mother liquor if reactant/solvent recycling is also desired. The identified optimal solvent (2-propanol) has a higher solubility compared to water for both the substrate and the API according to the model predictions. Even though a higher solubility for the substrate is favorable, the crystallization yield tends to be lower when the solubility of the API in the solvent is higher. Apparently, this adverse effect of 2-propanol on the crystallization yield was compensated by optimizing the crystallization medium composition, which contains both water and 2-propanol. In particular, the similarity between the values of the crystallization yield and the normalized reaction extent (see Table 2) suggest that the solubility of the API in the medium is sufficiently low to enable near-complete separation of the API. At the same time, the solvent medium affects the extent of the reaction as well, which is another factor that affects the final crystallization yield.

Split fraction 1 determines the fraction of reactants recycled. A higher reactant recycle stream is likely to allow for a larger reaction extent, but may also facilitate the reverse reaction due to the recycle flow of product into the crystallizer. A larger reactant recycle stream also results in a larger crystallizer volume to achieve a given residence time. The optimal value for split fraction 1 (0.56) shows the need to maintain a sufficiently large purge stream to avoid a strong impact of these negative effects on the objective function at the expense of more loss of reactant. Similarly, split fraction 2 determines the flow rate of the solvent recycle stream, where the solvent is mostly recovered due to its lower boiling point compared to water. This stream is closely related to the make-up solvent flow rate. The optimal value for split fraction 2 (1.00) indicates that it is more beneficial to minimize the make-up solvent flow rate (i.e., the solvent cost) compared to minimizing the energy penalty (for condensation) associated with a larger recycle stream. This case clearly shows how inherent trade-offs exist among the different solvent properties and the process operating conditions for continuous reactive crystallization processes with possible solvent and reactant recycle streams and why it is important to optimize the solvent type and operating conditions simultaneously.

Table 2: Optimal Operating Conditions

Yield (F_6/F_1)	0.9408
Normalized Reaction Extent (ξ/F_1)	0.9442
Make-Up Solvent Flow Rate (F_2/F_1)	0.0537
Flash Temperature (℃)	97.74
Split Fraction 1 (F_{11}/F_8)	0.56
Split Fraction 2 (F_9/F_7)	1.00

4. Conclusion

A thermodynamic approach is presented for the simultaneous optimization of solvent type and process operating conditions for continuous reactive crystallization processes including recycling of reactants and solvents with an economic objective function. The PC-SAFT equation of state can be used to construct a unified thermodynamic framework to model reaction, solid-liquid, and vapor-liquid equilibria within the overall process model. Continuous mapping method allows for the original MINLP to be converted into an NLP problem, which is computationally tractable at least for the investigated case in this work. The proposed approach has been successfully applied to the case of the API dalfampridine in which several inherent trade-offs between solvent properties and process conditions exist, which shows the potential of the proposed approach to improve continuous pharmaceutical processes that are industrially relevant.

Acknowledgment

This work was financially supported by the Research Grant Council of Hong Kong under Grant No. 16214418.

References

Chen C.-T., Lee C.-A., Tang M., Chen Y.-P., 2017, Experimental investigation for the solubility and micronization of pyridin-4-amine in supercritical carbon dioxide, Journal of CO2 Utilization, 18, 173–180.

Diedrichs, A., Gmehling, J., 2011, Solubility Calculation of Active Pharmaceutical Ingredients in Alkanes, Alcohols, Water and their Mixtures Using Various Activity Coefficient Models, Industrial & Engineering Chemistry Research, 50(3), 1757–1769.

Gross J., Sadowski G., 2001, Perturbed-Chain SAFT: An Equation of State Based on a Perturbation Theory for Chain Molecules, Industrial & Engineering Chemistry Research, 40(4), 1244–1260.

Gross J., Sadowski G., 2002, Application of the Perturbed-Chain SAFT Equation of State to Associating Systems, Industrial & Engineering Chemistry and Research, 41(22), 5510–5515.

Karunanithi A. T., Achenie L. E. K., Gani R., 2006, A computer-aided molecular design framework for crystallization solvent design, Chemical Engineering Science, 61(4), 1247–1260.

Li B., Wu Y., Zhu J., Chen K., Wu B., Ji L., 2016, Determination and correlation of solubility and mixing properties of isonicotinamide (form II) in some pure solvents, Thermochimica Acta, 627–629, 55–60.

Rane D. S., Sharma M. M., 1994, New strategies for the Hofmann reaction, Journal of Chemical Technology & Biotechnology, 59(3), 271–277.

Stavrou M., Lampe M., Bardow A., Gross J., 2014, Continuous Molecular Targeting–Computer-Aided Molecular Design (CoMT–CAMD) for Simultaneous Process and Solvent Design for CO_2 Capture, Industrial & Engineering Chemistry Research, 53(46), 18029–18041.

Wang J., Lakerveld R., 2018a, Integrated solvent and process design for continuous crystallization and solvent recycling using PC-SAFT, AIChE Journal, 64(4), 1205–1216.

Wang J., Lakerveld R., 2018b, Integrated Solvent and Process Optimization Using PC-SAFT for Continuous Crystallization with Energy-intensive Solvent Separation for Recycling, Computer Aided Chemical Engineering, 44, 1051–1056.

Sauro Pierucci, Flavio Manenti, Giulia Bozzano, Davide Manca (Eds.)
Proceedings of the 30th European Symposium on Computer Aided Process Engineering (ESCAPE30), May 24-27, 2020, Milano, Italy.
http://dx.doi.org/10.1016/B978-0-12-823377-1.50136-1

Synthesis of Complex Distillation Sequences with Multiple Feeds

José A. Caballero, Juan A. Labarta-Reyes, Juan A. Javaloyes-Anton

Institute of Chemical Process Engineering, University of Alicante. Carretera de San Vicente s.n. 03690, Alicante. Spain.
caballer@ua.es

Abstract

In this work, we address the problem of synthesizing sequences of distillation columns to sharply separate the components of multiple feeds of zeotropic mixtures in which each feed share at least one component with at least another feed.

We show that the space of feasible alternatives can be characterized by extending the concept of basic separation. The space of basic separations can be generated by combining the common sub-mixtures (or separation tasks) in the set of basic separations generated by each individual feed. However, the different composition and origin of repeated sub-mixtures can generate different arrangements in distillation columns with eventually very different performance even though the sequence of separations task be the same in some of them. We illustrate the procedure with an example involving two feeds and four components.

Keywords: Thermally coupled distillation, MINLP, separation sequences.

1. Introduction

The general separation problem was defined by Rudd and Watson (1968) as the transformation of several source mixtures into several product mixtures. In 1985 Westerberg (1985) claimed that this problem was essentially unsolved and after fifty years the general separation problem has not been completely solved and it is likely not to be solved in the near future. If we focus on the more specific problem of separation based on distillation, there is not a unified solution for the separation problem, instead, different researchers focused on specific problems based mainly on the physical characteristics of the mixture. Thus it is common to differentiate between mixtures containing azeotropes and mixtures that do not form azeotropes. While azeotropic mixtures are considerably more difficult to separate, the set of alternatives (sequences of columns) is considerably smaller (Górak and Sørensen 2014).

In the case of zeotropic separation we can differentiate two kinds of problems: when the product sets contain non-overlapping species with each other –referred to as sharp separations- and when there are overlapping species (non-sharp separations.) The nature of these problems requires different solution approaches. In the case of sharp separations, we can differentiate two cases. When a given separation task performs a separation between two key components consecutive in volatility (i.e. there is no other component with intermediate volatility between the selected key components) and when key components are not consecutive (Górak and Sørensen 2014).

Historically, sharp separation sequences were assumed to be performed by «conventional columns». A conventional column can be defined as columns having one feed, and producing two products and includes a condenser and a reboiler. Following this

assumption, the problem of developing an algorithm to enumerate the feasible separation sequences is straightforward (Westerberg and Wahnschafft, 1996), but the selection of the best alternative in terms of energy consumption, total cost or any other criteria is no so easy due to potential large number of feasible alternatives. The earliest attempts were based on heuristics extracted from case studies (Lorenz Biegler et al. 1997). The first models based on mathematical programming were linear MILP models and from that point, models evolved to MINLP using from shortcut to rigorous column models. A comprehensive review can be found in (José A. Caballero and Grossmann 2014).
For a single feed, the characteristics of the search space for the general zeotropic sharp split separation problem –feasible sequences that could include the optimal one- were established by different authors in the last 10-15 years (Caballero and Grossmann 2006; Giridhar and Agrawal 2010). Shah and Agrawal (2010) defined a «regular configuration» as a sequence formed by exactly N-1 columns (where N is the number of key components to be separated). A regular configuration in which each column has a condenser and a reboiler is a «basic configuration». Basic configurations are important because they can be generated only by relations between separation tasks and it allows separating the structural considerations associated with the separation from the heat transfer needed in distillation. The extension from basic to regular configuration only requires to substitute internal heat exchangers (those associated with a sub-mixture that is not a final product) by thermal couples. Shah and Agrawal (2010), and Caballero and Grossmann (2006) established that the search space must be formed by the set of regular configurations.
In this work, we present a discussion on how to generalize the concept of basic/regular configuration when we deal with the separation of multiple feeds that share some components. In the next sections first we clearly state the problem, then we include a discussion on how to generalize the concept of regular/basic configurations depending on the components present in each feed. Finally, we include some conclusions.

2. Structural considerations for distillation sequences with multiple feeds.

The problem we are dealing with can be stated as follows. Given is a set of zeotropic mixtures (feed streams) in which each stream shares at least one component with at least another stream. The objective consists of synthesizing a sequence of distillation columns to separate N key components (N ≤ total number of components) with the best performance in a given index (e.g. cost).
The first stage is determining with is the space of feasible alternatives, or alternatively which is the space of regular configurations. However, taking into account that all the regular configurations can be generated by the set of basic configurations just by removing condensers and/or reboilers associated with sub-mixtures connecting two distillation columns, the problem is reduced to determine the space of basic sequences.
The extension to basic sequences when there are multiple feeds can be done based on the following observations:

a. As a general rule, it is possible to generate all the basic sequences of a system with multiple feeds, from the combination of common separations (or common sub-mixtures) of each one of the single feed basic configurations.
b. When two sub-mixtures formed by the same components, but different compositions (i.e. each sub-mixture comes from a different feed) are merged in a single column, then we must avoid mixing the feeds and a two-feed column must be used. In another case, we generate a point of inefficiency due to the mixture of streams. An extra decision is determining the relative positions of both feeds in the new column.

c. Given k feeds each one with n_k key components, for a total of N different key components, in which a given feed shares at least one component with another feed. If we sort the components by volatility and in each one of the feeds there is not any component missing between the lightest and heaviest in that feed, it is possible to generate basic/regular configurations with could range from max(n_k-1) to (N-1) columns.
d. If in some of the feeds there are missing components between the lightest and the heavies one (e.g. The N components are A, B, C, D and we have a feed formed only by A and C), then we should consider the alternative of the general rule (separate A from C –A/C-) but also the possibility of adding the feed (or sub-mixture) AC as a second feed together with the sub-mixture ABC. While the first case will yield lower energy consumption, it also includes one more distillation column. Therefore, both situations must be considered.

3. Example

We will illustrate the generalization of basic sequences with multiple feeds with the following small example. We have two feed streams, the first formed by the components A, B and C (ABC) sorted by decreasing relative volatility and a second feed formed by a mixture of B, C, and D (BCD). The objective is generating the full space of basic alternatives for the sharp separation of the four components A, B, C and D. According to Giridhar and Agrawal (2010) for a three-component mixture, there are 3 basic configurations, shown in Figure 1 for the first feed.

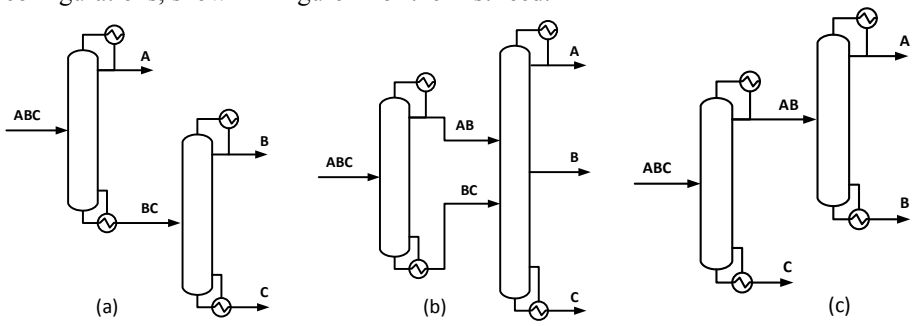

Figure 1. Basic sequences for a three component system. a) Direct; b) Pre-fractionator, c) Indirect.

The basic sequences for the second feed are the same simply changing the name of the components accordingly. The space of basic sequences can be generated by combining configurations (a), (b) and (c) in Figure 1 for Feed 1 and Feed 2. The simple combination produces initially 9 possible sequences. However, depending on the composition and the origin of the shared sub-mixtures new sequences arise. Figure 2 shows the alternatives for the example.

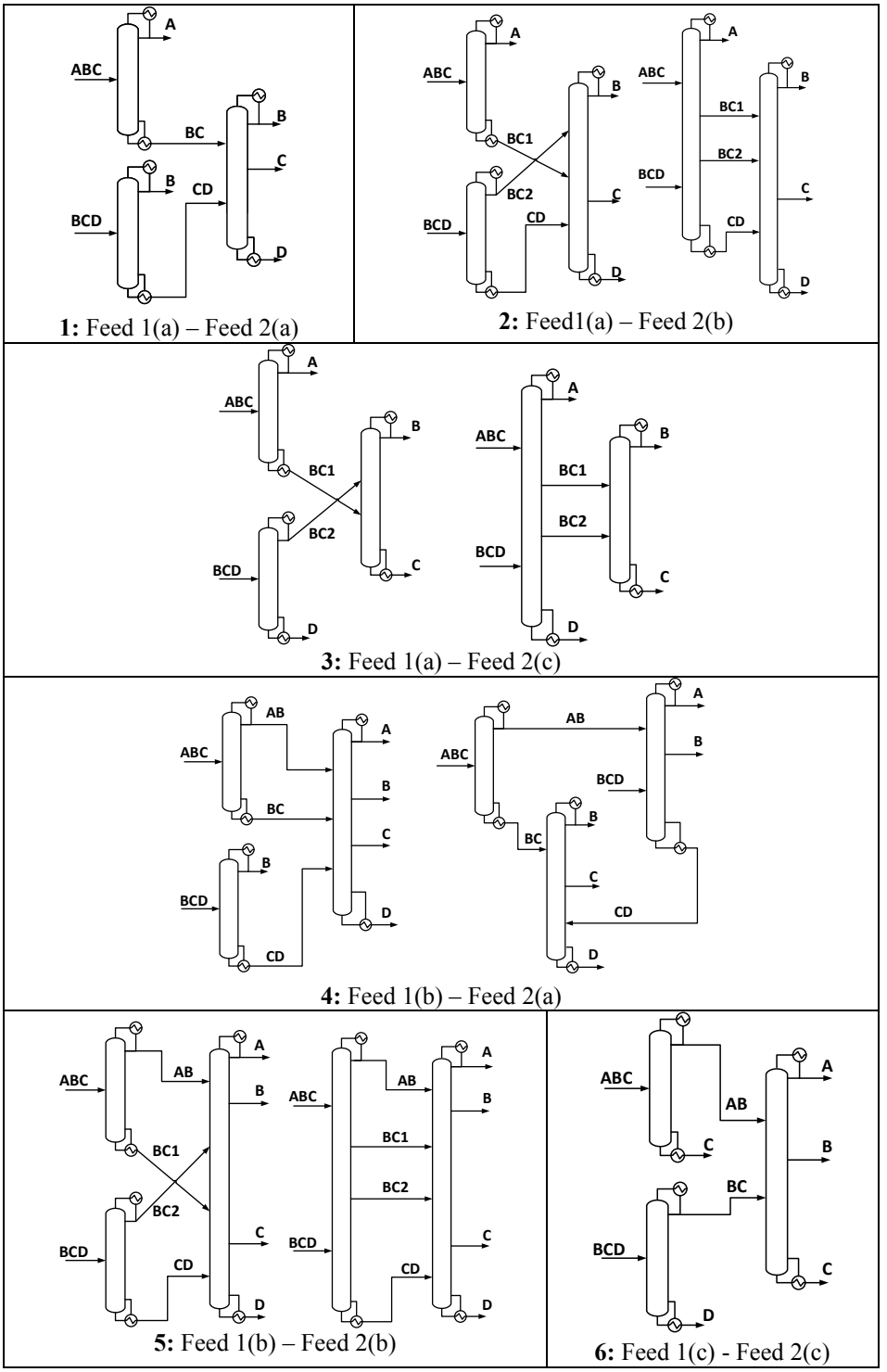

Figure 2. Basic sequences for the example. Feed 1 = ABC; Feed 2 = BCD.

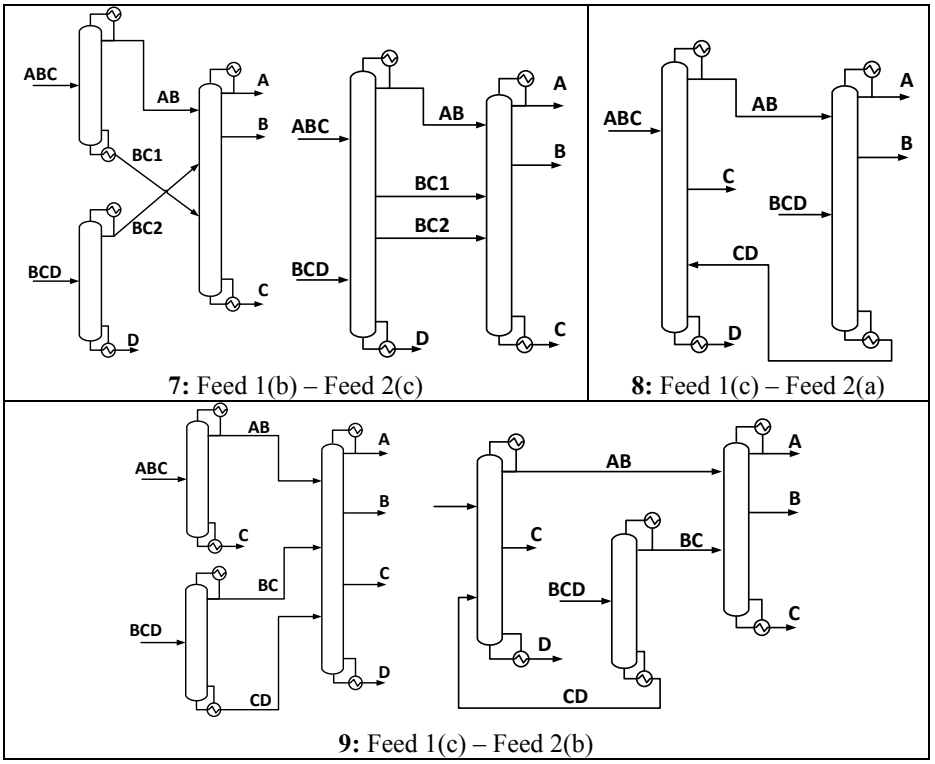

Figure 2. (cont) Basic sequences for the example. Feed 1 = ABC; Feed 2 = BCD.

In Figure (2), in the configuration 1, the Feed 1 and 2 share the final products B and C. (Feed 1 is performing the separation A/BC – B/C and Feed 2 B/CD – C/D). However, product B is produced by both sequences by a rectifying section, while product C is produced by a rectifying section (Feed 2) and a stripping section (Feed 1). Therefore it is possible to merge in a single column separations B/C and C/D. A similar situation occurs in configuration 6, but now the product C is produced by two stripping sections and product B by a rectifying section (Feed 2) and a stripping section (Feed 1). In configuration 8 again products B and C are shared by the two sequences, however, in this case, both B and C are produced by a rectifying and a stripping section and we can merge separation A/B with B/CD in a single column and AB/C with C/D in another column. The final result is that this configuration requires only two distillation columns.

Configuration 4 also share products B and C, however, Feed 1 produces product B simultaneously by a stripping and a rectifying section. And Feed 2 produced B just by a rectifying section. Product C is produced by a stripping section by Feed 1 and by a rectifying section by Feed 2. This situation gives a new degree of freedom because we can merge in a single column the separation that generates the stripping section of B: A/B with either B/C from Feed 1 or B/CD from Feed 2, while at the same time we merge in a single column the two contributions that form product C.

In configurations 2, 3, 5 and 7, sequences generated by Feed 1 and 2 share the sub-mixture BC. However at the difference of the previous cases in which the final products were pure components, now the compositions in both sub-mixtures (BC1 and BC2) can be very different. Therefore, depending on the relative compositions we can merge them in a single column or not. We have different alternatives: If the compositions are different but

when added to a second column (that should be a two feed column) they maintain its relative positions we can use a single column just adding a new column section between both feeds. If this is not the case, then we have a trade-off between the cost due to the extra energy consumption if we mix those two streams to reduce the number of columns or maintain two separated columns but avoiding the inefficiency of mixing those streams. If we take into account all the possibilities we finish, for this small example, with 15 basic configurations, 10 of them require 3 distillation columns and 5 can perform the separation using just 2 distillation columns. In larger problems, the space of alternatives is too large to be exhaustively generated. In those cases, previous results can be used to extend the logical relationships presented by Caballero and Grossmann (2006) and formulate the problem as a Generalized Disjunctive Programming problem.

4. Conclusions

In this paper, we have shown how to generalize the concepts of basic and regular configurations in thermally coupled distillation of zeotropic mixtures with a single feed to multiple feeds. As a general rule it is possible to generate all the basic sequences from the union of the sequences generated by individual feeds by merging the common parts. This procedure will produce basic sequences with different number of columns depending on the sub-mixtures and final products shared by the different feeds. Sub-mixtures involving the same components with different compositions generate multiple-feed columns. The relative position of those feeds could have important effect on energy consumption.

Acknowledgments

The authors acknowledge financial support to the Spanish «Ministerio de Economía, Industria y Competitividad» under project CTQ2016-77968-C3-2-P (AEI/FEDER, UE).

References

Caballero, J A, and Ignacio E. Grossmann. 2006. “Structural Considerations and Modeling in the Synthesis of Heat-Integrated−Thermally Coupled Distillation Sequences.” *Industrial & Engineering Chemistry Research* 45 (25): 84, 54–74.

Caballero, José A., and I. E. Grossmann. 2014. “Optimization of Distillation Processes.” In *Distillation: Fundamentals and Principles.*, edited by Andrzej Gorak and Eva Sorensen, 437–96. London: Elsevier.

Giridhar, Arun, and Rakesh Agrawal. 2010. “Synthesis of Distillation Configurations: I. Characteristics of a Good Search Space.” *Computers & Chemical Engineering* 34 (1): 73.

Górak, Andrzej., and Eva. Sørensen. 2014. *Distillation : Fundamentals and Principles*. London.

Lorenz Biegler; Ignacio Grossmann; Arthur Westerberg. 1997. *Systematic Methods of Chemical Process Design.* New Jersey: Prentice Hall PTR.

Rudd, D.F., and C.C. Watson. 1968. *Strategy of Process Engineering*. Edited by John Wiley & Sons Inc. New York.

Shah, Vishesh H, and Rakesh Agrawal. 2010. “A Matrix Method for Multicomponent Distillation Sequences.” *AIChE Journal* 56 (7): 1759–75.

Westerberg, A. 1985. “The Synthesis of Distillation-Based Separation Systems.” *Computers & Chemical Engineering* 9 (5): 421–29.

Westerberg, Arthur W., and Oliver Wahnschafft. 1996. “Synthesis of Distillation-Based Separation Systems.” *Advances in Chemical Engineering* 23 (C): 63–170.

Sauro Pierucci, Flavio Manenti, Giulia Bozzano, Davide Manca (Eds.)
Proceedings of the 30th European Symposium on Computer Aided Process Engineering (ESCAPE30), May 24-27, 2020, Milano, Italy.
http://dx.doi.org/10.1016/B978-0-12-823377-1.50137-3

Integrating Suppliers into the Simultaneous Process and Product Design of Formulated Products

Manuel Taifouris [a], Mariano Martín [a], Alberto Martínez [b] , Nats Esquejo[c].
[a] *Department of Chemical Engineering, University of Salamanca. Plz. Caídos. 1-5. 37008. Spain*
[b]*Procter and Gamble. Brussels Innovation Center. Temselaan 100. 1853 Strombeek-Bever . Belgium*
[c]*Procter and Gamble. Newcastle Technical Center. Whitley Rd, Longbenton, Newcastle Upon Tyne, Tyne And Wear, NE12 9SR*

Abstract

In this work, we present an extended pooling problem for the design of formulated detergents that includes process and product design and supplier's selection. It was a multiobjective, multiperiod and multiscale optimization product. The integrated problem presented was highly non-linear and non-convex. To address the problem, two different mathematical formulations have been compared. A traditional MINLP and a reformulation of the problem using a decision vector and the definition of penalties reducing the need for binary variables. To present the problem, a case study in Europe was formulated considering several ingredients, suppliers and price policies. The traditional formulation takes days to converge if it converges at all, while the reformulation, in spite of the larger problem size, achieves solution in 20 hours. Furthermore, it was demonstrated that when considering a multiobjective optimization (profit and environmental impact), the model can reduce the CO_2 emissions by 40% in the design of a set of detergents, maintaining the benefit within 1.39% of the maximum by selecting the detergent composition and the suppliers.

Keywords: Integrated process, product and supply chain, mutiobjective optimization, environmental friendly

1. Introduction

For a product to be competitive in a global market, it has to meet specific consumer needs and likes but also it has to be profitable and environmentally sustainable. In order to address all this issues simultaneously, the concept of process and product design (Ng and Gani, 2018) is gaining support. This integrated approach is particularly important in the design of formulated products, since, changes in the composition may result in difficulties in processing certain formulas, further limiting the feasible set of products and the selection of the ingredients also have marketing, logistics and environmental issues involved (Martín and Martínez, 2018). The manufacture of formulated products can be approached using an extended pooling problem. In the pooling problem, a series of ingredients, which can be supplied by different companies, are mixed to obtain a product with properties that meet the customers' expectations (Audet et al, 2004). The prices of these ingredients may have an associated uncertainty (Martín & Martínez, 2015) or be fixed by contracts depending on their variability during the year (Martín & Martínez, 2018). By further extending the pooling problem to integrate the product and process design and supply chain, the mathematical problem becomes a large non-linear, non complex problem that includes bilinear terms

In this work, a mathematical model is formulated to integrate suppliers selection, process and product design to determine the optimal formulation of three types of powdered detergents considering that the ingredients can come from different suppliers, each one at a distance from the manufacturer and with different prices depending on that distance. This distance affects the price of the ingredients, the cost of transport and the environmental impact.

2. Methodology

In this work, we develop a problem formulation for the integrated process and product design together with the supplier selection for the case of formulated products. The production process consists of 5 stages (Martín & Martínez, 2013): The homogeneous mixture of the ingredients, an atomization to avoid possible jams, a drying process in a spray drier, a cooling process and a finishing stage, where a series of additives are added to adjust the properties. The ingredients can be provided come from different suppliers. The distance affects the prices (the further away the supplier is, the cheaper the ingredients will be) and affects the environmental impact (the further away the supplier is, the higher the CO_2 emissions). In addition, some ingredients have their prices fixed by multiannual contracts while others will have associated market variability and average prices are computed using probability data. The model is multiobjective (profit and environmental impact) and multiperiod (three years). Two different formulations are developed to solve the extended pooling problem.

The first formulation is based on an extension to the work by (Martín and Martínez, 2015&2018) based on a mixed integer nonlinear programming (MINLP) formulation. We adapt that work to our problem. Our mathematical model is developed considering the mass balances, the process constraints, the final product's performance, the environmental impact of the ingredients and their transport, the pricing policies and the price of ingredients with associated uncertainty.

The ingredients of the current powder detergents can be classified into 7 groups (surfactant, builder, bleach, fillers, enzymes and polymers) and, following the open literature (European Ecaolabel, 2011), we consider the most typical ingredients of each group (2 o 3 ingredients per group) for a total of 17 ingredients. The work of Martín and Martínez (2015) is extended to include suppliers and this affects some variables such as ingredient cost, emissions of CO_2, etc. The amount purchased from any factory determines the cost and the CO_2 emissions due to transportation every year, for each ingredient and for each supplier. Supply capacity and process limits are included. In addition, all the variables depend on the temporal dimension because the model is multiperiod.

-Regarding product performance, we use the correlation from the work of Martín & Martínez (2013) but considering the 17 ingredients. We fix three types of detergents, Detergent A: High performance and high price, Detergent B: Medium performance and average price; Detergent C: Sufficient quality and low price.

- On the one hand, we consider four different types of price policies (1.-linear discount, 2.-logarithmic discount, 3.-constant elasticity and 4.-fixed discount) to calculate the final prices of the ingredients whose prices can be fixed using three-year contracts. The optimal selection of the price policies depends on the necessary amount to produce the optimal product. On the other hand, the probability values and the prices associated with that probability are used to calculate the average prices of the ingredients with associated uncertainty. Both of prices are calculated every year although the optimization chooses the best policy considering a temporal horizon of the three years. To evaluate the transportation cost, we use the distances between the factory and the

suppliers, the diesel price and the consumption of the truck. Using the loading capacity, we calculate the cost of unit transport and, therefore, the final transport cost depends on the distance and the purchased amount of each ingredient.
-The environmental impact is computed using the carbon footprint of each ingredient and the transportation.
-The main objective function accounts for the income for the sale of the three different detergents, the raw material costs, the transport costs and the cost of the intermediate tanks (to do the intermediate mixtures). The model is multi-objective and, therefore, the second objective (environmental impact) is added using the ε-constraint method considering different values of emissions of CO_2.

However, to select the best policy, we use binary variables in the first formulation, therefore, the model is an MINLP. It is a problem because, the model cannot be solved in a rational time and we have to reformulate the whole model to remove all the binary variables and only use continuous variable to facilitate the resolution of the problem. To achieve this, the dimension of the amount of raw material purchased variable is increased, which also depends on the price discount policy, $ccp_{(ye,i,sup,po)}$. In this reformulation, this variable is responsible for selecting and indicating the best policy through its indexes, in a similar way as already did in the previous case with the suppliers. For each year and for each ingredient, the variable $ccp_{(ye,\ i,\ sup,\ po)}$ will be equal to 0 for all combinations of 'sup' and 'po' except for one, which will be the optimal supplier and policy selection. The information provided by $ccp_{(ye,i,sup,po)}$ will be the amount purchased from ingredient 'i' in the year 'ye' and to the supplier 'sup' using the policy 'po'. Its value tells us the amount purchased and, its indexes, the supplier and the optimal policies. Therefore, we transform the initial MINLP into a nonlinear programming (NLP), in the second formulation. We have to change some equations and add some penalties into the model to avoid that the model selects different policies in different years, since the contract with the suppliers lasts 3 years and therefore, although the optimization evaluate the model every year, if the best policy is selected, this have to fixed during the 3 years.

3. Case of study

To show the use of the formulations, a case study in Europe is considered. Surfactants, polymers and antifoam prices are assumed to be subjected to market variability and the rest of the ingredients were fixed by contracts. Three inorganic suppliers, three organic suppliers and six enzyme suppliers are considered. The factory is located in Frankfurt (Germany) and all the suppliers are in Europe and represent actual factories of the important chemical companies. The solution of the optimization should show the optimal selection of the suppliers, ingredients, policies and the amount produced. The MINLP formulation consists of 5195 equations and 4320 variables (780 binary variables) and the NLP one consists of 11971 equations and 14083 variables. Although the MINLP model is much smaller in terms of equations and variables, the presence of integer variables make it much more difficult to solve, so that a valid solution is not found in more than 20 hours. Therefore, we proceed to evaluate the performance of the NLP model giving feasible results in the 20 hours established as a limit with a tolerance lower than 6%. A commercial solver, BARON is used for an Intel Core i7-7700 with 3.6 GHz and 32 Gb of RAM.
First, the model is optimized without environmental constraints to compare the detergent composition as the environmental objective is implemented, see Table 1. The

profit is 79.529 M€. Next, the profit and detergent composition are evaluated with different limits of carbon footprint. The pareto curve can be seen in Figure 1.

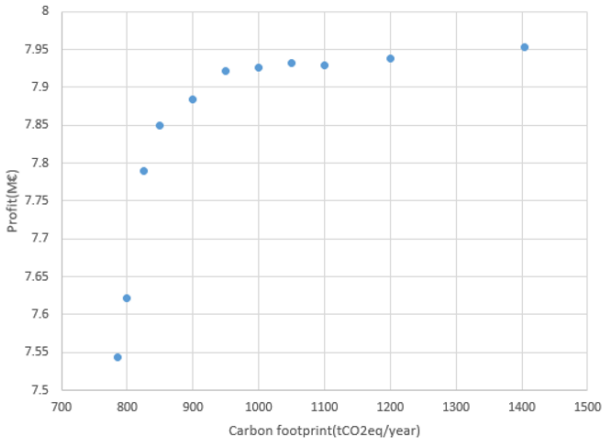

Figure 1.-Pareto curve for the profit as a function of the carbon footprint

When we add the environmental constraint, the model has to choose fewer polluting ingredients, however the system can still maintain a benefit close to the maximum. We can verify that between the value of 1400 tCO2eq/year and 850 tCO2eq/year (39% reduction of the emissions), the profit only decreased by 1.29%, However, from this point, the profit start to fall sharply. This is because the model lost the ability to compensate for environmental limitations with changes in the composition of the final product and changes in the selection of suppliers or in polities. The model have to select the less polluting ingredients and, in some cases (below 825 tCO2eq/year), the maximum demand cannot be met because combinations of ingredients that simultaneously meet the requirements of carbon footprint and yield cannot be found, so that by lowering the sold amount, the obtained profit fells. Therefore, the utopia point is 850 tCO2eq/year. For this point, the optimal selection of suppliers, ingredients, formulation and polities can be seen in the Table 1.

Most of the selected suppliers are the closest to the factory (the supplier 3 for inorganic ingredients and the supplier 4 for organic ingredients). Most of the ingredients that are purchased through contracts are very abundant, regarding their upper limits, so the linear and logarithmic policies are used. Regarding the composition, the requirement performance of each type of detergent is different and, therefore, their composition is different too. Each detergent tries to achieve the goals (performance, profit and environmental) with different set of possible compositions. As it can be seen in Table 1, the requirement of enzymes and polymers (the ingredients which more influent in the performance) is the highest in the case of A detergent and the lowest in the case of C detergent, since, the performance of the A detergent have to be higher than the performance of the C detergent, however in the intermediate case, the B detergent have a higher amount of polymers than the A detergent to compensate the lower amount of enzyme and achieve its performance requirement. The rest of the compositions are similar between the three detergents. However, in the case of the C detergent did not require the same amount of polymers, since its performance is expected to be lower than B detergent. The locations of the selected suppliers can be seen in the Figure 2 for both the economic (b) and multiobjective economic-environmental (a) solutions where a change in suppliers is shown.

Table 1.-Optimal detergent composition and selection of suppliers and policies

Without environmental constraints					
HC (tCO2e/year)	**Ingredient**	**Amount(t/year)**	**Carbon FootPrint (t/ti)**	**Price policy**	**Profit(M€)**
1404	**LAS LINEAR ALKYL ARYL SULFONATES**	120.00	4.20	-	**7.95**
	ZEOLITE	427.00	1.76	Logarithmic	
	SODIUM PERBORATE TETRAHYDRATE	95.50	0.40	Logarithmic	
	SODIUM SULFATE	80.00	0.30	Constant elasticity	
	ANTIFOAM	0.80	1.76	-	
	CELLULOSE	12.67	3.69	Logarithmic	
	CARBOXYMETHYL CELLULOSE	0.80	2.22	-	
	WATER	63.37	0.00	-	
	Optimal formulation(ti/tp)				
	Type of detergent				
		A	**B**	**C**	
	LAS LINEAR ALKYL ARYL SULFONATES	15%	15%	15%	
	ZEOLITE	56%	50%	60%	
	SODIUM PERBORATE TETRAHYDRATE	5%	19%	5%	
	SODIUM SULFATE	10%	10%	10%	
	ANTIFOAM	0%	0%	0%	
	CELLULOSE	3%	1%	1%	
	CARBOXYMETHYL CELLULOSE	0%	0%	0%	
	WATER	12%	5%	8%	
With environmental constraints					
HC (tCO2e/year)	**Ingredient**	**Amount(t/year)**	**Carbon FootPrint (t/ti)**	**Price policy**	**Profit(M€)**
850	**ALCOHOL ETHOXYLATE**	120.00	3.70	-	**7.85**
	POLYPHOSPHATES	240.69	1.02	Linear	
	SODIOUM PERBORATE	200.00	0.40	Logarithmic	
	XYLENE SULPHONATE	200.00	0.03	Logarithmic	
	ANTIFOAM	0.80	1.76	-	
	PROTEASE	104.13	3.69	Logarithmic	
	POLYMERS	145.20	0.17	-	
	WATER	135.82	0.00	-	
	Optimal formulation(ti/tp)				
		Type of detergent			
		A	**B**	**C**	
	ALCOHOL ETHOXYLATE	15.00%	15.00%	15.00%	
	POLYPHOSPHATES	31.07%	28.72%	32.58%	
	SODIOUM PERBORATE	25.00%	25.00%	25.00%	
	XYLENE SULPHONATE	25.10%	24.94%	24.92%	
	ANTIFOAM	0.10%	0.10%	0.10%	
	PROTEASE	1.99%	0.97%	0.54%	
	POLYMERS	0.10%	3.53%	0.10%	
	WATER	1.63%	1.74%	1.75%	

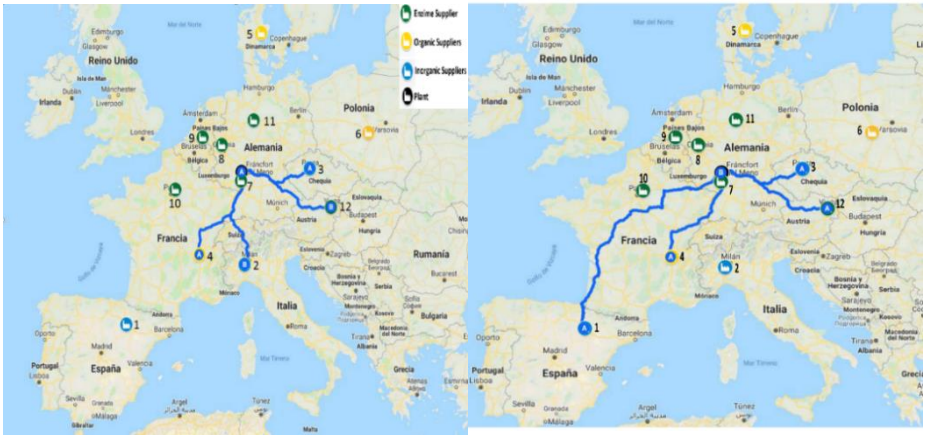

Figure 2.-Optimal solution for the design of powder detergents. a: Environmental friendly; b: Economic

4. Conclusion and future work

In this work, we have developed a mathematical formulation for the optimal design of formulated products. This framework can be applied to any formulated product present in the food industry, pharmaceutical and cosmetics among others. It has been shown that through the correct selection of ingredients and suppliers, the CO_2 emissions of the production process could be substantially reduced to more than 35% without significantly affecting the benefit. Being able to simultaneously select suppliers, ingredients and discount policies provides flexibility to adapt to different environmental limits. However, there is a limit value from which the profit starts to fall sharply since it is no longer possible to compensate for the environmental impact without reducing the production or having to use more expensive ingredients.

Acknowledgement:

P&G and PSEM3 USAL for funding the research

Reference

Audet, C., Brimberg, J., Hansen, P., Le Digabel, S., Mladenovi, N., 2004. Pooling Problem: Alternate Formulations and Solution Methods. Manag. Sci. 50, 761-776.

Calfa, B.A., Grossmann, I.E., 2015. Optimal procurement contract selection with price optimization under uncertainty for process networks. Comp. Chem Eng. 82, 330–343.

European Ecolabel, 2011 Revision of Ecolabel Criteria for Laundry Detergents 2008-2010 Background report. http://ec.europa.eu/environment/ecolabel/documents/Laundry%20Detergents%20technical%20report.pdf (Accessed 07 October 2019)

Karuppiah, R., Martín, M., Grossmann, I.E., 2010. A simple heuristic for reducing the number of scenarios in two-stage stochastic programming. Comput. Chem. Eng. 2010, 34, 1246−1255.

Martín M., Martínez A., 2015. Addressing Uncertainty in Formulated Products and Process Design. Ind Eng Chem Res. 54 (22), 5990-6001.

Martín M., Martínez A., 2018. On the effect of price policies in the design of formulated products. Comput. Aided Chem. Eng. 109, 299-310.

Martín, M., Martínez, A., 2013. Methodology for simultaneous process and product design in the consumer products industry: The case study of the laundry business. Chem. Eng. Res. Des. 91 .795–809

Ng K.M., Gani R., 2018 . Chemical Product Design: Advances in Research and Teaching. Computer Aided Chemical Engineering. 40, 21-32.

Sauro Pierucci, Flavio Manenti, Giulia Bozzano, Davide Manca (Eds.)
Proceedings of the 30th European Symposium on Computer Aided Process Engineering (ESCAPE30), May 24-27, 2020, Milano, Italy.
http://dx.doi.org/10.1016/B978-0-12-823377-1.50138-5

Modeling Framework for Joint Product and Process Synthesis with Material Recovery Opportunities

Ana Somoza-Tornos[a], Qi Chen[b], Moisès Graells[a], Antonio Espuña[a], Ignacio E. Grossmann[b*]

[a]*Department of Chemical Engineering, Universitat Politècnica de Catalunya Escola d'Enginyeria de Barcelona Est, C/ Eduard Maristany 16, 08019 Barcelona, Spain*
[b]*Center for Advanced Process Decision-making, Department of Chemical Engineering, Carnegie Mellon University, Pittsburgh, PA 15213, USA*
grossmann@cmu.edu

Abstract

The circular economy paradigm requires process synthesis to be expanded beyond the consideration of production activities aimed at market needs and to integrate valorization processes upcycling waste from different sources (industrial and urban). With this aim, this contribution presents a modeling approach for the joint synthesis of production processes and products from a waste-to-resource perspective.
The system is modeled through a superstructure with features from state-task network (i.e. the activation/deactivation of units) and state-equipment network (i.e. multiple tasks in a unit) representations. The problem is formulated using a Generalized Disjunctive Programming approach (GDP).
The proposed approach is tested with a case study addressing the synthesis problem of polyethylene pyrolysis, as a central step required to address the need to close the associated material loops. Decisions are made on the separation and reuse of the pure or mixed light gases from the reactor outlet (material reuse vs. energy valorization).
Results demonstrate the ability of the proposed approach to represent alternatives that cannot be considered if only STN or SEN models were used.

Keywords: process modeling, synthesis, superstructure, optimization, generalized disjunctive programming, circular economy.

1. Introduction

State-task network (STN, (Kondili et al., 1993)) and state-equipment network (SEN, (Smith, 1996)) are two process representations commonly used as a base for the superstructure representation required to address the conventional problem of process synthesis. While the STN representation is easier to formulate, the SEN representation is more suitable for modeling equipment networks, as it reduces the number of process nodes and prevents zero-flow singularities (Chen and Grossmann, 2017).
However, both conceptual models generally rely on the premise that product specifications are narrowly bounded (i.e. final products are single-component with a defined purity), and fail to consider other decisions that would affect the final result (i.e.

solutions in which intermediate products or mixtures may be sold or recycled into the process). This problem becomes crucial in the synthesis of processes addressing the circular economy paradigm, where material recovery alternatives are numerous and diverse. Hence, this work presents a novel modeling approach for the optimal synthesis of processes with flexible product composition, including equipment activation/ deactivation, and the possibility of selling/recycling mixed streams.

This is particularly interesting for the application of circular economy principles to process design, which has been gaining importance in recent years (Avraamidou et al., 2020). Processes for the chemical upgrading and recycling of polymers, such as the pyrolysis of plastics, lead to hydrocarbon mixtures similar to those from crude oil cracking but with different compositions. The two main alternatives for these products include their use as fuels (i.e. waste-to-energy, Honus et al., 2016) and their separation to recover the monomers that can be used to produce new chemicals or polymers (Hong and Chen, 2017), which results in a more efficient use of valuable resources and may increase incentives for recycling and closing material loops.

2. Problem statement

The problem addressed in this paper can be stated as follows: given is a set of raw materials (usually subproducts/waste) and process alternatives (equipment and tasks), the objective is to find the path to convert these materials into the most valuable resources, taking into account current market requirements.

In order to achieve this objective, these elements have to be represented in a flexible superstructure that considers different alternatives for pure or mixed products (i.e. selling or recycling) and also different flowsheeting alternatives and equipment design.

3. General framework for joint process and product synthesis of

The proposed general framework for addressing the synthesis problem consists of a three-step approach based on the work by Yeomans and Grossmann (1999): superstructure representation, modeling (Generalized Disjunctive Programming - GDP), and model resolution.

3.1. Superstructure representation

Separation processes are generally modeled considering that the inlet is separated in all the products that integrate it. STN leads to easier problem formulations, whereas SEN is more easily solved since it prevents zero-flow singularities (Chen and Grossmann, 2017). However, the synthesis of waste-to-resource processes requires a more flexible superstructure representation of separation sequences, including the activation and deactivation of equipment (as in STN) and the flexible assignment of tasks to equipment (as in SEN). This is done through the implementation of the most general form of SEN network (Yeomans and Grossmann, 1999) which does not avoid zero-flow singularities.

A generic example of superstructure representation of a process flowsheet including flexible product composition and material recovery is shown in Figure 1.

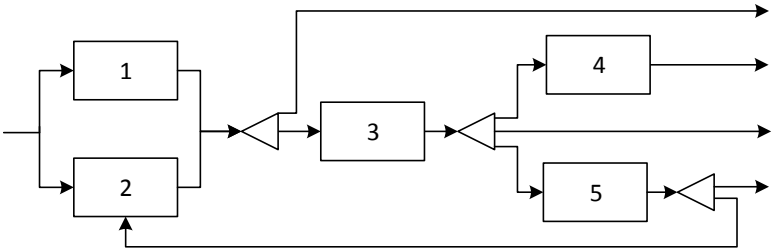

Figure 1. Example of superstructure for joint product and process synthesis.

3.2. GDP formulation

The superstructure defined in the previous step is now modeled and formulated using GDP (Raman and Grossmann, 1994). Let $j \in J$ define the set of equipment in the superstructure and $k \in I_j$ the set of tasks that can be performed in each equipment j. x_j and z_{jk} denote the continuous variables representing the operating conditions of the system, while the Boolean variables Y_j and W_{jk} represent whether equipment j is active and whether task k is assigned to it, respectively. The resulting formulation is as follows:

$$\min z = \sum_{j \in J} c_j + f(x_j, z_{jk}) \tag{1}$$

$$\text{s.t.} \quad f(x_j, z_{jk}) \leq 0 \tag{2}$$

$$\begin{bmatrix} Y_j \\ \vee \\ k \in I_j \end{bmatrix} \begin{bmatrix} W_{jk} \\ f_{jk}(x_j, z_{jk}) \leq 0 \\ c_j = \gamma_{jk} \end{bmatrix} \vee \begin{bmatrix} Y_j \\ x_j = z_{jk} = 0 \\ c_j = 0 \end{bmatrix} \quad \forall\, j \in J \tag{3}$$

$$\Omega(W_{jk}) = True \tag{4}$$

$$Y_j \in \{True, False\} \quad \forall\ j \in J \tag{5}$$

$$W_{jk} \in \{True, False\} \quad \forall\, j \in J, k \in I_j \tag{6}$$

The objective function to be minimized (Eq. 1) includes the fixed cost associated to the active equipment units and a function of the continuous variables (i.e. variable costs and income from selling the products). Algebraic constraints in Eq. (2) are equalities and inequalities that must be satisfied for any realization of the discrete variables, typically including mass balances that define the connections among the nodes of the superstructure. On the other hand, constraints that are inherent to equipment activation and task assignments are modeled in nested disjunctions. The external ones are based on the existence of equipment j, while the internal ones define task selection. Thus, if equipment j is active ($Y_j = True$) and task k is selected ($W_{jk} = True$), constraints $f_{jk}(x_j, z_{jk}) \leq 0$ are applied and the related fix costs are considered in the objective function $c_j = \gamma_{jk}$. Conversely, if equipment j is not selected ($Y_j = False$) continuous variables and fix costs are set to 0. Finally, logical constraints among the nodes of the superstructure are given by $\Omega(W_{jk})$ (Eq. (4)). These include enforcements of consecutive tasks in order to meet recipe-based constraints.

3.3. Model resolution

The model is implemented in Pyomo and solved with DICOPT after its reformulation to a MINLP using the Big M method. The MINLP involves 36 binary variables, 2353 continuous variables and 4280 constraints and was solved in 34 CPUs on an Intel Xeon processor operating at 2.20GHz.

4. Case study

The proposed framework has been applied to the synthesis of the process of polyethylene pyrolysis for the recovery of hydrocarbons. Experimental data from the literature is used to model the outlet from the pyrolysis furnace. Kannan et al. (2014) reported high conversions (>99%) of the polymer to gas when operating at 1000ºC, leading to outlet compositions of: 5% methane, 46% ethylene, 18% propylene, 3% propyne, 2% 1-butene, 13% 1,3-butadiene and 13% benzene. The main objective is to identify to which extent the gas resulting from the pyrolysis of polyethylene at such conditions should be separated into its compounds, according to the cost of separation and the market price for pure or mixed compounds. The model should also identify if any of the streams could be used as fuel to satisfy the energy requirements of the furnace used to maintain the operating conditions.

5. Results and discussion

In this section, the results for the synthesis of the case study are presented following the methodology described in section 3.

5.1. Superstructure representation

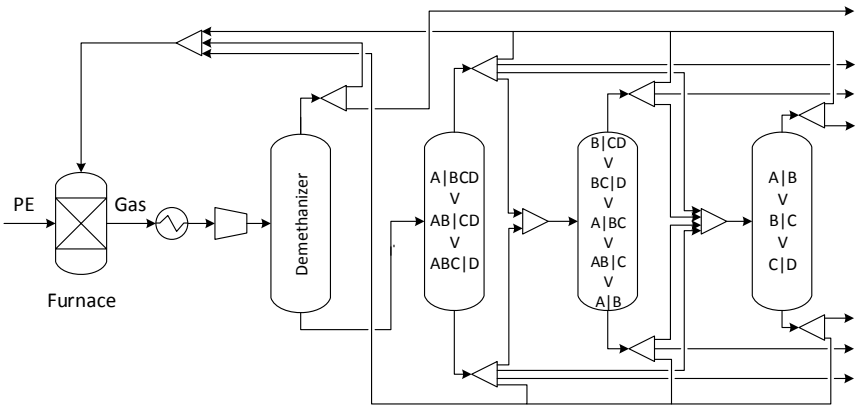

Figure 2. Superstructure representation of the process.

Figure 2 shows the superstructure for the proposed case study. The outlet of the pyrolysis reactor is cooled and compressed to enter the distillation sequence where the different hydrocarbons may be recovered. For the sake of simplicity and due to the different boiling point of methane compared to the rest, the stream is demethanized before entering the distillation sequence. After this step, a four component mixture distillation train is considered, in order to split the inlet into its fractions of ethylene (A), propylene (B), 1,3-butadiene (C) and benzene (D). Propyne and 1-butene are recovered with 1,3-butadiene

since their low concentration would not justify two extra separation stages. The first column considers the three possible tasks for the first level separation of the four-component mixture. The second one includes the three-component separations of the streams resulting from the previous column, plus the separation A|B in case AB|CD is selected in column one. Finally, column 3 can perform the two-component separation of outlet streams from column two. All three distillation columns can be active or inactive, but the existence of one implies that the previous ones need to exist. All outlet streams can be introduced to the next separation level, sold as final product, or reused in the process as fuel for the furnace.

5.2. Model formulation

The model is formulated following the GDP described in section 3.2 with the following considerations:

- The objective function is the profit maximization taking into account: the income for product sales (proportional to its purity), fix and variable costs for the active distillation columns, and fresh fuel savings.
- $f(x_j, z_{jk}) \leq 0$ include the mass balances at the nodes of the superstructure (e.g. the distillate of column one can be sold as a product, used as fuel at the furnace or go to column two if AB or ABC mixes are produced).
- $f_{jk}(x_j, z_{jk}) \leq 0$ represent the equations that depend on the column activation and task selection (e.g. mass balance of the distillation columns or reflux ration calculation).
- $\Omega(W_{jk})$ denotes the logical constraints that should be enforced (e.g. column 3 can only be active if column 1 and 2 are also active).

5.3. Solution

Figure 3 depicts the optimal solution for the flowsheet design for the material recovery from polyethylene pyrolysis. In this particular case all units were selected, so zero-flow singularities are not present.

The methane from the gas demethanization is sold, and the bottoms are sent to column 1. Here, task A|BCD is active, leading to the production of ethylene. Likewise, propylene and 1,3-butadiene are recovered in the distillates of columns 2 and 3, respectively. Thus, direct distillation was found to be the optimal option. Ethylene, propylene and benzene are sold, while 1,3-butadiene is burned as fuel at the furnace due to its low purity.

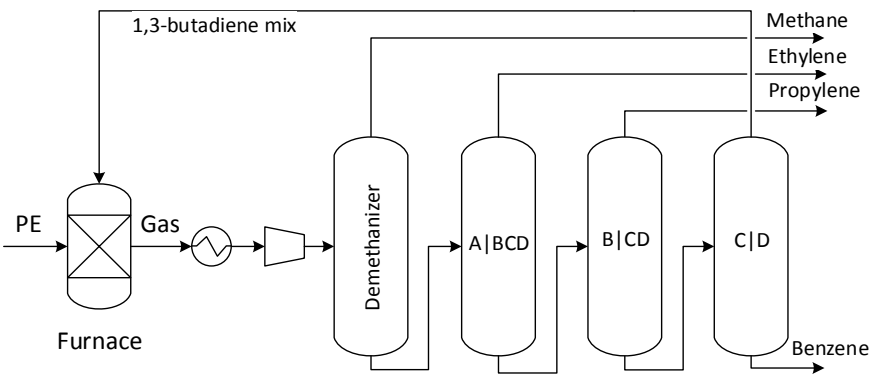

Figure 3. Optimal flowsheet design for the material recover from polyethylene pyrolysis.

6. Conclusions

This paper has introduced a general framework to represent, model and solve the joint product and process synthesis problems resulting from the consideration of waste-to-resource transformations. To achieve this objective, the work has followed the three-step method proposed by Yeomans and Grossmann (1999). First, the model is represented through the generalized version of a SEN, including task selection and equipment activation and deactivation to address the singularities of processes for material recovery. Second, we formulate the model as a GDP. Finally, the model is transformed into a MINLP through the Big M method and solved in Pyomo/DICOPT. The capabilities of the model have been tested through its application to the synthesis of a flowsheet for the recovery of hydrocarbons from the pyrolysis of polyethylene. The proposed methodology has been proven useful to identify the optimal extent of separation and the most economically profitable products in a systematic way. Future work will include the implementation of decomposition techniques to address the cases which present zero-flow singularities.

Acknowledgements

Financial support received from the Spanish "Ministerio de Economía, Industria y Competitividad" and the European Regional Development Fund, both funding the research Project AIMS (DPI2017-87435-R) is fully acknowledged.

Ana Somoza-Tornos thankfully acknowledges financial support received from the Spanish Ministry of Education, Culture and Sport (Ayuda para la Formación de Profesorado Universitario - FPU15/02932).

References

Avraamidou, S., Baratsas, S.G., Tian, Y., Pistikopoulos, E.N., 2020. Circular Economy - A challenge and an opportunity for Process Systems Engineering. Comput. Chem. Eng. 133, 106629. https://doi.org/10.1016/j.compchemeng.2019.106629

Chen, Q., Grossmann, I.E., 2017. Recent Developments and Challenges in Optimization-Based Process Synthesis. Annu. Rev. Chem. Biomol. Eng. 8, 249–283. https://doi.org/10.1146/annurev-chembioeng-080615-033546

Hong, M., Chen, E.Y.X., 2017. Chemically recyclable polymers: A circular economy approach to sustainability. Green Chem. https://doi.org/10.1039/c7gc01496a

Honus, S., Kumagai, S., Němček, O., Yoshioka, T., 2016. Replacing conventional fuels in USA, Europe, and UK with plastic pyrolysis gases – Part I: Experiments and graphical interchangeability methods. Energy Convers. Manag. 126, 1118–1127. https://doi.org/10.1016/j.enconman.2016.08.055

Kannan, P., Al Shoaibi, A., Srinivasakannan, C., 2014. Temperature effects on the yield of gaseous olefins from waste polyethylene via flash pyrolysis. Energy and Fuels. https://doi.org/10.1021/ef500516n

Kondili, E., Pantelides, C.C., Sargent, R.W.H., 1993. A general algorithm for short-term scheduling of batch operations—I. MILP formulation. Comput. Chem. Eng. 17, 211–227. https://doi.org/10.1016/0098-1354(93)80015-F

Raman, R., Grossmann, I.E., 1994. Modelling and computational techniques for logic based integer programming. Comput. Chem. Eng. 18, 563–578. https://doi.org/10.1016/0098-1354(93)E0010-7

Smith, E.M., 1996. On the optimal design of continuous processes, Ph.D. Dissertation, under supervision of C. Pantelides. Imperial College of Science, Technology and Medicine, London, UK.

Yeomans, H., Grossmann, I.E., 1999. A systematic modeling framework of superstructure optimization in process synthesis. Comput. Chem. Eng. 23, 709–731. https://doi.org/10.1016/S0098-1354(99)00003-4

Sauro Pierucci, Flavio Manenti, Giulia Bozzano, Davide Manca (Eds.)
Proceedings of the 30th European Symposium on Computer Aided Process Engineering (ESCAPE30), May 24-27, 2020, Milano, Italy.
http://dx.doi.org/10.1016/B978-0-12-823377-1.50139-7

Value Chain Synthesis in Algae Biorefineries under Uncertainty

Melina Psycha, Lorenzo-Andreas Mamos, Antonis Kokossis

School of Chemical Engineering, National Technical University of Athens, Zografou Campus, 9, Iroon Polytechniou Str., GR-15780 Athens, Greece
akokossis@mail.ntua.gr

Abstract

The work focuses on exploring the uncertainties concerning the prices of chemicals and the involved markets regarding algae biorefineries. A product-oriented approach is analyzed which directly links the customization of product portfolios with market needs and behaviors. For this purpose, the microalga Dunaliella is selected leading to four interested markets (pharmaceuticals, nutraceuticals, cosmetics and food). A number of scenarios are studied referring to different market behaviors and the Cauchy distribution is used for the uncertainty analysis. The combination of markets is taken into consideration focusing on the achievement of a potential investment with high profitability and low risk. The combination of the cosmetic and the food sector constitutes the most suitable field to steer future investments and the carotenoids group includes the target-products to be considered during the formulation of product portfolios.

1. Introduction

The merits of microalgae as an alternative source of biomass are well established over the years, especially because of their versatility in terms of products. This potential in addition to the utilization of carbon dioxide, which microalgae need for their growth, render the development of a large-scale application extremely promising either as a standalone venture or in integration with other plants (Galanopoulos et al., 2019). Specifically, the co-production of specialty chemicals from microalgae is gaining ground as the related markets expand and profit margins grow (García Prieto et al., 2017; Psycha and Kokossis, 2017). A plethora of microalgae has been studied and researched, especially for applications in the pharmaceutical, nutraceutical and cosmetic sector (Chua and Schenk, 2017; Panis and Rosales Carreon, 2016; Psycha et al., 2018).

The volatility of markets and prices regarding the specialty chemicals present in algae value chains constitutes a great challenge and adds to the uncertainty of the value chain synthesis (Psycha and Kokossis, 2016). Uncertainty analysis is imperative considering the high-value chemicals involved and the risk that concerned markets can show. Several studies have been conducted to address this issue based on performance measures of potential investments (Gong et al., 2016) as well as processing paths optimization (Rizwan et al., 2015). This paper deals with the alignment of the interested market sectors with the respective product portfolios and proposes a product-oriented approach in order to reach potential investments characterized as flexible, profitable and of low risk.

2. Product-oriented approach

The methodology follows a five-step course keeping in mind the challenges related to chemicals pricing, product synthesis and the evolution of markets according to Figure 1.

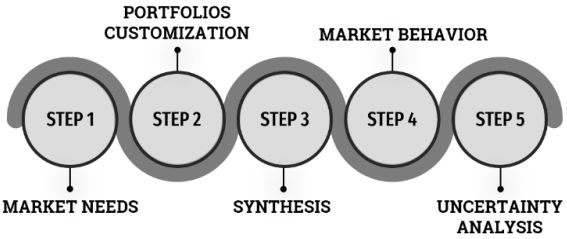

Figure 1. Step-by-step methodology of the product-oriented approach

2.1. Market needs

The first step refers to the identification of interested markets related to the specialty chemicals extracted from microalgae as products. Such products can find applications in the pharmaceutical sector (anti-inflammatories, antidepressants, anti-metastatic action etc.), the nutraceutical sector (antioxidants, food supplements etc.), the cosmetic sector (sunscreens, creams, scrubs etc.) and the food sector (natural colorants, functional ingredients such as emulsifiers etc.).

2.2. Portfolios customization

The second step relates to the customization of product portfolios based on the market needs of Step 1. The products are classified according to their possible applications on each market sector.

2.3. Synthesis

The synthesis step refers to a simultaneous screening of the processing paths instead of evaluating each path separately. The representation of all the available options is achieved by the development of a superstructure involving feedstocks, processes, intermediate mixtures or fractions and products. The synthesis model as well as the mathematical formulation of the problem follow the guidelines of Psycha and Kokossis (2016) and deal with profit maximization. The model is formulated into a MILP model, it is optimized by employing commercial software and is resolved with the use of integer cuts in order to provide multiple solutions to the problem.

2.4. Market behavior

Market behavior plays a significant role in order to address additional challenges related to prices fluctuations. On that note, three scenarios are established that depict patterns of future chemicals prices compared to current numbers (base-price):

- *Scenario 1:* Optimistic behavior. The prices are considered constant and no change is reported. As a result, the chemicals prices are assumed to be 100% of the base-price.
- *Scenarios 2 (a and b):* Realistic behavior. Prices are decreased by 20% and 40% in Scenario 2a and Scenario 2b respectively.
- *Scenarios 3 (a and b):* Pessimistic behavior. Prices are decreased by 50% and 60% in Scenario 3a and Scenario 3b respectively.

Table 1 summarizes behaviors and scenarios as well as the respective percentages of the base-price.

Table 1. Summary of price percentage in each scenario

	% of base-price				
Market behavior	Scenario 1	Scenario 2a	Scenario 2b	Scenario 3a	Scenario 3b
Optimistic	100%	-	-	-	-
Realistic	-	80%	60%	-	-
Pessimistic	-	-	-	50%	40%

2.5. Uncertainty analysis

The final step follows the Monte Carlo method and combines market needs with market behaviors. For the purposes of this paper, the Cauchy distribution is used for each scenario and for the different market sector described in Step 1. Random numbers are produced for the prices of the products with the initial numbers being those presented in Step 4 for each scenario.

3. Real-life case study

This study refers to the processing of the microalga Dunaliella for the production of high-value chemicals in a real-life biorefinery undertaken by the D-Factory, an FP7 collaborative project aiming at a commercial scale biorefinery process. Following the product-oriented approach, the abovementioned market sectors are taken into consideration, four different product portfolios are constructed considering the value chain of Dunaliella (Figure 2) and uncertainty analysis is applied following the scenarios of Step 5. According to the individual product portfolios, all sectors include 7 products except nutraceuticals, which includes 6.

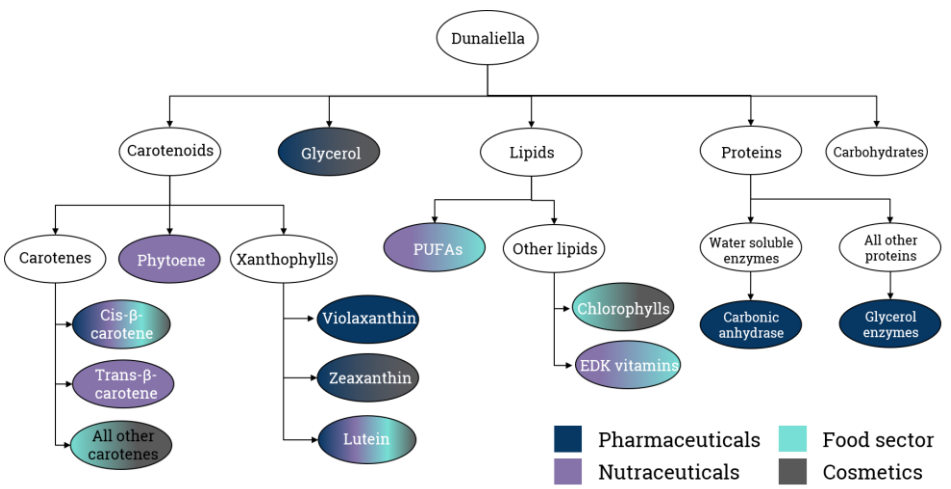

Figure 2. Value chain of the microalga Dunaliella indicating product portfolios for each market sector

4. Comparative results

Figure 3 depicts profits for each market sector following the market-behavior scenarios. For the purposes of this study, Scenarios 3 (a and b) are not listed due to the unsustainable solutions they produce. The larger margin of profit is observed in the cosmetic sector since all scenarios, including the ones following the realistic behavior, provide sustainable solutions. On the other hand, nutraceuticals offer a small profit margin but they stand with one product less in their portfolio.

According to the results, the markets could be arranged in order of decreasing profitability as follows: Cosmetics → Food sector → Pharmaceuticals → Nutraceuticals. Similarly, they could be arranged in order of decreasing risk: Pharmaceuticals → Food sector → Nutraceuticals → Cosmetics.

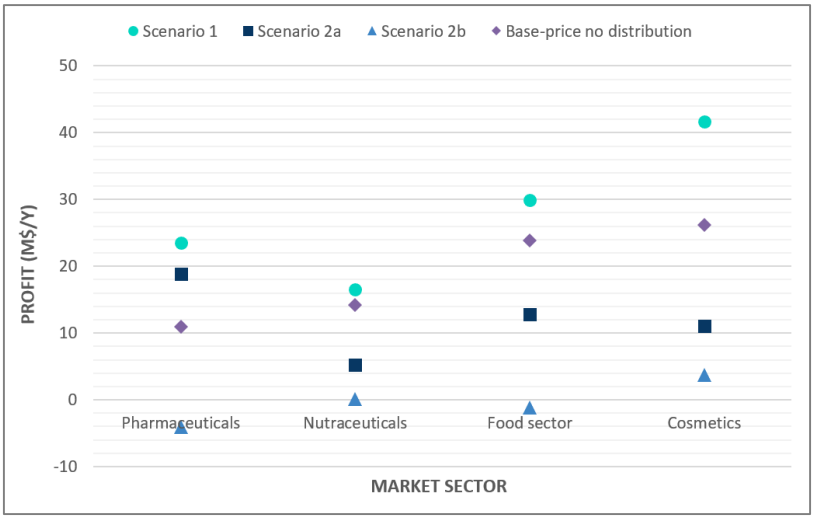

Figure 3. Profit chart for each market sector according to the scenarios

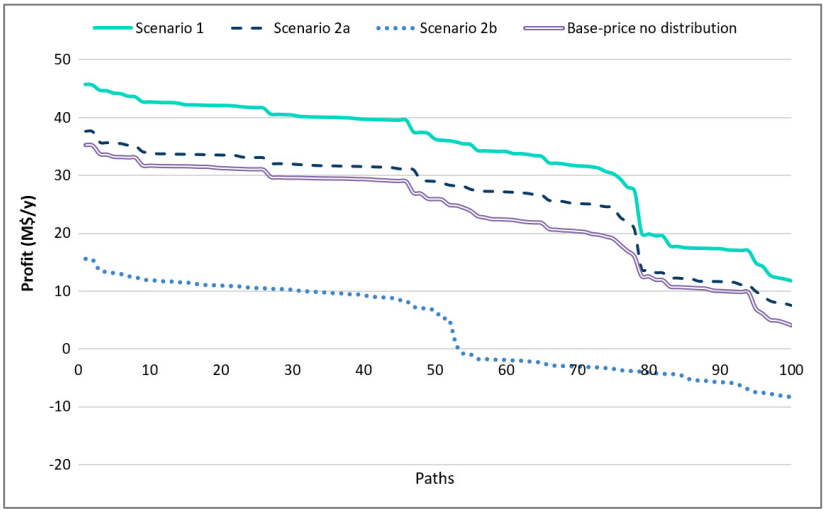

Figure 4. Profit chart for the entire value chain (13 products)

Taking into consideration the existence of common products in the different portfolios, the opportunity arises for combinations of markets to establish flexibility, profitability and less risky options. An additional incentive to explore this option emerges from the results depicted in Figure 4. According to the profit evolution in multiple solutions, one can draw the conclusion that for the entire value chain the potential biorefinery would be economically sustainable. Thus, more chemicals in the product portfolio yield to more sustainable options (even for Scenario 2b for the first fifty paths).
Considering the results of Figures 3 and 4, combinations of markets are proposed based on profitability and risk. Indications on profitability and risk for different combinations of markets are presented in Figure 5. More suitable combination yielding to more profitable and less risky options appears to be the cosmetic and the food sector, which have five common products and three of them belong to the carotenoid fraction (cis-β-carotene, lutein, carotenes as a mixture).

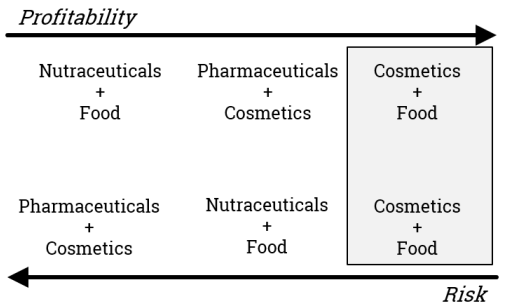

Figure 5. Profitability and risk indications on combinations of markets

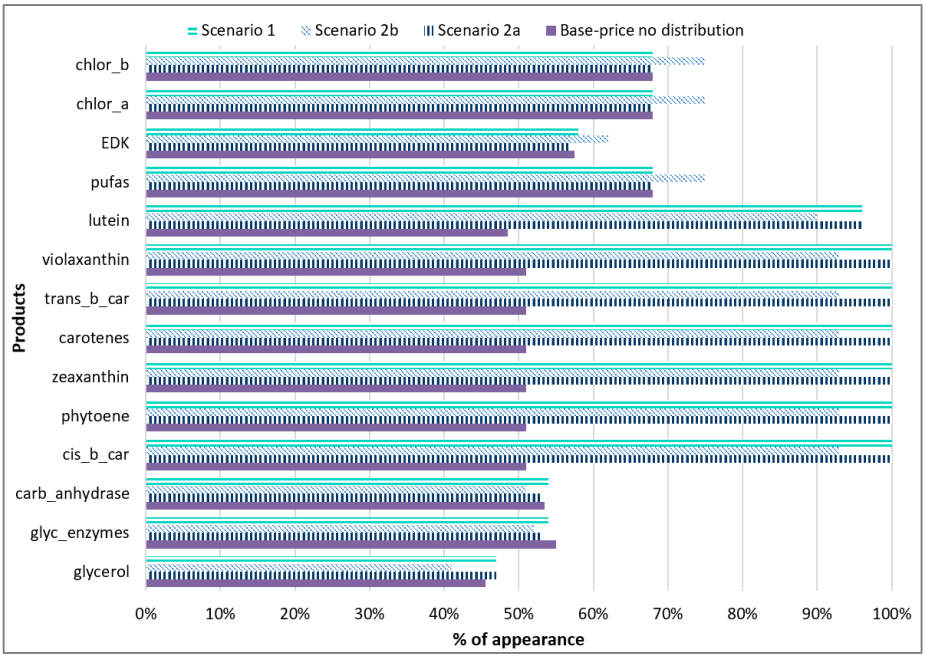

Figure 6. Appearance of products amongst model solutions

Following on the study of the total value chain of Dunaliella, Figure 6 presents the appearance of all products amongst the generated paths for each scenario. It is noteworthy that for the fraction of carotenoids (lutein, violaxanthin, trans-β-carotene, carotenes, zeaxanthin, phytoene and cis-β-carotene) a 50% increase in appearance is observed if one compares the base-price (no use of distribution) percentages with the ones of each scenario (with the use of the Cauchy distribution). This leads to the conclusion that carotenoids play the key role to the formulation of product portfolios and yield to higher profits. Moreover, markets with more carotenoids in their portfolios provide more profitable and less risky options, which confirms that the proposed combination of the cosmetic and the food sector as target-markets is the most suitable selection for future investment.

5. Conclusions and future work

The present work addresses challenges related to the uncertainty of markets and prices regarding the specialty chemicals present in algae value chains. The proposed product-oriented approach provides insight into the profitability and risk of a potential investment highlighting the importance of product selection and markets involved. Uncertainty analysis is conducted which combines market needs with market behaviors. The combination of the cosmetic and the food sector leads to the most suitable results in terms of high profitability and low risk and constitutes a fruitful field to steer a potential investment. Carotenoids are considered target-products and play the key role to the formulation of product portfolios. More research is required focusing on the use of more distributions customized for each individual market and on a more detailed investigation regarding the combination of markets.

References

C. Galanopoulos, P. Kenkel, E. Zondervan, 2019, Superstructure Optimization of an Integrated Algae Biorefinery, Computers and Chemical Engineering, 130, 106530

C.V. García Prieto, F.D. Ramos, V. Estrada, M.A. Villar, M.S. Diaz, 2017, Optimization of an Integrated Algae-based Biorefinery for the Production of Biodiesel, Astaxanthin and PHB, Energy, 139, 1159-1172

E.T.Chua, P.M. Schenk, 2017, A Biorefinery for Nannochloropsis: Induction, Harvesting, and Extraction of EPA-rich Oil and High-value Protein, Bioresource Technology, 244, 2, 1416-1424

G. Panis, J. Rosales Carreon, 2016, Commercial Astaxanthin Production Derived by Green Alga Haematococcus pluvialis: A Microalgae Process Model and a Techno-economic Assessment all through Production Line, Algal Research, 18, 175-190

J. Gong, F. You, 2016, Optimal Design and Synthesis of Algae Processing Network under Uncertainty based on Return on Investment, Computer Aided Chemical Engineering, 38, 2301-2306

M. Psycha, A.C. Kokossis, 2016, Synthesis and Optimization of Microalgae Biorefineries, Computer Aided Chemical Engineering, 38, 325-330

M. Psycha, A.C. Kokossis, 2017, Techno-economic Evaluation of an Integrated Microalga Biorefinery Targeting the Co-production of Specialty Chemicals, Computer Aided Chemical Engineering, 40, 1981-1986

M. Psycha, M. Kapnisi, A.C. Kokossis, 2018, Extended Value Cahin Synthesis towards the Design of Multi-Feedstock Algae Biorefineries, Computer Aided Chemical Engineering, 43, 645-650

M. Rizwan, M. Zaman, J.H. Lee, R. Gani, 2015, Optimal Processing Pathway Selection for Microalgae-based Biorefinery under Uncertainty, Computers and Chemical Engineering, 82, 362-373

Sauro Pierucci, Flavio Manenti, Giulia Bozzano, Davide Manca (Eds.)
Proceedings of the 30th European Symposium on Computer Aided Process Engineering (ESCAPE30), May 24-27, 2020, Milano, Italy.
http://dx.doi.org/10.1016/B978-0-12-823377-1.50140-3

Effect of Flue Gas Composition on the Design of a CO_2 Capture Plant

Ana Gabriela Romero-García,[a] Nelly Ramírez-Corona,[b*] Eduardo Sánchez-Ramírez,[a] Heriberto Alcocer-García,[a] Juan Gabriel Segovia-Hernández[a]

[a]*Departamento de Ingeniería Química, Universidad de Guanajuato, Noria Alta s/n, Guanajuato, Gto., 36050, México.*

[b]*Departamento de Ingeniería Química, Alimentos y Ambiental, Universidad de las Américas Puebla. ExHda. Santa Catarina Mártir s/n, San Andrés Cholula, Puebla, México, 72820*
nelly.ramirez@udlap.mx

Abstract

According to studies conducted by the International Energy Agency, the energy sector is the biggest producer of greenhouse gas emissions (CO_2), having important environmental consequences. Various alternatives have been sought to reduce CO_2 emissions during electric production, highlighting as an alternative, the implementation of CO_2 capture and storage plants. In this work, it is shown the global optimization of a coupling CO_2 capture plant to an electric power plant, having as objective function minimize the energetic requirements of the process. For this study, it was considered four different fuels in the power plant; biogas, coal, non- associated natural gas, and associated natural gas. Two operating scenarios are considered: in the first, generate the same combustion gas flow for all the proposed fuels and in second, obtain the same energy demand with the 4 fuels. For the design and simulation, the software ASPEN Plus simulator was used.

Keywords: CO_2 Capture plant, biogas, coal, non- associated natural gas.

1. Introduction

In recent years demand for electricity has been rapidly increased, the International Energy Agency reported that 65% of the energy produced worldwide was obtained from the burning of fossil fuels, which are the main sources of CO_2 emissions, generating climate change as the main consequence (IEA, 2018). From 37.1 trillion tonnes of CO_2 produced in 2018, 35 trillion tonnes are related to the energy sector (EIA,2019), in that way, the production of energy by fossil fuels is considered unsustainable processes in accordance with the principles of green chemistry and circular economy. Considering the aforementioned, the production of greenhouse gases and their relationship with the energy sector is of significant importance. Understanding a thermoelectric generator (TEG) as an apparatus that produces electricity from waste heat. There are several ways to produce electricity, the first of them is by a conventional thermal power plant that works with a simple thermal cycle, with a yield of 33%, the rest of the energy is dissipated in the form of heat. On the other hand, there are combined cycle thermoelectric plants where electric and thermal energy is produced simultaneously from the same fuel. The advantage of these over conventional plants is that they take better advantage of the energy produced, thus achieving greater efficiencies and in turn have lower CO_2 emissions. Globally,

several alternative solutions have been sought to reduce CO_2 emissions turning electricity production into cost-effective and sustainable processes. To achieve this goal, some authors propose different possibilities to reduce CO_2 emissions: 1) reduce the intensity of energy; 2) reduce the intensity of coal; for example, the use of carbon-free fuel; and 3) improve CO_2 capture. highlighting the implement of CO_2 Capture and Storage plants (CCS). Where post-combustion CO_2 capture is the most feasible technology than other alternatives; by reacting with alkanolamines as solvents, post-combustion capture technology is the best choice for CO_2 separation, because it has high efficiency, low cost, and facility to be adapted to existing power plants.

In order to have a positive environmental impact on CO_2 capture processes, it is necessary to highlight the technical challenges involved in the separation method of CO_2 due to the use of amine aqueous solutions, as well as consider using new ionic liquids solvents to CO_2 separation. To achieve high efficiency, low environmental impact and the best operating cost, it is important to consider two different aspects: first is needed to have a high concentration of CO_2 which depends on the type of fuel used in the power plant and second the election of the solvent used to CO_2 capture so as its proportions.

As discussed in Nagy and Mizey (2013), changing flue gases conditions significantly influence the optimal operation of the capture process, particularly the solvent and energy requiments. These authors evaluated the influence of type and flowrate of seven fuels (including 3 coals, 2 gasses, and one biomass) during capture process by means of a parametric study. Their findings indicate that different ratios absorbent/gas are required in order to operate the capture plant in optimum conditions. According to their results, the optimal L/G ratio shows a linear correlation with the CO_2 content of the flue gas.

In this work, we present a global optimization for the design of a CO_2 capture process coupled to a power generation plant (see Figure 1). The use of four different fuels in the power plant was considered; biogas, coal, non- associated natural gas, and associated natural gas. Two operating scenarios were considered; in the first, the same fuel flow was considered for all the plants and in the second, the same energy demand was specified. The design and simulation of the process plants were developed through the use of the ASPEN Plus simulator. Study Cases and Methodology: for the simulation of the power plant and the CO_2 capture plant, the ASPEN PLUS process simulator is used. In order to model the thermodynamic properties involved in the power generation plant, the Peng-Robinson method is used according to the reported by Hasan et al. (2012). For the combustion chamber, a RGibbs type reactor was selected, considering a molar ratio of air to the fuel of 30: 1 and a fuel flow of 1000kmol/h for all analyzed cases. Table 1 shows the mass percentages of the fuels used for the simulation. For the CO_2 capture process, it was considered a chemical absorption using as solvent an aqueous solution of monoethanolamine (MEA) with a weight of 30% in a RadFrac equilibrium stage block for the absorber and regenerator. The reactions involved in the CO_2 capture process are shown below from Eq. (1) to Eq. (5).

$$MEAH^+ + H_2O \leftrightarrow MEA + H_3O^+ \tag{1}$$

$$2H_2O \leftrightarrow OH^- + H_3O^+ \tag{2}$$

$$HCO_3^- + H_2O \leftrightarrow CO_3^{2-} + H_3O^+ \tag{3}$$

$$OH^- + CO_2 \xleftrightarrow{k1} HCO_3^- \tag{4}$$

$$MEA + CO_2 + H_2O \overset{k2}{\longleftrightarrow} MEACOO^- + HCO_3^- \quad (5)$$

Table 1. Fuel composition

	Natural Gas	Associated Gas	Biogas	Coal
CH_4	96.00	87.20	60.00	-
C_2H_6	1.80	4.50	-	-
C_3H_8	0.40	4.40	-	-
i-C_4H_{10}	0.15	1.20	-	-
N_2	0.70	2.70	2.00	-
CO_2	0.95	-	38.00	-
C	-	-	-	78.20
H	-	-	-	5.20
O	-	-	-	13.60
N	-	-	-	1.30
S	-	-	-	1.70

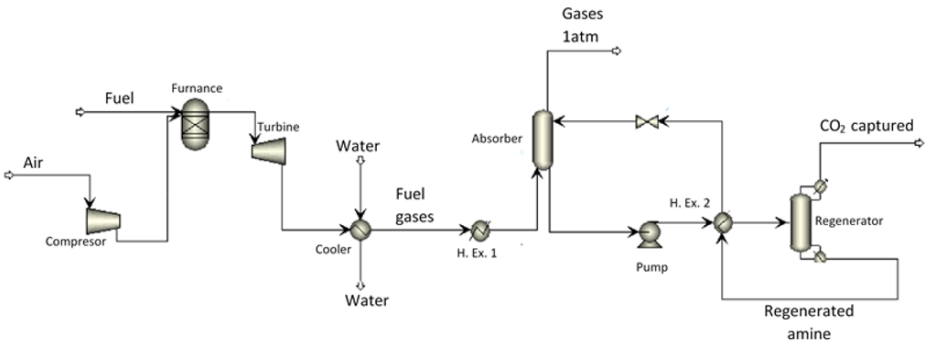

Figure 1. Representation of a thermoelectric power plant and the CO2 capture plant in post-combustion using chemical absorption with monoethanolamine

Because of the components present in the absorption are dissociate, it is necessary to achieve a CO_2 recovery in the gas output stream of the same equipment. In the case of the regenerator, the distillate flow and the reflux ratio were manipulated to capture the greatest amount of CO_2 from the flue gas stream from the thermoelectric plant and thus reduce CO_2 emissions into the atmosphere and the environmental impact that they generate For this reason, in all the cases analyzed, they were standardized to a purity of 99 mol% CO_2 and recovery of at least 95% of CO_2

2. Global Optimization

Once the Aspen Plus simulation is completed, a multi-objective optimization technique is employed having as objective function the minimization of energy requirement as

reboiler heat duty. The minimization of this objective was subject to the required recoveries and purities in each product stream (Eq. 6).

$$Min(Q) = f(N_{tn}, N_{fn}, R_m, D_{rf}, F_{rn}) \quad (6)$$

Where N_{tn} is the total number of column stages, N_{fn} is the feed stage in the column, R_{rn} is the reflux ratio, F_{rn} is the distillate/bottoms flux, and D_{cn} is the column diameter. This minimization considered 10 continuous and discrete variables.

To optimize the process route for CO_2 capture, a stochastic optimization method, Differential Evolution with Tabu List (DETL) was used, which has shown being robust to optimize intensified separation systems. This technique works as a combined system between the biological evolution from Differential Evolution technique and the random search method from the Tabu search technique. Sharma & Rangaiah, (2007) showed that the use of some concepts of the metaheuristic tabu could improve the performance of DE algorithm. The implementation of this optimization approach was made using a hybrid platform where the DETL method was coded using Microsoft Excel (ME). Initially, the method proposes a vector which is sent to Aspen Plus by means of dynamic data exchange (DDE). In there the separation process was rigorously simulated. For the optimization of process routes analyzed in this study, the following parameters for DETL method were used: 200 individuals, 500 generations, a tabu list of 50% of total individuals, a tabu radius of 0.0000025, 0.80 and 0.6 for crossover and mutation fractions, respectively.

3. Results

In this section, it is presented the results of the study cases where the operating conditions were varied for both constant fuel flow and energy demand. Both cases were analyzed for four different fuels. It is important to remark that the selection of fuel is very important because it has a direct impact not only on energy production but also on the fuel gas composition that is obtained (Nagy and Misey, 2013). Besides the concentration of the gases obtained will have a direct impact on the energy and solvent requirements used for the CO_2 capture plant. When it is presented the lower concentration of gases the capture efficiency will decrease, then the energy and solvent requirements for the capture will increase.

After the optimization process for reducing energy demand in the capture process, the optimum designs of absorber and desorber colums for Case 1 are presented in Table 2. For Case 2 the columns structure remains close to that obtained in Case 1, the operating parameters, however, shown important differences. The optimum operating parameters for both scenarios are shown in Table 3. For both cases, the CO_2 generated by GJ of energy produced in the power plant (CO_{2GEN}/E_{PP}) is larger when burning mineral coal and biogas than for the natural gasses. This is more noticeable for the scenario in which energy demand is specified, since it is necessary to adjust the feed flows of each fuel in order to reach the specified demand. It is important to highlight that CO_2 concentration in flue gases coming from burning mineral coal and biogas have lower values in the first scenario, but it significantly increases in the second case, which directly influences the capture effectiveness.

The optimum ratios of absorbent to flue gas (L/G), absorbent to CO_2 recovered ($L/CO_{2\,REC}$) and the reboiler duty to CO_2 recovered ($Q_R/CO_{2\,REC}$), are reported in Table 2. In Case 1, the largest value for $L/CO_{2\,REC}$ is obtained for the mineral coal, while for the other three fuels this ratio ranges between 13 and 15. The reboiler duty in the regenerator column (desorber) highly depends on the L/G ratio, so the largest requirement is also observed

for this fuel. These results dramatically changed in Case 2, as the CO_2 concentration in the flue gas importantly increases, such that the absorbent and energy requirements during CO_2 capture diminishes.

Table 2. Optimal designs for constant fuel flow considering the best 3 fuels

Design Variables	Mineral coal	Biogas	Non associated gas	Associated gas*
Columns Topology				
Stages (Absorbed)	48	20	46	19
Stages (Desorbed)	25	39	37	17
Feed flue gas stage (Absorbed)	48	20	46	19
Feed solvent stage (Absorbed)	1	1	1	1
Feed stage (Desorbed)	3	3	3	3
Operation Specifications				
Top pressure (kPa)	88	88	88	88
Reflux ratio (Absorbed) Reflux ratio (Desorbed) Heat duty (Desorbed) (GJ/h)	1.103	0.691	0.792	0.794
	0.9006	0.809	0.839	0.796
	173.067	126.567	155.224	143.99
Streams mass flow				
Flue gas (kg s^{-1})	267.68	271.055	268.25	268.78
Feed solvent (kg s^{-1})	251	140.49	176.950	161.88

*****Associated gas was taken as basis for the initial design*

Table 3. Optimization results for all scenarios

Fuel type	$CO_{2\,GEN}/E_{PP}$ (Power plant)	L/G	$L/CO_{2\,REC}$	$Q_R/CO_{2\,REC}$
	kg/GJ	*kg/kg*	*kg/kg*	*GJ/t CO2*
	Constan fuel in power plant			
Mineral coal	55.25	0.94	27.68	5.30
Biogas	60.13	0.58	13.93	3.09
Non associated gas	42.91	0.68	15.50	3.65
Associated gas	44.84	0.71	13.77	3.02
	Constant energy in power plant			
Mineral coal	71.04	0.598	7.812	2.950
Biogas	71.23	1.023	13.524	3.694
Non associated gas	44.24	0.672	13.848	3.214
Associated gas	44.88	0.705	13.773	3.017

Nagy and Misey (2013) found optimum operating parameters for CO_2 capture plants by considering seven fuels and two operating cases (similar to those here considered).After a parametric searching, they reported L/G values ranging between 1 to 4, with $Q_R/CO_{2\,REC}$ close to 4. For the studied cases in this work, L/G ratio took values between 0.58 and 1.023. From the overall results, it is clear that the optimum designs obtained through a global optimization, wherein the column structures are considered, may significantly

reduce not only the energy requirement but also the absorbent flowrate. Given the interest in CO_2 capture processes as an alternative to reduce the environmental impact during the generation of electricity, the implementation of this additional objective to the optimization problem may be considered in future works, in order to identify optimum solutions beyond the techno-economic point of view.

4. Conclusions

The implementation of the CO_2 capture process in power plants has been considered so far, the most mature technology to reduce the environmental impact associated with electricity production. Most research efforts in this field have been focused on performing techno-economic analysis and optimizing the energy efficiency of the capture process. There is a clear incentive to analyze the process from a holistic point of view, considering not only the CO_2 capture as a strategy to reduce the negative effects of the power plant but also by identifying new environmental effects due to the implementation of such capture process

References

EIA- U.S. Energy Information Administration - Independent Statistics and Analysis, 2019, “U.S. Energy-Related CO2 Emissions Expected to Rise Slightly in 2018”, Remain Flat in 2019, U.S. Energy Information Administration (EIA). Taken from: www.eia.gov/todayinenergy/detail.php?id=34872.

International Energy Agency, 2018, “Electricity Information 2018 overview”, International Energy Agency. Taken from: https://www.iea.org/statistics/electricity/

M. F. Hasan, R. C., Baliban, Elia, J. A. and C.A. Floudas, 2012, “Modeling, simulation, and optimization of postcombustion CO2 capture for variable feed concentration and flow rate. 1. Chemical absorption and membrane processes”, Industrial & Engineering Chemistry Research, 51, 48, 15642-15664.

S., Sharma, and G.P. Rangaiah, 2013, "An improved multi-objective differential evolution with a termination criterion for optimizing chemical processes", Computers & Chemical Engineering 56, 155-173.

T. Nagy and P. Mizsey, 2013, “Effect of fossil fuels on the parameters of CO2 capture”, Environmental science & technology,47, 15, 8948-8954.

Sauro Pierucci, Flavio Manenti, Giulia Bozzano, Davide Manca (Eds.)
Proceedings of the 30th European Symposium on Computer Aided Process Engineering (ESCAPE30), May 24-27, 2020, Milano, Italy.
http://dx.doi.org/10.1016/B978-0-12-823377-1.50141-5

Deterministic Global Optimization of Multistage Membrane Gas Separation Using Surrogate Models

Marius Hörnschemeyer[a*], Christian Kunde[b]

[a]*Max Planck Institute for Dynamics of Complex Technical Systems, Sandtorstraße 1, 39106 Magdeburg, Germany*
[b]*Otto von Guericke University Magdeburg, Universitätsplatz 2, 39106 Magdeburg, Germany*
hoernschemeyer@mpi-magdeburg.mpg.de

Abstract

This paper deals with deterministic global optimization of multistage membrane gas separation processes that are described by spatially distributed models. The computational tractability of the optimization problem is improved by approximating the spatially distributed models with data-driven surrogates. The resulting problems are solved globally using BARON/GAMS. The binary separation of a mixture containing CO_2 and CH_4 is considered as a case study for multistage membrane gas separation processes. The influence of the feed composition on the globally optimal multistage configurations is studied.

Keywords: gas permeation, multistage, binary separation, deterministic global optimization, surrogate modeling.

1. Introduction

Selective membranes enable the separation of gas mixtures without energy-intensive phase changes. The product purity and recovery demands for gas separations are often beyond the limits of single stage systems. To overcome these limitations, configurations comprising multiple stages of membrane-based gas separation modules and recycles can be employed (Ismail et al., 2015).

The optimization of such processes typically leads to the solution of nonlinear problems with continuous and discrete variables. Utilizing deterministic global optimization to solve those mixed-integer nonlinear programs (MINLP) avoids suboptimal local solutions that may otherwise result in poor process design decisions. However, the large number of complex nonlinear expressions and the auxiliary variables make detailed models of spatially distributed processes, e. g. based on finite volume discretization, unfavorable for deterministic global optimization.

In this contribution, replacing a spatially distributed model of a membrane module by a data-driven surrogate is studied as an option to trade some model accuracy for better computational tractability of the global optimization. The required data for the surrogate generation is provided by simulation runs with a fully discretized model of the membrane-based separation process. The developed optimization method is demonstrated for the membrane-based removal of CO_2 from biogas. A parameter study is carried out to investigate the influence of the feed composition on the globally optimal configurations of membrane modules. This way, the findings on multistage binary separations in (Kunde and Kienle, 2018) are extended to membrane-based gas separation.

2. Model description

2.1. Spatially distributed model / Membrane module model

The membrane module model describes the purification of a binary gas mixture due to a selective flow through a membrane. A membrane module operating in countercurrent flow pattern is modeled. The feed flow $\dot{N}_\alpha^{\mathrm{F}}$ enters the module and is transported along the membrane surface, while a part of it permeates through the membrane. The remaining gas on the retentate side leaves the module via the retentate flow $\dot{N}_{\alpha,\mathrm{out}}^{\mathrm{R}}$. The permeated gas is collected at the permeate side, transported in the opposing direction to the bulk flow at the retentate side and leaves via the permeate flow $\dot{N}_{\alpha,\mathrm{out}}^{\mathrm{P}}$. The permeating flux j_α^{m} is modeled according to the solution-diffusion-mechanism (Wijmans and Baker, 1995) assuming a constant permeance Q_α of the membrane. The fast permeating gas component A is enriched at the permeate side, while the slow permeating component B is enriched at the retentate side. Acting as a driving force for the flux

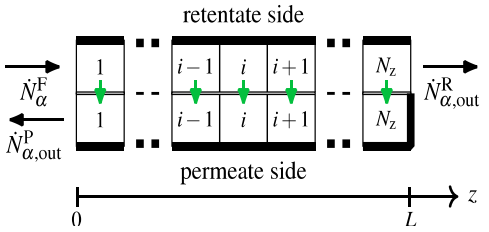

Figure 1: Finite volume discretization of the membrane module with $2N_z$ control volumes.

$$j_\alpha^{\mathrm{m}} = Q_\alpha (x_\alpha^{\mathrm{R}} P^{\mathrm{R}} - x_\alpha^{\mathrm{P}} P^{\mathrm{P}}),\ \alpha = \mathrm{A,B} \tag{1}$$

the difference in partial pressure between both sides is determined using ideal gas behavior with mole fractions x_α and constant total pressures at retentate side P^{R} and permeate side P^{P}. The permeate flow is increased by increasing the membrane area A^{m}. The opposing bulk flows at retentate and permeate side are assumed to be driven only by advection and ideally mixed except in their flow direction. The bulk flows are modeled using mass balances coupled by the permeating flux j_α^{m} of Eq. (1).

$$\begin{aligned} \frac{\partial}{\partial z}\dot{N}_\alpha^{\mathrm{R}}(z) &= \frac{-A^{\mathrm{m}}}{L} j_\alpha^{\mathrm{m}}(z),\ \dot{N}_\alpha^{\mathrm{R}}(z=0) = \dot{N}_\alpha^{\mathrm{F}} \\ \frac{\partial}{\partial z}\dot{N}_\alpha^{\mathrm{P}}(z) &= \frac{A^{\mathrm{m}}}{L} j_\alpha^{\mathrm{m}}(z),\ \dot{N}_\alpha^{\mathrm{P}}(z=L) = 0 \end{aligned} \tag{2}$$

A numerical solution for the spatially distributed model is obtained by using the finite volume method as shown in Figure 1. Linear concentrations profiles are assumed in each control volume. The first-order upwind scheme is applied to the differential equation system, which is discretized by $N_z = 150$ control volumes for each flow channel, i. e. the retentate side and the permeate side.

2.2. Superstructure model

The superstructure model is adopted from Kunde and Kienle (2018) and allows to optimize cascades as well as a more complex superstructure called network (see Figure 2). Superstructures with membrane modules $s = 1,\ldots,N_{\mathrm{MO}}$ are considered. Both superstructures have one overall feed $\dot{N}_\alpha^{\mathrm{FF}}$, an overall retentate outlet $\dot{N}_\alpha^{\mathrm{RR}}$, enriched in component B, and an overall permeate outlet $\dot{N}_\alpha^{\mathrm{PP}}$, enriched in component A. Each module s has a feed flow $\dot{N}_{\alpha,s}^{\mathrm{F}}$ and two product flows $\dot{N}_{\alpha,s}^{\mathrm{R}}$ and $\dot{N}_{\alpha,s}^{\mathrm{P}}$. No stream splitting is allowed. In the presented case study, minimum product purities $x_{\mathrm{B}}^{\mathrm{RR}}$ and $x_{\mathrm{A}}^{\mathrm{RR}}$ are required at the overall retentate and permeate outlet.

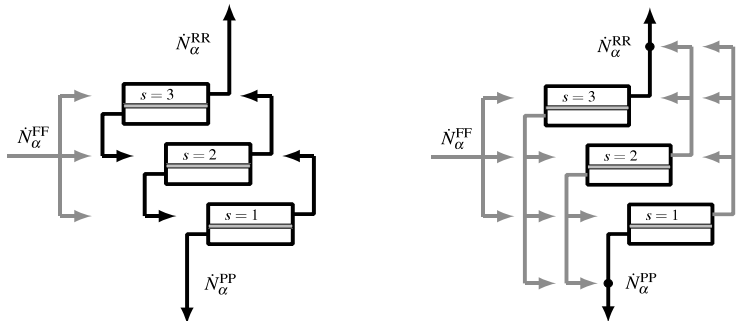

Figure 2: Superstructure models cascade (left) and network (right). Black arrows indicate locked connections and grey arrows potential connections, of which one has to be realized.

2.3. Objective function

As proposed by Kunde and Kienle (2018) a general performance indicator is chosen to serve as an objective function. The permeation effort

$$E_{\mathrm{P}} = \frac{\sum_{s=1}^{N_{\mathrm{MO}}} \sum_{\alpha=\mathrm{A,B}} \dot{N}_{\alpha,s}^{\mathrm{P}}}{\sum_{\alpha=\mathrm{A,B}} \dot{N}_{\alpha}^{\mathrm{FF}}} \tag{3}$$

is defined as the ratio of total amount of permeate to overall amount of feed. It is increased by repeated permeation, which requires larger membrane areas and additional gas compression. The permeation effort is therefore also an indicator for economic viability.

3. Surrogate modeling

Data-driven surrogate methods are applied here to obtain surrogates that accurately approximate the original model but require much less computational effort. The original model is treated as a black box with input and output data.

3.1. In- and outputs

In- and output variables are selected from the original model. This determines the properties of the input-output data and thereby affects accuracy and size of the surrogate. Here, we use the feed composition $x_{\mathrm{A}}^{\mathrm{F}}$ and permeate yield Y^{P} as inputs.

$$x_{\mathrm{A}}^{\mathrm{F}} = \frac{\dot{N}_{\mathrm{A}}^{\mathrm{F}}}{\sum_{\alpha=\mathrm{A,B}} \dot{N}_{\alpha}^{\mathrm{F}}} \qquad Y^{\mathrm{P}} = \frac{\sum_{\alpha=\mathrm{A,B}} \dot{N}_{\alpha}^{\mathrm{P}}}{\sum_{\alpha=\mathrm{A,B}} \dot{N}_{\alpha}^{\mathrm{F}}} \tag{4}$$

At high retentate purities the flux j_α^{m} permeating through the membrane contains predominantly component B, thus reducing the permeate purity as well as the amount of retentate product. Therefore, combinations of $x_{\mathrm{A}}^{\mathrm{F}}$ and Y^{P} that lead to a retentate purity well above product specifications are excluded from the data that is used to train the surrogate models. The corresponding input space Ω is defined as

$$\Omega = \left\{ x_{\mathrm{A}}^{\mathrm{F}} \in [0,1],\, Y^{\mathrm{P}} \in [0,1] \,|\, x_{\mathrm{A}}^{\mathrm{F}} \geq \kappa_1 Y^{\mathrm{P}} + \kappa_2,\, x_{\mathrm{A}}^{\mathrm{F}} \geq \kappa_3 Y^{\mathrm{P}} + \kappa_4 \right\} \tag{5}$$

with linear inequalities that remove most of the undesired input combinations.

The choice of the surrogate output is based on the authors previous evaluation of a number of alternative model formulations. Only the best performing model formulation from this evaluation is presented here. The model equations for each membrane module read

$$\begin{aligned}\dot{N}_{\mathrm{B}}^{\mathrm{R}} &= (1-Y^{\mathrm{P}})^{f(x_{\mathrm{A}}^{\mathrm{F}},Y^{\mathrm{P}})}\,\dot{N}_{\mathrm{B}}^{\mathrm{F}},\\ \dot{N}_{\mathrm{A}}^{\mathrm{P}} &= Y^{\mathrm{P}}(\dot{N}_{\mathrm{A}}^{\mathrm{F}}+\dot{N}_{\mathrm{B}}^{\mathrm{F}})-\dot{N}_{\mathrm{B}}^{\mathrm{P}},\\ \dot{N}_{\mathrm{A}}^{\mathrm{F}} &= \dot{N}_{\mathrm{A}}^{\mathrm{R}}+\dot{N}_{\mathrm{B}}^{\mathrm{P}},\ \alpha=\mathrm{A},\mathrm{B}\end{aligned} \tag{6}$$

with values for f obtained from the spatially distributed membrane module model. The mapping f is considered to be the original model and approximated by a surrogate model $\tilde{f}$ that is parameterized with a set of sample points $S=\left\{\left(\left(x_{\mathrm{A,k}}^{\mathrm{F}},Y_{\mathrm{k}}^{\mathrm{P}}\right),f\left(x_{\mathrm{A,k}}^{\mathrm{F}},Y_{\mathrm{k}}^{\mathrm{P}}\right)\right)\,|\,k=1,\ldots,N_{\mathrm{S}}\right\}$ generated on a dense grid for the input space Ω.

3.2. Surrogate method

A broad range of data-driven surrogate methods is available in the literature. For noise-free data sets, such as generated by deterministic simulation models, Razavi et al. (2012) recommend interpolation methods. In the work at hand a radial basis function model is chosen. The radial basis function model $\tilde{f}(\mathbf{x})$, with $\mathbf{x}=(x_{\mathrm{A}}^{\mathrm{F}},Y^{\mathrm{P}})^{\mathrm{T}}$, is constructed as a sum of a trend function $g(\mathbf{x})$ and a weighted sum of radial basis functions $\varphi(\mathbf{x}_i,\mathbf{x})$.

$$\tilde{f}(\mathbf{x})=g(\mathbf{x})+\sum_{i=1}^{N_{\mathrm{R}}}w_i\varphi(\mathbf{x}_i,\mathbf{x}) \tag{7}$$

The trend function $g(\mathbf{x})$ is calibrated on all sample points $(\mathbf{x}_k,f(\mathbf{x}_k))$ by least square fitting. The remaining difference between $g(\mathbf{x})$ and $f(\mathbf{x})$ is approximated by the radial basis functions. We choose a linear radial basis function $\varphi(\mathbf{x}_1,\mathbf{x}_2)=\|\mathbf{x}_1-\mathbf{x}_2\|$ with a weighted euclidean distance $\|\ \|$. The distance weights are empirically selected to reduce the maximum approximation error over all sample locations $\mathbf{x}_k$. The reference points $(\mathbf{x}_i,f(\mathbf{x}_i)),\ i=1,\ldots,N_{\mathrm{R}}$, of the radial basis function model are selected from the set of sample points S by an adaptive greedy sampling method that minimizes the maximum approximation error. In each step of the adaptive algorithm, the weights w_i are obtained by solving a linear equation system resulting from the interpolation conditions at the reference points $\tilde{f}(\mathbf{x}_i)=f(\mathbf{x}_i)$.

3.3. Accuracy measures

The accuracy of the surrogate model is evaluated in terms of the errors between the original function f and the surrogate $\tilde{f}$ at all sample locations $\mathbf{x}_k$. The maximum approximation error $e_{\max}$ and the mean approximation error e_{mean} are defined as

$$e_{\max}=\frac{\max\limits_k\left|f(\mathbf{x}_k)-\tilde{f}(\mathbf{x}_k)\right|}{\max\limits_k f(\mathbf{x}_k)-\min\limits_k f(\mathbf{x}_k)} \qquad e_{\mathrm{mean}}=\frac{\frac{1}{N_{\mathrm{S}}}\sum_{k=1}^{N_{\mathrm{S}}}\left|f(\mathbf{x}_k)-\tilde{f}(\mathbf{x}_k)\right|}{\max\limits_k f(\mathbf{x}_k)-\min\limits_k f(\mathbf{x}_k)}. \tag{8}$$

The error measures $e_{\max}$ and e_{mean} do not account for error propagation to other variables that are important for the overall process. Thus we define additional error measures $e_{\max}^{x_{\mathrm{B}}^{\mathrm{R}}}$, $e_{\max}^{x_{\mathrm{B}}^{\mathrm{P}}}$, $e_{\mathrm{mean}}^{x_{\mathrm{B}}^{\mathrm{R}}}$ and $e_{\mathrm{mean}}^{x_{\mathrm{A}}^{\mathrm{P}}}$ for the product purities by replacing f in Eq. (8) with $x_{\mathrm{B}}^{\mathrm{R}}$ and $x_{\mathrm{A}}^{\mathrm{P}}$, respectively.

4. Results

The present case study considers biogas upgrading as a separation of CO_2 (component A) from CH_4 (component B). Table 2 comprises all parameters and process requirements necessary to generate sample points and to carry out the superstructure optimization. The input space Ω contains 6262 equally spaced sample points, to which an empirically selected trend function is fitted. To keep the computational effort for parameter studies with many optimization runs feasible, we chose $N_R = 50$ reference points. The resulting approximation of the retentate outlet purity for a single module is shown in Figure 3. Table 1 presents the achieved approximation accuracy. Note that errors in process variables, such as the product purities, can be larger than the approximations errors of the surrogate due to error propagation.

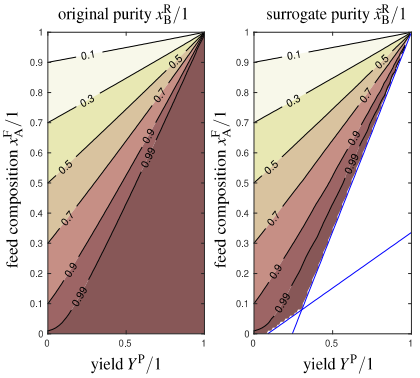

Figure 3: Retentate product purity obtained from the fully discretized model (left) and from the model formulation including $\tilde{f}$ (right). The straight lines indicate the input space restriction.

A parameter study is carried out to investigate the influence of the overall feed composition x_A^{FF} on the minimized permeation effort and corresponding optimal structures. The results are obtained using the solver BARON 15.9.22. (Tawarmalani and Sahinidis, 2005) and the subsolvers CPLEX and CONOPT in GAMS 24.2.1. Options are kept at default values except setting the relative termination tolerance to 1×10^{-3}. Optimizations of the cascade and network superstructure are performed at thirty values of x_A^{FF}. Each superstructure is optimized for 1, 2 and 3 modules. Solution times are in the order of minutes for each run. The lowest permeation efforts E_P achieved by these superstructures are depicted in Figure 4. There, the roman numerals indicate regions of x_A^{FF} that yield different optimal cascades. In region I, a two-staged cascade with a feed at stage $s = 2$ is optimal, whereas in region II, a two-staged cascade with a feed at stage $s = 1$ is optimal. The feed compositions in region III allow a single membrane module to be optimal. The permeation effort of optimal network configurations is significantly lower than that of optimal cascades at feed compositions close to the border between region I and II. These reductions are achieved by a single three-staged configuration, shown in Figure 4. At the feed composition $x_A^{FF} = 0.236$, a maximum relative reduction of 15.9 % between an optimal cascade with $E_P = 0.466$ and the optimal network configuration with $E_P = 0.392$ is observed.

Table 1: Accuracy of the model formulation that includes the surrogate.

error	e_{max}	$e_{max}^{x_B^R}$	$e_{max}^{x_A^P}$	e_{mean}	$e_{mean}^{x_B^R}$	$e_{mean}^{x_A^P}$
value	0.0119	0.0440	0.0105	0.0041	0.0014	0.0018

Table 2: Process parameters and requirements based on (Scholz et al., 2015).

parameter	permeance Q_A	permeance Q_B	retentate pressure P^R	permeate pressure P^P
value	$2.01\times10^{-8}\ \frac{\text{mol}}{\text{s m}^2\ \text{Pa}}$	$3.35\times10^{-10}\ \frac{\text{mol}}{\text{s m}^2\ \text{Pa}}$	16×10^5 Pa	1×10^5 Pa
variable	purity retentate x_B^{RR}	purity permeate x_A^{PP}		
domain	$[0.96,1]$	$[0.96,1]$		

5. Conclusion

In this contribution, the application of surrogate modeling allows for extensive parameter studies using deterministic global optimization, despite the high computational cost of the original spatially distributed process model. Results of the parameter study strongly suggests that the findings on multistage binary separation in (Kunde and Kienle, 2018) also extend to membrane-based gas separation: In certain parameter regions, countercurrent cascades are suboptimal compared to the alternative structure depicted in Figure 4. These parameter regions are located where the feed position of optimal cascades changes.

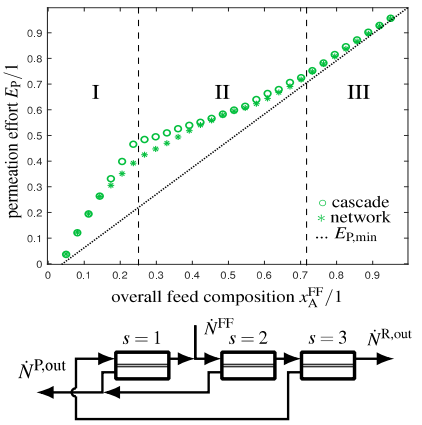

Figure 4: Minimized permeation effort of optimal structures and the theoretical minimum permeation effort $E_{P,min}$, i. e. for $Q_B = 0$, as functions of the feed composition (top). Alternative structure emerging from the network (bottom).

References

A. F. Ismail, K. C. Khulbe, T. Matsuura, 2015. Gas Separation Membranes : Polymeric and Inorganic. Springer International Publishing.

C. Kunde, A. Kienle, 2018. Global optimization of multistage binary separation networks. Chemical Engineering and Processing: Process Intensification 131, 164–177.

S. Razavi, B. A. Tolson, D. H. Burn, 2012. Review of surrogate modeling in water resources. Water Resources Research 48 (7).

M. Scholz, M. Alders, T. Lohaus, M. Wessling, 2015. Structural optimization of membrane-based biogas upgrading processes. Journal of Membrane Science 474 (Supplement C), 1–10.

M. Tawarmalani, N. V. Sahinidis, 2005. A polyhedral branch-and-cut approach to global optimization. Mathematical Programming 103, 225–249.

J. G. Wijmans, R. W. Baker, 1995. The solution-diffusion model: a review. Journal of Membrane Science 107, 1–21

Sauro Pierucci, Flavio Manenti, Giulia Bozzano, Davide Manca (Eds.)
Proceedings of the 30th European Symposium on Computer Aided Process Engineering (ESCAPE30), May 24-27, 2020, Milano, Italy.
http://dx.doi.org/10.1016/B978-0-12-823377-1.50142-7

An Innovative and Fully Automated System for Gel Electrophoresis

Konstantinos Theodoridis[(a,*)], Fotis Stergiopoulos,[a] Dimitrios Bechtsis,[a] Nikolaos Nikolaidis,[a] Dimitrios Triantafyllidis,[a] Apostolos Tsagaris,[a] Anastasios Filelis,[b] Asterios Papaikonomou,[b]

[a]*International Hellenic University (IHU), Department of Industrial Engineering & Management, PO Box 141, Sindos, Thessaloniki, 57400, Greece*

[b]*Evresis S.A, DA 12a Block:39b Industrial Area, 57400, Sindos, Thessaloniki*
kostastheod82@yahoo.gr

Abstract

Electrophoresis is a standard technique used in medical laboratories and research institutions worldwide, for DNA, RNA and protein analysis. Various methodologies and techniques have been developed over the past decades. The common ground used in all approaches is the separation of molecule particles based on their movement on a substrate under the existence of an electric field. Relevant research is assisted by the advancement of technology and focuses on the development of innovative and fully automated electrophoresis systems that use robotic systems and advanced programming techniques. To this extent, the proposed paper focuses on the presentation of an innovative fully automated electrophoresis system, currently being developed within the framework of a research project funded by the Greek National Programme for Competitiveness Entrepreneurship and Innovation. The system can process multiple protocols of gel electrophoresis, on a precast agarose film, utilizing a combination of hardware and software, with minimal intervention by humans. Healthcare professionals could significantly benefit from this system by obtaining fast and accurate results in a fully automated fashion, by eliminating human errors during the process.

Keywords: automated capillary gel electrophoresis, automated medical machine, prototype design, mechanical equipment

1. Introduction

Electrophoresis has been known for nearly a century, and various electrophoretic techniques have been developed over the decades. The basic principle is based on the separation of proteins, when an electrical field is applied across a compartment, filled with medium of different pH (Aslam et al., 2017). The first fundamental electrophoretic principle for the separation of acids and metals, was introduced as “isotachophoresis” (ITP) or “ion migration method” (Kendall et al., 1923). With the ITP method it was evident that when an electric field is applied, the charged protein components are separated according to the differences in their electrophoretic mobilities. A few years later, Tiselius constructed a U-tube system, that managed to separate two protein components, because of the thermal diffusion and convection phenomenon (Tiselius, 1937). Later on, several studies described ITP as “moving boundary electrophoresis” (Longsworth et al., 1939) or “displacement electrophoresis”, and a successful separation of amino acids and proteins like asparate, glutamate, chloride and acetate, was conducted.

A widely used type of electrophoresis is Gel Electrophoresis (GE), in which a compartment is filled with a gel medium, usually a natural anticonvective polymer like

agarose or on polyacrylamide gel (PAGE). PAGE is used for complex protein analysis that is found in human tissues, cells, or other biological samples. The major advantage of this method is that it separates hundreds to thousands proteins located in a single gel (Magdeldin et al., 2014). Polyacrylamide gel is made up of chains of acrylamide monomers that are cross linked with *N*, also commonly known as "bis". The concentration of "bis" determines the pore size of the polyacrylamide gel (Holmes et al., 1991).

Another established electrophoresis method is Capillary Electrophoresis (CE), which usually takes place within a glass tube (Vesterberg, 1989), filled with a simple buffered aqueous electrolytes solution (FSCE) (Altria et al., 2006). It provides efficient separation analysis within a certain time window, low consumption of chemicals and limited operational and maintenance procedures (Jarvas et al., 2020). This method gained a lot of popularity especially in the pharmaceuticals industry. CE can be used for determining drug-related impurities, physicochemical measurements of drug molecules, counter-ion analysis for drug discovery and the separation of drug enantiomers.

Development of the CE led to more efficient systems, like the microchip electrophoresis (Durney et al., 2015; Jarvas, Guttman et al., 2020; Lacher et al., 2001; Masár et al., 2020). The microchip system provides a fast and effective analysis as it contains various microchannels that are made of glass and/or fused silica substrates with optimal thermal characteristics. The advantages of CE provided the opportunity to researchers to develop reliable, fast and economic fully automated systems (Bodnar et al., 2016) or semi-automated portable devices (Nguyen et al., 2014).

Nowadays, in the pharmaceutical industry, ongoing research focuses on the development of innovative and automated medical devices. Electrophoresis automated devices can execute analytical protocols with high precision, low operational costs and shorter delivery times. To this extend, our research team, has focused on fabricating an innovative and fully automated electrophoresis system, based on capillary gel electrophoresis. A user-friendly machine that efficiently carries out various kinds of electrophoresis (protein, haemoglobin, lipoprotein, immunoelectrohoresis, DNA/RNA) on precast agarose films has been successfully designed and manufactured as a prototype. The system uses state of the art information and automation technology methods together with ergonomic design characteristics.

2. Electrophoresis main components

The study of the prototype's design was based on commercial agarose precast films and commercial blood tubes, with standard dimensions. The agarose film's dimensions are 102x69 mm and can contain up to thirty blood deposits (samples), using a layout pattern of three columns by ten rows. Emphasis was given on designing quality moving mechanisms and smart automation systems for the final device. The overall assembly of the electrophoresis system is illustrated in figure 1, including the following subsystems, referred to thereafter as mechanical components: (i) tube drawer system, (ii) bar code scanner, (iii) wash tank, (iv) robotic arm/gripper, (v) sample carrier, (vi) electrophoresis chamber, (vii) frame/film manipulator, (viii) staining-unstaining chamber, (ix) drying chamber, (x) camera analysis chamber.

In addition, the proposed electrophoresis system will also include embedded computer systems, microcontrollers and microprocessors, a sophisticated software that can run multiple electrophoretic procedures, a user-friendly interface and a customized power-supply system. This manuscript is focusing on the product design characteristics and thus extensively discussing the mechanical components, their functionalities and the developed processes.

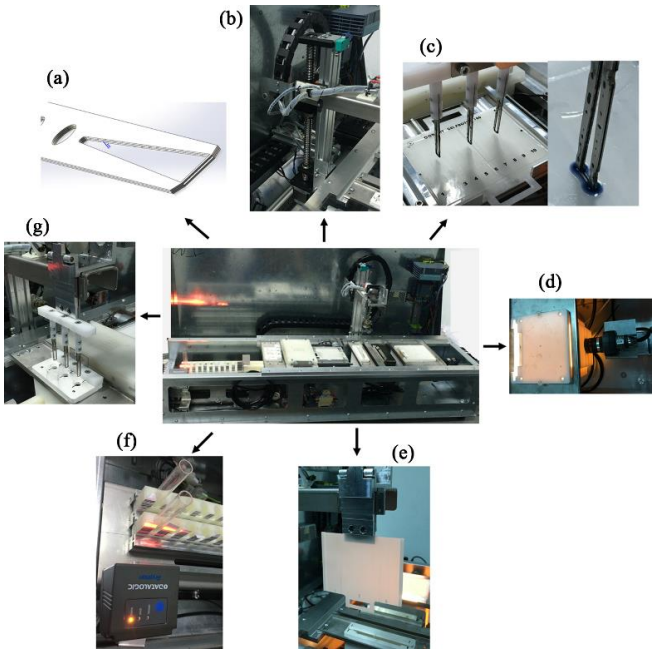

Figure 1, Automated Electrophoresis Machine layout. Design of the (a) V-shaped 316-SS finish, (b) screw drive mechanism of the robotic arm/gripper, (c) deposit of stained sample on the agarose film, (d) camera/analysis chamber, (e) gripper and film/frame manipulator, (f) sample tubes inside the drawer system and barcode scanner, (g) sample carrier and wash tank

2.1. Tube drawer system

The "tube drawer system" consists of three (3) drawers, each containing ten (10) positions for sample tubes. They were manufactured from polypropylene (PP) on a SLS 3D-printer (fig.1, f). These drawers are guided throughout aluminium profiles of shape type I and II, with specific tolerance-based dimensions. Each drawer has a hole underneath it, in order to allow a solenoid rod to engage and/or disengage automatically. The solenoids are mounted on a galvanized metal base and the whole base is fixed onto a rack which is driven by a belt drive system.

2.2. Electrophoresis chamber

The "electrophoresis chamber" subsystem was fabricated out of polypropylene (PP) by a CNC machine, and contains two opposite deeper compartments. On both compartments, two platinum electrodes were installed at the bottom edges, to apply the corresponding voltage. The internal design of the chamber has the appropriate shape dimensions allowing for a slight bending of the "frame/film manipulator". This task is accomplished by a cam-shaft mechanism that delivers a small force to the lid of the chamber which is fixed on coil springs. Furthermore, during electrophoretic processes, the film must have a steady state temperature of 20°C regardless of the outside ambient temperature. For this reason, a peltier sensor, two temperature sensors and a small fan were installed. The small fan was placed on the top surface of the lid, which has the appropriate openings for a straightforward airflow.

2.3. Main drive mechanism, robotic arm/gripper

The main drive system is the "robotic arm" and its guide rails were installed in parallel to the longitudinal X-axis of the system. The arm slides and moves by a belt drive system.

It also moves on the Z axis by a screw-drive system (fig.1, b). The gripping system, consists of two specially designed aluminium profiles that engage/disengage by a solenoid mechanism. The gripper is used to manipulate both the "frame/film manipulator" and the "sample carrier".

2.4. Chambers for the completion of the electrophoresis procedure

The "wash tank" with its lid was designed and fabricated with polypropylene (PP) material on a SLS 3D-printer. The lid consists of two rows by three holes each. This container is filled up with ethanol-based liquid and serves to wash the "sample carrier" and as a rest position for the "sample carrier", (fig.1, g).

Staining–unstaining chamber with its lid was also fabricated with polypropylene (PP) material on a SLS 3D-printer. Inside the chamber, an inner wall was built in, to separate it on two different compartments for staining and unstaining media.

The drying chamber was CNC machined out of aluminium. On the inner side of the chamber and along its perimeter, a thermal resistance was installed and covered with thermal isolation material. This system was built to work using the simple process of an oven.

The camera/analysis chamber and its lid were also designed and fabricated with polypropylene (PP) material on a SLS 3D-printer. A high-resolution camera is used to capture a clear photo of the film. For this reason, at the opposite side of the film's place, a 28mm diameter hole was opened to ensure that the camera can work properly. In addition, underneath the lid, two led tapes were installed for providing adequate light at the inner side of the chamber (fig.1, d).

3. System's operational principles

After designing the above described components and taking into consideration several dimension restrictions and requirements, it was decided to perform all movements along the "X" and "Z" axes. The machine operation starts over when the user places the agarose film into the "frame/film manipulator". Then it rotates 90° counter clockwise (CCW), by its vertical axis in to the horizontal position and stays still (standby position), as shown in figure 1, c.

The drawers of the "tube drawers' system, are exported instantaneously with the help of the solenoid mechanisms, and the operator/user places up to thirty (30) sample tubes. These tubes, have already a barcode tape on them which has been placed manually by the user, to distinguish each sample. Thereafter, each drawer is automatically inserted individually allowing for scanning and storing the data of the tubes, using a barcode scanner system.

The "sample carrier" has a custom designed V-shaped 316L-SS finish with a small opening and it is fixed on rods made of polypropylene PP (fig.1, a, c). Two sample carriers were fabricated and placed into the "wash tank" that is also used as a resting point. As soon as all the tubes are placed inside the drawer system, the "robotic arm/gripper" grabs the first of the two sample carriers, lifts it up and drags it to a predefined distance along the X axis and towards the first row of the tubes. Then it sinks inside the tubes, and a quantity of the stained medium (~1.2μl/rod) is entrapped inside the small opening. Simultaneously, the "sample carrier" moves backwards and stops above the agarose film. Then it moves downwards, until it touches the agarose film, and the stained medium is left on the film's surface, due to the surface tension (fig.1, c). After that the "robotic arm" returns the first "sample carrier" to its initial position ("wash tank") to be washed out, until it is ready to be used again. Immediately, the "robotic arm" grabs the second "sample

carrier" and the same process is repeated until all the samples are safely deposited on the film.

After automatically depositing all samples (up to 30), the "robotic arm" grabs and pushes the "frame/film manipulator" inside the "electrophoresis chamber". The chamber is filled up with electrolyte buffer. The cam-shaft mechanism applies a small force to the lid which in turn compresses the edges of the "frame/film manipulator", and the film's edges are slightly immersed into the electrolyte buffer. Depending on time and voltage settings, the electrophoretic process starts until all the appropriate molecules are separated (fig.2, a). After the electrophoretic separation, the force described above is released, and the "robotic arm" returns the "frame/film manipulator" to its initial position.

The staining/unstaining, drying of the film and the analysis of the samples are procedures of major significance during an electrophoresis process. These procedures can be accomplished inside the shaped chambers described above. The robotic arm moves the "frame/film manipulator" towards X axis, from one box to the other, with the following order: to the "staining-unstaining" box and then to the "drying" box at specific time intervals. Afterwards, the "frame/film manipulator" ends up inside the camera/analysis box for a clear photo of the film by a CMOS camera and a CCTV lens. Eventually, the robotic arm returns the "frame/film manipulator" to its home position and the user pulls out the agarose film.

4. Results of the pilot testing

Based on the above operational process, our effort was to test the reliability of the sample carrier and the electrophoresis chamber. For this pilot experiment the tubes were filled with experimental stained medium (approximately of the same viscosity as of the blood). The "sample carrier" was successfully entrapped and deposited the appropriate quantity of the stained medium on the agarose film. The stained film inserted inside the electrophoresis chamber, where 100Volts were applied for a period of 15 minutes, resulting to the accomplishment of molecular separation of the stained medium. To analyze the results, a picture of the agarose film is captured from the high-resolution CMOS camera kit (fig.1, d), The final photo of the film, were further analysed, and a histogram plot with fraction analysis is illustrated in figure 2, b.

5. Conclusions

A prototype automated electrophoresis system, that can execute electrophoresis processes on precast gel agarose films, has been designed and manufactured. As a next step, the robustness of the machine has been evaluated by executing a full electrophoresis process involving a protein analysis. From the results acquired, the mechanical integrity of the main components of the system has been confirmed. In addition, the full automated electrophoretic process, provides accurate results and minimizes delivery times. The developed prototype system constitutes a major progress as regards to the development of state of the art fully automated electrophoresis systems. Further work in the future will

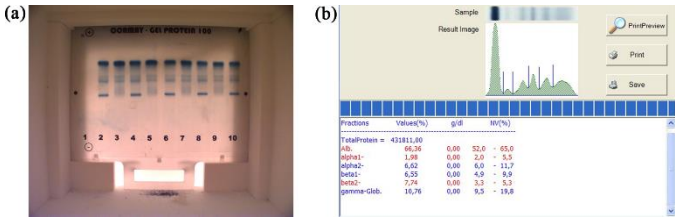

Figure 2, Photo of the film inside the camera/analysis chamber (a), results of the protein analysis (b)

focus on the optimisation of the design in terms of mechanical and electronic design.

Funding

This research has been co-financed by the European Regional Development Fund of the European Union and Greek national funds through the Operational Program Competitiveness, Entrepreneurship and Innovation, under the call RESEARCH–CREATE–INNOVATE (project code: T1EDK-02403)

References

Altria, K., Marsh, A., & Sänger-van de Griend, C. (2006). Capillary electrophoresis for the analysis of small-molecule pharmaceuticals. *ELECTROPHORESIS, 27*(12), 2263-2282. doi: 10.1002/elps.200600030

Aslam, B., Basit, M., Nisar, M. A., Khurshid, M., & Rasool, M. H. (2017). Proteomics: Technologies and Their Applications. *Journal of Chromatographic Science, 55*(2), 182-196. doi: 10.1093/chromsci/bmw167

Bodnar, J., Hajba, L., & Guttman, A. (2016). A fully automated linear polyacrylamide coating and regeneration method for capillary electrophoresis of proteins. *ELECTROPHORESIS, 37*(23-24), 3154-3159. doi: 10.1002/elps.201600405

Durney, B. C., Crihfield, C. L., & Holland, L. A. (2015). Capillary electrophoresis applied to DNA: determining and harnessing sequence and structure to advance bioanalyses (2009–2014). *Analytical and Bioanalytical Chemistry, 407*(23), 6923-6938. doi: 10.1007/s00216-015-8703-5

Holmes, D. L., & Stellwagen, N. C. (1991). Estimation of polyacrylamide gel pore size from Ferguson plots of normal and anomalously migrating DNA fragments. I. Gels containing 3 % N, N′-methylenebisacrylamide. *ELECTROPHORESIS, 12*(4), 253-263. doi: 10.1002/elps.1150120405

Jarvas, G., Guttman, A., Miękus, N., Bączek, T., Jeong, S., Chung, D. S., Pätoprstý, V., Masár, M., Hutta, M., Datinská, V., & Foret, F. (2020). Practical sample pretreatment techniques coupled with capillary electrophoresis for real samples in complex matrices. *TrAC Trends in Analytical Chemistry, 122*, 115702. doi: https://doi.org/10.1016/j.trac.2019.115702

Kendall, J., & Crittenden, E. D. (1923). The Separation of Isotopes. *Proc Natl Acad Sci U S A, 9*(3), 75-78. doi: 10.1073/pnas.9.3.75

Lacher, N. A., Garrison, K. E., Martin, R. S., & Lunte, S. M. (2001). Microchip capillary electrophoresis/ electrochemistry. *ELECTROPHORESIS, 22*(12), 2526-2536. doi: 10.1002/1522-2683(200107)22:12<2526::aid-elps2526>3.0.co;2-k

Longsworth, L. G., Shedlovsky, T., & MacInnes, D. A. (1939). ELECTROPHORETIC PATTERNS OF NORMAL AND PATHOLOGICAL HUMAN BLOOD SERUM AND PLASMA. *The Journal of Experimental Medicine, 70*(4), 399-413. doi: 10.1084/jem.70.4.399

Magdeldin, S., Enany, S., Yoshida, Y., Xu, B., Zhang, Y., Zureena, Z., Lokamani, I., Yaoita, E., & Yamamoto, T. (2014). Basics and recent advances of two dimensional- polyacrylamide gel electrophoresis. *Clinical Proteomics, 11*(1), 16. doi: 10.1186/1559-0275-11-16

Masár, M., Hradski, J., Nováková, M., Szucs, R., Sabo, M., & Matejčík, Š. (2020). Online coupling of microchip electrophoresis with ion mobility spectrometry for direct analysis of complex liquid samples. *Sensors and Actuators B: Chemical, 302*, 127183. doi: https://doi.org/10.1016/j.snb.2019.127183

Nguyen, T. A., Pham, T. N., Doan, T. T., Ta, T. T., Saiz, J., Nguyen, T. Q., Hauser, P. C., & Mai, T. D. (2014). Simple semi-automated portable capillary electrophoresis instrument with contactless conductivity detection for the determination of beta-agonists in pharmaceutical and pig-feed samples. *J Chromatogr A, 1360*, 305-311. doi: 10.1016/j.chroma.2014.07.074

Tiselius, A. (1937). A new apparatus for electrophoretic analysis of colloidal mixtures. *Transactions of the Faraday Society, 33*(0), 524-531. doi: 10.1039/TF9373300524

Vesterberg, O. (1989). History of electrophoretic methods. *Journal of Chromatography A, 480*, 3-19. doi: https://doi.org/10.1016/S0021-9673(01)84276-X

Sauro Pierucci, Flavio Manenti, Giulia Bozzano, Davide Manca (Eds.)
Proceedings of the 30th European Symposium on Computer Aided Process Engineering (ESCAPE30), May 24-27, 2020, Milano, Italy.
http://dx.doi.org/10.1016/B978-0-12-823377-1.50143-9

Integrated Design of Process Configuration and Scheduling for Hydrogen Peroxide Decontamination in Biopharmaceutical Injectable Manufacturing

Keisho Yabuta[a], Haruka Futamura[b], Koji Kawasaki[b], Hirokazu Sugiyama[a,*]

[a]*Department of Chemical System Engineering, The University of Tokyo, 7-3-1, Hongo, Bunkyo-ku, 113-8656, Tokyo, Japan*

[b]*Airex Co., Ltd., 14-13, Tsubaki-cho, Nakamura-ku, Nagoya-shi, 453-0015, Aichi, Japan*

sugiyama@chemsys.t.u-tokyo.ac.jp

Abstract

We present integrated process design and scheduling for hydrogen peroxide decontamination, a time-intensive change-over in biopharmaceutical injectable manufacturing. Models were developed that can (i) configure process parameters, e.g., loading amount of hydrogen peroxide in the isolator, and (ii) deal with the scheduling of filling and change-over of multiple batches/products under shift- and weekend-constraints. Sterility assurance level (SAL) of products and the required time for producing all batches were defined as the objective functions for quality and productivity, respectively. The models were applied to multiobjective optimization of process configuration and scheduling for producing 15 batches consisting of different product numbers, characteristics, and batch sizes. Pareto optimal solutions could be obtained that minimized both objectives. The trade-off became more significant when the product became more vulnerable to the residual hydrogen peroxide after decontamination and the product change-over became more frequent, which is the trend in the industry. Thus, the study motivates collaborative design of process and scheduling for the decontamination process in biopharmaceutical manufacturing.

Keywords: biopharmaceuticals, sterile manufacturing, multiobjective design, change-over, process performance

1. Introduction

In recent years, the number of approval for biopharmaceuticals, e.g., monoclonal antibodies, has increased drastically (Grilo and Mantalaris, 2019). Biopharmaceuticals are provided as injectables, and are produced batch-wise in a sterile environment such as isolator. Among various change-over operations between batches/products, decontamination of isolators is known as time-consuming. Because hydrogen peroxide (H_2O_2) is typically used as a decontaminant, the residual has a potential to oxidize the protein-based products. Figure 1 shows the typical H_2O_2 concentration profile. In the decontamination phase, the concentration increases up to 400 ppm by loading vaporized H_2O_2 into the isolator. In the aeration phase, the concentration is decreased down to a target concentration by ventilation. The process configuration, e.g., H_2O_2 loading amount, influences the level of the sterility assurance and the total time required.

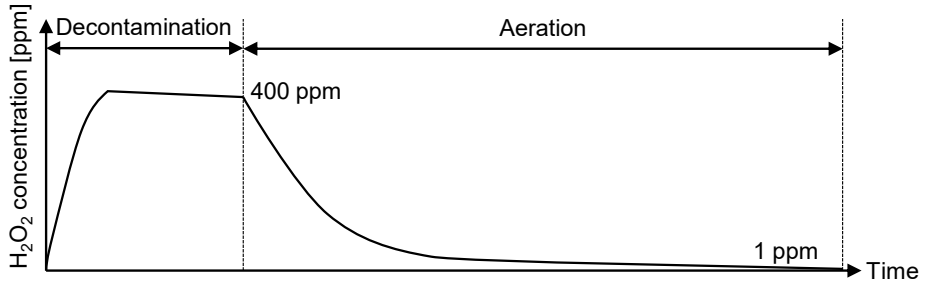

Figure 1. Typical concentration profile of vapor H2O2 in decontamination process (adapted from Yabuta et al., 2018b)

Radl et al. (2009, 2011) presented mechanistic models for describing distribution of H_2O_2 in the isolator considering condensation and absorption. Vuylsteke et al. (2019) developed a mechanistic model for predicting the concentration of H_2O_2 in the product filled after decontamination. We constructed a regression-based model, by progressively expanding the functionality to determine optimal configuration regarding rapidity and sterility (Yabuta et al., 2018a and 2018b). However, these previous studies have been focusing on one-time execution of the process, without considering the scheduling aspect. Thus in this work, we present a novel approach for designing H_2O_2 decontamination processes by integrating parameter configuration and scheduling. The work presents the model development and a case study on multiobjective optimization.

2. Method

2.1. Overview

Figure 2 shows task flow chart for sterile drug product manufacturing. Each task has a task ID *j* from one to seven. Production begins with the conditioning of temperature and humidity in the isolator. Decontamination and aeration are performed sequentially (see Figure 1), and then products are filled. If the next batch is not scheduled, the production ends. Otherwise, cleaning in place (CIP) is conducted for the manufacturing equipment, which is followed by format change if necessary, e.g., if the product of the next batch has a different vial size. If there is an interruption in the time line, e.g., weekend, the next batch is scheduled to a later time, e.g., Monday.

Two indicators are defined for evaluating the impact of the decision-making regarding process configuration and scheduling on productivity and product quality. One is the total time, *T* [h], required for producing the planned batches; the other is sterility assurance level, *SAL* [–]. *SAL* is the probability that a surviving microorganism exists in the product. Smaller values of *SAL* indicate lower probability, and thus are favorable for the product quality.

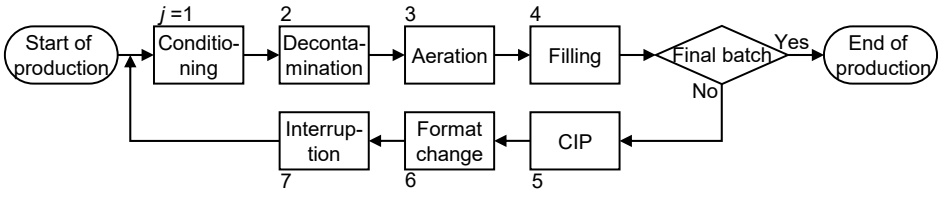

Figure 2. Task flow chart for sterile drug product manufacturing

2.2. Scheduling model

The scheduling model produces T as the objective function of productivity, by summing the durations of all tasks:

$$T = \sum_{n=1}^{nmax} \sum_{j=1}^{jmax} \tau_{n.j} \tag{1}$$

where $nmax$, n, $jmax$, j, and $\tau_{n,j}$ [h] are the total number of batches to be manufactured, the batch number, the total number of tasks, the task ID, and the duration of task j of batch n, respectively. The durations of decontamination and aeration ($\tau_{n,2}$ and $\tau_{n,3}$) are calculated by the decontamination process model explained in section 2.3. Constant values were used for the durations of conditioning, CIP, format change, and interruptions (defined as $\tau_{n,1}$, $\tau_{n,5}$, $\tau_{n,6}$, and $\tau_{n,7}$, respectively). The duration of filling, $\tau_{n,4}$, was converted from the batch size, q_n [vial batch^{-1}], as follows:

$$\tau_{n,4} = N \frac{q_n}{r_{\text{filling}}} \tag{2}$$

where N [–] and r_{filling} [vial h^{-1}] are the number of filling needles in the filling machine and filling rate, respectively.

Two types of input parameters are necessary for calculating T: product-related information and calendar information. Product-related information further consists of a set of batches and the target concentration of aeration. A set of batches is the list of batches to be manufactured, and is used for generating scheduling options by rearranging the production orders based on permutations with repetition. Each batch has information of product type, p_n [–], batch size, q_n, and target concentration, c [ppm]. Product type is used to judge the necessity of format change, i.e., format change is not conducted if p_{n+1} is equal to p_n. The target concentration represents the resistance of the product to oxidation by H_2O_2. While the current standard value is in the neighborhood of 1 ppm, a stricter value would be required for more sensitive products. As for calendar information, a set of days is used. Here, binary parameters distinguish the operation day and the non-operation day, i.e., interruption.

The basic tasks in Figure 2, namely, filling, CIP, format change, and interruption in scheduling, are defined with referring to Eberle et al. (2016). We newly added the durations of conditioning, decontamination, and aeration in this work to highlight more of the decontamination process.

2.3. Decontamination process model

Decontamination process model calculates the durations of decontamination, $\tau_{n,2}$, and aeration, $\tau_{n,3}$, as a part of the productivity objective T. Also, the model yields SAL as the product quality objective. The key variables of decontamination process are the injection rate of H_2O_2aq, x_i [g min^{-1} m^{-3}], and the target concentration, c, in aeration. Typically, the injection rate has stepwise values of x_1 and x_2 with the corresponding time spans of t_{d1} [min] and t_{d2} [min]. The models presented in our previous work (Yabuta et al., 2018b) have been modified to fit to the purpose of the current study:

$$SAL = 10^{6-\frac{t_{d1}+t_{d2}}{3.71-1.72x_1}} \tag{3}$$

$$\tau_{n,2} = \frac{t_{\mathrm{d}1} + t_{\mathrm{d}2}}{60} \tag{4}$$

$$\tau_{n,3} = \begin{cases} \dfrac{-24.2 + 1.39(x_1 t_{\mathrm{d}1} + x_2 t_{\mathrm{d}2}) + 0.765 H_0}{60} & \text{if } c = 1 \text{ ppm} \\ \dfrac{25.7 + 2.93(x_1 t_{\mathrm{d}1} + x_2 t_{\mathrm{d}2})}{60} & \text{if } c = 0.2 \text{ ppm} \end{cases} \tag{5}$$

where H_0 [%] is the relative humidity at the start of decontamination. These regression-based models were developed with experimental results using a medium-size isolator with the volume of 2.4 m^3. Decontamination options can be generated by changing the value of the injection rate x_1.

3. Case study

The models were applied to two design cases where 15 batches consisting of different product characteristics are produced. The design problem is:

$$\begin{cases} \min\limits_{d} SAL(d) \\ \min\limits_{s,d} T(s,d) \end{cases} \tag{6}$$

where d and s are the options of decontamination and scheduling, respectively. Table 1 shows the summary of the input information in the two cases. Case 1 corresponds to small product variety with large scale production, and Case 2 to wide product variety with small scale production, i.e., the future industrial trend. The target concentration set as 1 ppm in Case 1 was reduced to 0.2 ppm in Case 2, to simulate future products that are more vulnerable to the residual H_2O_2. The numbers of the generated scheduling options for Cases 1 and 2 were 3,003 and 6,306,300, respectively. The durations of conditioning, CIP, format change, and interruption ($\tau_{n,1}$, $\tau_{n,5}$, $\tau_{n,6}$, and $\tau_{n,7}$) were set as 0.5, 3, 2, and 48 h, respectively. As for decontamination, 10 options were set by raising the value of x_1 from 1.1 to 1.4 linearly. The filling machine was assumed to have six filling needles with the filling rate of 3,000 vial h^{-1} inside a 2.4 m^3 isolator. Calendar information was defined as the iteration of five operation days and two non-operation days. The operation time in one week was from 0:00 a.m. on Monday (starting point of T) to 12:00 p.m. on Friday with three shifts.

Figure 3 shows the multiobjective evaluation result of Cases 1 and 2. Each marker shows one combination of the scheduling and decontamination options. The scattering of the markers in the horizontal direction is caused by the decontamination options, and that in the vertical direction is caused by the scheduling options. The maximum vertical range was ca. 40 h. The worst points were the options with many format changes.

Table 1. Summary of input information in Cases 1 and 2

	Case 1	Case 2
Total number of batches to be manufactured, *nmax* [–]	15	15
Average batch size, $\overline{q_n}$ [vial]	20,667	14,933
Number of product types [–]	2	4
Target concentration in aeration, c [ppm]	1	0.2
Total number of scheduling options [–]	3,003	6,306,300

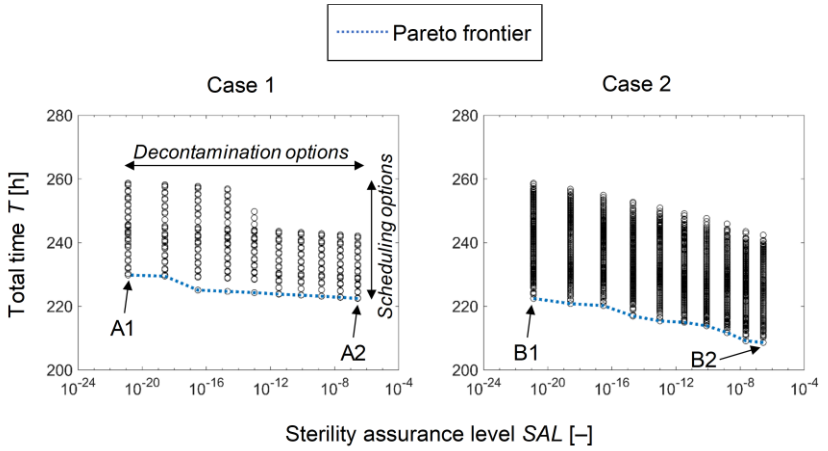

Figure 3. Multiobjective evaluation result

The Pareto frontier is indicated with the dotted line. In both results, the trade-off between *SAL* and *T* was observed, which became more significant in Case 2.

Figure 4 shows the breakdown of *T* at the points of A2 and B1 on the Pareto frontier in Figure 3. For simplification, conditioning, CIP, and format change were summarized as "other change-over". The values of *T* at A2 and B1 were almost the same (ca. 222.4 h) while the values of *SAL* were different (ca. 10^{-6} and 10^{-21}, respectively). The difference in the breakdown of A2 and B1 is in aeration and filling. The contribution of aeration drastically increased from 4.1 % to 16 % while that of filling decreased from 46 % to 34 %.

In order to assess the impact of the choice of the scheduling and decontamination options on the Pareto frontier, ratio *r* was defined as follows:

$$r = \frac{T_1 - T_2}{T_1} \tag{7}$$

where T_1 and T_2 are the leftmost and the shortest *T* (point A1 and B1 in Figure 3), and the rightmost and the shortest *T* (point A2 and B2), respectively. From Case 1 to Case 2, the ratio doubled from 3.2 % to 6.2 %. This result clearly indicates the increasing importance of decontamination in case of (i) strict target concentration, (ii) small batch sizes, and (iii) large number of products. These characteristics are exactly the trend in the biopharmaceutical manufacturing, and thus, integrated design approach of scheduling and decontamination will become more useful.

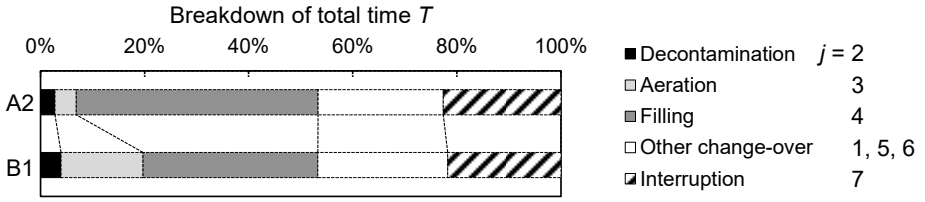

Figure 4. Breakdown of *T* at two points

The CPU time to obtain the results of Case 2, i.e., evaluating ca. 6 million generated options, was 343 s on Matlab® with parallel computing toolbox™ using 6 physical cores of Intel® Core™ i7-8700CPU@3.2GHz with 64.0 GB RAM.

4. Conclusions and outlook

We presented a novel approach for designing H_2O_2 decontamination processes by integrating parameter configuration and scheduling. Models were developed that can configure process parameters and deal with the scheduling of filling and change-over of multiple batches/products. SAL of products and the required time for producing all batches were defined as the objective functions for quality and productivity, respectively. Multiobjective evaluation was performed for two design cases with varying product numbers, characteristics, and batch sizes. Pareto optimal solutions could be obtained that minimized both objectives. The shift of the Pareto frontier was assessed, which indicated the increasing importance of decontamination in case of (i) strict target concentration, (ii) small batch sizes, and (iii) large number of products. This is exactly the trend in the biopharmaceutical industry, and thus, the work motivates collaborative design of process and scheduling for H_2O_2 decontamination in biopharmaceutical manufacturing. For future, more rigorous investigation of the decontamination process will be required, e.g., debottlenecking of aeration by effective removal of H_2O_2. Hybrid modelling would be effective to tackle complicated and dynamic phenomena during the entire process.

Acknowledgements

The authors would like to thank the experts from Airex Co., Ltd. for the contribution in the fruitful discussions. Financial supports by Grant-in-Aid for Young Scientists (A) No. 17H04964 as well as Grant-in-Aid for Research Fellow (DC2) No. 19J14085 from Japan Society for the Promotion of Science are also acknowledged.

References

L. Eberle, E. Capón-García, H. Sugiyama, A. Graser, R. Schmidt, K. Hungerbühler, 2016. Rigorous approach to scheduling of sterile drug product manufacturing, *Comput. Chem. Eng.*, 94, 221–234

A. Grilo and A. Mantalaris, 2019. The increasingly human and profitable monoclonal antibody market, *Trends Biotechnol*., 37, 9–16

S. Radl, S. Ortner, R. Sungkorn, J. G. Khinast, 2009. The engineering of hydrogen peroxide decontamination systems, *J. Pharm. Innov.*, 4, 51–62

S. Radl, S. Larisegger, D. Suzzi, J. G. Khinast, 2011. Quantifying absorption effects during hydrogen peroxide decontamination, *J. Pharm. Innov.*, 6, 202–216

B. Vuylsteke, I. Luyckx, G. de Lannoy, 2019. The diffusion of hydrogen peroxide into the liquid product during filling operations inside vaporous hydrogen peroxide–sterilized isolators can be predicted by a mechanistic model, *J. Pharm. Sci.*, 108, 2527–2533

K. Yabuta, H. Futamura, K. Kawasaki, M. Hirao, H. Sugiyama, 2018a. Models for designing hydrogen peroxide decontamination processes in sterile drug product manufacturing, *Comput. Aided Chem. Eng.*, 43, 1613–1618

K. Yabuta, H. Futamura, K. Kawasaki, M. Hirao, H. Sugiyama, 2018b. Design-oriented regression models for H_2O_2 decontamination processes in sterile drug product manufacturing considering rapidity and sterility, *Int. J. Pharm*., 548, 466–473

Sauro Pierucci, Flavio Manenti, Giulia Bozzano, Davide Manca (Eds.)
Proceedings of the 30th European Symposium on Computer Aided Process Engineering (ESCAPE30), May 24-27, 2020, Milano, Italy.
http://dx.doi.org/10.1016/B978-0-12-823377-1.50144-0

Social Life Cycle Assessment of Pulp and Paper Production – A Portuguese Case Study

Andreia Santos[a,*], Catherine Benoît Norris[b], Ana Barbosa-Póvoa[a], Ana Carvalho[a]

[a]*CEG-IST, Av. Rovisco Pais 1, Lisbon 1049-001, Portugal*
[b]*NewEarth B, Lois Ln, York, Maine 03909, United States of America*
andreia.d.santos@tecnico.ulisboa.pt

Abstract

Due to its size and intense use of resources, the pulp and paper industry is responsible for many devastating environmental impacts such as carbon pollution and wildlife species' extinction. While these environmental impacts have been investigated in numerous studies through environmental life cycle assessment, little attention has been given to the equally devastating social impacts. For this reason, the main goal of this work is to carry out a social life cycle assessment (S-LCA) to quantify the social impacts that a Portuguese pulp and paper supply chain has on its stakeholders. These impacts are aggregated into five different social categories, including labor rights and decent work, community infrastructure, governance, health and safety, and human rights. In this work, data extracted from the Social Hotspots Database accessed through SimaPro will be used. The results of the S-LCA conducted will be discussed to identify which part of the pulp and paper supply chain is responsible for most of the social impacts and which of these impacts are more critical. Based on this discussion, recommendations for improving the social sustainability of the supply chain analyzed will be provided.

Keywords: Social life cycle assessment, Social Hotspot Database, Supply chain, Paper production, Social hotspots

1. Introduction

As one of the largest industrial sectors in the world, the pulp and paper industry is responsible for the intense use of resources, including the consumption of over 40 percent of all industrial wood traded globally. Furthermore, this industry is one of the world's most energy-intensive industries and the single largest consumer of water used in industrial activities in developed countries (WWF, 2019). This intense use of resources, along with unsustainable operations such as discharging pollutants in surrounding water bodies, makes the pulp and paper industry responsible for many devastating environmental impacts. These environmental impacts have been investigated in different studies using the environmental life cycle assessment (E-LCA) methodology including a study by Silva et al. where the environmental impacts associated with offset paper production in Brazil were estimated (Silva, et al., 2015); the work by Santos et al. where the environmental impacts associated with the life cycle of different products, such as tissue paper, produced in Portugal were assessed (Santos, et al., 2018); and the study by Corcelli et al. where an environmental assessment of papermaking from chemical pulp in Finland was conducted (Corcelli, et al., 2018). Besides the environmental impacts, the pulp and paper industry is also responsible for equally devastating social impacts (WWF, 2019). However, contrary to the environmental impacts, little attention has been given to

the social impacts of this industry. Thus, the objective of this paper is to analyze the social impacts associated with the pulp and paper industry using the Portuguese printing and writing paper supply chain as an illustrative case study due to the relevance of this industrial sector in the Portuguese economy. In Portugal, the pulp and paper industry is responsible for 4 % of the gross value added generated by the manufacturing industry, 0.45 % of the gross domestic product, and 4.5 % of all exports (DGAE, 2017). The social impact will be analyzed using the social life cycle assessment (S-LCA) methodology to complement the existing E-LCA of the paper supply chain. The S-LCA will be implemented through the Social Hotspots Database (SHDB) in SimaPro. The remaining of this paper is organized into four sections. In Section 2, the S-LCA methodology and its application through the SHDB are described. In the following sections, the case study is presented (Section 3), and the results of applying the S-LCA methodology through the SHDB to the case study are discussed (Section 4). Finally, in Section 5, the main conclusions and some suggestions for future research are provided.

2. Methodology

Social life cycle assessment is a methodology mostly used to assess the potential social impacts of products along their life cycle from raw materials' extraction to final products' disposal (UNEP/SETAC, 2009). This methodology is similar to the environmental life cycle assessment methodology as both follow the ISO 14040 framework (ISO, 2006). Thus, S-LCA is comprised of four steps (Garrido, 2017):

Goal and Scope Definition – where the main objectives of the study, the functional unit, and the boundary of the product system are defined. The functional unit is a representative element of the system being study and provides a point of reference to quantify the magnitude of the social impacts associated with the product considered.

Inventory Analysis – consists of the collection of data using different indicators through questionnaires, literature review, and/or databases. The Social Hotspots Database is a database developed specifically for the purposes of supporting S-LCA. This database has generic social data for 160 indicators at country and sector levels based on statistics and information issued by governments and international organizations such as the World Health Organization.

Impact Assessment – the social data gathered in the previous step is converted into potential social impacts (named "impact subcategories"). Most S-LCA studies (Wu, et al., 2014) accomplished this by comparing the social data with performance reference points. In the SHDB, the social impacts are mostly determined by comparing the data obtained for each country-specific sector (e.g., data for "sector average wage" in "Wheat sector in China") involved in the product system under study with the worldwide distribution of data on this issue. Based on this comparison, a level of risk (low, medium, high, or very high risk) and a respective characterization factor (0.1, 1, 5, 10) (Benoît-Norris, et al., 2012) is attributed. The processes in a product system, which are more significant (i.e., where more hours of work are invested), will have a higher contribution to each impact subcategory. The labor intensity information is used together with the social risk levels, to express social impacts in terms of medium risk hours equivalent.

Results Interpretation – analysis of the results obtained in the previous step, which includes identifying the most critical social impacts (impact subcategories) and in which country-specific sector this social issue is most likely to arise (social hotspot).

In the next section, the application of the first three steps of the S- LCA methodology to this case study are presented. The last step is presented in Section 4.

3. Case Study

The first industrial process involved in the printing and writing paper production is pulping (i.e., pulp production). Pulp is mainly composed of cellulose fibers, which can be obtained from wood, fiber crops, or recycled paper. In this work, we focus on wood pulp production. After the trees are harvested, their trunks are bucked into logs that are delivered to mills where the logs are debarked and chipped. The next stage consists in separating the cellulose fibers from the other wood components such as lignin (the "glue" that cements the fibers together) and hemicelluloses. Several processes can be used in this stage, but the most common is the Kraft (sulfate) process where the wood chips are mixed and cooked with chemicals, caustic soda (NaOH) and sodium sulfate (Na_2S), and water under high pressure in a digester. The resulting raw pulp has a brown coloration caused by the presence of lignin that was not removed during cooking. The brown-colored raw pulp is then bleached to produce printing and writing paper. To improve the strength and optical properties of the paper, additives are added to the bleached pulp, which is then spread onto a traveling metal screen or plastic mesh (known as the "wire"). Water is drawn through the wire, leaving a web of fibers (paper sheet), which is passed through a series of rotating rolls to squeeze out water and air. The remaining water is removed by floating the sheet through a series of steam-heated rolls. After this stage, the paper sheet is usually wound onto jumbo reels, which can then be processed into smaller reels used for processing into various formats (The Navigator Company, 2019).

Following the methodology presented in the previous section:

Goal and Scope Definition – The main objective of this study is to assess the social impacts of Portuguese printing and writing paper supply chain to identify the critical hotspots. A cradle-to-gate boundary was considered, which includes the stages of the products' life cycle from growing and harvesting trees to paper production (including). The functional unit selected was 1 t of printing and writing paper produced from Kraft pulp.

Inventory Analysis – As mentioned in the previous section, the SHDB has social data for 160 indicators at the country and sector levels. For this reason, to conduct an S-LCA using this database, information on the country and sectors involved in the production of a product are required. The information needed is: 1) the materials used to produce a product, 2) which of the 57 GTAP (Global Trade Analysis Project) sectors the materials belong to, 3) in which country were the materials sourced from, and 4) what is the cost of the materials (Benoît-Norris, et al., 2018). Table 1 presents this information for the case study analyzed.

Table 1 - Main materials involved in the production of printing and writing paper

Materials	Costs (%)	GTAP Sector	Portugal	France	Germany	Spain	UK	USA	Algeria	Turkey
Wood	32 %	FRS	86.44 %	1.08 %	-	9.85 %	-	0.73 %	-	-
Chemicals	27 %	CHM	44.44 %	4.56 %	4.67 %	23.03 %	4.18 %	-	-	3.53 %
Water	18 %	WTR	100.0 %	-	-	-	-	-	-	-
Electricity	21 %	ELY	82.82 %	-	-	17.2 %	-	-		-
Fuels	3 %	GAS	0.0 %	-	-	77.84 %	-	-	22.16 %	-

The costs related to each one of the main materials identified in Table 1 were supplied by a Portuguese company operating in the printing and writing industrial sector. Due to the confidential nature of cost-related information, this data is shown in the table for each material as a percentage of the total production cost. The GTAP sectors involved in paper

production are forestry (FRS), chemicals (CHM), water supply (WTR), electricity (ELY), and gas (GAS). To determine from which countries the main materials were sourced, the atlas of economic complexity was used considering a cut-off of 5% (i.e., countries that contributed less than 5% in the importation share were not included). From the countries identified in Table 1, the SHDB does not have data available for Algeria. For this reason, we use its neighboring country Morocco to approximate the social context of natural gas production.

Impact Assessment – The SHDB is used to conduct this step of the S-LCA. This database includes information on 146 indicators covering 24 impact subcategories aggregated into 5 impact categories: (1) Labor Rights & Decent Work, (2) Health & Safety, (3) Human Rights), (4) Governance), and (5) Community.

4. Results

From the application of the S-LCA methodology to the case study using the SHDB, different results were obtained for the different indicators, subcategories, and impact categories. Figure 2 presents, for each impact category, the percentage of social impacts that they are responsible for.

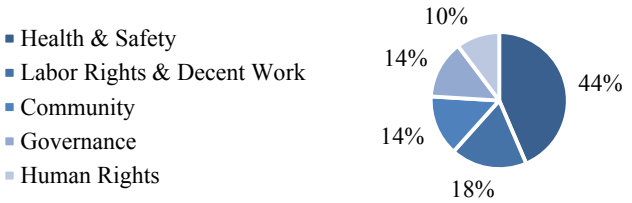

Figure 1 - Percentage of overall social impacts per impact category.

From the analysis of Figure 1, it can be concluded that the most critical social issues in the Portuguese printing and writing supply chain are related to health & safety, and labor rights & decent work. To analyze these issues in more detail, the contribution of each of the two impact subcategories that contribute to the health & safety and the contribution of each of the 11 impact subcategories that contribute to the labor rights & decent work is investigated (see Figure 2 and Figure 3).

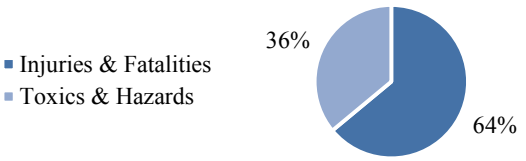

Figure 2 - Contribution of each of the two impact subcategories that contribute to the health & safety impact category.

From the analysis of Figure 2, it can be concluded that the most critical social issues in the Portuguese printing and writing supply chain related to health & safety belong to the Injuries and Fatalities impact subcategory. Each impact subcategory is categorized according to an indicator or a set of indicators that represent different social issues. The SHDB contains information for these indicators at a country and sector level. For the Injuries and Fatalities impact subcategory, the social issues addressed are the risk of having a fatal or non-fatal injury.

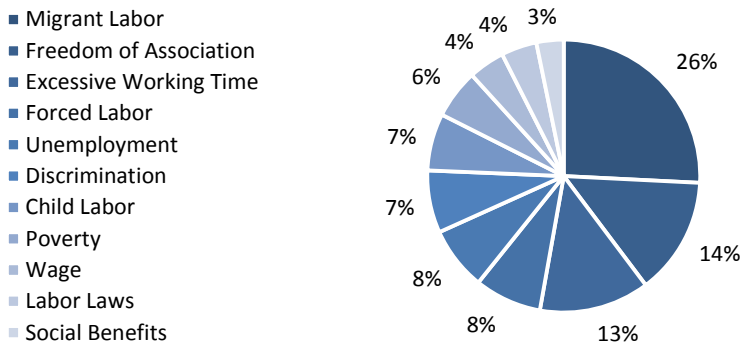

Figure 3 - Contribution of each of the 11 impact subcategories that contribute to the labor rights & decent work impact category.

From the analysis of Figure 3, it can be concluded that the most critical social issues in the Portuguese printing and writing supply chain related to labor rights & decent work belong to the Migrant Labor, Freedom of Association, and Excessive Working Time impact subcategories. The social issues addressed by these impact categories are the evidence of risk to migrant workers, the risk of not having the freedom of association, and the risk of having a high percentage of the population working more than 60 hours a week, respectively.

Figure 4 represents the contribution of each country and sector involved in the Portuguese printing and writing paper production to the four critical impact subcategories identified.

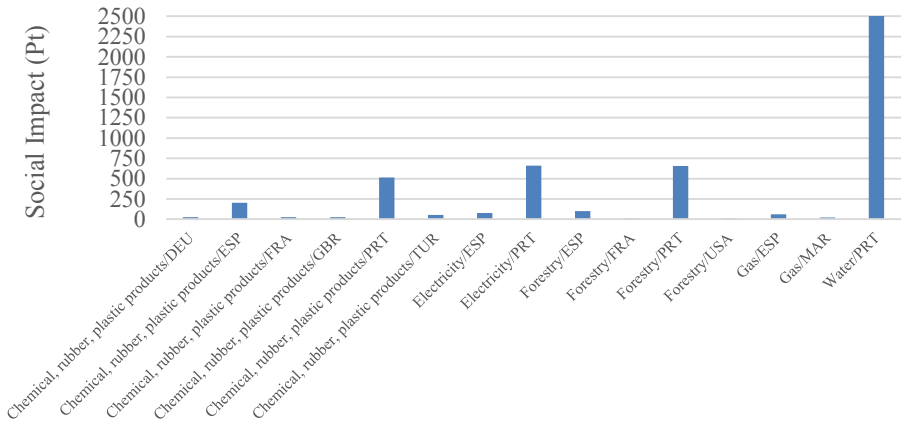

Figure 4 - Contribution of each country and sector involved in the Portuguese printing and writing paper production to the four critical impact subcategories.

From Figure 4, it is possible to conclude that the social impacts associated with the four most critical impact subcategories can be attributed to the Portuguese sectors since most of the materials used in the production of Portuguese printing and writing paper are produced in Portugal. Therefore, the social impacts associated with this region have a greater weight in the overall social impacts associated with the system under study in comparison with other countries included in the analysis, such as Spain, for example.

Consequently, the Portuguese printing and writing paper industrial sector can show rapid improvements if it addresses the social issues within the country, primarily in the arena of health and safety (the most critical impact category).

5. Conclusions

Although some research exists where E-LCA was applied to the paper industry, there was no literature found where the S-LCA was applied to the same industry. This work provided the first step in closing this gap by applying the S-LCA methodology through the SHDB to the Portuguese pulp and paper industry. Most social impacts identified were related to health & safety and labor rights & decent work issues mostly attributed to the Portuguese sectors. To improve its social impacts, the Portuguese printing and writing paper industrial sector should address the social issues within the country, including, among others, the risk of having a fatal or non-fatal injury.

This data could be used by different Portuguese companies that operate in the pulp and paper industry to benchmark the social impacts of their operations and determine whether they are performing better or worst them the national average. Future work should include the integration of environmental and social life cycle assessment to identify the impacts and hotspots of this industry from these two sustainability dimensions.

Acknowledgments

The authors gratefully acknowledge the project funding (PTDC/AGR-FOR/2178/2014_LISBOA-01-0145-FEDER-016733) and Ph.D. grant SFRH/BD/134479/2017.

References

Benoît-Norris, C., Bennema, M. & Norris, G., 2018. *The Social Hotspots Database,* Maine, USA: NewEarth B.

Benoît-Norris, C., Cavan, D. A. & Norris, G. A., 2012. Identifying Social Impacts in Product Supply Chains - Overview and Application of the Social Hotspot Database. *Sustainability,* 4(9), pp. 1946-1965.

Corcelli, F., Fiorentino, G., Vehmas, J. & Ulgiati, S., 2018. Energy efficiency and environmental assessment of papermaking from chemical pulp - A Finland case study. *Journal of Cleaner Production,* pp. 96-111.

DGAE, 2017. *Síntese de Indicadores Económicos.* [Online] Available at: https://www.dgae.gov.pt/documentacao/estatisticas/sintese-de-indicadores-economicos.aspx [Accessed 29 November 2019].

Garrido, S. R., 2017. Social Life-Cycle Assessment - An Introduction. *Encyclopedia of Sustainable Technologies,* pp. 253-265.

ISO, 2006. *Life Cycle Assessment – Principles and Framework,* Geneva, Switzerland: International Organization of Standardization.

Santos, A., Barbosa-Póvoa, A. & Carvalho, A., 2018. Life cycle assessment of pulp and paper production – A Portuguese case study. In: A. Friedl, et al. eds. *28th European Symposium on Computer Aided Process Engineering.* Graz, Austria: s.n., pp. 809-814.

Silva, D. A. L., Pavan, A. L. R., Oliveira, J. A. & Ometto, A. R., 2015. Life cycle assessment of offset paper production in Brazil - hotspots and cleaner production alternatives. *Journal of Cleaner Production,* 15 April, Volume 93, pp. 222-233.

The Navigator Company, 2019. *How paper is made.* [Online] Available at: http://en.thenavigatorcompany.com/Pulp-and-Paper/Paper/How-Paper-is-Made [Accessed 30 November 2019].

UNEP/SETAC, 2009. *Guidelines for Social Life Cycle Assessment of Products,* Paris, France: United Nations Environment Programme.

Wu, S., Yang, D. & Chen, J., 2014. Social life cycle assessment revisited. *Sustainability,* 6(7), p. 4200–4226.

WWF, 2019. *Pulp and Paper - Overview.* [Online] Available at: https://www.worldwildlife.org/industries/pulp-and-paper [Accessed 29 November 2019].

Sauro Pierucci, Flavio Manenti, Giulia Bozzano, Davide Manca (Eds.)
Proceedings of the 30th European Symposium on Computer Aided Process Engineering (ESCAPE30), May 24-27, 2020, Milano, Italy.
http://dx.doi.org/10.1016/B978-0-12-823377-1.50145-2

Determining the Design Parameters of Reactive Distillation Processes by a Quick Mapping Method

Rahma Muthia,[a] Megan Jobson,[a] Anton A. Kiss[a,b]

[a] *Department of Chemical Engineering & Analytical Science, The University of Manchester, Sackville St, Manchester, M13 9PL, United Kingdom*
[b] *Sustainable Process Technology, Faculty of Science and Technology, University of Twente, PO Box 217, 7500 AE Enschede, The Netherlands*
tony.kiss@manchester.ac.uk

Abstract

The application of reactive distillation in the chemical process industry promises significant benefits, such as boosting energy efficiency and reducing the overall cost. However, assessing and designing a reactive distillation process is still challenging as these tasks usually demand time-consuming procedures. To overcome this problem, the present work proposes a quick approach to determine the design parameters for a kinetically-controlled reactive distillation process according to the ratio between the Damköhler (Da) number and the chemical equilibrium constant (K_{eq}) – thus relating reaction kinetics and chemical equilibrium. This study employs a mapping method featuring an applicability graph that conveniently plots the reflux ratio vs. the number of theoretical stages and extends it to account for kinetically-controlled reactions. The method is demonstrated using the map for a generic quaternary reaction system, described as A + B ⇌ C + D, considering constant relative volatilities (α_{AB} = 2 and α_{CD} = 6) and various reaction equilibrium constants (K_{eq} = 0.01, 0.1, 1). For validation purposes, the applicability of reactive distillation is examined in two case studies – hydrolysis of methyl lactate and synthesis of methyl acetate. Modelling of both the generic and real systems suggests that, with a ratio Da/K_{eq} of 5 or more, the generic map can provide initial values for the design parameters of a reactive distillation column. Ultimately, the insights gained save time in effectively assessing the feasibility of reactive distillation at the conceptual design stage.

Keywords: reactive distillation, mapping method, Damköhler number, equilibrium constant, conceptual process design.

1. Introduction

Reactive distillation is an attractive and efficient process intensification method in the chemical industries. This technology combines reaction and separation functions in a single distillation column; the reaction converts feeds to products, while simultaneous separation enables removal of products. Reactive distillation has many advantages, such as reducing cost and energy consumption, enhancing conversion and selectivity, and overcoming unwanted azeotropes (Luyben and Yu, 2008). To gain these benefits, appropriate parameters for column design (e.g. number of stages, reflux ratio, liquid residence time and catalyst loading) must be determined. Over-design might result in an expensive and ineffective unit, while poor selection of the design parameters can lead to weak separation and reaction performance, or even an infeasible design. Therefore, a

good understanding of the interplay between the design parameters of reactive distillation is crucial at the early phase of conceptual design.

The present work proposes a quick approach to determine the design parameters of reactive distillation using the simple ratio of the Damköhler (Da) number over the chemical equilibrium constant (K_{eq}), along with a mapping method for RD applicability. The work aims to find whether the generic maps can be applied for kinetically-controlled reactions, characterized in terms of the Da/K_{eq} ratio, to narrow the range of possible reactive distillation design parameters, namely liquid residence time, catalyst selection and catalyst loading. In this case, these inputs for reactive column design could expedite development of feasible designs.

2. Problem statement

For almost a century, reactive distillation columns have been designed and optimized, but reactive distillation design, simulation and evaluation remains time consuming (Li et al., 2016): obtaining a feasible reactive distillation column is not an easy or quick task, while column optimization is even more demanding. To overcome this problem, this work employs a mapping method to provide a rule of thumb for the ratio Da/K_{eq} that guides engineers to quickly determine the liquid residence time, catalyst selection (affecting kinetics) and catalyst loading for designing a reactive distillation column.

3. Overall approach to determine reactive distillation design parameters

3.1. Overview of the mapping method

The mapping method was originally introduced to visualize the applicability of equilibrium-controlled reactive distillation, using pre-defined applicability graphs of generic cases (Muthia et al., 2018a, 2018b). The method was then employed for preliminary economic ranking of RD designs and to investigate the feed locations of RD columns (Muthia et al., 2019). The mapping method utilizes a so-called applicability graph for RD, i.e., a plot of reflux ratio (RR) vs. the number of theoretical stages (NTS), depicted in Figure 1(a). A boundary line limits the applicability area of reactive distillation for products of specified purity (99 mol% in this study). The applicability graph, generated using Aspen Plus process simulator and displayed in Figure 1(a) for a quaternary system, A + B ⇌ C + D, approximates the region of feasible operation for a single reactive distillation column – see RD configuration in Figure 1(b).

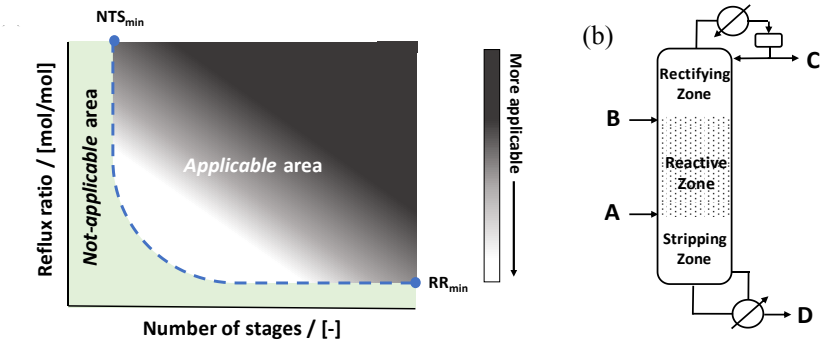

graph of reactive distillation used in the mapping method, and (b) a schematic reactive distillation column.

3.2. Use of mapping method to select the Da/K_{eq} ratio

The mapping method graphically correlates the performance of equilibrium-controlled reactive distillation processes, where each stage achieves the maximum possible conversion. This work extends the approach to consider kinetically-controlled reactions, where a smaller applicability area is observed (Muthia et al., 2018b). Finite reaction rates limit conversion on each stage, for example due to poor catalyst selection, poor catalyst performance, insufficient quantity of catalyst, or insufficient liquid residence time. The dimensionless Damköhler number, Da, captures these issues quantitatively:

$$Da = k_f \cdot M_r \cdot \beta \cdot \tau \tag{1}$$

where k_f is the forward reaction rate constant (mol g_{cat}^{-1} min^{-1}), M_r the average molar mass of components ($g_{mixture}$ mol^{-1}), β the catalyst loading (g_{cat} $g_{mixture}^{-1}$) and τ the liquid residence time per stage (min). The Da number is defined in terms of average conditions in the column. A large Da value improves the performance of reactive distillation, increasing the applicability area, and *vice versa*. Moreover, when Da is large enough, the applicability area is similar to that of an equilibrium-controlled operation. Therefore, it is crucial to find a quick approach to estimate what Da number is 'large enough'. To do so, the sensitivity of the applicability area to the ratio Da/K_{eq} is explored.

In this work, two groups of generic quaternary systems with different volatility orders are chosen: group I_p ($T_{b,C} < T_{b,A} < T_{b,B} < T_{b,D}$) and group III_p ($T_{b,C} < T_{b,A} < T_{b,D} < T_{b,B}$). The classification follows the convention proposed by Luyben and Yu (2008). The two selected groups are beneficial in chemical industries because products can be easily collected at the top and bottom streams of a reactive distillation column. Here, constant relative volatilities ($\alpha_{AB} = 2$ and $\alpha_{CD} = 6$) and a range of fixed equilibrium constants (K_{eq} = 0.01, 0.1, 1) are assumed.

To validate the approach, two case studies are investigated – hydrolysis of methyl lactate and synthesis of methyl acetate by esterification; these represent typical non-ideal systems relevant to the chemical industries. As in Muthia et al. (2018b), the representative Damköhler number and chemical equilibrium constant in the case studies are calculated at the average boiling point of the reactants.

4. Results and discussion

4.1. Assessment of generic cases

Group I_p ($T_{b,C} < T_{b,A} < T_{b,B} < T_{b,D}$) is the predominant class of quaternary systems for the application of reactive distillation, as the products are the lightest and the heaviest compounds. Therefore, high purity products can be anticipated in the top and bottom outlets. In this assessment, relative volatilities α_{CA} and α_{BD} are set to 2.0 and 1.5, respectively, to be consistent with the specified volatilies $\alpha_{AB} = 2$, $\alpha_{CD} = 6$).

Figure 2 depicts the applicability graphs of group I_p in equilibrium-controlled and kinetically-controlled conditions, for values of the chemical equilibrium constants of 0.01, 0.1 and 1, respectively. For each graph, the equilibrium-limited case gives the largest applicability area (bounded by the solid line), as expected. Other lines indicate the applicability boundaries for kinetically-controlled reactive distillation processes. Clearly, the applicability area for RD decreases as the ratio Da/K_{eq} (i.e. the Damköhler number) is reduced.

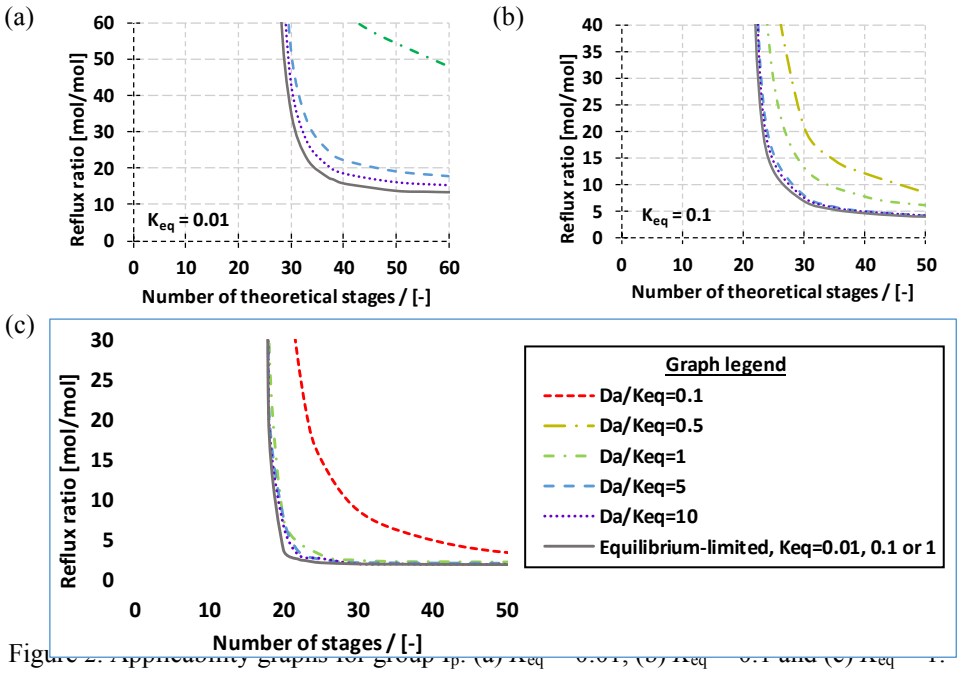

Figure 2. Applicability graphs for group I_p: (a) K_{eq} = 0.01, (b) K_{eq} = 0.1 and (c) K_{eq} = 1.

The applicability area is determined as the ratio Da/K_{eq} is varied from 0.1 to 10; Figure 2 shows that the high Da/K_{eq} ratios have a similar applicability area to that of equilibrium-controlled columns. The applicability bounds are almost equivalent when Da/K_{eq} is at least 5, except where the equilibrium constant is relatively low (e.g. K_{eq} = 0.01). In general, as K_{eq} increases, the kinetically-controlled and equilibrium-controlled boundaries become more similar. It is conclused that, in this case, Da/K_{eq} = 5 can be used as an initial criterion for determining reactive distillation design parameters.

Next, the assessment is performed for another group of quaternary systems – group III_p ($T_{b,C} < T_{b,A} < T_{b,D} < T_{b,B}$), with relative volatilities α_{CA} = 4, α_{AD} = 1.5 and α_{DB} = 1.4. That product D is an intermediate-boiling compound in the reactive distillation column potentially causes more reaction and separation challenges, relative to group I_p. Hence, the number of theoretical stages and reflux ratio of a reactive distillation column for this group are usually larger than those for group I_p (Muthia et al., 2018a, 2019).

Figure 3 depicts the applicability graphs of group III_p for chemical equilibrium constants of 0.01, 0.1 and 1. The application of reactive distillation is not beneficial for K_{eq} = 0.01 as the minimum reflux ratio is too high to be practical (RR_{min} > 50); therefore, this assessment only concerns chemical equilibrium constants of 0.1 and 1. As observed for group I_p, Da/K_{eq} values of 5 or greater have applicability areas that are only slightly smaller than those for equilibrium-limited reactive distillation. Again, for lower values of the equilibrium constant, the kinetically-controlled column under-performs more. An initial criterion for selecting reactive distillation design parameters is to design for Da/K_{eq} ≥ 5; this finding is consistent with that for group I_p.

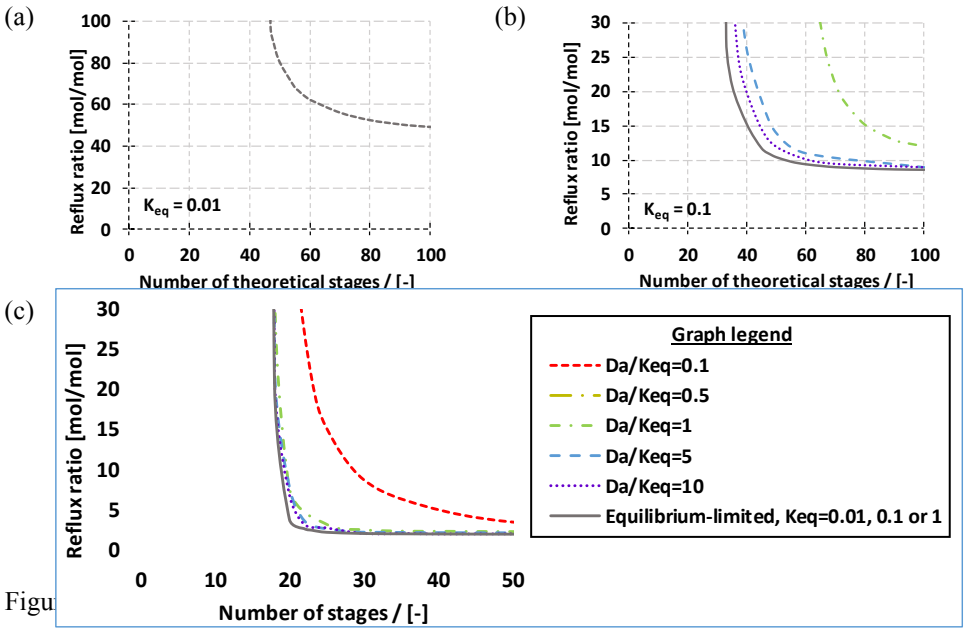

Figu

4.2. Case studies

Figure 2 and Figure 3 demonstrate the approach for generic cases, where relative volatilities and the equilibrium constant are assumed constant in the column. Two case studies aim to validate the findings for the generic cases: hydrolysis of methyl lactate (Eq. 2) and synthesis of methyl acetate by esterification (Eq. 3), representing groups I_p and III_p, respectively. Unlike ideal generic systems, the azeotropes present in these cases are expected to hinder the reactive distillation.

	Water **(A)** + methyl lactate **(B)** ⇌ methanol **(C)** + lactic acid **(D)**				(2)
T_b (°C)	100	144.8	64.7	216.9	

	Methanol **(A)** + acetic acid **(B)** ⇌ methyl acetate **(C)** + water **(D)**				(3)
T_b (°C)	64.7	118	56.9	100	

Sanz et al. (2004) present temperature-dependent K_{eq} and k_f (mol g_{cat}^{-1} min^{-1}) relationships for the hydrolysis of methyl lactate, where an azeotrope forms between water (97 mol%) and methyl lactate (3 mol%) at 99.8 °C.

$$\ln(K_{eq}) = 2.6 - 1954.2/T \tag{4}$$

$$k_f = 1.65 \cdot 10^5 \cdot \exp(-50{,}910/R \cdot T) \tag{5}$$

In the second case, two homogeneous azeotropes exist (methyl acetate (65.9 mol%)–methanol (34.1 mol%) at 53.7°C and methyl acetate (89 mol%)–water (11 mol%) at 56.4 °C. Pöpken et al. (2000) present correlations for K_{eq} and k_f (mol g_{cat}^{-1} min^{-1}) as:

$$\ln(K_{eq}) = -3.82 + 2408.65/T \tag{6}$$

$$k_f = 4.94 \cdot 10^2 \cdot \exp(-49{,}190/R \cdot T) \tag{7}$$

Figure 4 presents reactive distillation applicability graphs for both case studies generated via extensive simulation studies using Aspen Plus. It may be observed that the proposal to use $Da/K_{eq} \geq 5$ as an initial criterion for designing a reactive distillation

column applies very well: in both cases, the boundary line of the applicability region is very close to that in equilibrium-controlled conditions.

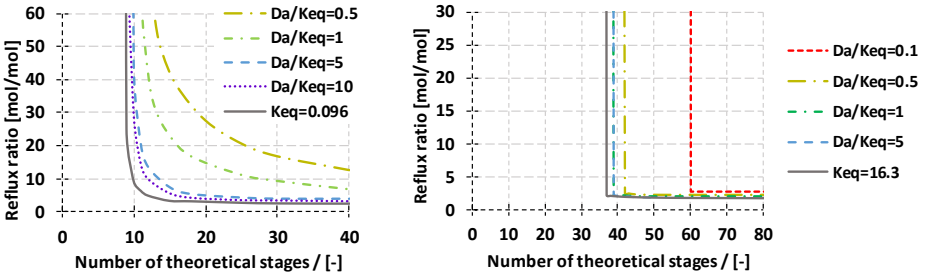

Figure 4. Applicability graphs for validation studies: (a) Hydrolysis of methyl lactate; (b) Synthesis of methyl acetate

5. Conclusions

The mapping method has been successfully employed to visualize the performance of reactive distillation in equilibrium-limited and kinetically-controlled reactions. This work proposes $Da/K_{eq} \geq 5$ as a criterion to initialise reactive distillation design parameters, namely liquid residence time, catalyst selection and catalyst loading, for groups I_p and III_p. This approach should enable the range of design parameters selection to be narrowed, to avoid time-consuming exploration of options at the conceptual design stage. This heuristic may also be useful for other groups of quaternary systems.

Acknowledgements

RM gratefully acknowledges full fund support from LPDP (Indonesia Endowment Fund for Education). AAK is thankful for the Royal Society Wolfson Research Merit Award.

References

H. Li, Y. Meng, X. Li, X. Gao, 2016, A fixed point methodology for the design of reactive distillation, Chemical Engineering Research and Design, 111, 479-491.

W. L. Luyben and C.-C. Yu, 2008, Effects of Boiling Point Rankings on the Design of Reactive Distillation, Reactive Distillation Design and Control, 487-518, USA, John Wiley & Sons Ltd.

R. Muthia, A. G. J. van der Ham, A. A. Kiss, 2018a, Preliminary economic ranking of reactive distillation processes using a navigation method, Computer Aided Chemical Engineering, 43, 827-832.

R. Muthia, A. G. T. Reijneveld, A. G. J. van der Ham, A. J. B. ten Kate, G. Bargeman, S. R. A. Kersten, A. A. Kiss, 2018b, Novel method for mapping the applicability of reactive distillation, Chemical Engineering and Processing: Process Intensification, 128, 263-275.

R. Muthia, A. G. J. van der Ham, M. Jobson, A. A. Kiss, 2019, Effect of boiling point rankings and feed locations on the applicability of reactive distillation to quaternary systems, Chemical Engineering Research and Design, 145, 184-193.

T. Pöpken, L. Götze, J. Gmehling, 2000, Reaction kinetics and chemical equilibrium of homogeneously and heterogeneously catalyzed acetic acid esterification with methanol and methyl acetate hydrolysis, Industrial & Engineering Chemistry Research, 39, 2601-2611.

M. T. Sanz, R. Murga, S. Beltrán, J. L. Cabezas, J. Coca, 2004, Kinetic study for the reactive system of lactic acid esterification with methanol: methyl lactate hydrolysis reaction, Industrial & Engineering Chemistry Research, 43, 2049-2053.

Sauro Pierucci, Flavio Manenti, Giulia Bozzano, Davide Manca (Eds.)
Proceedings of the 30th European Symposium on Computer Aided Process Engineering (ESCAPE30), May 24-27, 2020, Milano, Italy.
http://dx.doi.org/10.1016/B978-0-12-823377-1.50146-4

Conceptual Design Based on Superstructure Optimization in GAMS with Accurate Thermodynamic Models

David Krone[a], Erik Esche[a], Norbert Asprion[b], Mirko Skiborowski[c], Jens-Uwe Repke[a]

[a]*Technische Universität Berlin, Process Dynamics and Operations Group, Straße des 17. Juni 135, 10623 Berlin, Germany*
[b]*BASF SE, Chemical Process Modeling, Carl-Bosch-Strasse 38, 67056 Ludwigshafen am Rhein, Germany*
[c]*TU Dortmund University, Department of Chemical and Biochemical Engineering, Laboratory of Fluid Separations, Emil-Figge-Straße 70, 44227 Dortmund, Germany*
david.krone@tu-berlin.de

Abstract

Conceptual design based on superstructure optimization is a complex task that neither commercial simulators nor dedicated modeling and optimization environments like GAMS, AMPL, and AIMMS are able to perform well by themselves: the first lack interfaces to state-of-the-art solvers, the latter do not provide accurate thermodynamic models. While previous research shows that GAMS can be interfaced with an external thermo engine, this interfacing requires additional C++ code, whose manual generation and consistent implementation is tedious, making the approach both error prone and impractical for larger design problems. By using MOSAICmodeling as a modeling environment, this shortcoming of the existing approach is eliminated by automatically generating all code needed for interfacing GAMS with an external CAPE-OPEN thermodynamic property package.

Keywords: conceptual design, automated code generation, CAPE-OPEN

1. Introduction

Conceptual design based on superstructure optimization involving nonlinear process models remains a challenging task. Commercial simulators do not allow for the formulation and optimization of large-scale superstructure models or do not have interfaces to suitable solvers, whereas dedicated modeling and optimization environments like GAMS, AMPL, and AIMMS do not provide accurate thermodynamic models, which are required to properly describe the behavior of a multicomponent system. Several authors have shown how to interface GAMS with accurate thermodynamic models, e.g., by using external equations (Skiborowski et al., 2015) or extrinsic functions (Manassaldi et al., 2019). Both approaches depend on additional C++ code which is compiled as a dynamic link library (DLL). However, a successful application of these approaches for the optimization of complex process models in GAMS, like the ones for conceptual design, is still hampered by the manual generation of the code for the DLL.

This shortcoming is addressed in this contribution as we demonstrate an enhancement of the approach by Skiborowski et al. (2015), in which the code necessary for interfacing GAMS with accurate thermodynamic models via CAPE-OPEN is generated

automatically. This is achieved by a combination of a robust implementation of an equilibrium stage-based process model and the novel CAPE-OPEN Binary Interop Architecture (COBIA). The process model in GAMS and the additional C++ files for incorporating thermodynamics via COBIA are generated automatically by MOSAICmodeling (Technische Univerisät Berlin, 2019) via separate user-defined language specifications (UDLS). The concept of UDLS is described in detail in Tolksdorf et al. (2019). We demonstrate the ability of the automated code generation by presenting the results from a case study of the separation of the ternary mixture *n*-pentane, *n*-hexane and *n*-heptane by a sequence of vapor-liquid equilibrium-stage models, in which the resulting NLP is solved in GAMS using thermodynamic calculations in TEA (AmsterCHEM, 2019).

This work is an intermediate step towards a fully automated optimization-based approach for conceptual design, in which the MINLP describing the superstructure of a process network is solved in GAMS. Within this contribution, a superstructure formulation is employed, but optimization problems are reduced to NLP form by specifying the structural / binary variables within MOSAICmodeling prior to code export. Hence, the following sections focus on the development of the underlying robust superstructure that is used to create the NLP for the case study in hand.

2. Optimization Approach and Implementation

A state-space representation for the superstructure of a process network is chosen, originally introduced by Bagajewicz and Manousiouthakis (1992). Several equilibrium-stage-based vapor-liquid-separation-units (VL-U) are assembled into the superstructure by connecting their input and output streams to a distribution network that defines the interconnections between the separation units by a set of binary variables. Similar to the approach of Kuhlmann and Skiborowski (2017), inlet streams to the distribution network are allowed to be only split twice, in order to reduce the combinatoric complexity of the overall problem. The VL-U models are based on MESH equations, single phase enthalpies and distribution coefficients are implemented as external functions, which are formulated separately. A VL-U with an exemplary number of four equilibrium stages and a superstructure that connects six of those VL-Us for the separation of a ternary mixture of components A, B, and C is shown in Fig. 1.

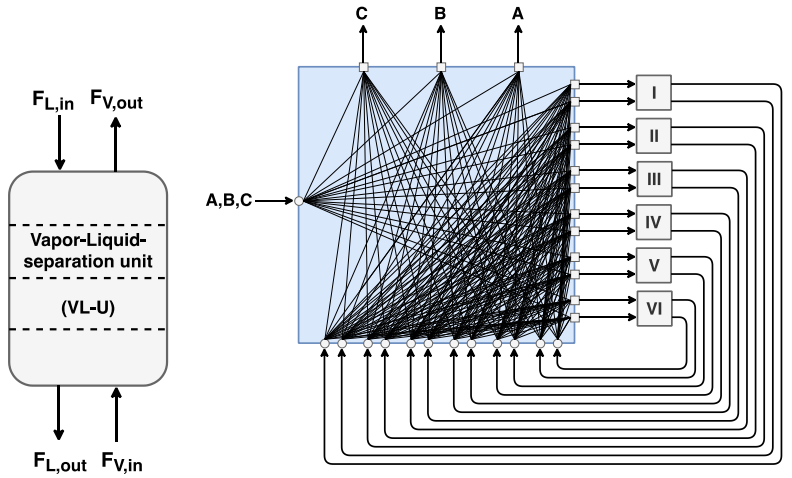

Figure 1: Vapor-liquid-separation unit (VL-U) and superstructure of six VL-Us

The figure shows all possible stream connections in the distribution network. The remainder of this section focuses on the three major features that are implemented in our approach to ensure both successful interfacing with the external thermodynamic property package and robust convergence of the superstructure during optimization in GAMS.

2.1. Robust superstructure formulation

By nature, superstructures for optimization-based conceptual design are highly complex systems. Applying the approach to complex distillation configurations, VLE models like the VL-U can frequently break down, i.e., in intermediate solutions there is no vapor or no liquid, or no phase at all present in some parts of the column. Model validity from "all liquid" to "all vapor" conditions is ensured in this approach by a robust formulation of the superstructure, relaxing all existing VLE by introducing additional complementary constraints (Gopal and Biegler, 1999), leading to the following model equations that describe the phase equilibrium on the ith stage of one VL-U

$$y_{\mathrm{i,j}} = \beta_{\mathrm{i}} \cdot K_{\mathrm{i,j}} \cdot x_{\mathrm{i,j}}, \tag{1}$$

$$\beta_i - 1 = s_i^V - s_i^L, \tag{2}$$

$$s_i^L \cdot F_i^L = 0, \tag{3}$$

$$s_i^V \cdot F_i^V = 0, \tag{4}$$

$$F_i^L, F_i^V, s_i^L, s_i^V \geq 0. \tag{5}$$

$$0 \leq x_{i,j}, y_{i,j} \leq 1 \tag{6}$$

The phase equilibrium (1) is updated by introducing the corrector β_{i} and adding complementarity constraints given by (3), (4), and (5). These constraints make sure that either the flow of a phase or its corresponding slack variable is at zero. Hence, if one phase disappears, the complementary constraint ensures that the corresponding slack variable takes a positive value. Then, via Eq. (2), β_{i} has a value different from one and the VLE is relaxed.

For a consistently robust behavior at phase transitions, NCP functions (3) and (4) are themselves relaxed by an inexact smoothening technique, while (5) is removed (Kanzow and Schwartz, 2013), resulting in the following updated versions:

$$(s_i^L + t_i) \cdot (F_i^L + t_i) - (t_i)^2 \geq 0, \tag{7}$$

$$s_i^L \cdot F_i^L - (t_i)^2 \leq 0, \tag{8}$$

$$(s_i^V + t_i) \cdot (F_i^V + t_i) - (t_i)^2 \geq 0, \tag{9}$$

$$s_i^V \cdot F_i^V - (t_i)^2 \leq 0. \tag{10}$$

Hence, during optimization a sequence of the same problems is solved while parameter t_i is reduced until reaching a small tolerance of, e.g., 1e-7. By this formulation, we can

ensure that any requests for thermodynamic calculations to the external thermo engine are both always feasible and do not lead to issues with problem convergence, while at the same time providing accurate derivatives to GAMS.

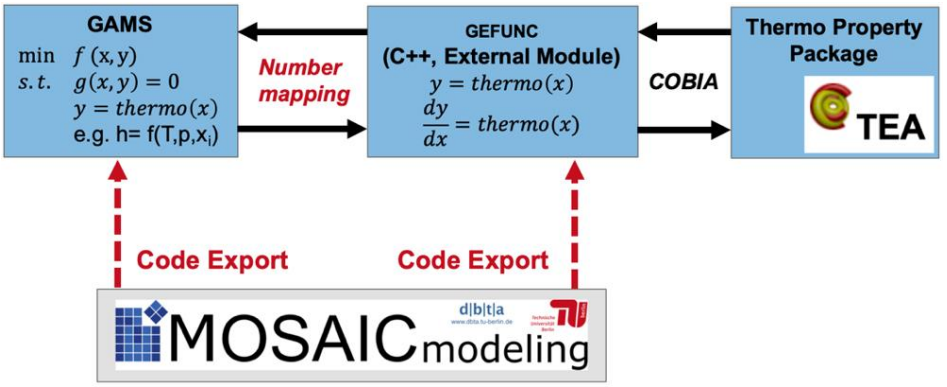

Figure 2: Interface between GAMS and a CAPE-OPEN property package

2.2. Interfacing GAMS with a CAPE-OPEN property package

Accurate thermodynamic property calculations are performed by a CAPE-OPEN thermo property package and provided to GAMS via the interface shown in Fig. 2. It consists of four parts: the external function calls in the program file of GAMS; a number mapping between this file and the C++ file of the external module; the function GEFUNC that is contained within the external module, where the actual calculations and thermo calls to the property package are performed (Skiborowski et al., 2015) and COBIA as the socket to the thermo package.

2.2.1. External function calls

In the GAMS model, all thermodynamic properties such as enthalpies, distribution coefficients, or dew / bubble point temperatures are defined in a separate block of external equations by specifying all input and output variables for each thermo call.

2.2.2. Number mapping

All external equations and variables defined within this block of external equations receive a unique number. These two sets of numbers ensure the implementation consistency of the external function calls made in GAMS and the calculations performed in the external module.

2.2.3. GEFUNC / External module (C++)

As described by Skiborowski et al. (2015), the function calculates the residual of every external equation and, in addition to that, calculates all first order derivatives with respect to all present output and input variables. For most property calls, input variables are temperature T, pressure p, and compositions x_j. All thermodynamic properties needed for these calculations are either provided by the property or flash routines of the property package or calculated implicitly. The latter is true for all first order derivatives of properties that are determined by flash routines, since the property package does not provide direct derivatives for these. Here, these missing values are computed by applying the implicit function theorem to the valid flash conditions and solving the resulting linear equation system by LU decomposition of the C++ library Eigen 3 (Guennebaud and Jacob, 2019).

2.2.4. COBIA

COBIA is relied upon to call the property package from GAMS' external module. All COBIA headers are added to the C++ project of the external module. The project is compiled as a DLL and added to the current GAMS workspace.

2.3. Implementation consistency

To facilitate the formulation of complex superstructure models and ensure implementation consistency across all program files, our own modeling environment MOSAICmodeling (Technische Universität Berlin, 2019) is applied and extended to allow for full COBIA support. The superstructure is fully formulated within MOSAICmodeling, wherein the calls for external computation of, e.g., enthalpies and separation coefficients are generically marked as "CAPE-OPEN" calls. Subsequently, as shown in Fig. 2, code is generated by two separate UDLS for both GAMS and the external module of GAMS, wherein the full COBIA calls and the generation of derivatives for GAMS is described depending on the exact structure of the GAMS model.

3. Case Study: Separation of a Ternary Mixture by a Dividing Wall Column

The capabilities of the approach are shown by generating an instance of the superstructure of six VL-Us introduced in Fig. 1, each VL-U consisting of 20 equilibrium stages, for the separation of a ternary mixture *n*-pentane, *n*-hexane, and *n*-heptane. The binary variables of the distribution network are specified so that the resulting instance of the superstructure serves as a surrogate model of a dividing wall column (DWC) as shown in Fig. 3.

The NLP problem is then solved in GAMS by CONOPT 3. All thermodynamic calculations are performed by a property package provided by TEA (AmsterCHEM, 2019). All variables are initialized arbitrarily within their bounds in order to test the robustness of the system. The reboiler duty is chosen as the objective function which is minimized in order to determine the most energy-efficient configuration of the DWC for the separation of the mixture. Extra inequality constraints ensure that the compositions of the desired products in each outlet stream remain above 0.9995. The saturated liquid feed stream of 20 kmol h^{-1} has the molar composition $x_1^F = 0.333$, $x_2^F = 0.333$ and $x_3^F = 0.334$ and the DWC operates at a pressure of 1 bar. The following five molar split ratios (cf. Fig. 3) are chosen as decision variables: reflux ratio ν_R, boil up ratio ν_{BU}, removal ratio of product stream B ν_B, vapor split fraction ν_V, and liquid split fraction ν_L. The optimal ratios are determined by CONOPT 3 after 554 iterations and a CPU time of 4460 seconds at $\nu_R = 0.266$, $\nu_{BU} = 0.233$, $\nu_B = 0.528$, $\nu_V = 0.550$ and $\nu_L = 0.229$ with product purities of $x_1^A = 1.000$, $x_2^B = 0.9995$, and $x_3^C = 0.9995$ for a reboiler duty of 194.6 kW. The resulting temperature profiles of all column sections (I to VI) are presented in Fig. 3.

4. Conclusions and Outlook

This work presents the enhancement of an optimization approach in GAMS using accurate thermodynamic models via CAPE-OPEN by automated code generation. The results from a case study, in which the NLP resulting from a process model of six VL-Us is solved in GAMS, indicate that the automated code export works well for interfacing GAMS with the external thermo package and that the robust model formulation ensures convergence even for systems that are poorly initialized. The

process model of the case study is an instance of the robust superstructure of the process network, which is already formulated in MOSAICmodeling, Hence, the next step towards optimization-based conceptual design is to export the entire superstructure to GAMS and investigate how the resulting MINLP can be solved effectively.

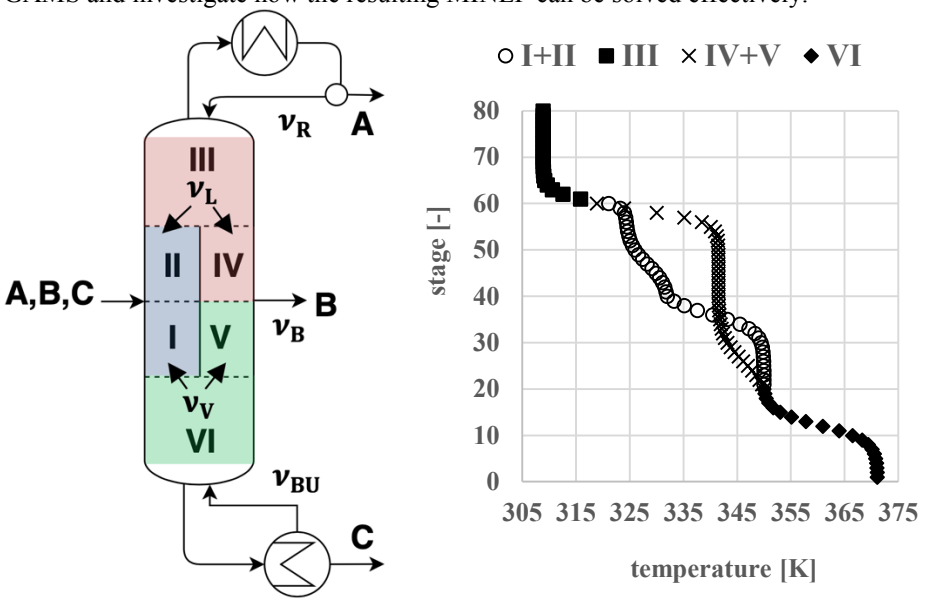

Figure 3: left: Combination of six VL-Us (I-VI) as a surrogate model of a DWC, right: Temperature profiles in the DWC for the optimized system

References

AmsterCHEM, 2019, COCO [WWW Document], URL https://www.amsterchem.com/coco.html (last accessed 25.11.19)

M. Bagajewicz, V. Manousiouthakis, 1992, AIChE Journal, Mass/heat-exchange networkd representation of distillation networks, 38, 11, 1769–1800

V. Gopal, L. T. Biegler, 1999, AIChE Journal, Smoothing methods for complementarity problems in process engineering, 45, 1535–1547

G. Guennebaud, B. Jacob, and others, 2019, Eigen v3 [WWW Document], URL http://eigen.tuxfamily.org (last accessed 25.11.19)

C. Kanzow, A. Schwartz, Comput. Optim. Appl. 2014, Convergence properties of the inexact Lin-Fukushima relaxation method for mathematical programs with complementary constraints, 59, 249–262

H. Kuhlmann, M. Skiborowski, 2017, Industrial & Engineering Chemistry Research, Optimization-Based Approach To Process Synthesis for Process Intensification: General Approach and Application to Ethanol Dehydration, 56, 45, 13461–13481

J. I. Manassaldi, M. C. Mussati, N. J. Scenna, S. G. Mussati, Computers & Chemical Engineering, 2019, Development of extrinsic functions for optimal synthesis and design – Application to distillation-based separation processes, 125, 532–544

M. Skiborowski, A. Harwardt, W. Marquart, 2015, Computers & Chemical Engineering, Efficient optimization-based design for the separation of heterogeneous azeotropic mixtures, 72, 34–51

Technische Universität Berlin, 2019, MOSAICmodeling [WWW Document], URL http://mosaic-modeling.de (last accessed 25.11.19)

G. Tolksdorf, E. Esche, G. Wozny, J.-U. Repke, 2019, Computers & Chemical Engineering, Customized code generation based on user specifications for simulation and optimization, 121, 670–684

Sauro Pierucci, Flavio Manenti, Giulia Bozzano, Davide Manca (Eds.)
Proceedings of the 30th European Symposium on Computer Aided Process Engineering
(ESCAPE30), May 24-27, 2020, Milano, Italy.
http://dx.doi.org/10.1016/B978-0-12-823377-1.50147-6

A Multiperiod Approach for Flexible Work and Heat Integration

Leandro V. Pavão,* Mauro A. S. S. Ravagnani, Caliane B. B. Costa[a]

Department of Chemical Engineering, State University of Maringá
Av. Colombo, 5790, Bloco D90, CEP 87020900, Maringá, PR, Brazil
leandropavao@gmail.com

Abstract

Industrial plants are constantly subject to undergoing operating condition variations. Those may be due to, for instance, ambient temperature changes, altering feed temperatures or to reactants and raw material quality changes, which may lead to certain stream flow fluctuations. Those scenarios require that equipment involved in the process is sized accordingly for reaching target outlet parameters and maintain the process feasible. In heat integration, several works have proposed methodologies for synthesizing heat exchanger networks (HEN) with equipment that is able to operate properly regardless of changes in temperatures or flowrates. A methodology that achieved considerable success for designing flexible HEN is the multiperiod approach. In it, a finite number of extreme scenarios is considered and a HEN, feasible in all of them, is synthesized. In simultaneous work and heat integration, however, flexibility has not yet been explored in the literature. The solutions presented so far are obtained for nominal conditions, which may lead to equipment that is undersized when the process undergoes inlet pressure, temperature or flowrate variations. In that sense, the present work proposes an optimization-based methodology for automatically synthesizing work and heat exchange networks (WHEN) that are flexible for operating under a finite set of varying conditions, as proposed in multiperiod approaches. A work and heat integration case study is proposed with a finite number of scenarios. Then, a meta-heuristic solution approach is applied to the new proposed multiperiod model, and a single solution is obtained. The identified solution is able to perform feasibly under all the proposed extreme scenarios. Moreover, units were only slightly oversized in comparison to the nominal conditions, representing a relatively small additional capital investment.

Keywords: Optimization; Multiperiod; Work and Heat Integration; Work and Heat Exchange Networks; Meta-heuristics

1. Introduction

Material streams in industrial facilities typically face temporary alterations in nominal operating conditions. These changes may be due to variations in raw material quality, weather conditions, control system issues, fouling, among others. Consequently, some degree of flexibility is required when sizing the employed equipment.

Under the scope of industrial flexibility studies, much attention has been given to the design of flexible heat exchanger networks (HEN). These systems must be able to operate under variable temperature and heat capacity flowrate conditions. Note that heat exchanger areas are fixed, and it is required that these areas are able to handle different operating conditions. In general, this leads to some additional heat exchange surface

requirement in the heat exchangers, which implies a greater capital investment than in a solution for the nominal state only. It is thus important to synthesize a network having this overdesign issue in mind in order to mitigate this additional capital investment.
A widely used approach for flexible HEN synthesis is the multiperiod concept. Under this consideration, a finite set of operating conditions is defined according to their duration probabilities throughout a year of operation. A pioneer mathematical programming approach for multiperiod HEN synthesis is the sequential framework of Floudas and Grossmann (1987). More recent contributions include the MINLP simultaneous models of Verheyen and Zhang (2006) and Pavão et al. (2018). The former employs deterministic methodologies as solution approach, while the latter uses hybrid meta-heuristic methods. Both models use as basis the stagewise superstructure (SWS) for HEN synthesis, developed by Yee and Grossmann (1990).
Another important field of energy integration regards the simultaneous integration of pressure and temperature change units, that is, work and heat integration. Although not as mature as heat integration literature, this new trend has shown in several recent studies that work and heat integration may lead to important energy savings in plants. The problem is similar to heat integration, but streams may also require compression or expansion. Work recovery may be performed, for instance, by means of single-shaft-compressor-turbine (SSTC) couplings or simply by power generation from turbines, which can be supplied to compression tasks.
Simultaneous optimization models have been proposed for designing networks with optimal placement and sizing of pressure manipulators (compressors, turbines, valves, SSTC units) as well as of temperature ones (heat exchangers and utility heaters and coolers). Onishi et al. (2014) proposed a WHEN synthesis MINLP model considering SSTC units. The model allowed a stream to pass multiple times through a heat recovery area, which was modelled with Yee and Grossmann's (1990) SWS. Nair and Karimi (2018) presented a model without streams pre-classification and assuming temperature-dependent properties. Based on the idea of multiple passes through a heat recovery area, Pavão et al. (2019) presented a matrix-based approach suitable for the use of a meta-heuristic solution method. The heat integration region was modelled with the enhanced SWS of Pavão et al. (2018).
Although efficient frameworks have been presented for work and heat integration, so far, the flexibility issue has not been approached, and remains an interesting opportunity (Yu et al., 2018). It is notable that stream pressure conditions may vary from the nominal ones, as well as temperatures and flowrates, due to the same factors mentioned previously. Hence, it is appropriate to design pressure manipulators having in mind some degree of flexibility. Hence, in this work, we propose a multiperiod WHEN synthesis framework able to perform pressure/temperature change tasks under multiple operating condition scenarios.

2. Problem statement

A set of process streams is given with supply and target temperature/pressure conditions, as well as heat capacity flowrates and heat transfer coefficients. Supply and target temperature and pressure, as well as heat capacity flowrates may vary. Therefore, a finite number of condition sets is known, and to each of these a duration time over a year is associated. A network of pressure manipulators (compressors, turbines, valves and SSTC units for work exchange among streams) and temperature manipulators (heaters, coolers and heat exchangers) must be designed so that all streams reach their target conditions in all periods. In case a SSTC unit requires additional power, an auxiliary motor is used.

Conversely, an auxiliary generator uses work surplus and produces electricity, which is sold to the grid.
Streams are assumed as ideal gases. Polytropic exponents, isentropic efficiencies and Joule-Thompson coefficients are known.

3. Mathematical model

The model proposed in this work is based on the master matrix concept of Pavão et al. (2019). That is, a matrix contains information of all stream passes through the heat exchange area, as presented in Figure 1.

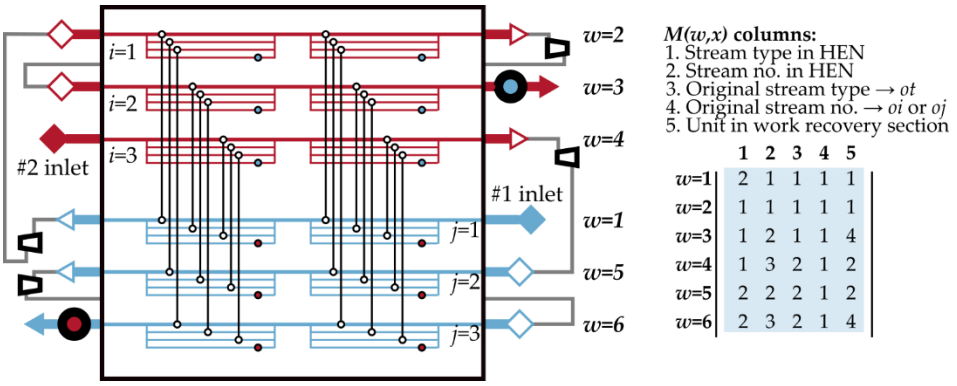

Figure 1. Master matrix-based structure for WHEN synthesis

Note that, in the superstructure, a given stream may have either hot or cold passes through the heat recovery region. The matrix contains information for correct stream identification and for the unit placed between passes through heat integration region (e.g., 1 for compressor, 2 for turbine, 3 for valves and 4 for final temperature correction heater/cooler). The algorithm reads the matrix data and is able to link the master superstructure to the heat integration superstructure in order to perform energy-related calculations and equipment sizing.
In order to consider multiple operating periods, several design-related variables must have individual values at each of these periods. For instance, heat exchanger areas, represented in the single period model as $A_{i,j,k}$, with indexes that represent hot and cold streams (i and j) and superstructure stage (k) must have an additional t index for periods. It is worth noting that associated with area calculations are all energy- and temperature-related variables, which also require the additional t index. Pressure manipulator variables require the index as well. In brief, illustrative equation forms for operating and capital costs (which are summed up as total annual costs to be minimized in the optimization model) are calculated as follows (a detailed single period model derivation can be found in Pavão et al. (2019)):

$$OC = \sum_{t \in NP} D_t (UC_t + WC_t) \tag{1}$$

where D_t is the period duration, UC_t are total utility costs for a given period and WC_t is the total electricity costs (which is negative if there is power surplus revenue) for a period. NP is the periods set.

$$
\begin{aligned}
CC = & \sum_{i\in NH}\sum_{j\in NC}\sum_{k\in NS} Afun[\max_t(A_{i,j,k,t})] + \\
& \sum_{m\in NHU}\sum_{j\in NC}\sum_{k\in NS} Afun[\max_t(Ahui_{m,j,k,t})] + \\
& \sum_{i\in NH}\sum_{n\in NCU}\sum_{k\in NS} Afun[\max_t(Acui_{i,n,k,t})] + \\
& \sum_{oj\in NOC} Afun[\max_t(Ahu_{oj,t})] + \sum_{oi\in NOH} Afun[\max_t(Acu_{oi,t})] + \\
& \sum_{w\in NW} Wfun[\max_t(Work_{w,t})] + MGfun[\max_t(MGWork_t)]
\end{aligned} \tag{2}
$$

where *Afun* is the area capital costs function, *Wfun* is the pressure changer capital costs function, which automatically identifies the unit as compressor/expander (standalone or coupled via SSTC), or valve and uses the appropriate capital cost estimation formula and *MGfun* is the auxiliary motor/generator capital costs function, which automatically identifies whether a helper motor or generator is needed in the SSTC coupling and calculates its capital costs. *NH* and *NC* are hot and cold stream sets. *NS* is the HEN superstructure stages set. *NOH* and *NOC* are original hot and cold stream sets. *NW* is the general streams set. Input values in these functions are functions as well: max_t identifies the greater value within those with *t* index. That is, in order to feasibly operate in all periods, the unit must be sized according to the greatest period requirement. *A*, *Ahui* and *Acui* are areas for heat exchangers and inner stage utility units in Pavão et al.'s (2018) superstructure. *Ahu* and *Acu* are areas for final temperature correction heaters/coolers. Only one of these units can be placed at the end of a stream, regardless of how many times it passes through the heat recovery area. That is why these areas have *oi* and *oj* index, which regard the original stream index. *Work* is the shaft-work in compressors/turbines, or the energy relief in valves. These units have the generic stream index *w*, which is translated to/from the *i*/*j* notation for the heat integration region by the algorithm. *MGWork* is the total net power required/generated in the SSTC coupling. Power lack or surplus is automatically identified for sizing a helper motor/generator.

4. Case study

The case study tackled here has one hot, low-pressure stream, one cold, constant-pressure stream and one cold, high-pressure stream. Four operation periods with equal durations are considered. Stream data is presented in Table 1. Parameters that vary in each period are supply temperatures (Ts1-Ts4), heat capacity flowrates (F1-F4) and supply pressures (ps1-ps4). Temperatures are given in K, heat capacity flowrates in kW/K and pressures in bar. Heat transfer coefficients are of 0.1 kW/(m^{2}K) for process streams and 1.0 kW/(m^{2}K) for hot and cold utilities (HU and CU). Hot and cold utilities cost 337 $/(kWy) and 100 $/(kWy). Electricity cost is 455.04 $/(kWy) and its revenue price is 364.03 $/(kWy). The polytropic exponent is 1.352; isentropic efficiency is assumed as 1.0 for compressors and turbines and Joule-Thompson coefficient value is 1.961 K/MPa. The annualizing factor is 0.18. The exchanger minimal approach temperature (EMAT) is 1 K. The algorithm used for solving the multiperiod model for this case study is based on the SA-RFO implementation for WHEN synthesis (Pavão et al., 2019). The code was revamped so that the multiple periods were considered. The implementation was in C++

in Microsoft Visual Studio 2019. All optimization runs were carried out on a computer with an Intel® Core™ i7-8750H CPU @ 2.20 GHz and 8.00 GB of RAM.

Table 1. Case study stream data

St.	Ts1	Ts2	Ts3	Ts4	Tt	F1	F2	F3	F4	ps1	ps2	ps3	ps4	pt
1	288	274	274	302	123	3.0	3.2	2.9	3.2	1.0	0.9	0.9	1.1	4.0
2	213	224	202	224	288	2.0	2.1	2.1	1.9	-	-	-	-	-
3	113	119	107	119	288	1.7	1.8	1.8	1.6	4.0	4.2	3.8	4.2	1.0
HU	383	383	383	383	383	-	-	-	-	-	-	-	-	-
CU	93	93	93	93	93	-	-	-	-	-	-	-	-	-

$Afun(Area) = 71{,}337.07 + 747.9931\ (Area)$;
$Wfun(Work) = 51{,}104.85\ (Work)^{0.62}$ (standalone compressor);
$Wfun(Work) = 2585.47\ (Work)^{0.81}$ (standalone turbine);
$Wfun(Work) = 51{,}104.85\ (\text{Work})^{0.62} - 985.47\ (\text{Work})^{0.62}$ (SSTC compressor);
$Wfun(Work) = 2585.47\ (Work)^{0.81} - 985.47\ (\text{Work})^{0.62}$ (SSTC turbine);
$MGfun(MGWork) = 985.47\ (MGWork)^{0.62}$ (for both aux. motor or generator);

A considerable problem in multiperiod solutions is overdesign. In that sense, an important parameter to measure a multiperiod HEN solution efficiency are "required to available" ratios. In heat integration, these ratios refer to heat exchange surface. That is, the ratio between the required area in a given heat exchanger at a period, versus the maximum area among all periods in that unit. Considering temperature manipulating units (heat exchangers, heaters and coolers), the methodology was able to find a solution with an average total required to total available area ratio of 97.4% (if only heat exchangers are considered, the ratio is of 99.1%). We can extend that idea to compressors and expanders. For the former, the average required to available compressing capacity ratio is of 88.0%. For the latter, the required to available expansion capacity is of 91.6%. The helper motor is designed with 105.5 kW power, leading to an average required to available power ratio of 84.4%. The multiperiod WHEN solution is presented in Figure 2.

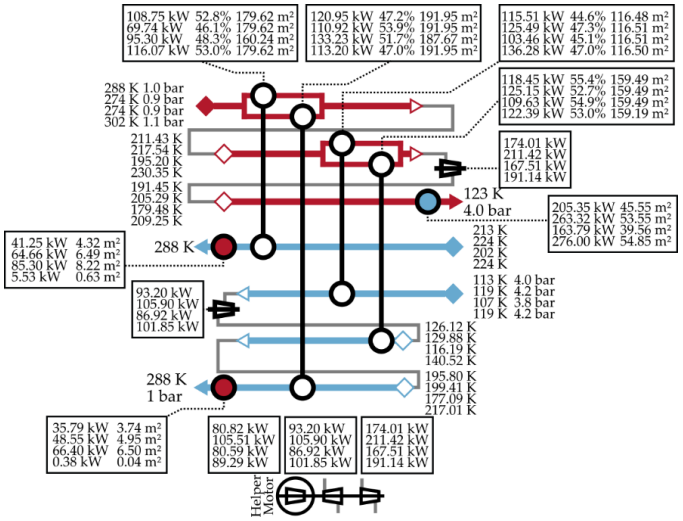

Figure 2. Multiperiod WHEN solution for the case study. For each unit, each row of values refers to calculated variables in a period of operation (heat duty/work in kW, stream split fraction in % and area in m^2).

The multiperiod solution found has TAC of 753,083 \$/y, with capital costs of 456,137 \$/y and operating costs of 296,946 \$/y. For comparison purposes, when the algorithm was

run for the nominal case only (i.e., period 1), TAC was 689,892 $/y, with capital costs of 421,557 $/y and operating costs of 268,336 $/y. Hence, the implementation of a WHEN able to operate feasibly at multiple conditions in this case led to a small additional capital investment of 34,580 $/y (8.2 % increase). Moreover, the aforementioned ratio values are similar to those presented in multiperiod case studies comprising heat integration only (see Pavão et al. (2018)), which means the methodology extension to work and heat integration was satisfactory. The processing time was of 4,084 s.

5. Conclusions

A novel framework for multiperiod work and heat exchange network synthesis was proposed. The method is based on an extension of a matrix-based model and a meta-heuristic approach is used to solve such a model. Tests were conducted for a case study. The methodology was able to identify a solution with small additional investments in comparison to the nominal case solution. The algorithm was able to identify a single work and heat exchange network configuration able to operate feasible in all periods. The design also has good "required to available" ratios for all units. The method found a solution with little overdesign. That is, all units have similar requirements for area, compression/expansion capacity and auxiliary motor power in all periods.

Acknowledgements

The authors gratefully acknowledge the financial support from CAPES (88887.360812/2019-00 and 88881.171419/2018-01) and CNPq (305055/2017-8, 428650/2018-0 and 311807/2018-6).

References

Floudas, C.A., Grossmann, I.E., 1987. Automatic generation of multiperiod heat exchanger network configuration. Comput. Chem. Eng. 11, 123–142.

Nair, S.K., Karimi, I.A., 2018. Exploiting the Synergy between Work and Heat for Holistic Energy Integration, in: Computer Aided Chemical Engineering. Elsevier B.V., pp. 403–408.

Onishi, V.C., Ravagnani, M.A.S.S., Caballero, J.A., 2014. MINLP Model for the synthesis of heat exchanger networks with handling pressure of process streams. Comput. Aided Chem. Eng. 33, 163–168.

Pavão, L.V., Miranda, C.B., Costa, C.B.B., Ravagnani, M.A.S.S., 2018. Efficient multiperiod heat exchanger network synthesis using a meta-heuristic approach. Energy.

Pavão, L. V., Costa, C.B.B., Ravagnani, M.A.S.S., 2019. A new framework for work and heat exchange network synthesis and optimization. Energy Convers. Manag. 183, 617–632.

Pavão, L. V, Costa, C.B.B., Ravagnani, M.A.S.S., 2018. An enhanced stage-wise superstructure for heat exchanger networks synthesis with new options for heaters and coolers placement. Ind. Eng. Chem. Res. 57, 2560–2573.

Verheyen, W., Zhang, N., 2006. Design of flexible heat exchanger network for multi-period operation. Chem. Eng. Sci. 61, 7730–7753.

Yee, T.F., Grossmann, I.E., 1990. Simultaneous optimization models for heat integration—II. Heat exchanger network synthesis. Comput. Chem. Eng. 14, 1165–1184.

Yu, H., Fu, C., Gundersen, T., 2018. Work and Heat Exchange Networks – Opportunities and Challenges. Comput. Aided Chem. Eng. 44, 481–486.

Sauro Pierucci, Flavio Manenti, Giulia Bozzano, Davide Manca (Eds.)
Proceedings of the 30th European Symposium on Computer Aided Process Engineering (ESCAPE30), May 24-27, 2020, Milano, Italy.
http://dx.doi.org/10.1016/B978-0-12-823377-1.50148-8

Multi-Objective Evolutionary Algorithm based on Decomposition (MOEA/D) for Optimal Design of Hydrogen Supply Chains

Victor H. Cantú,[a,*] Catherine Azzaro-Pantel,[a] Antonin Ponsich[b]

[a]*Laboratoire de Génie Chimique, Université de Toulouse, CNRS, INPT, UPS, 4 allée Emile Monso, 31432 Toulouse Cedex 4, France*
[b]*Departamento de Sistemas, Universidad Autónoma Metropolitana Azcapotzalco, Av. San Pablo Xalpa 180, Ciudad de México, Mexico*
vcantume@inp-toulouse.fr

Abstract

This work introduces an efficient tool for the design of sustainable hydrogen supply chains (HSCs), considering both economic and environmental concerns, through an appropriate multi-objective strategy. Within this hybrid strategy, a multi-objective evolutionary algorithm deals with integer variables and Pareto front construction, which reduces the original mixed-integer linear programming (MILP) to multiple linear programming (LP) sub-problems. The proposed methodology is validated through the comparison of the true Pareto fronts given by CPLEX, for three increasing size instances. Numerical results prove that the hybrid approach reproduces accurately the optimal fronts while reducing drastically (up to 20 times) the CPU time with respect to the MILP solver.

Keywords: Hydrogen supply chain, Multi-objective optimization, Hybrid evolutionary algorithm.

1. Introduction

Hydrogen is expected to play a significant role in low-carbon energy landscape. According to the Hydrogen Council (2017), hydrogen will cover 18% of global energy demand by 2050. However, much of the future expansion of hydrogen utilization depends not only on technological developments and energy policies, but also on the hydrogen supply chain (HSC) deployment. In this way, designing a cost-efficient infrastructure, encompassing the wide spectrum of production and distribution options that may evolve over time with growing demand, is a significant challenge.

The HSC deployment has been studied from different perspectives. One of the most popular approaches found in the dedicated literature is that proposed in Almansoori and Shah (2006), in which the HSC design problem is tackled through a mathematical programming (MP) model considering production, storage and distribution echelons. The resulting mixed-integer linear programming (MILP) problem consists in minimizing the total daily cost (*TDC*), which includes infrastructural, operating and transportation costs. The optimization problem is then efficiently solved by MP techniques. Yet, comprehensive analysis is needed to evaluate and optimize the sustainability of hydrogen energy systems and, in particular, the environmental aspects through the potential impacts associated with hydrogen production, distribution and storage. In this vein, the minimization of the environmental impact of supply chains (SCs) through Global Warming Potential (*GWP*), has received much attention. This indicator has thus been

proposed as a second objective in Almaraz et al. (2014a). The resulting bi-objective problem is solved by CPLEX by means of the ε-constraint method within GAMS environment. This methodology has now been used for different case studies in France (Almaraz et al., 2014b), Germany (Almansoori and Betancourt-Torcat, 2016) and Portugal (Câmara et al., 2019).

Even if the optimization problems derived from the above-cited works have been solved to optimality, it is worth mentioning that their computational complexity involves solution times that might rapidly rise with the instance size. In addition, for more than one objective, the construction of the Pareto front by MP techniques is usually a time-consuming task, since each Pareto solution requires at least one scalar optimization. An alternative to the solution of Process Engineering optimization problems is to use metaheuristics, and specifically, Multiobjective Evolutionary Algorithms (MOEAs). MOEAs are stochastic population-based nature-inspired algorithms, able of handling multiple objectives, continuous and discrete variables, nonlinear and multimodal functions. However, as these search algorithms are designed to work over unconstrained search spaces, they generally exhibit a poor performance when solving highly constrained problems, even if sophisticated constraint-handling techniques have been proposed.

The scientific objective of this work is thus to propose a hybrid methodology to solve the HSC problem, which decomposes the global problem in such a way that advantages can be taken of the strengths of each single approach, mitigating simultaneously their disadvantages: the construction of the Pareto front is carried out by the evolutionary algorithm, whereas the equality constraints are treated by the exact technique. Besides, the integer variables are handled by the MOEA, so that the original MILP problem is reduced to multiple LP sub-problems, which can be efficiently solved.

The remainder of this work is as follows: in the next section, a brief definition of the HSC problem is provided. Then, the proposed solution strategy is explained in section 3. Section 4 presents three case studies used for validation, while the computation experiments are described and discussed in section 5. Finally, some conclusions and perspectives for future work are proposed in section 6.

2. Problem definition

The mathematical model considered in this work is taken from Almansoori and Shah (2006) and from its adaptation proposed in Almaraz et al. (2014a). Accordingly, the total geographic area is divided into grids (nodes). Each grid has a total hydrogen demand that has to be satisfied. In addition, hydrogen can be transported between grids so that one grid cannot simultaneously import and export hydrogen. For instance, in the example shown in Figure 1, the geographic area is divided into 9 grids and grids 4, 6 and 7 cannot export hydrogen to other grids because they already import from grid 5. For each grid (g), a number of plants (N_{pig}) for each production type (p) and product physical form (i) must be determined, as well as the corresponding total production rates (P_{pig}) and the inlet/outlet hydrogen flows $Q_{ilgg'}$, where l accounts for the type of transportation mode. Three types of production plants (steam reforming, coal and biomass) and two storage types (liquid, gaseous) have been considered.

The two objectives to be minimized are (1) the total daily cost (*TDC*), which includes investment costs related to plant installation (*FCC*) and transportation (*TCC*), and operation costs for production (*FOC*), transportation (*TOC*) and storage (*FOC*); and (2) the *GWP*, formulated in Almaraz et al. (2014a) as indicated in Eq. (2). The *GWP* accounts

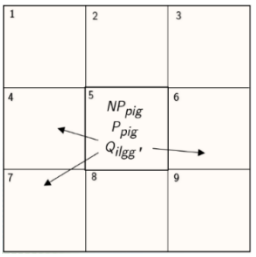

Figure 1. Example of grid discretization of geographic area.

for gas emission due to production (GW^{prod}), storage (GW^{stock}), and transportation (GW^{transp}). It is worth mentioning that the resulting problem is NP-hard. The complete formulation, particularly regarding constraints related to storage and transportation, the bounded production capacity of each plant and the satisfaction of hydrogen demand in each grid, can be found in Almansoori and Shah (2006) and Almaraz et al. (2014a).

$$TDC = \frac{FCC + TCC}{\alpha CCF} + FOC + TOC \tag{1}$$

$$GWP = \sum_{pg} P_{pg} \left(GW^{prod} + GW^{stock} \right) + \sum_{gg'} \left(\frac{2WL_{gg'} Q_{gg'}}{TCap} \right) GW^{transp} \tag{2}$$

3. Methodology

The complexity due to the combinatorial and multi-objective nature of the HSC problem deserves the development of an adapted solution strategy. The original MILP problem is decomposed into two parts (see Figure 2): the integer (master) sub-problem and the continuous (slave) sub-problem. The master sub-problem is treated by the multi-objective evolutionary algorithm, in which the integer variables (number of production units) are encoded in every individual in the population. For each individual, which is now a partial solution, a linear programming sub-problem is solved to determine the corresponding optimum production rates and transportation flows. This LP problem is constructed according to the values of the integer variables provided by the MOEA in such a way that it is almost a canonical transportation problem. The integer variables produced by the MOEA may be repaired to ensure that this problem is feasible. Subsequently, the MOEA recovers the continuous variables (P_{pig}, $Q_{ilgg'}$) from the LP solver, in order to compute the *TDC* and *GWP* objectives. Once evaluated, each individual has its fitness function value assigned by the MOEA, which evolves the population to the next generation. The proposed methodology is presented in an algorithmic scheme as follows:

1. Assign integer variables (NP_{pig}) using a stochastic operator.
2. Construct the transportation problem, identifying demand and source grids.
3. Solve the multi-objective transportation problem (LP).
4. Compute the TDC and GWP objectives for the current solution.
5. Evolve population according to MOEA.
6. If the termination criterion is not reached, go to step 1.

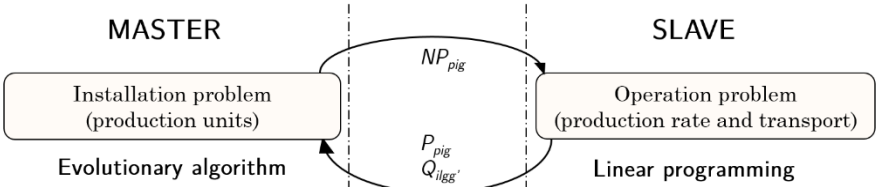

Figure 2. Hybrid (master - slave) approach.

The first key point of this methodology is the construction of a feasible transportation problem using the integer variables provided by the evolutionary module. The set of grids G is divided into importing (G^I) and exporting (G^E) grids according to the number of plants installed and their production capacity: if, for a given grid, the production capacity of all plants installed is lower than the grid demand, the grid is considered as a "source" (G^E). If the total production capacity (over all grids) does not meet the total demand, plant units are randomly added in order to ensure feasibility of the transportation problem.

Besides, to handle multiple objectives within the LP sub-problem, both criteria (*GWP* and *TDC*) are integrated in the objective function through a scalarizing function (such as the weighted sum or the Tchebycheff function). These functions involve weight vectors associated to each objective priority. In this way, the LP can be easily hybridized with the Multi-Objective Evolutionary Algorithm based on Decomposition (MOEA/D) (Zhang and Li, 2007). Indeed, this MOEA assigns a scalarization (like the LP formulated here) of the original multi-objective problem to every individual in the population, with a specific weight vector each. Then, each individual solves its respective scalar sub-problem through a collaboration with the neighbour solutions in the population. Consequently, each LP to be solved inherits its weight vector (used in the scalarizing function) from the individual, establishing a direct relationship between the objective space explored by the individual and by the LP.

In this work, the weighted Tchebycheff function (Coello et al., 2007) is used, so that the resulting LP sub-problem is formulated as follows:

$$\begin{aligned}
\min \quad & \max_{k\in K}\left\{\lambda_k \left| f_k(x) - f_k^* \right|\right\} & & \\
\text{s.t.} \quad & \sum_{p} P_{pig} = \sum_{\lg'} \left(Q_{i\lg g'} - Q_{i\lg' g}\right) + D_{ig}^T & & \forall i \in I, g \in G \\
& PCap_{pi}^{\min} NP_{pig} \le P_{pig} \le PCap_{pi}^{\max} NP_{pig} & & \forall p \in P, i \in I, g \in G \\
& Q_{i\lg g'} \ge 0 & & \forall i \in I, l \in L, g, g' \in G
\end{aligned} \tag{3}$$

where λ_k is the k-th weight vector (k =1,…, K), x represents the set of real decision variables (P_{pig}, $Q_{ilgg'}$), $f_k(x)$ the objective functions and f_k^* is the reference point (composed of single-objective optima). NP_{pig} are considered as constants in Eq. (3). It is to note that the optimum for the original MILP problem and the new one remains the same.

4. Case study

In this work, three increasing size instances are considered that correspond to the data for the Great Britain case study (Almansoori et al., 2006). Instances 1 and 2 represent a part of the entire geographic area of Instance 3. Please note that the number of decision

variables in Table 1 represents the actual decision variables of the hybrid methodology, although those for the original MILP formulation might be greater.

Table 1. Case study.

	Instance 1	Instance 2	Instance 3
Number of grids	6	12	34
Number of integer variables	18	36	102
Number of continuous variables	48	168	1224

5. Results

For the evolutionary algorithm, the population size and number of generations are 51 and 510, respectively. Likewise, 51 weight vectors are used for CPLEX using the Tchebycheff decomposition. The obtained Pareto fronts are presented in Fig. 3-5. As can be observed, the approximations of the Pareto front for both approaches are similar, as most solutions are overlaid. The stair shape of the Pareto front is due to the discrete nature of the problem, and precisely, to the constraint on maximum production capacity. Furthermore, Table 2 shows that, for the hypervolume indicator (which represents the hyper-space dominated by a Pareto front approximation, i.e., the higher, the better), both strategies perform similarly for all instances (results in accordance with Fig. 3-5). However, the computational time increases drastically for the deterministic algorithm, both because of the need for solving the problem multiple times and to the combinatorial aspect.

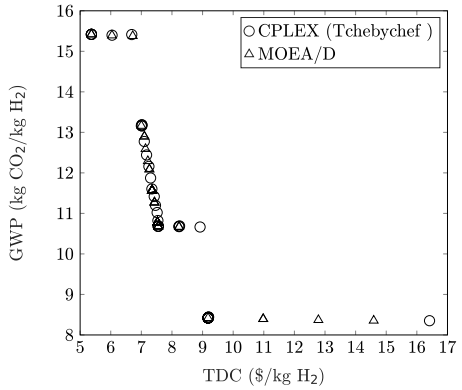

Figure 3. Obtained Pareto front for Instance 1.

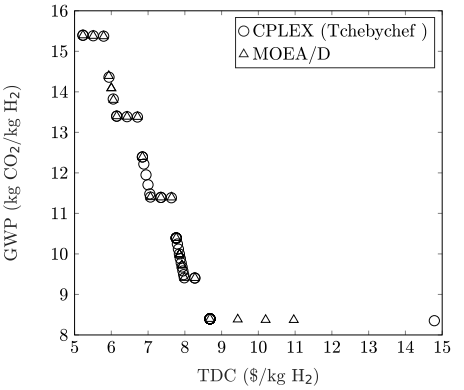

Figure 4. Obtained Pareto front for Instance 2.

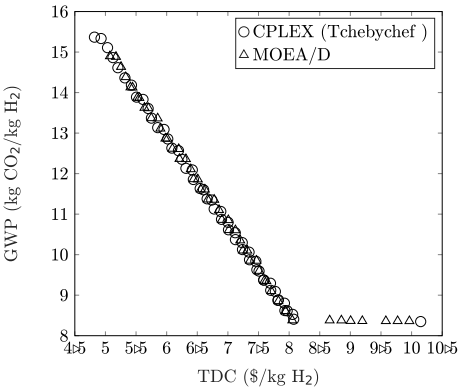

Figure 5. Obtained Pareto front for Instance 3.

Table 2. Numerical comparison of results for the hybrid and classical approaches.

	Instance 1		Instance 2		Instance 3	
	Hybrid	CPLEX	Hybrid	CPLEX	Hybrid	CPLEX
CPU time(s)[a]	164.65	**52.87**	**226.08**	4577.76	**1908.96**	45094.32
Hypervolume	**63.29**	63.04	**54.27**	54.26	14.80	14.80

[a] Computational experiments were carried out with a processor Intel Xeon E3-1505M v6 and 32 Go RAM.

The CPU time for the hybrid strategy remains yet acceptable even for the largest instance (lower than one hour), while the time required by the classical approach is prohibitive (more than 12 hours). In addition, note that the time proportion devoted to the solution of the LP sub-problems is practically the same in the three instances. To conclude, the solution strategy proposed in this work is able to accurately reproduce the optimal Pareto front, with CPU times up to 20 times lower than those required by the MILP approach.

6. Conclusions and perspectives

A hybrid approach combining MOEA and linear programming has been developed to overcome the main drawbacks that are present in MP techniques when solving multi-objective problems, and taking full advantage of MOEAs for the construction of the Pareto front for the solution of HSC design. The proposed methodology is capable to efficiently solve the multi-objective HSC problem as has been validated with the exact solutions given by CPLEX for three increasing size instances. Besides, the computational times for the proposed methodology are significantly inferior to that of the classical approach. This is promising for the solution of larger size instances and for a more realistic (nonlinear) model of the HSC to be considered.

References

The Hydrogen Council (2017) Hydrogen scaling up: A sustainable pathway for the global energy transition.

Almansoori, A., and Shah, N. (2006). Design and operation of a future hydrogen supply chain: snapshot model. *Chemical Engineering Research and Design, 84*(6), 423-438.

Almaraz, S. D. L., Azzaro-Pantel, C., Montastruc, L., and Domenech, S. (2014a). Hydrogen supply chain optimization for deployment scenarios in the Midi-Pyrénées region, France. *International Journal of Hydrogen Energy, 39*(23), 11831-11845.

Almaraz, S. D. L., Boix, M., Azzaro-Pantel, C., Montastruc, L., and Domenech, S. (2014b). Spatial-based approach of the hydrogen supply chain in the Midi-Pyrénées region, France. In *Computer Aided Chemical Engineering* (Vol. 33, pp. 307-312). Elsevier.

Almansoori, A., and Betancourt-Torcat, A. (2016). Design of optimization model for a hydrogen supply chain under emission constraints-A case study of Germany. *Energy*, 111, 414-429.

Câmara, D., Pinto-Varela, T., and Barbósa-Povoa, A. P. (2019). Multi-objective optimization approach to design and planning hydrogen supply chain under uncertainty: A Portugal study case. In *Computer Aided Chemical Engineering* (Vol. 46, pp. 1309-1314). Elsevier.

Zhang, Q., and Li, H. (2007). MOEA/D: A multiobjective evolutionary algorithm based on decomposition. *IEEE Transactions on Evolutionary Computation*, *11*(6), 712-731.

Coello, C. A. C., Lamont, G. B., & Van Veldhuizen, D. A. (2007). Evolutionary algorithms for solving multi-objective problems (Vol. 5, pp. 79-104). New York: Springer.

Sauro Pierucci, Flavio Manenti, Giulia Bozzano, Davide Manca (Eds.)
Proceedings of the 30th European Symposium on Computer Aided Process Engineering (ESCAPE30), May 24-27, 2020, Milano, Italy.
http://dx.doi.org/10.1016/B978-0-12-823377-1.50149-X

Integrated In Silico Design of Catalysts and Processes based on Quantum Chemistry

Christoph Gertig[a], Lorenz Fleitmann[a], Carl Hemprich[a], Janik Hense[a], André Bardow[a,b], Kai Leonhard[a,*]

[a]*Institute of Technical Thermodynamics, RWTH Aachen University, 52062 Aachen, Germany*
[b]*Institute of Energy and Climate Research (IEK-10), Forschungszentrum Jülich, 52425 Jülich, Germany*
Kai.Leonhard@ltt.rwth-aachen.de

Abstract

Most chemical processes rely on suitable catalysts. Thus, selecting the right catalyst for a process is an important task in chemical process design. However, searching new catalysts can be very tedious. Therefore, computer-aided molecular design (CAMD) methods are very desirable to identify promising candidate catalysts *in silico* and thereby minimize experimental effort. However, methods for computational catalyst design are still in their infancy and often focus on the catalyst turnover number and frequency only while the best catalyst is the one that maximizes the overall process performance. In this work, we therefore propose a method for computer-aided molecular and process design (CAMPD) of catalysts and the corresponding process. A key element is the efficient but accurate prediction of reaction kinetics with advanced quantum chemical methods. We demonstrate the design method for catalytic carbamate cleavage and show that only the integrated catalyst and process design identifies the catalysts that maximize process performance.

Keywords: catalysis, reactions, computer-aided molecular design, process design

1. Introduction

Catalysts are indispensable in the production of chemicals: More than 90 % of newly developed chemical processes require catalysts (Hagen, 2015). Therefore, finding a suitable catalyst is a very important task in chemical process design. Still, catalysts are usually found by experimental screenings or combinatorial chemistry. Such search methods are usually not target-oriented and often lead to huge experimental effort. In many fields of chemistry, experiments can already today (partly) be replaced by quantum chemical (QC) predictions. QC methods have even been combined with computer-aided molecular design (CAMD) methods e.g., for solvent design (Gertig et al., 2020).
However, the *in silico* design of catalyst molecules is still regarded as one of the "Holy Grails in Chemistry" (Poree and Schoenebeck, 2017). Only few approaches have been proposed for the *in silico* design of molecular catalysts. Some authors study catalytic effects in an abstract catalytic environment. The "Theozymes" approach (Tantillo et al.,1998) places functional groups representing the catalyst around reacting molecules. Subsequently, the spatial positions of the functional groups are optimized e.g., to decrease the activation energy of the reaction. Dittner and Hartke (2018) optimize an abstract environment of reacting molecules to study the effect of optimal catalysts. Such

approaches are very valuable to understand the influence of catalysts, but do not design real catalyst molecules. Rarely, approaches have been proposed that optimize real catalyst structures *in silico*. Lin et al. (2005) design transition metal catalysts based on a set of functional groups as building blocks using a tabu search algorithm. Quantitative structure-property relationships (QSPR) are fitted to experimental data and used for performance prediction. The design is based on objectives like density and toxicity. Thus, an optimized catalytic effect is not directly predicted. Chang et al. (2018) design Ni catalyst complexes for catalytic CO/CO_2 conversion. Selected groups of the ligands are optimized to lower the activation energy of the rate-limiting reaction step. Semi-empirical QC methods are used to predict activation energies during design. Promising candidates are subsequently investigated using quantum mechanical density functional theory (DFT).

Despite these encouraging first approaches to *in silico* design of molecular catalysts, two important elements are still missing (Gertig et al., 2020): First, a reliable prediction is required for the acceleration of chemical reactions by candidate catalysts to ensure reliable design results. Thus, reaction rate constants should be predicted using advanced quantum chemical methods. Second, acceleration of chemical reactions is not the ultimate objective of catalyst design but maximum performance of the chemical process. Consequently, catalyst design should be integrated with process design.

In this work, we present the CAT-COSMO-CAMPD method for computer-aided molecular and process design that integrates the optimization of catalyst structures and processes. We calculate reaction rate constants for the designed catalysts based on transition state theory (TST) (Eyring, 1935) and advanced QC methods. A hybrid optimization scheme determines optimal catalyst structures and process conditions: Catalyst structures are designed and optimized using the genetic optimization algorithm LEA3D (ligand by evolutionary algorithm) (Douguet et al., 2005). Optimal process conditions are determined by deterministic process optimization, thus enabling a process-based assessment of all candidate catalysts. The proposed integrated design method is presented in Section 2. The method is demonstrated for the integrated catalyst and process design for a carbamate cleavage process (Section 3).

2. Computer-Aided Catalyst and Process Design

Based on the generic CAMD problem (Gani, 2004), we formulate the computer-aided catalyst and process design problem as optimization problem:

$$
\begin{aligned}
& \max_{x,y} f(x,y) && \text{process-based objective} \\
\text{s.t.} \quad & h_1(x,y) = 0 && \text{thermodynamics, kinetics and process} \\
& h_2(x,y) \leq 0 && \text{inequality constraints on properties and process} \\
& g(y) \leq 0 && \text{(in)equality constraints on molecular structure} \\
& x \in X \subset \mathbb{R}^n && \text{process degrees of freedom} \\
& y \in Y && \text{molecular structure}
\end{aligned}
\tag{1}
$$

In Problem (1), the process-based objective $f(x,y)$ depends on process degrees of freedom x and the molecular structure of the catalyst y. Equality constraints $h_1(x,y)$ model the reaction kinetics, equilibrium thermodynamics and processes. Inequality constraints $h_2(x,y)$ are used on thermodynamic and kinetic properties as well as process conditions. (In)equality constraints $g(y)$ ensure the design of chemically feasible structures and may also limit the explored molecular design space.

To solve the integrated catalyst and process design problem (Problem (1)), we propose the CAT-COSMO-CAMPD method. Following our integrated solvent and process design method COSMO-CAMPD (Gertig et al., 2019a), we solve the integrated design problem in a hybrid optimization scheme (Figure 1): Catalyst structures are designed and optimized using the genetic optimization algorithm LEA3D (Douguet et al., 2005) based on a given library of 3D molecule fragments as building blocks. Optimal process conditions are determined by deterministic process optimization.

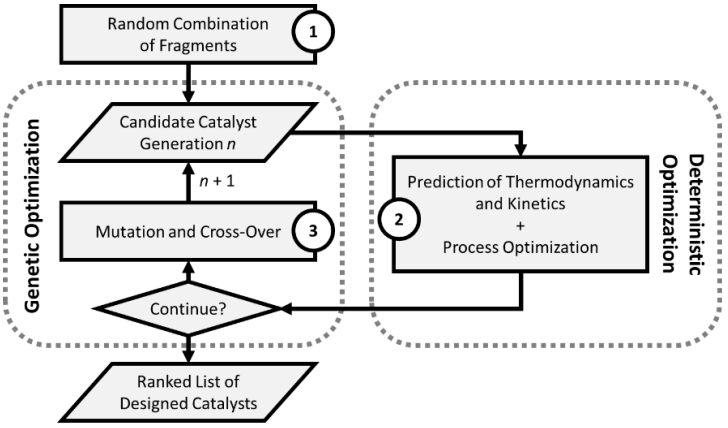

Figure 1: CAT-COSMO-CAMPD method for solution of the integrated catalyst and process design problem using a hybrid optimization scheme combining genetic optimization of molecular catalyst structures and deterministic process optimization.

In step 1 of CAT-COSMO-CAMPD (Figure 1), 3D molecule fragments from the fragment library are combined randomly to obtain an initial generation of candidate catalysts. It is important to ensure that all candidates contain a catalytically active group. In step 2, all candidates from the initial generation are evaluated. This evaluation requires the QC-based prediction of thermodynamic equilibrium properties as well as the prediction of reaction rate constants with transition state theory (TST) (Eyring, 1935). Geometry optimization and frequency analysis are performed for each candidate catalyst molecule as well as for transition states of the catalyzed reactions. The identification of transition states works reliably since the transition states are similar for all carboxylic acid-catalyzed reactions and the optimizations start from a general template. These calculations use the DFT method B3LYP with TZVP basis set and the software Gaussian 09 (Frisch et al., 2013). ORCA (Neese, 2018) is employed to calculate accurate electronic energies with DLPNO-CCSD(T) (Riplinger and Neese, 2013) and aug-cc-pVTZ basis set. We found that this combination of QC methods yields excellent results for different kinds of reactive systems (Gertig et al., 2019a; 2019b). Thermochemical calculations of ideal gas properties are performed with GoodVibes (Funes-Ardoiz and Paton, 2018) based on the rigid rotor harmonic oscillator (RRHO) approximation and quasi-harmonic treatment of low vibrational frequencies (Grimme, 2012). COSMO-RS (Eckert and Klamt, 2002) is used to account for solvation effects. This approach allows to predict both the required thermodynamic equilibrium properties as well as activation barriers between reactant states and transition states in gas and liquid phases. The predicted activation barriers are

used in TST to calculate the rate constants of reactions catalyzed by the candidate catalysts.

All candidate catalysts are assessed based on their process performance. For this purpose, process models are formulated from balance and kinetic equations. These process models are used together with the property prediction methods described above in deterministic optimizations to optimize the process performance for each candidate catalysts. Process optimization employs the interior-point algorithm available in the MatLab (The MathWorks, Inc., 2015) function *fmincon*. The optimized process performance of the candidate catalysts is forwarded to the genetic algorithm. In step 3, the genetic algorithm performs mutations and crossovers for promising candidate catalysts to obtain a new generation of candidates. This new generation of candidate catalysts is again evaluated using QC methods and process optimization (step 2). Steps 2 and 3 are repeated for a predefined number of cycles. Subsequently, a ranking of designed catalysts is returned based on their process performance.

3. Case Study: Integrated Catalyst and Carbamate Cleavage Process Design

The proposed CAT-COSMO-CAMPD method is demonstrated for the design of catalyst and process for carbamate cleavage. Carbamate cleavage is part of a possible production route of industrially important isocyanates (Six and Richter, 2000). The reaction is slow and endothermic (Leitner et al., 2018) and continuous removal of the volatile by-product methanol is required to avoid instantaneous limitation by reaction equilibrium (Kaiser et al., 2018). As discussed in our previous work on solvent design for carbamate cleavage (Gertig et al., 2019a), this constant methanol removal can be achieved by a process comprising of a 2-phase batch reactor and a flash (Figure 2). The catalytic cleavage takes place in a liquid reaction phase that is flushed by inert N_2 to strip out the formed methanol. The flash is used to recycle stripped out solvent, isocyanate and catalyst. Here, we study the cleavage of methyl phenyl carbamate (MPC) to phenyl isocyanate and methanol.

As design objective $f(x,y)$, we choose the yield Y defined as the final amount of isocyanate divided by the initial amount of MPC in the reactor. The degrees of freedom x for process optimization are the flow of nitrogen $\dot{V}_{N_2}$, and the temperature T^F in the flash. The catalytically active group in the designed catalyst structures y is the carboxyl group as carboxylic acids are known to be catalytically active (Satchell and Satchell, 1975). It is important to note that the design method could also work with other catalytically active groups. As further building blocks for catalyst design, the fragment library contains various alkyl and aryl as well as keto, ether, ester, nitrile, amino, halide, sulfide and sulfene fragments. The constraints $h_1(x,y)$ include all equations for property prediction and the process model. Constraints $h_2(x,y)$ limit the flash temperature T^F between 280 and 380 K and the nitrogen flow $\dot{V}_{N_2}$ between $5\text{x}10^{-5}$ and $1.5\text{x}10^{-1}$ m^3/s. Constant parameters are the reactor volume V^R of 1 m^3, the reactor temperature T^R of 473.15 K and a reaction time of 12 h. The reactor is loaded with 15 m-% MPC and 5m-% catalyst. The solvent is diphenyl ether. LEA3D inherently ensures chemical feasibility of designed structures. Further constraints $g(y)$ limit the number of non-hydrogen

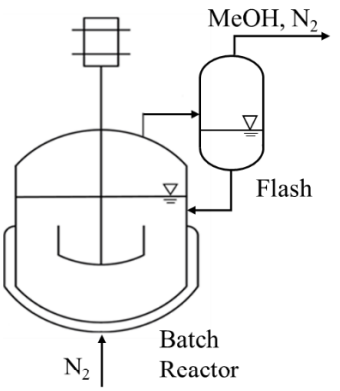

Figure 2: MPC cleavage process.

atoms in the catalysts to a maximum of 13 and ensure that each designed catalyst contains exactly one catalytically active group. The design is run for 6 generations of candidate catalysts after the random initial generation, with 12 candidate catalysts per generation.
The results of the integrated catalyst and process design are shown in Figure 3. 33 catalysts are designed that meet all constraints. The best designed catalyst (shown left in Figure 3) achieves an isocyanate yield of 21 % after 12 h. After few hours, complete conversion cannot be expected due to the slow nature of carbamate cleavage. The optimized process settings are: $\dot{V}_{N_2}$ = 5.4x10^{-2}, T^F = 281.1 K.
Besides the top catalyst, the design suggests several near-optimal candidates. Thus, the final choice could consider additional criteria like commercial availability and environmental properties.
Importantly, the top candidate from the integrated catalyst and process design differs from a simpler catalyst design with a high reaction rate constant as objective. The highest reaction rate is achieved by brominated formic acid. While brominated formic acid is expected to be unstable, it points here to the problem that a high reaction rate can still lead to poor performance in the MPC cleavage process (Figure 3). The reason is that besides the acceleration of the cleavage reaction, high process performance requires further criteria. Examples of such criteria are catalyst volatility leading to stripping by N_2 or the impact of the catalyst on the activity coefficient of methanol which influences the amount of methanol condensed and recycled in the flash. Only the integrated catalyst and process design accounts for the trade-offs between different properties and finds overall optimal solutions.

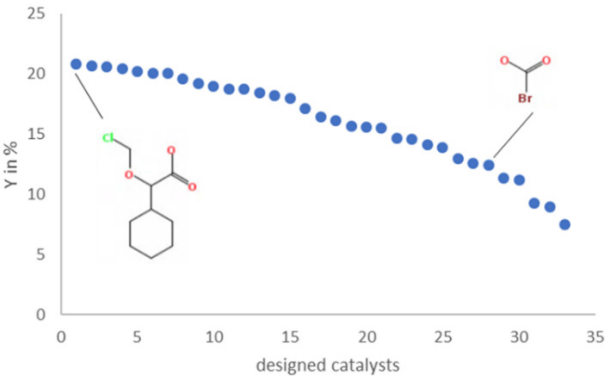

Figure 3: Ranking of catalysts from integrated design.

4. Conclusion

We propose the CAT-COSMO-CAMD method for computer-aided catalyst and process design. Equilibrium properties and kinetics are predicted based on advanced quantum chemical methods and transition state theory. A hybrid optimization scheme is employed to solve the integrated catalyst and process design problem: the genetic algorithm LEA3D is used to optimize catalyst structures and a deterministic algorithm is used for process optimization. The method is demonstrated for a catalytic carbamate cleavage process and identifies several promising catalyst molecules. The results show that catalyst design maximizing only the reaction rate may be misleading whereas the integrated catalyst and process design finds the catalysts that actually maximize process performance.

Acknowledgements

We thank the German Federal Ministry of Education and Research for funding of the project Carbon2Polymers (03EK30442C). Simulations were performed with computing resources granted by RWTH Aachen University under projects rwth0284 and rwth0478.

References

A. M. Chang, B. Rudshteyn, I. Warnke, V. S. Batista, 2018, Inverse Design of a Catalyst for Aqueous CO/CO_2 Conversion Informed by the NiII–Iminothiolate Complex, Inorganic Chemistry, 57(24), 15474-15480.
M. Dittner, B. Hartke, 2018, Globally Optimal Catalytic Fields–Inverse Design of Abstract Embeddings for Maximum Reaction Rate Acceleration, Journal of Chemical Theory and Computation, 14(7), 3547-3564.
D. Douguet, H. Munier-Lehmann, G. Labesse, S. Pochet, 2005, LEA3D: a Computer-Aided Ligand Design for Structure-Based Drug Design, J. Med. Chem., 48(7), 2457-2468.
F. Eckert, A. Klamt, 2002, Fast solvent screening via quantum chemistry: COSMO-RS approach, AIChE Journal, 48, 369–385.
H. Eyring, 1935, The activated complex in chemical reactions, J. Chem. Phys., 3(2), 107-115.
M. J. Frisch et al., 2013, Gaussian 09, Revision D.01.
I. Funes-Ardoiz, R. Paton, 2016, GoodVibes: GoodVibes v1.0.2, DOI: 10.5281/zenodo.595246.
R. Gani, 2004, Chemical product design: challenges and opportunities, Computers & Chemical Engineering, 28(12), 2441-2457.
C. Gertig, K. Leonhard, A. Bardow, 2020, Computer-Aided Molecular and Process Design based on Quantum Chemistry: Current Status and Future Prospects, Current Opinion in Chemical Engineering, 27, 89-97.
C. Gertig, K. Leonhard, A. Bardow, 2019a, Integrated Design of Solvents and Processes based on Reaction Kinetics from Quantum Chemical Prediction Methods, Computer Aided Chemical Engineering 46, 415-420.
C. Gertig, L. C. Kröger, L. Fleitmann, J. Scheffczyk, A. Bardow, K. Leonhard, 2019b, Rx-COSMO-CAMD: Computer-Aided Molecular Design of Reaction Solvents based on predictive Kinetics from Quantum Chemistry, Industrial & Engineering Chemistry Research, 58, 22835-22846.
S. Grimme, 2012, Supramolecular Binding Thermodynamics by Dispersion- Corrected Density Functional Theory, Chemistry–A European Journal, 18(32), 9955-9964.
J. Hagen, 2015, Industrial Catalysis, WILEY-VCH.
T. Kaiser, A. Rathgeb, C. Gertig, A. Bardow, K. Leonhard, A. Jupke, 2018, Carbon2Polymer–Conceptual Design of a CO_2- Based Process for the Production of Isocyanates. Chemie Ingenieur Technik, 90(10), 1497-1503.
W. Leitner, G. Franciò, M. Scott, C. Westhues, J. Langanke, M. Lansing, C. Hussong, E. Erdkamp, 2018, Carbon2Polymer–Chemical Utilization of CO_2 in the Production of Isocyanates, Chemie Ingenieur Technik 90 (10), 1504–1512.
B. Lin, S. Chavali, K. Camarda, D. C. Miller, 2005, Computer-aided molecular design using Tabu search, Computers & Chemical Engineering, 29(2), 337-347.
The MathWorks, Inc., 2015. MATLAB R2015b.
F. Neese, 2018, Software update: the ORCA program system, version 4.0, Wiley Interdisciplinary Reviews: Computational Molecular Science, 8, e1327.
C. Poree, F. Schoenebeck, 2017, A holy grail in chemistry: Computational catalyst design: Feasible or fiction?, Accounts of Chemical Research 50 (3), 605-608.
C. Riplinger, F. Neese, 2013, An efficient and near linear scaling pair natural orbital based local coupled cluster method,The Journal of Chemical Physics,138, 034106.
D. Satchell, R. Satchell, 1975, Acylation by ketens and isocyanates. A mechanistic comparison, Chemical Society Reviews, 4(2), 231-250.
C. Six, F. Richter, 2000. Isocyanates, organic. Ullmann's Encyclopedia of Industrial Chemistry.
D. J. Tantillo, C. Jiangang, K. N. Houk, 1998, Theozymes and compuzymes: theoretical models for biological catalysis, Current Opinion in Chemical Biology, 2(6), 743-750.

Sauro Pierucci, Flavio Manenti, Giulia Bozzano, Davide Manca (Eds.)
Proceedings of the 30th European Symposium on Computer Aided Process Engineering (ESCAPE30), May 24-27, 2020, Milano, Italy.
http://dx.doi.org/10.1016/B978-0-12-823377-1.50150-6

In silico Screening of Metal-organic Frameworks for Acetylene/ethylene Separation

Yageng Zhou[a], Teng Zhou[a,b,*], Kai Sundmacher[a,b]

[a] *Process Systems Engineering, Otto-von-Guericke University Magdeburg, Universitätsplatz 2, D-39106 Magdeburg, Germany*

[b] *Process Systems Engineering, Max Planck Institute for Dynamics of Complex Technical Systems, Sandtorstr. 1, D-39106 Magdeburg, Germany*

zhout@mpi-magdeburg.mpg.de

Abstract

Ethylene, used as feedstocks for producing polyethylene, is a valuable chemical in the petroleum industry. The separation of acetylene from ethylene in the ethane cracking process to produce high-purity ethylene is conventionally carried out by energy intensive partial hydrogenation or solvent absorption. Over the last decade, Metal-Organic Frameworks (MOFs) have emerged as a promising class of porous adsorbents. They are reported to have high performances in many gas separation applications thus could potentially lead to energy-efficient process alternatives (Li et al., 2012). In this work, a large-scale computational screening of 4764 different MOFs for the ethylene/acetylene separation is performed. As a result, 10 potential MOF candidates are identified as the best separation materials, which are targeted for further experimental synthesis and validation.

Keywords: metal-organic framework, acetylene/ethylene separation, GCMC simulation, adsorbent screening

1. Introduction

In the petrochemical industry, acetylene and ethylene are two important intermediate chemicals for producing consumer products. In the ethane cracking and biomass and coal pyrolysis processes, a mixture of C_2H_2 and C_2H_4 gases needs to be separated (Cui et al., 2016). Traditional separation methods, such as solvent absorption and partial hydrogenation, are quite energy-consuming (Studt et al., 2008).

Over the last few decades, metal-organic frameworks (MOFs), formed by inorganic centers and organic linking groups, have emerged as novel porous materials for gas storage and separation. It has been found that many MOFs exhibit high capacity and selectivity for the C_2H_2/C_2H_4 separation. Xiang et al. (2011) first reported a set of tunable mixed-metal-organic framework materials, among which M'MOF-3a showed the highest selectivities 25.5, 4.1 and 5.2 at 195 K, 273 K and 295 K, respectively. Bloch et al. (2012) demonstrated the high performance of FeMOF-74 with the C_2H_2 equilibrium uptake of 6.8 mmol/g and C_2H_2/C_2H_4 selectivity 2.08 at 318 K and 1 bar. Yang et al. (2014) reported that at 293 K and 1 bar the C_2H_2 uptake and C_2H_2/C_2H_4 selectivity of NOTT-300 are 6.34 mmol/g and 2.3, respectively. Hu et al. (2015) found that the suitable pores and opening windows of UTSA-100a can lead to a satisfying C_2H_2 uptake of 4.27 mmol/g and a high C_2H_2/C_2H_4 selectivity of 10.72 at 296 K and 1 bar. Cui et al. (2016) reported two new MOFs, SIFSIX-2-Cu-i (C_2H_2 uptake outperformed UTSA100a under 0.025 bar) and

SIFSIX-1-Cu (C_2H_2 uptake 8.5 mmol/g), and found their C_2H_2/C_2H_4 selectivities were in the ranges of 39.7 − 44.8 and 7.1 − 10.6, respectively, depending on the feed gas conditions. Recently, Wang et al. (2017) discovered BUT-11 that displayed a C_2H_2 uptake of 159.4 cm^3/g (≈ 7.12 mmol/g) at 298 K and 1 bar.

Given the structural diversities of MOFs, experimental synthesis and screening of MOFs for the separation of C_2H_2/C_2H_4 is costly and time-consuming. Fortunately, the significant progress of molecular simulation techniques makes it possible to utilize computational methods to discover promising MOFs for various gas separations, such as $CO_2/N_2/CH_4$ (Haldoupis et al., 2010; Wilmer et al., 2012a; Qiao et al., 2016), H_2/CH_4 (Wu et al., 2012; Altintas et al., 2018), C_2H_2/CH_4 and C_2H_2/CO_2 (Nemati Vesali Azar and Keskin, 2018), C_2H_6/C_2H_4 and C_2H_6/CH_4 (Altintas and Keskin, 2016), CO_2/H_2 (Avci et al., 2018), C_3H_8/C_3H_6 (Yeo et al., 2016), alkane isomers (Dubbeldam et al., 2012; Chung et al., 2017).

In this work, we perform a large-scale computational screening of 4764 experimentally synthesized MOFs for the separation of an equimolar C_2H_2/C_2H_4 gas mixture. First, we validate the accuracy of grand canonical Monte Carlo (GCMC) simulations by comparing the simulated and experimental adsorption uptakes of pure C_2H_2 and C_2H_4 gases. Next, the adsorption of the C_2H_2/C_2H_4 mixture in different MOFs is examined using GCMC simulations, based on which the working capacity and selectivity of each MOF are calculated. Finally, a separation performance index (SPI) is defined and determined for each material. Based on the ranking of SPI, the most promising MOFs are identified.

2. Materials and simulation details

2.1 MOF database

In this work, the computation-ready, experimental metal-organic framework (CoRE MOF) database developed by Chung et al. (2014) is utilized as the screening database due to the following considerations: first, the database consists of a variety of MOFs structures, which provide a rich search space for finding promising adsorbents; second, the structures in the database are immediately suitable for molecular simulation without any further modifications; third, all the MOFs have already been experimentally reported so that the screened materials can be synthesized and applied. There are totally 4764 MOFs in the CoRE MOF database.

2.2 Simulation details

Grand canonical Monte Carlo (GCMC) simulation is widely used for investigating gas adsorption in porous materials. In this study, we rely on GCMC for the simulation of C_2H_2/C_2H_4 adsorption in MOFs using RASPA software (Dubbeldam et al., 2016). Specifically, we consider equal probabilities for four types of Monte Carlo moves, which are translation, rotation, reinsertion, and swap. A cut-off radius of 12.0 Å is used and the simulation cell is expanded to at least 24.0 Å along each dimension where periodic boundary conditions are applied. Each simulation is carried out with first 30,000 cycles for equilibration and subsequent 20,000 cycles for production. More details of these simulations settings can be found in the literature (Dubbeldam et al., 2016).

Among the various C_2H_2 molecular models, the one proposed in Fischer et al. (2010) is used due to its validated accuracy. Similarly, the C_2H_4 molecular model is adopted from Liu et al. (2008). The model parameters of both molecules are listed in Table 1, including Lennard-Jones (LJ) potential parameters (σ and ε), partial charge (q), and bond length (l).

Table 1. Molecular model parameters of the C_2H_2 and C_2H_4 molecules

	Atoms	σ (Å)	ε (K)	q (e)	Bond length l (Å)
C_2H_2	C in C_2H_2	3.800	57.875	−0.278	1.2111 (C–C)
	H in C_2H_2	0	0	0.278	1.0712 (C–H)
C_2H_4	CH_2 (sp^2)	3.685	93.0	0	1.3300 (C–C)

Due to charged atoms in C_2H_2, Columbic forces cannot be omitted. Thus besides the LJ 12-6 potential for describing Van der Waals force, the force field function should also include the Columbic potential and be formulated as follows:

$$U = \sum 4\,\varepsilon_{ij}\left[\left(\frac{\sigma_{ij}}{r_{ij}}\right)^{12} - \left(\frac{\sigma_{ij}}{r_{ij}}\right)^{6}\right] + \sum \frac{q_i q_j}{4\pi\varepsilon_0 r_{ij}} \tag{1}$$

where ε_{ij} is well depth, σ_{ij} is collision diameter, r_{ij} is the distance between atoms i and j, q_i is the atomic charge of atom i, and ε_0 is 8.8542×10^{-12} ($C^2N^{-1}m^{-2}$). The employed LJ potential parameters are taken from the DREIDING force field (Mayo et al., 1990) with those of the missing atoms taken from the UFF force field (Rappe et al., 1992). The cross LJ parameters are computed using Lorentz-Berthelot combing rules (Maitland et al., 1981) except those between Cu and C of C_2H_2 that are modified according to Fischer et al. (2010) to account for the interactions with unsaturated metal sites. In order to calculate Columbic interactions, partial charges on every framework atoms are estimated using the EQeq method proposed by Wilmer et al. (2012b). Additionally, all MOFs are assumed to be rigid with the purpose of saving a large amount of computational time. Although this assumption is made at the cost of the sacrifice in simulation accuracy, it is a generally accepted practice in large-scale screening.

3. Evaluation metrics

It is well known that selectivity and working capacity are two key indicators for evaluating separation performance. Selectivity is defined as the ratio of equilibrium constant K. For the separation of component i from j, $S_{i/j}$ is determined as follows:

$$S_{i/j} = \frac{K_i}{K_j} = \frac{y_i}{x_i}\Big/\frac{y_j}{x_j}$$

where y and x are the gas and adsorbed phase compositions, respectively.

The working capacity of the adsorbent with respect to component i is defined as the difference between the equilibrium adsorption, $N_{i,ads}$, and desorption, $N_{i,des}$, loadings:

$$C_i = N_{i,ads} - N_{i,des}$$

Considering the significance of both selectivity and working capacity, we defined a separation performance index (SPI), the product of both criteria, to evaluate and rank the separation capabilities of MOFs:

$$SPI = S_{i/j} \times C_i$$

4. Results and discussion

Before large-scale MOF screening, it is necessary to first validate the accuracy of GCMC

simulations. For this purpose, we collect reported, experimental C_2H_2 and C_2H_4 adsorption uptakes in different MOFs (Xiang et al., 2009; Bao et al., 2011; He et al., 2012) under 298 K and 1 bar. For these MOFs we perform GCMC simulations at the same condition to compute pure gas equilibrium adsorption uptakes. The detailed simulation settings are described in Section 2. As illustrated in Figure 1, a good agreement between experimental and simulated gas uptakes can be found. The average relative deviations of acetylene and ethylene uptakes are 0.147 and 0.138, respectively. The results confirm that our selection of molecular models and force field parameters is appropriate and the molecular simulation setup is reasonable for MOF screening.

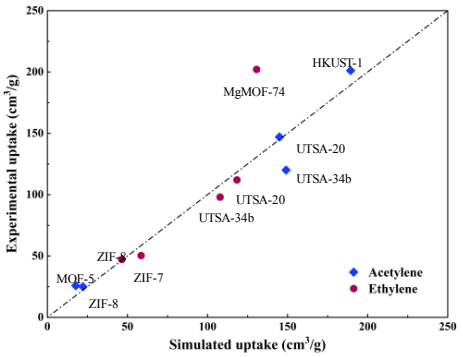

Figure 1: Comparison between experimental and GCMC simulated pure gas (C2H2 and C2H4) adsorption uptakes at 298 K and 1 bar

For the 4764 MOFs in the CoRE MOF database we conduct GCMC simulations and compute their selectivities and working capacities for C_2H_2 and C_2H_4 separation. In order to mimic the industrial adsorption process, the simulation temperature is fixed to 298 K and the adsorption and desorption pressures are set to 1 bar and 0.1 bar, respectively. The C_2H_2/C_2H_4 gas composition is specified to 50%/50% (mol/mol), a typical scenario in the biomass pyrolysis process (Cui et al., 2016). It is worth noting that for separating such an equimolar gas mixture, two different strategies can be employed. We can find either an adsorbent with a high $S_{C2H2/C2H4}$ and C_{C2H2} that selectively remove C_2H_2 from C_2H_4, or one preferentially adsorbs C_2H_4 with a high $S_{C2H4/C2H2}$ and C_{C2H4}. For better illustration, two separate plots corresponding to each strategy are presented in Figure 2.

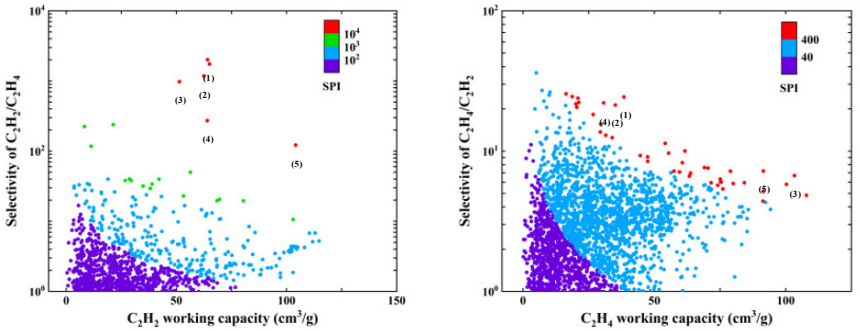

(a) **(b)**

Figure 2: (a) GCMC simulated C2H2 working capacity and C2H2/C2H4 selectivity (b) GCMC simulated C2H4 working capacity and C2H4/C2H2 selectivity

As indicated in Figure 2(a), there are in total 975 C_2H_2-selective MOFs with $S_{C2H2/C2H4}$ ranging from 1.0 to 2005.6 and C_{C2H2} up to 114.8 cm^3/g. Among the 975 MOFs, 0.7% are found to have SPI value above 10^4, 1.7% between 10^3 and 10^4, 25.4% between 10^2 and 10^3, and 72.4% below 10^2. A trade-off between the selectivity and working capacity in the selection of MOFs can be observed. The top 5 MOFs with the highest SPI values are listed in Table 2, together with their important physical properties. The density ρ, pore limiting diameter (PLD), and porosity ϕ of the top 5 MOFs have been found to vary in limited ranges around 1.079 g/cm^3, 5.157 Å, and 0.561, respectively. Additionally, the Cu atom in MOF is found to be very favorable for the C_2H_2/C_2H_4 separation, mainly due to the strong interactions between C_2H_2 and the Cu open metal site. This finding agrees well with the experimental observations (Xiang et al. 2009).

Table 2. Top 5 MOFs for the separation of C2H2 from C2H4

Rank	CSD code	Metal	ρ (g/cm^3)	PLD (Å)	ϕ	C_{C2H2}	$S_{C2H2/C2H4}$
1	DOLXOR	Cu	1.087	5.360	0.559	64.2	2005.6
2	DOLXOR02	Cu	1.079	5.365	0.559	62.5	1177.1
3	KAHNOX	Cu	1.085	5.407	0.562	51.4	978.0
4	UBUROY	Cu, Zn	1.081	5.389	0.573	64.0	271.5
5	TANBOZ	Cu	1.061	4.265	0.550	104.2	121.8

As depicted in Figure 2(b), there are 2477 C_2H_4-selective MOFs with $S_{C2H4/C2H2}$ ranging from 1.0 to 36.1 and C_{C2H4} up to 107.9 cm^3/g. 1.7% of the MOFs are found to possess SPI value above 400, 66.3% between 40 and 400, and 32.0% below 40. Likewise, the top 5 MOFs with the highest C_2H_4 separation potentials are recognized and listed in Table 3. Large variations in the MOF's physical properties ($0.774\ g/cm^3 \le \rho \le 1.511\ g/cm^3$, $2.593\ Å \le PLD \le 4.441\ Å$, $0.432 \le \phi \le 0.708$) are observable and no strong evidence on the metal-dependence can be found among the top MOFs.

Table 3. Top 5 MOFs for the separation of C2H4 from C2H2

Rank	CSD code	Metal	ρ (g/cm^3)	PLD (Å)	ϕ	C_{C2H4}	$S_{C2H4/C2H2}$
1	SETFUT	Cd	1.511	2.593	0.444	38.4	24.3
2	BEXTUV	Mn	1.305	3.789	0.486	35.2	21.3
3	QUQPOI	Zn	0.774	4.340	0.667	103.3	6.7
4	ADIQEL	Co	1.238	3.914	0.432	30.7	22.1
5	DEYVUA	Zn	0.961	4.441	0.708	91.5	7.2

5. Conclusions

In order to address the challenge in the discovery of advanced materials for the energy-efficient acetylene/ethylene separation, we have systematically screened 4764 MOFs by use of GCMC simulations. Very promising MOFs are identified and the relevant physical properties of these materials are analyzed. In our future work, a detailed study on the adsorption kinetics will be carried out to identify adsorbents featuring high mass transfer

rates. A rigorous evaluation of high-potential MOFs in a pressure or temperature-swing adsorption process will also be performed.

References

C. Altintas, I. Erucar, S. Keskin, 2018, ACS Appl Mater Interfaces, 10, 4, 3668-3679
C. Altintas, S. Keskin, 2016, Chem Eng Sci, 139, 49-60
G. Avci, S. Velioglu, S. Keskin, 2018, ACS Appl Mater Interfaces, 10, 39, 33693-33706
Z. Bao, S. Alnemrat, L. Yu, I. Vasiliev, Q. Ren, X. Lu, S. Deng, 2011, Langmuir, 27, 22,13554-13562
E.D. Bloch, W.L. Queen, R. Krishna, J.M. Zadrozny, C.M. Brown, J.R. Long, 2012, Science, 335, 6076, 1606-1610
Y.G. Chung, P. Bai, M. Haranczyk, K.T. Leperi, P. Li, H. Zhang, T.C. Wang, T. Duerinck, F. You, J.T. Hupp, O.K. Farha, J.I. Siepmann, R.Q. Snurr, 2017, Chem Mater, 29, 15, 6315-6328
Y.G. Chung, J. Camp, M. Haranczyk, B.J. Sikora, W. Bury, V. Krungleviciute, T. Yildirim, O.K. Farha, D.S. Sholl, R.Q. Snurr, 2014, Chem Mater, 26, 21, 6185-6192
X. Cui, K. Chen, H. Xing, Q. Yang, R. Krishna, Z. Bao, H. Wu, W. Zhou, X. Dong, Y. Han, B. Li, Q. Ren, M. J. Zaworotko, B. Chen, 2016, Science, 353, 6295, 141-144
D. Dubbeldam, S. Calero, D.E. Ellis, R.Q. Snurr, 2016, Mol Simul, 42, 2, 81-101
D. Dubbeldam, R. Krishna, S. Calero, A.Ö. Yazaydın, 2012, Angew Chem Int Ed, 51, 47, 11867-11871
M. Fischer, F. Hoffmann, M. Fröba, 2010, ChemPhysChem, 11, 10, 2220-2229
E. Haldoupis, S. Nair, D.S. Sholl, 2010, J Am Chem Soc, 132, 21, 7528-7539
Y. He, R. Krishna, B. Chen, 2012, Energy Environ Sci, 5, 10, 9107-9120
T.L. Hu, H. Wang, B. Li, R. Krishna, H. Wu, W. Zhou, Y. Zhao, Y. Han, X. Wang, W. Zhu, Z. Yao, S. Xiang, B. Chen, 2015, Nat Commun, 6, 7328
J.R. Li, J. Sculley, H.C. Zhou, 2012, Chem Rev, 112, 2, 869-932
B. Liu, B. Smit, F. Rey, S. Valencia, S. Calero, 2008, J Phys Chem C, 112, 7, 2492-2498
G.C. Maitland, M. Rigby, E.B. Smith, W.A. Wakeham, 1981, Oxford Clarendon Press
S.L. Mayo, B.D. Olafson, W.A. Goddard, 1990, J Phys Chem, 94, 26, 8897-8909
A. Nemati Vesali Azar, S. Keskin, 2018, Front Chem, 6, 36
Z. Qiao, C. Peng, J. Zhou, J. Jiang, 2016, J Mater Chem A, 4, 41, 15904-15912
A.K. Rappe, C.J. Casewit, K.S. Colwell, W.A. Goddard, W.M. Skiff, 1992, J Am Chem Soc, 114, 25, 10024-10035
F. Studt, F. Abild-Pedersen, T. Bligaard, R.Z. Sørensen, C.H. Christensen, J.K. Nørskov, 2008, Science 320, 1320-1322
X. Wang, L. Li, Y. Wang, J.R. Li, J. Li, 2017, CrystEngComm, 19, 13, 1729-1737
C.E. Wilmer, O.K. Farha, Y.S. Bae, J.T. Hupp, R.Q. Snurr, 2012a, Energy Environ Sci, 5, 12, 9849-9856
C.E. Wilmer, K.C. Kim, R.Q. Snurr, 2012b, J Phys Chem Lett, 3,17, 2506-2511
D. Wu, C. Wang, B. Liu, D. Liu, Q. Yang, C. Zhong, 2012, AIChE J, 58, 7, 2078-2084
S.C. Xiang, Z. Zhang, C.G. Zhao, K. Hong, X. Zhao, D.R. Ding, M.H. Xie, C.D. Wu, M.C. Das, R. Gill, K.M. Thomas, B. Chen, 2011, Nat Comm, 2, 204
S. Xiang, W. Zhou, J.M. Gallegos, Y. Liu, B. Chen, 2009, J Am Chem Soc, 131, 34, 12415-12419
S. Yang, A.J. Ramirez-Cuesta, R. Newby, V. Garcia-Sakai, P. Manuel, S.K. Callear, S.I. Campbell, C.C. Tang, M. Schröder, 2014, Nat Chem, 7, 121
B.C. Yeo, D. Kim, H. Kim, S.S. Han, 2016, J Phys Chem C, 120, 42, 24224-24230

Sauro Pierucci, Flavio Manenti, Giulia Bozzano, Davide Manca (Eds.)
Proceedings of the 30th European Symposium on Computer Aided Process Engineering (ESCAPE30), May 24-27, 2020, Milano, Italy.
http://dx.doi.org/10.1016/B978-0-12-823377-1.50151-8

Process Synthesis and Simultaneous Heat and Electricity Integration to Reduce Consumption of Primary Energy Sources

[a]Andreja Nemet*, [b]Timothy Gordon Walmsley, [c]Elvis Ahmetović, [a]Zdravko Kravanja

[a]*Faculty of Chemistry and Chemical Engineering, University of Maribor, Smetanova ulica 17, Maribor 2000, Slovenia*
[b]*Sustainable Energy and Water Systems Group, School of Engineering, University of Waikato, New Zealand*
[c]*Faculty of Technology, University of Tuzla, Tuzla 75000, Bosnia and Herzegovina*
andreja.nemet@um.si

Abstract

A synthesis of an industrial utility system considering cogeneration options together with heat exchanger network synthesis has been developed. It consists of boilers at different temperature and pressure levels, steam turbines, condensers, cooling tower, deaerator and a heat exchanger network system, connecting the utility system with the process heat and electricity requirements. A mixed-integer nonlinear programming (MINLP) model was used for synthesis. A sensitivity analysis has been performed considering the price ratio of natural gas to electricity, while also estimating primary energy consumption and GHG emissions. The results indicate that the cogeneration is economically viable at different ratios of natural gas and electricity price. In addition, the sensitivity analysis shows the relationship between cogeneration and electricity purchase for obtaining the minimal primary energy consumption and consequently to reduce GHG emissions.

Keywords: cogeneration; utility system; heat exchanger network; primary energy source reduction; GHG emissions

1. Introduction

Process synthesis is usually performed sequentially, obtaining the optimal design for the reactors at first, followed by the design of the separation subsystem, and, finally, designing the heat recovery system and the utility system, according to an Onion diagram. On the other hand, there are existing examples using the simultaneous approach where processes are optimized or their flowsheets synthesized by performing simultaneous heat integration, for example, using the model by Duran and Grossmann (1986), or even synthesizing their heat exchanger networks (HENs) simultaneously, such as using the simultaneous HEN synthesis model by Yee et al. (1990). The solutions obtained are in many cases significantly superior to those obtained by the sequential approach, often featuring smaller consumption of utilities, lower capital investment, and reduced consumption of raw materials. However, simultaneous utility system synthesis has been studied to a rather limited extent so far, as follows.

Goh et al. (2016) developed an automated targeting model considering both the HEN and utility system utilizing a steam and power cascade as well as the heat and utility cascade. This approach presents a targeting method considering HEN and utility system

simultaneously obtaining a “minimum” total operating cost, however, without synthesis of the utility system and HEN design. Luo et al. (2012) presented a hybrid targeting model, based on Pinch technology, and mathematical modeling. The study connected the utility system of a regenerative Rankine cycle based steam power plant with surplus heat from the process, presenting a way to include hot streams into the utility system. Lira-Barragán et al. (2014) presented a scheme for design optimization of process energy system integration considering a trigeneration system. In this study, the design of organic Rankine cycles, absorption refrigeration cycles and the heat exchanger network are considered. The streams of each utility system are considered in additional stages in a superstructure with fixed temperatures, in this way including the utility system into HEN synthesis. Luo et al. (2016) presented a model where the utility system, consisting of one boiler, a multi-stage turbine, a deaerator and a condenser, and the HEN synthesis were considered simultaneously. Elsido et al. (2019) performed a simultaneous heat integration and synthesis of steam and organic Rankine cycles, creating a connection between HEN and utility system synthesis. Martelli et al. (2017) considered HEN and utility synthesis in their work. A two-stage algorithm was developed, where in the first stage a targeting method was applied, while in the second stage the MINLP optimization occurred aided by the results from first stage. However, in their work, only a different presentation of utility streams is applied, not the trade-off between primary energy source and the utility and HEN system synthesis. Later a similar approach was used for heat recovery steam cycle optimization (Elsido et al., 2019). Liu et al. (2018) presented a HEN synthesis model accounting for a cooling water system. It should be noted that only Luo et al. (2016) considered the trade-off between the operating and investment costs and determined the primary energy sources actually bought by companies, e.g. natural gas and electricity, rather than steam, which is an intermediate energy carrier produced by a utility system. In this study, the system borders of HEN synthesis is widened to achieve more holistic and realistic trade-offs. Firstly, the HEN optimization is performed by simultaneously considering the synthesis of hot utility generation system. By this the trade-off between heat consumption “at-the-gate” of the company and the investment is established for the entire heat system. Secondly, the heat and electricity systems are considered simultaneously. This simultaneous handling of entire energy system leads to proper trade-off between energy utilization “at-the-gate” of the company and the investment. This wider scope of system borders enables achieving appropriate trade-offs between operating cost, considering primary energy source, and investment required for the utility system and HEN. In order to enable the evaluation of the mentioned trade-offs, the HEN superstructure is extended by: i) steam production system with boilers at different temperature ranges, ii) options with and without cogeneration, iii) hot and cold utility streams considered in each stage of the HEN superstructure, allowing better optimization of the entire HEN including heat exchangers between utility and process streams, and iv) both mass and energy flows and balances to appropriately track mass and heat losses in the (sub)systems. Note that temperatures and pressures of the steam headers (including superheated steam) are optimization variables, taking the advantages of interactions between steam production system, cogeneration system and steam utilization system (HEN).

2. Method

A superstructure approach applying MINLP model formulation has been formulated as represented in Figure 1. It consists of three boilers representing options for steam production at three different levels of superheated steam.

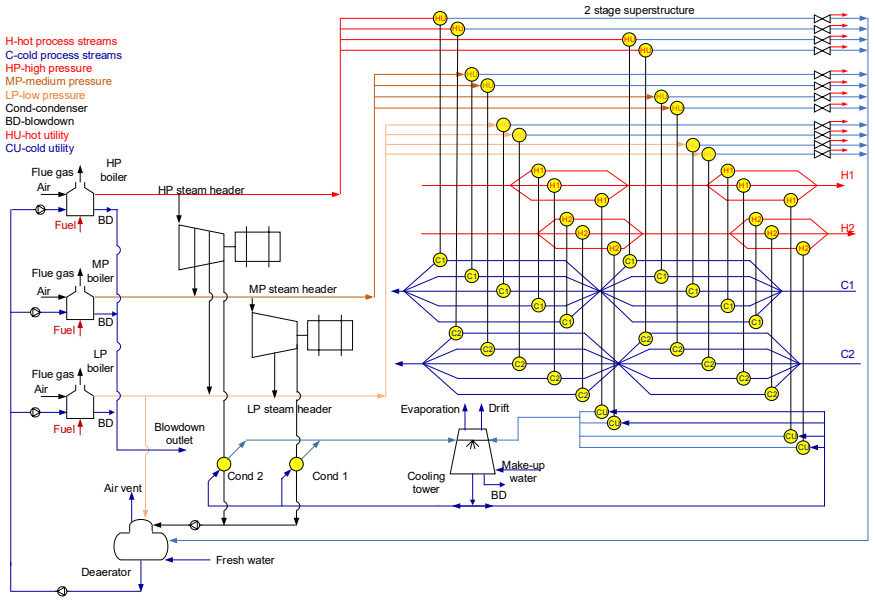

Figure 1: Superstructure of the cogeneration and simultaneous HEN synthesis.

It should be noted that the temperatures of steam headers are not fixed, and they are treated as optimization variables. Furthermore, the superstructure consists of two multi-stage turbines. The first is utilizing steam from the high pressure (HP) level, optionally releasing steam at medium pressure (MP), low pressure (LP), and/or condenser levels. The second turbine utilizes MP level steam, while releasing steam at LP level, if needed, before being sent to a condenser. The steam condensates released from condensers are directed to the deaerator. The superheated steam produced in the utility system is utilized in the process to heat cold process streams. The heat exchanger network (HEN) optimization is performed by the superstructure based on Yee and Grossmann (1990), while considering each utility stream in every stage of the superstructure as suggested by Isafiade and Fraser (2010). The condensate return is assumed to be returned in a vented pipeline at atmospheric pressure, causing both heat and mass loss from the system. Throttle valves are used to achieve atmospheric pressure in the pipelines. In this way, the loss due to flash steam is considered. The condensate is then returned to the utility system via the deaerator. Two cooling water cycles are presented in the superstructure in connection with a cooling tower: i) the first one supplies cooling water to the condensers after steam turbines and ii) the second one supplies cooling water to coolers in the HEN to cool hot process streams. The make-up water needs, as a result of evaporation, drift and blowdown water, are also considered. The water cycles of utility and process parts are closed via the deaerator. In the deaerator, the condensate from the condenser, condensate recovered from the process and fresh water inlet are considered as inlets. To operate the deaerator LP steam is used in the deaerator to operate the equipment and to preheat the water. The water from the deaerator is used in the selected boiler(s).

3. Case study

3.1. Input data

The process studied consisted of two hot and two cold streams with three different levels of intermediate utility available. The input data for streams are presented in Table 1. The

electricity requirement of the process was 1.5 MW. The fuel and utility prices are assumed as 40 €/MWh for natural gas, 8.75 €/MWh for cooling, and 80 €/MWh up to 140 €/MWh for electricity depending on the scenario. The fix charge for heat exchangers is 550 €, while the variable charges 15 €/m^2. The area exponent is set at 1. The fix charge for turbine is 18,200 €, and the variable charge is 2,173 €/MWh. For the boiler, the fixed charge is 28,400 € and the variable component is 2,220 € kg^{-1} s.

Table 1: Input data

Stream	T^{in}/ °C	T^{out}/ °C	FC/ MW °C^{-1}	h/ MW °C^{-1} m^{-2}
H1	377	40	0.5	0.00033
H2	317	97	0.4	0.0004
C1	137	277	17	0.00045
C2	77	127	16	0.00038
IU-saturated state	T_{lo}/°C	T_{up}/°C		h/MW °C^{-1} m^{-2}
LPS	120	148		10
MPS	148	208		10.5
HPS	208	252		11
IU-superheated state	T_{lo}/°C	T_{up}/°C		
LPS	130	497		
MPS	158	497		
HPS	218	497		

To determine the primary energy consumption of electricity bought from the grid network, the efficiency of the electricity production and transmission from natural gas is assumed to be 30.4 %. The GHG emission factor is taken as the LCA emission factors for the EU average. For natural gas, it is 0.237 $t_{CO2\text{-}eq}$/MWh and, for the electricity consumed, it is 0.578 $t_{CO2\text{-}eq}$/MWh$_e$ (EU, 2010).

3.2. Results

We compared a solution obtained by performing HEN optimization simultaneously with the synthesis of utility system excluding electricity generation and solution including electricity cogeneration. The first solution was obtained at electricity price of 80 €/MWh, while the second at 140 €/MWh. The selected heat exchangers are presented in Table 2. The heat consumptions in both cases were similar (1,904 MW no electricity generation vs. 1,929 MW in the case of cogeneration); however, lower temperature level of intermediate utility and larger areas of utility exchangers were selected when cogeneration was considered. As can be seen, the electricity price heavily effected the final HEN design, showing the significance of simultaneous consideration of the entire energy generation system with cogeneration and the HEN optimization.

Table 2: Area of heat exchangers in m^2 when considering HEN optimization and cogeneration

HE	**H1-C1**	**H2-C1**	**H2-C2**	**H1-CW**	**H2-CW**	**IU-C1**	**IU-C2**
No cogeneration	4,288	3,128	926	3,352	-	HPS 18,286	HPS 14,680
Cogeneration	3,910	2,444	-	3,455	573	MPS 24,023	MPS 20,329

Figure 2 presents the results of the sensitivity analysis, where the price of electricity was varied from 80 €/MWh up to 140 €/MWh. In Figure 2a, the cost distribution between annual investment, natural gas, electricity and cooling is presented, together with the TAC

of utility system and HEN. As can be observed at lower price ratios, the TAC is lower, and the largest proportion of TAC is the electricity cost.

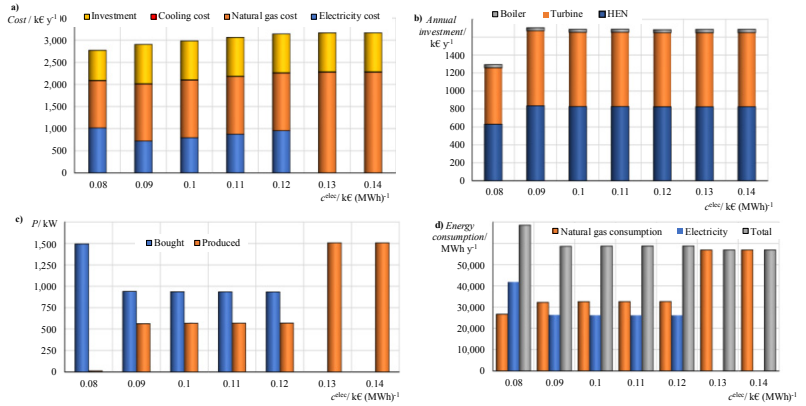

Figure 2: Results of the sensitivity analysis. a) Cost distribution between parts of TAC, b) cost distribution of annual investment, c) the amount of electricity produced via cogeneration and electricity bought from network, and d) "at-the-gate" energy consumption for various ratios between the electricity and natural gas prices

By increasing the electricity price, it becomes more economically viable to produce a larger amount of electricity compared to buying it. This is clearly visible in Figure 2c, where the electricity produced versus the one bought is presented. Figure 2b presents the further distribution of annual investment between HEN, turbines and boilers. As can be seen, the largest proportion of investment is in the HEN, and it is increasing with any increase of the electricity price. The boiler and turbine annual investment is also increasing with the increase of the price, which is a consequence of the basic trade-off between the operating cost and annual investment. Figure 2d presents the energy consumption within the company of the energy carriers supplied "at-the-gate". The trade-off between primary energy consumption and the investment is studied by determining the primary energy consumption and Greenhouse Gas (GHG) emission under various electricity prices. For the electricity bought from the network, it was assumed that the power plant operates at 30.4 % efficiency. As can be seen from Figure 3a, a minimum primary energy consumption occurred in the case with higher electricity prices. These results clearly show the reduction of primary energy consumption, when cogeneration of heat and electricity is used. This is a consequence of the shared heat and electricity production cycle that requires less primary energy. From a sustainability point of view, the optimal solutions should consider the transformations and distributions/transmissions of energy types from the primary energy source to minimize overall emissions. Figure 3b presents the GHG emission, which does lead to the conclusion that the lowest GHG emission matches the case with the lowest primary energy consumption.

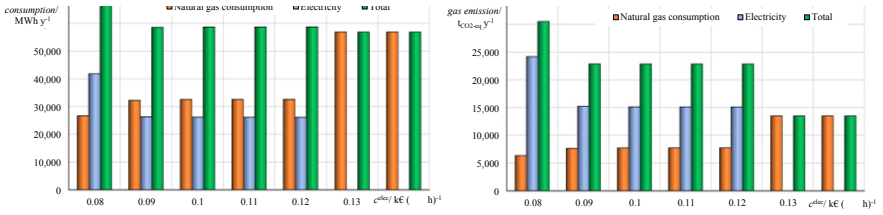

Figure 3: a) Primary energy consumption and b) GHG emission at various ratio between the electricity and natural gas prices

4. Conclusions

The study presents an attempt to simultaneously synthesize the utility system with HEN, taking advantage of the interactions among them. It is an important step in an appropriate evaluation of the optimal design considering the energy carriers "at-the-gate" of the company, rather than estimated prices of intermediate energy carriers (e.g. steam) within the company. In the case study presented, different HEN designs were obtained when considering only HEN optimization with utility system compared to the system with cogeneration. This result shows the significance of simultaneous consideration of energy generation system and HEN.

From a sustainability point of view, the trade-off should be widened to the overall primary energy source consumption of different alternatives. In the case study presented, it is shown that the lower primary energy consumption can be achieved, when the cogeneration is applied either partially of fully. The difference is even more significant in the case of GHG emission analysis of the cogeneration versus a separate heat and power generation.

References

E. Martelli, C. Elsido, A Mian, F. Marechal, 2017, MINLP model and two-stage algorithm for the simultanous synthesis of heat exchanger network, utility system and heat recovery cycles, Computers and Chemical Engineering, 106, 663-689.

W.S Goh., Y.K.Wan, C. K. Tay, R.T.L. Ng, D.K.S. Ng, 2016, Automated targeting model for synthesis of heat exchanger network with utility systems, Applied Energy, 162, 1272-1281.

C. Elsido, E. Martelli, T. Kreutz, 2019, Heat integration and heat recovery steam cycle optimization for a low-carbon lignite/biomass-to-jet fuel demonstration project, Applied Energy, 239, 1322-1342.

X. Luo, B. Zhang, Y. Chen, A. Mo, 2012, Heat integration of regenerative Rankine cycle and process surplus heat through graphical targeting and mathematical modeling technique, Energy, 556-569.

X. Luo, X. Huang, M.M. El-Halwagi, J.M. Ponce-Ortega, Y. Chen, 2016, Simultanous synthesis of utility system and heat exchanger network incroporating steam condensate and boiler feedwater, Energy, 875-893.

F. Liu, J. Ma, Y. Feng, Y. Wang, 2018, Simultanous integrated design for heat exchanger network and cooling water system, Applied Thermal Engineering, 128, 1510-1519.

C. Elsido, E. Martelli, I. E. Grossmann, 2019, A bilevel decomposition method for the simultanous heat integration and synthesis of steam/organic Rankine cycles, Computers and Chemical Engineering, 128, 228-245.

A.J. Isafiade, D.M. Fraser, 2010, Interval based MINLP superstructure synthesis of heat exchanger networks for multi-period operations, Chemical Engineering Research and Design. 88, 1329-1341.

M.A. Duran, I.E. Grossmann, 1986, Simultaneous optimization and heat integration of chemical processes. AIChE Journal, 32, 123-138.

T.F. Yee, I.E. Grossmann, Z. Kravanja,1990, Simultaneous optimization models for heat integration - III. Process and heat exchanger network optimization. Computers and Chemical Engineering, 14, 1185-1200.

L.F. Lira-Barragán, J.M. Ponce Ortega, M. Serna-González, M.M. El-Halwagi, 2014, Optimal desing of process energy systems integrating sustainable consideration, Energy, 76,139-160.

European Union, 2010, Covenant of Mayors, How to develop a Sustainable Energy Action Plan Part 2, https://conventiondesmaires.eu/support/funding-instruments_el.html, accessed 26.11.2019.

Sauro Pierucci, Flavio Manenti, Giulia Bozzano, Davide Manca (Eds.)
Proceedings of the 30th European Symposium on Computer Aided Process Engineering (ESCAPE30), May 24-27, 2020, Milano, Italy.
http://dx.doi.org/10.1016/B978-0-12-823377-1.50152-X

Coproduction of Ethylene and Propylene based on Ethane and Propane Feedstocks

H. Alejandro Pedrozo[a]; S. Belen Rodriguez Reartes[a,b]; Maria Soledad Diaz[a,b,*], A. R. Vecchietti[c], Ignacio E. Grossmann[d]

[a] *Planta Piloto de Ingeniería Química (PLAPIQUI CONICET-UNS), Camino La Carrindanga km. 7, Bahía Blanca, Argentina*
[b] *Departamento de Ingeniería Química, Universidad Nacional del Sur (UNS), Bahía Blanca, Argentina*
[c] *Institute of Design and Development (INGAR CONICET-UTN), Avellaneda 3657, Santa Fe, Argentina*
[d] *Center for Advanced Process Decision Making, Carnegie Mellon University, 5000 Forbes Avenue, Pittsburgh, PA 15213, USA*
sdiaz@plapiqui.edu.ar

Abstract

In this work, we develop a mathematical model to make decisions about the optimal scheme and operating conditions of an olefin plant. We formulate a superstructure that includes ethane and propane steam cracking, propane dehydrogenation and olefins metathesis process for the co-production of ethylene and propylene. Furthermore, considering the relevance of the separation scheme, the state equipment network (SEN) representation is considered and rigorous equations to model distillation columns (MESH) are formulated. This model is implemented in GAMS to maximize the project net present value (NPV). Numerical results show that the combination of ethane steam cracking and olefin metathesis is the most profitable configuration under the price scenario considered in this work.

Keywords: olefin production, superstructure optimization, propane dehydrogenation, metathesis, steam cracking

1. Introduction

The shale gas revolution has led to a high availability of natural gas liquids (NGLs), which are excellent feedstocks for chemical industries. In particular, there are economic advantages of using NGLs for olefin production instead of naphtha feedstock (Siirola, 2014). Thus, there is a general trend to turn reactive furnaces to work with ethane for ethylene production, even in countries that do not have shale gas exploitation, since they can import ethane at competitive prices (U.S. Energy Information Administration, 2019). This feedstock switch has also promoted a propylene yield reduction since propylene selectivity from naphtha is higher than from ethane. In addition, propylene demand continues rising mainly due to polypropylene consumption (Baker, 2018). The combination of both facts encouraged the development of on purpose technologies for propylene production (Lavrenov, Saifulina, Buluchevskii, & Bogdanets, 2015).
There are numerous process alternatives to produce propylene from both, petrochemical raw material and chemical intermediates, such as methanol into olefins, methanol into propylene, olefin metathesis, propane dehydrogenation, and deep catalytic cracking. Among these alternatives, both propane dehydrogenation and olefin metathesis are

particularly interesting technologies since either could be used with ethane steam cracking to produce ethylene and propylene more efficiently.
To the best of our knowledge, an optimal design of a plant producing ethylene and propylene that includes propane dehydrogenation and metathesis of olefins as process alternatives has not been studied in the literature. In addition, numerous papers that address optimal plant designs use short-cut models in distillation columns (Chen & Grossmann, 2017). While these approaches allow simplifying the optimization model, unfortunately, they are much less accurate in comparison to rigorous mass balances, equilibrium, summation and heat (MESH) equations, and consequently, may provide only rough estimations that directly affect economic indicators.
In this work, we formulate a superstructure to determine the optimal scheme of an olefin plant. Raw materials include both ethane and propane, and the superstructure embeds steam cracking furnaces, propane dehydrogenation, and metathesis as potential technologies. Furthermore, taking into account the relevance of the separation scheme, the state equipment network (SEN) representation (Chen & Grossmann, 2017), and rigorous equations (MESH) to model distillation columns are formulated. Numerical results show that the optimal scheme includes a combination of ethane steam cracking and olefin metathesis.

2. Process description

The present work addresses the optimal design of a plant producing ethylene and propylene at a rate of 500 kt/year for each olefin. Figure 1 shows the plant sections, where the different alternatives for the reactive pathways are presented. The raw materials are ethane and propane, and the entire process can be represented through three different sections: alkane conversion, separation train, metathesis section.

2.1. Alkane conversion

2.1.1. Ethane conversion

The commercial technology to produce ethylene from ethane feedstock is steam cracking. We should note that the reactor capacity for ethylene production is not fixed. This olefin is required to satisfy market demand, but it could also be transformed into propylene in the plant. Thus, discrete decisions are related to the number of furnaces included in the optimal design.

2.1.2. Propane conversion

We consider three different reaction pathways for handling propane feedstock, which are: steam cracking of propane, Pt-based propane dehydrogenation (Pt-PDH), and Cr-based propane dehydrogenation (Cr-PDH).
Steam cracking of propane mainly produces ethylene. It employs complex furnaces operating at high temperatures, as in steam pyrolysis of ethane. There are also discrete decisions associated to propane production furnaces in the plant.
Pt-PDH is a commercial process, developed by UOP Oleflex, with a 36 % propane conversion per pass, and an 85 % propylene selectivity (Maddah, 2018).
Cr-PDH is another propane dehydrogenation technology, commercialized as Catofin Process, which has a 40 % propane conversion per pass, and its selectivity towards propylene is around 88 % (Maddah, 2018).

2.2. Separation train

Since the output streams from ethane and propane processing reactors have roughly the same chemical species, both streams can be mixed and processed through the same

separation train to purify the olefin products. Thus, this strategy comprises process intensification.

The separation train consists of a quench tower to reduce the temperature reactor output stream, a series of compression stages, an acid gas removal unit to eliminate carbon dioxide and hydrogen sulfide, a dehydration process, a reactor for acetylene hydrogenation, a cold box for hydrogen separation, and a sequence of distillation columns to perform the final product purification.

In the representation of Fig. 1, the "main separation" block includes demethanizer, deethanizer, and depropanizer columns, and acetylene reactor; their interconnections are modeled with discrete variables. C2 and C3 splitters purify the main products, ethylene, and propylene, respectively, and the separated ethane and propane are recycled to "Alkane conversion" section. The debuthanizer column produces a butene stream that can be either sold or fed to the "Metathesis section". In addition, pyrolysis gasoline is obtained from debutanizer column bottom, but for the sake of clarity in Fig. 1, this product is omitted.

2.3. Metathesis section

An alternative process to produce propylene is the metathesis of ethylene and butenes. The propylene selectivity is about 95 %, and the butenes per-pass conversion is over 60 % (Ondrey, 2004). This technology employs a mixture of WO_3/SiO_2 and MgO as a catalyst for the metathesis and isomerization reactions.

A hydrogenation unit is used to eliminate diene and enyne compounds from the butene mixture. Then, the resulting stream is fed to an isomerization reactor to increase the composition of trans-2-butene. Next, ethylene and butene streams are fed to a fixed bed catalytic reactor where the metathesis reaction takes place. The output of this reactor is a mixture of ethylene, propylene, butenes and C_5^+ components. This mixture is treated in a series of distillation columns for propylene purification, which also involves discrete decisions regarding the separation scheme. From this set of columns, three output streams are obtained. First, the ethylene stream can be recycled or mixed with ethylene product stream. Second, the propylene stream is mixed with propylene product stream. Finally, the C_4^+ stream is sent to the debuthanizer column in the separation train section. Thus, in "Propylene purification" block (Fig. 1), there are also discrete decisions regarding the separation sequence.

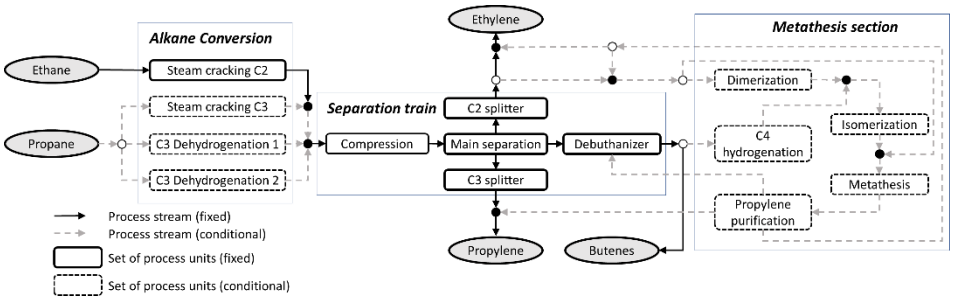

Figure 1: Plant sections for ethylene-propylene co-production

3. Mathematical modeling

We formulate process unit models within the superstructure representation and streams are defined by the connection between two units. The problem complexity of finding the optimal scheme increases with the number of units and tasks considered in the

superstructure. In order to tackle this issue, Yeomans and Grossmann (Yeomans & Grossmann, 1999) have proposed the state equipment network (SEN) representation, which allows addressing the problem systematically. In addition, this representation allows presetting the number of columns, avoiding nonexistent process units in the superstructure. Consequently, the number of flow and size variables forced to be zero is reduced, as well as the potential issues regarding numerical singularities. In SEN, the fed and produced states of equipment units depend on potential tasks that can be performed in each unit. In this work, the tasks assignment is based on the location of the separation cut for the distillation column.

Figure 2a shows the state equipment network for the main separation block (see Fig. 1). In this work, states are characterized by their composition. After compression, the reactor output stream is sent to the main separation block which includes the columns: demethanizer, deethanizer and depropanizer separating the stream in component groups. The identified component groups are: H_2 (hydrogen), C_1 (methane); C_2 (ethane and ethylene); C_2^a (ethane, ethylene, and acetylene); C_3 (species with 3 carbon atoms), and C_4^+ (species with 4 or more carbon atoms). Therefore, the discrete decisions associated with the separation scheme focus on task assignments in the demethanizer, deethanizer and depropanizer (based on the separation cuts). In addition, the acetylene hydrogenation is an important process in this section that also has discrete tasks associated. In this work, only front-end configurations were considered for acetylene hydrogenation unit since they are more energy-efficient (Zimmermann & Walzl, 2009). Consequently, H_2, C_1 and C_2 species must be in the acetylene reactor feed stream. Propylene purification (in metathesis section) also includes discrete decisions associated with column separation tasks, as Fig. 2b shows. In this case, the mixture to be processed is composed of ethylene (Et), propylene (Pr), and species with 4 or more carbon atoms (C_4^+).

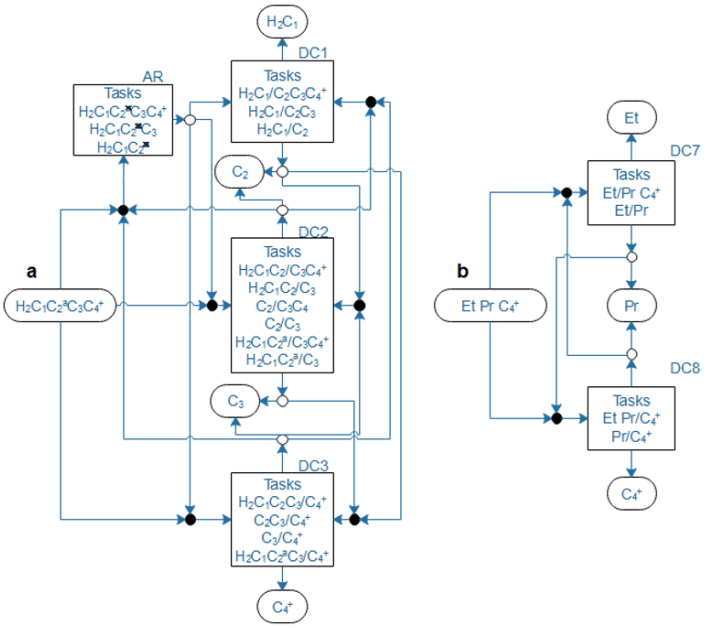

Figure 2: States equipment network. a) main separation train. b) propylene purification in the metathesis section. DC1: demethanizer. DC2: deethanizer. DC3: depropanizer. DC7: Deethylenizer. DC8: Depropylenizer. ●: mixer. ○: splitter

The corresponding disjunctions for the STN representation are as follows:

$$\bigvee_{t\in Ta_u}\left[\begin{array}{l} W_{u,t} \\ \left.\begin{array}{l} F_{s,u',c}=F_{u',u,c} \\ T_{s,u'}=T_{u,u'} \\ P_{s,u'}=T_{u,u'} \\ H_{s,u'}=T_{u,u'} \end{array}\right\} \begin{array}{l} c\in C \\ s\in SI_{u',u,t} \\ u'\in UI_u \end{array} \\ \left.\begin{array}{l} F_{u,s,c}=F_{u,u',c} \\ T_{u,s}=T_{u,u'} \\ P_{u,s}=P_{u,u'} \\ H_{u,s}=H_{u,u'} \end{array}\right\} \begin{array}{l} c\in C \\ s\in SO_{u,u',t} \\ u'\in UO_u \end{array} \end{array}\right] u\in\{DC1,DC2,DC3,AR,DC7,DC8\}$$

where $W_{u,t}$ is the Boolean variable that is true if the task t is performed in unit u, and false otherwise; $F_{s,u',c}$ is the molar flow from state s to u' of the chemical compound c; $T_{s,u'}$, $P_{s,u'}$ and $H_{s,u'}$ are the temperature, pressure and enthalpy flow from state s to u', respectively; C is the set of chemical species; Ta_u is the set of tasks that can be performed in unit u; $SI_{u',u,t}$ is the state that is fed through mixer u' and processed in unit u when the task t is selected; $SO_{u,u',t}$ is the state that is delivered through splitter u and produced in unit u' when the task t is selected; UI_u and UO_u are the sets of input mixer and output splitter corresponding to unit u, respectively.

In the superstructure, we include different reactor types, heat exchangers, flash, pumps, compressors, mixers, splitters, and distillation columns. Each type of process unit has equations to describe its physical behavior and to calculate its costs when applicable. We formulate a Generalized Disjunctive Programming mode (Vecchietti & Grossmann, 2000); thus, the presence of each unit is associated with Boolean variables as follows

$$\left[\begin{array}{l} Y_u \\ h(x)\le 0 \\ Ax\le b \end{array}\right] \veebar \left[\begin{array}{l} \neg Y_u \\ Bx=0 \end{array}\right]$$

where Y_u is the Boolean variable that is true if the unit u is present, and false otherwise; and the continuous variables x include material flows, operating temperature and pressure, enthalpy flows, unit internal variables, and unit capital cost. To solve the problem, we used the logic-based outer approximation algorithm (Turkay & Grossmann, 1996), in which the problem is decomposed into reduced NLP subproblems and the master MILP problem. In this way, NLP subproblems only include the nonlinear equations related to the disjunction active terms, avoiding potential issues regarding singularities. The master MILP is formulated based on the outer approximation with equality relaxation and augmented penalty approach (Viswanathan & Grossmann, 1990).

4. Case study

USA data prices reported in the literature (Boulamanti & Moya, 2017) were considered for the present case of study. Due to the active exploitation of shale gas resources in this country, ethane feedstock (146 EUR/t) is quite more economical than propane (394 EUR/t). When we solve the problem with the logic-based approach in GAMS 24.2.3, we found the optimal solution after solving three NLP subproblems and two Master problems, as Table 1 shows. The resulting Master MILP problems have 140 binary variables. Table 2 shows the most important economic indicators for the optimal scheme.

Numerical results indicate that the optimal scheme includes four steam cracking furnaces to produce ethylene from ethane in the alkane conversion section. Neither furnaces for propane steam cracking nor propane dehydrogenation technologies were selected. That means, propane feedstock was not employed in the optimal design. Instead, ethane feedstock is used to produce more ethylene for its further conversion in propylene through the metathesis process, whose section is included in the plant. Regarding the separation scheme, Table 3 shows the tasks assigned for each equipment unit. It is observed that a deethanizer first configuration was selected in the optimal solution scheme.

Table 1: Summary of iterations with the logic-based outer approximation algorithm

Iteration/subproblem	Objective	CPU time (s)	Constraints	Continuos vars.
NLP 1 (CONOPT)	1526	74	38847	38783
Master MILP 1 (Cplex)	2006	3921	71699	86919
NLP 2 (CONOPT)	2040	784	37681	37233
Master MILP 2 (Cplex)	1475	59075	115362	132362
NLP 3 (CONOPT)	2037	1104	37764	37316

Table 2: Economic indicators for the optimal solution

Net present value (MM$)	2040	Revenues (MM$/year)	1229
Investment (MM$)	1142	- Ethylene (MM$/year)	569
Net income (MM$/year)	564	- Propylene (MM$/year)	603
		- By-products (MM$/year)	57

Table 3: Selected tasks for equipment in the optimal scheme

Equipment	DC1	DC2	DC3	AR	DC7	DC8
Task	C_1/C_2	$C_1C_2^a/C_3$ C_4	C_3/C_4	$C_1C_2^x$	Et/Pr	Et Pr/C_4

5. Conclusions

This work addresses the optimal design of an olefin plant producing ethylene and propylene. The optimal plant design includes four ethane steam cracking furnaces, and no propane feedstock is employed. The selected reactive pathway to produce propylene was the metathesis of olefins and the optimal configuration includes the deethanizer column as the first separation step.

References

Baker, I. (2018). Polypropylene. In *Fifty Materials That Make the World* (pp. 169–173). Springer.
Boulamanti, A., Moya, J. A. (2017). *Renewable and Sustainable Energy Reviews*, *68*, 1205–1212.
Chen, Q., Grossmann, I. E. (2017). *Annu. Rev. Chem. Biomol. Eng.* 8 (1), 249–283.
Lavrenov, A., Saifulina, L., Buluchevskii, E. , Bogdanets, E. N. (2015). *Catal. Ind. 7*(3), 175–187.
Maddah, H. A. (2018). *ASRJETS*, *45*(1), 49–63.
Ondrey, G. (2004). *Chem. Eng.*, *111*(3), 20–24.
Siirola, J. J. (2014). *AIChE Journal*, *60*(3), 810–819
Turkay, M., Grossmann, I.E. (1996)," *Comp Chem Eng*, 20, 959-978.
U.S. EIA (2019). https://www.eia.gov/todayinenergy/detail.php?id=38232
Vecchietti, A., Grossmann, I.E. (2000). *Comput. Chem. Eng.* 24, 2143-2155.
Viswanathan, J., Grossmann, I. E. (1990). *Comput. Chem. Eng.* 14 (7) 769-782
Yeomans, H., Grossmann, I. E. (1999). *Comput. Chem. Eng.*, *23*(6), 709–731.
Zimmermann, H., Walzl, R. (2009). Ullmann's Encyclopedia of Industrial Chemistry, Ethylene. John Wiley & Sons, Inc., New York.

Sauro Pierucci, Flavio Manenti, Giulia Bozzano, Davide Manca (Eds.)
Proceedings of the 30th European Symposium on Computer Aided Process Engineering (ESCAPE30), May 24-27, 2020, Milano, Italy.
http://dx.doi.org/10.1016/B978-0-12-823377-1.50153-1

Circular Economy Analysis of Helium Recovery from Sales Gas Product

Ahmed AlNouss, Saad A. Al-Sobhi *

Chemical Engineering Department, College of Engineering, Qatar University. Doha, Qatar

saad.al-sobhi@qu.edu.qa

Abstract

The helium presence in natural gas (NG) is usually low, thus it seems infeasible economically to recover it. However, the continuous increase in helium demand with a growing rate of about 5%, industrial projects are searching for economic approaches to recover helium from sales gas at the earlier stages of the liquefaction process. This work investigates the techno-economic and environmental benefits of recovering helium from sale gas product. Among the available recovery technologies, namely, cryogenic fraction, adsorption-based processes, and membrane-based processes, the cryogenic fractionation is considered for analysis due to its wide use in industry. The cryogenic fractionation represented by three different configurations; single column, double columns fractionation, and cold box are developed using Aspen HYSYS to perform the steady-state simulation with a basis of 1400 MMSCFD of natural gas. Aspen Process Economic Analyzer and Aspen Energy Analyzer, are then used to carry out the economic evaluation and utility optimization steps. The results for all alternatives are compared in terms of helium recovery, emissions reduction, energy savings, and economic profitability. An illustrative case study is presented for the assessment of helium recovery for different helium molar composition in the NG feedstock and various helium selling prices. The results demonstrate cold box as the optimal technology for 3.5 vol% helium recovery with approximately $25.4 per kg of helium produced (PHP) compared to approximately $24.2 and $24.3 PHP for double column and single column options, respectively. Moreover, higher concentration of helium at around 7% indicates a profitability profile with lower overall net economic value of approximately $11.7 PHP for cold box alternative. The results for all options indicate high purity for helium with more than 98% and a recovery of more than 99%.

Keywords: Sustainable design, Helium recovery, Sales gas, Process Simulation, liquefied natural gas (LNG)

1. Introduction

The importance of helium comes for its unique properties such as inertness, high thermal conductivity, low solubility, low density and low boiling point. In addition, it has irreplaceable industrial and research applications where helium is used in critical technologies such as nuclear facilities, fiber optics and electronics fabrication, leak detection systems, aircraft manufacturing, magnets production and MRI scanners (Hamedi et al., 2019). Cryogenic separation is used heavily in natural gas liquefaction (NGL) processes to separate hydrocarbons, nitrogen and helium. Majority of newly established NGL plants utilize cryogenic separation technology. It is considered as a conventional process to produce crude helium from natural gas (NG) stream (Mehrpooya

and Shafaei, 2016). It can be divided into two main categories: high-pressure distillation processes and multi-stage flash systems (Ansarinasab et al., 2018).
Although helium is considered the second most common element in the universe, recoverable known helium reserves may get depleted within a few decades. Therefore, efficient processes should be implemented to recover this vital resource. In addition, the technical and economic performance along with environmental compliance must be enhanced to increase the benefits from the recovery process and decrease the environmental impacts. This research paper explores the techno-economic and environmental analysis of recovering helium from sale gas product for various concentration levels. The cryogenic fractionation represented by three different configurations; single column, double columns fractionation, and cold box are developed using Aspen HYSYS software to perform the steady-state simulation with a basis of 1400 MMSCFD of natural gas.

2. Model development

The extraction of helium from NG follows four main steps as highlighted in Figure 1. First, the gas feed is purified from acid gases, mercury and water. The heavier hydrocarbons are then extracted from the gas stream before entering nitrogen rejection unit (NRU) where most of the remaining methane gas is separated from nitrogen and helium mixture. Finally, helium is recovered from the nitrogen-rich stream in one or two steps to produce crude (50-70 mol%) or purified (99.99 mol%) helium (Hamedi et al., 2019).

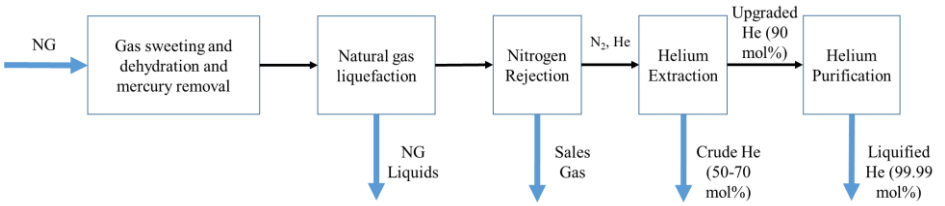

Figure 1: Block flow diagram of helium production for LNG with high nitrogen content

Given a typical LNG process, with desirable products as shown above, it is desired to investigate the economic and environmental benefits of recovering helium from the sale gas product. It is assumed in this paper that a 50% split of sales gas product is to be directed to liquefaction section. Aspen HYSYS software is used to simulate the three configurations; single column, double columns fractionation, and cold box with a basis of 1400 MMSCFD of natural gas (NG). The basic NGL configuration is based on Recycle split-vapor (RSV) technology, which has been described in an earlier study (AlNouss et al., 2018) and investigated more in (Al-Sobhi and AlNouss, 2018) using a sustainability metric. In the single column process, the purified NG product from the RSV unit is precooled to around -130 ^{o}C before being fed to a high-pressure distillation column operating at 20 bar. The overhead product of the column containing helium and nitrogen is further cooled to around -225 ^{o}C and enters a two-phase separator. The top stream from the separator is the helium product and the bottom is the nitrogen product. The bottom product from the column is considered as LNG stream. The simulated Aspen HYSYS model for single column process is illustrated in Figure 2.

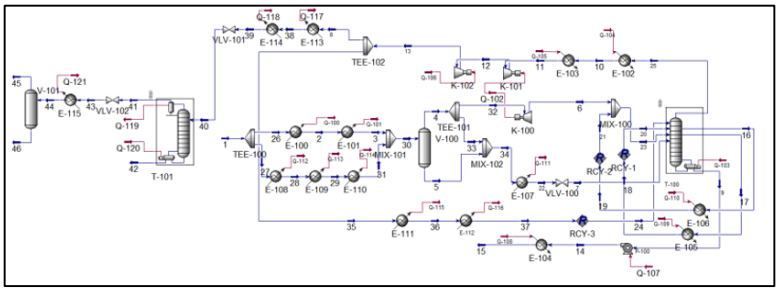

Figure 2: Simulation process flowsheet for single column helium recovery.

The double-column process starts with a heat exchanger to cool the NG product from the RSV NG recovery unit to around -130 ^{o}C. The stream then enters a two-phase separator to flash the gas from liquid and both enters the distillation column operating at 20 bar. The overhead stream is directed to a heat exchanger to cool the helium and nitrogen stream to around -225 ^{o}C before entering a second two-phase separator. The separator flash out helium from the top and leaves nitrogen in the bottom stream. Similar to the single-column, the bottom product from the column is considered as LNG stream. Figure 3 illustrates the simulated Aspen HYSYS model for double-column process.

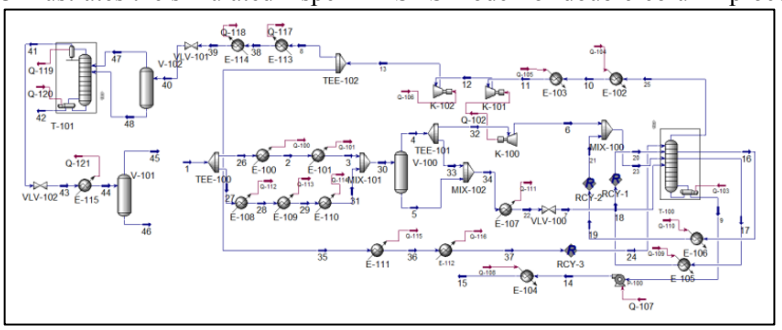

Figure 3: Simulation process flowsheet for double column helium recovery.

The last configuration is the cold box technology. NG product from the RSV NG recovery unit enters the cold box unit where it is first cooled to around -148 ^{o}C before entering a two-phase separator. The top stream from the separator is cooled to around -193 ^{o}C and enters a second two-phase vessel. The top stream is further cooled to around -220 ^{o}C and then flashed into helium top product and nitrogen bottom product. The bottom product form the second vessel is recycled back to the first vessel. Whereas the bottom product from the first vessel is cooled to around -193 ^{o}C and flashed to yield a bottom LNG product. Figure 4 illustrates the simulated model for the cold box technology.

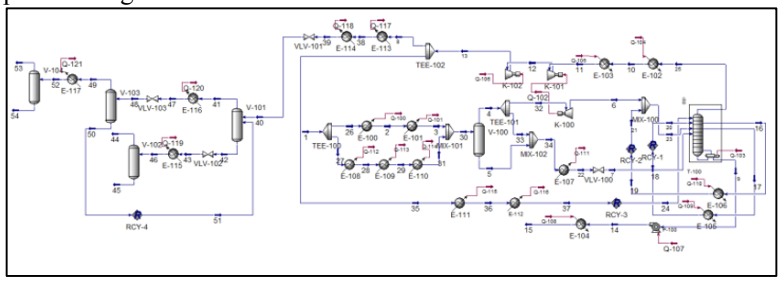

Figure 4: Simulation process flowsheet for cold box helium recovery.

After the simulation of the three cryogenic processes represented by single column, double columns fractionation, and cold box configurations, Aspen Process Economic Analyzer and Aspen Energy Analyzer, are used to carry out the economic evaluation and utility optimization steps with the prices of the main products and feeds as demonstrated in Table 1.

Table 1: Prices of main feeds and products.

Stream	Sales Gas	LNG	NGL	NG Feed	Helium
$/tonne	274.38	426.59	213.3	137.19	137.19

In order to perform a circular analysis, certain parameters have been varied. The percentage of helium in the feed has been varied between 1 and 7 mol%. The NG feed compositions of the three cases are illustrated in Table 1.

Table 2: NG feed composition for the three scenarios.

Component	Case a	Case b	Case c
Feed Composition (Vol%)			
Methane	85%	79%	82.3%
Ethane	5%	5%	5.4%
Propane	2%	2%	2.1%
i-Butane	1%	1%	0.7%
n-Butane	0%	0%	0.4%
i-Pentane	0%	0%	0.2%
n-Pentane	0%	0%	0.2%
n-Hexane	0%	0%	0.2%
Nitrogen	5%	5%	5.0%
Helium	1%	7%	3.5%

3. Results and discussion

The results for the single and double columns alternatives have demonstrated promising helium recovery with up to 99.9% compared to Sales gas product split and up to 49.9% compared to NG feed as illustrated in Figure 5. High percentages of energy savings and environmental emissions reduction approximated at 74% are observed for the single and double columns alternatives from the actual and target total utilities requirement and carbon emissions in Figures 6. In addition, with the increase of helium presence in sales gas, the cold box alternative demonstrated a constant and higher increase in the recovery of helium compared to the other two alternatives.

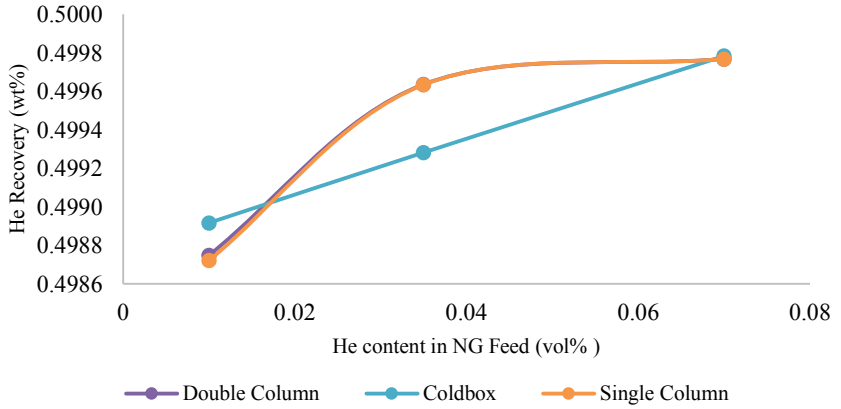

Figure 5: Helium recovery trend with the change in He content in NG feed.

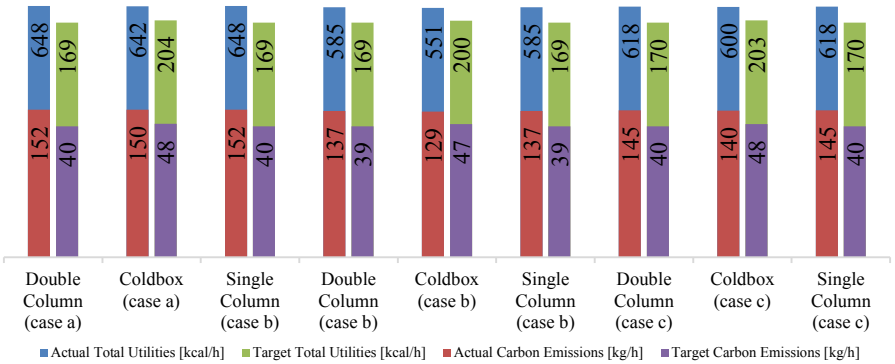

Figure 6: Actual and target total utilities requirement and carbon emissions for the three cases.

Nevertheless, the cold box alternative has shown higher net profit per kg of He product with around $25.4 at 3.5vol% helium content, compared to approximately $24.2 and $24.3 for double column and single column options, respectively. This profitability decreases with the increase in helium content in NG as indicated in Figure 7. These profitability figures are calculated from the different costs and revenues associated with the studied cases and technologies presented in Figure 8.

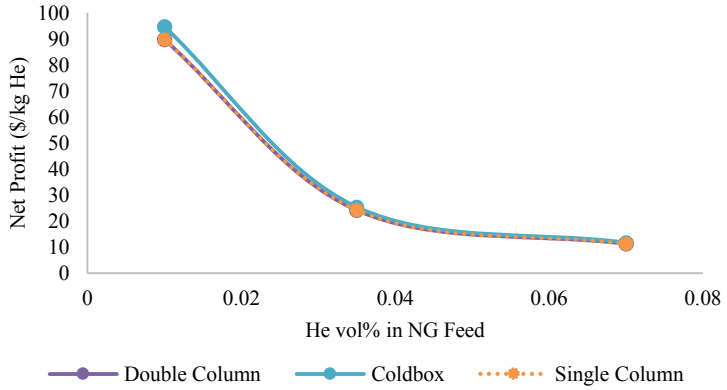

Figure 7: Helium recovery trend with the change in He content in NG feed.

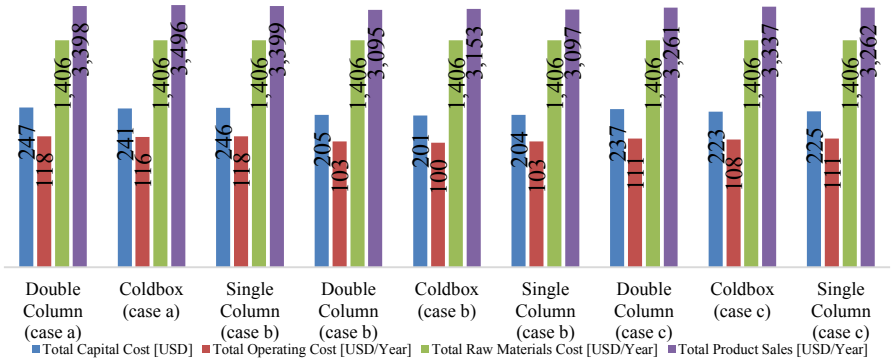

Figure 8: Revenue and costs associated with the different helium recovery cases and technologies.

These results indicate the potential of helium recovery as a key figure to enhance circular economy. More analysis can be done to find the optimal ratio of the Sales gas split that maximizes profit and minimizes environmental damages. Moreover, the investment in helium recovery can be investigated through sustainability metrics to ensure the long term profitability.

4. Conclusions

The global demand of helium reached approximately 5.9 billion cubic feet (Bcf) in 2016 with a global supply estimated at 6.0 Bcf. The major global reserves approximated at 8 million tons are located in US, Qatar, Algeria and Russia. These known helium reserves may get depleted within a few decades striking the need for efficient processes to be implemented to recover this vital resource. This work explores the techno-economic and environmental analysis of recovering helium from sale gas product for various concentration levels. The cryogenic fractionation represented by three different configurations; single column, double columns fractionation, and cold box are developed using Aspen HYSYS to perform the steady-state simulation with a basis of 1400 MMSCFD of natural gas (NG) and to perform profitability and environmental studies. The results demonstrate cold box as the optimal technology for 3.5 vol% helium recovery with approximately $25.4 per kg of helium produced (PHP) compared to approximately $24.2 and $24.3 PHP for double column and single column options, respectively. This profitability decreases with the increase in helium content in NG. These results demonstrate the potential of helium recovery as a key figure to enhance circular economy. However, more investment analysis needs be done through sustainability metrics to ensure the long term profitability of helium recovery.

References

S.A. Al-Sobhi, and A. AlNouss, 2018, Applying New Sustainability Metric in Different Natural Gas Liquid (NGL) Recovery Configurations to Extend Investment Decision and Incorporate Sustainability Analysis, Computer Aided Chemical Engineering, 43, 145-50.

A. AlNouss, M. Ibrahim, and S.A. Al-Sobhi, 2018, Potential energy savings and greenhouse gases (GHGs) emissions reduction strategy for natural gas liquid (NGL) recovery: Process simulation and economic evaluation, Journal of Cleaner Production, 194, 525-39.

H. Ansarinasab, M. Mehrpooya, and M. Pouriman, 2018, Advanced exergoeconomic evaluation of a new cryogenic helium recovery process from natural gas based on the flash separation – APCI modified process, Applied Thermal Engineering, 132, 368-80.

H. Hamedi, I.A. Karimi, and T. Gundersen, 2019, Optimization of helium extraction processes integrated with nitrogen removal units: A comparative study, Computers & Chemical Engineering, 121, 354-66.

M. Mehrpooya, and A. Shafaei, 2016, Advanced exergy analysis of novel flash based Helium recovery from natural gas processes, Energy, 114, 64-83.

Sauro Pierucci, Flavio Manenti, Giulia Bozzano, Davide Manca (Eds.)
Proceedings of the 30th European Symposium on Computer Aided Process Engineering (ESCAPE30), May 24-27, 2020, Milano, Italy.
http://dx.doi.org/10.1016/B978-0-12-823377-1.50154-3

Optimal Design and Operation of Flexible Polygeneration Systems using Decomposition Algorithms

Avinash S. R. Subramanian[a], Thomas A. Adams II[b], Truls Gundersen[a], Paul I. Barton[c,*]

[a] *Department of Energy and Process Engineering, Norwegian University of Science and Technology (NTNU), NO-7491, Trondheim, Norway.*
[b] *Department of Chemical Engineering, McMaster University, Hamilton, ON, Canada.*
[c] *Process Systems Engineering Laboratory, Department of Chemical Engineering, Massachusetts Institute of Technology, Massachusetts 02139, United States.*
pib@mit.edu

Abstract

A flexible design solution for a polygeneration system that utilizes a hybrid waste tire and natural gas feedstock to produce a mix of electricity, fuels and chemicals is presented. The optimal design and operation under uncertainty problem is formulated as a scenario-based two-stage stochastic MINLP. The problem is modeled using the recently developed GOSSIP software framework and solved using two methods: ANTIGONE to solve the full-space problem or NGBD with a decomposition strategy. The scaling of solution times of these two methods with number of scenarios is compared. The results of the stochastic formulation are compared with the deterministic approach to demonstrate the improvement in economic performance as a result of taking uncertainty into consideration (the value of the stochastic solution).
Keywords: Polygeneration System, Decomposition Algorithms, Flexible Design, Stochastic Programming, Global Optimization.

1. Introduction

Polygeneration systems produce more than one kind of product, typically a mix of electricity, fuels and chemicals and as such offer several economic and environmental advantages over single product systems. Polygeneration processes that utilize multiple feedstocks may enable the exploitation of certain synergies, for instance, heat integration of exothermic and endothermic processing units or blending the different qualities of syngas generated to provide the correct H_2/CO ratio for downstream synthesis processes (Adams and Barton, 2011). Furthermore, implementing a flexible design may enable polygeneration systems to maintain competitiveness in the face of uncertainties (such as in product prices or environmental policies) (Chen et al., 2007). Flexible design involves oversizing process equipment in order to allow adjustment of operating conditions so as to produce the most valuable product mix for a given realization of uncertainty. Thus, the optimal design and operation problem involves determining the best trade-off between the increased capital cost associated with larger equipment capacities (modeled with `here-and-now' variables fixed before realization of uncertainty) and the expected increase in net present value (NPV) due to operational flexibility (modeled with `wait-and-see' variables after realization of uncertainty). Previous work by Chen et al. (2011) studied the optimal design and operation of a

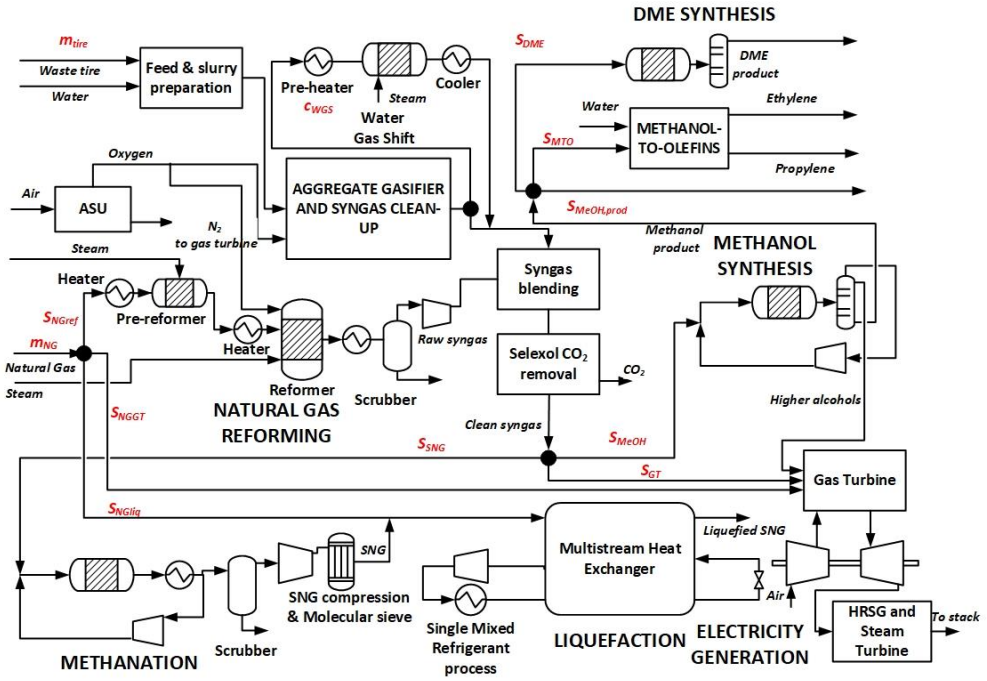

Figure 1: Superstructure of the hybrid feedstock flexible energy polygeneration process

flexible energy polygeneration process in which coal and biomass are co-gasified to produce a mix of naphtha, diesel, methanol or electricity. The flexible design problem was formulated first as a scenario-based two-stage stochastic NLP and solved with BARON and later as an MINLP and solved using the nonconvex generalized Benders decomposition algorithm enhanced with additional dual information (Chen et al., 2012).

In this work, a process that uses a hybrid of a waste tire and natural gas feedstock to produce electricity, liquefied (synthetic) natural gas (LNG), methanol, dimethyl ether (DME) or olefins is studied. 100% operational flexibility is assumed, thus no limits are imposed on the turndown ratios of the product trains. The two feedstocks produce syngas streams of different quality, thus syngas blending to achieve the correct H_2/CO ratio for downstream synthesis is considered. The optimization problem is formulated as a two-stage stochastic MINLP using the recently developed GOSSIP software framework that contains implementations of different decomposition algorithms such as NGBD (Li et al., 2014), Lagrangian Relaxation and Modified Lagrangian Relaxation, as well as a link to ANTIGONE (Misener and Floudas, 2014) to solve the deterministic equivalent problem and primal subproblems in NGBD (Kannan, 2018).

2. Process Description

Figure 1 presents a superstructure of the polygeneration system that utilizes a hybrid of waste tire and natural gas feedstocks to produce the following products: electricity, liquefied (synthetic) natural gas (LNG), sulfur, methanol, dimethyl ether (DME) or olefins. The key operational decision variables for the optimal design and operation problem are presented in Figure 1.

The overall plant scale is determined by two decision variables representing the tire and natural gas mass flow rates: m_{tire} and m_{NG}. The pulverized waste tire slurry is fed to an oxygen-blown entrained flow gasifier operating at 1250 °C and 56 bar to generate syngas which typically has a low H_2/CO ratio (~ 0.7). The syngas can be upgraded using a water gas shift (WGS) reactor in order to get the appropriate ratio for downstream synthesis sections. The conversion of CO (c_{WGS}) in the WGS reaction is a decision variable; high conversion results in hydrogen-rich syngas at the expense of higher steam consumption and lower energy efficiency. Sulfur-containing compounds are removed in a Selexol unit and converted to elemental sulfur in a Claus plant. The tire-derived syngas then heads to a blending section. The natural gas feedstock follows one of three routes. The first branch leads to an autothermal reforming section to generate (a higher quality of) syngas for blending and downstream synthesis, the second branch leads to a liquefaction section and leaves as LNG, while the third branch is fed to a gas turbine for electricity generation. The S_{NGref}, S_{NGliq} and S_{GT} decision variables determine the fraction of natural gas sent to the reforming, liquefaction or gas turbine sections. The optimal reformer operating conditions recommended by Adams and Barton (2011) are used resulting in an H_2/CO ratio of ~3.0.

After CO_2 removal using Selexol, the blended syngas heads to one of three downstream sections: Methanation, Methanol synthesis, or a gas turbine with the syngas split fractions given by S_{SNG}, S_{MeOH}, and S_{GT} respectively. The methanol produced could either be sold as a final product or be further converted to DME or olefins with the methanol split fractions given by $S_{MeOH,prod}$, S_{DME} and S_{MTO} respectively. Off-gases from methanol, DME synthesis and the methanol-to-olefins process are fed to the gas turbine. Heat from the gas turbine exhaust as well as from exothermic process units is used to generate steam for further electricity production in the steam turbine.

Mass and energy balances are first implemented using rigorous models in Aspen Plus v10 for most unit operations except for the Selexol-based H_2S and CO_2 removal sections which are modeled using Aspen HYSYS v10. The surrogate process model was then regressed using sample data points generated by the rigorous simulation in order to keep the optimization problem tractable for global optimization solvers. Further details of the polygeneration process and mathematical model are available in Subramanian et al. (2019 a,b).

3. Optimization problem formulation

The flexible design problem is formulated as a scenario-based two-stage stochastic nonconvex MINLP which takes the general form given below, where: $\boldsymbol{y}$ denotes discrete design decision variables (equipment capacities) which can take on values in $\boldsymbol{Y}$, $\boldsymbol{x}_h$ are operational decision and state variables in scenario h which can take on values in $\boldsymbol{X}$, $\mathbf{g}^{(1)}$ and $\mathbf{h}^{(1)}$ are constraints on the design variables (such as the capital cost model and budget constraints) while $\mathbf{g}^{(2)}$ and $\mathbf{h}^{(2)}$ are operational constraints such as process mass and energy balances, the operating cost model, scale and throughput constraints. The term $\boldsymbol{\omega}_h$ denotes the realization of the uncertain parameters in scenario h, while p_h denotes the probability of occurrence of scenario h, where h can take on values in $\{1,..,N_{scen}\}$. The function $f^{(1)}$ denotes the part of the objective function dependent on design variables while $f^{(2)}$ denotes the part dependent on operational variables.

For the flexible design problem, the objective function is the NPV. The equipment capacities are discretized as detailed in (Chen et al., 2012) because the current version of NGBD is only guaranteed to converge to ε-optimality with binary first-stage variables. The prices of the different products are uncertain parameters and

are assumed to belong to a normal distribution with mean and standard deviations calculated from historical data (Table 1).

$$\max_{\boldsymbol{y},\boldsymbol{x}_h} \quad f^{(1)}(\boldsymbol{y}) + \sum_{h=1}^{N_{scen}} p_h f^{(2)}(\boldsymbol{x}_h, \boldsymbol{y}, \boldsymbol{\omega}_h)$$

$$\begin{aligned}
\textbf{s.t.:} \quad & \mathbf{g}^{(1)}(\boldsymbol{y}) \le \mathbf{0}, \\
& \mathbf{h}^{(1)}(\boldsymbol{y}) = \mathbf{0}, \\
& \boldsymbol{y} \in \boldsymbol{Y}, \\
& \left.\begin{aligned} & \mathbf{g}^{(2)}(\boldsymbol{x}_h, \boldsymbol{y}, \boldsymbol{\omega}_h) \le \mathbf{0}, \\ & \mathbf{h}^{(2)}(\boldsymbol{x}_h, \boldsymbol{y}, \boldsymbol{\omega}_h) = \mathbf{0}, \\ & \boldsymbol{x}_h \in \boldsymbol{X}. \end{aligned}\right\} \quad \forall h \in \{1, \ldots, N_{scen}\},
\end{aligned} \tag{1}$$

Two-stage stochastic MINLPs exhibit a decomposable structure and thus are amenable to solution using duality-based decomposition algorithms such as nonconvex generalized Benders decomposition (NGBD) as detailed by Li et al. (2014). Motivated by the need for versatile implementation of the NGBD algorithm to a general application, recent work involved the development of the GOSSIP software framework (Kannan, 2018). GOSSIP includes subroutines for reformulating user input, detecting special structure, automatic construction of the subproblems required by the NGBD algorithm, bounds tightening techniques, automatic scenario generation, as well as links to several state-of-the-art solvers for solution of the various sub-problems.

In this work, the flexible design problem is formulated using GOSSIP as a nonconvex MINLP problem with 90 binary 1st stage variables and 321*N_{scen} continuous 2nd stage variables, and 18 1st stage constraints and 338*N_{scen} 2nd stage constraints. The nonconvexities arise due to bilinear terms in the mass balance model. The problem formulation is augmented with reformulation-linearization technique (RLT) equations which yield tighter convex relaxations as detailed by Sherali (2002).

Two cases are studied with 32 scenarios (2 scenarios for each of the 5 uncertain parameters) and 72 scenarios (3 scenarios for P_{Elec} and P_{NG}, and 2 scenarios for the other uncertain parameters). The optimization problem is solved using two methods: ANTIGONE to solve the full-space problem or NGBD as a decomposition strategy. The scaling of solution times of these two methods with number of scenarios compared.

Table 1: Uncertain parameters and values. *The prices of propylene and ethylene are assumed to be linearly correlated.

Uncertain Parameter	Description	Units	Mean	Std. dev.
P_{NG}	Henry hub Natural gas price	$/MMBtu	5.5	3.0
P_{Elec}	Hourly Electricity price	$/MWh	96.1	22.1
P_{MeOH}	Methanol price	$/kg	0.5	0.2
P_{DME}	DME price	$/kg	0.8	0.2
$P_{Ethylene}$	Ethylene price	$/kg	1.05	0.37

Table 2: Results of the flexible design optimization problem. *ANTIGONE did not converge in 5000 seconds in either case.

	Mean Value Problem	Case 1	Case 2
N_{scen}	1	32	72
Capital Costs (M$):			
Aggregate tire gasifier	-	279.7	342.1
Air Separation Unit	-	178.7	178.7
Water Gas shift	-	10.4	10.4
Natural Gas reformer	-	45.1	-
Selexol for CO2 removal	-	24.2	39.3
Methanation	-	-	-
Methanol synthesis	-	57.0	57.0
DME synthesis	-	87.2	87.2
Methanol To Olefins	-	-	-
Electricity generation section	385.0	194.4	194.4
Liquefaction	-	-	-
Water systems & Miscellaneous	58.1	109.8	109.8
Total Capital investment (M$)	443.2	986.5	1018.9
Operation mode:			
Natural Gas to Electricity (%)	100.0	-	-
Tire to DME & Electricity (%)	-	6.3	47.2
Tire & NG to DME & Electricity (%)	-	43.8	2.8
Tire to Methanol & Electricity (%)	-	-	50.0
Tire and NG to Methanol & Electricity (%)	-	50.0	-
Mean Annual Net Profit (M$)	127.8	236.0	221.5
NPV (M$)	559.8	884.1	753.5
EEV (M$)		589.3	320.8
VSS (M$)	-	294.8	432.7
Total wall time (s) – ANTIGONE	3.0	*	*
Total wall time (s) – NGBD	106.83	241.7	260.4

4. Results and Discussion

Table 2 presents the results of the flexible design optimization problem. The NPV increases as a result of considering uncertainty since the increase in annual profit due to operational flexibility exceeds the higher capital investment required. The value of stochastic solution (VSS) increases as more scenarios are considered in Case 2 compared to Case 1 since the expectation of the expected value problem (EEV) is much lower in Case 2. Thus, the nominal design (corresponding to the solution of the mean value problem) performs much worse under the uncertainties characterized by Case 2 than Case 1. Solving the mean value problem results in building only a natural gas to power plant. However, considering the substantial variation in hourly electric prices (Case 1 and Case 2) results in also building tire gasification, natural gas reforming, methanol and DME synthesis sections. We note that, for the characterization of uncertainty considered, the production of liquefied (synthetic) natural gas or olefins is never preferred. In addition, representing the variability of natural gas prices with 3 scenarios in Case 2 results in a solution in which natural gas is only used a small percentage of the time. Figure 2 illustrates the favorable scaling of the NGBD algorithm compared with ANTIGONE as the number of scenarios is increased. However, the

NGBD algorithm performs worse than ANTIGONE for a small number of scenarios since the set of feasible candidate solutions of the 1st-stage variables is relatively large compared to cases in which several scenarios are considered. We also note that adding RLT cuts results in a substantial improvement in the convergence time of the NGBD algorithm.

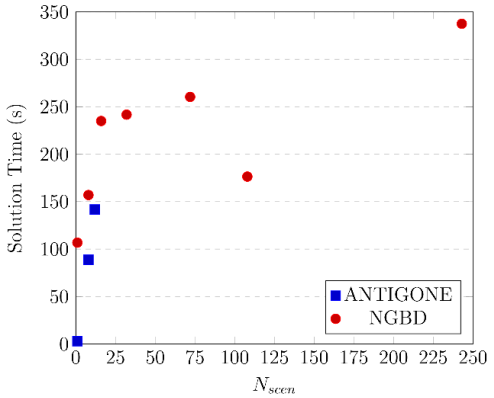

Figure 2: Scaling of solution times of NGBD and ANTIGONE with N_{scen}

5. Conclusions and Future Work

A flexible design solution for an energy polygeneration system that utilizes a hybrid waste tire and natural gas feedstock to produce a mix of products has been developed using a two-stage stochastic programming approach. The results suggest substantial value in taking uncertainty into account. In addition, the results show a favorable computational performance of using the NGBD decomposition algorithms over a state-of-the-art MINLP solver. Future work will involve adding complexity to the model by considering the gasifier and reformer operating conditions as decision variables.

References

T. A. Adams II, P. I. Barton, Combining coal gasification and natural gas reforming for efficient polygeneration, Fuel Processing Technology 92 (2011) 639-655.
Y. Chen, T. A. Adams II, P. I. Barton, Optimal design and operation of flexible energy polygeneration systems, Industrial & Engineering Chemistry Research 50 (2011) 4553-4566.
Y. Chen, X. Li, T. A. Adams II, P. I. Barton, Decomposition Strategy for the Global Optimization of Flexible Energy Polygeneration systems, AIChE Journal 58 (2012) 3080-3095.
X. Li, A. Sundaramoorthy, P. I. Barton, Nonconvex generalized benders decomposition, in: Optimization in Science and Engineering, Springer, 2014, pp. 307-331.
R. Misener, C. A. Floudas, ANTIGONE: Algorithms for Continuous/Integer Global Optimization of Nonlinear Equations, Journal of Global Optimization 59 (2014) 503-526.
R. Kannan, Algorithms, analysis and software for the global optimization of two-stage stochastic programs, Ph.D. thesis, Massachusetts Institute of Technology, 2017.
A. S. R. Subramanian, T. A. Adams II, T. Gundersen, Technoeconomic Analysis of a Waste Tire to Liquefied Synthetic Natural Gas (SNG) Energy System, Submitted (2019a).
A. S. R. Subramanian, T. A. Adams II, P. I. Barton, T. Gundersen, Optimal Design and Operation of a Hybrid Solid Waste and Natural Gas Feedstock Energy Polygeneration System, In Preparation (2019b).
H. D. Sherali, Tight Relaxations for Nonconvex Optimization Problems using the Reformulation-Linearization/Convexification Technique (RLT), in: Handbook of global optimization, Springer, 2002, pp. 1-63.

Sauro Pierucci, Flavio Manenti, Giulia Bozzano, Davide Manca (Eds.)
Proceedings of the 30th European Symposium on Computer Aided Process Engineering (ESCAPE30), May 24-27, 2020, Milano, Italy.
http://dx.doi.org/10.1016/B978-0-12-823377-1.50155-5

Computational Shape Optimization of Microreactors based on CFD Simulation and Surrogate Model driven Optimization

Runzhe Liang, Zhihong Yuan*

Department of Chemical Engineering, Tsinghua University, Beijing 100084, China

zhihongyuan@mail.tsinghua.edu.cn

Abstract

Pharmaceutical industry has become an emerging industry worldwide. However, the automation level and the production efficiency of pharmaceutical manufacturing are relatively low because of the large-scale utilization of batch mode. In the context of the rise of microdevices, this paper investigated the shape optimization of Y-shape microreactors for the production of the optically pure chiral product (S)-1-phenylethylamine. We established the computational fluid dynamics (CFD) based automatic simulation platform to obtain a large number of simulation data sets. We built the data-driven surrogate model based on support vector machine (SVM). Then, we formulated the optimization framework to obtain the optimal shape parameters. By shape optimization of microreactors, the yield of the main product can be increased to about 4.3 times as high as that of the initial microreactor.

Keywords: microreactor, shape optimization, data-driven model, CFD automatic simulation

1. Introduction

The traditional batch operation mode is widely adopted in the pharmaceutical industry. Although batch processes have a few advantages such as equipment flexibility, product recovery ability, practicality and so on, it often means the waste of resources and low operational asset efficiencies. To solve the problem, continuous processes can be utilized which means to feed and transform the input materials continuously, and to remove the processed output materials continuously from the system (U.S. Food and Drug Administration, 2019). In general, continuous processes can be considered to have great application potential in improving the flexibility, robustness and reducing operating cost of pharmaceutical manufacturing, which can realize the modernization of pharmaceutical manufacturing better.

The rise of microdevices provides a potential way of continuous pharmaceutical manufacturing. As one of the methods of process intensification, due to large specific surface area, microdevices usually have better mass transfer and heat transfer, which can significantly improve the selectivity and yield of the reaction (Tian et al., 2018). Consequently, operation under microfluidic conditions can be expected to greatly improve the operability and stability of the system (Plutschack et al., 2017). The development of additive manufacturing also provides conditions for precise processing of microdevices (Addison, 2018), however, the design and manufacturing of microdevices mainly follow the trial-and-error approach at present and usually require a large number of experiments and capital to seek the desirable candidate without any

guarantee of optimum solutions. There are relatively few studies on systematic shape optimization of microreactors, most of which only focus on the simulation of single microreactor. Inspired by the aforementioned issues, the presented work combines the computational fluid dynamics (CFD) simulation and data-driven optimization methods to formulate the framework for the shape optimization of microreactors to obtain the highest yield of main products. In our work, the synthesis of S-1-phenylethylamine by the reaction of acetophenone and isopropylamine is used as an example. In detail, our investigations can be divided into three parts: the establishment of automatic CFD simulation platform, the establishment of the data-driven model and the model optimization. Via the CFD simulation platform, a large number of simulation results can be obtained automatically within a certain period of time. CFD simulation results then feed to the building of the data-driven surrogate model based on support vector machine (SVM) method. The surrogate model will replace the original partial differential equations of the microreactor to represent the relationship between main product yield and geometric and shape conditions. Hence, the optimization model can be built to obtain the optimal parameters.

2. Reaction Information

In this paper, an enzymatic reaction is carried out as an example, to produce the optically pure chiral product (S)-1-phenylethylamine (PEA) since this product is an important pharmaceutical intermediate from acetophenone (APH) and isopropylamine (IPA) catalyzed by amine transaminase (ATA), with acetone (ACE) as a by-product, as shown in Figure 1:

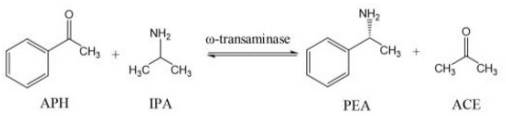

Figure 1. Reaction producing (S)-1-phenylethylamine from acetophenone

The reason why the reaction is chosen for study is that it is a typical and important reaction with unfavorable thermodynamic conditions. The reaction follows a ping pong bi-bi mechanism in which isopropylamine (IPA) binds to the enzyme first, and after acetone (ACE) is released acetophenone (APH) binds next, and finally the product (S)-1-phenylethylamine (PEA) is released from the enzyme (Al-Haque, 2012). As a transaminase-catalyzed reaction, the reaction is heavily influenced by inhibition of the substrate APH and the product PEA, with a small equilibrium constant. The kinetic model is described as Eq. (1):

$$
\begin{aligned}
r_{PEA} &= \frac{d[PEA]}{dt} \\
&= \frac{[E_0]k_{cat}^{f}k_{cat}^{r}([APH][IPA]-\frac{[PEA][ACE]}{K_{eq}})}{\{k_{cat}^{r}K_M^{APH}[IPA](1+\frac{[PEA]}{K_{Si}^{PEA}}+\frac{[IPA]}{K_{Si}^{IPA}})+k_{cat}^{r}K_M^{IPA}[APH](1+\frac{[APH]}{K_{Si}^{APH}}+\frac{[ACE]}{K_{Si}^{ACE}})+} \\
&\quad k_{cat}^{f}\frac{K_M^{PEA}[ACE]}{K_{eq}}(1+\frac{[APH]}{K_{Si}^{APH}}+\frac{[ACE]}{K_{Si}^{ACE}})+k_{cat}^{f}\frac{K_M^{ACE}[PEA]}{K_{eq}}(1+\frac{[PEA]}{K_{Si}^{PEA}}+\frac{[IPA]}{K_{Si}^{IPA}}) \\
&\quad +k_{cat}^{r}[APH][IPA]+k_{cat}^{f}\frac{K_M^{PEA}[IPA][ACE]}{K_{eq}K_i^{IPA}}+\frac{k_{cat}^{f}[ACE][PEA]}{K_{eq}}+k_{cat}^{r}\frac{K_M^{IPA}[APH][PEA]}{K_i^{PEA}}\}
\end{aligned}
\tag{1}
$$

Al-Haque et al. (2012) determined the parameters of the reaction system in detail through a large number of experiments and data fitting. At the same time, the mass transfer coefficient is also the key to affect the mixing and reaction rate. In this case, two compounds involved in the reaction are regarded as slow diffusion compounds: ATA ($D = 1 \times 10^{-11}$ m^2/s) and APH ($D = 1 \times 10^{-12}$ m^2/s), while other compounds are regarded as fast diffusion compounds, with the same diffusion coefficient ($D = 1 \times 10^{-9}$ m^2/s) (Grundtvig et al., 2017).

3. Method Description

3.1. Microreactor Information

The initial microreactor type studied is the Y-shape microreactor (Figure 2), where APH and IPA enter from one end of the microreactor, while the enzyme ATA enters from the other end of the microreactor, and they mix and react in the main reaction channel.

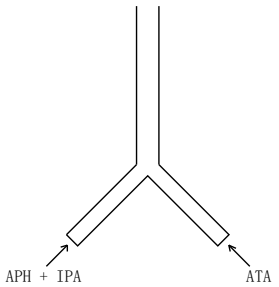

Figure 2. Initial configuration of the microreactor

Because of the low flow velocity and the existence of two slow diffusion substances, APH and ATA, although there is an intersection in the microreactor, the overall mixing effect is still poor, and the characteristics of laminar flow pattern and slow diffusion also make the radial diffusion of reactants difficult, so it is difficult for APH and ATA to reach a relatively uniform distribution. The reaction can only take place at the interface between the two parallel flows, which greatly affects the overall reaction rate and the yield of PEA.

3.2. Research Method

The idea of this work is to improve the mixing situation by optimizing the shape of the microreactor, and to interfere with the original laminar flow pattern so that the slow diffusion substances can achieve better radial mixing effect. For example, a depression on the wall of the microreactor is designed in this paper, which can influence the flow condition to some extent. When there is a depression on the wall, there will be two main effects: on the one hand, the depression can disturb the original flow pattern, and it is equivalent to reducing the distance of radial diffusion needed in a certain length range, which contribute to the improvement of conversion greatly; on the other hand, the occurrence of the depression will reduce the cross-sectional area of the microreactor. According to the continuity principle, the flow rate will accelerate, so that the residence time will reduce, which is not conducive to the improvement of conversion. In order to get a higher yield, it is necessary to design relevant parameters of the depression, such as the location of the depression x, the length of the depression l, the depth of the depression h and so on (Figure 3).

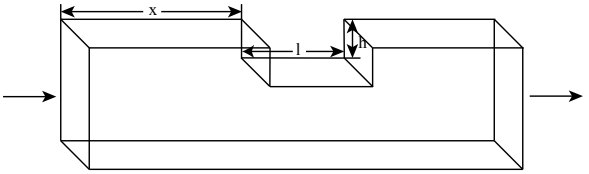

Figure 3. Determining parameters when introducing a depression

Due to existence of the grey box model of CFD simulation, a large number of data can be generated by CFD simulation, and then a surrogate model can be built based on SVM method, and the optimal solution with the highest product yield can be also obtained through optimization of related models. The flow chart is shown as Figure 4:

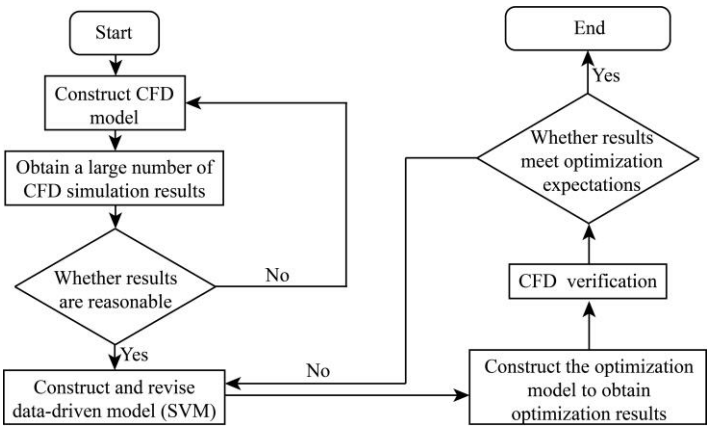

Figure 4. Research flow chart

4. Results and Discussion

The length, width and height of the main reaction channel of the initial microreactor are set as 10 mm, 0.3 mm and 1 mm respectively. The length and width of inlet passages are 3 mm and 0.15 mm respectively. The angle of the intersection is 90 °. The mass fractions of ATA, APH and IPA in the feed are 0.2 %, 0.3 % and 5 %, respectively, and the flow rate is 0.1 mm/s.

Considering the manufacturing difficulty, the distance between the beginning position of the depression and the intersection should not be less than 0.1 mm, the length of the depression should not be less than 0.1 mm, and the depth of the depression should not be more than 0.25 mm. According to the established surrogate model, we can get the objective function and constraints as Eq. (2):

$$\begin{aligned} &\max\ y = f(x,l,h) \\ &s.t.\ x \geq 0.1 \\ &\quad l \geq 0.1 \\ &\quad x + l \leq 10 \\ &\quad 0 \leq h \leq 0.25 \end{aligned} \tag{2}$$

Where $y = f(l,x,h)$ is the regression model obtained by SVM.

In order to build the above optimization model, the first step is to build an automatic simulation platform to get a large number of simulation results. In this work, ANSYS is utilized as the computational fluid simulation software, and the structured mesh is used for mesh generation to ensure mesh quality. In order to balance simulation time and simulation accuracy, the number of volume meshes divided in each simulation is about 1,000,000, so as to ensure that each solution time is not too long (about one hour). In this study 670 simulations are included in total, 530 of which are used as training sets with 121 boundary conditions (for example, when the length of the depression is zero, the yield is the same as that of the initial microreactor) while the others are used as test sets.

The second step is to set up the SVM-based surrogate model. After all data are normalized, radial basis function is used as kernel function for nonlinear regression, and appropriate parameters such as values of λ and penalty factor C are selected to ensure the regression effect and avoid over fitting. The regression results are listed in Table 1:

Table 1. SVM regression results

Number of support vectors	Regression coefficient R^2 (for training sets)	Regression coefficient R^2 (for test sets)
193	0.957	0.938

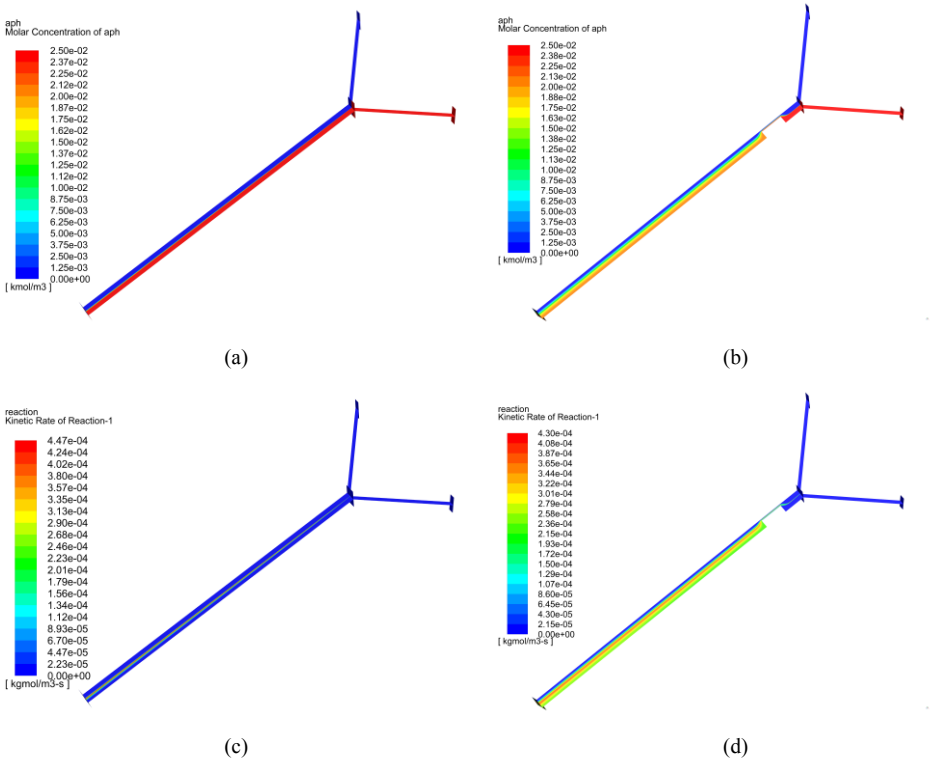

Figure 5. Concentration distribution of APH of a) initial microreactor b) microreactor with the optimal depression parameters and reaction zone distribution of c) initial microreactor d) microreactor with the optimal depression parameters

After the establishment of the data-driven surrogate model, the last step is to obtain the optimal parameters via optimization of Eq. (2), and then check the optimization result by CFD simulation. Because support vector theory is generally sensitive to missing data, if the simulation result is basically consistent with the optimization result, it is proved that the optimal parameters of depression have been obtained; if they are inconsistent, the simulation result is fed back to the training set and the model needs to be retrained, so as to obtain a new surrogate model and new optimal depression parameters, which will be checked again, until they are basically consistent.

To deal with this NLP problem, the software GAMS is utilized in this study to obtain the optimal solution, with CONOPT solver. After gaining several groups of inconsistent results and updating, the optimization result can be considered equal to the simulation result, where x, l and h are 0.72 mm, 0.77 mm and 0.25 mm, respectively, and the yield can be increased to 4.3 times of that of initial microreactor. Comparison figures are shown in Figure 5.

It can be observed from the figures above that there is almost no radial diffusion of APH in the initial microreactor, however in the optimized microreactor, diffusion effect has greatly improved after a short and deep depression. Things are the same for ATA. Because the radial diffusion effect of substances with small diffusion coefficient is improved, and the mixing condition of reactants is improved, the reaction zone is obviously expanded, resulting in a large increase in the yield.

5. Conclusion and Prospect

A systematic shape optimization method of microreactors based on CFD simulation and the surrogate model was proposed in this work. Through the establishment of the CFD based automatic simulation platform, a large number of simulation data can be obtained within a certain period of time, and a data-driven surrogate model can be also built by SVM regression, so as to determine the objective function and constraints, which can be solved by the reliable optimization algorithm to obtain the optimal parameters of geometry. The yield of the optimized microreactor has been greatly improved in the work, and in the future, the work will focus on the following two points: 1) to verify the results by a series of experiments; 2) to include more arguments to prove the general applicability of the optimization method.

References

U.S. Food and Drug Administration, 2019, Quality Considerations for Continuous Manufacturing.

Tian Y, Demirel S E, Hasan M M F, Pistikopoulos E N, 2018, An overview of process systems engineering approaches for process intensification: State of the art, Chemical Engineering and Processing - Process Intensification, 133:160-210.

Plutschack M B, Pieber B, Gilmore K, Seeberger P H, 2017, The Hitchhiker's Guide to Flow Chemistry, Chemical Reviews, 117(18):11796-11893.

Addison K, Stark, 2018, Manufactured Chemistry: Rethinking unit operation design in the age of additive manufacturing, AIChE Journal, 64: 1162-1173.

Al-Haque N, Santacoloma P A, Neto W, Tufvesson P, Gani R, Woodley J M, 2012, A robust methodology for kinetic model parameter estimation for biocatalytic reactions, Biotechnology Progress, 28(5):1186-1196.

Grundtvig I P R, Daugaard A E, Woodley J M, Gernaey K V, Krühne U, 2017, Shape optimization as a tool to design biocatalytic microreactors, Chemical Engineering Journal, 322:215-223.

Sauro Pierucci, Flavio Manenti, Giulia Bozzano, Davide Manca (Eds.)
Proceedings of the 30th European Symposium on Computer Aided Process Engineering (ESCAPE30), May 24-27, 2020, Milano, Italy.
http://dx.doi.org/10.1016/B978-0-12-823377-1.50156-7

High-purity DMC Production by Indirect Alcoholysis of Urea: Optimal Design and Control

Iulian Patrașcu,[a] Costin Sorin Bîldea,[a] Anton A. Kiss [b,c*]

[a] *University "Politehnica" of Bucharest, Polizu 1-7, 011061 Bucharest, Romania.*
[b] *The University of Manchester, Department of Chemical Engineering and Analytical Science, Sackville Street, The Mill, Manchester M13 9PL, United Kingdom.*
[c] *University of Twente, Sustainable Process Technology, PO Box 217, 7500 AE Enschede, The Netherlands.*
a.a.kiss@utwente.nl , tony.kiss@manchester.ak.uk

Abstract

This work shows that it is feasible to convert a greenhouse gas to a green solvent. Dimethyl carbonate (DMC) is an eco-friendly chemical compound which can be obtained by indirect alcoholysis of urea with propylene glycol, followed be the trans-esterification of propylene carbonate (PC) with a large excess of methanol. However, this process route requires the energy-intensive separation of the DMC-methanol azeotrope. Here, we propose a new process in which the transesterification reaction is performed with excess of PC, which allows obtaining high purity DMC (99.8%wt) in a less complex process. By optimizing the new process, the total annual cost is minimized to 4.71 M$/year (for a production capacity of 32 ktpy DMC), and by heat integration the energy requirement is reduced to only 2.64 kWh/kg DMC. The dynamics and control of the process show that ±10% changes of the production are easily accommodated.
Keywords: Alkyl carbonate, Process design, Process optimization, Plantwide control

1. Introduction

Carbon dioxide, available from CCS activities, can be used as feedstock for producing various chemicals. Dimethyl carbonate (DMC) is an essential chemical used in the production of polycarbonates, batteries and fuel additive (Keller et al., 2010). In contrast to solvents such as dimethyl sulphate and phosgene, DMC has low toxicity and fast biodegradability (Santos et al., 2014). DMC can be produced by various methods: phosgenation, urea esterification, ethylene carbonate esterification, methanol oxy-carbonylation, and direct synthesis from CO_2 and methanol (Kongpanna et al., 2015; Kuenen et al., 2016; Tan et al., 2018). The best reported process is the indirect urea alcoholysis (Figure 1), in which urea (produced by the CO_2-ammonia reaction) is used for the carbonylation of propylene glycol (PG) to make propylene carbonate (PC), which is further used in the transesterification with methanol (MeOH) to yield DMC (Wang et al., 2016). Recently, this process was used to obtain DMC/MeOH azeotrope (14.07 %mole DMC) using excess methanol for the transesterification step (Shi et al. 2017). This process requires 1.75 kWh/kg DMC as azeotrope with MeOH, to which one should add 2.55 kWh/kg DMC needed to break this azeotrope by extractive distillation with methyl isobutyl ketone (MIBK) as solvent (Hu and Cheng, 2017).

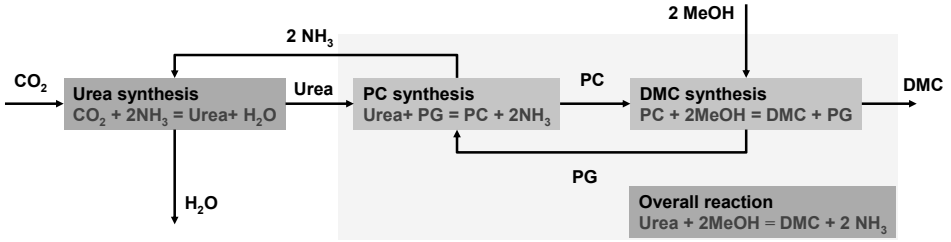

Figure 1. DMC synthesis by urea alcoholysis and transesterification of propylene carbonate

This study presents a new process that is specifically developed to produce high purity DMC (99.8 %wt). Process optimization is carried out to minimize the total annual cost, and heat integration is used to drastically reduce the energy usage, while an adequate process control structure is proposed to ensure controllability of the DMC plant.

2. Problem statement

The most important step of the DMC production by indirect alcoholysis of urea is the transesterification reaction of PC with methanol, followed by DMC purification by extractive distillation (Figure 2). A high PC conversion can be achieved if the reaction takes place with excess methanol (Figure 3 left). However, the composition of the reactor effluent is such that high purity methanol and DMC/MeOH azeotrope (Figure 3 right) can be obtained by conventional distillation. Thus, DMC purification and methanol recovery are achieved by extractive distillation (Figure 2), leading to high energy requirements. To solve this problem, this work proposes to carry out the transesterification reaction with excess PC instead of methanol, such that methanol is the limiting reactant and the DMC concentration in the reactor effluent exceeds the azeotropic value. Therefore, DMC can be obtained with high purity, while the azeotrope can be recycled to the process. Performing the reaction in this way, it is no longer necessary to use other costly separation techniques for breaking the azeotrope.

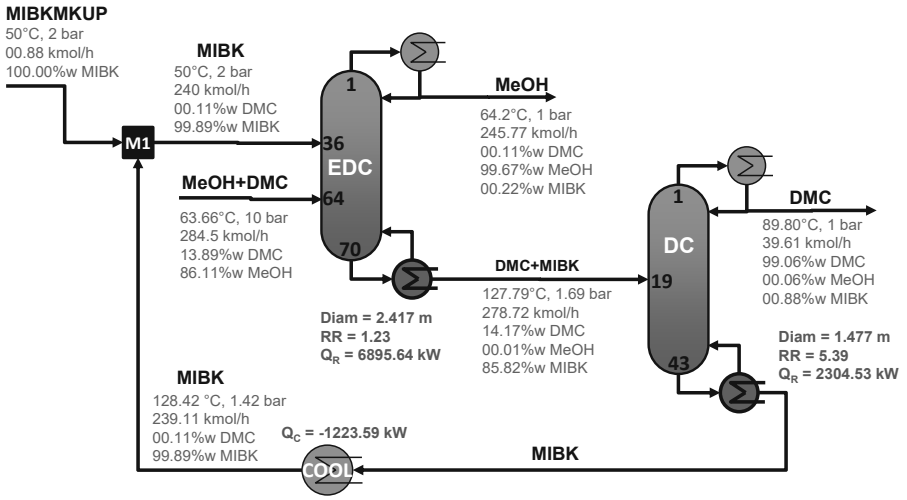

Figure 2. Process design for DMC purification by extractive distillation

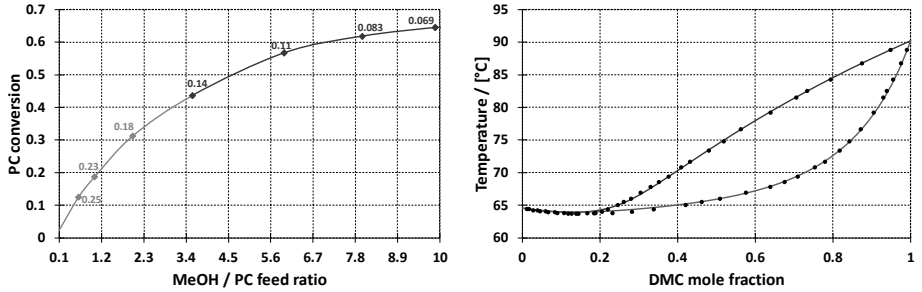

Figure 3. Dependence of the PC equilibrium conversion (40 °C) vs MeOH/PC feed ratio (left). VLE experimental data vs. values predicted by the NRTL model for MeOH / DMC (right).

3. Chemistry and kinetics

The process design developed in this work considers urea and methanol as raw materials. PC is obtained in the reaction of urea with PG, while DMC is obtained in the reaction of PC with methanol. The reaction rate for the PC synthesis step is given by (Shi et al. 2017):

$r_{PC} = k \cdot c_{PG} \cdot c_{Urea}$, with $k(T)/[m^3/(kmol/s)] = 0.02646 \cdot \exp(-562.6/T)$ (1)

For the DMC synthesis step, experimental data (Pyrlik et al. 2011) has been regressed to yield the following reaction rate:

$r_{DMC} = k\left(x_{MeOH}^2 x_{PC} - x_{PG} x_{DMC} / K_x\right)$, with $k_{(313\ K)}$=0.4166×10^{-3} kmol/kg/s, $K_{x(313\ K)} = 0.2$.

4. Results and discussion

Figure 4 presents the novel process design for DMC production, along with the mass balance and key design and operating parameters. Two stirred reactors are necessary to achieve a high conversion of urea. These reactors contain the MgO catalyst (2 %wt, about 400 kg), have 20 m^3 each and operate at 180 °C and 10 bar. PG and urea are fed in stoichiometric ratio in the first stirred reactor (CSTR1). The ammonia produced here is removed as vapour by using a flash vessel (V-L). The second stirred reactor (CSTR2) achieves over 99.3% conversion of PG. The first distillation column (C1) removes completely the ammonia to avoid its accumulation in the DMC/MeOH recycle loop.

Note that the stoichiometric ratio of MeOH/PC for DMC synthesis is 2, but to obtain high purity of DMC this ratio is kept at 1 such that there is an excess of PC. The PC previously produced and the fresh MeOH are fed in a tubular reactor (RPLUG), containing 1270 kg of catalyst. The effluent of the reactor is separated in the second distillation column (C2) into a distillate containing DMC and MeOH, and a bottom product consisting of PG and PC. DMC is obtained as a high purity (99.8 %wt) bottom product of the third column (C3), while the distillate (MeOH/DMC azeotrope) is recycled to the transesterification reactor. The separation of PG from PC takes place in the fourth column (C4). The PC is recycled from its bottom to DMC synthesis, while PG with some PC is sent to the first reactor for PC synthesis.

The total number of stages (*NT*) and the feed tray location (*NF*) of each distillation column were determined by optimization, where the minimum of the total annual cost was the objective function. Figure 5 shows results concerning the distillation column C-3: optimal number of stages (left), temperature and concentration profiles (right).

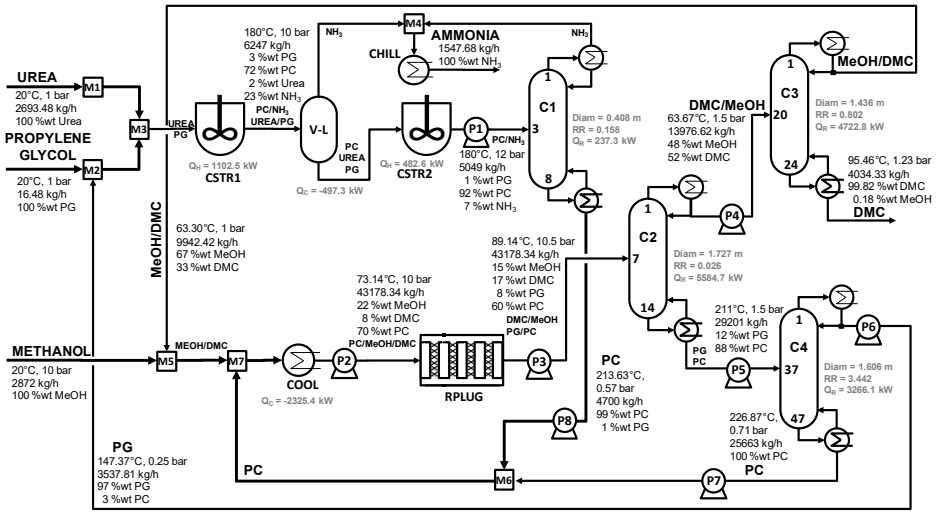

Figure 4. Process design for DMC production

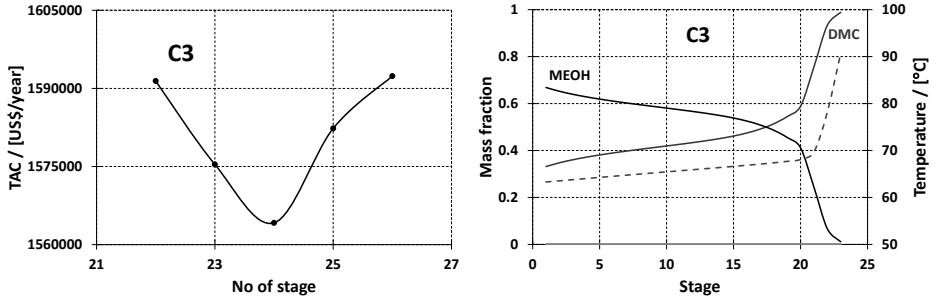

Figure 5. Column optimization (left). Temperature and mass composition profiles (right).

The dynamic simulation is built in Aspen Dynamic using a flow driven dynamic model. The basic control includes several pressure, liquid level, and temperatures control loops (for the stirred reactors, distillation columns, and various heat exchangers). More important, feeding the reactants in the correct amounts and avoiding their accumulation or depletion is the key to successful plantwide control. Thus, fresh urea sets the production rate. The ratio between reactants is kept constant at the inlet of the reactors, while fresh methanol and PG makeup flows are set by level control loops. Figure 6 shows the plantwide control structure of the heat integrated plant for DMC production, while the dynamic results are shown in Figure 7.

The performance of the plantwide control structure is tested by introducing feed flow rate disturbances. After two hours of steady state operation, the urea flow rate is increased in 1h ramp by 10%. The ratio controller increases the PG flow rate. As a result, more PC is produced. As the ratio MeOH/PC at the inlet of RPLUG is constant, more methanol is added to the process. Afterwards, the production of DMC is returned to initial value and the further decreased by 10%, by decreasing the fresh urea flow. During these changes, the PG flow rate is reduced, less PC is produced, and less MeOH is brought into the process. The control structure is clearly able achieve 10% production rate changes while maintaining high quality of the DMC product.

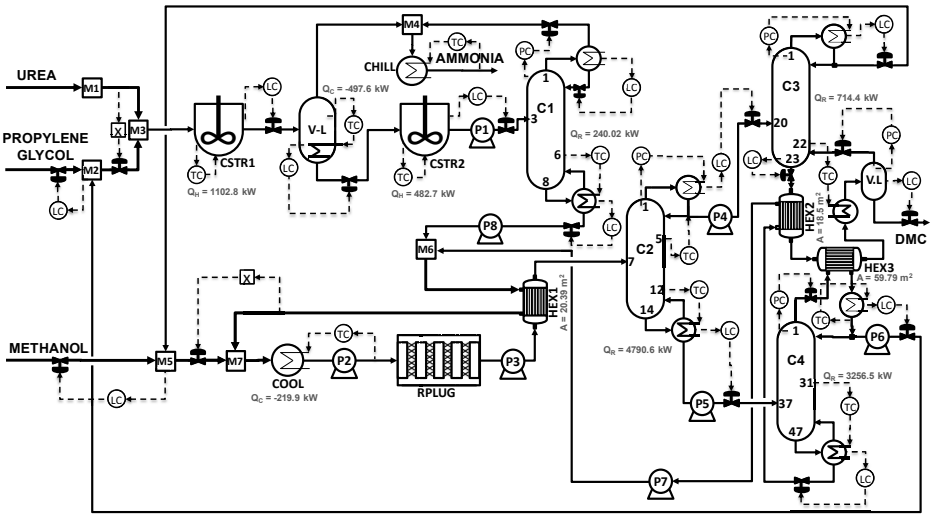

Figure 6. Control structure of heat integrated process design for DMC production

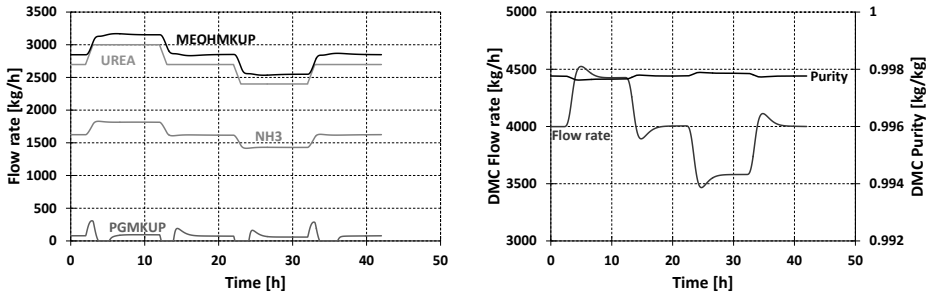

Figure 7. Dynamic results for production changes in the heat integrated DMC process

5. Process evaluation

The heat integration potential was analysed by Pinch Analysis, which revealed that up to 38% energy savings is possible. Using only a few process-process heat-exchangers, the energy requirement was reduced by 31%. Table 1 provides an overview of the economic evaluation, assuming a payback period of 3 years and 8000 hours/year operating time. The capital cost was evaluated according to Dimian (2003). The heating and cooling costs taken into account are: LP steam (6 bar, 160 °C, $7.78/GJ), HP steam (41 bar, 254 °C, $9.88 /GJ), and cooling water (1bar, 25 °C $0.72/GJ).

Table 1. Economic evaluation of the novel heat integrated DMC process

Item description *(unit)*	***C1***	***C2***	***C3***	***C4***	***React***	***HEX***	***Cool***	***Mixer***
Shell / [10^3 $]	25.0	199.5	336.0	457.6	589.5	199.9	291.9	407.9
Trays / [10^3 $]	1.1	16.4	35.0	55.6	–	–	–	–
Condenser / [10^3 $]	82.3	553.8	123.3	580.4	–	–	–	–
Reboiler / [10^3 $]	23.4	422.2	540.2	57.5	–	–	–	–
Heating / [10^3 $/year]	53.8	1363.1	160.1	926.6	384.5	–	–	–
Cooling / [10^3 $/year]	1.4	65.5	94.7	10.7	–	–	14.9	–
TAC / [10^3 $/year]	99.1	1826.0	599.6	1321.0	581.0	66.6	112.1	136.0

The total investment cost (including heat exchangers, distillation columns, reactors, vapor-liquid vessels and coolers) is $4998.5 \cdot 10^3$ US$, while the total operating cost is $3075.1 \cdot 10^3$ US$/year, with a total annual cost of $4712.3 \cdot 10^3$ US$/year. The total net carbon tax for 2506 kg/h CO2 emissions is evaluated at 13.81 $/h. The specific energy requirement is reduced to only 2.64 kWh/kg DMC for the new heat integrated process.

6. Conclusions

High purity DMC can be effectively produced by indirect alcoholysis of urea in the new process proposed in this study, by performing the transesterification reaction with excess PC (instead of methanol – as in a conventional process). This avoids the energy intensive DMC purification from the DMC/MeOH azeotrope. Moreover, the energy requirement is significantly reduced (by heat integration) to only 2.64 kWh/kg DMC, minimizing also the total annual cost to $4712.3 \cdot 10^3$ US$/year. The new process is easily controllable, ±10% changes of the production flow rate being easily achieved.

Acknowledgment

Financial support of the European Commission through the European Regional Development Fund and of the Romanian state budget, under the grant agreement 155/25.11.2016 Project POC P-37-449 (ASPiRE) is gratefully acknowledged. AAK gratefully acknowledges the Royal Society Wolfson Research Merit Award.

References

A. C. Dimian, 2003, Integrated design and simulation of chemical processes, Elsevier, Amsterdam.

C.-C. Hu, S.-H. Cheng, 2017, Development of alternative methanol/dimethyl carbonate separation systems by extractive distillation - A holistic approach, Chemical Engineering Research and Design, 127, 189-214.

N. Keller, G. Rebmann, V. Keller, 2010, Catalysts, mechanisms and industrial processes for the dimethylcarbonate synthesis, Journal of Molecular Catalysis a-Chemical, 317, 1-18.

P. Kongpanna, V. Pavarajarn, R. Gani, S. Assabumrungrat, 2015, Techno-economic evaluation of different CO2-based processes for dimethyl carbonate production, Chemical Engineering Research and Design, 93, 496-510.

H. J. Kuenen, H. J. Mengers, D. C. Nijmeijer, A. G. J. van der Ham, A. A. Kiss, 2016, Techno-economic evaluation of the direct conversion of CO_2 to dimethyl carbonate using catalytic membrane reactors, Computers & Chemical Engineering, 86, 136-147.

A. Pyrlik, W. Hoelderich, K. Müller, W. Arlt, J. Strautmann, D. Kruse, 2011, Dimethyl carbonate via transesterification of propylene carbonate with methanol over ion exchange resins, Applied Catalysis B: Environmental, 125, 486-491.

B. A. V. Santos, V. M. T. M. Silva, M. J. Loureiro, A. E. Rodrigues, 2014, Review for the direct synthesis of dimethyl carbonate, ChemBioEng Reviews, 1, 214-229.

L. Shi, S.-J. Wang, D.S.-H. Wong, K. Huang, 2017, Novel process design of synthesizing propylene carbonate for dimethyl carbonate production by indirect alcoholysis of urea, Industrial & Engineering Chemistry Research, 56, 11531-11544.

H-Z. Tan, Z-Q. Wang, Z-N. Xu, J. Sun, Y-P. Xu, Q-S. Chen, Y. Chen, G-C. Guo, 2018, Review on the synthesis of dimethyl carbonate, Catalysis Today, 316, 2-12.

M. Y. Wang, H. B. Wang, Q. H. Qu, L. N. He, 2016, Industrial production of dimethyl carbonate from CO_2 in China, in P. Tundo, L. N. He, E. Lokteva, C. Mota (Eds) Chemistry beyond chlorine, Springer, Cham.

Sauro Pierucci, Flavio Manenti, Giulia Bozzano, Davide Manca (Eds.)
Proceedings of the 30th European Symposium on Computer Aided Process Engineering (ESCAPE30), May 24-27, 2020, Milano, Italy.
http://dx.doi.org/10.1016/B978-0-12-823377-1.50157-9

Optimization of Shell and Tube Heat Exchangers Sizing with Heat Transfer Enhancement

Zekun Yang, Yingjie Ma, Nan Zhang,* Robin Smith
Centre for Process Integration, School of Chemical Engineering and Analytical Science, The University of Manchester, Manchester M13 9PL, UK
nan.zhang@manchester.ac.uk

Abstract

Heat transfer enhancement (HTE) is an efficient technology to improve the performance of shell and tube heat exchangers (STHEs). However, even though there are widely accepted commercial software packages being used in heat exchanger design combined with HTE, such as HTRI and Aspen EDR, the design procedure still requires extensive user manipulation and fine tuning, which not only is time-consuming but also leads to varied qualities due to human factors. Therefore, a systematic optimization methodology is required in order to achieve an efficient and accurate design solution. This paper presents a generalized disjunctive programming (GDP) model for the optimization of STHE design. The model is formulated as a mixed integer non-linear programming (MINLP) problem using GAMS (General Algebraic Modeling System), involving selection for 12 technology combinations (four tube-side techniques, three shell-side techniques) and all discrete decisions for each selection are modeled by disjunctions. The model is then applied to a case study to minimize the total capital cost. Both global optimization solver BARON, and general MINLP solver DICOPT are tested. The results show the developed HTE optimization method provides a better design solution compared with conventional STHE design procedure.

Keywords: Mathematical programming, heat transfer enhancement, shell and tube heat exchanger design

1. Introduction

Shell and tube heat exchanger (STHE) is a common heat transfer device widely used in oil, gas and chemical industries because of the simple structure and high capability of pressure drop. To increase the economic benefits, reducing the cost of STHE is always a challenge for industrial fields. Many conventional heat exchanger design methods, which are based on the plain tube and normal segmental baffle, have been developed for STHE sizing. These methods apply various algorithms and optimization approaches, which involve SA (simulated annealing) (Chaudhuri et al., 1997), MINLP (mixed integer nonlinear programming) (Mizutani et al., 2003), algorithm based on tube count table (Costa & Queiroz, 2008), GA (genetic algorithms) (Ponce-Ortega et al., 2009), MILP (Mixed-Integer Linear Programming) (Gonçalves et al., 2017). Nevertheless, a relatively high exchanger area under large heat duties is led, since a low utilization efficiency of exchanger geometries, followed by demanding a high capital investment.

To break geometry bottlenecks, heat transfer enhancement (HTE) techniques are developed to improve the performance of STHE through modifications of surface or structure. The main advantages of the HTE applications in different fields involve: (a) Reduce the required exchanger area for STHE design. (b) Avoid additional area, repiping

work and installing new exchangers for heat exchanger network retrofit. (c) Increase the conversion from pressure drop to heat transfer coefficients to avoid exceeding the limitation of process pump capacity.

HTE techniques can be categorized into tube-side and shell-side enhancement. Tube-side enhancement techniques include tube inserts (coiled-wire, twisted-tape) and internal fins, which are respectively able to increase heat transfer performance and geometrical area of STHE. Helical baffles and external fins are generally used as the shell-side intensified techniques. Compared with segmental baffles, the conversion from pressure drop to heat transfer rate can be significantly increased by using helical baffles. For external fins, it is similar to internal fins and can extend the surface area to 2-4 times. Relevant correlations have been developed by numerous papers (Jiang et al., 2014; Pan et al., 2013; Smith, 2016; Wang et al., 2012).

In recent years, human factors normally lead to different qualities of design as using the existing STHE design methods, because different users have to carry out various operations to converge the software, such as the selection of baffle type and tube inserts, adjusting tube pitch, tube diameter and twisted pitch. These operations cause various degrees of deviations for different users, and further increase computation time. In order to overcome the existing drawbacks, this paper aims to extend the existing mathematical models that have been developed for STHE to achieve automated heat exchanger sizing with using HTE. GDP is introduced in this model to select all discrete decisions, which mainly include the number of tube passes, TEMA tube sizes, helical angle and tube configurations.

2. Mathematical Model

2.1. Assumption

The assumptions below are required for this mathematical model, as described:

1. Single phase heat transfer in STHEs.
2. Baffles with 20-45% cut.
3. Straight tube bundle.
4. Fluid properties are assumed constant.
5. Constant fouling resistance.

2.2. Design Variables

The main decision variables in the configuration of STHE involve: continuous variables (tube pinch PT, tube number N_t, , tube length L, tube inside and outside diameter D_i, D_O, tube inlet and outlet nozzle diameter $D_{TN,inlet}$, $D_{TN,outlet}$, shell inner diameter D_{SI}, tube outside bundle diameter D_{SB}, shell inlet and outlet nozzle diameter $D_{SN,inlet}$, $D_{SN,outlet}$, , baffle spacing B_S, baffle inlet and outlet spacing B_{in}, B_{out} and baffle cut B_c) and Integer variable (baffle number N_b, the number of tube passes N_{TP}). Additionally, Boolean variables are applied in expressing the disjunctions and transformed into equivalent numbers of binary variables. Cost is defined as a free variable to formulate the objective function.

2.3. Design Equations

Tube-side modeling involves plain tube (PT), coiled-wire (CW), twisted-tape (TT) and internal fins (IF). GDP is developed to select the discrete decisions, which include: tube outside diameter D_O, number of tube passes N_{TP}, tube-side velocity V_T and total tube-side pressure drop ΔP_T. The required Boolean variables and logic propositions for each disjunction are demonstrated in detail.

For the selection of the tube diameters, the general TEMA tube outside diameters of STHE are respectively 0.01905m and 0.02550m. The tube wall thickness of 0.002108m can be used for steel tube. The following disjunction D1 is used to select the tube sizes, as shown:

$$\begin{bmatrix} De_1 \\ D_O = 0.01905 \\ D_i = 0.01483 \end{bmatrix} \quad \vee \quad \begin{bmatrix} De_2 \\ D_O = 0.02550 \\ D_i = 0.02128 \end{bmatrix} \tag{D1}$$

Where De_1 and De_2 are Boolean variables, and corresponding to binary variables de_1 and de_2. If selection De_1 is true ($de_1 = 1$), D_O and D_i are respectively equal to 0.01905m and 0.01483m, otherwise ($de_1 = 0$) D_O and D_i are assigned 0.02550m and 0.02128m. Eqs. (1-2) are used to model D1:

$$D_O = 0.01905\ de_1 + 0.02550\ de_2 \tag{1}$$

$$D_i = 0.01483\ de_1 + 0.02128\ de_2 \tag{2}$$

In order to only select one type of tube sizes, logic equation Eq. (3) is presented:

$$de_1 + de_2 = 1 \tag{3}$$

Similarly, the number of tube passes can be arranged in 1, 2, 4 and 6 passes. Disjunction D2 is presented to select one type of tube pass:

$$\begin{bmatrix} N_1 \\ N_{TP} = 1 \\ V_T = V_{T1} \\ \Delta P_T = \Delta P_{T1} \end{bmatrix} \vee \begin{bmatrix} N_2 \\ N_{TP} = 2 \\ V_T = V_{T2} \\ \Delta P_T = \Delta P_{T2} \end{bmatrix} \vee \begin{bmatrix} N_3 \\ N_{TP} = 4 \\ V_T = V_{T3} \\ \Delta P_T = \Delta P_{T3} \end{bmatrix} \vee \begin{bmatrix} N_4 \\ N_{TP} = 6 \\ V_T = V_{T4} \\ \Delta P_T = \Delta P_{T4} \end{bmatrix} \tag{D2}$$

Where N_1, N_2, N_3 and N_4 are Boolean variables, and then are transformed to binary variables: n_1, n_2, n_3 and n_4. V_{T1}, V_{T2}, V_{T3} and V_{T4} respectively are the tube-side velocity under 1, 2, 4 and 6 tube passes. Similar to the selection of tube sizes, the disjunctions are able to be formulated by logic equations.

Additionally, the tube-side velocity V_T is affected by different tube passes. To avoid directly multiply the N_{TP} by the correlation of V_T, the big-M method is applied in determining the V_T based on D2. The value for M depends on the maximum value of variable which need to be selected in disjunction and is equal to 10 for V_T selection. The correlation of V_T can be found by Wang et al. (2012).

Next, the design models of PT, CW, TT and IF can be respectively found in the literatures (Wang et al., 2012; Jiang et al., 2014; Pan et al., 2013). The tube-side heat transfer coefficient h_T and pressure drop in straight section ΔP_{TS} can be respectively formulated through these models. Finally, total tube-side pressure drop ΔP_T can be obtained based on the sum of ΔP_{TS}, the pressure drop in the tube entrances, exists and reversals ΔP_{TR} and the pressure drop in tube-side nozzles ΔP_{TN}. Smith (2016) presented the correlations to calculate ΔP_{TR} and ΔP_{TN}. The big-M method is used to selectΔP_T. The values of M are equal to 200000 for (N_1 and N_2) and 150000 for (N_3 and N_4). Shell-side model covers three shell-side intensified techniques which are segmental baffles (SSB), helical baffles

(HB) and external fins (EF). Moreover, tube-layout angle T_A, helical angle β_{HB}, shell-side Nusselt number Nu_{HB} and friction factor f_{HB} for helical baffle are automatically selected through disjunction D3 and D4.

For the selection of tube layout angle, general tube configurations include square ($T_A = 90^\circ$), rotated square pitch ($T_A = 45^\circ$), triangular ($T_A = 30^\circ$) and rotated triangular ($T_A = 60^\circ$). Various tube arrangements tend to lead significant impacts for shell-side velocity V_S, shell-side diameter D_{SI}, heat transfer coefficient h_S and equivalent diameter D_{SE}. The following disjunction D3 demonstrates the selection for tube configurations.

$$\begin{bmatrix} TA_1 \\ T_A = 90 \\ F_P = 0.85 \\ P_{CF} = 1 \\ P_C = 1 \\ C_{De} = 4/\pi \end{bmatrix} \vee \begin{bmatrix} TA_2 \\ T_A = 45 \\ F_P = 1 \\ P_{CF} = \sqrt{2}/2 \\ P_C = 1 \\ C_{De} = 4/\pi \end{bmatrix} \vee \begin{bmatrix} TA_3 \\ T_A = 30 \\ F_P = 1 \\ P_{CF} = 1 \\ P_C = 0.866 \\ C_{De} = 2\sqrt{3}/\pi \end{bmatrix} \vee \begin{bmatrix} TA_4 \\ T_A = 60 \\ F_P = 1 \\ P_{CF} = \sqrt{3}/2 \\ P_C = 0.866 \\ C_{De} = 2\sqrt{3}/\pi \end{bmatrix} \quad \text{(D3)}$$

Where F_P is the pitch factor and it is able to impact the correlations of h_S, P_{CF} is the pitch correction factor for flow direction and it directs different V_S, P_C is the pitch configuration factor which impacts D_{SI}. C_{De} is the pitch factor which leads different values for D_{SE}. Corresponding to Boolean variables, binary variables ta_1, ta_2, ta_3 and ta_4 direct the logic equations to achieve the selection of various layout angle.

Design model of SSB has been demonstrated by Wang et al. (2012) and Smith (2016), involving detailed equations which are able to calculate shell side heat transfer coefficient h_S and pressure drop ΔP_S. Pan et al. (2013) summarized the design method for the helical baffle to predict the shell-side heat transfer performance and friction factor. Based on Pan's (2013) approach, the correlations of shell-side Nusselt number Nu_{HB} and friction factor f_{HB} depend on the baffle configurations which are categorized as a various helical angle ($\beta_{HB} = 20^\circ$, 30°, 40° and 50°). Disjunction D4 demonstrate the selection for β_{HB}.

$$\begin{bmatrix} HA_1 \\ \beta_{HB} = 20 \\ Nu_{HB} = Nu_{HB,HA1} \\ f_{HB} = f_{HB,HA1} \end{bmatrix} \vee \begin{bmatrix} HA_2 \\ \beta_{HB} = 30 \\ Nu_{HB} = Nu_{HB,HA2} \\ f_{HB} = f_{HB,HA2} \end{bmatrix} \vee \begin{bmatrix} HA_3 \\ \beta_{HB} = 40 \\ Nu_{HB} = Nu_{HB,HA3} \\ f_{HB} = f_{HB,HA3} \end{bmatrix} \vee \begin{bmatrix} HA_4 \\ \beta_{HB} = 50 \\ Nu_{HB} = Nu_{HB,HA4} \\ f_{HB} = f_{HB,HA4} \end{bmatrix} \quad \text{(D4)}$$

Boolean variables (HA_1,HA_2,HA_3 and HA_4) respectively formulate the helical baffle model under different β_{HB}. Binary variables (ha_1, ha_2, ha_3 and ha_4) are transformed form Boolean variables and construct the logic equations through the big-M approach. The values of M are respectively equal to 200 for Nu_{HB} and 100 for f_{HB} formulation.

The relevant correlations of EF haven been demonstrated by Pan et al. (2013) to predict the performance of finned tube in STHE in which the shell-side coefficient and pressure drop at finned tube are tested, as related to fin geometries. The overall heat transfer coefficient U_O is the important criterion for evaluating the performance of STHXs and

can be calculated based on h_T, h_S which are simultaneously optimized with considering heat transfer enhancement techniques.

2.4. Constraints and Objective Function

The design of STHEs must respect the relevant constraints to direct the feasible results. Smith (2016) proposed the required constraints, which involve the popular size, the limitations for pressure drops and velocities. Additionally, the actual geometrical area supplied by tubes is necessary to satisfy the required area obtained from the thermal performance of exchanger, as demonstrated:

$$A' \geq A \tag{4}$$

Where A' is the geometrical area based on design techniques of tube and shell. The objective of this optimisation model is to minimize the capital cost. Pan et al. (2013) proposed the correlation to calculate the capital cost, as shown:

$$\text{Cost} = \left(K_0 + \sum K_i\right) EA^{0.8} \tag{5}$$

Where K_0 is the economic coefficient of PT-SSB exchanger, K_i is the economic coefficient for various heat transfer enhancement techniques. EA is the exchanger area related to the number and types of tube.

3. Case Study

In this section, the fluid properties and geometrical details of required base case can be found by Pan et al. (2013). The applied model includes 1175 variables, 1532 equations and is then operated on PC i5-3570. The optimum results are used to evaluate the performance of proposed model with different heat transfer enhancement technologies, through comparison with the results reported by Pan et al. (2013). Figure 1 shows the comparison of results based on the percentage of capital cost reduction. The pressure drop constraint is set at the same value between optimization and simulation for each technique combination.

As expected, the diagram shows that the optimization models lead to a higher enhancement level than the results of Pan et al. (2013), and the differences between the two involve: PT-SSB (-2.2%), PT-EF (-3.2%), CW-SSB (-3.8%), CW-EF (-6.3%), TT-

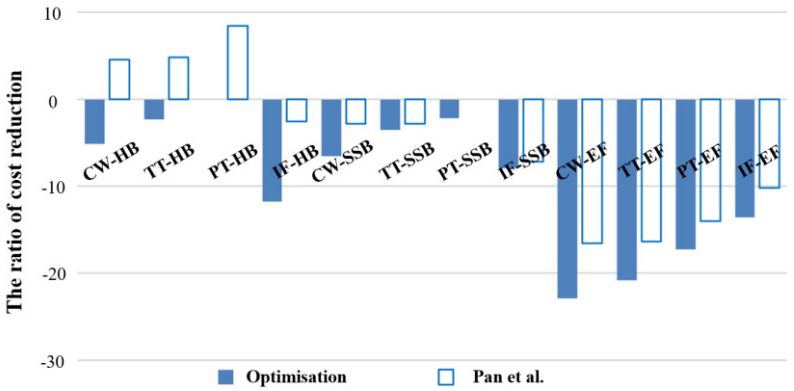

Figure 1. Reduced percentage of capital cost between Pen et al. and proposed model

SSB (-0.7%), TT-EF (-4.5%), IF-SSB (-0.8%) and IF-EF (-3.4%). It is obvious that there is an improvement using the proposed model. Compared with the results in case study-2, the helical baffle models are able to lead a dramatically decrease of capital cost (PT-HB -8.4%, TT-HB -7.1%, CW-HB -9.7% and IF-HB -9.2%), since a higher upper bound of shell-side pressure drop raises the space of optimization in this case. Moreover, an error that appeared in Pan et al. (2013) causes the wrong results for using helical baffles. In their work, helical baffle spacing should be equal to 0.252m, but Pan et al. used a special value 0.043 for baffle spacing, which is not practical. For the HB models in this paper, the baffle spacing is rigorously calculated and modified.

4. Conclusions

A disjunctive mathematical model for STHE optimization is proposed in this paper, which provides the selection for applying 5 types of heat transfer enhancement technique, and then applied in sizing an actual STHE under the given heat duty and streams properties. In GAMS, all variables are optimized simultaneously under detailed constraints and the objective: minimizing the total capital cost. The discrete decisions, which are formulated by disjunctions (D1-D4), are automatically selected to achieve the optimal solution.

Consequently, the optimization implemented by proposed model shows a better performance than that obtained from Pan et al. (2013). Furthermore, this model not only eliminates the influence by human factors, but also achieves the optimal solution under less time, which is possible to improve the performance of software packages through combining with the rigorous model.

References

Chaudhuri, P. D., Diwekar, U. M., & Logsdon, J. S. (1997). An automated approach for the optimal design of heat exchangers. *Industrial & engineering chemistry research*, *36*(9), 3685-3693.

Costa, A. L., & Queiroz, E. M. (2008). Design optimization of shell-and-tube heat exchangers. *Applied Thermal Engineering*, *28*(14-15), 1798-1805.

Gonçalves, C. D. O., Costa, A. L., & Bagajewicz, M. J. (2017). Alternative Mixed-integer linear programming formulations for shell and tube heat exchanger optimal design. *Industrial & Engineering Chemistry Research*, *56*(20), 5970-5979.

Jiang, N., Shelley, J. D., & Smith, R. (2014). New models for conventional and heat exchangers enhanced with tube inserts for heat exchanger network retrofit. *Applied Thermal Engineering*, *70*(1), 944-956.

Mizutani, F. T., Pessoa, F. L., Queiroz, E. M., Hauan, S., & Grossmann, I. E. (2003). Mathematical programming model for heat-exchanger network synthesis including detailed heat-exchanger designs. 1. Shell-and-tube heat-exchanger design. *Industrial & engineering chemistry research*, *42*(17), 4009-4018.

Ponce-Ortega, J. M., Serna-González, M., & Jiménez-Gutiérrez, A. (2009). Use of genetic algorithms for the optimal design of shell-and-tube heat exchangers. *Applied Thermal Engineering*, *29*(2-3), 203-209.

Pan, M., Jamaliniya, S., Smith, R., Bulatov, I., Gough, M., Higley, T., & Droegemueller, P. (2013). New insights to implement heat transfer intensification for shell and tube heat exchangers. *Energy*, *57*, 208-221.

Smith, R. (2016). *Chemical process design and integration*. Second edition ed.; John Wiley & Sons, Inc.: Chichester, West Sussex, United Kingdom.

Wang, Y., Pan, M., Bulatov, I., Smith, R., & Kim, J. K. (2012). Application of intensified heat transfer for the retrofit of heat exchanger network. *Applied Energy*, *89*(1), 45-59

Sauro Pierucci, Flavio Manenti, Giulia Bozzano, Davide Manca (Eds.)
Proceedings of the 30th European Symposium on Computer Aided Process Engineering (ESCAPE30), May 24-27, 2020, Milano, Italy.
http://dx.doi.org/10.1016/B978-0-12-823377-1.50158-0

The Evaluation of Combined Heat and Mass Exchanger Network Synthesis using Novel Stage-Wise Superstructure

Eleonora Amelia, Kitipat Siemanond
[a]*The Petroleum and Petrochemical College, Chulalongkorn University, Soi Chulalongkorn 12, Phayathai road, Pathumwan, Bangkok 10330, Thailand*
kitipat.s@chula.ac.th

Abstract

The Combined Heat and Mass Exchanger Network Synthesis (CHAMENS) comprising a win-win strategy for simultaneously diminishing the emission alongside maximizing the profits of the whole systems has been accomplished in this work. The novelty comes from the development of the original Stage-Wise Superstructure (SWS) to be able to overcome the CHAMENS problem by using more accurate formula to determine the exchanger configurations, initialisation strategies, favourable boundaries to solve the complexities, eradicate a number of the heat and mass exchangers, and decrease the Total Annualized Cost (TAC). The purpose of this work is to generate the new applicable method which is noticeable and flexible to be implemented with a better accuracy output for the small, moderate, and large chemical process plants using GAMS. The TAC, several units required, some advantages and limitations of each method have been compared and analysed. The result for the application of this work in CHAMENS achieves the significant TAC reduction € 2,591,720 compared to the current best result of the previous literature.

Keywords: CHAMENS, Novel Stage-Wise Superstructure, Total Annual Cost.

1. Introduction

Nowadays, a circular economy exists as a critical mission for any industries to afford the infeasibility of the conventional linear economy since the industries and population growth increase together with the expansion of the pollutants. It demonstrates that the energy and environmental problem are determined as the eminent parts in the distinctive industrial worldwide. Hence, a poor energy system alters the environmental destructions such as uncontrollable air pollution, high GHG emission, and global warming. According to the BP energy outlook, the primary energy consumption is expected to grow up about 18 billion toe in 2040. However, LCIB scenario cut down CO_2 emission of the industries and buildings to 15 % (3.9 Gt by 2040) associated by the expansion of circular economy activities (*BP Energy Outlook*, 2019). The current restrictions such as the conventional linear economy, inefficiency energy usage, energy crisis, costly energy price, and sustainability of the process plant needed lead to the advancement of optimum integration in both heat and mass exchanger network. Therefore, the circular economy should not only be a theoretical system but also an implementation of the circular economy's principles including the regeneration of all waste liabilities to become the assets which satisfy the standard setters i.e. the government regulations, customer demanding satisfaction regarding to minimize the cost, waste, and diminish the energy usage.

Figure 1. The Circular Economy of CHAMENS.

Based on Figure 1, CHAMENS contributes to the implementation of the circular economy. It has been applied to the Carbon Capture Storage (CCS), bioethanol production process, calcium looping systems, and COG sweetening (Yoro, Sekoai, Isafiade, & Daramola, 2019). The green and sustainable Heat Integration-Azeotropic Dividing Wall Column (HI-ADWC) in (Yang et al., 2019) has been generated to recycle solvent tert-butanol in ADWC separating binary azeotropic mixtures. However, the literature distributions about CHAMENS are still limited about 9 % (Yoro et al., 2019). The objective of this work is to invent a reliable optimization for CHAMENS with acceptable accuracy modeling of the novel Stage-Wise Superstructure (SWS) by developing the original SWS from (Yee T. F, 1990) to be able to solve the CHAMENS problems, to achieving the minimum material usage and competitive TAC compared to the other optimization methods.

2. Methodology

2.1. Mass Exchanger Network Synthesis (MENS)

After inputting all known data, deciding the variables and the boundaries is necessary to provide a good result. DICOPT is used to solve MINLP in this part.

2.2. Heat Exchanger Network Synthesis (HENS)

After completing the data extraction, CPLEX, MIP solver, is applied to avoid all nonlinearities and provide good initialization for the next step. Secondly, all accurate formularies and considerations are contemplated to avert the underestimation of the heat exchanger configurations, and the optimal solutions are produced by using DICOPT as MINLP solver. Then, the optimal solutions of this second step are taken to determine the types of the hot and cold utilities required at the minimum TAC.

2.3. Combined Heat Exchanger Network Synthesis (HENS)

In this part, MENS is solved firstly to get the flowrates at each hot and cold stream with the minimum mass exchanger matchings and costs of the external Mass Separating Agent (MSA), fresh source, and waste. The boundaries and constraints depend on the concentrations and the flowrate in each stream. Then, the HENS is applied in the same way as the HENS step above. In the end of this step, the results of MENS and HENS are combined and analyzed to validate their reliabilities before designing the network. All the methodologies in this work are resolved in GAMS 24.2.1 (General Algebraic Modeling System), and the platform server with 1.80 GHz Intel ® Core TM i7-8550 and 20 GB of RAM are operated.

2.4. Mass Exchanger Network Synthesis (MENS)

2.4.1. Case study 1. Ammonia removal using water based MSA in the packed column.

Based on the case study in PhD. Thesis (Jide, 2007), the process lean streams, L_1 and L_2, are used to remove contaminants from 5 gaseous rich streams. One external high-priced MSA L_3 is also allocated when using only two free process lean streams is not adequate. Our task is to provide the minimum TAC as it can be seen in Figure 2. The minimum composition difference is 0.0007. The IBMS method (Jide, 2007) provided the result of using external MSA 2.809 kg.s^{-1} impacting to their TAC \$ 133,323 y^{-1}, and The Total Capital Cost (TCC) \$ 196,358. This TAC was affected by the cost coefficient that they used was \$ 14,670 s.kg^{-1} with the operational time 8150 hours per year and \$ 0.0005 s.kg^{-1} for the cost coefficient of the external MSA. Moreover, FLM-SWS method (Jide, 2007) has the result TAC \$ 134,000 y^{-1} and TCC \$ 218,000 using external MSA 2.904 kg.s^{-1}. Using the same parameter to make equitable comparison, the result of MSA required by using our work is 2.595 kg. s^{-1}, with TCC \$ 103,411 and TAC \$ 49,160 y^{-1}. Our result has lower TAC than the IBMS method in (Jide, 2007) due to the target concentration of L3 is not counted at their objective function and our method has the lowest total height of the mass exchangers 743m. The FLM-SWS cited in (Jide, 2007) for the cost coefficient of the external MSA should be corrected to \$ 0.0005 s.kg^{-1}. Moreover, our method still has the lowest TCC and TAC in comparison to both IBMS model and FLM-SWS because the number of its mass exchanger is only 7 units and the external MSA required is still the lowest. The flowrates of MSA_1 and MSA_2 are 1.46 kg. s^{-1}, and 1 kg. s^{-1}. The result using IBMS method has the larger TAC because heat exchange of HENS in IBMS method cannot occur freely, and it only depends on the hot streams at the supply and target temperature. Moreover, our work does not have the splitting at both the rich streams and the lean streams, so it is safe and reliable to be applied in the real industrial application.

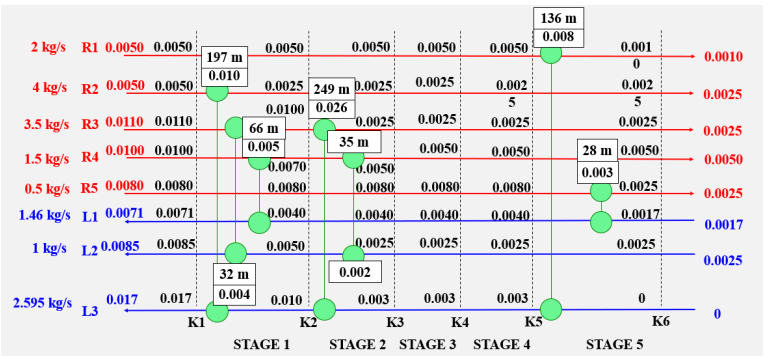

Figure 2. The MENS result of the case study 1 by using this work.

2.5. Heat Exchanger Network Synthesis

2.5.1. Case Study 2 HENS problem of a chemical cluster using three-plants.

In this case study (Hong et al., 2019), the three plants are possible to exchange heat across the plant. The distance among the plants is constant 0.25 km. EMAT is set at 10 ℃. The 7 stages are used to get high degree of freedom in the stream matchings. The pressure drop is neglected. The optimal solution provided in this work is compared to the other literatures which used the advancement of SWS (Chang, Chen, Wang, & Feng, 2017) and Transshipment model (Hong et al., 2019) currently. The TAC of this work exhibited in Table 1 is 65 % lower than the current best of the advancement transshipment model in (Hong et al., 2019). Based on this result, several heat exchanger matchings, hot and cold utilities which are the lowest cause the TAC reduction. When the stream matchings are needed, the binary variable in this case equals to 1. Moreover, the binary variable is zero, if the stream matchings do not appear. To get the minimum number of heat exchanger, our program will force the binary variable to be zero until getting the minimum units required at the minimum TAC. The three perceived interplant heat exchangers facilitate the network to diminish the energy demand by utilizing the excess of energy in the plant becoming the additional heating/cooling source for the other plant. The number of heat exchanger units in this work is the fewest in contrast to the other literatures, and the heat exchanger cost of this work is still the lowest due to the fewest units required.

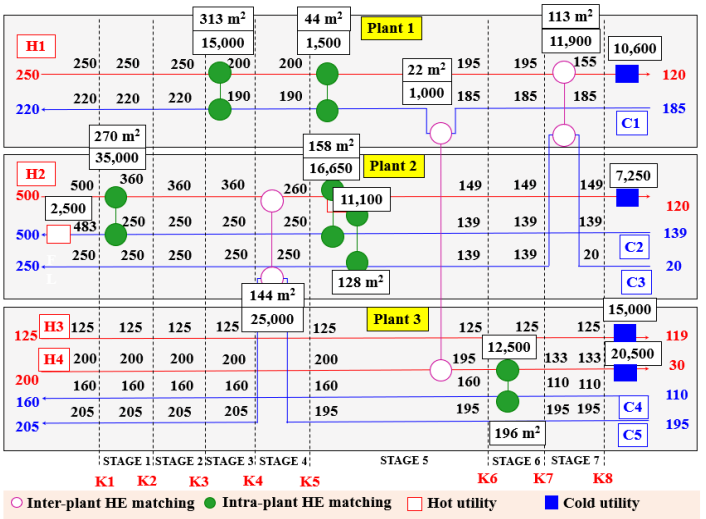

Figure 3. The HENS result of the case study 2 by using this work.

Table 1. The result comparisons of the case study 2 among the other literatures.

Parameters/ Methods	Modified SWS (Chang et al., 2017)	Modified SWS (Chang et al., 2017)	New Transhipment (Hong et al., 2019)	This Work
Heat exchanger units	20	14	14	9
Inter-plant heat exchangers	0	2	5	3
Hot utilities/HUC (kW/$)	15,500/-	6,250/-	2,776/427,620	2,500/500,000
Cold utilities/CUC (kW/$)	66,400/ 664,000	57,100/571,000	53,626/536,262	53,350/ 533,350
TAC, $/y	3,856,860	2,143,444	1,671,023	1,091,166

2.6. Combined Mass and Heat Exchanger Network Synthesis

2.6.1. Case study 3 CHAMENS problem of ammonia recovery.

This case study is obtained from PhD. thesis (Ghazouani, 2018). The ammonia waste from the calcium chloride plant is allocated. Noticing the distinctive of this work among the other previous works, the objective functions are minimizing the TAC. The Exchanger Minimum Approach Temperature (EMAT) is set at 35 ℃. The TAC produced by our work is still the lowest because the cold utilities are not needed. The 4 heat exchanger matchings and 5 heating utilities satisfy the heating and cooling demand. The result in (Ghazouani, 2018) has higher heating and cooling demand because HENS is not resolved while the result in (Tan, Ng, Foo, El-Halwagi, & Samyudia, 2014) deals with HENS using EMAT 35 ℃ having the total area of the heat exchangers 8,544.2 m^2 with 8 heat exchanger matchings while the results of our work successfully defeat their results using the same conditions. The total area of the heat exchangers provided by our results 2,971 m^2 with 7 heat exchanger matchings. The novel SWS successfully provides the result of the CHAMENS with the fewest TAC and the energy demand required. After avoiding the non-linearities by using MIP, the results using MINLP tend to decrease the number of the heat exchangers and minimize their areas, and the energy demand for the heating and cooling utilities.

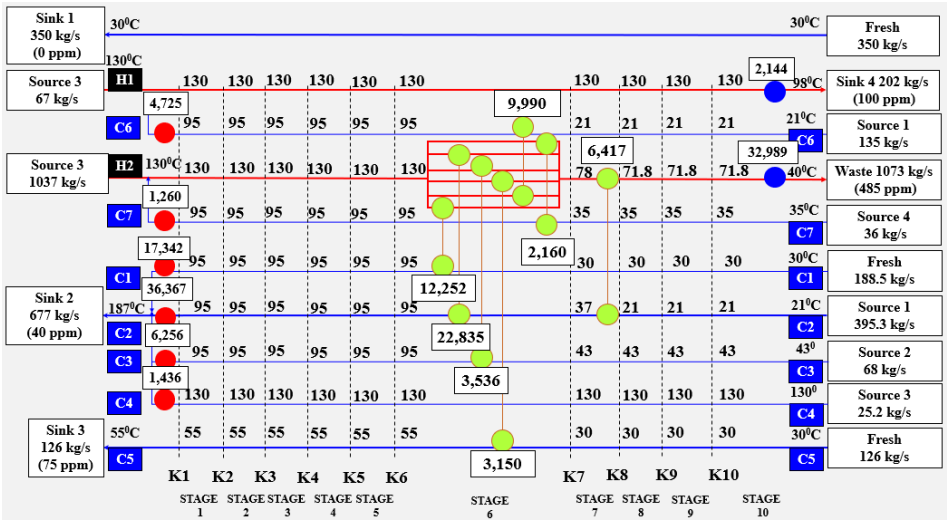

Figure 4. The CHAMENS result of the case study 3 by using this work.

Table 2. The result comparisons of the case study 3 among the other literatures.

Parameters/ Methods	Superimposed mass and energy curves, SMEC (Tan et al., 2014)	New Transhipment (Ghazouani, 2018)	This Work
Flowrate Fresh/ Waste (kGs-1)	654.9/ 1063.9	655/ 1063.9	664.5/ 1073
Total fresh cost (€)	327.5	327.5	332
Hot Utilities / HUC (kWs-1 / €)	132,927/ 4,785,372	131,883.5 / 4,747,806	67,386/2,425,896
Cold Utilities / CUC (kWs-1 / €)	79,228/ 713,052	78,184.5 / 703,660.5	35,133/ 316,197
TAC (€)	5,498,751	5,451,794	2,860,074

3. Conclusion

In this paper, the three case studies MENS, HENS, and CHAMENS have been accomplished due to validate the models contributing to the optimal solutions compared to the different methods FLM-SWS, IBMS, SMEC, and Transhipment model. The results shown are economically viable as the significant TAC reduction can be obtained. This novelty of SWS contains different solving strategy than the original SWS as the initialization step can help the model to get better local optimal solution. It takes the problems to MINLP optimization. This work has been accomplishing the CHAMENS problem with the significant TAC reduction € 2,591,720 compared to the current best result of the previous literature.

Acknowledgements

We would like to express our best gratitude to Chulalongkorn University's Rachadapisaek Sompote Fund (2017) for supporting this research, and The Petroleum and Petrochemical College (PPC) for partially funding support. Moreover, we would like to thank to Mr. Natchanon Angsutorn for his guidance.

References

BP Energy Outlook. (2019). Retrieved from https://www.bp.com/content/dam/bp/business-sites/en/global/corporate/pdfs/energy-economics/energy-outlook/bp-energy-outlook-2019.pdf

Chang, C., Chen, X., Wang, Y., & Feng, X. (2017). Simultaneous synthesis of multi-plant heat exchanger networks using process streams across plants. *Computers & Chemical Engineering, 101*, 95-109. doi:10.1016/j.compchemeng.2017.02.039

Ghazouani, S. (2018). *Linear optimization models for the simultaneous design of mass and heat networks of an eco-industrial park.* Université Paris Sciences et Lettres Paris, France. (HAL Id: tel-01699284)

Hong, X., Liao, Z., Sun, J., Jiang, B., Wang, J., & Yang, Y. (2019). Transshipment type heat exchanger network model for intra- and inter-plant heat integration using process streams. *Energy, 178*, 853-866. doi:10.1016/j.energy.2019.04.112

Jide, I. A. (2007). *Interval Based MINLP Superstructure Synthesis of Heat and Mass Exchange Networks.* Rondebosch, South Africa.

Tan, Y. L., Ng, D. K. S., Foo, D. C. Y., El-Halwagi, M. M., & Samyudia, Y. (2014). Heat integrated resource conservation networks without mixing prior to heat exchanger networks. *Journal of Cleaner Production, 71*, 128-138. doi:10.1016/j.jclepro.2014.01.014

Yang, A., Jin, S., Shen, W., Cui, P., Chien, I. L., & Ren, J. (2019). Investigation of energy-saving azeotropic dividing wall column to achieve cleaner production via heat exchanger network and heat pump technique. *Journal of Cleaner Production, 234*, 410-422. doi:10.1016/j.jclepro.2019.06.224

Yee T. F, G. I. (1990). Simultaneous Optimization Models for Heat Integration II. Heat Exchanger Network Synthesis. *Computers and Chemical Engineering, 14*(10), 1165-1184. doi:10.1016/0098-1354(90)85010-8

Yoro, K. O., Sekoai, P. T., Isafiade, A. J., & Daramola, M. O. (2019). A review on heat and mass integration techniques for energy and material minimization during CO2 capture. *International Journal of Energy and Environmental Engineering, 10*(3), 367-387. doi:10.1007/s40095-019-0304-1

Sauro Pierucci, Flavio Manenti, Giulia Bozzano, Davide Manca (Eds.)
Proceedings of the 30th European Symposium on Computer Aided Process Engineering (ESCAPE30), May 24-27, 2020, Milano, Italy.
http://dx.doi.org/10.1016/B978-0-12-823377-1.50159-2

An Improved Superstructure-Based Model for Integrating an Organic Rankine Cycle into Total Site

Zheng Chu, Nan Zhang*, Robin Smith
Centre for Process Integration,Department of Chemical Engineering and Analytical Science, the University of Manchester, M13 9PL,Manchester, United Kingdom
nan.zhang@manchester.ac.uk

Abstract

The organic rankine cycle (ORC) could be a promising technology for the further exploitation of the industrial low-grade waste heat. This paper aims to present an improved superstructure-based mixed integer non-linear program (MINLP) model for the integration of an ORC within a total site to recover low-grade waste heat. The model can consider energy-capital trade-off, which includes utility cost, ORC power output, relevant capital cost for ORC and heat exchangers. By using this model, the selection of matches between waste heat streams and the ORC and the operating conditions of ORC could be determined simultaneously. A case study is presented to illustrate the application of this method.

Keywords: Organic Rankine Cycle, Heat integration, MINLP model, Stage-wise superstructure

1. Introduction

The common problem featured in industrial operations is that large quantities of low-grade waste heat are rejected to environment even though, in some cases, the maximum heat recovery through utilisation of all process streams has been reached. With the improvement of low-grade heat exploitation technologies such as Compression Heat Pumps (CHP), Absorption Heat Transformers (AHT), Absorption Heat Pumps (AHP), Absorption Chillers (AbC) and Organic Rankine Cycles (ORC), further exploitation of low temperature waste heat could have economic potentials (Oluleye, 2016). Among these technologies, ORC is becoming a promising technology for commercial applications in industrial fields.

Desai and Bandyopadhyay (2009) proposed a sequential method to integrate an ORC with background processes. Waste heat streams are firstly identified by pinch analysis, and then an ORC is integrated in a heuristic way. Another sequential method was proposed by Chen et al. (2014). First, they synthesized a stand-alone heat exchanger network (HEN) for background processes. Then, an ORC is incorporated into the HEN by using a stage-wise superstructure-based model. Yu et al. (2017) integrated ORC with background processes in an indirect way. In their work, hot water is used as an intermediate between heat sources and an ORC. They presented a nonlinear program (NLP) model which could determine the integration strategy of hot water simultaneously with the techno-economic optimization of ORC. Yu et al. (2018) extended their work by considering different configurations of ORC architectures when integrate an ORC with background processes.

This paper aims to provide an improved superstructure-based MINLP model for the integration of an ORC with multiple waste heat streams. The superstructure is firstly proposed by Yee and Grossman (1990) and is improved by the authors for ORC integration. The annualized cost for ORC integration is considered as the objective to be minimized. By using this model, the selection of matches between waste heat streams and ORC with its corresponding operating conditions can be determined simultaneously.

2. Problem Statement

In the problem statement, waste heat streams are defined directly with the assumption that the background processes have already been integrated. Given a set I= {i|1, 2 ... I} of waste heat streams to be cooled from their supply temperatures $T_{i,in}$ to their target temperatures $T_{i,out}$. The heat capacity flow rates of waste heat streams are also given as CF_i. The cold utility is set as cooling water with its supply temperature $T_{cw,in}$ and outlet temperature $T_{cw,out}$. For the sake of simplicity, multiple choices of cold utilities are not considered. In this paper, waste heat streams are regarded as heat sources for evaporation of ORC working fluid, which is represented by the upper part of Figure 1. And as for condensation, cooling water is used, which is represented in the lower part of Figure 1.

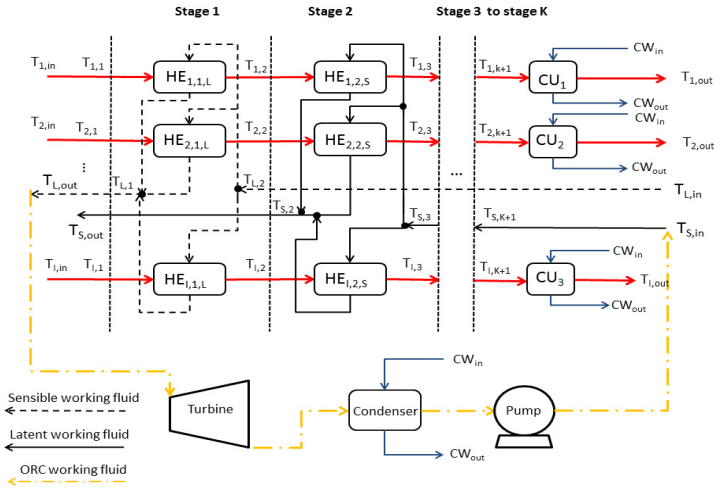

Figure 1. Schematic diagram of the superstructure

3. The Stage-wise Superstructure

Isothermal mixing is assumed for the outlet streams at each stage in this superstructure. To deal with the phase change, in this superstructure, the working fluid is divided into two sub-flows to carry the sensible heat and latent heat separately (shown in Figure 1). For the sake of simplicity, this superstructure matches these two heat flows sequentially, i.e. the latent flow is considered after the sensible heat requirement is fulfilled. In this case, from stage K to stage 2, the sensible heat flow is matched, and in stage 1 matched the latent heat flow. Using only one stage for latent heat transfer is reasonable due to the evaporation process is isothermal. In this way, the criss-cross matches for latent heat flow will be ignored. However, according to Linnhoff and Ahamd (1990), in the most cases, vertical heat transfer can obtain the minimum heat transfer area rather than criss-cross. The superstructure is then derived as follows:

1. Assume the suitable number of stages, normally:
$$K = 1 + I$$
Where K is the number of stages, I is the number of waste heat streams.
2. From stages K to 2, represent all of the potential matches between the sensible heat flow and waste heat streams. At the outlet of one stage, streams are isothermally mixed which then defines the inlet for the next stage.
3. At stage 1, both of the outlet and inlet temperatures are equal to the saturated temperature at that pressure.

4. Model formulation

4.1. The superstructure-based network

In this section, the model formulation for the evaporation network (shown in the upper side of Figure 1 will be discussed. The network model is developed in the steps as follows:

1) Overall energy balance for each stream
2) Energy balance at each stage
3) Cold utility load
4) Temperature assignment for the network inlet/outlet
5) The feasibilities of the second law of thermodynamics at each stage
6) Set the binary variables to determine the existence of process match
7) The minimum approach temperature feasibilities
8) The calculation of heat exchanger area for each feasible match
9) Calculate the split ratio of the ORC working fluid for each feasible heat transfer at each stage
10) Determine the excess heat exchanger unit

The model formulation from step 1 to step 8 is adopted from Yee and Grossman (1990). In the superstructure, as we split the phase-change stream into two sub-streams, i.e. the sensible heat stream and the latent heat stream, excess heat exchanger units may be created. One instance is presented in Figure 2. It could be realised that the two heat exchangers in dashed box could have potential to be merged into one. The case showed in Figure 2 could also appear in the network. Therefore, steps 9 and 10 are developed to deal with excessive heat exchanger units. In step 9, the split ratio is calculated as:

$$R_{S,i,k} = \frac{q_{S,i,k}}{CF_S \cdot (T_{S,k} - T_{S,k+1})}, i \in WS, k \in [2, K] \tag{1}$$

$$R_{L,i,k} = \frac{q_{L,i,k}}{(H_{L,out} - H_{L,in}) \cdot m_L}, i \in WS, k = 1 \tag{2}$$

Where R represents the spilt ratio, the subscripts S and L mean sensible heat stream and latent heat stream separately, the subscripts i and k represent waste heat stream and stage separately, CF is heat capacity flow rate, T is temperature, H is enthalpy, m is mass flowrate, and q is heat transfer amount. Eq. 1 calculates the spilt ratio R for sensible heat stream matches with each waste heat stream i at each stage from 2 to k. Similar, Eq. 2 calculates the spilt ratio R for latent heat stream matches with waste heat stream i at stage 1. In step 10, the excess heat exchanger unit is identified as:

$$(1-\xi) \cdot (R_{S,i,k} - R_{L,i,k-1}) + Z_{S,i,k} + Z_{L,i,k-1} - 2 \cdot Y_{i,k} \geq 0, i \in WS, k = 2 \tag{3}$$

Where ξ is a very small constant number which could be 10^{-3}, Z is a binary variable which represents the existence of heat exchanger, Y is a binary variable to determine if the excess heat exchanger unit exists and is incorporated in the objective function.

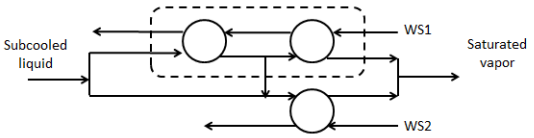

Figure 2. Excess heat exchanger units

4.2. ORC thermodynamic model

The ORC model is established by using Peng-Robinson equation of state (EoS) with the concept of state points (presented in Figure 3). The EOS can calculate the working fluid conditions (temperature, pressure, specific volume, enthalpy, entropy, etc.) at each state point, so that the performance of each component (condenser, pump, evaporator and turbine) could be calculated. The specific formulations are omitted in this paper due to the limitation of pages. The ORC model used in this paper is also adopted by Yu et al. (2017). However, it should be mentioned that the evaporator is incorporated with the network, which has:

$$T_{S,in} = T_4 \tag{4}$$

$$T_{L,out} = T_1 \tag{5}$$

$$H_{S,in} = H_4 \tag{6}$$

$$H_{L,out} = H_1 \tag{7}$$

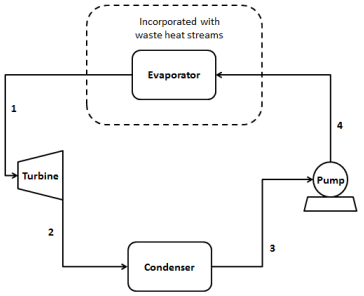

Figure 3. ORC schematic diagram with state points

4.3. Capital cost correlation

The capital cost of heat exchangers could be calculated by Equation (8) & (9), which are also adopted by Yu et al. (2017). Equation (8) calculates the heat exchanger manufacture cost CA_{he}; Equation (9) calculates the fixed charge FC_{he} for implementing heat exchangers.

$$CA_{he} = 190 + 310 \cdot A \tag{8}$$

$$FC_{he} = 5000 \cdot UN_{he} \tag{9}$$

The capital cost of the ORC pump C_{pump} is calculated by Equation (10), which is given by Hung et al. (2010).

$$C_{pump} = 900 \cdot (\frac{W_{pump}}{300})^{0.25} \tag{10}$$

The turbine cost C_{tur} is correlated with the turbine outlet volume V_2 in this paper. Equation (11) is taken from Quoilin et al. (2011).

$$C_{tur} = 1.5 \cdot (225 + 170 \cdot V_2) \tag{11}$$

4.4. Objective function

In this paper, the objective function OBJ includes utility cost, annualized capital cost, the fixed charge of heat exchangers and the profit from ORC operating.

$$\min : OBJ = C_{cu} + AF \cdot \sum C_{capital} - profit \tag{12}$$

Where C_{cu} is utility annual cost, AF is annualized factor, $C_{capital}$ is capital cost of each component.

5. Case study

In this case study, it is assumed that the background processes have been integrated, so that the waste heat stream data are given directly in Table 1.

Table 1. Waste heat stream candidates

Waste heat streams	Supply temperature (K)	Target temperature (K)	Heat capacity flow rate (kW/K)
stream 1	430.15	350.15	45
stream 2	410.15	300.15	35
stream 3	399.15	325.15	20

For this study, the following parameters are given as background data:

- Isentropic efficiency of the turbine and the pump is assumed as 75% and 90% separately.
- The heat transfer coefficients U between waste heat streams and ORC working fluid are set as $150\ W/(m^2 \cdot °C)$, and that between cooling water and ORC working fluid are set as $300\ W/(m^2 \cdot °C)$.
- The fixed charge FC of each heat exchanger is assumed as 5000 \$/unit.

Rest of the fixed parameters which include the annualized factor AF, the annual operating hours OH, the electricity price, the cold utility cost are assumed as the same value as those used in Yu et al. (2017). The working fluid of ORC is set as R245ca. To solve the MINLP model, the General Algebraic Modeling System (GAMS) is used as our solution platform with DICOPT as the MINLP solver. The optimized results of the overall objective function are listed in Table 2, and the optimized operating conditions of ORC are presented in Table 3. The corresponding configuration of the network is shown in Figure 4.

Table 2. Overall optimal results

OBJ (\$/year)	Cold utility (kW)	Network total area (m^2)	Network unit number	Power output (kW)
-364829	1382.12	1911.44	4	774.12

Table 3. Optimal operating conditions of ORC

Variable	Optimal value	Variable	Optimal value
working fluid mass flow rate (kg/s)	30.23	turbine shaft work output (kW)	830.20
turbine inlet pressure (kPa)	741.33	pump work input (kW)	13.85
turbine inlet temperature (K)	363.65	condensation temperature (K)	300.00
turbine outlet pressure (kPa)	107.25	evaporation temperature (K)	363.65
turbine outlet temperature (K)	322.57	thermal efficiency	10.82%

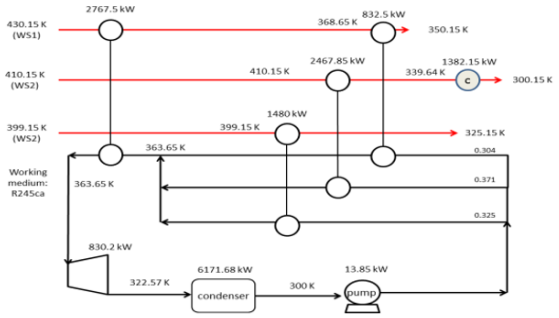

Figure 4. Configuration of the evaporation network

6. Conclusion

A superstructure-based MINLP model for the integration of an ORC with multiple waste heat sources is proposed in this paper. By using this model, the selection of matches between ORC working fluid and waste heat streams, the operating conditions of the ORC and the cold utility cost can be simultaneously determined with an optimal energy-capital trade-off. A simple case is given to illustrate the application of this model.

References

Chen, C., Chang, F., Chao, T., Chen, H. and Lee, J. (2014). Heat-Exchanger Network Synthesis Involving Organic Rankine Cycle for Waste Heat Recovery. *Industrial & Engineering Chemistry Research*, 53(44), pp.16924-16936.

Desai, N. and Bandyopadhyay, S. (2009). Process integration of organic Rankine cycle. *Energy*, 34(10), pp.1674-1686.

Hung, T., Wang, S., Kuo, C., Pei, B. and Tsai, K. (2010). A study of organic working fluids on system efficiency of an ORC using low-grade energy sources. *Energy*, 35(3), pp.1403-1411.

Linnhoff, B. and Ahmad, S. (1990). Cost optimum heat exchanger networks—1. Minimum energy and capital using simple models for capital cost. *Computers & Chemical Engineering*, 14(7), pp.729-750.

Quoilin, S., Declaye, S., Tchanche, B. and Lemort, V. (2011). Thermo-economic optimization of waste heat recovery Organic Rankine Cycles. *Applied Thermal Engineering*, 31(14-15), pp.2885-2893.

Yee, T. and Grossmann, I. (1990). Simultaneous optimization models for heat integration—II. Heat exchanger network synthesis. *Computers & Chemical Engineering*, 14(10), pp.1165-1184.

Yu, H., Eason, J., Biegler, L. and Feng, X. (2017). Simultaneous heat integration and techno-economic optimization of Organic Rankine Cycle (ORC) for multiple waste heat stream recovery. *Energy*, 119, pp.322-333.

Yu, H., Gundersen, T. and Feng, X. (2018). Process integration of organic Rankine cycle (ORC) and heat pump for low temperature waste heat recovery. *Energy*, 160, pp.330-340.

Sauro Pierucci, Flavio Manenti, Giulia Bozzano, Davide Manca (Eds.)
Proceedings of the 30th European Symposium on Computer Aided Process Engineering (ESCAPE30), May 24-27, 2020, Milano, Italy.
http://dx.doi.org/10.1016/B978-0-12-823377-1.50160-9

MINLP Synthesis of Flexible Process Flow Sheets under Variable Carbon Tax Rates

Klavdija Zirngast, Zdravko Kravanja, Zorka Novak Pintarič

University of Maribor, Faculty of Chemistry and Chemical Engineering, Smetanova 17, 2000 Maribor, Slovenia

zorka.novak@um.si

Abstract

This contribution presents methodology for inclusion of uncertain carbon tax rates into a mixed integer nonlinear programming (MINLP) process synthesis. Several approaches were developed and tested: two sequential deterministic methods with either fixed or increasing first-stage variables, and two stochastic approaches based on simultaneous Gaussian quadrature method for one- and multi-period process synthesis. Case study process flow sheet synthesis demonstrates that increased carbon tax rate leads to higher conversion, lower emission, lower raw material and utility consumptions, and improves process performance synergistically with process heat integration. Synthesis of optimal heat exchanger network shows that multi-period stochastic method produced around 5 % lower expected cost than sequential deterministic method which indicates a value of simultaneous stochastic process synthesis under uncertain carbon tax rate.
Keywords: MINLP synthesis, process flow sheet, carbon tax rate, stochastic two-stage with recourse

1. Introduction

European Union Emissions Trading System promotes reduction of greenhouse gas emissions in economically efficient manner (European Commission, 2019). Fossil fuels used for process heat and power are presently the largest contributors to global CO_2 emissions (Mahmoud and Sunarso, 2018). In order to curtail pollution, governments have created various policy mechanisms for pricing emissions, such as standards, carbon tax, energy tax, and emission trading systems (Lin and Li, 2011). Taxes on carbon emissions have proved useful for encouraging the emitters to reduce the emissions (OECD, 2018). Synthesis of efficient, optimal and flexible process flow sheets over the entire life cycle is important for reducing the emissions, however, long-term carbon tax rates are difficult to predict. A few recent works discuss design of process plants (Shahandeh and Li, 2017), production of syngas (Hernández and Martín, 2019) and supply chains (Alizadeh et al., 2019) under uncertain carbon tax rates. Novak Pintarič et al., 2019, developed an indicator for more detailed multi-objective analysis of Pareto process solutions with respect to variable carbon tax rates. They showed that increasing the carbon tax rate encourages the reduction of utility use and increases the savings and the net present value of heat exchanger network.

The effects of carbon tax rate are usually studied by parametric evaluations or optimizations of various process alternatives. This contribution, however, presents some novel insights into: a) impacts of carbon tax rates on topology, design, operation, economic and environmental efficiencies of optimal processes obtained during Mixed Integer Nonlinear Programming (MINLP) synthesis, and b) development of a

systematic methodology which would generate optimal process flow sheets under variable carbon tax rates over longer time period.

2. Methodology for MINLP process synthesis under uncertain carbon tax

MINLP process synthesis problem with uncertain carbon tax rate can be described as a two-stage stochastic problem with recourse. First stage (topology and design) variables are equal for several future carbon tax rates and determined in advance, while second stage (operating and control) variables can be adjusted later after the uncertainty is resolved. Several approaches were developed and applied for solving such problems.

2.1. Deterministic approach

In deterministic approach, first stage variables are determined at an initial value of carbon tax rate (θ_d in MINLP model P1).

$$
\begin{aligned}
&Z = \max\left(c^\mathrm{T} y + f(d,x,\theta_\mathrm{d})\right)\\
&\text{s. t.}\quad h(d,x,\theta_\mathrm{d}) = 0\\
&\qquad g(d,x,\theta_\mathrm{d}) + By \le 0\\
&\qquad Ay \le a\\
&d,x \ge 0,\ \ y \in \{0,1\}
\end{aligned}
\qquad \text{(P1)}
$$

Z scalar objective variable
c fixed costs
f variable cost function
y binary variables for process topology
d design variables for capacities and sizes of process units
x operating variables
θ uncertain carbon tax rate
h equality constraints
g inequality constraints
A, B and a matrices and vector of constants

The obtained values of binary and design variables (y and d) are then fixed, and one-scenario NLP problems are solved for operating and control variables at a finite number of discrete tax rate values (θ_t, $t \in T$). Objective values obtained (Z_t) are multiplied by the probability of each tax rate (pr_t) yielding a deterministic expected value of objective function, E(Z^deter), Eq. 1.

$$\mathrm{E}(Z^\mathrm{deter}) = \sum_{t \in T} pr_t \cdot Z_t \tag{1}$$

2.2. Modified deterministic approach

The approach described in previous section assumed that first stage variables remain unchanged during the entire process lifetime. In practice, however, initial process design can be retrofitted to some extent at specific realization of uncertain parameters. Previous approach was therefore modified in a way that first-stage variables obtained at an initial value of carbon tax rate (d_d) can change by (Δd_t) at specific realization of uncertain tax rate (θ_t), and the increase can be limited by an upper bound (U) (model P2). The expected value is then calculated by Eq. 1.

$$
\begin{aligned}
&Z_t = \max\left(c^\mathrm{T} y + f(d_\mathrm{d} + \Delta d_t, x_t, \theta_t)\right)\\
&\text{s. t.}\quad h(d_\mathrm{d} + \Delta d_t, x_t, \theta_t) = 0\\
&\qquad g(d_\mathrm{d} + \Delta d_t, x_t, \theta_t) + By \le 0\\
&\qquad Ay \le a,\ \ \Delta d_t \le U\\
&\Delta d_t, x_t \ge 0,\ \ y \in \{0,1\}
\end{aligned}
\qquad \begin{matrix}\text{(P2)}\\ t \in T\end{matrix}
$$

2.3. Stochastic approach – one-period Gaussian quadrature

In stochastic approach, a distribution function of carbon tax rate is assumed during a specific time period. MINLP synthesis is formulated as one-period multi-scenario problem in which carbon tax rates are assumed at Gaussian quadrature points, i.e. roots of the Legendre polynomials of specified order. The objective function of this model is an expected value in which the objectives derived at various tax rates are weighted by their probabilities, pr_t.

$$
\begin{aligned}
& E(Z) = \max\left(c^{\mathrm{T}} y + \sum_t pr_t \cdot f(d, x_t, \theta_t) \right) \\
& \text{s. t.} \quad h(d, x_t, \theta_t) = 0 \\
& \qquad g(d, x_t, \theta_t) + By \le 0 \qquad\qquad t \in T \\
& \qquad Ay \le a \\
& d, x_t \ge 0, \;\; y \in \{0,1\}
\end{aligned}
\tag{P3}
$$

2.4. Stochastic approach – multi-period Gaussian quadrature

In this method, a multi-period two-stage stochastic model with recourse is formulated in order to perform process synthesis simultaneously for multiple carbon tax rates over several time periods. A goal is to generate process configuration that would be optimal for a more extended time period during which carbon tax rate is expected to change. The problem (P3) is extended into a two-stage multi-period multi-scenario stochastic problem with recourse (P4).

$$
\begin{aligned}
& E(Z) = \max\left(c^{\mathrm{T}} y + \sum_t \sum_p pr_{t,p} \cdot f(d, x_{t,p}, \theta_{t,p}) \right) \\
& \text{s. t.} \quad h(d, x_{t,p}, \theta_{t,p}) = 0 \\
& \qquad g(d, x_{t,p}, \theta_{t,p}) + By \le 0 \qquad\qquad t \in T, \;\; p \in P \\
& \qquad Ay \le a, \;\; d, x_{t,p} \ge 0, \;\; y \in \{0,1\}
\end{aligned}
\tag{P4}
$$

3. Case studies

The aim of the first case study wass to demonstrate the effects of carbon tax rate on topology, design and operation of optimal process flow sheets obtained by MINLP synthesis. The heat exchanger network (HEN) case study demonstrates the applications of several methods described in Section 2.

3.1. Synthesis of optimal process flow sheet

First case study is a process for production of chemical B from reactant A (Figure 1). There are two alternative feed streams available: expensive Feed1 with lower content of impurity C and cheaper Feed2. The selected feed stream is mixed with the recycle stream, preheated and fed into the reactor. There are two alternative reactors in which reactant A is converted into product B: cheaper RCT1 with lower conversion and more expensive RCT2. Component C in purge stream is assumed to be a greenhouse gas (GHG). Consumptions of hot utility in heaters C1, C2 and C3 also contribute to total GHG emission of the process. The superstructure was modelled as an MINLP problem with maximization of profit at various carbon tax rates. Two synthesis options were considered for parametric analysis at various carbon tax rates: without and with heat integration using a model by (Duran and Grossmann, 1986).

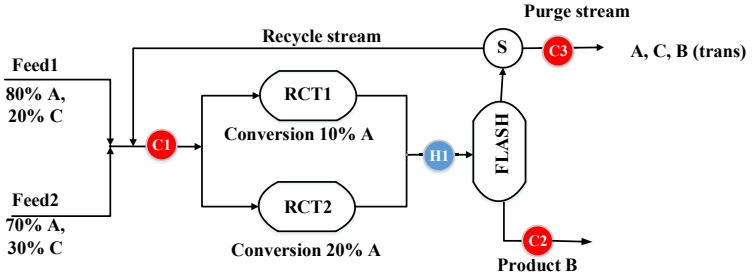

Figure 1: Process superstructure

Figures 2 to 5 demonstrate that increasing carbon tax rate leads to decreased GHG emission, increased overall conversion of reactant, reduced consumption of raw materials and decreased percentage of purge stream. Moreover, the synergies are established between the effects of carbon tax rate and heat integration as the effects are higher in heat integrated solutions. Higher carbon tax rates force the selection of more efficient process units, such as reactor RCT2 with higher conversion, and feed stream with lower content of impurities. In the heat integrated processes, cheaper feed stream Feed2 was selected only at low tax rates (up to 10 €/t), while at higher tax rates more expensive Feed1 with lower amount of impurity was selected.

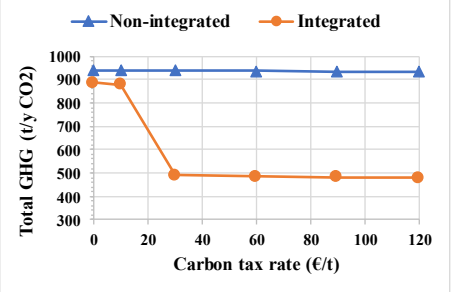

Figure 2: Total GHG emission vs carbon tax rate

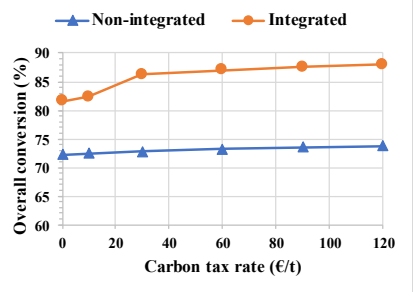

Figure 3: Overall conversion vs carbon tax rate

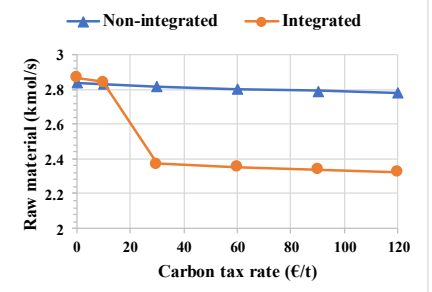

Figure 4: Raw material consumption vs carbon tax rates

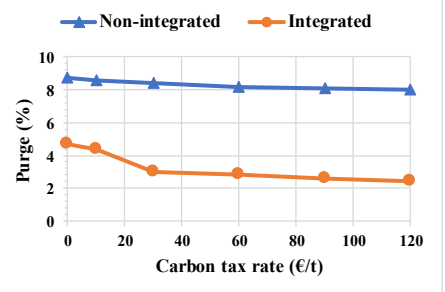

Figure 5: Purge stream percentage vs carbon tax rates

In the next step a MINLP synthesis of process flow sheet was performed under uncertain carbon tax rate by applying sequential one-scenario deterministic approach and simultaneous multi-scenario approach. Three carbon tax rates (10, 60 and 120) €/t with different probabilities within three periods were assumed. The expected profit of

heat integrated the stochastic solution (110,972 k€/a) was slightly higher than the profit of deterministic solution (110,917 k€/a), indicating a value of simultaneous multi-scenario approach.

3.2. Synthesis of optimal Heat Exchanger Network

Heat exchanger network (HEN) consisted of 2 hot and 3 cold streams (Novak Pintarič et al., 2019). Supply and target temperatures, heat capacity flow rates (*CF*), and heat transfer coefficients (α) are shown in Figure 6. The network was modelled based on a multi-stage superstructure by (Yee and Grossmann, 1990). The objective function was minimum Total Annual Cost (TAC) composed of annualized investment cost, utility costs and carbon tax rate cost. The latter included emissions from hot utility production and construction of HEN which was proportional to HEN capital cost.

Future carbon tax rates were assumed within an interval from 10 €/t to 60 €/t during three time periods. Five quadrature points within this interval were (12.3, 21.5, 35.0, 48.5, 57.7) €/t CO_2. It was assumed that lower taxes would be more probable during the first period while in the last period probability would concentrate at higher values. Two shape parameters of Beta distribution (α, β) for periods 1, 2, and 3 were assumed as follows: (2, 6), (3, 3) and (7, 3). The numerical results obtained by applying four methods described in Section 2 are presented in Table 1.

Table 1: TAC and GHG emission of HENs obtained with different methods

	Deterministic methods		Stochastic methods	
	Fixed first-stage variables	Modified first-stage variables	One-period quadrature	Multi-period quadrature
Period	TAC ($/y)	TAC ($/y)	TAC ($/y)	TAC ($/y)
1	1,471,251	1,471,243	1,396,198	1,465,382
2	1,550,941	1,550,863	1,470,393	
3	1,614,693	1,614,491	1,529,735	
Average	1,545,628	1,545,532	1,465,442	
GHG (t/y)	6375	6364	5936	5926

Optimal HEN obtained by deterministic method (Figure 6) had the total area 1,077 m^2, expected hot utility consumption 4,358 kW, and an average TAC over three periods 1,545,628 $/y. The network obtained by modified deterministic approach had the same topology while total HEN area increased by 6 %, i.e. for 63 m^2, which lead to slightly lower TAC. Optimal HEN obtained by simultaneous three-period Gaussian quadrature (Figure 7) had the total heat transfer area 946 m^2, expected hot utility consumption 4,040 kW, and the expected TAC 1,465,382 $/y. Its total GHG emission is by 7 % lower than GHG emission of HEN obtained by deterministic method.

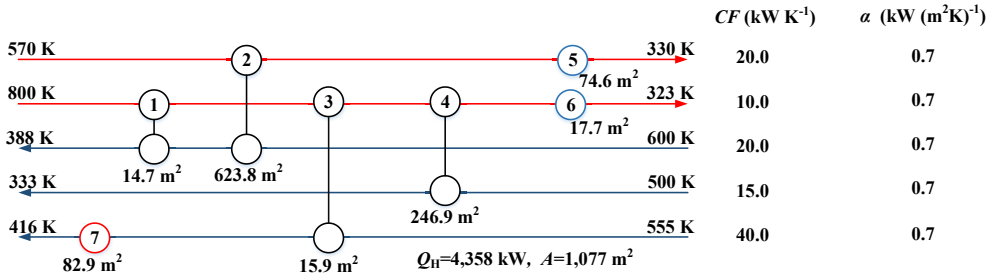

Figure 6: Optimal HEN obtained by deterministic method

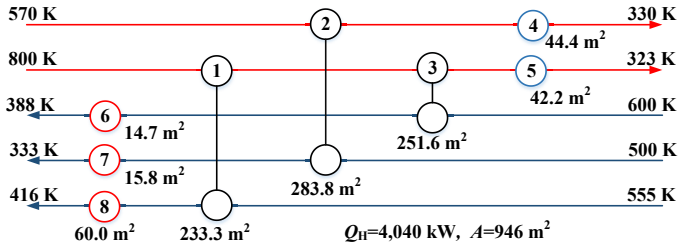

Figure 7: Optimal HEN obtained by three-period Gaussian quadrature

4. Conclusions

This study presented the effects of variable carbon tax rate on topology, design, operation, economics and environmental impacts of optimal processes obtained by MINLP synthesis. Several approaches were developed and tested for inclusion of uncertain carbon tax rate into process synthesis. Multi-period stochastic approach which considered various possible tax rates simultaneously yielded economically and environmentally better results than sequential deterministic approach, which indicates a value of stochastic solutions in process synthesis under uncertain carbon tax rate. The advantage of deterministic approach, however, is that the size of the model does not increase with the numbers of scenarios and periods.

Acknowledgment
The authors acknowledge financial support from the Slovenian Research Agency (PhD research fellowships MR-39209, program P2-0032, and project J7-1816).

References

Alizadeh, M., Ma, J., Marufuzzaman, M., Yu, F. 2019. Sustainable olefin supply chain network design under seasonal feedstock supplies and uncertain carbon tax rate. Journal of Cleaner Production, 222, 280-299.

Duran, M.A., Grossmann, I.E. 1986. Simultaneous optimization and heat integration of chemical processes. AIChE Journal, 32, 123-138.

European Commission. 2019. European Union Emissions Trading System (EU ETS). Available at: https://www.emissions-euets.com/carbon-market-glossary/872-european-union-emissions-trading-system-eu-ets. Accessed: 11.7.2019.

Hernández, B., Martín, M. 2019. Optimal production of syngas via super-dry reforming. Analysis for natural gas and biogas under different CO2 taxes. Chemical Engineering Research and Design, 148, 375-392.

Lin, B., Li, X. 2011. The effect of carbon tax on per capita CO2 emissions. Energy Policy, 39, 5137-5146.

Mahmoud, A., Sunarso, J. 2018. A new graphical method to target carbon dioxide emission reductions by simultaneously aligning fuel switching, energy saving, investment cost, carbon credit, and payback time. International Journal of Energy Research, 42, 1551-1562.

Novak Pintarič, Z., Varbanov, P.S., Klemeš, J.J., Kravanja, Z. 2019. Multi-Objective Multi-Period Synthesis of Energy Efficient Processes under Variable Environmental Taxes. Energy, 116182.

Shahandeh, H., Li, Z. 2017. Optimal design of bitumen upgrading facility with CO2 reduction. Computers & Chemical Engineering, 106, 106-121.

Yee, T.F., Grossmann, I.E. 1990. Simultaneous optimization models for heat integration II. Heat exchanger network synthesis. Computers and Chemical Engineering, 14, 1165 - 1184.

Sauro Pierucci, Flavio Manenti, Giulia Bozzano, Davide Manca (Eds.)
Proceedings of the 30th European Symposium on Computer Aided Process Engineering (ESCAPE30), May 24-27, 2020, Milano, Italy.
http://dx.doi.org/10.1016/B978-0-12-823377-1.50161-0

Design Space Investigation for Development of Continuous Flow Syntheses of Active Pharmaceutical Ingredients

Samir Diab, Dimitrios I. Gerogiorgis*

Institute for Materials and Processes (IMP), School of Engineering, University of Edinburgh, The Kings Buildings, Edinburgh, EH9 3FB, United Kingdom
D.Gerogiorgis@ed.ac.uk

Abstract

Continuous flow chemistry and synthesis have received significant attention over the past two decades for their potential for enhancing yields, selectivities, productivities, smaller operation and implementation of otherwise difficult/dangerous reactions. Recent demonstrations applied to a variety of different reaction types have highlighted the potential for continuous manufacturing technologies for fine and speciality chemical production, including many critical Active Pharmaceutical Ingredients (APIs) but also many biopharmaceuticals and therapeutics. This study discusses recent demonstrations from the literature on design space elucidation for continuous API production and further highlights attainable regions of recoveries, material efficiencies, flowsheet complexity and cost components for upstream (reaction + separation) via modelling, simulation and nonlinear optimisation studies, providing insight into optimal regions of operation.

Keywords: Continuous flow synthesis; Active Pharmaceutical Ingredients (APIs); pharmaceutical manufacturing; design space investigation; comparative evaluation.

1. Introduction

1.1 Continuous flow synthesis

The development of continuous flow technology and synthetic strategies by chemists and engineers has been the focus of significant research attention over the past two decades due to the wide variety of chemical processes whose performance can be improved or intensified by switching from batch to continuous flow operation. Operating continuously allows for smaller equipment dimensions, wherein mixing and heat transfer are significantly enhanced and thus improving yields, selectivities, productivities and allowing access to operating windows (e.g., high pressure/temperature, avoiding prolonged presence of hazardous intermediates, circumventing requirements for cryogenic conditions) that would be otherwise unsafe if implemented in batch mode.

1.2 Continuous manufacturing of active pharmaceutical ingredients

There has been significant research focus on continuous Active Pharmaceutical Ingredient (API) production due to pressure on the pharmaceutical industry to reduce drug development times, minimise product quality variation, process performance deviations, overall costs and environmental impact via lower capital and operating expenditures that are inherent of the smaller equipment and material usage reductions with continuous operations. The chemistry, chemical engineering and process systems engineering

communities have approached both unit operation and plantwide Continuous Pharmaceutical Manufacturing (CPM) processes from both experimental (lab-based and pilot plants) and theoretical (mathematical modelling, simulation and optimisation) perspectives to elucidate promising designs for optimal continuous API synthesis.

1.3 This work: Integrated upstream continuous pharmaceutical manufacturing

The majority of design space investigation studies in the literature focus on the attainment of optimal unit operation performance or specified product quality attributes. Consideration of technoeconomic and environmental impacts of different designs are also important for the selection of feasible and viable process operating regions. Modelling and simulation aids design space elucidation without labour-intensive experiments. In this study, we discuss design space investigation efforts for various upstream continuous reaction + separation processes for different APIs, encompassing both technoeconomic and material efficiency considerations of upstream CPM plantwide design considerations.

2. Relevant Literature

2.1 Design space investigation of flow reactors

The demonstration of continuous flow chemistry of an API is the foundation of any CPM process; however, subsequent purification, separation (upstream) and drug product formulation (downstream) unit operations are often challenging and expensive processes that must be considered in the comparative evaluation of different designs. Establishing feasible operating regions to the meet desired product quality and process performance targets is an important stage of design that has been implemented in various CPM studies. Development of automated continuous flow systems for reaction optimisation has been a recent hot topic of research. Bédard et al. (2019) developed a continuous synthesis system composed of reagent/feedstocks and pumps and interchangeable reactor and separator modules with online analytics and a software interface for process control and reaction monitoring. The authors demonstrated a variety of pharmaceutically-relevant reactions in flow, elucidating optimal regions of operation regarding operating temperature, residence time, reagent ratios, catalyst and base loading. Wyvratt et al. (2019) characterised the design space of a Knoevenagel condensation by varying residence time and catalyst loading whilst minimising the number of experiments and material consumption required to adequately map the design space. Comparative evaluation of batch vs. continuous syntheses are also useful in quantifying technical and economic benefits of different production paradigms and flowsheet configurations. Ott et al. (2016) performed a Life Cycle Assessment (LCA) of different flowsheet configurations of batch vs. flow microreactor networks for rufinamide synthesis, considering various metrics related to plant material efficiencies and environmental impacts of different production options.

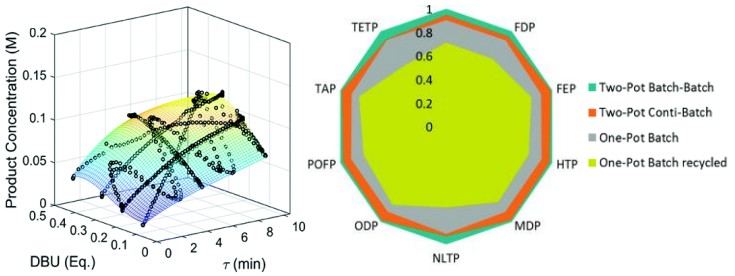

Figure 1: Flow synthesis design spaces: (a) Wyvratt et al., 2019, (b) Ott et al., 2016.

2.2 Design space investigation of separation processes

Design space investigation of separation options is also important when considering continuous API production. Gonzalez et al. (2019) used probabilistic modelling to establish the design space of a reaction and crystallisation to enhance process robustness and impurity control in the final product. The authors found a crystallisation combined with wet milling allowed greater robustness than a design without milling. Ridder et al. (2014) performed experiments and modelled the antisolvent crystallisation of flufenamic acid in a multisegment, multiaddition-plug flow crystalliser, where antisolvent feed rate to different tubular crystalliser segments was varied in order to either maximise the mean crystal size or minimise the product size distribution coefficient of variation. The authors presented Pareto fronts to show trade-offs between the two product quality attributes.

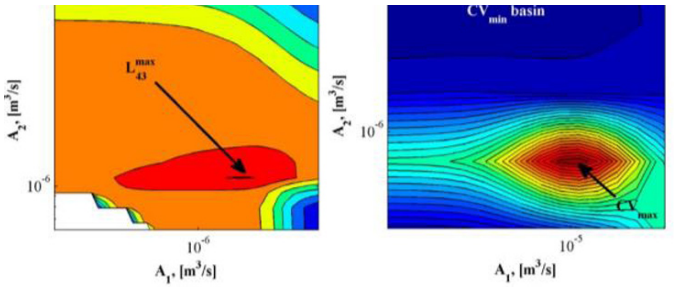

Figure 2: Design space of crystal quality vs. antisolvent addition (Ridder et al., 2014).

3. Plantwide design space investigation

In this study, we concentrate on upstream plantwide CPM studies we have previously done, encompassing both reaction (flow synthesis) and separation (continuous Liquid-Liquid Extraction (LLE) or antisolvent crystallisation) phenomena and unit operations as well as detailed Capital (CapEx) and Operating (OpEx) Expenditures cost components.

3.1 Upstream plantwide design case studies

Ibuprofen (analgaesic): three flow reactions followed by continuous Liquid-Liquid Extraction (LLE) with hexane (nHex) or toluene (PhMe) (Jolliffe and Gerogiorgis, 2016).

Artemisinin (antimalarial): two reactions and cooling-antisolvent crystallisation using ethanol (EtOH) or ethyl acetate (EtOAc) as antisolvents (Jolliffe and Gerogiorgis, 2016).

Diphenhydramine (antihistamine): one reaction followed by LLE with heptane (nHep), cyclohexane (CyHex) or methyl cyclohexane (MeCyHex) (Diab and Gerogiorgis, 2017).

Warfarin (anticoagulant): one reaction followed by continuous LLE with EtOAc, isopropyl acetate (iPrOAc) or isobutyl acetate (iBuOAc) (Diab and Gerogiorgis, 2018).

Atropine (nerve agent effects): three flow reactions followed by LLE utilising either diethyl ether (Et_2O), *n*-butyl acetate (nBuOAc) and PhMe (Diab and Gerogiorgis, 2019).

Nevirapine (HIV treatment): considers three flow reactions followed by crystallisation via pH change with different Solvent Recovery (SR) assumptions (Diab et al., 2019).

The extent of simulation/optimisation differs for each API case study. For ibuprofen, artemisinin and diphenhydramine, simulation studies are considered; for warfarin and

nevirapine, nonlinear optimisation of the upstream plants have been implemented. Modelling, simulation and optimisation details are in the relevant literature references.

3.2 Technoeconomic analysis methodology

Process performance metrics encompassing technical performance, process intensity and costs are compared for different APIs and selected separation option. The process metrics considered are: plantwide API recovery, Mass Productivity (MP = 100 / E-factor, a measure of how efficiently material is used in a process), number of reaction and separation stages (a measure of process intensity) and CapEx and OpEx cost components per unit mass of API produced. Fig. 3 shows a radar plot of these metrics for each API.

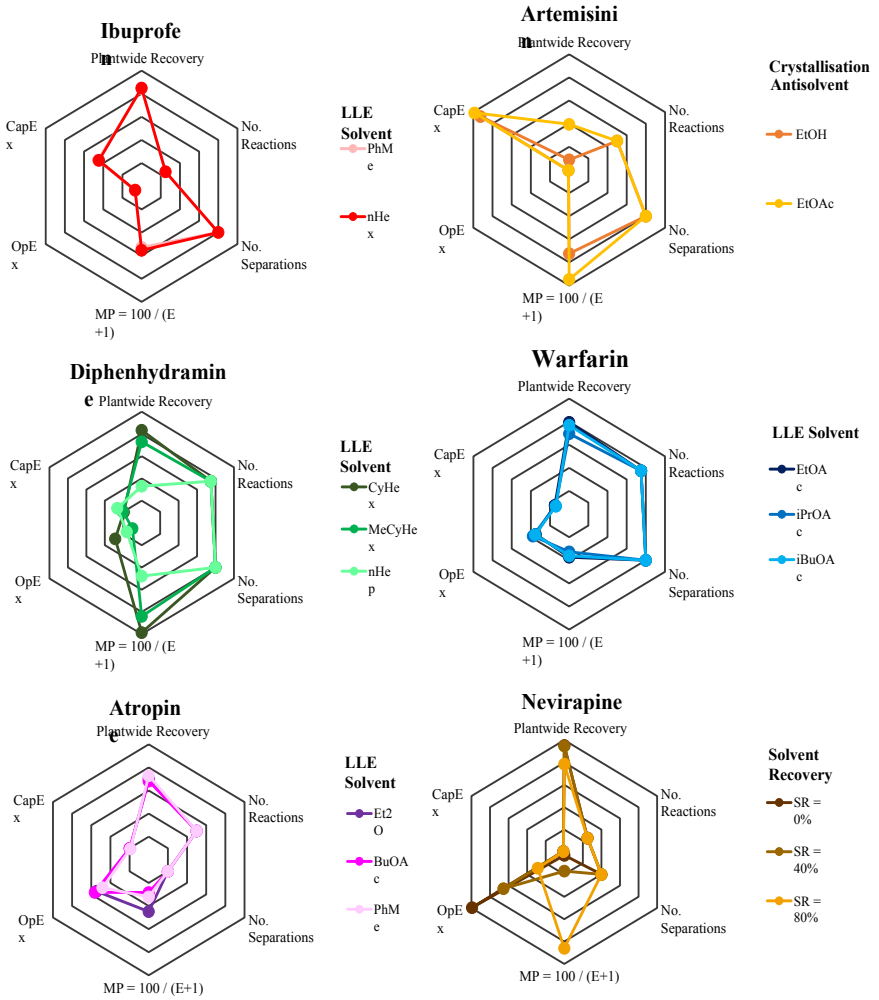

	Plantwide Recovery (%)	MP (%)	Reactions (#)	Separations (#)	CapEx (10^3 GBP kg^{-1})	OpEx (10^3 GBP kg^{-1})
min	30	0.6	3	4	10	0
max	100	3.6	1	1	420	230

Figure 3: Performance metrics of various CPM processes for different APIs.

Each axis (process performance metric) in Fig. 3 bear different meaning depending on whether they have a high or low value. Clearly, high plantwide recoveries and MP but lower cost components are desirable. For the number of reaction and separation stages, reverse-ordered axes are used to illustrate that lower values are preferable (i.e., fewer unit operations equate to lower process complexity). The maximum and minimum values of each axis in these axes are also provided in Fig. 3. For each API, the number of reactions and separation stages have the same coordinates for each different separation option.

3.3 Separation process design option selection

For ibuprofen, the different separation options (LLE solvent = {nHex, PhMe}) give similar results and thus the LLE solvent with the lower environmental/EHS impact (i.e., PhMe) is preferable (Jolliffe and Gerogiorgis, 2016). Similarly, for warfarin and atropine, each considered LLE solvent performs similarly, however, each also have similar EHS characteristics; solvent selection should thus be informed by subsequent crystallisation process design (Diab and Gerogiorgis, 2018; 2019). For artemisinin and diphenhydramine, plantwide technoeconomic performance varies more drastically with separation solvent choice; for artemisinin, EtOH as antisolvent allows for lower costs and is more environmentally friendly that EtOAc (Jolliffe and Gerogiorgis, 2016), and for diphenhydramine, nHep has both poorer EHS characteristics than either CyHex or MeCyHex as well as incurring higher costs (Diab and Gerogiorgis, 2017). For nevirapine CPM, various values of solvent recovery are considered (SR); whilst high SR (= 80%) is attainable in lab-scale conditions, lower values are likely to be possible at larger scale operation. The assumed SR drastically affects OpEx, thus inducing the significant contribution of the latter towards total costs: here, OpEx >> CapEx (Diab et al., 2019).

3.4 Comparative evaluation and discussion

While comparing different APIs for their performance on a detailed level may not be considered so valuable given the widely varying process phenomena, highlighting typical regions of operation for different processes is useful. For example, the CPM designs for the considered APIs in this study have typical plantwide recoveries = 70–80%; although total cost components and material efficiencies vary, this highlights that beyond this API recovery, cost benefits are incremental at best and not worth the extra effort with respect to material consumption and increased equipment volumes required for higher flow rates. Quantification of dimensionless numbers for different continuous processes for different APIs may also provide valuable insight into the most promising regions of operation.

Total cost components (i.e., CapEx and OpEx) have been scaled per unit mass of API produced in the product streams of each upstream CPM plant for fair comparison where different plant capacities are considered. Each case study considered upstream plant total costs as the economic metric for comparative evaluation of different process designs. Comparison of optimal Net Present Values (NPVs) can also provide valuable insight and alternative process designs for different APIs, but are subject to API sales price variation, which may be quite significant for certain drugs (e.g., artemisinin). Ultimately, when choosing whether to switch to continuous operation, clear operational and economic benefits must be clear over traditional / current manufacturing methods for the API.

4. Conclusions

Demonstrated continuous flow synthesis of APIs pave the way for the design of CPM processes for lean and efficient production. Various demonstrations in the literature have elucidated operating regions and mapped design spaces on a technical basis at unit operation level. We have conducted technoeconomic plantwide analyses for upstream CPM (reaction + separation) for various APIs. Separation design is informed by technical, economic and EHS criteria. Currently, strategic pharma decisions on whether to design (or adopt) continuous operation are made on a case-by-case basis. Elucidating operating regions for demonstrated CPM for different APIs is an important step towards more systematic selection and screening of promising candidates for continuous production.

Acknowledgements

The authors acknowledge the support of the Engineering and Physical Sciences Research Council (EPSRC)/IAA, the Japan Society for the Promotion of Science, the Great Britain Sasakawa and Nagai Foundations and the Royal Academy of Engineering (RAEng).

References

A.-C. Bédard, A. Adamo, K.C. Aroh, M.G. Russell, A.A. Bedermann, J. Torosian, B. Yue, K.F. Jensen and T.F. Jamison, 2018, Reconfigurable system for automated optimization of diverse chemical reactions, *Science*, 361, 6408, 1220–1225.

S. Diab and D.I. Gerogiorgis, 2017, Process modeling, simulation, and technoeconomic evaluation of separation solvents for the continuous pharmaceutical manufacturing (CPM) of diphenhydramine, *Org. Process Res. Dev.*, 21, 7, 924–946.

S. Diab and D.I. Gerogiorgis, 2018, Process modelling, simulation and technoeconomic optimisation for continuous pharmaceutical manufacturing of (*S*)-warfarin, *Comput. Aided Chem. Eng.*, 43, 1643−1648.

S. Diab and D.I. Gerogiorgis, 2019, Technoeconomic mixed integer nonlinear programming (MINLP) optimization for design of liquid-liquid extraction (LLE) cascades in continuous pharmaceutical manufacturing of atropine, *AIChE J.*, 65, 11, e16738. DOI: 10.1002/aic.16738.

S. Diab, D.T. McQuade, B.F. Gupton and D.I. Gerogiorgis, 2019, Process design and optimization for the continuous manufacturing of nevirapine, an active pharmaceutical ingredient for HIV treatment, *Org. Process Res. Dev.*, 23, 3, 320–333.

F.L. Gonzalez, J.E. Tobora, B. Mack and E.C. Huang, 2019, Development and implementation of a quality control strategy for an atropisomer impurity grounded in a risk-based probabilistic design space, *Org. Process Res. Dev.*, 23, 2, 211–219.

H.G. Jolliffe and D.I. Gerogiorgis, 2016, Plantwide design and economic evaluation of two continuous pharmaceutical manufacturing (CPM) cases: ibuprofen and artemisinin, *Comput. Chem. Eng.*, 91, 269–288.

M.B. Plutschack, B. Pieber, K. Gilmore and P.H. Seeberger, 2017, The hitchhiker's guide to flow chemistry, *Chem. Rev.*, 117, 18, 11796–11893.

B.J. Ridder, A. Majumder and Z.K. Nagy, 2014, Population balance model-based multiobjective optimization of a multisegment multiaddition continuous plug-flow antisolvent crystallizer, *Ind. Eng. Chem. Res.*, 53, 11, 4387–4397.

B.M. Wyvratt, J.P. McMullen and S.T. Grosser, 2019, Multidimensional dynamic experiments for data-rich process development of reactions in flow, *React. Chem. Eng.*, 4, 1637–1645.

Sauro Pierucci, Flavio Manenti, Giulia Bozzano, Davide Manca (Eds.)
Proceedings of the 30th European Symposium on Computer Aided Process Engineering (ESCAPE30), May 24-27, 2020, Milano, Italy.
http://dx.doi.org/10.1016/B978-0-12-823377-1.50162-2

Optimization of Liquid Air Energy Storage (LAES) using a Genetic Algorithm (GA)

Zhongxuan Liu,[a] Haoshui Yu,[b] Truls Gundersen[a*]

[a]*Norwegian University of Science and Technology, Kolbjørn Hejes v1B, NO-7491 Trondheim, Norway*
[b]*Massachusetts Institute of Technology, 77 Massachusetts Ave, Cambridge, MA, 02139, USA*
truls.gundersen@ntnu.no

Abstract

Renewable energy sources have a growing share in the energy market due to the threat from climate change, which is caused by emissions from fossil fuels. A future energy scenario that is likely to be realized is distributed energy systems (DES), where renewable energy sources play an increasing role. Energy storage technologies must be adopted to achieve these two expectations. Liquid Air Energy Storage (LAES), is a cryogenic technology that is discussed in this paper. Two cases are considered in this work to represent different operating modes for the LAES process: with and without an extra amount of hot oil in the discharging process. The performance of the LAES system will be analyzed with different number of compression stages and expansion stages in each mode. A Genetic Algorithm (GA) is used to optimize the LAES process. The round-trip efficiency is 63.1 % after flowsheet improvement and optimization.

Keywords: Liquid air energy storage, round-trip efficiency, flowsheet improvement, genetic algorithm

1. Introduction

With the increasing focus on the environment, a lot of measures have been taken to reduce the emission of greenhouse gases. Renewable energy technologies are considered to replace traditional fossil fuels. However, once renewable energy is introduced in the energy market, the most important challenge is to keep the stability of energy supply due to the intermittent nature of renewable energy sources such as wind and solar.

Another likely trend for future energy systems is decentralization in the form of distributed energy hubs. These hubs are located close to available energy forms and specific energy demands. The advantages of distributed energy systems mainly include the flexibility to utilize various energy conversion technologies and the improved reliability of energy supply (or reduced vulnerability of the overall system) by operating these distributed energy systems in networks and integrating with local energy resources (Alanne and Saari, 2006).

Energy storage technologies must be adopted to smoothen variations in supply (typical for renewable energy sources) and demand (daily or seasonal variations) and to guarantee supply during energy deficit periods. Pumped hydroelectric energy storage (PHES) (Rehman et al., 2015), compressed air energy storage (CAES) (Bullough et al., 2004), and battery energy storage (BES) (Aneke and Wang, 2016) are mature energy storage technologies. However, because of the geographical constraints of PHES and CAES and capital considerations for BES, the application of these technologies is still limited.

Energy storage technologies that can overcome the drawbacks of the existing technologies are more likely to be adopted in future energy systems. Among the proposed energy storage technologies, liquid air energy storage (LAES) seems to be a promising option (Guizzi et al., 2015), since LAES can benefit from established technologies, such as gas liquefaction and air separation units, and it is not geographically constrained.
Until now, the largest reported LAES implementation is a plant with 15 MWh storage capacity that was built in the UK (Highview Power, 2019). The round-trip efficiency of the standalone process is around 60 %. Li et al. (2014) studied the integration of LAES and a nuclear power plant, and the round-trip efficiency was claimed to reach 70 %. An approach with a liquid air Rankine cycle was proposed by Ameel et al. (2013), and a round-trip efficiency of 43 % was achieved. A standalone LAES plant was simulated with a round-trip efficiency of 55 % (Guizzi et al., 2015). None of these studies have been applied in large scale. In addition, since the round-trip efficiency of a standalone LAES plant is lower than 60 %, there is still considerable need for improvement before the technology can be industrialized. However, very few papers are trying to optimize standalone LAES systems. Instead, the integration of LAES with external heat sources have been gaining more focus recently. A standalone LAES with optimal design integrated with external heat sources should be tested to further enhance the round-trip efficiency of the process. Thus, the LAES first needs investigation to increase overall efficiency, store hot and cold thermal energy efficiently, and obtain good response times, so that the technology with its potential advantages can be used in practical applications. In this paper, two operating modes are studied for the LAES process: with or without introducing extra amounts of hot oil in the discharging process. A genetic algorithm (GA) is adopted to optimize the LAES process. GA is a search method used to find approximate solutions and is based on the concepts of "natural selection" and "genetic inheritance". The objective function is the round-trip efficiency (RTE, η_{RT}), which is the ratio of work output (W_{out}) in the discharging process and the work input (W_{in}) in the charging process. Results show that optimization with η_{RT} as objective function gives modest improvements compared with the original case.

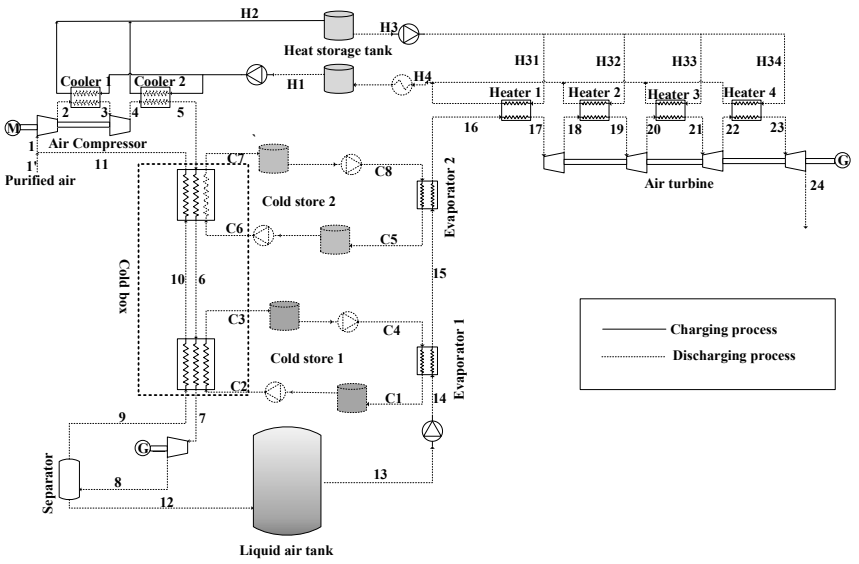

Figure 1: Flow diagram for the liquid air energy storage process

2. Design basis and optimization

The process in Figure 1 shows the liquid air energy storage process, having hot and cold thermal energy storages (Guizzi et al., 2015). The process is simulated in Aspen HYSYS V10.0 (Aspen HYSYS, 2017). The air, consisting of 78.82 % nitrogen, 21.14 % oxygen and 0.04 % argon, is assumed as the feed gas and is liquefied through this modified Claude process. The pre-purification unit (PPU) for the removal of CO_2, H_2O and other trace components is not included in the simulation. Other design conditions and assumptions used in this work are shown in Table 1.

The simulation model is optimized to maximize round-trip efficiency of the process. The pressures after the last-stage compressor and pump are set as variables. In addition, the operating temperatures and mass flow rates of hot oil, methanol and propane are defined as variables in order to manipulate the duty of heat exchangers during optimization. The inlet temperatures of compressors and turbines are also considered as variables, and this has direct effects on electricity consumption and generation in the process. The constraints applied in the optimization problem are the minimum temperature differences for heat exchangers, where 10 K for coolers and heaters and 3 K for evaporators and heat exchangers in the cold box have been assumed.

Table 1: Simulation conditions and assumptions

Parameter	Value	Unit
Ambient temperature	293	K
Ambient pressure	101.325	kPa
Cooling water temperature	288	K
ΔT_{min} of cooler	10	K
ΔT_{min} of heater	10	K
ΔT_{min} of cold box	3	K
ΔT_{min} of evaporator	3	K
Relative pressure drops of heat exchanger	1	%
Isentropic efficiency of compressor	85	%
Isentropic efficiency of turbine	90	%
Isentropic efficiency of cryo-turbine	75	%
Isentropic efficiency of pump	80	%

3. Results

3.1. Key performance indicators

In order to evaluate the performance of the different processes, two parameters will be introduced in this section: liquid yield and round-trip efficiency. Liquid yield η_{LA} is defined as the ratio between the mass flow rate of liquid air (m_{liq}) and the total mass flow rate of compressed air (m_{comp}) that includes the recycle of air:

$$\eta_{LA} = \frac{m_{liq}}{m_{comp}} \tag{1}$$

The most important parameter is the round-trip efficiency η_{RT} that is defined as the work output (W_{out}) in discharge mode divided by the work input (W_{in}) in charge mode:

$$\eta_{RT} = \frac{W_{out}}{W_{in}} = \frac{m_{liq} w_T}{m_{comp} w_C} = \eta_{LA} \cdot \frac{w_T}{w_C} \quad (2)$$

where w_T and w_C represent the specific work [kJ/kg] of the expanders and the compressors, respectively.

3.2. Effects of different number of compression stages and expansion stages on the round-trip efficiency

Minimum compression work for a compressor is obtained by isothermal operation, thus multi-stage compression at low temperature with inter-stage cooling is used to minimize work consumption. Likewise, expansion at high temperature with inter-stage reheating maximizes work production. However, from an economic point of view, the number of compressors and expanders affects the capital cost, which increases with number of units and flowsheet complexity.

In the LAES process, when the number of compressor stages (with interstage cooling) is increased, the compression heat that can be recovered by hot oil and utilized in the discharging process decreases. The achieveable temperature of the hot oil is decreased, however, since cooling of air after compressor stages is repeated, the mass flow rate of hot oil increases. These two changes have opposite effects on the round-trip efficiency and power generation. Reduced temperature of hot oil has a negative effect, while increased mass flow rate of hot oil has a positive effect. The trade-off between the number of compressors, capital cost and compression heat (temperature and mass flow rate of the hot oil) should be balanced. In this section, two operating modes are discussed: with or without introducing extra amounts of hot oil in the discharging process. The performance of the LAES system will be analyzed with different number of compression stages and expansion stages in each mode. First, the case without extra amounts of hot oil is studied.

3.2.1. Without extra amounts of hot oil in the discharging process

Figure 2 demonstrates the effects of different number of compression stages and expansion stages on the RTE of the process without extra amounts of hot oil in the discharging process. As can be seen from the figure, the highest RTE (58.2 %) is obtained with 2-stage compressor and 3-stage expander. Common for all cases without extra hot oil, is the fact that the pinch points in the expansion heat exchangers are in the cold end. The reason why the combination of 2-stage compressor and 3-stage expander has the best performance with respect to RTE, is that the composite curves are closer to parallel than for other combinations. For 3-stage expansion, the RTE is reduced with increased number of compression stages. This is due to the fact that the reduction of hot oil temperature leads to a decreased temperature of inlet air to the expanders, even if the pinch points in the expansion heat exchangers are in the hot end when the number of compression stages is equal to or larger than 3. The decreasing temperature of hot oil has a decisive influence on the RTE in the case with 3-stage compressor and 3-stage expander.From the previous discussion, both temperature and mass flowrate of hot oil are affected by the number of compressor stages in the charging process. Since hot oil is used to transfer compression heat to the expansion section in the discharging process in order to increase work production, there is a strong link between the number of compression stages and the number of expansion stages. The location of the pinch points in the heat exchangers also plays an important role. As a result, for a given number of compressor stages, there exists

an optimal number of expansion stages. This optimal matching can be found in Figure 2. Even though 4-stage expansion has a maximum RTE for 3-stage compression and similar for 5-stage expansion and 4-stage compression, these combinations have lower RTE than the simpler case with 3-stage expansion and 2-stage compression, which is the best combination overall.

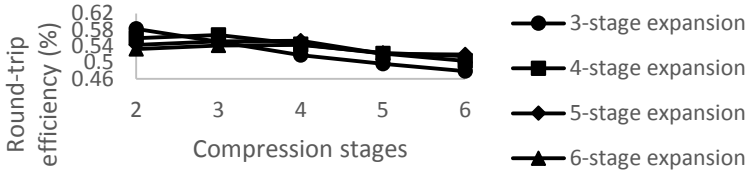

Figure 2: RTE of the LAES for combinations of compression and expansion stages

3.2.2. With extra amounts of hot oil in the discharging process

The pinch point analysis for the LAES process with 2-stage compression and 3-stage expansion indicates that the RTE can be further improved by shifting the pinch points to the hot end to reach a higher inlet temperature to the expanders. This can be achieved by providing enough hot oil in the discharging process. The effect of increasing the number of expansion stages on the RTE when the number of compression stages is fixed at 2, while other variables (such as pressure after the pump and inlet temperature to the expanders) are unchanged, is illustrated in Figure 3. There is a diminishing return on investment when increasing the number of expansion stages. When combining the economic considerations with the RTE, for 2-stage compression in the charging process, 4-stage expansion is recommended in the discharging process when sufficient amounts of hot oil is available. Key performance indicators are listed in Table 2. In this case, an extra amount of hot oil (731 kg/h) is added in the discharging process.

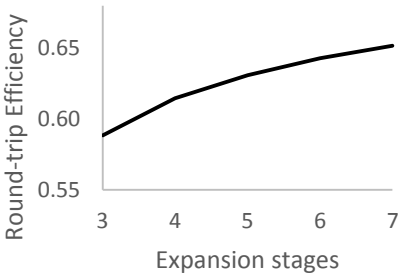

Figure 3: Analysis of the RTE when changing the number of expansion stages

Table 2: Key performance indicators for the LAES process with a 2-stage compressor and a 4-stage expander

Parameter	LAES	
	Charging	Discharging
Work (kW)	499.3	309.3
Liquid yield	0.865	
Round-trip efficiency	61.9 %	

Table 3: Genetic algorithm results

Parameter	LAES	
	Charging	Discharging
Work (kW)	498.9	314.8
Liquid yield	0.865	
Round-trip efficiency	63.1 %	

3.3. Optimization results

The work consumed in the charging process and produced in the discharging process, liquid yield, and the round-trip efficiency are shown in Table 3. Based on the results, the round-trip efficiency has been slightly improved from 61.9 % to 63.1 % by using GA.

4. Conclusions

Liquid air energy storage (LAES) is a viable option for grid-scale electrical energy storage, with the advantage that it is not geographically constrained. However, a low round-trip efficiency has limited the application of this technology. In this study, the cases without introducing extra hot oil in the discharging process is first studied, and the LAES process with a 2-stage compressor and 3-stage expander has the highest round-trip efficiency of 58.2 %. There is an optimal combination of number of compression stages and expansion stages. The combinations corresponding to 4 to 6 expansion stages are 3-stage, 4-stage and 4-stage compression, respectively. However, when introducing an extra amount of hot oil in the discharging process, the LAES process with a 2-stage compressor and 4-stage expander is recommended. An optimization method (Genetic Algorithm) is used to further improve the round-trip efficiency from 61.9 % to 63.1 %.

Acknowledgements

This publication has been funded by HighEFF - Centre for an Energy-Efficient and Competitive Industry for the Future. The authors gratefully acknowledge the financial support from the Research Council of Norway and user partners of HighEFF, an 8-years' Research Centre under the FME-scheme (Centre for Environment-friendly Energy Research, 257632).

References

K. Alanne and A. Saari, 2006, Distributed energy generation and sustainable development, Renewable and Sustainable Energy Reviews, 10(6): 539-558.

S. Rehman, L. M. Al-Hadhrami and M. M. Alam, 2015, Pumped hydro energy storage system: A technological review, Renewable and Sustainable Energy Reviews, 44: 586-598.

C. Bullough, C. Gatzen, C. Jakiel, M. Koller, A. Nowi and S. Zunft, 2004, Advanced adiabatic compressed air energy storage for the integration of wind energy. Conference Advanced Adiabatic Compressed Air Energy Storage For the Integration of Wind Energy, London, UK.

M. Aneke and M. Wang, 2016, Energy storage technologies and real life applications–A state of the art review, Applied Energy, 179: 350-377.

G. L. Guizzi, M. Manno, L. M. Tolomei and R. M. Vitali, 2015, Thermodynamic analysis of a liquid air energy storage system, Energy, 93: 1639-1647.

Highview Power, 2019, < https://www.highviewpower.com/technology/ >.

Y. Li, H. Cao, S. Wang, Y. Jin, D. Li, X. Wang and Y. Ding, 2014, Load shifting of nuclear power plants using cryogenic energy storage technology, Applied Energy, 113: 1710-1716.

B. Ameel, C. T'Joen, K. De Kerpel, P. De Jaeger, H. Huisseune, M. Van Belleghem and M. De Paepe, 2013, Thermodynamic analysis of energy storage with a liquid air Rankine cycle, Applied Thermal Engineering, 52(1): 130-140.

Aspen HYSYS, Version 10.0, 2017, Aspen Technology Inc., Burlington, MA.

Sauro Pierucci, Flavio Manenti, Giulia Bozzano, Davide Manca (Eds.)
Proceedings of the 30th European Symposium on Computer Aided Process Engineering (ESCAPE30), May 24-27, 2020, Milano, Italy.
http://dx.doi.org/10.1016/B978-0-12-823377-1.50163-4

Sensitivity Analysis of Desulfurization Costs for Small-Scale Natural Gas Sweetening Units

Yushi Deng[a], Shuang Xu[a], Kylie Webb[b], Harrison Wright[b], Paul S. Dimick[b], Selen Cremaschi[a]*, Mario R. Eden[a]

[a]*Department of Chemical Engineering, Auburn University, Auburn, AL 36849, USA*
[b]*IntraMicron, Inc., Auburn, AL 36832, USA*
selen-cremaschi@auburn.edu

Abstract

Natural gas from stranded sources are vented or flared rather than being utilized due to high gathering and processing costs. One of the hurdles that must be overcome for utilizing these stranded resources is the lack of scalable and easily deployable gas sweetening technologies. In this paper, three gas sweetening technologies, triazine-based absorption, a liquid redox process called LO-CAT®, and a newly developed process called SourCat™, that can be operated at smaller scales necessary for sweetening sour gas from stranded resources are compared in terms of their desulfurization costs. A sensitivity analysis using the Morris-One-At-a-Time (MOAT) method is performed to investigate the sensitivity of desulfurization cost to process and economical parameters. The results revealed that the desulfurization cost of triazine-based absorption is most sensitive to raw material costs. The parameters that determine the sulfur content inside the system have the strongest impact on the cost of the LO-CAT® process. The desulfurization cost of the SourCat™ process is most dependent on the parameters related to sulfur that needs to be removed and H_2S that needs to be adsorbed by the sorbent.

Keywords: Sensitivity analysis, Morris One-At-a-Time (MOAT), small-scale, desulfurization

1. Introduction

Natural gas, a colorless and odorless fossil fuel, is the second largest source of energy in the United States, which contributed 31% of the total primary energy consumption in the U.S. in 2018 (Dudley, 2018). Based on its hydrogen sulfide concentration, natural gas can be classified as sour gas (more than 4 ppm of H_2S) or sweet gas (no or a negligible amount of H_2S) (Faramawy et al., 2016). Hydrogen sulfide in sour gas has health and environmental effects, causes safety and corrosion issues, and should be eliminated below the sales gas specification limits (typically 4 ppm). Hence, removing hydrogen sulfide from natural gas, which is also called gas sweetening, is common practice.

Natural gas produced in small quantities or at remote locations is considered stranded gas. These natural gas resources are vented or flared because of high gathering and processing costs. The amount of stranded gas was over 200 Billion Cubic Feet (BCF) in 2017 (EIA, 2019). Processing stranded sour gas resources requires the development of scalable and easily deployable gas sweetening processes.

In this paper, we compare three gas sweetening processes that can potentially be deployed at capacities relevant for processing stranded gas resources. They are triazine-based absorption, a liquid redox process (modeled after the LO-CAT® process) and a new process called SourCat™. A process simulation model is developed for each technology,

and desulfurization cost is calculated using an economic analysis software called ECON (Kalakul et al., 2014). A systematic sensitivity analysis (SA) is carried out using the Morris One-At-a-Time (MOAT) method to identify process and economic parameters for each technology that the desulfurization cost is most sensitive to.

2. Process Simulations and Desulfurization Cost Calculations

2.1. Triazine-based Absorption Process

Triazines are composed of three nitrogen and three carbon atoms in a six-membered ring, and 1,3,5-tris-(2-hydroxyethyl) hexahydro-s-triazine (also known as MEA triazine) is the triazine used most commonly for removing H_2S (Taylor et al., 2019).Triazine-based absorption is commercially used for sweetening sour gas when its H_2S concentration is below a few hundred ppm (Lozano, 2000). Here, we consider triazine-based absorption using flooded systems because they are designed to operate continuously and have lower capital expense (CAPEX) than batch systems (Lozano, 2000). A simplified process flow diagram (PFD) of the Aspen Plus simulation for the triazine-based absorption process is given in Figure 1. Sour gas is injected into an absorber with a triazine-based scavenger, and the liquid-gas mixture is separated in a tower where sweet gas is collected from the top and spent liquid scavenger from the bottom.

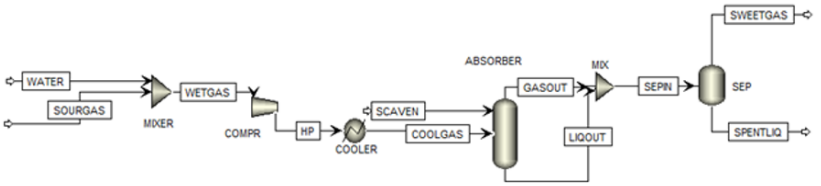

Figure 1: Process flow diagram of Aspen Plus simulation for triazine-based absorption process

2.2. Liquid Redox (LO-CAT®) Process

In the LO-CAT® process, H_2S is oxidized to elemental sulfur using a chelated iron solution. This process is primarily used for desulfurization at small scales (Speight, 2018). The PFD of the LO-CAT® process simulation is given in Figure 2. In the absorber vessel (T-1), H_2S from sour gas is absorbed by sodium ferric ethylenediaminetetraacetate (EDTA FeNa) solution. Ferric ion oxidizes H_2S to solid sulfur and is reduced to ferrous ion, which is oxidized back to ferric ion by oxygen in air in the oxidizer vessel (T-2). Ferric ion is then recycled back to the absorber. Sweet gas is the top product from the absorber. Fresh EDTA FeNa solution is added to the absorber to compensate for the solution loss with wet sulfur cake. To prevent iron precipitation and accelerate H_2S absorption, NaOH or KOH is used to control the solution pH between 8 and 9.

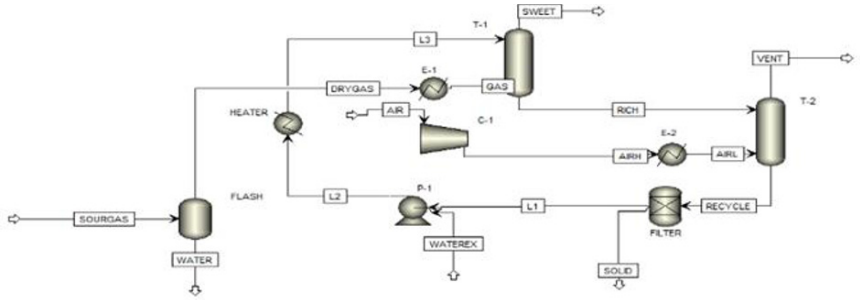

Figure 2: Process flow diagram of Aspen Plus simulation for LO-CAT® process

2.3. Chemical Oxidation (SourCat^{TM}) Process

The SourCat^{TM} process is a new desulfurization process developed by IntraMicron, Inc., an Auburn University spin-off company. It utilizes a patented solid oxidative sulfur removal catalyst to convert H_2S to elemental sulfur. A simplified PDF of the process simulation is given in Figure 3. Sour gas and air are injected into the fixed-bed catalyst reactor, where H_2S is converted to solid sulfur and SO_2 with a selectivity to elemental sulfur over 90%. The reactor effluent is washed with water to remove solid elemental sulfur, which is collected by a filter. The small amount of SO_2 produced is carried by the gas steam (G and G2) and is separated from the sweet gas by an adsorption bed.

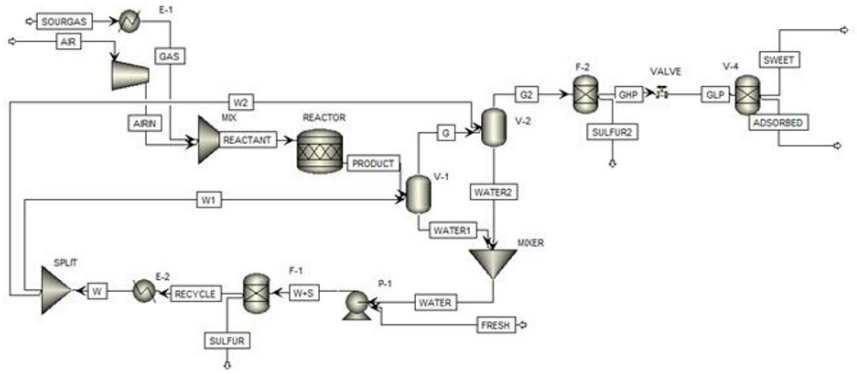

Figure 3: Process flow diagram of Aspen Plus simulation for SourCat^{TM} process

2.4. Desulfurization Cost Calculations

Desulfurization cost (DC) is defined as the cost of sweetening one thousand standard cubic feet (MSCF) natural gas. Aspen Plus process simulations are used to calculate raw material and utility requirements, and equipment sizes for each process. Given these, the CAPEX and the operating expenses (OPEX) are estimated using ECON (Kalakul et al., 2014). Then, DC in \$/MSCF natural gas is calculated with (DF_{wp}) and without (DC_{wop}) payoff using Eqns. (1) and (2), respectively. In Eq. (1), the annual interest rate, r, is 10% and the payoff time, t, is 3 years. The variable $capacity$ represents the sour gas flow rate in thousand standard cubic feet per day (MSCFD).

$$DC_{wp} = \frac{CAPEX \times \frac{r(1+r)^t}{(1+r)^t - 1} + OPEX}{Capacity} \tag{1}$$

$$DC_{wop} = \frac{OPEX}{Capacity} \tag{2}$$

3. Sensitivity Analysis of Desulfurization Cost

Sensitivity analysis (SA) is an approach for identifying important parameters that dominate model behaviour. A global SA method, Morris One-At-a-Time (MOAT) method, is chosen to study the sensitivity of desulfurization cost to process and economic parameters due to its efficiency and effectiveness (Gan et al., 2014). To apply the MOAT method, only one parameter is changed to a new value at each model evaluation. For an n-dimensional p-level orthogonal parameter space, the elementary effect, d_i, of the i^{th} parameter, X_i, is defined by Eq. (3),

$$d_i = \frac{f\left(X_1,\ldots,X_{i-1},X_i+\Delta,X_{i+1},\ldots,X_n\right) - f(X)}{\Delta} \tag{3}$$

where Δ is a predetermined multiple of $\frac{1}{[p-1]}$. When p is even, $\Delta = \frac{p}{[2(p-1)]}$. The final Morris measures for the i^{th} parameter are the mean (μ_i) and the standard deviation (σ_i) of d_i, and are calculated using Eqns. (4) and (5),

$$\mu_i = \sum_{j=1}^{k} \frac{d_i(j)}{k} \quad (4)$$

$$\sigma_i = \sqrt{\sum_{j=1}^{k} \frac{(d_j(j)-\mu_i)^2}{k}} \quad (5)$$

where k is the iteration number, which varies from 5 to 20. The higher the value of μ_i, the more sensitive the model response is to changes in parameter X_i. The higher the value of σ_i, the more interaction parameter X_i has with other parameters. The number of model evaluations for applying MOAT method is $k(n+1)$.

Process and economic parameters considered for SA of the desulfurization cost are summarized in Tables 1, 2, and 3. For SA, p is set to 4, and k was equal to 20 which required 160, 160, 200 desulfurization cost calculations for triazine-based absorption, LO-CAT®, and SourCat™ processes, respectively.

Table 1: Potential sensitive parameters for triazine-based absorption process

Parameters	Nominal Value	Range
Temperature	80°F	50-160°F
Pressure	300 psi	300-600 psi
Water Fraction	100 %	0 – 100 %
Gas flow rate	100 MSCFD	100 – 100000 MSCFD
H_2S Concentration	500 ppm	500-2000 ppm
Triazine Concentration	52 wt%	20 wt%-80 wt%
80wt% Triazine Scavenger Price	$2/kg	$1/kg – $2.3/kg

Table 2: Potential sensitive parameters for LO-CAT® process

Parameters	Nominal Value	Range
Pressure	14.7 psi	14.7-600 psi
Temperature	80°F	60-110°F
EDTA-FeNa Concentration	250ppm	250-3000 ppm
Sulfur Cake Water Fraction	50wt%	50-90 wt%
EDTA-FeNa Price	$2.15	$1.6 - $2.36/kg
Gas Flow Rate	100MSCFD	100-100000 MSCFD
H_2S Concentration	500 ppm	500-2000 ppm

Table 3: Potential sensitive parameters for SourCat™ process

Parameters	Nominal Value	Range
Gas Flow Rate	100 MSCFD	100 - 100000 MSCFD
H_2S Concentration	500 ppm	500 – 2000 ppm
Conversion of SO_2	1.96%	0 – 20%
Conversion of Sulfur	96%	80 - 98%
V-3 Split Fraction	99%	80 - 100%
F-2 Split Fraction	100%	90 - 100%
Sorbent Price	$2 /lb	$2 - $5/lb
Sorbent Capacity	0.03 g H_2S/g Sorbent	0.03 - 0.1 g H_2S/g Sorbent
Catalyst Price	$26/lb	$20 - $30/lb

3.1. Sensitivity of Desulfurization Cost for Triazine-based Absorption Process

The values of mean and standard deviation for all potential sensitive parameters are plotted in Figure 4 for the triazine-based absorption process. The gas flow rate and triazine concentration are the most significant parameters for this process' desulfurization cost. Gas flow rate determines the consumption rate of triazine solution, and triazine concentration determines the solution flow rate. For the triazine-based absorption process, 90% of desulfurization cost is raw materials, i.e., triazine solution cost. The SA results for desulfurization costs with and without payoff are very close (Figure 4) because CAPEX only contributes 1% to desulfurization cost for this process.

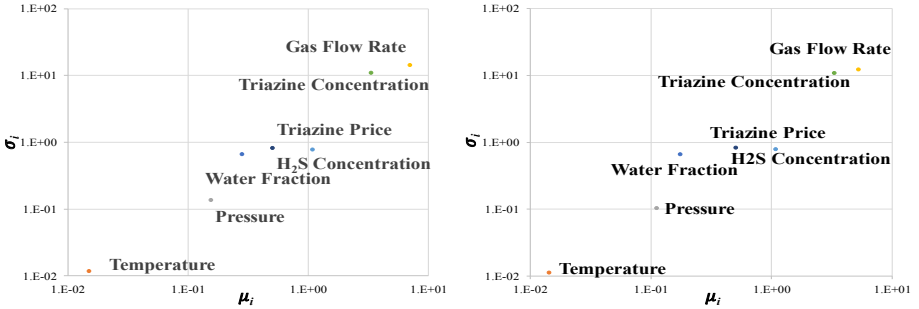

Figure 4: SA results for triazine-based absorption process. Mean and standard deviation values for potential sensitive parameters for desulfurization cost (a) with 3-year payoff and (b) after payoff.

3.2. Sensitivity of Desulfurization Cost for LO-CAT® Process

Similar plots to Figure 4 are provided for SA results of the LO-CAT® process in Figure 5. The gas flow rate, sulfur cake water fraction and H_2S concentration, which determine the sulfur amount inside the system, are the most sensitive parameters for desulfurization costs with and without payoff. This is because the sulfur amount influences the EDTA FeNa solution usage and air flow rate, which determine the size and utility of heat exchanger and compressor.

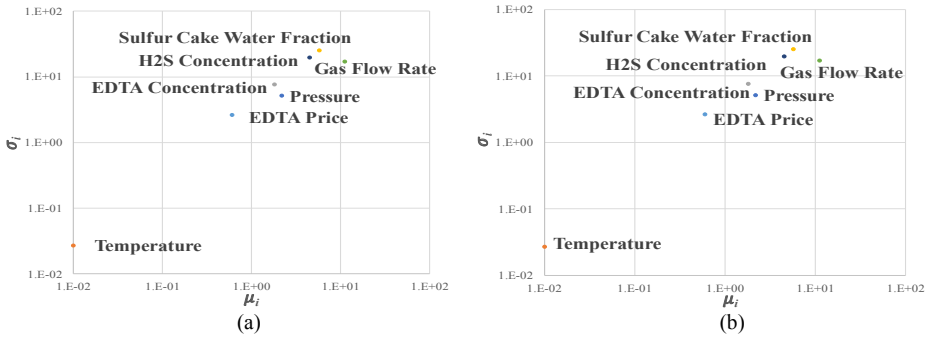

Figure 5: SA results for LO-CAT® process. Mean and standard deviation values for potential sensitive parameters for desulfurization cost (a) with 3-year payoff and (b) after payoff.

3.3. Sensitivity of Desulfurization Cost for SourCat™ Process

The sensitivity analysis results for SourCat™ process are compiled in Figure 6. The gas flow rate and H_2S concentration are the most sensitive parameters. Sulfur conversion, sorbent price, sorbent capacity and SO_2 conversion, which determine the total sorbent cost, also impact the desulfurization cost. This is because these parameters affect how

much H_2S is left in the reactor effluent. Adsorption of the left H_2S is much more expensive compared to converting it to solid elemental sulfur in the reactor.

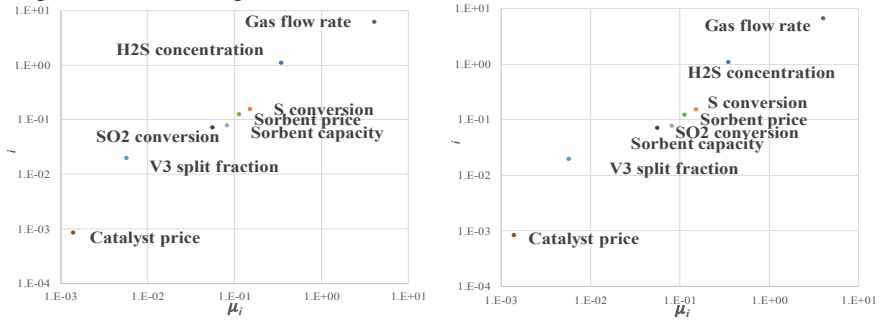

Figure 6 SA results for SourCat™ process. Mean and standard deviation values for potential sensitive parameters for desulfurization cost (a) with 3-year payoff and (b) after payoff.

4. Conclusions

A systematic sensitivity analysis using MOAT method is performed to investigate which parameters have the most significant impact on desulfurization costs of three small-scale desulfurization processes. For triazine-based absorption, gas flow rate, triazine concentration and H_2S concentration that determine the raw material cost are the most sensitive ones because raw material makes up 90% of the desulfurization cost. For LO-CAT® process, parameters that determine the sulfur amount inside the system are the most sensitive ones, such as gas flow rate and H_2S concentration. For this process, parameters that are related to EDTA FeNa cost also have an impact on desulfurization cost. For SourCat™ process, parameters controlling the sulfur content and H_2S amount that needs to be adsorbed by sorbent are the most sensitive ones. Gas flow rate and H_2S concentration are sensitive parameters for all three small-scale desulfurization processes.

Acknowledgements

The authors are grateful for the financial support provided by the DOE-RAPID Process Intensification Institute under contract DE-EE0007888-10-6.

References

Dudley, B. (2018). BP statistical review of world energy. *BP Statistical Review of World Energy*, 1–56.

EIA. (2019). U.S. Natural Gas Vented and Flared. Retrieved November 27, 2019, from https://www.eia.gov/dnav/ng/hist/n9040us2a.htm

Faramawy, S., Zaki, T., & Sakr, A. A.-E. (2016). Natural gas origin, composition, and processing: A review. *Journal of Natural Gas Science and Engineering*, *34*, 34–54.

Gan, Y., Duan, Q., Gong, W., Tong, C., Sun, Y., Chu, W., … Di, Z. (2014). A comprehensive evaluation of various sensitivity analysis methods: A case study with a hydrological model. *Environmental Modelling and Software*, *51*, 269–285.

Hugo Lozano, E. A. T. (2000). Re-generable H_2S Scavenger. *Laurance Reid Gas Conditioning Conference*.

Kalakul, S., Malakul, P., Siemanond, K., & Gani, R. (2014). Integration of life cycle assessment software with tools for economic and sustainability analyses and process simulation for sustainable process design. *Journal of Cleaner Production*, *71*, 98–109.

Speight, J. G. (2018). Gas cleaning processes. In *Natural Gas*. https://doi.org/10.1016/b978-0-12-809570-6.00008-4

Taylor, G., Smith-Gonzalez, M., Wylde, J., & Oliveira, A. P. (2019). *HS Scavenger Development During the Oil and Gas Industry Search for an MEA Triazine Replacement in Hydrogen Sulfide Mitigation and Enhanced Monitoring Techniques Employed During Their Evaluation*. https://doi.org/10.2118/193536-ms

Sauro Pierucci, Flavio Manenti, Giulia Bozzano, Davide Manca (Eds.)
Proceedings of the 30th European Symposium on Computer Aided Process Engineering (ESCAPE30), May 24-27, 2020, Milano, Italy.
http://dx.doi.org/10.1016/B978-0-12-823377-1.50164-6

Synthesis of Heat Pump Enhanced Solar Thermal for Low and Medium Temperature Operations

Ben Abikoye,[a,*] Lidija Čuček,[b,*] Danijela Urbancl,[b] Adeniyi Jide Isafiade,[a] Zdravko Kravanja[b]

[a]*Department of Chemical Engineering, University of Cape Town, Private Bag X3, Rondebosch 7701, Cape Town, South Africa*
[b]*Faculty of Chemistry and Chemical Engineering, University of Maribor, 2000 Maribor, Slovenia*
abksem001@myuct.ac.za, lidija.cucek@um.si

Abstract

This study presents a multi-period mathematical programming approach for the design and optimization of heat pump-enhanced solar thermal for low and medium temperature applications in industrial, residential and other sectors. Mathematical models which capture the dynamic operating properties and thermodynamic features of combined solar thermal and multi-stage vapour compression heat pump cycle have been developed. The multi-period optimization context of the model accounts for the intermittent variability of relevant meteorological conditions and their effects on heat output from the heat pump. The design and optimization of the integrated system is implemented and solved in GAMS and analysis of the system shows good prospect for enhanced thermal energy from solar. The results obtained show significant increase in the amount of heat recovered from the heat pump as solar collector area increases up to 6,511 m^2 with average heat duty of about 1,615 kW and coefficient of performance of 1.81 obtained for that same collector size.

Keywords: Solar thermal, Heat pump, Solar-driven heat pump synthesis, Low and medium temperature level applications, Design and optimization.

1. Introduction

Due to the urgent need to reduce energy-related emissions as well as increasing supports for stringent environmental regulations, energy system designs that showcase the synergy between energy efficiency measures and renewable energy technologies have received global interests and considerable research attention (IRENA, 2017). One of such technologies is integrated design of solar thermal and heat pump system which has been widely described to be a relatively preferred sustainable source of heat (Allouhi et al. 2017) especially for low and medium temperature operations. One of the captivating features of solar thermal is its natural availability at diverse ambient temperature levels without any mechanical work input (Abikoye et al. 2019a). Heat pump on the other hand is an energy efficient technology that is used to upgrade heat from a relatively low temperature heat source and eventually deliver more heat than the total work input (Carbonell et al. 2014). These attributes provide the platform for using the combined technology to circumvent the low energy output limitation of solar thermal systems (especially in periods with low solar irradiation and ambient temperature). It also provides a sustainable means to overcome the start-up problem in most heat pump applications thereby enhancing the performance of heat pumping cycle.

While numerous studies have been carried out on heat pump technologies, less information is available in literature on the synthesis of solar-driven heat pump and on the application of combined solar thermal and heat pump for low and medium temperature level applications (Grubbauer et al. 2018). This is especially the case for studies that include optimization of the integrated systems. Most previous research contributions combining solar thermal and heat pump designs have been largely applied to residential buildings, while few other available cases of industrial heat pump design and optimization are based on industrial waste heat recovery through thermoelectric devices and organic Rankine cycles (Mateu-Royo et al. 2019).

Utilization of solar thermal in any form is a task that is highly challenging due to considerable intermittent supply and multi-period variability features of its energy output. Even with modern synthesis techniques, the general requirements for achieving optimal design solution is still a challenge. More so, if a moderately-sized solar design with simple technology is considered, not much higher temperature level can be reached for typical industrial streams (Abikoye et al. 2019a). However, integrating heat pump with such simple design could enhance the thermal output of the system, but combination of the two technologies is not trivial considering the transient nature of solar resource and its influence on the heat output from the combined technology. This is in addition to the complexities at the heat pump side of the integrated network when a high temperature lift is desired. Such intricacies are generally unavoidable due to the wide difference between evaporator and condensing temperatures while trying to maximize the heat load recoverable from condensing vapour in the heat pump.

To the best of authors' knowledge, study on combined heat pump/solar thermal utility system that incorporate the aforementioned features using a simultaneous design and optimization approach is still lacking. Hence, this study presents a comprehensive synthesis method for the utilization of combined solar thermal and heat pump technologies for low and medium temperature level heat generation.

2. Methodology

2.1. System description

The integrated system presented in this paper consists of solar thermal system (which supplies heat to the evaporator side of the heat pump) and the heat pump cycle (having multi-stage vapor compression features with successive condensation and sub-cooling for maximum heat recovery) and low/medium temperature heat production for potential integration with the industrial or residential heat network.

Figure 1 presents the structure of the combined solar thermal and heat pump technology. The integrated design comprises three loops: i) closed loop solar collector – heat pump – solar collector; ii) closed loop of heat pump alone; and iii) open loop heat pump – industrial process – heat pump. The heat transfer fluid (HTF) that runs through solar collector – evaporator – solar collector loop (first loop) is a mixture of water and ethylene glycol. In the second loop (closed loop of heat pump cycle), R-245CA refrigerant is used as the working media, while circulating pressurized water is used to recover heat from the hot refrigerant gas which is then further used in the industrial process loop (third loop). In Figure 1 the third loop is presented with a dashed line, as it is modelled as an open loop.

Having increased in temperature, the HTF from solar collector is used to vaporize the low-pressure refrigerant within the sealed compartment of the evaporator. Thereafter, the

vaporized refrigerant goes through multi-stage vapor compression which further increases the pressure and temperature of the gas. The hot refrigerant gas is then finally used to raise the temperature of the circulating HTF on the heat recovery side of the heat pump cycle (i.e. condenser and sub-cooler). The advantage derived from an efficient heat pumping system is that more heat is delivered to the system than the total work input. In the conceptual framework of the design, the recovered heat can be used directly in the plant or stored in the tank to be used at a later time within the industrial heat network as shown in the integrated system (Figure 2) or for other potential uses such as space and water heating as demonstrated by Abikoye et al. (2019b). However, it should be noted that only the multiperiod integration between solar thermal and heat pump components of the integration is discussed in this paper.

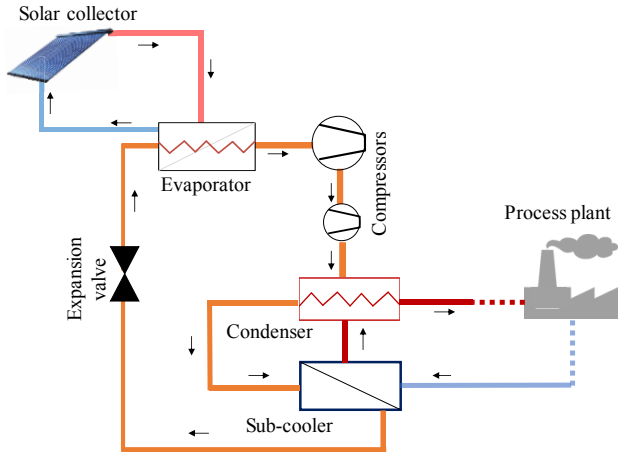

Figure 1: Integrated heat pump-enhanced solar thermal system

2.2 Model approach

The objective of the presented study is to maximize the total heat recovered from the vaporized refrigerant at the heat recovery side of the heat pump. The objective function is developed as shown in Eq. (1), where $\dot{Q}^{gen}_{mp,dp,hp}$ represents the total heat generated from the sub-cooler and condenser and delivered to the HTF in the process plant – heat pump – process plant loop. Sets *mp, dp* and *hp* represent monthly, daily and hourly periods, while *DPM* represents set of pairs of days and months as in Egieya et al. (2018).

$$\max\left(\sum_{mp\in MP}\sum_{dp\in DP}\sum_{hp\in hP}\bigwedge_{(mp,dp)\in DPM}\dot{Q}^{gen}_{mp,dp,hp}\right) \quad (1)$$

The main variables considered in the model include temperatures, flowrates and energy flows of streams across the system, mass enthalpies across the heat pump loop, the area of solar collector and efficiencies (for both solar collector and compressors). An important factor in modelling of combined solar thermal and heat pump system is the intermittent changes in ambient conditions and its effects on the heat output from the system. Hence, the mathematical model is formulated as a multi-period model. The model accounts for the dynamic behavior of the operating and thermodynamic features of the combined solar thermal-heat pump systems. The multi-periodicity framework of the model captures the

time-dependency disposition of all the integration features. These characteristics are accounted for on hourly, daily and monthly time periods in the model.

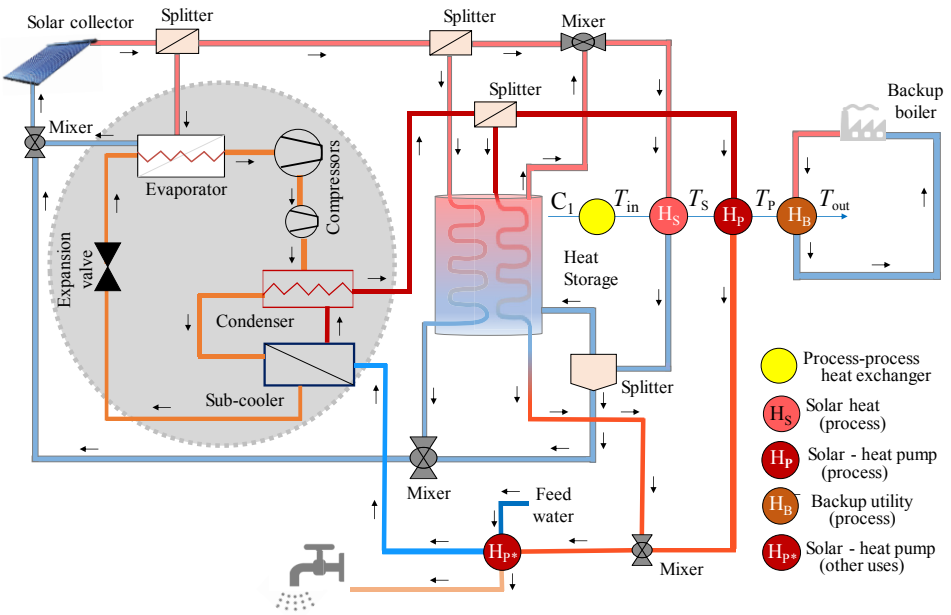

Figure 2: Industrial integration of combined solar thermal and heat pump system incorporated with periodic heat storage

To evaluate the periodic features on the heat pump side, correlations are developed for the changes in mass enthalpy with changes in temperature and pressure across the two-phase region of the refrigerant as shown in Figure 3 for R245CA. Thermodynamic data for the refrigerant are obtained from Aspen Plus V10 using REFPROP property method (Aspen Technology, 2019).

The periodic heat duty ($\dot{Q}$) and work ($\dot{W}$) required across units t such as evaporator (*evap*), compressors (*comp*), condenser (*cond*), sub-cooler (*cool*) and expander, are obtained by multiplying the flowrate (F) and the difference in mass enthalpy $(h^{out} - h^{in})$:

$$Q_{t,mp,dp,hp},\ W_{t,mp,dp,hp} = F_{t,mp,dp,hp} \cdot \left(h^{out}_{t,mp,dp,hp} - h^{in}_{t,mp,dp,hp}\right), \quad \forall\, mp \in MP, dp \in DP, hp \in HP, \quad t \in \{\text{evaporator, compressor, condenser, sub-cooler, expander}\} \tag{2}$$

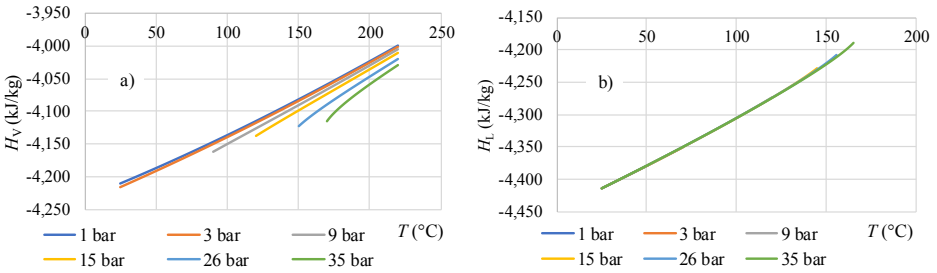

Figure 3: Mass enthalpy changing with temperature and pressure for a) vapor and b) liquid phase

3. Case Study and Results

The developed model is implemented based on the previous design of industrial integration of solar thermal by Abikoye et al. (2019a). The integrated solar thermal design is now modified by including the heat pump enhanced solar loop. The design is then simultaneously optimized for the maximum amount of heat energy that can be obtained from heat pump. Most integration parameters (such as flowrates, temperatures, pressures, energy flows, work required, mass enthalpies, mass fractions of liquid and vapor, efficiencies, collector area, heat capacities and cp/cv ratio) are variables which are then optimized to satisfy the objective of the design.

A reference location in Maribor, Slovenia, is used as the case study. Meteorological data (hourly solar irradiation and ambient temperature) of the location for the year 2016 are obtained from EC JRC PVGIS project (2017). To reduce the complexity of the model and computational time, the discretization of hourly, daily and monthly time periods follows the same techniques as used by Abikoye et al. (2019a). Readers are referred to the study for more details on solar thermal utilization in industrial process stream without heat pump. The resulting model consists of 9,971 single equations and 11,186 single variables. Solutions to the model was obtained in 60 minutes using SBB solver in GAMS (GAMS Development Corporation, 2019) with 0.1 % optimality gap on a personal computer with an Intel® Core™ i7-8700K CPU @ 3.70 GHz processor with 64 GB of RAM.

Figures 4 and 5 and Table 1 present summary of the results obtained. An example of the variability in the properties of streams in specific time period and collector area is shown in Figure 4 (e.g. when $A_{collector}$ = 5,000 m^2 and period is M8, D1, H2 i.e. August 8-10 am). Figure 5 shows the relationship between the average $\dot{Q}^{gen}$ obtained and solar collector sizes ($A_{collector}$). From Figure 5, a steady increase in the amount of heat recovered from the heat pump can be observed up to $A_{collector} \approx$ 6,510.6 m^2. A summary of the results showing this relationship is presented in Table 1 for different variables such as heat duty, power required, heat generated, and coefficient of performance (COP).

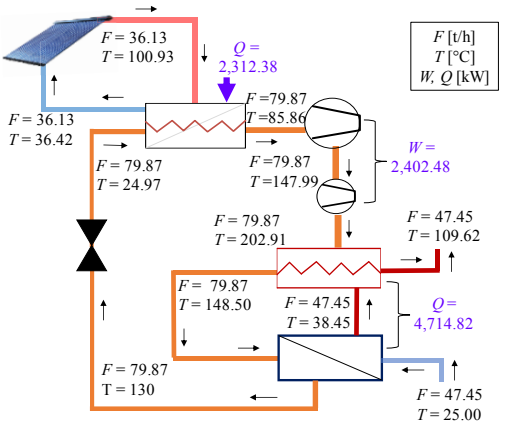

Figure 4: Values of variables in selected period and collector area (A = 5,000 m^2, M8, 8-10 am)

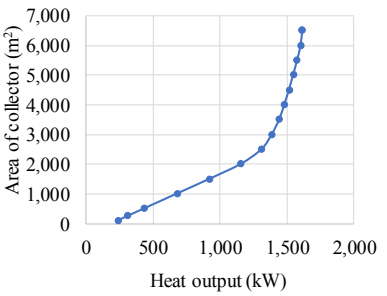

Figure 5: Average heat output with different sizes of solar collector

4. Conclusions and Recommendations

In this study, an integrated design and optimization framework that combined solar thermal and heat pump technologies has been proposed for enhanced thermal

performance. The framework and method is based on a multi-period model formulation where the dynamic features of solar integration and heat output from the system are evaluated and accounted for on hourly, daily and monthly time periods. The obtained results show that combining heat pump with solar thermal can enhance the thermal performance and reliability of the solar system. Future work will include integration of the proposed design with industrial and residential heat network for maximum heat delivery, and economic and sustainability objectives for the integrated design.

Table 1: Average values of some integration variables for different collector areas

$A_{\text{collector}}$ (m^2)	$\dot{Q}_{evap}$(kW)	$\dot{Q}_{cond}$(kW)	$\dot{Q}_{cool}$(kW)	$\dot{W}_{comp}$(kW)	$\dot{Q}^{gen}$(kW)	COP
100	11.94	-40.12	-8.85	37.04	237.20	1.32
500	59.67	-200.61	-44.26	185.20	433.10	1.32
1,000	119.35	-401.22	-88.52	370.40	677.99	1.32
2,000	236.94	-792.23	-175.18	730.46	1,155.44	1.33
4,000	440.49	-1,090.49	-239.24	889.24	1,480.20	1.50
6,000	629.90	-1,263.52	-245.33	878.95	1,601.92	1.78
6,510.6	672.60	-1,328.97	-256.08	912.46	1,614.58	1.81

Acknowledgements

The authors wish to acknowledge the supports received from the Erasmus+ programme of the European Union, Postgraduate Research Office and Faculty of Engineering and the Built Environment at the University of Cape Town, South Africa, and the Slovenian Research Agency (research core funding No. P2-0412 and P2-0032).

References

B. Abikoye, L. Čuček, A. Isafiade, Z. Kravanja, 2019a, Integrated design for direct and indirect solar thermal utilization in low temperature industrial operations, Energy, 182, 381-396

B. Abikoye, L. Čuček, A. Isafiade, Z. Kravanja, 2019b, Synthesis of Solar Thermal Network for Domestic Heat Utilization, Chem Eng Trans, 76, 1015-1020

A. Allouhi, Y. Agrouaz, M. Benzakour Amine, S. Rehman, M.S. Buker, T. Kousksou, A. Benbassou, 2017, Design optimization of a multi-temperature solar thermal heating system for an industrial process, Appl Energy, 206, 382–392

Aspen Technology, 2019, Aspen Plus, The Chemical Industry's Leading Process Simulation Software. <www.aspentech.com/en/products/engineering/aspen-plus> Accessed: 29.11.2019

D. Carbonell, M.Y. Haller, D. Philippen, E. Frank, 2014, Simulations of combined solar thermal and heat pump systems for domestic hot water and space heating, Energy Procedia, 48, 524–534

J.M. Egieya, L. Čuček, K. Zirngast, A.J. Isafiade, B. Pahor, Z. Kravanja, 2018, Biogas supply chain optimization considering different multi-period scenarios, Chem Eng Trans, 70, 985-990

GAMS Development Corporation, 2019, GAMS – Documentation, <gams.com/latest/docs/gams.pdf> Accessed: 29.11.2019

A. Grubbauer, J. Fluch, C. Brunner, T. Ramschak, V. Wilk, T. Fleckl, 2018, Renewable and highly efficient energy systems through innovative combination of solar thermal and heat pump systems, Chem Eng Trans, 70, 745-750

IRENA, 2017, Synergies between renewable energy and energy efficiency, <irena.org/-/media/Files/IRENA/Agency/Publication/2017/Aug/IRENA_REmap_Synergies_REEE_2017.pdf> Accessed 8.6.2019

C. Mateu-Royo, A. Mota-Babiloni, J. Navarro-Esbrí, B. Peris, F. Molés, M. Amat-Albuixech, 2019, Multi-objective optimization of a novel reversible High-Temperature Heat Pump-Organic Rankine Cycle (HTHP-ORC) for industrial low-grade waste heat recovery, Energy Conversion and Management, 197, 111908

Sauro Pierucci, Flavio Manenti, Giulia Bozzano, Davide Manca (Eds.)
Proceedings of the 30th European Symposium on Computer Aided Process Engineering (ESCAPE30), May 24-27, 2020, Milano, Italy.
http://dx.doi.org/10.1016/B978-0-12-823377-1.50165-8

Protein from Renewable Resources: Mycoprotein Production from Agricultural Residues

Thomas Upcraft[a], Rob Johnson[a], Tim Finnigan[a], Jason Hallett[a], Miao Guo[a,b]

[a] *Department of Chemical Engineering, Imperial College London, London, SW7 2AZ*
[b] *Department of Engineering, King's College London, Strand campus*

J.hallett@imperial.ac.uk, miao.guo@kcl.ac.uk

Abstract

As concerns intensify over the increasing impact of human activities on the environment, efforts are underway in several areas in order to mitigate the worst effects. In recent years agricultural systems have received intense public scrutiny and if the global population increases, then the risk to food security is of real concern. Food-grade Single Cell Proteins (SCPs), produced through microbial fermentation, are an alternative to traditional livestock protein sources. This study presents a conceptual design and economic evaluation of SCP production from cellulosic-derived sugars from agricultural wastes. We modelled an SCP biorefinery, with ionic liquid pretreatment, enzymatic hydrolysis and fermentation to convert rice straw to food-grade protein. A Techno-Economic Analysis (TEA) was performed to assess the feasibility and compare the minimum selling price (MSP) to meat protein sources. Technical constraints were evaluated, in addition to evaluating the impact of reagent prices to the commercial success of the process.

Keywords: Biorefinery, single cell protein, process design, techno-economic analysis

1. Introduction

Globally, 113 million people still exist in a state of 'crisis' over food security, with 109 million of those requiring humanitarian intervention, in part due to climate-related events (FAO et al., 2019). Agriculture accounts for 29% of global GHG emissions(Vermeulen et al., 2012) with livestock responsible for a significant proportion of emissions and land-water resource scarcity. There is now growing interest in meat-alternative protein sources with minimal environmental damage, such as food-grade single cell proteins (SCPs).

SCPs refer to edible unicellular microorganisms that can be used as a protein supplement for human consumption or animal feeds. Mycoprotein, an SCP success story, is derived from the fungus *Fusarium venenatum* and has been produced by Marlow Foods Ltd under the name Quorn™ since 1985, with current annual sales of over £200m(Quorn, 2018).

Mycoprotein is produced through the aerobic fermentation of glucose syrup with *F. venenatum*(Wiebe, 2002). Replacement of starch-derived glucose as a feedstock with cellulose-derived glucose offers potential reduced land-use through agro-residue waste utilisation coupled with partial carbon emission mitigation. One such agricultural residue is rice straw. Rice feeds over 45% of the world and is the staple food in Asia representing between 30-70% of the average person's caloric intake(IRRI, 2019). Much of the rice straw is burned causing air, land, and water pollution, severe health problems and decreased soil quality. Several pretreatment technologies are currently under investigation in tandem with hydrolysis and fermentation to convert rice straw to

bioproducts, amongst which, the use of ionic liquids (ILs) is one of the most promising due to its high sugar release, low production of saccharification inhibitors and prevention of toxins accumulating. Furthermore, the use of promising low-cost food-grade ILs may eliminate many hurdles relating to food safety, thereby enabling lignocellulosic-SCP.

Biorefinery models for biochemicals have been widely studied at both the conceptual and detailed design phases, such as for bioethanol production (Humbird et al., 2011) and Acetone-Butanol-Ethanol. However, biorefinery models with IL pretreatment are a scarcity. Baral and Shah (2016) investigated IL pretreatment for ethanol production and concluded that IL recovery and cost were significant economic factors. Similarly, SCP production models are uncommon. Strong et al. (2016), highlighted a potential process pathway, whilst Molitor et al. (2019) developed a two-stage power-to-protein process economic model, fixing CO_2 as the carbon source. However, a research gap remains on modelling of lignocellulosic derived protein.

In this paper, a conceptual biorefinery model was developed to investigate the feasibility of the lignocellulose-to-SCP process based on in-house experimental data on lignocellulosic sugar extraction with food-grade ionic liquid choline hydrogen sulphate [Ch][HSO_4] and enzyme. Sensitivity analyses were conducted to highlight the performance-limiting factors to inform the process design and optimisation.

2. Methodology

2.1. Process Synthesis

2.1.1. Process Design

A hypothetical lignocellulosic SCP biorefinery was modelled in Aspen Plus V9 for 40,000t/a production of SCP paste, where IL pretreatment, enzymatic hydrolysis and fermentation processes were simulated based on our experimental results and publicly available information. Table 1 defines the process areas and their design basis/targets.

2.1.2. Modelling framework for performance evaluation

A framework was developed to integrate Aspen Plus with MATLAB for economic performance evaluation and sensitivity analysis (Figure 1). MATLAB was used to initialise the simulation, equipment sizing and costing and subsequent economic analysis.

Table 1. The overall goals and design basis of each process hierarchy

Area	Goal	Basis
Feed Handling	Fresh ionic liquid (IL) is mixed with recycled IL and water to specified composition. Biomass feed processed through solid handling infrastructure.	(Humbird et al., 2011)
Pretreatment	Biomass delignification, pulp washing and recovery, lignin precipitation.	(Brandt-Talbot et al., 2017), experiments
Enzymatic Hydrolysis	Saccharification of pulp to recover glucose-rich hydrolysate stream.	(Humbird et al., 2011), experiments
Fermentation	SCP fermentation, RNA reduction and centrifugation to achieve SCP paste product.	(Wiebe, 2002)
Separation	Flashing of volatiles and water from IL mixture to recover IL. Separation and recovery of furfural.	(Brandt-Talbot et al., 2017) + >98.5% furfural purity
Combustor	Combustion of recovered lignin, and other 'waste' streams for energy recovery in boiler.	(Humbird et al., 2011)
WWT	Wastewater treatment producing purified water.	(Humbird et al., 2011)
Utilities	Tracks utility demands around the plant: process water, cooling water, chilled water and electricity.	

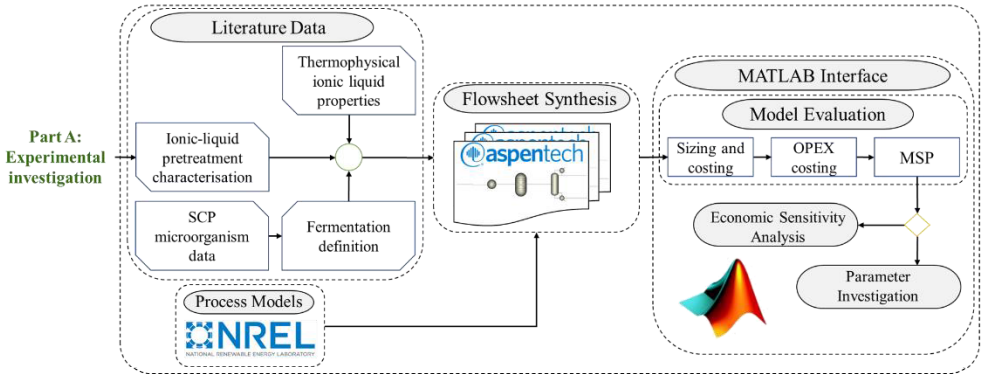

Figure 1. Modelling methodology highlighting the integration of MATLAB with the process simulator Aspen Plus.

2.1.3. Process Costing

The equipment sizing and costing were performed using two methods. For original design, factorial-based costing equations defined in Seider et al. (2017) were used. For the process design based on NREL hierarchy models (Combustor, WWT, (partial) Feed Handling), the cost was scaled based on a scaling variable as shown in Eq. (1).

$$Cost_2 = Cost_1\left(\frac{Capacity_2}{Capacity_1}\right)^{0.6} \quad (1)$$

Utility costs were estimated via the procedure defined by Ulrich and Vasudevan (2006) in which a two-factor cost equation accounts for both inflation and energy costs.

2.2. Economic Evaluation

A Minimum Selling Price (MSP) was used for economic comparison, which is defined as the selling price of the SCP paste for which the Net Present Value is 0.

2.3. Scenario Evaluation

Experimental data was fed into the model for the evaluation of four different scenarios. The input parameters and scenarios are given in Table 2 and Table 3 respectively.

Table 2. Universal model input parameters across the scenarios based upon experimental work

Parameter	Value	Composition	%	Reactant	Cost ($/kg)
Temperature (K)	423	Cellulose	40.07	Rice straw	0.049
Biomass/IL (%)	10	Xylan	18.21	IL	1.24
Water loading of IL (%)	20	Lignin	23.37	Cellulase	6.27
Cellulase/cellulose (mg/g)	20	Mannan	0.68	Ammonia	0.61
Glucan recovery (%)	100	Arabinan	4.04	Nutrient	0.74
		Galactan	1.92		
		Acetate	1.7		
		Ash	10.00		

* IL = Ionic liquid; Composition = dry biomass feedstock composition, 20% moisture added

Table 3. Comparison between 4 experimental scenarios summarising the main differences for model input.

Scenario	1	2	3	4
Ionic Liquid	[Ch][HSO_4]	[Ch][HSO_4]	[TEA][HSO_4]	[TEA][HSO_4]
Novozymes® Enzyme	Food grade	CTEC 2	Food grade	CTEC 2
Pulp Yield (%)	70.9	70.9	50.8	50.8
Saccharification Yield (%)	45.2	59.1	93.0	97.0

3. Results

3.1. Food-grade Scenario

Evaluation of the process area investment costs as a share of the Fixed Capital Investment (FCI), reactant and utility costs, water demand and heat duty for scenario 1 are presented in Figure 2. Fermentation dominates over half of total FCI. Second and third main contributors are wastewater treatment (WWT) and combustion. Figure 2.b shows the weighting of reagent and utility costs. The nutrient, electricity, cellulase and feedstock are the most significant cost contributors. Process water contribution is marginal (0.03% of manufacturing costs). Heat duty demands are dominated by heating of the pretreatment feed and IL recovery (Figure 2.d), due to the large quantity of water in the system. Implementation of a multi-effect evaporation system for recovering the IL reduced the

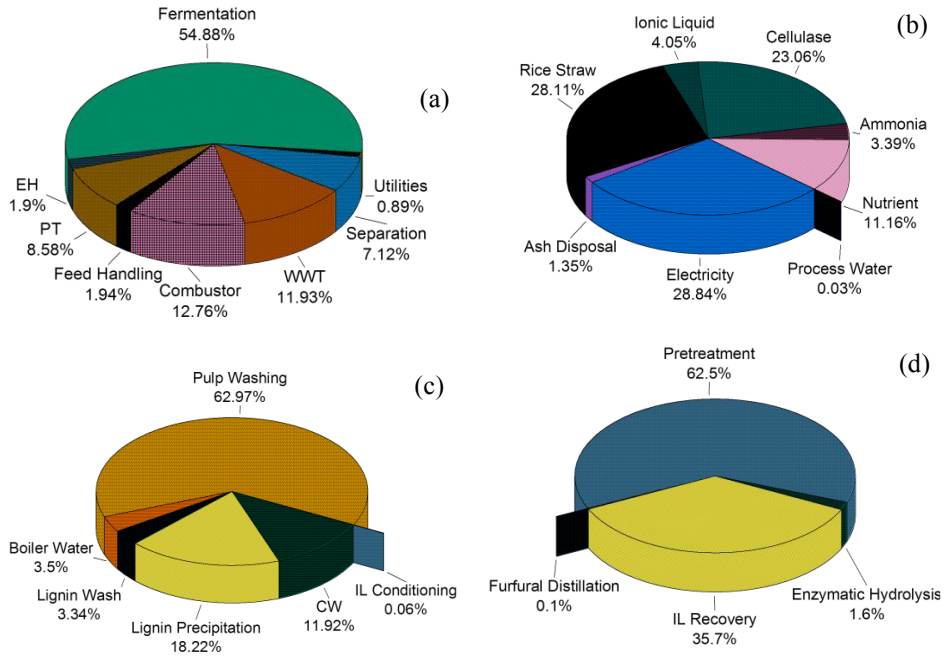

Figure 2. Scenario assessment showing (a) the proportion of fixed capital investment of process areas; (b) reagent and utility costs as a percentage of overall operating expenses; (c) water consumption in certain process tasks and (d) hot utility demand percentage between process tasks. EH = Enzymatic hydrolysis; PT = Pretreatment; CW = Cooling water

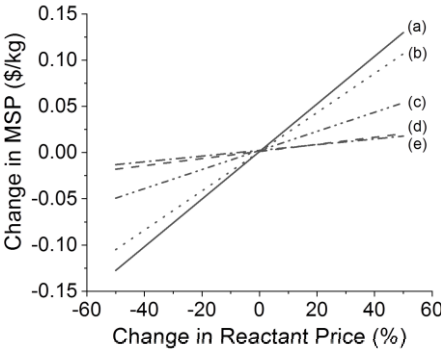

Figure 3. The % change in Net Present Value (NPV) as the % price of reactants changes. (a) rice straw; (b) cellulase; (c) nutrient; (d) [Ch][HSO_4]; (e) ammonia

heat burden significantly. Focus should be placed on reducing water usage throughout the process, through increasing biomass loading (biomass/IL) and reduction of water used in lignin precipitation.

Sensitivity analysis of the NPV to reactant prices is given in Figure 3. Feedstock costs are the most sensitive factor, followed by cellulase and nutrient. This highlights the improvement space in nutrient formulation and the importance to screen resilient feedstock, whose yield and price are less sensitive to environmental variation. Another sensitive factor is cellulase. Typical cellulase dosages range from 10-50+ mg cellulase/g cellulose, with higher rates achieving greater saccharification, therefore, scope for improvement exists through dosage optimisation. Interestingly, for a reasonable [Ch][HSO_4] price ($1.24/kg), IL price has a low impact on overall economics. Often, in stand-alone pretreatment processes, IL costs have a significant impact on economic performance, in this integrated biorefinery process, their significance is reduced. Production capacity also impacts MSP, as significant reductions in the MSP can be achieved for larger production volumes (Figure 4). The current Quorn production capacity is greater than 40,000 t/a.

3.2. Scenario Comparison

The evaluation of the MSP of the four scenarios is summarised in Table 4. The MSP is significantly reduced for scenarios 3 and 4 in which triethylamine hydrogen sulphate ([TEA][HSO_4]) was used. This is due to the higher saccharification yield which increased SCP production for similar production costs. Our experimental results suggest cellulase activity affects saccharification yield, where Cellic® CTEC 2 performed better for both ILs than food-grade enzyme, however, the most significant factor was IL performance. A lower pulp yield was obtained for [TEA][HSO_4] pretreatment, indicating greater delignification and hemicellulose removal, increasing cellulose accessibility to enzymes during saccharification.

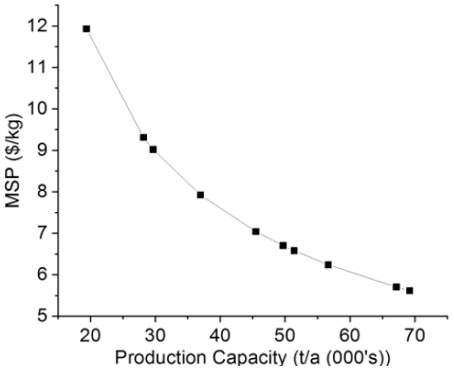

Figure 4. Minimum Selling Price (MSP) of SCP as a function of annual capacity production capacity for scenario 1.

3.3. Can we meet the meat-free protein supply with agro-residues?

The MSP was used as an indicator to compare to other protein sources, and Quorn™ mince based on retail market price. Table 5. Shows the price per kg of

Table 4. Minimum Selling Price (MSP) of the four scenarios at 40,000 t/a production capacity

Scenario	1	2	3	4
MSP $/kg	7.47	7.01	6.30	6.25

Table 5. Cost of products per kg of protein adjusted through Net Protein Utilisation ($/kgP)

Product	Egg	Beef [a]	Tofu	Chicken	Quorn™, [b]	SCP [c]
Cost ($/kgP)	15.37	39.06	109.14	41.67	55.71	54.35

[a] Beef mince 10-15% fat; [b] Quorn mince; [c] Mycoprotein paste (wet-basis) MSP of $6.25/kg

protein (adjusted through Net Protein Utilisation, NPU) which shows that, for a current supermarket selling price of Quorn™ mince ($6.5/kg), protein costs are comparable with beef and chicken. It must be noted that the Mycoprotein (SCP) paste represents the crude protein product that is expected to undergo further texturisation. However, it is positive that the protein cost of the paste is comparable to other protein sources. Scenario 1 yields an SCP protein cost of $64.96/kgP and is the only one which uses both food-certified IL and cellulase, therefore, the adoption of this process technology may depend on food-certification of the reagents. However, this suggests a promising outlook on the economics of lignocellulosic mycoprotein.

4. Conclusions

Overall this study highlights the significant factors in lignocellulosic mycoprotein production. Fermentation dominates capital costs (over 50%). Feedstock, cellulase, and nutrient contribute significantly to operating costs, but ILs show low impact on overall economics. Large heating duties for the pretreatment reactor and IL recovery place a burden on economics through large steam demands, but process optimisation offers scope for improvement. Scenarios 2, 3 and 4 gave an MSP less than scenario 1, in which both food-certified cellulase and IL were used, but would require food-certification of the IL and/or cellulase for technology adoption. All MSPs were comparable to meat protein sources and scenarios 3 and 4 produce a mycoprotein paste for less than the supermarket price for select Quorn™ products, leaving room for further processing to the final consumer product. Our results demonstrate the economic feasibility of lignocellulosic mycoprotein and highlight the performance-limiting steps for future research efforts.

References

Baral, N.R., Shah, A. (2016) Techno-economic analysis of cellulose dissolving ionic liquid pretreatment of lignocellulosic biomass for fermentable sugars production. Biofuels, Bioproducts and Biorefining 10, 70-88.

Brandt-Talbot, A., Gschwend, F.J.V., Fennell, P.S., Lammens, T.M., Tan, B., Weale, J., Hallett, J.P. (2017) An economically viable ionic liquid for the fractionation of lignocellulosic biomass. Green Chemistry 19, 3078-3102.

FAO, IFAD, UNICEF, WFP, WHO, (2019) The State of Food Security and Nutrition in the World 2019, Safeguarding against economic slowdowns and downturns. FAO, Rome.

Humbird, D., Davis, R., Tao, L., Kinchin, C., Hsu, D., Aden, A., Schoen, P., Lukas, J., Olthof, B., Worley, M., Sexton, D., Dudgeon, D., (2011) Process Design and Economics for Biochemical Conversion of Lignocellulosic Biomass to Ethanol: Dilute-Acid Pretreatment and Enzymatic Hydrolysis of Corn Stover. National Renewable Energy Laboratory

IRRI, (2019) Our Work. International Rice Research Institute.

Molitor, B., Mishra, A., Angenent, L.T. (2019) Power-to-protein: converting renewable electric power and carbon dioxide into single cell protein with a two-stage bioprocess. Energy & Environmental Science.

Quorn, (2018) Quorn Foods sees 16% Global Growth in 2017.

Seider, W.D., Lewin, D.R., Seader, J.D., Widagdo, S., Gani, R., Ng, K.M. (2017) Product and process design principles : synthesis, analysis, and evaluation.

Strong, P.J., Kalyuzhnaya, M., Silverman, J., Clarke, W.P. (2016) A methanotroph-based biorefinery: Potential scenarios for generating multiple products from a single fermentation. Bioresour Technol 215, 314-323.

Ulrich, G., Vasudevan, P. (2006) How to estimate utility costs. Chem. Eng. 113, 66-69.

Vermeulen, S.J., Campbell, B.M., Ingram, J.S.I. (2012) Climate Change and Food Systems. Annual Review of Environment and Resources 37, 195-222.

Wiebe, M.G. (2002) Myco-protein from Fusarium venenatum: a well-established product for human consumption. Appl Microbiol Biotechnol 58, 421-427.

Sauro Pierucci, Flavio Manenti, Giulia Bozzano, Davide Manca (Eds.)
Proceedings of the 30th European Symposium on Computer Aided Process Engineering (ESCAPE30), May 24-27, 2020, Milano, Italy.
http://dx.doi.org/10.1016/B978-0-12-823377-1.50166-X

Energy Efficient Distillation by Combination of Thermal Coupling and Heat Integration

Mirko Skiborowski

TU Dortmund University, Department of Biochemical and Chemical Engineering, Laboratory of Fluid Separations, Emil-Figge-Strasse 70, 44227 Dortmund, Germany

mirko.skiborowski@tu-dortmund.de

Abstract

Conventional heat-integration between adjacent columns, as well as thermal coupling and the equipment-integrated implementation in a dividing wall column are successful concepts for the improvement of the energy efficiency of distillation processes. While especially dividing wall columns have made a considerable impact in industrial application, further heat integration is prevented by the bidirectional transfer of liquid and vapor streams that impede a necessary pressure variation for modification of the boiling temperatures. This limitation can however be overcome by the modification of thermal couplings to one-directed liquid only transfer. While this concept has been proposed almost 20 years ago, it has received limited attention so far. In order to evaluate the prospect of this combination, the current article exploits a combination of a shortcut-based screening and a rigorous economic optimization, in order to evaluate a heat-integrated side-rectifier with liquid only transfer modification in comparison with a range of alternative options. The application to an exemplary case study highlights the huge potential of this combination, showcasing the possibility to save half of the energy required for a non-integrated configuration and even more than 30% compared to fully thermally coupled configurations, depending on the feed composition.

Keywords: distillation, thermal coupling, heat integration, rectification body method

1. Introduction

Despite serious concerns about the low thermodynamic efficiency, distillation processes remain the working horse for fluid separations, especially in case of large scale continuous production processes. Besides the exploitation of hybrid separation processes, combining distillation with other technologies such as extraction and membrane separations, a number of options for improving the energy efficiency in distillation processes have been established. These include e.g. direct heat integration and multi effect distillation, thermal coupling and the equipment integrated dividing wall columns (DWC), mechanical vapor recompression (MVR) and internally heat integrated columns, so called HiDiC (Kiss et al., 2012). The individual concepts allow for energy savings of up to 50% compared to the non-integrated distillation processes. Yet, choosing the right option requires a case specific evaluation of the different process concepts, which can be performed by means of shortcut methods (Skiborowski, 2018), as well as rigorous economic optimization of MESH based superstructure models (Waltermann and Skiborowski, 2019).

While some combinations of these concepts have recently been considered in case-specific evaluations, such as the combination of MVR and DWC (Jana, 2019; Patraşcu et al., 2018) or the extension of a HIDiC with further MVR through intermediate heat

exchangers (Kiran and Jana, 2016), such evaluations are still scarce. An interesting combination of thermal coupling and heat integration has been proposed by Agrawal (2000a) almost two decades ago. However, despite the indicated prospect of these so-called double-effect thermally coupled configurations, which were evaluated based on very approximate calculation for theoretical mixtures with constant relative volatility, the concept has received little attention so far. While thermal coupling itself and DWC in specific are considered as one of the most prominent examples of process intensification in fluid separations, with more than 130 industrial-scale DWC implementations (Staak et al., 2014), a direct extension of these configurations to the aforementioned combination is infeasible, due the standard bidirectional transfer of liquid and vapor streams between thermally coupled column sections that impedes the necessary pressure variation. This variation only becomes feasible in case of a transformation of the thermal coupling to a one-directed liquid only transfer (LOT), as introduced by Agrawal (2000b) and more recently considered in a systematic generation of DWC configurations with LOT modifications that allow for an independent control of the vapor flow rate in each partitioned zone of the DWC (Madenoor Ramapriya et al., 2014). Apart from the improved operability, Jiang and Agrawal (2019) conclude that the possibility to combine heat-integration with thermal couplings is another major opportunity offered by the LOT modification, since even double-effect systems for basic configurations can oftentimes outperform the best DWC configurations.

In order to evaluate this potential, the current study performs an optimization-based evaluation of a heat-integrated side-rectifier with LOT modification with various competing process concepts. The evaluation is based on a combination of pinch-based shortcut models, as well as rigorous equilibrium-stage models for an economic process optimization. The results obtained for a representative case study on the separation of a benzene, toluene, ethylbenzene mixture illustrates the significant potential for process intensification by showcasing energy savings of more than 30% in comparison to the fully thermally coupled DWC and the superiority for a wide range of feed compositions.

2. Improved side-rectifier configuration with heat integration

Following the initial idea of (Agrawal, 2000a, 2000b) an improved side-rectifier configuration with heat integration is derived in a sequence of steps, starting from the direct split configuration, as illustrated in Figure 1.

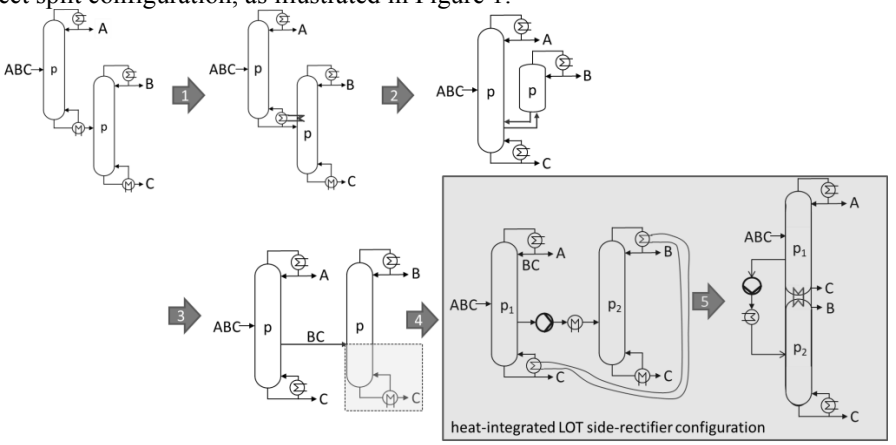

Figure 1: Transformation from direct split sequence over the thermally-coupled side rectifier to a heat-integrated LOT side-rectifier (HI-LOT-SR) configuration.

First, the direct split is converted to a thermally coupled side-rectifier, by an initial heat transfer of the reboiler of the first column (step 1) and a consecutive replacement of the reboiler by means of the bidirectional transfer of liquid and vapor (step 2). Subsequently the side-rectifier is modified to a LOT configuration, by exchanging the bidirectional transfer with a one-sided liquid transfer from the first to the second column, while extending the second column with an additional stripping section (step 3). Finally, a pump and heat exchanger are introduced into the liquid side stream in order to modify the operating pressure (p_2) of the second column (step 4). Pressure p_2 is determined such that the boiling temperature of the intermediate boiling product B is raised sufficiently above the boiling temperature of the heavy boiling product C at the operating pressure of the first column (p_1), enabling direct heat integration between both columns. According to Agrawal (2000a), this heat-integrated LOT side-rectifier (HI-LOT-SR) configuration could also be implemented in a consecutive column shell, when locating the second column on top of the first one (step 5).

3. Shortcut-based screening of alternative process configurations

In order to evaluate the potential benefits of the introduced HI-LOT-SR configuration, its performance has to be compared with alternative process configurations. For this purpose a shortcut-based screening method, developed in previous work (Skiborowski, 2018), is applied and extended, in order to include the HI-LOT-SR configuration. The initially developed algorithmic framework enables the evaluation of the minimum energy requirement (MED) of the simple column configurations (direct, indirect and intermediate split), six thermally coupled versions of these simple configurations, a heat integrated alternative for each of the simple configurations, as well as six configurations that consider MVR for either one or both columns in the direct and indirect split. Together with the LOT-SR and HI-LOT-SR a total number of 20 process configurations are evaluated by means of the Rectification Body Method (Bausa et al., 1998), while additional flash calculations and parametric optimizations are performed to evaluate the optimal distribution of the medium boiling product in the prefractionator, the distribution of heat loads in the LOT design, as well as the pressure levels in the heat-integrated and MVR designs (Skiborowski, 2018).

4. Economical optimization through MESH-based superstructure models

In order to evaluate the economic performance a MESH-based superstructure model is implemented and solved in GAMS, based on the previously developed superstructure models for simple and energy-integrated distillation processes (Waltermann and Skiborowski, 2019). The resulting mixed-integer nonlinear programming problem is solved in terms of a polylithic solution approach by means of a series of continuously relaxed nonlinear programming problems with the aid of additional nonlinear complementary constraints. The superstructure model for the HI-LOT-SR is a direct extension of the heat-integrated direct split configuration presented by (Waltermann and Skiborowski, 2019), for which an additional side stream is introduced for the first column, which is further connected to the second column, passing through the intermediate pump and heat exchanger, instead of the bottoms product. The latter is supposed to provide the heavy boiling product with the required purity specifications, as illustrated in Figure 1. The respective equation-oriented model for the superstructure and the economic model are described in further detail by (Waltermann et al., 2019; Waltermann and Skiborowski, 2019).

5. Case study

In the scope of the current study the separation of a zeotropic mixture of benzene, toluene and ethylbenzene is investigated. The thermodynamic properties are determined based on the Wilson model, the extended Antoine equation, as well as DIPPR correlations for the specific heat capacities and heat of vaporization. While the separation of this mixture, with a feed composition of 70 mol% benzene, 20 mol%, toluene and 10 mol% ethylbenzene was considered in the previous development of the shortcut screening approach (Skiborowski, 2018), the extended algorithmic framework is now used to evaluate potential feed compositions, for which the HI-LOT-SR provides potential MED savings in respect to all considered process configurations. Furthermore, an economic evaluation of the HI-LOT-SR is performed for the feed composition for which the largest MED savings are determined.

5.1. Shortcut-based screening

The MED of the 20 considered process configurations is evaluated for 171 feed compositions, resulting from an equidistant scattering of the composition space with variations in single component compositions of 5 mol%. Despite an energy conversion factor of 2 and isentropic and mechanical efficiencies of 80% and 90%, the MVR configurations provides generally the lowest MED. However, when considering the depreciation of the necessary compressor in the calculation of an estimate of the annual operating costs (AOC), MVR configurations are not the favorable choice for any of the feed compositions. Therefore, the following evaluation of the MED is first limited to the 14 configurations, excluding the MVR configurations. The results of this evaluation are illustrated in Figure 2, which indicates by means of different symbols, which process configuration provides the lowest MED for a specific feed composition.

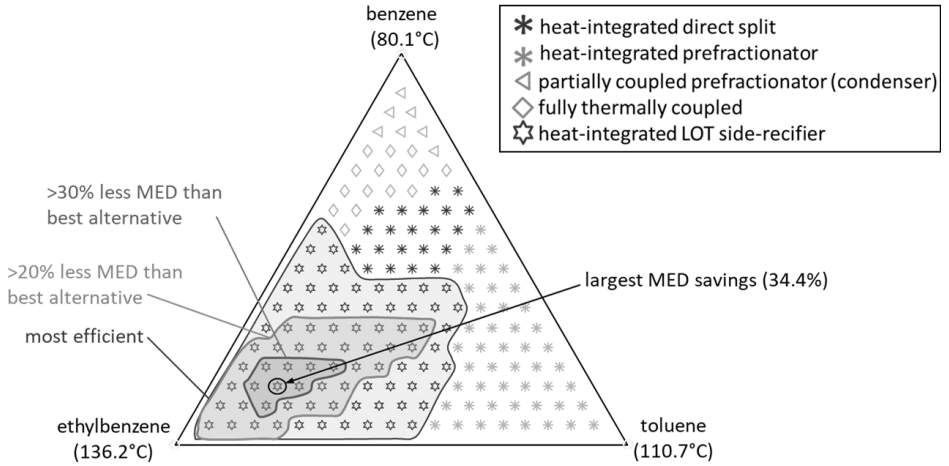

Figure 2: Illustration of favorable process configurations in terms of MED for different feed compositions (symbols indicate favorable process configuration at the specific feed composition).

While partially and fully thermally coupled configurations are preferred for high concentrations of benzene and low concentrations of toluene, heat-integrated direct split and prefractionator configurations are preferred for medium to high concentrations of toluene and low concentrations of ethylbenzene. The HI-LOT-SR provides the lowest MED for all feed compositions with medium to high concentrations of ethylbenzene. It has the lowest MED for 47% of the evaluated feed compositions, allowing for a

reduction of more than 20%(30%) in respect to the best alternative configuration for 38(8) of the considered feed composition, with 34.4% saving potential for a feed composition of 15 mol% benzene, 15 mol%, toluene and 70 mol% ethylbenzene.
For the separation of a feed stream of 10 mol/sec and this feed composition, the required MED and the according AOC estimates of all 20 considered process configurations are illustrated in Figure 3. As highlighted, the fully thermally coupled DWC is the next best configuration in terms of MED, apart from the MVR configurations. Yet, it requires 52% more energy, which translates into similar savings in AOC, assuming that both processes are heated with the same high pressure steam.

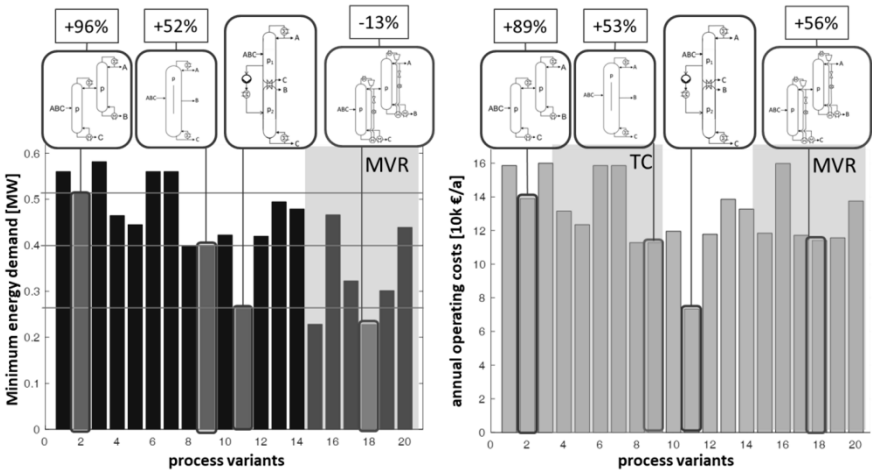

Figure 3: Illustration of single process performance for the selected feed composition in terms of MED (left) and estimated AOC (right)

5.2. Economic optimization

For further comparison the HI-LOT-SR configuration and the fully thermally coupled DWC are evaluated on the basis of an economically optimized design, making use of the aforementioned superstructure optimization approach (Waltermann and Skiborowski, 2019, 2017). The results are illustrated in Figure 4, considering a depreciation period of 5 years, an interest rate of 6% and an annual operating time of 8000h.

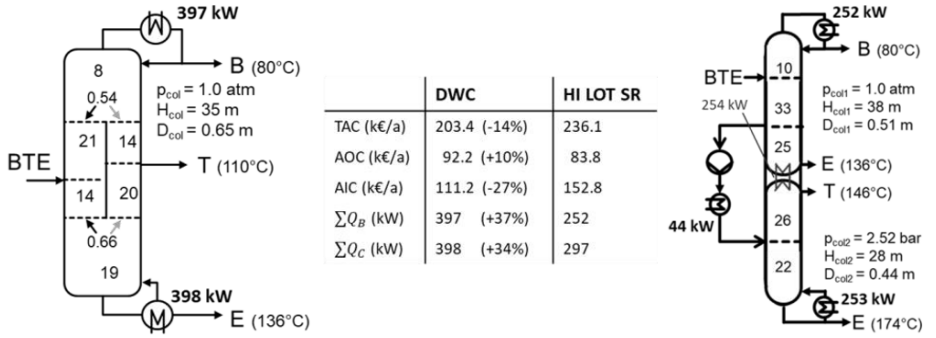

	DWC	HI LOT SR
TAC (k€/a)	203.4 (-14%)	236.1
AOC (k€/a)	92.2 (+10%)	83.8
AIC (k€/a)	111.2 (-27%)	152.8
$\sum Q_B$ (kW)	397 (+37%)	252
$\sum Q_C$ (kW)	398 (+34%)	297

Figure 4: Illustration of the results of the economic process optimization.

All products are required to be of 99.9 mol% purity. Given these assumptions, the DWC is still the most economic process, with a significantly lower investment. Yet, the rigorous design optimization confirms the potential energy savings determined by means of the shortcut screening, which however do not directly translate to AOC savings, since 20 bar steam is required for the reboiler of the second column in the HI-LOT-SR configuration, while 10 bar steam suffices for the DWC. Although the DWC is deemed economically superior under the current assumptions, the HI-LOT-SR configuration becomes more attractive in case of higher depreciation and utility costs.

6. Conclusions

The combination of thermal coupling and heat integration, enabled by the LOT modification, provides a promising option for further improvement of the energy efficiency of distillation processes. The comparative evaluation of multiple energy integrated process configurations highlights the significant improvement potential offered by the considered HI-LOT-SR configuration. The outlined combination of a shortcut-based screening and a subsequent economic optimization enables a time-efficient and case-specific evaluation of possible applications as well as a detailed economic comparison of the most promising options. As illustrated in the current case study such evaluation is of significant importance in order to determine the most effective process configuration for a specific application and economic scenario.

References

R. Agrawal, R., 2000a. Multieffect distillation for thermally coupled configurations. AIChE J 46 (11), 2211–2224.

R. Agrawal, 2000b. Thermally coupled distillation with reduced number of intercolumn vapor transfers. AIChE J 46 (11), 2198–2210.

J. Bausa, R.V. Watzdorf, W. Marquardt, 1998. Shortcut methods for nonideal multicomponent distillation: 1. Simple columns. AIChE Journal 44 (10), 2181–2198.

A.K. Jana, 2019. Performance analysis of a heat integrated column with heat pumping. Separation and Purification Technology 209, 18–25.

B. Kiran, A.K. Jana, 2016. Thermal integration of vapor recompression in a heat-integrated distillation: Impact of multiple intermediate reboilers. Chem. Eng. Res. Des. 114, 171–179.

A.A. Kiss, S.J. Flores Landaeta, C.A. Infante Ferreira, 2012. Towards energy efficient distillation technologies – Making the right choice. Energy 47 (1), 531–542.

G. Madenoor Ramapriya, M. Tawarmalani, R. Agrawal, 2014. Thermal coupling links to liquid-only transfer streams: A path for new dividing wall columns. AIChE J 60 (8), 2949–2961.

I. Patraşcu, C.S. Bîldea, A.A. Kiss, 2018. Heat pump assisted azeotropic DWC for enhanced biobutanol separation, in: Friedl, A., Klemeš, J.J., Radl, S., Varbanov, P.S., Wallek, T. (Eds.), 28th European Symposium on Computer Aided Process Engineering, vol. 43. Elsevier, Amsterdam, pp. 791–796.

M. Skiborowski, 2018. Fast screening of energy and cost efficient intensified distillation processes. Chemical Engineering Transactions 69, 199–204.

D. Staak, T. Grützner, B. Schwegler, D. Roederer, 2014. Dividing wall column for industrial multi purpose use. Chemical Engineering and Processing: Process Intensification 75, 48–57.

T. Waltermann, S. Sibbing, M. Skiborowski, 2019. Optimization-based design of dividing wall columns with extended and multiple dividing walls for three- and four-product separations. Chem. Eng. Process. 146, 107688.

T. Waltermann, M. Skiborowski, 2017. Conceptual Design of Highly Integrated Processes - Optimization of Dividing Wall Columns. Chemie Ingenieur Technik 89 (5), 562–581.

T. Waltermann, M. Skiborowski, 2019. Efficient optimization-based design of energy-integrated distillation processes. Comp. Chem. Eng. 129, 106520.

Sauro Pierucci, Flavio Manenti, Giulia Bozzano, Davide Manca (Eds.)
Proceedings of the 30th European Symposium on Computer Aided Process Engineering
(ESCAPE30), May 24-27, 2020, Milano, Italy.
http://dx.doi.org/10.1016/B978-0-12-823377-1.50167-1

Optimization-Based Design of Rotating Packed Beds with Zickzack Packings

Kai Fabian Kruber, Hina Qammar, Mirko Skiborowski*

TU Dortmund University, Department of Biochemical and Chemical Engineering, Laboratory of Fluid Separations, Emil-Figge-Straße 70, 44227 Dortmund, Germany
mirko.skiborowski@tu-dortmund.de

Abstract

Due to the fast development of the market in the chemical industry, more flexible and efficient equipment is obligatory. High-gravity contactors in form of Rotating Packed Beds (RPBs) have the potential to meet these needs since they offer an enhanced mixing by imposing centrifugal forces resulting in an intensified mass and energy transport. With the rotational speed as an additional degree of freedom, RPBs offer faster start-up times and an enlarged operating window. Despite the increasing scientific work in the areas of experimental investigations and modeling, industrial applications are still limited due to a lack of reliable methods for scale-up and design. In respect to the latter, this work presents a nested superstructure approach for the optimization-based design of RPBs with zickzack packings that is further demonstrated for the dehydration of methanol.

Keywords: optimization, process intensification, rotating packed bed, zickzack packing

1. Introduction

During the last decades, the chemical industry started to face a transition to more flexible production plants motivated by a constant change in feedstock towards sustainable resources, as well as a more fluctuating market caused by globalization and steady cultural development. In the same period, high-gravity contactors, like Rotating Packed Beds (RPBs), have gained increasing attention to meet these challenges via process intensification (Neumann et al., 2018). RPBs enable intense mixing, as well as heat and mass transfer intensification between the contacted phases through the application of centrifugal forces, several times larger than earth's gravity. Besides shorter residence time and reduced equipment size, RPBs have considerably shorter start-up times compared to gravity-based static contactors. The rotational speed in an RPB offers an additional degree of freedom that enlarges the operating window and aids flexibility during operation.

While substantial research on RPBs is conducted with particular emphasis on feasibility studies, general process development and operation in absorption, stripping, and distillation, with a steadily increasing number of publications, most studies focus on experimental evaluation (Cortes Garcia et al., 2017) Only a few articles address general design guidelines (Agarwal et al., 2010; Sudhoff et al., 2015), while so far, only a single optimization-based design approach for RPBs was introduced by Qian et al. (2017). The presented method focused on the design of a single-stage rotor equipped with a wire-mesh packing for H_2S-removal by absorption. However, especially for complex separation problems, the necessary rotor sizes may result in impractical designs and high uncertainty related to the varying loadings along the radial distance in the annular-shaped packing.

Especially for distillation, an alternative rotor design termed Rotating Zigzag Bed (RZB) has been promoted by Wang et al. (2008), which contrary to the single block packing, implements a tray-like structure of alternating baffles mounted on a rotating and a stationary disc. For the RZB, several hundred industrial applications for distillation have been reported primarily in Asia (Xu et al., 2012). The possibility of adjusting the distance between the baffles as well as the baffle size allows for the establishment of more uniform hydrodynamic conditions. However, the alternation of static and rotating baffles results in an increased pressure drop and power consumption. To overcome the latter limitations, Qammar et al. (2019) have recently introduced a single block Zickzack (ZZ) packing, which employs the same tray-like structure as in an RZB but can be implemented in a single-block RPB (see Figure 1), allowing for a reduced pressure drop and approximately constant F-Factors along the radial length. It was shown that the pressure drop for a 3D-printed ZZ packing was reduced by ten times compared to the equivalent RZB setup, also resulting in a considerable decrease in the electrical power consumption.

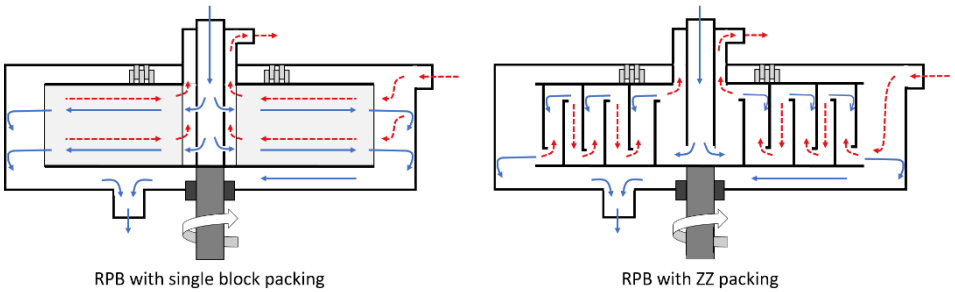

Figure 1: Schematic depiction of an RPB with a single block packing and an RPB with a ZZ packing including vapor (dashed lines) and liquid (solid lines) flows

Unlike the superstructure model of Qian et al. (2017), which evaluates the performance of a single stage RPB based on an HTU-NTU approach without further discretization along the radial length, the current work introduces an optimization-based approach for the conceptual design of a multi-stage RPB with ZZ packing, building on an efficiency-based equilibrium stage approach to represent the tray-like contacting in the ZZ packing. Therefore, a nested superstructure is developed, which enables the sizing of an RPB with a variable number of rotors and a variable diameter of each rotor, based on a rigorous equilibrium-tray model in combination with classical Murphree efficiencies. Additionally, the model is further complemented by general sizing constraints (Agarwal et al., 2010; Sudhoff et al., 2015) as well as an economic model, which allows for the minimization of the total annualized costs (TAC). The developed approach is further demonstrated for the dehydration of methanol.

2. Methodology

The optimization-based design approach for the RPB with ZZ packing builds on four elementary parts. First, a superstructure needs to be defined, which allows for a flexible sizing of the RPB in terms of the number and size of rotors, while the number of iterating baffles in the ZZ packing has to be matched to the number of equilibrium stages via an efficiency model and the specific hydrodynamic. Furthermore, a cost model and a strategy for initialization and optimization need to be specified.

2.1. Superstructure Model

The ZZ structure of the considered packing allows for a modeling approach based on equilibrium trays where two baffles are termed as a baffle pair represented by one equilibrium tray with a certain efficiency. Figure 2 illustrates the respective nested superstructure, showing only a radial intersection through the axisymmetrical RPB. While vapor streams are indicated by dotted lines, liquid streams are depicted by solid lines. There is an outer superstructure representing the number of rotors and an inner superstructure accounting for the number of baffle pairs in each rotor. This leads to the possibility of bypassing single stages in a rotor and bypassing of complete rotors resulting in different rotor diameters and different overall rotor setups, respectively. Analogously to the superstructure of a conventional column (CC) (see e.g. Kraemer et al., 2009), the reflux and the reboil stream can enter each rotor in the rectifying and stripping section, respectively, which is modeled by additional binary decision variables. The size of each rotor is determined by a decision variable for the location of the vapor stream coming from the rotor below. Since the rotor diameter can vary significantly, the current design assumes that the rectifying and stripping sections are implemented in separate housings, which however requires additional motor and shaft work. For the RPB design, the feed is always introduced at the eye of the rotor since the rotor is in constant rotational movement, while in an RZB, the upper plate is stationary, such that an intermediate feed position would be feasible.

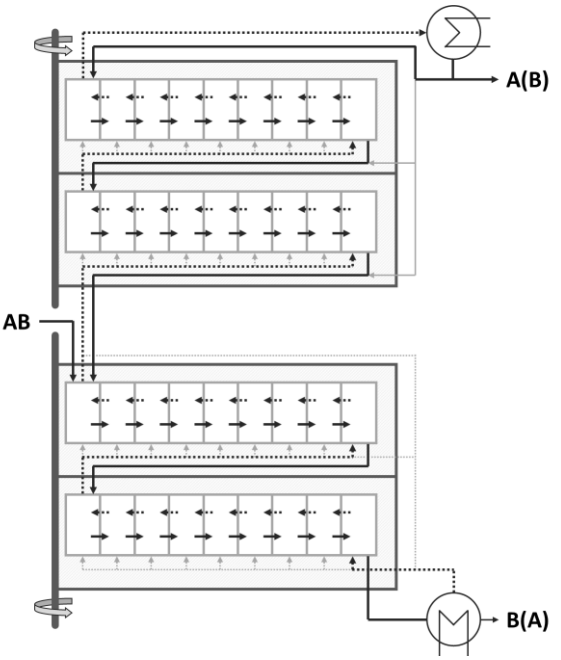

Figure 2: Superstructure representation of a Rotating Packed Bed (RPB) with Zickzack (ZZ) packings

2.2. Murphree Efficiency

Referring to Qammar et al. (2019), the efficiency of a baffle pair in a ZZ packing with 25 baffles is assumed to be about 15% - 30%. Therefore, the concept of Murphree stage efficiencies (ME) is utilized (Murphree, 1925), in order to account for the respective mass transfer limitation by a departure of the vapor composition from the equilibrium composition for each baffle pair. As a result, the vapor composition y leaving a baffle pair is determined from the equilibrium composition y^* and the ME η, cf. Equation (1).

$$y_{n,i} = y_{n+1,i} + \eta\left(y^*_{n,i} - y_{n+1,i}\right) \tag{1}$$

The ME is specific for the considered equipment and the investigated mixture, but also the considered rotational speed. For the explicit packing design, investigated system and specified hydrodynamics it is assumed to be constant. Aside from the mass transfer inside

the packing, each existing rotor provides additional mass transfer in the casing, for which a ME of 90% is assumed, based on the experimental results by Qammar et al. (2019).

2.3. Sizing and costing

In order to appropriately design the multi-stage RPB, different aspects of the equipment have to be considered apart from the external heat exchangers and heat duties, which are common to the design of a distillation column, i.e., the rotors and casing, as well as the motor and the respective electrical power consumption.

Initially, the rotor geometry is determined based on the inner diameter at the eye of the rotor as well as the desired F-Factor within the rotor, which are required as model inputs. Based on the F-Factor and approximated vapor flowrates, the spacing between the baffles and the height of the rotor are calculated. The outer radius of the rotor is determined by the sum of the baffle radii depending on the superstructure decision variables. A correlation between the rotor and casing heights and diameters links the two geometries. With these geometric constraints, the cost for the RPB body is calculated based on an adjusted form of the cost correlations for a pressure vessel according to Biegler et al. (1997). The rotor costs are currently based on lab-scale equipment due to a lack of reliable data for industrial-scale applications. The costs for the motor and the drive are calculated by correlations from Woods (2007), as suggested by Sudhoff (2015).

2.4. Optimization approach

The initialization and optimization of the superstructure model is conducted similarly to the design of distillation columns, according to the approach presented by Skiborowski et al. (2015). The model was implemented in the optimization software GAMS and solved as a sequence of successively relaxed nonlinear programming problems with additional nonlinear complementary constraints, in order to solve the mixed-integer nonlinear programming problem. The thermodynamic models, including flash and enthalpy computations, are integrated via the use of external functions, as described in Skiborowski et al. (2015).

3. Results

The proposed optimization-based design approach is used to investigate the well-known case study of methanol dehydration with an equimolar feed flow of about 6.7 $mol \cdot s^{-1}$ (600 $kg \cdot h^{-1}$) introduced as boiling liquid. A purity of 99 mol-% methanol for the distillate and 99 mol-% water for the bottom product are set as constraints. For the calculations, a depreciation time of five years with an interest rate of 6% is assumed. The necessary utilities are cooling water at 288 K (0.05 $€ \cdot t^{-1}$), 3 bar steam with a temperature of about 406 K (12 $€ \cdot t^{-1}$), and electricity (0.076 $€ \cdot (kWh)^{-1}$). For the RPB, a ME within the rotor of 30% is assumed, while the casing has an efficiency of 90%. As an initial setup for the RPB, four rotors for the rectifying section, two rotors for the stripping section, a maximum diameter of 1.2 m, and maximum F-factors within the rotors of up to 6 $Pa^{0.5}$ (Wang et al., 2019) are chosen, resulting in 15 baffle pairs per rotor based on approximated vapor flowrates. In contrast, the initial column setup consists of 30 trays per section and an ME of 70% per tray (Bausa and Steimel, 2018).

The optimization results for the RPB with ZZ packing are presented in Figure 3 with an additional comparison of the TAC of both RPB and CC. The structural depiction of the RPB indicates the bypassed regions (grey) and the used rotors and baffle pairs (white). For this case study, the rectifying section consists of three rotors with 15 baffle pairs each, and the stripping section comprises two rotors with 7 baffle pairs. Note that an additional constraint enforces equal sizes for the rotors in one section, in order to avoid empty casing volume. Besides the depicted structural decisions, the optimization also considers continuous operational degrees of freedom, i.e. the reboiler and the condenser duty. Based on the current cost correlations, the RPB is evaluated as the more expensive option in terms of operational and capital expenditures (CAPEX, OPEX). The increase in OPEX is about 8.9% compared to the CC related to the additional electricity input for the motor, while the necessary reboiler and condenser duties are comparable. The increase in CAPEX for the RPB compared to the CC is about 31.5% and almost entirely related to the rotors within the RPB. They account for an increase of 45.4% of the CAPEX, while the smaller casing saves about 18.6% of the costs. It should be noted that the cost increase for motor, drive and electricity is further enlarged by the consideration of two separate RPBs for rectifying and stripping section.

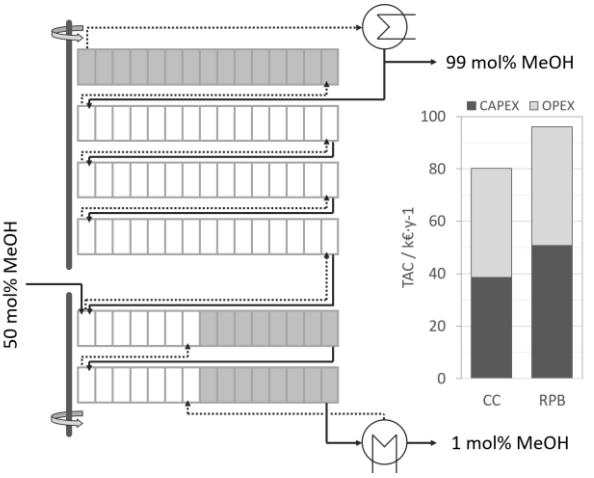

Figure 3: Optimized RPB structure and corresponding TAC compared to the CC

Despite the cost deficiency, a significant reduction in the apparatus height and volume can be achieved by the RPB. The height was reduced by approximately 91.6% considering a combined height for both RPBs (rectifying; stripping), while the overall equipment volume of the column shell is reduced by 13.4% through the RPBs.

4. Conclusion

The current work presents for the first time an equilibrium-stage based superstructure optimization approach for the design of RPBs with ZZ packings, which may also be used for the design of an RZB. The approach considers multiple rotors in individual RPBs for rectifying and stripping section. Furthermore, the model was extended by Murphree efficiencies in order to consider the characteristics of RPBs with ZZ packings. Applying a reliable polylithic modeling and solution approach similar to that of classical distillation columns, the approach effectively determines locally optimal solutions to an intricate multi-stage RPB design for the dehydration of methanol. The results indicate a potential for size reductions by means of the RPB, however, the applied cost model for the RPB needs further refinement since it is based on a currently available limited data set for sizing and costing of lab-scale equipment. Therefore, it is suggested that not too much emphasis is placed on the economic comparison. Besides the refinement of the cost model, additional pressure drop correlations, as well as an extended ME model should be

considered in future improvements of the model for deriving a more general and reliable model for RPB design. Apart from these modifications, the superstructure model already presents a suitable platform that can further be exploited in the development of RPB-based processes.

Acknowledgment

Dr.-Ing. Mirko Skiborowski gratefully acknowledges financial support from the Max-Buchner Research Foundation.

References

Agarwal, L., Pavani, V., Rao, D. P., Kaistha, N., 2010, Process Intensification in HiGee Absorption and Distillation: Design Procedure and Applications, Ind. Eng. Chem. Res., 49, 20, 10046-10058

Bausa, J., Steimel, J., 2018, Extending Murphree Tray Efficiency from Mass to Heat Transfer in Distillation, Chem. Eng. Trans., 69, 451-456

Biegler, L. T., Grossmann, I. E., Westerberg, A. W., 1997, Systematic methods for chemical process design, Prentice Hall, Old Tappan, New Jersey, United States

Cortes Garcia, G. E., van der Schaaf, J., Kiss., A. A., 2017, A review on process intensification in HiGee distillation, J. Chem. Technol. Biotechnol., 92, 6, 1136-1156

Mondal, A., Paramanik, A., Bhowal, A.,Datta, S., 2012, Distillation studies in rotating packed bed with split packing, Chem. Eng. Res. Des., 90, 4, 453-457

Murphree, E. V., 1925, Rectifying Column Calculations, J. Ind. Eng. Chem., 17, 7, 747-750

Neumann, K., Gładyszewski, K., Groß, K., Qammar, H., Wenzel, D., Górak, A., Skiborowski, M., 2018, A guide on the industrial application of rotating packed beds, Chem. Eng. Res. Des., 134, 443-462

Qammar, H., Gładyszewski, K., Górak, A., Skiborowski, M., 2019, Towards the Development of Advanced Packing Design for Distillation in Rotating Packed Beds, 91, 11, 1663-1673

Qian, Z., Chen, Q., Grossmann, I. E., 2017, Optimal synthesis of rotating packed bed reactor, Comput. Chem. Eng., 105, 152-160

Skiborowski, M., Harwardt, A., Marquardt, W., 2015, Efficient optimization-based design for the separation of heterogeneous azeotropic mixtures, Comput. Chem. Eng., 72, 34-51

Sudhoff, D., Leimbrink, M., Schleinitz, M., Górak, A., Lutze, P., 2015, Modelling, design and flexibility analysis of rotating packed beds for distillation, Chem. Eng. Res. Des., 94, 72-89

Wang, G. Q., Xu, Z. C., Yu, Y. L., Ji, J. B., 2008, Performance of a rotating zigzag bed - A new HIGEE, Chem. Emg. Process, 47, 2131-2139

Wang, G. Q., Zhou, Z. J., Li, Y. M., Ji, J. B., 2019, Qualitative relationships between structure and performance of rotating zigzag bed distillation, Chem. Eng. Process., 135, 141-147

Woods, D. R., 2007, Rules of Thumb in Engineering Practice, Wiley-VCH Verlag, Weinheim, Germany

Xu, Z. C., Ji, J. B., Wang, G., Li, X. H., Li, Y., 2012, Rotating Zigzag Bed Application in Extractive Distillation Process of THF-Methanol-Water System, AIChE Spring Meeting & Global Congress on Process Safety

Sauro Pierucci, Flavio Manenti, Giulia Bozzano, Davide Manca (Eds.)
Proceedings of the 30th European Symposium on Computer Aided Process Engineering (ESCAPE30), May 24-27, 2020, Milano, Italy.
http://dx.doi.org/10.1016/B978-0-12-823377-1.50168-3

Design Concepts for Pressurized LNG Storage Tanks

Marian Krol

Linde AG, Engineering Division, Dr.-Carl-von-Linde-Straße 6-14, D-82049 Pullach, Germany

Abstract

The containment philosophy has been well defined by European and North American regulations e.g. EN 1473, NFPA 59A for the flat bottom LNG storage tanks. However, such established definition is missing for the pressurized storage tanks. An outlook will be given to the latest development of the prEN 1473 regarding the containment philosophy and the related safety design of the pressurized LNG storage tanks. The definition of the possible tank leakage will be discussed based on fracture mechanics and event probabilities for both atmospheric and pressurized storage tanks.

1. Main Text

The current version of EN 1473 is valid for plants with LNG storage at pressure lower than 0.5 bar(g) and a capacity above 200 t. The plants with storage inventories ranging from 50 t up to 200 t and a pressure higher than 0.5 bar(g) are covered by EN 13645.

Due to the lack of safety concept definitions for pressurized LNG vessels having storage capacities exceeding 200 tons and 0.5 barg and the failed integration of these tanks into EN 13645, it was required to trump up a new guideline for the more and more increasing demand of large pressurized storage capacities over 200 tons.

At the beginning a finding process for the definition of safety concepts and related selection criteria was required.

In the publication “Comparative Risk Assessment for Different LNG-Storage Tank Concepts” (Stefan Rath, Marian Krol, both from Linde AG) presented on the 14th International Symposium on Loss Prevention and Safety Promotion in the Process Industry in Florence 2013 it was proposed to replace the existing containment definition of atmospheric storage tanks in favor of a new definition based on integrity safety levels and to use it for atmospheric as well as for pressurized storage tanks:

“LNG can be stored either in flat bottom storage tanks or pressurized storage tanks such as bullets or spheres. Safety levels of atmospheric storage tanks are classified by codes as "single containment", "double containment" and "full containment". For spherical and bullet tanks an analogical definition by codes is missing and containment philosophies for atmospheric storage cannot be applied to pressurized storage. Therefore, a new definition is proposed to describe the safety levels of pressurized tank types and flat-bottom tank types consistently.

It is supposed to use the definitions single, double and full integrity instead of single, double and full containment in order not to mix up definitions. The integrity level a storage tank has been assigned to give a direct link to the consequences that would have to be taken into account in case the primary container fails totally. The advantage of these new containment definitions is having available a normalized basis for the comparison of different tanks fulfilling similar requirements on safety design."

This publication demonstrates that "*in general the risk to external population is the higher the lower the integrity level of the LNG storage*".

After many presentations of the new concept authors received both positive and negative feedback, but the idea to classify atmospheric and pressurized tanks in a comparable manner was found mostly interesting.

Unfortunately, many discussions in the TC 282 WG 5 responsible for EN 1473 ("Installation and equipment for liquified natural gas - Design of onshore installations"), the TC 265 WG10 responsible for EN 14620 ("Design and manufacture of site built, vertical, cylindrical, flat-bottomed steel tanks for the storage of refrigerated, liquefied gases with operating temperatures between 0 °C and -165 °C") and the NFPA 59A ("Standard for the Production, Storage, and Handling of Liquified Natural Gas") showed that this integrity level classification of storage tanks was not supported by the majority of specialists involved in the standardization process. However, after a certain time it was astounding to notice a mind change within the TC 282 committee responsible for the EN 1473 Standard towards the preference of the well-known "containment" term instead of "integrity level". Now the proposed idea was suddenly accepted having changed the wording.

A further development of the idea took place after studying the fracture mechanics behaviour of atmospheric and pressurized cryogenic vessels and comparing probabilities of leak scenarios for both storage types. Several internationally recognized publications in equipment probability approaches area were compared.

The "Handbook of Scenarios for Assessing Major Chemical Accident Risks" issued in 2017 by Joint Research Centre (JRC) gives recommendations on possible major accident scenarios in the form of scenario trees. It is expected that the scenario recommendations will be useful to EU Member States and third countries to assess the Land-Use Planning cases, in complying with the requirements of the Seveso Directive. Unfortunately, there is no scenario for LNG pressurized tank, but due to the circumstance that the K_{IC} values for materials used in LPG service are generally comparable to those of the materials for LNG service the following conclusion may follow: "the leak in the tank shall be considered for both atmospheric and pressurized vessels".
The "Handbook" specifies for pressure vessel an annual probability of catastrophic failure as instantaneous release with 5E-7and a 10 mm diameter hole with 1E-5.

The "Failure Rate and Event Data for use within Risk Assessments" published on 02.02.2019 by HSE (Health and Safety Executive) presents the annular failure rates for LNG atmospheric and LPG pressurized vessel. According to this publication a catastrophic annular failure probability for the atmospheric LNG vessel is assumed to be

5E-8and a minor failure 3E-6. But this source inappropriately defines the minor leak as a 300 mm diameter hole for tanks bigger 12,000 m³. This is not probable since a crack having this rate would be much bigger than the critical one and at the end a zipping of tank would happen. The 13 mm diameter hole for pressurized LPG vessel shows the probability of 1E-5 what confirms previous JRC data.

The "Guidelines for quantitative risk assessment" 'Purple book' CPR 18E (2005 edition) Publication Series on Dangerous Substances (PGS 3) confirms the above rates for pressure vessel, i.e. annual probability of catastrophic failure as instantaneous release with 5E-7 and a 10 mm diameter hole with 1E-5. In contrast atmospheric cryogenic tanks possess the following annular failure probability of instantaneous release to the atmosphere:

- single containment: 5E-6
- double containment: 1.25E-8
- full containment 1E-8

The 10 mm diameter hole with release to the atmosphere for a single containment tank and release to the secondary container for a double containment has a probability of 1E-4.

It may be understood this value is also valid for full containment tank for the release

to the outer container due to the materials and equivalent stress level for double and full containment tank systems.

The "Risk Assessment Data Directory" Report No. 434 – 3 of March 2010 issued by International Association of Oil & Gas Producers OGP (Storage incident frequencies) describes the annular probability of primary containment catastrophic rapture for cryogenic atmospheric tanks with:

- 2.3E-6 – single containment
- 1E-7 – double and full containment.

The general annual leak frequency without definition for all containments tanks is 1E-5. Pressurized vessels with the hole of 10 mm diameter have an annular leak frequency of 3,5E-5 and for the catastrophic rupture the failure rate is 4.7E-5 per year.

The last 2019 edition of NFPA 59A "Standard for the Production, Storage, and Handling of Liquified Natural Gas (LNG)" in the chapter Release Probabilities and Conditional Probabilities also describes failure rates for different equipment. The annular probability of catastrophic rupture for cryogenic atmospheric tanks is:

- 1E-6 – single containment,
- 1.25E-8 – double containment, and
- 1E-8 - full containment.

The annual leak frequency for cryogenic tanks is not defined. Pressurized vessels leaking from a hole with 10 mm diameter have an annular probability of 1E-5 and for a catastrophic rupture it is 5E-7.

In contrast to the probabilistic approach, the German's deterministic approach to safety design of chemical plants discusses a few selected sources especially for possible leak area of pressurized vessels as basis for the consequence study. The mentioned extent of leak ranges from 20 mm² up to 100 mm², corresponding to an approximate hole diameter of 10 mm (refer to „Auswirkungsbetrachtungen bei störungsbedingten Stoff- und Energiefreisetzungen in der Prozessindustrie", Januar 2017).

From a fracture mechanics point of view it reveals that some possible leak scenarios require refinement. After analyzing the magnitudes of critical cracks, it can be said that the design requirement for atmospheric storage tanks in particular the dimensioning of Safety Valves should be done for a 20 mm diameter hole in the lower part of shell as specified in EN14620. This value corresponds very well to the fracture toughness properties of low alloyed Ni steels and the applied stress levels in the above-mentioned standard.
In the same it can be argued on the pressure vessels and the suggested hole diameter of 10 mm as leak source.

After a careful check of above publications on determining accident probabilities it came out that the likelihood of such an event like loss of containments is indeed comparable for atmospheric and pressurized tanks. The general tendency may be understood as the result of defining the possible leak for an atmospheric tank with diameter of 20 mm in the shell and for a pressurized tank with hole of 10 mm diameter.

This awareness has been taken as the basis for the new definition of "containment" in the prEN 1473 currently under revision. Both types of LNG storage, i.e. atmospheric and pressurized tanks, now possess a common definition as shown in the following excerpts from prEN 1473:

7.8.4.2 Single Containment
A single containment storage system is designed not to preclude the possibility of product spillage within the defined impounding area (see 7.2.2) in case of leakage.

7.8.4.3 Double Containment
A double containment storage system is designed to preclude the possibility of product spillage over the surrounding area in case of leakage from its primary container. Thus, a liquid tight secondary liquid container which is an integral part of the storage system is required to retain the full liquid inventory of LNG if drained from the primary container; while not intended to prevent the escape of product vapours resulting from that internal upset.

7.8.4.4 Full Containment
A full containment tank system is designed to both containing the full liquid inventory and controlling the vapour release in the event of product leakage from the primary liquid container. Transient product losses in case of product leakage from the primary liquid container due to outer container permeability are acceptable and subject to consistent limitations after consequence analysis.

The difference between the two storage concepts then turns out in the performance behavior, which is described in the following excerpts of prEN 1473:

7.8.5 Performance of atmospheric storage concepts
7.8.5.1 Gradual loss of containment
Leakage rates of equipment shall be established by the risk assessment based on the storage concept. For storage tanks, as a minimum, the scenario of a gradual loss of containment shall be considered:

- leak of 20 mm diameter as defined by EN 14620 for steel-steel or steel-concrete flat-bottom tank of atmospheric storage concepts;

7.8.5.4 Impounding
In case of single containment flat-bottom tanks, the impounding basin is required with a capacity of at least 110% of the largest tank.

7.8.6 Performance of pressurized storage concepts
7.8.6.1 Gradual loss of containment
Leakage rates of equipment shall be established by the risk assessment based on the storage concept. For pressure vessels, as a minimum, the scenario of a gradual loss of containment shall be considered:
- leak of a 8 mm diameter hole, unless demonstrated otherwise e.g. by the risk assessment. A broken instrument connection is considered a credible scenario.

7.8.6.4 Impounding
In case of single containment design, the spill from a liquid leak from the tank shall be handled by having a paved area with slope toward a safe location to avoid flammable liquid accumulation below the tank. The remote impounding basin shall have a capacity of minimum 20 % of the largest storage tank capacity and in addition shall observe requirements from Table 1 (below).

Table 1 — Pool fire sizing as function of tank types

Type of tank containment [a]	Atmospheric storage		Pressurized storage
	Metallic or with metallic roof only	Prestressed concrete with concrete roof	
Single containment	Impounding area	n/a	Remote impounding [b,c]
Double containment	Secondary container	n/a	Secondary container
Full containment	Secondary container	No pool fire	Remote impounding [c]

Remarks:
[a] For definition, see 7.8.4.
[b] For definition, see 7.8.6.4
[c] Sized for full line break prior to closure of the internal or integrated shut-off valve.

Considering that for pressurized LNG tanks the discharge connection is arranged below the liquid level in contrast to atmospheric tanks, the pipe break must be considered in the impounding basin design. The API Standard 625 (“Tank Systems for Refrigerated Liquified Gas Storage”) serves as a good solution for this accidental scenario. The prEN 1473 asks for an additional requirement to size the remote impounding pit for a full line break before the internal or integrated shut-off valve will be closed.

In the following figure, examples of pressurized single and full containment vessels above 200 tons are presented. Note that the double containment requirements are still under discussion and the finalized draft of the new EN 1473 is planned to be published before end of 2020.

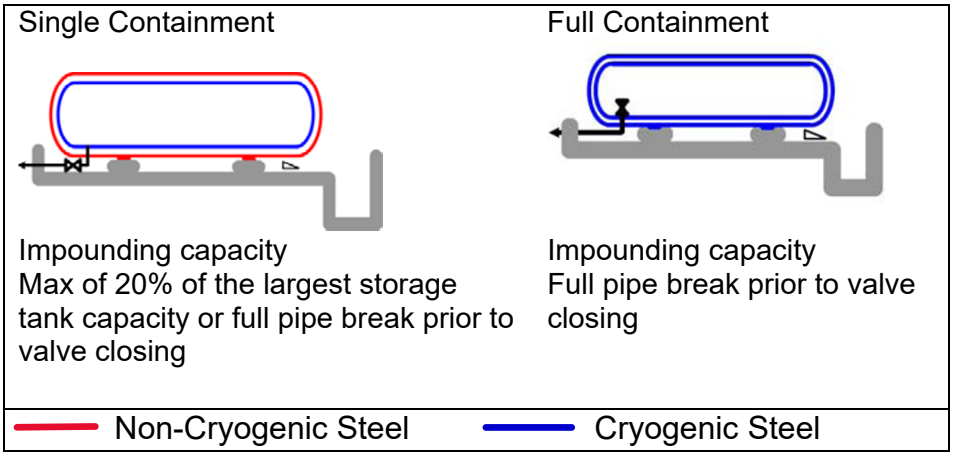

Figure 1 - Examples for pressurized vessels above 200 tons

References

Stefan Rath, Marian Krol, Comparative Risk Assessment for Different LNG-Storage Tank Concepts, CHEMICAL ENGINEERING TRANSACTIONS, VOL. 31, 2013
EN 1473:2016
prEN 1473:2019
NFPA 59A:2019
Handbook of Scenarios for Assessing Major Chemical Accident Risks, 2017, Joint Research Centre
Failure Rate and Event Data for use within Risk Assessments, 2019, HSE
Guidelines for quantitative risk assessment 'Purple book', CPR 18E, 2005
Risk Assessment Data Directory" Report No. 434 – 3 of March 2010, OGP
Auswirkungsbetrachtungen bei störungsbedingten Stoff- und Energiefreisetzungen in der Prozessindustrie", Januar 2017, VDI DECHEMA

Sauro Pierucci, Flavio Manenti, Giulia Bozzano, Davide Manca (Eds.)
Proceedings of the 30th European Symposium on Computer Aided Process Engineering (ESCAPE30), May 24-27, 2020, Milano, Italy.
http://dx.doi.org/10.1016/B978-0-12-823377-1.50169-5

Automatic Synthesis of Distillation Processes for the Separation of Heterogeneous Azeotropic Multi-component Mixtures

Thulasi Sasi, Kai Kruber, Moreno Ascani, Mirko Skiborowski*

TU Dortmund University, Department of Chemical and Biochemical Engineering, Laboratory for Fluid Separations, Emil-Figge-Strasse 70, Dortmund 44227, Germany

Abstract

The separation of azeotropic mixtures is a complex task that is frequently addressed by means of graphical analysis of residue curve maps and trial-and-error flowsheet simulations. While miscibility gaps in heterogeneous mixtures result in considerably more complex phase behaviour, the possible exploitation of a combination of decantation and distillation bears the potential for efficient separation processes. In order to enable an automatic generation of alternative separation sequences with closed recycle loops the current article presents an extension of a previously developed algorithmic framework for process synthesis of homogeneous distillation processes. This extension includes the computation and characterization of heterogeneous azeotropes and the analysis of the topology of the system, as well as an extended split feasibility algorithm, which also accounts for decantation at different temperature levels. The approach is fully algorithmic and includes a shortcut-based computation of the energy demand of the generated flowsheet variants.

Keywords: conceptual design, flowsheet optimization, heteroazeotropic distillation.

1. Introduction

Distillation is one of the most applied fluid separation process and contributes significantly to the energy requirement of the chemical industry. While energy efficiency and corresponding operational cost of separation processes are largely fixed during conceptual design, the prevailing method for process synthesis is based on expert knowledge in combination with graphical analysis and flowsheet simulation. In order to accelerate and simplify process synthesis a systematic and at best automatic identification of separation processes is required, which so far is not offered by any commercial flowsheet simulation software.

However, quite a few studies have addressed this synthesis problem in the past. Yet, the graphical analysis is still most popular, while being restricted to ternary mixtures. The first systematic methods for separation process synthesis were so-called expert systems, such as the blackboard system SPLIT (Wahnschafft et al. 1991). While the separation of multi-component mixtures was addressed, flowsheet generation was performed based on the evaluation of binary sub-systems, confirming split feasibility only in subsequent rigorous flowsheet simulation. Unlike SPLIT, the knowledge-based expert system PROSYN® (Schembecker and Simmrock 1997) is still available. The combined heuristic-numeric approach implements a concept of collaborating distributed expert systems that combines a variety of heuristic rules and physical property computations, including multi-component azeotrope computations (Schembecker and Simmrock

1995), with artificial intelligence. An algorithmic approach towards process synthesis based on the analysis of the mixture topology was first proposed at the end of the 1990s by Poellmann and Blass (1994) and Rooks et al. (1998), who proposed a matrix method to determine the topological distillation regions. This concept was further exploited by Tao et al. (2003) and Wasylkiewicz and Castillo (2001). Wasylkiewicz et al. (2003, 2006) implemented the matrix method in the software DISTIL, evaluating possible recycle structures based on the concept of preferred distillation regions, while checking the feasibility of heteroazeotropic distillation based on the boundary value method (BVM) (Pham et al. 1989). The BVM was also used by Prayoonyong and Jobson (2011) for more complex configurations of heterogeneous azeotropic distillation, while being limited to ternary mixtures due to the graphical analysis. Tao et al. (2003) developed a direct extension of the matrix method for the analysis of recycle structures, based on a different form of reachability matrix and a set of reachability rules, considering decantation alongside distillation. Yet, the approach focusses primarily on feasibility of distillation at total reflux, evaluating only residue curves.

Consequently, despite the reported efforts towards the synthesis of process alternatives for heteroazeotropic mixtures, there is still a need for an efficient algorithmic approach, which can be applied to arbitrary azeotropic multi-component mixtures and which considers split feasibility in a more general form. This paper combines proven methods with novel features to algorithmically generate process variants based on rigorous thermodynamic models, and include feasibility of distillation at total reflux and reversible distillation.

2. Methodology

The present work is an extension to the synthesis method for homogeneous azeotropic mixtures (Sasi et al. 2019). It builds solely on mathematical models for thermodynamic equilibrium computations, on which basis first a topological analysis of the mixture is performed and furthermore algorithms for split feasibility are exploited to generate and store flowsheet variants in terms of a tree structure.

2.1. Topological analysis

The topological structure of the mixture is defined based on the set of singular points and their allocation to distillation regions (DR) and compartments, which also results in the definition of distillation boundaries (DB). While the matrix method described by Rooks et al. (1998) can directly be applied to heterogeneous mixtures, it is important to first determine all relevant azeotropes and classify them in respect to their stability. The latter is accomplished by means of a dedicated homotopy continuation approach (Skiborowski et al. (2016)), which includes an efficient phase stability test (Bausa and Marquardt, 2000).

2.2. Split feasibility of separation

In order to generate possible flowsheets possible splits are evaluated algorithmically for a separation by either distillation or decantation. Split feasibility for distillation is determined based on the information of topological DR, residue curve and pinch line computations are used to determine the maximum recovery of potential sharp splits (Sasi et al. 2019). Thereby an explicit representation of DB is avoided, while split feasibility at total reflux and reversible distillation are considered. Further application of the rectification body method (RBM), checks for an intersection of rectifying and stripping profiles, while additionally providing an estimate of the minimum energy demand (MED) (Bausa et al. 1998). Feasible decanter splits are evaluated based on the phase stability test of Bausa and Marquardt (2000), while temperature sensitivity of the

miscibility gap is evaluated as well. Potential cooling considers available utilities, while subsequent heating to saturation temperatures for downstream columns is added to the MED computation.

2.3. Generation of tree structure

Starting from the initial feed composition, potential splits are evaluated by the aforementioned split feasibility criteria. Each split is introduced as new branch in a tree structure, for which the two product compositions result in subsequent nodes of the branch. Each node is considered as new feed stream for split generation, unless the products are either the desired products or pure component, or no further separation is feasible. During the generation of the tree structure additional nodes are introduced by consideration of mixing with potential recycle streams. These are either SP, in case of homogeneous azeotropes or pure components, or the equilibrium liquid phases of heterogeneous azeotropes. Unlike the recycle of homogeneous SP, the recycle ratio for equilibrium liquid phases is determined geometrically. This mixing point is the point of intersection of the line joining the desired product and the heteroazeotrope, and the line joining the feed and the recycled liquid phase. Consequently, the recycle of a liquid phase results in a configuration of a distillation column followed by a decanter, which indicates the possibility of replacing it with a heteroazeotropic distillation column. The possible substitution is illustrated in Figure 1. While the integrated heteroazeotropic distillation column can offer a lower MED, the current synthesis approach is for now restricted to the identification of the variant with standalone decanter, for which the distillation column and decanter are evaluated individually in terms of split feasibility and MED.

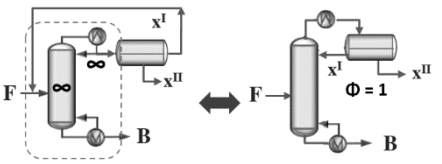

Figure 1: Standalone and integrated decanter

After the generation of the tree structure is finished, a post-processing step is performed, which evaluates for each branch, if suitable destinations for end streams that do not correspond to desired products can be determined using the recycle reachability method developed by Tao et al. (2003). This involves the evaluation of adjacency and reachability matrices, similar for each stream in a flowsheet instead of SP. Using these matrices, it is determined if there is an exit point for each component, such that the mass balance is not violated while recycling streams within a flowsheet. Since this rule cannot be applied to processes involving entrainers that are regenerated within the flowsheet, the initial feed is considered as the recycle destination for such cases. Figure 2 illustrates the tree structure and an example process for the separation of a mixture of ethanol and water using toluene as an entrainer that introduces heterogeneity in the system at saturation conditions. Starting from a binary ethanol-water feed, two possible splits using distillation are determined. Split 1 recovers water, while split 2 recovers ethanol by initial mixing of the feed with the organic phase (OP) of the ternary heteroazeotrope. The necessary recycle ratio of the OP is determined geometrically such that the separation of ethanol and the ternary heteroazeotrope is established. The process obtained from the shaded branch of the tree successfully separates ethanol and water, but also generates a potential waste stream corresponding to the aqueous phase (AP). To maximize the recovery of the products, AP is recycled to the initial feed and the flowsheet is converged iteratively during post-processing. Similarly, another process alternative can be obtained from the second branch (Split 2) by recovering water from AP, and subsequently recycling the product on the DB to the initial feed.

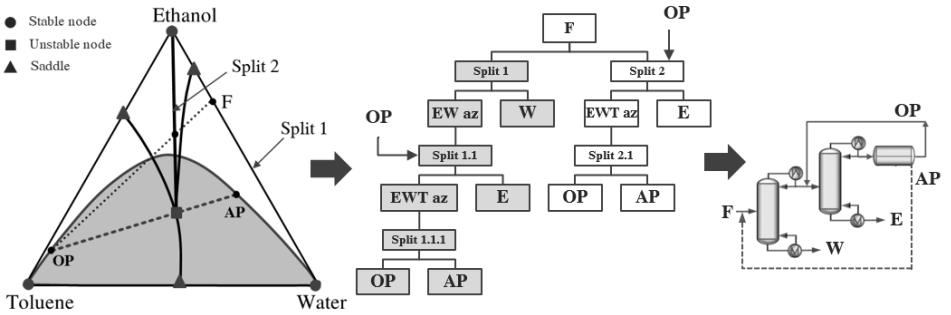

Figure 2: Illustration of tree structure with addition of decanter and a resulting process variant

3. Case Studies

The application of the approach is further illustrated for two case studies. The first case considers the separation of a ternary mixture of tetrahydrofuran (THF), methanol and hexane. Figure 3 illustrates the topology of the mixture, which is completely homogeneous at saturation conditions at atmospheric pressure, showing 3 binary azeotropes and 3 DR. However, at sub-cooled condition a miscibility gap originates from the binary methanol-hexane mixture, which is also indicated for 25°C and 15°C in Figure 3. For a feed consisting of 55 mol% THF, 35 mol% methanol and 10 mol% hexane, the current methodology generates two feasible flowsheets. The one with lower MED, shown in Figure 3, first performs a direct split of the feed for the separation of THF, followed by a decanter and the recovery of methanol and hexane from the subsequent liquid phases. The THF-methanol azeotrope is recycled to the initial feed based on the recycle reachability rule, and the methanol-hexane azeotrope is recycled to the decanter in the post-processing step. By reducing the decanter temperature from 25 to 15°C, the MED reduces by 5.6% due to the reduced recycle stream of the hexane-methanol azeotrope. Anyhow, the operating temperature of the decanter should be further optimized in an economic optimization of the feasible flowsheet, which is the main result of the presented synthesis approach.

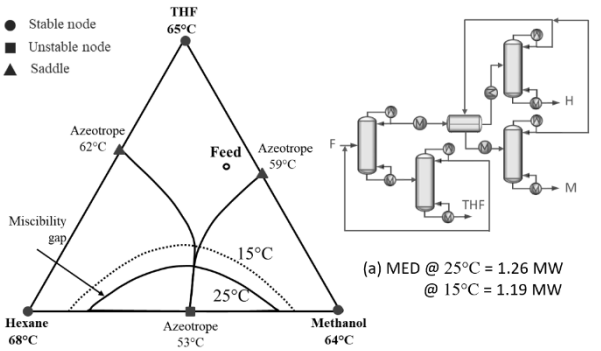

Figure 3: Topology and process alternative for the separation of the THF, methanol, hexane mixture at 1 bar.

The developed methodology is further applied to the separation of a quaternary mixture of methanol, ethanol, butanol and water, which was also investigated by Wahnschafft et al. (1992). Butanol and water are partly immiscible at saturation conditions, as illustrated in Figure 4.

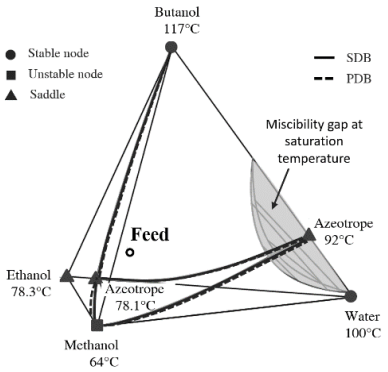

Figure 4: Topology of the methanol, ethanol, butanol, water mixture at 1 bar.

While the illustrated miscibility gap represents saturation conditions at 1 bar pressure, it is hardly affected by temperature modifications, according to the employed NRTL model. The mixture exhibits one homogeneous and one heterogeneous binary azeotropes that result in the separation of the composition space into two DR. Considering the same feed composition as investigated by Wahnschafft et al. (1992), i.e. 60 mol% methanol, 20 mol% ethanol and 10 mol% each of water and butanol, a total of 11 flowsheet variants are generated. The five variants that are able to retrieve all four pure components are further illustrated in Figure 5 together with their computed MED. The first three flowsheet variants involve the separation of the feed into two binary mixtures in the first column, followed by the separation of pure methanol and ethanol in a subsequent column. While flowsheet variant (c) resembles the only flowsheet proposed by Wahnschafft et al. (1992), the MED estimates of the generated flowsheets (a) and (b) are presumably offering a little over 10% energy savings with the same number of unit operations. Unlike variants (a)-(c), variants (d) and (e) start with the indirect split, where pure benzene is recovered first. In variant (d) the binary homogeneous ethanol-water azeotrope is recycled to the initial feed based on the recycle reachability algorithm during post-processing step, while pure methanol is recycled to the ternary feed of the second column to enable the complete recovery of water by exploiting the feasibility at finite reflux, since the PDB intersects the ethanol-methanol binary edge. While both variants operate without a decanter, they are evaluated with considerably larger MED.

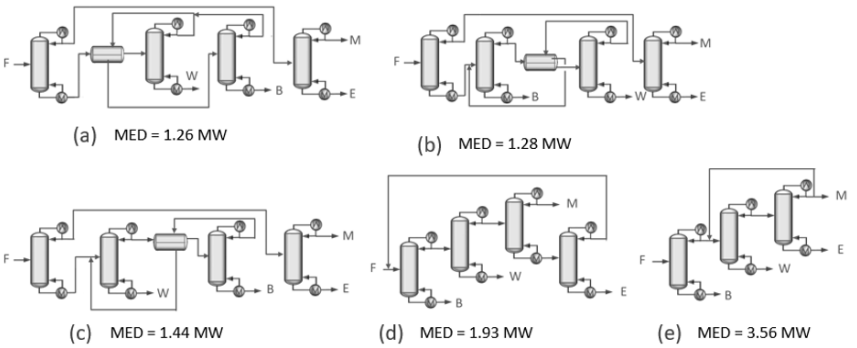

Figure 5: Process variants generated for the separation of the methanol, ethanol, butanol and water mixture.

4. Conclusion and outlook

The current article extends the previously developed algorithmic approach for the synthesis of distillation processes to the separation of heterogeneous azeotropic mixtures. The method is not restricted with respect to the number of components and incorporates general feasibility tests, which examine both limiting operational modes for distillation, total reflux as well as reversible distillation and decantation.

Although the current implementation only identifies combinations of simple columns and decanters, integrated heteroazeotropic distillation columns can be considered in a subsequent design study of promising flowsheet variants. Besides the connection to such a design optimization, future work will focus on the extension of the method towards alternative and more complex recycle options, pressure variations, as well as other process options, like extractive distillation.

References

J. Bausa, R. Watzdorf, W. Marquardt (1998): Shortcut methods for nonideal multicomponent distillation: I. Simple columns. In AIChE J 44 (10), pp. 2181–2198.

J. Bausa, W. Marquardt (2000): Quick and reliable phase stability test in VLLE flash calculations by homotopy continuation. In Computers & chemical engineering 24 (11), pp. 2447–2456.

P. Poellmann, E. Blass (1994): Best products of homogeneous azeotropic distillations. In Gas Sep. Purif. 8 (4), pp. 194–228.

P. Prayoonyong, M. Jobson (2011): Flowsheet synthesis and complex distillation column design for separating ternary heterogeneous azeotropic mixtures. In Chemical Engineering Research and Design 89 (8), pp. 1362–1376.

R. Rooks, V. Julka, M.F. Doherty, M.F. Malone (1998): Structure of Distillation Regions for Multicomponent Azeotropic Mixtures. In AIChE J 44 (6), pp. 1382–1391.

T. Sasi, J. Wesselmann, H. Kuhlmann, M. Skiborowski (2019): Automatic synthesis of distillation processes for the separation of azeotropic multi-component systems. In : Computer Aided Chemical Engineering, vol. 46: Elsevier, pp. 49–54.

G. Schembecker, K.H. Simmrock (1995): Azeopert-a heuristic-numeric system for the prediction of azeotrope formation. In Computers & chemical engineering 19, pp. 253–258.

G. Schembecker, K.H. Simmrock (1997): Heuristic-numeric design of separation processes for azeotropic mixtures. In Computers & chemical engineering 21, S231- S236.

M. Skiborowski, J. Bausa, W. Marquardt (2016): A Unifying Approach for the Calculation of Azeotropes and Pinch Points in Homogeneous and Heterogeneous Mixtures. In Industrial & Engineering Chemistry Research 55 (24), pp. 6815–6834.

L. Tao, M.F. Malone, M.F. Doherty (2003): Synthesis of Azeotropic Distillation Systems with Recycles. In Industrial & Engineering Chemistry Research 42 (8), pp. 1783–1794.

O.M. Wahnschafft, J.P. Le Rudulier, P. Blania, A.W. Westerberg (1992): Split: II. Authomated synthesis of hybrid liquid separation systems. In Computers & chemical engineering 16, S305- S312.

O.M. Wahnschafft, T.P. Jurain, A.W. Westerberg (1991): SPLIT: a separation process designer. In Computers & chemical engineering 15 (8), pp. 565–581.

S.K. Wasylkiewicz (2006): Synthesis of separation systems for azeotropic mixtures: Preferred distillation region. In Comput.-Aided Chem. Eng. 21, pp. 1033–1038.

S.K. Wasylkiewicz, F.J.L. Castillo (2001): Automatic synthesis of complex separation sequences with recycles. In : Computer Aided Chemical Engineering, vol. 9: Elsevier, pp. 591–596.

S.K. Wasylkiewicz, L.C. Kobylka, F.J.L.Castillo (2003): Synthesis and design of heterogeneous separation systems with recycle streams. In Chemical Engineering Journal 92 (1-3), pp. 201–208.

Sauro Pierucci, Flavio Manenti, Giulia Bozzano, Davide Manca (Eds.)
Proceedings of the 30th European Symposium on Computer Aided Process Engineering (ESCAPE30), May 24-27, 2020, Milano, Italy.
http://dx.doi.org/10.1016/B978-0-12-823377-1.50170-1

Technical and Economic Feasibility of Direct Methane Conversion for Hydrocarbon Production: Process Design and Techno-economic Analysis

Thai Ngan Do[a], Yong Tae Kim[b], Jiyong Kim[a]

[a]*Department of Energy and Chemical Engineering, Incheon National University, 119 Academy-ro, Yeonsu-gu, Incheon, 22012, South Korea*
[b]*C1 gas Separation and Conversion Research Center, Carbon Resources Institute, Korea Research Institute of Chemical Technology, Daejeon 34114, Republic of Korea*
jykim77@inu.ac.kr

Abstract

In this study, we have developed a modelling and evaluation framework of a direct conversion of methane (CH_4) to value-added chemicals including light hydrocarbons, FT fuels, and aromatics. As novel catalysts for a direct CH_4 conversion are targeted to adapt to industrial applications, it is important to access the technological and economic feasibility. Various techniques in process systems engineering play a crucial role here in the application of the current or extended methodologies to support R&D targets and planning: identification of major cost- and energy-drivers, preliminary process scheme and debottleneck strategies. In this framework, we developed a conceptual conversion process, which consists of a reaction section of directly converting CH_4 into hydrocarbons, and a separation section of sequentially integrated technologies for recycles of CH_4, purifying ethylene, other C_{2+} hydrocarbon, and aromatics production. Then, the technical and economic feasibility of the process was evaluated, included a sensitivity analysis for identifying the bottleneck factors. Outstandingly, the direct methane conversion process achieves high energy efficiency (58.9 %), consumed a large amount of utility but still overcomes the intensive-energy penalty as in other petrochemical processes that are primarily due to the contribution of hydrogen as a by-product. The ethylene as one of main products was produced at 0.97 $/kg that can be reduced and competitive to the market in promised scenarios. Otherwise, the study provides the perspective on improving catalyst performance (e.g. higher yield of ethylene), which is critical to achieve high technical performance and economic benefits.

Keywords: process design, direct methane conversion, ethylene production, techno-economic evaluation.

1. Introduction

Ethylene is one of the important building blocks in petrochemical industries for a variety of derivatives such as polyethylene, ethylene glycol, ethyl-benzene, and styrene. As predicted, the global market demand has significantly grown, increases approximately 3.6 %/y to reach 184 MMt by 2022 (Rentech, 2018). To meet the growing demand of ethylene, ethylene production facilities are being on the increase, and alternative ethylene production routes has been developed. Typically, ethylene is produced by steam cracking of gas hydrocarbon (e.g. ethane, propane, butane) and liquid hydrocarbon (e.g. naphtha, gasoil, condensate), which is an intensive-energy penalty route (Amghizar et al., 2017). Many alternative routes are considered such as methanol-to-olefin or coal-to-olefin.

Interestingly, the direct methane conversion is a promising route to produce ethylene from natural gas (Oh et al, 2019), along with other high-value chemicals such as acetylene, benzene, naphthalene, and hydrogen as by-products. As novel catalysts for the direct methane conversion have been developed, it is important to examine and evaluate the technical and economic feasibility for real industrial applications. Herein, techniques in process systems engineering, such as process synthesis and techno-economic analysis, play an important role to identify the major cost- and energy-drivers, preliminary process scheme and debottleneck strategies that supports R&D and planning (Vooradi et al., 2018).

In this work, we developed the direct methane conversion process which converts a natural gas into ethylene and other high-value chemicals, and evaluated the techno-economic performance. Therein, the novel catalyst of Fe-based, which presents the outstanding performance (e.g. yield) in the laboratory-scale experiment was used. The data of the methane conversion and the selectivity to each hydrocarbon were obtained and input in the catalytic conversion model in the process. In the separation section, several technologies were integrated to separate and purify ethylene, other C_{2+} hydrocarbon and H_2 product, and recycle CH_4. The techno-economic evaluation for the process was performed via the carbon efficiency, process energy efficiency, and minimum selling price of ethylene. Most of natural gas was converted into ethylene and acetylene besides the small amount of aromatics (e.g. naphthalene and benzene). Interestingly, hydrogen as a by-product positively contributes on in both energy efficiency and economic benefit due to its high heating value and high selling price. Besides, the sensitivity analysis of the ethylene minimum selling price (MSP) on major economic parameters was examined to identify the debottleneck solutions for the improvements of economic feasibility.

2. Methodology

2.1. Process simulation

The process models of the direct methane conversion for the hydrocarbon production, included catalytic conversion and separation sections, was developed using Aspen Plus V10.0. The property method of Peng Robinson-Boston Martin (PR-BM) was applied, which is recommended for the hydrocarbon processing (Huang et al., 2018). In the catalytic conversion section, the reactor is simulated using a black-box model for simplify performing the convergences of the novel catalyst performance. The reactions were operated at the atmosphere pressure and at very high temperature (over 1200°C) that required a large amount of fuel gas for heating, beside the heat recovery from heat exchanger network and burning the formed coke among the reactions (de-coking). In the separation section, the reaction outlet stream was compressed, then and separate naphthalene and benzene before entering to the very low temperature separation for purification of ethylene, hydrogen and other light hydrocarbon (i.e. acetylene, ethane). Therein, the heat exchanger network was installed to enhance the energy efficiency. Finally, the methane-rich gas emitted from the column was recycled back to reactor.

2.2. Techno-economic analysis

The proposed process was evaluated in various criteria such as carbon and energy efficiency, and minimum selling price (MSP). In the technical performance of the direct methane conversion to hydrocarbon, the terms of carbon element efficiency (η_C) and energy efficiency (η_E) presents how efficiently fed carbon source (e.g. CH_4) and supplied energy (i.e., utilities such as electricity, heat, and refrigeration) was utilized and captured in the products (Do et al., 2019) as expressed in Eqns. (1) and (2).

$$\eta_C = \frac{Total\ carbon\ element\ in\ products}{Fed\ CH_4} \times 100\% \quad (1)$$

$$\eta_E = \frac{Heat\ flow\ of\ products + Consumed\ utilities}{Heat\ flow\ of\ fed\ CH_4} \times 100\% \quad (2)$$

In the economic evaluation, the production cost considered the capital expenditures (*CAPEX*), operating expenses (*OPEX*), and tax. The return on investment (*ROI*) was estimated based on the interest rate at 8 %, and tax rate at 35 % within 30 years of economic plant life. Thereby, the minimum selling price (MSP) of ethylene was indicated after excluding the sale credits from other products (e.g. hydrogen, acetylene, crude naphthalene, benzene) as shown in Eqn. (3). Notably, the price of hydrogen and other hydrocarbons were indicated in the correlation with the price of natural gas and ethylene (Huang et al., 2018).

$$MSP_{ethylene} = \frac{(ROI + OPEX + Tax) - \sum Sale\ credit\ of\ other\ products}{Amount\ of\ ethylene}, [\$/kg] \quad (3)$$

3. Results and discussion

3.1. Process simulation

The process simulation of the direct methane conversion resulted that 0.33 million cubic m^3/h of natural gas was converted to the main product of ethylene at 0.49 Mt/y, and various hydrocarbon of raw acetylene, naphthalene, and benzene at 0.57, 0.03 and 0.09 Mt/y respectively. Hydrogen, which is one of the high-value heating components, was also produced at 0.35 Mt/y.

3.2. Techno-economic analysis

3.2.1. Technical performance

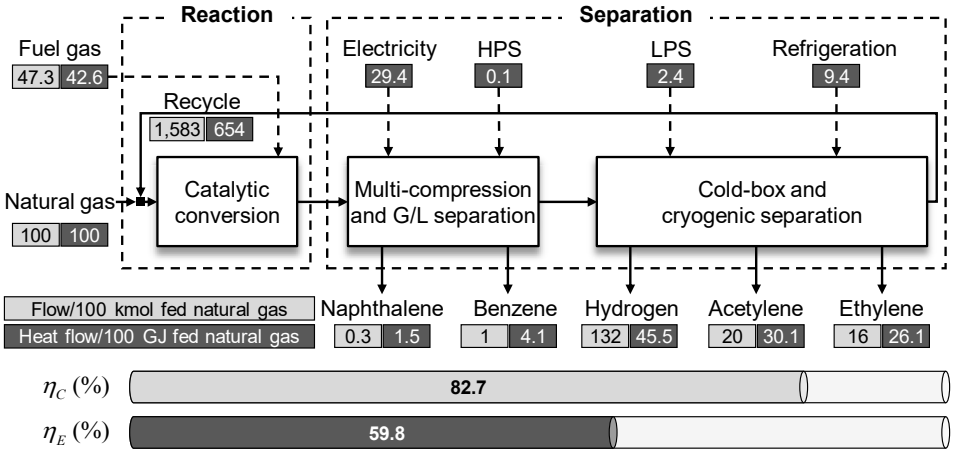

Figure 1. Simplified process scheme with the technical performance

Figure 1 presents the carbon element efficiency and energy efficiency together with the mass and energy balance among the process sections, presented on the basis of fed natural

gas. Therein, 82.7 % of natural gas was converted into hydrocarbon products with 59.8 % in the energy conversion. As shown in Figure 1, 16 units of ethylene, 20 of acetylene, and the small volumes of naphthalene and benzene are produced from 100 units of natural gas material. On the energy basis, the process consumes 83.9 units in utilities to convert 100 units in fed natural gas into 107.2 units in products. Several types of heating utility such as fuel gas, high- and low-pressure steam (HPS and LPS), and cryogenic utilization are used in the process. However, the direct methane conversion process performs high energy efficiency compared to the typical petrochemical process (Salaheldin et al., 2017). It is primarily due to the large energy contribution of high heating value hydrogen product.

3.2.2. Minimum selling price

For the economic evaluation, this study examined the total production cost and the minimum selling price of ethylene besides other hydrocarbon products and hydrogen. Therein, the major component costs (e.g. capital cost and operating cost) were estimated using Aspen Process Economic Analyzer. The assumptions of material and utility prices are shown in Table 1. Consequently, the total production cost was around 1,408 MM$ that included *ROI*, *OPEX*, and tax is shown in Table 2.

Table 1. Raw materials and utilities price

Parameter	Value
CH_4 ($/MMBTU)	3.27
O_2 ($/ton)	40
Refrigeration ($/GJ)	8.85
Electricity ($/kWh)	0.07
Cooling water ($/m^3)	0.03
High pressure steam ($/ton)	14.5
Low pressure steam ($/ton)	10.5

Table 2. Total production cost

	Value
(a) *CAPEX* (MM$)	1,128
Direct plant cost	806
Indirect plant cost	322
(b) *ROI* (MM$/y)	100.2
(c) *OPEX* (MM$/y)	1,274
Raw materials	303.1
Utilities	937
(d) Tax (MM$/y)	33.7
(e) Total production cost [=(b)+(c)+(d)] (MM$/y)	1,407.9

Table 3. Minimum selling price and sale credits of products

	Price ($/kg)	Sale credit (MM$)
Ethylene	0.97	474.6
Hydrogen	1.42	499.0
Raw acetylene	0.63	358.8
Crude naphthalene	0.49	17.0
Benzene	0.64	58.5

Figure 2 presents the breakdown of total production cost and revenue from the sale of products. In the total production cost, the utility cost is a dominant component, accounts for 66.6 %, followed by raw material cost (21.5 %). It can be explained by the large consumptions of heating utility in the catalytic conversion section, and electricity and cryogenic utility in the separation section. The *ROI* budgets only 7.1 % while tax income and fixed-operating cost (*OPEX - FOC*) account for the same value at 2.4 %. In a revenue breakdown, the ethylene and hydrogen sale credits are the large portions with relatively similar value, at 33.7 % and 35.5 %, in accordance with the selling production cost at 474.6 MM$/y and 499.0 MM$/y as present in Table 3. Followed, the raw acetylene credit at 25.5 % and benzene credit at 4.2 %.

The hydrogen and hydrocarbon products are sold at relatively low prices, as shown in Table 3, while the minimum selling price of ethylene is 0.97 $/kg, which is relatively higher than the market price (around 0.84 $/kg). The MSP of ethylene can be reduced in case of higher selling price of by-product. Another critical insight is to improve catalyst performance as increasing the yield of ethylene from methane. If the strategy could obtain, it significantly improved not only technical performance but also the economic benefits. However, at the moment of the novel catalyst performance, the MSP of ethylene can be reduced as other products are sold at higher prices, or reduce material or utility cost.

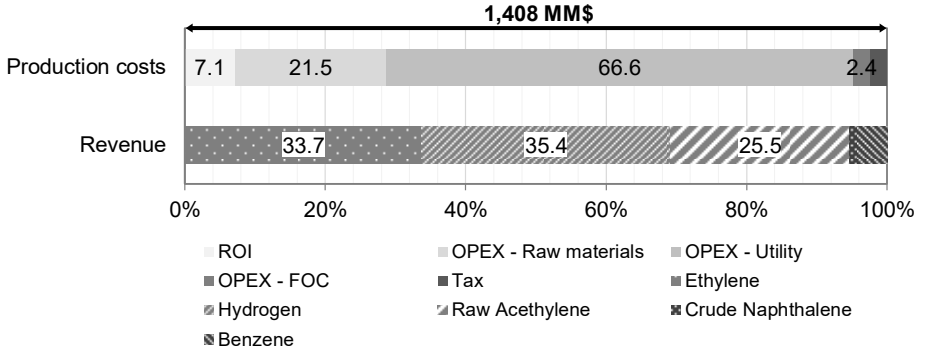

Figure 2. The breakdown of Production cost and Revenue

3.2.3. Sensitivity analysis

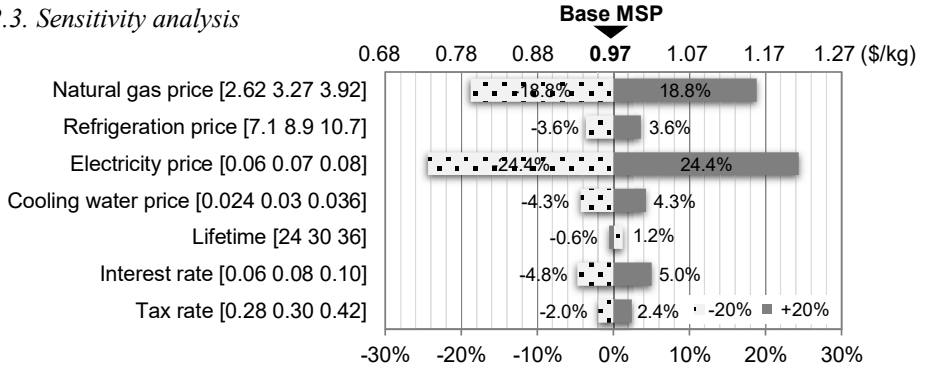

Figure 3. Sensitivity analysis of major economic parameter on Production cost

The sensitivity analysis of the ethylene MSP on the 20% changes of major economic parameters, in the case of other product prices are remained as in Table 3, is presented in Figure 3. It indicates that electricity price is the largest impact factor on MSP, which reduces by 24.4 % resulting in 0.74 $/kg of ethylene with a 20% reduction in electricity price. Natural gas price is the second sensitive parameter, which results in the MSP is from 0.79 to 1.12 $/kg within the examined range. Other factors are little effect on MSP, below 5%. As a result, the ethylene can be very competitive to the current market as reducing the price of natural gas or utility cost (e.g. electricity).

4. Conclusions

In this study, we developed the process of direct methane conversion to ethylene, C_{2+} hydrocarbon and aromatics production and conducted the techno-economic evaluation that identifies the major cost- and energy-drivers, and debottleneck strategies to improve the economic feasibility. The major findings and contributions of this study are as follows:

- The process performed carbon conversion at 82.7 % and energy efficiency at 59.8 %. Therein, H_2 has a large contribution on the energy efficiency besides the main product of ethylene and other hydrocarbon products due to its high heating value.
- Ethylene can be very competitive to the market as MSP is feasible to reduce with a lower price of electricity or natural gas (20% reduction), at 0.74-0.79 $/kg.
- The study also provides insight or targets for future research on catalyst development. In a scenario of higher ethylene yield, means achieved more ethylene production, the technical performance and economic feasibility significantly improve.

Acknowledgment

This work was supported by “Next Generation Carbon Upcycling Project” (Project No. 2017M1A2A2043137) through the National Research Foundation (NRF) funded by the Ministry of Science and ICT, Republic of Korea.

References

Rentech, 2019, Hydrocarbon processing: Petrochemical Technology - April 2018, 97, 4, https://www.hydrocarbonprocessing.com/magazine/2018/april-2018

I. Amghizar, L.A. Vandewalle, K. M. Van Geem, G. B. Marin, 2017, New Trends in Olefin Production, Engineering, 3, 171-178

S. C. Oh, E. Schulman, J. Zhang, J. Fan, Y. Pan, J. Meng, and D. Liu, 2049, Direct Non-Oxidative Methane Conversion in aMillisecond Catalytic Wall Reactor, Angew. Chem., 131, 7157-7160

R. Vooradi, M.O. Bertran, R. Frauzem, S.B. Anne, R. Gani, 2018, Sustainable chemical processing and energy-carbon dioxide management: Review of challenges and opportunities, Chem. Eng. Res. Des., 131, 440-464

K. Huang, J. B. Miller, G. W. Huber, J. A. Dumesic, and C. T. Maravelias , 2018, A General Framework for the Evaluation of Direct Nonoxidative Methane Conversion Strategies, Joule, 2, 2, 349-365

T. N. Do, J. Kim, 2019, Process development and techno-economic evaluation of methanol production by direct CO_2 hydrogenation using solar-thermal energy, J CO2 Util, 33, 461-472

M. Salaheldin, A.F. Abdul Moneim, M. Nashat Fors, 2017, Energy efficiency evaluation in petrochemicals industry, Proc. Int. Conf. Ind. Eng. Oper. Manag.,1058–1069.

Sauro Pierucci, Flavio Manenti, Giulia Bozzano, Davide Manca (Eds.)
Proceedings of the 30th European Symposium on Computer Aided Process Engineering (ESCAPE30), May 24-27, 2020, Milano, Italy.
http://dx.doi.org/10.1016/B978-0-12-823377-1.50171-3

Optimization Study of H2/CO Ratio in the Steam Gasification of PKS using Coal Bottom ash for fuel Production through Response Surface Methodology

Muhammad Shahbaz[a,b*], Tareq Al- Ansari[a], Gordon Mckay[a], Suzana Yusup[b], Muddasser Inayat[c]

[a]*Division of Sustainable Development, College of Science and Engineering, Hamad Bin Khalifa University (HBKU), Qatar Foundation, P.O. Box 5825, Doha, Qatar*
[b]*Institute of Sustainable living, Centre of biomass and biochemical Center, Department of Chemical Engineering, Universiti Teknologi PETRONAS, Bandar Seri Iskandar 32610, Perak Darul Ridzuan, Malaysia*
[c]*Department of Mechanical Engineering, Universiti Teknologi PETRONAS, Bandar Seri Iskandar 32610, Perak Darul Ridzuan, Malaysia*
mshahbaz@hbku.edu.qa

Abstract

H_2 and CO are the most critical components within the product gas obtained from the gasification of biomass. The composition of H_2 and CO is of significant importance as their ratio defines the utilization of the syngas. Application of syngas can include power generation, chemical products such as methanol, NH_3, and FT diesel. The objective of this study to optimize the parametric conditions for H_2/CO ratio in the gasification of PKS in TGA-MS set up using coal bottom ash as a catalyst and CaO as adsorbent. The experiments were designed using RSM and the effect of parameters such as temperature from (650-750 °C), particle size (0.5-1.0 mm), CaO/biomass ratio (0.5-2.0), and CBA wt % (0.02-0.10). The study demonstrates that the H_2/CO ratio is mostly influenced factor followed by the temperature and particle size, whereas the CaO/biomass ratio and CBA wt% are third and fourth influencing factors on H_2/CO ratio. The maximum H_2/CO ratio of 1.47 at optimum temperature of 715 °C, Particle size of 0.65 mm, CaO/biomass ratio of 1.45, and CBA wt % of 0.09%. H_2/CO ratio is important for its conversion into many products, such as methane, methanol, and FT diesel.

Keywords: H_2/CO ratio, gasification, RSM, optimization, TGA-MS.

1. Introduction

Energy is the backbone of modern human life. Fossil fuels are the primary source of the existing energy mix that contributed 81.7% of total energy needs (Inayat et al., 2020b). The progress of any country is highly dependent on reliable, affordable, and sustainable energy sources (Inayat et al., 2020b). It is forecasted by International Energy Agency that global energy consumption will increase by 53% in 2030 (Pang et al., 2010). Ever-increasing energy demand and limited fossil fuels motivate researchers to find alternative source of energy which are cheap and reliable to fulfill the future deficiency of fossils fuels. In this context biomass appears as cheap environmental friendly option of energy through thermal and biological conversion processes(Zeng et al., 2016). Among many, gasification is efficient and fast process that converts the biomass into gaseous fuel, which is sophisticated form of energy factor. The gasification process converts into syngas by

partial oxidation of biomass at high temperatures. Syngas is consists of H_2, CO, CH_4, and CO_2 (Inayat et al., 2020a). Syngas can be utilized for different purposes such as liquid fuel production (Fisher Tropsch) or used as alternative fuel (Ma et al., 2015).

The quality and utilization of syngas depend on its H_2/CO ratio. Zeng et al. (Zeng et al., 2016) reported the production of high H_2/CO ratio from steam gasification of sawdust and achieved 0.279 $Nm^3\ kg^{-1}$ of the H_2 yield in the steam reactor by chemical looping gasification. (Ma et al., 2015) used hybrid catalyst to synthesized the hydrocarbons and Ft diesel from syngas using having H_2/CO ratio less than 1 and 2 respectively. (Saad and Williams 2017) investigated two-stage pyrolysis-catalytic reforming of plastics for producing good quality syngas comprised of H_2 and CO. (Inayat et al., 2019) reported the H_2/CO under the effect of temperature, biomass ratio, ER, and catalyst loading in catalytic and non-catalytic co-gasification. The utilization of PKS for the steam gasification have been reported in our previous study (Herman et al.,.2016).Literature shows that reported studies focus only a normal investigation of H_2/CO ratio under catalytic and nan-catalytic gasification. However, there is lacking systematic investigation of the H_2/CO ratio in catalytic steam biomass gasification using RSM.

In this present work, catalytic steam gasification of PKS was performed using coal bottom ash as a catalyst for maximum H_2/CO ratio. The aim of this investigation to optimize and study the systematic combined effect of gasification parameters such as temperature range of 650-750 °C, CaO/biomass ratio of 0.5-2.0, CBA wt% of 0.02-0.10, and Particle size of 0.5-1.0 mm , on H_2/CO ratio. This study will be a contribution towards utilization of waste biomass PKS for energy production to replace fossil fuel.

2. Methodology

PKS used as a feedstock in this study was collected from Kilang Sawit Nasarudin Sdn. Bhd PKS was dried in the oven to remove excess moisture content (Shahbaz et al., 2017). The dried PKS was grounded in size range of 20.5 to 1.0 mm. The thermochemical properties of PKS are presented in Table.1. The CBA is the residue of boiler of power plant located in Selangor Malaysia used as a catalyst, and CaO used as adsorbent was acquired from Kinetic Chemical Sdn Bhd.(Shahbaz et al., 2016) Table 1 presented the XRF analysis of CBA that detected Fe, Ca, Mg, and Al oxides, which makes CBA good candidate as catalyst for gasification. A multivariate design of experiment approach, Response Surface Methodology (RSM) with Central Composite Design (CCD) was applied by using Design-Expert Version 8.® software for the TGA-MS experiment design matrix (Inayat et al., 2020a). ANOVA analysis helps to quantify individual and interactive effect of process parameters on the response with the help of response surface (Shahbaz et al., 2017). Moreover, the process could be optimized with the help of tool present inside it (Shahbaz et al., 2016). In current study, the effect of four operating was chosen to see their effect on H_2/CO ratio. The range of process parameters is selected on the basis of trial runs and literature as follows, temperature (650-750 ºC), particle size (0.1-1 mm), CaO/biomass ratio (0.5-2) and coal bottom ash wt% (0.02-0.10) (Shahbaz et al., 2017). Total twenty-one experiments were designed, which include five central runs, eight axial runs, and seven factorial runs.

A thermogravimetric analyzer EXSTAR TG/DTA 3200 attached a mass spectrometer (Pfeiffer Vacuum Thermostar) incorporated with setup of steam generation system was used for the gasification of PKS (Shahbaz et al., 2016). 20 mg of sample was used for each run, and all other materials (CBA and CaO) added according to the experiment design matrix. The experiments were repeated thrice in order to reduce the experimental error. The sample was heated up to 150 °C using N_2 rate of 100 ml/min. The

sample was heated at heating rate of 25 ºC/min in inert condition. The N_2 was replaced with the steam when temperature reached at 110 ºC. The sample was heated up to the desired temperature according to designed matrix (Shahbaz et al., 2017). The biomass to steam ratio was 0.5 for each experiment.

Table.1 Proximate and ultimate analysis of PKS and XRF of CBA (Shahbaz et al., 2017)

Proximate analysis			Ultimate analysis			
Volatile matter (%)	80.81		C (%)		48.78	
Fixed carbon (%)	14.25		H (%)		5.70	
Ash content (%)	4.94		N (%)		1.01	
			S (%)		0.21	
HHV MJ/kg	18.82		O (%) (by a difference)		44.3	
Compound	SiO	Fe_2O_3	CaO	Al_2O_3	MgO	K_2O_3
Coal Bottom Ash	44.1	24.3	13	9.21	1.88	1.25

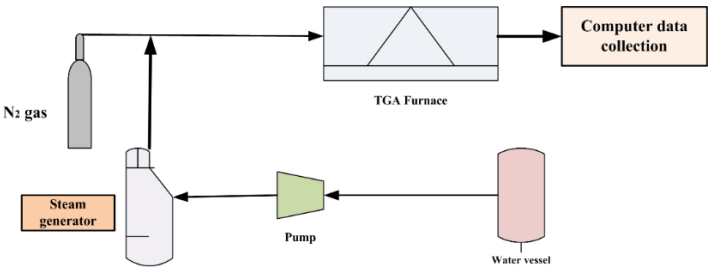

Figure1: Process Flow diagram of TGA-MS set up

Table.2: Experimental design and response results

Run	Temperature °C	Particle Size mm	CaO/Biomass ratio	CBA wt %	H_2/CO Ratio
1	700	0.75	1.25	0.003	1.431
2	700	0.75	1.25	0.06	1.470
3	650	0.50	2.00	0.02	1.218
4	700	0.75	2.30	0.06	1.334
5	650	1.00	2.00	0.10	1.237
6	700	0.75	0.18	0.06	1.407
7	700	0.75	1.25	0.06	1.468
8	700	0.75	1.25	0.06	1.477
9	700	0.75	1.25	0.06	1.470
10	750	1.00	2.00	0.02	1.252
11	700	0.75	1.25	0.06	1.470
12	650	0.50	0.50	0.02	1.295
13	700	1.10	1.25	0.06	1.253
14	700	0.39	1.25	0.06	1.356
15	630	0.75	1.25	0.06	1.182
16	650	1.00	0.50	0.10	1.254
17	750	0.50	0.50	0.10	1.355
18	700	0.75	1.25	0.12	1.450
19	750	0.50	2.00	0.10	1.430
20	770	0.75	1.25	0.06	1.315
21	750	1.00	0.50	0.02	1.294

3. Result and discussion

3.1. Statistical analysis

The functional relationship has been developed between process parameters and response (H_2/CO ratio) using RSM in catalytic steam gasification of PKS. The second-order quadratic model is found best for experimental data and a regression equation is developed in terms of coded factor, as shown in Table 3. From the ANOVA analysis it shows that model is significant as *P*–values are less than 0.05, and regression coefficient is 0.95 that shows the model fitted the data very well. Figure 2 shows that the predicted and experimental values are in close agreement. From ANOVA analysis it can be seen that temperature (A) and particle size (B) are more influencing variables towards H_2/CO ratio is due to having higher *F*-value and lower *P*-values as shown in Table 3. Whereas the CaO/biomass ratio and CBA show less effective as compared to it.

Table. 3 ANOVA for H2/CO in steam gasification of PKS

Source	*F*-value	*P*-value	Source	*F*-value	*P*-value
Model	9.026	0.006	AB	0.115	0.745
A-Temperature ºC	6.072	0.048	AC	0.767	0.414
B-Particle size mm	3.665	0.104	AD	1.373	0.285
C-CaO/biomass ratio	1.546	0.259	BC	0.029	0.869
D-CBA wt%	0.115	0.745	BD	0.286	0.612
Pure error	4.3E-05	0.767	CD	0.073	0.795
Lack of Fit	0.008	R^2	0.95	Adj-R^2	0.85

Regression equation using coded factor:

H_2/CO ratio = 1.45 + 0.047A - 0.036B - 0.013C + 0.006D - 0.020AB + 0.016AC - 0.004AD - 0.007BC + 0.006BD + 0.022CD - 0.089A² - 0.061B²- 0.0281C² + 0.006D²

3.2. Parametric analysis

The ANOVA analysis and 3-Dimensional response surface are generated to describe the effect of the individual and interactive impact of parameters on H_2/CO ratio. As temperature and particle size shows more influence on response. From Figure.2 it can be seen that H_2/CO ratio is increased from 1.1 to 1.467 by increased in temperature from 650 to 715 ºC and then dropped to 1.4 at smaller particle size. A similar trend shows a larger particle size with larger dropped at higher temperatures. The increase in H_2/CO ratio is due to increase in H_2 content, which enhances the activation of endothermic reactions such as water gas shift reaction methane reforming reaction (Shahbaz et al., 2016). The H_2/CO ratio varied in a similar pattern n when it investigated with CaO/biomass ratio and CBA wt %. The increase in ratio with the increase in CaO/biomass ratio and temperature is due to activation of endothermic reaction, and reduction of CO_2 is due to carbonation reaction (Shahbaz et al., 2017). The dropped in H_2 at elevated temperature is due to the reverse carbonation that observed by many researchers (Shahbaz et al., 2017). From figure 2 it can be seen that H_2/CO ratios are increased from 1.2 to 1.3 at small and higher particle size with the increased in CBA wt%. CBA also shows a similar effect when it is investigated with temperature. High H_2 yield causes increase in H_2/CO ratio that is due to the catalytic activity of Fe, Al, Ca, and Mg oxides of CBA, which have been used as a conventional catalyst in gasification (Inayat et al., 2020a).

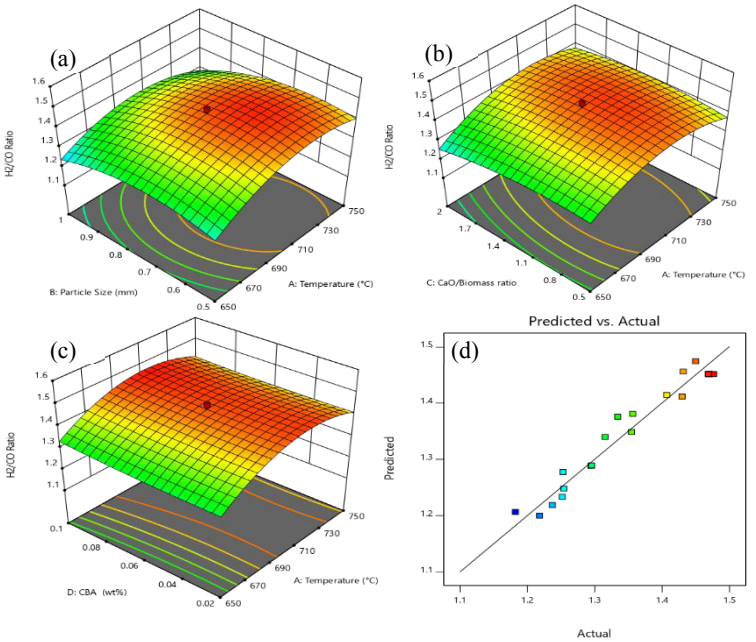

Figure 2: (a-c) 3-Dimension surface for the combined effect of process parameters H2/CO ratio for maxim and (d) Predicted vs Actual values from model

3.3. Optimization study

The obtained experimental results were utilized to optimize the parameters using the tool inside RSM for the maximize H_2/CO ratio yield (Shahbaz al., 2017). The predicted optimum parameters were summarized in Table 4. The predicted optimum parameters were performed thrice for the confirmation of predicted parameters. The standard deviation was found 0.005 shows the predicted and actual values are in close agreement.

Table 4. Optimization and predicted and experimental validation

Number	Temperature °C	Particle Size mm	CaO/Biomass ratio wt%	CBA wt%	H_2/CO Ratio
Predicted	715	0.66	1.45	0.09	1.4766
Exp. Run1	715	0.66	1.45	0.09	1.4650
Exp. Run 2	715	0.66	1.45	0.09	1.4699
Exp. Run 3	715	0.66	1.45	0.09	1.4799
Standard deviation					0.005

4. Conclusion

The catalytic steam gasification of PKS has been instituted in TGA-MS set up using CBA and CaO as a catalyst and adsorbent to investigate the H_2/CO ratio. The effect of four process parameters and interaction was studied by using RSM. The temperature and particle size have more influence on H_2/CO ratio as the ratio are increased from 1.1 to 1.4 by increasing the temperature from 650 to 710 °C and increased from 1.1 to 1.21 by increasing the particle size from 0.5 to 0.7 mm. Whereas, the CaO/biomass ratio and CBA wt% also shows a marginal effect on H_2/CO ratio.02-0.10. The optimum parameters were determined using tool inside RSM are temperature of 715 °C, CaO/biomass ratio of 1.45, particle size of 0.66mm, and CBA wt% of 0.9 for the maximum H_2/Co ratio of 1.47. The

variation in H_2/CO ratio with the increase of CBA shows the catalytic activity of Al, Fe, Mg, and Ca oxides as detected in CAB using XRF analysis.

Acknowledgment

The authors are grateful to Universiti Teknologi PETRONAS, Malaysia, and Hamad Bin Khalifa University, Doha, Qatar, for providing financial and technical assistance.

References

A. Inayat, M. Inayat, M. Shahbaz, S. A. Sulaiman, M. Raza and S. Yusup, 2020a, Parametric Analysis and Optimization for the Catalytic Air Gasification of Palm Kernel Shell ssing Coal Bottom Ash as Catalyst, Renewable Energy, 145, 671-681.

A. P. Herman, S. Yusup, M. Shahbaz, 2016, Utilization of Bottom Ash as Catalyst in Biomass Steam Gasification for Hydrogen and Syngas Production, Chemical Engineering Transactions, 52, 1249-1254.

M. Inayat, S. A. Sulaiman, J. C. Kurnia, and M. Y. Naz, 2019, Catalytic and Noncatalytic Gasification of Wood–Coconut Shell Blend under Different Operating Conditions, Environmental Progress & Sustainable Energy, 38, 688-698.

M. Inayat, S. A. Sulaiman, M. Shahbaz, and B. A. Bhayo, 2020b,. Application of Response Surface Methodology in Catalytic Co-Gasification of Palm Wastes for Bioenergy Conversion using Mineral Catalysts, Biomass and Bioenergy, 132, 105418.

T. Ma, H. Imai, T. Shige, T. Sugio, and X. Li, 2015, Synthesis of Hydrocarbons from H 2-Deficient Syngas in Fischer-Tropsch Synthesis over Co-Based Catalyst Coupled with Fe-Based Catalyst as Water-Gas Shift Reaction. Journal of Nanomaterials, 2015, 2.

T. Oh, S. Y. Pang, and S. C. Chua, 2010, Energy Policy and Alternative Energy in Malaysia: Issues and Challenges for Sustainable Growth, Renewable and Sustainable Energy Reviews, 14(4), 1241-1252.

J. Saad, and P. T. Williams, 2017, Manipulating the H_2/CO Ratio from Dry Reforming of Simulated Mixed Waste Plastics by the addition of Steam, Fuel Processing Technology, 156, 331-338.

M. Shahbaz, S. Yusup, A. Inayat, D. O. Patrick, and A. Pratama, 2016, Application of Response Surface Methodology to Investigate the Effect of Different Variables on Conversion of Palm Kernel Shell in Steam Gasification using Coal bottom Ash, Applied Energy, 18, 1306-1315.

M. Shahbaz, S. Yusup, A. Inayat, D. O. Patrick, A. Pratama, and M. Ammar, 2017, Optimization of Hydrogen and Syngas Production from PKS Gasification by using Coal Bottom Ash, Bioresource Technology, 241, 284-295.

J. Zeng, R. Xiao, D. Zeng, Y. Zhao, H. Zhang, and D. Shen, 2016, High H_2/CO Ratio Syngas Production from Chemical Looping Gasification of Sawdust in a Dual Fluidized Bed Gasifier.Energy & fuels 30(3), 1764-1770.

Sauro Pierucci, Flavio Manenti, Giulia Bozzano, Davide Manca (Eds.)
Proceedings of the 30th European Symposium on Computer Aided Process Engineering (ESCAPE30), May 24-27, 2020, Milano, Italy.
http://dx.doi.org/10.1016/B978-0-12-823377-1.50172-5

CO_2-based Acetic Acid Production Assessment

Kelvin A. Pacheco*, Antonio E. Bresciani, Claudio A. O. Nascimento, Rita M.B. Alves

Departamento de Engenharia Química, Escola Politécnica, Universidade de São Paulo, São Paulo, Brazil
kelvinpac@usp.br

Abstract

New synthetic routes to acetic acid production using CO_2 have been studied, such as methanol hydrocarboxylation, reaction of methane with CO_2, lignin with CO_2 and CO_2 hydrogenation. They represent a significant progress in synthetic chemistry, with the novel approach to acetic acid production and CO_2 transformation. These innovative routes can replace fossil raw materials by CO_2, additionally promote CO_2.abatement. This study presents an assessment of acetic acid production from CO_2 and identification of the most promising route by a multicriteria decision analysis, including process demand and characteristics, and a shortcut exergy criterion. Methanol hydrocarboxylation has demonstrated to be the best one. The process was designed based on hierarchical approach process synthesis in Aspen Plus simulator to verify its technical feasibility. An exergetic analysis was carried out in the proposed process design to evaluate thermodynamic inefficiencies. The gas recompression and the gas separation system presented the highest exergy destruction, in which possible process intensification or enhancements potentially improve the process.

Keywords: CO_2 routes to acetic acid, methanol hydrocarboxylation, process design, chemical reaction stoichiometry, exergetic analysis.

1. Introduction

Acetic acid is an important industrial chemical. According to the Mordor Intelligence Report (Intelligence, 2017), the global market was 14.2 Mt in 2017 and is expected to reach 18.2 Mt by 2023. The preferential route for glacial acetic acid production is methanol carbonylation which accounts for over 65% of the global capacity. New synthetic routes to acetic acid production using CO_2 have been studied, namely the reaction of methane with CO_2 (Wilcox et al., 2003), methanol hydrocarboxylation (Qian et al., 2016), lignin with CO_2 (Wang et al., 2019) and the hydrogenation of CO_2 (Jia et al., 2016). However, manufacturing C_{2+} carboxylic acids from CO_2 poses a commercial and innovative challenge: to reduce the production impact, lower cost raw materials and industrial design and engineering (Li et al., 2018).

The conversion of methane and CO_2 into acetic acid has received much attention recently, due to the improvement potential (100% atom economy, *i.e.* the total conversion of reactants to the desired product and avoiding the CO production step), but it presents thermodynamic restrictions. Wilcox, Roberts and Spivey (2003) synthesized acetic acid using a heterogeneous catalyst (Pd/carbon and Pt/alumina). So far, however, there has not been an efficient catalyst for acetic acid production from methane and CO_2 (Montejo-Valencia et al., 2017).

The second route is the methanol hydrocarboxylation. Qian *et al.* (2016) proposed the reaction of methanol, CO_2 and H_2 over bimetallic Ru-Rh homogeneous catalyst, the

ligand was imidazole, the promoter was LiI and 1,3 dimethyl-2-imidazolidinoe as solvent. The reported yield was 77%, the TON exceeded 1000.

Within the context of biomass conversion and to valorize lignin as a renewable source of aromatics, Wang *et al.* (2019) proposed a synthesis of acetic acid from lignin, CO_2 and H_2 over ionic liquid (**e.g.**, [BMIm][Cl])-based catalytic system containing Ru–Rh bimetal catalyst and LiI. The yield achieved was 94%.

The hydrogenation of CO_2 was studied by Jia et al. (2016), who evaluated the thermodynamics, which results showed a favorable production of higher-carbon acids (acetic acid, propionic acid) over formic acid, nonetheless kinetic constraints in C-C coupling is difficult in practice. In order to design and synthesize a process, a multicriteria analysis was performed and the most promising route was selected. A process synthesis by hierarchical approach leads to a detailed flowsheet and an exergy analysis reveals the exergy inefficiencies locations.

2. Methods

2.1. Multi-Criteria Analysis for Route Selection

Multiple criteria decision analysis (MCDA) refers to making preference decisions (*e.g.* evaluation and selection) over the alternatives available characterized by multiple attributes. The four different routes were compared through a MCDA using the Technique for Order Preference by Similarity to Ideal Solution method The elicitation of weights was obtained by the Shannon Entropy method (Shannon, 1948) and a sensitivity analysis was carried out using Monte Carlo Simulation (10% variability in weights with 100,000 runs).

Three criteria were used: (**i**) the procedure proposed by Audus and Oonk (1997) (Table 1); (**ii**) short-cut exergy demand of the chemical reaction proposed by Müller and Arlt (2014); and (**iii**) Gibbs energy of reaction.

Table 1 – Process Characteristics and their values.

Characteristic	**Value**	
	1	**2**
Number of Processes	Reaction/Sep	React/H2/Sep
Operating Conditions	Mild	Mild/Medium
Discontinuities in the process	No	Yes
Change of phase	No	Yes
possibility for process integration	Yes	No
Catalytic System	Adequate	Limited

2.2. Process Synthesis by Hierarchical Approach

Chemical process synthesis is a complex scheme, which comprises process modeling and design; it can be solved in a sequential scheme, by decomposing the hierarchy of elements (reactor, separation, heat recovery and utility). Dimian and Bildea (2008) proposed an improved hierarchical approach, reducing interactions between levels leading to a more efficient design, and it was used in this study.

2.3. Exergy Analysis

An exergy analysis based on the simulation results was carried out. Exergy refers to the maximum capacity of a system to produce useful work when balanced with its surroundings (Szargut et al., 1987). The standard chemical exergy table defined by Szargut, Morris and Steward (1987) was used; for non-reference components, the method proposed by Haghbakhsh and Raeissi (2019) was used to estimate. The methodology described in Szargut, Morris and Steward (1987) was used to calculate the chemical exergy, work and heat for a given unit operation.

3. Results and Discussions

3.1. MCDA Results

Table 2 shows the performance of each alternative for a specific criterion and its relative weight. The criterion Gibbs energy of reaction exhibited negative values for three out of four of the production process alternatives evaluated. The same behavior was observed for exergy demand; only the production process using methane and CO_2 displayed a positive value. The process characteristics criterion demonstrated similar values for all the production processes evaluated (note the smaller the value, the better).

Table 2 – Decision matrix for the acetic acid production.

Production Process	**$\Delta_r G$ (kJ/mol)**	**Exergy Demand (kJ/mol)**	**Process Characteristics[a]**
Relative weight[b]	*0.149*	*0.148*	*0.704*
CO_2 and Methane	70.19	10.77	8
Methanol Hidrocarboxylation	-46.54	-28.31	9
Lignin Oxidation	-35.92	-23.43	9
CO_2 Hydrogenation	-21.54	-30.53	9

a – The process characteristics are present in Table 1, the summation of a specific characteristic yielded the stated value in this table.
b - The relative weights were calculated using the Shannon Entropy method (Shannon, 1948).

The most promising route is methanol hydrocarboxylation (score = 0.843, std deviation = 0.007), followed by lignin oxidation (score = 0.802, std deviation = 0.008), CO_2 hydrogenation (score = 0.772, std deviation = 0.009) and lastly CO_2 and methane (score = 0.153, std deviation = 0.009). The selected route is used throughout the study.

3.2. Process Synthesis

3.2.1. Basis of Design

Considering the chemical plants in operation, the proposed plant is 200 kton/year as a target production. The methanol hydrocarboxylation route was studied in terms of catalyst availability and literature data. Two studies reported experimental data. Qian *et al.* (2016), employed a Ru–Rh bimetallic catalyst, while the second Cui *et al.* (2017) used a Rh-based catalyst. The catalyst system reported in the latter was selected because the amount of corrosive LiI used was reduced by 1/3 and effectively yield acetic acid under relative mild conditions was achieved.

3.2.2. Chemical Reaction Analysis

Chemical Reaction Stoichiometry deals with constraints placed on changes in compositions of a closed system. It can be expressed as a set of linear equations, taking the conservation of atom types into account. The algorithm proposed by Smith and Missen (1982) was used to simultaneously determine the number of independent equations and a complete set of chemical equations. The system is represented by CH_3OH, CO_2, H_2, H_2O, CH_3COOH, CH_4, C_2H_5OH, $C_3H_6O_2$, $C_4H_8O_2$. An additional restriction was imposed, CO_2 and H_2 do react, under certain conditions, in an equal amount (Cui et al., 2017). This restriction was incorporated into the general description explicitly. A complete stoichiometric matrix in canonical form is presented in Eq. (1)-(5).

$$CH_3OH + CO_2 + H_2 \rightarrow CH_3COOH + H_2O \quad (1)$$
$$3CH_3OH \rightarrow 2CH_4 + CO_2 + H_2 + H_2O \quad (2)$$
$$2CH_3OH \rightarrow C_2H_5OH + H_2O \quad (3)$$
$$2CH_3OH + CO_2 + H_2 \rightarrow C_3H_6O_2 + 2H_2O \quad (4)$$
$$3CH_3OH + CO_2 + H_2 \rightarrow C_4H_8O_2 + 3H_2O \quad (5)$$

3.2.3. Reactor/Separator/Recycle

The reactor was simulated in Aspen Plus (RStoic module), the reactions in Eq (1) – (5) were used (180ºC and 100 bar). The conversion for Eq (1) and (2) were adjusted according to the logistic fit of experimental data (Cui et al., 2017) as a function of temperature. For the conversion of Eq (3) – (5) a thermodynamic analysis was performed, and the maximum values were assumed. The solvent 1,3-dimethyl-2-imidazolidinone (DMI) (Cui et al., 2017) was also included in the simulations. The recycling of solvent and the catalyst and unreacted gases is considered.

3.2.4. Separation System

The first separation step permits the decomposition of the complex separation system into subsystems of separations, taking only monophasic streams into account. After examining the phase condition at the reactor outlet, a heterogeneous gas/liquid stream is present. The outlet stream of the reactor was cooled, goes pass through a valve to reduce the pressure and enters the flash. The temperature and pressure are optimized to recover at least 94% of CO_2 and more than 99% of hydrogen in the vapor stream and 97% of acetic acid in the liquid stream of the flash tank.

Gas Separation System

For generating separation sequences inside the subsystems (gas separation or liquid separation), the formalism of the task-oriented approach proposed by (Barnicki and Fair, 1992, 1990) was used.

An enrichment was coupled with purification to obtain a recycle stream with CO_2 and H_2 from the outlet of vapor split. The first part of the gas separation system is the removal of condensables, which are send to the liquid separation system, while the non-condensable stream enters the membrane module to remove methane. To simulate the membrane module, a model proposed by Pettersen and Lien (1994) was employed; it uses an analogy with the fundamental equation of heat exchangers. The permeability and selectivity values for the polyimide membrane were obtained from Abetz et al. (2006). The outlet stream from the membrane module is recompressed and feeds the reactor.

Liquid Separation System

A shortcut distillation column model was firstly used to estimate the parameters for a rigorous distillation column (RadFrac), in which the parameters were optimized to meet the purity requirement for acetic acid.

3.2.5. Process Analysis

In the proposed flowsheet design (Figure 1) methanol (16.3 t/h), carbon dioxide (28.9 t/h) and hydrogen (0.8 t/h) react in a solvent media yielding acetic acid (25.1 t/h). The gas separation system removes condensables using compressors (6.5 MW), coolers (7.4 MW) and a membrane module (pressure drop of 23.9 bar) yielding a stream of 57.5 %mol of hydrogen and 42.4 %mol of carbon dioxide, requiring 14.8 MW of power for the recompression system. In the liquid separation system, the solvent recovery column (17 stages and the reflux ratio of 0.09) is followed by the second column (10 stages with a reflux ratio of 2.46) to remove the lights. The dehydration column has 40 stages and reflux ratio of 5.71. Similar results were found by Feyzi and Beheshti (2017).

3.2.6. Exergy Analysis Results

An exergetic balance was performed for each subsystem of the flowsheet (Feed conditioning and recompression, reaction system, liquid-vapor split, gas separation system and liquid separation system) for identifying the magnitude and location of the inefficiencies (Figure 2). The thermodynamic inefficiencies occur mainly within the gas separation system and the gas recompression, indicating the units to be optimized.

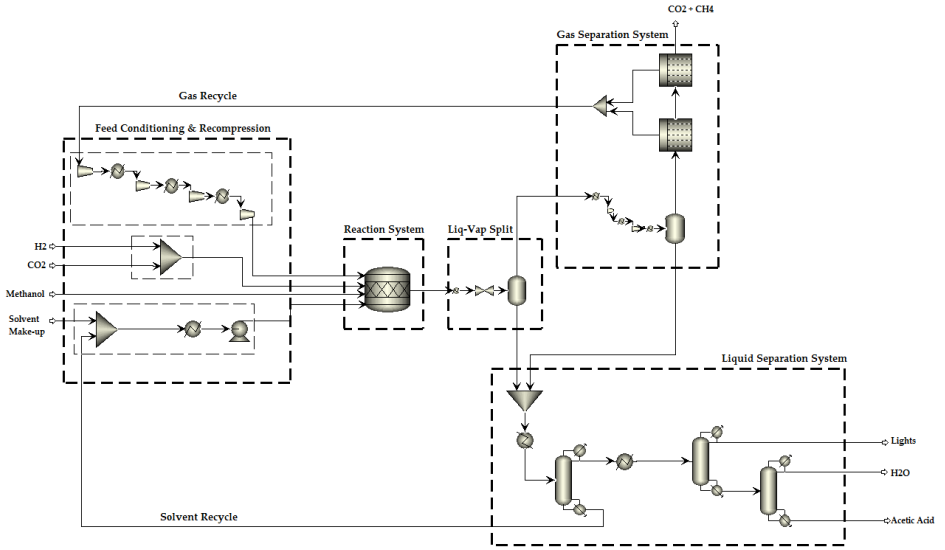

Figure 1 – Acetic acid from CO_2 flowsheet implemented in Aspen Plus.

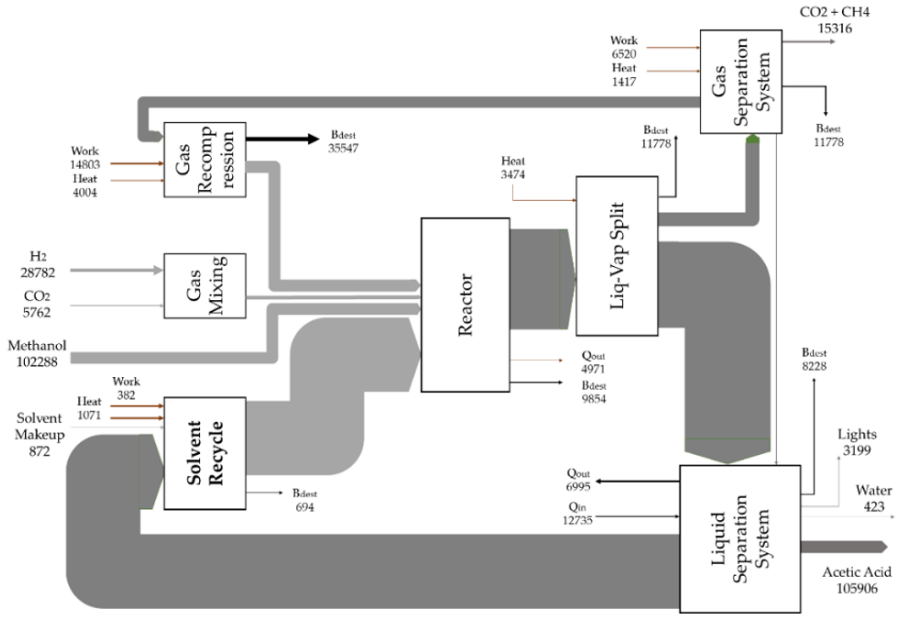

Figure 2 - True to scale exergy flow diagram (*Grassmann* chart) for acetic acid production. The main flows are shown.

4. Conclusions

This study presented an assessment of acetic acid production routes from CO_2 and a multicriteria analysis was used to select the most advantageous route in terms of process characteristic and energy demand. The methanol hydrocarboxylation route demonstrated to be the most promising and it was deeper studied. To the best of our knowledge there are no literature data regarding the process design of acetic acid production from CO_2. So, this work contributes to the field of process synthesis of CO_2 conversion to high added

value products. The flowsheet of the production process was designed based on process synthesis and demonstrated to be feasible. The exergy analysis pointed out the locations and magnitude of thermodynamic inefficiencies that can be improved for better design.

Acknowledgment

The authors gratefully acknowledge the support from FAPESP and SHELL Brasil through the Research Centre for Gas Innovation (FAPESP Proc. 2014/50279-4), hosted by the University of São Paulo, and the support given by ANP (Brazil's National Oil, Natural Gas and Biofuels Agency) through the R&D levy regulation. This study was financed in part by the Coordenação de Aperfeiçoamento de Pessoal de Nível Superior - Brasil (CAPES) - Finance Code 001. The authors acknowledge FAPESP for a PhD scholarship grant (FAPESP Proc. 2017/26683-8).

References

V. Abetz, T. Brinkmann, M. Dijkstra, K. Ebert, D. Fritsch, K. Ohlrogge, D. Paul, K. Peinemann, S. Nunes, N. Scharnagl, M. Schossig, M., 2006. Developments in membrane research: From material via process design to industrial application. Adv. Eng. Mater. 8, 328–358.

H. Audus, H. Oonk, 1997. An assessment procedure for chemical utilisation schemes intended to reduce CO2 emissions to atmosphere. Energy Convers. Mgmt 38, S409–S414.

S.D. Barnicki, J.R. Fair, 1992. Separation system synthesis: a knowledge-based approach. 2. Gas/vapor mixtures. Ind. Eng. Chem. Res. 31, 1679–1694.

S.D. Barnicki, J.R. Fair, 1990. Separation system synthesis: a knowledge-based approach. 1. Liquid mixture separations. Ind. Eng. Chem. Res. 29, 421–432.

M. Cui, Q. Qian, J. Zhang, C. Chen, B. Han, 2017. Efficient synthesis of acetic acid via Rh catalyzed methanol hydrocarboxylation with CO2 and H2 under milder conditions. Green Chem. 3558–3565.

A.C. Dimian, C.S. Bildea, 2008. Chemical process design: Computer-aided case studies. John Wiley

V. Feyzi and M. Beheshti, 2017. Exergy analysis and optimization of reactive distillation column in acetic acid production process. Chem. Eng. Process. Process Intensif. 120, 161–172.

R. Haghbakhsh and S. Raeissi, 2019. A novel atomic contribution model for the standard chemical exergies of organic compounds. Fluid Phase Equilib. 112397.

Intelligence, M., 2017. Acetic Acid Market - Segmented by Application, and Geography https://www.mordorintelligence.com/industry-reports/global-acetic-acid-market-industry (accessed 4.2.18).

C. Jia, J. Gao, Y. Dai, J. Zhang, Y. Yang, 2016. The thermodynamics analysis and experimental validation for complicated systems in CO2 hydrogenation process, J. Energy Chem., 25, 1027–1037.

J. Li, L. Wang, Y. Cao, C. Zhang, P. He, and H. Li, 2018. Recent advances on the reduction of CO2 to important C2 + oxygenated chemicals and fuels. Chinese J. Chem. Eng. 26, 2266–2279.

B. D. Montejo-Valencia, Y. J. Pagán-Torres, M. M. Martínez-Iñesta, and M. C. Curet-Arana, 2017. Density functional theory (DFT) study to unravel the catalytic properties of M-exchanged MFI for the conversion of methane and carbon dioxide to acetic acid. ACS Catal. 7, 6719–6728.

K. Müller and W. Arlt, 2014. Shortcut evaluation of chemical carbon dioxide utilization processes. Chem. Eng. Technol. 37, 1612–1615.

T. Pettersen and K. M. Lien, K.M., 1994. A new robust design model for gas separating membrane modules, based on analogy with counter-current heat exchangers. Comput. Chem. Eng. 18, 427–439.

Q. Qian, J. Zhang, M. Cui, and B. Han, 2016. Synthesis of acetic acid via methanol hydrocarboxylation with CO2 and H2. Nat. Commun. 7, 11481.

C.E. Shannon, 1948. A mathematical theory of communication. Bell Syst. Tech. J. 27, 379–423.

W.R. Smith, R.W. Missen, 1982. Chemical reaction equilibrium analysis: theory and algorithms. Wiley New York.

J. Szargut, D. R. Morris, and F. R. Steward, 1987. Exergy analysis of thermal, chemical, and metallurgical processes. Hemisphere, New York.

H. Wang, Y. Zhao, Z. Ke, B. Yu, R. Li, Y. Wu, Z. Wang, J. Han, Z. Liu, 2019. Synthesis of renewable acetic acid from CO_2 and lignin over an ionic liquid-based catalytic system. Chem. Commun. 55, 3069–3072.

E. M. Wilcox, G. W. Roberts, and J. J. Spivey, 2003. Direct catalytic formation of acetic acid from CO2 and methane. Catal. Today 88, 83–90.

Sauro Pierucci, Flavio Manenti, Giulia Bozzano, Davide Manca (Eds.)
Proceedings of the 30th European Symposium on Computer Aided Process Engineering (ESCAPE30), May 24-27, 2020, Milano, Italy.
http://dx.doi.org/10.1016/B978-0-12-823377-1.50173-7

CO_2 Conversion into Formates/Carbamates in an Electrolyte System

Maria C. M. Silva,[a*] Alessandra de C. Reis,[a] Antonio E. Bresciani,[a] Newton L. Ferreira,[b] Rita M. de B. Alves[a]

[a]*Universidade de São Paulo, Escola Politécnica, Depart.de Engenharia Química Professor Luciano Gualberto, travessa 3, 380 - São Paulo-SP 05508-010, Brazil.*

[b]*Centro Universitário FEI, Department of Chemical Engineering, Av. Humberto Alencar Castelo Branco, 3972-B - Assunção, São Bernardo do Campo - SP, 09850-901, Brazil*

mclaramendes@usp.br

Abstract

This paper explores the production of two intermediate chemicals with wide uses in industrial scale. The CO_2 hydrogenation using ammonia as an alkyl base produces ammonium formate and carbamate suitable for formic acid and urea synthesis. For this, an investigative simulation study was carried out to explore the possible operating conditions for each product. The given results pointed out that 50 °C and 1 bar favour the production of carbamate, obtaining 99% of yield and decrease formate one to less than 1%. However, low temperature (10 °C) and high pressure (50 bar) promote the formate yield to 81% and smaller quantities of carbamate, around 8%. CO_2 conversion is around 99% at 50 °C and 1 bar, when H_2O/ NH_3 ratio is 2.

Keywords: CO_2 hydrogenation, ammonia, ammonium formate, ammonium carbamate.

1. Introduction

Notably, climate change and the increase in temperature is directly caused by the increase in CO_2 emission, due to the greenhouse effect. To minimize this pollutant (CO_2) can be converted into valuable chemical products such as, methanol, acetic acid, dimethyl ether, formic acid and urea (Alper and Yuksel Orhan, 2017). To produce formic acid and urea, formates and carbamates are usually produced, as intermediates of the reaction. Methyl Formate is an intermediary in formic acid conventional production, which is mainly obtained by reacting carbon monoxide with methanol (Eq. 1 and 2) (Hietala et al., 2016).

$$CH_3OH + CO \rightarrow HCOOCH_3 \quad (1)$$

$$CH_3OOCH + H_2O \leftrightarrow CH_3OH + HCOOH \quad (2)$$

Carbamates are part of the urea synthesis, normally obtained from CO_2 and ammonia reaction (Eq. 3 and 4) (Morgan, 2013).

$$2NH_3 + CO_2 \leftrightarrow H_2NCOONH_4 \quad (3)$$

$$H_2NCOONH_4 \leftrightarrow (NH_2)_2CO + H_2O \quad (4)$$

Jessop et al. have suggested that the addition of ammonia (NH_3) in the CO_2 hydrogenation improves the production of formate and carbamate (Jessop et al., 1995). In this work, the ammonia reacts with CO_2 and H_2 to produce ammonium formate and carbamate. This route will be modeled in aqueous solution, characterized as an electrolyte system. In general, an electrolyte system is made of chemical species that can dissociate partially or totally into ions in a polar liquid medium (i.e., solvent). The presence of ions in the liquid phase requires non-ideal solution thermodynamics.

2. Modeling

The set of independent reactions of the electrolyte system was defined by applying the Chemical Reaction Stoichiometry (CRS) method developed by Smith and Missen (1998). This method is able to identify the number of independent chemical reactions associated with each reaction step in the manufacture of the desired product, including intermediates that can be separated and recycled. This method defined the reactions that occur, the intermediates and the products of the reactions. After that, the thermodynamic analysis was performed to convert CO_2 into formate and carbamate. This step was simulated by an equilibrium reactor model (*RGibbs*) in Aspen Plus V9® process simulator, considering all the species involved in the reactions, being three gaseous species (H_2, CO_2, NH_3), liquid water (H_2O) and aqueous species (CO_3^{-2}, NH_4^+, OH^-, H_3O^+, $HCOO^-$, HCO_3^-, NH_2COO^-).

The inlet reactor was at 25 °C temperature and 1 bar. The thermodynamic behavior was predicted by the ElecNRTL model, which is proper to treat electrolyte species in the simulator and the activity coefficients of the ions are based on infinite dilution in pure water.The Gibbs energy of a system at a given temperature and pressure is minimum for the state of equilibrium. Thus, the equilibrium composition can be estimated by minimizing the Gibbs energy subject to constraints of the conservation elements. The choice of species present is an important consideration in the non-stoichiometric approach. All possible major products must be included for a realistic composition profile of a process. A sensitivity analysis was carried out conducted to evaluate the influence of temperature, pressure and ratio of the reactants on the system to convert the CO_2 into formate and carbamates. All the results are reported in terms of CO_2 and H_2 conversion and product yield. Table 1 provides the parameter definitions for the process.

Table 1. Definition of conversion and yield parameters

Parameter	Definition
CO_2 conversion	$\left(\frac{F_{CO_{2,out}} - F_{CO_{2,in}}}{F_{CO_{2,in}}}\right) x100$
H_2 conversion	$\left(\frac{F_{H_{2,out}} - F_{H_{2,in}}}{F_{H_{2,in}}}\right) x100$
$HCOO^-$ yield	$\left(\frac{F_{HCOO^-_{out}}}{F_{CO_{2,in}}}\right) x100$
NH_2COO^- yield	$\left(\frac{F_{NH_2COO^-_{out}}}{F_{CO_{2,in}}}\right) x100$

The effect of three variables was evaluated: temperature, pressure and reactants ($NH_3/H_2O/H_2/CO_2$) ratio. Initially, all the reactants were in the ($NH_3/H_2O/H_2/CO_2$ =1) ratio at 1 bar and 25 °C. The temperature and pressure of the reactor were varied from 10 to 100 °C and from 1 to 50 bar, with 10 units of increment.

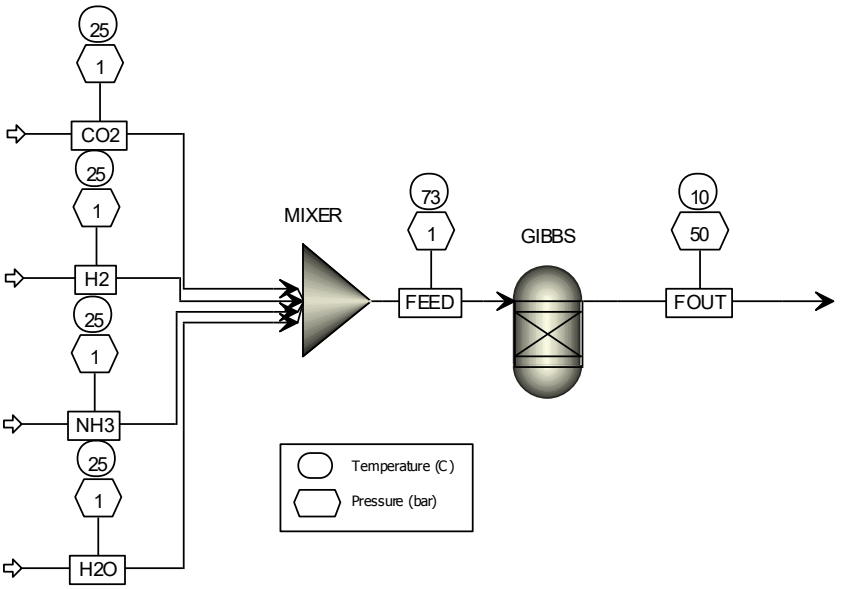

Figure 1. Simplified scheme of the process, initially at 25 °C, 1 bar and ($NH_3/H_2O/H_2/CO_2$ =1).

3. Results and Discussion

The procedure implemented by the Chemical Reaction Stoichiometry method resulted in 6 independent chemical reactions, which represent the electrolyte system of this study. Table 2 indicates all the reactions with their enthalpy and Gibbs energy of reaction and their remarks, respectively.

Table 2. Set of independent reactions for the electrolyte system

	Reaction	ΔH_R°	ΔG_R°	Remark
1	$CO_{2g} + 2NH_{3_g} + H_2O_l \leftrightarrow 2NH_{4aq}^{+} + CO_{3_{aq}}^{-2}$	170.67	-22.14	Endothermic, reversible, favored by high temperature
2	$H_2O_l + CO_{3_{aq}}^{-2} \leftrightarrow 2OH_{aq}^{-} + CO_{2g}$	109.46	56.14	Endothermic, reversible, favored by high temperature
3	$3H_2O_l + CO_{2g} \leftrightarrow CO_{3_{aq}}^{-2} + 2H_3O_{aq}^{+}$	2.58	104.10	Endothermic, reversible, favored by high temperature
4	$2H_{2_g} + CO_{2g} + CO_{3_{aq}}^{-2} \leftrightarrow 2HCOO_{aq}^{-} + 2H_2O_l$	-66.32	-17.00	Exothermic, reversible, favored by low temperature
5	$CO_{2g} + H_2O_l + CO_{3_{aq}}^{-2} \leftrightarrow 2HCO_{3_{aq}}^{-}$	-27.51	-14.27	Exothermic, reversible, favored by low temperature
6	$CO_{2g} + 2NH_{3_g} + CO_{3_{aq}}^{-2} \leftrightarrow 2NH_2COO_{aq}^{-} + H_2O_l$	115.29	-93.88	Endothermic, reversible, favored by high temperature

3.1. Sensitivity Analysis

In this process, CO_2 conversion is affected by the temperature and pressure applied to the system. Figure 2 a-b shows how these two variables influence the conversion of the reactants and products yields, respectively. The equilibrium conversion for both CO_2 and H_2 is high at lower temperature and higher pressure and decreases for higher temperature.

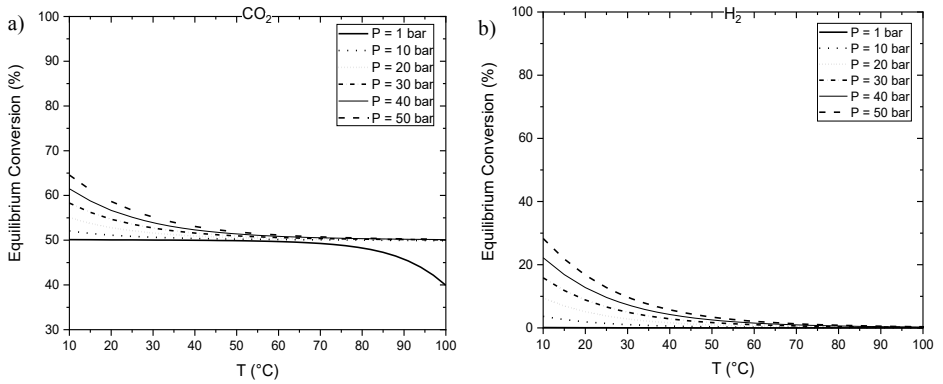

Figure 2. Effect of temperature and pressure on: a) CO_2 conversion, b) H_2 conversion at CO_2/H_2/NH_3/H_2O ratio = 1.

The highest CO_2 conversion (Fig. 2a) is 64% at 10 °C and 50 bar and (NH_3/H_2O/H_2/CO_2 =1) ratio. However, H_2 is less consumed at the same conditions, almost 30% conversion (Fig 2b). This difference is due to the numbers of reactions that CO_2 and H_2 participate in. CO_2 is consumed to produce ammonium formate and carbamate, while H_2 only reacts with ammonia and CO_2 to produce formate. Figure 3a-b are relative to the products yields.

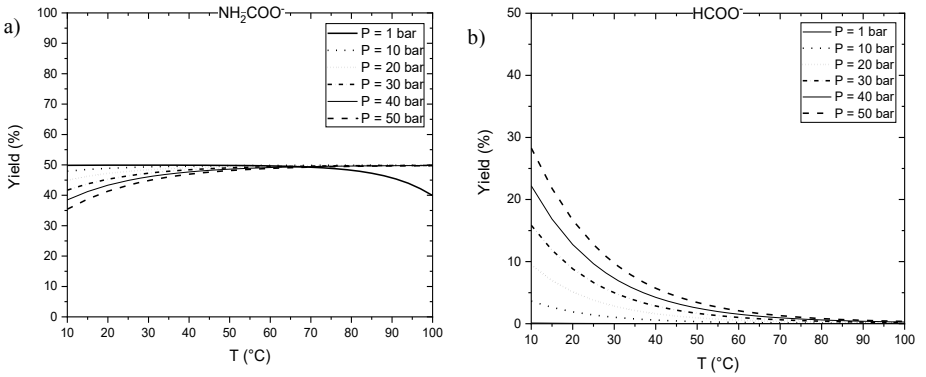

Figure 3. Effect of temperature and pressure on: a) Ammonium carbamate yield, b) Ammonium Formate yield at CO_2/H_2/NH_3/H_2O ratio = 1.

The ammonium formate yield increases at lower temperatures (10 °C) and higher pressure (50 bar), whereas ammonium carbamate yield is favoured at temperatures starting with 50 °C and room pressure (1 bar), according to Le Chatelier's Principle the formate reaction is exothermic, while, carbamate reaction is endothermic as shown in Table 3. From all the reactants variation relatively to water, ammonium carbamates concentrations in solution is higher when H_2O/NH_3 ratio is 2. Figure 4 shows that the highest yield is obtained by fixing temperature and pressure at 50 °C and 1 bar, respectively, and varying H_2O/NH_3 ratio.

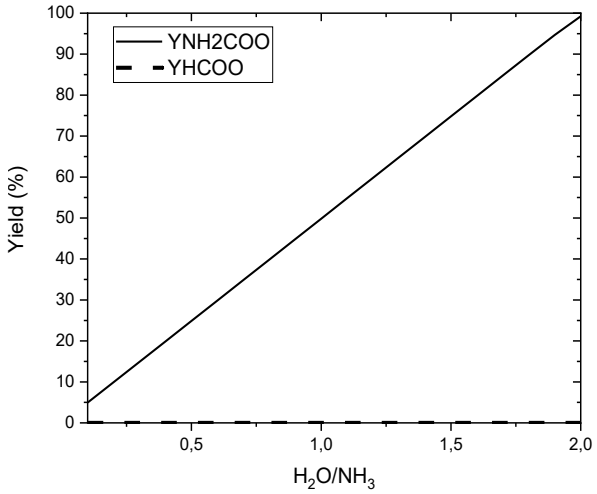

Figure 4. Effect of H2O/NH3 ratio on ammonium carbamate and ammonium formate yield at 50 °C and 1 bar.

Almost 99% of ammonium formate is obtained by fixing temperature and pressure at 10 °C and 50 bar, respectively, and increasing the H_2O/NH_3 ratio to 2. Figure 5 shows the conditions that the highest ammonium formate yield is reached.

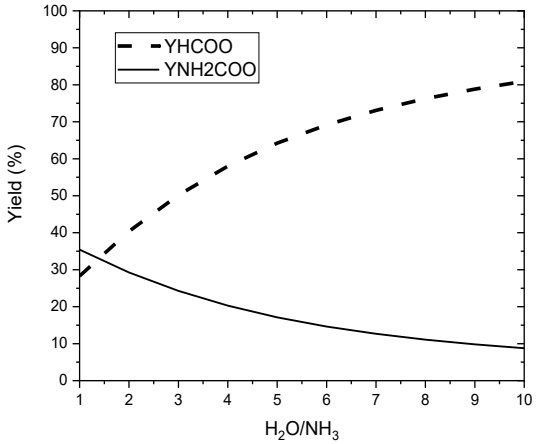

Figure 5. Effect of H2O/NH3 ratio of 10 on ammonium carbamate and ammonium formate yield at 10 °C and 50 bar.

This phenomenon occurs because a large quantity of water in the system enables the dissolution of the gases in the solution, which can increase the concentration of its ions. When there is less amount of ammonia in the solution, H_2 is free to reacts with CO_2, and produce more ammonium formate. As shown in Table 2, the reaction of ammonium formate production is exothermic.

4. Conclusions

The addition of ammonia makes the reaction thermodynamically viable for both ammonium formate and carbamate products. To detail the study on thermodynamic equilibrium on CO_2 and H_2 conversion into the products, the set of independent reactions was calculated through the Chemical Reaction Stoichiometry method. The influence of the variables studied, temperature, pressure and H_2O/NH_3 ratio were observed into both products yield. The results indicate that ammonium carbamate is favoured when temperatures are above 50 °C, low pressures, such as 1 bar, and H_2O/NH_3 ratio of 2 are applied. However, to shift the equilibrium to ammonium formate, lower temperature (10 °C), higher pressure and a H_2O/NH_3 ratio of 10 are required, reaching almost 81% of formates in the solution.

Acknowledgements: The authors would like to thank the sponsorship of Shell and FAPESP through the "Research Centre for Gas Innovation – RCGI" (FAPESP Proc. 2014/50279-4), hosted by the University of São Paulo, and the strategic importance of the support given by ANP (Brazilian National Oil, Natural Gas and Biofuels Agency) through the R&D levy regulation.

This study was financed in part by the Coordenação de Aperfeiçoamento de Pessoal de Nível Superior - Brasil (CAPES) - Finance Code 001.

References

Alper, E., Yuksel Orhan, O., 2017. CO2utilization: Developments in conversion processes. Petroleum 3, 109–126. https://doi.org/10.1016/j.petlm.2016.11.003

Hietala, J., Vuori, A., Johnsson, P., Pollari, I., Reutemann, W., Kieczka, H., 2016. Formic acid. Encycl. Ind. Chem. ULLMANN'S. https://doi.org/10.1002/14356007.a12_013.pub3

Jessop, P.G., Ikariya, T., Noyori, R., 1995. Homogeneous Hydrogenation of Carbon Dioxide. Chem. Rev. 95, 259–272. https://doi.org/10.1021/cr00034a001

Missen, R.W., Smith, W.R., 1998. Chemical Reaction Stoichiometry (CRS):

Morgan, E.R., 2013. Techno-Economic Feasibility Study of Ammonia Plants Powered by Offshore Wind. Univ. Massachusetts - Amherst, PhD Diss. 432.

Sauro Pierucci, Flavio Manenti, Giulia Bozzano, Davide Manca (Eds.)
Proceedings of the 30th European Symposium on Computer Aided Process Engineering (ESCAPE30), May 24-27, 2020, Milano, Italy.
http://dx.doi.org/10.1016/B978-0-12-823377-1.50174-9

Process Systems Design Framework for Resource Recovery from Wastewater

Alex Durkin[a], Marcos Millan-Agorio[a], Miao Guo[a,b,*]

[a] *Department of Chemical Engineering, Imperial College London, SW7 2AZ, UK*
[b] *Department of Engineering, Strand Campus, King's College London, WC2R 2LS, UK*
miao.guo@imperial.ac.uk

Abstract

A surrogate-based superstructure optimisation framework is presented and applied to the design of optimal flowsheets for the recovery of resources from wastewater. The process systems design framework involves training artificial neural networks (ANNs) using data sampled from commercial simulation software, where the sampling strategy incorporates Sobol sequences and support vector machines, ensuring good feasible design space coverage. A mixed integer linear programming (MILP) problem is formulated to solve the design problem for a set of optimal flowsheets highlighting the trade-offs between economic and environmentally focussed objective functions. However, despite the formulation of the MILP problem guaranteeing globally optimal solutions, this assurance comes at the expense of errors in the ANNs. These errors could become considerable for large design spaces, so exploration of the trade-off between optimality and accuracy is highlighted as a direction for future work.

Keywords: superstructure optimisation, resource recovery, surrogate modelling

1. Introduction

1.1. Background

Despite an explosion in process technology innovation, the successful deployment of these technologies is constrained by a lack of decision-making tools addressing the integration of technologies within optimal flowsheets. This process synthesis problem can be addressed by computer-aided process design, whereby evaluation of different flowsheets is achieved without the time and capital investments required for experimental or pilot scale studies. Specifically, superstructure optimisation can be used to rigorously search the design space for an optimal flowsheet, given a set of modular process units and possible interconnections (Yeomans and Grossmann, 1999).

Superstructure optimisation is a mathematical method whereby a flowsheet-wide performance indicator is optimised by determining the selection of process units, the design of these process units, and the interconnections between them. Binary variables are used for the selection of process units and interconnections, resulting in mixed integer programming (MIP) problems. However, there are many degrees of freedom in how to formulate and solve these MIP problems, including the choice of rigorous versus surrogate models. The former refers to complex models based on fundamental equations, whilst the latter addresses simpler reformulations to represent the complex underlying models in a more tractable form. Inherent in this decision is a trade-off between model complexity and tractability, where the use of accurate yet complex models lends to more computationally expensive optimisation problems, while more tractable surrogate models often come at the expense of solution accuracy.

Rigorous models are often embedded within black-box simulation software, allowing the user to observe input-output data but not the underlying model formulations. In these cases, computer experiments can be used to sample input-output data, providing training data for surrogate model formulations (Caballero and Grossmann, 2008). However, challenges associated with this approach include: choosing which variables to sample; assigning bounds to design variables; selecting a sampling strategy; and choosing surrogate model formulations which are accurate yet tractable. Further challenges with the superstructure optimisation methodology include: postulating the design space within a mathematical optimisation problem; formulating a tractable MIP problem; and solving the optimisation problem for the globally optimal flowsheet design. It is therefore beneficial to have methodological frameworks in place to assist in superstructure optimisation of process flowsheets.

1.2. Research Objectives

This research addressed the research objectives: develop a process systems design framework for the multi-criteria optimisation of process flowsheets; and application of the framework to resource recovery from wastewater, requiring tractable surrogate model formulations to represent complex process unit models. By addressing these objectives, this study provided a decision-making tool to assess process viability within integrated flowsheets, thereby assisting in resource recovery technology deployment.

Section 2 presents the methodology framework developed in this study. Section 3 applies the methodology to systems design for recovery of resources from a fermentation process wastewater. Finally, Section 4 presents some concluding remarks.

2. Methodology

Figure 1 shows the methodological framework developed in this study. The framework consists of 3 stages: an initialisation phase in which the flowsheet design space is posed; a surrogate modelling stage to generate the reduced-order surrogate models used to represent individual process units within the MIP problem; and the superstructure optimisation which solves the MIP problem for the optimum flowsheet.

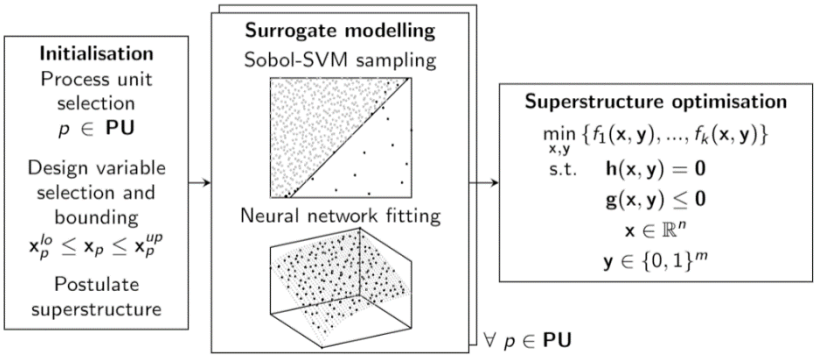

Figure 1. Process systems design framework.

2.1. Initialisation

In the initialisation phase, a set of process units were selected for consideration in the flowsheet optimisation. For each process unit within this set, design variables were chosen and bounds selected, thereby defining a hypercube representing the process unit design spaces. Connectivity between process units was then facilitated by connectivity

constraints, thereby formulating the superstructure within the mathematical optimisation problem. Together, the individual process unit design hypercubes and superstructure connectivity constraints defined the entire flowsheet design space, within which the flowsheet configuration and active process unit designs were optimised.

2.2. Surrogate modelling

For each process unit, surrogate models were formulated to calculate output variables given different combinations of input variables. Output variables include process unit output stream flows and compositions as well as economic and environmental performance indicators. Input variables refer to the process unit design variables and the flows and compositions of influent streams. The surrogate models therefore facilitate the superstructure optimisation by relating different flowsheet designs to performance variables appearing in the objective function being optimised. Surrogate models can also be of a reduced order, relative to their rigorous counterparts, which is particularly useful when the rigorous models are highly dimensional and the input-output variables of interest are relatively few.

2.2.1. Sampling

The surrogate modelling phase begins with sampling input-output data from commercial process simulators embedding state-of-the-art rigorous models and costing functions. Sobol sequences were used to generate samples with good design space coverage with a minimum number of samples (Munoz Zuniga et al., 2013). Additionally, by ensuring information was sampled at the vertices of the design space, the surrogate model accuracy for these critical designs was increased. This is important due to the tendency for optimal solutions to exist at the bounds of the design space hypercube.

The modularity of the superstructure required not only design variables to be sampled, but also interdependent influent stream variables. The interdependencies were represented by calculating the covariance matrix for effluent variables from upstream process units. Then, by generating Sobol samples from an assumed underlying normal distribution, influent variable samples were extrapolated using the covariance matrix. This allowed influent variable interdependencies to be mapped between process units, ensuring meaningful influent compositions were being sampled.

2.2.2. Support vector machines (SVMs)

SVMs were integrated within the sampling strategy to simultaneously increase feasible design space coverage, and construct feasibility constraints. Feasibility of a given process unit design was determined by the successful or failed convergence of the black-box simulator, giving rise to a binary classification problem to which SVMs could be applied to determine the optimum separating hyperplane. By activating the SVMs after a few initial samples, subsequent infeasible design samples were substituted by samples at feasible designs. Specifically, SVMs with linear classification functions were used to generate linear feasibility constraints for use in the optimisation.

2.2.3. Surrogate models

The input-output data sampled from computer experiments was used to train surrogate models which represent the underlying complex black-box functions in a more tractable formulation for use in optimisation. Artificial neural networks (ANNs) were used as surrogate models due to their ability to model multiple input-output relations with good accuracy. Specifically, two-layer feed-forward ANNs were exploited due to their layered structure being representable by a set of linear constraints directly implemented in the mathematical optimisation. Additionally, formulation as a mixed integer linear

programming (MILP) problem was facilitated using symmetric saturating linear functions and linear functions as activation functions in the hidden and output layer, respectively (Figure 2). The resulting ANN surrogate model constraints were therefore able to capture complex non-linearities from the rigorous models with a set of layered linear functions. ANN training and evaluation was performed in Python using Neurolab.

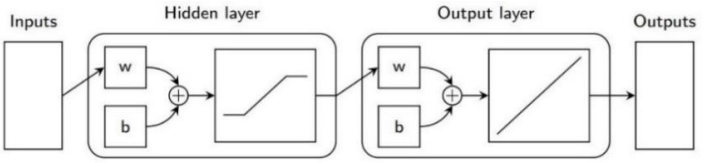

Figure 2. Two-layer feed-forward ANN configurations. Activation functions in the hidden and output layer are: symmetric linear saturating functions and linear functions, respectively.

2.3. Superstructure optimisation

The resulting MILP problem has the general formulation shown by Eq. (1) to Eq. (5),

$$\min_{x,y} z \tag{1}$$

$$s.t. \quad h(x,y) = 0 \tag{2}$$

$$g(x,y) \leq 0 \tag{3}$$

$$x \in \Re^n \tag{4}$$

$$y \in \{0,1\}^m \tag{5}$$

where z denotes the objective function optimising flowsheet-wide performance indicators dependent on the flowsheet configuration and active process unit designs. x and y are continuous design variables and binary selection variables, respectively. Both x and y are bounded by equality constraints, h, and inequality constraints, g, that enforce flowsheet connectivity and process unit surrogate models. The superstructure optimisation was formulated as a MILP problem in Pyomo and solved to global optimality using Gurobi (Hart et al., 2011; Gurobi Optimization, LLC, 2019).

3. Application

The methodology presented in Section 2 was applied to the design of an optimal process system to recover resources from wastewater. Specifically, the wastewater being considered comes from an industrial-scale fermentation process and is high in chemical oxygen demand (COD) and nutrients. The mathematical optimisation problem was posed to solve for a set of flowsheets representing the trade-off between economic and environmental objective criteria. Constraints implemented within the MIP problem also ensured that final effluent concentrations of total COD, total nitrogen (TN), and total suspended solids (TSS) were below environmental regulation limits. The application presented herein therefore explored: the trade-offs between recovering energy and/or nutrients; trade-offs between different flowsheets for recovering these resources; and the economic-environmental trade-offs between different flowsheet design focuses.

3.1. Process unit selection

Anaerobic reactors were considered for the recovery of biogas via decomposition of the wastewater COD. Specifically, two different reactor configurations were included in the superstructure, namely an upflow anaerobic sludge blanket (UASB) reactor and an

anaerobic membrane bioreactor (AnMBR). For these reactors, the volumes and design of subsequent settling processes (surface area and waste sludge pumping rate) were optimised simultaneously within the flowsheet.

To ensure that final effluent constraints were met by the designed flowsheets, further processes units were considered to remove TN and TSS from the wastewater, namely: nitrification-denitrification (ND), anammox (AX), and secondary clarifiers (SC). Design variables for these process units included: volumes (ND, AX, SC), aeration rates (ND, AX), COD dosing rate (ND), and waste sludge pumping rate (SC).

The superstructure resulting from the initialisation phase is shown by Figure 3. Input-output data were sampled from GPS-X and CapdetWorks, which are state-of-the-art commercial simulators embedding rigorous wastewater treatment models and costing functions, respectively (Hydromantis, 2019).

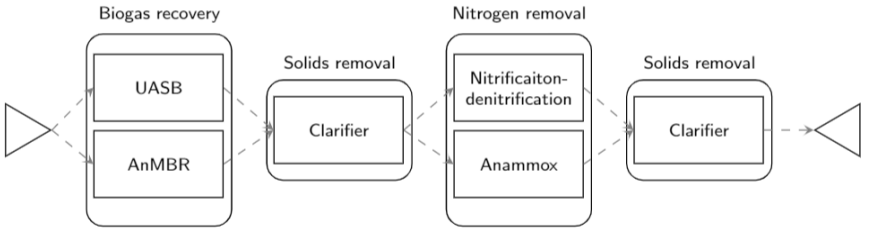

Figure 3. Superstructure of process units considered in application. Each functional stage (biogas recovery, solids removal, nitrogen removal) can also be bypassed.

3.2. Surrogate models

The input-output data was split into a training set, used to train the ANNs, and a test set used to validate the ANN performances (Table 1).

Table 1. Mean absolute error (MAE) and mean relative error (MRE) in ANN predictions.

Process unit	MAE	MRE / %
UASB	1.4	5.8
AnMBR	0.07	1.0
ND	7.7	19.9
AX	3.2	19.7

Some errors were accepted in the ANNs to avoid overfitting and maintain smooth input-output relations that well represented the underlying rigorous model trends. ANNs exhibited good performance for UASB and AnMBR models; AnMBR MAEs were particularly small due to the membrane resulting in small output concentrations. ND and AX models were less well represented by the ANNs due to the introduction of influent stream variables as inputs, thereby increasing the dimensionality of the design space.

3.3. Superstructure optimisation

The resulting MILP problem, containing connectivity constraints, process unit surrogate models, design variable bounds, and binary selection variables, consisted of 247 continuous variables, 195 binary variables, and 1060 linear constraints. Using Pyomo and Gurobi, the problem was solved to global optimality in 23.6 seconds, on a computer running 64-bit Linux on Dual 12-Core Intel Xeon 2.2 GHz processors with 96 GB RAM.

3.4. Solutions

The set of Pareto optimal flowsheets representing the tradeoff between economic and environmental objectives are shown in Figure 4a. The economic objective function was

to minimise annual cost, incorporating fixed and operating costs (data obtained from CapdetWorks) as well as revenues from selling recovered biogas. The environmental objective function was to minimise annual greenhouse gas (GHG) emissions, with any produced biogas modelled as substituting natural gas production. The embedded GHGs, expressed as CO_2-eq per material, were obtained as life cycle impact factors from the ecoinvent database, using the ReCiPe Midpoint characterisation method. The optimum flowsheet designs for the economic and environmental objective function are shown in Figure 4b and 4c, respectively.

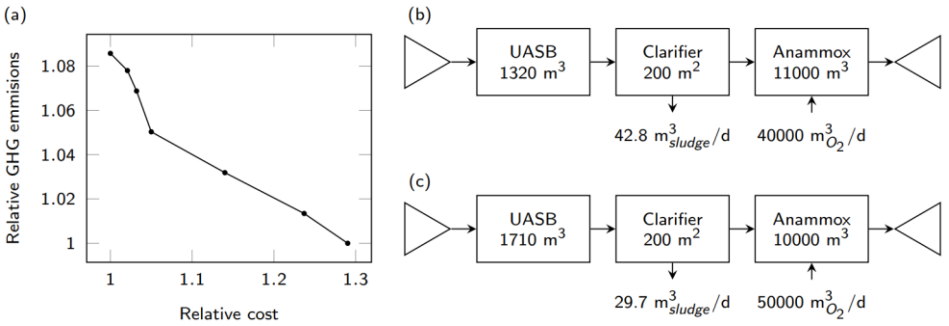

Figure 4. (a) Set of Pareto-optimal solutions representing the economic-environmental trade-off where data is shown relative to the optimum designs; (b) economic optimal flowsheet design; (c) environmental optimal flowsheet design.

Figure 4a depicts the trade-off between the different design criteria: the environmental optimum design is almost 30 % more expensive than the economic optimum; yet the cost optimal flowsheet emits more than 8 % CO_2-eq. Figure 4b and 4c only differ in the comprising process unit designs as a result of the limited feasible design space that meets final effluent constraints.

4. Conclusions

The presented design framework allows for MILP formulations for the optimisation of process systems, allowing for globally optimal flowsheets to be highlighted despite the incorporation of complex process units. However, as demonstrated, this guarantee of global optimality comes at the expense of some accuracy in the surrogate models. For larger superstructure postulations with many process units in series, the errors in the surrogate models propagate through the process train and become significant. Future work will aim to increase accuracy by: integrating the framework within an iterative approach; or exploring other surrogate models and their accuracy-tractability trade-off.

References

J. Caballero, I. Grossmann, 2008, An algorithm for the use of surrogate models in modular flowsheet optimization, AICHE Journal, 54, 10, 2633-2650

Gurobi Optimization, LLC, 2019, http://www.gurobi.com

W. E. Hart, J. P. Watson, D. L. Woodruff, 2011, Pyomo: modeling and solving mathemtical programs in Python, Mathematical Programming Computation, 3, 3, 219-260

Hydromantis Environmental Software Solutions, Inc., 2019, http://www.hydromantis.com

M. Munoz Zuniga, S. Kucherenko, N. Shah, 2013, Metamodelling with independent and dependent inputs, Computer Physics Communications, 184, 6, 1570-1580

H. Yeomans, I. E. Grossmann, 1999, A systematic modeling framework of superstructure optimization in process synthesis, Computers and Chemical Engineering, 23, 6, 709-731

Sauro Pierucci, Flavio Manenti, Giulia Bozzano, Davide Manca (Eds.)
Proceedings of the 30th European Symposium on Computer Aided Process Engineering (ESCAPE30), May 24-27, 2020, Milano, Italy.
http://dx.doi.org/10.1016/B978-0-12-823377-1.50175-0

Intensified green process for synthesizing non-phosgene hexamethylene-1,6-dicarbamate

San-Jang Wang,[a,*] David Shan-Hill Wong,[b] Yu-Zhang Chen,[b] En-Ko Lee[a]

[a]*Center for Energy and Environmental Research, National Tsing Hua University, Hsinchu 30013, Taiwan*
[b]*Department of Chemical Engineering, National Tsing Hua University, Hsinchu 30013, Taiwan*
wangsj@mx.nthu.edu.tw

Abstract

Hexamethylene diisocyanate (HDI) is an important chemical building block in the production of high value-added polyurethane because of its some excellent properties. Traditionally, the HDI synthesis route involves extremely toxic phosgene as an industrial scale reagent. Recently, thermal decomposition of hexamethylene-1,6-dicarbamate (HDC) has been considered as the most attractive non-phosgene process for the HDI synthesis because HDC can be synthesized by reacting 1,6-hexamethylene diamine (HDA) with a green compound, dimethyl carbonate (DMC), instead of toxic phosgene. Therefore, the intermediate HDC synthesis is crucial to the whole process. In the study, design of two plant-wide processes is explored for green HDC synthesis. In the first process, HDC is produced in two reactive distillation (RD) columns in series. Complete conversion of HDA is designed and excess DMC reactant is used to increase the reaction conversion. The mixture of un-reacted DMC and by-product methanol from RD column tops is separated by a series of conventional distillation columns containing a pre-concentrator column and an extractive distillation system comprising an extractive distillation column and a solvent recovery column. In the second process, RD is enhanced by vapor recompression (VR) to reduce energy consumption. The key cost saving from VR is attributed to fully take advantage of small temperature difference between RD column bottom and top, and higher RD column top temperature rendering condenser duty totally utilized by RD column bottom. Furthermore, additional latent heat of RD overhead vapor is released to the extractive distillation system by external heat integration, which can then achieve significant saving in the operation cost of this system. Compared to the RD intensified process, total annual cost of the RD+VR intensified process can be reduced by 35%.

Keywords: process intensification, reactive distillation, vapor recompression, green process.

1. Introduction

Hexamethylene diisocyanate (HDI) is an important chemical building block in the production of high value-added polyurethane products because of its excellent properties. HDI is traditionally synthesized by the phosgenation of 1,6-hexanediamine (HDA). Recently, a non-phosgene method, comprising two steps, has attracted much attention. The first step is the synthesis of hexamethylene-1,6-dicarbamate (HDC) and the second one is the decomposition of HDC to HDI. In this method, HDC is an intermediate and its synthesis is critical in the whole HDI production process. There are some routes to

synthesize HDC. However, these routes suffer from strict reaction conditions, use of expensive catalysts, and production of some byproducts. In recent years, the reaction of HDA with dimethyl carbonate (DMC) under mild operation conditions has become an attractive and popular route to synthesize HDC. DMC is a green compound and used as an important building block for various organic synthesis. The HDC synthesis from DMC is considered as a promising means because DMC can replace phosgene for the methoxycarbonylation of HDA.

Recent research of producing HDC by reacting HDA with DMC mostly concentrated on catalyst screening (Li et al., 2014; Ammar et al., 2017). However, very few literatures investigated the process design of non-phosgene HDC synthesis. In this study, we present the plant-wide process design of non-phosgene HDC synthesis by the reaction of HDA with DMC. Reactive distillation (RD) and vapor recompression (VR), two promising technologies of process intensification, are employed here in the green HDC synthesis process. The stoichiometric molar ratio of two reactants, DMC and HDA, is equal to 2. In most experimental studies, the molar ratio of DMC to HDA is mainly in the range of 4 to 8. Excess DMC reactant is used in our study to increase reaction conversion and complete HDA reaction conversion is achieved by two tandem RD columns. Un-reacted DMC and by-product MeOH can form a minimum-boiling homogeneous azeotrope with temperature of 63.8 °C and DMC composition of 13.3 mol% at atmospheric pressure. This azeotrope is separated by a pre-concentrator column and an extractive distillation system (EDS) using aniline as the solvent. In addition, the RD column is enhanced by VR to reduce energy consumption by fully taking advantage of a narrow temperature difference between bottom and top streams of HDC synthesis RD column. Finally, the VR effect on the economic performance of RD process is evaluated.

2. Design of RD intensified process for HDC synthesis

The HDC synthesis by HDA and DMC consists of two reactions given below.

$$\mathrm{HDA + DMC \rightarrow HMC + MeOH} \quad (1)$$

$$\mathrm{HMC + DMC \rightarrow HDC + MeOH} \quad (2)$$

The overall reaction is

$$\mathrm{HDA + 2DMC \rightarrow HDC + 2MeOH} \quad (3)$$

DMC is first reacted with HDA to form an intermediate HMC (dimethylhexane-1,6-monocarbamate). Then DMC is reacted with HMC to produce the main product HDC. Recently, Cao et al. (2018) screened several catalysts in the reaction of HDA with DMC, concluded that $Mn(OAc)_2$ was the most effective catalyst, and gave a kinetic model using $Mn(OAc)_2$ as a catalyst.

In the design of HDC synthesis process, the economic objective is to minimize the total annual cost (TAC) by adjusting design variables. TAC comprises annual capital cost and operation cost. Annual capital cost takes into account the annual costs of column, condenser, reboiler, compressor, and heat exchanger. Payback period is assumed to be eight years in this calculation. An annual operating time is assumed to be 8322 hours. The operation cost contains the costs of cooling water, steam, and electricity. The unit costs of these utilities are adopted from the formulas given by Turton et al. (2012).

In this study, a commercial simulator, ChemCad, is used to execute the process simulation of non-phosgene HDC synthesis. The pure components sorted in the order of increasing normal boiling temperature are as follows: MeOH (64.7 ºC) < DMC (90.3 ºC) < aniline (184.4 ºC) < HDA (201.9 ºC) < HMC (290.2 ºC) < HDC (371.8 ºC). Two reactants, HDA and DMC, are two intermediate boilers while the main product HDC and by-product MeOH are the heaviest and lightest boilers, respectively. This boiling point arrangement is the most favorable case for RD. Reactants can be easily kept within the RD column to proceed reaction while HDC and MeOH can be simply withdrawn from bottom and top, respectively, of the RD column. In the studied system, vapor-liquid equilibrium relationships for three pairs of binary components in a DMC-MeOH-aniline mixture can be described by UNIQUAC model (Hsu et al., 2010). The modified UNIFAC model is utilized to determine the phase equilibrium relationships of other pairs not built in the ChemCad database.

The optimal configuration of RD intensified HDC synthesis process cab be achieved by sequential iterative steps to minimize TAC. There are two RD columns and three conventional distillation (CD) columns in this configuration. Reflux ratio and reboiler duty are two operation variables in every column. However, there are many design variables in this process. Due to the scope limit, the optimization steps for different configurations are omitted. In the optimal RD intensified process, two reactants, HDA with 50 kmol/h and DMC with 235 kmol/h, are fed into the first RD (RD1) column at stages 8 and 9, respectively. This column has a rectification zone of 8 stages and a reaction zone of 39 stages. The RD1 column is chosen to be operated at 1 atm, the same value as that in the kinetic study of Cao et al. (2018). Because the boiling point of DMC is 90.3 °C, the temperature for liquid-phase reaction of HDA with DMC is limited in our study to be not greater than 90 °C. The maximum reaction conversion can be obtained when reaction temperature is set at 90 °C. Thus, the RD column base is designed to be operated at 90 °C. The catalyst is fed together with DMC into the RD1 column because of the consideration of reaction temperature constraint.

The bottom product of RD1 column contains by-product, intermediate, and main products (MeOH, HMC, and HDC) together with un-reacted HDA and DMC. In the patent of Wang et al. (2006), HDC can be separated from the reaction mixture by crystallization. Thus, in our study, HDC is assumed to be completely separated from the bottom product by crystallization. HDC with 29.9 kmol/h can be crystallized from the bottom stream of RD1 column. The mixture other than HDC is next fed into the second RD column (RD2) at stage 7 for further reaction. The RD2 column, operated at 1.09 atm, contains a rectification zone of 6 stages and a reaction zone of 43 stages. RD2 column base is also operated at 90 °C. HDA is completely reacted and HDC of 50 kmol/h is achieved by RD1 and RD2. The reboiler duties of RD1 and RD2 are 3.48 GJ/h and 1.11 GJ/h, respectively.

The overhead products of the RD1 and RD2 columns, with top HDA composition set to be 10^{-5} mol%, are almost the mixture of DMC and MeOH and sent into the first distillation column (CD1) at stage 9. This column contains 17 stages and is operated at 0.65 atm. Because the MeOH composition (42.5 mol%) of this mixture is much lower than that (86.7 mol%) of the DMC-MeOH azeotrope, CD1 is designed to achieve high-purity DMC (99.9 mol%) from column bottom and concentrate the MeOH composition of column top. A DMC-MeOH mixture with a MEOH composition (76 mol%) closer to that of DMC-MeOH azeotrope is distilled from CD1 column top and then entered into an EDS involving an extractive distillation column (CD2) and a solvent recovery column (CD3).

CD2 and CD3 columns have 36 and 25 stages, respectively. DMC-MeOH mixture from the top of CD1 column is entered into the CD2 column at stage 27. Aniline, employed as a solvent to improve the relative volatility of DMC and MeOH, is fed into the 4th stage and takes DMC towards CD2 column bottom. MeOH with purity 99.9 mol% is obtained from CD2 column top. The ratio of MeOH to the sum of DMC and MeOH from CD2 column bottom is set to be 9.5×10^{-4} for ensuring 99.9 mol% DMC separated from CD3 column top. The bottom product of CD2 column is sent into the 8th stage of CD3 column. Aniline with purity 99.99 mol% is removed from CD3 column bottom and recycled back to the aniline feed location in the CD2 column. To reduce the energy consumption of these CD columns, aniline stream releases sensible heat first to the feed stream of CD1 column through the heat exchanger 1 (HX1), then to the feed stream of CD2 column through the heat exchanger 2 (HX2), and finally to be cooled down at 54.5 °C (Hsu et al., 2010) through the heat exchanger 3 (HX3). A makeup stream of aniline is added to compensate for solvent loss in the EDS. The high-purity DMC products from CD1 column bottom and CD3 column top are recycled back to DMC feed location of RD1. The reboiler duties of CD1, CD2, and CD3 columns are 5.23, 5.67, and 1.70 GJ/h, respectively. Heat duties released by the CD3 bottom stream to HX1, HX2, and HX3 are 0.95, 0.11, and 0.07 GJ/h, respectively. Total annual capital cost, total operation cost, and TAC are 458.0×10^3, 1966.1×10^3, and 2424.1×10^3 US$/year, respectively. The total operation cost accounts for the major part (81%) of the TAC.

3. Design of RD+VR intensified process for HDC synthesis

VR is an intensification technology to reduce energy consumption by increasing thermodynamic efficiency. It is particularly effective when the temperature difference between column bottom and top is small. In the studied RD1 and RD2 columns given in the HDC synthesis process intensified by RD, column bottoms are operated at 90 °C while the top temperature of RD1 and RD2 columns are about 72 °C and 69 °C, respectively. This small temperature difference between column bottom and top makes VR a practical method to reduce energy consumption of RD1 and RD2 columns. Similar optimization steps for HDC synthesis process intensified by RD are employed to the one intensified by RD and VR. Figure 1 shows the optimal configuration of HDC synthesis process intensified by RD and VR. RD1 and RD2 columns are divided into top and bottom sections. In the RD1 column, top section has the stages above HDA feed. In the RD2 column, top section has the stages above this column feed. Bottom section is operated at low pressure while top section is operated at high pressure. The vapor from the bottom section is compressed by a compressor into the vapor with high temperature and pressure and then entered into the top section. The overhead vapor from top section can be used as a heating medium and release latent heat to the reboiler of bottom section. Blue dotted line represents the path of latent heat released. In this study, a temperature difference between two outlet streams leaving a reboiler is limited to be 10 °C. The pressure of compressor outlet is adjusted to satisfy this requirement of 10 °C temperature difference. Because DMC composition of DMC-MeOH azeotrope decreases when pressure increases, some amount of un-reacted DMC in top section is more easily moved downwards the reaction zone to increase reaction conversion when top section is operated at high pressure. The latent heat of overhead vapor from top section of RD1 column is totally released to the reboiler of RD1 column. The latent heat of overhead vapor from top section of RD2 column can be released to not only the reboiler of RD2 column but also the auxiliary reboiler of RD1 column and the HX4 for feed preheating of CD2 column. Aniline stream also releases sensible heat first to the feed stream of CD1 column through

the HX1, then to the feed stream of CD2 column through the HX2, and finally to be cooled down at 54.5 °C through the HX3. This heat integration path from the CD3 bottom to the aniline feed is denoted by cyan dotted line shown in Figure 1.

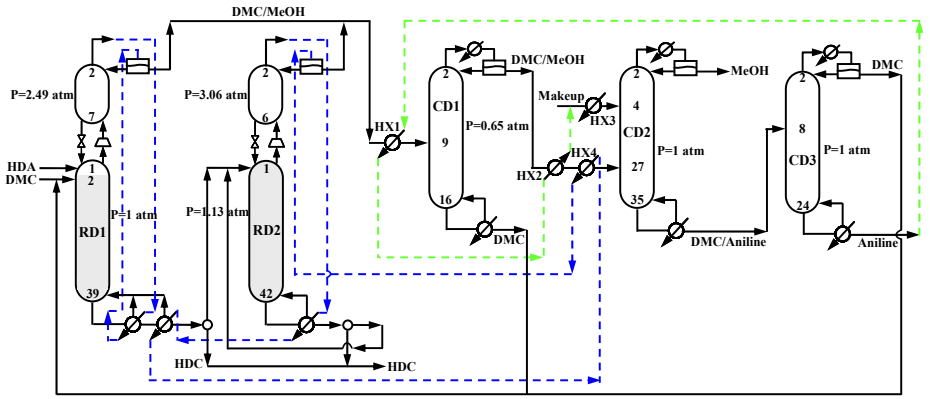

Figure 1. Configuration of HDC synthesis process intensified by RD and VR.

In the optimal configuration of HDC synthesis process intensified by RD and VR, top sections of RD1 and RD2 columns are operated at 2.49 atm and 3.06 atm, respectively. The optimal numbers of stages in the top sections of RD1 and RD2 columns are 7 and 6, respectively. The minimum TAC is achieved when the numbers of stages in the bottom sections of RD1 and RD2 columns are 40 and 43, respectively. The corresponding pressure at bottom section of RD2 column is 1.13 atm. The configuration of these designed CD columns is similar to that in the RD intensified process. CD1 column is operated at 0.65 atm. The number of total stages and number of feed stage are equal to 17 and 9, respectively. Overhead MeOH composition is set to be 76 mol%. Aniline (40 kmol/h) and the product distillated from CD1 column top are entered into stages 4 and 27, respectively, of CD2 column with 36 stages. In the CD3 column, the optimal feed location is the 8th stage under the number of total stage equal to 25 stages.

In comparison with the RD intensified process, the reboiler duties of RD1 and RD2 columns can be completely saved for the RD+VR intensified process. Furthermore, the reboiler duty of CD2 column can be substantially reduced from 5.67 GJ/h to 2.01 GJ/h because of the large latent heat released to the feed of CD2 column through HX4. The reboiler duty of CD1 column is also reduced from 5.23 GJ/h to 4.60 GJ/h because of the feed of CD1 column, from the overhead products of RD1 and RD2 columns, with higher temperature and pressure in the RD+VR intensified process. Only 49.9% of the steam cost in the RD intensified process is required in the RD+VR intensified process. The capital cost for compressor and electricity cost are the extraneous expenses under VR. All the costs except capital cost of HX are decreased by VR effect in the HDC synthesis process. Total annual capital cost, total operation cost, and TAC are 456.4×10^3, 1128.0×10^3, and 1584.4×10^3 US$/year, respectively. Compared with the process designed by RD, total operation cost and TAC can be reduced by 43% and 35%, respectively, for the process designed by RD+VR.

4. Conclusions

Some routes were used to synthesize HDC, an intermediate to manufacture HDI. Green HDC synthesis by reacting HDA with DMC has attracted much attention recently because of DMC usage to substitute toxic phosgene. In the study, we concentrate on the green HDC synthesis route by the reaction of HDC with DMC. Two plant-wide processes are proposed to produce HDC and separate the azeotrope of DMC and MeOH. In the optimal RD intensified process, two tandem RD columns are designed to achieve 100% HDA conversion by using excess DMC reactant. Because of small temperature difference between RD column bottom and top, an optimal reactive VR distillation process is designed to reduce energy consumption. Each RD column is divided into high pressure and low pressure sections by installing a compressor between these two sections. The latent heat of overhead vapor products from RD column tops can not only totally supply the heat duties of two RD column bottoms but also reduce substantial energy demand of CD columns. Simulation results demonstrate that the total operation cost and TAC of the RD intensified process can be substantially reduced by the effect of reactive VR.

References

M. Ammar, Y. Cao, L. Wang, P. He, H. Li, 2017, Synthesis of hexamethylene-1,6-dicarbamate by methoxycarbonylation of 1,6-hexamethylene diamine with dimethyl carbonate over bulk and hybrid heteropoly acid catalyst, Res. Chem. Intermed., 43, 6951-6972.

Y. Cao, L. Zhao, G. Zhu, L. Wang, P. He, H. Li, 2018, Kinetic study of methoxycarbonylation of 1,6-hexanediamine with dimethyl carbonate using $Mn(OAc)_2$ catalyst, Int. J. Chem. Kinet., 50, 767-774.

K. Y. Hsu, Y. C. Hsiao, I. L. Chien, 2010, Design and control of dimethyl carbonate-methanol separation via extractive distillation in the dimethyl carbonate reactive-distillation process, Ind. Eng. Chem. Res., 49, 735-749.

H. Q. Li, Y. Cao, X. T. Li, L. G. Wang, F. J. Li, G. Y. Zhu, 2014, Heterogeneous catalytic methoxycarbonylation of 1,6-hexanediamine by dimethyl carbonate to dimethylhexane-1,6-dicarbamate, Ind. Eng. Chem. Res., 53, 626-634.

R. Turton, R. C. Bailie, W. B. Whiting, J. A. Shaeiwitz, 2012, Analysis, Synthesis, and Design of Chemical Processes, Pearson Education, Boston.

G. Wang, J. Cheng, J. Yao, 2006, Method for Synthesizing Hexamethylene 1,6-Diamino Methyl Formate, China Patent CN1727330A.

Sauro Pierucci. Flavio Manenti, Giulia Bozzano, Davide Manca (Eds.)
Proceedings of the 30h European Symposium on Computer Aided Process Engineering (ESCAPE30), May 24-27, 2020, Milano, Italy.
http://dx.doi.org/10.1016/B978-0-12-823377-1.50176-2

Heat Exchanger Network Optimization including Detailed Heat Exchanger Models using Trust Region Method

Saif R. Kazi[a], Michael Short[a,b], Lorenz T. Biegler[a,*]

[a]*Department of Chemical Engineering, Carnegie Mellon University, Pittsburgh, PA 15213, USA*
[b]*Department of Chemical and Process Engineering, University of Surrey, Guildford, GU2 7XH, UK*
lb@andrew.cmu.edu

Abstract

A trust region framework is presented to synthesize heat exchanger network with detailed exchanger designs. The heat exchanger network (HEN) is first synthesized using the stage wise superstructure (SWS) formulation of Yee and Grossmann (1990). After a topology is found in this step the heat exchangers and the connections, flows and intermediate temperatures are designed, using the first principles based differential algebraic (DAE) model presented in our previous work. These detailed DAEs for heat exchanger design are incorporated within a nonlinear programming (NLP) model using reduced order models and solved using NLP solver IPOPT with a trust region method. The results show that the new method is faster than the previous approaches while providing comparable results.

Keywords: Heat Exchanger Network, Trust Region, Mathematical Programming

1. Introduction

Optimization of HENs has been an archetypal problem in the process system engineering community for many years. The problem has been researched for more than 50 years with more than 400 research articles until 2002 (Furman and Sahinidis (2002)). Advances in mathematical programming have enabled solving large scale heat exchangers in reasonable time. Most recently-developed HENs models are derived from the formulation presented in Yee and Grossmann (1990) with many extensions proposed for stream splitting, non-isothermal mixing, and stream bypass.

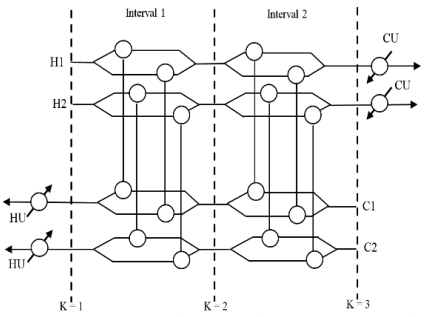

Figure 1: Superstructure formulation by Yee and Grossmann (1990)

Solutions obtained using these models are difficult to implement for real cases as the exchangers inside these networks are designed using shortcut models which are physically inaccurate.

Recent studies have addressed this issue by attempting to incorporate detailed design of exchangers within the MINLP HEN model. Liporace et al. (1999, 2000) derived the HEN

using pinch analysis and removed exchangers which were very small or had many shells from subsequent iterations. Their study concluded that it is vital to include aspects of detailed design in designing the HEN. Mizutani et al. (2003b) developed an MINLP model for heat exchanger design using Bell-Delaware method. They subsequently used their MINLP model to design heat exchangers in the network and updating the individual stream heat transfer coefficients in the SWS model (Mizutani et al. (2003a)). Results indicated that the heat transfer coefficients for the converged solution were very different from their initial guesses. The MINLP models for exchanger design are nonconvex in nature and thus tend to suffer from convergence issues.

For this reason, Ponce-Ortega et al. (2009) used a genetic algorithm with a fitness function to filter out networks with detailed exchanger designs. Their approach used the sum of total annual cost (TAC) and temperature constraint violations as the fitness function. They used binary variables in the HEN model and the heat duties in the detailed exchanger model to verify convergence. As no information was passed between the detailed model and the networking model, the method cannot guarantee feasible designs. Ravagnani and Caballero (2007) improved upon the MINLP model of Mizutani et al. (2003a) by including TEMA standard values for number of tubes, tube lengths and diameters along with other constraints. This makes the model more nonlinear, nonconvex and difficult to converge with deterministic optimization algorithms. Although they were able to solve two example HEN problems in their follow-up paper, it required custom initialization to solve the highly nonconvex MINLPs for exchanger design.

Short et al. (2016a,b) devised a two-step strategy, where correction factors are used to update the number of shells, pressure drops and heat transfer coefficients in the MINLP HEN model. Individual heat exchangers are designed using the Bell-Delaware method manually after solving the SWS model. The method ensures that the TAC is the same for both the network design step and the detailed model, and also guarantees that the final network design is feasible with detailed models. The method, however suffers from lack of automation in the detailed design step, making it impractical for large-scale HEN problems. In addition, the Bell-Delaware method for multiple shells includes calculation of F_T correction factor and log mean temperature difference (LMTD) which are numerically unstable for optimization purposes and are based on empirical correlations.

Our previous work (Kazi et al. (submitted, 2019a)) addressed these shortcomings by introducing a novel method of exchanger design using first principles without F_T correction and LMTD terms. Subsequently, this method was combined with the two step strategy and with a more stable LMTD approximation to design network with detailed exchanger designs based on first principles discrete model (Kazi et al. (submitted, 2019b)). However, it was found that the method is computationally expensive as many iterations obtain the same solution. Additionally, the individual unit designs were solved for fixed heat and mass balances, thus neglecting the optimization of unit mass and heat balances.

In this study, we present a trust region based framework to simultaneously design HENs with detailed designs of individual exchangers. This method is inspired from previous work by Agarwal and Biegler (2013) and Eason and Biegler (2018), which use a filter-based strategy and reduced order models to create the trust region framework.

2. Methodology

In our method we first use the SWS model of Yee and Grossmann (1990) to obtain a HEN topology and initializations for the mass and energy balances of the network. Note that parameters in the MINLP for heat transfer coefficients are chosen such that the solution will underestimate the objective function and that an isothermal mixing assumption is used to avoid bilinearity in this step. After obtaining this network structure, we formulate an NLP representation that includes bilinear stream splitting and mixing equations that were excluded in the original MINLP.

To represent the heat exchangers in this NLP formulation we use reduced order models that are obtained via a trust region approach. In trust region optimization we can utilize external, black box or glass box models within a larger optimization problem. In our approach, the detailed exchanger models are obtained using the method presented by Kazi et al. (submitted, 2019a) whereby the heat and mass balances of the unit are given from the NLP suboptimization layer and a Bell-Delaware method is first used to enumerate designs in order to find the best configuration for the discrete decisions.

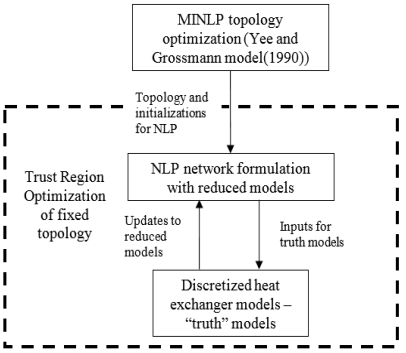

Figure 2 : Proposed algorithm for incorporating detailed designs into HEN synthesis

Following this, first principles equations are used to derive a set of DAEs based on the number of shell passes, number of tube passes, and number of baffles obtained in the Bell-Delaware optimization/enumeration. From this detailed discretized model we can easily obtain derivative information from the solution and use this to generate reduced order models that can be embedded within the network-level NLP.

2.1. Network-level NLP

The stream splitting and non-isothermal mixing constraints are added along with fixing the binary variables to the SWS solution to obtain the network level NLP. The NLP is formulated with reduced order models for detailed exchanger designs with trust region. After solving the NLP represented by Eq.(1), the solution is passed through the trust region filter to obtain the new trust region radius (Δ) for the next iteration. This is done until the infeasibility $\theta = \|y\text{-}d(x)\|$ and the trust region radius (Δ) are below threshold.

$$\begin{aligned} &\min_{x,y} f(x,y) \\ &s.t.\ \ c(x,y) = 0 \\ &\quad g(x,y) \le 0 \\ &\quad y = r_k(x) \\ &\quad \| x - x_k \| \le \Delta_k \end{aligned} \tag{1}$$

2.2. Reduced Order Model(ROM)

The reduced order modelsin the network-level NLP are generated by using the solution of the detailed DAE models and its sensitivity with the inputs from the NLP. The reduced order models are of the following form:

$$r_k(x) = \tilde{r}(x) + (d(x_k) - \tilde{r}(x_k)) + (\nabla_x d(x_k) - \nabla_x \tilde{r}(x_k))^T (x - x_k) \quad (2)$$

where r - reduced order model, $\tilde{r}$ -low fidelity model, d - detailed model and x – reduced order variables

The models are updated at each iteration with the solution ($d(x_k)$) and sensitivity ($\nabla_x d(x_k)$) from the detailed models. The reduced order model satisfies a useful property of exactly matching function and gradient values with the detailed model at xk ($r_k(x_k) = d(x_k)$ and $\nabla_x r(x_k) = \nabla_x d(x_k)$).

2.3. Filter

A trust-region filter is used to determine the trust region radius (Δ) by comparing the descent in the objective value (f) and infeasibility (θ) in each iteration step. A step (s_k) is considered acceptable to the filter if for all $(\theta_j, f_j) \in F_k$

$$\theta(x_k + s_k) \le (1 - \gamma_\theta)\theta_j \quad or \quad f(x_k + s_k) \le f_j - \gamma_j \theta_j \quad (3)$$

where $\gamma_\theta, \gamma_j \in (0,1)$ are fixed parameters. The update is done by first calculating the ratio of reduction in infeasibility $(\rho_k = 1 - \theta(x_k + s_k) / \theta(x_k))$. The trust region radius is determined by following rule:

$$\Delta_{k+1} = \begin{cases} \gamma_c \Delta_k & if \ \rho_k < \eta_1, \\ \Delta_k & if \ \eta_1 \le \rho_k < \eta_2, \\ \gamma_e \Delta_k & if \ \rho_k \ge \eta_2, \end{cases} \quad (4)$$

where $0 < \eta_1 \le \eta_2 < 1$ and $0 < \gamma_c < 1 < \gamma_e$

3. Results

Table 1: Example data, from Mizutani (2003a)

	m (kg/s)	T_{in} (K)	T_{out} (K)
H1	8.15	368	348
H2	81.5	353	348
C1	16.3	303	363
C2	20.4	333	343
HU		500	500
CU		300	320

where ΔT_{min} is 10 K, Area cost = $1000(NS) + 60(Area/NS)^{0.6}\$/year$. Pumping cost = $0.7(\Delta P_t m_t/\rho_t + \Delta P_s m_s/\rho_s)$, where ΔP = Pa, m = kg/s, and $\rho = kg/m^3$. CU cost = 6 \$/kW year and HU costs = 60 \$/kW year. Overall heat-transfer coefficients of process stream with utility matches = 444 W/m^2K.

To demonstrate the proposed optimization approach we solve a simple HENS problem from Mizutani et al. (2003a). The stream data is shown in Table 1, with stream properties like viscosity, density, specific heat capacity and conductivity equal to [2.4e-04 Pa.s, 634 kg/m3, 2454 J/(kg.K), 0.114 W/(m.K)]. The dirt resistance factor r_d on both sides of the exchanger is assumed to be 1.7e-04 m2.K/W. The problem is modeled in the python based environment Pyomo and solved with NLP solver IPOPT 3.12. DICOPT and BARON are used as MINLP solvers

Table 2: Summary of solutions obtained for Example in comp arison with other studies

	This Study	Kazi et al.(submitted)	Short et al.(2016a)
Total Annual Cost ($/a)	96,596.17	97,360.94	97,159.3
Utility Costs ($/a)	90,000	90,000	90,036
Area Costs ($/a)	1,301.17	1,604.67	1,631.68
Pumping Costs ($/a)	1,295	1,756.26	1,491.63
Fixed Costs ($/a)	4,000	4,000	4,000
Number of matches	2	2	2
Number of exchangers	4	4	4

The results obtained from this strategy are reported in Table 2 along with the results from previous studies. The optimal network is presented in Figure 3. The total annual cost (TAC) and pumping costs obtained by the proposed strategy is less than reported in Kazi et al. (submitted, 2019b) and Short et al. (2016a). The optimal network in Figure 3 shows that two process and two hot utility heat exchangers are required to obtain desired outlet temperatures. The optimal network obtained is different from the network reported in our previous study.

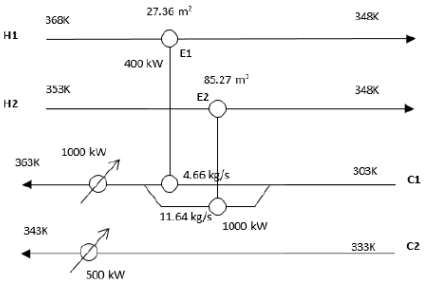

Figure 3: Proposed algorithm for incorporating detailed designs into HEN synthesis

In this network, the cold stream C1 undergoes splitting into two streams of flow rate 4.66 and 11.64 kg/s respectively. The total heat duty and area of process heat exchangers in the network are (400 kW, 27.36 m^2) and (1000 kW, 85.27 m^2) respectively.

Table 3 : Detailed heat exchanger results

	Exchanger 1	Exchanger 2
Area(m^2)	27.36	85.27
Duty(kW)	400	1000
Tube flowrate (kg/s)	8.15	81.5
Shell flowrate (kg/s)	4.66	11.64
Tube Pass	2	2
Baffles	11	6
Shell Dia(m)	0.32	0.81
Tube Count	150	438
Tube Length(m)	3.66	2.438
Overall Heat Transfer($W/m^2.K$)	478.9	439.9
$\Delta P_t(kPa)$	11.98	12.18
$\Delta P_s(kPa)$	5.85	5.12
Hot fluid	Tube	Tube

The detailed exchanger designs are reported in Table 3 along with allocation of hot and cold streams. Results show that both exchangers are designed with one shell and two tube passes heat exchanger. The pressure drops on tubeside and shellside streams are (11.98kPa, 12.18kPa) and (5.85kPa, 5.12kPa) respectively.

Future work will be aimed towards accelerating the convergence of the trust region algorithm. This will be aided by adding a compatibility check (see Eason and Biegler (2018)) such that the trust region NLP will always be feasible.

4. Conclusions

We present a new methodology for HEN synthesis which includes detailed heat exchanger design models. The new formulation uses the MINLP stagewise superstructure model to obtain a topology based on simplified exchanger models. This topology is then used as the basis of the NLP suboptimization with detailed heat exchanger models incorporated with a trust-region framework. The suboptimization provides optimal flow splits and detailed exchanger designs for the HENS based on detailed unit models. The heat exchanger design models are obtained through a rigorous optimization procedure whereby a DAE model is solved based upon a small enumeration of potential topologies based on Bell-Delaware equations. The new method is demonstrated on a small example and is shown to obtain excellent results in shorter times than other techniques while still providing guarantees on optimality. Future work is planned for application to larger problems and more advanced trust region strategies to decrease iterations.

References

A. Agarwal, L. T. Biegler, 2013. A trust-region framework for constrained optimization using reduced order modeling. Optimization and Engineering 14 (1), 3-35.

J. P. Eason, L. T. Biegler, 2018. Advanced trust region optimization strategies for glass box/black box models. AIChE Journal 64 (11), 3934–3943.

K. C. Furman, N. V. Sahinidis, 2002. A critical review and annotated bibliography for heat exchanger network synthesis in the 20th century. Ind. Eng. Chem. Res. 41 (10), 2335-2370.

S. R. Kazi, M. Short, L. T. Biegler, submitted, 2019a. Heat Exchanger Network Synthesis with Detailed Exchanger Designs - 1. A Discretized Differential Algebraic Equation (DAE) Model for Shell and Tube Heat Exchanger Design.

S. R. Kazi, M. Short, A. J. Isafiade, L. T. Biegler, submitted, 2019b. Heat Exchanger Network Synthesis with Detailed Exchanger Designs - 2. Hybrid Strategy for Optimal Synthesis of Heat Exchanger Networks with Detailed Individual Heat Exchanger Designs.

F. S. Liporace, F. L. P. Pessoa, E. M. Queiroz, 1999. Automatic Evolution of Heat Exchanger Networks with Simultaneous Heat Exchanger Design. Brazilian Journal of Chemical Engineering 16, 25–40.

F. S. Liporace, F. L. P. Pessoa, E. M. Queiroz, 2000. The influence of heat exchanger design on the synthesis of heat exchanger networks. Brazilian Journal of Chemical Engineering 17, 735–750.

F. T. Mizutani, F. L. Pessoa, E. M. Queiroz, S. Hauan, I. E. Grossmann, 2003a. Mathematical programming model for heat-exchanger network synthesis including detailed heat-exchanger designs. 2. Network synthesis. Ind. Eng. Chem. Res. 42 (17), 4019–4027.

F. T. Mizutani, F. L. P. Pessoa, E. M. Queiroz, S. Hauan, I. E. Grossmann, 2003b. Mathematical Programming Model for Heat–Exchanger Network Synthesis Including Detailed Heat–Exchanger Designs. 1.{Shell}–and–tube Heat–Exchanger Design. Ind. Eng. Chem. Res. 42 (17), 4009–4018.

J. M. Ponce-Ortega, M. Serna-González, A. Jiménez-Gutiérrez, 2009. Use of genetic algorithms for the optimal design of shell-and-tube heat exchangers. Applied Thermal Engineering 29 (2), 203 - 209.

M. A. S. S. Ravagnani, J. A. Caballero, 2007. Optimal heat exchanger network synthesis with the detailed heat transfer equipment design. Comp and Chem Eng 31 (11), 1432 -1448.

M. Short, A. Isafiade, D. Fraser, Z. Kravanja, 2016a. Two-step hybrid approach for the synthesis of multi-period heat exchanger networks with detailed exchanger design. Applied Thermal Engineering 105, 807-821.

M. Short, A. J. Isafiade, D. M. Fraser, Z. Kravanja, 2016b. Synthesis of heat exchanger networks using mathematical programming and heuristics in a two-step optimisation procedure with detailed exchanger design. Chemical Engineering Science 144, 372-385.

T. F. Yee, I. E. Grossmann, 1990. Simultaneous optimization models for heat integration—II. Heat exchanger network synthesis. Computers & Chemical Engineering 14, 1165–1184.

Sauro Pierucci, Flavio Manenti, Giulia Bozzano, Davide Manca (Eds.)
Proceedings of the 30th European Symposium on Computer Aided Process Engineering (ESCAPE30), May 24-27, 2020, Milano, Italy.
http://dx.doi.org/10.1016/B978-0-12-823377-1.50177-4

MINLP Model for Reliability Optimization of System Design and Maintenance Based on Markov Chain Representation

Yixin Ye[a], Ignacio E. Grossmann[a,*], Jose M. Pinto[b], Sivaraman Ramaswamy[b]

[a]*Department of Chemical Engineering, Carnegie Mellon University, Pittsburgh, PA 15213*

[b]*Business and Supply Chain Optimization, Linde.digital, Linde plc, Danbury, CT 06810*
grossmann@cmu.edu

Abstract

This paper proposes an MINLP model that represents the stochastic process of system failures and repairs as a continuous-time Markov chain, based on which it optimizes the selection of redundancy and the frequency of inspection and maintenance tasks for maximum profit. The model explicitly accounts for every possible state of the system. A decomposition method and a scenario reduction method are applied to this example to drastically reduce the computational effort. We show by an example that the proposed model and algorithms are capable of solving a practical problem based on the air separation process example that motivated our work, which features multiple stages, potential units and failure modes.

Keywords: reliability design, maintenance, optimization, Markov Chain, MINLP

1. Introduction

Plant availability has been a critical consideration for the design and operation of chemical processes as it represents the expected fraction of normal operating time, which directly impacts the ability of making profits. In practice, discrete-event simulation tools are used to examine the availability of a few selected designs of different redundancy levels under various maintenance and spare parts inventory policies (Sharda and Bury, 2008). However, the best plan selected through simulation is usually suboptimal because the list of design alternatives is often not exhaustive. Thus, there is a strong motivation for systematic optimization tools of redundancy design considering operational factors.

Several works have been reported regarding reliability considerations at the design phase (Kuo and Wan (2007)). In order to obtain a more comprehensive optimal design, it is important to consider the impact of operational factors such as maintenance on plant availability and their costs (Ding and Kamaruddin (2015)). Alaswad and Xiang (2017) provide a review for condition-based maintenance optimization models for stochastically deteriorating system with either discrete or continuous states. Pistikopoulos et al. (2001) and Goel et al. (2003) formulate MILP models for the selection of units with different reliability and the corresponding production and maintenance planning for a fixed system configuration.

Markov chain is a powerful mathematical tool that is extensively used to capture the stochastic process of systems transitioning among different states. Shin and Lee (2016) formulate the planning level problem of a procurement system as an Markov Decision Process to account for exogenous uncertainties coming from lead time and demand. Lin et al. (2012) model a utility system using Markov chain and carry out RAM (reliability, availability & maintainability) analysis iteratively to decide the optimal reliability design.

Terrazas-Moreno et al. (2010) use Markov chain as an uncertainty modeling tool for the optimal design of production site network considering reliability and flexibility. Kim (2017) presents a reliability model for k-out-of-n systems using a structured continuous-time Markov chain, which is solved with a parallel genetic algorithm.
Given the aforementioned research gaps and knowledge basis, this work extends our recent mixed-integer framework (Ye et al., 2017) and introduces a systematic approach to model the stochastic failure and repair process of the superstructure system as a continuous-time Markov chain. The new framework explicitly accounts for the long term property of each possible reliability scenario. Therefore, it is able to incorporate various kinds of decision making processes. Especially, comparing to Terrazas-Moreno et al. (2010) and Kim (2017), corrective maintenance and condition-based maintenance are incorporated in order to find the overall optimal selection of parallel units.

2. Motivating Example and Problem Statement

Consider an air separation unit (ASU) shown in Figure 1 as a motivating example. Critical processing units include the main air compressor, the pre-purifier, the booster air compressor, and the liquid O_2 pump.

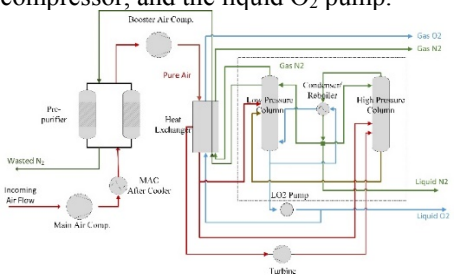

Figure 1. Typical flowsheet of an ASU

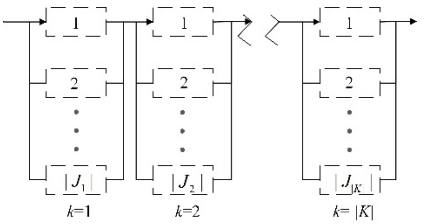

Figure 2. System topology and notations

The failure of any one of these processing stages can result in the failure of the entire system, which will compromise its ability to meet customer demands. In order to effectively increase the system availability, two strategies are considered.

2.1. Redundancy selection

The first strategy is to install parallel units for the critical stages. In Figure 2, the availability superstructure is formulated as a serial system of sequential stages, where each stage k has several potential design alternatives. The number and selection of parallel units have impacts on system reliability as well as capital costs.

2.2. Inspection Interval and Condition-based Maintenance

The second strategy is to carry out condition-based maintenance (CBM). Specifically, the units go through periodic inspections, and follow-up maintenance if the inspection result indicates that the equipment is going to fail shortly. The intervals between the periodic inspections impact individual unit failure rates and operational costs.
The ultimate goal is to achieve the optimal overall net present value for the system.

3. Mathematical Formulation

3.1. Markov Chain Representation

As mentioned in section 2.1, for each processing stage k, there is a set of potential units indexed by j. It is assumed that the time to failure and time to repair of each potential unit j follow exponential distributions with respective rate parameters $\lambda_{k,j}^{0}$ and $\mu_{k,j}$, which

constitutes the transition matrix Q_k of the continuous-time Markov Chain of stage k. The system transition matrix W is then calculated as follows.

$$W = I_{(n_{|K|}n_{|K|-1}\cdots n_2)} \otimes Q_1 + I_{(n_{|K|}n_{|K|-1}\cdots n_3)} \otimes Q_2 \otimes I_{n_1} + \cdots + Q_{|K|} \otimes I_{(n_{|K|-1}n_{|K|-2}\cdots n_1)} \quad (1)$$

Element $W(\bar{s},\bar{r})$of matrix $W$is the transition rate from state $\bar{s}$ to state $\bar{r}$, which belongs to the system state space $\bar{S}$.

3.2. Logical constraints

Binary variable $y_{k,j}$ indicates whether unit *j* in stage *k* is selected.

$$\sum_{j\in J_k} y_{k,j} \geq N_k \quad (2)$$

Each possible combination of the potential units of one stage is called a stage design alternative indexed by *h*. Binary variable $z_{k,h}$ indicates the selection of stage design *h* for stage *k*. Set *D* contains the tuples of (j,k,h) where unit *j* is selected in design *h* of stage *k*, based on which $z_{k,h}$ and $y_{k,j}$are connected as shown in (3), (4) and (5).

$$z_{k,h} \leq y_{k,j}, (j,k,h) \in D \quad (3)$$

$$z_{k,h} \leq 1 - y_{k,j}, (j,k,h) \notin D \quad (4)$$

$$z_{k,h} \geq \sum_{(j,k,h)\in D} y_{k,j} + \sum_{(j,k,h)\notin D} (1-y_{k,j}) - |J_k| + 1, k \in K, h \in H_k \quad (5)$$

Equation (6) requires that one and only one design is selected for each stage.

$$\sum_{h\in H_k} z_{k,h} = 1, \forall k \in K \quad (6)$$

The combination of certain stage designs of each stage k is called a system design, which is indexed with $\bar{h}$. Set HC contains the tuples of $(k,h,\bar{h})$ where system design $\bar{h}$ contains stage design h of stage k. Binary variable $\bar{z}_{\bar{h}}$ indicates the existence of system design $\bar{h}$, and is related to the values of $z_{k,h}$.

$$\bar{z}_{\bar{h}} \leq z_{k,h}, \forall (k,h,\bar{h}) \in HC \quad (7)$$

$$\bar{z}_{\bar{h}} \geq \sum_{k\in K} \sum_{h\in H_k, (k,h,\bar{h})\in HC} z_{k,h} - |K| + 1, \forall \bar{h} \in \bar{H} \quad (8)$$

Binary variable $\bar{z}\bar{z}_{\bar{s}}$ indicates the existence of system state $\bar{s}$, which is required to be equal to $\bar{z}_{\bar{h}}$, if $\bar{s} \in \bar{T}_{\bar{h}}$, the subspace supported by system design $\bar{h}$.

$$\bar{z}\bar{z}_{\bar{s}} = \bar{z}_{\bar{h}}, \forall \bar{s} \in \bar{T}_{\bar{h}} \quad (9)$$

$\pi_{\bar{s}}$ is the stationary probability of state $\bar{s}$, which has an upper bound of 1, and equals zero if state $\bar{s}$ does not exist.

$$\pi_{\bar{s}} \leq \bar{z}\bar{z}_{\bar{s}}, \forall \bar{s} \in \bar{S} \quad (10)$$

The stationary probability distribution satisfies (11) and (12), which are based on the system transition matrix W and the existence of each system state.

$$\sum_{\bar{s}\in\bar{S}} \pi_{\bar{s}} \mathbf{W}(\bar{s},\bar{r}) \leq M(1-\bar{z}\bar{z}_{\bar{r}}), \forall \bar{r} \in \bar{S} \quad (11)$$

$$\sum_{\bar{s}\in\bar{S}} \pi_{\bar{s}} \mathbf{W}(\bar{s},\bar{r}) \geq M(\bar{z}\bar{z}_{\bar{r}} - 1), \forall \bar{r} \in \bar{S} \quad (12)$$

Finally, the availability of the system is one minus the sum of the stationary probability of all failed states:

$$A = 1 - \sum_{\bar{s}\in\bar{S}^f} \pi_{\bar{s}} \quad (13)$$

3.3. Consideration of Inspections

The range of possible inspection intervals t_k^{insp} is discretized into a finite set of choices, T_l^{insp}. The selection of inspection intervals for each stage k is represented with binary variables $x_{k,l}$, where $x_{k,l} = 1$ when time length T_l^{insp} is selected for stage k.

$$\sum_{l \in L} x_{k,l} = 1, \forall k \in K \tag{14}$$

$$t_k^{insp} = \sum_{l \in L} x_{k,l} T_l^{insp}, \forall k \in K \tag{15}$$

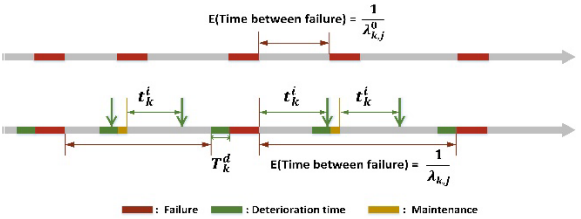

Figure 3. The impacts of inspections and maintenance

The equivalent failure rate $\lambda_{k,j}$with inspections and maintenance is calculated in (16). Figure 3 shows a sketch of how $\lambda_{k,j}$can be different from $\lambda_{k,j}^0$.

$$\lambda_{k,j}^0 - \lambda_{k,j} = \sum_{l \in L} x_{k,l} (e^{-\lambda_{k,j}^0 T_l^{insp}} - e^{-\lambda_{k,j}^0 (T_l^{insp} + T_k^d)}) / T_l^{insp}, \forall k \in K, j \in J_k \tag{16}$$

Each stage k has a inspection cost c_insp_k. Equation (17) enforces that the inspection cost for stage k is proportional to its inspection frequency and cost rate.

$$inspCost = \sum_{k \in K} c\_insp_k \sum_{l \in L} x_{k,l} \frac{T}{T_l^{insp}} \tag{17}$$

The repair cost is calculated according to the failure states. The repair cost in each state $\bar{s} \in \bar{S}$ is equal to the frequency of $\bar{s}$: $-W(\bar{s}, \bar{s})\pi_{\bar{s}}$, times the summation of the repair costs of all the units that are failed in state $\bar{s}$.

$$repaCost = -T \sum_{\bar{s} \in \bar{S}} W(\bar{s}, \bar{s}) \pi_{\bar{s}} \sum_{(k,j) \in KJ_{\bar{s}}^f} c\_repa_k \tag{18}$$

The number of times for follow-up maintenance to take place in a single unit relative to its number of repairs is calculated by the relative difference between the equivalent failure rate and the original failure rate.

$$mainRatio_k \geq y_{k,j} (\lambda_{k,j}^0 - \lambda_{k,j}) / \lambda_{k,j}, \forall j \in J_k \tag{19}$$

Equation (20) follows the same logic as in (18) to calculate costs according to failure states. Here, $c_repa_k$is replaced by c_main_k times $mainRatio_k$, which is the number of follow-up maintenance relative to the number of repairs.

$$mainCost = -T \sum_{\bar{s} \in \bar{S}} W(\bar{s}, \bar{s}) \pi_{\bar{s}} \sum_{k \in K_{\bar{s}}^f} mainRatio_k c\_main_k \tag{20}$$

In addition to the costs, maintenance also causes downtime, which will result in the decrease of availability. Equation (21) calculates the downtime caused by maintenance in terms of the failure states $\bar{s} \in \bar{S}^f$ and those stages that fail in $\bar{s}$. The net system availability A is calculated as A minus the ratio of downtime caused by maintenance to the entire time horizon T.

$$mainTime = -T \sum_{\bar{s} \in \bar{S}^f} W(\bar{s}, \bar{s}) \pi_{\bar{s}} \sum_{k \in K_{\bar{s}}^f} mainRatio_k T\_main_k \tag{21}$$

$$A^{net} = A - \frac{mainTime}{T} \tag{22}$$

3.4. Objective Function

The objective to be maximized is the Net Present Value NPV, the present value of net cash flow minus the investment costs. The yearly net cash flow is equal to revenue RV minus all the operational costs, and divided by number of years T. It is discounted by $\sum_{i=1}^{T} \frac{1}{(1+r)^i}$, where r is the rate of return (RoR) of cash flow. $instCost$ is the investment cost for installing the units depending on binary variables $y_{k,j}$. The revenue RV is proportional to system availability.

$$\max NPV = \frac{1}{T}\left(\frac{1-(1+r)^{-T}}{r}\right)(RV - repaCost - inspCost - mainCost) - instCost \tag{23}$$

$$inst\,\mathrm{Cos}\,t = \sum_{k\in K}\sum_{j\in J_k} y_{k,j} c\_inst_{k,j} \tag{24}$$

$$RV = A^{net} \cdot rv \tag{25}$$

4. Example

The model is applied to the motivating example of ASU (air separation unit) introduced in section 2, where the compressors have six failure modes and at least 2 units are needed for the pre-purifier. A time horizon of 10 years is considered. The exact numbers of relevant cost and reliability parameters of the units are proprietary information. Mean time between failures (MTBF) range from 5-25 years. Mean time to repair (MTTR) range from 8 - 1080hours. Capital cost of each unit range from \$85k - \$800k. Repair costs range from \$2k - \$20k per time. Inspection costs range from \$0.05k - \$0.5k per time. Maintenance costs range from \$1k -\$10k per time. Maintenance times range between 1 and 2 days. Inspection window lengths range between 5 and 6 day.

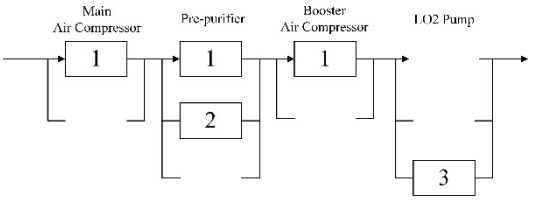

Figure 4. The optimal design

We propose an algorithm (Ye et al., 2019) that solves upper bounding MILPs and lower bounding MINLPs iteratively until the gap is closed. The algorithm converges in 7 rounds (ϵ= 1.7%) to the flowsheet shown in Figure 4. Only the least number of units are selected for each stage. For the main air compressor and the booster air compressor, more reliable and expensive units are selected, while for the LO2 pump, the solution selects the cheapest one. The expected system availability is 0.9866. The expected net present value is \$15,649.4k, with a revenue of \$29,597.8k and a penalty of \$421.9k. \$2,083k is spent on unit investment, \$262.7k is spent on inspections, \$7.4k is spent on maintenance, and \$48.9k on repair. Qualitatively speaking, this solution tends to spend more effort on reducing the failure rates for those failure modes with longer repair time.

The MILP models are solved with Xpress 29.01(748.8 CPUs), and the MINLP models are solved with SBB 25.1.1(492.0 CPUs).

5. Conclusions

In this paper, the stochastic process of system failures and repairs is modeled as a continuous-time Markov chain. Moreover, the impact of maintenance is incorporated.

With a general air separation unit as the motivating example, two strategies are considered to increase the availability of the system. The first strategy is to install parallel units for certain processing stages. The second strategy is to carry out periodic inspections, and condition-based maintenance if the inspection results indicate that the equipment will fail shortly. A non-convex MINLP model is proposed accordingly.

The non-convex MINLP model does not scale well, and has a large number of bilinear and multilinear terms. A decomposition scheme was proposed to reduce the size of the model and the computational time (Ye et al., 2019). The motivating example of the air separation unit is solved with the proposed specialized solution method.

References

Alaswad, S. and Xiang, Y. (2017). A review on condition-based maintenance optimization models for stochasticallydeteriorating system.Reliability Engineering & System Safety, 157:54–63.

Ding, S.-H. and Kamaruddin, S. (2015). Maintenance policy optimizationliterature review and directions.TheInternational Journal of Advanced Manufacturing Technology, 76(5-8):1263–1283.

Goel, H. D., Grievink, J., and Weijnen, M. P. (2003). Integrated optimal reliable design, production, and maintenanceplanning for multipurpose process plants.Computers & Chemical Engineering, 27(11):1543–1555.

Grossmann, I. E. and Trespalacios, F. (2013). Systematic modeling of discrete-continuous optimization modelsthrough generalized disjunctive programming.AIChE Journal, 59(9):3276–3295.

Kim, H. (2017). Optimal reliability design of a system with k-out-of-n subsystems considering redundancy strategies.Reliability Engineering & System Safety, 167:572 – 582.

Kuo, W. and Wan, R. (2007). Recent advances in optimal reliability allocation. InComputational intelligence inreliability engineering, pages 1–36. Springer.

Lin, Z., Zheng, Z., Smith, R., and Yin, Q. (2012). Reliability issues in the design and optimization of process utilitysystems.Theoretical Foundations of Chemical Engineering, 46(6):747–754.

Moubray, J. (1997).Reliability-centered maintenance. New York : Industrial Press, 2nd ed edition. "RCM II"–Cover.

Neuts, M. F. (1981).Matrix-geometric solutions in stochastic models: an algorithmic approach. Courier Corporation.

Pistikopoulos, E. N., Vassiliadis, C. G., Arvela, J., and Papageorgiou, L. G. (2001). Interactions of maintenance andproduction planning for multipurpose process plants a system effectiveness approach.Industrial & engineeringchemistry research, 40(14):3195–3207.

Sericola, B. (2013).Markov Chains: Theory and Applications. John Wiley & Sons.

Sharda, B. and Bury, S. J. (2008). A discrete event simulation model for reliability modeling of a chemical plant. InProceedings of the 40th Conference on Winter Simulation, pages 1736–1740. Winter Simulation Conference.

Shin, J. and Lee, J. H. (2016). Multi-time scale procurement planning considering multiple suppliers and uncertaintyin supply and demand.Computers & Chemical Engineering, 91:114–126.

Terrazas-Moreno, S., Grossmann, I. E., Wassick, J. M., and Bury, S. J. (2010). Optimal design of reliable integratedchemical production sites.Computers & Chemical Engineering, 34(12):1919–1936.

Weibull, W. et al. (1951). A statistical distribution function of wide applicability.Journal of applied mechanics,18(3):293–297.

Ye, Y., Grossmann, I. E., and Pinto, J. M. (2017). Mixed-integer nonlinear programming models for optimal designof reliable chemical plants.Computers & Chemical Engineering.

Ye, Y., Grossmann, I. E., Pinto, J. M., & Ramaswamy, S. (2019). Modeling for reliability optimization of system design and maintenance based on Markov chain theory. Computers & Chemical Engineering, 124, 381-404.

Sauro Pierucci, Flavio Manenti, Giulia Bozzano, Davide Manca (Eds.)
Proceedings of the 30th European Symposium on Computer Aided Process Engineering
(ESCAPE30), May 24-27, 2020, Milano, Italy.
http://dx.doi.org/10.1016/B978-0-12-823377-1.50178-6

Synthesis of Sustainable Integrated Process, Water Treatment and Power Generation Networks

Yue Li,[a] Zhihong Yuan,[a*] Rafiqul Gani[b]

[a]*Department of Chemical Engineering, Tsinghua University, Beijing10084, China*
[b]*PSE for SPEED company Ltd, Skyftemosen 6, DK 3450 Allerod, Denmazk*
zhihongyuan@mail.tsinghua.edu.cn

Abstract

In this paper, we propose the concept of sustainable synthesis, design and innovation of integrated processes that include water and power generation networks with the overall objective to achieve zero or negative carbon emissions as well as wastes. A superstructure-based framework is developed and leads to the formation of a new consolidated optimization problem, which represents multiple networks at different scales and includes environmental impacts as constraints. Problem was solved step by step using a decomposition-based solution strategy and leads to the design of a totally integrated and sustainable process. The applicability of the framework and solution steps is demonstrated through a realistic conceptual case study under different scenarios to obtain and analyze different sustainable solutions

Keywords: synthesis of processes, power generation, water networks

1. Introduction

Environmental and energy issues have received widespread attention, which has made demand for more environmentally friendly and sustainable production processes. Chemical processes convert selected raw materials to desired chemical products, by-products and waste, while requiring also utility such as water and energy. Usually the process synthesis problem is solved considering the cost of energy and water but without considering their availability limits or their sources. Different sources and generation processes of water and energy (such as electricity) will cause different investment costs, operating costs, carbon emissions and pollutant emissions, which should be optimized along with the production process.

Traditionally chemical processes, power generation processes and water treatment processes are optimized sequentially to find the most profitable production route and the most environmentally friendly or cheapest power generation technology, and the most reasonable water treatment method. This approach does not take into account the interaction of the three networks which cause infeasible solution. Synthesis and design of the production process water network and generation network with specific production targets will lead to a more suitable and comprehensive solution. Inspired by the superstructure-optimization based integrated process and water network design (Handani et al., 2015), in this contribution, we expand the existing framework (Quaglia et al., 2012a) by integrating the process with water treatment and power generation networks. In addition, we also expand the developed generic model (Bertran et al., 2017) to synthesis the integrated process, water treatment and power generation networks. The applicability of proposed multi-network integration is demonstrated by a conceptual example.

2. Concept and Modeling

We propose concepts and modeling methods for integrating process, water treatment and power generation networks to obtain the sustainable solution considering the economic benefit and environmental factor. The systematically description will be shown in this section.

2.1. Concept of integration problem

The process requires the electricity heat and water supplement during production. Usually the optimal design problem is solved by computing the cost of them to maximize the economic benefit. Although some environmentally friendly solutions will also consider carbon emissions and pollutant emissions from the production process, potential carbon emissions and pollutant emissions from the process of energy generation and water treatment are ignored. In order to get the optimized sustainable production route in a more comprehensive and meticulous method. It is necessary to optimize the power generation and water treatment networks while optimizing the production process. As can be seen in Figure 1a, the electricity heat and water, which touch upon different techniques and sources, will be considered as products of power networks and water networks respectively. The waste water can be treated and recycled by water networks. Moreover, the recovery of carbon dioxide and the use of excess energy will also be considered.

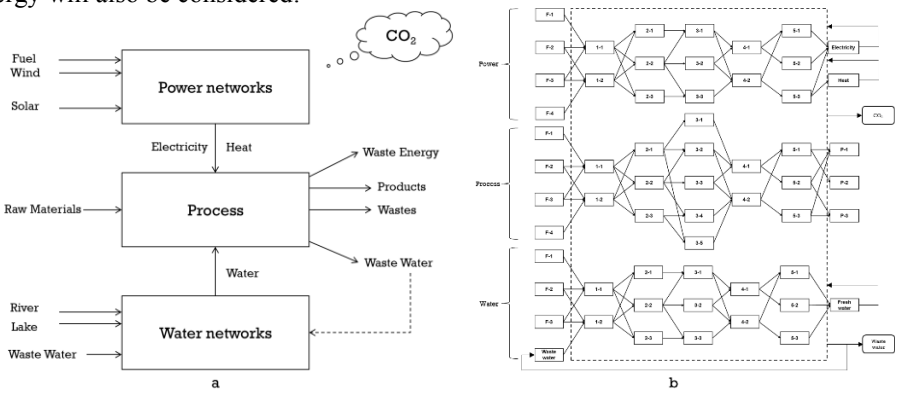

Figure1. Concept of integrated process water treatment and power generation networks Superstructure of synthesis and design of integrated problem

2.2. Modeling

The systematic framework for processing networks (Quaglia et al., 2012b) and industrial waste water treatment (Quaglia et al., 2014) are extended in this paper. The superstructure-based optimization approach is carried out to simultaneously synthesize and design a chemical process with related power generation and water treatment networks to find optimal process production flowsheet and power generation and water treatment process path.

2.2.1. Superstructure

Figure 1b. illustrates a superstructure of three networks. Each interval of a sub-network represents an alternative technique in different steps. The electricity and heat are presented as two products of power generation networks and supply to the whole process network. The water produced by water treatment networks is used to provide for production and utility consumption.

2.2.2. Generic interval model

The generic model for each interval (Bertran et al. 2017) is adapted to the problem of synthesis and design of integrated process power generation and water treatment networks.

Shown by Figure 2. The flow added to the interval $g_{i,M}^{M}$ can be divided to chemicals and water. additionally, the consumption of utilities can be divided to the electricity heat and water consumption. For each sub-networks the generic interval model is given in Eqs. 1-12.

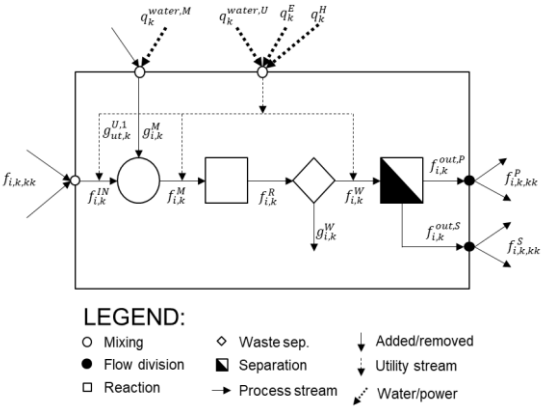

Figure 2. Generic structure of interval

$$g_{i,k}^{M} = \sum_i f_{i,k}^{IN} \mu_{i,ii,k} \quad (1)$$

$$g_{i,k}^{M} = \sum_i f_{i,k}^{IN} \mu_{i,ii,k} \quad (2)$$

$$f_{i,k}^{M} = f_{i,k}^{IN} + g_{i,k}^{M} \quad (3)$$

$$f_{i,k}^{R} = f_{i,k}^{M} + \sum f_{react,k}^{M} \theta_{react,r,k} \gamma_{i,r,k} \frac{MW_i}{MW_{react}} \quad (4)$$

$$f_{i,k}^{W} = f_{i,k}^{R}\left(1 - \delta_{i,k}\right) \quad (5)$$

$$g_{i,k}^{W} = f_{i,k}^{R} - f_{i,k}^{W} \quad (6)$$

$$f_{i,k}^{out,P} = f_{i,k}^{W} \sigma_{i,k} \quad (7)$$

$$f_{i,k}^{out,S} = f_{i,k}^{W} - f_{i,k}^{out,P} \quad (8)$$

$$g_{ut,k}^{U,j} = \sum_i \beta_{ut,k}^{j} f_{i,k}^{IN}\ ,\ j = 1,2,3 \quad (9)$$

$$q_k^{water} = q_k^{water,M} + q_k^{water,U} = g_{water,k}^{M} + \sum_j \varphi_{water,ut} g_{ut,k}^{M,j} \quad (10)$$

$$q_k^{E} = \sum_j \varphi_{E,ut} g_{ut,k}^{M,j} \quad (11)$$

$$q_k^{H} = \sum_j \varphi_{H,ut} g_{ut,k}^{M,j} \quad (12)$$

In Eq. (9), parameter $\beta_{ut,k}^{j}$ can be estimated by energy balance of mixing reaction and separation process considering heat transfer and loss.

2.2.3. Optimization problem

The new framework combining process, power generation water and treatment allows us to find environmentally friendly solutions while guaranteeing the economic benefit. The Objective function and environmental constraints are given in Eqs. 13-16.

Objective function:

$$Z = S^{PROD} - C^{RAW} - C^{C} - C^{T} - \frac{CAPEX}{\tau} \quad (13)$$

Environmental constraints:

$$\sum CO_2(kk) \leq CONS_{CO2} \quad (14)$$

$$\sum Waste_{solid}\ (kk) \leq CONS_{solid} \quad (15)$$

$$\sum Waste_{water}\ (kk) \leq CONS_{water} \quad (16)$$

2.3. Solution step.

In order to obtain a solution to a specific problem through the proposed framework, the following four steps are recommended.

Step1: Problem definition. The first step is the definition of the goal of optimization problem including the determination of objective function, environmental constraints and other conditions based on the exact scenario.

Step2: Superstructure representation and data collection. In this step, various alternatives of process, water treatment and power generation are specified to obtain the superstructure in 2.2.1. The process data and physical data of all intervals in each network are collected or estimated.

Step3: model development. The next task is the development of generic model in 2.2.1 using collected process data. Then generate the MI(N)LP model o in optimization software i.e. GAMS.

Step4: Solve MI(N)LP problem. The sustainable solution can be obtained by solving the MI(N)LP model with environmental constraints and objective function designed in different scenarios.

2.4. Solution strategy

We recommend a decomposition-based solution strategy to solve the proposed integration problem to obtain sustainable solution. First solve the process network with assumption of unlimited utilities. Then add constraints of available water and energy. Water treatment network and power generation network need to be solved independently and then combine with the process sequentially to obtain the result.

3. Conceptual Case Study

3.1. Problem definition

The production of xylitol is considered as an example in our work. The current methods of producing xylitol include chemical hydrogenation and biological fermentation (Jain and Mulay 2014). The conceptual case study aims to demonstrate the effectivity of combining process, power generation and water treatment. The object is to check the economic benefit while considering the limitation of carbon dioxide emission and waste water disposal.

3.2. Superstructure and data collection

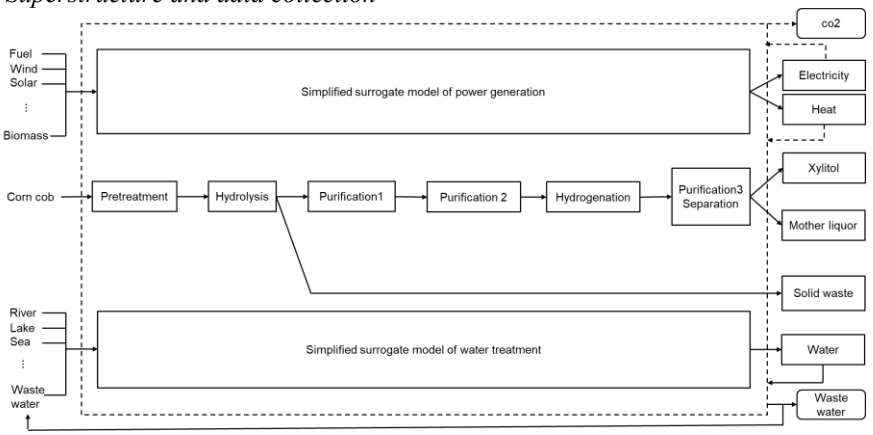

Figure 3. Superstructure of conceptual model

The chemical process converts the xylose from corn cob by Hydrolysis and then convert the xylose to xylitol while requiring a lot of electricity and steam. Different power generation, water supply methods and potential waste water recycle are integrated into this framework based-one simplified surrogate model of power generation and water treatment. The water sources include river, lake, sea, underground water and waste water. Power generation methods include thermal, wind, hydro, solar, nuclear and biomass. Different fuels are considered to generate steam.

3.3. Result and discussion

Market demand for xylitol is fixed at 12,000 t/y. For the first three scenarios, constraints are restricted in different degree. In scenarios 1 and 2, CO_2 emissions are restricted to be less than 390,000 t/y and 480,000 t/y while the waste water disposals are less than 1800,000t/y. In scenario 3 the problem is solved without environmental constraints. In scenario 4, the problem is solved in conventional method without considering the power and water networks. The results are given by Table 1. The radiation pattern of result 1-3 is shown in Figure 4.

Table 1. Xylitol production result in different scenarios

Result	1	2	3	4
Output (t/y)	9,727	12,000	12,000	12,000
Economic benefit ($/y)	8,103,785	11,602,450	14,139,542	9,544,956
Investment($/y)	81,331,530	100,301,888	100,301,888	100,301,888
CO2 emission (t/y)	390,000	479,737	541,084	\
Waste water disposal (t/y)	1800,000	1,800,000	3,662,130	3,662,130
Electricity (kwh)	50,328,788	62,073,333	61,347,100	60,246,710
Water consumption (t/y)	1,804,736	1,805,843	3,667,970	3,667,970
Steam consumption (t/y)	878,330	1,080,430	1,080,430	1,080,430
Electricity source	Wind	Wind	Thermal	\
Steam fuel	Coal	Coal	Coal	\
Water source	River	River	River	\

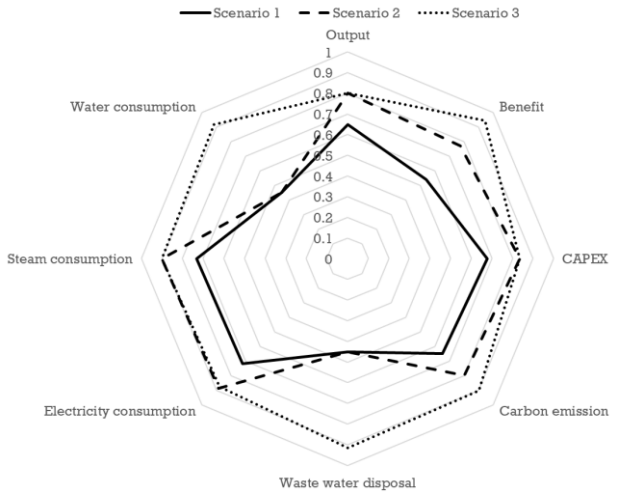

Figure 4. Radiation pattern of scenario 1-3

The scenario 3 has more economic benefit than result 4 since the new framework allows to get power and water at lower cost. By comparing scenarios 1-3, as can be seen in Figure 5, the environmental constraints can significantly influence the results. Strict environmental constraints will lead to environmentally friendly solutions while reducing productivity and economic benefits.

4. Conclusion and Future work

The concept of simultaneous design of process, water network and power generation network was proposed to obtain the sustainable solution. Superstructure-based framework were extended and generic interval model were developed to help construct new optimization problem in a generic approach. Solve the integration problem step by step can lead to sustainable solution with less carbon emission and waste water which has been demonstrated in conceptual case. Furthermore, this concept and method can be used for the synthesis and design of multiple networks to fixed optimal technical route of process, power generation water treatment and carbon recovery. The future work will focus on the design problem of multi-network of various cases and scenarios.

References

Z B. Handani, A. Quaglia, R. Gani, 2015, Synthesis and Design of Integrated Process and Water Networks. Computer Aided Chemical Engineering, 37:875-880.

A. Quaglia, B. Sarup, G. Sin, R. Gani, 2012a, Integrated Business and Engineering Framework for Synthesis and Design of Enterprise-wide Processing Networks, Computers & Chemical Engineering, 38, 213-223.

A. Quaglia, B. Sarup, G. Sin, R. Gani, 2012b, Synthesis and design of processingnetworks: stochastic formulation and solution, Comput. Aided Chem. Eng. 30,467–471.

A. Quaglia, A. Pennati, M. Bogataj, Z. Kravanja, G. Sin, R. Gani, 2014, Industrialprocess water treatment and reuse: a framework for synthesis and design, Ind.Eng. Chem. Res. 53, 5160–5171.

M O. Bertran, R. Frauzem, A S. Sanchez-Arcilla, et al., 2017, A generic methodology for processing route synthesis and design based on superstructure optimization, Computers & Chemical Engineering:S0098135417300303.

H. Jain, S.Mulay, 2014, A review on different modes and methods for yielding a pentose sugar: xylitol, International Journal of Food Sciences and Nutrition, 65(2):135-143.

Sauro Pierucci, Flavio Manenti, Giulia Bozzano, Davide Manca (Eds.)
Proceedings of the 30th European Symposium on Computer Aided Process Engineering (ESCAPE30), May 24-27, 2020, Milano, Italy.
http://dx.doi.org/10.1016/B978-0-12-823377-1.50179-8

Non-Newtonian Analysis of a Counter-flow Mixing Reactor for Fast Hydrothermal Liquefaction

Khanh-Quang Tran
Department of energy and process engineering Norwegian University of Science and Technology, NO-7491 Trondheim, Norway
Khanh-quang.tran@ntnu.no

Abstract

A CFD (computational fluid dynamics) model has been developed in ANSYNS Fluent for studying the use of the nozzle reactor concept for fast HTL of biomass. A Newtonian system was first assumed to make it possible to utilize data in the literature for calibration, which was then followed by a non-Newtonian assumption to simulate flows containing biomass particles. This paper presents and analyses results from the study.

Keywords: Hydrothermal liquefaction; Fast HTL; Nozzle reactor; Process intensification; Wet biomass.

1. Introduction

Fast hydrothermal liquefaction (HTL) may be defined as fast processing of biomass in hot compressed water (below 374°C, 22.1 MPa) for production of HTL oil or bio-crude. Similar to fast pyrolysis, the process of fast HTL requires heating rates higher than hundreds degrees per minute, aiming at maximized bio-crude yields and minimized coke formation of biomass HTL. Recently, the concept of fast HTL has been validated (Bach, Sillero et al. 2014, Bach, Tran et al. 2016). The possibility to improving the conversion efficiency and product selectivity of HTL by fast heating up to 585°C/min has been successfully demonstrated, using sealed capillary quartz reactors with a volume of approx. 0.5 cm^3 per reactor (Bach, Sillero et al. 2014, Bach, Tran et al. 2016). More recently, it has been identified that the concept of nozzle reactor may be suitable for fast HTL of biomass at both laboratory and industrial scales (Tran, Håkansson et al. 2017). A CFD (computational fluid dynamics) study on the nozzle reactor design for fast HTL has been performed (Tran, Håkansson et al. 2017) using ANSYS FLUENT. The results show that the mass flowrate ratio of hot and cold flows plays the most important role in establishing high heating rates in the reactor. Tests for pure water (viscosity = 0.001 Pa.s), the mass flowrate ratio of 60:20 (hot/cold, mil/min) gave very good mixing and thus high heating rate. Effect of the total mass flow on the temperature profile in the reactor was not significant. However, an analysis of the model for fluid flow with elevated viscosities was not in agreement with the experimental validation. The reason of the disagreement is probably due to the Newtonian assumption to make it possible to utilizing the validation data from the literature. Therefore, new attempts to study the reactor for fast HTL using ANSYS Fluent, assuming non-Newtonian fluid flows have been made, which will be presented in this present paper.

2. Reactor and study methods

2.1. Reactor and process

Figure 1 presents schematically the concept of nozzle reactor, which has been succesfully developed for production of nanoparticles from equaeous solution of metal salts (Lester, Blood et al. 2006, Sierra-Pallares, Huddle et al. 2016). The reactor 1 is essentially a pipe-in-pipe concentric setup in which the internal pipe has an open-ended nozzle with a cone attached (optional). The "hot" stream (or flow) of preheated water is fed downwards through the internal pipe, reaching out at the exit end (nozzle) of the pipe. The "cold" stream is fed upwards through the outer pipe. The reactor outlet is situated on top of the outer pipe, leading the reactant mixture to a cooling unit. Because of the impingement of the hot and cold streams, the forced counter-current mixing process is enhanced by the natural convection due to the difference in density between the two steams. As a result, very good mixing and thus high heating rates can be achieved in the reactor.

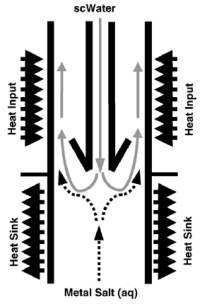

Figure 1: Schematic diagram of the nozzle reactor for hydrothermal synthesis of nanoparticles (Lester, Blood et al. 2006, Sierra-Pallares, Huddle et al. 2016)

2.2. Computational fluid dynamic approach

2.2.1. Geometry and messing

In this work, a full geometry similar to Figure 1B was created and presented in Figure 2, of which the main dimensions are given in Table 1.

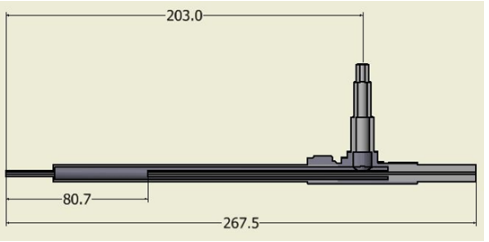

Figure 2. Geometry of the reactor used for CFD modelling

Table 1: Main dimensions of the reactor

Tube	Outer diameter (mm)	Thickness (mm)	Length (mm)
Hot flow inlet	3.175	0.89	186.72
Outer reactor tube	9.53	1.65	157.5
Cold flow inlet	3.175	0.89	20
Outlet flow	6.35	1.65	25

Due to the symmetry, only half of the reactor was meshed, using a hexahedral cell mesh with a maximum cell size of 0.2 mm. For meshing the fluids flowing through the reactor. a Virtual Body Group was added to the geometry of the reactor. For this purpose, the commercial CFD software ANSYS FLUENT, version 18.0 was used. Each analysis consisted of two steps; first a steady state run that established the flow and temperature fields of the entire reactor, and then a subsequent transient analysis to establish the *residence time distribution* (RTD) of the mixing zone. During the transient analyses, the flow and temperature fields were left unchanged at their steady state values; only the evolution of an inert scalar was simulated.

2.2.2. Governing equations and turbulence model

The behaviour of a fluid flow is governed by the fundamental set of Navier-Stokes equations for conservation of mass, momentum and energy. When modelling turbulent fluid flows, a suitable averaging method must be used (Sierra-Pallares, Huddle et al. 2016). For flow and mixing of fluids under supercritical conditions, it is convenient to use density or Favre averaging method, which applies fluctuation to average values instead of actual flow parameter in order to derive a time averaged solution (H.K.Versteeg and W.Malalasekera 2007, Sierra-Pallares, Huddle et al. 2016). The density averaged conservation equations for momentum, mass and energy are represented as

$$\frac{\partial \bar{\rho}}{\partial t} + \frac{\partial (\bar{\rho}\tilde{u}_i)}{\partial x_i} = 0 \tag{1}$$

$$\frac{\partial (\bar{\rho}\tilde{u}_i)}{\partial t} + \frac{\partial}{\partial x_j}(\rho u_i u_j) = -\frac{\partial \tilde{p}}{\partial x_i} + \frac{\partial}{\partial x_j}\left(\tilde{\sigma}_{ij} - \bar{\rho}\widetilde{u_i'' u_j''}\right) + \rho g_i \tag{2}$$

$$\frac{\partial (\bar{\rho}\tilde{e})}{\partial t} + \frac{\partial}{\partial x_j}\left(\bar{\rho}\tilde{u}_j\left[\tilde{e} + \frac{\tilde{p}}{\bar{\rho}}\right]\right) = \frac{\partial}{\partial x_j}\left[\lambda\frac{\partial \bar{T}}{\partial x_j} + \tilde{u}_j\left(\tilde{\sigma}_{ij} - \bar{\rho}\widetilde{u_i'' u_j''}\right) - \bar{\rho}\widetilde{e'' u_j''}\right] \tag{3}$$

$$\frac{\partial (\bar{\rho}\tilde{\phi})}{\partial t} + \frac{\partial}{\partial x_j}(\bar{\rho}\tilde{u}_i\tilde{\phi}) = \frac{\partial}{\partial x_j}\left[\bar{\rho}\mathcal{D}\frac{\partial \tilde{\phi}}{\partial x_j} - \bar{\rho}\widetilde{\phi'' u_j''}\right] \tag{4}$$

where u_j is the fluid velocity in direction x_j; p is the fluid pressure; ρ is the fluid density; e is the internal energy of the fluid; ϕ is a passive scalar; σ_{ij} is the viscous tress tensor of the fluid; and g_i is gravitational acceleration constant in direction x_i. If the viscosity fluctuation is neglected, the viscous tress tensor σ_{ij} will reduce to Eq. (5) where η is the molecular viscosity of the fluid and δ_{ij} is the unit matrix.

$$\sigma_{ij} = \eta\left[\left(\frac{\partial \tilde{u}_i}{\partial x_j} + \frac{\partial \tilde{u}_j}{\partial x_i}\right) - \frac{2}{3}\delta_{ij}\frac{\partial \tilde{u}_k}{\partial x_k}\right] \tag{5}$$

The set of equations Eq. (1-3) is not closed because the averaging procedure creates new variables for the Reynolds stress tensor $-\bar{\rho}\widetilde{u_i'' u_j''}$. In order to close the equation set, the Reynolds stress tensors is modelled and calculated, adopting the Reynolds-averaged Navier–Stokes (RANS) method and the Realizable k- ε turbulent model, of which further details can be found in the literature (Sierra-Pallares, Huddle et al. 2016) .

3. Results and discussion

In the first instance, the thermodynamic and fluid dynamic setup was defined with a Newtonian assumption. A RTD-based validation was performed, which gave similar results as for the simplified geometry assumption presented earlier (Tran, Håkansson et al. 2017). In addition, the mixing and thus reactor temperature profile, is in good agreement with the literature (flow ratio of 20:10 ml/min) (Sierra-Pallares, Huddle et al. 2016). Then the power law non-Newtonian model was adopted to simulate the cold flow

of biomass slurry. Three investigations were performed using the developed non-Newtonian model. The first looked at the effect of the flow ratio on the mixing and thus temperature profile of the reactor. The second analyzed the effect of the viscosity change of the cold flow of biomass slurry. Third studied the effect of the total mass flow.

3.3.1 Effect of the flow ratio

Two simulations were performed and analyzed for the hot flow of the same pressure (25 MPa) and temperature (450ºC) and a cold flow of 10% wt lignin slurry solution. The flows analyzed have been 20:10 and 30:10 ml/min. The results are shown in Figure 3.

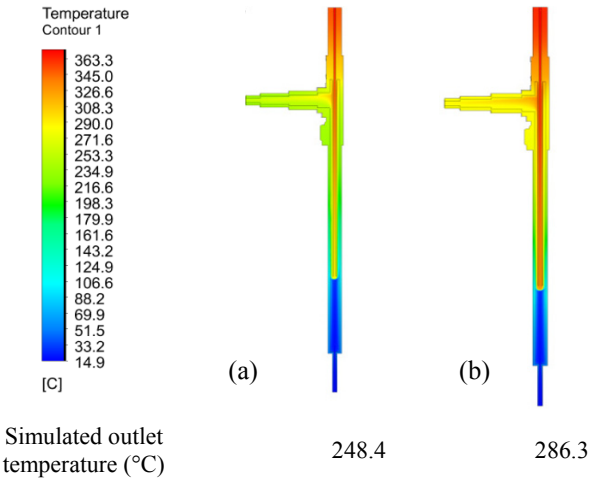

Figure 3. Temperature profile of the 20:10 (a) and 30:10 (b) ml/min for non-Newtonian model

It is clearly shown from the simulation result that the temperature at the outlet of the reactor is strongly dependent on the flow ratio. In addition, the temperature profile obtained from the non-Newtonian model is lower than that from the Newtonian. For example, comparing the 20:10 ml/min contours (Figure 3a and 3b) it can clearly be seen that for non-Newtonian fluid, the temperature of the hot inlet arriving the mixing point has drastically been reduced to an around value of 280°C compared to the 340°C obtained from the Newtonian one. On the other hand, as presented in Figure 4, clear differences in the shape of the mixing between the Newtonian and non-Newtonian simulations were observed. Indeed, the mixing of the fluids occurs in a point nearer to the hot inlet tube outlet in the non-Newtonian model than in the Newtonian simulation. In addition, the heat transfer takes place in a smaller space although the mixture temperature is notably lower.

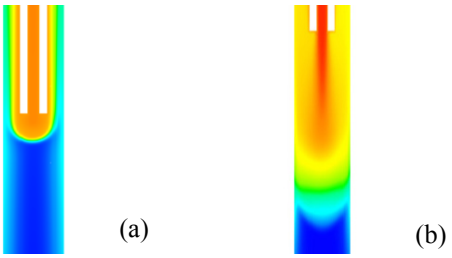

Figure 4: a) Mixing zones for non-Newtonian (a); and b) Newtonian model. (Flow ratios of 30:10 ml/min)

3.3.2 Effect of viscosity of the cold flow

The effect of viscosity of non-Newtonian fluid was used to simulate the effect of lignin concentration and particle size in the cold flow. The investigation was performed for the flow ratio of 30:10 ml/min and the result is presented in Figure 6. It is interesting to see that the temperature profiles obtained from the simulations are pretty similar, with their outlet temperatures of 286.32°C and 288.3°C, respectively. The main difference between them resides in the asymmetry which appears along the reactor in the 12.5%wt case (Figure 5d). Furthermore, the hot mixing zone appearing in the 10%wt is considerably longer than the one for 12.5%wt although being the same flow rates.

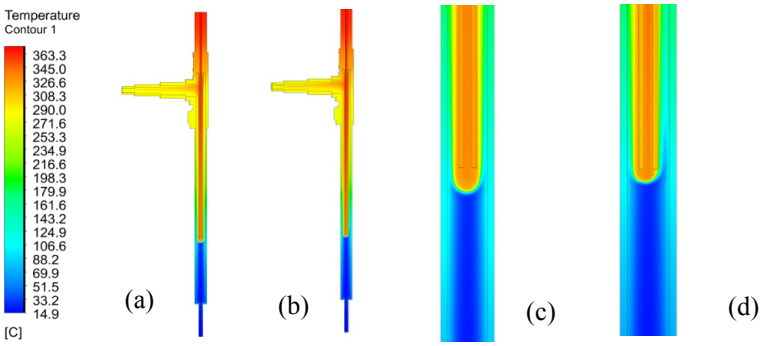

Figure 5: Temperature contour and c) mixing point for 10% wt (a and c), and 12.5%wt (b and d) lignin

3.3.3 Effect the total mass flow rate

For this study, the total mass flow rate were varied within 30:10, 60:20, 90:30 and 120:40 ml/min to insure a constant flow rate ratio of 3:1. In addition, a cold flow containing 10% wt lignin was employed all cases. In Figure 6 the obtained temperature contours for these flows and their outlet temperature are shown. The temperature in the mixing zone increases and this mixing zone moves downwards with increased total mass flow rate.

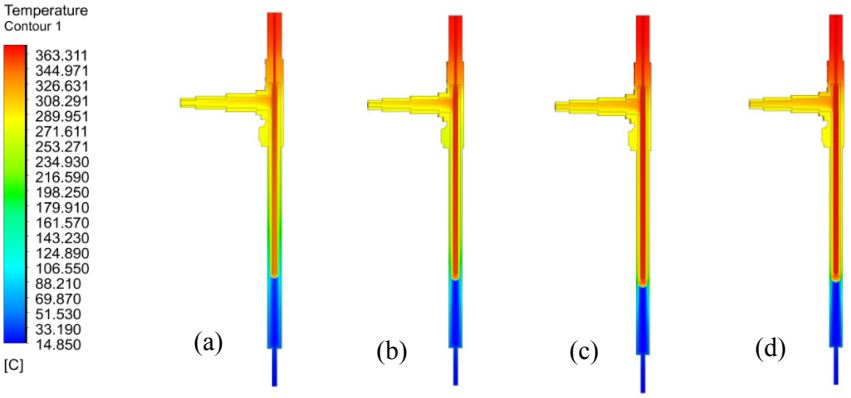

Simulated outlet temperature (°C)	286.3	290.82	302.16	305.49

Figure 6: Temperature profile for 30:10 (a), 60:20 (b), 90:30 (c) and 120:40 (d) ml/min, 10%wt lignin cold flow

4. Conclusions

In this study, a full geometry of the nozzle reactor design was developed and modelled for Newtonian and non-Newtonian fluids. The Newtonian assumption was used for model validation. The non-Newtonian assumption was used for studying the effects of the flow rate ratio, total mass flow rate, and the viscosity of the cold flow on the mixing the thus temperature profile of the reactor. The results indicated that

- Non-Newtonian fluids behave in a different way of Newtonian ones in important terms such as viscosity, temperature or flow.
- An important reduction in the temperatures along the reactor appears when working with non-Newtonian fluid compared to the results obtained with Newtonian one.
- The temperature profiles suffer very little change in value with the change of the viscosity.
- The mixing zone shape suffers a big change compared to the Newtonian fluid.
- Higher content of solid in the cold flow cause a bigger asymmetry in the temperature along the cross sections of the reactor. This fact can be solved using higher hot:cold flow ratios.
- The outlet temperature increases with the increment of the total mass flow rate.

Acknowledgement

The data presented in this paper is extracted from the master thesis of my ex-student, Gastón Mauricio Cocco, whose efforts are acknowledged.

References

Bach, Q.-V., M. V. Sillero, K.-Q. Tran and J. Skjermo (2014). "Fast hydrothermal liquefaction of a Norwegian macro-alga: Screening tests." Algal Research 6(B): 271-276.

Bach, Q. V., K. Q. Tran and K. Q. Lystad (2016). Fast hydrothermal liquefaction of macro-alga: Characterization of products. Chemical Engineering Transactions. 50: 97-102.

H.K.Versteeg and W.Malalasekera (2007). An Introduction to Computational Fluid Dynamics: The Finite Volume Method, Pearson Education Limited.

Lester, E., P. Blood, J. Denyer, D. Giddings, B. Azzopardi and M. Poliakoff (2006). "Reaction engineering: The supercritical water hydrothermal synthesis of nano-particles." The Journal of Supercritical Fluids 37(2): 209-214.

Sierra-Pallares, J., T. Huddle, J. García-Serna, E. Alonso, F. Mato, I. Shvets, O. Luebben, M. J. Cocero and E. Lester (2016). "Understanding bottom-up continuous hydrothermal synthesis of nanoparticles using empirical measurement and computational simulation." Nano Research 9(11): 3377-3387.

Tran, K.-Q., L. Håkansson and T. T. Trinh (2017). "CFD pre-study of Nozzle reactor for fast hydrothermal liquefaction." Energy Procedia 142: 861-866.

Sauro Pierucci, Flavio Manenti, Giulia Bozzano, Davide Manca (Eds.)
Proceedings of the 30th European Symposium on Computer Aided Process Engineering (ESCAPE30), May 24-27, 2020, Milano, Italy.
http://dx.doi.org/10.1016/B978-0-12-823377-1.50180-4

Techno-economic Analysis of Heat Pumping Technology for Oleochemical Fatty Acid Fractionation

Norul M. Sidek,[a,b*] Mohamad R. Othman[a,b]

[a]*Process Systems Engineering & Safety Research Group, Faculty of Chemical & Process Engineering Technology, Universiti Malaysia Pahang, 26300 Gambang, Pahang, Malaysia.*
[b]*Department of Chemical Engineering, College of Engineering, Universiti Malaysia Pahang, 26300 Gambang, Pahang, Malaysia.*
norulmalakiah.sidek@gmail.com

Abstract

Distillation unit is often known as a major energy consumer in chemical refineries. Recent researches have shown an increased interest in heat pumping technology. So far, previous studies of heat pump integrated column have not dealt with industrial oleochemical separation. The aim of this research paper has therefore been to investigate the implications of using heat pumping technology on oleochemical fractionation. This work takes the form of an industrial case-study of palm kernel oil (PKO) fatty acid fractional distillation. Two different arrangements of mechanical vapour recompression (MVR); namely direct vapour recompression (VRC) and bottom flashing heat pump (BFHP), were introduced to the process and their performances were assessed for technological efficacy as well as cost effectiveness. All simulations were carried out using Aspen Plus process simulator and UNIQUAC was chosen as the most suitable thermodynamic package. Economic analysis in terms of capital expenses (CAPEX) and operational expenses (OPEX) was evaluated. Though both MVR systems have shown relative reduction in energy load, however the CAPEX performance demonstrated in this study was not very appealing due to the additional equipment to satisfy the energy requirement. One anticipated finding was that the OPEX for the VRC showed only 50% from the conventional column (CC). On the contrary, the BFHP was ruled out for its CAPEX and OPEX, which showed twice as much as the CC.

Keywords: Oleochemical, vapour recompression, bottom flashing, fractional distillation.

1. Introduction

In the new global economy, energy consumption has become a central issue in chemical plants. One of the most significant discussions in this alarming issue is the energy utilization in major separation units. Distillation is commonly known as a prominent technology for separation process; however, it suffers from low thermodynamic efficiency which directly contributes to a large energy consumption. In view of this, any method of minimizing this associated energy would be of great advantage. Apparently, there is a large volume of published studies describing the important role of heat integration in energy saving. A number of mature heat-integrated technologies have already made a debut decade ago in chemical refineries. Heat pump assisted distillation has evolved to become one of those promising technologies that is commercialized for industrial practice.

In principle, application of heat pumping system would be worthwhile in an effort to reduce the associated external utility consumption, by recovering heat from column top vapour to aid the evaporation process in the reboiler. The state-of-the-art heat pump system used in many distillation operations worldwide is known as MVR. The typical MVR configuration, VRC, utilizes the overhead vapour as a heat transfer medium entering the compressor and will be compressed to a higher pressure and enters the bottom reboiler to heat the liquid. The other way is by flashing the liquid leaving the bottom reboiler and will be used to cool the overhead vapour, termed as BFHP.

To date, however, research on the subject has been mostly focused on petroleum processes. No previous study has investigated the influence of heat pumping system in energy saving for oleochemical separation thus far. As claimed by McKetta Jr. (1997) in his book, columns with the operation pressure of less than 100 mbar, which is common in oleochemical separation, are not suitable for VRC unless the system uses an auxiliary working fluid as to save the compressor cost. In addition to this, it was reported that most oleochemicals sustain limited familiarity and flexibility (Faessler et al., 2007). In this regard, far too little attention has been paid to heat integration measures in oleochemical separation due to the intricacy of low-pressure operation. This study therefore set out to assess the effect of MVR technology on the oleochemical separation particularly in fatty acid fractionation process. The findings of this study should make an important contribution to the oleochemical sector towards energy-efficient operation. The performance, external utility usage and capital investment were evaluated accordingly once the simulations were successfully established.

2. Process Simulations

2.1. Conventional column

Fat splitting of PKO generates crude fatty acid that can either be purified by distillation, giving a whole-cut purified fatty acid or separated into individual fatty acids by fractional distillation. In fractionation process, crude fatty acid is separated into its narrower cuts; light cut (C8-C10), medium cut (C12-C14) and heavy cut (C16-C18) (Illner and Othman, 2015; Othman and Rangaiah, 2020). Conventionally, the separation of low boiling point fatty acid component is commonly achieved by employing two units of fractionation columns. For the purpose of simplifying the process simulation in this study, only one fractionation column was used to separate the desired component, which in this case is 99% of lauric acid in distillate. Table 1 indicates the PKO fatty acid compositions obtained from an industrial oleochemical refinery.

Table 1: Compositions of PKO fatty acid (Othman and Rangaiah, 2020).

Component	Formula	Mole Fraction
Caproid acid	$C_6H_{12}O_2$	0.00121
Caprylic acid	$C_8H_{16}O_2$	0.03320
Capric acid	$C_{10}H_{20}O_2$	0.03420
Lauric acid	$C_{12}H_{24}O_2$	0.47681
Myristic acid	$C_{14}H_{28}O_2$	0.16296
Palmitic acid	$C_{16}H_{32}O_2$	0.07947
Oleic acid	$C_{18}H_{34}O_2$	0.15713
Linoleic acid	$C_{18}H_{32}O_2$	0.02615
Stearic acid	$C_{18}H_{36}O_2$	0.01891
Triglyceride (methyl-oleate)	$C_{19}H_{36}O_2$	0.00996

The process with a feed flow rate of 9000 kg/h was operated under high vacuum, 50 mbar. It is very important to keep the operating temperature below 250 °C to avoid chemical decomposition of fatty acid. The pressure drops in the column, condenser and reboiler throughout this work were taken to be zero due to too low operating pressure. For the simulation, the shortcut model in Aspen Plus, DSTWU was used to estimate the column performance such as number of stages and reflux ratio, which was later used for rigorous distillation (RADFRAC). 20 stages were needed for this separation process with a reflux ration of 0.75. In all simulations, the suitable model, UNIQUAC was chosen to predict the thermodynamic properties of the system (Sidek and Othman, 2019). The MVR assisted column configurations were also simulated based on the same column conditions and desired product specifications as the CC to promote a fair comparison.

2.2. MVR-assisted column with VRC

Various VRC configurations can be constructed depending on the process conditions. The latest novel VRC configuration was proposed by Cong et al. (2018) for a number of petroleum separation by introducing a middle VRC system. For this study, a typical VRC configuration will be adopted by Kazemi et al. (2016) but with some modification made based on the process conditions. The flow diagram of this scheme is shown in Figure 1. In this heat pump configuration, the low-quality heat of overhead vapour stream was upgraded by raising the temperature such that it was hotter than that in the reboiler. The elevated vapour temperature allowed the utilization of the latent heat for bottom liquid reboiling (Parhi et al., 2019). This was done by introducing the vapour into the compressor (C-101), eliminating the use of the condenser unit. Prior to that, the top vapour stream underwent superheating in order to prevent partial condensation from occurring. Moreover, it was appeared that even by using maximum practical compression of 3.0 as suggested by Felbab et al. (2014) without superheating, the compressor outlet temperature was not sufficiently hot for heat exchange with the bottom liquid. In view of this, the overhead vapour was superheated in the superheater (SH-101) at a temperature increase of 20 °C, while the compression ratio was taken as 3.0 to guarantee maximum heat was supplied to the heat exchanger (HX-101).

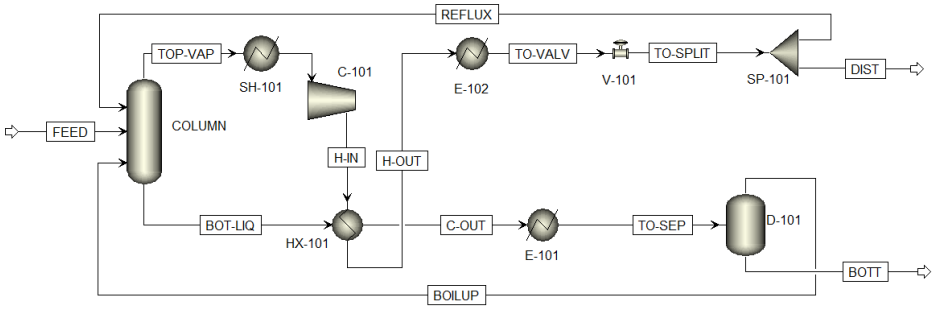

Figure1: Simulation flow diagram of the VRC

The early precaution of not letting the process temperature exceeded 250 °C was complied. The temperature difference in the heat exchanger was kept at a range of 5-8 °C for a cost-effective process. It was somewhat surprising to note that even with the aid of superheating and application of maximum compression ratio, the recovered heat could not provide required heat to evaporate the liquid. As a result, a trim-reboiler (E-101) was needed to supply the low-pressure steam to satisfy the remaining energy requirement.

The heated stream was flashed in the flash drum (D-101), where the vapour stream was routed to the column as boil-up, while the remaining liquid was drawn as a bottom product. On the other hand, the effluent stream from the heat exchanger was air-cooled in the trim-cooler (E-102) and expanded in the throttle valve (V-101) before being split in the splitter (SP-101). Part of the liquid was returned to the column as reflux, while the remaining was discharged as distillate.

2.3. MVR-assisted column with BFHP

This heat pump system is almost similar to the VRC, only in the BFHP, bottom liquid was flashed and used as working fluid in the compressor. In this configuration, the temperature of the bottom column outlet stream is normally reduced in the expansion valve (V-201). In that way, both condensation and evaporation can be fulfilled despite the omission of the reboiler and the condenser. The pressure drop during the expansion was determined such that the temperature difference between the hot inlet and cold inlet temperatures was exactly the same as in the VRC. Part of the reboiler duty was met during heat transfer in the heat exchanger (HX-201) and the remaining part was provided by the trim-reboiler (E-201). For similar reason as the VRC system, the stream was first routed to the superheater (SH-201) to avoid condensation. In Figure 2, it can be seen that the superheated cold outlet stream was recompressed to column operating pressure in the compressor (C-201) and sent to the flash drum (D-201) for vapour-liquid separation. The resulting vapour returned to the column as boil-up. Meanwhile, the liquid was subcooler in the air-cooler (E-202) and pumped out as final bottom product. The hot outlet stream from the heat exchanger was divided into two streams; reflux and distillate streams.

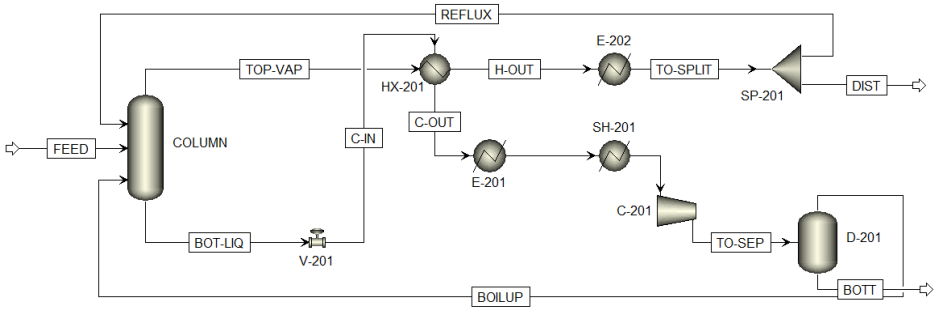

Figure 2. Simulation flow diagram of the BFHP.

3. Techno-economic analysis

3.1. Energy and utility requirement

Based on the results tabulated in Table 2, it was apparent that application of both MVR configurations to the column can reduce energy load despite the addition of the superheater unit in each system. On average, the CC reboiler duty was not entirely replaced by the heat exchangers, instead trim reboilers were employed to satisfy the remaining duty. The BFHP was shown to have a greater demand in energy consumption as only 40% of reboiler duty can be satisfied during heat exchange. This is due to the limitation set in temperature difference between the shell and tube inlet temperatures. As a result, overall heating duty for the BFHP was escalated to almost 20% close to what was needed in the CC. Operation of the BFHP also required even more extreme vacuum condition which is unfavourable, owing to its operation complexity.

On top of that, the MVR-assisted columns needed mechanical work to drive the compressor which accounts for the highest utility expenses. Taken together, it would be uneconomical to adopt the BFHP for this oleochemical separation, given that the mechanical compression work was twice the number reported in the VRC. To further validate this claim, a simple economic analysis will be discussed in the next section. Table 2 also reveals that there is a clear trend of decreasing in cooling utility to half of the number recorded by the CC condenser.

Table 2. Summary of utility requirements.

System	CC	VRC	BFHP
Cold utility requirements (kW)	969.25	423.36	496.16
Hot utility requirements (kW)	1185.83	556.06	965.32
Mechanical work requirements (kW)	-	94.58	192.40

3.2. Economic analysis

The economic performances of MVR-assisted columns were assessed in terms of CAPEX and OPEX. Sizing of individual equipment was primarily obtained from the calculated value in the simulator to determine the cost. These equipment details were then specified in the free capital cost estimation program, CAPCOST to determine the CAPEX for all configurations. Since all equipment was in contact with fatty acid, material of construction used in this study was 316 Stainless Steel for all units. The CAPEX mainly consists of major equipment; column tower, condenser, reboiler, heat exchanger, compressor, heaters and cooler costs. The Chemical Engineering Plant Cost Index (CEPCI) was used for cost adjustment from CAPCOST base year to a current year (2019). It was assumed that the plant was operated approximately 10 years, with 8000 operating hours per year. To calculate the OPEX, utility prices were taken from Parhi et al. (2019), where the electricity tariff for industry was \$0.084/kWh, high-pressure (HP) steam was \$17/t and cooling water \$0.06/t. The cost breakdown is detailed in Table 3.

Table 3. Summary of cost estimation for the CC and MVR configurations.

Configuration	**CC**	**VRC**	**BFHP**
CAPEX (x10^6 \$)			
Column tower	1.240	1.240	1.240
Column condenser	0.188	-	-
Column reboiler	0.475	-	-
Trim-reboiler	-	0.173	0.205
Trim-cooler	-	0.144	0.144
Superheater	-	0.271	0.487
Compressor	-	0.388	1.310
Heat exchanger	-	0.532	0.225
Total	***1.903***	***2.748***	***3.611***
OPEX (x10^6 \$/y)			
Electricity	-	0.064	0.129
High-pressure steam	0.338	0.158	0.275
Cooling water	0.080	-	-
Total	***0.418***	***0.222***	***0.404***

The findings of the current study in reviewing the performance of the MVR system in oleochemical fractionation are not very consistent with the previous researches. Both MVR configurations showed higher CAPEX than the CC. Nonetheless, it was somehow predictable because there were an additional equipment unit employed such as superheater and trim-reboiler to meet the energy requirement. In the typical configuration in most previous studies, liquid reboiler duty was entirely achieved during heat exchange, hence, no trim-boiler was needed and lower CAPEX recorded. Whilst, the estimated CAPEX of the BFHP was the highest amongst the three configurations, which was doubled the cost in the CC. This rather contradictory result may be due to the expensive compressor cost that was installed with high compression ratio to recompress the bottom stream to column operating pressure. On the other hand, it is interesting to note that, no cold utility was calculated for the MVRs. Since the trim cooler used in this study was an air-cooler, the cooling utility cost can be eliminated for both MVR systems. The VRC experienced 50% less utility expenses than the CC, and surprisingly, the higher utility was not coming from the electricity but HP steam. Approximately 1164 kg/h of HP steam was supplied to the superheater and the trim reboiler in the VRC and 2021 kg/h in the BFHP. The similar pattern was observed in the BFHP, only it was twice the amount of the utility used in the CC. Looking at the bigger picture, there is a strong possibility that in 10 years of the VRC operation, plant earnings can be increased by the amount saved on utility consumption. It is undoubtedly that a significant increase in profitability could be achieved in years to come, despite higher CAPEX recorded during the start of the operation.

4. Conclusions

The present study was designed to determine the implication of heat pumping technology application in PKO fatty acid fractionation. The energy usage evaluation suggests that the VRC was capable to operate excellently at lower heat load. Despite the VRC excellent performance in utility reduction, this thermal integration technology, however, relies greatly on the mechanical compression, which entails high costs. Furthermore, the use of the trim-reboiler with HP steam has also affected both CAPEX and OPEX performances. It is expected that the saving in utility consumption could contribute to the increase in future earnings in 10 years of the VRC operation and that it could exceed the CAPEX value. Meanwhile, the results for the BFHP was not very encouraging, not only it was costly, but it also worked under extreme vacuum condition which is not preferable. It is important to keep in mind that these simulations were only for a comparative study and the selected configurations might not be the most optimal design for fatty acid fractionation process. Further study is necessary to design the VRC system specifically for this process that works under vacuum condition.

References

A. Kazemi, A. Mehrabani-Zeinabad and M. Beheshti, 2018, Appl. Energy, 221, 1261-81.
H. Cong, J. P. Murphy, X. Li, H. Li, and X. Gao, 2018, Ind. Eng. Chem. Res., 57, 6317-29.
J. J. McKetta Jr., 1997, Encyclopedia of Chemical Processing and Design, Volume 61, 406-407.
M. Illner and M. R. Othman, 2015, PERINTIS e-Journal, 5, 34-44.
M. R. Othman and G. P. Rangaiah, 2020, J. of Oil Palm Res., In Press.
N. Felbab, B. Patel, M. El-Halwagi, D. Hildebrandt and D. Glasser, 2013, AIChE J., 59, 2977-92.
N. M. Sidek and M. R. Othman, 2019, Mat. Sci. Eng., In Press.
P. Faessler, K. Kolmetz, K. W. Seang and S. H. Lee, 2007, Asia- Pacific J. Chem. Eng., 2, 315-321.
S. S. Parhi, G. P. Rangaiah and A. K. Jana, 2019, Sep. Purif. Technol., 213, 553-570.

Sauro Pierucci, Flavio Manenti, Giulia Bozzano, Davide Manca (Eds.)
Proceedings of the 30th European Symposium on Computer Aided Process Engineering (ESCAPE30), May 24-27, 2020, Milano, Italy.
http://dx.doi.org/10.1016/B978-0-12-823377-1.50181-6

GHG Emission Reduction Assessment for Desalination Systems through Carbon Capture and Renewable Energy Options

Rachid Klaimi[a,b], Sabla Y. Alnouri[a,*]

[a]*The Baha and Walid Bassatne Department of Chemical Engineering and Advanced Energy, American University of Beirut, PO Box 11-0236, Riyad El-Solh, Beirut, Lebanon*

[b]*Department of Mechanical Engineering, American University of Beirut, PO Box 11-0236, Riyad El-Solh, Beirut, Lebanon*
sa233@aub.edu.lb

Abstract

Many existing desalination plants are energy intensive, relying on fossil fuels to provide the energy requirements of the process. In the long run, such desalination operations are unsustainable, and result in excessive carbon dioxide emissions. Since shifting towards renewable energy technologies has been identified as a plausible remedy for carbon dioxide emission reduction in the desalination market, the ability to invest in the most appropriate desalination/renewable energy technologies calls for the need to assess the many different options that do exist. When it comes to switching over to renewable energy options, policy makers are always concerned about the relatively high cost of renewable energy technologies compared to fossil fuels. Hybrid energy systems usually offer a relatively good compromise between conventional and renewable energy technologies, since such energy systems can address carbon footprint reduction to some extent. Moreover, carbon capture can be coupled with hybrid and conventional energy sources to reduce the carbon dioxide emission associated with their operation. To date, there exist no assessment methods that have captured the effects of imposing different carbon reduction targets on the optimal design of desalination systems, and their respective energy sources. Hence, the main objective of the model is to minimize the total desalination network cost, while satisfying a set of conditions and constraints related to water recovery, as well as heat and power production. Most importantly, the associated carbon emission levels may be controlled through renewable energy or a combination of conventional and hybrid energy options, in addition to the possibility of combining those options together with standard carbon capture methods.

Keywords: Desalination, Carbon dioxide emissions, Renewable energy, Hybrid energy systems, Carbon capture

1. Introduction

In light of the increased global water demand, due to population growth and excessive water use in the industrial and domestic sectors, the need to address eminent water shortage problems has become vital. Several studies have looked into potential solutions that could alleviate water scarcity through wastewater treatment and water reuse. By

looking into ways that can help design Zero Liquid Dicharge (ZLD) systems, brine wastewater can potentially be utilized to recover treated water for reuse (Mansour and Alnouri 2019). Many other studies tackled water scarcity from a different perspective. For instance, some focused on utilizing industrial symbiosis strategies for this purpose (Somoza-Tornos et al. 2019). However, seawater desalination remains one of the most appealing techniques for alleviating water scarcity, even though most desalination technologies are energy intensive. Desalination systems that rely on the use of conventional energy sources, such as fossil fuels, are often associated with high levels of GHG emissions (Mannan et al. 2018). Therefore, many desalination industries are trying to shift into more renewable energy sources that have recently invaded the markets, in an attempt to reduce emissions and abide by the international regulations (Klaimi et al. 2019). Since renewable technologies are often associated with high costs, hybrid energy systems are gaining more attention due to their ability of meeting required energy demands while easing off some of the environmental limitations that are often faced when using conventional fuel sources only. Moreover, their moderate costs when integrated with desalination technologies also make hybrid systems quite attractive (Khan, Rehman, and Al-Sulaiman 2018). Similarly, carbon capture and storage (CCS) is one of the most common techniques utilized for emission reduction, and has been widely utilized due to its maturity and moderate costs compared to renewable energy (Al-Mohannadi and Linke 2016). The question of whether investing in carbon capture or renewable energy in order to achieve desalination operations still remains a challenge, especially due to the lack of tools that can help assess such situations. Hence, this paper presents a Mixed Integer Nonlinear Problem (MINLP) optimization model that enables a generic assessment of those carbon emission reduction methods, when coupled with desalination systems.

2. Methodology

The proposed model, shown in Figure 1 below, consists of four different sets of technologies: thermal desalination units (set T), membrane (set M), renewable energy (set R) and hybrid systems (set H), in addition to a carbon capture unit.

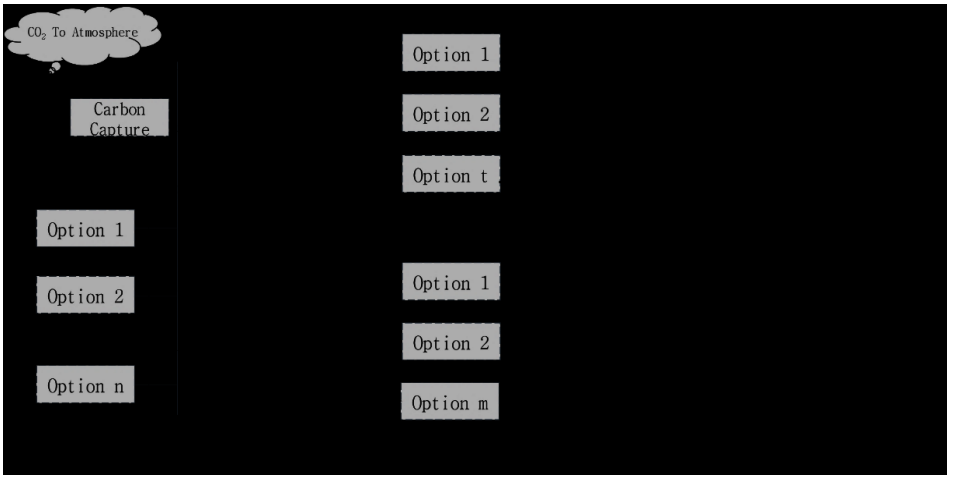

Figure 1: Desalination Network Structure

A seawater feed stream is mainly fed into the system and split between the thermal and membrane technologies. Two streams leave each desalination unit: a water product stream, and a concentrated brine stream. The system is designed such that a portion of the concentrated brine streams can be recycled back and mixed with the original feed stream, as this could potentially enhance the performance of the system. Additionally, the model allows for renewable energy and hybrid systems options to be available for providing the respective desalination units with their heat and power requirements. Unlike renewable energy sources, hybrid systems and conventional fuel energy sources are associated with certain amounts of carbon dioxide emissions. Therefore, the emissions resulting from those systems can be captured using CCS, which must undergo a treatment stage in order to reduce the environmental harm with respect to the imposed net carbon reduction target.

Designing an optimal desalination network integrated with renewable and hybrid energy systems requires a complete assessment of all the available technology options. This assessment is based on the specifications of each technology, which differ between desalination and energy units. For instance, the specifications of desalination units include the capacity limit, water recovery, salt rejection, heat and power requirements, in addition to the feed water characteristics, while those of energy sources include the capacity limit, capital and operational costs, as well as the amount of CO_2 associated with their operation, which is mainly based on the type of utilized fossil fuel. Different constraints can be imposed on those entities, as well as on the overall network. This makes the proposed approach very flexible, since it can be then modified based on the user specifications. Such constraints fall under one of the following categories: i) capacity constraints (the maximum flowrate that a desalination unit can withstand or the maximum amount of energy that can be produced by an energy unit), ii) composition constraints (the inlet and outlet brine concentrations), iii) water production (the required amount of product water), iv) and emission constraints (the maximum allowable carbon emissions).

3. Mathematical Formulation

The proposed optimization model is a MINLP, in which the cost objective function, represented by Eq. (1), is defined subject to various equality and inequality constraints:

$$\text{Minimize } Cost^{therm} + Cost^{mem} + Cost^{energy} + Cost^{carbon\ capture} \quad (1)$$

The objective function is to minimize the total network cost of the desalination system, which includes the capital and operational costs of desalination technologies, renewable and hybrid energy systems, as well as the carbon capture cost. The decision variable in the objective function refers to the flowrate vector which includes the flows into thermal and membrane units, the flows into technologies of the same type, and for the flows of the recycled streams. The objective function is subjected to two types of constraints: equality and inequality constraints. The equality constraints cover the mass and energy balances of different material throughout the system. The mass balance equations include total (Eq. (2)) and component (Eq. (3)) balances for brine and water streams in the system, while the energy balance equations, described by Eq. (4), target the amount of energy produced by the energy sources and integrated with the desalination technologies. In the following equations, F^{in} refers to the inlet feed flowrate, $F^{P}$is the flow entering desalination units, R refers to recycled streams, x_c is the concentration of component c,

E_r is the total energy produced by source r, and the subscripts t and m refers to thermal and membrane units.

$$F^P = (F^{in} + R^{therm} + R^{mem}) - B^{purge} \quad (2)$$

$$F^P x_c^P = \left(F^{in} x_c^{in} + R^{therm} x_c^{B,therm} + R^{mem} x_c^{B,mem}\right) - B^{purge} x_c^{purge} \quad (3)$$

$$E_r = \sum_{t \in T} E_{r,t} + \sum_{m \in M} E_{r,m} \ \ for \ \forall r \in R \quad (4)$$

On the other hand, the inequality constraints, represented by the capacity of desalination units and energy sources, maximum inlet salinity of desalination units, water production rate, and the net carbon reduction target, are described by Eq. (5-8), respectively, where PW refers to product water flow, χ_{PW} is the water recovery, while F_{CO2}^{total} is the exact CO_2 emission rate, F_{CO2}^{conv} is the CO_2 emissions of the base case and NCRT is the net carbon reduction target.

$$F^{min} \leq F \leq F^{max} \quad \forall t \in T, \ \forall m \in M \quad (5)$$

$$x_c^{min} \leq x_c \leq x_c^{max} \quad \forall c \in C, \forall t \in T, \ \forall m \in M \quad (6)$$

$$PW^{total} \geq \chi_{PW} F^{in} \quad (7)$$

$$F_{CO2}^{total} \leq NCRT * F_{CO2}^{conv} \quad (8)$$

4. Case Study Illustration

This case study features the desalination of Mediterranean seawater with TDS content of 38,600 ppm. Various thermal and membrane-based technologies have been considered as options for desalination, while renewable technologies and hybrid energy systems have been considered besides the conventional fuel option for energy production. A list of all the options that were included in this study is provided in Table 1. As for the carbon capture unit, only one technology has been assessed, which involves chemical adsorption using amine solvents due to its high level of maturity and easy application.

Table 1: List of Technology Options

Desalination technologies		Energy Production Technologies	
Thermal	Membrane	Renewable	Hybrid
Multi-Stage Flashing (MSF)	Seawater Reverse Osmosis (SWRO)	Photovoltaic Cells (PV)	PV-Wind
Multi-Effect Distillation (MED)	Brackish Reverse Osmosis (BWRO)	Wind	PV-Natural gas (PV-NG)
Mechanical Vapor Compression (MVC)	Electrodialysis (ED)	Concentrated Solar Power (CSP)	CSP-Natural gas (CSP-NG)
		Geothermal	

As previously mentioned, each of those technologies are associated with their own specifications and constraints, such as capacity limits, water recovery, and salt rejection, in addition to the carbon footprint parameters associated with energy production from natural gas. All these parameters and the technologies associated costs are obtained from (Klaimi et al. 2019). It should be noted that BWRO and ED options were not considered in this specific case, since their maximum inlet TDS is 12,000 ppm which is much lower than seawater TDS. On the other hand, a carbon removal efficiency of 90 % has been set on the carbon capture unit, and an overall water recovery of 50 % has been imposed on the system in all the studied cases. The model has been solved for different Net Carbon Reduction Targets (NCRT) that range from 0 % to 100 %. This Mixed Integer Non-Linear problem has been implemented using "What's Best 16.0" LINDO Global Solver for Microsoft Excel 2016 via a laptop with Intel Core i5 Duo Processor, 8 GB RAM and a 64-bit Operating System. In the first scenario, the system has been solved for 0 % NCRT. The obtained results showed that MVC and SWRO are the optimal technologies for desalination. This is mainly due to the high recovery of these two units and their lower cost compared to the thermal technologies which require both thermal and electrical energy. Only one energy source has been selected in this case which is the conventional fuel (natural gas), since it has the lowest cost among the available options and no carbon reduction target has been imposed on the system. The estimated amount of carbon emission was found to be 20.59 t/d, which is also used as the base case value for carbon reduction. When the NCRT is increased to 20 %, natural gas remains the only selected source of energy. However, the carbon reduction appears by the selection of the carbon capture option, as illustrated in Figure 2, where 4.58 t/d of CO_2 has been considered for capture to end up with a total carbon emission of 16.47 t/d.

Figure 2: Desalination network for 20 % NCRT

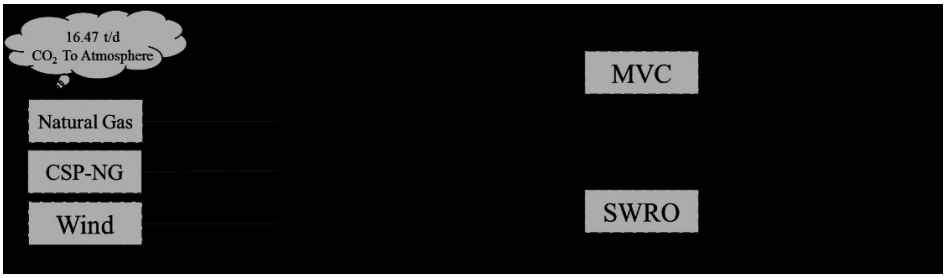

Figure 3: Desalination network for 20 % NCRT with model relaxation

When the NCRT is further increased to 40 %, a combination of wind energy and natural gas has been selected for power supply, in addition to carbon capture of 3.15 t/d of the resulted emission. At 60 % NCRT, the carbon capture option is no longer selected, while wind energy and natural gas remain the optimal energy sources until 80 % where only renewable wind energy has been selected to satisfy the stringent constraint on carbon emission. On the other hand, the water production cost associated with 100 % NCRT is estimated by 21.93 USD/m^3. Regarding the second scenario, the model has been relaxed by allowing the desalination units to be integrated with more than one energy source. This results in a completely different integration network regarding energy sources. The new obtained results (shown in Figure 3) witness the absence of carbon capture in all NCRT studied cases. The trend observed after model relaxation highlights the system's ability of selecting hybrid energy as a third party solutions, besides renewable and conventional energy options, and this helps achieve lower total network costs. Wind, CSP-NG and natural gas were the selected energy sources for NCRT values between 20 % and 80 %, while only wind energy has been selected for at 100 % NCRT.

5. Conclusions

The proposed approach presents an assessment of different carbon reduction strategies for seawater desalination systems. It was found that the selection of the optimal carbon reduction techniques depends on the net carbon reduction target imposed by the user. Carbon capture is highly recommended for reduction targets up to 40 % after which renewable energy, especially wind, gains higher attention. Moreover, hybrid energy systems were found to be a good compromise between renewable and conventional energy for carbon reduction targets that range between 0 % and 80 %.

Acknowledgment

The authors would like to acknowledge the financial support received from the University Research Board (Award# 103187; Project# 23308) and (Award# 103780; Project# 25352) at the American University of Beirut.

References

Al-Mohannadi, Dhabia M, and Patrick Linke. 2016. 'On the systematic carbon integration of industrial parks for climate footprint reduction', *Journal of Cleaner Production*, 112: 4053-64.

Khan, Meer AM, S Rehman, and Fahad A Al-Sulaiman. 2018. 'A hybrid renewable energy system as a potential energy source for water desalination using reverse osmosis: A review', *Renewable and Sustainable Energy Reviews*, 97: 456-77.

Klaimi, Rachid, Sabla Y Alnouri, Mahmoud Al-Hindi, and Fouad Azizi. 2019. 'Optimization techniques for coupling renewable/hybrid energy options with desalination systems for carbon footprint reduction', *Chemical Engineering Research and Design*, 151: 270-90.

Mannan, Mehzabeen, Tareq Al-Ansari, Hamish R Mackey, and Sami G Al-Ghamdi. 2018. 'Quantifying the energy, water and food nexus: A review of the latest developments based on life-cycle assessment', *Journal of Cleaner Production*, 193: 300-14.

Mansour, Fatima, and Sabla Y Alnouri. 2019. 'End-of-Pipe Zero Liquid Discharge Networks for different brine water qualities.' in, *Computer Aided Chemical Engineering* (Elsevier).

Somoza-Tornos, Ana, Manuel Rives-Jiménez, Antonio Espuña, and Moisés Graells. 2019. 'A circular economy approach to the design of a water network targeting the use of regenerated water.' in, *Computer Aided Chemical Engineering* (Elsevier).

Sauro Pierucci, Flavio Manenti, Giulia Bozzano, Davide Manca (Eds.)
Proceedings of the 30th European Symposium on Computer Aided Process Engineering (ESCAPE30), May 24-27, 2020, Milano, Italy.
http://dx.doi.org/10.1016/B978-0-12-823377-1.50182-8

NMPC based Temperature Control in Fed-batch Reactor to Avoid Thermal Runaway

Alex Kummer, Lajos Nagy, Tamás Varga

Department of process engineering, University of Pannonia, H-8200 Veszprém, Hungary
kummera@fmt.uni-pannon.hu

Abstract

Numerous fatal accidents occurred in the recent past caused by thermal reactor runaway, despite the fact, that the phenomenon of thermal runaway is well-known. However, accidents caused by runaway can be foreseen by using correct model and proper reactor runaway criteria, hence the operators can intervene in time in the system to prevent undesired events. Model Predictive Control (MPC) methodology is proposed to avoid reactor runaway during the optimal operation of fed-batch reactors. Fed-batch reactors are applied to carry out highly exothermic reactions safely, where the reactor and the sequence of process steps in normal operation are designed model-based. However, some of the parameters of reactor system (e.g. heat transfer coefficient) can change slightly over time or operators can make mistakes which can lead to trigger a runaway reaction. MPC can support the safe production by keeping the reactor controllable zone during the whole operation, in which also reactor runaway criteria can be implemented to predict the development of thermal runaway. Since the heat removal is limited the temperature is controlled by the inlet rate of feeding reactant and the cooling capacity is operating almost at maximum. To avoid thermal runaway, the feed rate of reactant is constrained by runaway criterion (namely Modified Dynamic Condition) which increases the safety of the process operation. Modified Dynamic Condition is implemented in NMPC algorithm as a penalty term, and also the criterion is used to define the minimal length of the considered prediction horizon based on process safety time. Moreover, the variable feed rate has an impact on economic of the operation since with decreasing the reactant concentration the feed rate increases to keep the reactor temperature close the optimal. Reactor efficiency is increased while the whole operation stays in controllable zone. The objective is to maximize productivity under the whole region of parameter uncertainty.

Keywords: thermal runaway, safe operation, early indication, process safety time

1. Introduction

Although the phenomenon of thermal reactor runaway is well-known, unfortunately lethal accidents still occurred in recent-past. In 2001 a polymerization reactor exploded because of a reactor runaway [1] and in 2007 an explosion occurred at T2 Laboratories caused death of four people. Thermal runaway results a rapid and significant temperature increase in the reactor which can lead to explosion due to the pressure increase in the reactor. Therefore it is highly important to keep the whole path of reaction under control to avoid the development of runaway. Fortunately, thermal runaway can be predicted by applying runaway criteria. Several runaway criteria exists which classify the reaction operation states as runaway or non-runaway, hence these

equations can be applied to predict the development of thermal runaway [2]. Tailored runaway criteria were developed also to get a more specific critical equation [3]. Thermal runaway criteria can be successfully implemented in NMPC to keep the reactor always in the controllable regime, where the impact of parameter uncertainty was also investigated [4], although the prediction horizon has to be long enough to capture the development of runaway.

It is difficult to obtain a perfect model of the plant, hence there always will be some model-plant mismatch. A lot of method can be found in the literature to handle this problem, like taking into account uncertain parameters or applying state observers. These methods lead to a robust controller which satisfies the constraint for all possible realizations of the uncertainty [5]. Parameter uncertainty can be considered by applying the well-known min-max formulation [6], multi-stage methods [7], or tube-based methods [8]. Min-max MPC taking into account the worst-case realization of the parameter uncertainty, although it is conservative and it may results an infeasible optimization problem [9]. The conservativeness of min-max MPC was reduced by taking into account the future feedback information [5]. Multi-stage NMPC realizes the uncertainty by a tree of discrete scenarios, where each scenario has to satisfy the predefined constraints [7].

Our goal is to propose a method which is able to handle potential runaway reactions under parameter uncertainty, hence a Multi-Stage NMPC algorithm with implemented thermal runaway criterion is proposed.

2. Case study

Williams-Otto process has been used for years to test different control and optimization algorithms. We optimize the fed-batch version of this process as it is presented in [10]. In Williams-Otto process three exothermic reactions take place, which are presented in Eq. 1-3 followed by the equation of reaction rates.

$$A + B \rightarrow C \qquad r_1 = k_{0,1} exp\left(-\frac{E_1}{RT}\right) c_A c_B \tag{1}$$

$$B + C \rightarrow P + E \qquad r_2 = k_{0,2} exp\left(-\frac{E_2}{RT}\right) c_B c_C \tag{2}$$

$$C + P \rightarrow G \qquad r_3 = k_{0,3} exp\left(-\frac{E_3}{RT}\right) c_C c_P \tag{3}$$

Two reactants (component *A* and *B*) are fed into the process, component *A* is preloaded and component *B* is continuously fed into the reactor. The desired product is component *P*, while two by-products are component *E* and *G*. The following differential equations (Eq. 4-8) describe the behaviour of the reactor system:

$$\frac{dc}{dt} = \frac{F^{in}}{V_R}\left(c_i^{in} - c_i\right) + \sum_{l=1}^{N_R} v_{il} R_l \;\; i = 1 \ldots N_C \tag{4}$$

$$\frac{dV_R}{dt} = F^{in} \tag{5}$$

$$\frac{dT_R}{dt} = \frac{4U}{D_R \sum_{i=1}^{N_C} c_i cp_i}\left(T_j - T_R\right) + \frac{F^{in} \sum_{i=1}^{N_C} c_i^{IN} cp_i}{V_R \sum_{i=1}^{N_C} c_i cp_i}\left(T^{in} - T_R\right) - \frac{\sum_{l=1}^{N_R} \Delta H_{r,l} R_l}{\sum_{i=1}^{N_C} c_i cp_i} \tag{6}$$

$$\frac{dT_j}{dt} = \frac{4UV_R}{D_R V_j \rho_j cp_j}\left(T_R - T_j\right) + \frac{F_j}{V_j}\left(T_j^{in} - T_j\right) \tag{7}$$

The kinetic parameters, component properties and reactor constructional and operating parameters can be found in [10], [11].

3. Formulation of Multi-Stage NMPC

The goal is to maximize the productivity while thermal runaway does not develop, hence the conversion of component *A* (x_A) and selectivity of component *P* (S_P) are considered in the objective function next to that runaway states should be avoided (I_k) and reactor temperature cannot exceed Maximum Allowable Temperature (*MAT*). Also the significant changes in the manipulated variables are penalized. We have applied Modified Dynamic Condition (Eq. 8) to operate the semi-batch reactor [2], where the slope of generated and removed heat, generated and removed heat and the decrease of reaction rate due to decrease of reagents concentration are considered to identify runaway states.

(8)

Formulation of nominal open-loop optimization problem can be seen in Eq. 9-12.

$$e^+ = max\left(T_{R,k} - MAT; 0\right) \tag{9}$$

$$L = -w_x x_A - w_s S_p + w_u|u_k - u_{k-1}| + w_I I_k + w_T e^+ \tag{10}$$

$$\min_{u} \sum_{0}^{t_{pred}} L(x_k, u_k) \tag{11}$$

subject to

$$0 \le u_k \le 100\ \% \tag{12}$$

where u_k is the control input at *k*-th time step, I_k is the sum of runaway states in the prediction horizon.

In case of Multi-Stage NMPC combination of maximal, minimal and nominal values of uncertain parameters are considered, which usually results a robust behaviour of the controller [5]. Each path of the scenario tree is called a scenario and indicated as *i*, and it contains all the states x_k^j and control inputs u_k^j that belong to scenario *i*. The set of all occurring indices (*j*,*k*) is denoted by *I* [12]. Formulation of Multi-Stage NMPC can be seen in Eq. 13.

$$\min_{u^j} \sum_{i=1}^{N} \frac{1}{N} L_i(x_k^i, u_k^i, d_k^i) \tag{13}$$

subject to

$$0 \le u_k^j \le 100\ \% \qquad \forall (j,k) \in I \tag{14}$$

$$u_k^j = u_k^l \; if \; x_k^{p(j)} = x_k^{p(l)} \quad \forall (j,k),(l,k) \in I \tag{15}$$

where $x_k^{p(i)}$ is the parent node. Eq. 15 represents the non-anticipativity constraints, which is about to equal all the control inputs at the same node.

The optimization problem was solved by modified progressive hedging algorithm, which is a decomposition algorithm, where non-anticipativity constraints are relaxed by

penalizing the difference between the control inputs that should satisfy the non-anticipativity constraints. Its advantage that the scenarios can be solved independently, hence the following (Eq. 16) optimization problem has to be solved. Since the length of robust horizon is one in this case, only the first control inputs (u_0^i) of different scenarios have to satisfy the non-anticipativity constraint.

$$\min_{u^j} L_i\left(x_k^i, u_k^i, d_k^i\right) + \lambda^i\left(u_0^i - \hat{u}_0^i\right) + \rho^i\left(u_0^i - \hat{u}_0^i\right)^2 \qquad (16)$$

subject to

$$0 \le u_k^j \le 100\ \% \quad \forall (j,k) \in I \qquad (17)$$

$$\hat{u}_0^i = \sum_{i=1}^{N} \frac{1}{N} u_0^i \qquad (18)$$

where $\hat{u}_1^i$ is the fictious value towards which the control input converge to satisfy the anticipativity constraints. Parameters λ^i and ρ^i are updated at each iteration to improve the convergence, where the update rule is the following:

$$\lambda^i = \lambda^i + \rho^i\left(u_0^i - \hat{u}_0^i\right) \qquad (19)$$

$$\rho^i = min(\beta\rho^i, \rho_{max}) \qquad (20)$$

where β determines the increase of ρ^i. Eq. 16-20 are solved iteratively until $max\left(u_1^i - \hat{u}_1^i\right) < \varepsilon$. After several iterations the non-anticipativity constraints are satisfied with a desired tolerance ε.

4. Results of reactor control with full feedback information

This section presents the results of comparison between Nominal NMPC and Multi-Stage NMPC, where the results are shown in Figure 1-2. The reactor temperature is controlled by manipulating the feed rate of reagent, while the cooling proceeds almost at maximum. Open-loop optimization problem has been solved by the classical SQP optimization algorithm, and the algorithm proceeds with a moving horizon. The sampling time was 100 second, length of control horizon was 500 seconds and length of prediction horizon was 2200 seconds.

Weights for equation 10 are summarized in Table 1.

Table 1 Weight factors in Eq. 10

w_x	1
w_s	1
w_u	0.001
w_I	100
w_T	100

As it can be seen in Figure 2, the uncertain parameters decrease the productivity. In our case the kinetic parameters of the first reaction ($k_{0,1}$, E_1) have ±10% uncertainty, hence the control of reactor becomes conservative. This two uncertain parameters result nine scenarios. This is understandable since runaway cannot occur at none of the scenarios, because the implemented MDC criterion penalizes the objective if runaway states occur. Results of Multi-Stage NMPC can be seen in Figure 2, and it does not allow to feed the reagents with high rate, and also there are no runaway states during the whole period of reactor operation, means that the method resulted a safe operation under parameter uncertainty.

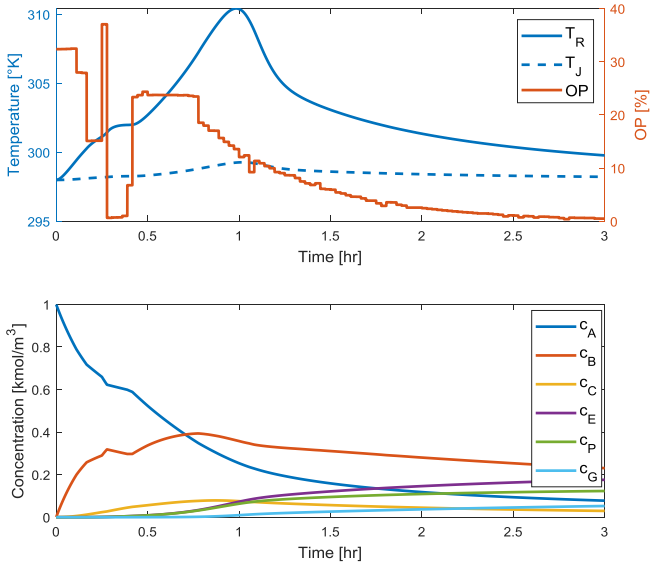

Figure 1 Results of Nominal NMPC

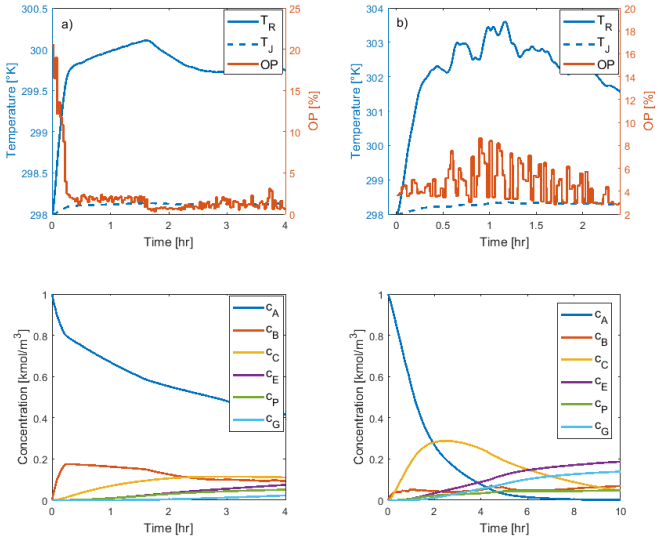

Figure 2 Results of Multi-Stage NMPC – a) Nominal values, b) $k_{0,1}$ +10%, E_1-10% (T_R – Reactor temperature, T_J – Jacket temperature, OP – Output Variable)

5. Conclusions

A nonlinear model predictive control approach has been analyzed in case of a fed-batch reactor which is carrying out a highly exothermic reaction. Modified Dynamic Condition was implemented in NMPC to avoid the development of thermal runaway under parameter uncertainty. The length of the prediction horizon was defined based on the process safety times of the system, which were calculated for the worst cases. Two different algorithms were compared to each other, which are nominal NMPC without any uncertain parameter and Multi-Stage NMPC with parameter uncertainty. The

kinetic parameters ($k_{0,1}$, E_1) of the first reaction were chosen as uncertain to analyze the behavior of different control algorithms, whose possible min and max values were ±10%. Uncertain parameters resulted a conservative operation of the reactor, because runaway cannot develop at any of parameter combination. Our future research will be about to decrease the possible region of uncertain parameters during the reactor operation and to apply state estimation methods to estimate the different states.

Acknowledgment

We would like to express our acknowledgement for the financial support of Széchenyi 2020 under the GINOP-2.2.1-15-2017-00059.

References

[1] C.-S. Kao and K.-H. Hu, "Acrylic reactor runaway and explosion accident analysis," *Journal of Loss Prevention in the Process Industries*, vol. 15, no. 3, pp. 213–222, May 2002, doi: 10.1016/S0950-4230(01)00070-5.

[2] A. Kummer and T. Varga, "Completion of thermal runaway criteria: Two new criteria to define runaway limits," *Chemical Engineering Science*, vol. 196, pp. 277–290, Mar. 2019, doi: 10.1016/j.ces.2018.11.008.

[3] A. Kummer, T. Varga, and J. Abonyi, "Genetic programming-based development of thermal runaway criteria," *Computers & Chemical Engineering*, p. 106582, Sep. 2019, doi: 10.1016/j.compchemeng.2019.106582.

[4] A. Kanavalau, R. Masters, W. Kähm, and V. S. Vassiliadis, "Robust thermal stability for batch process intensification with model predictive control," *Computers & Chemical Engineering*, vol. 130, p. 106574, Nov. 2019, doi: 10.1016/j.compchemeng.2019.106574.

[5] S. Thangavel, S. Lucia, R. Paulen, and S. Engell, "Dual robust nonlinear model predictive control: A multi-stage approach," *Journal of Process Control*, vol. 72, pp. 39–51, Dec. 2018, doi: 10.1016/j.jprocont.2018.10.003.

[6] P. Kühl, M. Diehl, A. Milewska, E. Molga, and H. G. Bock, "Robust NMPC for a Benchmark Fed-Batch Reactor with Runaway Conditions," in *Assessment and Future Directions of Nonlinear Model Predictive Control*, vol. 358, R. Findeisen, F. Allgöwer, and L. T. Biegler, Eds. Berlin, Heidelberg: Springer Berlin Heidelberg, 2007, pp. 455–464.

[7] S. Lucia, T. Finkler, and S. Engell, "Multi-stage nonlinear model predictive control applied to a semi-batch polymerization reactor under uncertainty," *Journal of Process Control*, vol. 23, no. 9, pp. 1306–1319, Oct. 2013, doi: 10.1016/j.jprocont.2013.08.008.

[8] D. Q. Mayne, M. M. Seron, and S. V. Raković, "Robust model predictive control of constrained linear systems with bounded disturbances," *Automatica*, vol. 41, no. 2, pp. 219–224, Feb. 2005, doi: 10.1016/j.automatica.2004.08.019.

[9] P. O. M. Scokaert and D. Q. Mayne, "Min-max feedback model predictive control for constrained linear systems," *IEEE Transactions on Automatic Control*, vol. 43, no. 8, pp. 1136–1142, Aug. 1998, doi: 10.1109/9.704989.

[10] F. Rossi, F. Manenti, C. Pirola, and I. Mujtaba, "A robust sustainable optimization & control strategy (RSOCS) for (fed-)batch processes towards the low-cost reduction of utilities consumption," *Journal of Cleaner Production*, vol. 111, pp. 181–192, Jan. 2016, doi: 10.1016/j.jclepro.2015.06.098.

[11] M. Sriram and W. F. Stevens, "An Example of the Application of Nonlinear Programming to Chemical-Process Optimization," *Operations Research*, vol. 21, no. 1, pp. 296–304, Feb. 1973, doi: 10.1287/opre.21.1.296.

[12] Sergio Lucia, *Robust Multi-stage Nonlinear ModelPredictive Control*. 2014.

Sauro Pierucci, Flavio Manenti, Giulia Bozzano, Davide Manca (Eds.)
Proceedings of the 30th European Symposium on Computer Aided Process Engineering (ESCAPE30), May 24-27, 2020, Milano, Italy.
http://dx.doi.org/10.1016/B978-0-12-823377-1.50183-X

A Framework for Application of Forward Iterative Dynamic Programming to Mixed Integer Control and Sequencing Problems

Michael Mulholland

Chemical Engineering, University of KwaZulu-Natal, Durban 4041, South Africa
mulholland@ukzn.ac.za

Abstract

A stepwise receding horizon predictive controller was arranged to use the Forward Iterative Dynamic Programming (FIDP) method to optimise the forward trajectory on each step. This format allowed for a completely arbitrary predictive model specification. Non-linear and hybrid systems with logical mode-changes and recipe-based decisions could be accommodated because it is only required to solve the model in the forward direction. In this paper the method is demonstrated in two situations, together with the interventions required to accommodate conditional mode sequences.

Keywords: MPC, FIDP, hybrid, batch, scheduling.

1. Introduction

In Model Predictive Control (MPC) one seeks to optimise a future dynamic path. Bellman (1957) made a succinct observation that simplifies this task: If an optimal policy has been established from one state onwards, then any other trajectory arriving at that state would have to continue with that policy in order to be optimal. This Dynamic Programming technique is made far more efficient if it focuses on the "reachable" zones of the state-space, thus reducing the "curse of dimensionality" (Bellman, 1957). In Iterative Dynamic Programming (Luus, 1989) this is done by sending out random complete trajectories from the first point in time, and considering only nearby parts of the *state grid*. A variation of this is Forward Iterative Dynamic Programming (FIDP – Lin and Hwang, 1996) where the random complete trajectories themselves actually constitute the *path grid* of points available at each time. Thus the grid point becomes defined not so much as a state, but by the fact that it is possible to get there.

In the present work, FIDP will be used as the path optimiser, in conjunction with stepwise receding horizon MPC to offer a flexible dynamic control solution (Rusnák et al., 2001). FIDP as a forward calculation easily accommodates dead-time and constraints, and it will be seen later that logical branches, modes, schedules and recipes can be included.

2. Method

The process model is represented as the arbitrary input-output step

$$\boldsymbol{y_i} = \boldsymbol{f}(\boldsymbol{y_{i-1}}, \boldsymbol{y_{i-2}}, \dots, \boldsymbol{u_i}, \boldsymbol{u_{i-1}}, \boldsymbol{u_{i-2}}, \dots) \tag{1}$$

This step has a cost

$$\boldsymbol{c_i} = \boldsymbol{g}(\boldsymbol{y_i}, \boldsymbol{y_{i-1}}, \boldsymbol{u_i}, \boldsymbol{u_{i-1}}) \tag{2}$$

where $\boldsymbol{u}_i$ is the piecewise-constant input vector in the interval which *ends* with the output vector at $\boldsymbol{y}_i$.

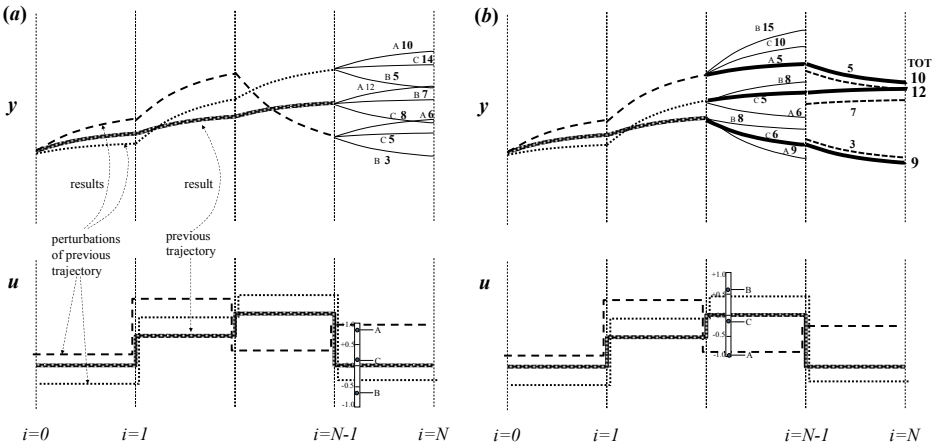

Figure 1. Building lowest cost trajectories using best combined trajectories established sequentially from (a) *i=N-1*, (b) *i=N*-2, etc.

On each time-step, *P* random forward trajectories of length *N* are generated by shifting the previous best trajectory one step back, and subjecting it to random input perturbation according to a specified sensitivity. Any trajectories violating input or output bounds are discarded. At each of the *P path grid* points thus established at each time, a further *M* input perturbations are applied for one time-step (Figure 1). In this way, moving backwards from the last step, the best combined trajectory from each *path grid* point is established through the "nearest" *path grid* point at the next step. The result is *P* improved trajectories. That with the lowest overall cost is selected, and its first control action implemented on the plant. The reference frame then moves forward one time-step, and actual plant data is gathered to repeat the entire calculation.

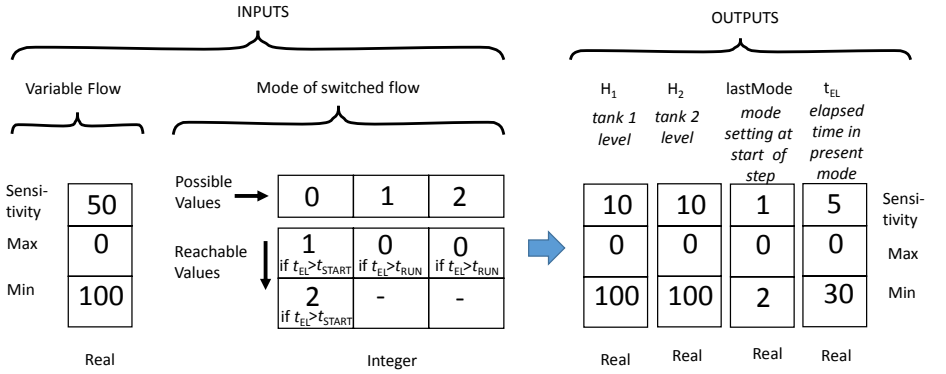

Figure 2. Pump/Tank system: Inputs: one continuous flow and one discrete (switched) flow; Outputs: four (including two tank levels). *t*EL is the elapsed time so far in a mode.

The proposed framework is best illustrated by previewing the IO table of the simple Pump/Tank system in section 3. Discrete variables are declared in a "possible-value / "reachable-value" table (Figure 2). Here one notes that modes 1 and 2 can only change by passing through a standby mode 0. In the perturbation of trajectories, both the present

possible value, and its associated reachable values, are available for random selection, unless other conditions are stipulated.

(a) Viewing possible values as "modes", sometimes additional variables play a part in determining the reachable values, eg. reactor contents must be cooled before discharge.
(b) Bearing (a) in mind, there is an obvious complication in Bellman's "backward stepping" outlined above, where the *M* one-step perturbations are applied: Arrival points need to lie within the set of reachable values.

The product of the backward-stepping above is effectively a vector-field, with an optimal vector direction determined at each *path grid* point. Rather than simply accepting the best of the *N* adjusted trajectories, we rather integrate through the vector field from the start to create a properly compliant "best" trajectory as the basis for the next time-step.

3. Applications

3.1. Pump/Tank system

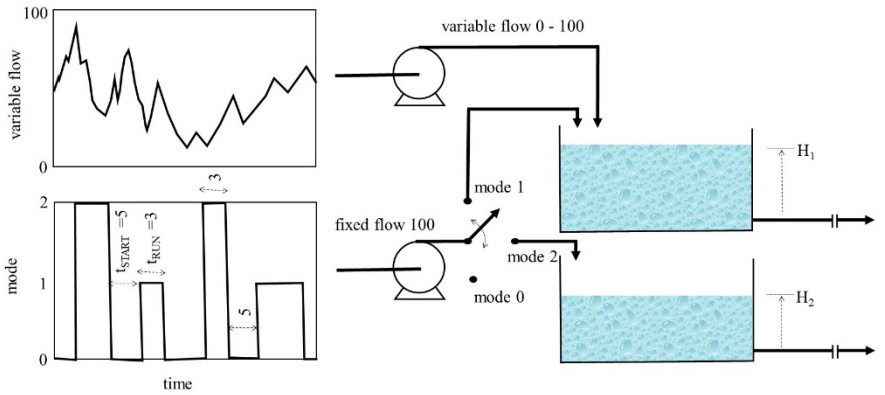

Figure 3. Example: Pump/Tank system: Level control of two tanks using one variable flow and one switched flow with a restart delay of 5, and minimum runtime of 3.

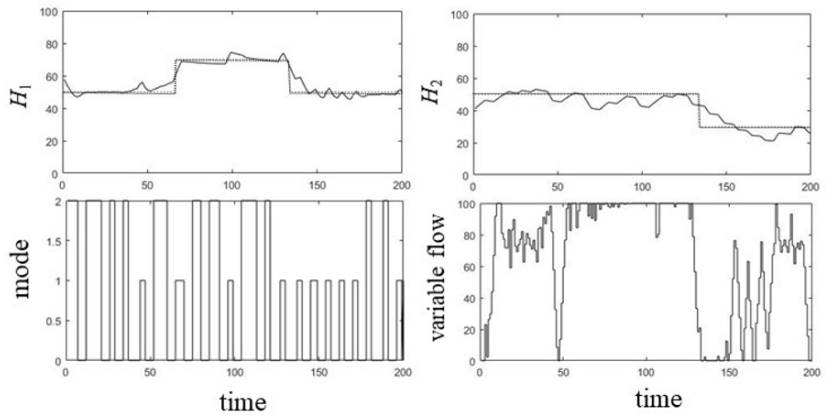

Figure 4. Pump/Tank system: Set-point step responses of the two levels using a 30-point model predictive control horizon.

3.2. Multiple batch reactors sharing utilities

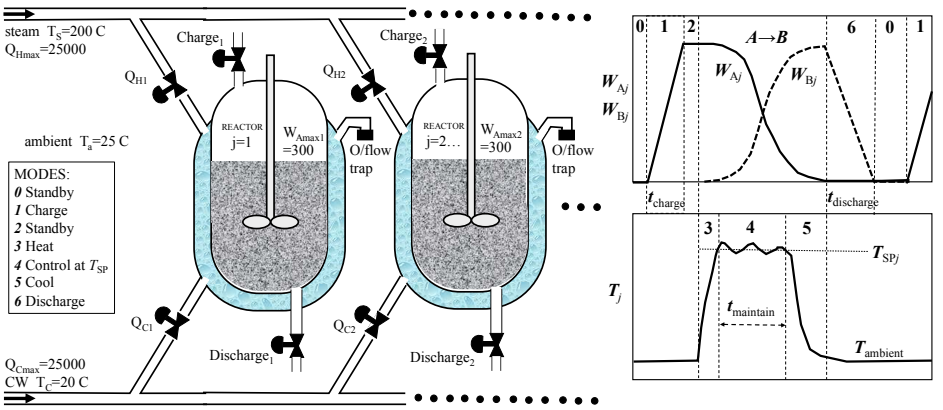

Figure 5. Multiple batch reactors converting A to B using common heating and cooling utilities.

Figure 5 shows a typical situation where multiple batch reactors, potentially having different sizes and different recipes, share common resources such as heating and cooling utilities. Each reactor must progress through a series of "modes". Conditions will determine whether a mode can start or end, and usually only a specified mode can follow. In the FIDP algorithm one wishes to provide a series of *different* trajectories, and then to allow a trajectory to borrow parts of other trajectories to improve itself. Only a few modes involve discretionary lengths, which allow one to generate random shifts (modes 0 and 2 in Figure 5). Furthermore, even at such "break-out" points, preceding and following conditions must be met in the combined trajectory.

A simple exothermic 1st order reaction is simulated as follows for reactor *j* over interval *i*
Mass balance:

$$\Delta W_{Aji} = -\left[k_0 + k_1\left(T_{ji} - T_a\right)\right] W_{Aji-1} \Delta t \tag{3}$$

$$W_{Aji} = W_{Aji-1} + \Delta W_{Aji} \tag{4}$$

$$W_{Bji} = W_{Bji-1} - \Delta W_{Aji} \tag{5}$$

Mutually exclusive heating/cooling selector Q_{Sj} : 0=Cool; 1=Standby; 2=Heat

$$\Delta Q_{Hji} = \begin{cases} (UA)_j \left(T_S - T_{ji}\right) & \text{if } Q_{Sj} = 2 \\ 0 & \text{otherwise} \end{cases} \tag{6}$$

$$\Delta Q_{Cji} = \begin{cases} (UA)_j \left(T_{ji} - T_C\right) & \text{if } Q_{Sj} = 0 \\ 0 & \text{otherwise} \end{cases} \tag{7}$$

$$\Delta Q_{aji} = (uA)_j \left(T_{ji} - T_a\right) \quad \text{ambient loss} \tag{8}$$

Heat balance:

$$T_{ji} = T_{ji-1} + \left[(-\Delta H_A)(-\Delta W_{Aji}) + (\Delta Q_{Hji} - \Delta Q_{Cji} - \Delta Q_{aji})\Delta t\right] / [Mc_P]_j \quad (9)$$

Total heating/cooling demand and production for n reactors in interval i-1 to i:

$$Q_{Hi} = \sum_{j=1}^{n} \Delta Q_{Hji} \qquad Q_{Ci} = \sum_{j=1}^{n} \Delta Q_{Cji} \qquad P_i = \sum_{j=1}^{n} \Delta W_{Bji} \quad (10)$$

Total trajectory production up to interval i:

$$P_{TOTi} = \sum_{k=1}^{i} P_k \quad (11)$$

		Standby	Charge	Wait	Heat	React	Cool	Discharge
Modes	Possible Values	$0\times n_0$	1 $t_{EL} < t_{charge}$	$2\times n_2$	3 $T < T_{SP}-\Delta T$	4 $t_{EL} < t_{maintain}$	5 $T > T_a+\Delta T$	6 $t_{EL} < t_{discharge}$
	Reachable Values	1	2 $t_{EL} \geq t_{charge}$	3	4 $T \geq T_{SP}-\Delta T$	5 $t_{EL} \geq t_{maintain}$	6 $T \leq T_a+\Delta T$	0 $t_{EL} \geq t_{discharge}$
Heat/ Cool selector Q_S	Possible Values	0 1 2	0 1 2	0 1 2	0 1 2	0 1 2	0 1 2	0 1 2
	Reachable Values	1 1 1 always	1 1 1 always	1 1 1 always	2 2 2 always	1 0 1 2	0 0 0 always	1 1 1 always

Figure 6. IO table for a single reactor - Inputs: possible (present) and reachable values.

For a single reactor j stepping from interval i-1 to i, the discrete values in the input vector $\boldsymbol{u}_i$ are randomly selected according to the possible-value/reachable-value tables in Figure 6. Here t_{EL} is the elapsed time so far in a mode, and T_{SP} is the set-point reaction temperature. The conditions shown force the associated choice. The multipliers "$\times n$" repeat the presence of the choice in the random selection vector to make it more likely, thus generating a greater range of standby periods.

A two-reactor example is demonstrated over 200 time-steps with a 100 step horizon. The cost function is formulated to maximise cumulative production and minimise deviations from the set-point temperature whilst in reaction mode (4). The primes below indicate normalisation according to the specified sensitivity.

$$c_i = -100P_{TOTi} + \left\{10^2\left(T'_{ji} - T'_{jiSP}\right)^2 + 10\sum_{k=1}^{i}\left(T'_{jk} - T'_{jkSP}\right)^2\right\}_{IF\ MODE=4\ ONLY} \quad (12)$$

In Figure 7, an output constraint of 15000 has been specified on the total steam heating power consumed Q_H at any time. This effectively allows only one instance of mode 3 or mode 4 amongst the reactors. The algorithm correctly manipulates the available standby periods to prevent such a clash, at the same time attempting to reduce these periods to maximise production. Enough break-out scope was provided by an extra n_0=2 and n_2=2 repeats in Figure 6.

Figure 7 includes at bottom right an example of the P random forward trajectories at an intermediate solution time – in this case for T_2, the temperature of reactor 2. The shifts in

these responses provide the scope for the dynamic programming optimisation. As one steps backwards from the horizon, the randomised starts at these *path grid* points provide the opportunity to start the next mode earlier or later.
The particular model under investigation is only distinguished *within* service functions such as those that evaluate equations (1) and (2). An IO table as in Figures 2 and 6 must be provided to the core solution for input choice prior to each step. This is achieved by a prior "dummy" call of (1) which reconfigures the IO table for current *start* conditions. This would be a "forward" match. A flag is set if a "backwards" match is required, and the required *end* condition is specified in this case. If this is not achievable with the given input, an alternative input is sought and returned to the core solution.

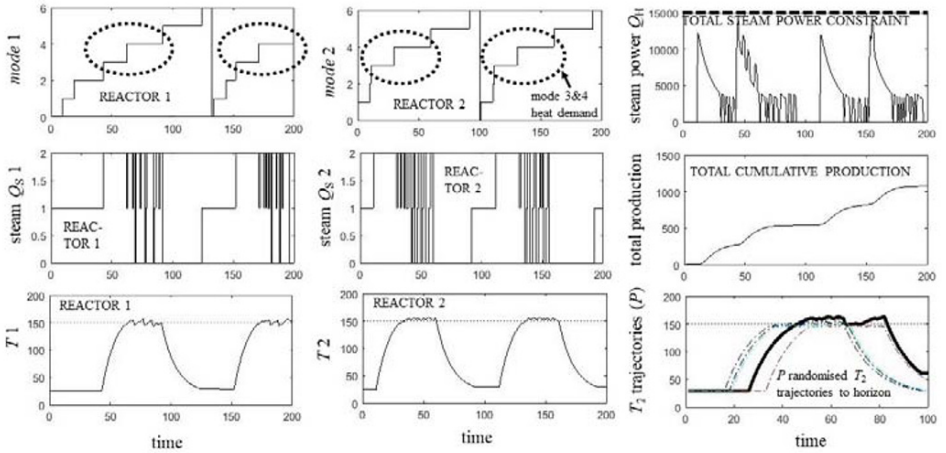

Figure 7. Two batch reactors sharing utilities with a constraint on heat demand.

4. Conclusions

In this framework a core FIDP solution loop is serviced on each time step by a set of functions (Step, Cost, Set-point, IO table) which index particular applications. These functions provide data in a fixed format (eg. Figure 6). Various mixed integer control problems have been dealt with, as well as dead time, integral action, and instantaneous set-point objectives. Sequencing requirements may hamper the dynamic programming, possibly causing some degrading to an evolutionary solution.

The forward modelling of FIDP allows the "mode" of a plant to be manipulated as a control input – a useful feature for flow-rerouting, start-up, recipe changes, etc.

References

R. Bellman, 1957, Dynamic Programming, Dover edition 2003.

J.-S. Lin and C. Hwang, 1996, Optimal control of time-delay systems by forward iterative dynamic programming, Industrial and Engineering Chemical Research, 35 (8) ,2795-2800

R. Luus, 1989, Optimal control by dynamic programming using accessible points and region reduction. Hung. J. Ind. Chem., 17, 523–543.

A. Rusnák, M. Fikar, M.A. Latifi and A. Mészáros, 2001, Receding horizon iterative dynamic programming with discrete time models", Computers and Chemical Engineering, 25 (1), 161-167.

Sauro Pierucci, Flavio Manenti, Giulia Bozzano, Davide Manca (Eds.)
Proceedings of the 30th European Symposium on Computer Aided Process Engineering (ESCAPE30), May 24-27, 2020, Milano, Italy.
http://dx.doi.org/10.1016/B978-0-12-823377-1.50184-1

Robust Short-term Planning of Combined Heat and Power Plants Participating in the Spot Market

Lise Mallier[a*], Gilles Hétreux[a], Raphaele Théry-Hétreux[a], Philippe Baudet[b]

[a]*Laboratoire de Génie Chmique (LGC), Université de Toulouse, CNRS, INPT, UPS, Toulouse, France*
[b]*Proesis SAS, 42 avenue du Général de Croutte, Toulouse 31100, France*
lise.mallier@toulouse-inp.fr

Abstract

Following the liberalization of the electricity market, many private producers have come into play through trading mechanism to ensure the balance between production and needs. This context is particularly beneficial for utilities plants such as Combined Heat and Power (CHP) plants. In this context, a previous work has shown the economic and environmental benefits of implementing a decision support tool for short-term planning of CHPs using a *Mixed Integer Linear Programming* (MILP) formulation. However, planning is subject to uncertainty about the steam demand that the plant must meet. A methodology is therefore put in place to obtain a robust production plan. The accuracy of this work is demonstrated with an industrial case study and shows significant improvements to obtain feasible plans under steam demand uncertainty.
Keywords: Combined Heat and Power, Robust Planning, Uncertainty, MILP

1. Introduction

Combined Heat and Power (CHP) plants represent an interesting solution to improve the energy efficiency of industrial sites while reducing greenhouse gas emissions. Indeed, it consists in simultaneously producing electricity and hot utilities (steam, hot water) from the same primary energy and within the same installation. In addition, following the liberalisation of the energy market, CHP plants have become both interesting contributors to electricity production and a significant source of profit (Santos and Uturbey, 2018). However, these new challenges have made the management of these facilities noticeably more complex (Figure 1). Indeed, similar to trading offers, the energy market is very time-sensitive (Mitra et al., 2013), forcing production units to be increasingly flexible and responsive. As a result, the management of CHP plants plays a key role in taking advantage of these opportunities. In this context, a good survey on short-term cogeneration planning has been published (Salgado and Pedrero, 2008), showing the value of implementing a planning model. However, scheduling is highly susceptible to unexpected events and uncertain input data such as demand fluctuations. These uncertainties often make the schedule generated under the deterministic assumption suboptimal or even infeasible. Uncertainty consideration, thus, is very important to preserve plant feasibility and viability during operations. Some excellent reviews in scheduling under uncertainty can be found in (Li et Ierapetritou, 2008b) and in (Verderame et al., 2010). Typical techniques used are stochastic scheduling that handle future uncertainty through recourse decision according to different uncertainty scenarios (De Ridder and Claessens, 2014) and robust scheduling that focuses on building the preventive scheduling ensuring that the predictive and realized scheduled do not differ drastically (Zhang et al., 2015).

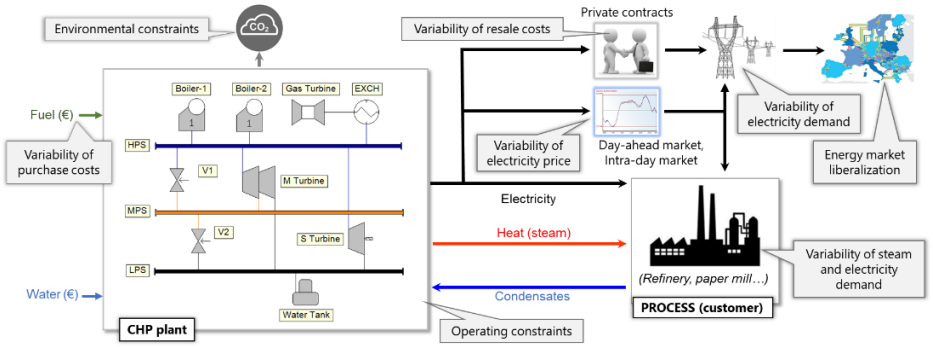

Figure 1: The Context of the Management of a Combined Heat and Power Plant

The work presented in this communication concerns a part of the methodology carried out in a prototype software named *PLANENER* dedicated to the management of the CHP plant. A previous work (Mallier et al., 2019) has introduced a methodology which implements MILP formulation and has shown significant improvements for the site's economic profitability as wells as its environmental impact. However, to ensure that the CHP plant's scheduling remains feasible, a robust counterpart problem has to be solved to deal with the presence of demand uncertainty. The remainder of this paper is organized as follows. Given the problem statement in Section 2, the uncertain scheduling model is presented in Section 3. In Section 4, an industrial case study is presented based on realistic data and results are discussed in Section 5.

2. Problem statement

The main objective of the *PLANENER* project is to propose a decision making tool dedicated to the management of CHP plant able to:

• take into account the real and multiple constraints of production (operational, economic, environmental, etc.) in order to build feasible planning,

• integrate the various opportunities for electricity sales into these plans, by evaluating them at the same time as production constraints,

• evaluate and manage short and medium strategies, as well as near-real-time decisions.

The short-term planning model is a generic scheduling model described in (Hétreux et al., 2011). Given the size of the problem, this model is based on a Mixed Integer Linear Programming (MILP) formulation for its qualities of computational stability and convergence. As shown in (Théry et al., 2012), the scheduling model can be instantiated by using the graphical formalism *ERTN* that allows an unambiguous modeling of production recipes.

Among the model's input parameters, forecast electricity prices and forecast demand (e.g steam demand) are subject to uncertainty. Many techniques have been used to forecast electricity prices such as artificial neural networks (Conejo et al., 2005) and time series model (Dimoulkas and Amelin, 2014). In this communication, the price of electricity sold on the Day-ahead market is assumed to be fixed by this type of forecast model. While the resale price of electricity influences the economic profitability of the utility plant, the demand to be met is a real constraint for the site. In all cases, the demand must be met by the CHP plant, otherwise the operation of the process will be affected. Thus, the forecast demand is not considered as a well-defined value but as an interval with bounded values. For this reason, a small number of variables and additional constraints have been

introduced into the original MILP problem, generating a robust counterpart problem that provides the optimal and feasible solution given the magnitude of the uncertain demand.

3. Robust Short-term planning

The robust planning approach has been adopted and implemented through a sliding horizon (24-hour rescheduling periodicity) decision-making structure divided into two levels (Figure 2) named respectively *forecast level* and *operational level*. These two decision-making levels are necessary in order to take into account the variety of constraints and data dynamics. Indeed, some organizational constraints are defined on specific time horizons. Similarly, some production data, initially defined with uncertainty, are periodically updated and become deterministic data.

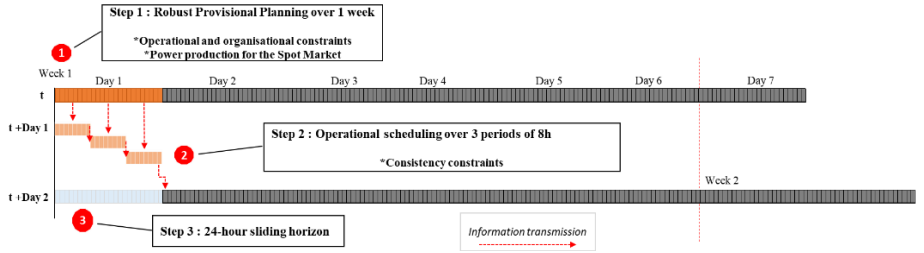

Figure 2: Decision-making process

3.1. Forecast scheduling

A first so-called *forecast scheduling model* $\mathcal{M}^{forc}$ establishes a plan for a week by taking into account the uncertainty on the steam demand, in an analytical way via specific capacity constraints. One of the objectives of this plan is to determine the state in which "critical" equipment should be positioned in order to satisfy any need within the uncertainty range. Critical equipment are defined as equipment subject to operational or organisational constraints. For example, the boiler has non-instantaneous shutdown and start-up phases. For this purpose, the minimum and maximum steam production capacities are evaluated for each possible configuration combination of these critical devices by calculating the minimum and maximum flow in the network thus constituted (preliminary calculation carried out only once). At this decision-making level, particular operating constraints (see case study) are taken into account. This first level makes it possible to anticipate the operating status of critical equipment by ensuring that production can satisfy steam demand regardless of its effective value. In addition, the operation of the Day-ahead market, also known as Spot, requires power producers to make a production offer the day before for each hour of the following day. The objective of the forecast plan is to establish a technically and economically viable power offer.This production offer, if accepted by the market, becomes a production order for the power plant. The 24-hour sliding horizon allows the electricity price and steam demand forecasts to be updated daily before sending the production offer to the Day-ahead market.

3.2. Operational scheduling

A second model, known as the *operational scheduling model* $\mathcal{M}^{oper}$, establishes the effective workload plan for the equipment over an 8-hour cycle (shift rotation cycle and period over which the actual utility needs are known and fixed). The decisions made by the forecast plan are the input data for the operational scheduling. Consistency constraints

make it possible to define the initial state of the system at each planning level. The degrees of freedom are associated with non-critical equipment: activation, deactivation and load.

4. Case Sudy

The CHP plant shown in Figure 1 is set up as an industrial case. This plant produces steam at three pressure levels and electricity by means of various equipment. Two gas boilers (Boiler-1 and Boiler-2) and one cogeneration train (Gas Turbine coupled to the heat recovery exchanger EXCH) generate High Pressure Steam (HPS) from deaerated water. The desuperheating valve V1 converts HPS into Medium Pressure Steam (MPS) whereas the desuperheating valve V2 converts MPS into Low Pressure Steam (LPS). In addition, the multi-stage steam turbine M-Turbine convert HPS into MPS and LPS, and the steam turbine S-Turbine converts HPS into LPS. Deaerated water is produced in a tank from LPS and demineralized water. The Gas Turbine, M-Turbine and S-Turbine equipment generate electricity, sold on the Spot market. All steam producers use natural gas as fuel. Figure 3 depicts the electricity prices in the Epex Spot forecast for a coming week. The price of gas fuel is set at 280 €/t and the price of demineralised water is set at 8 €/t. Finally, the utility plant must satisfy the steam demand of a production unit. Figure 4 shows the global steam demand, ranging from 10 t/h to 28 t/h, that is forecast for the coming week with an uncertainty of 15%.

Several operating constraints are taken into account. First of all, the number of boiler starts is set at 3 per week. Then, there can be no more than 3 changes in the cogeneration train production regime in 8 hours. These constraints have an impact on *forecast* and *operational* decision-making levels. In particular, the boiler start-up periods established in the *forecast* scheduling must be respected in the *operational* scheduling.

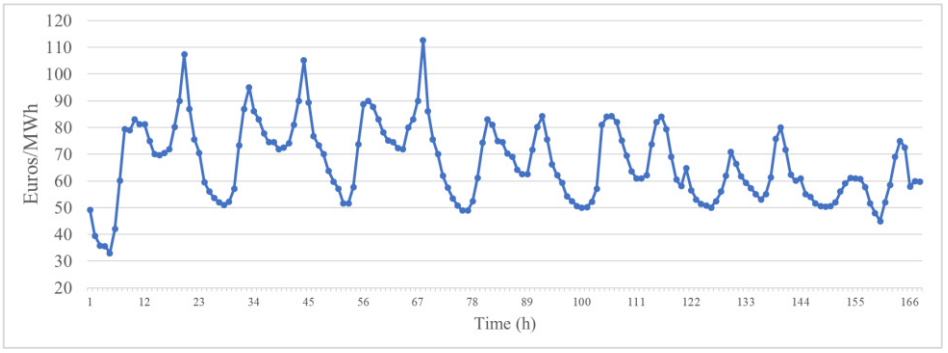

Figure 3: Forecast EPEX Spot Electricity Prices

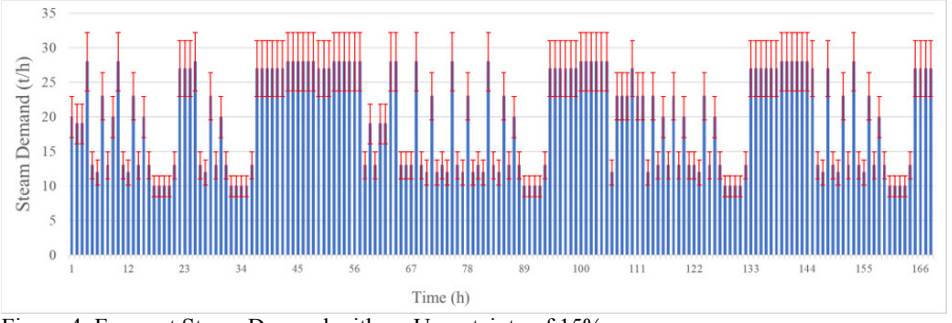

Figure 4: Forecast Steam Demand with an Uncertainty of 15%

5. Results and Discussion

The objective function aims to minimize the operating cost of the CHP plant (i.e. minimize fuel purchase cost and water purchase cost minus the profit resulting from the sale of the electricity produced).

5.1 Forecast schedule

The resolution of the planning model is performed on IntelCore i7 (2.8 GHz, 16 Go RAM). The preventive schedule of the CHP is presented in Figure 5, in the form of a GANTT chart, over 1 week (168 periods of 1 h). Taking into account the steam demand with its uncertainty and the Spot market price, the model $\mathcal{M}^{for}$ determines the optimal power production, as shown in Figure 6, and the periods during which the boilers can be shut down without risk on the satisfaction of the steam demand. The maximum of 3 starts in the week is reached for Boiler-1 and Boiler-2. Without this long-term vision, the shutdown and restart of the boilers cannot be foreseen. Taking into account the operational constraint of the cogeneration train ensures the feasibility of the plan.

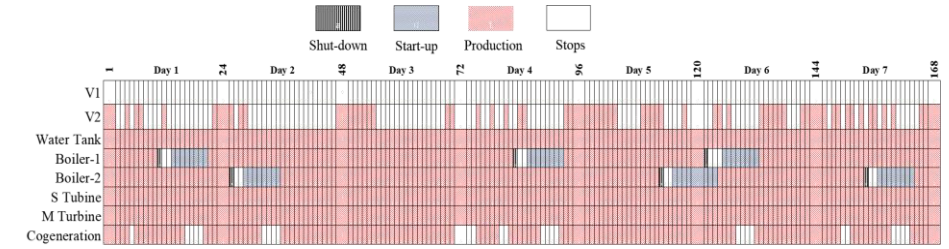

Figure 5: Provisional Schedule over 1 week (275,908 constraints, 146,348 variables with 6552 binary / CPU time = 83.80 s)

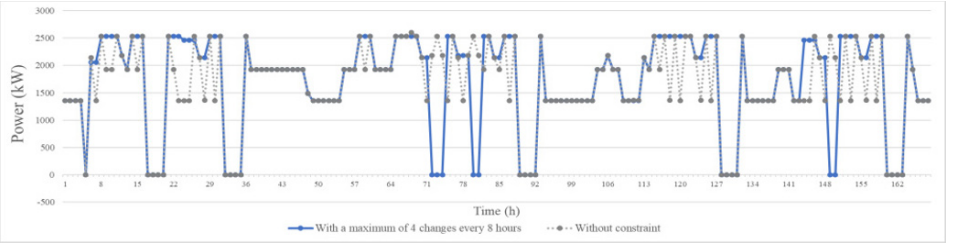

Figure 6: Power Produced by the Cogeneration Train over 1 week

5.2 Operational schedule

At this level of decision, the steam demand is known for sure. Decisions made by the *forecast* level become input data for the *operational* level. Thus, electricity production is dictated by the production supply sent to the Spot market and the load plan of the cogeneration train as well boiler shut-downs and starts are imposed to respect the operational constraints. The degrees of freedom are found in the activation/deactivation of valves and turbines and in the production load of boilers, valves and turbines. The production load is optimized according to the effective steam demand. In addition, the boiler may be in an alternative state called the *Low Boiling* mode. This mode is a conservation mode in which the boiler does not produce steam and consumes a small amount of fuel (5% of its nominal consumption) to be able to switch without transition to a production mode. This mode provides more flexibility in the operation of the plant. Figure 7 shows the operational schedule for the first day of the horizon. The model $\mathcal{M}^{oper}$

is run consecutively for the 3 periods of 8 hours. The operational schedule respects the decisions taken at the forecast level by allowing production to be adjusted to the effective value of steam demand to minimize the plant's operating cost.

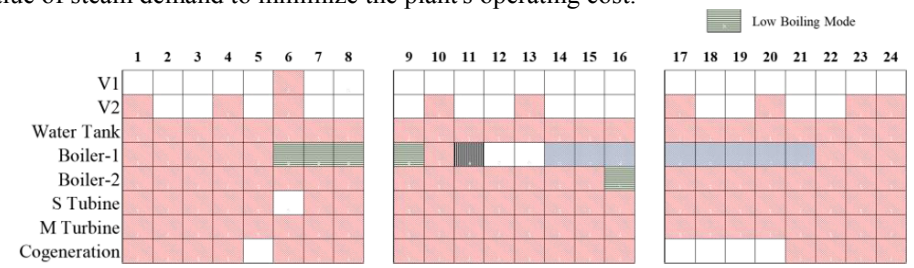

Figure 7 : Operational Schedule for the first day, over 8 hours

6. Conclusions

The methodology implemented makes it possible to establish a robust production plan for a utility plant that interacts with the *Day-ahead* electricity market. The *forecast level* smooths the load of the cogeneration train while regulating the operation of the boilers. The *operational level* then optimizes the production of *CHP* based on actual data and within the framework defined by the higher level. If the offer accepted by the market must be made by the power plant, it is nevertheless possible to value an overproduction of electricity on the market called *Intra-Day*. It would also be interesting to include financial penalties for non-compliance with the *Spot* offer.

References

A.J. Conejo, J. Contreras, R. Espinola, M.A. Plazas, 2005, Forecasting Electricity Prices for a Day-Ahead Pool-Based Electric Energy Market, International Journal of Forecasting, 21 (3), 435–462.

F. De Ridder, B. Claessens, 2014, A Trading Strategy for Industrial CHPs on Multiple Power Markets, International Transactions on Electrical Energy Systems, 24 (5), 677–697.

I. Dimoulkas, M. Amelin, 2014, Constructing Bidding Curves for a CHP Producer in Day-Ahead Electricity Markets, Energycon Conference, 487–494.

G. Hétreux, F. Fabre , J. LeLann, P. Zaraté, 2011, Dynamic Hybrid Simulation of Batch Processes Driven by a Scheduling Module, Computers and Chemical Engineering, 35 (10), 2098-2112.

Z. Li, M. Ierapetritou, 2008, Process Scheduling under Uncertainty: Review and Challenges, Computers & Chemical Engineering, 32 (4), 715–727.

L. Mallier, G. Hétreux, R. Théry, P. Baudet, 2019, Short-term Planning of Combined Heat and Power Plants Participating in the Electricity Day-ahead Market, 22nd Conference on Process Integration, Modelling and Optimisation for Energy Saving and Pollution Reduction

S. Mitra, L. Sun, I.E. Grossmann, 2013, Optimal Scheduling of Industrial Combined Heat and Power Plants under Time-Sensitive Electricity Prices, Energy, 54, 194–211.

F. Salgado, P. Pedrero, 2008, Short-Term Operation Planning on Cogeneration Systems: A Survey, Electric Power Systems Research, 78 (5), 835–848.

M.I. Santos, W. Uturbey, 2018, A Practical Model for Energy Dispatch in Cogeneration Plants, Energy, 151, 144–159.

R. Théry, G. Hétreux, M.H. Agha, A. Hait, J.M. Le Lann, 2011, The Extended Resource Task Network : a Framework for the Combined Scheduling of Batch Processes and CHP Plant, International Journal of Production Research, 50 (3), 623-646.

P. Verderame, J. Elia, J. Li, C. Floudas, 2010, Planning and Scheduling under Uncertainty: A Review Across Multiple Sectors, Industrial Engineering Chemistry Research, 49 (9), 3993–4017

Q. Zhang, M.F. Morari, I.E. Grossmann, A. Sundaramoorthy, J.M. Pinto, 2016, An Adjustable Robust Optimization Approach to Scheduling of Continuous Industrial Processes Providing Interruptible Load, Computers & Chemical Engineering, 86, 106–119.

Sauro Pierucci, Flavio Manenti, Giulia Bozzano, Davide Manca (Eds.)
Proceedings of the 30th European Symposium on Computer Aided Process Engineering (ESCAPE30), May 24-27, 2020, Milano, Italy.
http://dx.doi.org/10.1016/B978-0-12-823377-1.50185-3

Plantwide Control Structure Selection Methodology based on Economics: a Quadratic Approximation

Christos S. Patilas [a,b], Ioannis K. Kookos [a,b*]

[a]*University of Patras, Department of Chemical Engineering,Patras, Greece*

[b]*Research Infrastructure for Waste Valorisation and Sustainable Management of Resources, Patras, Greece*

i.kookos@chemeng.upatras.gr

Abstract

The back-off methodology has been developed and refined in the last decades and offers a systematic tool for solving the simultaneous design and control problem. The first formulation of the methodology was based on linear process and control models. In previous work an improved formulation was proposed where use is made of a nonlinear process model that ensures improved accuracy but increases the complexity and the computational cost of the final problem. In this work, another formulation is presented which is based on the quadratic approximation of the objective function, resulting in a Mixed Integer Quadratic Programming (MIQP) formulation. This approximation can offer greater accuracy than the linear counterpart with a reasonable increase in the computational complexity. The three formulations are evaluated in a reactor-separator-recycle process.

Keywords: process control, control structure selection, mathematical programming

1. Introduction

In industry, processes are designed to operate at specific conditions dictated by economics, equipment capacity constraints and environmental and safety considerations. However, a wide range of disturbances may cause process operation to deviate from the optimal operating point which can not only cause performance deterioration but also operation infeasibility. These phenomena are treated with corrective actions in the form of control mechanisms. In designing those systems, the objective is to develop control structures that satisfy the constrains under the effect of disturbances with minimum performance loss. This is known as the Control Structure Selection Problem (CSSP) and refers to the synthesis of optimal regulatory control structures by considering both structural and parametric optimization issues.

A systematic method, that is known as the back-off methodology for simultaneous design and control, has been proposed and latter refined by Heath et al. (2000). More recently Psaltis et al. (2013) proposed some implementation improvements that made the application of the methodology possible to plantwide control problems.

The initial formulation of the method was based on linearized economics that ensure quick determination of the optimal solution at the expense of a possible loss in the accuracy due to the nonlinearities. In (Kookos and Perking, 2016) a new formulation is proposed which uses the nonlinear model of the process assuming that all design (structural) decisions have been made. This new formulation ensures improved accuracy

and also offers the opportunity for the simultaneous consideration of process design and control. The nonlinear formulation increases the complexity and the computational cost of the final problem. Therefore, a new formulation based on the quadratic approximation of the objective function (economic penalty) is introduced resulting in a Mixed Integer Quadratic Programming (MIQP). This approximation can be more accurate when compared with the linear counterpart at reasonable increase in computational effort.
A short review of the back-off methodology is first presented followed by the formulation of the quadratic approximation. Finally, all three formulations are evaluated in a case study involving a reactor-separator-recycle process (Luyben and Floudas ,1993).

2. Mathematical Framework and Formulation

Operation of chemical process systems may be modeled by a set of nonlinear differential and algebraic equations and inequality constraints that involve an n_x vector of state variables $\mathbf{x}(t)$, an n_z vector of algebraic variables $\mathbf{z}(t)$, an n_u vector of control variables $\mathbf{u}(t)$, a vector of design variables that consist of continuous ($\mathbf{d}$) as well as integer ($\mathbf{\Delta}$) variables and an n_p vector of disturbances $\mathbf{p}(t)$ (variables that are determined exogenously). Finally, J is the objective function usually used to evaluate the economic performance of the process. The control structure selection problem can be modeled as a Mixed Integer Non-Linear Programming (MINLP) and described by the following set of equations:

$$\begin{aligned} \min_{\mathbf{x}(t),\mathbf{z}(t),\mathbf{u}(t),\mathbf{p}(t);\mathbf{d},\mathbf{\Delta}} \quad & J(\mathbf{x}(t),\mathbf{z}(t),\mathbf{u}(t),\mathbf{p}(t);\mathbf{d},\mathbf{\Delta}) \\ s.t. \quad & \\ \mathbf{h}(\dot{\mathbf{x}}(t),\mathbf{z}(t),\mathbf{u}(t),\mathbf{p}(t);\mathbf{d},\mathbf{\Delta}) &= 0 \\ \mathbf{g}(\mathbf{x}(t),\mathbf{z}(t),\mathbf{u}(t),\mathbf{p}(t);\mathbf{d},\mathbf{\Delta}) &\le 0 \end{aligned} \tag{1}$$

For the ideal case, in which the uncertain parameters are set to their nominal values the above formulation is restricted to steady state. The solution of the steady state problem yields the optimum steady-state operating point which usually lies at the intersection of active constraints. In general, the uncertain parameters deviate from their nominal values and therefore the process operation may shift to the infeasible region.
In order to ensure the feasibility of the operation under the effect of disturbances, the back-off vector $\boldsymbol{\mu}$ is introduced:

$$\mu_k = \max_t \left| g_k - g_k^N \right|, \; k = 1, 2, ..., n_g \tag{2}$$

where, g_k^N is the value of the k-th constraint at the nominal optimal operating point. Each element of the back-off vector is defined as the maximum violation of the corresponding constraint over the time horizon. The magnitude of the back-off vector depends not only on the disturbance characteristics but also on the structure and the parameters of the regulatory control system.
The dynamic behavior of a process under the effect of disturbances, in a region close to a steady state point can be described with adequate accuracy by the linearization of Eq. (1) at the optimal operating point. Furthermore, to avoid the complexity of solving a dynamic problem, the system of differential and algebraic equations can be transformed into the frequency domain. The latter is performed by taking the Laplace transformation of the system and decompose the transformed variables into real (superscript R) and

imaginary (superscript I) parts. The final system of equations is described below in Eq. (3):

$$\begin{aligned} 0 &= \mathbf{A}\mathbf{X}^R + \mathbf{B}\mathbf{U}^R + \mathbf{E}\mathbf{P}^R + \omega\mathbf{X}^I \\ 0 &= \mathbf{A}\mathbf{X}^I + \mathbf{B}\mathbf{U}^I + \mathbf{E}\mathbf{P}^I - \omega\mathbf{X}^R \\ \mathbf{Y}^R &= \mathbf{C}\mathbf{X}^R + \mathbf{D}\mathbf{U}^R + \mathbf{F}\mathbf{P}^R \\ \mathbf{Y}^I &= \mathbf{C}\mathbf{X}^I + \mathbf{D}\mathbf{U}^I + \mathbf{F}\mathbf{P}^I \\ \mathbf{\Sigma}^R &= \mathbf{H}\mathbf{X}^R + \mathbf{P}\mathbf{U}^R + \mathbf{S}\mathbf{P}^R \\ \mathbf{\Sigma}^I &= \mathbf{H}\mathbf{X}^I + \mathbf{P}\mathbf{U}^I + \mathbf{S}\mathbf{P}^I \end{aligned} \tag{3}$$

If we set P^R =1 and P^I =0, we can obtain the frequency response of the system (i.e. the asymptotic response to sinusoidal variation of the disturbances with frequency ω). However, the system of linear equations is undetermined as $2n_u$ equations are missing. These are the equations that are needed to describe the controller in the frequency domain. To resolve this issue and simultaneously avoid the introduction of the controller design problem, the implementation of perfect control was proposed. Integer variables Ψ_j are introduced to denote the selection (Ψ_j =0) or not (Ψ_j =1) of potential controlled variable (CV) y_j. In a similar way the integer variables Θ_j are introduced to select (Θ_j =1) or not (Θ_j =0) a potential manipulated variable (MV) u_j in the regulatory control structure and perfect control is implemented through the following linear inequalities. Finally, consideration is also restricted to square control structures. The equations of the controller are presented in Eq. (4).

$$\left.\begin{aligned} -y_j^U\Psi_j \le Y_j^R \le y_j^U\Psi_j \\ -y_j^U\Psi_j \le Y_j^I \le y_j^U\Psi_j \end{aligned}\right\} j=1,2,...,n_y \qquad \left.\begin{aligned} -u_j^U\Theta_j \le U_j^R \le u_j^U\Theta_j \\ -u_j^U\Theta_j \le U_j^I \le u_j^U\Theta_j \end{aligned}\right\} j=1,2,...,n_u$$

$$\sum_{j=1}^{n_y}\Psi_j + \sum_{j=1}^{n_u}\Theta_j = n_y \tag{4}$$

Psaltis et al. (2013) have shown that the back-of vector can be determined accurately through a set of linear inequalities that avoid the need for the iterative application of the algorithm used earlier by Heath et al (2000).

$$\mathbf{\Pi}^R\mathbf{\Sigma}^R + \mathbf{\Pi}^I\mathbf{\Sigma}^I \le \boldsymbol{\mu} \tag{5}$$

For the linear formulation equations Eq. (3) - Eq. (5) can be combined with the state space model of the process and can be written in Eq. (6), where $\mathbf{J_x}$ and $\mathbf{J_u}$ are the gradients of the objective function with respect to the state and control vectors accordingly and EP_{lp} is the economic penalty resulting from the occurrence of the disturbances. Additionally, the non-linear formulation is also presented in Eq. (6) and makes use of the linear approximation for the back-off estimation and the initial formulation Eq. (1) for the estimation of the economic penalty.

$$\min_{\delta\mathbf{x},\delta\mathbf{u},\Theta,\Psi,\boldsymbol{\mu}} EP_{lp} = \mathbf{J}_x^T\delta\mathbf{x} + \mathbf{J}_u^T\delta\mathbf{u} \qquad \min_{\mathbf{x}_s,\mathbf{z}_s,\mathbf{u}_s,\mathbf{d},\boldsymbol{\Delta},\Theta,\Psi,\boldsymbol{\mu}} EP_{nlp} = J\big|_{\mu\neq 0}(\mathbf{x}_s,\mathbf{z}_s,\mathbf{u}_s,\mathbf{p}_N;\mathbf{d},\boldsymbol{\Delta}) - J\big|_{\mu=0}$$

s. t.

$$\mathbf{A}\delta\mathbf{x} + \mathbf{B}\delta\mathbf{u} = 0$$
$$\mathbf{C}\delta\mathbf{x} + \mathbf{D}\delta\mathbf{u} = \delta\mathbf{y}$$
$$\mathbf{g}_N + \mathbf{H}\delta\mathbf{x} + \mathbf{P}\delta\mathbf{u} \le -\boldsymbol{\mu}$$
$$-\delta\mathbf{x}^u \le \delta\mathbf{x} \le \delta\mathbf{x}^u$$
$$-\delta\mathbf{u}^u \le \delta\mathbf{u} \le \delta\mathbf{u}^u$$
$$\Theta_j, \Psi_j \in \{0,1\}$$
$$Eqs\ 3-5$$

s. t.

$$\mathbf{h}(\mathbf{x}_s,\mathbf{z}_s,\mathbf{u}_s,\mathbf{p}_N;\mathbf{d},\boldsymbol{\Delta}) = 0$$
$$\mathbf{g}(\mathbf{x}_s,\mathbf{z}_s,\mathbf{u}_s,\mathbf{p}_N;\mathbf{d},\boldsymbol{\Delta}) \le -\boldsymbol{\mu}$$
$$\Theta_j, \Psi_j \in \{0,1\}$$
$$Eqs\ 3-5 \qquad (6)$$

The proposed formulation has the same set of equations as the linear and a quadratic approximation of the economic penalty. The objective function of this formulation is stated below in Eq. (7), where **Q** is the hessian matrix.

$$EP_{qp} = \mathbf{J}_x^T\delta\mathbf{x} + \mathbf{J}_u^T\delta\mathbf{u} + \frac{1}{2}\begin{bmatrix}\delta\mathbf{x}^T & \delta\mathbf{u}^T\end{bmatrix}\mathbf{Q}\begin{bmatrix}\delta\mathbf{x}^T \\ \delta\mathbf{u}^T\end{bmatrix} \qquad (7)$$

3. Case Study

The reactor-separator-recycle process examined in this case study is presented in Figure 1. Fresh feed of 90% A is fed into the reactor, where the first order irreversible reaction A → B takes place. The reactor product is then fed to the distillation column. The main product B is obtained as the bottom product, while unreacted A is recycled back to the reactor.

The design strategy of the process was based on a structural optimization problem for finding the optimal steady state regarding the topology and the operating point (Luyben and Floudas ,1993) and (Viswanathan and Grossmann ,1992).

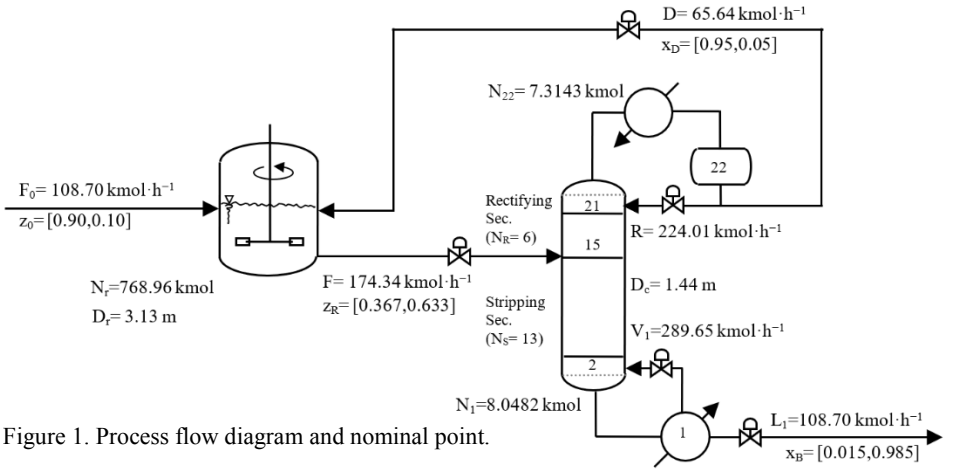

Figure 1. Process flow diagram and nominal point.

Table 1. Results of the CSSP- Nonlinear, Linear and Quadratic for 5% variation in Disturbances

N_o	EP_{nlp}	N_o	EP_{lp}	N_o	EP_{qp}	Manipulated	Controlled
1	0.01 %	1	0.00 %	1	0.00 %	F, L_1, V_1, R, D	N_r, x_B, x_D, N_1, N_{NT}
2	0.14 %	2	0.08 %	2	0.21 %	F, L_1, V_1, R, D	N_r, x_2, x_{21}, N_1, N_{NT}
3	0.32 %	3	0.21 %	3	0.21 %	F, L_1, V_1, R, D	N_r, x_3, x_{21}, N_1, N_{NT}
4	0.56%	5	0.36 %	4	0.37 %	F, L_1, V_1, R, D	N_r, x_4, x_{21}, N_1, N_{NT}
5	0.58 %	4	0.34 %	9	0.56 %	F, L_1, V_1, R, D	N_r, x_2, x_{20}, N_1, N_{NT}
6	0.85 %	9	0.77 %	6	0.77 %	F, L_1, V_1, R, D	N_r, x_2, x_{19}, N_1, N_{NT}
7	0.85 %	8	0.61 %	7	0.77 %	F, L_1, V_1, R, D	N_r, x_4, x_{20}, N_1, N_{NT}
8	0.85 %	7	0.55 %	5	0.56 %	F, L_1, V_1, R, D	N_r, x_5, x_{21}, N_1, N_{NT}
9	1.22 %	-	-	8	0.79 %	F, L_1, V_1, R, D	N_r, x_6, x_{21}, N_1, N_{NT}
10	1.22 %	6	0.46 %	10	1.08 %	F, L_1, V_1, R, D	N_r, x_3, x_{20}, N_1, N_{NT}

The mathematical problem for the optimal design of the process is a MINLP problem which was solved using the SBB solver available in GAMS. The optimal solution is presented in Figure 1.

The state vector consists of the mole fractions of component A and the molar holdups in the reactor and the column. The potential MV are the reactor product flowrate F, the vapor boilup V_1, the bottom's product flowrate L_1, the reflux rate R and the recycle stream flow D. The potential CV are the reactor's holdup N_r and composition x_r, the holdup of the reboiler N_1 and condenser N_{NT} and finally the composition of component A in all trays. It should be noted that for this case study the choice of compositions as CV rather than temperatures will not make any difference because it is well known that both of them are equivalent for binary mixtures. As a result, there are 5 potential MV and 26 CV giving rise to an exploding size of potential control structures. The CSSP was then solved applying the three formulations to determine the 10 most promising structures and to examine if the quadratic performs better when compared to the linear. Table 1 summarizes the results.

All structures make use of all MV resulting in 5x5 control structures. An RGA analysis was performed to design the interconnection between the variables. In all cases, the reactor holdup is controlled by the reactor's outflow, the reboiler's holdup by the bottom's product flow and the condenser's holdup by the reflux rate. Finally, the boilup is connected with a composition in the stripping section and the recycle stream flow (distillate) with a composition in the rectifying section. The best structure was identified by all formulations and makes use of the compositions of the bottom and distillate product streams. Direct control of variables that appear in design specifications is often unrealistic therefore, these were eliminated as CV to examine structures based on the compositions of the internal trays.

Based on the results, the quadratic formulation managed to identify all of the structures produced by the non-linear and rank them more accurately than the linear. Some selected structures were evaluated in closed loop simulations in a rather aggressive disturbance scenario, where the inlet flow F_0 to the reactor was increased by 10 %, then decreased by 20 % and finally returned to the nominal point. The same procedure was followed for the composition z_0. In the closed loop system, PI controllers were implemented and tuned via the ATV method. In Figure 2, the deviation of the composition in the bottom's product is

presented. As expected, the most promising structure is CS1 in which the purity specifications are directly controlled. Apart from that, the performance of the other three structures is also smooth with small deviations of order 10^{-3}.

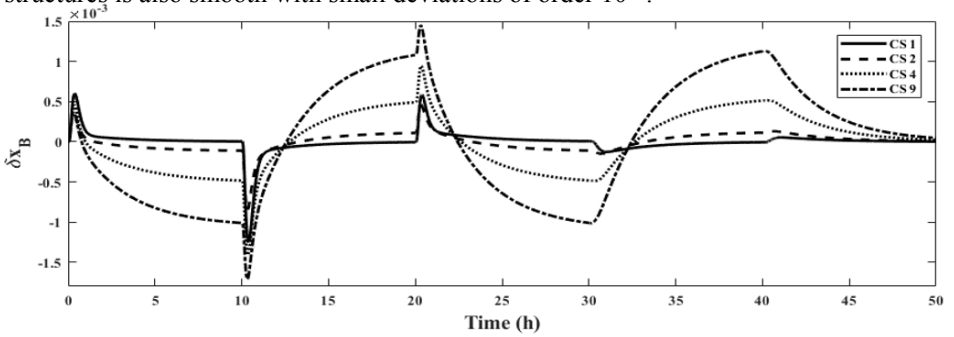

Figure 2. Deviation of bottom's product composition.

Finally, in order to evaluate the economic performance of the structures, the cost of utilities regarding the examined time domain was calculated. More specifically, the examined structures resulted in 2001.4$, 2001.5$, 2001.6$ and 2001.7 $ accordingly. Considering the order of the resulted economic penalties, it can be said that all structures feature in the same cost. The difference between the cost although insignificant, manages to ascertain the ranking of the structures presented in Table 1. These findings prove that the proposed formulation is successful in identifying promising control structures in a systematic way based on economic performance and not on rules of thumb and heuristics.

Conclusions

This paper presents, the main concepts of the back-off methodology for the CSSP problem. A new formulation is presented and evaluated for the reactor-separator-recycle process. The results are very promising and the new formulation may offer advantages in the study of even more aggressive non-linear processes. The back-off methodology in general, handles efficiently the CSSP and based on the size of the current case the proposed methodology is not size-limited.

Acknowledgement

This work was supported by the project "INVALOR: Research Infrastructure for Waste Valorization and Sustainable Management" (MIS 5002495) which is implemented under the Action "Reinforcement of the Research and Innovation Infrastructure", funded by the Operational Programme "Competitiveness, Entrepreneurship and Innovation" (NSRF 2014-2020) and co-financed by Greece and the European Union (European Regional Development Fund).

References

1. J. Heath,I. Kookos,J. Perkins, 2000, Process control structure selection based on economics, AIChe J., 46, 10, 1998-2016.
2. I. Kookos,J. Perkins, 2016, Control Structure Selection Based on Economics: Generalization of the Back-Off Methodology, AIChE J., 62, 9, 3056-3064
3. M. Luyben, C. Floudas, 1994, Analyzing the interaction of design and control-2. Reactor-Separator-Recucle system, Comp. Chem. Eng, 18, 10, 971-944
4. A. Psaltis,I. Kookos, C. Kravaris, 2013, Plant-wide control structure selection methodology based on economics, Comp. Chem. Eng.,52, 240-248
5. J. Viswanathan, I. Grossmann, 1993, An alternate minlp model for finding the number of trays required for a specified separation objective, Comp. Chem. Eng.,17, 9, 949-955

Sauro Pierucci, Flavio Manenti, Giulia Bozzano, Davide Manca (Eds.)
Proceedings of the 30th European Symposium on Computer Aided Process Engineering (ESCAPE30), May 24-27, 2020, Milano, Italy.
http://dx.doi.org/10.1016/B978-0-12-823377-1.50186-5

Optimal Design and Planning of Biomass-to-Biofuel Supply Chain Considering Economic Dimension under Strategic and Tactical Levels: a Case Study in Ethiopia

Brook Tesfamichael[a,b,c], Ludovic Montastruc[a,b,*], Stéphane Negny[a,b], Abubeker Yimam[c]

[a.] *Université de Toulouse, INP-ENSIACET, 4, allée Emile Monso, F-31432 Toulouse Cedex 04, France*
[b.] *CNRS, LGC (Laboratoire de Génie Chimique), F-31432 Toulouse Cedex 04, France*
[c.] *Addis Ababa University, Addis Ababa Institut e of Technology, School of Chemical and Bio Engineering, Addis Ababa, Ethiopia*
ludovic.montastruc@ensiacet.fr

Abstract

Biofuel derived from biomass on account of being renewable energy source and having high potential to substitute fossil fuels, have attracted considerable interest in both developed and developing countries like Ethiopia. However, the lack of optimal design and planning of the biomass-to-biofuel projects in countries like Ethiopia results in poor economic attractiveness of the sector. Therefore, this study presents a novel economic optimization model to design and plan biomass-to-biofuel supply chain (BBSC) at strategic and tactical level simultaneously. The problem is formulated as spatially explicit, multi-feedstock, multi-period and multi-echelon mixed integer linear programming model that seeks to maximize the NPV of the entire supply chain. The proposed model covers all the entities along the supply chain including biomass cultivation, feedstock pretreatment, conversion into bioethanol or biodiesel, as well as distribution, transportation and storage of the biomass, products and byproducts. A county-level case study in Ethiopia is provided to demonstrate the applicability of the model. Results show the effectiveness of the model as a quantitative decision-making or planning tool to design different BBSC configurations. Optimal location, technology, and capacity of the preprocessing facility, biorefinery and biofuel distribution centers are determined simultaneously with inventory levels, material flows and transportation capacities between network nodes of the supply chain.

Keywords: Biomass-to-biofuel supply chain (BBSC), economic optimization, strategic and tactical level.

1. Introduction

Biomass-to-biofuel industry has been grown in recent years since it has a tremendous potential to reduce oil imports and greenhouse gas (GHG) emissions, support agricultural and forestry growth, and foster social benefits like job creation. As a result of this, biofuel targets have been set by many developed and developing nations including Ethiopia. Biomass based biofuel production particularly bioethanol production from sugar byproducts - Molasses and Bagasse and biodiesel production from the nonedible oil seed bearing plants - Jatropha curcas and Castor seed - is a key strategic direction outlined in

the biofuels strategy of the Government of Ethiopia. The main objective underlying the strategy include substitution of imported gasoline and diesel oil used in the transport sector while at the same time contributing to the local and global greenhouse gasses (GHG) reduction efforts (Gabisa et al., 2018).

To demonstrate the feasibility and validate the economic interest in the production of biofuel from biomass, the development of systematic studies is becoming imperative. Accordingly, many Process Systems Engineering (PSE) approaches focusing on Biomass-to-Biofuel Supply Chain (BBSC) optimization through mathematical programming have been recently developed, considering mostly the economic dimension (Espinoza Pérez et al., 2017a). However, these studies have some drawbacks: a) the strategic level decision has been the center of investigation in most researches (Akhtari et al., 2018; Barbosa-Povoa et al., 2018). However, tactical and operational level studies are also essential to provide comprehensive information and realistic representation to support decisions; b) most of the BBSC studies considered only one type of biofuel product. The simultaneous bioethanol and biodiesel production in one supply chain has not been considered so far; and c) Most of the BBSC researches deal the system complexity in a fragmented and partial manner, either on the upstream biomass supply chain, from the biomass cultivation site to the production plant or on the downstream biofuel supply chain, from the production plant to the end customer (Yu et al., 2013). Moreover, because of not incorporating some important components while planning the BBSC, the project incurs high amount of cost that discourages investors, government and other stakeholders (Espinoza Pérez et al., 2017a). For instance, overlooking a pre-processing operation in the BBSC may bring an increment of transportation cost due to the higher moisture content and large size of the raw biomass.

Henceforth, to overcome the above drawbacks, this study presents a decision-support optimization model that maximizes the net present value (NPV) of the entire BBSC considering: a) both strategic and tactical level planning and decisions; b) BBSC with two-product (bioethanol and biodiesel) processing plants those are located at different sites; and c) comprehensive supply chain which incorporates all relevant components from biomass feedstock supply to biofuel end-users: namely, biomass feedstock supply centers, preprocessing centers, bio-Refineries, biofuel (bioethanol & biodiesel) distribution centers, biofuel and by-product market zones

The proposed approach will be applied for Ethiopia's case to provide decision or planning support tool for the policy makers, investors and other pertinent stakeholders in order to bring the biomass-to-biofuel sector economically sustainable.

2. Problem Statement

The core driver of this study is to deal with the strategic and tactical design and planning of BBSC for the production of bioethanol and biodiesel in Ethiopia over 30-years' time horizon. The problem addressed in this paper is presented schematically on **Figure 1** and the problem is described as follows. The BBSC optimization model proposed in this work considers different types of biomass b that can be procured from a variety of supply sources h. In each candidate location i, there are preprocessing facilities that can be installed for pretreating the biomass with candidate technologies f and capacities c. The technologies are mainly drying and size reduction for bioethanol feedstocks and oil extraction for biodiesel feedstocks. Then the preprocessed feedstock d goes to a

biorefinery located at j, where there are g candidate technologies with capacities e that can be installed for the production of biofuel u and generation of byproduct v. There are two possibilities for the biofuel u to reach to the demand zone m from the biorefinery j; either it goes to the distribution center k with capacity a and then to the demand zone m or it directly goes to the demand zone m without going to distribution center k, whereas the byproduct v directly goes to the demand zone n from the biorefinery j.

The deterministic parameters used in the proposed BBSC are the following:

- Biomass supply location and amount over a fixed time horizon
- Bioethanol and biodiesel demand location and amount over a fixed time horizon.
- The procurement cost of biomass and selling price of the biofuels and useful by-products.
- The candidate locations, capital and operating costs, and maximum capacities of the pre-processing, biorefinery, and biofuel distribution facilities.
- The transport logistics (distances, availability, costs and modes).
- Government policies relating to the BBSC, e.g. taxation and subsidies.

Having the above parameters, the key variables of the model that need to be optimized, refer to both strategic and tactical decisions for the entire supply chain. Precisely, the strategic decisions regard the location of biomass procurement sites and location, technology, and capacity of the preprocessing facility and biorefinery as well as location and capacity of biofuel distribution sites, whereas the tactical decisions deal with inventory levels, material flows and transportation capacities between network nodes.

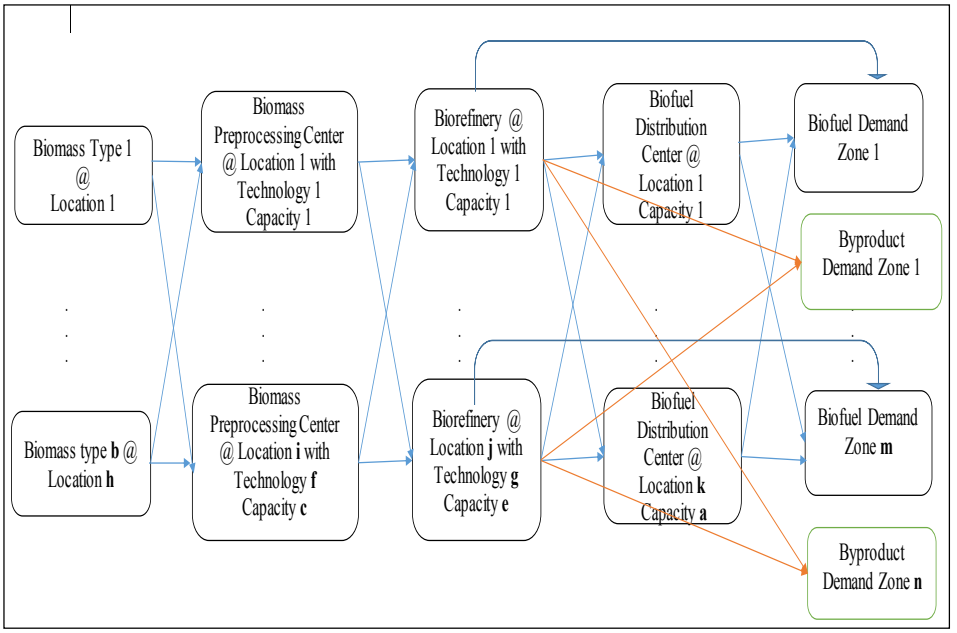

Figure 1: Model Superstructure

3. Model Formulation

In order to address the entire behavior of BBSC, the mathematical modeling framework has been formulated as an MILP problem. The design process is conceived as a single-

objective optimization problem targeting at NPV maximization of the entire supply chain. The problem is formulated as a spatially explicit multi-period, multi-feedstock, multi-product and multi-echelon modeling framework. Precisely, the objective function, as illustrated in eq. 1, comprises of cash inflows, cash outflows and initial investment. Revenues obtained by selling, and tax credit for producing the desired products and byproducts are considered as the cash inflows whereas cash outflows comprised of biomass procurement, operational, inventory and transportation costs along the supply chain. The initial investment considers the capital investments for the preprocessing, biorefinery and product storage facilities, and government incentive for biorefinery installation. In this work, the cash inflow and outflow are calculated for a lifetime project of 30 years ($y \in Y$, $Y = \{1,2,\ldots,30\}$), based on the planning years optimized over 12 months ($t \in T$, $T = \{1,2,\ldots,12\}$).

$$NPV = \left\lfloor \sum_{n=1}^{Y} \frac{1}{(1+\partial)^{y}} \left(CashInflow^{y} - CashOutflow^{y} \right) \right\rfloor - InitalInvestment \tag{1}$$

The design process is also subjected to logical constraints that must be satisfied at each of the supply chain nodes; including feedstock availability constraints, mass balances in the preprocessing facility for the feedstock and preprocessed biomass, mass balances in the biorefinery for the preprocessed biomass, biofuel product and byproducts, mass balances in the distribution center for the biofuel, and biofuel and byproduct demand satisfaction. The model also takes into account the biomass seasonality and biomass degradation over time.

4. Case Study

The developed model in this study will be applied to a case study in Ethiopia to support the government and other stakeholders engaged in the country's biomass-to-biofuel projects. In this study, the candidate locations of the biomass collection, pre-processing, biorefinery, and biofuel and byproduct storage and distribution facilities were restricted to the nine regions (Afar, Amhara, Benishangul, Gambella, Harari, Oromia, SNNP, Somali and Tigray) and two city administrations (Addis Ababa and Diredawa) of the country due to the availability of data. The prior feedstocks for biofuel development in Ethiopia are considered in this study; sugar cane molasses, bagasse and corn stover for bioethanol and jatropha and castor bean for biodiesel production. Annual productions of sugar cane molasses and bagasse are acquired from Ethiopian Sugar Corporation since sugar industries are the only place where these two biomass feedstocks are released from. The amount of corn stover produced was estimated using corn grain yield values which are available on Ethiopia Statistical Agency reports. The stover mass to grain mass ratio of 1:1 (i.e., a dry weight harvest index [HI] of 0.5) (Graham et al., 2007) and taking in to consideration if 50 % of the stover in each region is used for bioethanol production. Having the amount of suitable land available in each region of the country for jatropha and castor plantation from Ministry of Agriculture, bibliographic data were used to determine the average amount of seed produced per hectare of suitable land. The pre-processing mechanism considered for the two bioethanol feedstocks; bagasse and corn stover is only drying and size reduction. However, no preprocessing is required for the molasses. On the other hand, technologies considered for the pre-processing facility of the biodiesel feedstocks are steam explosion and acid hydolysis. Biochemical and thermo-chemical conversion processes for bioethanol production (Hamelinck et al., 2005) and

homogenous and heterogenous catalysis transesterification for biodiesel production (Saifuddin et al., 2015) are considered as biorefinery technologies in this study. These technologies are chosen for their relative practice in current Ethiopia biofuel industries and availability of detailed techno-economic data. The six capacity levels of the preprocessing facilities considered in this study are 65, 125, 190, 250, 320 and 380 kton of wet biomass per year and the biorefinery capacities are 25, 50, 75, 100, 125 and 150 kton of biofuel per year. Due to the lack of real preprocessing and biorefinery investment and production costs data from commercial plant within Ethiopia, these costs were estimated with bibliographic data, assuming that the components follow the economy of scale, and then corrected with the available information and recent data. The biofuels demand was calculated based on the current government plan to blend bioethanol and biodiesel at a rate of 15 and 5% in the gasoline and diesel respectively. Based on the case study area features, only road transportation mode is assumed for transporting different materials within the supply chain.

5. Result and Discussion

The proposed MILP model was solved using the ILOG CPLEX solver. The model for this case study had 21,242,485 constraints and 315,161 decision variables of which 44,352 were binary variables. An optimal solution was found in 17 hours, after 132,326,057 iterations on an Intel 2.60-GHz processor.

Aiming the maximization of the NPV of the entire BBSC, the model decides the installation of biorefinery with technology of biochemical conversion with acid pretreatment and homogenous catalysis transesterification for the bioethanol and biodiesel production respectively. The optimal solution showed that, from the eleven different allocation options, one of them (Oromia), two of them (Oromia and Amhara) and three of them (Oromia, Amhara and Afar) for the first 10, 11-20, and 21-30 years respectively are feasible locations for bioethanol production. The optimal capacity of both the Oromia and Amhara plants is 125 kton/year, and 50 kton/year for the Afar plant. Meanwhile, two allocations (Addis Ababa and Oromia), four allocations (Addis Ababa, Oromia, SNNP and Tigray), and five allocations (Addis Ababa, Oromia, SNNP, Tigray and Benishangul) are the best alternatives to have biorefinery producing biodiesel for the first 12, 13-23, and 24-30 years respectively. The optimal capacity of both Addis Ababa and Oromia plants is 150 kton/year, and 125, 50 and 25 kton/year for the SNNP, Tigray and Benishangul plants respectively to address the required biodiesel demand.

Regarding the pre-processing facility, the optimal solution showed that, installation of drying and size reduction for the bioethanol feedstocks are required in Oromia, Amhara, Afar, SNNP and Tigray regions for the years 7-30. Solvent extraction is the best option starting from year 1 to pretreat the biodiesel feedstocks and the selected location for the plant are all the regions except Harari. Moreover, the best selected locations for the distribution centers are Addis Ababa, Amhara and Diredawa.

The optimal result also show that, molasses is the only biomass feedstock to fulfill the bioethanol demand of the country for the next 6 years, whereas molasses and bagasse for the years 7-15, and corn stover is also required with the previous two feedstocks for the years 16-30. Regardless of the biodiesel feedstocks, all the demand of the biodiesel for the next 26 years can be fulfilled by using jatropha as a feedstock if the country utilizes

only 10% of the highly suitable land for jatropha cultivation. Castor seed is required together with jatropha for the years 27-30 to address the biodiesel demand.

Although the availability and price of biomass, and price of products were assumed to be fixed over the planning period, revenue shows increment over the 30-year period due to increasing demand of the products. Biomass purchase, transport, operating, and storage costs are accounted for about 23.48 %, 17.08 %, 54.94 % and 4.49 % of the total cash outflow respectively for the first 10 years. In the last 10 years, biomass procurement cost decreased by 8.8 %, transportation cost increased by 42.44 %, operating cost decreased by 9 %, and insignificant change on storage cost compared with those first 10 years.

6. Conclusions

In this work, a novel optimization model has been developed as a decision-making tool for the strategic and tactical design and planning of BBSC. A spatially explicit, multi-period MILP modeling framework for optimization of multifeedstock and multiechelon BBSC, has been presented and discussed. To demonstrate the applicability of the model, it is implemented to determine the optimal supply chain, in terms of maximizing NPV, of the abundant residual biomass available in Ethiopia to produce bioethanol and biodiesel. Results showed that the design and planning of economically sustainable biofuel production and utilization can be enhanced significantly through the optimization of all the entities involved in the BBSC. Finally, future extensions of this work will incorporate the integration of other sustainability dimensions: environment and social, to come-up with comprehensive decision-making tool.

References

E.W. Gabisa, S.H. Gheewala, 2018. Potential of bio-energy production in Ethiopia based on available biomass residues. Biomass and Bioenergy 111, 77-87.

A. Espinoza Pérez, M. Camargo, P.C. Narváez, M. Alfaro, 2017a. Key challenges and requirements for sustainable and industrialized biorefinery supply chain design and management: A bibliographic analysis. Renewable and Sustainable Energy Reviews 69, 350-359.

S. Akhtari, T. Sowlatia, V.C. Griess, 2018. Integrated strategic and tactical optimization of forest-based biomass supply chains to consider medium-term supply and demand variations. Computers and Chemical Engineering 113, 11-31.

A.P. Barbosa-Póvoa, C. Silva, A. Carvalho, 2018. Opportunities and challenges in sustainable supply chain: An operations research perspective. European Journal of Operational Research 268, 2, 399-431.

M. Yu, F. Cecelja, S.A. Hosseini, 2013. Design and optimization of biofuel supply chain network in UK. Computer Aided Chemical Engineering 32, 673-678.

R.L. Graham, R. Nelson, J. Sheehan, R.D. Perlack and L.L. Wright, 2007. Current and Potential US Corn Stover Supplies. Agronomy Journal 99, 1-19.

C.N. Hamelinck, G.V. Hooijdonk, A.C. Faaij, 2005. Ethanol from lignocellulosic biomass: Techno-economic performance in short-, middle- and long-term. Biomass Bioenergy 28, 384-410.

N. Saifuddin, A. Samiuddin, P. Kumaran, 2015. A Review on Processing Technology for Biodiesel Production. Trends Applied Sciences 10, 1, 1-37.

Sauro Pierucci, Flavio Manenti, Giulia Bozzano, Davide Manca (Eds.)
Proceedings of the 30th European Symposium on Computer Aided Process Engineering (ESCAPE30), May 24-27, 2020, Milano, Italy.
http://dx.doi.org/10.1016/B978-0-12-823377-1.50187-7

Modelling a Penicillin Fermentation Process Using Attention-Based Echo State Networks Optimized by Covariance Matrix Adaption Evolutionary Strategy

Kai Liu, Jie Zhang

School of Engineering, Merz Court, Newcastle University, Newcastle upon Tyne NE1 7RU, UK.
jie.zhang@newcastle.ac.uk

Abstract

Echo state network (ESN) has emerged as an effective alternative to conventional recurrent neural networks due to its simple training process and good modelling ability for solving a variety of problems, especially time-series modelling tasks. To improve modelling capability and to decrease the reservoir topology complexity, a new attention mechanism based ESN optimised by covariance matrix adaption evolutionary strategy (CMA-ES) is proposed in this paper. CMA-ES is a stochastic and derivative-free algorithm for solving non-linear optimization problems. Attention mechanism is incorporated to guide ESN to focus on regions of interest relevant to the modelling task. The proposed optimised ESN with attention mechanism is used to model a fed-batch penicillin fermentation process and the results are better than those from the standard ESN and ESN with attention mechanism.

Keywords: Echo State Network, Attention Mechanism, CMA-ES, Fed-batch Bioprocess

1. Introduction

Fed-batch fermentation processes are widely used in the pharmaceutical industry. In fed-batch fermentation processes, the maximization of yield is often regarded as the main objective, but the features of fed-batch fermentation processes including strong nonlinearity, non-steady-state condition, batch-to-batch variations, and strong time-varying condition make the yield hard to be predicted (Ashoori et al., 2009).

Due to the increasing demand on product quality and safety, optimization of fed-batch fermentation processes is becoming very important. One optimization approach is to use first principle models and stochastic optimisation algorithms such as evolutionary algorithm (EA), differential evolution (DE) and particle swarm optimization (PSO) (bin Mohd Zain et al., 2018). Another optimization approach for fed-batch bioprocesses is to use data-driven models such as artificial neural networks. Yu (2012) presented a Bayesian inference based two-stage support vector machine for soft sensor development in batch bioprocesses. Chen et al. (2004) proposed a cascade recurrent neural network combining with modified genetic algorithm for the modelling and optimisation of fed-batch fermentation processes.

In recent years, recurrent neural networks (RNNs) attracted a mass of attention because of its dynamic temporal nonlinear behaviour and processing arbitrary sequences of

inputs by its internal memory. RNNs are appropriate for modelling complex dynamic processes such as fed-batch fermentation processes. RNNs include but no limit to long short-term memory networks (LSTM), gated recurrent unit (GRU) and reservoir computing (RC). Comparing to LSTM and GRU, the benefit of RC is lower computational training cost and faster convergence with excellent performance. Due to the randomly generated input scaling matrix, the normal ESNs are not able to distinguish the different property of input elements. The concept of "attention mechanism", which allows models to learn alignments between different modalities, has drawn significant attention in the training of neural networks. Attention mechanisms have been successfully used in speech translation and image caption generation (Luong et al., 2015), but have rarely been used in modelling complex bioprocesses, especially fed-batch fermentation process with a large number controllable and monitoring variables.

In this paper, an input elements scaling method based on the attention mechanism is integrated with ESN which is optimized by covariance matrix adaption evolutionary strategy (CMA-ES). Three global reservoir parameters in ESN are optimized by CMA-ES and they are reservoir size, spectral radius, and leak rate.

2. Methodology

2.1. Echo state networks

An ESN is composed of a reservoir and a linear output layer which maps the reservoir states to the network output. Figure 1 shows the original ESN. The input weights are generated randomly. The internal weights between reservoir neurons can be created with a sparse connection density which means that internal neurons may not be fully connected to each other but connected sparsely. The weights mentioned above will not change during the training process and only the readout output weights need to be learned. The reservoir states of ESN with leak rate are shown in Eq(1) (Lukoševičius and Jaeger, 2009):

$$\boldsymbol{x}(t) = (1-\alpha)\cdot\boldsymbol{x}(t-1) + \alpha\cdot\boldsymbol{f}(\boldsymbol{W^{in}}\cdot\boldsymbol{u}(t) + \boldsymbol{W}\cdot\boldsymbol{x}(t-1) + \boldsymbol{W^{back}}\cdot\boldsymbol{y}(t-1) \quad (1)$$

where $\boldsymbol{u}(t)$ and $\boldsymbol{x}(t)$ are the inputs and the reservoir states at time t respectively, α is the leak rate, $\boldsymbol{f}()$ is the general activation function, and the weights donated by $\boldsymbol{W^{in}}$, $\boldsymbol{W^{back}}$, and $\boldsymbol{W}$ represent the weights for inputs, feedback, and reservoir respectively. Then $\boldsymbol{W}$ needs to be rescaled by a spectral radius (the largest absolute eigenvalue of $\boldsymbol{W}$, $|\boldsymbol{\theta_{Max}}|$) and then multiplied by a spectral radius factor $\boldsymbol{\delta}$ as shown in Eq(2) to keep its echo state property.

$$\boldsymbol{W} \leftarrow \boldsymbol{\delta W}/|\boldsymbol{\theta_{Max}}| \quad (2)$$

The readout matrix is then obtained by solving a linear regression problem:

$$\boldsymbol{X}\cdot\boldsymbol{W^{out}} = \boldsymbol{Y} \quad (3)$$

where $\boldsymbol{X}$ is a matrix of hidden states which are updated at discrete time steps using Eq(1) and $\boldsymbol{Y}$ is the corresponding target outputs.

Ridge regression has been shown to be an efficient method to calculate the readout matrix (Dutoit et al., 2009). Ridge regression is a shrinkage method that consists of adding a penalty term proportional to the Euclidean norm of the readout matrix:

$$\boldsymbol{W^{out}} = arg\min_{w}(\|\boldsymbol{Xw} - \boldsymbol{Y}\|^2 + \gamma\|\boldsymbol{w}\|^2) \quad (4)$$

where $\gamma \geq 0$ is the ridge parameter determined on a hold-out validation set. The solution of readout matrix is given as:

$$\boldsymbol{W^{out}} = (\boldsymbol{X^T X} + \gamma^2\boldsymbol{I}_N)^{-1}\boldsymbol{X^T Y} \quad (5)$$

where $\boldsymbol{I}_N$ is the identity matrix of size N.

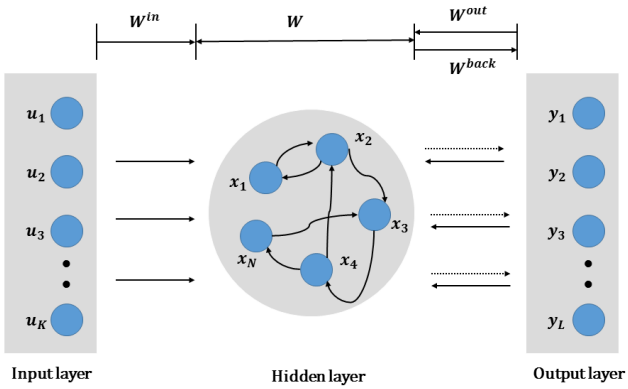

Figure 1. Typical structure of an echo state network

2.2. Covariance matrix adaption evolution strategy

CMA-ES is a well-established evolutionary algorithm for real-valued optimization with many successful applications. The main advantages of CMA-ES lie in its invariance properties, which are achieved by carefully designed variation and selection operators and its efficient adaptation of the mutation distribution. The CMA-ES is invariant against order-preserving transformations of the fitness function value and in particular against rotation and translation of the search space. It has been demonstrated by experiments that the covariance matrix $\boldsymbol{C}^{(g)}$ is similar to the inverse of the Hessian matrix of the problem at the optimum point. CMA-ES is particularly useful on non-smooth and ill-conditioned problems as it estimates a covariance matrix using an iterative procedure.

In CMA-ES, the population of new search offspring $\boldsymbol{x} \in \mathbb{R}n$ is generated by sampling a multivariate normal distribution (Hansen et al., 2003):

$$\boldsymbol{x}_k^{(g+1)} \sim \boldsymbol{m}^{(g)} + \sigma^{(g)} \cdot \aleph\left(0, \boldsymbol{C}^{(g)}\right) \ for\ k = 1, \ldots, l \tag{6}$$

where $\boldsymbol{x}_k^{(g+1)}$ denotes the kth offspring at the (g+1)th generation; $\boldsymbol{m}^{(g)}$ is the mean value of the search distribution at generation g; $\aleph\left(0, \boldsymbol{C}^{(g)}\right)$ is a multivariate normal distribution with zero mean and covariance matrix $\boldsymbol{C}^{(g)}$; and $\sigma^{(g)}$ is the step-size at generation g.

After those l individuals have been created, they are evaluated on the objective function which is the mean squared errors (MSE) of the ESN and sorted according to their objective function values.

2.3. Attention mechanism

Attention mechanism in neural networks was proposed to guide networks to focus on regions of interest relevant for a particular modelling task. This prunes the network search space and avoids computing features from irrelevant input data (Luong et al., 2015). In order to make predictions based upon the relative input data, a variable-length alignment vector $\boldsymbol{a_t}$, whose size equals the input dimension, is derived by comparing the current target state $\boldsymbol{s_t}$ with input hidden state $\boldsymbol{h}_{ut}$:

$$\boldsymbol{a_t} = align(\boldsymbol{s_t}, \boldsymbol{h}_{ut}) = sigmoid[score(\boldsymbol{s_t}, \boldsymbol{h}_{ut})] \tag{7}$$

Here, score is obtained as:

$$score(\boldsymbol{s_t}, \boldsymbol{h}_{ut}) = \boldsymbol{s}_t^T W_a \boldsymbol{h}_{ut} \tag{8}$$

where W_a is a rescale matrix of $\boldsymbol{s_t}$ and $\boldsymbol{h}_{ut}$.

The original input matrix is pruned by $\boldsymbol{a_t}$ and updated input data $\widehat{\boldsymbol{u_t}}$ is calculated as:

$$\widehat{\boldsymbol{u_t}} = \boldsymbol{a_t} \odot \boldsymbol{u}_t \tag{9}$$

where $\odot$ denotes element-wise multiplication.

3. Proposed modelling strategy

This paper proposes using CMA-ES to optimize the structure parameters of ESN with attention mechanism (Atten-ESN) for nonlinear process modelling. Figure 2 shows the flow chart of the proposed algorithm. The procedure can be summarized as follows:

1. Data for model building are divided by into three sets: training data, testing data, and unseen validation data, and then they are normalized to have zero mean and unit variance.
2. Prune the input matrix by global attention mechanism.
3. Establish an ESN with random R, α, and δ in the range based on sufficient internal units as default. The activation function used here in the hidden layer (reservoir) is $f = tanh$ and the input weights and reservoir weights are generated randomly.
4. Train the established ESN with training data using ridge regression.
5. Optimize the Atten-ESN by CMA-ES. The MSE on the testing data is used as objective function. The optimization objective is to upgrade the values of R, α, and δ to minimize the MSE on the testing data.
6. Test the optimized Atten-ESN (O-Atten-ESN) on the unseen validation data.

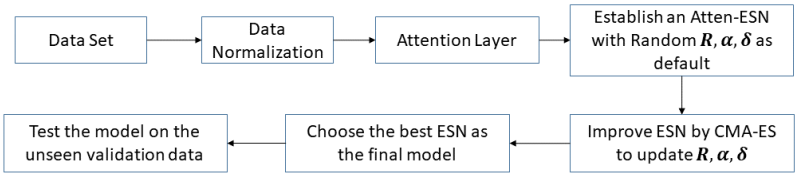

Figure 2. Graphical illustration of the proposed approach

4. Experiments

The benchmark industrial penicillin fermentation simulator, IndPenSim (Goldrick et al., 2015), is used to produce simulated process operation data. The simulator code in Matlab R2013b is available to download at www.industrialpenicillinsimulation.com. Three benches of data generated by IndPensim are used in model development. One batch is used as training data, the second batch is used as testing data, and the third batch is used as the unseen validation data. The penicillin concentration is taken as the target output and 30 controllable and monitoring variables are used as model inputs.
The fitness function to minimize is the MSE of the ESN on the training data:

$$MSE = \frac{\sum_{i=1}^{N}(y_i - \hat{y}_i)^2}{N} \tag{10}$$

where y_i and $\hat{y}_i$ are target value and predicted value at sample i respectively, and N is the number of data samples.

5. Results and discussion

In order to investigate the performance of O-Atten-ESN, it is compared with standard ESN, Atten-ESN, and standard LSTM. The comparison between standard ESN and Atten-ESN is to investigate the effect of integrating attention mechanism with ESN. The comparison between Atten-ESN and O-Atten-ESN is to illustrate the effect of optimization using CMA-ES. In all ESNs, the three structural parameters, reservoir size, leak rate, and special radius, are randomly generated in the ranges of [1-1000], [0-1], and [0-1.5] respectively. The initial step size of CMA-ES is 0.1 and the ridge regression parameter is 0.005.

The prediction results on unseen validation batch with different methods are shown in Figure 3 with the MSE of each method shown in the legend. Figure 4 shows the corresponding prediction errors. It can be seen in Figure 3, comparing to the predictions of the standard ESN, predictions of both O-Atten-ESN and Atten-ESN are closer to target values, especially when the slope of the target values is steep. This illustrates that the attention mechanism can take out some irrelevant input signals to reduce their influence. In other words, attention mechanism can increase the model robustness. Figure 4 shows that the errors of O-Atten-ESN are much smaller than those of the other two methods, demonstrating that high dimensional optimized algorithm such as CMA-ES can optimize ESN by searching better structure parameters. Table 1 gives the average MSE values and standard deviations of the three methods which were run 50 times with different random parameters. In summary, the attention mechanism and CMA-ES can improve ESN on predicting penicillin concentration in the fed-batch fermentation process in terms of prediction accuracy and robustness.

Table 1. Average MSE and standard deviation of different ESNs

Methods	Average MSE	Standard deviation
O-Atten-ESN	0.0781	0.0122
Atten-ESN	0.9723	0.1740
Standard ESN	1.6871	0.4116

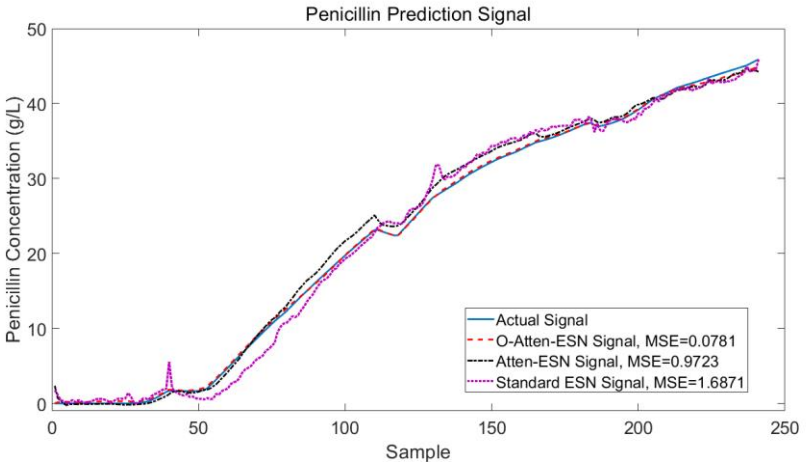

Figure 3. Predictions of penicillin concentration

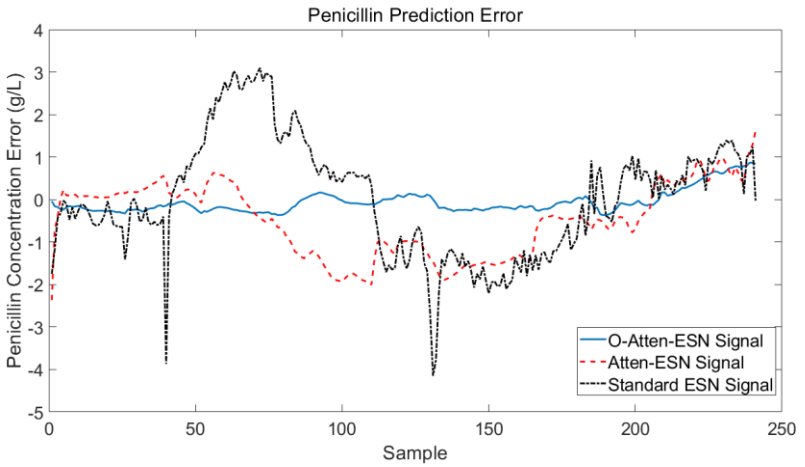

Figure 4. Prediction errors of penicillin concentration

6. Conclusions

An ESN with attention mechanism and optimized by CMA-ES is proposed in this paper to model a fed-batch penicillin fermentation process. Based on the preliminary results, the attention mechanism and CMA-ES can improve standard ESN on modelling complex bioprocesses with enhanced accuracy and reliability. It is expected that the proposed method will be effective for modelling other complex bioprocesses.

References

Ashoori, A., Moshiri, B., Khaki-Sedigh, A., and Bakhtiari, M. R., 2009. Optimal control of a nonlinear fed-batch fermentation process using model predictive approach. Journal of Process Control, 19(7), 1162-1173.

bin Mohd Zain, M. Z., Kanesan, J., Kendall, G., and Chuah, J. H., 2018. Optimization of fed-batch fermentation processes using the Backtracking Search Algorithm. Expert Systems with Applications, 91, 286-297.

Chen, L., Nguang, S. K., Chen, X. D., and Li, X. M., 2004. Modelling and optimization of fed-batch fermentation processes using dynamic neural networks and genetic algorithms. Biochemical Engineering Journal, 22(1), 51-61.

Dutoit, X., Schrauwen, B., Van Campenhout, J., Stroobandt, D., Van Brussel, H., Nuttin, M., 2009. Pruning and regularization in reservoir computing. Neurocomputing, 72(7-9), 1534-1546.

Goldrick, S., Stefan, A., Lovett, D., Montague, G., Lennox, B., 2015. The development of an industrial-scale fed-batch fermentationsimulation. Journal of Biotechnology, 193, 70–82.

Hansen, N., Müller, S. D., Koumoutsakos, P., 2003. Reducing the time complexity of the derandomized evolution strategy with covariance matrix adaptation (CMA-ES). Evolutionary Computation, 11(1), 1-18.

Lukoševičius, M., Jaeger, H., 2009. Reservoir computing approaches to recurrent neural network training. Computer Science Review, 3(3), 127-149.

Luong, M. T., Pham, H., and Manning, C. D., 2015. Effective approaches to attention-based neural machine translation. Conference on Empirical Methods in Natural Language Processing, EMNLP 2015, Lisbon; Portugal, 17 - 21 September 2015, 1412-1421.

Yu J., 2012. A Bayesian inference based two-stage support vector regression framework for soft sensor development in batch bioprocesses. Computers & Chemical Engineering, 41, 134-144.

Sauro Pierucci, Flavio Manenti, Giulia Bozzano, Davide Manca (Eds.)
Proceedings of the 30th European Symposium on Computer Aided Process Engineering (ESCAPE30), May 24-27, 2020, Milano, Italy.
http://dx.doi.org/10.1016/B978-0-12-823377-1.50188-9

Tailored Time Grids for Nonlinear Scheduling Subject to Time-variable Electricity Prices by Wavelet-based Analysis

Pascal Schäfer,[a] Alexander Mitsos[b,a,c,*]

[a]*Process Systems Engineering (AVT.SVT), RWTH Aachen University, 52074 Aachen, Germany*
[b]*JARA-CSD, 52056 Aachen, Germany*
[c]*Forschungszentrum Jülich, Energy Systems Engineering (IEK-10), 52425 Jülich, Germany*
amitsos@alum.mit.edu

Abstract

Typically, the consideration of nonlinear process models in discrete-time scheduling is limited to short planning horizons and/or coarse discretizations due to a linear scaling of the problem size with the number of considered scheduling intervals. To overcome this limitation, we recently proposed a wavelet-based algorithm focusing on scheduling problems with time-variable electricity prices, which iteratively adapts the time grid (Schäfer et int., Mitsos, doi:10.1016/j.compchemeng.2019.106598). In this work, we extend our approach by presenting a systematic method for the identification of promising initial aggregated time grids based on the analysis of the wavelet representation of the time series of electricity prices. We apply the procedure to a literature example addressing the scheduling of a seawater reverse osmosis (Ghobeity and Mitsos, doi: 10.1016/j.desal.2010.06.041). We demonstrate that substantial reductions in the number of optimization variables in a reduced-space formulation are possible, while furnishing feasible schedules that lead to insignificant deviations below 0.05 % in the objective value compared to the global optimum using the full time grid.

Keywords: Demand side management, Discrete-time scheduling, Reduced-space, Global optimization, Adaptive refinement

1. Introduction

The adjustment of the electricity consumption to time-variable electricity prices is an important measure to increase the competitiveness of industrial consumers (Mitsos et al., 2018). Consequently, sophisticated methodologies for discrete-time scheduling with time-variables prices have been proposed, mostly aiming at formulating mixed-integer linear programs (MILPs) that can be handled efficiently by state-of-the-art solvers (e.g., Ierapetritou et al., 2002; Mitra et al., 2012; Zhang et al., 2015). In contrast, although many processes are governed by strongly nonlinear characteristics, only few authors tried to consider nonlinear models in discrete-time scheduling (e.g., Ghobeity and Mitsos, 2010), as this leads to nonlinear programs (NLPs) with potentially multiple local solutions. Consequently, solving these problems requires global solution approaches that currently prohibit long planning horizons and/or fine discretizations. To overcome this limitation and allow for nonlinear scheduling with relevant horizons and sufficiently fine discretizations, we recently proposed an iterative algorithm combining

three key ideas (Schäfer et al., 2019): a reduced-space scheduling formulation, a time series aggregation, and a wavelet-based grid adaptation procedure.

In this work, we extend our approach by a systematic method to identify a promising initial aggregated time grid. In particular, we perform an analysis of the wavelet representation of the time series of electricity prices to derive the initial grid. The proposed procedure is examined and benchmarked against state-of-the-art solution approaches for a case study. Therein, we consider the scheduling of a seawater reverse osmosis (SWRO) formulated as a mixed-integer nonlinear program (MINLP).

2. Case study and solution approaches

2.1. Process model and problem description

We focus on the same case study as Ghobeity and Mitsos (2010), cf. Figure 1. All modeling equations, parameters and operating bounds can be found in their work. The SWRO model comprises eleven variables and ten nonlinear equations. The operation of the SWRO is hence fully determined by specifying one degree of freedom, e.g., the recovery ratio. As in the original reference, we further introduce a disjunction represented by an additional binary variable that allows for shutting down the plant. Discrete-time scheduling of the SWRO consequently corresponds to solving an MINLP with potentially multiple local minima, thus global solution approaches are preferred. We further assume an hourly discretization considering historic time-variable German Day-Ahead spot electricity prices retrieved from EPEX SPOT SE (https://www.epexspot.com/en/). The objective is to achieve lowest electricity costs for fulfilling a given production target, i.e., a fixed cumulated permeate production. Furthermore, the SWRO's operation is constrained by bounds on the key variables: transmembrane pressure, high-pressure pump shaft frequency, recovery ratio and salt concentration in concentrate.

2.2. Solution approaches using the full time grid

When considering the full time grid, i.e., one grid point per hour of the horizon, we apply two different solution approaches for the MINLP. In the first one – referred to as full-space (FS) – all model variables and equations of each scheduling interval are exposed to the optimizer, as it is common practice in the formulation of discrete-time scheduling problems. In this case, model equations simply correspond to equality constraints and operating bounds to box-constraints on selected variables.

In the second approach – referred to as reduced-space (RS) – only a truncated set of

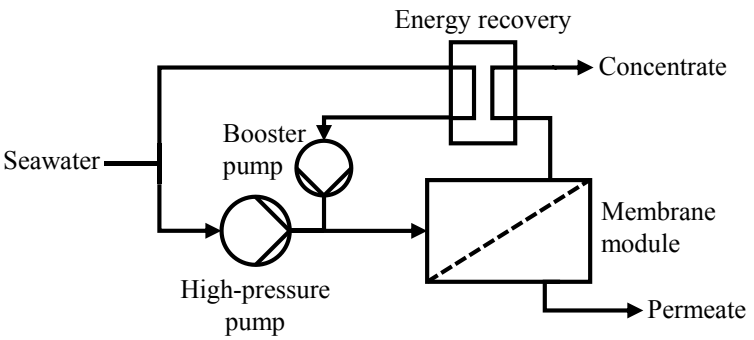

Figure 1: Schematic flowsheet of the considered process configuration for seawater reverse osmosis from Ghobeity and Mitsos (2010).

model variables is exposed to the optimizer; objective and constraints are expressed as functions thereof. This concept has been shown promising for global optimization of process flowsheets (Bongartz and Mitsos, 2017). In the considered case study, we expose two model variables per scheduling interval to the optimizer, although the SWRO's operation would be fully determined by specifying only one, as the model equations cannot be solved analytically. We herein select the high-pressure pump shaft frequencies and the recovery ratios as optimization variables. All other model variables are expressed as explicit functions thereof. One equality constraint per scheduling interval ensures that the selected values of the optimization variables comply with the process model. We remark that, like in the FS formulation, the disjunction introduces an additional binary optimization variable per scheduling interval.

2.3. Solution approaches using an aggregated time grid

Using an RS scheduling formulation allows for the application of our recently proposed time series aggregation scheme (Schäfer et al., 2019), which aims at tailored time grids and thus avoids a global optimization considering the full grid with individual optimization variables in each interval. This is achieved by mapping one optimization variable to multiple intervals with similar electricity prices Thereby, the number of optimization variables in RS is reduced and thus decoupled from the number of considered scheduling intervals, enabling substantial savings in computational time. However, due to the mapping, all scheduling intervals and consequently all constraints are considered further on, ensuring that feasible schedules are furnished. In the computational study below, we make furthermore use of the proposed iterative grid adaptation. Therein, a wavelet transform of the solution from the previous iteration using a coarser grid is conducted and the obtained coefficients are analyzed as proposed by Schlegel et al. (2005), allowing for a systematic adjustment of the mapping procedure by inserting promising new and deleting insignificant grid points.

In this work, we extend our approach by a systematic method to identify promising initial grids for the adaptation algorithm. More precisely, we first perform a wavelet transform of the input time series of electricity prices. Those wavelet coefficients with absolute values above a defined threshold are identified. Then, we use only the set of significant coefficients for the construction of the initial aggregated time grid following the procedure described in our previous work. Note that starting from this initialized grid, the same iterative adaptation algorithm as described above could be applied. However, for illustration purposes, we herein omit this possibility, so that we confine to one single optimization using the initial aggregated grid.

3. Computational results

3.1. Implementation and solver settings

The FS formulation (full time grid) is implemented in GAMS version 26.1.0 (GAMS Development Corp.) and corresponding optimization problems are solved globally using BARON version 18.11.12 (Tawarmalani and Sahinidis, 2005) with standard settings. For RS formulations (full time grid, grid adaptation, and grid initialization), the model is implemented as sequential C++ code and global optimizations are conducted using our in-house open-source software MAiNGO (Bongartz et al., 2018). Inside MAiNGO, CPLEX (IBM Corp.) is used for the lower bounding procedure and KNITRO (Exler and Schittkowski, 2007) for the upper bounding. Apart from that, we apply standard settings. For all optimizations, we set the relative optimality tolerance to

0.005. Furthermore, we apply a time limit of 100,000 s of CPU time. For the grid adaptation algorithm, threshold values of 0.0001 for deletion and 0.7 for insertion are used. Concerning the construction of the initial aggregated grid, we apply a threshold value of 0.03. All threshold values are relative to the Euclidean norm of the considered vector of wavelet coefficients. For the grid adaptation approach, three iterations of the algorithm starting from an equally distributed initial grid (6 grid points) are conducted.

3.2. Day-ahead scheduling

First, we consider a day-ahead scheduling, i.e., 24 intervals of one hour, targeting the exploitation of price spreads between day and night. Table 1 summarizes the results for all solution approaches described in Section 2. Note that in all cases, the best feasible schedule is obtained within negligible time. Reported CPU times thus primarily stem from the lower bounding procedures. Due to the good performance of local solvers in the upper bounding even when considering the full time grid (in both FS and RS), the reported solution in this case is considered as the global optimum and thus used as the benchmark for all solutions with aggregated grids. We emphasize that in contrast to the approaches considering the full grid, the approaches using aggregated grids lead to converged solutions within the defined time limit. In particular, savings in computational time when using the aggregated grids are more than two orders of magnitude. Moreover, we find that substantial reductions in the number of considered grid points are possible, while causing only minor deviations in the objective value. For instance, when applying the initial aggregated grid using only eight grid points, a feasible schedule is furnished with a difference in the objective value of ~0.025 % compared to the global optimum. Likewise, the final schedule after the third iteration of the adaptation algorithm starting from an equally distributed grid leads to only ~0.01 % deviations compared to the global optimum by using ten grid points.

Consequently, the corresponding final schedules obtained when using the aggregated grids look highly similar to the globally optimal schedule, as can be seen in Figure 2 (left). In contrast, the intermediate results of the grid adaptation using 6 and 8 grid points respectively lead to inferior schedules that do not make use of the possibility for a temporary shutdown during peak hours. The reason for this finding lies in a distinct price peak at 21 h, which can only be exploited by assigning individual optimization variables to that hour, which is not possible in the first two iterations of the adaptation, as they are limited to aggregating at least four (first) or two (second) intervals.

Table 1: Summary for solution approaches addressing a day-ahead scheduling (24 intervals). Asterisks indicate converged solutions.

Solution approach	**Solver**	**#Grid points** [-]	**CPU time** [s]	**Optimality gap** [%]	**Objective value** [%]
RS-grid initialization	MAiNGO	8	273	0.005*	100.025
RS-grid adaptation iteration 1	MAiNGO	6	47	0.005*	100.66
RS-grid adaptation iteration 2	MAiNGO	8	1,027	0.005*	100.65
RS-grid adaptation iteration 3	MAiNGO	10	3,055	0.005*	100.01
FS-full time grid	BARON	24	100,000	0.006	100
RS-full time grid	MAiNGO	24	100,000	0.021	100

Table 2: Summary for solution approaches addressing a week-ahead scheduling (168 intervals). Asterisks indicate converged solutions.

Solution approach	Solver	#Grid points [-]	CPU time [s]	Optimality gap [%]	Objective value [%]
RS-grid initialization	MAiNGO	10	22,334	0.005*	100.041
FS-full time grid	BARON	168	100,000	0.077	100

We highlight that we successfully resolve this issue by following the proposed grid initialization procedure. In particular, we thereby a priori identify the most significant parts of the horizon requiring fine discretizations, while relying on coarser discretizations in insignificant parts.

3.3. *Week-ahead scheduling*

We also consider an hourly planning for one week, which allows for further exploiting weekly price patterns, such as lower prices on weekends. For the sake of brevity, we confine ourselves to comparing the proposed procedure for identifying an initial aggregated grid to the FS approach considering the full time grid. A solution summary is given in Table 2. Again, local searches perform exceptionally well, so that the best feasible solution is found in the upper bounding within short time. Thus, the reported solution using the full time grid is again assumed to be the globally optimal schedule.

As in case of day-ahead scheduling, applying the initial aggregated grid from wavelet analysis of the price time series leads to a feasible schedule, while limiting losses in the objective value to <0.05 % compared to the global optimum and schedules look highly similar, cf. Figure 2 (right). Most impressively, this is achieved by using only ten grid points for the scheduling problem, corresponding to a reduction of the temporal dimensionality by 94 %, illustrating the efficacy of the approach for a priori identifying promising tailored aggregated time grids. Moreover, whereas the RS formulation using the aggregated grid results in a converged solution within the time limit, the approach considering the full grid leaves a substantial remaining optimality gap after exceeding the time limit. Comparing Tables 1 and 2 finally illustrates the superior scaling behavior

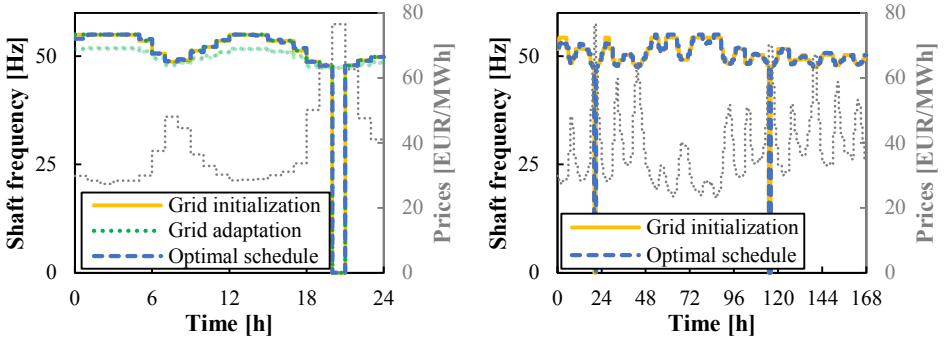

Figure 2: Final production schedules from the different solution approaches for day-ahead (left) and week-ahead (right) scheduling. Orange solid lines: result of a single optimization using an initial aggregated grid following the proposed procedure. Green dotted line: outcome after three iterations of the grid adaptation algorithm when using an equally distributed initial grid (transparent lines correspond to intermediate results). Blue dashed lines: globally optimal production schedule considering the full time grid. Light dotted grey lines: electricity prices.

of solution approaches using aggregated time grids. More precisely, decoupling the number of optimization variables from the number of scheduling intervals avoids the typically exponential scaling with the horizon length when using full time grids.

4. Conclusions

We extend our previously proposed algorithm for adaptive grid refinements in scheduling problems with time-variable electricity prices by a systematic method for the identification of promising initial aggregated time grids. The presented case study is suitable for assessing the efficacy of the approach due to a good performance of local solvers on this problem even for long horizons. Our results show that substantial reductions in the number of grid points and hence in the dimensionality of the scheduling problem are possible, enabling promising speed-ups in the optimization, while leading to only insignificant deviations in the objective value. Future work should focus on the application of the procedure to more challenging problems, where generating favourable feasible points is already difficult if considering the full time grid.

Acknowledgment

The authors gratefully acknowledge the financial support of the Kopernikus project SynErgie by the Federal Ministry of Education and Research (BMBF) and the project supervision by the project management organization Projektträger Jülich.

References

D. Bongartz, A. Mitsos, 2017. Deterministic global optimization of process flowsheets in a reduced space using McCormick relaxations, Journal of Global Optimization 69 (4), 761-796.

D. Bongartz, J. Najman, S. Sass, A. Mitsos, 2018. MAiNGO – McCormick-based Algorithm for mixed-integer Nonlinear Global Optimization. http://permalink.avt.rwth-aachen.de/?id=729717.

O. Exler and K. Schittkowski, 2007. A trust region SQP algorithm for mixed-integer nonlinear programming. Optimization Letters 1 (3), 269-280.

A. Ghobeity, A. Mitsos, 2010. Optimal time-dependent operation of seawater reverse osmosis. Desalination 263 (1), 76-88.

M.G. Ierapetritou, D. Wu, J. Vin, P. Sweeney, M. Chigirinsky, 2002. Cost minimization in an energy-intensive plant using mathematical programming approaches. Industrial & Engineering Chemistry Research. 41 (21), 5262-5277.

S. Mitra, I.E. Grossmann, J.M. Pinto, N. Arora, 2012. Optimal production planning under time-sensitive electricity prices for continuous power-intensive processes. Computers & Chemical Engineering 38, 171-184.

A. Mitsos, N. Asprion, C. A. Floudas, M. Bortz, M. Baldea, D. Bonvin, A. Caspari, P. Schäfer, 2018. Challenges in process optimization for new feedstocks and energy sources. Computers & Chemical Engineering 113, 209-221.

P. Schäfer, A.M. Schweidtmann, P.H.A. Lenz, H.M.C. Markgraf, A. Mitsos. Wavelet-based grid-adaptation for nonlinear scheduling subject to time-variable electricity prices. Computers & Chemical Engineering 132, 106598.

M. Schlegel, K. Stockmann, T. Binder, W. Marquardt, 2005. Dynamic optimization using adaptive control vector parameterization. Computers & Chemical Engineering 29 (8), 1731-1751.

M. Tawarmalani, N.V. Sahinidis, 2005. A polyhedral branch-and-cut approach to global optimization, Mathematical Programming 103 (2), 225-249.

Q. Zhang, I.E. Grossmann, C.F. Heuberger, A. Sundaramoorthy, J.M. Pinto, 2015. Air separation with cryogenic energy storage: Optimal scheduling considering electric energy and reserve markets. AIChE Journal 61 (5), 1547-1558.

Sauro Pierucci, Flavio Manenti, Giulia Bozzano, Davide Manca (Eds.)
Proceedings of the 30th European Symposium on Computer Aided Process Engineering (ESCAPE30), May 24-27, 2020, Milano, Italy.
http://dx.doi.org/10.1016/B978-0-12-823377-1.50189-0

Troubleshooting an Industrial Batch Process for the Manufacturing of Specialty Chemicals using Data Analytics

Federico Zuecco,[b] Pierantonio Facco,[a] Stefan R. Hoeser,[b] Mattia R. Fogli,[b] Matteo Cicciotti,[b] Fabrizio Bezzo,[a] Massimiliano Barolo[a*]

[a]*CAPE-Lab – Computer-Aided Process Engineering Laboratory), Department of Industrial Engneering, University of Padova, via Marzolo 9, 35131 Padova, Italy*
[b]*BASF Italia S.p.A., via Pila 6/3, 40037 Pontecchio Marconi, Italy*
max.barolo@unipd.it

Abstract

The troubleshooting of an industrial, multi-unit, multi-phase batch process for the manufacturing of specialty chemicals is considered in this study. The investigated problem is inconsistency in the final product quality, leading to the need of applying "corrections" to some batches with consequent significant increase of the processing time. Product quality information is scarce and available only for the last unit in the process flow diagram. It is shown that, by coupling the use of multivariate statistical methods to engineering understanding, one can step back in the process flow diagram to identify the unit wherein the problem originates, and to single-out the root-cause of the fault. For the process under investigation, fault isolation led to reduction of the cycle times and increase of productivity.

Keywords: troubleshooting; data analytics; batch processes; multivariate analysis

1. Introduction

Batch processing is common in the manufacturing of specialty chemicals due to its flexibility and ability to process relatively small amounts of materials. Batch processes are typically operated through a sequence of prescribed operations resulting in a recipe. While a recipe can be automated easily, it basically results in open-loop operation of the plant. This is the main reason why product quality control in a batch process is typically more difficult than in a continuous one, an issue that is often tackled by adjusting the recipe in real time through a "correction" (i.e., a recipe modification) if the product quality is found not to be on specification at an assigned manufacturing step. Although a correction can be effective in bringing the product to specification in a given batch, it typically results in an increase of the batch time, hence in productivity decrease. Additionally, if the root-cause of the fault causing the product off-specification is not isolated, the product quality issue can manifest again in subsequent batches.

Multivariate statistical methods have found many applications in batch process monitoring (Nomikos and MacGregor, 1995; Ündey and Cinar, 2002; Garcia-Muñoz et al., 2003; Faggian et al., 2009). However, most of the reported studies are related to fault detection and isolation in single processing units, whereas plantwide analyses are lacking. In this study we show how, even in the absence of real-time quality measurements, a complex industrial batch process can be troubleshooted using multivariate statistical methods, in such a way as to find out the root causes leading to product quality inconsistency across batches.

2. Process, data and methods

2.1. Process description

An industrial batch process for the manufacturing of a specialty chemical to be used for polymer stability enhancement is considered. The reaction scheme involves two main liquid-phase reactions:

$$C + D \rightarrow E + N \quad (1)$$

$$E + D \rightarrow F + N \quad (2)$$

where C and D are the reactants, E an intermediate, F the desired product, and N a by-product. Some secondary reactions also occur, which are responsible for the consumption of both the reactants and the final product. However, they can be disregarded for the purpose of this study.

A simplified block flow diagram of the process is shown in Figure 1. The plant layout involves five main units connected in a series-parallel arrangement. Due to limitations in the vessel sizes, each batch is operated according to a two-step recipe. The first step (called "part A") comprises three sub-steps: *i*) a suspension of reactant C in solvent S is obtained in unit R101; *ii*) the suspension is sent to reactor R201, to which also reactant D (through intermediate tank T201-A) and other species are fed to carry out the synthesis of F in an assigned time; *iii*) the resulting reaction mixture is sent to R202, where a decantation occurs followed by the separation of the aqueous solution from the desired organic phase (which then remains on hold in R202). In the second step of the recipe ("part B"), a second charge of reactants (with the same amount and composition of that of part A) is fed to R201, and the reaction is left to occur for an assigned time; after that, the product is transferred directly to reactor R203; then, the R202 content is also transferred to R203, and the reaction is completed for an assigned time. Finally, a product sample is taken and sent to the lab for quality analysis.

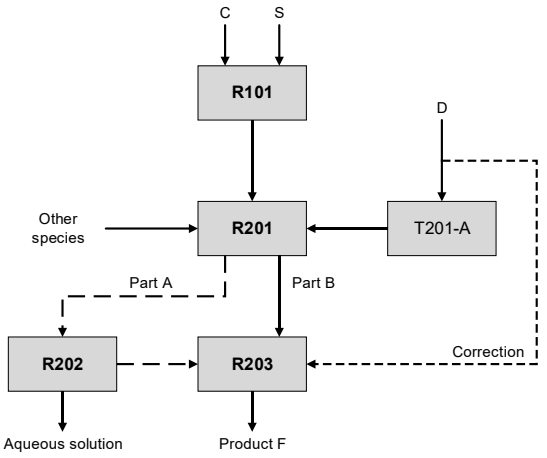

Figure 1. Simplified block flow diagram of the units involved in the analyzed process.

If the product is found to be out of specification, an additional amount of reactant D (namely, a correction) is fed to R203 according to a semi-empirical law based on the impurity levels in the product, and the reaction is left to proceed further. A second quality sample is then taken at a given time, and if the product is still not on specification, a

second correction is applied, and the product is sampled again after a prescribed time. At this point, typically additional corrections are not required anymore.
Since the process is recipe-driven and the recipe is automated, there is no apparent reason why some batches do not require a correction, whereas some others may require one or even two corrections. The net result is that the overall batch length is strongly variable and, if two corrections are required, R203 becomes the bottleneck of the entire manufacturing process. Finding the root-cause of the product quality variability is the objective of this study.

2.2. Available data

Data from 116 batches from the same production campaign were extracted from the historians, and divided into three categories: process data, recipe data, and quality data. With respect to the process data, the measurements available on-line from each unit were organized in three-dimensional arrays $\underline{\mathbf{X}}$ [116×J×K_i], where J is the number of measurement sensors available for the unit, and K_i is the total number of observations for batch i (the batches have different lengths). The recipe data for a given unit were arranged in matrix **Z** [116×N], where N is the number of parameters through which the recipe can be characterized for that unit. Finally, the quality variables (compositions) related to the first product sample were arranged into a **Y** matrix [116×5]. Overall, the analyzed dataset comprised over 3.5 million data entries.

2.3. Mathematical methods

To extract meaningful information from the available data, two multivariate statistical techniques were used: principal component analysis (PCA; Jackson, 1991) and projection to latent structures (PLS; Geladi and Kowalski, 1986).
PCA finds A maximum variability directions (called principal components or PCs) in a bidimensional matrix **X** [I×S]. A notable characteristic of the PCs is that they are orthogonal linear combinations of the original data that allow to summarize the data in a reduced-order subspace with no major loss of information. PCA can be used to represent **X** as:

$$\boldsymbol{X} = \boldsymbol{T}\boldsymbol{P}^T + \boldsymbol{E} \quad , \tag{3}$$

where **T** [I×A] is the scores matrix, **P** [S×A] is the loadings matrix, and **E** [I×S] is the residuals matrix.
PLS is used to correlate an input matrix **X** [I×S] and a response matrix **Y** [I×M]. Similarly to PCA, the relationship is based on the projection on a common space of A maximum variability directions (called latent variables or LVs) that are most predictive for the responses according to the model structure composed of Eq. (3) and of:

$$\boldsymbol{Y} = \boldsymbol{U}\boldsymbol{Q}^T + \boldsymbol{F} \tag{4}$$

$$\boldsymbol{T} = \boldsymbol{X}\boldsymbol{W}^* \tag{5}$$

where **Q** [M×A] is the loadings matrix, **F** [I×M] is the residuals matrix, and **W*** [S×A] is the weights matrix.
In both techniques, the scores matrix **T** represents the coordinates of the I observations in the new space of the LVs, which describe how different observations relate to each other. Information about the relation between the original variables is provided by the loadings and weights matrices.

3. Results and discussion

In the following sections, the main steps followed to troubleshoot the process will be discussed.

3.1. Data pre-processing

Data pre-processing is important because it prepares the data in the most meaningful way for the subsequent detailed analysis. In particular, missing process observations were replaced by interpolating the observations that bracket them; some feature variables (e.g., heat removed from a reactor) were calculated from the available measurements and added to the $\underline{\mathbf{X}}$ dataset. Trajectories in $\underline{\mathbf{X}}$ were synchronized over a fixed number K of samplings using dynamic time warping (Kassidas et al., 1998). This allowed batch-wise unfolding $\underline{\mathbf{X}}$ into $\mathbf{X}$, with $S = J \cdot K$.

3.2. Quality data analysis

Analysis of the available quality data ($\mathbf{Y}$ matrix) was used to uncover the inherent multivariate nature of product quality (Duchesne and MacGregor, 2004). The main results of a PCA model that uses 2 PCs (explaining 80% of the overall variance in the quality data) are shown in Figure 2.

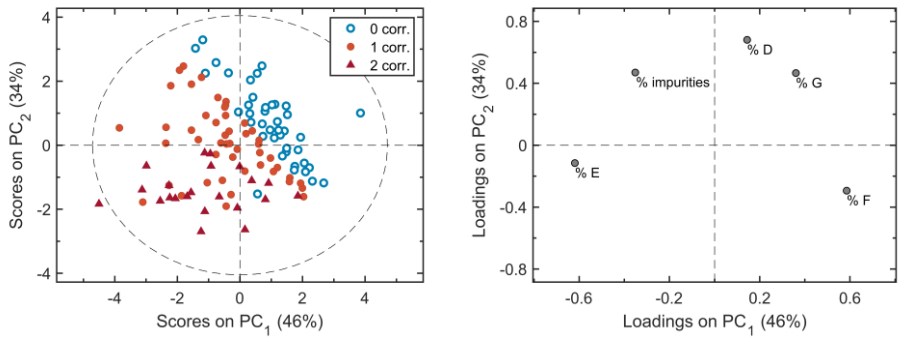

Figure 2. (a) Scores plot and (b) loadings plot resulting from the PCA model on the quality matrix $\mathbf{Y}$. In (a) the dashed ellipse indicates the 99% confidence limit. The percentages on the axis represent the explained variance of the $\mathbf{Y}$ matrix for each PC.

The scores plot (Figure 2*a*) shows the clustering of the on-spec batches (0 corrections) with respect to the off-spec ones (1 or 2 corrections). In particular, from the loadings plot (Figure 2*b*), the off-spec batches are characterized by a greater amount of intermediate species E (% E) and a smaller amount of reactants D and G (% D, % G) in the product. The desired species concentration (% F) and the amount of impurities (% impurities) in the product do not particularly contribute to the batch separation in the scores plot and, therefore, to the batch clustering.

3.3. Single-unit analysis

The subsequent step is to analyze the behavior of each unit separately by comparing the process data available for that unit across all batches carried out in the unit. In fact, even if product quality is assessed only in reactor R203, information about the final product quality may in principle be available even earlier, both in R203 and in upstream units, in the form of time profiles of the process measurements. Therefore, by stepping back through the process equipment (starting from R203), one can track how the fault propagates across the units until it manifests itself as an off-specification product in R203.

For each unit, multi-way PLS discriminant analysis (PLS-DA) was used to classify on-spec and off-spec batches using the time profiles of the available process measurements. To this purpose, a Boolean vector **y** identifying the two classes (on-spec batches vs. off-spec ones, as seen in R203) was defined. The PLS-DA models could correctly classify the batches for units R203, R202, and R201; instead, correct batch classification was not possible for R101. This suggested that R201 (and, more specifically, part B in that reactor) is the unit where the batch anomalies originate.

The PLS-DA modeling results for part B of R201 are shown in Figure 3. As can be noticed from the scores plot (Figure 3*a*), the process variable time profiles can indeed cluster most of the batches according to the number of corrections they underwent. Interestingly, the separation between normal batches and a large fraction (about two thirds) of the anomalous batches occurs along the direction of the bisector of the first and third quadrants, and the first quadrant collects anomalous batches only. This suggests that a large fraction of the batches that undergo at least one correction are characterized by a time evolution of the measured process variables that is different from that of the regular batches.

The importance of each variable in defining the direction of maximum variability in the process data can be assessed by analyzing the weights plot for the first LV. Figure 3*b* shows that the contributions of variables no. 6, 7 and 11 dominate over those of the remaining variables. The dominating variables are two mass measurements (coming from two distinct flowrate totalizers) and level in tank T201-A. All these variables refer to the load of reactant D in R201. Since the weights for these variables are negative, it can be concluded that most of the off-spec batches (namely, those located in the first off-spec quadrant) are characterized by a smaller load of reactant D in reactor R201 during part B.

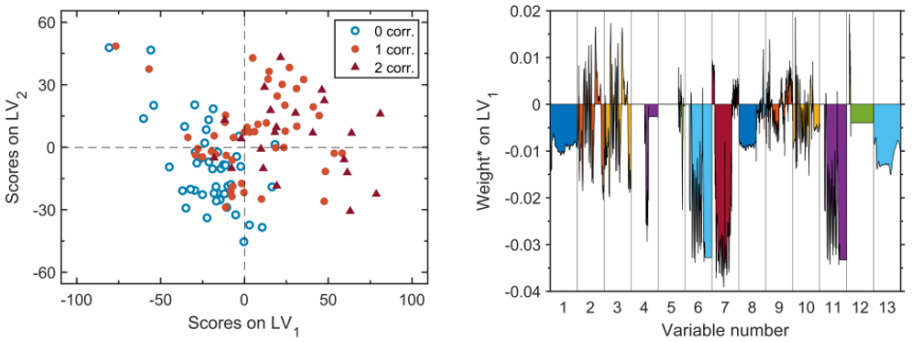

(a) (b)

Figure 3. (a) Scores plot and (b) weights plot resulting from the PLS-DA modeling of part B in R201. In (b), the time evolutions of the weights of the first latent variable are reported for each process variable included in the **X** array.

3.4. Root-cause analysis

The single-unit analysis suggested that most of the batch anomalies are related to a lower load of reactant D to R201. The final step of the troubleshooting exercise is therefore to identify the root-cause of the problem. To this purpose, the process line responsible for the feeding of reactant D was investigated in detail. Three mass flowrate totalizers (FQ-001, FQ-002 and FQ-003) are installed in the line, and each of them measures the amount of reactant D fed to R201. The mass measured by FQ-001 comes from reactant D storage tank; this mass is fed to tank T201-A, which is subsequently fully discharged into R201; the mass fed to R201 is measured by FQ-002 and FQ-003, which are installed at the end of the feeding line. Inspection of the data showed that, during part B of the

manufacturing recipe, FQ-001 provided a wrong measurement, as highlighted by the correlation matrix in Table 1. The correlation coefficients between the measurements from FQ-001 and all other sensors are very low, meaning that sensor FQ-001 is not working appropriately.

Table 1. Correlation matrix between the amounts of reactant D measured by the mass totalizers and the level in the intermediate tank T201-A for the part B of the process.

	FQ-001	**FQ-002**	**FQ-003**	**LI-201A**
FQ-001	1.000	0.465	0.474	0.452
FQ-002	0.465	1.000	0.999	0.885
FQ-003	0.474	0.999	1.000	0.885
LI-201A	0.452	0.885	0.885	1.000

A faulty sensor in the feed line to R201 was therefore the reason of product quality inconsistency in most of the batches that later required a correction in R203. Namely, the faulty sensor caused a defect in the reactant D load with respect to the on-specification batches.

4. Conclusions

Although product quality data in a batch process may be scarce, process data are typically abundant and embed information that can be very useful for process troubleshooting. In this study we have shown how a complex, multi-unit, multi-phase batch process can be troubleshooted by coupling multivariate statistical methods to engineering understanding of the process. By stepping back from the unit where quality data are intermittently available to each of the upstream units, the unit where the fault originates can be identified. Then, engineering inspection of the data in that unit and of the relevant plant section layout can provide a reliable indication of the root-cause of the batch anomalies. In the problem under investigation, the root-cause was identified in a faulty sensor, which was responsible for the feeding of the reactant in the main reactor. Fixing this problem significantly reduced the number of batches requiring corrections.

References

C. Duchesne, J. F. MacGregor, 2004, Establishing multivariate specification regions for incoming materials, J. Qual. Technol., 36, 78-94.

A. Faggian, P. Facco, F. Doplicher, F. Bezzo, M. Barolo, 2009, Multivariate statistical real-time monitoring of an industrial fed-batch process for the production of specialty chemicals, Chem. Eng. Res. Des., 87, 325-334.

S. García-Muñoz, T. Kourti, J. F. MacGregor, 2003, Troubleshooting of an industrial batch process using multivariate methods, Ind. Eng. Chem. Res., 42, 3592-3601.

P. Geladi, B. R. Kowalski, 1986, Partial least-squares regression: a tutorial, Anal. Chim. Acta, 185, 1-17.

J. E. Jackson, 1991, A user's guide to principal components, John Wiley & Sons Inc., New York (USA).

A. Kassidas, J. F. MacGregor, P. A. Taylor, 1998, Synchronization of batch trajectories using dynamic time warping, AIChE J., 44, 864-875.

P. Nomikos, J. F. MacGregor, 1995, Multi-way partial least squares in monitoring batch processes, Chemometr. Intell. Lab., 30, 97-108

C. Ündey, A. Cinar, 2002, Statistical monitoring of multistage, multiphase batch processes, IEEE Contr. Syst. Mag., 22, 40-52.

Sauro Pierucci, Flavio Manenti, Giulia Bozzano, Davide Manca (Eds.)
Proceedings of the 30th European Symposium on Computer Aided Process Engineering
(ESCAPE30), May 24-27, 2020, Milano, Italy.
http://dx.doi.org/10.1016/B978-0-12-823377-1.50190-7

On the Role of State Estimation in Real-time Scheduling

Venkatachalam Avadiappan, Christos T. Maravelias*

Department of Chemical and Biological Engineering, University of Wisconsin –Madison, 1415 Engineering Drive, Madison, WI 53706, USA
christos.maravelias@wisc.edu

Abstract

We formally introduce the concept of "state" of a batch in production scheduling, we examine how this state impacts the scheduling process, and propose an approach to estimate it based on real-time plant information. We present an online scheduling algorithm based on a state-space resource task network (RTN) formulation and show why and how the resource-task interaction coefficients (which have always been thought to be constants) should be updated based on the state of the executed batches, using real-time information, to obtain better implemented solutions.

Keywords: State estimation, online scheduling, resource task network

1. Introduction

Scheduling plays a crucial role in many industrial sectors such as pharmaceutical, petrochemical and food industries. Optimization-based scheduling methods can lead to multi-million dollars increase in profits, compared to schedules generated by heuristics. In a dynamic environment, disturbances or new information may render a computed schedule sub-optimal or infeasible, thereby necessitating rescheduling (Gupta and Maravelias, 2016). Therefore, it is important to exploit all the available real-time information from the plant during (re)scheduling. However, while the incorporation of such information through the modeling of process dynamics has been explored, there are no methods available for standalone scheduling approaches. Accordingly, we propose the first systematic methods that account for the state of the system, at real-time, and propose generalize models that exploit such information.

In most scheduling models, a single task has been used to approximate the entire batch recipe. However, in reality, task is composed of a sequence of steps (say, filling of raw material, heating, reaction, quality control and draining of product) with step transitions guided by logic conditions (Rawlings et al., 2019). In this work, we present a discrete-time RTN model in which a task encompasses information regarding the steps involved. We develop an online scheduling algorithm based on the RTN model, and update equations, used for calculating the initial state of the plant based on real-time data. Furthermore, we introduce features that have not been examined before, such as considering delays in batch processing as optimization decisions, to avoid infeasibility.

In section 2, we present a brief overview of the features of the scheduling model. In section 3, we propose the online scheduling algorithm involving the recalculation of the resource-task interaction coefficients coupled with initial state estimation. In section 4, we illustrate the need to consider delays as optimization decisions through a motivating example and in section 5, we apply the proposed methods to a case study.

2. Scheduling Model

2.1. State-space representation

The standard discrete-time state-space models popular in model predictive control (MPC) approaches have the following general form for state-evolution constraints:

$$x(t+1) = Ax(t) + Bu(t) + B_d d(t) \tag{1}$$

where $x(t)$ indicates the state of the plant, t is the index of time and A, B, B_d are coefficient matrices.

In this work, we pose the scheduling model in state-space form so that the complete status of the plant can be interpreted from the states at any given point of time (Subramanian et al., 2012, and Gupta and Maravelias, 2016). The scheduling decisions or inputs $u(t)$ are whether to start a new task and the amount of material to ship. The state of the plant $x(t)$ includes the progress of the task, the amount of inventory and backlog of materials and the resources engaged/available at that time.

2.2. Resource task network framework

The Resource Task Network (RTN) is a popular framework to represent the different elements of the scheduling problem. It consists of resources $r \in \mathbf{R}$ that include materials, equipment, and utilities and tasks $i \in \mathbf{I}$, which consume and/or release certain resources during its execution.

2.3. Mathematical formulation of state-space RTN model

The state of a batch of task i is indicated by the progress status $k \in \mathbf{K}_i$. The progress status of task i varies from $k = 0$ at the start, to $k = \tau_i$ at the end, where τ_i is its processing time. As opposed to state estimation in MPC approaches, wherein the vector of states is estimated based on the actual inputs and measured outputs, here the state of a batch is solely determined by its progress status k, calculated based on measurements. The main decision variables (inputs) are $N_{it} \in \{0,1\}$, which equals 1, when task i starts at time t. These inputs have a lagged effect on the state of the system, say, the inventory of material produced after τ_i periods. So, these inputs are lifted forward and augmented with states $\bar{N}_{it}^{k} \in \{0,1\}$, which equals 1, when task i has progress status k at time t. The evolution of the progress status is achieved through equations (2) and (3), where $\hat{N}_{it}^{0}$ is determined from real-time data as explained later.

$$\bar{N}_{it}^{0} = N_{it} + \hat{N}_{it}^{0} \quad \forall i, t \tag{2}$$

$$\bar{N}_{i(t+1)}^{k} = \bar{N}_{it}^{k-1} \quad \forall i, t, k \in \{1, \dots, \tau_i\} \tag{3}$$

Equation (4) expresses the resource balance, wherein the resource level in a given period depends on the level in the previous period, consumption/production resource-task interactions, and the shipment quantity V_{rt}. The consumption/production of resource r by task i at progress status k is represented by μ_{irk}. The bounds on the resource levels are given by constraint (5) and the backorder quantity, U_{rt}, in cases where the demand α_{rt} cannot be met, is determined based on equation (6).

$$S_{rt} = S_{r(t-1)} + \sum_{i \in \mathbf{I}} \sum_{k=0}^{\tau_i} \left(\mu_{irk} \bar{N}_{it}^{k}\right) - V_{rt} \quad \forall r, t \in \{1,2, \dots\} \tag{4}$$

$$0 \leq S_{rt} \leq \lambda_r^{\mathrm{M}} \quad \forall r, t \tag{5}$$

$$U_{rt} = U_{r(t-1)} - V_{rt} + \alpha_{rt} \quad \forall r, t \in \{1,2, \dots\} \tag{6}$$

2.3.1. Update equations

The update equations (7), (8) and (9) are written at $t = 0$ based on real-time data. The initial resource levels S_r^0 and the backorder quantity U_r^0 are determined based on real-time information from the plant. In equation (9), the progress status of currently executed tasks $\hat{N}_{i(t=0)}^k$ is determined from real-time data as explained in section 3, and assigned to the appropriate task state binary variable $\bar{N}_{it}^k$.

$$S_{rt} = S_r^0 + \sum_{i \in \mathbf{I}} \sum_{k=0}^{\tau_i} \left(\mu_{irk} \bar{N}_{it}^k\right) - V_{rt} \quad \forall r, t = 0 \tag{7}$$

$$U_{rt} = U_r^0 - V_{rt} + \alpha_{rt} \quad \forall r, t = 0 \tag{8}$$

$$\bar{N}_{it}^k = \hat{N}_{it}^k \quad \forall i \in \mathbf{I}^C, t = 0, k \in \{1, \dots, \tau_i\} \tag{9}$$

We assume that the measurements are error free and the system is observable (i.e., current state of the system can be determined from measurements/outputs).

2.3.2. Objective function

The objective function as given in (10), is to minimize the total cost composed of the backorder cost and fixed cost of executing tasks.

$$\min \sum_{r \in \mathbf{R}^P} \sum_{t \in \mathbf{T}} \gamma_r^U U_{rt} + \sum_{i \in \mathbf{I}} \sum_{t \in \mathbf{T}} \gamma_i^F N_{it} \tag{10}$$

3. Online Scheduling Algorithm

3.1. Motivating example

The system consists of two batch reactors U1 and U2, and two tasks I1 and I2 representing the conversion of raw material M1 into products P1 and P2, respectively. The tasks are composed of various steps, namely, *Feed, React, Filter, Sample,* and *Empty.* In the *Feed* step in I1, raw material M1 is fed to the reactor U1 at a flow rate of 50 kg/min and a total quantity of 600 kg is required for executing I1, so the *Feed* step spans $\left(\left\lceil \frac{600}{50} \right\rceil = \right)$ 12 min. In the *React* step, the raw material is converted to the product. The solid particles in the product mixture are removed using a filter F in the *Filter* step. The product quality is analyzed by an operator O in the *Sample* step and finally, the product is drained from the reactor in the *Empty* step. There is a demand for a batch of task I1 at 40 min, so task I1 starts at time 0 and requires equipment resource U1, material resource M1, filter resource F and operator resource O during its execution (refer to Figure 1 (**A**)). Similarly, task I2 has its own sequence of steps and associated resources, which are not described here. We use a time grid with a discretization (δ) of 5 min in the scheduling model and we reschedule every 5 min.

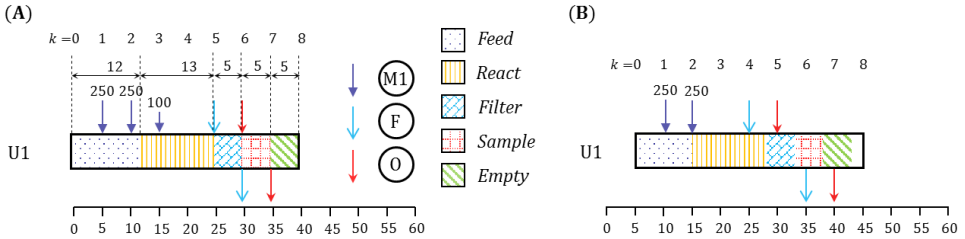

Figure 1. Schedule showing steps and resource interactions (i.e. consumption/release) for task I1. (**A**) Nominal optimal schedule at time 0. (**B**) Schedule obtained while rescheduling after 5 min.

3.2. Re-computation of resource-task interaction coefficients

Given the batch recipe, we know the different resources that are associated with the different steps. There can be a variety of reasons such as delays or resource unavailability, that may lead to steps in the batch not starting at their prescribed times. When a particular step is delayed, the subsequent steps shift forward in time, resulting in an increase in the batch end time. Therefore, the resource-task interaction coefficients need to be recalculated to account for the shift in steps.

A detailed explanation of the algorithm to recalculate the resource-task interaction coefficients is not possible given the limited space, so we illustrate selected modules of the algorithm using the motivating example. A source of delay could be disruptions in raw material flow rates. In the nominal case, 250 kg of M1 is supposed to flow into U1. However, after 5 min, when we reschedule, we realize that only 100 kg has flown in. So, the remaining 500 kg would flow as 250 kg in the two subsequent periods as shown by the arrows and the numbers in Figure 1 (**B**). The *Feed* step is supposed to end at 15 min as opposed to the nominal end time of 12 min.

After determining the end time of the current step, we determine the start and end times of the subsequent steps as well as the (revised) batch end time. Here, the batch of task I1 ends at 45 min. The discrete renewable resources are consumed at the start of a step and released at its end. The *Filter* step is supposed to start at 28 min and end at 33 min. Since δ =5 min, the filter resource F is consumed at 25 min and released at 35 min which is different from the nominal resource-task interactions shown in Figure 1 (**A**). Similarly, the resource-task interactions for the operator resource O also need to be re-computed.

3.3. Initial state estimation

The current state of the batch represented by the status indicator $\widehat{N}_{i,k(t=0)}$ is determined based on periods remaining for the batch to end. Note that when we reschedule after 5 min, $t = 0$ in the scheduling model corresponds to the absolute time of 5 min. In the motivating example, in the nominal case, the batch would have progressed to a status of $k = 1$ after 5 min. Since, we determined the revised batch end time to be 45 min, 8 periods still remain for the batch to end and the progress status remains at $k = 0$, owing to disruptions in flow rates.

We introduce a parameter β_{irk} to capture the dependence of resource-task interactions on the current state indicated by the progress status k. For the filter resource F in task I1, consumption is at $k = 4$ (i.e., $\beta_{\mathrm{I1,F},4} = -1$) and release is at $k = 6$ (i.e., $\beta_{\mathrm{I1,F},6} = 1$). Whereas in the nominal case, the *Filter* step was supposed to start at 25 min and end at

30 min. So, the consumption was at $k = 5$ (i.e., $\mu_{\mathrm{I1,F},5} = -1$) and release at $k = 6$ (i.e., $\mu_{\mathrm{I1,F},6} = 1$). Therefore, we clearly see the distinction between the nominal μ_{irk} and "updated" β_{irk} resource-task interaction coefficients.

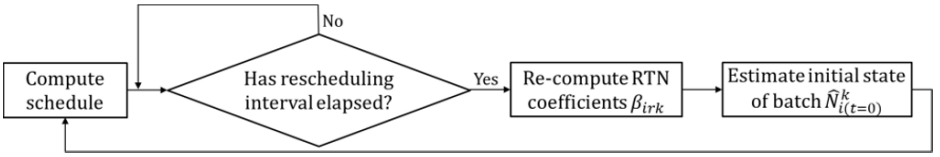

Figure 2. Online scheduling algorithm.

To summarize, in the online scheduling algorithm (refer to Figure 2), we compute a schedule and after the rescheduling interval has elapsed, we re-compute the resource-task interaction coefficients β_{irk}, estimate the initial state $\widehat{N}^k_{i(t=0)}$ based on the revised batch end time, and re-solve the scheduling model with the updated state and parameters. Importantly, we have illustrated the necessity and the methodology to update the models in real-time. This is a major departure from all previous standalone scheduling approaches for real-time scheduling, in which models were assumed to remain unchanged.

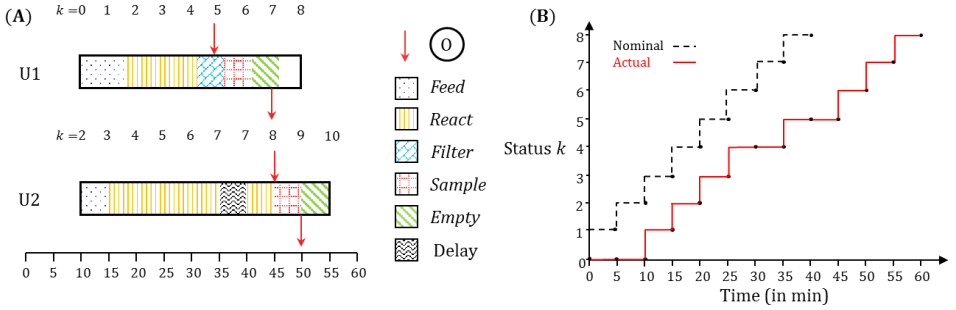

Figure 3. (**A**) Schedule showing delays triggered by optimizer in task I2 to avoid schedule infeasibility. (**B**) Plot showing the comparison between the nominal and actual evolution of progress status of batch of task I1 with time.

4. Delays as Optimization Decisions

To account for delays in other tasks and maintain schedule feasibility, we introduce delays as optimization decisions (provided that pre-emption is allowed at some steps of a task). For example, when steps in different tasks require the same shared resource at a given point in time, one of the steps will have to be delayed. To model delays as decisions, we introduce $E^k_{it} \in \{0,1\}$, which equals 1, if a batch of task i with progress status k at time t is delayed. The progress status evolution (equation (3)) and resource balance (equation (4)) are modified as follows:

$$\bar{N}^k_{i(t+1)} = \bar{N}^{k-1}_{it} - E^{k-1}_{it} + E^k_{it} \quad \forall i, t, k \in \{1, \dots, \tau_i\} \tag{11}$$

$$S_{rt} = S_{r(t-1)} + \sum_{i \in \mathbf{I}} \sum_{k=0}^{\tau_i} \left\{\hat{\mu}_{irkt}\left(\bar{N}^k_{it} - E^k_{it}\right)\right\} - V_{rt} \quad \forall r, t \in \{1,2, \dots\} \tag{12}$$

where $\hat{\mu}_{irkt}$ is assigned the value of β_{irk} for currently executed batches and μ_{irk} for the batches scheduled in the future.

In the motivating example, after 10 min, we observe that there is an overlap in the *Sample* step in tasks I1 and I2. Since both *Sample* steps require an operator and there is only one operator available, the schedule is infeasible. To maintain feasibility, the start of *Sample* in I2 is delayed as shown in Figure 3(**A**). The differences in progress status evolution for a batch of I1 for the nominal and actual cases are shown in Figure 3(**B**).

5. Case Study

We apply the proposed methods to a case study consisting of 3 reactors, 15 resources of different types (i.e., continuous/discrete and renewable/non-renewable) with demands for various products. Here, the steps in tasks are associated with multiple resources and the limiting resource determines the step duration. In Figure 4, we show the difference between the nominal predicted and actual implemented schedule for the first batch in each reactor.

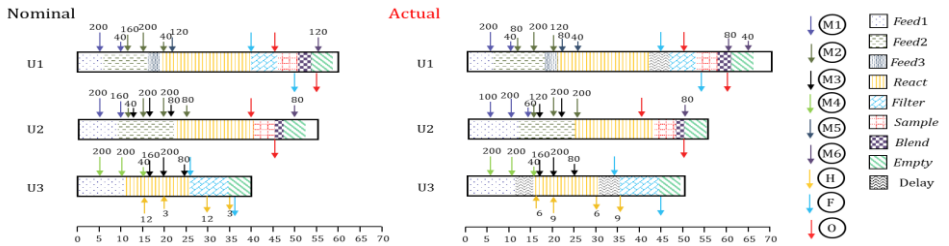

Figure 4. Gantt charts showing the nominal predicted and actual implemented schedule for the case study.

6. Conclusions

Although state-space models for production scheduling are available, the concept of state estimation, unlike in process control, has not been studied in the context of scheduling. In this paper, we introduced progress status as the key state, and discussed, for the first time, how it should be used in real-time. Specifically, we showed that real-time information can be used to calculate the progress status and, importantly, update the resource-task interaction parameters which, in all previous approaches, were thought to be constant. Finally, motivated from the mismatch between the predicted and actual progress status, we introduced delays as optimization decisions, thus allowing the seamless execution of real-time scheduling. The proposed work is a major departure from previous real-time scheduling approaches in which the scheduling model was assumed to remain the same between iterations.

References

Gupta, D. and Maravelias, C.T., 2016, On deterministic online scheduling: Major considerations, paradoxes and remedies, Computers & Chemical Engineering, 94, 312-330.
Rawlings, B.C., Avadiappan, V., Lafortune, S., Maravelias, C.T., and Wassick, J.M., 2019, Incorporating automation logic in online chemical production scheduling, Computers & Chemical Engineering, 128, 201-215.
Subramanian, K., Maravelias, C. T., and Rawlings, J.B., 2012, A state-space model for chemical production scheduling, Computers & Chemical Engineering, 47, 97-110.

Sauro Pierucci, Flavio Manenti, Giulia Bozzano, Davide Manca (Eds.)
Proceedings of the 30th European Symposium on Computer Aided Process Engineering (ESCAPE30), May 24-27, 2020, Milano, Italy.
http://dx.doi.org/10.1016/B978-0-12-823377-1.50191-9

Augmenting Heat Balance of the Wastewater Treatment Plant Model and Improving Plant Control by Counteracting Temperature Disturbances

Daniel Crîstiu, Melinda Simon-Várhelyi, Alexandra Veronica Luca, Marius Adrian Brehar, Vasile Mircea Cristea*

Babeș-Bolyai University, Faculty of Chemistry and Chemical Engineering, 11 Arany János Street, Cluj-Napoca 400028, Romania

mcristea@chem.ubbcluj.ro

Abstract

Municipal wastewater treatment has become one of the most challenging environmental problems due to the volume increase of urban wastewaters and stricter regulations imposed to effluent pollutants concentration. Besides the tough pollutants concentration and flow rate influent disturbances, the influent temperature changes also affect the complex biochemical processes taking place in WWTP bioreactors. As a result, the WWTP dynamic behavior description relying on the mass balance needs to be completed either with temperature correction factors or by comprehensive heat balance equations. The latter approach was considered in the present research, addressing a municipal WWTP using the activated sludge technology in the Anaerobic-Anoxic-Oxic (A^2O) configuration. The heat balance enhanced WWTP model was developed on the basis of the Activated Sludge Model No. 1 (ASM1), coupled with a modified version of the Benchmark Simulation Model no. 1 (BSM1). The wastewater temperature changes were evaluated and a control system structure was proposed in order to counteract the negative effects of the influent temperature associated to other typical influent disturbances. Simulation results performed with the calibrated municipal WWTP model and the proposed control system demonstrate twofold benefits. They may reduce the aeration and pumping energy costs by 12 % and improve the effluent quality by 5 %.

Keywords: wastewater treatment, heat balance, temperature disturbances, control system design

1. Introduction

Explorations based on dynamic mathematical models of the biological wastewater treatment plants (WWTPs) are valuable tools for investigating the process performance. This capability leads to straightforward evaluation of potential improvements produced by the design of different operating and control strategies within a municipal wastewater treatment plant (Makinia, 2010).

The Activated Sludge Model No. 1 made available a coherent framework for describing biological processes in activated sludge systems taking into consideration the mass balances for substrate utilization and microbial growth (Henze et al., 2002). For further improvements in performance predictability, besides the dynamics of the flow and pollutants load, the temperature dynamics could be also taken into consideration. Hence, an accurate heat balance model may be incorporated in the simulator in order to predict the changes of the activated sludge wastewater temperature (Lippi et al., 2009).

Temperature variations affect the efficiency of wastewater treatment plant due to their influence on microbial kinetics and physic-chemical parameters (Fernández-Arévalo et al., 2014). Based on a previous study it was shown that the WWTP process is negatively affected by temperature drops, especially for the nitrogen removal (Brehar et al., 2019). Model based predictions of the WWTP behavior may be considerably influenced by temperature disturbances, although this issue is not always taken into consideration. When performing simulation studies the water temperature is often assumed constant or, at the most, temperature changes are only considered by empirical factors.

The changes in basins wastewater temperature are frequently caused by a combination of various factors. Several literature sources present the development of temperature models. They have been incorporated into integrated models which contain the mass balance and energy balance as well (Arnell et al., 2017). A steady-state model was developed by Novotny and Krenkel (1973) in which four terms of the heat transfer were introduced. They are the short wave (solar) radiation (Q_s), long wave (atmospheric) radiation (Q_{lr}), surface evaporation heat (Q_e) and surface convection heat (Q_c). An extension of this model was presented by Argaman and Adams (1977) by adding mechanical energy input (Q_p), biochemical reaction heat (Q_b) and heat loss through basin walls (Q_{tw}). Talati and Stenstrom (1990), with the support of the existing models, enhanced the accuracy of the temperature predictions and reduced the required site-specific information. Sedory and Stenstrom (1995) developed a dynamic model for estimating the wastewater temperature in aerated basins, in the form shown in Eq. (1):

$$\rho_w \cdot V \cdot c_{pw} \frac{dT_w}{dt} = Q_t + \rho_w \cdot q_w \cdot c_{pw} \cdot (T_i - T_w) \tag{1}$$

where (V) is the basin volume, (q_w) flow rate, (ρ_w) density, (c_{pw}) specific heat and (T_i) water inlet temperature. Net sum of the heat gains and losses (Q_t) is presented in Eq. (2).

$$Q_t = Q_s + Q_p + Q_b - Q_{lr} - Q_e - Q_c - Q_a - Q_{tw} \tag{2}$$

The heat gains produce the increase of the basin temperature (T_w) while heat losses determine its decrease.

2. WWTP model development

The Benchmark Simulation Model No. 1 (BSM1) and the Activated Sludge Model No. 1 (ASM1) are the roots of the dynamic WWTP model developed in this work. Appropriate changes to BSM1 were applied to the model in order to fit it to the investigated municipal WWTP having an Anaerobic-Anoxic-Oxic (A^2O) configuration. The dynamic WWTP model consists of a primary settler model based on the equations proposed by Otterpohl and Freund (1992), five ASM1 bioreactor models connected in series and a secondary clarifier model incorporating the double exponential velocity function introduced by Takács et al. (1991).

The developed WWTP model, relying on the mass balance equations, was previously calibrated based on plant size information and measured data collected from the investigated municipal WWTP during the month of May 2016 (Várhelyi et al., 2019).

In this research, additional meteorological and construction data were collected in order to describe the temperature dynamics in the bioreactors. For each of the five bioreactors the heat balance was introduced according to Eq. (1) by considering the net heat gain or loss described by Eq. (2). Matlab software and Simulink graphical extension were used for the model development. The process mass and heat balance equations were coded in C programming language and incorporated in the simulation environment as S functions.

3. Implemented control strategy

The calibrated and heat balance enhanced WWTP simulation model was augmented with two feedback control loops. They are the ammonia concentration control in the last aerated bioreactor (reactor no. 5) and the nitrates concentration control in the anoxic bioreactor (reactor no. 2). The proposed control system design is presented in Figure 1.

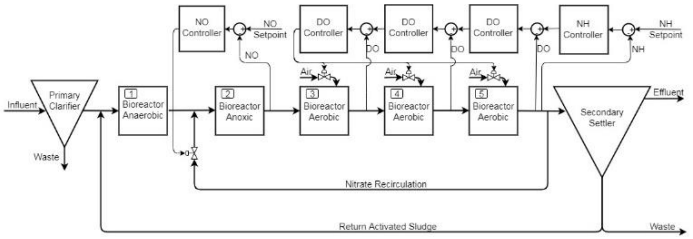

Figure 1. Structure of the proposed control system

The ammonia control loop includes an ammonia controller and three dissolved oxygen controllers arranged in a cascade setup. Proportional-Integral (PI) control law was considered for all four controllers. Based on the difference between the ammonia concentration setpoint value and the actual ammonia concentration value in the last bioreactor, the master ammonia (NH) controller computes the setpoint value for the first dissolved oxygen (DO) slave controller. This setpoint value is compared to the dissolved oxygen concentration in the last bioreactor and the control signal of the first DO controller is sent as setpoint to the second DO controller. The other two DO slave controllers work in a similar way. Consequently, the third DO controller computes the control signal which is distributed equally to the air control valves in order to change the air flow rate entering the three aerobic bioreactors. Ammonia concentration was measured with the AMTAX^{TM} sc ammonia analyzer, based on the colorimetric method.
The nitrates and nitrites feedback control loop also uses a PI controller. The controlled variable is the nitrates and nitrites concentration in the anoxic bioreactor, while the manipulated variable is the nitrate recirculation flow rate. The nitrates and nitrites concentration was determined with the patented 2-beam NITRATAX^{TM} clear sc sensor, using the UV absorption method of measurement.

4. Investigated influent temperature disturbances

Influent temperature disturbances can act for a short or a long period of time. The season originating temperature changes result in weeks or months long lasting variations of the wastewater temperature. Rapid changes in influent temperature, occurring during a few hours or days, can be the consequence of sudden weather changes (e.g. storm, rain, snowing, snow melting). The effect of influent temperature disturbances needs to be minimized for preserving the desired WWTP performance. The temperature influences processes in the activated sludge plant. For example, the heterotrophic and autotrophic biomass growth, ammonification rate, dissolved oxygen saturation and mass transfer rates are all temperature dependent. The influent temperature disturbances may be also accompanied by flow rate and influent pollutants concentration disturbances. Different cases were investigated in the present work for the effects of the influent temperature disturbances. Case 1 represents a reference simulation with the WWTP measured influent temperature data collected during the first 22 days of May 2016. Based on the measured influent temperature, different influent temperature profiles were created. The second case incorporates the disturbance

of 2 °C influent temperature decrease for the whole 22 days period of time (Case 2). Additionally, changes in the influent flow rate and influent Chemical Oxygen Demand (COD) concentration were considered in Case 3. The investigated cases are presented in Table 1. Simulations were performed for all three considered cases, both with and without the operation of the proposed control system.

Table 1. Investigated cases for effects of influent temperature and typical disturbances

CASE	DESCRIPTION
Case 1	Simulation using the municipal WWTP measured influent temperature data
Case 2	Simulation with influent temperature decreased by 2 °C
Case 3	Simulation with influent temperature decreased by 2 °C, associated to 10% influent flow rate increase and 10% influent COD concentration decrease

5. Results and discussion

5.1. Simulation results for the heat balance extended WWTP model

The previously calibrated model was extended with the heat balance equations and simulation was performed with the influent measured data from the municipal WWTP under study. The solar radiation heat, mechanical power heat and biological reaction heat are the heat gain terms, while the long-wave (atmospheric) radiation heat, surface convection heat, surface evaporation heat, aeration heat and basin wall heat are responsible for the heat losses. Representative simulation results shows for the last bioreactor that the most significant heat component proved to be the solar radiation heat, which corresponds to 32.1 % of the total heat gains and heat losses. The biological reaction heat component represents 29.2 %, while the mechanical power heat component represents 10.2 % of the total heats. All these three components are corresponding to the heat gains. From the heat losses components, the surface evaporation heat is the most significant (15.2 %), while the heat losses through the basin wall are almost negligible. The net heat exchange has a positive value. The distribution of the heat components in the fifth bioreactor is presented in Figure 2.

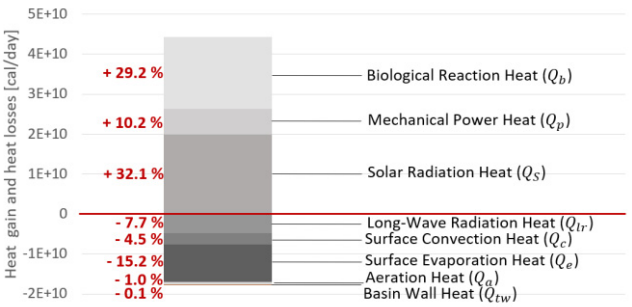

Figure 2. Representative distribution of the heat terms, for the last of the bioreactors

According to the simulation with the extended WWTP model, the Celsius temperature in the last aerobic bioreactor increased by 4 % compared to the inlet wastewater temperature. The average value of the influent temperature is of 15.8 °C, while the temperature predicted in the last aerated bioreactor by the extended WWTP model is of 16.5 °C. The variations of the measured influent wastewater temperature and the predicted temperature in the fifth bioreactor are presented in Figure 3.

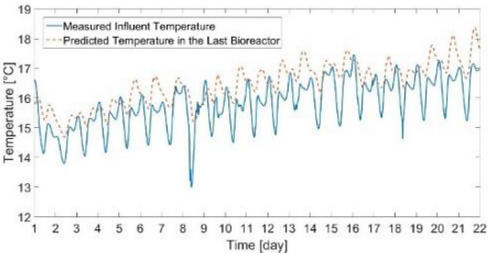

Figure 3. Measured influent and model predicted water temperature in the last reactor

Figure 3 reveals the increase in the wastewater temperature along the WWTP and the buffer effect of the bioreactors for the influent temperature changes.

5.2. Simulation results for the WWTP performance without the proposed control system

For all of the three presented cases, simulations were firstly run with the extended WWTP model but without the proposed control system. The performance indices (aeration energy (AE), pumping energy (PE) and effluent quality (EQ)) were calculated according to Eqs. (3-5).

$$AE = C_{AE} \cdot \frac{SO_{sat}}{T \cdot 1.8 \cdot 1000} \int_0^T \sum_{aerated\ bioreactor} \left[V_{bioreactor} \cdot K_L a_i(t) \right] dt \tag{3}$$

$$PE = C_{PE} \cdot \frac{1}{T} \int_0^T \left[0.004 \cdot Q_{NR}(t) + 0.08 \cdot Q_{RAS}(t) + 0.05 \cdot Q_{waste}(t) \right] dt \tag{4}$$

$$EQ = \frac{1}{T \cdot 1000} \int_0^T [PU_{TSS}(t) + PU_{COD}(t) + PU_{BOD}(t) + PU_{TKN}(t) + PU_{NO}(t)] Q_{effluent}(t)\, dt \tag{5}$$

The values of the performance indices obtained by simulation for the municipal WWTP are presented in Table 2, when temperature and the other typical disturbances are acting.

Table 2. Results of the performance indices for the different influent disturbance cases, without the proposed control system

Performance index	Case 1	Case 2	Case 3
AE [kWh/day]	14,886.4	14,775.4	14,781.5
PE [kWh/day]	8,831.7	8,831.7	8,831.7
Total Energy [kWh/day]	23,718.1	23,607.1	23,612.5
EQ [kg P.U./day]	18,412.0	19,681.3	21,387.4
AE+PE+EQ	42,130.1	43,288.4	44,999.9

Table 2 shows that in the presence of disturbances the effluent pollutant concentrations increase. The worst case is Case 3 when the influent temperature decreases, the influent flow rate increases and influent COD concentration decreases, revealing an overall WWTP performance (sum of AE, PE and EQ) deterioration of about 7%.

5.3. Simulation results for the WWTP performance with the proposed control system

The three disturbance investigated cases were tested on the enhanced WWTP model with the proposed control system. The simulation results are shown in Table 3.

Table 3. Results of the performance indices for the different influent disturbance cases and with application of the proposed control system

Performance index	Case 1	Case 2	Case 3
AE [kWh/day]	10,003.4	11,872.7	12,243.2
PE [kWh/day]	8,720.8	8,486.1	8,464.1
Total Energy [kWh/day]	18,724.2	20,358.8	20,707.3
EQ [kg P.U./day]	13,988.6	18,068.5	20,249.0
AE+PE+EQ	32,712.8	38,427.3	40,956.3

Results presented in Table 3 show that by implementing the proposed control system, the performance of the municipal WWTP can be improved by reducing the energy costs and enhancing the effluent quality, in all cases. When comparing the simulation results in the presence and absence of the proposed control system, the overall performance was improved by 9 % for the most challenging Case 3. This is owing to the reduction of operational energy (AE+PE) by 12 % and improvement of the effluent quality by 5 %.

6. Conclusions

The dynamic WWTP calibrated model including the mass balance was enhanced with the heat balance equations. Effluent wastewater temperature changes were investigated in the presence of different influent wastewater temperature, flow rate and COD concentration disturbances. Simulations of the enhanced model showed as most significant heat component for the month of May the solar radiation heat, followed by the biological reaction heat. In the studied month the net heat exchange has a positive value and the mean water temperature is increasing along the WWTP basins by 0.7°C. The negative effect of the influent temperature decrease, coupled with other typical disturbances, can be minimized by implementing the proposed control system. Control simulation results demonstrate an overall performance improvement for the spent energy and for the effluent quality of about 9 %. The proposed control system shows potential benefits for the implementation in the municipal WWTP in order to achieve efficient operation in the presence of temperature disturbances.

References

Y. Argaman, C.E. Adams, 1977, Comprehensive temperature model for aerated biological systems, Progress in Water Research, 9, 397-409

M. Arnell, E. Lundin, U. Jeppsson, 2017, Sustainability Analysis for Wastewater Heat Recovery Literature Review, Lund, Sweden, 1-40

M.A. Brehar, M. Várhelyi, V.M. Cristea, D. Crîstiu, Ş.P. Agachi, 2019, Influent temperature effects on the activated sludge process at a municipal wastewater treatment plant, Studia UBB Chemia, 64, 1, 113-123

T. Fernández-Arévalo, I. Lizarralde, P. Grau, E. Ayesa, 2014, New systematic methodology for incorporating dynamic heat transfer modelling in multi-phase biochemical reactors, Water Research, 60, 141-155

M. Henze, W. Gujer, T. Mino, M. van Loosdrecht, 2002, Activated Sludge Models ASM1, ASM2, ASM2d and ASM3, Padstow, Cornwall, UK, 1-121

S. Lippi, D. Rosso, C. Lubello, R. Canziani, M.K. Stenstrom, 2009, Temperature modelling and prediction for activated sludge systems, Water Science & Technology, 59, 1, 125-131

J. Makinia, 2010, Process temperature model, Mathematical Modelling and Computer Simulation of Activated Sludge Systems, IWA Publishing, London, UK, 98-118

V. Novotny, P.A. Krenkel, 1973, Simplified Mathematical Model of Temperature Changes in Rivers, Journal of the Water Pollution Control Federation, 45, 240-248

R. Otterpohl, M. Freund, 1992, Dynamic Models for Clarifiers of Activated Sludge Plants with Dry and Wet Weather Flows, Water Science and Technology , 26, 5-6, 1391-1400

P.E. Sedory, M.K. Stenstrom, 1995, Dynamic prediction of wastewater aeration basin temperature, Journal of Environmental Engineering, 121, 609-618

I. Takács, G.G. Patry, D. Nolasco, 1991, A Dynamic Model of the Clarification-Thickening Process, Water Research, 25, 20, 1263-1271

S.N. Talati, M.K. Stenstrom, 1990, Aeration-Basin Heat Loss, Journal of Environmental Engineering, 16, 70-86

M. Várhelyi, V.M. Cristea, M. Brehar, E.D. Nemeş, Abhilash Nair, 2019, WWTP Model Calibration Based on Different Optimization Approaches, Environmental Engineering and Management Journal, 18, 8, 1657-1670

Sauro Pierucci, Flavio Manenti, Giulia Bozzano, Davide Manca (Eds.)
Proceedings of the 30th European Symposium on Computer Aided Process Engineering (ESCAPE30), May 24-27, 2020, Milano, Italy.
http://dx.doi.org/10.1016/B978-0-12-823377-1.50192-0

Optimal Start-Up of Air Separation Processes using Dynamic Optimization with Complementarity Constraints

Adrian Caspari[a], Steffen R. Fahr[a], C. Offermanns[a], Adel Mhamdi[a], Lorenz T. Biegler[d], Alexander Mitsos[b,a, c,*]

[a] *Process Systems Engineering (AVT.SVT), RWTH Aachen University, 52074 Aachen, Germany*

[b] *JARA-CSD, RWTH Aachen University, 52056 Aachen, Germany*

[c] *IEK-10, Forschungszentrum Jülich, 52425 Jülich, Germany*

[d] *Carnegie Mellon University, Department of Chemical Engineering, Pittsburgh, PA 15213, USA*

amitsos@alum.mit.edu

Abstract

Fluctuating electricity prices create an incentive for the flexible operation of electricity intensive processes, such as air separation units (ASUs). Shutting down an ASU during times with peak electricity prices has been claimed economically attractive but requires an efficient and largely automated start-up procedure. Previous works have considered simulations of plant start-ups and dynamic optimization of load scheduling near the nominal operation mode. Discrete events like the appearance of a liquid phase have impeded any rigorous ASU start-up optimization. In this work, we formulate the optimal start-ups as dynamic optimization problems with regularized algebraic complementarity constraints (Caspari et al., 2019b) using a mechanistic dynamic process model in Modelica. Our approach captures physical effects appearing during start-up like the appearance and disappearance of phases. We solve the resulting optimization problems with direct single-shooting using the dynamic optimization framework DyOS. We perform in-silico dynamic offline optimizations of an ASU start-up and consider different process modifications. We consider cold start-up optimizations, where the process medium is initialized at cryogenic conditions just before liquefaction. The results illustrate that the proposed approach can be applied to large-scale processes. The results show further that liquid assist operation reduced the optimal start-up time by about 70 % compared to the start-up without this modification.

Keywords: dynamic optimization, complementarity constraints, air separation, optimal start-up

1. Introduction

The flexible operation of continuous processes in the presence of fluctuating electricity prices enable economic benefits (Daryanian et al., 1989). Since air separation units (ASUs) are large-scale electricity consumers, they are well suited for exploiting electricity price fluctuations (Caspari et al., 2019c). Irrespective of the different

perspectives on flexible operation, whether scheduling (Zhang et al., 2015) or control (Huang et al., 2009), the start-up or shut-down of processes have been either assumed to be known or neglected; estimates of the start-up or shut-down times are used in the transitional constraints in scheduling and the control approaches assume the process to be in operation around nominal conditions. However, start-up and shut-down are crucial for the exploitation of the economic potential when the electricity price dynamics and process dynamics are in the same range, like in the case of ASUs (Miller et al., 2008b). While start-ups are currently performed with a fixed recipe under the surveillance of skilled workers, a rigorous optimization-based approach would be desirable leading to faster commissioning, higher energy efficiency, and reduced labour (Vinson, 2006). While simulations of an ASU start-up has been reported in literature, e.g, (Kender et al., 2019; Miller et al., 2008a), the optimization of a start-up process has not yet been considered. The optimization has to deal with discrete events like the appearance and disappearance of phases. The ASU can be described by a nonsmooth differential algebraic equation (DAE) system and the start-up optimization can be formulated as a dynamic optimization problem with complementarity constraints (CCs). Optimization problems of this form have been solved using full discretization leading to a nonlinear program (NLP) with equilibrium constraints, e.g., (Raghunathan et al., 2004). Recently, we proposed an approach for the efficient solution of such problems based on direct shooting (Caspari et al., 2019b). In this work, we apply this approach for the start-up optimization of an ASU. The start-up optimizations allow us to evaluate different process designs regarding their impact on the start-up. We therefore consider liquid assist operation in addition to a basic process design and perform start-up optimizations for both designs. We consider a cold process start-up, i.e., we assume the medium in the process to be already at cryogenic conditions, just before liquefaction. A warm start-up would assume that the medium inside the process is at ambient conditions. The cold start-up occurs when the plant was shut down for no more than several hours up to a few days (Miller et al., 2008a), which covers most of the scenarios occurring during flexible operation of an ASU. This could be the case in an operation scenario where the process is turned-off in the presence of very high electricity prices and turned-on otherwise. We briefly describe the process and its model in Section 2 and summarize the problem formulation and solution approach in Section 3. We show the results in Section 4 and conclude in Section 5.

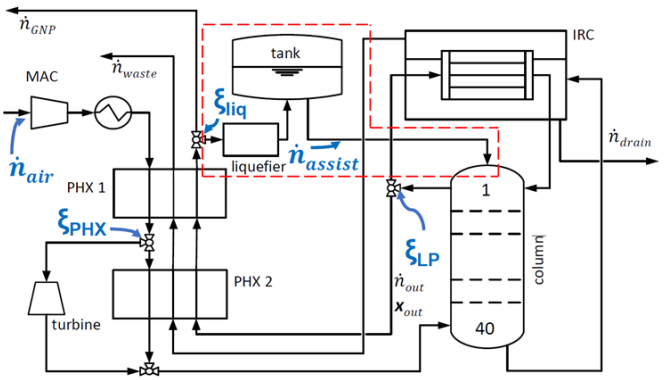

Figure 1 ASU flowsheet. Liquid nitrogen assist operation option indicated by dashed, red frame.

2. Process and Model

We consider the ASU depicted in Figure 1, which is similar to the process we used in (Caspari et al., 2018).Ambient air (nitrogen, oxygen, argon) enters the process,is

compressed to 11 bar, inter-cooled to 298 K and fed to the heat exchanger. There, the air stream is cooled in counter current with the waste and the gaseous nitrogen product (GNP) stream. A part is split-up and expanded to the column feed pressure in a turbine. The remaining part enters zone 2 of the heat exchanger, where it is further cooled and may be liquefied. Both streams are mixed and fed to the column. The condenser pressure is 5.5 bar whereas the reboiler outlet pressure is 1.5 bar. We adapt the liquid assist modification proposed in Miller et al. (2008a) for an ASU with an argon column; the GNP stream is liquefied and stored in a tank and can be fed into the column top stage to accelerate the process start-up. We implement a mechanistic dynamic model that is able to represent the transient process behaviour during the ASU start-up. The model includes CCs for modelling the appearance and disappearance of vapour-liquid equilibria (VLEs), overflow weirs and valves. It uses a relaxed VLE formulation similar to (Raghunathan et al., 2004), which includes CCs of the form $0 \leq y_{i_k}(t) \perp y_{i_k'}(t) \geq 0$. We apply similar formulations with CCs for overflow weirs and vapor outlet streams valves of the column trays. We briefly summarize the model and refer to previous works. We use the unit models from (Caspari et al., 2019b), the column model and the relaxed VLE formulation from (Raghunathan et al., 2004), and the physical property models from Johansson (2015). Thermodynamics: The vapour phase is modelled as an ideal gas and the liquid phase as a nonideal liquid. We apply standard models for the physical properties. We refer to Johansson (2015). Distillation Column: We use the same distillation column model as in (Raghunathan et al., 2004) with 40 trays. The model includes vapour and liquid holdups. Every tray has an overflow weir. The vapour outlet is calculated based on the pressure difference between the trays. Every tray includes 4 CCs: for the liquid outlet, the gas outlet, and two for the relaxed VLE. Consequently, the column model includes 160 CCs. PHX: We use a 1-dimensional distributed model for the heat exchangers. The fluid behaves quasistationary. We consider dynamic energy balances for the wall. Liquefaction can take only place in the PHX2 in the feed air stream, justified by several simulations. The PHX1 has 50 finite elements. We use 1 finite element for the PHX2. The PHX 2 include 2 CCs for the VLE. Compressor/Turbine: The compressor and turbine are modelled with an adiabatic efficiency of 0.8. The turbine includes 2 CCs for the relaxed VLE. Integrated reboiler and condenser: We model the reboiler as an equilibrium tray with a heat supply and the condenser as pseudo-steady-state. Reboiler and condenser are energetically integrated using a heat transfer correlation. The reboiler includes 4 CCs. The condenser includes 2 CCs for the VLE. Liquefier: We model the liquefier with a liquefaction efficiency of 0.8. The resulting process model is a differential index 1 DAE including 270 differential and about 3060 algebraic states. The model includes 170 CCs.

3. Problem Formulation and Solution Approach

The optimal start-up problems are formulated as a dynamic optimization problem with algebraic CCs. We described how to handle these in single shooting in detail in our previous work (Caspari et al., 2019b): We substitute each CCs using a regularized Fischer-Burmeister function of the form $0 = y_{i_k}(t) + y_{i_k'}(t) - \sqrt{y_{i_k}(t)^2 + y_{i_k'}(t)^2 + \varepsilon}, \varepsilon > 0$. The Fischer-Burmeister function is directly used as model equation. Regularization of the Fischer Burmeister function leads to a smooth DAE, enabling the application of standard integrators and optimizers to solve the optimization problems using direct shooting. We minimize the deviation of the GNP purity $x_{GNP}^{N_2}$, the GNP flowrate $\dot{n}_{GNP}$, the liquefier splitfactor ξ_{liq}, and the tank holdup n_{tank} from there desired setpoints by using the following objective function: $\Phi =$

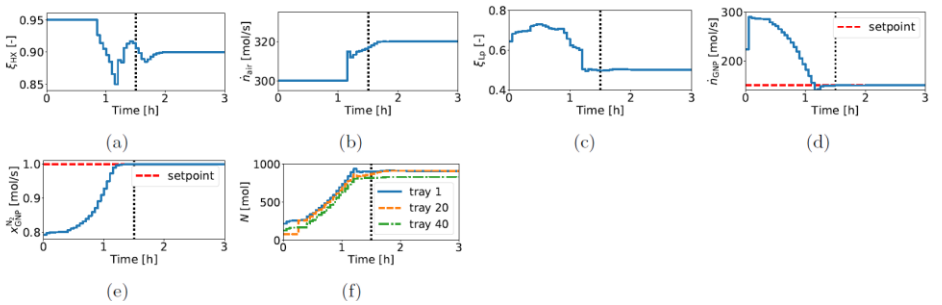

Figure 2: Optimal control and state variable profiles for start-up without liquid assist operation. Start-up range indicated by vertical, dotted lines. (a) PHC split factor to turbine. (b) Feed air flowrate. (c) Column split factor. (d) GNP flow rate. (e) GNP purity. (f) Column tray holdups.

$\int_0^{t_f} w_{purity}\left(x_{GNP}^{N_2}(t) - x_{GNP}^{N_2,set}\right)^2 + w_{flow}\left(\dot{n_{GNP}}(t) - \dot{n_{GNP}^{set}}\right)^2 + w_{liq}\left(\xi_{liq}(t)\right)^2 + w_{tank}\left(n_{tank}(t) - n_{tank}(t=0h)\right)^2 \mathrm{d}t$, with the weight parameters $w_{purity} = 10^{-3}$, $w_{flow} = 10^{-3}$, $w_{liq} = 10^{-4}$, $w_{tank} = 10^{-10}$, $x_{GNP}^{N_2,set} = 0.99995$, $\dot{n_{GNP}^{set}} = 150$ mol/s. We penalize the liquefier stream, since the liquefication uses electricity and could thus just be used as a bonus reflux for the column; we aim to minimize the liquefier activity in order to keep the electricity demand as low as possible while still allowing its use for the tank refill. We penalize the deviation of the tank holdup from the initial value to avoid unnecessary tank withdrawal. We use the following controls and bounds: $\xi_{PHX}(t) \in [0.85,0.95]$, $\xi_{LP}(t) \in [0.2,0.8]$, $\xi_{liq}(t) \in [0.5,1]$, $\dot{n_{air}}(t) \in [300,340]$ mol/s, $\dot{n_{assist}}(t) \in [0,30]$ mol/s. The control variables are initialized with the constant profiles $\xi_{PHX}(t) = 0.9$, $\xi_{LP} = 0.5$, $\xi_{liq} = 1$, $\dot{n_{air}} = 320$mol/s, $\dot{n_{assist}} = 0$ and are discretized piecewise constant with 60 intervals. We use the path constraints $\varphi_{turbine}(t) \in [0.95,\infty)$ and $x_{tank}^{N_2}(t) \in [0.99995,1]$. The turbine vapour fraction $\varphi_{turbine}$ is constrained due to technical limitations of the turbine. The tank purity $x_{tank}^{N_2}$ is constrained to the nominal product purity to avoid contamination in the tank. The last two summands of the objective function with the respective weights, the liquefier split factor, and the liquid assist flowrate are used only in the case with liquid assist operation. We assumed the start-up procedure to be finished when the product purity and the product flowrate are at their desired setpoints. We implement the process model in Modelica and use direct single-shooting (Brusch and Schapelle, 1973) to solve the optimization problems with the shooting framework DyOS (Caspari et al., 2019a). The DAE integrator is NIXE (Hannemann et al., 2010) and the NLP solver is SNOPT (Gill et al., 2005). We use integration tolerances of 10^{-6}, NLP tolerances of 10^{-4}.

4. Numerical Results

4.1. Start-Up without Liquid Assist Operation

Figure 2 shows results from the dynamic optimization of the start-up without liquid assist operation. The start-up time is about 1.5 h (Figures. 2d and 2e). At the beginning, the turbine activity is at the maximum (Figure 2a), while the air feed flowrate is at the lower bound (Figure 2b), and the column split factor is increased (Figure 2c) leading to a higher column reflux. This supports the cooling of the medium in the process since the turbine withdraws energy from the process and the reduced feed air flowrate reduces the energy fed to the process through the air feed. We see that the amount of liquid in the column increases

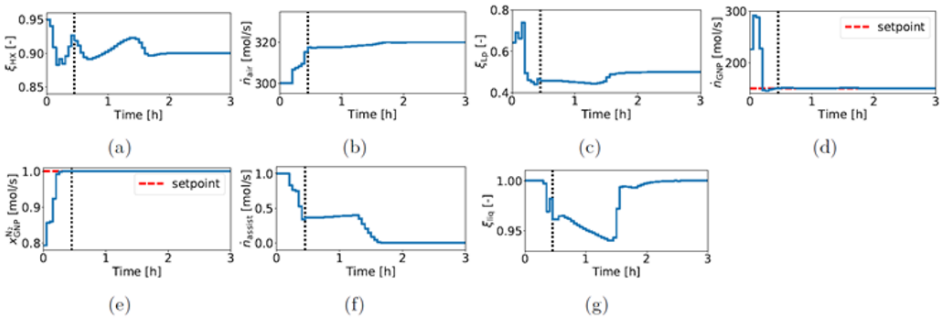

Figure 3: Optimal control and state variable profiles for start-up using liquid assist operation. Start-up range indicated by vertical, dotted lines. (a) PHC split factor to turbine. (b) Feed air flowrate. (c) Column split factor. (d) Liquid assist flowrate. (e) Liquefier splitfactor. (f) GNP flow rate. (g) GNP purity.

starting with the first tray followed by the other trays (Figure 2f). With the optimal control profiles, the product flowrate increases in the beginning before it settles down to the setpoint (Figure 2d). The product purity begins from ambient conditions and increases until it reaches the desired setpoint (Figure 2e).

4.2. Start-Up with Liquid Assist Operation

Figure 3 shows results from the dynamic optimization of the start-up with liquid assist operation. The optimal start-up takes about 24 min (Figures 3d and 3e), which corresponds to a reduction of the optimal start-up time of about 70 % compared to the optimal startup without liquid assist operation. The control variable profiles for the PHX splitfactor (Figure 3a), the feed air flowrate (Figure 3b), and the column splitfactor (Figure 3b) look qualitatively similar to the case without liquid assist operation (Figure 3c). The start-up is clearly supported by the liquid assist operation; The assist stream is at the upper bound in the beginning before it is reduced and set to zero at the end (Figure 3f). Remember that we penalize the liquid assist flowrate. The liquefier is used to refill the tank, in which the holdup is decreased due to the liquid assist stream. The tank refill is induced by the holdup penalization. However, due to the tank purity constraint, the liquefier can only be activated if the GNP purity is suitable and does not pollute the tank. The liquefier is thus activated as soon as the GNP purity is at the desired value (Figures 3g and 3e). The state variable profiles, e.g., for the product flowrate and purity (Figures 3d and 3e) look qualitatively similar as for the case without liquid assist option, though the operating level is obtained faster.

5. Conclusions

We use dynamic optimization with CCs to optimize start-ups of an ASU. The optimizations allow to evaluate process design modifications with respect to the effect on the process start-up time. We therefore perform cold start-up optimizations for ASU designs with and without liquid assist option. The results demonstrate the applicability of the approach to large-scale processes. They show further the effectiveness of liquid assist operation. This modification reduces the optimal process start-up time by about 70 % compared to a start-up without this modification. Further work can consider the start-up of ASUs with additional design modifications, other topologies, a warm process start-up starting from ambient conditions, and the application of the obtained start-up procedure

to a real process. Future work can use the approach to obtain start-up and shut-down times as required for transitional constraints in scheduling, and for online control.

Acknowledgement: The authors gratefully acknowledge the financial support of the Kopernikus project SynErgie by the Federal Ministry of Education and Research (BMBF) and the project supervision by the project management organization Projektträger Jülich (PtJ). The authors thank Anna-Maria Ecker, Florian Schliebitz, Gerhard Zapp from the Linde AG for fruitful discussion.

References

R. G. Brusch, R. H. Schapelle, 1973. Solution of highly constrained optimal control problems using nonlinear programing. AIAA Journal 11 (2), 135–136.

A. Caspari, J. M. Faust, P. Schäfer, A. Mhamdi, A. Mitsos, 2018. Economic nonlinear model predictive control for flexible operation of air separation units. IFAC-PapersOnLine 51 (20), 295–300.

A. Caspari, J. M. M. Faust, F. Jung, C. Kappatou, S. Sass, Y. Vaupel, R. Hannesmann-Tamás, A. Mhamdi, A. Mitsos, 2019a. Dyos - a framework for optimization of large-scale differential algebraic equation systems. Computer-Aided Chemical Engineering 46.

A. Caspari, L. Lüken, P. Schäfer, Y. Vaupel, A. Mhamdi, L. T. Biegler, A. Mitsos, 2019b. Dynamic optimization with complementarity constraints: Regularization for direct shooting. Optimization Online.

A. Caspari, C. Offermanns, P. Schäfer, A. Mhamdi, A. Mitsos, 2019c. A flexible air separation process: 2.optimal operation using economic model predictive control. AIChE Journal 65 (11).

B. Daryanian, R. E. Bohn, R. D. Tabors, 1989. Optimal demand-side response to electricity spot prices forstorage-type customers. IEEE Power Eng. Rev. 9 (8), 36–36.

P. E. Gill, W. Murray, M. A. Saunders, 2005. SNOPT: An SQP algorithm for large-scale constrained optimization. SIAM Rev. 47 (1), 99–131.

R. Hannemann, W. Marquardt, U. Naumann, B. Gendler, 2010. Discrete first- and second-order adjoints and automatic differentiation for the sensitivity analysis of dynamic models. Procedia Comput. Sci. 1 (1), 297–305.

R. Huang, V. M. Zavala, L. T. Biegler, 2009. Advanced step nonlinear model predictive control for air separation units. J. Process Control 19 (4), 678–685.

T. Johansson, 2015. Integrated scheduling and control of an air separation unit subject totime-varying electricity prices. Master's Thesis. KTH Royal Institute of Technology, Stockholm, Sweden.

R. Kender, B. Wunderlich, I. Thomas, A. Peschel, S. Rehfeldt, H. Klein, 2019. Pressure-driven dynamic simulation of start up and shutdown procedures of distillation columns in air separation units. Chem. Eng. Res. Des. 147, 98–112.

J. Miller, W. L. Luyben, P. Belanger, S. Blouin, L. Megan, 2008a. Improving agility of cryogenic air separation plants. Ind. Eng. Chem. Res. 47 (2), 394–404.

J. Miller, W. L. Luyben, S. Blouin, 2008b. Economic incentive for intermittent operation of air separation plants with variable power costs. Ind. Eng. Chem. Res. 47 (4), 1132–1139.

A. U. Raghunathan, M. S. Diaz, L. T. Biegler, 2004. An MPEC formulation for dynamic optimization of distillation operations. Comput. Chem. Eng. 28 (10), 2037–2052.

D. R. Vinson, 2006. Air separation control technology. Comput. Chem. Eng. 30 (10-12), 1436–1446.

Q. Zhang, I. E. Grossmann, C. F. Heuberger, A. Sundaramoorthy, J. M. Pinto, 2015. Air separation with cryogenic energy storage: Optimal scheduling considering electric energy and reserve markets. AIChE J. 61 (5), 1547–1558.

Sauro Pierucci, Flavio Manenti, Giulia Bozzano, Davide Manca (Eds.)
Proceedings of the 30th European Symposium on Computer Aided Process Engineering (ESCAPE30), May 24-27, 2020, Milano, Italy.
http://dx.doi.org/10.1016/B978-0-12-823377-1.50193-2

Scheduling of a Large-scale Industrial Make-and-Pack Process with Finite Intermediate Buffer using Discrete-time and Precedence-based Models

Christian Klanke[a]*, Vassilios Yfantis[a], Francesc Corominas[b], Sebastian Engell[a]

[a]*TU Dortmund University, Faculty of Biochemical and Chemical Engineering, Process Dynamics and Operations Group, Emil-Figge-Straße 70, 44227 Dortmund, Germany*
[b]*Procter & Gamble, Temselaan 100, 1853 Strombeek-Bever, Belgium*
christian.klanke@tu-dortmund.de

Abstract

We address the short-term scheduling of a two-stage continuous make-and-pack process with finite intermediate buffer and sequence-dependent changeovers from the consumer goods industry. In the current layout of the plant under consideration, the two stages, product formulation and packing, are directly coupled, i.e. the products of the formulation stage go directly to the packing stage. As for different products either one of both stages can be the bottleneck, a gain in productivity can be obtained if the two stages are decoupled by a buffer so that the formulation lines and the packing lines can both run at full capacity. The disadvantage of this setup is an increased complexity of the scheduling problem, so that support for the schedulers must to be provided. We employ a mixed-integer programming problem formulation for this purpose. The problem at hand is characterized by a large number of products in several product families, product specific order quantities and deadlines, product dependent production times, sequence-dependent changeover times, and a finite intermediate buffer. As the problem turned out to be intractable for the planning horizons of interest, a solution approach that employs a discrete-time scheduling model, a precedence-based presorting model and a decomposition strategy that is enhanced by several heuristics was developed.

Keywords: MILP modelling, Industrial scheduling, Heuristic decomposition, Make-and-Pack processes, Shifting bottlenecks, Precedence-based models.

1. Introduction

In the consumer goods industry, satisfying rapidly growing product demands poses a challenge to the decision makers: It needs to be decided whether to invest into new processing lines or to increase the productivity of an existing production plant either by improved operation or by revamping it to ensure market demand satisfaction.
In the make-and-pack plant under consideration, the two stages, formulation and packing, are closely coupled, i.e. the products of each line of the formulation stage flow directly to the corresponding packing line. A limitation of the current layout is the necessity to synchronize the production rates of the two stages within a line. Since the processing rate of the packing lines can be larger or smaller than the processing rate of the formulation lines, depending on the product, the bottleneck of the plant can either be the formulation or the packing stage. In order to reduce the total changeover time and to utilize the higher processing rates in each stage, an option is to decouple the two stages via an intermediate buffer. To establish such a buffer requires a significantly smaller investment than to add additional processing or packing lines. The scheduling of the different products in the

layout with such a buffer is even more challenging than the scheduling of the plant with a direct feed of the packing lines from the formulation lines, that was addressed in Elekidis et al. (2019), due to the larger number of degrees of freedom. In both cases, decomposition strategies are necessary to solve the problem for realistic problem sizes in reasonable computation times.

In this paper, we extend a discrete-time formulation for the scheduling problem with an intermediate buffer by a precedence-based model which is used for presorting the jobs which are then scheduled sequentially. The efficiency of the extension is demonstrated for relevant problem instances. The solution quality is measured by the total idle time, total changeover time, and total completion time.

This contribution is composed as follows: In Section 2 the case study is presented in detail. In Section 3 the proposed iterative solution procedure is introduced. Finally, the results for an exemplary case are discussed in Section 4 before final conclusions are drawn in Section 0.

2. Case study

In this section, a possible new layout of the plant under consideration is presented. In the first stage, a formulation process takes place on parallel, identical machines, and the formulated products can be, but do not necessarily have to be, stored in an intermediate buffer. The formulated products are fed to the second stage where they are packed on parallel, non-identical machines. The number of different products in the formulation stage is considerably less than the number of final packed products. Changeovers that require sequence-dependent changeover times occur in both stages of the process. Figure 1 shows a scheme of the plant layout that is considered here.

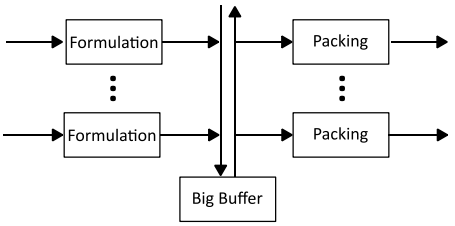

Figure 1: Layout of the make-and-pack production plant.

The buffer can store any product of the first stage, and only the total content of the buffer is limited. Any product can be withdrawn from the buffer at any time. There are two types of packing lines which are dedicated to specific types of products, those packed into large and those packed into small containers. The processing rates of small containers are lower than those of large containers. The assignment of the products to the two sets of packing lines is fixed, due to the lack of flexibility of the equipment. The formulated products feed a significantly larger number of differently packaged products. A single type of formulated product, hereinafter denoted a product family, can be used for a variety of final products. Each product has to be produced prior to a delivery date (deadline), but there are only up to three deadlines within the scheduling horizon. The transfer times between the formulation stage and the buffer and between the buffer and the packing stage are assumed to be small compared to the production times and are therefore neglected. The production rates and the order sizes are fixed and known for each product.

3. Solution approach

The MILP-based solution that we present here is based on the discrete-time mixed-integer linear programming (MILP) model from Yfantis et al. (2019). It is augmented by a precedence-based MILP presorting model. The discrete time MILP model solves the timing and allocation problem iteratively for sets of products. The inventory of each product family in the buffer is tracked at each discrete time point and the total buffer content is constrained. As the planning time horizon usually is three days of non-stop production, the problem instances become large, e.g., weekend schedules with around ninety products are generated. Due to the high number of decision variables that results from the high temporal resolution of the discrete-time model, a tailored decomposition strategy is applied. The decomposition approach is based on splitting the original set of orders into smaller subsets I^{k} with $|\mathrm{I}^{k}| = N$ which are scheduled in each iteration k. After each iteration, the timing and allocation decisions of the set of orders considered are fixed. For a detailed description of the decomposition algorithm, the reader is referred to Yfantis et al. (2019).

The discrete-time model does not provide explicit sequencing information for the different production lines, therefore the changeover times cannot be optimized directly. As stated by Harjunkoski et al. (2014), considering changeovers in a discrete-time model would significantly increase its size. This is undesirable because of limitations of the computation time and memory. Therefore, in addition to the discrete-time model of the overall problem, an immediate precedence-based model, that bears similarities to the one introduced by Cerda et al. (1997), has been developed. The precedence-based model is solved in each iteration of the decomposed solution process and the allocation and sequencing decisions of certain packing lines are fixed prior to the solution of the discrete-time model. The precedence-based model has a much smaller size compared to the discrete-time model, and therefore larger sets of products and longer prediction horizons can be considered than in the solution of the full model. In order to maintain enough degrees of freedom in the discrete-time model, e.g. to still be able to satisfy the buffer mass balance and buffer capacity constraint, the precedence-based model is only applied to a subset of packing lines $\mathrm{J}^{prec} \subset \mathrm{J}$ and the formulation stage is not considered in this model. The buffer mass balance is ignored because the discrete-time model takes care of it in the second step. Based on the results of the precedence-based model, a heuristic chooses the final subset of products that is scheduled by the discrete-time model.

The iterative procedure of presorting and choosing appropriate products to be scheduled in the discrete-time model is shown in Figure 3. The set I^{k}_{prec} denotes the products that are scheduled with the precedence-based model in iteration k. I^{k}_{prec} is generated iteratively from those orders from the initial set of orders I which are not scheduled yet. For the order decomposition a totally ordered set I_{j} of orders is created prior to the optimisation. Details on the computation of I_{j} are described in Yfantis et al. (2019). The order heuristic picks products either from I_{j} or seq_{j} in each iteration. The totally ordered set seq_{j} contains the sequence of orders in line j and is calculated from the solution of the precedence-based model. Deadlines are accounted for in the following manner: For lines $j \notin \mathrm{J}_{prec}$ the set I_{j} is sorted with respect to the deadlines. For lines $j \in \mathrm{J}_{prec}$, the heuristic chooses a product with the closest deadline, if not all products in seq_{j} have the same deadline. Otherwise deadlines pose no issue in the respective iteration and the first product from seq_{j} is taken. After the timing of the products has been determined by the discrete-time model, the allocation and timing information for each line is fed back to compute co_{ij}^{k-1}, C_{max}^{k-1} and the line-specific completion time C_{j}^{k-1}.

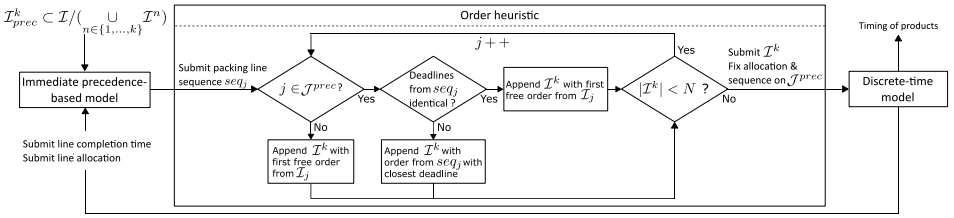

Figure 2: Iterative interaction of the immediate precedence-based model, the discrete-time model, and the order heuristic.

The precedence-based model makes use of binary line-specific immediate precedence variables $X_{ii'j}$, line allocation variables Y_{ij} and first/last-scheduled variables Z^f_{ij}/Z^l_{ij}. The variable $X_{ii'j}$ is active if product i precedes product i' on line j.
In the following the most important equations of the precedence-based model are given:

$$2\cdot(X_{ii'j}+X_{i'ij}) \le Y_{ij}+Y_{i'j}, \quad \forall j \in \mathrm{J}^{prec}, i \in \mathrm{I}^k_{prec}, i' \in \mathrm{I}^k_{prec} \setminus \{i\} \tag{1}$$

$$Z^f_{ij} + \sum_{i' \in \mathrm{I}^k_{prec} \setminus \{i\}} X_{ii'j} \le 1, \quad \forall i \in \mathrm{I}^k_{prec}, j \in \mathrm{J}^{prec} \tag{2}$$

$$Z^l_{ij} + \sum_{i' \in \mathrm{I}^k_{prec} \setminus \{i\}} X_{i'ij} \le 1, \quad \forall i \in \mathrm{I}^k_{prec}, j \in \mathrm{J}^{prec} \tag{3}$$

$$M \sum_{i \in \mathrm{I}^k_{prec}} Z^f_{ij} \ge \sum_{i \in \mathrm{I}^k_{prec}} Y_{ij}, \quad \forall j \in \mathrm{J}^{prec}, M \sum_{i \in \mathrm{I}^k_{prec}} Z^l_{ij} + 2 \ge \sum_{i \in \mathrm{I}^k_{prec}} Y_{ij}, \quad \forall j \in \mathrm{J}^{prec} \tag{4}$$

$$Z^l_{ij} + Z^f_{ij} \le 1, \quad \forall j \in \mathrm{J}^{prec}, i \in \mathrm{I}^k_{prec} \tag{5}$$

$$X_{ii'j} + Z^l_{i'j} + Z^f_{ij} \le 2, \quad \forall j \in \mathrm{J}^{prec}, i \in \mathrm{I}^k_{prec}, i' \in \mathrm{I}^k_{prec} \setminus \{i\} \tag{6}$$

$$2\cdot(2 - Z^f_{ij} - Z^l_{i'j}) + \sum_{\hat{i} \in \mathrm{I}^k_{prec} \setminus \{i',\tilde{i}\}} X_{\tilde{i}ij} + \sum_{\hat{i} \in \mathrm{I}^k_{prec} \setminus \{i,\tilde{i}\}} X_{\tilde{i}ij} \ge 2, \quad \forall i \in \mathrm{I}^k_{prec}, i' \in \mathrm{I}^k_{prec} \setminus \{i\}, \tilde{i} \in \mathrm{I}^k_{prec} \setminus \{i,i'\}, j \in \mathrm{J}^{prec} \tag{7}$$

$$\min_{X_{ii'j}, Y_{ij}, Z^f_{ij}, Z^l_{ij}} -C^{k-1}_{max} + C_{max} + \rho \cdot co^{tot} \tag{8}$$

$$co^{tot} := \sum_{j \in \mathrm{J}^{prec}} \sum_{i \in \mathrm{I}^k_{prec}} co^{k-1}_{ij} Z^f_{ij} + \sum_{l \in \mathrm{L}} \sum_{j \in \mathrm{J}^{prec} \cap \mathrm{J}^l} \sum_{i' \in \mathrm{I}^k_{prec}} \sum_{i \in \mathrm{I}^k_{prec} \setminus \{i'\}} co_{ii'l} X_{ii'j} \tag{9}$$

$$C_{max} \ge C_{il}, \quad \forall i \in \mathrm{I}^k_{prec}, \forall l \in \mathrm{L} \tag{10}$$

$$C_{il} \ge \sum_{j \in \mathrm{J}^{prec} \cap \mathrm{J}^l} (co^{k-1}_{ij} + p_{il}) Z^f_{ij} + \sum_{j \in \mathrm{J}^{prec} \cap \mathrm{J}^l} C^{k-1}_j Y_{ij}, \quad \forall i \in \mathrm{I}^k_{prec}, l \in \mathrm{L} \tag{11}$$

$$C_{i'l} \ge C_{il} + co_{ii'l} + p_{il} - M(1 - X_{ii'j}), \quad \forall j \in \mathrm{J}^{prec} \cap \mathrm{J}^l, i \in \mathrm{I}^k_{prec}, l \in \mathrm{L} \tag{12}$$

Constraint (1), as given in Elekidis et al., (2019), states that if product i' is followed by product i both allocation variables have to be active. Eqs. (2) and (3) prohibit that products which are the first respectively last on their line can be the successor respectively predecessor of another product. Eqs. (4) make sure that there is a first product on every line with at least one product and a last product on every line with at least three products. This is complemented by Eq. (5) allowing each product to either be the first or the last on a line. If there is just one product on a line, Z^f_{ij} is one, as Z^f_{ij} accounts for the changeover with products from previous iterations in the objective function. Eq. (6) prevents that on a line with two products i and i' all three variables Z^f_{ij}, Z^l_{ij} and $X_{ii'j}$ are active. Finally, constraint (7) enforces two different products i and i' being the first and the last product on a line to be the predecessor and successor of at least one other product. For all other combinations of two products not being the first and the last one, the constraint is relaxed. In addition to the above constraints, simple logic constraints, for example prohibiting that

a line can contain more than one first product or that a product is scheduled twice, are imposed.

The objective function Eq. (8) minimizes the makespan and the weighted total changeover time. Eq. (9), which also considers changeover times with previously scheduled products co_{ij}^{k-1}, defines the total changeover time. The objective function is normalized by the parameter C_{max}^{k-1} which is the makespan of the previous iteration to maintain a consistent effect of ρ throughout the iterations. Eq. (10) defines the makespan. Eq. (11) constraints the completion of a product to be at least the previous completion time C_j^{k-1} of the line where product i is allocated plus the processing time p_{il} of this product in the respective stage l. Eq. (12) transforms the precedence relations into the completion time of each product, similar to the completion time constraints in Elekidis et al. (2019).

4. Example

The resulting schedule for an exemplary case is shown in Figure 3. Six formulation lines (Line1L to Line6L) and six packing lines (Line1P to Line6P) are considered. The numbers above the bars indicate the product family of which products are produced respectively consumed by the packing lines. The bars in the formulation lines are not distinguished by different colours, as they do not represent different final products like in the packing lines. Black bars between the product bars indicate changeover times, while dotted lines indicate idle times. The vertical bold dashed grey line represents a deadline at 2019-03-16 08:00 PM. To solve this problem instance $N = 6$ products per iteration and stage were scheduled by the discrete-time model and $N_{prec} = 15$ by the precedence-based model. The time resolution was set to 6 minutes and the penalty parameter ρ was linearly decreased from 20 to 0 to favour a reduced makespan over reduced changeovers and therefore balanced packing lines in later iterations. The buffer was initialised at 50 % of the maximum value. The proposed approach was implemented in Julia 1.1.1 with Gurobi 8.1.0 as the MILP solver on a MS Windows 10 desktop PC (Intel Core i7-3770 CPU @ 3.40 GHz, 32 GB RAM).

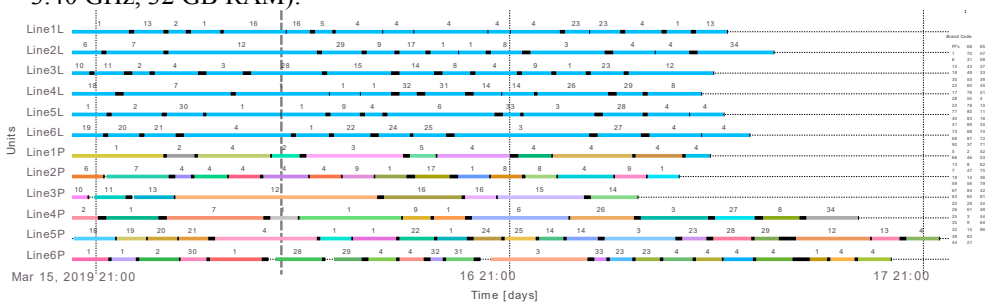

Figure 3: Optimised schedule for the case study.

Due to the demand structure, the last three packing lines, although producing only products that are packed faster, take significantly longer. The algorithm managed to balance the formulation lines well. As can be seen, idle times could not be fully avoided. This is a consequence of significantly different processing rates in the formulation and packing lines which could not be compensated fully by the utilization of the intermediate buffer or from the initially available product families.

In Table 1 the main quality measures for the exemplary case with and without precedence-based presorting are summarized. The precedence-based presorting could improve all criteria listed. While improvements in changeover times are an obvious consequence from

the presorting approach, the reduction in idle times results from dynamically choosing the products on non-presorted lines within the iterations. Also, the computation times could be reduced, as the optimizer that solved the discrete-time model is given less degrees of freedom by fixing the allocation and sequencing decisions for the presorted lines.

Table 1: Comparison of relevant quality measures and computation time of the optimized schedule with and without precedence-based presorting.

Presorting?	Makespan [min]	Completion time packing stage [min]	Changeover time total [min]	Idle time total [min]	Computation time [s]
No	3,042	15,204	2,670	186	739
Yes	3,024	14,940	2,628	120	636
Improvements	0.59 %	1.74 %	1.57 %	35.48 %	13.92 %

5. Conclusions

We presented an iterative solution of a challenging real-world two-stage scheduling problem with intermediate buffer based on a discrete-time formulation. The discrete-time model was extended by a precedence-based presorting algorithm that directly minimizes the changeover times. The precedence-based presorting is used to split the set of orders into tractable subproblems. A heuristic coordinates the proposed sequences from the precedence-based model with the eligibility and deadline constraints to obtain the set of orders that are scheduled in each iteration. The extension improves the quality of the schedules while at the same time reducing the computational time.
The main drawback of the proposed strategy is that it employs only a very limited look-ahead horizon. It would be desirable to enlarge the horizon of the precedence-based optimization but for more than 15 products per iteration a rapid growth of the solution times was observed.

Acknowledgements

The project leading to this publication has received funding from the European Union's Horizon 2020 research and innovation programme under grant agreement No 723575 (CoPro, spire2030.eu/copro) in the framework of the SPIRE PPP.

References

J. Cerda, G. Henning, I. Grossmann, 1997, A Mixed-Integer Linear Programming Model for Short-Term Scheduling of Single-Stage Multiproduct Batch Plants with Parallel Lines, Industrial and Engineering Chemistry Research, 36, 5, 1695-1707
A. Elekidis, F. Corominas, M. Georgiadis, 2019, Optimal short-term Scheduling of Industrial Packing Facilities, Computer Aided Chemical Engineering, 46, 1183-1188
I. Harjunkoski, C. Maravelias, P. Bongers, P. Castro, S. Engell, I. Grossmann, J. Hooker, C. Méndez, G. Sand, J. Wassick, 2014, Scope for industrial applications of production scheduling models and solution methods, Computers and Chemical Engineering, 62, 161-193
V. Yfantis, F. Corominas, S. Engell, 2019, Scheduling of a Consumer Goods Production Plant with Intermediate Buffer by Decomposition and Mixed-integer Linear Programming, Proc. IFAC MIM, Berlin 2019, to appear in IFAC-PapersOnLine

Sauro Pierucci, Flavio Manenti, Giulia Bozzano, Davide Manca (Eds.)
Proceedings of the 30th European Symposium on Computer Aided Process Engineering (ESCAPE30), May 24-27, 2020, Milano, Italy.
http://dx.doi.org/10.1016/B978-0-12-823377-1.50194-4

Optimization of Business Transactional Processes in a Digital Supply Chain

Hector D. Perez,[a] Satyajith Amaran,[b] Esra Erisen,[b] John M. Wassick,[b] Ignacio E. Grossmann[a*]

[a]*Carnegie Mellon University, Pittsburgh 15213, USA*
[b]*The Dow Chemical Company, Midland 48674, USA*
grossmann@cmu.edu

Abstract

A new continuous time multistage scheduling Mixed-Integer Linear Programming (MILP) model is proposed to optimize the business transactional processes in supply chains. The novelty of this approach is in using techniques from the Process Systems Engineering (PSE) and Operations Research (OR) communities to address a side of supply chain optimization (information flow) that has not been targeted previously. This model accounts for the allocation of resources in processing orders at each of the stages of a business transactional process. The objective of the model is to improve customer experience, using on-time-delivery (OTD) as a surrogate metric for this target. An illustrative example, featuring a subset of the business transactional steps in the Order-to-Cash (OTC) process is presented, showing the potential of using mathematical programming to improve supply chain performance. The model enables identifying bottlenecks in the processes and determining where additional resources should be allocated. The model can also be used as a valuable tool to assist customer service representatives in establishing realistic promise-to-delivery dates for their clients.

Keywords: scheduling, MILP, supply chain, optimization, business transactions.

1. Introduction

Supply chains have been traditionally modelled and optimized by the Process Systems Engineering (PSE) (Grossmann, 2012) and Operations Research (OR) (Owen and Daskin, 1998) communities, with the focus being on the optimization of material flow within the supply chain network. Literature has shown the need to expand this vision to also include the financial flows in supply chain optimization. Jahangiri and Cecelja (2014) show how financial models of supply chain can be used to understand the effect of supplier penalty and manufacturer lead time on the company profit. Kees et al. (2019) show the benefits of integrating material and financial flows to improve both the availability of drugs in a hospital supply chain as well as the hospital economic performance. Yi and Reklaitis (2004) show the impact that an integrated material and cash flow model can have on the design of chemical plants. Guillen et al. (2006) show the economic benefits of integrating process operations and financial decisions when optimizing a chemical supply chain. However, there is another type of flow that has been overlooked by the optimization communities: information flow. Supply chains are commonly managed via Enterprise Resource Planning (ERP) systems, which log the data associated with business processes. Previous work in this regard has focussed on

the simulation (Villarraga et al., 2017) and design (Niedermann and Schwarz, 2011) of business processes, rather than the optimization of its operations.

The purpose of this paper is to propose a mathematical programming model for optimizing the transactional processes in a supply chain. As an example, the model is applied to the Order-to-Cash (OTC) business process. The OTC process is one of the business processes present in virtually all companies, involving the transactions that occur between the time when an order is placed by a client, to the time when payment is received for the goods delivered. The objective is to minimize the occurrence of late product deliveries and thus reduce the time between when orders are placed, and payment is received for the delivered products. Additional benefits of the model include helping to inform production order due dates as well as promise-to-delivery dates for order fulfilment. The model presented in the paper is analogous to the sequential multistage models used by the PSE community for scheduling multistage batch plants (Mendez et al., 2006), but it differs in several important respects from the traditional multistage scheduling models. Although the model is a new model for modelling multistage processes, the novelty of this project is in using techniques from the PSE and OR communities to address an aspect of supply chain optimization that has been largely overlooked by the optimization communities.

2. Problem Statement

The OTC process is analogous in its structure to a flowshop problem. When a company receives a set of orders, $o \in O$, from its clients, there are a set of tasks, $l \in L$, that need to be performed by agents, $a \in A$, until products are delivered to the clients and payment of invoices is received. Each agent has a queue with positions $p \in P$ to which orders are assigned for processing. The system can be described as a directed graph of queues that map the trajectory of each order within the supply chain. The overall goal is to assign orders to agents and reorder the queue positions to maximize the number of orders delivered on time. Thus, the problem seeks to find an optimal order processing policy, as opposed to the traditional queue management policies of first-in-first-out (FIFO), last-in-first-out (LIFO), smallest-to-largest, or largest-to-smallest (Villarraga et al., 2017).

3. Mathematical Model

The mathematical model for the OTC process is based on the following assumptions,

1. Order release dates, due dates, and processing times are deterministic. In practice orders are placed dynamically, but in the base model, the system is assumed to be static.
2. There are no transition times for orders between steps or stages in the OTC process. Unlike chemical plants, which require waiting times for materials to be transferred between units, instantaneous transitions are possible since data (information) are available to all agents in the OTC process via the company's ERP system.
3. There are no transitions times between orders in an agent's queue. Unlike chemical processing units, which often require transition times for changeovers, business processing units (agents) can process orders back to back due to their non-material nature.

4. Each order can only be processed at most once at each stage. Inefficiencies in the OTC process may lead to orders being processed multiple times by an agent. However, this degree of complexity is not included in the base model.
5. Each order represents one batch of product. In industrial systems, orders can correspond to multiple sub-orders, and sub-orders can correspond to multiple batches, fractions of batches, or even entire production campaigns in some cases. The assumption of one batch per order is made for simplification purposes.
6. No resource constraints are considered aside from human personnel constraints.

The model described in this section uses continuous time via time slots (Mouret et al., 2011) to model the time events, and is analogous to the model presented by Pinto and Grossmann (1995) for scheduling multistage batch plants. Some differences with the latter model are:

- The model allows for the possibility of not all orders being processed on time. When this occurs in a real scenario, the promise-to-delivery dates would be adjusted by the customer service representatives.
- Order transfers between stages are instantaneous due to the use of ERP systems.
- Based on the agent type, processing times may or may not depend on the quantity ordered.
- Time matching of order stages and unit slots is not required. The assignment of units (agents) to stages is defined *a priori* by the structure of the OTC process steps.
- Instead of minimizing the earliness of an order's end time, the proposed formulation targets maximizing the on-time completion of orders.

3.1. Model Constraints

3.1.1. Time Bounds

There is a start time, $t^s_{o,p,a} \in \mathbb{R}^+$, and an end time, $t^f_{o,p,a} \in \mathbb{R}^+$, for each order assigned to a queue position. The start time occurs between the release date, T^r_o, and due date T^d_o of the order (**Eq. 1**). The binary variable $x_{o,p,a}$ denotes when an agent a has order o in queue position p. The time an order leaves a queue is the sum of the start time and the order processing duration and must occur before the due date of the order (**Eq. 2**). $\tau_{o,a}$ is the average processing time of agent a for order o and can depend on the material quantity requested as well as the material type.

3.1.2. Assignment Constraints

Eqs. 3-4 allow each order to be processed at most once at each stage and allow at most one order to occupy each queue position in the queue of each agent.

3.1.3. Precedence Constraints

Eq. 5 ensures that queue positions are used consecutively in each agent's queue. Agent precedence relations are given in **Eq. 6**. **Eq. 7** enforces that if there is an order present in a queue position, then its start time must be after the end time of the order in the queue position immediately ahead of it. T_{max} is the scheduling horizon. **Eq. 8** ensures that if an order is scheduled to be processed at a downstream stage, it can only be processed after the previous stage, has finished processing it.

$$x_{o,p,a} \cdot T_o^r \leq t_{o,p,a}^s \leq x_{o,p,a} \cdot T_o^d \qquad \forall o \in O, p \in P, a \in A \tag{1}$$

$$t_{o,p,a}^s + \tau_{o,a} \cdot x_{o,p,a} = t_{o,p,a}^f \leq x_{o,p,a} \cdot T_o^d \qquad \forall o \in O, p \in P, a \in A \tag{2}$$

$$\sum_{a \in A_l} \sum_{p \in P} x_{o,p,a} \leq 1 \qquad \forall o \in O, l \in L \tag{3}$$

$$\sum_{o \in O} x_{o,p,a} \leq 1 \qquad \forall p \in P, a \in A \tag{4}$$

$$\sum_{o \in O} x_{o,p_1,a} \geq \sum_{o \in O} x_{o,p_2,a} \qquad \forall p_1, p_2 \in P, p_1 + 1 = p_2, \forall a \in A \tag{5}$$

$$\sum_{a \in A_{l_1}} \sum_{p \in P} x_{o,p,a} \geq \sum_{a \in A_{l_2}} \sum_{p \in P} x_{o,p,a} \qquad \forall l_1, l_2 \in L, l_1 + 1 = l_2, \forall o \in O \tag{6}$$

$$\sum_{o \in O} t_{o,p_1,a}^f \leq \sum_{o \in O} t_{o,p_2,a}^s + T_{max} \cdot \left(1 - \sum_{o \in O} x_{o,p_2,a}\right) \qquad \forall p_1, p_2 \in P, p_1 + 1 = p_2, \forall a \in A \tag{7}$$

$$\sum_{p \in P} \sum_{a \in A_{l_1}} t_{o,p,a}^f \leq \sum_{p \in P} \sum_{a \in A_{l_2}} t_{o,p,a}^s + T_o^d \cdot \left(1 - \sum_{p \in P} \sum_{a \in A_{l_2}} x_{o,p,a}\right) \qquad \forall l_1, l_2 \in L, l_1 + 1 = l_2, \forall o \in O \tag{8}$$

3.2. Objective Function

The On-Time-Delivery (OTD, percentage of orders fulfilled before their due date) metric is a key performance indicator of the OTC process. Since the model is intended for dynamic implementation, the objective function to be maximized is the total number of business transactions (**Eq. 9**), which measures the sum of orders processed by all agents. This is the objective function of choice since it increases the chances of obtaining a high OTD throughout the optimization horizon. Customer segmentation dictates order priority, such that orders from high priority customers have a higher w_o.

$$OTD = \sum_{a \in A} \sum_{p \in P} \sum_{o \in O} w_o \cdot x_{o,p,a} \tag{9}$$

4. Illustrative Example

The MILP model was applied to a subset of the OTC process with three stages and four agents (see **Figure 1**). The order and system details are given in **Tables 1-2**. The illustrative example was run using JuMP 0.19.2 (Julia 1.2.0) with Gurobi 8.1.0 as the MIP solver using a PC with an Intel i7, 1.9 GHz, 64-bit processor, and 24 GB of RAM.

Solution time was 0.07 s to full optimality. To show the benefits of using the model over traditional scheduling, the model results were compared to those of a human scheduler using the priority-first approach (orders are scheduled based on customer priority). The results given in **Figure 2** show that for this case, the human scheduler only attains a 60% order fulfilment, whereas the model provides a schedule with 100% order fulfilment. Thus, the benefits of using the model to schedule the operations of the OTC process are evident in even small cases with five orders. Although a human scheduler could potentially come up with the same schedule as that of the optimizer after much trial and error, such a task becomes virtually impossible as the number of orders increases.

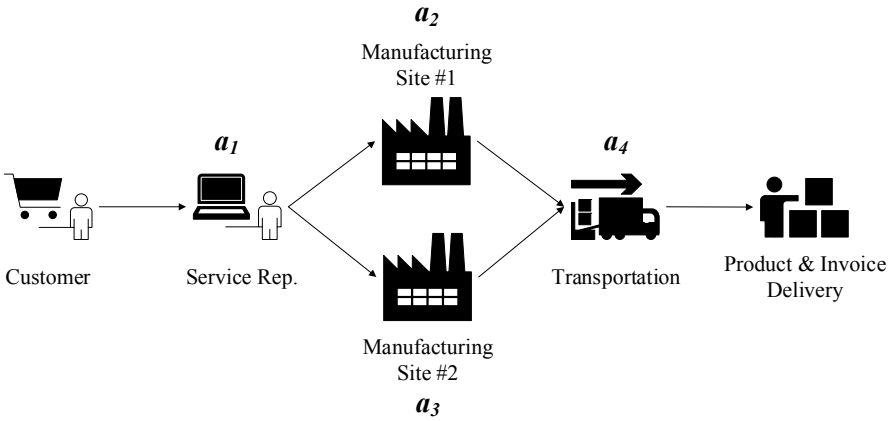

Figure 1. Simplified OTC process flow for illustrative example

Table 1. Order specifications in the illustrative example

Order	1	2	3	4	5
Day Released	0	1	2	2	7
Day Due	10	10	10	12	14
Priority	Medium	High	High	Low	Low

Table 2. OTC agent processing times

Agent	a_1	a_2	a_3	a_4
Processing Time (d)	1	3	3	2

5. Conclusions

A new sequential multi-stage process model is presented to optimize the queues of the agents involved in the OTC business process to improve on-time delivery. An illustrative example is given, which shows that the allocation of resources is key in orders fulfilment. The proposed model can be used to identify bottlenecks in the process and determine which stages need an increase in personnel or a decrease in processing times to improve system performance. Future work in this area includes integrating the business transactional model with manufacturing scheduling models to account for the details involved in the manufacturing and logistic stages of the supply chain. In terms of implementation, a rolling horizon approach can be used for dynamic optimization. Scaling to industrial sized problems, which also contain additional complexities such as rework, and variable processing times will also be addressed in the future.

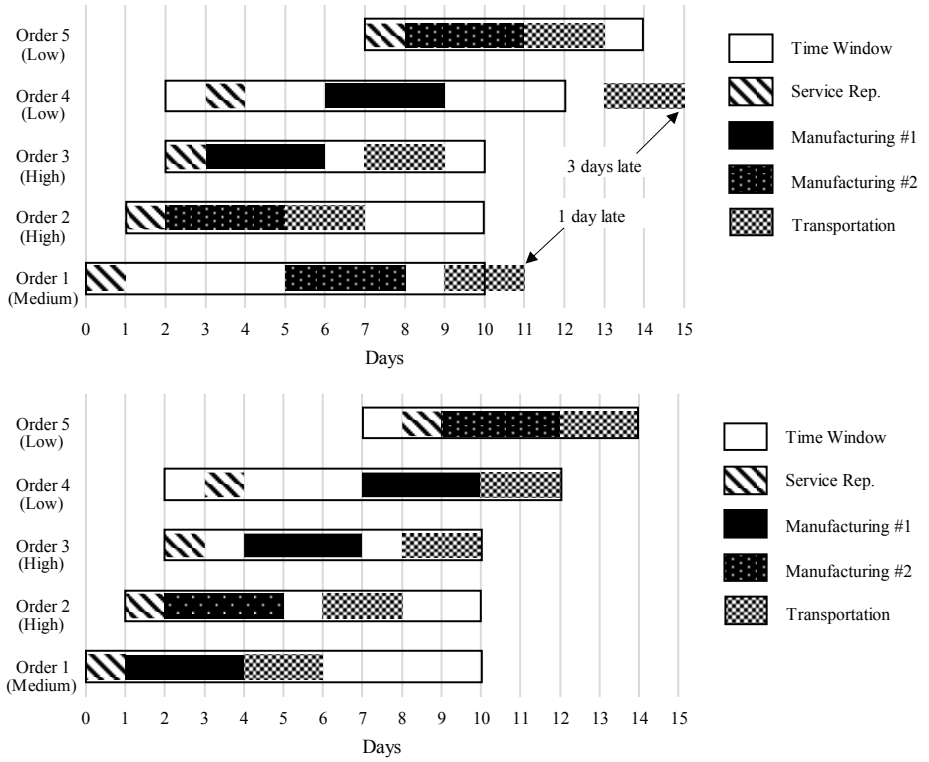

Figure 2. Priority-first human scheduler (top) and model optimized schedule (bottom)

References

I. Grossmann, 2012. Advances in mathematical programming models for enterprise-wide optimization, *Comput. Chem. Eng.*, 47, 2-18.

G. Guillen, M. Badell, A. Espuña, L. Puigjaner, 2006, Simultaneous optimization of process operations and financial decisions to enhance the integrated planning/scheduling of chemical supply chains, *Comput. Chem. Eng.*, 30, 3, 421-436.

M. Jahangiri, F. Cecelja, 2014, Modelling financial flow of the supply chain, IEEE IEEM.

M. Kees, J. Bandoni, M. Moreno, 2019, An optimization model for managing the drug logistics process in a public hospital supply chain integrating physical and economic flows, *Ind. Eng. Chem. Res.*, 58, 9, 3767-3781.

C. Mendez, J. Cerda, I. Grossmann, I. Harjunkoski, M. Fahl, 2006, State-of-the-art review of optimization methods for short-term scheduling of batch processes, *Comput. Chem. Eng.*, 30, 913-946.

S. Mouret, I. Grossmann, P. Pestiaux, 2011, Time representations and mathematical models for process scheduling problems, *Comput. Chem. Eng.*, 35, 6, 1038-1063.

F. Niedermann, H. Schwarz, 2011, Deep Business Optimization: Making Business Process Optimization Theory Work in Practice, *BPMDS 2011, EMMSAD 2011*, Berlin, 88-102.

S. Owen, M. Daskin, 1998, Strategic facility location: A review, *Eur. J. Oper. Res.*, 111, 423-447.

J. Pinto, I. Grossmann, 1995, A Continuous Time Mixed Integer Linear Programming Model for Short Term Scheduling of Multistage Batch Plants, *Ind Eng. Chem. Res.*, 34, 3037-3051.

J. Villarraga, K. Carley, J. Wassick, N. Sahinidis, 2017, Agent-based Modeling and Simulation for an Order-To-Cash Process using NetLogo. Pittsburgh, USA.

G. Yi, G. Reklaitis, 2004, Optimal design of batch- storage network with financial transactions and cash flows, *AIChE J.*, 50, 11.

Sauro Pierucci, Flavio Manenti, Giulia Bozzano, Davide Manca (Eds.)
Proceedings of the 30th European Symposium on Computer Aided Process Engineering (ESCAPE30), May 24-27, 2020, Milano, Italy.
http://dx.doi.org/10.1016/B978-0-12-823377-1.50195-6

Fault Propagation Path Inference in a Complex Chemical Process Based on Time-delayed Mutual Information Analysis

Cheng Ji, Fangyuan Ma, Xuebing Zhu, Jingde Wang, Wei Sun*

College of Chemical Engineering, Beijing University of Chemical Technology, North Third Ring Road 15, Chaoyang District, Beijing, 100029, China
sunwei@mail.buct.edu.cn

Abstract

Process monitoring plays more and more important role in modern process industry. Early root cause isolation is the most attractive character to process operators. Currently, the signed directed graph (SDG) is a widely used method for fault diagnosis, in which graphs are employed to represent the causality between process variables. In most cases, the SDG model is obtained from expert experience. The challenge of this approach is that it is hard to include all knowledge required in complex chemical process operation, which may not be available to experts and operating professionals, as they can be significantly different with changing control strategies, even to same set of process operation. With the universal application of distributed control system (DCS), operation data have been recorded for a certain long time, which contain comprehensive information regarding the process itself. It can be expected that the logic and time dependence among all variables can be extracted with proper analysis method. Mutual information is a commonly used data-based method for measuring the interaction of two objects. The initiator and responder between a pair of variables can be identified by adding an appropriate time lag. In this paper, the identification of fault propagation path is achieved based on a time-delayed mutual information method. When a fault occurs, the response information among variables will be used to explore the propagation path, which provides a more objective information for fault diagnosis. The methodology is applied to a simulated process and a practical industrial case, an ethylene cracking process. The result illustrates that the proposed data-based method shows a good capability for identifying the fault propagation path.

Keywords: fault diagnosis, mutual information, causal analysis, ethylene cracking process

1. Introduction

Abnormal operating conditions in chemical process industry may lead to economic losses and safety accidents. With the ever-increasing concern on safety and economic benefits, early isolation of fault propagation path is of great significance, but on the other side, the complexity of chemical process as well as the large-scale of chemical equipment make it extremely challenging. Generally, the process fault detection and diagnosis methods can be classified into three categories: the first principle model-based methods, the knowledge-based methods and the data-based methods (Frank, 1990).

The first principle model-based methods can show good performance in some simplified ideal processes, but it is almost impossible to establish for an industrial chemical process due to its high complexity. Knowledge-based methods, such as fault tree analysis and expert system, are generally obtained from causal model established by expert

knowledge. As an example tool of expert system, the signed directed graph (SDG) model is widely used for fault diagnosis. However, the challenge of this method is that it is unable to get sufficient knowledge about the process to establish an objective causality model. In contrast, with the wide application of DCS system, the data-based methods have received more and more attention of researchers. Under this category, the contribution plots are widely used for fault diagnosis in industrial processes (Miller, et al., 1998). Generally, the variable with the largest contribution are considered as the root cause of the fault, but sometimes the variable with the largest contribution may be a state variable, which is a result caused by the fault. Vedam and Venkatasubramanian (1999) combined the advantages of the contribution plots and the SDG model, and proposed a model based on the principal component analysis (PCA) and SDG to solve the above problem. However, due to the difference of automatic control strategies applied to a particular system, causal relationship between variables may be inconsistent with previous obtained expert knowledge, which will lead to incorrect fault diagnosis result. The mutual information analysis, as a completely data-based variable correlation identification method, is able to reflect the actual situation of the process. In addition, the mutual information algorithm has an advantage in detecting both linear and nonlinear relationships between variables (Li et al, 2018), making it suitable for fault diagnosis in nonlinear processes, such as chemical processes.

In this work, sufficient historical data is used to obtain the mutual information threshold matrix, the correlation between process variables is identified by comparing the mutual information value in the abnormal state with the threshold, and then the diagnosis of fault propagation path under different control strategies is achieved in a simulated process. An ethylene cracking process as a practical case is studied using the proposed method.

2. Methodology

2.1. Time-delay mutual information(TDMI)

The concept of mutual information is derived from Shannon entropy, which is a measurement of the uncertainty of a random variable proposed by Shannon (Shannon C E, 1948). For two-dimensional random variables X, Y, the independence between them can be measured using the formula as follows:

$$I(X,Y) = -\iint_{xy} p(x,y) \log \frac{p(x,y)}{p(x)p(y)} dydx \tag{1}$$

where $p(x, y)$ is the joint probability of variables X and Y. According to the formula, mutual information is symmetric. In order to establish causal relationships between two variables, TDMI can be applied by adding a time lag to the calculation:

$$I(X,Y,\tau) = -\iint_{xy} p(x+\tau,y) \log \frac{p(x+\tau,y)}{p(x+\tau)p(y)} dydx \tag{2}$$

where $p(x + \tau, y)$ is the joint probability distribution of $X = x + \tau$ and $Y = y$. The time lag parameter τ indicates the time delay when the value of mutual information reaches its peak. A positive τ indicates that the information is transferred from Y to X, which means X is affected by Y, while a negative τ indicates that Y is affected by X.

2.2. Estimation of probability density

The key point or difficulty of the calculation of TDMI lies in the estimation of joint probability. In this work, kernel density estimation model is applied to estimate the

probability by considering each sample value of a variable (Silverman, 1986). A kernel function K is centered at every sample point and summed to give an estimation:

$$p(x) = \frac{1}{n}\sum_{i=1}^{n} K(x - x_i) \tag{3}$$

where $K(x)$ is the kernel function, Gaussian function is selected here as the kernel function:

$$K(x - x_i) = \frac{1}{\sqrt{2\pi}d}\exp\left(-\frac{(x - x_i)^2}{2d^2}\right) \tag{4}$$

where d is the bandwidth determined by the number of samples N and the standard deviation of the variable X. The estimation of joint probability density distribution can be constructed in a similar way.

2.3. Significant control limit and fault propagation path

According to the definition of mutual information, the value of mutual information has no upper bound. In order to identify the fault propagation path, it is significant to set up a confidence limit. When the system is under normal condition, each variable is in the vicinity of the set value range and can be regarded as independent of each other. The value of mutual information is at a small value other than 0 due to the presence of noise, and a threshold can be determined from the normal operating state. Once a fault occurs, the value of mutual information between two variables exceed this threshold, indicating that they have an interaction relationship, and the direction of the fault propagation path can be obtained from the time lag.

3. Application of the proposed methodology

In this chapter, the proposed methodology is applied to a continuous stirred tank heater (CSTH) simulation process and an ethylene cracking unit.

3.1. Continuous stirred tank heater (CSTH)

The CSTH is a common unit in the chemical process industry. It is built using the first principal models and the real disturbance data (Thornhill, et al., 2008). There are totally six variables as shown in Table 1. In the stirred tank, the cold water and the hot water are mixed together, and the mixture is heated by steam. Finally, the heated mixed water is discharged from the bottom of the heating tank.

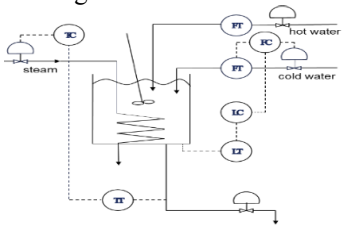

Figure 1: The CSTH: control strategy 1

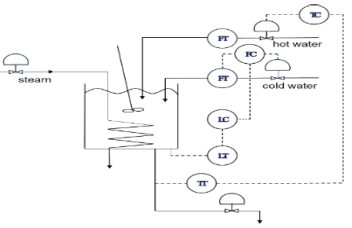

Figure 2: The CSTH: control strategy 2

There are two different control strategies. In Figure 1, the temperature is controlled by steam valve demand. And in Figure 2, the temperature is controlled by the hot water valve demand. Each condition contains 4,500 sample points with a sampling frequency of 1 second and a step fault on the steam flow valve occurs at 3,500th sample.

Table 1: Variables in the CSTH

Variables	Description	Variables	Description
CW	cold water valve demand	LEVEL	level of the tank
HW	hot water valve demand	STEAM	steam valve demand
OW	output water flow rate	TEMP	temperature

3.2. Ethylene cracking furnace

The process of naphtha steam cracking to produce ethylene plays an important role in chemical industry. In pyrolysis furnace, the mixture of naphtha and steam are preheated in convection section and crack in radiation section. The information of major variables is shown in Table 2. The application of the proposed TDMI based fault diagnosis methodology is demonstrated on this process.

Table 2: Variables in ethylene cracking furnace

Variables	Description	Variables	Description
F	Naphtha mass flow rate	P2	Crossover section pressure
COT	Coil outlet temperature	TA	Temperature in furnace A side
P1	Naphtha pressure	TB	Temperature in furnace B side
DS	Diluted steam mass flow rate	QL	Total fuel gas calorific value

3.3. Implement procedure

As mentioned above, the value of mutual information between some pairs of variables will fluctuate with the occurrence of the fault. The fault propagation path model is established based on this principle. As is shown in the figure 3, a PCA model and a significance threshold matrix of mutual information are first established with the historical data in steady state. Once a fault occurs, the value of mutual information between each pair of variables is calculated and compared with the threshold. If the value exceeds the threshold, the corresponding position of the matrix is taken as 1, otherwise 0. The final causal matrix is represented by a SDG and the root cause of the fault is obtained.

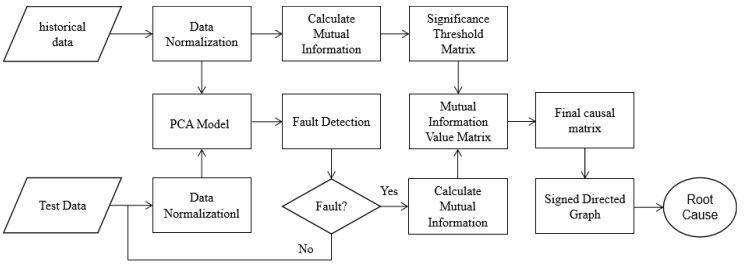

Figure 3: Fault detection and diagnosis procedure

4. Result and discussion

4.1. Results of the CSTH simulation process

For the first condition, the result of the fault detection is shown in Figure 4. It can be seen that the value of T^2 statistic exceeds the 99% control limit at 500th sample, indicating that a fault has been detected. The mutual information value between each pair of variables is shown with the significance thresholds in Table 3.

Variables	CW	OW	LEVEL	HW	TEMP	STEAM
CW		-0.147(0.318)	0.031(0.288)	0.043(0.280)	-0.049(0.252)	-0.193(0.277)
OW			-0.055(0.343)	-0.041(0.248)	-0.099(0.242)	-0.188(0.420)
LEVEL				-0.024(0.247)	0.023(0.366)	0.013(0.355)
HW					0.038(0.242)	-0.001(0.253)
TEMP						0.584(0.231)
STEAM						

Table 3: Mutual information value matrix

It can be seen from the Table 3 that only the mutual information value between the temperature and the steam flow exceeds the threshold. A SDG is depicted in Figure 5 and the time lag is 12 seconds, indicating that the direction of fault propagation is from the steam flow to the temperature. Therefore, it can be concluded that the root cause of the fault is the steam flow, which is verified by operation record.

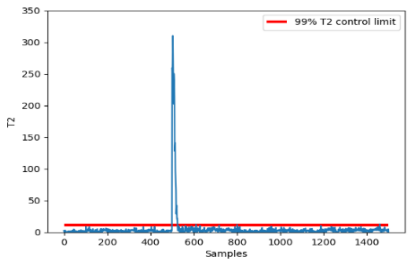

Figure 4: Fault detection result 1

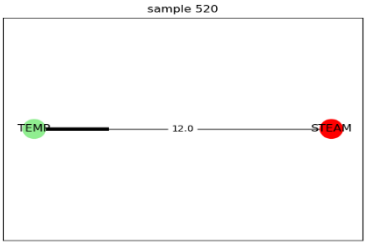

Figure 5: Fault diagnosis result 1

For the second condition, in the similar way, the fault detection result is shown in Figure 4. The mutual information matrix and its threshold are shown in Table 4.

Table 4: Mutual information value matrix

Variables	CW	OW	LEVEL	HW	TEMP	STEAM
CW		-0.284(0.318)	0.302(0.288)	0.260(0.280)	-0.224(0.252)	0.233(0.277)
OW			0.134(0.343)	-0.145(0.248)	-0.136(0.242)	0.138(0.420)
LEVEL				0.302(0.247)	0.245(0.366)	0.195(0.355)
HW					0.329(0.242)	0.366(0.253)
TEMP						0.331(0.231)
STEAM						

According to the fault diagnosis result in Figure 7, it can also be concluded that the steam valve is the root cause of the fault. However, the fault propagation path is different due to the difference in control strategy. In this condition, when the temperature is fluctuated by the fault in the steam valve, the hot water valve is controlled to restore the temperature. Then the level is affected by the fluctuation of the hot water flow and the cold water valve is controlled to restore the level. It can be noted in this case that the interrelationships between variables vary when the same fault occurs under different control strategies.

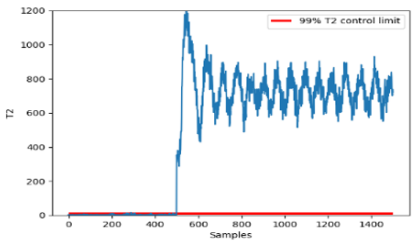

Figure 6: Fault detection result 2

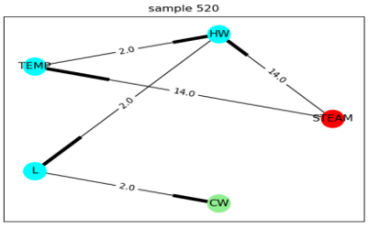

Figure 7: Fault diagnosis result 2

4.2. Results of the ethylene cracking process

In this section, data for a complete production cycle in ethylene cracking process with one-minute interval is selected to test the applicability of the proposed method. As shown in Figure 8, the fault is detected since the 87489th sample. The mutual information between variables is then calculated. The result of part of the variables and the threshold

obtained from steady state are shown in Table5, and the fault diagnosis result is shown in Figure 9.

Table 5: Mutual information value matrix

Variables	F	DS	COT	TA	TB	QL
F		-0.103(0.153)	-0.033(0.154)	0.031(0.122)	0.096(0.165)	0.046(0.160)
DS			-0.046(0.192)	-0.051(0.151)	0.050(0.203)	-0.023(0.152)
COT				0.186(0.315)	0.409(0.309)	1.035(0.258)
TA					-0.178(0.327)	-0.173(0.324)
TB						0.506(0.244)
QL						

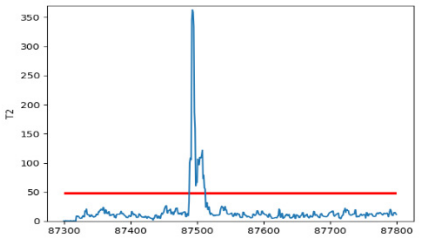

Figure 8: Fault detection result

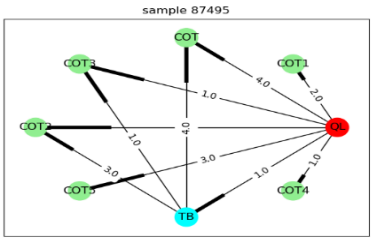

Figure 9: Fault diagnosis result

The result indicates that temperature in furnace B side rises due to high total fuel gas calorific value. And the high total COT and COT in whole coil 6 caused by high temperature in furnace B side lead to the alarm. Therefore, the root cause of this fault is the fluctuation of fuel gas feed flow. As shown above, with comparing the TDMI value with the threshold, the fault propagation path and the root cause of the fault is recognized.

5. Conclusions

In this work, the interaction between variables is correctly identified by TDMI analysis. By the proposed method, the fault diagnosis in both a simulated CSTH under different control strategies and an ethylene cracking unit has been implemented. Not only the root cause of the fault can be isolated, but also the fault propagation path can be identified, which is consistent with process operation record. The method provides a brand new way to obtain the causal relation between variables for fault propagation path identification solely based on the historical data, which makes the online fault diagnosis more feasible.

References

P. M. Frank, 1990, Fault diagnosis in dynamic systems using analytical and knowledge-based redundancy: A survey and some new results, Automatica, 26(3), 459-474.

P. Miller, R. Swanson and C. Heckler, 1998, Contribution Plots: A missing link in multivariate quality control, Appl. Math. and Comp. Sci., 4(8), 775-792.

H. Vedam, V.Venkatasubramanian, 1999, PCA-SDG based process monitoring and fault diagnosis, Control engineering practice, 7(7), 903-917.

S. Li, Y. Xiao, D. Zhou, D. Cai, 2018, Causal inference in nonlinear systems: Granger causality versus time-delayed mutual information, Physical Review E, 97(5).

C. E. Shannon, 1948, A mathematical theory of communication, Bell Labs Technical Journal, 27(4):379-423.

B. W. Silverman, 1986, Density estimation for statistics and data analysis, London, U.K.: Chapman & Hall.

N. F. Thornhill , S. C. Patwardhan and S. L. Shah, 2008, A continuous stirred tank heater simulation model with applications, Journal of Process Control, 18(3-4):347-360.

Sauro Pierucci, Flavio Manenti, Giulia Bozzano, Davide Manca (Eds.)
Proceedings of the 30th European Symposium on Computer Aided Process Engineering (ESCAPE30), May 24-27, 2020, Milano, Italy.
http://dx.doi.org/10.1016/B978-0-12-823377-1.50196-8

Dynamic Optimization of an Emulsion Polymerization Process Using an Embedded Monte Carlo Model for Bimodal MWD

Johannes M. M. Faust, Lars Henrichfreise, Adel Mhamdi, Alexander Mitsos*

AVT Process Systems Engineering, RWTH Aachen University, 52056 Aachen, Germany
amitsos@alum.mit.edu

Abstract

The molecular weight distribution (MWD) of polymers affects many end-use properties and is therefore a major production target. The desired MWD can also be multi-modal, which can be achieved by using chain-transfer agents. As these products are specialty chemicals, they are most often produced in semi-batch operation leading to inherent non-linear dynamics. By using dynamic optimization, production time can be reduced while producing the targeted quality. In this work, we consider the model-based dynamic optimization of an emulsion polymerization process to achieve a bimodal MWD while reducing the batch time. The degrees of freedom consist of the isothermal reactor temperature, feed rates of monomer, initiator and chain-transfer agent. We use a combined model consisting of a deterministic kinetic model and a stochastic Monte Carlo polymer architecture model. The kinetic model describes macroscopic variables, such as concentrations. Distinct chains are simulated in a polymer particle using the Monte Carlo model, and many particles are computed in parallel. The time-varying reaction rates used in the Monte Carlo model are computed in the kinetic model. By taking all simulated chains and their respective weights, the MWD can be constructed. A Monte Carlo approach is chosen as it allows to simulate properly the transfer to polymer and branching reactions. To solve the dynamic optimization problem, we select a derivative-free surrogate model based optimizer due to the stochastic nature of the Monte Carlo model. For the Monte Carlo model, gradients are not readily available. The results show a reduction of the batch time between 6.2 and 7.5 % compared to the base recipe while the product quality is satisfied.

Keywords: Dynamic Optimization, molecular weight distribution, derivative-free optimization, Monte Carlo simulation

1. Introduction

Polymers produced via emulsion polymerization have various applications such as paints, adhesives or drug delivery. For each use case, the polymer product should have usually different properties like viscosity, stickiness, etc. An important quality attribute of polymers is the molecular weight distribution (MWD), which can be narrow or broad, unimodal or bimodal. Due to strong competition among manufactures, optimal process operations can save cost and therefore protect operating margins. Especially polymer products are affected heavily by process operations, as they are known to be products-by-process (Asua, 2007). Therefore, optimal process operations must both increase the economic benefit and achieve the same customer demanded quality. Several authors have

addressed the problem of optimal control of polymerization processes. Sayer et al. (2001) use iterative dynamic programming to optimize the operations of a semicontinuous emulsion process with fixed batch time to reach a desired MWD in-silico. The MWD is computed via an adaptive collocation technique. Vicente et al. (2001) decompose the MWD into instantaneous MWD distributions over the global conversion, which is possible as only linear polymer chains are considered. They optimize the total process time. Vicente et al. (2002) also use iterative dynamic programming to achieve a desired composition and MWD, which is modeled by adaptive orthogonal collocation. They test the computed optimal feed rates in a lab scale reactor and achieve MWDs fairly close to the desired ones. Saliakas et al. (2007) optimize for minimal batch time and the deviation to the desired MWD is added as quadratic penalty to the objective function. Two models describing the MWD of the homopolymerization are compared, one model with fixed pivots and one using orthogonal collocation on finite elements. Pontes et al. (2011) model the MWD with orthogonal collocation for a continuous steady state operation and optimize operations for an economic objective function, consisting of the cost of raw materials and sale price of product.

All the works mentioned so far use deterministic models to describe the MWD. Despite the vast use of Monte Carlo models for polymerization systems, there is little work on the optimization with such models embedded. Gao et al. (2018) compare three derivative-free optimizers in case studies with a kinetic Monte Carlo process embedded. A free-radical polymerization is modeled which allows to describe microstructural aspects of the copolymer such as the dyad fractions. Ma et al. (2018) employ a steady-state Monte Carlo simulation in a derivative-free optimization environment. The chemical composition distribution is used as a micro-structural quality attribute. Overall the optimization problem consists of seven degrees of freedom. Mohammadi et al. (2018) use the outputs of a Monte Carlo model to train an artificial neuronal network which is optimized using a genetic algorithm to find optimum reaction conditions consisting of the monomer ratio, catalyst composition and chain shutting agent concentration.

In this contribution, a typical industrial setting is considered, where a given recipe should be optimized. The desired MWD is known from a reference batch. Using this recipe as starting point, an optimal process operation scheme is computed achieving the same MWD as quality while reducing the batch time. The contribution is structured as follows. In Section 2, the model and its extensions are briefly described. The dynamic optimization problem is formulated in Section 3 and its solution approach is presented. A case study with a bimodal MWD is dealt with in Section 4 and the contribution is summarized and conclusions are drawn in Section 5.

2. Model description and model extensions

The considered copolymerization is modeled by a hybrid model consisting of a deterministic kinetic model and Monte Carlo model describing the polymer chains described by Chaloupka et al. (2017) and shortly introduced here. The macroscopic variables, like concentrations, are solved using a deterministic kinetic model of the emulsion polymerization. Then, the computed trajectories of reaction rates are used in the Monte Carlo simulation, where each single particle is computed and individual chains are simulated. The Monte Carlo simulation is sped up by considering the propagation reaction separately. The models are implemented in Matlab. As it is assumed that the polymer particles do not influence each other, they can be computed easily in parallel. For this contribution, this model is extended by chain-transfer agent (CTA) and its related reactions. Therefore, bimodal distributions can be simulated and optimized. Chain

transfer agents increase the chain transfer reaction rate and lead in general to shorter chains. For a bimodal distribution, the CTA is added in a later stage to produce shorter chains while the long chains have already been generated. The new chain transfer reaction is added to the overall scheme:

$$M_n^{\bullet} + R - X \rightarrow M_n - X + R^{\bullet}, \tag{1}$$

where Mn, R-X, the superscript $^{\bullet}$ define a polymer chain with n monomeric units, the chain transfer agent and a radical, respectively. The parameters for the CTA kinetics are chosen from literature. An isothermal operation is assumed.
In the overall simulation scheme, the kinetic part cannot be parallelized in the same fashion as the Monte Carlo part. However, for different inputs, different ODE integrators compute the solution faster. Matlab offers six different integrators, each with different advantages and disadvantages. There is no additional cost to integrate the kinetic model with all available integrators in parallel and the simulations are stopped after the first result is available. All integrators use the same integration tolerances and the same model. Compared to (Faust et al., 2019), a new binning strategy for the computed chains is applied which increases the exactness of the MWD calculation. Here, the computed polymer chains from all particles are taken and binned into the MWD. Therefore, the computation accuracy increases.

3. Dynamic optimization problem formulation and solution approach

The goal of the dynamic optimization is to find an operating scheme that minimizes the batch time while producing the desired MWD, which is given by the base recipe operation (2). In Faust et al. (2019) the reactor temperature, batch time, monomer and initiator feed are optimized. Here, the CTA feed is added to the degrees of freedom.

$$\min_{\dot{m}_M(t),\dot{m}_I(t),\dot{m}_{CTA}(t),T_R,t_f} \quad t_f \tag{2a}$$

$$\text{s.t. kinetic ODE model} \tag{2b}$$

$$\text{stochastic MWD model} \tag{2c}$$

$$\int_{t_0}^{t_f} \dot{m}(t)_M dt = m_M^{total} \tag{2d}$$

$$T_R^{min} \leq T_R \leq T_R^{max} \tag{2e}$$

$$\epsilon_{MWD}^{max} \geq \sum_{k=1}^{N_k} (MWD(k) - MWD^{ref}(k))^2 \tag{2f}$$

$$X^{ref} \leq X(t_f) \tag{2g}$$

where $\dot{m}_M(t), \dot{m}_I(t), \dot{m}_{CTA}(t), T_R, t_f$ refer to the monomer feed rate, initiator feed rate, CTA feed rate, reactor temperature and total time, respectively. ϵ_{MWD}^{max} denotes the absolute squared deviation to the reference MWD and is constrained in (2f). Constraint (2g) refers to the minimum conversion at the end of the batch.

In this work, the open source solver MaTSumoTo, developed by Müller et al. (2013), is used. A thin-plate spline with a polynomial tail is used as surrogate function. Matlab's fmincon is used as local optimizer of the surrogate function. Two new sample points are

generated for each version of the surrogate function. If these two sample points are close to each other or close to already evaluated inputs, the search space is explored by maximizing the distance the evaluated points. As we optimize the surrogate with a local gradient-based optimizer, we can add constraints if we know the underlying function in terms of the degrees of freedom. Of course, the reformulation using penalties would not be necessary, if we have a functional expression of all constraints using the degrees of freedom. One could argue that at least the conversion constraint (2g) could be added as nonlinear constraint as it depends only on the evaluation of the ODE system. However, this would slow down the optimization of the surrogate with such an embedded ODE problem. Therefore, only the ratio feeds are used as linear inequality constraints (3b) to the optimization problem to be solved:

$$\min_{\substack{x_j^M, x_j^I, \hat{m}_I^{total}, x_j^{CTA}, \hat{m}_{CTA}^{total}, \hat{T}_R, \hat{t}_f \\ j\in[2,\ldots,N]}} \sum_{k=1}^{N_k} (MWD(k) - MWD^{ref}(k))^2 + w_{time} t_f^2 + w_{conv} (\min(0, X(t_f) - X^{ref}))^2 \quad (3a)$$

$$\text{s.t.} \sum_{j=2}^{N} x_j^p \leq 1 \quad \forall p \in \{M, I, CTA\} \quad (3b)$$

4. Case study with bimodal target MWD

In this case study, a given reference batch recipe is optimized for batch time while achieving the same quality measures, such as the molecular weight distribution and the overall monomer conversion at the end of the batch. The desired bimodal molecular weight distribution is a result of the use of CTA.

The reference process operation takes 12600 seconds. The monomers are fed for the first 9000 seconds, and the CTA is fed from that time point on for one hour. The initiator feed is stopped after 7200 seconds. The problem is discretized using seven piecewise constant control profiles for each controlled feed rate. No CTA is fed during the first two control intervals, as it is known that the CTA will shorten the chains and the long chains will not be generated. Together with the reactor temperature and the total batch time, the problem consists of 20 degrees of freedom for optimization. The number of function evaluations is limited to 1000. In Table 1, an overview of the numerical results is given, both for the reference case and three optimization runs. As the model is stochastic and the optimization of the surrogate is started from random points, the optimization is started three times to check the consistency of the result. In total, 100 particles are simulated in parallel with the Monte Carlo model.

Compared to the reference, the batch time is reduced between 6.2 and 7.4% for the three runs by the optimization. The trajectories for different key states and inputs are shown in Figure 1. The reactor temperature is more or less unchanged compared to the reference, which is an indication that the quality is affected strongly by the reactor temperature. The reactor temperature difference between the runs is less than 0.2 K. In a pure batch time minimization with an inequality constraint on the overall conversion only, it is expected that the reactor is operated at the maximum allowed temperature. The overall conversions for the three runs differ in the first interval, but are relatively similar from that point on. The monomer feed for the optimized cases is higher than in the reference case leading to a faster reaction rate. Qualitatively, the optimized CTA feed very similar to the reference, only the total amount is increased.

Table 1 Numeric values of reference and optimization runs

	Conversion[-]	Time[s]	Objective value	Time saving[%]
Reference	0.984	12600	1.68	-
Run 1	0.983	11777	1.47	6.5
Run 2	0.983	11815	1.47	6.2
Run 3	0.982	11662	1.47	7.4

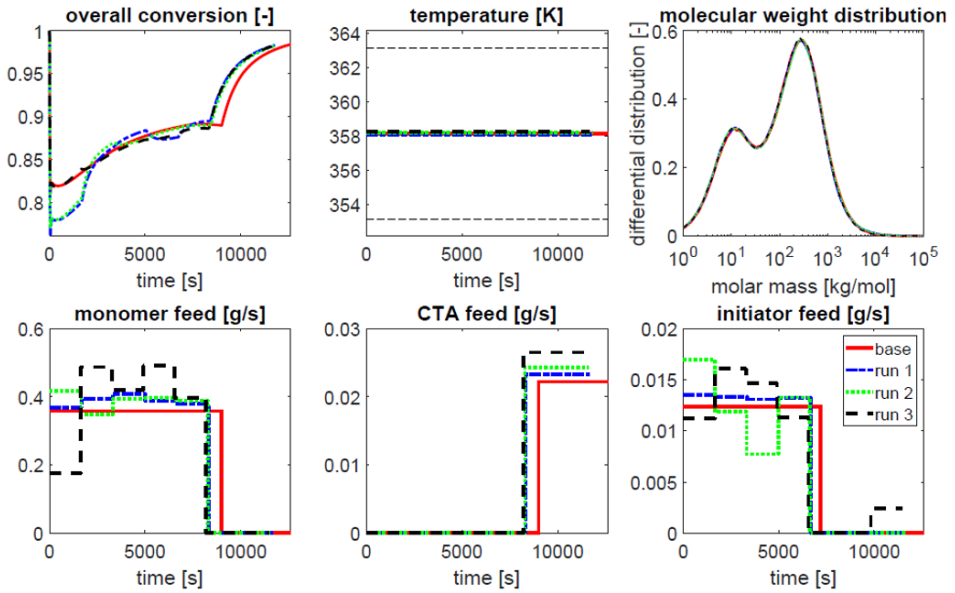

Figure 1 Trajectories of the conversion, reactor temperature, molecular weight distribution, monomer, initiator and chain transfer agent feed for the reference case and the three optimization runs.

The initiator in the base recipe is stopped after 57% of the batch time. This behavior is still observed for the best solutions found, while the total initiator amount is larger.

5. Summary and Conclusion

We presented an approach to optimize the process operation of a semi-batch reactor while achieving desired product specifications. The molecular weight distribution defines the product quality and is bimodal due to the use of chain transfer agent being added during the end of the batch. As the underlying model has embedded Monte Carlo simulations, a gradient-free optimization solver is used. A surrogate model is built from objective function evaluations, which consists of the objective and penalty terms for the nonlinear constraints where no algebraic function of degrees of freedom is known. Using random starting points, the surrogate model is optimized locally to generate new sample points and which are used to update the surrogate function. For the case study considered, the batch time is reduced between 6.2 and 7.2 % while achieving the same polymer properties. The optimization problem formulation is flexible and does allow for integrated

product and process development. It can be tested whether for a given new molecular weight distribution, a process producing this quality can be found.

Acknowledgement

The financial support of the RECOBA project (funding from European Framework Horizon 2020, No. 636820) and the support of the KoPPonA 2.0 project of the German Federal Ministry for Economic Affairs and Energy (BMWi) under grant number 03EN2004L and the project supervision by the project management organization Projektträger Jülich (PtJ) is gratefully acknowledged.

References

Asua, J. M., 2007. Polymer Reaction Engineering. Blackwell Pub, Oxford, UK and Ames, Iowa, USA.

Chaloupka, T., Zubov, A., Kosek, J., 2017. Real-time hybrid monte carlo method for modelling of 4 monomer semi-batch emulsion copolymerization. In: 27th European Symposium on Computer Aided Process Engineering. Vol. 40 of Computer Aided Chemical Engineering. Elsevier, pp. 259–264.

Faust, J. M. M., Chaloupka, T., Kosek, J., Mhamdi, A., Mitsos, A., 2019. Dynamic optimization of an emulsion copolymerization process for product quality using a deterministic kinetic model with embedded monte carlo simulations. Computers & Chemical Engineering 130, 106566.

Gao, H., Waechter, A., Konstantinov, I. A., Arturo, S. G., Broadbelt, L. J., 2018. Application and comparison of derivative-free optimization algorithms to control and optimize free radical polymerization simulated using the kinetic Monte Carlo method. Computers & Chemical Engineering 108, 268–275.

Ma, Y., Chen, X., Biegler, L. T., 2018. Monte-Carlo-simulation-based optimization for copolymerization processes with embedded chemical composition distribution. Computers & Chemical Engineering 109, 261–275.

Müller, J., Shoemaker, C. A., Piché, R., 2013. SO-MI: A surrogate model algorithm for computationally expensive nonlinear mixed-integer black-box global optimization problems. Computers & Operations Research 40 (5), 1383–1400.

Mohammadi, Y., Saeb, M. R., Penlidis, A., Jabbari, E., Zinck, P., Stadler, F. J., Matyjaszewski, K., 2018. Intelligent Monte Carlo: A new paradigm for inverse polymerization engineering. Macromolecular Theory and Simulations 6, 1700106.

Pontes, K. V., Embiruçu, M., Maciel, R., Hartwich, A., Marquardt, W., 2011. Optimal process operation for the production of linear polyethylene resins with tailored molecular weight distribution. AIChE Journal 57 (8), 2149–2163.

Saliakas, V., Chatzidoukas, C., Krallis, A., Meimaroglou, D., Kiparissides, C., 2007. Dynamic optimization of molecular weight distribution using orthogonal collocation on finite elements and fixed pivot methods: An experimental and theoretical investigation. Macromolecular Reaction Engineering 1 (1), 119–136.

Sayer, C., Arzamendi, G., Asua, J., Lima, E., Pinto, J., 2001. Dynamic optimization of semicontinuous emulsion copolymerization reactions: composition and molecular weight distribution. Computers & Chemical Engineering 25 (4-6), 839–849.

Vicente, M., Leiza, J. R., Asua, J. M., 2001. Simultaneous control of copolymer composition and MWD in emulsion copolymerization. AIChE Journal 47 (7), 1594–1606.

Vicente, M., Sayer, C., Leiza, J. R., Arzamendi, G., Lima, E., Pinto, J., Asua, J. M., 2002. Dynamic optimiza- tion of non-linear emulsion copolymerization systems Open-loop control of composition and molecular weight distribution. Chemical Engineering Journal 85 (2-3), 339–349.

Sauro Pierucci, Flavio Manenti, Giulia Bozzano, Davide Manca (Eds.)
Proceedings of the 30th European Symposium on Computer Aided Process Engineering (ESCAPE30), May 24-27, 2020, Milano, Italy.
http://dx.doi.org/10.1016/B978-0-12-823377-1.50197-X

A Hybrid Model Predictive Control Strategy using Neural Network Based Soft Sensors for Particle Processes

Rasmus Fjordbak Nielsen, Krist V. Gernaey, Seyed Soheil Mansouri*

Process and Systems Engineering Centre, Department of Chemical and Biochemical Engineering, Technical University of Denmark, Kongens Lyngby, 2800, Denmark
seso@kt.dtu.dk

Abstract

Particle processes, such as crystallization, flocculation and emulsification constitute a large fraction of the industrial processes for removal of insolubles, product isolation, purification and polishing. The outcome of these processes typically needs to comply with a given set of quality attributes related to particle size, shape and/or yield. With recent technological advances in commercially available on-line/at-line particle analysis sensors, it is now possible to directly measure the particle attributes in real-time. This allows for developing new direct control strategies. In this work, a model predictive control (MPC) strategy is presented based on a hybrid machine-learning assisted particle model. The hybrid model uses mechanistic models for mass and population balances and machine learning for predicting the process kinetics. In the presented approach, the hybrid model is trained in real-time, during process operation. Combined with MPC, this allows for continuous refinement of the process model. Thereby, the calculated control actions are provided robustly. This approach can be employed with limited prior process knowledge, and allows for directly specifying the target product properties to the controller. The presented control strategy is demonstrated on a theoretical case of crystallization to show the potential of the presented methodology.

Keywords: Hybrid model, Machine learning, Soft-sensor, On-line particle analysis, Model predictive control (MPC)

1. Introduction

Particle processes, including crystallization, fermentation and flocculation play an important role in many chemical and biochemical industries. However, due to their complexity, these processes also pose a number of challenges when it comes to monitoring and process control. The outputs of many of these processes are required to comply with a number of quality attributes related to particle size, shape and/or yield. However, due to a historical lack of on-line sensor data on these attributes, the processes have historically been controlled using heuristics and based on indirect process variables. At the same time, the kinetics behind these processes are highly non-linear and multivariable, which results in process variations in industry, and in the end also significant product losses.

In the last two decades, a number of on-line and at-line particle analysis sensors have become commercially available, opening up for the development of new control strategies for particle processes. This includes flow-cell system based dynamic particle analysis (QicPic, ParticleTech), in-line dynamic particle analysis (PVM from Mettler Toledo) and

laser based techniques such as Focused Beam Reflectance Measurement (FBRM). Especially FBRM has been examined in new control strategies, especially within control of crystallization processes. FBRM allows for obtaining a relative count of particles in a given liquid suspension, and a chord-length size distribution. The chord-length size distribution gives an estimate of the mean particle size distribution, along one axis, and thus not a direct measure of the particle dimensions.

Both model-based and model-free control approaches have been suggested using these new monitoring tools (Nagy et al. (2013)). Amongst the model-free control approaches, direct nucleation control (DNC) has shown acceptable results for several crystallization cases, using only little prior process knowledge, by controlling the FBRM count of crystals to a given set-point. However, this approach only gives an indirect control over the particle size properties, as it is the count that is controlled. Model-based control approaches have also been suggested, where the process kinetics have been assumed to follow a number of mathematically simple kinetic expressions, where a number of parameters are estimated based on experimental data. Eren et al. (2019) have also shown how these approaches can be combined.

Nielsen et al. (2019a, 2019b) have suggested a systematic hybrid modelling framework that uses a machine learning assisted approach for estimating the process kinetics instead of using fixed kinetic expressions. The remaining part of the model, including mass and population balances are retained, ensuring physical constraints not to be violated. This allows for increased flexibility towards capturing complex dynamics and relations between measured process variables, which have an impact on the process kinetics.

In the present work, a model based control strategy is presented, using a hybrid model suggested by Nielsen et al. (2019a). It is shown how the hybrid model can be trained continuously during process operation, and thus incorporating the latest obtained process sensor data. The real-time updated process model is used in parallel for calculating the optimal control, by solving a shrinking horizon model predictive control problem. By combining the continuous training and model predictive control, the hybrid model will continuously be refined, thus also refining the process control.

2. Hybrid model

The hybrid model used in this work is created based on the hybrid model framework by Nielsen et al. (2019a), consisting of a machine learning model f, in this work, a deep feed-forward neural network, and a mechanistic population balance model g, as illustrated in Figure 1. The hybrid model is flexible towards incorporating multiple process sensors, physical or soft, that may have an impact on the process kinetics. Here, $\bar{x}$, is the measured process variable(s), $\bar{z}$, is the controlled process variable(s) and N is particle population discretized by one or more particle properties. The output of the machine learning model is one or more kinetic rates, related to general particle phenomena. This includes nucleation rate, α, bin-specific growth, β, bin-specific shrinkage, γ, bin-specific agglomeration, ε, and bin-specific breakage κ, and the corresponding daughter particle distribution, θ.

The machine learning model is trained indirectly using time-series measurement pairs of particle size distributions from two time-stamps, N_0 and $N(t+\Delta t)$. By implementing the hybrid model in a math library that allows for rapid calculation of derivatives, using methods such as Automatic Differentiation (AD), one can train the model in real-time and continuously update the machine learning weights to the latest measurements.

Note here that case specific models needs to be specified for the measured variables, $\bar{x}$, to allow for long-term predictions of the particle properties. These are specified based on prior process knowledge, or simply set to be constant.

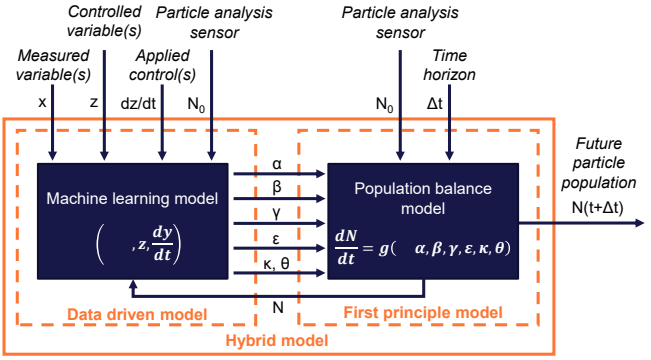

Figure 1: Hybrid model structure

Nielsen et al. (2019a) have previously successfully applied this hybrid modelling framework on two experimental cases of crystallization, including lab-scale food crystallization and industrial scale pharmaceutical crystallization.

3. Model predictive control

In this work, a model predictive control (MPC) is applied to the hybrid model structure presented in the previous section. As many of the mentioned particle processes are carried out in batch operation in industry, it is intended to demonstrate the application using a shrinking horizon MPC. For every new measurement of the particle distribution N, the following optimization problem is solved:

$$\min_{d\bar{z}/dt} \sum_{i=1}^{M} \omega_i \cdot (p_i(N^{end}) - r_i) \tag{1}$$

Here, M is the number of controlled particle properties, denoted p, that are either directly related to the predicted particle distribution N, or any derivative thereof. r_i is here the corresponding controller set point. Each of the controlled variables is furthermore weighted by a factor $\bar{\omega}$, reflecting the relative importance of the controlled variables.

The hybrid model is used to predict the final particle distribution, N^{end}, given the calculated control slopes, $d\bar{z}/dt$. The hybrid model is solved, $\Delta t = t^{batch}\text{-}t^{current}$, into the future where t^{batch} is the batch duration. Note that the presented approach requires a fixed batch duration wherein that target particle properties should be obtained.

A differential evolution algorithm (DE/rand/1/bin), implemented in the Tensorflow framework (Abadi et al. (2015)), is used in this work to solve the MPC optimization problem. The reason for using a differential evolution algorithm is to reduce the risk of converging to local minima. This carries a risk when using heavily parametric machine learning models.

As the case for any MPC, the computational time for solving the MPC optimization problem should be less than the sampling rate. The kinetics for many of the particle processes mentioned previously are relatively slow and only require sampling rates of

approximately 0.5 min^{-1} – 0.2 min^{-1}. The choice of particle analysis sensor may limit this sampling rate.

4. Parallel training and MPC

A continuous learning approach is suggested (see Figure 2) to run together with the model predictive control algorithm. This allows for the MPC not only to use the current process measurements, but also to use the data to refine the process model and to refine the future calculated process control actions. Due to the computational time of both model training and solving the MPC problem, it is suggested to run these processes in parallel. The number of training iterations (epochs) is fixed to 2 per cycle.

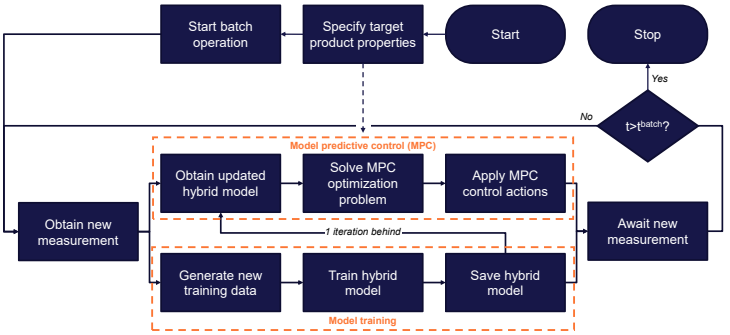

Figure 2: Parallelized model training and model predictive control

Note that the MPC optimization problem will be using the hybrid model from the last training iteration to reduce the time from current state to calculated MPC control actions. This structure allows distributed computing in cases where the hybrid model may be computationally expensive to evaluate and train concurrently.

5. Application example

The continuous learning and model predictive control strategy is demonstrated through a theoretical crystallization case. This is to showcase the feasibility of the presented approach. The given example is a temperature-controlled crystallization of α-lactose. An in-silico crystallizer is utilized, which is based on the crystallization model by Wong et al. (2012). An overview of the in-silico experimental setup can be seen in Figure 3.

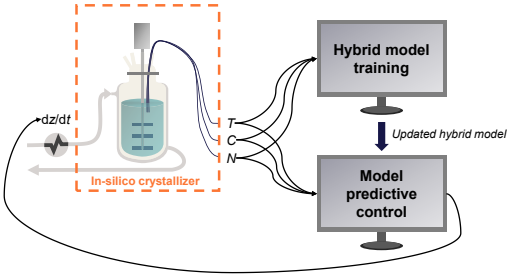

Figure 3: In-silico experimental setup for demonstrating the feasibility of the suggested control strategy

The in-silico crystallizer constitutes a real crystallizer, where a number of sensors are fitted. This includes a temperature sensor, solute concentration sensor and a particle

analysis sensor (emulating image analysis of 1 µL sample). To make this feasibility study as realistic as possible, Gaussian noise is added to the sensor readings corresponding to realistic measurement uncertainties of these sensors. Furthermore, the maximum sampling rate is set to 0.2 min^{-1}, corresponding to a measurement every 5 minutes.

In the hybrid model, the evolution in temperature is modelled assuming ideal temperature control, and the concentration of the solute is modelled using a simple mass balance, knowing the approximate density of lactose crystals ρ and given a bin characteristic size L_i, as shown in Equation (2).

$$\frac{dC}{dt} = \rho \cdot \sum_{i=1}^{m} \frac{dN_i}{dt} \cdot L_i^3 \tag{2}$$

The control performance is now examined for two controlled variables; final temperature (1) and the mean crystal size (2).

The batch duration is here fixed to be 2.5 hours. The initial batch conditions are the same for each batch, but with random uniformly distributed disturbances in both seed mass and mean seed size, to illustrate the controller performance. Furthermore, the hybrid model is initialized without any prior training, which means that the first control iterations are expected to be erroneous.

To evaluate on the presented control strategy, the case is compared to a simple benchmark control with a linear cooling profile. The details of initial conditions, disturbances, control targets and objective function weights can be found in Table 1 and Table 2, respectively. Note that the target mean particle size of 41 µm corresponds to the final particle size of the benchmark control without any process disturbances.

Table 1: Initial conditions and disturbances for feasibility study

T_0 [°C]	C_0 [g/mL]	Seed mass fraction [%]	Seed mean size [µm]	Disturbance seed mass fraction [%]	Disturbance seed mean size [µm]
50	0.337	0.5	10	[-0.2; 0.2]	[-5; 5]

Table 2: Control targets and objective function weights

Final temperature control		Final mean particle size control	
ω_1 [°C^{-1}]	r_1 [°C]	ω_2 [μm^{-1}]	r_2 [µm]
1/10	10	10/41	41

The controller performance over 10 batch operations is presented in Figure 4 on the following page, where the hybrid model is initialized from the first batch without any prior training. The employed MPC achieves stable control of the final temperature within +/- 0.01 °C for all batches. For the final mean particle size, the MPC performs equally good compared to the reference control in the first two batches. After this, it can be seen that the hybrid model has been trained to an extent that results in the MPC outperform the reference control. This is especially evident in batch 9.

One should be aware that overfitting of the hybrid model may occur after a number of batches. Thus, the model prediction accuracy will decrease, which has a negative effect on the model predictive control performance. Steps to mitigate this must be taken to stabilize the presented approach. This is subject to future investigations.

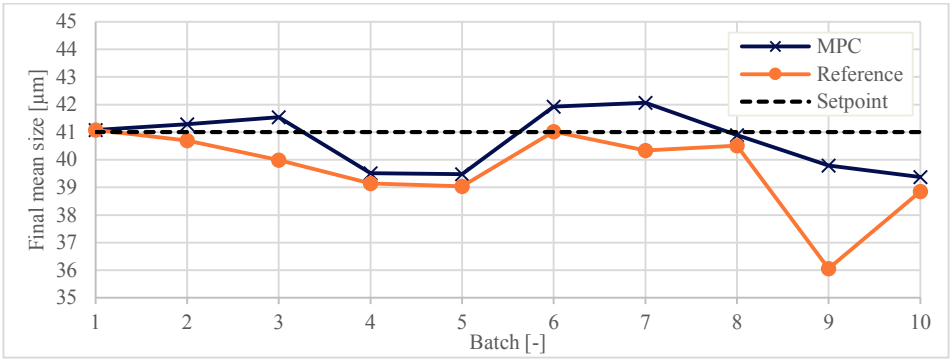

Figure 4: Controller performance of MPC vs reference control

6. Conclusions

A new hybrid model based control strategy has been presented, that allows for direct specification of the ideal particle product properties, by measuring the particle properties on-line. The approach is flexible towards use of multiple process sensors, and requires little prior process knowledge. The control strategy has been illustrated on a theoretical food crystallization. The case study shows that it is possible to obtain an accurate control with only little process data. However, overfitting of the hybrid model must actively be mitigated to obtain a more stable training and control approach.

Acknowledgments

This work partly received financial support from the Greater Copenhagen Food Innovation project (CPH-Food), Novozymes, from EU's regional fund (BIOPRO-SMV project) and from Innovation Fund Denmark through the BIOPRO2 strategic research center (Grant number 4105-00020B).

References

R. F. Nielsen, K. V. Gernaey, S. S. Mansouri, 2019a. Hybrid machine learning assisted modelling framework for particle processes, submitted to Computers & Chemical Engineering.

R. F. Nielsen, N. K. Arjomand, L. C. Freiesleben, K. V. Gernaey, S. S. Mansouri, 2019b. Novel strategies for predictive particle monitoring and control using advanced image analysis, Computer Aided Chemical Engineering, 46, 1435-1440.

Z. K. Nagy, G. Fevotte, H. Kramer, L. L. Simon, 2013. Recent advances in the monitoring, modelling and control of crystallization systems, Chemical Engineering Research and Design Volume, 91, 1903-1922.

A. Eren, B. Szilágyi, J. Quon, M. Furuta, C. Papageorgiou, Z. Nagy. 2019, Development of a Model-Based Quality-by-Control Framework for Crystallization Design, Computer Aided Chemical Engineering, 46, 319-324.

M. Abadi, A. Agarwal, P. Barham, E. Brevdo, Z. Chen, C. Citro, G. Corrado, A. Davis, J. Dean, M. Devin, S. Ghemawat, I. Goodfellow, A. Harp, G. Irving, M. Isard, R. Jozefowicz, Y. Jia, L. Kaiser, M. Kudlur, J. Levenberg, D. Mané, M. Schuster, R. Monga, S. Moore, D. Murray, C. Olah, J. Shlens, B. Steiner, I. Sutskever, K. Talwar, P. Tucker, V. Vanhoucke, V. Vasudevan, F. Viégas, O. Vinyals, P. Warden, M. Wattenberg, M. Wicke, Y. Yu, X. Zheng. TensorFlow: Large-scale machine learning on heterogeneous systems, 2015. Software available from tensorflow.org.

S. Wong, R. Bund, R. Connelly, R. Hartel. 2012. Designing a lactose crystallization process based on dynamic metastable limit. Crystallization Growth Design, 111, 642–654.

Sauro Pierucci, Flavio Manenti, Giulia Bozzano, Davide Manca (Eds.)
Proceedings of the 30th European Symposium on Computer Aided Process Engineering (ESCAPE30), May 24-27, 2020, Milano, Italy.
http://dx.doi.org/10.1016/B978-0-12-823377-1.50198-1

Water Distribution Network Optimization Considering Uncertainties in the Nodes Demands

R. Salcedo-Díaz[a*], R. Ruiz-Femenia[a], J. A. Caballero[a], M. A. S. S. Ravagnani[a,b]

[a]*Chemical Process Engineering Institute, University of Alicante, Spain*
[b]*Chemical Engineering Department, State University of Maringá, Brazil*
raquel.salcedo@ua.es

Abstract

The design of Water Distribution Networks (WDN) can be formulated as an optimization problem for the minimization of the total network cost, which depends on the pipe diameters and the pumping power required. The variability in water demand at nodes can be modelled as a set of finite scenarios generated from a multivariate normal distribution assuming correlations between the selected pair nodes of the network. A disjunctive stochastic Mixed Integer Nonlinear Programming (MINLP) model is proposed for the optimal synthesis of WDN considering correlated uncertainties in nodal demands. Strategies for avoiding nonconvex nonlinearities in the equations are applied to avoid unnecessary complexities. We analyse the effect of different correlation matrices to gather insight into how the model faces uncertainty. A case study was used to test the model and the optimization techniques proposed. Results show that under uncertainty the stochastic solution of the WDN improves the deterministic one (i.e. the design obtained for nominal values of nodes demand), evincing that neglecting uncertainty in the optimization process may lead to suboptimal or, even worse, infeasible design of WDNs.

Keywords: Water distribution networks, nodes demand uncertainty, stochastic optimization.

1. Introduction

Water Distribution Networks (WDN) are important systems in urban centers and in industrial facilities. The design of WDN can be formulated as an optimization problem, involving, generally, the minimization of the total network cost, which depends on the pipe diameters and flow directions known a priori (Caballero & Ravagnani, 2019).
In some WDN, there exist variations in the nodal water demands, which could exert a huge influence on the optimal network. In such cases, it is reasonable to account for such uncertainty in the design phase of the WDN. Following this approach, it is guaranteed that the WDN designed under uncertainty is able to cope once the unknow water nodal demands are unveiled, otherwise a design of the WDN assuming nominal values could offer an economically inadequate behaviour. The design under uncertainty one of the key area of Process Systems Engineering, and consequently has been applied to different cases studies (Carrero-Parreño et al., 2019; Ruiz-Femenia et al., 2013). Some authors have considered nodal water demand uncertainty (uncorrelated) in the WDN design, and have used genetic algorithms to find the optimal solution (Branisavljević et al., 2009). Other approach is to handle uncertainty (uncorrelated) through fuzzy logic (Geranmehr et al., 2019). Furthermore, the variability of the water demand (and head) has been represented using log-normal probability distribution uncorrelated functions (Marquez Calvo et al., 2018), but to best our knowledge water demand uncertainty implemented by a set of correlated scenarios with desired marginal distributions for each uncertain

parameter has not been considered in WDN optimization (for an exhaustive list of works in WDN optimization see Mala-Jetmarova et al, 2018).

2. Problem statement

In this work we consider the design of a generic WDN that includes a set of water demand nodes with a set of pipes connecting them (i.e. edges) with fixed flow directions. Given are a set of nodes, described by their elevation and by the expected values and variance of the water flow demand; a set of pipes characterized by their initial and final nodes, their length and whose diameters must be assigned from a set of commercial diameters (with its corresponding price per unit of length); minimum and maximum velocities allowable; and a set of pumps than can provide head at each pipe.

The goal is to determine the configuration of the WDN that minimizes the Total Annualized Cost (TAC) under nodal water demand uncertainty, which is modeled by random variables with the special feature of being correlated. Decisions to be made are of two types: structural and operational. The former includes the diameter and capital cost of each selected pipe, whereas the operational decisions are effective pressure (i.e. total pressure at each node), the velocity, volumetric flow rate and pressure drop at each pipe, and the pump head and its operational cost for each pump.

3. Representation of the uncertainty

We model the water demand uncertainty by a set of correlated scenarios, generated by Monte Carlo sampling and with the key feature that each random variable follows the desired marginal distribution (we assume lognormal distribution for the water demand at each node). To enable this flexibility in the scenario modelling, we implement a two-step transformation algorithm (Reyes-Labarta et al., 2014). Given are the expected value and the variance for each nodal water demand, and the correlation matrix. These three inputs define the covariance matrix, whose diagonal elements contain the variances for each variable, while the off-diagonal elements the covariance between variables. First, we apply a standard multivariate normal probability distribution function for each pair of the uncertain parameters to obtain a correlated sampling (Onishi et al., 2017), where each random variable follows a normal marginal distribution (Figure 1a). Then, we apply a transformation to each random variable using the normal cumulative distribution function with the corresponding expected mean and standard deviation to obtain a correlated distribution with uniform marginal distributions on the interval (0,1). And finally, we apply the inverse cumulative distribution of the lognormal distribution (i.e., the desired marginal distribution) to each random variable (Figure 1b).

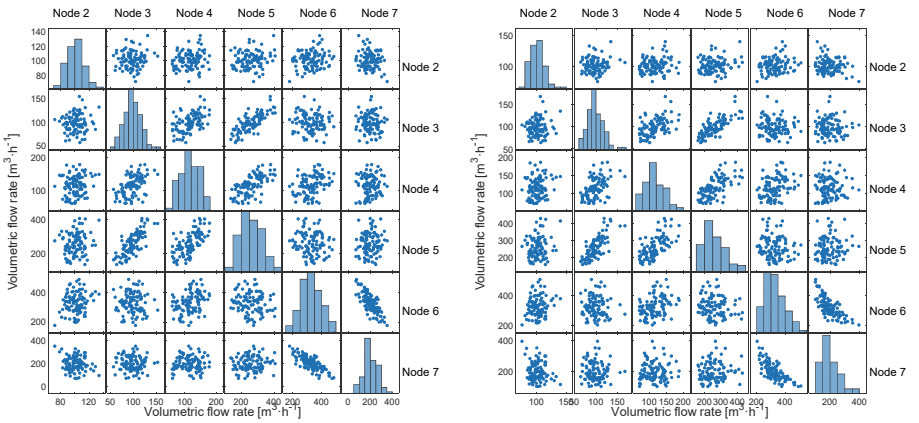

Figure 1. Correlated scenarios between every pairs of nodes for the water demand: a) normal marginal distribution; b) lognormal marginal distributions.

4. Stochastic mathematical model

The approach proposed in this work relies on stochastic programming, in particular a two-stage stochastic model. In our case, stage-1 decisions, which are taken before the uncertainty is resolved, are given by the design variables, like establishing a new plant or warehouse. In contrast, stage-2 decisions, which are made after the uncertainty is revealed, model operational variables (mainly production levels and transportation flows) that can be adjusted according to the uncertainty resolution. We assume that the uncertain parameters are described by a set of explicit scenarios with given probability of occurrence. Such scenarios together with their associated probabilities must be provided as input data to the model. In our case, these scenarios are generated from probability distributions using sampling methods.

4.1. Objective function

The WDN design is assessed by the Total Annualized Cost (TAC), which includes the annualized pipe capital cost and the pump operation cost. For each scenario s, a TAC value is computed, and to collect the performance of the WDN in face of uncertain in a single metric, we minimize the expected value of the TAC, which is compute as follows:

$$E\left[\mathrm{TAC}\right] = \sum_{p} prob_s TAC_s \tag{1}$$

where $prob_s$ is the given probability of occurrence of scenario s.

4.2. Constraints

A logic equation is included in the model to assign a diameter for each pipe:

$$\sum_{k} \mathrm{y}_{i,j,k} = 1, \forall i, j \in R_{i,j} \tag{2}$$

where $R_{i,j}$ define all the pipes by their starting node i and ending node j.

In addition, the minimization of the expected value is subject these set of equality and inequality constraints that must be satisfy in each scenario: mass balance at each node; flowrate velocity relation (linearized) at each pipe; mechanical energy balance at each pipe; and the Hazen-Williams at each pipe, that in its linearized form is as follows:. The expression for the last constraint is as follows:

$$\ln\_\text{pressureDrop}_{i,j,s} = \log(10.674) + 1.852\ln\_\text{flowRate}_{i,j,s} + \log(\text{LENGTH}_{i,j}) - \sum_{k}(1.852\log(\text{RUGOSITY}\_\text{COEFFICIENT}_{i,j,k})\,y_{i,j,k}) - \sum_{k}(4.871\log(\text{DIAMETER}_{i,j,k})\,y_{i,j,k}) \quad (3)$$

where we use the variable logarithmic transformations of the variables, named $\ln\_\text{pressureDrop}_{i,j,s}$ and $\ln\_\text{flowRate}_{i,j,s}$, instead of their current variables. Also, remark that Eq. (3) arises from a convex hull reformulation of the initial disjunctive model in order to activate only the contribution corresponding to the selected diameter k.

5. Case Study

The case study is a WDN with seven nodes and eight pipes forming two loops. Figure 2 shows its topology, the node elevations and the direction of the flow. We generate the correlated scenarios with the expected values and variances for water demand shown in Table 2. Node 1 represents the initial water reservoir which flow rate is the summation of water demands in nodes 2 to 7. The correlation matrix elements between two nodes ρ different from 0: $\rho_{2,3} = 0.6$, $\rho_{2,4} = 0.8$, $\rho_{3,4} = 0.7$, $\rho_{3,5} = 0.4$ and $\rho_{5,6} = -0.8$.

Table 1. Water demand expected values in nodes.

Water demand (m^3/h)	Node 2	Node 3	Node 4	Node 5	Node 6	Node 7
Expected value of the	100	100	120	270	330	200
Standard deviation	9.6	18.3	32.0	72.1	74.6	69.2

All pipes have 1000 m length and the velocities are bounded between 0.3 m/s and 3 m/s. Pipe diameters are selected from a set of available commercial ones (Table 2). Hazen–Williams dimensionless roughness coefficient C is 130 for all pipes. The use of pumps is considered in case it is necessary to satisfy the nodes demand in any of the scenarios generated. The pumping operational cost is calculated using an electricity cost of 0.24 $/kWh.

Table 2. Set of available pipe diameters and costs.

Diameter (m)	0.0254	0.0508	0.0762	0.1016	0.1524	0.2032	0.254
	0.3048	0.3556	0.4064	0.4572	0.508	0.5588	0.6096
Cost ($/m)	2	5	8	11	16	23	32
	50	60	90	130	170	300	550

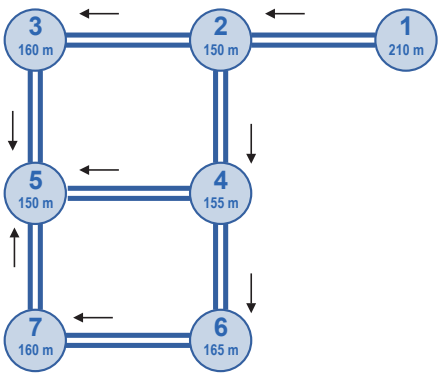

Figure 2. Topology of the WDN studied.

6. Results and discussion

The stochastic Mixed Integer Nonlinear Programming (MINLP) problem is solved in GAMS using BARON (version 18.11.12). To confirm the suitability of accounting for the uncertainty in the WDN, the problem has been solved again against all the scenarios but fixing the network topology (i.e. binary variables) according to the solution obtained from a deterministic problem, where there is no uncertainty in the nodal water demand (i.e., a unique scenario with water demand equal to the expected value). In addition, the problem has been solved for the case that nodal demands are uncorrelated and correlated according to the above-mentioned correlations coefficients.

Figure 3 shows this comparison in terms of the TAC ($/y). In both cases the expected TAC for stochastic designs is smaller than the expected TAC for the deterministic ones, which refers to the solution for all scenarios fixing the WDN topology (pipe diameters). Therefore, in some scenarios the system is forced to make use of pumps to satisfy the respective demands of some nodes, thus increasing the cost of the WDN. Another issue with the deterministic solution is that could lead to infeasible solutions as in some scenarios the velocity in pipes must be greater than the imposed upper bound (3 m/s) in order to satisfy nodal demands.

Regarding data correlation, both stochastic and deterministic designs yield lower expected TAC when the uncertain parameters are correlated (

Figure 3). Moreover, when distances between nodes are not too large (1000 m), it is expected a certain correlation between nodes demands. Figure 4 shows the optimal topology (pipe diameters) for the stochastic and deterministic WDN designs with correlated scenarios.

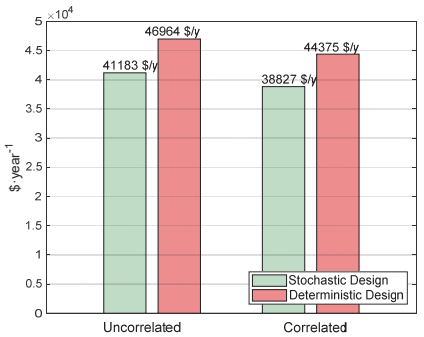

Figure 3. Comparison of the WDN expected total annualized cost between the stochastic and deterministic designs, and for uncorrelated and correlated and nodes demands.

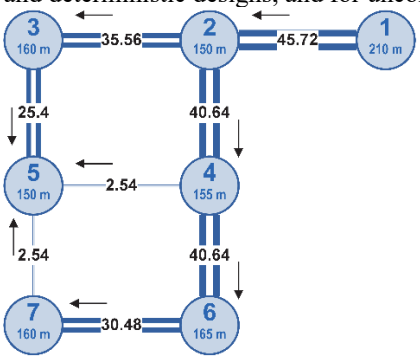

a) Stochastic Design

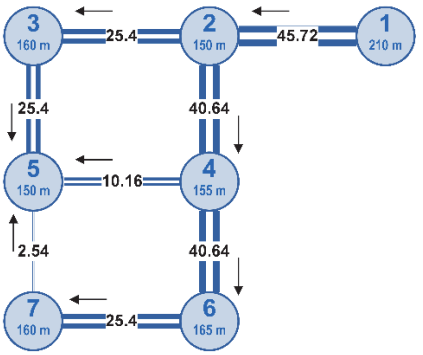

b) Deterministic design

Figure 4. WDN topology for the stochastic and deterministic designs with scenario correlation (pipe diameters in cm).

7. Conclusions

A stochastic MINLP optimization model has been developed for the optimal design of water distribution networks under nodal water demand uncertainty. The model has been applied to a case study with 7 nodes seeking to minimize the expected total annualized cost, which includes the pipe capital cost and the pumping operational cost. The solution of the stochastic problem is compared with that obtained fixing the pipe diameters according to the solution of the problem that assumes no variability in water demand at nodes. The results show that the stochastic design reduces the expected TAC by more than 12 % with respect to the deterministic one. This is mainly due to the need of using pumps to satisfy the nodes demand in some scenarios in the deterministic design. Additionally, the deterministic design could become infeasible due to the excessive water velocity in pipes needed to satisfy the water demand in some scenarios. These facts demonstrate that neglecting uncertainty in the optimization process may lead to suboptimal or, even worse, infeasible design of WDNs.

Acknowledgements

The authors acknowledge financial support to the Spanish «Ministerio de Economía, Industria y Competitividad» under project CTQ2016-77968-C3-2-P (AEI/FEDER, UE).

References

Branisavljević, N., Prodanović, D., & Ivetić, M. (2009). Uncertainty reduction in water distribution network modelling using system inflow data. Urban Water Journal, 6, 69-79.

Caballero, J. A., & Ravagnani, M. A. S. S. (2019). Water distribution networks optimization considering unknown flow directions and pipe diameters. Computers & Chemical Engineering, 127, 41-48.

Carrero-Parreño, A., Quirante, N., Ruiz-Femenia, R., Reyes-Labarta, J. A., Salcedo-Díaz, R., Grossmann, I. E., & Caballero, J. A. (2019). Economic and environmental strategic water management in the shale gas industry: Application of cooperative game theory. AIChE Journal, 65, e16725.

Geranmehr, M., Asghari, K., & Chamani, M. R. (2019). Uncertainty analysis of water distribution networks using type-2 fuzzy sets and parallel genetic algorithm. Urban Water Journal, 16, 193-204.

Mala-Jetmarova, H., Sultanova, N., & Savic, D. (2018). Lost in optimisation of water distribution systems? A literature review of system design. Water (Switzerland), 10.

Marquez Calvo, O. O., Quintiliani, C., Alfonso, L., Di Cristo, C., Leopardi, A., Solomatine, D., & de Marinis, G. (2018). Robust optimization of valve management to improve water quality in WDNs under demand uncertainty. Urban Water Journal, 15, 943-952.

Onishi, V. C., Ruiz-Femenia, R., Salcedo-Díaz, R., Carrero-Parreño, A., Reyes-Labarta, J. A., & Caballero., J. A. (2017). Optimal Shale Gas Flowback Water Desalination under Correlated Data Uncertainty. Computer Aided Chemical Engineering, 40, 943 - 948.

Reyes-Labarta, J. A., Salcedo-Díaz, R., Ruiz-Femenia, R., Guillén-Gosálbez, G., & Caballero, J. A. (2014). Handling of uncertainty in life cycle inventory by correlated multivariate lognormal distributions: Application to the design of supply chain networks. Computer Aided Chemical Engineering, 33, 1075-1080.

Ruiz-Femenia, R., Guillén-Gosálbez, G., Jiménez, L., & Caballero, J. A. (2013). Multi-objective optimization of environmentally conscious chemical supply chains under demand uncertainty. Chemical Engineering Science, 95, 1-11.

Sauro Pierucci, Flavio Manenti, Giulia Bozzano, Davide Manca (Eds.)
Proceedings of the 30th European Symposium on Computer Aided Process Engineering (ESCAPE30), May 24-27, 2020, Milano, Italy.
http://dx.doi.org/10.1016/B978-0-12-823377-1.50199-3

Enabling Dynamic Real-Time Optimization under Uncertainty using Data-Driven Chance Constraints

Joris Weigert, Christian Hoffmann, Erik Esche, Jens-Uwe Repke

Technische Universität Berlin, Process Dynamics and Operations Group, Straße des 17. Juni 135, 10623 Berlin, Germany
joris.weigert@tu-berlin.de

Abstract

Dynamic real-time optimization has been suggested in the past to ensure feasible and economic trajectories. These approaches typically neglect uncertainty, which may lead to constraint violation. However, the introduction of uncertainty significantly increases computational demand and thus makes these approaches non-applicable to real-time applications. In this contribution, we present a framework for chance-constrained (CC) optimization with online capability for dynamic real-time optimization (D-RTO) under uncertainty in which fast recurrent neural networks replace the rigorous dynamic process models. To demonstrate the performance and the online applicability of the presented framework, it is applied on a dynamic model of a simplified Williams-Otto process.

Keywords: Dynamic Real-time Optimization, Optimization under Uncertainty, Chance-constrained Optimization, Data-driven Models, Recurrent Neural Networks

1. Introduction

The application of dynamic real-time optimization (D-RTO) instead of a two layer approach based on steady-state real time optimization combined with model predictive control has been suggested for process operation tasks in the past. This suggestion is motivated by the need to describe the nonlinear dynamic system behaviour of complex processes (Biegler, 2009).

Process models describing real systems always contain a certain amount of uncertainty (Sahinidis, 2004), even though it is scarcely ever quantified. Uncertainty can originate, e.g., from little known or uncertain physical properties, from uncertainty in thermodynamic models, from neglected phenomena, or from over-simplification. This fact may lead to safety relevant constraint violations or unstable operation resulting from determninistic optimization.

A possible approach to include uncertainty in optimization problems is the application of chance-constrained (CC) optimization (Charnes and Cooper, 1962). Nevertheless, existing frameworks cannot be used for online application given that the computational effort is still a major challenge (Esche et al., 2016).

In a previous contribution we presented a framework for CC optimization with online capability for steady-state systems, in wich fast data-driven models are used instead of rigorous models (Weigert et al., 2019). In this work, we extend the existing framework to dynamic systems.

In the next section, we give a general definition of dynamic chance-contrained optimization. In section 3 and 4 we present the developed framework in detail. Finally, we apply this framework to a case study of a simplified Williams-Otto process, in which the activation energies are assumed uncertain.

2. Dynamic Chance-Constrained Optimization

One appoach for solving optimization problems under uncertainty is chance-constrained optimization (Charnes and Cooper, 1962). Here, the uncertainty information is incorporated into the optimization problem by ensuring that inequality constraints are fulfilled by a desired minimum probability level α. For the present case, the dynamic optimization problem can be formulated as

$$\begin{aligned} \min_{u(t)} \quad & E[\phi(x(t), y(t), u(t), \xi, t)] \\ s.t. \quad & \dot{x} = f(x(t), y(t), u(t), \xi, t) \quad , \dim x = \dim f \\ & 0 = g(x(t), y(t), u(t), \xi, t) \quad , \dim y = \dim g \\ & Pr\{h_i(x(t), y(t), u(t), \xi, t) \geq 0\} \geq \alpha \\ & 0 \leq h_j(x(t), y(t), u(t), E[\xi], t) \\ & u^{LB} \leq u(t) \leq u^{UB} \end{aligned} \tag{1}$$

where the expected value of ϕ represents the objective function, x are the differential variables corresponding to f, y the variables corresponding to the algebraic system g and u the decision variables of the optimization problem. The variables ξ and t describe the uncertain parameters and time, respectively. The fourth term in Eq. (1) introduces a lower bound on the probability of the fulfilment Pr of the inequality constraint h_i into the optimization problem. h_j represent the inequality constraints that are not enforced with a user-defined probability, but are evaluated at the expected value of the uncertain parameters.

To solve optimization problems as given by Eq. (1), a sequential optimization approach with an additional layer for the probability computation is used conventionally. The basic idea of this additional layer is to map inequality constraints $h_i(x, y, u, \xi, t) \geq 0$ into the uncertain parameter space. Then, the probability is calculated by integrating over the multivariate probability distribution of the uncertain parameters in the feasible region of the uncertain parameter space (Esche et al, 2016). For this purpose, multiple additional simulations and numerical integrations are carried out at every iteration step of the optimization. Especially for high dimensional parameter spaces, this leads to rapidly increasing computational effort, which is the reason why existing frameworks for CC optimization are not suitable for online application.

3. Dynamic Data-Driven Optimization under Uncertainty

Within the proposed approach, two classes of data-driven models for usage in chance-constrained optimization problems are set up. The in- and output dependencies of both model types are shown in Figure 1. A more detailed description of the recursive neural network structure shown in Figure 1 will be given below (see section 4.3.).

The data-driven process model is generated to describe a dynamic input-output relationship of variables based on a rigorous dynamic process model. It describes the relationship between the decision variables u and the predefined output variables z_i at a certain time step k. The output variables z_i in general include the expected values of the objective function $E[\phi(t)]$ and the inequality constraints $E[h(t)]$, but additional variables of the rigorous model can also be added as outputs.

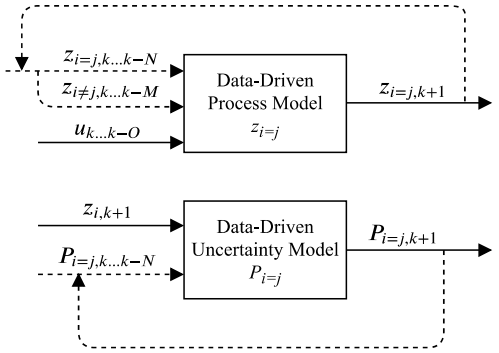

Figure 1: In- and output specifications of the data-driven process and the uncertainty model (solid lines). Additionally, the input specifications of the utilized recurrent neural networks are shown (dashed lines)

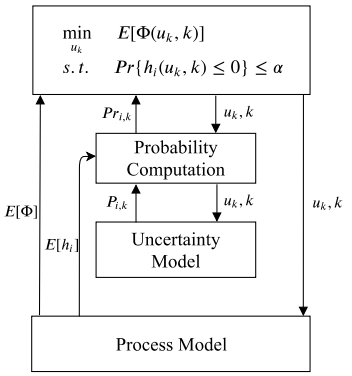

Figure 2: Dynamic data-driven chance-contrained optimization framework

The uncertainty model (UM) is generated to describe uncertainty included in the rigorous dynamic process model. It relates decision variables u and probability distribution parameters P_i of the predefined output variables z_i at a certain time k. Depending on which probability distribution model is chosen for the uncertainty description, the number of parameters in P_i can vary. In the moment a normal, a beta or a gamma distribution can be selected. In case the output uncertainty is, e.g., assumed to be normally distributed, $P_{i,k}$ contains the variance of z_i at the time point k.

By combining the expected value of $h_{i,k}$ with the paramters from $P_{i,k}$ the cumulative density function (CDF) of h_i at time step k can be approximated to calculate the probability of the inequality constraint fulfilment $Pr_{i,k}$ directly.

By applying the data-driven process and uncertainty model to a CC optimization problem, the general dynamic optimization problem from Eq. (1) can be simplified to

$$\begin{aligned} \min_{u_k} \quad & E[\phi(u_k,k)] \\ s.t. \quad & Pr\{h_i(u_k,k)\leq 0\}\leq\alpha \\ & u^{LB}\leq u_k\leq u^{UB} \end{aligned} \tag{2}$$

Here, the equation system of f and g, the corresponding variables x and y, and the uncertain parameters ξ from Eq. (1) are replaced by the data-driven process and uncertainty models. Additionally, time t is now described as discrete points k. The discretization step size is predefined in the artificial data generation procedure (see section 4.1.).

In Figure 2 the optimization workflow of the dynamic data-driven CC optimization is shown. At each iteration step the optimization layer calls the process model and the requested objective function is returned. Additionally, the expected values of the inequality contraints are returned to the probability computation layer. Here, the probability $Pr_{i,k}$ is calculated by evaluating the CDF based on $E[h_i]$, and the probability distribution parameters $P_{i,k}$. In contrast to traditional CC optimization, only explicit data-driven models and cumulative densitiy functions have to be evaluated during the optimization calculations, which leads to a significant decrase of computation time with a minimum factor of 7^{n_ξ}, where n_ξ describes the number of uncertain parameters.

4. Modeling Workflow

The presented modeling workflow is carried out in a framework implemented entirely in Python. Different rigorous process models, formulated and solved in different programming languages, can be connected to the framework. The utilized recurrent neural networks are trained and tested in the machine learning toolbox Scikit-learn (Pedregosa et al., 2011) and the probability distribution analysis and fitting capabilities are used from the Python toolbox Scipy.stats. A simplified flowchart of the presented modeling workflow is shown in Figure 3.

4.1. Artificial Data Generation

In a first step, artificial data for training and testing of the data-driven models needs to be created based on a dynamic rigorous process model. For this purpose, three different sampling methods are used. For the predefined uncertain parameters ξ samples are generated by sampling from a pseudo-random normal distribution. The time dependent decision variables u are sampled from an amplitude pseudo random binary sequence (APRBS). This method ensures high information content in training data for identification of input-output relationships within the recurrent neural networks (Nelles, 2001). Additionally, a well-distributed sampling method (e.g., Hammersley sequence sampling (HSS)) can be used on the initial conditions of the output variables (h, ϕ), which increases the valid space of the output variables in the data-driven models. Based on the created samples, dynamic simulations with time dependent decision variable changes (APRBS) are carried out at every sample point in the parameter and initial condition space and the resulting dynamic simulation results are stored at predefined equidistant time points. This step size defines the discretiziation step size between the discrete time points k in the data-driven models (see Figure 1).

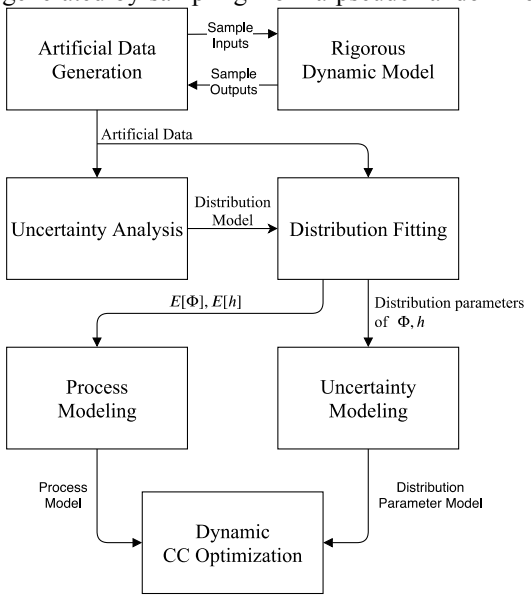

Figure 3: Simplified flowchart of the developed modeling workflow, which is applied offline.

4.2. Uncertainty Analysis and Distribution Fitting

The obtained dynamic simulation results are clustered with respect to the uncertain parameter sampling. For every output variable a qualified probability distribution model is found and fitted at each time point accordingly. Based on these distributions, the expected values of h and ϕ at ever time point, and the respective distribution parameters are handed over to the subsequent modeling steps

4.3. Recurrent Neural Networks

To create independent data sets for training and testing of the data-driven models, the aforemetioned steps need to be carried out twice with two independent sets of APRPS

samples for the decision variables. The in- and output specifications of the recurrent neural networks are shown in Fig. 1. For each output, a single process and a single uncertainty model is generated. Each process model uses O past values of the decision variables, N past values of the associated output variable and M past values of the remaining output variables to predict the output at the next time step. Each uncertainty model uses the past N values of the corresponding probability parameters and the current values of the output variables to predict the parameter at the next time step.

5. Case Study

To demonstrate the performance and the applicability in D-RTO under uncertainty, the presented framework is applied on a dynamic model of a Williams-Otto process (Hoffmann et al., 2019). This process consists of a continously-stirred tank reactor, a decanter, and a distillation column. Part of the bottom product of the column is recycled into the reactor. The activation energies of the three reactions are assumed to be uncertain with a standard deviation of 1% of the specified value.
The following optimization problem has been specified for the case study

$$\begin{aligned} \min_{T_j, \alpha_{recycle}} \quad & -\sum_{k=1}^{120} E\left[w_{product}(T_j, \alpha_{recycle}, k)\right] \\ s.t. \quad & Pr\{T_{reactor}(T_j, \alpha_{recycle}, k) \leq 172°C\} \\ & 56°C \leq T_j \leq 64°C \\ & 0.52 \leq \alpha_{recycle} \leq 0.63 \end{aligned} \tag{3}$$

where $w_{product}$ is the mass fraction of the product in the reactor, $T_{reactor}$ and T_j are the temperatures in the reactor and its cooling jacket, and $\alpha_{recycle}$ is the ratio of recycled bottom product.
Based on the decision variable bounds, artificial training and testing data sets are generated. A simulation time of 10,000 seconds with a step size of 1 second, 500 APRBS changes and 500 samples in the parameter space are used. The process and uncertainty models are based on the specifications shown in Fig. 1 with $= 3$, $M = 1$, and $O = 3$. The uncertainty in the data is found to be normally distributed. The resulting recurrent neural networks have a normalized mean squared error of around $1 \cdot 10^{-4}$ regarding the testing data, which is accurate enough to predict the 10,000 seconds of testing data with a mean deviation of around 1%.

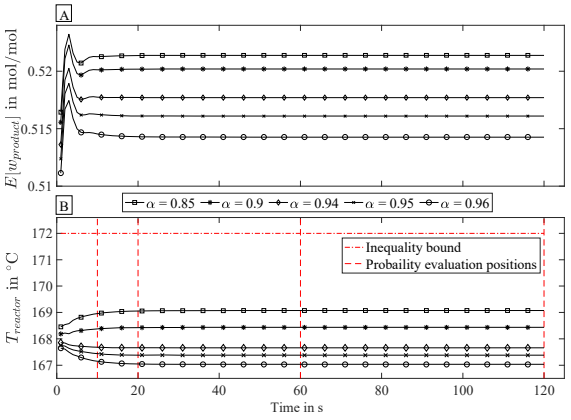

Figure 4: Results of the CC optimization at different probability levels. (A) objective function, (B) inequality contraint

The Optimization is carried out in Scipy.optimize using the method SLSQP for a time horizon of 120 seconds with a

tep size of 1 second. The decision variables are set to be constant over the whole horizon and the probability constraint is evaluated at 10, 20, 60, and 120 seconds. In Fig. 4, the resulting objective variable (A) and the chance-constrained variable (B) are shown for different probability levels α. It is apparent that an increasing probability level for the fulfilment of the temperature constraint leads to a lower product mole fraction in the reactor. This is the expected behavior given that a high probability level is supposed to shift the optimum to a more conservative solution.
The computation for an entire CC optimization run with the developed framework takes about 1 second (9 iterations), which is definitely fast enough for real-time application.

6. Conclusion and Outlook

A framework for generating dynamic data-driven process and uncertainty models for enabling dynamic real-time optimization under uncertainty is presented. The framework generates recurrent neural networks based on a dynamic rigorous process model and uses these data-driven models to compute the objective function and the probability contraints in a CC optimization framework.
To demonstrate the performance and the applicability in D-RTO under uncertainty, the presented framework is applied on a dynamic model of a simplified Williams-Otto process. It can be shown that the computation time for the CC optimization is suitable for application in online environments.
In future work, we will focus on developing techniques to update the data-driven models based on online measaurements from the real process.
Additionally, the framework will be tested extensively with a variety of different process models and a precise comparison with other CC optimization techniques regarding the computational effort will be performed.

References

Biegler, L. T., 2009. Technology advances for dynamic real-time optimization. In Computer Aided Chemical Engineering (Vol. 27, pp. 1-6). Elsevier.

Charnes, A., Cooper, W., 1962. Chance constraints and normal deviates. Journal of the American Statistical Association, 57(297), 134-148.

E. Esche, D. Müller, S. Werk, I. E. Grossmann, G. Wozny, 2016. Solution of chance-constrained mixed-integer non- linear programming problems. In: Z. Kravanja, M. Bogataj (Eds.), Proceedings of the 26th European Symposium on Computer Aided Process Engineering - ESCAPE 26. No. 38. Elsevier, pp. 91–94.

Hoffmann, C., Esche, E., Repke, J.-U., 2019. Integration of Design and Control Based on Large-Scale Nlp Formulations and An Optimal Economic NMPCs. In: Proceedings of the 9th International Conference on Foundations of Computer-Aided Process Design, vol. 47. Elsevier, pp. 125–130.

Nelles, O., 2001. Nonlinear system identification: From classical approaches to neural networks and fuzzy models. Springer, Berlin, 785 S.

Pedregosa, F., Varoquaux, G., Gramfort, A., Michel, V., Thirion, B., Grisel, O., Blondel, M., Prettenhofer, P., Dubourg, V., Vanderplas, J., 2011. Scikit-learn: Machine learning in Python. Journal of machine learning research, *12(Oct)*, 2825-2830.

Sahinidis, N.V., 2004. Optimization under uncertainty: state-of-the-art and opportunities. Computers & Chemical Engineering 28 (6-7), 971–983. 10.1016/j.compchemeng.2003.09.017.

Weigert, J., Esche, E., Hoffmann, C., Repke, J.-U., 2019. Generation of Data-Driven Models for Chance-Constrained Optimization, Proceedings of the 9th International Conference on Foundations of Computer-Aided Process Design, Elsevier, 311-316.

Sauro Pierucci, Flavio Manenti, Giulia Bozzano, Davide Manca (Eds.)
Proceedings of the 30th European Symposium on Computer Aided Process Engineering (ESCAPE30), May 24-27, 2020, Milano, Italy.
http://dx.doi.org/10.1016/B978-0-12-823377-1.50200-7

Flexibility Analysis of High-dimensional Systems via Cylindrical Algebraic Decomposition

Chenglin Zheng,[a] Fei Zhao,[a] Lingyu Zhu,[b] Xi Chen[a*]

[a]*State Key Laboratory of Inductrial Control Technology, College of Control Science and Engineering, Zhejiang University, Hangzhou, Zhejiang, 310027, China*
[b]*College of Chemical Engineering, Zhejiang University of Technology, Hangzhou, Zhejiang, 310014, China*
xi_chen@zju.edu.cn

Abstract

In process design, flexibility analysis is an important technique for evaluating the operability of a chemical process. The cylindrical algebraic decomposition (CAD) method has been proposed for flexibility analysis to derive analytical expressions of a feasible region. Due to the heavy computational burden caused by symbolic computation, this method can only handle small-scale problems currently. To overcome this limitation, a novel method is proposed for high-dimensional systems in this work. As the inequality constraints for flexibility analysis are usually limited in most cases, a surrogate model is first built to correlate the inequality constraints based on an initial sample set. Then, the flexibility region is obtained with explicit expressions via the CAD method. Next, the sampling validation is conducted on the boundary. For any violation, a refinement will be activated by taking an iterative process of data sampling, surrogate modelling, and region deriving, until the correctness condition is satisfied. The case study shows the proposed method can effectively describe the flexibility region for high-dimensional systems.

Keywords: Flexibility analysis, surrogate model, cylindrical algebraic decomposition.

1. Introduction

All chemical plants are subject to the uncertainties and variations during their design and operation. Given this fact, it is clearly important to conduct flexibility analysis of a system in the presence of the uncertainties. The main purpose of the flexibility analysis is to determine and describe the feasible region for a feasible and safe operation. The existing methods for describing flexibility region can mainly be divided into four categories: (1). formulating the flexibility analysis model into a global or parametric optimization problem (Bansal et al. 2002); (2). constructing boundary iteratively by simple approximation method (Goyal and Ierapetritou, 2003); (3). generating polygonal representation by appropriate sampling points (Banerjee and Ierapetritou, 2005); (4). establishing response surface of flexibility functions via the surrogate models (Wang and Ierapetritou, 2017). The aforementioned methods mainly rely on numerical calculation methods to estimate the outer envelope of a flexibility region. They cannot provide analytical descriptions for flexibility regions. Recently, a novel method based on quantifier elimination was proposed by Zhao and Chen (2018). The cylindrical algebraic decomposition (CAD) method (Collins, 1975) was utilized for analytically representing the flexibility region, which is suitable for both convex and nonconvex systems. However, due to the heavy computational burden caused by symbolic

computation, the CAD method is more applicable to small-scale problems. Regarding high-dimensional systems, how to apply the CAD method to analytically depict the flexibility region is still an open challenge. In this work, a novel method integrating the surrogate modeling technique and the CAD method is proposed to analytically depict the flexibility region for high-dimensional systems. In many cases, most of the constraints in a high-dimensional system are equalities. Thus, the number of the inequalities for the flexibility analysis is usually limited. A surrogate model is first built to approximate the inequality constraints, where only uncertain parameters and control variables are involved. Then, the CAD method is applied to the surrogate system to derive the flexibility region with explicit expressions. Next, the boundary check is conducted. Once a sampling point on the boundary violates constraints, additional points will be gathered and the process will be repeated, until the correctness condition is satisfied.

2. Cylindrical algebraic decomposition

A given design system can be described by the following set of constraints.

$$F = \begin{cases} \boldsymbol{h}(\boldsymbol{\theta}, \boldsymbol{z}, \boldsymbol{x}) = 0 \\ \boldsymbol{g}(\boldsymbol{\theta}, \boldsymbol{z}, \boldsymbol{x}) \le 0 \end{cases} \tag{1}$$

where $\boldsymbol{h}$ is the vector of equations (e.g., mass or energy balance equation); $\boldsymbol{g}$ is the vector of inequalities (e.g., physical operating limit); $\boldsymbol{x}$, $\boldsymbol{\theta}$, and $\boldsymbol{z}$ represent vectors of the state variables, the uncertain parameters and the control variables, respectively.

The CAD method is a symbolic computation method, which can depict the flexibility region with explicit expressions. It regards the flexibility analysis problem as an existential quantifier formula shown in Eq. (2).

$$\exists(\boldsymbol{\theta}, \boldsymbol{z}, \boldsymbol{x}) \left[\begin{array}{l} \boldsymbol{h}(\boldsymbol{\theta}, \boldsymbol{z}, \boldsymbol{x}) = 0 \wedge \\ \boldsymbol{g}(\boldsymbol{\theta}, \boldsymbol{z}, \boldsymbol{x}) \le 0 \end{array} \right] \tag{2}$$

Based on the quantifier elimination, the CAD method can eliminate the quantifier in Eq. (2) and generate an equivalent quantifier-free formula, which is the solution space of Eq. (2). There are two phases, namely the projection phase and lifting phase, in the CAD method. In the projection phase, through calculating discriminates and resultants on each dimension, variables are eliminated one by one with the predefined elimination order. In the lifting phase, through repeatedly sampling points within the cells, checking the signs and substituting the sampled points, the valid cells can be lifted, which constitute the feasible region of Eq. (2).

3. Flexibility region based on surrogate model and CAD

Instead of conducting the elimination, the surrogate-based method is utilized to approximate the inequality constraints $\boldsymbol{g}$ with explicit expressions. First, the initial sampling set ($\boldsymbol{\theta}^{ini}$, $\boldsymbol{z}^{ini}$) can be obtained within the design space of uncertain parameters and control variables. The corresponding state variables $\boldsymbol{x}^{ini}$ can be deduced by running the simulation. Based on the initial sample set, the inequality constraints can be represented as the function of uncertain parameters and control variables; Then, the surrogate system can be used to approximately describe the flexibility region.

$$F^s = \boldsymbol{g}^s(\boldsymbol{\theta}, \boldsymbol{z}) \le 0 \tag{3}$$

Noted that the surrogate system F^s only involves inequalities; thus, the computational burden for the CAD method will be alleviated due to the model reduction. Subsequently, the CAD method is applied to the surrogate system F^s. The projection order is specified as $\boldsymbol{\theta} \prec \boldsymbol{z}$, where the uncertain parameters are $\boldsymbol{\theta} = [\theta_1, \ldots, \theta_m]$ and control variables are $\boldsymbol{z} = [z_1, \ldots, z_n]$. Through the CAD method, the solution space of $\boldsymbol{\theta}$ and $\boldsymbol{z}$ can be split into a union set of finite k disjoint flexibility subspaces.

$$\varphi'(\theta, z) = \varphi'_1(\theta, z) \vee \varphi'_2(\theta, z) \vee \ldots \vee \varphi'_k(\theta, z) \tag{4}$$

where the kth subspace is

$$\varphi'_k(\theta, z) = \left| \begin{array}{l} p_{k,1} \le \theta_1 \le q_{k,1} \wedge \\ p_{k,2}(\theta_1) \le \theta_2 \le q_{k,2}(\theta_1) \wedge \\ \ldots \\ p_{k,m}(\theta_1, \ldots, \theta_{m-1}) \le \theta_{m-1} \le q_{k,m}(\theta_1, \ldots, \theta_{m-1}) \wedge \\ p_{k,m}(\theta_1, \ldots, \theta_{m-1}, \theta_m) \le z_1 \le q_{k,m+1}(\theta_1, \ldots, \theta_{m-1}, \theta_m) \wedge \\ \ldots \\ p_{k,m+n}(\theta_1, \ldots, \theta_m, z_1, \ldots, z_{n-1}) \le z_n \le q_{k,m+n}(\theta_1, \ldots, \theta_m, z_1, \ldots, z_{n-1}) \end{array} \right| \tag{5}$$

where p_k and q_k are continuous algebraic functions, $-\infty$ or $+\infty$. Thus, the flexibility region $\varphi'(\theta, z)$ can be depicted by the logical combination of the semi-algebraic system $\varphi'_k(\theta, z)$, which has the explicit expression. However, the accuracy of surrogate model depends on the number and location of samples in the design space. One must acknowledge that the surrogate model might result in an inaccurate description of flexibility region. A refined procedure should be executed to iteratively check and update the flexibility region until it satisfies the correctness condition in Eq. (6).

$$\forall(\boldsymbol{\theta}^{val}, \boldsymbol{z}^{val}) \ [\boldsymbol{g}(\boldsymbol{\theta}, \boldsymbol{z}, \boldsymbol{x})] \le 0 \tag{6}$$

where $(\boldsymbol{\theta}^{val}, \boldsymbol{z}^{val})$ are validation samples on the boundary of flexibility region. The correctness condition requires all the validation samples on the boundary should satisfy the inequalities $\boldsymbol{g}$ in Eq. (1). The refined procedure involves two parts: the boundary check, and the update of surrogate modeling and CAD solution.

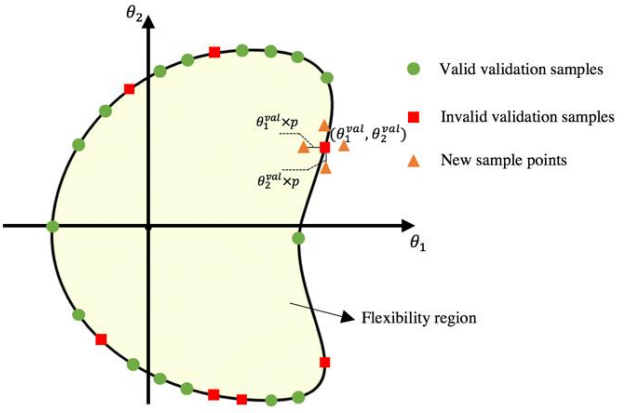

Figure 1. Geometric illustration of validation samples and new points for the proposed method.

3.1. Boundary check

Since the analytical expressions of the flexibility region have been obtained in Eqs. (4)-(5), validation points ($\boldsymbol{\theta}^{val}$, $\boldsymbol{z}^{val}$) can be sampled on the boundary through uniform sampling. For ease of understanding, an illustration for these validation samples on the boundary is provided in Figure. 1. It is a case with two uncertain parameters θ_1 and θ_2. When a validation sample on the boundary satisfies the inequalities $\boldsymbol{g}$ in Eq. (1), denote it as the valid sample marked by a circle; otherwise, denote it as the invalid sample marked by a square. The existence of the invalid samples indicates that the inaccurate surrogate model results in an incorrect derivation of the flexibility region around those sample points.

3.2. Iterative process of the surrogate modelling and CAD updating

Once the flexibility region does not hold the condition in Eq. (6), i.e., there exist invalid samples on the boundary, a refinement will be activated by taking an iterative process of surrogate modeling and CAD updating. First, new points ($\boldsymbol{\theta}^{new}$, $\boldsymbol{z}^{new}$) are sampled around invalid validation samples. Regarding the two-dimensional case as illustrated in Figure 1, four points located on the upper, lower, left and right sides of the invalid validation points are sampled as new points. Then, add validation samples and new points into the initial sample set. Based on the updated sample set, the updated surrogate model can be built. Subsequently, though applying the CAD method to the updated surrogate system, the new flexibility region can be depicted. After the iterative process of constructing a surrogate model based on the current sample set, applying the CAD method for the current surrogate system and doing the sampling validation on the boundary are converged, the final flexibility region can be obtained for high-dimensional systems.

4. Results and discussion

Flexibility analysis problem of a vacuum distillation is studied in this paper. The distillation process can be described by a rigorous tray-by-tray MESH model which includes a total of 917 variables. The uncertain parameter lies in the flowrate of the feed stream, F, which is bounded within 1000 kg/h $\le F \le$ 3000 kg/h. The control variable is the operating pressure P of vacuum distillation. The bounds of P are 3.7 kPa $\le P \le$ 39.7 kPa. In addition, it also involves several inequalities for capacity or quality restrictions: $y_B \le 850$, $T_{oil} \le 265$ and $0.5 \le \sigma \le 2$, where y_B is the residue in the bottoms (ppm), T_{oil} is the inlet temperature of thermal oil (℃), and σ is the flooding factor of the column.

$$
F^s = \begin{cases} g_1: 1000 \le F \le 3000, \\ g_2: 3.7 \le P \le 39.7, \\ g_3: y_B = -188.639 + 0.604F - 11.437P - 2.749\times10^{-4}F^2 + 1.992P^2 \\ -0.025FP + 1.340\times10^{-7}F^3 - 0.094P^3 - 1.258F^2P + 0.002P^2F \le 850, \\ g_4: T_{oil} = 220.134 + 0.002F + 3.248P + 1.797\times10^{-8}F^2 - 0.088P^2 + 4.122\times10^{-5}FP \\ +1.278\times10^{-11}F^3 + 0.001P^3 - 6.083\times10^{-9}F^2P + 2.018\times10^{-7}P^2F \le 265, \\ g_5: 0.5 \le \{\sigma = 1.884 + 1.149\times10^{-5}F - 0.188P + 1.552\times10^{-8}F^2 + 0.011P^2 + 7.044 \\ \times10^{-7}FP - 5.421\times10^{-12}F^3 - 2.070\times10^{-4}P^3 + 9.103\times10^{-10}F^2P - 2.123\times10^{-7}P^2F\} \le 2 \end{cases} \tag{7}
$$

The proposed method carries out the sampling in the space of uncertain parameter and control variable first. The number of samples in the initial sample set is 75. Based on the initial sample set, inequality constraints can be represented as a function of the

uncertain parameter and control variable using the cubic polynomials. The surrogate system can be represented in Eq. (7). The computational time of the surrogate system is 9.18 s. Then, the projection order is defined as $F \prec P$. Applying the CAD method to the surrogate system F^s, the flexibility region can be described by $\{(F,P) \in \mathrm{R}^2 \mid \varphi'\}$. The computational time of the CAD method is 0.117 s.

$$\varphi' = \left[\begin{array}{l} 1: \left[\begin{array}{l} 1000 \le F \le 2204.81 \wedge \\ 3.7 \le P \le Root[f_1(F,\#1)\&,1] \end{array} \right] \vee \\ 2: \left[\begin{array}{l} 2204.81 \le F \le 2896.91 \wedge \\ Root[f_2(F,\#1)\&,1] \le P \le Root[f_1(F,\#1)\&,1] \end{array} \right] \end{array} \right] \tag{8}$$

where $f(F,\#1)$ is a pure function with a parameter F.

$$\begin{aligned} f_1(F,\#1) = & -3.51\times10^{10} + 1.21\times10^{8} F + 1406.43F^2 + F^3 + (2.54\times10^{11} + 3.23\times10^{6} F - 476.14F^2)\#1 \\ & + (-6.90\times10^{9} + 15799.3F)\#1^2 + 1.01\times10^{8}\#1^3 \\ f_2(F,\#1) = & 7.75\times10^{9} - 4.51\times10^{6} F + 2051.22F^2 - F^3 + (8.53\times10^{7} + 1.84\times10^{5} F + 93.83F^2)\#1 \\ & + (-1.49\times10^{7} - 13084.8.3F)\#1^2 + 700648\#1^3 \end{aligned}$$

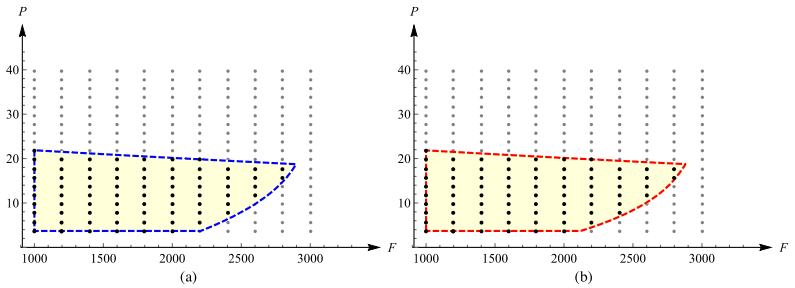

Figure 2. (a) Flexibility region φ'; (b) Final Flexibility region φ'_{final} for the vacuum distillation.

φ' shows that the flexibility region consists of two 2D cells. The complete flexibility region is depicted in Figure 2(a). However, since it is inevitable that the surrogate model will exist fitting error, the iterative process of the boundary check, surrogate modelling and CAD updating, is executed to refine the flexibility region. After 17 iterative processes, the final flexibility region φ'_{final} can be obtained, as shown in Figure 2(b).

$$\varphi'_{final} = \left[\begin{array}{l} 1: \left[\begin{array}{l} 1000 \le F \le 2121.2 \wedge \\ 3.7 \le P \le Root[f_1'(F,\#1)\&,1] \end{array} \right] \vee \\ 2: \left[\begin{array}{l} 2121.2 \le F \le 2880.96 \wedge \\ Root[f_2'(F,\#1)\&,1] \le P \le Root[f_1'(F,\#1)\&,1] \end{array} \right] \end{array} \right] \tag{9}$$

where $f'(F,\#1)$ is a pure function with a parameter F. The difference between φ'_{final} and φ' is on the depiction for the right boundary, which is illustrated in Figure 3(b). It should be noted that after the iterative refined process, the right boundary of flexibility region φ'_{final} is a little bit tighter than φ' since the validation samples on the right boundary of φ' is invalid. Thus, in order to obtain the flexibility region satisfying the correctness condition, the right boundary should be retracted.

$$f_1'(F,\#1) = -4.58\times10^{12} + 1.58\times10^{8}F + 1132.88F^2 + F^3 + (3.34\times10^{11} + 4.30\times10^{6}F - 507.06F^2)\#1 + (-9.29\times10^{9} + 13728.9F)\#1^2 + 1.40\times10^{8}\#1^3$$

$$f_2'(F,\#1) = 6.37\times10^{9} - 4.73\times10^{6}F + 2222.49F^2 - F^3 + (1.92\times10^{8} + 1.97\times10^{5}F + 102.56F^2)\#1 + (-2.75\times10^{7} - 15177.6F)\#1^2 + 1.14\times10^{6}\#1^3$$

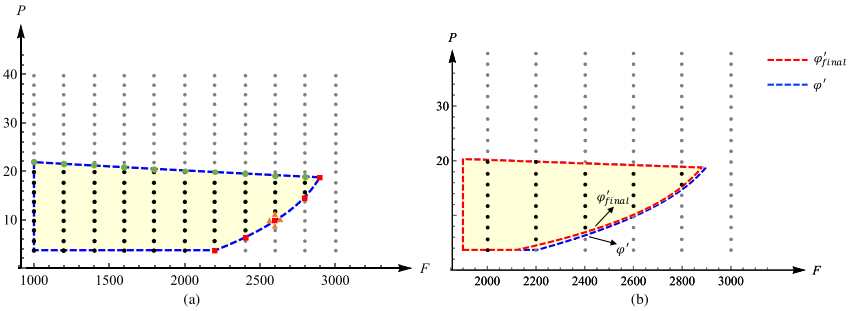

Figure 2. (a) Validation samples and new points; (b) The difference illustration of φ'_{final} and φ' .

5. Conclusions

In this study, a novel method is proposed to analytically describe the flexibility region for high-dimensional systems. First, based on the idea of model reduction, a surrogate model is built to approximate the inequality constraints and reduce the equalities. Then, the CAD method is utilized to depict the flexibility region with explicit expressions. Last, an iteratively refined procedure including the boundary check and the process of surrogate modelling and CAD updating is activated until the correctness condition is satisfied. The proposed method integrates the advantage of the surrogate model which is less computationally expensive and the CAD method which can describe the flexibility region analytically.

Acknowledgements

We gratefully acknowledge the financial support of the National Natural Science Foundation of China (No.61973268), the National Key Research and Development Program of China (No. 2017YFE0106700), and China Scholarship Council.

References

V. Bansal, J. D. Perkins, E. N. Pistikopoulos, 2002, Flexibility analysis and design using a parametric programming framework, AIChE Journal, 48, 2851-2868.

V. Goyal, M. G. Ierapetritou, 2003, Framework for evaluating the feasibility operability of nonconvex processes, AIChE Journal, 49, 1233-1240.

I. Banerjee, M. G. Ierapetritou, 2005, Feasibility evaluation of nonconvex systems using shape reconstruction techniques, Industrial & Engineering Chemistry Research, 44, 3638-3647.

Z. Wang, M. G. Ierapetritou, 2017, A novel feasibility analysis method for black-box processes using a radial basis function adaptive sampling approach, AIChE Journal, 63, 532-550.

F. Zhao, X. Chen, 2018, Analytical and triangular solutions to operational flexibility analysis using quantifier elimination, AIChE Journal, 64, 3894-3911.

G. E. Collins, 1975, Quantifier elimination for real closed fields by cylindrical algebraic decomposition, Lecture Notes in Computer Science, 33, 134-183.

Sauro Pierucci, Flavio Manenti, Giulia Bozzano, Davide Manca (Eds.)
Proceedings of the 30th European Symposium on Computer Aided Process Engineering (ESCAPE30), May 24-27, 2020, Milano, Italy.
http://dx.doi.org/10.1016/B978-0-12-823377-1.50201-9

Online Optimal Cleaning Scheduling and Control of Heat Exchanger Networks under Fouling with Large Disturbances

Federico Lozano Santamaria, Sandro Macchietto

Department of Chemical Engineering, Imperial College London South Kensington Campus, London SW7 2AZ, UK

Abstract

Fouling in refining applications reduces the energy recovery in the pre heat train, increasing the overall cost of the operation. To mitigate fouling, cleanings of the exchangers are scheduled, and the flow distribution in the network modified. Usually, these two decisions are considered independently, and the dynamic behavior and disturbances affecting the network are ignored. Without considering process variability, fouling mitigation alternatives will become suboptimal or infeasible over time. This work builds on our previous research where an online NMPC-MHE multiloop approach was developed for fouling mitigation and tested under nominal model mismatch. Here, the performance of the framework for simultaneous optimal online flow control and cleaning scheduling is demonstrated for large and realistic disturbances found in refining operations (+/- 50% inlet temperatures and flow changes, and processing different types of crudes). A realistic case is used to demonstrate the advantages of the framework, and results show its effectiveness to react to disturbances over various time scales while minimizing the total operating cost.
Keywords: integrated scheduling and control, NMPC, MHE, heat exchanger network, crude oil fouling, large disturbances.

1. Introduction

Fouling reduces the efficiency of energy recovery and has a large impact on refining applications. It increases the energy consumption, carbon emissions, and operating cost of the refinery. Mitigation alternatives are necessary for a reliable operation. The most important mitigation actions to reduce the deposition rate or recover heat transfer efficiency are: changing the flow distribution (e.g. flow splits between parallel branches) and periodic cleaning of the units. Modelling and mathematical programming have been used to solve independently for the optimal flow distribution (de Silva et al. 2015) or optimal cleaning schedule (Georgiadis et al. 2000). If formulated as an MINLP, the main limiting factor is the complexity and combinatorial nature of the optimal cleaning scheduling problem. Simplifications are usually made to solve it, using linear fouling models, linearization of the heat exchanger models (Lavaja and Bagajewicz 2004), or heuristic algorithms (Ishiyama et al. 2009). A simultaneous solution of the flow control and cleaning scheduling problems exploits the interactions and synergies between all decision levels, with large economic benefits (Lozano Santamaria and Macchietto 2018). However, in refining operations, the type of crude processed, inlet flow rates and streams temperature change frequently. These disturbances impact significantly the operation and performance of HEN, but are usually ignored. Furthermore, a single solution to the problem at some nominal conditions may rapidly become suboptimal or infeasible given

the large uncertainty and variability of the operation. In our previous research (Lozano Santamaria and Macchietto 2019a) we solved online the optimal cleaning scheduling and flow control problem of HEN using a NMPC-MHE (Nonlinear model predictive control – Moving horizon estimator) approach with multiple loops. It was shown that the method worked well with relative small noise (coefficient of variance of 5% - 8% in the inlet flow rates and 12% - 30% in the deposition rates). Here, we expand on that work, addressing the much more extreme disturbances which are usually observed in refining operations (+/- 50% change or greater in inlet flows). It is demonstrated that the proposed online fouling mitigation approach, that updates the prediction models and optimally reacts to the disturbances, is able to minimize operating cost and satisfy all constraints even in these more demanding and realistic situations.

2. Multi loop online integration of cleaning scheduling and control

The online integration of cleaning scheduling and control (Figure 1) is based on two feedback loops: the flow control problem which has a time scale of hours/days, and the cleaning scheduling problem which has a time scale of months/years. Each loop is composed by i) a MHE that estimates fouling model parameters and current HEN conditions by minimizing the error between measurements and predictions over a past estimation horizon (PEH), and ii) a NMPC controller that, using the model and conditions estimated, defines optimal future actions (flow distribution and/or cleaning scheduling) by minimizing the total operating cost over a (long) future prediction horizon (FPH). The measurements inputs to all MHE problems are flow rates, temperature, and pressure drops. As in standard NMPC, only actions in the first step are implemented, the rest are discarded, and the problem is solved again at the next sampling instance.
At the core of each MHE and NMPC problem there is a formulation and solution of an optimization problem: an MINLP (for the scheduling layer including binary decisions for the cleanings) or an NLP (for the control layer, where cleanings are known and fixed).

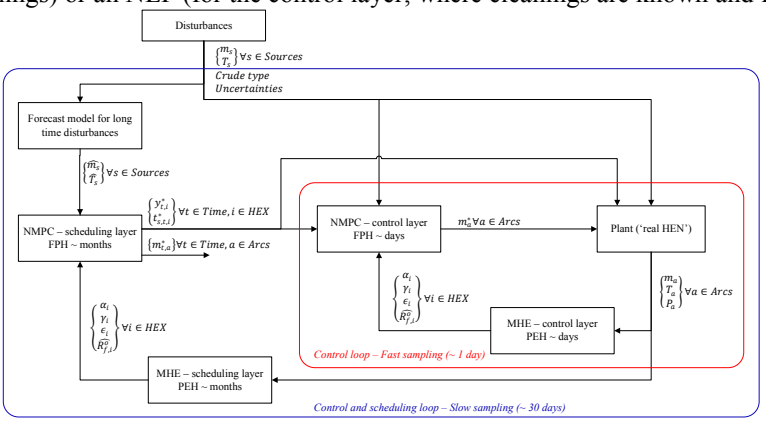

Figure 1. Schematic representation of the multi loop control scheme for the optimal cleaning scheduling and control in mitigating fouling.

The problem formulation (Lozano Santamaria and Macchietto 2018) includes: an axially lumped radially distributed model for shell and tube heat exchangers (P-NTU model) that accounts for radial temperature profiles in the tubes, the Ebert-Panchal model to characterize crude oil deposition (Ebert and Panchal 1995), a continuous time representation with variable length for the periods, tube side pressure drop correlations, and operational constraints (e.g. firing limit, pressure drop limits). The MINLP for the

simultaneous flow control and cleaning scheduling optimization is reformulated as a NLP using complementarity constraints and solved using an iterative ϵ regularization approach (Lozano Santamaria and Macchietto, 2019b). The control layer is updated frequently (~daily) to respond rapidly to changes, while the scheduling layer is updated less frequently (~ weekly or monthly). The disturbances considered are: changes in flow rates and temperatures of all inlet streams to the network, and changes in the type of crude processed. The latter are modelled by modifying the deposition constant in the fouling rate model. All these disturbances have a significant impact on the performance of the network, on the fouling rates of each exchanger, and thus on the optimal operation of the system. In the control layer, the current realization of the disturbances (last measured value at each update) is used as a constant forecast within the FPH in the NMPC problem. In the scheduling layer a moving average of each disturbance realization over the most recent month is used to forecast it over the FPH. These two different forecasting strategies are necessary because of the differences in time scales and frequency updates of each layer.

3. Refinery case study

Figure 2 shows the preheat train of a real refinery used as case study. It has 5 exchangers, of which 4 are double shell, arranged in two parallel branches. The flow control degree of freedom is the split fraction between the branches. Historical data collected daily from actual operations over 4 years were used as process inputs and to characterize their variability.

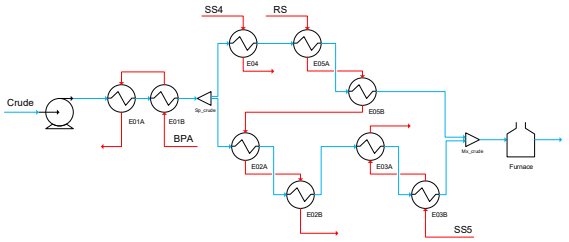

Figure 2. Heat exchanger network used for the case study.

A model for the actual operation of this plant was validated previously (Lozano Santamaria and Macchietto 2019b). Here, in order to "carry out" alternative operations, the 'plant' in the online scheme is defined artificially using the same predictive model as that of the optimization problems. To mimic changes in crude slates (no records were available), fouling parameters were changed in a pseudo random manner. The deposition constant of each exchanger of the plant model was modified, based on a normal probability distribution characteristic of the process variability. Because all exchanger processed the same crude, the deposition constants are positively correlated (i.e. heavier crudes increase the fouling rate in all exchangers). Two types of large disturbances were imposed representing large deviations from normal operation: a) changes in the type of crude (modelled as a change in the deposition constant of the Ebert-Panchal model), and b) changes in the inlet streams flow rates. These disturbances are modelled as step changes with +/- 50%, and +/- 30% with respect to their average value, respectively. Note that the nominal variability of these variables is characterized by a coefficient of variance of 21% for (a) and of 7% for (b), hence the disturbances represent a large departure from the operating point of the system. Figure 3 shows the disturbances imposed for three of the exchangers over 1 year. Flow rates exhibit a natural variability with significant step change deviations from normal operation. The parameters used in the multiloop scheme

are: a sampling frequency of 1 day for the plant and the control layer, and 15 days for the scheduling layer; a future prediction horizon (FPH) of 10 days for control and 90 days for scheduling; a past estimation horizon (PEH) of 20 days for control, and 60 for scheduling.

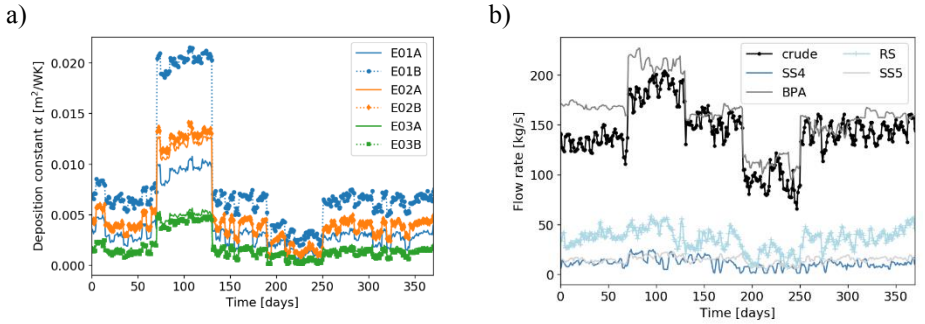

Figure 3. Large disturbances considered for the case study. a) deposition constants, b) inlet flow rates.

4. Results and analysis

The integrated cleaning scheduling and control problem is solved repeatedly online for 1 year of operation, with the actual refinery inputs to the network and the large disturbances as above. The optimal closed loop solution is compared to the actual mitigation strategies used in the refinery (records of cleanings and flow control). Figure 4 shows the closed loop cleaning schedule obtained at the end of the year, with the periods of step change disturbances highlighted (red area for a positive disturbance, blue area for a negative one), and the number of cleanings per exchanger on the right. For scenario a) (deposition changes), the number of cleanings is higher during the period of high fouling (+50% in deposition constants) than during periods of low fouling (-50% in deposition constants) or periods of nominal operating conditions. For scenario b) (flowrate changes), a higher number of cleanings is observed during the periods of high flow rates than during those of low flow rate. The time between cleanings (e.g. for E01) decreases when the inlet flow rate decreases. The online schemes reacts well to the higher/lower fouling caused respectively by higher/lower deposit rates and lower/higher flowrates (high flows increase shear stress, partially removing deposits or reducing the fouling rate in some exchangers).

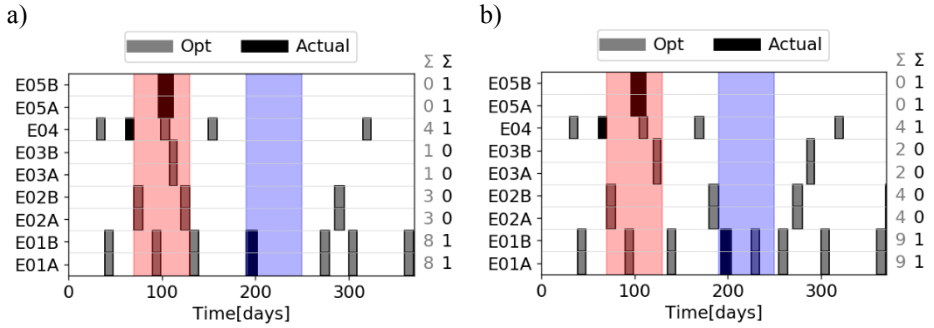

Figure 4. Closed loop cleaning scheduling considering large disturbances. a) Disturbance in the deposition constant, and b) disturbance in the inlet flow rates

Figure 5 shows the closed loop response of the split ratio to E02 branch (a) and fouling resistance in exchanger E03A/B (b) following large disturbances in the inlet flow rates

(scenario b). The effect of the natural variability is observed as small oscillations of the fouling resistance, while a larger departure from nominal behavior is introduced by the large disturbances. High crude flow rates (red area) increase the shear stress in the exchangers of branch E03A/B and the deposit is partially removed. The optimal flow distribution plays a key role in reducing deposition in some units, thus enabling to avoid or delay cleaning. This is not observed in the mitigation strategy previously used, where the benefits of the reacting to disturbances and integrating decisions are not observed. All these interactions and trade-offs are here considered implicitly at each update in the online methodology, at the two decision levels of control and scheduling.

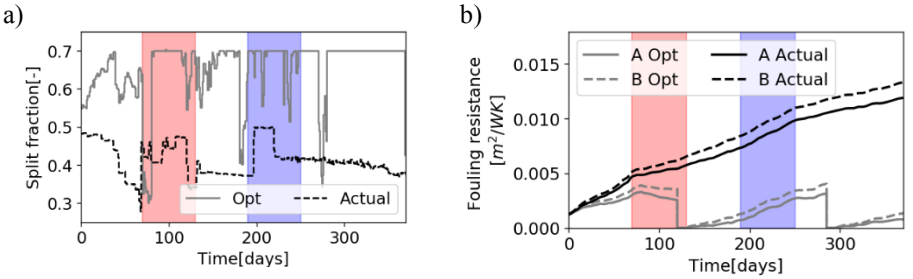

Figure 5. Closed loop response of split ratio profile a) and fouling resistance in exchanger E03A/B b) following large disturbances in the inlet flow rates (scenario b).

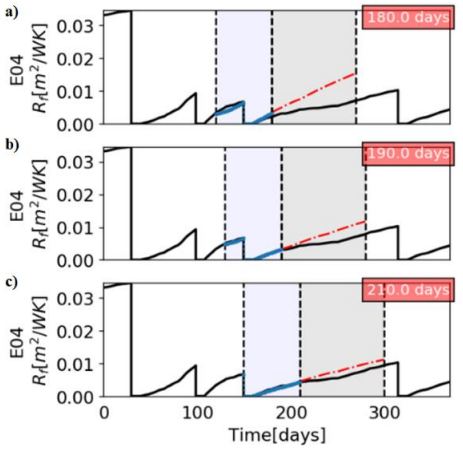

Figure 6. Fouling resistance of E04 in the PEH (light blue band) and the FPH (grey band) for three consecutive solutions of the scheduling layer, scenario (a). The top right corner of each figure indicates the current time (solution of MHE and NMPC).

Figure 6 shows the solution of the scheduling layer problems (MHE and NMPC) at three consecutives updates of scenario (a) around the second major step from nominal operation to low deposition rate. It shows the actual fouling resistance in E04 during the closed loop operation (black, continuous line), the values estimated by the MHE (blue, dotted line), and the predicted values by the NMPC solution (red, dashed line). This shows that large disturbances affect the prediction capabilities of the model, and that without any modification or update of the model, the predictions are erroneous and lead to suboptimal of infeasible operating modes. This figure also illustrates the excellent predictive capabilities achieved using the online framework, how the model adapts to large disturbances and how it improves the prediction at each update. Initially (Fig. 6a), the

MHE problem includes most of the points of the nominal operation, so the NMPC solution overestimates the effects of fouling during low deposition operation. Then (Fig. 6b), more recent information about the disturbances is available to the MHE problem and the NMPC prediction improves. Finally (Fig. 6c), with a larger data set from the current operation the prediction matches the actual realization observed in the plant. The adaptive solution of the scheduling layer problems allows improving the prediction capabilities and accuracy of the model faster in the presence of large disturbances. Overall, for scenario a) this approach reduces total operating cost from $ 12.3 MM (actual operation) to $ 11.4 MM, representing savings of $ 0.9 MM (7.3%) during one year of operation. If no cleanings are performed and the flow split is fixed at 50%, the total cost of the operation for this scenario is $ 13.0 MM, highlighting the need of mitigation strategies.

5. Conclusions

The online approach presented simultaneously and optimally defines the flow distribution and cleaning schedules of HEN under fouling. Its two feedback control loops accurately capture process variability over various time scales and react appropriately to it. It deals efficiently with both the nominal variability of the process and the large operational changes characteristic of actual refinery operation. Operational feasibility is maintained, and the total operating cost is minimized regardless of disturbances. Results for a realistic case study show the importance of considering disturbances, and how varying operating conditions – inlet flow rates and fouling rates – affect the optimal flow distribution and cleaning schedules. Future work will investigate other disturbances, the feedback loop specification, and the overall closed loop stability of the integrated solution.

References

Ebert, Richmond, and IL Panchal. 1995. “Analysis of Exxon Crude-Oil-Slip Stream Coking Data.” In . United States. http://www.osti.gov/scitech/servlets/purl/453433.

Georgiadis, Michael C, Lazaros G Papageorgiou, and Sandro Macchietto. 2000. “Optimal Cleaning Policies in Heat Exchanger Networks under Rapid Fouling.” *Industrial & Engineering Chemistry Research* 39 (2): 441–54. https://doi.org/10.1021/ie990166c.

Ishiyama, E M, W R Paterson, and D I Wilson. 2009. “Platform for Techno-Economic Analysis of Fouling Mitigation Options in Refinery Preheat Trains.” *Energy & Fuels* 23 (3): 1323–37. https://doi.org/10.1021/ef8005614.

Lavaja, Javier H, and Miguel J Bagajewicz. 2004. “On a New MILP Model for the Planning of Heat-Exchanger Network Cleaning.” *Industrial & Engineering Chemistry Research* 43 (14): 3924–38. https://doi.org/10.1021/ie034178g.

Lozano Santamaria, Federico, and Sandro Macchietto. 2018. “Integration of Optimal Cleaning Scheduling and Control of Heat Exchanger Networks Undergoing Fouling: Model and Formulation.” *Industrial & Engineering Chemistry Research* 57 (38): 12842–60. https://doi.org/10.1021/acs.iecr.8b01701.

Lozano Santamaria, Federico, and Sandro Macchietto. 2019a. “Online Integration of Optimal Cleaning Scheduling and Control of Heat Exchanger Networks under Fouling.” *Industrial & Engineering Chemistry Research*, November, acs.iecr.9b04531. https://doi.org/10.1021/acs.iecr.9b04531.

Santamaria, Federico Lozano, and Sandro Macchietto. 2019b. “Integration of Optimal Cleaning Scheduling and Control of Heat Exchanger Networks under Fouling: MPCC Solution.” *Computers & Chemical Engineering* 126 (July): 128–46. https://doi.org/10.1016/J.COMPCHEMENG.2019.04.012.

Silva, R. L. de, L.H. Costa, and Eduardo M Queiroz. 2015. “Stream Flow Rate Optimization for Fouling Mitigation in the Presence of Thermohydraulic Channeling.” In *Proceedings of International Conference on Heat Exchanger Fouling and Cleaning*, edited by M.R Malayeri, H Muller-Steinhagen, and A.P Walkinson, 384–91.

Sauro Pierucci, Flavio Manenti, Giulia Bozzano, Davide Manca (Eds.)
Proceedings of the 30th European Symposium on Computer Aided Process Engineering (ESCAPE30), May 24-27, 2020, Milano, Italy.
http://dx.doi.org/10.1016/B978-0-12-823377-1.50202-0

Integrated Planning of Industrial Gas Supply Chains

Yena Lee[a], Alba Carrero-Parreño[a], Lazaros G. Papageorgiou[a,*], Sivaraman Ramaswamy[b], Jose M. Pinto[b]

[a] *Centre for Process Systems Engineering, Department of Chemical Engineering, UCL (University College London), Torrington Place, London WC1E 7JE, UK*

[b] *Linde plc., 10 Riverview Drive, Danbury CT 06810, United States*

l.papageorgiou@ucl.ac.uk

Abstract

In this work, we propose a Mixed Integer Linear Programming (MILP) model for optimal planning of industrial gas supply chain, which integrates supply contracts, production scheduling, truck and rail-car scheduling, as well as inventory management under the Vendor Managed Inventory (VMI) paradigm. The objective used here is minimisation of the total operating cost consisting of purchasing of raw material, production, and transportation costs by trucks/rail-cars so as to satisfy customer demands over a given time horizon. The key decisions for production sites include production schedule and purchase schedule of raw material, while the distribution decisions involve customer to plant/depot allocation, quantity transported through rail network, truck delivery amounts, and times. In addition, a relaxation approach is proposed to solve the problem efficiently. An industrial case study is evaluated to illustrate the applicability of the integrated optimisation framework.

Keywords: Integrated supply chain planning, discount contract model, rail-car and truck scheduling, relaxation approach

1. Introduction

The optimisation of supply chain planning for the industrial gas business is a challenge when the supply chain structure integrates multiple decisions such as: supply contracts, inventory management, production and distribution scheduling, etc. As the level of detail increases, it becomes more difficult to optimally solve the model due to its complexity. However, optimal decisions considering a coordinated industrial gas supply chain have significant benefits (Marchetti et al., 2014). In their research, potential cost savings were identified with coordination between production and distribution in industrial gas supply chain. Nevertheless, expensive computational cost is required when dealing with large size examples. Recently, some efforts have been made to tackle this limitation. You et al. (2011) developed a mixed integer linear programming model which considers distribution and inventory decisions of industrial gas supply chain planning simultaneously. They also proposed two different approaches to solve the large-scale instances. The first one is based on a two-level decomposition method and the second one is based on a continuous approximation method. Additionally, Zamarripa et al. (2016) proposed a rolling horizon decomposition approach for full space optimisation problem which coordinate production-distribution decisions, and Zhang et al. (2017) proposed an MILP model and an iterative heuristic approach for the multiscale production routing problem which integrates production, distribution, and inventory decisions.

In this work, we investigate a problem of optimal integrated production and distribution planning that reliably produces CO_2 from a number of plants (and sourced from external third-party suppliers) and distributes high quality CO_2 product to a network of depots and customers. The problem is formulated as a mixed integer linear programming (MILP)model which can simultaneously deal with purchase contracts, inventory management, production, and truck/rail-car scheduling. Furthermore, we present a relaxation approach to handle the computational complexity of a large-scale industrial problem.

2. Problem Definition

This study considers an existing CO_2 supply chain network (schematized in Figure 1) located in the U.S. which comprises of external CO_2 suppliers, production plants, depots, third-party suppliers, and customers. The crude CO_2 is purchased from external suppliers by discount contracts and transformed into high purity CO_2 in the plants. This pure CO_2 can also be sourced from third-party suppliers. The distribution between different locations to satisfy the customers' demand is guaranteed via rail-cars or trucks. The rail-cars can distribute the CO_2 product from plants/third-parties to depots using existing rail infrastructure, and the trucks from the plants, depots and/or third parties to the customers. The customers' demand is controlled by the Vendor Managed Inventory (VMI) paradigm. Under this policy, each customer inventory level is monitored to deliver the product when it reaches close to the minimum level.

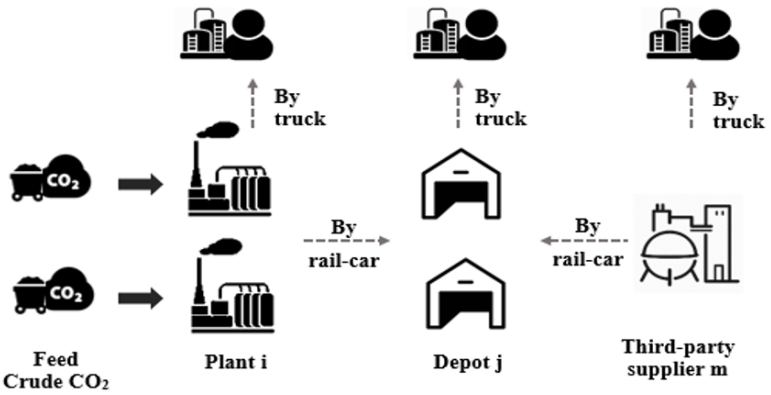

Figure 1. Network structure for the CO_2 supply chain planning problem

The problem can be stated as follows:

Given (a) for each plant: its location, maximum production capacities, and corresponding production and crude CO_2 purchasing costs; (b) for each depot: its location; (c) for each third-party supplier: its location, maximum purchasing amount, and purchasing costs; (d) for customers: their locations, and daily consumption rates; (e) for inventories: initial levels, minimum levels, and maximum levels; (f) for trucks and rail-cars: its loading capacities, maximum quantities, and transfer unit costs;

Determine (a) Production schedule; (b) Purchasing schedule of crude CO_2 and CO_2 product from external suppliers and third party suppliers, respectively; (c) Allocation of plant/depot/third party to customer; (d) Rail-car schedule;

So as to minimise the overall cost of integrated CO_2 supply chain planning by satisfying customer demands over a given time horizon.

3. Mathematical Framework

The overall problem is formulated as a Mixed Integer Linear Programming (MILP) model which integrates supply contracts, truck and rail-car scheduling, as well as inventory management under the Vendor Managed Inventory (VMI) paradigm. A brief outline of some of the model constraints is next given.

$$min.\ TC^{total} \tag{1}$$

$$TC^{total} = TC^{raw} + TC^{prod} + TC^{st} + TC^{os} + TC^{rail} + TC^{truck} \tag{2}$$

Eq. (1) is the objective function and considers the minimization of total cost which consists of crude CO_2 cost, production cost, plant start-up cost, product CO_2 purchasing cost, and transportation cost via rail-car and truck.

$$TC^{raw} = \sum_{in} C_{in}^{raw} F_{in} \tag{3}$$

$$\sum_{n} F_{in} = \sum_{t} R_{it} \qquad \forall\, i \tag{4}$$

$$(\lambda_{in} - \lambda_{i,n-1}) y_{i,n+1} \le F_{in} \le (\lambda_{in} - \lambda_{i,n-1}) y_{in} \qquad \forall\, i, n = \{1,2, \dots N-1\} \tag{5}$$

$$F_{in} \le M y_{in} \qquad \forall\, i, n = N \tag{6}$$

$$y_{in} \ge y_{i,n+1} \qquad \forall\, i, n = \{1,2, \dots N-1\} \tag{7}$$

Eq. (3)-(7) represent a discount contract model for crude CO_2. The proposed discount contract model follows the model published by Park et al. (2006). In their formulation, the purchasing cost is decided by a binary variable depending on both cost region *n* and time period *t*. However, as in our problem the discount is applied to the total cumulative purchasing amount, it is reformulated considering a non-time-dependent binary variable. Eq. (3) calculates the total cost for crude CO_2 which depends on the purchased amount in the cost region *n* (F_{in}), and the corresponding cost for plant *i* (C_{in}^{raw}). Eq. (4) indicates that the total purchased amount in each cost region is equal to the sum of the purchased amount in each time period *t*. Eq. (5) determines the amount corresponding on each cost region; i.e. y_{in} is equal to 1 when the total purchased amount $\sum_t R_{it}$ is in the cost region *n*. Here, λ_{in} is the breakpoint of cost region n, where the price is reduced when the total cumulative purchasing amount during a time horizon excess the breakpoint. Eq. (6) restricts the amount in the last lost region (*n*=*N*); i.e. F_{iN} has to be lower than the M value.

Finally, Eq. (7) is a logical relationship which avoid the selection of intermediate cost regions.

$$TC^{truck} = \sum_{s\in\{I,J,M\}} \sum_{k} \sum_{l\in l_{Truck}} \sum_{t} C^{truck}\ D_{sk}\ Q_{sklt} \tag{8}$$

$$\sum_{l\in l_{Truck}} \sum_{k} \alpha_{sk}\ Q_{sklt} \le NT_s^{max} Cap^{truck} \qquad \forall t, s \in \{I, J, M\} \tag{9}$$

Eq. (8)-(9) state the relaxed formulation for the truck scheduling problem to estimate the trucking cost and allocate plants/depots/third-parties to customers without considering the detailed scheduling. By using this formulation, the discrete variables associated with the detailed truck scheduling are relaxed; therefore, the computational efficiency is improved when dealing with a large number of customers, plants and time horizon. Eq. (8) calculates the transfer cost by trucks departing from plants *i*, depots *j*, and third-parties *m*. The truck cost is based on the unit transfer cost (C^{truck}), travelling distance (D_{sk}), and loading amount (Q_{sklt}). Constraint (9) limits the total product amount transferred by trucks. Because trucks can make multiple trips per time period *t*, not only the loading capacity but also the number of the multiple trips should be considered to limit the total amount transferred during a time period *t*. However, the complexity of the model increases if integer variables are introduced to consider the number of the multiple trips. Here, the duration of the round-trip between the locations (α_{sk}), which is formed as a fraction of a time period, is introduced to approximate the total transferred amount by the multiple trips instead of introducing the integer variables. By using the fraction of travelling time (α_{sk}), all the integer variables can be relaxed into continuous variables (Q_{sklt}). Finally, the total amount transferred by trucks during a time period *t* is restricted by the loading capacity (Cap^{truck}), and the number of trucks available at each plant, depot, and third-party (NT_s^{max}).

4. Case Study and Results

The proposed model is applied for a large-scale industrial supply chain planning problem given by Linde which includes 700+ customers, total 30+ of plants, depots, transshipments, third-parties, and one month discretised into 30 days. To compare the efficiency and validity of the relaxation approach, the case study is solved with the proposed MILP model (M^R), which includes the approach and the integrated one (M), which involves the discrete variables to indicate the multiple trips made by trucks. Both models are implemented into GAMS software and solved using Gurobi 8.1.0 on Intel 3.60 GHz, 16.0 GB RAM computer.

Table 1. Optimal solution and computational performance

Model	M	M^R
Equations	252,364	140,869
Continuous variables	138,253	138,253
Discrete variables	653,156	5,411
Optimality gap [%]	5	1
CPU time [s]	144,371	145
Total cost [M$]	5.73	5.25

Table 1 describes the problem size, optimal solution and computational performance of the rigorous and relax model. It can be observed that the case study cannot be solved with the rigorous formulation in an acceptable computational time since the large number of discrete variables. It requires 40 h to reach an optimal solution with 5 % of optimality gap. Conversely, the CPU time significantly decreases solving the relaxed formulation as the number of discrete decisions is reduced to 5,411. This enables the model to handle the large-scale problem by reducing computational time dramatically. Additionally, to validate the optimal solution, the gaps of the optimal costs generated by model M and model M^R are presented in Table 2. The table shows that these gaps are within 5 % except for the start-up and third-party cost, but they only account for 1 % and 2 % of the total cost, respectively as it can be shown in the total cost breakdown of Figure 2.

Table 2. Gaps between optimal solution from the model M and model M^R

Cost breakdown	TC^{raw}	TC^{prod}	TC^{st}	TC^{os}	TC^{rail}	TC^{truck}
Gap [%]	1	0	14	0	5	2

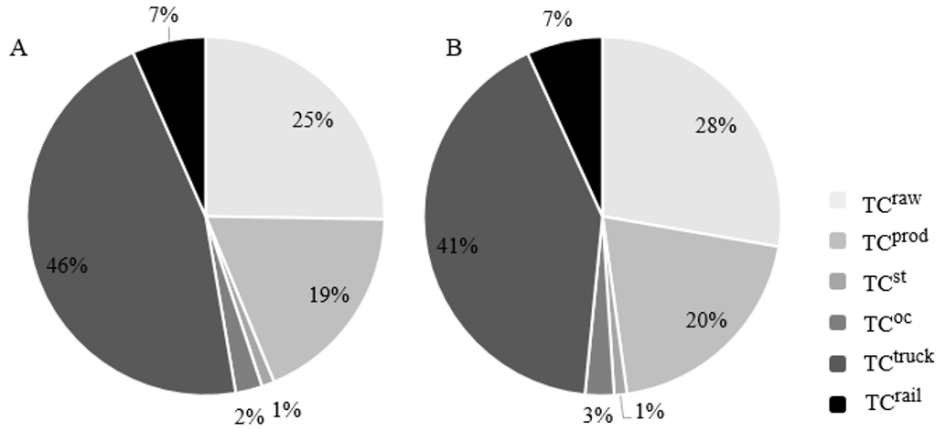

Figure 2. Total cost breakdown of (A) the model M and (B) the model M^R

In the figure, each breakdown cost of total cost obtained from each model account for almost the same percentage which means that the relaxed approach proposed can predict optimal costs without significant degradation of solution quality.

Figure 3 and Figure 4 illustrate part of the production and rail-car scheduling results gained from model M^R. In the production scheduling result, each value in the colored cells shows the production amount during a time period *t*. In the rail-car scheduling result, the solid cells represent one-way trip, whereas the vertical striped cells represent returning trip. The figures reveal that the proposed model is capable of providing detailed solutions for the production scheduling problem and rail-car scheduling problem without considering detailed truck scheduling.

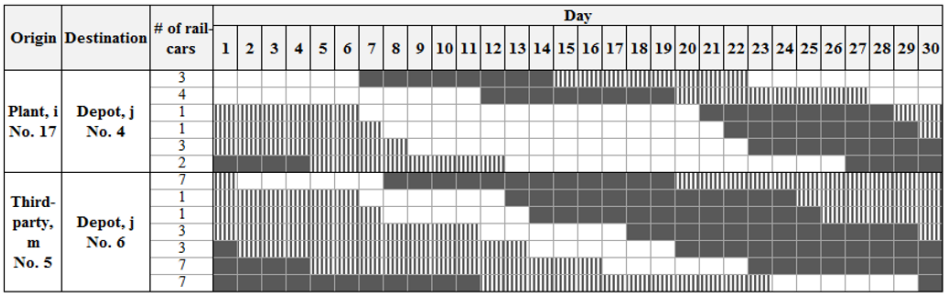

Figure 3. Gantt chart for rail-car schedule

Plant, i	Day																												
	1	2	3	4	5	6	7	8	9	10	11	12	13	14	15	16	17	18	19	20	21	22	23	24	25	26	27	28	29	30
No. 1	325	247	228	228	228	228	228	228	228	228	228	228	228	228	228	228	228	228	228	228	228	228	228	228	325	228				
No. 2	50	50	50	50	50	50	50	50	50	50	50	50	50	50	50	50	50	50	50	50	50	50	50	50	50	50	50	50	50	50
No. 3	430	372	301	420	430	362	301	301	301	351	301	376	308	301	301	301	368	338	301	311	301	301	301	301	301	403				
No. 4			161	161	161	161	161	161	190	230	230	230	230	230	230	230	161	230	161	161	161									
No. 5	400	284	400												318	400	280	400	305	280	280	280	280							
No. 6						209	170	188	154	154	168	220	220	154	154	154	154	154	154	164	154	154	154	154	154	154				
No. 7	263	263	263	263	263	263	263	263	263	263	263	263	263	263	263	263	263	263	263	263	263	263	263	263						
No. 8						350	350	350	350	350	350	350	305	350	350	350	350	350	350	350	350	350	245	350	350	350				

Figure 4. Production schedule

5. Conclusions

This work has introduced an MILP formulation which considers supply contracts, inventory management, production, rail-car and truck scheduling simultaneously. To handle the complexity of the integrated problem, a relaxation approach is applied in the truck scheduling problem where discrete variables associated with the detailed truck scheduling are relaxed to continuous variables. The proposed strategy successfully solve a real large-scale industrial gas supply chain planning case study given by Linde. The results prove that the proposed approach has the capability of finding an optimal solution without significant degradation of quality, as well as high computational efficiency.

References

P. A. Marchetti, V. Gupta, I. E. Grossmann, L. Cook, P.-M. Valton, T. Singh, T. Li, J. André, 2014. Simultaneous production and distribution of industrial gas supply-chains. Computers & Chemical Engineering 69, 39–58.

M. Park, S. Park, F. D. Mele, I. E. Grossmann, 2006. Modeling of purchase and sales contracts in supply chain optimization. Industrial & Engineering Chemistry Research 45 (14), 5013–5026.

F. You, J. M. Pinto, E. Capón, I. E. Grossmann, N. Arora, L. Megan, 2011. Optimal distribution-inventory planning of industrial gases. i. fast computational strategies for large-scale problems. Industrial & Engineering Chemistry Research 50 (5), 2910–2927.

M. Zamarripa, P. A. Marchetti, I. E. Grossmann, T. Singh, I. Lotero, A. Gopalakrishnan, B. Besancon, J. André, 2016. Rolling horizon approach for production–distribution coordination of industrial gases supply chains. Industrial & Engineering Chemistry Research 55 (9), 2646–2660.

Q. Zhang, A. Sundaramoorthy, I. E. Grossmann, J. M. Pinto, 2017. Multiscale production routing in multicommodity supply chains with complex production facilities. Computers & Operations Research 79, 207–222.

Sauro Pierucci, Flavio Manenti, Giulia Bozzano, Davide Manca (Eds.)
Proceedings of the 30th European Symposium on Computer Aided Process Engineering (ESCAPE30), May 24-27, 2020, Milano, Italy.
http://dx.doi.org/10.1016/B978-0-12-823377-1.50203-2

Advanced Process Control of an Industrial Depropanizer Column using Data-based Inferential Sensors

Martin Mojto[a], Karol L'ubušký[b], Miroslav Fikar[a] and Radoslav Paulen[a]

[a]*Faculty of Chemical and Food Technology, Slovak University of Technology in Bratislava, Bratislava, Slovakia*
[b]*Slovnaft, a.s., Bratislava, Slovakia*
martin.mojto@stuba.sk

Abstract

Inferential sensors are used in industry to infer the values of the imprecisely and infrequently measured (or completely unmeasured) variables from measured variables (e.g., pressures, temperatures). This work deals with the design of inferential sensors suitable for an advanced process control of a depropanizer column of the Slovnaft refinery in Bratislava, Slovakia. We design linear inferential models of top and bottom product compositions. Model calibration is performed using historical production data. We study the effectiveness of several data-based methods (PCA, PLS, LASSO) for the design of inferential sensors. Our results show that the methods, which promote model sparsity are more suitable. Validation using a rigorous mathematical model shows that the designed inferential sensors are sufficient for the advanced process control of the column.

Keywords: Inferential Sensors, Data-based Models, Process Control.

1. Introduction

Majority of advanced controllers in industry is based on linear input-output models (Qin and Badgwell, 2003). This is usually sufficient because of the existence of corrective feedback actions, i.e., receding-horizon principle. In many cases, the input-output models do not include main process characteristics, e.g., product quality, since they are often expensive or impossible to measure. The process performance can thus be improved by designing soft-sensors (also called inferentials), which can infer the values of the unmeasured variables from other measured variables (e.g., pressures, temperatures) and improve the overall process management (Weber and Brosilow, 1972; Joseph and Brosilow, 1978; Joseph, 1999).

The inferential sensor stands for a model designed to predict hard-to-measure variable according to other easily measured variables. In chemical industry, hard-to-measure variables are typically concentrations of products, since online concentration sensors are expensive or too slow for effective monitoring and control. Several works were devoted to state estimation and control of (chemical) process using inferentials (Mejdell and Skogestad, 1991, 1993; Zhang, 2001; Kano et al., 2003; Parvizi Moghadam et al., 2019). The approaches are ranging from simple enhancement of monitoring and control—by heuristically combining several variables to compensate the sensor-noise or external disturbance (e.g., pressure-corrected temperature control)—to the use of

Acknowledgements: This research received funding from the Slovak Research and Development Agency under the project APVV 15-0007 and from the Scientific Grant Agency of the Slovak Republic under the grant 1/0004/17.

Table 1: Composition of feed stream of the depropanizer column.

C3 fraction	C4 fraction			C5 fraction
Propane	n-Butane	Trans-2-Butene	1-Butene	Isopentane
Propylene	Isobutane	Cis-2-Butene	Isobutene	

sophisticated data-mining techniques, which select the optimal structure of the inferential sensor using available measured outputs and their historical records (Morari and Stephanopoulos, 1980).

This work deals with the design of inferential sensors for advanced process control (APC) of a depropanizer column of the Slovnaft refinery situated in Bratislava, Slovakia. We design linear inferential models of top and bottom product composition in order to provide a simple and appropriate structure of the soft-sensors for the APC of the plant. Model calibration is carried out using historical production data. We use various data-based modeling techniques, including principal component analysis (PCA), partial least-squares (PLS), and Least Absolute Shrinkage and Selection Operator (LASSO). We compare the accuracy and the effectiveness of the designed inferential sensors using the validation dataset from historical plant data and also using a rigourous mathematical model of a depropanizer column via gPROMS ModelBuilder. We also assess the appropriateness of the use of a linear soft-sensor for the control of the product quality.

2. Problem Description

The studied depropanizer column (see scheme in Fig. 1) contains 40 trays, operates in above-the-atmospheric pressure, and its feed composition is shown in Tab. 1. The column serves to separate feed mixture to C3-fraction-rich distillate product and to C4/C5-fraction-rich bottom product. The available operational degrees of freedom are feed flowrate F, bottom product flowrate B, distillate flowrate D, reflux flowrate R, heat duty in the reboiler Q_B, and heat duty in the condenser Q_D. Several of these variables are available as historical data. These are marked correspondingly in Fig. 1. The plant measurements, also available from historical data, are pressure at the top of the column p_D, pressure at the bottom of the column p_B, and temperatures of distillate T_D, at the 10^{th} tray T_{10}, at the 37^{th} tray T_{37} and at the bottom T_B.

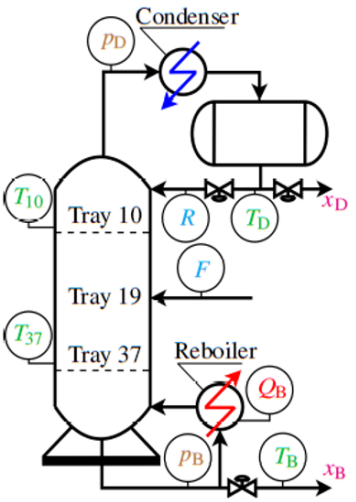

Figure 1: A schematic diagram of the depropanizer column.

It is evident that the use of thermodynamic properties model to monitor top/bottom stream compositions is prohibitive in this case, even under any appropriate ideality assumptions. This is because there are too many degrees of freedom for a seven-component mixture that cannot be inferred from plant data. According to previous paragraph, there are eleven possible input variables to select for the design of an inferential sensor. Current inferentials (denoted as ref), used in the refinery for monitoring/control of concentrations of C4/C5 fraction in the distillate (x_D) and of C3 fraction in the bottom stream (x_B), are designed according to King (2011) in the following form:

$$x_D = a_1 p_D + a_2 T_{10} + a_3 \frac{R}{F}, \qquad x_B = a_1 p_B + a_2 T_{37} + a_3 \frac{Q_B}{F}. \tag{1}$$

Our goal will be to identify models of inferential sensors in the following form

$$x = (a_1, a_2, \ldots, a_{n_p}) \left(F, R, Q_B, p_D, p_B, T_D, T_B, T_{10}, T_{37}, \frac{R}{F}, \frac{Q_B}{F} \right)^T = a^T m, \tag{2}$$

where m is the vector of available input variables for the inferential sensor and $a \in \mathbb{R}^{n_p}$ is the vector of parameters of the inferential sensor.

3. Identification of Inferential Models

Given n data points, we use various statistical methods in order to design the inferential sensors.

- The basic method is Ordinary Least-Squares (OLS) regression. This method estimates the parameters of an inferential sensor according to

$$\min_a \sum_{i=1}^{n} (x_i - a^T m_i)^2, \tag{3}$$

  which minimizes sum of squared errors between measured compositions and compositions estimated from inferential sensors.
- Principal Component Analysis (PCA) (Pearson, 1901) is a method of identifying a $\tilde{n}_p$-dimensional subspace ($\tilde{n}_p \leq n_p$) of orthogonal coordinates that exhibit a maximum variation in a given dataset. The principal components are identified by SVD decomposition of the covariance matrix of the input dataset MM^T, $M := (m_1, m_2, \ldots, m_n)$, taking the eigenvectors (for subset definition) and the associated eigenvalues (for measure of variance). The (PCA) regression is then done over the selected subspace using (3).
- Partial Least Squares (PLS) regression (Wold et al., 1984) is similar to PCA (Dunn et al., 1989) with the difference that it takes a cross-covariance matrix between inputs and outputs MX^T, $X := (x_1, x_2, \ldots, x_n)$.
- Least Absolute Shrinkage and Selection Operator (LASSO) (Santosa and Symes, 1986) is a method that simultaneously identifies the structure of the model and model parameters by

$$\min_a \sum_{i=1}^{n} (x_i - a^T m_i)^2 + \lambda \|a\|_1, \tag{4}$$

  where λ is a weight between model accuracy and model over-parameterization.

Note that among the presented methods, the PCA method comprises a certain distinct feature. As it does not require any output data, it can potentially be applied on much larger datasets in our general problem setup. This comes since the industrial data are usually available with much finer time granularity for the online sensors rather than for infrequent and expensive measurements.

4. Design of Inferential Sensors using Industrial Data

The design of inferential sensors is performed according to the data from more than two years of production (13.12.2016–21.2.2019) of the depropanizer column. The distillate composition is measured once per month and therefore only 28 measurements is available for the given period. Bottom inferential sensor is design according to 176 measurements as the concentration of this product is measured approximately once per week. The input data provided by online sensors are measured every 30 minutes, which gives an input dataset of 38,360 measurements.

A gross error detection and its subsequent reduction was performed on the given dataset by performing an SVD decomposition of the covariance matrix MM^T and by retaining only those data

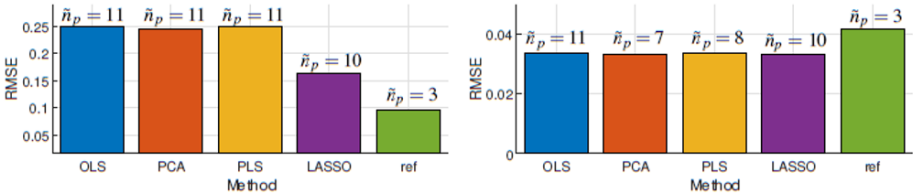

(a) Distillate composition.

(b) Bottom composition.

Figure 2: Accuracy of the designed inferential sensors according to the industrial validation data. The number of model input variables ($\tilde{n}_p$) is shown on top of each bar.

points that are inside the $\pm 3\sigma$ confidence ellipsoid given by the covariance matrix. The excluded points consist mostly of plant start-up, shutdown and upsets data.

When applying the methods mentioned in Section 3, we use 50 % of the data for training and 50 % of the data for validation. We use the implementations of the design methods available within MATLAB. We are interested in simplest possible structures, which is interesting for APC applications. For this reason, when using PCA and PLS to identify the model structure, we select only those input variables whose principal components explain 90 % of variance in the data. We use root mean square error (RMSE) to assess the accuracy of the designed inferential sensors.

We designed inferential sensors according to the OLS, PCA, PLS and LASSO. We repeated the design 1,000 times, each time randomly distributing the available data among the training and validation datasets. Presented results stand for mean values obtained. The results are shown in Fig. 2 in terms of accuracy of the sensors on the validation dataset for distillate and for bottom composition. Accuracy of the model is influenced by the ability of the method to escape from model over-parameterization. We show the number of variables that the model uses on the top of the bar that represents model accuracy.

Overall, we notice that the nature of the problem of designing the inferential sensors differs between distillate and bottom sensor. While the best distillate sensor uses only few (three) input variables, the most accurate bottom soft-sensors retain 7–11 out of eleven available input variables (all the temperatures and pressures). This is attributed to the small dataset available for the tuning of the distillate sensor and is subject of further analysis.

When comparing the different methods, we can find that OLS is not able to reduce the number of parameters/inputs of the inferential model in both cases. PCA and PLS perform similarly, although the promotion of model sparsity improves with the number of available data (bottom sensor). LASSO achieves slightly better results than OLS in both cases by being able to sparsify the model slightly, even if the dataset is small. The performance of the current on-site inferential sensor (ref) is very good in case of distillate composition inferential. However, there seems to be a room for improvement (around 20 %) of the inferential sensor for bottom composition.

5. Analysis of Inferential Sensors using Synthetic Data

In order to confirm our findings from the previous chapter and to analyse the further possible enhancements of inferential sensors, we designed the mathematical model of depropanizer column in gPROMS ModelBuilder. The model is built according to the parameters from the technical documentation of the depropanizer in the Slovnaft refinery and validated in the simulations with several step changes. We use 200 different (steady state) measurements for the design of inferential sensors. Compared to the historical data from the refinery, this is much larger dataset with many more different operating points (steady-states). The simulated measurements are corrupted with normally distributed random noise of similar magnitudes as present in the industrial data.

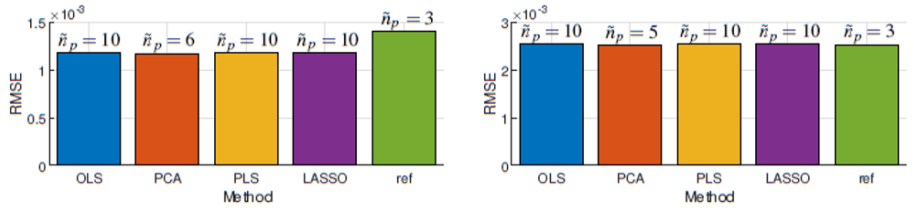

(a) Distillate composition. (b) Bottom composition.

Figure 3: Accuracy of the designed inferential sensors according to synthetic validation data. The number of model input variables ($\tilde{n}_p$) is shown on top of each bar.

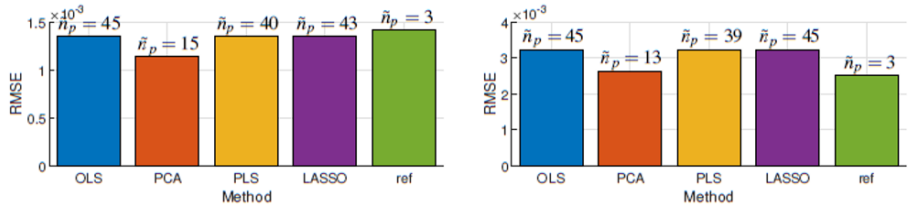

(a) Distillate composition. (b) Bottom composition.

Figure 4: Accuracy of the designed inferential sensors according to synthetic validation data for 49 possible input variables. The number of model input variables ($\tilde{n}_p$) is shown on top of each bar.

First, we use the information from the same sensors as in the previous section to mimic the case of studied column instrumentation. The results are shown in Fig. 3. We can mostly see that they confirm our previous conclusions. As the noise present in the data corresponds to the assumptions of the least-squares regression and variance analysis, all the methods exhibit an improved performance. Even the OLS method is able to sparsify the model to the extent of PLS and LASSO method. PCA can go even further without compromising the model quality. The slight improvement of the PCA-based distillate sensor w.r.t. ref is caused by adding variables R and F into the sensor structure.

Next, we consider data from more online sensors, 49 instead of 11. The input dataset is enriched by all the tray temperatures ($T_{1–40}$). In this case, we can conclude that bottom sensor cannot be much improved using new instrumentation. The optimal distillate inferential sensor seems to be 21 % more accurate that the current ref model but it is also much more complicated, one would need at least nine new sensors for the model by PCA. Lastly, we also see that the LASSO method does not cope well with situations when much dimension-reduction is needed.

At last, we tested the inferential control in the scenario, where the plant model is controlled by PI controllers using the following CV-MV pairs: p_D-Q_C, h_B-B, h_C-D, x_D-R, and x_D-Q_B. The results from the simulation of control using PCA-based inferential sensors are shown in Fig. 5. The prediction and steady-state error is indicated by evaluating the true plant response. We observe 90–95 % accuracy of the control, which is correspondence with the results from prediction accuracy analysis. The designed sensors are thus appropriate for control (APC) purposes.

6. Conclusions

We studied the design of linear inferential sensors for the top and bottom product composition of an industrial depropanizer column. We studied the accuracy and the effectiveness of several advanced data-based methods (PCA, PLS, LASSO). We used historical plant data for model calibration.

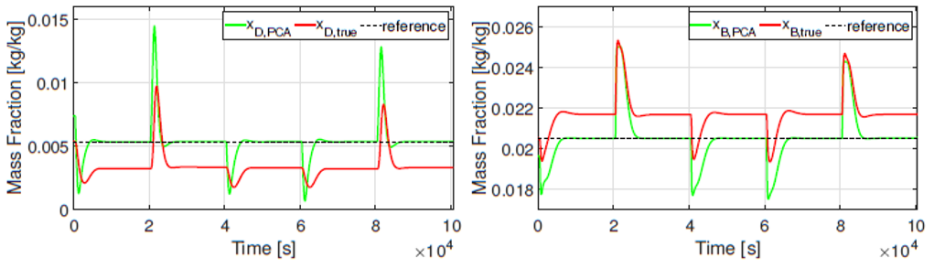

(a) The distillate product. (b) The bottom product.

Figure 5: The comparison of product concentrations from the simulation of depropanizer column with implemented PCA inferential sensors.

Further we used a rigorous process model to confirm our findings and to analyze appropriateness of inferential control of the depropanizer column and its potential further improvements. The results show that the designed inferential sensors are sufficient for the advanced process control of the column. The methods that separate model-structure identification and the model regression are found more suitable.

References

W. Dunn, D. Scott, W. Glen, 1989. Principal components analysis and partial least squares regression. Tetrahedron Computer Methodology 2 (6), 349 – 376.

B. Joseph, June 1999. A tutorial on inferential control and its applications. In: Proceedings of the 1999 American Control Conference. Vol. 5. pp. 3106–3118.

B. Joseph, C. B. Brosilow, 1978. Inferential control of processes: Part i. steady state analysis and design. AIChE Journal 24 (3), 485–492.

M. Kano, N. Showchaiya, S. Hasebe, I. Hashimoto, 2003. Inferential control of distillation compositions: selection of model and control configuration. Control Engineering Practice 11 (8), 927 – 933.

M. King, 2011. Process Control: A Practical Approach. John Wiley & Sons Ltd., iSBN: 978-0-470-97587-9.

T. Mejdell, S. Skogestad, 1991. Composition estimator in a pilot-plant distillation column using multiple temperatures. Industrial & Engineering Chemistry Research 30 (12), 2555–2564.

T. Mejdell, S. Skogestad, 1993. Output estimation using multiple secondary measurements: High-purity distillation. AIChE Journal 39 (10), 1641–1653.

M. Morari, G. Stephanopoulos, 1980. Studies in the synthesis of control structures for chemical processes: Part iii: Optimal selection of secondary measurements within the framework of state estimation in the presence of persistent unknown disturbances. AIChE Journal 26 (2), 247–260.

R. Parvizi Moghadam, J. Sadeghi, F. Shahraki, 2019. Optimization of time-variable-parameter model for data-based soft sensor of industrial debutanizer. Optimal Control Applications and MethodsIn Press.

K. Pearson, 1901. Liii. on lines and planes of closest fit to systems of points in space. The London, Edinburgh, and Dublin Philosophical Magazine and Journal of Science 2 (11), 559–572.

S. J. Qin, T. A. Badgwell, 2003. A survey of industrial model predictive control technology. Control Engineering Practice 11 (7), 733 – 764.

F. Santosa, W. W. Symes, 1986. Linear inversion of band-limited reflection seismograms. SIAM Journal on Scientific and Statistical Computing 7 (4), 1307–1330.

R. Weber, C. Brosilow, 1972. The use of secondary measurements to improve control. AIChE Journal 18 (3), 614–623.

S. Wold, A. Ruhe, H. Wold, W. J. Dunn, III, 1984. The collinearity problem in linear regression. the partial least squares (PLS) approach to generalized inverses. SIAM Journal on Scientific and Statistical Computing 5 (3), 735–743.

J. Zhang, 2001. Inferential feedback control of distillation composition based on PCR and PLS models. In: Proceedings of the 2001 American Control Conference. Vol. 2. pp. 1196–1201.

Sauro Pierucci, Flavio Manenti, Giulia Bozzano, Davide Manca (Eds.)
Proceedings of the 30th European Symposium on Computer Aided Process Engineering (ESCAPE30), May 24-27, 2020, Milano, Italy.
http://dx.doi.org/10.1016/B978-0-12-823377-1.50204-4

MPC for Process Heat Supply Systems: Considering Load Prediction Uncertainty Caused by Human Operators

Florian Fuhrmann*,Alexander Schirrer, Martin Kozek

Technische Universität Wien, Institute of Mechanics and Mechatronics,

Getreidemarkt 9/BA, 1060 Vienna, Austria
florian.fuhrmann@tuwien.ac.at

Abstract

The aim of this work is to define guidelines for model predictive control dealing with uncertain pulse-like disturbances caused by human operators. Measurement data of an industrial use case is utilized to carry out a simulation study to investigate the influence of control parameters on the robustness and efficiency of the controller. Special focus is laid on an efficient way to introduce suitable slack constraint formulations into the mixed-integer model predictive controller formulation to cope with uncertain peak loads. Methods to calibrate such a control structure with industrial operational data are given.

Keywords: Model predictive control, industrial application, uncertain load prediction;

1. Introduction and Motivation

Decarbonisation of power production induces an increasing share of renewable energy sources with fluctuating availability. Varying power availability has led to varying electricity prices, which can be utilized by consumers to reduce energy costs, by energy demand management (EDM). This is especially interesting for industry plants which accounted for 41.9% of the worldwide electricity demand in 2017 (International Energy Agency, 2019). The economic potential of EDM for industrial plants is shown in several studies, but is still rarely applied in industry (Ding and Hong, 2013; Schäfer *et al.*, 2018). According to McKane et al., 2008 this is, among other reasons, caused by the risk of affecting production safety. Efficient EDM and production safety can be realized simultaneously by utilizing model predictive controllers (MPC) in the energy supply systems. Crucial for the performance of an MPC is an accurate prediction of the disturbances, in this case the energy demand. In partially automated manufacturing plants, human operators are often responsible for the starting time of single process steps and thereby heavily influence the schedule of the energy load. This is of particular importance for energy-intensive batch processes where pulsed energy loads occur. Uncertain starting times of such batch processes lead to significant prediction errors, which can cause bottlenecks in the energy supply. Insufficient energy supply, in turn, affects the production safety and thereby has to be prevented under all circumstances. Typical examples of energy-intensive batch processes are heat treatments in which products undergo temperature trajectories in order to reach required quality attributes.

This work is motivated by an industrial use-case where human operators are responsible for preparatory works of heat treatment steps and thereby affect the starting times of these steps. In a previous work of the authors (Fuhrmann *et al.*, 2019) a load prediction method for pulsed heat loads was developed and tested on the very same industrial use case. The estimated predictions therein are accurate in disturbance and their temporal profile, but

rely on known starting times. In the present work, the influence of stochastic starting times of pulsed energy loads on the performance of a model predictive controller (MPC) is investigated. The main contributions of this paper are:

1. Modelling an industrial use case based on measurement data.
2. Executing a simulation study in which the performance of a mixed-integer MPC in the heat supply system is tested with:
    a. Varying controller settings for the slack variable and the prediction horizon N_p
    b. Varying random time shifts of the pulsed heat loads.
3. Deducing guidelines and hints to effectively adjust the MPC parameters for the case of time-varying pulse-like disturbances.

2. Problem Set-Up

The structure and characteristics of the considered industrial use case are illustrated in Figure 1 and Figure 2. The essential components are a heat source (HS), a thermal energy storage (TES), and N batch-like heat consumers (BC) with temperatures $T_{BC,n}$ ($n=1,2,..,N$) which demand pulsed heat loads. The sum of the heat loads $\dot{Q}_{BC,sum}$, is the disturbance affecting the heat stored in the TES Q_{TES}, which is controlled utilizing the heat supply unit's heat flow, $\dot{Q}_{HS}$ as manipulated variable. Typical BC are heat treatment steps in the manufacturing industry that are used to alter the physical or chemical properties of a material (e.g. annealing, tempering, pasteurization). Heat treatments start with a heating phase, were the treated material is brought from the initial temperature to a desired temperature level. The heating phases typically induce short pulse-like heat loads to accomplish fast temperature transients that are necessary for product quality. Delayed or incomplete heating phases, caused by insufficient heat supply, may affect product quality and thereby incur additional costs. One central heat source provides the heat. Thermal liquid and heat exchangers transport it to the BC. The maximum of $\dot{Q}_{BC,sum}$ is typically many times higher than the maximum heat production rate $\dot{Q}_{HS}$ Therefore, a TES is installed to buffer the transient heating process. In this setting, predictive control provides multiple economic benefits: 1. bottlenecks in the heat supply can be detected and prevented before the production process is affected, 2. the energy consumption can be shaped according to the objectives of EDM (e.g. reduce energy costs), 3. the usage of the HS can be evened out, which reduces wear, 4. better exploitation of TES and HS enables a smaller design of these components, lowering investment costs. A precise load prediction is crucial for the performance of a predictive controller. In Fuhrmann et al, 2019, a prediction method for pulse-like heat loads is presented and applied to the very same industrial use-case considered in the present publication. The prediction method shows good results but it is based on an assumption, which does not hold in many manufacturing plants: The starting time point t_0 of the heat treatments is known. In reality, the starting times are often defined by human operators and thereby have to be considered a stochastic quantity. Human operators usually try to follow a given schedule, but preparation steps may introduce delays, for example due to loading tasks or quality checks. In the present work, the influence of a stochastic starting time t_0 on the performance of a model predictive

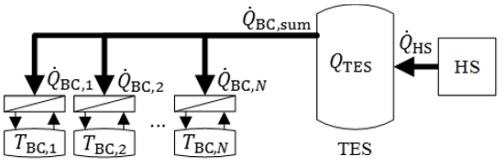

Fig. 1 Industrial use-case consisting of a heat source (HS), a thermal energy storage (TES) and N batch consumers (BC).

controller (MPC) is investigated. The influence of the controller settings for the slack variable and the prediction horizon N_p on robustness and efficiency of the MPC are tested and characterized in a simulation study. To incorporate the influence of human operators, the actual starting times of HT t_0 are altered by random time-shifts Δt_0. As conclusions of the simulation study, guidelines and hints to adjust the MPC parameters so that the control task can cope with the uncertainties efficiently are devised.

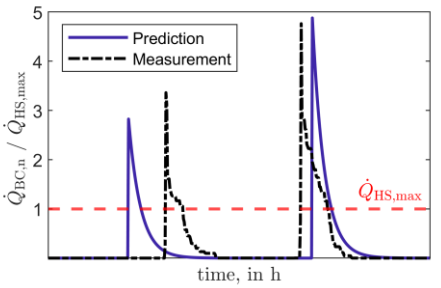

Fig. 2 Typical pulse-like heat loads of BC compared to the maximum heat production.

3. Methodology

The main control goals of the industrial use case are:

- Minimize the number of heat treatments affected by insufficient energy supply
- Minimize the total heat consumption

To decide whether a heat treatment is affected by insufficient energy supply, a critical state of charge $Q_{TES,crit}$ is defined. Heat treatments where $Q_{TES,crit}$ is exceeded at any time instant between starting time t_0 and the end time t_{end} of the heat treatment, such that

$$Q_{TES}(t) < Q_{TES,crit} \forall t \in [t_0, t_{end}] \tag{1}$$

is true, is considered as affected. Heat losses correspond to the temperature T_{TES} in the storage. By minimizing Q_{TES} and thereby T_{TES}, losses can be reduced. To quantify losses without knowledge of T_{TES}, the deviation Q_{dev} from the minimal allowed state of charge

$$Q_{dev} = \sum_{t_i=0}^{t_i=t_{max}} Q_{TES}(t_i) - Q_{TES,crit}(t_i) \tag{2}$$

is used where t_{max} is the duration of the used measurement-data. Equations 1 and 2 show a conflict of objectives, as Q_{TES} shall be as close to, but never fall below $Q_{TES,crit}$. Model predictive controllers (MPC) allow to weight different control goals and offer a convenient way to introduce constraints. The system is modelled as discrete linear state-space model. Defining the storage as simple integrator, $x = Q_{TES}$ as state, $u = \dot{Q}_{HS}$ as input $z = \dot{Q}_{BC,sum}$ as disturbance and T_s as sampling time, the system model is given by

$$Q_{TES}(t_i + 1) = Q_{TES}(t_i) + T_s \dot{Q}_{HS}(t_i) + T_s \dot{Q}_{BC,sum}(t_i) \tag{3}$$

The storage state must lie between bounds $x \in [x_{min}, x_{max}]$. The heat is supplied by a heat pump. The control input $\dot{Q}_{HS}$ can be either zero or between operational limits, such that

$$\dot{Q}_{HS} = \begin{cases} 0 \\ \dot{Q}_{HS,min} \le \dot{Q}_{HS} \le \dot{Q}_{HS,max} \end{cases} \tag{4}$$

holds.

To avoid a violation of the critical minimal storage level $Q_{\mathrm{TES,crit}}$ the slack cost C_{Slack} penalizes an undershoot of $r = Q_{\mathrm{Slack}} = Q_{\mathrm{TES,crit}} + Q_{\mathrm{Buffer}}$, where Q_{Buffer} is a safety margin (Figure 3). The resulting MPC formulation yields a mixed-integer quadratic programming problem, with δ_{k} as discrete variable describing whether the HP is on (δ_{k} =1) or off (δ_{k} =1) at step k. The optimization problem is defined as

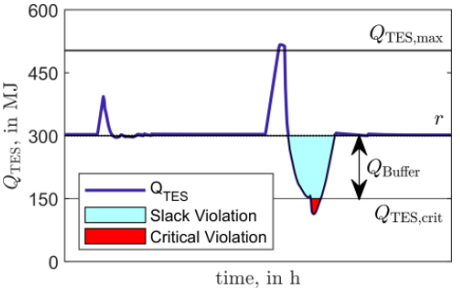

Fig. 3 Critical level of Q_{TES} and safety margin.

$$
\begin{aligned}
J_i = \frac{1}{2}\sum_{k=i}^{i+Np-1} & \left[(Q_{\mathrm{TES},k+1}-r)^T C_R \left(Q_{\mathrm{TES},k+1}-r\right)+\left(\dot{Q}_{\mathrm{HS},k}-\dot{Q}_{\mathrm{HS},k-1}\right)^T C_{dU}\left(\dot{Q}_{\mathrm{HS},k}-\dot{Q}_{\mathrm{HS},k-1}\right)+\right. \\
& \left. \dot{Q}_{\mathrm{HS},k}^T C_U \dot{Q}_{\mathrm{HS},k} + s_k C_{\mathrm{Slack}} + \mathrm{abs}\left(\delta_{k-1}-\delta_k\right) C_{\mathrm{on}}\right] \\
& s.t. \\
& Q_{\mathrm{Slack}} - s_k \le Q_{\mathrm{TES},k+1} \le Q_{\mathrm{TES,max}} \\
& \delta_k \cdot u_{\min} \le u_k \le u_{\max} \cdot \delta_k \\
& s_k \ge 0 \\
& \delta_k \in \{0,1\} \\
& k \in \left[i,\ldots,i+N_p-1\right]
\end{aligned}
\tag{5}
$$

where N_P is the prediction horizon, C_R, C_{dU}, C_U, C_{Slack} and C_{on} are weight factors and s_k are slack variables. A basic MPC, formulated in the Matlab toolbox YALMIP (Lofberg, 2019), was utilized and modified for this paper. Gurobi is used as solver (Gurobi, 2018).

Load Manipulation

To imprint the stochastic time shift, on the heat load, the starting time t_0 of each heat treatment was altered using random time shifts:

$$
t_{0,\mathrm{shifted}}^i = t_0^i + T_s \cdot \mathrm{ceil}\left(N_{\mathrm{Shift,max}} \cdot U(-1,1)\right) \tag{6}
$$

where U(-1,1) is a uniform distribution in interval [-1, 1]. Eleven deviated predictions with maximum time shifts $\Delta t_{0,\max}$ from 0 to 60 minutes were generated.

Simulation Study

The aim of the simulation study was to investigate the influence of the slack variable limit Q_{Buffer}, slack costs C_{slack}, and prediction horizon N_{p} on robustness and efficiency of the MPC, considering a varying accuracy of disturbance prediction. For this purpose, data of one week with 26 heat treatments is taken from the industrial measurement data and the basic parameters of the MPC were defined. Then simulations were made with different settings for Q_{Slack}, C_{Slack} and N_{p}. Table 1 shows the boundaries these parameters were varied in, the values of the basic parameters, and the constraints of Q_{TES} and $\dot{Q}_{\mathrm{HS}}$.

Table 1 MPC Parameter.

N_{p}	{5,10,…,60}
C_{Slack}	$\{10^0,10^1,\ldots,10^{10}\}$
Q_{Buffer}	{5,10,20,…,50, 75,100,150,200}
C_R	10^{-1}
C_U	2.5
C_{dU}	10^{-1}
C_{on}	10^1
$Q_{\mathrm{TES,max}}$	504 MJ
$\dot{Q}_{\mathrm{HS,max}}$	0.206 MW

The simulations were repeated for 13 different cases:

- Perfect information (PI): the applied load is equal to the load prediction
- No information (NI): the applied load does not correlate with the load prediction
- The eleven differently manipulated loads are applied and the predicted load used as load prediction.

4. Results & Discussion

The performance of the different controller settings is quantified by two quality attributes:

1. The number of heat treatments n_{aff} affected by insufficient heat supply.
2. Heat losses Q_{dev} quantified as deviation from the optimal state of charge.

As expected, a conflict of objectives is visible in the results. In Figure 4, pareto fronts for different $\Delta t_{0,max}$ are visible. Q_{Buffer} is the decisive control parameter to adjust the trade-off between Q_{dev} and n_{aff}. The diamond markers and the square markers show the results for constant values of Q_{Buffer} with different load prediction quality. For imprecise load predictions with high $\Delta t_{0,max}$, production losses occur more often (n_{aff} increases) while Q_{loss} shows only a slight increase. Furthermore, for high Q_{Buffer} a strong increase of Q_{dev} is detectable but little change on the production safety. To calculate the optimal trade-off between Q_{dev} and n_{aff}, the cost of production losses and the energy costs have to be compared. Figure 5 is a heatmap where the number of affected heat treatments for different values of Q_{Buffer} are displayed for all 13 different load prediction cases. Even with the applied heat load as load prediction, (PI) four heat treatments are affected by insufficient energy supply. This shows that the heat storage installed in the industrial use case is too small to guarantee production safety for all possible production plans. Still these production losses could be avoided utilizing an MPC, as the bottlenecks in energy supply would be detectable before they occur. A human machine interface could be installed to warn the operator, who then would have the opportunity to reschedule the heat treatments. Figure 5 further shows that even with perfect information (PI) a minimal Q_{Buffer} is needed to guarantee an acceptable production safety.

To deduce guidelines for the correct choice of Q_{Buffer} two variables proved appropriate: the average duration $t_{load>supply}$ of periods where the heat load $\dot{Q}_{BC,sum}$ is bigger than the maximum heat supply

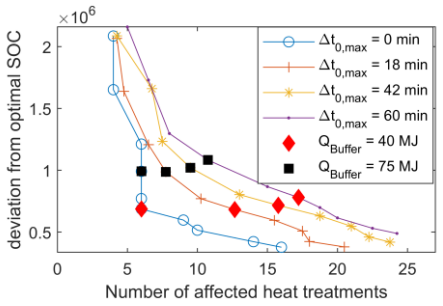

Fig. 4 Deviation from the optimal state of charge versus number of heat treatments with insufficient energy supply for varying $\Delta t_{0,max}$ and Q_{Buffer}.

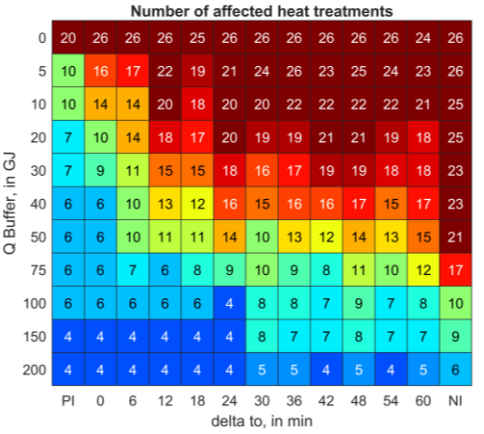

Fig. 5 Number of heat treatments with insufficient energy supply for different values of Q_{Buffer} and different load predictions: perfect information (PI) no information (NI) and predictions with varying maximum deviation of starting time points $\Delta t_{0,max}$.

$\dot{Q}_{\mathrm{HS,max}}$ and the average heat amount $Q_{\mathrm{load>supply}}$ which is delivered in these periods. For the simulation data $Q_{\mathrm{load>supply,avg}} = 22.94$ MJ which is a good choice as minimal Q_{Buffer} for processes with known starting time t_0. Further, $t_{\mathrm{load>supply,avg}} = 12{,}5$ min holds. Simulation results for varying slack weight C_{Slack} show that it needs to be a minimum of three magnitudes higher than the other weights to ensure production safety. The simulation results for varying prediction horizon N_P show that the optimal prediction horizon is dependent on the storage size $Q_{\mathrm{TES,max}}$ and the maximum heat production $\dot{Q}_{\mathrm{HS,max}}$. The heat source needs maximum $t_{load,max} = Q_{\mathrm{TES,max}}/\dot{Q}_{\mathrm{HS,max}}$ to charge the TES. Therefore, $N_{P,max} = t_{load,max}/T_s$ is sufficient for any occurring heat loads.

5. Conclusions

The following guidelines and hints to effectively adjust the MPC parameters for the case of time-varying pulse-like disturbances can be deduced from the results above:

1. Soft constraints with a slack variable are a proper method to avoid production losses caused by critical low state of charge $Q_{\mathrm{TES,crit}}$. Guidelines for tuning are:

   a) Define Q_{slack} as:

$$Q_{\mathrm{slack}} = Q_{\mathrm{TES,crit}} + Q_{\mathrm{Buffer}} = Q_{\mathrm{TES,crit}} + Q_{\mathrm{load>supply,avg}} \left(1 + \frac{t_{0,\max}}{t_{\mathrm{load>supply,avg}}} \right) \tag{7}$$

   b) Define slack costs C_{slack} as:

$$C_{\mathrm{slack}} \geq C_{\mathrm{slack,min}} = 10^3 \max\left(C_R, C_{dU}, C_U, C_{\mathrm{ON}}\right) \tag{8}$$

2. Define prediction horizon N_P as:

$$N_P \leq N_{P,\max} = t_{\mathrm{load,max}} / T_s \tag{9}$$

Acknowledgment

This work was supported by the project 'EDCSproof', which is part of the energy model region NEFI - New Energy for Industry and is funded by the Austrian Climate and Energy Fund (FFG, No.868837).

References

Ding, Y. and Hong, S. H. (2013) 'A model of demand response energy management system in industrial facilities', *2013 IEEE International Conference on Smart Grid Communications, SmartGridComm 2013*. IEEE, pp. 241–246. doi: 10.1109/SmartGridComm.2013.6687964.

Fuhrmann, F. *et al.* (2019) 'Prediction of pulsed heat loads in manufacturing plants', Puplication under review.

Gurobi, O. (2018) 'Gurobi Optimizer Reference Manual, Version 5.0', *www.Gurobi.Com*.

International Energy Agency (2019) *Electricity Statistics*. Available at: https://www.iea.org/statistics/electricity/ (Accessed: 25 October 2019).

Lofberg, J. (2019) *YALMIP standard MPC*. Available at: https://yalmip.github.io/example/standardmpc/ (Accessed: 6 November 2019).

McKane, A. T. *et al.* (2008) 'Opportunities, Barriers and Actions for Industrial Demand Response in California Environmental Energy Technologies Division'. Available at: https://industrialapplications.lbl.gov/sites/default/files/lbnl-1335e.pdf.

Schäfer, P. *et al.* (2018) *Nonlinear Dynamic Optimization for Improved Load-Shifting Agility of Cryogenic Air Separation Plants*, *Computer Aided Chemical Engineering*. Elsevier Masson SAS. doi: 10.1016/B978-0-444-64241-7.50086-0.

Sauro Pierucci, Flavio Manenti, Giulia Bozzano, Davide Manca (Eds.)
Proceedings of the 30th European Symposium on Computer Aided Process Engineering (ESCAPE30), May 24-27, 2020, Milano, Italy.
http://dx.doi.org/10.1016/B978-0-12-823377-1.50205-6

Swarm Optimisation for Shipping Fleet Scheduling, Routing and Delivery in Sustainable Liquified Natural Gas (LNG) Supply Chain Models

Sara Al-Haidous[a], Rajesh Govindan[b], Tareq Al-Ansari[a,b]

[a] *Division of Sustainable Development, College of Science and Engineering, Hamad Bin Khalifa University, Qatar Foundation. Doha, Qatar.*
[b] *Division of Engineering Management and Decision Sciences, College of Science and Engineering, Hamad Bin Khalifa University, Qatar Foundation. Doha, Qatar.*

talansari@hbku.edu.qa

Abstract

Natural gas is a relatively clean fuel when compared to other hydrocarbon fuels, such as oil and coal. It can be liquified into what is known as liquefied natural gas (LNG) with the potential for cost-effective transportation thereby allowing it to be adopted as a major energy source in many parts of the world. Whilst there exists an increasing global demand for LNG of up to 20 % annually, supply chains lack objective approaches that enable decision-making for planning and delivery, and encourage the global mobilisation of LNG reserves in an economically and environmentally sustainable manner. The objective of this study is to develop a multi-objective mathematical model for shipping fleet scheduling, routing and delivery for sustainable LNG supply chains. The model incorporates flexibility in delivery times; inventory management and berth availability constraints; and fuel consumption and carbon emissions. The model formulation is based on a real-case LNG supply chain in the state of Qatar, which represents the business-as-usual scenario, with polynomial number of variables and constraints corresponding to 248 cargoes spread across 90 days. The problem formulation is subsequently solved using the Binary Particle Swarm Optimisation (BPSO) algorithm. The solutions for scheduling, routing and delivery over the representative planning horizon obtained thus far demonstrate that the average total costs and emissions associated with a single cargo is approximately 1.6 million USD and 38 million kg CO_2/day respectively.

Keywords: LNG Supply Chain, LNG Shipping, Particle Swarm Optimisation, Natural gas

1. Introduction

Natural gas, is an important fuel bridging environmentally benign hydrogen and a renewable energy-based economy (Shively, and Ferrare, 2011). It can be liquified into what is known as liquefied natural gas (LNG), thus enabling more efficient transport through specialised carrier vessels over large distances and time horizons. Depending on its composition, natural gas is generally liquified at approximately -162 °C and atmospheric pressure. This liquefied state enables the natural gas to be shrunk to about 600

times its original volume. Currently, the state of Qatar has the largest chartered fleet of LNG vessels globally, including a new generation of state-of-the-art vessels enabling Qatari LNG to reach global markets in a safe, efficient, and reliable manner. Qatar provides 33 % of global LNG supply (IGU, 2014), representing 63 % of the government revenues. In addition, Qatar's customer portfolio is spread throughout the world in Asia, Europe, and America. Evidently, the optimal and sustainable delivery of hydrocarbon products to customers play is an important part of Qatar's economy.

Maritime transportation problems have unique practical and theoretical perspectives. Practical perspectives consider economies of scale making the case for the cheapest per unit transportation across all transport modes, fitting well with heavy industrial activities. From a theoretical perspective, however, maritime transportation is complex, and as such are difficult to solve within in a reasonable time frame. As with many energy supply chains, the transport of LNG is rather challenging. The producer is obligated to deliver a certain amount of LNG to re-gasification terminals each year because of a set of long-term contracts. These contracts have a duration of several years that specify the quantity and time for deliveries. They also state how the deliveries should be spread throughout the year; either evenly spread or if there are seasonal variations. Based on the mutually agreed information, the LNG producer needs to develop the annual delivery plan (ADP) accordingly. Variations in ADP may impact LNG inventories, and can occur due to fluctuations of production as a result of planned or unplanned shutdown, seasonality and slowdowns at the end of the planning horizon. Transport of LNG is particularly important as the associated costs represent 30 % of the total LNG supply chain (Cornot-Gandolphe *et al*., 2003). The LNG fleet is usually heterogeneous, with specific tank capacities and cruising speeds as scheduled and operated by the LNG producer. The duration of a voyage may also depend on the time of year, as sailing conditions may vary between summer and winter seasons. At the beginning of the planning horizon, there are several factors that affect the availability of vessels in the fleet. Whilst some vessels could serve other customers, others may be unavailable due to certain pre-planned activities, such as maintenance. It is technically possible for a vessel to sail between the liquefaction and a re-gasification terminals with partially filled-up tanks. In addition, there are several components that affect the transportation costs. Fixed costs are related to charter rates and cannot be changed during the time horizon. Variable costs relate to canal fees, load and discharge operation and fuel consumption for serving a scheduled voyage based on the vessel type and the duration of the voyage. Furthermore, cruising speeds affect the fuel consumption and exhaust gas emissions. Moreover, a vessel will also require re-fueling after each voyage.

The scheduling, routing and delivery problem for LNG supply could be more difficult to solve when further complexities are incorporated into the system, *e.g.* the consideration of sustainable development in terms of integrated environmental and economic objectives. The International Maritime Organization (IMO) aims to achieve a reduction of CO_2 emissions from shipping operations by 50% by 2050 (IMO, 2019). Incidentally, there is little published work pertaining to the overall planning of sustainable LNG supply chains. As such, developing sustainable LNG supply chains presents a large research opportunity as various quantitative models can be utilised to model and analyse such supply chains (Al Haidous. S. and Al Ansari, T, 2019). As such, (Al Haidous. S. and Al Ansari, T, 2019) introduces a model that integrated approaches to manage energy supply

chains to deliver cargo at minimal cost and environmental impact, and to ensure that supply chains can overcome vulnerabilities withstanding potential disruptions to the supply chain. The LNG inventory routing problem is a unique case in what is known as the maritime inventory routing problem (MIRP), which considers variable production, contractual obligations, and berth constraints at production and liquefaction terminals (Christiansen *et al*., 2004). Other studies have focused on single objectives. From an economic perspective, Mutlu *et al*. (2016) developed a model to minimise total operational costs considering production, inventory, and delivery routing decisions at the lowest possible cost for LNG. Meanwhile, from an environmental perspective, Fagerholt *et al*. (2010) developed a model to reduce fuel emissions by optimising speed on the shipping routes. As such, it has been identified that, from the perspective of sustainable planning of the LNG supply chain, the trade-offs involved in costs and environmental impacts have not been fully investigated, particularly in the case of supply chains served by large-sized heterogeneous delivery fleet. Evidently, there is a need to develop methods that integrate multiple dimensions of sustainability within a complex LNG supply chain. The aim of this study is thus to address the critical factors in the planning of a sustainable LNG supply chain management. It considers sustainability objectives within an integrated multi-objective optimisation-based methodology accounting for factors, including shipping fleet scheduling, flexibility in delivery times, inventory management, berth availability, fuel consumption and associated carbon emissions.

2. System Definition and Model Formulation

Developing models for LNG supply chain problems require defining the long-term contracts delivery dates and the assignment of the different type of the vessels to the cargoes, whilst accommodating several constraints including partial delivery, berth, and liquefaction terminal inventory and carbon emissions to achieve the objective by supporting innovative solutions that achieve greater efficiency, flexibility, and optimisation of resources whilst meeting customer needs. As such, the methodology adopted in this study includes a multi-objective mixed integer programming model for the problem to minimise both the total cost and environmental impact, treating them as competing objective functions. The notation that shall be used throughout the paper are introduced below, followed by the proposed model formulation for optimisation:

Sets:

- T: set of days that cover planning horizon; {1,...,T}.
- V: set of vessels indexed by v.
- C: set of cargoes indexed by c_{in}.
- V^i: set of vessels that can visit port i.
- P^v: set of ports that vessel v can visit.

Parameters:

- I^{min}/I^{max}: minimal and maximal inventory levels of the storage tank at the liquefaction terminal.
- P_t: daily production rate.
- B: number of available berths.
- q_{vit}: loaded or unloaded quantity from vessel v on day t.
- $[T^e_{in}, T^a_{in}]$: time window during which should be delivered cargo c_{in}.

- d_{voj}: Travel time of vessel v from port i to j.
- E: CO_2 emissions (ton/day)

Nodes:

- (i, j): any port including customer ports and loading port.
- o: source node.

Decision Variables:

- x_{vijt}: Binary variable, which is equal to 1 if the vessel v arrives at port j from port i on day t, and 0 otherwise.
- I_t: Inventory level of liquefaction terminal's storage tank on day t, $t \in T$

The formulation reads as follows.

$$Min \sum_{v\in V}\sum_{i\in p^v}\sum_{j\in p^{vi}}\sum_{t\in T} C_{vij}x_{vijt}$$
$$Min \sum_{v\in V}\sum_{i\in p^v}\sum_{j\in p^{vi}}\sum_{t\in T} E\, d_{ij}x_{vijt} \quad (1)$$

Subject to:

Initialization and termination constraints

$$x_{voo0} = 1 \qquad v \in V \quad (2)$$

$$\sum_{t\in T_o}\sum_{j\in p^{vo}\setminus\{0\}} x_{vojt} = 1 \qquad v \in V \quad (3)$$

$$x_{vojt} = 0 \qquad v \in V, j \in P^v\setminus\{0\}, t < d_{voj} \quad (4)$$

$$x_{vijt} = 0 \qquad v \in V, i \in P^v\setminus\{0\}, j \in P^v, t < d_{voi} + d_{vij} \quad (5)$$

Flow constraints

$$\sum_{k\in P_o^{vi}} x_{vkit} - \sum_{j\in P^{vi}} x_{vij(t+T_{vij})} = 0 \qquad v \in V, i \in P^v, t \in T_o \quad (6)$$

$$\sum_{i\in P^v}\sum_{j\in P^{vi}} x_{vijt} = 1 \qquad v \in V, t \in T \quad (7)$$

Inventory management constraints

$$I_t = I_{t-1} + P_t - \sum_{v\in V} q_{vlt}x_{vijt} \qquad t \in T \quad (8)$$

$$I^{min} \le I_t \le I^{max} \qquad t \in T \quad (9)$$

Berth constraint

$$\sum_{v \in \mathrm{V}} x_{vijt} \leq B \qquad t \in \mathrm{T} \qquad (10)$$

Vessel speed constraints

$$t_j - t_i - d_{vij} \geq 0 \qquad v \in \mathrm{V},\ i \in P^v \qquad (11)$$

$$\mathrm{T}_{in}^{e} \leq t_i \leq \mathrm{T}_{in}^{a} \qquad i \in P^v \qquad (12)$$

$$x_{vijt} \in \{0,1\} \qquad v \in \mathrm{V}, t \in T \qquad (13)$$

The objective is to minimise the overall operating costs and fuel consumption for the planning horizon of 90 days. Constraints (2-5) are initialisation constraints to ensure that all vessels originate from the origin port o and prevent any vessel going to two different ports during the same time intervals. Constraint (6) Controls the flow of each vessel during the planning horizon. In this constraint if a vessel arrived at port i at time t then it should go to another port j that is accessible from port i at time $t + \mathrm{T}_{vij}$. Where constraint (7) ensures that each cargo should be served only by one vessel. Constraints (8-9) are inventory balance and limits constraints for the liquefaction terminal. Berth capacity constraint at the loading port presented by constraint (10). Constraint (11) ensures that the ship does not start services prior to arrival at the node. Constraint (12) represents the time window limits, and finally constraint (13) demonstrates the binary nature of the decision variable. The average solution is determined from the Pareto front, representing the best trade-off obtained for the cost and environmental impact.

3. Computational experiments

The test instances are based on real data provided by an LNG producer. In this instance, three months for the planning horizon are considered for 248 cargoes using 6 berths, 70 vessels with different sizes and fuel consumption for each type of the vessel. The Binary Particle Swarm Optimisation (BPSO) algorithm was used to perform a heuristic search in the high-dimensional binary solution space for feasible solutions that solves the model formulation described above. The algorithm was implemented in a manner that it would work on balancing between the minimisation of the multi-objective functions and the number of constraints satisfied (Yazdi *et al*., 2019). As such, the implementation splits up the high-dimensional binary solution into multiple swarms and solve them locally using BPSO to determine local Pareto sets, before combining them to determine the global Pareto set. When compared to earlier studies that have looked at similar problems using single objective functions using MILP solvers that guarantee optimality as studied by Mutlu *et al*. (2016), the current implementation was able to provide a convergence of the Pareto set under one hour. However, the main limitation of the study is the lack of objective assessment of the quality of the solutions obtained, when compared to the optimal solutions obtained using exact methods with industry-standard solvers such as CPLEX. Table 1 provides illustrative numbers for the total cost and environmental impact for an average point on the preliminary Pareto front results obtained in this study.

Table 1. Results for Total costs and emissions for planning horizon, corresponding to an average solution from the Pareto front.

No. of cargoes	Time horizon (days)	No. of berths	No. of vessels	Total Costs ($)	Total CO2 emissions (kg/day)
248	90	6	70	0.4 Billion	38 Million

4. Conclusion

The volume of maritime transportation of LNG is expected to continue to grow in the coming years due to the accelerating supply and demand for natural gas. The expanding opportunities in this business require decision support systems that fit the specific problem characteristic. The main contribution of this paper is to introduce sustainability within the LNG supply chain model by considering economic and environmental dimensions using BPSO to solve the problem optimally. The results have been tested on real instance to ensure model validity and reliability. The model developed in this paper can be further developed by considering multi discharges on the same route, ship to ship transfer operation and alternative routing between Asia and Europe. Going forward, development of integrated sustainable LNG supply chain models should be further enhanced to capture all sustainability dimensions at higher resolutions.

References

B. Shively, and J. Ferrare, (2011), Understanding today's natural gas business. Enerdynamics.

IGU, 2014, Natural gas, the energy for today and the furure, Available on: https://www.igu.org/sites/default/files/node-document

S. Cornot-Gandolphe, O. Appert, R. Dickel, M.-F. Chabrelie, and A. Rojey, (2003), The challenges of further cost reductions for new supply options (pipeline, LNG, GTL). 5, 1-17.

IMO, 2019, Low carbon shipping and air pollution control, Available on: http://www.imo.org/en/MediaCentre/HotTopics/GHG/Pages/default.aspx

S. Al-Haidous, and T. Al-Ansari, (2019), Sustainable Liquefied Natural Gas Supply Chain Management: A Review of Quantitative Models, Sustainability, 12(1), 243.

M. Christiansen, K. Fagerholt, and D. Ronen, (2004), Ship Routing and Scheduling: Status and Perspectives. Transportation Science, 38(1), 1–18.

F. Mutlu, M. K. Msakni, H. Yildiz, E. Sönmez, and S. Pokharel, (2016). A comprehensive annual delivery program for upstream liquefied natural gas supply chain. European Journal of Operational Research, 250(1), 120–130. https://doi.org/10.1016/j.ejor.2015.10.031

K. Fagerholt, G. Laporte, and I. Norstad, 2010, Reducing fuel emissions by optimizing speed on shipping routes, Journal of the Operational Research Society, 61, 523-529.

A. Karbassi Yazdi, M. A. Kaviani, A. Emrouznejad, and H. Sahebi, H., (2019). A binary particle swarm optimization algorithm for ship routing and scheduling of liquefied natural gas transportation. Transportation Letters, 1-10. https://doi:10.1080/19427867.2019.1581485

Sauro Pierucci, Flavio Manenti, Giulia Bozzano, Davide Manca (Eds.)
Proceedings of the 30th European Symposium on Computer Aided Process Engineering (ESCAPE30), May 24-27, 2020, Milano, Italy.
http://dx.doi.org/10.1016/B978-0-12-823377-1.50206-8

Online Decoupled Data-Driven Estimation of Nonlinear Kinetic Parameters

Wilfredo Angulo, Dany De Cecchis, Santiago D. Salas*

Escuela Superior Politécnica del Litoral, ESPOL, Facultad de Ciencias Naturales y Matemáticas,Campus Gustavo Galindo Km 30.5 Vía Perimetral, P.O. BOX 09-01-5863, Guayaquil, Ecuador.

sdsalas@espol.edu.ec

Abstract

A data-driven parameter estimation strategy is assessed and tested for the estimation of nonlinear parameters in a classic continuous stir tank reactor (CSTR). A decoupled version of the retrospective cost model refinement (RCMR) algorithm serves as the estimation structure. The proposed method studies the simultaneous estimation of three kinetic parameters within a CSTR considering one available measurement. The decoupled RCMR algorithm is adapted and implemented as an efficient estimation structure for the proposed problem, and contrasted with its original structure.

Keywords: Continuous stirred tank reactor, decoupled RCMR, nonlinear parameter estimation, data-driven estimation.

1. Introduction

The chemical engineer requires to count with a reliable set of physicochemical, transport and kinetic parameters for the design and simulation of industrial reactors. The information related to the kinetics is required for the implementation of well-specialized laboratory or pilot scale experiments. For the proper adjustment of kinetic parameters, it is necessary to formulate and resolve an optimization problem, which minimizes the error between the variables measured experimentally and those calculated from the fundamental model. Due to the growth of computing power, nonlinear optimization methods have become an alternative for parameter estimation. Among these methods, gradient-based ones such as the Levenberg Marquardt (L-M) algorithm has demonstrated a good local performance (*A. Neumaier*, 2004). Other methods that include stochastic optimization require significantly higher computations, but have a relatively easy implementation. Eftaxias et al. (2002) tested separately the performance of L-M and Simulate Annealing to estimate the kinetic parameters that describe a catalytic oxidation. The stochastic method was competitive when compared with the L-M algorithm.

However, the use of such optimization methods in real-time is computationally expensive. Real-time estimation techniques are commonly based on the implementation of the extended Kalman filter, geometric observer or their variations which adapt to the problem under study (*Salas et al.*, 2017, 2018). Nonetheless, these methods have the limitation of requiring an adjoint model, or explicit knowledge of the dependence of the parameters. Hence, the mathematical model for the chemical kinetics must be computable and known by the estimation algorithm. In contrast, the retrospective cost model refinement (RCMR) algorithm overcomes these notable disadvantages. This algorithm has been applied in the estimation of parameters with nonlinear dependence considering single or multiple estimation, linear or nonlinear gray-box models, and first-principle

models for polymerization systems using real experimental data (*Goel and Bernstein*, 2018; *Salas et al*, 2019). Advantageous characteristics of this strategy are that it does not require the incorporation of the model to the estimation structure nor evinces to be CPU intensive. After applying a recursive computation based on the retrospective cost function, the coefficients of the estimator are updated for later calculating the estimated parameters. Salas, Angulo and De Cecchis (2020) proposed a decoupled version of this method (denoted by dRCMR) which improves the speed of convergence and stability for some cases in the estimation of strongly non-linear parameters.

The main contribution of this work is the implementation of the dRCMR algorithm for the online data-driven estimation of nonlinear kinetic parameters in a classic isothermal CSTR system, and to compare the obtained results when using the RCMR. This study analyses the dynamic behavior of the CSTR, and it can be approached by means of phenomenological-based semi-physical models coupled with expressions that represent the kinetics of the reaction (or reactions), with a strongly non-linear dependence among its parameters.

2. Background

2.1. Mathematical model of an isothermal CSTR

In this work, a classical isothermal CSTR is under consideration. It composes by a system of n chemical reactions, and m chemical species, with second order kinetics, that can be expressed in the form:

$$\sum_{j=1}^{m} \nu_{ij} A_j = 0; \;\; i = 1, \dots, n, \tag{1}$$

where A_j denotes the j-th chemical species and ν_{ij} is its stoichiometric coefficient in the i-th reaction. The component A_j is defined as the j-th reactant of the reaction i if $\nu_{ij} < 0$, and as the product of the reaction i if $\nu_{ij} > 0$. The information contained in the reaction mechanism (1) can be summarised as a matrix $C \in \mathbb{R}^{n \times m}$ where the elements are the stoichiometric coefficients of reactants and products. The reaction rate in each mechanism is a nonlinear function of the temperature T, and the vector of the concentrations of the reacting species $\boldsymbol{x}^r$. For (1), it is defined a vector $\boldsymbol{r}(\boldsymbol{x}^r, T) \in \mathbb{R}^n$ which contains the reaction rates, and it is a separable function with respect to its arguments, i.e.,

$$\boldsymbol{r}(\boldsymbol{x}^r, T) = \Theta(\boldsymbol{x}^r)\boldsymbol{G}(\boldsymbol{\mu}(T)), \tag{2}$$

where the vector $\boldsymbol{G}(\boldsymbol{\mu}(T)) \in \mathbb{R}^n$ is in general a nonlinear function of the specific speed vector (kinetic parameters) $\boldsymbol{\mu}(T) \in \mathbb{R}^n$, which is composed of bounded positive functions of the temperature while $\Theta(\boldsymbol{x}^r) \in \mathbb{R}^{n \times n}$ is a diagonal matrix which elements are functions of the vector $\boldsymbol{x}^r$. This vector is defined as $\boldsymbol{x}^r = (\boldsymbol{x}_1^r, \dots, \boldsymbol{x}_n^r)$, with

$$\boldsymbol{x}_i^r = \mathcal{P}_i^r \boldsymbol{x}; \;\; i = 1, \dots, n, \tag{3}$$

and $\mathcal{P}_i^r$ as the operator that projects the concentration vector $\boldsymbol{x} \in \mathbb{R}^m$ of the reactants in the i-th reaction into the vector $\boldsymbol{x}_i^r$, such that

$$\boldsymbol{r}(\boldsymbol{x}^r, T) = \begin{pmatrix} \phi_1(\boldsymbol{x}_1^r) & \cdots & 0 \\ \vdots & \ddots & \vdots \\ 0 & \cdots & \phi_n(\boldsymbol{x}_n^r) \end{pmatrix} \begin{bmatrix} g_1(\boldsymbol{\mu}(T)) \\ \vdots \\ g_n(\boldsymbol{\mu}(T)) \end{bmatrix}, \tag{4}$$

Then, the matrix $\Theta(\boldsymbol{x}^r)$ is related to the vector $\boldsymbol{x}$, which components are the m concentrations of chemical species involved in the reaction network (reactants and products), by the projection operator $\mathcal{P}_i^r$. The functions $\phi_i(\boldsymbol{x}_i^r)$, for $i = 1, \dots, n$, are nonlinear functions respecting the concentration of the reactants involved in the i-th reaction, i.e., $\phi_i(\boldsymbol{x}_i^r) = \prod_{j \in J_r} \psi_{ij}(x_j)$, $i = 1, \dots, n$, where, in the presence of an elementary reaction, $\psi_{ij}(x_j) = x_j^{\nu_{ij}}$, with $\nu_{ij} \in \mathbb{N}$, represents the mass action law, and J_r is the set of indices associated with the reactants.

The mathematical model of an isothermal CSTR reactor describes the relationships between the state variables given by the vector $\boldsymbol{x} \in \mathbb{R}^m$, the operation variables, and the kinetic parameters given in the vector $\boldsymbol{G}(\boldsymbol{\mu}(T))$. This model is in general very complex. However, in this study some assumptions are introduced in the attempt to reduce its complexity. In particular, it is assumed that the reactant inside the tank is perfectly mixed, the volume of the reactant is constant during the reactions, and the inlet flow rate is equal to the outlet flow rate. Then, using the dynamic material balances inside the reactor, the mathematical model of the system reactions-CSTR is the initial value problem:

$$\begin{cases} \dot{\boldsymbol{x}}(t) = d\left(\boldsymbol{x}^{in} - \boldsymbol{x}(\boldsymbol{t})\right) + C^T \boldsymbol{r}\left(\boldsymbol{x}^r(t)\right), & \forall t \in (0, +\infty), \\ \boldsymbol{x}(0) = \boldsymbol{x}^0, \end{cases} \tag{5}$$

where $\dot{\boldsymbol{x}}$ denotes the derivative of $\boldsymbol{x}$ with respect to the time t, $d \in \mathbb{R}_+$ is the dilution rate, which is the ratio between the feed stream flowrate and the volume of the reactor, $\boldsymbol{x}^{in} \in \mathbb{R}^m$ is the vector of non-negative reactor feed concentrations, and $\boldsymbol{x}^0 \in \mathbb{R}^m$ is the vector of non-negative initial concentrations. In this model, $\boldsymbol{r}(\boldsymbol{x}^r)$ does not depend on the temperature because the system is assumed to be isothermal. The vector $\boldsymbol{\mu} = (\mu_1, \dots, \mu_n)$ is, in fact, the vector of parameters estimated by the dRCMR.

2.2. Decoupled RCMR

The dRCMR is a variation of the RCMR; hence, the latter is introduced first to then describe the decoupled strategy.

The first step to use the RCMR for estimating the vector of kinetic parameters $\boldsymbol{\mu}$ consists on discretizing the mathematical model in (5) by means of a suitable numerical method, e.g., a fourth-order Runge-Kutta or a *stiff*-method among others. The purpose of this first step is to obtain a dynamic system in the form of:

$$\begin{aligned} \boldsymbol{x}_{k+1} &= \boldsymbol{f}(\boldsymbol{x}_k, \boldsymbol{u}_k, \boldsymbol{\mu}) + \boldsymbol{w}_k; \quad k \in \mathbb{N}, \\ \boldsymbol{y}_k &= \boldsymbol{h}(\boldsymbol{x}_k, \boldsymbol{u}_k, \boldsymbol{\mu}). \end{aligned} \tag{6}$$

where $\boldsymbol{u} \in \mathbb{R}^{l_u}$ is the input vector, $\boldsymbol{\mu} \in \mathbb{R}^{l_\mu}$ is the unknown parameters vector, $\boldsymbol{y} \in \mathbb{R}^{l_y}$ is the measurements vector, and $\boldsymbol{w} \in \mathbb{R}^{l_y}$ is the output error of the system. Here, $\boldsymbol{f}$ and $\boldsymbol{h}$ are known maps that depend non-linearly on the states $\boldsymbol{x}$, inputs $\boldsymbol{u}$ and parameters $\boldsymbol{\mu}$. Thereafter, at every step $k \in \mathbb{N}$, the RCMR calculates an estimated vector $\widehat{\boldsymbol{\mu}}$ based on an ARMA (Auto Regressive Moving Average) model. Specifically, the estimation problem consists of determining a vector $\boldsymbol{\theta} \in \mathbb{R}^{l_\theta}$, at each $k \in \mathbb{N}$, such that,

$$\widehat{\boldsymbol{\mu}}_k = \Phi_k \boldsymbol{\theta}_k; \quad k \in \mathbb{N}, \tag{7}$$

where $\Phi \in \mathbb{R}^{l_\mu \times l_\theta}$ is the regressor matrix, and $\boldsymbol{\theta} \in \mathbb{R}^{l_\theta}$ is an alternative representation of the adaptive integrator in the ARMA model. Here, $l_\theta = l_\mu^2 n_c + l_\mu l_y (n_c + 1)$, where the notation n_c refers to both the number of autoregressive terms and the moving-average terms. The vector $\boldsymbol{\theta} \in \mathbb{R}^{l_\theta}$ is approximated by a vector $\widehat{\boldsymbol{\theta}}_k \in \mathbb{R}^{l_\theta}$, which is determined by minimizing in every step $k \in \mathbb{N}$ the retrospective cost function defined as

$$J_k(\widehat{\boldsymbol{\theta}}_k) = \sum_{m=0}^{k-1} \lambda^{k-m} \hat{\boldsymbol{z}}_m^T R_z \hat{\boldsymbol{z}}_m + \lambda^k \widehat{\boldsymbol{\theta}}_k^T R_\theta \widehat{\boldsymbol{\theta}}_k, \tag{8}$$

where $0 < \lambda \leq 1$ is the forgetting factor, $R_z \in \mathbb{R}^{l_y \times l_y}$ and $R_\theta \in \mathbb{R}^{l_\theta \times l_\theta}$ are positive definite matrices. The vector $\hat{\boldsymbol{z}} \in \mathbb{R}^{l_y}$ in (8) is the retrospective performance variable defined as

$$\hat{\boldsymbol{z}}_k = (\hat{\boldsymbol{y}}_k - \boldsymbol{y}_k) + N\widetilde{\boldsymbol{\Phi}}_k \widehat{\boldsymbol{\theta}}_k - N\widetilde{\boldsymbol{U}}_k \widehat{\boldsymbol{\theta}}_k, \tag{9}$$

where $\hat{\boldsymbol{y}} \in \mathbb{R}^{l_y}$ is the estimated output vector corresponding to the dynamic system (6). When the output error $\boldsymbol{w}$ is neglected, $N = [N_1, \cdots N_{n_f}]$, with $N_i \in \mathbb{R}^{l_y \times l_\mu}$, are the coefficients associated to a finite impulse response (FIR) filter of order n_f, and the matrices $\widetilde{\boldsymbol{\Phi}}_k \in \mathbb{R}^{l_\mu n_f \times l_\theta}$ and $\widetilde{\boldsymbol{U}}_k \in \mathbb{R}^{l_\mu n_f}$ are, respectively,

$$\widetilde{\boldsymbol{\Phi}}_k = \begin{bmatrix} \Phi_{k-1} \\ \vdots \\ \Phi_{k-n_f} \end{bmatrix}; \quad \widetilde{\boldsymbol{U}}_k = \begin{bmatrix} \mu_{k-1} \\ \vdots \\ \mu_{k-n_f} \end{bmatrix}. \tag{10}$$

The dRCMR algorithm consists of using l_μ instances of a modified version of the RCMR to estimate every parameter of the system, as illustrated in Figure 1. The nonlinear parameter estimation structure compares two outputs, the one generated by the physical system and the one generated by the estimation model. Each parameter estimation box is an instance of the modified RCMR, which is set for estimation purposes with only two parameters, i.e., $l_\mu = 2$, and calculates one parameter as an element of the system parameters. The other parameter within the instance is kept constant, and its value can be tuned proportionally between the other parameters of the system.

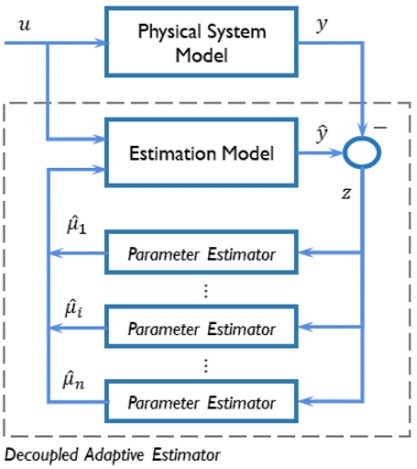

Figure 1: Nonlinear kinetic parameter estimation framework.

3. Results

For the numerical test, the model is a technological case taken from Kense et al. (2012). There are three chemical reactions, $n = 3$, involving five chemical spices, $m = 5$, and $\boldsymbol{G}(\boldsymbol{\mu}) = (10^{\mu_1}, 10^{\mu_2}, 10^{\mu_3})$. The parameter vector to be estimated is $\boldsymbol{\mu} = (\mu_1, \mu_2, \mu_3)$, and its exact value is $(-3.301, -1.301, -1.699)$.

Figure 2 portrays the results for the RCMR only, which is the structure proposed by Goel & Bernstein (2019). It is implemented with $n_c = 1$, considering a sampling time of 0.1 s. The initial values of the state vector and parameters is zero. For 20,000 iterations the estimated parameters remain trapped at a similar value.

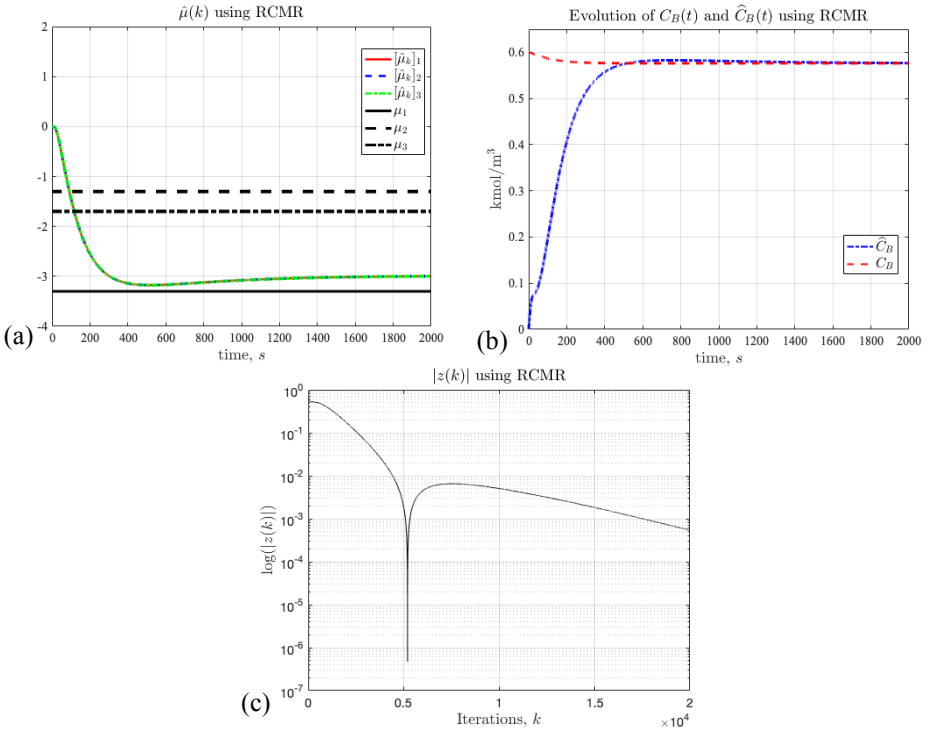

Figure 2: RCMR results when estimating three kinetic parameters and C_B as measurement: (a) the evolution of the kinetic parameters; (b) measured variable evolution; (c) Evolution of $|z(k)|$ at each iteration.

Figure 3 portrays the results for the dRCMR, $n_c = 1$ remains considering a sampling time of 0.1 s. The initial values of the state vector and parameters is zero. When using the decoupled version, the estimated parameters vector converges to its theoretical value after 800 iterations. The proposed approach shows a stable convergence.

4. Discussion and Conclusions

In this contribution, a decoupled data-driven methodology based on the RCMR algorithm was introduced for estimating nonlinear kinetic parameters. The proposed dRCMR attains good parameter estimates while the original RCMR remains trapped in unrepresentative values.

For estimating kinetic parameters in CSTRs, typically an optimization formulation is required for its subsequent kinetic parameter estimation. Nonetheless, dynamic methods such as the dRCMR open the possibility to immediately estimate kinetic parameters of nonlinear systems while or right after running experiments. Additionally, the proposed methodology could be applied in other pieces of equipment including heat exchangers. Yet, the use of a first-principles model might be mandatory for understanding the physical meaning of the estimated parameters. Grey-box models might be useful for certain applications although they lack of a fully descriptive structure.

Future steps in the subject include to test the performance of the algorithm with multiple parameters and observations in polymerization systems.

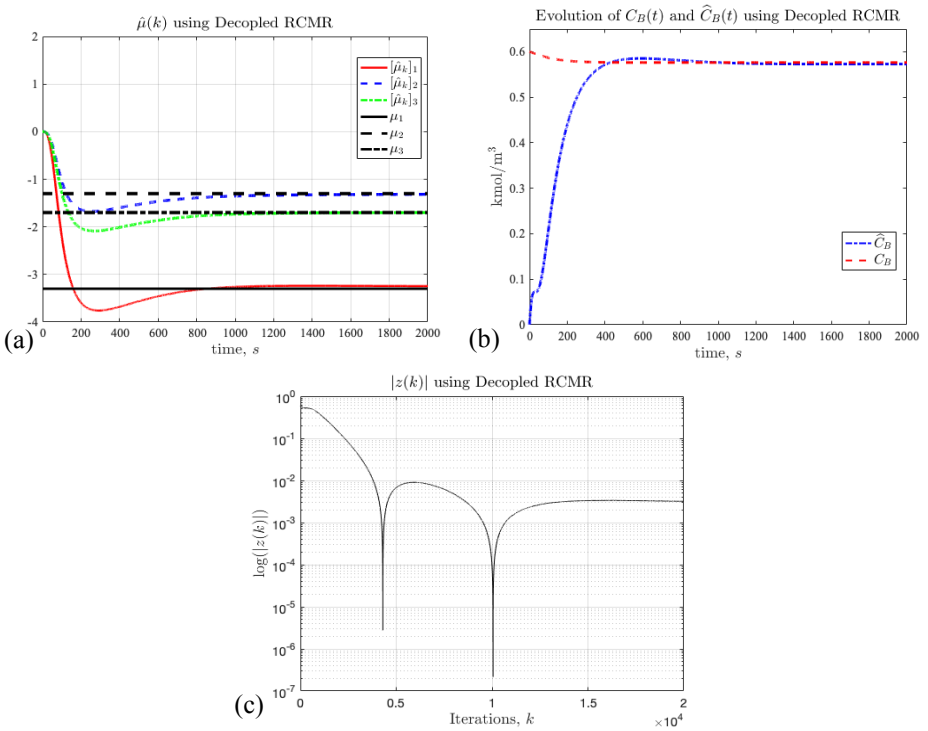

Figure 3: dRCMR results when estimating three kinetic parameters and C_B as measurement: (a) the evolution of the kinetic parameters; (b) measured variable evolution; (c) Evolution of $|z(k)|$ at each iteration.

References

Neumaier A. 2004. Complete Search in Continuous Global Optimization and Constraint Satisfaction. in Acta Numerica (A. Iserles, ed.), Cambridge University Press, Cambridge.

Eftaxias A., Font J., Fortuny A., Fabregat A., Stüber F. 2002. Nonlinear kinetic parameter estimation using simulated annealing. Computers and Chemical Engineering, (26), 1725-1733.

Goel A., & Bernstein D. S. 2018. Data-Driven Parameter Estimation for Models with Nonlinear Parameter Dependence. In 2018 IEEE Conference on Decision and Control (CDC) (pp. 1470-1475). IEEE.

Kanse N. G., Dhanke P. B., & Thombare A. 2012. Modeling and Simulation Study of the CSTR for Complex Rection by Using Polymath. Research Journal of Chemical Sciences, 2(4) 79-85.

Salas S. D., Angulo W. , & De Cecchis D. 2020. A Decoupled Data-Driven Strategy for Estimating Parameters with Nonlinear Dependence. In ICIT 2020 (accepted). IEEE.

Salas S. D., Brandão A. L., Soares J. B., & Romagnoli J. A. 2019. Data-Driven Estimation of Significant Kinetic Parameters Applied to the Synthesis of Polyolefins. *Processes*, 7(5), 309.

Salas S. D., Chebeir J., Tronci S., Baratti R., & Romagnoli J. A. 2018. Real-Time Nonlinear State Estimation in Polymerization Reactors for Smart Manufacturing. In *Computer Aided Chemical Engineering* (Vol. 43, pp. 1207-1212). Elsevier.

Salas S. D., Ghadipasha N., Zhu W., Romagnoli J. A., Mcafee T., & Reed W. F. 2017. Online DEKF for State Estimation in Semi-Batch Free-Radical Polymerization Reactors. In *Computer Aided Chemical Engineering* (Vol. 40, pp. 1465-1470). Elsevier.

Sauro Pierucci, Flavio Manenti, Giulia Bozzano, Davide Manca (Eds.)
Proceedings of the 30th European Symposium on Computer Aided Process Engineering
(ESCAPE30), May 24-27, 2020, Milano, Italy.
http://dx.doi.org/10.1016/B978-0-12-823377-1.50207-X

Linear Combination of Gradients as Optimal Controlled Variables

Dinesh Krishnamoorthy and Sigurd Skogestad

Department of Chemical Engineering, Norwegian University of Science and Technology, Trondheim 7491, Norway
dinesh.krishnamoorthy@ntnu.no

Abstract

In this paper, we show that optimal economic operation can be achieved using feedback control, by controlling the right variables that translate economic objectives into control objectives. We formulate a generic framework for selecting the controlled variables based on the Karsh-Kuhn-Tucker (KKT) conditions, that can be used to select the optimal controlled variables for different operating conditions. The proposed generalized framework is given as a linear combination of cost gradients. Furthermore, we also show that, the proposed linear gradient combination framework can be used to select the economically optimal controlled variables for parallel operating units. The proposed linear gradient combination framework can be used with any gradient estimation scheme. A benchmark Williams-Otto reactor example is used to demonstrate the effectiveness of the proposed CV selection framework.

Keywords: Measurement-based optimization,self-optimizing control, gradient

1. Introduction

One of the challenges that impede practical implementation of traditional real-time optimization is the need to solve numerical optimization problems online. In order to avoid the need to solve numerical optimization problems, there is an increasing interest in a class of methods for real-time optimization, known as "feedback-optimizing control" or "direct-input adaptation". Here the objective is to indirectly move the optimization into the control layer, thereby converting the optimization problem into a feedback control problem.

The idea of achieving optimal operation using feedback control predates 1980s, where Morari et al. (1980) proposed a "feedback optimizing control" structure that translates the economic objectives into process control objectives. This idea was further studied in detail by Skogestad (2000), where the objective was to find a simple feedback control strategy,with near optimal cost subject to constraints.

When converting the optimization problem into a feedback control problem, one of the most important question that arises is "*What to control?*". In other words, one has to find appropriate controlled variables that translates the economic objectives into control objectives. Addressing this problem, Skogestad (2000) advocates that it is important to control the constraints tightly that are optimally active. This is known as active constraint control and results in zero loss. In fact, the feedback optimizing control structure presented by Morari et al. (1980) also resulted in active constraint control. If there are

any unconstrained degrees of freedom, Skogestad (2000) advocates that one should find self-optimizing variables, which when kept at a constant setpoint, leads to acceptable loss.

The simplest and the earliest methods to find a self-optimizing CV was using a brute-force method that evaluates the performance loss of different possible candidate CVs (Skogestad, 2000). Since then there has been several developments in methods to select the optimal measurements or linear measurement combinations $\mathbf{c} = \mathbf{H}\mathbf{y}$ as self-optimizing CVs, where $\mathbf{H}$ is known as the optimal selection matrix. Some notable approaches of finding the optimal selection matrix $\mathbf{H}$ include the nullspace method (Alstad and Skogestad, 2007) and the exact local method (Alstad et al., 2009), which are based on linearized models around some nominal operating point.

The main drawback of using a linear measurement combination is that the loss increases as the optimal point moves away from the point of linearization. Using linear measurement combination also involves selecting a subset of all the available measurements that one wants to include in the measurement combination $\mathbf{c} = \mathbf{H}\mathbf{y}$, which may require additional offline analysis and/or process insight.

In this paper, we consider the linear combination of cost gradients as self-optimizing variables instead of linear measurement combination. By using a linear *gradient* combination, we show that one can achieve zero loss even when disturbances occur. To this end, we propose a generalized framework for selecting the self-optimizing variables based on the Karush-Kuhn-Tucker (KKT) conditions that can be used for different operating scenarios.

2. Selection of controlled variables

Consider the steady-state economic optimization problem

$$\begin{aligned} \min_{\mathbf{u}} \quad & J(\mathbf{u},\mathbf{d}) \\ \text{s.t. } & \mathbf{g}(\mathbf{u},\mathbf{d}) \leq 0 \end{aligned} \tag{1}$$

where $\mathbf{u} \in \mathbb{R}^{n_u}$ denotes the vector of manipulated variables (MV) and $\mathbf{d} \in \mathbb{R}^{n_d}$ denotes the vector of disturbances, $J : \mathbb{R}^{n_u} \times \mathbb{R}^{n_d} \to \mathbb{R}$ is the scalar cost function and $\mathbf{g} : \mathbb{R}^{n_u} \times \mathbb{R}^{n_d} \to \mathbb{R}^{n_g}$ denotes the vector of constraints. The Lagrangian of the optimization problem is given by

$$\mathscr{L}(\mathbf{u},\mathbf{d}) = J(\mathbf{u},\mathbf{d}) + \lambda^{\mathsf{T}}\mathbf{g}(\mathbf{u},\mathbf{d}) \tag{2}$$

where $\lambda \in \mathbb{R}^{n_g}$ is the vector of Lagrangian multipliers for the constraints. The Karush-Kuhn-Tucker conditions for optimality states that the first order necessary conditions are satisfied when

$$\nabla_{\mathbf{u}}\mathscr{L}(\mathbf{u},\mathbf{d}) = \nabla_{\mathbf{u}}J(\mathbf{u},\mathbf{d}) + \lambda^{\mathsf{T}}\nabla_{\mathbf{u}}\mathbf{g}(\mathbf{u},\mathbf{d}) = 0 \tag{3a}$$

$$\mathbf{g}(\mathbf{u},\mathbf{d}) \leq 0 \tag{3b}$$

$$\lambda^{\mathsf{T}}\mathbf{g}(\mathbf{u},\mathbf{d}) = 0 \tag{3c}$$

$$\lambda \geq 0 \tag{3d}$$

Depending on the disturbances realization, different constraints may be active. By active constraints, we mean a set of constraints $\mathbf{g}_{\mathbb{A}} \subseteq \mathbf{g}$ that are optimally at its limiting value. Let $n_a \leq n_g$ denote the number of active constraints $\mathbf{g}_{\mathbb{A}}(\mathbf{u},\mathbf{d})$. The complementary

slackness condition (3c) states that, for the active inequality constraints $\mathbf{g}_{\mathbb{A}}(\mathbf{u},\mathbf{d}) = 0$, the corresponding Lagrange multipliers are positive $\boldsymbol{\lambda}_{\mathbb{A}} > 0$ and for the constraint $\mathbf{g}_{\mathbb{I}}(\mathbf{u},\mathbf{d}) < 0$ that are not active, the corresponding Lagrange multipliers are zero, $\boldsymbol{\lambda}_{\mathbb{I}} = 0$.

The Lagrangian (2) can be re-written as

$$\mathscr{L}(\mathbf{u},\mathbf{d}) = J(\mathbf{u},\mathbf{d}) + \begin{bmatrix}\boldsymbol{\lambda}_{\mathbb{A}} & \boldsymbol{\lambda}_{\mathbb{I}}\end{bmatrix}^{\mathsf{T}} \begin{bmatrix}\mathbf{g}_{\mathbb{A}}(\mathbf{u},\mathbf{d}) \\ \mathbf{g}_{\mathbb{I}}(\mathbf{u},\mathbf{d})\end{bmatrix} \Rightarrow J(\mathbf{u},\mathbf{d}) + \boldsymbol{\lambda}_{\mathbb{A}}^{\mathsf{T}} \mathbf{g}_{\mathbb{A}}(\mathbf{u},\mathbf{d}) \tag{4}$$

For a system with n_g constraints, we can have at most 2^{n_g} active constraint regions. To convert the optimization problem into a feedback control problem, we need to find optimal controlled variables for each active constraint region.

Active constraint control: As mentioned in Skogestad (2000), if there are any active constraints, we control the active constraints tightly. For each active constraint, we choose an associated CV, usually the constraint itself, i.e. CV = $\mathbf{g}_A$ which is controlled to its limit. If the number of active constraints is the same as the number of MVs, then active constraint control is sufficient to achieve optimal operation.

Unconstrained degrees of freedom: After controlling the active constraints, we need to find CVs for any remaining $(n_u - n_a)$ unconstrained degrees of freedom. In this case, from (3) and (4), the necessary conditions of optimality is given by

$$\nabla_{\mathbf{u}} \mathscr{L}(\mathbf{u},\mathbf{d}) = \nabla_{\mathbf{u}} J(\mathbf{u},\mathbf{d}) + \boldsymbol{\lambda}_{\mathbb{A}}^{T} \nabla_{\mathbf{u}} \mathbf{g}_{\mathbb{A}}(\mathbf{u},\mathbf{d}) = 0 \tag{5}$$

$$\Rightarrow \nabla_{\mathbf{u}} J(\mathbf{u},\mathbf{d}) = -\boldsymbol{\lambda}_{\mathbb{A}}^{T} \nabla_{\mathbf{u}} \mathbf{g}_{\mathbb{A}}(\mathbf{u},\mathbf{d}) \tag{6}$$

Since $\boldsymbol{\lambda}_{\mathbb{A}}$ is unknown in (6), we can eliminate it by looking into the nullspace of the active constraint gradients $\nabla_{\mathbf{u}} \mathbf{g}_{\mathbb{A}}(\mathbf{u},\mathbf{d})$. (Jäschke and Skogestad, 2012). $\mathbf{N}$ is defined as the nullspace of $\nabla_{\mathbf{u}} \mathbf{g}_{\mathbb{A}}(\mathbf{u},\mathbf{d})$ if $\mathbf{N}^{\mathsf{T}} \nabla_{\mathbf{u}} \mathbf{g}_{\mathbb{A}}(\mathbf{u},\mathbf{d}) = 0$.

Theorem 1 (Linear combination of gradients as self-optimizing variables)**.** *Given a steady-state optimization problem* (1) *with $n_a < n_u$ active constraints $\mathbf{g}_{\mathbb{A}}(\mathbf{u},\mathbf{d})$. Let $\mathbf{N} \in \mathbb{R}^{n_u \times (n_u - n_a)}$ be the nullspace of the active constraint gradients $\nabla_{\mathbf{u}} \mathbf{g}_{\mathbb{A}}(\mathbf{u},\mathbf{d})$, such that $\mathbf{N}^{\mathsf{T}} \nabla_{\mathbf{u}} \mathbf{g}_{\mathbb{A}}(\mathbf{u},\mathbf{d}) = 0$. Then the necessary conditions of optimality can be achieved by controlling the linear combination of the gradients*

$$\mathbf{c} = \mathbf{N}^{\mathsf{T}} \nabla_{\mathbf{u}} J(\mathbf{u},\mathbf{d}) \tag{7}$$

to a constant setpoint of zero.

Proof. Pre-multiplying (6) by $\mathbf{N}^{\mathsf{T}}$ gives

$$\mathbf{N}^{\mathsf{T}} \nabla_{\mathbf{u}} J(\mathbf{u},\mathbf{d}) = -\mathbf{N}^{\mathsf{T}} \nabla_{\mathbf{u}} \mathbf{g}_{\mathbb{A}}(\mathbf{u},\mathbf{d})^{\mathsf{T}} \boldsymbol{\lambda}_{\mathbb{A}} \tag{8}$$

Since $\mathbf{N}^{\mathsf{T}} \nabla_{\mathbf{u}} \mathbf{g}_{\mathbb{A}}(\mathbf{u},\mathbf{d})^{\mathsf{T}} = 0, \Rightarrow\ \mathbf{N}^{\mathsf{T}} \nabla_{\mathbf{u}} J(\mathbf{u},\mathbf{d}) = 0$ □

Therefore, controlling $\mathbf{c} = \mathbf{N}^{\mathsf{T}} \nabla_{\mathbf{u}} J(\mathbf{u},\mathbf{d}) \in \mathbb{R}^{(n_u - n_a)}$ to a constant setpoint of zero satisfies the necessary condition of optimality (Krishnamoorthy and Skogestad, 2019). Since $n_a < n_u$, Linear independent constraint qualification (LICQ) is satisfied (i.e. $\nabla_{\mathbf{u}} \mathbf{g}_{\mathbb{A}}(\mathbf{u},\mathbf{d})$ has full row rank) and $\mathbf{N}$ is well defined. If $n_a = 0$ (fully unconstrained case), $\mathbf{N} = I_{n_u \times n_u}$, which means that the n_u self-optimizing CVs are simply the cost gradients $\mathbf{c} =$

$\nabla_{\mathbf{u}} J(\mathbf{u},\mathbf{d})$. Therefore, for any active constraint region, $(n_u - n_a)$ CVs can be chosen as $\mathbf{c} = \mathbf{N}^\top \nabla_{\mathbf{u}} J(\mathbf{u},\mathbf{d})$ which by construction is of size $(n_u - n_a)$.

The proposed framework also enables us to select the CVs without having to develop reduced models for each active constraint region. One the CVs are chosen from each active constraint region, one can switch between the different active constraint regions using simple logic blocks such as selectors or split-range, as demonstrated by Krishnamoorthy and Skogestad (2019) and Reyes-Lúa et al. (2018). Although the gradients are ideal self-optimizing CVs, they are not readily available measurements. One has to estimate the gradients using the measurements. There are several model-based and model-free gradient estimation algorithms, which are briefly summarized by Srinivasan et al. (2011).

3. Illustrative example: Williams-Otto reactor

Consider the benchmark Williams-Otto reactor example, where the raw materials A and B are converted to useful products P and E through a series of reactions

$$\begin{aligned} A + B &\rightarrow C & k_1 &= 1.6599 \times 10^6 e^{-6666.7/T_r} \\ B + C &\rightarrow P + E & k_2 &= 7.2177 \times 10^8 e^{-8333.3/T_r} \\ C + P &\rightarrow G & k_3 &= 2.6745 \times 10^{12} e^{-11111/T_r} \end{aligned}$$

The feed stream F_A with pure A component is a disturbance to the process and the manipulated variables are the feed stream F_B with pure B component and the reactor temperature T_r. The objective is to maximize the production of valuable products P and E, subject to some purity constraints on G and A in the product stream,

$$\begin{aligned} \min_{T_r, F_B} \; & -1043.38 x_P (F_A + F_B) - 20.92 x_E (F_A + F_B) + 79.23 F_A + 118.34 F_B \\ \text{s.t.} \quad & x_G \leq 0.08, \qquad x_A \leq 0.12 \end{aligned} \tag{9}$$

Since we have two constraints, we can have at most $2^2 = 4$ active constraint regions, namely, 1) x_A and x_G active, 2) only x_G active, 3) only x_A active, and 4) unconstrained. However, the max limit on x_G is so low that x_G will always be active. Therefore, we can eliminate regions 3 and 4, and we only need to choose CVs for regions 1 and 2. In region 1, we simply control the concentration of x_A to its limit of $0.12 kg/kg$ and x_G to its limit of $0.08 kg/kg$. In region 2, we control x_G to its limit of $0.08 kg/kg$, and control the linear gradient combination $c := 0.9959 \nabla_{F_B} J + 0.0906 \nabla_{T_r} J$ to a constant setpoint of zero.

Region 1 ($F_A = 1.8275 kg/s$): - When the disturbance is $F_A = 1.8275 kg/s$, we are operating in region 1, with both the constraints active. This is the simplest case, where optimal operation is achieved using active constraint control.

Region 2 ($F_A = 1.3 kg/s$): - When the disturbance is $F_A = 1.3 kg/s$, we are operating in region 2, with only x_G constraint active. We use the reactor temperature T_r to control this constraint tightly and use F_B to control the linear gradient combination $c := 0.9959 \nabla_{F_B} J + 0.0906 \nabla_{T_r} J$. In this case, we use a model-based gradient estimation method proposed by Krishnamoorthy et al. (2019). The simulation results are shown in Fig. 2, where it can be seen that the proposed CVs are able to drive the process ot its true optimum.

Switching between x_A and c can automatically be achieved using a selector block. Additional results such as, comparison of the proposed approach with the linear measurement

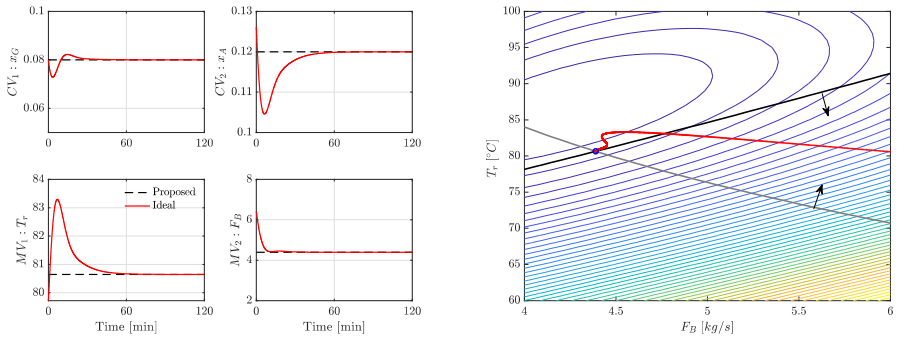

(a) (b)

Figure 1: Region 1: Simulation results using the proposed CVs when $F_A = 1.8275 kg/s$.

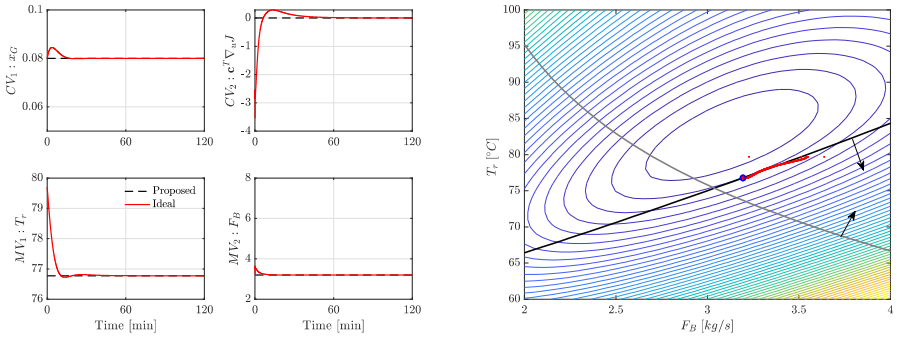

(a) (b)

Figure 2: Region 2: Simulation results using the proposed CVs when $F_A = 1.3 kg/s$.

combination and brute force method, including automatic CV-CV switching between x_A and c using a selector block can be found in the first author's PhD thesis (Krishnamoorthy, 2019, Appendix D).

4. Optimal operation of parallel operating units

In this section, we show how the proposed linear gradient combination framework can be used to choose the CVs for optimal operation of parallel operating units. Often in practice, when a plant capacity expands, this is done by simply adding new units in parallel to the existing units. The parallel units often share common resources such as feed, hot water etc. The different units may have different capacities, different equipment condition and different efficiencies.

Consider the optimal operation of p parallel units each with a cost function $\ell_i(u_i)$ and a given total feed U^{max}. The optimization problem is given as

$$\min_{u_i} J = \sum_{i=1}^{p} \ell_i(u_i) \quad \text{s.t.} \sum_{i=1}^{p} u_i - U^{max} = 0 \tag{10}$$

In this case, $\nabla_{\mathbf{u}}\mathbf{g}_{\mathbb{A}} = \mathbb{1}^p$ and $\mathbf{N} \in \mathbb{R}^{(p-1)\times p}$ is chosen such that $\sum_{j=1}^{p} \eta_{i,j}\nabla_{\mathbf{u}_j}J$ and $\sum_{j=1}^{p} \eta_{i,j} = 0 \quad \forall i = 1,\ldots,p-1$ where $\eta_{i,j}$ is the i and j^{th} element in $\mathbf{N}$. This implies $\nabla_{\mathbf{u}_i}\ell_i = \nabla_{\mathbf{u}_j}\ell_j$ for all $i \neq j$. That is the optimal operation of parallel units occur when the marginal cost is the same for all the units, which was also proved by Downs and Skogestad (2011) and commonly used in practice.

To illustrate this, consider a process with $p = 3$ parallel units. Using the nullspace of $\nabla_{\mathbf{u}}\mathbf{g}_{\mathbb{A}} = [1,1,1]^T$, we get

$$c_1 : -0.5774\nabla_{\mathbf{u}_1}J + 0.7887\nabla_{\mathbf{u}_2}J - 0.2113\nabla_{\mathbf{u}_3}J = 0$$
$$c_2 : -0.5774\nabla_{\mathbf{u}_1}J - 0.2113\nabla_{\mathbf{u}_3}J + 0.7887\nabla_{\mathbf{u}_3}J = 0$$

Adding $c_1 + c_2$ yields $-\nabla_{\mathbf{u}_2}J + \nabla_{\mathbf{u}_3}J = 0$. Substituting this in c_1 gives $-0.5774\nabla_{\mathbf{u}_1}J + 0.5774\nabla_{\mathbf{u}_2}J = 0$, which results in $\nabla_{\mathbf{u}_1}J = \nabla_{\mathbf{u}_2}J = \nabla_{\mathbf{u}_3}J$. Although this is not a new result and is a well known concept, this re-iterates the general applicability of the proposed linear gradient combination framework.

5. Conclusion

In this paper, we proposed a generalized framework for selecting *what to control* in order to achieve optimal economic operation. An optimization problem can be converted into a feedback control problem by controlling:

- Active constraints $\mathbf{g}_{\mathbb{A}} \to 0$
- Linear gradient combination $\mathbf{c} = \mathbf{N}^{\mathsf{T}}\nabla_{\mathbf{u}}J \to 0$ (with $\mathbf{N}^{\mathsf{T}}\nabla_{\mathbf{u}}\mathbf{g}_{\mathbb{A}} = 0$)

References

V. Alstad, S. Skogestad, 2007. Null space method for selecting optimal measurement combinations as controlled variables. Industrial & engineering chemistry research 46 (3), 846–853.

V. Alstad, S. Skogestad, E. S. Hori, 2009. Optimal measurement combinations as controlled variables. Journal of Process Control 19 (1), 138–148.

J. J. Downs, S. Skogestad, 2011. An industrial and academic perspective on plantwide control. Annual Reviews in Control 35 (1), 99–110.

J. Jäschke, S. Skogestad, 2012. Optimal controlled variables for polynomial systems. Journal of Process Control 22 (1), 167–179.

D. Krishnamoorthy, 2019. Novel approaches to online process optimization under uncertainty. Ph.D. thesis, Norwegian University of Science and Technology.

D. Krishnamoorthy, E. Jahanshahi, S. Skogestad, 2019. A feedback real time optimization strategy using a novel steady-state gradient estimate and transient measurements. Industrial and Engineering Chemistry Research 58, 207–216.

D. Krishnamoorthy, S. Skogestad, 2019. Online process optimization with active constraint set changes using simple control structures. Industrial & Engineering Chemistry Research.

M. Morari, Y. Arkun, G. Stephanopoulos, 1980. Studies in the synthesis of control structures for chemical processes: Part i: Formulation of the problem. process decomposition and the classification of the control tasks. analysis of the optimizing control structures. AIChE Journal 26 (2), 220–232.

A. Reyes-Lúa, C. Zotică, T. Das, D. Krishnamoorthy, S. Skogestad, 2018. Changing between active constraint regions for optimal operation: Classical advanced control versus model predictive control. In: Computer Aided Chemical Engineering. Vol. 43. Elsevier, pp. 1015–1020.

S. Skogestad, 2000. Plantwide control: the search for the self-optimizing control structure. Journal of process control 10 (5), 487–507.

B. Srinivasan, G. François, D. Bonvin, 2011. Comparison of gradient estimation methods for real-time optimization. In: 21st European Symposium on Computer Aided Process Engineering-ESCAPE 21. No. EPFL-CONF-155235. Elsevier, pp. 607–611.

Sauro Pierucci, Flavio Manenti, Giulia Bozzano, Davide Manca (Eds.)
Proceedings of the 30th European Symposium on Computer Aided Process Engineering
(ESCAPE30), May 24-27, 2020, Milano, Italy.
http://dx.doi.org/10.1016/B978-0-12-823377-1.50208-1

Optimisation of Petroleum Production Well Placement under Geological Uncertainty

Emmanuel I. Epelle, Dimitrios I. Gerogiorgis

Institute for Materials and Processes (IMP), School of Engineering, University of Edinburgh, The Kings Buildings, Edinburgh, EH9 3FB, United Kingdom
D.Gerogiorgis@ed.ac.uk

Abstract

Large investments are required for the positioning and drilling of oil and gas wells, implying that decisions related to these activities may be significantly aided by sound and proven mathematical-oriented methods. The use of intuitive engineering judgement alone cannot guarantee sustainable profitability over long periods, especially under geological (reservoir model) uncertainty. To capture significant uncertainty sources in the subsurface geology of the reservoir considered in this study, geostatistical model realisations are obtained using available information (permeabilities and porosities). We use specialised algorithms of the MATLAB Reservoir Simulation Toolbox (MRST, interfaced with PETREL™) in order to determine optimal petroleum production well locations and production rates and thus maximise the field oil recovery. The developed computational workflow has been applied to a realistic case study, for which robust optimality is demonstrated using the worst-case realisation for determining optimal well locations.

Keywords: Production optimisation; optimal well placement; geological uncertainty.

1. Introduction

Well placement optimisation at the early planning stages of field development is necessary to achieve the best possible economic benefits. Reservoir simulations that quantify fluid flow behaviour with respect to well positions can be used to describe subsurface flow phenomena over a long time horizon. However, these simulations can be computationally expensive and this limits the number of iterations that can be performed in the search for an optimal operation strategy. The application of mathematical optimisation to well placement problems usually includes gradient-based methods, mixed integer programming, genetic algorithms and particle swarm optimisation (Bangerth et al., 2006; Onwunalu and Durlofsky, 2010). The complexity of this problem is aggravated by geological uncertainty, which can be accounted for by incorporating multiple geological realisations in the optimisation formulation. The use of the entire superset and a subset of equiprobable geological realisations for well placement optimisation has been carried out by Yeten et al. (2003) and Wang et al. (2012), with intense computational efforts. However, the application of flow diagnostics adopted in this work for well placement optimisation, utilises an adjoint code for gradient evaluations (Møyner et al., 2015), thus enabling faster and accurate computations compared to previous studies. The objective of the present study is to offer a systematic exploration of different operational strategies (with flow visualisations) for optimal oil recovery, demonstrated on a realistic field using the functionalities of the MATLAB Reservoir Simulation Toolbox (MRST).

2. Methodology

Static modelling: The first step in this stage involves the mapping of horizons and faults from the available seismic data in PETREL™ (Figs. 1a and 1b). This is followed by the creation of surface maps that mark the reservoir's boundary (Fig. 1c). Well log interpretations are carried out next to identify the productive geological zones based on the reservoir's lithology, porosity and fluid resistivity (Fig. 1d). The result of this interpretation is the final static model as shown in Fig. 1e, which is upscaled for dynamic simulation purposes (Fig. 1f). The field contains 5 injection wells and 3 production wells.

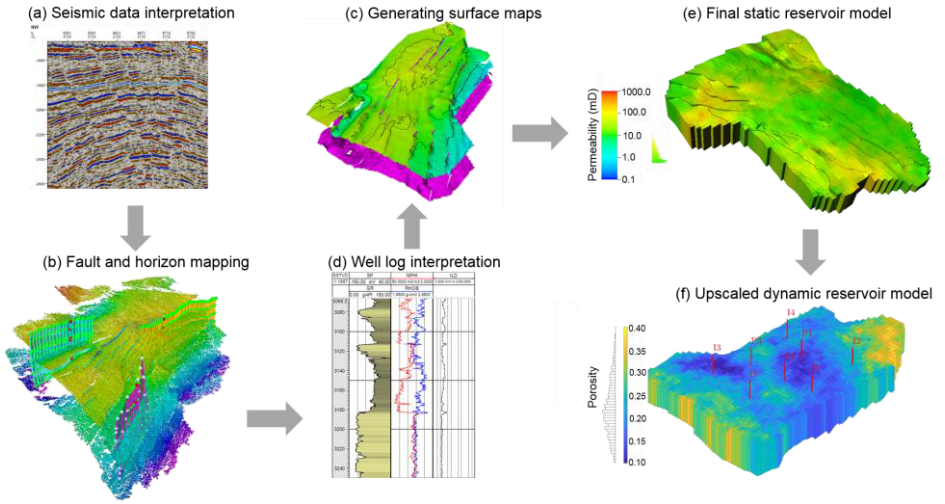

Figure 1: Static and dynamic reservoir model development procedure.

Incorporating uncertainty: Geological uncertainty exists because it is difficult to know the exact properties of every section of the realistic reservoir (Rahim and Li, 2015). Using the sequential Gaussian simulation functionality of PETREL™, 50 realisations of the reservoir's permeability (horizontal and vertical) are generated. The grid structure and the fluid and rock properties of each realisation are imported into MATLAB (where optimisation tasks are performed using the MRST toolbox). The Lorenz coefficient (L_c) is the main ranking metric applied and the worst realisation is that with the highest L_c.

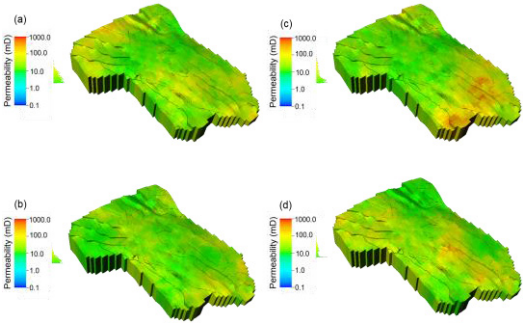

Figure 2: 4 out of 50 geological realisations.

Dynamic modelling and optimisation formulation: Optimisation tasks are carried out over the worst case scenario after ranking the geological realisations, thus ensuring robust feasibility of the obtained solution (worst-case optimisation). The mathematical formulation of the reservoir model, objective function, operational constraints and adopted solution strategy (Møyner et al., 2015) are shown in Table 1. The dynamic reservoir model (Eqs. 1–3) describes the flow field in the reservoir and the time-of-flight (TOF, the time required for a fluid particle to travel along a streamline from its starting

point to the current position). The pressure is denoted as p, the TOF as τ, the Darcy velocity as $\vec{v}$, the reservoir's storage capacity as ϕ, the permeability tensor as **K**, and the fluid mobility as λ_f. Flow in the reservoir can be driven by wells, n_{bh}, which are controlled by the bottomhole pressure (BHP), but also by other wells, n_r, which are rate controlled. Both well types, n_w, have perforations, n_{pf}, through which fluid flows from the reservoir into the wellbore. All wells are modelled using the Peaceman well model (Eq. 4) in which the well perforation fluxes are denoted by q_{pf}. The index of the well to which perforation number j belongs is denoted as $N_w(j)$. Moreover, k is the well index and W^j_{pf} is the Peaceman well index. Furthermore, a set of manipulations (controls), in the form of closure relations, are specified for each well type (Eqs. 5–6); **u** is the control vector.

Table 1: Modelling and optimisation framework for well placement optimisation.

Reservoir Model

$$\mathcal{P}(q,\vec{v}) = \nabla \times \vec{v} - q = 0 \quad (1)$$

$$\mathcal{V}(p,\vec{v}) = \vec{v} + \mathbf{K}\lambda_f \nabla p = 0 \quad (2)$$

$$\mathcal{T}(\tau,\vec{v}) = \vec{v} \times \nabla\tau - \phi = 0 \quad (3)$$

$$\mathcal{Q}^j(q_{pf}, q_{pf}, p) = q^j_{pf} - W^j_{pf}\lambda_f\left[p^{N_w(j)}_{bh} - p\right] = 0; j = 1, \dots, n_{pf} \quad (4)$$

$$\mathcal{C}_{bh} = u^k_{bh} - p^k_{bh} = 0; k = 1, \dots, n_{bh} \quad (5)$$

$$\mathcal{C}_r = u^k_r - \sum_{j \in N_{pf}(k)} q^j_{pf} = 0; k = n_{bh}+1, \dots, n_{bh} \quad (6)$$

Objective Function & Constraints

$$L_{c,o} = 2\int_0^1 [F(\phi) - \phi]\, S_o d\phi \quad (7)$$

$$NPV(T) = \int_{t=0}^{T} \sum_{c=o,w} (r_c q_c + r_{ci} q_{ci})\,(1+d)^{-1} dt \quad (8)$$

$$u \leftarrow u - P\left(\alpha \frac{dG_\lambda}{d\boldsymbol{u}}\right)^T \quad (9)$$

Solution Strategy

$$\begin{bmatrix} 0 & \partial_v \mathcal{P} & \partial_q \mathcal{P} & 0 \\ \partial_p \mathcal{V} & \partial_v \mathcal{V} & 0 & 0 \\ \partial_p \mathcal{Q} & 0 & \partial_q \mathcal{Q} & \partial_{p_{bh}} \mathcal{Q} \\ 0 & 0 & \partial_q \mathcal{C} & \partial_{p_{bh}} \mathcal{C} \end{bmatrix} \begin{bmatrix} \mathbf{p} \\ \mathbf{v} \\ \mathbf{q} \\ \mathbf{p_{bh}} \end{bmatrix} = \begin{bmatrix} 0 \\ 0 \\ 0 \\ 0 \end{bmatrix} \quad (10)$$

Adjoint Formulation

$$G_\lambda = G[\boldsymbol{x}(\boldsymbol{u}), \boldsymbol{u}] + \lambda^T g[\boldsymbol{x}(\boldsymbol{u}), \boldsymbol{u}] \quad (11)$$

$$\frac{dG_\lambda}{d\boldsymbol{u}} = \frac{\partial G}{\partial \boldsymbol{u}} + \left(\frac{\partial G}{\partial \boldsymbol{x}} + \lambda^T \frac{\partial g}{\partial \boldsymbol{x}}\right)\frac{\partial x}{\partial \boldsymbol{u}} + \lambda^T \frac{\partial g}{\partial \boldsymbol{u}} + \boldsymbol{g}^T \frac{\partial \lambda}{\partial \boldsymbol{u}} \quad (12)$$

$$\left(\frac{\partial g}{\partial \boldsymbol{x}}\right)^T \lambda = \mathbf{J}^T \lambda = -\left(\frac{\partial G}{\partial \boldsymbol{x}}\right)^T \quad (13)$$

$$\frac{dG_\lambda}{d\boldsymbol{u}} = \frac{\partial G}{\partial \boldsymbol{u}} + \lambda^T \frac{\partial g}{\partial \boldsymbol{u}} \quad (14)$$

Besides the well placement optimisation, rate control optimisation is subsequently performed on the optimally located wells. The first objective function (Eq. 7) is applied to the well placement optimisation task; the objective function is based on the Lorenz coefficient (Eq. 7), which is written in terms of the flow capacity, F, and the storage capacity, ϕ. This coefficient measures how the oil displacement efficiency for a given well pattern differs from that of an ideal (piston-like) displacement pattern in the reservoir. Thus, this coefficient is a measure of the optimality of the water flooding operation and hence the oil recovery in the reservoir. However, a simplified Net Present Value (*NPV*) expression (without installation cost of wells and other factors) is utilised as the objective function of the rate control procedure (Eq. 8). T represents the length of the time horizon, q_c and q_{ci} are the field production and injection rates of components c (oil and water) respectively. The revenues and costs of production and injection of components c are r_c and r_{ci} respectively and d is the discount rate. Furthermore, we note that $\boldsymbol{\mathcal{C}}$, $\boldsymbol{\mathcal{T}}$, $\boldsymbol{\mathcal{V}}$, $\boldsymbol{\mathcal{Q}}$ and $\boldsymbol{\mathcal{P}}$ represent the discretised system in terms of variables, q_{pf}, p_{bh}, p, v, τ.

To perform optimisation computations, the primary variables (pressure, rates and TOF) in Eqs. 1–3 are solved for, and the objective function gradients are computed for a set of controls. The solution strategy (two-point flux approximation for spatial discretisation – Eq. 10) minimises computational workload and makes it adaptable to different linear

algebraic solvers. The adjoint equations comprises the Lagrange function for the problem (Eq. 11), its derivatives (Eq. 12) and simplifications (Eqs. 13–14) that yield an objective function which depends on the state variables, **x** and not on the control variables **u**. $\mathbf{x}^T$ is a vector of the solution quantities $\mathbf{p}^T$, $\mathbf{v}^T$, τ^T, $\mathbf{q}^T$ and $\mathbf{p}_{bh}{}^T$. G[**x**(**u**)] represents the objective function and **g**[**x**(**u**),**u**] = 0 represents a set a constraints; λ is the Lagrange multiplier, **J** is the Jacobian, and superscript *T* denotes the vector/matrix transpose, as applicable above.

Optimal well controls: A steepest-descent algorithm is implemented for finding optimal controls (Eq. 9). This utilises the supplied *NPV* objective function, the well rate bounds (maximum and minimum) and voidage replacement; α represents the step size and *P* is a projection to the constraints. While evaluating the objective, the value of α is adjusted and the algorithm stops when the improvement in the objective function between two successive iterations is less than the specified tolerance (in this case, equal to: 5×10^{-4}).

Well placement algorithm: The algorithm begins by adding pseudowells with a zero-rate in the region around each injector and computes the gradients of the added wells (based on the Lorenz coefficient). The original well is then replaced by the pseudowell with the largest gradient. The process is repeated until all wells remain stationary.

3. Simulation and optimisation results

In carrying out the optimisation procedure it is assumed that the production wells have been drilled whereas the injection wells are yet to be drilled. Thus, the aim of the optimisation task to determine the optimal injection well positions that yields the best possible oil displacement in the reservoir. In our case study, the reservoir model contains 2,726 cells with an initial pressure of 500 bar; two phases are present (oil and water). Densities and viscosities of both phases are 859 kg m^{-3}, 1014 kg m^{-3}, 2 cP and 0.5 cP respectively; the relative permeability exponents of both phases were set as 2. All 5 injection wells and 3 production wells are assumed to have vertical geometries. The initial injector placement was done such as to maintain good hydraulic connectivity between the injection and production wells given the faulted nature of the reservoir – this is based on reservoir engineering judgement (Fig. 3a). However, on applying the well placement algorithm, optimal injector locations that guarantee improved oil sweep are obtained. This can be observed in the oil saturation plots for both placement patterns (unexplored regions of the reservoir - the yellow patches in Fig. 3a are absent in Fig. 3b). The well paths taken by the algorithm during the search for optimal injector well position are shown in Fig. 3c.

The Lorenz coefficient (a measure of reservoir heterogeneity and the efficiency of oil displacement) is also shown for the two placement scenarios. A smaller value of this parameter represents a better displacement scenario; this is the case with the optimised well positions as shown in Fig. 3b compared to Fig. 3a. F/ϕ denotes the ratio of the reservoir's flow capacity to its storage capacity (Fig. 4a). For a perfect/idealised oil displacement in the reservoir, the F/ϕ ratio = 1. It is observed that the optimised well placement yields an F/ϕ curve closer to an idealised displacement scenario compared to initial well positions. In order to further validate the optimality of the new well configurations determined by the algorithm, we run multiphase flow simulations for a production timeframe of 5 years and obtain the oil recovery over this period. It is shown in Fig. 4b that the oil recovery of the optimised well placement far supersedes that of the initial well placement (twice the recovery of the initial placement at the end of the production forecast – Fig. 4b). This indicates that intuitive-based well placements will hardly yield similar performance and oil recovery (field profitability) to that obtained by

sound mathematical techniques. The well placement algorithm thus capitalises on the underlying permeability distribution for optimal determination of injection well locations.

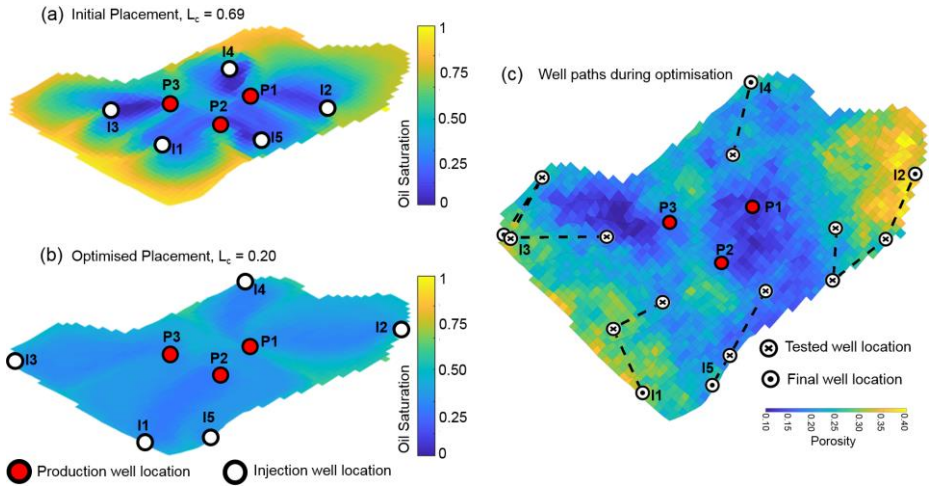

Figure 3: Oil saturation distribution before and after well placement optimisation.

The optimal control configurations (injection and production rates for respective wells) based on the new well placements are thus illustrated in Fig. 4c and 4d, respectively.

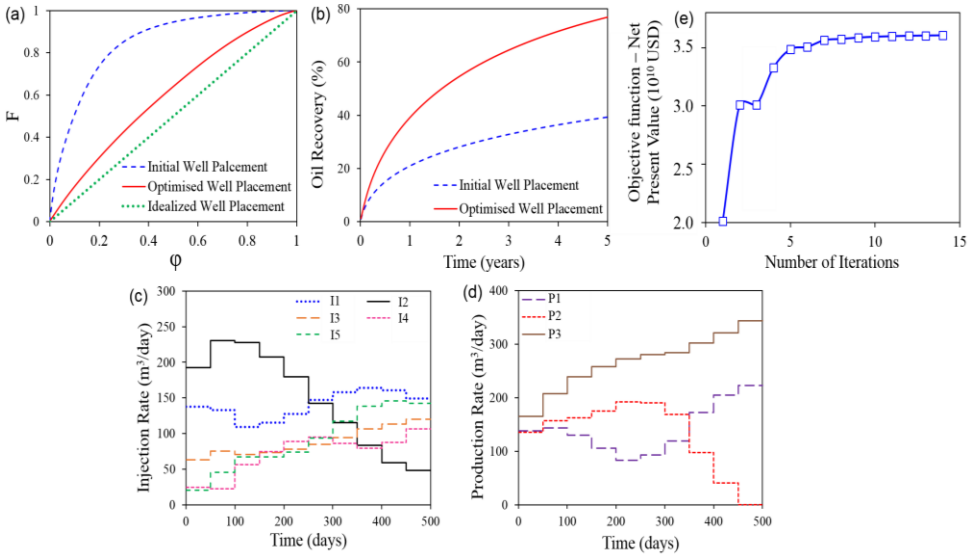

Figure 4: (a) Oil displacement efficiency F/ϕ diagram, (b) percentage oil recovery, optimal manipulations for injection (c) and production (d) wells in the field considered, (e) NPV evolution.

The application of the rate optimisation algorithm, which is based on the *NPV* indicates that injection well I2 with a steady decreasing injection rate at each timestep should be allocated the highest injection rate at the start of production. Next in magnitude is I1 with a relatively lower injection rate. I4 has the lowest injection rate compared to other injection wells and may be considered the least performing. Since operators have control over the injection rates at the surface, it can be said that the rate optimisation algorithm also inherently solves a rate allocation problem. The production rate responses from the

different wells indicates that P3 is the most productive well and significantly contributes to the overall field *NPV*. The evolution of the *NPV* objective function is shown in Fig. 4e. It is observed that within the first 5 iterations, the algorithm is able to find a near optimal solution. Compared to a methodology that requires numerous direct calls to a high-fidelity simulator or an approximation of the simulator's output (Epelle and Gerogiorgis, 2019a; b), the implemented algorithm attains optimality in fewer iterations (within 2 min of run time). Although the presented case study is somewhat small (in terms of the number of wells), such rapid computational performance is also expected when the problem size increases. Beyond the computational time required for the rate control optimisation step, we present the time required for the entire workflow (Fig. 5). Most of the time is spent on static model development and preliminary dynamic simulations to ascertain performance.

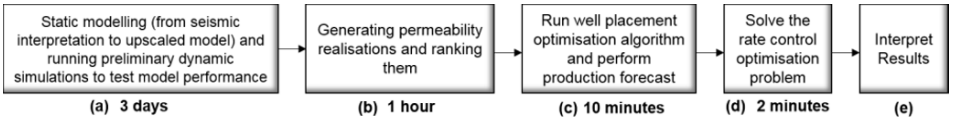

Figure 5: Time requirement for each step of the computational workflow.

4. Conclusion

This study presents an injection well placement and rate control problem of a realistic oil field under geological uncertainty. A worst-case scenario optimisation is performed based on 50 geological realisations obtained from static reservoir modelling, via Sequential Gaussian Simulation. By implementing a well placement optimisation algorithm, oil recovery in the field is boosted to twice the value obtained via intuition-based methods (for a 5-year forecast period). Furthermore, the robust computational methodology for rapid determination of gradients enables rate control (using *NPV* is the objective function) and well placement optimisation (using the Lorenz coefficient as the objective function). These tasks are performed in a matter of minutes, thus demonstrating the applicability of the implemented approach towards real-time decision support in reservoir management.

References

W. Bangerth, H. Klie, M.F. Wheeler, P.L. Stoffa and M.K. Sen, 2006. On optimization algorithms for the reservoir oil well placement problem. *Comput. Geosci.*, 10, 3, 303–319.

E.I. Epelle and D.I. Gerogiorgis, 2019a. A multiperiod optimisation approach to enhance oil field productivity during secondary petroleum production. *Comput. Aided Chem. Eng.,* 46, 1651–1656.

E.I. Epelle and D.I. Gerogiorgis, 2019b. Optimal rate allocation for production and injection wells in an oil and gas field for enhanced profitability. *AIChE J.*, 65, 6 (DOI: 10.1002/aic.16592).

O. Møyner, S. Krogstad and K.A. Lie, 2015. The application of flow diagnostics for reservoir management. *SPE J.*, *20*(02), 306–323.

J.E. Onwunalu and L.J. Durlofsky, 2010. Application of a particle swarm optimization algorithm for determining optimum well location and type. *Comput. Geosci.*, 14, 1, 183–198.

S. Rahim and Z. Li, 2015. Reservoir geological uncertainty reduction: an optimization-based method using multiple static measures. *Math. Geosci.*, 47, 4, 373–396.

H. Wang, D. Echeverría-Ciaurri, L.J. Durlofsky and A. Cominelli, 2012. Optimal well placement under uncertainty using a retrospective optimization framework. *SPE J.*, 17, 1, 112–121.

B. Yeten, L.J. Durlofsky and K. Aziz, 2003. Optimization of nonconventional well type, location, and trajectory. *SPE J.*, 8, 3, 200–210.

Sauro Pierucci, Flavio Manenti, Giulia Bozzano, Davide Manca (Eds.)
Proceedings of the 30th European Symposium on Computer Aided Process Engineering (ESCAPE30), May 24-27, 2020, Milano, Italy.
http://dx.doi.org/10.1016/B978-0-12-823377-1.50209-3

Oil Production Optimisation using Piecewise Linear Approximations (MILP): Computational Performance Comparison vs. MINLP Formulation

Emmanuel I. Epelle, Dimitrios I. Gerogiorgis

Institute for Materials and Processes (IMP), School of Engineering, University of Edinburgh, The Kings Buildings, Edinburgh, EH9 3FB, United Kingdom
D.Gerogiorgis@ed.ac.uk

Abstract

Typical daily operations of oil and gas production systems are characterised by numerous decisions that must be carefully made if field profitability is to be sustained. These systems are usually nonlinear, nonconvex and involve binary decision variables; hence, the application of mathematical optimisation often results in an MINLP formulation. Piecewise linearisation techniques based on Special Ordered Sets of type 2 (SOS2) constraints have been used to approximate the nonlinear functions of the optimisation problem for complexity reduction. However, a computational analysis of these MILP-based formulations in comparison to their MINLP equivalents in oil production systems is scarce in literature. In this study, the benefits of MILP reformulation are applied to a synthetic but realistic case. In comparing both formulations, we evaluate solution sensitivity to the number of breakpoints, solution time, accuracy, and ease of automation.

Keywords: Mixed-integer optimisation; piecewise linear approximation; oil production.

1. Introduction

The application of mathematical optimisation for the recovery improvement of hydrocarbon reserves is vital for a field's sustainability (Gunnerud and Foss, 2010; Epelle and Gerogiorgis, 2019a). Novel algorithmic advancements have enabled engineers model, simulate and optimise complex nonlinear phenomena characterising the production activities in the petroleum industry (Codas et al., 2012). This results in Mixed Integer Nonlinear Programs (MINLP) which can be difficult to solve. A simplification approach involves reformulating the MINLP to a Mixed Integer Linear Program (MILP) via piecewise linear approximations (Silva and Camponogara, 2014; Kronqvist et al, 2018). Nonlinearities in the formulation are mainly attributable to the multiphase flow rate relationships in the wells, pipelines and valves (Epelle and Gerogiorgis, 2019b). These complex relationships are usually not explicitly known and are dependent on several operational parameters estimated via high fidelity simulators. Piecewise linear models have the advantage of establishing linear relationships directly from the simulator sample points; a property that reduces problem complexity. This study explores this benefit and compares the computational performance of the MILP with the corresponding MINLP. The novel analysis presented herein also enables quality assessment of the optimisation formulation on the overall oil production. Furthermore, another novel

element of this study is the combination of operationally distinct well behaviours with complex flow physics and bi-level flow routings within the optimisation formulation.

2. Methodology

The surface network model is first constructed in a steady state multiphase flow simulator (PIPESIM®). As shown in Fig. 1, the model consists of the wells, chokes, flowlines, manifolds, pipelines and separators, which are all connected. Robust multiphase flow correlations are adopted to capture complex flow physics in the respective network components. Some of these phenomena include: water coning behaviour in well (W1), non-vertical/deviated well trajectories (W2 and W4), and downhole pressure assistance to maintain production by means of Progressive Cavity Pumps (PCPs) and Electrical Submersible Pumps (ESPs), as seen in Fig. 1 (denoted as W3 and W4, respectively).

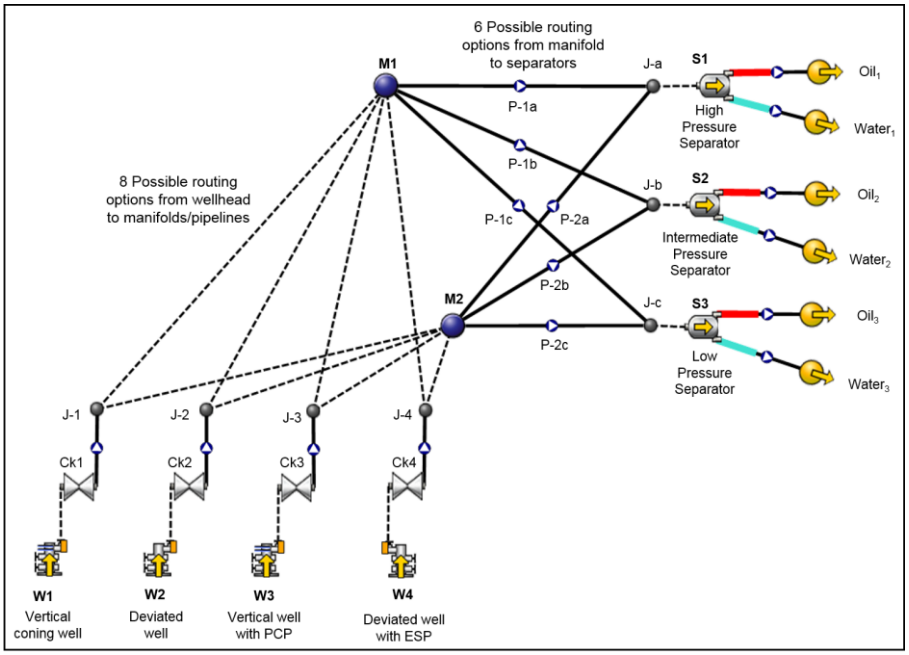

Figure 1: Surface production network and routing superstructure for optimisation.

Although water coning (a change in well inflow that occurs when the water-oil interface changes to a bell shape in the reservoir) is a transient process, the steady state simulator is capable of modelling this process using data tables (implemented herein) that describe oil production rate as a function of the water cut. Several design considerations are also made during the selection of the PCP and ESP for optimal oil delivery from the wells. The surface network design procedure was followed by the generation of large data tables. This involved performing several simulations at different well and pipeline conditions, which correspond to different wellhead pressures (300 – 380 psia) and liquid production rates. Using these data, algebraic (polynomial) proxy models are developed for each network component. These proxy models are then utilised together with an objective function (Eq. 1) to optimise the oil production rate. This methodology takes advantage of the decomposable nature of the production network, in that separate equations can be written for each component, which constitute the optimisation constraints. The complexity of the optimisation problem herein also stems from the presence of discrete

routing variables at different levels: the well to manifold level and the pipeline to separator level. The nonlinear pressure-rate responses of the wells and pipelines coupled with these routing decisions inevitably result in an MINLP model, described in Table 1.

Table 1: Mathematical formulations (MINLP and MILP) for oil production optimisation.

Objective function

$$\text{Max } (NPV) = ROP - CWP \quad (1)$$

$$ROP = r_o \times \sum_{w=1}^{Nprod} q_o \quad (2)$$

$$CWP = r_{wt} \times \sum_{w=1}^{Nprod} q_w \quad (3)$$

Constraints of the MINLP formulation

$$P_{w,min}^{wh} \le P_w^{wh} \le P_{w,max}^{wh} \quad \forall\, w \quad (4)$$

$$q_{i,w,NF} = f(P_w^{wh}) \;\; \forall\, i, \forall\, w \quad (5)$$

$$q_{i,w,ESP} = f\left(P_w^{wh}, f_{i,w,ESP}\right) \;\; \forall\, i, \forall\, w \quad (6)$$

$$q_{i,w,PCP} = f\left(P_w^{wh}, \Omega_{i,w,PCP}\right) \;\; \forall\, i, \forall\, w \quad (7)$$

$$\Delta P_p = f\left(q_{p,o}, q_{p,wt}\right) \;\; \forall\, p \quad (8)$$

$$x_{w,p} P^m \le P_w^{wh} \quad \forall\, w, \forall\, p \quad (9)$$

$$z_{p,s} P^s \le P^m \quad \forall\, p, \forall\, s \quad (10)$$

$$Q_{i,p} = \sum_w (x_{w,p} \times q_{i,w}) \;\; \forall\, i, \forall\, p \quad (11)$$

$$LC^s = \sum_p (z_{p,s} \times Q_{i,p}) \;\; \forall\, i, \forall\, s \quad (12)$$

$$\sum_p x_{w,p} = 1 \quad (13)$$

$$\sum_s z_{p,s} = 1 \quad (14)$$

$$P^s = P^m - \Delta P \quad (15)$$

$$\sum_p q_p \le LC^s \quad (16)$$

Piecewise linearization in 2 dimensions

$$P_w^{wh} = \sum_{j\in J} \sum_{k\in K} \lambda_{j,k} P_{(w)j}^{wh} \quad (17)$$

$$f_{w,ESP} = \sum_{j\in J} \sum_{k\in K} \lambda_{j,k} f_{(w,ESP)k} \quad (18)$$

$$q_{w,ESP} = \sum_{j\in J} \sum_{k\in K} \lambda_{j,k} q_{(w,ESP)j,k} \quad (19)$$

$$\sum_{j\in J} \sum_{k\in K} \lambda_{j,k} = 1 \quad (20)$$

$$\delta_j = \sum_{k\in K} \lambda_{j,k} \quad \forall\, j \quad (21)$$

$$\delta_k = \sum_{j\in J} \lambda_{j,k} \quad \forall\, k \quad (22)$$

$$\lambda_{j,k}, \delta_j, \delta_k \ge 0 \quad (23)$$

$$\delta_j \text{ and } \delta_k \text{ are } SOS2 \quad (24)$$

Piecewise linearization in 1 dimension

$$P_w^{wh} = \sum_{j\in J} \lambda_j P_{(w)j}^{wh} \quad (25)$$

$$q_w = \sum_{j\in J} \lambda_j q_{(w)j} \quad (26)$$

$$\sum_{j\in J} \lambda_j = 1 \quad (27)$$

$$\lambda_j \text{ is } SOS2 \quad (28)$$

Linearizing bilinear terms of type ($C_1 \cdot C_2$ and $B \cdot C$)

$$C_1 \cdot C_2 = \xi_1^2 - \xi_2^2 \quad (29)$$

$$L_1 \le C_1 \le U_1; \quad L_2 \le C_2 \le U_2 \quad (30)$$

$$\xi_1 = 0.5(C_1 + C_2); \quad 0.5(L_1 + L_2) \le \xi_1 \le 0.5(U_1 + U_2) \quad (31)$$

$$\xi_1 = 0.5(C_1 - C_2); \quad 0.5(L_1 - U_2) \le \xi_2 \le 0.5(U_1 - L_2) \quad (32)$$

$$\tau = B \cdot C; \;\; 0 \le C \le U \quad (33)$$

$$\tau \le U \cdot B \quad (34)$$

$$\tau \ge \mathrm{C} - U(1 - B) \quad (35)$$

$$\tau \ge 0; \quad \tau \le \mathrm{C} \quad (36)$$

Proxy model structure

$$q_{o,ESP} = \alpha_0 + \alpha_1 P_{wh} + \alpha_2 f_{ESP} + \alpha_3 P_{wh}^2 + \alpha_4 f_{ESP}^2 + \alpha_5 P_{wh} f_{ESP} \quad (37)$$

This MINLP formulation is linearised in 3 ways to generate MILPs; the computational performance of these 4 formulations (including the MINLP) are compared. The first MILP formulation (MILP-3) applies standard algebraic transformation and Special Ordered Sets of type 2 (SOS2) to linearise nonlinear terms (quadratic and bilinear terms – products of 2 continuous variables and products of a continuous and binary variable) in the MINLP formulation using 3 breakpoints. The second MILP formulation (MILP-5) uses 5 breakpoints instead; the third (MILP-LKT) directly utilises the look-up data tables for linear interpolation in 1 and 2 dimensions. Table 1 presents the detailed formulations for the MINLP and MILP, respectively. The aim is to maximise the objection function

(in terms of the Net Present Value – *NPV*, Eq. 1); where the Revenue from Oil Production (ROP) and Cost of Water Production (CWP) are given by Eqs. 2 and 3 respectively; r_o is the oil price (USD/STB), r_{wt} denotes the water production unit cost (USD/STB) and N_{prod} is the number of wells. Eq. 4 ensures that the wellhead pressure (P^{wh}) is tightly bounded. The proxy models for Naturally Flowing (NF) well, ESP well, PCP well and pipelines are given by Eqs. 4–7 respectively; q represents the flowrate, f_{ESP} the ESP frequency, Ω, the PCP impeller rotation speed and ΔP_p, the pipeline pressure drop. Indices o, wt, i, w, p, wh, m, s denote oil phase, water phase, all phases, wells, pipelines, wellheads, manifolds, and separators, respectively. P_m and P_s are manifold and separator pressure, respectively.

Binary variables $x_{w,p}$ assigned to each well, ensure that the produced fluids from a well are routed by the choke (Eq. 9) to one of the pipelines. Similarly, $z_{p,s}$ in Eq. 10 ensures that the pipelines are routed to the separator. The mass balance constraint between wells and pipelines is represented by Eq. 11; Eq. 12 ensures material balance between the pipelines and the separators (which operate at a fixed pressure). The selection of only 1 binary variable is enforced using Eqs. 13–14. The constraint defined by Eq. 15 ensures the target separator pressure is met, while the liquid capacity constraints of the separators are represented by Eqs. 16. The procedure for linearising functions in 2D and 1D are shown in Eqs. 17–28 respectively; where j and k represent the breakpoints associated with the different variables. Bilinear terms which occur in the MINLP formulation as shown in the typical proxy model structure (Eq. 37) are linearised using Eqs. 29–36. In these equations, C represents, a continuous variable, and B a binary variable; L and U denote the lower and upper bounds of a continuous variable. ξ and τ are additional variables introduced in the linearisation procedure. BONMIN (v.1.8.6) and CPLEX (v.12.8.0.0) have been employed in order to solve the MINLP and MILP formulations, respectively.

3. Optimisation results

The proposed formulations were programmed in MATLAB® R2016a (using OptiToolbox v2.28) and solved with BONMIN and CPLEX on an Intel Core i7-6700 processor at 3.40 GHz running on a 64 bit Windows workstation with 16GB of RAM. The MILP-LKT formulation consists of 25 polytopes (squares) for the well performance function (5 breakpoints for the ESP frequency/rotational speed and 5 breakpoints for the wellhead pressure). For the pipelines, 144 polytopes (squares) were adopted (12 breakpoints for the oil and water phases respectively). This resulted in a total of 8,740 variables; this is significantly larger than the number of variables required in the other formulations (as shown in Table 2). Despite this considerably large number of variables, the MILP model is solved in a shorter time, compared to the MINLP formulation which has 36 variables. This increase in problem size (number of constraints and variables) that ensues with an increasing number of data points is a major drawback of the SOS formulation; hence, it is only suitable for low-dimensional problems. With the MINLP, the increase in number of data points would hardly affect the approximations of the simulator output. In this regard, the MINLP formulation can be regarded as more robust and scalable compared to the MILP reformulation. The convergence of proposed formulations to different optimal solutions (Table 1) is an indication of the non-convexity of the optimisation problem. Nevertheless, high-quality, reliable solutions have been obtained from all formulations as demonstrated in the relative gap obtained (Table 2). The MINLP formulation has provided the best solution in terms of the NPV. Our computational analysis has also shown that the improvement in resolution quality affects the solution quality of both formulations. With 5 breakpoints (MILP-5), the NPV obtained is closer to that of MINLP compared to the lower resolution formulation, consisting of 3 breakpoints (MILP-3).

Table 2: Computational performance of optimisation formulations

Optimisation formulation	MINLP	MILP-3 (SOS2)	MILP-5 (SOS2)	MILP-LKT (SOS2)
Solver used	BONMIN	CPLEX	CPLEX	CPLEX
Number of constraints	34	184	184	340
Number of variables	36	134	170	8702
Relative gap (%)	0.00	0.00	0.00	0.00
Solution time (s)	0.536	0.111	0.152	0.287
Number of nodes	0	229	253	292
NPV (USD)	989,228	979,934	986,832	979,261
Total oil production rate (STB/day)	15,219	15,076	15,182	15,066
Total water production rate (STB/day)	3,803	3,767	3,794	3,766

The MILP-LKT formulation has provided the lowest NPV (1% lower than the MINLP). This may be attributed to the fact the solutions are always approximated by linear segments (in the SOS formulation – with inherently limited extrapolation capabilities when flowing conditions change), which are generated between nonlinear data points. Water coning behaviour is a broadly known source of nonlinearity in the wellbore model. Another important observation from results is that the high-pressure separator with lower capacity (S1) is the least preferred option for routing fluids from manifolds (Fig. 2).

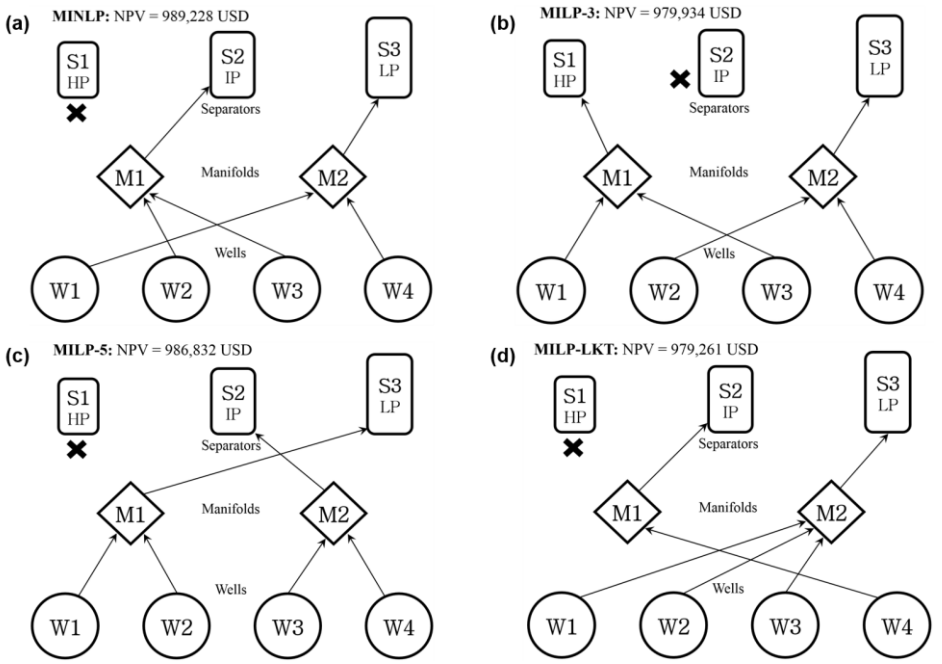

Figure 2: Optimal discrete routing structure for all optimisation formulations considered.

The pipeline diameter and length, and the high pressure drop that ensues, makes it difficult for fluids to be delivered to S1 which operates at 45 psia, compared to S2 and S3 at 35 psia and 25 psia respectively. The algorithm has shown good utilisation of separator

capacities for routing the fluids. As shown in Table 2, the MILP formulations converge faster than the MINLP. Furthermore, the time required for proxy model development if incorporated will further make the MINLP slower compared to the MILP (which directly uses the table data points). It can also be observed that the differences between the oil and water production rates of the respective formulations are minimal. Despite this, very different optimal routing structures are obtained. This indicates that the algorithmic treatment of discrete variables is complicated, especially when they exist at different levels. However, the low number of nodes utilised for finding the optimal solution in all formulations reflects the efficiency of the CPLEX solver (which uses the Branch and Bound algorithm). On applying the CBC solver (based on the Branch and Cut algorithm) to our problem, the number of nodes reduces by an order of magnitude, although with a higher relative gap and a longer computational time. While a detailed comparison of solver performances is beyond the scope of this study, such analysis may be conducted to further evaluate the performances of these formulations especially for bigger-sized problems. Although the computational time requirement is expected to increase with larger production networks, the fast solution times obtained herein should be attributed to the nature of our optimisation formulation, rather than just problem size. On performing a network optimisation task (on Fig. 1) using PIPESIM's v2019.3® optimisation module, we observed the required runtime is over 30 s, resulting in a 10% lower NPV obtained: this attests to the superior performance of our proposed and implemented formulation.

4. Conclusion

This study proposes MINLP and MILP formulations for optimising production from a synthetic oil field consisting of 3 separators, 2 manifolds and 4 wells with complex downhole/multiphase flow physics. The nonlinear models were developed using regression analysis that resulted in algebraic polynomial models; whereas piecewise linear models were developed from production points sampled from a look-up table. A computational analysis performed on the formulations showed superior performance of the MILP formulation in terms of the runtime despite the significantly increased number of variables involved in comparison to the MINLP. Improved resolution of the MILP formulation from 3 to 5 breakpoints resulted in a better NPV. However, compared to other formulations, the MINLP yielded the highest NPV. Despite the similarity in the production rates, different optimal routing strategies are obtained for each formulation.

References

A. Codas, S. Campos, E. Camponogara, V. Gunnerud and S. Sunjerga, 2012. Integrated production optimization of oil fields with pressure and routing constraints: The Urucu field. *Comput. Chem. Eng.,* 46, 178–189.

E.I. Epelle and D.I. Gerogiorgis, 2019a. Optimal Rate Allocation for Production and Injection Wells in an Oil and Gas Field for Enhanced Profitability. *AIChE J.,* 65, 1, (DOI: 10.1002/aic.16592).

E.I. Epelle and D.I. Gerogiorgis, 2019b. Mixed-Integer Nonlinear Programming (MINLP) for production optimisation of naturally flowing and artificial lift wells with routing constraints. *Chem. Res Des.*, 152, 134–148.

V. Gunnerud and B. Foss, 2010. Oil production optimization—A piecewise linear model, solved with two decomposition strategies. *Comput. Chem. Eng.,* 34, 11, 1803–1812.

J. Kronqvist, D.E. Bernal, A. Lundell, and I.E. Grossmann, 2018. A review and comparison of solvers for convex MINLP. *Optimization Eng.*, 1–59.

T.L. Silva, and E. Camponogara, 2014. A computational analysis of multidimensional piecewise-linear models with applications to oil production optimization. *Eur. J. Op. Res.*, 232, 3, 630–642.

Sauro Pierucci, Flavio Manenti, Giulia Bozzano, Davide Manca (Eds.)
Proceedings of the 30th European Symposium on Computer Aided Process Engineering (ESCAPE30), May 24-27, 2020, Milano, Italy.
http://dx.doi.org/10.1016/B978-0-12-823377-1.50210-X

A Fuzzy Control Approach for an Industrial Refrigeration System

Robert Menzhausen[a], Manuel Merino[b], Bogdan Dorneanu[a,c], José José Manrique Silupú[b], William Ipanaqué Alama[b], Harvey Arellano-Garcia[a,c,*]

[a]*LS Prozess- und Anlagentechnik, Brandenburgische Tecnische Universität Cottbus-Senftenberg, Cottbus, D-03046, Germany*
[b]*Departamento de Ingeneria Mecánico Eléctrica, Universidad de Piura, Piura, Peru*
[c]*Department of Chemical Process Engineering, University of Surrey, Guildford, GU2 7XH, United Kingdom*
arellano@b-tu.de

Abstract

This contribution presents the development of a model for the refrigeration plant used for mangos, which is able to simulate both the chamber and the fruit temperatures. The model is developed from energy balances for each section of the refrigeration system and the fruits, and is the basis for the setup of a fuzzy controller, capable of regulating continuously the compressor's frequency to achieve the desired temperature. The model is able to accurately predict the chamber temperature profiles, but is more sensitive when simulating the fruit temperature. The fuzzy controller is able to achieve the set-point more accurately and in a shorter time than the on/off control, achieving a decrease in energy consumption as well.

Keywords: modelling, refrigeration system, fuzzy control.

1. Introduction

Tropical fruits are important products on the global market. The change to a healthier nutrition, the development of new products and great availability let to a rise in their consumption during the last decade (Provido, 2016). For example, the worldwide production of mangos rose by about 4.5% between 2007 and 2016 (Provido, 2016).
Piura is a region in the north of Peru, with a very diverse economy. Agriculture is the second biggest sector in the region, with main products such as mangos (8%), bananas (6%) and grapes (12%). Due to their perishable nature, fruits are stored in cooling chambers until they reach the distribution stations. To achieve rapid and efficient decrease in fruit's temperature, refrigeration systems are employed, using vapor compression refrigeration plants. They consist of four main components: the compressor, the condenser, the expansion valve and the evaporator. Within the system a refrigerant is circulating. Though designed to satisfy maximum load, these plants usually work at part-load for much of their life, generally regulated by on/off cycles of the compressor (Aprea, et al., 2004). The fast growth of fruit exports lead to an increase demand of reliable and efficient refrigeration systems.
A big disadvantage of cooling systems is that they count as the biggest consumers of electricity today (IIR, 2015). This implies a high cost in operating cold storage or controlled atmosphere storage systems, which becomes a pressing problem for developing countries (Aprea, et al., 2004).

Research into these challenges enabled development in the area of cooling systems in the past years, especially in the field of energy efficiency (Basediya, et al., 2013). Among these achievements is the use of variable speed compressors, which allow the use of new and more beneficial control approaches, such as fuzzy or PID controllers, where the applied frequency takes values between a minimum and maximum (Saleh & Aly, 2015). The following sections will present the development of a model for a refrigeration plant used for mangos, starting from first principles, as well as of a control system to enable the operation of the plant, to improve the fruit conservation and reduce the energy consumption. The resulting models are tested experimentally on a refrigeration plant located on the campus of the University of Piura (Peru).

2. Mathematical model of the refrigeration system

Starting from energy balances for each section of the refrigeration system and the fruits, a simple model is developed to simulate the temperature in the cooling chamber and for approximating the fruits' temperature.

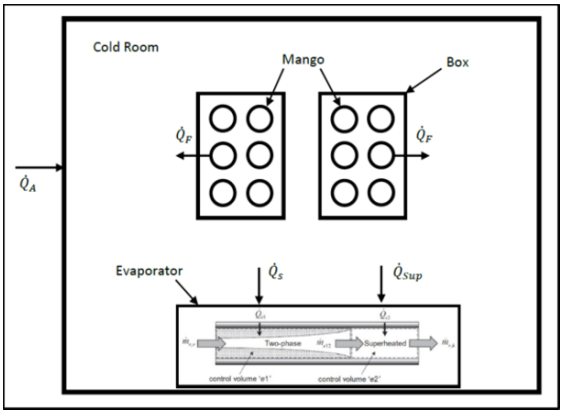

Figure 1. Heat flows inside the cooling chamber

2.1. Refrigeration chamber temperature

The cooling chamber temperature is determined by balancing the heat flows inside the room. Fig.1 shows the individual heat sources and sinks around the cooling chamber.

The energy balance for the refrigeration chamber is expressed as:

$$\frac{dQ_{CR}}{dt} = \dot{Q}_{F,total} + \dot{Q}_A - \dot{Q}_S - \dot{Q}_{Sup} \quad (1)$$

With Q_{CR} the energy stored in the cooling chamber [J]; $\dot{Q}_{F,total}$ the total heat flow of the fruits [J/s]; $\dot{Q}_A$ the heat flow equivalent from the ambient [J/s]; $\dot{Q}_S$ the heat flow of the saturation section [J/s]; $\dot{Q}_{Sup}$ the heat flow of the superheated section [J/s].

Writing the terms in Eq.1 in terms of the temperatures, the following equations are obtained:

$$\frac{dQ_{CR}}{dT_{CR}} = V_{CR} \cdot \rho_{A,CR} \cdot c_{p,A,CR} \quad (2)$$

$$\dot{Q}_{F,total} = \alpha_F \cdot A_{F,total} \cdot (T_F - T_{CR}) \quad (3)$$

$$\dot{Q}_A = \dot{V}_A \cdot \rho_A \cdot c_{p,A} \cdot (T_A - T_{CR}) \quad (4)$$

$$\dot{Q}_S = U_S \cdot A_S \cdot (T_S - T_{CR}) \quad (5)$$

$$\dot{Q}_{Sup} = U_{Sup} \cdot A_{Sup} \cdot \left(T_{Sup} - T_{CR}\right) \quad (6)$$

Where V_{CR} is the volume of the cooling chamber [m^3]; $\rho_{A,CR}$ the air density in the cooling chamber [kg/ m^3]; $c_{p,A,CR}$ the air specific heat capacity in the chamber [J/(kgK)]; T_{CR} the cooling chamber temperature [K]; α_F the overall fruit heat transfer coefficient [J/(m^{2}K]; $A_{F,total}$ the total heat transfer area of the fruits [m^2]; T_F the fruit temperature [K]; $\dot{V}_A$ the ambient air volume flow [m^3/s]; ρ_A the ambient air density [kg/ m^3]; $c_{p,A}$ the ambient air

specific heat capacity [J/(kgK)]; T_A the ambient air temperature [K]; U_S the overall heat transfer coefficient of the saturation section [W/(kgK]; A_S the heat transfer area of the saturation section [m^2]; T_S the saturation section temperature [K]; U_{Sup} the overall heat transfer coefficient of the superheated section [W/(kgK)]; A_{Sup} the heat transfer area in the superheated section [m^2]; T_{Sup} the superheated section temperature [K].

Replacing the heat flows in Eq.1 results in the following equation for the cooling chamber temperature:

$$\frac{dT_{CR}}{dt} = \alpha_F \cdot \frac{A_{F,total}\cdot(T_F - T_{CR}) + U_S\cdot A_S\cdot(T_S - T_{CR}) + U_{Sup}\cdot A_{Sup}\cdot(T_{Sup} - T_{CR}) + \dot{V}_A\cdot\rho_A\cdot c_{p,A}\cdot(T_A - T_{CR})}{V_{CR}\cdot\rho_{A,CR}\cdot c_{p,A,CR}} \quad (7)$$

As fruits are heterogeneous, with different shapes, sizes and weight, their heat transfer area was determined using an averaged fruit diameter, and assuming spherical shape.

2.2. Fruit temperature

The energy balance for the fruits stored inside the cooling chamber follows:

$$\frac{dQ_F}{dt} = \dot{Q}_{F,total} \quad (8)$$

With Q_F the energy stored inside the fruits [J].

Eq.8 can be rewritten in terms of the fruit temperature as:

$$\frac{dT_F}{dt} = \frac{\alpha_F\cdot A_F\cdot(T_F - T_{CR})}{m_F\cdot c_{p,F}} \quad (9)$$

Where m_F is the fruit mass [kg]; $c_{p,F}$ the fruit specific heat capacity [J/(kgK)].

2.3. Model parameters

The values of the refrigeration chamber and heat transfer areas of the saturation and the superheated sections were measured. For the average values of the mango diameter and weight, 20 mangos were measures and the average was calculated. Other values such as the mango heat transfer coefficient, or the saturated and superheated section heat transfer coefficients were assumed. The values used are presented in Table 1.

Table 1. Model parameters

Parameter	**Value**	**Parameter**	**Value**
Chamber volume, V_{CR}	34.24	*Heat transfer area superheated section, A_{Sup}*	0.27
Chamber air density, $\rho_{A,CR}$	1.2	*Ambient air density, ρ_A*	1.2
Chamber air heat capacity, $c_{p,A,CR}$	1.4	*Ambient air heat capacity, $c_{p,A}$*	1.4
Overall heat transfer coefficient saturation section, U_S	0.1	*Fruit heat transfer coefficient, α_F*	0.0005
Heat transfer area saturation section, A_S	0.27	*Fruit average mass (one mango), m_F*	0.3
Overall heat transfer coefficient superheated section, U_{Sup}	0.1	*Fruit average diameter (one mango), D_F*	0.1

3. Control of the refrigeration cycle

The aim of the refrigeration cycle is to ensure a pre-set temperature in the cooling chamber. The most common and simple method to control refrigeration system is the on/off controller (Saleh & Aly, 2015), which works with a fixed speed compressor.

The controller transmits a fixed frequency to the compressor if the temperature is higher than the set-point, or the compressor is turned off if the temperature is lower than the pre-set temperature. An on/off controller is easy to design and use, and it is not expensive to implement (Mosayebi, 2011). The disadvantages of these controllers are that they consume a lot of energy, they have low accuracy due to oscillating overshooting and undershooting temperature and they reduce the compressor life by attrition of the continuous on/off mode operation. Variable speed compressors are becoming more popular, as they have the ability to improve the energy efficiency and allow the use of more complex control systems that provide more accuracy.

3.1. Fuzzy control

The main idea of fuzzy control is to use human knowledge for creating the controller by describing the state of system with fuzzy variables, using words and gradings such as very hot, hot, warm, medium, cold, very cold, freezing to describe the temperature. These variables are connected by IF-clauses defining actions. For example, if the room temperature is cold, the heater will be running a little bit. Fuzzy controllers are structured in four blocks: the fuzzification, which receives the input variables and transforms the information into fuzzy variables the inference mechanism is able to interpret; the rule-base, which contains defined rules as IF-clauses; the inference mechanism, which checks which rules are complied and passes the output variable to the defuzzification; the defuzzification, which transforms the output to process values.

The fuzzy controller for the refrigeration plant (Fig.2) has the frequency applied to the compressor as its output variable, $u(t)$. As its inputs it takes the error, $e(t)$, defined as the difference between the desired temperature and the actual cooling chamber temperature, and the derivative of the error with the time, $\partial e/\partial t$. This is done to improve the control accuracy.

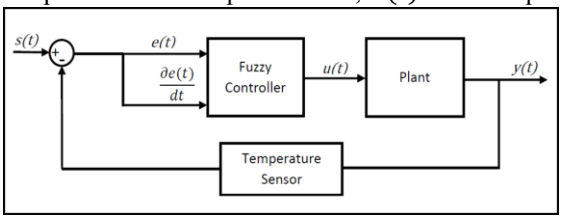

Figure 2. Block diagram of the control system

The rule-base connecting the membership functions are shown in Table 2, with values between the available functions of 25 and 70 Hz. Experimental investigations showed that the separation into small sections improve the control accuracy.

Table 2. Rule base for the fuzzy controller

Frequency $u(t)$		$\frac{\partial e(t)}{\partial t}$		
		positive	zero	Negative
$e(t)$	big	70	70	70
	small	55	60	65
	tiny	45	50	55
	zero	35	40	45
	minus	25	25	25

The next step in developing the control system is to establish membership functions for the input variables. Triangular membership functions are considered, shown in Fig.3a, with values developed by experimental investigation. Trapezoidal functions are considered for the beginning and the end of the intervals, as in these cases

a fast approach is desired. In case of the output variable (the compressor frequency), ten membership functions (Fig.3b) are defined over small sections, to improve the control accuracy. The range of the membership functions was chosen to be high, leading to a crossing with each other. This overlap results in a smooth gradient from the highest to the lowest frequency, and benefits the control.

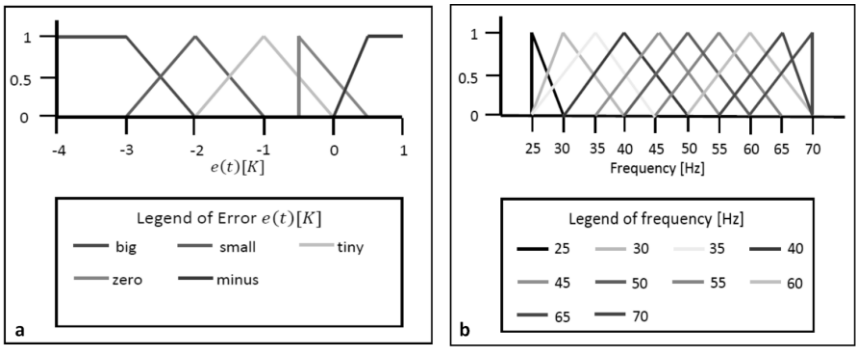

Figure 3. Membership functions of the a) input variable (error); b) output variable (frequency)

4. Results

The models developed in the previous sections have been tested experimentally in a refrigeration plant located on the campus of the University of Piura (Peru). It is divided into two rooms covered with a simple corrugated sheet roof, for protection against environmental impact. The walls and the top of the refrigeration room are insulated to reduce the heat flow from the ambient. The control room is located next to the refrigeration chamber. And contains a computer used to run and control the refrigeration system. The fruits are stored in boxes and stacked on palettes, located right under the evaporator. The arrangement of the temperature sensors is fixed during the experiments, in the top and the bottom boxes of a stack.

4.1. Control of the refrigeration system

The model developed in the previous sections is used to validated a set of experiments performed in the refrigeration plant. The first experiments are done implementing an on-off controller and using 230 kg mangos, assuming a set-point of 9 ^{0}C. The results for the cooling chamber temperature (Fig.4) show that the model is able to predict very well the experimental data, and the set-point is reached after 2,700 seconds. An energy consumption of 18.97 kWh is recorded in this case.

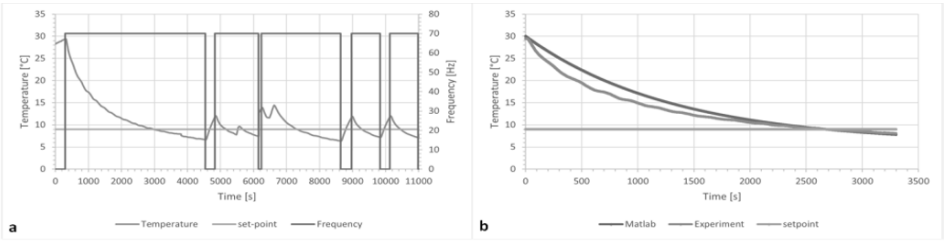

Figure 4. a) Experimental results for on/off control with 230 kg mango; b) Model vs. experimental results for on/off control and 230 kg mango

Furthermore, further experiments were performed to investigate the performance of the fuzzy control on the refrigeration plant. The initial temperature was set to 25 ^{0}C and the refrigeration process was started to achieve a set-point of 9 ^{0}C. When the equilibrium for the chamber temperature is achieved for about 10 minutes, a disturbance is introduced by opening the door for 4 minutes. Then the door is closed again, and the procedure repeated once equilibrium is reached. At this point, the set-point was changed to 8 ^{0}C. For the fuzzy control experiments, a total mass of 200 kg of mangos is considered.

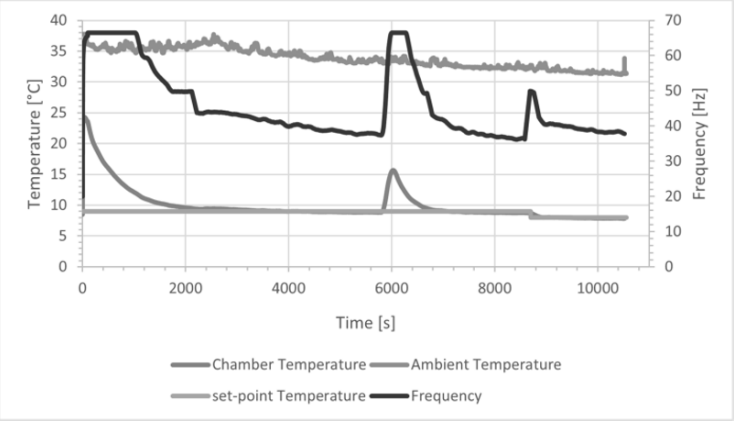

Figure 5. Results for fuzzy control of the refrigeration plant with 200 kg mango

The experiment (Fig.5) was run between 3:41 and 6:38 PM. The results show that the controller is able to achieve both set-point temperatures quite well even after the disturbance was introduced. The experiment consumed 10.92 kWh.

5. Conclusions

A simplified model to determine the temperature of the cooling chamber and the fruit in a refrigeration plant is presented. The model starts from energy balances for the different components of the plant, and is able to predict the temperatures with a good accuracy. Furthermore, the model is used in the development of a fuzzy controller of the refrigeration system. This controller is then implemented in the plant, being able to achieve a good performance and a reduced energy consumption compared to PID controllers. Future work will consider more accurate representation of the heat transfer coefficients to improve the temperature predictions, as well as other types of control approaches, such as model predictive control.

References

Aprea, et al., 2004, International Journal of Refrigeration 27, pp. 639-648
Basediya, et al., 2013, J Food Sci Technol 50 (3), pp. 429-442
IIR, 2015, The role of refrigeration in the global economy, pp. 1-16
Mosayebi, 2011, On/off control, Australia: AQUARIUS Technologies PTY Ltd.
Provido, 2016, Business Mirror, https://businessmirror.com.ph/2016/09/06/global-demand-for-tropical-fruits-increasing-international-network-says
Saleh & Aly, 2015, International Journal of Control, Automation and Systems 4 (1), pp. 14-25

Sauro Pierucci, Flavio Manenti, Giulia Bozzano, Davide Manca (Eds.)
Proceedings of the 30th European Symposium on Computer Aided Process Engineering (ESCAPE30), May 24-27, 2020, Milano, Italy.
http://dx.doi.org/10.1016/B978-0-12-823377-1.50211-1

Online Process Monitoring in SMB Processes

Stefanie Gerlich,* Yannik-Noel Misz, Sebastian Engell
Process Dynamics and Operations Group, Department of Biochemical and Chemical Engineering, TU Dormund University, Emil-Figge-Str. 70, 44227 Dortmud, Germany
stefanie.gerlich@tu-dortmund.de

Abstract

Conventionally, preparative chromatographic separation processes are operated in batch mode. For more efficient separation, the simulated moving bed (SMB) process has been introduced. Due to its hybrid dynamics, optimal operation of the SMB process is challenging. For increased process efficiency, model-based optimizing control schemes can be applied. These schemes require online information about the states and the parameters of the plant. The online process monitoring strategy presented here is based on the transport dispersive model of the SMB process and simultaneously estimates the states and the parameters of the individual columns by exploiting the switching nature of the SMB process. The scheme can be activated before the process reaches its cyclic steady state (CSS). The strategy is demonstrated for the separation of two amino acids.

Keywords: state estimation, parameter estimation, SMB process, chromatography

1. Introduction

In the production of fine chemicals, pharmaceuticals and biotechnological products chromatography is an important separation technique due to its high selectivity, low operating temperatures and ability to handle of aqueous solutions (Schmidt-Traub et al., 2012). Preparative chromatographic processes are usually operated in batch mode. In order to use the stationary phase more efficiently, the continuously operated simulated moving bed (SMB) process can be used (Rajendran et al., 2009). This multi-column chromatographic process simulates a counter-current flow of the stationary and mobile phase by periodically switching the inlet and outlet ports between the individual columns (Schmidt-Traub et al., 2012). It is schematically depicted in Figure 1.

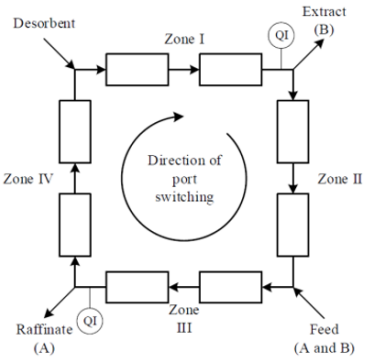

Figure 1: Schematic representation of a 4-zone SMB process with 2 columns per zone.

Due to the hybrid dynamics of the SMB process that lead to discontinuities and sharp fronts in the state trajectories, the optimal operation of the SMB process is challenging.

To improve performance, model-based optimizing control schemes can be used, which adjust the manipulated variables of the process such that the operating point moves towards an optimal operation. Such schemes have been demonstrated successfully at real SMB plants (Toumi and Engell, 2004, Küpper and Engell, 2007). These schemes require online information about the states and the parameters of the plant. In Toumi and Engell (2004) the states were computed by forward simulation of a plant model with identical columns. Küpper and Engell (2009) employed a moving horizon estimator for state and parameter estimation assuming identical columns. The estimation of individual column parameters can help to optimize the operation and online monitoring of individual column parameters is important to detect degrading columns.

The main problem in the estimation of individual column parameters is that only scarce measurement information is available in SMB processes. Küpper and Engell (2006) developed an Extended Kalman Filter-based scheme for estimating parameters of each column individually using concentrations measurements at the two outlet ports and at one fixed location between the columns. An optimization-based scheme for estimating individual column parameters one by one was presented in Lemoine-Nava and Engell (2014). This scheme only relies on concentration measurements in the extract and raffinate streams.

In this contribution, we apply the latter scheme to the online estimation of states and parameters of each individual column for a separation of amino acids. Compared to previous work which was based on the general rate model (GRM) for describing the dynamic behavior of each individual column, the transport dispersive model (TDM) and the weighted essentially non-oscillatory (WENO) scheme for its numerical solution are employed. The TDM contains less parameters compared to the GRM resulting in a decreased experimental effort for determining them. The GRM contains the particle diffusion as a parameter which cannot be identified accurately from experiments indicating that the GRM is over-parameterized (Toumi and Engell, 2004). The TDM is applicable for low molecular weights of the solutes(Schmidt-Traub et al., 2012) which applies here. The two amino acids are tryptophan and phenylalanine. Concentration measurements are only available at the extract port and at the raffinate port (see Figure 1). We demonstrate that the state and parameter estimation can already be activated during the start-up phase of the process before a cyclic steady state (CSS) is reached.

The remainder of the paper is structured as follows: First, the employed first principle model, the TDM, is briefly explained. Second, the state and parameter estimation scheme that is considered here is described. Afterwards, the scheme is applied to the continuous separation of two amino acids, phenylalanine and tryptophan. We conclude the paper with a summary, a discussion of outcomes and future research.

2. Modeling of the SMB process

Here the SMB process is modeled by directly considering its switched dynamics. Models describing the dynamics of the individual columns in the system are connected through mass and component balances at the inlet and outlet ports:

$$0 = -Q_I + Q_{IV} + Q_{Des} \tag{1}$$

$$0 = -Q_{II} + Q_I - Q_{Ex} \tag{2}$$

$$0 = -Q_{III} + Q_{II} + Q_{Fe} \tag{3}$$

$$0 = -Q_{IV} + Q_{III} - Q_{Raf} \tag{4}$$

$$0 = -c_{i,in,I}Q_I + c_{i,out,IV}Q_{IV} \tag{5}$$

$$0 = -c_{i,in,III}Q_{III} + c_{i,out,II}Q_{II} + c_{i,Fe}Q_{Fe} \tag{6}$$

Where Q represents the flow rate in the respective zone or at the respective port. c_i refers to the concentration of component i.
For dynamic modeling of the individual chromatography columns, the TDM is chosen and the adsorption behavior is described by a multi-component Langmuir isotherm. The respective model equations can be found in Schmidt-Traub et al. (2012). The model consist of a set of two partial differential equations (PDEs) per component present in the system. The PDEs here are spatially discretized using a finite volume approach combined with the WENO scheme (von Lieres and Andersson, 2010). The method is suitable for handling systems with steep concentration gradients as they appear in chromatography columns.

3. State and Parameter Estimation Scheme for the SMB process

A scheme for estimating the states and the parameters of each column individually was proposed by (Lemoine-Nava and Engell, 2014) and is illustrated in Figure 2. The scheme consists of two main parts, a state estimation and a parameter estimation routine.

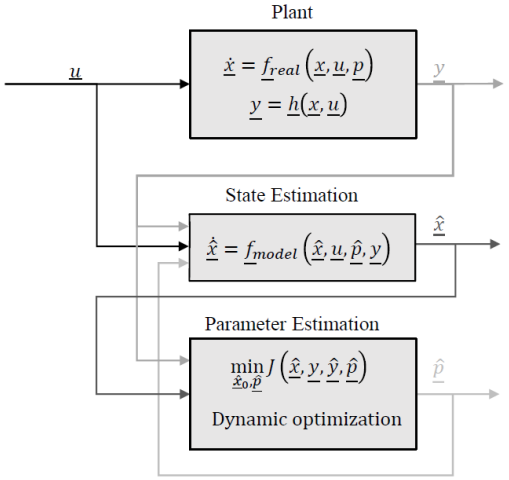

Figure 2: Structural overview of the state and parameter estimation scheme

In the state estimation routine, the process is simulated based on the current process inputs and the parameters from the parameter estimation routine. Additionally, measured concentrations at the extract and raffinate port are fed to the process model as inlet concentrations for the column behind the measurement location.
For the parameter estimation routine, a least-squares optimization problem is solved periodically that aims at minimizing the deviations between measured and simulated concentrations. It estimates the model parameters separately for each column. During one full cycle of the SMB process, two virtual batch experiments can be identified for each individual column of which each has a length of two periods. For the first experiment, the respective column is located next to the extract port and measurements are collected at the column inlet during period k. For the next period k+1, measurements are then collected at the column outlet. This procedure is repeated for the periods when the respective column is connected to the raffinate node, generating the second experiment.
Thus, individual optimization problems for parameter estimation are set up for each column exploiting the switching nature of the SMB process. The formulation of the optimization problem is given in Lemoine-Nava and Engell (2014). Each period, the parameter estimation is started for one column leading to updating the parameters once

per cycle. The first parameter estimation is activated after six periods of operation as this marks the time when enough measurement information is available for the first column.
Regarding the implementation, the symbolic math framework CasADi is employed that provides derivatives using automatic differentiation (Andersson et al., 2019). For the process simulation in the state estimation routine, the integrator CVODES from the Sundials suite is used.
The underlying dynamic optimization problem is solved using direct collocation, in which both, inputs and states are fully discretized in the time domain. The time domain is discretized using orthogonal collocation on finite elements (OCFE). The resulting non-linear program (NLP) is solved with the interior point solver IPOPT.
The parallel execution of state and parameter estimation is realized using Matlab's Parallel Computing toolbox. After each complete period, the parameter estimation for the column with the extract port at its outlet is started on a parallel worker as a background Matlab process without a user interface. In total four parallel workers are available. To prevent jobs from forming long queues on the workers, a parameter estimation is only started, if the result of the previous estimation step for the same column is available. The results from all finished optimizations are transferred to the state estimation model after each period.

4. Case Study: Continuous Amino Acid Separation using the SMB process

The continuous separation of two amino acids, phenyalanine and tryptophane, on an eight column SMB pilot plant with 2 columns per zone is studied in this contribution. For this case study, the estimated parameters are the parameters H_{Phe} and H_{Trp} in the multicomponent Langmuir isotherm as these have sensitivity strong influence on the outlet concentration profile of a column. Their initial estimates as well as all other model parameters that are needed for modeling are presented in Table 1. Unless otherwise indicated, it is assumed that all 8 columns in the system are described by the same set of parameters although slight deviations occur from column to column in real plants.

Table 1: Model parameters (Phe = phenylalanine, Trp = tryptophane)

Parameter	Description	Value
d_c	Column diameter	8 mm
L_c	Column length	125 mm
r_p	Solid phase particel radius	7.5 µm
ε	Void fraction	0.80
ε_p	Solid phase porosity	0.26
ρ	Liquid phase density	1 g/mL
η	Liquid phase viscosity	1 mPa s
$k_{eff,phe}$	Mass transfer coefficient (Phe)	28.38 µm/s
$k_{eff,trp}$	Mass transfer coefficient (Trp)	156.80 µm/s
b_{Phe}	Isotherm parameter (Phe)	0.0682 L/g
b_{Trp}	Isotherm parameter (Trp)	0.2697 L/g
$H_{i0,Phe}$	Initial estimate for the Henry coefficient (Phe)	8.1858
$H_{i0,Trp}$	Initial estimate for the Henry coefficient (Trp)	36.2682

As $H_{Phe} > H_{Trp}$, tryptophan represents the stronger adsorbing component and thus it is retrieved at the extract port, while the less retained component phenylalanine is withdrawn at the raffinate port. The solvent is a methanol/water mixture with 5 vol.-% of methanol and a phosphate buffer. The feed contains 0.2 g/L of phenylalanine and tryptophane each and ports are shifted every three minutes giving a period length of

τ = 3 min. The process is operated with Q_I = 13.32 g/L, Q_{Des} = 9.75 g/L, Q_{Ex} = 6.82 g/L, and Q_{Fe} = 4.72 g/L.

5. Results and discussion

The performance of the state and parameter scheme described in section 3 is tested for two different scenarios that are relevant for applications at real plants. All results shown are simulation results.

5.1. Tracking offsets in all parameters

In a real plant, differences in the parameters of all columns have to be expected. Here, it is assumed that the initial estimates of the parameters H_{Phe} and H_{Trp} for each column deviate up to ±30 % from their true values. The resulting accuracy of the state estimation, measured by the sum of the squared errors between the estimated and the true states, is depicted in Figure 3. Here, the true states of the plant are available as the measurement data is obtained from a process simulation with the true parameter values.

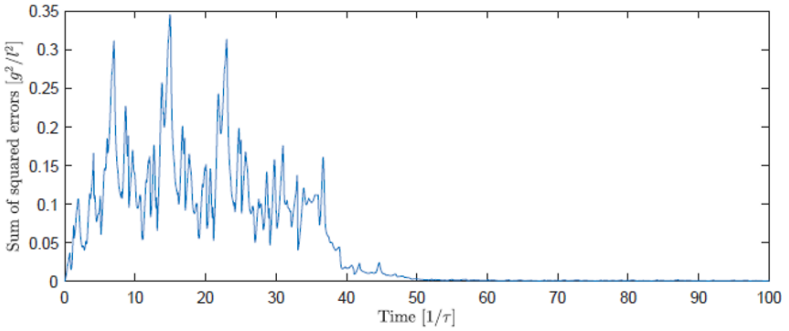

Figure 3: Sum of squared errors in the state estimation over 100 periods of operation with adaptation of the individual Henry parameters of the columns when all initial Henry parameter estimates deviate up to ±30 % from their true values. The initial error of the state estimation is zero as the plant is initially empty, meaning that all concentrations are zero. The peaks in the state estimation error that can be observed over the first 35 periods are caused by the deviations in the initial parameter estimates from column to column leading to larger or smaller deviations in the state trajectories if components are traversing through the respective column. After period 48, the state error is negligible, as the parameter estimates for each individual column have converged to their true values.

5.2. Plant-model mismatch in the void fractions of the columns

Here a mismatch of ±5 % between the true column void fraction and the column void fraction used in the estimation model is assumed, leading to different flow velocities inside the columns. The void fractions are not estimated, only the Henry coefficients as in the simulation in the previous section. The initial estimates for H_{Phe} and H_{Trp} are at their true values. The accuracy of the state estimation is depicted in Figure 4. Again, the initial error is zero as all concentrations in the process are initially zero. During the first 30 periods of operation, the error increases and exhibits many peaks resulting from the deviations in the void fraction from column to column. Around period 30, the state and parameter estimation has converged. In order to compensate for the plant-model mismatch in the column void fraction, the estimated values of H_{Phe} and H_{Trp} converged to values that are different from their true values. Due to the high sensitivity of the outlet concentration profile to H_{Phe} and H_{Trp}, effects from other model parameters can be lumped into H_{Phe} and $H_{Trp,}$ if the deviations are not too large. It is remarkable that the state estimation is almost perfect after convergence of the parameters.

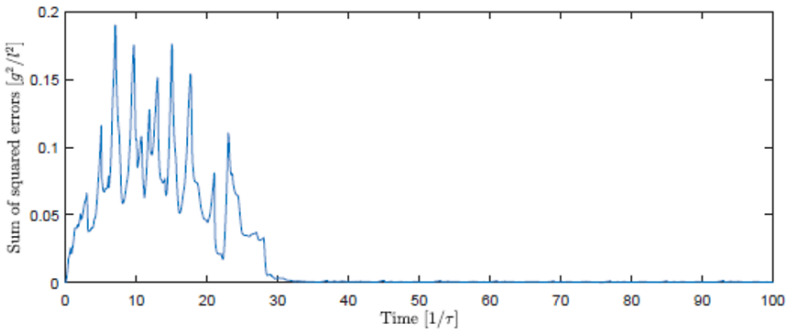

Figure 4: Sum of squared errors in the state estimation over 100 periods of operation in the presence of plant-model mismatch in the column void fractions with adaptation of the Henry coefficients

6. Conclusion and Future Works

In this work, a state and parameter estimation scheme for individual columns has been presented that is based on the work by Lemoine-Nava and Engell (2014). Modifications to original scheme include the use of the simpler TDM model that is sufficient for most practical applications with the WENO scheme for the numerical solution, and the activation of the estimation scheme before the CSS is reached. It is shown that the state and parameter estimation scheme is capable of successfully estimating the process states if all isotherm parameters have different but constant values or if plant-model mismatch in the column porosities is present. This is the basis for combining the estimation scheme with a model-based optimizing control scheme to ensure optimal SMB process operation for not exactly known or slowly varying column parameters.

References

J. Andersson, J. Gillis, G. Horn, J. Rawlings, M. Diehl, 2019, CasADi: a software framework for nonlinear optimization and optimal control, Mathematical Programming Computation, 11, 1, 1-36

A. Küpper, S. Engell, 2006, Parameter and state estimation in chromatographic SMB processes with individual columns and nonlinear adsorption isotherms, IFAC Proceedings Volumes, 39, 2, 611-616

A. Küpper, S. Engell, 2007, Optimizing Control of the Hashimoto SMB Process: Experimental Application, IFAC Proceedings Volumes, 40,5, 149-154

A. Küpper, M. Diehl, J. Schröder, H. Bock, S. Engell, 2009, Efficient moving horizon state and parameter estimation for SMB processes, Journal of Process Control, 19, 5, 785-802

R. Lemoine-Nava, S. Engell, 2014, Individual Column State and Parameter Estimation in the Simulated Moving Bed Process: an Optimization-based Method, IFAC Proceedings Volumes, 47, 3, 9376-9381

E. von Lieres, J. Andersson, 2010, A fast and accurate solver for the general rate model of column liquid chromatography, Computers & Chemical Engineering, 34, 8, 1180-1191

A. Rajendran, G. Paredes, M. Mazzotti, 2009, Simulated moving bed chromatography for the separation of enantiomers, Journal of Chromatography A, 1216, 4, 709-738

H. Schmidt-Traub, M. Schulte, A. Seidel-Morgenstern, 2012, Preparative Chromatography, Wiley-VCH, Weinheim, Germany

A. Toumi, S. Engell, 2004, Optimization-based control of a reactive simulated moving bed process for glucose isomerization, Chemical Engineering Science, 59, 18, 3777-3792

Sauro Pierucci, Flavio Manenti, Giulia Bozzano, Davide Manca (Eds.)
Proceedings of the 30th European Symposium on Computer Aided Process Engineering (ESCAPE30), May 24-27, 2020, Milano, Italy.
http://dx.doi.org/10.1016/B978-0-12-823377-1.50212-3

Conceptual Design of Novel Processes for 4-Hydroxybutyl Acrylate Production

Mihai Daniel Moraru[a,b,*], Elena Zaharia[b], Costin Sorin Bildea[b]

[a]*Department of Technology, Engineering and Projects, Hexion, Seattleweg 17, 3195 ND Pernis, The Netherlands*
[b]*Department of Chemical and Biochemical Engineering, University Politehnica of Bucharest, Str. Gh. Polizu 1-7, 011061 Bucharest, Romania*
mihai.moraru@hexion.com

Abstract

This paper is the first to present novel solid-based catalytic processes for the production of 4-hydroxybutyl acrylate (HBA): three conventional reaction-separation-recycle (RSR) systems, and one reactive distillation-based (RD) process. Each of them tackles the selectivity and difficult separations in various ways, achieving a final HBA product within the required specification. While the RD process is less capital and energy intensive, each process has its trade-offs that are worth further optimization, followed by a rigorous comparison on economic basis.

Keywords: Aspen, esterification, hydrolysis, reactive-distillation, side-reactor

1. Introduction

4-Hydroxybutyl Acrylate (HBA) is used to obtain homopolymers and copolymers with end-use in a variety of products. HBA is also used in chemical syntheses, because it readily undergoes addition reactions with a wide variety of organic and inorganic compounds (BASF, 2016). The patent literature (Tanaka et al., 2017, and the references therein) describes that HBA is produced by esterification of acrylic acid (AA) and 1,4-butanediol (BD), with formation of water as byproduct, using acidic catalysts as sulfonic acid, para-toluene sulfonic acid or dibutyltin oxide.

A relatively recent journal article (Yang et al., 2007a) shows that this esterification reaction can be performed using an ion-exchange resin as solid catalyst, overcoming the well-known issues of the liquid catalysts (e.g. side reactions, difficult product recovery, corrosion, and other environmental problems during the disposal of waste).

This work presents the conceptual design of several process alternatives for HBA production, using solid catalysis. The reaction scheme consists of two consecutive reactions: (1) formation of the desired HBA in the reaction between AA and BD, and (2) formation of the undesired 1,4-butanediol diacrylate (BDA) from HBA and AA; water is formed in both reactions.

$$AA + BD \rightleftarrows HBA + H_2O \quad (1)$$

$$AA + HBA \rightleftarrows BDA + H_2O \quad (2)$$

We develop three reaction–separation–recycle (RSR) and one reactive distillation (RD) processes. Each process has a capacity of roughly 20 kt/y of 99.4 %mass HBA. The

RSR processes use fixed-bed reactors and common distillation equipment for separation of product and recycle of reactants; the very difficult HBA/BD separation is achieved by pressure-swing distillation. The RD process uses a standard column (i.e., the fresh reactants are fed at the top and bottom of a catalytic section located in the middle of the column). The bottom product stream contains both HBA and BDA (the heaviest components). Therefore, an additional column is required to perform the HBA/BDA split. Finally, BDA is hydrolyzed in a side-reactor and recycled to the RD column.

2. Thermodynamics and Reaction Kinetics

The chemical system in this study has 5 components, namely, H_2O, AA, BD, HBA and BDA. The pure component physical properties for H_2O, AA and BD are available in the Aspen databanks. The properties of HBA and BDA are estimated using group contribution methods by the Property Constant Estimation System (PCES) in Aspen. For HBA, the parameters of the Antoine vapor pressure equation are regressed from experimental data (4 data points, BASF brochures). The UNIQUAC model is selected to model the phase equilibria, using one set of binary interaction parameters. The H_2O/AA and H_2O/BD interaction parameters are available in Aspen; for all the remaining binary systems, they are estimated with the UNIFAC method. The vapor pressure of all components and the azeotropes at 0.05 and 0.8 bar are presented in Figure 1, left. In a mixture in which all components are present, H_2O and AA are easily separated due to their low boiling points and not forming azeotropes; H_2O does form a heterogeneous azeotrope with BDA, however it does not play an essential role in the separation processes described here. From the mixture of the remaining components (i.e., BD, HBA and BDA), it may seem that BDA can be easily separated because it has the highest boiling point throughout the whole range of pressure (say, above 0.003 bar). However, the BDA/BD and BD/HBA azeotropes are important for the separation of this mixture. In addition, BD and HBA have close vapour pressure, which makes the BD/HBA split to be very challenging. This difficult separation was observed in the experiments reported by Yang et al. (2007b), where they state that, after the reaction, it is very difficult to obtain a high purity of HBA by general separation techniques such as distillation and extraction. Consider Figure 3, top-left diagram: from a mixture having the composition in region I (point F), BD can be removed by distillation as a bottom product, but neither HBA nor BDA can be separated; if the composition is in region II, HBA and BDA can be separated, in a two-column sequence, but not BD (or one should accept sending back to the reactor a large recycle stream containing large amounts of HBA, using one distillation column less). Independent of the choice, the separation of this mixture remains challenging.

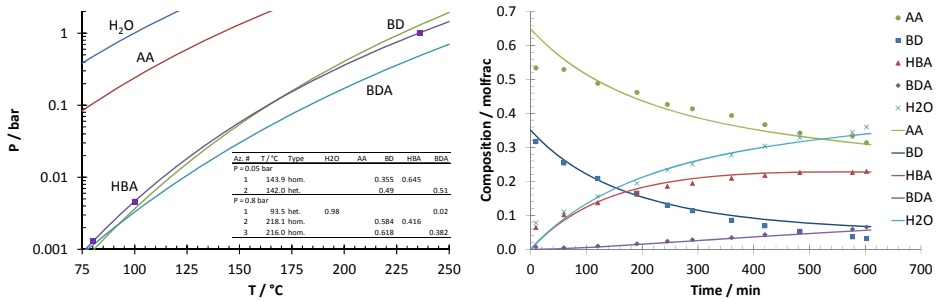

Figure 1. Left: Vapor pressure and azeotropes (by *Distillation Synthesis* tool in Aspen Plus); Right: Comparison between experimental and regressed composition during reaction at 100 °C.

The course of reaction catalyzed by Amberlyst 15 can be described by the kinetic model given by equations (3)-(5) proposed by Yang et al. (2017a); the pre-exponential factors were determined by regression using the data reported in the same reference. The comparison between experimental and regressed data at 100 °C is presented in Figure 1, right; a good agreement is observed.

$$r_1 / \left[kmol/kg_{cat}\cdot s\right] = 91.49 \exp\left(-\frac{58300}{8.314\cdot T}\right)\left(C_{AA}C_{BD}\text{-}(1/K_{eq,1})C_{HBA}C_{H_2O}\right) \quad (3)$$

$$r_2 / \left[kmol/kg_{cat}\cdot s\right] = 181625 \exp\left(-\frac{86700}{8.314\cdot T}\right)\left(C_{AA}C_{HBA}\text{-}(1/K_{eq,2})C_{BDA}C_{H_2O}\right) \quad (4)$$

$$K_{eq,1} = \exp\left(1457.6/T - 2.0212\right);\ K_{eq,2} = \exp\left(810.4/T - 0.4614\right) \quad (5)$$

3. Process Concepts and Design

3.1. Reaction–Separation–Recycle (RSR)

Three RSR process concepts are developed, starting with their basic process structure as presented in Figure 2; while all processes share many similarities, there are also key differences between these process concepts. Consider first the **RSR-A** concept: The fresh ($F_{AA,0}$, $F_{BD,0}$) and recycled reactants ($F_{AA,RCY}$, $F_{BD,RCY}$) are mixed and fed to a fixed-bed tubular reactor (PFR) operated adiabatically, with an inlet temperature of 100 °C and an inlet molar ratio BD/AA of 3. The reactor is modeled using the kinetic model (3) –(5). From the separation section (SEP), H_2O, HBA and BDA are removed from the system, while AA and BD are recovered and recycled to the reaction section as two separate streams. This structure with two recycles is possible since AA can be easily separated from the mixture, while BD can be separated by pressure–swing distillation as it will be described later. In the RSR-A, the selectivity to HBA is about 97.8 %mole, therefore a loss of reactants. **RSR-B** achieves 100% selectivity recycling the BDA back to PFR; hence, this process has 100 % selectivity to HBA. A particularity of this concept, important for designing the separation section, is that the reactions are performed at high concentrations of BDA (the composition of key streams around the reactor is shown in Figure 2).

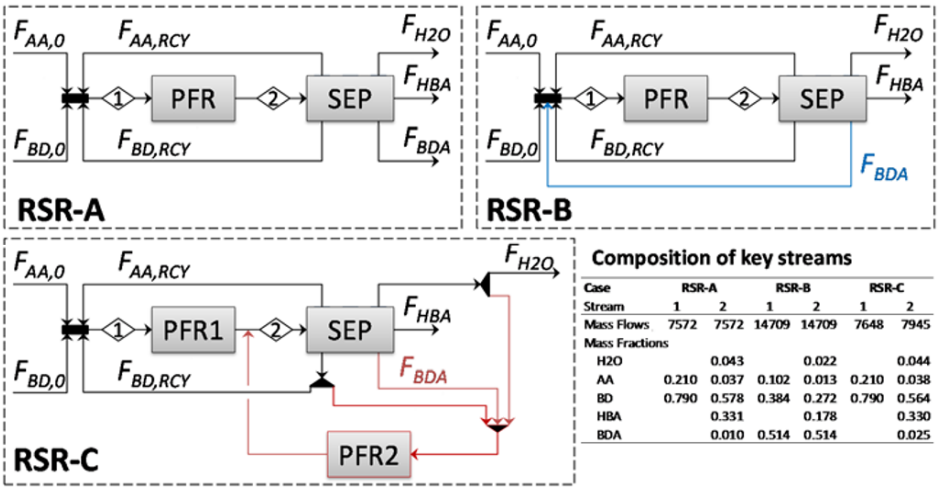

Composition of key streams

Case	RSR-A		RSR-B		RSR-C	
Stream	1	2	1	2	1	2
Mass Flows	7572	7572	14709	14709	7648	7945
Mass Fractions						
H2O		0.043		0.022		0.044
AA	0.210	0.037	0.102	0.013	0.210	0.038
BD	0.790	0.578	0.384	0.272	0.790	0.564
HBA		0.331		0.178		0.330
BDA		0.010	0.514	0.514		0.025

Figure 2. Structure of three RSR process concepts and composition of key streams.

Another alternative is to convert BDA back to AA, HBA and BD in a hydrolysis reactor; this is shown in **RSR-C**, where BDA is mixed with part of the H_2O and part of the BD streams and reacted in a second reactor (PFR2).

While developing the RSR concepts using the rigorous reactor modeling and black-box separation, a rough sensitivity analysis (not presented here) showed that, in the RSR-A and RSR-C processes, 2,500 kg of catalyst are sufficient for complete reactants conversion, while RSR-B requires 10,000 kg; hence, a four-times larger reactor; PFR2 of RSR-C, requires roughly 1,500 kg of catalyst. As expected, trade-offs exist and are worth future exploration: utilization of reactants versus larger recycle and larger reactor (RSR-A/RSR-B); utilization of reactants versus a second reactor (RSR-A/RSR-C).

The structure of each separation system is developed starting with the composition of stream 2 (see table in Figure 2) and making use of thermodynamic insights. Consider first the RSR-A process. The low-boiling H_2O and AA are removed first, by simple distillation. The remaining components are separated in a series of three distillation columns. The first two columns operated at different pressures overcome the minimum boiling homogeneous azeotrope BD-HBA by pressure-swing, as explained by the ternary diagrams (Figure 3, top) and the block scheme of the system (Figure 3, bottom). At 0.05 bar (top-left diagram), the concentration of the feed (F) entering the distillation column C-3 (bottom-left) falls in region I. Thus, BD is obtained as bottoms stream (B) and recycled to the reaction section, while the distillate (T*, containing all three components) is near the distillation boundary connecting the two binary azeotropes. At 0.8 bar, the locations of the binary azeotropes and distillation boundary change and the composition of the C-3 distillate (T*), which is the same as C-4 feed (F*), falls in region II (top-right diagram). Having crossed the distillation boundary, it is possible to obtain a bottoms stream (B) containing HBA and BDA, and a distillate (T) close to the distillation boundary. The former can be easily separated. The later falls back in region I at lower pressure, and can be recycled as feed to C-3.

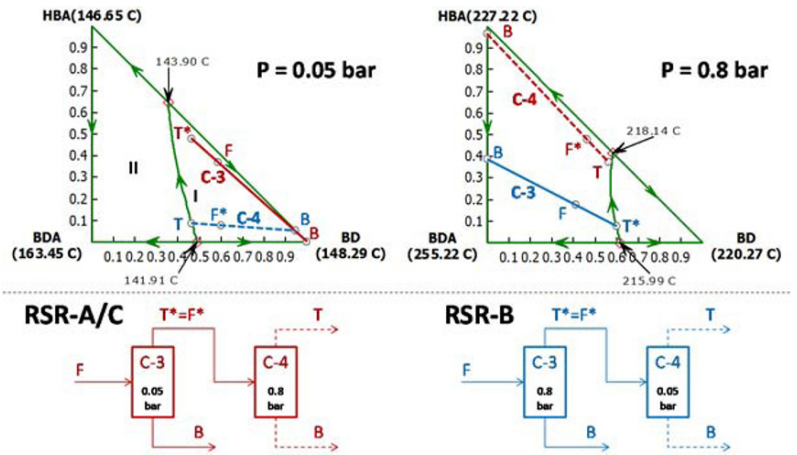

Figure 3. Top: Ternary diagrams showing the singular points (boiling and azeotropes) for the ternary system BD/HBA/BDA at two pressures, and mass balance for columns C-3 and C-4 that form the Pressure–Swing distillation system. Bottom: Columns sequence for each RSR processes.

With respect to RSR-B, sending back the BDA stream to the reactor brings a major change in the mass balance. As BDA is not allowed to leave the process, its overall generation rate (reaction-outlet vs. reaction-inlet) must be zero. For this reason, the

BDA concentration in the reactor is high, hence a composition of the stream leaving the reactor which is significantly different compared to RSR-A and RSR-C (see table in Figure 2). Given this change, the separation system is different. After H_2O and AA removal, the feed (F) to C-3 falls in region II of the ternary diagram at 0.8 bar (Figure 3, top-right diagram). Now, it is possible to obtain the binary mixture HBA/BDA, free of BD, as bottoms of C-3 (B in Figure 3, bottom-right diagram); this mixture can be easily split in a next distillation column. Changing the pressure to 0.05 bar, the concentration of the C-3 distillate (T*) crosses the distillation boundary. Thus, the feed of C-4 (F*) falls in region I. Here, BD is obtained as bottoms product (high purity is not required) being recycled to the reactor, while the C-4 distillate is sent back as feed to C-3.

The RSR-C process follows the same sequence as RSR-A, the difference being that the BDA is mixed with part of the H_2O and BD, and hydrolysed in a second reactor (PFR2) back to AA, HBA and BD. The outlet stream, containing all components, is returned to the separation section. The complete process flow diagram of RSR-C process, together with a mass balance and key sizing and operating parameters, is shown in Figure 4.

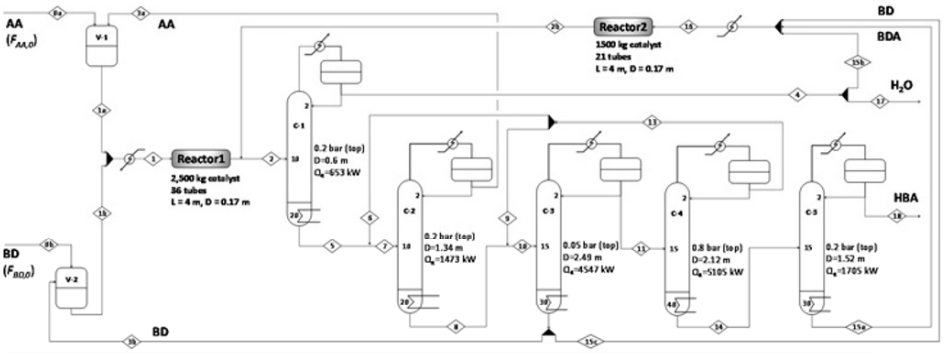

Stream	0A	0B	1	1A	1B	2	2B	3A	3B	4	5	6	7	8	9	10	11	13	14	15A	15B	15C	16	17	18
T / C	30	30	100	39.9	126.8	73.6	105.4	67	161.5	60.1	117.2	237.6	138.2	178.4	237.6	200.2	143.6	237.6	228.7	207.3	60.3	161.5	50	60.1	182.3
P / bar	2	2	2	2	2	2	2	0.2	0.09	0.29	0.21	0.80	0.90	0.21	0.8	0.80	2	0.8	0.8	0.21	0.2	0.09088	2	0.2	0.2
flow / m³/h	1.26	1.62	8.17	1.65	6.62	8.14	0.27	0.39	5.06	0.36	8.38	2.55	10.68	10.79	34.44	25.20	18.43	16.99	3.57	0.20	0.087	0.08	0.27	0.34	2.96
flow / kg/h	1330	1635	7760	1695	6074	8026	258	385	4439	345	7683	2304	9785	9401	31921	23122	16835	14025	2790	174	16	68	258	329	2616
Mass Fractions																									
H2O			0.010	0.045	0.000	0.052	0.052	0.200	0.000	0.995	0.010	0.000	0.008	trace	0.000	trace	0.000	0.000	0.000	0.000	0.995	0.000	0.068	0.995	
AA	1		0.208	0.955	trace	0.038	0.036	0.800	trace	0.002	0.060	447 PPM	0.012	100 PPM	447 PPM	299 PPM	571 PPM	447 PPM	trace	0.000	0.002	trace	307 PPM	0.002	
BD		1	0.783	trace	0.999	0.561	0.336	trace	0.999	trace	0.586	0.541	0.577	0.600	0.541	0.567	0.451	0.541	0.001	trace	trace	0.999	0.261	trace	0.001
HBA			571 PPM	trace	731 PPM	0.325	0.319	trace	1000 PPM	12 PPB	0.339	0.379	0.348	0.362	0.379	0.371	0.471	0.379	0.933	24 PPM	12 PPB	1000 PPM	250 PPM	12 PPB	0.995
BDA			trace	trace	trace	0.071	0.407	trace	trace	0.003	0.024	0.080	0.076	0.038	0.080	0.061	0.078	0.080	0.066	1.000	0.003	trace	0.675	0.003	0.004

Figure 4. Process flow diagram and mass balance (selected streams) of the RSR-C process.

3.2. Reactive Distillation (RD)

HBA can be conveniently produced also in a RD-based process. The process flow diagram is showed in Figure 5, together with a mass balance, operating conditions and main equipment sizes. The RD column has a standard configuration with the catalytic bed in the middle and standard addition of the fresh feeds: the light reactant as vapor at the bottom of the catalytic bed, the heavy reactant as liquid at its top. The heavier HBA and BDA exit the column with the bottoms, and are further split in the ideal separation block SEP; the HBA/BDA split is easy, and a column as C-5 of RSR-C can be used. The key to obtain HBA at the required specification is avoiding the contamination of the RD bottoms with reactants; otherwise, during the HBA/BDA separation, these low-boiling components will end up in the lighter product, HBA. At the top of RD, high-purity H_2O (99.99 %mass) is obtained. BDA is mixed with part of the H_2O stream and fresh BD, and hydrolyzed back to AA, HBA and BD. The reactor outlet stream is fed to the RD below the catalytic bed, providing in this way the necessary separation of the heavier HBA and BDA from the lighter reactants AA and BD, and side-product H_2O.

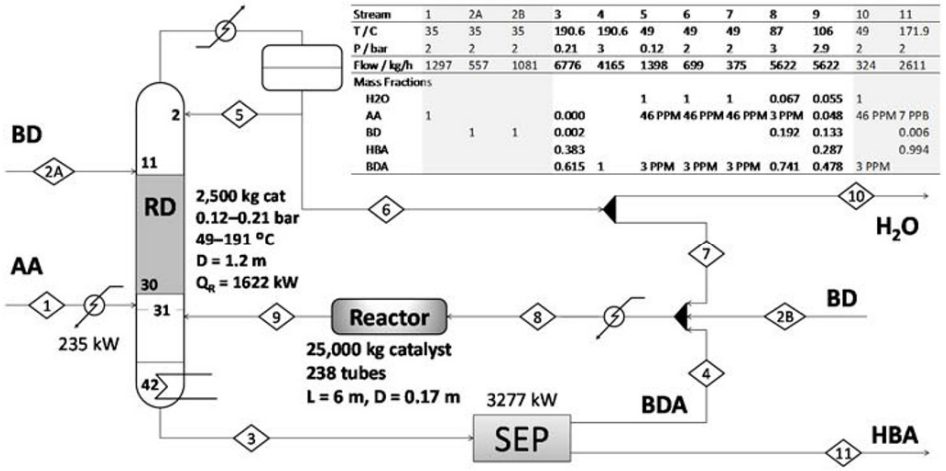

Stream	1	2A	2B	3	4	5	6	7	8	9	10	11
T/C	35	35	35	190.6	190.6	49	49	49	87	106	49	171.9
P/bar	2	2	2	0.21	3	0.12	2	2	3	2.9	2	2
Flow/kg/h	1297	557	1081	6776	4165	1398	699	375	5622	5622	324	2611
Mass Fractions												
H2O						1	1	1	0.067	0.055	1	
AA	1			0.000		46 PPM	46 PPM	46 PPM	3 PPM	0.048	46 PPM	7 PPB
BD		1	1	0.002					0.192	0.133		0.006
HBA				0.383						0.287		0.994
BDA				0.615	1	3 PPM	3 PPM	3 PPM	0.741	0.478	3 PPM	

Figure 5. Process flow diagram and mass balance (selected streams) of the RD process.

4. Conclusions

Production of HBA at industrial scale using Amberlyst 15 as solid catalyst is feasible. Due to the nature of the chemical system and reaction conditions, the chemistry is not 100 % selective towards HBA, important amounts of BDA being formed. In the RSR-C process, the per-pass HBA selectivity in the esterification reactor is 98 %mol. Conveniently, a second reactor is used to hydrolyze BDA back to AA, HBA and BD, achieving in this way an HBA overall process selectivity of 100 %. The difficult split of the BD/HBA/BDA mixture is achieved by pressure-swing distillation. This process is capital and energy intensive: 2 reactors, 4000 kg catalyst, 5 distillation columns and about 13.5 MW heating. In the RD process, the reaction conditions in the catalytic column favor even more the BDA production, the per-pass HBA selectivity being only 48 %mol. As in the previous process, the BDA is hydrolyzed back, achieving overall an HBA process selectivity of 100 %. The RD process overcomes the BD/HBA/BDA separation difficulty by reacting BD completely in the column, and therefore achieving the required HBA specification in a subsequent distillation column for HBA/BDA split. This process requires 1 reactor, 27500 kg of catalyst, 2 columns, and about 4.9 MW heating. Hence, triggered by their trade-offs, these processes should be optimized and rigorously compared on economic basis.

References

BASF, 2016, Petrochemicals specialty monomers, Technical information, TI/CP 1331 e.

BASF, Specialty monomers, Technical data, E-CPI/M 1610 booklet.

Y. Tanaka, K. Okamura, K. Ito, 2017, Process for preparing 4-hydroxybutyl acrylate, Patent No. US009670129B2.

J. I. Yang, S. H. Cho, H. J. Kim, H. Joo, H. Jung, K. Y. Lee, 2007a, Production of 4ˇ hydroxybutyl acrylate and its reaction kinetics over Amberlyst 15 catalyst, Can. J. Chem. Eng., 85, 83-91.

J. I. Yang, S. H. Cho, J. Park, K. Y. Lee, 2007b, Esterification of acrylic acid with 1,4-butanediol in a batch distillation column reactor over Amberlyst 15 catalyst, Can. J. Chem. Eng., 85, 883-888.

Sauro Pierucci, Flavio Manenti, Giulia Bozzano, Davide Manca (Eds.)
Proceedings of the 30th European Symposium on Computer Aided Process Engineering (ESCAPE30), May 24-27, 2020, Milano, Italy.
http://dx.doi.org/10.1016/B978-0-12-823377-1.50213-5

Physically Consistent Machine Learning Models Using Artificial Data for MISO Systems and Model Predictive Control

Jia-Lin Kang[a], Shi-Shang Jang[b*], Fan-Kai Sun[b], Po-Hsun Chang[b]

a Department of Chemical and Material Engineering, National Yunlin University of Science and Technology, Yunlin, 64002, Taiwan
b Department of Chemical Engineering, National Tsing Hua University, Hsinchu, 30013, Taiwan
ssjang@mx.nthu.edu.tw

Abstract

This work presents a novel artificial data assisted machine learning modelling approach to guarantee the correct physical gain signs between manipulated variables (MV)/controlled variable (CV) in a multi-input-single-output (MISO) model predictive control system (MPC). These industrial systems, such as polymerization reacting systems, are basically controlled based on the operators' experiences due the lack of the trustworthy models. The purpose of this work is to provide an implementable machine learning model for MPC purposed by the aid of artificial data. This approach is shown valid through a numerical problem, real plant test data and plant test.

Keywords: Machine Learning Models, Artificial data, Gain sign consistency, Model predictive Control

1. Introduction

Multi-Input-Single –Output (MISO) systems exist in many problems for example, grade transition and quality control problems in chemical engineering. In many cases, due to the lack of reliable physical model, these operations strongly depend on the experiences of the field operators. These cases result unstable qualities, loss of raw materials and products. In many cases, the on-line quality data can be directly or indirectly detected such as intrinsic viscosity, melting index,… etc.. In case of non-direct measurement, online soft senor is an active research topic and the plant applications (Zhang et al., 2016). Model predict control (MPC) hence becomes a possible solution to these problems. Basically, MPC approaches implement data-driven linear/nonlinear models. In nonlinear cases, machine learning dynamic models are highly active research topics among chemical engineering researchers (Wu et al., 2019). Machine learning models are most likely derived based on historical plant data. However, historical data do not guarantee to cover complete dynamical territories of many MISO systems. These models can be trained well and tested well without any physical consistency due to the existences of many local minima. With a trustworthy model, MPC approaches can be easily implemented to solve the above problems. Back-propagation-neural-network (BNPP) has been mature for many decades (Aglodiya, 2017). It is conceptually easy to understand and implement, but it might cause a large number of inputs and complicated structure if one implements them as a dynamic model with long time lags. Recurrent neural network hence becomes a rather wide spread approach among chemical engineering researchers because of its dynamic and deep learning natures. On the other

hand, XGBoost is a most popular machine learning approach in case of large amount of training data. In this paper, the above three different approach are used to show the generality of this artificial data approach. In the area of machine learning approaches, there have been other approaches that have claimed able to solve physical consistent problem of these data-driven models, such as sequence-to-sequence approaches (Hsiao et al.) or model transfer learning (Cho et al., 2014). However, these approaches are either trained with tricky arrangements of network arrangements or with a rather complicated physical model. This work is to propose an easy reasoned approach without changing the general structure of original machine learning models with very limited domain knowledge. This paper is to pursue a physically consistent MISO machine learning model using an artificial data approach. The artificial data matched to the physical properties are created and added to the plant data into the training set. These artificial data should be derived to ensure the gain signs of the output and inputs corrected but the accuracy of the model is not sacrificed. Note that types of these artificial data should depend on different types of machine learning models. In this work, most common implemented models such as artificial neural network (ANN), recurrent neural network (RNN) as well as XGBoost models will be studied. The models should be accurate enough for the implementation of MPC. This modelling approach as well as MPC will be demonstrated using a numerical benchmark problem. A real industrial example is presented to show the applicability and efficiency of this novel approach. Plant test results are also included.

2. Artificial Data Approach for MISO machine learning models

Consider Multi-Input-Single-Output (MISO) system, with a set of manipulated inputs, $U = \{U_1, U_2, \dots, U_N\}$, a set of measurable outside-determined inputs or disturbance inputs, $D = \{D_1, D_2, \dots, D_M\}$, and a single out output variable *Y*. Let us denote a set of historical operating data:

$$S_H = \begin{Bmatrix} (u_{11}, u_{21}, \dots, u_{N1,} d_{11}, d_{21}, \dots, d_{M1}, y_1), \dots, \\ (u_{1S}, u_{2S}, \dots, u_{NS,} d_{1S}, d_{2S}, \dots, d_{MS}, y_S) \end{Bmatrix} = \{R_1, R_2, \dots, R_S\} \quad (1)$$

where lower case of *U, D* and *Y* represent the numerical data of the inputs and outputs, *S* is the size of the historical data set and the second sub-index indicates the time sequence of the historical data, while R_i represents each event at time *i*. It is our purpose to obtain a machine learning model G such that each sequence $\{R_{k-K}, R_{k-K+1}, \dots, R_k\}$ with:

$$y_{k+1} = G(R_{k-K}, R_{k-K+1}, \dots, R_k) \quad (2)$$

Assume that the domain knowledge or plant operators knowledge lead to the gains for each inputs are known, i.e. the signs of $\frac{\partial Y}{\partial U_1}, \frac{\partial Y}{\partial U_2}, \dots, \frac{\partial Y}{\partial U_N}, \frac{\partial Y}{\partial D_1}, \dots, \frac{\partial Y}{\partial D_M}$ can be obtained. The problem on the field is that the machine learning model *G* such that the prediction of y_{k+1} using (2) are correct inside the historical data set S_H with wrong input signs. This would lead to physically unrealizable control actions and even regulatory operations. In this work, we propose to create the following artificial data set:

$$S_A = S_{AH} \cup S_{AI} = \{R_1, R_2, \dots, R_{AH}\} \cup \{R_1, R_2, \dots, R_{AA}\} \quad (3)$$

Note that each element of S_{AH} is termed half artificial data such that $R_i = (u_{1i}, u_{2i}, \dots, u_{Ni,} d_{1i}, d_{2i}, \dots, d_{Mi}, y_i)$ with its next elements $R_{i+1} = R_i$. With these S_{AH} set, the artificial steady state of the system will hence exist in the training set. Then N+M elements of S_{AI} are created corresponding to each element of S_{AH} in a fashion shown in Figure 1. Note that the increments B and C in Figure 1 are tuning factors as proposed below. These data sets are added to guarantee the correct gain sign existed in the model. The following is the proposed artificial data approach:

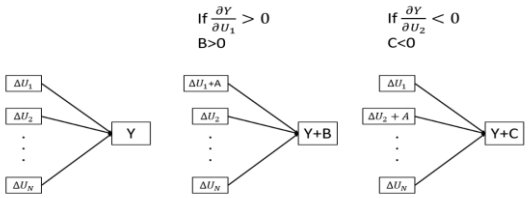

Figure 1. The increment set of the artificial data set

(1) Define the following original loss function:

$$L_0 = \frac{1}{S}\sum_{i=1}^{S}(y_i - \hat{y_i})^2 \quad (4)$$

where y_i is the plant data while $\hat{y_i}$ is the model prediction of the data in the prediction set.

(2) Perform the following training

Step 1: Create S_{AH} and S_{AI} by assuming that the increment of each variable from artificial steady state $U_i = U_i + \alpha$ yields $Y = Y + \beta$. Note that β can be positive or negative depending on the known gain sign.

Step 2: Train the ANN, RNN and XGBoost model by adding the artificial data set to the original data set.

Step 3: Fine tune the increment β based on the value of loss function (4), and go back to step 2 until the optimal of L_0 is obtained.

It can be well understood that there exists no general rule for the size of the artificial data as well as the tuning factor β. We propose that for the particular industrial case N=4, M=2 with total data set of 13000 time series data (10 minutes/sampling and three months duration), the appropriate size of artificial data $S_{AH} \cup S_{AI}$ should be around 2600 (i.e. 20% of original data set). Besides, as the first trial of β, we implemented 4α and α should be a small value.

3. Model Predictive Control of MISO Systems

Given the machine learning model (2), the following model predictive control is implemented:

$$\min J = \alpha\sum_{n-1}^{H}(y_{SP}(t+n) - \hat{y}(t+n))^2 + \beta\sum_{n=1}^{H}\sum_{i=1}^{M}(u_i(t+n))^2 \quad (5)$$
$$\text{s.t. } \hat{y}(t+k+1) = \quad G(R_{t+k-K}, R_{t+k-K+1}, \dots, R_{t+k}), \quad k = 0, \dots, H$$
$$u_{i,min} < u_i(t+n) < u_{i,max}, i = 1, \dots, M$$

where H is the horizon of the forward prediction, α and β are the penalties of the set point trajectory and the control actions, respectively. Note that in this particular case, only control action lower and upper bounds are implemented. Of course, in many cases, some output properties should also be bounded if they are either measurable or predictable. However, this work is aiming at solving a popular industrial case. Equation (5) can be easily extended to more general situations.

4. The Numerical Example

4.1. The numerical problem

In order to demonstrate the validity of the above approach, the following numerical example was implemented to demonstrate the proposed artificial data method:

$$f_1 = sigmoid(u_1), f_2 = \tanh(u_2), f_3 = -0.2 * u_3, f_4 = \sin(u_4) - 1 < u_i(i = 1,2,3,4) < 1 \quad (6)$$

$y_{t+1} = \tanh(f_1 + f_2 + f_3 + f_4 - \sin(f_2 * f_3) + f_2 * f_1) + y_t$

We randomly generated 10000 data sets, and three machine learning models ANN, RNN and XGBoost are trained using 9000 data sets. The remained 1000 data sets were implemented as testing sets

4.2. Traditional Training Approaches

One of 1000 fittings including ANN, RNN and XGBoost of the testing set is shown in Figure 2. Most machine learning models result satisfied fittings as Figure 2 however, none of 1000 gives correct gain sign and MPC to change the set point from 0. 5 to 0.65 is failed as shown in Figure 3.

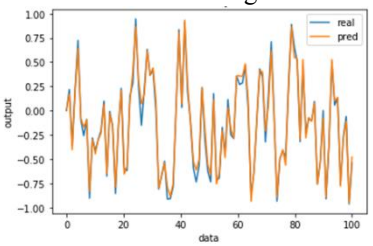

Figure 2. Comparison of the machine learning predictions without artificial data and testing set

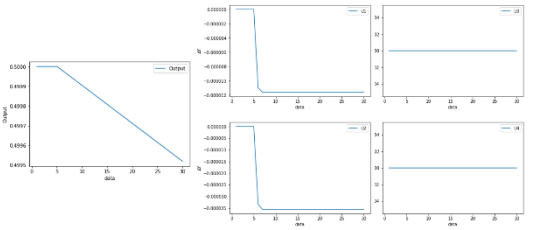

Figure 3. MPC of the numerical example using the machine-learning model without artificial data.

4.3. Traditional Training Approaches

We implemented 2000 artificial data set as described in the previous section, and retrained the model using three different machine learning models. Figure 4 compares the predictions of the testing set. Table 1 shows the fitting results of the testing set in terms of RMSW and R^2. The gain signs are all correct as shown in Figure 5. The MPC control gives correct control results with correct gain signs as shown in Figure 6.

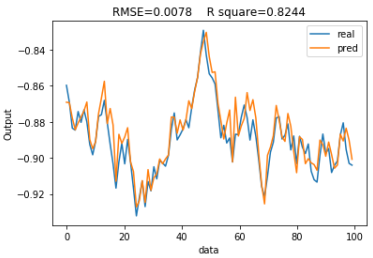

Figure 4. Comparison of the proposed machine learning predictions and testing set.

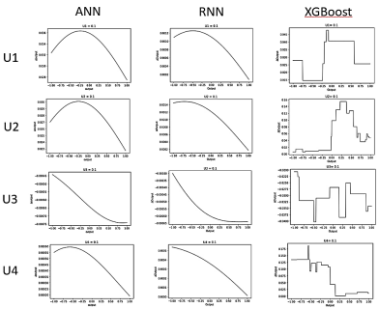

Figure 5. Gain signs of model with artificial data and Model predictive control of the numerical example

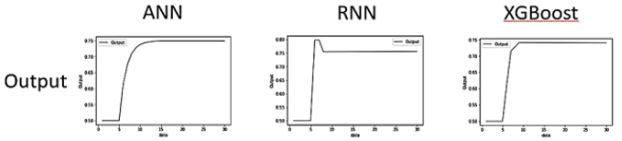

Figure 6. Model predictive control using the proposed model.

Table 1. RMSE and R^2 of the numerical testing set

	RMS	**R**
ANN	0.026	0.898
RNN	0.037	0.824
XGBoost	0.0074	0.9858

5. The Polymerization Reactor

5.1. The Proposed Approach

The models derived using artificial data can also fit the testing set as shown in Figure 7. All three models can fit the testing set well, and Table 2 gives the RMSE and R^2 of three models.

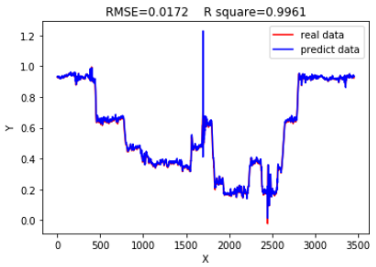

Figure 7. The comparison of plant data and model predictions (the proposed approach) of the testing set

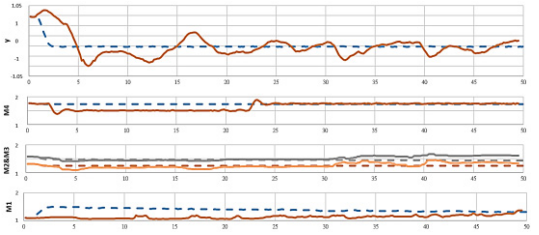

Figure 8 Comparisons of the solution of MPC to the historical set point change operations using the proposed machine learning model

Table 2 RMSE and R^2 of the reactor testing set

	RMSE	**R square**
ANN	0.0180	0.9875
RNN	0.0172	0.9961
XGBoost	0.0093	0.9990

Figure 8 demonstrates the validity of the proposed modelling approach. In this simulation, the plant and model are all the same machine learning model. Note that in Figure 8, the MPC controller took very different actions compared to the field operators. Interestingly, M4 was discarded by the MPC as a manipulated variable, and it is clearly correct if one observes the field operators adjusted it initially but set it back to the original value as shown in Figure 10.

5.2. Plant Test

Plant test was performed 8 hour duration. In Figure 9, during the time zone before the dash line, the plant was controlled by the field operators. The plant was rather stable compared to their historical data. The plant hence was taken over by ANN-MPC after the dash line, the control actions taken by MPC were quite different from the field operators. It is quite interesting if the readers observe the patterns of M1, M2 and M3 are all different from the manual approaches with much smaller oscillations even the disturbances of the plant (D1 and D2) were bigger than the period in manual period.

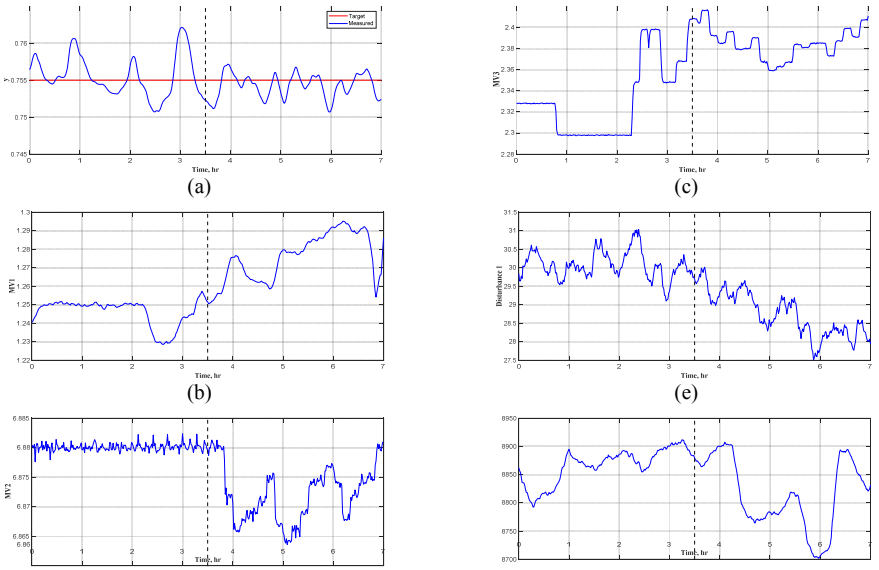

Figure 9. Plant test of the proposed approach. (a) the quality variable, (b) M1, (c) M2, (d) M3, (e) D1, (f)D2 v.s. time

6. Conclusions

A novel artificial data machine learning approach is proposed for MISO control system. The proposed approach demonstrates ability to converge to correct gain sign solutions in these multi-solution cases by adding artificial data sets. The approach also shows versatile in terms different training algorithms such as ANN, RNN and XGBoost. Numerical example and real plant examples are performed to show the validity of the proposed approach. The simulations and plant tests all show that the models derived from this approach is valid in MPC applications, while the machine learning without special treating may fail in these MISO systems.

References

Aglodiya, A. (2017). Application of Artificial Neural Network (ANN) in Chemical Engineering: A Review. *IJARIIE, 3*(2), 5322-5328.

Cho, K., Van Merriënboer, B., Gulcehre, C., Bahdanau, D., Bougares, F., Schwenk, H., & Bengio, Y. (2014). Learning phrase representations using RNN encoder-decoder for statistical machine translation. *arXiv preprint arXiv:1406.1078*.

Hsiao, Y.-D., Chou, C.-H., Wu, H.-b., Kang, J.-l., Wong, D. S. H., Yao, Y., . . . Ou, J. D.-Y. PHYSICALLY CONSISTENT DATA-DRIVEN SOFT-SENSOR DEVELOPMENT.

Wu, Z., Tran, A., Rincon, D., & Christofides, P. D. (2019). Machine learning- based predictive control of nonlinear processes. Part I: Theory. *AIChE Journal, 65*(11).

Zhang, M., Liu, X., & Zhang, Z. (2016). A soft sensor for industrial melt index prediction based on evolutionary extreme learning machine. *Chinese journal of chemical engineering, 24*(8), 1013-1019.

Sauro Pierucci, Flavio Manenti, Giulia Bozzano, Davide Manca (Eds.)
Proceedings of the 30th European Symposium on Computer Aided Process Engineering (ESCAPE30), May 24-27, 2020, Milano, Italy.
http://dx.doi.org/10.1016/B978-0-12-823377-1.50214-7

CO_2 Reduction by Advanced Process Control in Gasification Processes

Moein Mighani,[a] Karsten Covella,[a] Evrim Örs,[a] Jean-Francois Rauch,[b] Hans-Peter Mönch,[c] Martin Gräbner[a,*]

[a] *AIR LIQUIDE Forschung und Entwicklung GmbH, Frankfurt Innovation Campus, Gwinnerstrasse 27-33, Frankfurt am Main 60388, Germany*

[b] *AIR LIQUIDE Large Industries, 57 avenue Carnot BP 313, Champigny-Sur-Marne 94503, France*

[c] *AIR LIQUIDE Global Management Services GmbH, Olof-Palme-Strasse 35, Frankfurt am Main 60439, Germany*

Martin.Graebner@Airliquide.Com

Abstract

Improvement in energy efficiency and operation of production units plays a key role in reducing carbon intensity of production processes. Entrained-flow gasification is a prevalent technology for converting coal to syngas. However, due to highly nonlinear interactions between process variables and inherent fluctuations, the operation and control of these gasifiers are difficult. This results in often suboptimal gasifier operation and therefore presents significant opportunity for optimization. In this work an advanced process control strategy for improving the operation and control of entrained-flow gasification is developed. This solution involves different components including online coal properties measurement and analysis, real time optimization engine and model predictive control. Finally, it is shown how implementation of this advanced process optimization and control solution improves the production stability and efficiency presenting opportunities for reduction of CO_2 per unit production.

Keywords: Advanced Process Control, CO_2 Emission Reduction, Gasification, Model Predictive Control

1. Introduction

A significant portion of global greenhouse gases and subsequently CO_2 emissions arise from energy conversion and process emissions in the industry. Accelerated worldwide demand of energy and substantial materials including steel, plastic, paper, etc., is accompanied by an increase in emissions. Therefore, effective measures are needed to mitigate CO_2 emissions from industrial activities. Among the existing measures, increasing the energy efficiency of processes via maximizing the production efficiency and reducing the CO_2 intensity per unit production is considered as one the most significant strategies (Allwood et al., 2010).

Partial oxidation is one of the most important processes for hydrogen production from any carbonaceous feedstock. Coal is identified as one of the most abundant carbon sources which can be converted to synthesis gas (syngas) using gasification processes. Among different existing coal gasification technologies, entrained-flow (ETF) gasification is currently the most widely employed choice. It is due to its ability to process a wide variety of coal types and its high syngas yield (Gräbner, 2015). However, the

presence of highly nonlinear interactions among relevant process parameters coupled with long dynamic response times make the operation and control of a gasifier complex and challenging. Moreover, fluctuations in the quality of the coal feedstock affecting the operational parameters and efficiency of the gasification (Emami Taba et al., 2012) are not measured in real time and become available much later as laboratory results. These normally lead to suboptimal control and operation of the gasifier. This effect can be traced in noticeable fluctuations of monitored variables such as gasifier reactor wall temperature, CH_4 and CO_2 concentrations in the produced syngas (Gräbner, 2015). Therefore, reducing such fluctuations via implementing an optimized control methodology presents a remarkable opportunity for improving the efficiency of the operation. Consequently, this results in reduction in CO_2 emissions previously caused by suboptimal operation of gasifier (Gräbner, 2015).

In the industrial processes, advanced process optimization and control strategies involve hierarchy of different layers. These layers from a top to bottom sequence can include product scheduling and supply chain, real time optimization (RTO) engine, model predictive control (MPC) and finally, regulatory controllers interacting with process measurements. The RTO layer in general is equipped with high fidelity process models. The function of RTO engine is to calculate the optimum operational window and set points of controlled variable sets in given specific steady-state process conditions (Marchetti et al., 2011). MPC is a process control methodology involving the process knowledge through different process models in order to improve the process controllability and performance. During the recent years MPC has become an attractive and accepted method along the industry due to its ability to handle both process nonlinearities and constraints in multivariate systems (Morari and Lee, 1999).

The current work explains how the fluctuations in ETF gasification are identified and used to build up an advanced process control (APC) strategy benefiting from RTO and MPC to improve the production efficiency of the gasifier. Tools like Python™ and Matlab® were employed for operational data segmentation and signal processing. Moreover, an in-house developed and verified ETF gasification model was used as RTO engine while the Platform for Advanced Control and Estimation (PACE) (Amrit et al., 2015) was the main core of MPC development and implementation. Finally, this work can serve as a practical example to demonstrate how improving the efficiency of gasification processes can lead to CO_2 emission reductions.

2. Computational Methodology

2.1. Advanced Process Control for ETF Gasification

Operation and control of ETF gasification is a challenging task due to highly nonlinear interactions between the process variables and presence of fluctuations caused by changes in coal properties. In order to improve the operation and performance of this process, an APC strategy comprising different components with specific tasks has been developed. The primary component of this solution is a coal online analyzer measuring, calculating and recording the properties of coal feed such as ash content, lower heating value (LHV) and other parameters of relevance (Gräbner et al., 2019). The output information of this online measurement device together with information recorded from process measurements like gasifier pressure, shell steam production rate, carrier gas flow rate, etc., are fed into the RTO engine. Based on this information, the RTO engine calculates the operation window for process control variable sets. This operation window includes allowable high and low limits of controlled variables (operation constraints) as well as

optimal steady state set points. This RTO engine is based on a thermodynamic first principle model and was developed and verified in-house (Örs and Gräbner, 2019). The model assumes equilibrium and applies a carbon conversion rate to account for the fuel reactivity and residence time in the ETF gasifier. Details are described elsewhere (Sasi et al., 2018). The last piece of this strategy is MPC. This key player performs the task of stable operation of the gasifier and mitigation of fluctuations while driving the operation towards the optimal set points. A schematic view of this solution can be seen in Figure 1.

2.2. Model Predictive Control

The main idea of MPC is to incorporate the process knowledge in the process control via employing different types of process models. Platform for Advanced Control and Estimation was used for all the development and simulations in the MPC part. The primary step in MPC development is to define the control variable sets and their

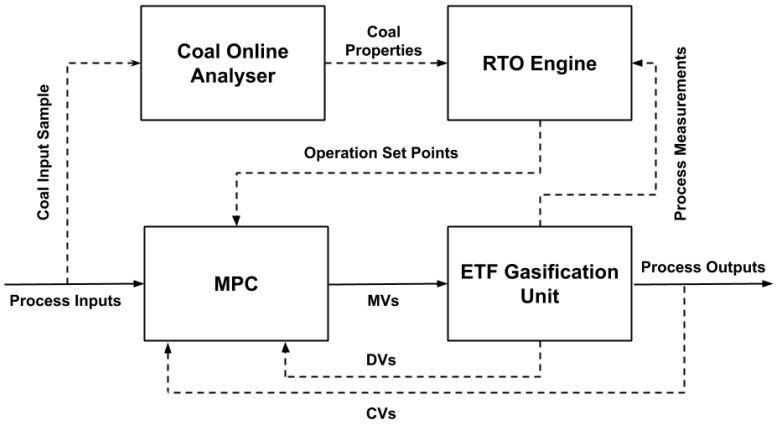

Figure 1. APC Solution Scheme

relationship. Controlled variables (CVs), manipulated variables (MVs), and disturbance variables (DVs) are among possible control variable sets can be defined in PACE. Table 1 represents the employed process parameters and their role in the process control variable set.

Table 1. Control variable set

CVs	O_2/Total Coal (wt/wt), Effective Syngas Production (Nm^3/h), CH_4 Slip in Syngas (p.p.m), CO_2 in Syngas (vol. %), Gasifier Wall Temperature (°C)
MVs	Coal Flow Line 1 (kg/h), Coal Flow Line 2 (kg/h), Coal Flow Line 3 (kg/h), O_2 Flow (Nm^3/h)
DVs	Feeding tank ΔP (kPa), Shell Steam Density (kg/m^3)

After assigning the control variables, the next step is to define the dynamic models and correlations defining the relationships between these variables. Primarily, the relationship between each MV and CV or DV and CV is modeled in single input single output (SISO) mode benefiting from first or second order parametric transfer function models. Then, the developed models are embedded in a control matrix known as dynamic matrix control for calculating the dynamic behavior of the system in multi input multi output (MIMO) mode.

This step is known as dynamic system identification. In the current work, the identification of dynamic models was carried out in closed loop manner exploiting operational data. In the closed loop system identification it has to be made sure that the data lies within acceptable process conditions and is of enough mathematical excitation for effective model identification. Finding the suitable operational data for system identification which is called data segmentation was carried out in Python™ over more than a year of historical data from the operation. This was done by applying different process filters like acceptable gasifier load and stable steam injection (always kept constant; not used as control parameter due to significant temperature moderating effect of conveying CO_2) together with mathematical filters to ensure the suitability of the data set. During the identification period the accuracy of identified models was evaluated using the following formula:

$$1 - \frac{\mathrm{var}(y_i - y_{pred})}{\mathrm{var}(y_i)} \tag{1}$$

Where, y_i is the real data and $y_{pred.}$ is the model output. This accuracy metric explains how good the model performs in explaining the dynamic behavior of the output response. Practically, the models with accuracy of over 0.5 are suitable to be used in control matrix.

After developing the control matrix and corresponding dynamic models, the controller parameters need to be set and fine-tuned. In this stage, parameters related to CVs such as constraints and set points are received from RTO engine based on feeding coal properties. The other constraints related to MVs like maximum and minimum movements and rate of changes are normally set according to process operation manuals and safety prerequisites. Afterwards, the aggressivity and robustness of the controller have to be determined based on the expected control actions. PACE employs a nonlinear solver with infinite horizon formulation which permits the use of nonlinear models (Amrit et al., 2015). The final step is to simulate various process control scenarios in order to evaluate the performance of the designed controller. All the explained steps can be reiterated several times to result in a desired and effective designed MPC application.

3. Results and Discussion

All the developed models are whether first order or second order continuous transfer functions. Employing the formula (1) as the accuracy metric, all the models scored higher than 0.5 and proved to be suitable for MPC usage. Figure 2 illustrates an example of a CV response simulated via identified dynamic model using one MV and one DV as inputs.

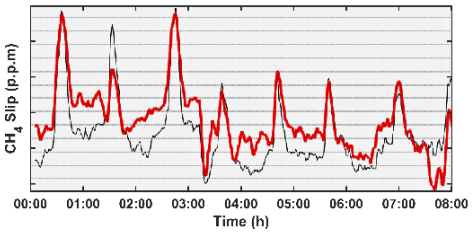

Figure 2.a. Dynamic model response for CH4 Slip in Syngas (p.p.m). Black solid line is real data. Red line is model output.

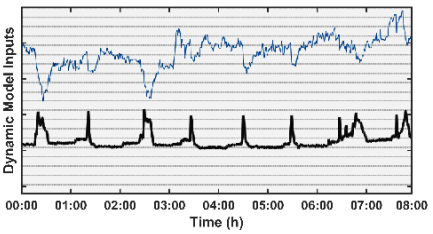

Figure 2.b. Inputs for CH4 Slip Model. Black line is feeding tank ΔP (kPa). Blue line is O2 / Total Coal (wt/wt).

After successful dynamic system identification and development of desired MPC application, a production scenario was simulated to show the benefits of developed APC solution. For doing this, a 42 hours simulation was carried out and the outcomes were compared to real operational data recorded in DCS. The results of this simulation can be seen in Figure 3.a-d (red lines are simulated APC responses while blue lines are real DCS data).

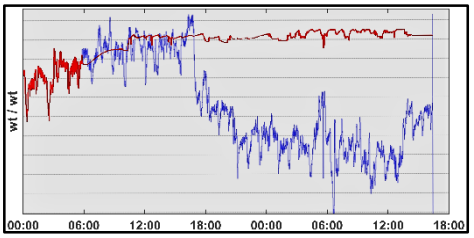

Figure 3.a. O_2 / Total Coal (wt/wt)

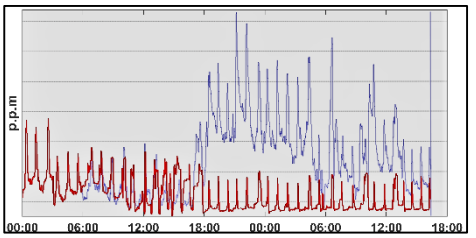

Figure 3.b. CH_4 Slip in Syngas (p.p.m)

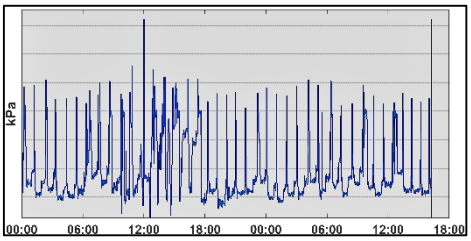

Figure 3.c. Feeding Tank ΔP (kPa)

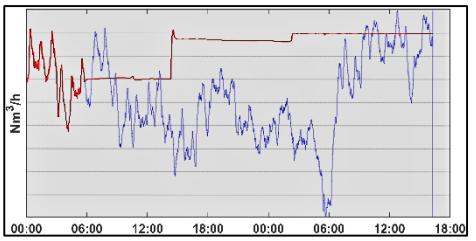

Figure 3.d. Effective Syngas (Nm^3/h)

In the first 6 hours of simulation the APC is off and the shown data is solely real operational data taken from DCS. After around 6 hours, the APC solution is turned on with the primary focus of stabilizing the operation with regard to O_2/Total Coal, CH_4 slip in syngas and effective syngas production. After 10 hours of stable operation, when the stability is ensured, the optimization objective which is the maximization of produced effective syngas is applied (Figure 3.d). During the overall simulation, signals for DVs were taken from real operational data and were fed as feed forward signals (Figure 3.c). As it can be seen in Figure 3.a, after turning the APC on, the fluctuations in O_2/Total Coal have been mitigated by around 80 % which corresponds to tighter and smoother control actions over available MVs related to oxygen and coal input flows.

Real operational data in Figures 3.a, 3.b and 3.d after the first 18 hours of operation reflect suboptimal operation and control actions. The effect of deviation from optimal O_2 / Total Coal set point (seen in Figure 3.a) can be traced in higher amount of CH_4 slip in syngas production for a long period (Figure 3.b) which corresponds to low temperature operation of gasifier leading to inefficiency and reduced conversion. Such deviations from optimal operational window coupled with high bandwidth of unmitigated fluctuations have resulted in highly oscillating and reduced amounts of effective produced syngas which can be seen in Figure 3.d. On the other hand, by looking at same figures for operation with APC on during the same time period, a stable and smooth operation of O_2 / Total Coal around optimum calculated set point is observed while continuously mitigating the effects of fluctuations (Figure 3.a). As it is seen in Figure 3.b, this can lead to lowered and tightly controlled amounts of CH_4 slip in syngas translating to hot gasifier operation and high conversions. Finally, the result of this optimal control and operation can be observed in Figure 3.d, where the amount of effective syngas production is kept at a

constant and stable maximum of output while ensuring both operation safety and efficiency.

Ultimately, it was calculated that the developed APC solution delivers on average more than 1 % savings on O_2 input per unit effective syngas production (Nm^3 O_2 / Nm^3 effective syngas) as well as up to 3 % savings in total coal input per unit effective syngas production (kg coal / Nm^3 effective syngas). These savings present a significant opportunity for reduction of both direct and indirect CO_2 emissions related to the gasification process.

4. Conclusions

The growing global demand for energy and substantial matters has made the industry to take measures for mitigating the CO_2 emissions corresponding to industrial activities. Here in this work, an APC solution was developed and tested for ETF coal gasification to optimize the operation control and production efficiency targeting the abatement in associated CO_2 emissions. The resulted savings in oxygen input per unit effective syngas production and total coal input per unit effective syngas production suggest considerable savings in direct and indirect CO_2 emission caused by the gasification process. At the end, application of advanced process control and optimization for CO_2 emissions reduction utilizing various objective functions in gasification processes shows a significant potential for further investigations.

References

J. M. Allwood, J. Cullen, R. Milford, 2010, Options for Achieving a 50 % Cut in Industrial Carbon Emissions by 2050, Environmental Science & Technology, Volume 44, 1888-1894.

R. Amrit, W. Canney, P. Carrette, R. Linn, A. Martinez, A. Singh, T. Skrovanek, J. Valiquette, J. Williamson, J. Zhou, B. J. Cott, 2015, Platform for Advanced Control and Estimation (PACE): Shell's and Yokogawa's Next Generation Advanced Process Control Technology, IFAC-PapersOnLine, Volume 48, 1-5.

L. Emami Taba, M. F. Irfan, W. A. M. W. Daud, M. H. Chakrabartial, 2012, The Effect of Temperature on Various Parameters in Coal, Biomass and CO-Gasification: a Review, Renewable and Sustainable Energy Reviews, Volume 16.

M. Gräbner, 2015, Industrial Coal Gasification Technologies Covering Baseline and High-Ash Coal, Wiley.

M. Gräbner, M. Mighani, K. Covella, E. Örs. 2019, CO_2 Reduction by Implementing Online Fuel Analysis in Gasification Processes, International Conference on Coal Science & Technology, Krakow, Poland.

A. Marchetti, P. Luppi, M. Basualdo, 2011, Real-Time Optimization via Modifier Adaptation Integrated with Model Predictive Control, IFAC Proceedings Volumes, Volume 44, 9856-9861.

M. Morari, J. H. Lee, 1999, Model Predictive Control: Past, Present and Future, Computers & Chemical Engineering, Volume 23, 667-682.

E. Örs, M. Gräbner, 2019, FuALadvisor 1 - A Model-Based Fuel Procurement Tool for Gasification, International Conference on Coal Science & Technology, Krakow, Poland.

T. Sasi, M. Mighani, E. Örs, R. Tawani, M. Gräbner, 2018, Prediction of ash fusion behavior from coal ash composition for entrained-flow gasification, Fuel Processing Technology, Volume 176, Pages 64-75.

Sauro Pierucci, Flavio Manenti, Giulia Bozzano, Davide Manca (Eds.)
Proceedings of the 30th European Symposium on Computer Aided Process Engineering (ESCAPE30), May 24-27, 2020, Milano, Italy.
http://dx.doi.org/10.1016/B978-0-12-823377-1.50215-9

A Deep Learning Approach on Surrogate Model Optimization of a Cryogenic NGL Recovery Unit Operation

Wenbo Zhu, Jorge Chebeir, Zachary Webb, Jose Romagnoli

Department of Chemical Engineering, Louisiana State University, Baton Rouge, Louisiana, 70803, United States

jose@lsu.edu

Abstract

Natural gas liquids (NGL) are utilized in nearly all sectors of the economy such as feedstock for petrochemical plants and blended for vehicles fuel. In this work, the operation of a cryogenic expansion unit for the extraction of NGL is optimized through the implementation of data-driven techniques. The proposed approach is based on an optimization framework that integrates dynamic process simulations with two deep learning based surrogate models. The first model utilizes a recurrent neural network (RNN) based surrogate model to disclose the dynamics involved in the process. The second regression model is built to generate profit predictions of the process. The integration of these models allows the determination of the process operating conditions that maximize the hourly profit. Results from two case studies show the capabilities of the proposed optimization framework to find optimal operating conditions and improve the process profits.

Keywords: Cryogenic expansion unit, Deep learning, Dynamic process simulation, Surrogate model

1. Introduction

Natural gas is a naturally occurring hydrocarbon mostly constituted by methane. The relevance of this energy commodity resides in its abundance, relatively easy transportation and clean burning in comparison to other fossil fuels. As natural gas flows out of the ground, it may also contain reduced amounts of other hydrocarbons such as ethane, propane, butanes and natural gasoline. These heavier hydrocarbon liquids are commonly referred to as NGL. The extraction of NGL components from the raw gas is not only required for hydrocarbon dew point control in a natural gas stream, but also represents a source of revenue, as NGL normally have significantly greater value as separate marketable products than as part of the natural gas.

The extraction of heavier hydrocarbon liquids constitutes a mature and well-known process with a broad literature covering its particular features. The different variants of this process are normally based on external refrigeration, turbo-expansion, Joule-Thompson expansion, and absorption. In the natural gas industry, one of the most common recovery schemes is the industry-standard single stage (ISS). This process replaces the utilization of a Joule-Thompson valve by a turbo-expander in order to enhance the feed gas cooling (Campbell and Wilkinson, 1981). A major drawback of this configuration is the relatively low NGL recovery achieved and the problematic issue of the carbon dioxide freezing (Lynch et al., 2002). These limitations have led to more advanced process schemes, such as the gas sub-cooled process (GSP), cold residue reflux

(CRR) process, and recycle split vapor (RSV) process among others. These processes are based on the implementation of a cold recycle by bypassing a portion of the gas fed to the turbo-expander. The NGL recovery, energy consumption, and economic benefits of each process scheme are not only affected by the efficiency of the process, but also by the operating conditions, including the outlet chiller temperature, column pressure, turboexpander by-pass flow, etc. Surrogate models offer the capability of simplifying large-scale complex process models to perform the optimization. Significant works have been done on applying surrogate models in process optimization. Nevertheless, most of these methods build the predictive models using the correlations among different variables (spatial correlations), while the serial correlations that represents the correlations at different time steps are rarely taken into consideration. Nevertheless, process dynamics commonly exists in chemical systems, which suggests that serial features should also be included into the construction of surrogate models. Recent development of deep learning techniques, particularly recurrent neural network (RNN) have displayed promising performance in sequential data analysis. Compared with traditional methods such as Kriging models, and quadratic best-fit models, the RNN approach can provide additional insights into the time-correlation information (process dynamics). In this work, a simulated-based optimization framework is proposed to determine the optimal operating conditions of an NGL cryogenic unit. A simulation model is developed to emulate the dynamics involved in the operation of a CRR unit utilizing a commercial process simulator. Since the detailed expression of the process model is not available directly in algebraic form, the simulation is treated as an input-output black box. In order to optimize such simulated process, an optimization algorithm based on the utilization of surrogate models is proposed in this work. An RNN-based surrogate model is used to learn the discrete process dynamic behaviors from eight control loops in the NGL process. Based on the system status, e.g. set points (SPs) and present values (PVs), a second regression model is constructed to predict the expected profit at each time step incorporating the current market price of feeds and products. After that, a differential evolution (DE) algorithm is applied to find the optimal operating conditions based on the proposed discrete surrogate model.

2. Dynamic Process Simulation and Control

The CRR process scheme was first introduced in the original design of GSP by Campbell et al. (1981) to improve the ethane recovery efficiency. The model to emulate the real CRR configuration is constructed in the process simulator Aspen HYSYS®. The default values of set-points in the different control loops, operating conditions, and design parameters in the process are based on previous literature, and realistic industrial conditions, which can be referred in Chebeir et al. (2019).

A dynamic simulation of the CRR process scheme is developed for the implementation of the different control strategies. A critical step for the generation of a realistic simulation model is the definition of the equipment design involved in the system. Following the criteria of previous works (Chebeir et al., 2019; Luyben, 2013), the demethanizer column is built with a total number of 30 stages plus a reboiler. The reboiler (E-104) of the column (regular heater and separator reboiler in process simulator) has a diameter of 1.193 m and a length of 1.789 m. The diameter of the column is 1.72 m with a tray space of 0.5 m. In the case of the heat exchangers, the UA for E-100, E-102 and E-103 are $2.038 \cdot 10^5$ kJ/·°Ch, $1.961 \cdot 10^5$ kJ/·°Ch and $1.576 \cdot 10^5$ kJ/·°Ch, respectively. The chiller (E-101) has a volume of 0.10 m^3 and a duty of $1.275 \cdot 10^7$ kJ/h. The flash separator, TK-100, have a diameter of 1 m and a height of 2.5 m. The expansion and compression sections of the

turboexpander TE-100, recompressor K-101 and cryogenic compressor K-102 (CRR process) have an adiabatic efficiency of 75%. Joule-Thompson valves (JTV-100 and JTV-101) are also included in the process scheme in order to generate a sudden expansion of the fluids (pressure decrease) to enter into the demethanizer column at the stage pressure. The control structure implemented in the CRR configuration scheme is summarized as follows:

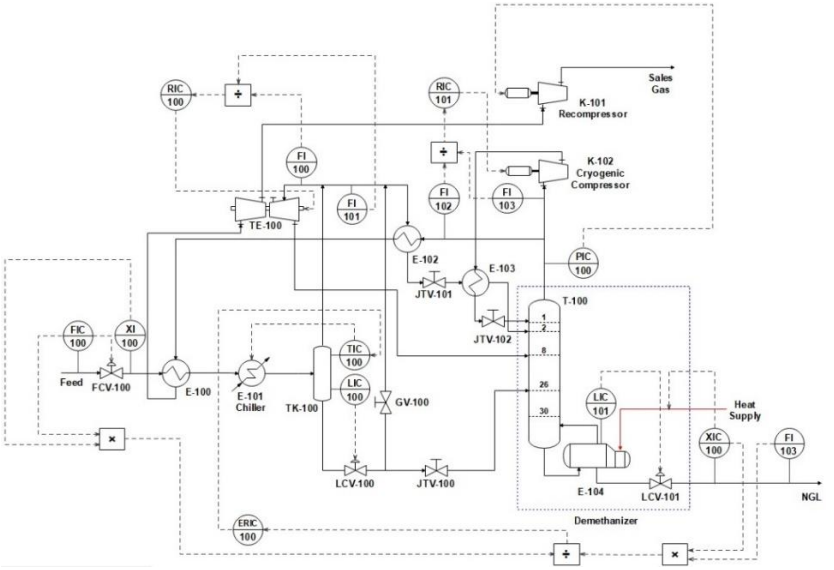

Figure 1. Control structure of the CRR process configuration.

3. Surrogate Modeling and Optimization

In this section, the implementation of the surrogate model that predicts process profit will be discussed. In order to maximize the CRR process profit by the manipulation of the operating conditions, the problem is separated into two main parts namely the CRR system side and the market side.Since the simulation is treated as a black-box, a dynamic surrogate model is implemented to represent the complex dynamics involved in the process. In this sense, a special type of RNN called long short-term memory (LSTM) neural network (Hochreiter and Schmidhuber, 1997) is opted to represent the process simulation in a discrete term. This means that the model would compute the process response at a fixed time interval, instead of representing the dynamics in a continuous-time form. The time interval utilized in this work is 43 seconds, considering the Python-Simulator connection delay and the inherent dynamics of the CRR process. After modelling the CRR process dynamics, the market side information is incorporated into the framework to generate the entire surrogate model of the system. A regression model is built to map the expected profit at each time step from market price of natural gas and NGL, as well as the process operating conditions. Once the surrogate model is completely defined, the optimizer is implemented to guide the operating conditions.

3.1. Data Preparation

Before implementing the surrogate model, data at different operating conditions has to be collected. The initial data was collected randomly from perturbations generated in the eight SP values inside the process and the market prices of sales gas and NGL. The corresponding responses on all eight control loops are recorded through their PVs readings until reaching a new steady state which takes roughly about 6300 seconds in the

simulation. The surrogate model is designed to predict process responses at fixed discrete time intervals, where the time interval in the discrete system is 43 second and total time step is set 150.

3.2. Surrogate Model

In this work, a LSTM-based regression model is opted to learn the time sequential dynamics in the CRR process. The basic idea here is that the PVs at next time step are predicted using the SP and PV in previous time steps. Besides the basic LSTM layout, recent developed techniques namely, bidirectional RNN structure (Schuster and Paliwal, 1997) and attention mechanism (Rocktaschel et al., 2015) are also incorporated in the regression model. After incorporating the different elements mentioned above, a schematic representation of the surrogate model is depicted by Figure 2.

Once the dynamic surrogate model is accurate enough to mimic the process dynamics, then a feed-forward neural network is trained separately to predict profit using current market prices of natural gas and NGL, as well as the SP and PV values that represent the current status of the system.

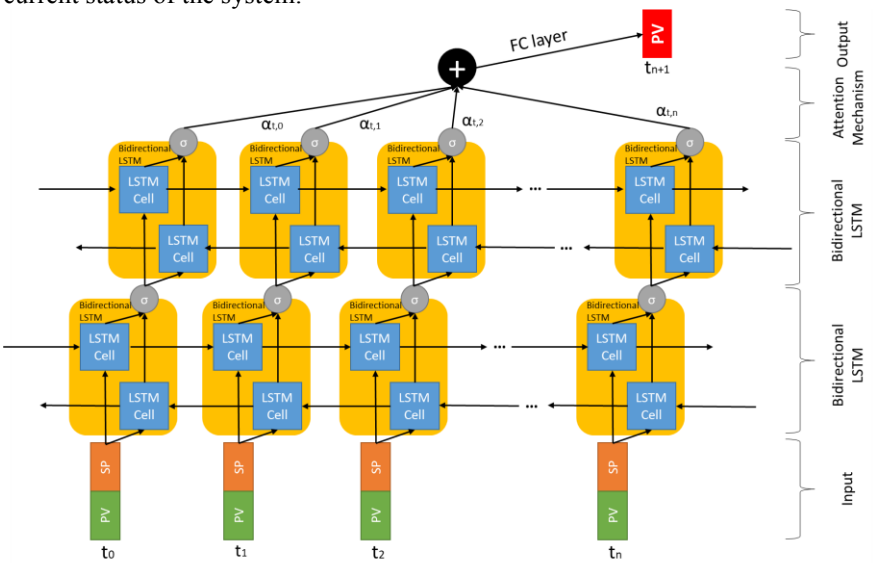

Figure 2. The LSTM based surrogate model

3.3. Optimization Framework

Considering the above information of the surrogate model, the entire surrogate model can be written as:

$$PV_{n+1} = f_d\left(PV_{n_{-L}} \cdots PV_n, SP\right) \tag{1}$$

$$Profit_{n+1} = g_P\left(PV_{n+1}, SP, d_p\right) \tag{2}$$

where d_p is the disturbance from the market price, n is the discrete time index, f_d is the dynamic surrogate model, and g_p is the profit regression model. Hence, the optimization model can be written as:

$$\arg max \sum_{i=t_1}^{t_n} Profit \tag{3}$$

s.t. $SP_1 \dots SP_j \in \left[SP_j^L, SP_j^H\right]$

where the constraints are the ranges of each SP. The objective of the optimizer is to find proper SPs that can maximize profit profile in a following time period (6300 seconds), in order to bring the process into a new steady state operation. The optimizer used in this work is differential evolution (Storn and Price, 1997), which is a metaheuristic optimization method that find optimal solution from iterative trials.

4. Result and Discussion

4.1. Surrogate Model Results

To initiate the training of the dynamic surrogate model, 330 batches (with 150-time steps in each batch) from different operating conditions were collected by choosing random SPs within their corresponding ranges. Hence, a total of 42,570 training samples are provided in the model training. A validation set was generated separately with alternative time step length to avoid the model overfitting during the training. After that, the error maximization sampling is opted to further improve the model accuracy. The model accuracy is then evaluated by testing data consisting of 40 batches of different operating conditions (5,160 samples), which is summarized in Table 1. The results from a simple two-layer LSTM model without bidirectional layer or attention mechanism are also included to verify the effectiveness of these additional elements. The bidirectional layer and attention mechanism narrow down the averaged relative error from 10.53% to 0.93% compared with the simple LSTM model.

Table 1. Relative error comparison

	Two-layer LSTM	Proposed architecture
Relative Error (%)	10.53	0.93
Std of Error (%)	±2.95	±0.76

4.2. Optimization Results

Two case studies are performed to validate the proposed optimization framework. In Case Study I, the prices are set high for the different products to mimic a profitable scenario. In Case Study II, a feed gas with a high cost is set to create a scenario of losses. The corresponding prices for the different case studies are listed in Table 2, and the optimized results for both scenarios are summarized in Table 3. The optimized SP values for both cases studies were verified through the simulation, which is illustrated in Figure 3. In Case Study I, the optimized operating condition improves the hourly profit by $50.92 in average, while in Case Study II, the optimized operating conditions reduce the hourly loss by $120.17 in average.

Table 2. Market price setting (unit in USD/MMBtu) for two scenarios

	Raw Material	Methane	Ethane	Propane	Butanes	Pentanes
Case I	3.6	3.6	4.5	7.0	7.8	9.7
Case II	4.1	3.1	4.6	7.5	7.8	8.8

Table 3. Optimized SP values for two scenarios

	FIC-100	RIC-100	LIC-100	LIC-101	RIC-101	PIC-100	XIC-100	ERIC-100
Case I	5112	0.621	43.97	51.44	0.451	1101.1	0.009	0.738
Case II	4697	0.624	36.51	46.39	0.453	1076.9	0.009	0.738

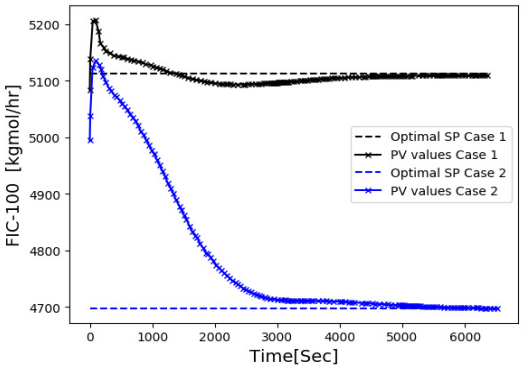

Figure 3. Illustration of the optimized SP values and their corresponding responses for FIC-100 control loop.

5. Conclusion

In this work, an optimization framework based on the use of surrogate models is implemented for optimizing the operating conditions of a CRR unit. Two sub-models are utilized to build the correlation between the profit and the operating conditions of the process. The dynamic surrogate model is established using deep learning techniques, namely a bidirectional LSTM with attention mechanism, which gives accurate predictions of the dynamic behavior. After that, another regression model (a neural network) is opted to incorporate market prices with system status for profit prediction. Utilizing the entire surrogate model, the optimal operating conditions are determined by a differential evolution optimizer that maximizes the profit corresponding to market price.

Reference

J. Chebeir, S. Salas, J. Romagnoli, 2019, Operability assessment on alternative natural gas liquids recovery schemes, Journal of Natural Gas Science and Engineering 71, 102974

J. Lynch, C. Cairo, H. Hudson, J. Wilkinson, 2002, Unique design challenges in the aux sable NGL recovery plant, presented at the 81st Annual Convention of the Gas Processors Association, Dallas, T.

M. Schuster, K. K. Paliwal, 1997, Bidirectional recurrent neural networks, IEEE Transactions on Signal Processing 45 (11) 2673-2681

R. Campbell, J. Wilkinson, 1981, Hydrocarbon gas processing (U.S. Patent 4 278 457).

R. Storn, K. Price, 1997, Differential evolution-a simple and efficient heuristic for global optimization over continuous spaces, Journal of global optimization 11 (4) 341-359

S. Hochreiter, J. Schmidhuber, 1997, Long short-term memory, Neural computation 9 (8) 1735-1780

T. Rocktaschel, E. Grefenstette, K. M. Hermann, T. Kocisky, P. Blunsom, 2015, Reasoning about entailment with neural attention, arXiv preprint arXiv:1509.06664 (2015)

W. Luyben, 2013, NGL demethanizer control, Industrial and Engineering Chemistry Research 52 (33) 11626-11638.

Sauro Pierucci, Flavio Manenti, Giulia Bozzano, Davide Manca (Eds.)
Proceedings of the 30th European Symposium on Computer Aided Process Engineering (ESCAPE30), May 24-27, 2020, Milano, Italy.
http://dx.doi.org/10.1016/B978-0-12-823377-1.50216-0

Control Strategies for Natural Gas Liquids Recovery Plants

Stefania Tronci[b]*, Jorge A. Chebeir[a], Marta Mandis[b], Roberto Baratti[b], José A. Romagnoli[a]

[a]*Department of Chemical Engineering, Louisiana State University,Baton Rouge, LA 70809, United States of America*
[b]*Dip. di Ingegneria Meccanica, Chimica e dei Materiali, Università degli Studi di Cagliari, Cagliari 09123 Italy*
stefania.tronci@dimcm.unica.it

Abstract

Nowadays the improvements on the extraction methods of natural gas has increased the availability of natural gas liquids (NGL), which represent a valuable source of energy and industrial feedstock. Several process schemes have been developed in the past for an economical, safe and efficient recovery of these components including the conventional, cold residue recycle (CRR), and gas subcooled process (GSP), each comprising a range of competing advantages. In the present work, the control problem of the NGL extraction in a CRR process scheme is addressed aiming to achieve a recovery of at least 84% of ethane while maintaining low the level of methane impurity in the bottom of the demethanizer. Considering the high cost of composition analyzers, different temperature control structures are assessed. The temperature direct control and cascade control are proposed to improve the rejection of the disturbances. The operability of these NGL recovery technologies is evaluated under typical disturbances.

Keywords: natural gas liquids recovery, multivariable control, controllability, dynamic process simulation, pressure-compensated temperature.

1. Introduction

The technological advancement of recent years on fracking methods for the extraction of natural gas has brought to the access to huge volumes of gas trapped in shale formations. This has led to an increase in the quantities of natural gas available and a consequent decrease in its selling price, fallen drastically to less than 30% of their previous highs (Luyben et al., 2013). Natural gas liquids (NGL) are a valuable commodity consisting of the hydrocarbon fractions of ethane, propane, butane and heavier hydrocarbons contained in natural gas. These compounds have a higher selling price than the raw gas, justifying the construction and implementation of separation plants for their recovery. For this reason, different process configurations have been developed and analyzed for the separation of NGL from the raw natural gas. The conventional NGL recovery process has been modified to improve the separation and reduce the operating costs through the energy integration of flows. Among the new configurations proposed, Cold Residue Recycling Process (CRR) and Gas Subcooled Process (GSP) are the best known and most used in gas treatment plants (Kherbeck and Chebbi, 2015). The first separation equipment used is a high-pressure cryogenic distillation column for the separation of methane (the most important fraction in the raw gas), which is called demethanizer. In the literature, several works covering different NGL recovery processes have been presented by

Manning and Thompson (1991), Kidnay and Parrish (2011), Chebbi et al. (2010), and Park et al. (2015).
The control of concentrations achieved through the separation process under typical disturbances such as changes in flow rate or input compositions, has been investigated in contributions by Luyben et al. (2013) and Chebeir et al. (2019). The latter represents the starting point of this work. The dynamic response of the CRR process scheme is analyzed in terms of achieving the control objectives and reducing process upsets under typical disturbances, considering two alternative control strategies. In particular, a ratio flow rate controller in cascade with temperature controller in the demethanizer column, to reduce the methane concentration in the column bottom flow, and a pressure compensator in the separator to improve ethane recovery were considered. The purpose of this article is to formulate and implement a control strategy for the NGL process avoiding the use of costly concentration analyzers.

2. Background

2.1 Flowsheet
The dynamic simulation of CRR process was developed in the process simulator Aspen HYSYS® and based on realistic operating conditions optimized under nominal operation (Chebeir et al., 2019). The raw gas was fed to the separation units with a molar flow rate of 4980 kmol/h and a composition with a low content of liquids (Table 1), with the following inlet conditions: pressure equal to 5818 kPa and temperature equal to 35 °C.

Table 1: Feed composition (Chebbi et al., 2010)

Components	Mol fractions
Nitrogen	0.01
Methane	0.93
Ethane	0.03
Propane	0.015
Butanes	0.009
Pentanes	0.003
Hexanes	0.003
$\%C_{2+}$	6

The main component of the separation unit was the demethanizer column, with 30 stages and three feed streams introduced at Stages 2, 8 and 26. Another important unit was the separator, positioned upstream of the demethanizer. Variations in inlet flow rate induced a change in its pressure and then, at constant temperature, changes in outflow composition that was fed to the column. In this context, the specifications required by the CRR configuration were 84% ethane recovery and 1% mol methane composition at the base of the demethanizer column.

2.1 Temperature sensor placement
As a first step, the optimal sensor temperature location to control the column temperature profile and consequently the concentration has been carried out. To this aim, an analysis of the temperature and composition gradients inside the column was performed. The temperature and the composition profiles are flat in the main part of the column. This means that separation takes place in the last few stages of the stripping section and in the top of the column. Through the analysis of the temperature gradient with per-component

contribution diagram (Porru et al., 2013), it was found that the most appropriate location for the sensor is on tray 28.

3. System Dynamics and Control structure

Different control strategies were compared with two main objectives: to maintain a methane composition of 1% mol in the bottom product stream, to maintain the recovery of ethane at 84 %. In this contribution, the control structure proposed by Chebeir et al. (2019) was modified to consider the possibility of attaining the composition and recovery goals without the utilization of composition analyzers.

3.1 Ethane Recovery

First, the possibility of removing the ethane recovery controller, which manipulated the set point of the separator's temperature controller, was studied. A constant recovery of ethane was maintained by compensating the pressure changes in the separator. This has been achieved by modifying the separator temperature control. The process variable was adapted based on the pressure changes. The pressure-compensated temperature (PCT) was determined by the relation reported below, which is derived from Antoine's Equation: (Brambilla, 2014):

$$PCT = T^m - C \ln \frac{P}{P^{rif}}$$

Here, T^{m} and P were respectively the measured separator temperature and pressure; P^{rif} was the nominal separator pressure; C was the compensation coefficient determined by obtaining temperature values for pressure variations at constant composition in the Aspen HYSYS® simulation.

3.2 Methane bottom impurity

The responses obtained through the action of two different control structures to maintain the methane concentration at the bottom of the demethanizer were compared. The first structure was a direct control of the temperature on the 28th stage by means of reboiler duty. The second structure was a cascade control, where the temperature on the 28th stage was controlled by means of a temperature primary controller that gave the set point to a ratio controller that maintained constant the ratio between the boilup and the bottom stream, manipulating the reboiler duty. The boilup flow rate measurement, not available in practice, was estimated by knowledge of the measures of bottom flow rate and reboiler duty. The estimation was computed assuming that the boilup was only composed by ethane and considering that only a fraction (correlated to the variation of the duty by means of a regression, estimated under different operating conditions) of the reboiler duty was used to generate the vapor fed back to the column. This was the result of using part of the reboiler duty to bring the mixture to saturation conditions when methane gas solute was present. The control loops were tuned independently once the process transfer function matrix has been evaluated. The tuning was conducted through the step test model identification and using the IMC approximate model rules for PI controllers (Rivera et al., 1986). The tuning parameters for the different structures are reported in Table 2.

Table 2: *Control structures tuning parameters*

Controllers	Kc	τi
Direct	1.33	15.2
Primary Cascade loop	4.04	13.8
Secondary Cascade loop	1.53	0.287

4. Results

4.1 Ethane Recovery

The dynamic response of the ethane recovery in the CRR separation process was investigated considering step changes in the feed flow rate. An increase of 10% and a decrease of the same percentage on the nominal value of 4980 kmol/h were considered. The flow rate changes induced pressure variations in the separator, and the temperature was maintained constant by a temperature controller. In this work, it has been attempted to limit the impact of these pressure variations on the ethane recovery, with a target value of 0.84, through the control of the temperature compensated in pressure on the separator. The results obtained in terms of the ethane recovery objective, performed without concentration control, for a decreasing of 10% in the inlet feed stream are showed in Figure 1. This variation produces a decrease in the separator pressure of 3.87 bar, with a maximum initial variation of 5.71 bar with the temperature controller and a decrease in the pressure separator of 4.26 bar, with a maximum initial variation of 6.35 bar with the pressure compensated temperature controller.

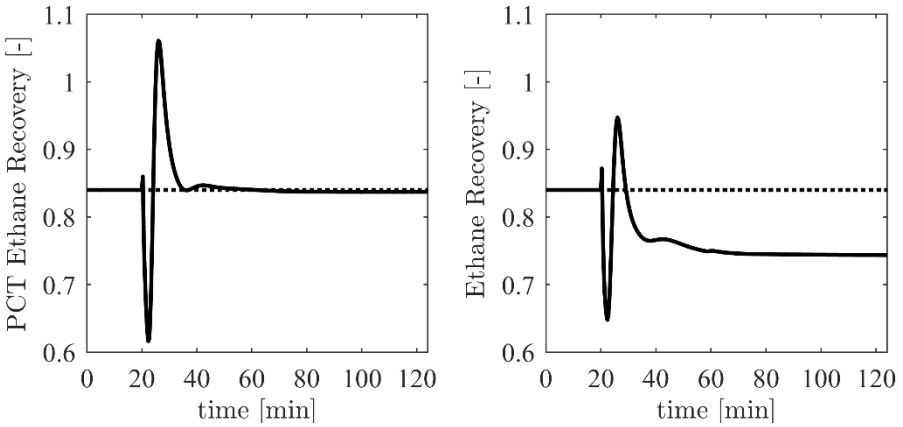

Figure 1: Ethane recovery for a decreasing of 10% in the feed flow rate with the separator pressure compensated temperature control (on the left panel) and with the separator temperature control (on the right panel)

As depicted by Figure 1 (right panel), the process is not able to maintain the recovery target when the ethane recovery control is removed from the configuration. The new steady state reached a value of 0.7437 with an offset of 0.0963. However, with the modification proposed on the separator temperature controller, even without an ethane concentration analyzer and an ethane composition controller, it is possible to bring the ethane recovery to the value 0.8372 with an offset of 0.0028, near to the target value of 0.84. The recovery stays off specification for about 20 minutes from the initial variation. Analog results are obtained with the increasing of 10% in the feed flow rate, that are reported in Table 3.

Table 3: Ethane recovery results for an increasing of 10% in the feed flow rate

	Final DP	**Max DP**	**New steady states value**	**Offset**
PCT control	4.18 bar	7.97 bar	0.838	0.0020
T control	3.66 bar	7.21 bar	0.898	0.0582

4.2 Methane bottom impurity level

The dynamic response of the methane concentration in the demethanizer bottom was investigated by step changes in the feed flow rate. For an increase/decrease of 10% on the nominal value of 4980 kmol/h, the response obtained through the action of the cascade and temperature direct controllers were compared. The results obtained for of 10% decrease in the inlet feed stream for methane concentration, 28th tray temperature and reboiler duty, are depicted by Figure 2.

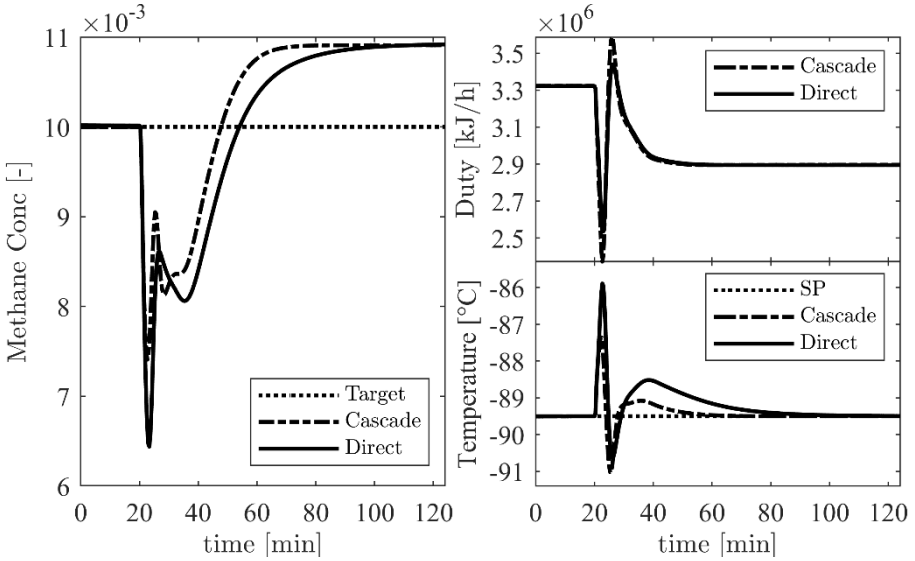

Figure 2: Dynamic response obtained by cascade and temperature direct controls for a decreasing of 10% in the feed flow rate: methane concentration profile (left panel); reboiler duty profile (top right panel); 28th Tray temperature profile (bottom right panel)

Observing the concentration profile in Figure 2 (left panel), obtained by the cascade temperature control, it is possible to appreciate a lower initial deviation and a higher speed of convergence to the new steady state value when compared to the direct temperature control. None of the two configurations can bring back the methane impurity to the target value of 1% mol. In both approaches, the methane concentration achieves a new value of 0.0109 at different times: the temperature direct control after around 65 min with a final off-set of 0.0009; the approximate cascade after around 43 min, with an off-set of 0.0009. In the right-hand side panels of Figure 2, the temperature profiles on the 28th tray are displayed in the bottom. In this case, it can also be concluded that the cascade control structure has a faster response (it reaches the set point value of 89.5°C around 35 minutes earlier) and a lower initial variation. This behaviour could be explained by considering that the column internal flow rates have faster dynamics than the temperature ones and consequently, the ratio controller action is more aggressive (see top right panel of Figure 2). After an initial time, the response of the manipulated actions in these controllers are comparable. Similar results are obtained with an increase of 10% in the feed flow rate (reported in Table 4).

Table 4: Methane bottom impurity level results for an increasing of 10% in the feed flow rate

Controller	New steady states value	Offset	Response time
Direct	0.0094	0.0006	76 min
Cascade	0.0094	0.0006	52 min

5. Conclusions

Several control strategies were compared with the main objective of achieving the methane composition of 1% mol, while maintaining ethane recovery at 84% in the demethanizer bottom in presence of changes in the inlet flow rate. It was shown that even without ethane recovery controller, it was possible to achieve the same recovery when using pressure compensated temperature in the separator as controlled variable. Comparing the impurity control of methane concentration with cascade control and direct temperature control for step changes in the inlet flow rate, we concluded that the cascade configuration had the best control performance. This controller had the fastest response and maximum convergence speed for controlling the temperature and composition of the methane in the bottom product stream.

References

A. Brambilla, 2014. *Distillation Control and Optimization*. McGraw-Hill Education.

A. J. Kidnay, W. R. Parrish, D.G., McCartney, 2011. *Fundamentals of natural gas processing*. Second ed., CRC press. Boca Raton, FL.

D. E. Rivera, M. Morari, S. Skogestad, 1986. *Internal Model Control 4. PID Controller Design*. I&C Process Design Development, 25,252.

F. S. Manning, R. E. Thompson, 1991.*Oilfield Processing: Natural Gas*; PennWell Publishing Co. Tulsa, USA.

J. Chebeir, S. D. Salas, J. A. Romagnoli, 2019. *Operability assessment on alternative natural gas liquids recovery schemes*. Journal of Natural Gas Science and Engineering Volume 71, 102974.

J.H. Park, M.S. Khan, R. Andika, M. Getu, A. Bahadori, M. Lee, 2015. *Techno-economic evaluation of a novel NGL recovery scheme with nine patented schemes for offshore applications*. J Nat Gas Sci Eng. 27, 2-17.

L. Kherbeck, R. Chebbi, 2015. *Optimizing ethane recovery in turboexpander processes*. Ind Eng Chem Res. 21, 292-297.

M. Porru, J. Alvarez, R. Baratti, 2013. *Composition Estimator Design for Industrial Multicomponent Distillation Column*. Chemical engineering transactions vol. 32.

R. Chebbi, N. S. Al-Amoodi, N. A. Jabbar, G. A. Husseini, & K. A. Al Mazroui, 2010. *Optimum ethane recovery in conventional turboexpander process*. Chemical engineering research and design, 88(5-6), 779-787N.

W.L. Luyben, 2013. *NGL demethanizer control*. Ind Eng Chem Res. 52(33), 11626-11638.

Sauro Pierucci, Flavio Manenti, Giulia Bozzano, Davide Manca (Eds.)
Proceedings of the 30th European Symposium on Computer Aided Process Engineering (ESCAPE30), May 24-27, 2020, Milano, Italy.
http://dx.doi.org/10.1016/B978-0-12-823377-1.50217-2

Global Optimization of Refinery – petrochemical Operations via Process Clustering Decomposition

Ariel Uribe-Rodriguez[a,b], Pedro M. Castro[c], Benoît Chachuat[b,*], Gonzalo Guillén-Gozálbez[d]

[a] *Colombian Petroleum Institute, ECOPETROL, Colombia*
[b] *Centre for Process Systems Engineering, Department of Chemical Engineering, Imperial College London, United Kingdom*
[c] *Centro de Matemática Aplicações Fundamentias e Investigação Operacional, Faculdade de Ciências, Universidade de Lisboa, Portugal*
[d] *Institute for Chemical and Bioengineering, Department of Chemistry and Applied Biosciences, ETH Zürich, Switzerland*
b.chachuat@imperial.ac.uk

Abstract

We consider the short-term planning of an integrated refinery and petrochemical complex using a mixed-integer nonlinear optimization. The process network is represented by input-output relationships based on bilinear and trilinear expressions to estimate yields and stream properties, fuels blending indices and cost functions. Binary variables select the operating modes for the process units. Our global optimization algorithm decomposes the network into small clusters according to their functionality. For the constraints inside a given cluster, we formulate a mixed-integer linear relaxation based on piecewise McCormick envelopes. The partitions for the variables are updated dynamically and their domain is reduced applying optimality-based bound tightening. For the constraints outside the cluster, we use the standard McCormick envelopes. Our approach is demonstrated on an industrial-size case study representing a typical planning scenario in Colombia. Results show that it outperforms the state-of-the-art commercial solvers ANTIGONE and BARON not only in terms of optimality gap (8 vs. 58 and 48%, respectively) but also the quality of the solution itself.

Keywords: planning, refinery-petrochemical, process-clustering, global optimization.

1. Introduction

The integration of refinery and petrochemical operations exploits the synergy between various processes, optimizing utility requirements, reducing operating costs and ensuring the fulfilment of environmental regulations, all together increasing the profitably margin of a wide range of products, from fuels to petrochemicals. Recently, deterministic global optimization and Lagrangean decomposition have been applied to short-term planning of integrated refining and petrochemical operations. These problems were formulated as large-scale nonconvex mixed-integer nonlinear programs (MINLP). Along these lines, Li et al. (2016) reported a profit improvement of 30%–65%, and Zhao et al. (2017) between 14%–53%, compared to optimizing sequentially the refinery and then the ethylene plant.

Herein, we propose a deterministic global optimization algorithm for such large-scale MINLP based on a two-stage procedure, alternating the solution of a mixed-integer linear

program (MILP) relaxation and a nonlinear program (NLP) restriction of the original MINLP. Our approach decomposes the process network into small clusters (i.e. crude oil unloading, refining operations and fuels blending), which are then explored sequentially. The bilinear terms present into the constraints of the active cluster are relaxed with piecewise McCormick envelopes (Bergamini, Aguirre, and Grossmann 2005), after reducing the domain of their variables through optimality-based bound tightening (Puranik and Sahinidis, 2017). Outside the active cluster, McCormick envelopes (McCormick, 1976) relax the bilinear terms.

2. Elements for global optimization

The short-term planning problem can be cast as the following nonconvex MINLP, where x represents a $n-$ dimensional vector of non-negative continuous variables for flowrates and stream properties, constrained between given lower x^L and upper x^U bounds; y is a $r-$ dimensional vector of binary variables to determine operating conditions. The functions f_q: $\mathbb{R}^n \times \mathbb{R}^r \to \mathbb{R}$, with $q = 0, \dots, Q$, comprising the objective functions and the constraints, are quadratic in x and linear in y: $f_q(x,y) \coloneqq \sum_{(i,j)\in BL_q} a_{ijq} x_i x_j + B_q x + C_q y + d_q$; BL_q is an (i,j)-index set defining the bilinear terms $x_i x_j$ present in quadratic function f_q; parameters a_{ijq} and d_q are scalars, whereas B_q and C_q are row vectors:

$$\begin{aligned} &\max f_0(x,y) \\ &\text{s.t.} \\ &\quad f_q(x,y) \le 0\,, \forall q \in \{1,\dots,Q\} \\ &\quad x \in [x^L, x^U] \subseteq \mathbb{R}^n_+, y \in \{0,1\}^r \end{aligned} \tag{P}$$

In order to solve problem P, our deterministic global optimization algorithm solves a series of upper and lower bounding problems, named respectively PR and PF.

2.1. Process clustering

Following the workflow, the physical system is first clustered into process sections dealing with crude unloading and blending, crude distillation, refining processes, petrochemical processes and fuel blending. For example, crude allocation and blending determine the crude distillation unit's feed streams (flowrate and quality) and hence their operation. Crude fractionation then determines the performance of petrochemical and refining processes, which generate all intermediate streams needed for fuel blending.

2.2. Lower bounding

The NLP restriction PF is a version of P with fixed binary variables $\hat{y}$, obtained from solving PR.

$$\begin{aligned} z^{PF} \coloneqq \max\ & f_0(x,\hat{y}) \\ \text{s.t. } & f_q(x,\hat{y}) \le 0, \forall q \in \{1,\dots,Q\} \\ & x \in [x^L, x^U] \subseteq \mathbb{R}^n_+ \end{aligned} \tag{PF}$$

If feasible, solution z^{PF} provides a lower bound on the optimal value of P.

2.3. Upper bounding

The MILP relaxation is obtained by substituting bilinear terms $x_i x_j$ in P with new variables w_{ij}, thus linearizing $f_q(x,y)$ into $f_q^R(x,y,w)$. It also includes either standard (SME) or piecewise McCormick (PWME) envelopes, relating w_{ij} to the x_i and x_j variables and their bounds:

$$\begin{aligned} z^R := \ & \max f_0^R(x,y,w) \\ & \text{s.t.} f_q^R(x,y,w) \le 0\ , \forall q \in \{1,\dots,Q\} \\ & x \in [x^L, x^U] \subseteq \mathbb{R}_+^n, y \in \{0,1\}^r \end{aligned} \tag{PR}$$

PWME is tighter but since it uses binary variables to partition the domain of one of the variables (e.g. x_j) in every $x_i x_j$ term, it may lead to an intractable MILP even with a moderate number of partitions N_j. We compromise by partitioning x_j only if j belongs to the current cluster ($j \in CL$). Otherwise, we use SME. Since, PR is a relaxation of P, PR will be feasible whenever P is feasible and its optimal value z^R of PR will provide a finite upper bound UB on that of P.

2.4. Bounds contraction

The PR relaxation is improved by solving optimality-based bound tightening problems (OBBT). The bounds on a variable x_h appearing in a bilinear term of cluster CL can be tightened by solving two optimization problems.

$$\begin{aligned} x_h^L / x_h^U := \ & \min/\max x_h \\ & \text{s.t.} f_0^R(x,y,w) \ge LB \\ & f_q^R(x,y,w) \le 0\ , \forall q \in \{1,\dots,Q\} \\ & x \in [x^L, x^U] \subseteq \mathbb{R}_+^n, y \in \{0,1\}^r \end{aligned} \tag{OBBT}$$

As PR, OBBT linearizes the bilinear terms and relaxes the problem using the SME and PWME relaxations. The number of partitions N_j is set to 2 for all partitioned variables inside cluster CL so as to keep the problem tractable.

2.5. Dynamic partitions updating

The maximum normalized deviation $\lambda_j \in [0,1]$ between the exact value of the bilinear term $x_i x_j$ and its relaxation w_{ij} drives the partitions update:

$$\begin{aligned} \delta_j &= \begin{cases} \Delta \ if\ \lambda_j > \tau \\ 0 \text{ Otherwise} \end{cases} \\ N_j^* &= \min(N_j + \delta_j, N^{max}) \end{aligned} \tag{1}$$

For each $j \in CL$. We use the threshold τ to determine the increasing in the number of partitions δ_j. Thus, the number of partitions N_j^* is updated by Δ until reaching its maximum number N^{max}.

2.6. Global optimization algorithm

The models described in sections 2.1 to 2.4 and the dynamic partition scheme showed in section 2.5 are combined into the following global optimization algorithm based on process cluster-decomposition. The model size for PR increases dynamically as a function

of CL and N_j (see steps 5.1 and 5.7). Consequently, the runtime for solving PR increases across the iterations until reaching the $MaxRunTimePR$ or ε^{PR}. The algorithm outputs are the lower LB and upper UB bounds on the global objective value of P, as well as a feasible short-plan corresponding to LB.

1. Initialize $MaxRunTime$, $MaxRunTimePR$, $MaxNumIter$, ε, ε^{PR},N, N^{max}.

2. Set $UB = -\infty$, $LB = +\infty$, $Iter = 0$.

3. Solve problem P and update $LB \leftarrow z$.

4. Solve relaxed problem PR (using the McCormick relaxation for all bilinear terms since there are no active clusters at this point) and update $UB \leftarrow z^R$.

5. For each cluster k do:

5.1. Set active cluster(s) $CL = \bigcup_{l=1}^{k} CL^l$.

5.2. Define $N_j = N$ for every partitioned variable x_j belonging to cluster CL^l. If $l \geq 2$ set the number of partitions in clusters $CL^1, \ldots CL^{l-1}$ to their final values N_j^* determined in previous iterations.

5.3. Generate a population with up to PFS feasible solutions of PR and select the best solution, z^Ramong them. If $z^R < UB$, update $UB \leftarrow z^R$

5.4. Fix binary variables in P ($y \leftarrow \hat{y}$). Solve up to PFS instances of problem PF where the binary variable $\hat{y}$ are set to the feasible solutions of PR, and select the best feasible solution z^{PF}. If $z^{PF} > LB$, update $LB \leftarrow z^{PF}$.

5.5. If the cluster relative optimality gap $\varepsilon_{CL} = (UB - LB)/UB$ does not decrease continue to step 5.8.

5.6. Tighten the variable bounds by solving the OBBT problems.

5.7. Update N_j via Eq. (1). The optimal number of partitions N_j^* for the current cluster is propagated, so it is used as initial number of partitions for the next cluster. Return to step 5.3.

5.8. Do $Iter \leftarrow Iter + 1$. If $MaxRunTime$ is reached, or $Iter > MaxNumIter$, or $\varepsilon_{CL} \leq \varepsilon$, stop. Otherwise, increase cluster index k and loop.

3. Case Study

The industrial complex under study is composed of a medium conversion refinery for manufacturing several grades of gasoline, diesel and fuel oil, and a set of petrochemical processes for providing BTX, polyethylene, propylene, waxes and specialty solvents (see Figure 1). These commodities mostly supply the Colombian market, while a small part is exported. The total refining capacity is 240 kbbl/day. We assume a domestic petroleum production equal to 297 kbbl/day, involving 17 types of crude oil distributed over 8 geographical regions. The refinery can also import 7 types of crude, with up to 15 kbbl/day per crude. The logistic system comprises four river fleet routes and a system of nine pipelines. It deliveries crude oil from the production wells and import ports to the industrial complex as well as commodities from/to the industrial facility to/from the markets. The process network is composed of 60 industrial plants which are represented by about 155 models aggregated into six clusters defined using engineering insight: logistic and crude allocation (8 models), crude distillation units (13), vacuum and debutanizer columns (11), refining (53), petrochemical (48) and fuels blending (22). In

total, 88 intermediate refined streams are routed to produce up to 22 different fuels grades (see Table 1) with a given quality specifications as indicated in Table 2. The network has four recycles: (i) LCO recycling from FCC for the fulfillment of diesel HDT feedstock; (ii) in the separation of BTX mix; (iii)-(iv) in the solvent extraction to produce waxes.

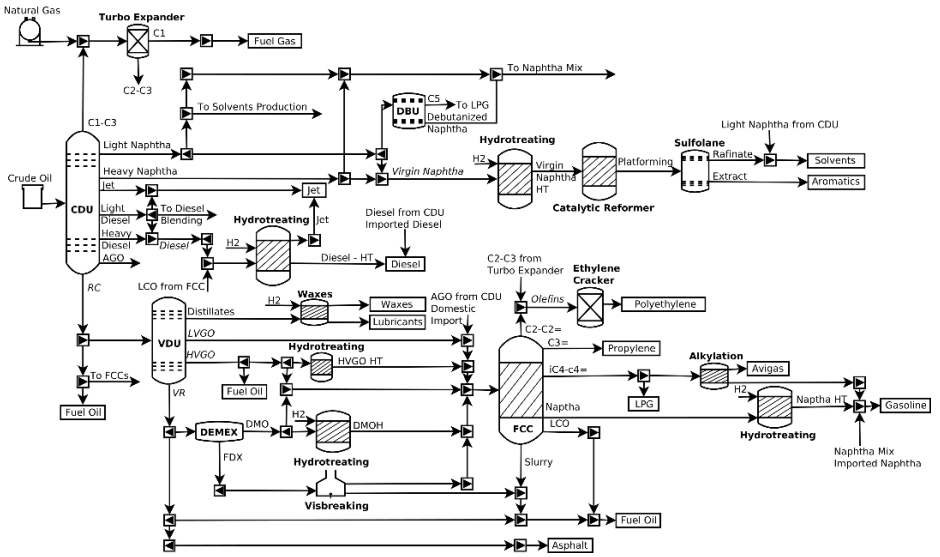

Figure 1. Integrated refinery - petrochemical complex

Table 1. Intermediate refined streams for fuels blending.

Fuel	LPG	Gasoline	Medium distillate	Fuel Oil	Asphalt
Streams to blend	24	23	25	10	6
Products grade	3	7	6	4	2

Table 2. Fuels quality specifications.

Fuel/Quality	Specific gravity	Sulphur content	Cetane number	RON	RVP	Viscosity
LPG	x					
Gasoline	x	x		x	x	
Medium distillate	x	x	x			
Fuel Oil	x	x				X
Asphalt	x	x				X

Figure 2 compares the clustering approach with the two most widely used commercial global optimization solvers, showing the progress of the profit (LB) and best-possible solution (UB) with the computational time. Both ANTIGONE and BARON are able to quickly identify a feasible solution, but no bound improvements are observed up to the maximum runtime (10 CPU hours). On the other hand, our approach starts with the same profit as ANTIGONE, but with a tighter UB, corresponding to $\epsilon = 42\,\%$. After processing Cluster I, our approach can reduce the optimality gap to 8%. This is accomplished through the OBBT step, which reduces the domain of the decision variables in CL^I by 23% on average, and by increasing the number of partitions for the variables in

this sub-system. More importantly, the profit increases sharply from 2.634 to 2.928 MM$/day. During Clusters II and III, ϵ remains unchanged, while the profit increases to 2.964 MM$/day, after going through Cluster IV. This value is 11 % and 10% greater than the figures reported by ANTIGONE and BARON, respectively.

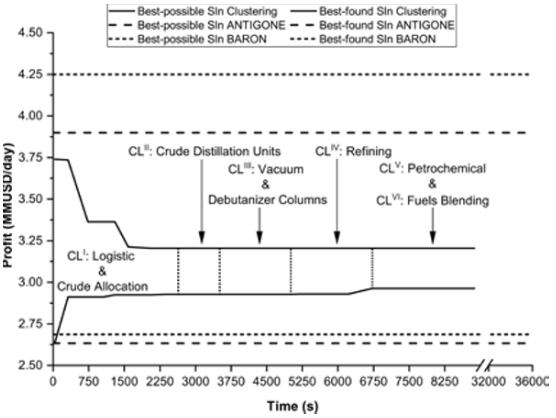

Figure 2. Solvers performance for the case study.

4. Conclusions

This paper has presented a novel cluster-based decomposition approach for the short-term planning of an integrated refinery-petrochemical facility. The problem is formulated as a large-scale MINLP, with the binary variables selecting the optimal operating mode of conversion processes. Nonconvexities also arise from the correlations used to predict yields and stream properties, cost functions, intermediate pooling and fuels blending constraints. The topology complexity of the real-life case study addressed in this work, logistic considerations for the reception and delivery of commodities as well as the complexity of the crude basket selection and product allocation tasks, altogether made it challenging to find high-quality solutions within a reasonable optimality gap. While all algorithms were able to identify feasible solutions, our approach outperformed BARON and ANTIGONE, in terms of profit, optimality gap and computational runtime.

Acknowledgments

The authors would like to acknowledge the financial support from the Colombian Science Council (COLCIENCIAS) and the Colombian Petroleum Company (Ecopetrol S.A.).

References

Bergamini, M. L., Aguirre, P. and Grossmann, I.E. 2005. “Logic-Based Outer Approximation for Globally Optimal Synthesis of Process Networks.” *Computers and Chemical Engineering* 29 (9): 1914–33.

Li, J., Xin X., Boukouvala F., Floudas, C.A., Zhao, B., Du, G., Su, X. and Liu, H. 2016. “Data-Driven Mathematical Modeling and Global Optimization Framework for Entire Petrochemical Planning Operations.” *AIChE Journal* 62 (9): 3020–40.

McCormick, G. P. 1976. “Computability of Global Solutions to Factorable Nonconvex Programs: Part I - Convex Underestimating Problems.” *Mathematical Programming* 10 (1): 147–75.

Puranik, Y. and Sahinidis N.V. 2017. “Domain Reduction Techniques for Global NLP and MINLP Optimization.” *Constraints* 22 (3): 338–76.

Sauro Pierucci, Flavio Manenti, Giulia Bozzano, Davide Manca (Eds.)
Proceedings of the 30th European Symposium on Computer Aided Process Engineering (ESCAPE30), May 24-27, 2020, Milano, Italy.
http://dx.doi.org/10.1016/B978-0-12-823377-1.50218-4

A Robust Nonlinear Estimator for a Yeast Fermentation Biochemical Reactor

Silvia Lisci, Massimiliano Grosso*, Stefania Tronci
Dipartimento di Ingegneria Meccanica, Chimica e dei Materiali, Università degli Studi di Cagliari, Cagliari I-09123, Italy
massimiliano.grosso@dimcm.unica.it

Abstract

Nonlinear state estimation is an active research area, particularly to address monitoring and control problems in continuous processes. Recently, literature evidenced that bioproduction of chemicals and pharmaceuticals, which usually employs batch manufacturing, can have significant product quality and financial benefits when using continuous mode. In this paper, the geometric approach is used to address the estimation problem of a bioreactor for ethanol production. The work is based on a detailed model reported in the literature, hereafter considered as the virtual plant. The main objective is to compare different estimation solutions depending on the available measurements and the characteristics of the considered sensors.

Keywords: soft-sensing, bioprocessing, nonlinear observer

1. Introduction

Continuous processes are generally quite common in chemical industries, but biomanufacturing, like pharmaceutical industry, still prefers batch processes (Croughan et al., 2015). However, because of the necessity to be more competitive, also biotechnology processes are starting to consider the use of continuous operation (Galvanauskas et al., 2019). The main issue when dealing with continuous process is that an adequate monitoring and control system is required, because possible deviations need to be detected in time and counteracted, leading to a robust production with constant performance (Tronci et al., 2011; Baratti et al., 2018). Product quality indexes of bioprocesses such as biomass, substrate, product or by-product, dissolved oxygen concentrations need to be measured in order to ensure that requirements are met. Unfortunately, those variables are often difficult to measure in real-time, resulting from the complex nature of biological systems (Spigno and Tronci, 2015) and a lack of adequate measuring device (Holzberg et al., 2018). It is worth noting that several disturbances can affect the system and that the states' dynamics are in general governed by complex and nonlinear processes. This means that the application of a continuous mode cannot be considered if a proper monitoring and control system is not applied and this cannot be satisfied if proper sensors are not available.

A nonlinear estimator can be a possible approach to deal with a lack of in-line measurements. The combination of a process model and a measurement processor allows the reconstruction of all the states of the process if the considered system is observable at the given conditions. In this paper, the geometric approach is used to address the estimation problem of a bioreactor for the production of ethanol. The work is based on the model proposed by Nagy (2007), which is considered as the virtual plant. The main

objective is to compare different estimation solutions depending on the available measurements and the characteristics of the sensors.

2. Process model

The biochemical process considered in the present paper is a fermentation reactor for ethanol production. The model has been carefully developed by Nagy (2007) and subsequently extended by other authors (Lawrýnczuk, 2008; Imtiaz et al., 2013).
The reactor is modeled as a continuous stirred tank (CSTR) with a constant feed rate. The device contains three different components (Eqs. 1-3): the biomass (C_x), namely a yeast suspension fed to the system and continuously removed from it; the substrate (C_s), which is the glucose solution that feeds the microorganisms; the product (i.e. the ethanol, C_P) that is removed from the reactor together with other components. Dissolved oxygen is also present in the reactor (C_{O2}) and it is consumed during the fermentation (Eq. 4). A low dilution rate (F_e/V) is necessary in order to have a quasi-stationary state for biomass and the consequence is the quite slow dynamics of the process. The heat balances in the reactor and in the jacket are also considered (Eqs. 4-5), describing the dynamics of the reactor temperature (T_r) and the coolant temperature (T_{ag}). For sake of brevity, only the mass and energy balances describing the process are reported in the present paper (Eqs.1-6). More details and the values of the parameters can be found in Nagy (2007).

$$\frac{dC_X}{dt} = \mu_X\, C_X\, \frac{C_S}{K_{S1}+C_S} e^{-K_{P1}C_P} - \frac{F_e}{V} C_X \tag{1}$$

$$\frac{dC_P}{dt} = \mu_P C_X \frac{C_S}{K_{S1}+C_S} e^{-K_{P1}\,C_P} - \frac{F_e}{V}\, C_P \tag{2}$$

$$\frac{dC_S}{dt} = -\frac{1}{R_{SX}} \mu_X C_X \frac{C_S}{K_S+C_S} e^{-K_P C_P} - \frac{1}{R_{SP}} \mu_P C_X \frac{C_S}{K_{S1}+C_S}\, e^{-K_{P1}C_P} + \frac{F_i}{V} C_{S,in} - \frac{F_e}{V} C_S \tag{3}$$

$$\frac{dT_r}{dt} = \left(\frac{F_i}{V}\right)(T_{in} + 273) - \left(\frac{F_e}{V}\right)(T_r + 273) + \frac{r_{O_2}\,\Delta H_r}{32\,\rho_r\, C_{heat,r}} - \frac{K_T A_T\,(T_r - T_{ag})}{V\,\rho_r\, C_{heat,r}} \tag{4}$$

$$\frac{dT_{ag}}{dt} = \left(\frac{F_{ag}}{V_j}\right)\left(T_{in,ag} - T_{ag}\right) + \frac{K_T A_T (T_r - T_{ag})}{V_j \rho_{ag} C_{heat,ag}} \tag{5}$$

$$\frac{dC_{O_2}}{dt} = k_l a\left(C^*_{O_2} - C_{O_2}\right) - r_{O_2} \tag{6}$$

3. State estimation

Consider a non-linear dynamic system that can be represented as follows:

$$\frac{dx}{dt} = f\big(x, u(t)\big) \tag{7}$$

$$y = h(x, u) \tag{8}$$

where $x \in \mathbb{R}^n$ is the vector of states, which is indicated as x_0 at the initial instant t_0, $u \in \mathbb{R}^q$is the input vector, $y \in \mathbb{R}^m$ is the output vector, while f is the vector field of n dimension and h is the non-linear vector of m dimension that relates outputs to inputs. As reported in Salas et al. (2019), it is possible to consider a non-linear map ϕ, whose components are the measured outputs and some of their directional derivatives, as reported in Eqs. (9-10)

$$\Phi(x, u) = [\Phi_1, \dots, \dots, \Phi_i, \dots, \dots, \Phi_m]^T \tag{9}$$

$$\Phi_i = \left(h_i(x), L_f^1 h_i(x), \dots, \dots, L_f^{\kappa_i - 1} h_i(x)\right) \tag{10}$$

where $L_f^j h_i(x)$ are the recursive j^{th} Lie derivatives of the time-varying scalar field $h_i(x)$ along the vector field time-variant $f(x, u(t))$, and κ_i is the observability index of the i^{th} output. If the sum of the m observability indices κ_i is equal to the dimension of the state vector and the map $\Phi(x, u)$ is invertible with respect to x, it is possible to relate the measured outputs to the states and to reconstruct the system dynamics. This issue can be assessed by evaluating the rank of the matrix $\partial_x \Phi(x, u)$ for given trajectories, meaning that the system is observable if

$$rank(\partial_x \Phi(x, u)) = n \tag{11}$$

It is important to underline that robust observability can be detected by evaluating the condition number of the observability matrix and its minimum singular value. Such metrics are important tools for choosing the best estimator structure (López and Alvarez, 2004; Salas et al., 2019).

3.1 Geometric observer

If the observability condition is fulfilled then the unmeasured states can be reconstructed at any time, through information obtained from measurements and their derivatives. The estimator used in this work is in the form developed by López and Alvarez (2004)

$$\frac{d\hat{x}}{dt} = \hat{f}(\hat{x}, u(t)) + \Phi_x^{-1} K \left(y - h(\hat{x})\right) \tag{12}$$

$$y = h(\hat{x}) \tag{13}$$

where $\Phi_x^{-1}$is the inverse of the Jacobian Φ_x of the map calculated with respect to system states, K is the observer gain matrix, the components of which are tuning parameters and their values are calculated using the procedure suggested in Alvarez and Fernández (2009).

4. Problem statement

The main purpose of the present investigation is to assess if soft sensors have the potential to solve problems related to the monitoring of bioprocesses with the available transducers. The selected algorithm is the geometric observer, because it includes a robust local convergence and a systematic construction-tuning procedure, making it applicable in nonlinear problems (López and Alvarez, 2004; Alvarez and Fernández 2009). Because a real plant is not available for the present investigation, the study is based on the simulation of the bioprocess. In order to mimic a real situation, two sources of errors are present. The first is an additive white noise which behaves like a uniformly distributed random number in the interval (0,1) and that corrupts the available measurements. The second source is responsible for a model mismatch, which implies that the model used in the estimator is different from the model used to simulate the 'virtual plant'. In particular, it is assumed that the kinetic parameters used in the estimator algorithm are different from the ones reported in Nagy (2007). Model mismatch and measurement noise make the estimation problem more demanding and more representative of an industrial plant.

4.1. Estimator structure

In order to select the best estimator configuration, different tests were carried out considering alternative structures, according to the combinations of observability indexes and innovated states, starting from the full order estimator. For the purpose of the study, it is important to specify that all tests have been carried out by making step variations on three inputs of the model. More specifically, the temperature of the feed entering the bioreactor (T_{in}) was changed after 100 h of simulation, the concentration of substrate inlet ($C_{s,in}$) after 150 h and finally the coolant inlet temperature ($T_{in,ag}$) after 250 h (cf. Table 1).

Table 1 - Model parameters submitted to step-change

T_{in} [°C]	25	30
$C_{s,in}$ [g/l]	60	75
$T_{in,ag}$ [°C]	15	10

The first case analyed is that of a hypothetical ideal situation in which five measurements are available (C_x, C_s, C_{O2}, T_r, T_{ag}), while the product (C_P) is not measured. Temperature measurements and oxygen sensors are usually present in the real plants, while biological related measurements are seldom available (Randek and Mandenius, 2018). The choice of considering substrate and biomass as measured variables has been accomplished by considering the literature on sensors for biomanufacturing (Holzberg et al., 2018). In more detail, robustness, stability, and costs have been considered. The first scenario considering five measured outputs is the less demanding because almost all variables can be monitored on-line.

The second case considers only 4 measured outputs and, for this purpose, only one of the components' measurements is considered. For guaranteeing the observability property, the substrate concentration is used, while the biomass concentration is not a measured output. This situation is more demanding because less information on the states is accessible. Because the condition to be fulfilled is that the sum of the observability indexes associated with each measurement is equal to n, the second case will require the evaluation of one more Lie derivative in order to compensate the lack of the measured output.

5. Results

The dynamic of the estimator in both the cases described above is here reported. When considering five measured outputs, observability property is satisfied with two configurations (Eqs. 14a-b).

$$\Phi_1 = \left[C_x, L_f C_x, C_s, C_{O_2}, T_r, T_{ag}\right], \Phi_2 = \left[C_x, C_s, L_f C_s, C_{O_2}, T_r, T_{ag}\right] \quad \text{(14a-b)}$$

The best structure between (14a) and (14b) can be selected by considering the minimum singular value and condition number of the Jacobian matrix for the two maps. The mean values of the selected indexes calculated along a reference trajectory are reported in Table 2, and they indicate that the second configuration should be the better choice in terms of robustness (lower condition number) and the relationship between measured outputs and states (highest minimum singular value).

Table 2 - Minimum singular values and condition number with five measurements.

	Φ_1	Φ_2
κ	133.29	28.9358
σ	0.0076	0.069

The choice based on Table 2 has been confirmed by the dynamic simulations, where it is evident that the second configuration allows a better reconstruction of the product composition, which is the only unmeasured state (Figure 1). Indeed, the nonlinear estimator (dotted line) is able to reduce the mismatch between the model without correction (dashed line), indicated as open-loop model, and virtual plant (continuous line). The response is highly corrupted by noise, because of the amplification of the measurement error due to the high gain values used to reduce the offset in the ethanol composition estimation.

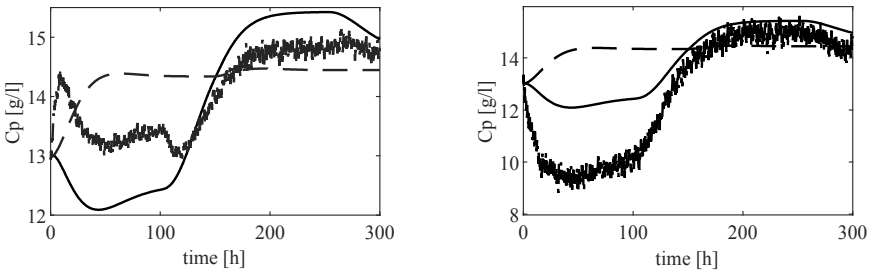

Figure 1. Comparison of the ethanol dynamic behavior between virtual plant (continuous line), open-loop model (dashed line) and estimator (dotted line) for structure with map Φ_1 (left panel)and Φ (right panel).

The same procedure can be used to select the best configuration when only four measured outputs are available. The observability property is satisfied for the following structures (Eqs. 15a-b):

$$\Phi_3 = \left[C_s, L_f C_s, C_{O_2}, L_f C_{O_2}, T_r, T_{ag}\right],\ \Phi_4 = \left[C_s, L_f C_s, C_{O_2}, T_r, L_f T_r, T_{ag}\right] \qquad (15a\text{-}b)$$

The means of the minimum singular value and condition number along the reference trajectory are reported in Table 3.

Table 3 - Minimum singular values and condition number with four measurements.

	Φ_3	Φ_4
κ	1814.8	54.29
σ	0.0842	0.0332

The reconstructed dynamic behavior for the two unmeasured states is reported in Figure 2. Results show that the offset is slightly lower with the map Φ_3, confirming the higher value for σ. This indicates that the directional derivative of substrate concentration with respect to oxygen concentration gives more information on the product dynamics.

6. Conclusions

This work was focused on the development of a soft-sensor for estimating the states of a bioprocess. Results show that the states of the bioreactor can be efficiently reconstructed

using four measurements and that observability was fulfilled if the substrate concentration was measured. The procedure discussed in this paper can be used to select which is the sensor that can give more information on the whole system if a choice is required for reducing costs related to monitoring and control of the process.

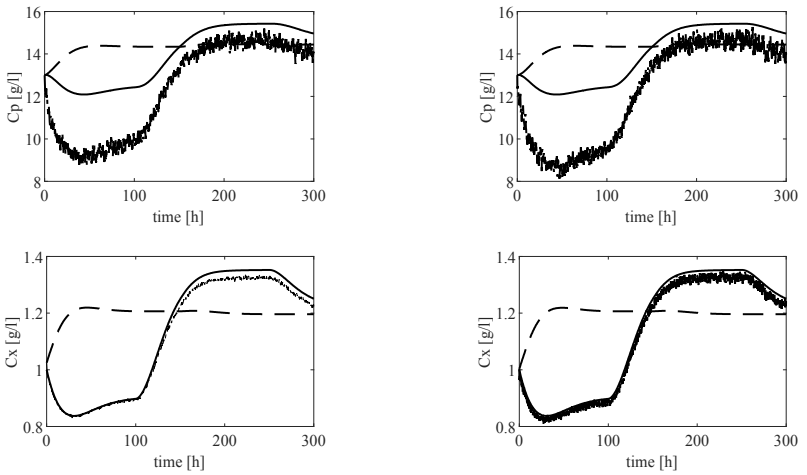

Figure 2. Comparison of the ethanol and biomass dynamic behavior between virtual plant (continuous line), open-loop model (dashed line) and estimator (dotted line) for structure with map Φ_3 (left panel) and Φ_4 (right panel).

References

J. Alvarez, C. Fernández, 2009, Geometric estimation of nonlinear process systems, J. Process Control, 19, 247-260.

R. Baratti, S. Tronci, A. Schaum, J. Alvarez, 2018, Open and closed-loop stochastic dynamics of a class of nonlinear chemical processes with multiplicative noise. Journal of Process Control, 66, 108-121.

M.S. Croughan, K.B. Konstantinov, C. Cooney, 2015, The future of industrial bioprocessing: batch or continuous? Biotechnol Bioeng, 112, 648-651.

V. Galvanauskas, R. Simutis, D. Levišauskas, R. Urniežius, 2019, Practical Solutions for Specific Growth Rate Control Systems in Industrial Bioreactors, Processes, 7(10), 693.

T.R. Holzberg, Timothy R., V. Watson, S. Brown, A. Andar, X. Ge, Y. Kostov, L. Tolosa, G. Rao, 2018, Sensors for biomanufacturing process development: facilitating the shift from batch to continuous manufacturing, Current opinion in chemical engineering, 22, 115-127.

U. Imtiaz, A. Assadzadeh, S.S. Jamuar, J.N. Sahu, 2013, Bioreactor temperature profile controller using inverse neural network (INN) for production of ethanol. Journal of Process Control, 23(5), 731-742.

M. Ławryńczuk, 2008, Modelling and nonlinear predictive control of a yeast fermentation biochemical reactor using neural networks. Chemical Engineering Journal, 145(2), 290-307.

T. López, J Alvarez, 2004, On the effect of the estimation structure in the functioning of a nonlinear copolymer reactor estimator, J. Process Control, 14, 99-109.

Z.K. Nagy, 2007, Model based control of a yeast fermentation bioreactor using optimally designed artificial neural networks, Chemical engineering journal, 127(1-3), 95-109.

S. D., Salas, J.A. Romagnoli, S. Tronci, R. Baratti, 2019, A geometric observer design for a semi-batch free-radical polymerization system. Computers & Chemical Engineering, 126, 391-402.

J. Randek, C.F. Mandenius, 2018, On-line soft sensing in upstream bioprocessing. Critical reviews in biotechnology, 38(1),106-121.

G. Spigno, S. Tronci, 2015, Development of hybrid models for a vapor-phase fungi bioreactor, Mathematical Problems in Engineering, Article ID 801213, 11 pages.

S. Tronci, M. Grosso, J. Alvarez, R. Baratti, 2011, On the global nonlinear stochastic dynamical behavior of a class of exothermic CSTRs, Journal of Process Control, 21(9), 1250-1264.

Sauro Pierucci, Flavio Manenti, Giulia Bozzano, Davide Manca (Eds.)
Proceedings of the 30th European Symposium on Computer Aided Process Engineering (ESCAPE30), May 24-27, 2020, Milano, Italy.
http://dx.doi.org/10.1016/B978-0-12-823377-1.50219-6

Big Data Generation for Time Dependent Processes: The Tennessee Eastman Process for Generating Large Quantities of Process Data

Emil B. Andersen[a], Isuru A. Udugama[a], Krist V. Gernaey[a], Christoph Bayer[b,*], Murat Kulahci[c,d]

[a]*Technical University of Denmark, Department of Chemical and Biochemical Engineering, Process and Systems Engineering Center (PROSYS), Building 229, 2800 Kongens Lyngby, Denmark*
[b]*TH Nürnberg, Department of Process Engineering, Wassertorstraße 10, 90489 Nürnberg, Germany*
[c]*Technical University of Denmark, DTU Compute, Richard Petersens Plads 324, 2800 Kongens Lyngby, Denmark*
[d]*Luleå University of Technology, 97817 Luleå, Sweden*
christoph.bayer@th-nuernberg.de

Abstract

The concept of applying data-driven process monitoring and control techniques on industrial chemical processes is well established. With concepts such as Industry 4.0, Big Data and the Internet of Things receiving attention in industrial chemical production, there is a renewed focus on data-driven process monitoring and control in chemical production applications. However, there are significant barriers that must be overcome in obtaining sufficiently large and reliable plant and process data from industrial chemical processes for the development of data-driven process monitoring and control concepts, specifically in obtaining plant and process data that are required to develop and test data driven process monitoring and control tools without investing significant efforts in acquiring, treating and interpreting the data. In this manuscript a big data generation tool is presented that is based on the Tennessee Eastman Process (TEP) simulation benchmark, which has been specifically designed to generate massive amounts of process data without spending significant effort in setting up. The tool can be configured to carry out a large number of data generation runs both using a graphical user interface (GUI) and through a .CSV file. The output from the tool is a file containing process data for all runs as well as process faults (deviations) that have been activated. This tool enables users to generate massive amounts of data for testing applicability of big data concepts in the realm of process control for continuously operating time dependent processes. The tool is available for all researchers and other parties who are interested.

Keywords: Data generation, Statistical process control, Data-driven control

1. Introduction

With an ever increasing demand for the generation of large amounts of process data that is required for enabling concepts such as Industry 4.0, Big Data and the Internet of Things there is a need for finding efficient ways to generate large amounts of plant and process data. However, researchers who work in the area of data analytics often face significant barriers in obtaining sufficiently large and reliable plant and process data sets from industrial chemical processes for the development of data-driven process monitoring and control concepts. The main barriers can be summarized as follows:

1. Restrictions on the use of industrial plant and process data by corporations due to confidentiality and intellectual property rights issues. Many researchers find it difficult to obtain realistic plant and process data as they are unable to identify industrial partners willing to share data. In other situations researchers may have access to plant and process data, but will be barred from publishing such data sets or required to publish a partially redacted or altered data set (Udugama et al., 2018).

2. Insufficient quality of available process data due to data compression practices which dates back to the era of limited data storage capacity. Similarly, the general lack of regard for past plant data results in key changes to plant and process not being clearly logged with the plant data.

3. The operational doctrine of a production plant is to ensure on-specification production and safe plant operation at all times. Therefore, the plant operators generally prefer to keep their actions to a minimum and to maintain steady state operations. As a result, a large amount of process data logs may contain little to no process movement, which in turn will not reveal key process features.

4. Many chemical engineering processes have nuances and practical limitations which must be considered, particularly if findings made are to be used for control and corrective purposes. This requires the interlinking of key phenomena, which need to be controlled, with process variables that indeed can be manipulated in practice. Hence, to have an adequate presence of domain knowledge and understanding is a key requirement as this is not a trivial exercise (Gajjar et al., 2018).

One method that has been employed to remedy this lack of process data is the use of process simulations that have a proven track record in being applicable in many process control applications in chemical processes (Udugama et al., 2017a, 2017b). Even though the use of dynamic flowsheet simulators to generate vast amounts of process data is a valid approach, it requires in-depth domain knowledge understanding for the simulation set-up as well a tedious process to set up multiple processes runs required for big data-based approaches. By contrast, industrial benchmark simulations like the Tennessee Eastman Process (TEP) are widely regarded particularly in the area of process control as a realistic and a challenging problem since it was released in the early 1990s (Downs and Vogel, 1993; Udugama et al., 2020). However, it is important to note that this process simulation benchmark was not created for the purpose of generating large amounts of process data. In this manuscript a tool is presented to specifically tackle the requirement of generating large amounts of process data, employing the TEP benchmark process as the simulation engine, while mitigating the above-mentioned barriers.

2. TEP simulation

The Tennessee Eastman Process consists of a reactor, a product condenser, a separator and a stripping column with the objective of reacting feed streams into products. In simple terms, the TEP takes four feed streams (streams 1-4) and partially converts the contents in the reactor into products, including the valuable compounds G and H. The resulting stream is cooled down and partially condensed using the product condenser. The resulting liquid stream, which predominantly contains the products of interest (compounds G and H), is then introduced to a stripping column, where dissolved gaseous compounds and middle-boiling compounds can be removed to meet the required product specifications. Modelled on an actual industrial process, the TEP is valuable as a simulation tool due to its complexity and realistic nature. The model contains 28 predefined fault scenarios that can be applied to the process.

3. Converting the TEP simulation into a data generation tool

The original TEP simulation introduced by Downs and Vogel in the 90's was written in the software language FORTRAN (Downs and Vogel, 1993). In the early 2000's, this original FORTRAN file was augmented with the capabilities of MATLAB Simulink by Ricker (Bathelt et al., 2015) where the control variables (Inputs) to the FORTRAN file can be manipulated via MATLAB while process variables (outputs) are sent back to MATLAB. While this implementation makes the use of the original FORTRAN code much more convenient, the following shortcomings render this implementation in its current form impractical for the purpose of massive data generation.

- The model terminates soon after start up due to lack of control on safety critical variables.
- The data output is generated for a single run and is not available in an easy to export process format such as .CSV or .SQL.
- The data structure requires the user to explicitly track the state of the 28 process disturbances that can influence the operations and record other critical process parameters.
- Prior experience with Simulink and MATLAB is necessary.
- A detailed understanding of the TEP is necessary.

The focus of the TEP tool presented here is on facilitating the fast and simple generation of reliable fault scenario data sets, which can be used by data scientists in fault detection, process monitoring and ultimately process control. From a data generation point of view, the TEP code itself contains a random element (seed) to it which means that no two TEP runs would produce the exact same data set, while still retaining the fundamental characteristics. Hence, the TEP is geared towards the generation of a large number of non-repeating data sets. Moreover, the TEP code and the subsequent TEP big data tool have been developed so that all relevant information related to the process is clearly recorded in the data set, as opposed to most industrial data sets.

3.1. Process control

TEP is an open loop unstable process, and as discussed in the previous section, the simulation reaches shutdown limits and terminates soon after start-up. This does not provide useful results, and for this reason a layer of process control has been implemented. The five safety variables that must remain in a strict interval have each been equipped with a PID controller. It is important to keep in mind the effect that closed loops

may have on process dynamics when evaluating the data generated by the tool. The variables used in PID controllers are given in Table 1. The user may implement their own control scheme in the Simulink file that contains the process model.

Table 1 - Process control

Controlled variable	**Manipulated variable**
Reactor pressure (XMEAS 7)	Purge valve (XMV 6)
Reactor level (XMEAS 8)	Condenser cooling water flow (XMV 11)
Reactor temperature (XMEAS 9)	Reactor cooling water flow (XMV 10)
Product separator level (XMEAS 12)	Separator pot liquid flow (XMV 7)
Stripper base level (XMEAS 15)	Stripper liquid product flow (XMV 8)

3.2. User input

The user may enter the following information in the GUI to tailor the simulations to their needs.

- Runs - How many times should the same setup be simulated?
- Duration – How many hours of operation should be simulated?
- Disturbance – Which fault scenarios should be applied?
- Start time – At what time during the simulation should the fault scenario start?
- End time – At what time during the simulation should the fault scenario stop?
- Seed – What should be the random generator seed for the first simulation?

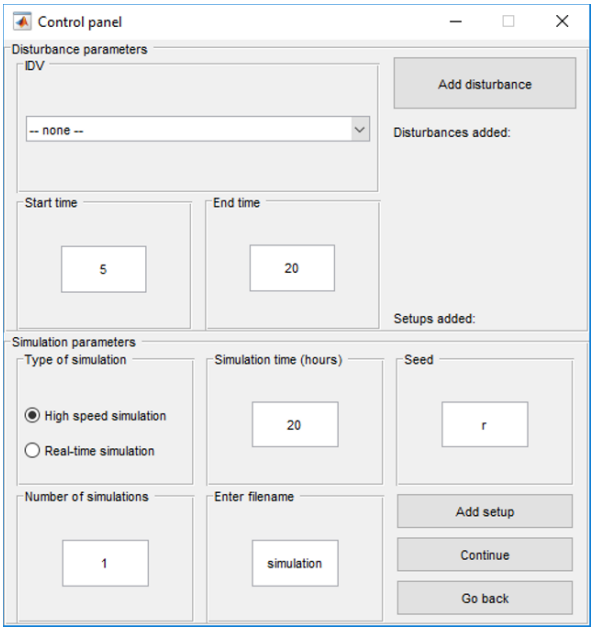

Figure 1 - Graphical User Interface of the TEP tool

The ability to enter the random generator seed allows for reproducibility of results. Alternatively, the user may let the program generate a random number as a seed for the simulation. When simulating multiple runs of the same setup, the seed will increase by one for each simulation to produce distinct data sets.
Inputting the information to the program can be done through loading a .CSV file based on a template, or through the user-friendly interface.

3.3. Output of GUI

The default setting of the GUI is to run the desired simulations as quickly as possible. This generates a set of .CSV files and a .TXT file. Each .CSV file contains the simulation result for a single run of the process and the .TXT file contains a summary of the simulations that have been run. This ensures that the user can keep track of which .CSV contains the results for a given simulation setup and allows for easy reproduction of the data. The simulation produces 81 time-dependent variables. There are 12 input variables, 41 output variables and 28 disturbance variables that indicate whether or not a disturbance scenario is active. The columns in the .CSV files are named to avoid confusion about what a given column of data represents. As an alternative to a quick simulation, the user may run a single simulation in 'real-time'. This will give the user an operator view of the process with displays of the input variables and safety variables. Figure 2 shows the structure of the result files and Figure 3 shows the real time simulation view.

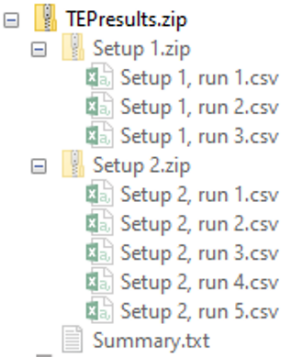

Figure 2 - Result files

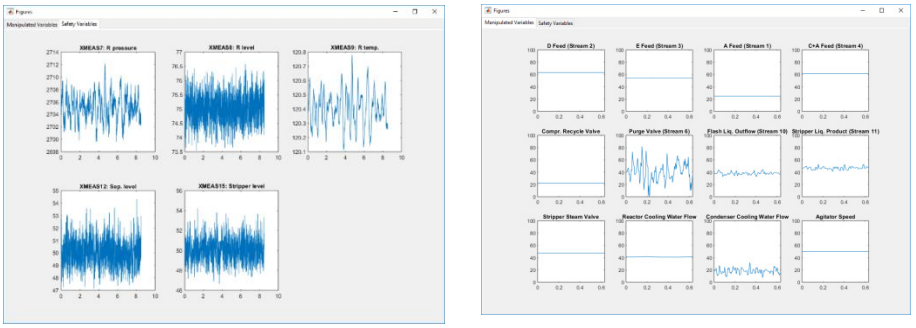

Figure 3 - Real time simulation view

4. Conclusions

In this work a big data tool is presented that can generate a large amount of realistic process data using the well-established Tennessee Eastman process simulation as the data generation engine. The tool addresses the need in the data science and process control community for large amounts of realistic process data to formulate new data-driven solutions for process control and fault detection. The tool is designed such that data can be generated with minimum interaction with MATLAB programming where the input to the tool can be carried out using either a csv-file and/or an easy to use graphical user interface while the output from the tool is also in the form of a csv-file. This allows an interested user to request, generate and process the desired data with minimum interaction with MATLAB. It is expected that the tool will lead to better understanding of process characteristics by data scientists and result in the development of fit-for-purpose data driven process monitoring and diagnosis concepts.

References

Bathelt, A., Ricker, N.L., Jelali, M., 2015. Revision of the Tennessee Eastman Process Model. IFAC-PapersOnLine 48, 309–314.

Downs, J.J., Vogel, E.F., 1993. A plant-wide industrial process control problem. Comput. Chem. Eng. 17, 245–255.

Gajjar, S., Kulahci, M., Palazoglu, A., 2018. Real-time fault detection and diagnosis using sparse principal component analysis. J. Process Control 67, 112–128.

Udugama, I.A., Gernaey, K. V., Taube, M.A., Bayer, C., 2020. A novel use for an old problem: The Tennessee Eastman challenge process as an activating teaching tool. Educ. Chem. Eng. 30, 20–31.

Udugama, I.A., Taube, M.A., Mansouri, S.S., Kirkpatrick, R., Gernaey, K. V., Yu, W., Young, B.R., 2018. A Systematic Methodology for Comprehensive Economic Assessment of Process Control Structures. Ind. Eng. Chem. Res. 57, 13116–13130.

Udugama, I.A., Wolfenstetter, F., Kirkpatrick, R., Yu, W., Young, B.R., 2017a. A comparison of a novel robust decentralised control strategy and MPC for industrial high purity, high recovery, multicomponent distillation. ISA Trans. 69, 222–233.

Udugama, I.A., Zander, C., Mansouri, S.S., Kirkpatrick, R., Yu, W., Young, B.R., 2017b. A novel back-up control structure to manage non-routine steam upsets in industrial methanol distillation columns. Comput. Aided Chem. Eng. 40, 1597–1602.

Sauro Pierucci, Flavio Manenti, Giulia Bozzano, Davide Manca (Eds.)
Proceedings of the 30th European Symposium on Computer Aided Process Engineering (ESCAPE30), May 24-27, 2020, Milano, Italy.
http://dx.doi.org/10.1016/B978-0-12-823377-1.50220-2

Floating Pressure Control of Vapor Recompression Distillation in Propane-propylene Separation

Jan Marvin Frias,[a] San-Jang Wang,[b,*] David Shan-Hill Wong,[a]

Cheng-Huang Chou,[a] Shi-Shang Jang,[a] En-Ko Lee[b]

[a]*Department of Chemical Engineering, National Tsing Hua University Hsinchu 30013, Taiwan*
[b]*Center for Energy and Environmental Research, Natioinal Tsing Hua University Hsinchu 30013, Taiwan*
wangsj@mx.nthu.edu.tw

Abstract

The separation of propylene from propane is an energy-intensive distillation process. Vapor recompression is commonly used for the separation of propylene and propane. Most studies of vapor recompression were carried out at a given pressure. It is well known that the lower the pressure, the higher the volatility difference and less energy is required to perform the separation. In a traditional column, energy of the distillation can be minimized by operating at the lowest pressure possible. The limit is usually determined by the maximum cooling capacity in the condenser, which is in turn determined by the temperature of the cooling water. Such a practice is known as floating pressure control. In a vapor-recompression column, the condenser and reboiler were replaced by a heat exchanger. Auxiliary condenser and reboiler may or may not be present. The operating constraint is determined by the anti-surge control of the compressor. Furthermore, it is necessary to ensure that the compressed vapor which acts as steam in the reboiler is not substantially subcooled to avoid the vibration of the heat exchanger.

In this study, the implementation of floating pressure control for a vapor-recompression propane-propylene column with an auxiliary condenser is studied using ASPEN Plus dynamics. A control scheme that includes basic inventory control and quality control was proposed. To keep the operation within safe region of the compressor surge curve, the split of the compressed vapor going to the bottom as heating medium and passing through the auxiliary condenser is adjusted. It is shown that the column can be operated under product purity requirements of top and bottom when column pressure is reduced by 1 kg/cm2.

Keywords: vapor recompression, floating pressure control, energy optimization

1. Introduction

Global demand of propylene has been increasing from recent years to present. This makes the industry more viable for technology improvements and energy minimization strategies to make the profits more promising. Propylene is an essential raw material in the production of its various derivatives requiring high purity polymer-grade propylene. In the refinery, it usually comes along propane which is very close to its boiling point making it a very energy-consuming separation process. There is a growing need to

improve efficiencies of propylene production due to enlarging gap between supply and demand making it more attractive for businesses to invest in this industry.
Distillation is an energy consuming separation process in chemical process industries. Vapor recompression is one of the energy efficient technologies employed to harness all the heat circulating in a distillation system. For systems where boiling point difference of separated components is small, energy saving obtained is more improved because at decreased system pressure, relative volatility is enhanced. This makes separation process more convenient and economical. However, reduction of column pressure is constrained by the cooling capacity of the condenser, thus it shall be optimized. In this study, the column pressure effect for a vapor-recompression propane-propylene column with an auxiliary condenser is studied by implementing floating pressure control using ASPEN Plus dynamics to minimize energy consumption. Compressor performance curve and anti-surge curve are also involved in the design and control of this column.

2. Review of Related Literatures

2.1. Vapor recompression distillation
A major advantage of vapor-recompression system is that the column can be operated with minimized pressure condition due to independence from cooling or heating media conditions since process fluids heat and cool each other at the same time. With changing feed rates and column overhead pressure, we shall study here how to achieve lowest energy consumption while keeping operation as close to anti-surge curve. According to Ma et al. (2019), the optimal pressure needs to be determined by balancing cost and control. They claim in this study that pressure had different effects on the dynamic controllability of different systems.

Annakou and Mizsey (1995) used two schemes to investigate propylene-propane splitter assisted by a heat pump: single and double compressor schemes. They found that with the double compressor, column pressure is independent of threshold temperature of condenser. They claim both processes are 37% cheaper when compared to conventional column. The literature did not discuss the anti-surge operation of the compressor with every pressure change which we now include in our study. Keeping the operation as near as possible to anti-surge curve will optimize inventory and help minimize energy consumption. Optimum valve conditions are also employed in this study.

2.2 Floating pressure control
In vapor recompression distillation, condenser maximum cooling capacity is the common constraint dictated by the cooling water conditions. In previous studies, most distillation columns are in fixed pressure operation. However, floating pressure control is advantageous in many processes according to Hoffman et al. (2006). Since analyzers are now substituting temperature-based controls, fixed pressure operation argument is also becoming less. One of the major advantages of floating pressure control is the capability of operation at minimum column pressure within system constraints. We know that at low pressure, volatility is improved which entails reduction of heat input and energy to achieve separation. Moreover, if we can operate at the lowest possible pressure, there will be increased reboiler capacity and reboiler fouling can be prevented.

According to Mauricio-Iglesias et.al. (2014), information available in the open literature on pressure control design is scarce and sometimes contradictory. Most distillation systems are at fixed pressure to minimize the compensation of temperature control preventing column flood and weep, optimization of column capacity and operation

stability. On the other hand, dynamic pressure control is very advantageous in terms of energy reduction.

2.3 Research Motivation

Floating pressure control has never been employed in vapor recompression distillation. To get minimum energy consumption, it is desired to operate at lowest pressure possible. This FPC shall integrate all quality, inventory and pressure controls such that pressure is optimized, energy is minimized, and purity requirements are satisfied. Along with this is inclusion of performance curve to compressor during simulation which had never been done in recent studies. This paper shall present a control study.

3. Methods of Study

3.1 Process flow diagram

Process flow diagram of this study is shown in Figure 1. Two columns represent just one very high column with 214 stages in the actual scenario. The Aspen Plus steady state file is exported to Aspen Plus Dynamics as a pressure-driven simulation after all required parameters are specified. Conventional PI controllers are used for all controllers except the liquid level controllers which are proportional controllers.

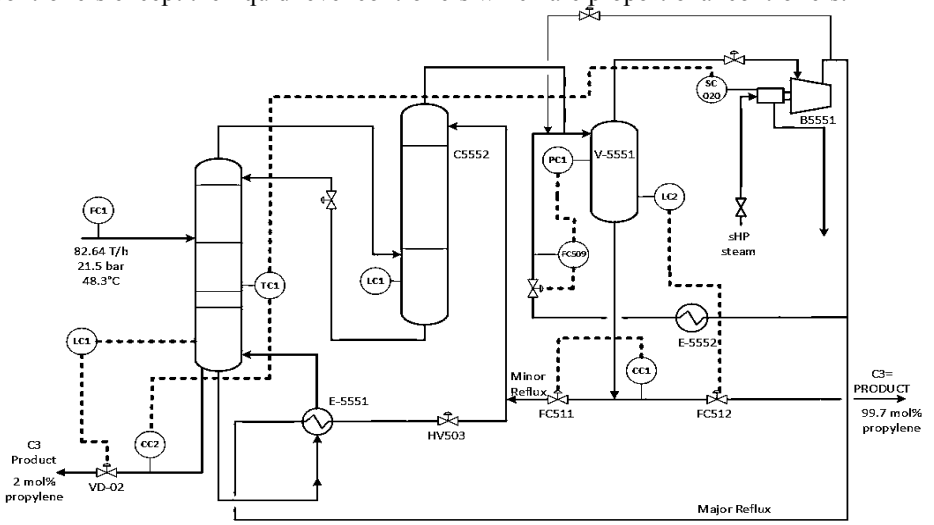

Figure 1. Process flow diagram.

In this study, we employed two kinds of control: inventory control (PC_1, FC_1, LC_1, and LC_2) and quality control (CC_1 and CC_2). Remaining degree of freedom shall be the HV503 valve opening which affects both reflux rate and compressor energy consumption. The features of the loops are outlined as follows: (1) The feed rate is flow-controlled via FC1 (reverse-acting); (2) The pressure in the column is controlled (direct-acting) through FC509 valve at the trim condenser outlet via PC1; (3) The bottom composition control CC2 is cascaded to TC1 column temperature control, output of which dictates the shaft speed of compressor B5551; (4) The top composition is controlled (reverse-acting) through FC511 valve of the minor reflux stream via CC1; (5) Level of column is controlled (direct-acting) through bottom product valve VD-02 via LC1; (6) Level of vessel is controlled (direct-acting) through top product valve FC512 via LC2.

4. Results and Discussion

In this section, we will examine the effects of reducing pressure to compressor power, speed, top and bottom purity, suction flow, pressure ratio, operating point in the anti-surge curve, operating point in the dew point curve of the condenser-reboiler hot stream exit, and the column top and bottom pressure and temperature profiles. Aspen dynamic simulation is used to produce results. Reflux flow rate has a huge effect on both product purity and compressor energy consumption. In this section, it is desired to observe the effects of HV503 reflux valve opening to steam economy. Results show that a certain reflux valve opening will give an operation at which the steam consumption per ton feed is minimized.

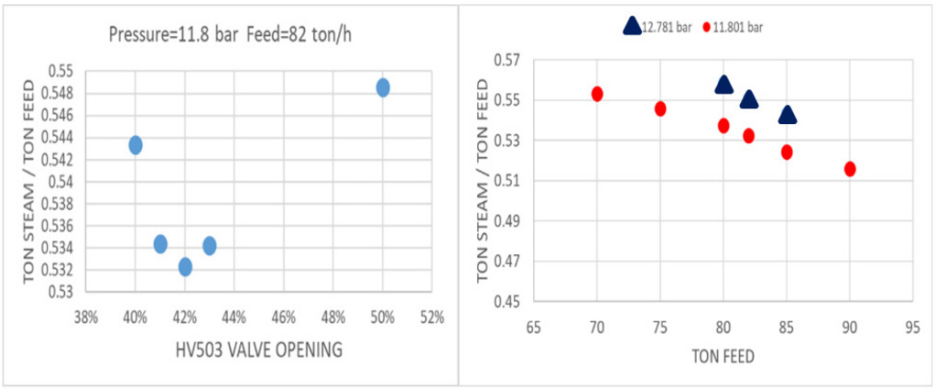

(a) (b)

Figure 2. (a) Optimum energy consumption as function of HV503 valve opening, (b) Optimum energy consumption at different feed mass-column pressure case.

Figure 2a shows that at a certain feed mass rate and column top pressure, the optimum HV503 opening is 42 %. To verify results, we checked different cases of ton feed rates and pressure and find minimum steam consumption at each case. Moreover, we tried to check the behavior for both high pressure (12.781 bar) and low pressure (11.801 bar). At a specific pressure, if feed rate is changed to 80, 82.6, 85, and 87 tons per hour, there exists an optimum HV504 opening % (which is around 42 to 43 %). The optimum ton steam/ton feed results in every case are shown above. This figure shows that with different feed flow rates and column top pressure fixed, we can obtain a trend line of optimum energy consumption for both high pressure and low pressure. Therefore, our floating pressure control shall operate the reflux valve HV503 at this optimum opening.

We can see from Figure 4a that transition from high to low pressure is in the safe region of the anti-surge curve. Also, HV503 adjustment gears the operating point to the left slightly nearer the anti-surge curve making it more ideal for operation. This proves that the reflux valve opening should be in optimum position to minimize energy consumption while operating as close as possible to anti-surge line. The compressed overhead vapor entering the reboiler-condenser should not be substantially subcooled so that it can be ensured that the heat exchanger will not suffer vibration. This monitor can be traced by observing the operation against the dew point curve of the fluid as shown in Figure 4b. Proposed strategy did not cause pulling away of the operating point from the dew point curve so this process is operated within a safe operation for the heat exchanger.

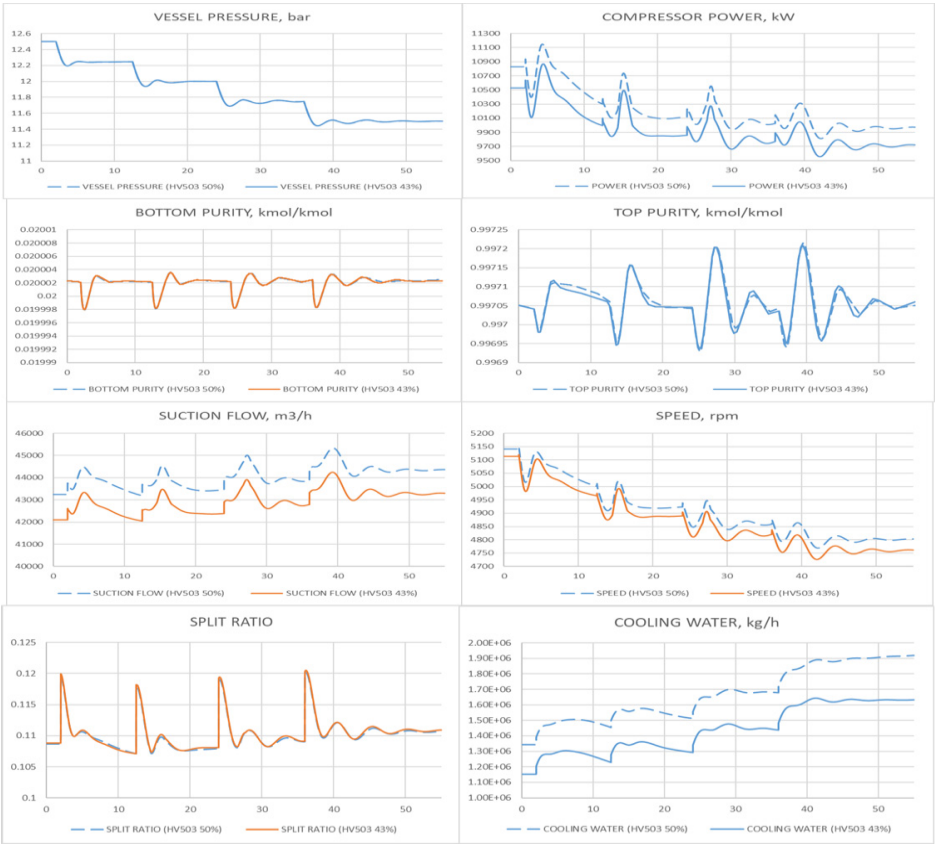

Figure 3. System profile for HV503 opening of 50 % (broken lines) and 43 % (solid lines)

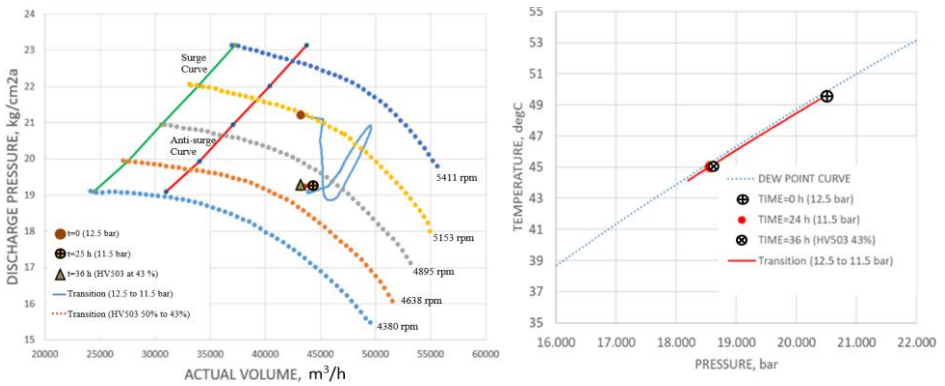

(a) (b)

Figure 4. (a) Operating points in compressor anti-surge curve during pressure reduction (b) Operating points in reboiler-condenser dew point curve during pressure reduction

5. Conclusion

In this study, we provided a steady state simulation of propane-propylene splitter system employing vapor recompression distillation. With a feed mass rate of 82.64 ton/h composed of propane and propylene, it is desired to obtain a top distillate product of at least 99.7 mol % propylene and a bottoms product of at most 2 mol % propylene. All equipment are sized using Aspen plus software. Performance curve of the compressor is employed. The converged steady state simulation is translated to dynamic simulation in a pressure-driven mode. The control system includes inventory control and quality control. The remaining degree of freedom, which is the HV503 opening, is examined. It is found that there must be a desirable opening at which optimum conditions will be achieved such as minimized energy consumption and nearness of operation to compressor anti-surge curve and heat exchanger dew point curve.

In the future work, it is intended to make a control study considering preceding results of how floating pressure control can be employed in a vapor recompression distillation process. This includes determination of the pressure limit constrained by the cooling capacity of the trim condenser. The automatic control system shall encompass all inventory and quality control. Observation of operation behavior in the compressor performance curve shall be implemented. To our knowledge, this is the first time a control study like this will be done in literature.

A double compressor scheme given by Annakou and Mizsey (1995) may allow the compressor worked at even smaller pressure. Its performance will be compared with our study's results in the future.

References

O. Annakou, P. Mizsey, 1995, Rigorous investigation of heat pump assisted distillation, Heat Recovery Systems and CHP, 15, 241-247.

A. Choudhari, J. Divey, 2012, Distillation optimization by vapor recompression, Chemical Engineering, 119(3), 43-47.

C.C.E. Christopher, A. Dutta, S. Farooq, I.A. Karimi, 2017, Process synthesis and optimization of propylene/propane separation using vapor recompression and self-heat recuperation, Industrial and Engineering Chemistry Research, 56(49), 14557-14564.

H.L. Hoffman, D.E. Lupfer, L.A. Kane, B.A. Jensen, B.G. Liptak, 2006, Control and Optimization of Unit Operations, Distillation: Basic Controls, Taylor and Francis.

S.S. Jogwar, P. Daoutidis, 2009, Vapor recompression distillation: Multi-scale dynamics and control, American Control Conference, IEEE, 647-652.

Y. Ma, Y. Luo, X. Yuan, 2019, Towards the really optimal design of distillation systems: Simultaneous pressure optimization of distillation systems based on rigorous models, Computers and Chemical Egnineering, 126, 54-67.

M. Mauricio-Iglesias, T. Bisgaard, H. Kristensen, K.V. Gernaey, J. Abildskov, J.K. Huusom, 2014, Pressure control in distillation columns: a model-based analysis, Industrial and Engineering Chemistry Research, 53(38), 14776-14787.

W.L. Luyben, 2013, Distillation design and control using Aspen simulation, John Wiley and Sons.

Sauro Pierucci, Flavio Manenti, Giulia Bozzano, Davide Manca (Eds.)
Proceedings of the 30th European Symposium on Computer Aided Process Engineering (ESCAPE30), May 24-27, 2020, Milano, Italy.
http://dx.doi.org/10.1016/B978-0-12-823377-1.50221-4

Modern Process Monitoring and Optimization Methods Integrating a Process Simulator into a Distributed Control System

Corinna Busse,[a] Ewa Bozek,[a] Bernd-Markus Pfeiffer,[a] Sreekumar Maroor,[b] Mathias Oppelt[a]

[a] *Siemens AG, Werner-von-Siemens- Str. 60, Erlangen 91052, Germany*
[b] *PSE – A Siemens business, 26-28 Hammersmith Grove, London W6 7HA, UK*
corinna.busse@siemens.com

Abstract

On the one hand, process simulation has become an inherent part of design, engineering and operation of chemical production plants. On the other hand, process industry is moving to highly automated plants, with a distributed control system (DCS) at the core of these facilities. Considering both trends the integration of a process model into a DCS is the consecutive next step, which enables the online use of process models during plant operation. The details of technical integration as well as specific use cases such as soft-sensors and real-time optimization will be presented in this contribution. As introduction, a brief review of applications of simulation along the life-cycle of a process plant is given, leading to a vision for a digital twin concept.

Keywords: digital twin, dynamic process modelling, soft sensor, real-time optimization

1. Introduction

As part of progressing digitalization in process industry, the term “digital twin” is an increasingly popular expression. Although various definitions of this term exist, a common understanding is that a digital twin is a digital counterpart of a physical object. (Kritzinger, et al., 2018) state that within the existing definitions, the expressions such as digital model, digital shadow and digital twin are often used synonymously, although the level of data integration differs for these terms. The authors suggest a classification into three subcategories depending on the level of data integration: a digital model does not use any form of automated data exchange, whereas a digital shadow incorporates an automated data exchange from the physical to the digital world and a digital twin offers a bidirectional automated data flow between real and virtual environment.
Furthermore, there exist various types of digital twins addressing different aspects of a chemical production plant e.g. assets, the product itself, the automation system or the overall production. (Pfeiffer, et al., 2019) described a concept for a digital twin of a process plant as a consistent framework which evolves along the plant life-cycle and contains a representation of the product, assets and the performance of process and product. The new perspectives in this framework is opened by the idea to integrate the individual models and simulation tools to a holistic, semantically integrated system, integrated across different hierarchy levels of the plant, and integrated along all phases of plant life-cycle.
Within this contribution a key part of this overall framework is addressed: the digital process twin, which combines a high-fidelity predictive process model with plant data to

generate high-value information enabling online decision support for the operators via the distributed control system (DCS) of the plant. Since process modeling is a core aspect of this contribution, a brief review of its application in the plant life-cycle is given first. Subsequently incorporation of process models into a DCS is presented using the example of an ethylene cracking furnace.

2. Process modeling in the life-cycle of a process plant

Within the life-cycle of a chemical production plant, modeling has become an invaluable tool (Oppelt, 2016). A variety of applications for process models exists, while the modeling rigor depends on the designated purpose of the model.

2.1. Design phase

For continuous processes, the development of a steady-state process model during the design phase has become a standard task and is mandatory for hand-over to engineering phase. These steady-state models are used for conceptual process and equipment design (e.g. column equipment), the generation of a heat and mass balance and detailed simulation e.g. including reaction kinetics. A workflow for developing and validating a high-fidelity predictive model of a catalytic reactor in the design phase is given by (Spatenka, et al., 2019). The authors demonstrate how this model can be used to explore many aspects of the decision space for both design and operation, leading to a more comprehensive workflow than experimentation alone.

2.2. Engineering and commissioning phase

The developed steady-state model can also be used for the development of the overall control scheme and to determine optimal set-points. Transferring this model into a dynamic simulation enables open-loop and closed-loop step tests as well as controller tuning. Furthermore, operability analysis like scenario simulation including start-up and shutdown, or early detection of operational challenges is possible with a dynamic process model.

Simulation can also be used for the validation and testing of an automation system, which is a demanding task, usually executed under very tight schedules. Therefore, the use of simulations to check-out the automation system earlier in the engineering phase can be very beneficial (Oppelt, et al., 2014). Another application of simulation are operator training systems. Based on a detailed process model created in the design and extended in the engineering phase, plant operators can be trained for their job, even before the real plant is up and running.

2.3. Operation phase

During plant operation the application of models can be distinguished between off- and online use. Offline applications can include operational optimization, troubleshooting and debottlenecking. As stated by (Spatenka, et al., 2019) significant additional benefit can be achieved if the model is used to provide day-to-day economic performance improvements online, executing within or in conjunction with the plant automation system. These online applications range from plant monitoring and forecasting to open-loop decision support and closed-loop control (Pantelides & Renfro, 2013).

2.4. Challenges for the application of process modeling along the plant life-cycle

The status quo for most chemical companies and EPCs is that all modeling activities typically start from scratch and the re-use of process models is not yet established (Oppelt, 2016). The only fully-established modeling activity occurs in the initial design phase of a new production facility. Challenges for the uniform application of process models along the whole life-cycle are for instance the higher engineering effort to create a dynamic

process model, the divergent development of the real-world process plant from the initial design due to revamps, and changing plant performance due to long-term degradation processes (e.g. catalyst deactivation, fouling, coke formation).
A conceptual workflow to overcome some of these challenges is described by (Labisch, et al., 2019). Here the initial steady-state process model is connected to a data-based plant design tool, where the P&IDs are developed and transferred back to a process simulator to create a dynamic process model. This model can be used in closed-loop form for conceptual control design and as open-loop version for online applications during operation. This concept of a digital twin would ensure consistency between the simulation and planning tool and would reduce the effort to create a process model, since model development would not start from scratch anymore. The challenge of long-term degradation processes effecting the predictive capability of an offline process model can be overcome by the transformation of a digital process model into a digital process twin, which will be explained in the next section using the example of steam cracking furnace in an ethylene plant.

3. Use case: Ethylene production through steam cracking

3.1. Challenges during operation

Thermal cracking of hydrocarbons is still the major process to produce the key intermediate product ethylene in the petrochemicals value chain. Due to the large-scale production capacity of this process, small improvements in efficiency can already yield significant annual savings. The steam cracking furnace is the heart of the ethylene production process and its optimal operation is key to maximizing profitability. Coke buildup within the furnace coils leads to higher pressure drop and lower residence time, thereby affecting the conversion and product yields. It also increases the tube metal temperature and reduces the heat transfer efficiency resulting in higher energy costs. Once the state of coking reaches to a certain limit, the furnace needs to be taken offline for decoking.
Feedstock availability and prices change with time and it hence it is necessary to operate the steam cracking furnaces in the ethylene plant at optimal conversions to maximize profitability and to ensure operation within the plant constraints. Hence reliable information of conversion, product yields and state of coking is key to ensuring optimal operation of the steam cracking furnace. However, measuring conversion and product yields accurately and reliably using gas analyzers is often a challenge due to the process conditions at the point of measurement. Analyzers used to measure composition at the outlet of the furnace are subject to fouling and tend to fail often, making frequent maintenance and calibration necessary. Information on current state of coking and coking rates are useful for better planning of de-coke schedules. However, these are not directly measurable and thus need to be indirectly inferred from the operating data from the furnace.
Due to the economic relevance and the complexity of the aforementioned challenges, academia (Savu, et al., 2010) as well as industry (Goethem, et al., 2001) have addressed this issue over the past. In this contribution a solution is presented which demonstrates and evaluates the combination of a rigorous process model of a steam cracking furnace with the distributed control system.

3.2. Modern process monitoring and optimization methods to overcome these challenges

As discussed by (Pantelides & Renfro, 2013) the online use of first-principle models offers a broad range of possibilities to support operators regarding day-to-day decisions.

The realized infrastructure for combining a rigorous process model with the plant automation is given in Figure 1.
The core element of this infrastructure is a process master model, which is coupled to regularly-updated plant data to enable real-time calibration of the model. Based on this digital model, several model-based applications like e.g. soft-sensing, run length prediction and real-time optimization can be realized.

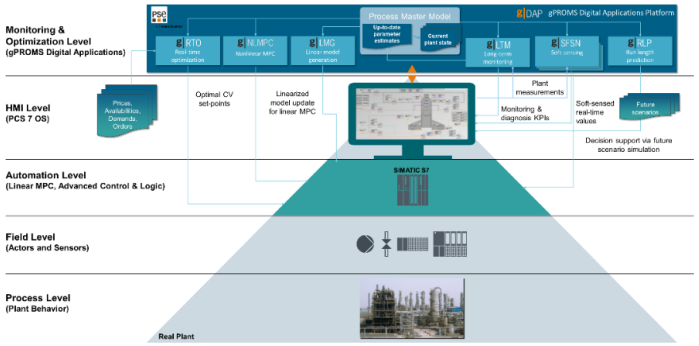

Figure 1: Realized infrastructure to combine a rigorous process model (process master model) with the plant automation system to enable several model-based online applications.

3.2.1. Process master model

As discussed by (Pantelides & Renfro, 2013) one major challenge for the online deployment of process models is to find the best trade-off between modeling rigor and life-cycle sustainability of the online solution. Due to complexity increasing with model rigor, the maintenance of the online solution becomes also more difficult. Therefore, a model which is "fit-for-purpose" should be developed or adjusted from previously developed models. Another requirement for the model is that it is robust and fast solving.
The first-principle model used in this contribution was previously described by (Spatenka, et al., 2017). It includes a mass and energy balance as well as kinetics of cracking and coking. A grey-box (or hybrid) modeling approach, which combines rigorous and data-driven model, for this application is currently evaluated by *PSE* within the CoPro project (Nauta, 2019).
The model was developed within the gPROMS ProcessBuilder environment, which offers custom modeling capabilities as well as powerful optimization technology, using an equation-oriented approach. The steam cracking furnace is the core unit of the ethylene production process and is therefore discussed here in more detail. The hydrocarbon feedstock (e.g. ethane) and steam are fed to the convection section of the steam cracking furnace where they are first pre-heated before entering the radiant coils where thermal cracking of the hydrocarbon takes place. The heat input necessary for the cracking is provided by burning fuel gas in the firebox of the furnace. The cracked gas from the radiant coil is subsequently quenched in transfer line exchanges (TLEs) to prevent undesired side reactions.
The olefins model libraries in gPROMS ProcessBuilder allow detailed representation of steam cracking furnaces and support all standard radiant coil configurations. They also provide a framework and workflow for incorporating proprietary knowledge such as custom coil configurations, cracking and coking kinetic models etc. The libraries include cracking kinetic models adopted from literature as well as coking kinetic models to represent the coke build up in the coils. The parameters associated with the cracking and coking kinetic models can be tuned to laboratory or plant data.

3.2.2. Long term monitoring

Plant data (historical and current) is used in conjunction with the described model to track coke build-up in the furnace. The online calibration of this model is a core element of the demonstrated architecture, since it is a crucial input for all other online applications. The current coking state of the furnace is determined by periodically tuning the model using plant data from start of the run until the current time.

3.2.3. Soft sensor

As described in section 3.1, obtaining accurate and reliable measurements of KPIs such as conversion and product yields through direct measurement challenging. The soft sensor application makes use of the up-to-date coke profile and coking kinetics information from the long-term monitoring activity above and provides accurate and real-time estimates of KPIs such as conversion, product yields, coking rates etc. This application runs 24/7 on plant computers and it can be closely coupled to the plant automation systems. The soft sensed KPIs can be displayed as "normal" process variable in the operator station (OS). Therefore, the soft-sensor variables can be directly used as controlled variables for process automation, providing key new information that can be used to implement for improved conversion control.

3.3. Run length prediction

Optimal de-coke planning and scheduling is key to maintain furnace availability and to maximize production. The up-to-date coking information from the long-term monitoring activity above can be used to determine the remaining length of run for each individual furnace in the plant, depending on one or more specified operation scenarios. This information helps in deciding consequences of different operational choices on run length and it can help in better planning and scheduling of decoke operation.

This "what-if" simulation of future operation can be started and adjusted directly from the OS of the DCS, which is offering a common user interface for the operators and therefore could increase acceptance. The results of the simulation are displayed in the OS as well and plant operation can directly be adjusted based on the simulation study.

3.4. Linear model generation for model predictive control (MPC)

Since the conversion and yield is affected by several factors (feed composition, hydrocarbon-to-steam ratio, cracking temperature and furnace residence time) the implementation of a model predictive controller (MPC) is promising to improve operation. The rigorous model can once again be used to derive a linear model which is needed for the MPC. The realization is explained in more detail by (Pfeiffer, et al., 2019).

3.5. Real-time optimization (RTO)

Optimizing the economic performance of a process plant is one of the ultimate goals for operation. The up-to-date plant model together with the current market situation (e.g. feedstock availability, product demand, prices) can be used to determine optimal setpoints for key operational decision variables such as allocation of fresh feed and recycles to the furnaces, and operating conditions for each furnace to maximize economic performance.

The optimization can be started from the operator stations of the DCS and the operator can decide whether the optimized process variables are acceptable. The transition from one steady-state to the other is done by the sub-ordinated control structures by writing the setpoint combinations to the MPC.

3.6. System architecture

The system architecture to realize the described online applications based on a rigorous process model is as follows: real-time input variables for the model-based applications

e.g. flow rates, compositions, temperatures, stem positions etc. are transferred via OPC-UA from the DCS or historian (OPC-UA server) to the application (OPC-UA client). The calculated outputs from the different applications such as soft sensed KPIs, optimal conversion set points for each furnace etc. are sent back to the DCS via OPC-UA. Through the DCS these process variables are used for monitoring and control.

4. Conclusion

The incorporation of a process model into a plant automation system offers a broad range of opportunities for decision support of operators. Using the steam cracker of an ethylene production as example, several online applications of the process model are demonstrated, such as soft sensing, run length prediction and real-time optimization. The integration of first-principles models into the DCS offers several advantages like improved acceptance of operators for advanced solutions and use of calculated process variables as "normal" controlled variables for feedback control, interlocks, recipe control or alarming. Please note that the purpose of these online applications is to support the operator and not to replace him or her. The typical focus is optimization, not moving towards autonomous plant operation. Sustainable implementation of such online solutions can be supported by an integrated engineering approach to keep manual maintenance activities as infrequent as possible.

References

Goethem, M., Kleinendorst, F., Leeuwen, C. & Velzen, N., 2001. Equation-based SPYRO (R) model and solver for the simulation of the steam cracking process. *Computers & Chemical Engineering,* 5, Band 25, pp. 905-911.

Hall, S. & Matzopoulos, M., 2018. *Using digital process twin technology to drive Operational Excellence,* s.l.: s.n.

Kritzinger, W. et al., 2018. Digital Twin in manufacturing: A categorical literature review and classification. *IFAC-PapersOnLine,* 1, Band 51, pp. 1016-1022.

Labisch, D. et al., 2019. Evolution eines Digital Twin am Beispiel einer Ethylen-Anlage - Konzept und Umsetzung. *atp magazin,* 6, Band 2019, pp. 70-85.

Nauta, M., 2019. *D1.1 Efficient construction of efficient models,* s.l.: s.n.

Oppelt, M., 2016. *Towards an integrated use of simulation within the life-cycle of a process plant,* s.l.: s.n.

Oppelt, M. et al., 2014. *Automatische Generierung von Simulationsmodellen für die virtuelle Inbetriebnahme auf Basis von Planungsdaten. Vorstellung eines generischen Konzepts und einer prototypischen Implementierung.*. s.l., s.n.

Pantelides, C. & Renfro, J., 2013. The online use of first-principles models in process operations: Review, current status and future needs. *Computers & Chemical Engineering,* 4, Band 51, p. 136–148.

Pfeiffer, B.-M., Oppelt, M. & Leingang, C., 2019. *Evolution of a Digital Twin for a Steam Cracker.* s.l., s.n., pp. 467-474.

Savu, A. V., Lazea, G. & Agachi, P.-Ş., 2010. Optimization and advanced control for thermal cracking processes. *Computers & Chemical Engineering.*

SIMATIC PCS 7, V., 2018. *PCS 7 Unit Template "Stirred tank reactor with Kalman filter" using the example of the Chemical Industry,* s.l.: s.n.

Spatenka, S. et al., 2017. Model-Based Real-Time Monitoring of Ethylene Cracking Furnaces. *2017 Spring Meeting and 13th Global Congress on Process Safety.*

Spatenka, S., Matzopoulos, M., Urban, Z. & Cano, A., 2019. From Laboratory to Industrial Operation: Model-Based Digital Design and Optimization of Fixed-Bed Catalytic Reactors. *Industrial & Engineering Chemistry Research,* 6.Band 58.

Sundaram, K. & Froment, G. F., 1977. Modeling of thermal cracking kinetics—I. *Chemical Engineering Science,* 12, Band 32, p. 609–617.

Sauro Pierucci, Flavio Manenti, Giulia Bozzano, Davide Manca (Eds.)
Proceedings of the 30th European Symposium on Computer Aided Process Engineering (ESCAPE30), May 24-27, 2020, Milano, Italy.
http://dx.doi.org/10.1016/B978-0-12-823377-1.50222-6

A European Optimisation Tool for Carbon Capture and Storage, Accounting for Delays in Public Procurement

Federico d'Amore, Leonardo Lovisotto, Fabrizio Bezzo

CAPE-Lab – Computer-Aided Process Engineering Laboratory, Department of Industrial Engineering, University of Padova, via Marzolo 9, 35131 Padova PD (Italy).
fabrizio.bezzo@unipd.it

Abstract

The global anthropogenic generation of greenhouse gasses experienced an exponential increase compared to pre-industrial levels and, among these, CO_2 is the most abundant, with an emission that rose globally from 2 Gt/year in 1850 to over 35 Gt/year in 2010. Carbon capture and storage has been highlighted among the most promising options to decarbonise the energy sector, especially considering the European context which heavily relies on fossil fuels. When dealing with the strategic design and planning of an international carbon capture and storage infrastructure, the necessity of taking into account the differential behaviour among the European countries in terms of public procurement and assignation delays emerges as a key requirement for attaining an effective implementation of the network. This contribution proposes a mixed integer linear programming modelling framework for the economic optimisation of a multinational European carbon capture and storage supply chain, including the effects of countrywide delays in public procurement. Assignation lags are implemented as an additional cost for the installation of the network. Results show that only minor modifications in the supply chain design should be taken into account with respect to an equivalent non-delayed scenario, with a consequent just moderate increase in transport costs (+3 %). Moreover, it is shown that capture and sequestration stages are barely not affected by the introduction of assignation lags among countries.

Keywords: carbon capture and storage, mixed integer linear programming, supply chain optimisation, delay in public procurement.

1. Introduction

In the last 50 years, CO_2 constituted nearly the 80 % of overall anthropogenic greenhouse gases (GHGs) emissions thus, global actions are needed to tackle the increase of carbon concentration in the atmosphere (IPCC, 2018). Carbon capture and storage (CCS) has emerged among the most promising options, considering its capability at directly decarbonising the energy generation and industry without necessitating a complete rethinking of these sectors (IPCC, 2005). However, in order to attain major environmental benefits, CCS has to be done at scale and across many borders (Bui et al., 2018). To this purpose, mixed integer linear programming (MILP) has often been employed as an effective modelling approach for the optimisation of large-scale networks (Heuberger et al., 2018). For instance, Han and Lee (2012) optimised a CCS supply chain (SC) for North Korea under uncertainty in market prices, Hasan et al. (2015) developed a tool for the optimal design of a CCS system in the United States, while d'Amore and Bezzo (2017)

minimised the costs of a European CCS network, also considering social acceptance and risk perception (d'Amore and Bezzo, 2020).
However, one aspect, which typically is not considered in the optimisation of CCS supply chain, is the impact of delays in the public procurement on the overall costs. Public procurement is governments' most commonly employed methodology to assign the construction of an infrastructure to a private company (EC, 2011). The European Commission (EC) keeps track of all the assigned procurements by including them in the Tenders Electronic Daily (TED) dataset and measures the efficiency in procurement timing and cost over the years through different indicators. Among these indicators, the national assignation lag is the most commonly employed to quantify the procurement performance of each European country (EC, 2018). As a matter of facts, a positive assignation lag generates a procurement delay, defined as the overall time for the assignation procedure, which varies in Europe form a minimum of 90 days in Poland to a maximum of 278 days in Greece (EC, 2011). Considering a large-scale international CCS SC, discrepancies in assignation lags may generate differential procurement delays among the European countries.
This contribution proposes a MILP modelling framework for the economic optimisation of a time-dependent, spatially-explicit, multi-echelon European CCS SC, including the effects of delays in public procurement across different countries. In particular, delays in projects assignations are here formulated as an additional cost for the construction of the infrastructure. Only sequestration basins and pipeline networks will be affected by the additional cost, whereas capture facilities will not be included in the delayed-affected formulation, as these are assumed to be placed in existing industrial area, and their project is likely to be only marginally affected by public procurement delays.

2. Material and methods

A multi-echelon, spatially-explicit, time-dependent, MILP model for the economic optimisation of a European CCS SC is presented, with the aim of providing a financial tool that evaluates the additional cost due to delays in countrywide public procurement. In particular, the model provides an optimal European CCS infrastructure (in terms of selection, positioning, and operation of capture nodes, transport routes and sequestration sinks), whilst considering the differential behaviour and characteristics among European countries in terms of infrastructural assignation lags.
The spatial framework is geographically described through a grid of 134 squared cells g, whose size ranges from 123 km to 224 km. This discretisation includes the European continent, few regions of North Africa and some offshore regions in the North Sea, where offshore sequestration basins are located and may be exploited (along with onshore storage options). Data and location of emission sources of CO_2 are obtained from the Emission Database for Global Atmospheric Research (EDGAR) published by Joint Research Centre (JRC, 2016). In particular, only large stationary emission sources (i.e., emitting more than 10^6 t of CO_2/year, corresponding to 37 % of overall European CO_2 emissions) are considered, and include coal- and gas-fired power plants. These emissions can be captured according to a set of technologies k including post-combustion from either coal or gas power plants, oxy-fuel combustion applied to coal power plants, and pre-combustion capture applied to gas power plants. CO_2 flowrates can be transported from region g to region g' by mean of either onshore or offshore pipelines l, towards sequestration in geological basins. The techno-economic characterisation (i.e., costs, efficiencies, feasibility) of capture and transport options is given in d'Amore and Bezzo (2017), while data on the type, location and capacity of the most promising formations

for CO_2 storage (i.e., deep saline aquifers, hydrocarbon and coal fields) is obtained from the EU GeoCapacity Project (2009).
The delay in the assignation of projects is here interpreted as an additional cost for the construction of the CCS system. Accordingly, the total cost of the European CCS SC is here revised with respect to d'Amore and Bezzo (2017) in order to include the additional cost generated by a delayed investment, which penalises the installation of the SC nodes and arcs in regions with high assignation lags. In particular, assignation lags generating procurement delays D_g [days] in region g within country c are evaluated from the countrywide lags producing delays D_c [days] according to data provided by the EC (EC, 2011).
Overall, given: the size and location of European large stationary sources of CO_2, the techno-economic characteristics of capture and transport options, the feasible transport links, the capacity and location of geological basins suitable for sequestration, the total European carbon reduction target to be pursued, and the countrywide characteristics in terms of procurement lag; the model is capable at providing: the optimal scale and location of the infrastructural nodes (capture and sequestration) and arcs (transport) according to the additional costs due to national delays.

3. Mathematical formulation

The objective is the minimisation of total cost *TC* [€] to install and operate the network, given by the sum of capture (*TCC* [€]), transport (*TTC* [€]) and sequestration (*TSC* [€]) costs, including the effect of delays in public procurement:

$$TC = TCC + TTC + TSC \tag{1}$$

On the one hand, the cost for capture *TCC* of Eq. (1) is calculated from the unitary capture cost UCC_k [€/t] and the captured amount $C_{k,g,t}$ [t] through technology k:

$$TCC = \sum_{k,g,t} (UCC_k \cdot C_{k,g,t}) \tag{2}$$

where costs and flowrates calculations are described in d'Amore and Bezzo (2017) according to the equations reported in the capture problem model. On the other hand, the cost of transport *TTC* and sequestration *TSC* of Eq. (1) are evaluated through the transport problem model and the sequestration problem model, respectively. In particular, *TTC* and *TSC* include the additional costs due to delays in public procurement. The transport cost *TTC* is given by two contributions, i.e. the inter-connection cost TTC_t^{inter} [€] and the intra-connection cost TTC_t^{intra} [€]:

$$TTC = \sum_{t} (TTC_t^{inter} + TTC_t^{intra}) \tag{3}$$

The term TTC_t^{inter} of Eq. (3) accounts for yearly pipelining cost between region g and g' according to the transport size Q_p [t/year] and length $LD_{g,g'}$ [km] as described in d'Amore and Bezzo (2017):

$$TTC_t^{inter} = \sum_{p,g,l,g'} \left[\lambda_{p,g,l,g',t} \cdot UTC_{p,l} \cdot Q_p \cdot LD_{g,g'} \cdot \tau_g \cdot \left(1 + \overline{AC}_{g,g'}\right)\right] \quad \forall t \tag{4}$$

where $UTC_{p,l}$ [€/t/km] (i.e., unitary transport cost) and τ_g (i.e., regional tourtuosity factor) are taken from d'Amore and Bezzo (2017), while $\lambda_{p,g,l,g',t}$ is a binary planning variable representing whether an infrastructure of size p is installed and operated between regions g and g' through a transport mean l at time period t, or not. Besides, $\overline{AC}_{g,g'}$ of Eq. (4) represents the average additional cost due to procurement delays between region g and g'. The term TTC_t^{intra} of Eq. (3) describes the yearly short-distance transport cost within region g according to the flowrate of CO_2 captured $C_{k,g,t}$ [t] through technology k in region g at time period t and the size LD_g [km] of cell g:

$$TTC_t^{intra} = \sum_{k,g} \left[C_{k,g,t} \cdot \overline{UTC} \cdot LD_g \cdot \tau_g \cdot \left(1 + AC_g\right) \right] \qquad \forall t \tag{5}$$

where $\overline{UTC}$ [€/t/km] (i.e., average unitary transport cost) is taken from d'Amore and Bezzo (2017), while AC_g represents the additional cost due to a procurement delay occurring in region g. The sequestration cost TSC of Eq. (1) is proportional to the number of injection wells $N_{g,t}$ that need to be installed and operated in region g at time period t:

$$TSC_t = \sum_{g} \left[N_{g,t} \cdot USC_g \cdot \left(1 + AC_g\right) \right] \qquad \forall t \tag{6}$$

where USC_g [€/well] is the unitary sequestration cost (d'Amore and Bezzo, 2017). The additional cost AC_g assigned to the construction of either a pipeline through Eqs. (4,5) or sequestration basin through Eq. (6) depends on the annual interest rate IR and the public procurement delay D_g for the assignation of a project of region g:

$$AC_g = IR \cdot D_g \qquad \forall g \tag{7}$$

In particular, IR is set equal to 10 % in analogy with the typical values employed for industrial projects in the oil and gas sector (Lise et al., 2008), whereas D_g is retrieved from data provided by the EC (EC, 2011) (Table 1).

Table 1. Time delay for public procurement D_C [days] in country c (EC, 2011). Regional delays D_g [days] have the same value in cells g belonging to country c.

C	D_c	c	D_c	c	D_c
Poland	90	Norway	123	Belgium	166
Hungary	92	Netherlands	130	Ireland	170
Latvia	93	Average	133	Bulgaria	171
Romania	104	France	133	Italy	174
Lithuania	112	Spain	134	Portugal	184
Slovakia	119	Czech Rep.	135	United Kin.	193
Sweden	120	Denmark	139	Greece	278
Germany	121	Austria	145		
Estonia	122	Finland	160		

4. Results and discussion

The model was implemented in GAMS software and optimised through CPLEX solver on a 2.60 GHz (32 GB RAM) computer in less than 1 hour. Two scenarios have been investigated: Scenario 0 optimised the CCS SC in absence of delay in public procurement

and constitutes a reference case to compare the results from Scenario A, in which conversely assignation lags were taken into account as described before.

Table 2. Scenarios 0-A. Total cost *TC* [G€, €/t], capture cost *TCC* [G€, €/t], transport cost *TTC* [G €, €/t], and sequestration cost *TSC* [G€, €/t]. Specific values refer to a t of geologically sequestered CO_2.

Scen.	*TC*		*TCC*		*TTC*		*TSC*	
	[G€]	[€/t]	[G€]	[€/t]	[G€]	[€/t]	[G€]	[€/t]
0	462.8	38.19	433.1	35.75	26.2	2.16	3.4	0.28
A	463.8	38.27	433.4	35.76	27.0	2.23	3.4	0.28

The economic results depict an almost identical situation between the optimised scenarios (Table 2). That for transport *TTC* is the only cost component to be affected by delays in public procurement, since it raises from 26.2 G€ (i.e., 2.16 €/t) in Scenario 0 to 27.0 G€ (i.e., 2.23 €/t) in Scenario A, with an increase of +3.05 %. Besides, capture cost *TCC* (at most slightly higher than 433.1 G€, i.e. 35.8 €/t) and sequestration cost *TSC* (almost steadily equal to 3.4 G€, i.e. 0.28 €/t) are barely not affected by assignation lags. Furthermore, a sensitivity analysis on *IR* was performed in order to test the model response to the chosen level of interest rate attributed to the additional cost of procurement delay. As a result, even when imposing *IR* = 20 %, *TTC* exhibits a moderate increase until 28.1 G€ (i.e., 2.32 €/t, corresponding to +7.25 % with respect to Scenario 0), whereas the growth of *TSC* is still as marginal as it is in Scenario A (+0.37 % with respect to Scenario 0).

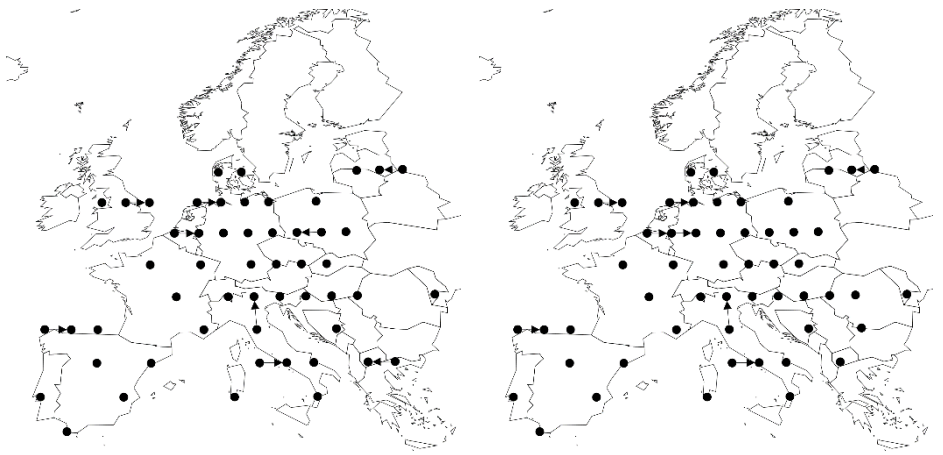

(a) **(b)**

Figure 1. Final SC configuration for Scenario 0 (a) and Scenario A (b).

The slight costs differences between Scenario 0 and Scenario A are a consequence of the minor design modifications in the resulting SC configurations. Differently from Scenario 0 (Figure 1a), Scenario A (Figure 1b) limits (e.g., in the case of Bulgaria) or totally avoids (e.g., in the case of Greece) the installation of transport and sequestration infrastructures in those countries characterised by particularly large assignation lags. Apart from this, the main driver for the installation and operation of the CCS network is still constituted by

capture costs, which are here assumed to neglect the effects of public procurement given the installation of this SC stage onto already existing power plants. Accordingly, the model solution exploits almost the same capture nodes in both Scenario 0 and Scenario A thus, the final configurations are almost identical.

5. Conclusions

This contribution presented a mixed integer linear programming modelling framework for the strategic optimisation of a European carbon capture and storage supply chain, considering the effects of delays in public procurement among European countries. In particular, countrywide assignation lags were interpreted as an additional expenditure for the installation of the transport and sequestration infrastructures. As a result, only minor design modifications were found between the delayed and non-delayed supply chains, which reflected in a just slight increase in transport costs in the case of the network optimised while taking into account the effects of public procurement. Countrywide delays in public procurement should not constitute an obstacle towards the installation of a European carbon capture and storage network.

On the flip side, the effects of delays in public procurement may affect further aspects beyond the mere increase in investment costs, e.g. difficulties for companies in properly scheduling and planning building works, a growth in uncertainty in the effectiveness of implementation of the overall system, difficulties among stakeholders in terms of transnational cooperation. These issues were not discussed in this contribution and might represent future perspectives to improve the formulation presented in this work.

References

M. Bui, C.S. Adjiman, A. Bardow, E.J. Anthony, A. Boston, et al., 2018, Carbon capture and storage (CCS): The way forward, Energy Environ. Sci., 11, 1062-1176.

F. d'Amore, F. Bezzo, 2017, Economic optimisation of European supply chains for CO_2 capture, transport and sequestration, Int. J. Greenh. Gas Control, 65, 99-116.

F. d'Amore, L. Lovisotto, F. Bezzo, 2020, Introducing social acceptance into the design of CCS supply chains: a case study at a European level, J. Clean. Prod, https://doi.org/10.1016/j.jclepro.2019.119337

EC, 2011, Public procurement in Europe Cost and effectiveness Annex: Detailed methodology and data.

EC, 2018, Single Market Scoreboard, Public Procurement.

EU GeoCapacity Project, 2009, Assessing European Capacity for Geological Storage of Carbon Dioxide.

J.H. Han, I.B. Lee, 2012, Multiperiod Stochastic Optimization Model for Carbon Capture and Storage Infrastructure under Uncertainty in CO_2 Emissions, Product Prices, and Operating Costs, Ind. Eng. Chem. Res., 51, 11445-11457.

M.M.F. Hasan, E.L. First, F. Boukouvala, C.A. Floudas, 2015, A multi-scale framework for CO_2 capture, utilization, and sequestration: CCUS and CCU, Comput. Chem. Eng., 81, 2-21.

C.F. Heuberger, I. Staffell, N. Shah, N. Mac Dowell, 2018, Impact of myopic decision-making and disruptive events in power systems planning. Nat. Energy, 3, 634-640.

IPCC, 2005, IPCC Special Report on Carbon Dioxide Capture and Storage. Prepared by Working Group III of the Intergovernmental Panel on Climate Change.

IPCC, 2018, Global warming of 1.5°C. An IPCC special report on the impacts of global warming of 1.5°C above pre-industrial levels and related global greenhouse gas emission pathways, in the context of strengthening the global response to the threat of climate change.

JRC, 2016, Emission Database for Global Atmospheric Research (EDGAR).

W. Lise, B.F. Hobbs, F. van Oostvoorn, 2008, Natural gas corridors between the EU and its main suppliers: Simulation results with the dynamic GASTALE model, Energy Policy, 36, 1890-1906.

Sauro Pierucci, Flavio Manenti, Giulia Bozzano, Davide Manca (Eds.)
Proceedings of the 30th European Symposium on Computer Aided Process Engineering (ESCAPE30), May 24-27, 2020, Milano, Italy.
http://dx.doi.org/10.1016/B978-0-12-823377-1.50223-8

Wind and Thermal Generation Portfolio: Optimal strategies in Energy-only Pool Markets under Wind Production Uncertainty

Evangelos G. Tsimopoulos, Michael C. Georgiadis*

Aristotle University of Thessaloniki, Department of Chemical Engineering, 54124 Thessaloniki, Greece

mgeorg@auth.gr

Abstract

This work considers a power producer with dominant position in electricity market. A bi-level model is constructed to derive optimal offering strategies for this producer. The bi-level model is reformed into a mathematical programming with equilibrium constraints (MPEC) model which is then recast into a mixed integer linear program using strong duality theorem and Karush-Kuhn-Tacker first order optimality conditions. The proposed algorithm results in optimal scheduled thermal and wind energy production as well as reserve deployments for the strategic producer. It also provides endogenous formation of local marginal prices and optimal offers under network constraints and wind generation uncertainty.

Keywords: generation portfolio, MPEC, withholding strategies, LMPs, wind uncertainty.

1. Introduction

This work investigates the capacity withholding strategies for an electricity producer whose generation portfolio consists of thermal and wind power production to avoid profit losses due to high penetration of renewable resources. The assumption is made that this producer (strategic) can exercise market power and can therefore impact the prices in the market (price maker). The producer competes with other non-strategic producers (price takers) in a jointly cleared energy and balancing market. The market is cleared by the independent system operator (ISO) one day in advance and on an hourly basis providing local marginal prices (LMP's) and energy quantities which are bought and sold.

2. Problem Statement

In the above context, a bi-level complementarity model is designed following the Stackelberg hypothesis of the single leader-follower game. The upper level establishes the expected profits optimization of the relevant strategic producer (leader). Conversely, the lower level is representative of the market clearing procedure conducted by the ISO (follower). The aim of the ISO is to determine the dispatch amount of production and consumption maximizing the social welfare, the difference between the total consumption utility bids, and the total production cost offers, or equivalently to minimize the total social cost. The lower-level of the model is constructed in the form of a linearized direct current (DC) network as two-stage stochastic programming. The first stage enables the day-ahead (DA) market and leads to optimization of the anticipated dispatch (DA

scheduled energy production) while the DA market clearing prices are received as dual variables. The second stage is representative of the balancing or real-time (RT) market in which the stochastic nature of wind generation is considered through the realization of all the plausible wind power production scenarios (Tsimopoulos and Georgiadis, 2018). The clearing of the balancing market results in balancing dispatch (reserve deployments) and RT market prices.

For the following formulation the indices *i* and *j* indicate the conventional units, and the wind farms respectively while the index *d* indicates the demands of the system. Additionally, the indices *b* and *f* refer to power blocks offered by the conventional units *i* and the wind farms *j*, the index *k* refers to power blocks consumed by load *d* and the index *ω* refers to wind power production scenarios. The sets I^s and J^s define units and wind farms owned by the strategic producer while the sets I^o and J^o define units and wind farms owed by non-strategic producers. The set I_n^s, I_n^o ,J_n^s, J_n^o and D_n map generation units, wind farms and loads onto the system and the set Θ_n defines the connection of the bus *n* with the other buses of the network. The parameters c_{ib}, c_{jf}^{DA} and u_{dk} represent the marginal cost of offered power blocks of generation units and wind farms, and the marginal utility of load blocks. In addition, the parameters c_i^{up},c_i^{down} and $c_{j\omega}^{RT}$ indicate the cost of offered regulations and wind power realization at balancing stage. In addition, the parameter B_{nm} denotes the susceptance of the line *n-m*. The *here* and *now* decision variables P_{ib}^{DA} and W_{jf}^{DA} represent the scheduled production of conventional units and wind farms respectively and the δ_n^o represents the voltage angle at DA stage. The *wait* and *see* variables $r_{i\omega}^{up}$ and $r_{i\omega}^{down}$ refer to upward and downward reserves offered by units *i,* the $W_{j\omega}^{sp}$ indicates the wind power production spillage of wind farm *j* under scenario *ω,* the $L_{d\omega}^{sh}$ indicates the load shedding of demand *d* under scenario *ω* and the $\delta_{n\omega}$ indicates the voltage angle at RT stage. Finally, O_{ib}^{DA} and O_{jf}^{DA} define the price offer of generation block *b* and *f* of strategic unit *i* and wind farm *j* in DA market while O_i^{up}, O_i^{down} and O_j^{RT} define the price offer of upward, downward reserves and surplus or shortfall of strategic unit *i* and wind farm *j* respectively in RT market.

2.1 Bi-level Formulation

Upper level problem

$$\begin{aligned} max \quad & \sum_{(i\in I_n^S)b} \lambda_n^{DA} P_{ib}^{DA} - \sum_{(i\in I^S)b} c_{ib} P_{ib}^{DA} + \sum_{(j\in J_n^S)f} \lambda_n^{DA} W_{jf}^{DA} \\ & + \sum_{(i\in I_n^S)\omega} \lambda_{n\omega}^{RT} r_{i\omega}^{up} - \sum_{(i\in I^S)\omega} \pi_\omega c_i^{up} r_{i\omega}^{up} - \sum_{(i\in I_n^S)\omega} \lambda_{n\omega}^{RT} r_{i\omega}^{down} \\ & + \sum_{(i\in I^S)\omega} \pi_\omega c_i^{down} r_{i\omega}^{down} + \sum_{(j\in J_n^S)\omega} \lambda_{n\omega}^{RT} \left(W_{j\omega}^{RT} - \sum_f W_{jf}^{DA} - W_{j\omega}^{sp} \right) \end{aligned} \tag{1}$$

Lower level problem

$$min \quad \sum_{(i\in I^S)b} O_{ib}^{DA} P_{ib}^{DA} + \sum_{(i\in I^S)\omega} \pi_\omega O_i^{up} r_{i\omega}^{up} - \sum_{(i\in I^S)\omega} \pi_\omega O_i^{down} r_{i\omega}^{down}$$

$$+\sum_{(j\in J^S)f} O_{jf}^{DA}\,W_{jf}^{DA}+\sum_{(j\in J^S)\omega}\pi_\omega\,O_j^{RT}\left(W_{j\omega}^{RT}-\sum_f W_{jf}^{DA}-W_{j\omega}^{sp}\right)$$
$$+\sum_{(i\in I^o)b} c_{ib}\,P_{ib}^{DA}+\sum_{(i\in I^o)\omega}\pi_\omega\,c_i^{up}r_{i\omega}^{up}-\sum_{(i\in I^o)\omega}\pi_\omega\,c_i^{down}r_{i\omega}^{down}$$
$$+\sum_{(j\in J^o)f} c_{jf}^{DA}\,W_{jf}^{DA}+\sum_{(j\in J^o)\omega}\pi_\omega\,c_{j\omega}^{RT}\left(W_{j\omega}^{RT}-\sum_f W_{jf}^{DA}-W_{j\omega}^{sp}\right)$$
$$-\sum_{dk} u_{dk}\,L_{dk}^{DA}+\sum_{d\omega}\pi_\omega\,vLOL_d L_{d\omega}^{sh} \qquad (2)$$

s.t.

$$-\sum_{(i\in I_n)b} P_{ib}^{DA}-\sum_{(j\in J_n)f} W_{jf}^{DA}$$
$$+\sum_{(d\in D_n)k} L_{dk}^{DA}+\sum_{m\in\Theta_n} B_{nm}(\delta_n^o-\delta_m^o)=0 \quad :(\lambda_n^{DA}) \quad \forall n \qquad (3)$$

$$-\sum_{(i\in I_n)} r_{i\omega}^{up}+\sum_{i\in I_n} r_{i\omega}^{down}-\sum_{d\in D_n} L_{d\omega}^{sh}$$
$$-\sum_{(j\in J_n)} W_{j\omega}^{RT}+\sum_{(j\in J_n)f} W_{jf}^{DA}+\sum_{j\in J_n} W_{j\omega}^{sp}$$
$$+\sum_{m\in\Theta_n} B_{nm}(\delta_{n\omega}-\delta_n^o+\delta_m^o-\delta_{m\omega})=0 \quad :(\lambda_{n\omega}^{RT}) \quad \forall n,\forall\omega \qquad (4)$$

$$\sum_b P_{ib}^{DA}+r_{i\omega}^{up}\le\sum_b P_{ib}^{MAX} \quad :(\mu_{i\omega}^{max}) \quad \forall i,\forall\omega \qquad (5)$$

$$r_{i\omega}^{down}-\sum_b P_{ib}^{DA}\le 0 \quad :\left(\mu_{i\omega}^{min}\right) \quad \forall i,\forall\omega \qquad (6)$$

$$0\le W_{j\omega}^{sp}\le W_{j\omega}^{RT} \quad :\left(\kappa_{j\omega}^{min},\kappa_{j\omega}^{max}\right) \quad \forall j,\forall\omega \qquad (7)$$

$$0\le L_{d\omega}^{sh}\le\sum_k L_{dk}^{DA} \quad :\left(\nu_{d\omega}^{min},\nu_{d\omega}^{max}\right) \quad \forall d,\forall\omega \qquad (8)$$

Objective function (1) optimizes the expected profit of the strategic producer, and it is defined by the revenues from the DA and RT market minus the actual incurred cost. The market prices λ_n^{DA} and $\lambda_{n\omega}^{RT}$ are created endogenously and received as dual variables from the lower level problem. Objective function (2) optimizes the expected cost of the power system operation conducted by ISO. It consists of the scheduled production cost and the scenario dependent reserve deployment, spilling wind power and shedding load cost in real time operation. Constraint (3) enforces the energy balance at each node and the transmission capacity limits between them at DA. Thus, the total power flowing into bus *n*, which is the algebraic sum of generation and load at the bus, should be equal to the power flowing away from the bus. Constraint (4) counterbalances the imbalance occurred in RT due to the uncertain wind production arranging the reserve deployment and the load curtailments. Constraint (5) ensures that scheduled energy and upward reserve cannot exceed unit capacity. Constraint (6) ensures that downward reserve cannot exceed scheduled production. Actually, these two constraints express the strong coupling between scheduled energy and reserves (Morales et al. 2012). Constraints (7) and (8) indicate that the wind energy spillage cannot exceed the scenario dependent actual wind energy production $W_{j\omega}^{RT}$ and the involuntary load curtailment cannot exceed the actual

load consumption. Each constraint is followed by its relevant dual variable in parenthesis. Finally, other constraints enforce unit generation limits, transmission capacity limits between two buses, upper and lower bounds of voltage angle at each bus.

2.2 MPEC formulation and linearization

Considering the continuity and the convexity of the lower level problem, the latter is characterized convex therefore it can be replaced by its Karush - Kuhn - Tacker (KKT) first order optimality conditions. Thus, the bi-level model is reduced to a single MPEC model. However, the MPEC is still non-linear due to non-linear KKT complementarity constraints and objective function (1). The former are replaced by linear disjunctive constraints (Fortuny-Amat and McCarl, 1981) while the latter is linearized by applying the strong duality theorem to the lower level problem in combination with some of the KKT equality constraints (Tsimopoulos and Georgiadis, 2018). Hence, the MPEC is reformed in an equivalent MILP solvable by commercial solvers such as GAMS/CPLEX.

3. Illustrative example

The proposed clearing market formulation is applied in a six-node system sketched in Figure 1. The conventional units i1, i2, i3, i4 and the wind farm j1 belong to the strategic producer and the i5, i6, i7,i8 and j2 belong to non-strategic producers. The technical data of the units is taken from Ruiz and Conejo (2009). Two wind farms j1 and j2, located at bus n2 and n5, have installed capacity of 100 MW and 70 MW, and their scheduled power production is offered in one block with zero marginal cost. Wind farms' uncertain power production is realized through three scenarios, ω1 (high production) with 100 MWh and 70 MWh, ω2 (medium production) with 50 MWh and 35 MWh, and ω3 (low production) with 20 MWh and 15 MWh while occurrence probability of each scenario is 0.2, 0.5 and 0.3 respectively. A total demand of 1 GWh is allocated according to Figure 1. Demand d1 accounts for 19 % and demands d2, d3 and d4 account for 27 % of the total demand each. Additionally, data about demand bids (energy and utility marginal cost) for each period of time comes from Ruiz and Conejo (2009). Finally, the value of the involuntary load reduction is 200 euro/MWh for all demands and all the connecting lines have a transmission capacity of 500 MW with susceptance equal to 9.412 per unit.

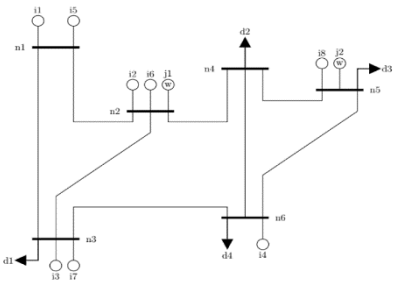

Figure 1. six-bus system

4. Results

4.1. Uncongested network

Based on the above information the proposed MILP model is applied to the system and solved using GAMS/CPLEX. Under cost offer (black) the expected DA price is constant and low at the floor of 11.26 €/MWh throughout the 24-hour period. However, when the producer exercises market power (red) the price moves away from the competitive equilibrium and fluctuates between 16.130 and 19.200 €/MWh (Figure 2). Similarly, the expected real-time prices move upwards when the producer exercises market power in all wind scenarios. Especially, in low wind scenario when the producer offers strategically the RT prices rocket at the level of 37 €/MWh (Figure 3). Note that, the LMP's

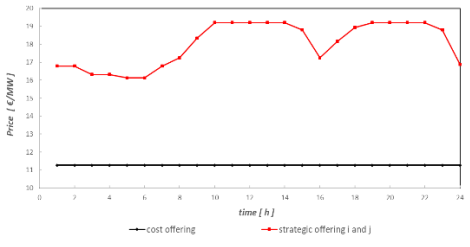

Figure 2. DA clearing prices [€/MWh]

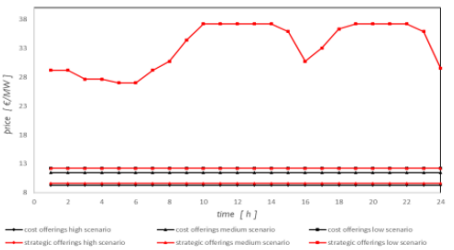

Figure 3. RT clearing prices [€/MWh]

are the same in all buses at each time period, as there is enough line capacity to keep the system uncongested in all wind scenarios. Having a closer look at time period *t12* in Table 1, when the producer offers strategically the scheduled production decreases in all units *i*, giving space for more scheduled wind energy. However, now the production is paid at

Table 1. Energy [MWh] and price outcomes [€/MWh] at time period t12

units *i*	$\sum_b P_{ib}^{DA}$	λ_n^{DA}	r_ω^{up}			r_ω^{down}			$\frac{\lambda_{n\omega}^{RT}}{\pi_\omega}$		
			high	medium	low	high	medium	low	high	medium	low
i1	132.2 [108.8]	11.260 [19.200]	.	.	.	15.0 [0.0]	.	.	9.280 [9.570]	11.470 [12.230]	12.230 [37.237]
i2	.		.	.	.	.	.	.			
i3	155.0 [124.0]		.	.	0.0 [10.0]	.	.	.			
i4	157,6 [118.2]		.	0.0 [15.0]	15.0 [40.0]	40.0 [40.0]	.	.			
wind j	$\sum_f W_{jf}^{DA}$										
j1	15.0 [60.0]										

a higher price. Considering the reserves, in low wind scenario where now the energy shortage is bigger the upward reserve supply increases compared to cost offering and it is paid almost at triple price. On the other hand, in high wind scenario, although the producer is charged at a higher price the downward reserve supply is lower. The proposed model results in an increase in the total expected profit from 23,286 € to 91,950 € even though the scheduled power production of strategic conventional units *i* decreases.

4.2. Offer building process

Considering unit *i1*, it can be seen in Table 2 that under cost offer the unit is fully dispatched as all the energy blocks are accepted by ISO. However, under strategic offer the first two blocks are fully accepted, the third is partially accepted and the fourth is not accepted at all. To create an upward offer curve; the first two blocks are offered at their marginal cost. The third block is offered at a price slightly lower than the clearing price.

Table 2. Day-ahead offer building process for unit i1 at time period t12

block	c_{ib}	P_{ib}^{MAX}	cost offers		strategic offers			
			P_{ib}^{DA}	λ_n^{DA}	P_{ib}^{DA}	λ_n^{DA}	O_{ib}^{DA*}	
b1	9.92	54.25	54.25	11.26	54.25	19.20	9.92	
b2	10.25	38.75	38.75		38.75		10.25	
b3	10.68	31.00	31.00		15.80		19.20 - ε	→ Financial withholding
b4	11.26	31.00	31.00		.		19.20	→ Physical withholding

Actually, this offer defines the DA market price. With this offer the producer exercises financial withholding, raising the offer of block 3 from 10.680 to slightly below 19.200

€/MWh. Now the last block is offered at a price 19.200 €/MWh or higher. In this way the producer guarantees block's rejection, exercising physical withholding (production curtailment).

4.3. Congested line 3-6

Under cost optimization the maximum power flow in line 3-6 is 208 MW. If the capacity is reduced to 220 MW, the system remains uncongested. However, under strategic offer the producer changes the mixture of production rendering the line congested. As a result, LMP's appear at certain time periods, as shown in Figure 4, and the total expected profits compared to those of uncongested system increase at the level of 92,759 €.

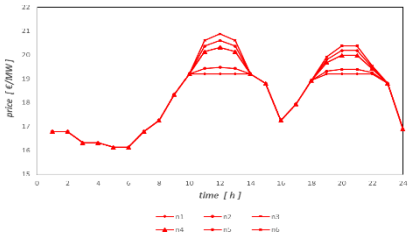

Figure 4. DA LMP's [€/MWh]

4.4. Wind power production increment

The wind power capacity increases from 10% to 14% of the total installed capacity. More specifically, the power production of the wind farms *j*1 and *j*2 is now 150 MW and 100 MW respectively in high wind scenario 1, 75 MW and 50 MW in medium wind scenario 2, and 30 MW and 20 MW in low wind scenario 3. In this case the strategic units *i* and the wind warm *j1* incur losses under cost offer as the price formation is lower. Only the units *i4* shows increased profits because now it is more involved in supply of upward reserves due the higher volatility of wind generation. However, when the producer exercises market power by means of capacity withholdings the expected profits of all units *i* and *j1* raise as depicted in Figure 5.

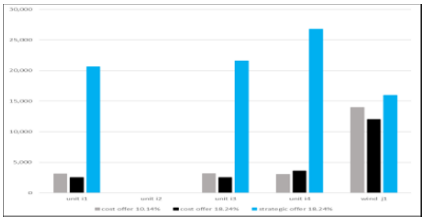

Figure 5. Units' expected profits [€]

5. Conclusions

This work proposes a bi-level complementarity model to derive capacity withholding strategies for power producer participating in a pool-based market. A representative case study is used to illustrate the applicability of model and how the producer can increase its expected profits considering wind generation uncertainty and line capacity limitations.

References

E.G. Tsimopoulos and M.C. Georgiadis, 2018. Strategic offers in day-ahead market co-optimizing energy and reserve under high penetration of wind power production: An MPEC approach. AIChE Journal.

J. M. Morales, A. J. Conejo, K. Liu and J. Zhong, (2012), Pricing electricity in pools with wind producers. IEEE Transactions on Power Systems, 27(3), 1366-1376.

J. Fortuny-Amat and B. McCarl, (1981). A representation and economic interpretation of a two-level programming problem. Journal of the operational Research Society, 32(9), 783-792.

C. Ruiz and A. J. Conejo, (2009), Pool strategy of a producer with endogenous formation of locational marginal prices, IEEE Transactions on Power Systems, 24(4), 1855-1866.

Sauro Pierucci, Flavio Manenti, Giulia Bozzano, Davide Manca (Eds.)
Proceedings of the 30th European Symposium on Computer Aided Process Engineering (ESCAPE30), May 24-27, 2020, Milano, Italy.
http://dx.doi.org/10.1016/B978-0-12-823377-1.50224-X

Supply chain optimization for the production of biofuels and bioproducts from lignocellulosic biomass in Mexico

Yulissa M. Espinoza-Vázquez, [a] Fernando Israel Gómez-Castro [a,*], José María Ponce-Ortega [b]

[a] *Departamento de Ingeniería Química, División de Ciencias Naturales y Exactas, Campus Guanajuato, Universidad de Guanajuato, Noria Alta S/N, Col. Noria Alta, Guanajuato, Guanajuato, 36050, México.*
[b] *División de Estudios de Posgrado, Facultad de Ingeniería Química, Universidad Michoacana de San Nicolás de Hidalgo, Francisco J. Múgica S/N, Morelia, Michoacán. 58060, México.*

fgomez@ugto.mx

Abstract

Lignocellulosic biomass is a raw material to produce biofuels and bioproducts. Thus, the proper use of such materials may help to development of a bio-based industry, additionally giving a second use to such waste material. Mexico is a country with a high agricultural production, implying a high production of agricultural residues. Since there are many possibilities for making use of the residues, the question arising is: which are the best products to be obtained from the lignocellulosic biomass available in the country? To answer this question, in this work a mathematical model for the supply chain of the production of biofuels/bioproducts is proposed. The mathematical model is formulated using generalized disjunctive programming (GDP) and relaxed through the convex hull approach. The resulting MILP is solved using the software GAMS, aiming to maximize the profit.

Keywords: lignocellulosic biomass, supply chain, disjunctive programming.

1. Introduction

The production of renewable fuels has taken growing importance on the last years, due to the concerns around the availability of petroleum and the environmental impact due to the use of its derivatives. According to British Petroleum, if the present demand of petroleum remains constant, the reservoirs will be enough for other 50.2 years (British Petroleum, 2018). Among the renewable fuels, those derived from sugar-rich materials, as bioethanol and biobutanol, can be used to partially replace gasoline in engines. Nevertheless, the industrial-scale production of such fuels must take place using non-edible raw materials, as lignocellulosic residues. Particularly, Mexico is a country with a high agricultural production, with corn, sorghum, and wheat as main products. Such crops generate lignocellulosic residues, with a reported production of 75.73 million ton in 2006 (Saval, 2012). Those residues contain cellulose, hemicellulose and lignin, and, as aforementioned, can be used as raw materials to produce biofuels as bioethanol, biobutanol, among others. On the other hand, such residues have also potential to produce high value-added bioproducts, as lactic acid, furfural, levulinic acid, among

others, which are the basis for the generation of several derivatives. The production of biofuels may not be profitable by itself, and the success of a biofuel production facility may strongly depend on the politics of each country, in terms of the subsidies offered by the governments. Thus, the use of lignocellulosic materials to produce both, biofuels and bioproducts, may enhance the economy of the biofuel industry. Nevertheless, among the different biofuels and bioproducts which can be obtained from lignocellulosic biomass, a given combination of products must have the highest profitability, making use of as much residues as possible and satisfying the demand for fuels and for a given bioproduct. Maximizing the profit will also depend on the location of the raw material, the production facilities and the markets. To determine the best supply chain for the production of biofuels/bioproducts from lignocellulosic residues, a mathematical model is proposed, considering the distribution of the raw materials, the potential locations for the facilities, the unitary cost for the production of each potential product, and the potential markets for the products. The mathematical model is formulated using generalized disjunctive programming (GDP) and relaxed using the convex hull approach, obtaining a MILP equivalent. The model is then codified in the software GAMS and optimized.

2. Case Study

As a first step, the availability of agricultural residues in Mexico is determined for four main crops: corn, sorghum, wheat and barley. Data for the distribution of such crops in all the country, and their contribution to the production of lignocellulosic residues, has been collected from the Service of Agrifood and Fisheries Information (SIAP, 2018). It has been determined that Mexico has a mean production of 1,394.8 kt/y of corn residues, 264.6 kt/y of sorghum residues, 93.0 kt/y of wheat residues and 40.4 kt/y of barley residues, distributed along the national territory. These raw materials are proposed to be used for the production of bioethanol and/or biobutanol, as biofuel alternatives, and levulinic acid and furfural as high-value added products. As a simplification, a single municipality has been selected as representative for each of the 32 states in Mexico. The selected municipality is the one with the highest production of residues in the spring/summer season. The effect of the change in the production of lignocellulosic materials in the autumn/winter season will be studied in a future work. For the potential location of the facilities, the states with the highest industrial infrastructure have been selected. Finally, the production of each potential product is constrained by its national demand. For bioethanol, mean national demand is 1,748,525.8 m^3/y, assuming covering 10% of the gasoline demand. For biobutanol, demand is set as 2,797,641.2 m^3/y, assuming covering 16% of the gasoline demand. For levulinic acid, demand is 1,667.9 m^3/y; while for furfural is 11.6 m^3/y.

3. Mathematical Model

The mathematical model represents the selection of the four raw materials (i) from the 32 states in Mexico (j). The raw materials from the different states are transported to one of the five states with highest industrial infrastructure (k), where the facilities can be located. On each facility, four products (m) can be obtained: bioethanol, biobutanol, levulinic acid and furfural. Finally, the products can be distributed to ten markets (n), selected among the 32 states because they are the locations with higher demand for gasoline. Figure 1 shows the superstructure for the supply chain. The mathematical model involves the transportation costs for the biomass from the source to the facilities,

in terms of the distance between locations, and the transportations costs from the facilities to the markets.

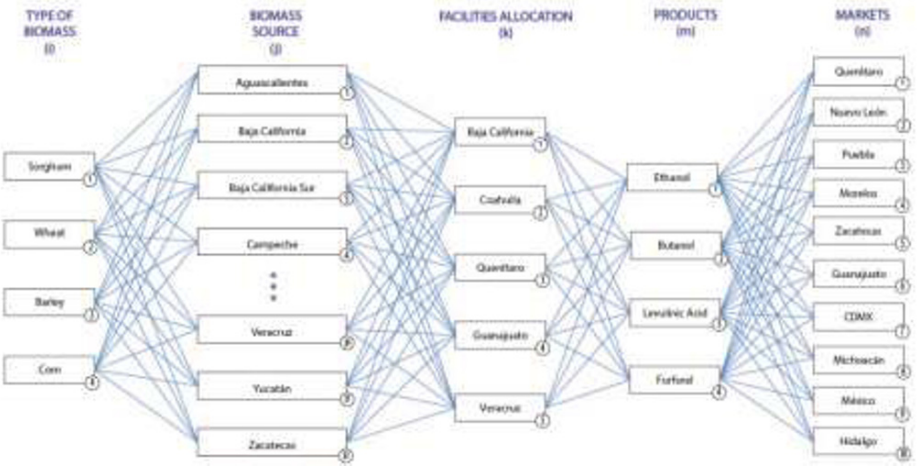

Figure 1. Superstructure for the supply chain of biofuels and bioproducts.

In the proposed model, it is assumed that the production for each product does not exceed the demand:

$$\sum_k MP(m,k) \leq \sum_n DP(m,n) \tag{1}$$

Where MP(m,k) is the mass production of the product m in the facility k, and DP(m,n) is the demand for product m in the market n. Additionally, MPAT(i,j,k), the quantity of raw material i from the source j entering to the plant k, cannot be higher than the availability of such raw material in the source j, MPA(i,j):

$$\sum_k MPAT(i,j,k) \leq MPA(i,j) \tag{2}$$

Transportation cost CP(j,k) for biomass from a source j to the facility k is given by:

$$CP(j,k) = \sum_i MPAT(i,j,k) * D1(i,j,k) * UPST \tag{3}$$

Where D1(i,j,k) is the distance from the source j of the biomass i to the facility k, and UPST is the transportation cost for solid biomass, which is taken as 0.00508 USD/km·ton. Similarly, the cost for the transportation of the product m obtained in the facility k to the market n, CD(k,m,n) is given by:

$$CD(k,m,n) = MPTM(k,m,n) * D2(k,n) * UPLT \tag{4}$$

Where MPTM(k,m,n) is the quantity of product m obtained in the facility k which is transported to the market n, D2(k,n) is the distance from the facility k to the market n, and UPLT is the unitary transportation cost for the liquid products, which is taken as 0.00671 USD/km·ton.

For the cost of the facilities, the unitary cost of raw material is assumed a 280 USD/t. The unitary cost for the production of bioethanol and the yield have been computed from the results reported by Sassner et al. (2008). For the production of biobutanol, the information given by Alavijeh and Karimi (2019) has been used. For levulinic acid and furfural, the data reported by Gozan et al., (2017) and Cai et al. (2013), respectively, have been taken. The cost of the land has also been included. The selection of the location of the facility and the obtained product(s) on each facility has been modelled through disjunctions, as the following:

$$\begin{bmatrix} \begin{matrix} Y(k) \\ TCP(k) = \left\{\left[\sum_m \left[\frac{MP(m,k)}{\rho(m)} \times 0.66 \times 0.4048\right]\right]\right\} \\ + \left[\sum_i \sum_j MPAT(i,j,k) \times \left(280 + PC(m)\right)\right] \end{matrix} \\ \begin{bmatrix} S(m,k) \\ MP(m,k) = \sum_i \sum_j MPAT(i,j,k) \times Yield_m \end{bmatrix} \vee \begin{bmatrix} \neg S(m,k) \\ MP(m,k) = 0 \end{bmatrix} \end{bmatrix} \\ \vee \begin{bmatrix} \neg Y(k) \\ MP(m,k) = 0 \\ MPAT(i,j,k) = 0 \\ TCP(k) = 0 \end{bmatrix} \tag{5}$$

where Y(k) is a logical variable associated with the construction of the plant in the location k, and S(m,k) is a logical variable associated with the production of a given product m in the plant k. TCP(k) is the total cost of the production, PC(m) is the cost for processing the raw material to obtain the product m, and SP(m) is the selling price for the product m. The value of 0.66 represents an estimation of the land surface, in m^2, required per liter of product. This value is estimated using the data reported for the refinery "Francisco I. Madero" in Ciudad Madero, Tamaulipas, Mexico (El Informador, 2019). The cost of the land required to build the facilities is taken as 0.4048 USD/m^2. The disjunctions have been relaxed through the convex hull approach (Lee and Grossmann, 2000). Additionally, the following implication is established to ensure that the products will be obtained only if the facility is built:

$$Y(k) \Leftrightarrow S(BE,k) \vee S(BB,k) \vee S(LA,k) \vee S(F,k) \tag{6}$$

Where BE represents bioethanol, BB is the biobutanol, LA stands for lactic acid and F is the furfural. The objective function implies the maximization of the profit, given by:

$$Profit = \sum_m \sum_k [MP(m,k) \times SP(m)] - \sum_k TCP(k) - \sum_j \sum_k CP(j,k) - \sum_n \sum_k CD(k,n) \tag{7}$$

The relaxed disjunctions, together with the constraints which are not dependent of the disjunctions, are codified in the software GAMS. The resulting MINLP problem consists of 448 equalities and 134 inequalities. The model has been optimized with the solver DICOPT, in a Dell WorkStation with a Inter Core i5-9300H CPU, 4.00 GB of RAM.

4. Results

According to the obtained results, a single plant must be installed in Querétaro. Table 1 shows the distribution of raw materials to the facility. It can be seen that, for this scenario, wheat and corn are the only raw materials used for the generation of biofuels and bioproducts.

Table 1. Distribution of raw materials (t/yr).

Facility location/Raw material	Sorghum	Wheat	Corn	Barley
Querétaro	--	Querétaro (10)	Querétaro (19)	--

Table 2 shows the products obtained on the plant. It can be seen that the facility produces mainly furfural.

Table 2. Products obtained on the facility (t/yr).

Facility location/Product	Bioethanol	Biobutanol	Levulinic acid	Furfural
Querétaro	2	3	6	13

All the obtained products are used to satisfy the local demand of the city of Queretaro. In this case, only the furfural demand is completely satisfied, with the production of small quantities of the other products. Since the objective function implies the maximization of the profit, the solution implies satisfying the demand of the product with the highest yield, being also the second product with the highest selling prize. With this solution, the profit is 65,289 USD/yr. Further constraints must be added to ensure a better use of the great production potential in the country.

5. Conclusions

A supply chain model is proposed for the production of two biofuels, namely bioethanol and biobutanol, and two bioproducts, levulinic acid and furfural, using the available biomass in Mexico. The supply chain has been optimization in terms of the annual profit. As expected, most of the biofuels and bioproducts are obtained from corn residues. On the other hand, the model predicts the need of a facility in the center on Mexico, only satisfying the demand of furfural. The model can be enhanced to look for a better use of the biomass to satisfy the demand of fuels and chemicals.

References

M.K. Alavijeh, K. Karimi, 2019, Biobutanol production from corn stover in the US, Industrial Crops and Products, 129, 641-653.

British Petroleum, 2018, BP Statistical Review of World Energy, at https://www.bp.com/content/dam/bp/en/corporate/pdf/energy-economics/statistical-review/bp-stats-review-2018-full-report.pdf. Last visited August 19, 2019.

C.M. Cai, T. Zhang, R. Kumar, C.E. Wyman, 2013, Integrated furfural production as a renewable fuel and chemical platform from lignocellulosic biomass, Journal of Chemical Technology and Biotechnology, 89, 1, 2-10.

El Informador, 2019, Serán siete las refinerías de México en 2022, at https://www.informador.mx/Seran-siete-las-refinerias-de-Mexico-en-2022-t201905090003.html. Last visited January 24, 2020.

M. Gozan, B. Ryan, Y. Krisnandi, 2017, Techno-economic assessment of levulinic acid plant from *Sorghum Bicolor* in Indonesia, IOP Conference Series: Materials Science and Engineering, 345, 012012.

S. Lee, I.E. Grossmann, 2000, New algorithms for nonlinear generalized disjunctive programming, Computers and Chemical Engineering, 24, 9, 2125-2141.

P. Sassner, M. Galbe, G. Zacchi, 2008, Techno-economic evaluation of bioethanol production from three different lignocellulosic materials, Biomass and Bioenergy, 32, 5, 422-430.

S. Saval, 2012, Aprovechamiento de residuos agroindustriales: pasado, presente y futuro, BioTecnología, 16, 2, 14-16 (Spanish).

Service of Agrifood and Fisheries Information (SIAP), 2018, Anuario Estadístico de la Producción Agrícola, at https://nube.siap.gob.mx/cierreagricola/ (Spanish). Last visited October 29, 2019.

Sauro Pierucci, Flavio Manenti, Giulia Bozzano, Davide Manca (Eds.)
Proceedings of the 30th European Symposium on Computer Aided Process Engineering (ESCAPE30), May 24-27, 2020, Milano, Italy.
http://dx.doi.org/10.1016/B978-0-12-823377-1.50225-1

Total Site Synthesis: Selection of Processes to Save Energy and Boost Cogeneration

Konstantinos A. Pyrgakis, Antonis C. Kokossis

School of Chemical Engineering, National Technical University of Athens, Iroon Polytechneiou 9, GR-15780, Greece
akokossis@mail.ntua.gr

Abstract

The design of biorefineries is challenged by new chemistries that need to be evaluated and properly integrated across industrial sites. Process and energy integration are necessary to maximize performance and sustainability margins. In a previous work, the authors addressed the combinatorial nature of the biorefinery synthesis and integration problem (Pyrgakis and Kokossis, 2019) introducing systems and an optimization model (MILP) to systematically screen and integrate value chain paths highlighting energy promising and high profitable biorefinery solutions. This work presents an updated version of the previous model to simultaneously address cogeneration and utility levels optimization. The previous version is also combined with cogeneration models to select processes that benefit energy savings and electricity production, as necessary co-product to offset price volatilities of upcoming biochemicals. New strategies are proposed to improve accuracy of Turbine Hardware Model (THM), in light of variable processes and utility levels, and revise regression parameters of turbine modules and predictions of input specific heat load. The optimization model (MILP) was used to examine 20 candidate chemistries and revealed biorefinery solutions with high energy savings (10.5%), shaft work production (25.6 MW) and profitability margins (9.3 M€/yr).

Keywords: Total Site integration, Turbine Hardware Model, Cogeneration, Utility levels optimization, Biorefineries.

1. Introduction

Chemical engineering is challenged by new bio-based chemistries that need to be tested in the contexts of building Industrial Biotechnology and Circular economy. Common, but still questionable, solutions are solely focusing on bio-ethanol and bio-fuels that hold few evidences for sustainable production. Value chains provide new options towards numerous biochemicals (commodities and specialties) to examine and integrate across biorefinery sites. It is still challenging to screen and optimize value chain options in the scope of recovering sources and securing sustainable production (Kokossis et al., 2015). Process and energy integration technologies are essential to propose engineering solutions against high production costs and uncertainties of upcoming markets.

Process integration is commonly provided by means of superstructure optimization to synthesize chemical paths with common input-output chemicals scoping for complete biorefining routes form raw materials (biomass) to intermediate and end-bioproducts. Energy integration is called to improve and evaluate the performance of candidate process portfolios (Pyrgakis and Kokossis, 2017) by means of (i) direct heat source-to-sink integration, (ii) indirect process-to-process integration via steam and (iii)

cogeneration optimization. Though not visible through value chains, electricity still counts as a valuable co-product to offset price volatilities of upcoming biochemicals.

In (i), integration is provided by well-known heat cascade technologies. The analysis in (ii) is challenged by the use of graphical tools and multi-stage computational analyses that examine given, rather than variable, process portfolios. The previous work of Pyrgakis and Kokossis (2019) faced these challenges by proposing a new heat cascade concept and an enhanced transshipment model to systematize the analysis in (ii) and simultaneously address (i) and (ii) in light of unknown/variable value chain processes. This paper presents an updated version of previous work to simultaneously address (i), (ii) and (iii) along with utility levels optimization. The enhanced transshipment model is extended with cogeneration technologies and strategies to improve accuracy of turbine models. The biorefineries design is formulated as an MILP problem to select value chain processes that maximize energy performance, cogeneration and profitability.

2. The Cross-Interval Transshipment (CIT) model

Direct integration refers to heat exchange of hot-cold streams belonging to each process, while indirect applies among streams of different processes selected for the industrial site by valorizing available process heat for generation steam utilities. Indirect integration is commonly conducted by means of Site Sources & Sinks Profiles (SSSP) that one should prepare by combining the Grand Composite Curves (GCC) of individual processes. The conventional graphical approach apparently applies for fixed processes by first applying direct integration on GCCs and, then, indirect (process-to-process) integration based on SSSPs. However, the biorefineries design faces with candidate value chain processes (not fixed options) to be properly selected and integrated to optimize performance. A previous work of authors (Pyrgakis and Kokossis, 2019) systematized the graphical procedure through an enhanced heat transshipment model (Figure 1.a) that simultaneously implements direct and indirect integration considering processes (and their hot/cold streams) as additional degrees of freedom in integration.

In Figure 1.a, heat flows (solid lines) around nodes 1, 2 and 3 still count for direct integration along the proposals of Papoulias and Grossmann (1983). Nodes 4 and 5 have been added by Pyrgakis and Kokossis (2019) to simultaneously describe indirect heat exchange of hot-cold streams. Indirect integration exploits excess heat to generate steam, which is introduced to the utilities of the whole plant. Node 4 applies as a pseudo-cold utility level to extract available heat from intervals. The extracted heat load is translated into steam, which travels to lower-temperature intervals providing heat along with fresh utilities through node 5. The proposed CIT transshipment describes the energy balances along the Total Site Cascade (TSC) of Figure 1.b, which is configured by the temperature intervals of all candidate processes that are possible to get integrated across the under-construction biorefinery site. The updated version of CIT further involves options to use fresh and generated steam for shaft work production.

Figure 1.b explains the operation of TSC for a two-process site. Hot-cold streams of Process A are directly integrated along the intervals of TSC, while excess heat from Process A generates steam of level 1. The transshipment addresses energy trade-offs concerning the use of steam either to save fresh steam (indirect integration of Processes A-B) or to generate shaft work by expanding steam to lower steam level 2. The CIT is combined with a turbine model and a strategy to simultaneously optimize utility levels.

3. Integration and cogeneration strategies

Steam utility levels act as energy gates for process-to-process integration by gathering/supplying heat from/to intervals of TSC (Figure 1.b). They also define the

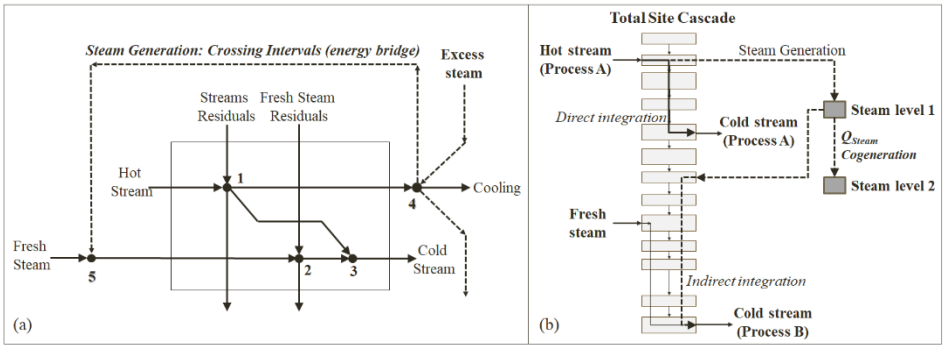

Figure 1: Cross-Interval Transshipment (a) and Total Site Cascade (b)

expansion zones (the span between levels) of turbines operations. Steam savings are estimated by connecting nodes 4 and 5 (Figure 1.a), while steam residuals exiting node 4 correspond to turbines steam loads; nodes 4 and 5 apply for each utility level. This work considers a set of candidate utility levels (Figure 2.a), between the upper and lower temperatures of TSC, to select with a scope to maximize benefits from steam savings and cogeneration. The Turbine Hardware Model (THM) of Mavromatis and Kokossis (1998) is used to describe complex turbines through an equivalent cascade of simple turbines (one inlet and outlet), as shown in Figure 2.b. The THM applies for simple turbines providing a linear approximation of power output (E^{max}) as a function of steam load (M^{max}) facing non-linearities between isentropic efficiency (n_{is}^{max}) and steam load, as shown through Eq.(1).

$$n_{is}^{max} = \frac{\overline{\Delta H}_{real}}{\overline{\Delta H}_{is}} = \frac{E^{max}}{\overline{\Delta H}_{is} \cdot M^{max}} \tag{1}$$

where $\overline{\Delta H}_{is} = \frac{\Delta T^{SAT}}{1854-1931 \cdot q_{in}}$ is the isentropic enthalpy change, q_{in} the specific heat load, ΔT^{SAT} the saturation temperature difference and $M^{max} = \frac{Q}{q_{in}}$, where Q corresponds to the steam residuals of node 4 of the transshipment model (Figure 1.a).

The THM is based on the transformation of turbine efficiency data vs power output of Peterson and Mann (1985) into piecewise linear expressions (see Figure 2.c), as: $\overline{\Delta H}_{is} \cdot M^{max} = \frac{E^{max}}{n_{is}} = A + B \cdot E^{max}$, where A, B are regression parameters. Finally, the THM takes the form of:

$$E^{max} = \frac{1}{B}(\overline{\Delta H}_{is} \cdot M^{max} - A) \tag{2}$$

Existing literature strategies use linear expressions for the estimation of A, B as a function of inlet saturation temperature T_{in}^{SAT} (Mavromatis and Kokossis, 1998), or ΔT^{SAT} (Varbanov et al., 2004), or inlet pressure P_{in} (Medina et al., 2010). Also, q_{in} is generally assumed approximately constant at 0.557 MWh/tn (VHP-90 bar, 500 ºC) to preserve linearity of THM. However, the existing strategies are not enough to combine

Eq.(2) with the transshipment of Figure 1.a and utility levels optimization. The accuracy of THM is not enough to model turbines operating at extreme conditions (e.g. small ΔT^{SAT} and M^{max} and large T_{in}^{SAT}). For example, let a turbine expanding 5 tn/hr of VHP steam from 90 to 80 bar. The regression parameters (A, B) of Mavromatis and Kokossis

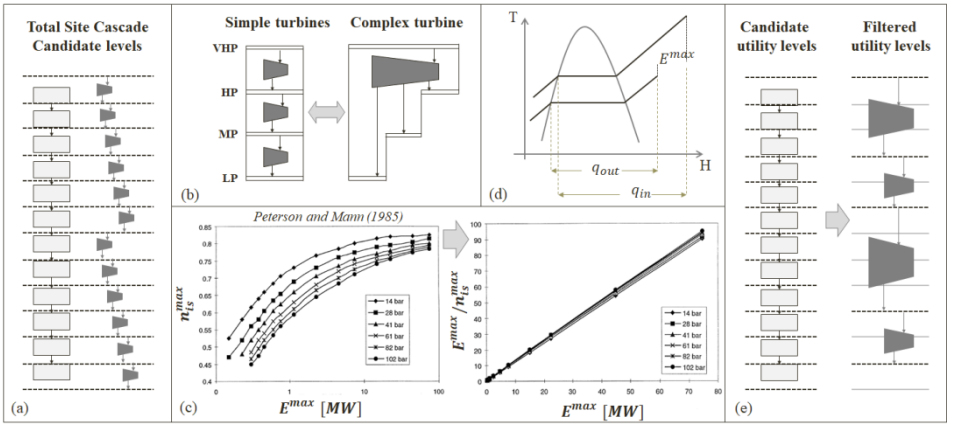

Figure 2: Candidate utility levels (a), Simple turbines cascade (b), Turbine efficiency data (c), T-H diagram (d), Candidate and filtered utility levels (e).

(1998) and Medina et al. (2010) resulted in negative power outputs, while the model of Varbanov et al. (2004) results in the same power output regardless P_{in} or T_{in}^{SAT} variations. The following strategies are proposed to increase accuracy of the THM and the prediction of q_{in}, as well as to prepare a linear optimization model to address the combinatorial nature of process synthesis, integration and shaft work cogeneration.

3.1. Revision of THM regression parameters

The data of Figure 2.c are revisited and regressed preparing a new approach for the estimation of regression parameters A and B as a function of T_{in}^{SAT}, ΔT^{SAT} and q_{in}, as follows: $A = a_1 \cdot \Delta T^{SAT}$ and $B = a_2 + a_3 \cdot T_{in}^{SAT} + a_4 \cdot \Delta T^{SAT} + a_5 \cdot q_{in}$, where a_1=0.0011, a_2=1.0079, a_3=0.00114, a_4=0.00054, a_5=0.001, when E^{max}<3.26 MW; a_1=0.0039, a_2=1.0878, a_3=0.00049, a_4=0.00017, a_5=0.0012, when E^{max}>3.26 MW. The revised parameters return E^{max}=0.037 MW for the above example (90→80 bar).

3.2. A formulation for the prediction of input specific heat load

The input specific heat loads of a turbines cascade are estimated by: $q_{out} = q_{in} + c_p \cdot \Delta T^{SAT} - \frac{E^{max}}{M^{max}}$, where q_{out} of a turbine corresponds to q_{in} of the next one, based on the T-H diagram of Figure 2.d. The common practice of using constant q_{in} for each expansion zone would aggregate multiple errors at the design of the equivalent complex turbine. This work revisits the above expression providing conservative predictions for q_{in}, ahead of optimization.

The term $\frac{E^{max}}{M^{max}}$ of the above expression is replaced by $\eta_{is}^{max} \cdot \overline{\Delta H}_{is}$, based on Eq.(1). A conservative approximation of q_{in} is obtained, if the turbine operates at maximum feasible performance. Drawing on Eq.(1) and Eq.(2), that performance is considered by term $\frac{1}{B}$, which counts for ΔT^{SAT}, T_{in}^{SAT} and q_{in} variations (see Section 3.1). Given a set

of utility levels, q_{in} at each level *n* is approximated, as: $q_{in}^{n+1} = q_{in}^{n} + c_p \cdot \Delta T^{SAT^n} - \frac{1}{B} \cdot \frac{\Delta T^{SAT^n}}{1854-1931 \cdot q_{in}^{n}}$, where q_{in}^{1} refer to the known steam level (VHP) supplied by the boiler house.

3.3. THM variations

When turbines design is constructed as an optimization problem, additional non-linearities are introduced due to A, B variations with power output; e.g. over/under 3.26 MW (see Section 3.1). The non-linearities are regularly faced by using same values for parameters a_1-a_5 regardless the power output estimations. These inaccuracies are faced by considering changes in parameters a_1-a_5 and by introducing linear logical constraints to switch over different THM formulations, each adjusted with the appropriate parameters, according to power output variations over/under 3.26 MW.

3.4. Turbines cascade optimization

The method assumes a set of candidate utility levels to optimize as shown on the left of Figure 2.e. The use of THM over the multiple narrow expansion zones would aggregate multiple errors at the approximation of power output of the equivalent complex turbine. Inaccuracies are minimized by filtering selected levels against discarded, building a parallel, yet dynamic, cascade of expansion zones, where THM is applied, as shown on the right of Figure 2.e. Processes are treated as degrees of freedom to configure the intervals of TSC, while candidate utility levels are tested to optimize steam savings and cogeneration. The biorefinery is not given at early design stages; steam savings and cogeneration are benefited by the selection of value chain processes and utility levels.

4. Mathematical formulation

The domain is formulated by continuous variables for the capacities of value chain process, the heat flows of the CIT model and the turbines power output. Binary variables are used for the selection of processes and utility levels, to switch among alternative THM formulations and to build the expansion zones, where THM is applied. The optimization model includes mass balances along the value chain, energy balances of CIT and logic constraints to select and filter utilities and address changes of turbine parameters (a_1-a_5). The objective function is formulated by the utilities cost and the profits from cogeneration to maximize energy performance; otherwise, economic data of candidate processes and products are also included to maximize profitability.

5. Case study

The optimization approach was used to address a value chain of 20 candidate chemistries (Figure 3.a) considering both objectives to optimize the use of energy or profitability. In the first case, the integration of xylitol, itaconic acid and poly-urethanes production processes results in 9.3% steam cost savings (due to process-to-process integration), while cogeneration rises to 25.6 MW. In the second case, xylitol, PVC and poly-urethanes production maximized annual profitability to 9.3 M€; steam cost savings rise to 10.5%, while 20.3 MW of electricity are generated. Figure 3.b shows the optimized utility levels and the power output resulted in each case. The selection of narrow expansion zones at lower temperature steam levels justifies the revision of cogeneration modeling strategies; otherwise, the accuracy of existing literature models would not be enough to predict shaft work at those levels, as discussed in Section 3.

6. Conclusions

A modified heat transshipment model is combined with THM to maximize steam savings and cogeneration of shaft work in light of unknown processes. New strategies

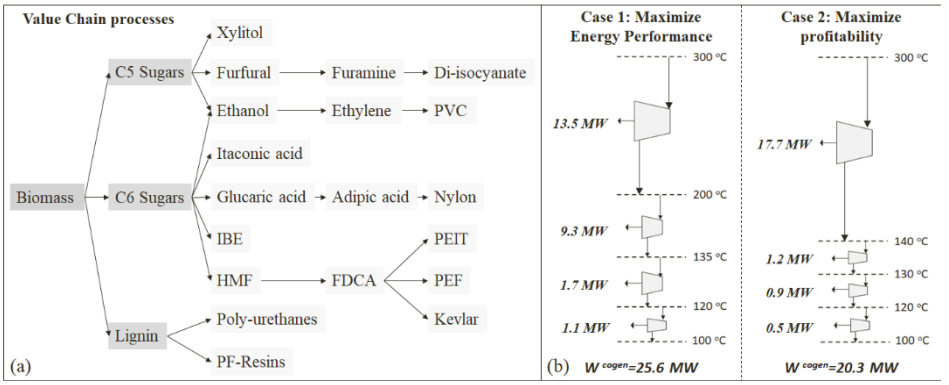

Figure 3: Candidate value chain processes (a), Optimal utility levels and turbines (b).

are proposed to improve accuracy and face limitations at the implementation of THM. The analysis resulted in new formulations to predict THM regression parameters, and approximate q_{in} instead of being considered as constant. The model builds the optimal expansion zones, where THM is accurately applied, also in light of variable utility levels. The model was applied to investigate 20 candidate value chain processes highlighting the most promising bio-based chemistries in terms of energy savings (10.5%), cogeneration potential (25.6 MW) and sustainability margins (9.3 M€/yr).

References

A. Kokossis, M. Tsakalova, K. Pyrgakis, 2015, Design of Integrated Biorefineries, Comp & Chem Eng, 81, 40–56

S.P. Mavromatis, A.C. Kokossis, 1998, Conceptual Optimisation of Utility Networks for Operational Variations-I. Targets and Level Optimisation, Chem Eng Sci, 53, 8, 1585–1608

J.M. Medina-Flores, M. Picon-Nunez, 2010, Modelling the Power Production of Single and Multiple Extraction Steam Turbines, Chemical Engineering Science, 65, 2811–2820

S.A. Papoulias, I.E. Grossmann, 1983 A Structural Optimization Approach in Process Synthesis-I Utility Systems, Comp & Chem Eng, 7, 6, 695–706

J.F. Peterson, W.L. Mann, 1985, Steam-System Design: How it Evolves, *Chem Eng*, 92, 21,62–74

K.A. Pyrgakis, A.C. Kokossis, 2017, Total Site Integration as a Process Synthesis and Scheduling Tool in Multiple-feedstock Biorefineries, CACE, 40, 1825–1830

K.A. Pyrgakis, A. Kokossis, 2019, A Total Site Synthesis Approach for the Selection, Integration and Planning of Multiple-Feedstock Biorefineries, Comp & Chem Eng, 122, 326–355

P.S. Varbanov, S. Doyle, R. Smith, 2004, Modelling and Optimization of Utility Systems, Chemical Engineering Research and Design, 82, A5, 561–578

Sauro Pierucci, Flavio Manenti, Giulia Bozzano, Davide Manca (Eds.)
Proceedings of the 30th European Symposium on Computer Aided Process Engineering (ESCAPE30), May 24-27, 2020, Milano, Italy.
http://dx.doi.org/10.1016/B978-0-12-823377-1.50226-3

An Extended Approach for the Integration of Heat Pumps into HENS Multi-Period MILP Superstructure Formulation for Industrial Applications

Leopold Prendl [a], René Hofmann [a,b*]

[a]*Technische Universität Wien, Institute for Energy Systems and Thermodynamics, Getreidemarkt 9/BA, 1060 Vienna, Austria*
[b]*AIT Austrian Institute of Technology GmbH, Center for Energy, Sustainable Thermal Energy Systems, Giefinggasse 2, 1210 Vienna, Austria*
rene.hofmann@tuwien.ac.at

Abstract

This paper deals with the extension of the linearized superstructure formulation for heat exchange network synthesis (HENS) proposed by Beck and Hofmann (2018a). The energy consumption of heat pumps as a function of the temperature lift and the thermal energy flow is approximated by a convex linearization. This allows for a linear extension of the cost function that takes the size and the energy consumption of heat pumps into account. As given problem an existing process and a predetermined heat pump characteristic is assumed. A test case consisting of two hot and two cold process streams has been constructed to investigate the proposed optimization method. The test case has been optimized with and without the extended approach for comparable results. The HEN resulting from the newly developed approach has 16.1 % lower total annual costs (TAC) and a 48.1 % lower external energy demand than the network resulting from the HENS without storages or heat pumps. This improvements come with the drawback of a more complex HEN with 15 installations compared to the simple HEN with 7 installations.

Keywords: Mathematical Programming, Linearization, Heat Recovery, Heat Pump, HENS

1. Introduction

The recovery of thermal energy is becoming more and more important, taking into account the overall objective of the reduction of primary energy consumption and thus reduction of greenhouse gas emissions. One way towards achieving this goal is the enhancement of energy exchange and conversion networks. Heat exchange network synthesis (HENS) was broadly investigated and approached with many different approaches over the last decades as recapitulated by Escobar and Trierweiler (2013). The integration of heat pumps into non continuous processes has also been the subject to a number of scientific publications as, for example, by Stampfli et al. (2019). Nonetheless, the integration of heat pumps into HENS for the economic optimization of batch processes with multiple time steps was not being thoroughly investigated. An existing paper from Becker and Maréchal (2012) uses the heat cascade formulation as approach. In contrast to this, a superstructure formulation was used as starting point for this work.

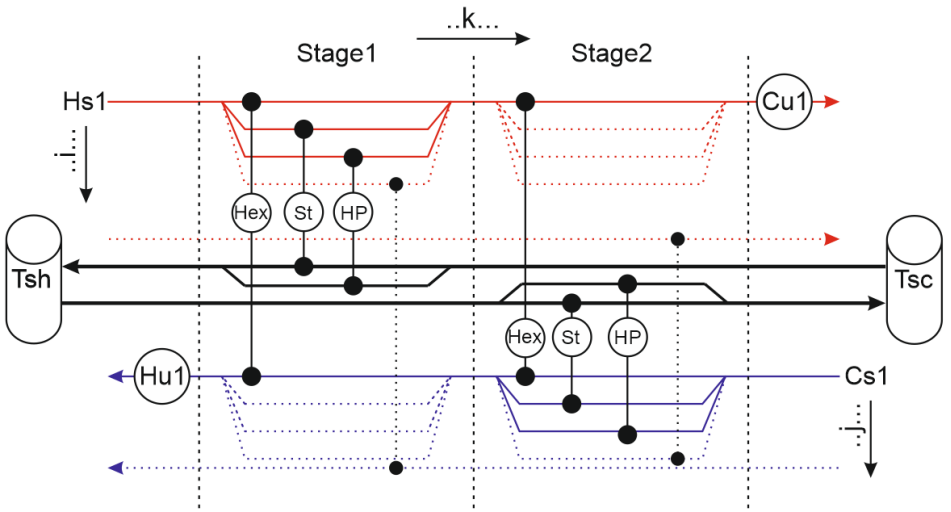

Figure 1: Extended Superstructure with possible Stream-Stream Hex (Hex), Stream-Storage Hex (St), Heat Pumps (HP), Hot/Cold Streams (Hs/Cs), Hot/Cold Storage Temperatures (Tsh/Tsc), Hot/Cold Utilities (Hu/Cu), Stage Subscript (k) and Hot/Cold Stream Subscripts (i/j).

2. Extended Mathematical Model

The superstructure is based on the formulation by Beck and Hofmann (2018a), which is a linearization of the superstructure proposed by Yee and Grossmann (1990). The objective function as shown in Eq. (1) uses the same nomenclature and constraints as Beck and Hofmann (2018a). The extension considers a two tank liquid thermal storage, heat exchangers between the streams and the storage and heat pumps between the streams and the storage. The possible connections for every stream in every stage are exemplarily represented in Figure 1. The two tank storage is modelled according to Beck and Hofmann (2018b). The multiple time periods during the cyclic process are realized by using the time slice model for cutting the process into different time slices in which the process parameters are constant. Isothermal mixing after every stream split is assumed. If heat exchangers occur at the same spot in different time periods p, the largest heat exchanger area A is taken into account for the calculation. In the other time steps the isothermal mixing is assured by bypasses. Furthermore, as a simplification to keep the problem linear, the heat transfer coefficients are assumed to be constant.

$$\begin{aligned}\min\ TAC = &\sum_i\sum_j\sum_k c_f Z_{ijk} + \sum_i c_f Zcu_i + \sum_j c_f Zhu_j + \sum_i\sum_j\sum_k cA_{ijk}^{\beta} \\ &+\sum_i cAcu_i^{\beta} + \sum_j cAhu_j^{\beta} + \sum_i\sum_p c_{cu} qcu_{ip}\tau_p + \sum_j\sum_p c_{hu} qhu_{jp}\tau_p \\ &+C_{fixst} + C_{varst} Size_{st} + \sum_i\sum_j\sum_k c_f Zst_{ijk} + \sum_i\sum_j\sum_k cAst_{ijk}^{\beta} \\ &+\sum_i\sum_j\sum_k c_{hp} Zhp_{ijk} + \sum_i\sum_j\sum_k cAhp_{ijk}^{\beta} + \sum_i\sum_j\sum_k\sum_p c_{Pel} Pel_{ijkp}\tau_p\end{aligned} \quad (1)$$

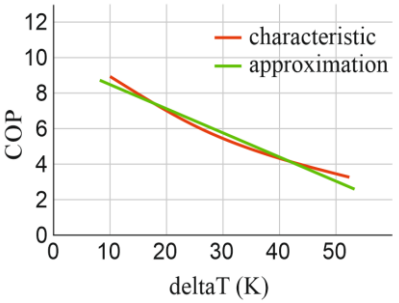

Figure 2: Linearized COP over deltaT

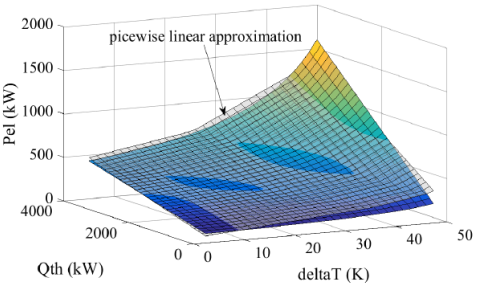

Figure 3: Linear Approximation of P_{el}

3. Linearization

For the integration of heat pumps into the MILP superstructure several linearizations are necessary. In the following chapter the chosen approach is explained in detail.
The coefficient of performance (COP) of heat pumps is defined in Eq. (2) as the ratio of useful heat supplied by the heat pump (Q_{th}) to the required work (P_{el}).

$$COP = \frac{Q_{th}}{P_{el}} \tag{2}$$

In this work it is assumed that the heat pump characteristic curve of the COP over the temperature lift of the heat pump (deltaT) is known. For the linearization this characteristic curve is approximated by a polynomial of first order. In Figure 2 an example for a characteristic curve with its associated linear approximation is shown. From Eq. (2) it is visible that P_{el} can be calculated as the ratio of Q_{th} to COP. This nonlinear relation is linearized with an approach inspired by the linearization of the heat exchange area by Beck and Hofmann (2018a). The nonconvex, nonlinear feasible solution space is split into three regions. Each of these regions is then approximated by a linear equation which is fitted with least squares methods. This piecewise linear approximation is shown in Figure 3 with the underlying solution space. The linear approximations are used as constraints for P_{el} with the help of big-M formulations. In these constraints Γ is a sufficient large number to activate or deactivate Eq. (3) dependent on whether a Heat Pump exists on this position or not.

$$P_{el} \geq P_{el,approx} - (1 - Zhp_{ijk})\Gamma \tag{3}$$

The heat exchanger area between the streams and heat pumps is approximated with the same procedure as for the heat exchangers between the streams. As measure to keep the objective function linear, the heat pump approach temperature, which is the minimum temperature difference between stream or storage and heat pump operation temperature, gets set to a fixed value. Due to the preset storage temperatures it is possible to linearize the reduced heat exchange area between storage and heat pump as function of the heat flow Q_{hpst} as shown in Eq. (4) because the denominator remains constant.

$$A_{hpst}^{\ \beta} = \left(\frac{Q_{hpst}}{U \ LMTD_{hpst}} \right)^{\beta} \longrightarrow A_{hpst}^{\ \beta} \approx c_{A1} + c_{A2} Q_{hpst} \tag{4}$$

4. Test Case

Table 1: Stream data and cost coefficients

Stream	Tin (°C)	Tout (°C)	CP (kW/K) period 1	CP (kW/K) period 2	CP (kW/K) period 3	h (kW/m^2K)
H1	120	40	18	50	9	0.5
H2	90	30	22	22	1	0.5
C1	20	100	20	10	10	0.5
C2	50	90	50	40	70	0.5
UT h	150	150	-	-	-	1
UT c	5	10	-	-	-	1

exchanger cost = $4000+500[A(m^2)]^{\beta}$ €y^{-1}, storage cost = 7000+0.15[kg] €y^{-1},
hot utility cost = 0.07 €$kW^{-1}h^{-1}$, cold utility cost = 0.007 €$kW^{-1}h^{-1}$, cost exponent β = 0.83,
electrical power costs = 0.06 €$kW^{-1}h^{-1}$, dTmin = 5 °C, Heat Pump cost = 11000 €y^{-1}

As test case an example which consists of two hot and two cold process streams was investigated. The assumed cyclic process has a duration of three hours and is split into three periods of one hour each. It is assumed that the process is operated annually for 8600 h. The superstructure model was set up with two stages. The cost coefficients and stream data used are given in Table 1. A two tank storage which operates at 70 °C and 100 °C with thermo-oil as storage medium with an specific heat capacity of cp_{oil} = 2 $kJkg^{-1}K^{-1}$ and an heat transfer coefficient of h_{oil} = 0.5 $kWm^{-2}K^{-1}$ was chosen. The assumed heat pump has a power consumption range from 400 kW to 2000 kW and a given approach temperature of $T_{hpaproach}$ = 5 K. The linearized COP characteristic is given as COP = 10 – 0.15 K^{-1} deltaT and the heat transfer coefficient as h_{hp} = 5 $kWm^{-2}K^{-1}$. A lower boundary of the COP of COPmin = 1 was set as constraint. As solver for the MILP Gurobi 8.1.0 was used.
The plausibility of the optimization was tested with the variation of different cost coefficients. With increasing costs for electrical power or decreasing costs for utilities, the size and number of heat pumps gets reduced until no more heat pumps get chosen for the system. Similarly increasing costs for storage material lead to smaller storage sizes and finally the exclusion of solutions containing storages. This behavior matches the results expected from the structure of the used cost function.

5. Results

The test case was optimized in two different configurations. In the first configuration the HEN was optimized without heat pumps or storages in order to be able to obtain comparable results. In the second configuration the test case was optimized with the extended approach including a storage and heat pumps.

5.1. Configuration 1: Test case without heat pumps and storage

For this setup, the solver found a solution after 0.02 s with total annual costs of TAC = 1,120,500 €y^{-1}. The obtained heat exchange network which is shown in Figure 4 consists of three stream – stream heat exchangers and four utility heat exchangers. The obtained heat flows for the different time periods are given in Table 2. The high amount of needed cold utility in period 2 and needed hot utility in period 3 shows potential for temporal energy shifting. The total utility energy demand adds up to 20.869 GWh y^{-1}.

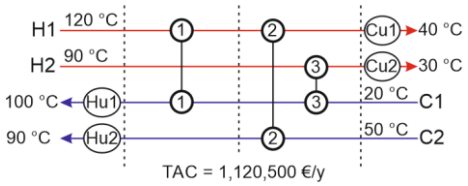

Figure 4: Hen obtained without Heat Pump

Table 2: Heat Flows without Heat Pump (kW)

	p1	p2	p3
1	294.3	150.00	720.00
2	875.70	1600.00	-
3	1300.00	650.00	-
Hu1	5.72	-	80
Hu2	1124.3	-	2800.00
Cu1	270.00	2250.00	-
Cu2	20.00	670.00	60.00

5.2. Configuration 2: Test case with integrated heat pumps and storage

For the extended case a solution was found after 54.12 s with total annual costs of TAC = 940,260 €y^{-1}. The extended heat exchange network which is shown in Figure 6 consists of five stream – stream heat exchangers, two stream – storage heat exchangers, four utility heat exchangers, two heat pumps and a storage tank with 192334 kg of thermo-oil which has a storage capacity of 3.206 MWh. The obtained heat flows and the electrical power demands for the different time periods are given in Table 3. The total utility energy demand is 6.074 GWh y^{-1} and the electrical energy demand for the heat pumps is 4.755 GWh y^{-1}. This adds up to a total external energy demand of 10.829 GWh y^{-1}. The charging state of the storage over the cycle time is given in Figure 5. The storage has a variable storage charge at the beginning of the cycle which has to be reached again at the end of the cycle. This is ensured by suitable boundary conditions.

5.3. Comparison:

The TAC of the extend network are 16.1 % lower compared to the simple network and the total external energy demand of the obtained extended structure is only 51.9 % of the total energy demand of configuration 1. From Table 2 and Table 3 it is visible that the utilities are significantly smaller for configuration 2 and that a big part of the energy is supplied by the heat pumps instead. Although configuration 2 has lower TAC and energy demand it has to be noticed that it is much more complex with 15 installations and a storage compared to the simple configuration 1 with 7 installations.

6. Conclusion

An extension for the integration of heat pumps into HENS for multi-period MILP superstructures by linearizing the energy consumption of heat pumps has been developed. A test case consisting of two hot and two cold process streams with varying mass flows for different time steps has been constructed to demonstrate the proposed method. This test case was optimized with and without the possibility of including a storage and heat pumps to compare the gained results. The obtained extended HEN has 16.1 % lower TAC and 48.1 % lower external energy demand compared to the conventional HEN which comes with the drawback of a higher complexity of the network. The test case was chosen rather small because the target was to check if the optimization results are plausible which is hardly possible for bigger problems. From the results of the optimization without storage and heat pumps it can be concluded that a storage device that shifts energy between the time periods is able to reduce the TAC if the costs of the storage, the heat pumps and the electrical energy are low enough compared to the utility costs. This is consistent with the results of the second configuration. When comparing results it has to be taken into account that the results of these optimizations are strongly dependent on the

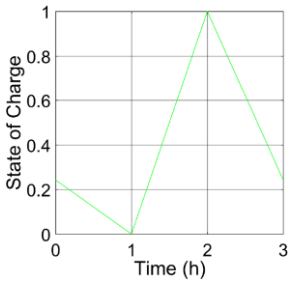

Figure 5: Storage Charging State over Cycle Time

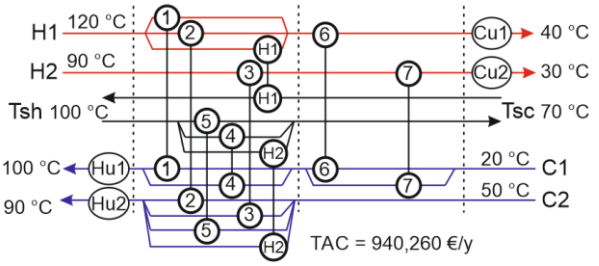

Figure 6: Hen obtained with Heat Pumps and Storage

Table 3: Heat Flows and P_{el} results with Heat Pump (kW)

	p1	p2	p3
1	549.38	456.93	216.24
2	577.21	630.00	368.76
3	770.00	770.00	-
4	373.64	-	398.76
5	402.79	-	262.44
6	265.58	343.07	135.00
7	311.41	-	-

	p1	p2	p3
Hu1	100.00	-	50.00
Hu2	250.00	200.00	-
Cu1	47.84	622.29	-
Cu2	238.59	550.00	60.00
Hp1	-	1947.70	-
Hp2	-	-	2168.80
Pel Hp1	-	1257.80	-
Pel Hp2	-	-	400.90

chosen coefficients. Small changes of cost coefficients or physical parameters can result in very different network solutions because of the nature of mixed integer programming.

Acknowledgment

The idea of this paper was initiated by the endowment professorship of the Technical University of Vienna (TUW), Institute for Energy Systems and Thermodynamics – Industrial Energy Systems, and the Austrian Institute of Technology (AIT) – Center for Energy – Energy in Industries. This work was funded by the cooperation doctoral school Smart Industrial Concept (SIC!). The authors want to express their great acknowledgment.

References

Beck, A., Hofmann, R. (2018a). A Novel Approach for Linearization of a MINLP Stage-Wise Superstructure Formulation. *Computers & Chemical Engineering*, *112*, 17–26.

Beck, A., Hofmann, R. (2018b). Extensions for Multi-Period MINLP Superstructure Formulation for Integration of Thermal Energy Storages in Industrial Processes. *Computer Aided Process Engineering*, *43*, 1335–1340.

Becker, H., Maréchal, F. (2012). Targeting industrial heat pump integration in multi-period problems. *Computer Aided Chemical Engineering*, *31*, 415–419.

Escobar, M., Trierweiler, J. O. (2013). Optimal heat exchanger network synthesis: A case study comparison. *Applied Thermal Engineering*, *51*, 801–826.

Stampfli, J. A., Atkins, M. J., Olsen, D. G., Walmsley, M. R.W., Wellig, B. (2019). Practical heat pump and storage integration into non-continuous processes: A hybrid approach utilizing insight based and nonlinear programming techniques. *Energy*, *182*, 236–253.

Yee, T. F., Grossmann, I. E. (1990). Simultaneous optimization models for heat integration—II. Heat exchanger network synthesis. *Computers & Chemical Engineering*, *14*, 1165–1184.

Sauro Pierucci, Flavio Manenti, Giulia Bozzano, Davide Manca (Eds.)
Proceedings of the 30th European Symposium on Computer Aided Process Engineering (ESCAPE30), May 24-27, 2020, Milano, Italy.
http://dx.doi.org/10.1016/B978-0-12-823377-1.50227-5

Enabling Renewable Base Load Generation via Chemical Energy Storage

Antonio Sánchez[a], Mariano Martín[a], Qi Zhang[b,*]

[a]*Departamento de Ingenieria Quimica, Universidad de Salamanca, Salamanca, Spain*
[b]*Departament of Chemical Engineering and Material Science, University of Minnesota, Minneapolis, USA*
qizh@umn.edu

Abstract

Energy storage plays a key role in the modern power system. Recently, the use of chemicals for energy storage, especially in long-term applications, has attracted significant attention. In this work, the potential benefit of using different chemicals – namely methane, methanol, dimethyl ether (DME), and ammonia – as energy carriers is evaluated. For a region of Spain, the optimal locations of plants to supply a portion of the local base-load power demand are determined as well as the transportation modes used to deliver the chemicals to the different demand locations. Moreover, a scheduling optimization is carried out to analyse the system's dynamic performance.

Keywords: energy storage, chemical storage, renewable energy

1. Introduction

Power generation is currently responsible for about 40% of the world's total CO_2 emissions. The main means to reduce the emissions will be the use of renewable energy sources for power generation. The penetration of renewables into the power grid has increased significantly in the last few decades. According to recent predictions (BloombergNEF, 2019), the share of renewables in 2050 will be about 62%, with 48% of solar and wind generation. At this point, energy storage is the main bottleneck for the effective deployment of the intermittent renewable energy sources.

A large number of alternatives to store power have been proposed with different levels of development. Diverse electrical, mechanical, thermal, chemical or electrochemical technologies are being evaluated. Pumped hydro storage (PHS) is the most commonly used technology today, contributing to about 95% of the total storage capacity installed (Christensen et al., 2013). Batteries have been used in a wide spectrum of devices and their integration at the power grid level is being investigated. The use of chemicals is one of the most promising alternatives to store energy in a wide range of capacities and for long time horizons. Besides power generation, these chemicals can also be used as fuels for the transportation sector and as feedstock for the chemical industry. A suitable combination of all the alternatives could be the solution to meet all the requirements for a particular storage application (Gur, 2018).

Different chemicals have been studied for energy storage applications. One of those chemicals that has received considerable attention is hydrogen. However, the use of hydrogen faces two main challenges: the low volumetric energy density and the cost for storage and transportation. To overcome these issues, the synthesis of a wide range of hydrogen derivate chemicals has been proposed. Methane has the advantage that the

infrastructure for its storage, transport and supply is already in place. The use of liquid chemicals is also attractive due to the easy storage and transportation and higher energy density. Such liquid chemicals include methanol, dimethyl ether (DME), and ammonia. In the case of ammonia, no carbon sources are involved in its synthesis or utilization.

The objective of this work is to evaluate the storage of solar/wind power in the form of chemicals to provide a source for stable production of electricity out of them on demand. In Spain, due to more restrictive legislation regarding nitrogen and carbon dioxide emissions, coal-based power plants are expected to be decommissioned within the next few years. Hence, there is an urgent need to enable renewable power generation for meeting base load. In this work, we consider two levels of decision making: design at the supply chain level and operation at the scheduling level. At the supply chain level, the production and storage facilities and the transportation network are determined. Then, the impact of the intermittent wind and solar availability on the process performance is analyzed at the scheduling level. The remainder of this paper is organized as follows. In Section 2, the problem to be solved is presented. Section 3 includes the mathematical formulation of the problem. Section 4 presents results from the case study. Finally, some concluding remarks are provided in Section 5.

2. Problem Description

The power-to-chemicals alternative for energy storage is evaluated in this work. The synthesis of four chemicals is considered: methane, methanol, DME, and ammonia. The first three are produced using hydrogen and carbon dioxide. Ammonia does not require a carbon source for its synthesis; instead, nitrogen is needed. Hydrogen is produced using electrolysis of water. Carbon dioxide can be obtained from carbon capture, and different technologies to separate air (distillation, adsorption and membranes) are considered to produce nitrogen. Methane, methanol and DME are produced by CO_2 hydrogenation, and ammonia through the well-stablished Haber-Bosch process. As power collection units, wind turbines and solar PV panels are considered. In Figure 1, a schematic with the different processes and resources involved in this work is presented.

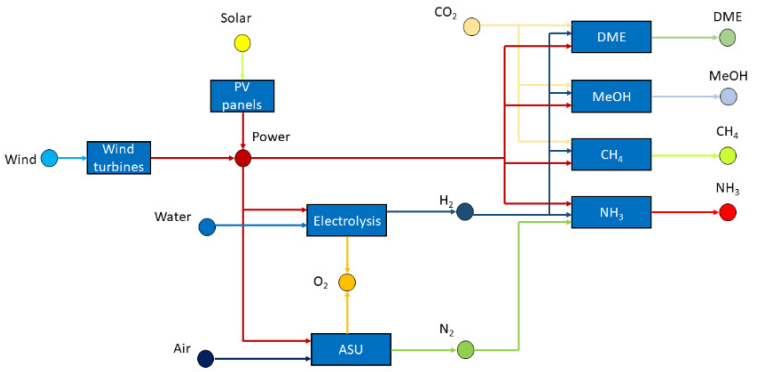

Figure 1: Simplified flowsheet for the proposed superstructure

The supply chain analysis is carried out for Leon, a province of Spain. This region is divided into 29 different sub-regions (see Figure 2). The city/town with the highest population is selected as the representative point for each region. Three different transportation modes are evaluated: truck, rail and pipeline. Truck and rail can be

selected for transporting all chemicals, but pipeline is only available for methane. Truck connections are available for transportation between each sub-region and its neighbouring sub-regions. The available rail and pipeline connections are shown in Figure 2.

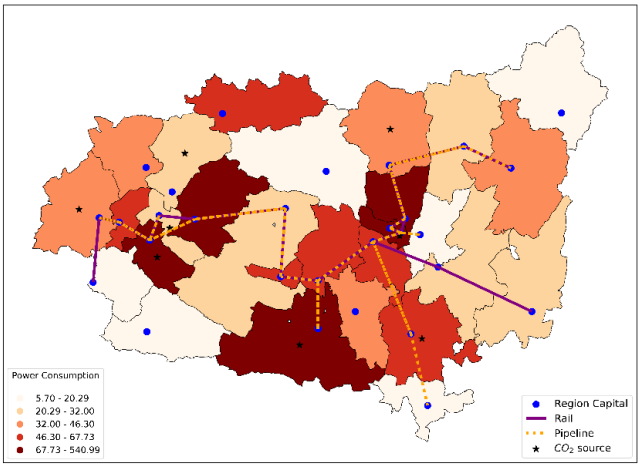

Figure 2: Rail and pipeline connections in a map where the color of the different region represent the power consumption intensity. The CO_2 sources are also presented.

The synthesis of the carbon-based chemical products (methane, methanol and DME) is mainly limited by the availability of CO_2. Figure 2 also shows the sub-regions where there are carbon dioxide sources. It is assumed that water and air are available with no restrictions.

The objective is to determine the optimal plant and transportation network to meet a portion of the base-load power demand, which we assume to be 10% of the total power demand, in each sub-region. After this supply chain analysis, the operation of the installed plants is evaluated. The goal in this second analysis is to determine the required oversize capacity to meet the power demand with the hourly fluctuations in solar and wind availability.

3. Problem Formulation

The multiperiod supply chain optimization is conducted for a time horizon of a year and a monthly time discretization. The problem is formulated as an MILP (Guillén-Gosálbez & Grossmann, 2008). The main equations are presented in the following.

The mass balance for each resource j at each location k in each time period t is formulated as follows:

$$Q_{jkt} = B_{jkt} - S_{jkt} + \sum_i \rho_{ij} P_{ikt} + \sum_{k' \in \bar{K}_{jk'k}} W_{jk'kt} - \sum_{k' \in \bar{\bar{K}}_{jkk'}} W_{jkk't} \qquad \forall j,k,t \tag{1}$$

where Q_{jkt} is the storage level for resource j at location k at time t, B_{jkt} is the amount of resource j consumed by the system and $W_{jkk't}$ is the amount transported from location k to k'. The production level, P_{ikt}, for each process i is limited by its capacity, C_{ik}:

$$P_{ikt} = \eta_{ikt} C_{ik} \quad \forall i \in \{1,2\}, k, t \tag{2}$$

$$P_{ikt} \le \eta_{ikt} C_{ik} \quad \forall i \in \{3,10\}, k, t$$

The inventory level, Q_{jkt} is limited by the storage capacity ($\overline{C}_{jk}$):

$$Q_{jkt}^{total} \le \overline{C}_{jk} \quad \forall j, k, t$$

$$Q_{jkt}^{total} = Q_{jkt-1}^{total} + Q_{jkt} \cdot 3600 \cdot 24 \cdot 30 \quad \forall j, \mathrm{k}, \mathrm{t} \tag{3}$$

The process capacity is limited by a maximum value ($C_i^{\max}$):

$$C_{ik} \le C_i^{\max} x_{ik} \quad \forall i, k \tag{4}$$

The maximum storage capacity ($\overline{C}_{jk}$) is also bounded by an upper bound ($\overline{C}_j^{\max}$):

$$\overline{C}_{jk} \le \overline{C}_j^{\max} x_{jk} \quad \forall j, k \tag{5}$$

The resource availability, B_{jkt} is limited by an upper bound ($B_{jkt}^{\max}$):

$$B_{jkt} \le B_{jkt}^{\max} \quad \forall j, k, t \tag{6}$$

The power consumption ($D_{power,k,t}$) must be met by the combination of different chemical productions. The heating value, H_j, is used to compute the energy available in each chemical (S_{jkt}):

$$\sum_{j \in \overline{J}} S_{jkt} H_j \ge D_{power,k,t} \quad \forall k, t$$

$$S_{jkt} = 0 \quad \forall j \in \overline{\overline{J}}, k, t \tag{7}$$

There are three kinds of transportation modes to transfer the chemicals between locations:

$$W_{jkk't} = \sum_{m \in \overline{M}_{jkk'\mathrm{m}}} T_{jkk'mt} \quad \forall j, k, k', t \tag{8}$$

The transported amount, $T_{jkk'mt}$ is limited by an upper bound ($T_{jkk'm}^{\max}$) as a function of the transportation mode:

$$T_{jkk'mt} \le T_{jkk'm}^{\max} \quad \forall j, k, k', t \tag{9}$$

The production in each plant and time period (P_{ikt}) is limited by a lower and an upper bound:

$$P_i^{\min} y_{ikt} \le P_{ikt} \le P_i^{\max} y_{ikt} \quad \forall i, k, t \tag{10}$$

The capital costs (CC) are calculated using a linear approximation. The objective value is the operating cost (OP) of the entire grid, including the cost of the processes, the cost of storage of the different chemicals and the transportation cost.

$$OP = \sum_k \left(\sum_t \sum_i J_{ikt} + \sum_i \sigma_i CC_{ik}^p \right) + \sum_k \sum_j \left(\frac{CC_{jk}^{st}}{lifetime} \right) + \sum_j \sum_k \sum_{k'} \sum_m \sum_t T_{jkk'mt} C_{jm}^{transp} Dist_{kk'} \tag{11}$$

In this equation, J_{ikt} includes the operating cost of the different processes not related to the capital cost, C_{jm}^{transp} is the cost of the different modes of transport and $Dist_{kk'}$ is the distance between the different locations.

After the supply chain analysis, for each of the facilities set up in the region, a scheduling problem is solved to determine the operation of the facility and to determine the oversize in the production capacity and storage with respect to the supply chain

results when the wind and solar availabilities are considered on an hourly basis. The scheduling model is adapted from Zhang et al. (2019).

4. Results

The supply chain results are presented in Figure 3. Two plants are set up to meet the power demand of the entire region (blue stars on the map). These two facilities have solar PV panels as energy collection units. Wind turbines are not selected. Only two of the chemicals are produced: methane and methanol. The total capital cost for the production and storage of the system is $393 MM where about 99% corresponds to the investment in the production processes. About 50% is due to the investment in the PV panels, 45% is due to the capital cost of the electrolyzers and 5% due to methane and methanol production units. To transport the methane and methanol produced to the different sub-regions, truck, rail and pipeline are selected. The pipeline is the main option to transport the methane. The storage of chemicals is built up next to the production facilities. Only methanol is stored. The total operating cost of the network is equal to $45 MM/year. As depicted in Figure 3, the transportation links change depending on the month of the year.

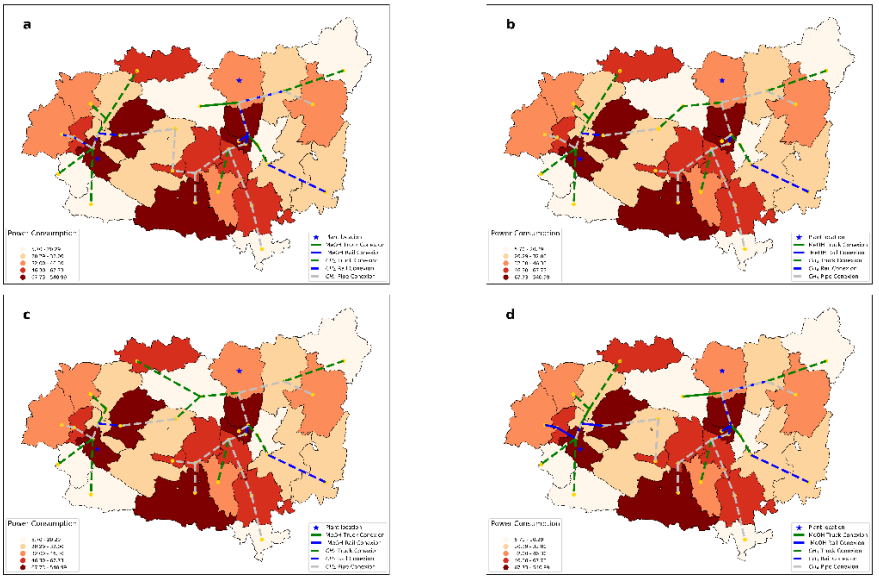

Figure 3: Plant locations and transportation modes for different months: a) January b) June c) September d) December

Considering fluctuations in the solar irradiance and wind speed profiles, the production schedules for the two plants are optimized on an hourly basis for the entire year. To meet the demand calculated in the supply chain stage, it is necessary to increase the capacity of the plant by about 35%. During the day, a fraction of the power produced in the PV panels has to be sold to the local power grid due to the limited capacity in the electrolyzer and other chemical units. Hydrogen storage is also allowed in the scheduling optimization. Figure 4 shows the production schedule for one of the plants over the course of a week. Methane production is kept constant while methanol production fluctuates according to the solar availability. As previously mentioned,

methanol is used to storage energy. The production of methanol takes place mainly during the summer where solar energy is more abundant. Methanol is consumed during the winter to meet a fraction of the power demand. In Figure 3, it is also shown that the methanol transportation takes place only during the winter months (January and December).

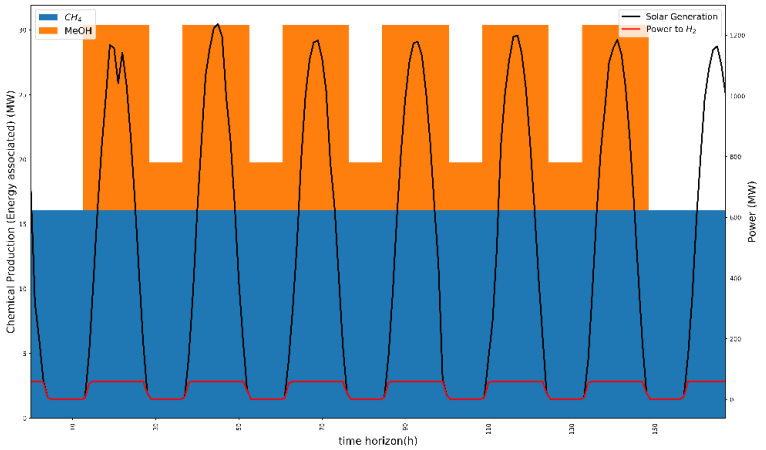

Figure 4: Scheduling results for a representative week in June

5. Conclusions

In this work, an MILP framework has been developed to optimize power-to-chemicals supply chains and the scheduling of the production plants to supply based load power generation. A real-world case study considering a specific region in Spain has been conducted. The results show that methane and methanol production are selected to meet the power demand. The scheduling problem determines the operation of the facility on an hourly basis. Methanol is stored during the summer when more power is generated, and used in the winter when the solar-based power generation is lower. Future work involves the process design and integration of the transformation of these chemicals into electricity.

Acknowledgements: The authors acknowledge the FPU, Spain grant (FPU16/06212) from MECD to AS, and JCYL for S026G18.

References

BloombergNEF, 2019. New Energy Outlook 2019. https://about.bnef.com/new-energy-outlook/

J.M. Christensen, P.V. Hendriksen, J.D. Grunwaldt, A.D. Jensen, 2013, Chemical energy storage. In H. Hvidtfeldt Larsen, L. Sønderberg Petersen (Eds.), DTU International Energy Report 2013: Energy storage options for future sustainable energy systems, 47-52, Technical University of Denmark.

T.M. Gur, 2018, Review of electrical energy storage technologies, materials and systems: challenges and prospects for large-scale grid storage, Energy & Environmental Science, 11, 2696-2767.

G. Guillén-Gosálbez, I.E. Grossmann, 2018, Optimal design and planning of sustainable chemical supply chains under uncertainty, AIChE Journal, 55, 1, 99-121.

Q. Zhang, M. Martín, I.E. Grossmann, 2019, Integrated design and operation of renewables-based fuels and power production networks, Computers & Chemical Engineering, 122, 80-92.

Sauro Pierucci, Flavio Manenti, Giulia Bozzano, Davide Manca (Eds.)
Proceedings of the 30th European Symposium on Computer Aided Process Engineering (ESCAPE30), May 24-27, 2020, Milano, Italy.
http://dx.doi.org/10.1016/B978-0-12-823377-1.50228-7

On the Benefit of Modular and Mobile Production Units in Biomass Waste-to-energy Supply Chains

Andrew Allman[a], Che Lee[a], Mariano Martín[b], Qi Zhang[a,*]

[a]*Department of Chemical Engineering and Materials Science, University of Minnesota, Twin Cities, 421 Washington Ave SE, Minneapolis, MN, USA 55455*
[b]*Universidad de Salamanca, Departamento de Ingeniería Química. Pza. Caídos 1-5, 37008 Salamanca, España.*
qizh@umn.edu

Abstract

Upgrading biomass waste to energy is a promising technology which enhances the economic values of crop residues such as wheat straw and corn stover, which are typically present in excess in highly agricultural regions such as the United States Midwest. In this work, gasification of biomass to turn a gas turbine is considered as a technology for upgrading biomass waste to energy. We propose to use modular and mobile production units to limit the transportation cost of moving biomass to energy production facilities in a distributed supply chain. We present a generic optimization framework for determining the optimal location and relocation of gasifier and turbine modules over time. To demonstrate the efficacy of our framework, we apply it to a case study where biomass residue in Minnesota is converted to energy. The results show the economic benefits of considering mobility of modules in processing biomass waste, which is produced at different times in different parts of the state.

Keywords: modular manufacturing, distributed manufacturing, biomass waste-to-energy, circular economy, process intensification

1. Introduction

Crop residues, or inedible parts of plants such as stalks, leaves, husks, and straw, account for more than 50% of the biomass present in common agricultural plants such as corn and wheat (Smil 1999). Some of this biomass is necessary for farming: much of it is burned in the fields to replenish the soil with nutrients or left in fields to prevent soil erosion, while some other biomass can be processed into animal feed or bedding. Even still, about 40% of this waste can be sustainably extracted from farms without sacrificing these needs (Batidzirai et al 2016). While exact statistics on the amount of crop residue produced annually are not maintained, it is estimated that by 2030, 155 million tons of biomass waste will be produced in the United States, with more than half coming from the four Midwestern states of Iowa, Illinois, Minnesota, and Nebraska (UCS 2014). The fact that such an abundant resource is readily available without need to change current land use patterns offers immense opportunity for sustainable manufacturing; however, many technical and logistical challenges need to be addressed to make processing biomass waste to more valuable commodities economically feasible.

Biomass is a naturally occurring hydrocarbon resource which has been proposed as a replacement for fossil fuels in energy production. As energy represents an essential resource in modern society, the upgrading of biomass waste to energy offers the potential to convert a low value resource into one of high value. Many different technologies can

be used for this conversion, including gasification to turn a gas turbine, gasification with further upgrading to methane or methanol, fermentation to ethanol, or anaerobic digestion to biogas (Iakovou et al. 2010). Recent research has shown that processing agricultural waste to energy can address food-energy-water-waste nexus concerns (Garcia et al. 2019). Other work has analyzed the tradeoff of economies of scale versus efficient resource management in biomass gasification networks (Zetterholm et al. 2018). Ultimately, the low density of biomass can make transportation costs high, providing a key logistical challenge in developing biomass waste-to-energy supply chains. Distributed manufacturing, whereby manufacturing facilities are built at a small scale and located close to supply and demand sites, offers a promising approach to address the aforementioned logistical challenge. Recent research has shown the benefits in using distributed manufacturing to address the challenge of using crop production as an industrial supply, as in the production of biofuels (Marvin et al. 2013), or demand, as in the production of ammonia (Palys et al. 2019). Modular production units, which can be constructed off-site, and then shipped to and assembled at a production site into a working facility, act as an enabling technology for distributed manufacturing (Baldea et al. 2017). Individual unit modules can be relocated between different production sites over time; however, to the best of our knowledge, no previous work exists which analyzes the economic benefits of doing so in a practical waste-to-energy case study. In this work, we present an optimization framework for determining the optimal location and relocation of modular production facilities in a distributed biomass waste-to-energy supply chain, and apply the framework to the case study of biomass waste-to-energy production in Minnesota. The remainder of the paper is structured as follows: in Section 2, a broad problem statement is defined and the mathematical framework is presented. Next, Section 3 introduces the data used for the particular case study considered. Section 4 presents the results of this case study and showcases the benefit of modular mobility. Finally, we provide concluding remarks and areas of future research in Section 5.

2. Problem Statement and Formulation

The objective of this problem is to determine the location and relocation of biomass gasifier and gas turbine modules, as well as the transportation of biomass from farm to energy production site, minimizing a sum of capital and operating costs such that a given amount of biomass waste is processed from each farm over multiple time periods. The mathematical framework for solving this problem is presented in this section, with definitions for the symbols used provided in Table 1.

The objective function of this optimization problem is to minimize a sum of fixed and variable operating costs, capital costs, and module relocation costs:

$$\zeta = \sum_{t\in\mathcal{T}}\left(\sum_{j\in\mathcal{J}}\sum_{m\in\mathcal{M}}\left(g_{jmt}z_{jmt} + \sum_{j'\in\bar{\mathcal{J}}_j} h_{jj'mt}w_{jj'mt}\right) + \sum_{j\in\mathcal{J}}\sum_{l\in\mathcal{L}}\left(\sum_{i\in\mathcal{I}} c_{ijlt}d_{it}x_{ijlt} + f_{jlt}y_{jlt}\right)\right). \tag{1}$$

The problem is constrained such that all of a given biomass waste supply must be processed. As x is a fractional supply, this equation takes the form:

$$\sum_{j\in\mathcal{J}}\sum_{l\in\mathcal{L}} x_{ijlt} = 1 \quad \forall\, i \in \mathcal{I},\, t \in \mathcal{T}. \tag{2}$$

It is important to keep track of the number of modules installed at each energy production site during each time period. This is done according to the following unit conservation

Table 1. Nomenclature for problem formulation.

Symbol	Description
Sets	
$\mathcal{I}$	Set of farms supplying biomass waste
$\mathcal{J}$	Set of candidate energy production sites
$\bar{\mathcal{J}}_j$	Set of sites to which modules can be moved from site j, $\bar{\mathcal{J}}_j \subseteq \mathcal{J} \setminus \{j\}$
$\hat{\mathcal{J}}_j$	Set of sites from which modules can be moved to site j, $\hat{\mathcal{J}}_j \subseteq \mathcal{J} \setminus \{j\}$
$\mathcal{L}$	Set of facility configurations
$\mathcal{M}$	Set of modules
$\bar{\mathcal{M}}_l$	Set of modules required for configuration l, $\bar{\mathcal{M}}_l \subseteq \mathcal{M}$
$\mathcal{T}$	Set of time periods
Parameters	
b_{jl}	Minimum fractional operating capacity of configuration l at production site j
c_{ijlt}	Relative operating cost of processing biomass from farm i at site j in configuration l at time t, \$/t
d_{it}	Total biomass waste supply from farm i in time period t, t
f_{jlt}	Fixed operating cost of producing in configuration l at site j in time t, \$
g_{jm}	Capital cost of installing module m at site j in time t, \$
$h_{jj'mt}$	Cost of relocating module m from site j to site j' in time t, \$
n_{lm}	Number of units of module m operating in configuration l
u_{jl}	Processing capacity of configuration l at production site j, t
v_{jm}^0	Initial number of units of module m present at production site j
v_{jmt}^{max}	Maximum number of units of module m allowed at production site j during time period t
Decision Variables	
$v_{jmt} \in \mathbb{N}$	Number of units of module m present at production site j during time period t
$w_{jj'mt} \in \mathbb{N}$	Number of units of module m moved from site j to site j' during time period t
$0 \le x_{ijlt} \le 1$	Fraction of biomass from farm i processed by energy production site j operating in configuration l during time period t
$y_{jlt} \in \{0, 1\}$	Binary variable, 1 if production site j operates in configuration l during time period t
$z_{jmt} \in \mathbb{N}$	Number of units of module m built at production site j during time period t

equation, which states that this value will equal the number of modules present at the start, plus the number of modules built, plus the number of modules relocated from other locations, minus the number of modules relocated to other locations:

$$v_{jmt} = v_{jm}^0 + \sum_{t'=1}^{t} \left(z_{jmt'} - \sum_{j' \in \bar{\mathcal{J}}_j} w_{jj'mt'} + \sum_{j' \in \hat{\mathcal{J}}_j} w_{j'jmt'} \right) \quad \forall\, j \in \mathcal{J},\, m \in \mathcal{M},\, t \in \mathcal{T}. \tag{3}$$

A configuration is defined as a fixed number of modules that are actively used to process biomass waste during a specific time period. A production site is only able to operate in a specific configuration if the requisite modules for that configuration are installed, and the total number of modules installed cannot exceed a predefined maximum:

$$n_{lm} y_{ilt} \le v_{jmt} \le v_{jmt}^{\max} \quad \forall\, j \in \mathcal{J},\, l \in \mathcal{L},\, m \in \bar{\mathcal{M}}_l,\, t \in \mathcal{T}. \tag{4}$$

Each facility can only process as much biomass waste as the capacity of its operating configuration allows. Additionally, some configurations may have a minimum capacity at which they can operate:

$$b_{jl} u_{jl} y_{jlt} \le \sum_{i \in \mathcal{I}} d_{it} x_{ijlt} \le u_{jl} y_{jlt} \quad \forall\, j \in \mathcal{J},\, l \in \mathcal{L},\, t \in \mathcal{T}. \tag{5}$$

Furthermore, each facility can only operate in a single configuration at a time:

$$\sum_{l \in \mathcal{L}} y_{jlt} \le 1 \quad \forall\, j \in \mathcal{J},\, t \in \mathcal{T}. \tag{6}$$

The optimization problem to be solved is to minimize the total cost ζ, defined by Eq. (1), subject to Eqs. (2)-(6). The formulation is a mixed-integer linear program that can be readily solved by an off-the-shelf solver such as CPLEX.

3. Case Study Data

In this work, the framework presented in the previous section to determine the optimal supply chain for processing 1% of total biomass waste produced in Minnesota, or 2.5% of available biomass waste, equal to 562,000 tons of biomass per year. While this percentage seems small, we note that it is unlikely that a single entity would be able to process all available biomass, and more likely that individual farms will supply to different entities or different technologies; thus, processing this fraction of demand is reasonable for a base case. Biomass waste is assumed to be proportional to the amount of corn, wheat, and soy harvested, for which annual data is available at a county scale (USDA 2019). As such, each of Minnesota's 87 counties is considered as a farm supply site for the purpose of this study, with demands derived from 2017 harvesting data. We further consider that different crops are harvested at different times using data provided by the USDA (USDA 2019), considering four time periods which give the biomass produced in August, September, October, and November, respectively. This data is displayed in Figure 1. In each time period, a supply center of mass (SCM) is calculated, which is a supply-weighted average of farm supply locations, given by coordinates ℓ_i:

$$\mathbf{SCM}_t = \frac{\sum_{i \in I} d_{it} \ell_i}{\sum_{i \in I} d_{it}} \tag{7}$$

The supply center of mass for each month is denoted by a star in Figure 1. Its movement from northwest to south central Minnesota suggests that mobile modules are likely to be economically beneficial for this case study.

To determine candidate production sites, we separate the state of Minnesota into 9 regions and choose the largest city in each region. These locations are also shown in Figure 1. Each candidate site can install a set of gasifier and gas turbine modules, both of which are needed to process biomass waste to electricity. For both module types, units that can process either 2 kg/s or 30 kg/s biomass can be installed. The smaller units can be easily relocated through the supply chain as needed, and are also assumed to be able to operate completely flexibly at any capacity below their maximum. Meanwhile the larger units are assumed to be too large to move or operate flexibly; they can operate at a minimum of 75% of their rated capacity. Because of the 1 month-long time periods considered, we constrain the problem to only allow for building new units in August, the first time period; however, module mobility is allowed at any time. Capital costs for the modules are taken from correlations presented by Larson et al. (2005), while operating costs are taken from Martín and Grossmann (2018). Transportation costs for biomass and relocation costs for modules are determined using driving distances using the Google Maps distance matrix API, and assuming a truck capacity of 10 m^3, fuel economy of 6 mpg, and fuel cost of \$3/gal, and negligible module reinstallation costs.

4. Results

The case study for processing Minnesota's biomass waste is solved using CPLEX 12.8 in Julia 0.6.4 using the JuMP v0.18.5 package (Dunning et al. 2017). Computations were performed on a 3.2 GHz Intel Core i7-9700 processor. To determine the practical economic effects of module mobility, the optimization is performed twice, once when small modules are allowed to move, and once where no mobility is allowed (i.e. w is fixed to zero). The optimization problem consists of 70,689 variables (1476 integer), and 77,616 constraints. The mobile supply chain is solved to optimality in 1091 s, while the immobile supply chain is solved to optimality in 455 s.

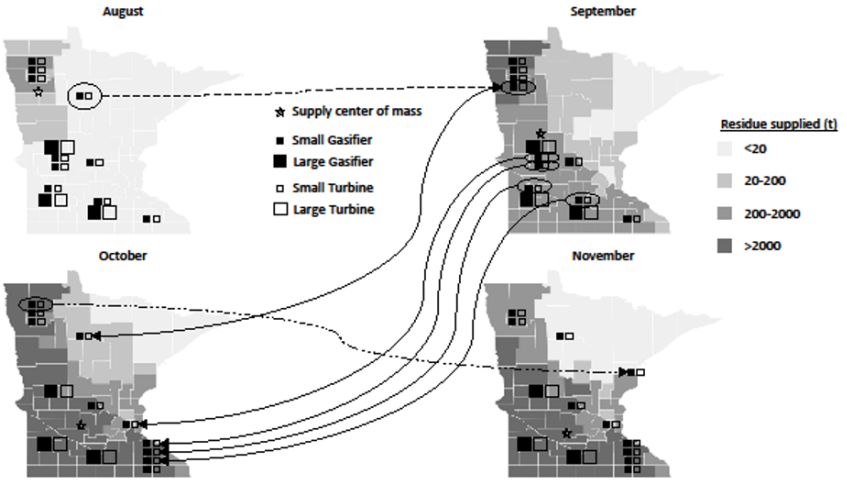

Figure 1. Supply of biomass residue over 4-month period in Minnesota, with optimal facility location and relocation in mobile module case.

The optimal location and relocation of gasifier and turbine modules for the mobile module case is shown in Figure 1. In the mobile supply chain case, the optimal solution builds 3 large gasifier and turbine modules, and 10 small modules. Interestingly, in the immobile supply chain case, the optimal solution builds more small modules, choosing to build 19 small modules and only 2 large modules. We hypothesize that this is because flexibility is essential to optimally responding to the spatiotemporal changes in supply. In the immobile case, the only flexibility that is present is the ability of small modules to operate at any capacity, which is important with supply moving from northwest to southeast over the year. When mobility is allowed, this implements an extra degree of flexibility, nonintuitively also enabling the introduction of additional units which are not flexible, as each small unit provides greater ability for the supply chain to agilely respond to changes. This effect is clear when considering the operating configurations of the mobile system: in August and September, the larger modules are not used since the supply of biomass residue is not yet high enough; as such, smaller modules are also located and operated in the southwestern production sites. In October and November, the larger modules are turned on which enables moving the smaller modules to other locations in the supply chain. In the immobile supply chain, this movement is not allowed but there is not enough supply to run the larger units in the early months. Thus, 5 small modules are installed at the west central production site instead of a large module.

The optimal annualized supply chain cost for the mobile case is determined to be \$87.8 MM/y, equivalent to an electricity cost of 10.4 ¢/kWh power produced (assuming 35% efficiency in the energy conversion process). Both results are on the same order of magnitude with those reported in similar biomass-waste to energy works (Garcia et al. 2019, Zetterholm et al. 2018). When units are not mobile, the optimal annualized cost is \$89.0 MM/y, equivalent to an electricity cost of 10.6 ¢/kWh, or a 1.4% increase in cost from the mobile case. Surprisingly, this reduction mainly comes from a reduction in capital costs, which are 5.4% lower in the mobile supply chain case, whereas operation and transportation costs are roughly equal. This again results from the added flexibility of mobility also enabling the construction of larger, immobile units in the locations where supply is highest.

5. Conclusions

In this paper, a supply chain optimization framework determining the location and relocation of modular and mobile production units was presented. This framework was then applied to the case study of a biomass waste-to-energy supply chain using gasification and a gas turbine in the state of Minnesota. The results of this work showcased the economic benefits of module mobility in a practical case study. Here, annualized supply chain costs were reduced by 1.4%, driven by a reduction in capital costs when mobile units were considered.

In the future, we aim to extend this work by considering the effects of uncertainty in crop yields and harvesting time, in a multi-year, multi-stage stochastic supply chain planning problem. We anticipate that module mobility will be even more valuable for providing an agile supply chain response to such uncertainty. We also plan to consider additional technologies, such as mobile driers and compactors present at individual farms to increase the density of transported biomass waste. Finally, we intend to consider how different public policies, such as a carbon tax, can also act as a driving force for module mobility.

Acknowledgements

The authors gratefully acknowledge financial support from the University of Minnesota.

References

Baldea, M., Edgar, T.F., Stanley, B.L., Kiss, A.A., 2017. Modular manufacturing processes: Status, challenges, and opportunities. AIChE Journal 63, 4262–4272.

Batidzirai, B., Valk, M., Wicke, B., Junginger, M., Daoiglou, V., Euler, W., Faaij, A.P.C., 2016. Current and future technical, economic, and environmental feasibility of maize and wheat residues supply for biomass energy application: Illustrated for South Africa. Biomass and Bioenergy 92, 106-129.

Dunning, I., Huchette, J., Lubin, M., 2017. JuMP: A modeling language for mathematical optimization. SIAM Review 59, 295–320.

Iakovou, E., Karagiannidis, A., Vlachos, D., Toka, A., Malamakis, A., 2010. Waste biomass-to-energy supply chain management: A critical synthesis. Waste Management 30, 1860-1870.

Larson, E.D., Jin, H., Celik, F.E., 2005. Gasification-based fuels and electricity production from biomass, without and with carbon capture and storage. URL: https://acee.princeton.edu/wp-content/uploads/2016/10/LarsonJinCelik-Biofuels-October-2005.pdf

Martin, M., Grossman, I.E., 2018. Optimal integration of renewable based processes for fuels and power production: Spain case study. Applied Energy 213, 595-610.

Marvin, W.A., Schmidt, L.D., Benjaafar, S., Tiffany, D.G., Daoutidis, P., 2012. Economic optimization of a lignocellulosic biomass-to-ethanol supply chain. Chemical Engineering Science 67, 68–79.

Palys, M.J., Allman, A., Daoutidis, P., 2019. Exploring the benefits of modular renewable-powered ammonia produciton. Industrial and Engineering Chemistry Research 58, 5898-5908.

Smil, V., 1999. Crop residues: Agriculture's largest harvest: Crop residues incorporate more than half of the world's agricultural phytomass. BioScience 49, 299-308.

UCS, 2014. Turning agricultural residues and manure into bioenergy. URL: https://www.canr.msu.edu/uploads/files/Agricultural-Residue-Ranking.pdf

USDA, 2019. National Agricultural Statistics Service. URL: https://www.nass.usda.gov/Statistics_by_State/Minnesota/Publications/County_Estimates/index.php

Zetterholm, J., Pettersson, K., Leduc, S., Mesfun, S., Lundgren, J., Wetterlund, E., 2018. Resource efficiency or economy of scale: Biorefinery supply chain configurations for co-gasification of black liquor and pyrolysis liquids. Applied Energy 230, 912-924.

30TH SYMPOSIUM ON COMPUTER AIDED PROCESS ENGINEERING

PART C

Edited by

SAURO PIERUCCI, FLAVIO MANENTI, GIULIA LUISA BOZZANO AND DAVIDE MANCA

COMPUTER-AIDED CHEMICAL ENGINEERING, 48

ELSEVIER

30TH EUROPEAN SYMPOSIUM ON COMPUTER AIDED PROCESS ENGINEERING

PART C

30TH EUROPEAN SYMPOSIUM ON COMPUTER AIDED PROCESS ENGINEERING

PART C

Edited by

Sauro Pierucci
AIDIC Servizi s.r.l.,
Milano, Italy,
sauro.pierucci@polimi.it

Flavio Manenti
SuPER Team, Sustainable Process Engineering Research
Dipartimento di Chimica, Materiali e Ingegneria Chimica,
Politecnico di Milano, Milano, Italy,
flavio.manenti@polimi.it

Giulia Luisa Bozzano
SuPER Team, Sustainable Process Engineering Research
Dipartimento di Chimica, Materiali e Ingegneria Chimica,
Politecnico di Milano, Milano, Italy,
giulia.bozzano@polimi.it

Davide Manca
PSE-Lab - Process Systems Engineering Laboratory,
Dipartimento di Chimica, Materiali e Ingegneria Chimica,
Politecnico di Milano, Italy,
davide.manca@polimi.it

ELSEVIER

Amsterdam – Boston – Heidelberg – London – New York – Oxford
Paris – San Diego – San Francisco – Singapore – Sydney – Tokyo

Elsevier
Radarweg 29, PO Box 211, 1000 AE Amsterdam, Netherlands
The Boulevard, Langford Lane, Kidlington, Oxford OX5 1GB, UK
50 Hampshire Street, 5th Floor, Cambridge, MA 02139, USA

Notices
Knowledge and best practice in this field are constantly changing. As new research and experience broaden our understanding, changes in research methods, professional practices, or medical treatment may become necessary.

Practitioners and researchers must always rely on their own experience and knowledge in evaluating and using any information, methods, compounds, or experiments described herein. In using such information or methods they should be mindful of their own safety and the safety of others, including parties for whom they have a professional responsibility.

To the fullest extent of the law, neither the Publisher nor the authors, contributors, or editors, assume any liability for any injury and/or damage to persons or property as a matter of products liability, negligence or otherwise, or from any use or operation of any methods, products, instructions, or ideas contained in the material herein.

British Library Cataloguing in Publication Data
A catalogue record for this book is available from the British Library

Library of Congress Cataloging-in-Publication Data
A catalog record for this book is available from the Library of Congress

ISBN (Part C): 978-0-12-823513-3
ISBN (Set) : 978-0-12-823377-1
ISSN: 1570-7946

Publisher: Susan Dennis
Acquisition Editor: Kostas Marinakis
Editorial Project Manager: Lena Sparks
Production Project Manager: Paul Prasad Chandramohan
Designer: Greg Harris

Typeset by SPi Global, India

Contents

BIORESOURCES, BIOPROCESSES AND BIOMEDICAL SYSTEMS

EDUCATION IN CAPE AND KNOWLEDGE TRANSFER

Sauro Pierucci, Flavio Manenti, Giulia Bozzano, Davide Manca (Eds.)
Proceedings of the 30th European Symposium on Computer Aided Process Engineering (ESCAPE30), May 24-27, 2020, Milano, Italy.
http://dx.doi.org/10.1016/B978-0-12-823377-1.50229-9

Assessment of Innovative Carbon Capture Technologies Applied for Flexible Energy Vectors Poly-generation

Calin-Cristian Cormos*, Ana-Maria Cormos, Ionela Dumbrava

Babes-Bolyai University, Faculty of Chemistry and Chemical Engineering, Arany Janos 11, Cluj-Napoca, RO-400028, Romania
cormos@chem.ubbcluj.ro

Abstract

Reducing CO_2 emissions from energy-intensive industrial applications is of paramount importance today. Various carbon capture, utilisation and storage (CCUS) technologies can be applied to reduce the carbon footprint of industrial processes. This paper is presenting, through various illustrative gasification-based examples, some innovative carbon capture technologies used for decarbonised flexible energy vectors poly-generation (e.g. power, hydrogen, methanol etc.). The reactive gas-liquid and gas-solid methods are evaluated as CO_2 capture methods with emphasize on innovative energy-efficient chemical looping systems. The overall carbon capture rate of the plant is set to min. 90 %. The proposed conceptual designs were simulated using process flow modelling, the generated mass & energy balances as well as the various thermal integration tools (e.g. pinch method) were used to quantify and optimize the key technical and environmental plant performance indicators. The assessments show that flexible carbon capture technologies have significant advantages in reducing the environmental impact of energy-intensive industrial applications as well as the CO_2 capture energy penalty, increasing the overall energy efficiency, improving plant cycling capabilities (flexible energy vectors poly-generation) with clear benefits in the modern energy systems where time-irregular renewable sources have an increase share.

Keywords: Flexible energy vectors poly-generation, Carbon Capture, Utilisation and Storage (CCUS) technologies, Reactive gas-liquid and gas-solid systems.

1. Introduction

Climate change and energy are one of the most important topics in the modern society. Greenhouse gas emissions (mainly CO_2) resulted from human activity are the main contributor to the global warming. To efficiently combat climate change, the fossil CO_2 emissions needs to be drastically reduced e.g. at European Union level the power generation is foreseen to be fossil CO_2 neutral by 2050 (European Commission, 2018). To achieve the global target of reducing CO_2 emissions a wide range of technical measures are to be used e.g. boosting renewable energy sources, increase energy conversion and end-use efficiencies, large scale deployment of CCUS technologies etc. (International Energy Agency, 2015).This paper is evaluating potential technical and environmental benefits of reactive gas-liquid (physical and chemical absorption) and gas-solid (chemical looping) systems used in conjunction with gasification technology for decarbonised flexible energy vectors poly-generation. The evaluations are focused on the conceptual design and the technical & environmental assessment of CCUS technologies with potential applications in heat & power generation as well as

chemicals (e.g. hydrogen, methanol, substitute natural gas etc.). Gasification was chosen as energy conversion technology for its multi-fuel multi-product capability (Cormos et al., 2015). The ability of energy conversion system to adjust its energy carriers over time would be a great asset for future energy systems where time-irregular renewable sources are predicted to have an increase share (Szima et al., 2019). The key innovative element of this paper towards the current state of the art in the field is the assessment of technical and environmental performance indicators of flexible energy vectors poly-generation based on gasification process with carbon capture.

2. Gasification-based flexible energy vectors poly-generation with CCUS

The conceptual design of gasification plant operated in a flexible energy vectors poly-generation scenario with CO_2 capture is presented in Figure 1. This plant concept can timely adjust the generated energy carriers considering the current situation in the energy system (e.g. power grid). A period with high production of renewable electricity implies that the plant will produce mostly chemicals (to be used either as energy carriers or as chemicals) since a period with low renewable electricity implies that the plant will generate mostly power. In both situations, most of the plant will operated base load with benefic technical and economic consequences (Mikulčić et al., 2019).

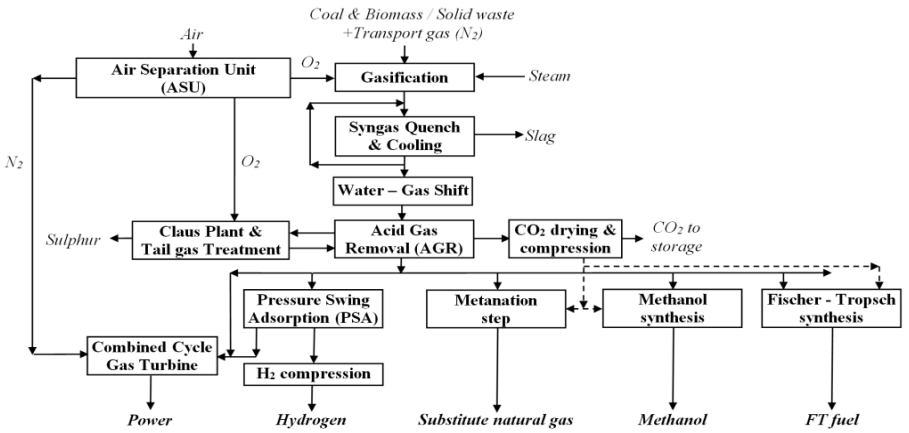

Figure 1. Layout of gasification-based flexible energy vectors poly-generation

Pre-combustion syngas decarbonisation can be done either by reactive gas-liquid absorption or reactive gas-solid system based on chemical looping cycle. For gas-liquid absorption, alkanolamines are mostly used, for instance Methyl-Di-Ethanol-Amine (MDEA) for which the chemical reaction is the following:

$$MDEA + CO_2 + H_2O \leftrightarrow MDEAH^+ + HCO_3^- \quad (1)$$

For reactive gas-solid system, the Calcium Looping (CaL) cycle was used in a pre-combustion capture scenario as Sorbent Enhanced Water Gas Shift (SEWGS) being based on the carbonation - calcination cycle (Mantripragada and Rubin, 2017):

$$CO + H_2O + CaO \leftrightarrow CaCO_3 + H_2 \quad (2)$$

$$CaCO_3 \leftrightarrow CaO + CO_2 \quad (3)$$

3. Plant concepts, model assumptions and process integration aspects

Shell gasifier was chosen as gasification reactor to take advantage of dry feed design and gas quench configuration (which both increase the overall energy efficiency). The gasification plant without carbon capture was also considered as benchmark concept (Case 1). As pre-combustion carbon capture options the reactive gas-liquid (Case 2) and gas-solid (Case 3) systems presented above were evaluated. After syngas decarbonisation, the hydrogen-rich gas can be used for generation of total (e.g. power, hydrogen) or partial decarbonised (methanol, SNG, FT fuel) energy carriers. As illustrative example, flexible hydrogen and power co-generation is presented in details. As evaluated fuels, coal alone or in mixture with renewable biomass (sawdust) were considered. Table 1 is presenting the main design assumptions of evaluated cases.

Table 1. Design assumptions of evaluated gasification-based poly-generation systems

Process unit	Design assumptions
Fuels	Coal: 25.35 MJ/kg calorific value (as received)
	Biomass: 16.05 MJ/kg calorific value (after drying)
Air Separation Unit (ASU)	Composition (% vol.): 95 % O_2, 3 % N_2, 2 % Ar
	ASU power consumption: 200 kWh/t oxygen
Gasification island	Shell gasification reactor operated at 40 bar
	Gas quench design to 800 ^oC final temperature
Water gas shift conversion	Sour catalyst (cobalt-molybdenum catalyst)
(Case 1)	High & low temperature shift: 400 – 500 °C / 250 – 350 °C
	CO conversion efficiency: >98 %
Syngas desulphurization unit	Gas-liquid absorption cycle coupled with Claus plant
	Sulphur removal efficiency: >98 %
Gas-liquid CO_2 capture unit	50 wt.% MDEA aqueous solution
(Case 1)	Absorption/desorption columns: 20/10 stages
Gas-solid CO_2 capture unit	Calcium-based sorbent: natural limestone
(Case 2)	Carbonation reactor temperature: 500 – 650 °C
	Calcination reactor temperature: 850 – 950 °C
CO_2conditioning unit	TEG gas-liquid absorption dehydration unit
(drying and compression)	Final delivery purity and pressure: >95 % (vol.) / 120 bar
	Multi-stage inter-cooling compressor with 85 % efficiency
Hydrogen purification unit	Pressure Swing Adsorption (PSA) system
	Final hydrogen purity and pressure: 99.95 % vol. / 60 bar
Power block	Combined cycle based on one M701G2 gas turbine
	Steam cycle pressure: HP 120 bar / MP 34 bar / LP 3 bar
	Final steam expansion pressure: 45 mbar

The evaluated gasification-based poly-generation systems were simulated using ChemCAD and Thermoflex software packages. The assessed designs were subject of detailed energy integration analysis using pinch method for maximisation of overall energy efficiency. As illustrative example for Case 2 (pre-combustion CO_2 capture based on reactive gas-liquid design), Figure 2 present the hot and cold composite curves for the gasification island and syngas conditioning train (left) and the combined cycle gas turbine - CCGT (right). In addition of heat (steam) integration across the plant, other heat and power integration analysis were performed e.g. air integration between gas turbine compressor and air separation unit, ancillary energy consumptions for the carbon capture unit (both assessed options). The mass and energy balances of all evaluated gasification-based systems were then used for quantification of main technical and environmental performance indicators presented in next section of the paper.

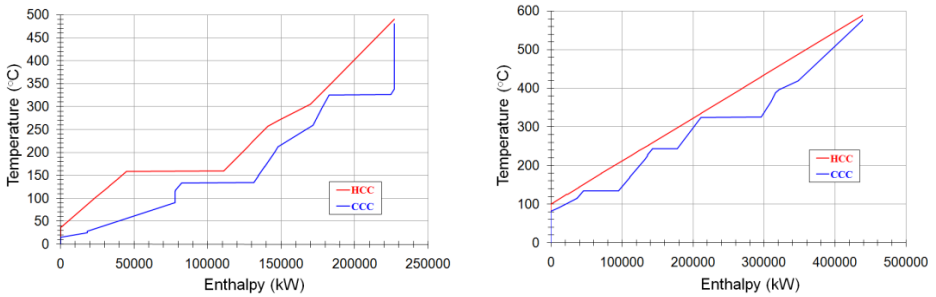

Figure 2. Composite curves for the syngas treatment line (left) and the combined cycle (right)

4. Results and discussions

The following Integrated Gasification Combined Cycle (IGCC) conceptual designs with and without carbon capture capability were evaluated:

Case 1 – Coal-based IGCC without carbon capture (benchmark case);
Case 2.a – Coal-based IGCC with CO_2 capture by MDEA process;
Case 2.b – Coal and biomass-based IGCC with CO_2 capture by MDEA process;
Case 3.a – Coal-based IGCC with CO_2 capture by CaL process;
Case 3.b – Coal and biomass-based IGCC with CO_2 capture by CaL process.

The above mentioned designs were evaluated firstly in power generation only conditions (corresponding to base load conditions). Table 2 presents the most important technical and environmental performance indicators.

Table 2. Main technical and environmental indicators of evaluated cases (power only)

Key parameter	UM	Case 1	Case 2.a	Case 2.b	Case 3.a	Case 3.b
Fuel flowrate	t/h	147.80	165.70	180.45	226.71	246.89
Calorific value	MJ/kg			25.35 / 16.05		
Fuel thermal input	MW_{th}	1,040.88	1,166.98	1,177.68	1,596.60	1,611.24
Gas turbine output	MW_e	334.00	334.00	334.00	334.00	334.00
Steam turbine output	MW_e	224.00	200.50	199.25	410.55	408.75
Gross power output	MW_e	558.50	535.75	533.85	745.95	743.75
Power consumption	MW_e	74.10	109.85	113.01	154.82	155.12
Net power output	MW_e	484.40	425.90	420.84	591.13	588.63
Gross efficiency	%	53.36	45.91	45.74	46.72	46.16
Net efficiency	%	46.53	36.49	35.73	37.02	36.53
Carbon capture rate	%	0.00	91.20	92.25	95.80	95.75
CO_2 emissions	kg/MWh	741.75	85.65	74.12	33.25	35.10

As can be noticed from Table 2, there is an energy penalty for CO_2 capture in the range of 9.5 - 10.8 net energy efficiency percentage points. The coal-based gasification concepts are slightly more efficient than the combined coal & biomass gasification concepts by about 0.5 to 0.75 net energy efficiency points. Also, calcium looping option is more energy efficient than reactive gas-liquid absorption. The major benefit of CCS concepts is the substantial reduction of the specific CO_2 emissions. The carbon capture rates and CO_2 emission values presented in Table 2 were calculated considering that the whole carbon as fossil, when consider that for biomass the carbon is renewable, the CO_2 emissions are lower by about 15 - 18 %.

After evaluating the plant concepts in a fixed operation scenario (power only base load conditions), the flexible hydrogen and power co-generation option was assessed. The flexible evaluation was done considering that the gas turbine is turned down gradually to displace a hydrogen stream to be purified and send to external customers (corresponding to the situation when power requirements from the grid are decreasing). The plant flexibility in this concept was restricted to 75 – 100 % from the nominal gas turbine power output (334 MW net). Table 3 presents the variation of key performance indicators vs. hydrogen output for Case 2.a considered as illustrative example.

Table 3. Main technical and environmental indicators of hydrogen and power co-generation

Key parameter	UM	Power only	Hydrogen and power co-generation	
Fuel flowrate	t/h		165.70	
Calorific value	MJ/kg		25.35	
Fuel thermal input	MW_{th}		1,166.98	
Gas turbine power output	MW_e	334.00	293.00	252.00
Steam turbine power output	MW_e	200.50	180.10	159.85
Gross power output	MW_e	535.75	474.35	413.52
Hydrogen thermal output	MW_{th}	0.00	100.00	200.00
Ancillary power consumption	MW_e	109.85	110.25	110.80
Net power output	MW_e	425.90	364.10	302.72
Net power efficiency	%	36.49	31.20	25.94
Hydrogen thermal efficiency	%	0.00	8.57	17.13
Cumulative energy efficiency	%	36.49	39.77	43.08
Carbon capture rate	%	91.20	91.20	91.20
Specific CO_2 emissions	kg/MWh	85.65	78.00	72.01

As can be noticed from Table 3, the overall plant performance indicators (e.g. cumulative energy efficiency, specific CO_2 emissions) are improving with the hydrogen output. The cumulative energy efficiency is increasing by about 3.3 net percentage points for each 100 MW_{th} hydrogen output. The specific CO_2 emissions are also decreasing with hydrogen output because more energy is produced by the plant. Another positive aspect is that the ancillary energy consumption of the plant is not changing much with hydrogen output. The flexible hydrogen and power co-generation evaluated here is just partial by changing the gas turbine load in a range that not affect its performances. If a fully flexible scenario is desirable, a separate steam turbine is needed to cover the ancillary energy consumption (see Starr et al., 2007).

The next evaluated operational scenario for gasification plants was based on co-generation of power and various partial decarbonised energy vectors (e.g. methanol, synthetic natural gas, Fischer-Tropsch fuel). For these concepts, the gasification island is producing the syngas which is then partially decarbonised by capturing a part of carbon dioxide stream, the rest being used for synthetic fuel production. As for the case of hydrogen and power co-generation, these concepts can be used very efficiently to make the overall power plant more flexible to the variations imposed by the electricity grid. The main performance indicators for these concepts (considering coal and biomass processing - Case 2.b) are presented in Table 4. As can be noticed, the co-generation of various partially decarbonised energy carriers is beneficial for increasing the overall energy efficiency although these concepts do not have very high carbon capture rates as for power and hydrogen and power co-generation (40 - 60 vs. 90 %).

Table 4. Co-generation of power and various energy carriers based on gasification with CCS

Key parameter	UM	Methanol	SNG	FT fuel
Fuel flowrate	t/h	36.60	200.00	200.00
Fuel thermal input	MW_{th}	282.60	1,235.50	1,235.50
Steam turbine power output	MW_e	36.90	163.25	192.00
Methanol thermal output	MW_{th}	141.50	-	-
SNG thermal output	MW_{th}	-	800.00	-
FT fuel thermal output	MW_{th}	-	-	700.00
Ancillary power consumption	MW_e	21.85	115.35	74.85
Net electrical efficiency	%	15.05	3.87	9.48
MeOH / SNG / FT efficiency	%	50.00	64.75	56.65
Cumulative energy efficiency	%	65.05	68.62	66.13
Carbon capture rate	%	48.20	60.75	47.50
Specific CO_2 emissions	kg/MWh	25.75	7.05	40.05

Several important conclusions can be drawn from this evaluation: (i) combination of chemical routes with heat & power production will give an increased overall plant energy efficiency; (ii) once-through poly-generation plants will provide synthetic fuels at much lower cost than recycle plants designed to maximize the fuel output and (iii) poly-generation plants can provide decarbonised power at lower costs of greenhouse gas emissions avoided than stand alone fossil fuel power plants.

5. Conclusions

Flexible production of power and other energy carriers (hydrogen, synthetic fuels) was evaluated based on coal and coal & biomass gasification systems. As carbon capture options, two reactive gas-liquid (MDEA) and gas-solid (CaL) systems were evaluated, the calcium looping option having superior energy efficiency (by about 0.5 - 0.75 net electricity points) and carbon capture rate (95-96 vs. 91-92 %). The flexible power and hydrogen co-generation has also significant advantages in term of higher cumulative energy efficiency, lower specific CO_2 emissions, plant cycling etc.

References

A.M. Cormos, C. Dinca, C.C. Cormos, 2015, Multi-fuel multi-product operation of IGCC power plants with carbon capture and storage (CCS), Applied Thermal Engineering, 74, 20-27

European Commission, 2018, A European strategic long-term vision for a prosperous, modern, competitive andclimate neutral economy, COM(2018) 773 final, Brussels, Belgium

International Energy Agency, 2015, Energy Technology Perspectives 2015 - Mobilising Innovation to Accelerate Climate Action, Paris, France

H.C. Mantripragada, E.S. Rubin, 2017, Chemical looping for pre-combustion and post-combustion CO_2 capture, Energy Procedia, 114, 6403-6410

H. Mikulčić, I.R. Skov, D.F. Dominković, S.R. Wan Alwi, Z.A. Manan, R. Tan, N. Duić, S.N. Mohamad, X. Wang, 2019, Flexible Carbon Capture and Utilization technologies in future energy systems and the utilization pathways of captured CO_2, Renewable and Sustainable Energy Reviews, 114, 109338

F. Starr, E. Tzimas, S. Peteves, 2007, Critical factors in the design, operation and economics of coal gasification plants: The case of the flexible co-production of hydrogen and electricity, International Journal of Hydrogen Energy, 32, 1477-1485

S. Szima, S.M. Nazir, S. Cloete, S. Amini, S. Fogarasi, A.M. Cormos, C.C. Cormos, 2019, Gas switching reforming for flexible power and hydrogen production to balance variable renewables, Renewable and Sustainable Energy Reviews, 110, 207-219

Sauro Pierucci, Flavio Manenti, Giulia Bozzano, Davide Manca (Eds.)
Proceedings of the 30th European Symposium on Computer Aided Process Engineering (ESCAPE30), May 24-27, 2020, Milano, Italy.
http://dx.doi.org/10.1016/B978-0-12-823377-1.50230-5

Holistic Approach for the Optimization of Industrial Hybrid Energy Hubs with MILP

Verena Halmschlager [a] and René Hofmann [a,b]

[a]*Technische Universität Wien, Institute for Energy Systems and Thermodynamics, Getreidemarkt 9/E302, 1060 Vienna, Austria*
[b]*AIT Austrian Institute of Technology GmbH, Center for Energy, Sustainable Thermal Energy Systems, Giefinggasse2, 1210 Vienna, Austria*
rene.hofmann@tuwien.ac.at

Abstract

This work presents a holistic approach for the optimization of Energy Hubs with mixed integer linear programming for industrial applications. As a use case, a chipboard production plant is used, which produces different products depending on current orders. The use case includes units for power and steam generation, energy conversion, energy and material storages as well as continuous and batch production machines. Additionally, power is sold to the grid and energy in form of heat covers the demand of two district heating suppliers. To model and optimize such extensive industrial systems efficiently, a generic and modular modelling approach is proposed. The entire process is modelled based on five generic modules, which can be configured for specific tasks. To evaluate the viability of the proposed approach, three different scenarios within the industrial use case (without storage, with thermal energy storage, with material storage) were optimized. The results show, that this approach is well suited for scheduling and the assessment of process design improvements of existing industrial plants, due to its easily adaptable modular structure and the ability to use simple data-driven models.

Keywords: Industrial Energy Hub (IEH), Optimization, Mixed Integer Linear Programming (MILP), Scheduling, Demand Side Response (DSR)

1. Introduction

The increased application of renewable energies, combined with the complex energy market and new flexible technologies, challenges today's industry. This increases the need for holistic energy efficiency solutions. In industry, optimal production scheduling - discussed in (Merkert et al., 2015) - and Demand Side Response (DSR) - discussed in (Lindberg et al., 2014) - are promising solutions. However, in many processes, other energy carriers like steam, oil or gases need to be considered as well as the product and electric power. (Hybrid) Energy Hubs (EH) are an option for integrated management of these Multi Energy Systems, where different energy carriers can be converted, coupled and stored. Only few publications deal with the optimization of EHs, most of them focusing on the residential or commercial buildings sector (Sadeghi et al., 2019).
The idea of the EH was first expressed in (Favre-Perrod, 2005) and further researched in several papers. (Mohammadi et al., 2017) and (Sadeghi et al., 2019) provide a good overview of recent publications within this topic. Terms such as "Multi-Energy System", "Multi-Carrier Energy Systems" and "Natural Gas Multi Energy Services" usually describe systems that are all based on the concept of the EH.

In this work, a concept for the modelling and optimization of an Industrial Energy Hub is proposed. The optimization of the Industrial Energy Hub is intended to be used for optimal production and energy scheduling as well as the analysis of different scenarios within an industrial process. The work is structured as follows: Section 2 describes the general concept of the Industrial Energy Hub. Section 3 deals with the holistic and modular modelling and optimization approach. In Section 4, the industrial use case - a chipboard production plant - is modelled and optimized and results are shown. The conclusion is presented in Section 5.

2. Industrial Energy Hub Concept

In contrast to the commonly used EH concept presented in (Geidl et al., 2007; Mohammadi et al., 2017; Sadeghi et al., 2019), we propose the Industrial Energy Hub (IEH) that also takes into account the production in an industrial plant. Thus, in addition to different energy carriers like electrical and thermal power, also the product acts as a carrier in the IEH. Figure 1 illustrates the concept of the IEH. This approach emphasizes the importance of energy in production processes and enables the integration of different energy carriers and networks into the modelling and optimization of an industrial production plant.

In analogy to a classification of general EH systems in (Mohammadi et al., 2017), the parts of the IEH can be divided into four units: *conversion, storage, input* and *output.* In contrast to the general EH system, the product is taken into account in each of these units in the IEH system. In *conversion* units, the characteristics and quality of a carrier can be changed (adapting converters) or a carrier can be transformed into other forms (changing converters). Both types of converters can be either operated continuously or in (semi-)batch mode. In the IEH, typical *conversion* units for energy are generators, thermal power plants or heat exchangers. *Conversion* units for the product are all machines or devices that are part of the production chain. *Storage* units in the IEH can be energy storages, but also material storages. *Input* and *output* units in the IEH are process requirements or limits that need to be considered. Typical *inputs* are energy from the grid, fuel for production machines and energy converters, as well as primary product materials. Typical *outputs* of the IEH are heat for district heating (DH) supply, power for the electricity grid, gas that is fed into the gas network as well as the product of the plant. Thus, the IEH concept and its classification to the four units *conversion, storage, input* and *output* enables a generic description of a variety of different industrial processes and can be used as a basis for the optimization of IEH systems.

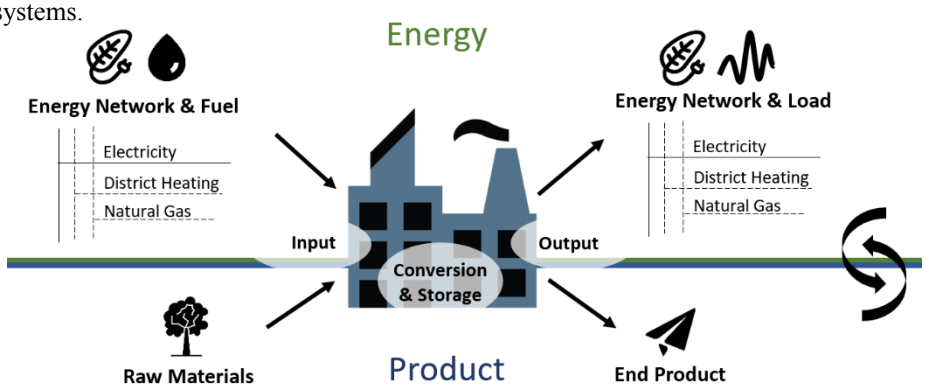

Figure 1: Illustration of the IEH concept

3. Modelling and Optimization Approach

The optimization of the IEH aims to determine the optimal energy and product flow in order to achieve minimal costs over a time horizon, whilst taking into account production specifications and external requirements.The approach is intended to be used for scheduling of existing industrial processes, but also for the assessment of different process design scenarios, e.g. to evaluate the implementation of additional machines/devices or storages. However, in existing industrial processes, the creation of detailed models is often not possible because only little data is available. Thus, simple and easily adaptable models are chosen for this applied approach. For this reason, the approach is based on an adaptable modular structure and uses a mixed integer linear programming (MILP) formulation with only linear, mostly data-based correlation. This way, modelling and optimization of an existing process and different design scenarios can be done in a time-saving manner with available process data.

3.1. MILP Formulation

The optimization problem is formulated as a MILP problem with linear constraints and a linear objective function. The optimization is set up in Matlab® with an object oriented approach. Process variables that can be varied and therefore optimized are called decision variables. These decision variables can be restricted by constraints. Binary decision variables (0 or 1) are used to indicate, if a device is switched on (1) or off (0). The objective function includes real costs, as well as penalties or rewards on decision variables to shift the optimization towards a desired goal. By using a MILP problem formulation, the optimization can be solved with state-of-the-art solvers (e.g. GUROBI) and results in a global optimum.

3.2. Holistic Modular Approach

To create an optimization model of the IEH with the MILP formulation, the industrial process is split into part models, called units. Based on the previous classification of the IEH system, all parts of the IEH can be divided in four units: *conversion, storage, input* and *output*. In addition to the former described first four units, also a *connection* unit is used in the optimization approach. For each of the five units, a generic module exists that acts as a basis model for all its parts/devices. Each generic module has an adaptable structure and offers the option to implement different preconfigured constraints and objectives. These are used to tailor a generic module to a specific device. The main advantage of this holistic approach is, that all part models can be easily adapted, omitted or added anywhere in the overall process model. In the following paragraphs, the structure, constraints and objectives of each module and its carriers (e.g. heat, product) are described in detail.

Conversion modules are used to model units that can adapt or transform a carrier in the IEH. Thus, converters are all machines/devices that consume or generate energy or a product. All converters are based on a generic input/output module and configured in detail by linear constraints. In the case that linear correlations are not capable to describe the behavior of the converter adequately, non-linear behavior can be approximated by piecewise linear relations and a differentiation in two or more operation modes. Constraints for converters can be divided into adaption/conversion constraints, carrier constraints and technical constraints. Constraints for adaption/conversion are used to describe the internal behavior of the converter, e.g. the amount of input that is required to generate a certain output. Carrier constraints are used to restrict the carriers when entering or exiting a converter. They include minimal and maximal constraints,

as well as ramp up and ramp down constraints and represent limitations of the converter itself or the connection between different converters (e.g. pipes, conveyors). To model a converters technical limitations, start up and shut down times as well as minimal and maximal up and down times of a converter can be implemented. In addition to the constraints, the costs (start up or shut down costs, operation costs, material costs) of the converter can be added in the objective function.

Storage (energy or material) modules can have the same constraints as *conversion* modules. Additionally, constraints to model the integrative and dynamic charging and discharging behavior as well as thermal losses are added in the *storage* module.

The *input and output* module includes minimal and maximal constraints, as well as ramp up and ramp down constraints. If the input or output restriction varies over time, time sequence or integrative constraints can be used. Time sequence constraints can model demands or forecasts that need to be met by a certain carrier of a converter or storage. Integrative constraints are used to implement a production schedule over the time horizon. Both sequence and integrative constraints can be implemented directly as constraints, or added to objective function with a penalty or reward term.

The *connection* module connects the input and output streams of every module (converter, storage, in/outputs) with a mass or energy balance constraint.

The modelling of an IEH with the modular approach can be summarized as follows: Any carrier can be adapted and transformed in converters as well as stored in storages. Different converters and storages are connected with each other by connecting the according input and output streams of their carries with connections. External process inputs and outputs can be connected to converters or storages. They can represent time-dependent demands or a production sequence.

4. Use Case - Chipboard Production

To demonstrate the capability of the IEH approach, a simplified industrial chipboard production plant is considered as a use case, which is presented in Figure 2. The optimization model of the chipboard production is based on the IEH approach and uses industrial process data. A fictive district heating (DH) demand and a fixed price for electrical power are used. The optimization minimizes the overall process costs over a time horizon of 50 hours. For a design analysis of the process, three scenarios A, B and C are optimized.

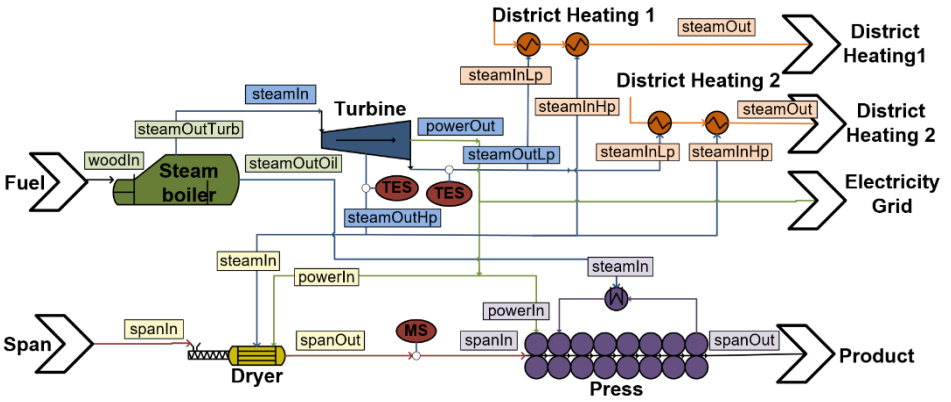

Figure 2: Use case - Flowchart of the simplified chipboard production

4.1. Analyzed Scenarios

In all scenarios, thermal and electrical energy that is required for the production is generated by a steam boiler and a steam turbine. As the amount of energy produced exceeds the demand of the production process, heat is fed into two DH networks with changing demands over time and electric power is sold to the grid. A production schedule defines the generation of two different products in two time intervals (product 1: 9-16 h, product 2: 23-38 h). Satisfying the production limits has highest priority in the process. The described external requirements are equal in all scenarios. The three scenarios only differ in the availability of storages. In the standard scenario A, no storages are available. In scenario B, two thermal energy storages (TES - steam accumulators for high and low pressure steam) with an efficiency of 99% are implemented. In scenario C, a material storage (MS) for dried span is added to scenario A. The location of the storages can be seen in the flowchart in Figure 2.

4.2. Optimization Results

Figures 3, 4 and 5 show the cumulative thermal energy (TE) that is used for the production process and fed into the DH network over a time horizon of 50 hours for the optimized scenarios A, B and C. Additionally, the charging and discharging behavior of the storages is depicted for scenarios B and C. In scenario A, the DH demand cannot be met over the entire time horizon (~93 % energy coverage), because not enough TE can be generated in times of high DH demand (after ~10 and 35 h) and production. In scenario B with the TES, more TE is produced in times of little production and used in times of high TE demand. In scenario C with the material storage, the generation of TE is shifted in time and used to process and store the chipboards in times of low DH demand. Hence, both storages can improve the processes efficiency by increasing its flexibility and enable the full coverage of DH demand.

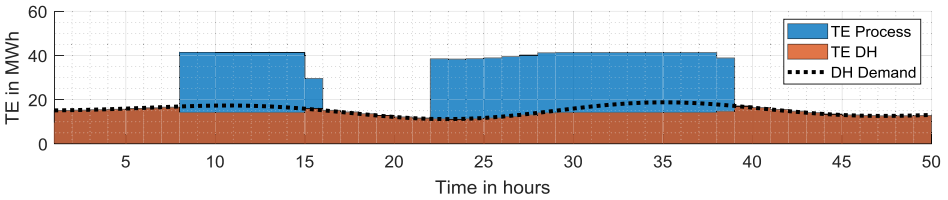

Figure 3: Optimization results of scenario A (no storage)

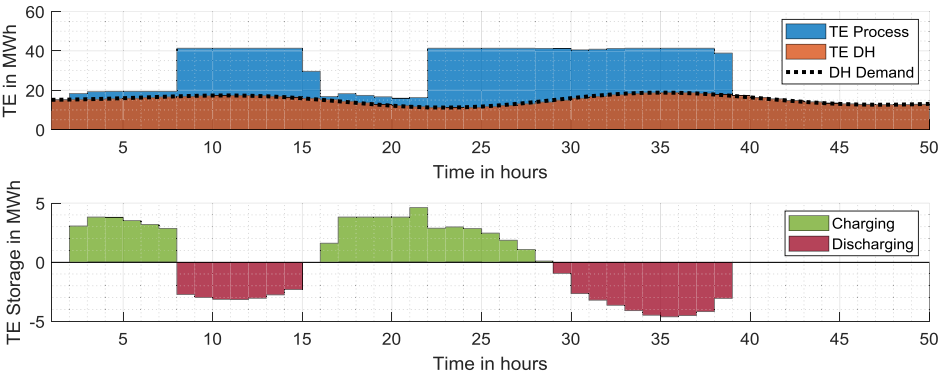

Figure 4: Optimization results of scenario B (thermal energy storage)

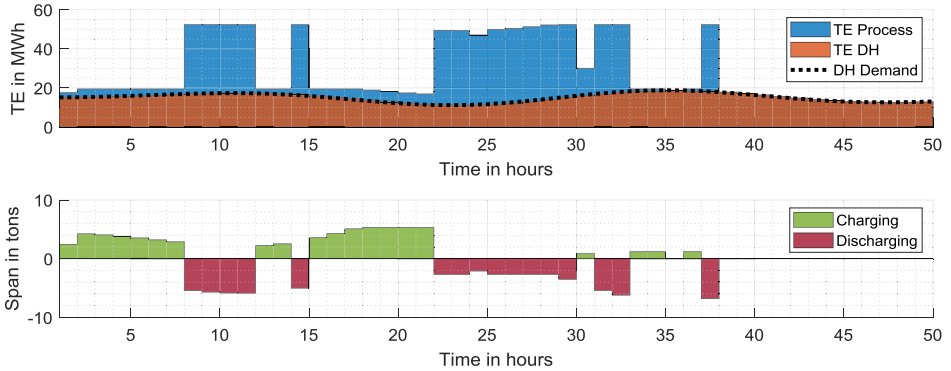

Figure 5: Optimization results of scenarios C (material storage)

5. Conclusion

The concept of the IEH and a holistic modelling and optimization approach were proposed. In the IEH, energy as well as the production of an industrial plant is considered. This enables the integration of different energy carriers and networks into the modelling and optimization of industrial plants. With the proposed approach, an industrial process can be modelled and optimized with five generic modules (converter, storage, input, output, connection). The generic and modular structure enables a fast implementation, combined with a high model adaptability. The results of the optimization can be used for scheduling, as well as for process design improvements. The viability of the approach was demonstrated with a use case. It confirms, that this holistic approach offers a straightforward and fast method to model and optimize industrial plants with process data. Future work will analyze the application of the proposed approach to extensive use cases and more comprehensive scenarios.

Acknowledgment

This work was funded by the cooperation doctoral school Smart Industrial Concept (SIC!). We particularly like to thank our industrial partner FunderMax, who enabled the analysis of the chipboard production and provided the required data. The authors want to express their great acknowledgment.

References

Favre-Perrod P 2005. A vision of future energy networks. Proceedings of the inaugural IEEE PES conference and exposition in Africa. Piscataway, NJ: IEEE Service Center; 13–17.

Geidl M, Koeppel G, Favre-Perrod P, Klöckl B, Andersson G, Fröhlich K 2007. The energy hub-A powerful concept for future energy systems. Third Annual Carnegie Mellon Conference on the Electricity Industry: 13–4.

Lindberg C-F, Zahedian K, Solgi M, Lindkvist R 2014. Potential and Limitations for Industrial Demand Side Management. Energy Procedia; 61: 415–8.

Merkert L, Harjunkoski I, Isaksson A, Säynevirta S, Saarela A, Sand G 2015. Scheduling and energy – Industrial challenges and opportunities. Computers & Chemical Engineering; 72: 183–98.

Mohammadi M, Noorollahi Y, Mohammadi-ivatloo B, Yousefi H 2017. Energy hub. Renewable and Sustainable Energy Reviews; 80: 1512–27.

Sadeghi H, Rashidinejad M, Moeini-Aghtaie M, Abdollahi A 2019. The energy hub. Applied Thermal Engineering; 161: 114071.

Sauro Pierucci, Flavio Manenti, Giulia Bozzano, Davide Manca (Eds.)
Proceedings of the 30th European Symposium on Computer Aided Process Engineering
(ESCAPE30), May 24-27, 2020, Milano, Italy.
http://dx.doi.org/10.1016/B978-0-12-823377-1.50231-7

Agile Operation of Renewable Methanol Synthesis under Fluctuating Power Inputs

Christopher Varela,[a,*] Mahmoud Mostafa,[a] Elvis Ahmetovic,[b] Edwin Zondervan[a]

[a]*Laboratory of Process Systems Engineering, Faculty of Production Engineering, University of Bremen, Leobener Str. 6, 28359 Bremen, Germany*

[b]*Faculty of Technology, University of Tuzla, Univerzitetska 8, 75000 Tuzla, Bosnia and Herzegovina*

varela@uni-bremen.de

Abstract

The fluctuating production of renewable energy constraints the operation of Power-to-X processes such that steady-state conditions are unattainable without energy storage. It seems eminent to establish operation strategies considering significant disturbances along the process and to determine those scenarios where the operation becomes unfeasible. In this work, an industrial methanol Lurgi-type reactor, embedded in a Power-to-Jet process (Figure 1), is evaluated under fluctuating feed conditions. The simulated scenarios consist of step functions up to 20 % (w/w) increments in the feed flowrate as consequence of the fluctuating power input on the electrolysis stage. A one-dimensional dynamic model for a multi-tubular fixed bed reactor is implemented, considering both the gas and catalyst phase. The mathematical model is solved numerically using orthogonal collocation at the spatial domain and backward differences at the time domain. The system shows rapid response to disturbances, reaching steady state conditions in 1.5 minutes. Furthermore, it is evidenced that the feasible region to increase the production of methanol is narrowed down by rises of carbon dioxide feed flowrate up to 5 % (w/w).

Keywords: Power-to-X, methanol synthesis, renewable energy, process dynamics.

1. Introduction

By the conversion of electric power into chemicals, denoted as Power-to-X, renewables can substitute petrol-based feedstock in energy intensive industries with high greenhouse gas emissions. Methanol, with a global demand of 40 million tons per year (Olah et al., 2009), is one of the most relevant products for Power-to-X technologies as energy carrier and building block for a wide range of products, namely plastics, paints or synthetic fuels. By the Mobil process, methanol is converted into gasoline and a range of distillates (Tabak et al., 1986) with a distribution highly dependent on the zeolite catalyst shape (Schmidt et al., 2018). Hence aviation fuel, whose annual growth rate is 4.5 %, can be produced through the synthetic methanol pathway (Schmidt et al., 2016) as alternative to its conventional fossil-based production. The proposed route for the Power-to-Jet process is presented in Figure 1, where renewable power (photovoltaic, wind) and water are used to produce hydrogen on the electrolysis stage. Carbon dioxide is captured from concentrated sources and converted into methanol by hydrogenation. On the final stage, methanol is transformed into aviation fuel, gasoline and other distillate fractions by the MTGD (methanol to gasoline and distillates) process.

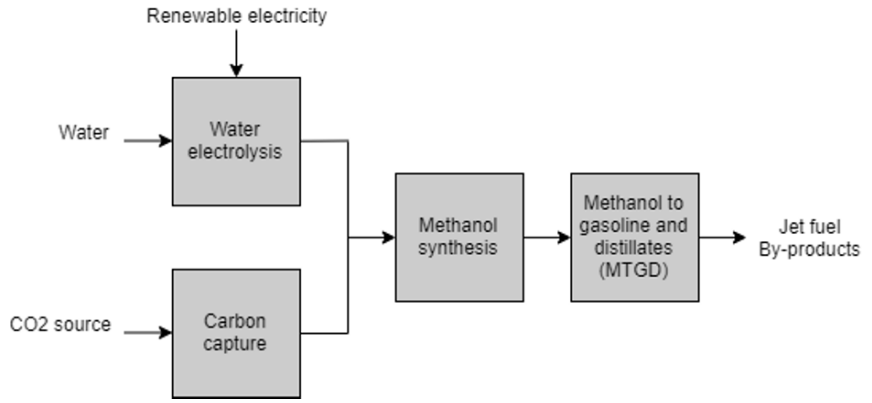

Figure 1 – Power-to-Jet process block diagram.

Such a process has the capability to directly convert excess renewable energy into commodities, although with high investment and operation costs mainly on the electrolysis stage (Schmidt et al., 2018). The fluctuating power input in the Power-to-Jet technologies introduces new challenges to the process design and operation.
Some effort has recently been put into finding optimal process conditions for the synthesis of renewable methanol; aiming to combine hydrogen produced through electrolysis with carbon dioxide captured from either air or concentrated sources such as flue gas streams (Schmidt et al., 2018; Van-Dal et al., 2013; Leonzio et al., 2019). A kinetic model that accounts for catalyst activity under different carbon dioxide to hydrogen ratios (Seidel et al., 2018) gives precise information on the reaction dynamics. Figure 2 describes the renewable methanol synthesis from the Power-to-Jet process (Figure 1), in which the fluctuations of renewable power cause a variation of hydrogen feed flowrate.

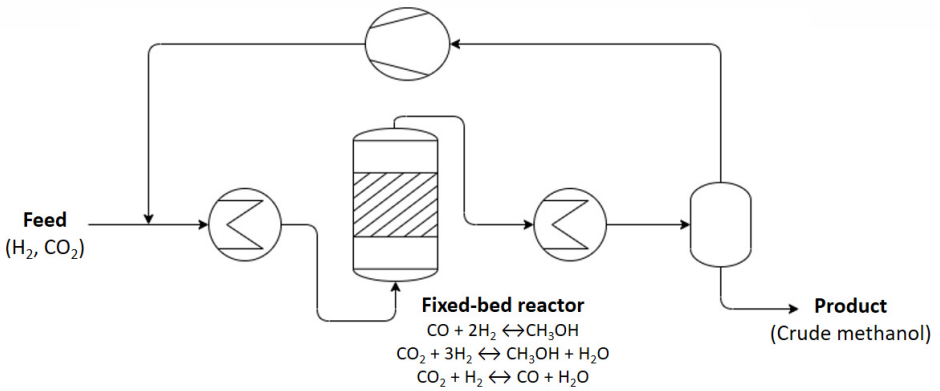

Figure 2 – (Crude) Methanol synthesis process from renewable energy.

2. Model development

2.1. Fixed-bed reactor model

The reactor model consists of a one-dimensional component and energy differential balance for the fluid and solid (catalyst) phase, considering convection, mass and heat transfer at the interphase, and reaction at the catalyst surface. To account for the porous

catalyst ($Cu/ZnO/Al_2O_3$), the effectiveness factor is calculated by a diffusion-reaction balance within the catalyst cylindrical pellet (Lommerts et al., 2000).

$$\varepsilon \frac{\partial c_g^i}{\partial t} = -v \frac{\partial c_g^i}{\partial z} + a_v k_g^i \left(c_s^i - c_g^i \right) \tag{1}$$

$$\left(1-\varepsilon\right) \frac{\partial c_s^i}{\partial t} = a_v k_g^i \left(c_g^i - c_s^i \right) + \rho_b \sum_{j=1}^{N} \nu_j^i \eta_j R_j \tag{2}$$

$$\varepsilon \frac{\partial \left(\rho_g Cp_g T_g \right)}{\partial t} = -v \frac{\partial T_g}{\partial z} + a_v h_f \left(T_s - T_g \right) + \frac{4U_w}{d_i} \left(T_w - T_g \right) \tag{3}$$

$$\rho_b \frac{\partial \left(Cp_s T_s \right)}{\partial t} = a_v h_f \left(T_g - T_s \right) + \rho_b \sum_{j=1}^{N} \eta_j \left(-\Delta_R H_j \right) R_j \tag{4}$$

$$\frac{1}{x} \frac{d}{dx} \left(D_i^{eff} x \frac{dc_x^i}{dx} \right) = \rho_b \sum_{j=1}^{N} \nu_j^i R_j \tag{5}$$

Empirical correlations for mass and heat transfer, and commercial catalyst characteristics are conveniently provided by Rezaie et al. (2005).

2.2. Reaction kinetics

The kinetics are the most relevant part of the model since the aim of this work is to evaluate the reactor under varying feed compositions. To study the dynamic behavior, the detailed kinetic model proposed by Seidel et al. (2018) is used. It follows the general Langmuir-Hinshelwood kinetics:

$$R_j = \left[\text{kinetic factor} \right] \frac{\left[\text{driving force} \right]}{\left[\text{adsorption term} \right]} \tag{6}$$

The adsorption term includes the variable "ϕ" that accounts for the morphological changes in the catalyst surface for disturbances in the feed composition. Its transient behavior is described as follows:

$$\frac{d\phi}{dt} = k_1^+ \left(y_{H_2} \left(1-\phi\right) - \frac{1}{K_1} y_{H_2O} \phi \right) + k_2^+ \left(y_{CO} \left(1-\phi\right) - \frac{1}{K_2} y_{CO_2} \phi \right) \tag{7}$$

2.3. Numerical solution

The partial differential equations from the original model (Equations 1 to 4) are converted into ordinary differential equations using orthogonal collocation with 9 collocation points at the axial domain of the reactor. The collocation points correspond to the zeros of Jacobi polynomials (Rice et al, 1995). The solution of the ODE system is obtained using backward differences while the balance within the catalyst pellet (Equation 5) is solved with a three-points orthogonal collocation and Powell's method. Python is used as simulation environment.

3. Transient behaviour analysis

The open loop response to the hydrogen step changes of 5 %, 10 %, 15 % and 20 % (w/w) feed flowrate denotes a moderate variation in the production of methanol and no effect in the temperature at the fluid phase. The response for a hydrogen feed step change of 20 % in 20 seconds is shown in Figure 3.

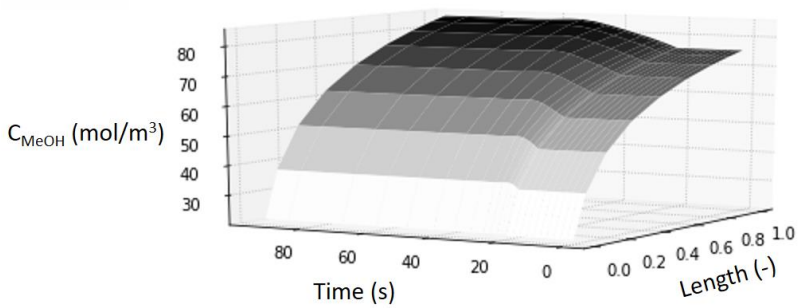

Figure 3 – Concentration profile of methanol for hydrogen feed step change of 20 % at t = 20 s.

To overcome the thermodynamic limitations of the chemical system, large recycle streams are required for the methanol synthesis. This excess of components being present in the reactor reduces the disturbance effects. However, during the simulation time of 90 seconds (Figure 3), the production of methanol increases by 11.26 %. Assuming a low-price electricity due to excess generation from renewables, the profit is expected to increase. In that case, the complete process has to be simulated, including the electrolysis stage. The concentration profile of methanol and hydrogen at the outlet of the reactor are shown in Figure 4.

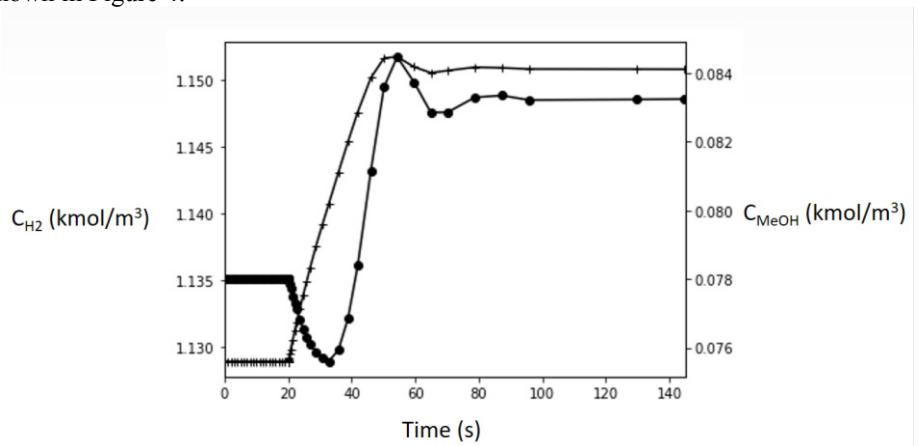

Figure 4 – Concentration profiles at reactor outlet for hydrogen feed step change of 20 % at t = 20 s for methanol (+) and hydrogen (•).

After 15 seconds of the applied disturbance (from t = 20 s to t = 35 s) methanol is diluted at the gas phase, still taking 55 seconds (from t = 35 s to t = 90 s) to balance the complex reaction system and transfer phenomena at the two phases. The relative fast dynamics and the proportional increase on the methanol production offers the opportunity to convert excess renewable energy into hydrogen and, consequently, into methanol.

4. Reactor operation strategy

For the operation of the Power-to-Jet process (Figure 1), more aspects have to be investigated along with the fluctuating hydrogen feed such as temperature and carbon dioxide to hydrogen ratio at the reactor feed stream. In this work, scenarios for carbon dioxide feed step change of 5 %, 10 %, 15 %, 20 % and 50 % (w/w) are chosen. A combination with the former scenarios for hydrogen feed step change (5 %, 10 %, 15 %, 20 %) results in twenty additional simulated scenarios. The results are shown in Figure 5, where the greyscale represents the conversion of carbon atoms into methanol along the reactor, the horizontal axis is the increment of carbon dioxide and the vertical axis the increment of hydrogen at the feed stream.

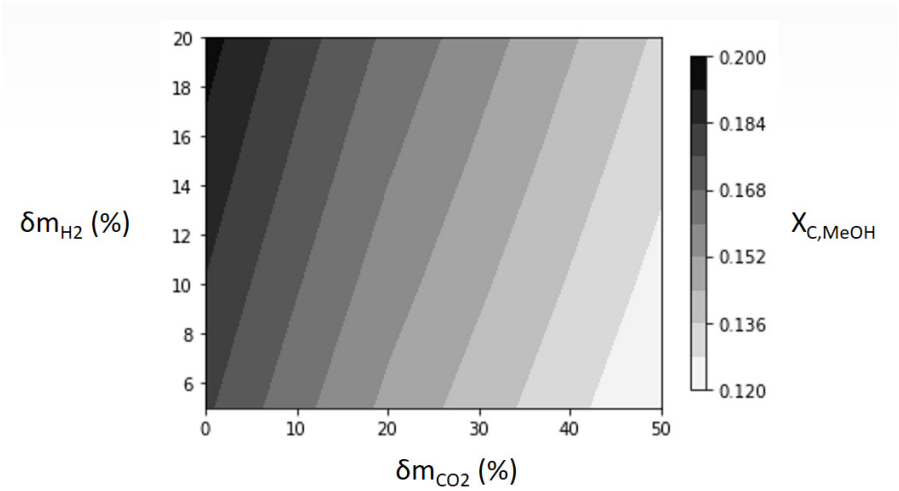

Figure 5 – Reactor performance in terms of conversion of carbon into methanol for different increments of hydrogen and carbon dioxide at the reactor feed.

It is proved that after a 10 % increase of the carbon dioxide intake, the reactor exhibits suboptimal operation conditions despite of any additional increment of hydrogen feed flowrate. Furthermore, it is shown that the operation window should be limited at 5 % extra carbon dioxide for the highest disturbance of hydrogen flow rate. This way, the performance of the reactor is not compromised in terms of conversion of carbon atoms into methanol, while the production of methanol is increased due to the fluctuations at the generation of renewable energy.

5. Conclusions and future work

The heterogeneous model for the catalytic reactor with tailor-made kinetics for dynamic simulation can be used to describe the transient behaviour of the methanol synthesis reactor under varying renewable energy inputs. The reactor reaches steady-state in roughly 90 seconds which is a relatively fast response for the significant disturbance at the feed of 20 % (w/w) hydrogen. An operation strategy considering the ratio of carbon dioxide to hydrogen was investigated. By simulating several scenarios, a suitable operating region for up to 5 % of carbon dioxide and up to 20 % hydrogen feed flowrate is identified. The renewable methanol synthesis is feasible in terms of short reaction times and smooth profiles with open loop response.

The effects of the disturbances on the temperature of the fluid and solid phase were negligible. Besides the reason stated at Section 3 related to dilution of the components, a one-dimensional model is less adequate in computing accurately the energy balance due to significant radial heat transport. Therefore, the model presented in this work can be extended to a two-dimensional model to account for the radial heat transfer on the reactor. In future work, different stages of the Power-to-Jet process (Figure 1) have to be simulated together in order to evaluate the opportunities for a dynamic renewable energy-driven operation. Regarding renewable methanol synthesis, the operation with different types of fixed-bed reactor are to be investigated, including scenarios for the long-run operation.

Acknowledgments

Funding of this research by the German Federal Ministry of Economic Affairs and Energy within the KEROSyN100 project (funding code 03EIV051A) is gratefully acknowledged.

References

G. Olah, A. Goeppert, G.K. Surya (2009), Beyond Oil and Gas: The Methanol Economy, 118

P. Schmidt,W. Weindorf (2016), Power-to-Liquids Potentials and Perspectives for the Future Supply of Renewable Aviation Fuel, German Environmental Agency Background no. Septemeber 2016, 10

S.A. Tabak, A.A. Avidan, F.J. Krambeck (1986), Production of synthetic gasoline and diesel fuel from nonpetroleum resources, American Chemical Society Volume 31:2, 293-299

P. Schmidt, V. Batteiger, A. Roth, W. Weindorf, T. Raksha (2018), Power-to-Liquids as Renewable Fuel Option for Aviation: A Review, Chem. Ing. Tech. 2018, 90 No. 1-2, 127-140

E. Van-Dal, C. Bouallou (2013), Design and simulation of a methanol production plant from CO2 hydrogenation, Journal of Cleaner Production 57 (2013), 38-45

G. Leonzio, E. Zondervan, P. Foscolo (2019), Methanol production by CO2 hydrogenation: Analysis and simulation of reaction performance, International Journal of Hydrogen Energy 44 (2019), 7915-7933

C. Seidel, A. Jörke, B. Vollbrecht, A. Seidel-Morgenstern, A. Kienle (2018), Kinetic modeling of methanol synthesis from renewable resources, Chemical Engineering Science 175 (2018), 130-138

N. Rezaie, A. Jahanmiri, B. Moghtaderi, M.R. Rahimpour (2005), A comparison of homogeneous and heterogeneous dynamic models for industrial methanol reactors in the presence of catalyst deactivation, Chemical Engineering and Processing 44 (2005), 911-921

B.J. Lommerts, G.H. Graaf, A.A.C.M. Beenackers (2000), Mathematical modeling of internal mass transport limitations in methanol synthesis, Chemical Engineeering Science 55 (2000), 5589-5598

R.G. Rice, D.D Do (1994), Applied Mathematics and Modeling for Chemical Engineers, John Wiley & Sons Inc., Chapter 8

Sauro Pierucci, Flavio Manenti, Giulia Bozzano, Davide Manca (Eds.)
Proceedings of the 30th European Symposium on Computer Aided Process Engineering (ESCAPE30), May 24-27, 2020, Milano, Italy.
http://dx.doi.org/10.1016/B978-0-12-823377-1.50232-9

Power-to-Syngas Processes by Reactor-Separator Superstructure Optimization

Andrea Maggi[a], Marcus Wenzel[b], Kai Sundmacher[a,b,*]

[a]*Max Planck Institute for Dynamics of Complex Technical Systems, Department Process Systems Engineering, Sandtorstr. 1, 39106 Magdeburg, Germany*
[b]*Otto-von-Guericke University Magdeburg, Process Systems Engineering, Universitätplatz 2, 39106 Magdeburg, Germany*
sundmacher@mpi-magdeburg.mpg.de

Abstract

The effects of global warming and the depletion of fossil resources call for technological solutions. Syngas, a mixture of carbon dioxide and hydrogen, can bridge chemicals and fuels production with renewable feedstocks and energy sources. In this contribution, a reactor-separator network for syngas production is proposed by superstructure optimization based on thermodynamics. Interactions among the network elements are quantitatively explored for different H_2/CO ratios and electricity production scenarios: zero-carbon and power plant operations.

Keywords: Syngas, Separation, Process Network

1. Introduction and Motivation

The transition from fossil (coal, oil, gas) to renewable feedstocks and energy carriers (solar, wind, water, biomass) has become a matter of importance in industry. Prompt actions are required to face arising challenges, such as the intermittency and geographical displacement of resources, resulting in storage and transportation issues. Schack et al. (2018) identified cost-optimal conversion pathways from renewables to valuable target products. Syngas, a mixture of hydrogen and carbon monoxide, is an ideal candidate due to its versatility as a reactant for different, well-known, downstream conversion systems, characterized by high production volumes. Table 1 exemplifies the composition requirements for such applications. Therefore, syngas represents a strategic hub between state-of-the-art processes and sustainable power and carbon sources. In this contribution, possible synergies among methane steam reforming (SR), reverse water-gas shift (RWGS) and water electrolysis (EL) are explored based on thermodynamics. All together, they allow for flexibility in terms of raw materials. SR can either be fed by CH_4 from biogas or, if not available, by natural gas. Similarly, RWGS can be fed by H_2 from water electrolysis and CO_2 from external sources (e.g. air capture, capture from flue gases etc.) or by excess H_2 from SR. Alternative separation techniques are proposed within an optimization framework.

Table 1: Downstream applications and typically required compositions, adapted from Wenzel et al. (2017)

Process	H2/CO
Phosgene Monsanto	0.0
Hydroformylation	0.0-0.02
Direct Reduction of Iron Ore	1.0-1.2
FischerTropsch	1.3-1.5
Alcohol Synthesis	1.6-2.3
	2.0-2.3

2. Methods

2.1. Conversion steps

RWGS and SR are endothermic conversion steps ($\Delta H°_{R,RWGS}$ = 41 kJ/mol, $\Delta H°_{R,SR}$ = 206 kJ/mol at 298 K). For the electrochemical conversion of H_2O into H_2, an electrical power input of 385 kJ/mol$_{H2}$ for 60% stack efficiency is accounted for in a low-pressure electrolyzer as in Bensmann et al. (2013). CH_4 is provided by the anaerobic digestion of biomass (AD), resulting in a mixture of CH_4 and CO_2 (biogas). As stated in Section 1, syngas is used as feed stream for different downstream applications, each requiring a well-defined ratio of r=H_2/CO. Therefore, syngas conditioning is required and achieved by flowrate adjustment at the reactors and at the electrolyzer. High syngas ratios can be attained by conversion of CO into CO_2 within an oxy-combustion step (COMB), where O_2 is provided as a by-product of the electrolyzer. In principle, a WGS reactor can be combined with SR, which is the typical solution for H_2 production plants, also reported in LeValley et al. (2014). For pure H_2 production, such a configuration leads to consistent energy savings but larger CO_2 emissions with respect to its alternative, water electrolysis. Nonetheless, for syngas ratios lower than three, an additional capital investment on a WGS reactor is not justified.

2.2. Feasible separation methods

Separation sequences of gas-phase mixtures might be negatively affected by the presence of H_2O, which can condense along the process pathways, thus leading to clogging. Therefore, most of the moisture should be removed at the reactor outlets by temperature-driven condensation (CD). Feasible separation methods for specific feed mixtures are identified from the literature. For the sake of brevity, a generic ternary mixture will be denoted as (A,B,C), while the task of separating A out of (A,B,C) is denoted as A/(B,C). Hydrogen, CH_4 and O_2 can leave the plant after compression or cryogenic condensation.

2.2.1. RWGS separation sequences

After condensation, the outlet stream from RWGS comprises of CO, unreacted CO_2 and H_2, and traces of H_2O (ca. 0.3%$_{vol}$). Metz et al. (2005) reported high permeability of water in poly-dimethylsiloxane. Lower permeabilities for the other components of the mixture were reported by Merkel et al. (2001). Therefore, a membrane separator (MS) can be implemented for gas dehydration followed by a tree of alternatives for the final product separation and conditioning: 1. CO/(CO_2,H_2) (Gao et al., 2016) followed by CO_2/(H_2) on activated carbons or by recycle of the reactants (CO_2,H_2), both steps via vacuum pressure swing adsorption (VPSA); 2. H_2/(CO_2,CO) and CO/(CO_2) via VPSA; 3. CO_2/(H_2,CO) by amine absorption (AA) and H_2/(CO) (VPSA) and/or bypass to the product.

2.2.2. SR separation sequence

As for the RWGS separation train, SR requires water condensation followed by a membrane dehydration step. Afterwards, CH_4/(CO,H_2) is performed by cryogenic condensation (CR), possibly followed by recycle of CH_4. Lastly, VPSA (possibly by-passed) al-

lows for syngas conditioning. Biogas provides methane to SR: after anaerobic digestion, it is separated into CH_4 and CO by VPSA.

2.3. Modeling strategies

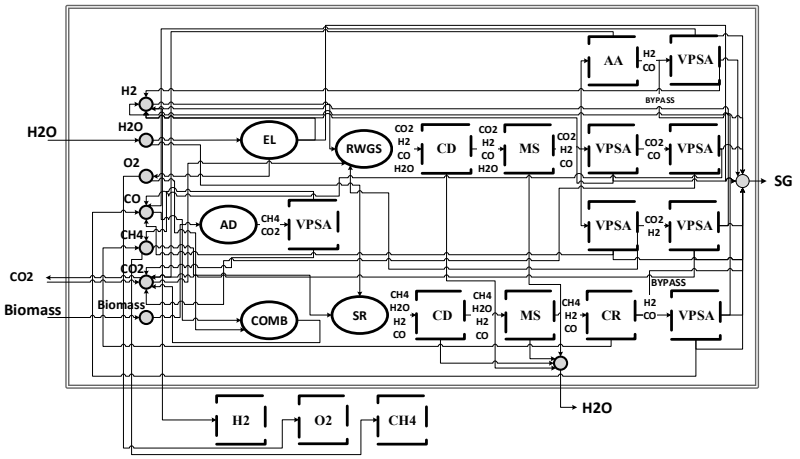

Figure 1 Fully connected superstructure.

Reactors and separators are assembled into a superstructure (see Figure 1). Nodes for the chemical components receive and deliver process streams. The outlets of the reactors are at their equilibrium compositions. Besides, the assumption of sharp-split separators allows to calculate each process stream flowrate as a function of the mole fractions after condensation at the reactor outlet,

$$\dot{n}_A = \dot{n}_{(A,B,C)} \frac{x_A}{x_A + x_B + x_C} = \dot{n}_{(A,B,C)} \xi_{A/(B,C)}, \tag{1}$$

where component A is separated from a feed stream (A,B,C), whereas $\dot{n}$ and x are the mole flowrates and mole fractions, respectively, of the stream leaving from the condensation steps. The split factor for the separation task A/(B,C) is denoted by $\xi_{A/(B,C)}$. Temperature and pressure levels are fixed. Moreover, a stoichiometric feed is assigned to the reactors. As a result, ξ is fixed and Equation 1 is linear with respect to the mole flowrates. Given that no compression is considered before water is condensed, the selected pressure level at the reactors also defines the amount of water fed to the membrane separators. The partial pressure of water in the membrane separator must be less than its vapor pressure to avoid condensation. For RWGS and SR, the thermal energy requirements are calculated from the reaction enthalpy at T_{RWGS} and T_{SR}, respectively. Normalized temperature and pressure (i.e. normal conditions) are assigned to the substance nodes. Therefore, a recycle stream will reach the normal conditions before being heated and compressed to the actual conditions at the reactors. Separation methods such as VPSA and AA comprise sequences of operation and regeneration steps, each being associated with pre-defined (T,p) values. Changes in T and p between consecutive tasks are performed via adiabatic compression and heating from external utilities. Expansion and cooling are not energetically considered. An exception is made for cryogenic condensation and storage, whose power demand is calculated from the definition of coeffi-

cient of performance (COP) which is 60% of its ideal value. The ideal COP corresponds to the ratio between T_L and ($T_H - T_L$), where T_H and T_L are the condensation and evaporation temperature of the refrigerant fluid, respectively. Furthermore, vacuum is normalized by adiabatic expansion.

2.4. Optimization problem

Three different optimization problems are defined:

$$\min \quad \dot{W} + \dot{Q} \tag{I}$$

$$\min \quad \frac{1}{LHV_{CH4}} \dot{Q} \tag{II}$$

$$\min \quad \frac{1}{LHV_{CH4}} \frac{1}{\eta_{PP}} \dot{W} + \frac{1}{LHV_{CH4}} \dot{Q} \tag{III}$$

Problem (I) represents the minimization of the total power requirement, where no distinction is made between electrical ($\dot{W}$) and thermal power ($\dot{Q}$). As stated earlier, neither thermal nor electrical power recovery is considered: gas expansion and cooling are not accounted for by the objectives. Problem (II) represents the CO_2 generated with a reference fuel (methane) as thermal power source, where *LHV* stands for lower heating value: the electricity is provided via zero-emissions sources, i.e. solar and wind. The minimization of CO_2 emissions is given by (III), where electricity is provided by a reference power-plant of assigned efficiency η_{PP}=34%, fueled by methane (see Descamps et al. (2008)). Linear programs are implemented and solved by the dual-simplex algorithm. In the post-processing of results from objectives (II) and (III), the CO_2 flowrate required as a chemical reactant at RWGS is subtracted from the CO_2 generated by combustion and process-streams emissions: the direct inclusion of this term in the objectives would lead to unboundedness, i.e. infinite flowrate at RWGS.

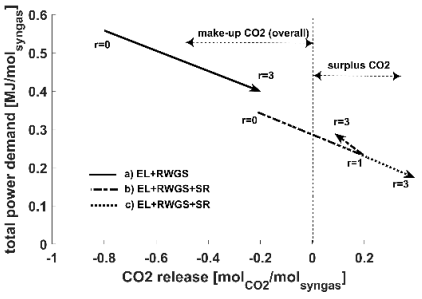

(B) Renewable electricity: objectives (I) and (II)

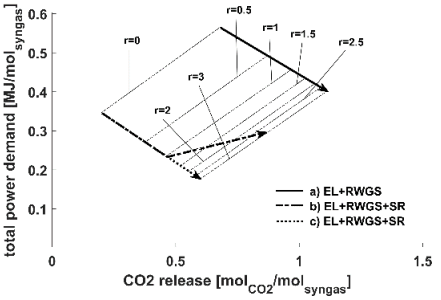

(B) Electricity from power plant: objectives (I) and (III); a) and b) suboptimal.

Figure 2: Identification of the optimal process patterns.

3. Results and discussion

Figure 2A illustrates the results from a combination of objectives (I) and (II) into a single multi-objective optimization problem, which accounts for totally renewable electrical power. The syngas ratio r spans between zero and three. Three process configurations a), b), and c) are determined and their relevant flowrates are shown in Figure 3A, 3B, and 3C, respectively. Configuration a) implements EL + RWGS, followed by water condensation, membrane dehydration and VPSA separation of CO which recycles (CO_2,H_2); b) and c) allow for SR and the associated separation scheme: they coincide for $r \in [0,1)$ and diverge with respect to energy consumption and carbon dioxide generation for $r \in [1,3]$. The combination of objectives (I) and (III) results in optimal configuration c), whereas a) and b) are suboptimal (see Figure 2B).

Configuration a) requires the largest amount of power due to the high electrical duty for EL. If electricity is provided via renewables, the CO_2 generated within the plant is not sufficient to fulfill the feed requirements at RWGS: an external carbon source must be allowed for, i.e. direct air capture or CO_2 from industrial flue gases. Configuration a) represents the least attractive solution if electricity is provided by power plants, both energy-wise and in terms of CO_2 generation. The inversely proportional trends between total power duty and r can be explained by Figure 3A: the outlet flowrate from EL is constant regardless of the value of r, which implies a constant power demand at this unit. On the other hand, the energy duty at RWGS decreases for increasing r. Part of the

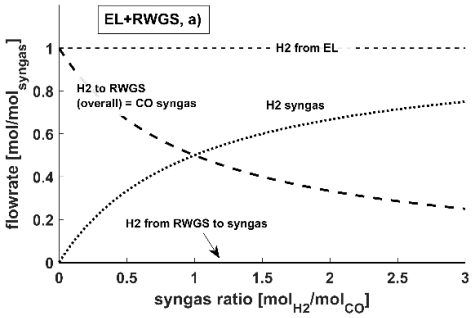

(C) Relevant flowrates, EL+RWGS, a)

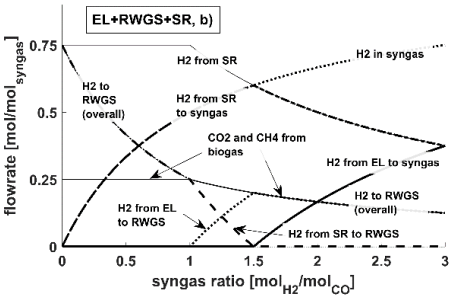

(B) Relevant flowrates, EL+RWGS+SR, b

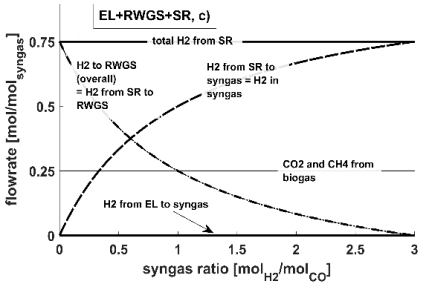

(A) Relevant flowrates, EL+RWGS+SR, c)

Figure 3: Flow-patterns.

H_2 generated by EL leaves as syngas, whereas the remaining amount is converted into CO by RWGS. Consequently, to preserve a fixed syngas flowrate, the productivity of RWGS must decrease, and so does its energy demand. Since RWGS is a sink for carbon dioxide, the system behavior with respect to the CO_2 generation in Figures 2A and 2B is also explained: the less CO is produced, the less CO_2 is consumed by RWGS. SR can substitute EL as a producer of H_2 for RWGS. Process configurations allowing for SR are only suboptimal: it is less energy-intensive and more sustainable to generate part of the CO by RWGS. For $r \in [0,1)$ in b) and $r \in [0,3]$ in c), SR provides all the H_2 required at RWGS and syngas. In this case, the outlet flowrate from SR does not change for different values of r. For $r \geq 1$ in b) (see Figure 3B), the electrolyzer starts to feed H_2 to RWGS, gradually substituting SR, whereas for $r \geq 1.5$ it totally replaces it. Furthermore, the biogas generated from AD is entirely converted within the battery limits according to the overall stoichiometry $CH_4+CO_2=2H_2+2CO$. Therefore, RWGS is always operated.

4. Conclusions

In this contribution, a reactor-separator superstructure for the syngas production is proposed. Optimization results identify possible synergies between EL, SR and RWGS. Unreacted H_2 and CO_2 are recycled by VPSA after RWGS, whereas CO and H_2 leave as syngas. EL is highly energy demanding and only sustainable if renewable electricity is available. Thus, if electricity is provided via conventional power plants, EL is not a favourable option. Therefore, the implementation of EL and RWGS would be unable to ensure a sustainable production for scenarios where renewable electricity is not sufficiently available. In such cases, process systems comprising EL, RWGS and SR allow for lower CO_2 generation levels and energy demand because SR can substitute or complement EL as H_2 source for RWGS.

References

B. Bensmann, R. Hanke-Rauschenbach, I. P. Arias, K. Sundmacher, 2013. Energetic evaluation of high pressure pem electrolyzer systems for intermediate storage of renewable energies. Electrochimica Acta 110, 570–580.

C. Descamps, C. Bouallou, M. Kanniche, 2008. Efficiency of an integrated gasification combined cycle (igcc) powerplant including co2 removal. Energy 33 (6), 874–881.

F. Gao, Y. Wang, S. Wang, 2016. Selective adsorption of co on cucl/y adsorbent prepared using cucl2 as precursor: Equilibrium and thermodynamics. Chemical Engineering Journal 290, 418–427.

T. L. LeValley, A. R. Richard, M. Fan, 2014. The progress in water gas shift and steam reforming hydrogen production technologies–a review. International Journal of Hydrogen Energy 39 (30), 16983–17000.

T. Merkel, R. Gupta, B. Turk, B. D. Freeman, 2001. Mixed-gas permeation of syngas components in poly (dimethyl-siloxane) and poly (1-trimethylsilyl-1-propyne) at elevated temperatures. Journal of Membrane Science 191 (1-2),85–94.S.

J. Metz, W. Van de Ven, J. Potreck, M. Mulder, M. Wessling, 2005. Transport of water vapor and inert gas mixtures through highly selective and highly permeable polymer membranes. Journal of Membrane Science 251 (1-2), 29–41.

M. Wenzel, L. Rihko-Struckmann, K. Sundmacher, 2017. Thermodynamic analysis and optimization of rwgs processes for solar syngas production from co2. AIChE Journal 63 (1), 15–22.

Sauro Pierucci, Flavio Manenti, Giulia Bozzano, Davide Manca (Eds.)
Proceedings of the 30th European Symposium on Computer Aided Process Engineering (ESCAPE30), May 24-27, 2020, Milano, Italy.
http://dx.doi.org/10.1016/B978-0-12-823377-1.50233-0

Search Space Analysis in Work and Heat Exchange Networks Synthesis using MINLP Models

Lucas F. Santos,[a*] Caliane B. B. Costa,[a] José A. Caballero,[b] Mauro A. S. S. Ravagnani[a,b]

[a]*Chemical Engineering Graduate Program, State University of Maringá, 5790 Colombo Av., Maringá – 87020900, Brazil*
[b]*Department of Chemical Engineering, University of Alicante, Ap. Correos 99, Alicante – 03080, Spain*
lfs.francisco.95@gmail.com

Abstract

Superstructure-based optimization models have been used as important approaches in solving process systems engineering problems. Despite its promising results, mixed-integer nonlinear programming (MINLP) optimization models are usually complex, once they involve integer and continuous variables, and nonlinear, non-convex functions. For work and heat exchange networks (WHEN) synthesis, even in problems of few process streams, the derived MINLP models have large combinatorial and continuous search spaces. In the present paper, the search spaces of two equivalents MINLP models for WHEN synthesis are analyzed to test their influence on optimization performance. The models are derived from the same superstructure, but one of those uses strategies to reduce the number of decision variables that provides a considerable diminution of combinatorial problem. The same bi-level meta-heuristic optimization approach in which Simulated Annealing deals with the combinatorial level and Particle Swarm Optimization with the continuous one is used to solve both MINLP problems. The mean values of total annualized cost and elapsed time from several optimization runs of both models are compared. The results show that the decision-variable-reduced model is more efficient and consistent than the standard-decision-variable one. It can be concluded that combinatorial search space reduction is important for optimization performance of highly complex decision-making problems such as WHEN synthesis and should be addressed in WHEN modeling because the problem's complexity increases exponentially with the number of the model binary variables.
Keywords: Work and heat exchange networks. MINLP. Search space. Optimization performance. Combinatorial analysis.

1. Introduction

Energy has fundamental importance in chemical processes as it fuels the transformation of matter into desired products. However, consuming energy sources implies costs and environmental footprint. One way to use this resource with less waste is by means of energy integration. The synthesis of optimal work and heat exchange networks (WHEN) performing work and heat integration is deeply important to guarantee economic competitiveness and viability of chemical processes that demand high energy consumption for compression, heating, and cooling tasks. WHEN synthesis is a rather complicated decision-making task because it comprises choosing existence, sequence, and sizes of heat exchangers, heaters, cooler, compressors, turbines, single-shaft-turbine-compressors (SSTC), and valves and considering thermal identity change due to

pressure manipulation, phase transition, and thermodynamic cycles. Since decisions must be taken to reduce a value of interest, such as total annualized cost (TAC), it is intuitive and useful to use mathematical optimization. In this context, superstructures help systematizing possible WHEN configurations from which mixed-integer nonlinear programming (MINLP) models can be derived. The resulting MINLP models are usually large scale, non-convex problems; therefore, difficult to solve to global optimality.

In recent years, many researchers have employed superstructure-based optimization for WHEN synthesis. Wechsung et al. (2011) published the first paper on this subject. Those authors proposed a heat exchanger network (HEN) superstructure that allowed streams to compress and expand in pre-defined routes based on heuristics for appropriate placement of compressors and turbines from Gundersen et al. (2009). Razib et al. (2012) proposed a multi-stage work exchange network (WEN) superstructure that considered heating and cooling streams using utilities. They introduced in their superstructure the possibility of direct work integration via single-shaft-turbine-compressors (SSTC). Onishi et al. (2014a; 2014b) extended previous superstructures by implementing the well-known stage-wise HEN superstructure from Yee and Grossmann (1990) to improve heat integration. Onishi et al. (2018) proposed a superstructure and disjunctive-MINLP model that did not pre-classify streams with respect to its temperature and pressure, so that heating, cooling, compression, and expansion had no fixed routes. This improvement made WHEN superstructures more generic to deal with non-trivialities such as thermal identity change, and thermodynamic cycles, at the price of making the mathematical problem more complicated. Pavão et al. (2019) presented interesting WHEN results using a new superstructure and MINLP model and a bi-level meta-heuristic optimization approach. In their framework, simplified routes of temperature and pressure manipulations were fixed, but complicated heat integration configurations were allowed based on a new HEN superstructure (Pavão et al., 2018).

In the above-mentioned works, the complexity of the MINLP problems was reduced by means of simplifications in the superstructures and models. These considerations simplify the problem, but reduce its generality and exclude possible promising WHEN configurations. Based on that, Santos et al. (2020) reported interesting and non-trivial WHENs using a new superstructure and MINLP model that included strategies to reduce the number of decision variables by means of changes of variables and third-level optimization. Mathematical simplifications based on additional calculations and extra information that did not necessarily reduce the model generality were introduced.

Given this background of different MINLP models for WHEN synthesis, the current literature lacks on mathematical characterization of these models via, for instance, search space, combinatorial, and convex analyzes. Therefore, the purpose of the present paper is to analyze the search space of two MINLP models for WHEN synthesis and its influence on the optimization performance. Both models are equivalent and derived from the same superstructure. One of them, however, is in a more intuitive formulation, whereas the other presents strategies for reducing the number of decision variables.

2. WHEN models

The superstructure and MINLP models analyzed in the present paper were proposed by Santos et al. (2020). Authors presented a multi-stage WHEN superstructure divided into four sections: classification, heat integration, temperature adjustment, and work exchange network, as illustrated in Figure 1.

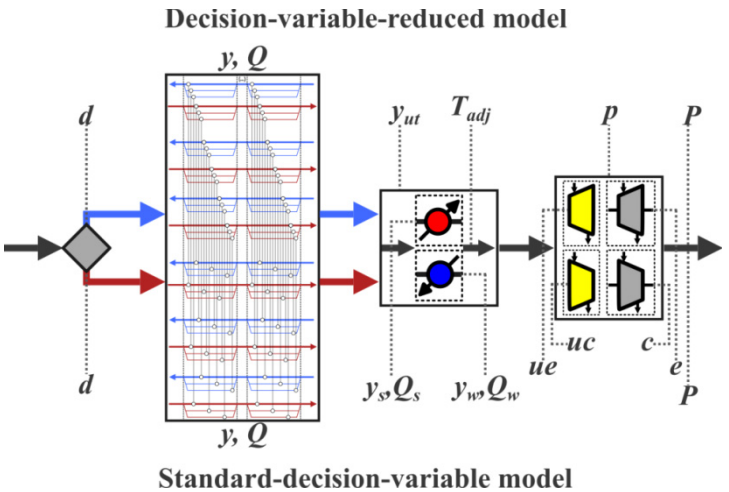

Figure 1. Stages of WHEN superstructure with decision variables of both models.

Using changes of variables and third level optimization to reduce the optimization search space, their MINLP model (Eq. (1)) aims to minimize total annualized cost (*TAC*) and has the following decision variables: d, y, y_{ut}, p, Q, T_{adj}, and P. These variables stand for thermal classification, existence of heat exchanger, activation of temperature adjustment section, activation of pressure manipulation section, heat load of heat exchanger, adjusted temperature, and manipulated pressure, respectively. Notice that d, y, y_{ut}, and p are binary variables, and Q, T_{adj}, and P are continuous ones. The reader is referred to Santos et al. (2020) for more information regarding the model and superstructure.

$$\begin{aligned} \min \quad & TAC(d, y, y_{ut}, p, Q, T_{adj}, P) \\ & \text{Thermodynamic and operating constraints} \\ \text{s.t.} \quad & \begin{array}{lll} d \in \{0,1\}^{n_1}, & & n_1 = S \cdot Ns \\ y \in \{0,1\}^{n_2}, & Q \in \mathbb{R}^{n_2}, & n_2 = S^2 \cdot Ns^2 \cdot K \\ y_{ut} \in \{0,1\}^{n_3}, & T_{adj} \in \mathbb{R}^{n_3}, & n_3 = S \cdot (Ns - 1) \\ p \in \{0,1\}^{n_4}, & P \in \mathbb{R}^{n_4}, & n_4 = S \cdot (Ns - 2) \end{array} \end{aligned} \tag{1}$$

Note that S is the number of process streams, Ns the number of WHEN stages in the superstructure, and K the number of heat integration stages. Now, by simply removing the strategies of reducing the number of decision variables, the resulting and equivalent MINLP (Eq. (2)) has the following decision variables: d, y, Q, and P and y_s, y_w, e, c, ue, uc, Q_s, and Q_w. The latter set of variables contains those that represent the existence of heater (y_s), cooler (y_w), turbine coupled to work integration shaft (e), compressor coupled to the shaft (c), electric turbine (ue), electric compressor (uc), heater heat load (Q_s), and cooler heat load (Q_w). Notice that d, y, y_s, y_w, e, c, ue, and uc are binary variables, and Q, P, Q_s, and Q_w are continuous ones.

$$\begin{aligned} \min \quad & TAC(d, y, y_s, y_w, e, c, ue, uc, Q, Q_s, Q_w, P) \\ & \text{Thermodynamic and operating constraints} \\ \text{s.t.} \quad & \begin{array}{lll} d \in \{0,1\}^{n_1}, & & n_1 = S \cdot Ns \\ y \in \{0,1\}^{n_2}, & Q \in \mathbb{R}^{n_2}, & n_2 = S^2 \cdot Ns^2 \cdot K \\ y_s, y_w \in \{0,1\}^{n_3}, & Q_s, Q_w \in \mathbb{R}^{n_3}, & n_3 = S \cdot (Ns - 1) \\ e, c, ue, uc \in \{0,1\}^{n_4}, & P \in \mathbb{R}^{n_4}, & n_4 = S \cdot (Ns - 2) \end{array} \end{aligned} \tag{2}$$

2.1. Search space analysis

A degrees of freedom (DoF) analysis of these models shows that (1) has $2 \cdot S^2 \cdot Ns^2 \cdot K + S \cdot (5 \cdot Ns - 6)$ DoF and (2) has $2 \cdot S^2 \cdot Ns^2 \cdot K + S \cdot (10 \cdot Ns - 14)$ DoF. Although each DoF must be fulfilled with a decision variable, increasing the problem dimension, it is not enough to measure the MINLP search space by the number of decision variables. One reason for that is because continuous space is determined by the binary configuration that activates and deactivates continuous variables. Therefore, not all continuous variables are considered, but only the ones activated by binary configuration. Another reason is that the number of binary combinations is more relevant to determine the combinatorial search space than the number of binary variables. Given that, let us consider that the search space can be divided into continuous and combinatorial (binary).

The continuous search space of both standard-decision-variable model (SDVM) (2) and decision-variable-reduced model (DVRM) (1) are equivalent. Even though the number of continuous decision variables is $S \cdot (Ns - 1)$ higher in the SDVM, the number of active continuous variables at equivalent topologies is always the same. For example, Q_s and Q_w cannot coexist; therefore, they are analogous to the single variable T_{adj}.

The combinatorial search spaces change considerably from SDVM to DVRM. The resulting combinations of temperature adjustment in SDVM are $3^{S\,(Ns\,-\,1)}$, which come from three possible binary results of y_s, y_w = {[0,0], [1,0], [0,1]} for each stream s = 1, …, S, and stage n = 1, …, N_s – 1. On the other hand, for DVRM the combinations in this section are $2^{S\,(Ns\,-\,1)}$ from two possible results of y_{ut} = {0, 1} for the same s and n. In the work exchange section, the difference is even stronger. In the SDVM there are $5^{S\,(Ns\,-\,2)}$ combinations from e, c, ue, uc = {[0,0,0,0], [1,0,0,0], [0,1,0,0], [0,0,1,0], [0,0,0,1]} for each stream s = 1, …, S, and stage n = 1, …, N_s – 2. The same section in DVRM presents only $2^{S\,(Ns\,-\,2)}$ combinations from p = {0, 1} for the same s and n. The heat integration section is the same for both models. Thus, SDVM has $3^{S \cdot (Ns-1)} \cdot 5^{S \cdot (Ns-2)} / 2^{S \cdot (2Ns-3)}$ times more binary combinations than DVRM. For a simple example of S = 4 and Ns = 4, SDVM binary combinations are 197,977 times higher than those of DVRM, and it clearly escalates exponentially with S and Ns.

3. Case study

Both models were implemented in C++ language in a computer with a 3.20 GHz Intel® Core™ i5-4460 processor and 8.00 GB of RAM. The models were used to solve a two-stream work and heat integration case study, whose data are presented in Table 1. This case study is inspired by Onishi et al. (2014a), and was used by Pavão et al. (2019). However, in order to complicate the problem, the pressure differences and heat capacity flow rate were increased by a factor of 10.

Table 1. Process streams and utilities data

Stream	T_{in} [K]	T_{out} [K]	CP [kW.K^{-1}]	h [kW.m^{-2}.K^{-1}]	P_{in} [MPa]	P_{out} [MPa]
$s1$	650	370	30	0.1	0.1	5
$s2$	410	650	20	0.1	5	0.1
HU	680	680	–	1.0	–	–
CU	300	300	–	1.0	–	–

The superstructure parameters for this case study are S = 2, Ns = 4, K = 2. Thus, the resulting optimization problems (*1*) and (*2*) has 284 (146 binary) and 308 (164 binary) decision variables, respectively. The problem is solved using a bi-level meta-heuristic optimization approach with Simulated Annealing (SA) in the combinatorial problem

and Particle Swarm Optimization (PSO) in the NLP, as proposed by Santos et al. (2020). This solution approach was selected instead of deterministic global solvers because, as reported in the literature (Onishi et al., 2018), they are too time-consuming when applied to MINLP problems from WHEN synthesis. However, the same search space analysis using deterministic methods for global optimization will be the subject of future work. Considering the non-deterministic behavior of meta-heuristic techniques, each optimization was run 50 times and the resulting *TAC* and elapsed time (τ) were saved for further analysis. The reader is referred to case study 1 of Santos et al. (2020) for more information about the problem as well as solver parameters. The mean value and standard deviation of *TAC* and τ obtained for both SDVM and DVRM are presented in Table 2.

Table 2. Optimization results of SDVM and DVRM.

	SDVM			DVRM		
	TAC ($.y^{-1})	τ (min)	Failure (%)	TAC ($.y^{-1})	τ (min)	Failure (%)
Mean	9.304.802	10	2	8.637.935	9	0
Standard deviation	339.964	0.4	-	225.777	0.9	-

As presented in Table 2, DVRM performed better and more consistently, *i.e.* lower *TAC* mean value and standard deviation and less failure (infeasible solution). One reason for that is the combinatorial analysis of these models. Let the search space of binary variables be all possible configurations of binary variables as explained in 2.1. Then, the binary search space of SDVM is 445 times greater than DVRM, considering the superstructure parameters used (*S*, *Ns*, and *K*). Knowing that the number of topologies evaluated in SDVM was 2480 and DVRM was 930, which are far from all combinations possible, it can be inferred that the reduction of 445 times guarantees the solver to investigate proportionally more of the whole binary search space. The difference between the numbers of topologies evaluated in each model is because of the DVRM third-level optimization. In order to approximate elapsed time for a fair comparison, more SA trials were available for SDVM.

These results show the importance of not only evaluating the degrees of freedom of a problem for decision variables choice, but also paying attention to the number of binary combinations of a MINLP model. Knowing that the latter grows exponentially, it increases the problem complexity a lot and quickly.

4. Conclusions

Two MINLP models for WHEN synthesis are compared regarding their search spaces. These models are equivalent and derived from the same superstructure, but strategies for reducing the number of decision variables are applied in one of them (Santos et al., 2020). One finding of search space comparison is that the ratio of binary combinations between SDVM and DVRM increases exponentially ($3^{S\cdot(Ns-1)} \cdot 5^{S\cdot(Ns-2)}/2^{S\cdot(2Ns-3)}$) with respect to the number of streams (*S*) and stages (*Ns*) of the work and heat integration superstructure. It means that the higher is *S* and *Ns*, the more significant is the combinatorial search space diminution due to the strategies. The optimization results showed that the DVRM outperformed the SDVM in both performance (lower mean *TAC*), and consistency (lower *TAC* standard deviation and failures). Regarding elapsed time, DVRM was slower than SDVM because of its time-consuming third-level

optimization. Therefore, it can be concluded that, in WHEN synthesis MINLP models, combinatorial search space reduction is extremely important for optimization performance as it simplifies the complexity of decision-making problem.

Acknowledgements

The authors acknowledge the National Council for Scientific and Technological Development – Brazil, processes 440047/2019-6, 311807/2018-6, 428650/2018-0 148184/2019-7, 305055/2017-8, and Coordination for the Improvement of Higher Education Personnel – Brazil for the financial support.

References

T. Gundersen, D. O. Berstad, and A. Aspelund, 2009, Extending Pinch Analysis and Process Integration into Pressure and Fluid Phase Considerations, Chemical Engineering Transactions, 18, 33–38.

V. C. Onishi, M. A. S. S. Ravagnani, and J. A. Caballero, 2014a, Simultaneous Synthesis of Heat Exchanger Networks with Pressure Recovery: Optimal Integration between Heat and Work, AIChE Journal, 60, 3, 893–908.

V. C. Onishi, N. Quirante, M. A. S. S. Ravagnani, and J. A. Caballero, 2018, Optimal Synthesis of Work and Heat Exchangers Networks Considering Unclassified Process Streams at Sub and Above-Ambient Conditions, Applied Energy, 224, 8, 567–81.

V. C. Onishi, M. A. S. S. Ravagnani, and J. A. Caballero, 2014b, Simultaneous Synthesis of Work Exchange Networks with Heat Integration, Chemical Engineering Science, 112, 6, 87–107.

L. V. Pavão, C. B. B. Costa, and M. A. S. S. Ravagnani, 2019, A New Framework for Work and Heat Exchange Network Synthesis and Optimization, Energy Conversion and Management, 183, 3, 617–632.

L. V. Pavão, C. B. B. Costa, and M. A. S. S. Ravagnani, 2018, An Enhanced Stage-Wise Superstructure for Heat Exchanger Networks Synthesis with New Options for Heaters and Coolers Placement, Industrial & Engineering Chemistry Research, 57, 7, 2560–73.

M. S. Razib, M. M. F. Hasan, and I. A. Karimi, 2012, Preliminary Synthesis of Work Exchange Networks, Computers & Chemical Engineering, 37, 2, 262–277.

L. F. Santos, C. B. B. Costa, J. A. Caballero, M. A. S. Ravagnani, 2020, Synthesis and optimization of work and heat exchange networks using an MINLP model with a reduced number of decision variables, Applied Energy, 262, 114441.

A. Wechsung, A. Aspelund, T. Gundersen, and P. I. Barton, 2011, Synthesis of Heat Exchanger Networks at Subambient Conditions with Compression and Expansion of Process Streams, AIChE Journal, 57, 8, 2090–2108.

T. F. Yee, and I. E. Grossmann, 1990, Simultaneous Optimization Models for Heat Integration-II. Heat Exchanger Network Synthesis, Computers & Chemical Engineering, 14, 10, 1165–1184.

Sauro Pierucci, Flavio Manenti, Giulia Bozzano, Davide Manca (Eds.)
Proceedings of the 30th European Symposium on Computer Aided Process Engineering (ESCAPE30), May 24-27, 2020, Milano, Italy.
http://dx.doi.org/10.1016/B978-0-12-823377-1.50234-2

Modelling and Simulation of the Conversion of Chicken Fat to Produce Renewable Aviation Fuel through the Hydrotreating Process

Ana Laura Moreno Gómez[a], Claudia Gutiérrez-Antonio[a*], Fernando Israel Gómez-Castro[b], Salvador Hernández[b]

[a] *Facultad de Química, Universidad Autónoma de Querétaro, Av. Cerro de las Campanas s/n, Col. Las Campanas,76010, Querétaro, Mexico*

[b]*Departamento de Ingeniería Química, División de Ciencias Naturales y Exactas, Campus Guanajuato, Universidad de Guanajuato, Noria Alta S/N. Col. Noria Alta, 38010, Guanajuato, Guanajuato, México*
claudia.gutierrez@uaq.mx

Abstract

In the transport sector, aviation has the higher growth; thus, more fuel will be required for its operation in the forthcoming years. In order to guarantee the sustainable development of the aviation sector, the use of renewable fuels has been proposed. The renewable aviation fuel can be produced from different types of biomass through several conversion processes. One of these processes is the hydrotreating, where triglyceride feedstock is converted to renewable aviation fuel, light gases, naphtha and green diesel, which are later separated by distillation; in hydroprocessing, the cost of raw material contributes around 80% to the final cost of the biojet fuel. Due to this, the use of waste oils and fats represents an interesting alternative to produce biojet fuel with competitive prices. In addition, this kind of raw material is available all the year, and its generation is in constant increasing due to the population growth. Therefore, in this work the modelling and simulation of the hydrotreating process to produce biojet fuel, considering chicken fat as raw material, is presented. The study is performed using the software Aspen Plus. Two conventional hydrotreating processes are defined and evaluated in terms of total annual costs, CO_2 emissions and price of biojet fuel. It has been found that the hydrotreating process that includes the direct conventional sequence has the lowest energy consumption. Also, a significantly decrease in the price of biojet fuel is observed when chicken fat is used as raw material, in comparison with oils from *Jatropha curcas*, castor bean and micro-algae. The use of chicken fat represents a promissory raw material to produce biojet fuel, considering its low-cost and constant availability along the year.

Keywords: Biojet fuel, hydrotreating process, chicken fat, renewable aviation fuel.

1. Introduction

Nowadays the aviation sector faces two important challenges: the decrease of oil reserves and the global warming. The forecasts indicate that the growth of aviation sector will be of 4.8 % for each year until 2036 (Chacin, 2010); thus, more fuel will be required for its operation in the forthcoming years, with the consequent increase in CO_2 emissions. Moreover, considering that the fuel represents around 30% of the total operation costs of airlines, the fluctuations in the price of aviation fuel affect considerably the profitability. On the other hand, the global warming is associated with the excessive use of fossil fuels;

in this context, the growth of aviation sector will contribute to the global warming problem. Thus, in order to guarantee the sustainable development of the aviation sector, the International Air Transport Association (IATA) promotes the development of renewable biofuels, also known as biojet fuel or biokerosene. Biojet fuel can be produced from several types of biomass through different conversion processes; one of them is the hydroprocessing of triglyceride feedstock. In this process, triglyceride are converted through hydrodeoxygenation to generate long chain lineal hydrocarbons, which later are cracked and isomerized to generate hydrocarbons in the boiling point range of biojet fuel; these reactions are carried out at high pressure and temperature, and they also required hydrogen as another reactant (Shalaby et al., 2015). In addition, other hydrocarbons are produced such as light gases, naphtha, and green diesel, which are separated by distillation. Several raw materials have been explored to produce renewable aviation fuel, including oils from second and third generation. From these studies, it can be concluded that the processing of these raw materials is technically feasible to produce renewable aviation fuel, but their cost is the major contributor to the biofuel price (at least 80%. Gutiérrez-Antonio et al., 2018). Thus, the use of waste triglyceride feedstock is a promissory alternative to produce biojet fuel with a competitive selling price, in comparison to its fossil counterpart. Therefore, this work presents the modelling and simulation of the hydroprocessing of chicken fat to produce renewable aviation fuel. This kind of raw material offers the opportunity to reduce the production cost of biojet fuel and, consequently, its selling price.

2. Methodology

The selected raw material is chicken fat, which consists on free fatty acids (6%) and triglycerides (94%) (Kaewmeesri et al., 2014). The composition of the raw material is shown in Table 1.

Table 1. Composition for the raw material (Hanafi et al., 2016)

Component	Composition (%mass)
Palmitic Acid	1.48
Estearic Acid	0.35
Oleic Acid	2.68
Linoleic Acid	2.18
Tripalmitin	20.62
Triestearin	4.91
Triolein	37.32
Linolein	30.44

The oil derived from chicken fat is converted to biojet fuel through the hydrotreating process, which includes three main sections: conditioning zone, reactive zone, and distillation zone, as shown in Figure 1. In the conditioning zone, the temperature and pressure of the reactants (hydrogen and oil) is increased, through heat exchangers, a pump and a compressor, to reach the adequate conditions (480 °C and 6 MPa) to be fed in the reactive zone. The reactive zone is integrated by two reactors: hydrodeoxygenation/hydrocracking and hydroisomerization. In the first reactor, the conversion of the oil derived from chicken fat is modelled according to the data reported by Hanafi et al. (2016), where hydrodeoxygenation and hydrocracking reactions are carried out; moreover, H_2 is fed in a proportion of 450 v/v H_2/oil, and 100 kg/h of oil are

fed to the reactive zone. The hydrotreating reactor was modelled using the RYield module of Aspen Plus.

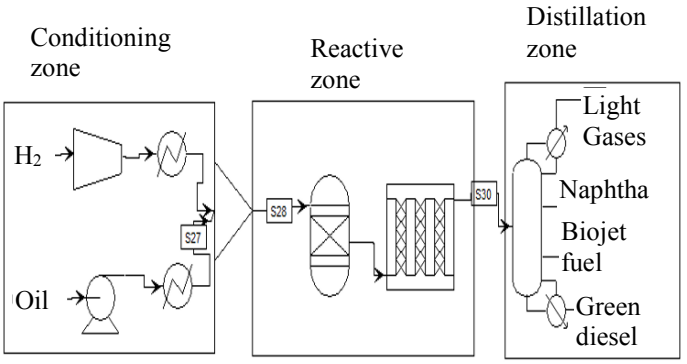

Figure 1. Main zones of the hydrotreating process.

The effluent of the first reactor is fed to the hydroisomerization reactor, which was modelled with the RPlug module based on the kinetic model reported by Calemma et al. (2000); it is considered an activation energy of 3,500 cal/mol, and the reactions proposed by Romero-Izquierdo (2015), which are shown in Table 2. The hydroisomerization reactor operates at 480 °C and 8 MPa; from the second reactor, a mixture of four products was obtained in the effluent: light gases, naphtha, biojet fuel, and green diesel.

Table 2. Reactions used to model the hydroisomerization reactor (Romero-Izquierdo, 2015)

$C_5H_{12} \rightarrow isoC_5\ H_{12}$
$C_6H_{14} \rightarrow isoC_6\ H_{14}$
$C_7\ H_{16} \rightarrow isoC_7\ H_{16}$
$C_8H_{18} \rightarrow isoC_8H_{18}$
$C_9H_{20} \rightarrow isoC_9H_{20}$
$C_{10}H_{22} \rightarrow isoC_{10}\ H_{22}$
$C_{11}\ H_{24} \rightarrow isoC_{11}H_{24}$
$C_{12}\ H_{26} \rightarrow isoC_{12}\ H_{26}$
$C_{16}H_{36} \rightarrow isoC_{16}\ H_{36}$

The effluent of the hydroisomerization reactor was conditioned to reduce its pressure and temperature using a turbine, which allows to generate electricity. After that, the hydrocarbon stream is fed to the distillation zone. Several alternatives for the separation of the mixture are possible, since there are four products; however, only two sequences allow the separation in the first column of the light gases, which is necessary to avoid the excessive use of refrigerants. Therefore, only two sequences are analysed in this work: the direct and the direct-indirect schemes. In both schemes, a partial condenser was used in the first distillation column, while the second and third distillation columns employ total condensers. The use of each one of these distillation schemes defines two scenarios, where the conditioning and reactive zones are the same; the difference lies in the use of the direct sequence in scenario 1, while the direct-indirect sequence is considered in scenario 2. The simulation was performed in Aspen Plus V10. The employed

thermodynamics methods were Peng-Robinson for the conditioning and reactive zones, and BK10 for the distillation zone.
The price of the raw material was obtained from a market study taking as suppliers the local merchants of the poultry line. In order to calculate the biojet fuel price, the methodology proposed for Romero-Izquierdo (2015) has been used. The methodology of Guthrie (Turton et al., 2004) is used to calculate the cost of the equipment. Finally, to obtain the CO_2 emissions the methodology proposed by Romero-Izquierdo (2015) is used.

3. Results

This section shows the results of both scenarios in terms of total annual costs, biojet fuel price and CO_2 emissions. Table 3 shows the yield and mass flow of the products generated in the hydrotreating reactor. As it can be observed, the obtained yield of hydrocarbons in the jet fuel range is the highest, compared with the yield of the other three products.

Table 3. Yield and mass flow of hydrotreating reactor

Products	Total flow (kg/h)	Yield
Light gases	12.8	0.1227
Naphtha	20.33	0.1948
Biokerosene	31.52	0.3020
Green diesel	25.84	0.2477

In the hydroisomerization reactor it was possible obtain 44% of isomers in the effluent; therefore, a total biokerosene flow of 40 kg/h. The total electricity consumed in the process was 25.31 kW; if the energy produced with the turbine is used, the electricity consumption can be reduced by 88.4%. The energy requirements in both distillation sequences are shown in Table 4.

Table 4. Reboiler energy consumptions of both distillation sequences.

Equipment	Energy requirement (kW)	Distillation sequence
Reboiler of distillation column 1	5.25	Direct
Reboiler of distillation column 2	8.23	
Reboiler of distillation column 3	8.30	
Total	21.78	
Reboiler of distillation column 1	5.25	Direct-Indirect
Reboiler of distillation column 2	14.57	
Reboiler of distillation column 3	6.07	
Total	25.89	

The summary of economic and environmental parameters for both scenarios is presented in Table 5. The price of raw material represents only 6.83% of the total processing cost, which makes it very attractive since a significant price reduction is observed; this reduction is up to 97% in comparison with microalgae oil and *Jatropha Curcas* oil (Gutiérrez-Antonio et al., 2018; Gutiérrez-Antonio et al., 2016). In the Scenario 2, CO_2

emissions are higher than in scenario 1, due mainly to the high energy requirement in the second reboiler of the distillation scheme.

Table 5. Summary of economic and environmental parameters for scenarios 1 and 2.

Scenario	Cost of equipment (USD/ year)	Processing Cost (USD/year)	CO_2 emissions (Ton/year)	Cost of raw material (USD/year)	Biojet fuel price (USD/L)
1	$1,963,384.12	$1,864,701.78	66,199.1397	$127,500.00	$0.543
2	$2,215,893.95	$1,867,003.31	79,339.4034		$0.557

4. Conclusions

The modelling and simulation of the hydroprocessing of chicken fat has been presented. Results shown that a considerable decrease in the biojet fuel price is obtained, as result of the low price of the raw material. The high energy requirements in the process opens enhancement opportunities, as the implementation of strategies as energy integration or process intensification to reduce those requirements.

Acknowledgements

Financial support provided by CONACyT, grant 279753, for the development of this project is gratefully acknowledged.

Also, A.L. Moreno Gómez was supported by a scholarship from CONACYT for the realization of her postgraduate studies.

References

R. Turton, R.C. Bailie, W.B. Whiting, J.A. Shaeiwitz, D. Bhattachayya, 2012, Analysis, synthesis, and design of chemical processes, 4th edition, Prentice Hall, New Jersey, 850-872.

E. Chacin, 2010, La OACI y los combustibles alternativos sustentables de aviación, Taller de Financiamiento, Legislación, Logística y Distribución, Plan de Vuelo, 21 (Spanish).

V. Calemma, S.Paratello, C. Perego, 2000, Hydroisomerization and hydrocracking of long chain n-alkanes on Pt/amorphous SiO2-Al2O3 catalyst, Applied Catalyst A, 190, 207-218.

S.A. Hanafi, M.S.Elmelawy, N.H.Shalaby, H.A.El-Syed, G.Eshad, M.S.Mostafa, 2016, Hydrocracking of waste chicken fat as a cost effective feedstock for renewable fuel production: A kinetic study, Egyptian Journal of Petroleum, 25, 531-537.

International Energy Agency (IEA), 2017, Key World Energy Statistics, 1,7 -97.

C. Gutiérrez-Antonio, F.I. Gómez-Castro, G.A. de Lira-Flores, S.Hernandez, 2017, A review on the production process of renewable jet fuel, Renewable and Sustainable Energy Reviews, 79, 709-729.

C. Gutiérrez-Antonio, A.G. Romero-Izquierdo, F. I. Gómez-Castro, S. Hernández, 2016, Energy Integration of a Hydrotreatment Process for Sustainable Biojet Fuel Production, Industrial and Engineering Chemestry Research, 55, 8165–8175.

C. Gutiérrez-Antonio, A.G. Romero-Izquierdo, F. I. Gómez-Castro, S. Hernández, 2018, Modeling, simulation and intensification of hydroprocessing of micro-algae oil to produce renewable aviation fuel, Clean Technologies and Enviromental Policy, 20, 1589-1598

C. Gutiérrez-Antonio, F.I. Gómez-Castro, S. Hernández, 2018, Sustainable production of renewable aviation fuel through intensification strategies, Chemical Engineering Transactions, 69, 1-6.

A.G. Romero-Izquierdo, 2015, Integración energética de un proceso para la producción de combsutible renovable para aviación, Thesis, Universidad de Guanajuato (Spanish).

R. Kaewmeesri, A.Srifa, V. Itthibenchapong, K. Faungnawakij, 2014, Deoxygenation of Waste Chicken Fats to Green Diesel over Ni/Al_2O_3: Effect of Water and Free Fatty Acid Content, energy and fuels, 29, 833-840.

N.Shalaby, S.H. Harap, M.S. Elmelawy, 2015, Hydrocracking of waste cooking oil as renewable fuel on NiW/SiO2-Al2O3, Journal of Advanced Catalyst Science and Technology, 2, 27-37.

Sauro Pierucci, Flavio Manenti, Giulia Bozzano, Davide Manca (Eds.)
Proceedings of the 30th European Symposium on Computer Aided Process Engineering (ESCAPE30), May 24-27, 2020, Milano, Italy.
http://dx.doi.org/10.1016/B978-0-12-823377-1.50235-4

Mixed-Integer Dynamic Scheduling Optimization for Demand Side Management

Florian Joseph Baader[a], Maximilian Mork[a], André Xhonneux[a], Dirk Müller[a,b], André Bardow[a,c], Manuel Dahmen[a,*]

[a]*Institute of Energy and Climate Research - Energy Systems Engineering (IEK-10), Forschungszentrum Jülich GmbH, 52425 Jülich, Germany*
[b]*E.ON Energy Research Center, Institute for Energy Efficient Buildings and Indoor Climate, RWTH Aachen University, 52074 Aachen, Germany*
[c]*Institute of Technical Thermodynamics, RWTH Aachen University, 52056 Aachen, Germany*
m.dahmen@fz-juelich.de

Abstract

With fluctuating electricity prices, demand side management (DSM) promises to reduce energy costs. DSM of processes and energy supply systems requires scheduling optimization to consider transient behavior and binary on/off-decisions resulting in challenging mixed-integer dynamic programs. In this work, we present an efficient scheduling optimization approach that captures scheduling-relevant dynamics in a linear scale-bridging model and relies on collocation for time discretization. The resulting mixed-integer linear program (MILP) can be solved with state-of-the-art solvers. We apply the approach to a case study on building DSM. A detailed simulation model represents an office building, which allows load shifting through dynamic concrete core activation and is heated by a heat pump with minimum part-load. The DSM scheduling optimization approach reduces energy cost significantly compared to a rule-based scheduler without DSM if electricity price volatility is high. At the same time, the optimization is sufficiently fast to perform online scheduling.
Keywords: Mixed-Integer Dynamic Optimization, Demand Side Management, Mixed-Integer Linear Programming

1. Introduction

Many policies to reduce greenhouse gas emissions aim for increasing renewable electricity supply. The intermittency of renewable electricity sources increases volatility in prices. This volatility gives flexible power-intensive processes and building energy systems the opportunity to reduce costs via demand side management (DSM) (Zhang and Grossmann, 2016). Conceptually, DSM of building energy systems is similar to DSM of chemical processes: Energy supply is needed to maintain a controlled variable (the temperature) within a quality band (the occupant comfort range). The energy consumption can be shifted in time using the thermal inertia of building construction elements.

A promising DSM method is scheduling optimization that can account for transient process behavior, and on/off- decisions in the energy supply system; however, such scheduling optimization requires solving computationally challenging mixed-integer dynamic optimization problems. Scheduling or real-time optimization are decision layers that typically consider time-scales from hours to weeks and optimize set-points for the

underlying control (Daoutidis et al., 2018). Online scheduling optimization in receding horizon allows to react to changing prices and model plant mismatch, however, necessitates optimization runtimes to be in the order of minutes. Therefore, efficient problem formulations are needed. A particularly promising approach is to use scale-bridging models introduced by Baldea and co-workers (Du et al., 2015) that – in contrast to first-principle models – only account for the slow closed-loop process dynamics.
For DSM, we propose to extend the scale-bridging model concept by Du et al. (2015) to the domain of energy systems with its many discrete on/off-decisions. To this end, we change the formulation from continuous to discrete time. Thereby, we can integrate the scale-bridging dynamics in mixed-integer linear programming (MILP). We use this MILP-based approach for DSM of building energy systems. In section 2, we explain our approach for DSM scheduling optimization with a scale-bridging model. In section 3, we apply the approach to a case study on building DSM through concrete core activation to demonstrate its capabilities. Section 4 concludes the paper.

2. DSM Scheduling Optimization with Scale-Bridging Model

Operational optimization of energy systems is often approached with MILP formulations (Voll et al., 2013). For DSM, we need to represent the process dynamics. To still retain a MILP formulation, we propose to use a linear scale-bridging model of the scheduling-relevant closed-loop process dynamics (Du et al., 2015). The linear closed-loop response is enforced by an underlying control that also ensures stability. In contrast to Du et al. (2015), we formulate the scheduling optimization problem in discrete instead of continuous time, because (i) discrete time often performs better for varying energy prices (Castro et al., 2009), and (ii) linear differential algebraic equations (DAEs) discretized with collocation in discrete time lead to linear constraints (Biegler, 2010). The resulting scale-bridging model consists of linear mixed-integer DAEs:

$$\frac{d\boldsymbol{x}}{dt} = \boldsymbol{f}_{SBM}(\boldsymbol{x}, \boldsymbol{y}, \boldsymbol{z}, \boldsymbol{w}_{SP}, t) \tag{1 a}$$

$$0 = \boldsymbol{g}_{SBm}(\boldsymbol{x}, \boldsymbol{y}, \boldsymbol{z}, \boldsymbol{w}_{SP}, t) \tag{1 b}$$

with differential states $\boldsymbol{x}$, algebraic variables $\mathbf{y}$, discrete variables $\mathbf{z}$, set-points $\boldsymbol{w}_{SP}$, time t, and linear functions $\boldsymbol{f}_{SBM}, \boldsymbol{g}_{SBM}$. In the following, we describe the three main steps of our approach.

2.1. Adapt Control System to Achieve Linear Closed-Loop Response

Whereas Du et al. (2015) use input-output feedback linearization control to enforce a linear closed-loop response, we propose to place a linear set-point filter before the control. The advantage is that we can also use classical non-model-based tracking controls like PID control. The set-point filter converts a piecewise constant set-point trajectory to the desired linear closed-loop response, which can then be tracked by the underlying control. A set-point filter of order r can be modelled as a cascade of first-order filters for which the filtered set-point $w_{SP,fl,1}$ evolves depending on the current set-point w_{SP} and the filter constant $\tau_{SP,1}$:

$$\frac{dw_{sp,fl,1}}{dt} = \frac{1}{\tau_{SP}}(w_{SP} - w_{SP,fl,1}) \tag{2}$$

The resulting control loop including the set-point filter is visualized in Fig. 1. The control manipulates inputs u such that the controlled variable y_{cv}, e.g., product quality in a reactor or temperature in a building, follows the filtered set-point $w_{SP,fl,r}$. The set-points w_{SP} are

determined in scheduling optimization, where we assume $y_{cv} = w_{SP,fl,r}$, i.e., the desired linear closed-loop response is tracked sufficiently accurate. To ensure $y_{cv} = w_{SP,fl,r}$ with good accuracy, the set-point filter must be sufficiently slow such that system and control can follow. Note that a too slow set-point filter would deteriorate process performance. The filter constants are therefore tuning factors.

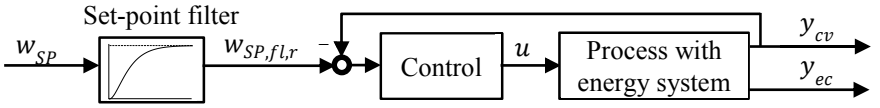

Figure 1: Control loop and set-point filter. y_{ec} denotes the resulting energy costs.

2.2. Set Up of the Scale-Bridging Model

The scale-bridging model represents the slow dynamics of the control loop in Fig. 1. Therefore, the scale-bridging model receives the set-point w_{SP} as input and has the controlled variable y_{cv} and the energy costs y_{ec} as outputs. Because $y_{cv} = w_{SP,fl,r}$ on the scheduling timescale, the set-point filter equations essentially model the dynamics of the controlled variable y_{cv}. The energy costs y_{ec} depend on the process energy demand and the efficiencies of the energy system components. For nonlinear part-load efficiencies, we use piecewise-linear approximations (Voll et al., 2013). To compute the energy demand of the process, we use a linear data-driven or gray-box model. We refer to Tsay and Baldea (2019) who review data-driven models for process systems, and Li and Wen (2014) who review gray-box models for building energy systems.

2.3. Set Up of the Scheduling Optimization Problem

Based on the scale-bridging model, we create the scheduling optimization problem by adding an objective function, performing time discretization, and adding problem constraints. The objective function minimizes the integral over the energy costs y_{ec}. For time discretization, we use three time grids: Grid 1 is given by the market and contains piece-wise constant electricity prices with a fixed time step. Grid 2 is used to discretize the discrete variables $\boldsymbol{z}$ as piece-wise constant. Grid 3 is used to discretize the continuous variables $\boldsymbol{x}, \boldsymbol{y}$ via collocation polynomials. Grids 2 and 3 are discretized finer, i.e., the number of time steps for grid 2 and 3 is a multiple of the number of time steps for grid 1. As constraints, we consider upper and lower variable bounds, problem-specific constraints, and on/off-constraints to account for the minimum part-load of energy system components. The resulting scheduling optimization problem is a MILP and can be solved with state-of-the-art solvers.

3. Case Study: Building Energy System

Flexible building energy systems can perform DSM because the thermal inertia of building construction elements allows to shift load in time. For the purpose of optimization and control, building energy systems can often be modeled sufficiently well by linear DAE models called gray-box or resistor-capacitor models (Li and Wen, 2014). For buildings operated in a market with an on-/off-peak pricing structure, Touretzky and Baldea (2016) propose to use an integrated scheduling and control architecture that avoids binary decision variables through a slot-based continuous-time reformulation. In contrast, here we consider a pricing structure with hourly changing electricity prices and thus need to consider binary decisions in every time step. To test our scheduling optimization approach, we simulate an office room with concrete core activation in detail. The virtual office has a temperature control that receives the optimized set-point trajectory from scheduling optimization. We assume that the air temperature T_{air} has to be in a comfort

range from minimum temperature $T_{min} = 20$ °C to maximum temperature $T_{max} = 22$ °C from 08:00 to 20:00 o'clock. During the night (20:00 to 08:00 o'clock), the room temperature is allowed to drop to $T_{min} = 16$ °C. For comparison, we also assess the performance of a rule-based scheduler that sets the set-point temperature equal to $T_{min} = 20$ °C during the day and equal to $T_{min} = 16$ °C during the night.

3.1. Virtual Office

To construct the detailed simulation model of a corner office room (Fig. 2) and PI temperature controllers for air and concrete core, we use the AixLib Modelica modeling library (Müller et al., 2016). The AixLib provides models of building components and parametrized controllers. The zero-dimensional corner office is surounded by two outside walls, two inside walls, a ceiling, and a concrete core. Outside walls exchange heat with the environment. We only consider half of the wall volume for inside walls and assume zero heat transfer in the middle of these walls. This assumption is reasonable if the temperature in the neighboring rooms is controlled similarly. An air-source heat pump with minimum part-load of 12.5 % (Bischi et al., 2014) heats a fluid system which transports the heat to a radiator and the concrete core. As the concrete core has a considerable thermal inertia, it offers a high DSM potential. In total, the detailed model has 122 differential states. Time-varying model inputs are: ambient temperature, room occupancy, and electricity price. We distinguish three electricity price scenarios. Scenario 1 uses historical German EPEX-spot day-ahead prices from 25th and 26th February 2019. For scenario 2, we increase the deviation between the prices and the arithmetic mean of the historical time series by a factor of two. For scenario 3, we apply a factor of three to the deviation in the historical data.

3.2. Building DSM

To apply the DSM scheduling optimization approach, we follow the three steps presented in section 2. First, we adapt the underlying control by placing second-order set-point filters before the PI-controllers. We choose second-order filters such that the transitions forwarded to the tracking control start and end smoothly. Second, for the scale-bridging model, we use the set-point filter equations (Equation (2)) as a model for the room and concrete core temperatures. The efficiency of the energy system is given by the coefficient of performance (COP) of the heat pump. Since we consider an air-source heat pump and assume that the ambient temperature is known, the COP is a predefined time-varying parameter. To compute the energy demand of the building, we derive linear differential equations for the temperatures of air, walls, radiator, ceiling, and concrete core by assuming constant heat transfer coefficients fitted to simulation data. Such a model is commonly called resistor-capacitor model (Li and Wen, 2014). The resulting scale-bridging model has only 16 differential states: the temperatures, the filtered set-points, and the integrated electricity cost of the heat pump.

For setting up the scheduling optimization problem, we introduce an objective function that minimizes the integrated electricity costs. The considered time horizon lasts 33 hours starting at 0:00 o'clock on day one and ending at 09:00 o'clock on day two. Thereby, we end in the occupancy period where the temperature has to be within the comfort range. Electricity prices vary hourly and we use four discretization elements per hour for the discrete and continuous variables. For the continuous variables, we use fourth-order collocation polynomials within the discretization elements. We add on/off-constraints describing the heat pump minimum part-load. Furthermore, we add constraints to account for the fact that we can only heat the air and the concrete core but we cannot cool them. In the following, we describe this effect for the air temperature T_{air}. If heating is required

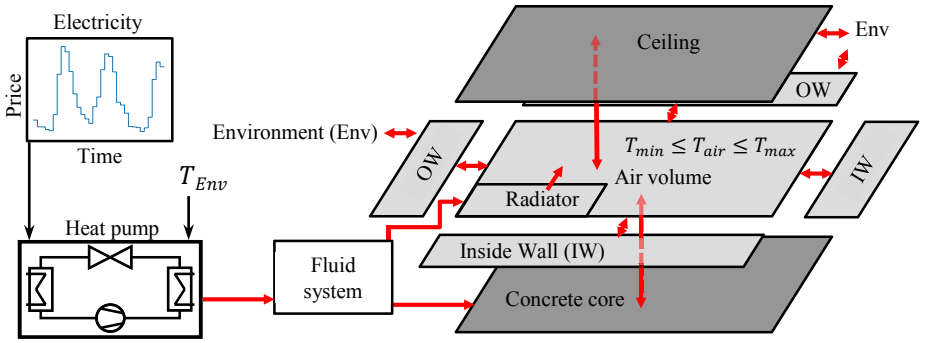

Figure 2: System considered in case study: Corner-office with concrete core and radiator heated by a heat pump; heat flows are denoted by thick red arrows (↔); OW: Outside wall

($T_{air} \leq T_{air,SP,fl,2}$), the temperature-control is *active* and regulates the heat flow to the radiator Q_{rad} such that the air temperature increases to the filtered set-point $T_{air,SP,fl,2}$. In contrast, if heating is not required ($T_{air} > T_{air,SP,fl,2}$), the temperature-control is *inactive* ($Q_{rad} = 0$). We implement these two operating regimes with a binary variable and big-M constraints. The same logic applies to the temperature-control of the concrete core. The scheduling optimization problem is solved with IBM CPLEX 12.8.0 on an Intel Core i5-8250U processor. We limit the optimization runtime to 5 minutes, which is well below the interval length of the decision variables (15 minutes).

3.3. Results

The results show that the DSM potential strongly depends on the electricity price volatility. In scenario 1 (historical prices), DSM scheduling optimization does not reduce cost compared to the rule-based scheduler. With the stronger price fluctuations, DSM scheduling optimization reduces electricity costs by 6.8 % (scenario 2) and by 20.8 % (scenario 3). Fig. 3 shows exemplarily the results for scenario 2. Our approach for DSM scheduling optimization is able to shift energy consumption to times of lower prices in

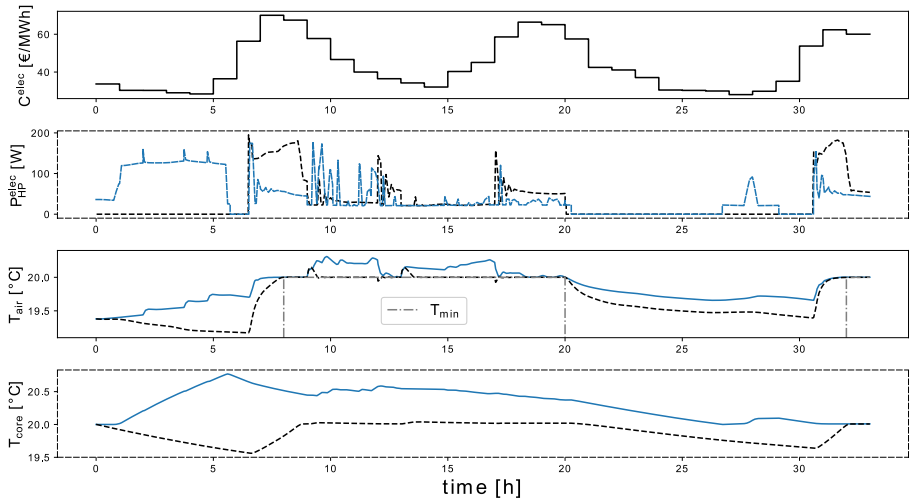

Figure 3: Results for building energy system in scenario 2 (top to bottom): electricity price C^{elec}, electric power of heat pump P_{HP}^{elec}, room temperature T_{air}, and core temperature T_{core}. Rule-based scheduler (black dashed line) and DSM scheduling optimization (blue solid line).

the morning (1:00 – 5:00 o'clock, day 1; 2:00 – 5:00 o'clock, day 2) mainly by increasing the concrete core temperature. Consequently, the electricity consumption is reduced in times of high prices (6:00 – 9:00 and 17:00 – 20:00 o'clock, day 1; 6:00 – 7:00 o'clock, day 2). Like the rule-based scheduler, the DSM scheduling optimization ensures that the air temperature is always above the minimum comfort temperature. After the maximum runtime of 5 minutes, the optimization returns a near-optimal solution with a remaining optimality gap of 3.3 %.

4. Conclusion

Scheduling optimization for demand side management (DSM) of dynamic processes is computationally challenging, as it needs to account for process dynamics and a large number of binary on/off-decisions in the energy supply system. To tackle such problems, we propose a linear scale-bridging model of the closed-loop process dynamics in discrete time combined with a linear model of the energy supply system. Thereby, we obtain a mixed-integer linear program (MILP) that can be solved efficiently with state-of-the-art solvers. Applied to a virtual office with concrete core activation, our DSM approach improves the economic performance of the building energy system compared to a rule-based scheduler, if energy price fluctuations are sufficiently large. The optimization is fast enough to allow for online scheduling.

Acknowledgements

The present contribution is supported by the Helmholtz Association under the Joint Initiative 'Energy Systems Integration'.

References

L. T. Biegler, 2010, Nonlinear programming, SIAM, Philadelphia

A. Bischi, L. Taccari, E. Martelli, E. Amaldi, G. Manzolini, P. Silvam, S. Campanari, E. Macchi, 2014, A detailed MILP optimization model for combined cooling, heat and power system operation planning, Energy, 74, 12-26

P. M. Castro, I. Harjunkoski, I. E. Grossmann, 2009, New continuous-time scheduling formulation for continuous plants under variable electricity cost, Industrial & Engineering Chemistry Research, 48, 6701-6714

P. Daoutidis, J. H. Lee, I. Harjunkoski, S. Skogestad, M. Baldea, C. Georgakis, 2018, Integrating operations and control: A perspective and roadmap for future research, Computers & Chemical Engineering, 115, 179-184

J. Du, J. Park, I. Harjunkoski, M. Baldea, 2015, A time scale-bridging approach for integrating production scheduling and process control, Computers & Chemical Engineering, 79, 59-69

X. Li, J. Wen, Review of building energy modeling for control and operation, Renewable and Sustainable Energy Reviews, 37, 517-537

D. Müller, M. Lauster, A. Constantin, M. Fuchs, P. Remmen, 2016, AixLib - An open-source Modelica library within the IEA-EBC Annex 60 Framework, Proceedings of the CESBP and BauSIM 2016, Ed. J. Grunewald, Dresden, 3-9

C. R. Touretzky, M. Baldea, A hierarchical scheduling and control strategy for thermal energy storage systems, Energy and Buildings, 110, 94-107

C. Tsay, M. Baldea, 2019, 110th Anniversary: Using data to bridge the time and length scales of process systems, Industrial & Engineering Chemistry Research, 58, 16696-16708

P. Voll, C. Klaffke, M. Hennen, A. Bardow, 2013, Automated superstructure-based synthesis and optimization of distributed energy supply systems, Energy, 50, 374–388

Q. Zhang, I. E. Grossmann, 2016, Planning and scheduling for industrial demand side management: Advances and challenges, Alternative Energy Sources and Technologies, Ed. M. Mariano, Cham: Springer International Publishing, 383-414

Sauro Pierucci, Flavio Manenti, Giulia Bozzano, Davide Manca (Eds.)
Proceedings of the 30th European Symposium on Computer Aided Process Engineering (ESCAPE30), May 24-27, 2020, Milano, Italy.
http://dx.doi.org/10.1016/B978-0-12-823377-1.50236-6

Design of a Sustainable Power-to-methanol Process: a Superstructure Approach Integrated with Heat Exchanger Network Optimization

Philipp Kenkel,[a*] Timo Wassermann,[a] Edwin Zondervan[b]

[a]*University of Bremen, Advanced Energy Systems Institute , Enrique-Schmidt-Straße 7, 28359 Bremen, Germany*
[b]*Univeristy of Bremen, Advanced Energy Systems Institute, Leobener Straße 6, 28359 Bremen, Germany*
kenkel@uni-bremen.de

Abstract

This work presents a bi-criteria superstructure optimization of a PtM (power-to-methanol) design regarding techno-economic and environmental key figures. The general modeling approach based on mass- and energy balances is applied to a case study depicting a potential plant located in the region of northern Germany Schleswig-Holstein. The selected case study demonstrates minimal net production costs of 1,346 €/t of methanol and minimal net production emissions of -2.29 t_{CO2}/t of methanol. Hence, PtM concepts are not cost competitive as compared to conventional methanol. However, utilizing renewable electricity, PtM can contribute to CO_2 abatement in the process sector.

Keywords: Superstructure optimization, power-to-methanol, CO_2 utilization

1. Introduction

To counter climate change, Germany has set out a strategy to considerably reduce its greenhouse gas emissions by 2050. A transition in the mobility-sector, as well as the process industry poses major challenges due to their inert behavior and strong dependency on fossil fuels. As long as there are no other near zero-emission alternatives for these sectors, innovative concepts for renewable production of synthetic liquid fuels and other hydrocarbons are a viable option for defossilization. One promising option is the production of methanol from renewable hydrogen and carbon dioxide via the power-to-methanol (PtM) process. Methanol is an important platform chemical as well as a potential liquid fuel and intermediate for kerosene or gasoline synthesis.
The PtM process requires 5 process steps which are 1) hydrogen production via electrolysis, 2) carbon dioxide preparation using carbon capture technologies, 4) the methanol synthesis step itself as well as 4) upgrading and 5) waste stream management [1], [2]. Each of these steps can be designed using various technological alternatives for example carbon can be captured from the ambient air or from power plant flue gases. In addition, some process steps are exothermic and others are highly endothermic. Therefore, a major challenge is the design of a cost-optimal PtM process from the given myriad of possibilities including the options to reach a suitable degree of heat recovery. It is noted however that even such PtM concepts are not emission free due to energy demand in terms of electricity and process heat as well as emissions related to required solvents and other chemicals. Ergo, the process should not only be optimized in terms of methanol costs but also in terms of life cycle CO_2 emissions, this leads to a bi-criterion optimization problem.

2. Methodology

The work at hand presents a practical way for the assessment and optimization of a PtM process design comparing different technology alternatives for techno-economic as well as environmental key figures, utilizing the concept of superstructure optimization. A superstructure is a representation of all possible combinations of technologies from raw materials up to the final products. This formulation enables the investigation of energy- and mass integration potentials, leading to a multi-energy system which could also be interpreted as an energy hub specialized on the production of liquid fuels [3], [4]. The superstructure representation is converted into a mathematical program, which can be solved using well-known software packages and optimization solvers.

2.1. Mathematical approach

The mathematical program utilizes general mass- and energy balances inspired by Galanopoulos et al. [5]. Mass balances are defined using a three-step methodology of mixing, reaction and separation by means of fixed split factor parameters (cf. Figure 1).

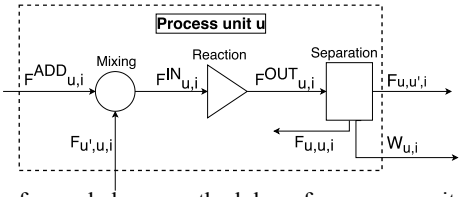

Figure 1: Representation of mass balance methodology for process unit u. The inlet flow $F^{IN}_{u,i}$ is calculated as the sum of entering streams from other units $F_{u',u,i}$ and added chemicals $F^{ADD}_{u,i}$. The outlet flow is calculated using stoichiometric or yield reactions. Unit connecting flows ($F_{u,u',i}$) are calculated from the outlet flow using predefined split parameters, while waste streams $W_{u,i}$ are determined by balance.

The energy balance for utility *Ut* is based on specific energy demands (τ_u^{Ut}) as well as specific flows (M_u^{Ut}) as shown exemplary for electricity in Eq. 1-3. Non-linearities resulting from the use of integer decision variables (Y_u) are linearized by means of Big-M constraints using upper bound parameters (α_u).

$$E_u^{EL} \leq \alpha_u \cdot Y_u \tag{1}$$

$$E_u^{EL} \leq M_u^{EL} \cdot \tau_u^{EL} + \alpha_u \cdot (1 - Y_u) \tag{2}$$

$$E_u^{EL} \geq M_u^{EL} \cdot \tau_u^{EL} - \alpha_u \cdot (1 + Y_u) \tag{3}$$

The generated mass- and energy balances are used for calculation of the equipment, utility, raw material and fixed operating costs [5]. This leads to a mixed-integer linear programming (MILP) problem, which can be solved using open source modeling software as well as open source optimization algorithms.

2.2. Objective functions

The superstructure optimization is performed independently for two different objective functions. The first one is the total annual costs (TAC) of a fixed amount of methanol (200,00 t/y). The TAC are calculated by the sum of the annualized capital costs (CAPEX) and the annualized operational costs (OPEX), using the approach of Peters et al. The OPEX arise from the usage of utilities such as electricity, raw materials like water as well as fixed costs like maintenance expenses [6]. Profits from sold by-products like oxygen (PROFITS) are subtracted from the costs (cf. Eq. (4)).

$$TAC = CAPEX + OPEX - PROFITS \tag{4}$$

The second objective represents an environmental quantity. The total annual CO_2 emissions (TAE) are calculated by means of mass- and energy balances. The CO_2 emissions ($W_{u,CO2}$) in all process units u are added to the emissions which can be assigned to the used utilities (Ut). This is done by multiplying emission factors (ζ) with the actual amount of consumed goods E_{Ut}^{tot}. Using the approach of avoided burden, CO_2 that enters the system from carbon capture ($F_{CO_2}^{IN,CC}$) as well as reference emissions for oxygen production ($F_{O_2}^{PROD}$) are subtracted (cf. Eq. (5)) [7].

$$TAE = \sum_{u} W_{u,CO_2} + \sum_{Ut} \zeta_{Ut} \cdot E_{Ut}^{tot} - \zeta_{O_2} \cdot F_{O_2}^{PROD} - F_{CO_2}^{IN,CC} \tag{5}$$

3. Case study

The generic formulation offers the possibility to investigate different technologies and process designs based on the implemented data. In this work a power-to-methanol process design is examined for a specific location in northern Germany, Schleswig-Holstein. This special location leads to unique carbon sources such as the flue gases of a local oil refinery as well as CO_2 from a nearby cement factory. In addition, the choice of location defines the studied sources of electricity.

3.1. Investigated technologies

The case study at hand investigates the production of methanol from electricity and captured CO_2. Electricity is used to produce hydrogen and oxygen (which can be sold as by-product). Five different water electrolysis technologies are considered, namely ambient / high pressure proton-exchange membrane electrolysis (LP / HP-PEMEL), ambient / high pressure alkaline electrolysis (LP / HP-AEL) and high temperature solid oxide electrolysis (SOEL). CO_2 can be either captured from ambient air using low temperature direct air capture (LT-DAC), or it can be obtained from point sources such as the refinery power plant flue gas using monoethanolamine in absorption-based carbon capture (MEA-CC) as well as from a nearby cement factory using oxyfuel combustion with subsequent CO_2 purification technology (CEMENT-OXY). The raw materials H_2 and CO_2 are pressurized to 70 bar and converted to methanol via direct hydrogenation at 250 °C (MeOH SYN). Arising off gas, containing unreacted raw materials as well as carbon monoxide (CO) and methanol (MeOH), is separated using a series of flash separators combined with compressors and intercoolers (cumulated in FLASH) and either burned to produce heat in form of steam (FURNACE) or electricity using a combined power circle (GAS TUR). The crude methanol is purified in a last step using a distillation column (DC 1). Figure 2 displays the superstructure representation of the given case study.

3.1.1. Main assumptions

Two specific cases are considered in this study. The main difference is the source of the applied electricity. In both cases, all prior mentioned technologies are investigated. However, CASE 1 uses electricity from the German energy grid, while CASE 2 investigates the use of a direct power supply by offshore wind energy which could be especially interesting for the location of northern Germany, where a lot of wind energy is produced resulting in high amounts of surplus energy.

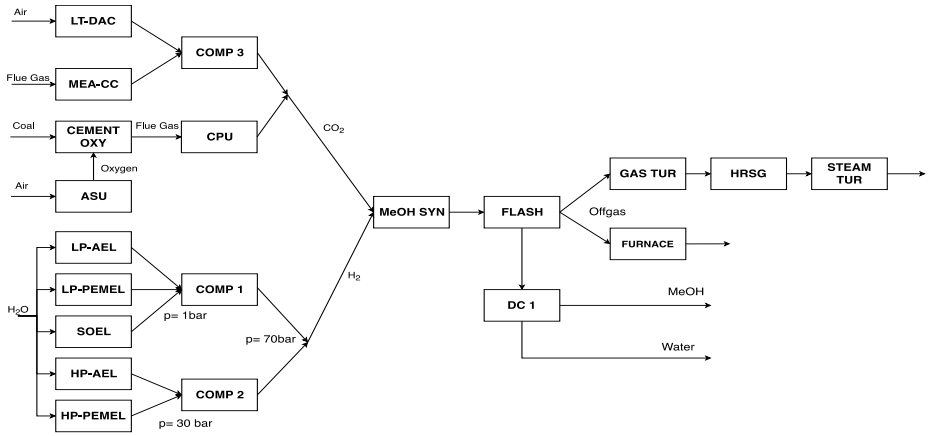

Figure 2: Case study superstructure representation with technologies: LT-DAC: Low temperature direct air capture, MEA-CC: Amine based carbon capture from refinery power plant flue gases, CEM OXY: Cement factory oxyfuel process, ASU: Air separation unit, CPU: CO_2 purification unit, COMP 1-3: Compression for hydrogen and CO_2, LP / HP-AEL: Ambient pressure / High pressure alkaline electrolysis, LP / HP-PEMEL: Ambient pressure / High pressure proton exchange membrane electrolysis, SOEL: Solid oxide electrolysis, MeOH SYN: Methanol synthesis reactor, FLASH: Flash unit, DC 1: Distillation column, GAS TUR: Gas turbine, HSRG: Heat recovery and steam generation unit, STEAM TUR: Steam turbine, FURNACE: Furnace for heat generation.

The assumptions of CASE 1 and 2 lead to different full load hours (FLH) of the plant as well as different emission factors for the provided electricity [8]. Other parameters such as utility costs, yearly methanol production or oxygen selling price are constant. A list of the most important assumptions for both cases is given in Table 1.

Table 1: Main assumptions for the different cases: CASE 1: Electricity purchase from the German electricity grid, CASE 2: Electricity purchase from direct supply of offshore wind energy [8]–[10]

Parameter	CASE 1	CASE 2
Full load hours per year (h/y)	8,260	4,500
CO_2-eq. of electricity (t/MWh)	0.628	0.015
Electricity price (€/MWh)	87.7	
External heat price (€/MWh)	55	
Cooling water costs (€/MWh)	0.22	
Yearly methanol production (t/y)	200,000	
Oxygen selling price (€/t)	26.3	
Interest rate (%)	5	
CO_2-eq. of heat (t/MWh)	0.294	
CO_2-eq. of reference O_2 production (t/t)	0.695	
CO_2-eq. of reference MeOH production (t/t)	0.525	
Cost of reference MeOH Production (€/t)	333	

4. Results and discussion

4.1. Mathematical programming results

Each case of the presented study is an optimization problem with 11,763 constraints, 10,876 variables of which 2,082 are binary and 8,794 are continuous. These MILP problems are implemented in python PYOMO version 5.6.6 and solved within 32 seconds on a MacBook Pro with a 2 GHz Intel Core i5 processor using the open source GNU linear Programming Kit (GLPK) independently for both objective functions. This leads to four optimization calculations and four main results.

4.2. Optimization results

The results of the optimization for CASE 1 and 2 for either the techno-economic objective function (a) or the environmental objective function (b) are shown in Table 2.

A techno-economic optimized design with electricity from the German grid (CASE 1a) with 8,260 FLH per year uses an ambient pressure alkaline electrolyser with subsequent compression for hydrogen supply. CO_2 is captured at the cement factory using oxyfuel combustion, while arising off gas is combusted in order to produce electricity in a combined power cycle. Relating the TAC and TAE of this design to the overall production of 200,000 t/y of methanol yields net production costs (NPC) of 1,346 €/t and net production emissions (NPE) of 4.67 t_{CO2}/t.

When optimized for minimal CO_2-emissions (CASE 1b), the alkaline electrolyser is replaced by a solid oxide electrolyser, resulting in higher NPC of 1,642 €/t but lower NPE of 1.19 t_{CO2}/t. Both cases are neither cost competitive nor environmentally beneficial as compared to the reference methanol produced from natural gas. This is due to high specific emission factors of the electricity from the German electricity grid as well as high electricity prices and installation costs for electrolyser technologies. Due to higher emissions compared to the reference process a calculation of CO_2 abatement costs is not reasonable for CASE 1a and 1b.

Table 2: Main results from optimization: CASE 1a/b: Electricity from the German electricity grid optimized for TAC/TAE, CASE 2a/b: Electricity from direct offshore wind energy supply optimized for TAC/TAE

Parameter	Case 1a	Case 1b	Case 2a	Case 2b
Total annualized costs (TAC) in M€/y	269.3	314.8	309.4	328.5
Total annualized emissions (TAE) in Mt_{CO2}/y	0.934	0.383	-0.389	-0.459
Net production costs (NPC) in €/t	1,346	1,642	1,547	1,574
Net production emissions (NPE) in t_{CO2}/t	4.67	1.19	-1.95	-2.29
CO_2 abatement costs (CAC) in €/t_{CO2}	-	-	490	440

Switching the electricity supply from grid electricity to direct power supply from an offshore wind farm shows a different picture. A cost optimal design (CASE 2a) utilizes CO_2 directly captured at the refinery, H_2 produced from ambient pressure alkaline electrolysis as well as off gas combustion for electricity production purposes. This design leads to NPC of 1,547 €/t of methanol with NPE of -1.95 t_{CO2}/t. If optimized for minimal emissions (CASE 2b), CO_2 is captured again from the cement factory while the remaining design is constant. This leads to a marginally higher NPC of 1,574 €/t but a lower NPE of -2.29 t_{CO2}/t. Using reference costs and emissions for conventional methanol the CO_2 abatement costs (CAC) are 490 €/t_{CO2} and 440 €/t_{CO2} for case 2a and 2b, respectively. It is apparent that a PtM process shows possibilities to reduce the greenhouse gas emissions only if renewable electricity is applied. However, in the case of northern Germany the overall renewable PtM process is not cost competitive related to conventional methanol production.

4.3. Sensitivity Analysis:

Due to the large influence of the energy supply to the costs and environmental impact a sensitivity analysis was performed varying the costs of external heat and external electricity. Figure 2 shows the dependency of the NPC from the external heat costs. The effect on the NPC is quite weak; resulting in a cost decrease of only around 5 % even if heat is free of charge. However, the effect of the electricity costs is much higher (cf. Figure 4). NPC drop to around 550 €/t if wind energy is free of charge. This indicates, that with cost reductions in offshore wind energy production as well as electrolysis combined with rising CO_2 taxes a renewable PtM concept could be cost efficient.

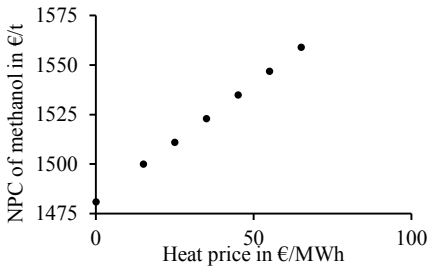

Figure 3: Sensitivity analysis for varying heat prices for electricity price of 87.7 €/MWh and 4500 FLH

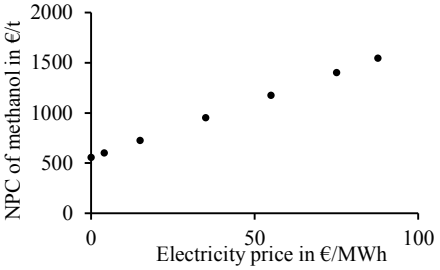

Figure 4: Sensitivity analysis for varying electricity prices for heat price of 55 €/MWh and 4500 FLH

5. Conclusion

A superstructure model was developed and tested on a PtM process located in northern Germany, Schleswig-Holstein using either electricity from the German electricity grid or from direct supply of offshore wind energy. The optimization indicates, that only PtM concepts utilizing renewable electricity are environmental beneficial compared to conventional methanol resulting in net production emissions of -1.95 t_{CO2}/t (conv. 0.525 t_{CO2}/t). This however comes at a price of higher net production costs of 1,547 €/t of methanol compared to conventional 333 €/t of methanol. The performed sensitivity analysis demonstrates a large influence of the electricity price on the net production costs with minimal costs of around 550 €/t if electricity is free of charge. This suggests a potential business model for the utilization of surplus energy if CO_2-certificates become more expensive.

Funding

Funding of this research by the German Federal Ministry of Economic Affairs and Energy within the KEROSyN100 project (funding code 03EIV051A) is gratefully acknowledged.

References

[1] D. Bongartz *et al.*, "Comparison of light-duty transportation fuels produced from renewable hydrogen and green carbon dioxide," *Appl. Energy*, vol. 231, no. May, pp. 757–767, 2018.

[2] M. Martín and I. E. Grossmann, *Enhanced production of methanol from switchgrass : CO 2 to methanol*, vol. 38. Elsevier Masson SAS, 2016.

[3] M. Mohammadi, Y. Noorollahi, and B. Mohammadi-ivatloo, "Energy hub : From a model to a concept – A review," vol. 80, no. July, pp. 1512–1527, 2017.

[4] A. Quaglia, C. L. Gargalo, S. Chairakwongsa, G. Sin, and R. Gani, "Systematic network synthesis and design : Problem formulation , superstructure generation , data management and solution," *Comput. Chem. Eng.*, vol. 72, pp. 68–86, 2015.

[5] C. Galanopoulos, P. Kenkel, and E. Zondervan, "Superstructure optimization of an integrated algae biorefinery," vol. 130, 2019.

[6] M. S. Peters, K. D. Timmerhaus, and R. E. West, *Plant Design and Economics for Chemical Engineers*, Fifth Edit. New York: McGraw-Hill, 2003.

[7] N. Von Der Assen, J. Jung, and A. Bardow, "Life-cycle assessment of carbon dioxide capture and utilization: Avoiding the pitfalls," *Energy Environ. Sci.*, 2013.

[8] C. Kost, T. Schlegl, and F. Ise, "Stromgestehungskosten Erneuerbare Energien," 2018.

[9] F. G. Albrecht, D. H. König, N. Baucks, and R. Dietrich, "A standardized methodology for the techno-economic evaluation of alternative fuels – A case study," *Fuel*, vol. 194, pp. 511–526, 2017.

[10] G. Wernet, C. Bauer, B. Steubing, J. Reinhard, E. Moreno-ruiz, and B. Weidema, "The ecoinvent database version 3 (part I): overview and methodology," *Int. J. Life Cycle Assess.*, vol. 3, pp. 1218–1230, 2016.

Sauro Pierucci, Flavio Manenti, Giulia Bozzano, Davide Manca (Eds.)
Proceedings of the 30th European Symposium on Computer Aided Process Engineering
(ESCAPE30), May 24-27, 2020, Milano, Italy.
http://dx.doi.org/10.1016/B978-0-12-823377-1.50237-8

Optimization of Retrofit and Cleaning Schedules for Heat Exchanger Networks Subject to Fouling

Federico Lozano Santamaria, Edward Honein, Sandro Macchietto

Department of Chemical Engineering, Imperial College London South Kensington Campus, London SW7 2AZ, UK

Abstract

Retrofit of heat exchanger networks (HEN) is commonly done to increase their efficiency or respond to changing operational needs. It involves modifying the structure of the network and/or the design of individual units. Decisions are usually based on simplified, steady state models, ignoring performance decay due to fouling, the system dynamics, and possible mitigation actions during operation. However detailed dynamic simulations show all these aspects are important. Here, a mathematical formulation and solution are presented for the optimal retrofit of HEN under fouling that consider realistic exchanger models, fouling dynamics, and cleaning scheduling at the same time. A case study for a refinery preheat train demonstrates that simultaneous optimization of retrofit and cleaning schedules significantly reduces operating cost and capital investment.
Keywords: heat exchanger networks, energy recovery, fouling, optimal retrofit, optimal cleaning scheduling.

1. Introduction

Heat exchanger networks (HEN) are extensively used to recover energy. Because of operational or production changes, or inadequate performance, they are often retrofitted to increase energy recovery or to reach a different operating target. Retrofit options include: i) changing the configuration of the network (i.e. connectivity among existing units), ii) introducing new units in key locations of the network, or iii) modifying the heat transfer area or flow pattern of existing units (e.g. by changing the number of tubes, introducing heat transfer enhancement technology). These are capital investment decisions in a large complex system with many feasible alternatives. Extensive research using Pinch analysis and mathematical optimization has been done to address the retrofit and the related HEN synthesis problems (Bagajewicz et. al 2013; Sreepathi et. al 2014). Most approaches assume that the HEN operates at steady state and use simple exchanger models. However, in many cases (e.g. refining and food applications) fouling, a dynamic process, significantly affects performance, reducing heat transfer and increasing operational cost over time. Using detailed dynamic models in simulation, it has been shown (Coletti et. al 2011) that ignoring fouling when deciding on retrofit alternatives for the network structure may well lead to wrong choices or benefits substantially smaller than expected. In other studies the problem of area retrofit or including inserts has been addressed considering fouling (Wang and Smith 2013; Pan et. al 2013), but they ignore any fouling mitigation action, their cost, and how they affect the retrofit alternatives.

The optimal operational strategies to mitigate fouling (e.g. periodic cleanings, flow distribution control) are directly related to the HEN configuration after retrofitting. Conversely, the best retrofit alternative depends on the future fouling mitigation actions. Although these two problems are intimately connected, they have typically been assumed

to be independent and considered separately. The optimal retrofit problem has been studied using pinch analysis or mathematical programming, mainly considering steady sate conditions (Bagajewicz et. al 2013). Georgiadis et al.,1998 addressed the optimal design of HEN subject to fouling using detailed dynamic models, but not their retrofit. For an existing HEN, the simultaneous operations optimization of cleaning schedules and flow control with detailed dynamic exchanger models was considered (Lozano Santamaria and Macchietto 2018). In principle, optimal operation and retrofit can be considered together in a MINLP formulation. However, size, combinatorial nature, and strong interactions and trade-offs between operational and retrofit decisions, make finding a suitable formulation and solution rather challenging.

This work presents an integrated formulation and efficient solution of the optimal retrofit and cleaning scheduling problems, with application to HEN used in refining applications. Section 2 presents the models and formulation, Section 3 introduces a realistic case study, Section 4 discusses results and benefits, and Section 5 summarizes the main conclusions.

2. Heat exchanger and network models for retrofit

The main application considered here is the retrofit of the preheat train of a refinery. The problem formulation is an extension of previous work (Lozano Santamaria and Macchietto 2018) dealing with the optimal cleaning scheduling and flow control problems for an *existing* HEN. The complete formulation is not presented because of space limitation, however the new elements regarding optimal retrofit are described. In that case, all exchangers and the network structure are fully defined. The network is represented as a directed multigraph where the nodes are the exchangers, mixers, splitters, sources and sinks. The exchangers, of shell and tube type, are modelled using an axially lumped P-NTU representation, but a radial temperature distribution is included to capture the effect of the various thermal resistances, including the (time-varying) deposit layer. The radial distribution also determines the changes in pressure drop due to deposition. The time representation is key to consider the process dynamics, while reducing the number of binary time dependent decisions. A continuous time representation with variable length periods is employed. The reader is referred to (Lozano Santamaria and Macchietto 2018; Lozano Santamaria and Macchietto 2019) for details of formulation, and numerical solution aspects, respectively.

The above formulation is used as a basis for defining the optimal retrofit and fouling mitigation problem. The additional retrofit decisions considered are: i) the addition of new heat exchangers of specified geometry (and related connecting streams) in specified network locations (binary variables $y_{h,i} \in \{0,1\} \forall i \in HEX_R$), and ii) the percent increase or decrease of heat transfer area (here limited to +/-50%) in selected existing units, for example by increasing the number of tubes (continuous variables $x_{a,i} \in [0.5,1.5] \forall i \in HEX_R$). HEX_R is the set of heat exchangers considered as retrofit alternatives to include/remove or modify, and is a subset of all the exchangers in the network (set HEX). All exchangers (including the retrofit options) are thus included in the HEN. The retrofit decisions regarding the existence of exchangers are modelled using the variables $y_{p,i} \in \{0,1\} \forall i \in HEX, p \in Periods$ associated with the cleanings in the cleaning scheduling formulation, where index p is related to the periods used in the time discretization. That is, when an exchanger does not exist, it is modelled as being in cleaning mode at all times. To include retrofit decisions in the cleaning scheduling problem, Eq. 1 - Eq. 6 are added as constraints to the original problem formulation. Eq. 1 defines the retrofitted heat transfer area, which is used in the heat duty constraints, and in the calculation of the mass flux in the exchanger tube-side. Eq. 2 - Eq. 6 link the cleaning constraints of the original

formulation with the retrofit decisions. Eq. 2 states that if a unit does not exist, it is always being cleaned. Eq. 3 is a constraint to avoid consecutive ineffective cleanings modified according to the retrofit state of the unit. Eq. 4 and Eq. 5 are the lower and upper bounds for z_p, a binary variable representing whether one or more exchangers are being cleaned in a period $p \in Periods$. This binary variable is used to define the cleaning time and the bounds in the length of the periods when there are no cleanings It was modified relative to the original formulation to enable a retrofit alternative to be modelled as a cleaning. Finally, Eq. 6 is the modification of the maximum number of cleanings per unit allowed over the time horizon.

$$A_i = \pi d_i L N_T(x_{a,i}), \qquad \forall i \in HEX_R \qquad \text{Eq. 1}$$

$$1 - y_{h,i} \le y_{p,i}, \qquad \forall p \in Periods, i \in HEX_R \qquad \text{Eq. 2}$$

$$y_{p+1,i} \le 1 - y_{p,i} + 1 - y_{h,i}, \qquad \forall p \in Periods \backslash \{N_P\}, i \in HEX_R \qquad \text{Eq. 3}$$

$$y_{p,i} - (1 - y_{h,i}) \le z_p, \qquad \forall p \in Periods, i \in HEX \qquad \text{Eq. 4}$$

$$z_p \le \sum_{i \in HEX} \left(y_{p,i} - (1 - y_{h,i})\right), \qquad \forall p \in Periods \qquad \text{Eq. 5}$$

$$\sum_{p \in Periods} y_{p,i} \le N_{cl}^{max} y_{h,i} + N_P(1 - y_{h,i}), \qquad \forall i \in HEX \qquad \text{Eq. 6}$$

This set of new constraints is included in the original optimal cleaning scheduling and flow distribution problem so that retrofit decisions are simultaneously considered. For the retrofit alternatives regarding including or removing units of the network, the HEN graph represents a superstructure with more alternatives and combinations than those feasible. Some of the exchangers will never be in service at the final optimal solution of the problem. As in the original cleaning scheduling formulation, units out of service or being cleaned, and the non-existing ones are ignored using bypasses around them on both the tube and shell sides. The bypass flows are decision variables constrained by the binary variables defining the cleanings and the unit retrofit.

The objective function (Eq. 7) is modified from Coletti and Macchietto (2011) to include in the total cost both operating costs (for energy (P_E), cleaning (P_{cl}), and carbon emitted (P_{co})) and the capital cost of the retrofit alternatives. The cleaning cost is subject to the existence of the exchanger. The capital cost of the exchangers (P_{HEX}) is assumed to be fixed for new retrofit units (their area is known) and proportional to the increase in area for those units subject to a heat transfer area retrofit.

$$\min J = \int_0^{t_f} \left[P_E Q_f + P_{co} m_{co} Q_f\right] dt + \sum_{i \in HEX} \sum_{p \in Period} P_{cl}(y_{p,i} - 1 + y_{h,i}) + \sum_{i \in HEX_R} P_{HEX}\, y_{h,i} + \sum_{i \in HEX} P_{HEX}\,(x_{a,i} - 1) \qquad \text{Eq.7}$$

The problem thus defined for the simultaneous HEN retrofit, cleaning scheduling, and flow control is a large scale MINLP, which is combinatorial in nature due to the many possible cleaning sequences and network structures. For a given HEN, the cleaning scheduling problem was solved efficiently and quickly using a reformulation via complementarity constraints (Santamaria and Macchietto 2019). After relaxing the binary variables and imposing complementarity, it is solved sequentially using a regularized ϵ approach that converges to the solution of the original problem. The same solution strategy is used here for the combined retrofit and cleaning scheduling problem because it inherits the same structure from the previous formulation. As the modified constraints

are linear, and the number of new retrofit variables is much smaller than the cleaning variables, the algorithm is directly applicable without compromising its performance.

3. Case study

The case study, adapted from Coletti et al., (2011), considers the hot end of a preheat train in a small real refinery. Figure 1 shows the superstructure of the preheat train network including the retrofit alternatives. The original network (base case, C1) includes exchangers HEX1 to HEX7, the desalter and the furnace. Three new network structures are explored by possibly including a new exchanger in one of three different locations (exchangers with diagonal grey pattern). These are the same structures considered by simulation in Coletti et. al., (2011). HEX1, HEX2 and HEX3 do not exhibit fouling due to their low operating temperature, the desalter has a temperature drop of 4.5°C, and all other exchangers follow a deposition dynamics characterized by the Ebert-Panchal model. Note that this is a dynamic model where fouling depends on operating conditions, and all decisions involved consider the effect of time on the network performance.

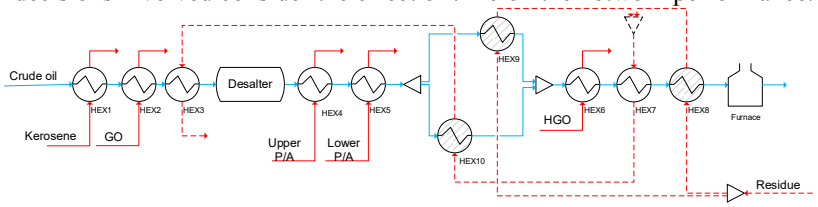

Figure 1. Network superstructure for the optimal retrofit case study

The main retrofit options considered are the inclusion of one of the exchangers HEX8, HEX9, or HEX10 (all with the same specifications) in the positions noted in Figure. 1, and a +/-50% change of the heat transfer area in all units. If the heat transfer area is decreased, there no additional capital cost. The two retrofit decisions are considered both separately and simultaneously in two scenarios. In all cases the decay in the heat transfer due to fouling, and the possible mitigation actions (cleanings) are accounted for. A time horizon of 600 days is considered, and the total capital cost of the retrofit alternatives is included in the objective function. The time horizon is discretized using 20 periods of variable length, and each period has 1 finite element and 3 Radau collocation points. It is expected that including an additional exchanger will increase the overall heat recovery, but there is a complex trade-off on the overall benefit because of fouling in the new unit, impact on fouling of other units, cost of cleanings, and extra capital cost.

The following retrofit scenarios are considered: i) retrofit of units, with and without scheduling of cleanings over the given horizon, and ii) retrofit of units and their heat transfer area, with and without scheduling of cleanings over the given horizon. These scenarios cover all combinations of decisions. The goal is to demonstrate the importance of considering retrofit and fouling mitigation decisions simultaneously, and that the dynamic formulation presented here can cope efficiently with it.

4. Results and analysis

Figure 2 and Figure 3 show the furnace duty profiles– the additional energy provided by the furnace – for the optimal retrofit, without and with cleanings, respectively. In both cases, the optimal network configuration is the one that includes HEX10. The figures also compare the optimal retrofit alternatives against the base case HEN configuration (C1). In all scenarios the energy consumed in the furnace is reduced significantly over all the operation, which represents significant economic savings. Including the retrofit options

to increase the heat transfer area of the exchangers leads to an even better performance of the network, reducing energy consumption further. The total operating cost for the base case, $ 5.04 MM, is reduced to $ 4.54 MM when HEX10 is introduced, and to $ 4.14 MM when area retrofit options are also included. The capital cost of these two alternatives are $ 0.17 MM and $ 0.43 MM, respectively, which for the time horizon considered still represent a more profitable operation than the base case.

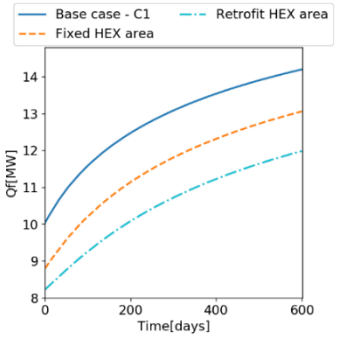

Figure 2. Furnace duty for Case1a - optimal retrofit options without cleanings

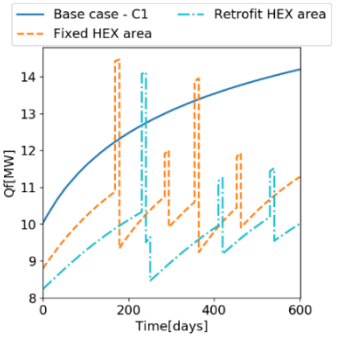

Figure 3. Furnace duty for Case1b - optimal retrofit options with cleanings

Introducing cleanings to mitigate fouling simultaneously with the network retrofit does not change the optimal structure of the network, but provides larger economic savings. With cleanings, selected units can recover their efficiency, hence reduce the overall energy requirements of the furnace. It is observed in Figure 3 that during cleanings the furnace duty increases significantly (as one or more units are out of service), but then it decreases for a long period thereafter. When cleanings are optimized together with retrofit alternatives, the operating cost is reduced to $ 4.26 MM for the optimal unit allocation, and to $ 3.92 MM when area retrofit is also included. These costs include the cost of the cleanings and in both cases the capital cost is much lower than the operating cost ($ 0.17 MM and $ 0.42 MM, respectively).

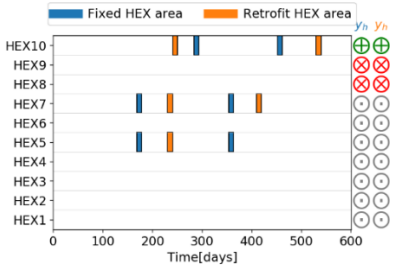

Figure 4. Optimal cleaning schedule for simultaneous cleaning and retrofit.

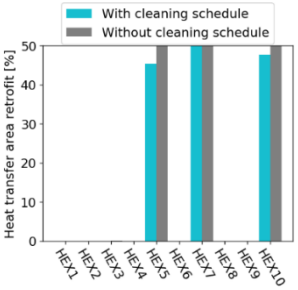

Figure 5. Optimal retrofit of heat transfer area

In this case study, optimizing cleanings together with the retrofits does not change the optimal structure of the network, but affects the optimal area retrofit decisions. Also, the optimal area retrofit affects the cleaning schedule of the units. Clearly, these two problems are strongly related and should not be decoupled to achieve the best possible operation and configuration of the heat exchanger network. Figure 4 shows the optimal cleaning schedule when both schedule and retrofit are optimized, with and without area retrofit. In both cases, only exchanges 5, 7, and 10 (new unit) are cleaned over the 600 days of operation. These exchangers have a larger duty and higher fouling rate than the others, because of the high temperature of the residue stream. When the heat transfer area of the

units is modified, the total number of cleanings is reduced from 6 to 5, and most of the cleanings are moved to later times, indicating that they can operate for longer between cleanings. Finally, the interaction between cleaning schedule and area retrofit is observed in Figure 5 that shows the optimal percent increase of the heat transfer area of all exchangers. The area of old exchangers 5, 7, and new exchanger 10 (the same units involved in the cleanings) is modified. The area of these units is increased by the maximum allowed 50% in the case without cleanings, but a lower increase is observed when cleanings are also optimized, i.e. smaller, and cheaper, modifications are required.

5. Conclusions

The optimization formulation presented allows to optimally retrofit heat exchanger networks, taking into account detailed models, fouling dynamics, cleaning of the units, the complex interactions caused at network level by both fouling, cleanings, and retrofit alternatives. The formulation, an extension of the optimal cleaning scheduling problem, considers network retrofit alternatives and area retrofit of individual units simultaneously with fouling mitigation strategies. The extension requires only few additional integer variables and constraints, and is therefore solved efficiently with the methods developed earlier for optimizing HEN operation and fouling mitigation. A realistic case study shows the ability of the formulation to handle problems of industrially relevant size, and that it can efficiently integrate retrofit and fouling mitigation decisions. It was demonstrated that such integrated solution allows to reduce the total cost of HEN operation. Future work will investigate the applicability of the formulation to larger networks with more retrofit alternatives and parallel branches, and a further extension to include optimal flow distribution in the formulation.

References

Bagajewicz, M., G. Valtinson, and D. Q. Nguyen Thanh. 2013. “Retrofit of Crude Units Preheating Trains: Mathematical Programming versus Pinch Technology.” *Industrial & Engineering Chemistry Research* 52 (42): 14913–26.

Coletti, F, and Macchietto, S. 2011. “Refinery Pre-Heat Train Network Simulation Undergoing Fouling: Assessment of Energy Efficiency and Carbon Emissions.” *Heat Transfer Engineering* 32 (3–4): 228–36.

Coletti, F., Macchietto, S, and G. T. Polley. 2011. “Effects of Fouling on Performance of Retrofitted Heat Exchanger Networks: A Thermo-Hydraulic Based Analysis.” *Computers & Chemical Engineering* 35 (5): 907–17.

Georgiadis, M. C, G. E Rotstein, and Macchietto, S. 1998. “Optimal Design and Operation of Heat Exchangers under Milk Fouling.” *AIChE Journal* 44 (9): 2099–2111.

Lozano Santamaria, F., and Macchietto, S. 2018. “Integration of Optimal Cleaning Scheduling and Control of Heat Exchanger Networks Undergoing Fouling: Model and Formulation.” *Industrial & Engineering Chemistry Research* 57 (38): 12842–60.

Lozano Santamaria, F., and Macchietto, S. 2019. “Integration of Optimal Cleaning Scheduling and Control of Heat Exchanger Networks under Fouling: MPCC Solution.” *Computers & Chemical Engineering* 126 (July): 128–46.

Pan, M., I. Bulatov, and R. Smith. 2013. “Exploiting Tube Inserts to Intensify Heat Transfer for the Retrofit of Heat Exchanger Networks Considering Fouling Mitigation.” *Industrial & Engineering Chemistry Research* 52 (8): 2925–43.

Sreepathi, B. K., and G P Rangaiah. 2014. “Review of Heat Exchanger Network Retrofitting Methodologies and Their Applications.” *Industrial & Engineering Chemistry Research* 53 (28): 11205–20.

Wang, Y., and R. Smith. 2013. “Retrofit of a Heat-Exchanger Network by Considering Heat-Transfer Enhancement and Fouling.” *Industrial & Engineering Chemistry Research* 52 (25): 8527–37.

Sauro Pierucci, Flavio Manenti, Giulia Bozzano, Davide Manca (Eds.)
Proceedings of the 30th European Symposium on Computer Aided Process Engineering (ESCAPE30), May 24-27, 2020, Milano, Italy.
http://dx.doi.org/10.1016/B978-0-12-823377-1.50238-X

Optimal Design of Integrated Urban Energy System Under Uncertainty and Sustainability Requirements

Zhihao Chen,[a,b] Styliani Avraamidou,[b] Pei Liu,[a*] Efstratios N. Pistikopoulos[b,c]

[a]*State Key Lab of Power Systems, Department of Energy and Power Engineering, Tsinghua University, Beijing, 100084, China*
[b]*Texas A&M Energy Institute, Texas A&M University, College Station, TX 77843, USA*
[c]*Artie McFerrin Department of Chemical Engineering, Texas A&M University, College Station, TX 77843, USA*
liu_pei@tsinghua.edu.cn

Abstract

Urban energy consumption and consequent environmental impacts such as the massive amount of energy-related greenhouse gas emission and water consumption are posing significant pressure on sustainable development. Energy systems of the future should satisfy the ever-increasing energy demand and reduce negative externalities. This paper proposes an integrated urban energy system modelling and optimisation approach. Based on the main features of urban energy systems, the model is established as a mixed-integer linear program. Multi-objective optimisation is used to reveal the trade-offs among economic and environmental concerns, and stochastic programming is adopted to treat the uncertainties rooted in energy supply. A new urban area is used as a case study to illustrate the functions of the model and to provide insights for energy system design.

Keywords: Integrated urban energy system, energy system design, carbon emission mitigation, energy-water nexus, stochastic programming.

1. Introduction

Energy underpins modern society. Large scale energy use in urban areas leads to several environmental problems. Cities are responsible for the majority of global energy-related greenhouse gas emissions, and water consumption of urban energy supply exacerbate water stress. These issues are expected to become more severe since the urbanisation trend is expected to continue. Therefore, the optimal design of urban energy systems is needed for the realisation of affordable and sustainable energy supply.

Recently, we have witnessed an increased research interest in energy system design. The energy hub (EH) concept has been widely used in multi-generation systems (Mohammadi et al., 2017). Superstructure-based modelling has become a general approach in process system design; combined with the EH concept, it provides a systematic way to consider all possible energy flow pathways, technology options, network configurations, and operation modes (Demirhan et al., 2019). Many planning models are either at the macroscopic scale (Guo et al., 2017) or microscopic scale (Zhou et al., 2013), but rarely at an urban scale. Growing attention has been paid to the externalities of energy supply, such as greenhouse gas emissions (Liu et al., 2010) and energy-water nexus (Allen et al., 2019). Also, many researchers have considered the stochastic nature of energy systems (Mavromatidis et al., 2018). However, very few models at the urban scale cover all the aspects above and incorporate the main features of urban systems in a holistic framework.

This work aims to build an integrated urban energy system modelling framework that is suitable for optimal system design. The core model is introduced in Section 2. Section 3 illustrates the main functions of the model through a case study, in which the uncertainty and sustainability requirements are considered. Conclusions are drawn in the final part.

2. Methodology

2.1. Superstructure representation

Urban energy systems should have commonalities of general energy systems and particularities of urban systems. In the past, different energy systems were designed separately and operated individually. However, urban energy systems are multi-energy systems that encompass a variety of energy sources, needs, and conversion paths. While centralised generation still dominates the energy supply, distributed generation is playing a more critical role. Energy systems of the future should utilise the strengths of both types of production. Planning decisions, usually made on an annual or longer basis, should be able to meet the energy demand in each time slot under real operating constraints, such as capacity range and ramping rate limit.

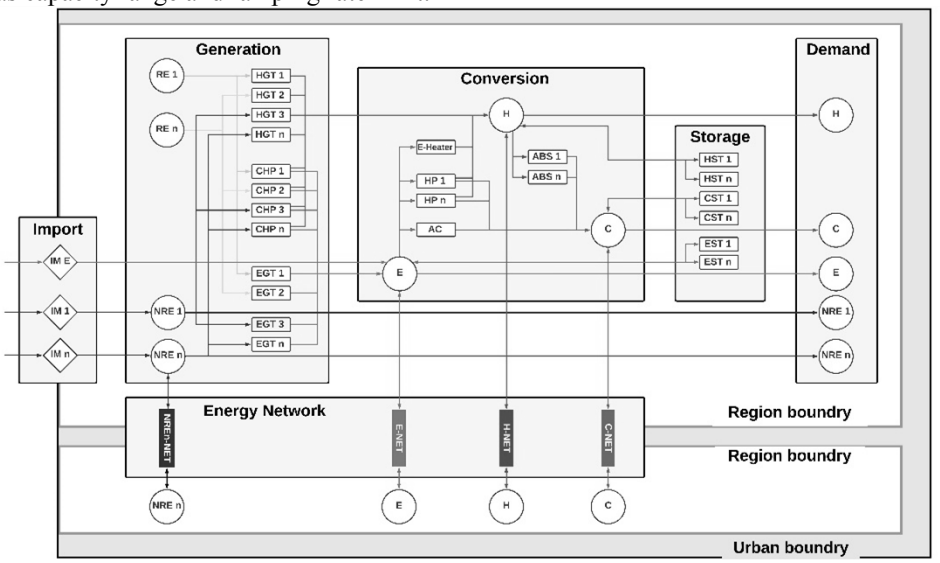

Figure 1. Structure of integrated urban energy systems

Figure 1 illustrates the superstructure representation of the integrated urban energy systems. We use the adjective 'integrated' to highlight the interaction of multiple energy forms, the synthesis of centralised and distributed generation, and the coordination of design and operation phases. The two white blocks represent two different regions inside the city, each of which can be considered as an energy hub. Energy can be imported from outside the city, collected on-site, or transmitted and distributed between regions through energy networks. Inside each energy hub, there are energy generation, conversion, and storage sectors. Different varieties of primary energy (both renewable and non-renewable) are transformed into secondary energy (e.g. electricity, heat, and cooling) in the generation sector. In the conversion sector, secondary energy can be converted from one form into other forms. Storage facilities help to store the excess energy at a time for later use. These three sectors, as well as energy import and energy networks, work together to meet the final energy demand in each region.

2.2. Mathematical formulation

The superstructure representation is expressed as an optimisation model comprised of algebraic equations. The equations include objective functions, design constraints, and operating constraints.

2.2.1. Objective functions

As a multiple criteria decision-making problem, it has several objective functions. The total cost of the system consists of capital expenditure, operating and maintenance cost, and fuel cost. And the total carbon dioxide emissions are derived from fossil fuel consumption and emission index. The ε-Constraint method is adopted for multi-objective optimisation. The total cost remains as the objective function, while the emission function is converted to a constraint. The optimal solution at each discretised emission point can be obtained by solving a single-objective problem.

2.2.2. Design constraints

Infrastructure selection, sizing and location are the core issues in energy planning. The installed capacities of different technologies in each region are determined by Eq. (1). The notations of the model are defined in Table 1 and Table 2.

$$ic_{t,r} = iu_{t,r} \cdot SCAP_t \tag{1}$$

2.2.3. Operating constraints

Energy balance is a fundamental principle. The balance of each form of energy is specified by Eq. (2) for primary energy and Eq. (3) for secondary energy.

$$x^{imp}_{s,h,r,pe} + \sum_{r'} \sum_n \left(x^{tri}_{s,h,r,r',pe} \cdot \eta_n - x^{tri}_{s,h,r',r,pe} \right) + x^{onsite}_{s,h,r,pe} - \sum_{gnt} x^{in}_{gnt,s,h,r,pe} = FED_{s,h,r,pe} \tag{2}$$

$$x^{imp}_{s,h,r,se} + \sum_{r'} \sum_n (x^{tri}_{s,h,r,r',se} \cdot \eta_n - x^{tri}_{s,h,r',r,se}) + \sum_{gnt} x^{out}_{gnt,s,h,r,se} + \sum_{cvt} (x^{out}_{cvt,s,h,r,se} - x^{in}_{cvt,s,h,r,se}) + \sum_{stt} (x^{out}_{stt,s,h,r,se} - x^{in}_{stt,s,h,r,se}) = FED_{s,h,r,se} \tag{3}$$

For energy generation and conversion components, the relation between input and output is expressed by Eq. (4). For energy storage devices, energy balance between adjacent time periods is given by Eq. (5).

$$\sum_e x^{in}_{t,s,h,r,e} \cdot \eta_{t,e'} = x^{out}_{t,s,h,r,e'} \tag{4}$$

$$str_{stt,s,h+1,r,e} = str_{stt,s,h,r,e} \cdot \eta_{stt} - \frac{x^{out}_{stt,s,h+1,r,e} \cdot \Delta h}{\eta^{out}_{stt}} + x^{in}_{stt,s,h+1,r,se} \cdot \Delta h \cdot \eta^{in}_{stt} \tag{5}$$

Technology can only be operated within a specific load range, as shown in Eq. (6) and (7). The output of renewable generation is restricted by resource availability, given by Eq. (8). Ramp-up and ramp-down rates are constrained by Eq. (9) and (10).

$$\sum_e x^{out}_{t,s,h,r,e} \le op^{operate}_{t,s,h,r} \cdot SCAP_t \tag{6}$$

$$\sum_e x^{out}_{t,s,h,r,e} \ge (op^{operate}_{t,s,h,r} - op^{startup}_{t,s,h,r}) \cdot SCAP_t \cdot \underline{LOL}_t \tag{7}$$

$$\sum_e x^{out}_{rgt,s,h,r,e} \le op^{operate}_{rgt,s,h,r} \cdot SCAP_{rgt} \cdot \overline{RA}_{rgt,s,h} \tag{8}$$

$$\sum_e (x^{out}_{t,s,h+1,r,e} - x^{out}_{t,s,h,r,e}) \le (op^{operate}_{t,s,h,r} + op^{startup}_{t,s,h+1,r}) \cdot \overline{RU}_t \cdot SCAP_t \tag{9}$$

$$\sum_e (x^{out}_{t,s,h,r,e} - x^{out}_{t,s,h+1,r,e}) \le (op^{operate}_{t,s,h,r} \cdot \overline{RD}_t + op^{shutdown}_{t,s,h+1,r}) \cdot SCAP_t \tag{10}$$

Each technology may have several units, and the status of each unit can be operating, starting up, shutting down, or closed. The number of units in use cannot exceed existing units at that period.

Energy can only be imported at specific locations under certain capacity limits. Cross-region energy flows can not exceed the capacity of the network in use. Land use constraints are also contained. The full detailed model formulation is not given in this work because of space limitations.

3. Illustrative example and results

3.1. Case specification

The model introduced in the previous section is applied to a new urban area in China. This new area consists of six regions. We consider three seasons (i.e. winter, mid-season, and summer), one typical day for each season, and 24 hours for each day, for a total of 72 time intervals. The hourly energy demands of the new area are exogenously specified. Here we consider 17 types of generation technologies (e.g. NGCC w/o CCS, Nuclear, PV, wind turbine, gas turbine CHP, NGCC CHP, coal boiler, and gas boiler), four conversion technologies (i.e. absorption chiller, air-source heat pump, ground-source heat pump, and AC), three storage technologies (i.e. battery, thermal storage, and ice storage), and four energy networks (i.e. gas pipe, heat pipe, cooling pipe, and power grid). Technical and economic parameters such as efficiency, lifetime, capital expenditure, fixed and variable operating cost, are mainly collected from IEA-ETSAP and 2019 Annual Technology Baseline (NREL 2019). Solar and wind resource data are found from Pfenninger and Staffell (2016). CO_2 emission index is adopted from 2018 Energy Data (Wang, 2018). Water consumption data are gathered from Gerdes and Nichols (2009) and UCS (2013).

3.2. Trade-offs among economic and environmental criteria

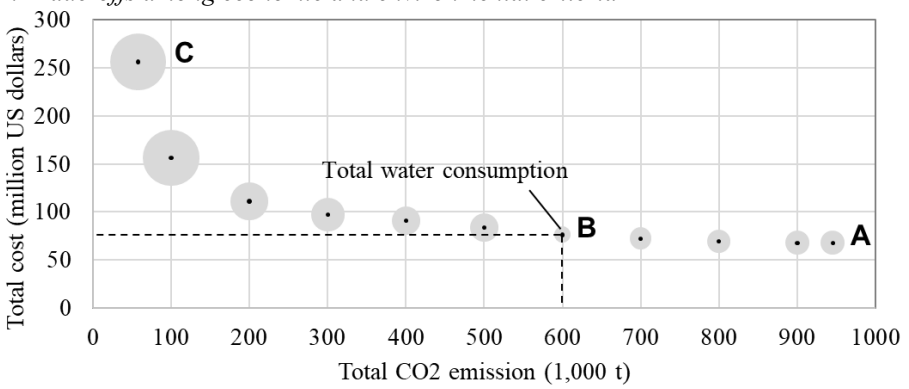

Figure 2. The Pareto Front of total cost and CO_2 emission

Figure 2 illustrates the results of multi-objective optimisation, taking cost and CO_2 emission as two conflicting interests. Each point corresponds to a Pareto optimal solution, while the area of each bubble represents the amount of water consumption. Along with the decline of CO_2 emission boundary, the total cost rises at an ever-increasing speed. The change in water consumption, however, is not monotonous. From cost minimum point A to point B, the water consumption decreases, because the system adopts more CHP and PV technologies that are less water consuming. To further reduce CO_2 emission, NGCC plants start to apply CCS technology and are finally replaced by nuclear plants, both of which are water hunger. In other words, less CO_2 emission does not necessarily mean less water consumption. The energy-water nexus shouldn't be overlooked, especially in areas that suffer from water shortage.

3.3. The deterministic and stochastic design plan of the new area energy system

Decision-makers can choose any point from the Pareto Front according to their design requirements or specific interests. Once their decision is made, the developed optimisation model can supply them with a holistic plan for the system design. Compared with point A, CO_2 emissions and water consumption at point B decreased by 36.5% and 52.6% respectively, and the total cost increased by only 13.7%. Figure 3(a) illustrates the energy network design solution of point B.

Previous discussions are based on the deterministic model. However, renewable generation technologies such as PV and wind turbine introduce uncertainty into the system. To simply address this problem, we assume that PV might operate at a lower output with a probability of 0.2 or at a higher output with a probability of 0.8 on each typical day. Similar settings are applied to wind turbines. Thus, we get $2^3 \times 2^3 = 64$ scenarios. In Figure 3(b), white rectangles represent the deterministic solution of energy technology design in region 1, and dark grey rectangles refer to extra technology capacity required to meet the energy demand and the CO_2 emission limit in all the scenarios. In response to the uncertainty, region 1 should adopt Li-Battery and build more gas turbine CHP and air-source heat pump (ASHP).

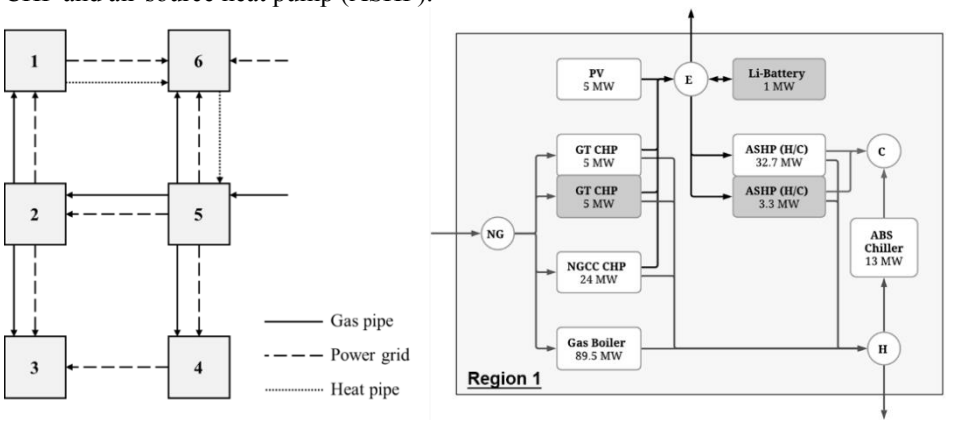

(a) Energy flow across regions (b) Energy technology deployment in region 1

Figure 3. The energy system design solution of point B

4. Conclusions

In this paper, we developed an optimisation approach for integrated urban energy system design under uncertainty and sustainability requirements. This approach has been applied to a new area in China. The results reveal that more stringent carbon emission limit requires a higher investment, while the relationship between carbon emission and water use is complicated. Decision-makers can choose the proper design point based on their specific interests and constraints. Once renewable technologies such as PV and wind turbine are to be deployed, the impact of uncertainty should be considered to avoid the suboptimal design.

Table 1. Definition of variables

Continuous Variables		Integer Variables	
x	Energy flow	ic	Installed capacity
str	Energy stored in storage facilities	iu	Installed units
		op	Units in use

Table 2. Definition of sets, superscripts, and parameters

Sets and superscripts		Parameters	
s	Season	η	Efficiency
h	Hour	FED	Final energy demand
r	Region	$SCAP$	Single unit capacity
e	Energy	Δh	Length of a time-slot
pe	Primary energy	$\underline{LOL}$	Lower operating level limit
se	Secondary energy	$\overline{RA}$	Renewable availability limit
t	Technology	$\overline{RU}$	Ramping up limit
gnt	Generation technology	$\overline{RD}$	Rampin down limit
cvt	Conversion technology		
stt	Storage technology		
imp	Energy imported from outside		
tri	Energy transmitted across regions		
$onsite$	Renewables collected onsite		
in/out	Technology inlet/outlet		

Acknowledgements

The authors gratefully acknowledge financial supports from National Natural Science Foundation of China (71690245), the Program of China Scholarship Council (201806210214), and U.S. NSF under INFEWS project 1739977. Portions of this research were conducted with the advanced computing resources provided by Texas A&M High Performance Research Computing.

References

Allen R. C., Nie Y., Avraamidou S., Pistikopoulos E. N., 2019. Infrastructure Planning and Operational Scheduling for Power Generating Systems: An Energy-Water Nexus Approach. In Computer Aided Chemical Engineering (Vol. 47, pp. 233-238). Elsevier.

Demirhan C. D., Tso W. W., Ogumerem G. S., Pistikopoulos E. N., 2019. Energy systems engineering-a guided tour. BMC Chemical Engineering, 1(1), 11.

Gerdes K., Nichols C., 2009. Water requirement for existing and emerging thermoelectric plant technologies. Office of Systems, Analysis & Planning, National Energy Technology Laboratory, DOE/NETL-402/080108, p13.

Guo Z., Cheng R., Xu Z., Liu P., Wang Z., Li Z., Jones I., Sun Y., 2017. A multi-region load dispatch model for the long-term optimum planning of China's electricity sector. Applied Energy 185, 556–572.

Liu P., Pistikopoulos E. N., Li Z., 2010. An energy systems engineering approach to the optimal design of energy systems in commercial buildings. Energy Policy, 38(8), 4224-4231.

Mavromatidis G., Orehounig K., Carmeliet J., 2018. Design of distributed energy systems under uncertainty: A two-stage stochastic programming approach. Applied Energy, 222, pp.932-950.

Mohammadi M., Noorollahi Y., Mohammadi-Ivatloo B., Yousefi H., 2017. Energy hub: from a model to a concept–a review. Renewable and Sustainable Energy Reviews, 80, 1512-1527.

NREL (National Renewable Energy Laboratory). 2019. 2019 Annual Technology Baseline. Golden, CO: National Renewable Energy Laboratory.

Pfenninger S., Staffell I., 2016. Long-term patterns of European PV output using 30 years of validated hourly reanalysis and satellite data. Energy, 114, 1251-1265.

UCS (Union of Concerned Scientists), 2013. How it Works: Water for Nuclear.

Wang Q., 2018. 2018 Energy Data. Beijing: Innovative Green Development Program.

Zhou Z., Liu P., Li Z., Ni W., 2013. An engineering approach to the optimal design of distributed energy systems in China. Applied Thermal Engineering, 53(2), pp.387-396.

Sauro Pierucci, Flavio Manenti, Giulia Bozzano, Davide Manca (Eds.)
Proceedings of the 30th European Symposium on Computer Aided Process Engineering (ESCAPE30), May 24-27, 2020, Milano, Italy.
http://dx.doi.org/10.1016/B978-0-12-823377-1.50239-1

Optimal Integration of a Stratified Thermal Energy Storage into a Multi-Component Industrial Energy System

Karl Schenzel [a], René Hofmann [a,b*]

[a]*Technische Universität Wien, Institute for Energy Systems and Thermodynamics, Getreidemarkt 9/BA, 1060 Vienna, Austria*
[b]*AIT Austrian Institute of Technology GmbH, Center for Energy, Sustainable Thermal Energy Systems, Giefinggasse 2, 1210 Vienna, Austria*
rene.hofmann@tuwien.ac.at

Abstract

One way of balancing the increasing shares of fluctuating renewables in the energy mix are flexible consumers. For utilizing system flexibility and load shifting, thermal energy storages are of vital importance. Concerning optimal operation, the use of optimization becomes inevitable, as decisions for optimal storage management are based on future energy prices and demand predictions. Due to the nonlinear character, the formulation of stratified thermal energy storage models in optimization problems are crucial, especially when temperature distributions inside the storage are of interest.
Inspired by a specific industrial use case this work aims to analyze the flexibility of the corresponding energy system through proper storage management based on load predictions and profiles of energy prices using mathematical optimization. Considering the selection of a suitable modelling approach, stratification and convection inside the centrally located sensible water storage were of special interest, thus a detailed nonlinear approach was chosen. Based on the comparison of three scenarios the outcomes of this work demonstrate the usefulness and strength of applied mathematical optimization for both economic operation and prediction of system states and conditions for multi-connected sensible thermal energy storages.

Keywords: Flexible Consumer, Demand Response, Thermal Energy Storage, Stratification, Operation Optimization

1. Introduction

Sensible water storages can be found in almost any industrial process, nevertheless they are used in most cases more as hydraulic switch rather than acting as a storage in the proper sense. By making use of their storage potential through a proper and predictive storage management, consumers can be timely more flexible in their energy demand and can thus benefit from cheaper off-peak energy prices. Considering the entire industrial sector, this shows huge unused potential that can be utilized to increase demand side flexibility.
The industrial plant of the considered use case consists of several different components surrounding a centrally located and multi-layer-connected hot water storage tank. As it represents the most complex and decisive component in terms of system flexibility, the storage is of main focus. Concerning optimal operation the use of optimization models becomes inevitable as decisions for optimal storage management are based on future energy prices and demand predictions. In Schütz et al. (2015) and Baeten et al. (2015) different optimization formulations for stratified thermal storage were compared.

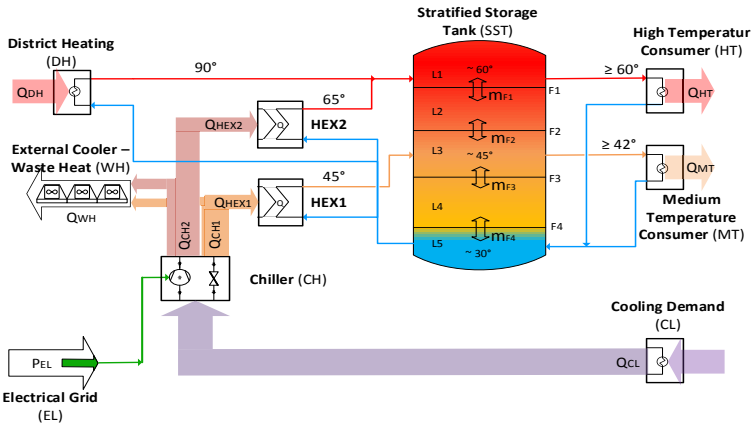

Figure 1: Flow-Scheme of the considered energy system: Having a closer look at the storage it is discretized into five equally sized layers: Three layers in which it has inputs and outputs and one intermediate layer each. In the following the layers are identified with the letter L, the faces, which letter F.

However, in the considered energy systems, the storage had only one inlet and one outlet what results in a uniform flow distribution. In order to be able to model the different inflows and outflows at different vertical positions, the nonlinear model approach was extended in this work in order to be able to consider uneven flow distributions within the stratified water storage.

2. Use Case

At present, instead of using predictive control tools, single components as well as storage management are operated by human plant managers only based on their experience. Consequently also the overall system of this industrial plant is operated inefficiently. In general a too large amount of waste heat cannot be used and has to be released to the environment by the external coolers. Also the control of the district heating supply does not work properly what often results in too high temperatures inside the storage tank. This is followed by negative impacts on both, the production quality and energy costs.

As the storage is of main interest in this work a simplified subsystem of the real complex industrial plant was derived. The corresponding energy system is shown in Figure 1 and consists of two heat consumers on different temperature levels (HT and MT), a Chiller (CH) for cooling services (CL), a district heating supply (DH) and an external cooler for waste heat release. All of them are connected to the stratified storage tank (SST) at three different temperature levels. This work aims to be an introductory contribution as basis of developing an operation planning and predictive control tool for the whole industrial site with its complex interconnected system.

3. Method and Approach

With special focus on the storage, the aim was to use a detailed nonlinear approach - mainly for the following reasons: On the one hand the precise temperature distributions are of central interest as they are of importance for the quality of the production process. Also, the current control system is only based on temperature measurements.

On the other hand, since there are currently no flow measurements available, this model can also be used to calculate mass flow rates. Furthermore the model considers the convection and heat conduction inside the storage as well as the heat losses to the ambient what makes the model more complex. Regarding the surrounding components, the goal was to model them as simply as possible, but to provide the connections to the storage in

sufficient detailed. If not stated explicit in the text, all considered variables are defined positive and unbounded. Due to a lack of existing measurements, the model validation could not be done using real component data. As a workaround another stratified storage tank, similar in size and geometry, was taken for parameter estimation and validation.

3.1. Storage Model

A stratified thermal storage physically consists of various temperature layers having different temperatures with the highest on the top and the lowest on the bottom. A suitable way of modelling stratification is to vertically divide the storage in N volumes, with each having a constant mass and a uniform temperature that can vary over time. Each volume can have several input and output flows which impact the convection flow rates to and from the neighboring layers. Depending on the combination of the different inlet and outlet flows, from one layer simultaneously flows into the upper and lower neighboring layers can occur. Because both, layer temperatures which represent the states of the transient model, as well as flow rates are considered variables of the optimization problem this is a nonlinear model. Heat conduction between layers and heat losses to the ambient are modeled using a constant heat conduction coefficient. The layer energy balances are the governing equations regarding transient system behavior. Considering all features described above, this state constraint equation can be - for an exemplary layer - read as followed in Eq.(1).

$$\begin{aligned}\frac{Mc_w(T_{(L)}^{t+1} - T_{(L)}^{t})}{\Delta t} &= \dot{m}_{(F+)}c_w(T_{(L+1)}^{t^*} - T_{(L)}^{t^*}) + \dot{m}_{(F-)}c_w(T_{(L-1)}^{t^*} - T_{(L)}^{t^*}) \\ &+ \sum_{i,in}(\dot{m}_{i,in}\, c_w(T_{i,\,in} - T_{(L)}^{t^*})) + k_{amb}\, A_{amb}(T_{amb} - T_{(L)}^{t^*}) \\ &+ k_F\, A_F(T_{(L+1)}^{t^*} - T_{(L)}^{t^*}) + k_F\, A_F(T_{(L-1)}^{t^*} - T_{(L)}^{t^*})\end{aligned} \tag{1}$$

The upper indices refer to the time at which the respective value is taken. The marker* stands for the central interpolated timepoint: $T_{(L)}^{t^*} = 0.5(T_{(L)}^{t+1} - T_{(L)}^{t})$

Table 1: Abbreviations used in Eq. (1)

Abbreviation	Definition	Abbreviation	Definition
M	*Mass content*	*k*	*Heat conduction coefficient*
$\dot{m}$	*massflow rate*		
c_w	*heat capacity water*	*A*	*Surface*
T	*Temperature*	*amb*	*Ambient*

3.2. Cooling and Heat Recovery System

The chiller that provides cooling services performs similar to a heatpump. After the enthalpy increase due to the compression the refrigerant releases heat at a higher temperature (Q_{CH2}) in a desuperheater and at a lower temperature in a condenser (Q_{CH1}). By varying the electrical power input the compressor unit offers some flexibility in operation. Increasing the electric power input leads to higher superheating of the refrigerant and so the proportion of heat released at high temperature level (Q_{CH2}) is increased. Thus the ratio of heat released at the higher temperature to the total heat released by the chiller can vary between 0.2 and 0.25. Eq.(4) states this constraint. When superheating is at its maximum the total COP is 2.5, with minimal superheating the total COP is 3.2. In between, there is linear interpolation. The waste heat from the chiller can either be released to the environment level (Q_{WH}) or supplied to the stratified tank via the two heat exchangers HEX1 and HEX2, which have a maximum capacity of 500kW and 100kW respectively.

$$Q_{CL} + P_{EL} = Q_{CH2} + Q_{CH1} \quad (2) \qquad COP = \frac{Q_{CH1}+Q_{CH2}}{P_{EL}} \quad (3) \qquad 0.2 \le \frac{Q_{CH2}}{Q_{CH1}+Q_{CH2}} \le 0.25 \quad (4)$$

3.3. Consumers, Electricity- and District Heating Suppliers

These components represent the boundaries of the system. The corresponding load and price profiles which are the same for the first and second 24hours of the observation period are specified in Figure 2.

According to observations of the real operation a constant outflow temperature of 90°C is assumed for the district heating supply. As indicated in Figure 1 the inflow temperature of the HT- and MT-Consumer correspond to its sources, Layer 1 and Layer 3. At minimum 60°C and 42°C are required by the HT-and MT- Consumers. Although too high inflow temperatures can cause quality losses in the attached processes no upper boundaries are considered in the consumers. However, in scenario 3 this is taken into account by a soft constraint. As measurement data show almost constant temperature drops between the different distribution and collection networks in the consumption side, constant temperature drops ΔT_{HT} and ΔT_{MT} are assumed for the consumers.

3.4. Optimization and Objective Function

The system was modelled and implemented in MATLAB using the toolbox YALMIP. The described nonlinear program was solved using the IPOPT algorithm. The optimization was executed for an observation period of 48 hours with a discrete time-step of 5 minutes. At this point it should be noted that the observation period refers to a finite horizon rather than a periodic time cycle.

To analyze the systems flexibility three different scenarios are compared, with each having the same load and price profiles as boundary conditions (shown in Figure 2) but different optimization objectives. In scenario A only the minimization of total operation costs is taken into account (c_{WH}=0, c_{TL1}=0).In scenario B Waste Heat release is minimized (c_{WH}=1000, c_{TL1}=0). In scenario C the temperature of the highest layer is tried to be kept as low as possible (c_{WH}=0, c_{TL1}=1000). The optimization problem is stated with the objective function given in Eq.(5) where pr_{El} pr_{DH} stand for the prices for electricity and district heating.

$$Min \quad z = Q_{DH}\ pr_{DH} + P_{EL}\ pr_{EL} + c_{WH}\ \|Q_{WH}\| + c_{TL1}\ \|T_{(L1)} - T_{HT\,min}\| \qquad (5)$$

4. Results and Discussion

The results shown in Table 2 give a comparison of the overall performance of the three scenarios. Immediately it can be seen that scenario A, where cost minimization is the only objective, has the lowest energy costs. This means that the additional objectives in the other scenarios can only be met by accepting higher energy costs.

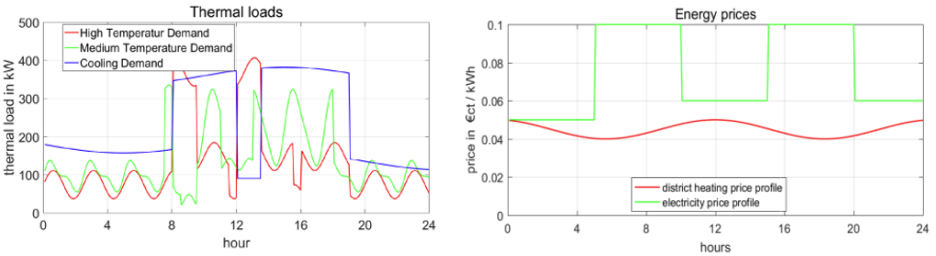

Figure 2: Loads and prices – valid for the first and second 24h-period

Table 2: Comparison of the three scenarios

Scenario/ Objective	A-Minimization of operation costs	B-Minimization of Waste Heat	C-Minimization of Temperature in Layer 1
Operation Costs in €	572.5	596.8	647.8
Waste Heat in kWh	6854.1	6649.3	8545.5
District Heat in kWh	3556.0	4072.7	5250.3
Electricity in kWh	5142.9	5142.2	5142.2

The waste heat reduction of 3% in scenario B can be achieved by a cost increase of 4.2%. When looking at the temperature behaviors shown in Figure 3, layer 1 and layer 3 are of particular interest as these are also the inflow temperatures of the consumers which have to be at least 60°C and 42°C, respectively. In the cost-effective scenario A the consumption peaks in the morning and midday lead to higher temperatures than actually required. As the behavior in scenario B shows only minor difference to scenario A, a further comparison here is neglected. The optimization strategy in scenario C aims at improving the operation of the HT-consumer and reduces the influence of the consumption peaks for the highest layer. However, in the other layers constantly higher temperatures are observed over the whole observation period, what is also reflected in a significant increase in energy consumption (19.5%), operating costs (+15%) and waste heat release to the environment(+24%).

It should be noticed that the beginning and end of the first and second 24h period show different behavior although the boundaries are the same. This is due to the finite horizon optimization, where only the initial and final constraints are considered. Instead a periodic horizon would include the consideration of the entire previous and subsequent periods and result in identical profiles.

Considering the interconnections of the storage and taking into account the layer mass balances, it becomes clear that the vertical flows of the two lower and the two upper faces must be equal. Especially the flow rate in the upper section is of interest, as it gives indication how the different suppliers are co-operating.

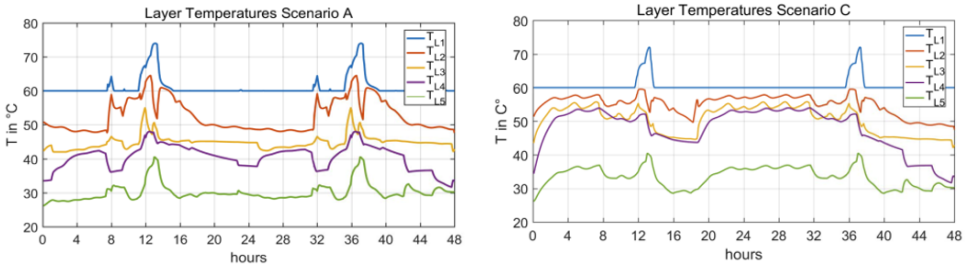

Figure 3: Layer temperatures for scenario A (left) and scenario C (right)

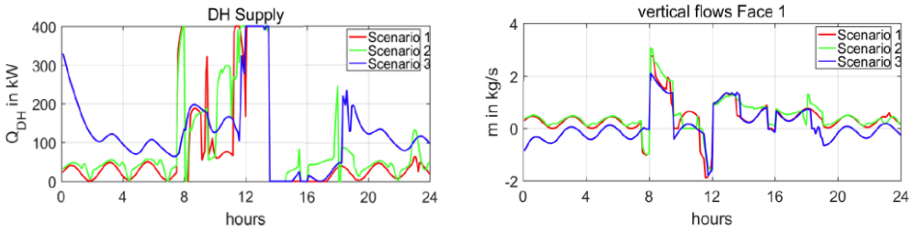

Figure 4: District heating supply (left) and upper section vertical flows (right), for first 24h-period

For example Figure 4 shows that in scenario C district heating is used most frequently, especially during off-peak periods. This causes an increased inlet flow entering the highest layer, what results in the upper vertical flow to be directed downwards (shown as negative values in figure 4). By looking at Figure 3, it can also be analyzed well how the temperatures of neighboring layers affect each other through the appearing vertical flows.

5. Conclusion

According to proven static analytical methods and energy-economic aspects, optimal storage management means storing energy from off-peak periods as well as waste heat in order to save energy and costs. Away from this, the presented results show that optimal operation of the considered hot water storage tank does not entirely follow these rules. Reduction of waste heat release has not been identified as a cost-effective objective and a more stringent temperature control is associated with considerable increase in costs and waste heat. Regarding the analysis of the systems flexibility, it can be derived from the scenarios that the identical energy demand can be met by very different ways of operating the suppliers. Under the given circumstances a potential of about 20% of the energy consumption can be utilized and offered for demand side flexibility by this process.
Especially when intricately integrated into diversified systems, the optimal management of stratified storages is a complex problem and requires advanced methods of predictive control as well as suitable and problem specific modelling approaches. The example demonstrates the usefulness and strength of mathematical optimization for operational planning in addition to common analytical methods such as pinch and exergy analysis.

In Outlook to further work the considered energy system will be extended to represent the whole industrial site. Of particular focus is the introduction of a CHP-plant and a high-temperature heat pump as well as the derivation and analysis of alternative linearized models in order to execute operational optimization with subject to design aspects.

References

Baeten, B., Rogiers, F., Patteeuw, D., Helsen, L. (2015). Comparison of optimal control formulations for stratified sensible thermal energy storage in space heating applications In: The 13th International Conference on Energy Storage.

Schütz, T., Streblow, R., Müller, D. (2015). A comparison of thermal energy storage models for building energy system optimization. In: Energy and Buildings 93, S. 23–31.

Sauro Pierucci, Flavio Manenti, Giulia Bozzano, Davide Manca (Eds.)
Proceedings of the 30th European Symposium on Computer Aided Process Engineering (ESCAPE30), May 24-27, 2020, Milano, Italy.
http://dx.doi.org/10.1016/B978-0-12-823377-1.50240-8

Portfolio Optimisation of Integrated Renewable Energy Cogeneration Systems

Houd Al-Obaidli,[a] Ahmed AlNouss,[a] Yusuf Bicer,[a] Tareq Al-Ansari[a,b*]

[a]*Divison of Sustainable Development, College of Science and Engineering, Hamad Bin Khalifa University, Qatar Foundation, Doha, Qatar.*

[b]*Division of Engineering Management and Decision Sciences, College of Science and Engineering, Hamad Bin Khalifa University, Doha, Qatar.*

talansari@hbku.edu.qa

Abstract

The global energy sector is predominated by fossil fuels for the production of electricity and freshwater. This is more pronounced in the Gulf Cooperation Council (GCC) region experiencing fast economic growth driven by major oil and gas infrastructure. Conventional cogeneration systems typically encounter higher operational efficiencies and relatively lower costs compared to renewables-based systems. Their use of fossil fuels as a primary energy source generates high levels of CO_2 emissions resulting in a substandard environmental performance per capita. Renewable energy sources can be integrated into the energy portfolio mix to improve overall resilience and diversification, whilst improving on overall sustainability as environmental emissions are restrained. In this study, an integration of solar and biomass renewable energy into existing energy infrastructure is proposed and analysed using Aspen Plus. The focus is to compare different water and power cogeneration configurations and identify the optimal configuration using MATLAB's optimisation toolbox. A techno-economic assessment is performed to review the effects of renewable energy integration on the overall performance of the grid. The optimal configuration indicate overall levelised costs and emissions approximated at \$0.79 and 184.78 gCO_2e per unit output, respectively, compared to \$2.61 and 350.01 gCO_2e per unit output for the base case. The results demonstrate improvements in the environmental and economic performance. The integration of renewable energy into a portfolio mix offer significant economic and environmental advantages and can be considered a promising and viable option for the provision of water and electricity in the GCC region.

Keywords: Solar, Biomass, Cogeneration, Techno-economic, Portfolio optimisation.

1. Introduction

The Gulf Cooperation Council (GCC) region, like many developing regions in the world, is facing an ever-growing demand for vital services such as electricity and water. This demand is fuelled by rapid economic growth coinciding with population expansion within the local and expatriate communities to meet the monumental development needs of the region. The GCC, which is located in the Arabian desert, is home to some of the largest fossil-fuel reservoirs. However, many areas are vulnerable to severe climate conditions exerting further pressure on essential amenities such as freshwater and energy for space cooling throughout the year. As a result of the vast reserves, fossil fuels dominate the energy sector where utilisation is protected from fuel price volatility through heavy government subsidies. Over-reliance on carbon technologies for power and water

production over the last few decades result in fossil fuel-based economies result in large CO_2 emissions per capita metrics for this region (World Bank, 2019). As such, there is an opportunity to explore the integration of renewable energy sources into the energy portfolio mix to reduce these emissions. The GCC nations along with many countries in the global community have supported climate action plans and are signatories to the Kyoto protocol and Paris COP agreement. Initial investment projects in renewable energy began recently in the region (IRENA, 2019), where Abu Dhabi has completed the Shams-1 100 MW CSP project and a 1,177 MW solar PV farm is under construction. A large-scale solar PV facility is underway in Dubai with a capacity exceeding 2,000 MW. The state of Qatar is also embarking on solar energy through its first solar PV project with a planned capacity of 700 MW. Moreover, many other small-to-medium-scale renewable energy projects are either planned or under construction in Saudi Arabia, Kuwait, Oman and Bahrain. However, the adoption of renewable energy induces particular challenges; government subsidies for fossil-fuels and household utility services such as water and electricity; inefficient use of resources especially water, considering the desert climate conditions and the increasingly depleting physical freshwater resources; and lack of a clear and firm government targets/commitments to curb down carbon emissions.

Previous studies evaluated techno-economic metrics of integrated portfolio configurations with regional context. Seawater desalting methods applied to fourteen combined power and desalting plant (CPDP) configurations in Kuwait were analysed by Darwish *et al.* (2009). A techno-economic study was conducted using energy and fuel cost together with GHG emissions. Thermal driven desalination technologies were identified as the most inefficient while the combination of combined-cycle gas turbine (CCGT) and seawater reverse-osmosis (SWRO) proved to be the most economic configurations. Kaya *et al.* (2019) proposed a renewable based energy desalination technology for the emirate of Abu Dhabi to reduce emissions and improve sustainability. A reverse-osmosis plant driven by solar PV was modelled and analysed using levelised cost of water (LCW) methodology. Their results indicate levelised costs of 0.28 \$/m^3 for the best case and 0.35 \$/m^3 for the most conservative case. The intermittent nature of the solar resource and its implication on total costs outside of a portfolio mix was however neglected. Abdul-Wahab *et al.* (2019) used HOMER to identify the most economic PV system for the Sultanate of Oman. It was estimated that the application of PV technology instead of natural gas or diesel power generation will reduce carbon emissions by 9.7 and 13.1 million kg/year, respectively. The cost of energy was also estimated to witness a reduction to 0.085 \$/kWh. Al-Obaidli *et al.* (2019) reviewed several CPDP configurations within the GCC region. A rigorous genetic algorithm optimisation technique was used and an optimal configuration was proposed based on most favourable economic and environmental results. The study made a case supporting renewable energy infusion into existing infrastructure to promote sustainability and resilience. AlNouss *et al.* (2019) compared a blend of biomass feedstock application to produce: methanol, urea, liquid fuels and power. The techno-economic-environmental approach demonstrated that methanol production was the most economic while the urea process resembled the lowest environmental emissions. The study didn't identify biomass integrated gasification combined-cycle (BIGCC) particularly favourable in terms of economic and environmental performance especially in the case of standalone operation outside of an energy portfolio mix. Based on the review above, a limited number of integrated technology options were analysed. The aim of this paper is to evaluate multiple electricity and water cogeneration schemes through a techno-economic evaluation and to identify the optimal portfolio mix which can promote a more sustainable coupled energy and water sector. Four configurations are considered: base reference case; renewable energy

integration using 3 renewable energy options; a renewable energy exclusive configuration; and an optimal portfolio mix based on the outcome of the optimisation method.

2. Methodology

Integration of efficient and clean renewable energy sources with fossil-based systems in a portfolio mix is a common approach for achieving sustainability targets. Many integrated configurations are possible to provide the necessary demand targets in a sustainable manner. Due to primary energy resource availability, and environmental and operational considerations, the following five production technologies were selected for this study: CCGT; BIGCC; concentrated solar power (CSP); multi-stage flash (MSF); and SWRO. An integrated model was developed using the listed technologies. The process flow diagram of the model describing the different components of the system and the main inputs and outputs is shown in Figure 1.

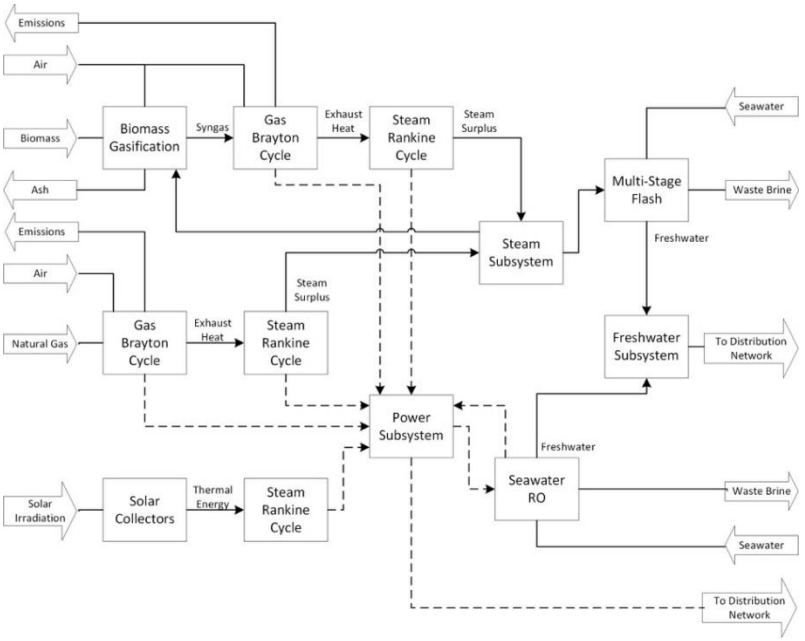

Figure 1. Process flow diagram of the integrated cogeneration system.

The CCGT is the predominant power generation technology in the GCC and in Qatar due to the vast natural gas reserves. It consists of a gas Brayton cycle combined with a steam Rankine cycle to increase the power yield and improve overall energy efficiency. The BIGCC is a renewable energy source based on biomass gasification process which can be used to generate power whilst reducing organic waste. As with the CCGT, it utilises a combined cycle in which syngas, rather than natural gas, is combusted in a gas Brayton cycle and the exhaust heat is used to drive a steam Rankine cycle. The CSP, also, has a great potential for power production due to solar resource availability throughout the year. A parabolic trough collector (PTC) system is used in which the parabolic mirrors concentrate direct irradiation from the Sun into a focal line which coincides with a pipe carrying heat transfer fluid (HTF) which absorbs thermal energy and transports it to the rest of the system. A direct steam Rankine cycle at the end is used to generate power.

MSF is used widely for water desalination in a cogeneration configuration due to availability of surplus steam from the power block. Seawater in the MSF passes through multiple stages of flash drums in which the temperature rises causing seawater to boil. The resultant water vapour is then condensed and collected as freshwater. The process also produces high-salinity seawater brine which is typically diverted to waste disposal. The SWRO is a popular and promising desalination technology due to its improved water recovery ratio and utilisation of high-pressure waste brine to recover energy. Feed seawater passes through a high-pressure pump to a set of special membranes that separate freshwater from salty brines through reverse-osmosis process. The design specifications for the five systems are listed in Table 1. The model is designed under the assumption of stable and ideal economic and operational conditions.

Table 1. Design specifications for production technologies.

Quantity	Value	Quantity	Value
CCGT			
Mass flow (natural gas)	0.5 kg/s	Air-fuel ratio	26.9
High heating value	51.74 MJ/kg	Pressure Ratio (gas)	20
Pressure Ratio (steam)	72.5	Efficiency (isentropic)	90 %
Efficiency (overall)	65 %		
BIGCC			
Mass flow (syngas)	1.1 kg/s	Air-fuel ratio	15
Low heating value	23.72 MJ/kg	Pressure Ratio (gas)	20
Pressure Ratio (steam)	72.5	Efficiency (isentropic)	90 %
Efficiency (overall)	60 %		
CSP			
Absorbed solar irradiation	594 W/m^2	Aperture area	91 m^2
Mass flow (HTF)	10 kg/s	Pressure Ratio (steam)	100
Efficiency (isentropic)	90 %	Efficiency (overall)	18 %
MSF & SWRO			
Mass flow (seawater)	83.3 kg/s	Recovery Ratio (MSF)	12
Salinity (seawater)	30,000 ppm	Recovery Ratio (SWRO)	20
Pressure Ratio (pump)	20	Efficiency (isentropic)	90 %

Key operational design assumptions were made to suit the regional climate conditions such as reference temperature and pressure and solar irradiation. A techno-economic multi-objective-genetic-algorithm (MOGA) method was used to identify the optimal portfolio configuration where two optimisation objectives were envisaged: levelised costs (equivalent to discounted lifecycle costs over lifecycle throughput) and global warming potential (GWP) for each of the five technologies:

$$Minimise \sum_i c_i x_i \quad (1)$$

$$Minimise \sum_i e x_i \quad (2)$$

Where, c and e are levelised cost and GWP emission factors per technology, respectively. The optimisation problem was subject to the following constraints:

$$x_{CCGT} + x_{BIGCC} + x_{CSP} = \quad (3)$$

$$x_{MSF} + \quad x_{SWRO} = 1 \quad (4)$$

$$0 \leq x_i \leq 1 \quad (5)$$

3. Results and Discussion

Five generation technologies were selected based on suitability for operations within the region and were modelled in Aspen Plus which is a commonly used process modelling software in academia and industry. The models contained both technical and economic data relevant to each of the technologies. As part of the techno-economic analysis, four power and water cogeneration system configurations were selected for comparison and are presented in Table 2.

Table 2. Power and water cogeneration configurations.

Configuration	Power	Water
0 – Base	1.0 CCGT (100%)	1.0 MSF
1 – All renewables	0.5 BIGCC + 0.5 CSP	1.0 SWRO
2 – All technologies	0.33 CCGT + 0.33 BIGCC + 0.33 CSP	0.5 MSF + 0.5 SWRO
3 – Optimal mix	x CCGT + y BIGCC + z CSP	p MSF + q SWRO

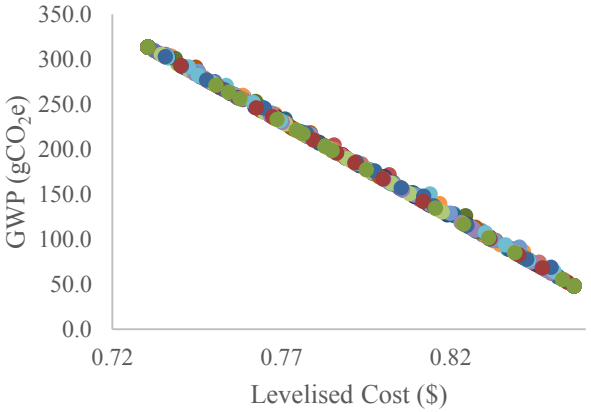

Figure 2. Optimisation function Pareto curves (20 iterations).

Application of the model resulted in levelised costs and GWP factors for each technology and integrated system configuration. A multi-objective genetic algorithm (MOGA) optimisation function in MATLAB was used to compute the optimal cogeneration configuration. In order to improve the reliability of the results, 20 iterations were made and the pareto curve results of the optimisation are presented in Figure 2. Due to the choice of generation technologies and configurations, the apparent linear behaviour of the pareto set indicate that a global optimal configuration is not feasible as normally observed in pareto solutions. However, several configurations that were relatively optimal in comparison to the two extreme points were possible and an optimal configuration was selected from the middle of the pareto set. The optimal configuration predominately consisted of CCGT and CSP for power and SWRO for water. A comparison of total

levelised costs and GWP for each scenario is presented in Figure 3. From the results, it is evident that the base configuration is the most suboptimal with the highest cost and the worst environmental performance whereas configuration 2 performed moderately. Configurations 1 and 3 offered the best combination of low-cost and environmental performance, where configuration 3 had a slight advantage in terms of carbon emissions since BIGCC, which emits more CO_2 compared to CCGT, was excluded from the mix by the optimisation algorithm.

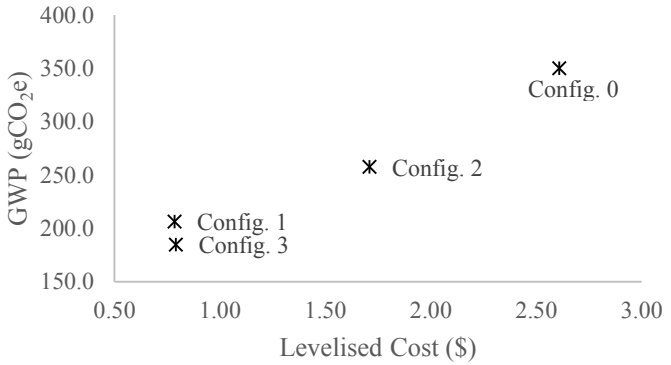

Figure 3. Levelised costs and GWP results for all scenarios.

4. Conclusions

A techno-economic assessment was conducted to evaluate levelised costs and CO_2 emissions from four different electricity and water cogeneration configurations. The configurations represented current installations and future renewable portfolio mixes for the GCC region. An optimisation based on MOGA was applied to identify the optimal cogeneration portfolio configuration. The results show 70 % and 47 % improvement in economic and environmental performance, respectively, for the optimal configuration compared to the base configuration. The integration of renewable energy into the cogeneration portfolio mix proves to deliver substantial benefits to the sector improving overall sustainability.

References

S. Abdul-Wahab, Y. Charabi, A. M. Al-Mahruqi, I. Osman, S. Osman, 2019, Selection of the best solar photovoltaic (PV) for Oman, Sol. Energy, 188, 1156–1168.

A. AlNouss, G. McKay, T. Al-Ansari, 2019, A techno-economic-environmental study evaluating the potential of oxygen-steam biomass gasification for the generation of value-added products, Energy Convers., 196, 664–676.

H. Al-Obaidli, S. Namany, R. Govindan, T. Al-Ansari, 2019, System-Level Optimisation of Combined Power and Desalting Plants, Comput. Aided Chem. Eng., 46, 1699–1704.

M. A. Darwish, N. M. Al-Najem, N. Lior, 2009, Towards Sustainable Desalting in the Gulf Area, Desalination, 235, 58–87.

IRENA, 2019, Renewable Energy Market Analysis: GCC 2019.

A. Kaya, M. E. Tok, M. Koc, 2019, A Levelised Cost Analysis for Solar-Energy-Powered Sea Water Desalination in The Emirate of Abu Dhabi, Sustainability.

World Bank, 2019, CO2 Emissions (metric tons per capita), https://data.worldbank.org.

Sauro Pierucci, Flavio Manenti, Giulia Bozzano, Davide Manca (Eds.)
Proceedings of the 30th European Symposium on Computer Aided Process Engineering (ESCAPE30), May 24-27, 2020, Milano, Italy.
http://dx.doi.org/10.1016/B978-0-12-823377-1.50241-X

Techno-Economic Assessment of Conceptual Design for Methanol Production Using Coal and Natural Gas Based Parallel Process Configuration

Usama Ahmed[*a], Umer Zahid[a], Nabeel Ahmad[b]

[a]*Chemical Engineering Department, King Fahd University of Petroleum and Minerals, Dhahran, Saudi Arabia*
[b]*Department of Chemical Engineering, COMSATS University Islamabad, Lahore Campus, Pakistan*
usama.ahmed@kfupm.edu.sa

Abstract

Methanol production has gained a lot of attention due to its wide application in both the process and product industries. This study aims to investigate the coal/methane based process for simultaneous methanol and power generation. Two process models were developed in Aspen Plus and techno-economically compared. Case 1 is taken as a base case model that represents the coal to methanol (CTM) technology. Case 2 represents the sequential integration between the coal gasification and methane reforming technologies to enhance both the synthesis gas and methanol production capacity. It has been seen from results that case 2 design has a potential to boost up the methanol production compared to the case 1 design. In terms of process performance, the overall process efficiencies for the case 1 and case 2 is calculated as 63.2% and 70.0%, respectively. Moreover, the carbon conversion efficiency for case 2 design is nearly 6% higher than the case 1 design. In terms of methanol production cost, case 1 and case 2 offered 0.25€/kg and 0.23€/kg, respectively. While evaluating other process performance and environmental quality control indicators, it has been analysed from results that case 2 offers higher process feasibility compared to the case 1 design.

Keywords: Gasification, Reforming, Methanol Synthesis, Synthesis Gas.

1. Introduction

During the last many decades, fossil fuels remained the main source of energy and power generation that not only increased the greenhouse gas emissions to unsafe levels but also caused global warming. The damaged caused by fossil fuels to environment especially by the coal based systems can be minimized using an alternative energy conversion technologies. The conventional routes of producing the methanol from fossil fuel includes two stages. In the first stage, the synthesis gas is generated from fuel which is then cleaned prior to its conversion into methanol. Natural gas to methanol (NGTM) technology has been extensive utilized around the world to meet the methanol production and supply demand. The synthesis gas can be efficiently converted to methanol if the HCR (hydrogen to carbon) ratio in the synthesis gas is between 2-2.05. Usually, steam methane reforming (SMR) technology is used to generate synthesis gas from natural gas which offers higher HCR in the synthesis gas. On the other hand, coal to methanol (CTM) converts the coal into synthesis gas by the gasification technologies. The synthesis gas generated from the coal has a lower value HCR and contains more CO_2 and CO. The synthesis gas from the coal gasification process is usually integrated with the water gas shift (WGS) reactors to

convert the CO in the synthesis gas to H_2 on reaction with the H_2O. Yi et al. (2015) reported that CTM technologies produces 2.6 ton of CO_2 for each ton of methanol (MeOH) production, whereas, SMR technologies offers higher HCR ratio in the synthesis gas and shows very less CO_2 emissions. Comparing the current prices and reserves of natural gas and coal, the opportunities to develop the dual fuel conversion technologies have gained a lot of attention. The SMR and coal derived synthesis gas can be mixed to regulate the higher HCR ratio at the inlet of methanol synthesis reactor. Recently, Blumberg et al. (2019) integrated the different methane reforming technologies for enhancing the H_2 production, which offers higher exergetic efficiency for methanol synthesis. Ahmed et al. (2017, 2019) also showed an improvement in the power and H_2 production by integrating the gasification and reforming technologies in the series design configuration. Similarly, Kler et al. (2018) proposed a model for simultaneous production of methanol and electricity from coal. Chen et al. (2019) developed a model using multiple feed-stocks for MeOH synthesis while reducing the CO_2 emissions. In this study, coal and natural gas feed-stocks are used for the MeOH synthesis and electricity production by using the parallel design integrations between the gasification and reforming technologies. The key idea of this research is to utilize the heat energy from the gasification unit into the reforming unit to sustain the high enthalpy SMR reactions. This integration not only reduces the overall process energy requirements but also enhances the syngas production with the higher HCR ratio. The focus of this research article is to perform the techno-economic analysis of the proposed design and its comparison with the conventional processes.

2. Process Simulation and Methodology

The process models were developed in Aspen Plus v10 where Peng Robinson with Boston Mathias equation of state is selected as an effective thermodynamic package. Coal is usually considered as an unconventional component and its composition is defined in terms of key components through Proximate, ultimate and sulfanal analysis. RGibbs reactor model is selected for the modelling of gasification, water gas shift, reforming and methanol synthesis reactor which generates the reaction products on the principle of Gibbs free energy minimization. Table 1 highlights some of the design assumptions for the design of major unit processes.

Table 1: Design Assumptions for Model Development

Unit/Component/System	Modelling Unit	Parameter
Gasification Reactor	RGibbs (Reactor)	Coal flow rate= 62.01kg/s Temp/Press: 1350-1370°C/56 bar
Reformer	RGibbs (Reactor)	NG flow rate: 5.5 kg/sec H_2O:CH_4 = 3:1 Temp/Press: 900°C/ 32 bar
Air Separation Unit (ASU)	HeatX, Compr	Oxygen Purity 95% (vol)
Methnanol Reactor	RGibbs (Reactor)	Cu based catalyst Pressure/Temp: 55bar/200°C

2.1. Case 1- Conventional Coal to Methanol (CTM) Process

Case 1 is considered as a conventional CTM where coal water slurry is fed to the coal gasification unit at 56bar, which is partially oxidized to generate synthesis gas at the

temperature of 1370°C. The synthesis gas is then cooled in the radiant and convective heat exchangers followed by H_2S removal. The sulphur free synthesis gas is then passed over the Cu based catalyst in the methanol reactor at the standard temperature and pressure of 200°C and 55 bar. Figure 1 represents the conventional methanol production process from coal. Finally, series of flash drums and distillation columns are sequentially used in the downstream process chain to enhance the purity of methanol in the product stream to 99%.

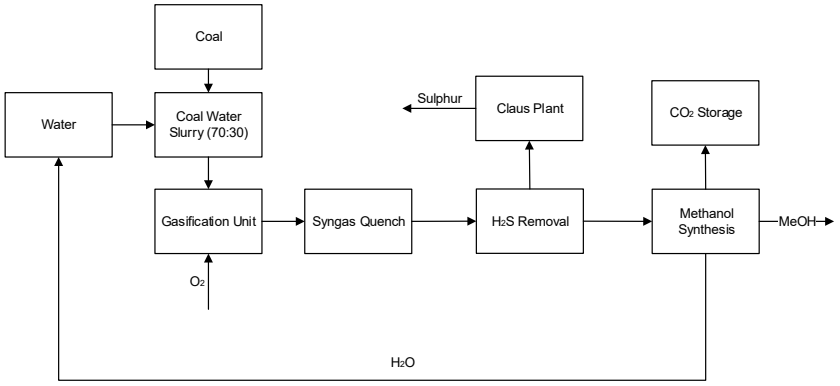

Figure 1: Coal to Methanol (CTM) Process

2.2. Case 2- Coal and Natural Gas based Process for Methanol Production (CNPM)

Case 2 is considered as a conceptual design where coal and natural gas feed-stocks are used for methanol synthesis as represented in Figure 2. The coal gasifier derived synthesis gas usually contains high amounts of sulphur which must be removed in the H_2S removal section prior to its mixing with the reformed natural gas. The temperature and pressure of the syngas at the inlet of the methanol reactor is also maintained at 200°C and 55 bar, respectively, as done in the case 1 design. This parallel design configuration of integrating the gasification unit with the reforming unit not only reduces the process energy requirements but also helps in increasing the overall methanol production.

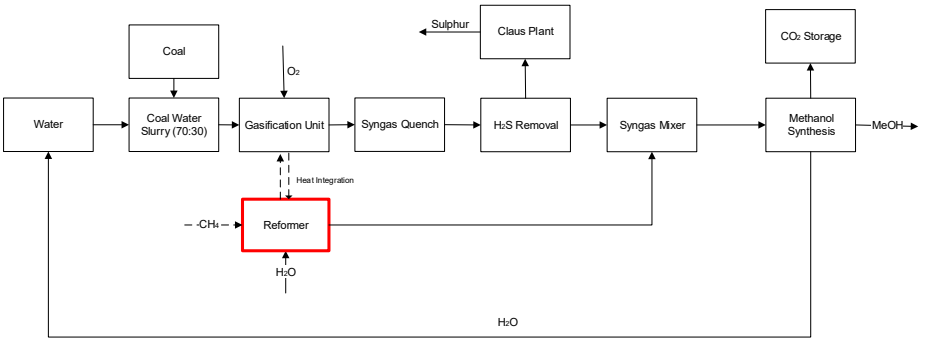

Figure 2: Coal and Natural Gas based Methanol Production Process

3. Results and Discussion

Case 1 was modelled as the conventional CTM process where cold gas efficiency (CGE) of the syngas is based on the gasifier operational conditions, type of feed and the heat

integration network. The case 1 design is then retrofitted with the SMR technology to generate the case 2 design to utilize the key technical benefits of both the gasification and reforming technologies. This retrofitting of SMR unit in the parallel design configuration not only allowed to utilize the high enthalpy heat from the gasifier derived synthesis gas but also helps in increasing the HCR ratio at the inlet of the methanol reactor. In both the cases, 62.19kg/s of the bituminous coal has been used as a feedstock for the gasification unit. Unlike case 1, the case 2 design consumes an additional natural gas at the rate of 5.5kg/s in the reforming unit. The coal to natural gas ratio of 5.5:1 is maintained in the case 2 design to utilize maximum heat from the gasification unit for the reforming of natural gas without any additional heat supply. The results showed that there is a signification increase in syngas production capacity in the case 2 design compared to the case 1. The HCR (hydrogen to carbon ratio) obtained in the case 2 design is also higher than case 1 design. Figure 3 shows the synthesis gas composition at the inlet of methanol reactor for case 1 and case 2 designs.

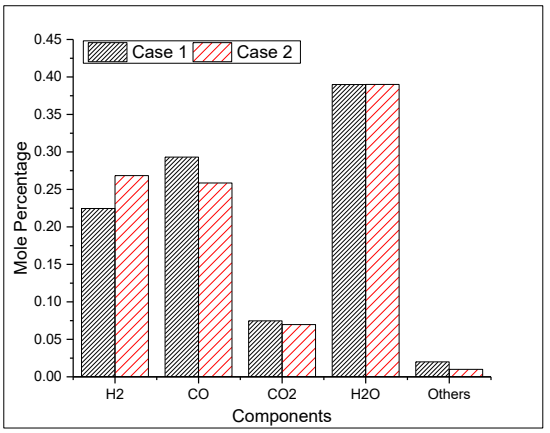

Figure 3: Synthesis gas composition at the inlet of Methanol Reactor

To ensure the unbiased analysis, the process performance indictor for calculating the overall process efficiency has been used as given in the equation 1. The overall energy efficiency is a function of heat input rates in the form of thermal energy and the heating value of the produced methanol along with the power generation potential for each case.

$$\text{Energy Efficiency} = \frac{\text{Produced electricity + Heat of Produced MeOH}}{\text{Feed stock heating value + Energy Consumed}} \ [\%] \qquad (1)$$

The results showed that the process efficiency calculated for case 1 and case 2 is 63% and 70%, respectively. The heat generated from both the cases has been utilized for electricity generation using steam turbine cycle. The results showed that the electricity generation potential from the case 1 and case 2 is calculated as 11.26MW_e and 16.70MW_e, respectively. Methanol production capacity and energy requirement from a specific fuel is also an important criterion to analyze the process technical and economic feasibility. The difference in the process configuration and the heat exchanger network highly effects the overall production capacity. The simulation results showed that the methanol production capacity from case 1 and case 2 is calculated as 171 MT/hr and 212 MT/hr, respectively, where the case 2 design shows 24% higher methanol production capacity compared to case 1. Figure 4 also represents the comparison between two cases in terms of process efficiency (%), methanol production energy (kg/kW_e) and methanol production

capacity (ton/hr). The results showed that the the specific methanol production for case 1 and case 2 is calculated as 0.7 kg/watt and 0.8 kg/watt, respectively.

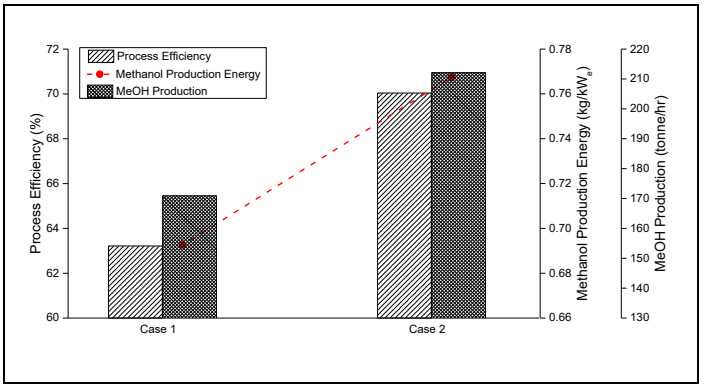

Figure 4: Comparison of Methanol Production Rates and Energy for Case 1 and Case 2

The estimation of capital (CAPEX) and operational (OPEX) expenditures are important factors to analyze the sustainability of any chemical process. The fixed CAPEX includes the cost of equipment, cost of land, installation costs etc. The OPEX involve the cost of feedstocks, catalysts and the utilities. The CAPEX for both the cases is calculated using the power law of capacity as shown in the equation 2, where, *x* represents the capacity factor which is taken as 0.6 in this research.

$$\mathrm{Cost_{New}} = \mathrm{Cost_{Old}} \times \left(\frac{\mathrm{Capacity_{New}}}{\mathrm{Capacity_{Old}}}\right)^{x} \times \frac{\mathrm{CEPCI_{New}}}{\mathrm{CEPCI_{Old}}} \qquad (2)$$

The results showed that the CAPEX required for case 1 and case 2 is 2594.89M€ and 2895.06M€, respectively. Similarly, the OPEX calculated on the yearly basis for case 1 and case 2 is calculated as 190M€ and 225M€, respectively. Despite the higher value of the overall OEPX and CAPEX for case 2 design, the per unit cost for methanol production is lower than the case 1 due to its higher methanol production capacity. In terms of specific cost for methanol production, case 1 and case 2 offers nearly 275.2 €/ton and 258.4 €/ton, respectively. In terms of cash flow analysis throughout the lifetime of the project, the minimum payback time of the project and the expected profit has been also calculated.

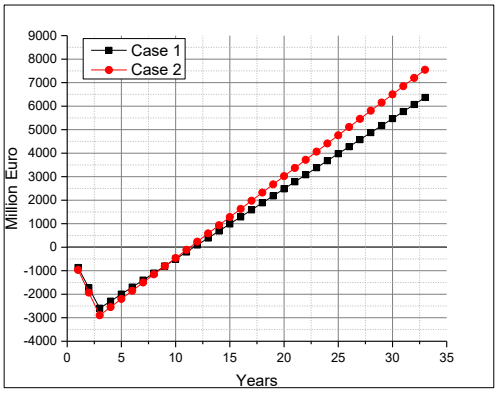

Figure 5: Cumulative cash flow for Case 1 and Case 2

Figure 5 represents the cumulative cash flow analysis for both case 1 and case 2 design where the life time of the project is assumed to be 33 years. It has been analyzed from the results that the payback time for both the case 1 and case 2 is calculated as 11 years, where the case 2 design showed a higher profit potential of 2600-2700M€ as compared to the case 1 design throughout the life time of the project.

4. Conclusion

This paper represents the techno-economic analysis of two processes for methanol production. Case 1 is taken as a conventional coal to methanol (CTM) processes, whereas, case 2 represent the conceptual design of integrating of the reforming unit with the gasification unit to utilize the maximum heat to sustain the reforming reactions. It has been analyzed from the results that the case 2 design offers higher process performance and economics compared to the case 1 design in terms of methanol production. Case 2 design not only represents higher methanol production rates but also showed a reduction in the per unit production energy requirements. Moreover, case 2 design offers higher rate of return on the investments, which makes its design more sustainable compared to the conventional process.

Acknowledgement

The authors would like to acknowledge the support provided by the King Fahd University of Petroleum & Minerals (KFUPM) for funding this work through project No. SR181006.

References

Ahmed U, Zahid U, Lee Y. Process simulation and integration of IGCC systems for H_2/syngas/electricity generation with control on CO_2 emissions. International Journal of Hydrogen Energy. 2019;44(14):7137-48.

Ahmed U, Kim C, Zahid U, Lee C-J, Han C. Integration of IGCC and methane reforming process for power generation with CO_2 capture. Chemical Engineering and Processing: Process Intensification. 2017;111:14-24.

Blumberg T, Morosuk T, Tsatsaronis G. CO_2-utilization in the synthesis of methanol: Potential analysis and exergetic assessment. Energy. 2019.

Chen J, Yang S, Qian Y. A novel path for carbon-rich resource utilization with lower emission and higher efficiency: An integrated process of coal gasification and coking to methanol production. Energy. 2019;177:304-18.

Kler AM, Tyurina EA, Mednikov AS. A plant for methanol and electricity production: Technical-economic analysis. Energy. 2018;165:890-9.

Yi Q, Li W, Feng J, Xie K. Carbon cycle in advanced coal chemical engineering. Chemical Society Reviews. 2015;44(15):5409-45.

Sauro Pierucci, Flavio Manenti, Giulia Bozzano, Davide Manca (Eds.)
Proceedings of the 30th European Symposium on Computer Aided Process Engineering
(ESCAPE30), May 24-27, 2020, Milano, Italy.
http://dx.doi.org/10.1016/B978-0-12-823377-1.50242-1

Sustainable Exergoeconomic Optimization of Petroleum Production Systems

Meziane Akchiche[a,b], Jean-Louis Beauquin[a], Sabine Sochard[b], Sylvain Serra[b], Jean-Michel Reneaume[b], Pascal Stouffs[b]

[a]*Production & Well Performance Department, TOTAL SA, France*
[b]*Universite de Pau et des Pays de l'Adour, E2S UPPA, LaTEP, 64000, Pau, France*
meziane.akchiche@univ-pau.fr

Abstract

This paper presents a new methodology to improve the conception of petroleum production systems by incorporating environmental perspectives, in addition to energy and economic aspects, over their entire life-cycle. We first proposed generic oil production system configurations that include the most common technologies. In this work, two objective functions are suggested to evaluate the performance of an oil production system, which can be operated by different equipment during its whole life-cycle: i) Cumulative Net Exergy (CNE), ii) Cumulative Net Profit (CNP). In this dynamic optimization problem, considering that optimization variables may be continuous, binary, or discrete, that most of the production systems have a non-linear response and that the imposed constraints make the problems non-convex, we are usually dealing with Mixed Integer Non-Convex Non-Linear Optimization Problems (MINLP). The stated problem is then solved using a multiphase flow simulator, coupled with a thermodynamics calculator for the exergy analysis. The Genetic Algorithm included within the chosen software is then used to solve the multiperiod MINLP problem. The optimization results show that for a non-eruptive oil well, the most energy-efficient artificial lift and boosting methods are not always the most cost-effective. It therefore appears that it is necessary to combine exergy and economics (exergoeconomics) for the optimization purposes at the level of petroleum production system components for designing sustainable systems.

Keywords: Oil & Gas production system, Exergy, MINLP, Superstructure, Optimization

1. Introduction

In accordance with the International Energy Agency (IEA, 2018), fossil fuels will remain relevant to the energy system for decades. In 2018, global oil supply exceeded 100 million barrels per day for the first time, and world natural gas demand increased by 4.9 percent compared to 2017 (IEA, 2018). The growing need for hydrocarbons is driving petroleum exploitation to cross new borders: technical borders, economic borders, and also environmental borders. Oil and gas companies are increasingly going after deep and/or complex petroleum reservoirs to meet hydrocarbon demand. Developing these fields requires the construction of more elaborate production systems and the implementation of fluid and power processing, transportation, and delivery systems. Also, power generation is a high source of greenhouse gas (GHG) emissions. Therefore, the main challenge for oil and gas companies is to select the most economically viable and, at the same time, the least GHG emitting development scheme.

Fig.1 illustrates a typical oil production profile that we can split into three distinct periods. First, the start-up period corresponds to the extent of time during which producing wells are sequentially brought into production. Then, the plateau period begins when the full installed capacity is used, and a constant production rate is maintained by using a choke valve. This production restriction is imposed by technical and economic criteria, while the real production potential may be more significant. Finally, the decline period refers to the time when producing wells, and more generally, the overall field production falls at a rate of 1% to 10% per year.

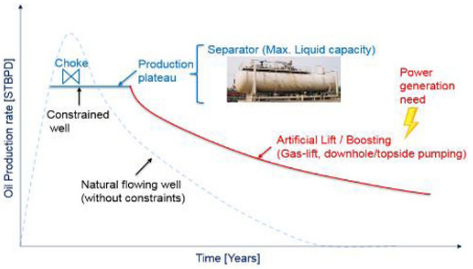

Fig.1 : Oil production profile

Fig 2 shows some of the most common configurations of oil production systems. As long as the natural energy of a reservoir (P_{Res}, T_{Res}) is sufficient to achieve the production plateau, fluids flow naturally from the reservoir to surface facilities (Fig.2a) and may be restrained by a choke valve (THC). When this natural energy is not or no longer sufficient to maintain production due, for example, to reservoir depletion over time, it becomes necessary to provide an external energy boost by using artificial lift and boosting equipment. Fig.2b depicts an oil production system equipped with gas-lift. The pressurized gas injection lightens the gradient in the tubing resulting in a lower Bottom Hole Pressure (P_{BH}) that increases the liquid production rate (G. Takacs, 2005). Fig.2c and Fig.2d show two different downhole pumping technologies. The first one is an Electrical Submersible Pump (ESP) that is made of centrifugal pump stages (G.Takacs, 2009), while the second one called Electrical Submersible Progressing Cavity Pump (ESPCP) is a positive displacement pump (H. Cholet et al., 2012). These two pumping technologies can be equipped with a separator or not, depending on the nature of the produced effluents. In addition to the downhole artificial lift technologies, it is also possible to use surface artificial lift methods, such as, for example, Progressive cavity pumping (PCP) systems.

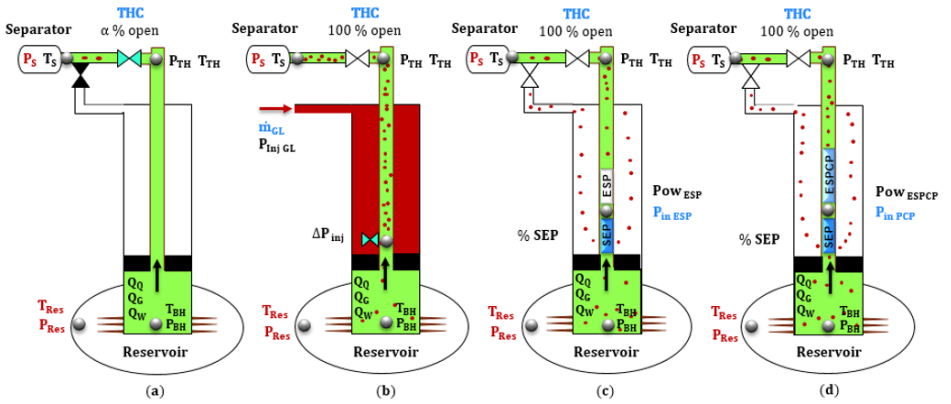

Figure 2. Oil Production system models

2. Methodology

2.1. Objective functions

We want to evaluate the influence of selecting two different objective functions on the whole life-cycle of an oil production system. The first objective function is a Cumulative Net Profit (CNP) to be maximized, while the second one is a Cumulative Net Exergy (CNE) to be also maximized. The objective functions are defined as follows:

$$F_1 = \mathrm{CNP}\ [\mathrm{MM\$}] = \mathrm{CHS} - \mathrm{CBE} \quad (1)$$

$$F_2 = \mathrm{CNE}[\mathrm{GWh}] = \mathrm{Ex}^{\mathrm{ch}}_{\mathrm{oil+gas}} - \mathrm{Ex}^{\mathrm{ch}}_{\mathrm{inv}} \quad (2)$$

Where CHS [MM$] is the Cumulative Hydrocarbon Sales, CBE [MM$] is the Cumulative Boosting Expenses (CAPEX + OPEX), $\mathrm{Ex}^{\mathrm{ch}}_{\mathrm{oil+gas}}$ [GWh] is the cumulative chemical exergy of produced hydrocarbons, $\mathrm{Ex}^{\mathrm{ch}}_{\mathrm{inv}}$ [GWh] is the cumulative exergy invested (as an example, the artificial power generation). The CBE term includes the costs of switching from one technology to another between two periods. The different changes in reservoir conditions and fluid properties over time require more flexible petroleum production systems. Fig.3 shows the evolution of the petroleum production system during different time steps.

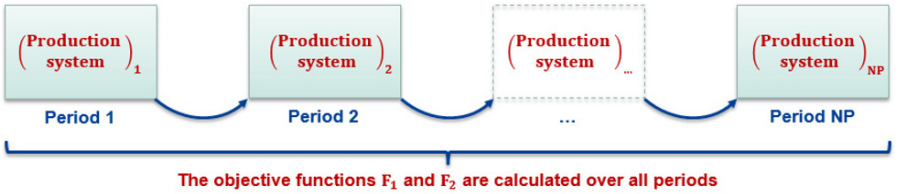

Figure 3. Optimization of the objective functions over all periods

Fig.4 shows the superstructure of alternative configurations of the oil production system that includes all the artificial lift and boosting methods mentioned in Fig.2. At each period, topological variables will be used to select a production system among all the possible topologies offered by the superstructure. For example, a possible configuration is to have an ESP pump equipped with a downhole separator at the subsurface level and no boosting method at the surface level (ESP + D-SEP + Natural F).

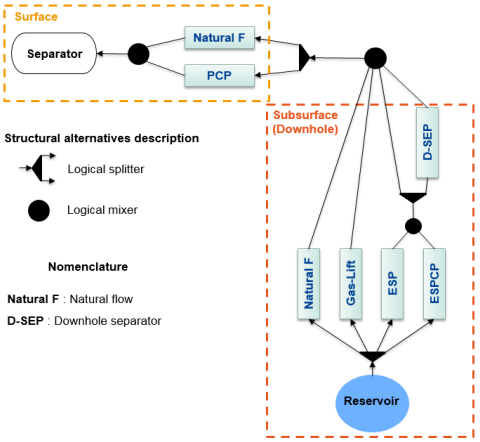

Figure 4. The superstructure of alternative configurations of the oil production system

2.2. Resolution strategy

Usually, we model each part of the petroleum production system within the dedicated tools to catch the complexity of the physical-chemical phenomena involved at each step of the production chain. These specialized tools that model the different parts of the field can, therefore, be connected and exchange data dynamically to implement a full field model. This combined architecture is called Integrated Production Modeling (IPM). In this study, the Petex IPM suite of tools (MBAL®, PROSPER®, GAP®, RESOLVE®) was used to model and optimize the entire production system (Petex, 2019). The nodal analysis of petroleum production systems is the method used within the IPM suite to evaluate the flow performance of the oil production system for a given configuration and design parameters as well as a set of steady-state operating parameters. The production system is split into several discrete nodes that separate the system components. Flow correlations and thermal models are then used to calculate pressure, flow rates, and temperature at each node. A Black oil method and an enthalpy balance temperature model were used to describe the fluid flow through the entire oil production system.

RESOLVE® is the platform that brings together external applications, such as, for example EXCEL, in addition to including multiple optimization modules. Exergy calculations were carried out with Simulis thermodynamics® that is available as a Microsoft Excel® add-in (ProSim, 2019). The same Excel model was used for economic calculations. We have then formulated the MINLP problem using the optimization module (GIRO) at the RESOLVE® level, allowing to have GAP®, MBAL®, and EXCEL as underlying applications. GIRO is based on Genetic Algorithm (GA) principles and does not allow using continuous variables, nor does it handle constraints. To solve the formulated problem with the GIRO algorithm, we have discretized (in the sense of encoding) the continuous variables and developed a workflow to meet the constraints. The methodology described in Fig.5 was used to solve the formulated MINLP problem.

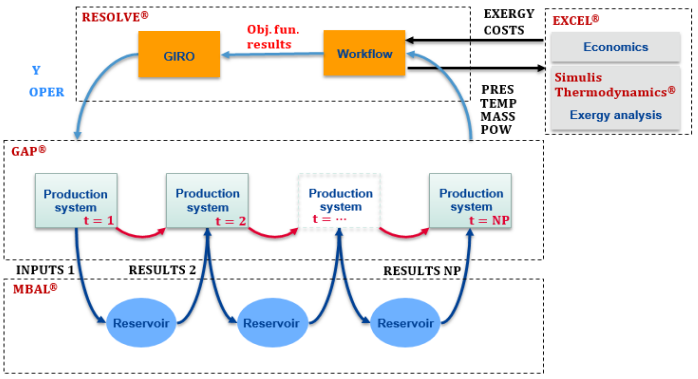

Figure5. Workflow for formulation and solution of dynamic MINLP problem

At each GIRO iteration, topological and operating variables are provided. For each period, the knowledge of the chosen technology (linked to topological variables **Y**) and the operating variables (**OPER** in Fig.5 and variables in blue in Fig.2), together with (P_{Res}, T_{Res}) and P_S (in red in Fig.2) enable GAP® to calculate, in quasi-static state, the produced flow rates (oil, gas, and water), temperatures, and pressures for all the nodes (in black in Fig.2). P_S is the fixed pressure of the surface facilities' first separator. At the end of the period, these results are provided to MBAL®, which calculates the new reservoir conditions. At the end of this calculation sequence, all the temperatures, pressures, and

mass flow rates at each node for each period are sent back to RESOLVE® level. The workflow checks the constraints (maximum production, open choke valve if an artificial lift method is used, etc.): if a constraint is not met, the objective function of this iteration is not considered. Then, the excel model calculates economics and exergy functions, and the results are sent to the workflow, which estimates the objective function.

3. Results & discussion

The studied case is based on a realistic reservoir model. The separator pressure (P_s) was fixed to 30 bars for all cases, and the maximum production constraint (Qmax) set at 5000 STBPD. Table 1 shows the results of the optimized objective functions. The whole period is 12 years, simulated with quasi-static approximation with periods of 6 months.

Table 1: optimization results

Objective function	Cumulative Net profits (CNP) MM$	Cumulative Net Exergy (CNE) Gwh	Cumulative production MMSTB[1]	CO2 emissions kt	Topologic variables **Y**
Max. Cumulative Net Profit (CNP)*	613*	19594	12.4	9.8	Natural F + GL
Max. Cumulative Net Exergy (CNE)**	610	19947**	12.6	6.7	Natural F + ESP

[1] MMSTB: Millions Standard (1bar, 60°F) Barrels

In both cases of maximizing the CNP or the CNE, the oil production system is first producing naturally (Natural Flow) while respecting the maximum production constraint. After some time, water progressively gains access to the producing well at the expense of hydrocarbons and increases the weight of the fluid column (density). Therefore, the total liquid flow decreases, and an artificial lift or boosting system is needed to maintain production and prevent the well shutdown.

When the CNP was maximized, the optimizer has selected the gas-lift system as it ensures to maintain the liquid production rate as high as possible while being less expensive than an ESP that produces the same flow rate. On the other side, when it is a matter of improving energy efficiency by maximizing the CNE, an ESP is selected. It is not only due to increased cumulative chemical exergy of produced hydrocarbons, but also because Gas-lift systems are high energy consumers. However, it can be pointed out that a decrease of 0.5% in CNP leads to an increase of 1.8% in CNE but, above all, a reduction of about 32% in CO_2 emissions. From the two objective functions point of view, the optimum solution may be a compromise.

4. Conclusion & perspectives

Due to their high pressure (P_{Res}), petroleum reservoirs give the essential part of the energy required to extract and transport hydrocarbons to surface facilities. Once this pressure is not sufficient to overcome the sum of pressure losses occurring along the flow path to the separator, artificial lifting and boosting methods are used to provide the additional mechanical exergy. The cost (OPEX+ CAPEX), as well as the GHG emissions of these methods, are directly linked to the mechanical exergy to be delivered to the fluid vein and the overall performance of the artificial lifting and boosting systems.

In the present work, we succeeded in solving a dynamic optimization problem to select suitable technologies over the life cycle of an oil production system. To our knowledge, it is the first study of this kind. It has been done in the IPM suite of tools used by many petroleum companies. The objective functions were economic and exergy functions. The exergy analysis by itself does not make it possible to choose the most suitable production system as it does not include the economic aspect. The most important criterion to select a suitable development scheme is the economic viability of the development.
On the other hand, the cheapest technologies are not always the most energy-efficient (ex. Gas-lift). It may be interesting to formulate a multiobjective optimization problem taking into consideration both economics and energy efficiency (via exergy analysis). Moreover, it appears essential to add, within the superstructure, technologies that reduce exergy losses and, above all, that recover some of the lost exergies to reduce the power needed by the production facilities, and therefore, reduce GHG emissions.

Nomenclature

Variables		Vectors*	
$\dot{m}$	mass rate	**COSTS**	Cost results
P	pressure	**EXERGY**	Exergy results
Pow	Power	**PRES**	Node pressures
T	Temperature	**TEMP**	Node temperatures
THC	Tubing Head Choke	**MASS**	Node mass flow rates
ΔP	Pressure drop	**POW**	Equipment powers
%SEP	Separation percentage	**Y**	Topological variables
Subscript		**OPER**	Operating variables
GL	Gas-Lift	**INPUTS**	Input variables
inj	injection	**RESULTS**	Results
Res	Reservoir		
s	separator	* these vectors include, for each iteration, all the variables of interest over all the periods	
TH	Tubing Head		

References

G. Takacs, 2005, Gas Lift Manual, PennWell Books
G. Takacs, 2009, Electrical Submersible Pumps Manual Design, Operations, and Maintenance, Gulf Professional Publishing
H. Cholet et al., 2012, Progressing Cavity Pumps, Technip
IEA, 2018, Global Energy & CO2 Status Report
IEA, 2018, Energy Technology Perspectives
Petex. (2019, Novembre). Integrated Production Modelling Software for Oil and Gas Fields. Récupéré sur Petroleum Experts Oil, Gas, Structural Geology Software: http://www.petex.com/products/ipm-suite/
ProSim. (2019, November). Simulis Thermodynamics - Mixture properties and fluid phase equilibria calculations. Récupéré sur PROSIM: chemical process simulation software and services: http://www.prosim.net/fr/logiciels-simulis-thermodynamics-calculs-proprietes-melanges-dequilibres-entre-phases--3.php

Sauro Pierucci, Flavio Manenti, Giulia Bozzano, Davide Manca (Eds.)
Proceedings of the 30th European Symposium on Computer Aided Process Engineering (ESCAPE30), May 24-27, 2020, Milano, Italy.
http://dx.doi.org/10.1016/B978-0-12-823377-1.50243-3

Power-to-Methanol at Refineries as a Precursor to Green Jet Fuel Production: a Simulation and Assessment Study

Timo Wassermann [a,*], Christian Schnuelle [a], Philipp Kenkel [a], Edwin Zondervan [b]

[a] *University of Bremen, Advanced Energy Systems Institute, Enrique-Schmidt-Straße 7, 28359 Bremen, Germany*
[b] *University of Bremen, Advanced Energy Systems Institute, Leobener Straße 6, 28359 Bremen, Germany*
timo.wassermann@uni-bremen.de

Abstract

The growing interest in power-to-methanol (PtM) in policy, industry and academia illustrates the need for studies assessing the concept's potential in the context of energy transition. Although there are already studies, which evaluate PtM in a generic way, application-specific analyzes for refineries considering the option of further jet fuel synthesis are lacking. This study provides a unique assessment of the techno-economic feasibility and the environmental impacts of PtM plants at refineries as a precursor to green jet fuel production. The utilization of the flue gas of a single refinery, the Heide refinery, is sufficient for the production of 415,095 t_{MeOH}/y. As methanol production via PtM avoids 2.50 kg_{CO2eq}/kg compared to conventional methanol, it is favorable in terms of greenhouse gas emissions. However, net production costs are 2.9-4.6 times higher than the market price. Subsequent jet fuel synthesis allows a production of at least 83 kt_{Jet}/y on basis of the refinery's flue gas.

Keywords: CO_2 utilization, power-to-methanol, jet fuel, refinery

1. Introduction

Ongoing climate change is one of the most urgent socio-ecological problems as well as one of the most demanding socio-techno-economic challenges confronting humanity. To face this problem, Germany declared to reduce greenhouse gas (GHG) emissions by 80-95 % until 2050 compared to 1990 levels (BMU, 2016). In this context, substitution of conventional chemicals and fuels by synthetic electricity-based products seems to be a viable alternative, as it allows an extensive reduction of GHG emissions. A prominent option is the production of synthetic methanol. Such methanol is identical in chemical structure and composition to its conventional counterpart and can be utilized as chemical feedstock, as fuel or for synthesis of drop-in fuels (Bertau et al., 2014). Conventional crude oil refineries could serve as breeding hub for the realization of commercial PtM plants. They are experienced in the processing of hydrocarbons and their flue gas streams have significant carbon capture potential. In addition, refinery operators in Germany are facing increasingly restrictive emission regulations that require a realignment towards renewable products, e.g. electricity-based methanol and derived drop-in jet fuel.

2. Case study

The state of Schleswig-Holstein, Germany, with its significant on- and offshore wind energy potential is particularly suited as model region for power-to-liquid plants (Flachsbarth and Kasten, 2017). Within this work, the Heide refinery is studied as specific site for a PtM plant. The flue gases emitted by its in-house combined heat and power (CHP) plant, catalytic reformer and steam cracker are considered as CO_2 point source and limiting factor for the PtM plant's production capacity. These facilities are responsible for about 70 % of the refinery's CO_2 emissions. The main properties of the merged flue gas stream are listed in Table 1, neglecting trace components like NO_X and SO_X.

Table 1: Mass flow and composition of the merged flue gas stream based on Finnern (2019)

Facilities	$\dot{m}_{Flue\ gas}$ [t/h]	w_{CO2} [wt%]	w_{H2O} [wt%]	w_{O2} [wt%]	w_{N2} [wt%]
CHP plant, catalytic reformer and steam cracker	570.1	13.9	8.8	4.1	73.2

3. Methodology

Rigorous techno-economic analysis (TEA) and life-cycle assessment (LCA) are conducted based on process modeling and simulation using Aspen Plus V11. The technologies considered are primarily selected according to their maturity level: Alkaline electrolysis (TRL 9), CO_2 extraction via absorption with monoethanolamine (TRL 9) and methanol synthesis via direct CO_2 hydrogenation (TRL 8).

3.1. Process concept: alkaline electrolysis

Alkaline electrolysis (AEL) is represented by literature data. An efficiency of 4.8 kWh/Nm^3_{H2} is assumed at the electrolyzer-system level, i.e. including periphery (Buttler and Spliethoff, 2018). Hydrogen is provided to the methanol unit with a purity of 99.9 vol%, at a pressure of 30 bar and at 25 °C.

3.2. Process concept and modeling: carbon capture

The modeled carbon capture concept via MEA scrubbing builds on the work disseminated by Nguyen and Zondervan (2018). Flow-sheet modifications have been implemented, which include a relocation of the flue gas blower as well as the integration of two recycle/inter-cooling streams within the absorber column (Figure 1). These modifications are primarily based on findings at the Niederaussem pilot plant (Schmidt, 2014).

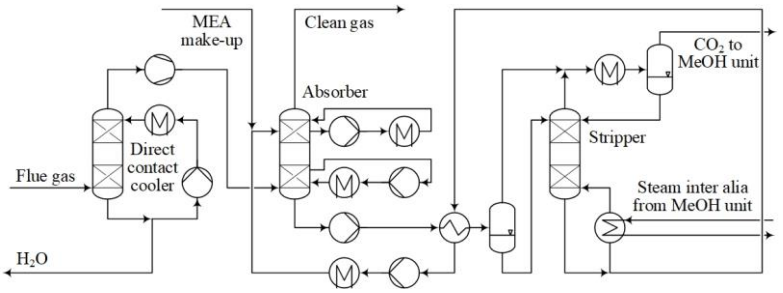

Figure 1: PFD carbon capture unit

A rigorous rate-based model of the carbon capture process is developed using FLEXIPAC 250Y as structured packing. The unsymmetrical electrolyte NRTL property method (ENRTL-RK) is applied as thermodynamic model, while the electrolyte solution chemistry of the MEA-CO_2-H_2O system is modeled considering equilibrium and kinetic

reactions. The respective equilibrium constants are calculated from Gibbs-free energy and power law equation is applied for calculation of the reaction rates (Li et al., 2016). The model is calibrated for 90 % capture efficiency and the characteristics of the captured CO_2 stream (T=40 °C, p=1.75 bar, w_{CO2}=95.7 wt%) are used for methanol synthesis modeling.

3.3. Process concept and modeling: methanol synthesis

Methanol synthesis is considered via the direct CO_2 hydrogenation process concept proposed by Bongartz et al. (2019) (Figure 2). AA-grade methanol is produced at a reaction pressure of 70 bar, a reaction temperature of 250° C, a molar H_2:CO_2 ratio of 3.0 and application of commercial $Cu/ZnO/Al_2O_3$ catalyst. An isothermal fixed bed reactor is modeled as a plug flow reactor using kinetics of Van-Dal and Bouallou (2013). NRTL is considered as thermodynamic model for units operating below 10 bar, while the Redlich-Kwong-Soave equation of state with modified Huron-Vidal mixing rules is applied for units operating above 10 bar. It is noted, that one percent of the recycle stream is purged to prevent accumulation of inert gases. The combustion of the purge stream together with heat from the exothermic methanol synthesis is used for steam generation, with the steam being integrated in the carbon capture unit's stripper.

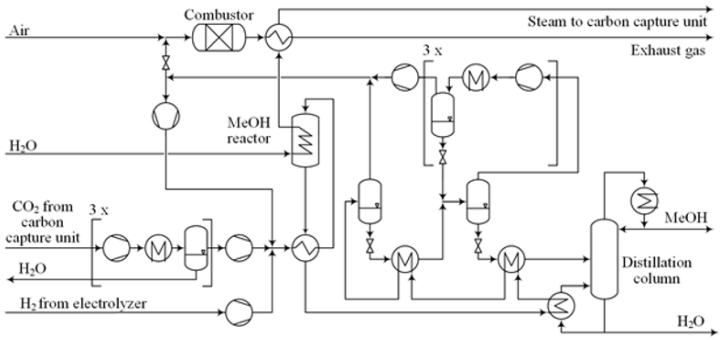

Figure 2: PFD methanol synthesis unit adopted from Bongartz et al. (2019)

3.4. Techno-economic analysis

The TEA is carried out according to a standard methodology proposed by Peters et al. (2003). It yields the net production costs (NPC), defined as the ratio of the total annualized costs of production (TAC) by the annual product output. Table 2 lists the main assumptions for the TEA. The CAPEX are based on the component's specific acquisition costs (C_i). For the carbon capture and the methanol unit Aspen Economic Analyzer is applied for generation of C_i, while a value of 500 €/kW_{el} is assumed for the AEL (IEA, 2019). A ratio factor is applied to take account of further capital requirements, i.e. to calculate the total capital investment. For the electrolysis unit, a decreased ratio factor is sufficient as it is not a thermo-chemical (TC) but an electro-chemical process (EC), being delivered as skid-mounted unit.

Table 2: Basic assumptions of the TEA

Parameter	Value	Unit
Year of comparison	2018	-
Plant lifetime	25	y
Plant availability	8,260	h/y
Interest rate	5	%
Ratio factor	EC: 1.81, TC: 5.93	-
Electricity	87.00	€/MWh
Medium pressure steam	55.00	€/MWh

Parameter	Value	Unit
Catalyst	95.24	€/kg
MEA	1,450.00	€/t
Deionized water	1.00	€/t
Cooling water	0.00125	€/t
Waste water	0.40	€/t
Oxygen	26.30	€/t
CO_2 certificate	24.00	€/t

3.5. Life-cycle assessment

LCA is conducted by application of openLCA V1.8 software for modeling and calculating, while ecoinvent V3.3 database is used in background processes. A comparison of the global warming potential of conventionally produced methanol from natural gas with methanol based on renewable electricity is intended. The system boundaries are defined according to the cradle-to-gate approach, the production of 1 kg methanol is considered as functional unit and CML 2001 is taken as impact assessment method.

The life cycle inventory data builds on the generated mass- and energy balance and takes account of plant construction. The CO_2 provision processes, i.e. the refinery facilities, are not taken into account, as the uncaptured CO_2 is classified as waste. Thus, the environmental impacts of the conventional refinery process are not affected.

4. Results and discussion

4.1. Power-to-methanol

Utilization of the refinery's flue gas output results in a synthetic methanol production capacity of 415,095 t_{MeOH}/y. This corresponds to 0.1 tons of synthetic methanol per ton of crude oil processed and equals 22 % of German methanol production. The energy requirements of the PtM process as well as its mass in- and outputs are shown in Table 3. The steam generated in the methanol unit covers 27.0 % of the heat demand of the stripper of the carbon capture unit and thus improves the efficiency of the overall process. The energy conversion efficiency of the process is 46.4 % based on the lower heating value of methanol. In terms of energy input, the electrical power demand is most significant. It corresponds to a rated power supply of 531 MW_{el} for electrolysis and 545 MW_{el} for the overall process, being in the order of magnitude of a typical German offshore wind farm's nominal load.

Table 3: Energy, utilities and outputs of the integrated PtM process

Stream	Energy MJ/kg_{MeOH}	Stream	Mass kg/kg_{MeOH}	Stream	Mass kg/kg_{MeOH}
Electricity	39.07	Deionized water	1.98	Waste water	-0.57
Medium pressure steam	3.77	Cooling water	136.19	Oxygen	-1.57
		Flue gas	11.34	Exhaust	-0.50
		MEA	2.13E-03		

The net production costs are 1,146 €/t_{MeOH}. This corresponds to a ratio of 2.9-4.6 to the price of conventional methanol in the European market, considering its price level in the last 8 years (Methanex, 2019). Based on the bare acquisition costs of 265.5 M€ for the electrolyzer, 14.7 M€ for the CO_2 capture unit and 26.1 M€ for the methanol unit, the plant's total capital investment is 723.3 M€, including 15 % working capital. A breakdown of the TAC is shown in Figure 4. 88 % of the TAC can be attributed to the electrolyzer unit. These costs are in turn primarily attributable to electricity purchase, while electricity accounts for 82 % of the TAC at the overall process level.

Sensitivity of the NPC on the electricity price is shown in Figure 5, while its sensitivity on full load hours (FLH) is displayed in Figure 6. At electricity purchase costs of about 2 ct/kWh, while keeping the other assumptions constant, electricity-based methanol actually becomes competitive. However, since OPEX are dominant, reduction of the FLH has rather small effect on the NPC. When adjusting the TEA assumptions for direct power purchase from an offshore wind farm (FLH: 4,500 h/y), the product output decreases to 226,141 t_{MeOH}/y, while the net production costs reach 1,324 €/t_{MeOH}.

A comparison of the global warming potential (GWP_{100}) of offshore wind energy based PtM methanol from refinery flue gas with methanol from natural gas is shown in Figure 3. At -1.97 kg_{CO2eq}/kg, the net emissions of the PtM route are much lower than those of the conv. alternative with 0.53 kg_{CO2eq}/kg. Thus, production via PtM avoids 2.50 kg_{CO2eq}/kg, although GHG emissions are still present, in particular for steam provision. The negative value for PtM results from the avoided burden approach, where captured CO_2 as well as reference emissions for oxygen production are considered as credit.

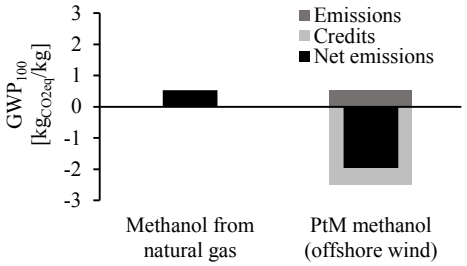

Figure 3: GWP conventional methanol vs. PtM methanol

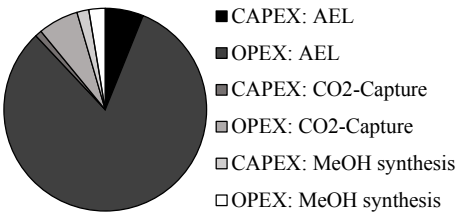

Figure 4: Total annualized costs of production breakdown

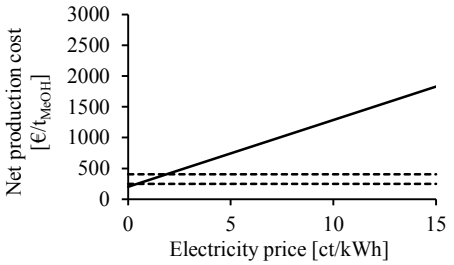

Figure 5: NPC sensitivity on electricity price; dashed lines: conv. methanol price range

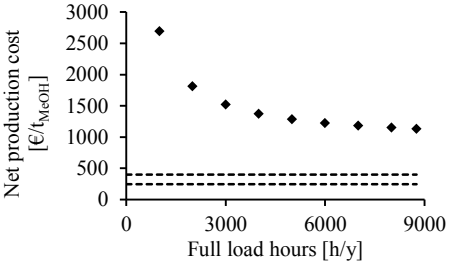

Figure 6: NPC sensitivity on full load hours; dashed lines: conv. methanol price range

4.2. Outlook methanol-to-jet (MtJ)

The general capability of methanol-based jet fuel synthesis was demonstrated in the early 1980's by Mobil's MtO/MOGD technology and by Lurgi's MtSynfuels technology in the early 2000's (Tabak et al., 1986; Liebner and Wagner, 2004). These processes are built on the following sequence: olefin synthesis, olefin oligomerization, hydrogenation and fractionation. However, in contrast to alcohol-to-jet via ethanol and isobutanol, the route via methanol has not yet been approved by the relevant specification for aviation turbine fuel containing synthesized hydrocarbons, namely ASTM D7566.

According to Liebner and Wagner (2004) 0.200 kg_{Jet}/kg_{MeOH} can be yielded with 0.163 kg_{Diesel}/kg_{MeOH}, 0.046 $kg_{Gasoline}/kg_{MeOH}$ and 0.039 kg_{LPG}/kg_{MeOH} as by-products. Assuming this product distribution, 83 kt_{Jet}/y can be produced via synthetic methanol on basis of the flue gas of the Heide refinery. This corresponds to a max. blending ratio of 18.7 % taking into account the refinery's jet production of 360 kt_{Jet}/y in 2018 (Finnern, 2019). A substitution of the German jet fuel production of 5,110 kt_{Jet}/y would require 25,602 kt_{MeOH}/y as intermediate and 278 TWh electricity for synthetic methanol production, which even surpasses Germanys renewable energy generation of 225 TWh in 2018 (Statistisches Bundesamt, 2019; UBA, 2019). The prior given numbers are highly

reliant on the jet fuel selectivity and the MtJ synthesis is expected to have improvement potential with respect to this parameter.

5. Conclusion

Utilization of the flue gas of a single refinery, namely Heide refinery, is sufficient to cover 22 % of German methanol production. Production of such electricity-based methanol allows the avoidance of 2.50 kg_{CO2eq}/kg compared to its conventional production, provided that renewable electricity is applied. From an economic point of view, however, it should be noted that the net production costs of 1,146 $€/t_{MeOH}$ are 2.9-4.6 times the methanol market price. The implementation of PtM at refineries therefore requires far-reaching regulatory measures for emission avoidance or incentive mechanisms. For the subsequent MtJ synthesis it is found that at least 83 kt_{Jet}/y can be produced from Heide refinery's flue gas. Although this concept is promising, substitution of the entire German jet fuel production via power-to-jet is not realistic on a national level, but must be accompanied by imports.

Funding - Funding of this research by the German Federal Ministry of Economic Affairs and Energy within the KEROSyN100 project (funding code 03EIV051A) is gratefully acknowledged.

Acknowledgement - This paper is dedicated to Prof. Dr. Stefan Gößling-Reisemann, who inspired us, shared his knowledge with us and unfortunately cannot be with us today.

References

M. Bertau, H. Offermanns, L. Plass, F. Schmidt, H.-J. Wernicke, 2014. Methanol: The Basic Chemical and Energy Feedstock of the Future. Springer, Berlin, Heidelberg.

BMU, 2016. Klimaschutzplan 2050 - Klimaschutzpolitische Grundsätze und Ziele der Bundesregierung. Berlin.

D. Bongartz, J. Burre, A. Mitsos, 2019. Production of Oxymethylene Dimethyl Ethers from Hydrogen and Carbon Dioxide - Part I : Modeling and Analysis for OME 1. Industrial & Engineering Chemistry Research, 58, 4881–4889.

A. Buttler, H. Spliethoff, 2018. Current status of water electrolysis for energy storage , grid balancing and sector coupling via power-to-gas and power-to-liquids: A review. Renewable and Sustainable Energy Reviews. 82, 2440–2454.

S. Finnern, 2019. Personal data provision. Raffinerie Heide.

F. Flachsbarth, P. Kasten, 2017. Aktuelle Potenziale der Produktion von PtX-Kraftstoffen auf Basis von zusätzlich integrierten Erneuerbaren Energien. Öko-Institut Working Paper, 3.

IEA, 2019, The Future of Hydrogen. Paris.

K. Li, A. Cousins, H. Yu, P. Feron, M. Tade, W. Luo, J. Chen, 2016. Systematic study of aqueous monoethanolamine-based CO2 capture process: model development and process improvement. Energy Science & Engineering, 4, 23–39.

W. Liebner, M. Wagner, 2004. MtSynfuels, die effiziente und wirtschaftliche Alternative zu Fischer-Tropsch-Treibstoffen. Erdoel Erdgas Kohle, 120, 10, 323–326.

Methanex, 2019. Durchschnittlicher Preis für Methanol auf dem europäischen Markt in den Jahren von 2012 bis 2019. Statista.

T. B. H. Nguyen, E. Zondervan, 2018. Ionic Liquid as a Selective Capture Method of CO2 from Different Sources: Comparison with MEA. ACS Sustainable Chemistry & Engineering, 6, 4845–4853.

M. S. Peters, K. D. Timmerhaus, R. E. West, 2003. Plant Design and Economics for Chemical Engineers. McGraw-Hill, New York.

S. Schmidt, 2014. Optimierung und experimentelle Untersuchung der CO2-Abtrennung mit Monoethanolamin für braunkohlegefeuerte Kraftwerke. Technische Universität München.

Statistisches Bundesamt, 2019. Statistisches Jahrbuch 2019. Wiesbaden.

S. A. Tabak, A. A. Avidan, F. J. Krambeck, 1986. Production of synthetic gasoline and diesel fuel from non-petroleum resources. Am. Chem. Soc., Div. Gas Fuel Chem., 31, 293–299.

UBA, 2019. Zeitreihen zur Entwicklung der erneuerbaren Energien in Deutschland. Dessau-Roßlau.

É. S. Van-Dal, C. Bouallou, 2013. Design and simulation of a methanol production plant from CO2 hydrogenation. Journal of Cleaner Production, 57, 38–45.

Sauro Pierucci, Flavio Manenti, Giulia Bozzano, Davide Manca (Eds.)
Proceedings of the 30th European Symposium on Computer Aided Process Engineering (ESCAPE30), May 24-27, 2020, Milano, Italy.
http://dx.doi.org/10.1016/B978-0-12-823377-1.50244-5

Optimizing the Capacity of Thermal Energy Storage in Industrial Clusters

Mandar Thombre,[a] Sandeep Prakash,[a] Brage Rugstad Knudsen,[b] Johannes Jäschke[a*]

[a] *Norwegian University of Science and Technology, Trondheim 7491, Norway*
[b]*SINTEF Energy Research, Trondheim 7491, Norway*
johannes.jaschke@ntnu.no

Abstract

A key factor for energy-efficient industrial clusters is the recovery of waste heat. To this end, thermal energy storage (TES) is an appealing technology that facilitates dynamic heat integration between supplier and consumer plants. A long-term strategy for energy savings must involve adequate consideration for the optimal design of the TES. From an industrial perspective, finding the capacity of the TES unit is often based on heuristic rules which may lead to suboptimal design. This approach does not account for the short-term variability in operation of the TES system. Scenario-based stochastic programming approaches, where the operational uncertainty is described in form of discrete scenarios, can be used to find the best design for the TES system. We present two problem formulations for finding the optimal capacity of the TES unit. The first is a single-level formulation where the design and operating constraints are combined for all scenarios, with the objective of minimizing the combined cost of design and operation. The second is a bilevel formulation where the design decisions are taken on the upper level to minimize overall system cost, whereas the lower level problems (one per scenario) represent the optimal operation for the chosen design variables, each minimizing the operating cost for their respective scenarios. We compare the results of the two approaches with an illustrative case study of an industrial cluster with one supplier plant and one consumer plant exchanging heat via a TES unit.
Keywords: thermal energy storage, bilevel programming, industrial cluster

1. Introduction

Storage and reuse of industrial waste heat is vital for improving energy efficiency of many energy-intensive processes. When multiple industrial plants operate in close proximity of each other, waste heat can be recovered from one plant and supplied to another plant in need of it. Thermal energy storage (TES) can mitigate the issue of asynchronous heat supply and demand by storing energy during off-peak periods and discharging it during peak demands, leading to savings in operating costs. The capital investment costs for installing a TES system are proportional to the capacity of the TES, and may become significantly high. In order to find a trade-off between high capital costs (large capacity) and high operating costs (small capacity), it is worth investigating methods for optimally sizing the TES. A well designed TES system has to contend with operational uncertainty, for example the daily/weekly fluctuations in heat supply and demand. By incorporating this uncertainty information in the design phase itself, it is possible to size a TES system that is robust against this uncertainty. Solving a single deterministic optimization problem that spans across the entire operation horizon of the TES (typically multiple years), and accounts for all the heat profile fluctuations therein,

is computationally intractable. To overcome this, stochastic programming approaches can be used to optimize the design decisions over a set of representative scenarios.

Our aim is to find a measure for the optimal sizing of the TES equipment - the volume of a TES unit and the areas of the HEX delivering/extracting heat from the TES unit - by rigorously accounting for the uncertain heat supply and demand in operation phase. For the TES system, the decisions can be divided into two stages - design and operation. In the extensive form of stochastic programming (Birge and Louveaux, 2011), the design variables are “here-and-now", whereas the “wait-and-see" operation variables are assigned to each scenario. This results in a single-level optimization problem, where the objective function represents the overall system cost. The design constraints and the operating constraints for each scenario are all imposed together in this formulation.

Another stochastic approach is the bilevel formulation, based on a Stackelberg leader-follower hypothesis. The upper level problem (leader) identifies the optimal design decisions that minimize the overall cost over a set of scenarios. On the other hand, the lower level problems (followers), representing different scenarios, aim to minimize their corresponding operating cost (see Xu et al. (2017), for example). Bilevel problems are typically nonconvex and NP-hard. However, for cases where the lower level problems are convex and follow some constraint qualifications, the lower level problems can be replaced with their Karush-Kuhn-Tucker (KKT) optimality conditions (Dempe and Franke (2019)). The KKT reformulation turns the bilevel problem into a single-level mathematical program with complementarity constraints (MPEC). The complementarity constraints can be further linearized using disjunctive programming (Fortuny-Amat and McCarl, 1981), rendering the problem a mixed-integer program.

In this paper, we develop a linear model for the TES system and present the two formulations for optimizing the TES design. The results are compared with the help of a case study that is motivated from an industrial district heating network in northern Norway. We compare the results of the two approaches in terms of design parameters for the TES - its volume, the HEX area and the associated capital investment.

2. Methodology

Topology of a TES system with one supplier and one consumer is shown in Figure 1. We employ a simplified linear model in terms of heat duties (MW) to represent the TES system. The heat supplier needs to reject $Q_{supply}(t)$ amount of duty, whereas the consumer has a heat demand $Q_{demand}(t)$ to be met. If the TES cannot meet the total demand of the consumer, the excess energy $Q_{peak}(t)$ is imported from an external peak heating source. Similarly, if all of supplied heat cannot be extracted from the supplier, the excess energy $Q_{dump}(t)$ is rejected into a cooling water system. The resulting heat flows in and out of the tank are denoted by $Q_{tes}^{in}(t)$ and $Q_{tes}^{out}(t)$. The energy in the TES unit is denoted by $E_{tes}(t)$ (MWh). Heat losses from the TES unit to the surroundings are denoted by $Q_{loss}(t)$, which proportional to its energy content. The peak heating and heat dumping duties, along with the energy in the TES unit represent the operating variables in the system. $x_{opr} := \{Q_{peak}(t),\ Q_{dump}(t),\ E_{tes}(t)\}$ The associated costs (NOK/MWh) of importing and dumping heat are $C_{peak}(t)$ and $C_{dump}(t)$ respectively. Considering an operating period from t_0 to t_f, the total operating cost can be shown as

$$C_{opr} := \int_{t_0}^{t_f} \left(C_{peak}(t) Q_{peak}(t) + C_{dump}(t) Q_{dump}(t) \right) dt \tag{1}$$

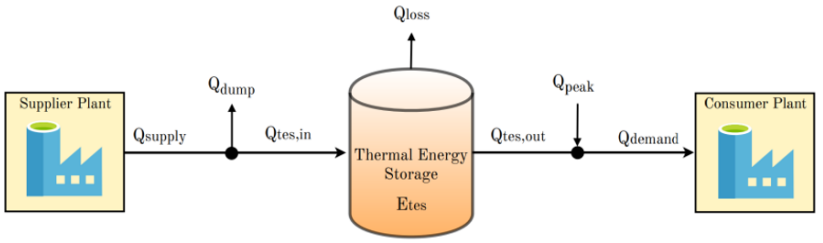

Figure 1: Industrial cluster with one supplier and one consumer exchanging heat through TES.

In context of the system design, the required total energy capacity of the TES unit (MWh) is denoted by CAP_{tes}, whereas the required maximum power rating for heat exchange with the TES unit (MW) is POW_{tes}. For taking design decisions, the former gives the basis for choosing the total volume of the tank. Similarly, the maximum power rating, often serving as the heat exchanger (HEX) design point is related to the HEX area required to deliver and withdraw heat from the TES unit. Thus, CAP_{tes} and POW_{tes} represent the design variables in the system. $x_{des} := \{CAP_{tes}, POW_{tes}\}$. The prices associated with these variables are C_{cap}(NOK/MWh) and C_{pow}(NOK/MW) respectively. The total design cost is: $C_{des} := C_{cap}CAP_{tes} + C_{pow}POW_{tes}$.

Our aim is to identify optimal design parameters for TES system under some information about the operational uncertainty. Uncertainty is modeled in terms of N scenarios, each representing a discrete combination of the heat supply and demand profiles $Q_{supply}(t)$ and $Q_{demand}(t)$ across the operating period. We consider two different formulations of the design optimization problem, a single-level formulation and a bilevel formulation.

2.1. Single-Level formulation

Considering N scenarios of operation, the single-level problem is formulated as (2).

$$\min_{x_{des}, x_{opr}} \quad C_{des} + \sum_{n=1}^{N} \omega_n \, C_{opr,n} \tag{2a}$$

$$s.t. \quad CAP_{tes} \geq 0 \tag{2b}$$

$$POW_{tes} \geq 0 \tag{2c}$$

$$\dot{E}_{tes,n}(t) = Q^{in}_{tes,n}(t) - Q^{out}_{tes,n}(t) - Q_{loss,n}(t) \qquad n = 1,...,N \tag{2d}$$

$$0 \leq Q_{peak,n}(t) \leq Q_{peak,max} \qquad n = 1,...,N \tag{2e}$$

$$0 \leq Q_{dump,n}(t) \leq Q_{dump,max} \qquad n = 1,...,N \tag{2f}$$

$$0 \leq Q^{in}_{tes,n}(t) \leq POW_{tes} \qquad n = 1,...,N \tag{2g}$$

$$0 \leq Q^{out}_{tes,n}(t) \leq POW_{tes} \qquad n = 1,...,N \tag{2h}$$

$$0 \leq E_{tes,n}(t) \leq CAP_{tes} \qquad n = 1,...,N \tag{2i}$$

Here, the subscript n represents the nth scenario of operation. In the objective (2a), ω_n is the probability associated with the nth scenario. Equation (2d) is the energy balance equation for the TES, where $\dot{E}_{tes,n}(t)$ is the derivative of the energy in the TES unit. The heat flows in and out of the TES unit are upper bounded by the POW_{tes}, and energy in TES unit is upper bounded by its capacity CAP_{tes}. For implementation, we discretize all the continuous variables in (2) using constant time steps. The integral in the objective (2a) is thus replaced by summation over all the discretized time steps.

Moreover, we employ a forward Euler scheme to discretize the energy balance equation (2d). This transforms (2) into an LP, solvable by MILP solvers like Gurobi and CPEX.

2.2. Bilevel formulation

In the bilevel formulation (3), the lower level operating variables are constrained to be the optimal solutions of the lower level problems (3d), corresponding to their respective scenarios of operation. The upper level objective function is the overall cost (same as (2)), whereas the objective function of each lower level problem is the operating cost for the corresponding scenario.

$$\min_{x_{des},x_{opr}} \quad C_{des} + \sum_{n=1}^{N} \omega_n \, C_{opr,n} \tag{3a}$$

$$s.t. \quad CAP_{tes} \geq 0 \tag{3b}$$

$$POW_{tes} \geq 0 \tag{3c}$$

$$x_{opr,n} \in \arg\min_{x_{opr,n}} \quad C_{opr,n} \qquad n = 1,\ldots,N \tag{3d}$$

$$s.t. \quad \dot{E}_{tes,n}(t) = \dot{Q}^{in}_{tes,n}(t) - \dot{Q}^{out}_{tes,n}(t) - \dot{Q}_{loss,n}(t)$$

$$0 \leq \dot{Q}_{peak,n}(t) \leq \dot{Q}_{peak,max}$$

$$0 \leq \dot{Q}_{dump,n}(t) \leq \dot{Q}_{dump,max}$$

$$0 \leq \dot{Q}^{in}_{tes,n}(t) \leq POW_{tes}$$

$$0 \leq \dot{Q}^{out}_{tes,n}(t) \leq POW_{tes}$$

$$0 \leq E_{tes,n}(t) \leq CAP_{tes}$$

The notation used for various variables is the same as in (2). Note that the lower level constraints involve the upper level variables. We also use the same discretization scheme as (2) to convert (3) into a linear bilevel program. This linear bilevel program is still nonconvex is nature owing to the constraints (3d). However, since the lower level problems (3d) are LPs after discretization, the bilevel problem (3) can be reformulated as an MILP as explained in Section 1, and can thus be solved by solvers like Gurobi and CPLEX. The formulation (3) has tighter feasible set than (2). Problem (3) is thus expected to result in more conservative solutions than (2). However, the bilevel formulation is more representative of the design problem since in practice the problem has a hierarchical nature with the operator's decisions following those of the designer's, with both trying to optimize their respective objectives.

3. Case study – design basis

An industrial TES system with one supplier and one consumer of heat is studied. To formulate the design problem, 5 years of operation is assumed for the TES unit. The overall objective function (Equations (2a) and (3a)) in the formulation then consists the design cost and the operating cost for 5 years of operation. On the operation level, we consider only hourly variation in the heat duties and, to maintain computational tractability, an operating horizon of one week (168 hours). On the design level, we approximate the total 5-year operating cost by extrapolating the weekly operating cost from the operation level over 5 years of operation. The scenarios for weekly operation are taken from the 2017 winter data for heat supply/demand provided by Mo Fjernvarme, a district heating company in northern Norway. Further, all scenarios are considered equally likely in the formulations (2) and (3). The prices for peak heating,

C_{peak} are taken to be the corresponding hourly 2017 electricity prices in northern Norway. The prices for heat dumping, C_{dump}, are assumed to be 1/10th of the peak heating prices. The maximum peak heating and heat dumping rates $Q_{peak,max}$ and $Q_{dump,max}$ are set to be 50 MW each. The design basis for calculating the TES volume and HEX area is as follows. The maximum energy storage capacity CAP_{tes} is related to the TES volume and depends on the total enthalpy change of the TES fluid in the tank between the fully charged and fully discharged state, $CAP_{tes} = \rho C_p V_{tes} \Delta T$. Assuming water as the storage medium and an operating window of $20^{\circ}C$ for the storage tank, the following relation is obtained:

$$V_{tes}\ (\mathrm{m}^3) = 43.06\ CAP_{tes}\ (\mathrm{MWh}) \tag{4}$$

The maximum power rating POW_{tes} corresponds to the maximum duty transferred across the HEX to and from the TES unit, given by $Q = UA(\Delta T)_{LMTD} = mC_p \Delta T$. Charging to a nearly fully charged TES or discharging from a nearly discharged TES unit would give the maximum area requirement of the HEX. We assume that the TES unit is large enough to have a nearly flat profile across the HEX and use a $10^{\circ}C$ approach temperature in the HEX. Using the fluid properties of water, we estimate the lowest $(\Delta T)_{LMTD}$ to be $19.5^{\circ}C$, and get the relation between POW_{tes} and an upper bound for the area required for the HEX as:

$$A_{hex}\ (\mathrm{m}^2) = 60.24\ POW_{tes}\ (\mathrm{MW}) \tag{5}$$

Finally, we use a linearized approximation of the total purchased equipment cost as provided by Sinnott and Towler (2009), to estimate our design costs C_{cap} and C_{pow}. Following the factorial method to convert the purchase costs to total design costs, we get the following approximate relations:

$$C_{cap}(\text{mil. NOK 2017}) = 0.7 + 0.11\ CAP_{tes}\ (\mathrm{MWh}) \tag{6}$$

$$C_{pow}(\text{mil. NOK 2017}) = 0.095 + 0.3\ POW_{tes}\ (\mathrm{MW}) \tag{7}$$

4. Results and discussions

We compare the results between the two formulations while considering 5, 10 and 20 weekly scenarios, chosen from the 2017 winter data. Also, when considering real data, care has to be taken to avoid any outliers that may skew the results of the design optimization. Figure 2 shows that the single-level formulation results in higher TES capacities, whereas the bilevel formulation emphasizes higher HEX areas for efficient heat transfer. This implies that, at higher TES capacities, optimal lower level solutions result in a higher design cost for the bilevel formulation. The bilevel formulation prioritizes minimizing the design objective at the expense of operation objective. Although this results in a higher operation cost for the bilevel formulation (Figure 3), it ensures that the chosen design parameters lead to optimal operation on the lower level. Also interesting to note is that the design costs from the bilevel formulation remain unchanged when scenarios are increased from 10 to 20. The single-level formulation leads to lower overall costs, but optimal operation is not guaranteed explicitly for any of the chosen scenarios. Including more scenarios seems to reduce the design cost in single-level formulation. Availability of more data would allow us to check if this cost converges to a particular value.

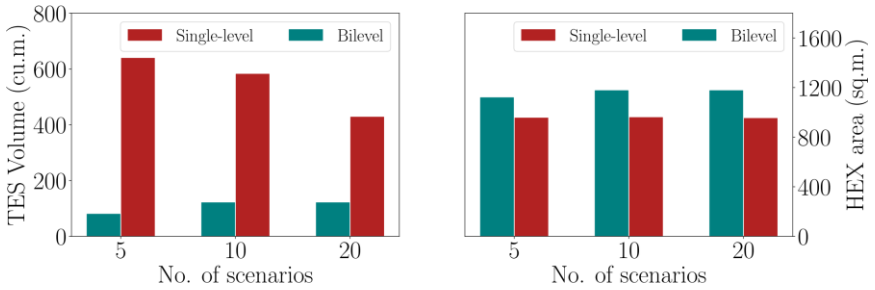

Figure 2 : TES volume and HEX area for the two formulations

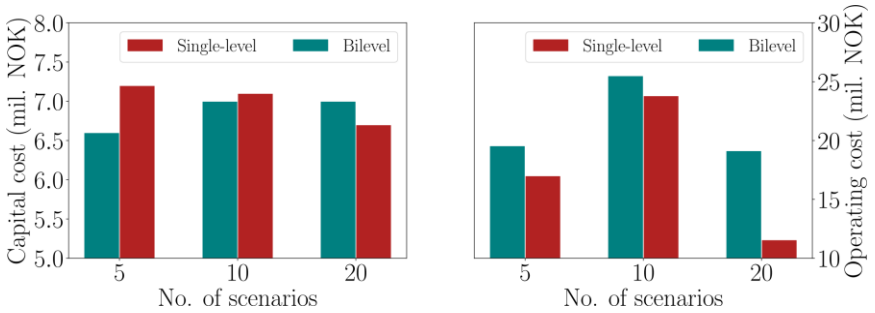

Figure 3 : Design and operating cost for the two formulations

5. Conclusion

In this paper, we compared two stochastic formulations for design optimization of TES systems. The results show that the bilevel formulation prioritizes minimizing the design cost, leading to higher operating costs. On the other hand, the single-level formulation minimizes the overall cost, but does not explicitly account for optimal operation.

Acknowledgements

This publication has been funded by HighEFF - Centre for an Energy Efficient and Competitive Industry for the Future, an 8-year Research Centre under the FME-scheme (Centre for Environment-friendly Energy Research, 257632). The authors gratefully acknowledge the financial support from the Research Council of Norway and user partners of HighEFF. The authors thank Mo Fjernvarme AS in particular for providing industrial data on heat supply and demand.

References

J. R. Birge, F. Louveaux, 2011. Introduction to Stochastic Programming, 2nd Edition. Springer Publishing Company, Incorporated.

S. Dempe, S. Franke, 2019. Solution of bilevel optimization problems using the KKT approach. Optimization 68 (8), 1471–1489

J. Fortuny-Amat, B. McCarl, 1981. A representation and economic interpretation of a two-level programming problem. Journal of the Operational Research Society 32 (9), 783–792

R. Sinnott, G. Towler, 2009. Chemical Engineering Design. Butterworth-Heinemann/IChemE series. ButterworthHeinemann.

B. Xu, Y. Wang, Y. Dvorkin, R. Fernández-Blanco, C. A. Silva-Monroy, J. Watson, D. S. Kirschen, 2017. Scalable planning for energy storage in energy and reserve markets. IEEE Transactions on Power Systems 32 (6), 4515–4527.

Sauro Pierucci, Flavio Manenti, Giulia Bozzano, Davide Manca (Eds.)
Proceedings of the 30th European Symposium on Computer Aided Process Engineering (ESCAPE30), May 24-27, 2020, Milano, Italy.
http://dx.doi.org/10.1016/B978-0-12-823377-1.50245-7

Heat Decarbonisation Pathways in the UK: Modelling and Policy Insights

Vassilis M. Charitopoulos[a,b], Chi Kong Chyong[a], David Reiner[a*]

[a]*Judge Business School, Energy Policy Research Group, University of Cambridge, Trumpington Street, Cambridge CB2 1AG, United Kingdom*

[b]*Department of Chemical Engineering, Centre for Process Systems Engineering, University College London, Torrington Place, London WC1E 7JE, United Kingdom.*

dmr40@cam.ac.uk

Abstract

Although most progress on decarbonisation in the UK has been made in the power sector, heat accounted for 44% of total energy consumption and approximately 37% of GHG emissions in 2017. Given the efficiency and cost-competitiveness of the incumbent gas-based system, decarbonising the heat sector signals a transition that requires judicious planning and defensible policy intervention. We present a novel spatially explicit MILP model for integrated optimisation of heat and power to assess the implications of heat electrification. For the first time, real-world regional hourly heat demand data are employed and the optimal share of regional heat electrification is explored by taking into account operational and investment decisions. Finally, we propose the concept of heat carbon budgets to assist policy interventions and systematically assess the transition to a low-carbon heat system.

Keywords: heat decarbonisation, spatially explicit modelling, energy systems, unit commitment, heat electrification.

1. Introduction

1.1. Background and motivation

By 2017, the UK managed to reduce its greenhouse gas (GHG) emissions by 43% compared to 1990 levels, with 75% of those reductions coming from the power sector, the decarbonisation of the heat and transportation sectors remains a big challenge (CCC, 2018). The need for addressing all sectors of a carbon-neutral economy has been reinforced when the UK government adopted a net-zero target in June 2019. Heat was the biggest energy consumer in the UK, accounting for 44% of total energy consumption in 2017, producing 37% of UK's GHG emissions (BEIS, 2018). Peak heat demand in the UK can reach 300 GW, approximately five times greater than the current electricity system's peak demand (Ofgem, 2016; Eyre & Baruah, 2015). Owing to the existing gas infrastructure system in the UK, balancing between the demand and supply sides can be achieved without excessive capacity investments (Dodds, 2014). However, for the electricity system this is not the case since instantaneous balancing is required to avoid power outages.

1.2. Literature review

Sansom & Strbac (2012) examined the impact of electrifying heat for different settings. Later on, Quiggin & Buswell (2016) presented a model for estimating the impact of heat electrification in the UK from a demand-supply viewpoint. Heinen et al. (2017) examined the impact of exploiting thermal building inertia and the effect of weather events on heat demand in Ireland. Qadrdan et al. (2019) presented a linear programming model with electricity dispatch consideration to study the impact of heat electrification on the UK gas

and electricity system. A common shortcoming of the aforementioned works is that the spatial dimension is restricted to single-node representations. A spatially-explicit, multi-period MILP model was developed by Jalil-Vega & Hawkes (2018) to investigate the heat supply and network infrastructure trade-offs in the City of Bristol. Recently, Zhang et al. (2018) presented a whole-system study on the decarbonisation of heat in the UK so to optimally decide on the end-use heat generation system design involving heat-pumps, district heat networks (DHN) and hybrid deployment of heat pumps with gas boilers (HP-B). The authors concluded that the HP-B pathway presents economic and operational benefits over the other alternatives, due to the lower capital cost of decommissioning existing domestic gas-boilers and the avoidance of reinforcing the electricity network because of heat peak demand.

Thus, to date, most studies examine heat decarbonisation by considering aggregate representations of the spatial and temporal scales of problem on a national level. Moreover, region-specific hourly heat demand data, detailed transmission capacities and interconnection have not been considered so far. It is the goal of this article to address these issues and present a novel model to investigate the impact of heat electrification in future integrated power and gas systems. The remainder of the article is organized as follows: in Section 2 the key modelling contributions of the present work are outlined while details about heat demand data and energy data processing are given in Section 3. In section 4, we employ the proposed model to investigate the impact of heat electrification in a future scenario for the UK while conclusions are drawn in section 5.

2. Integrated heat and power systems optimisation model

2.1. Spatially explicit modelling & power system

In the present work, the UK was divided in 13 regions based on the established local distribution zones of the gas network as shown in Fig. 1 while electricity network transmission capacities where derived by National Grid's Ten Year Statement (National Grid, 2018a). The electricity demand in each region (g) as shown in eq. (1), comprises of two parts: (i) non-heat demand ($DemElec_{g,c,h}$) and (ii) heat-related demand ($P^{heat}_{g,r,c,h}$) which results from the optimised electrification share of the regional heat demand and is an endogenous model decision.

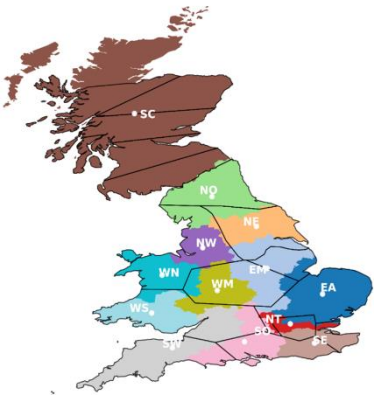

Figure 1. Spatially explicit modelling of the UK by local distribution zone (LDZ)

$$Dem_{g,c,h} = DemElec_{g,c,h} + \sum_r P^{heat}_{g,r,c,h} \qquad \forall g,c,h \qquad (1)$$

The electricity balance in each region is given by eq. (2) and can be envisaged in Fig. 2. In each region we consider power generation within the region ($P_{g,j,c,h}$), grid level storage charging ($CH_{g,j,c,h}$) and discharging ($DC_{g,j,c,h}$), bidirectional power transmission with other regions ($TR_{g,g',c,h}$), renewables curtailment for the case of excessive generation ($L^{curtail}_{g,c,h}$), load shedding for unmet power demand ($L^{shed}_{g,c,h}$) and bidirectional interconnection with third countries ($PIM_{g,i,c,h}$).

$$\begin{aligned} &\sum_{j\in je} P_{g,j,c,h}\left(1-PL_j\right) + \sum_{g'\in N_{g,g'}} TR_{g',g,c,h}\left(1-\alpha\cdot LDD_{g'g}\right) + \\ &\sum_{j\in j_{es}} DC_{g,j,c,h} + \sum_{i\in IG_{i,g}} PIM_{g,i,c,h}\left(1-\gamma_{i,g}\right) = Dem_{g,c,h} + \\ &\sum_{g'\in N_{g',g}} TR_{g,g',c,h} + \sum_{j\in j_{es}} CH_{g,j,c,h} + L^{curtail}_{g,c,h} - L^{shed}_{g,c,h} \qquad \forall g,r,c,h \end{aligned} \qquad (2)$$

Notice that for thermal generators we consider a parasitic load factor (PL_j) to account for the net power production as well as a linear loss factor (α) proportional to the transmission distance when power is transmitted across regions and the related losses in interconnection through the factor $\gamma_{i,g}$. Further to these constraints, we formulate the security and ramp-rate constrained unit commitment problem for thermal generators by explicitly accounting for: (i) start-ups/shut-downs, (ii) minimum uptime/downtime, (iii) ramp-rate constraints (up/down), (iv) upward & downward short term operating reserve provision and (v) minimum/maximum generation limits building on our previous work (Chyong et al., 2019).

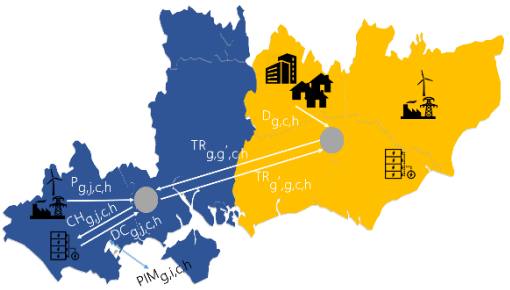

Figure 2. Visual representation of different electricity flows within and across two regions

2.2. Heat supply chain modelling

With regards to the heat supply chain, eq. (3) represents the spatiotemporal energy balance where the heat demand at each region (g) representative day (c) and hour (h) ($HDem_{g,r,c,h}$) is equal to the heat supplied ($Q^{heat}_{g,r,j,c,h}$) by the different heating technologies ($j \in J_h$) minus the thermal energy discharged at each time period ($Q^{dheat}_{g,r,c,h}$) plus the thermal energy stored ($Q^{sheat}_{g,r,c,h}$). Notice that in each region (g) we differentiate between areas (r) that are connected to the gas grid.

$$HDem_{g,r,c,h} = \sum_{j \in J_h} Q^{heat}_{g,r,j,c,h} - Q^{dheat}_{g,r,c,h} + Q^{sheat}_{g,r,c,h} \qquad \forall g,r,c,h \qquad (3)$$

Eqs. (4)-(5) describe the resulting demand in electricity ($P^{heat}_{g,r,c,h}$) and fuel ($V^{heat}_{g,r,f,c,h}$) that result by the heat demand respectively by taking into account the efficiency of each heating technology ($\eta_{g,r,j,c,h}$).

$$P^{heat}_{g,r,c,h} = \sum_{j \in J_{he}} \frac{Q^{heat}_{g,r,j,c,h}}{\eta_{g,r,j,c,h}} \qquad \forall g,r,c,h \qquad (4)$$

$$V^{heat}_{g,r,f,c,h} = \sum_{j \in J_h \wedge JF_{f,j}} \frac{Q^{heat}_{g,r,j,c,h}}{\eta_{g,r,j,c,h}} \qquad \forall g,r \in R_{grid},f,c,h \qquad (5)$$

For an air-source heat pump (ASHP), efficiency is not constant but rather temperature-dependent and we assume that eq. (6) holds following the work of Zhang et al. (2018).

$$\eta_{g,r,'ASHP',c,h} = 0.07T_{g,r,c,h} + 2.07 \ (-5℃ \leq T_{g,r,c,h} \leq 25℃) \quad \forall g,r,c,h \qquad (6)$$

To model the thermal energy storage technologies we employ eqs. (7)-(13) which represent the energy content balance, storage duration limits and charging/discharging limits respectively. In the present work we consider as thermal energy storage technology hot water tanks with self-discharge rate (β) 1%/h and ratio of capacity to the power rating (TES) of 4h.

$$S^{heat}_{g,r,c,h} = S^{heat}_{g,r,c,h-1}(1-\beta) - Q^{dheat}_{g,r,c,h} + Q^{sheat}_{g,r,c,h} \qquad \forall g,r,c,h \qquad (7)$$

$$S^{heat}_{g,r,c,h} \leq S^{cap}_{g,r} TES \qquad \forall g,r,c,h \qquad (8)$$

$$Q^{dheat}_{g,r,c,h} \leq S^{cap}_{g,r}, \ Q^{sheat}_{g,r,c,h} \leq S^{cap}_{g,r} \qquad \forall g,r,c,h \qquad (9)\text{-}(10)$$

$$S^{heat}_{g,r,c,h} = 0 \qquad \forall g,r,c,h = \{0,23\} \qquad (11)$$

Finally, investment-related decisions on the capacity of the heat-end technology capacities are calculated based on eq (12)-(13).

$$Q^{heat}_{g,r,c,h} \leq Heat^{cap}_{g,r} \quad and \quad Q^{sheat}_{g,r,c,h} \leq S^{cap}_{g,r} \qquad \forall g,r,c,h \qquad (12)\text{-}(13)$$

2.3. Overall model formulation

In summary, the model is formulated as a mixed integer linear program (MILP) with a total system cost minimisation objective and the overall formulation is given below in brief.

$$\min \text{TotalCost} = \text{OPEX} + \text{CAPEX} + \text{CIMP} + \text{CEM} + \text{CSHED}$$

$$\text{Subject to:} \begin{cases} \text{Security \& Ramp-rate constrained unit commitment} \\ \text{Transmission \& Interconnection bounds} \\ \text{Grid-level storage constraints} \\ \text{Heat supply chain constraints} \\ CO_2 \text{ emissions constraints} \end{cases}$$

The total system cost comprises of the operating cost for power and heat generation and storage (OPEX), the capital cost for the final portfolio of heating technologies (CAPEX), the cost of interconnection (CIMP), the cost related to environmental penalties for emissions (CEM) and the cost of shedding demand or operating reserve (CSHED).

3. Data preparation and processing

3.1. Regional heat demand data

In order to capture seasonality and volatility of heat demand, several years (2014-18) of historical regional hourly gas consumption data were collected from the UK gas distribution companies. The data accounted for industrial, domestic and commercial loads which were further disaggregated so as to segment heat-related demands. A key novelty and benefit of this approach is that (i) we do not rely on synthetic data, (ii) the after-diversity demand factors do not need to be calculated to provide realistic loads (Sansom & Strbac, 2012) and (iii) the derived heat demands represent the actual energy load that will be considered for electrification within each region. In Fig. 3, an overview of region-specific heat load characteristics are provided.

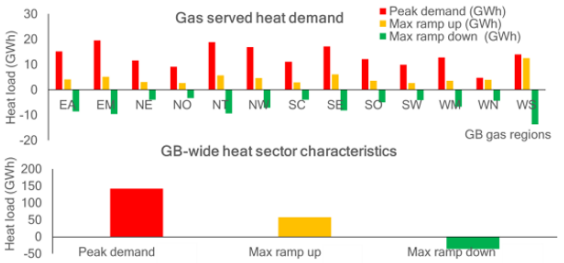

Figure 3. Regional heat demand operational characteristics

3.2. Regional power sector data

The incumbent power generation fleet is mapped in the different regions under study together with the related transmission capacity of interconnections with third countries. The base year of our study is 2015 where UK generation capacity consists of 10% nuclear, 23% unabated coal, 37% unabated gas, 3% biomass and 27% renewables (DUKES, 2018).

3.3. Chronologically-ordered spatiotemporal data clustering

Data clustering techniques have been widely used in optimisation models for energy systems because of their ability to reduce the related computational burden while at the same time provide a good approximation to the full-dimensional problem (Heuberger et al., 2017). We employ K-means clustering to select ten representative days of the year but, in contrast to previous works, we modify the clustering algorithm so as to impose the chronological order of the resulting days since this is important in preserving the heat demand seasonality. On top of the aforementioned 10 days we also include two additional days, accounting for peak electricity and peak gas demand days.

4. Case study: Heat electrification options for a 2030 UK system

In this section, we employ the capacity mix of National Grid's "Two degrees" future energy scenario for 2030 (National Grid, 2018b) to demonstrate the model's capabilities. First, we investigate the simultaneous decarbonisation of the heat and power sector under a single "carbon-budget" with a reduction goal of 15% for heat-related emissions compared to their 2015 levels (BEIS, 2018) in addition to the existing carbon budget for the incumbent power sector. The optimal generation schedule is shown in Fig. 4 and the impact of electrifying heat becomes obvious on the second representative day which in the original time-series was the peak (gas) heat demand day. There is a great increase in the marginal price of electricity during "Day 2" due to operating reserve shedding so as to meet the resulting additional heat-related demand. For this case, the regional change in gas-fuelled properties from 2015 to 2030 can be seen in Fig. 5.

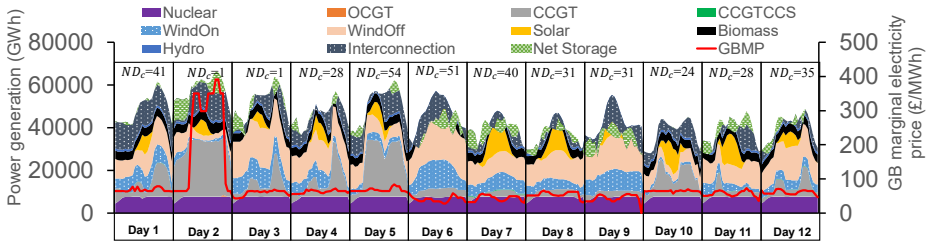

Figure 4. Optimal generation schedule and the resulting GB-wide marginal price of electricity in 2030 under a single carbon budget and 15% reduction in heat emissions. (ND_c: frequency of day)

Finally, motivated by the fact that for the case of single carbon budget the heat-related emissions reduction goal was never achieved but rather a deeper decarbonisation of the electricity sector was preferred as optimal, we investigate and propose for the first time the stipulation of heat-specific carbon budgets so as to guide and surveil the decarbonisation more efficiently. The impact of stipulating a single carbon budget different carbon budgets and the role of intraday heat storage can be seen in Fig. 6 where sector-specific carbon budgets and intraday heat storage enable a deeper level of decarbonisation to be achieved at more reasonable costs.

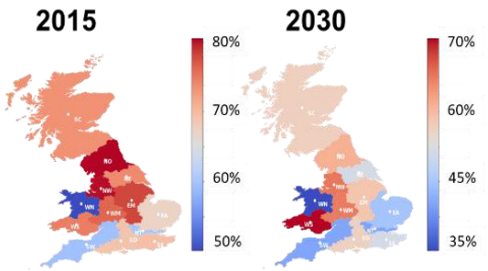

Figure 5. Regional percentages of gas-fueled properties in 2015 vs optimal 2030 scenario for 15% reduction in heat emissions.

5. Conclusions

Our novel spatially-explicit MILP model allows us to investigate the impact of different levels of heat electrification in the UK. The model accounts for investment decisions for the heat supply chain while a security & ramp-rate constrained unit commitment formulation allows for evaluation of the adequacy and operability of the power system. For the first time, real-world heat demand data are employed to analyse heat decarbonisation and we propose a novel clustering framework to preserve seasonality, account for bidirectional interconnection and propose the notion of "heat carbon budgets".

Going forward, we plan to investigate the role of hydrogen in heat of heat as well as incorporating generation capacity expansion planning decisions in heat decarbonisation.

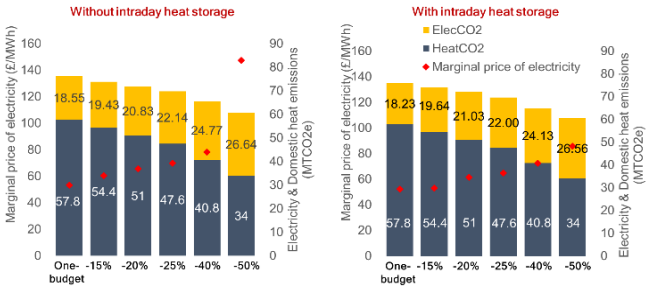

Figure 6. Impact of heat storage and the stipulation of "heat carbon budgets" on the cost of decarbonisation. The yellow and blue columns represent power and heat-related CO2 emissions respectively, while the red diamonds indicate the resulting average GB marginal price of electricity.

Acknowledgements: Financial support for this project from the Engineering and Physical Sciences Research Council (EPSRC Grant EP/P026214/1) is gratefully acknowledged. We also gratefully acknowledge the hourly historical data supplied to us by the gas distribution networks: Cadent Gas, Northern Gas Networks, Wales & West Utilities and SGN.

References

CCC, 2018, Reducing UK emissions 2018 progress report to parliament, London: Committee on Climate Change.

BEIS, 2018, Clean growth: Transforming heating- overview of current evidence, London: Department for Business, Energy & Industrial Strategy.

Ofgem, 2016, The decarbonisation of heat, Ofgem's Future Insights Series, 1-16.

Eyre, N., & Baruah, P., 2015, Uncertainties in future energy demand in UK residential heating. Energy Policy, 87, 641-653.

Dodds, P. E., 2014, Integrating housing stock and energy system models as a strategy to improve heat decarbonisation assessments. Appl. Energy, 132, 358-369.

Sansom, R., & Strbac, G., 2012, The impact of future heat demand pathways on the economics of low carbon heating systems. In *BIEE-9th Academic conference*, 2-10.

Quiggin, D., & Buswell, R. (2016). The implications of heat electrification on national electrical supply-demand balance under published 2050 energy scenarios. *Energy*, *98*, 253-270.

Heinen, S., Turner, W., Cradden, L., McDermott, F., & O'Malley, M. (2017). Electrification of residential space heating considering coincidental weather events and building thermal inertia: A system-wide planning analysis. *Energy*, 127, 136-154.

Qadrdan, M., Fazeli, R., Jenkins, N., Strbac, G., & Sansom, R. (2019). Gas and electricity supply implications of decarbonising heat sector in GB. *Energy*, *169*, 50-60.

Jalil-Vega, F., & Hawkes, A.D. (2018). Spatially resolved model for studying decarbonisation pathways for heat supply and infrastructure trade-offs. *Appl. Energy*, *210*, 1051-1072.

Zhang, X., Strbac, G., Teng, F., & Djapic, P. (2018). Economic assessment of alternative heat decarbonisation strategies through coordinated operation with electricity system–UK case study. *Appl. Energy*, 222, 79-91.

Chyong, C., Newbery, D., & McCarty, T., 2019, A Unit Commitment and Economic Dispatch Model of the GB Electricity Market – Formulation and Application to Hydro Pumped Storage, Energy Policy Research Group Working Paper 1924. Cambridge: University of Cambridge.

Heuberger, C.F., Rubin, E.S., Staffell, I., Shah, N., & Mac Dowell, N., 2017, Power Generation Expansion Considering Endogenous Technology Cost Learning, *Comput. Aid. Chem. Eng*, 40, 2401-2406

National Grid, 2018a, Electricity Ten Year Statement.

National Grid, 2018b, Future Energy Scenarios.

Sauro Pierucci, Flavio Manenti, Giulia Bozzano, Davide Manca (Eds.)
Proceedings of the 30th European Symposium on Computer Aided Process Engineering (ESCAPE30), May 24-27, 2020, Milano, Italy.
http://dx.doi.org/10.1016/B978-0-12-823377-1.50246-9

Energy System Design for the Production of Synthetic Carbon-neutral Fuels from Air-captured CO_2

Lukas Weimann[a], Alexa Grimm[a], Janet Nienhuis[a], Paolo Gabrielli[b], Gert Jan Kramer[a], Matteo Gazzani[a*]

[a]*Copernicus Institute of Sustainable Development, Utrecht University, 3584 CS Utrecht, The Netherland*
[b]*Institute of Process Engineering, ETH Zurich, 8092 Zurich, Switzerland*
m.gazzani@uu.nl

Abstract

In this work, we investigate the design and operation of an energy system for the production of a carbon-rich CO_2-neutral fuel, i.e. where hydrogen reacts with CO_2 from air to give synthetic methane. As the systems consists of multiple energy conversion and storage technologies, we make use of the energy hub approach coupled with MILP optimization to identify optimal plant designs and operation. We investigate the effect of flexible vs. steady operation of the fuel synthesis and direct air capture, as well as the effects of different geographical locations. We find that if the system is optimized for cost, electricity is mainly supplied by the grid, and therefore the electricity prices and grid emission factors determine the economic and environmental performance. Moreover, the location plays a minor role in the cost of the minimum emissions point, as the direct air capture cost largely control the total plant costs. Along this line, the optimal design was found to rely on steady operation of the synthesis and direct air capture ensemble, as this allows for the lowest associated capital expenditure.

Keywords: multi energy system, MILP, direct air capture, net-zero, negative emissions technologies

1. Introduction

One of the biggest technical challenges society is facing in its endeavor to meet the goals set by the Paris Agreement is the decarbonization of (i) high temperature endothermic processes in heavy industry and (ii) transportation, especially aviation. While renewable energy sources can rather easily substitute fossil fuels for electricity generation and household energy demands, (part of) the sectors mentioned above will keep requiring energy-dense carbon-based fuels. Therefore, in a system compliant with net-zero CO_2 emission, as the one depicted by the IPCC 1.5 °C report (IPCC, 2018) for approximately 2050, a CO_2-neutral production of carbon-rich fuel will be needed. One such possibility – others being indeed the use of fuels derived from biomass or CCS – is producing synthetic fuels via using CO_2 recovered from air (direct air capture, or DAC) and H_2, provided that the energy required to drive the whole process has no CO_2 footprint. While the advocates of the synthetic fuel route typically identify this process as viable when cheap and abundant green electricity will be available, the design and operation of the

fuel production process and the associated energy system remain largely an open question. Therefore, with this contribution we aim at understanding (i) how the production of a synthetic fuel is optimally designed and operated, (ii) what are the associated CO_2 emissions and production costs, and (iii) how electricity import and onsite generation are controlled for various designs along a cost-emission pareto front. To this end, we have modified an existing MILP framework so as to take into account the performance and energy input/output of a synthetic fuel production unit coupled with a direct air capture plant. Due to the inherent aleatory nature of renewable power generation (i.e. PV and wind turbines), and to the large variations in the annual electricity cost profile, we explore the effect of pursuing a static vs. a flexible operation of the ensemble DAC+fuel synthesis. Moreover, we investigate the effect of the geographical plant location by considering different sites with different weather profiles and electricity costs: (i) the Netherlands, (ii) Spain, (iii) California (US), and (iv) United Arabic Emirates.

2. Background and Methodology

In the following, we focus on the novelties of this contribution, namely the application of the modelling framework developed by (Gabrielli et al., 2018b, 2018a) to a system lacking detailed analysis so far (section 2.1) and the required extension of the framework to realize this (section 2.2).

2.1. System description

The investigated system is sized considering that the direct air capture unit delivers 1 Mt/y of high purity CO_2. This was chosen as an exemplary large scale production plant. The CO_2 is utilized for fuel production (FP), here represented with a methanation step (Sabatier reaction). For simplicity, the FP unit is modeled via mass and energy balances (see section 2.2.1), fulfilling a constant synthetic natural gas (SNG) demand of 22.1 MW or 194 GWh annually. The required amount of hydrogen is produced via a polymer electrolyte membrane (PEM) electrolyzer. It is important to note that DAC and FP are simulated as coupled units, i.e. sizing and operation is proportionate.

Electricity is provided through photovoltaic panels, wind turbines, or the grid, while heat is provided by solar thermal panels or hydrogen boilers. Hence, the only source of CO_2 derives from the carbon footprint of the electricity grid, which is here considered as location-dependent. In addition to these conversion technologies, batteries for electricity storage and pressurized tanks for hydrogen storage are considered. Moreover, the installation of a PEM fuel cell in combination with the PEM electrolyzer and the hydrogen storage can work as a power-to-gas-to-power system. Finally, the sole purpose of the SNG storage is to allow for flexible production, i.e. vary the output of the DAC-FP unit,

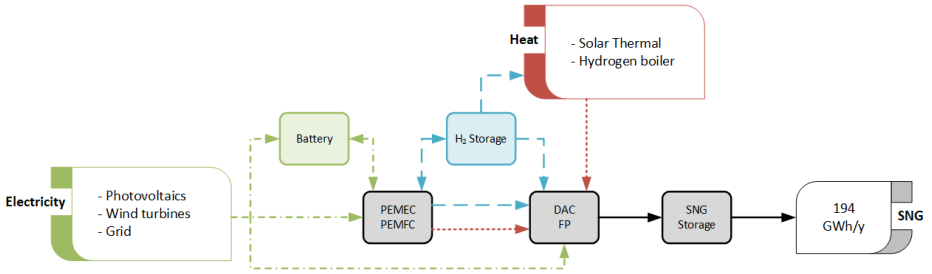

Figure 1: Schematic representation of the system investigated in this study

despite having a constant SNG demand profile. Figure 1 shows a graphic representation of the described system and its possible configuration.
The system optimization was carried out via mixed integer linear programming (MILP) as framed in the energy hub approach (Geidl et al., 2007) and as implemented by Gabrielli et al. (Gabrielli et al., 2018b, 2018a). The framework allows for optimizing the design – via technology selection and sizing – and the operation of multi-energy systems (MES), while also retaining adequate description of the technology performance. The considered time span is the full year 2018 at hourly resolution. The various locations are accounted for through their wind speed, solar irradiation, and electricity price profiles.

2.2. Modeling of direct air capture and SNG production

2.2.1. Performance parameters

In order to simulate the combined DAC-FP unit, it was assumed that the CO_2 capture process follows the CO_2 demand of the methanation process. For the electricity and heat input for the DAC the values reported in (Sutter et al., 2019) are used. The inputs for the methanation process are obtained from Müller et al. (Müller et al., 2011), who conducted thermodynamic simulations based on an existing methanation plant. The performance parameters are summarized in Table 1.

2.2.2. Cost parameters

Because of the large uncertainties associated with estimating the costs of new technologies (e.g. fuel synthesis and DAC), the cost results presented in this paper should be regarded mainly as preliminary estimates and as a way to distinguish between the different operating points. Currently, there exist two main technological pathways for DAC, which rely either on the use of an aqueous solutions or on the use of solid sorbents as means to capture CO_2. For the former chemical sorbents like potassium hydroxide are used which strongly bind the CO_2. This process benefits from the experience gained in post-combustion CO_2 capture but requires high quality fuels for regeneration. On the other hand, solid sorbent processes shows more favorable thermodynamics during the regeneration step, and requires low quality heat. For this reason, they are a good fit with renewable-based technologies, and are therefore assumed as DAC process here.

Table 1: Performance parameters for direct air capture (DAC), fuel production via methanation (FP) and the coupled DAC-FP unit

	DAC	FP	DAC-FP
Heat [kWh/kWh_{SNG}]	0.366	-0.167	0.199
Electricity [kWh/kWh_{SNG}]	0.052	0.023	0.076
Hydrogen [kWh/kWh_{SNG}]	-	1.198	1.198
CO_2 [kg/kWh_{SNG}]	-	0.209	0.209
Efficiency			0.679

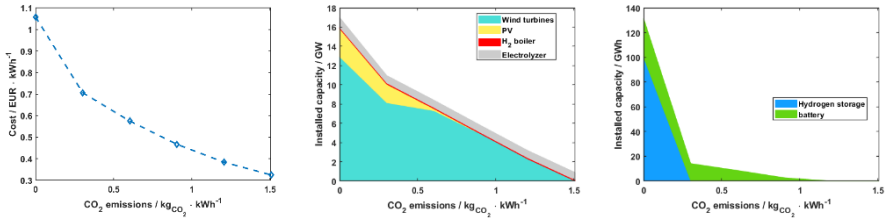

Figure 2: Graphic summary of the system design in the Netherlands, used as base case in this work. (left) pareto front, (middle) sizes of installed conversion technologies along the pareto front, (right) sizes of installed storage technologies along the pareto front

To estimate the CAPEX and O&M of an adsorbtion-based direct air capture system, the commonly used value of 600 EUR/t_{CO2} (Socolow et al., 2011) is applied to the Climeworks pilot plant of 1000 t_{CO2}/y, i.e. total unit cost of 12'000 EUR/(t_{CO2}/y) assuming 20 years lifetime. The values reported in (Alhajaj et al., 2016) for heat, electricity, and labor cost and an additional 10 % of CAPEX for maintenance and other financial factors, together with the performance parameters described in the previous section, allow to extract the CAPEX from the known total cost, giving 5294 EUR/(t_{CO2}/y) or 9699 EUR/kW_{SNG}. For the methanation, a value of 130 EUR/kW_{SNG} was assumed (Götz et al., 2016) resulting in total CAPEX of 9829 EUR/kW_{SNG} for the DAC-FP unit.

3. Results

Henceforth, we define the Netherlands with static production, i.e. without SNG storage (compare with Figure 1), as base case. Figure 2 shows the pareto front and the technology sizing for all optimal designs of this base case, i.e. ranging from minimum cost to minimum emissions. The total system costs range from 0.33 to 1.06 EUR/kWh_{SNG}. While all electricity is imported for the cheapest design (high-emission side of the pareto front), wind turbines are the main source of electricity upon emission reduction. Given Dutch weather conditions, photovoltaics are only used when very low emissions are aimed for. Looking at the storage technologies, it can be observed that hydrogen storage clearly dominates for low emissions and even hits the arbitrarily set cap of 100 GWh for the emission-free scenario. The correlation between installed wind power capacity and hydrogen storage is in accordance with the scientific consensus that the seasonal character of renewable power generation favors seasonal storage solutions like power-to-hydrogen (Gabrielli et al., 2020). Along those lines, hydrogen storage also dominates for UAE, where the system relies entirely on photovoltaics and electricity from the grid. However, with a maximum installed capacity of 36 GWh it does not hit the cap. This indicates that the costs, 21 EUR/kWh for hydrogen storage compared to 150 EUR/kWh for batteries, are another significant driver for the dominance of hydrogen storage over batteries given that supporting facilities like electrolyzers have to be installed anyway in this setting. Flexible operation of the DAC-FP unit facilitated by SNG storage was not observed. This can be explained by the high investment cost of DAC-FP, resulting in a situation where the gain through flexible operation does not justify the increase in costs due to required oversizing of the DAC-FP unit.

3.1. Effect of location

Differences in solar irradiation and wind speed profiles but also in electricity prices and electricity grid emission factors are the drivers for local differentiation of the results.

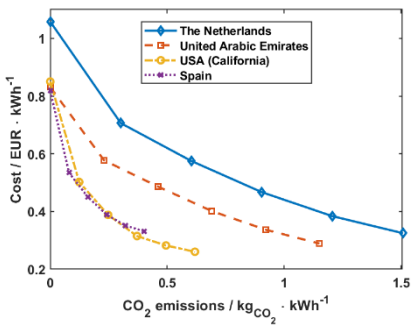

Figure 3: Pareto fronts for the 4 locations considered in this work

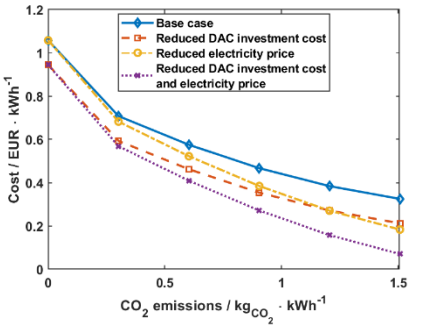

Figure 4: Pareto fronts for the Dutch system design using different cost assumptions. The reduced DAC investment cost is 1453 EUR/kW_{SNG} and the electricity price is reduced by a factor 100

From Figure 3 it can be observed that the emissions for the cheap designs vary significantly, driven by the difference in emission factors. Nevertheless, as the electricity import from the grid gradually reduces upon emission reduction, and given the high contribution of the DAC's costs to the total system costs, the minimum emission specific cost is similar for all considered locations despite differences in the energy system design. In the Netherlands, the total system costs are higher along the full pareto front, mainly due to higher oversizing of wind turbines and photovoltaics to compensate for more volatile wind and irradiation profiles.

3.2. Effect of DAC investment cost and electricity price

To investigate the effect of the highly uncertain costs of DAC and electricity, the base case was simulated with lowered costs. For the DAC, costs of 1453 EUR/kW_{SNG} (Keith et al., 2018) were used, resulting in a cost reduction for the coupled DAC-FP unit of 85 %. The electricity price was lowered by a factor 100.

As can be seen in Figure 4, decreasing both DAC investment cost and electricity price decreases the system cost to a range of 0.07 (high-emission) to 0.95 (low-emission) EUR/kWh_{SNG}. Comparing this with the household retail price for conventional national gas of roughly 0.06 EUR/kWh (EU-28 average 2019) shows that the investigated system can be economically competitive if cheap clean electricity is available and carbon tax is factored in.

As expected, decreasing the DAC cost facilitated flexible operation. Nevertheless, with technology oversizing of just 2.9 % the effect was minor.

4. Conclusion

In this work, we investigated the economic and environmental performance of SNG production from air-captured CO_2 and hydrogen, and its related energy supply system for four different locations. With the current electricity price and DAC cost, and if the system is optimized for cost, electricity is mainly supplied by the grid. Hence, electricity prices and emission factors determine the economic and environmental performance, ranging from 0.26 to 0.33 EUR/kWh_{SNG} and 0.4 to 1.5 kgCO2/kWh_{SNG} for the four locations. From those figures, it can be concluded that the location affects the environmental

performance and the exact energy system design, but the influence on the final economic performance is limited. Decreasing the cost of DAC by 85 % leads to a cost reduction for an emission free design of about 11 % (0.95 compared to 1.07 EUR/kWh$_{SNG}$). Further reduction of investment cost for DAC is necessary to make this system economically feasible, though unlikely to happen in the short/medium term. Moreover, it was found that cheap clean electricity will be key to bring the costs down, especially as the contribution of the DAC investment cost decreases. Finally, a flexible DAC system, which is capable of operating following the electricity and demand as best for the objective function, was found to have limited effects on the costs. Indeed, more severe reduction on the investment cost would be necessary to justify the required oversizing.

References

Alhajaj, A., mac Dowell, N., Shah, N., 2016. A techno-economic analysis of post-combustion CO2 capture and compression applied to a combined cycle gas turbine: Part II. Identifying the cost-optimal control and design variables. International Journal of Greenhouse Gas Control 52, 331–343.

Gabrielli, P., Gazzani, M., Martelli, E., Mazzotti, M., 2018a. Optimal design of multi-energy systems with seasonal storage. Applied Energy 219, 408–424.

Gabrielli, P., Gazzani, M., Mazzotti, M., 2018b. Electrochemical conversion technologies for optimal design of decentralized multi-energy systems: Modeling framework and technology assessment. Applied Energy 221, 557–575.

Gabrielli, P., Poluzzi, A., Kramer, G.J., Spiers, C., Mazzotti, M., Gazzani, M., 2020. Seasonal energy storage for zero-emissions multi-energy systems via underground hydrogen storage. Renewable and Sustainable Energy Reviews 121, 109629.

Geidl, M., Koeppel, G., Favre-Perrod, P., Klöckl, B., Andersson, G., Fröhlich, K., 2007. Energy hubs for the future. IEEE Power and Energy Magazine 5, 24–30.

Götz, M., Lefebvre, J., Mörs, F., McDaniel Koch, A., Graf, F., Bajohr, S., Reimert, R., Kolb, T., 2016. Renewable Power-to-Gas: A technological and economic review. Renewable Energy 85, 1371–1390.

Keith, D.W., Holmes, G., st. Angelo, D., Heidel, K., 2018. A Process for Capturing CO2 from the Atmosphere. Joule 2, 1573–1594.

IPCC, 2018. Global Warming of 1.5 °C. An IPCC Special Report on the impacts of global warming of 1.5°C above pre-industrial levels and related global greenhouse gas emission pathways, in the context of strengthening the global response to the threat of climate chan.

Müller, B., Müller, K., Teichmann, D., Arlt, W., 2011. Energiespeicherung mittels Methan und energietragenden Stoffen ein thermodynamischer Vergleich. Chemie-Ingenieur-Technik 83, 2002–2013.

Socolow, R., Desmond, M., Aines, R., Blackstock, J., Bolland, O., Kaarsberg, T., Lewis, N., Mazzotti, M., Pfeffer, A., Sawyer, K., Siirola, J., Smit, B., Wilcox, J., 2011. Direct Air Capture of CO2 with Chemicals: A Technology Assessment for the APS Panel on Public Affairs, APS physics.

Sutter, D., van der Spek, M., Mazzotti, M., 2019. 110th Anniversary: Evaluation of CO2-Based and CO2-Free Synthetic Fuel Systems Using a Net-Zero-CO2-Emission Framework. Industrial and Engineering Chemistry Research 58, 19958–19972.

Sauro Pierucci, Flavio Manenti, Giulia Bozzano, Davide Manca (Eds.)
Proceedings of the 30th European Symposium on Computer Aided Process Engineering
(ESCAPE30), May 24-27, 2020, Milano, Italy.
http://dx.doi.org/10.1016/B978-0-12-823377-1.50247-0

Computational Tools used in Hybrid Renewable Energy Systems Optimization-An overview

H. O. Guelleh, I. M. Mujtaba*, R. Patel

School of Engineering, Faculty of Engineering and Informatics.,

University of Bradford. Bradford, West Yorkshire BD7 1DP, UK

I.M.Mujtaba@bradford.ac.uk

Abstract

In nowadays, renewable energy has become a key area of interest for solving many problems such as climate changes, security of energy supply, and poverty reduction. To face these challenges and issues, the penetration and the implementation of renewable energy technologies have been done through Hybrid energy systems (HES). The aim of this work is to highlight an overview of software tools used in HES to get an optimum design of HES to get a better reliability and efficiency of electricity generated and to save the cost of installation. Within this context, the most software tools used widely in terms of techno-economic design of HES are so far HOMER, iHOGA, and RETScreen. This paper will help policy makers, academic researchers and energy planners to take a better decision for the paradigm shift of renewable energy.

1. Introduction

Concerns about climate change with GHG emissions, energy security supply and depletion of fossil fuel resources have certainly contributed the urgent search for alternative renewable energies. However, one of the United Nations Sustainable Development Goals (SDGs), Goal#7, which defines global goals for sustainable, affordable, and clean energy, and Kyoto protocol, a part of United Nations Framework Convention on Climate Change (United Nation, 2018), are not the only factors pushing developing countries in the direction of renewable and clean energy. But, developing countries see this opportunity to compensate their insufficient electricity-production capacity, in order to reduce fossil fuel dependence, and imported electricity from neighbouring countries for their energy security supply by developing their potential indigenous renewable resources. Moreover, these renewable resources are mostly intermittent such as solar, wind, and wave energy resources. But if they are combined of two or more renewable energy unit and fossil fuel unit (Diesel generators), they form Hybrid Energy System (HES). These HES could be stand alone or grid-connected HES such as wind-hydro-PV, Solar-Wind-Diesel generator, Solar-Wind-Battery, Solar-Wind-Biomass, or solar-wind grid connected. In electricity sector, HES improves the reliability, efficiency and the production of electricity generated (Abhishek, et al, 2018). To avoid high installation cost, having adequate sizing, simulation and optimization software tools are very essential for the efficient utilization of hybrid energy systems.

This paper presents an overview of software tools used in hybrid energy systems optimization. The extensive approaches of optimization in hybrid energy system are beyond the scope of this paper. The structure of this paper will be as follows. Section 2 describes literature review. In section 3, software tools for hybrid energy systems are

presented. In section 4, the results and a brief discussion are presented, and section 5 will conclude the work proposed in this paper.

2. Literature overview

2.1 Overview of hybrid energy systems optimization techniques

Combining different renewable energy units in HES can be costly and technically difficult to be feasible. Therefore, an optimal planning of HES design is deemed necessary in order to minimise the cost of the installation. The first process of optimizing of the hybrid energy system is creating an appropriate model which, in turn, will determine the objective function of a problem mathematically. After modelling, the next step is to choose the appropriate software tool in order to make the simulation and find the optimal solution (Tezer et al. 2017).

In the literature, to solve the optimization problem for HES, various optimization techniques have been used in hybrid Energy systems (Connolly et al. 2010). Some various optimizations methods or techniques are listed in table 1.

Table 1. Various optimization techniques used in hybrid energy system design

• Neural Networks	• Linear programming methodology
• Parametric and numerical approaches	• Iterative and probabilistic approaches
• Quasi-Newton methodology	• Evolutionary algorithm
• Response surface methodology	• Dynamic programming
• Simplex algorithm	• Design space based approach
• Stochastic approach	• "Energy hub" concept
• Matrix approach	

Negi and Matthew (2014) highlighted also that several optimization techniques available for sizing optimization of HES in order to minimize the cost while maintaining the reliability. These techniques are probabilistic approach, graphical construction method, iterative technique, artificial intelligence method, etc.

2.2. Software tools for hybrid Energy Systems

The online market is sometimes a daunting place to find suitable software energy tools for the integration of renewable energy into energy systems or hybrid renewable energy systems (HRES). Many tools have been developed and applied to energy sector that is itself divided into electricity sector, heat sector and transport sector. Right in the beginning of a project, the researcher or the energy planner needs to define the job that the software tool is going to perform, the kind of software tool they require to perform the job and how the software tool is going to perform that job. The following example in table 2 is given to understand better.

Table 2. Example of choice for software energy tool selection

Energy capability categorization	External process of software tool selection	Technical process of software tool requirements to complete the job needed.
Example: -Pre-feasibility study -Short-term energy planning -Future energy planning	Example: -Energy software tool must be freely available without charge for downloading -It must support technical and economic analysis -Complete software package -Short software training –1 to 3 days	Example: -Energy model -Simulation and optimization - Technical and economic analysis -Greenhouse gas analysis -Financial summary -Sensitivity and risk analysis

Suresh and Meenakumari (2018) have discussed briefly 17 energy software tools for. Out of these 17 energy software tools, HOMER, iHOGA, and IGRYHSO simulate and optimise as hybrid energy systems software tools.
Connolly et al. (2010) had done an extensive research and reviewed 37 computer energy tools out of 67 outlining briefly their application. The goal of their study was to provide the individual description of these 37 computer energy tools so that the reader or the decision-maker can choose the right energy tool suitable to accomplish the primary goal of their project. In this regard, Connolly et al. (2010) highlighted that HOMER can perform techno-economic optimization for hybrid energy systems. In another study,
Bernal-Agustin and Dufo-Lopez (2009) revised some of the simulation and optimization software tools of hybrid systems. HOMER, HYBRID2, HOGA, TRNSYS, HYGROGEMS, INSEL, ARES, RAPSIM, SOMES, SOLSIM. Out of these hybrid systems software tools, HOMER, HOGA, and HYDROGEMS can only perform economical optimization. However, HYDRGOGEMS has got some limitations. It is not a whole program but series of libraries. It can only perform optimization if it goes with TRNSYS.

3. Software tools for Hybrid Energy Systems

The following figure1 represents an example of HES's schematic configuration.

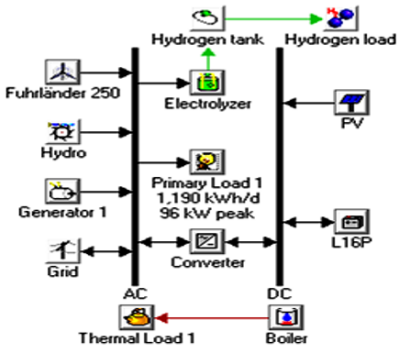

Figure 1. Hybrid Renewable Energy System configuration

From literature review and academic experience, the following table 3 gives an overview of software tools for simulation and optimization of hybrid energy systems

Table 3. Up to date Software tools for simulation and optimization of Hybrid Energy Systems

Software tools	Simulation	Economic Optimization	Availability on the market	Free of charge or commercial
HOMER	YES	YES	YES	FREE
RETScreen	YES	YES	YES	FREE
EMPS	YES	NO	YES	PRICED
EnergyPRO	YES	NO	YES	PRICED
TRNSYS	YES	NO	YES	PRICED
HYBRIDS2	YES	NO	YES	DEMO version with password free
INSEL	YES	NO	NO	-
SOLSTOR	YES	YES	NO	-
HySim	YES	NO	NO	-
HybSim	YES	NO	NO	-
HySys	YES	NO	NO	-
IPSYS	YES	NO	NO	-
RAPSIM	YES	NO	NO	-
SOLSIM	YES	NO	NO	-
iHOGA	YES	YES	YES	EDU version free.
iGRYHSO	YES	YES	Spanish version	PRICED

4. Results and Discussions

4.1. Results: software tools for HRES optimization

The following table 4 summarizes software tools which have the capability to do optimization for hybrid energy systems techno-economic design. As it can be noticed from table 3, most software tools supporting hybrid energy system have the capability of performing simulation. However, three of them support only their optimization in order to reduce the cost of their installation and to get the best optimum design for their technicality.

Table 4. Software tools supporting Hybrid Energy Systems optimization

TOOLS	Free of charge or commercial?	Duration of training
HOMER	Download Free of charge from https://www.homerenergy.com	1 day
iHOGA	EDU version is free from https://ihoga.unizar.es/en/descarga/	1 day
RETScreen	free-of-charge from https://www.nrcan.gc.ca/energy/retscreen/7465	1 day

The following points give a brief explanation of HOMER, iHOGA, and RETScreen capable of supporting HES optimization.

- ***HOMER***

Hybrid Optimization Model for Electric Renewable (HOMER) is developed by National Renewable Energy Laboratory (NREL) in USA. It is available on the market. Many researchers have used it for the prefeasibility, sizing HES technologies, and techno-economic analysis of their projects. The newest version HOMER Pro and HOMER Grid can be downloaded with a 21 free trial days and a variety of licences. However, older versions such as HOMER 2.68 beta can be freely downloaded through permission by contacting Homer Energy.

- ***iHOGA***

Improved Hybrid Optimization by Genetic Algorithm is a hybrid system optimization tool developed by University of Zaragoza, Spain. It has replaced the older version HOGA. iHOGA is available in English. It has got two versions namely PRO+ and EDU. EDU version is freely downloadable. However, it can only simulate a maximum daily load of 10kWh.

- ***RET Screen***

Renewable Energy Technologies Screen (RETScreen) is developed by Ministry of Natural Resources in Canada. It helps to determine the techno-economic viability of hybrid energy systems (HES) or integrated renewable energy systems (IRES). Mostly it is used to perform the feasibility study of simulation of cogeneration projects but it can also perform optimization of hybrid energy systems. However, RETScreen Expert is available free of charge in viewer mode as an advanced premium version. To get the ability options to save, print or export files, RETScreen Expert in professional mode is necessary and it needs to be purchased.

4.2. Discussions

Many researchers have given an extensive literature review on software tools. Essential constraints that were included such as the availability these tools on the market or whether they are free-of-charge or commercial and the duration of the training in order to use the model tool. This information is important for the academic researchers if their educational institutions do not provide these tools to save some time. This is due to the fact that some software tools can be very expensive and it can take also up to several months of training to use the software. For example, according to Connolly et al. (2010) EPMPS costs NOK 500, 000 (€54,930) and takes one month of training to use it. Moreover, some energy tools for HES are no longer used or maintained such as SOLSTOR, HySim, and SOMES. Besides, some of them are not available for external users or they are not for sale such as AELIUS, H2RES. Hybrid 2 software is free to be downloaded. However, it does not work on windows platforms later than Windows XP such as Windows 10. And iHOGA can simulate only a maximum 10kWh of daily load.

5. Conclusion

Hybrid Energy Systems have the following advantage:

- To save fossil fuel
- To have a higher reliability and a better efficiency in electricity generation
- To save the cost of HES technologies when optimum design is used.

In this study, an overview of HES simulation and optimization is given. It has been concluded that only few software tools have the capability so far of giving an optimum design for the implementation of hybrid renewable energy systems. These tools are HOMER (widely used), iHOGA, and RETScreen. The following figure 2 shows the screens of these three software tools.

References

K.S.N.Abhishek ,M.K.V.Kiran Kumar, R.S.Mansoor Ali, 2018.Analysis of Software Tools for Renewable Energy Systems. International Conference on Computation of Power, Energy, Information and Communication (ICCPEIC), IEEE:pp. 179-185, ISBN: 1538624478

José L., Bernal-Agustín, and Rodolfo Dufo-López, 2009. Simulation and optimization of stand-alone hybrid renewable energy systems. Renewable and Sustainable Energy Reviews, 13(8):pp. 2111-2118

D. Connolly, H. Lund , B.V. Mathiesen , M. Leahy, 2010. A review of computer tools for analysing the integration of renewable energy into various energy systems. Applied Energy, 87 (4) , pp. 1059-1082.

Samir M. Dawoud, Xiangning Lin, Merfat I. Okba, 2018. Hybrid renewable micro-grid optimization techniques: A review. Renewable and Sustainable Energy Reviews. Volume 82:p. 2039-2052

S., Negi, and L., Matthew, 2014. Hybrid renewable energy system: a review. International Journal of Electronic and Electrical Engineering, 2014. Volume 7, Issue 5: P. 535-542.

M., Suresh, and R., Meenakumari, 2018. Software Tools for Analyzing the Integration of Various Renewable Energy Systems, . Issue 2456-8449:p. 135-140

T. Tezer, Tuba, R. Yaman, and G.Yaman, 2017. Evaluation of approaches used for optimization of stand-alone hybrid renewable energy systems. Renewable and Sustainable Energy Reviews, Volume 73: P.840-853.

United Nations, The Sustainable Development Goals 2018. New York, United Nations, P.40.

https://unstats.un.org/sdgs/files/report/2018/TheSustainableDevelopmentGoalsReport2018-EN.pdf [Access Date: 15 September 2019]

Sauro Pierucci, Flavio Manenti, Giulia Bozzano, Davide Manca (Eds.)
Proceedings of the 30th European Symposium on Computer Aided Process Engineering
(ESCAPE30), May 24-27, 2020, Milano, Italy.
http://dx.doi.org/10.1016/B978-0-12-823377-1.50248-2

Sour Gas Sweetening Technologies for Distributed Resources – A Process Simulation Study

Shuang Xu[a], Yushi Deng[a], Kylie Webb[b], Harrison Wright[b], Paul S. Dimick[b], Selen Cremaschi[a] , Mario R. Eden[a]

[a]*Department of Chemical Engineering, Auburn University, Auburn, AL 36849, USA*
[b]*Intramicron, Inc., Auburn, AL 36832, USA*
edenmar@auburn.edu

Abstract

With increasing natural gas consumption, a wider range of gas fields/resources is being explored, however utilization of distributed natural gas resources remains a challenge. The primary reasons are that the cost of processing/treatment and transport, which can be higher than the natural gas selling price. Furthermore, distributed/stranded gas resources are typically limited in volume/capacity, which may them uneconomic to recover. Therefore, the identification of low cost small scale gas treatment processes is a key enabling step in utilization of distributed natural gas resources. Desulfurization is a critical natural gas treatment process, as it removes H_2S, which is a catalyst poison and also avoids the formation of SO_2. In order to identify a suitable small scale desulfurization process, we evaluate three technologies, triazine absorption, LOCAT, and SourCat, and analyze their techno-economic performance at different conditions.

Keywords: Natural gas desulfurization, small scale operation, process simulation

1. Introduction

Desulfurization is a very important step in utilization of natural gas resources, not only in terms of preventing the formation of SO_2 after combustion, but also to avoid catalyst poisoning in subsequent processing steps. It is estimated that 30% of the global natural gas reserves are distributed, i.e. located away from the processing infrastructure and/or market demand (Baldea et al., 2017). In Alaska, for example, there are large amounts of natural gas stranded in oil fields, and the gas is not being utilized due to both the cost of recovery and required pipeline construction. Current practice for transporting distributed gas resources to market is either by pipeline or as liquefied natural gas (LNG). Wood et al. (2008) have shown that the most economic transportation mode is actually through gas to liquid (GTL) processing, when the production rate is small and the gas well is far away from the intended market. As a result, identification of low cost small scale desulfurization processes can stimulate utilization of stranded natural gas through scalable GTL processes. In this paper, we briefly review current desulfurization processes and present a simulation-based economic study for three small scale processes along with the preferred operational scale for each.

2. Background

In general, desulfurization processes can be classified by three primary types, i.e. absorption, chemical oxidation, and adsorption. Absorption processes use a solvent to absorb (either chemically or physically) the sulfur component(s) and then the solvent is regenerated in a stripping column. The concentrated gas leaving the stripping column is

typically sent to a chemical oxidation process. Current industrial practice involves the use of various solvents including amines, caustic, triazine, and methanol. It should be noted that while the triazine based process does not regenerate the solvent, but it exhibits very good performance at small scale. As mentioned above, the concentrated sulfur stream is fed to a chemical oxidation step to produce elemental sulfur or sulfuric acid. Typical processes include solid bed oxidation (Claus, SourCat), liquid redox (LOCAT/Sulferox), and wet sulfuric acid (WSA), some of which are widely applied at commercial/large scale. SourCat and LOCAT/Sulferox have shown potential for small scale operation (Catalyst Commercialization, 2017; Echt et al., 2017). Therefore, triazine absorption, LOCAT, and SourCat were selected for this study.

3. Process Simulation

The sour gas feedstream is at 95°C and 115 psi and the sulfur concentration should be reduced to less than 4 ppm (Faramawy et al., 2016) before it can be sent to downstream processing. Furthermore, to illustrate the process performance at different scales the feed flow rate is varied from 100,000 standard cubic feet per day (MSCFD) to 100,000,000 standard cubic feet per day (MMSCFD), and the H_2S content ranges from 500 to 2000 ppm. All three desulfurization processes are simulated using Aspen Plus and the Aspen Process Economic Analyzer is used to calculate equipment sizes etc.

3.1. Triazine-based Absorption

Three reactions take place in the absorption column (Eqs. 1-3) with the primary reaction given in Eq. (1). The product of the reaction in Eq. (2) forms a solid inside the vessel, which may cause plugging problems. To avoid the formation of solids, the triazine feed is kept at 20% excess. The process flowsheet is given in Figure 1. The feed gas is first mixed with water to mimic the actual saturated sour gas conditions. Next, the saturated gas is cooled to the reaction temperature. After that, the sour gas along with a 52 wt% triazine solution is fed to an absorber, where the sulfur components are captured at temperatures ranging from 10 to 70°C. The sweet gas stream leaving the absorber contains less than 4 ppm sulfur, and the liquid stream consists of spent triazine, which will be sent to disposal. As such, the process costs are primarily related to the solvent usage and thus the triazine price will greatly influence the operating costs.

$$C_9H_{21}N_3O_3 + 3H_2S \rightarrow C_3H_6O_3 + 3C_2H_7NO \quad (1)$$

$$C_9H_{21}N_3O_3 + H_2S \rightarrow C_7H_{16}N_2O_2S + C_2H_7NO \quad (2)$$

$$C_7H_{16}N_2O_2S + H_2S \rightarrow C_5H_{11}NOS_2 + C_2H_7NO \quad (3)$$

3.2. Liquid Redox (LOCAT)

The LOCAT process (shown in Figure 2) uses a liquid catalyst (chelate iron) to convert the sulfur component(s) to elemental sulfur and then the catalyst is regenerated using oxygen. The reactions are show in Eqs. (4-5). Because of the ferric ions in the system, the pH of the solution should be strictly maintained between 8 and 9. Typically, sodium is added to the system to help with pH control. The inlet iron concentration is 250 ppm and the Fe^{3+}: H_2S molar ratio is kept at 4:1. Different to the triazine process above, the saturated sour gas is cooled to remove the water to avoid diluting the liquid catalyst. Next, the dry sour gas along with the liquid catalyst solution is fed to an absorber to generate elemental sulfur at temperatures ranging from 27 to 55°C and pressures from 1 to 34 atm. The gaseous stream leaving the absorber contains the sweetened gas, while the liquid phase contains sulfur and ferrous ions is fed to the regeneration column, where the ferric ions are regenerated by reaction with oxygen. Finally, the solid sulfur is captured using a

filter, and the liquid catalyst along with makeup catalyst material is recycled to the absorber. Depending on the type of filter used, the sulfur cake mass fraction varies from 30% to 90%. To balance the accumulation of water and catalyst recovery, the sulfur cake mass fraction is specified at 48%.

$$2Fe^{3+} + HS^- \rightarrow 2Fe^{2+} + S + H^+ \quad (4)$$

$$2Fe^{2+} + \tfrac{1}{2}O_2 + H_2O \rightarrow 2Fe^{3+} + 2OH^- \quad (5)$$

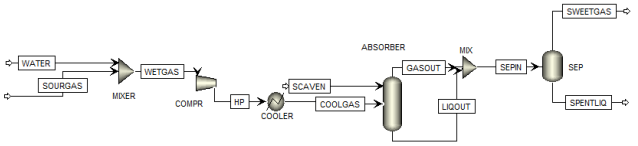

Figure 1. Triazine absorption process flow diagram.

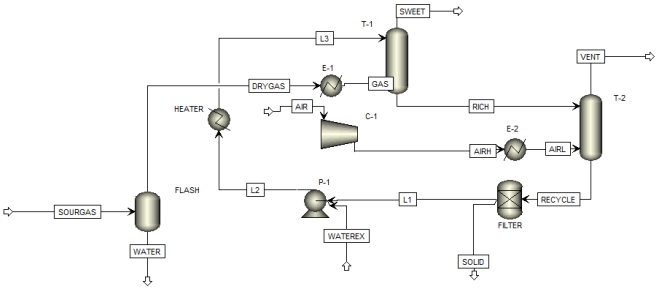

Figure 2. Liquid redox (LOCAT) process flow diagram.

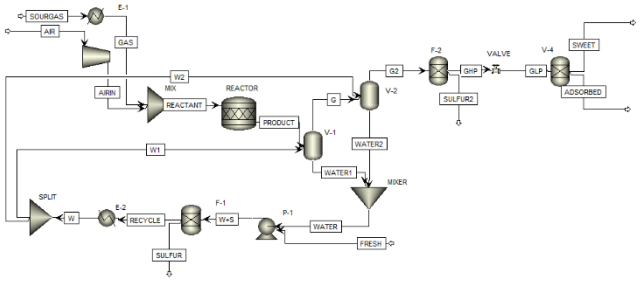

Figure 3. Process flow diagram of SourCat process.

3.3. Chemical Oxidation (SourCat)

The SourCat process (shown in Figure 3) directly converts H_2S to elemental sulfur with SO_2 as a side product as shown in Eqs. (6-7). The catalyst exhibits more than 90% conversion and selectivity. Because of the side product and remaining H2S, a sorbent bed is needed. Similar to the Triazine process, the saturated sour gas can be directly fed to the system without first removing the water. First, the sour gas and oxygen feeds are heated to 200°C at 115 psi and then fed to a solid bed reactor to generate elemental sulfur. The reaction is highly exothermic, so tight temperature control is needed, especially when scaling up the process. Following the reaction, the elemental sulfur is captured by a water quench and then separated by a filter. A 20% water loss is specified for the filter, and the rest of the water along with makeup fresh water is recycled back to the quench system.

The gaseous product can be sent to downstream processing after passing through a sorbent bed.

$$\frac{1}{2}O_2 + H_2S \rightarrow H_2O + S \quad (6)$$

$$\frac{3}{2}O_2 + H_2S \rightarrow H_2O + SO_2 \quad (7)$$

4. Economic Analysis

Following the simulation studies, equipment sizes from Aspen Process Economic Analyzer are input to a process economics tool ECON (Kalakul et al., 2014) to calculate the capital (CAPEX) and operating (OPEX) costs. These values are then used to calculate the desulfurization cost as defined in Eqs. (8-9), where the annual interest (i) is set at 10% and the payoff period (n) is three years.

$$\text{Desulfurization cost before pay off} = \frac{CAPEX \times \frac{i(1+i)^n}{(1+i)^n - 1} + OPEX}{Capacity} \quad (8)$$

$$\text{Desulfurization cost after pay off} = \frac{OPEX}{Capacity} \quad (9)$$

4.1. Validation of Simulation Results

In order to verify the results from the simulation and economic analyses, a comparison with reference data is performed. The LOCAT reference data (Echt et al., 2017; Judd and Eng, 2006) along with the simulation results are shown in Table 1. It can be seen that our results fall within the ranges of the reference data and as such indicates that the simulation and cost estimation models can reasonably represent the actual processes. The same comparison is performed for the triazine absorption process and the results, which have confirmed by our collaborators, are shown in Table 2. It should be noted that the triazine prices can fluctuate significantly, and since the process cost depends almost entirely on the triazine cost, the operating cost in this study should be considered a general case not necessarily the optimal one.

Table 1. Validation of Results for LOCAT process (TPD: tons per day; ST: standard ton).

Parameter	Reference Data	Simulation Data
Capacity (sulfur removal)	0.5 – 20 TPD	3.8 TPD
H_2S concentration	10000 ppm	10000 ppm
Gas flow rate	0.01 – 200 MMSCFD	10 MMSCFD
Iron concentration	250 – 1000 ppm	250 ppm
OPEX (chemicals and electricity)	$250 - $1000 per ST	$436 per ST

Table 2. Validation of Results for Triazine Absorption Process.

Parameter	Reference Data	Simulation Data
H_2S concentration	100 ppm	100 ppm
Gas flow rate	1 MMSCFD	1 MMSCFD
OPEX	$1	$1.1

4.2. Cost Estimation at Different Conditions

After verifying the appropriateness of the simulation and economic models, we can evaluate the three desulfurization processes at different scales. Figure 4 shows the capital

and operating costs of the three processes at 0.1 MMSCFD. It can be seen that the LOCAT process has the highest capital and operating cost at this scale. The triazine process has the lowest capital and operating costs, but the latter increases rapidly as the sulfur concentration goes up. The SourCat process exhibits medium capital cost and the operating cost remains fairly stable as a function of sulfur concentration as it uses a solid bed reactor and the primary contributor to the operating costs are utilities.

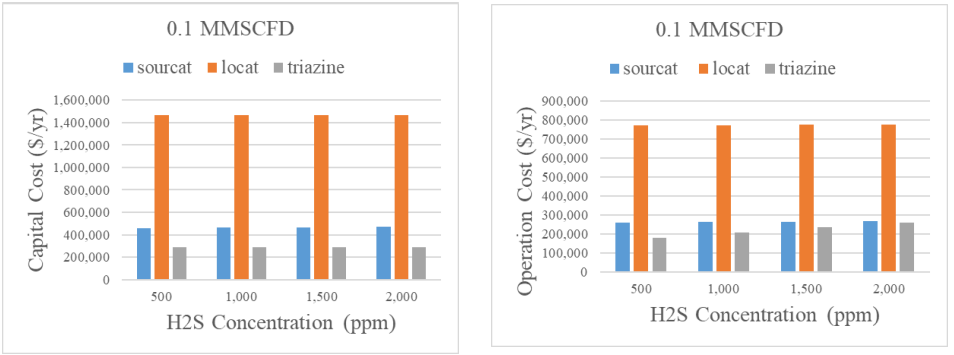

Figure 4. Capital and operating cost of desulfurization processes at 0.1 MMSCFD flow rate.

Next, the process economics are evaluated at flowrates of 1 MMSCFD, 10 MMSCFD, and 100 MMSCFD. Figure 5 shows the desulfurization cost for all three processes at the four different gas flowrates. For small scale conditions (gas flowrate less than 0.1 MMSCFD), the triazine process shows the lowest desulfurization cost, however as the gas flowrate increases (1-10 MMSCFD), the SourCat process shows the best performance. At the largest scale evaluated (100 MMSCFD), the results show that the SourCat and LOCAT processes have similar desulfurization costs, however it would appear that the LOCAT process could be favored if the flowrate was increased even further.

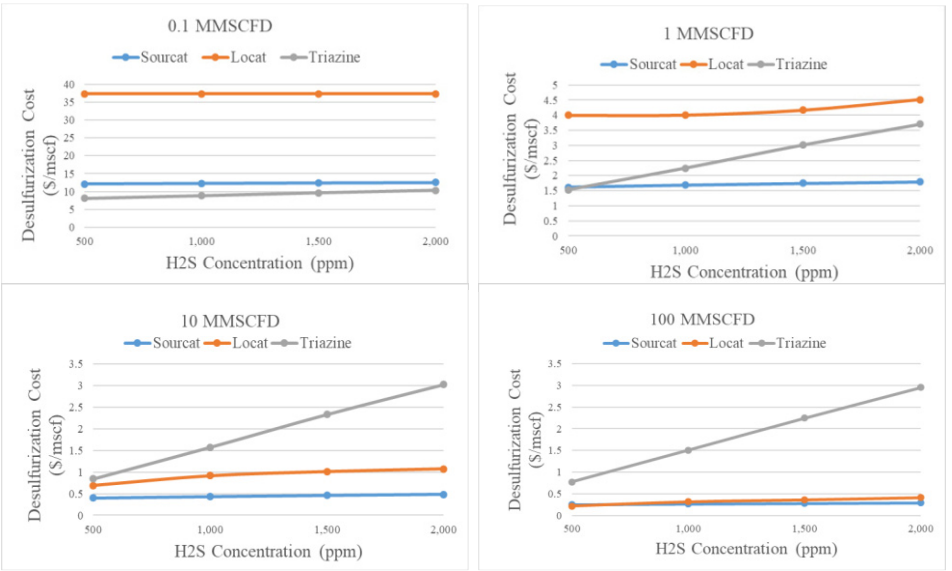

Figure 5. Desulfurization cost (with 3 year payoff) at different gas flowrates.

5. Conclusions

In this work, we have compared the performance of a novel small scale desulfurization process to two commercial industrial implementations. Following a detailed simulation study and subsequent cost estimation of all three processes (and validation against reference data where available), it was found that the triazine absorption process shows the best performance at very small scale (0.1 MMSCFD corresponding to a sulfur removal rate of 0.02 TPD), while the SourCat process has the lowest desulfurization cost at flowrates between 1 and 10 MMSCFD (corresponding to sulfur removal rates of 0.02-2 TPD). Finally, the LOCAT process is found to be better suited for large scale processes (over 100 MMSCFD). As new intensified/modular technologies for GTL and other valorization strategies for stranded gas resources are developed, the ability to remove sulfur from the feed gas will be of critical importance. This study provides a foundation for insightful selection of the appropriate desulfurization technology for small scale natural gas conditioning.

Acknowledgements

The authors are grateful for the financial support provided by the DOE-RAPID Process Intensification Institute under contract DE-EE0007888-10-6.

References

Baldea, M., Edgar, T.F., Stanley, B.L., (2017). Modular manufacturing processes: status, challenges, and opportunities. AIChE journal, 63(10), 4262-4272.

Catalyzing Commercialization: Sour Gas Has a Sweeter Future. (2017). Retrieved from https://www.aiche.org/resources/publications/cep/2017/january/catalyzing-commercialization-sour-gas-has-sweeter-future.

Echt, B., Leppin, D., Mamrosh, D., Mirdadian, D., Seeger, D., Warren, B., (2017). Fundamentals of low-tonnage sulfur removal and recovery. In Proceedings of 2017 Laurance Reid Gas Conditioning Conference.

Faramawy, S., Zaki, T., Sakr, A.A.E., (2016). Natural gas origin, composition, and processing: A review. Journal of Natural Gas Science and Engineering, 34, 34-54.

Judd, B., Eng, P., (2003). Fundamentals - gas sweetening. In Proceedings of 2003 Laurance Reid Gas Conditioning Conference.

Kalakul, S., Malakul, P., Siemanond, K., Gani, R., (2014). Integration of life cycle assessment software with tools for economic and sustainability analyses and process simulation for sustainable process design. Journal of Cleaner Production, 71, 98-109.

Wood, D., Mokhatab, S., Economides, M.J., (2008). Technology options for securing markets for remote gas, In Proceedings of 87th Annual Convention of the Gas Processors Association (GPA).

Sauro Pierucci, Flavio Manenti, Giulia Bozzano, Davide Manca (Eds.)
Proceedings of the 30th European Symposium on Computer Aided Process Engineering (ESCAPE30), May 24-27, 2020, Milano, Italy.
http://dx.doi.org/10.1016/B978-0-12-823377-1.50249-4

Supply Chain Design Optimization within Planetary Boundaries

Jonathan Wheeler,[a,b] Ángel Galán Martín,[b] Fernando D. Mele,[a] Gonzalo Guillén-Gosálbez [b].

[a] *Consejo Nacional de Investigaciones Científicas y Técnicas, FACET-UNT, Av. Independencia 1800, T4002BLR S. M. de Tucumán, Tucumán, República Argentina.*
[b] *Institute for Chemical and Bioengineering, Swiss Federal Institute of Technology in Zurich, Vladimir-Prelog-Weg 1, Zurich, 8093, Switzerland.*
gonzalo.guillen.gosalbez@chem.ethz.ch

Abstract

The recently emerged Planetary Boundaries framework establishes global limits to human activities in order to avoid highly deleterious events that could shift the current state of the Earth. Here, for the first time we address the strategic design of sustainable supply chains (SCs) considering their absolute sustainability level using PBs. To this end, an MILP model is developed where the mass and energy flows of the network are linked to PBs, thereby enabling the maximization of their absolute environmental sustainability. To illustrate our approach, we studied the supply of sugarcane-based bioethanol in Argentina, considering local policies seeking to increase the gasoline-ethanol blend from 12% to 20% in the upcoming years. We found that none of the SC configurations can meet the eight downscaled PBs concurrently, although their transgression would be reduced significantly in the optimal solution. Our results highlight the need for incorporating PBs in the design of sustainable SCs in a globalized world.

Keywords: Planetary Boundaries, Supply Chain, Optimization, Bioethanol

1. Introduction

The growth in trade of goods and services resulting from increased globalization over the past decades has posed new challenges for the design, planning and operation of value chains. In the area of PSE, the strategic planning of SCs has attracted increasing interest in the last decades. This has led to a plethora of decision-support tools, most of which are based on optimization methods. In essence, the task of optimizing SCs requires: (i) building models for representing the network precisely; (ii) algorithms to solve these models efficiently; and (iii) analysis tools to interpret their optimal solutions insightfully. The latter cover activities from raw materials acquisition to the delivery of final products passing through all manufacturing, transportation and storage stages, which should be coordinated effectively for optimal operation of the network.

Traditional SC models focused on optimizing economic performance as a unique criterion, yet the recent quest for sustainability requires enlarging the scope of the analysis to embrace environmental and societal concerns as well. This has been accomplished through the integration of Life Cycle Assessment (LCA) and optimization tools, which allows covering the three sustainability pillars when optimizing SC decisions (*i.e.*, societal-human health, environmental-ecosystems quality, and economic-resources). The main drawback of the so-called Life Cycle Optimization (LCO) approach is that it allows

comparing and optimizing solutions in terms of a set of impact metrics, but as such cannot answer the questions of whether they are "truly" sustainable.

Here we present an approach that overcomes this limitation by integrating the planetary boundaries (PBs) concept (Steffen et al., 2015; Rockström et al., 2009) into SC models to assist in the optimal design of sustainable SCs. In essence, the PBs framework identifies nine biophysical boundaries that define a "safe operating space" (SOS) for the Planet (*e.g.*, climate change, freshwater use or land-use change boundaries). Operating outside the SOS could lead to catastrophic events and a shift from the current Anthropocene state (where humanity flourished) to an unknown (most likely, much less friendly) state.

Our proposed framework provides a theoretical and methodological basis to evaluate SCs considering the carrying capacity of the Earth. This is accomplished by imposing limits on the SC operation, whose activities are linked to impacts on PBs. To illustrate the capabilities of the proposed framework, we applied it to the design of a biomass-to-biofuels SC that produces bioethanol from sugarcane in Argentina. Our framework aims at guiding practitioners, researchers and governments in the design and planning of SCs aligned with global sustainable development.

2. Modelling Framework

A general design problem of sustainable SCs can be mathematically expressed as follows:

$$\begin{aligned} &min\ \{f_{econ}, f_{env}, f_{soc}\} \\ &s.t. \quad f(x,y,z) = 0 \\ &\qquad g(x,y,z) \leq 0 \\ &x \in \Re, y \in \mathrm{N}, z \in \mathrm{Z}^{+} \end{aligned} \tag{M1}$$

where f_{econ}, f_{env} and f_{soc} are the economic, environmental and societal objective functions, and, x, Y and Z represent continuous, binary and integer decision variables, respectively, related to the design and operation of the SC. In essence, we incorporate PBs into this model by following LCA principles combined with a recently published damage assessment model that converts inventory flows into impacts on PBs. The overall approach is outlined in Figure 1. The PBs, defined globally, are first downscaled to the SC level. Next, LCA is applied to derive equations that link the SC operation to its performance in terms of PBs. Finally, M1 is solved with these equations embedded to find solutions that minimize the PBs transgression.

2.1. Environmental assessment using Planetary Boundaries

A total of 14 global and regional PBs have been defined, including climate change due to energy imbalance and CO_2 emissions, stratospheric ozone depletion, biogeochemical flows of nitrogen and phosphorus (global and regional), land-system change (global and biome), freshwater use (global and basin), atmospheric aerosol loading (global and regional), introduction of novel entities and biosphere integrity. While there is no full consensus on their exact values, there seems to be a general agreement on most of them and their global relevance (Steffen et al., 2015; O'Neill et al., 2018).

Here we are interested in assessing the performance of a SC in terms of these PBs. To this end, we include constraints in the optimization model that link any activity in the SC with its corresponding impact on PBs.

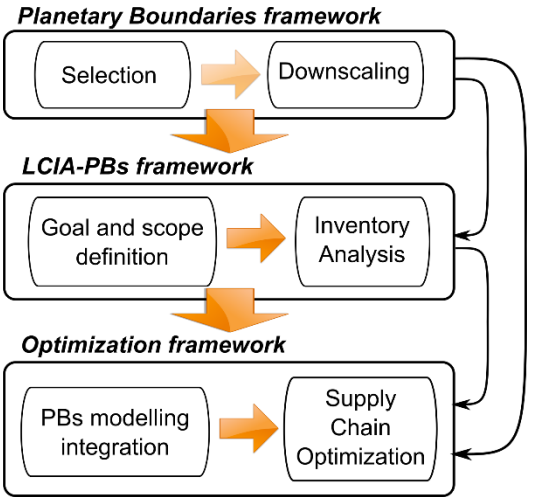

Figure 1. Flowsheet of the proposed modelling framework.

2.1.1. Step 1: Selection of Planetary Boundaries and downscaling

Due to some methodological gaps highlighted in previous work by some of us (Alguinabet et al., 2019), we omit here regional PBs on freshwater use, land system change and phosphorus flow, as well as the one defined on biodiverse integrity. We also omit atmospheric aerosol loading, as current values refer to the Indian subcontinent. Finally, the PB on the introduction of novel entities was also left out of the analysis because it has not been fully defined yet. A partition principle needs to be applied first to define an allowable budget for the SC activities (considering a given functional unit, FU) in each PB (Ryberg et al., 2018a). If the environmental impact of the activity remains below the value of the assigned share, it is deemed fully sustainable, while the converse would imply that it is unsustainable. Assigning a share of the SOS (SoSOS) is controversial. Without loss of generality, an Egalitarian principle is applied to calculate the share assigned (aS) from the final consumption expenditure (FCE) for the functional unit (FU) and the total FCE worldwide:

$$aS = \frac{FCE_{FU}}{FCE_{world}} \tag{1}$$

Next, the SoSOS for a PB b is calculated using the selected sharing principle and the value of the SOS, according to Eq. (2).

$$SoSOS_b = SOS_b \times aS_b \quad \forall b \tag{2}$$

Here $SoSOS_b$ is the quota of the SOS_b assigned to the FU considered following the sharing principle chosen (aS_b). The absolute sustainability level of a system is given by the ratio between the impact score in PBs and the $SoSOS_b$, as shown in Eq. (3).

$$FSoSOS_b = \frac{ES_b}{SoSOS_b} \quad \forall b \tag{3}$$

ES_b is the impact score of the activity measured in the units of a PB b, and $FSoSOS_b$ represents the occupied fraction of the SoSOS. Therefore, if this value is equal to or lower than one, the activity can be considered fully sustainable.

2.1.2. Step 2: Linking SC activities to their performance in PBs

The life cycle inventory entries are linked to PBs using the characterization factors (CF) in (Ryberg et al., 2018b). Therefore, we can calculate the environmental impact of an SC in terms of PBs as in Eq. (4):

$$ES_b = \sum_i F_i \sum_j LCI_{j,i} \,.\, CF_{j,b} \quad \forall b \tag{4}$$

where ES_b is the total environmental flow in PB b, F_i is the material flow of product i, $LCI_{j,i}$ is the elementary flow j in the life cycle inventory of activity i (represented by a mass or energy flow) and $CF_{j,b}$ is the characterization factor that links the elementary flow j to PB b. We can define the transgression on a PB (PBT_b) as the difference between the environmental score of the SC (ES_b) and the downscaled value of the PB b ($SoSOS_b$).

2.1.3. Step 3: Solving the optimization model with embedded constraints on PBs

Finally, to solve the sustainable SC optimization problem, we add up the transgression level across PBs, as follows:

$$f_{env} = \sum_b \frac{PBT_b}{SoSOS_b} \tag{5}$$

$$PBT_b \geq 0 \quad \forall b \tag{6}$$

$$EP_b \leq SoSOS_b + PBT_b \quad \forall b \tag{7}$$

In Eq. (5-7), PBT_b is the transgression in PB b. If a PB is transgressed, the transgression level corresponds to the difference between the SC environmental impact EP_b and the downscaled PB ($SoSOS_b$). Otherwise, the transgression in that PB would be zero. Note that here f_{env} quantifies how many times the $SoSOS_b$ is exceeded.

3. Case study

We test the proposed framework by addressing the design of a biomass-to-biofuels SC. Specifically, we search for the optimal design of a three-echelon SC to produce bioethanol from sugarcane in Argentina considering its environmental and economic performance simultaneously and a ten-year time horizon. To this end, we modified a previous model (Wheeler et al., 2018) to introduce current industrial and transport practices as well as the PBs equations required to calculate the environmental performance of the SC .

3.1. Life cycle impact assessment

We adopt a well-to-wheel approach, where the FU is defined as *"the annual passenger transport in conventional cars using a gasoline and sugar cane ethanol blend in Argentina*". Inventories for the agricultural and ethanol production stages were obtained from previous studies of the sugar-ethanol production in Argentina (Nishihara et al., 2017; Amores et al., 2013). Life cycle inventories to calculate PBs ($LCI_{j,i}$) were acquired from the Ecoinvent LCA database. LCI for ethanol transport and gasoline market were directly obtained from Ecoinvent 3.5®. Elementary flows for passengers transport were taken from GREET® (Wang et al., 2018).

3.2. Share of the safe operating space

We calculated first the SoSOS based on the FCEs in Argentina and the world (Eq. (1) and Eq. (2)). The domestic FCE for passenger transport in Argentina is 24 billion US$, while the FCE of the world is 43900 billion US$. Thus, the share of the SOS for to the FU (aS_{AR}-

Thus, the share of the SOS for to the FU *(aSAR-transp)* is 0.0274%. The values of the PBs studied in this work, their background level and the SOS can be found in Ryberg et al.

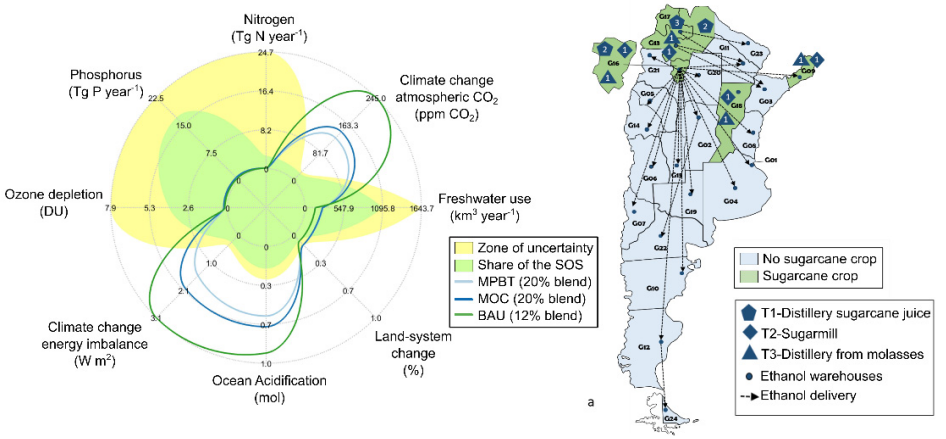

Figure 2. Supply chain performance in PBs for the MPBT, MOC and BAU solutions. Full lines show the environmental performance in eight planetary boundaries; the darker area is the safe operating space and the lighter one, the uncertainty zone. a) Supply chain topology for the MPBT solution.

3.3. Results

Fig. 2 depicts the environmental performance relative to the downscaled PBs of the minimum cost and minimum transgression solutions together with the BAU solution. Although there are significant improvements in the environmental performance in the MPBT solution, no SC configuration meets all PBs concurrently. Three PBs were transgressed beyond the uncertainty zone: climate change (in CO_2 concentration and energy imbalance), and ocean acidification. Here, fossil emissions (gasoline) are the main contribution to the environmental scores, where the amount of bioethanol in gasoline blends is limited to 20%. The score in land system change also transgresses the downscaled PB; meanwhile, values for MOC and MPBT remained in the uncertainty range. The worsening in this PB compared to the BAU solution is mainly related to a more extensive agricultural activity needed to increase bioethanol production.

Concerning the SC design decisions, we find by minimizing the PBs transgression, that the model decides to change the current technologies (T2 and T3) to direct ethanol production from sugar cane (T1), in the central crop regions (G13, G16 and G17). Moreover, in crop regions that only produce sugar (G09 and G18) currently, the model decides to produce ethanol from molasses (T3). This investment scheme for the MPBT solution, reports a 23.12% higher total costs compared to the topology results for the MOC solution, but a 71.56% improvement in the total transgression of PBs.

4. Conclusions

We proposed here a novel framework to assist in the design of SCs within the safe operating space of the Earth System. Our approach relies on the use of optimization models that incorporate equations to link the SC activities with its performance in terms of PBs. We applied our approach to the design of a real SC producing bioethanol from

sugarcane in Argentina to satisfy increased fuels demands in the transportation sector. Overall, our results show that despite significant improvements in PBs performance compared with the business-as-usual scenario, there is no configuration capable of meeting all PBs considering a 20% gasoline blend. This highlights the need for higher-blends, which should be promoted through government mandates, or alternative transportation technologies. The proposed framework provides a sound tool to support practitioners and researchers in the development of optimization models for the design of sustainable SCs entirely consistent with the carrying capacity of our Planet.

References

I.M. Algunaibet, C. Pozo, Á. Galán-Martín, M.A. J. Huijbregts, N. Mac Dowell, G. Guillén-Gosálbez. 2019. Powering sustainable development within planetary boundaries. Energy Environ. Sci., 12, 1890.

M.J. Amores, F.D. Mele, L. Jiménez, F. Castells, 2013. Life cycle assessment of fuel ethanol from sugarcane in Argentina. Int J Life Cycle Assess., 18, 1344–1357.

Z. Kravanja, L. Čuček, 2013. Multi-objective optimization for generating sustainable solutions considering total effects on the environment. Appl.Energy 101, 67–80Z.

A.L. Nishihara Hun, F.D. Mele, G.A. Pérez, 2017. A comparative life cycle assessment of the sugarcane value chain in the province of Tucumán (Argentina) considering different technology levels. Int J Life Cycle Assess, 22:502–515.

D.W. O'Neill, A.L. Fanning, W.F. Lamb, J.K. Steinberger. 2018. A good life for all within planetary boundaries. Nature Sustainability,Volume 1, (2), 88-95.

J. Rockstrom, W. Steffen, K. Noone, A. Persson, F. S. Chapin, E. F. Lambin, T. M. Lenton, M. Scheffer, C. Folke, H. J. Schellnhuber, B. Nykvist, C. A. de Wit, T. Hughes, S. van der Leeuw, H. Rodhe, S. Sorlin, P. K. Snyder, R. Costanza, U. Svedin, M. Falkenmark, L. Karlberg, R. W. Corell, V. J. Fabry, J. Hansen, B. Walker, D. Liverman, K. Richardson, P. Crutzen and J. A. Foley, 2009. A safe operating space for humanity. Nature, 461, 472–475

M.W. Ryberg, M. Owsianiak, J. Clavreul, C. Mueller, S. Sim, H. King and M. Z. Hauschild, 2018a. How to bring absolute sustainability into decision-making: An industry case study using a Planetary Boundary-based methodology, Sci. Total Environ., 634, 1406–1416.

M.W. Ryberg, M. Owsianiak, K. Richardson and M. Z.Hauschild, 2018b. Development of a life-cycle impact assessment methodology linked to the Planetary Boundaries framework Ecol. Indic., 88, 250–262.

M.W. Ryberg, M. Owsianiak, K. Richardson, M.Z. Hauschild, 2016. Challenges in implementing a planetary boundaries based life-cycle impact assessment methodology. J. Clean. Prod. 139, 450–459.

W. Steffen, K. Richardson, J. Rockström, S.E. Cornell, E. M. Bennett, R. Biggs, S. R. Carpenter, W. de Vries, C. A. de Wit, C. Folke, D. Gerten, J. Heinke, G. M. Mace, L. M. Persson, V. Ramanathan, B. Reyers, S. Sörlin. 2015. Planetary boundaries: guiding human development on a changing planet. Science 347, 1217.

J. Wheeler, M.A. Páez, G. Guillén-Gosálbez, F.D. Mele, 2018. Combining multi-attribute decision-making methods with multi-objective optimization in the design of biomass supply schains. Computers and Chemical Engineering 113, 11–31.

M. Wang, A. Elgowainy, A., P. T. Benavides, A. Burnham, H. Cai, Q. Dai, ... & U. Lee. 2018. Summary of Expansions and Updates in GREET® 2018 (No. ANl-18/23). Argonne National Lab.(ANL), Argonne, IL (United States).

Sauro Pierucci, Flavio Manenti, Giulia Bozzano, Davide Manca (Eds.)
Proceedings of the 30th European Symposium on Computer Aided Process Engineering (ESCAPE30), May 24-27, 2020, Milano, Italy.
http://dx.doi.org/10.1016/B978-0-12-823377-1.50250-0

Simultaneous Multiperiod Optimization of Rankine Cycles and Heat Exchanger Networks

Cristina Elsido,[a] Emanuele Martelli,[a*] Ignacio E. Grossmann[b]

[a] *Politecnico di Milano, Dipartimento di Energia, Via Lambruschini 4, Milano, IT*

[b] *Department of Chemical Engineering, Center for Advanced Process Decision-Making, Carnegie Mellon University, Pittsburgh, PA, USA*

emanuele.martelli@polimi.it

Abstract

This work addresses the multiperiod synthesis and optimization of integrated Heat Exchanger Networks (HEN) and Rankine cycles for plants with demanding operational flexibility requirements. A general and systematic synthesis methodology has been developed to optimize simultaneously the utility systems, Rankine cycles and HENs considering different expected operating modes, seeking for the solution with the minimum Total Annual Costs (TAC). Heat exchangers have been modelled with different approaches depending on the type of control measure (with/without by-pass) in off-design operation. The problem is formulated as a challenging nonconvex MINLP and solved with a bilevel decomposition method, specifically developed to address this class of problems. We present the results of the proposed methodology applied to an extremely challenging problem, with 35 streams and 2 operating modes (periods), consisting in the design of an Integrated Gasification Combined Cycle (IGCC).
Keywords: Heat integration, Nonconvex MINLP, Bilevel decomposition, Multiperiod, Utility systems, Rankine cycle superstructure.

1. Introduction

Given the increasing share of intermittent renewable energy sources and the use of novel energy technologies, a new challenge for these energy systems and poly-generation plants is to deal with the increased requirement of operational flexibility. This includes the capability of achieving stable and efficient operation in different operating modes. Among the operational issues, when dealing with plants featuring large volumetric flows of high-temperature gases, it is not possible to control the heat exchanger in the off-design conditions by using bypass streams, as typically done in chemical processes. Examples of this issue are the steam tube banks (superheaters and reheaters) of coal-fired boilers and combined cycles, for which it is impractical to install a bypass duct for the stream of flue gases. Moreover, in steam generators, the steam acts as temperature moderator, as it keeps the metal temperature of the tubes exposed to high-temperature flue gases lower than the maximum allowed value of the material (Spliethoff, 2010). Thus, it is not feasible to use a bypass on the steam side, because the reduced flow of steam would cause an excessive increase in the steam outlet temperature and consequent overheating of the tubes. For the same reason, if steam is used as temperature moderator of the heat exchanger tubes and the hot stream (e.g., the flue gases) cannot be bypassed, the heat exchanger must exchange heat for all operating periods. The heat exchanger featuring this

kind of operational issue needs to be modelled with ad-hoc constraints called "no-bypass HX" constraints (see Section 2).
In the process system engineering community, the design optimization approaches which can consider different expected operating modes and operating issues (e.g., off-design control measures of heat exchangers) are referred to as "multiperiod" design/synthesis methods. Among these methods, three main categories can be distinguished: multiperiod HEN synthesis approaches, multiperiod utility design/synthesis approaches, multiperiod HEN & utility synthesis approaches. Previous studies mainly focused on the first two approaches, optimizing only the HEN synthesis, or only the utility synthesis. Only recently, some authors started to address both problems simultaneously in the multi-period version (Mian et al., 2016; Isafiade et al., 2015).
In this work, we propose an MINLP formulation of the multiperiod HEN & utility synthesis problem, starting from an extension of the single-period model proposed by Martelli et al. (2017) and further extended in Elsido et al. (2019), that enables the automated generation of Rankine cycles recovering heat from one or more heat sources, and the HEN of the overall heat integration.

2. Mathematical model

The general problem for the multi-period simultaneous synthesis of utilities, Rankine cycles and HENs, is formulated as follows:
"Given

- *a set of hot/cold process streams to be cooled/heated, with their heat capacity flow rates, input and output temperatures and heat transfer coefficients for different operating conditions,*
- *a set of hot and cold utility streams, with their specific heat capacity, input and output temperatures and heat transfer coefficients,*
- *information on process needs of hot water/liquid and steam/vapor, technical limitations (e.g., forbidden/forced matches, no stream splitting, etc.) and economic data (e.g., price of fuels, price of electricity, cost models of units, etc.),*

determine

- *the optimal arrangement and design of the heat recovery cycle, of the installed energy systems (e.g., gas turbines, boilers, etc.), and the design of the HEN,*
- *the optimal commitment (on/off status) and operation (loads) of the installed utility and energy systems for each period,*
- *the optimal load and mass flow rates of the Rankine cycle in each period,*

while taking into account a finite set of expected operating conditions of the process with their duration".

The model is based on the SYNHEAT superstructure (Yee and Grossmann, 1990) for the optimal design of heat exchanger networks. The SYNHEAT model is extended to include the streams of the heat recovery cycle, with variable mass flow rate. It should be noted that a steady state condition is assumed in each working period (i.e., no dynamics).
The thermodynamic cycles are modelled with a very general "*p-h* superstructure" (Elsido et al., 2017a, 2017b), capable of embedding many configurations of Rankine cycles, both power cycles and inverse cycles (refrigeration cycles or heat pumps), steam cycles or organic Rankine cycles, with single or multiple pressure levels, as well as heat/steam distribution networks. The proposed approach allows to explicitly consider both technical design constraints (i.e., the "no stream splitting" constraint, forbidden matches, etc.),

which are extremely important when dealing with the detailed design of power plants and chemical processes, and heat integration equipment costs.

The multiperiod problem can be formulated as a non-convex MINLP problem (P1), that comprises Eqs. (1)-(10), extending the single-period formulation of Elsido et al. (2019) to the multiperiod case. Two types of variables are defined: "operational" variables, depending on the periods, and "design" variables, for the selection of the components of the cycle and the layout of the network of heat exchangers. All the constraints are period-dependent, and they are linked by the design constraints defining the calculation of the installed areas and the logical constraints on the binary variables (i.e., complicating constraints). The multi-period objective function (Eq. (1)) is the sum of the annualized investment costs and the weighted sum of the operational costs and revenues of the plant at the different operating conditions, weighted for their expected duration.

$$\begin{aligned}\min TAC = &\sum_r C_{F,r} y_r + \sum_{i,j,k} C_{F,i,j} z_{i,j,k} + \sum_i C_{F,CU,i} z_{CU,i} + \sum_j C_{F,HU,j} z_{HU,j} \\ &+ \sum_r C_{S,r} S_{REF,r} \left(\frac{S_r}{S_{REF,r}}\right)^{\alpha_r} + \sum_{i,j,k} C_{A,i,j} A_{REF,i,j} \left(\frac{A_{i,j,k}}{A_{REF,i,j}}\right)^{\beta_{i,j}} \\ &+ \sum_i C_{A,CU,i} A_{REF,CU,i} \left(\frac{A_{CU,i}}{A_{REF,CU,i}}\right)^{\beta_{CU,i}} \\ &+ \sum_j C_{A,HU,j} A_{REF,HU,j} \left(\frac{A_{HU,j}}{A_{REF,HU,j}}\right)^{\beta_{HU,j}} \\ &+ \sum_{i,p} h_{EQ,p} C_{CU,i,p} q_{CU,i,p} + \sum_{j,p} h_{EQ,p} C_{HU,j,p} q_{HU,j,p} \\ &- \sum_p h_{EQ,p} p_{EL,p} \left(\sum_{r \in TURB} \Gamma_{r,p} \Delta h_{r,p} - \sum_{r \in (PUMP \cup COMPR)} \Gamma_{r,p} \Delta h_{r,p} \right)\end{aligned} \tag{1}$$

$$\text{s.t. } B_1 \begin{bmatrix} \boldsymbol{z} \\ \boldsymbol{y_p} \end{bmatrix} + B_2 \begin{bmatrix} \boldsymbol{t_p} \\ \boldsymbol{dt_p} \\ \boldsymbol{\Gamma_p} \\ \boldsymbol{q_p} \\ \boldsymbol{A} \\ \boldsymbol{S} \end{bmatrix} - \boldsymbol{b} \leq \boldsymbol{0} \tag{2}$$

$$\left(t_{ic,k,p} - t_{ic,k+1,p}\right) \Gamma_{ic,p} c_{P,ic,p} = \sum_j q_{ic,j,k,p} \quad \forall k, ic \notin ISO, p \tag{3}$$

$$\left(t_{jc,k,p} - t_{jc,k+1,p}\right) \Gamma_{jc,p} c_{P,jc,p} = \sum_i q_{i,jc,k,p} \quad \forall k, jc \notin ISO, p \tag{4}$$

$$q_{i,j,k,p} \leq U_{i,j,p} A_{i,j,p} \left(dt_{i,j,k,p} dt_{i,j,k+1,p} \frac{dt_{i,j,k,p} + dt_{i,j,k+1,p}}{2} \right)^{1/3} \quad \forall i, j, k, p \tag{5}$$

$$q_{CU,i,p} \leq U_{i,CU,p} A_{CU,i} \left(dt_{CU,i,k,p} dt_{CU,i,k+1,p} \frac{dt_{CU,i,k,p} + dt_{CU,i,k+1,p}}{2} \right)^{1/3} \quad \forall i, last(k), p \tag{6}$$

$$q_{HU,j,t} \leq U_{HU,j,p} A_{HU,j} \left(dt_{HU,j,k,p} dt_{HU,j,k+1,p} \frac{dt_{HU,j,k,p} + dt_{HU,j,k+1,p}}{2} \right)^{1/3} \quad \forall j, first(k), p \tag{7}$$

$$q_{i,j,k,p} \leq \left(1 + \left(\frac{\Delta A}{A}\right)_{MAX,i,j}\right) U_{i,j,t} A_{i,j,p} \left(dt_{i,j,k,p} dt_{i,j,k+1,p} \frac{dt_{i,j,k,p} + dt_{i,j,k+1,p}}{2} \right)^{1/3} \tag{8}$$

$$\forall (i,j) \in MP, p$$

$$\left(1 - \left(\frac{\Delta A}{A}\right)_{MAX,i,j}\right) U_{i,j,t} A_{i,j,k} \left(dt_{i,j,k,p} dt_{i,j,k+1,p} \frac{dt_{i,j,k,p} + dt_{i,j,k+1,p}}{2}\right)^{1/3} \leq q_{i,j,k,p} \quad (9)$$

$$\forall (i,j) \in MP, p$$

$$z_{i,j,k}, z_{CU,i}, z_{HU,j}, y_{ic}, y_{jc}, y_r \in \{0,1\}$$

$$\Gamma_{ic,p}, \Gamma_{jc,p}, \Gamma_{r,p}, q_{i,j,k,p}, q_{CU,i,p}, q_{HU,j,p}, A_{i,j,k}, A_{CU,i}, A_{HU,j}, S_r, dt_{i,j,k,p} \in \mathcal{R}_+$$

$$t_{i,k}, t_{j,k} \in \mathcal{R}$$

The linear constraints (synthetically represented by Eq. (2)) of the multiperiod model are: the energy balances for each hot and cold stream for each period, the energy balances of non-isothermal process streams in each stage for each period, assignment of inlet temperatures, monotonic temperature variation, load of and utilities, logical constraints on the existence of heat exchangers, calculation of approach temperatures, "no stream splitting" constraint, forbidden matches, restricted/required matches, activation/ deactivation of utility streams, mass and enthalpy balances of the "*p-h* superstructure", calculation of nominal size of Rankine cycle units and utility, constraints for thermal energy storage system, logical constraints for heat exchanger areas.

The nonlinear constraints of the multiperiod model are: the objective function (Eq. (1)), the energy balances of non-isothermal "HEN utility" streams in each stage for each period (Eq. (3)-(4)), the calculation of the installed areas of heat exchangers (Eq. (5)-(7)), and the areas for "no-bypass HXs" (Eq. (8)-(9)). Eq. (8) and (9) impose that the areas of the heat exchangers between hot stream i and cold stream j in temperature stage k can only vary within a certain tolerance. This margin of error to the heat transfer rate equation allows avoiding possible numerical issues due to the adopted linearization technique of the equation (i.e., the Taylor expansion) and take into account the fact that in practice the outlet temperatures of streams can vary by some degrees.

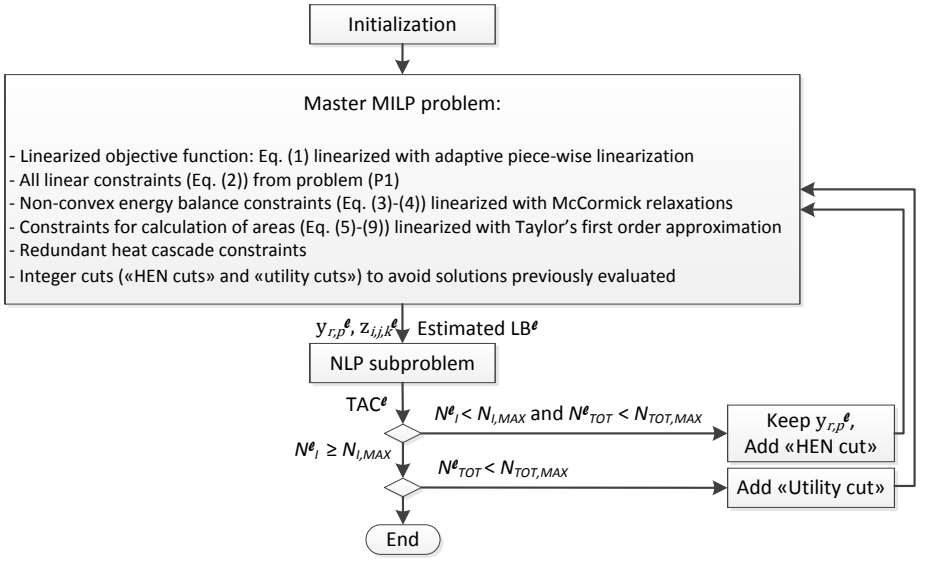

Figure 1: Scheme of the bilevel decomposition algorithm for the multiperiod MINLP problem.

3. Bilevel decomposition

The solution of the challenging nonconvex MINLP problem is tackled with a bilevel decomposition algorithm, extended from the single-period version of Elsido et al. (2019). The algorithm, represented in Figure 1, is based on an upper level (i.e., the "master" problem), comprising a linearized and relaxed version of the original problem (MILP) is solved, to minimize a linearized version of the original objective function; then a lower level problem is solved, in which the binary variables are fixed, and the continuous variables are re-optimized solving a non-convex nonlinear program (NLP). The master problem is obtained by the integration of multiple linearization techniques and the addition of redundant constraints and integer cuts to improve the algorithm convergence.

4. Case study

The methodology is applied to optimize the design and the Heat Recovery Steam Cycle (HRSC) and HEN of an Integrated Gasification Combined Cycle (IGCC) plant with 9 hot and 4 cold process streams in addition to the streams of the superstructure. The HRSC superstructure includes 3 levels of evaporation (HP, MP, LP) and reheating. The single-period analysis of the same process is reported in Elsido et al. (2019).
Here we consider that the IGCC must operate in two different modes:

- "IGCC mode" (5256 h/year): full load condition with gasifier and process at the nominal operating mode;
- "GT-only mode" (2628 h/year): Gas Turbine (GT) is running on natural gas following the electric market/grid requirements, while the gasification island is off (e.g., due to maintenance of the gasifier).

Technical limitations are taken into account as additional constraints in the model: the "no stream splitting" constraint is imposed to the GT flue gases; forbidden matches are imposed so that the high-temperature syngas cooler can be matched only with the HP evaporator or the MP evaporator; the gasifier can be coupled only with the MP evaporator (Elsido, Martelli, & Grossmann, 2019). Besides, the "no-bypass HX" constraints have been imposed to the GT flue gases stream with a critical temperature level of 300°C. The full multiperiod MINLP problem has 30,680 equations and 19,930 variables (3,130 binaries). The proposed algorithm reached convergence to a promising solution in 9,000 s, while BARON, state-of-the-art general purpose MINLP solver, did not provide any feasible solution in 20,000 s. The scheme of the optimal plant is represented in Figure 2.

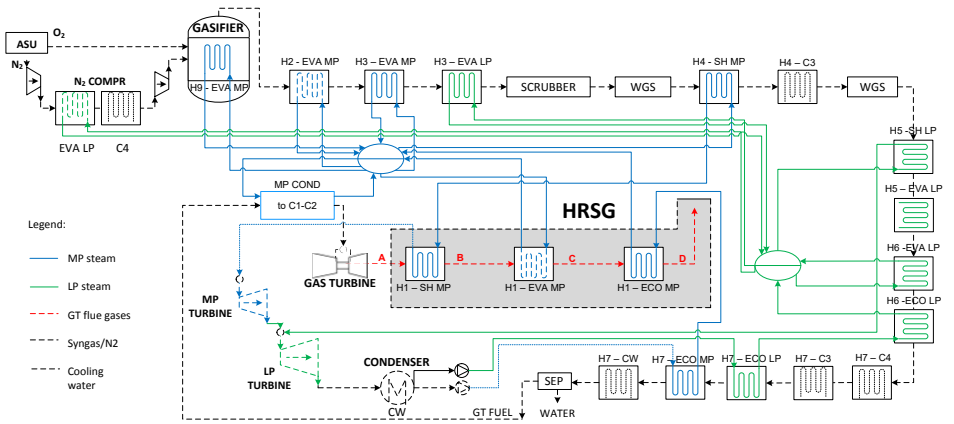

Figure 2: Scheme of the optimal solution of the multiperiod IGCC case study.

The solution obtained by the proposed methodology is a double-level steam cycle (only the MP and LP levels are activated). Thanks to the flexible design, the HRSC can operate 90 % of the yearly hours, both in the "IGCC mode", with net power output equal to 203.7 MW and 31.9 % net electric efficiency, and in the "GT-only mode", with net power output equal to 106.7 MW and 34.0 % net electric efficiency of the HRSC. The MP steam is raised in the Heat Recovery Steam Generator (HRSG) with heat from GT flue gases, the gasifier cooling, and the high-temperature, low-temperature, and post-first WGS syngas coolers. During the "GT-only mode" the MP level flow rate decreases considerably (31.7%) compared to the "IGCC mode", due to the reduction of heat available from the process, and the LP level is de-activated. The outlet temperature of the flue gases is 110°C in "IGCC mode" and 130°C in "GT-only mode".

5. Conclusions

We have presented a multiperiod MINLP model and an ad-hoc bilevel decomposition method to solve complex optimization problems for the simultaneous design of utility systems, Rankine cycles and HEN considering multiple operating conditions. The proposed method is effectively applied to the design of an Integrated Gasification Combined Cycle featuring 10 hot process streams and 14 cold process streams. The design of the HEN and HRSC considers two different expected operating modes ("IGCC mode" and "GT-only mode") making the problem extremely challenging for general purpose MINLP solvers. Nevertheless, the proposed MINLP model can include all the key design and operational constraints, and the ad hoc bilevel decomposition algorithm can find promising solutions within a limited computational time.

Nomenclature

Indices
i, j hot/cold process or utility stream
k index for temperature stage
r component of Rankine cycle
p period
Parameters
T_{IN}, T_{OUT} inlet/outlet temperature of a stream
U heat transfer coefficient
h enthalpy, h_{EQ} duration of periods
C, α, β specific cost and exponent for component/area cost
Binary Variables
z existence of heat exchanger
y existence of utility/Rankine cycle component
Continuous variables
Γ mass flow rates of streams
t temperature of streams at a stage
dt approach temperature difference
q, q_{CU}, q_{HU} heat exchanged
A, A_{CU}, A_{HU} heat transfer areas
S_r nominal size of a Rankine cycle component

References

C. Elsido, A. Mian, F. Marechal & E. Martelli, 2017a. A general superstructure for the optimal synthesis and design of power and inverse Rankine cycles. Computer Aided Chemical Engineering, 40, 2407–2412.
C. Elsido, A. Mian & E. Martelli, 2017b. A systematic methodology for the techno-economic optimization of Organic Rankine Cycles. Energy Procedia, 129, 26–33.
C. Elsido, E. Martelli & I.E. Grossmann, 2019. A Bilevel Decomposition Method for the Simultaneous Heat Integration and Synthesis of Steam/Organic Rankine Cycles. Computers & Chemical Engineering, 228-145.
A. Isafiade, M. Bogataj, D. Fraser & Z. Kravanja, 2015. Optimal synthesis of heat exchanger networks for multi-period operations involving single and multiple utilities. Chemical Engineering Science, 175–188.
E. Martelli, C. Elsido, A. Mian & F. Marechal, 2017. MINLP Model and two-stage Algorithm for the Simultaneous Synthesis of Heat Exchanger Networks, Utility Systems and Heat Recovery Cycles. Computers & Chemical Engineering, 106, 663–689.
A. Mian, E. Martelli & F. Marechal, 2016. Framework for the Multiperiod Sequential Synthesis of Heat Exchanger Networks with Selection, Design, and Scheduling of Multiple Utilities. Industrial & Engineering Chemistry Research, 55, 168–186.
H. Spliethoff, 2010. Power Generation from Solid Fuels. Springer-Verlag Berlin Heidelberg.
T. Yee & I.E. Grossmann, 1990. Simultaneous optimization models for heat integration—II. Heat exchanger network synthesis. Computers & Chemical Engineering, 14(10), 1165–1184.

Sauro Pierucci, Flavio Manenti, Giulia Bozzano, Davide Manca (Eds.)
Proceedings of the 30th European Symposium on Computer Aided Process Engineering (ESCAPE30), May 24-27, 2020, Milano, Italy.
http://dx.doi.org/10.1016/B978-0-12-823377-1.50251-2

A MILP Model for the Operational Planning of Multi-Energy Systems Accounting for variable Delivery/Return Temperatures and Non-Isothermal Mixing in Headers

Luca Moretti*, Giampaolo Manzolini, Emanuele Martelli**
Politecnico di Milano, Piazza Leonardo da Vinci, 32, Milano, 20133, Italy
**luca1.moretti@polimi.it* ***emanuele.martelli@polimi.it*

Abstract

This work presents a MILP formulation for the optimal operation planning of Multi-Energy Systems serving district heating networks. In particular, the work focuses on Multi-Energy Systems (MES) featuring thermal generation units connected in series and/or parallel, units with limitations on the operating temperature range of inlet/outlet water, and headers in which occurs the non-isothermal mixing of water flows. The model accounts for both dispatchable (e.g. CHP engines) and non-dispatchable (e.g. thermal solar panels) generation units, as well as for the presence of stratified thermal storages. To avoid the nonlinearity and nonconvexity associated to the variable stream temperatures and non-isothermal mixing, each water flow is represented as a linear combination of at most two virtual flows at discrete temperature levels, imposing a Type 2 Special Ordered Set (SOS2) condition to identify the two flows with closest temperatures. The model is used to optimize the operation of an integrated MES designed to serve the electric and thermal loads of a University Campus.

Keywords: Multi-Energy Systems (MES), Unit Commitment and Economic Dispatch, Heating Network, Mixed Integer Linear Programming.

1. Introduction

Multi-Energy Systems (MES) have been identified as a fundamental concept in the undergoing transition of the energy sector towards a more flexible, efficient and greener paradigm [1]. A MES is an integrated energy system utilizing different types of primary energy sources by means of a diversified set of energy conversion and storage technologies, to supply different energy vectors (e.g., electricity, heating, cooling). The heating and cooling power are typically transferred to the final users via a district heating/cooling network (DHN). By exploiting synergies in the energy conversion processes, the coordinated management of the MES units can lead to an overall performance relevantly higher than for a system addressing the supply of the energy vectors independently. MES typically feature various types of generators consuming different forms of internal / external inputs (including poly-generation units such as Combined Heat and Power (CHP) generators), intermittent Renewable Energy Sources (RES), and energy storage system technologies [2]. The large number of units and control degrees of freedom makes the definition of an optimal control strategy non-trivial [3]. Numerous MILP formulations have therefore been proposed in the literature to solve the Unit Commitment (UC) and Economic Dispatch (ED) of these type of systems (e.g. [3]).

However, these approaches do not account for the topology of the hydraulic network connecting thermal generators, Thermal Energy Storage Systems (TESS) and the thermal load, relying on the assumption that all units are placed in parallel (i.e., directly connected to return and delivery water headers). In many plants, units are connected to intermediate headers arranged in series/parallel with respect to the flow of water (i.e., the heat transfer medium to be sent to the thermal users) with the aim of operating each generation technology in the range of temperatures best suited to their technical features (see Figure 1). As an example, Solar Thermal (ST) panels are typically placed to warm-up the water from the return header to an intermediate header so as to maximize their efficiency. Similarly, heat pumps are used to heat-up water to an intermediate temperature (lower than the delivery temperature required by the final user) so as to operate with a high coefficient of performance. Boilers are typically placed in series to heat pumps and ST panels to raise the water temperature from the that of the intermediate headers to the final delivery temperature because their thermal efficiency is not appreciably affected by the water temperature. As a result, units may be placed in series or parallel with respect to the flow of water (heat carrier fluid), each unit may have a different outlet water temperature, non-isothermal mixing of water flows may occur in the headers, and the temperature of the headers may vary in time depending on the water flow rates and temperatures supplied by each unit. Since the flow rate, return and delivery temperatures of the water to be sent to the DHN may vary throughout the day, considering only the thermal power provided by each unit in the operational planning problem may lead to infeasible solutions (e.g., the ST panels or the heat pump may provide all the thermal power required by the users but their maximum water outlet temperature is lower than required by the DHN). This calls for the need of considering also the maximum/minimum inlet/outlet water temperatures and flow rates of each unit as well as the non-isothermal mixing occurring within the headers.

The bilinear terms arising when modelling non-isothermal mixing make the energy balance equations of the headers nonlinear and nonconvex, a well-known problem in the literature [4], leading to a challenging nonconvex MINLP which may not be tractable for operational planning problems due to the large number of time steps. This work proposes a novel linear approach, formulated as a Mixed Integer Linear Program (MILP), for approximating the solution of the non-isothermal mixing occurring in headers and for accounting for the detailed topology of the water network between thermal generation units, limitations on the inlet/outlet temperatures of the units and non-isothermal mixing. Stratified thermal storages (thermoclines) are also accounted for in the model.

2. Problem Statement

The scheme of a typical MES with the connections between the different water headers is shown in Figure 1. Delivery temperature $\tilde{T}_t^D$, return temperature $\tilde{T}_t^R$ and circulating water flow $\widetilde{m}_t^{CIRC}$ are linked by the energy balance of the thermal user served by the DHN:

$$\widetilde{m}_t^{DHN}\tilde{c}_{H_2O}\left(\tilde{T}_t^D - \tilde{T}_t^R\right) = \tilde{Q}_t^{DHN} \quad (1)$$

Considering a MES supplying a heat load through a thermal network as the one depicted in Figure 1, and given:

- the topological description of the water network (connections between units and headers, bypass flows, etc.);
- the profiles of water flow rates, delivery temperature and return temperatures of the DHN;
- the production profiles from the intermittent RES generators;

- the performance maps of all units, including part-load curves of generators, maximum / minimum load constraints and ramping limits, and capacity (in terms of contained water mass) of the thermal energy storage systems (TESS);
- the minimum and maximum inlet / outlet temperatures of the water heated by each generator;
- the value of selling / purchasing energy from external networks (e.g. electric grid);

we aim at determining the optimal Unit Commitment (UC) and Economic Dispatch (ED) of all units for each hour of the day, defined by:

- commitment plan (on/off status), input consumption and energy production rate for all generators;
- elaborated water mass flow (for thermal generators) and corresponding outlet temperature;
- outlet temperature from each header;
- mass of water in the hot and cold region of thermoclines, and their temperature;
- bypass flow rate between connected headers.

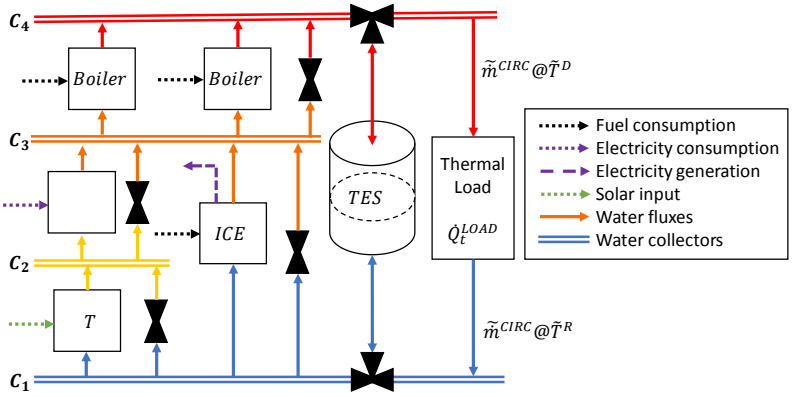

Figure 1: topological scheme of the MES heat generation and supply network.

The typical control strategy of DHNs consists in keeping a fixed water delivery temperature $\tilde{T}^D$ throughout the day while the return temperature $\tilde{T}^R$ changes with time according to the thermal load and to the circulating water mass flow control strategy. It is worth noting, the proposed model is suited for any DHN control strategy.

3. Mathematical Formulation

The general idea of the proposed formulation is to avoid bilinear terms in the energy balance equations of headers and units by defining a set of pre-defined temperature levels for the water flows. Each water flow $\dot{m}$ at temperature T is represented as an ordered set of virtual flows $\dot{m}_{i,h,t}$ at discrete increasing temperature levels $\tilde{T}_h$ spanning the temperature range in which the flow temperature can vary. Streams of water delivered by a unit at an arbitrary temperature T (potentially different from the discrete temperature levels $\tilde{T}_h$) is represented as the linear combination of two or more virtual mass flows of water at discrete temperatures. Each thermal generator is connected to an inlet and an outlet header, C_i^{IN} and C_i^{OUT}. In this formulation, for each unit $\mathcal{M}_i$, for each temperature level $h \in \boldsymbol{\mathcal{H}}_i \backslash last(\boldsymbol{\mathcal{H}}_i^{out})$ (excluding the highest temperature level), the mass flow variable $\dot{m}_{i,h,t}$ denotes the amount of water heated up by the machine from the virtual temperature level h to the subsequent one (h+1). If a generator has limitations on the

maximum/minimum inlet/outlet temperatures of the elaborated water flow, it is sufficient to restrict the set of inlet/outlet virtual flows $\dot{m}_{i,h,t}$ to a proper subset encompassing the feasible thermal operating range of the unit (as denoted by the dashed rectangles in Figure 1 for the depicted units).

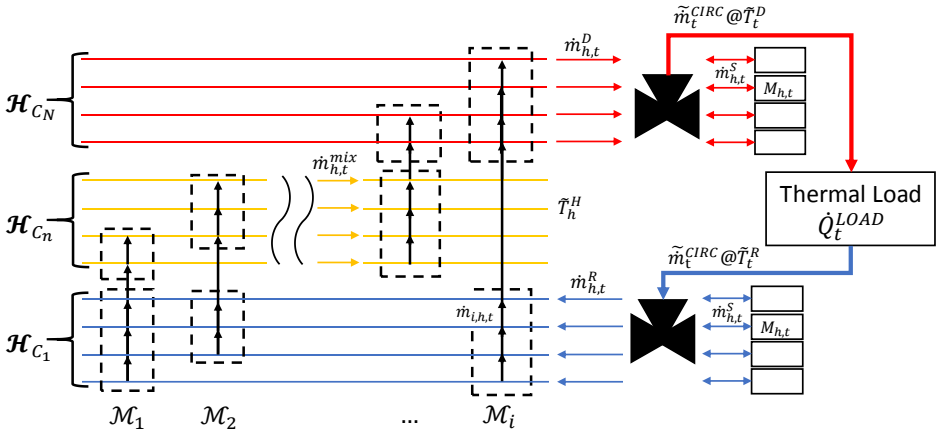

Figure 2: modelling approach for the thermal network of variable temperature headers: the colored group of lines identify the set of virtual headers associated to a physical header. Thermal generators can promote water from their inlet to their outlet set of headers.

Machines can only withdraw water from the inlet headers, and deliver it on the outlet headers: therefore, $\dot{m}_{i,h,t}$ can only increase on $\boldsymbol{\mathcal{H}}_i^{in}$ and decrease on $\boldsymbol{\mathcal{H}}_i^{out}$. The overall thermal power supplied by the generator can then be computed by Eq. (2):

$$\dot{Q}^{out}_{i,t} = \sum_{h \in \boldsymbol{\mathcal{H}}_i \setminus last(\boldsymbol{\mathcal{H}}_i^{out})} \dot{m}_{i,h,t} \tilde{c}_{H_2O} \left(\tilde{T}^{H}_{h+1} - \tilde{T}^{H}_{h}\right) \quad \forall i \in \boldsymbol{\mathcal{M}}^{th}, t \in \boldsymbol{\mathcal{T}} \tag{2}$$

Since each header can receive water at different temperatures (generated by two or more units and/or coming from the by-pass valves), the resulting mixing temperature of the water exiting the header must be modelled. This is done by writing the mass and energy balance equation on the header, in which the header outlet flow (resulting from the perfect mixing of all inbounds flows and either directed to the DHN or available to the units fed by the header) is modelled as at most two flows at discrete temperature levels, by imposing a Type 2 Special Ordered Set (SOS2) condition on the mass flow variables at the discrete temperature levels $\dot{m}^{mix}_{c,h,t}$. The SOS2 condition guarantees that the header outlet stream is represented as at most two flows at adjacent discrete temperature levels. Since the two fractions of water are determined according to the energy and mass balances, they are equivalent to the real outlet flow at a continuous temperature level in terms of energy content. Although introducing a non-physical separation of the flow in a warmer and a colder stream violates the second law of thermodynamics, the proposed approach preserves the energy balance and the entity of approximation can be controlled by adopting a finer temperature discretization (i.e., increasing the number of discrete temperature levels).

Similarly to units and headers, the masses of water associated to the hot and cold zones of TESS are represented by a set of virtual masses $M_{h,t}$ at discrete temperature levels $h \in \boldsymbol{\mathcal{H}}_{C^{IN}_{TESS}} \cup \boldsymbol{\mathcal{H}}_{C^{OUT}_{TESS}}$. To model the average temperature of the hot and cold zones of the TESS, an SOS2 condition ensures that at most two virtual masses with adjacent

temperature levels are active. For sake of simplicity, the model presented in this work only considers a single TESS connecting the delivery and return headers, but the approach be easily extended to account for an arbitrary number of TESS placed in between any pair of headers. Each TESS virtual mass $M_{h,t}$ can exchange a virtual water flow $\dot{m}^S_{h,t}$ with the header to which it is connected: $\dot{m}^S_{h,t}$ can assume both positive (outbound) or negative (inbound) value. The total mass stored in the hot and cold storage zone can be computed according to the following mass balance (shown for the cold zone):

$$\sum_{h \in \mathcal{H}_{C^{IN}_{TESS}}} M_{h,t+1} = \sum_{h \in \mathcal{H}_{C^{IN}_{TESS}}} M_{h,t} - \sum_{h \in \mathcal{H}_{C^{IN}_{TESS}}} \dot{m}_{h,t} \quad \forall t \in \mathcal{T} \tag{3}$$

The dynamic evolution of each single virtual $M_{h,t}$ is determined by the energy balance on each TESS zone (assuming a perfect mixing with any inlet flow):

$$\sum_{h \in \mathcal{H}_{C^{IN}_{TESS}}} M_{h,t+1}\tilde{T}^H_h = \sum_{h \in \mathcal{H}_{C^{IN}_{TESS}}} M_{h,t}\tilde{T}^H_h - \sum_{h \in \mathcal{H}_{C^{IN}_{TESS}}} \dot{m}_{h,t}\tilde{T}^H_h \quad \forall t \in \mathcal{T} \tag{4}$$

While the storage can be charged with water at any temperature level, it can discharge water only from the active virtual masses (due to the SOS2 condition):

$$M_{h,t} - \dot{m}_{h,t} \geq 0 \quad \forall t \in \mathcal{T} \tag{5}$$

The storage is always filled with water, therefore discharging a given water flow from the cold zone of the storage implies charging an equivalent flow to the hot zone and vice-versa. As shown in Figure 1, the hydraulic connection considered for the TESS consists in two three-way valves that allow directing part of the delivery (return) flow respectively to the hot (cold) region of the thermal storage, while at the same time mixing an outlet flow from the TESS cold (hot) region with the flow coming from (directed to) the thermal user. Respectively, the two described operating modes correspond to charging / discharging the storage. The values of $\dot{m}^D_{h,t}$and $\dot{m}^R_{h,t}$ are respectively linked to the mixing balance (both energy and mass) on the delivery header C_N and on the three-way valve.

4. Case Study

The proposed formulation is used to determine the optimal management of an integrated MES designed to supply heat and electricity to the university campus. The system architecture is the one shown in Figure 1 featuring Solar Thermal (ST) panels in series with a Heat Pump (HP), and in parallel with a natural gas CHP Internal Combustion Engine (ICE). A natural gas boiler further increases the water temperature in case of thermal demand peaks. The electricity and heating demand profiles, the delivery temperature (constant at 80°C), return temperature and DHN water flow rate derive from operational data of a real plant. ST and HP both discharge at a constant outlet temperature respectively of 60 and 75°C, whereas the ICE can discharge in the temperature range 60°C to 90°C. The solution yield by the proposed model was compared with the solution yield by a traditional UC and ED formulation, not accounting for the hydraulic connections and the temperature limitations of the units. The new formulation properly foresees the need of using the natural gas boiler to attain the required delivery temperature also during thermal demand peak hours, when the return temperature is lowest and the circulating mass flow higher, therefore making it impossible to ensure the 80 °C delivery temperature relying only on the parallel configuration of ICE and ST + HP. Conversely,

the traditional model yields a commitment solution that provides an equivalent amount of thermal energy but at a thermal level lower than the target delivery temperature $\tilde{T}^D$.

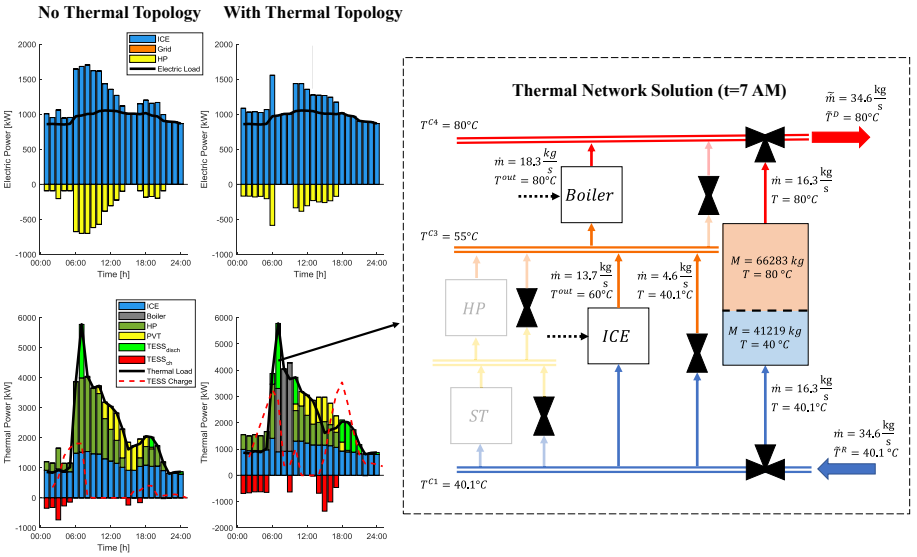

Figure 3: comparison of dispatch profiles when accounting / neglecting thermal topology and units' temperature limitations (left). Temperature and flow distributions are shown for the simulation accounting for thermal topology in a specific timestep (right).

5. Conclusions

This work proposes a formulation of the Unit Commitment and Economic Dispatch problem for the optimal management of a Multi-Energy System featuring units with limited inlet/outlet temperatures, multiple headers and variable return/supply temperatures of the DHN flows. The topology of the water network connecting the units and headers is defined and the nonlinearities (bilinear products due to the non-isothermal mixing) are avoided by representing water flows with variable temperature as linear combinations of virtual flows at discrete temperatures. The mixing temperature in the headers and in the hot/cold regions of the thermoclines are determined by enforcing energy and mass balances and by imposing SOS2 conditions on the virtual water masses / mass flows. The model is tested on a real-life case study, showing how explicitly accounting for the topology and for the temperature limitations of units in terms of inlet/outlet temperature range is essential to avoid infeasible solutions.

Acknowledgements: The authors acknowledge SIRAM for supporting the research activity and for the useful discussions about the operational issues of MESs.

References

[1] P. Asmus, "Microgrids, Virtual Power Plants and Our Distributed Energy Future," *Electr. J.*, vol. 23, no. 10, pp. 72–82, Dec. 2010.

[2] P. Mancarella, "MES (multi-energy systems): An overview of concepts and evaluation models," *Energy*, vol. 65, pp. 1–17, Feb. 2014.

[3] A. Bischi *et al.*, "A detailed MILP optimization model for combined cooling, heat and power system operation planning," *Energy*, vol. 74, pp. 12–26, 2014.

[4] K. A. Pruitt, S. Leyffer, A. M. Newman, and R. J. Braun, "Optimal Design and Dispatch of Distributed Generation Systems," 2012.

Sauro Pierucci, Flavio Manenti, Giulia Bozzano, Davide Manca (Eds.)
Proceedings of the 30th European Symposium on Computer Aided Process Engineering (ESCAPE30), May 24-27, 2020, Milano, Italy.
http://dx.doi.org/10.1016/B978-0-12-823377-1.50252-4

Optimal Operation and Control of a Thermal Energy Storage System: Classical Advanced Control versus Model Predictive Control

Cristina Zotica[a], David Pérez-Piñeiro[a], Sigurd Skogestad[a]*

[a]*Department of Chemical Engineering, Norwegian University of Science and Technology,Trondheim, NO-7491, Norway*
Sigurd.Skogestad@ntnu.no

Abstract

The objective of this work is to define the optimal operation and control for a thermal storage system with heat sources and a consumer, which exchange utilities using one hot water thermal energy storage tank. In this work, we compare a decentralized control structure using classical advanced control with PID controllers and logic blocks (split-range control and selectors) and a centralized control structure (model predictive control) to implement optimal operation for a simple thermal energy storage system, which is a multivariable system with constraints. We analyze a varying heat supply profile over a horizon of 24 hours. We show that the supply and demand can be balanced, and we achieve optimal operation by using the energy stored in the tank while minimizing the heat from the market.

Keywords: thermal storage, optimal operation, split range control, model predictive control

1. Introduction

Thermal energy storage has the potential to save energy in many applications by balancing the asynchronous supply and demand of heating and cooling. Furthermore, it can enhance the use of uncertain and highly fluctuating heat sources (e.g., power generation from solar thermal plants and/or re-utilization of industrial waste heat).

A large emphasis in the literature on energy storage has been placed on technology advances, design and applications (Arteconi et al., 2012; International Energy Agency, 2014). From an operational and control perspective, model predictive control has become the multivariable control technique of choice in several papers for controlling thermal energy storage systems in buildings, combined heat and power plants, and solar thermal power plants (Ma et al., 2009; Cole et al., 2012; Knudsen et al., 2019). Although less extensively, classical advanced control structures have also been studied in the context of thermal energy storage in buildings (de Oliviera et al., 2016). In this work, we show how to use classical advanced control using PID controllers and logic blocks (split-range control and selectors) to control a simple thermal energy storage system, which is a multivariable system with constraints. The control performance of the proposed solution is compared with model predictive control (MPC).

This paper is organized as follows. In Section 2, we describe a typical thermal storage system, in Section 3 we describe both a decentralized and a centralized control structure

for the system, in Section 4, we present a simulation case study, and we make our final remarks in Section 5.

2. Thermal storage system

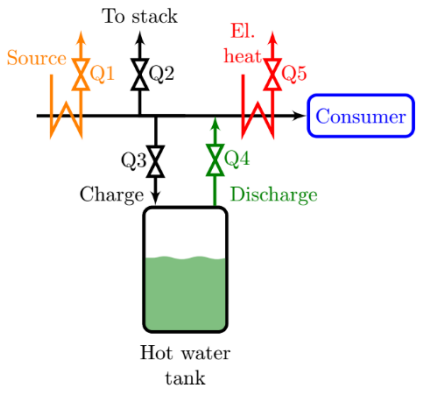

Figure 1. Process flowsheet indicating the five degrees of freedom for operation.

The process studied in this work is a thermal storage system illustrated in Figure 1. For example, this can be a district heating network, or an industrial cluster formed of heat sources and heat sinks. We consider a general system, composed of a variable heat source (Q_0) that utilizes industrial waste heat, an electric boiler that employs electricity from the market (Q_5), one consumer plants with heat demand (Q), and a hot water tank used for energy storage. The tank can either be charged (Q_3) or discharged (Q_4). The tank acts as a buffer between a varying heat supply and demand to minimize electric heating. Note that we may also heat the tank directly with electric heating (not shown in the figure). Excess heat is sent to the stack (Q_2).

Considering the relationship between demand and supply we can identify three cases:

Case 1. Low demand. No storage tank $\Rightarrow$ send excess heat to the stack (Q_2).
Case 2. Intermediate demand. Use tank to balance heat demand and supply.
Case 3. High demand. No storage tank $\Rightarrow$ buy electric heating (Q_5).

We analyse case 2, and we consider a scenario with constant electricity prices. Note that with constant electricity prices we would not gain from charging the tank with electric heating and discharge it subsequently to the consumer. We should instead supply the consumer directly with electric heat to minimize heat losses.

2.1. Process model

We discuss optimal operation on a simple thermal storage example, and we start by deriving a model based on first principle. On the consumer side, we assume that the dynamics are considerable faster compared to the slow tank dynamics, and we write the steady-state energy balance, given by Eq. (1).

$$Q = Q_1 + Q_4 + Q_5 \tag{1}$$

We assume constant density (ρ), heat capacity (c_p), and volume (V). The energy balance in temperature (T) form for the tank is given by Eq. (2).

$$\frac{dT}{dt} = \frac{1}{\rho c_p V}(Q_3 - Q_4) \tag{2}$$

where, Q3 is the excess heat, given by a static energy balance in Eq. (3).

$$Q_3 = \max(0, (Q_0 - Q_1 - Q_2)) \quad (3)$$

3. Optimal operation and control

We analyse the system in the setting of plantwide control (Skogestad 2004), and we systematically define the operational objective, manipulated variables (MVs) (i.e. degrees of freedom for optimal operation), operational constraints, main disturbances and controlled variables (CVs). The operational objective of the system is to keep the heat demand setpoint, while minimizing electric heating. Table 1 shows the MVs (also shown in Figure 1. Process flowsheet indicating the five degrees of freedom for operation., CVs, and main disturbances.

Table 1 Manipulated variables, controlled variables and disturbances

Manipulated variables	Controlled variables	Disturbances
MV1: Heat directly to consumer (Q1)	CV1: Consumer heat demand	D1: Heat supply
MV2: Heat to stack (Q2)	CV2: Tank temperature	D2: Electricity prices (not considered in this work)
MV3: Heat to tank (Q3) (not independent)		
MV4: Heat from tank (Q4)		
MV5: Electric heating (Q5)		

Furthermore, during operation the tank water temperature must satisfy the following constraints, as given by Eq. (4).

$$T^{\min} < T < T^{\max} \quad (4)$$

where T^{min} is given by the consumer process specifications and T^{max} is the allowed maximum temperature in the tank given by operation constraints.

With the constant electricity prices assumption, optimal operation is trivial, and three regions can be defined:

R 1. $Q < Q_0$. Charge the tank with surplus heat until $T = T^{\max}$.

R 2. $Q > Q_0$. Discharge the tank.

R 3. $Q > Q_0$ and $Q_3 = 0$ (fully discharged tank). Buy electric heat from the market.

The operational challenge arises from the fact that the degrees of freedom are dynamic, that is, they are not available at all time (i.e. once the tank is discharged is can no longer supply the consumers). The question we want to answer is: what is the simplest way to implement optimal operation? We compare a decentralized control structure using

classical advanced control using PID-controllers and logic, and centralized control structure using Model Predictive Control (MPC).

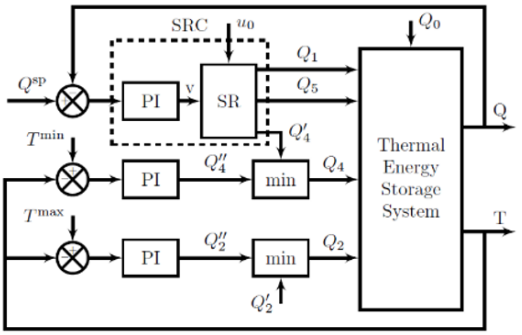

Figure 2 Decentralized control structure with split range control and min selectors. The split range (SR) block is represented in Figure 3

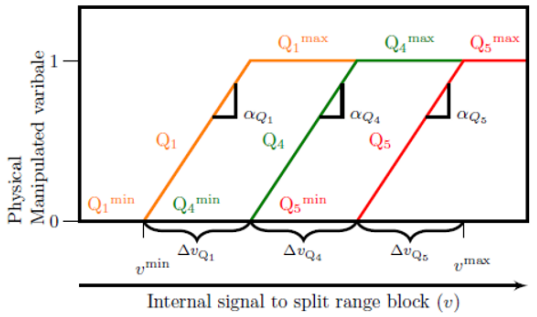

Figure 3 . Split range block

3.1. Decentralized control with classical advanced control structures

Optimal operation can be implemented in practice using classical advanced control structure, i.e. cascade, feedforward, valve position control or split range control together with logic elements (selectors) (Reyes-Lua and Skogestad, 2019). Split range control is a multiple-inputs single-output control structure that allows to use one input at a time and extends the steady-state operating range for the controlled variable. In this work we propose a control structure with split range control (SRC) and selectors, which can be used for active constraints changes (Reyes-Lua et al., 2018). Figure 2 shows the block diagram of the proposed decentralized control structure. The SRC keeps the heat demand setpoint Q^{sp} by manipulated the heat flows Q_1, Q_4, and Q_5. However, when $T \leq T^{min}$, and the active set constraints changes, we use a min selector to give-up discharging the tank. Similarly, when $T \geq T^{max}$, we use a min selector to give-up charging the tank.

Figure 3 shows the split range block. Note that this is not a typical split range controller because of the dynamic degrees of freedom. Consider a case when the tank is fully discharged (Q_3=0), there is no heat supply (Q_0=0), and we operate on the red line in the split range block in Figure 3. If the heat demand decreases, we could in theory operate on the green line using Q_3, but this is not physically possible because the tank is discharged. To solve this issue, we propose to update the maximum values (Q_1^{max} and Q_3^{max}) in the split range block to reflect the operational constraints. We set Q_3^{max}=0, when the tank is discharged (i.e. $T=T^{min}$), and $Q_1^{max} = Q_0$. We follow the systematic design procedure from the work of (Reyes-Lua 2019) to design the split range controller. In the split range block, the split value is set at v*=0, which corresponds to maximum Q_1, and minimum Q_3 and Q_4. The slopes ± in the split block are equal, because the process gains from MVs to CV are equal. To tune the PI-controllers, we use the SIMC tuning rules (Skogestad2003). Note that Eq. 3 is static, and we need to use a pure I-controller. The tuning parameters for

the split range controller are: slope ±=3, and integral gain K_I=0.033. The other PI-controllers are tuned following the SIMC rules for integrating processes.

3.2. Centralized control. Model predictive control

Model predictive control solves an open loop control problem subject to constraints with a finite horizon at each sampling time to determine an optimal control sequence, and the first control is applied to the plant (Mayne et al., 2000). It's main advantage it that it handles constraints and interactive processes by design, while it's disadvantage is that it required a details model.

We formulate the optimal control problem as to minimize electric heating (Q_5), heat discharged (Q_3) and heat sent to stack (Q_2) subject to model equations and operational constraints, as given in Eq. (5).

$$
\begin{aligned}
&\min \sum_{k=1}^{N} \omega_2 Q_{2_k}^2 - \omega_4 Q_{4_k}^2 + \omega_5 Q_{5_k}^2 \\
&s.t. Q_k - Q_k^{sp} = 0 \\
&Q_k = f(Q_{i_k}), \forall i \in \{1,4,5\} \\
&T_k = g(Q_{i_k}), \forall i \in \{3,4\} \\
&0 < Q_{i_k} < Q_{i_k}^{\max}, \forall i \in \{1,3,4,5\} \\
&T_k^{\min} < T_k < T_k^{\max} \\
&\forall k \in \{1,\ldots,N\}
\end{aligned}
\qquad (5)
$$

where, ω_j are the weights in the optimization problem and $Q_1^{max} = Q^0$.

4. Simulation results

We anaylze a varying heat supply profile over a horizon of 24 hours with a constant heat supply, as shown in Figure The tank volume is V = 100, the initial tank temperature is T_0=105 °C. The MPC is solved in CasADi (Andersson et al., 2013), and IPOT is used to solve the NLP (Wächter and Biegler, 2005). We use N = 60 control intervals and a sampling time of 60 s and $\omega_2 = 10, \omega_4 = 10^3, \omega_j = 10^4$

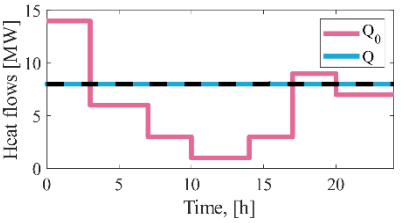

Figure 4. Variable heat supply in pink, and constant heat demand in blue

Figure 4, Figure 5, and 6 show the simulations results. Full lines show SRC and the dotted lines MPC.

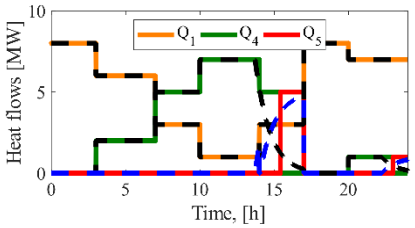

Figure 5. Input usage for SRC and MPC

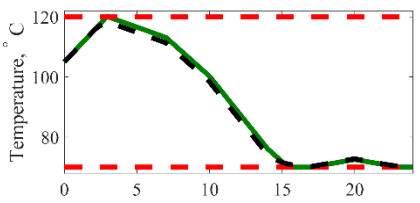

Figure 6. Temperature profile for SRC and MPC

5. Discussion and conclusions

In this work we identify optimal operation for a simple thermal energy storage system with constant electricity prices. We compare a decentralized control structure using PID controllers and logic blocks (split-range control and selectors) and a centralized control structure using MPC to implement optimal operation. For this example, we have shown that a systematically designed advanced control structure using SRC and selectors gives similar performance compared to MPC. The simulation results from Figures 4, 5 and 6 shows that the tank is discharging heat when the heat supply is not enough, and electric heat is used when the tank is fully discharged, while satisfying the operational constraints. Comparing both alternatives, SRC is considerable easier to implement in practice and tune and does not require as full detail model as MPC. However, for a larger scale process, PID-controllers and logic might not provide a simple implementation.

Acknowledgment - This publication has been partly funded by HighEFF - Centre for an Energy Efficient and Competitive Industry for the Future, an 8-years' Research Centre under the FME-scheme (Centre for Environment-friendly Energy Research, 257632). The authors gratefully acknowledge the financial support from the Research Council of Norway and user partners of HighEFF.

References

J. Andersson, 2013. A General Purpose Software Framework for Dynamic Optimization. Phd thesis, KU Leuven.

A. Arteconi, N. J. Hewitt, F. Polonara, 2012. State of the art of thermal storage for demand-side management. Applied Energy 93, 371–389.

W. J. Cole, K. M. Powell, T. F. Edgar, 2012. Optimization and advanced control of thermal energy storage systems, Reviews in Chemical Engineering. 28. 10.1515/revce-2011-0018.

International Energy Agency, 2014. Technology Roadmap. Energy storage. Tech. rep., International EnergyAgency.

B. R. Knudsen, H. Kauko, T. Andresen, 2019. An Optimal-Control Scheme for Coordinated Surplus-Heat Exchange in Industry Clusters. Energies.

Y. Ma, F. Borrelli, B. Hencey, A. Packard, S. Bortoff, 2009. Model predictive control of thermal energy storage in building cooling systems. In: Proceedings of the 48h IEEE Conference on Decision andControl (CDC) held jointly with 2009 28th Chinese Control Conference. IEEE, pp. 392–397.

D.Q. Mayne, J.B. Rawlings, C.V.Rao, and P. O. M Scokaert (2000). Constrained model predictive control: Stability and optimality. Automatica, 36(6):789–814.

A. Reyes-Lua, C. Zotica, S. Skogestad, 2018. Optimal Operation with Changing Active Constraint Regions using Classical Advanced Control. IFAC-PapersOnLine 51 (18), 440–445.

A. Reyes-Lúa, A. and Skogestad, S., 2019. Systematic Design of Active Constraint Switching Using Classical Advanced Control Structures. Industrial & Engineering Chemistry Research (In Press)

A. Reyes-Lúa, C. Zotica, S. Skogestad, 2019. Systematic Design of Split Range. IFAC-PapersOnLine 53 (1), 898–903.

S. Skogestad, 2003. Simple analytic rules for model reduction and PID controller tuning. Journal of Process Control 13 (4), 291–309.

S. Skogestad, 2004, Control structure design for complete chemical plants, Computers and Chemical Engineering 28 (1-2) 219-234.

A. Wächter, L. T. Biegler, Apr. 2005. On the implementation of an interior-point filter line-search algorithm for large scale nonlinear programming. Mathematical Programming 106 (1), 25–57.

Sauro Pierucci, Flavio Manenti, Giulia Bozzano, Davide Manca (Eds.)
Proceedings of the 30th European Symposium on Computer Aided Process Engineering (ESCAPE30), May 24-27, 2020, Milano, Italy.
http://dx.doi.org/10.1016/B978-0-12-823377-1.50253-6

A Robust Rolling-Horizon Algorithm for the Optimal Operation of Multi-energy Systems with Yearly Constraints and Seasonal Storage

Alessandro Francesco Castelli, Luca Moretti, Giampaolo Manzolini, Emanuele Martelli*

Politecnico di Milano, Dipartimento di Energia, Via Lambruschini 4, Milano, IT
emanuele.martelli@polimi.it

Abstract

This work proposes an affinely adjustable robust optimization model and rolling horizon algorithm to optimize the day-ahead unit commitment and economic dispatch problem of Multi Energy Systems (MES) featuring seasonal storage systems and/or yearly basis constraints on the performance of the installed units and/or yearly limits on the electricity import/export. The algorithm is applied to optimize the operation of a MES designed to serve the district heating network of the university campus. Results indicate that the proposed approach is able to operate the MES and the seasonal storage system in an efficient way while meeting the yearly basis constraints.

Keywords: robust optimization, unit commitment, seasonal storage, MILP, CHP.

1. Introduction

Buildings are characterized by thermal demands which vary according to daily path, mainly related to the control strategy of the building internal temperatures (i.e., to guarantee the desired comfort temperature within certain hours of the day) and habits of the users, and a yearly path related to the ambient temperature and sun radiation. In order to reduce fossil fuels consumption and the related CO2 emissions, three strategies are typically adopted: (i) integrating the use of intermittent renewable sources, such as solar photovoltaic (PV) panels and solar thermal (ST) panels, (ii) adopting efficient Combined Heat and Power (CHP) systems and heat pumps (HP), (iii) use thermal storage (TS) systems. The integrated energy system is referred to Multi-Energy System (MES). For MES featuring a large capacity of solar thermal panels, seasonal TS can be considered so to exploit the heat stored during the warmer months during the colder periods of the year (Shah et al. 2018). On the other hand, the seasonal TS can be used with daily charge/discharge cycles to operate the CHP and HP units in a more efficient/economic way. As a further challenge, in several EU countries the operation of CHP units must meet yearly basis constraints to guarantee that they are operated efficiently (and not just to maximize the revenues from the electricity sales): the total electric energy generated during the year must be smaller than the total consumption of the buildings/users, the average (yearly basis) primary energy efficiency (PES) and first–law efficiency (η_I) must be above certain threshold values (Bischi et al., 2017). In Italy and other EU countries, fiscal incentives are given to the owner of the yearly targets on the average yearly efficiency $\eta_I$and PES. Since these incentives have a considerable impact on the economic balance of the MES, meeting the yearly performance targets is of primary relevance.
This paper addresses the Unit Commitment (UC) and Economic Dispatch (ED) problem of MESs featuring CHP with yearly basis performance constraints, intermittent renewable

sources and seasonal TS systems by proposing an ad hoc affine adjustable robust optimization MILP model. Uncertainty factors related to short-term (day-head) and long-term (till the end of the year) forecasts are considered. Since the Robust MILP cannot be applied to optimize the whole year of operation, a Rolling Horizon algorithm is adopted. The algorithm has been applied to optimize the operation of a MES designed to serve the university campus.

2. Problem statement

A scheme of the type of MES under investigation is represented in Figure 1.

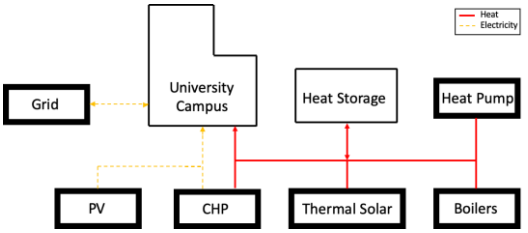

Figure 1. Scheme of the MES under investigation.

The MES may include one or more CHP units (e.g., internal combustion engines), boilers, PV panels, ST panels, Heat Pumps, conventional energy storage systems (hot tanks, batteries, etc.) as well as seasonal storage systems (e.g. Underground Thermal Energy Storage). Being connected to the electric grid, electricity can be sold or bought depending on the electricity balance. The excess heat generated by the CHP unit can be wasted (rejected to the environment). Provided the data of the MES, the general problem is formulated as follows:

"Given:

- *The part-load performance curves and operational limitations (ramp-up rates, start-up time, etc.) of the machine and boilers,*
- *the 24h ahead (short-term) forecasts of daily profiles of heating and electricity demands, PV and Thermal Solar production, electricity selling and buying prices for each day of the year*
- *the estimate for the electricity import/export, the electricity, the useful heat and the fuel consumed by each CHP for the future days of the year (long-term estimates required by the yearly constraints).*

determine for each hour of the following day:

- *the amount of electricity bought and sold to the grid,*
- *the management of the storage system (charge/discharge rate),*
- *the Unit Commitment (on/off) and economic dispatch (loads) of the units,*

which minimize the total operating costs of the MES taking into account:

- *the energy demand of the users*
- *the yearly limit on the amount of electricity which can be exported,*
- *the constraint on the average yearly η_l and PES ("CHP incentive constraints") of the CHP units,*
- *the optimal seasonal management of the seasonal storage system*
- *the uncertainty of the short-term forecast and long-term estimates."*

3. Rolling Horizon and Forecast generation

The proposed Rolling Horizon algorithm is shown in Figure 2. The basic idea is to proceed optimizing a single day of operation (so as to have a computationally tractable RO MILP), one day after the other, with estimates for the short-term and long-term forecasts and with historical data of the past days. The short-term forecasts are day-ahead forecasts of the profiles of electric consumption, heating demand and production from PV and ST panels while the long-term forecasts are estimates for the optimal management of the seasonal storage system, the fuel consumption, electric energy and heat generated by the CHP unit from the optimized day k to the end of the year (parameters involved in the calculation of the PES, η_I and net electricity export constraints).

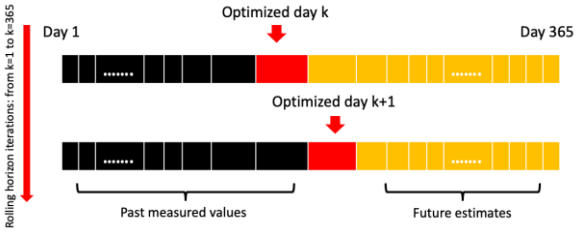

Figure 2. Rolling Horizon algorithm scheme.

The short-term forecasts of energy demand are determined using the Persistence method (properly accounting for weekends and holydays), while the short-term PV and ST previsions are obtained by means of the artificial neural network proposed in Dolara et al. (2015).

As far as the long-term forecast are concerned, it is necessary to determine the optimal management of the seasonal storage and CHP unit from the beginning to the end of the year. The basic idea is to determine the optimal yearly solution considering the past years. For representation of the whole year of operation and modelling of the yearly cycles of the seasonal storage in a computationally tractable way, we adopted the approach proposed by Gabrielli et al. (2018) relying on the definition of. “typical days”. First, for each of the past years, twelve typical days are determined by means of the k-means clustering algorithm considering the profiles of solar production, heat and electricity demands and electricity prices. Then, a deterministic MILP UC and ED optimization model is formulated to obtain the yearly operational solution with the lower operational cost. In such MILP, all the yearly constraints on CHP units (PES, η_I and limit on the electricity export) can be easily included while the seasonal variation of the charge of the seasonal storage system can be modelled with the approach proposed by Gabrielli et al. (2018): the storage charge variable is defined for every hour of the year (thus 8760 variables) and a cyclic constraint is imposed to have the same storage charge level at the beginning and end of the year. While the year is represented as a sequence of typical days, this allows having different storage charge levels at the beginning and end of each typical day (needed to allow seasonal variations of the storage state of charge). Unfortunately for the university campus only the energy demand profiles of the years 2017 and 2018 are available, making it difficult to analyze the year-by-year variability of the yearly performance indexes and seasonal storage management. Thus, it has been necessary to reconstruct the heating and electricity demand profiles of the last 10 years (2008-2017) from the measured weather data using a model similar as the one described by Gambarotta et el. (2017). The parameters of the model have been regressed to best fit the thermal demand profiles of the years 2017-2018.

Once optimization is done for all the available past years, it is possible to calculate the profiles of the average expected fuel consumption, electricity and useful heat generated by the CHP unit and average optimal profile of the state of charge of the seasonal TS. Calculating the average over multiple past years allows filtering atypical periods which could have affected some of the past years. Similarly, it is possible to calculate the average cumulative profiles of electricity import/export, fuel consumption and number of operating hours of the ICE from the current day k to the end of the year. The average profiles obtained considering the past 10 years are shown in Figure 3. Since years may differ considerably in terms of average yearly ambient temperature ($\pm$5°C), the expected (average) profiles of fuel consumption, electricity and heat generation must be treated as uncertain parameters in the robust optimization of the MES operation.

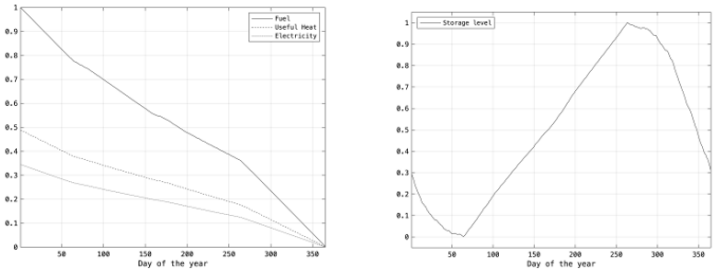

Figure 3. On the left: estimates on the future CHP consumption and generation (normalized to the total fuel consumption), on the right: yearly average profile of the seasonal storage (normalized to the storage capacity).

4. Affinely Adjustable Robust Optimization model

The optimization of the UC and ED of the MES is performed 24h ahead using as input the day-ahead forecasts of heating demand, production from ST, electric demand and PV production for the next day (the k-th day of the year to be optimized), the expected future fuel consumption and operating hours of the CHP unit (from day k+1 to the end of the year), the expected future electricity import/export, and the average optimal charge level of the seasonal storage at the end of day k. All the above listed short-term and long-term forecasted profiles are considered as independent uncertain data for the RO MILP model. It is worth noting that the estimate of future electric energy and useful heat generated by the CHP unit, terms of the yearly incentive constraints, can be expressed as linear functions of the future fuel consumption and operating hours of the CHP unit thanks to the linearity of the performance map of the CHP unit. As a consequence, they must not be considered as independent uncertain parameters. Similarly, to the model recently published by Moretti et al. (2019), for the uncertainty related to the short-term forecasts, an affine piecewise linear recourse decision rule is defined so as to adjust the loads of the units and the management of the storage system depending on the realization of the uncertain data. The model mimics the fact that real MES are operated defining the scheduling of the units on a day-ahead basis (here and now decisions) and then the loads of the units are corrected during operation (recourse) so as to meet the demands. On/off status of the units are “here and now” decision variables (the recourse does not involve any binary/integer decisions) while the loads of the units and the charge level of the storage have a “here and now” component (the expected set point decided the day-ahead) and an adjustable one. As far as the long-term forecasts are considered, the realization of their uncertainty of the forecast does not occur within the optimized day but it is revealed

only at the end of the year. So, it is not possible to define a recourse decision rule: the operational solution found for the optimized day must meet the yearly operational constraints under any possible realization of the long-term forecast uncertainty. Thus, the proposed RO model is adjustable only for the subset of the uncertain parameters related to the short-term forecasts (energy demands and production from renewables). A polyhedral uncertainty set is defined for the forecasted parameters. As for the short-term forecasted parameters, in addition to the upper/lower bounds, a budget of uncertainty limiting the cumulated absolute error of each forecast is defined so as to encompass the 99^{th} percentile of the forecast errors observed in the past year. For the long-term forecasted parameters, their uncertainty set is a simple box with bounds assessed by looking at the variability of the optimal profiles computed for the past years available. As far as the seasonal storage charge is concerned, the RO model guarantees that at the state of charge at the end of the *k*-th day is higher or equal to the average optimal storage profile computed for the previous years. This allows storing more heat than expected if the sun radiation or the optimal loads of the ICE turn out to be higher than the same period of the previous years. The piecewise affine decision rules and the polyhedral uncertainty set have been selected because of the possibility of reformulating the affinely adjustable robust counterpart into a tractable MILP (using to the duality theorem of linear programming (Ben-Tal et al., 2009)) and the good results obtained by Moretti et al. (2019) for the operation of MESs.

5. Case study

The rolling horizon algorithm with RO MILP model has been applied to optimize the day ahead UC+ED and real-time operation of an MES designed to serve the district heating network of the university campus. The MES features a CHP ICE unit sized to meet 7% of the peak heating demand and 14% of the peak electricity one, two equal boilers (each covering 32% of the peak demand), PV panels with a capacity equal to the 40% of the peak electricity demand, ST panels with capacity covering 21% of the peak heating demand, and a heat pump sized to provide up to 23% of the peak demand. The CHP unit and the boilers use natural gas. The seasonal storage has a capacity equal to 25% of the total expected yearly heating demand. The university campus is connected to the grid, such that electricity can be sold or bought. For the optimization of a single day, the RO MILP model is solved with an average computational time of 120 sec in an Intel Xeon E5 workstation. The historical data of years 2008-2017 have been used to derive the long-term forecasts and average optimal management strategy of the seasonal storage while the rolling horizon algorithm is tested in the year 2018. Once determined (day-ahead), the optimized affine decision rules are used to adjust the loads of the units to meet the real demand profiles and the simulated system performance are recorded.

6. Results and conclusions

The operational results for the second week of January 2018 are shown in Figure 4. The peak demand is met by using the CHP ICE and the TES (which, according to the optimal seasonal strategy, must be discharged in that period). It is worth noting that the electricity produced by the engine is always smaller than the demand of the campus and the use of the boiler is minimized. Figure 5 shows the comparison between the day-ahead commitment plan (left-hand bars) and the real-time operation (right-hand bars) of the MES. Uncertain variations of the heating demand profiles are a compensated by the affine decision rules by adjusting the discharge rate of the storage and loads of the HP and boiler.

As far as the yearly performance indexes are concerned, the rolling horizon algorithm does not deviate from the average optimal seasonal storage charge profile and it meets all the yearly basis constraints on CHP incentives and electricity export.
The proposed affinely adjustable robust optimization MILP model and rolling horizon algorithm appears to be a promising and effective approach to optimize the day-ahead UC and ED of Multi-Energy Systems featuring seasonal storage systems and/or yearly basis constraints on the performance of the units.

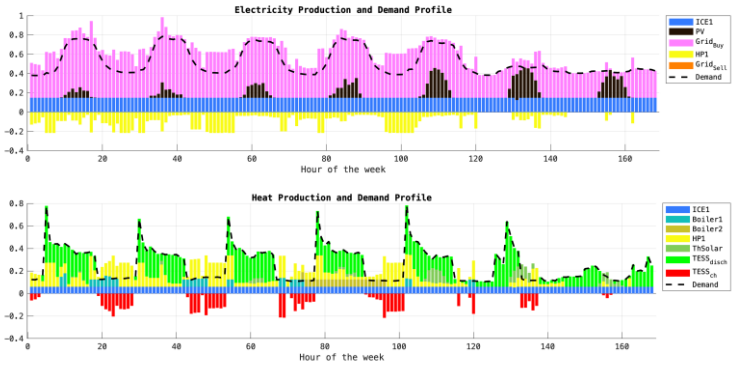

Figure 4. Operation of the second week of January 2018. Dashed black line show the actual demand profiles.

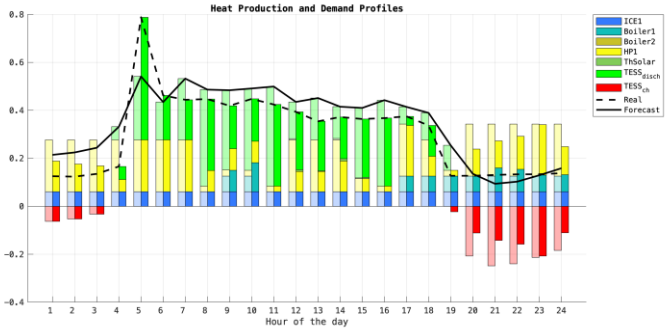

Figure 5. Heat production in a working day of January. Solid black line is the forecast, while the dashed one is the actual demand. For each hour, the bar on the right is the recourse, on the left is the day ahead set point.

References

A. Ben-Tal, L. El Ghaoui, A. Nemirovski, Robust Optimization, Princeton Series in Applied Mathematics, Princeton University Press, 2009.

A. Bischi et al., A rolling-horizon optimization algorithm for the long term operational scheduling of cogeneration systems, Energy, 184, Pages 73-90, 2017.

A. Dolara, F. Grimaccia, S. Leva, M. Mussetta, E. Ogliari, A Physical Hybrid Artificial Neural Network for Short Term Forecasting of PV Plant Power Output, Energies, 8, 2015.

P. Gabrielli, M. Gazzani, E. Martelli, M. Mazzotti, Optimal design of multi-energy systems with seasonal storage, Applied Energy, Volume 219, Pages 408-424, 2018.

A.Gambarotta, M. Morini, M. Rossi, M. Stonfer, A Library for the Simulation of Smart Energy Systems: The Case of the Campus of the University of Parma, En. Proc, 105, 1776-1781, 2017

L. Moretti, E. Martelli, G. Manzolini, An efficient robust optimization model for the unit commitment and dispatch of multi-energy systems and microgrids, Applied Energy, 261, 2020

S. K. Shah, L. Aye, B. Rismanchi, Seasonal thermal energy storage system for cold climate zones: A review of recent developments, Ren. and Sust. En, Rev., 97, 2018, 38-49.

Sauro Pierucci, Flavio Manenti, Giulia Bozzano, Davide Manca (Eds.)
Proceedings of the 30th European Symposium on Computer Aided Process Engineering (ESCAPE30), May 24-27, 2020, Milano, Italy.
http://dx.doi.org/10.1016/B978-0-12-823377-1.50254-8

Global Sensitivity Analysis for Design and Operation of Distributed Energy Systems

Ishanki De Mel,[a*] Panagiotis Demis,[a] Bogdan Dorneanu,[a,b] Oleksiy Klymenko,[a] Evgenia Mechleri,[a] Harvey Arellano-Garcia[a,b]

[a]*Department of Chemical and Process Engineering, University of Surrey, Guildford GU2 7XH, United Kingdom*
[b]*LS Prozess- und Anlagentechnik, Brandenburgische Technische Universität Cottbus-Senftenberg, Cottbus, Germany*
i.demel@surrey.ac.uk

Abstract

Distributed Energy Systems (DES) are set to play a vital role in achieving emission targets and meeting higher global energy demand by 2050. However, implementing these systems has been challenging, particularly due to uncertainties in local energy demand and renewable energy generation, which imply uncertain operational costs. In this work we are implementing a Mixed-Integer Linear Programming (MILP) model for the operation of a DES, and analysing impacts of uncertainties in electricity demand, heating demand and solar irradiance on the main model output, the total daily operational cost, using Global Sensitivity Analysis (GSA). Representative data from a case study involving nine residential areas at the University of Surrey are used to test the model for the winter season. Distribution models for uncertain variables, obtained through statistical analysis of raw data, are presented. Design results show reduced costs and emissions, whilst GSA results show that heating demand has the largest influence on the variance of total daily operational cost. Challenges and design limitations are also discussed. Overall, the methodology can be easily applied to improve DES design and operation.

Keywords: Distributed energy system, optimisation, design and operation, global sensitivity analysis, mixed-integer linear programming.

1. Introduction

In the UK, the National Grid has predicted that high energy demands can be met through decentralised and local Distributed Energy Systems (DES) and a smart grid using renewable and low-carbon energy resources, leading to a decarbonised energy sector by 2050 (National Grid, 2018). Optimisation-based models are often employed for the design and operation of DES; these usually minimise objective functions related to total cost and/or carbon emissions (Flores and Brouwer, 2018). Design involves selecting suitable distributed technologies and their capacities for energy generation and storage for each user whilst operation involves scheduling these technologies based on the recommended design (Mehleri *et al.*, 2013). Mixed-Integer Linear Programming (MILP) has been commonly used for both design and operation models as it can achieve a good balance between complexity, accuracy and solver-time that is suitable for real-time operation of DES (Nosratabadi, et al., 2017). However, when formulating MILP, modellers tend to assume that input variables can be measured accurately and there is no natural variability. Consequently, when real-time data is fed, uncertainties associated with these variables can lead to unexpected issues such as increased costs that may prevent

wider implementation of DES. Identifying these input variables, quantifying their uncertainties, and evaluating the influence of these variables on the outputs can lead to the design of more robust models.

Quantitative methods to analyse uncertainties have been frequently used in DES studies, particularly Local Sensitivity Analysis (LSA) (Di Somma *et al.*, 2018). LSA varies only one parameter at a time whilst remaining parameters are prescribed fixed nominal values. Global Sensitivity Analysis (GSA) has been less frequently used; however, it is generally preferred over LSA because it allows simultaneous variations of multiple uncertain parameters and considers those variations over the joint probability distribution of all uncertain parameters (Saltelli *et al.*, 2008). This provides measures of overall influence of input uncertainties over that of the output. Although a framework to conduct GSA has been presented by Mavromatidis, et al. (Mavromatidis, *et al.*, 2018) for design models, no such methodology exists for operational models. This paper addresses the gap by presenting a methodology that can be easily applied to other DES models, helping modellers identify areas for improvement and limitations within their designs.

2. Methodology

2.1. Overview

The overall methodology is summarised in Figure 1. The design model is formulated using input data from a test case for the lifetime of the DES. The design and input data are then used to formulate an operational model, which is optimised for a smaller period, such as 24 hours, in a given season. Uncertain inputs are identified and quantified by creating empirical models from past data using relevant distributions; this is detailed using data from a case study. Variance-based methods of GSA require the computation of multidimensional integrals, which are estimated using Monte Carlo methods. This is done by employing a sample of random or quasi-random points based on the joint probability distribution of all uncertain parameters (Saltelli *et al.*, 2008). The operational model is updated to feed these random samples as inputs, which then generate random outputs for each sample. Sampled inputs and outputs are then used to conduct GSA, which quantifies the influence of uncertain variables on the variance of the model output, in the form of sensitivity indices. The dashed feedback arrows in Figure 1 represent how results from GSA can be used to make improvements in design and operational models.

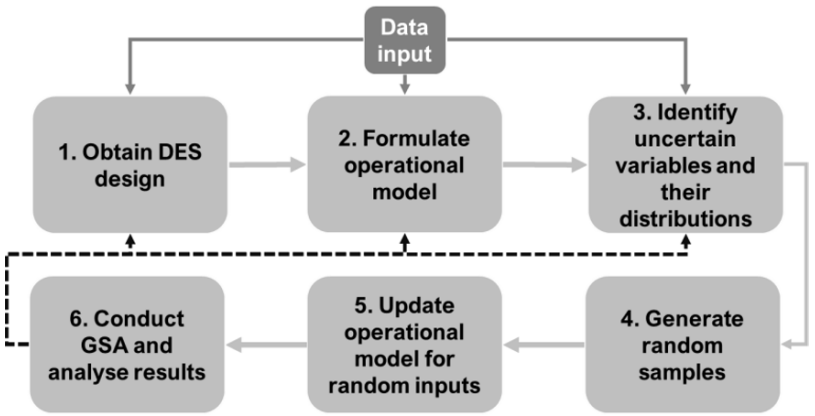

Figure 1. Flow diagram summarising the methodology used in this work.

2.2. Model formulation

The design of the DES is modelled as a Mixed-Integer Linear Programming (MILP) problem, as presented in Mehleri et al. (Mehleri *et al.*, 2012a). Distributed technologies include photovoltaic (PV) arrays, mini combined heat and power (CHP) units and boilers. The objective function minimises total annualised cost. The MILP operational model is based on the work of Mehleri (Mehleri *et al.*, 2012b), where Model Predictive Control (MPC) rolling horizon is used. MPC is a strategy which predicts the current state of the model at each timestep (hourly, in this case) over the total horizon (24 hours). The objective function minimises total daily operational cost. Both design and operational models are tested on the General Algebraic Modelling System (GAMS) (GAMS Development Corporation, 2019).

The operational model has been updated to account for a design limitation, which is applicable to all models, particularly those that do not incorporate heat storage. When heating demand exceeds the maximum generation capacity of the design, the model is rendered infeasible. This is avoided by introducing a set of equations instructing the generation technologies (such as CHPs and boilers) to produce the maximum heat, based on their capacities, whilst the additional demand is recorded for future analysis.

2.3. Uncertain variables

In this study, a subset of model inputs, which include electricity demand, heating demand and solar irradiance, is treated as uncertain. The objective to be optimised, C_{Total}, which is the total daily operational cost in this study, is presented as a function of these uncertain input variables as shown in Eq. 1.

$$minimise \quad C_{Total} \quad where \quad C_{Total} = f(X_{elec,t}, X_{heat,t}, X_{insol,t}) \tag{1}$$

where $X_{elec,t}$, $X_{heat,t}$, and $X_{insol,t}$ are the input variables for electricity, heating and irradiance, respectively. Note that index *t* has been used to denote a variable or parameter as a function of time.

3. Case study

3.1. Description

Data from nine residential areas at the University of Surrey is used to test the methodology. It is assumed that the DES is operating under the Feed-In-Tariff (FIT) scheme (Ofgem, 2019); design and operational model equations have been updated accordingly. Some model inputs data include electricity consumption, heating consumption, FIT tariffs, current electricity and gas prices, and solar irradiance. Currently residential DES in the United Kingdom are exempt from carbon taxes.

Figure 2 shows real data for $X_{elec,t}$, $X_{heat,t}$, and $X_{insol,t}$ and their means over a 24-hour period for electricity demand, heating demand and irradiance, respectively. Analysis of raw data at each timestep show that electricity and heating demand appear to be normally distributed, whilst irradiance has a beta distribution. Uncertain parameters for each input variable are assigned the corresponding distribution.

Inputs for electricity and heating demand are modelled using the following equations:

$$X_{v,t} = \mu_{v,t}(1 + k_v) \tag{2}$$

$$k_v = \frac{\mu_{v,t}}{\sigma_{v,t}} \tag{3}$$

where k_v is the uncertain parameter (index *v* indicates for either electricity or heat), $\mu_{v,t}$ is the expected time-dependent variation, $\sigma_{v,t}$ is the standard deviation. A constant relative variance model is assumed. Distribution of k_v, is assumed to be $N(0,\sigma_v)$ as given in Table 1.

Irradiance is modelled by:

$$X_{insol,t} = l_{max,t} * \alpha \tag{4}$$

where $l_{max,t}$ is the maximum recorded irradiance as a function of time in winter. The uncertain parameter α describes the variability of irradiance due to weather conditions; it is modelled using a beta distribution fitted to the data, as seen in Table 1.

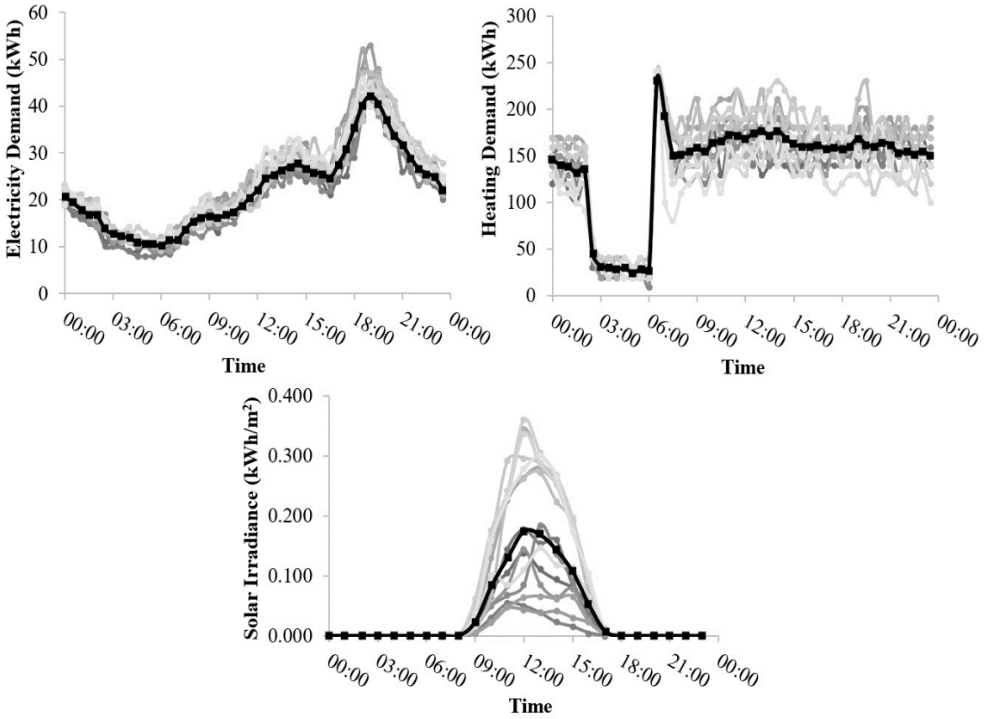

Figure 2. Electricity demand, heating demand and insolation from real data (noise). The mean is shown by the black line.

Random sampling points are generated using SobolGSA (Kucherenko and Zaccheus, 2018), software which was also used to conduct GSA of outputs (total daily operational cost) simulated for each random sample and each scenario. These are fed into the operational model to calculate inputs using Eq. (2) and (4), which then generates the optimised output, total daily operational cost, for each scenario.

Table 1. Uncertain parameters and their distributions. Under distribution parameters, μ, σ, α, β are mean, standard deviation, alpha and beta parameters, respectively.

Uncertain Parameter	Assigned distribution	Distribution parameters
$k_{electricity}$	Normal	μ = 0, σ = 0.14
$k_{heating}$	Normal	μ = 0, σ = 0.12
α	Beta	α = 0.56, β = 0.60

4. Design and operational results

Optimal capacities for solar panels, CHPs and boilers are obtained for each of the nine residential areas. When compared to a conventional design, i.e. electricity from the grid and heat from boilers only, a cost saving of over 30% is obtained for the DES. Carbon emissions are reduced by 4.5% for the same DES design.

The operational model is run for 1,023 scenarios, which take a total computational time of 15 hours and 42 minutes on an Intel® Core™ i3-7130U processor at 2.70 GHz, solved to 5% optimality using the CPLEX solver. Each scenario solves 135 single equations with 171 single variables. Figure 3 presents the results from conducting GSA, in the form of first-order sensitivity indices.

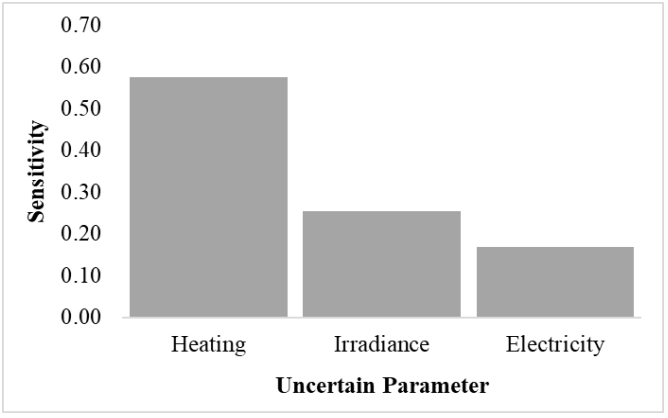

Figure 3. Sensitivity of model output, total daily operational cost, to uncertain input parameters.

5. Discussion and Conclusions

Results from the test case shows that heating demand has the largest influence on the variance of total daily operational cost in winter. Solar irradiance and electricity demand have minor influences (note that these conclusions may not hold for other seasons). With respect to the case study, the large influence of heating demand highlights the need for better heating regulation within the DES.

Key limitations of the study are high computational expense, consideration of data from the recent past only (for the development of empirical models), and lack of energy storage in the DES design.

Despite these limitations, the methodology can be applied to other operational models and a larger number of uncertain inputs. As illustrated through the test case, these findings

undoubtedly can help modellers to explore the design limitations and thus lead to the development of more robust DES for the future.

References

R. J. Flores and J. Brouwer, 2018, Optimal design of a distributed energy resource system that economically reduces carbon emissions, Applied Energy. Elsevier, 232, pp. 119–138.

GAMS Development Corporation, 2019, General Algebraic Modeling System (GAMS). Fairfax, VA, USA,. Available at: https://www.gams.com/download/ (Accessed: 14 November 2018).

S. Kucherenko and O. Zaccheus, 2018, SobolGSA Software, Imperial College London. Available at: https://www.imperial.ac.uk/process-systems-engineering/research/free-software/sobolgsa-software/ (Accessed: 10 November 2018).

G. Mavromatidis, K. Orehounig, and J. Carmeliet, 2018, Uncertainty and global sensitivity analysis for the optimal design of distributed energy systems, Applied Energy. Elsevier, 214, pp. 219–238.

E. D. Mehleri, H. Sarimveis, N. C. Markatos, and L. G. Papageorgiou, 2012, A mathematical programming approach for optimal design of distributed energy systems at the neighbourhood level, Energy, 44(1), pp. 96–104.

E. D. Mehleri, L. G. Papageorgiou, N. C. Markatos, and H. Sarimveis, 2012, A Model Predictive Control Framework for Residential Microgrids, Computer Aided Chemical Engineering, 30(June), pp. 327–331.

E. D. Mehleri, H. Sarimveis, N. C. Markatos, and L. G. Papageorgiou, 2013, Optimal design and operation of distributed energy systems: Application to Greek residential sector, Renewable Energy. Elsevier Ltd, 51, pp. 331–342.

National Grid, 2018, Future Energy Scenarios. Available at: http://fes.nationalgrid.com/media/1363/fes-interactive-version-final.pdf (Accessed: 25 May 2019).

S. M. Nosratabadi, R. A. Hooshmand, and E. Gholipour, 2017, A comprehensive review on microgrid and virtual power plant concepts employed for distributed energy resources scheduling in power systems, Renewable and Sustainable Energy Reviews. Elsevier, 67, pp. 341–363.

Ofgem, 2019, About the FIT scheme, Ofgem. Available at: https://www.ofgem.gov.uk/environmental-programmes/fit/about-fit-scheme (Accessed: 18 March 2019).

A. Saltelli, M. Ratto, T. Andres, F. Campolongo, J. Cariboni, D. Gatelli, M. Saisana, and S. Tarantola, 2008, Global sensitivity analysis : The Primer. Online. Chichester, United Kingdom: John Wiley & Sons, Ltd.

M. Di Somma, G. Graditi, E. Heydarian-Forushani, M. Shafie-khah, and P. Siano, 2018, Stochastic optimal scheduling of distributed energy resources with renewables considering economic and environmental aspects, Renewable Energy. Pergamon, 116, pp. 272–287.

Sauro Pierucci, Flavio Manenti, Giulia Bozzano, Davide Manca (Eds.)
Proceedings of the 30th European Symposium on Computer Aided Process Engineering (ESCAPE30), May 24-27, 2020, Milano, Italy.
http://dx.doi.org/10.1016/B978-0-12-823377-1.50255-X

Retrofit of Heat Exchanger Networks with Temperature and Flowrate Uncertainties

Yossaral Charnkhuang,[b] Jui-Yuan Lee,[a] Dominic Chwan Yee Foo[c,*]

[a]*Chemical Engineering Practice School, King Mongkut's University of Technology Thonburi, 126 Prachautid Road, Bangmod, Thoongkru, Bangkok 10140, Thailand*

[b]*Department of Chemical Engineering and Biotechnology, National Taipei University of Technology, 1, Sec. 3, Zhongxiao E. Rd., Taipei 10608, Taiwan, R.O.C.*

[c]*Department of Chemical & Environmental Engineering/Centre of Excellence for Green Technologies, University of Nottingham Malaysia, 43500 Semenyih, Selangor, Malaysia*
Dominic.Foo@nottingham.edu.my

Abstract

This work presents a fuzzy optimisation model for HEN retrofit design incorporating parametric uncertainties. The basic model is based on a stage-wise superstructure with non-isothermal mixing. Fuzzy set theory is used with max-min aggregation to provide a robust, more conservative design with maximum overall degree of satisfaction of fuzzy constraints. An illustrative example is presented to demonstrate the application of the proposed approach. Results obtained for the deterministic and fuzzy cases are discussed and compared with the literature.

Keywords: process integration, mathematical programming; fuzzy optimisation, energy recovery.

1. Introduction

After four decades of development, process integration techniques are well established for heat exchanger network (HEN) synthesis, particularly for grassroots design, i.e. for new processes at the conceptual design stage. However, a significant breakthrough still remains to be made for the retrofit of HENs in existing process plants. In most cases, HENs not designed using a systematic approach tend to involve cross-pinch heat transfer. This could result in much higher consumption of hot and cold utilities, as compared to the best grassroots design targets. Such ill-designed HENs may thus be retrofitted for better energy efficiency. Also, it is often the case that the existing HEN needs to be retrofitted to accommodate process changes. Retrofitting an existing HEN can entail significant costs, and it is important to ensure a reasonable payback period for a retrofit project. Apart from the economic aspect, uncertainties in process stream data such as flowrates and temperature should also be taken into account.

There have been many research works on HEN retrofit based on pinch analysis and mathematical programming. In the seminal work of Tjoe and Linnhoff (1986), grassroots design targets were used to guide retrofit. More recently, Lal et al. (2018) developed an HEN retrofit method based on bridge analysis. Their method identifies retrofit bridges corresponding to energy saving modifications using the heat surplus-deficit table and the modified energy transfer diagram. Jiang et al. (2018) proposed an HEN retrofit methodology with performance reassessment. The authors incorporated performance simulation into the HEN retrofit model to reassess the performance of reused heat exchange units, and adopted genetic algorithm for the optimization problem.

Most of the works on HEN retrofit do not consider uncertainties in process stream data. Although Monte Carlo simulation can be used to analyse the effect of stream data variations on the performance of retrofitted HENs, and to assess the sensitivity and robustness of the HEN and individual heat exchangers (Lal et al., 2019), uncertainties should be incorporated in retrofit design to better guide the decision making. In this paper, a new mathematical technique is proposed for robust HEN retrofit design under parametric uncertainties. The basic model formulation is based on a stage-wise superstructure with non-isothermal mixing streams. Uncertainties in stream flowrates and supply temperatures are allowed for using fuzzy optimisation, which has been applied to water network synthesis problems (Tan, 2011). An illustrative example is presented to illustrate the proposed approach.

2. Problem statement

The HEN retrofit problem addressed in this paper can be formally stated as follows. A given process has a set of hot streams $i \in \mathbf{I}$ and a set of cold streams $j \in \mathbf{J}$. Hot and cold utilities are available to meet the cooling and heating demands of the process. There has been an existing HEN for the process to reduce its utility consumption. This HEN is, however, to be retrofitted for further energy efficiency improvements. Knowing stream data and parameters for utilities and equipment, the objective is to determine the optimal HEN retrofit design with maximum profit.

3. Model formulation

The basic model for the HEN retrofit problem is adapted from Jiang et al. (2018). Based on the stage-wise superstructure with non-isothermal mixing, the formulation consists mainly of energy balances (for each stream, in each stage and for each heat exchanger), mass balances (for each stream in each stage) and temperature constraints.

To improve energy efficiency whilst ensuring economic feasibility, the objective is to maximise the total retrofit profit (g_{TRP}), which is defined as the difference between the utility cost savings (g_{UCS}) and the annualised capital cost (g_{ACC}), as given in Eq. (1).

$$g_{\mathrm{TRP}} = g_{\mathrm{UCS}} - g_{\mathrm{ACC}} \tag{1}$$

$$g_{\mathrm{UCS}} = AOH\left[C_{\mathrm{CU}}\sum_{i\in\mathbf{I}}\left(Q^{0}_{i,\mathrm{CU}} - q_{i,\mathrm{CU}}\right) + C_{\mathrm{HU}}\sum_{j\in\mathbf{J}}\left(Q^{0}_{\mathrm{HU},j} - q_{\mathrm{HU},j}\right)\right] \tag{2}$$

$$\begin{aligned} g_{\mathrm{ACC}} = {} & AF\sum_{i\in\mathbf{I}}\sum_{j\in\mathbf{J}}\sum_{k\in\mathbf{K}}\left[C^{\mathrm{ex}}_{\mathrm{fix}}z^{\mathrm{ex}}_{ijk} + C^{\mathrm{new}}_{\mathrm{fix}}z^{\mathrm{new}}_{ijk} + C_{\mathrm{var}}\left(a^{\mathrm{add}}_{ijk}\right)^{\beta}\right] \\ & + AF\sum_{i\in\mathbf{I}}\left[C^{\mathrm{ex}}_{\mathrm{fix}}z^{\mathrm{ex}}_{i,\mathrm{CU}} + C^{\mathrm{new}}_{\mathrm{fix}}z^{\mathrm{new}}_{i,\mathrm{CU}} + C_{\mathrm{var}}\left(a^{\mathrm{add}}_{i,\mathrm{CU}}\right)^{\beta}\right] \\ & + AF\sum_{j\in\mathbf{J}}\left[C^{\mathrm{ex}}_{\mathrm{fix}}z^{\mathrm{ex}}_{\mathrm{HU},j} + C^{\mathrm{new}}_{\mathrm{fix}}z^{\mathrm{new}}_{\mathrm{HU},j} + C_{\mathrm{var}}\left(a^{\mathrm{add}}_{\mathrm{HU},i}\right)^{\beta}\right] \end{aligned} \tag{3}$$

where AOH is the annual operating hours; C_{CU} and C_{HU} are the costs of cold and hot utilities; $Q^{0}_{i,\mathrm{CU}}$ and $Q^{0}_{\mathrm{HU},j}$ are the cold utility load for hot stream i and the hot utility load for cold stream j in the existing HEN; $q_{i,\mathrm{CU}}$ and $q_{\mathrm{HU},j}$ are the cold utility load for stream i and the hot utility load for stream j in the retrofitted HEN; AF is the annualisation factor; $C^{\mathrm{ex}}_{\mathrm{fix}}$ and $C^{\mathrm{new}}_{\mathrm{fix}}$ are the fixed area cost coefficients for existing and new heat exchangers; C_{var} is the variable area cost coefficient; β is the area cost exponent; a^{add}_{*} (∗

$= \{(ijk), (i,\text{CU}), (\text{HU}, j)\}$) represents the additional heat transfer area required for the match; z_*^{ex} and z_*^{new} are binary variables indicating the use of an existing heat exchanger or a new one for the match in the retrofitted HEN.

The additional heat transfer areas are calculated using Eqs. (4)-(6).

$$a_{ijk}^{\text{add}} \geq a_{ijk} - A_{ij}^{0} z_{ijk}^{\text{ex}} \quad \forall i \in \mathbf{I}, j \in \mathbf{J}, k \in \mathbf{K} \tag{4}$$
$$a_{i,\text{CU}}^{\text{add}} \geq a_{i,\text{CU}} - A_{i,\text{CU}}^{0} z_{i,\text{CU}}^{\text{ex}} \quad \forall i \in \mathbf{I} \tag{5}$$
$$a_{\text{HU},j}^{\text{add}} \geq a_{\text{HU},j} - A_{\text{HU},j}^{0} z_{\text{HU},j}^{\text{ex}} \quad \forall j \in \mathbf{J} \tag{6}$$

where A_*^0 and a_* ($*= \{(ijk), (i,\text{CU}), (\text{HU}, j)\}$) represent the heat transfer areas required for the match in the existing and retrofitted HENs. Furthermore, the binary variables are correlated in Eqs. (7)-(12).

$$z_{ijk} = z_{ijk}^{\text{ex}} + z_{ijk}^{\text{new}} \quad \forall i \in \mathbf{I}, j \in \mathbf{J}, k \in \mathbf{K} \tag{7}$$
$$z_{i,\text{CU}} = z_{i,\text{CU}}^{\text{ex}} + z_{i,\text{CU}}^{\text{new}} \quad \forall i \in \mathbf{I} \tag{8}$$
$$z_{\text{HU},j} = z_{\text{HU},j}^{\text{ex}} + z_{\text{HU},j}^{\text{new}} \quad \forall j \in \mathbf{J} \tag{9}$$
$$\sum_{k \in \mathbf{K}} z_{ijk}^{\text{ex}} \leq Z_{ij}^{0} \quad \forall i \in \mathbf{I}, j \in \mathbf{J} \tag{10}$$
$$z_{i,\text{CU}}^{\text{ex}} \leq Z_{i,\text{CU}}^{0} \quad \forall i \in \mathbf{I} \tag{11}$$
$$z_{\text{HU},j}^{\text{ex}} \leq Z_{\text{HU},j}^{0} \quad \forall j \in \mathbf{J} \tag{12}$$

where z_* ($*= \{(ijk), (i,\text{CU}), (\text{HU}, j)\}$) is the binary variable indicating the existence of the match in the retrofitted HEN; Z_*^0 is the binary parameter denoting the match in the existing HEN. It should be noted that this formulation applies to a specific case in which there is at most one match between any pair of hot and cold process streams in the existing HEN.

To allow for uncertainties in process stream flowrates and temperatures, the basic model is extended using fuzzy set theory (Zimmermann, 1978). The objective function of the fuzzy model is to maximise the overall degree of satisfaction (λ) of the fuzzy goals and constraints, as given in Eq. (13).

$$\max \lambda \tag{13}$$
$$0 \leq \lambda \leq 1 \tag{14}$$

Eq. (15) represents the fuzzy profit goal, for which a high value is desirable, assuming a linear membership function. Note that g_{TRP} reaches its lower bound (TRP^{L}) when the degree of satisfaction of the profit goal (λ^{TRP}) is equal to zero (unsatisfactory), and reaches its upper bound (TRP^{U}) when $\lambda^{\text{TRP}} = 1$ (completely satisfactory).

$$g_{\text{TRP}} = TRP^{\text{L}} + \lambda^{\text{TRP}}(TRP^{\text{U}} - TRP^{\text{L}}) \tag{15}$$
$$0 \leq \lambda^{\text{TRP}} \leq 1 \tag{16}$$

The fuzzy parameters are redefined and treated as variables in the fuzzy constraints given in Eqs. (17)-(20).

$$F_i = F_i^{\text{U}} - \lambda_i^{\text{F}}\left(F_i^{\text{U}} - F_i^{\text{L}}\right) \tag{17}$$
$$T_i^{\text{in}} = T_i^{\text{in,U}} - \lambda_i^{\text{T}}\left(T_i^{\text{in,U}} - T_i^{\text{in,L}}\right) \tag{18}$$
$$F_j = F_j^{\text{L}} + \lambda_j^{\text{F}}\left(F_j^{\text{U}} - F_j^{\text{L}}\right) \tag{19}$$
$$T_j^{\text{in}} = T_j^{\text{in,U}} - \lambda_j^{\text{T}}\left(T_j^{\text{in,U}} - T_j^{\text{in,L}}\right) \tag{20}$$
$$0 \leq \lambda_i^{\text{F}}, \lambda_i^{\text{T}}, \lambda_j^{\text{F}}, \lambda_j^{\text{T}} \leq 1 \tag{21}$$

where F_i and F_j are the flowrates of hot stream i and cold stream j; T_i^{in} and T_j^{in} are the supply temperatures of hot stream i and cold stream j. For hot streams, lower values of flowrates and supply temperatures are considered more conservative and thus more desirable, whilst higher values are riskier and less desirable. Likewise, for cold streams, higher values of flowrates and lower values of supply temperatures are considered to be more conservative and more desirable.

Eq. (22) ensures that the overall degree of satisfaction is less than all individual degrees of satisfaction. The satisfaction degrees of these fuzzy goal and constraints can be maximised simultaneously using max-min aggregation, where λ is equal to the degree of satisfaction of the least satisfied fuzzy goal/constraint.

$$\lambda \leq \lambda^{\text{TRP}}, \lambda_i^{\text{F}}, \lambda_i^{\text{T}}, \lambda_j^{\text{F}}, \lambda_j^{\text{T}} \tag{22}$$

4. Illustrative example

A four-stream problem adapted from Lal et al. (2018) is used to illustrate the proposed approach. The models are implemented in GAMS and solved using BARON. Figure 1 shows the existing HEN (Lal et al., 2018). There are two coolers (C1 for stream F2; C2 for stream F4), two process-process heat exchangers (E1 for match F4-F1; E2 for match F2-F1) and one heater (H1 for stream F3). This HEN has a hot utility load of 2,700 kW (H1) and a total cold utility load of 2,950 kW (C1 and C2). Table 1 shows the stream data.

This example assumes a $\Delta T^{\min}$ of 10 °C. The total utility cost is based on 8,000 h of operation per year. The ACC is calculated using the following parameters: $C_{\text{fix}}^{\text{ex}}$ = 2,000 NZD; $C_{\text{fix}}^{\text{new}}$ = 4,000 NZD; C_{var} = 500 NZD/m^2; β = 0.83.

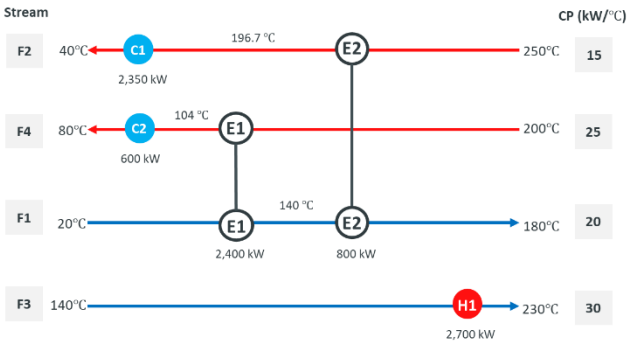

Figure 1. Existing HEN for the Four-stream Example

Table 1. Stream Data for the Illustrative Example

Stream	Supply temperature (°C)	Target temperature (°C)	Heat capacity flowrate (kW/°C)	Cost (NZD/kWh)
F1	20	180	20	-
F2	250	40	15	-
F3	140	230	30	-
F4	200	80	40	-
Steam	250	250	-	0.035
Cold utility	20	40	-	Negligible

U = 0.25 kW/m^2/°C for all heat exchangers, heaters and coolers.

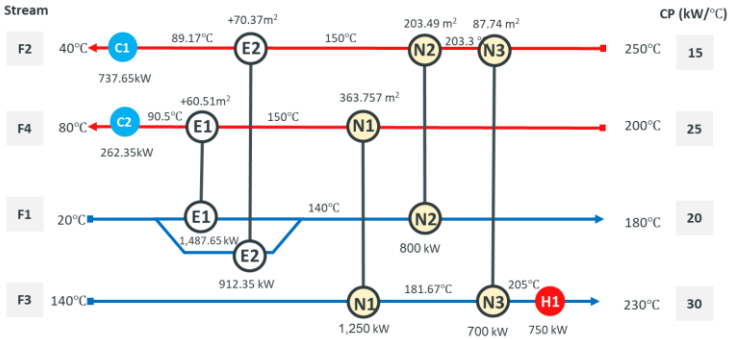

Figure 2. Retrofitted HEN without Considering Parametric Uncertainties

Table 2. Fuzzy Limits for Stream Flowrates and Temperatures

Stream	Heat capacity flowrate (kW/°C)		Supply temperature (°C)	
	Lower bound	Upper bound	Lower bound	Upper bound
F1	19	21	19	21
F2	10	20	240	255
F3	27	32	120	165
F4	15	37	190	210

Solving the basic model gives the retrofit design in Figure 2. The retrofitted HEN uses three new exchangers (N1 for match F4-F3, N2 for match F2-F1 and N3 for match F2-F3) together with the existing units, requiring a total additional area of 758.87 m^2. Thus, the hot utility and cold utility loads are reduced to 750 kW and 1,000 kW, respectively. The corresponding TRP is about 0.526 million NZD/y.

Table 2 shows the fuzzy range for each of the uncertain parameters in this example. These fuzzy ranges are taken from Lal et al. (2019). Wider fuzzy intervals in these data represent greater parametric uncertainty. The lower and upper limits of the fuzzy profit goal are based on the TRP before HEN retrofit (= 0), and the maximum TRP of 0.5 million NZD/y in the case without considering uncertainties, respectively.

Solving the fuzzy model gives the optimal retrofit design in Figure 3. It can be seen that a new exchanger (N1 for match F2-F3) and a new heater (NH1 for stream F1) are used in the retrofitted HEN, requiring a total additional area of 372.56 m^2, whilst the existing cooler C2 and exchanger E2 are no longer used. The resulting hot utility and cold utility loads are 1,711.25 kW and 1948.6 kW respectively, with a TRP of 0.269 million UZD/y. This is only half the TRP to be achieved in the deterministic (non-fuzzy) case, with an overall degree of satisfaction of 0.5. The decrease in TRP is the penalty incurred to provide a margin of safety based on process energy balances, particularly with regard to the heating demand.

Table 3 shows the results comparison. When parametric uncertainties are not considered, the solution obtained using the basic model results in a much higher TRP than the solution of Lal et al. (2018). However, the fuzzy model provides a conservative HEN retrofit design, from which the TRP is lower than that reported by Lal et al. (2018). The number of heat exchange units used and hence heat recovery is also reduced with the consideration of parametric uncertainties in stream flowrates and temperatures.

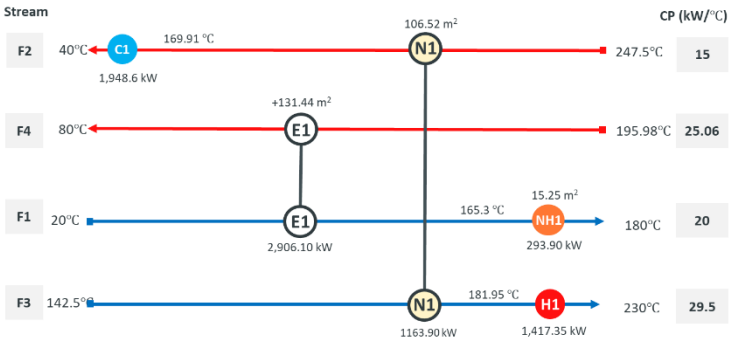

Figure 3. Retrofitted HEN Considering Parametric Uncertainties

Table 3. Results Comparison

Parameter	Existing HEN	Lal et al. (2019)	Basic model	Fuzzy model
Hot utility (kW)	2,700	1,500	750	1,711
Cold utility (kW)	2,950	1,750	1,000	1,948
Utility cost (NZD/y)	7.56×10^5	4.2×10^5	2.1×10^5	4.79×10^5
Additional area (m^2)	0	298.3	758.87	372.56
TRP (NZD/y)	0	3.27×10^5	5.26×10^5	2.69×10^5
Number of units	5	6	8	5

5. Conclusions

A fuzzy optimisation model for HEN retrofit design under parametric uncertainties has been developed in this paper, based on a stage-wise superstructure with non-isothermal mixing. An illustrative example was solved to illustrate the proposed approach. Future work will extend the current model to more general HEN retrofit problems with a more detailed evaluation of the cost incurred by HEN retrofits. Monte Carlo simulation may then be performed to verify the results obtained from the improved model.

References

N. S. Lal, T. G. Walmsley, M. R. W. Walmsley, M. J. Atkins, J. R. Neale, 2018, A Novel Heat Exchanger Network Bridge Retrofit Method Using the Modified Energy Transfer Diagram, Energy, 155, 190-204

N. S. Lal, M. J. Atkins, T. G. Walmsley, M. R. W. Walmsley, J. R. Neale, 2019, Energy, 181, 1129-1141

N. Jiang, W. Han, F. Guo, H. Yu, Y. Xu, N. Mao, 2018, A Novel Heat Exchanger Network Retrofit Approach Based on Performance Reassessment, Energy Conversion and Management, 177, 477-492

R. R. Tan, 2011, Fuzzy Optimization Model for Source-sink Water Network Synthesis with Parametric Uncertainties. Industrial and Engineering Chemisrty Research, 50, 3686-3694

T. N. Tjoe, B. Linnhoff, 1986, Using Pinch Technology for Process Retrofit, Chemical Engineering, 93, 47-60

H-J. Zimmermann, 1978, Fuzzy Programming and Linear Programming with Several Objective Functions. Fuzzy Sets and Systems, 1, 45-55

Sauro Pierucci, Flavio Manenti, Giulia Bozzano, Davide Manca (Eds.)
Proceedings of the 30th European Symposium on Computer Aided Process Engineering (ESCAPE30), May 24-27, 2020, Milano, Italy.
http://dx.doi.org/10.1016/B978-0-12-823377-1.50256-1

Probabilistic Performance Evaluation of Small-Scale Organic Rankine Cycle Power Plants for Waste Heat Recovery

Giuseppina Di Lorenzo* , Ambra Giovannelli

Department of Engineering - University of Roma Tre, via della Vasca Navale 79, Rome 00146, Italy
giuseppina.dilorenzo@uniroma3.it

Abstract

The performance of Organic Rankine Cycles (ORC) plants is subject to uncertainties deriving from several factors. Such uncertainties are unavoidably propagated through the model to the outputs, affecting predictions of the commercial-scale performance and cost of this technology. The aim of this work is to analyse how the uncertainties associated with the performance of the expander, one of the main ORC components, propagate to the relevant thermodynamic and economic outputs and affect their final value. The analysis was performed for three different expander options (a single-stage turbine, a twin screw and a two-stage turbine) to generate a full spectrum of possible outputs rather than exact figures. Overall, a considerable variability of the output metrics was highlighted compared to the results from the deterministic analysis.

Keywords: Monte Carlo simulation, stochastic analysis, mini Organic Rankine Cycle, techno-economic modelling and analysis.

1. Introduction

Organic Rankine Cycle (ORC) plants are a promising technical solution for recovering and converting low-to-medium grade waste heat into electricity, as they present several advantages compared to other technologies in terms of improved thermal performance, flexibility and maintainability (Tchanche et al., 2011). However, the introduction of this advanced solution at a small scale, although technically interesting, is not always economically attractive. As a matter of fact, the small-scale application of ORCs is hindered by their uncompetitive specific cost, which is too high compared to other existing technologies. For this reason, a core issue for the development of the small-scale ORC systems is the assessment and optimization of their techno-economic feasibility. More specifically, considerable research efforts have been channelled into the technical performance optimization of different cycle layouts (including selection of the most appropriate organic fluids) and improvement of the performance of the individual components, with the ultimate aim of maximizing the power production of ORC plants while keeping their specific total capital requirement as low as possible. (Tocci et al., 2017). In all of the existing studies and analyses, however, the models devised and applied are essentially deterministic (i.e., they use best estimates of model input parameters, without inclusion of any uncertainties, and generate exact figures for the output parameters). This is a concern because the input values characterizing such process models can have significant uncertainties, stemming from several factors (e.g., material properties, variable operating conditions, design factors, low technological readiness level). Such uncertainties will be unavoidably propagated through the model to the

outputs, thus affecting predictions of the commercial-scale performance and cost of this technology. Combining the techno-economic evaluation of energy conversion systems with a stochastic analysis has proved helpful in dealing with such uncertainties and thus providing a more comprehensive understanding of their technical and economic feasibility and their operation (Di Lorenzo et al., 2012; Maccapani et al., 2014).The aim of this study is to evaluate, by means of a stochastic approach, the impact of uncertainties in model input parameters on the performance of the ORC power plants. In particular, the stochastic method has been used in this work to systematically and explicitly analyse how the uncertainties related to the expander performance propagate to the relevant thermodynamic and economic outputs and affect their final value. The proper selection of the expander for small-scale ORC systems remains an outstanding issue (Tocci et al., 2017), as can be deduced from the existing literature. For small-scale applications different expander options are available, each with its own advantages and disadvantages. The selection process is complicated further by the fact that, among all of the ORC components, the expander is the one whose performance is most negatively affected when downscaling to kW (Tocci et al, 2017). The analysis in this work has been performed on three different expander options that were previously comparatively studied by the authors (Di Lorenzo et al., 2019). By including uncertainties in the techno-economic evaluation, a full spectrum of possible outputs is made available rather than exact figures, thus quantifying the confidence in the results from the previous work.

2. Description of the ORC Plant

The plant considered in this analysis is an ORC plant for Waste Heat Recovery (WHR) applications with a power output of less than 100 kWe based on a subcritical cycle. Three different expanders have been considered, i.e. a one-stage radial turbine (Case A), a twin-screw expander (Case B) and a two-stage radial turbine (Case C). On one hand, the twin-screw expanders display lower speed and higher nominal pressure ratios compared to a single-stage turbomachine, which theoretically fits well ORC requirements. However, the performance of twin-screw expanders for small-scale applications is considerably reduced by under- or over-expansions in off-design conditions, leakage and clearance gap losses, and lubrication issues. On the other hand, radial-inflow turbomachines are robust and reliable machines and could provide higher performances in a wide range of operating conditions, though high rotational speeds, low pressure ratio per stage, clearance and windage losses, and choking conditions hinder the design of an efficient turbine for ORC applications.

In the ORC system considered in this work, a feed pump compresses and pumps the working fluid up to 17.5 bar into the Primary Heat Exchanger (PHE), where the waste heat is transferred to the working fluid, which is pre-heated, evaporated and then super-heated. An expander is connected to a generator, so that the thermal energy of the working fluid is converted into useful work and then into electricity. After the expansion (down to 6 bar for Case A, 4 bar for Case B and 2.2 bar for Case C, according to the expander's features), the thermodynamic cycle is closed by condensing the fluid in the condenser. The resulting three power plants were designed for the same reference waste heat source with the same refrigerant used as the working fluid. They were compared from a thermodynamic and economic performance viewpoint in a previous study by the same authors (Di Lorenzo et al., 2019), using only a deterministic approach and delivering the following key results. Case C, with a two-stage turbine, resulted in efficiency (11.6%) and power output (87.4 kWe) well above those achieved by the plants with a one-stage turbine (7% and 45kWe) and a twin-screw expander (8.5% and 58.5 kWe). The plant

specific cost figure for the two-stage turbine plant is also considerably below those for the other two plants ($6188 USD_{2016} against $9889 USD_{2016} and $8221 USD_{2016}). These results were obtained assuming exact figures for the input variables with no consideration of their stochasticity. Among these input variables is the efficiency of the expander (Case A: η_{is}=75%; Case B: η_{is}=72%; Case C: η_{is}=75% for the first stage, η_{is}=72% for the second stage), which has a strong impact on the cycle performance.

3. Methodology

In this analysis, the approach adopted was the Monte Carlo method, an established stochastic approach that has been used extensively to model and study uncertainty in engineering system behaviour evaluation. In a Monte Carlo simulation a sufficiently large number of samples of the uncertain input variables are randomly generated based on the defined probability distributions. The samples are input into the model of the system being considered and the resulting output variables chosen as indices of the performance of the system are collected and stored. The analysis of these results ultimately produces a quantitative estimate of the impact of the uncertainty of the input variables on the system behaviour. The three ORC plant variants were modelled with a simulation routine developed in-house (Di Lorenzo et al., 2019), estimating their design-point performance. The thermodynamic and transport properties of the organic fluid were determined using the RefProp database (Lemmon et al., 2002). The stochastic analysis was performed assuming as a stochastic input the isentropic efficiency of the expander. The uncertainty of this input parameter was described by means of triangular and normal distributions with the features presented in Table I. The deterministic on-design value was assumed to be the central value of the distribution, while the standard deviation stemmed from information and data collected from the open literature and critically reviewed: for the single stage turbine the values suggested by (Costall et al., 2015; Kang, 2012; Han et al., 2014; Sung et al., 2016; Wong et al., 2013; Shao et al., 2017; Giovannelli et al., 2019) were examined, while for the twin-screw expander, the figures proposed by (Hsu et al., 2014; Stošić et al., 1997; Lee et al., 2017; Platell, 1993; Astolfi, 2015) were evaluated. For the two-stage turbine, in contrast, not many values are currently available in the literature, apart from the one resulting from the work by Kang (2016). A summary of the other main assumptions used for the calculation of the heat and mass balances of the ORC systems is reported elsewhere (Di Lorenzo et al., 2019). The performance metric that was monitored to evaluate the effect of the uncertainty in the expander performance on the ORC system was the thermal efficiency.

Table I - Probability distributions for the expander efficiency

Case – Expander Type	Distribution	Min and Max Values
Case A – Single Stage Turbine	Triangular	68% - 83%
Case B – Twin Screw	Triangular	70% - 85%
Case – Two Stage Turbine (second stage)	Normal	65% - 79%

[1]For the first stage the probability distribution adopted for the single stage case was used.

Furthermore, the uncertainty in the expander performance was propagated through economic parameters. The Specific Unit Cost ($\$_{2016}$/kW) was used as an indicator representative of the economic performances of the power plants being investigated. The work aimed primarily to assess the propagation of uncertainty from the expander to the

economic parameters. For this reason, the impacts that the variability of expander η_{is} can have on the sizing and design of the other components (e.g., the condenser) were not taken into account, but rather, all of the other components were assumed to be as estimated in the previous work and unchanging. Nevertheless, the final results are yet informative, as they reflect changes in economic expectations based on expander performance variability.

4. Key Results

The results are presented as cumulative probability distributions (Figures 1-3), which provide the analyst with the likelihood of random variable X, evaluated at $\bar{x}$, being equal to or less than the specified value $\bar{x}$; the complement (one minus the cumulative probability) is the probability that the variable will exceed the specified value $\bar{x}$. The deterministic evaluation is represented in the same figures by a vertical dotted line.

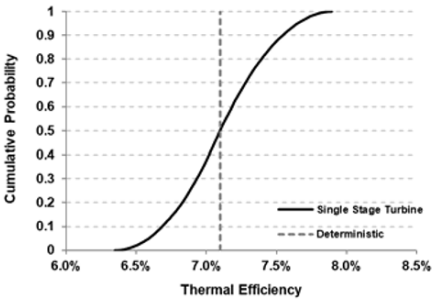

Figure 1 -Cumulative probability distribution for case A

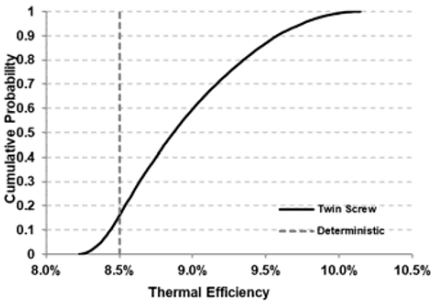

Figure 2 -Cumulative probability distribution for case B

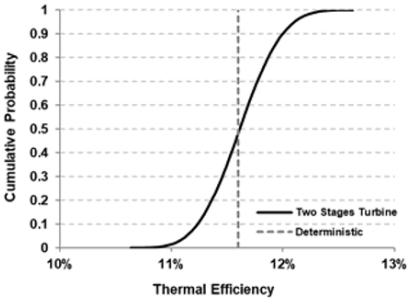

Figure 3 -Cumulative probability distribution for case C

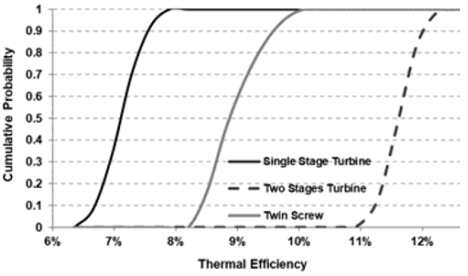

Figure 4 -Cumulative probability distribution for the three cases

According to the simulation results, the probability that the thermal efficiency for Case A could be less than the deterministic value of 7.1% is approximately 50%. It could range between 6.3% and 7.9% with a standard deviation of 0.003 and a relative standard deviation of 0.045. The median value was equal to 7.1% in line with the deterministic prediction. For Case B, the resulting efficiency displays a median value of 8.9% close to the deterministic value of 8.5%. It could vary within a range of 8.2% to 10.1%, with a standard deviation of 0.004 and a relative standard deviation of 0.048. The probability that the final figure of plant efficiency could exceed the deterministic value is quite high (85%). The results indicate that a considerable level of uncertainty is also associated with the variation of the expander performance in Case C. The likelihood that the forecast efficiency value can exceed the deterministic value is approx. 52%, with a remaining 48% probability that the final value could be lower than the deterministic one. The variation in

the expander efficiency in Case C causes the plant efficiency to vary between 10.6% and 12.6%, with a median value of 11.6% (well aligned with the deterministic result), a standard deviation of 0.003 and a relative standard deviation of 0.025. It is of paramount importance to highlight that these results (like the results of any Monte Carlo simulation analysis) rely on the initial assumptions, especially the statistical distributions selected and assigned to the uncertain input variables. A deterministic analysis only provides the decision maker with information on deterministic efficiencies, with no suggestion of the above-mentioned likelihood of a higher (or lower) value. Figure 4 shows the cumulative probability distributions of the plant efficiency for the three cases. It is evident that there are not any intersection points among the three curves; therefore, Case C (the two stage turbine) should be selected, as its probability distribution curve spreads further to the right (higher values of efficiency), although the results (i.e., same chance of observing a lower or higher value compared to the deterministic one) suggest that additional research should be undertaken in order to reduce uncertainty in the expander performance.

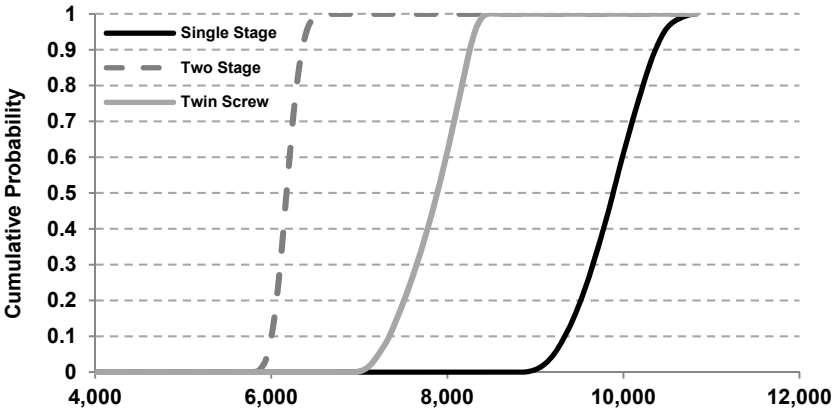

Figure 5 -Cumulative probability distribution for the three cases for the economic results

Figure 5 reports the cumulative probability distributions for the Specific Unit Cost for the three cases. Like the plant efficiency results, the three cumulative probability distributions do not intersect at any point, confirming the superior economic performance of Case C already highlighted by the deterministic analysis.

5. Conclusions

The research effort presented in this paper focuses on the inclusion of uncertainties in the techno-economic evaluation of ORC power plants. The Monte Carlo simulation technique was employed to quantify the impact of uncertainties associated with three different expanders on key techno-economic performance outputs (plant efficiency and specific unit cost). By including uncertainties in the techno-economic evaluation of the three plant options, it was found that the plant efficiency was equally likely to be lower or higher than the deterministic value for Cases A and C, while it could exceed the forecasted value with an 85% probability in Case B. The economic results are indicative of how the probability distribution of specific unit cost is affected by the uncertainty in the expander performance and confirm that the two-stage turbine outperforms the other

two cases. Overall, a considerable variability of the output metrics was highlighted compared to the results from the deterministic analysis. A full spectrum of possible outputs was made available, rather than exact figures. This type of analysis allows the decision-maker to make more informed decisions on the evaluation of the ORC technology and, in particular, on what options to pursue for further R&D activities by establishing the least expensive and the best-performing solution among those analysed.

References

M. Astolfi, 2015, Techno-economic Optimization of Low Temperature CSP Systems Based on ORC with Screw Expanders, Energy Procedia, 69, 1100-1112.
A.W. Costall, A. Gonzalez Hernandez, P.J. Newton, R.F. Martinez-Botas, 2015, Design methodology for radial turbo expanders in mobile organic Rankine cycle applications, Applied Energy, 157, 729-743.
G. Di Lorenzo, P. Pilidis, J. Witton, D. Probert, 2012, A Framework for the Evaluation of Investments in Clean Power-Technologies, Computer Aided Chemical Engineering, 30, 492-496.
G. Di Lorenzo, A. Giovannelli, P. Bartocci, F. Fantozzi, 2019, Comparison of Mini Organic Rankine Cycle Plants for Waste Heat Recovery, AIP Conference Proceedings 2191, 020066.
A. Giovannelli, E.M. Archilei, C. Salvini, 2019, Full-admission radial turbine for waste heat recovery organic Rankine cycles, Energy Reports, https://doi.org/10.1016/j.egyr.2019.09.043.
S. Han, J.B. Seo, B.-S. Choi, 2014, Development of a 200 kW ORC radial turbine for waste heat recovery, Journal of Mechanical Science and Technology, 28, 12, 5231-5241.
S.-W. Hsu, H.-W.D. Chiang, C.-W. Yen, 2014, Experimental investigation of the performance of a hermetic screw-expander organic rankine cycle, Energies, 7, 9, 6172-6185.
S.H. Kang, 2012, Design and experimental study of ORC (organic Rankine cycle) and radial turbine using R245fa working fluid, Energy, 41, 1, 514-524.
S.H. Kang, 2016, Design and preliminary tests of ORC (organic Rankine cycle) with two-stage radial turbine, Energy, 96, 142-154.
Y.-R. Lee, L.-W. Liu, Y.-Y. Chang, J.-C. Hsieh, 2017, Development and application of a 200 kW ORC generator system for energy recovery in chemical processes, Energy Procedia, 129, 519-526.
E. W. Lemmon, M. O. McLinden and M. L. Huber, 2002, NIST Reference Fluid Thermodynamic and Transport Properties – REFPROP, NIST Standard Reference Database 23, Version 7.0.
M. Maccapani, R.S.R. Khan, P.J. Burgmann, G. Di Lorenzo, S.O.T. Ogaji, P. Pilidis, I. Bennett, 2014, A TERA based comparison of heavy duty engines and their artificial design variants for liquified natural gas service, Journal of Engineering for Gas Turbines and Power, 136, 2, 022001.
P. Platell, 1993, Displacement expanders for small-scale cogeneration, Lic. Thesis, KTH Stockholm.
L. Shao, J. Zhu, X. Meng, X. Wei, X. Ma, 2017, Experimental study of an organic Rankine cycle system with radial inflow turbine and R123, Applied Thermal Engineering, 124, 940-947.
N. Stošić, I.K. Smith, A. Kovačević, C.A. Aldis, 1997, The Design of a Twin-screw Compressor Based on a New Rotor Profile, Journal of Engineering Design, 8, 4, 389-399.
T. Sung, E. Yun, H.D. Kim, S.Y. Yoon, B.S. Choi, K. Kim, J. Kim, Y.B. Jung, K.C. Kim, 2016, Performance characteristics of a 200-kW organic Rankine cycle system in a steel processing plant, Applied Energy, 183, 623-635.
B.F. Tchanche, G. Lambrinos, A. Frangoudakis, G. Papadakis, 2011, Low-grade heat conversion into power using organic Rankine cycles–a review of various applications, Renewable and Sustainable Energy Reviews, 15, 8, 3963-3979.
L. Tocci, T. Pal, I. Pesmazoglou and B. Franchetti, 2017, Small Scale Organic Rankine Cycle (ORC): A Techno-Economic Review, Energies, 10, 4, 413.
C. S. Wong, D. Meyer, S. Krumdieck, 2013, Selection and conversion of turbo-expander for organic Rankine cycle (ORC), 35th New Zeland Geothermal Workshop Proceedings, 17-20 November 2013, Rotorua, New Zeland.

Sauro Pierucci, Flavio Manenti, Giulia Bozzano, Davide Manca (Eds.)
Proceedings of the 30th European Symposium on Computer Aided Process Engineering
(ESCAPE30), May 24-27, 2020, Milano, Italy.
http://dx.doi.org/10.1016/B978-0-12-823377-1.50257-3

Optimum Installation of Heat Recovery Devices in Biomass Boiler

Somchart Chantasiriwan

Department of Mechanical Engineering, Thammasat University, Pathum Thani 12121, Thailand
somchart@engr.tu.ac.th

Abstract

Biomass boiler uses thermal energy from the combustion of biomass fuel and air to produce superheated steam from feed water. Biomass fuel usually has a high moisture content, which leads to low boiler efficiency. The boiler efficiency can be increased by using heat recovery devices to decrease the temperature of flue gas before it is exhausted from the boiler. Three heat recovery devices found in a typical installation of biomass boiler are economizer, air heater, and flue gas dryer. Economizer increases feed water temperature, air heater increases air temperature before combustion, and flue gas dryer decreases the moisture content of fuel. Limited available thermal energy of flue gas means that a decision must made in selecting the sizes of these devices. The main objective of this paper is to use a biomass boiler model, in which the boiler consists of as a furnace and a set of heat exchangers, to determine the optimum sizes of economizer, air heater, and flue gas dryer that minimize the total cost of installing them in biomass boiler system.

Keywords: Heat exchangers, Biomass drying, Energy system, Modelling

1. Introduction

Biomass fuels are usually characterized by high-moisture content. Combustion of a moist fuel in a biomass boiler results in low boiler efficiency because a large amount of thermal energy released from fuel combustion is required for the evaporation of moisture in the fuel. Drying of fuel requires an energy source. A high-temperature source like flue gas seems to be ideal for this purpose. Flue gas dryer is a heat recovery device that may be installed in a boiler to decrease flue gas temperature and increase boiler efficiency. Other heat recovery devices that are normally installed in a boiler are economizer and air heater. Thermal energy from flue gas increases feed water temperature in economizer and air temperature in air heater. All three heat recovery devices can effectively increase boiler efficiency. However, since all three devices require thermal energy from flue gas, there are limits to their sizes if they are installed together in a biomass boiler.

Studies of integrating flue gas dryer into biomass boiler system have been carried out by several investigators. Andersson et al. (2006) evaluated different methods of drying biomass in a pulp mill, and found that flue gas dryer was the most attractive. Sosa-Arnao and Nebra (2009) analyzed different energy recovery configurations in boilers fired by bagasse, and showed that the configuration consisting of economizer, air heater, and flue gas dryer had the lowest optimized cost. Li et al. (2012) compared energy saving resulting from the integration of flue gas dryer in a power plant that used pine

chips as fuel and the cost of drying, and concluded that 3 - 4 years of operation was expected to give a return on the investment. Gebreegziabher et al. (2014) proposed a multi-stage process for biomass drying that combines hot air dryer, superheated steam dryer, and flue gas dryer. Liu (2017) determined the limit for the cost of flue gas dryer under which the integration of the dryer was economically justified. Although some previous works have considered the economic aspect of the integration of flue gas dryer and the comparison between flue gas dryer and other dryers, none of the previous works have considered the constraint of flue gas dryer installation in presence of economizer and air heater and the optimum installation of these devices.

In this paper, a model of biomass boiler is used to determine the optimum installation of heat recovery devices in biomass boiler. The boiler is required to generate superheated steam at specified flow rate, pressure, and temperature. It is shown that, under the constraint that boiler efficiency is fixed, there are the optimum sizes of economizer, air heater, and flue gas dryer that minimize the total cost of installing these devices.

2. Biomass boiler system

Analysis of a thermal energy system usually requires a boiler model. A widely used model is the black-box model. This model considers only the inputs to the boiler, which are feed water, fuel, and air, and the outputs, which are superheated steam and flue gas. Using this model requires that either boiler efficiency or flue gas temperature is known. Although the black-box model is sufficient in an analysis that does not consider effects of heating surface areas, it is insufficient for the current investigation. A more suitable model must take into account components of the boiler. An illustration of biomass boiler system with flue gas dryer is shown in Fig. 1. Solid lines denote fuel, air, and flue gas, whereas and dashed lines denote feed water and steam. The main components of the system are furnace (F), evaporator (EV), steam drum (SD), superheater (SH), boiler bank (BB), economizer (EC), air heater (AH), and flue gas dryer (FD).

Combustion of fuel in F results in thermal energy that is used to evaporate water in EV and increase steam temperature in SH from the saturated steam temperature (T_v) to T_s. Flue gas leaving F at T_{g1} flows successively SH, BB, EC, AH, and FD, and its temperature is reduced, respectively, to T_{g2}, T_{g3}, T_{g4}, T_{g5}, and T_{g6}. Heat transfer from flue gas causes the increase of feed water temperature from T_{wi} to T_{we} in EC, the increase of air temperature from T_{ai} to T_{ae} in AH, the increase of fuel temperature from T_{ai} to T_f, and the reduction of fuel moisture content from x_{Mi} to x_M in FD. Subcooled feed water at a mass flow rate m_w from EC and saturated steam at mass flow rates m_{s1} and m_{s2} from EV and BB enter SD, which returns saturated liquid water at the same mass flow rates to EV and BB, and sends saturated steam at a mass flow rate m_s to SH. Water evaporation in EV is due to radiative heat transfer from flue gas in F, whereas water evaporation in BB is due to convective heat transfer from flue gas. In order to maintain the concentration of dissolved solids in feed water at a safe level, it is assumed that some of the feed water is blowdown water. It should be noted that, in an actual operation, the inputs to SD from EV and BB are mixtures of saturated steam and saturated liquid water, which are separated in SD. In other words, most saturated liquid water is recirculated through SD. In this simplified model, the recirculated saturated liquid water is ignored, and inputs to SD from EV and BB are assumed to be saturated steam. Mathematical models for F, EV, SD, SH, BB, EC, and AH are provided by Chantasiriwan (2019).

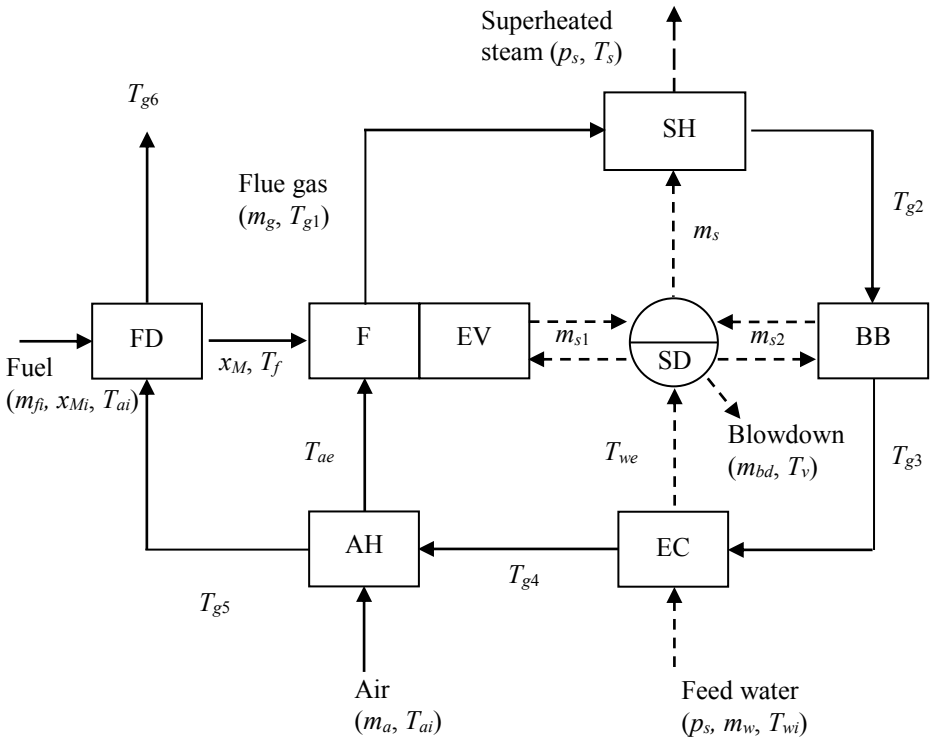

Figure 1. Bagasse boiler model.

The model of FD is shown in Fig. 2. Assume that fuel is divided into 2 parts with mass fractions y and $(1 - y)$. The mass fraction y of fuel is completely dried in FD, as reported in Eq. (1).

$$y = \frac{m_g c_{pg}\left(T_{g5} - T_{g6}\right)}{m_{fi}\left\{\left[\left(1 - x_{Mi}\right)c_{pf} + x_{Mi}c_{pw}\right]\left(T_{g6} - T_a\right) + x_{Mi}\left[c_{pw}\left(T_r - T_{g6}\right) + \Delta i_r + c_{pv}\left(T_{g6} - T_r\right)\right]\right\}} \tag{1}$$

where c_{pg}, c_{pf}, c_{pw}, and c_{pv} are specific heat capacities of flue gas, fuel, water, and vapor, T_r is the reference temperature (25°C), and Δi_r is the latent heat of evaporation at the reference temperature. The dried fuel is then mixed with the rest of the fuel. The mass flow rate, the moisture content, and the temperature of fuel at the dryer outlet are determined from Eqs. (2) – (4).

$$m_f = m_{fi} - y m_{fi} x_{Mi} \tag{2}$$

$$x_M = \frac{\left(1 - y\right)x_{Mi} m_{fi}}{m_f} \tag{3}$$

$$T_f = \frac{m_{fi}\left\{c_{pf}(1-x_{Mi})\left[yT_{g6}+(1-y)T_a\right]+c_{pw}(1-y)x_{Mi}T_a\right\}}{m_f\left[c_{pf}(1-x_M)+c_{pw}x_M\right]} \tag{4}$$

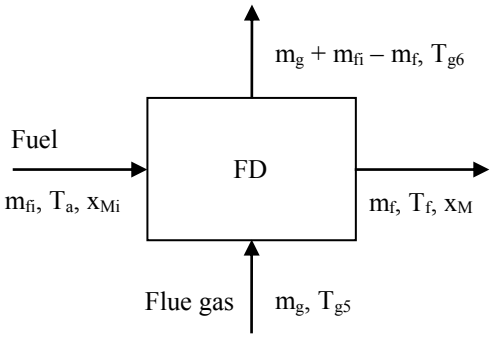

Figure 2. Flue gas dryer model.

Heating surface areas of F are A_v and A_t, whereas A_{SH}, A_{BB}, A_{EC}, and A_{AH} are, respectively, heating surface areas of SH, BB, EC, and AH. Unlike these heat exchangers, which are characterized by heating surface areas, FD is characterized by the amount of moisture removed from fuel (M) in kg/h, which is determined from Eq. (5).

$$M = 3600 y x_{Mi} m_{fi} \tag{5}$$

3. Optimization procedure

The 25 primary variables in this boiler system are A_v, A_t, A_{SH}, A_{BB}, A_{EC}, A_{AH}, M, p_s, T_s, m_s, m_{s2}, m_{fi}, m_a, x_{Mi}, x_M, T_{ai}, T_{ae}, T_{wi}, T_{we}, T_{g1}, T_{g2}, T_{g3}, T_{g4}, T_{g5}, and T_{g6}. The other variables are secondary variables, which may be expressed in terms of primary variables. The system is governed by 12 energy and heat transfer equations. Therefore, the values of 13 primary variables must be specified values so that the solution of the system can be found. Known variables are A_v, A_t, A_{SH}, A_{BB}, A_{EC}, A_{AH}, M, p_s, m_{fi}, m_a, x_{Mi}, T_{ai}, and T_{wi} in a boiler system analysis. In a boiler design for the minimum installation cost of heat recovery devices, however, A_{EC}, A_{AH}, and M are unknown, and must be determined for given design conditions, which include a fixed value of boiler efficiency. Boiler efficiency (η) is defined in Eq. (6).

$$\eta = \frac{m_s\left(h_s - h_{fw}\right)}{m_f HHV} \tag{6}$$

where m_s is the mass flow rate of steam, h_s is the enthalpy of superheated steam at pressure p_s and temperature T_s, h_{fw} is the enthalpy of feed water, m_f is the mass flow rate of fuel, and HHV is the fuel higher heating value. This design requires the specified values of m_s and T_s. The other known variables are A_v, A_t, A_{BB}, A_{EC}, M, p_s, m_a, x_{Mi}, T_{ai}, and T_{wi}. In order to find the minimum installation cost, only A_{EC} and M are allowed to vary. As a result, heating surface area A_{AH} becomes a function of A_{EC} and M. It is assumed that the nominal unit installation costs of economizer and air heater are, respectively, 120 \$/m^2, and 100 \$/m^2. Furthermore, the unit installation cost of flue gas

dryer is assumed to be 50 $/(kg/h). Therefore, the total installation cost of heat recovery devices is determined from Eq. (7).

$$C_{total} = 120A_{EC} + 100A_{AH} + 50M \tag{7}$$

The minimum value of C_{total} corresponds to the optimum values of A_{EC} and M.

4. Results and discussion

The fuel for the boiler system is bagasse of which composition is provided by Rein (2017). The boiler design parameters are p_s = 4.5 MPa, T_s = 500°C, and m_s = 100 kg/s. The fuel moisture content is 52%. The inlet air and fuel temperatures are 30°C. The inlet feed water temperature is 120°C.

By fixing η at 70%, it is found that A_{AH} decreases as either A_{EC} or M increases. Furthermore, C_{total} varies with only A_{EC} and M. The minimum value of C_{total} may be found by using a line-search method. First, the optimum value of A_{EC} that yields the minimum installation cost at a specified value of M ($C_{min,M}$) is determined. Figure 3 shows variations of C_{total} with A_{EC} for four values of M. $C_{min,M}$ is found to be \$1.144 × 10^6, \$1.128 × 10^6, \$1.124 × 10^6, and \$1.132 × 10^6 for M = 0, 2000, 4000, and 6000 kg/h, respectively. Next, $C_{min,M}$ is plotted as a function of M as shown in Fig. 4. It can be seen that the minimum installation cost (C_{min}) of \$1.125 × 10^6 results from the optimum value of 3550 kg/h for M. The corresponding values of A_{EC} and A_{AH} are, respectively, 4685 m^2 and 3844 m^2. Therefore, the installation of flue gas dryer in addition to economizer and air heater results in 1.7% less total installation cost than the installation of only economizer and air heater. It should be noted that this result is obtained for the value of 50 $/(kg/h) for the unit cost of flue gas dryer. The minimum installation cost is quite sensitive to the unit cost of flue gas dryer. When the unit cost reaches 61 $/(kg/h), the installation of flue gas dryer is not justified because C_{min} is equal to $C_{min,0}$, and the installation of flue gas dyer increases the total installation cost.

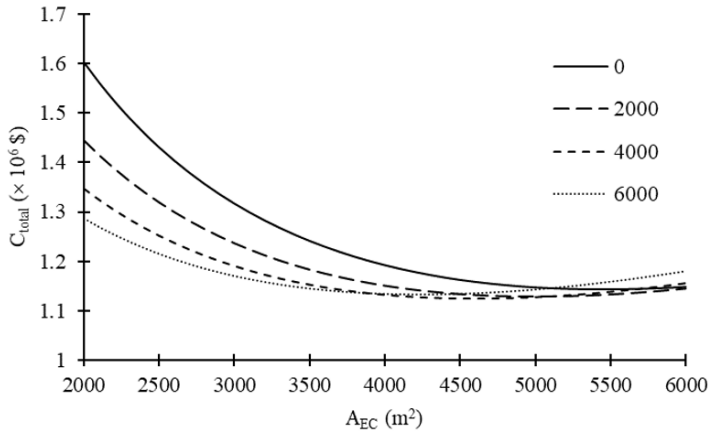

Figure 3. Variations of total installation cost (*Ctotal*) with the economizer surface area (*AEC*) and the amount of removed moisture (*M*).

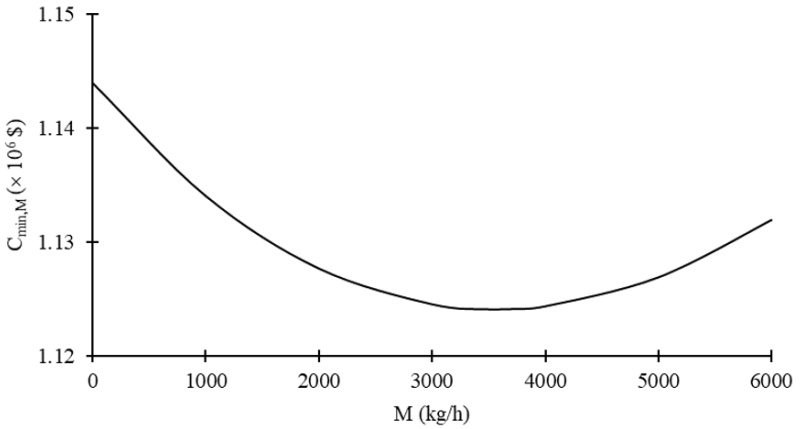

Figure 4. Variation of minimum installation cost at a fixed M value ($C_{min,M}$) with M.

5. Conclusion

Three heat recovery devices that may be installed in a biomass boiler are economizer, air heater, and flue gas dryer. They decrease flue gas temperature, and increase boiler efficiency. Since all three devices require thermal energy from high-temperature flue gas that results from combustion of biomass fuel, there are limits to the sizes of these devices under given boiler operating conditions if they are installed together. For a fixed value of 70% for the boiler efficiency, a boiler model can be used to demonstrate that there are the optimum sizes of these devices that result in the minimum installation cost. Simulation results indicate that the optimum installation of economizer, air heater, and flue gas dryer can reduce the installation cost by 1.7% compared with a non-optimum installation, in which there are only economizer and air heater. Cost reduction increases with decreasing unit cost of dryer.

References

E. Andersson, S. Harvey, T. Berntsson, 2006, Energy efficient upgrading of biofuel integrated with a pulp mill, Energy, 31, 1384-1394.

S. Chantasiriwan, 2019, Effects of heating surface areas on the performance of bagasse boiler, Chemical Engineering Transactions, 74, 139-144.

T. Gebreegziabher, A. O. Oyedun, Z. Yu, W. Maojian, Z. Yi, L. Jin, C. W. Hui, 2014, Biomass drying for an integrated power plant: Effective utilization of waste heat, Computer Aided Chemical Engineering, 33, 1555-1560.

H. Li, Q. Chen, X. Zhang, K. N. Finney, V. N. Sharifi, J. Swithenbank, 2012, Evaluation of a biomass drying process using waste heat from process industries: A case study, Applied Thermal Engineering, 35, 71-80.

M. Liu, X. Zhang, X. Han, G. Li, J. Yan, 2017, Using pre-drying technology to improve the exergetic efficiency of bioenergy utilization process with combustion: A case study of a power plant, Applied Thermal Engineering, 127, 1416-1426.

P. Rein, 2017, Cane Sugar Engineering, 2nd Ed., Verlag, Berlin.

J. H. Sosa-Arnao, S. A. Nebra, 2009, Bagasse dryer role in the energy recovery of water tube boilers, Drying Technology, 27, 587-594.

Sauro Pierucci, Flavio Manenti, Giulia Bozzano, Davide Manca (Eds.)
Proceedings of the 30th European Symposium on Computer Aided Process Engineering (ESCAPE30), May 24-27, 2020, Milano, Italy.
http://dx.doi.org/10.1016/B978-0-12-823377-1.50258-5

Thermogravimetric Analysis of Individual Food Waste Items and their Blends for Biochar Production

Samar Elkhalifa,[a] Omar Elhassan,[c] Prakash Parthasarathy,[a] Hamish Mackey,[a] Tareq Al-Ansari, [a,b] , Gordon McKay[a]*

[a]*Divison of Sustainable Development, College of Science and Engineering, Hamad Bin Khalifa University, Qatar Foundation, Doha, Qatar.*

[b]*Division of Engineering Management and Decision Sciences, College of Science and Engineering, Hamad Bin Khalifa University, Doha, Qatar.*

[c]*Qatar Environment and Energy Institute, Doha, Qatar.*

gmckay@hbku.edu.qa

Abstract

Food waste is generated in enormous quantities globally. Due to its organic- and nutrient-rich composition, food waste is a potential feedstock for the production of energy and value-added products. In many countries, food wastes are currently landfilled or incinerated together with other combustible municipal wastes for possible recovery of energy, but these two approaches are facing more and more economic and environmental pressures. Moreover, food waste can be converted into energy using waste to energy technologies. The use of thermochemical technologies has become an acceptable practice that is undergoing widespread research. The ultimate goal of the current research work is to produce value-added biochar products from food waste, hence providing an option to tackle the previously addressed problems of effective waste management. Prior to the production of biochars, three selected food items are studied under Thermogravimetric analysis (TGA). The analysis involves the single food items, a binary mixture, and a blend of the three. The studied food wastes are tomatoes, cucumbers, and carrots. Moreover, TGA revolves around measuring the weight of sample continuously in a controlled temperature program. This, in turn, allows the physical and chemical properties of the sample to be obtained based on the variation of sample weight with respect to time and temperature using the DTG curve resulting from a differential TGA curve. The TGA technique can be helpful in determining the proximate analysis of food waste and to find out the thermal characteristics like ignition, burnout temperature and chemical kinetics of food waste by using the pyrolysis process. The results of TGA are of key importance as they suggest the thermal degradation patterns of food waste, and bio-char under air or an inert environment for succeeding kinetic studies. The configurations explain the response of heating rate, food waste properties, stability and compatibility of food waste to different processes. Furthermore, the results of the different experimental runs and TGA modelling are presented, analyzed and discussed. Very little information is available on the pyrolysis and understanding of individual food waste components.

Keywords: TGA, Food Waste, Modelling, Pyrolysis, Biochar.

1. Introduction

Thermogravimetric analysis (TGA) is based on the weight loss and the heat transfer rate of material and therefore the derivative difference peaks of each specific elements (e.g. C or N) are not available, which are key components for the characterization of biochar (Li & Chen, 2018).

Previous studies have investigated the TGA of different biomass waste like food waste (Jo et al., 2017), apricots stones (Nocera et al., 2016), and biosolids and plant-based biomass waste (Li & Chen, 2018). However, the use of mixed food items and binary mixtures have not been fully explored. The motivation behind the use of food waste is the huge quantities generated (Elkhalifa et al., 2019a), in addition to the unique properties of the value-added products produced from their conversion using waste to energy conversion methods such as pyrolysis (Elkhalifa et al., 2019b). Thus, this paper aims to investigate the TGA of different widely used food waste products and their different interactions and behavior. In particular, the study looks at tomatoes, cucumbers and carrots and their single, binary and ternary blends and mixtures.

2. Materials and Methods

In order to study the interaction between the components, all permutations of binary and tertiary mixture of components, which are mixed in an equal proportion by weight are prepared for TG analyses. Slow pyrolysis, which occurs at low heating rates, moderate temperatures and long residence times, was carried out in the presence of a nitrogen atmosphere until a temperature of 800 °C was reached. The effect of different heating rates (5 and 10 °C/min) has been studied.

2.1. Feedstock and Production of Biochar

The raw feedstock samples (i.e. carrots, cucumber and tomatoes) were oven-dried at 140 °C for 24 h before being chopped into smaller chunks. The dried samples were then ground to finer particles making them ready for TGA.

2.2. Thermogravimetric Analysis (TGA)

Both the feedstock and products of the pyrolysis were analyzed under inert atmosphere using a TA Discovery thermogravimetric analyzer with a continuous nitrogen flow of 100 ml/min. The TG analyzer was used to obtain the simultaneous mass loss and differential mass profile of the samples with respect to time and temperature.

Around 10 mg of the sample was weighed for the thermal weight-change analysis. Additionally, the temperature ramp was set as follows: (1) temperature equilibrium at 30 °C linearly heated to 100 °C at two different constant heating rates: 5 and 10 °C/min; (2) isotherm at 100 °C for 10 min; (3) two ramping rate of ramping of 5 and 10 °C/min from 100 °C to 800 °C.

An attached mass spectrometer was able to monitor the evolving gas samples while the TGA measured the thermal decomposition of the feedstock and biochar by monitoring the weight loss.

2.3. Kinetics Analysis Using the Friedman Method

The TGA/DTGA curves were then evaluated using the Friedman kinetics method that is described in White et al. (2011). The method determines the Arrhenius kinetic parameters from the non-isothermal TGA measurements as follows in Eq. (1):

$$\ln\left(\frac{d\alpha}{dt}\right) = \ln\left[HR\left(\frac{d\alpha}{dT}\right)\right] = \ln\left(A\left(1-\alpha\right)\right) - \frac{Ea}{RT} \tag{1}$$

Where α is the conversion degree of biomass and is computed from the TGA measurement of mass; t is the time, HR(dT/dt) is a linear heating rate; T is the absolute temperature; A is the frequency factor; Ea is the activation energy, and R is the universal constant of the ideal gases. Plotting ln(dα/dt) as a function of 1/T produces a straight line from which the activation energy can be obtained from the slope while the frequency factor can be obtained from the intercept of the equation.

3. Results and Discussion

Mass loss profiles, temperature ranges, and kinetic parameters of the decomposition of each component are presented in this section along with the approximate analysis that was also generated using TGA. Figure 1-3 show, for both food products and their blends, the mass loss (TGA) and the derivative of mass loss (DTGA) as a function of the pyrolysis temperature. The 3 figures are constructed based on the use of 2 different heating rates: 5 °C/min and 10 °C/min. Moreover, the approach for the kinetics analyses was demonstrated on the same selected food waste samples and for the hemicellulose decomposition region only.

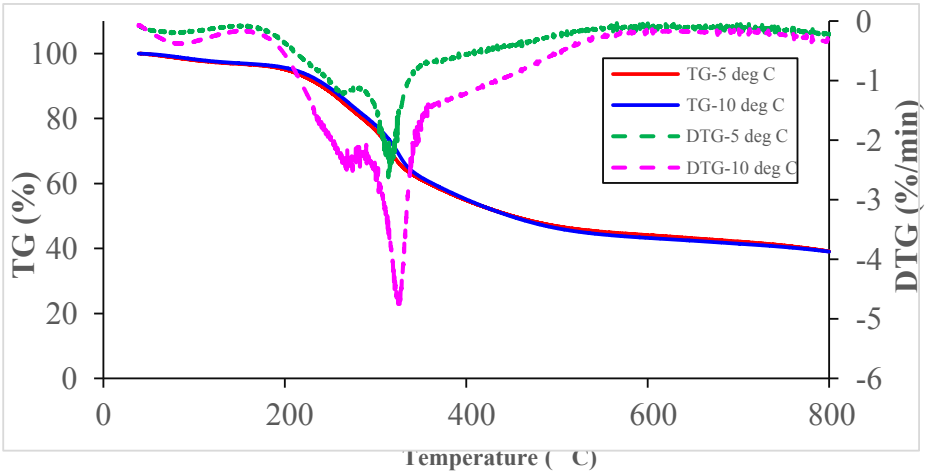

Figure 1. TGA/DTGA of the cucumber sample at heating rates of 5 °C/min and 10 °C

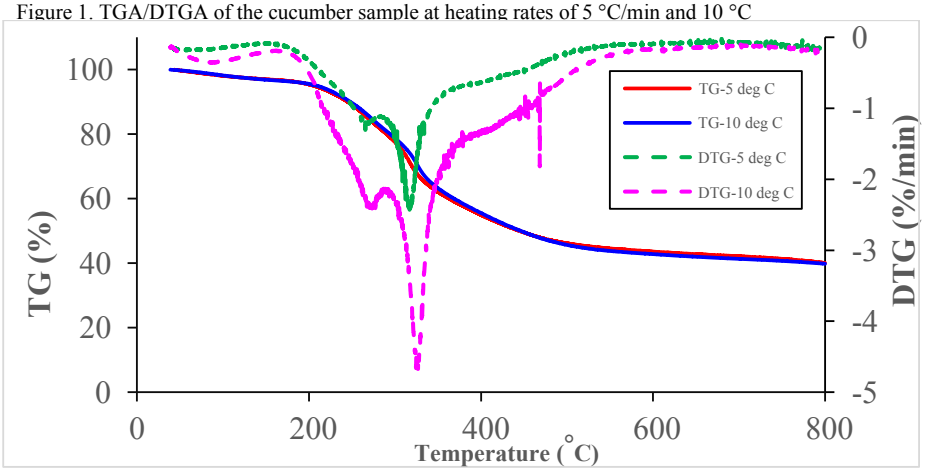

Figure 2. TGA/DTGA of the tomato sample at heating rates of 5 °C/min and 10 °C/min

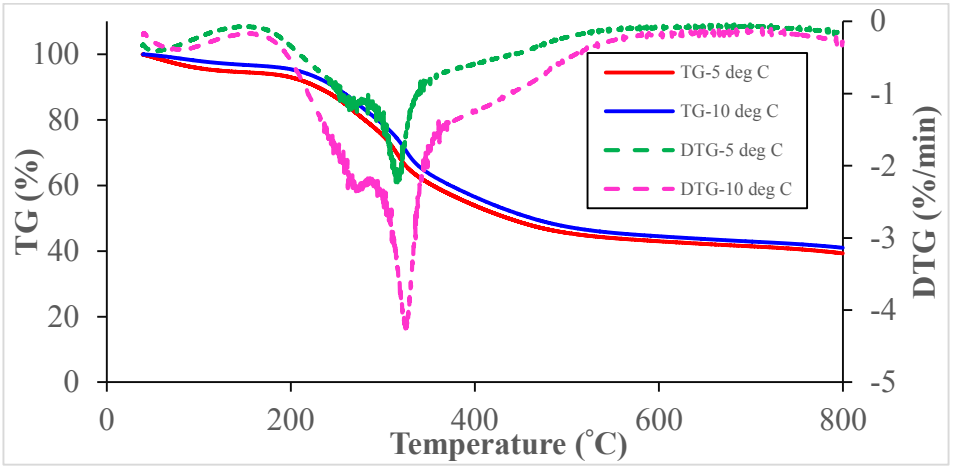

Figure 3. TGA/DTGA of the cucumber and tomato sample at heating rates of 5 °C/min and 10 °C/min

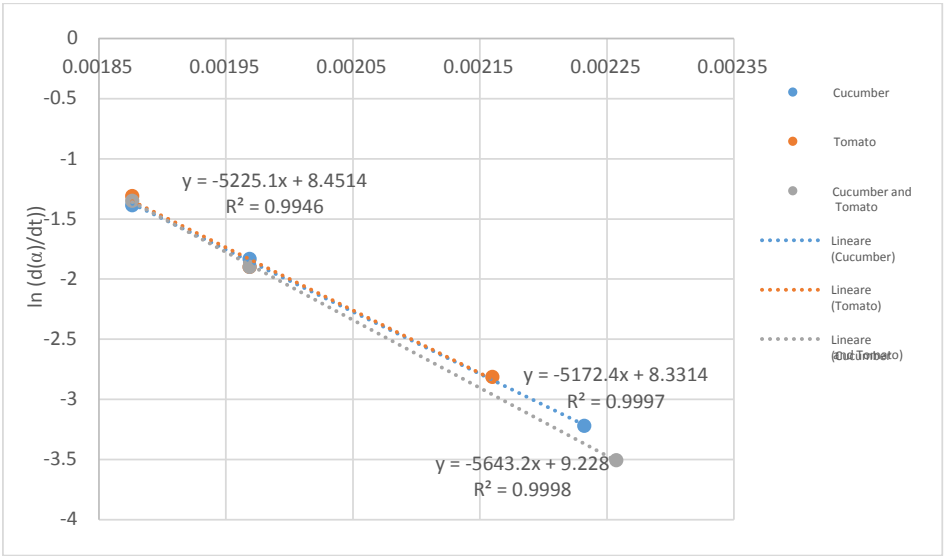

Figure 4. Results of the kinetics calculations using the Friedman method and the TGA/DTGA

Table 1. Proximate analysis of the raw materials (air-dried basis)

Vegetables	Moisture content (wt. %)	Volatile matter (wt. %)	Fixed carbon* (wt. %)	Ash content (wt. %)
Cucumber	8.32	63.97	25.87	1.84
Tomato	5.24	76.24	14.00	4.52
Carrot	8.75	80.14	5.87	5.24

*calculated by difference

Table 2. The kinetic parameters for hemicellulose decomposition region for selected samples

Sample	T_1 (°C)	T_2 (°C)	Conversion	Ea (kJ/mol.K)	A (min^{-1})
Cucumber	175.0	260.0	8.3-28.3%	43.0	4151.5
Tomato	190.0	260.0	8.3-25.0%	43.4	4680.9
Cucumber and Tomato	170.0	260.0	8.3-25.0%	46.9	10177.4

As can be seen from the figures, for both heating rates, the total weight loss at the final temperature is approximately 60-72%, however the larger part of biomass volatilization occurs between 200 °C and 500 °C. The volatilization of biomass can be attributed to the presence and thermal decomposition of three main biomass components, namely: lignin, cellulose and hemicellulose. These components are known to have a great influence on the behavior of the pyrolysis process (Hu et al., 2007).

Moreover, the occurrence of some peaks is observed in the DTGA curves, which represent maximum points of the reaction rates for both heating rates. The first peak is observed around 100 °C and is attributed to the moisture evaporation, which is associated with very low weight loss around 2-4%. The second peak of DTGA occurs at around 260 °C for both 5 °C/ min and 10 °C/min. This peak is primarily associated with hemicellulose pyrolysis. According to other studies that are found in the scientific literature, hemicellulose decomposes in the range 160 °C and 300 °C for orange peel residues (Aguiar et al., 2008), olive oil pomace (Özveren & Özdoğan, 2013), and biomass residuals mixtures with lignite (Vamvuka et al., 2003). The third peak of interest occurs at around 310 °C for both heating rates. This peak is mainly associated with cellulose, which normally degrades at high temperatures around 300 °C – 400 °C (Yang et al., 2007). Additionally, lignin is the first biomass component to decompose at low temperatures, however the degradation of this component takes place at very low rates and hence it continues for 800 °C. This indicates that a very small part of the second and third peaks of the DTGA curves are associated with the decomposition of lignin (Font et al., 2009). Furthermore, the results of the studies indicated some similarities between the two heating rates used in this study. The mass loss trends, amounts and peaks were very similar throughout all the samples. Differences in the DTGA peaks, for both heating rates, are negligible. According to the literature, however, varying the heating rate has a major influence on DTGA curves (Ounas et al., 2011). It should be noted that these low heating rates were chosen to study the slow pyrolysis which produces higher yields of the desired biochar product. The findings indicate that both heating rates are capable of producing the same TGA and DTGA curves. Hence, it is recommended to explore the effect of lower heating rates (e.g. 1 °C/min) and higher heating rates (e.g. 20 °C/min) to arrive at a better understanding of the behavior of the pyrolysis process in relation to the heating rates that are employed in the study.

With respect to the kinetics results, the Friedman method allowed the computation of both the activation energy and frequency factors as shown in Table 2 when assuming a first order reaction. In order to demonstrate the approach, the kinetics were only evaluated at the region of hemicellulose decomposition until the maximum decomposition is reached. As can be noticed, the activation energy was almost constant for the three samples with slight variations for the binary mixture, while the frequency factor increased significantly in the mixed binary sample. The activation energies of the two single component systems are 43 kJ/mol, but for the binary system there appears to be some form of interaction as the Ea value is slightly higher at 47 kJ/mol.

4. Conclusion

The current work is concerned with the understanding of the pyrolysis process and the production of biochars from food waste. The TGA is a convenient method that facilitates the understanding of such systems. The results of the use of two distinct heating rates indicated that further research is required employing higher and lower heating rates since both heating rates for slow pyrolysis generated identical TGA/DTGA results. According to the results, the peaks of hemicellulose and cellulose decomposition occurred at ranges typical to those reported in the literature. Finally, the kinetics analysis revealed that the interactions between the binary mixtures resulted in an activation energy of a similar magnitude to the energies of the individual food wastes, while the frequency factor was almost doubled.

References

L. Aguiar, F. Márquez-Montesinos, A. Gonzalo, J. L. Sánchez, & J. Arauzo, 2008, Influence of temperature and particle size on the fixed bed pyrolysis of orange peel residues. Journal of Analytical and Applied Pyrolysis, 83, 124–130. https://doi.org/10.1016/j.jaap.2008.06.009

S. Elkhalifa, T. Al-Ansari, H. R. Mackey, & G. McKay, 2019a, Food waste to biochars through pyrolysis: A review. Resources, Conservation and Recycling, 144. https://doi.org/10.1016/j.resconrec.2019.01.024

S. Elkhalifa, A. AlNouss, T. Al-Ansari, H. R. Mackey, P. Parthasarathy & G. Mckay, 2019b, Simulation of Food Waste Pyrolysis for the Production of Biochar: A Qatar Case Study. In Computer Aided Chemical Engineering (pp. 901–906). https://doi.org/10.1016/B978-0-12-818634-3.50151-X

R. Font, J. Moltó, A. Gálvez, & M.D. Rey, 2009, Kinetic study of the pyrolysis and combustion of tomato plant. Journal of Analytical and Applied Pyrolysis, 85, 268–275. https://doi.org/10.1016/j.jaap.2008.11.026

S. Hu, A. Jess, & M. Xu, 2007, Kinetic study of Chinese biomass slow pyrolysis: Comparison of different kinetic models. Fuel, 86, 2778–2788. https://doi.org/10.1016/j.fuel.2007.02.031

J. H. Jo, S. S. Kim, J. W. Shim, Y.E. Lee, & Y.S. Yoo, 2017, Pyrolysis characteristics and kinetics of food wastes. Energies. https://doi.org/10.3390/en10081191

S. Li, & G. Chen, 2018, Thermogravimetric, thermochemical, and infrared spectral characterization of feedstocks and biochar derived at different pyrolysis temperatures. Waste Management, 78, 198–207. https://doi.org/10.1016/j.wasman.2018.05.048

F. Nocera, A. Gagliano, F. Patania, M. Bruno, & S. Scirè, 2016, Slow pyrolysis kinetics of apricots stones by thermogravimetric analysis. In IREC 2016 - 7th International Renewable Energy Congress. https://doi.org/10.1109/IREC.2016.7478945

A. Ounas, A. Aboulkas, K. El harfi, A. Bacaoui, & A. Yaacoubi, 2011, Pyrolysis of olive residue and sugar cane bagasse: Non-isothermal thermogravimetric kinetic analysis. Bioresource Technology, 102, 11234–11238. https://doi.org/10.1016/j.biortech.2011.09.010

U. Özveren, & Z. S. Özdoğan, 2013, Investigation of the slow pyrolysis kinetics of olive oil pomace using thermo-gravimetric analysis coupled with mass spectrometry. Biomass and Bioenergy, 58, 168–179. https://doi.org/10.1016/j.biombioe.2013.08.011

D. Vamvuka, E. Kakaras, E. Kastanaki, & P. Grammelis, 2003, Pyrolysis characteristics and kinetics of biomass residuals mixtures with lignite. In Fuel (pp. 1949–1960). https://doi.org/10.1016/S0016-2361(03)00153-4

J.E. White, W. J. Catallo, & B.L. Legendre, 2011, Biomass pyrolysis kinetics: A comparative critical review with relevant agricultural residue case studies. Journal of Analytical and Applied Pyrolysis. https://doi.org/10.1016/j.jaap.2011.01.004

H. Yang, R. Yan, H. Chen, D. H. Lee, & C. Zheng, 2007, Characteristics of hemicellulose, cellulose and lignin pyrolysis. Fuel, 86, 1781–1788. https://doi.org/10.1016/j.fuel.2006.12.013

Sauro Pierucci, Flavio Manenti, Giulia Bozzano, Davide Manca (Eds.)
Proceedings of the 30th European Symposium on Computer Aided Process Engineering (ESCAPE30), May 24-27, 2020, Milano, Italy.
http://dx.doi.org/10.1016/B978-0-12-823377-1.50259-7

Analyzing Hydrogen Production Capacities to Seize Renewable Energy Surplus

Mariana Corengia, Nicolás Estefan, Ana I. Torres*

Instituto de Ingeniería Química, Facultad de Ingeniería, Universidad de la República, Montevideo, Uruguay
aitorres@fing.edu.uy

Abstract

Modern renewable energy sources such as wind or sunlight cannot be programmed to be available when needed. A robust design of electrical grids with high penetration of these usually imply the existence of energy surplus. This surplus can be taken advantage of by seeking integration with fuel hydrogen production systems. However, the surplus is neither constant nor periodic, hence there is a trade-off between usage resource and economic goals. For a given energy surplus vs time curve, this paper presents three different decision-making problems to find the optimal hydrogen production capacity that needs to be installed, and the associated hydrogen prices.

Keywords: renewable energy surplus, power to hydrogen, green fuels, optimization

1. Introduction

Decarbonization of the energy mix has two main objectives: one is the displacement of the fossil fuels from the electricity generation sector, the other one is their displacement from the transportation sector. The former can be considered at a mature stage: in many regions, electricity from wind and sunlight is already integrated into the power grid, and in some cases (e.g. Norway, Costa Rica, Uruguay) the power mix is now close to 100 % renewable (Kroposki et al., 2017; MIEM, 2018). Replacement of liquid fuels within the transportation sector lags behind. For short distance applications battery electric vehicles seem to be the most suitable solution. However, for medium-long distance or heavy load applications, battery sizes and their weight become a barrier; in these cases, electric vehicles fueled by hydrogen are promising alternatives (Hydrogen Council, 2017).

Hydrogen produced by electrolysis has several advantages over hydrogen produced by other means. First, it requires little downstream processing to be suitable for fuel cell electric vehicles (i.e. does not contain CO and other contaminants that are poisonous to the fuel cells). Second, as electrolyzers usually have fast on-off dynamics (Corengia and Torres, 2018), they can run intermittently.

The presence of large energy surplus is common in regions in which the power mix is now close to 100 % renewable, as to avoid failures due to the non-programmable nature of wind and sun, generation capabilities are usually oversized by design. In these regions, using the surplus to operate electrolyzers has been proposed to valorize the surplus. The overall renewable energy to hydrogen process is schematized in Figure 1. Power from non-programmable sources is incorporated into the electric grid when available; if the power required by users (households, industries, etc.) is larger than the amount produced,

programmable sources (such as hydroelectrical) are turned on. If users do not consume all the power produced by the non-programmable sources, the electrolyzer is turned on.

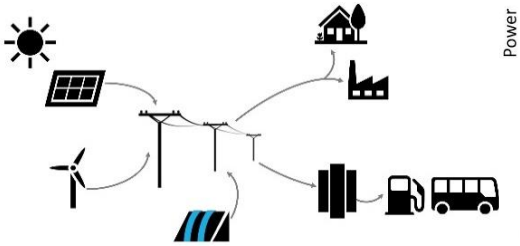

Figure 1. Schematic of the renewable energy (RE) to fuel-hydrogen process. RE is delivered to the grid whenever it is available, the electrolyzer is turned on in case of surplus.

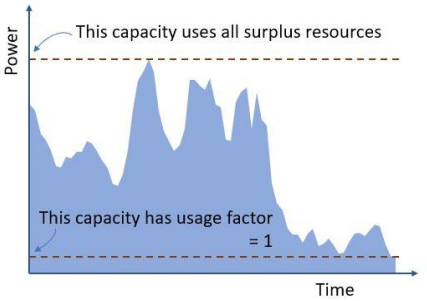

Figure 2. Energy surplus (dark area) is variable during time.

Questions pertinent to the design of hydrogen production systems include which technology to use, how many electrolyzers to install and which capacity to select. Among the technologies alkaline electrolyzers, proton exchange membranes and solid oxide cells are the most mature ones. The number of the electrolyzers to be installed and their capacity depends on the (expected) demand for hydrogen and the amount of energy that will be available. The latter largely depends on the climatic conditions as well as the consumption patterns of the region of interest. Figure 2 shows an example of variation of energy surplus with time, which, given a region, more or less cyclically repeats. As seen, there are two limiting design cases: one that takes maximum advantage of the energy surplus (low usage factor of the electrolyzer), the other takes maximum advantage of the installed capacity (low resource use).

The goal of our research is to design optimal grid-connected H_2 production plants. The novelty of the work lies in considering the energy surplus as a limiting factor, thus there is a trade-off between maximum usage of the resource and maximum usage of installed capacity. We focus on this trade off and analyze its effect on H_2 selling price and economic performance of the plant.

2. Mathematical model and relevant problem formulations

As mentioned above we will seek for economic solutions; we have chosen the Net Present Value (*NPV*) as the economic indicator. As usual, *NPV* is computed in terms of the installed equipment cost (*IC*), future revenues (*REV*) and operational expenditures (*OPEX*), assuming *N* years of operation and a discount rate *r*.

Installed equipment costs: mainly include the cost of the electrolyzer and the cost of the compressor(s) required to pressurize the hydrogen exiting to the electrolyzer to the standard vehicle charging pressures: 350 or 700 bars. These costs can be modeled as having a linear/piecewise linear dependence with production capacity (M_{H2} mass/time units) with factors to correlate H_2 mass with power ($f_{pwr,el}$ and $f_{pwr,comp}$) and investment factors ($f_{IC,el}$ and $f_{IC,comp}$) for the electrolyzer and compressor.

Revenues: are computed as the product of the hydrogen selling price ($\$_{H2}$ in USD/mass) and the total hydrogen produced during a year of operation. The latter is in turn computed

as the sum of the amount of hydrogen generated at each time step ($\dot{m}_{H2,t}$ and Δt respectively).

Operational expenditures: include the cost of energy and maintenance. Energy is consumed by the electrolyzer and the compressor(s) and depends on the amount of hydrogen generated. Maintenance costs are estimated as a fraction (f_M) of the installed equipment cost. Note that the price of energy ($\$_{energy,t}$) may be a time-dependent parameter, that varies according to local electricity tariffs.

Eqs. (1)-(4) present the mathematical formulation of these statements.

$$NPV = -IC + \sum_{i=1}^{N} \frac{REV - OPEX}{(1+r)^i} \tag{1}$$

$$IC = M_{H_2} \cdot \left(f_{pwr,el} \cdot f_{IC,el} + f_{pwr,comp} \cdot f_{IC,comp} \right) \tag{2}$$

$$REV = \$_{H_2} \cdot \sum_t \Delta t \cdot \dot{m}_{H_2,t} \tag{3}$$

$$OPEX = \sum_t \left(\Delta t \cdot \dot{m}_{H_2,t} \cdot \$_{energy,t} \cdot \left(f_{pwr,el} + f_{pwr,comp} \right) \right) + f_M \cdot IC \tag{4}$$

In addition, the designs have to guarantee that:

- At each time t the amount of H_2 produced has to be below the installed capacity.

$$\dot{m}_{H_2,t} \le M_{H_2} \tag{5}$$

- The power used for production of hydrogen and its compression cannot exceed the power that is available from the surplus of non-programmable sources (RE_t).

$$\dot{m}_{H_2,t} \cdot \left(f_{pwr,el} + f_{pwr,comp} \right) \le RE_t \tag{6}$$

- Achievement of hydrogen production targets ($H_{2,trgt}$) if required.

$$H_{2,trgt} \le \sum_t \Delta t \cdot \dot{m}_{H_2,t} \tag{7}$$

Based on these equations our interest lies in finding the answer for the following problems:

Problem 1: For a given target of H_2 selling price, find capacity and mode of operation that maximizes *NPV*.

$$\min_{M_{H_2}, \dot{m}_{H_2,t}} \; -NPV \tag{8}$$

$$\text{s.t. Eqs}: 1, 2, 3, 4, 5, 6$$

$$IC, OPEX, REV, M_{H_2}, \dot{m}_{H_2,t} \ge 0$$

Problem 2: For a given target of H_2 selling price, find capacity and mode of operation that maximizes surplus usage.

This problem formulation intends to capture the case of policy makers that would like to make maximum use of the resource without losing money.

$$\min_{M_{H_2}, \dot{m}_{H_2,t}} \sum_t RE_t - \dot{m}_{H_2,t} \cdot \left(f_{pwr,el} + f_{pwr,comp} \right) \tag{9}$$

$$\text{s.t. Eqs}: 1, 2, 3, 4, 5, 6$$

$$NPV, IC, OPEX, REV, M_{H_2}, \dot{m}_{H_2,t} \geq 0$$

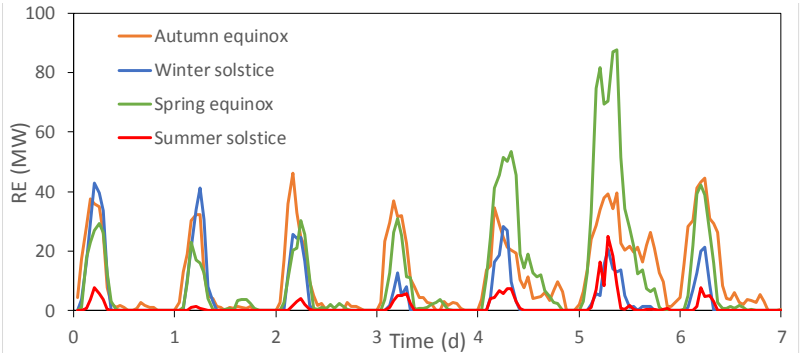

Figure 3. Surplus of renewable energy in four representative weeks.

Problem 3: Find capacity and mode of operation that minimizes the selling price of hydrogen and achieves a certain production goal.

This problem formulation again captures the case of policy makers. In this case we study the need to achieve a certain share of substitution of fossil-based fuels for long-distance transportation.

$$\min_{M_{H_2}, \dot{m}_{H_2,t}} \$_{H_2} \tag{10}$$

$$\text{s.t. Eqs}: 1, 2, 3, 4, 5, 6, 7$$

$$NPV, IC, OPEX, REV, M_{H_2}, \dot{m}_{H_2,t} \geq 0$$

The optimization problems described above were implemented in GAMS 24.8.5. It is easy to see that the first two problems are linear; the third problem is not linear as written as in this case both terms in Eq. (3) contain decision variables (price of hydrogen and flux rate). However, this problem can be linearized by considering that Eq. (7) will be always be satisfied as an equality thus the term $H_{2,target}$ (a parameter) can substitute the sum. Then, all problems are LP and were solved using CPLEX.

3. Case Study

The case study focuses in Uruguay, a country in which 98% of the electricity is generated from renewable sources: 26 % is eolic 2 % is solar (MIEM, 2018), and the next milestone is decarbonization of the transportation sector. Pilot projects for production of hydrogen for heavy duty and long-distance fleet have recently been approved.

Figure 3 shows the surplus of renewable energy in the country. The surplus was obtained in the following way: (1) we generated 100 year-long random scenarios of production of electricity from wind and solar sources using the software SimSEE version iee19.193: a locally built software that loads historical data of solar irradiance, wind speed and precipitations and simulates probable renewable electricity generation with current installed capacities; (2) we considered a representative electric energy demand for the country which is available in ADME (2019); (3) for each of the 100 scenarios we computed the non-programmable renewable energy surplus by adding wind and solar generation at each hour and subtracting the power consumed (demand) at the same time, if demand was larger than generation, a zero was placed; (4) The average of the 100 scenarios was considered. Overall, we found that the mean value of the surplus is 10

MW, with a maximum of 130 MW (in spring), and that periods without any surplus account for 37 % of the time. As expected, larger surplus usually occurs at night.

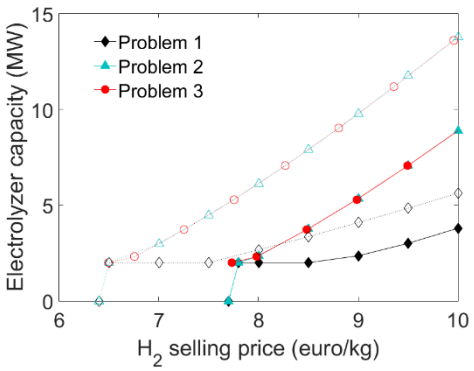

Figure 4: Optimal installed capacity vs H_2 prices. Filled/empty symbols indicate 0.022/0 euro/kWh surplus cost.

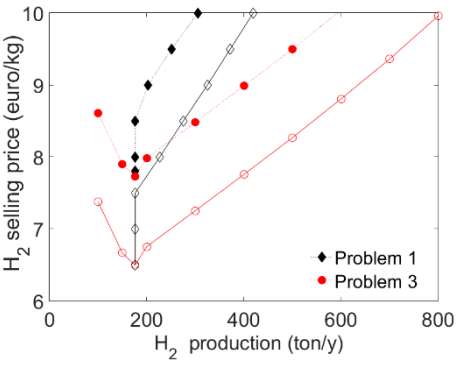

Figure 5: H_2 selling price an annual production. Filled/empty symbols indicate 0.022/0 euro/kWh surplus cost.

In terms of technologies, PEMs were selected as they provide the most flexible operation due to faster start-ups and the possibility of working under different loads. Hydrogen produced in PEMs is already partially pressurized; for design purposes we have assumed that PEM stacks self-pressurize up to 15 bar, which is conservative. The compression system was designed offline using the software Aspen Plus. From the two standard pressures used to fuel H_2-based vehicles, in this article, we have assumed service at 350 bar, as this is the most favorable situation in terms of the economics. From the compression system designs analyzed so far, a three-stage compressor with intermediate cooling provided the best performance.

4. Results and discussion

Simulations of the problems were run by considering surplus data for ten years with an hourly time step. Surplus costs in the 0-0.022 € /kWh range (usual lowest energy prices for current day-ahead Uruguayan tariffs (UTE, 2019)) were assumed. Following the electrolyzer costs in Proost (2019) we proved that the $6/10^{th}$ rule is satisfied for the cost/capacities pairs up to 2 MW reported in the paper. For multiple stacks, i.e. when more than 2 MW are needed, it can be shown that a linear relation that considers a cost of 1238 € per kW installed reasonably approximates the composite cost. Note that as mentioned in Proost (2019) this cost already includes the water demineralizer, the gas separators and vessels, the purifying system and the required peripherals. Investment costs for the compressor were estimated with Aspen Process Economics Analyzer. In both cases we assumed a location factor of 1.14. Energy consumptions were assumed as 58.2 kWh/kg H_2 for the electrolyzer (Proost, 2019) and 77 kW/kg H_2 for the compressor (Aspen simulations).

The results of the simulations are shown in Figures 4, 5 and 6. As expected H_2 selling price is the key parameter. As seen in Figure 4, the program choses to install capacity only if the H_2 selling price is above 6.5 €/kWh, this is the most favorable case and assumes that the surplus of energy is available at no cost. This threshold implies installation of a single 2 MW electrolyzer. Beyond this threshold, Problem 1 can initially increase its NPV

without increasing its production rate. whereas Problem 2 and 3 are required to increase their production. The latter is achieved by providing a solution at the *NPV=0* restriction. When hydrogen price becomes large enough, Problem 1 has an incentive to install more capacity to increase its NPV.

Figure 5 shows a particular feature of Problem 3. As this problem needs to satisfy a set production target, when the target is lower than that of a single 2 MW equipment, small and costly units are installed, which result in larger H_2 selling price, whereas Problems 1 and 2 just cannot produce for low capacities. In addition, note that the minimums in the curves for Problem 3 coincide with the capacity production threshold for the other problems.

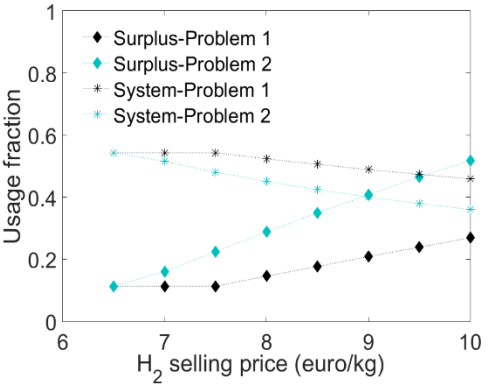

Figure 6: Optimal usage factors for both resource and installed capacity at several H_2 prices. Surplus cost = 0 euro/kWh.

Figure 6 shows the fraction of usage of electrolyzer and compressor (i.e. amount of hydrogen produced in a year over the maximum they can produce based on their capacity), and the fraction of usage of the renewable energy surplus (amount of energy used in a year over what was available). The curves indicate that as H_2 price increases, it is more favorable to capture the resource, which is achieved by installing more capacity. On the other hand, large capacities imply lower usage of the system due to the natural fluctuation of the surplus. In all cases, it should not be forgotten that 37 % of the time there is no energy available, hence the usage is capped at 63 %. This cap was not achieved in any of these problems due to effects of the capital cost. This discussion is left out of this paper due to space restrictions.

5. Conclusions

Three different decision-making problems to produce fuel hydrogen from surplus of renewable energy were presented and appropriate optimization problems proposed for their solution. For the numerical demonstration, Uruguay was taken as the case study. For these instances we found that H_2 prices are too high to compete with classical fuels, mainly due to the intermittence of the resource, that tends to install large capacities which even at the optimal have an usage factor of less than 55 %.

References

ADME (Administración del mercado eléctrico). https://adme.com.uy/ acceded on Oct. 2019.

M. Corengia, A. I. Torres, 2018. Two-phase dynamic model for PEM electrolyzer. In: 13th International Symposium on Process Systems Engineering (PSE 2018). Elsevier, 1435–1440.

Hydrogen Council, 2017. How hydrogen empowers the energy transition.

B. Kroposki, B. Johnson, Y. Zhang, V. Gevorgian, P. Denholm, B.-M. Hodge, B. Hannegan, 2017. Achieving a 100% renewable grid: Operating electric power systems with extremely high levels of variable renewable energy. IEEE Power and Energy Magazine 15 (2), 61–73.

MIEM (Ministerio de Industria, Energía y Minería), Dirección Nacional de Energía, 2018. Energy Balance 2017. Historical Series 1965-2017.

J. Proost, 2019. State-of-the art CAPEX data for water electrolysers, and their impact on renewable hydrogen price settings. International Journal of Hydrogen Energy 44 (9), 4406–4413.

UTE. Plan 24 horas. https://portal.ute.com.uy/ Last access Nov.

Sauro Pierucci, Flavio Manenti, Giulia Bozzano, Davide Manca (Eds.)
Proceedings of the 30th European Symposium on Computer Aided Process Engineering (ESCAPE30), May 24-27, 2020, Milano, Italy.
http://dx.doi.org/10.1016/B978-0-12-823377-1.50260-3

Characterizing the Dynamic Behaviour of a WtE Plant through Start-up Data

Elisa Magnanelli,[a]* Jostein Mosby,[b] Cansu Birgen,[a] Per Carlsson,[a] Michaël Becidan[a]

[a]*SINTEF Energy Research, Sem Sælands vei 11, Trondheim 7034, Norway*
[b]*Returkraft AS, Setesdalsveien 205, Kristiansand 4618, Norway*
elisa.magnanelli@sintef.no

Abstract

Municipal Solid Waste is a highly heterogenous fuel, with physical and chemical properties that change over time. When describing the dynamic behaviour of a waste-to-energy plant, physical parameters such as thermal inertia of the different plant components play an important role when determining the plant response to fluctuations in waste properties. In this work, we used process data collected during plant start-ups to experimentally determine these parameters for an existing plant. Identification of these parameters during normal operation is challenging due to lack of information on physical and chemical properties of waste entering the process. However, fossil fuels are burned during start-up due to EU regulations. By using process data from a plant start-up where a chemically and physically defined fuel was used, we could establish mass and energy balance over the whole system and estimate plant specific parameters. The parameters were further validated using data from a second start-up. The error between model prediction and experimental data was below 6%, and prediction was better for conditions closer to plant normal operation.

Keywords: Waste-to-Energy, Dynamic modelling, Start-up.

1. Introduction

One of the main factors that challenges stable operation of waste-to-energy (WtE) plants is the feedstock properties. Municipal Solid Waste (MSW) is a highly heterogenous fuel, with physical and chemical properties that change over time. Hence, despite advanced control systems, the process remains subject to large fluctuations in both heat production and emissions. Different works in the literature have focused on modelling steady state operation of WtE plants, e.g. Yang et al. (2004) described steady state combustion in grate furnace, while Shin and Choi (2000) modelled waste particle combustion. However, this approach is not suitable when the goal is to identify measures to improve process stability, and a dynamic model should be used instead (Alobaid et al. 2018). In the dynamics of a system, parameters such as components' thermal inertia play an important role. Due to fluctuations in MSW properties, it is difficult to estimate these parameters during normal plant operation. However, to satisfy current EU regulation, conventional fuel is burned during plant start-ups (Directive 2010). In this work, we developed a dynamic model that describes the boiler of a WtE plant and use process data to estimate plant specific parameters. Since the start-up fuel has known chemical and physical properties, data from start-up are used to determine plant parameters that describe the dynamic behaviour of the process. A second set of start-up data is used to validate the dynamic model.

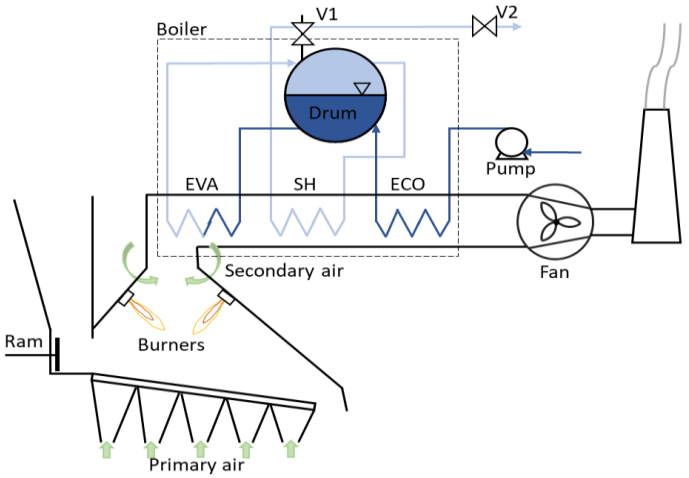

Figure 1: A schematic illustration of the Returkraft WtE plant in Kristiansand, Norway. Burners warm up the air and materials in the combustion chambers. Thanks to the fan, the flue gas leaves the combustion chamber passing through the boiler section. In the boiler, heat is recovered from the flue gas by a series of heat exchangers (EVA, SH, and ECO), and accumulated in the drum.

2. System

The dynamic model is based on Returkraft WtE plant in Kristiansand, Norway. It is a grate-fired plant with a capacity of 130,000 t/y (Figure 1). During normal operation, MSW is incinerated to produce electricity and/or heat. To comply with regulations, during start-ups, fossil fuel is burned instead. To minimize fuel usage, neither electricity nor district heating are produced during start-up, and a smaller number of components can hence be considered when modelling the start-up.

2.1. Process overview

During start-up, oil-burners heat the combustion chamber and boiler circuit in a controlled and gradual way. Well-established procedures must be followed depending on the nature of the stop and on the state of the system when start-up is initiated. A general and simplified procedure can be described as follows:

P1. The combustion chamber and flue gas system are vented to ensure that no combustible gas is present. If the boiler circuit is cold and not under pressure, steam system drainage and ventilation valves are opened (valve V1 in Figure 1 is opened and V2 is closed) before starting the burners, so that water/vapor can only circulate in the evaporator circuit (EVA).
P2. Burners are started to achieve the desired temperature increase in the drum.
P3. Once the boiler reaches 100 °C, the boiler is kept at 100 °C for at least 1 hour.
P4. Valve V1 is closed and V2 is opened to let steam circulate in the superheater (SH).
P5. When the steam production equals the heat recovered from the flue gas, valve V2 is regulated to allow the pressure in the drum and boiler circuit to build up at a predefined rate.
P6. When the pressure has reached the desired value and the temperature of the flue gas in the combustion chamber is such to satisfy regulations, MSW can be introduced in the combustion chamber.

During the whole procedure, water is pumped in the drum to keep the water level constant. Figure 2 shows the temperature evolution in the boiler drum during a start-up.

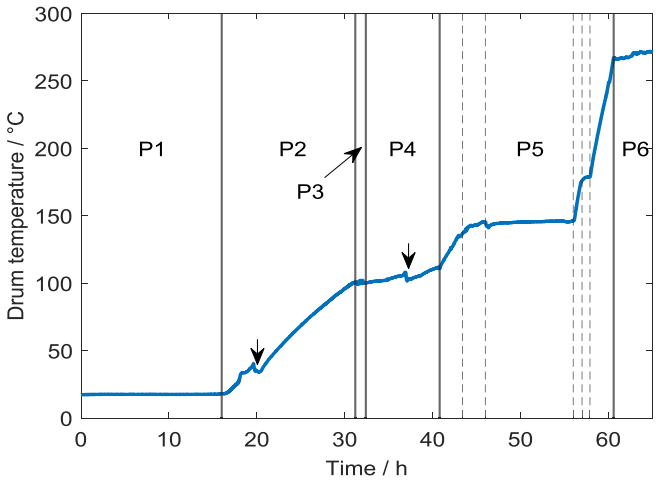

Figure 2: Temperature evolution in the boiler drum during a start-up procedure. The vertical solid lines delimit the startup phases described in Section 2 (P1-P6). The vertical arrows point at the effect of sudden water level drop in the drum and subsequent pumping of water.

The temperature profile during each phase is linear. Deviations from the linear behaviour are caused by sudden water level drop and subsequent pumping of water (the two vertical arrows in Figure 2 point at two such instances). The profile that the drum temperature follows in P5 is piecewise linear, as in the illustrated case a more cautious warming up was carried out to reduce stress on the plant.

3. Model description

The model was implemented in Matlab Simulink® using a set of differential and/or algebraic equations describing each sub-process.

3.1. Combustion chamber

The mass of flue gas in the freeboard, M_{fg}, results from a balance of the flue gas from the burners, F_b, the combustion air entering the combustion chamber, F_a, and the flue gas flow that leaves the system thanks to the flue gas fan, F_{fg}:

$$\frac{dM_{fg}}{dt} = F_b + F_a - F_{fg}. \tag{1}$$

The temperature of the flue gas, T_{fg}, is given by:

$$M_{fg}c_{p,fg}\frac{dT_{fg}}{dt} = F_b c_{p,fg}(T_b - T_{fg}) + F_a c_{p,a}(T_a - T_{fg}) + Q_{rad} \tag{2}$$

where $c_{p,fg}$ and $c_{p.a}$ are the specific heat capacity of the flue gas and of the air respectively, T_b is the temperature of the flue gas from the burners, T_a is the temperature of the incoming air, and Q_{rad} is the heat exchanged by radiation between the flue gas and the walls of the combustion chamber. In order to account for the large thermal inertia of the combustion chamber materials, a separate energy balance was established:

$$M_c c_{p,c}\frac{dT_c}{dt} = -Q_{rad} \tag{3}$$

where T_c, M_c and $c_{p,c}$ are the temperature, mass and heat capacity of the combustion chamber materials, respectively.

3.2. Boiler drum

Boiler drum dynamics was modelled as described by Åström and Bell (2000). The global mass balance in the drum is given by the water flow entering the drum, F_w, and the steam leaving it, F_{st}:

$$\frac{d}{dt}(M_{st} + M_w) = -F_{st} + F_w \tag{4}$$

where M_{st} and M_w are the mass of steam/air and liquid water in the drum. The energy balances for the water inside the drum and for the materials of the drum are:

$$\frac{d}{dt}(M_{st}h_{st} + M_w h_w - pV) = -F_{st}h_{st} + F_w h_w + Q_{EVA} + Q_{wall} \tag{5}$$

$$M_{wall}c_{p,wall}\frac{dT_{wall}}{dt} = -Q_{wall} - Q_{loss,drum} \tag{6}$$

where h_{st} and h_w are the enthalpy of the steam/air and liquid water, p is the pressure in the drum, V is the drum volume, Q_{EVA} is the heat transferred to the water in the evaporator, Q_{wall} is the heat exchanged between the water and the drum walls, $Q_{loss,drum}$ is the heat lost to the environment, and M_{wall}, $c_{p,wall}$ and T_{wall} are the mass, heat capacity and temperature of the boiler drum materials.

3.3. Superheater, evaporator and economizer

The heat exchanged between a fluid and the walls of a heat exchanger, Q_{ex}, can be described as (Incropera et al. 2007):

$$Q = H_{ex}(T - T_{wall,ex}) \tag{7}$$

where H_{ex} is an empirical overall heat transfer coefficient between the fluid and the wall, and T and $T_{wall,ex}$ are the fluid and wall temperatures, respectively. To reduce the complexity of the model, the outlet temperature of the fuel was calculated as:

$$T_{out} = T - \frac{Q}{c_p F} \tag{8}$$

where the c_p is the specific heat capacity of the fluid and F is the fluid mass flow in the heat exchanger. To take into account the thermal inertia offered by the heat exchanger materials, a dynamic energy balance for the heat exchanger walls, where the temperature was given by a balance between the heat exchanged with the cold fluid, Q_c, and the heat exchanged with the hot fluid, Q_h was established:

$$M_{wall,ex}c_{p,wall}\frac{dT_{wall,ex}}{dt} = Q_c + Q_{\square} \tag{9}$$

3.4. Flue gas fan

The angular velocity of the flue gas fan, ω, is controlled to maintain the pressure in the combustion chamber at a desired value. Its dynamic response was described as:

$$I\frac{d\omega}{dt} = \tau_M - \tau_D \tag{10}$$

where I is the moment of inertia, and τ_M and τ_D are the motor and drag torque. The flue gas mass flow through the fan, F_{fg}, can be calculated from the fan angular velocity as:

$$F_{fg} = \rho_{fg} k \omega \tag{11}$$

where ρ_{fg} is the flue gas density and k is a fan constant.

4. Results

Two sets of start-up data were collected from Returkraft WtE plant. These data were used as calibration and validation data set, respectively. The plant start-ups considered were so-called *warm start-ups*, where the plant had been stopped for less than one day and the boiler drum temperature was above 100 °C. Phase P2 (see Section 2.1) was therefore not part of these start-ups. The parameters to be estimated were the mass of the different components, M_i, and the heat transfer coefficients between fluid and component walls, H_i. The parameters were estimated through an optimization procedure based on nonlinear least-squares algorithms, where the error between simulated and measured output was minimized. A sensitivity analysis was carried out to identify the parameters that had the largest influence on the model outputs and to find appropriate starting values for the optimization procedure (not reported in this work). Figure 3 shows some of the experimental data used for parameter estimation (solid lines) and the respective simulated response of the model with the calibrated parameters (dashed lines). Figure 4 shows the experimental data used for validation (solid lines) and the corresponding model response (dashed lines). The relative error between experimental and simulated data lies within 6% of the output absolute value. The good match between model prediction and validation data indicates that the model has not been overfitted and describes the dynamic behaviour of the plant well. In addition, the error is lower in the second part of the start-up (below 2 %). The larger discrepancy during the initial part of start-up is due to the fact that there are no data on the amount of steam being vented out through valve 1 (see Fig.1). This lack of information introduced some uncertainties on the mass and energy balance of the drum.

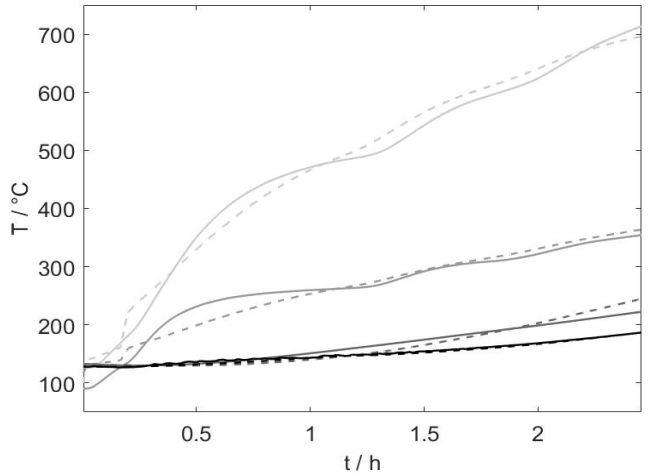

Figure 3: Temperature measurements during start-up (solid lines) and model response (dashed lines) for the boiler drum (black) and for the flue gas at 3 different positions (shades of gray). Calibration set: start-up on 12.03.19.

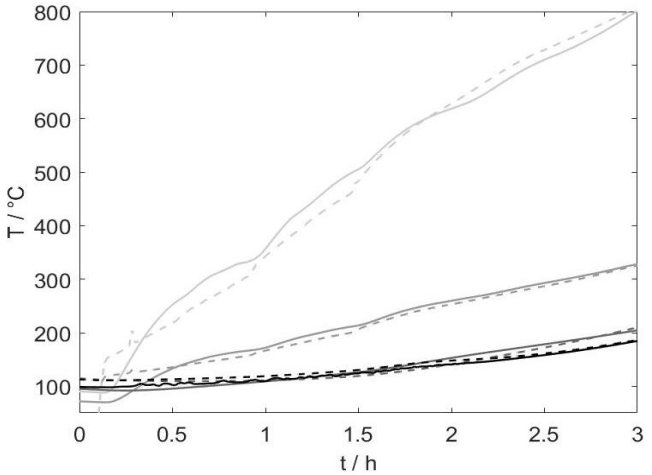

Figure 4: Temperature measurements during start-up (solid lines) and model response (dashed lines) for the boiler drum (black) and for the flue gas at 3 different positions (shades of gray). Validation set: start-up on 18.07.18.

On the other hand, complete mass and energy balance could be established when valve 1 was closed. For this reason, the model prediction was more accurate in the second part of start-up. Conditions during the final part of start-up are closer to those under normal plant operation, which indicates that the model can be used to describe MSW combustion.

5. Conclusions

In this work, a dynamic model describing the boiler of a WtE plant was developed. Data from a plant start-up, where conventional fuel is combusted, were used to determine plat specific parameters that describe the dynamic response of important plant components. The resulting dynamic model with calibrated parameters was further validated using data from a different start-up at the same plant. The good agreement between process data and model response suggests that the model describes the system dynamics well and that it can be used to simulate and study plant operation under normal conditions.

Acknowledgment

This work is part of the Waste-to-Energy 2030 project co-funded by industry partners and the Research Council of Norway under EnergiX program (WtE 2030, 280949).

References

F. Alobaid, W.A.K. Al-Maliki, T. Lanz, M. Haaf, A. Brachthäuser, B. Epple, I. Zorbach, 2018, Dynamic simulation of a municipal solid waste incinerator. Energy, 149, 230-249.

C. Directive, 2010. Directive 2010/75/EU of the European Parliament and of the Council. Official Journal of the European Union, 334, 17-119.

F.P. Incropera, A.S. Lavine, T.L. Bergman, D.P. DeWitt, 2007, Fundamentals of Heat and Mass Transfer, Wiley, Hoboken, New Jersey.

D. Shin, S. Choi, 2000, The combustion of simulated waste particles in a fixed bed, Combustion and flame, 121, 1, 167-180.

Y. Yang, C. Ryu, J. Goodfellow, V. N. Sharifi, J. Swithenbank, 2004, Modelling waste combustion in grate furnaces, Process Safety and Environmental Protection, 82, 3, 208-222.

K.J. Åström, R.D. Bell, 2000, Drum-Boiler Dynamics, Automatica, 36, 363-378.

Sauro Pierucci, Flavio Manenti, Giulia Bozzano, Davide Manca (Eds.)
Proceedings of the 30th European Symposium on Computer Aided Process Engineering (ESCAPE30), May 24-27, 2020, Milano, Italy.
http://dx.doi.org/10.1016/B978-0-12-823377-1.50261-5

Evaluating the Cleaning Routines in a Norwegian WtE Plant by Principal Component Analysis

Cansu Birgen[a], Elisa Magnanelli[a], Per Carlsson[a], Michaël Becidan[a], Jostein Mosby[b]

[a]*SINTEF Energy Research, 7034, Trondheim, Norway*
[b]*Returkraft AS, 4618 Kristiansand, Norway*
cansu.birgen@sintef.no

Abstract

Principal components analysis was performed using process data from a waste-to-energy plant (WtE), together with Hotelling's T^2 statistics and Q statistics, to evaluate the effect of maintenance routines on the performance of different units. The results showed that shower cleaning of evaporator units improves their efficiency while decreasing the heat exchanged in superheater and economizer. Q statistic detected the effects of maintenance earlier than Hotelling's T^2 statistics. The analysis could indicate which of the cleanings were less effective. Therefore, the proposed method can contribute to the design of a more effective cleaning strategy to prevent failures due to particle deposition. All in all, the fault detection and diagnosis proposed in this work can provide operational improvements, increased efficiency and reliability in WtE plants.
Keywords: Waste-to-Energy, Principal component analysis, fault detection, fault diagnosis, plant maintenance

1. Introduction

Heat or power can be produced from MSW that cannot be recycled. In 2016, the number of Waste-to-Energy (WtE) plants in Europe reached 512, with a potential for 248 new plants (Scarlat et al. 2019). WtE plants are confronted with strict regulations (Makarichi et al. 2018) as well as requirements for efficiency and reliability due to increasing load demands and strong process fluctuations. These can be attained by improving efficiency in steam boilers, which are critical units for heat recovery (Yu et al. 2017).

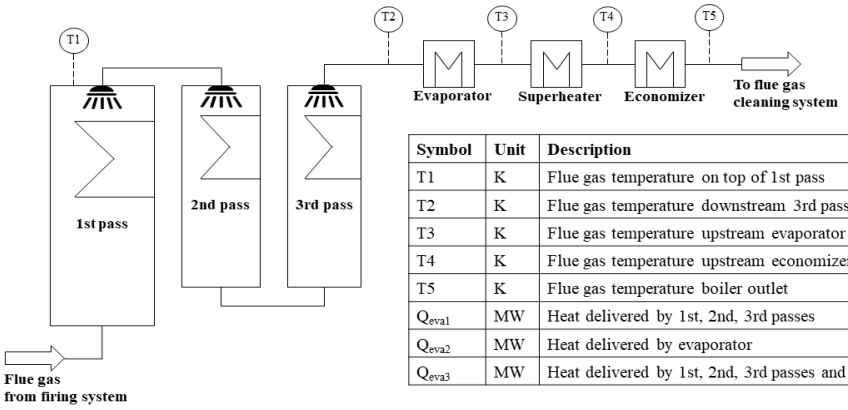

Symbol	Unit	Description
T1	K	Flue gas temperature on top of 1st pass
T2	K	Flue gas temperature downstream 3rd pass
T3	K	Flue gas temperature upstream evaporator
T4	K	Flue gas temperature upstream economizer
T5	K	Flue gas temperature boiler outlet
Q_{eva1}	MW	Heat delivered by 1st, 2nd, 3rd passes
Q_{eva2}	MW	Heat delivered by evaporator
Q_{eva3}	MW	Heat delivered by 1st, 2nd, 3rd passes and evaporator

Figure 1 Representative process flow sheet with process variables (in table).

Heat transfer efficiency deteriorates due to deposition of particles transported with the flue gas onto the boiler walls. To prevent this, a shower cleaning system is employed at the Returkraft WtE plant in Kristiansand, Norway (Fig.1). The evaluation of the boiler cleaning strategy will allow us to quantify its effectiveness and to propose improvements.

In this paper, Principal Component Analysis (PCA) was employed to study the effects of cleaning on the performance of the steam boiler unit. PCA is an advantageous method, since it provides robust performance due to elimination of random noise and uncontrollable disturbances by dimensionality reduction (Gao et al. 2016).

2. Methodology

The data used in PCA consisted of 8 variables and 11520 observation samples, which were recorded every minute for 8 days from 04.11.2019 to 12.11.2019 in Returkraft WtE plant. Temperature data (T1, T2, T3, T4 and T5) are direct sensor measurements, while heat delivered in evaporator units are calculated using sensor measurements.

First, the data was standardized using their median and median absolute deviation (Boudt et al. 2012), then PCA was performed. The amounts of heat delivered by the evaporator units were calculated using Eq. (1) to Eq. (3).

$$Q_{evap1} = F_{fg} Cp_{fg} (T1\text{-}T2) \quad (1)$$

$$Q_{evap2} = F_{fg} Cp_{fg} (T2\text{-}T3) \quad (2)$$

$$Q_{evap3} = F_{fg} Cp_{fg} (T1\text{-}T3) \quad (3)$$

where F_{fg} and Cp_{fg} are mass flow rate (kg/s) and specific heat capacity of the flue gas (J/kg/K). Raw data plots of the eight variables used in PCA are shown in Figure 2.

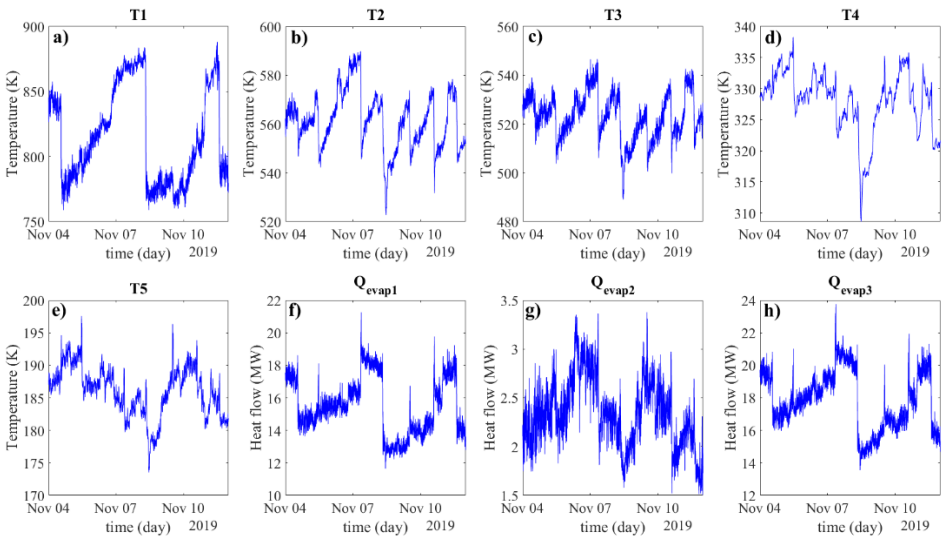

Figure 2 Raw data plots of the eight variables used in PCA (a-h).

2.1. Principal Component Analysis

The aim of PCA is to find latent variables called Principal Components (PCs) that capture important variations in the data that cannot be observed and measured directly; therefore, PCs should be chosen to preserve original information as much as possible (Yu et al. 2017). Let $X = [x_1 \dots x_n]^T \in R^{nxm}$ be an original data matrix composed of n observations, where each observation consists of m correlated variables, $x_n \in R^m$. The matrix X is decomposed as in Eq. (4).

$$X = T P^T \tag{4}$$

where the matrices $T = [t_1 \dots t_m] \in R^{nxm}$ and $P = [p_1 \dots p_m] \in R^{mxm}$ are composed of m score vectors $t_m \in R^n$ and m orthogonal loading vectors $p_m \in R^m$, respectively. The matrix P consists of eigenvectors of covariance matrix Σ, given in Eq. (5).

$$\Sigma = \frac{1}{n\text{-}1} X^T X = P \Lambda P^T \tag{5}$$

where $P P^T = P^T P = I_m$, I_m is a m×m identity matrix, and Λ is a diagonal matrix where the components consist of m eigenvalues sorted in descending order, $\lambda_1 > \lambda_2 > \dots > \lambda_m$, and $\Lambda = \text{diag}(\lambda_1, \dots, \lambda_m)$. Λ is given in Eq. (6).

$$\Lambda = \frac{1}{n\text{-}1} T^T T = \text{diag}(\lambda_1, \dots, \lambda_m) \tag{6}$$

2.2. Hotelling's T^2 statistic

Hotelling's T^2 statistic is a measure of variation in each sample within the PCA model (Bro & Smilde, 2014). Eq. (7) shows calculations of T^2.

$$T^2_n = \sum_{m=1}^{M} \frac{t^2_{nm}}{\lambda_m} \tag{7}$$

where T^2_n and t_{nm} are the Hotelling's T^2 value and the score value of the n^{th} sample on the m^{th} component. The Hotelling's T^2 contribution for a specific sample indicates variables causing the sample to have extreme score values, shown in Eq. (8).

$$\text{Tcont}_{nm} = \sum_{m=1}^{M} \frac{t_{nm} p_{nm}}{\sqrt{\lambda_m}} \tag{8}$$

where Tcont_{nm} is the Hotelling's T^2 contribution of the m^{th} variable on the n^{th} sample.

2.3. Q statistic

The lack of fit statistic in PCA models can be provided by Q statistics, which is a measure of how well each sample conforms to the PCA model and a measure of residuals, e_n. Eq. (4) can be written as Eq. (9) to include the residuals. Then Q for the n^{th} sample (Q_n) is calculated as the sum of squares of the n^{th} row of $E(e_n)$ as shown in Eq. (10).

$$X = T P^T + E \tag{9}$$

$$Q_n = e_n e^T_n \tag{10}$$

e_n represents the Q contributions, which define how much each variable contributes to the overall Q statistic for the sample. Confidence limits for both Q statistic and Hotelling's T^2 statistic are calculated for a significance level of α=0.01 by using the formulas given in Yu et al. (2017).

3. Results and Discussions

3.1. Principal Component Analysis

PCA results are summarized in Figure 3 in terms of explained variances. It is typical to decide on the number of PCs with a minimum cut-off point of explaining 70% variance (Yu et al. 2016). Figure 3.a shows that the first 4 PCs explain almost all the variance, and the first 3 PCs, which we selected as the number of PCs in our analysis, can explain more than 91% of variance in the system. Figure 3.b shows that the most important variable is T4, thus it can be beneficial to improve its measurement. For the model with 3 PCs, the most important variables are T5 and Q_{eva1}, while T3 and Q_{eva2} are the least important. Figure 3.b illustrates that PCA models with different number of PCs have different variable importance ranking.

3.2. Fault Detection and Diagnosis

Shower cleaning of the boiler walls affects the process; therefore, we refer to this disturbance as a "fault", to remain consistent with PCA terminology. Information on the cleaning strategy was obtained from the plant operators, while the data were received from the sensors in the plant. Table 1 shows the faults, i.e. cleaning locations and times. Cleaning location was determined using the cleaning hose position data.

Table 1 Fault descriptions in terms of hose cleaning locations and times.

	Fault1	Fault2	Fault3	Fault4	Fault5	Fault6	Fault7	Fault8
Location	3rdpass	1stpass	2ndpass	3rdpass	1stpass	2ndpass	3rdpass	1stpass
Time	Nov4 08:55	Nov4 13:13	Nov5 10:59	Nov7 08:14	Nov8 07:37	Nov9 12:19	Nov10 14:02	Nov11 14:14

As described in the methodology section, T^2 and Q statistics are complementary to provide information about faults observed in the system. 99% confidence limits are calculated for both statistics to define criteria for fault detection. The results are given in Figure 4.

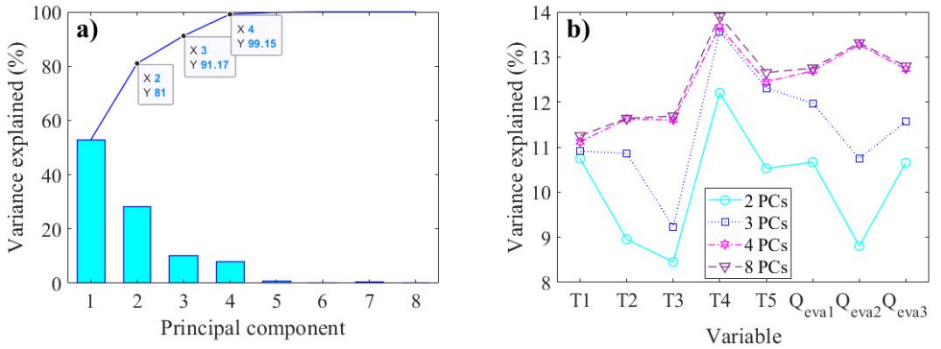

Figure 3 Variance explained by each principal component (a) and by each process variable (b).

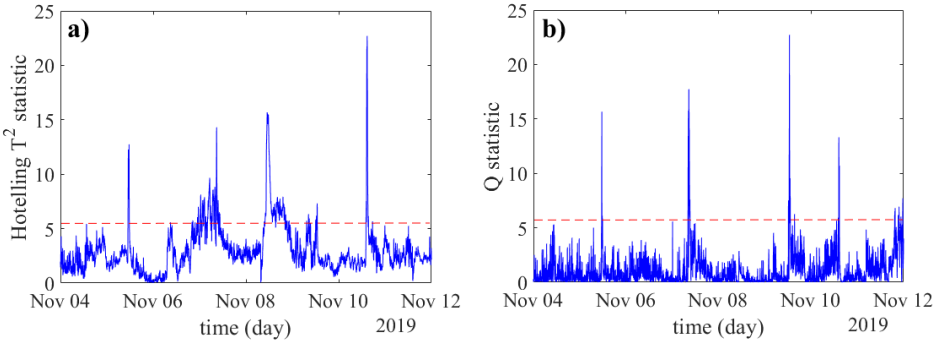

Figure 4 T² (a) and Q statistics (b) with 99% confidence limits shown by the dashed lines.

Figure 4 shows that Faults 1, 2, 5 and 8 are not detected (see Table 1); it seems that cleaning of 1st pass (i.e. Faults 2, 5 and 8) does not provide sufficient cleaning to result in a significant change in the system. This result is in line with the observations done in the plant, where there seems to be less deposit formation on the walls of the 1st pass compared to the 2nd and 3rd. Fault 1 was not detected since the cleaning did not actually take place; hose was placed but water was not sprayed. A fault on 08.11 at 11:11 is wrongly detected by T^2. Fault 3, 4, 6 and 7 are detected by both T^2 and Q. Moreover, Q statistic detected these 3 faults earlier than T^2. Because, the variances explained by Q and T^2 are composed of different process variables, and the effect of cleaning is observed in process variables measured by different sensors having different physical locations. This information becomes critical when a monitoring or a control system is installed in the plant.

Figure 5 shows the fault diagnosis results explaining the root causes of the faults happening in the system. T5 is the largest contributor to T^2 statistics for Fault 3. Q_{eva1} and Q_{eva3} have positive contributions due to improved the heat transfer efficiency.

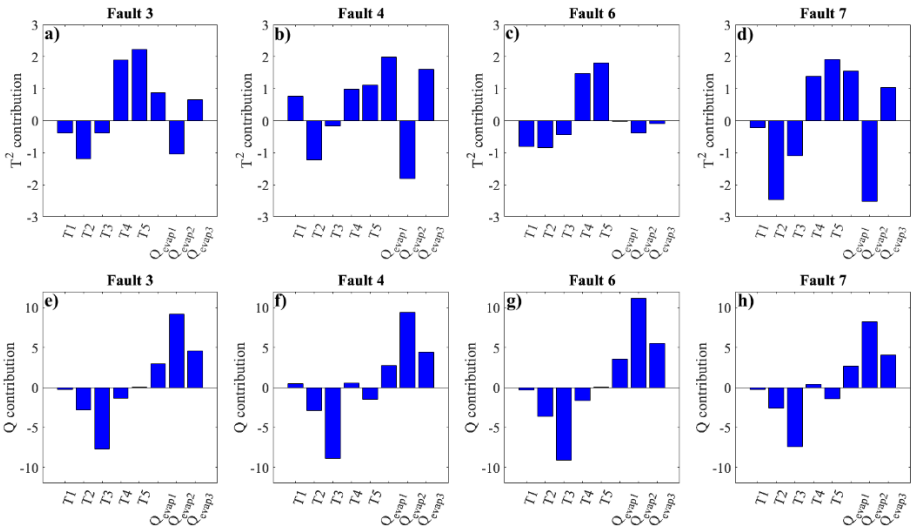

Figure 5 Variable contributions to T^2 (a-d) and Q statistics (e-h) for faults 3, 4 ,6 and 7.

Similarly, the larger the amount of heat exchanged in the evaporators, the lower their outlet temperatures become, as apparent in the negative contributions of T1, T2 and T3. However, T4 and T5 have large positive contributions to Fault 3, since the driving force to heat exchange in superheater and economizer (temperature difference between inlet hot and cold streams) becomes lower. Q statistic covers the rest of fault diagnosis showing that all Q_{eva1}, Q_{eva2} and Q_{eva3} are positive contributors to Fault 3 (Figure 5.e). Other faults show a similar contribution trend for both Q and T^2 statistics. Practically, this means that shower cleaning of the 2nd and 3rd pass of the evaporator unit improves its efficiency, consequently decreasing the heat exchanged in superheater and economizer. It is important to note that Q statistic detects the faults earlier, with the largest contributors being Q_{eva1}, Q_{eva2} and Q_{eva3}, while T4 and T5 have the largest contributions to T^2 statistics. This trend can be explained by the physical locations of sensors; cleaning impacts are seen first on the evaporator temperatures (T1, T2 and T3), then on Q_{eva1} Q_{eva2} and Q_{eva3} and lastly on T4 and T5. Therefore, the variable contributions to the overall variance needs to be combined with considerations on sensors' location in the system to effectively detect and diagnose faults.

4. Conclusions

Fault (i.e. cleaning) detection and diagnosis show that the proposed methodology can successfully identify the effect of maintenance on different units in the WtE process. Shower cleaning of 2nd and 3rd passes of the evaporator unit improves its efficiency while decreasing the heat exchanged in superheater and economizer. The analysis could indicate which of the cleanings were less effective. Therefore, the proposed method can help to design a more effective cleaning strategy, helping to prevent severe failures due to deposits on the evaporator walls. Moreover, Q statistic detects the faults earlier than Hotelling's T^2 statistics as a result of the physical locations of sensors. All in all, the fault detection and diagnosis proposed in this work can lead to operational improvements, increased reliability and better understanding of WtE plants.

Acknowledgements

This work is part of the Waste-to-Energy 2030 project co-funded by industry and public partners and the Research Council of Norway under the EnergiX program (WtE 2030 - 280949).

References

Boudt, K., Cornelissen, J., & Croux, C. (2012). The Gaussian rank correlation estimator: robustness properties. Statistics and Computing, 22(2), 471-483.

Bro, R., & Smilde, A. K. (2014). Principal component analysis, Analytical Methods.

Gao, Y., Wang, X., Wang, Z., & Zhao, L. (2016). Fault detection in time-varying chemical process through incremental principal component analysis. Chemometrics and Intelligent Laboratory Systems, 158, 102-116.

Makarichi, L., Jutidamrongphan, W., & Techato, K. A. (2018). The evolution of waste-to-energy incineration: A review. Renewable and Sustainable Energy Reviews, 91, 812-821.

Scarlat, N., Fahl, F., & Dallemand, J. F. (2019). Status and opportunities for energy recovery from municipal solid waste in Europe. Waste and Biomass Valorization, 10(9), 2425-2444.

Yu, J., Yoo, J., Jang, J., Park, J. H., & Kim, S. (2017). A novel plugged tube detection and identification approach for final super heater in thermal power plant using principal component analysis. Energy, 126, 404-418.Z.

Yu, H., Khan, F., & Garaniya, V. (2016). A sparse PCA for nonlinear fault diagnosis and robust feature discovery of industrial processes. AIChE Journal, 62(5), 1494-1513.

Sauro Pierucci, Flavio Manenti, Giulia Bozzano, Davide Manca (Eds.)
Proceedings of the 30th European Symposium on Computer Aided Process Engineering
(ESCAPE30), May 24-27, 2020, Milano, Italy.
http://dx.doi.org/10.1016/B978-0-12-823377-1.50262-7

Circular Economy in Banana Cultivation

Nicole Gehring[a], Bogdan Dorneanu[a,b], José José Manrique Silupú[c],

William Ipanaqué Alama[c], Harvey Arellano-Garcia[a,b,*]

[a]*LS Prozess- und Anlagentechnik, Brandenburgische Tecnische Universität Cottbus-Senftenberg, Cottbus, D-03046, Germany*
[b]*Department of Chemical and Process Engineering, University of Surrey, Guildford, GU2 7XH, United Kingdom*
[c]*Departamento de Ingeneria Mecánico Eléctrica, Universidad de Piura, Piura, Peru*
arellano@b-tu.de

Abstract

This paper examines the most important approaches that could be applied for the introduction of circular economy strategies for the banana production process in the region of Piura (Peru). Based on this, a framework for an optimized economic cycle that is able to conserve resources and minimize the capital investments of farmers, while simultaneously increasing their production, can be created. Challenges and potential solutions are discussed for the production stages.

Keywords: Circular economy, Banana production, Biomeiler, Digestor.

1. Introduction

Peru has experienced success in developing a strong export market for its organic bananas. This success has been built on a strategy for developing a strong niche market, especially in the European Union (Donahue, et al., 2011), in the face of large competitors in the non-organic market, such as Ecuador. Almost all of Peru's exported bananas are organic, accounting for around 3% of the global production. The region of Piura, in the north of the country, produces about 80 % of the national organic bananas. The production is characterized by small producers with farms of less than 3 ha of farmland, over a total of almost 170,000 ha.

The current approach in the production of bananas in Piura is that the trees are cut off after harvesting and left in the field. The fertilizer is expensive and is usually not dosed correctly, since measurements are scarce, hence a danger of under- or overfertilization exists, which can lead to a large loss of fruit. The water used for irrigation is taken from nearby rivers and fed into catchment basins and the plantation is flooded by means of joints in the soil, which are distributed over the field and connected to the basin. The water from giant washbasins used for washing the fruits is discarded, as it cannot be reused, being polluted.

Maintaining a strong growth in organic banana exports is important, as the industry is providing additional employment opportunities in rural areas of Peru. In order to access global markets, the farmers are required to meet demands for quality of produce, as well as for quantity and quality of supply. Organic producers in Peru face several challenges (FAO, 2017): providing an appropriate level of nutrients, in particular nitrogen, phosphorus and potassium; securing an adequate supply of quality planting material; securing sufficient water supply for irrigation; access to improved production technologies to increase yields. Moreover, organic bananas are more subject to disease

and insects than the conventional counterparts grown with herbicides and pesticides. To prevent insects, the organic banana bundles are covered in plastic bags until they are ready to be harvested.
The main costs for the banana producers relate to inputs and labour. The main inputs are manure and other organic fertilizers (island guano, sulfomag and potassium sulfate). The cost of fertilizers represents 43% of the total costs in a year (ODI, 2009). Although Piura has an excellent dry tropical climate and fertile soil for growth of the organic bananas, allowing the fruits to be produced year-round, the country is vulnerable to the effects of climate change. For these reasons it is important to keep focusing on sustainable practices to keep the organic banana sector a successful one. Efforts should be made to enhance investments leading to implementing modern farming techniques and improving the infrastructure around the plantations.
In the context of the agri-food chain, the circular economy (CE) aims to reduce waste while also making best use of the agricultural wastes, by-products and co-products produced, by using innovative technologies and profitable business practices to increase their value (Toop, et al., 2017). The development of CE requires the adoption of closed loop systems which work towards the goals of improved economic and environmental sustainability (Winkler, 2011).
The next sections present various CE approaches that can be applied in the organic banana sector that could significantly increase production, and the way they could be applied specifically to the farms in Piura. These include ways in which valuable resources, such as water or nutrients (Bertolucci Paes, et al., 2019; James Sherwood) can be protected or recycled, (Ngan, et al.,2019; Del Borghi, et al., 2020).

2. Methods

2.1. Parameter monitoring

How can these objectives be achieved? On one hand, by closely monitoring the plantations in order to record the necessary influencing variables, as shown in Table 1, and to be able to intervene if necessary.

Table 1. Parameters of optimal banana production

Parameter	Best conditions	Bad conditions	Measure with
Temperature	26 °C-30 °C	Less than 14 °C, more than 34 °C	Thermometer
Air humidity	50-80 %		Sensor Hygrometer
Sunshine hours		Less than 3 hours	
Soil moisture	Humidity	Not too wet for too long, as it is very sensitive to root rot.	Sensor Hygrometer
pH	5,6-7 pH	Die at more 7.5 pH	Measuring strips Sensor
Lime		Not too much because it's too bad for the plant.	Electrical conductivity Sensor
Nitrogen			Sensor
Phosphors			Sensor

Potassium			Sensor
Zinc			Sensor
Chlorine			Sensor
CO_2 or O_2 (presence of insects)			Sensor

Smart farming is important for tackling the challenges of agricultural production in terms of productivity, environmental impact, food security and sustainability. To address these challenges, the agricultural ecosystem needs to be better understood by monitoring, measuring and analysing it continuously. This implies analysis of big agricultural data and the use of new ICT technologies.

It is therefore necessary to develop comprehensive monitoring solutions of banana cultivation in order to achieve maximum yields with minimum use of resources. This not only makes sense for optimizing the use of resources, but also for saving capital. The aim of a CE approach is to ensure the optimal supply of resources to the plantations and to redesign existing processes in order to achieve better results with higher yields and minimal waste.

2.2. Waste (re)utilization

Currently, the banana plant waste remains in the field after harvest, to decompose, spreading diseases and polluting water supplies. This raises the question of whether there are no better alternatives or use for the banana plants waste, such as developing low-cost solutions to capitalize the banana waste through transformation into useful products such as solid or liquid fuels (Nazari, et al., 2019), organic fertilizers (Mohiuddin, et al., 2014), or precursors to other high value-added products (Tarrés, et al., 2017). This offers a possibility for a paradigm shift in the development of technological approaches for a complete conversion of the banana waste.

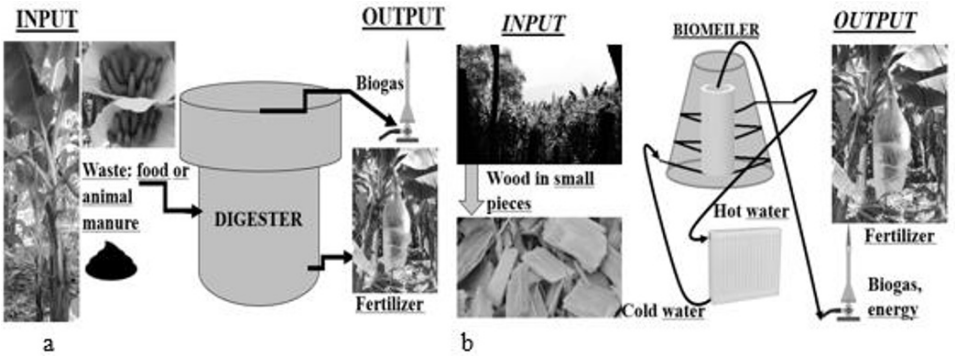

Figure 1. a) Digestor; b) Biomeiler

A low cost, stand-alone process to generate electricity for production and packing stations and at the same time, to produce a very good fertilizer for the plants would provide additional gain for the rural agricultural communities of Peru. A digestion tank (Figure 1a), or a Biomeiler (Figure 1b), could be used here.

In the digestion tank, the biological residues, such as bananas not suitable for trade and the harvested banana plant, can be disposed of. As a product for the recycling industry, fertilizer is obtained and biogas that can be further processed as electricity for the packaging station near the plantation.

In the Biomeiler the stem of the banana tree can be used as feed to produce fertilizers, as well as biogas. A further advantage of the Biomeiler is that a water pipe can be integrated into the system, which enables the automatic production of hot water through various biological processes.

2.3. Water treatment

The average water footprint of bananas produced in Peru corresponds to 11.4 m3 per standard 18.14 kg box (Clercx, et al., 2016). Approximately 1% of the blue water footprint corresponds to the washing, processing and packaging stage. Yet, the predominant irrigation practices in Peru imply a waste of water in the context of severe water scarcity. In order to increase the sustainability and the efficiency of the production process, the water resulting from the processing of bananas should be treated for reuse. This could be achieved with the aid of activated carbon filters, which can be produced from banana peels waste (Baloch & Mangi, 2019). Thus, the dirty washing water is treated and either used again for washing the bananas or for irrigation.

Furthermore, the recovery of the various nutrients, in particular of phosphorus, is very important as this resource is limited (Greuling, 2011). This could be achieved with the Stuttgart or the Gifhorn processes (Amann, et al., 2018). Thus, the phosphorus is recovered from digested sludge, with the aid of acid leaching.

3. Implementation

So how can the methods presented in the previous section be applied to improve the production of organic bananas in Peru?

3.1. Parameter monitoring

As can be seen in Table 1, there are several parameters that should be monitored more closely, in order to create optimal conditions for the plants' growth, especially with regard to nutrients such as:

- Phosphorus – essential in the DNA of all life on Earth
- Potassium – plants low in potassium are stunted in growth and have lower yields
- Nitrogen – important for photosynthesis and a significant component for amino acids, building blocks of proteins

Temperature and humidity have also great influence on the crops, as well as on the diseases and insects, hence affordable and reliable monitoring of these parameters is important as well. The recent developments in the Internet of Things and communication technologies enable the implementation of reliable, affordable wireless sensor networks, including RFID able to transmit stored information on various parameters such as soil, water, light, precipitation, temperature, humidity, etc., enabling producers to make better decision on how to handle the crops, when to add fertilizers or pest control, or when to irrigate.

3.2. Waste (re)utilization

The idea of using technologies such as the digestion tower is to supply energy to the plantation independently, without generating extra costs and to use the resulting biowaste profitably. This can be done with both methods. Fig.2 shows the implementation of these processes in the context of CE for the banana production process. Thus, all data from the sensors should be evaluated in order to compile the amounts of fertilizer and nutrients required. The nutrients or fertilizers should be produced from the biomass waste of the biomass resulted on the plantation, so that no further costs are incurred. To achieve this, after harvesting, the plants' unused parts are cut into small pieces and fed into the digestion tower. Fruit not suitable for sale can be added as well. The biological processes produce

both fertilizer and biogas. The biogas can be used to produce energy that can be used to produce hot water or to power various stages of the production process.

In case a Biomeiler is used, the unit can be equipped with a pipe that heats the water flowing through this pipe up to 55 °C. However, to start the fermentation process, the Biomeiler needs some water to be added to the shredded banana waste.

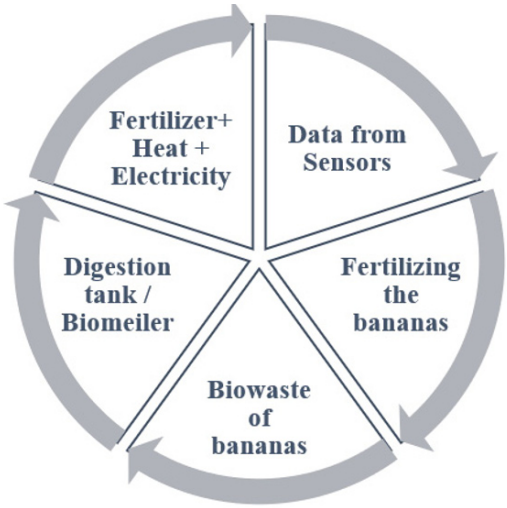

Figure 2 Circular economy in banana production

Both technologies do not require a lot of space and are not very expensive, which makes them suitable for any banana plantation, no matter how small.

3.3. Water treatment

As already mentioned in the Introduction section of this paper, the Piura region is an arid region in the north of Peru. Due to this fact the efficient use of water is of outmost importance.

The banana production, however, already requires a lot of water during cultivation, not to mention the post-harvest stage, when the banana bunches are taken directly to the packaging station, where they are first divided into the appropriate portions, and then washed in a very large basin filled with water. The bananas are then treated and packed in cartons and prepared for transport. For these reasons, it is particularly important to treat the used washing water appropriately so that the treated water can then be reused either as washing water, for soaking the banana plants or for irrigation. Sensors can be used to check the water quality and enable decisions on when to use treatment methods. Activated carbon filters can be used here as they remove chlorine and dirt from the water. A method has been developed in which the banana shells (Mahindrakar, et al, 2018) have been processed into activated carbon filters. Thus, the farmers have an opportunity for an extra income, by selling banana peels to the manufacturers of these filters, as well as having the possibility to acquire them to treat the waste water on their plantation.

The recovery of nutrients is also an important task, so that future generations can use it, as there is currently no alternative for this vital component in the DNA. The easiest way to recover it is to use technologies such as the digestion tower of the Biomeiler. Since phosphorus is found in the organic bananas and their residues, it can be recovered in the fertilizers produced from these feedstocks through composting. By fertilizing the plants, the phosphorus is returned to the natural cycle, and the plants can grow according to expectations. If more phosphorus is needed, there are further possibilities of phosphorus recycling from the sewage sludge (Amann, et al., 2018). However, some of these processes (e.g., the Stuttgart process) are very complex and require appropriately trained personnel and an expensive technical system.

4. Conclusions

Circular economy attempts to eliminate waste and reduce the impact of human activity on the environment. This paper explored several options for applying the CE concepts to optimize the banana cultivation in Peru, and showed that novel technologies could have an important impact in the activity of the banana producers. Furthermore, in the context of the unique conditions of the banana production in Peru (small-size farms, organic, low precipitation), parameter monitoring, waste (re)utilization and water treatment can offer solutions that can be realized with little effort and at low cost.

Thus, higher profits can be achieved by improving the control of the production, obtaining better crops, and additionally producing energy from the waste that can be used to decrease the operating costs.

Other technologies can be examined further to close the circle, among them the use of thermal processes on the banana biowaste, or the possibilities to replace the plastic used during the cultivation, which is currently not recycled due to its insignificant cost.

In this way, all materials introduced into the banana production process can be used several times, or nearly endlessly, with the ultimate goals not only to improve the quality of the crops while also protecting the environment for future generations, but also the livelihood of the rural communities where it takes place.

Furthermore, the CE would not be only limited to the banana cultivation, but it can also be transferred to other agricultural processes that may take place on the same farm (e.g., cocoa is often produced on many Peruvian banana plantations), or in other regions in Peru.

References

Amann, et al., 2018, Resources, Conservation and Recycling 120, pp. 127-139
Baloch & Many, 2019, Journal of Materials and Environmental Sciences 10 (10), pp. 966-986
Bertolucci Paes, et al., 2019, Journal of Cleaner Production 239, 118086
Clercx, et al., 2016, Acta Hortic. 1112, DOI: 10.17660/ActaHortic.2016.1112.1
Del Borghi, et al., 2020, Current Opinion in Environmental Science & Health, Volume 13, pp. 23-28
Donahue, et al., 2011, An examination of expanding Peru's organic banana exports to the United States, 21st Annual International Food and Agribusiness Management World Symposium, Frankfurt, Germany
FAO, 2017, Organic banana production in Peru, http://www.fao.org/3/a-i6870e.pdf
Greuling, 2011, Die Welt Bewegen, https://www.welt.de/dieweltbewegen/article13585089/Am-Phosphor-haengt-das-Schicksal-der-Menschheit.html
James Sherwood, Bioresource Technology
Mahindrakar, et al., 2018, Environmental Technology and Innovation 11, pp. 371-383
Mohiuddin, et al., 2014, The Agriculturists 12 (1), pp. 148-158
Nazari, et al., 2019, International Journal on Advanced Science Engineering Information Technology 9 (2), pp. 455-460
Ngan, et al., 2019, Renewable and Sustainable Energy Reviews 111, pp. 314-331
ODI, 2009, Organic banana cultivation and fair trade in Peru, https://www.odi.org/sites/odi.org.uk/files/odi-assets/publications-opinion-files/5652.pdf
Tarrés, et al., 2017, Industrial Crops and Products 99, pp. 27-33
Toop, et al., 2017, Energy Procedia 123, pp. 76-80
Winkler, 2011, CIRP Journal of Manufacturing Science and Technology 4 (3), pp. 243-246

Sauro Pierucci, Flavio Manenti, Giulia Bozzano, Davide Manca (Eds.)
Proceedings of the 30th European Symposium on Computer Aided Process Engineering (ESCAPE30), May 24-27, 2020, Milano, Italy.
http://dx.doi.org/10.1016/B978-0-12-823377-1.50263-9

The Value of Bioenergy with CO_2 Capture and Storage in an Electrified UK Heat Sector

Mathilde Fajardy[a], Vasileios Charitopoulos[b], David Reiner[a]

[a]*Energy Policy Research Group, Judge Business School, University of Cambridge, Trumpington Street, Cambridge CB2 1AG, UK.*
[b]*Department of Chemical Engineering, Centre for Process Systems Engineering, University College London, Torrington Place, London WC1E 7JE, UK.*
d.reiner@jbs.cam.ac.uk

Abstract

The electrification of heat in the UK offers an alternative to a heating system dominated by natural gas, but poses significant challenges for the current energy supply, both in terms of meeting peak heat demand, and in decommissioning existing infrastructure. The UK's recent adoption of a net zero target by 2050 signals an increase in ambition in heat decarbonisation targets. On the other hand, negative emissions from the power sector, in the form of bioelectricity with carbon capture and storage (BECCS), could provide both low-carbon firm power and CO_2 removal, to assist in this transition. Our study explores the role of CO_2 removal in least cost electrification pathways to net zero, using a spatially explicit hourly unit operation and capacity expansion optimisation model of the UK heat and power sectors. We model the full biomass and CCS value chains to account for potential geo-physical, sustainability and financial constraints to BECCS deployment at the regional level. Our contribution introduces the methodology to derive the biomass supply curve and CO_2 storage capacity and injectivity cost curves for the UK.

Keywords: electrification of heat, negative emissions, biomass supply curve, carbon capture and storage

Acronyms

AR: Agricultural Residues; BECCS: Bioenergy with CO_2 capture and storage; CCS: CO_2 capture and storage; DEC: Dedicated Energy Crop; FR: Forestry Residues; LDZ: Local Distribution Zone; SRF: Short Rotation Forestry; T&S: Transport and Storage; UK-GBRM: UK and Global Bioenergy Resource Model.

1. Introduction

The heat sector accounts for 37% of UK greenhouse gas emissions and will be instrumental in achieving the UK net zero target by 2050 (BEIS 2018a). However, the timing, approach (hydrogen, electrification, or hybrid), and extent to which CO_2 removal will be required to decarbonise the UK heat sector, remain unknown (CCC 2019). A range of CO_2 removal methods have been proposed (Royal Society 2018). One option, bioenergy with carbon capture and storage (BECCS), has been consistently featured in UK-level power systems modelling as a way to provide both low-carbon firm power and CO_2 removal to decarbonise the power sector (Daggash *et al.* 2019). This role could become increasingly important with the electrification of other sectors of the economy (*e.g.*, see Heuberger *et al.,* 2020 for the impact of electric vehicles). Knowing how much biomass can be sustainably produced in or imported to the UK, and at what cost, is

therefore key to quantifying the value of BECCS in the UK energy system. Studies have quantified the indigenous biomass potential by 2050 between 100 and 240 TWh (ETI 2018; Zhang *et al*. 2019; BEIS 2018b), depending on land availability, yield assumptions, and the range of feedstocks included. Open-access assessments of bioenergy potential at the regional level are, however, not readily available. While Zhang *et al.* (2019) curated biomass availability values for a range of feedstock types at a high resolution, this dataset did not account for potential competition with other biomass uses, and sustainability constraints restricting this supply, as included in the UK and Global Bioenergy Resource Model (UK-GBRM) (BEIS 2018b). Where, how much, at which rate, and at which cost, can the UK store CO_2, is also likely to impact the optimal investment decision to deploy BECCS (and fossil CCS) capacity across the UK. While the UK boasts ample CO_2 storage reserves in the North Sea, the affordability, capacity and injectivity of this reserve is not evenly distributed (ETI 2013). It is therefore important to integrate a spatially explicit CO_2 storage cost curve, for both capacity and injectivity, in the modelling framework. Our study aims to explore the potential role for BECCS in heat electrification scenarios, by integrating spatially-explicit biomass and CO_2 storage supply curves in a UK heat and power systems model, which operates at a high spatial and temporal resolution, using an actual hourly heat demand profile (Charitopoulos *et al.*, *under review*). This particular contribution presents the methodology to derive the biomass and CO_2 storage supply curves (Section 2), and discusses the spatial distribution of the UK's geophysical constraints on BECCS deployment (Section 3).

2. Derivation of supply curves

2.1 Biomass supply curve

In our modelling framework, the UK is divided into thirteen local distribution zones (LDZ) of the natural gas network (National Grid 2016). A biomass supply curve for each UK LDZ was derived based on local and imported biomass. The archetype chosen for the BECCS technology is a large scale (500 MW) biomass pulverised combustion plant combined with amine-based post-combustion CO_2. The following feedstock types were considered suitable for the use in a large scale BECCS plant: 1) dedicated energy crops (DEC) including miscanthus and short rotation coppice, 2) short rotation forestry (SRF), 3) wood forestry residues (FR), 4) agricultural residues (*e.g* cereals straw) (AR), and 5) wood pellet imports. The UK-GBRM was used to obtain the availability of these different feedstock at the national scale (BEIS 2018b). In assessing local bioenergy availability, the UK-GBRM accounts for competing uses and potential sustainability constraints. For imports, the model quantifies the availability of wood pellets from forestry in different producer countries, and assumes a share of that biomass will be available to the UK (based on the UK share of global energy use). The biomass is assumed to be sourced in the same proportions as the UK's current biomass imports are sourced. We find that the amount of global biomass available for imports to the UK decreases over time, from 240 TWh/yr in 2015 to 37 TWh/yr in 2050, as global demand for bioenergy increases.

In order to allocate these national assessments by UK region, we adopted tailored approaches for different feedstock types. For virgin biomass (DEC and SRF), regional marginal land availability for deploying energy crops and short rotation forestry was obtained using a 30 arc second resolution world map of "marginal mixed crop and vegetation land" (Cai *et al.* 2011). Such assessments are naturally highly uncertain and dependent on definitions of "marginal" land, and a sensitivity analysis will need to be performed to assess the robustness of the model outcomes. With this method, we find that marginal land availability in the UK is primarily concentrated in Scotland and southern

England, and sums up to 1.2 Mha. These findings are consistent with a previous assessment by the Energy Technology Institute (ETI), in which total land availability amounted to 1.4 Mha (ETI 2018). This map was then overlayed with a miscanthus, poplar and short rotation forestry yield map by Hastings *et al*. (2014). For each parcel of marginal land, the crop with the highest yield potential was selected. With this method, total DEC and SRF potentials were found to be 83 TWh/yr and 12 TWh/yr respectively. These values are considerably higher than in the UK-GBRM, where DEC availability ranges from 0.4 (2015) to 31 (2050) TW/yr, and SRF between 0 (2015) and 6 (2050) TWh/yr. Regional availability ratios were derived and applied to the more conservative national value obtained in the UK-GBRM model. For agricultural and forestry residues, cereal straw (Copeland and Turley 2008) and forestry residue (di Maio and Turley 2014) estimates were calculated by LDZ. Similarly, regional ratios were derived and applied to the national assessment value in the UK-GBRM. Costs and carbon footprint data from earlier calculations by DECC, curated by Element Energy and E4Tech (2018), were used for each biomass type. Pelleting and transport costs derived from Mobini *et al.* (2013) were added to obtain the cost of virgin biomass pellets at the point of use. The same methodology was applied for the carbon footprint. The biomass pellets can be used locally in each LDZ – in which case the transport distance is assumed to be 50 km (Bonilla and Whittaker 2009; DECC 2014) – or transported to another region. The cost and carbon footprint associated with biomass road transport from one LDZ to another were computed based on the Euclidean distance between the centroid of each LDZ, and emissions and cost factors from Lu *et al*. (2015). For biomass imports, the eight largest UK ports were represented in the model. For each LDZ, biomass imports are assumed to be available from the nearest port, with an added carbon and financial cost associated with biomass transport from the port to the centroid of the LDZ. Regional biomass availability are represented in *Figure 1*, while biomass supply curves in 2030 and 2050 are represented in *Figure 2*.

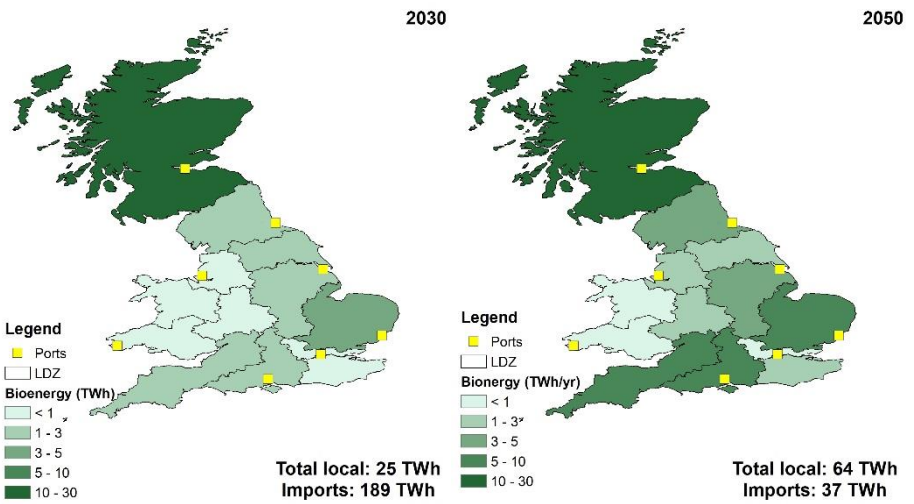

Figure 1 Representation of the UK in local distribution zones (cells), featuring ports for biomass imports (yellow squares) and regional bioenergy potential in TWh/yr (colouring).

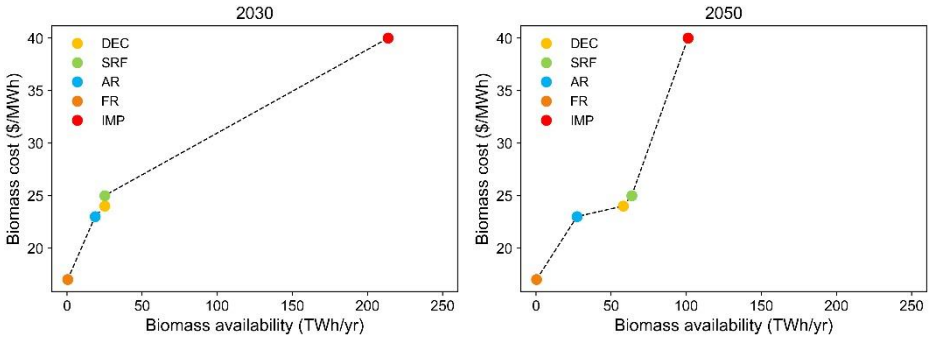

Figure 2 Representation the UK biomass cost curves in 2030 and 2050.

2.2 CO_2 storage

The British Geological Survey and ETI estimated the UK CO_2 storage capacity to 78 $GtCO_2$ with 50% confidence across 505 potential storage sites distributed around the UK in the North Sea and Irish Sea (Bentham *et al.* 2014). Out of 505 storage sites, ETI selected 20 sites for pre-feasibility studies (ETI 2013), and conducted economic analysis on 186 sites. We populated our CO_2 storage database with these 186 units, along with their characteristics, including latitude and longitude of storage centroid (assumed to be injection point), storage capacity (50% probability estimate), storage lifetime, storage injection rate, offshore CO_2 transport (T) capital and operating costs, and storage (S) capital and operating costs. For some of the storage units, T&S capital and operating costs were available for a range of injection rates (2 to 60 $MtCO_2/yr$) and lifetimes (10 to 40 years) in the database. When possible, the costs calculated for a lifetime of 30 years and the highest injection rate possible, were collected. When not available, costs for a lower lifetime (10-20 years) were used. Based on the lifetime and injection rate chosen, the undiscounted T&S cost for each selected storage site was calculated. The transport cost data in the CO_2Stored database only includes offshore CO_2 transport from an inland CO_2 terminal to the storage site. ETI identified 10 CO_2 terminals to cluster different incoming CO_2 flows and send the CO_2 offshore to the different CO_2 storage areas (ETI 2013). To account for inland CO_2 transport cost, the cost of transporting CO_2 between the centroid of each LDZ and the nearest CO_2 terminal was calculated based on pipeline capital and operating cost data from Johnson *et al.* (2014). A 26% (higher heating value) efficient 500 MW BECCS plant typically captures 3-4 $MtCO_2/yr$[1]. The CO_2 transport cost data for a flow rate of 3 $MtCO_2$/year was thus chosen. Figure 3a represents the location, capacity and undiscounted cost of the 186 CO_2 storage sites selected, while Figure 3b provides the cost of CO_2 T&S as a function of capacity and injectivity.

[1]Assuming 5 MWh/ton biomass (50% carbon content), 90% capture rate and 75% capacity factor.

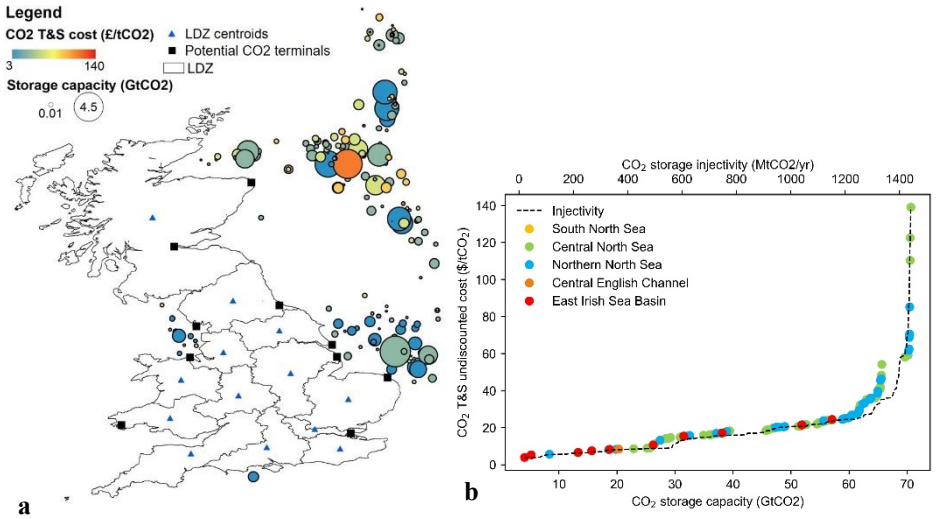

Figure 3 (a) Representation of the UK in local distribution zones (cells), featuring on-shore CO_2 terminals (black squares) and offshore CO_2 storage sites (coloured dots) selected for this analysis. (b) CO_2 storage capacity (each storage area is denoted by a different colour circle) and injectivity (line) cost curve. Data from the CO_2Stored database (Bentham *et al.* 2014).

3. Conclusions

Owing to the decrease in biomass imports over time, we find that bioenergy supply decreases between 2015 and 2050. This decline could be reversed if lower quality feedstock, particularly wastes (*e.g.,* municipal solid wastes, waste food) would be considered for use in smaller scale conversion plants (*e.g.,* combined heat and power) or in gasifiers. In terms of regional distribution, we observe that the primary bioenergy supply regions for the UK are Scotland followed by South East England. By 2050, the South West also becomes a key provider of bio-resources. These are also the regions with the highest installed renewable capacity today (National Grid 2018), and could therefore benefit from BECCS deployment, which would help balance the intermittency of renewables with firm load generation. By examining the CO_2 storage supply curve, we find that approximately 30 $GtCO_2$ of storage capacity and an injectivity of 600 $MtCO_2$/yr is available at a cost below £20/tCO_2, which is likely to be enough for the UK to meet its CCS needs by 2050 – in its 'Further Ambition' scenario, the Committee on Climate Change (CCC) estimates that achieving net zero would require up to 175 $MtCO_2$ to be captured annually (CCC 2019). Finally, we observe that 38% of CO_2 storage capacity with a cost below £20/tCO_2 is located in the Central and Northern North Sea areas, close to the main bioenergy providers. The spatial distribution of biomass resources and low cost CO_2 storage sites therefore offer, *a priori*, a good opportunity for biomass source and sink matching with CO_2 storage sites, which could have a determining impact on the optimal location of BECCS and fossil-CCS plants.

References

BEIS. 2018a. "Clean Growth - Transforming Heating, Overview of Current Evidence." https://assets.publishing.service.gov.uk/government/uploads/system/uploads/attachment_data/file/766109/decarbonising-heating.pdf.

———. 2018b. "The UK and Global Bioenergy Resource Model." 2018. Department for https://www.gov.uk/government/publications/uk-and-global-bioenergy-resource-model.

Bentham, M., J. Lowndes, and A. Green. 2014. "CO2 STORage Evaluation Database (CO_2Stored). The UK's Online Storage Atlas." *Energy Procedia* 63 (0): 5103–13.
Bonilla, D., and C. Whittaker. 2009. "Freight Transport and Deployment of Bioenergy in the UK," no. December: 1–23. http://www.tsu.ox.ac.uk/pubs/1043-bonilla-whittaker.pdf.
Cai, X., X. Zhang, and D. Wang. 2011. "Land Availability Analysis for Biofuel Production." *Environmental Science and Technology* 45 (January): 334–39.
CCC. 2019. "Net Zero - The UK' s Contribution to Stopping Global Warming." https://www.theccc.org.uk/publication/net-zero-the-uks-contribution-to-stopping-global-warming/.
Charitopoulos, V., C. K. Chyong, and D. Reiner. (under review). "The Prospect of Electrification for the Decarbonisation of Heat in the UK." *EPRG Working Paper*.
Copeland, J., and D. Turley. 2008. "National and Regional Supply/Demand Balance for Agricultural Straw in Great Britain." http://www.ruraldevelopment.org.uk/northwoods/files/2012/12/StrawAvailabilityinGreatBritain.pdf.
Daggash, H A, C F Heuberger, and N Mac Dowell. 2019. "The Role and Value of Negative Emissions Technologies in Decarbonising the UK Energy System." *International Journal of Greenhouse Gas Control* 81: 181–98.
Element Energy and E4Tech. 2018. "Cost Analysis of Future Heat Infrastructure Options Report for National Infrastructure Commission March 2018." https://www.nic.org.uk/wp-content/uploads/Element-Energy-and-E4techCost-analysis-of-future-heat-infrastructure-Final.pdf.
Energy Technology Institute (ETI). 2013. "A Picture of CO_2 Storage in the UK: Learnings from the ETI's UKSAP and Derived Projects." https://www.eti.co.uk/library/ccs-a-picture-of-co2-storage-in-the-uk.
Energy Technology Institute (ETI). 2018. "The Evidence for Deploying Bioenergy with CCS (BECCS) in the UK." *Energy Technologies Institute*. https://www.eti.co.uk/insights/the-evidence-for-deploying-bioenergy-with-ccs-beccs-in-the-uk.
Hastings, A., M. J. Tallis, E. Casella, R. W. Matthews, P. A. Henshall, S. Milner, P. Smith, and G. Taylor. 2014. "The Technical Potential of Great Britain to Produce Ligno-Cellulosic Biomass for Bioenergy in Current and Future Climates." *GCB Bioenergy* 6 (2): 108–22.
Heuberger, C. F., P. K. Bains, and N. Mac. 2020. "The EV-Olution of the Power System : A Spatio-Temporal Optimisation Model to Investigate the Impact of Electric Vehicle Deployment." *Applied Energy* 257 (June 2019): 113715.
Johnson, N., N. Parker, and J. Ogden. 2014. "How Negative Can Biofuels with CCS Take Us and at What Cost? Refining the Economic Potential of Biofuel Production with CCS Using Spatially-Explicit Modeling." *Energy Procedia* 63: 6770–91.
Lu, X., M. R. Withers, N. Seifkar, R. P. Field, S. R. H. Barrett, and H. J. Herzog. 2015. "Biomass Logistics Analysis for Large Scale Biofuel Production: Case Study of Loblolly Pine and Switchgrass." *Bioresource Technology* 183: 1–9.
Maio, D. di, and D. Turley. 2014. "Lignocellulosic Feedstock in the UK." www.nnfcc.co.uk.
Mobini, M., T. Sowlati, and S. Sokhansanj. 2013. "A Simulation Model for the Design and Analysis of Wood Pellet Supply Chains." *Applied Energy* 111: 1239–49.
National Grid. 2016. "Gas Demand Forecasting Methodology," https://www.nationalgrid.com/sites/default/files/documents/8589937808-Gas%20Demand%20Forecasting%20Methodology.pdf
National Grid. 2018. "Future Energy Scenarios." http://fes.nationalgrid.com/fes-document/.
Royal Society and Royal Academy of Engineering. 2018. *Greenhouse Gas Removal*. https://royalsociety.org/-/media/policy/projects/greenhouse-gas-removal/royal-society-greenhouse-gas-removal-report-2018.pdf.
DECC. 2014. "Life Cycle Impacts of Biomass Electricity in 2020." https://assets.publishing.service.gov.uk/government/uploads/system/uploads/attachment_data/file/349024/BEAC_Report_290814.pdf
Zhang, D., M. Bui, M. Fajardy, P. Patrizio, F. Kraxner, and N. Mac Dowell. 2019. "Unlocking the Potential of BECCS with Indigenous Sources of Biomass at a National Scale." *Sustainable Energy & Fuels*. (*advance article*).

Sauro Pierucci, Flavio Manenti, Giulia Bozzano, Davide Manca (Eds.)
Proceedings of the 30th European Symposium on Computer Aided Process Engineering (ESCAPE30), May 24-27, 2020, Milano, Italy.
http://dx.doi.org/10.1016/B978-0-12-823377-1.50264-0

Strategic Biorefining Supply Chain Design for Novel Products in Immature Markets

Anna Panteli,[a] Sara Giarola,[b*] Nilay Shah [a]

[a]*Chemical Engineering Department, Imperial College London, SW7 2AZ, UK*
[b]*Earth Science & Engineering Department, Imperial College London, SW7 2AZ, UK*
s.giarola10@imperial.ac.uk

Abstract

Castor oil is a key intermediate in the chemical and pharmaceutical industry, but its use as energy vector is hindered by high feedstock costs. However, it become a competitive fuel if a full market is also created for the by-products. Mixed Integer Linear Programs are effective tools to drive investment decisions in bio-based supply chains.

This paper proposes a Mixed Integer Linear Fractional Programming (MILFP) with the objective to minimise the levelised cost of the examined supply chain. Results produce the most economical supply chain solution which maximises the unit value of the supply chain feedstock rather than just proposing a solution where the system fulfills the demand at the minimum size possible.

Keywords: MILFP, castor oil, supply chain optimisation.

1. Introduction

Environmental and societal concerns regarding the mitigation of climate change (IPCC, 2007) have driven the research in renewable sources as they can improve energy security and reduce greenhouse gas (GHG) emissions. Biorefineries relying on processes and technologies producing high added value bio-fuels, chemicals and polymers can play a remarkable role in delivering energy security and emissions reduction.

With a yield of about 2,000 kg per ha, castor seeds have high oil potentials and lower plantation costs compared to competing crops. Being composed for about 90 % of rinoleic acid, castor oil has also an extraordinary purity compared to the majority of the bio-oils. The fluctuations of the castor seeds price due to biomass availability, has boosted the interest in assessing potentials for castor seeds to produce plant lipids for both energy and industrial applications (Severino et al., 2012).

The application of a system approach, embracing the entire supply chain (SC), is essential in the design of advanced biorefining networks over the long-term. The approach requires that every step, from biomass cultivation to delivery of the final bioproducts to the customers, should be considered, while integrated with a technology superstructure for the biomass transformation (Santos et al., 2019).

Most of the existing works considering the planning and optimizing of novel infrastructures, use an absolute (extensive) economic performance metric, such as maximizing the total profit or minimizing the total cost or a combination of absolute environmental and economic metrics (Patel et al, 2016). In the design of completely novel systems, multi-objective formulations are also widely used. Huang et al. (2019) proposed a multi-objective formulation including greenhouse gas emissions and systems cost

minimization in the design of a renewable jet fuel SC in US. Mandade et al. (2019) presented a multi-objective optimization approach to select the feedstock mix for ethanol production in India showing the trade-off among life cycle greenhouse gas emissions, energy return on investment, life cycle water use, and land use. All these approaches, implying the minimisation of an extensive metric, constrain the product demands with lower bounds, thus giving a SC configuration which would produce and sell the lowest quantity of biofuels as possible to reduce costs. The solution is not necessarily the most economical one. The advantage of unit objective is rarely acknowledged in the literature (Gao & You, 2017). In the past, only a few studies used intensive metric to support a supply chain design. In one of the most recent applications, Yue et al. (2013) proposed an optimization for (bio)-refining systems with two fractional objective functions. An economic objective guarantees the optimal sales amount between the demand upper and lower bounds to guarantee the lowest unit cost per functional unit. The environmental objective guarantees the lowest environmental impact per functional unit.

This paper addresses the problem of biorefining planning, specifically applied to a castor oil biorefinery, whose profitability might vary depending on the selling price of the bioproducts, which is unknown as there market is not developed yet. To plan a sustainable biorefinery, an optimization framework is proposed which maximises the bioproducts throughput and controls their costs through minimising the levelized costs. The rest of this article is organised as follows. The general problem statement is first presented followed by the mathematical formulation. A Romanian case study with modelling assumptions, numerical results and final considerations is then discussed.

2. Methods

2.1. Problem statement

Here we examine a bio-based supply chain system, involving the production of castor oil from castor seeds in Romania to meet the demand of oil in Marseille. The case study is based on a real industrial application with a focus on determining where the castor seeds transformation sites would be located and how the products would be channeled to the market, via either truck or ship. The SC optimization problem applies to 12 months of the biorefinery planning and operation.

2.2. Mathematical formulation

A multi-echelon multi-product biorefining supply chain is modelled as proposed in Panteli et al. (2018) where the upstream supply chain steps (such as biomass production, storage, transport, and processing) are optimized alongside the downstream supply chain steps (such as including bioproduct storage and transport to the market). The objective function (Eq. (1)), also known as the cost of goods per gram (COG/g), is equal to the total annualised cost, comprising of both capital and operating costs divided by the total annual demand of products.

The Mixed Integer Linear Programming (MILP) model proposed by Panteli et al. (2018) was reformulated into a MILFP, substituting the profit-based objective function with the levelised cost-based one, as given in Eq. (1).

$$min\ LC = \frac{TAC}{TAD} \tag{1}$$

$$s.t.\ TAC = TCC + \sum_t TOC_t \tag{2}$$

$$TAD = \sum_c \sum_t D_{c,g,t} \tag{3}$$

$$D_{c,g,t} \geq 0.15 \cdot \ MD_{c,g,t} \tag{4}$$

where *LC* (€M/kt of products) stands for the levelised cost, *TAC* (€M/y) refers to the total annualised costs, and *TAD* (kt of products/y) represents the total annual demand of bioproducts. As reported in Eq. (2), *TAC* includes the annualized capital costs (*TCC*) and the operating cost per month *t* (TOC_t). *TAD* is the total demand across all the commodities *c*, all the geographical subdivisions *g*, and time period *t* (Eq. (3)). Moreover, an additional demand-related constraint, Eq. (4), is included in the mathematical formulation, introducing a lower bound for the demand of the bioproducts $D_{c,g,t}$ equal to the 15% of the market demand value $MD_{c,g,t}$ by commodity *c*, region *g*, and time period *t*. As there is no consideration of potential profit to motivate the production of bioproducts, in this case a minimum level demand restriction is needed to enforce the production procedure.

The MILFP model is solved using the Dinkelbach algorithm (Liu et al., 2014). This solution procedure began as an application of the classical Newton method to solve convex non-linear fractional programming (NFP) models by solving a sequence of non-linear programming (NLP) models successively, and recently it has been implemented to solve MILFP optimisation problems.

The implementation of the Dinkelbach algorithm, relies on transforming the MILFP model as in EQ. (1) into an MILP model, by modifying the fractional objective function as:

$$min\, TAC - \ f \cdot TAD \tag{5}$$

Overall, the above MILP model is solved iteratively for different values of *f*, based on each iteration optimal solutions, until a termination criterion, based on the absolute objective value, is satisfied. The scheme of the employed Dinkelbach algorithm is presented in Figure 1.

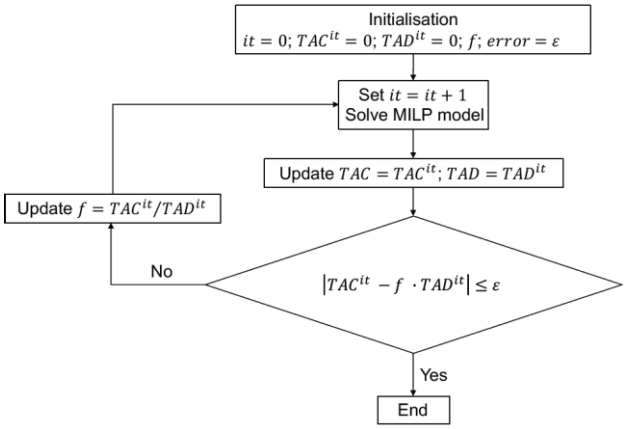

Figure 1. Flowchart for the Dinkelbach algorithm.

3. Case study

The EuroBioRef project (EuroBioRef, 2016) and Tsagkari et al. (2016) were the sources used for the agronomic and costs data. In the remaining part of the section, each SC step is further described.

3.1. Spatially-explicit features

The Romanian area of Constanţa (i.e., 150,000 ha) has been discretised into a grid of 60 square cells of equal size, i.e., 5 km of length. An additional cell represents the demand centre in Marseille. The fraction of cultivation area and fraction of arable land devoted to castor seeds were assumed based on the soil conditions and altitude differences of the examined region. As disaggregated data at the spatial scale of analysis were not available, the fraction of the arable land density was randomly distributed while the cultivation yield of castor seeds was assumed constant geographically, although available only two months in a year.

3.2. Transport

The model specifies whether and, if presents, what kind of transport link is available between two cells. Specifically, truck only was allowed within the Romanian area while trans-shipping was allowed between Romanian and Marseille ports.

3.3. Processing

A seed pressing followed by oil extraction technology was modelled. The technology produces castor oil and meal. The biorefining process consists of two sections. In the first section, the castor seeds undergo pretreatment through continuous dehulling, conditioning and flaking. In the second section, crude oil is separated from the seeds by hexane (solvent) extraction and the de-oiled meal is desolventised and toasted. Due to the small surface of the Romanian region and the low demand of castor oil, the installation of only one conversion facility was examined: the capacity of the investigated SC is assumed to be 150 kt/y.

3.4. Storage

Castor seeds were assumed to be stored on-fields, whereas castor meal and castor oil in drums. The cost and the maximum capacity of storage were calculated from Panteli et al. (2018).

3.5. Demand

Marseille is the market for the products and where the consumption of the bioproducts is assumed. In addition to castor oil, the by-product (i.e., castor meal) can be further utilised for field fertilisation or for power generation, and subsequently, contribute to the total profit of the examined SC system.

4. Results and discussion

The results obtained with the MILFP approach are presented and commented in comparison with the solution obtained solving the problem as a profit maximisation MILP. The MILFP with the use of several non-linear solvers failed, so that the MILP reformulation of the MILFP in CPLEX 12.7.0.0 was adopted. The optimality gap for each run was set to 0%.

4.1. Planning decisions

The obtained minimum levelised cost of 0.733 €M/kt of products resulted in 16.3 €M/y profit. As shown in Figure 2 the required processing plant is installed in Marseille (i.e., in cell g=61). As the maximum level of demand was set equal to the maximum capacity of the examined conversion facility, only one plant was expected to be installed for the conversion of castor seeds into castor oil and castor meal. Aiming at satisfying the targeted castor oil and meal demand in Marseille, the SC configuration showed that the

optimal location to build the examined seeds pressing and oil extraction plant would be in the port cell in Marseille. In addition, castor seeds were cultivated in the Romanian region. Except a 5 kt/y castor oil and a 22 kt/y castor meal storage facility in Marseille (i.e., in cell g=61, where the conversion facility would be planned), most of the storage would occur next to the biomass production fields. All the biomass stored in Romania would be then transhipped to Marseille. The relatively higher unit cost of transporting liquid compared to solids, explains the preference for moving solid biomass for most of the freights envisaged in the final solution.

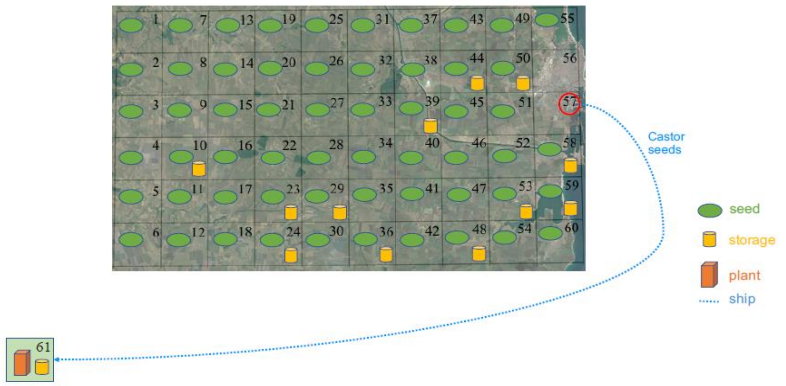

Figure 2. Optimal SC system configuration.

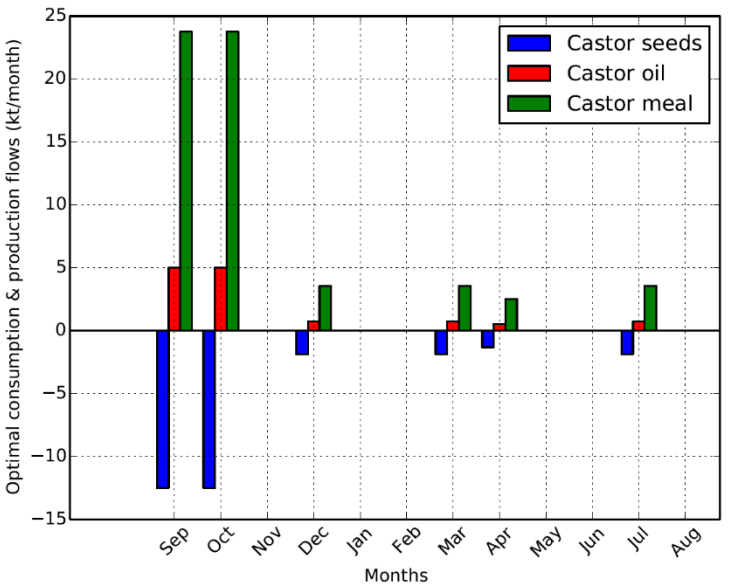

Figure 3. Optimal feedstock and product flows of the examined plant.

Figure 3 illustrates the optimal monthly flows of castor seeds, oil and meal of the facility. The plant of the current case would operate for four months (i.e., September, October,

December, March, April and July), and at full capacity just for the first two periods. The cost breakdown for the MILFP shows a dominant role of cultivation (49 % of total) and biomass pretreatment (37 %) costs. Transport and storage, 13 % and 1% of the total costs respectively, play a minor role.

4.2. Comparison between the MILFP and the MILP solution

The MILP and MILFP solutions appear very close in term of SC configuration, where the optimisation driven MILP sets all the storage facilities in the Romanian region. The cost breakdown between the MILP and the MILFP solutions is also comparable. The relative proximity in the results can be mainly explained with the constraints set on the SC demand due to the limits on biomass availability. However, the MILFP case produces a 2 % less profitable supply chain system than the MILP profit maximisation, where the difference depends on the implications of the assumptions on the product selling price.

5. Conclusions

A Mixed Integer Linear Fractional Programming (MILFP) approach is used to minimise the levelized cost of a castor seeds-to-oil supply chain and solved using the Dinkelbach approach. The methodology has the benefit that no assumptions would be required on product selling prices, which are hard to define when novel infrastructures introduce products for yet-to-developed markets. Overall, the examined castor seeds-to-oil supply chain network produces an interesting business case for investments even when land usage restrictions regarding plant allocation are applied.

Acknowledgements

The FP7 RENESENG project under grant agreement 607415 is acknowledged for funding this research.

References

EuroBioRef (2014). Available from: http://www.eurobioref.org/index.php/dissemination.

Gao, J., & You, F. (2017). Computers and Chemical Engineering, 107, 221–236.

Huang, E., Zhang, X., Rodriguez, L., Khanna, M., de Jong, S., Ting, K. C., Lin, T. (2019). Renewable and Sustainable Energy Reviews, 115, 109403.

IPCC. Intergovernmental Panel on Climate Change (IPCC) [online]. Available from: http://www.ipcc.ch/,page, 2017.

Liu, S., Simaria, A. S., Farid, S., and Papageorgiou, L. G. (2014). Computers & Chemical Engineering, 68:151–164, 2014. doi: 10.1016/j. compchemeng.2014.05.005.

Mandade, P. and Shastri, Y. (2019). Journal of Cleaner Production. Elsevier, 231, pp. 1226–1234. doi: 10.1016/J.JCLEPRO.2019.05.311.

Panteli, A., Giarola, S., and Shah (2018). Industrial & Engineering Chemistry Research, 57(30):9849–9865, 2018. doi: 10.1021/acs.iecr.7b05228

Patel, V. R., Dumancas, G. G., Viswanath, L. C. K., Maples, R., & Subong, B. J. J. (2016). Lipid Insights, 9(1), 1–12. https://doi.org/10.4137/LPI.S40233.

Santos, A., Carvalho, A., Barbosa-Póvoa, A. P., Marques, A., & Amorim, P. (2019). Forest Policy and Economics, 105, 112–135. https://doi.org/10.1016/J.FORPOL.2019.05.026.

Severino, L. S., Auld, D. L., Baldanzi, M., Cândido, M. J. D., Chen, G., Crosby, W., Zieler, H. (2012). Agronomy Journal, 104(4), 853–880. https://doi.org/10.2134/agronj2011.0210.

Tsagkari, M., Couturier, J. L., Kokossis A., and Dubois, J. L. ChemSusChem, 9(17): 2284–2297, 2016. doi: 10.1002/cssc.201600309

Yue, D., Kim, M. A., & You, F. (2013). ACS Sustainable Chemistry and Engineering, 1(8), 1003–1014. https://doi.org/10.1021/sc400080x

Sauro Pierucci, Flavio Manenti, Giulia Bozzano, Davide Manca (Eds.)
Proceedings of the 30th European Symposium on Computer Aided Process Engineering (ESCAPE30), May 24-27, 2020, Milano, Italy.
http://dx.doi.org/10.1016/B978-0-12-823377-1.50265-2

Optimization of Biomass Circulating Fluidized Bed Gasifier for Synthesis Applications using Simulation and Response Surface Methodology

Ingrid L. Motta, Andressa N. Marchesan, Rubens Maciel Filho, Maria Regina Wolf Maciel

Laboratory of Optimization, Design and Advanced Control, School of Chemical Engineering, University of Campinas, Av. Albert Einstein 500, Campinas, 13083-852, Brazil

ingridmotta2@gmail.com

Abstract

Biomass gasification is a complex process that uses heat and catalysts to convert biomass into syngas, which can be applied in Fischer-Tropsch (FT) synthesis to produce liquid fuels. As FT requires specific syngas compositions, this work performs an optimization of the operating conditions of a pressurized circulating fluidized bed (CFB) gasifier for such purposes. The CFB operated with sugarcane bagasse as a feedstock and steam as a gasifying agent and was simulated in Aspen Plus v8.6 based on Gibbs free energy minimization with restricted equilibrium. The optimization followed the response surface methodology (RSM), consisting of central composite designs performed in Statistica 7.0 at a 99.0 % confidence level to obtain simplified mathematical models between input factors (temperature, T; steam-to-biomass ratio, S/B; and moisture content, MC) and output factors (cold gas efficiency, CGE; H_2/CO ratio; gasifier heat duty, $Q_{gasifier}$; higher heating value, HHV; and H_2, CO, CO_2, and CH_4 contents). The models were used to generate four optimized cases of pressurized CFBs that returned H_2/CO ratios of 2.15, required for FT reactors. The optimized CFB operates at 916 ºC, 15 bar, S/B of 1.12, and 10 wt.% moisture, generating a syngas stream of low CO_2 and CH_4 contents, which may reduce the syngas cleaning and conditioning costs downstream the gasifier. The results agree with optimizations using other feedstocks and sets of objectives, showing the validity of the models.

Keywords: optimization, response surface methodology, biomass gasification, fluidized bed, Aspen Plus

1. Introduction

Biomass gasification is the conversion of biomass using heat and catalysts mainly into syngas, a gas mixture composed of H_2, CO, CO_2, CH_4, water, and light hydrocarbons (Sadhwani et al., 2017). Syngas can hold a variety of applications, from low-added-value uses in gas turbines to high-added-value uses in Fischer-Tropsch (FT) synthesis (Bain and Broer, 2011).

FT synthesis is an important group of catalytic reactions in which syngas polymerizes into a wide range of long-chain hydrocarbon fuels. To yield certain hydrocarbon fractions, the FT reactor must operate with specific catalysts (usually Fe and Co-based) (Bukur et al., 2016), temperatures, and pressures (Graves et al., 2011), and the syngas must have specific compositions. Thus, the first step consists of obtaining strict syngas compositions via the optimization of the biomass gasifiers' operating conditions.

This chapter continues a previous study on sugarcane bagasse gasification (Motta et al., 2019) and performs an optimization of a pressurized circulating fluidized bed (CFB) gasifier using simulation and response surface methodology (RSM) tools to achieve H_2/CO ratios of 2.15, suitable for FT synthesis. The results show the direct correlation between syngas composition and possible downstream applications.

2. Methodology

The CFB was simulated in Aspen Plus v8.6, and its flowsheet is depicted in Figure 1. The simulation includes a sugarcane bagasse dryer and a gasification stage based on Gibbs free energy minimization with restricted equilibrium. Details on the bagasse characterization and simulation parameters are described elsewhere (Motta et al., 2019).

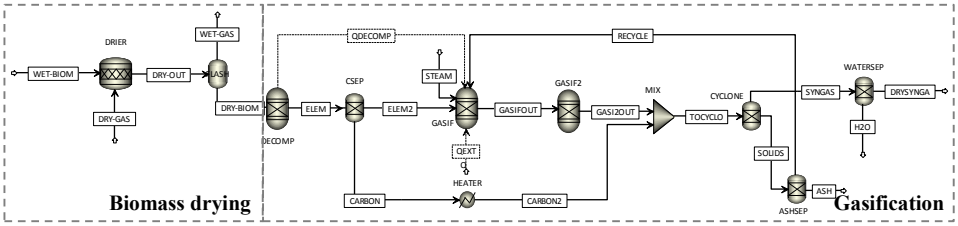

Figure 1 – Simulation flowsheet. Reproduced with permission from Elsevier (Motta et al., 2019).

In the RSM optimization, 2^4 face-centered central composite analyses were run in Statistica 7.0 at a 99 % confidence level. The analyses used coded input factors (Table 1) to ensure that the orders of magnitude of the latter did not influence the obtained models. The analyses were performed for each output factor: higher heating value (HHV), cold gas efficiency (CGE), gasifier heat duty ($Q_{gasifier}$), H_2/CO ratio, as well as H_2, CO, CO_2, and CH_4 contents.

Table 1 – Design matrix used in the RSM for CFB gasifier.

Input factor	2^4 face-centered central composite designs levels		
	-1	0	+1
T (°C)	750	850	950
P (bar)	1	8	15
S/B	0.5	1.0	1.5
MC (%)	10	20	30

In each analysis, the statistically significant parameters were determined using Pareto charts of effects, and full mathematical quadratic models using coded input factors were estimated. Later, the backward elimination methodology was used to obtain simplified models. If a parameter does not contribute to a model's description, its elimination will increase R^2_{adj} (adjusted R-squared). Therefore, the least significant parameters of each Pareto chart were removed one by one until R^2_{adj} no longer increased. The models were then tested for the F-test with 99.0 % confidence to verify their statistical significance.
The models were used to generate four optimized cases (max HHV, min $Q_{gasifier}$, max H_2 content, and min CH_4 content) that returned an H_2/CO ratio of 2.15 at a 15-bar pressure. The optimization cases represent desirable features for either gasifiers or FT reactors: higher HHV means that the syngas streams may also be used for efficient combustion purposes, increasing the process flexibility; minimum $Q_{gasifier}$ implies higher energy efficiencies and lower costs; higher H_2 and lower CH_4 contents are both desirable for FT

synthesis. The H_2/CO ratio of 2.15 was selected because it is a typical syngas ratio for FT synthesis. A 15-bar pressure was fixed because, as the FT reactor downstream of the gasifier works at high pressures, higher gasifier pressures will result in lower syngas compression costs (Spath et al., 2005). All cases had additional restrictions: H_2, CO, CO_2, and CH_4 concentrations must be higher than 0 to avoid negative values; and T, S/B, and MC must vary in the ranges defined for the central composite design ($-1 \leq X \leq 1$). Finally, the optimization was run using the SOLVER tool at Microsoft Excel using the GRG nonlinear solving method.

3. Results and Discussion

Table 2 presents the models obtained via RSM for a CFB at 15-bar pressure. Quadratic models were selected because they provide more accurate adjustments than linear models, as also experienced by Yusup et al. (2014). All models passed the F-test at a 99 % confidence level, indicating that they are statistically significant equations.

All models except for CGE present R^2 values higher than 0.97 and R^2_{adj} higher than 0.96, which shows satisfactory adjustment between the values simulated in Aspen Plus and those calculated by the mathematical models.

Table 3 presents the results obtained for the optimization scenarios. Max HHV and min $Q_{gasifier}$ require lower temperatures (~750 °C) and S/B (0.6–0.7), leading to gas mixtures of low H_2 and CO concentrations and high CH_4 contents. Such cases are comparable because extra gasifier heat duty is necessary to reform CH_4 and other hydrocarbons, and CH_4 is the component of the highest contribution to HHV. The syngas mixtures of max HHV and min $Q_{gasifier}$ are unsuitable for synthesis purposes but can find application in heat and power plants. On the other hand, max H_2 and min CH_4 require higher temperatures (> 900 °C) and S/B (1.12), producing syngas mixtures of appropriate composition for FT synthesis. Such scenarios are equivalent because high temperatures and steam feeds (S/B) shift the chemical equilibrium towards H_2 production and CH_4 consumption in the water-gas shift and steam-methane reforming reactions (Motta et al., 2019). In all cases, low moisture contents were obtained, being 18.4 wt.% advised for the max HHV case and values below 12 wt.% moisture for the other cases.

Figure 2 demonstrates the good agreement between predicted and simulated results of the selected scenarios (max H_2, min CH_4) for compositions (H_2, CO, CO_2, CH_4), H_2/CO ratios, HHV, and $Q_{gasifier}$. Slightly higher deviations for CGE are observed due to the model's lower regression coefficients (R^2 and R^2_{adj}), as shown in Table 3.

Figure 3 shows the response profiles for T, S/B, and some gasification parameters at 10-wt.% moisture content and 15-bar pressure. In the response profiles, dashed lines were used to highlight the areas in which the optimal values of max H_2 and min CH_4 (see Figure 2) could occur. The H_2/CO response profile shows a narrow region (highlighted with dashed lines) that leads to H_2/CO ratios of 2.15, occurring along the entire T range and at S/B values of 0.6 – 1.2. The overlapping of this H_2/CO region onto the other charts, represented by a transparent solid area, shows that the input conditions necessary to achieve the optimal parameters are much stricter and that the gasifier operation is sensitive to changes in parameters.

The response profiles also demonstrate the relationship between the parameters. Even though the T levels for higher H_2 production are opposite to those of higher CH_4 generation, both response profiles present similar shapes. H_2/CO ratios and $Q_{gasifier}$ present opposing effects in terms of S/B, but also similar shapes.

Table 2 – Mathematical coded models obtained via RSM.

Output factor and mathematical model	Eq.	R^2	R^2_{adj}
$CGE(\%) = 77.09 + 0.75T - 2.19S/B - 1.63MC + 0.84MC^2$	(1)	0.988	0.978
$H_2/CO = 2.37 - 0.57T + 0.39T^2 + 0.96S/B - 0.16(S/B)^2 - 0.25MC - 0.32T \times S/B - 0.09T \times MC$	(2)	0.889	0.843
$Q_{gasifier}(MJ/h\ kg_{bagasse}) = 5.74 + 1.09T - 0.62T^2 + 0.86S/B + 0.22(S/B)^2 + 0.61MC + 0.28MC^2$	(3)	0.992	0.985
$HHV(MJ/m^3) = 14.05 - 2.19T + 1.72T^2 - 0.97S/B - 0.34(S/B)^2 - 0.29MC - 0.64MC^2$	(4)	0.991	0.978
$H_2(vol.\%) = 32.69 + 14.68T - 11.45T^2 + 5.42S/B + 2.56(S/B)^2 + 1.64MC + 4.23MC^2$	(5)	0.976	0.961
$CO(vol.\%) = 14.03 + 8.81T - 6.49T^2 - 2.23S/B + 3.36(S/B)^2 - 1.00MC + 2.37MC^2 - 1.55T \times S/B - 0.47T \times MC$	(6)	0.977	0.962
$CO_2(vol.\%) = 30.84 - 10.18T + 7.65T^2 + 0.26S/B - 3.14(S/B)^2 + 0.35MC - 2.81MC^2 + 1.33T \times S/B + 0.39T \times MC$	(7)	0.992	0.982
$CH_4(vol.\%) = 22.25 - 13.27T + 10.25T^2 - 3.30S/B - 2.77(S/B)^2 - 0.98MC - 3.78MC^2 + 0.92T \times S/B$	(8)	0.989	0.978

Table 3 – RSM optimization results for a 15-bar CFB gasifier. P (predicted), S (simulated), *wet basis

Case	T (°C)	P (bar)	S/B	MC (%)	H_2/CO		CGE (%)		$Q_{gasifier}$ (MJ/h $kg_{bagasse}$*)		HHV (MJ/m^3)		H_2 (vol.%)		CO (vol.%)		CO_2 (vol.%)		CH_4 (vol.%)	
					P	S	P	S	P	S	P	S	P	S	P	S	P	S	P	S
Max HHV	750	15	0.60	18.4	**2.15**	1.98	75.6	73.6	3.4	4.8	18.6	17.5	3.7	10.3	1.6	5.2	47.5	42.9	47.4	41.3
Min $Q_{gasifier}$	750	15	0.68	11.3	**2.15**	1.95	77.1	73.9	3.2	4.7	18.2	17.5	5.9	10.2	3.1	5.2	46.0	42.9	45.3	41.4
Max H_2	916	15	1.12	10.0	**2.15**	2.14	78.5	69.9	6.1	8.3	12.8	13.1	41.4	39.3	20.0	18.4	24.1	26.0	14.4	16.2
Min CH_4	915	15	1.12	10.0	**2.15**	2.14	78.5	69.8	6.1	8.3	12.8	13.1	41.4	39.1	20.0	18.3	24.1	26.1	14.4	16.3

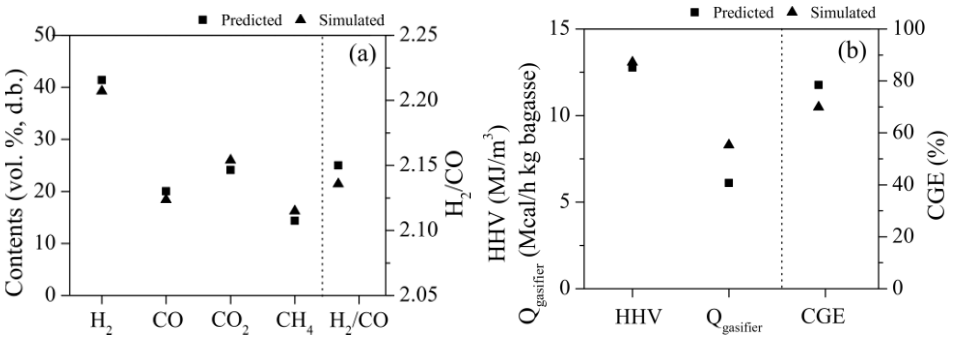

Figure 2 – Comparison of predicted (P) and simulated (S) gasification results of the selected optimization cases: (a) syngas composition; (b) HHV, $Q_{gasifier}$, and CGE.

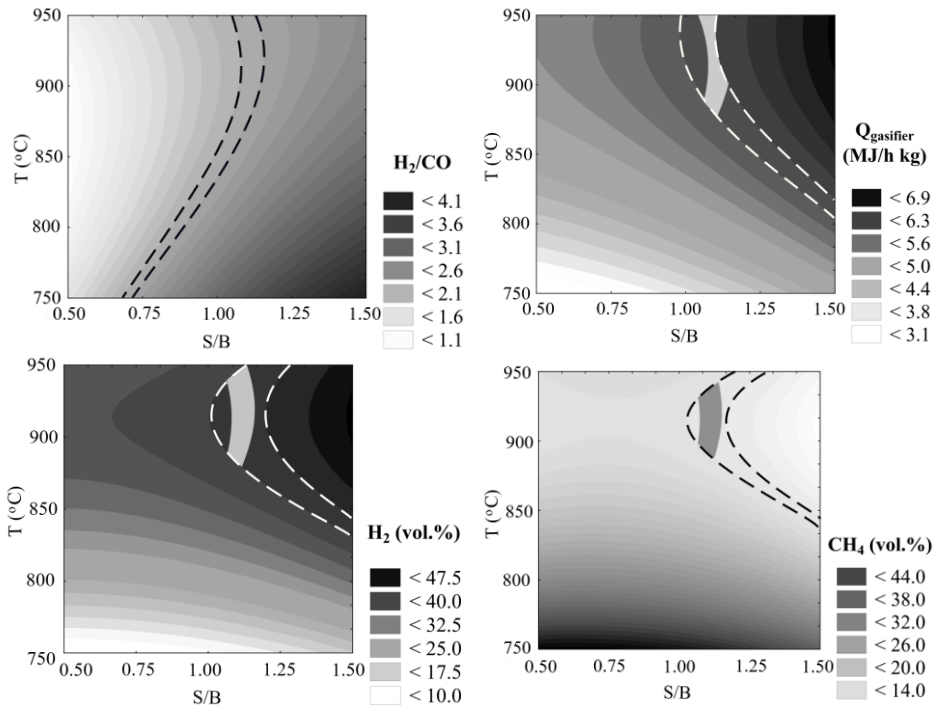

Figure 3 – Response profiles for the analyzed gasification parameters. Dashed lines and transparent areas refer to T and S/B for optimal values at any H_2/CO ratio and 2.15, respectively.

Although several simulation and experimental works have used RSM to optimize syngas composition, yields, heating values, and gasifier performances, none have optimized steam-blown CFB gasifiers for FT synthesis and with the same objective functions of our study. Therefore, the results obtained here can be compared to the literature only in part. In the optimization of an entrained-flow gasifier with rice husk as a feedstock, Gao et al. (2019) aimed at maximizing CO production and CGE, obtaining a 25.15 % CO content and 65.34 % CGE, similar to the results of max H_2 and min CH_4 of this work. In the attempt to maximize H_2 yield and CGE, Silva and Rouboa (2014)

found that and S/B of 1, temperature of 777 °C, and O content of 25 vol.% may produce 29.2 vol.% H_2 in the simulation o
f a steam-air-blown BFB gasifier operating with forest residues. Such an S/B is close to the one obtained in the selected optimized cases of our study. Yusup et al. (2014) found that, to produce syngas containing 82.11 vol.% H_2 in a pilot-scale fluidized bed gasifier, a much higher S/B of 2.0 was necessary.
Thus, the optimization of a biomass gasifier for a specific syngas downstream application requires the understanding of the correlation between input parameters (such as biomass properties and operating conditions) and output parameters (CGE, heating value, syngas composition).

4. Conclusions

The optimization of a sugarcane bagasse pressurized CFB gasifier for downstream synthesis purposes via RSM was performed in this work, analyzing scenarios of max HHV, min gasifier heat duty ($Q_{gasifier}$), max H_2 production, and min CH_4 generation. Although the cases of max HHV and min $Q_{gasifier}$ required lower temperatures and S/B, they resulted in low H_2 and CO concentrations and high CH_4 contents, which are unsuitable for synthesis purposes. On the other hand, the cases of max H_2 and min CH_4 levels produced syngas mixtures of appropriate starting composition for FT synthesis, requiring 916 °C, 15 bar, S/B of 1.12, and 10 wt.% moisture content. The results agree with other optimization studies and propose a new application for circulating fluidized bed gasifiers.

Acknowledgments

The authors would like to thank CNPq, Coordenação de Aperfeiçoamento de Pessoal de Nível Superior - Brasil (CAPES) - Finance Code 001, and São Paulo Research Foundation (FAPESP) grant #2015/20630-4 for the financial support.

References

R.L. Bain, K. Broer, 2011, Gasification, Thermochemical Processing of Biomass: Conversion into Fuels, Chemicals and Power, 1st ed, Chichester, John Wiley & Sons, 47-77.

D.B. Bukur, B. Todic, N. Elbashir, 2016, Role of water-gas-shift reaction in Fischer-Tropsch synthesis on iron, Catal Today, 275, 66-75.

X. Gao, F. Xu, F. Bao, C. Tu, Y. Zhang, Y. Wang, B. Li, 2019, Simulation and optimization of rice husk gasification using intrinsic reaction rate based CFD model, Renew Energy, 139, 611-620.

C. Graves, S.D. Ebbesen, M. Mogensen, K.S. Lackner, 2011, Sustainable hydrocarbon fuels by recycling CO_2 and H_2O with renewable or nuclear energy,Renew Sustain Energy Rev,15,2-23.

I.L. Motta, N.T. Miranda, R. Maciel Filho, M.R. Wolf Maciel, 2019, Sugarcane bagasse gasification: simulation and analysis of different operating parameters, fluidizing media, and gasifier types, Biomass Bioenergy, 122, 433-445.

N. Sadhwani, P. Li, M.R. Eden, S. Adhikari, 2017, Process Modeling of Fluidized Bed Biomass-CO_2 Gasification using ASPEN Plus, Computer Aided Chemical Engineering, 40, 2509-2514.

V. Silva, A. Rouboa, 2014, Optimizing the gasification operating conditions of forest residues by coupling a two-stage equilibrium model with a response surface methodology, Fuel Process Technol, 122, 163-169.

P. Spath, A. Aden, T. Eggeman, M. Ringer, B. Wallace, J. Jechura, 2005, Biomass to Hydrogen Production Detailed Design and Economics Utilizing the Battelle Columbus Laboratory Indirectly- Heated Gasifier, Golden, National Renewable Laboratory.

S. Yusup, Z. Khan, M.M. Ahmad, N.A. Rashidi, 2014, Optimization of hydrogen production in in-situ catalytic adsorption (ICA) steam gasification based on response surface methodology, Biomass Bioenergy, 60, 98-107.

Sauro Pierucci, Flavio Manenti, Giulia Bozzano, Davide Manca (Eds.)
Proceedings of the 30th European Symposium on Computer Aided Process Engineering (ESCAPE30), May 24-27, 2020, Milano, Italy.
http://dx.doi.org/10.1016/B978-0-12-823377-1.50266-4

Modelling and Analysis of Microbial Fuel Cells with a Two-species Anode Biofilm

Ziming Yang, Aidong Yang*

Department of Engineering Science, University of Oxford, Parks Road, Oxford, OX1 3PJ, United Kingdom

aidong.yang@eng.ox.ac.uk

Abstract

A mathematical model for continuous Microbial Fuel Cells (MFCs) with a two-species anode biofilm was developed, taking either Mediator-Based Extracellular Electron Transfer (MET) or Direct Conduction-Based Extracellular Electron Transfer (DET) as the electron transfer mechanism. The results of numerical simulation revealed the impact of key parameters on biofilm composition and current generation, several optimal settings for current generation, and a number of trade-offs between the impacts of different factors. These findings offer new insights on multi-species biofilms governed by bioelectrochemical kinetics and mass and electron transfer, and have the potential to guide the design and operation of multi-species MFCs or other similar systems.

Keywords: Microbial fuel cells, Two-species biofilm modelling, Extracellular electron transfer, Biofilm composition; Current generation

1. Introduction

Climate change and other environmental issues associated with the use of fossil fuels call for urgent exploration of green and renewable energy options, including bioelectrochemical systems such as Microbial Fuel Cells (MFCs). An MFC relies on the biofilm attached on the anode to convey electrons from substrate. The microorganisms that produce electrons in the biofilm and carry out Extracellular Electron Transfer (EET) are called Electron Active Bacteria (EAB). There are two EETs widely accepted so far: Mediator-Based Extracellular Electron Transfer (MET) and Direct Conduction-Based Extracellular Electron Transfer (DET). In MET, electron transfer is realised through the reduction and the oxidisation of soluble mediators at the EAB and the anode surface, respectively. In DET, electrons are transferred directly from the EAB to the anode surface by exchanging with the conductive biofilm matrix.

While an anode biofilm may comprise a single microbial species, it has been proven that synergy exists in a multispecies biofilm which enhances electron transfer efficiency and power output compared to pure culture (Logan, 2009; Liu et al., 2017). A particular type of multispecies consortium is “fermenter-EAB”, where the EAB achieves electrons generation and transportation, which relies on the Fermentative Bacteria (FB) as a fermenter to digest the primary substrate to an intermediate substrate that the EAB can consume.

In general, the spatial heterogeneity across a biofilm, the electron transfer mechanism and interactions between different microbial species ultimately determine the maximum power output of an MFC. However, the interplay between these factors under different process settings has not been systematically studied, particularly in the continuous MFCs. This study is therefore aimed at analysing the impact of key parameters on the

composition of the multispecies anode biofilm and power generation with two alternative EET mechanisms in continuous MFCs.

2. Mathematical model

A 1-D, time-dependent model for an MFC with a two-species 'fermenter-EAB' biofilm is established. The model constructed only considers the growth and characteristics of the biofilm in the x-axis, which is perpendicular to the anode surface. The higher-dimensional aspect is not considered as biofilm heterogeneity was reported to be higher in the direction proportional to substratum than in the horizontal direction (Zhou et al., 2009). The whole model comprises three domains: bulk liquid, biofilm and electrode. The model focuses on the biofilm; planktonic biomass (i.e. biomass in the bulk liquid) is not considered. In the following, the main kinetics and conservation equations are presented.

2.1. Bulk liquid

It is assumed that the bulk liquid sub-domain is well-mixed and the volumetric flowrates of the inlet (feeding) and outlet streams are identical. For a soluble component, mass balance that includes diffusion and convection is applied:

$$\frac{dC_{S,B}}{dt} = -\frac{1}{V_B} \cdot n_{S,F} \cdot A_F + \frac{V_f}{V_B} \cdot (C_{S,in} - C_{S,B}) \tag{1}$$

where $C_{S,B}$, $C_{S,in}$ are the concentration of a soluble component in the bulk liquid and inlet flow, respectively; V_B is the volume of the bulk liquid; V_f is the volumetric flowrate of inlet/outlet flow; $n_{S,F}$ denotes the molar flux of a soluble component across the biofilm/bulk liquid interface, of which area is A_F . According to the Fick's law and the assumption of constant concentration gradient in the diffusion layer, $n_{S,F}$ is expressed as:

$$n_{S,F} = -D_{S,F} \frac{\partial C_{S,F}}{\partial x}|_{x=L_F} = (\frac{D_{S,B}}{L_D}) \cdot (C_{S,B} \cdot \varepsilon - C_{S,F}|_{x=L_F}) \tag{2}$$

where $D_{S,F}$ is the diffusivity of a soluble component in the biofilm; $C_{S,F}$ is the concentration of a soluble component in the biofilm; L_F , L_D are the thickness of biofilm and diffusion layer, respectively; the biofilm porosity, ε is introduced to modify and indicate the actual soluble concentration at the biofilm/bulk liquid interface.

2.2. Biofilm

2.2.1. Growth kinetics

For FB, its specific growth rate, μ_{FB} can be modelled by the Monod Equation:

$$\mu_{FB} = \mu_{\max,FB} \cdot (C_{P,F} / (C_{P,F} + K_P)) \tag{3}$$

where $\mu_{\max,FB}$ is the maximum specific growth rate for FB; $C_{P,F}$ represents the concentration of primary substrate in the biofilm and K_P denotes half-saturation constant.

For EAB, its specific growth rate is controlled by both the substrate concentration and the concentration of the Electron Acceptor (EA). In MET, the oxidised mediator (*Mo*) serves as the primary EA and the EAB's specific growth rate, $\mu_{EAB,M}$ therefore can be given by the double Monod equation (Bae and Rittmann, 1996):

$$\mu_{EAB,M} = \mu_{\max,EAB} \cdot \frac{C_{I,F}}{C_{I,F} + K_I} \cdot \frac{C_{Mo,F}}{C_{Mo,F} + K_{Mo}} \tag{4}$$

where $\mu_{\max,EAB}$ is the maximum specific growth rate for EAB; $C_{I,F}$ and $C_{Mo,F}$ represent the concentration of intermediate substrate and *Mo* in the biofilm, respectively; K_I and K_{Mo} correspond to the half-saturation constant for intermediate substrate and *Mo*, respectively.
As for the DET mechanism, the only EA is the anode surface, which is non-soluble. In order to model the EAB's specific growth rate with DET, $\mu_{EAB,C}$, the Nernst-Monod equation is applied, using the anode potential, V_a to substitute the soluble EA's concentration (Marcus et al., 2007):

$$\mu_{EAB,C} = \mu_{\max,EAB} \cdot \frac{C_{I,F}}{C_{I,F} + K_I} \cdot \frac{1}{1+\exp(-F(V_a - E_{KA})/RT)} \tag{5}$$

where E_{KA} is the anode potential corresponding to the half $\mu_{\max,EAB}$; F is the Faraday constant; R is the ideal gas constant; T is the operating temperature.

2.2.2. Mass balance

Mass balance for any soluble component in the biofilm (including primary substrate, intermediate substrate and for MET case, oxidised and reduced forms of the mediator) is:

$$\frac{\partial C_{S,F}}{\partial t} = \frac{\partial}{\partial x}(D_{S,F}\frac{\partial C_{S,F}}{\partial x}) - R_{S,F} \tag{6}$$

where $R_{S,F}$ represents the consumption rate of a soluble component in the biofilm. At the biofilm/bulk liquid interface, Eq. (2) is applied. The boundary condition for the anode/biofilm interface is established by stating the equality between the production rate (per unit anode surface area) and the diffusion flux (Picioreanu et al., 2007).
For biomass, its mass balance is (Wanner and Gujer, 1986; Marcus et al., 2007):

$$\frac{\partial C_{X,F}}{\partial t} + \frac{\partial(vC_{X,F})}{\partial x} = R_{X,F} \tag{7}$$

where $C_{X,F}$ is the biomass concentration of any type of microbial species in the biofilm; $R_{X,F}$ is the net reaction rate of biomass in the biofilm, which is the product of biomass yield from its corresponding substrate and $R_{S,F}$; v is the advective velocity due to the growth of the biofilm, which is determined by the sum of $R_{X,F}$ (Wanner and Gujer, 1986; Marcus et al., 2007).

2.3. Electrode

In the case of MET, the current density, i_M is proportional to the net reaction rate of the mediator conversion process at the anode surface, r_E , which itself is given by the Butler-Volmer equation:

$$r_E = k_a C_{Mr,F}|_{x=0} \exp((1-\beta)nFV_a/RT) - k_c C_{Mo,F}|_{x=0} \exp(-\beta nFV_a/RT) \tag{8}$$

where k_a , k_c are the rate constant for oxidisation and reduction processes, respectively; $C_{Mr,F}|_{x=0}$, $C_{Mo,F}|_{x=0}$ denote the concentration of reduced and oxidised forms of the mediator at the anode surface, respectively; β is the transfer coefficient; n is the number of electrons transferred per redox mediator reaction.
With DET, the current density i_C is obtained based on the electron conservation and Ohm's law (Marcus et al., 2007; Renslow et al., 2013):

$$k\frac{\partial^2 V_a}{\partial x^2} = F \cdot R_C \tag{9}$$

where R_C is the electron generation rate via DET, which is proportional to the specific growth rate of EAB (see Eq. (5)).

2.4. Model implementation

The model is applied for the anodic biofilm with *Shewanella oneidensis* (as known as MR1) and *E. coli*. *E. coli* as a fermentor converts glucose to formate; the latter is treated as the only intermediate substrate to be utilised by MR1, the EAB in this case. All simulations were carried using COMSOL Multiphysics Software.

3. Results and discussion

3.1. The effect of feeding flowrate

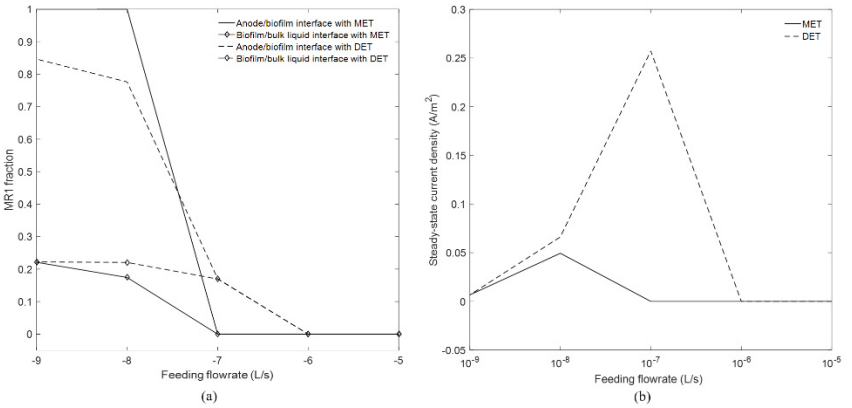

Figure 1 Impacts of the feeding flowrate. (a) MR1 fraction at the anode/biofilm interface (without 'diamond') and biofilm/bulk liquid interface (with 'diamond') via MET (solid line) and DET (dashed line) at the steady state; (b) Steady-state current density profiles with MET and DET.

As shown in Figure 1(a), with either MET or DET, there is more MR1 at the anode surface end of the biofilm than the end interfacing with the bulk liquid when flowrate is sufficiently low to allow MR1 to exist in the biofilm. In those cases, the combination of decreasing *Mo* (V_a for DET) and increasing glucose concentration weakens the competitiveness of MR1 from anode/biofilm interface, hence the level of MR1 fraction drops. The increase in the feeding flowrate generally leads to the decrease of MR1 fraction across the biofilm and eventually causes MR1 to disappear. The decline of MR1 is due to the dilution effect of a higher feeding flowrate, which results in a lower formate concentration that restricts the growth of MR1. On current generation, Figure 1(b) shows that current density in the case of DET is much higher compared to MET, which is due to the higher overall growth rate of MR1. However, the tendencies of steady-state current density change with the feeding flowrate are similar between the two cases: the current density initially rises as more formate is produced and subsequently descends due to the decrease in MR1 fraction. The above results suggest that biofilm composition and current density are affected by the trade-offs between substrate supply and dilution along with the changing feeding flowrate. The respective values of $1\times10^{-8} L/s$ and $1\times10^{-7} L/s$ for the flowrate with MET and DET are shown to be optimal for the maximization of the steady-state current density.

3.2. The effect of feed primary substrate (glucose) concentration

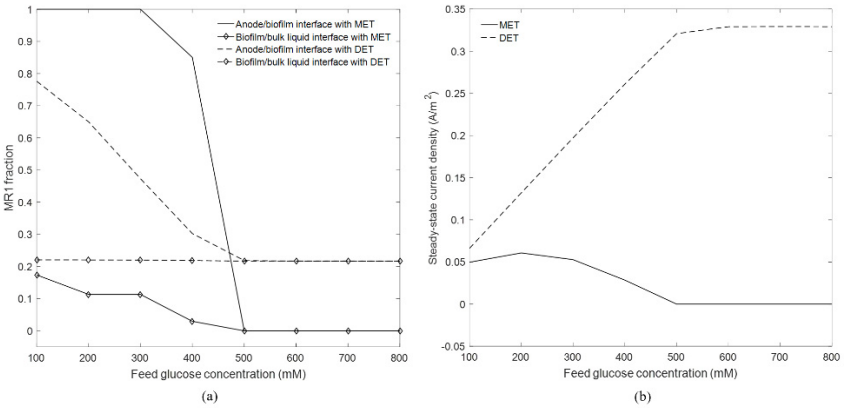

Figure 2 Impacts of the feed glucose concentration. (a) MR1 fraction at the anode/biofilm interface (without 'diamond') and biofilm/bulk liquid interface (with 'diamond') via MET (solid line) and DET (dashed line) at the steady state; (b) Steady-state current density profiles with MET and DET.

As shown in the Figure 2(a), for MET, overall MR1 fraction drops when the biofilm is fed with more concentrated glucose. There are two causes: (1) the specific growth rate of *E. coli* in the biofilm is promoted by reducing the glucose limitation. When glucose concentration is 500mM or higher, even the *E. coli* at the most remote location (i.e. anode/biofilm interface) grows faster than MR1 and eventually repels MR1 completely; (2) the specific growth rate of MR1 is restricted by the lower level of *Mo*, which will be illustrated in the following section. In the case of DET, the fraction of MR1 at the anode/biofilm interface has the similar declining trend with MET. It is noticeable, however, that the biofilm composition at the biofilm/bulk liquid interface almost remains constant. This is because of the identical specific growth rate of the two species at this interface (revealed by simulation results, not shown here). As mentioned in the *section* 3.1, the current generated via MET is determined by both biofilm composition and substrate supply. For feed glucose concentration, an optimal value corresponding to the maximum steady-state current density exists at 200mM in this case. With DET, Figure 2(b) shows that current density is primarily governed by the substrate concentration until it reaches a plateau.

3.3. The effect of initial concentration of Mo in the bulk liquid

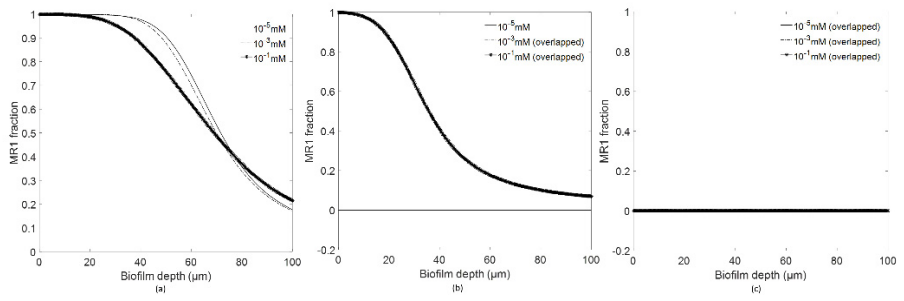

Figure 3 Impact of initial concentration of *Mo* in the bulk liquid on steady-state MR1 fraction, with the feed glucose concentration at (a) 100mM; (b) 300mM; and (c) 500mM.

The simulations with MET reveal that the impact of initial concentration of *Mo* in the bulk liquid on the steady-state biofilm composition varies with the values of the feed

glucose concentration. As shown in the Figure 3(a) and (c), the overall biofilm composition is independent of the initial concentration of *Mo* in the bulk liquid when the level of the feed glucose concentration is either the lowest (i.e. 100mM) or the highest (i.e. 500mM). With the lowest feed glucose concentration, *Mo* is consumed slowly and thus the specific growth rate of MR1 is maintained and it is able to co-exist with *E. coli*. Conversely, *Mo* is exhausted rapidly in the case of the higher feed glucose concentration. Coupled with the faster specific growth rate of *E. coli* resulting from better substrate (glucose) supply, MR1 is repelled completely from the biofilm. When the 'middle' value of the feed glucose concentration (i.e. 300mM) is selected, the increase of the initial concentration of *Mo* in the bulk liquid can change the steady-state biofilm from the '*E. coli only*' type to the '*E. coli*-MR1 co-existence' type. The value of $1\times10^{-3}mM$ marks this transition, being the lowest initial level of *Mo* to be able to sustain MR1 in the biofilm.

4. Conclusion

A two-species, 'fermenter-EAB' anode biofilm, modelled in this work as part of a continuous MFC, was shown by our simulation studies to be shaped by a number of factors, including the kinetics of microbial growth and electrochemical reactions, mass and electron transfer mechanisms. The modelling outcomes particularly implied that the biofilm composition would change with the feeding flowrate, feed concentration of the primary substrate and the initial concentration of mediators in the bulk liquid. Our results also showed the trade-offs between the impacts of various factors, and the existence of optimal settings for the purpose of improving current generation.

Acknowledgement

The financial support from China Scholarship Council (CSC) to Z. Y. is greatly appreciated

References

Andrew Kato Marcus, Ce´sar I. Torres, Bruce E. Rittmann. 2007. "Conduction-Based Modeling of the Biofilm Anode of a Microbial Fuel Cell." *Biotechnology and Bioengineering* 98 (6): 1171–82.

Bae, Wookeun, and Bruce E. Rittmann. 1996. "A Structured Model of Dual-Limitation Kinetics." *Biotechnology and Bioengineering* 49 (6): 683–89.

Liu, Ting, Yang Yang Yu, Tao Chen, and Wei Ning Chen. 2017. "A Synthetic Microbial Consortium of Shewanella and Bacillus for Enhanced Generation of Bioelectricity." *Biotechnology and Bioengineering* 114 (3): 526–32.

Logan, Bruce E. 2009. "Exoelectrogenic Bacteria That Power Microbial Fuel Cells." *Nature Reviews Microbiology* 7 (5): 375–81.

Picioreanu, Cristian, Ian M Head, Krishna P Katuri, Mark C M van Loosdrecht, and Keith Scott. 2007. "A Computational Model for Biofilm-Based Microbial Fuel Cells." *Water Research* 41 (13): 2921–40.

Renslow, Ryan, Jerome Babauta, Andrew Kuprat, Jim Schenk, Cornelius Ivory, Jim Fredrickson, and Haluk Beyenal. 2013. "Modeling Biofilms with Dual Extracellular Electron Transfer Mechanisms." *Physical Chemistry Chemical Physics* 15 (44): 19262–83.

Wanner, O., and W. Gujer. 1986. "A Multispecies Biofilm Model." *Biotechnology and Bioengineering* 28 (3): 314–28.

Zhou, Xiao-Hong, Yu-Qin Qiu, Han-Chang Shi, Tong Yu, Miao He, and Qiang Cai. 2009. "A New Approach to Quantify Spatial Distribution of Biofilm Kinetic Parameters by in Situ Determination of Oxygen Uptake Rate (OUR)." *Environmental Science & Technology* 43 (3): 757–63.

Sauro Pierucci, Flavio Manenti, Giulia Bozzano, Davide Manca (Eds.)
Proceedings of the 30th European Symposium on Computer Aided Process Engineering (ESCAPE30), May 24-27, 2020, Milano, Italy.
http://dx.doi.org/10.1016/B978-0-12-823377-1.50267-6

Development of Systems Modelling Framework for Waste-to-Resource Transformation

Ivan Robles[a], Miao Guo[a, b, *]

[a] *Department of Chemical Engineering, Impeiral College London, SW7 2AZ, UK*

[b] *Department of Engineering, Strand Campus, King's College London, WC2R 2LS, UK*

miao.guo@kcl.ac.uk

Abstract

Due to complex composition e.g. carbohydrates, lipids, protein, lignin, cellulose and hemicellulose, organic fraction municipal solid waste (OFMSW) represent nutrient and carbon rich resources. Full utilisation of OFMSW resources requires a value chain transformation towards pro-active resource recovery. This study focuses on the waste value chain optimisation to recover value added products from OFMSW.

Our research presents a systems modelling approach, which integrates spatial data analyses, mixed integer linear programming (MILP) optimisation and technology performance evaluation to inform the waste-to-resource value chain design. Variation in OFMSW quantity and composition across the UK and over 600 existing anaerobic digestion (AD) operational plants in the UK have been accounted for in the model. Based on the 2018 UK land cover map, potential sites for new waste-recovery facilities have been identified and the transportation and logistics were modelled based on the network analyses of existing UK road transport infrastructures. Furthermore, OFMSW generation scenarios were constructed, where the probability was estimated based on OFMSW correlation with environmental variables. The optimisation problems were solved to provide insights into the economically optimal design of OFMSW-recovery value chains, which highlight the spatially-explicit solutions on technology choice, sizing, location, and logistics of AD and thermochemical treatment facilities.

Keywords: OFMSW, waste recovery, MILP, value chain optimisation, anaerobic digestion

1. Introduction

Global municipal solid waste (MSW) growth is projected to exceed 11 million tons per day (59%-68% organic fraction (OFMSW)) by 2100 under 'business as usual' and a significant amount (330km^3 per year) of municipal wastewater (WW) is generated. Increasing waste trends are particularly intense in less developed countries and contribute to resource stress, greenhouse gases and environmental degradation. The transition from a linear fossil-based economy to a circular bio-based economy offers a mechanism to tackle environmental changes and degradation.

In conventional waste management value chains, OFMSW and WW along with other waste streams have been regarded as by-products (carrying zero or low-value). In fact, OFMSW and WW streams are not only carbon-rich resources as energy carrier but also contain high nutrient values. The waste sector represents promising opportunities for resources to be converted to value-added products under circular economy. To exploit waste resource value requires a transformative value chain, which calls for robust

projection of waste quantity and composition and waste recovery planning from whole systems perspectives. Efficient planning (e.g. sizing and logistics) and operation of waste recovery facilities requires continuous and consistent waste feedstock supply. However, it is complex to quantity waste feedstock due to highly varying composition and low traceability. These are dependent on spatially-explicit socio-economic factors and seasonally environmental variables. Despite the increasing interests in waste volume forecast by using material flow models, regression analysis, machine learning and artificial intelligence techniques, projection of waste composition remains open.

By far the most widespread resource recovery in the WW and OFMSW sector is anaerobic digestion (AD). The generated biogas i.e. carbon recovery, is often used for onsite combined-heat-and-power generation (CHP), but could be upgraded and injected into the natural gas grid (BtG), or used for methanol and biodegradable plastic production, or reformed to hydrogen. Other recovery technologies e.g. nutrient recovery and digestate utilization are also of interest. To maximize the waste resource recovery, existing AD facilities could be further optimized via systems design integrating biogas conversion with value-added carbon and nutrient resource recovery.

This study presents an OFMSW supply chain optimization model considering the existing AD plants and waste supply variability where the model application in UK case study is demonstrated.

2. Methodology

2.1. Spatial data analyses

Geographic Information Systems (GIS) is recognized as an efficient approach to analyze complex spatial phenomena and has been used to model various applications at multiple levels spanning from waste resource potential to conversion technologies. In this study, the UK was divided into 70 grid cells; ArcGIS v10.7 was applied to analyze spatial data to 1) map out OFMSW resource availability and existing AD facilities; 2) screen and identify the potential AD locations; 3) analyze networks and logistic data.

2.2. Deterministic optimization

For a given set of technology options and spatially explicit OFMSW resource distribution, this study aims to design the economic optimal strategies for technology integration, logistics and resource flows. A mixed integer linear programming (MILP) model is developed to solve the optimization problem.

The objective function (Eq. (1)) is to maximize the profit J, which is determined by the revenue (Rev^{Tot}), and the total costs including the capital costs (Cap^{Total}), operational costs (Opt^{ProDry}), and transport costs (Opt^{trans}).

$$J = Rev^{Tot} - Opt^{trans} - Opt^{ProDry} - Cap^{Total} \quad (1)$$

The transport cost is defined as Eq.(2), where variable $trans_{sp}^{Tot}$ denotes total transport costs for each chemical species present in waste stream sp. The total operational cost (Eq.(3)) is dependent on two variables i.e. operational costs of each technology $Opt_{\theta}^{Proc}$and costs for drying digestate Opt_{g}^{Dry} in cell g. The operational costs of existing AD plant, new AD plants with BtG and CHP as well as post-treatment of digestate are determined by amount of products generated from resource recovery ($Prd_{\theta,sp}$) and operational costs ($\delta_{\theta,sp}^{op}$) of each technology θ (Eq. (4)). The total cost of digestate drying in each cell prior to being transported to post-treatment is defined as Eq.(5), where variable $Prd_{g,sp}$ represents chemical species produced in cell g. The

total capital cost for new AD (JN) and posttreatment facilities (K) is defined in Eq.(6), where binary variable $y_{\theta,st}^{st}$ indicates the presence of a type/size (st) of a given technology (θ) and parameter δ_{st}^{cap} denotes the annualised capital costs for a given technology type st. As given in Eq. (7) the total revenue generated by selling the products is calculated by amount of products from waste recovery and unit price (δ_{sp}) of chemical specie sp.

$$Opt^{trans} = \sum_{sp\in\{W,D\}} trans_{sp}^{Tot} \quad (2)$$

$$Opt^{ProDry} = \sum_{\theta\in\vartheta} Opt_{\theta}^{Proc} + \sum_{g\in G} Opt_{g}^{Dry} \quad (3)$$

$$Opt_{\theta}^{Proc} = \sum_{sp} Prd_{\theta,sp}\delta_{\theta,sp}^{op}\,, \quad (4)$$

$$Opt_{g}^{Dry} = Prd_{g,sp}\delta^{dry} \quad (5)$$

$$Cap^{Total} = \sum_{\theta\in JN\cup K}\sum_{st\in St} y_{\theta,st}^{st}\,\delta_{st}^{cap} \quad (6)$$

$$Rev^{Tot} = \sum_{sp\in Pr}\sum_{\theta\in\vartheta} Prd_{\theta,sp}\,\delta_{sp} \quad (7)$$

A range of constraints have been introduced in the developed MILP model to bound the selection of technology locations, size and types and constrain transport network and resource and chemical species flows. The model was parameterized using the costs database we developed based on the publicly available information.

2.3. Stochastic optimization

A two-stage stochastic optimization model was developed to optimize the OFMSW supply chain under uncertainty, where Benders decomposition method was applied (Benders, 1962; Birge and Louveaux, 1988). Two sets of decision variables have been defined. The first-stage variables include selection of technology capacity and type and second-stage variables cover the flows of resource and chemical species and transport network. The objective function under master problem is to minimize the total capital costs of new AD plants (JN) as defined by Eq.(8), where STJ denotes the new AD subset of size/type. The new plant locations are constrained by Eq.(9) and Eq.(10), which define that only one location exists for any technology and new technologies can only be present in the potential cells identified by GIS analyses (binary parameter φ_g). The selection of size/type (st) of each technology (θ) is determined by binary variable $y_{\theta,st}^{st}$ (Eq.(11)). The continuous variable $Cpct_{sp,g,st}$ defines the capacity selected for each technology type and *sp* recovery, which is determined by given maximum capacity ($Cpt_{\theta,st,sp}^{max}$) of technology θ type *st* to recover *sp* and binary variable $z_{\theta,g,st}^{cpct}$ (Eq.(12)). By solving master problem, the optimal solution for capacity variable ($Cpct_{sp,g,st}$) is sent to the sub-problem as a constant. A set of logical constraints Eq.(13-15) were introduced to bound the capacity solution consistent with the type and location of technologies. In addition constraints were introduced in the master problem to bound 1) the operating capacity lower than the waste feedstock availability; 2) maximum landfilled waste not exceeding environmental regulation and non-negative.

$$Cap^{Total} = \sum_{\theta\in JN}\sum_{st\in STJ} y_{\theta,st}^{st}\,\delta_{st}^{cap} \quad (8)$$

$$\sum_{g\in G} y_{\theta,g}^{\theta} \le 1\,,\ \theta\in JN \quad (9)$$

$$y_{\theta,g}^{\theta} \le \varphi_g,\ \theta\in JN, g\in G \quad (10)$$

$$\sum_{st\in STJ} y_{\theta,st}^{st} = \sum_{g\in G} y_{\theta,g}^{\theta}, \ \theta \in JN \quad (11)$$

$$Cpct_{sp,g,st} = \sum_{\theta\in JN} Cpt_{\theta,st,sp}^{max} z_{\theta,g,st}^{cpct}, \ g \in G, sp \in \{elec, bgs\}, st \in STJ \quad (12)$$

$$z_{\theta,g,st}^{cpct} \leq y_{\theta,g}^{\theta} \qquad \theta \in JN, st \in STJ, \ g \in G \quad (13)$$

$$z_{\theta,g,st}^{cpct} \leq y_{\theta,st}^{st} \qquad , \theta \in JN, st \in STJ, \ g \in G \quad (14)$$

$$z_{\theta,g,st}^{cpct} \geq y_{\theta,st}^{st} + y_{\theta,g}^{\theta} - 1 \ , \theta \in JN, st \in STJ, \ g \in G \quad (15)$$

The objective function of sub-problem (Eq.(16)) is to maximize the profit, which is determined by the revenue, Rev^{Tot}, operational costs, Opt^{Pro}, transport costs Opt^{trans}, landfill cost, Lnd^{TX}, and the penalisation of the slack variable $Slck^{Pen}$. The landfill costs and slack variables are given in Eq.(17) and Eq.(18), where NP_g represents landfilled waste in cell g, δ^{LndTX} denotes the landfill tax, $Slck^{Pen}$ is the summation of all slack variables$(Slck_g)$ in a given cell. A set of constraints were introduced to constrain the technology capacities and resource flow balances and transport network.

$$J = Rev^{Tot} - Opt^{trans} - Opt^{Pro} - Lnd^{TX} - Slck^{Pen} \quad (16)$$

$$Lnd^{TX} = \sum_{g\in G} NP_g \, \delta^{LndTX} \quad (17)$$

$$Slck^{Pen} = \sum_{g\in G} Slck_g \, \mathcal{M} \quad (18)$$

3. Results

3.1. Spatial data analyses

OFMSW can be categorised as garden waste, food waste or other organic waste. The weighted averages waste composition produced under each categories in each authority were calculated (as shown in Figure 1) based on the 12-year data (April 1st 2006 to Januay 1st 2018) derived from (WDF, 2019). AD plants were categorised into five types based on the feedstock as shown in Figure 1.

To prevent issues with the installation of the new facilities, steep and elevated terrain was identified and excluded from the set of potential areas for plant construction (areas which have an incline larger than >10-15° and an elevation over 250m (Lovett et al., 2014). To achieve this, a digital elevation model (DEM) of the UK (EROS, 1996) is used. Numerous sample areas were constructed within each cell the elevation measurements from the DEM were extracted; only those under 250m were selected. The sensitive areas including forests, reserves, urban areas and water bodies are also identified and excluded as potential areas for waste-treatment site construction, where the CORINE land cover data were used. As plotted in Figure 2, the locations of the existing AD facilities correspond to feasible regions denoted by the black color, which verify the spatial data analyses. The road transport network was developed based on the UK road map obtained from Ordnance Survey (OS OpenData, 2019).

3.2. Deterministic optimization results

To obtain an optimal configuration of the technologies and distribution for OFMSW processing, the model presented in Section 2.2 was solved using the PuLP 1.6.9 library for Python 3.5. The optimal solution for baseline (waste generation remaining constant in future) is plotted out in Figure 3 as an example. Our results suggested that the optimal

solutions are sensitive to the quantity of waste produced in the future, where three scenarios were constructed to represent waste generation ranging from 50% to 150% of the 2018 level. For the baseline scenario (100% of 2018 level), the total cost for the system operation including annualized capital costs is 155.7 Million £/year, while the total revenue for selling the products made is 179.85 million £/year. This leads to a whole system profit of 24.1 million £/year and a specific profit of 13.7 £/tonne of waste processed. The cost of transporting waste and digestate, is relatively small (1.79 Million £/year) in comparison to operational and capital inputs for AD facilities. The ratio of OPEX to CAPEX decrease with the increase in future waste generation (4.59:1, 3.89:1 and 2.96:1 for 50%, 100% and 150% waste generation scenarios respectively).

3.3. Stochastic optimization results

We developed a projection model for waste generation considering environmental variables and building OFMSW scenarios for stochastic optimization. The effects of technology minimum capacity and landfilled waste threshold and landfill tax rates have been investigated. Our previous research has identified a strong correlation between temperature and OFMSW generation in the UK (Adeogba et al., 2019). In this study, based on the correlation between OFMSW and temperature, we estimated OFMSW production throughout the year 2018 with an equal time spacing of 1.2 million sample points (Figure 4A); a histogram with 5000 bins was then constructed to represent the probability distribution functions (Figure 4b) and used to calculate the probability of OFMSW generation scenarios (Figure 4 c) for stochastic optimization modelling.

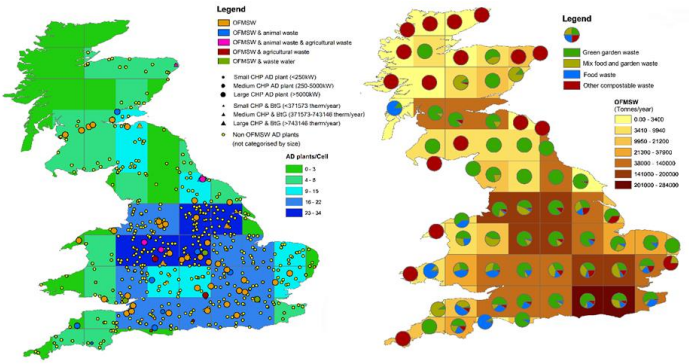

Figure 1 Characterization of anaerobic digestion plants which use OFMSW as feedstock in Great Britain and percentage category of OFMSW per area

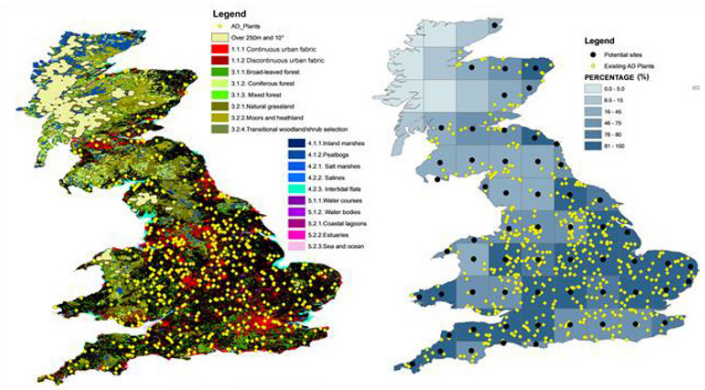

Figure 2 Suitable areas for AD locations overlaid by existing locations

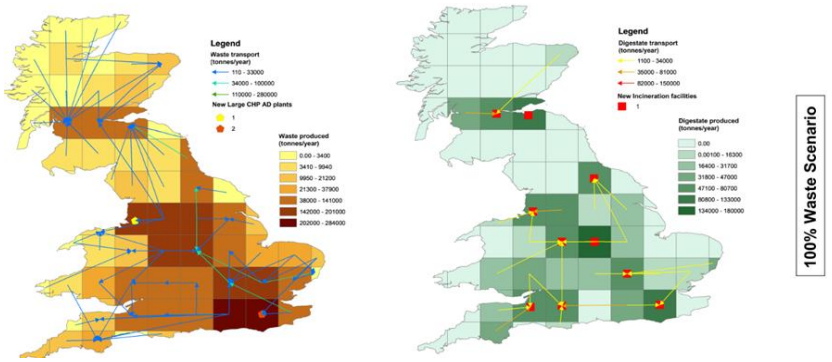

Figure 3 Spatially-explicit new technologies solutions and resource flow

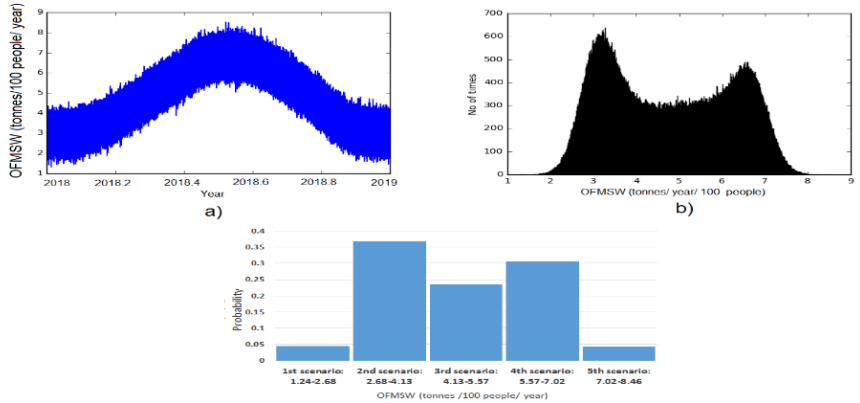

Figure 4: a) 2018 OFMSW estimation. b) OFMSW generation histogram (1.2 million samples and 5000 bins). c) probability for the 5 waste scenarios

Our modelling results suggested that i) waste generation variability has a negative impacts on OFMSW value-chain economic performances with profit decrease to 11.49 £/tonne OFMSW (13.78 £/tonne OFMSW in deterministic optimization). ii) despite that minimum capacity constraints avoid the competition of AD facilities for OFMSW supply, this leads to a cost-ineffective value chain design and loss in waste recovery. iii) constraining the maximum waste landfilled decrease profit; iv) 2018 landfill tax would lead to an optimal value chain design with 1.1% of the OFMSW ending in landfill.

References

Adeogba E, Barty P, O'Dwyer E, Guo M. Waste-to-Resource Transformation: Gradient Boosting Modelling for Organic Fraction Municipal Solid Waste Projection. 2019.

Benders, J. F. (1962) 'Partitioning procedures for solving mixed-variables programming problems', Numerische Mathematik, 4(1), pp. 238–252.

Birge, J. and Louveaux, F. (1988) 'A multicut algorithm for two-stage stochastic linear programs', European Journal of Operational Research, 34(3), pp. 384–392.

WDF, 2019. Data on organic fraction municipal solid waste. Waste Data Flow, Available at: http://www.wastedataflow.org/ (Accessed: 5 June 2019).

Lovett, A., Sünnenberg, G., Dockerty, T., 2014. The availability of land for perennial energy crops in Great Britain. GCB Bioenergy 6, 99–107.

EROS, 1996. 30 arc-second DEM of Europe (GTOPO30). U.S. Geological Survey's Center for Earth Resources Observation and Science (EROS)

OS OpenData, 2019. OS Open Roads. Ordenace Survey.

Sauro Pierucci, Flavio Manenti, Giulia Bozzano, Davide Manca (Eds.)
Proceedings of the 30th European Symposium on Computer Aided Process Engineering (ESCAPE30), May 24-27, 2020, Milano, Italy.
http://dx.doi.org/10.1016/B978-0-12-823377-1.50268-8

Time Scale Analysis and Optimization of a Continuous Microbial Bioprocess

Peter Sinner, Christoph Herwig, Julian Kager,*

Institute of Chemical, Environmental and Bioscience Engineering, Technische Universität Wien, Gumpendorfer Straße 1a, 1060 Vienna, Austria
julian.kager@tuwien.ac.at

Abstract

Continuous bioprocesses are widely used for quantitative strain characterization and industrial fermentations aiming for high space time yields and constant productivity. However, due to the presence of different biochemical reaction dynamics these processes can exhibit slow system behavior under certain conditions. This leads to extended start up times to reach a targeted steady state and impedes to detect and act on process disturbances. We applied a model-based approach to determine the time scale of a continuous *Corynebacterium glutamicum* bioprocess utilizing a lignocellulosic waste stream in dependence of operational parameters. Time scales were derived by Jacobian linearization of the nonlinear process model and used as an input for multi-objective process optimization. Hereby, operational points with high productivity as well as fast system response upon process disturbances could be obtained. In this way, model-based time scale analysis delivers valuable input for the design of efficient and robust bioprocesses.

Keywords: Bioprocess, dynamic modelling, time scale analysis, multi-objective optimization

1. Introduction

Model-based methods enable a targeted development of bioprocesses. Especially for continuous processes, quantitative understanding is important to select stable operational points. Besides of its relevance in biomanufacturing, continuous cultivation processes are also an important experimental method for the characterization of microbial strains. A three-residence-times rule of thumb is commonly used to reach a hypothetical steady state approximation of 95 % and to derive the corresponding process characteristics. However, this assumption is based on non-reactive tracer experiments and is only proven to be applicable to non-autocatalytic reactions (Heinrichs and Schneider, 1980; Zhang et al., 2007). For different chemical (Zhang et al., 2007) and biochemical systems (Lachmann and Schneider, 1983; Sonnleitner and Hahnemann, 1994) slow system behaviour was reported in the literature, showing a higher number of hydraulic residence times needed to reach a targeted steady state. Methods for time scale analysis based on eigenvalue analysis are well-established in the fields of systems biology (Kremling, 2013) and chemical engineering (Isaac et al., 2013). However, time scale analysis is so far not systematically included in bioprocess design applications. To show the potential and possible effects of time scale analysis within bioprocess development, a continuous *C. glutamicum* bioprocess utilizing the lignocellulosic waste stream spent sulfite liquor is analyzed in this work. *C. glutamicum* is a platform organism with high industrial importance and a wide potential product spectrum (Becker et al., 2018). Time scales of

this example process are analyzed in dependence of operational parameters and used as input for process design. In the first part of this work, the applied process model and the methodology for time scale analysis and model-based process design are outlined. Then, the effect of operational parameters on the time scale is shown. The practical relevance of time scale analysis for bioprocess design applications is discussed subsequently, with a focus on system response upon process disturbances.

2. Material and Methods

2.1. Dynamic Process Model

A dynamic process model describing the growth of wild-type *C. glutamicum* ATCC 13032 on spent sulfite liquor was used for simulations. The spent sulfite liquor composition of this study is typical for softwood pulping (Niemelä and Alén, 1999). A general vector form of a dynamic system of mass concentrations $\underline{c}$, inputs $\underline{u}$, parameters $\underline{\theta}$ and disturbances $\underline{d}$ is shown in Eq. (1).

$$\dot{\underline{c}} = \underline{f}(\underline{c}, \underline{u}, \underline{d}, \underline{\theta}, \mathrm{t}) \tag{1}$$

The model describes biomass (X) growth on the two main carbon substrates glucose (S_1) and mannose (S_2), as well as conversion of xylose (S_3) without detectable contribution to biomass formation. The ODEs describing mass concentrations (g L^{-1}) of biomass c_X and sugar states $c_{S,1}$, $c_{S,2}$, $c_{S,3}$ in a CSTR with constant reactor volume V_R (L) are shown in Eq. (2) and Eq. (3).

$$\dot{c}_X = \left(\sum_{i=1}^{3} q_{S,i} Y_{XS,i} - \frac{F_{in}}{V_R}\right) c_X \tag{2}$$

$$\dot{c}_{S,i} = \frac{F_{in}}{V_R}\left(c_{S,i,in} - c_{S,i}\right) - q_{S,i} c_X \tag{3}$$

Sugar uptake $q_{S,i}$ ($g_{S,i}$ g_X^{-1} h^{-1}) is governed by competitive interaction between different sugars and a non-competitive inhibitory effect (inhibition constant $K_{I,SSL}$ in g L^{-1}) of spent sulfite liquor concentration $c_{I,SSL}$ (g L^{-1}), see Eq. (4). Biomass growth and sugar uptake are linked by constant yield coefficients $Y_{XS,i}$ (g_X $g_{S,i}^{-1}$). The model parameters were previously determined using experimental data (Sinner et al., 2019). All calculations were performed in MATLAB R2017b (The MathWorks, Inc., United States).

$$q_{S,i} = q_{Smax,i} \frac{c_{S,i}}{K_{S,i}\left(1 + \sum_{j=1, j\neq i}^{3} \frac{c_{S,j}}{K_{S,j}}\right) + c_{S,i}} \frac{K_{I,SSL}}{K_{I,SSL} + c_{I,SSL}} \tag{4}$$

2.2. Time Scale Analysis

For time scale analysis, the Jacobian matrix J is used to linearize the nonlinear vector function $\underline{f}$ around a steady state operating point of interest, see Eq. (5). Hereby, $\underline{c'}$ denotes a deflection of the process variables around the steady state values $\underline{c}_{eq}$. The entries j_{ij} of the Jacobian are calculated according to Eq. (6).

$$\dot{\underline{c'}} = J\underline{c'} \tag{5}$$

$$j_{ij} = \left.\frac{\partial f_i}{\partial c_j}\right|_{\underline{c}=\underline{c_{eq}}} \tag{6}$$

By decomposing the Jacobian its eigenvalues λ_n are derived. The absolute value of the real part (*Re*) of the eigenvalue describes the reciprocal time scale τ_n (h) of a mode, see Eq. (7). The largest time scale τ_{max} was selected as the dominating time scale among τ_n.

$$\tau_n = |Re(\lambda_n)|^{-1} \tag{7}$$

As a reference, hydraulic residence times needed to approach a steady state with a certain accuracy were calculated numerically by nonlinear model simulations.

2.3. Model-based Process Optimization

Optimal process inputs for dilution rate (D) and spent sulfite liquor concentration in the feed medium ($c_{I,SSL}$) were selected using a multi-objective optimization procedure. Biomass space time yield was defined as a typical objective to be maximized in bioprocess development, see Eq (8). In addition to that, time scale of the system, see Eq (9), was included as an additional objective function to obtain regions with high biomass productivity and fast equilibration kinetics. Time scales at operating points of interest were scaled by the maximum time scale of the process design space.

$$\min_{D,c_{I,SSL}} \; J_1 = -c_{X,steady\ state} D \tag{8}$$

$$\min_{D,c_{I,SSL}} \; J_2 = \frac{\tau_{max,operating\ point}}{\tau_{max,design\ space}} \tag{9}$$

Pareto-optimal solutions were computed using a genetic algorithm (gamultiobj, MATLAB R2017b) based on NSGA-II (Deb et al., 2002).

3. Results and Discussion

3.1. Influence of Process Parameters and Reaction Kinetics on Time Scale

Time scales were determined based on eigenvalue analysis of the linearized process model. Figure 1 shows the effect of two main operational parameters for CSTR processes, dilution rate and feed concentration, on the time scale of the analyzed process. Each Jacobian eigenvalue corresponds to the time scale of a mode, as depicted by dashed lines in Figure 1. The mode with the largest time scale at a certain operating point dominates the time scale of the process in the respective region, as can be seen by comparison to the numerically calculated residence times needed to approach a steady state in Figure 1 (solid line). When the dilution rate of the CSTR is approaching the washout of the system, in the region around 0.05 h^{-1} in Figure 1, time scale is considerably increasing. This is in accordance with the phenomenon of critical slowing down of nonlinear systems close to phase transitions (Jähnig and Richter, 1976; Lachmann and Schneider, 1983).

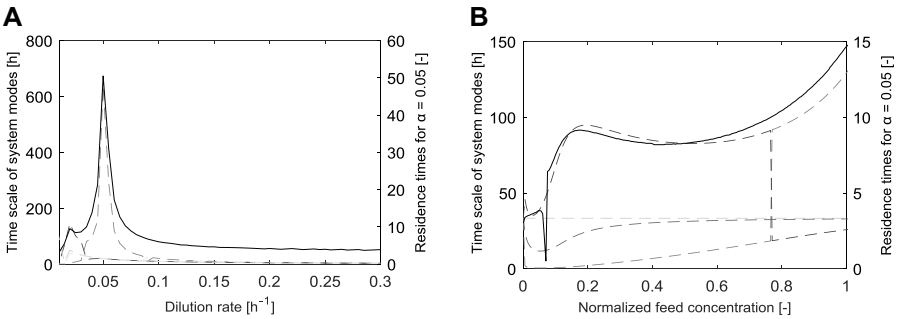

Figure 1: Eigenvalue based time scales of modes (dashed lines) and numerically derived residence times (solid line) needed to approach steady state with α = 0.05 in dependence of CTSR operational parameters dilution rate (A) and feed concentration (B).

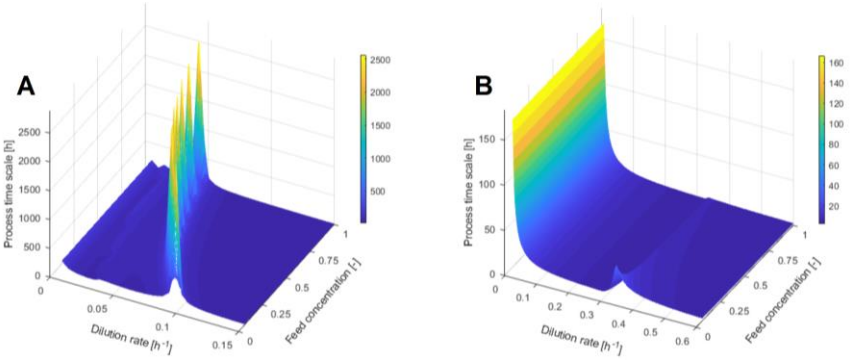

Figure 2: Eigenvalue based process time scale in dependence of CSTR operational parameters dilution rate and normalized feed concentration for different reaction systems. A: Multi-substrate process (spent sulfite liquor). B: Single carbon substrate process without inhibitory effects.

The concentration of spent sulfite liquor in the feed influences the time scale of the process as well. Different substrate and inhibitor levels can shift the boundary of the CSTR washout equilibrium and thereby the region of slow time scales. In general, it can be stated that residence times significantly above the commonly applied three-residence-times rule of thumb are necessary to approach a steady state in most operational regions of the studied CSTR process. 10 residence times are sufficient for a wide range of the design space. However, close to the washout state up to 100 theoretical residence times are necessary to fully reach a steady state. Equilibration of the CSTR bioprocess is not governed by hydraulic equilibration but by the time scale of the biochemical reaction system. In Figure 2 A the process time scale is visualized for the entire process design space, depicting critical slowing down in the region close to washout. In comparison to that, a single substrate CSTR without inhibitory effects as described in Doran (2013) is shown in Figure 2 B. For this simpler reaction system, lower time scales and a less pronounced slowing down close to washout can be observed. The type of underlying reaction mechanisms, such as substrate competition, strongly influences the reaction velocity of a bioprocess, making time scale analysis a necessity to determine steady state stabilization timepoints during strain and bioprocess characterization.

3.2. Time Scale Analysis in Model-based Optimization

Time scale analysis can be included as an objective function within an optimization problem. By defining a multi-objective optimization problem, maximum space time yields for biomass productivity and minimal time scales for fast system responses were defined for the examined bioprocess. In Figure 3 A the process design space based on the sum of equally weighted objective function values is shown. In accordance to the critical slowing down of the system, undesirably high objective function values are obtained close to washout equilibrium. Washout regions are excluded from the process design space. To obtain optimal operating conditions among the conflicting objective functions for high biomass formation rates and fast system response, Pareto optimal solutions were computed by a genetic algorithm, see Figure 3 B. A time scale threshold below 80 h was set as constraint. Thereby, a dilution rate of 0.018 h^{-1} and a normalized spent sulfite liquor feed concentration of 0.51 were selected as optimal process parameters yielding a CSTR bioprocess with predicted 0.70 g L^{-1} h^{-1} biomass space time yield and a time scale of 68.8 h. This corresponds to 8.4 residence times needed to reach a steady state when simulating the nonlinear process.

3.3. Dynamic Response to Process Disturbances

The dynamic behavior during CSTR process start up as well as upon process disturbances was analyzed for the operating point optimized in section 3.2. Variability in lignocellulosic raw material characteristics is an important challenge for industrial biotechnology (Kenney et al., 2013). Therefore, the transitory behavior after disturbances in the substrate feed composition (25 %) is simulated for the optimized (dilution rate 0.018 h^{-1}, normalized feed concentration 0.51, productivity 0.70 g L^{-1} h^{-1}) as well as for a time-scale suboptimal but equally productive operational point (dilution rate 0.018 h^{-1}, normalized feed concentration 0.84, productivity 0.71 g L^{-1} h^{-1}). The startup phase until steady state and behavior after disturbance in the feed composition are displayed in Figure 4 A for the biomass and B for the substrate concentration. The optimized operational point (black line) reaches its initial steady state faster than the operational point with comparable productivity (grey line). Also, its response upon process disturbances and the subsequent return to its targeted operational point is considerably faster. This shows that time scale information can be used to define process conditions leading to a stable and productive process.

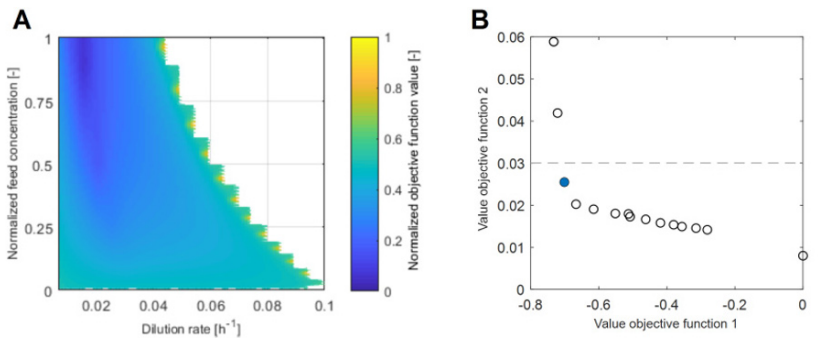

Figure 3: Multi-objective bioprocess optimization. A: Projection of surface plot of normalized sum of objective function value for equally weighted J_1 (productivity) and J_2 (time scale) in dependence of dilution rate and normalized feed concentration. B: Pareto-optimal solutions (black, circle) for objective functions J_1 and J_2 with maximum time scale threshold of 80 h (dashed lined), the selected point is highlighted (filled circle).

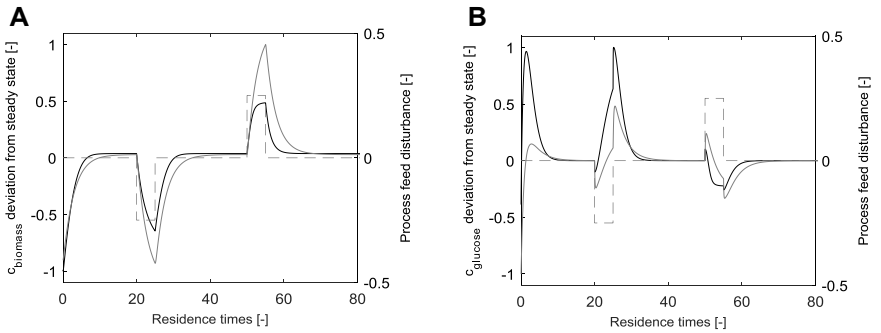

Figure 4: Dynamic response of CTSR states (left axis) upon process start up and subsequent disturbances in the substrate feed concentration level of glucose (dashed line, right axis) for the optimized operational point (black line) and a time scale suboptimal but equally productive operational point (grey line). A: Scaled biomass state deviation. B: Scaled carbon substrate state (glucose) deviation.

4. Conclusions

Time scale analysis delivered valuable insights into the dynamics of a wild-type *C. glutamicum* bioprocess utilizing lignocellulosic waste as a substrate. It could be shown that a high amount of residence times can be necessary to approach a steady state under certain operational parameters. This has implications for CSTR cultivations for strain characterization as well as industrial operations subject to process disturbances due to raw material fluctuations. Multi-objective optimization was performed to select operational points combining high productivity with fast steady state convergence. Time scale analysis is a straightforward, quantitative methodology and its inclusion within process design and development can help to correctly plan strain characterization experiments and to determine robust process conditions.

Acknowledgements

This project has received funding from the Bio Based Industries Joint Undertaking under the European Union's Horizon 2020 research and innovation program under grant agreement No 790507 (iFermenter).

References

J. Becker, C. M. Rohles, C. Wittmann, 2018, Metabolically engineered Corynebacterium glutamicum for bio-based production of chemicals, fuels, materials, and healthcare products, Metab. Eng., 50, 122-141

K. Deb, A. Pratap, S. Agarwal, T. Meyarivan, 2002, A fast and elitist multiobjective genetic algorithm: NSGA-II, IEEE Trans. Evol. Comput., 6 (2), 182-197

P. M. Doran, 2013, Chapter 14 - Reactor Engineering, In P. M. Doran (Ed.), Bioprocess Engineering Principles (Second Edition), London, UK, Academic Press, 761-852

M. Heinrichs, F. W. Schneider, 1980, On the Approach to Steady States of Reacting Systems in the Continuous Stirred Tank Reactor, Ber. Bunsenges. Phys. Chem., 84 (9), 857-865

B. J. Isaac, A. Parente, C. Galletti, J. N. Thornock, P. J. Smith, L. Tognotti, 2013, A Novel Methodology for Chemical Time Scale Evaluation with Detailed Chemical Reaction Kinetics, Energy Fuels, 27 (4), 2255-2265

F. Jähnig, P. H. Richter, 1976, Fluctuations in spatially homogeneous chemical steady states, J. Chem. Phys, 64 (11), 4645-4656

K. L. Kenney, W. A. Smith, G. L. Gresham, T. L. Westover, 2013, Understanding biomass feedstock variability, Biofuels, 4 (1), 111-127

A. Kremling, 2013, Systems biology: mathematical modeling and model analysis, Boca Raton, USA, CRC Press Taylor & Francis Group

H. Lachmann, F. W. Schneider, 1983, Phenomenon of slowing down in the autocatalytic trypsinogen to trypsin conversion in a continuous-flow stirred-tank reactor, J. Am. Chem. Soc., 105 (9), 2898-2900

K. Niemelä, R. Alén, 1999, Characterization of Pulping Liquors, In E. Sjöström & R. Alén (Eds.), Analytical Methods in Wood Chemistry, Pulping, and Papermaking, Berlin and Heidelberg, Springer, 193-231

P. Sinner, J. Kager, S. Daume, C. Herwig, 2019, Model-based Analysis and Optimisation of a Continuous Corynebacterium glutamicum Bioprocess Utilizing Lignocellulosic Waste, IFAC-PapersOnLine, 52 (26), 181-186

B. Sonnleitner, U. Hahnemann, 1994, Dynamics of the respiratory bottleneck of Saccharomyces cerevisiae, J. Biotechnol., 38 (1), 63-79

M. Zhang, T. W. Karjala, B. W. S. Kolthammer, 2007, Delayed Dynamics of Polymer Properties in Continuous Stirred Tank Polymerization Reactors, Ind. Eng. Chem. Res., 46 (18), 5922-5935

Sauro Pierucci, Flavio Manenti, Giulia Bozzano, Davide Manca (Eds.)
Proceedings of the 30th European Symposium on Computer Aided Process Engineering (ESCAPE30), May 24-27, 2020, Milano, Italy.
http://dx.doi.org/10.1016/B978-0-12-823377-1.50269-X

Integrated Design of Biopharmaceutical Manufacturing Processes: Operation Modes and Process Configurations for Monoclonal Antibody Production

Sara Badr,[a] Kozue Okamura,[a] Nozomi Takahashi,[a] Vera Ubbenjans,[b] Haruku Shirahata,[a] Hirokazu Sugiyama[a*]

[a]*Department of Chemical System Engineering, The University of Tokyo, 7-3-1 Hongo, Bunkyo-ku, 113-8656, Tokyo, Japan*
[b]*Faculty of Mechanical Engineering, RWTH Aachen University, Kackertstraße 9, 52072 Aachen, Germany*
sugiyama@chemsys.t.u-tokyo.ac.jp

Abstract

The market for monoclonal antibodies (mAb)s is rapidly expanding. They are however expensive, with complicated lengthy production processes. Process models for two bottleneck operating units up- and downstream of the production chain are presented. The models are validated using pilot scale and experimental literature data. Dynamic simulations of batch, continuous, and mixed mode operations are used to compare economic performance and productivity. A qualitative discussion of risk factors and possible operational hurdles is presented. Results show that continuous operations have a significant advantage in terms of processing times, but not regarding operating costs. To realize a cost advantage, careful consideration of process conditions and parameters is required. These simulations can be used to map the design space and show the range of favourable operating modes and conditions in a thorough sensitivity analysis study.

Keywords: Process design, Continuous operation, Techno-economic assessment, Upstream, Downstream

1. Introduction

Monoclonal antibodies (mAb)s are dominating the biopharmaceutical market, which is the fastest growing sector in the pharmaceutical industry (Butler and Meneses-Acosta, 2012; Walsh, 2018). They are used to treat, among others, certain types of cancer and auto-immune diseases and often with less side effects than available alternative treatments. The market for monoclonal antibodies has been rapidly expanding and is expected to double again over the next five years (Grilo and Mantalaris, 2019). These drug products are often expensive and have complicated lengthy production processes. To facilitate the expansion of the mAb market, to face the competition from biosimilars, and to ensure the availability of the required demand volume, the production process needs to be optimized to allow for higher production flexibility and lower costs. The production of mAbs is typically conducted through upstream cell cultivation processes and downstream purification processes to obtain the desired mAb product. Figure 1 shows a typical mAb production process.

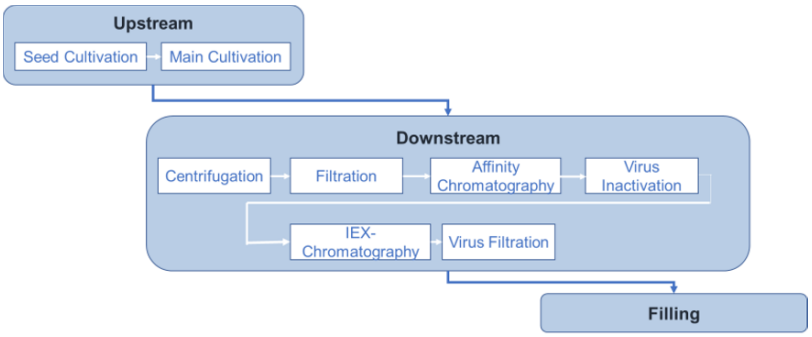

Figure 1: Typical mAb upstream cultivation and downstream purification processes

Generally, continuous production of biopharmaceuticals can offer significant advantages in terms of increased production efficiency. However, continuous production can also suffer from higher operational problems. Many factors affect the performance of the production process. This work aims to explore the available design options and map favourable production modes at different production scales and sizes. Process models are developed and validated with experimental data from literature and pilot scale runs in Japan. Two process units: the main cultivation unit, and the capture chromatography unit are chosen as the main focus of this work. These units represent bottleneck operations in terms of time and cost requirements. Dynamic simulations of batch, continuous, and mixed mode operations are used to compare economic performance and productivity. The impact of different process configurations and operating modes is evaluated in terms of operating costs and production time with a qualitative discussion of risk factors and possible operational hurdles.

2. Process modelling and simulation

Upstream processes comprise activities of cell cultivation. Three cultivation modes are commonly employed: conventional batch cultivation; fed-batch, where nutrients are fed throughout the production batch to maintain glucose concentrations thus increasing batch periods and productivity; and perfusion mode where the cultivation media is constantly fed and the reactor output is removed at the same rate with cell retention in the system achieving continuous operation. Multi-column processes, e.g. periodic counter current chromatography (PCC) with alternating column loading and regeneration stages can be used to simulate continuous flow in downstream capture chromatography processes. Simulated moving bed (SMB) operation can reduce the required number of columns to two (Angarita et al., 2015; Karst et al., 2018). Interconnected columns can thus provide longer loading times and higher column utilizations.

Production data has been obtained from a pilot scale research facility in Japan for the production of mAbs from Chinese hamster ovary (CHO) cells. Different models for the large-scale cultivation and chromatography have been fitted against the production data and the appropriate models were selected and further validated with more experimental data from literature. The obtained parameters were then used to simulate and assess further production scenarios.

2.1. Cultivation models

Cultivation models were developed based on mass balances of key process components and Monod type model for cell growth and death rates as previously presented in literature

(Kornecki and Strube, 2018; Xing et al., 2010). The models were adjusted based on pilot scale fed-batch production data and then validated with perfusion mode experimental data from Xu and Chen (2016) and from Zhang et al. (2015), which employed a temperature downshift within the process operation. Equations (1-7) show the perfusion model equations used:

$$\frac{d(VX_V)}{dt} = (\mu - \mu_d)VX_V - F_{bleed}X_V \tag{1}$$

$$\frac{d(VP)}{dt} = Q_P VX_V - (F_{harvest} + F_{bleed})P \tag{2}$$

$$\frac{d(V[GLC])}{dt} = -\left(\frac{\mu - \mu_d}{Y_{X_V/glc}} + m_{glc}\right)VX_V + F_{in}C_{in} \mp F_{suppl}C_{suppl} - (F_{harvest} + F_{bleed})[GLC] \tag{3}$$

$$\frac{d(V[LAC])}{dt} = Y_{lac/glc}VX_V - (F_{harvest} + F_{bleed})[LAC] \tag{4}$$

$$\frac{d(V)}{dt} = F_{in} + F_{suppl} - F_{harvest} + F_{bleed} \tag{5}$$

$$\mu = \mu_{\max}\left(\frac{[\mathrm{GLC}]}{K_{\mathrm{glc}}+[\mathrm{GLC}]}\right)\left(\frac{KI_{\mathrm{lac}}}{KI_{\mathrm{lac}}+[\mathrm{LAC}]}\right) \tag{6}$$

$$\mu_{\mathrm{d}} = k_{\mathrm{d}}\left(\frac{[\mathrm{LAC}]}{KD_{\mathrm{lac}}+[\mathrm{LAC}]}\right)\left(\frac{KD_{\mathrm{glc}}}{KD_{\mathrm{glc}}+[\mathrm{GLC}]}\right) \tag{7}$$

where, X_V is the viable cell density and V is the culture volume. F_{bleed}, $F_{harvest}$, F_{in}, and F_{suppl} are the bleed, harvest, main, and supplementary feed flows rates, respectively. P, $[GLC]$, and $[LAC]$ represent the antibody product, glucose and lactate concentrations, respectively. C_{in} and C_{suppl} are glucose concentrations in the main and supplementary feed streams, respectively. μ and μ_{d} are cell growth and death rates respectively, while $\mu_{\max}$ and k_{d} are their corresponding maximum values. Y is the yield coefficient, where $Y_{x/y}$ for example represents the change in the value of x with respect to variations in values of y. m_{glc}, KI_{lac}, K_{glc}, KD_{lac}, KD_{glc} are the Monod model parameters representing the glucose maintenance coefficient, the lactose and glucose half maximum rate concentrations for cell growth and cell death, respectively.

The pilot facility implemented single-use equipment for its runs. Changeover time was therefore calculated to be 1 day and changeover costs represented the costs of new reactor bags used. Run durations were assumed to be 7, 14, and 60 days for batch, fed-batch, and perfusion operations, respectively. The operating cost was calculated as the cost of media (basal and feed) and utilities (water, gas, and electricity) in addition to changeover costs (cost of reactor bags).

2.2. Capture chromatography models

The lumped kinetic model was used for the chromatography column (Felinger and Guiochon, 2004; Guélat et al., 2016). Equations (8-9) show the model equations:

$$\varepsilon\frac{\partial c_i}{\partial t} + (1-\varepsilon)\frac{\partial q_i}{\partial t} + u_{sf}\frac{\partial c_i}{\partial x} = u_{sf}d_{ax}\frac{\partial^2 c_i}{\partial x^2} \tag{8}$$

$$\frac{\partial q_i}{\partial t} = k_m\left(q_i^{eq} - q_i\right) \tag{9}$$

where, c_i and q_i are the concentrations of component i in the mobile liquid phase and in the resin, respectively. ε is the total porosity. x is the distance travelled along the column length, and u_{sf} is the superficial velocity. d_{ax} is the axial dispersion coefficient. k_m is the lumped mass transfer coefficient, while $q_i^{eq}$is the equilibrium concentration of component i in the resin.

Model parameters were fitted using data obtained from the pilot scale facility. Optimal superficial velocities and column lengths are determined based on input conditions from upstream operations in terms of total volume to be treated and product titer. In the pilot facility, approximately 200 loadings are assumed per column before it is disposed of. The required cost of resin is then accordingly calculated. Operating time for batch columns include: loading, washing, elution, and regeneration. Multiple column operations (PCC and SMB) take into account the parallel execution of the columns, but add the interconnected loading time.

3. Results and discussion

Figure 2 shows the model fit to two experimental perfusion runs. The figure shows the viable cell density, Glucose and lactate concentrations, in addition to the mAb product. In the experiment of Zhang et al. (2015) the total produced mAb was reported, while in the experiment of Xu and Chen (2016), the produced titer. Zhang et al. (2015) implemented a temperature shift in the experiment. Lowering temperatures in perfusion culture to inhibit cell growth has been shown to enhance productivity. The model developed and used here is independent of operating conditions. Therefore, three different phases are modelled for such an operation, the initial batch phase, the initial growth phase in perfusion mode, and the production phase after a temperature downshift. Model performance is reported independently for each phase. The model results match well to the experimental values, especially for viable cell density and produced mAb concentrations/amounts. Lactate concentrations are not well modelled in the perfusion growth phase though. Nevertheless, the fed-batch model (fitted to the pilot scale data) performed better for lactate prediction yielding an R^2 value of 0.75.

Figure 3 shows the simulated results of a comparison of the different cultivation modes in terms of operating costs and production time in a 200 L reactor. Perfusion simulation assumed conditions closer to those presented by Xu and Chen (2016), which resulted in a higher titer compared to Zhang et al. (2015). No scale-up effects were assumed in this work. Perfusion mode shows a definite advantage in terms of productivity. However, due to the higher costs of media in perfusion, it can also lead to higher costs with longer operation times as compared to the fed-batch operation. Further analysis of this result can show the sensitivity of the produced results to operating conditions and model assumptions.

Figure 4 shows the results of the comparison of batch and a 3-column PCC operation of chromatography columns in terms of the cost of resin needed and the processing time for a small, pilot and large-scale operation at an inlet titer of 3 g/L. PCC columns were assumed to be one third of the length of the batch. The higher column utilization observed in PCC can be seen at pilot and larger scales as benefits in operating costs. Continuous column operation once again shows a major advantage in processing time.

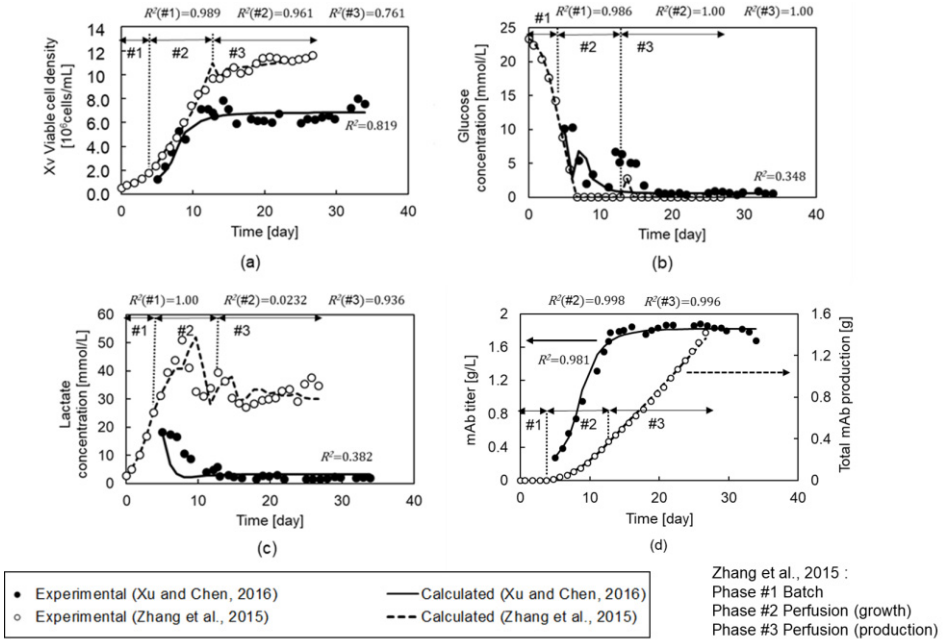

Figure 2: Model fitting results to perfusion experiments form Xu and Chen (2016) and Zhang et al. (2015)

Since column dimensions were not changed among scales, the processing time/g-mAb remains the same. The total processing time will then accordingly change with the scale; or the cost can change as more columns become needed at larger scales.

For the operation of an integrated continuous process, flowrates and productivities of upstream and downstream units need to be unified. Intermediate buffer tanks will be required to maintain flexibility, or in the case of implementing hybrid mode operations. Considerations of operational difficulties might also be encountered at larger scales for continuous operation. In cultivation mode, clogging might impede longer operation times, while in chromatography valve reliability will be a key issue for smooth operations.

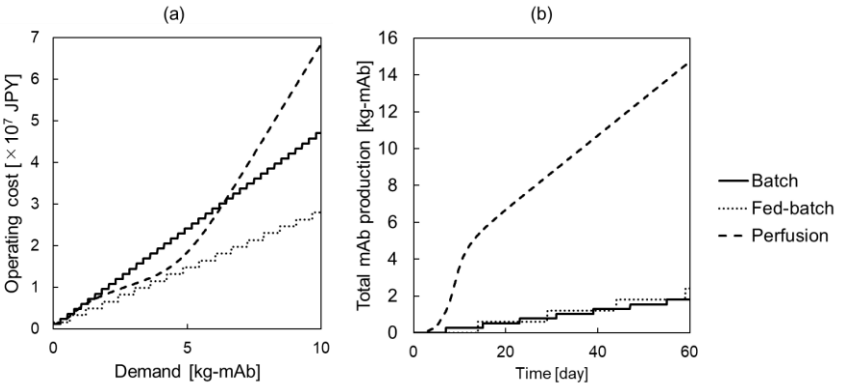

Figure 3: comparison of operating modes in terms of (a) operating cost and (b) production time using a 200 L reactor volume.

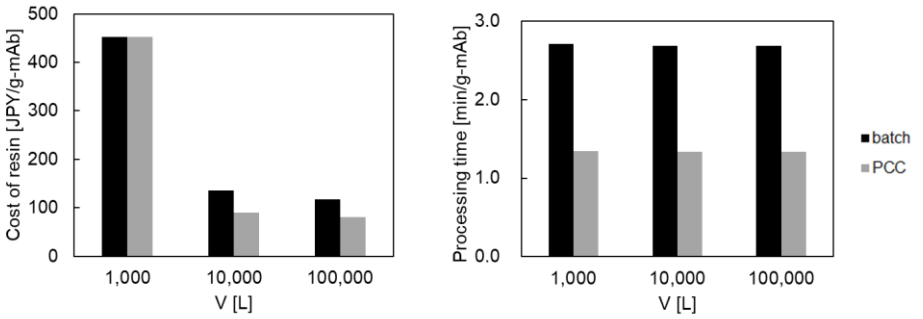

Figure 4: (a) cost of resin and (b) processing time for batch and PCC capture chromatography for a 3 g/L inlet titer

4. Conclusions

This work presents models developed for the main cultivation unit. The models are fitted and validated using pilot scale fed-batch data and experimental scale perfusion data from literature. Models for chromatography units are also fitted using pilot scale data. The produced models are used to simulate and compare different operating modes in terms of operating costs and processing times. Continuous operation was shown to have a clear advantage in terms of productivity, but the advantage in terms of costs still needs to be fully investigated and verified. A sensitivity analysis to model assumptions is still required to map out and characterize the design space.

Acknowledgements

This work was supported by the Japan Agency for Medical Research and Development (AMED) [grant No. JP19ae0101064, JP17ae0101003, JP18ae0101058].

References

Angarita, M., Müller-Späth, T., Baur, D., Lievrouw, R., Lissens, G., Morbidelli, M., 2015, Twin-column CaptureSMB: A novel cyclic process for protein A affinity chromatography. J. Chromatogr. A 1389, 85–95.

Butler, M., Meneses-Acosta, A., 2012, Recent advances in technology supporting biopharmaceutical production from mammalian cells. Appl. Microbiol. Biotechnol. 96, 885–894.

Felinger, A., Guiochon, G., 2004, Comparison of the kinetic models of linear chromatography. Chromatographia 60, 175–180.

Grilo, A.L., A. Mantalaris, 2019, The Increasingly Human and Profitable Monoclonal Antibody Market. Trends Biotechnol. 37, 9–16.

Guélat, B., Khalaf, R., Lattuada, M., Costioli, M., Morbidelli, M., 2016, Protein adsorption on ion exchange resins and monoclonal antibody charge variant modulation. J. Chromatogr. A 1447, 82–91.

Karst, D.J., Steinebach, F., Morbidelli, M., 2018, Continuous integrated manufacturing of therapeutic proteins. Curr. Opin. Biotechnol. 53, 76–84.

Kornecki, M., Strube, J., 2018, Process analytical technology for advanced process control in biologics manufacturing with the aid of macroscopic kinetic modeling. Bioengineering 5.

Walsh, G., 2018, Biopharmaceutical benchmarks 2018. Nat. Biotechnol. 36, 1136–1145.

Xing, Z., Bishop, N., Leister, K., Li, Z.J., 2010, Modeling kinetics of a large-scale fed-batch CHO cell culture by markov chain monte carlo method. Biotechnol. Prog. 26, 208–219.

Xu, S., Chen, H., 2016, High-density mammalian cell cultures in stirred-tank bioreactor without external pH control. J. Biotechnol. 231, 149–159.

Zhang, Y., Stobbe, P., Silvander, C.O., Chotteau, V., 2015, Very high cell density perfusion of CHO cells anchored in a non-woven matrix-based bioreactor. J. Biotechnol. 213, 28–41.

Sauro Pierucci, Flavio Manenti, Giulia Bozzano, Davide Manca (Eds.)
Proceedings of the 30th European Symposium on Computer Aided Process Engineering (ESCAPE30), May 24-27, 2020, Milano, Italy.
http://dx.doi.org/10.1016/B978-0-12-823377-1.50270-6

Robust Monitoring of Lactic Acid Bacteria with Sequential Monte Carlo

Ergys Pahija,[a] Robert Spann,[b] Gürkan Sin[a,*]

[a]*Process and Systems Engineering Research Center (PROSYS), Department of Chemical and Biochemical Engineering, Technical University of Denmark, 2800 Kgs. Lyngby, Denmark*
[b]*Chr. Hansen A/S, Hørsholm, Denmark*
gsi@kt.dtu.dk

Abstract

Lactic Acid Bacteria (LAB) are commonly utilised in the dairy industry. Although the process is well established, the conditions in which the fermentation process takes place can strongly influence the production of LAB.

The objective of this manuscript is to apply the Sequential Monte Carlo (SMC) method for monitoring the fermentation process. The online monitoring system is based on a statistical method for the estimation of model parameters using importance sampling technique, making use of limited data and predicting a number of relevant but unmeasured process variables such as biomass and product yields. The SMC technique was evaluated using two case studies one a simulation study and the other is a pilot-scale data from LAB fermentation. To describe the process, a mechanistic fermentation model was developed and validated comprehensively before being used in SMC for online monitoring. The results show the application of SMC makes effective use of online data as batch progress and the quality of the predictions (for unmeasured state variables) improve as more information becomes available. This indicates the principle of Bayesian update of prior information on model parameters through importance sampling successfully works. In addition to process monitoring using limited online knowledge, the SMC technique allows convergence to the real value of the parameters of interest in the model. In fermentation studies with a limited online sensor, SMC offers a flexible alternative to traditional soft-sensors especially when the measurement errors are not necessarily normally distributed.

Keywords: Lactic acid bacteria, fermentation, monitoring, sequential Monte Carlo.

1. Introduction

Parameter estimation problems are very common in engineering and science applications (Beck and Arnold, 1977). Possible approaches to solve the problem are the trial and error, the frequentists approach (e.g., MLE) and the Bayesian approach (e.g., Monte Carlo methods (Sin et al., 2008)). In our case, we will focus on the latter approach, being the application of Sequential Monte Carlo (SMC) method for updating of model parameters as a function of online data with an application for fermentation processes. The main motivation is that in fermentation process models, the biokinetic parameters are subject to vary hence motivating the application of online update/parameter estimation. The end application is to use the online update model as a soft-sensor/process monitoring purpose. Several approaches can be followed when applying sequential Monte Carlo for on-line monitoring, such as defining an extended state that includes state and parameters, and

then apply standard particle methods (Kantas et al., 2015). We present the methodology of applying SMC based on importance sampling which is a Bayesian inference/update method. We first demonstrate the concept of the SMC methodology using a simulation/test study by studying the effect of several degrees of freedom of the methodology. To this end, we use a biological process focusing on the ammonia-oxidizing bacteria. After the implementation of the methodology is demonstrated step by step for online updating and process monitoring, we present the application of the methodology for a LAB fermentation process.

2. Methodology

The ammonia-oxidizing bacteria represent the first step of the two-step nitrification process. The model has a total of 6 ODE equations, which corresponds to one mass balance for each variable of interest. The objective is to determine [Y_{AOO} μ_{maxAOB} $K_{s,AOB}$ $K_{o,AOB}$]. For a complete description of the model refer to the paper from Sin et al. (2010). Using matrix notation, each ODE can be formulated as shown by System of Equations (1).

$$\begin{cases} \frac{dC_{NH4}}{dt} = -\frac{1}{Y_{AOB}}\mu_{AOB} \\ \frac{dC_{NO2}}{dt} = \frac{1}{Y_{AOB}}\mu_{AOB} - \frac{1}{Y_{NOB}}\mu_{NOB} \\ \frac{dC_{NO3}}{dt} = \frac{1}{Y_{NOB}}\mu_{NOB} \\ \frac{dC_{DO}}{dt} = \left(1 - \frac{3.43}{Y_{AOB}}\right)\mu_{AOB} - b_{AOB}C_{AOB} + \left(1 - \frac{1.14}{Y_{NOB}}\right)\mu_{NOB} - b_{NOB}C_{NOB} + k_{la}(O_{2,sat} - C_O) \\ \frac{dC_{AOB}}{dt} = \mu_{AOB} - b_{AOB}C_{AOB} \\ \frac{dC_{NOB}}{dt} = \mu_{NOB} - b_{NOB}C_{NOB} \end{cases} \quad (1)$$

where AOB and NOB represent the ammonia-oxidizing bacteria and nitrite oxidizing bacteria performing the nitrification process.

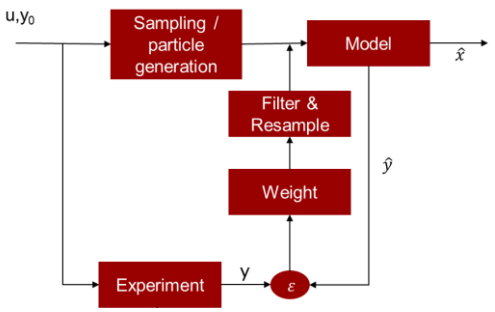

Figure 1 Schematic representation of the SMC for parameter estimation, x: unmeasured state variables, y: measured variable(s), epsilon is an error (different between model and measurements). The hat indicates it is an estimated value.

In order to follow the scheme shown in Figure 1, the following points have been implemented in MATLAB:

- Step 1 Initialization
- Step 2 Select experimental data and select the subset of parameters of interest
- Step 3 Select the sample size and apply a sampling technique

- Step 4 Apply the model of the defined problem
- Step 5 Compare (weight) the measured variable and compare to the ones estimated by the model
- Step 6 Overall weight, apply the filter
- Step 7 Update the parameters value and their uncertainty

In our case, we will make use of the importance sampling algorithm for updating the prior information on model parameters after new data/information becomes available (Gelman et al., 2013) (Doucet et al., 2006). We make use of the importance sampling as shown in Equation (3), where the weights are updated at each iteration by comparing the available data to the estimated variable. Note that in our case, the resampling is applied on the same initial particles.

$$E\big(f(x)\big) \approx \frac{1}{n}\sum_i f(x_i)\frac{p(x_i)}{q(x_i)} \tag{2}$$

where the estimation of a function *f(x)* depends on the number of particles (*n*) and on the "weight" obtained through the $p(x_i)/q(x_i)$ ratio, which allows a better convergence to the real solution at each iteration. The weight given to specific particle *i*, based on a certain measurement at time j, is calculated by using the likelihood function $1/\sqrt{2\pi\varepsilon}\exp\left(-\sum_i\frac{\left(\hat{y}_{i,j}-Data_{i,j}\right)^2}{2\varepsilon}\right)$, where ε represents the measurement error.

Below, we briefly introduce the LAB problem, that is currently under investigation and that will be included in the final version of this manuscript.

LAB is commonly used in the dairy industry for the production of yoghurt. This work focuses on *Streptococcus thermophilus*, which is gram-positive, aerotolerant, non-motile and used for the production of yoghurt, together with *Lactobacillus bulgaricus*, among others. The production process is well established, and mechanistic models can be found in the literature (Spann et al., 2018).

However, only a limited number of variables is commonly available at industrial scale. In our case, only pH and ammonia flowrate measurements are available. Temperature is kept constant, while other variables need to be calculated using the available models. Hence, it arises the necessity in having a robust monitoring system. The reaction defining lactic acid production is shown below.

$$Lactose + Ammonia + Phosphoric\ acid \rightarrow Biomass + Lactic\ acid + Galactose$$

The dynamic model that is used to determine the change of state variables like biomass, lactose and lactic acid is shown below in Equation (3) and Equation (4). The biomass growth rate is calculated as a function of the maximum specific growth rate μ_{max}, lag time f_{lag}, lactose limitation and inhibition f_s, lactate inhibition f_p and pH f_{pH}.

$$\frac{dC_x}{dt} = \mu_{max} f_{lag} f_s f_p f_{pH} C_x \tag{3}$$

$$\frac{dC_x}{dt} = \mu_{max}\cdot\left(1-e^{-\frac{t}{t_{lag}}}\right)\cdot\left(\frac{C_s}{C_s+K_s+\frac{C_s^2}{K_I}}\right)\cdot\left(\frac{1}{1-e^{K_{P,La}(C_{LA}-K_{La})}}\right)\cdot\left(e^{-\left(\frac{\left(pH_{opt}-pH\right)^2}{\sigma_{pH}^2}\right)}\right)\cdot C_x \tag{4}$$

For additional information on the applied model, refer to the paper written by Spann et al. (2018).

3. Results

3.1. Case study 1: Model parameter estimation/update using online data

For the first case study, a sample of 300 particles was randomly selected for each parameter of interest. The initial parameter values are assumed uniform as shown in Figure 3 (a). As data are collected over time, the information is updated on the prior with importance sampling, and the uncertainty on the monitored state variables decreases.

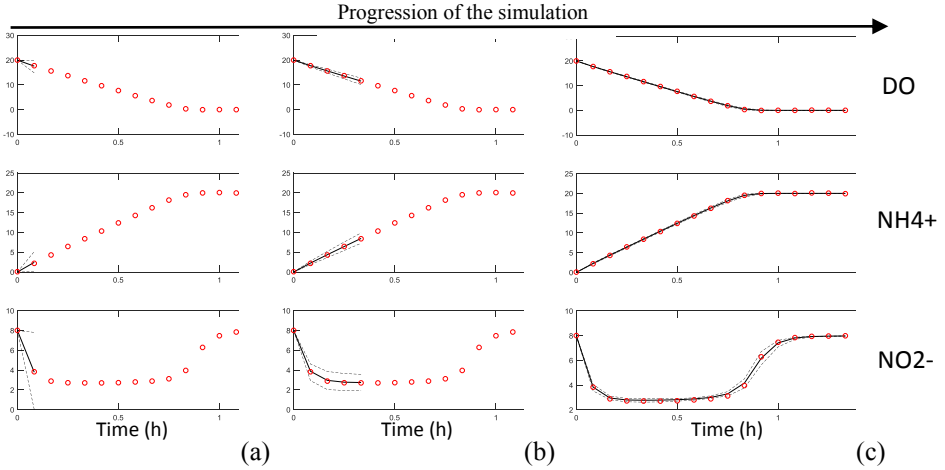

Figure 2 Representation of the model output at different times. (a) Time interval 1, (b) time interval 4, (c) time interval 16. Circles: measurements (based on a single set of data – benchmark); line: model predictions.

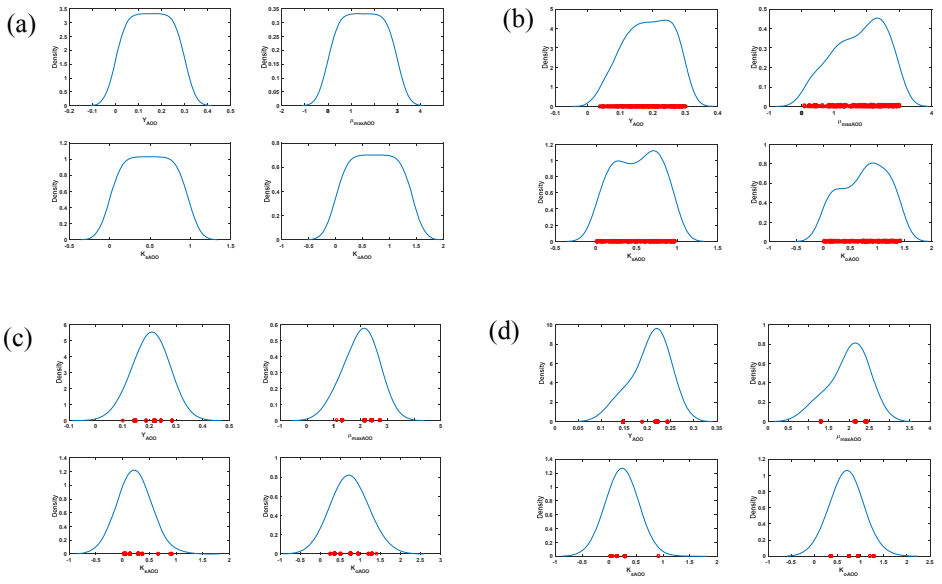

Figure 3 Representation of parameters sampling. (a) Initial distribution, (b) distribution after 5 time steps, (c) distribution after 9 time steps and (d) distribution after 15 time steps.

Figure 3 shows the effect of applying the filter. In our case, we assume that after the filter is applied to the initial distribution, the resampling is performed on the same set of numbers which was randomly sampled in the first place. It is possible to observe that the distribution of the particles starts with flat distributions and it converges to much sharper distributions, indicating that the value is converging. The red dots in Figure 3 represent the MC samples. They start from being uniformly distributed (flat distribution – a) to being concentrated around a specific value (bell-shaped distribution – d).

The covariance matrix of the evaluated parameters is shown below in Table 1. As a comparison, the estimated value of parameters by applying MLE ($\hat{\theta}_{MLE}$).

Table 1 Covariance matrix.

			Correlation matrix			
	$\hat{\theta}$	$\hat{\theta}_{MLE}$	Y_{AOO}	μ_{maxAOB}	$K_{s,AOB}$	$K_{o,AOB}$
Y_{AOO}	0.1983	0.14	1.0000	0.9897	-0.2992	0.3775
μ_{maxAOB}	2.0368	1.45	0.9897	1.0000	-0.2120	0.5022
$K_{s,AOB}$	0.5279	0.5	-0.2992	-0.2120	1.0000	0.4803
$K_{o,AOB}$	0.7950	0.69	0.3775	0.5022	0.4803	1.0000

3.2. Case study 2: Effect of considering only one measurement when calculating the weight in the importance sampling

Differently from Case study 1, in which we made use of all three measurements for the weight of particles, we are considering only the measurement from the dissolved oxygen. As shown in Figure 4, the results are still acceptable, and very similar to applying the MLE method, for the proposed problem.

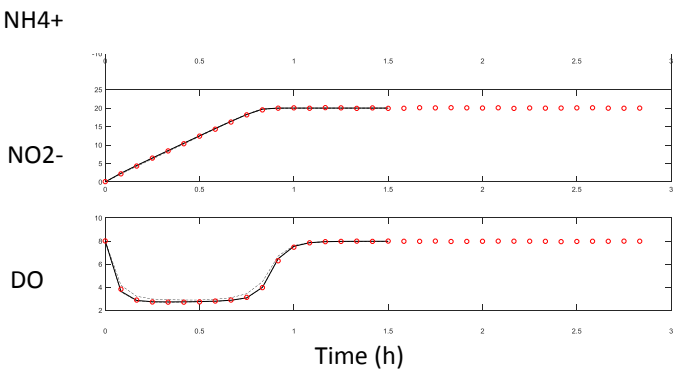

Figure 4 Concentration of ammonia, nitrite and dissolved oxygen over time (sample size: 300 particles).

Sensitivity analysis with the effect of the sample size of particles and the prior distribution of parameters (initial range of values) is studied and it is determined that it is better to start with relatively large uninformative prior (so that importance sampling can sample

and generate particles from a broader space). On the other hand, if the particle size is too small and the initial distribution (prior range) is wide, the model will tend to converge very quickly to a single value, which can diverge from actual measured values.
In the case of LAB monitoring, only pH and ammonia can be measured while all other variables are calculated and rely on the quality of the model and its parameters. Hence, the SMC provides an update on the unmeasured state variables. Figure 5 shows some preliminary results of the LAB monitoring. The model is applied to two sets of data.

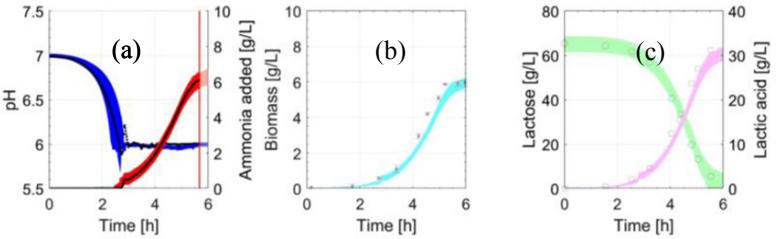

Figure 5 Monitoring of LAB, model prediction and data. (a) Online measurements: pH and ammonia addition, Offline measurements: (b) biomass and (c) lactose and lactic acid. Symbols: on- and off-line (time-delayed) measurements, filling: model prediction with 90% uncertainty interval.

4. Conclusions

The SMC is applied to the two-steps nitrification process. The SMC implementation is adapted for updating information on the model parameters, which is then used to estimate future states of the system and unmeasured outputs (this is different than the state space implementation, where particle filters are defined on the states themselves). When a parameter is unknown, one can start with a large uninformative prior (giving a "small" sampling range is not advised, as it risks limiting the input space covered during successive importance sampling). However, it is possible to define some limitations when applying such methodology: the sample size needed to have a good estimate of the problem can be quite large if the value of the required parameters is not known, and the number of parameters that need to be determined may affect the computational time.
The proposed work will be applied to LAB and several investigations on the effect of different filtering techniques as well as on the sample size will be investigated in future.

References

J. V. Beck, & K. J. Arnold, 1977, Parameter estimation in engineering and science.
A. Doucet, M. Briers, and S. Sénécal, 2006, Efficient block sampling strategies for sequential Monte Carlo methods. Journal of Computational and Graphical Statistics, 15(3), 693-711.
A. Gelman, J. B. Carlin, H. S. Stern, D. B. Dunson, A., Vehtari, & D. B., Rubin, 2013, Bayesian data analysis. Chapman and Hall/CRC.
N. Kantas, A. Doucet, S.S. Singh, J. Maciejowski, and N. Chopin, 2015, On particle methods for parameter estimation in state-space models. Statistical science, 30(3), 328-351.
G. Sin, D. J. De Pauw, S. Weijers, and P.A. Vanrolleghem, 2008, An efficient approach to automate the manual trial and error calibration of activated sludge models. Biotechnology and bioengineering, 100(3), pp.516-528.
G. Sin, A.S. Meyer, K.V. Gernaey, 2010, Assessing reliability of cellulose hydrolysis models to support biofuel process design—Identifiability and uncertainty analysis. Computers & Chemical Engineering, 34(9):1385-92.
R. Spann, C. Roca, D. Kold, A. E. Lantz, K. V. Gernaey, and G. Sin, 2018, A probabilistic model-based soft sensor to monitor lactic acid bacteria fermentations. Biochemical Engineering Journal, 135, 49-60.

Sauro Pierucci, Flavio Manenti, Giulia Bozzano, Davide Manca (Eds.)
Proceedings of the 30th European Symposium on Computer Aided Process Engineering (ESCAPE30), May 24-27, 2020, Milano, Italy.
http://dx.doi.org/10.1016/B978-0-12-823377-1.50271-8

Solvent Selection using CAMD for the Solid-liquid Extraction of Bioactive Compounds from Agroindustrial Waste from Avocado (Persea Americana)

Jorge Rodríguez-Iniesta,[a] Nancy Medina-Herrera,[a*] Guillermo Martínez-Ávila,[a] Romeo Rojas-Molina,[a] Salvador Tututi-Avila[b]

[a] *Universidad Autonoma de Nuevo León, Agronomy School, Francisco Villa s/n, Ex Hacienda el Canadá, General Escobedo, N.L, 66451, Mexico*

[b] *Universidad Autónoma de Nuevo León, Department of Chemical Engineering, Av. Universidad s/n, Ciudad Universitaria, San Nicolas de los Garza, N.L., 66455,Mexico*

nancy.medinahr@uanl.edu.mx

Abstract

The extraction of bioactive compounds is an interesting alternative to add value to agroindustrial waste, due to its demand in the pharmaceutical and food industry. The extraction of these compounds is highly dependent on the solvent used. The extraction of these compounds is limited by a small variety of solvents. Currently, there is no extraction model that accounts for thermodynamic behaviour. This manuscript presents a methodology to design a solid-liquid extraction system for bioactive compounds, from solvent selection generating candidates via computer aided molecular design (CAMD), model generation and process simulation in Aspen Custom Modeler (ACM). The approach was applied to a case study, which examines the extraction of bioactive compounds from avocado (*Persea americana*) agroindustrial waste. Results show how the extraction performance varies according to selected solvent, for instance conventional solvent (methanol) differs to the candidate solvent (1,2-propylene glycol) tested by process simulation. From simulation results, the candidate solvent presented flexible operating conditions, extracting 90.72% of the initial bioactive compound present in the agroindustrial waste in a single equilibrium stage. While working at a higher temperature, the solvent feed flowrate was decreased. The proposed strategy allows obtaining composition and temperature profiles for the extraction to select a proper solvent and operating conditions, although, it is still necessary to validate the results with experimental data.

Keywords: Bioactive compounds, CAMD, waste added value, solid-liquid extraction, solvent selection.

1. Introduction

Due to the population growth rate of the last decades, there has been a dramatic increment of agroindustrial waste worldwide. Thus, several works have reported that the agroindustrial waste is a valuable source of bioactive compounds, which are important on

the pharmaceutical and food industry due to their antioxidant potential and their uses in therapeutic treatments and nutrition (Morais, et al., 2015).
Currently, the extraction of this compounds is limited to just a few solvents, which do not perform optimally, resulting in a high solvent consumption in the extraction process (Jannatul, et al., 2013). Thus, a proper solvent selection is crucial for the extraction process, because the solvent determine the overall extraction yield, as well as product safety (de Matos, et al., 2018). Accordingly, there is an increasing need for a proper solvent selection for the extraction of bioactive compounds present in agroindustrial waste. A useful tool to achieve this goal is the implementation of CAMD to determine the optimal solvent candidates (Fedorova, et al., 2015).
Besides, a proper model for the extraction of this kind of compounds has not been fully developed in process simulators, limiting the evaluation of the extraction using different solvents. Therefore, there is a need to develop proper models and evaluate them within process simulators in order to save time and resources in experimental designs.
The goal of this work is to study the mathematical model for bioactive compounds extraction from agroindustrial waste and evaluate different potential solvents generated via CAMD in the software ICAS and extraction simulation in ACM on ASPEN Tech software.

2. Methodology

The proposed methodology uses ICAS 20.0 and AspenTech software, as illustrated on Figure 1. Based on literature survey, the main bioactive compounds present in agroindustrial waste tissue are identified. The ICAS 20.0 software is used for the generation of the candidate solvents for the extraction of bioactive compounds. Bioactive compounds are separated by families for optimal solvent selection. First, thermodynamic properties were estimated via the Marrero & Gani model for each bioactive compound, for better property estimation, experimental data can be added if it is available in literature.
Then, a solvent preselection is performed on ProCAMD tool within ICAS. The solvent design was carried out selecting the bioactive compounds of interest in such a way that there were no azeotropes between the selected compounds and the generated solvents. In the last step, the solvents are selected by analyzing the highest selectivity coefficients (β), and the lowest Octanol/Water partition coefficient, also the normal boiling point (T_b) was considered.
Finally, the model for the extraction of bioactive compounds is solved considering a single solid-liquid extraction (SLE) stage by means of simulation. By using Aspen Custom Modeler V11.0, the model was developed for the evaluation of the candidate solvents generated in ProCAMD. A comparison is made between the conventional solvents and the candidate solvents.

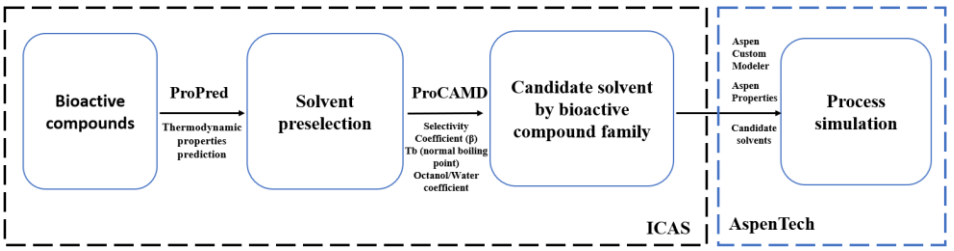

Figure 1 Methodology for the solid-liquid extraction.

3. Case of study

Avocado (*Persea americana*) is a tropical or subtropical fruit native from Mexico and South America, which has been referred as one of the most nutritious of all fruits. It is highly valuated due to its taste and healthy properties. Because of this it has gained worldwide recognition and its consumption has increased in the last years (Hurtado, et al., 2018).

It has been reported that their agroindustrial waste (seed and peel) are a rich source of bioactive compounds. The most abundant families present in *Persea americana* are phenolic acids, quinic acids, tyrosol derivatives, carboxylic acids and flavonoids. One of the most valuable is the carboxylic acids, due to their application in the pharmaceutical and food industry, such as anti-inflammatory, antioxidant, anti-microbial, food stabilizer and food flavouring.

The extraction of this compounds has been reported by typical conventional solvents, such as ethanol, methanol, acetone, chloroform, dioxane, which do not show very promising experimental yields.

It has been reported that for every 100 g of dry matter (DM), there are around 911 mg of this bioactive compounds (López, et al., 2016) as it is shown in Table 1. A bioactive compound was selected to represent each family according to the experimental properties data availability, expecting similar behaviour for compounds present in each chemical family, their economic and industrial potential. In this manuscript only carboxylic acids will be evaluated and presented.

Table 1 Bioactive compounds present in *Persea americana.*

Bioactive compound family	Weight per 100 g of DM (mg)	Compound of interest
Carboxylic acids	0.5189	Citric acid
Quinic acids	126.42	1-caffeoylquinic acid
Flavonoids	325.53	Rutin
Tyrosol derivatives	262.61	Hydroxytyrosol glucoside
Phenolic acids	196.79	3,4-Dihydroxybenzoic acid

4. Results

4.1. Candidate solvents for bioactive compounds extraction.

Solvent screening was performed by evaluating each family of bioactive compounds separately accordingly to Table 1 using the UNIFAC model. Conventional solvents were also considered for the analysis. Solvent selection criteria were based on safety of usage and operational thermodynamic properties, such as the normal boiling temperature (Tb), selectivity coefficient (β) and Octanol/Water partition coefficient as a safety coefficient. Regarding Tb, the upper limit was 175 °C to avoid thermal degradation of the desired bioactive compounds. Regarding to β coefficient, an indicator of optimal solvent affinity with the bioactive compound, the lower limit was fixed at 1, this value was obtained on a preliminary selection of candidate solvents. Octanol/Water coefficient was considered in an interval of -2 and 2 as an indicator for health safety. Thus, final candidate solvents were selected considering a higher Tb, a higher β coefficient and lower Octanol/Water coefficient values. The final candidate solvent list takes into consideration the potential

solvent performance with other bioactive compound families. As well, commercial availability was considered for industrial scale.

The candidate solvents for the extraction of bioactive compounds found by ProCAMD are shown in Table 2. It should be noted that the CAMD was performed considering no azeotropes formation. From results, it should be noted that only the acetone has been reported as a conventional solvent for bioactive compound extraction, whereas 1,2-Propylene glycol, succinic acid and cyclohexanol has not been reported to our knowledge for the extraction of these compounds.

4.2. Solid-Liquid extraction model in ACM.

Currently there is not an extraction model that consider thermodynamic behaviour within ASPEN Plus. Thus, for developing the SLE model, the extraction was considered in a single equilibrium stage, as it is shown in the flowsheet (Figure 2).

Table 2 Candidate solvents for the solid-liquid extraction for the selected bioactive compounds

Candidate solvent	Bioactive compound family	Selectivity coefficient (β)	Octanol/Water coefficient	Tb (°C)
1,2-Propylene glycol	Tyrosol derivatives	2.58	-0.43	172.34
	Phenolic acids	130.87		
	Carboxylic acids	1.14		
Acetone	Quinic acids	1.37	0.0674	32.22
	Tyrosol derivatives	3.69		
Cyclohexanol	Phenolic acids	7.85	1.93	162.53
	Quinic acids	1.03		
Succinic acid	Flavonoids	5.85	-0.347	258.92

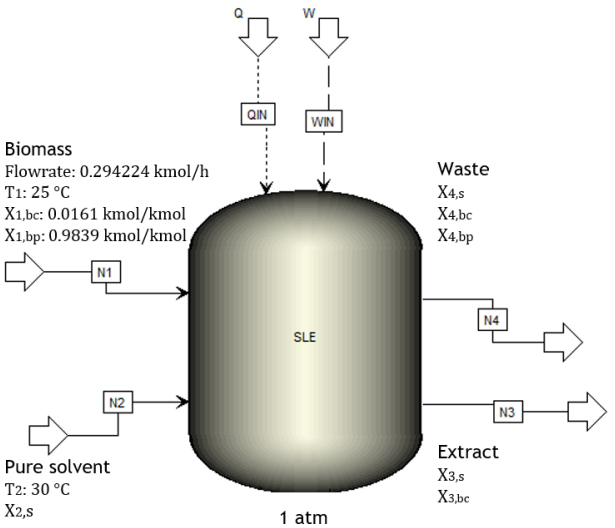

Figure 2 Process flow diagram for the solid-liquid extraction

The equations for the SLE model for bioactive compounds are presented in this section. Molar material balances represent that the sum of the inlet flowrates is equal to the sum of outlet flowrates (Equation 1-3).

$$n_1 * x_{1,i} + n_2 * x_{2,i} - n_3 * x_{3,i} - n_4 * x_{4,i} = 0 \qquad \forall i \in N \tag{1-3}$$

Where the solvent (s), the bioactive compound (bc) and the biopolymer (bp) represent the set N. The sum of composition fractions in the outlet streams are considered as well.

The energy balance considers the inlet and outlet enthalpy and heat and work required to perform the extraction, Equation 4.

$$n3*h3 + n4*h4 - n1*h1 - n2*h2 - Q - W=0 \tag{4}$$

According to Nevers (2016) the solid-liquid equilibrium in extraction can be represented by Equation 5. Where it is considered the activity coefficient, enthalpy of fusion, operating and melting temperatures.

$$\ln\left(\frac{1}{x_{3,bc}\gamma_{3,bc}}\right) = \left(\frac{H_{fus,bc}}{R}\right)\left(\left(\frac{1}{T_3}\right) - \left(\frac{1}{T_{m,bc}}\right)\right) \tag{5}$$

Additionally, thermal equilibrium was considered on the outlet streams. Enthalpies and activity coefficients are calculated through calling ASPEN Properties. Thus, the model has four degrees of freedom, the design specifications were the molar bioactive compound composition of extract stream and waste stream, the molar solvent composition fraction on the waste stream and the power of agitator. The model was codified within ACM and evaluated for solvent candidates.

4.3. Extraction process simulation.

A sensitivity analysis for 1,2-propylene glycol was performed with the design specification of molar bioactive compound composition of bioactive compounds for carboxylic acids can be seen at Figure 3.

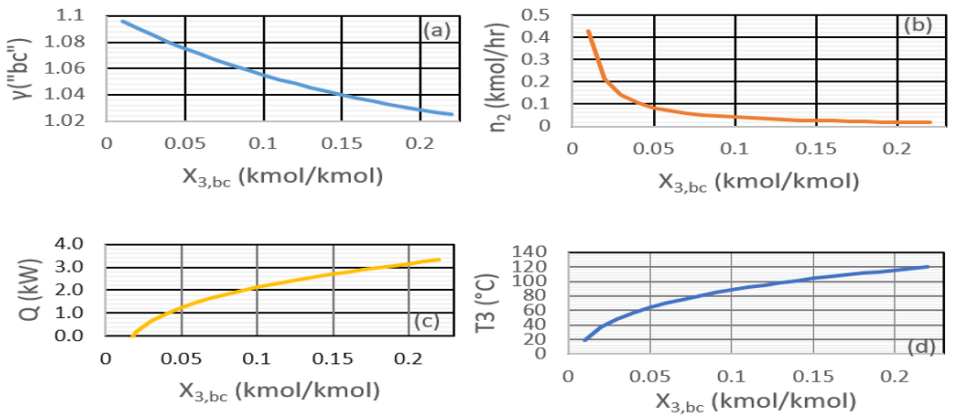

Figure 3 Sensitivity analysis for molar bioactive compound composition of extract stream for carboxylic acids. Results for (a) activity coefficient; (b) solvent feed flowrate; (c) heat duty; and (d) extraction temperature

The following design specifications were fixed: agitator power (0.00027 kW); molar solvent composition fraction on the waste stream (0.005 kmol/kmol); molar bioactive compound composition on the waste stream (0.0015 kmol/kmol).

The candidate solvent (1,2-propylene glycol) presented an activity coefficient greater than one. The amount of solvent used for the extraction decreases by increasing the operation temperature. This would require greater heat duty into the system. In comparison with conventional solvent (methanol), the trend is similar regarding solvent feed flowrate, operating temperature, and heat duty. However, the activity coefficient for the conventional solvent was calculated between 0.4-0.6. The operating temperature using the conventional solvent limits the extract composition of bioactive compounds, due to after a value of 0.09 the normal boiling point of methanol is reached. Therefore, operation using the candidate solvent is more flexible.

5. Conclusions

This methodology has the potential to be extrapolated to other agroindustrial waste. Potential candidate solvents can be obtained for the solid-liquid extraction of bioactive compounds present in *Persea americana* using CAMD. A solid-liquid extraction model has been developed for the simulation of the extraction process. The simulation performed in ACM showed promising results for the extraction of carboxylic acids, although a more reliable model considering mass and energy transfer is still required. The usage of candidate solvents may reduce the solvent consumption and ease of purification, on the other hand, extraction process may be performed into higher temperatures, consequently it should be performed a more detailed analysis for the energy consumption on the process in order to evaluate economic feasibility.

Acknowledgements

The authors acknowledge the software license support for ICAS 20.0 provided by Dr. Rafiqul Gani.

References

A. Jannatul, et al. 2013. Techniques for extraction of bioactive compounds from plant materials: A review. Journal of Food Engineering. 117. 10.1016/j.jfoodeng.2013.01.014.

A. López, et al. 2016.. HPLC-DAD-ESI-QTOF-MS and HPLC-FLD-MS as valuable tools for the determination of phenolic and other polar compounds in the edible part and by-products of avocado. LWT, 73, pp.505-513.

application. Computers & Chemical Engineering, 83, pp.232-247.

D. Morais, et al. 2015. Antioxidant activity, phenolics and UPLC–ESI(–)–MS of extracts from different tropical fruits parts and processed peels. Food Research International, 77, pp.392-399.

E. Hurtado, A. Fernández, A. Carrasco. 2018. Avocado fruit— Persea americana. Exotic Fruits, pp.37-48.

M. Fedorova, G. Sin, R. Gani. 2015. Computer-aided modelling template: Concept and

N. Nevers. 2013. Physical and chemical equilibrium for chemical engineers. Hoboken, N.J.: Wiley..

R. de Mattos, et al. 2018. Solvent use optimization on polyphenols extraction from grape marc involving economical aspects.

Sauro Pierucci, Flavio Manenti, Giulia Bozzano, Davide Manca (Eds.)
Proceedings of the 30th European Symposium on Computer Aided Process Engineering (ESCAPE30), May 24-27, 2020, Milano, Italy.
http://dx.doi.org/10.1016/B978-0-12-823377-1.50272-X

Development of a Computational Intelligence Framework for the Strategic Design and Implementation of Large-scale Biomass Supply Chains

Ahmed AlNouss,[a] Rajesh Govindan,[b] Gordon McKay,[a] Tareq Al-Ansari [a,b*]

[a] *Division of Sustainable Development, College of Science and Engineering, Hamad Bin Khalifa University, Qatar Foundation. Doha, Qatar*

[b] *Division of Engineering Management and Decision Sciences, College of Science and Engineering, Hamad Bin Khalifa University, Qatar Foundation. Doha, Qatar*

talansari@hbku.edu.qa

Abstract

Biomass utilisation has witnessed growing attention as a promising alternative to fossil fuels. However, the biomass supply chain is generally unstable due to the fluctuation of the supply and the difficulty to accommodate all the available biomass feedstock and utilisation pathways. This has made the optimisation of the supply chain a challenging task due to the complexities of modelling the different interconnected systems consisting of various production sources, intermediate processing methods, and utilisation sinks. The objective of this study is to develop a geospatial information systems (GIS)-based decision framework integrated with statistical learning and heuristic optimisation capabilities in order to establish the design solutions for biomass supply chains on a national scale and subsequent strategic decision-making. The artificial neural network (ANN)-based surrogate models for the biomass processing system were developed and validated to predict the synthesis gas flowrate and composition linked to the input parameters of biomass attributes in terms of their proximate and ultimate analysis, as simulated in previously developed Aspen Plus models. The surrogate models were then coupled with GIS, including information about biomass sources, candidate plant locations, and utilisation sinks. The optimal biomass utilisation routes were subsequently solved using the genetic algorithm (GA). The framework implementation is illustrated through a biomass gasification case study in the state of Qatar. The results demonstrate the importance of domestic biomass resources to support the local economy through the production of methanol as a final product, and utilising primarily manure-based biomass feedstock in an optimal blend with sludge and date pits. The economic optimisation of the biomass processing-plant locations reveals production routes supporting the generation of methanol and the utilisation of manure feedstock in Qatar.

Keywords: Biomass Supply Chain, Biorefinery Plant, Biomass Gasification, Artificial Neural Network, Genetic Algorithm, GIS

1. Introduction

Biomass gasification is witnessing growing attention as a result of the promising production of high-energy syngas from renewable sources and the reduction in carbon dioxide emissions (AlNouss et al., 2018). Nevertheless, the investment risk in biomass conversion is largely due to the complex nature of the process and the requirement of

quality biomass feedstock and cost-efficient biomass handling facility (Sharma et al., 2013). Moreover, the requirement of safely-operated experiments that are highly time-consuming hinders the progression in analysing the effect of key gasification parameters on the overall process performance. Mathematical simulation and modeling have the capabilities to mimic real operational processes and help in understanding the operational performance of complex natural processes (Salah et al., 2016). The highly integrated sequential operational processes involved in the conversion of biomass into value-added products that hinder its modelling using simple closed-form equations. Though, machine learning techniques (Salah et al., 2016) coupled with geospatial analysis methods (Rodríguez et al., 2017) can help in data-driven model induction for complex systems that aid in making decisions to solve the problems related to supply chain routing, productivity, resource efficiency and risk management. The state of Qatar depends purely on natural gas to run its entire power and petrochemical production sector. The national strategy supports the utilisation of the high waste per capita generation approximated at 7,000 tons per day of food waste only to diversify the energy mix and reduce the significant greenhouse gas (GHG) emissions (AlNouss et al., 2020). This research described in this paper looks at the development of a geospatial information systems (GIS)-based decision framework integrated with statistical learning and heuristic optimisation capabilities in order to establish the design solutions for biomass supply It is envisaged that the proposed framework will enable stakeholders to rapidly assess alternative designs under different scenarios for the biomass supply chains, in both the local and international context. The implementation of the framework is illustrated through a biomass gasification case study in the state of Qatar.

2. Methodology

The methodological framework developed in this study is illustrated in Figure 1. This framework combines the capabilities of GIS analysis, artificial neural network (ANN) modelling, and process simulation and optimization. In addition, it takes into account several important components in the biomass supply chain as illustrated in Figure 2. These components include: (a) procurement of biomass feedstock from the sources; (b) transportation of biomass raw material; (c) processing of biomass; (d) transportation of the intermediate product; and (e) processing of the value-added products.

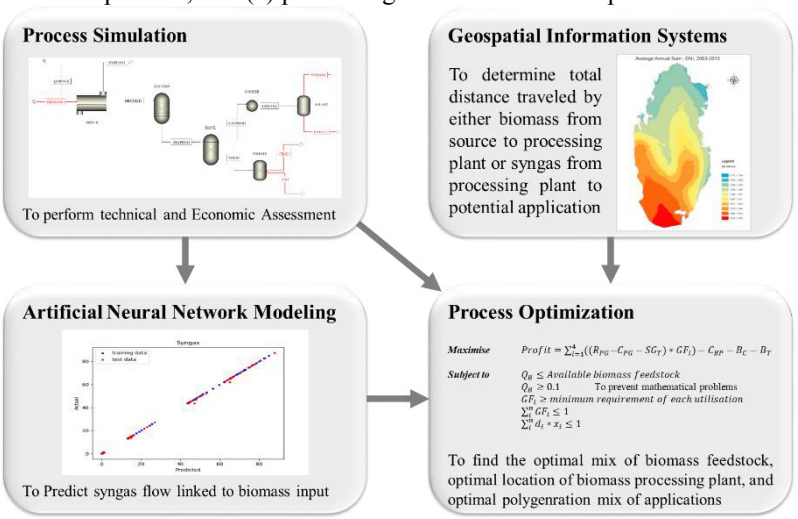

Figure 1: Methodological framework developed in this study.

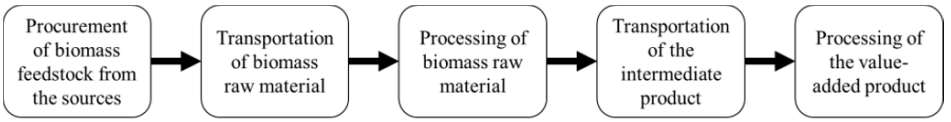

Figure 2: Biomass supply chain stages considered in this study.

The biomass feedstocks are first procured from the different sources. The biomass types involved in this study include date pits, manure, sludge and foodwaste. The prices associated with the biomass sources available in Table 1 are used to calculate the cost of raw materials through Eq (1).

$$B_c = \sum_{i=1}^{4} Q_{B,i} * B_{p,i} \quad (1)$$

Where Q_B = Biomass Quantity, and $B_{P,i}$ = Biomass price for each biomass type. The transportation of biomass raw material from the different biomass sources to the processing plant is assumed to take place using trucks. The cost associated with biomass transportation is calculated using Eq (2) through (4).

$$B_T = \sum_{i=1}^{4} n_{B_{T,i}} * T_{P,i} \quad (2)$$

$$T_{p,i} = d_i * C_d \quad (3)$$

$$n_{B_{T,i}} = \frac{Q_{B,i}}{C_T} \quad (4)$$

Where n_{BT} = number of biomass transportation, $T_{P,I}$ = price of one transportation, d = distance, C_d = cost per distance travelled, and C_T = Capacity of one biomass transportation. The cost of biomass processing plant is retrieved from previously simulated Aspen Plus models in (AlNouss et al., 2019b). The models are based on the gasification of the same biomass feedstock considered in this study using oxygen and steam as gasification agents to generate high-energy syngas. The cost of the processing plant is accounted for in the network using Eq (5).

$$C_{BP} = Cost\ of\ Biomass\ processing \quad (5)$$

The transportation of the intermediate syngas product from the biomass processing plant to the different utilisation applications is assumed to take place using a pipeline network. The cost of the pipeline construction to transport syngas based on a pipeline corridor specific to Qatar is calculated using Eq (6) through (8).

$$SG_T = Q_{SG} * C_Q \quad (6)$$

$$C_Q = C_{Seg} * n_{seg} \quad (7)$$

$$n_{seg} = \frac{d}{CP_{Seg}} \quad (8)$$

Where Q_{SG} = quantity of syngas, C_Q = cost per quantity, C_{Seg} = cost of one segment of pipline, n_{Seg} = number of segments needed, d = total distance, and CP_{Seg} = capacity of one segment. The prediction of syngas production quantity is governed through the use of ANN-based surrogate models. The ANN-based surrogate models for the biomass processing system are trained and validated to predict the synthesis gas flowrate and composition linked to the input parameters of biomass attributes in terms of their proximate and ultimate analyses as illustrated in Figure 3. The feed-forward back propagation technique is used to develop the network. A multi-layer perceptron (MLP) one of the classes of feed-forward neural network is utilised to model the network. It comprises three layers i.e. input layer, hidden layers and the output layer. The model utilises a non-linear least squares approach called the Levenberg-Marquardt (LM)

algorithm to determine the weights Biomass types, attributes and flowrate represent neurons in the input layer, while the effluent flowrate of CO_2, CO, H_2, CH_4, and N_2 represent neurons in the output layer. Before the training of the network, the data for input and output variables are normalised to improve the network efficiency. For the training of the network, 60% data points are used, while the remaining 40% of the data are used for the testing and the validation of the network respectively for the better indication of the model's performance on unseen data.

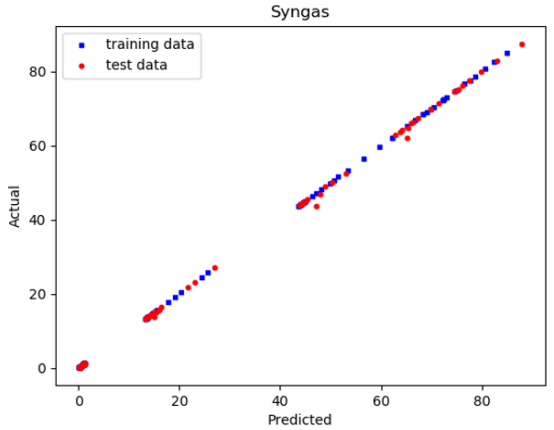

Figure 3: Training and test plots for ANN model.

The syngas in the case study is utilised in four different applications that include, urea, methanol, power, and liquid fuels production. The costs associated with product generation for each application are supplied from the simulated Aspen Plus models (AlNouss et al., 2019) and Eq (9) to demonstrate the representation of these costs in the model.

$$C_{PG} = Cost\ of\ product\ generation \quad (9)$$

Moreover, the revenue of from products generation is accounted using Eq (10).

$$R_{PG} = \sum_{i=1}^{4} Q_{Product,i} * P_{Product,i} \quad (10)$$

Where R_{PG} = revenue from product generation, Q = quantity of a certain product, and P_i = selling price of each product. The optimisation objective is then formulated to maximise the summation of the different costs subtracted from the revenue of each application as indicated in Eq (11).

Maximise $$Profit = \sum_{i=1}^{4}((R_{PG} - C_{PG} - SG_T) * GF_i) - C_{BP} - B_C - B_T \quad (11)$$

Where GF_i = Generation fraction of each product based on the required minimum quantity. These fractions limit the minimum requirement of each utilisation technique to the national needs where for the case of Qatar, urea is represented by 0.032, methanol by 0.0085, liquid fuels by 0.00032 and power by 0.042 (AlNouss et al., 2019a). The optimisation problem is subject to different constraints as specifiedby Eq (12) through (14).

Subject to

$$Q_B \leq Available\ biomass\ feedstock \quad (12)$$

$$Q_B \geq 0.1 \quad \text{To prevent mathematical problems} \quad (13)$$

$$GF_i \geq minimum\ requirement\ of\ each\ utilisation \quad (14)$$

$$\sum_i^n GF_i \leq 1 \quad (15)$$

$$\sum_i^n d_i * x_i \leq 1 \quad (16)$$

Where x_i represents the applicability of this distance in the geospatial information systems for a minimum distance to be traveled by either biomass source using the expressway and road network or syngas intermediate product using the service pipeline corridors. This is achieved through calculating the shortest distance between latitude and longitude points on the available network map over the earth's surface.

3. Case Study

The integrated (GIS)-based decision framework with statistical learning and heuristic optimisation capabilities is implemented in the case study of Qatar. Table 1 summarises the main raw data used in the case study.

Table 1: Raw data of Qatar's case study.

Parameter	Value	Unit
Biomass Price ($B_{p,i}$)	10	\$/Ton
Cost per distance (biomass) (C_d)	1	\$/km
Capacity of one transfer (C_T)	1000	Ton
Cost of one segment of pipline (syngas) (C_{Seg})	2	\$/km
Capacity of pipe (CP_{Seg})	1000	kg/s

The local biomass sources are identified by several map locations that include 11 locations for date pit procurement, 3 locations for manure procurement, 4 locations for sludge procurement and 1 location for food waste procurement. The potential biomass processing plant locations are located in the expressway and road network or in the service pipeline corridors where 2453 location points were identified and included in the optimization. The utilisation applications are identified by 2 locations for current gas to liquid (GTL) plants located in Ras Laffan industrial city (RLIC), 1 location for urea and 1 location for methanol located in Mesaieed industrial city (MIC), and 3 locations for power located in RLIC, MIC and Ras Abu Fontas power station. The optimisation problem is formulated as a mixed integer nonlinear programming (MINLP) and solved using the genetic algorithm (GA) in Matlab. The formulation consists of 63,786 decision variables, 2453 integers/binary and 44 constraints.

4. Results

The results of the optimisation problem are in the from of optimum biomass blended feedstock, optimum polygeneration mix and optimum locations of biomass sources, processing plant and application sinks. The optimum biomass blended feedstock presented in Figure 4 demonstrates a domination of manure-based biomass with around 60,118 kg/h. Whereas the optimum polygeneration mix illustrated in Figure 5 suggests methanol as the optimal biomass utilisation technique with more than 93%. The overall objective function highlights a net revenure \$6.5M per year coming mainly from methanol and power production. These results demonstrate the potential of manure utilisation and methanol production in supporting the national waste utilisation and emissions reduction in Qatar. The optimum locations of biomass sources, processing plant and application sinks are highlighted in the network map of Qatar in Figure 6. The location of the biomass processing plant is placed near to the manure procurement source. The applications sinks are mainly selected in MIC with only the GTL plant located in RLIC.

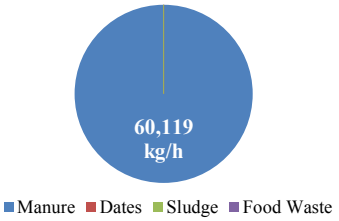

Figure 4: Optimum biomass blends.

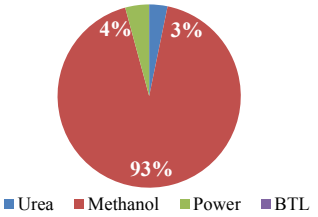

Figure 5: Optimum polygeneration mix.

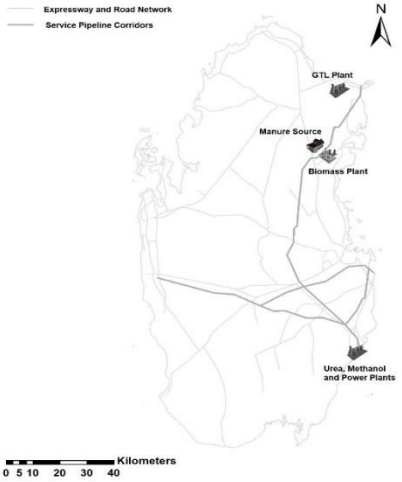

Figure 6: Optimum locations map.

5. Conclusions

This paper study the development of a geospatial information systems (GIS)-based decision framework integrated with statistical learning and heuristic optimisation capabilities in order to establish the design solutions for biomass supply chains on a national scale and subsequent strategic decision-making. The proposed framework potentially enables stakeholders to rapidly assess alternative designs under different scenarios of the biomass supply chains, in both the local and international context. The implementation of the framework is illustrated through a biomass gasification case study in the state of Qatar where manure utilisation and methanol production dominated the national biomass supply chain.

Acknowledgment

The authors acknowledge the support of Qatar National Research Fund (QNRF) (a member of Qatar Foundation) by GSRA grant No GSRA4-1-0518-17082.

References

A. AlNouss, G. McKay, and T. Al-Ansari, 2018, Optimum utilization of biomass for the production of power and fuels using gasification, Computer Aided Chemical Engineering, 43, 1481-86.

A. AlNouss, G. McKay, and T. Al-Ansari, 2019a, Superstructure Optimization for the Production of Fuels, Fertilizers and Power using Biomass Gasification, Computer Aided Chemical Engineering, 46, 301-06.

A. AlNouss, G. McKay, and T. Al-Ansari, 2019b, A techno-economic-environmental study evaluating the potential of oxygen-steam biomass gasification for the generation of value-added products, Energy Conversion and Management, 196, 664-76.

A. AlNouss, G. McKay, and T. Al-Ansari, 2020, Production of syngas via gasification using optimum blends of biomass, Journal of Cleaner Production, 242, 118499.

R. Rodríguez, P. Gauthier-Maradei, and H. Escalante, 2017, Fuzzy spatial decision tool to rank suitable sites for allocation of bioenergy plants based on crop residue, Biomass and Bioenergy, 100, 17-30.

A. Salah, L. Hanel, M. Beirow, and G. Scheffknecht, 2016, Modelling SER Biomass Gasification Using Dynamic Neural Networks, Computer Aided Chemical Engineering, 38, 19-24.

B. Sharma, R.G. Ingalls, C.L. Jones, and A. Khanchi, 2013, Biomass supply chain design and analysis: Basis, overview, modeling, challenges, and future, Renewable and Sustainable Energy Reviews, 24, 608-27.

Sauro Pierucci, Flavio Manenti, Giulia Bozzano, Davide Manca (Eds.)
Proceedings of the 30th European Symposium on Computer Aided Process Engineering (ESCAPE30), May 24-27, 2020, Milano, Italy.
http://dx.doi.org/10.1016/B978-0-12-823377-1.50273-1

Optimising Multi Biomass Feedstock Utilisation Considering a Multi Technology Approach

Tareq Al-Ansari [a,b*], Ahmed AlNouss[a], Mohammad Alherbawi , Nayla Al-Thani[a], Prakash Parthasarathy[a], Samar ElKhalifa[a], Gordon Mckay[a]

[a]*Divison of Sustainable Development, College of Science and Engineering, Hamad Bin Khalifa University, Qatar Foundation, Doha, Qatar.*
[b]*Division of Engineering Management and Decision Sciences, College of Science and Engineering, Hamad Bin Khalifa University, Doha, Qatar.*
talansari@hbku.edu.qa

Abstract

As effects of climate change and resource scarcity disturb the modern world, there is an urgent need to shift from the traditional fossil fuel-based economy towards a more sustainable future. Transitioning towards a bio-economy can serve waste reduction and energy diversification objectives. Whilst technologies continue to develop that are capable of processing a wide array of wastes as feedstock, it is necessary to devise methodologies that optimise strategic decisions within bio-economies and increase the competitiveness with traditional fossil fuel-based industries. As such, the objective of this study is to develop an integrated framework that can inform optimal technological pathways for the conversion of various biomass waste into value-added products. The biomass feedstock include: date seeds, municipal solid waste, food waste, camel manure, and sludge. To achieve this objective, a two stage optimisation framework is developed based on three technologies; gasification, pyrolysis, hydrothermal liquefaction. Outputs of process specific models are used in a multi-objective mathematical formulation model to identify optimal pathways that encompass technology pathways and corresponding value-added product for each waste type. The mathematical model maximises the total revenue and minimises total emissions within the waste to value added product pathways. The simulation results demonstrate that the process yield of syngas production using gasification is higher than the pyrolysis for the date seeds, MSW, food wastes, and camel manure by about 58.67%, 69.81%, 60.38%, and 58.32% respectively. The results of the optimisation indicate the need to improve the efficiency of the hydrothermal liquefaction process, which is the optimal pathway to produce bio-oil from date seeds alone. However, for the other waste types, the gasification process is the preferred technology discarding bio-oil quality.

Keywords: Bioenergy, Aspen Plus, Gasification, pyrolysis, hydrothermal liquefaction

1. Introduction

Extracting value from biomass, which would have otherwise been disposed of as waste is an important component of circular and bio-economies. By extension, bio-economies involve the sustainable transformation of renewable organic resources into food, energy, and other essential products. There are various types of waste that are produced from both urban and industrial ecosystems that have potential to be recycled into valued added

products such as food waste, animal manure, municipal solid waste, sewage sludge. As such, the objective of this paper is to explore the optimal pathways for which particular feedstock can be converted into value-added products through various technology options. However, the challenge is identify optimum technology pathway for the different feedstock determined by the quality of products, environmental and economic dimensions. The three processes considered in this study include gasification, pyrolysis, and hydrothermal liquefaction as illustrated in Figure 1 and will form the basis of process models developed. Pyrolysis is the thermal decomposition of biomass in the absence of oxygen to form bio-char and bio-oil. It has the potential to produce highly porous solids used as adsorbents and catalytic support materials (Elkhalifa et al., 2019). In this process, the pseudo-biomass components; hemicellulose, cellulose, and lignin, undergo thermal decomposition in the temperature ranges of 220-315 ^{o}C, 314-400 ^{o}C and 160-900 ^{o}C, respectively, to yield varying composition of the gaseous components (Yang et al., 2007). Gasification is a promising technique in the utilisation of biomass for the generation of high-energy combustible gas (Sikarwar et al., 2016). It is defined as the process of converting carbon-based materials thermochemically into synthesis gas using a gasifiying agent such as oxygen and steam. It can also generate pyrolysis products such as bio-fuels and bio-char. The gasification processes are usually distinguished by reactor conditions that ranges from low temperature (425-650 ^{o}C) to medium and high temperatures of (900-1050 ^{o}C) and (1250-1600 ^{o}C), respectively, and atmospheric pressure to high pressurised gasifiers. These conditions influence the oxygen and steam demand of the gasification process along with the H_2:CO ratio in syngas and the presence of the pyrolysis products (AlNouss et al., 2020). Hydrothermal Liquefaction (HTL) is a thermochemical conversion of wet biomass into liquid bio-crude using pressurised hot water operating at high temperatures between 250 – 400 °C and pressures between 50 – 200 bar (Ramirez et al., 2015). During HTL, water acts as a reactant, therefore, biomass can be converted directly without the need to the energy-intensive drying step as in pyrolysis technology (Toor et al., 2011).

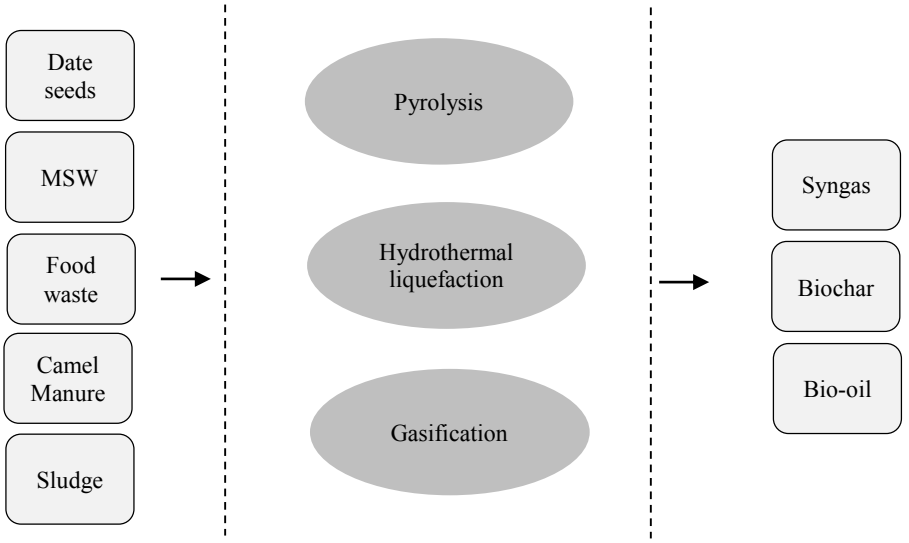

Figure 1: Biomass thermochemical conversion pathways considered in this study.

2. Methodology

2.1 Process descriptions

The gasification model in this paper is simulated using on the basis of atmospheric pressure with medium temperature gasification at 850 °C, isothermal and steady state operations. The fluid package is selected to be Peng-Robinson with Boston-Mathias modification to account for nonpolar and real components presented in the model. The main operation units considered in the model include a decomposition rector that uses a calculator block to convert the nonconventional attributes presented in Table 1 into conventional components. The stream is then introduced into a solid separator to remove ash content from the gaseous mixture that is sent to the gasification reactor. Steam is introduced in the gasifier as a gasifying agent with a steam to biomass ratio of 0.75. The gasifier is simulated as a Gibbs reactor where the equilibrium is restricted through minimisation of Gibbs free energy. The model is valeted against available literature models (AlNouss et al., 2019; 2018). Whereas, the pyrolysis model is simulated based on the assumptions of kinetic-free equilibrium, steady state operation, 500 °C decomposition temperature and atmospheric pressure. After decomposing the nonconventional attributes presented in Table 1 into conventional components, the stream enters a cyclone unit to separate ash and char solids from the gaseous species. The gaseous stream is cooled to separate the condensable components and yield the two products; syngas and bio-oil. The solid stream enters another solid separator to purify char product from ash (Elkhalifa et al., 2019).

Table 1: Feedstock Characteristics.

Biomass	**Date seeds**	**MSW**	**Food waste**	**Camel manure**	**Sludge**
Proximate analysis (%)	Air dried-basis	As-received	As-received	Air dried-basis	As received
Moisture	0.33	7.56	10	4.34	39.29
Fixed carbon	14.99	24.21	33.07	28.51	19.49
Volatile matter	83.61	57.99	61.14	51.56	18.07
Ash	1.40	17.80	5.79	19.94	62.44
Ultimate analysis (%)	Dry-basis	Dry-basis	Dry-basis	Dry-basis	Dry-basis
Ash	1.4	16.45	5.8	19.94	62.44
Carbon	46.48	49.02	43.99	36.73	7.63
Hydrogen	6.54	5.24	4.9	5.55	1.54
Nitrogen	0.89	1.23	2.07	2.62	1.2
Cl	0	0	0	0	0
Sulphur	0	0.3	0.19	0.42	0.28
Oxygen	44.69	27.76	43.05	34.74	26.91

Aspen Plus (V.9) ® is used to develop the different thermochemical conversion models. Whereby, biomass feeds are defined as nonconventional components based on their proximate and elemental values presented in Table 1. Biomass is defined based on Aspen's built-in enthalpy and density correlations of coal, identified as HCOALGEN and DCOALIGT respectively. Char is defined as 100% carbon. Biomass feeds initially undergo decomposition to breakdown nonconventional components into their corresponding conventional elements. Prediction of resulted elements' yield is calculated based on the Fortran code introduced by (AlNouss et al., 2018). Ash is then separated

from the mixture before processing the stream into the main reactors. In the HTL model, a slurry is created via mixing the biomass feed with a hot and pressurized water before being pumped into the HTL reactor. Besides, sodium hydroxide alkali catalyst is added to biomass slurry to increase the possibility of oil-like products formation (Cao et al., 2017). Block "RGibbs" is used to represent the HTL reactor, which operates based on the principle of minimizing Gibbs free energy. The reactor is operated at 300°C and 150 bars. At these reaction conditions, water is preserved in sub-critical state, thus, has lower viscosity and higher solubility of organic compounds. Possible products of the process are defined based on earlier reports (Pedersen et al., 2017). The downstream process is initiated with solids separation. Consecutively, gases are separated by partial cooling of products, while the aqueous phase is separated from the bio-crude using a distillation column that consists of 6 stages and operates at atmospheric pressure with a reflux ratio of 1.

2.2 Optimsation framework

The optimisation framework determines the optimum technology to treat each waste type into useful products i.e. syngas, char, and bio-oil. The problem was formulated as 0-1 integer programming with two objectives which were solved sequentially. The first objective is an economical objective that aims to maximise the profit, while the second objective in an environmental objective which aims to minimise the total emissions represented as tonnes of CO_2 equivalent per year. The problem is subject to a logical constraint which ensures that each waste type will be treated by only one technology.

Table 2: Optimisation variables.

indices	
$K = 1,2,\dots,k$	technology types
$J = 1,2,\dots,j$	product types
$I = 1,2,\dots,i$	waste types
Parameters	
C_{jki}	the cost associated with producing product j from waste i using technology k
P_{ijk}	the selling price of the product j from waste I using technology k
E_{jki}	the emissions associated with producing product j from waste i using technology k
Decision Variable	
x_{jki}	$\begin{cases} 1, & if\ technology\ k\ will\ be\ used\ to\ produce\ product\ j\ from\ waste \\ 0, & otherwise \end{cases}$

Objective function:

$$Economic\text{: } \max \sum_{I=1}^{i} \sum_{K=1}^{k} \sum_{J=1}^{j} \left[\left(P_{ijk} x_{jki} \right) - \left(C_{jki} x_{jki} \right) \right]$$

$$Envirnomental\text{: } \min \sum_{I=1}^{i} \sum_{K=1}^{k} \sum_{J=1}^{j} \left(E_{jki} x_{jki} \right)$$

Subject to:

$$\sum_{K=1}^{k} x_{jki} \leq 1 \qquad \forall\, I = 1,2,\dots,i; J = 1,2,\dots,j$$

3. Results

The results of the economical objective maximization illustrated in Figure 2 suggest that for the date seeds the gasification is the best option to produce syngas, while for the char and bio-oil, pyrolysis and HT liquefaction are the optimal conversion pathways, respectively. Additionally, gasification turned out to be the optimal option to produce both syngas and bio-oil from MSW, food waste, and the camel manure, while pyrolysis is the optimal option for the production of char. However, the results from the environmental objective maximisation illustrated in Figure 3 suggest that bio-oil is to be produced by pyrolysis while syngas and char to be produced by HT liquefaction for all waste types in order to minimise the environmental effect of the processes. These results represent overall production pathways discarding products quality, hence further analysis shall be done to explain and improve the results.

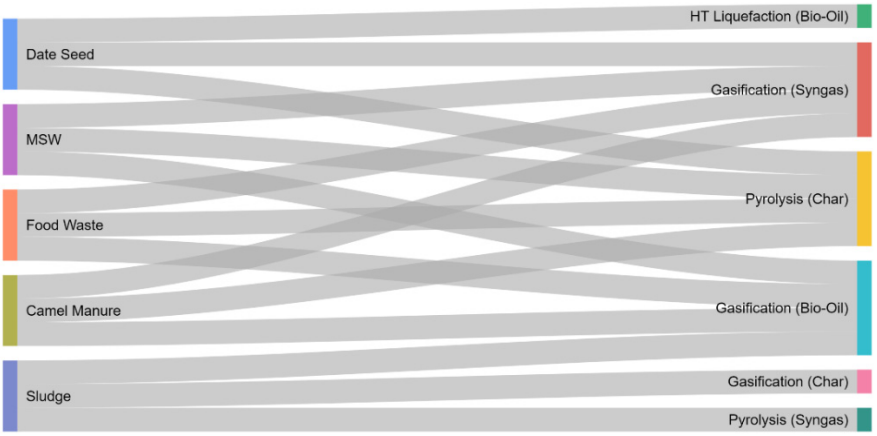

Figure 2: Feedstock and tehcnology selection pathways considering economic objective.

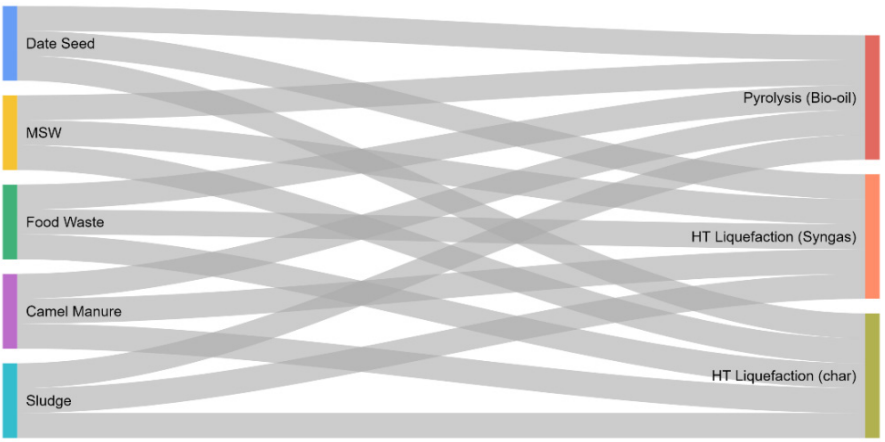

Figure 3: Feedstock and tehcnology selection pathways considering environmental objective.

4. Conclusion

Considering the development of multiple technologies that can treat similar feedstock, it is important to devise decision tools that determine the best pathway for a particular feedstock in terms of environmental impact and economic feasibility. Preliminary work introduced in this study formulated the problem using a 0-1 integer programming where the two objectives were solved sequentially. The results demonstrate that the gasification dominate the conversion pathway from economic prespective to produce syngas and bio-oil while pyrolysis is the optimal technology to produce char. From environmental perspective, HT liquefaction was found to be the optimal pathway to produce syngas and char, while pyrolysis is the optimal pathway to generate bio-oil. Future work will include development of the optimisation solver to solve environmental and economic objectives concurrently and study the effect on the technology selection. In addition, the model could be expanded to include more constraints such as water, and energy requirements for the processes and to pay more attention to the quality of generated products from the different conversion pathways.

References

A. AlNouss, G. McKay, and T. Al-Ansari, 2018, Optimum utilization of biomass for the production of power and fuels using gasification, Computer Aided Chemical Engineering, 43, 1481-86.

A. AlNouss, G. McKay, and T. Al-Ansari, 2019, A techno-economic-environmental study evaluating the potential of oxygen-steam biomass gasification for the generation of value-added products, Energy Conversion and Management, 196, 664-76.

A. AlNouss, G. McKay, and T. Al-Ansari, 2020, Production of syngas via gasification using optimum blends of biomass, Journal of Cleaner Production, 242, 118499.

L. Cao, C. Zhang, H. Chen, D.C.W. Tsang, G. Luo, S. Zhang, and J. Chen, 2017, Hydrothermal liquefaction of agricultural and forestry wastes: state-of-the-art review and future prospects, Bioresource technology, 245, 1184-93.

S. Elkhalifa, A. AlNouss, T. Al-Ansari, H.R. Mackey, P. Parthasarathy, and G. McKay, 2019, Simulation of Food Waste Pyrolysis for the Production of Biochar: A Qatar Case Study, Computer Aided Chemical Engineering, 46, 901-06.

T.H. Pedersen, C.U. Jensen, L. Sandström, and L.A. Rosendahl, 2017, Full characterization of compounds obtained from fractional distillation and upgrading of a HTL biocrude, Applied Energy, 202, 408-19.

J.A. Ramirez, R.J. Brown, and T.J. Rainey, 2015, A review of hydrothermal liquefaction bio-crude properties and prospects for upgrading to transportation fuels, Energies, 8, 7, 6765-94.

V.S. Sikarwar, M. Zhao, P. Clough, J. Yao, X. Zhong, M.Z. Memon, N. Shah, E.J. Anthony, and P.S. Fennell, 2016, An overview of advances in biomass gasification, Energy & Environmental Science, 9, 10, 2939-77.

S.S. Toor, L. Rosendahl, and A. Rudolf, 2011, Hydrothermal liquefaction of biomass: A review of subcritical water technologies, Energy, 36, 5, 2328-42.

H. Yang, R. Yan, H. Chen, D.H. Lee, and C. Zheng, 2007, Characteristics of hemicellulose, cellulose and lignin pyrolysis, Fuel, 86, 12, 1781-88.

Sauro Pierucci, Flavio Manenti, Giulia Bozzano, Davide Manca (Eds.)
Proceedings of the 30th European Symposium on Computer Aided Process Engineering (ESCAPE30), May 24-27, 2020, Milano, Italy.
http://dx.doi.org/10.1016/B978-0-12-823377-1.50274-3

Data-Driven Model Development for Cardiomyocyte Production Experimental Failure Prediction

Bianca Williams[a], Caroline Halloin[b], Wiebke Löbel[b],Ferdous Finklea[a], Elizabeth Lipke[a], Robert Zweigerdt[b], Selen Cremaschi[a]*

[a]*Auburn University, Department of Chemical Engineering, Auburn, AL, USA*
[b]*Leibniz Research Laboratories for Biotechnology and Artificial Organs (LEBAO), Department of Cardiac, Thoracic, Transplantation, and Vascular Surgery, Hannover Medical School, 30625 Hannover, Germany*
selen-cremaschi@auburn.edu

Abstract

Cardiovascular diseases (CVD) are the leading cause of death worldwide. Engineered heart tissue produced by differentiation of human induced pluripotent stem cells may provide an encompassing treatment for heart failure due to CVD. However, considerable difficulties exist in producing the large number of cardiomyocytes needed for therapeutic purposes through differentiation protocols. Data-driven modeling with machine learning techniques has the potential to identify factors that significantly affect the outcomes of these differentiation experiments. Using data from previous cardiac differentiation experiments, we have developed data-driven modeling methods for determining which experimental conditions are most influential on the final cardiomyocyte content of a differentiation experiment. With those identified conditions, we were able to build classification models that can predict whether an experiment will have a sufficient cardiomyocyte content to continue with the experiment on the seventh (out of 10) day of the differentiation with a 90% accuracy. This early failure prediction will provide cost and time savings, as each day the differentiation continues requires significant resources.

Keywords: cardiac differentiation, machine learning, random forests

1. Introduction

Cardiovascular diseases (CVD) are the leading cause of death worldwide, meaning there are more deaths annually due to CVD than any other cause. These diseases can lead to heart attacks, which can result in the loss of more than one billion heart cells, leading to congestive heart failure (Kempf, Andree, et al., 2016). Patients who suffer from advanced stages of heart failure have a poor prognosis for survival, and the large disparity between numbers of donors and recipients leaves few viable treatments. Artificial prosthetic hearts and heart assist devices have demonstrated some success in prolonging the lives of patients receiving treatment, but their development is slow and clinical trials have seen limited. Due to the nature of heart transplants and the stigma surrounding artificial organs, engineered heart tissue may provide an encompassing treatment for heart failure (Kempf, Andree, et al., 2016).

Mature cardiomyocytes, the contracting cells in the heart, are some of the least regenerative cells in the body. This characteristic carries over into the laboratory environment and thus limits in vitro expansion capabilities of cardiomyocytes.

Difficulties in direct culture of cardiomyocytes can be overcome by differentiation from human pluripotent stem cells (hiPSCs) (Kempf, Andree, et al., 2016). The indefinite turnover potential of pluripotent cells allows for the expansion of large quantities for differentiation into therapeutic engineered tissues. However, the differentiation of hiPSCs into specific cell types is a highly complex and costly process that is sensitive to the impact of a high number of factors (Gaspari et al., 2018), and significant difficulties exist in reliably and consistently producing the large number of cardiomyocytes needed for therapeutic purposes (Kempf, Andree, et al., 2016).

Data-driven modeling with machine learning techniques has the potential to identify factors and patterns that most significantly affect the outcomes of these differentiation experiments. Previously, machine learning techniques have successfully been used to identify key factors and assist in optimization for production of several proteins and cell lines (Sokolov et al., 2017; Zhou et al., 2018). The goal of this work is to use machine learning techniques to identify key process parameters to be used in predictive modeling of bioreactor cardiac differentiation outcomes. The high number of experimental factors that influence the differentiation results in a large set of possible inputs to be considered for modeling. This high data dimensionality, in addition to the low number of data points due to the time-consuming nature of these experiments, represent significant challenges for modeling the differentiation process. Our aim is to use machine learning models to predict whether or not the cardiomyocyte content at the end of differentiation process will be sufficiently high. We define insufficient production as having a cardiomyocyte content on the tenth day of differentiation (dd10) that is less than 90%, meaning less than 90% of the cells produced at the end of the differentiation are cardiomyocytes. Predicting if the cardiomyocycte content will be insufficient before the end of the differentiation will provide cost and time savings, as each day the differentiation continues requires significant resources.

Using existing data from bioreactor experiments, we have applied feature selection techniques, including correlations, principal component analysis, and built-in feature selection in machine learning models, to identify the conditions in the bioreactor, which we define as bioreactor features, are the most influential on and predictive of the cardiomyocyte content. Bioreactor features considered include values related to the cell concentration, size of cell aggregates, pH, dissolved oxygen concentration, and concentrations and timings of certain nutrients, such as glucose, and small molecules known to direct the differentiation. We then used the identified features as inputs to build models to classify the resulting cardiomyocyte content of a particular bioreactor run as being sufficient or insufficient to justify continuing with the differentiation.

2. Machine Learning Techniques for Cardiomyocyte Content Prediction

2.1. Multivariate Adaptive Regression Splines (MARS)

Multivariate adaptive regression spline (MARS) models are made up of a linear summation of basis functions. The three types of possible basis functions are a constant, a hinge function (or "spline"), or a product of two or more hinge functions. The training of a MARS model starts with an initial model that is a constant value equal to the mean of the data outputs. On its initial training pass, the model is overfit to the data using a greedy algorithm, adding basis functions to reduce the sum of the squared errors (SSE) between the given and predicted outputs. Then, a backward, pruning pass is performed to remove terms that have little effect on the SSE until the best model is identified based on generalized cross validation (GCV) criteria (Friedman, 1991). In order to make

cardiomyocyte content classifications, MARS models were trained to predict the value of the cardiomyocyte content using the selected bioreactor features as inputs, and a classification was assigned based on the predicted value.

2.2. Random Forests (RF)

Random forest (RF) models are machine learning models that make output predictions by combining outcomes from a sequence of regression decision trees. Each tree is constructed independently and depends on a random vector sampled from the input data, with all the trees in the forest having the same distribution. The predictions from the forests are averaged using bootstrap aggregation and random feature selection. RF models have been demonstrated to be robust predictors for both small sample sizes and high dimensional data (Biau & Scornet, 2016). RF classification models were constructed that directly classified bioreactor runs as having sufficient or insufficient cardiomyocyte content.

2.3. Gaussian Process Regression (GPR)

Gaussian process regression (GPR) is a method of interpolation where interpolated values are modeled by a Gaussian process governed by prior covariances. Under suitable assumptions on the priors, GPR gives the best linear unbiased prediction of the intermediate values (Rasmussen & Williams, 2005). It uses a kernel function as measure of similarity between points to predict the value for an unseen point from the training data. This method has been successfully used with small dataset sizes. In order to make cardiomyocyte content classifications, GPR models trained were similarly to the MARS models.

3. Data Collection and Feature Selection Methods

3.1. Experimental Data

Experimental data was generated and collected from 58 cardiac differentiation experiments performed by (Halloin et al., 2019). The differentiation experiments were carried out in chemically defined conditions in stirred tank bioreactors. Details of the experiments are described in Halloin et al. (2019). The set of independent variables include experimental conditions such as the rotation speed in the bioreactor and measurements such as differentiation day dependent cell densities and aggregate sizes, and continuous time measurements of dissolved oxygen (DO) concentration and pH. The set of independent variables measured from the experiments was expanded to include engineered features such as estimated gradients in cell densities and DO concentrations, resulting in a total of 101 variables, which we refer to as bioreactor features. The dependent variable is the percentage of the cells in the bioreactor that have differentiated into cardiomyocytes, or the cardiomyocyte content, on the last day of the differentiation experiment, dd10. Data from 42 of the experiments was designated as training data and used for feature selection and classification model construction. The remaining experiments were reserved as test data for testing the classification models.

3.2. Feature Selection Methods

We performed feature selection using the training data set in order to discover which of the bioreactor features were most influential on the cardiomyocyte content. The set of features considered consists of all the collected bioreactor features measured up until the seventh day of differentiation (dd7).

3.2.1. Correlations

The Pearson and Spearman correlations (Bonett & Wright, 2000) between the collected bioreactor features and the cardiomyocyte content were calculated. The Pearson

correlation measures the strength of the linear relationship between two variables. It has a value between -1 to 1, with a value of -1 meaning a total negative linear correlation, 0 being no correlation, and +1 meaning a total positive correlation. The Spearman correlation measures the strength of a monotonic relationship between two variables with the same scaling as the Pearson correlation.

3.2.2. Principal Component Analysis

Principal component analysis (PCA) converts a set of possibly correlated variables into a set of linearly uncorrelated ones through an orthogonal transformation (Hotelling, 1933). The resulting principal components (PCs) are linear combinations of the original set of variables.

3.2.3. Machine Learning Technique Built-In Feature Selection

Each of the machine learning techniques applied has its own method for selecting features and ranking their predictive importance. During the MARS model construction, a pruning pass is performed over the model that removes terms and features based on the level of their effect on GCV criteria. For RF models, features are selected based on how well they improve the separation of the data at each decision node. GPR selects features using its built-in automatic relevance determination method.

4. Classification Performance Metrics

The metrics used to evaluate the performance of the classification models (i.e., the classification of insufficient/sufficient cardiomyocyte content) are accuracy, precision, (Sokolova & Lapalme, 2009), and the Matthews correlation coefficient (MCC) (Matthews, 1975). The accuracy is the proportion of the classifications made by the models that were correct. Given that the classification model predicts an insufficient cardiomyocyte content for a bioreactor run, precision is the probability that the cardiomyocyte content of that run will actually be insufficient. The MCC is the correlation between actual and predicted classifications. It has the same range and scale of the Pearson and Spearman correlations. Figure 1 depicts the workflow of the process taken to construct the models and calculate the performance metrics.

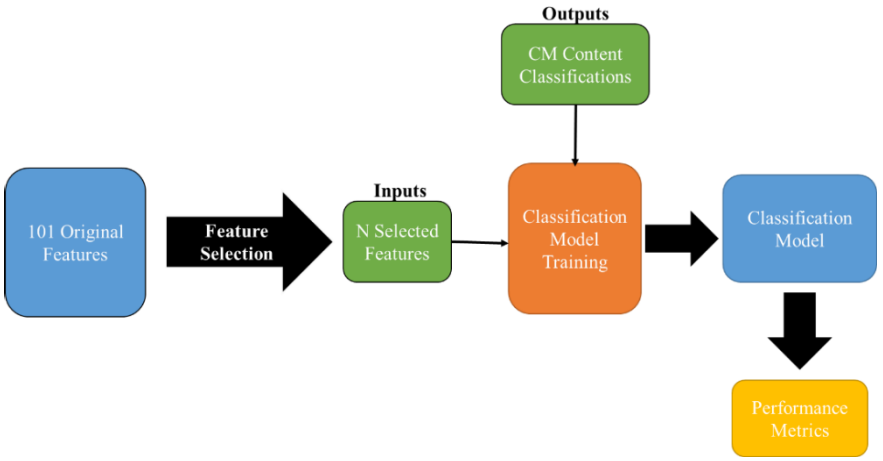

Figure 1-Feature selection and model training process (CM = cardiomyocyte)

5. Results and Discussion

5.1. Feature Selection Results

PCA of the collected feature set yielded five principal components that explained 94% of the variance in the input data. Correlations and PCA did not yield any results for significant features, with the strongest linear correlation between a feature and the cardiomyocyte content being -0.51, with the time that the IWP2 molecule remained in the bioreactor. The strongest linear correlation between the PCs and the cardiomyocyte content was 0.16. However, we had success in reducing the feature set using the built-in feature selection methods of each of the machine learning approaches investigated. From the original 101 features, MARS, RF and GPR identified 12, 12, and 7 significant features, respectively. Common features that were selected as significant include the cell densities and their gradients during the first two days of the differentiation protocol (dd0 and dd1). This selection agrees with previous experimental studies concluding that cell density during early differentiation influences differentiation into specific cell lineages (Kempf, Olmer, et al., 2016).

5.2. Classification Model Results

Results for classification model performance are summarized in Tables 1 and 2. The performance metrics in Table 1 were calculated using the leave one out (LOO) cross validation (Wong, 2015) on the training data. Two classification models were trained for each method. One model utilized the bioreactor features selected by the built-in feature selection as the inputs, and the other employed the PCs obtained from PCA as the inputs.

Table 1 – Performance of classification models on training data evaluated using LOO cross validation

	MARS		**RF**		**GPR**	
	Features	**PCA**	**Features**	**PCA**	**Features**	**PCA**
Accuracy	0.74	0.64	**0.90**	0.74	**0.90**	0.67
Precision	0.81	0.66	**0.90**	0.74	**0.93**	0.67
MCC	0.55	-0.11	**0.78**	0.36	**0.79**	0

For all of the machine learning techniques tested, the classification models using the model-selected features yielded better performance (Table 1). This suggests that while the principal components successfully explain the variance in the data, they fail to accurately characterize the relationship between the features and the cardiomyocyte content. RF models and GPR had similar performance with an accuracy and precision both of about 90%, while MARS models did not perform as accurately.

Table 2 – Performance of classification models on test data

	RF	**GPR**
Accuracy	0.89	0.89
Precision	0.92	0.87
MCC	0.72	0.72

The performances of the RF and GPR classification models trained using the model-selected features were evaluated on the test data (Table 2). Both classification models performed comparably for the test data with an accuracy of 89%, precisions near 90%, and MCC values of 0.72. The results obtained for the test data are comparable to those obtained from LOO cross validation on the training data, indicating that the models

accurately captured the relationship between the features and the cardiomyocyte content, while avoiding overfitting.

6. Conclusions and Future Directions

Using existing data from previously conducted cardiac differentiation experiments, we were able to identify on dd7 if an experiment would have an insufficient final cardiomyocyte content of less than 90% with accuracy and precision of about 90% with both RF and GPR models. We were able to make these predictions using less than 16% of the collected features. Future work with this data will focus on predicting the experimental outcomes at earlier timepoints in the differentiation. This modeling will enable the early interruption of failing experiments, providing cost and time savings.

Acknowledgements

This work was partially funded by Department of Education GAANN grant #P200A150075 and NSF grant #1743445.

References

Biau, G., & Scornet, E. (2016). Rejoinder on: A random forest guided tour. Test, 25, 264-268.

Bonett, D. G., & Wright, T. A. (2000). Sample size requirements for estimating Pearson, Kendall and Spearman correlations. Psychometrika, 65, 23-28.

Friedman, J. H. (1991). Multivariate Adaptive Regression Splines - Rejoinder. Annals of Statistics, 19, 123-141.

Gaspari, E., Franke, A., Robles-Diaz, D., Zweigerdt, R., Roeder, I., Zerjatke, T., & Kempf, H. (2018). Paracrine mechanisms in early differentiation of human pluripotent stem cells: Insights from a mathematical model. Stem Cell Res, 32, 1-7.

Halloin, C., Schwanke, K., Lobel, W., Franke, A., Szepes, M., Biswanath, S., Wunderlich, S., Merkert, S., Weber, N., Osten, F., de la Roche, J., Polten, F., Wollert, K., Kraft, T., Fischer, M., Martin, U., Gruh, I., Kempf, H., & Zweigerdt, R. (2019). Continuous WNT Control Enables Advanced hPSC Cardiac Processing and Prognostic Surface Marker Identification in Chemically Defined Suspension Culture. Stem Cell Reports.

Hotelling, H. (1933). Analysis of a complex of statistical variables into principal components. Journal of Educational Psychology, 24, 417-441.

Kempf, H., Andree, B., & Zweigerdt, R. (2016). Large-scale production of human pluripotent stem cell derived cardiomyocytes. Advanced Drug Delivery Reviews, 96, 18-30.

Kempf, H., Olmer, R., Haase, A., Franke, A., Bolesani, E., Schwanke, K., Robles-Diaz, D., Coffee, M., Gohring, G., Drager, G., Potz, O., Joos, T., Martinez-Hackert, E., Haverich, A., Buettner, F. F. R., Martin, U., & Zweigerdt, R. (2016). Bulk cell density and Wnt/TGFbeta signalling regulate mesendodermal patterning of human pluripotent stem cells. Nature Communications, 7.

Matthews, B. W. (1975). Comparison of Predicted and Observed Secondary Structure of T4 Phage Lysozyme. Biochimica Et Biophysica Acta, 405, 442-451.

Rasmussen, C. E., & Williams, C. K. I. (2005). Gaussian Processes for Machine Learning. Adaptive Computation and Machine Learning, 1-247.

Sokolov, M., Ritscher, J., MacKinnon, N., Souquet, J., Broly, H., Morbidelli, M., & Butte, A. (2017). Enhanced process understanding and multivariate prediction of the relationship between cell culture process and monoclonal antibody quality. Biotechnol Prog, 33, 1368-1380.

Sokolova, M., & Lapalme, G. (2009). A systematic analysis of performance measures for classification tasks. Information Processing & Management, 45, 427-437.

Wong, T. T. (2015). Performance evaluation of classification algorithms by k-fold and leave-one-out cross validation. Pattern Recognition, 48, 2839-2846.

Zhou, Y., Li, G., Dong, J., Xing, X. H., Dai, J., & Zhang, C. (2018). MiYA, an efficient machine-learning workflow in conjunction with the YeastFab assembly strategy for combinatorial optimization of heterologous metabolic pathways in Saccharomyces cerevisiae. Metab Eng, 47, 294-302.

Sauro Pierucci, Flavio Manenti, Giulia Bozzano, Davide Manca (Eds.)
Proceedings of the 30th European Symposium on Computer Aided Process Engineering (ESCAPE30), May 24-27, 2020, Milano, Italy.
http://dx.doi.org/10.1016/B978-0-12-823377-1.50275-5

Simulation of Multi-stage Lactic Acid Salting-out Extraction using Ethanol and Ammonium Sulfate

Andressa N. Marchesan, Ingrid L. Motta, Rubens Maciel Filho, Maria Regina W. Maciel

Laboratory of Optimization, Design and Advanced Control, School of Chemical Engineering, University of Campinas, Av. Albert Einstein 500, Campinas, 13083-852,Brazil
marchesan.andressa@gmail.com

Abstract

Lactic acid obtained through fermentation is an important chemical in the bioeconomy, especially for the production of the biodegradable polymer polylactic acid. However, its production in a larger scale is hindered by its low concentration in the fermentation broth, low volatility, and temperature sensitivity. These characteristics result in high cost for vacuum evaporation and distillation for water removal. Therefore, alternative methods for lactic acid separation have been studied in the literature, including liquid-liquid extraction methods. Salting-out extraction uses the addition of an inorganic salt to reduce the mutual solubility between water and a solvent, thus resulting in a two-phase system. In this work, salting-out extraction of lactic acid using ethanol as solvent and ammonium sulfate as salt was studied using process simulation to define the process conditions that lead to maximum lactic acid recovery and water removal at one-stage and multi-stage extraction scenarios. The simulations were performed using the electrolyte NRTL activity coefficient model (ELECNRTL) in Aspen Plus v8.6, and one-stage simulation was validated with experimental results published in the literature. The results demonstrate that one-stage extraction can yield up to 87 % lactic acid recovery with 35 % of water removal, while counter-current multi-stage extraction can provide more than 96 % recovery with water removal ranging from 47 % to 57 %, and yet requiring lower ethanol volumes, which demonstrates the need for multi-stage experiments in salting-out extraction to validate its performance.

Keywords: lactic acid, salting-out extraction, biorefinery, Aspen Plus, simulation

1. Introduction

The demand for bio-based and biodegradable materials has stimulated the growth of the lactic acid fermentative production and the research on methods to improve the economic competitiveness of this bioproduct. To that end, different approaches have been studied in the literature, including microbial technology, cheaper substrates (Méndez-Alva et al., 2018), and alternative separation methods (Gasca-González *et al.*, 2019). The latter is motivated by the low product concentration, lactic acid's high affinity for water, and low volatility, which result in high purification costs. In this context, salting-out extraction has been studied as an alternative separation method for bioproducts, which is based on the reduced mutual solubility of a solvent and water due to the presence of a salt. However, lactic acid salting-out extraction studies reported in the literature (Ayodogan *et*

al., 2011; Fu *et al.*, 2015) were limited to one-stage separation, which is not very attractive from a large-scale perspective. Considering that, the objective of this work is to use process simulation to assess the performance of multi-stage salting-out extraction.

2. Methods

2.1. Process Simulation

Simulations were performed in Aspen Plus v8.6 using the Electrolyte NRTL activity coefficient model (ELECNRTL) using the equilibrium reaction in Eq. (1), and its equilibrium constant as represented in Eq. (2) (Rumpf *et al.*, 1997) in the liquid-liquid equilibrium calculations. For the ethanol/ion pair parameters, these were assumed to be symmetric (GMELCC = 5), as per the software manual. The non-volatile characteristic of the salt was accounted for in the simulation by setting its natural log of the vapor pressure in N/m² (PLXANT) to -15 and the heat of vaporization (DHVLWT) to zero. To obtain the liquid-liquid equilibrium, the apparent components approach was used. However, in this approach, the salt saturation is not calculated. Therefore, to account for salt precipitation in the aqueous phase, the true components approach was used in the raffinate stream with the reaction represented in Eq. (1) and the salt equilibrium constant in Eq. (3). This approach allows the identification of unfeasible operating conditions.

$$(NH_4)_2SO_4 \;=\; 2NH_4^+ + SO_4^{2-} \tag{1}$$

$$\ln K = 8.7 \tag{2}$$

$$\ln K = -216.55 + 4262.38/T + 37.52 \cdot \ln(T) - 0.08 \cdot T \tag{3}$$

For model validation, a single equilibrium-stage separator (DECANTER) was used to generate the binodal curve and tie-lines for the system water + ethanol + ammonium sulfate and also single-stage extraction of lactic acid using the same components, which were used for comparison with experimental results reported in the literature.

2.2. Multi-stage extraction and Statistical analysis

Multi-stage extraction simulations were performed using a liquid-liquid extractor model (EXTRACT) at a constant temperature of 25 °C – the temperature has little effect on the lactic acid partition coefficient up to 60 °C for the system under study (Fu *et al.*, 2015). A face-centered composite design was used to assess the effects of the initial lactic acid concentration (**LA**), the mass ratios of ammonium sulfate (**SULF**) and hydrous ethanol (93 wt % ethanol) to water (**ETOH**) in the feed stream, and the number of equilibrium stages (**N-ST**) at a 95.0 % confidence level. This intends to maximize the lactic acid recovery (**LA REC**) and the amount of water removed (**WAT REM**). The mass fraction of precipitated salt (**W SULF**) is also calculated as a model output so that it can be used as a restriction in the optimization studies. Figure 1 presents the simulation flowsheet and the levels used in the statistical analysis. The statistical models were determined through backward elimination, assessed as per the F-test and applied for optimization using the GRG Nonlinear method.

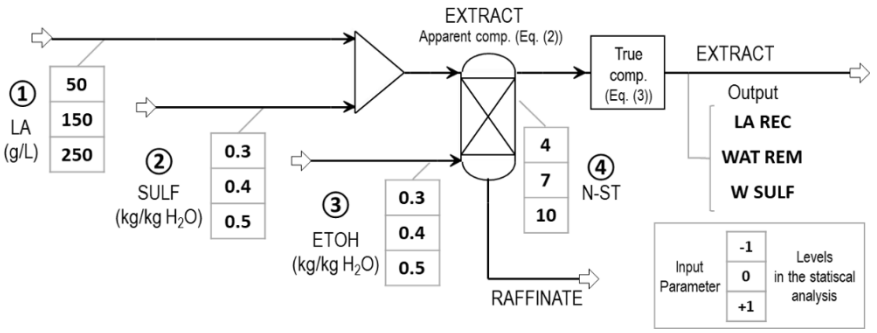

Figure 1: Simulation flowsheet and parameters. 1) Lactic acidc oncentration (g/L); 2) Sulfate to water mass ratio (kg/kg); 3) Ethanol to water mass ratio (kg/kg); 4) Number of equilibrium stages.

3. Results

The validation of results for the one-stage separation demonstrates a good agreement between simulation and experimental results, as shown in Figure 2. Although the LLE calculations underestimate the mass fraction of sulfate in the ethanol-rich phase (Figure 2a), it still provides good acid recovery estimates (Figure 2b).

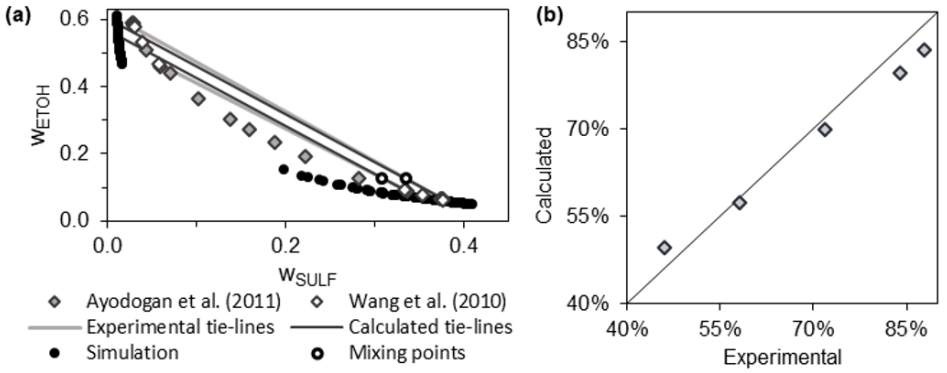

Figure 2: Validation of results: (a) LLE for the system ethanol + ammonium sulfate + water at 298.15 K (Wang *et al.*, 2010; Ayodogan *et al.*, 2011); (b) Lactic acid recovery in one-stage extraction for a 25 g/L solution, experimental results from Fu *et al.* (2015).

Figure 3 presents the simplified Pareto charts of the effects of parameters. The results show that the parameters studied have opposite effects on acid recovery and water removal, which are largely affected by the ethanol-to-water ratio (ETOH). Eq. (4) describes the model for each output (LA REC, WAT REM, W SULF), with their respective parameters listed in Table 1, and the models are illustrated by the response profiles in Figure 4. For each response profile, the other parameters were fixed at the central point. All models presented R^2 and R^2_{adj} above 0.96 and 0.95, respectively, and were significant to the F-test with 95 % confidence. Although ethanol- and sulfate-to-water ratios and lactic acid initial concentration have positive effects on acid recovery, it is possible to observe from Figure 4(c) that higher values for these parameters result in the precipitation of salt (W SULF) and, therefore, result in an unfeasible area of operation.

$$OUTPUT = a_0 + \sum_{i=1}^{4} a_i x_i + \sum_{i=1}^{4} b_i x_i^2 + \sum_{i=1}^{3} \sum_{j=i+1}^{4} c_{ij} x_i x_j \quad (4)$$

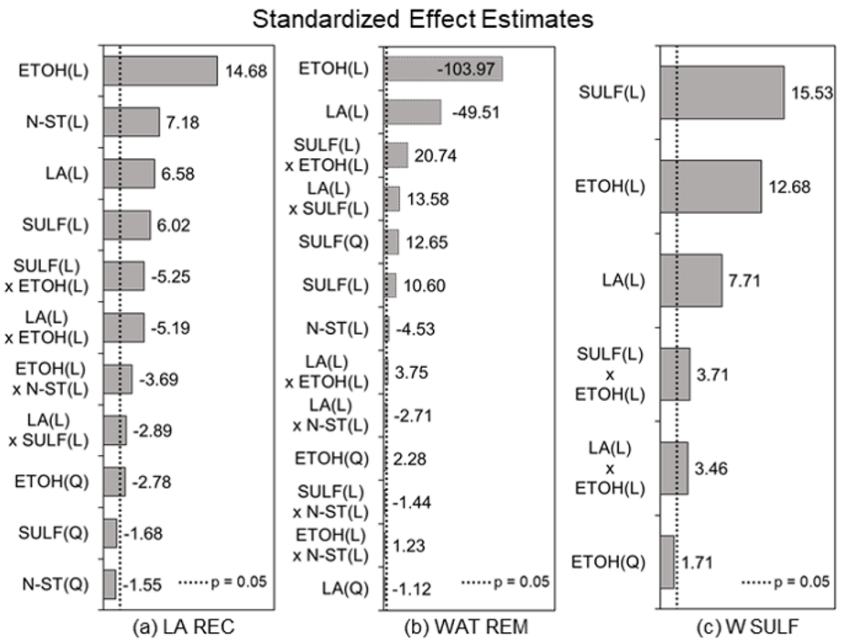

Figure 3: Pareto charts of parameters` effects on (a) Lactic acid recovery; (b) Water removal; (c) Mass fraction of salt precipitate.

Table 1: Parameters for statistical model (x_1 = LA, x_2 = SULF, x_3 = ETOH, x_4 = N-ST).

Param.	LA REC	WAT REM	W SULF	Param.	LA REC	WAT REM	W SULF
a_0	0.975	0.557	0.048	c_{12}	-0.019	0.018	0
a_1	0.041	-0.062	0.018	c_{13}	-0.035	0.005	0.009
b_1	0	-0.004	0	c_{14}	0	-0.004	0
a_2	0.038	0.013	0.037	c_{23}	-0.035	0.027	0.009
b_2	-0.027	0.040	0	c_{24}	0.000	-0.002	0
a_3	0.092	-0.129	0.030	c_{34}	-0.025	0.002	0
b_3	-0.045	0.007	0.008	R^2	0.973	0.999	0.965
a_4	0.045	-0.006	0	R^2_{adj}	0.951	0.998	0.953
b_4	-0.025	0.000	0				

The output models in Table 1 were used to maximize the acid recovery for each concentration level (50, 150, 250 g/L) with the restriction of a maximum fraction of precipitated salt in the raffinate (W SULF) of 0.01. For comparison, the same approach was used for a single-stage extraction. In this situation, the highest recovery (86.6 %) was obtained for a 50 g/L solution, with a water removal of 35.3 %, requiring the sulfate and ethanol to water ratios of 0.2 and 0.77, respectively. The results for the optimization in Table 2 demonstrate that multi-stage extraction yields higher acid recovery and water removal with lower ethanol use. Although higher recoveries are achieved for more dilute solutions, Case 1 requires larger volumes of salt and ethanol and also produces a more dilute extract (mass percentages: lactic acid – 5 %, water – 51 %, ethanol – 43%). On the other hand, Case 3 produces an extract with 30 wt % lactic acid, 43 wt % water, and 25 wt % ethanol, thus reducing heat duty for further extract concentration.

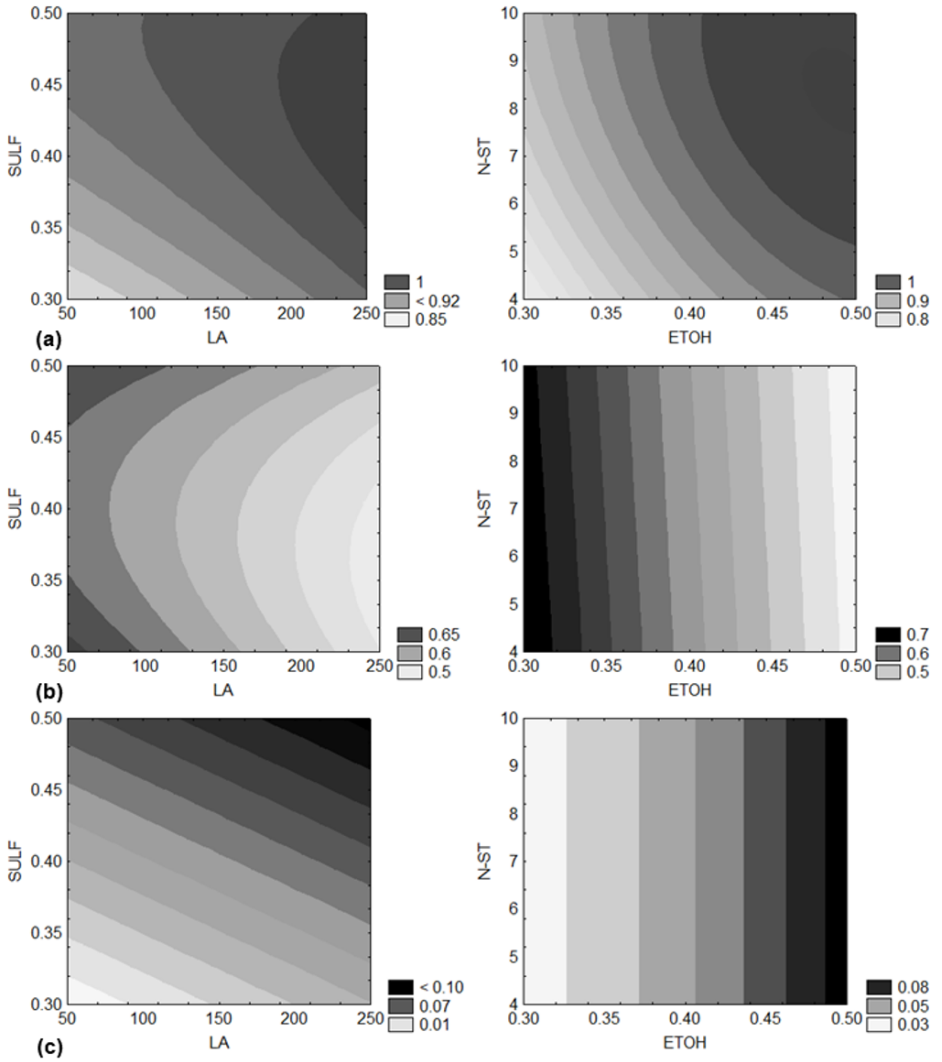

Figure 4: Response profiles of (a) Lactic acid recovery; (b) Water removal (c); Mass fraction of salt precipitate. For each response profile, the other parameters were fixed at the central point.

Table 2: Optimization results (M – statistical model outputs, S – simulation results).

					LA REC (%)		WAT REM (%)		W SULF	
Case	LA	SULF	ETOH	N-ST	M	S	M	S	M	S
1	50	0.3	0.491	8	96.5	98.6	51.9	47.2	0.01	0.03
2	150	0.3	0.395	10	92.6	98.0	58.4	54.4	0.01	0.00
3	250	0.3	0.317	10	90.4	96.0	62.4	57.0	0.01	0.00

To produce high-purity lactic acid, reactive distillation is employed to convert the acid in a more volatile ester by reaction with an alcohol, that is evaporated and then hydrolyzed back to the acid to reach a mass purity of 88 wt % (Gasca-González *et al.*, 2019). However, it requires a pre-concentration step to remove part of the water and drive the reaction equilibrium towards the products, and the entire reactive distillation process has

a high energy demand. Therefore, assuming that salting-out extraction is able to selectively separate the acid from fermentation residues, it could be employed as a pre-evaporation step, and simplify the following downstream steps. To illustrate this, a simple four-effect evaporation of the extract from Case 3 to obtain an 88 wt % lactic acid solution was simulated. Without heat integration, the multiple-effect evaporation, the ethanol recovery from the raffinate, and the hydrous ethanol distillation require a reboiler duty of 7235 kJ per kg of lactic acid final product, starting from 24 wt % (250 g/L) in the fermentation broth. For comparison, the reactive distillation process with ethanol reported by Su *et al.* (2013) for a 30 wt % initial lactic acid solution requires ca. 16300 kJ/kg. Although salting-out extraction of a real fermentation broth has been published in the literature (Ayodogan *et al.*, 2011), the distribution of other components present in the broth, such as residual sugars and metabolites were not assessed. Such studies should be performed to allow more detailed simulations and designs of salting-out processes.

4. Conclusions

In this work, process simulation was used to assess lactic acid multi-stage salting-out extraction in terms of the influence of initial acid concentration, salt and solvent amounts, and the number of stages. The results show that it is possible to obtain more than 96 % acid recovery while removing more than 50 % of the initial amount of water in the feed. A preliminary analysis also demonstrates the potential gains in terms of energy savings if such a process could replace more traditional options such as reactive distillation.

Acknowledgments

This work was executed with support from CNPq, Coordenação de Aperfeiçoamento de Pessoal de Nível Superior - Brasil (CAPES) - Finance Code 001, and São Paulo Research Foundation (FAPESP) grant #2015/20630-4.

References

Ö. Aydoğan, E. Bayraktar, Ü. Mehmetoğlu, 2011, Aqueous two-phase extraction of lactic acid: Optimization by response surface methodology, Sep. Sci. Technol., 46, 1164–1171.

H. Fu, Y. Sun, H. Teng, D. Zhang, Z. Xiu, 2015, Salting-out extraction of carboxylic acids, Sep. Purif. Technol., 139, 36–42.

R. Gasca-González, O. A. Prado-Rubio, F. I. Gómez-Castro, J. Fontalvo-Alzate, E. S. Pérez-Cisneros, R. Morales-Rodriguez, 2019, Techno-economic analysis of alternative reactive purification technologies in the lactic acid production process, Computer Aided Chemical Engineering, 46, 457-462.

J. A. Méndez-Alva, E. S. Perez-Cisneros, D. Rodriguez-Gomez, O. A.Prado-Rubio, B. Ruiz-Camacho, R. Morales-Rodriguez, 2018, Computer-aided process simulation, design and analysis: lactic acid production from lignocellulosic residues, Computer Aided Chemical Engineering, 44, 463-468.

B. Rumpf, F. Weyrich, G. Maurer, 1997, Enthalpy of dilution in aqueous systems of single solutes ammonia, sodium sulfate and ammonium sulfate: Experimental results and modeling, Therrnochimica Acta, 303, 77-91.

C. Y. Su, C. C. Yu, I. L. Chien, J. D. Ward, 2013, Plant-wide economic comparison of lactic acid recovery processes by reactive distillation with different alcohols, Ind. Eng. Chem. Res., 52, 11070–11083.

Y. Wang, Y. Yan, S. Hu, J. Han, X. Xu, 2009, Phase diagrams of ammonium sulfate + ethanol/1-propanol/2-propanol + water aqueous two-phase systems at 298.15 K and correlation, J. Chem. Eng. Data, 55, 876–881.

Sauro Pierucci, Flavio Manenti, Giulia Bozzano, Davide Manca (Eds.)
Proceedings of the 30th European Symposium on Computer Aided Process Engineering (ESCAPE30), May 24-27, 2020, Milano, Italy.
http://dx.doi.org/10.1016/B978-0-12-823377-1.50276-7

Improving the Calibration of Kinetic Growth Models using Dynamic Time Warping

Mhd Adnan Jouned[a,b], Julian Kager[a,c], Judit Aizpuru[b], Christoph Herwig[a,c] , Tilman Barz[b]

[a] *ICEBE, TU Wien, Gumpendorfer Straße 1a 166/4, 1060 Wien, Austria*
[b] *AIT Austrian Institute of Technology GmbH, Giefinggasse 2, 1210 Wien, Austria*
[c] *CD Laboratory on Mechanistic and Physiological Methods for Improved Bioprocesses, TU Wien, Gumpendorfer Straße 1a 166/4, 1060 Wien, Austria*
tilman.barz@ait.ac.at

Abstract

Off-gas measurements give valuable information on the respiratory activity of organisms during fermentation processes. Measured oxygen consumption and carbon dioxide production is usually linked to the overall metabolic activity of the cultivated cells. Together with offline measured nutrient and metabolite concentrations reaction parameters of growth models can be determined. Standard algorithms for parameter estimation use the least-squares (LSQ) error criterion for fitting model predictions to measured data. However, their application does not necessarily yield off-gas representative model predictions and parameters. This is especially true for off-gas signals with rapid variability and corresponding sharp bends and kinks. Off-gas signals include clear indicators for nutrient limitations and metabolic shifts of the culture. Using the LSQ error criterion the fitting tends to smooth out these informative details leading to poor model predictions and parameter estimates.

This contribution presents a comparative analysis of the performance of standard nonlinear LSQ algorithms and an adapted algorithm using the Dynamic Time Warping (DTW) criterion. Both algorithms are applied to fit off-gas signals for the calibration of the kinetic model of *Saccharomyces cerevisiae* (Sonnleitner and Käppeli 1986) on three experimental datasets. The data represents high dynamics with rapid variations and covers yeast fermentation through Batch and Fed-Batch phases including time windows where the organisms are forced to produce ethanol through the "Crabtree effect" by overfeeding. It turns out that, compared to results using LSQ criterion, the application of the DTW criterion yields a better shape matching of the data. In addition, results are also discussed comparing the performance in terms of convergence to the best fitting parameters and the robustness of algorithms against structural modelling errors.

Keywords: dynamic programming, signals matching, parameter estimation, kinetic modelling

1. Introduction

Kinetic modeling plays an essential role in bioprocess development because it provides not only information about changing quantities and rates, but also gives valuable insights about the underlying reactions scheme. Hence, the parameters reflect biological meaning apart from being mathematical coefficients. Model calibration is considered to be a complex task especially for problems with a high number of interdependent parameters and a low number of samples. In addition to that, available information is often

concentrated in certain time ranges or only available at distinct time points. For example, for practical reasons it is often the case that offline samples are concentrated in the Fed-batch phase while no/less data is available for the Batch-phase. The parameters estimated in these cases may not reveal the actual underlying behavior and may result in "Observation Biased" models where the quality of the model in experimental design and control can be questionable. This issue can be improved when semi-/continuous (online) data resources are introduced such as off-gas information or spectral information (Golabgir and Herwig 2016).

In yeast fermentations processes off-gas information proved to be used to identify different metabolic pathways and to provide information, like maximum growth rate (Petkov and Davis 1996, Anderlei et al. 2004, Gollmer and Posten 1996). On the other hand, off-gas signals are usually more complex than other states and contain both low and high frequency information where rapid changes represent mostly certain limitations or metabolic shifts and slower changes are usually corelated to the respiration of the culture. Moreover, off-gas signal errors arise completely from different sources compared to other states such as component concentrations. While for concentration samples, variance in the measurements is witnessed, off-gas signal suffers - among different errors types - from shifts, offsets and drifts. These usually caused by different factors including possible sensors delay, not-proper accounting for humidity and high interactions with other conditions/states such as pH and temperature (Frick and Junker 1999). Fitting criteria able to account for these characteristics are necessary to obtain representative model parameters.

Parameter estimation algorithms using Least-Squares (LSQ) as a criterion to fit off-gas signals, could potentially perform better if another criterion that accounts for these characteristics is used. The reason is that the standard criterion evaluates the quadratic fitting error by comparing measurements and predictions point-by-point. Interesting features like kinks and sharp bends in the measured signals are not in the focus. Accordingly, in the presence of structural model simplifications and measurement noise, off-gas signals are usually fitted by smooth curves (which are optimal in the sense of the quadratic error criterion, but do not mimic the shape of the measured signals). A possible solution to this is parameter estimation implementing an error criterion derived from Dynamic Time Warping (DTW) method (Gollmer and Posten 1996) (Srinivasan and Qian 2007). The method is applied in shape recognition. It has a high potential for yielding model predictions, which mimic the interesting features in the measured signals, and to overcome the limitations of algorithms using LSQ error criterion.

The applicability of DTW as a non-linear mapping tool between signals, which reduces the distance and matches the shape, has been shown in the field of chemistry and bioprocessing (Srinivasan and Qian 2007; González-Martínez, Ferrer, and Westerhuis 2011). (Gollmer and Posten 1996) actually used DTW to identify different phases of off-gas signals in *S. cerevisiae* fermentation two decades ago, but according to author knowledge, this concept has not been exploited to match simulation/observation signals to improve model parameters estimation consequently. This work exemplarily validates this improvement by a comparative analysis of the performance of standard nonlinear LSQ algorithms and an adapted algorithm using the Dynamic Time Warping (DTW) criterion.

2. Materials and Methods

To understand the effect of using an error criterion derived from DTW on parameters estimation, two algorithms with different error criteria are used to fit three different

experimental datasets. The well-known model for baker's yeast fermentation (Sonnleitner and Käppeli 1986) is used where we try to get best parameter-set ($q_{s,max}$,$\mu_{ethanol,max}$, $q_{O_2,max}$,K_s, $Y^{oxidative}_{biomass/glucose}$,$Y^{reductive}_{biomass/glucose}$,$Y_{biomass/ethanol}$). The selection of the parameters and initial values has been done recursively based on importance ranking and sensitivity information (López et al. 2013) (Ulonska et al. 2018). Details on the model structure, nomenclature and parameter values are shown in the original paper (Sonnleitner and Käppeli 1986).

Around thousand initializations with various initial guesses of selected parameter-set were established, passed to an optimizer *("fminsearch", MATLAB R2017b*, stopping criterion is set to 100 iterations, all other options are set to default) to find parameter values yielding lowest error criterion.

In order to find a reference base to compare both results, the solutions from both algorithms are accepted among best fitting parameters-set, when the metabolic states calculated back from the model match the ones that have been pre-identified by experts, error of the state estimation is between 0-5% NRMSD and the error of off-gas signals estimation is between 0-50% NRMSD of any off-gas signal of each metabolic state.

The three fermentation experiments consist of Batch and Fed-Batch phases where overfeeding is applied after some hours in the Fed-Batch phase to force the cells deliberately to produced ethanol through "Crabtree effect". Data presented in Figure 1 shows clearly high dynamics in the off-gas signals with some rapid changes reflecting the time-varying behavior of the cells.

2.1. S. cerevisiae fermentation model

In this model derived from (Sonnleitner and Käppeli 1986) the growth is described on two substrates glucose and ethanol with fermentative and oxidative pathways, based on three metabolic pathways with correspondent yield parameters $Y^{oxidative}_{biomass/glucose}$, $Y^{reductive}_{biomass/glucose}$ and $Y_{biomass/glucose}$. Total growth is the growth based on all forms of biomass specific intake ($q_s^{oxidative}$, $q_s^{reductive}$, $q_{ethanol}$) as:

$$\mu_{total} = Y^{oxidative}_{biomass/glucose} \cdot q_s^{oxidative} + Y^{reductive}_{biomass/glucose} \cdot q_s^{reductive} + Y_{biomass/ethanol} \cdot q_{ethanol} \quad (1)$$

Mass balances equations are (*x: biomass, s: glucose, e: ethanol, V: volume and F: feed)*

$$\begin{aligned}
\frac{dV}{dt} &= F_S + F_{Base} + F_{Acid} - F_{Gas} \\
\frac{d\,C_x}{dt} &= \mu_{total} \cdot C_x - \frac{F_S}{V} \cdot C_x \\
\frac{d\,C_s}{dt} &= -\left(q_s^{reductive} + q_s^{oxidative}\right) \cdot C_x - \frac{F_S}{V} \cdot C_s + \frac{F_S}{C_{s,in} \cdot V} \\
\frac{d\,C_e}{dt} &= \left(q_s^{reductive} - q_e\right) \cdot C_x - \frac{F_S}{V} \cdot C_e
\end{aligned} \quad (2)$$

Additionally, off-gas equations of Carbon Dioxide Evolution Rate (CER) and Oxygen Uptake Rate (OUR) can be derived from the original model taking into consideration elemental balance, which can be derived from oxidative and reductive reaction stoichiometry:

$$CER = (q_s^{oxidative} \cdot Y^{CO_2}_{s,ox} + q_{ethanol} \cdot Y_e^{CO_2} + q_S^{reductive} \cdot Y^{CO_2}_{s,Red}) C_x \cdot V \quad (4)$$

$$OUR = (q_s^{oxidative} \cdot Y_s^{O_2} + q_{ethanol} \cdot Y_e^{O_2})\, C_x \cdot V \quad (3)$$

2.2. Objective functions

Two objective functions are formulated, in which the first uses standard LSQ. The second uses a combination of LSQ and DTW derived terms. The two functions differ from each other by how they calculate the similarity of the off-gas signals, i.e. the sampled and simulated OUR, CER.

2.2.1. LSQ criterion

For *M* samples, $N = N_L + N_G$ liquid and gas states, and θ as unknown parameter vector, LSQ is defined as ϕ^{LSQ}. Assuming all model states have the same weight in the objective function the fitting problem reads:

$$\min_{\theta} \phi_{L+G}^{LSQ}(\theta)\,; \quad \text{with} \quad \phi_{L+G}^{LSQ}(\theta) = \sum_{i=1}^{M} \sum_{j=1}^{N_L+N_G} (Y_{i,j}^{m} - Y_{i,j}(\theta))^2 \tag{5}$$

2.2.2. Combined LSQ and DTW criterion

Replacing $\phi_G^{LSQ}(\theta)$ by $\phi_G^{DTW}(\theta)$ where all deviations from off-gas measurements are calculated based on DTW. For both, *OUR, CER,* two sequences are needed to build DTW distance matrix. The matrix size is defined by the sizes of both sequences Y_G^m and $Y_G(\theta)$, in which each matrix element $\varepsilon_{i,j}$ represents the distance according to the chosen metric, which is in our case the squared Euclidian distance. To get shape preserved matching between two sequences DTW seeks an optimal path *k* through the matrix which minimize the warping cost (Ratanamahatana and Keogh 2004)

$$\phi_G^{DTW} = \min_{k} \left(\sum^{I,J} \gamma_{i,j} \right)_k \tag{6}$$

Where γ are the elements of the warping path. The optimal path is found by calculating the minimum cumulative distance of the current element and the other three adjacent cells in DTW matrix

$$\gamma_{i,j} = \varepsilon_{i,j} + \min\left(\gamma_{i-1,j-1}, \gamma_{i-1,j}, \gamma_{i,j-1}\right) \tag{7}$$

Using α as a weighting coefficient to scale the DTW term to the same magnitude of the LSQ term, the combined objective function reads

$$\min_{\theta} \left(\phi_L^{LSQ}(\theta) + \alpha \cdot \phi_G^{DTW}(\theta) \right) \tag{8}$$

3. Results and discussion

Figure 1 shows model estimation results of two experiments after 100 optimization iterations. While the fitting of the states is similarly good for both objectives, larger differences can be seen when examining the off-gas signals and by comparing the active metabolic states. We can notice that the metabolic states sequence differs. It can be seen that with standard LSQ criterion the optimizer overlooks some intermediate details in order to get a good fitting along the whole time horizon.

This is problematic, as different metabolic states are assigned along the process, where metabolic states are indicated by sharp changes in the off-gas signal.

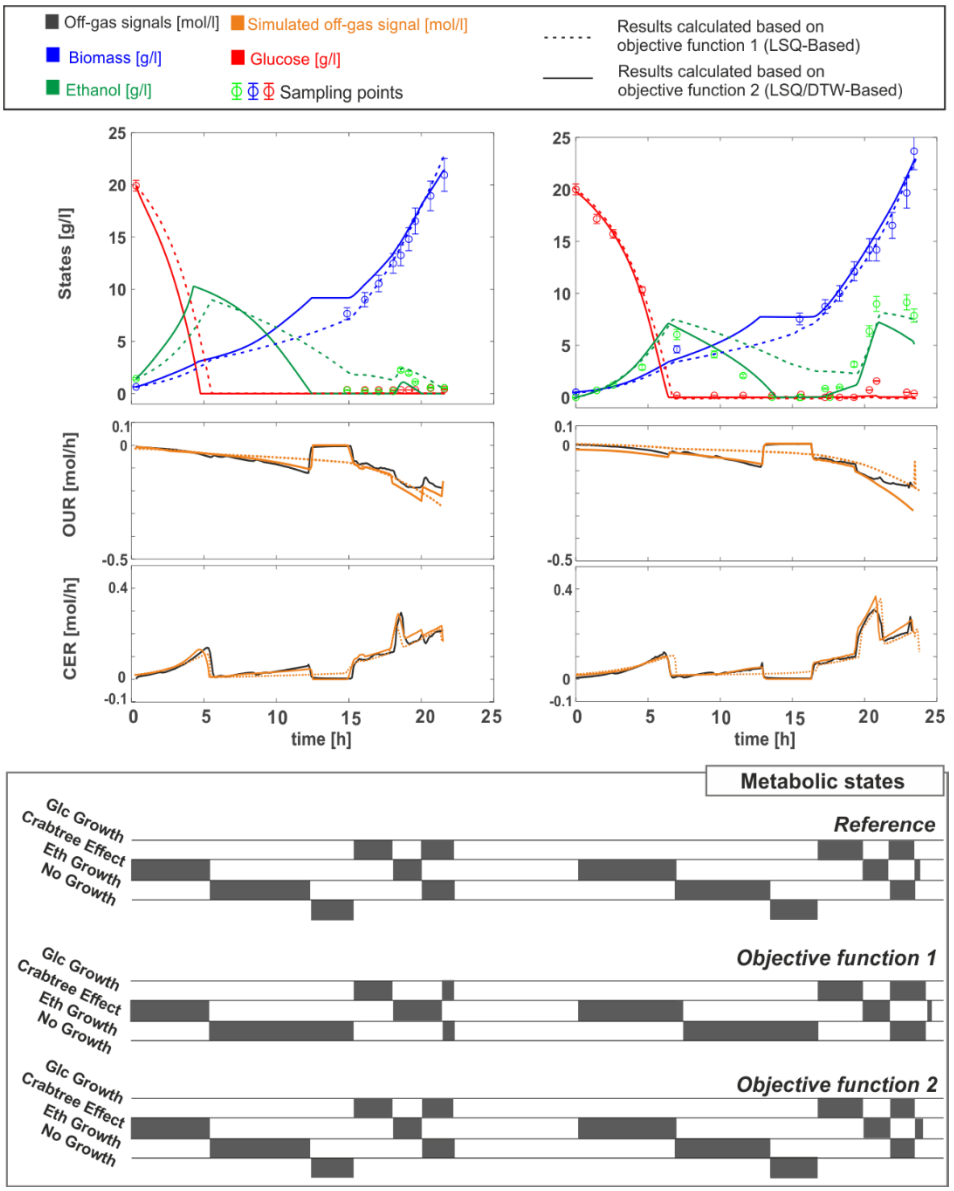

Figure 1: Model fits two experimental datasets out of three after 100 optimization iterations with standard LSQ-based objective function (dashed line) and LSQ/DTW-based objective function (solid line). The corresponding metabolic states are presented below with the reference solution (identified by an experienced field expert based on the visual inspection of CER, OUR signals and offline measurements).

The length of a metabolic state is strongly determined by the parameters related to maximum reaction rates and the corresponding conversion coefficients (yields), which needed to be correctly assigned during model parametrization. Figure 2 shows clearly that the algorithm using DTW/LSQ criterion had a twice higher success rate in finding the exact parameters out of 1000 model calibrations, each with differently perturbed initial parameter sets.

4. Conclusion

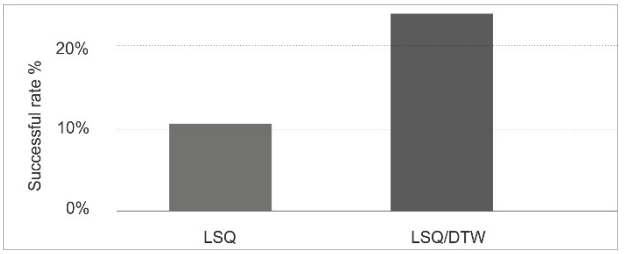

Figure 2: Success rate implementing the LSQ and the combined LSQ/DTW objective functions for parameter identification from off-gas and sampling data.

Using DTW (Dynamic Time Warping) as a fitting criterion for the identification of *S. cerevisiae* fermentation models clearly leads to more reliable parameters estimates compared with the standard LSQ fitting approach. This has been quantitatively proved for three experimental datasets with different metabolic states. For the presented case study, it is shown that model predictions generated by LSQ fitting tend to smooth out measured off-gas signals losing specific details of the signals shape that might represent important metabolic changes. The results clearly indicate a superior performance using DTW, i.e. the more accurate shape matching of the signals yields improved model predictive performance and provides more accurate model parameters.

Acknowledgment

This work was partially funded by the Austrian Research Funding Association (FFG) within the program Bridge 1 in the project ”AdaMo” (No. 864705).

References

Frick, and Junker. 1999. “Indirect Methods for Characterization of Carbon Dioxide Levels in Fermentation Broth.” *J. Biosci. Bioeng.* 87 (3): 344–51.

Golabgir, and Herwig. 2016. “Combining Mechanistic Modeling and Raman Spectroscopy for Real-Time Monitoring of Fed-Batch Penicillin Production.” *Chemie Ing. Tech.* 88 (6): 764–76.

Gollmer, and Posten. 1996. “Supervision of Bioprocesses Using a Dynamic Time Warping Algorithm.” *Control Eng. Pract.* 4 (9): 1287–95.

González-Martínez, Ferrer, and Westerhuis. 2011. “Real-Time Synchronization of Batch Trajectories for on-Line Multivariate Statistical Process Control Using Dynamic Time Warping.” *Chemom. Intell. Lab. Syst.* 105 (2): 195–206.

López, Barz, Peñuela, Villegas, Ochoa, and Wozny. 2013. “Model-Based Identifiable Parameter Determination Applied to a Simultaneous Saccharification and Fermentation Process Model for Bio-Ethanol Production.” *Biotechnol. Prog.* 29 (4): 1064–82.

Ratanamahatana, and Keogh. 2004. “Everything You Know about Dynamic Time Warping Is Wrong.” *Third Work. Min. Temporal Seq. Data*, no. January 2004: 22–25.

Sonnleitner, and Käppeli. 1986. “Growth of Saccharomyces Cerevisiae Is Controlled by Its Limited Respiratory Capacity: Formulation and Verification of a Hypothesis.” *Biotechnol. Bioeng.* 28 (6): 927–37.

Srinivasan, and Qian. 2007. “Online Temporal Signal Comparison Using Singular Points Augmented Time Warping.” *Ind. Eng. Chem. Res.* 46 (13): 4531–48.

Ulonska, Kroll, Fricke, Clemens, Voges, Müller, and Herwig. 2018. “Workflow for Target-Oriented Parametrization of an Enhanced Mechanistic Cell Culture Model.” *Biotechnol. J.* 13 (4): 1–11.

Sauro Pierucci, Flavio Manenti, Giulia Bozzano, Davide Manca (Eds.)
Proceedings of the 30th European Symposium on Computer Aided Process Engineering (ESCAPE30), May 24-27, 2020, Milano, Italy.
http://dx.doi.org/10.1016/B978-0-12-823377-1.50277-9

Dynamic Simulation and Visualisation of pH-Modulated Fed-batch Fermentation for mAb Production from CHO Cell Cultures

Samir Diab[a], Sara Badr[b], Hirokazu Sugiyama[b], Dimitrios I. Gerogiorgis[a*]

[a] *Institute for Materials and Processes (IMP), School of Engineering, University of Edinburgh, The Kings Buildings, Edinburgh, EH9 3FB, United Kingdom*
[b] *Department of Chemical System Engineering, University of Tokyo, Tokyo, 113-8656, Japan*
D.Gerogiorgis@ed.ac.uk

Abstract

Monoclonal antibodies (mAbs) are therapeutic proteins used for treating cancer, autoimmune diseases and many other critical ailments, thus constituting essential biopharmaceutical products in global healthcare. The mAb market turnover is predicted to significantly increase, with numerous new products and processes being developed each year. Current mAb processes often rely on Chinese Hamster Ovary (CHO) cell cultures, which are commonly implemented in batch and fed-batch modes, with some demonstrations of continuous/perfusion cultures in pursuit of much leaner manufacturing. Modelling and simulation can allow optimisation of different design and operating parameters towards achieving the most promising process configurations. The dynamic model for mAb fed-batch production from CHO cell cultures employed in this study describes cell growth and death, mAb production and culture volume as a function of time and pH, allowing for systematic simulation in order to elucidate promising dynamic pH modulations. Dynamic pH and state profiles for fed-batch production of mAbs from CHO cells via systematic simulation are presented. Comparisons of attained productivities, resulting concentration profiles and culture volumes are visualised and compared in order to quantitatively elucidate trade-offs in mAb production with a view to manufacturing.

Keywords: Dynamic simulation; monoclonal antibodies (mAbs); fed-batch production; Chinese Hamster Ovary (CHO) cells; pH modulation; comparative evaluation.

1. Introduction

Monoclonal antibodies (mAbs) represent approximately 50% of the rapidly growing biopharmaceuticals market and are important Drug Substances (DS) for their applications in cancer treatment, autoimmune diseases and many other therapies (Grilo and Mantalaris, 2019). The production of mAbs is most commonly implemented via fermentation of Chinese Hamster Ovary (CHO) cells in either batch, fed-batch or perfusion modes (Shukla et al., 2017), with the latter being pushed towards continuous mode by numerous recent research efforts towards leaner manufacturing campaigns (Schofield, 2019; Papathanasiou et al., 2019). Fed-batch mode is the industrial standard mode of operation for mAb manufacturing due to the ability to tune the nutrient dosing policy throughout the batch runtime (Bunnak et al., 2016). Optimisation of manipulation trajectories during fed-batch operation pinpoints promising process improvements over current experimental demonstrations, and foster manufacturing (Dafnomilis et al., 2019).

Dynamic simulation and optimisation of fermentation operations in bioprocessing is a useful tool in screening promising operating policies while circumventing time and financial investments in laborious experimental campaigns (Shirahata et al. 2019). A recently published dynamic model for the fed-batch production of mAb from a CHO cell culture utilised pH manipulation in order to control fermentation process performance (Hogiri et al., 2018); implementation of the model for optimisation subject to different process constraints can highlight improved pH control policies and trade-offs in performance vs. product quality. This study implements the published dynamic model for mAb production from CHO cells via pH variation for systematic comparative evaluation of different dynamic pH modulations to meet different production objectives. Dynamic pH profiles for fed-batch production of mAbs from CHO cells via systematic simulation are presented. Comparisons of productivities, concentration profiles, and culture volumes are visualised and compared to quantitatively elucidate trade-offs in mAb production.

2. Dynamic model for mAb production from CHO cells

The dynamic model for pH-dependent production of mAb from CHO cells is presented in Fig. 1 (Hogiri et al., 2018). The model describes the production of the mAb immunoglobulin G (IgG) from a CHO cell culture, where X_n, X_a and X_d are concentrations of viable, apoptotic and dead cells, respectively. The mAb is produced from viable (X_n) and apoptotic (X_a) cells, which consume nutrient and dictate the amount of dosing required vs. operation time, t, which affects the culture volume, V. The kinetic model equations are also presented in Fig. 1 (Eqs. 1–6). Here, ρ_1 and ρ_2 are production rate constants and g_1 and g_2 are production kinetic orders from viable and apoptotic cells, respectively. Parameters v_0, v_1, v_2, v_3 and v_4 describe cell growth, apoptosis onset, apoptotic cell death, viable cell death and cell lysis rates, respectively; μ and μ_{max} are specific cell growth rate as a function of cell concentration and its maximum value, respectively and x_{max} = maximum total cell density. Parameters x_{max}, μ_{max}, k_1, k_2, k_3, k_4, r_1, r_2 and r_3 are functions of $pH(t)$, which can be found in the literature (Hogiri et al., 2018).

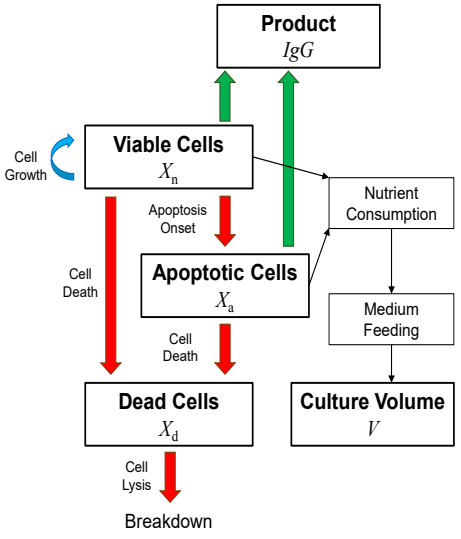

State Trajectories

$$\frac{dIgG}{dt} = \rho_1(pH - 6.4)^{g_1}X_n + \rho_2(pH - 6.4)^{g_2}X_a \quad (1)$$

$$\frac{X_n}{dt} = v_0 - v_1 - v_3 = \mu X_n - k_1 X_n \left(\frac{X_a}{V}\right)^{\alpha} - k_3 X_n \quad (2)$$

$$\frac{X_a}{dt} = v_1 - v_2 = k_1 X_n \left(\frac{X_a}{V}\right)^{\alpha} - k_2 X_a \quad (3)$$

$$\frac{X_d}{dt} = v_2 + v_3 - v_4 = k_2 X_a + k_3 X_n - k_4 X_d \quad (4)$$

$$\frac{dV}{dt} = r_1 v_0 + r_2 X_n + r_3 X_a = r_1 \mu X_n + r_2 X_n + r_3 X_a \quad (5)$$

$$\mu = \mu_{max}\left(1 - \frac{X_n + X_a + X_d}{x_{max} V}\right) \quad (6)$$

Figure 1: Dynamic model for mAb (IgG) production = $f(pH)$ (Hogiri et al., 2018).

3. Dynamic simulation of static pH operation

Dynamic simulation of the published model for mAb production is performed for varying $pH(t)$ = constant, as per the published experimental results (Hogiri et al., 2018); the dynamic model is valid within the range $6.6 \leq pH(t) \leq 7.2$ and thus constant values of $pH(t) = \{6.6, 6.8, 7.0, 7.2\}$ are considered for a maximum batch duration of $t_f = 350$ hr. As $pH(t)$ is increased, the final amount of mAb produced increases and then decreases beyond some intermediate pH value. Production of mAb is slow at first and then increases around $t = 50$ hr for all considered pH values. As pH is increased, dead cell concentrations increase. Viable cell concentrations reach a peak at different points during the batch run and then decrease; as pH is increased from 6.6 to 7.0, the time at which this is reached becomes later and the value and final viable cell concentration are higher, whereas for pH = 7.2, these values occur earlier and lower, respectively. Specific growth rates decrease and then increase to a plateau over the batch duration with final values decreasing with increasing pH. Culture volumes vary with cell densities, which both increase with pH.

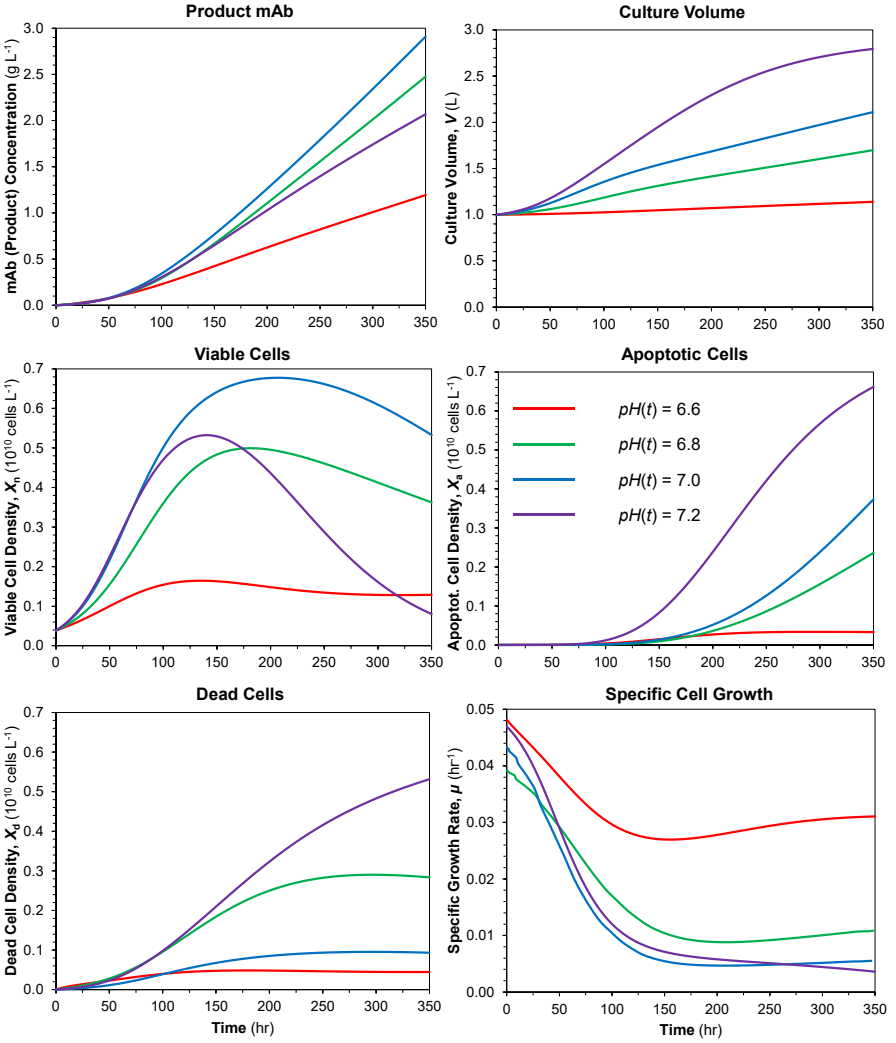

Figure 2: Dynamic simulation of different constant $pH(t)$ profiles on state trajectories.

4. Dynamic pH manipulation: process performances and trade-offs

From the previous static simulations, it is shown that there are trade-offs between variables in the considered system. The model can be used to investigate the effect of dynamic pH profile implementation on different production objectives. Previous work investigated dynamic manipulation to maximise mAb production (Hogiri et al., 2018), but did not consider effects on other variables, such as cell concentrations and culture volume, which can inform the design of more efficient processes, e.g., implementing recycle. Here, we consider the effect of dynamic pH on different process variables and then visualise production trade-offs. The considered pH profiles assume initial $pH(t = 0) = 6.8$, as per experimental demonstrations, and $\Delta pH = \{0.0, +0.2\}$ within each 24 hr period; the maximum possible batch duration is 384 hr. All considered limitations are in accordance with literature demonstrations (Hogiri et al., 2018). The number of time domain discretisation elements, $N = 16$; thus the number of considered pH profiles = 2^{16}.

Fig. 3 shows the considered pH profile attaining the highest final mAb concentration (IgG ($t_f = 384$ hr) = 3.35 g L^{-1}) and corresponding state variables. A gradual increase from the initial pH ($t = 0$) = 6.8 to pH ($t = 168$ hr) attains the maximum final mAb concentration of those pH profiles considered. The best pH profile of those considered lies in the middle of the applicable pH range, i.e. above the lower bound, ($pH_L = 6.6$) and below the upper ($pH_U = 7.2$). The likely reason for pH plateauing at this time is the decrease of viable cells producing mAb thereafter, which implies a concurrent increasing quantity of dead cells. Investigating the region of attainable production performance over the range of possible implemented pH manipulations gives an indication of where process improvement can be achieved, with excessive cell death (reduction in viable cell concentration) thus avoided.

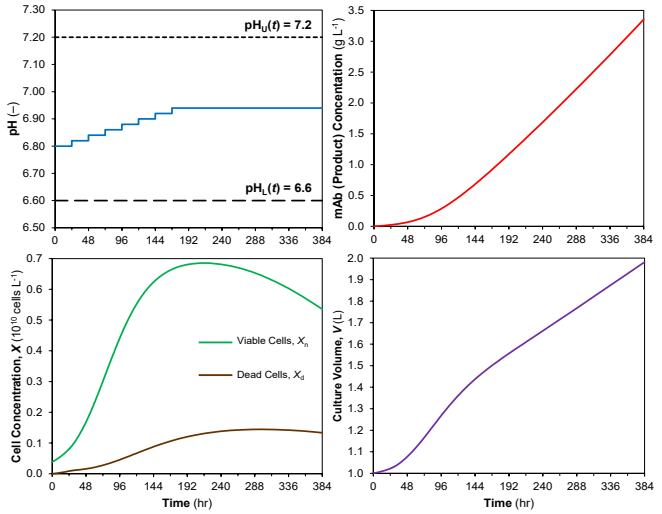

Figure 3: Manipulation (pH) and state profiles attaining maximum mAb concentration.

Fig. 4 visualises process variables vs. batch time for all pH profiles considered. While batch time increases productivity, the culture volume increases; although the considered scale is relatively small (initial volume, V ($t = 0$) = 1 L), increasing culture volumes at larger scales of operation may be undesirable due to the larger material handling requirements post-batch as well as the higher capital expenditures associated with larger equipment. With ongoing batch duration, viable cell concentrations begin to decrease as dead cell quantities increase; this makes potential cell recycling/separation less feasible.

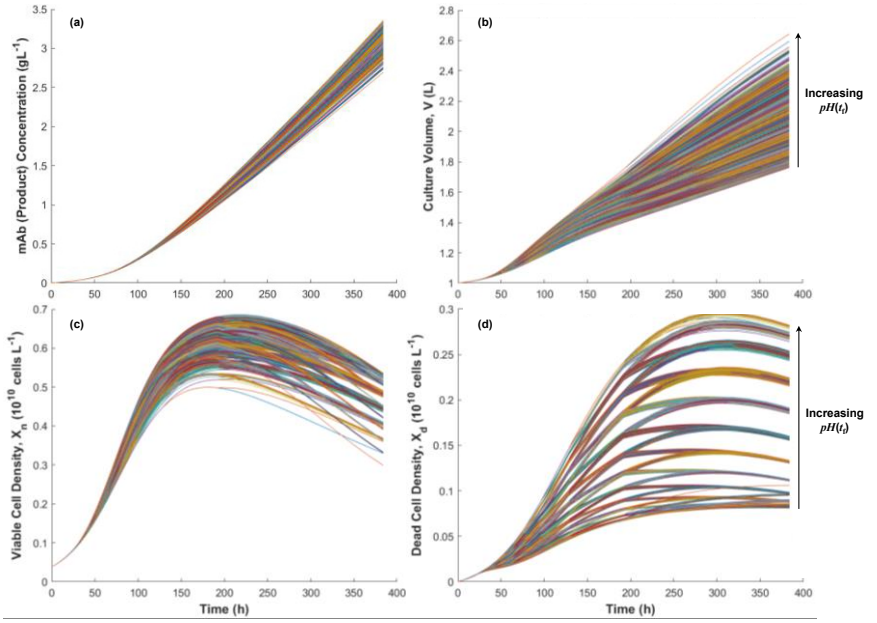

Figure 4: Trade-offs: (a) Product, (b) Volume, (c) Viable cells, (d) Dead cells vs. time.

Fig. 5 shows trade-offs between variables for all pH profiles. Banding is observed due to the constraints on the pH. Increasing productivity leads to lower viable and higher dead cell densities. There is a trade-off between viable and dead cell densities that must be considered if deciding to recycle. The considered pH profiles are limited in their pH step size, temporal discretisation, initial pH and their piecewise constant variation; piecewise linear variation is also possible. Formulation of a dynamic multiobjective optimisation problem of pH for optimal production will further elucidate productivity benefits.

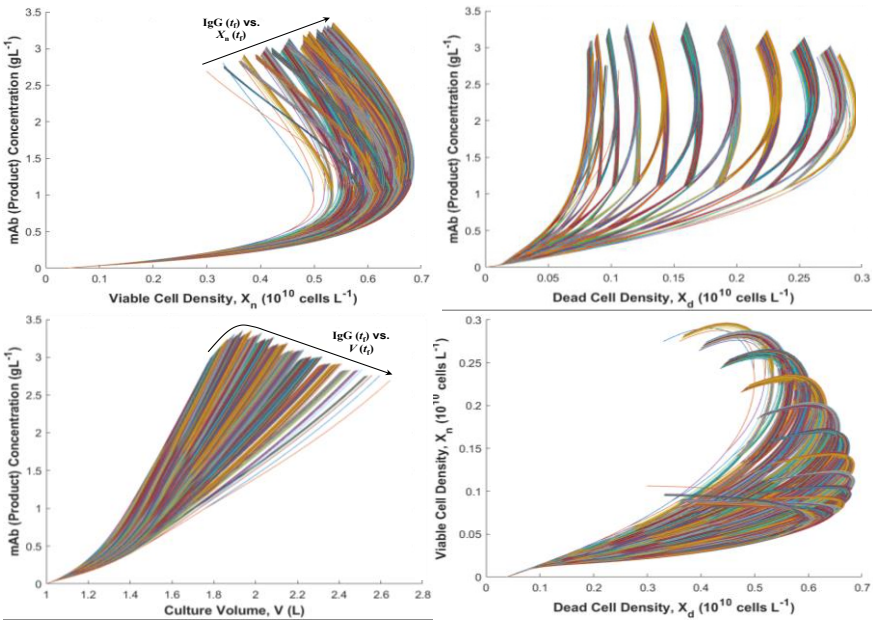

Figure 5: Pareto fronts exhibiting different trade-offs between different process variables.

5. Conclusions

The dynamic modelling and simulation of mAb production from CHO cell cultures can elucidate potential improvements in biopharmaceutical production compared to static pH culture conditions in terms of productivity, cell viability, culture volume and total batch duration. This study has visualised and compared trade-offs between mAb production, cell concentrations and culture volume. The pH manipulation attaining maximum productivity steadily increases until halfway through the batch and then remains steady for the remaining half. This manipulation profile lies in the middle of the applicable pH range of the model. Consideration of the effects of different pH manipulations on other state variables is also important for efficient process design. Trade-offs between mAb productivity as well as viable and dead cell concentrations elucidate the need for dynamic optimisation of pH variation, in order to design biopharma processes of high efficiency.

Acknowledgements

The authors acknowledge the support of the Engineering and Physical Sciences Research Council (EPSRC)/IAA, the Japan Society for the Promotion of Science, the Great Britain Sasakawa and Nagai Foundations and the Royal Academy of Engineering (RAEng).

References

P. Bunnak, R. Allmendinger, S.R. Ramasamy, P. Lettieri and N.J. Titchener-Hooker, 2016, Life-cycle and cost of goods assessment of fed-batch and perfusion-based manufacturing processes for mAbs, *Biotechnol. Prog.*, 32, 5, 1324–1335.

A. Dafnomilis, S. Diab, A.D. Rodman, A.G. Boudouvis and D.I. Gerogiorgis, 2019, Multiobjective dynamic optimization of ampicillin batch crystallization: sensitivity analysis of attainable performance vs product quality constraints, *Ind. Eng. Chem. Res.*, 58, 40, 18756–18771.

A.L. Grilo and A. Mantalaris, 2019, The increasingly human and profitable monoclonal antibody market, *Trends Biotechnol.*, 37, 9–16.

T. Hogiri, H. Tamashima, A. Nishizawa and M. Okamoto, 2018, Optimization of a pH-shift control strategy for producing mAbs in Chinese hamster ovary cell cultures using a pH-dependent dynamic model, *J. Biosci. Bioeng.*, 125, 2, 245–250.

C.D. Kappatou, A. Mhamdi, A.Q. Campano, A. Mantalaris and A. Mitsos, 2018, Model-based dynamic optimization of monoclonal antibodies production in semibatch operation—use of reformulation techniques, *Ind. Eng. Chem. Res.*, 57, 30, 9915–9924.

M.M. Papathanasiou, B. Burnak, J. Katz, N. Shah and E.N. Pistikopoulos, 2019, Assisting continuous biomanufacturing through advanced control in downstream purification, *Comput. Chem. Eng.*, 125, 232–248.

M. Schofield, 2019, Current state of the art in continuous bioprocessing, *Biotechnol. Lett.*, 40, 9–10, 1303–1309.

H. Shirahata, S. Diab, H. Sugiyama and D.I. Gerogiorgis, 2019, Dynamic modelling, simulation and economic evaluation of two CHO cell-based production modes towards developing biopharmaceutical manufacturing processes, *Chem. Eng. Res. Des.*, 150, 218–233.

A.A. Shukla, L.S. Wolfe, S.S. Mostafa and C. Norman, 2017, Evolving trends in mAb production processes, *Bioeng. Transl. Med.*, 2, 1, 58–69.

F. Steinebach, N. Ulmer, M. Wolf, L. Decker, V. Schneider, R. Wälchli, D. Karst, J. Souquet and M. Morbidelli, 2017, Design and operation of a continuous integrated monoclonal antibody production process, *Biotechnol. Prog.*, 33, 5, 1303–1313.

Sauro Pierucci, Flavio Manenti, Giulia Bozzano, Davide Manca (Eds.)
Proceedings of the 30th European Symposium on Computer Aided Process Engineering (ESCAPE30), May 24-27, 2020, Milano, Italy.
http://dx.doi.org/10.1016/B978-0-12-823377-1.50278-0

Surrogate Modelling Based Uncertainty and Sensitivity Analysis for the Downstream Process Design of a Xylitol Biorefinery

Nikolaus I. Vollmer,[a]* Krist V. Gernaey,[a] Solange I. Mussatto,[b] Gürkan Sin[a]

[a]*Process and Systems Engineering Center (PROSYS), Department of Chemical and Biochemical Engineering, Technical University of Denmark, Søltofts Plads, Building 229, 2800 Kgs. Lyngby, Denmark*
[b]*Biomass Conversion and Bioprocess Technology Group, Novo Nordisk Foundation Center for Biosustainability, Technical University of Denmark, Kemitorvet, Building 220, 2800 Kgs. Lyngby, Denmark*
nikov@kt.dtu.dk

Abstract

A rising number of diabetes patients and the urgent need for novel biotechnological process solutions are the instigation for this work. A biorefinery concept based on the valorization of the hemicellulosic sugar fraction is proposed by producing the sugar substitute xylitol. Its process design is supposed to be performed via superstructure optimization (SSO). In order to assess the viability, the downstream process unit operations are analyzed by a comprehensive uncertainty and sensitivity analysis. Monte Carlo methods and the *easyGSA* framework are applied. The output is twofold: the uncertainty in the output is assessed and shows improvement potential for the xylitol yield by serial crystallization and the sensitivity analysis of operational parameters indicates a serial crystallization in the downstream process. Overall, the biorefinery concept is viable and can contribute to the development of sustainable value chains.

Keywords: Biorefinery, Monte Carlo Methods, Surrogate Modelling, Process Design, Optimization.

1. Motivation and Outline

1.1 Motivation

By 2045, over ten percent of the human population will suffer from type II diabetes, while this group grows by around two percent per year (International Diabetes Federation, 2019). This is promoted enormously by the availability of sugar-rich convenience food and a general transition towards an unhealthy lifestyle (International Diabetes Federation, 2019). Hence, it is of major importance for the affected to facilitate a suitable diabetic nutrition with the use of sugar substitutes and to prevent the further build-up of insulin resistances in the population to stop the increase of the number of diabetics (Mussatto, 2012).

A good candidate for this is xylitol: it is a pentose sugar alcohol, showing anticariogenic properties and a low glycemic index, making it perfectly suitable for diabetic nutrition. In addition, it has a similar sweetening power to sucrose but 40% less calories (Mussatto, 2012). Currently, xylitol is produced in a chemical conversion process from wood biomass or corn, but due to exhaustive purification steps, this process is very expensive (Hernandez et al., 2019).

Because of this, amongst other reasons, the US Department of Energy lists xylitol as one of the top 12 bio-based molecules, indicating a high potential for biotechnological production (Hernandez et al., 2019).

The biorefinery concept describes the utilization of a single feedstock for the production of multiple biochemicals, biofuels and energy. Second-generation biorefineries aim to use agricultural or forestal residues as feedstock. This lignocellulosic biomass contains a lot of sugars in different fractions, which can be used as substrate for fermentation processes. In particular, the main fractions are the hemicellulosic fraction (HF) with xylose as main component, the cellulosic fraction (CF) with glucose as main component and the lignin fraction (LF) with different phenolic macromolecules as main compounds (Mussatto, Dragone, 2016). All of the fractions show a macromolecular structure. The major challenge in designing and operating these second-generation biorefineries in an economically viable way derives from the pretreatment of the biomass in order to break down the polymeric structure into monomers for their use in the fermentation processes (Mussatto, Dragone, 2016).

Therefore, we propose a strategy in order to surmount these economic hurdles: The production focus in the biorefinery is shifted towards the valorization of the HF sugars by producing xylitol in a biotechnological process. As the chemical production process is expensive, a viable biotechnological production indicates a promising economic potential. Building up on this, the CF can be valorized by producing bioethanol or another value-added product as e.g. succinic acid. Lastly, lignin is either used as energy source for the supply of heat in both downstream processes or valorized by producing high-value energy carriers as e.g. sustainable aviation fuels. In order to conceptually perform the process design for this biorefinery and to find an optimal overall design, a SSO approach is chosen (Gargalo et al., 2017). For this, mechanistic models for all the relevant unit operations in the refinery are developed, which guarantee flexibility and scalability due to their parametrization.
The US DoE state in their report that the major issue for a biotechnological production is the separation from other sugars (Hernandez et al., 2019). In order to assess this, the uncertainty and sensitivity of the models in the downstream process (DSP) of the suggested biorefinery concept is investigated. By quantifying this uncertainty, a robust process design in the SSO can be guaranteed, which ultimately is supposed to yield an economically resilient biorefinery.

1.2 Outline

First, the models employed in the DSP of xylitol are described, i.e. an evaporation and a crystallization unit. Other unit operations are not considered to have a crucial influence on the robustness of the design. Following this, the applied methods in uncertainty analysis and sensitivity analysis are presented, as well as the results from the model assessment. This ultimately allows drawing conclusions, which give necessary indications on how to best perform the process design as mentioned in 1.1.

2. Models and Surrogates

The employed main unit operations in the downstream operation are an evaporation unit and a crystallization unit. For the successful recovery of xylitol, these units become crucial in order to remove residual sugars and other impurities. Both models are mechanistic models and are described in detail in the following section.

2.1. Evaporation Model

The evaporation unit mainly serves the purpose of upconcentrating the fermentation broth, but also helps removing more volatile compounds from the bulk phase as e.g. ethanol which is inherently produced in the fermentation process, or acetic acid. Due to the high separation factor of water and xylitol, a single-stage evaporation is sufficient to fulfil this task. The employed model here is a simple evaporator model of the ASPEN Plus process simulation package. The underlying thermodynamic model for the modelling of the phase behavior in order to simulate the evaporation is NRTL.

2.2. Crystallization Model

The crystallization unit both yields the final product and also serves to remove less soluble compounds from the bulk phase. As xylitol shows an extraordinarily high solubility in comparison to other sugars (C=1.6 g/g H_2O), the assumption holds that all other present sugars will crystallize before xylitol.

The model itself is based on previous work (Öner et al., 2018): it is a mechanistic model based on mass and energy balances, as well as a population balance which is solved by the method of classes. The incorporated phenomena in the population balance are crystal nucleation and crystal growth. Both the operation as cooling crystallization or as anti-solvent crystallization are implemented. The underlying thermodynamic model for the modelling of the phase behavior for different solvent/anti-solvent ratios is based on experimental work measuring solubility curves. Equally, kinetic parameters for the population balance are determined from experimental data as described by Bandit and Pari (Bandit, Pari, 2018). The model is implemented in MATLAB.

2.3. Surrogate Models

In order to facilitate the performed analyses, a surrogate model of the evaporation unit in ASPEN Plus is created. For the generation and cross-validation of the surrogate models the *easyGSA* framework is used (Al et al., 2019). Different types of surrogate modelling techniques as e.g. Gaussian Process Regression (GPR), Artificial Neural Networks (ANN) or Polynomial Chaos Expansion (PCR) can be utilized by the toolbox.

3. Uncertainty and Sensitivity Analysis

Models have inherent uncertainties. Especially the propagation of these uncertainties when using several models in series of a simulation may lead to meaningless result. Therefore the uncertainties have to be assessed, which happens classically by a combined uncertainty and sensitivity analysis. The uncertainty analysis quantifies the influence of uncertainties in the model input on the model output, whereas the complementary sensitivity analysis quantifies the individual and combinatorial contribution of input parameters on the output uncertainty. A suitable technique for the named analysis are Monte Carlo methods. They are based on large random sampling numbers, which derive a numerical solution for the underlying deterministic problem by processing the random numbers in a stochastic process. In the case of the uncertainty and sensitivity analysis, the input space of the model is sampled and then the model output for each sample is calculated (Sin et al., 2009). For both analyses, the first step is the definition of the input uncertainty for the set of m subjected parameters. The parameters can be input parameters to the model, the model parameters itself or also design parameters.

3.1. Uncertainty Analysis

In the Uncertainty Analysis, a sampling technique is chosen in order to randomly sample the input space. The here applied methodology is Latin Hypercube sampling (LHS). The sampling number N has to be sufficiently high in order to guarantee randomness. The

output is a sampled input space $\boldsymbol{x}_{N\times m}$. By evaluating the model for every input in the input space, the output space $\boldsymbol{y}_{N\times n}$ for the set of n outputs is created. With this output space, the mean value μ_{y_i} and standard deviation σ_{y_i} of each respective output y_i are calculated (Sin et al., 2009)

3.2. Sensitivity Analysis

The applied Sensitivity Analysis is a variance-based method, assuming that a higher dimensional model representation (HDMR) for the underlying model $\boldsymbol{y} = f(\boldsymbol{x})$ exists. With this HDMR, the variance of the model output can be decomposed, which allows the calculation of first-order and total sensitivity indices (S_i and S_{Ti}) of each input x_i as described by (Saltelli et al., 2010). The first-order sensitivity index describes the reduction in the output variance by fixing parameter x_i, the total sensitivity index equivalently describes the reduction in the output variance by fixing all parameters but x_i. With this, the first-order sensitivity index helps identifying important model parameters, whereas the total sensitivity index helps detecting parameters, which possibly can be discriminated. In practice, the sampling technique applied here is quasi-random Sobol sampling, which provides four specific input space matrices being subsequently used for the Monte Carlo simulations as described by Sobol (Al et al., 2019). The sensitivity indices are calculated by the methodology described by Jansen et al. (Saltelli et al., 2010). The analysis itself is performed through the easyGSA framework (Al et al., 2019).

4. Model Assessment

By assessing both downstream models with the named Monte Carlo methods, two things can be investigated: the first is the model uncertainty in predicting the output yield of xylitol which helps classifying the viability of the downstream concept. Secondly, by assessing the operational parameters for both models by sensitivity analysis, important parameters for the implementation and the scale-up of this process can be detected. This yields answers to all the questions arising in section 2.

4.1. Output yield

As the downstream process is commonly the most cost-intensive process part, a high output yield becomes crucial in order to guarantee economic viability. In the upstream process, in the biomass pretreatment yields of around $Y_{Pret} = 90\%$ can be achieved. In the actual fermentation process, the yield is highly dependent on the employed cell factory. Hernandez et al. indicate an average yield $Y_{Ferm} = 70\%$ for different *Candida* species, including also engineered and evolved cell factories (Hernandez et al., 2019).

For the evaporation unit, it is assumed, that the yield of xylitol is $Y_{Evap} = 100\%$, as the separation factor of water and xylitol is sufficiently high. Furthermore the parameter uncertainties for the NRTL model implemented in ASPEN Plus are assumed to have low uncertainty, so that the model output can be considered robust.

The crystallization model uses solubility and kinetic parameters, which were estimated from experimental data. A realistic simulation scenario for a batch crystallization with ethanol as anti-solvent is selected. The simulation parameters are the nominal values μ in table 2. A sampling number of $N = 100$ is chosen for the simulations. The uncertainty bounds of the parameters are set according to the mean values and the standard deviations from the parameter estimation. The results on the xylitol concentration in the solute for only assuming the kinetic parameters uncertain, as well as assuming both kinetic and solubility parameters uncertain are illustrated in the following figure 1:

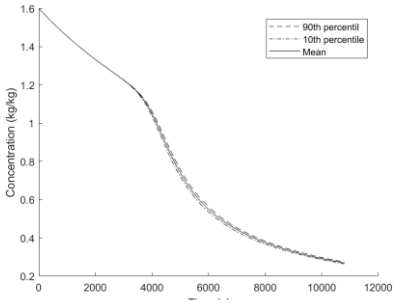

Figure 1a) Uncertainty analysis for kinetic parameters

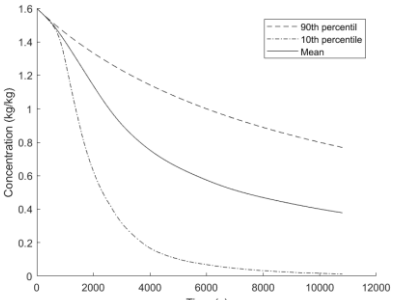

Figure 1b) Uncertainty analysis for kinetic and solubility parameters

The direct comparison of both analyses illustrates very clearly that the uncertainty in the kinetic parameters is very low compared to the uncertainty in the solubility parameters. The yield for both cases is $Y_{Cryst,a} = 65\%$ and $Y_{Cryst,b} = 51\%$.

4.2. Importance of Operational Parameters

For performing SSO in order to properly design a biotechnological production process of xylitol in a biorefinery, it is imperative to possess knowledge of the sensitivity of operational parameters of the employed models in order to define an expedient objective function. Therefore the operational parameters of both models are analyzed.

4.2.1. Sensitivity Analysis of the Evaporation Model

In order to perform the proposed analysis, a surrogate model is created. The considered operational parameters and their bounds are the feed rate F, the xylitol concentration according to the mentioned yields, the preheating temperature T_{Pre} and the vapor fraction γ within the range σ around their nominal value μ. Each parameter is sampled with $n = 4$ points. From this sampling, surrogate models are fitted to the data. With this, a sensitivity analysis as described in section 3.2 is performed with *N=2000* sampling points. The results for a GPR surrogate model are shown in the following table:

Table 1: Sensitivity of the operational parameters of the evaporation unit model

Parameter	μ	σ	S_i	S_{Ti}
F	$1000\ kg/s$	50 %	-0.0052	0
x_{XyOH}	0.08	62.5 %	0.8058	0.8209
T_{Pre}	80 °C	12.5 %	-0.0052	0
γ	0.75	10 %	0.1791	0.1942

4.2.2. Sensitivity Analysis of the Crystallization Model

The sensitivity analysis for the crystallization model as described in section 3.2 is equally performed with $N = 2000$ samples. All parameters are sampled within the range σ of their nominal values μ. The ranges and results are displayed in the following table 2:

Table 2: Sensitivity of the operational parameters of the crystallization unit model

Parameter	μ	σ	S_i	S_{Ti}
F_{AS}	$0.01\ kg/s$	10%	0.0106	0.0118
F_C	$1.6\ kg/s$	10%	0.0075	0
m_S	$0.0025\ kg$	10%	0.0075	0
t_B	$10800\ s$	25%	0.1847	0.2401
H	$0.5\ m$	10%	0.0072	0.0003
$C_{XyOH,0}$	$1.6\ kg/kg$	25%	0.7479	0.7902
$T_{C,0}$	10 °C	10%	0.0076	0
T_0	40 °C	25%	0.0078	0

5. Conclusion and Outlook

5.1. Conclusion

When assessing the yield of the downstream process, the following points become clear: as the yield for the pretreatment is very high and the yield in the fermentation process can only be elevated by engineering more compelling cell factories, it is crucial to increase the yield of the downstream process. Firstly, the solubility parameters should be improved by including more measurement data. Secondly, the superstructure should be set up including more than one crystallizer in series as a trade-off against uncertainties in the upstream units. The sensitivity analysis with the *easyGSA* framework proves to be a simple yet effective tool for the analysis. It shows for both unit operations, that the most important operational parameter on the output yield is the input concentration. This directly indicates further potential in developing a new cell factory, paving the way for higher recovery rates and also the employment of a serial crystallization in order to increase the overall yield. Overall, the performed Monte Carlo based analyses provide valuable insight into the downstream process design, show possible potential for improvement and prove the general viability of this setup for the downstream process.

5.2. Outlook

The following step now is the final implementation of the surrogate models created by the *easyGSA* framework in a superstructure in order to validate the concept by optimizing towards the objective of a maximum xylitol production under minimum capital and operational costs. Further research will study the effect of including a process train for the utilization of the CF and the LF on the optimal biorefinery concept. The overall aim is to improve the economic potential of integrated biorefineries for the biotechnological production of xylitol and creating more sustainable value chains as demanded by the sustainable development goals of the United Nations.

References

International Diabetes Federation, 2019, IDF Diabetes Atlas 9th Edition, acces: 19.11.2019.

S. Mussatto, in: D-Xylitol, S. da Silva, A. Chandel (Eds.), Springer, Heidelberg, Berlin; 2012; 309-323.

A. Hernandez et al., 2019, Xylitol bioproduction: state-of-the-art, industrial paradigm shift and opportunities for integrated biorefineries, *Critical Reviews in Biotechnology*, 39, 7, 924-943.

S. Mussatto, G. Dragone, 2016, Biomass Pretreatment, Biorefineries, and Potential Products for a Bioeconomy Development, in: Biomass Fractionation Technologies for a Lignocellulosic Feedstock Based Biorefinery, S. Mussatto (Ed.), Elsevier, 1-22.

C. Gargalo et al., 2017, Optimal Design and Planning of Glycerol-Based Biorefinery Supply Chains under Uncertainty, *Industrial & Engineering Chemistry Research*, 56, 41, 11870-11893.

M. Öner et al., 2018, Scale-up Modeling of a Pharmaceutical Crystallization Process via Compartmentalization Approach, *Computer Aided Chemical Engineering*, 44, 181-186.

A. Bari, A. Pandit, 2018, Sequential Crystallization Parameter Estimation Method for Determination of Nucleation, Growth, Breakage, and Agglomeration Kinetics, *Industrial & Engineering Chemistry Research*, 57, 5, 1370-1379.

R. Al et al., 2019, Meta-modeling based efficient global sensitivity analysis for wastewater treatment plants – An application to the BSM2 model, *Computers & Chemical Engineering*,

G. Sin et al., 2009, Good Modeling Practice for PAT Applications: Propagation of Input Uncertainty and Sensitivity Analysis, *Biotechnology Progress*, 25, 4, 1043-1053.

A. Saltelli et al., 2010, Variance based sensitivity analysis of model output. Design and estimator for the total sensitivity index, *Computer Physics Communications*, 181, 2, 259-270.

Sauro Pierucci, Flavio Manenti, Giulia Bozzano, Davide Manca (Eds.)
Proceedings of the 30th European Symposium on Computer Aided Process Engineering (ESCAPE30), May 24-27, 2020, Milano, Italy.
http://dx.doi.org/10.1016/B978-0-12-823377-1.50279-2

Process Modelling and Sensitivity Analysis of Roller Mill and Lauter Tun Subsystem Operation

Eduardo Andres Morales, Dimitrios I. Gerogiorgis

Institute for Materials and Processes (IMP), School of Engineering, University of Edinburgh, The Kings Buildings, Edinburgh, EH9 3FB, United Kingdom
D.Gerogiorgis@ed.ac.uk

Abstract

Industrial beer production faces many technical as well as economic challenges, with increased competition and trends towards craft beers and non-alcoholic beverages posing new challenges to brewers, who strive to minimise production costs and processing times whilst improving product quality. Milling, mashing and lautering are a major bottleneck in sweet wort production; however, mathematical models describing these unit operations remain elusive. This study focuses on modelling these unit operations as a subsystem, using a dataset compiled from a brewhouse pilot plant. A first-principles model using batch filtration theory is conceived for the lauter tun, with another statistical model based on Partial Least Squares (PLS) regression describes the milling and mashing operations. The first-principles model describes reasonably well lautering data; the PLS model offers reasonable accuracy for batch time prediction. A holistic view on the brewhouse is then emphasised through a sensitivity analysis, in which variables such as mashing agitation speed and pre-mashing, resting and mash-out temperatures have been found to have the greatest influence on subsystem batch time. Strategies for improved operating protocols are also presented, highlighting the strengths and limitations of the models proposed.

Keywords: Process modelling; Partial Least Squares (PLS); roller mill; lauter tun; beer.

1. Introduction

Beer is one of the most globally consumed alcoholic beverages, accounting for 74% of alcohol consumption in 2016. However, consumption per capita has decreased over the past 50 years in traditionally beer-drinking (mainly European) countries while consumption in the US has plateaued. These trends may be due to increased globalisation and competition, the rise of microbreweries and craft beer and the emergence of health-oriented drinks, which has shifted consumer preferences (Conen and Swinnen, 2016).

Milling, mashing and lautering operations in beer brewing are strongly linked due to the complex interactions and trade-offs arising between them. A very fine grist will increase starch conversion and sugar extraction rates, but at the cost of undesirable flavours such as bitterness in the finished beer. Moreover, it could lead to a “stuck mash” condition in the separation vessel, where the mash filter becomes clogged and cannot filter the wort and thus hindering its collection rate. On the other hand, coarser grists increase wort flowrates and reduce filtration times but with lower extraction yields. A balance must be struck between grist particle size and the obtained extraction efficiency (Crescenzi, 1987).

This study aims to analyse the milling-mashing-lautering operations in an industrial UK brewery, and improve their performance by means of formulating a mathematical model describing the subsystem and the main drivers behind wort separation. To this end, operational parameters and process variables contained in datasets collected from a pilot

plant are used to develop a validated model for the subsystem. The ultimate goal is to improve brewhouse efficiency via superior operating protocols towards minimising batch time whilst not compromising high product quality (Rodman and Gerogiorgis, 2019).

2. Roller Mill and Lauter Tun Subsystem Modelling

Model formulation for brewhouse subsystems must be pursued in accordance with plant size, sensor availability and process variables obtained or inferred from industrial data. The experimental data in this study is acquired from a pilot plant consisting of a roller mill, a mash conversion vessel and a lauter tun. Process variables are recorded at one-second (1 s) intervals over the entire subsystem batch duration. The experimental data has been compiled over 12 different days, with one batch produced per day. Process variables associated with the mashing and lautering operations (and raw material weights used) have also been recorded over the batch duration for each batch. The subsystem is therefore considered as two connected sub-processes, presented in Fig. 1; milling and mashing are described via the statistical (PLS) model and the lautering via a physics-based model.

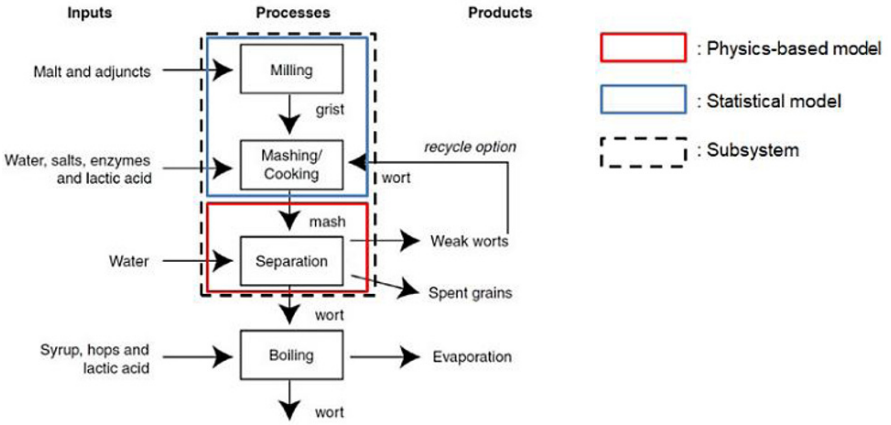

Figure 1: Modelling strategy for the sweet wort subsystem.

For the milling and mashing sub-process PLS model, 14 variables were chosen in order to develop the statistical model. The general linear regression model can be written in a compact form as Eq. 1, where $\boldsymbol{y}$ is the response vector, $\boldsymbol{X}$ is the process matrix, β is the regression coefficient vector and ε the residuals vector. PLS regression is based on the idea that while many predictor variables could be present, only a few variables, i.e., components or latent variables, account for most of the variation in the response, measured by the coefficient of determination, R^2. By projecting the information present to low-dimensional spaces as delineated by the number of PLS variables (n_{comp}), data redundancy is eliminated, giving structure to the process matrix formulated. To obtain the PLS components, initially the variables in $\boldsymbol{X}$ and $\boldsymbol{y}$ are normalised. Afterwards, a linear transformation for the original variables is performed, using an appropriate weight matrix $\boldsymbol{W}$, such that the covariance between the PLS components from the $\boldsymbol{T}$ matrix and the response variable $\boldsymbol{y}$ is maximised. Using the new latent variables obtained, OLS regression is performed to solve for the vector $\boldsymbol{Q}$ (Eq. 2), which represents the loading vector for the response variable. The original coefficients β are then determined (Eq. 4).

$$\boldsymbol{y} = \boldsymbol{X}\beta + \varepsilon \tag{1}$$

$$\boldsymbol{y} = \boldsymbol{T}\boldsymbol{Q} + \varepsilon \tag{2}$$

$$\boldsymbol{T} = \boldsymbol{XW} \tag{3}$$

$$\beta = \boldsymbol{WQ} \tag{4}$$

The PLS model (MacGregor et al., 1994) was implemented in MATLAB using a modified version of the SIMPLS algorithm (de Jong, 1993). To assess the PLS model, the cumulative R^2 vs. the number of PLS components was plotted to determine the range of optimal latent variables. Then, a detailed PLS regression was performed for the selected components, making use of the cross-validation technique, to test its capability against future observations. Following best practice and prior experience, the 'leave-one-out' cross-validation method has been selected. Along with the R^2 coefficient, the Root Mean Squared Error of Prediction (RMSEP) was also considered as a performance indicator.

Lauter tun vessels can be described by Darcy's law (Eq. 5), where Q : the volumetric flowrate, k the permeability constant, A: the filter area, ΔP the pressure differential, μ: the wort viscosity, and L: the filter bed thickness. The resulting differential form of the filtration equation is given by Eq. 6, defining α_{av}: average specific resistance accounting for compressible cake filtration, c: the corrected dry solids concentration in the filter cake, V: the cumulative filtrate volume, R: the medium resistance. To ensure optimal flowrate and to avoid filter blocking in a lauter tun, the differential pressure through the filter cake is often selected as the controlled variable. When ΔP is kept constant during filtration, Eq. 6 can be integrated analytically, assuming constant α_{av}, c and R to obtain Eq. 7: K_1 and K_2 are the cake and medium resistance factors, respectively. For the sake of filter size scaling, the cake resistance factor K_1 is converted to a filterability coefficient F_k (Eq. 8). A plot of t/V vs. V yields a linear trend if the Darcy model adequately fits industrial data.

$$Q = \frac{kA\Delta P}{\mu L} \tag{5}$$

$$\frac{1}{A}\frac{\mathrm{d}V}{\mathrm{d}t} = \frac{A\Delta P}{\mu(\alpha_{av} cV + AR)} \tag{6}$$

$$\frac{t}{V} = \frac{K_1}{2} V + K_2 \tag{7}$$

$$F_k = K_1 A^2 \tag{8}$$

3. Subsystem Model Validation

The PLS model results for the mashing-milling sub-process vs. industrial data for different numbers of PLS variables (n_{comp}) are shown in Fig. 2. With 6 or 7 PLS components, the PLS model does not accurately represent the data; however, when 9 components are used, the model represents the data accurately but may exhibit significant deviation when fitted to new data. Generally, one should avoid having too many variables (MacGregor et al., 1994; Shen et al., 2019). Thus, a selection of $n_{comp} = 8$ is used here, in order to ensure an adequately descriptive but not overly complex statistical formulation.

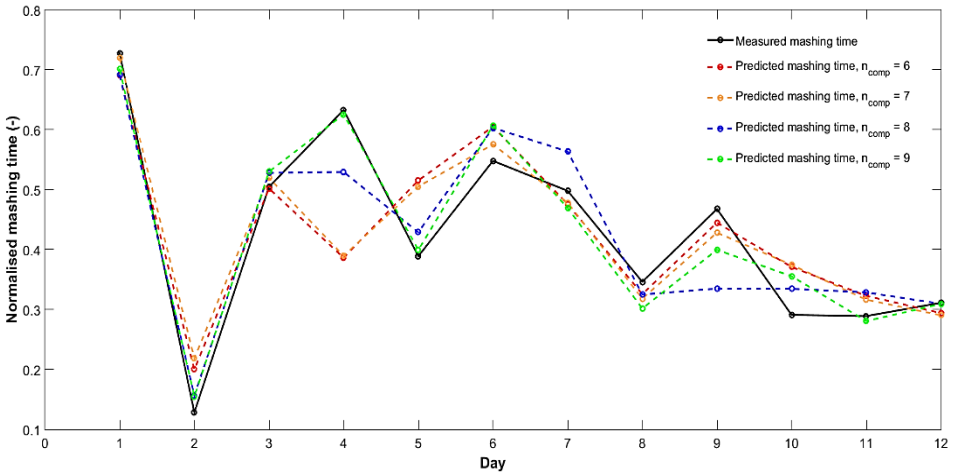

Figure 2: PLS components (n_{comp}) predictive assessment.

Lautering modelling results from the first-principles model are presented in Fig. 3. Experimental points from individual days follow a linear trend, as per the R^2 = 0.654–0.993 in this work, indicating reasonable fit. The variation may be attributed to equipment design or gradual filter blocking due to insufficient wort recirculation time. The resulting model coefficients K_1, K_2 and F_k and their standard deviations are listed in Table 1.

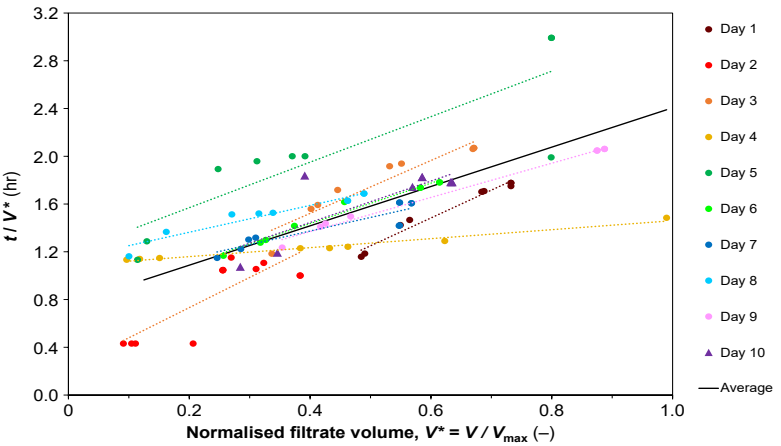

Figure 3: Lautering time vs. normalised volume for various operation days, and average.

4. Sensitivity Analysis

To detect the main drivers for the overall subsystem, a sensitivity analysis was performed, under a ±10% scenario. Following the method of Jørgensen and Fath (2011), sensitivity indices *S* were calculated. The values of *S*-indices remain constant regardless of the parameter relative perturbation if the model is linear. The perturbed subsystem variables, x_i, are listed in Table 2. Sensitivity analysis results are presented in Fig. 4 by illustration of *S*-values (Fig. 4a) and the effect of a ±10% variable deviation on the overall subsystem batchtime. The subsystem batch time is highly sensitive towards changes in the pre-mashing temperature (x_8), third resting temperature (x_{11}), mash-out temperature (x_{13}),

mashing agitation speed (x_{14}) and moderately sensitive to the amount of malted grain weight (x_1–x_4) and the wort volume collected (x_{15}), providing valuable hints for operation.

Table 1: Lautering model statistics summary.

Stats	K_1		K_2		F_k
Units	10^{-7} hr L^{-2}	10^{-4} hr m^{-6}	hr L^{-1}	hr m^{-3}	hr m^{-2}
Average	8.24	3.79	0.824	0.379	2.57
Std. dev.	3.26	1.84	0.326	0.184	1.02
Variation (%)	85.1	92.9	85.1	92.9	85.1

Fig. 4b shows an increase mash-out temperature (x_{13}), agitation speed (x_{14}) and wort volume (x_{15}) also increases the batch processing time. On the lower end of the tornado plots, increasing the malted grain weight (x_1), the pre-mashing temperature (x_8) and the third resting temperature (x_{11}) decrease the subsystem batch time significantly. Implementing a speed control system would improve mash filterability, because excessive stirring leads to increased batch times because of the increased shear forces exerted on the mash, in agreement with brewing theory (de Rouck et al., 2013). The wort volume can thus be controlled via a composition loop system so as to stop its collection and reduce batch times, once the sweet wort has achieved a desired sugar composition.

Table 2: Milling, mashing and lautering: subsystem process variables.

Variable	**Name**	**Units**	**Unit Op.**	**Variable**	**Name**	**Units**	**Unit Op.**
x_1	Material Weight 1	kg	Milling	x_9	Resting T_1	°C	Mashing
x_2	Material Weight 2	kg	Milling	x_{10}	Resting T_2	°C	Mashing
x_3	Material Weight 3	kg	Milling	x_{11}	Resting T_3	°C	Mashing
x_4	Material Weight 4	kg	Milling	x_{12}	Resting T_4	°C	Mashing
x_5	Initial tank T	°C	Mashing	x_{13}	Mash-out T	°C	Mashing
x_6	Pre-mash water volume	L	Mashing	x_{14}	Agitation speed	rpm	Mashing
x_7	Strike water volume	L	Mashing	x_{15}	Wort volume	L	Lautering
x_8	Pre-mash T	°C	Mashing				

Not all sensitive variables mentioned can be used as manipulations for process control. The mass of malted grain (MW1) and the wort volume are defined as design parameters for a specific brewing recipe and cannot change under normal conditions. The rest of the sensitive variables (x_3, x_8, x_{11}, x_{14}) can be conveniently used for batch process regulation.

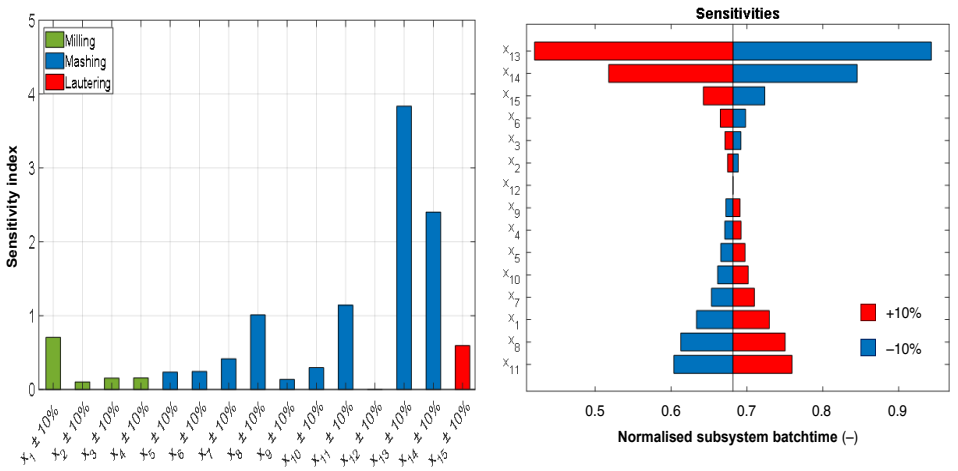

Figure 4: (a) Parameter sensitivity indices, (b) Batch times vs. ±10% parameter variation.

5. Conclusion

The modelling strategy conceived in this study resulted in the formulation of two mathematical models capable of capturing mashing and lautering behaviour, giving rise to operational protocols aimed at reducing batch times and increasing plant productivity. To gain mechanistic understanding of the wort separation processes, a first-principles model based on filtration theory has been formulated to describe lauter tun operation. Correlation of the coefficients K_1 and K_2 to other process parameters may further increase the fidelity of the presented model and the accuracy of the modelling results vs. the considered industrial datasets which can be analysed. This model can be used to predict lautering times as a function of the wort volume only, which is a key operating parameter. The optimal number of PLS latent variables for mashing-milling modelling is a compromise between model accuracy and reliability for future predictions. This model predicts milling-plus-mashing times with adequate accuracy for performance monitoring. The sensitivity analysis clearly indicates that significant reductions in batch time can be achieved by increasing the malted grain weight, pre-mashing temperature, resting temperature and decreasing the mash-out temperature, agitation speed and wort volume.

Acknowledgements

The authors acknowledge the support of the Engineering and Physical Sciences Research Council (EPSRC)/IAA, the Japan Society for the Promotion of Science, the Great Britain Sasakawa and Nagai Foundations and the Royal Academy of Engineering (RAEng). Previous discussions with Molson Coors colleagues are also gratefully acknowledged.

References

A.M. Crescenzi, 1987, Factors governing the milling of malt, *J. I. Brewing*, 93, 193–201.

L. Colen and J. Swinnen, 2016, Economic growth, globalisation and beer consumption, *J. Agric. Econ.*, 67, 1, 186-207.

S. de Jong, 1993, SIMPLS: An alternative approach to partial least squares regression, *Chemometr. Intell. Lab.*, 18, 3, 251–263.

G. de Rouck, B. Jaskula, B. de Causmaeckerm, S. Malfliet, F. van Opstaele, J. de Clippeleer, J. de Brabanter, L. de Cooman and G. Aerts, 2013, The influence of very thick and fast mashing conditions on wort composition, *J. Am. Soc. Brew. Chem.*, 71, 1, 1–14.

S.E. Jørgensen and B.D. Fath, Concepts of modelling. In *Fundamentals of Ecological Modelling*, S.E., Jørgensen, B.D. Fath, Eds. *Developments in Environmental Modelling*, Elsevier: 2011; 23, 19-93.

J.F. MacGregor, C. Jaeckle, C. Kiparissides and M. Koutoudi, 1994, Process monitoring and diagnosis by multiblock PLS methods, *AIChE J.*, 40, 5, 826–838.

A.D. Rodman and D.I. Gerogiorgis, 2019, An investigation of initialisation strategies for dynamic temperature optimisation in beer fermentation, *Comput. Chem. Eng.*, 124, 42–61.

Q. Shen, M. Weaser, L. Griffiths and D.I. Gerogiorgis, 2019, Statistical modelling for optimisation of mash separation efficiency in industrial beer production, *Comput. Aided Chem. Eng.*, 46, 1465–1470.

Sauro Pierucci, Flavio Manenti, Giulia Bozzano, Davide Manca (Eds.)
Proceedings of the 30th European Symposium on Computer Aided Process Engineering (ESCAPE30), May 24-27, 2020, Milano, Italy.
http://dx.doi.org/10.1016/B978-0-12-823377-1.50280-9

Dynamic Modelling and Simulation of Cold Contact Fermentation (CCF)

Dylan Pilarski, Dimitrios I. Gerogiorgis

Institute for Materials and Processes (IMP), School of Engineering, University of Edinburgh, The Kings Buildings, Edinburgh, EH9 3FB, United Kingdom
D.Gerogiorgis@ed.ac.uk

Abstract

The increased commercial presence and comparative health benefits of alcohol-free beer (AFB) provide a substantial impetus for research, particularly in the field of dynamic simulation whereby the development of accurate models can help reduce costs of experimentation. Cold Contact Fermentation (CCF) is an existing method of industrial-scale AFB production that utilises reduced fermentor temperatures and altered contact times compared to Warm Fermentation (WF), though requiring continual attention given the production of non-optimal organoleptic compositions, which drastically affect taste. In order to better understand the differences between Warm Fermentation (WF) and CCF, a DAE system is constructed based on previous WF studies whose responses are compared vis-à-vis to simulations of the same model under industrial CCF conditions. Given the significant discrepancies between dynamic results, industrial data can be for the parametrisation of a new CCF model, in order to accurately portray plant operation. Further to these simulations, the sensitivity of final species concentrations to parameter variation and the effect of hypothetical temperature profiles are studied with the aim of evaluating model system flexibility and opportunities for improvement based on changes to fermentor temperature profiles. Overall, disparate relative ethyl acetate sensitivity and clustering of hypothetical CCF responses reflect existing challenges with flavour composition but highlight opportunities for remarkable process improvements.

Keywords: Cold Contact Fermentation (CCF); Cold Contact Process (CCP); Alcohol-Free Beer (AFB); dynamic modelling; multivariate constrained dynamic optimisation.

1. Introduction

Cold Contact Fermentation (CCF) or Cold Contact Process (CCP) emerged in 1983 as novel method of producing beer with a reduced alcohol content by altering both fermentation duration and temperature from the conditions utilised in standard brewing practice (Perpète and Collin, 1999). Since that time, interest in alcohol-free beer (AFB) has surged, with an estimated global increase in consumption of 80% from 2007 to 2012 corresponding to an amount of $2.2 \cdot 10^9$ L yr^{-1} (Liguori et al., 2018). Despite this increase in consumption, the production of AFB is still beset by concerns with the issue of maintaining the balance between flavours such as butter/butterscotch (due to vicinal diketones, frequently denoted as VDKs, such as diacetyl), bitterness (due to aldehydes such as acetaldehyde) and fruitiness (due to esters, such as ethyl acetate) while retaining a consistent flavour profile with regard to sweetness (residual extract) and beer aroma.
While numerous research efforts regarding CCF at a laboratory scale have been undertaken since its inception, its dynamic modelling has not received the same attention

as the produced beverage. Dynamic modelling and optimisation have been applied for beer manufacturing (Rodman and Gerogiorgis, 2016); this work steers towards the implementation of not only a robust model but a sound platform for future optimisation on a broader industrial scale aimed at process cost reduction and flavour improvement. This study uses the kinetic model of de Andrés-Toro et al. (1998) as the basis for describing state responses under CCF conditions of suspended biomass (X_S), ethanol (C_E), sugar (C_S), diacetyl (C_{DY}) and ethyl acetate (C_{EA}) (see Fig. 1). This model splits the fermentation process into an initial lag phase and, upon adequate lag cell activation, transition to a fermentation phase where secondary flavour products are generated. The kinetic model equations (Eqs. 1–12) describing species profiles are shown in Fig. 1.

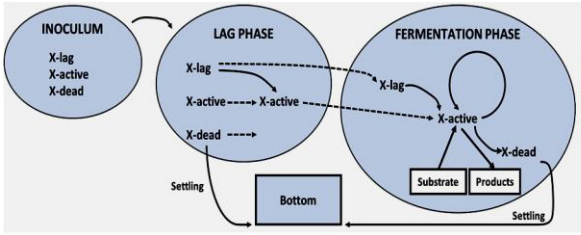

$$\frac{dX_A}{dt} = \mu_X X_A - \mu_{DT} X_A + \mu_L X_L \quad (1)$$

$$\frac{dX_D}{dt} = -\mu_{SD} X_{dead} + \mu_{DT} X_A \quad (2)$$

$$\frac{dC_S}{dt} = -\mu_S X_A \quad (3)$$

$$\frac{dC_E}{dt} = f \mu_E X_A \quad (4)$$

$$\frac{dC_{EA}}{dt} = Y_{EA} \mu_X X_A \quad (5)$$

$$\frac{dC_{DY}}{dt} = \mu_{DY} C_S X_A - \mu_{AB} C_{DY} C_E \quad (6)$$

$$\frac{dX_L}{dt} = -\mu_L X_L \quad (7)$$

$$\mu_X = \frac{\mu_{X0} C_S}{k_X + C_E} \quad (8)$$

$$\mu_{SD} = \frac{\mu_{SD0} 0.5 C_{S0}}{0.5 C_{S0} + C_E} \quad (9)$$

$$\mu_S = \frac{\mu_{S0} C_S}{k_S + C_S} \quad (10)$$

$$\mu_E = \frac{\mu_{E0} C_S}{k_E + C_S} \quad (11)$$

$$f = 1 - \frac{C_E}{0.5 C_{S0}} \quad (12)$$

Figure 1: Kinetic model for Warm Fermentation (WF) (de Andrés-Toro et al., 1998).

Arrhenius factors (μ_i) denote formation or consumption of corresponding model species while the stoichiometric factor (Y) and inhibition factor (f) guide ethyl acetate and ethanol formation, respectively. The full mathematical model has been expressed as a Differential Algebraic Equation (DAE) system and solved in MATLAB, to simulate key responses.

2. CCF Model Parameterisation

A comparison of dynamic simulation responses for the de Andrés-Toro et al. (1998) model (T = 13 °C) and implementation of new CCF operating (T = 5–6.5 °C) and initial conditions (CCFIC) demonstrated severe differences in model dynamic behaviours, i.e., differing trends aside from the differing initial (imposed via the CCFIC) and final species concentration values (Fig. 2). Because of anticipated response discrepancies between simulations of WF and CCF in respect to assumed initial conditions, final concentrations from industrial CCF batches were incorporated as numerical benchmarks for parameterisation of de Andrés-Toro (1998) kinetic model, now under CCF conditions.

Reparameterisation of temperature-dependent parameters of specific rates (μ_i, Eq. 13) has therefore been systematically conducted, and it was achieved through an algorithm targeting least squares regression (Eq. 14) with respect to each of the state variables $\theta_{i,\text{measured}}$ (for a total of N) and corresponding model responses, $\theta_{i,\text{model}}$ (Pilarski, 2019).

$$\mu_i = \exp\left(A_i + \frac{B_i}{T}\right) \quad (13)$$

$$\min_{\theta_i} J(\theta_i) \quad (14)$$

$$J = \sum_{i=1}^{N} \left(\theta_{i,\text{measured}} - \theta_{i,\text{model}}\right)^2 \quad (15)$$

Minimisation was performed using the Nelder-Mead direct search algorithm, whereby a subset of DAE parameters were allowed to vary in order for the algorithm to converge

and produce a solution set of parameters that diverged minimally from the WF parameters presented by de Andrés-Toro et al. (1998). Plausible industrial operating conditions and/or data encompassing processing, initial conditions and final concentrations for CCF simulations and parameterisation can be considered in this computational framework.

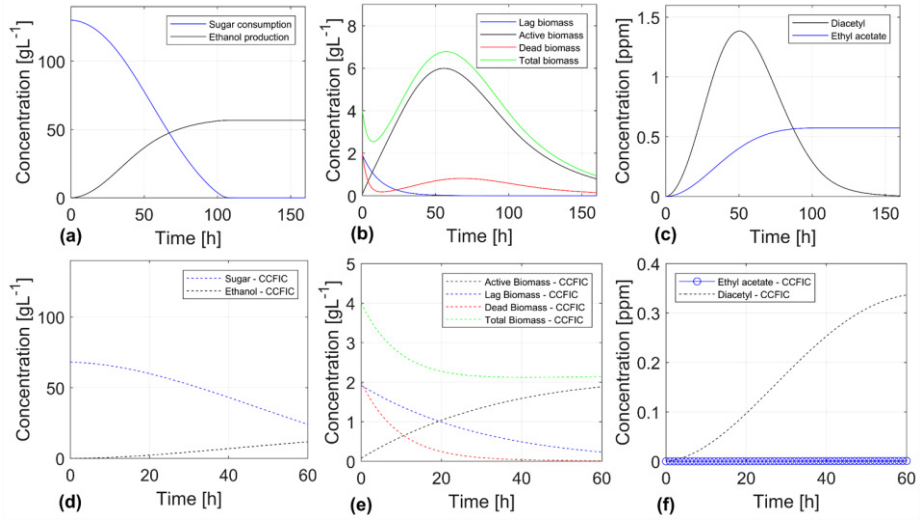

Figure 2: Key dynamic response comparisons between WF (a–c) and CCFIC (d–f).

Values of A_i and B_i for explicit kinetic model parameters which have properly converged have been then reparameterised to constrain the scope of the problem. This successfully allowed for parameterisation with respect to C_S, C_E, C_{EA} and C_{DY} based on limited pilot plant data, with all biomass responses remaining unconstrained (Fig. 3). Reparameterised CCF values, but also those kept as per the WF model, have been summarised in Table 1.

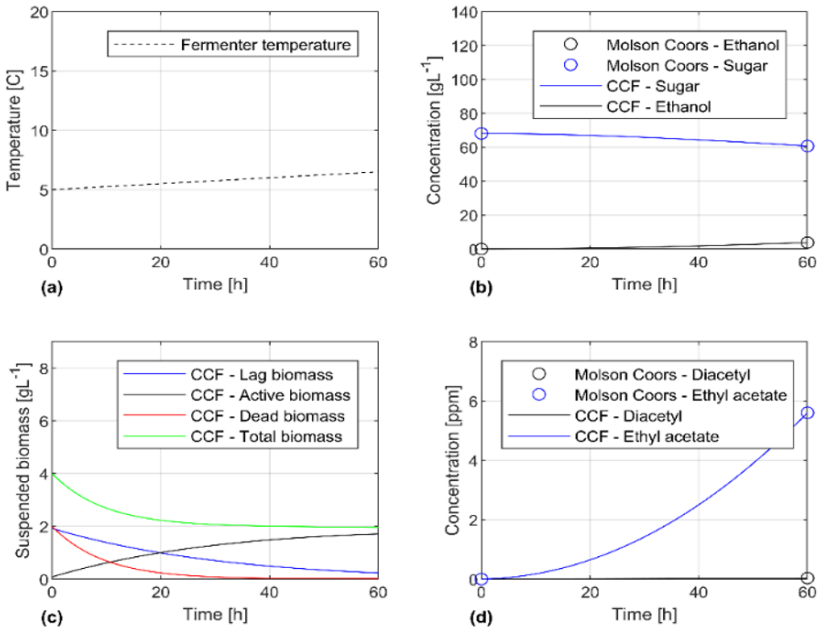

Figure 3: A plausible CCF temperature profile (a); parameterised CCF responses (b–d).

Table 1: Resulting CCF model parameters with * denoting values original to this study (our results).

Rates / Parameters	Description	A_i	B_i
μ_{SD0}	Maximum dead cell settling rate	33.820	–10,033.280
μ_{X0}	Maximum cell growth rate	37.450*	–31,934.090
μ_{S0}	Maximum sugar consumption rate	–41.920	11,754.776*
μ_{E0}	Maximum ethanol production rate	4.125*	–1,267.240
μ_{DT}	Specific cell death rate	130.160	–38,313.000
μ_L	Specific cell activation rate	30.720	–9,501.540
$k_E = k_S$	Affinity constant for sugar and ethanol	–119.630	35,203.709*
Y_{EA}	Stoichiometric factor - ethyl acetate production	169.130*	–26,589.000
		Value	
μ_{DY}	Rate of diacetyl production	$7.590 \cdot 10^{-6}$*	
μ_{AB}	Rate of diacetyl consumption	$1.138 \cdot 10^{-3}$	

3. Sensitivity Analysis

Sensitivity analyses offer great insight for batch and semi-batch processing that may require control policies of varying flexibility based on production progress/completion. Process response sensitivity S can be quantified in relation to the measured change in a state variable θ based on an intended change in a parameter P according to Eq. 15.

$$S = \frac{\partial\theta}{\theta} \Big/ \frac{\partial P}{P} \tag{15}$$

Parameter variations of ±5% were implemented and the resulting sensitivities of state variables (model responses) visualised for clarity (Fig. 4). Variations in parameters A_{kes} and B_{kes} produced large perturbations for all state variables, though final C_{EA} sensitivity to variation (particularly for A_{YEA}, B_{YEA}, $A_{\mu x0}$ and $B_{\mu x0}$) was most significant and a reflection of 'fruity' flavour issues described for AFB as a result of over or uncontrolled ester expression (Verstrepen et al., 2003). Thus, process variations (parameter values being a function of processing conditions) have the greatest impact on C_{EA}.

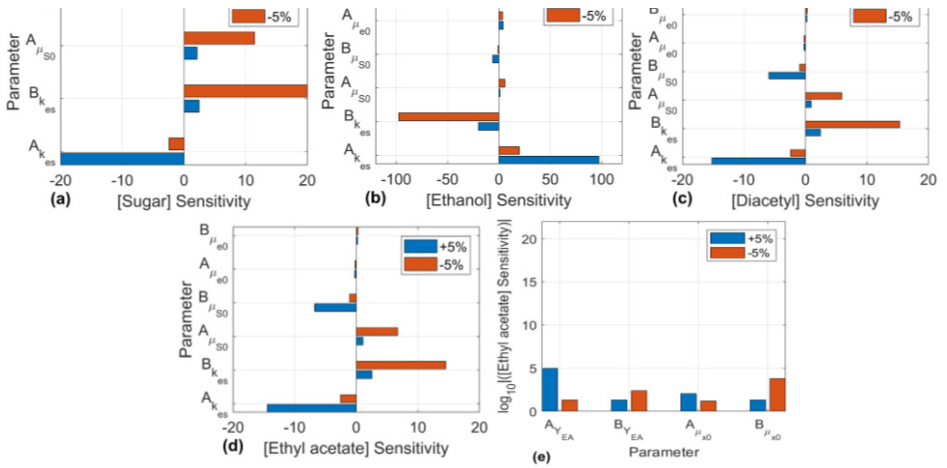

Figure 4: Sensitivities for (a) final sugar, (b) ethanol, (c) diacetyl and (d–e) ethyl acetate concentrations under ±5% variation for all parameters of non-negligible process impact.

4. Course Grid Enumeration of Hypothetical Temperature Profiles

Previous CCF industrial results were garnered via consideration of a 1.5 °C temperature band. However, it is known that CCF processes can make use of temperatures between 0–8 °C (Perpète and Collin, 1999; Montanari et al., 2009). In addition, by using existing cooling jackets, the fermentor temperature can be controlled provided the CCF progresses, through the exothermic reactions in the fermentor, or with future implementation of external heating. The effect of temperature variation was studied via coarse grid discretisation of the computational time (10 hr sub-grids for $t \in [t_0, t_f] = [0, 60]$ and temperature domains (1 °C sub-grids for 1–7 °C). Furthermore, different temperature profiles have been selected on the basis of ease of industrial implementation (Pilarski, 2019). This resulted in 29 hypothetical temperature profiles, ranked by total theoretical heat Q (Eq. 16). Here, m is the fermentation broth mass and C_P is the specific heat capacity at constant pressure. Results for all temperature profiles are given in Fig. 5.

$$Q = mC_P \int_{t_0}^{t_f} T(t)\mathrm{d}t \tag{16}$$

Of all enumerated results, C_{EA} and C_{DY} represent the largest and smallest spans of hypothetical outcomes, respectively. In addition, a general increase in consumption of final C_S and increased formation of C_E, C_{EA} and C_{DY} is noted. However, general trends for rates of change of each response are very different. When coupled with evident clustering (e.g., Trials 26–29) these trends show the potential for improvement based on changes to fermentor temperatures. Although the number of temperature profiles considered here is limited in comparison to the full scope of possibilities that could be implemented industrially, comparison of the effects of the theoretical Q limits the number of temperature profiles that allow one to stay within product specifications. Each Q may have multiple associated temperature profiles; the optimal manipulation may be established via dynamic optimisation attain target ethanol concentrations while also ensuring critical flavour component concentration constraints (Rodman et al., 2019).

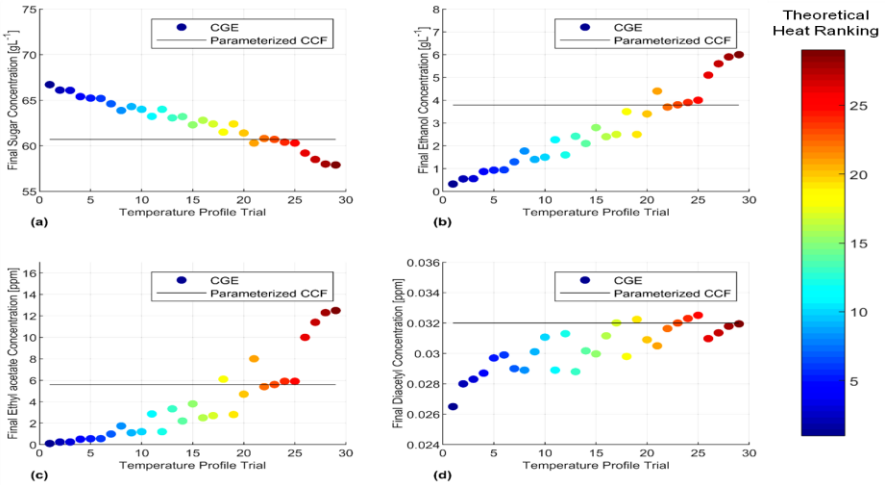

Figure 5: (a) Sugar, (b) ethanol, (c) ethyl acetate and (d) diacetyl final concentrations based on T- profile variation and ranking by a Q metric (CGE: Coarse Grid Enumeration).

5. Conclusion

This study used industrial data to formulate a newly parameterised model for CCF using the published de Andrés-Toro et al. (1998) kinetic model to compare model responses between WF and CCF. Differences in dynamic behaviour, aside from different initial and final species concentration values inherent of the different processing requirements of WF and CCF operations, necessitated reparameterisation of the Andrés-Toro model to accurately describe CCF. Subsequent parameterisation regarding industrial data points provided a solution set of parameters to follow the dynamic behaviour of the WF model. Sensitivity analyses based on a ±5% variation elucidated the most important model parameters with the highest sensitivity to changes in temperature-dependence, with ethyl acetate concentrations being the most impacted. Enumeration of CCF responses based on hypothetical temperature profiles confirmed that increased theoretical heat increased formation of ethanol, ethyl acetate and diacetyl during CCF, albeit at different rates. Future work will implement the newly parameterised CCF model for dynamic optimisation of temperature profiles in order for low-alcohol content beer subject to different end-point (related to flavour species) and interior-point (related to temperature boundaries and gradient limitations associated with controllers) constraints as well as heat transfer dynamics to account for different scales of fermentor operation and production.

Acknowledgements

The authors acknowledge the support of the Engineering and Physical Sciences Research Council (EPSRC)/IAA, the Japan Society for the Promotion of Science, the Great Britain Sasakawa and Nagai Foundations and the Royal Academy of Engineering (RAEng). Previous discussions with Molson Coors colleagues are also gratefully acknowledged.

References

B. de Andrés-Toro, J.M. Girón-Sierra, J.A. Lopez-Orozco, C. Fernández-Conde, J.M. Peinado and F. Garcia-Ochoa, 1998, A kinetic model for beer production: simulation under industrial operational conditions, *IFAC Proceedings Volumes*, 48, 65–74.

L. Liguori, P. Russo, D. Albanese and M. Di Matteo, 2018, Production of low-alcohol beverages: current status and perspectives, in *Food Processing for Increased Quality and Consumption,* Grumezescu, A.M.; Maria, A (eds.), Cambridge, USA, Academic Press, 347–382.

L. Montanari, O. Marconi, H. Mayer and P. Fantozzi, 2009, Production of alcohol-free beer, *Beer Heal. Dis. Prev.*, 274, 2016, 61–75.

P. Perpète and S. Collin, 1999, Fate of the worty flavours in a cold contact fermentation, *Food Chem.*, 66, 3, 359–363.

D. Pilarski, 2019, *Dynamic Modelling and Simulation of Cold Contact Fermentation*, Masters Thesis, The University of Edinburgh, UK.

A.D. Rodman and D.I. Gerogiorgis, 2016, Multi-objective process optimisation of beer fermentation via dynamic simulation, *Food Bioprod. Process.*, 100, 255–274.

A.D. Rodman, M. Weaser, L. Griffiths and D.I. Gerogiorgis, 2019, Dynamic optimisation and visualisation of industrial beer fermentation with explicit heat transfer dynamics, *Comput. Aided Chem. Eng.*, 46, 1459–1464.

K.J., Verstrepen, G., Derdelinckx, J-P., Dufour, J., Winderickx, J.M., Thevelein, I.S., Pretorius and F.R., Delvaux, 2003, Flavor-active esters: adding fruitiness to beer, *J. Biosci. Bioeng.,* 96, 2, 110–118.

Sauro Pierucci, Flavio Manenti, Giulia Bozzano, Davide Manca (Eds.)
Proceedings of the 30th European Symposium on Computer Aided Process Engineering (ESCAPE30), May 24-27, 2020, Milano, Italy.
http://dx.doi.org/10.1016/B978-0-12-823377-1.50281-0

Application of the "Distance to Target" Approach to the Multiobjective Optimization of Nutritional and Economic Costs due to Food Loss and Waste

Ricardo Abejón,[a] Ian Vázquez-Rowe,[b] Alba Bala,[c] Pere Fullana-i-Palmer,[c] María Margallo,[a] Rubén Aldaco[a*]

[a]*Departamento de Ingenierías Química y Biomolecular, Universidad de Cantabria. Avda. de Los Castros s/n, 39005, Santander, Spain*
[b]*Peruvian LCA Network, Department of Engineering, Pontificia Universidad Católica del Perú, Av. Universitaria 1801, 15088 San Miguel, Lima, Peru*
[c]*UNESCO Chair in Life Cycle and Climate Change ESCI-UPF. Pg. Pujades 1, 08003 Barcelona, Spain*
aldacor@unican.es

Abstract

Since about one third of all food produced worldwide is lost or wasted throughout the supply chain, measures to reduce food loss and waste (FLW) must be fostered to meet the increasing challenge of sustainable feeding of the world's population. In addition to the minimization of the total amount of FLW, two additional relevant aspects must be taken into account: the nutritional and economic costs caused by these losses. This point of view defines a more complex scenario with multiple sustainability targets, with different minimization objectives. A "distance to target" approach, based on the definition of a normalized weighted distance, has been selected to provide practical and effective optimization guidelines by measuring the magnitude towards the quantitative sustainable targets in the minimization of economic and nutritional costs associated to FLW. The results revealed that vegetables were the food category that showed the worst performance in terms of nutritional and economic costs due to the great amount of loss and waste generated, which highlights the importance of providing measures in this category.

Keywords: Multiobjetive optimization, Distance, FLW, Economic costs, Nutritional costs.

1. Introduction

The food supply chain is a key aspect to be considered for sustainable development of the Water-Food-Energy nexus. In addition, wastes must be integrated in this context, since food supply chains are particularly wasteful (García and You, 2018). About 30% of all food produced is lost or wasted worldwide throughout the supply chain. These losses have important consequences on the environment, implying significant impacts in terms of inefficient use of natural resources and energy, biodiversity and habitat loss, soil and water degradation, and climate change (Hoehn et al., 2019).

Efficient measures and future strategies are required to decrease FLW. In order to identify the most critical aspects, the simple quantification of the losses in terms of mass are insufficient and further tools to include the nutritional and economic characteristics of these losses must be taken into account (Vázquez-Rowe et al., 2019). Indexes that

consider the nutritional quality and economic cost of lost and wasted food can assist policy-makers, because these more complex metrics include additional relevant aspects to support the decision-making processes.

Although the definition of this type of indexes helps to measure the performance of different solutions, a high number of case studies related to sustainability assessment and impact reduction that must manage with multiple objectives are based on a "direction to target" approach, which defines the improving direction to a sustainable objective without quantitative guidelines. However, a "distance to target" approach results more effective, since it provides practical guidelines by measuring and quantifying the magnitude toward a previously defined sustainable target. This approach was applied to the minimization of the economic and nutritional costs due to FLW attributable to different food categories.

2. Case study

FLW along the supply chain of the Spanish food system was selected as the case study (García-Herrero et al. 2018). This work does not consider the nature of the supply chain models, since a previous study, which evaluated the economic and nutritional efficiency of 13 food categories, was used as the reference database (Vázquez-Rowe et al., 2019). This previous work applied a life cycle perspective to define two indexes that characterize the economic and nutritional losses: the economic FLW index (EFLW) and the nutrient-rich foods index (NFR9.3). In the current study, however, these indexes were transformed to normalized economic and nutritional factors (X_{EC} and X_{NUTR}, respectively) by dividing each value by the corresponding maximal value. The factors obtained are presented in Figure 1.

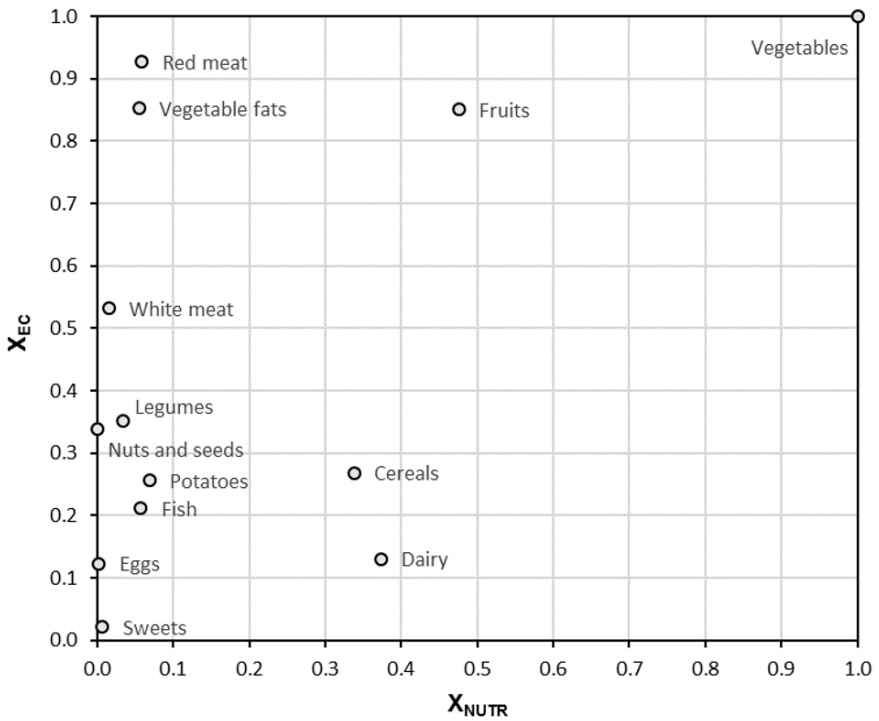

Figure 1. Economic factor X_{EC} versus nutritional factor X_{NUTR} for the food categories.

3. Modelling

The use of a "distance to target" approach provides some advantages when compared to standard multiobjective optimization methods like ε-constraints (Abejón et al., 2012). For instance, it provides a single Pareto solution, rather than a Pareto front of solutions. Moreover, it can be applied to identify the best way to improve suboptimal solutions by finding minimal projections onto the Pareto front (Limleamthong and Guillen-Gosálbez, 2017). The Euclidean distance between the individual solutions and the optimization targets can be used as base (Schadler et al., 2016). The Euclidean distance D in a n-dimension space can be defined by the following equation:

$$D = \sqrt{\sum_{i=1}^{n} |f_i(x) - g_i|^2} \quad (1)$$

where $f_n(x)$ is the vector to be optimized and g_n the specified target vector. In the current study, a normalized weighted distance D_n was employed as the main indicator to identify minimal nutritional and economic costs of different categories of food products:

$$D_n = \frac{\sqrt{\sum_{i=1}^{n} k_i |F_i(x) - G_i|^2}}{\sqrt{n}} \quad (2)$$

where $F_n(x)$ is the normalized vector to be optimized and G_n the normalized specified target vector, while k_n represents the weighting factor of each objective. This definition of D_n implies that the distance values are normalized in the range between 0 (closest to the target) and 1 (furthest to the target), so a direct and easily comparable outlook of the results is provided (another clear advantage over conventional multiobjective optimization methods). In this case, since both objectives must be minimized, the normalized target vector is the null vector (all components are equal to 0).

4. Results

First, normalized distances of each category were assessed when the contributions of both objectives were considered equally important ($k_{EC} = k_{NUTR} = 1$). The results obtained can be observed in Table 1 ($D_{n\ eq}$ column). Sweets appeared as the optimal category, with minimal distance to the defined sustainability target. In contrast, vegetables was the most distant category to the target due to the higher economic and nutritional factor values. Then, GAMS software was employed to manage the formulated NLP models using CONOPT3 solver (Abejón et al., 2016) to calculate the minimal and maximal values that the normalized distance could take ($D_{n\ min}$ and $D_{n\ max}$ respectively in Table 1). These optimization programs were subject to restrictions: the weighting factors were ranged between 0.2 and 1.8, and the sum of the weighting factors was equal to the number of objectives (i.e., 2):

$$\min D_n = f(k_i) \quad \text{or} \quad \max D_n = f(k_i)$$
$$\text{s.t.} \quad h(k_i) = 0$$
$$g(k_i) \leq 0$$
$$k_i \in \Re$$

Once again, when the minimal values were compared, sweets were the optimal category. When white meat, as the best example of a category with uncompensated economic and nutritional values, was compared to cereals, with more compensated values, different patterns were identified. White meat presented lower minimal distance because it was favored by its low X_{NUTR} value and high weighting factor of this objective improved its performance when compared to cereals. However, the range between minimal and maximal distances was lower for cereals. In addition to sweets, other two categories (i.e., eggs and nuts and seed) resulted non-dominated and these three categories formed the standard Pareto front (Figure 2). Therefore, the rest of categories can be considered sub-optimal points.

Table 1. Economic and nutritional factors, normalized distance under equal weighting factors (D_n eq), minimal (D_n min) and maximal (D_n max) normalized distances, and the normalized projection distances onto the Pareto front (D_n Front) or the distance to form a new front (D_n Pareto)

	X_{EC}	X_{NUTR}	$D_{n\ eq}$	$D_{n\ min}$	$D_{n\ max}$	$D_{n\ Front}$	$D_{n\ Pareto}$
Sweets	0.021	0.006	**0.016**	0.009	0.020	-	-
Eggs	0.123	0.002	**0.087**	0.039	0.117	-	-
Fish	0.212	0.057	**0.155**	0.086	0.202	0.039	0.039
Potatoes	0.256	0.069	**0.187**	0.104	0.244	0.048	0.048
Nuts and seeds	0.338	0.000	**0.239**	0.107	0.321	-	-
Legumes	0.351	0.033	**0.249**	0.115	0.333	0.025	0.023
Dairy	0.130	0.373	**0.279**	0.171	0.356	0.262	0.077
Cereals	0.268	0.338	**0.305**	0.276	0.332	0.239	0.175
White meat	0.532	0.015	**0.377**	0.169	0.505	0.138	0.010
Vegetable fats	0.853	0.055	**0.604**	0.275	0.809	0.366	0.039
Red meat	0.927	0.058	**0.657**	0.298	0.880	0.419	0.041
Fruits	0.850	0.476	**0.689**	0.526	0.820	0.494	0.336
Vegetables	1.000	1.000	**1.000**	1.000	1.000	0.848	0.692

These sub-optimal categories can be projected onto the Pareto front to establish the best improvement route to make them Pareto optimal. These projection distances ($D_{n\ Front}$) were assessed as the minimal normalized distance between a category and the front formed by the three Pareto optimal categories (Table 1). Legumes, which had a higher $D_{n\ eq}$ value when compared to fish or potatoes, resulted with a lower $D_{n\ Front}$ value because it was relatively close to an optimal category (i.e., seeds and nuts). Instead of becoming optimal solutions by projection onto the existing Pareto front, a sub-optimal category could be a new optimal point to extend the front. In this case, this situation resulted from the reduction of the X_{NUTR} value below that of sweets or the reduction of the X_{EC} value below that of seeds and nuts. These minimal distances ($D_{n\ Pareto}$) are also included in Table 1. In most cases, the D_n Pareto values were lower than $D_{n\ Front}$ values. The case of the categories with uncompensated factors (white meat as example) must be highlighted, because a slight decrease of the factor with lower value (X_{NUTR} in this case) resulted in a close transformation to optimal solution (0.010 is the lowest Dn Pareto value).

Finally, a detailed analysis of Figure 2 revealed that under particular weighting factor conditions, each of the three optimal categories could be those with the lowest distance to target.

However, as demonstrated in the results compiled in Table 1, the minimizationof these distances subject to restriction in the weighting factors (limited between 0.2 and 1.8) displayed sweets as the best option.

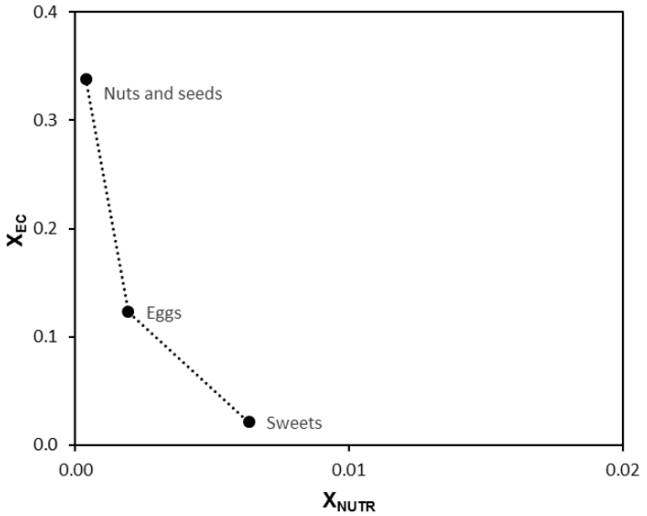

Figure 2. Detailed view of the Pareto front of optimal categories.

Therefore, a more complete sensitivity analysis of the influence of the weighting factors without restrictions was carried out. As observed in Figure 3, only extreme values of the weighting factors resulted in the discarding of sweets as the best performing category. When the k_{NUTR} value was higher than 1.995, the distance value of eggs was lower than that of sweets and it became the best performing category. To get nuts and seeds as the best category a more extreme situation was required: the k_{EC} value had to be lower than 7.8·10-5 to overpass eggs and attain the lowest distance. Consequently, the robustness of sweets as the optimal category according to the distance to target approach was clear.

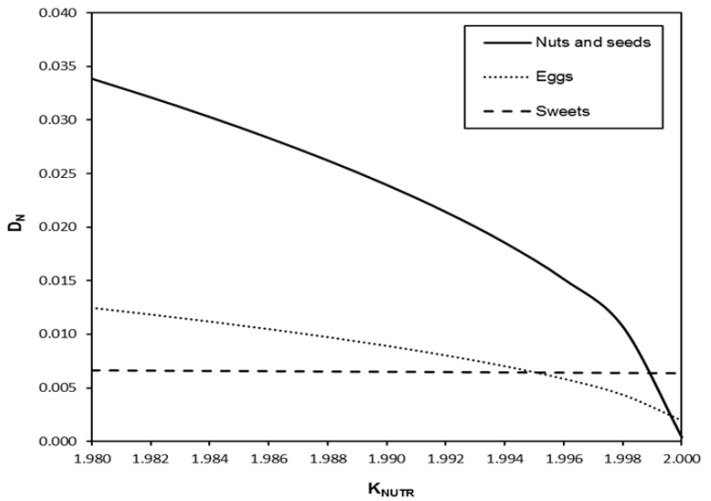

Figure 3. Evolution of the normalized distant of the three Pareto categories as a function of the weighting factors.

5. Conclusions

A “distance to target” approach, based on a normalized weighted distance, was applied to the simultaneous minimization of the nutritional and economic costs of FLW. On the one hand, the analysis of the different food categories demonstrated that vegetables resulted as the worst performing category, requiring urgent measures. On the other hand, sweets appeared as the best performer. Only the consideration of extreme weighting factors that practically cancel the economic costs made possible the transformation of eggs or nuts and seeds into the most preferable categories. This study can assist the decision-making process to design and select effective strategies and policies for the most adequate management of FLW. The applied approach is a useful tool to prioritize the most critical food categories and to measure the efficacy of the implementation of the proposed measures.

Acknowledgements

The authors are grateful for the funding of the Spanish Ministry of Economy and Competitiveness through the Ceres-Procom Project: Food production and consumption strategies for climate change mitigation (CTM2016-76176-C2-1-R) (AEI/FEDER, UE).

References

R. Abejón, A. Garea, A. Irabien, 2012, Multiobjective optimization of membrane processes for chemicals ultrapurification, , Computer Aided Chemical Engineering, 30, 542-546.

R. Abejón, A. Abejón, M.P. Belleville, J. Sánchez-Marcano, A. Garea, A. Irabien, 2016, Multiobjective optimization of membrane networks for fractionation of protein hydrolysate from fish by-products, Computer Aided Chemical Engineering, 38, 415-420.

D.J. Garcia, F. You, 2018, Including agricultural and organic waste in Food-Water-Energy-Waste nexus modelling and decision-making, Computer Aided Chemical Engineering, 43, 1475-1480.

I. García-Herrero, D. Hoehn, M. Margallo, J. Laso, A. Bala, L. Batlle-Bayer, P. Fullana, I. Vázquez-Rowe, M.J. González, M.J. Durá, C. Sarabia, R. Abajas, F.J. Amo-Setién, A. Quiñones, A. Irabien, R. Aldaco, 2018, On the estimation of potential food waste reduction to support sustainable production and consumption policies, Food Policy, 80, 24-38.

D. Hoehn, M. Margallo, J. Laso, I. García-Herrero, A. Bala, P. Fullana-i-Palmer, A. Irabien, R. Aldaco, 2019, Energy embedded in food loss management and in the production of uneaten food: seeking a sustainable pathway, Energies, 12, 767.

P. Limleamthong, G. Guillen-Gosálbez, 2017, Rigorous analysis of Pareto fronts in sustainability studies based on bilevel optimization: Application to the redesign of the UK electricity mix, Journal of Cleaner Production, 164, 1602-1613.

P. Schadler, J.D. Berdugo, T. Hanne, R. Dornberger, 2016, A distance-based Pareto evolutionary algorithm based on SPEA for combinatorial problems, 4th International Symposium on Computational and Business Intelligence Proceedings, 112-117.

I. Vázquez-Rowe, J. Laso, M. Margallo I. Garcia-Herrero, D. Hoehn, F. Amo-Setién, A. Bala,

R.aAbajas, C. Sarabia, M. J. Durá, P. Fullana-i-Palmer, R. Aldaco, 2019, Food loss and waste metrics: a proposed nutritional cost footprint linking linear programming and life cycle assessment, The International Journal of Life Cycle Assessment, in press.

Sauro Pierucci, Flavio Manenti, Giulia Bozzano, Davide Manca (Eds.)
Proceedings of the 30th European Symposium on Computer Aided Process Engineering (ESCAPE30), May 24-27, 2020, Milano, Italy.
http://dx.doi.org/10.1016/B978-0-12-823377-1.50282-2

A Step Closer to the Market for Poly-hydroxy-alkanoates (PHAs) through their Bacterial Production in Continuous Bioreactors in Series: a Model Investigation of Novel Operating Strategies

Christos Chatzidoukas,[a,*] Evgenios Karasavvas[b]

[a]*Department of Chemical Engineering, Aristotle University of Thessaloniki (AUTH), P.O. Box: 472, 54124, Thessaloniki, Greece*

[b]*Chemical Process & Energy Resources Intitute (CPERI), Centre for Research and Technology Hellas (CERTH), P.O. Box: 60361, 57001, Thermi, Thessaloniki, Greece*
chatzido@auth.gr

Abstract

The current work explores the dynamic optimization of a sequence of two continuous stirred-tank bioreactors for the production of poly-3-hydroxybutyrate (PHB) in *Azohydromonas lata* cultures using a credible and sophisticated mathematical model. The cumbersome problem of operating a microbial fermentation process continuously in a consistent, systematic and controllable manner is uncovered at its full dimension and addressed, pursuing in parallel the efficient substrate utilization and the optimization of the fermentation stage. Advanced optimization algorithms and well-posed optimization strategies with different subsets of control variables are implemented A notable improvement on the performance of the continuous optimal operating bioreactors is demonstrated via the maximization of key process factors, such as productivity, biopolymer content, final product concentration etc., under three different strategies

Keywords: Dynamic optimization of microbial processes, fermentation process design, bio-based polymer production, optimal operating profiles, fermentation modelling.

1. Introduction

The stiffness of the biochemical industry to change the operating mode of fermentation processes from a batch-wise profile to a continuous one is a well-known reason blamed for the large production cost of highly promising, green, renewable products with novel applications, deficient though to compete the respective fossil-based counterparts, massively fabricated in continuous chemical processes. This is currently the status quo of polyhydroxyalkanoates (PHAs), a group of biopolymers gaining global importance across different sectors (e.g., packaging, automotive, pharmaceutical, medical industry, etc.) due to their thermoplastic and mechanical properties (similar to polyolefins) combined with biocompatibility, biodegradability, and sustainability, holding though a modest position in the global polymer market ranking (Spierling et al., 2018). The large production cost is definitely the major drawback of PHAs, which suspends their commercialization. The complexity of the bio-processes and the interdependence of the decisions that should be taken simultaneously (Koller et al., 2017) to take care fermentation aspects make the development of reliable and rigorous mathematical models for dynamic simulation and model-based optimization of the PHAs production process indispensable. In the present study, the dynamic problem of the continuous

operation of two bioreactors in series for the production of poly-3-hydroxybutyrate (PHB) in *Azohydromonas lata* cultures is investigated. It is demonstrated that the establishment of a steady-state operation of the system is feasible, thus the continuous process operation guarantees a substantially productivity enhancement and provides the means for a truly sustainable production of PHB.

2. Dynamic Mathematical Model of Bioprocess

A two-compartment, structured, non-segregated macroscopic/kinetic and oxygen mass transfer model (Chatzidoukas et al., 2013, Papapostolou et al., 2019) is used in the present study for the fermentative intracellular production of PHB by *A. lata* bacteria. The integrated model enables the simulation and prediction of the time evolution of the residual biomass, X; the polymer intracellular content, w_P; the accumulation of polymer, P; the carbon (S) and nitrogen (N) source utilization, as well as the dynamic profile of oxygen concentration in both gas phase ($O_{2,g}$) and liquid culture phase ($O_{2,l}$). The derived validated model is employed as a rigorous and reliable mathematical tool for the optimal decision making towards the mitigation of the PHAs production cost, through the design of novel efficient continuous operating strategies of a two-bioreactor system.

3. Dynamic Optimisation Strategies

Continuous operation of a fermentative PHB production process practically means a continuous feeding of fresh nutrient medium to the culture with a simultaneous removal of culture broth, while holding the entire process at the desired steady state. The optimisation of the continuous two-stage process operation is practically meant as the investigation of the optimal steady state. However, the settlement of the optimal steady state cannot be sought independently of the selection of the optimal dynamic trajectory towards this *'static'* operation. Thus, the design of optimal operating policies of PHB-producing fermentation reactors, operating in continuous mode, is practically attained through the intelligent handling of the nutrient feeding, and the initial concentration of substrates as a means of regulating both the size of the cell population and their physiological state towards the efficient production of the product of interest. Properly formulated equality and/or inequality constraints representing rational and operational restrictions of the fermentation process are employed for a realistic statement of the dynamic optimization problem. Then the problem of the optimal continuous operation of the two bioreactors in series is explored via the design of three continuous operating scenarios **(*CO1-CO3*)** of gradually increasing number of control variables (CVs) summarized in Table 1. It is noted that for all three continuous operating policies a stock of sucrose aqueous solution and ammonium sulphate aqueous solution of fixed concentration (i.e., 50 g/l and 20 g/l, respectively) is employed for the feeding of both bioreactors. Primarily, the optimal initial substrates concentrations ($[S]_{0,i}$,$[N]_{0,i}$) as well as the respective optimal substrates feeding profiles and broth outflow rates, ($Q_{S,in,i}$, $Q_{N,in,i}$, $Q_{out,i}$) are sought separately for each bioreactor (i=1,2), under the scenario ***CO1***. Then ***CO2*** has been designed similarly to the first one, but the air flow rate, ($F_{air,i}$) and the set point value ($D.O_{sp,i}$) of the controller for the dissolved oxygen concentration in the medium, which is cascaded to the rate of agitation ($N_{r,i}$), supplement the set of CVs. Finally, ***CO3*** is identical to ***CO2*** and differs only in terms of the working volume of the second bioreactor. In ***CO1*** & ***CO2*** both bioreactors are of equal working volumes (i.e., 3 l), while in ***CO3*** the respective volume V_2 is 5 l, allowing for greater flexibility in culture's residence time in the reactor where polymer cellular accumulation is built.

Table 1: Set of control variables for the continuous operating scenarios of two bioreactors (i=1,2).

Scenarios	$[S_{o,i}]$ (g/L)	$[N_{o,i}]$ (g/L)	$Q_{S,in,i}$ (l/h)	$Q_{N,in,i}$ (l/h)	$Q_{out,i}$ (l/h)	$F_{air,i}$ (l/h)	$D.O_{sp,i}$ (-)	$t_{f,i}$ (h)
CO1	✓	✓	✓	✓	✓	—	—	✓
CO2 & CO3	✓	✓	✓	✓	✓	✓	✓	✓

The objective function employed to address the dynamic optimisation of the PHB production process operating in a continuous mode, is mathematically defined as:

$$Obj = w_1[P_2(t_f)]Q_{out,2}(t_f) + w_2 w_{p,2}(t_f) - w_3 \int_0^{t_f} Q_{out,2}(t)[S_2(t)]dt$$

The first two terms in the objective function clearly express the polymer mass rate exiting from the second bioreactor, and the respective polymer content in the cells. The last term though contributed detractively to the objective function and practically represents the cumulative amount of sucrose removed from the process (via the 2nd bioreactor outlet stream) and thus is wasted. Thus, the mathematical statement of the multi-objective dynamic optimization problem of the continuously operating process is written as shown below, while the entire problem is solved using the generic simulation platform gPROMS® (Process Systems Enterprise, Ltd.) combined with the embedded gOPT optimization tool.

$$\max_{[S_{0,i}],[N_{0,i}],Q_{S,in,i},Q_{N,in,i},Q_{out,i},F_{air,i},D.O_{sp,i},t_f} \quad Obj$$

$$w.r.t. \quad process \ \mathrm{mod}el \ equations$$

$$0 \le Q_{out,i}(t) \le 0.5 \ l/h; \ i = 1,2$$

$$V_{l,i}(t) \le 2.5 \ l; \ i = 1,2 \ (for \ CO1, \ CO2) \ or \ V_{l,1}(t) \le 2.5 \ l, \ V_{l,2}(t) \le 4.5 \ l, \ (for \ CO3)$$

$$0 \le D.O_{sp,i}(t) \le 100; \ i = 1,2$$

$$100 \le N_{r,i}(t) \le 1000 \ rpm; \ i = 1,2$$

$$t_j \ge 0.5 \ h; \ j = 1,...10$$

$$-10^{-7} \le \frac{dY_i(t_f)}{dt} \le 10^{-7}; \ i = 1,2 \ where \ Y_i = \{[X_i],[P_i],[S_i],[N_i],[O_{2g,i}],[O_{2l,i}],[V_{l,i}],[V_{g,i}]\}$$

4. Results and Discussion

Analysing the optimal policies calculated for the system of the two bioreactors in series it is important to illuminate the scope of each reactor unit in a continuous PHB production process and the pathway followed towards the establishment of the optimal steady state. High priority target for the optimizer is to build immediately a sufficiently dense population in the first reactor unit, which successively feeds the second reactor unit. This need unambiguously requires a culture medium rich in nitrogen source and adequacy in carbon source. At the same time avoidance of culture suffocation conditions, due to the high level of demanded oxygen and given the process limitations in culture aeration and mixing, is a major issue that an optimal strategy should take care of. On the other hand, the role attributed by the optimiser to the second bioreactor is mainly to raise the polymer content of the bacterial population and maintain (or ideally further increase) the population density. The reported values of the optimal initial bioreactor loadings (see Table 2) and the respective optimal control trajectories displayed in Fig. 1-3 for the three operating scenarios, demonstrate this operating plan.

Table 2. Optimal initial loadings of the two bioreactors and steady-state values of state variables for the 2nd reactor unit for each continuous operating scenario.

Scenarios	$[S_{0,1}]$ (g/l)	$[N_{0,1}]$ (g/l)	$[S_{0,2}]$ (g/l)	$[N_{0,2}]$ (g/l)	$[P_2]$ (g/l)	$[X_2]$ (g/l)	$[S_2]$ (g/l)	$[N_2]$ (g/l)	$[w_{p,2}]$ (%)	$D.O_2$ (%)	$V_{l,2}$ (l)
CO1	16.14	2.28	6.61	3.19	10.36	3.68	6.93	1.10	73.78	13.79	2.50
CO2	8.20	1.31	3.06	3.10	16.08	4.69	4.51	0.99	77.40	14.95	2.50
CO3	21.90	2.84	25.00	0.02	17.12	3.39	3.73	1.07	83.43	14.30	4.50

Note that in *CO1* & *CO2* operating scenarios, different initial loadings of the first reactor unit with the nitrogen source (resulted from our capacity to adjust in addition the F_{air} and $D.O_{sp}$, in the case of *CO2*) are combined with different complementary feeding policies of this nutrient to guarantee its sufficiency in the culture medium, throughout the transition period and at the final steady state. In the second reactor unit the respective initial loadings are even larger combined though with more conservative feeding policies, since for this unit the outflow stream is held close to zero (in order to minimise the wasted carbon) and only towards the completion of the transition strategy it is raised to its steady state value. In line with this tactic is the sucrose initial loading and feeding implemented in the process. In case though of the *CO3* operating scenario, where all the available CVs are employed, the larger volume of the second reactor unit steers the optimization problem towards a totally different solution approach (see Table 2 & Fig.3). Null nitrogen initial loading in the second reactor unit is applied and its repletion in the nitrogen source is practically regulated by the outflow stream from the first reactor. It is worth of pointing out that similar to *CO1* & *CO2* in this operating scenario the optimal profile of the bioreactor outlet stream, $Q_{\text{out},2}$, is held zero throughout the transient period and only in the last time interval raises to its maximum allowed value, driving the bioreactor to the optimal steady state. Finally, it should be emphasized

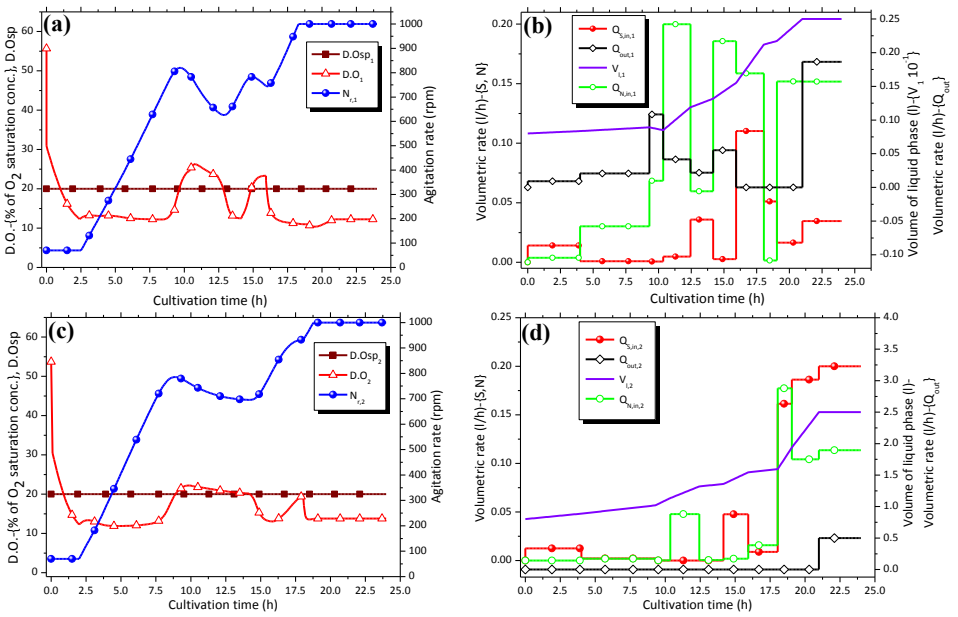

Figure 1: Dynamic transition to the optimal steady state of the 1st (a, b) and 2nd bioreactor (c, d) in a process of two continuously operating bioreactors in series under the optimized scenario *CO1*.

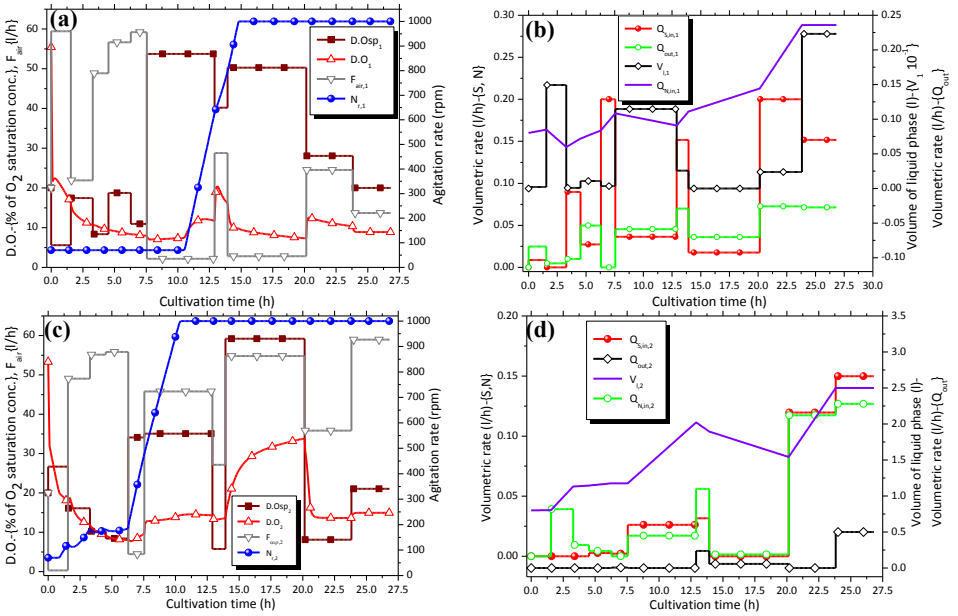

Figure 2: Dynamic transition to the optimal steady state of the 1st (a, b) and 2nd bioreactor (c, d) in a process of two continuously operating bioreactors in series under the optimized scenario *CO2*.

that the large culture needs in oxygen, restrains the optimal process performance no matter which one of the three operating scenarios is applied since in all cases, in both reactor units the agitation speed is bound to the maximum allowed value (i.e., 1000 rpm) in the final steady state, while the value of the D.O. in the culture cannot be fixed to the desired set point.

For the comparison of the three operating scenarios with respect the objective function and key performance indicators, their values are summarised in Table 3. The predominance of the operating scenario *CO3* against the other two is evident in terms of either the polymer production rate (8.56 g/h against 5.18 & 8.04 g/h) or yield or polymer content or even sucrose wasted rate ($Q_{out,2}[S_2]$). The only performance index where the *CO3* scenario is inferior is the productivity (1.9 g/(l h) against 2.07 & 3.21 g/(l h)) and this is because a larger working volume for the 2nd reactor (4.5 l) has been decided by the optimiser to increase the cells residence time and thus PHB content.

Table 3: Optimal values of objective function and individual performance indices for ***CO1-CO3***.

Scenarios	$Q_{out,2}$ (l/h)	$[P_2]Q_{out,2}$ (g/h)	$Q_{out,2}[S_2]$ (g/h)	$\int Q_{out,2}[S_2]dt$ (g)	*Productivity* (g/(l h))	*Yield* (g/g)	t_f (h)	*Obj* (-)
CO1	0.5	5.18	3.46	3.46	2.07	0.62	22.0	12.33
CO2	0.5	8.04	2.25	5.01	3.21	0.62	25.6	15.44
CO3	0.5	8.56	1.86	5.43	1.90	0.74	28.5	16.54

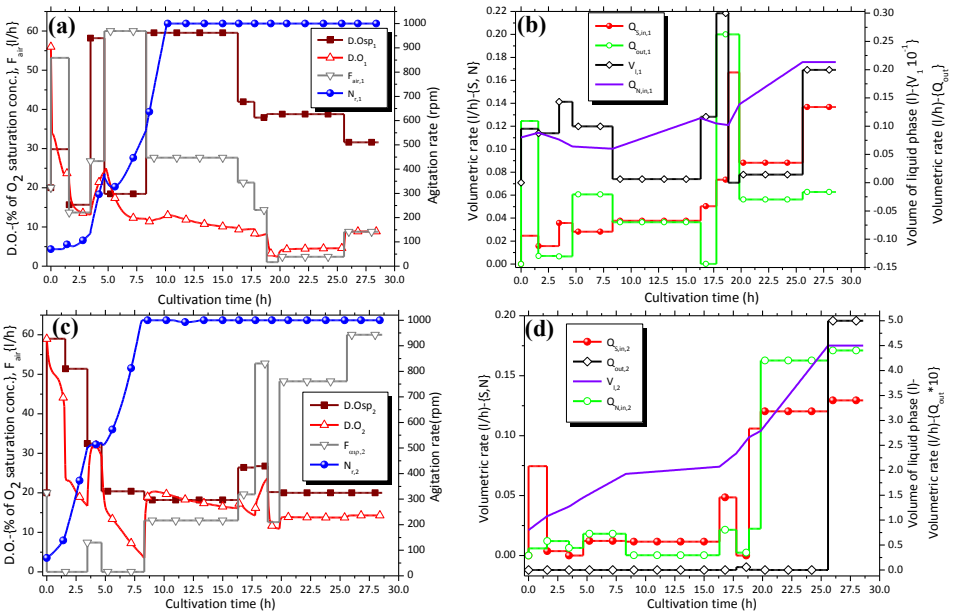

Figure 3: Dynamic transition to the optimal steady state of the 1st (a, b) and 2nd bioreactor (c, d) in a process of two continuously operating bioreactors in series under the optimized scenario *CO3*.

5. Conclusions

In the present study, a highly non-linear, sophisticated and validated dynamic mathematical model of *A. lata* bacterial culture was employed to develop a systematic optimization methodology and launch an innovative continuous PHB production strategy. For the first time, a configuration of two stirred tank bioreactors in series was modelled and optimized under three different policies seeking for the optimal steady state in terms of key process factors such as productivity, biopolymer content and final product concentration, which explicitly reflect prosperous financial indexes of the process operation. It was demonstrated that the decision of this optimal steady state is in essence not a matter of identifying the final optimal steady-stated culture conditions, but of dynamically optimising the system's operation during the transition from the initial loading and inoculation of the two reactor units up to the point where the process performance is stable (i.e., a steady state has been reached). The most promising among these strategies enabled the system operation at steady state values of PHB concentration and intracellular content in the outflow stream equal to 17.12 g/L and 83.43 % wt., respectively and a minimum substrate loss rate of 1.86 g/h. The proposed operating strategy is a strong evidence of the potential of continuous production processes of PHAs, of their restrictions and their capacity to help towards the commercial advancement of PHAs.

References

S. Spierling, E. Knüpffer, H. Behnsen, M. Mudersbach, H. Krieg, S. Springer, S. Albrecht, C. Herrmann, H. J. Endres, 2018, J. Cleaner Product. 185, 476-491
M. Koller, K. Maršálek, M.M. de Sousa Dias, G. Braunegg, 2017, N. Biotechnol. 37, 24-38.
C. Chatzidoukas, G. Penloglou, C. Kiparissides, 2013, Biochem. Eng. J., 71, 72-80.
A. Papapostolou, E. Karasavvas, C. Chatzidoukas, 2019, Biochem. Eng. J., 148, 224-238.

Sauro Pierucci, Flavio Manenti, Giulia Bozzano, Davide Manca (Eds.)
Proceedings of the 30th European Symposium on Computer Aided Process Engineering (ESCAPE30), May 24-27, 2020, Milano, Italy.
http://dx.doi.org/10.1016/B978-0-12-823377-1.50283-4

Modelling Ontologies for Biorefinery Processes - A Case Study

Robert Pujan,[a,b] * Roy Nitzsche,[a] Jakob Köchermann,[a] Heinz A. Preisig[b]

[a]*DBFZ Deutsches Biomasseforschungszentrum gemeinnützige GmbH, Torgauer Straße 116, 04347 Leipzig, Germany*
[b]*NTNU Norwegian University of Science and Technology, Høgskoleringen 5, 7491 Trondheim, Norway*
robert.pujan@dbfz.de

Abstract

This study introduces the systematic modelling approach of "visual modelling" to biorefinery processes by applying it to a concept from the demonstration project *KomBiChem*^{PRO}. The process consists of a hydrothermal conversion of hemicellulose-derived oligo sugars into monomeric C5 sugars, combined with purification steps of adsorption and nanofiltration. The experimental studies determine on model effluents hydrothermal conversion kinetics, adsorption isotherms and kinetics, as well as separation efficiencies of the nanofiltration. The paper shows an efficient graphical representation of the process topology, which is combined with an equation ontology.
Keywords: process modelling, ontology, topology, biorefinery

1. Motivation

Research and development in modern biorefinery concepts require the combination of multiple disciplines such as physics, biology, chemistry, and engineering. Correspondingly, one has to utilise the same large pool of interdisciplinary expertise when designing biorefinery models. That is a collection of fundamental principles, relations, and definitions taken from the different scientific roots - an equation ontology. Introducing the ontology- and topology-based approach to biorefinery modelling minimises modeller-caused errors and enables rapid design. The modelling suite *ProMo*, currently in development at the NTNU (Elve and Preisig, 2017), implements this approach. *ProMo* also compiles the equations into several target languages and generates with the help of a graph-based reasoner executable program code based on the user-defined topology. Due to this, the modeller has to only focus on the structural design. This paper presents the systematic modelling methodology implemented in *ProMo* and provides a first equation ontology for the discussed process. As a biorefinery-representative example, one of the concepts developed in the demonstration project *KomBiChem*^{PRO} is used. The model's performance is out of the scope of this methodology paper and will be assessed in a future study.

2. The process concept

Within a lignocellulose biorefinery, a pulping process separates the biomaterial into its main components cellulose, hemicellulose, and lignin. Due to relatively mild process conditions and easy to recover solvents, organosolv pulping with ethanol-water is a promising technology (Laure et al., 2014). During this pulping, a process stream rich in oligomeric and monomeric sugars, as well as other hemicellulose degradation products accrues - the so-called hemicellulose hydrolysate (HH). This stream is currently not

recovered due to its low concentration and inhomogeneity. However, utilizing the HH can be important for making lignocellulose processes economic feasible. Therefore, a part of *KomBiChem*^{PRO} focused on the development of processes for the hemicellulose conversion into C5 sugars for further processing. The result is the process concept shown in Figure 1, designed for the valorization and purification of xylose from HH. The process removes via adsorption residual lignin and its phenolic degradation products from the HH, which would otherwise cause impurities and inhibitors downstream. A continuous hydrothermal process hydrolyses the oligomeric xylose in the HH to monomeric xylose, while keeping the yield of products, like furfural and acetic acid, low. Finally, membrane nanofiltration removes furans and carboxylic acids from the treated solution and increases the concentration of xylose up to 12 %.

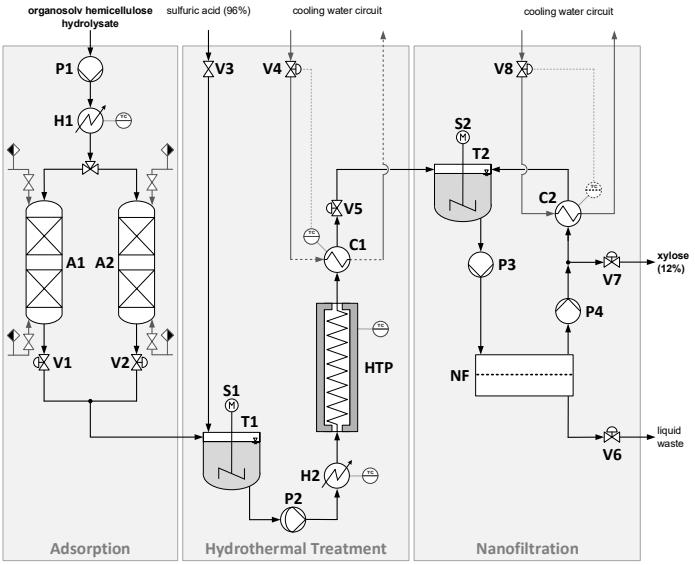

Figure 1: The exemplary process concept from *KomBiChem*^{PRO}

3. Experimental methods

While fundamental process parts like pipes, pumps, and heat exchangers can be modelled by theoretical methods, complex processes often require models to be fitted to experimental data. This paragraph discusses the experiments conducted for this purpose.

3.1. Adsorption

Batch experiments were carried out on the resin *SEPABEADS SP700* (*Mitsubishi Chemical Corporation*) to determine adsorption isotherms and kinetics. A binary-component model solution consisting of 3.1 g/L phenol and 4.2 g/L xylose was used. Detailed information of experimental setup, analytics, isotherm modelling, and preliminary desorption studies are given by Nitzsche et al. (2019). The adsorption of phenol and xylose is best described by the extended Freundlich isotherm in the model feed (Table 1, Eq. (37)). Hence, multi-layer adsorption, with non-uniform distribution of adsorption heat and affinities, seems to be predominant (Nitzsche et al., 2019).

3.2. Hydrothermal treatment

Hydrothermal conversion was performed in a continuous coiled tube reactor using HH with 70 g/L xylose as real substrate. To determine the best conditions, experiments

covered different reaction temperatures (160, 180, 200 °C) and residence times of 2.5 to 23 min. A back pressure valve at the reactor outlet regulated the process to 50 bar. The reaction model found best-fitting is represented in Eq. (1)-(4). The experiments are comprehensively described by Köchermann et al. (2018) and (2019).

$$\dot{c}_{Xos} = -k_0 c_{Xos} \quad (1)$$

$$\dot{c}_{Xy} = k_0 c_{Xos} - k_1 c_{Xy} \quad (2)$$

$$\dot{c}_{Int} = k_1 c_{Xy} - k_2 c_{Int} - k_3 c_{Int} c_{Fu} \quad (3)$$

$$\dot{c}_{Fu} = k_2 c_{Int} - k_3 c_{Int} c_{Fu} - k_4 c_{Fu} \quad (4)$$

3.2.1. Nanofiltration

The experimental set-up consisted of an *Alfa Laval LabStak M20* plate-and-frame membrane module, an *Alfa Laval NF* flat-sheet membrane, a feed tank, a diaphragm pump, and a shell-and-tube heat exchanger. A model solution of 50 g/L xylose, 6 g/L glucose, 2 g/L furfural, and 8 g/L acetic acid was used. In parameter screenings, transmembrane pressure (10-40 bar), temperature (25-55 °C) and cross-flow velocity v_z (0.5-1.5 m/s) were varied at pH = 2.5 and in total reflux mode. 40 bar, 25 °C, and 1.1 m/s were identified to be appropriate. The permeate flux J (Table 1, Eq. (24)) was measured by collecting permeate for 1 min at predetermined time intervals. With feed, retentate, and permeate samples (10 mL), the component concentrations c_i and the observed retention R_{obs} (Eq. (5)) were determined. At the appropriate process parameters and a filtration area A_M of 0.036 m², a J of 78.1 L/(m²h) and R_{obs} of 100 % for glucose, 93.6 % xylose, 14.1 % furfural, and 2.4 % acetic acid were achieved. 70 % of the feed solution was transferred into the permeate, yielding 20 g/L glucose, 159 g/L xylose, 2.7 g/L furfural, and 8.5 g/L acetic acid in the retentate. The average frictional pressure drop $\Delta p_{f,av}$, determined according to Jönsson et al. (2009), is 1.18 bar.

$$R_{obs} = \left(1 - {c_{Perm}}/{c_{Feed}}\right) \cdot 100\% \quad (5)$$

4. Topology and ontology design

The topology in Figure 2 is generated based on the plant sketch in Figure 1 by applying the methods established in (Preisig, 2014). In addition to the depiction of mass and energy balances, the graph also includes a process control domain and the pressure distribution model discussed by Pujan and Preisig (2020). Due to space limitations, we place the focus on the description of the physical domain.

The model is equipped with the equation ontology presented in Table 1, covering everything from pipe flows, heat transfer, adsorption, hydrothermal reactions, nanofiltration and pressure distribution. $\underline{\underline{F}}$ is the incidence matrix of the directed graph from Figure 2, while $\underline{\underline{D}}$ and $\underline{\underline{R}}$ refer to capacity-intern transport processes and internal reactions respectively. The state vectors are written as $\underline{x}$, while a dot decorator indicates accumulation and a hat a flow. The ontology also considers heat transfer and the thermal effect of reactions. Usually, the introduction of energy as a state variable requires the Legendre transformations, linking internal energy U, enthalpy H, and Helmholtz energy. In this case however, constant volume is the modus operando in the energy-exchanging parts of the model. Thus, only U is required. To convert reaction enthalpies into U, Eq. (32) is used. Eq. (31) uses the stoichiometry $\underline{\underline{N}}$ and reaction coefficients $\upsilon_{i,r}$ found in section 3.2.

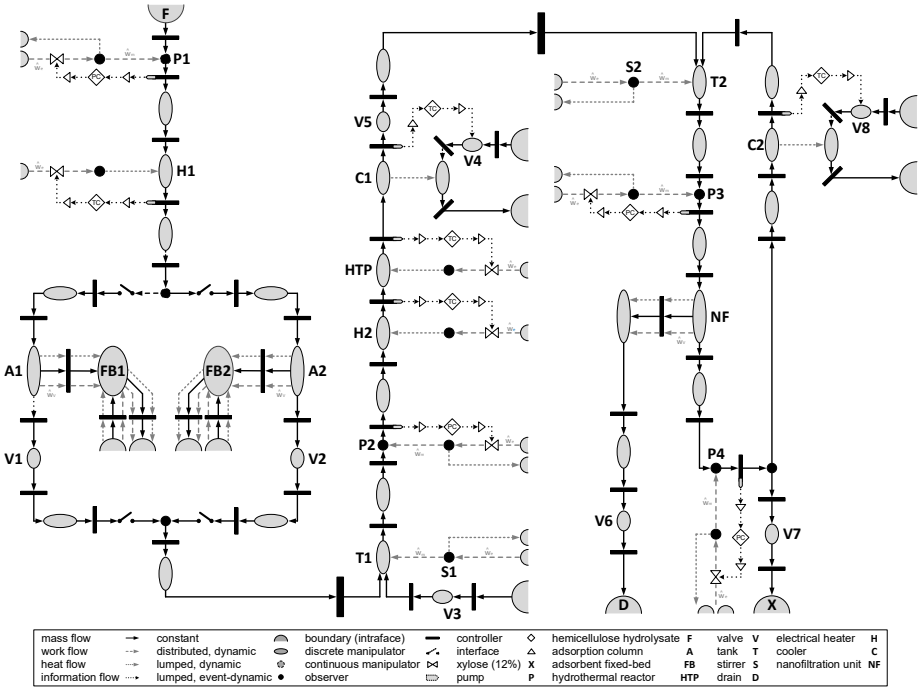

Figure 2: The initial topology of the exemplary process

Table 1: Equation ontology of the physical domain

Description	Equation	
Integrals		
Mass	$\underline{m} = \int_0^t \dot{\underline{m}}(\tau)d\tau + \underline{m}(0)$	(7)
Energy	$\underline{E} = \int_0^t \dot{\underline{E}}(\tau)d\tau + \underline{E}(0)$	(8)
Component mass	$\underline{m}_i = \int_0^t \dot{\underline{m}}_i(\tau)d\tau + \int_0^t \tilde{\underline{m}}_i(\tau)d\tau + \underline{m}_i(0)$	(9)
Component concentration	$\underline{c}_i = \int_0^t \dot{\underline{c}}_i(\tau)d\tau + \int_0^t \tilde{\underline{c}}_i(\tau)d\tau + \underline{c}_i(0)$	(10)
Balances		
Mass conservation	$\dot{\underline{m}} = \sum \dot{\underline{m}}_i$	(11)
Component conservation	$\dot{\underline{m}}_i = \underline{\underline{F}}\hat{\underline{m}}_i + \underline{\underline{D}}\hat{\underline{m}}_i^D + \underline{\underline{R}}\tilde{\underline{m}}_i$	(12)
Energy conservation	$\dot{\underline{E}} = \underline{\underline{F}}\hat{\underline{U}} + \underline{\underline{R}}\tilde{\underline{U}}_T^R + \underline{\underline{F}}\hat{\underline{K}} + \underline{\underline{F}}\hat{\underline{P}} + \underline{\underline{F}}\hat{\underline{w}}^y + \underline{\underline{F}}\hat{\underline{w}}^f$	(13)
Flows		
Mass flow	$\hat{\underline{m}} = \sum \hat{\underline{m}}_i$	(14)
Component mass flow	$\hat{\underline{m}}_i = \underline{c}_i\hat{V}$	(15)
Component adsorption	$\hat{\underline{m}}_i = \underline{m}_{Ads}\dot{\underline{q}}_i$	(16)
Diffusional flow	$\hat{\underline{m}}_i^D = \underline{J}_i^D\underline{A}$	(17)

Table 1: Equation ontology of the physical domain (continued)

Description	Equation	
Internal energy flow	$\hat{\underline{U}} = \underline{C}_V \hat{\underline{m}} \underline{T}$	(18)
Kinetic energy flow	$\hat{\underline{K}} = \frac{1}{2} \hat{\underline{m}} \underline{v}^2$	(19)
Potential energy flow	$\hat{\underline{P}} = \hat{\underline{m}} \underline{h} g$	(20)
Volume work flow	$\hat{\underline{w}}^y = \underline{p} \hat{\underline{V}}$	(21)
Friction work flow	$\hat{\underline{w}}^f = \Delta \underline{p}^f \hat{\underline{V}}$	(22)
Volume flow	$\hat{\underline{V}} = \hat{\underline{m}} \underline{\rho}^{-1}$	(23)
Permeate volume flow	$\hat{\underline{V}} = \underline{J}^{NF} \underline{A}_{Mem}$	(24)
Cross-sectional velocity	$\underline{v} = \hat{\underline{V}} \underline{A}^{-1}$	(25)
Material properties		
Cylindrical cross-section	$\underline{A} = \pi \left[\underline{r}(l) \right]^2$	(26)
Liquid level	$h_L := root[\underline{F}_L \underline{V} = \pi \int_0^{h_L} \left\{ \underline{F}_L \underline{r}(l) \right\}^2 dl]$	(27)
Voluminous property	$\underline{V} = \underline{m} \underline{\rho}^{-1}$	(28)
Component accumulation	$\dot{\underline{m}}_i = \dot{\underline{c}}_i \underline{V}$	(29)
Component transposition	$\tilde{\underline{m}}_i = \tilde{\underline{c}}_i \underline{V}$	(30)
Concentration transposition	$\tilde{\underline{c}}_i = \underline{\underline{N}}^T \underline{k} \underline{c}_i^{\lvert \underline{v}_i \rvert}$	(31)
Internal energy transposition	$\tilde{\underline{U}}_T^R = \left(\underline{C}_V \underline{C}_p^{-1} \underline{H}_m \right)_T$	(32)
Length of cylindrical body	$\underline{l} = \underline{V} \underline{A}^{-1}$	(33)
Void fraction fixed-bed	$\underline{\varepsilon} = \underline{V}_L \left(\underline{V}_L + \underline{V}_{Ads} \right)^{-1}$	(34)
Adsorption pseudo-2nd order kinetic model	$\underline{q}_i = \frac{\underline{q}_{e,i}^2 \underline{k}_{P2} t}{1 + \underline{q}_{e,i} \underline{k}_{P2} t} = \int_0^t \dot{\underline{q}}_i(\tau) d\tau + \underline{q}_i(0)$	(35)
Adsorption intra-particle diffusion kinetic model	$\underline{q}_i = \frac{3 \underline{q}_{e,i}}{\underline{d}_{Ads}} \sqrt{\frac{\underline{D}_P}{\pi}} t + \underline{B} = \int_0^t \dot{\underline{q}}_i(\tau) d\tau + \underline{q}_i(0)$	(36)
Multi-component extended Freundlich isotherm model	$\underline{q}_{e,i} = \frac{\underline{K}_{F,i} \underline{c}_{e,i}^{\underline{n}_i + \underline{x}_i}}{\underline{c}_{e,i}^{\underline{x}_i} + \underline{y}_i \underline{c}_{e,j}^{\underline{z}_j}}$	(37)
Fick's 1st law	$\underline{J}_i^D = -D_L \cdot \nabla \underline{c}_i$	(38)
Darcy-Weisbach model	$\Delta \underline{p}^f = \frac{1}{2} \underline{f}^i \underline{v}^2 \underline{\rho} \underline{l} \left[2 \underline{r}(l) \right]^{-1}$	(39)
Friction factor (laminar)	$f^i := f^{la} = 64 \,\mathrm{Re}^{-1}$ if $\mathrm{Re} \le 2{,}100$;	(40)
Friction factor (turbulent)	$f^i := f^t = f(\mathrm{Re}, \in)$ if $\mathrm{Re} > 2{,}100$	(41)
Reynolds number	$\mathrm{Re} = 2 \rho v r(l) \eta^{-1}$	(42)

Pujan and Preisig (2020) discuss extensively how to derive a reduced plant model from the ontology. Substituting Eq. (7), (9)-(12), (14)-(17), (25), (26), (29) and (33)-(38), as well as common assumptions, yields for example the mass balance for the fixed-bed adsorption in Eq. (6):

$$\dot{c}_i = D_L \frac{\partial^2 c_i}{\partial z^2} - v_z \frac{\delta c_i}{\delta z} - \rho_{Ads} \frac{(1-\varepsilon)}{\varepsilon} \dot{q}_i \tag{6}$$

5. Conclusions

Based on experimental studies and the process flowsheet, a model design was performed by applying the systematic methodology. This study shows that the introduced methodology enables rapid process modelling, also for multi-disciplinary, complex biorefinery processes like the one discussed. At this point, only assumptions, initial and boundary conditions to the ontology equations, and the implementation of a numerical solver are required, what will be the focus of future work to conclude with model fitting and a simulation study.

Acknowledgments

The process concept as well as the experiments were conducted as part of the demonstration project *KomBiChem*^{PRO}, funded by the *German Federal Ministry of Education and Research* (*BMBF*) under the grant number FKZ 031B0083B. The modelling was executed within the research centre *Bio4Fuels*, funded by the *Research Council of Norway* (*RCN*) under the support code 257622.

References

A.T. Elve, H.A. Preisig, 2019, From ontology to executable program code, Comput. Chem. Eng., 122, 383-394

A.-S. Jönsson, O. Wallberg, 2009, Cost estimates of kraft lignin recovery by ultrafiltration, Desalination, 237, 254-267

J. Köchermann, J. Mühlenberg, M. Klemm, 2018, Kinetics of Hydrothermal Furfural Production from Organosolv Hemicellulose and D-Xylose, Ind. Eng. Chem. Res., 57, 14417-14427

J. Köchermann, J. Schreiber, M. Klemm, 2019, Conversion of d-Xylose and Hemicellulose in Water/Ethanol Mixtures, ACS Sustain. Chem. Eng., 7, 12323-12330

S. Laure, M. Leschinsky, M. Fröhling, F. Schultmann, G. Unkelbach, 2014, Assessment of an organosolv lignocellulose biorefinery concept based on a material flow analysis of a pilot plant, Cell. Chem. Technol., 48, 793–798

R. Nitzsche, A. Gröngröft, M. Kraume, 2019, Separation of lignin from beech wood hydrolysate using polymeric resins and zeolites – Determination and application of adsorption isotherms, Sep. Purif. Technol., 209, 491-502

H.A. Preisig, 2014, Visual Modelling, Comput. Aided Chem. Eng., 34, 729-734

R. Pujan, H.A. Preisig, 2020, Systematic Modelling of Flow and Pressure Distribution in a Complex Tank, Proceedings of the 30th European Symposium on Comput. Aided Process Eng.

Sauro Pierucci, Flavio Manenti, Giulia Bozzano, Davide Manca (Eds.)
Proceedings of the 30th European Symposium on Computer Aided Process Engineering (ESCAPE30), May 24-27, 2020, Milano, Italy.
http://dx.doi.org/10.1016/B978-0-12-823377-1.50284-6

Life Cycle Assessment for Carbon Balance of a Wastewater Treatment Integrated Microalgae Biofuel Production Process

Peiyao Li,[a] Xigang Yuan, [a,b,c]*Yiqing Luo[a,c]

[a]*School of Chemical Engineering and Technology, Tianjin University, Tianjin 300350, China*
[b]*State Key Laboratory of Chemical Engineering, Tianjin University, Tianjin 300350, China*
[c]*Chemical Engineering Research Center, Tianjin University, Tianjin 300350, China*
yuanxg@tju.edu.cn

Abstract

Recent technology advances in carbon fixation via microalgae have shown increasing potentials in reducing net greenhouse gas emission. Carbon in the greenhouse gas is assimilated by photosynthesis in algal cell during the cultivation process, which can be carried out in wastewater environment as an alternative to conventional fertilizer feedstock-based processes. To improve the environmental performance of microalgae biofuel production process as well as increase the efficiency of nutrient biomass uptake in microalgae activities, the carbon balance is investigated by using the Life Cycle Assessment (LCA) for a separated nutrient delivery configuration in this study. In the proposed configuration, sewage sludge from wastewater treatment segment is reclaimed as supporting mediums to improve microalgae biogas production and a stream of pretreated nutrient-enriched wastewater is introduced to high rate algal ponds to satisfy the demand of microalgae-derived lipid productivities. Combined with the downstream process converting algal biomass into biofuel, the system termed as wastewater treatment integrated microalgae biofuel production process is formed. Our analysis showed the advantage of the separated nutrient delivery configuration in improving microalgae carbon fixation performance and the environmental impact of the biofuel production process. In the analysis, the mass and energy balances are achieved by process simulation, and the background data are taken from available databases and the literature. The LCA results show that the system proposed in this work can generate biofuel in energy self-sufficient condition with the carbon fixation effect.

Keywords: microalgae biofuel; life cycle assessment; wastewater treatment; carbon fixation

1. Introduction

Microalgae has been regarded as a promising approach to address climate change and greenhouse effect because of the carbon fixation capability in the microalgae photosynthesis activities (Enamala et al. 2018). Attempts to develop algal biomass conversion technologies and biofuel products to utilize the rich content of lipids, carbohydrates and proteins in algal cells as a cleaner and lower carbon footprint algal biofuel have been reported (Maria et al. 2019). However, the current technical pathways of microalgae biofuel production are in the limitation of nutrient resources from

ecological system. To address this challenge, nutrient loaded wastewater has been introduced to microalgae cultivation system as an alternative of make-up nutrient fertilizers to satisfy nutrient demands of algae culture.

As reported by Whitton et al. (Whitton et al. 2016), algae species are in high nutrient removal capacity of wastewater via biomass uptake to algal cells. Besides, lipid content and lipid accumulation rate of algae species could be regulated and controlled by adjustment of nutrient ratio. However, the wastewater-based microalgae cultivation is in risk of low nutrient recovery potentials. The previous researches have mainly focused on microalgae culture processes and the profitability in environmental impacts of wastewater integration to reduce eutrophication, whereas the issue of greenhouse gas (GHG) emissions improvement of the wastewater-integrated microalgae production design has been barely discussed.

Inspired by the work of de Wilt et al. (de Wilt et al. 2016) concerning different technological pathways of integration with algae cultivation for wastewater collected from different sources loaded with different concentrations of nutrient contents, the separated nutrient delivery configuration we proposed for the analysis are shown in figure 1. This configuration includes the primary and secondary treatment of wastewater, tertiary microalgae treatment, biomass conversion and combined heat and power unit. Municipal wastewater and urine influents are treated via microalgae from different pathways. To show the potential advantages of the separated nutrient delivery design in improving microalgae carbon fixation performance, the Life Cycle Assessment (LCA) method is employed in this study to make assessments on the environmental impacts of the integrated biofuel production process. The mass and energy balances are achieved by process simulation software Aspen Plus v8.6, and the background data are taken from Ecoinvent3.5 Database(Frischknecht 2011) and the literatures.

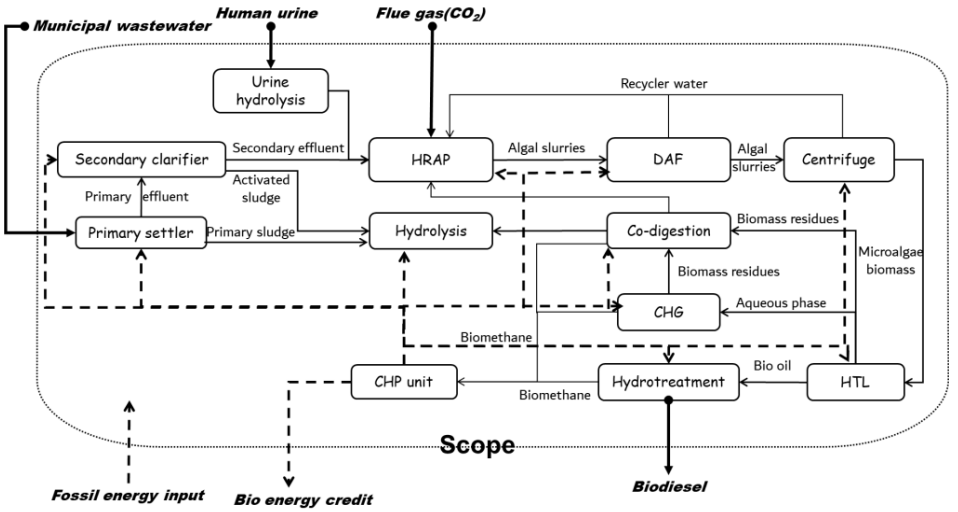

Figure 1 Configuration of the WWTP integrated microalgae biofuel production process.

2. Methods

2.1. Lifecycle inventory (LCI)

2.1.1. LCA goal, scope and function unit

The goal of this study is to reveal the potential impacts of source-separated nutrient delivery strategy to carbon balances in wastewater treatment integrated with microalgae biofuel production process. The GHG emissions of each part in the whole process is quantified as the output of LCI results. Besides, the LCA scope is from gate to gate, which includes the primary and secondary treatment of wastewater, algal tertiary treatment, algal biomass harvesting conversion, combined heat and power unit. The function unit in this LCA study is 1 MJ energy.

The main parameters of lifecycle inventory are shown in Table 1.

2.1.2. Lifecycle impact assessment

ReCiPe(Huijbregts et al. 2017) method is introduced in this study to evaluate global warming potentials (GWP). The GHG emission results, associated with the 100-year global warming equivalence factors, which, for carbon dioxide, methane and nitrogen oxide is 1,34 and 298 in turn, are involved to calculate the GWP index in g $CO2_{-eq}$ MJ^{-1}. This midpoint impacts in ReCiPe could explicitly show the GHG emissions of each section in the wastewater-microalgae integration process. In the analysis, the mass and energy balances are achieved by process simulation via Aspen Plus 8.6 software, and the background data are taken from Ecoinvent3.5 database(Wernet et al. 2016) and literatures.

Table 1: Background data of wastewater treatment integrated microalgae biofuel production process

Sub-process	Parameter	Value	Units
Cultivation			
Growth	Pond circulation energy	1.42	kwh·ha^{-1}
	Biomass productivity	25	g·m^{-2}·day^{-1}
	Cultivation Area	2000	ha
Harvest/Dewatering			
Bio flocculation	Biomass concentration	2%	wt.%
Dissolved air flotation	Biomass concentration	6%	wt.%
Centrifuge	Biomass concentration	20%	wt.%
Conversion & Upgrading			
Hydrothermal Liquefaction (HTL)	Bio-oil yield	35%	wt.%
Catalytic Hydrothermal Gasification (CHG)	Biogas yield	4%	wt.%
Hydrotreating	Diesel yield	61.90%	wt.%
	Naphtha yield	12.10%	wt.%
	Biogas yield	9.10%	wt.%
Combined Heat &Power Unit (CHP)	Electricity	35	%
	Heat	12	%
Primary wastewater treatment			
Primary settler	Electricity demand	0.00441	kwh·m^{-3}
Urine precipitation	Electricity demand	0.0004	kwh·m^{-3}
Pumping	Electricity demand	0.5	kwh·m^{-3}
Secondary wastewater treatment			
Secondary settler	Electricity demand	0.00252	kwh·m^{-3}
Thermal hydrolysis	Heat demand	0.000108	kwh·m^{-3}
Digester	Heat demand	0.0417	kwh·m^{-3}
	Electricity	0.015	kwh·m^{-3}

2.2. Scenario design

The plant layout of our study is partly based on the baseline assumptions of the carbon delivery engineering model given by Somers and Quinn (Somers and Quinn 2019). This study underlies the integration design with wastewater treatment to utilize separated alternative nutrient resources from municipal wastewater and urine instead of make-up nutrient. Primary and secondary treatment of wastewater are designed in this study as the upstream sub-processes of the whole process, biomass harvesting and dewatering, biomass conversion and upgrading, and combined heat and power unit in this study are designed as the downstream sub-processes of the whole process.

2.2.1. Primary and secondary treatment

In the primary treatment, hydrolyzed urine is mixed with primarily treated municipal wastewater as nutrients feedstock to supplement microalgae cultivation in high rate algae ponds (HRAPs). The primary treatment settles down the girds suspended in municipal wastewater influent and the primary influent is then further clarified in the secondary settler to remove sludge. The sewage sludge from primary and secondary settlers go through thermal hydrolysis and then enters anaerobic digestor to generate biogas, which is composed of CH_4 and CO_2 that could be utilized in combined heat and power unit to generate heat.

2.2.2. Algae tertiary treatment

Microalgae *Galdieria sulphuraria* biomass productivity in HRAPs is 25 $g \cdot m^{-2} \cdot day^{-1}$ with nutrient contents from wastewater influent and CO2 supply from flue gas injection. The HRAPs with paddle wheel circulation in electricity demand of 1.42 $kw \cdot ha^{-1}$, for on-site material flow, the pumping energy demand is 1.6 kJ kg^{-1}, for flue gas delivery is 37.1 $kJ \cdot kg^{-1}$.

2.2.3. Algae biomass harvesting and conversion

Algae harvesting and dewatering in this study is achieved by the state of art technology: bio-flocculation-dissolved air flotation-centrifuge. The biomass separation efficiencies of the three sections in algae harvesting and dewatering are 90 %, 95 %, and 95 % respectively, and the harvested biomass concentrations are 2 %, 6 % and 20 % (wt) respectively. The concentrated biomass is converted to bio oil via hydrothermal liquefaction (HTL), and then upgraded by hydrotreatment to generate final products: biodiesel and naphtha fuel. According to Somers and Quinn (Somers and Quinn 2019), the energy demand of HTL is 3 $kJ \cdot kg^{-1}$ AFDW algae. Slurries dehydrated from algal harvesting and dewatering are reclaimed to HRAPs to recover nutrients and freshwater. The gas co-generated with fuel products is sent to the combined heat and power unit to generate heat and electricity.

3. Results and discussion

3.1 Carbon balance results

Carbon balance relationship is based on the mass and energy balance relationship of the process configuration in this study. The results show that unit GHG emissions of the whole process are 0.09357 $kgCO2\text{-}eq. \cdot MJ^{-1}$, and 0.1913 $kgCO2\text{-}eq. \cdot MJ^{-1}$ GHG assimilation in function unit, so the unit credit of GHG emissions 0.09773 $kgCO2\text{-}eq. \cdot MJ^{-1}$ of GHG emissions credit, as shown in Table 2. The result in the carbon credit shows that although the downstream biomass harvesting, biomass dewatering, biomass conversion and upgrading are carbon-discharging processes, the carbon balance in our study comes across the neutral point and to reach positive carbon credit, in other words,

the process of the designed separated nutrient delivery configuration in this study could significantly reduce carbon emissions to environment. Comparing to GHG emissions reported in LCA research on conventional wastewater treatment (Rodriguez-Garcia et al. 2012), the microalgae-based wastewater treatment is notably more sustainable to ecosystem.

Table 2 :GWP results of wastewater treatment integrated microalgae biofuel production process.

Sub-process	**Unit GHG emissions / $kgCO_2$-eq. $\cdot MJ^{-1}$**
Cultivation	3.1681E-02
Harvest/Dewatering	5.1888E-04
Conversion & Upgrading	2.4665E-02
Primary WWTP	3.5529E-02
Secondary WWTP Electricity	1.2031E-03
Unit GHG emission	9.3597E-02
Unit GHG assimilation	1.9133E-01
Unit GHG credit	9.7737E-02

For the wastewater pretreatment, primary treatment is the biggest contributor to the GHG emissions, approximately 0.03553 kgCO2-eq.$\cdot MJ^{-1}$. The high carbon emission is the result of the highest fossil energy demand in wastewater influent pumping, which leads directly to the increase of the carbon emission. The secondary treatment only contributes less than 8 % of total GHG emissions, and the co-digestion of sludge and microalgal residues is accounted for a lower GHG emission, as it converts the organic carbon in sludge and algal residues to the biogas by co-digestion. Comparing to conventional secondary treatment of wastewater such as aerobic or anoxic digestion (Bonton et al. 2012), the separated nutrient recovery in secondary treatment in this study is significantly more sustainable. Among the downstream sub-processes, the biomass conversion and upgrading is the biggest fossil energy consumer, it generates thus approximately 27 %, the highest, of the total GHG emissions.

3.2 Separated nutrient delivery strategy impacts to carbon balance

Comparing to the high GHG emissions 0.40-1.18 kgCO2-eq.$\cdot MJ^{-1}$ of conventional treatment reported (Bonton et al. 2012), the separated nutrient delivery shows significantly more sustainable due to positive carbon credit result. Compared with sole source of nutrient delivery of microalgae-wastewater integration process presented in literature (Colzi Lopes et al. 2018), 0.1322 kgCO2-eq.$\cdot MJ^{-1}$of the separated nutrient delivery is lower than the reported 0.1947 kgCO2-eq.$\cdot MJ^{-1}$. The comparison results show the advantages of separated-nutrient delivery not only in improving sustainability performance of wastewater treatment, but also in microalgae biofuel production.

In LCA methodology, the GHG emission could be divided into two categories: direct GHG emissions and indirect GHG emissions. The separated nutrient delivery strategy proposed in this study reduces GHG emissions by recycling the direct and indirect GHG emissions. Direct GHG emissions, which is composed of bioCH_4 and bioCO_2, is generated from co-digestion and biomass conversion and upgrading. BioCO_2 is recovered by HRAPs as carbon resource for microalgae cultivation and bioCH_4 is recycled in CHP unit for energy supply. As for the indirect GHG emissions discharged by fossil energy usage of the whole system as flue gas, although unavoidable, it could be recycled and assimilated by microalgae in HRAPs.

4. Conclusion

In this study, we employed the LCA methodology to show the effectiveness of a separated nutrient delivery configuration of wastewater treatment integrated microalgae biofuel production in improving microalgae carbon fixation performance and the environmental impact of the biofuel production process. The LCA result shows that the primary treatment of wastewater is a major contributor to the carbon emission, and the carbon emission of secondary treatment could be significantly reduced by separated nutrient delivery design. Even though the carbon emission of the downstream process of biofuel production could not be avoided, the carbon utilization in the wastewater-based microalgae cultivation could make the carbon balance come across a neutral point achieving a positive effect in carbon credit.

References

Bonton, Alexandre, Christian Bouchard, Benoit Barbeau, and Stéphane Jedrzejak, 2012, Comparative Life Cycle Assessment of Water Treatment Plants, Desalination, 284, 42-54

Colzi Lopes, Alexandre, Antonio Valente, Diego Iribarren, and Cristina González-Fernández, 2018, Energy Balance and Life Cycle Assessment of a Microalgae-Based Wastewater Treatment Plant: A Focus on Alternative Biogas Uses, Bioresource Technology, 270, 138-146

Enamala, Manoj Kumar, Swapnika Enamala, Murthy Chavali, Jagadish Donepudi, Rajasri Yadavalli, Bhulakshmi Kolapalli, Tirumala Vasu Aradhyula, Jeevitha Velpuri, and Chandrasekhar Kuppam, 2018, Production of Biofuels from Microalgae - A Review on Cultivation, Harvesting, Lipid Extraction, and Numerous Applications of Microalgae, Renewable and Sustainable Energy Reviews, 94, 49-68

Huijbregts, Mark A. J., Zoran J. N. Steinmann, Pieter M. F. Elshout, Gea Stam, Francesca Verones, Marisa Vieira, Michiel Zijp, Anne Hollander, and Rosalie van Zelm, 2017, ReCiPe2016: A Harmonised Life Cycle Impact Assessment Method at Midpoint and Endpoint Level, International Journal of Life Cycle Assessment, 22, 2, 138-147

Maria Solé-Bundó, Fabiana Passos, Maycoll S. Romero-Güiza, Ivet Ferrera, Sergi Astalsd, 2019, Co-digestion strategies to enhance microalgae anaerobic digestion: A review, Renewable and Sustainable Energy Reviews, 112, 471–482

Rodriguez-Garcia, G., A. Hospido, D. M. Bagley, M. T. Moreira, and G. Feijoo, 2012, A Methodology to Estimate Greenhouse Gases Emissions in Life Cycle Inventories of Wastewater Treatment Plants, Environmental Impact Assessment Review, 37, 37-46

Somers, Michael D. and Jason C. Quinn, 2019, Sustainability of Carbon Delivery to an Algal Biorefinery: A Techno-Economic and Life-Cycle Assessment, Journal of CO2 Utilization, 30, 193-204

Wernet, Gregor, Christian Bauer, Bernhard Steubing, Jürgen Reinhard, Emilia Moreno-Ruiz, and Bo Weidema. 2016, The Ecoinvent Database Version 3 (Part I): Overview and Methodology, The International Journal of Life Cycle Assessment, 21, 9, 1218–1230

Whitton, Rachel, Amandine Le Mével, Marc Pidou, Francesco Ometto, Raffaella Villa, and Bruce Jefferson, 2016, Influence of Microalgal N and P Composition on Wastewater Nutrient Remediation, Water Research, 91, 371-378

de Wilt, Arnoud, Andrii Butkovskyi, Kanjana Tuantet, Lucia Hernandez Leal, Tânia V. Fernandes, Alette Langenhoff, and Grietje Zeeman, 2016, Micropollutant Removal in an Algal Treatment System Fed with Source Separated Wastewater Streams, Journal of Hazardous Materials, 304, 84–92

Sauro Pierucci, Flavio Manenti, Giulia Bozzano, Davide Manca (Eds.)
Proceedings of the 30th European Symposium on Computer Aided Process Engineering (ESCAPE30), May 24-27, 2020, Milano, Italy.
http://dx.doi.org/10.1016/B978-0-12-823377-1.50285-8

Economics of Climate Change: a Sensitivity Analysis Study Applied to Integrated First- and Second-Generation Ethanol Biorefinery

Roymel R. Carpio[a,*], Simone C. Miyoshi[b], Andrew M. Elias[b], Felipe F. Furlan[b], Roberto C. Giordano[b], Argimiro R. Secchi[a]

[a]*Chemical Engineering Program, Universidade Federal do Rio de Janeiro (UFRJ), Rio de Janeiro - RJ, 21941-914, Brazil*
[b]*Chemical Engineering Department, Universidade Federal de São Carlos (UFSCar), São Carlos - SP, 13565-905, Brazil*
roymel@peq.coppe.ufrj.br

Abstract

According to the Brazilian federal program called Renovabio, biofuels producers will earn a number of carbon credits, known as CBios, proportionally to the reduction of greenhouse gases emissions. These CBios will be sold by biorefineries to fuel distributors in Brazil. Thus, the environmental performance will have a direct impact on the economic profitability of the biorefinery. In this work we compared the sensitivity of the overall economic performance for ten key parameters of the second generation ethanol process, considering the current conditions and future scenarios with additional incomes of CBios selling. The most influent parameters for all scenarios were hydrolysed bagasse fraction, enzyme loading and pre-treatment solid fraction. The relative relevance of parameters does not change when considered the CBios selling incomes, but the absolute relevance of the hydrolysed bagasse fraction decreases significantly, especially for the optimist CBios price. The residence times of hydrolysis, pre-treatment and fermentation, and the xylose concentration have negligible effects for both current and future scenarios.

Keywords: Sugarcane biorefinery, sensitivity analysis, economical and environment evaluation.

1. Introduction

In a low-carbon economy and increasing energy demanding society, concerns about climate change and energy security are shifting the global energy matrix towards renewable energy technologies. In Brazil, as result of Paris agreement (COP 21, 2016), a federal program called Renovabio was issued. Thus, carbon credits, called CBios, will be sold by biofuels producers and the environmental performance will have an impact on the economic evaluation of the process.

Sugarcane biorefineries play an important role in this economic scenario due to the production of biofuel and bioelectricity. The quantification of how the application of Renovabio Program will affect the relative importance of operational parameters in an integrated first and second generation ethanol Biorefinery has not been sufficient assessed yet. Therefore, this work compares the sensitivity of the overall economic performance for ten key parameters of the second generation ethanol process, considering the current conditions and a future scenario with the additional incomes of CBios selling.

2. Methodology

2.1. Process modelling and simulation

The biorefinery was modelled based on a standard autonomous Brazilian distillery, with a process capacity of 500 t/h of sugarcane. The modelled biorefinery can produce first generation ethanol (E1G) from sugarcane juice, second-generation ethanol (E2G) from bagasse, and electricity from residues in an integrated process. The process data used in the base case simulation were based on Carpio et al. (2019). A simplified process diagram is presented in Figure 1.

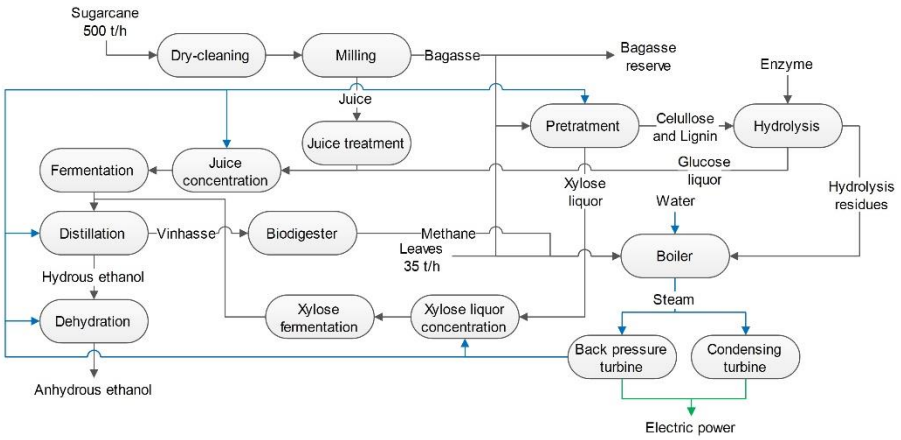

Figure 1. Simplified process diagram of the integrated biorefinery.

The bagasse obtained after milling is diverted into two fractions. The first one is fed in the boiler and the second one is used for E2G production. The bagasse diverted to E2G production undergoes a liquid hot water pre-treatment. After that, the liquid fraction, rich in xylose is separated from the solid fraction containing the cellulose. The xylose liquor is used for ethanol production by fermentation. On the other hand, the solid fraction containing cellulose is fed to the enzymatic hydrolysis. The coupling of the kinetic model of Angarita et al. (2015) into the whole steady-state simulation was made as described in Carpio et al. (2018).

After hydrolysis period, the solid fraction (mostly lignin) is sent to the boiler and the liquid fraction (glycose liquor) is mixed to the 1G treated juice and undergoes the traditional stages of E1G. The cogeneration system includes a boiler, a back-pressure turbine and a condensing one, and produces steam and electricity to supply process demands. The electricity surplus is sold to the grid. EMSO software (Soares and Secchi, 2003) was used to perform the modelling and simulation of the biorefinery.

2.2. Economic analysis

The economic analysis was also implemented in EMSO, coupled to the process model. This allows instant calculation of economic indexes for any feasible operational condition simulated, without requiring external or auxiliary sheet calculations. The main economic premises considered in this study are shown in Table 1.

The capital cost (CAPEX), operating costs (OPEX), cash flows (CF) and net present value (NPV) were calculated based on the methodology of Peters et al. (2003). The main

equipment purchase costs were estimated from industrial information (personal communication) and the literature (Humbird et al., 2011).

Table 1. Main premises considered in the economic analysis

Parameter	Value	Reference
Ethanol selling price (US$/m^3$)	584.61	MAPA (2018)
Electricity selling price (US$/MWh)	71.19	CCEE (2018)
CBios selling price (US$/CBio)	10 / 30	Conservative/Optimist estimates
Sugarcane costs (US$/t)	22.15	UDOP (2018)
Leaves cost (US$/t)	15	Bechara et al. (2016)
Enzyme cost (US$/kg)	1.25	Bechara et al. (2016)
Fresh water cost (US$/t)	0.06	Bechara et al. (2016)
Refrigeration cost (US$/kW)	0.04	Bechara et al. (2016)
Operation time (h/year)	4732	Furlan et al. (2013)
Project life time (years)	25	Longati et al. (2018)
Construction period (years)	2	Furlan et al. (2013)
Tax Rate (%)	34	Longati et al. (2018)
Discount rate (%)	10	Bechara et al. (2016)
Depreciation strategy (%/year)	10	Longati et al. (2018)

2.3. Life cycle assessment (LCA)

The Life Cycle Assessment considered the climate change impact category using the Global Warming Potential under a horizon of 100 years – GWP 100 (Myhre et al., 2013). It was performed an inventory of inputs, outputs and emissions based on process simulation and ethanol agricultural data (Seabra et al., 2011) under a cradle to grave scope. The characterization factor data base considered was IPCC (2006) for emissions in fuels burning and agricultural emissions and the Ecoinvent 3.1 (Wernet et al., 2016) database for raw materials inputs. The applied allocation method was energy based and the bagasse, as it is an agricultural residue, was considered to have zero emission as input. The quantity of CBios was determined by the annual tonnes of CO_2 equivalent savings of ethanol compared with gasoline.

2.4. Sensitivity analysis

A global sensitivity analysis was performed applying the modified method of Morris (Campolongo et al., 2007) with 200 trajectories and 8 levels. Ten parameters of E2G process were chosen as input variables, as shown in Table 2. Since E2G process is not fully developed, all selected parameter are related to different subareas of this process.

Table 2. Parameter considered in the sensitivity analysis

Parameter	Range	Parameter	Range
1 Hydr. bagasse fraction (wt %)	10-50	6 Pre-treat. yield (%)	40-60
2 Hydr. enzyme loading (FPU/g)	10-30	7 Pre-treat. residence time (min)	10-20
3 Hydr. solid fraction (wt %)	10-20	8 Xylose concentration (g/L)	40-60
4 Hydr. residence time (h)	48-72	9 Xylose ferment. yield (%)	60-80
5 Pre-treat. solid fraction (wt %)	10-20	10 Ferment. residence time (h)	12-24

3. Results and discussion

The indices μ, μ^*, e σ were calculated as described in Campolongo et al. (2007). The impact of opposite signs in the elementary effects, which may occurs when the model is

non-monotonic, were negligent, i.e., $|\mu| \approx \mu^*$. Thus, the measure μ can be used without affecting the factors' ranking. Figure 2 shows the results of the sensitivity analysis of NPV without considering CBios selling.

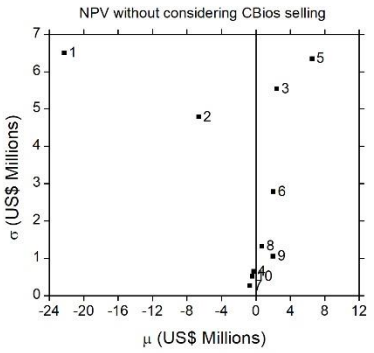

Figure 2. Result of the sensitivity analysis of NPV without considering CBios selling.

The parameter hydrolysed bagasse fraction (P1) has the greatest impact on NPV (highest absolute value of μ). The negative sign indicates an inversely proportional behaviour of NPV to P1, i.e., the NPV decreases as P1 increases. This behaviour may suggests that, in the studied configuration, it is more advantageous to produce electric energy (a larger proportion of bagasse going to cogeneration) than E2G.

The sensitivity of NPV to pre-treatment solid fraction (P5) and hydrolysis enzyme loading (P2) is approximately the same, being these parameters in the second place of importance. Nevertheless, they have opposite signs and consequently, an increase on P5 or/and a decrease on P2 will improve the NPV. All the cited parameters have nonlinear effects or/and interactions represented by the high value of σ.

The sensitivity analysis also indicates which parameters have non-significant effects. In this case, the influence of parameters residence times of hydrolysis (P4), pre-treatment (P7) and fermentation (P10), and xylose concentration (P8) on NPV is practically negligible. This information provides feedback to R&D teams, indicating the parameters which the efforts should focus on.

The results for the future scenarios, which consider additional incomes due to CBios selling, are shown in Figure 3. Two sale prices (conservative and optimist) of CBios were used.

When considered the additional incomes from CBios selling, the relative importance of the parameters does not change significantly, but it is notable that the absolute relevance of the hydrolysed bagasse fraction (P1) decreases sensibly, especially when the optimist price of CBios is used. This behaviour is caused by the trade-off between the economic and environmental performance, thus the CBios incomes tend to compensate the sensitivity of NPV on hydrolysed bagasse fraction.

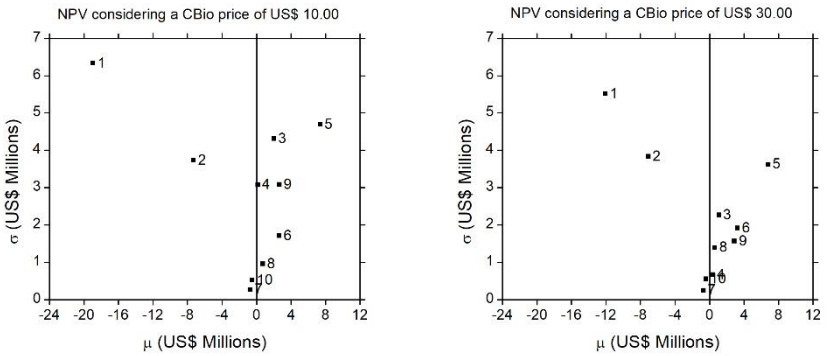

Figure 3. Result of the sensitivity analysis of NPV considering CBios selling.

4. Conclusions

For all scenarios, the most influent parameter is the hydrolysed bagasse fraction, showing a high sensitivity of NPV to 2G ethanol and bioelectricity production. When the higher CBios price is considered, the environmental impact of E2G production reduces significantly the effect of the bagasse fraction on economic results. These results indicate that the decision towards ethanol 2G and bioelectricity production has a key conflicting impact on both environmental and economic aspects: an improve on the NPV frequently implies an increase on the environmental impact of the E1G2G process.

The relative relevance of the analysed parameters does not change significantly when considered the implementation of Renovabio Program with two different CBios prices. Nevertheless, the absolute relevance of the hydrolysed bagasse fraction decreases significantly, particularly when the higher price of CBios is considered. Some parameters such as residence times of hydrolysis, pre-treatment and fermentation, and xylose concentration have negligible effects on NPV for both current and future scenarios.

Acknowledgements

Financial support from FAPERJ (grant #E012018-236117), FAPESP (grants #2017/13993-9, #2014/21252-0 and #2016/10636-8), and CAPES (finance Code 001) are gratefully acknowledged.

References

J. Angarita, R. Souza, A. Cruz, E. Biscaia, A. Secchi, 2015, Kinetic modeling for enzymatic hydrolysis of pretreated sugarcane straw, Biochemical Engineering Journal, 104, 10-19.

R. A. Bechara, A. Gomez, V. Saint-Antonin, J.-M. Schweitzer, F. Maréchal, 2016, Methodology for the optimal design of an integrated first and second generation ethanol production plant combined with power cogeneration, Bioresource Technology, 214, 441-449.

F. Campolongo, J. Cariboni, A. Saltelli, 2007, An effective screening design for sensitivity analysis of large models, Environmental Modelling & Software, 22, 1509-1518.

R. R. Carpio, F. F. Furlan, R. C. Giordano, A. R. Secchi, A kriging-based approach for conjugating specific dynamic models into whole plant stationary simulations, 2018, Computers & Chemical Engineering, 119, 190-194.

R. R. Carpio, R. C. Giordano, A. R. Secchi, 2019, Optimization of an Integrated First- and Second-Generation Ethanol Production Plant with Focus on Hydrolysis Parameters, Computer Aided Chemical Engineering, 46, 241-246.

CCEE, 2018, Public auction electricity prices, Electric Energy Commercialization Chamber, www.ccee.org.br.

F. F. Furlan, R. T. Filho, F. H. Pinto, C. B. Costa, A. J. Cruz, R. L. Giordano, R. C. Giordano, 2013, Bioelectricity versus bioethanol from sugarcane bagasse: is it worth being flexible?, Biotechnology for Biofuels, 6 (1), 142.

D. Humbird, R. Davis, L. Tao, C. Kinchin, D. Hsu, A. Aden, P. Schoen, J. Lukas, B. Olthof, M. Worley, D. Sexton, D. Dudgeon, 2011, Process design and economics for biochemical conversion of lignocellulosic biomass to ethanol, Tech. rep., NREL/TP-5100-47764.

IPCC. 2006 IPCC guidelines for national greenhouse gas inventories: v. 2-3 agriculture, forestry and other land use and industrial processes and product use. Prepared by the National Greenhouse Gas Inventories Programme, Eggleston H.S., Buendia L., Miwa K., Ngara T., and Tanabe K. Japan: IGES, 2006.

G. Myhre, D. Shindell, F.M. Bréon, W. Collins, J. Fuglestvedt, J. Huang, D. Koch, J.F. Lamarque, D. Lee, B. Mendoza, T. Nakajima, A. Robock, G. Stephens, T. Takemura and H. Zhang, 2013, Anthropogenic and Natural Radiative Forcing. In: Climate Change 2013: The Physical Science Basis. Contribution of Working Group I to the Fifth Assessment Report of the Intergovernmental Panel on Climate Change [Stocker, T.F., D. Qin, G.-K. Plattner, M. Tignor, S.K. Allen, J. Boschung, A. Nauels, Y. Xia, V. Bex and P.M. Midgley (eds.)]. Cambridge University Press, Cambridge, United Kingdom and New York, NY, USA. https://www.ipcc.ch/site/assets/uploads/2018/02/WG1AR5_Chapter08_FINAL.pdf

A. A. Longati, A. R. Lino, R. C. Giordano, F. F. Furlan, A. J. Cruz, 2018, Defining research & development process targets through retro-techno-economic analysis: The sugarcane biorefinery case, Bioresource Technology, 263, 1-9.

MAPA, 2018, Brazilian annual ethanol exports, Ministry of Agriculture, Cattle and Supply, www.agricultura.gov.br.

M. S. Peters, K. D. Timmerhaus, R. E. West, 2003, Plant design and economics for chemical engineers, 5th Edition, Vol. 5, McGraw-Hill.

J.E. Seabra, I.C. Macedo, H.L. Chun, C.E. Faroni, C.A. Sarto, 2011, Life cycle assessment of Brazilian sugarcane products: GHG emissions and energy use. Biofuels Bioprod. Bioref. 5, 519-532. https://doi.org/10.1002/bbb.289

R. P. Soares, A. Secchi, 2003, EMSO: A new environment for modelling, simulation and optimisation, Computer Aided Chemical Engineering, Vol. 14, pp. 947-952.

G. Wernet, C. Bauer, B. Steubing, J. Reinhard, E. Moreno-Ruiz, B. Weidema, 2016, The ecoinvent database version 3 (part I): overview and methodology. The International Journal of Life Cycle Assessment, 21(9), 1218-1230. http://doi.org/10.1007/s11367-016-1087-8

UDOP, 2018, Sugarcane prices, Union of Biofuel Producers, www.udop.com.br.

Sauro Pierucci, Flavio Manenti, Giulia Bozzano, Davide Manca (Eds.)
Proceedings of the 30th European Symposium on Computer Aided Process Engineering (ESCAPE30), May 24-27, 2020, Milano, Italy.
http://dx.doi.org/10.1016/B978-0-12-823377-1.50286-X

Assessing Parameter Relative Importance in Bioprocesses Mathematical Models through Dynamic Sensitivity Analysis

Julio Cesar Sánchez-Rendón [a], Ricardo Morales-Rodriguez [b], Luis Gerónimo Matallana-Pérez[c], Oscar Andrés Prado-Rubio [a*]

[a]*Departamento de Ingeniería Química, Universidad Nacional de Colombia, Km 9 vía al Aeropuerto La Nubia, 170003, Colombia.*
[b]*Departamento de Ingeniería Química, División de Ciencias Naturales y Exactas, Campus Guanajuato, Universidad de Guanajuato, Noria Alta S/N, Guanajuato, Gto. 36050, México*
[c]*Departamento de Ingeniería, Facultad de Ingeniera, Universidad de Caldas, Cl. 65 #26-10, Manizales, 170004, Colombia*
oaprador@unal.edu.co

Abstract

Fast global population growth has imposed an increasing demand for feedstock, food, energy and commodities; therefore, the industries are in constant development to optimize their processes. From the Process System Engineering (PSE) perspective this problem could be addressed employing mathematical models that describe the processes behaviour. However, it is common that mathematical models have parameters that must be estimated from experimental data, leading to the propagation of experimental uncertainty into the model. Several methods have been designed and used for uncertainty quantification and sensitivity analysis over the whole model output. In this work, the Standardized Regression Coefficient method has been applied for quantification of parameter relative importance profiles (PRIP) along the simulation time. The results show that parameter importance changes dynamically and the relevance of one parameter could be different for different state variables, which gives insights of the relevant processes taking place at one specific point in time. This methodology could also be used in experimental design and data selection to improve parameter estimation and parameter interpretability.

Keywords: mathematical models, bioprocess, parameter estimation, uncertainty analysis, sensitivity analysis.

1. Introduction

The fast-growing world population imposes an increasing demand on feedstock, food, energy and commodities (Jones & O'Neill, 2016). Therefore, industries are constantly under pressure to optimize and upgrade technology in order to have safer, cleaner, environmentally friendly and more profitable production to cope with the demand. From Process System Engineering (PSE) perspective, process optimization and more recently process intensification offer a systematic way to address the above-mentioned challenge (Prado-Rubio *et al*., 2016). Current methodologies highly rely on process models and system understanding, in order to achieve a substantial breakthrough in technology design and operation. Thus, there is a constant need to improve process mathematical models towards developing high fidelity representations with high parameter significance. This

task is particularly complex for bioprocesses due to the lack of process understanding and diverse sources of uncertainty.
In literature, there are several methods for quantifying the effect of uncertainty has over the model output such as differential sensitivity analysis, sensitivity index, subjective sensitivity analysis, the importance index, relative deviation methods, factorial design methods and regression methods (Hamby, 1994). Typically, sensitivity analysis has been applied to the whole model output, as like a stationary state, but the following question arises: is the importance of a parameter the same throughout the simulation time? Or does it changes dynamically according to the model dynamics? Therefore, this paper aims to identify and analyze the parameter relative importance over the simulation time, in order to identify the impact related with the physical interpretation, aiming to improve the process performance.

2. Methodology

2.1. Mathematical model

Xylitol is a highly versatile molecule with several uses like dental creams, sweeteners, pharmaceutics compounds, dietary supplements and has even been pointed out as a chemical building block for chemical or biochemical industries (Prado-Rubio *et al*., 2015). For this reason, the mathematical model of diauxic xylitol production from glucose and xylose proposed by Tochampa *et al.*,(2015) was analyzed. The experimental data used for parameter estimation was extracted from Sirisansaneeyakul *et al*. (2013).

2.2. Parameter estimation

The particle swarm optimization algorithm found in the Global optimization Toolbox of Matlab was used to obtain the parameter values of the above mentioned mathematical model. Additionally, these optimization algorithm was calibrated using the "IRACE" package available in R software.

2.3. Experimental design

To explore the sensitivity of the mathematical model to perturbations in its parameters it is necessary to analyze the totality of the parameter space of the mathematical model, considering all the possible combinations of parameter values. However, it is required an experimental design that leads to a finite set of experimental points that represent the whole parameter space. One approach to solve this problem consist in Latin Hypercube Sampling method (LHS) (Sheikholeslami & Razavi, 2017), followed by a Monte Carlo simulation to obtain the output of the models due to parameter perturbations.

2.4. Sensitivity analysis

Regression methods are often used to represent the complex behavior of the system in a simplified way through a response surface (Hamby, 1994). This representation is simply a regression equation that approximates the model output using only the most sensitive model parameters. Commonly the regression equation is of the form:

$$Y = b_0 + \sum_{i=1}^{p} b_i Z_i \tag{1}$$

where Z_i is predictor variable and a function of the parameters, b_i are the regression coefficients. The equation (1) corresponds to multiple linear regression. This technique allows the calculation of the sensitivity ranking based on the relative magnitude of the regression coefficients. These values are a measure of the amount of influence that a parameter has on the whole model output. However, because of differences in the numeric scale of the parameters, a standardization process is required. Standardized Regression Coefficients (SRC) (Morales-Rodriguez *et al*., 2012) then uses the standard deviation of the model output σ_y and the standard deviation of the uncertain parameters σ_{θ_i} according to the following equation:

$$B_i = \left(\frac{\sigma_{\theta_i}}{\sigma_Y} \right) b_i \tag{2}$$

3. Results and discussion

The parameter values obtained for the diauxic fermentation model for xylitol are listed in Table 1 and the model fitting is shown in Figure 1. Even though the glucose is consumed first, the growth of the biomass appears to be in a latent state, only when the glucose has been completely consumed the xylose is actively consumed by the microorganism as expected of a diauxic fermentation. However, the growth in the presence of xylose overcome this latent state and the exponential growth phase begin.

Table 1. Estimated parameter values for diauxic fermentation model for xylitol production

Parameter	Estimated value	Parameter	Estimated value
$\mu_{glu}^{\max}$	0.01907 h^{-1}	$q_{xyl}^{\max}$	0.23987 g xylose/DWG h
$\mu_{xyl}^{\max}$	0.99999 h^{-1}	$q_{glu}^{\max}$	1.81202 g glucose/DWG h
$K_{S,glu}$	2.38313 g/L	$K_{i,xyl}$	13.3963 g/L
$K_{S,xyl}$	0.02636 g/L	$K_{i,glu}$	0.00558 g/L
$K_{S,xyt}$	0.93634 g/L	P_{xyl}	9.5185×10^{-9} m/s
K_r	0.46133 g/L		

The global sensitivity of the diauxic fermentation model is shown on Figure 2. The bars represent the dispersion of the model output due to aleatory changes up to 25% in the model parameters. The uncertainty in the model output increase with time, except for glucose concentration. This is because both, the initial and the final state of this variable, are well known as the glucose is completely depleted before the active consumption of xylose. On the other hand, xylitol concentration has the mayor effect of uncertainty, this could be due to the high interaction of this molecule with the other metabolites through the metabolic pathway represented by the model.

The dynamic sensitivity analysis was performed on a diauxic fermentation model for xylitol production. This analysis was carried out through the calculation of the SRC in each experimental point, thought it could be done at any part of the integration time. This led to a profile of relative importance of the parameter in the model for that specific point. The calculated profiles are shown in Figures 3-5. A positive value in PRIP indicates that a parameter contributes to increase the variable value and vice versa.

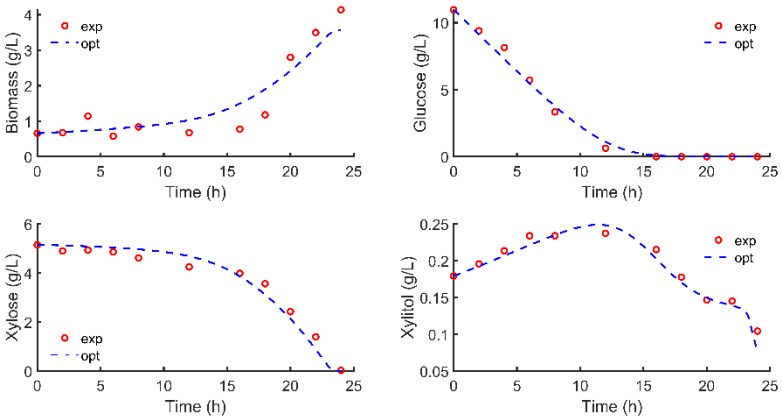

Figure 1. Diauxic fermentation model fitting to experimental data with particle swarm algorithm in MATLAB.

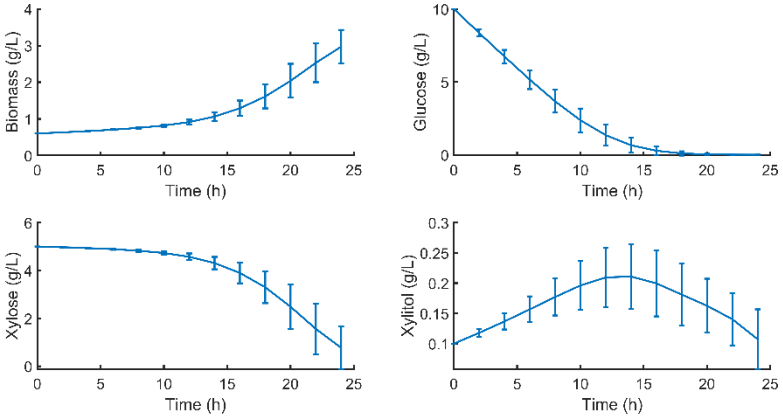

Figure 2. Uncertainty analysis with aleatory combinations of parameter values with LHS.

Figure 3 shows the effect to $\mu_{glu}^{\max}$, $\mu_{xyl}^{\max}$, $K_{S,glu}$ and $K_{S,xyl}$ on the system states. For biomass concentration, $\mu_{glu}^{\max}$ was the most important parameter with a relative weight of 1 at the beginning of simulation time but this value dropped at 12 h of fermentation when the glucose was completely depleted of the system. For the case of glucose concentration, the most important parameter was $K_{S,glu}$ whose value increased slowly through simulation time, the remainder parameters were not explanatory for this state. For xylose concentration $K_{S,glu}$ and $K_{S,xyl}$ were the most relevant parameters and exhibit a shift in their value when glucose was depleted, indicating metabolic shift required for a change in the substrate uptake. Interestingly, the dynamic behavior of these parameters showed to have influence in the model output even after the first substrate is consumed, indicating the high interaction between parameters within the model. In the case of xylitol concentration, $\mu_{xyl}^{\max}$ and $K_{S,xyl}$ were the most relevant since xylose is consumed for biomass growth.

Fig 4 shows the PRIP for $K_{S,xyt}$, K_r, $q_{glu}^{\max}$ and $q_{xyl}^{\max}$. For the four state variables, $q_{glu}^{\max}$ and $q_{xyl}^{\max}$ are the most significant parameters as expected, since the substrates uptake are the fuel for the metabolic engine. K_r and $K_{S,xyt}$ are also important for xylitol concentration, as they are related to xylitol consumption for biomass production after glucose depletion.

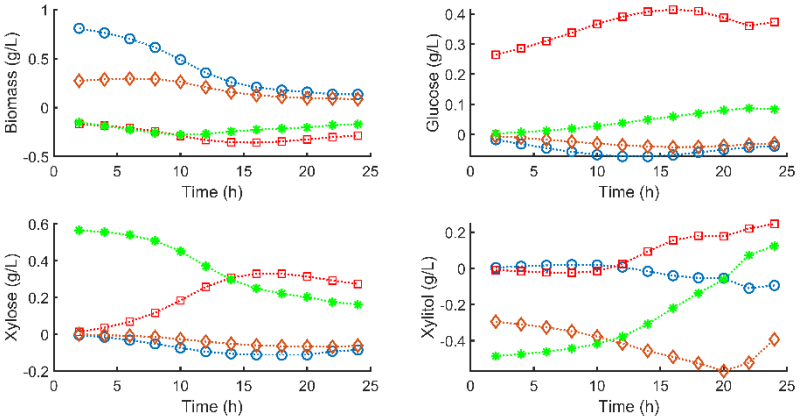

Figure 3. PRIP for $\mu_{glu}^{\max}$ (O), $K_{S,glu}$ (□), $\mu_{xyl}^{\max}$ (◊), $K_{S,xyl}$ (*)

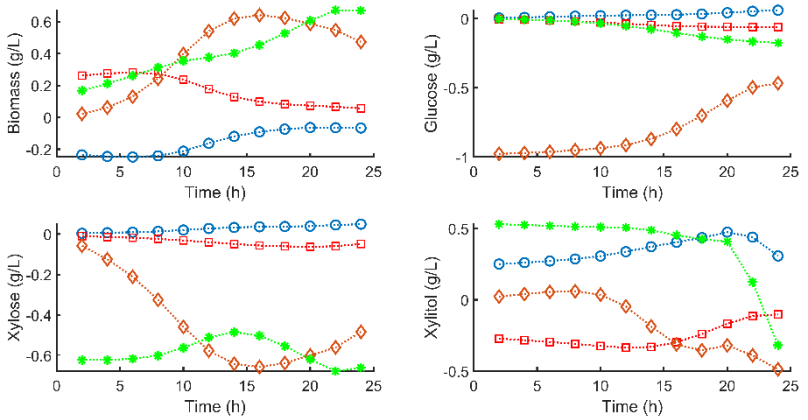

Figure 4. PRIP for $K_{S,xyt}$ (O), K_r (□), $q_{glu}^{\max}$ (◊), $q_{xyl}^{\max}$ (*)

Fig 5 shows the relative parameter importance profiles for $K_{I,glu}$ $K_{I,xyl}$ and PIt can be seen that these parameters are not relevant for biomass and glucose states but $K_{I,glu}$ is relevant for xylose and xylitol states. Once again, there is a shift in the parameter relevance after glucose depletion. $K_{I,glu}$ is relevant because it is linked to biomass production and represents the effect of the internal switch between glucose and xylose metabolism uptake(Lebeau *et al*., 2007).

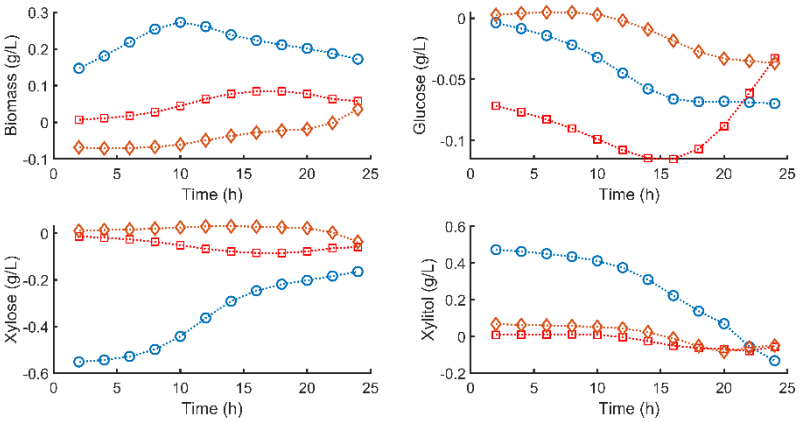

Figure 5. PRIP for $K_{i,glu}$ (O), $K_{i,xyl}$ (□), P_{xyl} (◊).

4. Conclusions

The relative parameter importance profiles shown in this work contradict the hypothesis that the influence of a certain parameter inside a mathematical model remains constant during the simulation time. Also, these results lead to a deeper level of understanding of the behavior of the system with the phenomena described by the mathematical model, thereby, improving parameter interpretability. Additionally, this methodology could be extended to be used in experimental design and data selection to optimize the information packed in the parameters, to analyze the model structure and then improve model accuracy.

References

Hamby, D. M. (1994). A review of techniques for parameter sensitivity analysis of environmental models. Environmental monitoring and assessment, 32(2), 135-154.

Jones, B., & O'Neill, B. C. (2016). Spatially explicit global population scenarios consistent with the Shared Socioeconomic Pathways. Environmental Research Letters, 11(8), 084003.

Lebeau, T., Jouenne, T., & Junter, G. A. (2007). Long-term incomplete xylose fermentation, after glucose exhaustion, with Candida shehatae co-immobilized with Saccharomyces cerevisiae. Microbiological Research, 162(3), 211-218.

Morales-Rodriguez, R., Meyer, A. S., Gernaey, K. V., & Sin, G. (2012). A framework for model-based optimization of bioprocesses under uncertainty: Lignocellulosic ethanol production case. Computers & Chemical Engineering, 42, 115-129.

Prado-Rubio, O.A., Morales-Rodriguez, R., Andrade-Santacoloma, P., Hernández-Escoto, H. (2016). "Process Intensification in Biotechnology Applications". In book "Process Intensification in Chemical Engineering", J.G. Segovia-Hernández, A. Bonilla-Petriciolet (eds.). Springer editorial ISBN: 978-3-319-28392-0. pp. 183-219.

Sheikholeslami, R., & Razavi, S. (2017). Progressive Latin Hypercube Sampling: An efficient approach for robust sampling-based analysis of environmental models. Environmental modelling & software, 93, 109-126.

Sirisansaneeyakul, S., Wannawilai, S., & Chisti, Y. (2013). Repeated fed- batch production of xylitol by Candida magnoliae TISTR 5663. Journal of Chemical Technology & Biotechnology, 88(6), 1121-1129.

Tochampa, W., Sirisansaneeyakul, S., Vanichsriratana, W., Srinophakun, P., Bakker, H. H., Wannawilai, S., & Chisti, Y. (2015). Optimal control of feeding in fed-batch production of xylitol. Industrial & Engineering Chemistry Research, 54(7), 1992-2000.

Sauro Pierucci, Flavio Manenti, Giulia Bozzano, Davide Manca (Eds.)
Proceedings of the 30th European Symposium on Computer Aided Process Engineering
(ESCAPE30), May 24-27, 2020, Milano, Italy.
http://dx.doi.org/10.1016/B978-0-12-823377-1.50287-3

Multi-objective Optimization of Co-processing of Bio-oil and Vacuum Gas Oil: a Survey of Gasoline Selling Price and Bio-oil Co-processing Ratio

Le Wu*, Zhaowei Qi, Yuqi Wang, Lan Zheng

School of Chemical Engineering, Northwest University, Xi'an 710069, China
lewu@nwu.edu.cn

Abstract

The prices of the bio-diesel and bio-gasoline are generally higher than those of petroleum based fuels. The co-processing of bio-oil and vacuum gas oil in a fluid catalytic cracker has been proposed to utilize the existing refinery infrastructures and decrease the prices of bio-fuels. According to our previous study, the techno-economic analysis of the co-processing process, there is a contradiction between the minimum gasoline selling price and bio-oil co-processing ratio. In this work, the relations between the two factors (objectives) are investigated via a multi-objective optimization. Two co-processing scenarios, fast pyrolysis scenario using fast pyrolysis make bio-oil and catalytic pyrolysis scenario adopting catalytic pyrolysis produce bio-oil, are proposed to obtain the trade-off solution between the two objectives using the evaluation function method. The minimum gasoline selling price is approximately \$3.1/gal if 20% bio-oil is co-processed for the two scenarios. The price is only about \$1.9/gal if the bio-oil ratio is 1%. The trade-off solution between the two objectives is strongly depended on the weight factor. Therefore, the relation and the compromise between the bio-oil co-processing ratio and the minimum selling price should be considered and determined before the co-processing technology industrializes.

Keywords: Co-processing, Multi-objective optimization, Bio-oil co-processing ratio, Minimum selling price

1. Introduction

The co-processing of bio-oil and vacuum gas oil (VGO) in a fluid catalytic cracker (FCC) to transportation fuels has been proposed for a decade to lower the production cost of bio-fuels (Bui et al. 2009). The modeling and analysis of the co-processing process has gained increased attention in recently years (Al Jamri et al. 2018 and 2019). Cruz et al. (2017) proposed a kinetic model for the co-processing in FCC. Wu et al. (2019a) built a superstructure model to obtain the optimal integration process between the bio-oil production process and the existing refining process. The techno-economic analysis of the co-processing product was carried out to attain the minimum selling price (MSP) of co-processing product, gasoline (Wu et al. 2019b). Furthermore, the sensitivity analysis was also conducted to investigate the effects of relevant parameters on MSP. It was found that there is a contradiction between the MSP and bio-oil co-processing ratio. A higher MSP as well as a higher bio-carbon content of gasoline would be obtained if more bio-oil and less VGO were co-processed. That is to say, a higher bio-carbon content of co-processing product usually has a higher price. Thus, the best compromise and the trade-off between the bio-carbon content i.e. bio-oil co-processing ratio and the price should be determined when design the process.

In this work, a multi-objective model is proposed to investigate the relation between the bio-oil co-processing ratio and MSP of co-processing product for the co-processing of bio-oil and VGO in an FCC. The evaluation function method is used to obtain the trade-off solution between the two objectives. The effect of the weight factor on trade-off solution is also discussed.

2. Mathematical model

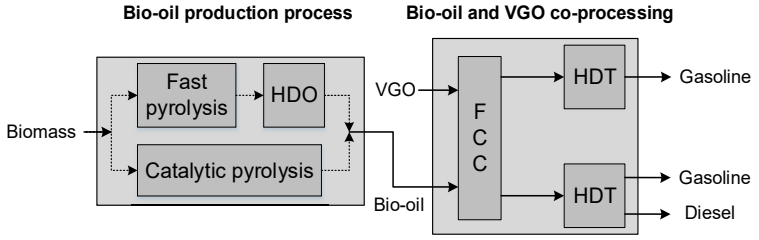

Figure 1 The co-processing flowsheet

According to Figure 1, the biomass is pyrolysised by a fast pyrolysis (FP) or a catalytic pyrolysis (CP) to produce bio-oil. The fast pyrolysis bio-oil is hydrotreated to remove extra oxygen impurities in a hydrodeoxygenation reactor (HDO). The obtained catalytic pyrolysis oil or the HDO bio-oil is then co-fed with VGO into an FCC to make gasoline and diesel with bio-carbon, which are hydrotreated in hydrotreators(HDT).

2.1. Objective functions

The main purpose of this work is to investigate the relations between the minimum selling price (MSP) of the co-processing product gasoline and the bio-oil co-processing ratio. Thus, the objectives are directly set as the minimization of the minimum gasoline selling price and the maximization of the bio-oil co-processing ratio as more bio-carbon would be detected in the products if more bio-oil were co-processed with VGO in an FCC.

$$\min MSP \tag{1}$$

where MSP denotes the minimum selling price of gasoline, in \$/gal.

The calculation of the MSP of gasoline is mainly according to our previous work (Wu et al. 2019b), which contains the mass balance and energy balance of the co-processing process, capital investment, operating cost, net present value (NPV), internal interest of rate (IRR) and double declining balance (DBB) for depreciation. The relevant equations are not shown in this work due to the page limitation.

$$\max BCR \tag{2}$$

where BCR is the bio-oil co-processing ratio, in %.

2.2. Constraints

The constraints in this work are the mass balance, which is shown as follows:

$$\sum_i m_i^{\text{in}} = \sum_j m_j^{\text{out}} \tag{3}$$

$$m_j^{\text{out}} = \sum_j \sum_i m_i^{\text{in}} y_j \tag{4}$$

where m is the mass flowrate of a stream, in t/h; Subscripts i and j denote the i^{th} inlet streams and the j^{th} outlet stream of a device; Superscripts in and out represent the inlet and outlet streams, respectively.

2.3. Trade-off between the MSP of gasoline and the bio-oil co-processing ratio

For a multi-objective optimization problem, each optimal solution on the Pareto fronts can be considered as the trade-off solution of the two objectives. The evaluation function method is used to obtain the trade-off solution. The summation of all the weight factors equals to one. The minimum value of u^s is the trade-off solution.

$$u_o^s = \left(f_o^s - f_o^{\min}\right) \Big/ \left(f_o^{\max} - f_o^{\min}\right) \tag{5}$$

$$u^s = \sum_o \varpi_o u_o^s \tag{6}$$

where u denotes the value of the evolution function; f is the value of the objective function; Superscript s, min and max are the s^{th} solution, the minimum solution and the maximum solution, respectively; Subscript o represents the o^{th} objective function; ω is the weight factor.

3. Case study

3.1. Basic data

The bio-oil and VGO are co-processed in an FCC with annual processing capability of 1.2 million tonnes. Different bio-oil co-processing ratio are used to obtain the corresponding minimum selling price (MSP) of gasoline. Two scenarios are proposed, as there are two bio-oil production technologies, fast pyrolysis and catalytic pyrolysis. Pulpwood is used as the biomass feedstock to make bio-oil. The product yields for the related processes (Wu et al. 2019b) are listed in Table 1.

Table 1 Yields for pyrolysis, FCC and HDT processes

Yield/%	FP	FP oil HDT	CP	FCC	Gasoline HDT	Diesel HDT
Bio-oil	52.5	/	33.0	/	/	/
Bio-gas	26.0	/	53.0	/	/	/
Bio-char	21.5	/	12.5	/	/	/
HDO oil	/	66.0	/	/	/	/
Gasoline	/	/	/	48.1	99.5	7.6
Diesel	/	/	/	23.0	/	91.2

3.2. Optimal results of fast pyrolysis scenario

3.2.1. Pareto fronts of fast pyrolysis scenario

The Pareto fronts of the bio-oil co-processing ratio and MSP of gasoline are shown in Figure 2. The MSP is increased with the increase of the bio-oil co-processing ratio. The MSP is \$3.08/gal when 20% bio-oil is co-processed while the MSP is only \$1.9/gal when the bio-oil co-processing ratio is 1%. That is to say, the co-processing product, gasoline, can be competed with the petroleum-based gasoline even the bio-oil ratio is

20%. The reason for the only \$1.9/gal gasoline is that the capital costs of the refinery existing infrastructures, FCC and hydrotreators, are ignored.

According to the breakdown of the gasoline price shown in the right figure of Figure 2, the raw material VGO contributes the largest proportion while the biomass is the least part. The tax takes about 40% to the price as the tax rate is set to 39%. The annual capital cost is strongly linked to the bio-oil co-processing ratio as the ratio decides the capital costs of the pyrolysis process and the HDO process, which are the only capital costs considered in the co-processing system.

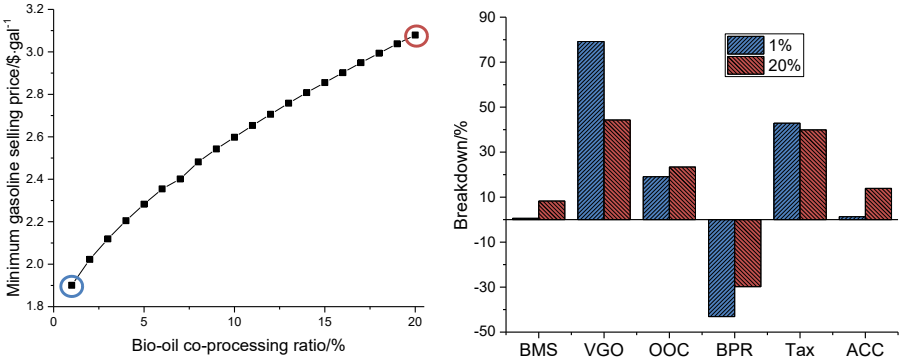

Figure 2 The Pareto fronts and the breakdowns of MSPs with 1% and 20% bio-oil co-processed (BMS=biomass, OOC=other operating cost, BPR=byproduct revenue, ACC=annual capital cost)

The Pareto fronts between the bio-oil co-processing ratio and the MSP of gasoline is not similar as usual. The reason is that the bio-oil co-processing ratio is preferred to be maximized while the gasoline selling price is to be minimized, the two different trends may lead to the curve as it is presented. The usual curve of traditional Pareto fronts would be obtained if the axis X was started from 20 to zero.

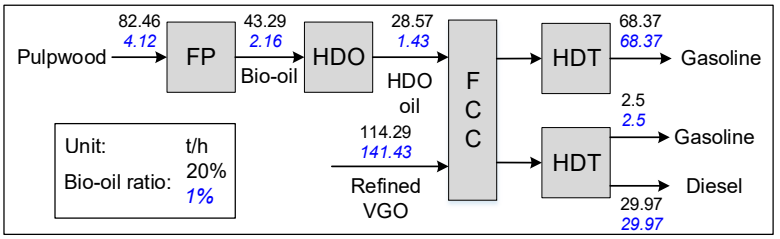

Figure 3 Mass balances of situations of the minimized MSP and the maximized bio-oil ratio

According to Figure 3 with bio-oil co-processing ratio of 20%, 82.46 t/h pulpwood is pyrolysised and hydrotreated to obtain 28.58 t/h HDO oil which is then co-fed with 114.29 t/h VGO into an FCC, gasoline HDT and diesel HDT. Finally, 70.88 t/h gasoline and 29.97 t/h diesel with bio-carbon are produced. For the situation of the minimum selling price with bio-oil co-processing ratio of 1%, 1.43 t/h bio-oil is produced by consuming 4.12 t/h pulpwood, which is then co-processed with 141.43 t/h VGO to make gasoline and diesel of 70.88 and 29.97 t/h, respectively.

3.2.2. Effect of the weight factor on the trade-off solution

The effect of the weight factor on the trade-off solution is also investigated. The result are shown in Table 2. The trade-off solution should be bio-oil ratio of 20% corresponding to the MSP of \$3.08/gal when the weight factor is less than 0.4. If the

factor is more than 0.7, the bio-oil of 1% and the MSP of \$1.9/gal should be the trade-off solution. The optimal bio-oil co-processing ratios should be 8% and 3% if the weight factors are 0.5 and 0.6, respectively.

Table 2 Effect of weight factor on the trade-off solution

Weight factor	0	0.1	0.2	0.3	0.4	0.5	0.6	0.7	0.8	0.9	1
Bio-oil ratio/%	20	20	20	20	20	8	3	1	1	1	1
MSP/\$·gal^{-1}	3.08	3.08	3.08	3.08	3.08	2.48	2.12	1.90	1.90	1.90	1.90

3.3. Optimal results of catalytic pyrolysis scenario

3.3.1. Pareto fronts of catalytic pyrolysis scenario

The Pareto fronts for the catalytic pyrolysis scenario is shown in Figure 4. Similar to the fast pyrolysis scenario, the MSP is also raised with the increase of the bio-oil co-processing ratio. The MSP is \$1.85/gal when 1% bio-oil is co-processed while the MSP is \$3.15/gal when the bio-oil co-processing ratio is 20%. No matter for which scenario, the co-processing product, gasoline, can be competed with the petroleum-based gasoline even the bio-oil ratio is 20%.

As for the breakdown of the gasoline price in the catalytic pyrolysis scenario, it is similar to the one in the fast pyrolysis scenario.

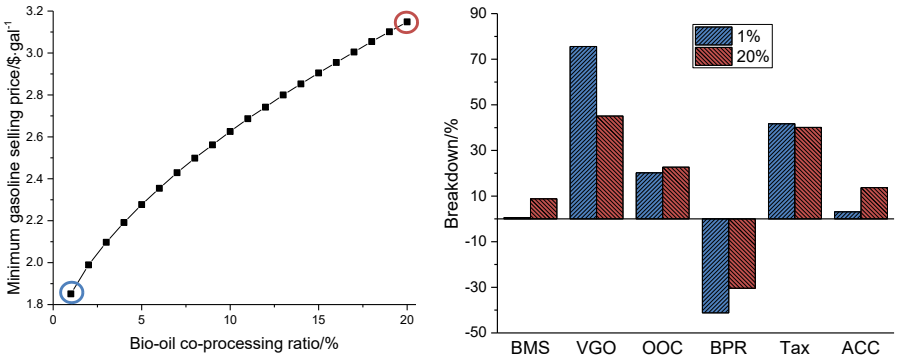

Figure 4 The Pareto fronts and the breakdowns of MSPs with 1% and 20% bio-oil co-processed (BMS=biomass, OOC=other operating cost, BPR=byproduct revenue, ACC=annual capital cost)

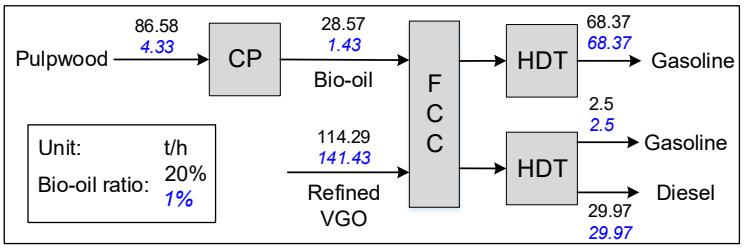

Figure 5 Mass balances of situations of the minimized MSP and the maximized bio-oil ratio

According to Figure 5 with bio-oil co-processing ratio of 20%, 86.58 t/h pulpwood is consumed to attain the bio-oil of 28.57 t/h in a catalytic pyrolysis. The 28.57 t/h bio-oil and 114.29 t/h VGO are then co-processing in an FCC to produce the gasoline and diesel with bio-carbon, which are hydrotreated in HDT to make gasoline of 70.88 t/h and diesel of 29.97 t/h. As for the 1% bio-oil co-fed with 99% VGO into an FCC, the

pulpwood consumption is 4.33 t/h, the product (gasoline and diesel) flowrates are the same with the one of 20% bio-oil co-processing ratio as the same yield data is used.

3.3.2. Effect of the weight factor on the trade-off solution

Table 3 Effect of weight factor on the trade-off solution

Weight factor	0	0.1	0.2	0.3	0.4	0.5	0.6	0.7	0.8	0.9	1
Bio-oil ratio/%	20	20	20	20	20	8	3	1	1	1	1
MSP/$·gal^{-1}	3.15	3.15	3.15	3.15	3.15	2.50	2.10	1.85	1.85	1.85	1.85

The effect of the weight factor on the trade-off solution in the catalytic pyrolysis scenario is same with the effect in the fast pyrolysis scenario.

4. Conclusions

A multi-objective optimization of the co-processing of bio-oil and VGO was proposed in this work. Two scenarios, fast pyrolysis scenario and catalytic pyrolysis scenario, were used to investigate the relation between MSP of gasoline and the bio-oil co-processing ratio. The MSP was increased with the increase of the bio-oil co-processing ratio. The MSP of gasoline was approximately $3.1/gal if 20% bio-oil was co-processed for the two scenarios. The MSP was only about $1.9/gal if the bio-oil ratio was 1%. The trade-off solution was strongly affected by the weight factor. Therefore, the best compromise between the MSP and bio-oil co-processing should be determined when designing the co-processing process.

Acknowledgments

The authors gratefully acknowledge funding by the project (No. 21808183) sponsored by the National Natural Science Foundation of China (NSFC) and the project (No. 20190602) sponsored by Young Talent Fund of University Association for Science and Technology in Shaanxi, China.

References

M. Al Jamri, R. Smith and J. Li, 2018, Integration of Renewable Resources into Petroleum Refining, Computer Aided Chemical Engineering, Elsevier, 43, 1439-1444.

M. Al Jamri, R. Smith and J. Li, 2019, Molecular Modelling of Co-processing Biomass Pyrolysis Oil with Vacuum Gasoil in an Oil Refinery Fluid Catalytic Cracking Unit, Computer Aided Chemical Engineering, Elsevier, 46, 991-996.

V. N. Bui, G. Toussaint, D. Laurenti, C. Mirodatos and C. Geantet, 2009, Co-processing of pyrolisis bio oils and gas oil for new generation of bio-fuels: Hydrodeoxygenation of guaïacol and SRGO mixed feed, Catalysis Today, 143, 1-2, 172-178.

P. L. Cruz, E. Montero and J. Dufour, 2017, Modelling of co-processing of HDO-oil with VGO in a FCC unit, Fuel, 196, 362-370.

L. Wu, Y. Wang, L. Zheng, M. Shi and J. Li, 2019, Design and optimization of bio-oil co-processing with vacuum gas oil in a refinery, Energy Conversion and Management, 195, 620-629.

L. Wu, Y. Wang, L. Zheng, P. Wang and X. Han, 2019, Techno-economic analysis of bio-oil co-processing with vacuum gas oil to transportation fuels in an existing fluid catalytic cracker, Energy Conversion and Management, 197, 111901.

Sauro Pierucci, Flavio Manenti, Giulia Bozzano, Davide Manca (Eds.)
Proceedings of the 30th European Symposium on Computer Aided Process Engineering (ESCAPE30), May 24-27, 2020, Milano, Italy.
http://dx.doi.org/10.1016/B978-0-12-823377-1.50288-3

From Screening to Production: a Holistic Approach of High-throughput Model-based Screening for Recombinant Protein Production

Niels Krausch,[a] Sebastian Hans,[a] Felix Fiedler,[b] Sergio Lucia,[b] Peter Neubauer,[a] Mariano N. Cruz Bournazou[c*]

[a]*Technische Universität Berlin, Bioprocess Engineering, Ackerstrasse 76, 13355 Berlin, Germany*
[b]*Technische Universität Berlin, Internet of Things for Smart Buildings, Einstein Center Digital Future, Einsteinufer 17, 10587 Berlin, Germany*
[c]*DataHow AG, Vladimir-Prelog-Weg 1, 8093 Zurich, Switzerland*
n.cruz@datahow.ch

Abstract

Efficient and robust screening of production strains in early bioprocess development is usually hampered by the limited cultivation resources and identification of dynamical cell parameters for the complete design space. Even though High-Throughput (HT) liquid handling stations enable a large number of strains to be tested, these experiments provide no insight into the dynamical phenotype of the strains. This is especially critical in scale-up, since cultivations in industrial bioreactors expose the microbial cell factories to significant stresses due to substrate, oxygen, and pH gradients among others. In an effort to address this challenge and reduce the risk of failure during scale-up, new HT scale down systems based on model-based operation strategies have been developed and extended to conditional screening experiments.

In this work we further extend the existing platform to enable a feedback control of the 24-parallel mini-bioreactor setting, using a recursive moving horizon parameter estimation combined with a model-predictive control approach to calculate an optimal feeding regime, which exposes the cells to stress conditions similar to those present in large-scale bioreactors. We present a case study showing the advantages of the framework by screening a set of *E. coli* strains for obtaining highest biomass at the end of the process. The results show that the prediction and selection of the most suitable strain for industrial production is significantly improved.

Keywords: High-throughput, MPC, bioprocess development, adaptive robot operation.

1. Challenges in early bioprocess development

The development of a process to produce e.g. a new chemical entity in biotechnology is characterized by long developmental times and high costs. The risk of failure is also high, especially in the early phases when screening for a potential producer strain (Neubauer et al., 2013). Hence, novel tools to shorten product development times are required in biomanufacturing. An important step to tackle this issue has been the introduction of High-Throughput (HT) liquid handling stations, which are able to perform several cultivations in parallel, using micro-well plates or even Mini-Bioreactors (MBR) (Hemmerich et al., 2018; Nickel et al., 2017). These MBRs share geometric similarities to large scale bioreactors and can be used to screen a fair number of possible strains at

low costs and effort. Consideration of specific cultivation conditions such as pulse-based glucose feeding regimes enables furthermore to perform scale-down studies with conditions also present in large scale bioreactors, characterized by significant oxygen and glucose gradients (Neubauer and Junne, 2016). Several studies have shown that intermittent feeding regimes with oscillating conditions regarding substrate and oxygen supply are an easy to implement yet powerful way of studying organisms under industrial-like stress conditions.

Successful bioprocess cultivations require a careful and well-tuned operation of the system which is currently performed with continuous manual tuning of the cultivation setpoints, while MBR systems are operated without exploiting state-of-the-art optimization and control methods. Model-based methods for process simulation, design, optimization, and control are required to maximize experimental efficiency and bioprocess understanding. Additionally, keeping conditions comparable to the production scale and promoting a consistent information flow while going through the developmental stages ensures robustness and decreases the risk of failure during scale-up (Haringa et al., 2018). The use of mechanistic models has proven to support and increase efficiency of experimental campaigns (Barz et al., 2018; Cruz Bournazou et al., 2017).

However, during the early screening stage, little is known about the phenotype and dynamical behavior of the mutants. This poses a challenge in the operation of fed-batches since the optimal feeding strategy is not known beforehand. The typical solution to this problem in parallel cultivations is a unique and very conservative feeding profile for all mutants. Using this strategy, it is not possible to compare the performance of each mutant at its optimal process conditions. By this, it is difficult to consider important differences between the mutants like the specific growth rate. Furthermore, relevant constraints are easily violated as would be strict aerobic conditions for all cultivations or avoiding cell starvation.

We tackle these issues implementing a Model Predictive Control (MPC) framework that assures a feeding strategy as close as possible to optimality for each individual mutant. A reduced macro-kinetic growth model with adaptive parameters for qSmax (maximum substrate uptake rate), pAmax (maximum specific acetate production rate), Yem (yield of biomass on glucose, excluding maintenance), and Yaof (yield of acetate on all other products of overflow routes), is used to compute the feeding strategy. The framework can interact with the robotic facility to run fed-batch like cultivations for different strains simultaneously.

As a proof of concept, we present a screening experiment of eight *E. coli* K 12 strains in 24 mini bioreactors in parallel, six of them knockout strains obtained from the well-known Keio collection of *E. coli* knockout strains. For all knockout strains there exists only very limited information regarding the growth behavior and no kinetic model parameters are available.

2. Problem Formulation

Eight different *E. coli* K-12 strains were cultivated in parallel with an industrial process-relevant feeding design consisting of batch and exponential fed-batch phases using a total of $n_r = 24$ mini bioreactors. Each one of the bioreactors $r \in \Re = \{1,\ldots,n_r\}$ can be described by the dynamics:

$$\begin{aligned} \dot{x}_r(t) &= f\left(x_r(t), u_r(t), \theta\right) \\ x_r(t_0) &= x_{0,r} \end{aligned} \tag{1}$$

Where the dynamic states are denoted by $x_r \in \mathbb{R}^{n_x}$ and include biomass, substrate, dissolved oxygen tension (DOT) as well as acetate. The control inputs for each mini bioreactor are $u_r \in \mathbb{R}^{n_u}$ and $\theta \in \mathbb{R}^{n_\theta}$ denotes the unknown parameters of the reactor and the strains. The available measurements for all the states can be obtained at each sampling time: this is 30 seconds for DOT, and 20 min for the remaining. At each iteration of the proposed framework, the inputs of the system (the optimal feeding rate for each mini bioreactor) is computed using an MPC controller (Rawlings and Mayne, 2009), that uses the dynamical model defined in (1) using the current estimation of the uncertain parameters $\hat{\theta}$. By using the MPC controller, it can be assured that all strains are cultivated based on their maximum capabilities to assure that the best performing strain is selected for further upscaling.

The optimization problem that the MPC controller with prediction horizon N_{mpc} needs to solve at each sampling time can be written as:

$$\min_{u_r} \sum_{r=1}^{n_r} -X_r\left(t_{end}\right) \tag{2}$$

$$\begin{aligned} & \dot{x}_r\left(t\right) = f\left(x_r\left(t\right), u_r\left(t\right), \hat{\theta}\right) \forall r \in \Re \\ \text{s.t.:} \; & x_r\left(t_0\right) = x_{0,r} \\ & \text{DOT}_r\left(t\right) \geq 20\% \end{aligned} \tag{3}$$

Since the estimation of the parameters plays an important role in the computation of the optimal inputs and they are known to vary throughout the cultivation, we iteratively estimate the parameters using a moving horizon approach, which uses a sliding time window and only considers the N_{mhe} last measurements (Haseltine and Rawlings, 2005). The optimization problem that needs to be solved at each sampling time to obtain a new estimate of the parameters can be written as:

$$\min_{\theta} \left\| \hat{\theta}_{old} - \hat{\theta} \right\|_{W_p}^2 + \sum_{k=0}^{N_{mhe}} \left\| h\left(x\left(k\right)\right) - y\left(k\right) \right\|_{W_y}^2 \tag{4}$$

$$\begin{aligned} & \dot{x}_r\left(t\right) = f\left(x_r\left(t\right), u_r\left(t\right), \hat{\theta}\right) \forall r \in \Re \\ \text{s.t.:} \; & x_r\left(t_0\right) = x_{0,r} \\ & \theta_{\min} \leq \theta \leq \theta_{\max} \end{aligned} \tag{5}$$

Where $h\left(x\left(k\right)\right)$ denotes the measurement equations, $y\left(k\right)$ denotes the measurement at time point k, $\hat{\theta}_{old}$ is the previously estimated parameters and the two terms that penalize the change in parameters and the residuals are weighted by the parameters W_p and W_y.

An overview of the iterative process is given in Figure 1. Based on the sampled measurements, the MHE parameter estimation is performed to generate an updated set of parameters $\hat{\theta}$. Based on this parameter set, an optimal glucose feed is calculated which yields the highest biomass, subject to the constraint that anoxic conditions (DOT < 20 %) should be avoided.

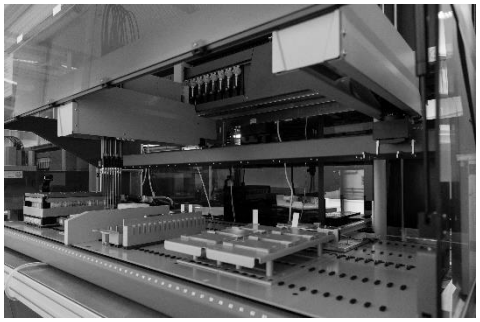

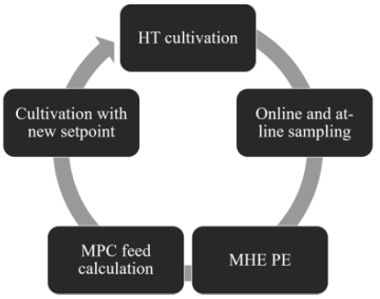

Figure 1: The high-throughput robotic facility (left) and the iterative workflow of the cultivation

3. Methods

3.1. HTBD facility

The results presented in this work are based on *in silico* data generated from 8 models validated with real experimental data, for further details on the experimental procedure the reader is referred to Hans et al. (2020). The framework has been developed to operate the high throughput bioprocess development facility, comprising of two liquid handling stations (Freedom Evo 200, Tecan, Switzerland; Microlab Star, Hamilton, Switzerland), a mini-bioreactor system (48 BioReactor, 2mag AG, Munich, Germany) and a Synergy MX microwell plate reader (BioTek Instruments GmbH, Bad Friedrichshall, Germany). Cultivations are carried out at 37 °C with 5 g L^{-1} initial glucose in the batch phase at a constant stirring speed of 3,000 rpm. Glucose is added as substrate in a pulse-based manner every 5 min after end of the batch. pH and Dissolved Oxygen Tension (DOT) are measured online, while measurements of glucose, acetate and OD600 are performed at-line on the Hamilton LHS using enzymatic kits. The reader is referred to Haby et al. (2019) for a detailed description of the facility and sampling procedure.

3.2. Computational methods

The *E. coli* macro-kinetic growth model used in this framework consists of 6 ordinary differential equations describing biomass, glucose, acetate oxygen, and enzymatic glucose release. The model contains 18 parameters from which 13 have been shown to vary with mutations and cultivation conditions. The reader is referred to the paper by Anane et al. (2017) for a detailed description of the model and to Anane et al. (2019) for a description of the procedure followed for the parameter estimation.

To allow for easier parameter identification, a subset of 4 important parameters (qSmax, pAmax, Yem, Yaof) is used, while the others are kept at constant values. All scripts were written in Matlab R2019a and ODEs were solved using the sundials CVODE solver.

4. Results

After an initial batch phase, the feed was started with 5 min pulses until the end of the process which was set to 11 h. Every hour, the framework performed an MHE based on the data generated during the previous hour. When the feed had started, the MPC part of the framework calculated the optimal feed rate based on the current parameter set $\hat{\theta}$ to obtain the highest biomass based on the different parameters for each strain. Moreover, it is assured that the cells are not overfed, considering that the substrate uptake capacity of

the cells is decreasing over time. To give a better insight into the procedure at this stage, we performed simulations based on the parameters obtained from fitting the model to the data of the experiment and describe the process based on *in silico* data. In Figure 2, the process is shown without usage of an MPC framework or MHE parameter adaption (dashed orange line), with usage of the MPC framework, but without parameter estimation (purple dash-dotted line). The blue dotted line represents the output of the simulation with adapted parameters and usage of the MPC framework, while the green solid line represents the simulation output based on the actual parameters that were estimated from the process data. It can be seen clearly, that with a predefined feed, the cells are overfed, glucose accumulates and acetate (an indicator for overflow feeding) is produced in large amounts. In contrast, within the MHE/MPC framework, optimal feeding regimes are calculated, so that overfeeding is prevented. It can be seen clearly, that the MPC approach ensures optimal feeding conditions which are close to the maximum growth capacity and excel traditional approaches with a predefined growth rate. Figure 2 clearly depicts that the constraint (DOT lower than 20 %) are maintained by the MPC framework.

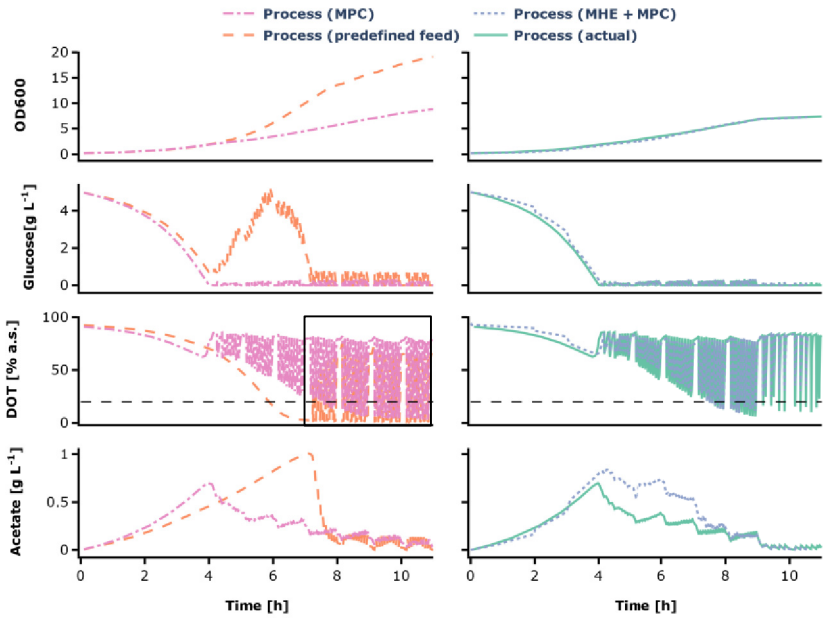

Figure 2: Exemplary results of mutant strain 1. Comparison of the process data, the simulation with the parameter set from the MHE and the simulation without parameter estimation. The black rectangle indicates a time frame in which the process without MHE violates the constraint.

5. Conclusions

In this work we present an adaptive framework comprising of an MHE for computational inexpensive parameter estimation and an MPC controller for optimal feeding calculation. The screening procedure is drastically improved by cultivating the strains at their maximum growth rates while at the same time ensuring that they will not be exposed to anoxic conditions. The results demonstrate the importance advanced control strategies in the operation of parallel dynamical cultivations due to the low *a priori* information of the mutants and the large variations in their phenotypes.

References

Anane E, García ÁC, Haby B, Hans S, Krausch N, Krewinkel M, et al. A model-based framework for parallel scale-down fed-batch cultivations in mini-bioreactors for accelerated phenotyping. Biotechnology and bioengineering 2019;116(11):2906–18. https://doi.org10.1002/bit.27116.

Anane E, López C DC, Neubauer P, Cruz Bournazou MN. Modelling overflow metabolism in Escherichia coli by acetate cycling. Biochemical Engineering Journal 2017;125:23–30. https://doi.org10.1016/j.bej.2017.05.013.

Barz T, Sommer A, Wilms T, Neubauer P, Cruz Bournazou MN. Adaptive optimal operation of a parallel robotic liquid handling station. IFAC-PapersOnLine 2018;51(2):765–70. https://doi.org10.1016/j.ifacol.2018.04.006.

Cruz Bournazou MN, Barz T, Nickel DB, Lopez Cárdenas DC, Glauche F, Knepper A, et al. Online optimal experimental re-design in robotic parallel fed-batch cultivation facilities. Biotechnology and bioengineering 2017;114(3):610–9. https://doi.org10.1002/bit.26192.

Haby B, Hans S, Anane E, Sawatzki A, Krausch N, Neubauer P, et al. Integrated Robotic Mini Bioreactor Platform for Automated, Parallel Microbial Cultivation With Online Data Handling and Process Control. SLAS technology 2019;24(6):569–82. https://doi.org10.1177/2472630319860775.

Hans S, Haby B, Krausch N, Barz T, Neubauer P, Cruz Bournazou MN. Automated conditional screening of Escherichia coli knockout mutants in parallel adaptive fed-batch cultivations. Microbial Cell Factories 2020 (submitted).

Haringa C, Mudde RF, Noorman HJ. From industrial fermentor to CFD-guided downscaling: what have we learned? Biochemical Engineering Journal 2018;140:57–71. https://doi.org10.1016/j.bej.2018.09.001.

Haseltine EL, Rawlings JB. Critical Evaluation of Extended Kalman Filtering and Moving-Horizon Estimation. Industrial & Engineering Chemistry Research 2005;44(8):2451–60. https://doi.org10.1021/ie034308l.

Hemmerich J, Noack S, Wiechert W, Oldiges M. Microbioreactor Systems for Accelerated Bioprocess Development. Biotechnology journal 2018;13(4):e1700141. https://doi.org10.1002/biot.201700141.

Neubauer P, Cruz N, Glauche F, Junne S, Knepper A, Raven M. Consistent development of bioprocesses from microliter cultures to the industrial scale. Engineering in Life Sciences 2013;13(3):224–38. https://doi.org10.1002/elsc.201200021.

Neubauer P, Junne S. Scale-Up and Scale-Down Methodologies for Bioreactors. In: Mandenius C-F, editor. Bioreactors. Weinheim, Germany: Wiley-VCH Verlag GmbH & Co. KGaA; 2016. p. 323–354.

Nickel DB, Cruz-Bournazou MN, Wilms T, Neubauer P, Knepper A. Online bioprocess data generation, analysis, and optimization for parallel fed-batch fermentations in milliliter scale. Eng. Life Sci. 2017;17(11):1195–201. https://doi.org10.1002/elsc.201600035.

Rawlings JB, Mayne DQ. Model predictive control: Theory and design. Madison, Wis.: Nob Hill Publ; 2009.

Sauro Pierucci, Flavio Manenti, Giulia Bozzano, Davide Manca (Eds.)
Proceedings of the 30th European Symposium on Computer Aided Process Engineering (ESCAPE30), May 24-27, 2020, Milano, Italy.
http://dx.doi.org/10.1016/B978-0-12-823377-1.50289-5

Techno-economic Assessment of a Hydrothermal Liquefaction Process for Energy Recovery from Food Waste

Enrique Medina-Martos[a*], Pablo Miranda-Rey[a,b], José-Luis Gálvez-Martos[a], Javier Dufour[a,b]

[a] *Systems Analysis Unit, IMDEA Energy. Avenida Ramón de la Sagra, 3. 28935 Móstoles, Madrid (Spain).*
[b] *Chemical and Environmental Engineering Group, Rey Juan Carlos University. Calle Tulipán s/n. 28933 Móstoles, Madrid (Spain).*
enrique.medina@imdea.org

Abstract

Hydrothermal technologies have been extensively studied over the last decade as promising pathways for energy recovery from bioresources. Feedstocks with a high moisture content, such as food waste, are particularly suitable to undergo hydrothermal conversion. In this work, we addressed a techno-economic study of the production of food-waste-derived biofuels via Hydrothermal Liquefaction (HTL), in a commercial scale facility. To that end, a simulation model encompassing the HTL conversion step (including the combination of two kinetic models from bibliography), bio-oil upgrading and products separation was implemented in Aspen Plus® V10. Results show that both the predicted biocrude mass yield in HTL (37 %) and its composition are consistent with those of previous experimental studies. Amongst the products, the annual volumetric production of gasoline triples that of diesel. In terms of the economic viability, under the studied assumptions, we found the project would only be profitable if a fee (27-39 €/t) accounting for waste treatment is adopted.

Keywords: Hydrothermal liquefaction, Techno-economic assessment, Process simulation, Aspen Plus.

1. Introduction

A better utilization of resources is currently a global concern. One aspect on this statement is related to exploring innovative uses for waste (Elkhalifa et al., 2019). Within the European Union (EU) context, the Circular Economy package includes diverse actions to that end. Municipal solid waste (MSW) management is one target of such policies. Within MSW, Food Waste (FW) represents a significant fraction, which has been estimated to amount 1.3 billion t/y globally. Thus, a great potential for energy production is associated if a proper management of FW is promoted (Elkhalifa et al., 2019; Pham et al., 2015). The conversion of FW to energy has been previously addressed by the application of thermochemical (incineration, pyrolysis, gasification) or biochemical (anaerobic digestion) technologies. First ones are energetically unfavorable due to high expenses for feedstock drying and the latter involve high investment costs due to extensive conversion times (Pham et al., 2015). As an alternative to these, hydrothermal technologies, which are performed in an aqueous medium and have shorter reaction times, arise as suitable alternatives. In particular, Hydrothermal Liquefaction (HTL) yields a crude-like viscous

liquid (biocrude) which can be further refined to produce biofuels. HTL is usually developed at 200-400 ºC and 40-220 bar (Gollakota et al., 2018). Together with the biocrude (30-50 %), an aqueous phase (~50 %), a carbonaceous solid called char (~10 %), and little gas (<5 %) are obtained. In this work we approach the conversion of food waste into biofuels (gasoline and diesel) via HTL by assessing economic implications for the deployment of a commercial scale facility. A process simulation model in AspenPlus® V10 served as the basis to retrieve meaningful parameters for such evaluation.

2. Process Description

The considered feedstock composition is reported in Table 1. Plant capacity was set to 161,000 t/y, similar to that reported for the anaerobic digestion facilities owned by the municipality of Madrid (Spain). Figure 1 depicts the studied process, whose main equipment specifications are summarized in Table 2.

Food waste is initially mixed with water so as to obtain a pumpable mixture (85 % moisture) and then sent to the HTL reactor, where it is isothermally converted. Required heating is provided by the exhaust gas resulting from the combustion of heavy hydrocarbons from bottom product of C-302. Afterwards, the produced char is separated in a cartridge filter, which operates at high pressure (Knorr et al., 2013). The liquid stream, made up by the biocrude and the aqueous phase, is headed to a decanter (S-101), where both phases separate. The aqueous phase leaves the process to wastewater treatment. The biocrude follows to the upgrading section to undergo deoxygenation. Such operation is performed in a fixed-bed type hydrotreating reactor (R-201). Most of the required H_2 is freshly introduced, but a certain amount is recovered H_2 which comes from a Pressure Swing Adsorption (PSA) unit (C-201), which is placed after light gases separation in flash unit S-201. The converted hydrocarbons continue to the refinery section, which comprehends two distillation columns, C-301 and C-302, where light gases, gasoline, diesel and heavier hydrocarbons (C_{20+}) are recovered. As previously stated, the latter fraction is combusted to furnish the heat for R-101. The combustion takes place in a furnace (R-401) where 10 % stoichiometric air excess is introduced. Due to environmental concerns, the NO_x concentration needs to be reduced (<0.5 ppm) in order to attain the Spanish national legislation. To that end, a Selective Catalytic Reduction (SCR) unit (R-402) is included, where NO_x reacts with NH_3 to give N_2 and H_2O.

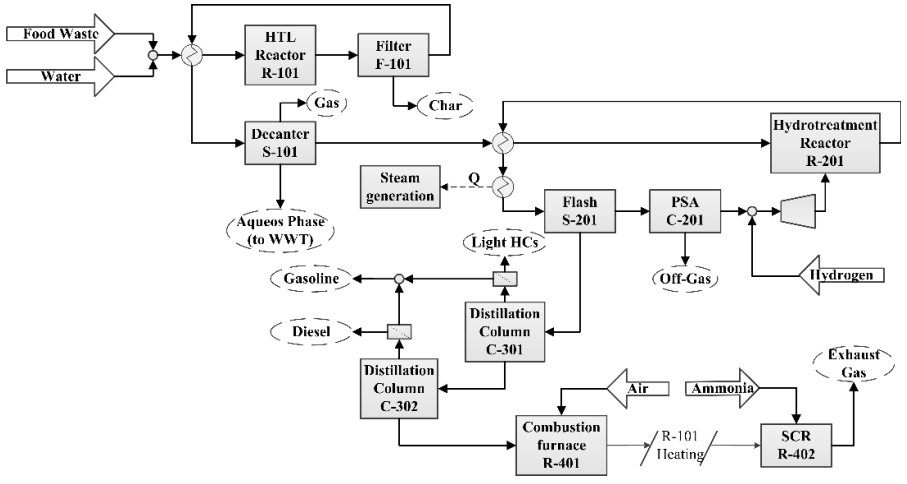

Figure 1. Block chart of studied process.

Table 1. Considered FW composition.

Fraction	Mass % (d.a.f)	Compound used in Aspen Plus®
Moisture	74.00	
Ash	1.15	
Organic Matter	24.85	
Protein	26.46	$CH_{1.57}O_{0.31}N_{0.29}S_{0.07}$ (Davis et al., 2014)
Carbohydrates	52.54	$C_6H_{12}O_6$ (Dextrose)
Lipids	2.00	$C_6H_{32}O_2$ (Palmitic acid)
Lignin	19.00	$C_{22}H_{29}O_9$ (LIG-H, Faravelli et al., (2010))

Table 2. Operating conditions for main process equipment.

Unit equipment	ID	Operating Condition
HTL Reactor	R-101	T = 300 ºC; P = 100 bar; t_r = 30 min. (Knorr et al., 2013)
Filter	F-101	T = 300 ºC; ΔP = 3.5 bar; (Knorr et al., 2013)
Decanter	S-101	T = 60 ºC; P = 40 bar
Hydrotreatment Reactor	R-201	T = 400 ºC; P = 138 bar; Catalyst: Co/Mo (Elliott, 2007)
Pressure-Swing Adsorption	C-201	T = 30 ºC; P = 1 – 13 bar
Distillation Column	C-301	$T_{reboiler}$ = 217 ºC; P = 1 bar; Stages = 10; Feed stage = 4; Reflux ratio = 0.5; Condenser: part.
Distillation Column	C-302	$T_{reboiler}$ = 337 ºC; P = 0.8 bar; Stages = 10; Feed stage = 5; Reflux ratio = 0.86; Condenser: part.
SCR Reactor	R-402	T = 350 ºC; P = 3.3 bar; (Sorrels et al., 2019)

3. Methodology

3.1. Process simulation

The process, as described in Section 2, was implemented in software Aspen Plus® V10 in order to obtain the most relevant design parameters to perform the economic analysis. Utilized property methods were *SOLIDS* for the HTL reaction (due to the presence of char), Non-Random Two-Liquid with the Redlich-Kwong equation of state (*NRTL-RK)* for the upgrading section and the Peng-Robinson equation of state with Boston-Mathias correction (*PR-BM)* for the distillation section.

The core of the simulation i.e. the HTL reactor, was based on the combination of two literature kinetic models. The first one (Sheehan and Savage, 2017; Valdez et al., 2014), describes the formation of the bio-crude, the aqueous phase and gas by taking as input the biochemical composition of the considered feedstock. Yet, this model lacks a description for the degradation of lignin and char formation. To fix this, we incorporated the model by Zhang et al. (2008), in which lignin kinetics are explained. The reactor was simulated by means of a *RYIELD* unit ruled by a *calculator block* in which the cited kinetics are developed. Products from the HTL reaction are further assigned, attending to the elemental composition, to common families of compounds reported in Wądrzyk et al. (2018).

The hydrotreating reactor was also simulated with a *RYIELD* block. Typical process yields and hydrogen consumption were set from those reported in previous works (Elliott, 2007; Peters, 2015). For the PSA unit, we utilized an ideal separator model with assumed efficiency of 85 % for H_2 separation (Spath et al., 2005). We simulated the SCR by a *RGIBBS* block in which the consumption of NH_3 is adjusted through a *DesignSpec* feature to meet the environmental limits on NO_x emissions. Finally, the distillation columns were both implemented as *RADFRAC* blocks, with internal parameters fitted so as to achieve optimized separation of gasoline and diesel.

3.2. Techno-economic assessment

Process economics were assessed with reference on the general methodology described in Towler and Sinnott (2013). Cost data were all updated to Euros (€) of year 2018. First, we estimated the individual equipment purchase cost by using either cost correlations or applying a capacity ratio (Williams' rule). Factors were applied to account for equipment construction in stainless steel and plant location in Spain. Then, the Total Investment Cost (TIC) was estimated by the Lang method. Fixed contributions to the Operating Expenditure (OPEX) were calculated as percentages of the Capital Expenditure (CAPEX). Revenues were obtained by multiplying the annual production of each product by its market price in Spain in late 2018. Based on this, a discounted cash flow analysis was performed assuming a 15-year plant lifespan. Inflation was set to 1.02 %, the assumed tax rate was 35 % and depreciation was calculated by considering the straight line method along project years from 1 to 10. We evaluated the influence of the selected discount rate (DR) on the Net Present Value (NPV) of the project and determined the Minimum Treatment Cost of Waste (MTCW) for it to be profitable.

4. Results and discussion

4.1. Process results

The evolution of mass composition in the HTL reactor is shown in
Figure **2**. We roughly obtained 10 % char, 35 % biocrude, 55 % aqueous phase and a negligible quantity of gas. Such results are in good concordance with those reported in previous works (Kruse et al., 2013), also when attending to the elemental composition of the biocrude and its characterization by families of compounds (Not shown).

For the upgrading section, a comparison between the elemental composition of the biocrude before and after the stage is shown in Table 3. Please note that light nitrogen and sulfur compounds are considered to leave the process by the off-gas stream.

Finally, the calculated annual production of gasoline and diesel was respectively of 5.74 and 1.94 ML/y.

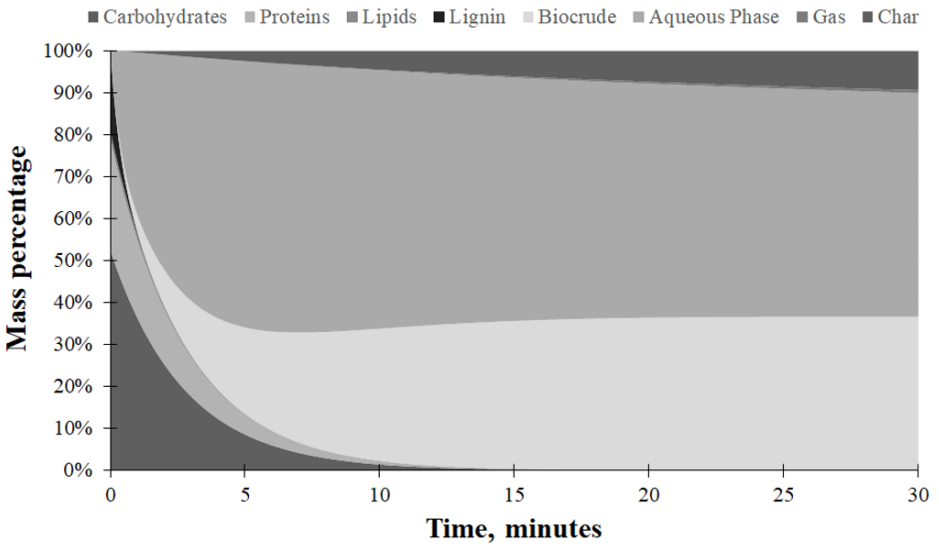

Figure 2. Kinetic profile of the simulated HTL reactor (R-101).

Table 3. Comparison of elemental composition (mass %) of biocrude before and after upgrading.

	C %	H %	O %	N %	S %
Before	69.32	9.73	13.83	6.41	0.71
After	85.2	13.5	1.3	-	-

4.2. Economic results

The economic breakdown of plant investment and operation are gathered in Table 4. OPEX is similarly participated by fixed and variable expenses, the latter being 70 % due to natural gas purchase, which is required to fill the heating necessities from the plant, and 14 % H_2 utilized in the upgrading section.

Results for NPV at the final year of the project for DR values between 6-12 % are presented in Figure 3. As proposed, the project is not profitable for any DR. To overcome this, a royalty accounting for the treatment cost of waste was adopted. The calculated MTCW (those values which make NPV=0) range 27-39 €/t. However, note that these are the values that would make the project neutral from an investor's perspective. If we took NPV=30 M€ as the minimum desired profit for investment, the required FW treatment cost would be >54 €/t.

Table 4. Estimated CAPEX, OPEX and revenues of simulated process.

Item	Value (€$_{2018}$)	Item	Value (€$_{2018}$)
CAPEX		**OPEX (annual)**	
Working capital	2,551,728	Fixed	2,963,363
ISBL	14,581,301	Variable	2,426,082
Purchased equipment	5,131,003	(If catalyst in SCR replaced – 3 years)	2,441,614
OSBL	5,832,520	**Revenues (annual)**	
Design & engineering	3,645,325	Gasoline (@ 0.533 €/L)	3,057,939
Contingency	1,458,130	Diesel (@ 0.587 €/L)	1,141,359
Total investment cost (TIC)	25,517,277	Steam (@) 7.3 €/t)	98,660

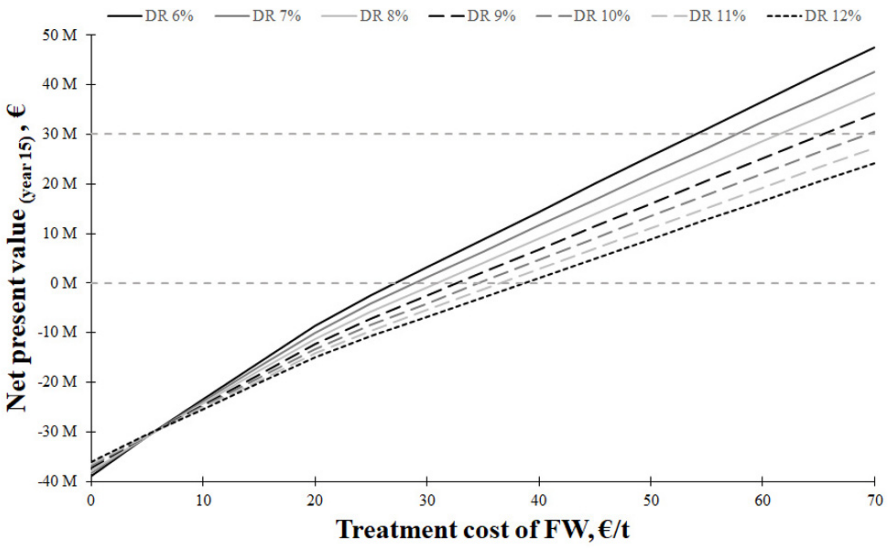

Figure 3. NPV (at final year of project lifespan) as a function of DR and FW treatment cost.

5. Conclusions

A techno-economic study based on process simulation has proven the economic feasibility of the hydrothermal conversion of food waste to biofuels in a commercial scale facility. The simulation of hydrothermal liquefaction and biocrude hydrotreating have shown good consonance with previous literature data. To ensure economic profitability, we calculated a Minimum Treatment Cost for Waste of 27-39 €/t.

Acknowledgements

The authors would like to thank financial support by the Spanish Ministry of Science, Innovation and Universities through the REDEFINERY project (RTI2018-097227-B-I00, AEI-FEDER/Retos Investigación 2018).

References

Davis, R., Kinchin, C., Markham, J., Tan, E.C.D., Laurens, L.M., 2014. Process Design and Economics for the Conversion of Algal Biomass to Biofuels: Algal Biomass Fractionation to Lipid- and Carbohydrate-Derived Fuel Products. Renewable Energy 110.

Elkhalifa, S., Al-Ansari, T., Mackey, H.R., McKay, G., 2019. Food waste to biochars through pyrolysis: A review. Resources, Conservation and Recycling 144, 310–320. https://doi.org/10.1016/j.resconrec.2019.01.024

Elliott, D.C., 2007. Historical Developments in Hydroprocessing Bio-oils. Energy Fuels 21, 1792–1815. https://doi.org/10.1021/ef070044u

Faravelli, T., Frassoldati, A., Migliavacca, G., Ranzi, E., 2010. Detailed kinetic modeling of the thermal degradation of lignins. Biomass and Bioenergy 34, 290–301. https://doi.org/10.1016/j.biombioe.2009.10.018

Gollakota, A.R.K., Kishore, N., Gu, S., 2018. A review on hydrothermal liquefaction of biomass. Renewable and Sustainable Energy Reviews 81, 1378–1392. https://doi.org/10.1016/j.rser.2017.05.178

Knorr, D., Lukas, J., Schoen, P., 2013. Production of Advanced Biofuels via Liquefaction - Hydrothermal Liquefaction Reactor Design: April 5, 2013 (No. NREL/SR-5100-60462, 1111191). https://doi.org/10.2172/1111191

Kruse, A., Funke, A., Titirici, M.-M., 2013. Hydrothermal conversion of biomass to fuels and energetic materials. Current Opinion in Chemical Biology 17, 515–521. https://doi.org/10.1016/j.cbpa.2013.05.004

Peters, J.F., 2015. Pyrolysis for biofuels or biochar? A thermodynamic, environmental and economic assessment. Rey Juan Carlos Univeristy, Madrid.

Pham, T.P.T., Kaushik, R., Parshetti, G.K., Mahmood, R., Balasubramanian, R., 2015. Food waste-to-energy conversion technologies: Current status and future directions. Waste Management 38, 399–408. https://doi.org/10.1016/j.wasman.2014.12.004

Sheehan, J.D., Savage, P.E., 2017. Modeling the effects of microalga biochemical content on the kinetics and biocrude yields from hydrothermal liquefaction. Bioresource Technology 239, 144–150. https://doi.org/10.1016/j.biortech.2017.05.013

Sorrels, J.L., Randall, D.D., Schaffner, K.S., Fry, C.R., 2019. Cost Reports and Guidance for Air Pollution Regulations - Section 4 - NOx Controls - Chapter 2 Selective Catalytic Reduction. US Environmental Protection Agency.

Spath, P., Aden, A., Eggeman, T., Ringer, M., Wallace, B., Jechura, J., 2005. Biomass to Hydrogen Production Detailed Design and Economics Utilizing the Battelle Columbus Laboratory Indirectly-Heated Gasifier (No. NREL/TP-510-37408, 15016221). https://doi.org/10.2172/15016221

Towler, G.P., Sinnott, R.K., 2013. Chemical engineering design: principles, practice, and economics of plant and process design, 2nd ed. ed. Butterworth-Heinemann, Boston, MA.

Valdez, P.J., Tocco, V.J., Savage, P.E., 2014. A general kinetic model for the hydrothermal liquefaction of microalgae. Bioresource Technology 163, 123–127. https://doi.org/10.1016/j.biortech.2014.04.013

Wądrzyk, M., Janus, R., Vos, M.P., Brilman, D.W.F., 2018. Effect of process conditions on bio-oil obtained through continuous hydrothermal liquefaction of Scenedesmus sp. microalgae. Journal of Analytical and Applied Pyrolysis 134, 415–426. https://doi.org/10.1016/j.jaap.2018.07.008

Zhang, B., Huang, H.-J., Ramaswamy, S., 2008. Reaction Kinetics of the Hydrothermal Treatment of Lignin. Appl Biochem Biotechnol 147, 119–131. https://doi.org/10.1007/s12010-007-8070-6

Sauro Pierucci, Flavio Manenti, Giulia Bozzano, Davide Manca (Eds.)
Proceedings of the 30th European Symposium on Computer Aided Process Engineering (ESCAPE30), May 24-27, 2020, Milano, Italy.
http://dx.doi.org/10.1016/B978-0-12-823377-1.50290-1

A Simulation Case Study for Bio-based Hydrogen Production from Hardwood Hemicellulose

Ville Tuppurainen[a]*, Jani Kangas[a], Juha Ahola[a], Juha Tanskanen[a], Atte Aho[b], Henrik Grénman[b], Dmitry Yu. Murzin[b], Tapio Salmi[b]

[a]*Chemical Process Engineering, University of Oulu, P.O. Box 4300, FI-90014 University of Oulu, Finland*
[b]*Laboratory of Industrial Chemistry and Reaction Engineering, Johan Gadolin Process Chemistry Center, Åbo Akademi University, Biskopsgatan 8, FI-20500 Åbo, Finland*
ville.tuppurainen@oulu.fi

Abstract

A novel bio-based hydrogen production process concept is simulated using Aspen Plus software. In the concept, hemicellulose is first extracted from birch wood using aqueous formic acid (FA). The dilute FA is then decomposed and used synergistically as a source of H_2. The hemicellulose monosaccharides in the dilute aqueous hydrolysate are hydrogenated to their corresponding sugar alcohols, which are further processed to H_2, various alkanes and carbon dioxide using aqueous phase reforming (APR). In addition to H_2 and electricity, cellulose and lignin rich solid wood fraction is produced. However, the case study revealed high heating requirements of dilute aqueous hydrolysate stream to APR reaction temperatures. High degree of APR effluent recycling to the extraction stage is considered, resulting in a relatively high concentration of the required fresh FA stream in the process concept.

Keywords: Bio-based Hydrogen, Hemicellulose Extraction, Aqueous Phase Reforming

1. Introduction

Hydrogen is an important raw material for chemical industry and is also considered as a potential energy carrier. H_2, used for various on-site hydrotreatment processes, is predominantly produced by steam reforming of fossil based natural gas and thus inherently producing nonrenewable carbon dioxide emissions. H_2 is an essential reagent in many lignocellulosic feedstock (LCF) valorization processes and its production from wood based raw material streams within an integrated biorefinery has been a subject of considerable interest. (Schüth 2014)

Hot water extraction of hemicellulose from hardwood typically produces a dilute aqueous mixture of mono- and oligosaccharides, furans, dissolved lignin and extractive derived compounds as well as acetic acid released from hemicellulose acetyl groups. However, usage of FA in the extraction of hemicellulose from hardwood has been shown to increase monosaccharide yields (Goldmann et al. 2017, van Heiningen et al. 2017). In addition, FA has been shown to suppress the formation of fouling lignin precipitates, a major bottleneck in the industrial recovery of hydrolysates during prehydrolysis in dissolving pulp production (van Heiningen et al. 2017). In APR, first introduced by Dumesic and colleagues (Davda et al. 2005), oxygenated biomass hydrocarbons are catalytically processed in liquid phase at relatively low temperatures (around 225 °C) and high pressure to H_2, various alkanes and CO_2. Kinetic studies with sugar alcohols, e.g. sorbitol

(Kirilin et al. 2012) and xylitol (Murzin et al. 2017, Kirilin et al. 2012, 2014), have highlighted the feedstock potential of these components for APR, which can be obtained from monosaccharides by commercial hydrogenation processes.

In this study, the concept of combining FA aided hemicellulose extraction (HCE) with APR to a complete integrated process concept is investigated using a simulation software. In the concept, FA, the catalyst of the HCE, is decomposed and used synergistically as an additional source of H_2. APR in turn enables the subsequent conversion of polyols to H_2. In addition to being an alternative source of bio-based H_2, the process concept enables more efficient use of hemicellulose hydrolysate. The aim of this paper is to evaluate the feasibility of the novel process concept by assessing its mass balance of the preliminary heat integrated flowsheet.

2. Methodology

The simulation case study was conducted using Aspen Plus. NRTL was used as the thermodynamic model, except in flash units NRTL-HOC was used to account for the non-idealities caused by the presence of carboxylic acids. H_2, CO and CO_2 were set as Henry components. Detailed description of the components in the birch and decomposition products formed in the HCE was based on the well-known National Renewable Energy Laboratory (NREL) report by Humbird et al. (2011). Palmitic and pimaric acids were used as model components for wood extractives. Solid 4-O-methylglucuronic acid substituent and its soluble monomer were defined by using the same solid enthalpy of formation as for cellulose and defining the molecular structure, respectively.

The simulation process flowsheet is described in Fig. 1. Solid debarked birch wood chips (stemwood composition compiled from Alakangas et al. (2016) with hemicellulose fraction based on Alén (2000)) with 50 wt-% moisture are fed to FA aided HCE reactor. The reactor is modeled using the R-STOIC model based on the fractional conversions of individual components. The fractional conversions were adjusted based on laboratory scale experiments done within this study using a Dionex ASE350 extractor (T=160 °C, t=60 min, Wood-to-solvent (W/S) mass ratio 1:4, 2 wt-% aqueous FA as the solvent) and analysed by HPLC, so that equal concentrations of the measured components in the hydrolysate are obtained. The behavior of unquantified components present in the hydrolysate in small amounts, most notably uronic acids and wood extractives, are subject to high uncertainty. It was assumed that 50 % of these components are solubilized. Oligosaccharides recycled back to the HCE from the APR section are completely hydrolysed to their corresponding monosaccharides. It must be noted that in the absence of detailed kinetic model, possible condensation or other degradation reactions of these components are not considered in the case study.

The HCE reactor outlet is flashed to 1 atm with the flash vapor recycled back to process feed. The solid fraction of the hemicellulose extracted wood is recovered completely but only 60 % of wood hydrolysate is recovered when draining by gravity as proposed by Saeed et al. 2012, while the rest is retained with the solid fraction. FA in the hydrolysate is first completely decomposed to H_2 and CO_2 in decomposition reactor. FA decomposition was experimentally tested to occur in the presence of a Pd/C catalyst for 2 wt-% FA aqueous solution during the study (T=150 °C, P=14 bar). The formed gas is directed to gas-liquid-separation (GLS) and pressure swing adsorption (PSA), from where

the amount of H_2 required to completely hydrogenate hemicellulosic monosaccharides to the corresponding sugar alcohols is circulated back to the hydrogenation reactor.
APR reactor is modelled as a RPLUG reactor model. The base of the APR reaction stoichiometries and kinetics of sugar alcohols was from Murzin et al. (2017). The kinetic parameters were adjusted to yield approximately the same product distribution and conversion of xylitol as observed in Murzin et al. (2017). The kinetics were extended to other sugar alcohols using the data of Duarte et al. (2017) and Kirilin et al. (2012, 2014). The heating requirements of the APR reactor are met with latent heat of condensing saturated high pressure steam (HPS).
As shown in Fig. 1, the APR reactor outlet stream is used as a heat source in the front end of the process before feeding it to GLS. The separated liquid is flashed to 1 atm to purge most of the dissolved gases before being recycled back to the HCE. The gas is directed to PSA, modelled as a simple component splitter, where 85 % of the H_2 is recovered. The alkane containing PSA tail gas is combusted together with birch bark, considered here as an available supplementary fuel. Combustion is modelled as a coupled system of RYIELD, where nonconventional component bark (attributes compiled from Alakangas et al. (2016)) is broken down to conventional components, and RGIBBS, where the most typical combustion products are specified as possible products. Superheated HPS is expanded through a turbine (isentropic, with 0.72 efficiency). Cooling water network was not rigorously simulated in the study, but was assessed using Aspen Plus utility estimates.

Due to the need of estimating formation enthalpies for wood and some products of extraction, reaction enthalpy values have significant uncertainties in HCE. In addition, the net heat formation was relatively low compared to other parts of the process. Thus, the HCE reactor duty was not included in the heat integration.

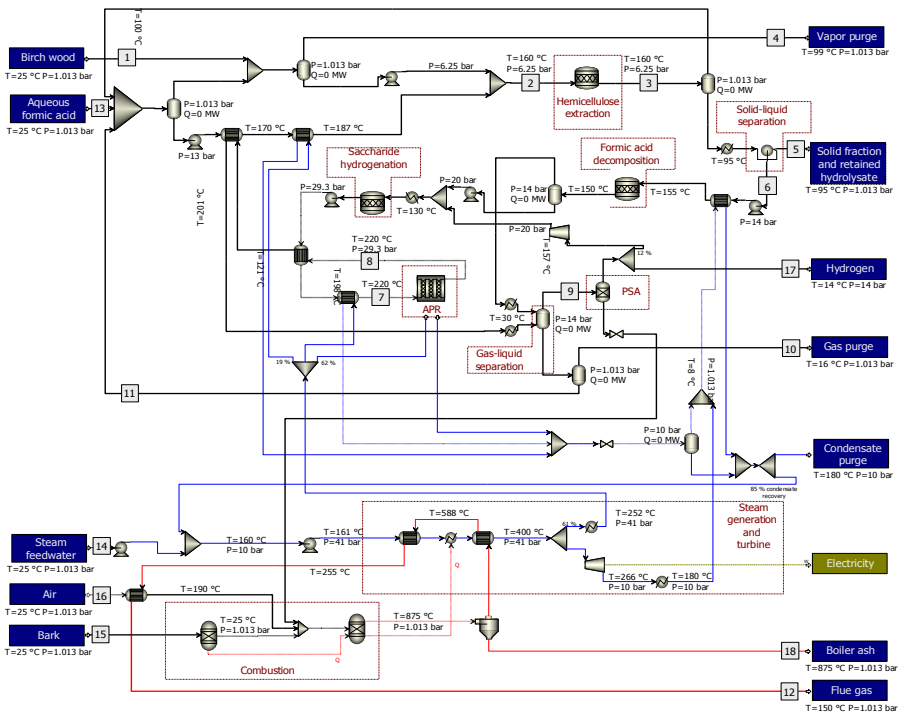

Figure 1. Simulation flowsheet of the integrated process

3. Results and discussion

Simulation results of the main process streams are presented in Table 1.

Table 1. Main process streams (numbered in Figure 1). Similar component groups are lumped.

Streams		**1**	**2**	**3**	**4**	**5**	**6**
Temperature [°C]		25.0	159.7	160.0	99.1	95.0	95.0
Pressure [bar]		1.013	6.25	6.25	1.013	1.013	1.013
Vapor frac		0	0	0	1	0	0
Total flow [kg/h]		134,460	346,637	346,637	6,893	153,702	150,069
Mass fraction	Water	0.5	0.76	0.76	0.90	0.58	0.89
	Monosaccharides	0	$3{\cdot}10^{-8}$	0.024	$2{\cdot}10^{-20}$	0.021	0.033
	Oligosaccharides	0	0.0058	0.0097	$7{\cdot}10^{-16}$	0.0088	0.013
	Soluble lign+extr	0	0.0063	0.010	$4{\cdot}10^{-7}$	0.009	0.015
	Furans	0	0.0074	0.0106	0.042	0.0052	0.0080
	Acetic acid	0	0.011	0.017	0.0013	0.014	0.021
	Formic acid	0	0.016	0.016	0.0004	0.014	0.021
	Cellulose	0.226	0.088	0.087	0	0.197	0
	Hemi polysac	0.132	0.051	0.022	0	0.049	0
	Lignin	0.104	0.040	0.040	0	0.090	0
	Acetyl	0.016	0.0063	$1{\cdot}10^{-4}$	0	$3{\cdot}10^{-4}$	0
	Extractives	0.020	0.0076	0.0038	0	0.0086	0
	Ash+tar	$2{\cdot}10^{-3}$	$8{\cdot}10^{-4}$	0.0017	0	0.0039	0
	CO_2	0	$4{\cdot}10^{-6}$	$4{\cdot}10^{-6}$	0.0382	$4{\cdot}10^{-9}$	$6{\cdot}10^{-9}$
	APR liquids	0	0.0022	0.0022	0.0174	$1{\cdot}10^{-3}$	$2{\cdot}10^{-3}$
	APR gases	0	$5{\cdot}10^{-8}$	$5{\cdot}10^{-8}$	$4{\cdot}10^{-4}$	$1{\cdot}10^{-10}$	$2{\cdot}10^{-10}$
Streams		**7**	**8**	**9**	**10**	**11**	**12**
Temperature [°C]		219.9	220.0	16.6	16.0	16.0	150.4
Pressure [bar]		29.3	29.3	14	1.013	1.013	1.013
Vapor frac		0.0027	0.241	1	1	0	1
Total flow [kg/h]		145,270	145,270	8,555	982	140,597	84,470
Mass fraction	Water	0.904	0.891	0.0016	0.0078	0.933	0.156
	Oligosaccharides	0.014	0.014	$2{\cdot}10^{-14}$	$2{\cdot}10^{-13}$	0.014	0
	Soluble lign+extr	0.015	0.015	$3{\cdot}10^{-9}$	$1{\cdot}10^{-8}$	0.016	0
	Furans	0.0079	0.0079	$1{\cdot}10^{-4}$	$4{\cdot}10^{-4}$	0.0086	0
	Acetic acid	0.022	0.022	$1{\cdot}10^{-5}$	$7{\cdot}10^{-5}$	0.023	0
	Sugar alcohols	0.034	$6{\cdot}10^{-5}$	$5{\cdot}10^{-18}$	$4{\cdot}10^{-17}$	$6{\cdot}10^{-5}$	0
	H_2	$1{\cdot}10^{-5}$	0.0035	0.075	0.0025	$1{\cdot}10^{-7}$	$3{\cdot}10^{-7}$
	CO	0	$1{\cdot}10^{-7}$	$2{\cdot}10^{-6}$	$7{\cdot}10^{-8}$	$3{\cdot}10^{-12}$	$3{\cdot}10^{-6}$
	CO_2	0.0010	0.041	0.883	0.974	0.0019	0.280
	O_2	0	0	0	0	0	$9{\cdot}10^{-8}$
	N_2	0	0	0	0	0	0.564
	APR alkanes	$2{\cdot}10^{-11}$	$2{\cdot}10^{-3}$	0.040	0.015	$2{\cdot}10^{-5}$	$4{\cdot}10^{-25}$
	APR liquids	$1{\cdot}10^{-3}$	$3{\cdot}10^{-3}$	$5{\cdot}10^{-5}$	$2{\cdot}10^{-4}$	0.0035	0

Stream **13** *T* [°C] = 25, *P* [bar] = 1.013, vfrac = 0, total flow [kg/h] = 35,608, massfr: H_2O = 0.85, FA = 0.15
Stream **14** *T* [°C] = 25, *P* [bar] = 1.013, vfrac = 0, total flow [kg/h] = 9,575, massfr: H_2O = 1
Stream **15** *T* [°C] = 25, *P* [bar] = 1.013, vfrac = 0, total flow [kg/h] = 14,560, specified HHV_{dry} [MJ/kg] = 24.2, [wt-%]: C = 56.6, H = 6.8, O = 34.166, S = 0.034, N = 0.8, ash = 1.6, moisture = 50, FC = 19.68, VM = 78.72
Stream **16** *T* [°C] = 25, *P* [bar] = 1.013, vfrac = 1, total flow [kg/h] = 62,020, massfr: O_2 = 0.233, N_2 = 0.767
Stream **17** *T* [°C] = 14, *P* [bar] = 14, vfrac = 1, total flow [kg/h] = 483, massfr: H_2 = 1
Stream **18** *T* [°C] = 875, *P* [bar] = 1.013, vfrac = 0, total flow [kg/h] = 116 massfr: ash = 1

The main results of the overall process are depicted in Fig. 2. The studied HCE step aims to selectively extract only hemicellulose from wood while maintaining the cellulose and lignin fraction mostly intact for further refining. Thus the amount of the cellulose and lignin rich solid fraction is clearly the largest process output and H_2 can be considered as a side product in the overall process concept. As can be seen in Fig. 2, in the HCE, 21 % of the total dry mass of wood is converted to soluble products present in the hydrolysate, corresponding to 62 % conversion of hemicellulosic material (glucan, mannan, xylan, uronic acids, acetyl groups). H_2 molar yield in APR is 70 % (calculated with an APR reforming ratio of 11/5 for C5 and 13/6 for C6 polyols), while the carbon of polyols is converted to alkanes and CO_2 with the yields of 15 % and 80 %, respectively.

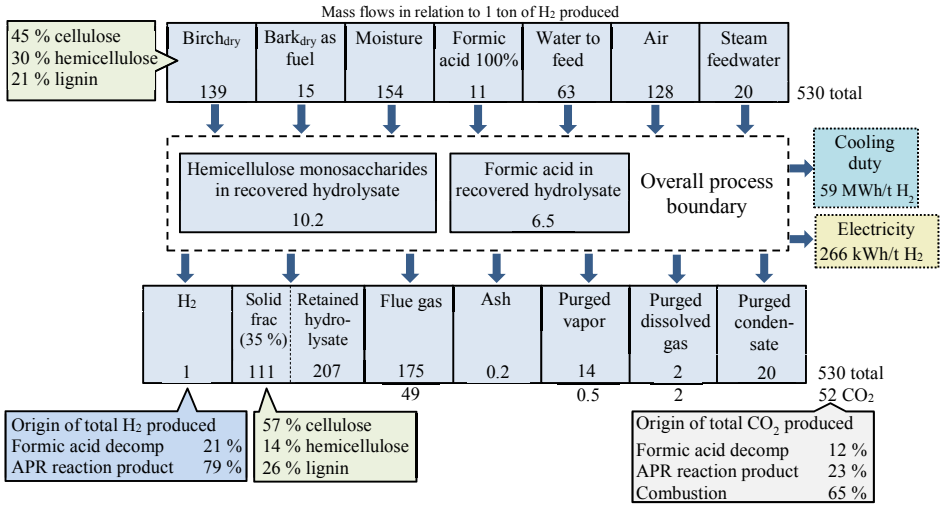

Figure 2. Overall process mass balance and summary of the most important findings.

40 % of FA and hemicellulosic saccharides in the hydrolysate are retained within the porous wood fraction, representing the most significant loss of potentially H_2 forming raw material. The needed amounts of FA and hemicellulose monosaccharides in the recovered dilute hydrolysate for processing them to H_2 through FA decomposition and APR are shown within the process boundary in Fig. 2. It is noteworthy that a relatively large fraction of the produced H_2 (21 %) originates from the FA decomposition.

Assuming 14 % of bark content in dry birch wood and perfect debarking, the bark requirement would correspond to 69 % of the bark that would be present in the total birch feedstock. Total electricity production from the turbine is 1,087 kWh/t H_2, of which 76 % is consumed by the pumps and compressors identified in Fig. 1. Total cooling duty in Fig. 2 corresponds to an estimated 10,200 t/t H_2 of cooling water utility requirement.

Due to the high degree of water recycle and relatively high feedstock moisture content, the minimum aqueous FA feed concentration to achieve the specified FA concentration and W/S ratio in the extraction reactor is 15 wt-% FA (stream 13, Table 1). Lower effluent recycling could permit the use of a more dilute, potentially waste based FA feed stream, but could, in turn, result in increased waste water treatment requirements.

4. Conclusions

A novel process concept for the production of bio-based hydrogen from wood hemicellulose was evaluated by a simulation case study focusing on the mass balance of the process. The largest product output of the process is the cellulose and lignin rich solid wood fraction, potentially suitable as a raw material for other biorefinery processes. H_2 produced originates both from FA used as the HCE catalyst and from hydrogenated hemicellulosic sugars through APR. In addition, net electricity is produced in the process. The APR reactor is operated at higher temperatures compared to HCE stage and thus heat integration of APR outlet stream is beneficial from the energy balance point of view. However, combustion of the alkanes produced in the APR does not provide enough heat to run the overall process and birch bark is exemplified as a supplementary fuel. The main drawbacks hindering the process performance according to this study is high heating requirements of dilute aqueous hydrolysate stream to APR reaction temperatures. Due to

the high degree of water recycle and relatively high feedstock moisture content, a relatively concentrated fresh FA feed is needed, hindering the economic attractiveness of the aqueous effluent recycle. As the total H_2 produced in the process consists also from H_2 produced from FA decomposition, the FA fed to the process should also be of bio- or waste-based origin for truly sustainable H_2 output. General development targets of the applied technologies are to increase the recovery of hydrolysate after the HCE and yield of H_2 and alkanes in the APR of complex hydrolysate components.

Acknowledgments

The authors are grateful for the financial support from Business Finland (Biohydrogen from wood hemicellulose hydrolysate, HemiH2, 2017-2019).

References

E. Alakangas, Hurskainen M., J. Laatikainen-Luntama, J. Korhonen, 2016, Properties of indigenous fuels in Finland, VTT Technology report 272, Espoo, Finland, 53, 54, 61

R. Alén, 2000, Structure and chemical composition of wood, In: P. Stenius (Eds.) Papermaking Science and Technology: Forest Products Chemistry, 11-57, Helsinki, Finland

R.R. Davda, J.W. Shabaker, G.W. Huber, R.D. Cortright, J.A. Dumesic, 2005, A review of catalytic issues and process conditions for renewable hydrogen and alkanes by aqueous-phase reforming of oxygenated hydrocarbons over supported metal catalysts, Applied Catalysis B: Environmental, 56, 1-2, 171-186

H.A. Duarte, M.E. Sad, C.R. Apesteguía, 2017, Production of bio-hydrogen by liquid processing of xylitol on Pt/Al2O3 catalysts: Effect of the metal loading, International Journal of Hydrogen Energy, 42 (7), 4051-4060

W.M. Goldmann, J. Ahola, M. Mikola, J. Tanskanen, 2017, Formic acid aided hot water extraction of hemicellulose from European silver birch (Betula pendula) sawdust, Bioresource Technology, 232, 176-182

D. Humbird, R. Davis, L. Tao, C. Kinchin, D. Hsu, A. Aden, P. Schoen, J. Lucas, B. Olthof, M. Worley, D. Sexton, D. Dudgeon, 2011, Process Design and Economics for Biochemical Conversion of Lignocellulosic Biomass to Ethanol: Dilute-Acid Pretreatment and Enzymatic Hydrolysis of Corn Stover, United States.

A.V. Kirilin, A.V. Tokarev, L.M. Kustov, T. Salmi, J-P. Mikkola, D.Y. Murzin, 2012, Aqueous phase reforming of xylitol and sorbitol: Comparison and influence of substrate structure, Applied Catalysis A: General, 435-436, 172-180

A.V. Kirilin, B. Hasse, A.V. Tokarev, L.M. Kustov, G.N.Baeva, G.O. Bragina, A.Y. Stakheev, A-E. Rautio, T. Salmi, B.J.M. Etzold, J-P. Mikkola, D.Y. Murzin, 2014, Aqueous phase reforming of xylitol over Pt/C and Pt/TiC-CDC catalysts: Catalyst characterization and catalytic performance. Catalysis Science & Technology, 4 (2), 387-401

D.Y. Murzin, S. Garcia, V. Russo, T. Kilpiö, L.I. Godina, A.V. Tokarev, A.V. Kirilin, I.L. Simakova, S. Poulston, D.A. Sladkovskiy, J. Wärnå, 2017, Kinetics, Modeling, and Process Design of Hydrogen Production by Aqueous Phase Reforming of Xylitol, Industrial and Engineering Chemistry Research, 56 (45), 13240-13253

A. Saeed, M.S. Jahan, H. Li, Z. Liu, Y. Ni, A. van Heiningen, 2012, Mass balances of components dissolved in the pre-hydrolysis liquor of kraft-based dissolving pulp production process from Canadian hardwoods, Biomass and Bioenergy, 39, 14-19

F. Schüth, 2014, Hydrogen: Economics and its Role in Biorefining, In: R. Rinaldi (Eds.) Catalytic Hydrogenation for Biomass Valorization, 1-21, Royal Society of Chemistry, Cambridge, UK

A. van Heiningen, Y. Yasukawa, K. Dido, R. Francis, 2017, Minimizing Precipitated Lignin Formation and Maximizing Monosugar Concentration by Formic Acid Reinforced Hydrolysis of Hardwood Chips, In: H.A. Ruiz, M.H. Thomsen, H.L.Trajano (Eds.) Hydrothermal Processing in Biorefineries, 421-441, Springer International Publishing

Sauro Pierucci, Flavio Manenti, Giulia Bozzano, Davide Manca (Eds.)
Proceedings of the 30th European Symposium on Computer Aided Process Engineering (ESCAPE30), May 24-27, 2020, Milano, Italy.
http://dx.doi.org/10.1016/B978-0-12-823377-1.50291-3

Computational Intelligence for Process-optimization Software

Paola P. Oteiza[a,b], Juan I. Ardenghi[a], Nélida B. Brignole[a, c]

[a]*Laboratorio de Investigación y Desarrollo en Computación Científica (LIDECC)-Departamento de Ciencias e Ingeniería de la Computación (DCIC), Universidad Nacional del Sur (UNS), Bahía Blanca, Argentina.*
[b]*Departamento de Ingeniería Química (DIQ), Universidad Nacional del Sur (UNS), B8000 Bahía Blanca, Argentina*
[c]*Planta Piloto de Ingeniería Química (Universidad Nacional del Sur - CONICET) Camino La Carrindanga km. 7 - 8000 Bahía Blanca – Argentina*
dybrigno@criba.edu.ar

Abstract

This work describes a general algorithm for a cooperative hyper-heuristics that enables the optimization of systems of nonlinear algebraic equations with algebraic constraints. The hyper-heuristics comprises the following agents: Genetic Algorithms, Simulated Annealing and Particle Swarm Optimization. Information exchanges take place effectively among them since the immediate incorporation of solution candidates speeds up the search. Algorithmic performance is illustrated with general test models, most of them corresponding to process systems that have currently been employed in PSE. When running in parallel, numerical results demonstrate that the collaborative hybrid structure with embedded intelligent learning contributes to improve results in terms of effectiveness and accuracy. The combination of several heuristic optimization approaches into a hyper-heuristics provides enhanced benefits over traditional strategies since this method helps to find proper comprehensive solutions, also contributing to achieve and accelerate convergence.

Keywords: optimization, meta-heuristics, hyper-heuristics, parallel programming.

1. Introduction

Computational Intelligence provides solutions for complex real-world problems by means of many biologically inspired computational approaches, which are known as Evolutionary Computation. Nature-inspired algorithms have recently become popular due to their simplicity and flexibility. The state-of-the-art for these algorithms is summarized in Yang (2015), while Huang (2019) has provided a survey of automatic parameter tuning methods for meta-heuristic algorithms. Though the quick advances in Evolutionary Algorithms (EAs) have resulted in a richer literature, there has been little emphasis on its application for large industrial problems. Therefore, a challenging promising topic is the exploration of the potential value of computational intelligence in process-engineering applications, aiming at the creation of alternative methods, such as hyper-heuristics, that can cope with tough problems.

An up-and-coming approach to solve complex optimization problems is the one of hyper-heuristics, whose agents can be posed as combinations of nature-inspired techniques. Regarding pipelining, Oteiza et al.(2018) presented a hyper-heuristic that employed a genetic algorithm (GA), an ant colony optimization (ACO) and a simulated

annealing algorithm (SA). It was noticed that when running SA and GA jointly, GA contributed to diversify the search by enlarging the search space. Later, Liu et al. (2019) analysed the case of West-East Natural Gas Pipeline II by optimizing this problem with the following meta-heuristics: GA, SA and particle swarm optimization (PSO). Their merits and drawbacks were discussed based on their optimization results. In their case they showed that although SA was the slowest algorithm, it yielded the best optimization results. The fastest behaviour was exhibited by GA, while in PSO each optimization problem was treated as a particle and an adaptive value was determined by the optimization function. Compared with GA, the information sharing mechanism was different in PSO and all the particles tended to converge to the best solution quickly in most cases (Lhotska et al., 2006).

Taking everything into consideration, GA, SA and PSO look like the three best candidates for team work. In turn, from an individual point of view, meta-heuristic algorithms have extensively been recognized as effective approaches for solving complex optimization problems (Mahdavi et al., 2015). Besides, it is widely accepted that the performance of EAs can be improved by parameter tuning (Karafotias et al., 2014). This task, which is sometimes very time consuming and tedious, has been carried out manually in the literature to suit specific problems. Moreover, parallel methods are also enticing for time-consuming meta-heuristics. In this sense, parallel computing together with meta-heuristic techniques are increasingly powerful to find swiftly solutions located near optimality.

Decision-making processes that involve optimization strategies play a vital role for modern industry, where there is a pervading trend towards the introduction of more realism in industrial modelling. In consequence, large constrained optimization problems, which can even be NP-hard, often arise since the integrated models usually become bigger when more details are introduced. Hence, efficient optimization procedures may help to maximise profitability. Therefore, an intelligent hyper-heuristics has been designed aiming at obtaining a high-quality solution with an emphasis on both problem search-space diversity and reasonable execution times. As to the strategy of generalisation pursued in this paper, parameter retuning has been automated in order to find adequate settings for efficient processing. In this sense, a generalised cooperative hybrid strategy with a novel learning technique is presented. It has the ability to explore and exploit the problem search space more effectively to solve any problem whose model can be defined as a system of nonlinear algebraic equations with algebraic constraints.

2. Fundamentals

In this optimizer we have employed the following well-known meta-heuristics: GA,SA and PSO. As explained in the introduction, their judicious combination looks promising when a general-purpose optimizer is desired. Figure 1 shows a schematic diagram of the proposed Master-Worker approach, where the Master is a central node and n meta-heuristics (Workers) are running. Hence, $p=n+1$ threads are being used. The Workers (agents) are heterogeneous and only communicate with the Master, who organises the cooperativism.

The computational process of the proposed hyper-heuristic algorithm is illustrated in Figure 1 for three agents: GA, SA and PSO. Firstly, the input is adapted to fit the model information needed by each agent. Then, all of them start working. During the whole procedure, a cooperative learning technique is applied to improve the search. Whenever a candidate solution has been found, all agents should be informed. The meta-heuristics that has succeeded in finding a new candidate solution, i.e. the winner, keeps its settings,

while the other agents are retuned. Then, the ranking, which is an ordered list based on fitness values, is updated with the new candidate. The process continues until 30 outer iterations are completed. It is important to remark that each agent carries out 15 inner runs, internally administrating his own termination criteria. Finally, the Master reports the best solution found. Moreover, optional inputs of suggested solutions have also been contemplated in the proposed algorithm, since in many cases the experienced user can envisage the approximate location of the optimum point from an engineering viewpoint.

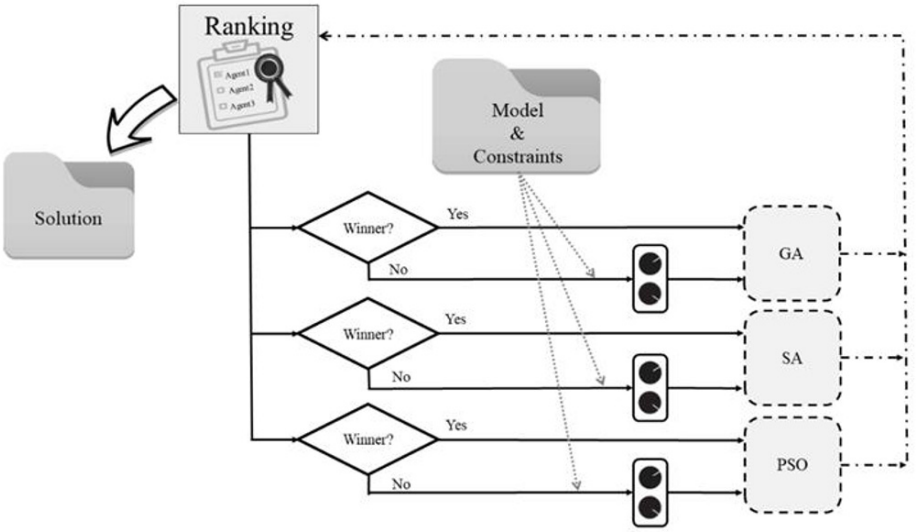

Figure 1. Schematic diagram of the optimizer.

Since the performance of EAs greatly depends on the values of their parameters and operators, on-line selection is carried out to adaptively choose them during the search. From a practical perspective, this strategy contributes to favor diversity. Whenever an agent has failed to be the winner, some of his settings are retuned based on his latest performance for the same problem. In the proposed algorithm the tunable parameters are the temperature for SA and the inertial weight for PSO. As to GA, Figure 2, which is an enlargement of a part of Fig.1, shows that both the crossover rate and the crossover mechanism are automatically adapted during GA evolution.

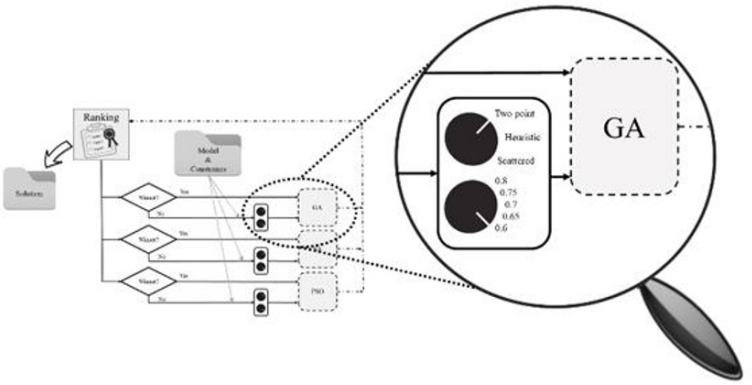

Figure 2. Parameter retuning for GA.

How the information is shared establishes the degree of cooperation among the agents. The update policy depends on the meta-heuristics. For PSO and GA the population is conveniently updated, whereas the initial point is changed for SA. Depending on its input, each meta-heuristics adopts a different behavior in order to include the best discovery so far. It should be taken into account that, in general terms, the shared information provides an idea of where the good areas of the space are. Hence, a new set of samples can be generated. Since the potential parent (i.e., the recently informed candidate solution) is more promising, the enriched set will provide diversity in the initial population for GA, thus favoring convergence.

In particular, SA iterates using a tunable parameter, always calculating energy values (i.e., fitness values) in order to keep the better solution. Given a newly-informed better candidate, the existing solution should be replaced so that the random walk continues from a newly-created point. In this way, the restart might potentially help to escape local optima. If SA remained stuck running towards a local optimum, restarting would be beneficial since both computational speed might be accelerated and the search would be guided to find the global optimum. In turn, for PSO the fitness of each particle is assessed and the best-discovered location is updated.

3. Discussion

For this testing n=3 (GA, SA and PSO) and p= 4 were chosen. Based on their intrinsic features and their potential for complementary behaviour, GA, PSO and SA have been adopted in order to evaluate the strengths and weaknesses of the hyper-heuristics. The results presented in Fig. 3 and Table 1 are based on 48 problems. For software testing all these problems were extracted from the traditional collections by Floudas and Pardalos (1990), Adjiman et al. (1998) and Hock and Schittkowski (1981) in order to have comparable results. These collections are useful for benchmarking purposes because they provide best-known solutions of the optimization problems. First of all, the initial strategy adopted is the cooperative learning technique explained in Section 2. When it was applied to 48 problems, the best-known solution was found for 19 problems. For the rest of them, the algorithm could reach a feasible non-optimal solution, having only two of those cases approached the optimum (i.e., $d \leq 1$). The distance d between points was calculated as the Euclidean norm of the difference between the best-known solution and the one given as final result by the hyper-heuristics. Then, an improvement became necessary.

As shown in Figure 1, the initial strategy implies that there is always a winner in every iteration and for the following outer run the winning agent will only modify his initial point without retuning his method. In fact, there is a tie whenever at least two agents obtain simultaneously the same fitness value. To take this case into account, an improved learning strategy was implemented. It consists in keeping the winner site vacant while all agents without exceptions retune their parameters or operators. Figure 3 shows that the improved strategy contributed to augment the number of solved problems to 25, while for other 6 problems the solutions were feasible points that approached the optimum ($d \leq 1$).

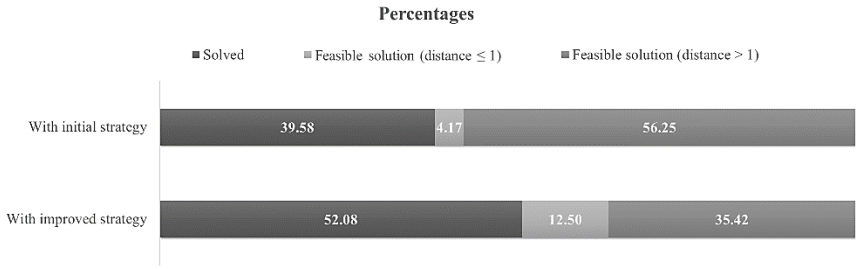

Figure 3 Performance analysis: percentages of successful executions.

Figure 4 shows the optimization results for problems where a braid has ensued in the plots, thus representing competitiveness. Problems 2V, 3V, 6V and 7V have 2, 3, 6 and 7 optimization variables, respectively. In all cases the improved learning strategy was applied and the best-known solution was satisfactorily reached. The best fitness values for all the agents is displayed for each execution. In general terms, it can be observed there is a braid behavior, which means that all the agents become competitive while the algorithm is running. How the learning strategy works can be noticed whenever the fitness value falls down suddenly overtaking the other agents. For example, in iteration 4 for problem 6V, GA exhibited the worst performance, whereas in the next iteration GA became the winner after a judicious retuning of his parameters. The braid behavior shows that all agents compete and learn, jumping out towards distinct fitness values to cope with different situations in the search space. Nevertheless, according to the results for all these problems, the best fitness value was reached between executions 10 and 20.

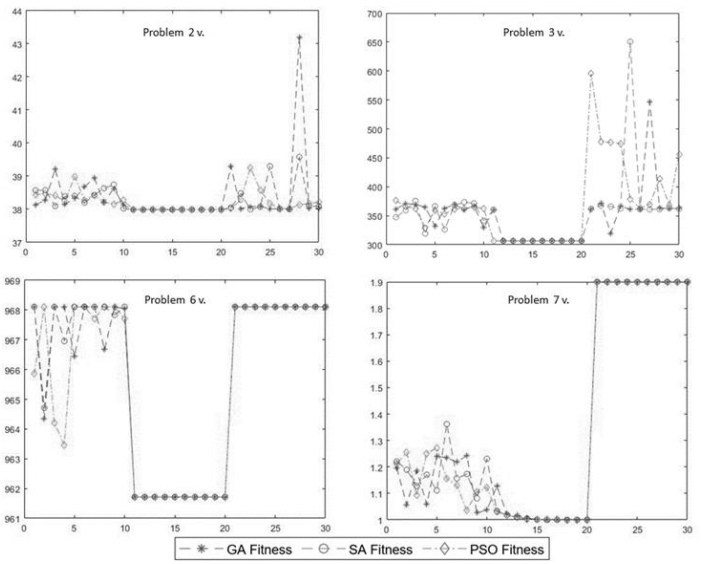

Figure 4. Disaggregated algorithmic performance: best fitness vs. number of executions.

Table 1 shows the average of the CPU times required by 48 test problems. For this analysis, forty-five medium-size (i.e., up to 20 degrees of freedom) problems and three large cases, which respectively involved 22, 30 and 48 degrees of freedom, were

evaluated. It was noticed that the coarse-grain parallel implementation led to a 20% average time reduction, yielding a speed-up of 0.3125. If more efficiency is desired, it is possible to increase the attainable speed-up by refining task distribution among workers.

Table 1. Average execution times expressed in seconds

Size	Sequential CPU mean time (s)	Paralell CPU mean time (s)
Medium	316.5	256.8
Large	1284.6	1025.4

4. Conclusions

The general framework of a parallel hyper-heuristic optimizer was developed and implemented. It solves predefined problems by means of various meta-heuristics working collectively and cooperatively. It was tested by using GA, SA and PSO, which contributed to the search with their intrinsic features. The results provided by each agent are administrated by means of an innovative learning mechanism, where improvements of the optimizer intelligence are achieved by including self-adaptive features in every meta-heuristics. General testing was carried out and the hyper-heuristics proved to be accurate and efficient due to the incorporation of self-adaptability.

In chemical engineering applications, this topic is nowadays open for active research. There are plenty of opportunities in Industry 4.0 mainly regarding process control and plant-wide design that might profit from the employment of hyper-heuristic methods. The hyper-heuristic strategy is innovative as a modelling tool. An adequate ad-hoc implementation of this approach may enrich the optimization platforms of traditional PSE packages in order to contribute to next-generation advanced process modelling environments. Aiming at an efficient optimizer to tackle with time-demanding problems, it would be interesting to explore how to combine traditional equation-oriented methods with the hyper-heuristics so that the new solver helps to find improved solutions and/or initializations in competitive CPU times. Moreover, since the prediction of properties can also be posed as problems of error minimization, the proposed algorithm might be useful as an efficient computational tool to provide accurate predictions in this field.

References

C.S. Adjiman, I.P. Androulakis, C.A. Floudas (1998). A global optimization method, αBB, for general twice-differentiable constrained NLPs-II. Implementation and computational results. Computers Chemical Engineering, 22 (9), 1159-1179.

C. A. Floudas, P. M. Pardalos, (1990). A collection of test problems for constrained global optimization algorithms Springer Science & Business Media. Vol. 455.

W. Hock, K. Schittkowski, (1981). Test examples for nonlinear programming codes. Lecture Notes in Economics and Mathematical Systems. Berlin: Springer-Verlag.

C. Huang (2019). A survey of automatic parameter tuning methods for meta-heuristics, IEEE Transactions on Evolutionary Computation.

G. Karafotias, M. Hoogendoorn, A.E. Eiben. (2014). Parameter control in evolutionary algorithms: Trends and challenges. IEEE Transactions on Evolutionary Computation, 19(2), 167-187.

L. Lhotska, M. Macaš, M. Burša, (2006) PSO and ACO in optimization problems. In: International Conference on Intelligent Data Engineering and Automated Learning, Springer, 1390-1398

E. Liu, L. Lv, Y. Yi, P. Xie, (2019) Research on the steady operation optimization model of natural gas pipeline. IEEE Access. 7, 83251-83265.

S. Mahdavi, M. E. Shiri, S. Rahnamayan, (2015). Meta-heuristics in large-scale global continues optimization: A survey. Information Sciences, 295, 407-428.

P.P. Oteiza, D.A. Rodriguez, N.B. Brignole, (2018). A parallel hyper-heuristic algorithm for the design of pipeline networks. Industrial & Engineering Chemistry Res., 57(42), 14307-14314.

X. S. Yang, (2015). Recent advances in swarm intelligence and evolutionary computation. Springer.

Sauro Pierucci, Flavio Manenti, Giulia Bozzano, Davide Manca (Eds.)
Proceedings of the 30th European Symposium on Computer Aided Process Engineering (ESCAPE30), May 24-27, 2020, Milano, Italy.
http://dx.doi.org/10.1016/B978-0-12-823377-1.50292-5

Identification and Localization of Cyber-Attacks in Industrial Facilities

Kathrin Reibelt, Jörg Matthes, Hubert B. Keller , Veit Hagenmeyer

Karlsruhe Institute of Technology, Hermann-von-Helmholtz-Platz 1, D-76344 Eggenstein-Leopoldshafen, Germany
kathrin.reibelt@kit.edu

Abstract

A new method for improving cyber-security of interconnected smart components of industrial systems is introduced and evaluated. Since usual informational security measures are often bypassed (in spite of existing IT security measures), the new proposed method is based on physical models for detecting manipulations resulting from cyber-attacks. The method builds on and goes beyond traditional ways of Data Reconciliation used in chemical facilities by extending it using prior knowledge on informational properties of components. Thereby, our approach is not restricted to a specific attacker model, which is a significant advantage for the detection of unknown cyber-attacks. The attack detection using the new method is demonstrated using the example of a cooling circuit - as it may be found in chemical processing facilities. Receiver operating characteristics (ROC-curves) are used to show and to quantify the improvement provided by our new method over the performance of traditional Data Reconciliation.

Keywords: cyber-security, Data Reconciliation, industry 4.0, cyber-physical systems

1. Cyber-Security for Cyber-Physical Systems

Cyber-attacks on cyber-physical systems are not new, already in 1986, a few years after the introduction of early internet technologies, a malicious software was discovered in the controlling system of a bevatron accelerator [Bellovin, 2019]. Since then several countermeasures were developed and introduced, always in competition with new attack technologies [Bellovin, 2019]. Until today almost all of the defence measures are based on informational technologies, e.g. monitoring of traffic and restriction of access [Bellovin, 2019]. The ongoing digitalization increases the number of targets. Most attacks target on cyber-physical systems like industry 4.0 facilities or components of the new energy system [Kaspersky Lab, 2018]. Attacker models, describing the limited abilities of the attacker, are not sufficient as attacks are today driven with almost unlimited capabilities, sometimes supported by governments. Hence, new approaches are needed that utilize physical constraints and component properties - that cannot be altered - instead of informational measures that are evadable by design [Cherepanov, 2017]. These new approaches should evidently surpass the very basic countermeasures on cyber-attacks utilizing physical properties using constant and uncorrelated constraints for variables.
One of these approaches could be e.g. using error models that describe patterns of errors. Traditionally these error models are set-up and tuned by experts knowledge. A new version of error models is pattern classification by neural networks. For the set-up of error models the effect of dedicated known errors are determined and described. Using neural networks, data of attacks has to be included and named in training datasets. Hence, for both cases detection using error models is always restricted to known types of errors,

which is very suitable for early detection of wearing, but does not work for complex and unknown cyber-attacks [Katipamula et al. 2005].
Furthermore, a possible detection method utilizing physical properties could be classic Data Reconciliation [Narasimhan et. al., 2000], in which the values of the systems variables are adjusted to the model. Deviations between measured and model values, arising for both set values at captured controls and measured values at false data injection for influencing controls are used for error detection and localization of the faults. However this detection is not sufficient for any system, as the sensor equipment may not be set-up for this use and - with few redundancy - some faults may not be distinguishable. In order to address this, the proposed model-based method for detection of cyber-attacks in the present paper is an extension of Data Reconciliation: The existing detection methods are extended by prior knowledge regarding properties related to cyber-attacks like exposition and commonalities in order to detect efficiently and suitably respective cyber-attacks.
The present paper is organized as follows: In section 2, the new detection method is introduced based on with Data Reconciliation. Section 3 shows the application using a standard example and section 4 gives an evaluation of the performance and the improvement by the extension using Receiver Operating Characteristic Curves (ROC-Curves).

2. Data Reconciliation with Extension for Cyber-Security

Data Reconciliation is based on a mathematical system model, which contains redundancy w.r.t. the information gained by respective measurements [Narasimhan et al., 2000; Schladt et al., 2007]. Considering all system variables $\boldsymbol{y}$, a system matrix $\boldsymbol{A}$ is determined that represents the conservation laws fitting the system equation $\boldsymbol{A} \cdot \boldsymbol{y} = \boldsymbol{0}$. Due to statistical errors, real measurement will not fulfil the system equation exactly. This is utilized by Data Reconciliation to optimize the measurements by adjusting them to the equation. For this adjustment different methods are available, the one used in the present paper is the utilization of Lagrange multipliers. The difference between measured values $\boldsymbol{y}$ and adjusted values $\hat{\boldsymbol{y}}$ is minimized satisfying the constraint of fulfilling the system equation. In this case the measurement deviation is scaled by the variance of the respective variable in order to take different accuracies of the variables into account. The optimization gives a closed solution for calculating $\hat{\boldsymbol{y}}$ from the measured $\boldsymbol{y}$ [Narasimhan et al., 2000].
Based on Data Reconciliation several gross error detection methods are available. Three methods are chosen in view of their adaptability for different systems, their sensitivity to different types of errors (especially to multiple errors), and their ability to localize errors:

1. The measurement test analyses the measurement deviation $\boldsymbol{d} = \boldsymbol{V}_y^{-1} \cdot (\boldsymbol{y} - \hat{\boldsymbol{y}})$ with variance matrix $\boldsymbol{V}_y$ [Tahamhane, 2010].
2. The global test evaluates the sum of the residuals $\boldsymbol{r} = \boldsymbol{A} \cdot \boldsymbol{y}$ and its reduction if measurements of suspected variables are removed and calculated as virtual sensors [Madron, 1985].
3. The hypotheses test compares the residuals to patterns prepared for every possible gross error and gross error combination [Narasimhan et al., 1987].

For normalization the variance matrices for residuals $\boldsymbol{r}$ and normalized deviation $\boldsymbol{d}$ have to be calculated by projecting the variance matrix $\boldsymbol{V}_y$ of the variables $\boldsymbol{y}$ to the basis of $\boldsymbol{r}$ respectively $\boldsymbol{d}$.
For conventional error detection applied in order to detect sensor outages the probability is decreasing with the number of conjointly affected sensors. For detection of cyber-attacks multiple manipulations have to be expected. The similar structure of many sensors and actors leads to effects on several components by one attack. Vice versa the attacks utilize properties of a component that might also be properties of other components. This

is why multiple manipulations for combinations with similar components are more probable than for combinations without commonalities. Subsets $X_i = \{Y|P_i\}$ of variables Y with commonalities P_i like common communication protocols, connection to the same network layer, same measurement principle, same operation system for smart sensors, common manufacturer of the software, high exposition to the network and so on are defined and associated with their common property P_i, an impact factor I_i expressing the weakness of the commonality or the grade of exposition and a class of countermeasures C_i referring to the commonality: $X_i \rightarrow (P_i, I_i, C_i)$. For manipulation detection, the tested combinations $T_k \epsilon Y$ are compared to all predefined subsets X_i, and in case $T_l = X_j$, the threshold for manipulation detection is adapted by factor I_j to be fulfilled more easily. If a group with commonalities is detected to be manipulated, the information about their commonality gives information on possible attack vectors. The class of countermeasures C_i contains targeted measures like blocking certain communication gates as well as safe measures like a shut-down. For every element, it defines conditions regarding system state as well as certainty of knowledge on system state. This enables targeted countermeasures and allows safe further operation during an attack in some cases.

3. Examples

Figure 1 shows the standard example of Data Reconciliation [Narasimhan et al., 2000], a cooling circuit with six devices, one fork and one join. The flow rate of the cooling liquids in the devices is measured. The total amount of cooling liquids is considered to be constant, which leads to conservation equations [Narasimhan et al., 2000]. With the array of 'real' variable values $\boldsymbol{y}$, a system matrix $\boldsymbol{A}$ is determined that represents the conservation laws fitting the system equation $\boldsymbol{A} \cdot \boldsymbol{y} = \boldsymbol{0}$.

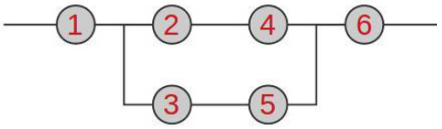

$$\boldsymbol{A} = \begin{bmatrix} 1 & -1 & -1 & 0 & 0 & 0 \\ 0 & 1 & 0 & -1 & 0 & 0 \\ 0 & 0 & 1 & 0 & -1 & 0 \\ 0 & 0 & 0 & 1 & 1 & -1 \end{bmatrix}$$

Figure 1: Standard example, cooling circuit with six connected devices.

Based on this cooling circuit example, the different detection methods and the effect of the adaption for cyber-attacks is used in the following scenario. The manipulation increases variables 1 and 5 with an amplitude of 5 additional to statistical errors (Table 1).

Table 1: Measurements of example.

Variable	True value	Measurement (with statistical errors)	Measurement manipulated	Reconciled values
1	100	100.54	105.54	102.37
2	36	37.83	37.83	37.09
3	64	61.74	61.74	65.28
4	36	36.31	36.31	37.09
5	64	64.32	69.32	65.28
6	100	98.69	98.69	102.37

For demonstrating the effect of adjusted thresholds high exposition to the internet is assumed for variables 1;3;6 and common properties are considered for combinations [4,6]; [1,5]; [2,3]; [1,2,3]; [3,5,6]; [2,4,6]; [3,4,5]. Note that in the following, thresholds for the detection of manipulated variables and combinations, as well as for the decision, if a tested variable or combination could be part of a manipulated combination with more variables are determined in section 4 using Receiver Operating Characteristic Curves (ROC-Curves). In the example, for all properties the same impact factor of 0.7 is used.

3.1. Measurement Test

For the measurement test the test statistics $\boldsymbol{z} = \boldsymbol{V}_d^{-1} \cdot \boldsymbol{d}$ is evaluated [Tahamhane, 2010]. High test statistics result from high deviations and indicate the presence of a gross error. For single manipulations a threshold of 19.76 is used. The adapted threshold is reduced by impact factor of 0.7 to 5.928. The difference to the individual threshold, given in the right column of Table 2, should be positive in case of a detection. A different threshold of 2.83 is used to decide whether single variables could be part of manipulated combinations. In this case no single manipulation is detected and combinations of 1, 3, 5 and 6 are further investigated.

For the detection of multiple errors, suspected variables are removed and the other variables are tested. Therefore test statistics for combination [3,6] is different from the one of [6,3]. Due to space limitation, in Table 2 only a few combinations are listed.

Table 2: Test statistics and difference to adapted threshold by measurement test.

Var	z	Δ
1	3.8804	-2.0476
2	0.9065	-18.8535
3	4.3288	-1.5992
4	0.2836	-19.4764
5	4.9518	-14.8082
6	4.5034	-1.4246
3 1	2.8900	-13.1100
3 2	2.0540	-2.7460
3 4	0.8248	-15.1752
3 5	3.2186	-12.7814
3 6	5.7688	-10.2312

Var	z	Δ
5 1	5.2862	0.48623
5 2	0.3423	-15.6577
5 3	2.1396	-13.8604
5 4	1.5714	-14.4286
5 6	3.3725	-12.6275
6 1	1.8807	-14.1193
6 2	0.2265	-15.7735
6 3	5.6336	-10.3664
6 4	1.4556	-3.3444
6 5	3.9514	-12.0486

For the detection of double combinations, a threshold of 16 and adapted threshold of 4.8 is used. This leads to a detection in combination [5,1]. For investigation for being part of triple manipulations, a threshold of 4.22 is used. The combinations [3,6] and [1,5] are qualified to be further investigated, whether they are part of triple combinations. For triple combinations the threshold 16 respective 4.8 is again used. However, none of the triple manipulations fulfils the detection criteria. Hence, for this example the measurement test would only detect the combination [5,1] that was manipulated indeed.

3.2. Global Test

For the global test the suspected variables are removed and the test statistics $\gamma = \boldsymbol{r}^T \cdot \boldsymbol{V}_r^{-1} \cdot \boldsymbol{r}$ is calculated [Madron, 1985]. As the tested combination is removed, the test statistics for the remaining variables should be small. The thresholds are 0.3 for single manipulations, 0.07 for double manipulations and 0.02 for triple manipulations. For adaption the thresholds are increased by impact factor of 0.7 to 0.51, 0.119 and 0.034.

Table 3: Test statistics and difference to adapted threshold by global test.

Var	γ	Δ
0	52.9998	53.1198
1	37.9422	37.4322
2	52.1780	51.8780
3	34.2610	33.9610
4	52.9194	52.4094
5	28.4793	28.1793
6	32.7192	32.2092
1 2	34.1856	34.1156
1 3	25.9091	25.8391
1 4	37.4394	37.3694
1 5	0.5351	0.4161
1 6	29.1822	29.1122
2 3	30.0422	29.9232

Var	γ	Δ
2 4	52.1395	52.0695
2 5	28.3622	28.2922
2 6	32.6679	32.5979
3 4	33.5807	33.5107
3 5	23.9016	23.8316
3 6	0.9821	0.9121
4 5	26.0100	25.9400
4 6	30.6003	30.4813
5 6	17.1053	17.0353
1 2 3	18.6932	18.6592
1 2 4	28.7101	28.6901
1 2 5	0.0026	-0.0174
…	…	…

The global test only identifies the combination [1,2,5] as manipulated (Table 3). Indeed variable 2 has a high statistical error compared to the other not manipulated variables.

3.3. Hypotheses Test

The hypotheses test compares the residuals to expectation values of residuals $\boldsymbol{F}_k$ for hypotheses $\boldsymbol{k}$ of manipulations in the tested variables. The test statistics [Narasimhan et al., 1987]

$$T = sup_{\boldsymbol{F}_k} \frac{(\boldsymbol{F}_k^T \cdot \boldsymbol{V}_r^{-1} \cdot \boldsymbol{r})^2}{\boldsymbol{F}_k^T \cdot \boldsymbol{V}_r^{-1} \cdot \boldsymbol{F}_k} \quad (1)$$

is normalized and is high for high similarity. The thresholds used for detection are 34 for single manipulations, 80 for double manipulations and 160 for triple manipulations. The reduced thresholds are 23.8, 56 and 112. According to Table 4 variables 1, 3, 6 and combinations [1,5] and [3,5,6] are considered to be manipulated. The highest difference to the individual threshold is shown by combination [1,5].

Table 4: Test statistics and difference to adapted threshold by hypotheses test.

Var	T	Δ	Var	T	Δ
1	15.0576	4.8576	2 5	24.6376	-55.3624
2	0.8218	-33.1782	2 6	20.3319	-59.6681
3	18.7387	8.5387	3 4	19.4191	-60.5809
4	0.0804	-33.9196	3 5	29.0982	-50.9018
5	24.5205	-9.4795	3 6	52.0177	-27.9823
6	20.2806	10.0806	4 5	26.9898	-53.0102
1 2	18.8142	-61.1858	4 6	22.3995	-1.6005
1 3	27.0907	-52.9093	5 6	35.8945	-44.1055
1 4	15.5604	-64.4396	1 2 3	34.3066	-13.6934
1 5	52.4647	28.4647	1 2 4	24.2897	-135.7103
1 6	23.8176	-56.1824	…	…	…
2 3	22.9575	-1.0425	3 5 6	52.5277	4.5277
2 4	0.8602	-79.1398	4 5 6	41.1488	-118.8512

4. Evaluation

For objectively evaluating the performance of the three detection methods and calculation of optimal thresholds that are already used for the examples, the receiver operating characteristics are determined [Fawcett, 2005]. In order to show the effect of the adaption for cyber-security and to quantify the improvement provided by our new method over the performance of the traditional Data Reconciliation, the ROC-curves are calculated for different shifts of the adapted threshold. Thereby shift of 0% represents the curve without adaption, which means incorporating no prior knowledge. For the determination, if the tested variables could be part of a manipulated combination, the ROC-curves a calculated by considering all subsets of the manipulated combination as ‘true’ manipulation. The referring curves are plotted in dark colour.

As high sensitivity as well as high specificity is desirable, the area between the curves and the diagonal determines the value of the test. The diagonal itself represents random results. Thresholds can either be determined by boundary conditions, e.g. a required specificity where the referring threshold can be read out at the ROC-curve, or by using the optimal threshold, that has the highest distance to the diagonal. The optimal thresholds are inscribed in the plots. The specificity decreases with higher numbers of involved variables. For hypotheses test and measurement test an extra threshold for the decision of investigating higher combinations including the referred variables is useful, for the global test this threshold is not meaningful as the ROC-curve almost follows the diagonal.

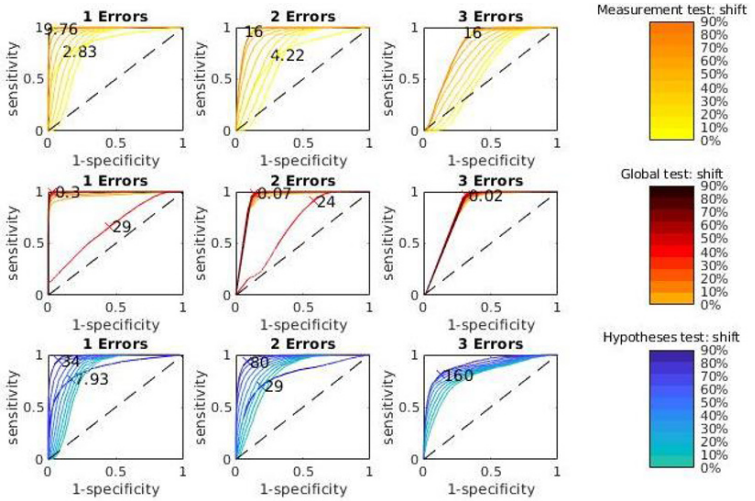

Figure 2: ROC-Curves for the three tests for different numbers of manipulated variables and different threshold shifts for commonalities. Optimal thresholds for detection and for examination for higher combinations are marked.

5. Conclusions

In this paper we introduce a new model-based method for detection of cyber-attacks. The new detection method extends Data Reconciliation by prior knowledge on informational properties of components. It is thus able to detect and localize cyber-attacks in a cyber-physical system. This adds a second layer of defence to industry 4.0 facilities, enables targeted countermeasures and reduces the risk of damages, outages and misproduction.

References

Steven M. Bellovin, 2019, 30 Years of Defending the Internet, Talk, Newark, Delaware, USA, https://www.cs.columbia.edu/~smb/talks/30-years-udel.pdf [Accessed 25 Nov. 2019]

Anton Cherepanov,2017, WIN32/INDUSTROYER, A new threat for industrial control systems, techreport, ESET

Tom Fawcett, 2005, An introduction to ROC analysis, Pattern Recognition Letters 27, pp. 861–874

Kaspersky Lab ICS CERT, 2018, Threat Landscape for Industrial Automation Systems in H2 2017, Moscow, Russia, ics-cert.kaspersky.com

Srinivas Katipamula, Michael R. Brambley, 2005, Methods for Fault Detection, Diagnostics, and Prognostics for Building Systems—A Review, Part I and II. HVAC&R RESEARCH. 11(1) pp. 3 – 26, 11(2) pp. 169 – 187

Frantisek Madron, 1985, ANew Approach to the Identification of Gross Errors in Chemical Engineering Measurements, Chemical Engineering Science - CHEM ENG SCI 40 (1985), pp. 1855–1860

Shankar Narasimhan, Cornelius Jordache, 2000, Data Reconciliation & Gross Error Detection, An Intelligent use of Process Data, Gulf Publishing Company, Houston Texas

Shankar Narasimhan, Richard S. H. Mah, 1987, Generalized Likelihood Ratio Method for Gross Error Detection, AIChE Journal 33 (1987), p. 1514 – 1521

Markus Schladt, Bei Hu, 2007, Soft sensors based on nonlinear steady-state data reconciliation in the process industry. Chemical Engineering and Processing: Process Intensification, 46(11), pp. 1107-1115

Ajit C. Tahamhane, 2010, A Note on the Use of Residuals for Detecting an Outlier in Linear Regression, Biometrika 69(2), pp. 488–489

Sauro Pierucci, Flavio Manenti, Giulia Bozzano, Davide Manca (Eds.)
Proceedings of the 30th European Symposium on Computer Aided Process Engineering (ESCAPE30), May 24-27, 2020, Milano, Italy.
http://dx.doi.org/10.1016/B978-0-12-823377-1.50293-7

Online Condition Monitoring: Sensors, Models and Software for a Safe Management of Aged Process Plants

Paolo Bragatto[a], Patrizia Agnello[a], Canio Mennuti[a], Maria Francesca Milazzo[b]

[a]*INAIL Dipartimento Innovazione Tecnologica, Via Fontana Candida,1; Monteporzio Catone 00078 Italy*

[b]*Università di Messina Dipartimento di Ingegneria, C.da di Dio, Sant'Agata, Messina 98166 Italy*

Abstract

The paper discusses a software application aiming at the dynamic assessment of the remaining useful life (RUL) of critical equipment in process plants. A number of advanced integrity sensors, including *ultrasound thickness* (UT) and *acoustic emissions* (AE) systems, are installed on vessels and pipe throughout the plant. They are able to detect in advance cracks and corrosion and gather continuous data, which feed a simple prognostic model and, in turn, is able to continuously update the information about the expected RUL, in order to support reasonable decisions about equipment life extension as well as inspection scheduling and stops planning. The software exploits an existing platform for communication, database and user interface. The prognosis module uses an easy model, which could be replaced by a more sophisticated algorithm, keeping the other modules.

Keywords: Remaining Useful Life, Major Accident Hazard, Equipment Ageing, Smart Sensors.

1. Context

The control of equipment integrity along the plant lifetime has been a major concern in process industries since a couple of decades ago. For this purpose, operators of major hazard establishments adopt successfully the Risk Based Inspection (RBI) techniques, which determine, based on the results of risk assessment, time and modes of integrity inspections, in order to prevent losses due to deteriorated equipment. The knowledge of deterioration mechanisms and related testing techniques is the core of the RBI methods. The RBI techniques are defined by different national and international standards and represent recognized industrial practices, which are implemented in a number of commercial software products. The main limit of most RBI implementations is the lack of a continuous dynamic update.

Risks related to aged equipment is an emerging concern in European major hazard industries, due to the evidences of many equipment related accidents (Wood & al. 2013), as well as to a few specific requirements of the legislation for the prevention of major accidents. This concern pushes the operators to adopt RBI techniques even with the known limits.

The recent development of innovative sensor technologies is providing the operators new instruments, able to gather and transmit data about material deterioration, allowing a real time monitoring of equipment conditions. The present technologies are able to provide continuous data for a number of deterioration mechanisms, but in the next future, further

sensors will be ready for industrial use. They have the potential to provide a real time control of the conditions of most critical equipment (Bragatto & al. 2018). The exploitation of such data is a new challenge, which involves different disciplines, including chemical engineering, corrosion science, electronic engineering and computer science.

2. Objectives

The use of innovative sensors could become very important to extent the equipment lifecycle at Seveso establishments, assuring a higher level of safety with low costs. In this way, the process industry could successfully face the challenge to continue the safe operating of aged plants. Innovative sensors are able to operate in a continuous way and create a huge a huge amount of data, for which special attention is required. The RBI procedures, as present in the recognized guidelines, were developed to deal data coming from punctual measurements, in most case performed just during periodical programmed stops. To evolve towards a new RBI, able to integrate also continuous monitoring data, a few problems have to be solved. The aim of the paper is to focus on these problems and propose a few solutions. In the detail, the objectives of the paper include a) the review of the emerging sensors technologies, b) the definition of a conceptual framework to use the data provided by these technologies for improving the present RBI techniques and c) the development of a simple application for the safe management of ageing in process plants.

3. Innovative sensors for equipment integrity monitoring

The present section discusses a few advanced sensors, based on non-destructive testing techniques, which have been demonstrated suitable to be used to monitor, even in a continuous way, the integrity of primary containment systems. A generic monitoring system is featuring a sensor and a few electronic components or subsystems, which provide services for identification, transmission, and processing of data. These systems can be used in many different contexts of process industry for monitoring the integrity and functionality of critical equipment, including vessels, pipes and rotating machines. The sensors suitable for monitoring system must be low cost, non-invasive, flexible, scalable and user friendly.

3.1. Vibration Monitoring

Accelerometers are devices that measure the vibration, or acceleration of motion of a structure. They have a transducer that converts mechanical force caused by vibration or a change in motion, into an electrical current using the piezoelectric effect. For monitoring and predictive maintenance applications, it is required a good frequency response, a long-term stability with minimum drift and a wide operating temperature range. These systems are already used to control rotating machines in many refineries.

3.2. Ultrasound Thickness Measurements

Techniques based on the ultrasonic (UT) method can be used to monitor the wall thickness at certain critical points of an equipment. The monitoring systems are essentially composed of high frequency ultrasound emitter (generally 1 ÷ 10 MHz), a localization device and a wireless communication system. The performance of monitoring systems based on UT technologies surpasses those of traditional systems. Monitoring always requires a number of sensors in the network in all critical units, so redundancy helps to increase the overall reliability of the solution. Sensors are installed on critical pipeline or vessels in a permanent or semi-permanent way and can be accessed

remotely. A few commercial systems for UT monitoring are already available for industrial applications.

3.3. Acoustic Emission Monitoring

Acoustic Emission (AE) refers to the generation of transient elastic waves (generally 20 KHz – 1 MHz) produced by a sudden redistribution of the stress state in a material. When a structure is subjected to an external stimulus (change in pressure, load or temperature), the localized sources trigger the release of energy, in the form of tension waves, which propagate to the surface and are recorded by the piezoelectric sensors array. The AE examination is a non-destructive method used for several decades to identify defects (e.g. cracks and micro cracks) in structures and components, both in civil and industrial engineering. The technology is particularly suitable to build a network of sensors across large structures, such as atmospheric storage tanks or pressure vessels. The system consists of a digital signal processor, standardized data transfer ports, reconfigurable logic and specific software. Even though AE monitoring is not yet popular in process industry, it has been demonstrated feasible by a few studies.

4. Dynamic approach to RBI, through innovative sensors

The Risk-Based Inspection approach is based on the concept that high-risk equipment is a limited number of critical items of the establishment (API, 2016a; API, 2016b). Accordingly, priorities and additional investments must be oriented to the maintenance of them. The approach includes the following steps: i) defining and measuring risk; ii) creating a risk-based ranking of critical equipment, and iii) optimizing inspections based on the probability of failure. All these steps require the management of numerous information, therefore, the execution of an RBI analysis is a highly time-consuming process. To support the manager in easily performing it, a number of applications has been developed. There are many software implementing the RBI approach. First of all, the API RBI software, which is based on the RBI quantitative approach as detailed in API RP 581, it was developed by subject matter experts from top multinational refiners and supported by the American Petroleum Institute. A RBI software popular in oil industry is *Credo*, which is an application, developed for the inspection management. A further product, worthwhile to be referred is Inspection Manager developed by *Antea*, an Italian firm and popular in Italian Process industry. It is a management software integrated with the RBI approach as detailed in API RP 581 (Vianello et al., 2016).

The revision of the RBI model identifies, besides various benefits, some limits that should be studied for a better optimization of inspection and maintenance activities. The adoption of the classical approach implies that the equipment prognosis is based on a number of a priori hypotheses (e.g. failure rates, factors associated with the damage mechanisms and complexity of the system under analysis and managerial factors, etc.), which are updated by inspection results. These hypotheses could lead to a false sense of safety and, thus, to unpredictable failures. For this reason, some international guidelines require the risk recalculation to achieve an effective management of changes inside the establishment (API, 2014). The RBI analysis could be imagined as a “frame” of the establishment, taken at time t, which guarantee, by accounting for the established level of reliability, the integrity of the system up to the time $t + \Delta t$ (where Δt is a number of years). This is obviously carried out, on the basis of consolidated knowledge, measurements, historical data of the equipment and a priori assumptions. This model followed by the API 581 is also valid for EEMUA159 and EN16991. The standard API 584 is more dynamic, because it also takes into account changes in operating parameters affecting the probability of

failure and, thus, modifies the operating time before the intervention. The monitoring of the actual equipment conditions would be the solution to avoid incidents related to equipment deterioration, as indicated Bathia et al. (2019). In this context, the monitoring of online conditions clearly offers, as main advantage, the opportunity for a more detailed and reliable prognosis, through the processing of the measurement of the variables performed in real time. Unfortunately, the tools that are currently available for the execution of RBI analyses do not integrate the dynamic concept introduced by API 584. However, the use of the innovative sensors, described in Section 3, could provide information related to time interval Δt, i.e. it would provide a lot of new data about the equipment integrity, which would update the forecasts, without having to wait for the next stop, in such a way that prognostics can be updated in real time.

5. A software framework for integrating innovative sensors

In order to develop a software to manage the data provided in a continuous way by the sensors distributed throughout the plant, it is essential to have a shared platform, able to handle different communication protocols and different format types of data and information. The platform should also manage other important aspects, such as the user interface and database access.

5.1. "Smartbench" platform

"Smartbench" platform was selected, as meeting the essential requirements. It was developed in the Smartbench research project (2017-2019) co-funded by INAIL, the Italian Workers Compensation Authority and a few major Italian universities, with the aim to promote the use of smart safety system in the process industries. The platform provides a distributed infrastructure where, equipment, machines, environment, and workers are connected each other in order to retrieve relevant data from the field and provide early warnings. Different types of sensors may be handled, including environmental, wearable and integrity sensors, installed on the equipment . The platform provides a high-level communication protocol, layered on the usual industrial protocols, such as BLE and NFC. It enables to access into the cloud, where a database deals with different information, including equipment identification, inspections' results, and workers' position. The platform includes an ontology-based knowledge management system to make it able to handle different deterioration mechanisms, depending on materials, operating parameters, environmental conditions and in service age. The platform provides also a user-interface and supports vertical application targeted to workers, supervisors, auditors and external inspectors. It is suitable for both smartphone and control-room applications.

5.2. The modules

The application layered on the "Smartbench" platform aims at demonstrating the feasibility of a "dynamic" assessment of the integrity condition of the whole plant and of any item of equipment. Minimal requirements are the evaluation of the equipment ageing condition and the forecast of remaining useful life. This forecast is used to support the decision making about the safe life extension and stops' planning. RUL is the length of time an equipment is likely to operate before it requires repair or replacement, with a reasonable safety margin. The evaluation of equipment ageing can be carried out by using a sort of virtual sensor, which exploits the results of equipment inspections and elaborates appropriate simplified ageing-related metrics (Milazzo et al., 2019). These make use of accelerating and slowing down factors, as defined in the *Ageing FishBone model* (Milazzo and Bragatto, 2019). By means of a simple prognostic model ageing factors may be

exploited to provide an estimation of the failure frequency and the remaining useful lifetime for each equipment. Input parameters are updated when an inspection is carried out by the competent authority or during a self-assessment by the operator. Taking advantage of the "SmartBench" platform, it is, however, possible to feed the virtual sensor with data from the online monitoring and, therefore, to obtain real-time updates of ageing metrics and, consequently, of RUL estimation. The overall framework is shown in fig. 1. The "Smartbench" platform provides already a few services for presenting the two-dimensional layout of the plant, highlighting equipment with relevant information and sensors. It may be used for presenting on mobile device (smartphone or tablet) the RUL associated with pipes or vessels. Augmented reality has been implemented as ageing indexes and related RUL may be displayed in a small sized screen (1.5 inch) embedded in a home-made smart helmet, interfaced with the platform. The helmet may be worn by the supervisor walking through the plant, in order to have an immediate feeling of the equipment integrity condition. There is, furthermore, a desktop application that shows the plant layout with the items characterized by different symbols and colours, to give a complete picture of the ageing indices. In order to evaluate the effects of different choices and support the decisions, future conditions are simulated and represented over the plant layout.

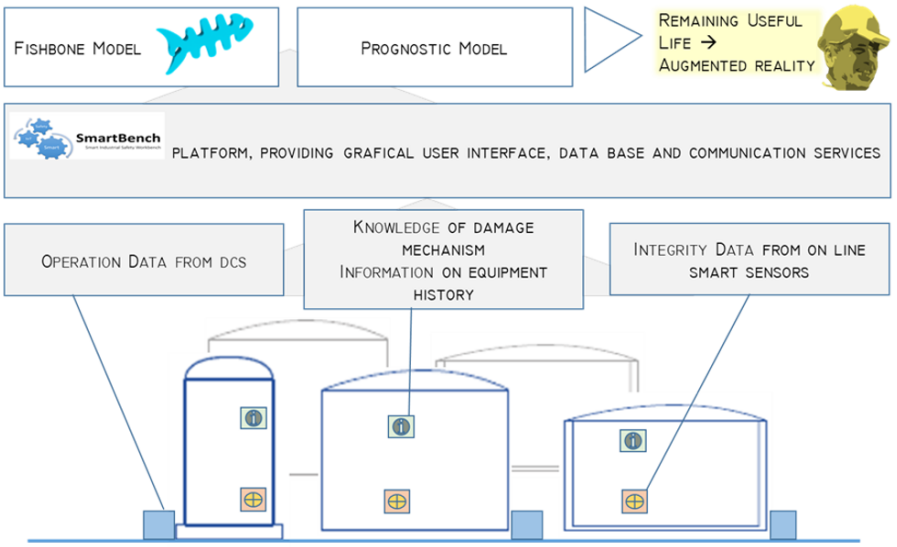

Figure 1 The software framework for the Dynamic Lifetime Extension of Ageing Equipment

6. First Results

As use case, a storage tank has been examined, whose prevalent damage mechanism is soil corrosion. To control the phenomenon, the tank is regularly inspected according to the standard EEMUA 159. In order to improve the control, the tank has been equipped with an AE monitoring system. The system is a network of connected sensors placed along the gunwale at a distance of some 1.5 meters. The system provides a signal for any minimal advance of cracking or thinning. It is robust enough to support outages that are frequent, due to external causes, including meteorological conditions. The ageing index is determined over the years by the *Ageing Fishbone model*. This index has the trend shown in Figure 1(a). Figure 1(b) gives the residual useful lifetime, calculated according

to the assumed corrosion rate (i.e. on the conditions detected at the last inspection by using EEMUA 159). As the tank is equipped with the continuous EA monitoring system, the prognosis may be more accurate and updated. The zero signal from the monitoring system assures, with adequate certainty, that there are no cracks and corrosion in progress and RUL, consequently, would be further extended. If, instead, a positive signal is detected by AE monitoring, automatically RUL would be reduced.

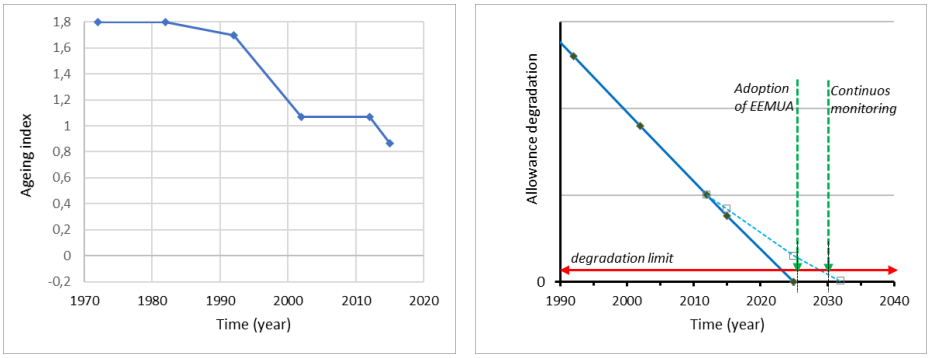

(a) (b)

Figure 2 (a) Ageing Index calculated by the Ageing FishBone model; (b) Residual Useful Lifetime

7. Conclusions

The software architecture discussed in the paper is suitable to exploit the mass of measurement data coming continuously from the integrity sensors distributed in the plant in order to have trustable and updated evaluation of the equipment RUL, adequate to make reasonable decisions on the safe extension of equipment lifetime as well as on inspection scheduling and stop planning. A clear limit of the application is the naivety of the prognostic module. It will be replaced, in the continuation of the research by algorithms much more sophisticated, keeping anyway the other modules. Even the home made smart helmet will be replaced by commercial smart glasses, as soon as they will become reliable and cheap enough.

Acknowledgement

Funded by INAIL in the framework of the call BRIC/2018/ID=11 *(project MAC4PRO)*

References

API, 2014 Integrity Operating Windows RP 584,Washington, US
API, 2019 Risk-based Inspection Methodology RP 581,Washington, US
API, 2016 Risk-based Inspection RP 580, Washington, US
Bhatia, K., Khan, F. Patel, H., Abbassi, R., 2019. Dynamic risk-based inspection methodology. Journal of Loss Prevention in the Process Industries, 62, 1-12.
Bragatto, P., Ansaldi, S.M., Mennuti, C., 2018, Improving safety of process plants, through smart systems for critical equipment monitoring Chemical Engineering Transactions, 67, 49-54.
Milazzo, M.F, Bragatto, P., 2019. A framework addressing a safe ageing management in complex industrial sites: The Italian experience in «Seveso» establishments. Journal of Loss Prevention in the Process Industries, 58, 70-81.
Milazzo, M.F., Scionti, G., Bragatto, P., 2019. Estimation of the Equipment Residual Lifetime in Major Hazard Industries by Using a Virtual Sensor. Proceeding of 29th ESREL, 1764-1771.
Wood, M.H., Arellano, A.V., Van Wijk, L., 2013 Corrosion Related Accidents in Petroleum Refineries. European Commission Joint Research Centre Report EUR 26331 EN

Sauro Pierucci, Flavio Manenti, Giulia Bozzano, Davide Manca (Eds.)
Proceedings of the 30th European Symposium on Computer Aided Process Engineering (ESCAPE30), May 24-27, 2020, Milano, Italy.
http://dx.doi.org/10.1016/B978-0-12-823377-1.50294-9

A Computational Workflow to Study Particle Transport in Porous Media: Coupling CFD and Deep Learning

Agnese Marcato, Gianluca Boccardo, Daniele L. Marchisio

Department of Applied Science and Technology - Politecnico di Torino, Corso Duca degli Abruzzi 24, 10129 Torino, Italy
gianluca.boccardo@polito.it

Abstract

In this work, we studied the coupling of CFD simulation with machine learning models, by using a large set of computational result as the training dataset of a simple fully-connected neural network. The focus of the CFD investigation is the flow and colloid transport in porous media models, both simple and complex, with the end result of obtaining a computationally inexpensive data-driven surrogate model able to replace the CFD simulation, while keeping the same accuracy. While considerable success was obtained in the case of simpler geometries, more sophisticated deep learning models are needed to treat cases characterized by non-trivial fluid dynamic structures.

Keywords: CFD, porous media, machine learning, packed bed reactors, filtration, deep learning

1. Introduction

The study of particle transport in porous media is of the utmost importance as it touches a wide variety of different fields: from the study of contaminant transport in aquifers to the design of effective packed bed reactors in chemical engineering. One very difficult problem in this context is the distinction between Fickian and anomalous transport, with important implications: be it on the estimation of the travel length of a toxic contaminant plume in an aquifer, or in the estimation of the residence time in a packed bed reactor. One of the difficulties lies in the many parameters characterizing the porous media (which are generally geometric), and whose impact and synergy of action can be impossible to analytically predict.

These particularities, which render the problem of particle transport in random media difficult to treat, at the same time make it a prime candidate for machine learning (ML) and specifically deep-learning (DL) approaches, which are particularly suited to extract essential features hidden in data. ML and DL have been notably extensively used in computer science, and some examples of applications of these techniques are making their way in from chemical engineering, from molecular classification (Chang et al. 2019) to pharmaceutical processes (Rolandi, 2019). In this work we couple our recent CFD work laying the groundwork of computational analysis for parameter identification of anomalous transport in porous media, explored by Crevacore et al. (2016), with a variety of different classes of deep neural networks (DNNs).

2. Methods and numerical details

As explored in the Introduction, the objective of this work is to investigate the problem of fluid flow and particle transport (and filtration) in porous media from a first-principle perspective in order to gain a deep insight on the fluid dynamic and transport structure in different models of porous media. The results of these simulations (each characterized by its distinctive features) are then fed to a simple, fully-connected, neural network in order to build a fast surrogate model of the fully-resolved CFD simulation.

2.1. Computational Fluid Dynamics simulations

The first step in this framework is to build the computational models. We explored several different geometrical models of porous media, increasing in complexity, starting from a simple channel with two identical spherical obstacles, to random arrangements of mono-disperse and finally polydisperse spherical objects (these can be seen in Figure 1). Then, two sets of CFD simulations are performed, using the open-source code OpenFOAM. First, the fluid flow is explored by solving the Navier-Stokes equation in the limit of very small Reynolds numbers: from each simulation conducted, the porous model permeability was extracted by way of the well-known Darcy's law. Then, considering the (steady-state) flow field, the transport of dilute colloid particles (characterized by a certain molecular diffusivity) is studied by solving the advection-diffusion equation. In order to study the filtration of this colloid by the solid grains of the porous media (on which the colloid may deposit), a sink boundary condition for the transported scalar is set on the solid surface, and a filtration efficiency extracted following our work by Boccardo et al. (2014).

2.2. Neural network and construction of the surrogate data-driven model

For each of these geometries, a large number (from 1000 to 7000) of CFD simulations are run, each differing randomly in their geometrical or physical conditions: width of the channel, porosity, spheres polydispersity, Reynolds number, and colloid diffusivity. The aggregate set of numerical input features coupled with simulation results are then fed to a fully-connected feedforward neural network, built with MATLAB, initially constituted by one hidden layer with ten neurons, which later evolved to different architectures, as specified in Table 1 in the Results section.

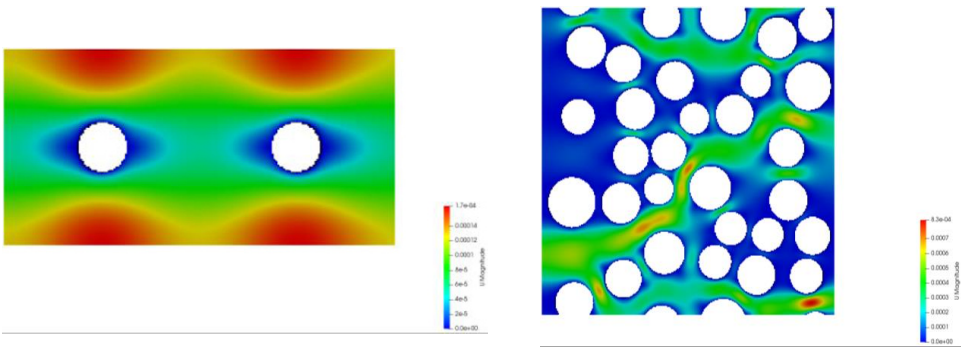

Figure 1. Geometrical model of a channel with two spherical obstacles (left), and of polydisperse periodic randomly arranged spheres (right). Shades of grey representing the fluid velocity contour plot.

3. Results and accuracy of the data-driven surrogate model

As it has been mentioned, the CFD results were analysed and post-processed with the purpose of obtaining, for each geometry considered, a set connecting the input features of the simulation with the result(s) obtained. The numerosity of this set is equal to the number of simulations performed to build the training set for the neural network (which, as mentioned, is numbering in the thousands).
In practical terms, this means that in the case of the polydisperse randomly placed media, each of the 1000 simulations performed was expressed (and fed to the network) as an array of chosen *input features*, namely mean sphere diameter, polydispersity index and porosity for the fluid flow simulations, to which pressure drop and colloid diffusivity are added in the case of colloid transport simulations. To these *input features* the corresponding *output values*, in the form of the Darcyan permeability and filtration efficiency, are then linked.
The full numerical details of computational results and the ranges of operating conditions explored can be found in the recent work from Marcato (2019).
After the neural network *training process*, the end result is a surrogate black-box model capable of predicting the output values when given a new set of input features, with varying accuracy depending on the geometric model considered and on the distance of the new input feature from the original set of features used in the training process. This accuracy is tested by choosing a new set of input parameters, performing CFD simulations and obtaining their results, which are then compared to the predictions of the neural network for that same set of input parameters.

In the case of the channel with obstacles, the network performance was tested both on predictions of Darcyan permeability and of deposition efficiency: its performance is very good, as it can be seen from the parity diagram presented in Figure 2, corresponding to prediction errors lower than 1% (in both cases); for brevity, the figure only shows deposition efficiency results, with an identical diagram in the case of permeability. Given these very good performance, we extended the range of operation of the neural network by testing its prediction accuracy outside of its training range, i.e., the range of operating conditions of the CFD simulations used in the network training.

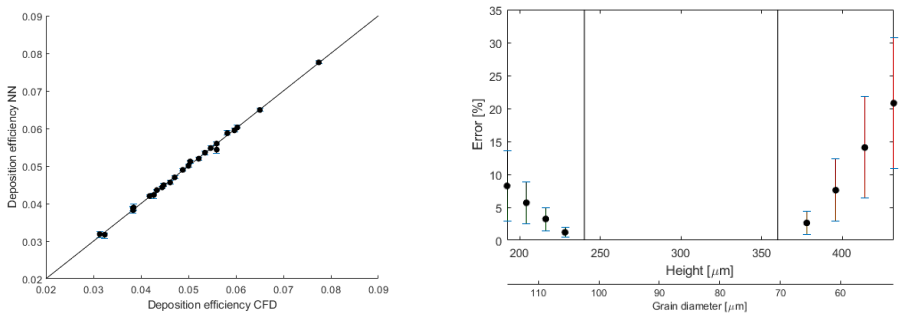

Figure 2. Channel with obstacles results: parity diagram between CFD results and surrogate model predictions (left) and prediction error for input features outside of the training range.

In the case of permeability prediction, the height of the channel and obstacles diameter were both varied, first in the same direction (increasing or decreasing both at the same time) and then one opposite to the other (increasing channel height while decreasing grain diameter), as Figure 2 shows. While the errors are still below 1% inside of the training range, they increase moderately the further the parameters move from the training range limits, reaching values between 10% and 20% for the cases considered; in the case of deposition efficiency prediction they reach larger values at the outer limits (between 20% and 60%). This exercise, which has a parallel in the practice of carefully extrapolating data trends outside of a range of experimental values, was done to better inform the trade-off between the cost of re-training a new network with a wider range of data (and thus, new CFD simulations to further populate the set), and the error of using an already trained network outside of its training range. In order to give an order of magnitude of these different simulation and training times, it is useful to note that (in our simple test cases) while the computational cost of a CFD simulation is of a few minutes, the equivalent network prediction is done in under one second, while the training of the full network takes under one minute.

Another thing to note is that, since the training of a neural network is not a deterministic process, different training runs result in slightly different parameterizations of the surrogate model, leading to a variation in the error prediction. This is expressed graphically in Figure 2 (and slightly less visibly in Figure 3) by means of error bars on the prediction errors, which were obtained by performing ten different network training runs on the same training set and calculating the average and the standard deviation of the ten resulting errors.

Then, a similar analysis was conducted for the case of the random media, whose results are shown in the parity diagram in Figure 3 (for the polydisperse case). As it can be seen, the prediction error is now noticeable, and is slightly higher in the case of the polydisperse media, most likely due to the additional input feature with respect to the monodisperse case (i.e.: the spheres polydispersity). In order to try to decrease this error (of the order of 29% and 17% for permeability and deposition efficiency respectively), two actions were taken.

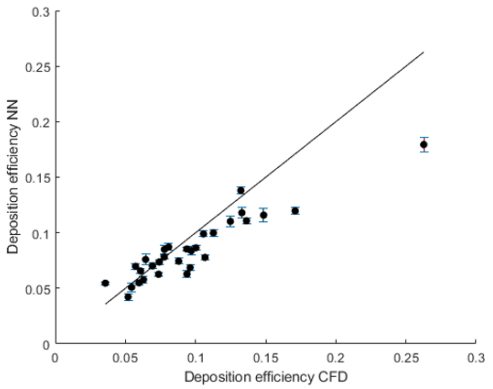

Figure 3. Polydisperse random spheres results: parity diagram between CFD results and surrogate model predictions.

First, the size of the training set (i.e. number of CFD simulations) was increased gradually from 1000 to 7000, in order to present a more feature-rich dataset to the training network.

As it is shown in Figure 4, the errors in both output values decrease appreciably but not in a significant way, with errors still higher than 20% and 10% respectively. Then, a few tentative steps in adjusting the network architecture were taken, specifically by changing the number of the hidden layers and the number of neurons in each one. The tested architectures are detailed in Table 1 along with the corresponding prediction errors for each of the networks: even with this technique some error reduction can be obtained (while noting that very deep networks, i.e. with more than 50 neurons per layer, suffer from higher overfitting errors), but it is clearly not possible to reach a confidence level equivalent to the data-driven surrogate model built on the simpler case, leading to the necessity of exploring more sophisticated techniques.

Table 1: surrogate model errors, in the case of the polydisperse porous media, for different neural network architectures. The number of components in each vector is the number of hidden layers, and their value the number of neurons; e.g. [5 5] means two layers constituted by five neurons each.

Architecture	Error on permeability prediction [%]	Error on deposition efficiency prediction [%]
[5]	24.9	15.9
[10]	28.8	17.1
[5 5]	28.3	15.3
[20]	26.8	16.2
[10 10]	27.2	16.4
[15 10 5]	31.4	17.4
[50]	28.9	18.4
[100]	34.5	21.1
[50 50]	35.6	23.1

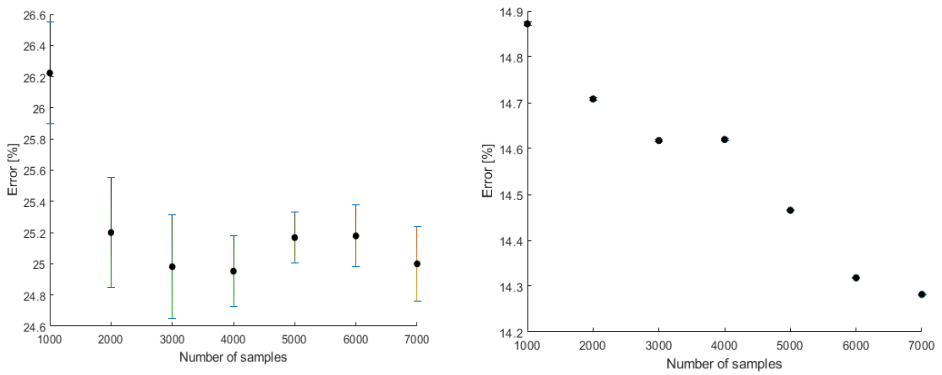

Figure 4. Trends of average prediction error on polydisperse random media by increasing number of training samples (permeability on the left and deposition efficiency on the right).

Conclusions and current work

In this work we have studied the coupling of CFD with machine learning models on different porous media models. In the first case, representing fluid moving in a channel past spherical objects, the performance of the data-driven model is very good, with errors below 1% between the surrogate model and CFD results: the network can also be used for extrapolation in ranges of operating conditions slightly outside the training range. On the other side, when considering more complex porous media, the surrogate model returns accuracies lower than 10% or 20% even by adjusting the network architecture.

The time required for the resolution of the advection diffusion equation (CFD simulation) is approximately 20 minutes, instead the training process of the neural network lasts less than 2 minutes and the response of the data-driven model to a new input is instantaneous. This simple data-driven models can then be reliably used in place of expensive CFD simulations (or in general, all "first principles" methods), as one single call of the neural network has a computational cost which is orders of magnitude lower than the full CFD simulation: in our test problems, under a second versus several minutes – with a total neural network training time of around one minute. This makes them attractive for all cases in which a quick (i.e. *real-time*) computation of the process impact of a change in operating conditions is desired or needed: examples are in-line industrial process control, or that of coupled multi-scale simulations, where lower-scale expensive models should be run many times in a single larger scale model (e.g.: a single process-scale CFD simulation instantiating several runs of a coupled mesoscopic simulation).

Instead, one promising avenue of research for more complex cases, which are now showing in lower accuracy, lies in turning to a "parameter-agnostic" approach, where instead of trying to calculate a set of relevant input parameters, the full geometry and CFD vector/scalar fields are used as training data. This is the approach taken with convolutive neural networks, which enjoyed particular success in the field of image recognition/classification/segmentation, and is the focus of our current research.

References

Chang, J.J., Kang, J.L., Wong, D.S.H., Chou, C.H., Hsu, H.H., Huang, C.H. and Lin, S.T., 2019. Machine Learning of Molecular Classification and Quantum Mechanical Calculations. In *Computer Aided Chemical Engineering* (Vol. 46, pp. 787-792).

Rolandi, P.A., 2019. The Unreasonable Effectiveness of Equations: Advanced Modeling For Biopharmaceutical Process Development. In *Computer Aided Chemical Engineering* (Vol. 47, pp. 137-150).

Crevacore, E., Tosco, T., Sethi, R., Boccardo, G. and Marchisio, D.L., 2016. Recirculation zones induce non-Fickian transport in three-dimensional periodic porous media. *Physical Review E*, *94*(5), pp. 053118.

Boccardo, Gianluca, Daniele L. Marchisio, and Rajandrea Sethi, 2014. "Microscale simulation of particle deposition in porous media." *Journal of colloid and interface science* 417 – pp. 227-237.

Marcato, A., 2019, "Coupling CFD and Machine Learning: two case studies in process engineering" [Original title: "Accoppiamento di CFD e Machine Learning: due casi nell'ingegneria di processo"], *M.Sc. Thesis, Politecnico di Torino, Italy*.

Sauro Pierucci, Flavio Manenti, Giulia Bozzano, Davide Manca (Eds.)
Proceedings of the 30th European Symposium on Computer Aided Process Engineering (ESCAPE30), May 24-27, 2020, Milano, Italy.
http://dx.doi.org/10.1016/B978-0-12-823377-1.50295-0

Hybrid Mechanistic Data-Driven Modeling for the Deterministic Global Optimization of a Transcritical Organic Rankine Cycle

Wolfgang R. Huster[a] , Artur M. Schweidtmann[a] and Alexander Mitsos[b,a,c*]

[a]*Process Systems Engineering (AVT.SVT), RWTH Aachen University, 52074 Aachen, Germany*
[b]*JARA - ENERGY, 52056 Aachen, Germany*
[c]*Institute of Energy and Climate Research: Energy Systems Engineering (IEK-10), Forschungszentrum Jülich GmbH, Wilhelm-Johnen-Straße, 52425 Jülich, Germany*
amitsos@alum.mit.edu

Abstract

Global optimization is desirable for the design of chemical and energy processes as design decisions have a significant influence on the economics. A relevant challenge for global flowsheet optimization is the incorporation of accurate thermodynamic models. A promising alternative to conventional thermodynamic property models is the integration of data-driven surrogate models into mechanistic process models and deterministic global optimization in a reduced space. In our previous works, we trained artificial neural networks (ANNs) on thermodynamic data and included the surrogate models in the global flowsheet optimization of subcritical organic Rankine cycles (ORC). In this work, we extend the framework to the optimization of transcritical ORCs operating at a supercritical high pressure level and subcritical low pressure level. We train separate ANNs for supercritical and subcritical thermodynamic properties. ANNs with a small number of neurons can learn the thermodynamic properties to sufficient accuracy. We identify the optimal working fluid among 122 available fluids in the thermodynamic library CoolProp via a deterministic global optimization of the hybrid process model using the solver MAiNGO. The results show that the process can be optimized efficiently and that transcritical operation can enable high power generation.

Keywords: Surrogate model, Artificial neural networks, MAiNGO, Geothermal power, Supercritical properties

1. Introduction

Numerical optimization of the design and operation of energy processes using renewable energy resources is a key element for the transition to a carbon neutral economy. Making use of low-temperature power resources, such as geothermal brine, will become a relevant part of future power generation. However, the most relevant processes for this energy transformation, organic Rankine cycles (ORCs), often suffer from low thermal efficiencies. This is, among other effects, caused by the isothermal evaporation of the working fluid (WF), which results in high exergy destruction. One way to circumvent is the evaporation at supercritical pressure, i.e., at a pressure level higher than the critical pressure of the working fluid p_c. Fluids at supercritical pressure levels exhibit different thermodynamic properties than at subcritical pressure.

Supercritical pressure levels in ORCs have been investigated in many studies (Chen et al., 2006; Schuster et al., 2010; Gao et al., 2012). Most authors perform a variation of

process parameters to improve the performance (Shengjun et al., 2011; Yağlı et al., 2016; Xu et al., 2016) or apply a local optimization solver (Le et al., 2014; Maraver et al., 2014). Although rare, experimental investigations validated the potential advantages of operating ORCs at supercritical pressure (Kosmadakis et al., 2016). A review on transcritical ORC studies, experimental data, and existing plants is given by Lecompte et al. (2019).

In our previous works (Schweidtmann et al., 2018; Huster et al., 2019a,b), we investigated the deterministic global optimization of ORCs employing pure fluids at subcritical pressure levels. Solving the optimization problem in a reduced-space using our in-house solver MAiNGO (Bongartz et al., 2018), we were able to illustrate the benefit of using surrogate models for the calculation of accurate thermodynamic properties. For this, we train artificial neural networks (ANNs) on subcritical thermodynamic data, which allow for an explicit model formulation. Together with tighter relaxations compared to the original thermodynamic equations, this drastically reduces CPU times (Schweidtmann and Mitsos, 2019; Schweidtmann et al., 2018).

Surrogate models and ANNs have been discussed in engineering literature for decades (Wang, 2006; Himmelblau, 2000). Furthermore, ANNs have been employed for the prediction of supercritical fluid properties by several authors (Mehdizadeh and Movagharnejad, 2011; Eslamimanesh et al., 2011). Arslan and Yetik (2011) and Rashidi et al. (2011) used ANNs to learn ORC process models in a black-box approach and optimized these. The novelty of this work compared to earlier works is that ANNs have not been used for learning supercritical fluid properties and subsequently used in a hybrid model that is to be optimized to guaranteed global optimality. In this work, we apply ANNs for the prediction of supercritical fluid properties within an ORC process optimization. Further, we select the most promising fluid candidates among a wide range of fluids available in the thermodynamic library CoolProp (Bell et al., 2014).

2. ORC process model

We adopt the geothermal set up presented in (Huster et al., 2019a) and adjust the model to transcritical operation. Figure 1 shows the ORC flowsheet, indicating the super- and subcritical pressure levels. The models of the pump, expander and condenser are identical to (Huster et al., 2019a). We model the evaporator as a single process unit due to the continuous phase change and assume a constant heat transfer coefficient. The supercritical phase change requires constraining the minimum temperature difference along the heat transfer, similar to the use of WF mixtures (Huster et al., 2020). For this, the evaporator is discretized along its length. In each discretization cell, we introduce an inequality on the minimum temperature difference to avoid unphysical temperature crossover. When choosing ten cells or less in the process optimization, temperature crossovers occurred at the optimal solution point, resulting in a relaxed solution. To ensure sufficient temperature difference for all WF candidates, we choose 50 cells in all further optimizations. We found that the influence of cell number on the CPU time of the process optimization is almost linear between 10 and 100 cells, ranging from 95 to 632 s. This is summed over six cores that are used for the parallelized branch-and-bound algorithm. Further, we ensure that the expansion process does not cross the two-phase region by setting a lower bound for the specific entropy at the outlet of the evaporator, as illustrated in Figure 2. For the lower bound of the high pressure level p_{HP}, we select $1.1 \cdot p_c$. This avoids pressure levels close to or below the critical point, which requires different models to account for the two-phase region.

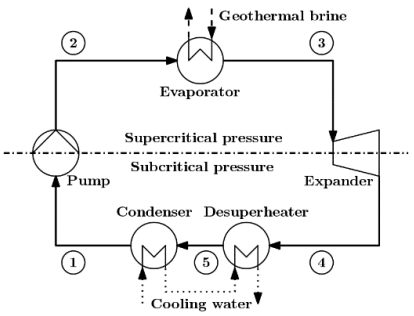

Figure 1: Flowsheet of the transcritical ORC. The circled numbers indicate fluid states. Above the dashed line, the process operates at supercritical pressure, below at subcritical pressure.

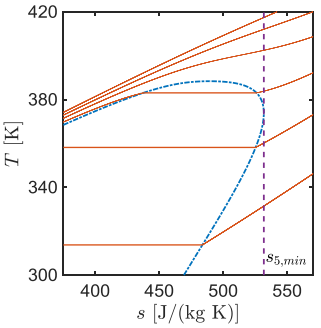

Figure 2: Lower bound for the minimum specific entropy of RC-318 (purple dashed line) for the superheated state at the expander inlet. Orange lines indicate isobars, the blue dash-dotted line indicates the two-phase region.

3. Method

CoolProp (Bell et al., 2014) provides accurate thermodynamic equations of state for 122 fluids. Many of these fluids are not suitable for the presented case study due to their thermodynamic properties. Thus, we only consider WF candidates that can be evaporated at supercritical pressure and condensed at the present conditions. We apply the following rigorous feasibility preselection criteria to all 122 fluids in CoolProp: critical temperature T_c < 400 K, saturation temperature at a pressure of 10 bar $T|^{sat}_{10\ \mathrm{bar}}$ > 260 K. For the preselected fluids, we perform an automated data generation using CoolProp, which we extend to transcritical properties. The procedure for subcritical properties is described in more detail in (Huster et al., 2019b). For supercritical properties, we generate 10^5 data points. We perform the ANN training in Matlab R2018b using the Bayesian backpropagation algorithm, 700 training epochs, and randomly split the data into 40% training data, 30% validation data, and 30% test data. In the training procedure, we minimize the mean-squared error (MSE) on the training data. We optimize the resulting hybrid model using our open-source deterministic global optimization solver MAiNGO (Bongartz et al., 2018).

4. Results

4.1. Artificial neural network accuracy

Table 1 shows that ANNs can learn temperature T as a function of pressure p and mass-specific enthalpy h in the supercritical region with high accuracy. Based on these results and desirable accuracy (Huster et al., 2019a), we select six neurons for both hidden layers for supercritical properties. For subcritical properties, we also select two hidden layers with six neurons each (Huster et al., 2019a,b).

Table 1: Mean-squared errors of the ANNs on the training data for the supercritical region, in dependence of the number of neurons in both hidden layers (input variables: p, h; output variable: T; fluid: RC318).

Number of neurons	5	6	7	8	9	10
MSE [K^2]	$5.3\cdot10^{-8}$	$6.0\cdot10^{-9}$	$6.1\cdot10^{-9}$	$1.1\cdot10^{-10}$	$4.7\cdot10^{-10}$	$1.4\cdot10^{-10}$

4.2. Process optimization results

The process optimization results of the five fluids with the highest net power generation P_{net} (Table 2) show that transcritical operation allows for much higher net power generation than using isobutane at subcritical conditions ($P_{net,max}$ = 16.5 MW, (Huster et al., 2019a)). However, no general claim can be made as we have not performed the WF selection procedure for subcritical operation for this case study. We give p^* as the ratio of high pressure level and critical pressure ($p^* = p_{HP}/p_c$), and the thermal efficiency η_{th}. Aside from high power generation in the turbine P_{turb}, high values of p_{HP} also strongly increase power consumption in the pump P_{pump} and investment costs Inv respectively levelized cost of electricity $LCOE$. The CPU times are between $2 \cdot 10^2$ and $2 \cdot 10^4$ s. Using six CPU cores, this corresponds to less than one hour of wall time. Five of the 21 preselected fluid candidates are infeasible.

Table 2: Results of the thermodynamic optimization for the five WF candidates with the highest P_{net}, sorted by decreasing P_{net}.

Fluid	$\dot{m}_{WF}$ [kg/s]	p_{HP} [bar]	p_{LP} [bar]	P_{net} [MW]	P_{pump} [MW]	η_{th} [%]	Inv [m US-$]	$LCOE$ [US-$/MWh]	p^* [-]
R507A	17.2	65.2	15.8	25.5	10.3	9.1	51.4	57.3	1.8
R125	20.7	71.8	16.9	25.5	12.2	8.8	53.3	59.5	2.0
R143a	14.5	62.2	15.5	25.4	9.3	9.3	50.1	56.3	1.7
R404A	16.7	64.1	15.5	25.4	9.9	9.1	50.9	57.1	1.7
R227EA	20.9	31.9	5.8	25.3	5.0	9.2	46.0	52.1	1.1

The thermoeconomic optimization, i.e., minimization of $LCOE$, takes the investment cost of the process units into account. The results reflect the increased cost of operating at high pressure levels (Table 3). For four of the five given WF candidates, operating the ORC at $p^* = 1.1$ is economically favorable. As this is the lower bound for p_{HP} of each respective WF, the results suggest that subcritical operation could be the most economic option. The CPU times for the thermoeconomic optimizations are between $3 \cdot 10^2$ and $4 \cdot 10^4$ s, summed over all cores. Although the CPU times are higher compared to the thermodynamic optimization, they are still viable for process design.

Table 3: Results of the thermoeconomic optimization for the five WF candidates with the lowest $LCOE$, sorted by increasing $LCOE$.

Fluid	$\dot{m}_{WF}$ [kg/s]	p_{HP} [bar]	p_{LP} [bar]	P_{net} [MW]	P_{pump} [MW]	η_{th} [%]	Inv [m US-$]	$LCOE$ [US-$/MWh]	p^* [-]
R227EA	19.9	31.9	6.2	24.6	4.7	9.4	44.2	51.5	1.1
R1234yf	14.1	36.8	9.0	23.4	4.6	9.5	43.0	52.6	1.1
Propylene	5.7	49.6	14.8	22.5	5.0	10.1	42.8	54.4	1.1
R143a	13.5	55.6	16.1	25.0	7.4	9.3	47.8	54.8	1.5
n-Propane	5.4	46.3	12.3	21.7	4.8	10.3	41.6	54.8	1.1

The T-Q-plots for the best-performing WFs of the thermodynamic and thermoeconomic optimization are given in Figure 3. For $P_{net,max}$, the temperature curve is almost parallel along the evaporator, which comes close to minimum exergy destruction. This is not the case for $LCOE_{min}$, and higher temperature differences between heat source and WF occur. Like this, the HX investment cost is reduced due to the decreased area and a smaller pressure factor.

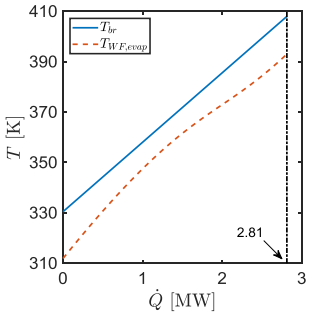

(a) Pnet,max (R507A)

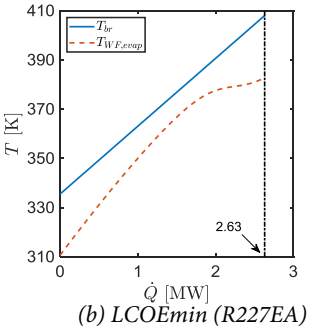

(b) LCOEmin (R227EA)

Figure 3: T-Q-plots for the WFs with the highest net power (R507A) and lowest LCOE (R227EA), illustrating the temperatures of the geothermal brine Tbr and WF in the evaporation TWF,evap.

5. Conclusion and outlook

We propose an approach for globally optimal WF selection and process design for transcritical ORCs. For this, we train ANNs on accurate supercritical thermodynamic data and subsequently integrate them into a mechanistic process model. We solve the resulting hybrid model using the deterministic global solver MAiNGO. We identify the optimal WF among 122 fluids that are available in CoolProp.

We show that ANNs with a small number of neurons (two hidden layers with six neurons each) can learn supercritical data with high accuracy, which is comparable to subcritical data. The thermodynamic optimization reveals the potential of operating ORC at supercritical pressure levels. The nonisothermal evaporation allows to adjust the slope of the evaporation curve towards the heat source, approaching minimal exergy destruction in the evaporation. In contrast, the thermoeconomic optimization can lower investment costs significantly for similar net power generation. All optimizations can be solved to global optimality within less than two hours of wall time using six CPU cores. This demonstrates the viability of the proposed approach.

Future work includes the optimization of more detailed models with heat transfer correlations embedded. It would further be relevant to take the influence of fluid stability at high pressure levels and environmental fluid properties into account.

Acknowledgments: The authors gratefully acknowledge the financial support of the Kopernikus project SynErgie by the Federal Ministry of Education and Research (BMBF) and the project supervision by the project management organization Projektträger Jülich (PtJ).

References

Arslan, O., Yetik, O., 2011. ANN based optimization of supercritical ORC-binary geothermal power plant: Simav case study. Applied Thermal Engineering 31 (17-18), 3922-3928.

Bell, I. H., Wronski, J., Quoilin, S., Lemort, V., 2014. Pure and pseudo-pure fluid thermophysical property evaluation and the open-source thermophysical property library CoolProp. Industrial & Engineering Chemistry Research 53 (6), 2498-2508.

Bongartz, D., Najman, J., Sass, S., Mitsos, A., 2018. MAiNGO - McCormick-based Algorithm for mixed-integer Nonlinear Global Optimization. Tech. rep., Process Systems Engineering (AVT.SVT), RWTH Aachen University.

Chen, Y., Lundqvist, P., Johansson, A., Platell, P., 2006. A comparative study of the carbon dioxide transcritical power cycle compared with an organic Rankine cycle with R123 as working fluid in waste heat recovery. Applied Thermal Engineering 26 (17-18), 2142-2147.

Eslamimanesh, A., Gharagheizi, F., Mohammadi, A. H., Richon, D., 2011. Artificial neural network modeling of solubility of supercritical carbon dioxide in 24 commonly used ionic liquids. Chemical Engineering Science 66 (13), 3039-3044.

Gao, H., Liu, C., He, C., Xu, X., Wu, S., Li, Y., 2012. Performance analysis and working fluid selection of a supercritical organic Rankine cycle for low grade waste heat recovery. Energies 5 (9), 3233-3247.

Himmelblau, D. M., 2000. Applications of artificial neural networks in chemical engineering. Korean journal of chemical engineering, *17*(4), 373-392.

Huster, W. R., Schweidtmann, A. M., Mitsos, A., 2019a. Impact of accurate working fluid properties on the globally optimal design of an organic Rankine cycle. Computer Aided Chemical Engineering 47, 427-432.

Huster, W. R., Schweidtmann, A. M., Mitsos, A., 2019b. Working fluid selection for organic Rankine cycles via deterministic global optimization of design and operation. Optimization and Engineering, in press.

Huster, W. R., Schweidtmann, A. M., Mitsos, A., 2020. Globally optimal working fluid mixture composition for geothermal power cycles, submitted September 6th, 2019.

Kosmadakis, G., Manolakos, D., Papadakis, G., 2016. Experimental investigation of a low-temperature organic Rankine cycle (ORC) engine under variable heat input operating at both subcritical and supercritical conditions. Applied Thermal Engineering 92, 1-7.

Le, V. L., Feidt, M., Kheiri, A., Pelloux-Prayer, S., 2014. Performance optimization of low-temperature power generation by supercritical ORCs (organic Rankine cycles) using low GWP (global warming potential) working fluids. Energy 67, 513-526.

Lecompte, S., Ntavou, E., Tchanche, B., Kosmadakis, G., Pillai, A., Manolakos, D., Paepe, M. D., 2019. Review of experimental research on supercritical and transcritical thermodynamic cycles designed for heat recovery application. Applied Sciences 9 (12), 2571.

Maraver, D., Royo, J., Lemort, V., Quoilin, S., 2014. Systematic optimization of subcritical and transcritical organic Rankine cycles (ORCs) constrained by technical parameters in multiple applications. Applied Energy 117, 11-29.

Mehdizadeh, B., Movagharnejad, K., 2011. A comparison between neural network method and semi empirical equations to predict the solubility of different compounds in supercritical carbon dioxide. Fluid Phase Equilibria 303 (1),40-44.

Rashidi, M. M., Bég, O. A., Parsa, A. B., Nazari, F., 2011. Analysis and optimization of a transcritical power cycle with regenerator using artificial neural networks and genetic algorithms. Proceedings of the Institution of Mechanical Engineers, Part A: Journal of Power and Energy 225 (6), 701-717.

Schuster, A., Karellas, S., Aumann, R., 2010. Efficiency optimization potential in supercritical organic Rankine cycles. Energy 35 (2), 1033-1039.

Schweidtmann, A. M., Huster, W. R., Lüthje, J. T., Mitsos, A., 2018. Deterministic global process optimization: Accurate (single-species) properties via artificial neural networks. Computers & Chemical Engineering 121, 67-74.

Schweidtmann, A. M., Mitsos, A., 2019. Deterministic global optimization with artificial neural networks embedded. Journal of Optimization Theory and Applications 180 (3), 925-948.

Shengjun, Z., Huaixin, W., Tao, G., 2011. Performance comparison and parametric optimization of subcritical organic Rankine cycle (ORC) and transcritical power cycle system for low-temperature geothermal power generation. Applied Energy 88 (8), 2740-2754.

Wang, G. G., Shan, S., 2006. Review of metamodeling techniques in support of engineering design optimization. Journal of Mechanical Design 129, 370-380.

Xu, H., Gao, N., Zhu, T., 2016. Investigation on the fluid selection and evaporation parametric optimization for sub- and supercritical organic Rankine cycle. Energy 96, 59-68.

Yağlı, H., Koç, Y., Koç, A., Görgülü, A., Tandiroğlu, A., 2016. Parametric optimization and exergetic analysis comparison of subcritical and supercritical organic Rankine cycle (ORC) for biogas fuelled combined heat and power (CHP) engine exhaust gas waste heat. Energy 111, 923-932.

Sauro Pierucci, Flavio Manenti, Giulia Bozzano, Davide Manca (Eds.)
Proceedings of the 30th European Symposium on Computer Aided Process Engineering (ESCAPE30), May 24-27, 2020, Milano, Italy.
http://dx.doi.org/10.1016/B978-0-12-823377-1.50296-2

A Discrete Multiple Shooting Formulation for Efficient Dynamic Optimization

Morgan T. Kelley[a], Ross Baldick[b], Michael Baldea[a,*]

[a]*McKetta Department of Chemical Engineering, The University of Texas at Austin (200 E Dean Keeton St. C0400, Austin, TX 78712)*

[b]*Electrical and Computer Engineering, The University of Texas at Austin (2501 Speedway C0803, Austin, TX 78712)*

mbaldea@che.utexas.edu

Abstract

The growing need for fast and efficient solution techniques for solving dynamic optimization problems is driven by a broad spectrum of applications in scheduling and control. We propose a novel framework for dynamic optimization that utilizes a multiple shooting "backbone" with discrete rather than continuous subproblems, thereby eliminating need for repeated time-integration. A Lagrangian relaxation (LR)-based decomposition scheme then dualizes the state continuity requirements between subproblems and enables parallel solution of the problem.

Keywords: dynamic optimization, multiple shooting, batch process control.

1. Introduction

Economic trends such as fast-changing electricity markets require that process operations increasingly rely on real-time decision-making based on dynamic models, motivating research in methods and tools for fast solution of dynamic optimization problems.

Existing methods fall into two broad categories. *Direct methods* utilize nonlinear programming (NLP) solvers for optimization of systems of equations via stepwise integration (Hargraves & Paris, 1987). In *single shooting,* the model equations are integrated over the entire time horizon, and only the decision variables are discretized in time (Vassiliadis et al., 1994). These methods enable the use of efficient solvers for differential algebraic equations (DAEs), but require repeated solution and integration over the time horizon. Furthermore, they cannot deal with open-loop unstable systems and path constraints are difficult to enforce. Conversely, *simultaneous methods* generate large nonlinear programs by discretizing the entire problem space (both state and decision variables). The accuracy of simultaneous methods increases with added discretization points, as does computational cost. However, simultaneous approaches are appealing due to their ability to deal with open-loop unstable systems. *Multiple shooting (MS)* can be regarded as a hybrid between single shooting and sequential methods, wherein the time horizon is divided into smaller intervals where the control vector is represented by simple functions; the solution of the differential constraints is sought for each interval and equality constraints enforce state continuity between time blocks (Bock et al. 1984). In this paper, we propose a new approach for dynamic optimization. Specifically, we further expand the symbiosis of MS and simultaneous methods by exploiting the parallelization

capabilities offered by MS while considering a full discretization of the state variables in each block.

2. Problem Description

The (continuous-time) general dynamic optimization problem to be solved (**PI**) and its discretized version (**PII**) are given below:

$$\max_{u} J = f(\boldsymbol{x}, \boldsymbol{y}, \boldsymbol{u}, t_f) \qquad \max_{u_i} J = f\left(\boldsymbol{x}_{N_i,N_j}, \boldsymbol{y}_{N_i,N_j}, \boldsymbol{u}_{N_i}\right) \quad (1a)$$

$$\text{s.t. } \frac{dx}{dt} = g(\boldsymbol{x}, \boldsymbol{y}, \boldsymbol{u}) \qquad \text{s.t. } \boldsymbol{x}_{i,j+1} = g\left(\boldsymbol{x}_{i,j+1}, \boldsymbol{y}_{i,j+1}, \boldsymbol{u}_i\right)\Delta j + \boldsymbol{x}_{i,j} \quad (1b)$$

$$\boldsymbol{y}(t) = h(\boldsymbol{u}) \qquad \boldsymbol{y}_{i,j} = h(\boldsymbol{u}_{i,j}) \quad (1c)$$

$$\boldsymbol{x}(t_o) = \boldsymbol{x}_o \qquad \boldsymbol{x}(t_o) = \boldsymbol{x}_o \quad (1d)$$

$$\boldsymbol{x}^L \le \boldsymbol{x} \le \boldsymbol{x}^U \qquad \boldsymbol{x}^L \le \boldsymbol{x}_{i,j} \le \boldsymbol{x}^U \quad (1e)$$

$$\boldsymbol{y}^L \le \boldsymbol{y} \le \boldsymbol{y}^U \qquad \boldsymbol{y}^L \le \boldsymbol{y}_{i,j} \le \boldsymbol{y}^U \quad (1f)$$

$$\boldsymbol{u}^L \le \boldsymbol{u} \le \boldsymbol{u}^U \qquad \boldsymbol{u}^L \le \boldsymbol{u}_{i,j} \le \boldsymbol{u}^U \quad (1g)$$

$$\boldsymbol{x}_{i-1,N_j} = \boldsymbol{x}_{i,1} \; \forall \; i > 1 \quad (1h)$$

$\boldsymbol{x}$ represents the differential variables with initial conditions x_o, $\boldsymbol{y}$ are algebraic variables, and $\boldsymbol{u}$ the control/input variables. The objective, J, is a function of these variables evaluated at the final time point, t_f. In our new approach, problem (1) is discretized using two time grids: one for the controls/inputs (set i of length N_i), and another to represent state variable dynamics (set j of length N_j), where $N_i N_j = t_f$. We impose continuity conditions Eq. (1h) and utilize the implicit (backward) Euler method for discretization, with time step length Δj. The structure of the resulting system is block-angular (Figure 1). **PII** can be solved directly using NLP solvers. We observe that the state continuity conditions are complicating constraints. Thus, the solution of the problem can be parallelized using a Lagrangian Relaxation (LR) strategy (Kelley et al., 2018a). In our recent work (Kelley et al., 2018b), we demonstrated that LR was able to significantly reduce the computation time of a dynamically-constrained scheduling problem with linear constraints. In this work, we extend our previous findings to nonlinear problems.

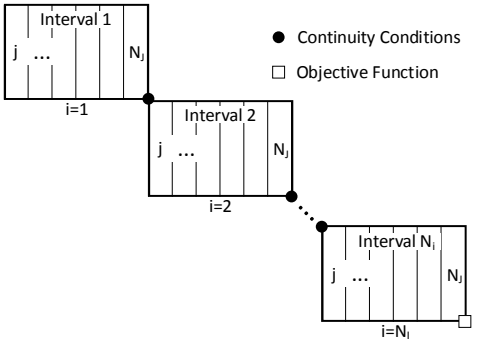

Figure 1: Block angular problem structure with an end-point objective, where control intervals are divided into dynamic time slots with state continuity conditions.

We propose a decomposition scheme based on Lagrangian relaxation (LR) (Fisher, 1981) that enables the solution of **PII** in parallel by decoupling the control intervals and creating N_i independent subproblems by dualizing the continuity conditions. We identify the continuity constraint violation with the variable $\boldsymbol{\gamma}_i$:

$$\boldsymbol{\gamma}_i = \left| \boldsymbol{x}_{i-1,N_j} - \boldsymbol{x}_{i,1} \right| \ \forall i > 1 \tag{3}$$

We represent the above absolute value calculation with Eq. (4), where ε is a sufficiently small number added to preserve the derivative continuity of **PII**.

$$\boldsymbol{\gamma}_{\mathrm{i}} = \sqrt{\left(\boldsymbol{x}_{\mathrm{i-1,N_j}} - \boldsymbol{x}_{i,1} \right)^2 + \epsilon} \ \forall i > 1 \tag{4}$$

The constraint violations, $\boldsymbol{\gamma}_i$, are then penalized in the objective function for **PII**, scaled by a fixed penalty variable, $\lambda_i > 0$:

$$L = J - \sum_i \boldsymbol{\lambda}_i \boldsymbol{\gamma}_i \tag{5}$$

The objective of the reformulated problem (**PIII**) becomes:

$$\max_{u_i} L = J - \sum_i \boldsymbol{\lambda}_i \boldsymbol{\gamma}_i \tag{6}$$

where all constraints besides the continuity constraints from **PII** are included Eq. (1b-g).

When $\gamma_i = 0$, **PII** and **PIII** are equivalent but are solved using different strategies which may result in different local solutions. If using fixed penalty multipliers (as in this work), the solution of **PIII** is relatively straightforward:

1. Initialize: Solve the process model in **PIII** Eq. (6, 1b-g) with bounds on continuity constraint violations, i.e. $\boldsymbol{\gamma}_i \leq \theta$ with fixed control inputs, $\overline{\boldsymbol{u}}_i$. The variable levels become initial guesses in the optimization step.
2. Optimize: Solve **PIII**, optimizing the controls/inputs to maximize objective L.

In the case of a linear program or a convex nonlinear program with equality constraints dualized, the optimality of **PIII** is guaranteed as long as **PII** is feasible and the continuity constraint violations are equal to zero (Guignard, 2003). However, for a nonconvex nonlinear problem, the equivalence of the optimal solution to **PII** and **PIII** cannot be proved. Nevertheless, the solution of **PIII** provides an upper bound on the optimal solution of **PII**, which in some cases is close to the optimal solution of **PII** (Fisher, 1981).

3. Case Study

The previously derived methods are applied to a batch reactor, whose model is an example supplied by Process Systems Enterprise with gPROMS Process Builder v1.3.1.

3.1. Process Description

Two exothermic reactions Eq. (7), with four total components, $\ell = \{A, B, C, D\}$, take place in the batch reactor over a time horizon of $t_f = 1000$ units, with desired product being C.

$$\begin{aligned} A + B &\rightarrow C \\ B + C &\rightarrow D \end{aligned} \tag{7}$$

The model equations for the batch reactor are given in Eq. (8), with the control input as the flow rate of the cooling water, F_{cw}. N_ℓ, C_ℓ, and h_ℓ are the number of moles, concentration, and enthalpy of each component, respectively. The volumetric holdup of the reactor is represented by V, the rate of reaction, r, is based on the temperature-dependent (T) rate constant, k, and C_A and C_B. Q_c is the rate of cooling, U is the

cumulative amount of cooling water used in the process, and H is the total enthalpy of the process.

$$\frac{dN_\ell}{dt} = Vr\nu_\ell \qquad N_{\ell,i,j+1} = \left(V_{i,j+1} r_{i,j+1} \nu_\ell\right)\Delta j + N_{\ell,i,j} \tag{8a}$$

$$r = kC_A C_B \qquad r_{i,j} = k_{i,j} C_{A,i,j} C_{B,i,j} \tag{8b}$$

$$k = Le^{-\frac{E}{RT}} \qquad k_{i,j} = L * \exp\left(-\frac{E}{RT_{i,j}}\right) \tag{8c}$$

$$\frac{dH}{dt} = -Vr\Delta H - Q_{cR} \qquad H_{i,j+1} = \left(-V_{i,j+1} r_{i,j+1} \Delta H - Q_{cR_i}\right)\Delta j + H_{i,j} \tag{8d}$$

$$Q_{cR} = MF_{cw} \qquad Q_{cR_i} = MF_{cw_i} \tag{8e}$$

$$\frac{dU}{dt} = F_{cw} \qquad U_{i,j+1} = \left(F_{cw_i}\right)\Delta j + U_{i,j} \tag{8f}$$

$$H = \sum_\ell N_\ell h_\ell \qquad H_{i,j} = \sum_\ell N_{\ell,i,j} h_{\ell,i,j} \tag{8g}$$

$$h_\ell = a_\ell(T - \bar{T}) + \frac{b_\ell T^2 - \bar{T}^2}{2} \qquad h_{\ell,i,j} = a\_\ell\left(T_{i,j} - \bar{T}\right) + \frac{b_\ell\left(T_{i,j}^2 - \bar{T}^2\right)}{2} \tag{8h}$$

$$VC_\ell = N_\ell \qquad V_{i,j} C_{\ell,i,j} = N_{\ell,i,j} \tag{8i}$$

$$V = \sum_\ell \frac{N_\ell}{\rho_\ell} \qquad V_{i,j} = \sum_\ell \frac{N_{\ell,i,j}}{\rho_\ell} \tag{8j}$$

The discretized model has additional constraints in the form of state continuity conditions:

$$N_{\ell,i-1,N_j} = N_{\ell,i,1} \tag{9a}$$

$$H_{i-1,N_j} = H_{i,1} \tag{9b}$$

$$U_{i-1,N_j} = U_{i,1} \tag{9c}$$

Table 1: Model parameters for the batch reactor case study.

Parameter	Value
a	$\{150,175,200,175\}$
b	$\{0,0,0,0\}$
ρ	$\{10000,8000,11000,11000\}$
ν	$-1,-1,1,1$
ΔH	-60000
E	19000
R	8.314
L	$7.5 * 10^{-4}$
$\bar{T}$	296
M	168000

Initial conditions are imposed on all differential state variables:

$$N(\ell, 0) = N_{\ell,0} \qquad N_{\ell,1,1} = N_{\ell,o} \tag{10a}$$

$$H(0) = H_o \qquad H_{1,1} = H_o \tag{10b}$$

$$U(0) = U_o \qquad U_{1,1} = U_o \tag{10c}$$

The cooling water flowrate, F_{cw} is bounded according to:

$$0.1 \le F_{cw} \le 3 \qquad 0.1 \le F_{cw_i} \le 3 \tag{11}$$

and the reactor temperature, T, is bounded by a path Eq. (12) and an end-point Eq. (13) constraint.

$$T(t) \le 400 \qquad T_{i,j} \le 400 \tag{12}$$

$$310 \le T(t_f) \le 321 \quad \Big| \quad 310 \le T_{N_i,N_j} \le 321 \tag{13}$$

The sequential optimization problem (referred to as **P1**) utilizes Eq. (8), (10)-(13), and the simultaneous optimization problem (referred to as **P2**) uses Eq. (8)-(13). The objectives, which seek to maximize the moles of the desired product, N_C while reducing the cumulative moles of cooling water used, U are given in Eq. (14).

P1	**P2**	
$\max_{F_{cw_i}} J = 2N_{C,t_f} - U_{t_f}$	$\max_{F_{cw_i}} \mathrm{J} = 2\mathrm{N}_{\mathrm{C,N_i,N_j}} - \mathrm{U}_{\mathrm{N_i,N_j}}$	(14)

In order to apply LR to **P2**, continuity constraints Eq. (9) were removed and used to calculate the constraint violation, $\gamma_{\mathrm{i}} = \{\gamma_N, \gamma_{\mathrm{U}}, \gamma_{\mathrm{H}}\}$, (following Eq. (4) with $\varepsilon = 10^{-8}$). Applying the LR scheme to Eq. (14) yields **P3**, which follows the format of **PIII** with Eq. (3), (8), and (10-13) and objective function:

$$\max_{F_{cw_i}} \mathrm{L} = \mathrm{J} - \sum_{\mathrm{i}} \left(\gamma_{\mathrm{i}}^{\mathrm{U}} \lambda_{\mathrm{i}}^{\mathrm{U}} + \gamma_{\mathrm{i}}^{\mathrm{H}} \lambda_{\mathrm{i}}^{\mathrm{H}} + \sum_{\ell} \gamma_{\ell,\mathrm{i}}^{\mathrm{N}} \lambda_{\ell,\mathrm{i}} \right) \tag{15}$$

3.2. Results and Discussion

P1-**P3** were solved on a 64 bit PC running Windows 10® with a 3.6 GHz Intel Core i7 processor with 32 GB of RAM and 8 threads available. **P1** was solved using gPROMS Process Builder v1.3.1 and **P2**-**P3** were solved using CONOPT3 version 3.17I in GAMS 25.0.3. In all cases, wall clock time is reported rather than CPU time since multiple threads were used to solve the decomposed problem, **P3**.

Figure 2 presents the solution times for **P2** and **P3** for N_j varied from 150 to 500 and $N_i = 4$ control intervals. The solution times of **P2** and **P3** are nearly equal for small subproblem sizes, demonstrating that the LR-based decomposition strategy in **P3** does not lead to added overhead solution time in the generation of independent subproblems. Furthermore, the solution time plot of **P3** stays relatively flat until the number of subproblem discretization points reaches 500. Conversely, solution time for **P2** increases almost exponentially with the number of discretization points used in each control interval. Figure 2 also demonstrates that the LR decomposition-based problem, **P3**, reaches nearly the same optimal solution as the non-decomposed problem, **P2**.

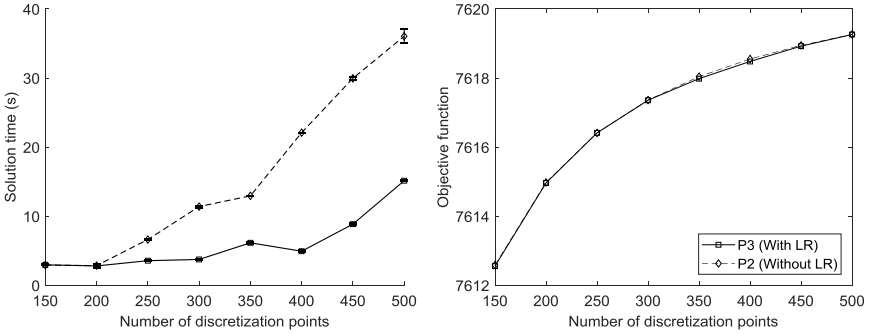

Figure 2: Solution time and optimal objective value versus problem size for **P2** and **P3**.

The optimization problems **P1**-**P3** were also solved considering different control intervals, $N_i = [2,10]$ with the total number of time points kept constant ($\mathrm{N_i N_j} = 1000$). Figure 3 demonstrates that the solution of the sequential optimization problem (**P1**) is consistently slower than simultaneous methods, **P2** and **P3**. The simultaneous method

using LR (**P3**) consistently solves fastest up until 10 intervals are used. This is expected with a constant number of time points, given that the size of the subproblems decreases as the number of intervals, N_i, grows, thereby increasing the number of penalty terms in the objective and the number of γ_i variables to calculate for each state variable. The sequential problem **P1** achieves a higher objective function value than the two simultaneous problems (**P2** and **P3**). This can possibly be attributed to the variable time step utilized by the single-shooting solver for **P1**, whereas the discretization of the time variable in **P2** and **P3** is based on a constant time step. However, the original problem (**P2**) and the relaxed problem (**P3**) achieve nearly the same result, demonstrating that it is possible to significantly reduce the computation time required to get the same solution by employing a LR-based decomposition strategy.

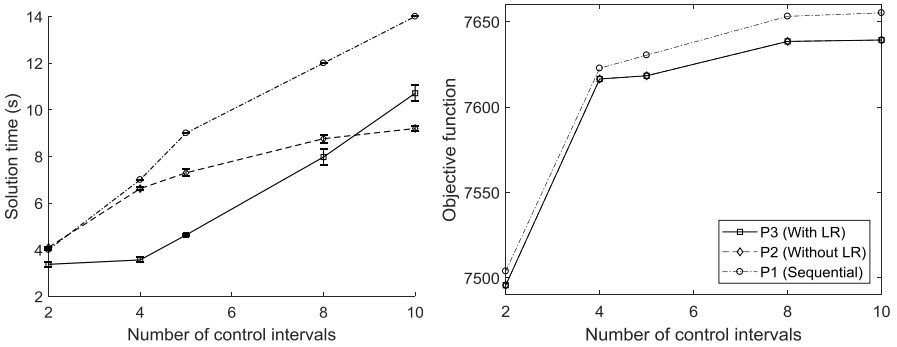

Figure 3: Solution time and optimal objective function value versus problem structure for **P1**-**P3**.

4. Conclusions and future work

We have supplied a general framework for dynamic optimization of nonlinear problems utilizing the structure of multiple shooting, but replacing the continuous subproblems with discrete subproblems, negating the need for repeated time-integration. We have applied an LR-based decomposition scheme which enables parallel solution of the problem, resulting in a solution time that remains low despite increasing problem size and is relatively resilient to increases in problem complexity (i.e. the addition of control intervals)

References

H.G. Bock, & K.J. Plitt, 1984, A Multiple Shooting Algorithm for Direct Solution of Optimal Control Problems. IFAC Proceedings, Vol. 17, 1603–1608.

M.L. Fisher, 1981, The Lagrangian Relaxation Method for Solving Integer Programming Problems. Management Science, 27, 1–18.

M. Guignard, 2003. Lagrangean relaxation. Top, 11(2), 151–200.

C.R. Hargraves, & S.W. Paris, 1987, Direct trajectory optimization using nonlinear programming and collocation. Journal of Guidance, Control, and Dynamics, 10, 338–342.

M.T. Kelley, R.C. Pattison, R. Baldick, & M. Baldea, 2018a, An efficient MILP framework for integrating nonlinear process dynamics and control in optimal production scheduling calculations. Computers & Chemical Engineering, 110, 35–52.

M.T. Kelley, R.C. Pattison, R. Baldick, & M. Baldea, 2018b, An MILP framework for optimizing demand response operation of air separation units. Applied Energy, 222, 951–966.

V.S. Vassiliadis, R.W.H. Sargent, & C.C Pantelides, 1994, Solution of a Class of Multistage Dynamic Optimization Problems. 1. Problems with Path Constraints. Industrial and Engineering Chemistry Research, 33(9), 2123–2133.

Sauro Pierucci, Flavio Manenti, Giulia Bozzano, Davide Manca (Eds.)
Proceedings of the 30th European Symposium on Computer Aided Process Engineering
(ESCAPE30), May 24-27, 2020, Milano, Italy.
http://dx.doi.org/10.1016/B978-0-12-823377-1.50297-4

Backoff-Based Model-Based Design of Experiments Under Model Mismatch

Panagiotis Petsagkourakis , Federico Galvanin*

Department of Chemical Engineering, University College London (UCL), Torrington Place,

WC1E 7JE London, United Kingdom

f.galvanin@ucl.ac.uk

Abstract

Kinetic modelling has become an indispensable tool in industry for a quantitative understanding of reaction systems. In the presence of parametric and structural mismatch, the constraints that maintain safe experiments, e.g. solubility of a chemical may well turn out to be violated when that optimally designed experiment is performed, leading in the best case to less informative data sets or worse to an unsafe experiment. In this work, a Gaussian process is utilised to quantify the uncertainty realisation of the physical system to calculate the explicit back-offs through Monte Carlo stochastic simulations. The method provides a theoretical guarantee for the robust satisfaction of the constraints. The proposed method can be used for the design of optimal experiments starting from limited preliminary knowledge of the parameter set, leading to a safe exploration of the parameter space. The performance of this method is demonstrated through an illustrative case study regarding the parameter identification of the transient behaviour a nucleophilic aromatic substitution (SNAr).

Keywords: Gaussian Process, Uncertainty Propagation, Safe Design.

1. Introduction

A wide range of reaction systems are too complex for allowing the identification of exact mathematical laws governing the phenomena. The identification of model structures is affected by limitations related to the observability of the natural phenomena or/and systematic errors affecting the system. A trustworthy kinetic model can potentially be used to predict the behaviour of the system outside of the experimental conditions used in the model validation and then be utilized for design, optimisation and control in process systems engineering applications. Model-based design of experiments (MBDoE) has been widely used for the purposes of improving parameter precision in highly nonlinear dynamic systems (Franceschini & Macchietto, 2008). Several methods have been proposed in the literature for maximizing the collection of information for a limited amount of resources available for conducting the experiments (Galvanin et al., 2009; Telen et al., 2018). However, the robust satisfaction of potential constraints on the system (for example restrictions on the solubility of chemicals or on the reaction temperature in exothermic transformations) can still be challenging, since the model realisation of the physical system is uncertain at the stage of the experimental design. Various methods have been proposed for the probabilistic satisfaction of constraints, in the presence of parametric uncertainty (Galvanin et al. 2010; Mesbah & Streif, 2015; Telen et al., 2018), however constraint satisfaction that are based on the uncertainty set of the parameters may cause very conservative designs. The structural mismatch may cause large confidence ellipsoids, that subsequently may over-constrain or falsely constrain the

feasibility set of the design. To accommodate this issue, a nonparametric probabilistic model, specifically Gaussian Process (GP), is proposed in this paper to approximate the physical system and propagate the uncertainty to future time instances. GP has been proven to accurately approximate the probability density function of a system and propagate the uncertainties effectively (Deisenroth & Rasmussen, 2011). GP allows us to run Monte Carlo simulation to compute the tightened constraints that will result in a probabilistic satisfaction of the constraints under the uncertainty scenario. The performance of this method is demonstrated through an illustrative case study, in which the optimal experimental design approach is tested on a flow reactor system, where transient experiments are designed and executed (Hone et al., 2017).

2. Problem Statement

We assume that a process model is described by a set of differential and algebraic equations (DAEs) in the form

$$\begin{aligned}\dot{\mathbf{x}} &= \mathbf{f}(\mathbf{x}, \mathbf{u}, \boldsymbol{\theta}, t)\\ \mathbf{y} &= \mathbf{h}(\mathbf{x}, \mathbf{u}, \boldsymbol{\theta}, t),\end{aligned} \tag{1}$$

where $\mathbf{x} \in \mathbb{R}^{n_x}$ is the time dependent vector of state variables, $\mathbf{u} \in \mathbb{R}^{n_u}$ is the vector of the manipulated variables, $\boldsymbol{\theta} \in \mathbb{R}^{n_\theta}$ is the set of unknown model parameters to be estimated within a continuous realizable set Θ which is unknown and to be identified in the present problem, $\mathbf{y} \in \mathbb{R}^{n_y}$ are the responses measured in the process, $t \in \mathbb{R}_+$ is the time and $\hat{\cdot}$ represents the variables that are predicted by the model. In this work, we assume that there is plant-model mismatch, where the physical system is represented by $\mathbf{f}_{\text{real}}$ and $\mathbf{h}_{\text{real}}$ in (1), and the process model by $\mathbf{f}$ and $\mathbf{h}$. Given this mismatch, this work focuses on the safe exploration of the design space with a probabilistic guarantee of constraint satisfaction $\mathbb{P}(g_i(\mathbf{x}, \mathbf{u}) \leq 0) \geq 1 - \alpha$, where g_i is *i-th* constraint and $1 - \alpha$ is the probability for the constraint satisfaction. The MBDoE optimisation problem can then be defined in terms of maximizing a metric of the Fisher information matrix (FIM), $\sum_{t=1}^{N} \mathbf{y}_{\boldsymbol{\theta}}^{\mathbf{T}} \boldsymbol{\Sigma}^{-1} \mathbf{y}_{\boldsymbol{\theta}} + \mathbf{M_0}$, or the variance-covariance matrix FIM^{-1}, where $\boldsymbol{y_\theta}$ is the sensitivity of the measured responses, $\boldsymbol{\Sigma}$ is the variance-covariance matrix of the measurement error, $\mathbf{M_0}$ is the FIM of the previous experiments and N the total number of measured instances. The MBDoE problem can be formulated as

$$\begin{aligned}&\mathbf{u}^* = arg\, \max_{\mathbf{u}} \psi \left(\sum_{t=1}^{N} \hat{\mathbf{y}}_{\boldsymbol{\theta}}^{\mathbf{T}} \boldsymbol{\Sigma}^{-1} \hat{\mathbf{y}}_{\boldsymbol{\theta}} + \mathbf{M_0} \right)\\ &s.t.\\ &\hat{\mathbf{x}}(t = 0) = \mathbf{x}(t = 0)\\ &\dot{\hat{\mathbf{x}}} = \mathbf{f}(\hat{\mathbf{x}}, \mathbf{u}, \boldsymbol{\theta})\\ &\hat{\mathbf{y}} = \mathbf{h}(\hat{\mathbf{x}}, \mathbf{u}, \boldsymbol{\theta})\\ &\dot{\hat{\mathbf{x}}}_{\boldsymbol{\theta}} = \frac{\partial \mathbf{f}}{\partial \mathbf{x}} \hat{\mathbf{x}}_{\boldsymbol{\theta}} + \frac{\partial \mathbf{f}}{\partial \boldsymbol{\theta}}\\ &\hat{\mathbf{y}}_{\boldsymbol{\theta}} = \frac{\partial \mathbf{h}}{\partial \mathbf{x}} \hat{\mathbf{x}}_{\boldsymbol{\theta}}\\ &\mathbb{P}(g_i(\hat{\mathbf{x}}, \mathbf{u}) \leq \mathbf{0}) \geq 1 - \alpha \; \forall i \in \{1, \dots, n_g\}.\end{aligned} \tag{2}$$

However, the probabilistic constraints in (2) are subject to the presence of structural uncertainty. This is a two-sided intractable problem, since the probabilities are infinite dimensional and the uncertainty due to mismatch is not defined. To accommodate these issues, first a probabilistic model (GP) is proposed to approximate the physical system

such that the uncertainty propagation can be performed efficiently. Subsequently, the tightening of the g_i constraints is performed to satisfy the probabilistic guarantee.

3. Gaussian Process Regression and Uncertainty Propagation

In this section, we briefly introduce the fundamentals of GPs (Rasmussen & Williams, 2006). GPs generalize multivariate Gaussian distribution to a distribution over infinite dimensional vector of functions. A GP is a collection of random variables of which any finite subset follows a Gaussian distribution. GP regression aims to model an unknown function $\mathbf{f}$: $\mathbb{R}^{n_x} \rightarrow \mathbb{R}^{n_y}$ given some noisy observations. For $\mathbf{f} = [f_1, \dots, f_{n_y}]$, this could be expressed as:

$$f_i(\cdot) \sim \mathcal{GP}(m_i(\cdot), k_i(\cdot,\cdot)), \tag{3}$$

with m and k are the prior mean and covariance functions. The mean and covariance function define the prior GP and, in this work, we choose zero mean function and squared exponential covariance function:

$$k_i(\mathbf{x}, \mathbf{x}') = \sigma_{f_i}^2 \exp(-\frac{1}{2}(\mathbf{x} - \mathbf{x}')^T \boldsymbol{\Lambda_i}(\mathbf{x} - \mathbf{x}')), \tag{4}$$

where $\sigma_{f_i}^2$ is the covariance magnitude and $\boldsymbol{\Lambda_i} = \frac{1}{\lambda_i^2}\mathbf{I}$ is a scaling matrix. Given the acquired n data points $\mathcal{D}$: $\{\mathbf{X}, \mathbf{y}\}$, with $\boldsymbol{X} = [\mathbf{x_1}, \dots, \mathbf{x_n}]$ and $\boldsymbol{y} = [\boldsymbol{y_1}, \dots, \mathbf{y_n}]$, the mean and variance of the posterior $p(f_i(\mathbf{x}^*)|\mathbf{x}^*)$ can be computed for a deterministic test data point $\mathbf{x}^*$,

$$\begin{aligned} \mu_i(\mathbf{x}^*) &= \mathbb{E}[f_i(\mathbf{x}^*)] = \mathbf{k}_*^{\mathrm{T}}(\mathbf{K} + \sigma_\epsilon^2\mathbf{I})^{-1}\mathbf{y} = \mathbf{k}_*^{\mathrm{T}}\beta \\ \sigma_i(\mathbf{x}_*) &= \mathbb{V}\big(f_i(\mathbf{x}^*)\big) = k_{**} - \mathbf{k}_*^{\mathbf{T}}(\mathbf{K} + \sigma_\epsilon^2\mathbf{I})^{-1}\,\mathbf{k}_*\,, \end{aligned} \tag{5}$$

where $\mathbf{k}_* = k_i(\mathbf{X}, \mathbf{x}^*)$, $k_{**} = k_i(\mathbf{x}^*, \mathbf{x}^*)$ and $K_{m,j} = k(\mathbf{x_m}, \mathbf{x_j})$. In the case of uncertain $\mathbf{x}_*$ that follows a distribution, then (5) is not suitable. This is observed when predictions are conducted for time series and the previous output is the input of the next time instant, since the output of the GP follows a normal distribution. Now if $\mathbf{x}^* \sim \mathcal{N}(\boldsymbol{\mu}^*, \boldsymbol{\Sigma}^*)$ then the posterior $p(f_i(\mathbf{x}^*)|\boldsymbol{\mu}^*, \boldsymbol{\Sigma}^*) = \int p(f_i(\mathbf{x}^*)|\boldsymbol{\mu}^*, \boldsymbol{\Sigma}^*)p(\mathbf{x}^*)d\mathbf{x}^*$ needs to be computed. As this is an analytically intractable problem, a numerical approach based on MC simulations is used where approximation methods are applied. An analytical Gaussian approximation can be conducted using moment matching, the law of iterated expectations and conditional variance, then the mean and variance of the predictions can be approximated using detailed expressions as in (Deisenroth & Rasmussen, 2011).

4. Proposed Methodology

In this section, the proposed methodology is described where the physical system is approximated using a GP and then MC are used to approximate the tightened constraints. First the probabilistic constraints are substituted by a deterministic one in the form of $\tilde{\boldsymbol{g}}_{\boldsymbol{i}} = \boldsymbol{g}_{\boldsymbol{i}} + \boldsymbol{b}_{\boldsymbol{i}} \leq \mathbf{0}$ and $\boldsymbol{b}_{\boldsymbol{i}}$ is selected such that condition (7) is satisfied:

$$g_i(\hat{\mathbf{x}}, \mathbf{u}) + b_i = 0 \rightarrow \mathbb{P}(g_i(\mathbf{x}, \mathbf{u}) \leq 0) = 1 - \alpha. \tag{7}$$

When a constraint is active, the corresponding probabilistic constraint is also active. To compute b_i the inverse cumulative density function (CDF) is used and the exact expression can be derived

$$b_i = F_{g_i}^{-1}(1 - \alpha) - g_i(\hat{\mathbf{x}}, \mathbf{u}) \tag{8}$$

where F_{g_i} is the CDF of g_i. The estimation of F_{g_i} is not trivial, since the distribution of the close loop does not have a known special structure. The CDF is defined as

$$F_{g_i}(0) = \mathbb{P}(g_i \leq 0) = \mathbb{E}(\mathbf{1}_{g_i \leq 0}), \tag{9}$$

where $\mathbf{1}_{g_i \leq 0} = \begin{cases} 1, \text{ if } g_i \leq 0 \\ 0, \text{otherwise} \end{cases}$ is the indicator of $g_i \leq 0$. A nonparametric inference method was proposed in (Bradford et al., 2019; Paulson & Mesbah, 2018) to avoid any assumption regarding the distribution. An empirical CDF (ECDF) can be computed using MC simulations,

$$\hat{F}_{g_i}(0) = \frac{1}{N_{MC}} \sum_{k=1}^{N_{MC}} \mathbf{1}_{g_i^k}, \tag{10}$$

with N_{MC} being a sample size of independent and identically distributed samples. The inverse ECDF can subsequently be computed using the quantile of the N_{MC} samples. Now that (8) can be approximated, the computation of the tightened constraints can follow. A GP is trained to describe the dynamic behaviour of the physical system, and an initial value for the backoffs is given (b_i^0) The optimal experimental design is computed using (2) and predictions for the time horizon are conducted using the GP, where the mean and variance are propagated through time using moment matching (Deisenroth & Rasmussen, 2011); constraints are evaluated using N_{MC} MC simulations. Subsequently, the inverse CDF is computed using the predictions from the GP, and the $g_i(\hat{\mathbf{x}}, \mathbf{u})$ using the nominal model. Then, the backoffs are computed (8) and this process is repeated (see Algorithm 1). It should be noted that the GP is trained with scarce data which may result in conservative constraints, however as new data are becoming available the GP can be updated increasing the accuracy.

Algorithm 1: Backoff Computation

Input	$\mathcal{GP}$, N_{iter}, Optimisation Problem (2), b_i^0	**Output:**	b_i
1.	**for** $m = \{1, \dots, N_{iter}\}$ **do**		
	a. **for** $k = \{1, \dots, N_{MC}\}$ and each sampling time **do** solve (2) using (7) with $b_i^m \ \forall i$ and get u^*. Simulate $\mathcal{GP}$ using u^*		
2.	b. $b_i^m = F_{g_i}^{-1} - g_i(\hat{\mathbf{x}}, \mathbf{u}) \ \forall i$		

5. Case study

The proposed methodology is tested on an online (re)-design of transient experiments case study involving nucleophilic aromatic substitution (SNAr) of 2, 4- difluoro nitrobenzene {1} with pyrrolidine {2} in ethanol (EtOH) to give a mixture of the desired product ortho-substituted {3}, para-substituted {4} and bis-adduct {5} as side products. This case study has been adopted from Hone et al. (2007) and the schematic of the reaction is depicted in Fig 1. A model mismatch is assumed to present and the experimental design was carried out by comparing *1*) a standard MBDoE approach (Galvanin et al., 2010) (SD); *2*) the proposed methodology (GP-BACKOFF). In this case study in-silico experiments were conducted, where {1}, {2} and EtOH have a decreasing flowrate given by a ramp. This allows us to use the residence time instead of time and length of reactor, namely if the flowrates are given as $v = \beta(v_0 - at)$ then the residence time τ for given length of reactor L and time t is $\tau(t, L) = \frac{-(v_0 - at) + \sqrt{(v_0 - at)^2 + 2aL/\beta}}{a}$.

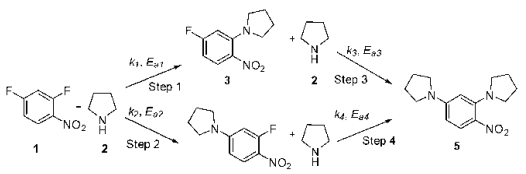

Figure 1: Reaction schematic of case study (Adopted from Hone et al. (2007))

As a result, the molar balance of the reactor can be written as:

$$\frac{dc_1}{d\tau} = -r_1 - r_2, \frac{dc_2}{d\tau} = -r_1 - r_2 - r_3 - r_4, \frac{dc_3}{d\tau} = r_1 - r_3,$$
$$\frac{dc_4}{d\tau} = r_2 - r_4, \frac{dc_5}{d\tau} = r_3 + r_4, \quad (11)$$

where the $i-th$ reaction rate for the real experiment is:

$$r_i = k_i \exp\left(-\frac{E_i}{R}\left(\frac{1}{T} - \frac{1}{T_{ref}}\right)\right) c_i c_2 \text{ and } r_4 = k_4 \exp\left(-\frac{E_4}{R}\left(\frac{1}{T} - \frac{1}{T_{ref}}\right)\right) \frac{c_4 c_2}{1+c_4}, i = \{1,2,3\} \quad (12)$$

with E_i, k_i are the kinetic parameters to be identified, $T_{ref} = 90^o C$. The design variables are the initial conditions for the $\{1\}$, $\{2\}$, and the temperature of the reactor. The assumed *true* kinetic parameters of (11) & (12) have the same values as in Hone et al. (2007). Additionally, a model mismatch is introduced, where the modeller constructed r_4 to be $r_4 = k_4 \exp\left(-\frac{E_4}{R}\left(\frac{1}{T} - \frac{1}{T_{ref}}\right)\right) c_4 c_2$. Since $\{5\}$ is soluble only when $c_5 \leq 0.01M$, a chance constraint is applied to force the satisfaction of this constraint with probability 99% under the presence of the structural mismatch and 5% Gaussian noise of all the measurements. After the computation of the backoffs (offline), an online re-design is performed where the parameter estimation is conducted every time an additional measurement becomes available and the experiment is re-designed (Galvanin et al. 2009) maximizing the determinant of FIM. Six initial experiments were conducted using latin hypercube sampling where the design variables (temperature, and initial concentration of $\{1\}$ and $\{2\}$) are assumed to be bounded with $30\,(^oC) \leq T \leq 150(^oC)$, $0.2(M) \leq c_1^0 \leq 0.3(M)$ and $0.3(M) \leq c_2^0 \leq 2.(M)$. After the first measurements, a maximum likelihood estimation (MLE) is performed together with GP regression. Predictions for one set of experiments are shown in Fig 2. After 5 iterations of 1000 MC simulations the backoffs converged to produce 99% constraint satisfaction. Then, 3000 MC simulations were performed and the results are shown in Fig. 3 (a) and compared with the ones obtained from the SD case. The value of the tightened constraints that are needed in order to satisfy the chance constraints are also illustrated, where the shaded areas correspond to the 99.9% and 0.1 % quantiles. Subsequently, 8 loops of redesign and MLE have been performed, where after each experiment the parameters are estimated using MLE and then MBDoE is computed to result in a new set of experimental conditions. In Fig 3 (b) all 8 profiles of concentrations of $\{5\}$ are depicted, where is clear that none of them violates the respective constraint.

6. Conclusions

In this work, a new backoff-based model-based design of experiments strategy is presented where the chance constraints are effectively satisfied under the presence of structural model mismatch. GP regression is utilized to accommodate the issue of the structural uncertainty and guarantee the feasibility of optimal experiments. The tools described in this work focus on the safe exploration of the design space, where new acquired experimental points can help to identify the "true" structure of the model. Results clearly show that the computed experimental conditions allow a safe conduction

of experiments. Future work will concentrate on improving the accuracy of parameter estimation.

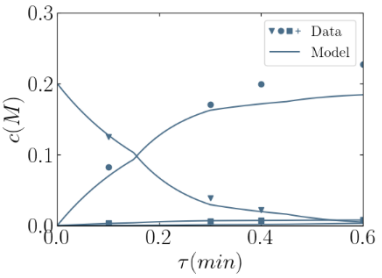

Figure 2: Predictions of experimental conditions for $T = 30.^{o}\,C$, $c_1 = 0.2\,M$ and $c_2^0 = 1.4\,M$

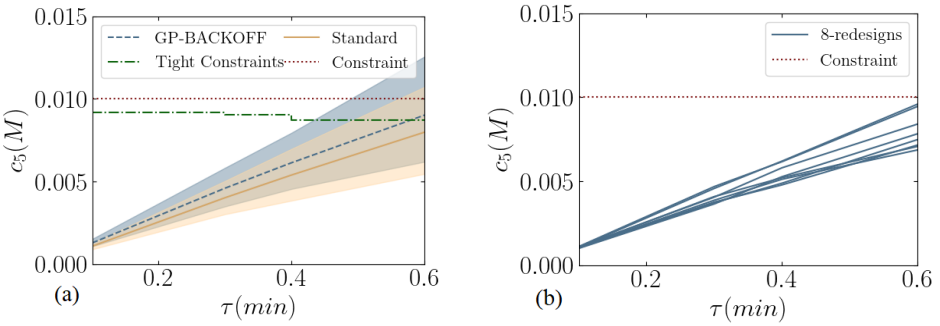

Figure 3:(a) Probabilistic satisfaction of constrain of the proposed method and comparison with nominal satisfaction of constraints (b) Constraint satisfaction after 8 additional redesigns and parameter estimations in a closed loop operation. Each line corresponds to a different redesign.

References

E. Bradford, L. Imsland, D. Zhang, & E.A. del Rio Chanona, 2019, Stochastic data-driven model predictive control using Gaussian processes, http://arxiv.org/abs/1908.01786

M.P. Deisenroth, & C.E. Rasmussen, 2011, PILCO: A Model-Based and Data-Efficient Approach to Policy Search, in Proceedings of the 28th International Conference on Machine Learning.

G. Franceschini, & S. Macchietto, 2008. Model-based design of experiments for parameter precision: State of the art, Chemical Engineering Science, 63(19), 4846–4872.

F. Galvanin, M. Barolo & F. Bezzo, 2009, Online model-based redesign of experiments for parameter estimation in dynamic systems, Industrial & Engineering Chemistry Research, 48, 9, 4415-4427.

F. Galvanin, M. Barolo, F. Bezzo, & S. Macchietto, 2010, A backoff strategy for model-based experiment design under parametric uncertainty, AICHE, 56, 8, 2088-2102.

C.A. Hone, N. Holmes, G.R. Akien, R.A. Bourne, & F.L. Muller, 2017. Rapid multistep kinetic model generation from transient flow data, Reaction Chemistry and Engineering, 2, 103–108.

A. Mesbah, & S. Streif, 2015. Probabilistic approach to robust optimal experiment design with chance constraints, IFAC-PapersOnLine, 28, 8, 100–105.

J.A Paulson, & A. Mesbah, 2018, Nonlinear Model Predictive Control with Explicit Backoffs for Stochastic Systems under Arbitrary Uncertainty. IFAC-PapersOnLine, 51, 20, 523–534

C.E. Rasmussen, & C.K.I Williams, 2006, Gaussian Processes for Machine Learning.

D. Telen, Nimmegeers, Philippe, & J. Van Impe, 2018, Uncertainty in optimal experiment design: comparing an online versus offline approaches, IFAC-PapersOnLine, 51, 2, 771–776.

Sauro Pierucci, Flavio Manenti, Giulia Bozzano, Davide Manca (Eds.)
Proceedings of the 30th European Symposium on Computer Aided Process Engineering (ESCAPE30), May 24-27, 2020, Milano, Italy.
http://dx.doi.org/10.1016/B978-0-12-823377-1.50298-6

Computer-Aided Hazop: Ontologies and Ai for Hazard Identification and Propagation

Johannes I. Single, Jürgen Schmidt, Jens Denecke

CSE Center of Safety Excellence (CSE Institut), Joseph-von-Fraunhofer-Str.9, 76327 Pfinztal, Germany
Johannes.single@cse-institut.de

Abstract

The Hazard and Operability (HAZOP) study is an accepted hazard identification technique in the chemical process industry. It is a time and labor-intensive process and it can be prone to human error. Computer-aided HAZOP systems can be used to support human experts. In this research approach a semantically connected knowledge structure in the form of an ontology was developed that stores process safety engineering knowledge. Based on ontologies artificial intelligence methods and semantic reasoners are used to analyze the knowledge structure. Preliminary results show that an ontology-based reasoning algorithm in combination with case-based reasoning or a support vector machine algorithm is well-suited to infer hazards including their propagation.

Keywords: Computer-aided HAZOP studies, safety engineering ontologies, inference-based hazard identification, case-based reasoning, support vector machine

1. Introduction

During the entire life cycle of a chemical process plant, safety assessments are conducted during the process and plant design phase, plant revisions or in order to comply with amended legal regulations. Hazard and Operability (HAZOP) studies are conducted to identify and assess hazards and malfunctions that arise from processes and process plants. The HAZOP methodology is a human-centered and moderated technique and it is conducted by an interdisciplinary team of experts. The capabilities of the HAZOP practitioners can be reduced by repetitive tasks, stressful conditions and large amounts of data. Also, it is time and labor-intensive while the results of the study depend on the personal experience, level of training, moderation of the study, communication and safety culture. Computer-aided systems allow an experience-independent, completely systematic and uniform approach. They can assist HAZOP practitioners and serve as a decision support system. For over 30 years, different research groups proposed rule-based expert systems or graph-based approaches in order to automate HAZOP studies, see (Single et al., 2019). Some approaches make use of promising technologies, such as ontologies (Rodríguez and Laguía, 2019), case-based reasoning (Zhao et al., 2009), and model-based reasoning, but in many cases requirements from a process safety engineer's point of view are not considered. Thus, none of these approaches have been used in the process safety engineering community so far. In this paper an ontology-based computer-aided HAZOP systems (CAHS) approach to automatically identify hazards is proposed. The focus of this paper is on the ontology and the usage of artificial intelligence methods to detect the propagation of potential hazards.

2. Method

The proposed research approach consists of the following components: an ontology framework to store knowledge, process safety engineering knowledge that is fed into the framework, algorithms that use the knowledge to infer hazards.

2.1. Knowledge models

The hazard identification process is knowledge intensive where knowledge domains, such as substances, processes including chemical reactions, process plants, equipment, hazards and malfunctions, causes and consequences must be covered. In this research approach knowledge models in the form of ontologies are used due to their expressiveness, domain rules and the possibility to model knowledge unambiguously. The developed concepts (upper classes), such as HAZOP deviations, causes, hazardous events and consequences and their relations are shown in Figure 1. They are based on the following guiding principles that are developed to ensure a careful definition of the semantic context:

- Deviation + Context ⇒ Cause,
- Cause + Context ⇒ SuperCause,
- Deviation + Context ⇒ Effect,
- Effect + Context ⇒ Consequence.

For example, the deviation "LowFlow" and the equipment "Pump" could have the cause "IncreasedDifferentialPressure", while it could have the super-cause "IncreasedBackpressurePressureSide". The same applies to effects and consequences. The designed ontologies were formalized using the Web Ontology Language (OWL) that was recommended by the World Wide Web Consortium (W3C) in 2004, see (Hitzler et al., 2010). This means, it is specified using a set of classes, properties, individuals, property values and axioms. Therefore, the Python module Owlready2 by (Lamy, 2019). Owlready2 is also used to infer logical consequences based on the asserted facts and axioms that are defined through the formal specification of the ontology. This is done using semantic reasoners, such as HermiT (Glimm et al., 2014). Thus, ontologies can be queried to receive query answers and thereby make use of the modeled knowledge.

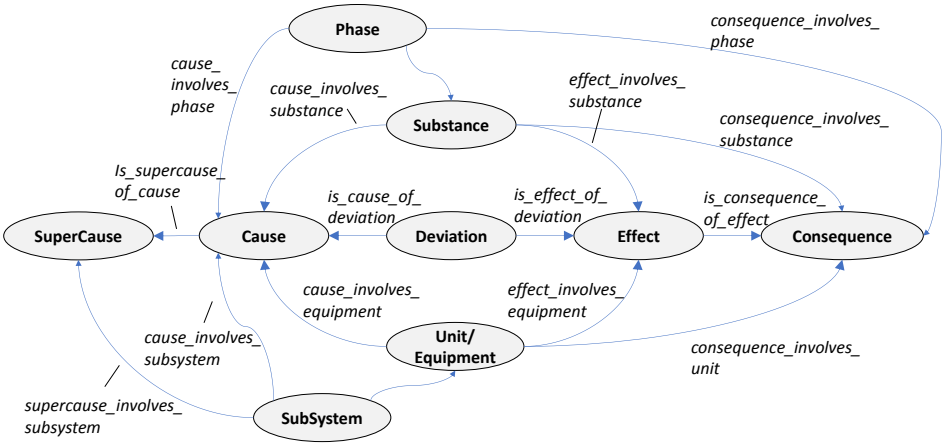

Figure 1 Semantic relationships between concepts

2.2. Hazard identification

The ontology is the foundation for an algorithmic hazard identification. It is queried to infer equipment-specific hazards and malfunctions using a reasoner, such as HermiT, as mentioned above. The influence of the equipment-specific conclusions on adjacent equipment of the process plant is analyzed using case-based reasoning (CBR) and support vector machine (SVM) algorithms. CBR is an established paradigm of Artificial Intelligence, see (Richter and Weber, 2013). It is a pattern-based problem-solving method where knowledge from past situations (cases) are reused in new situations (cases). This means the cases are compared while their similarity is measured using a similarity measure. For instance, for the cases A and B it is calculated from:

$$sim(A,B) = \sum_{i=0}^{n} sim(attr_{Ai}, attr_{Bi}) \cdot w_i \qquad (1)$$

A similarity measure of 1 would mean a perfect match between cases. In this work the case with the highest similarity measure is accepted. A case consists of various attributes and associated weights. Some exemplary cases of the case base are shown in Figure. 2 (a). For instance, case 1 is relatively simple and states that a "NoFlow" deviation is directly propagated downstream to the downstream equipment if there is one inlet and outlet. Case 2 describes a case where a "MoreFlow" deviation in a pump leads to an increased filling level in a downstream container. Case 3 describes a case where a "LowLevel" in a deviation leads to a "NoFlow" deviation in a downstream equipment. This means, the case-base serves as a memory.

a)

Cases for case-based reasoning

Case attributes	weight	Case 1	Case 2	Case 3
Current deviation	10	NoFlow	More Flow	Low Level
Current equipment/ subsystem	10	-	Pump	Vessel
Equipment (up/downstream)	10	-	Vessel (down)	-
Number of inlets/outlets	1	1/1	1/1	-
Substance property/phase	5	-	Phase: liquid	Phase: liquid
Propagated deviation	-	NoFlow (down)	HighLevel (down)	NoFlow (down)

c)

Training data for vector support machine

Features	Case 1	Case 2	Case 3
Current deviation	1	2	3
Current equipment	0	1	3
Equipment (up)	0	0	0
Equipment (down)	0	3	0
Number of inlets	1	1	0
Number of outlets	1	1	0
Substance phase	0	1	1

b)

Encoding the cases

Deviation		Equipment		Substance phase	
Not defined	0	Not defined	0	Not defined	0
NoFlow	1	Pump	1	Liquid	1
MoreFlow	2	Pipe	2	Vapor	2
LowLevel	3	Vessel	3	TwoPhase	3

Figure 2 Cases and encoding of the cases

As an alternative to CBR a support vector machine (SVM) algorithm was also used. The machine learning algorithm SVM is used here for the classification and therefore identification of propagations. It can be used for linear and non-linear classification problems and is applied in this work using the Scikit-learn library for Python, see (Pedregosa et al., 2011).

For this purpose, the categorical features (case attributes) from Figure 2 (a) were encoded (using Figure 2 (b)) into a numeric matrix that serves as training data, see Figure 2 (c). In this example only three cases are shown for illustration purposes. The SVM is trained using the training data that is represented by the encoded cases. Afterwards, the SVM classifier is used to make a prediction regarding a potential propagation. For the training data (cases) in this research, the application of CBR and SVM provided equivalent results, i.e. the same propagations were identified. Using the CBR approach the determination of the similarity measure requires the tuning of the attribute weights to uniquely identify cases. This carries the risk that several identical similarity measures may occur. On the contrary SVM is particularly suitable for finding unique solutions.

2.3. Handling propagations using the propagation stack method

In order to identify propagating deviations, the so-called Propagation Stack Method is developed in this work. This means, propagating deviations are detected using CBR or SVM, see Figure 2. Afterwards, the detected deviation is pushed into an equipment specific stack, see Figure 3. There can be several propagating deviations per equipment. From the stack, where the deviation was detected, every deviation is propagated downstream until the last equipment/unit of the system. For instance, in case the deviation "NoFlow" is detected in the pump it is propagated through the pipe into the vessel, see Figure 3. Thus, the effects of this deviation are evaluated in the equipment: pipe and vessel.

A flow chart of the overall method is shown in Figure 4. First, the process plant is analyzed equipment-wise (beginning to end) in order to detect equipment specific hazards and to fill the propagation stacks with the propagating deviations (equipment-specific inference using a semantic reasoner). Afterwards, the deviations within the propagation stacks are consecutively propagated downstream through the system (see propagation stack-based inference in Figure 3). Based on the propagated deviations super-causes, causes, effects and consequences are inferred. This is repeated until all deviations in the propagation stacks are considered. The proposed propagation stack method solves the problem that some hazards cannot be inferred solely based on equipment-specific relationships but only with consideration of adjacent equipment and units.

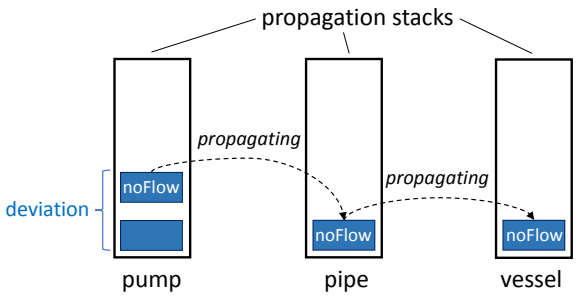

Figure 3 Hazard propagation using the propagation stack method

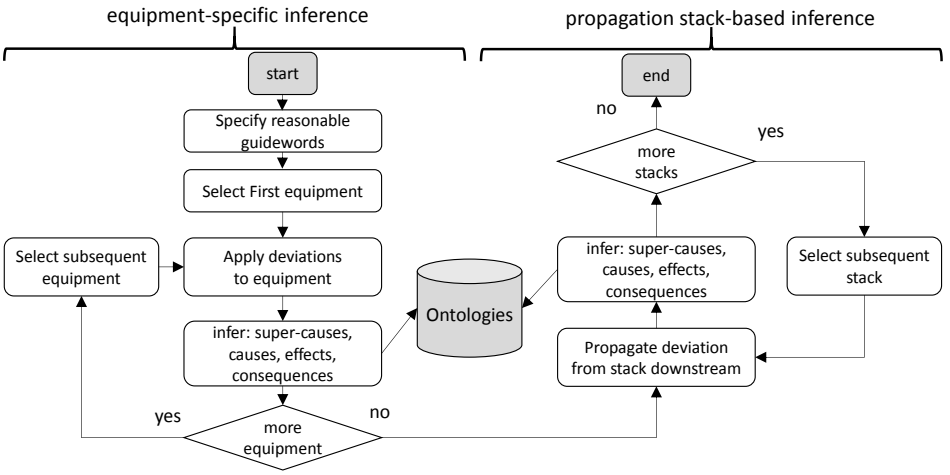

Figure 4 Flow chart of the proposed methodology

3. Case-study

The proposed methodology is applied to an exemplary process plant consisting of two pumps, an open vessel containing the solvent methanol in liquid phase and a downstream scrubber, see Figure 5. The first pump (P1) supplies the vessel (V) with the liquid solvent (methanol), while the second pump (P2) transports methanol from the vessel (V) and supplies the scrubber (S) which cleans the unspecified process gas. In this case-study the focus is on the capabilities of the propagation stack method. Thus, only propagating hazards are considered in the following and equipment specific deviations, effects or consequences are not considered here. By applying the proposed methodology various propagating deviations were identified and are shown in Table 1. The detected causal relationships of propagating deviations can be described as follows:

- No flow in pump (2) ⇒ no flow in scrubber (solvent feed),
- Low flow in vessel (V) ⇒ no flow in scrubber (solvent feed),
- More flow in pump (1) ⇒ high level in vessel (overflow),
- No flow in pipe after pump (2) ⇒ high pressure in pipe after pump 2.

This case-study demonstrates, that causes that lie upstream in the system can be detected using the propagation stack method.

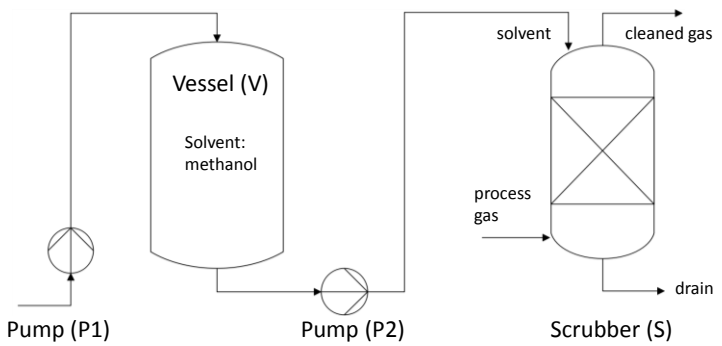

Figure 5 Process plant of the case study

Table 1 Exemplary HAZOP results of the case study considering only propagated circumstances

Equip-ment	Deviation	Super-Cause	Cause	Effect	Consequence
Scrubber (solvent feed)	NoFlow	propa-gated	propagated (P2 not working)	no solvent; no cleaning effect	release of untreated process gas
Scrubber (solvent feed)	NoFlow	propa-gated	propagated (V empty)	no solvent; no cleaning	release of untreated process gas
Vessel	HighLevel	propa-gated	propagated (P1 high flow)	overflow vessel	loss of containment, fire, explosion
Pipe after P2	HighPressure	propa-gated	propagated (Pipe blocked)	leakage, pipe bursting	loss of containment, fire, explosion

4. Conclusions

In this research approach ontologies are used to model process and plant safety knowledge. Based on that, different reasoning techniques are used to identify hazards in a HAZOP like manner. For the identification of hazards that propagate across equipment case-based reasoning or support vector machine algorithms were used. Therefore, the propagation stack method is developed and applied in a case-study. The first results show, that the proposed method is well-suited to identify propagating hazards. More research is needed regarding the backpropagation of deviations and effects, propagation effect on non-neighborly equipment and multi-failure propagation effects. The application limits of machine learning, such as support vector machine must be further explored. Finally, this research approach contributes to establish computer systems for HAZOP studies in the chemical process industry.

References

B. Glimm, I. Horrocks, B. Motik, G. Stoilos, Z. Wang, 2014, HermiT: An OWL 2 Reasoner, Journal of Automated Reasoning, 53, 3, pp. 245-269

P. Hitzler, M. Kroetzsch, S. Rudolph, 2010, Foundations of Semantic Web Technologies, CRC Press, New York

J. B. Lamy, 2017, Owlready: Ontology-oriented programming in Python with automatic classification and high level constructs for biomedical ontologies, Artificial Intelligence In Medicine, 80, pp. 11-28

F. Pedregosa, G. Varoquaux, A. Gramfort, V. Michel, B. Thirion, O. Grisel, M. Blondel, and P. Prettenhofer, R. Weiss, V. Dubourg, J. Vanderplas, A. Passos, D. Cournapeau, M. Brucher, M. Perrot, E. Duchesnay, 2011, Scikit-learn: Machine Learning in Python. Journal of Machine Learning Research, 12, pp. 2825-2830

R. R. Richter, R. O. Weber, 2013, Case-Based Reasoning: A Textbook, Springer Publishing Company, Incorporated

M. Rodríguez, J. Laguía, 2019, An Ontology for Process Safety, Chemical Engineering Transactions, 77, pp. 67-72

J. I. Single, J. Schmidt, J. Denecke, 2019, State of research on the automation of HAZOP studies, Journal of Loss Prevention in the Process Industries, https://doi.org/10.1016/j.jlp.2019.103952

J. Zhao, L. Cui, L. Zhao, T. Qiu, B. Chen, 2009, Learning HAZOP expert system by case-based reasoning and ontology, Computers & Chemical Engineering, 33, 1, pp. 371-378

Sauro Pierucci, Flavio Manenti, Giulia Bozzano, Davide Manca (Eds.)
Proceedings of the 30th European Symposium on Computer Aided Process Engineering (ESCAPE30), May 24-27, 2020, Milano, Italy.
http://dx.doi.org/10.1016/B978-0-12-823377-1.50299-8

Machine Learning-aided Process Design for Formulated Products

Liwei Cao[a,b], Danilo Russo[a], Werner Mauer[c], Huan Huan Gao[d], Alexei A. Lapkin[a,b *]

[a]*Department of Chemical Engineering and Biotechnology, University of Cambridge, Cambridge CB3 0AS, UK*
[b]*Cambridge Centre for Advanced Research and Education in Singapore, CARES Ltd. 1 CREATE Way, CREATE Tower #05-05, 138602, Singapore*
[c]*BASF Personal Care and Nutrition GmbH, 40589 Duesseldorf-Holthausen, Germany.*
[d]*BASF Advanced Chemical Co., Ltd., No. 300 Jiangxinsha Road, 200137 Shangai, China.*
aal35@cam.ac.uk

Abstract

Robotic experiments were coupled with the previously published Thompson Sampling Efficient Multiobjective Optimization (TS-EMO) algorithm, using a batch sequential design approach, in order to optimize the composition and the process conditions of a commercial formulated product. The algorithm was trained with a previously collected data set used to optimize the formulation without taking into account the influence of the process conditions. The target was to obtain a clear homogeneous formulation within a certain viscosity range, minimizing the cost of the adopted ingredients. The GP surrogate models used in the algorithm were found suitable to model the complex unknown relationship between the input space and the outputs of interest, identifying suitable samples with a general decrease in the formulation price, needed mixing power, and process time. The proposed methodology can lead to quicker product design and therefore can generate considerable profit increase with an early product release time.
Keywords: robotic experiments, closed loop optimization, multiobjective optimization, formulated product, process design.

1. Introduction

Formulated products are ubiquitous in the chemical industry, ranging from household detergent to synthetic fuels. They are obtained by mixing selected ingredients in order to get the desired product functions. The design of formulated products is a complex multidisciplinary process, especially when specific product microstructural attributes strongly depend on the selected manufacturing technologies and operating conditions. The integration of product and process design is crucial (Martin and Martinez, 2013; Bernardo, 2016). Grossmann (2004) introduced product-process design as one of the future challenges of chemical engineering. Since then, various attempts have been made to develop systematic methodologies. There are mainly three approaches to the design of formulated products (Ng et al., 2006). Many formulated products are developed through trial-and-error experiments by specialists with extensive experience in producing the specific product under consideration. Cussler and Moggridge (2011) proposed a four-step generic framework to guide such an integrated problem from

needs, ideas and selection to manufacture. Although heuristics and experiments often lead to the successful development of the, it is practically impossible to screen a large number of product prototypes experimentally when there are few alternative ingredients to choose. Moreover, this approach is not suitable for engineers with limited experience in formulating a new type of product.

The orthogonal approach is design by simulations. For relatively simple molecules and homogenous mixtures with well-defined target properties, design methods are available, known as computer-aided product design, which is a combination of computer-aided molecular design and computer aided mixture/blend design techniques (Gani and Ng, 2015). These tools consist of mathematical programming and hybrid methods and provide a promising framework for the development of new chemicals, formulations and methods to estimate different target properties. A large number of computer-aided methods were developed and successfully applied to solvent design (Gani et al., 1991; Macchietto et al., 1990; Pretel et al., 1994; Gani et al., 2005), mixture design (Eden et al., 2004), refrigerant design (Joback and Stephanopolous, 1989; Churi and Achenie, 1996), chemical (Kalakul et al., 2016, Gani et al., 2014) and formulated products (Martin and Martinez, 2013, Arrieta-Escobar et al., 2017, Martin and Martinez, 2016, Arrieta-Escobar et al., 2019). However, this approach is highly depended on validated mathematical models for the estimation of all desired properties. For the cases where no suitable physical model is available the role of model-based design is limited.

A hybrid experiment- and model-based techniques was proposed when mathematical models are not available for all desired properties and/or product-process performance evaluations (Conte et al., 2012). According to this approach, physical models can be used to generate and test alternatives in order to identify a small number of candidates, which may be further investigated through the experiment-based trial and error approach. However, a physical model is still needed in the integrated approach, which can be a limitation to some extent. Here we ask a question, *is it possible to train a surrogate statistical model to describe the desired product properties in the absence of a physical model, and use it to optimize the product and process design in an automated fashion*?

With the increase in computational power, machine learning methods become available to many new application areas and present a transformative approach to optimization. The application of machine learning in chemical engineering is a rapidly developing field (Venkatasubramanian, 2019). Important advances were made within the area of catalyst design (Goldsmith et al., 2018; Medford et al., 2018), chemical synthesis (Amar et al., 2019), process optimization (Lee et al., 2018) and so on. In this work, we present an integrated approach, which is a combination of a machine learning algorithm and a robotic experimental platform for the optimization of a formulated product. To achieve the optimal design of a product and a process, a Bayesian multi-objective optimization algorithm was adopted, specifically. Thompson Sampling Efficient Multi-Objective (TS-EMO) (Bradford et al., 2018). The algorithm trains Gaussian processes (GPs) as the surrogate models on the experimental dataset and then identifies new samples based on the predictions and uncertainty of the surrogates. The TS-EMO algorithm was incorporated in the robotic experimental platform to guide the next-run experiments.

The experimental results were then used as inputs for the TS-EMO algorithm for the next iteration of optimization till the set criterion of the formulated product is met.

2. Materials and Methods

The formulated product under consideration is a real industrial case study. The formulation consists of a mixture of three surfactants (S1 = Texapon SB3, S2 = Dehyton AB30, S3 = Plantacare 818), a polymer (P1 = Dehyquart CC7), a thickener (T1 = Arlyon TT), and water at a specific pH.

A scheme of the experimental system is shown in Fig. 1. The robotic system was developed at University of Glasgow, in the group of Prof. Leroy Cronin. At each iteration of the optimization procedure, 8 new formulation recipes and process conditions are suggested by the algorithm. These conditions are summarized in a .csv file, triggering the Robotic Platform no. 1 for the samples preparation. Automated syringe pumps (Tricontinent, Gardner Denver, C-Series) dispense the proper amount of each ingredient in 20 mL vials placed on a rotating wheel. At each iteration a batch of 8 samples is prepared. They are then moved into an incubator, where they are shaken at a fixed temperature, mixing power, and time. Process conditions were also suggested by the algorithm. The processed samples are then cooled to room temperature and analyzed using the robotic platform no. 2. In this platform turbidity of each sample is measured and pH is tested to ensure it is constant. No pH variations were observed after processing in any of the samples. Sample viscosity at a shear rate of 10 s^{-1} is finally measured off-line with a rotational viscometer (controlled strain rheometer, ARES Rheometric Scientific, couette configuration) and the results exported to a new .csv file for the next iteration of the TS-EMO algorithm. A batch-sequential design was used to suggest the next 8 experiments (Bradford et al., 2018). The three target functions to minimize were chosen as turbidity value, the squared distance of the measured viscosity from the target viscosity (3,000 mPa·s), and price, calculated as the sum of the unit price of each ingredient multiplied by the dispensed amount. The variables of interest were concentrations of the 5 ingredients S1, S2, S3, T1, P1, and three process variables (temperature T, mixing power MP, and time t). Constraints suggested by process knowledge were: S1+S2+S3 = 15 g/L; T1 < 2 g/L; P1 < 2 g/L; 30 < T < 60 °C; 30 < MP < 300 rpm; 10 < t < 120 min. Surrogate GPs model were used to model the unknown outputs, i.e. viscosity and turbidity.

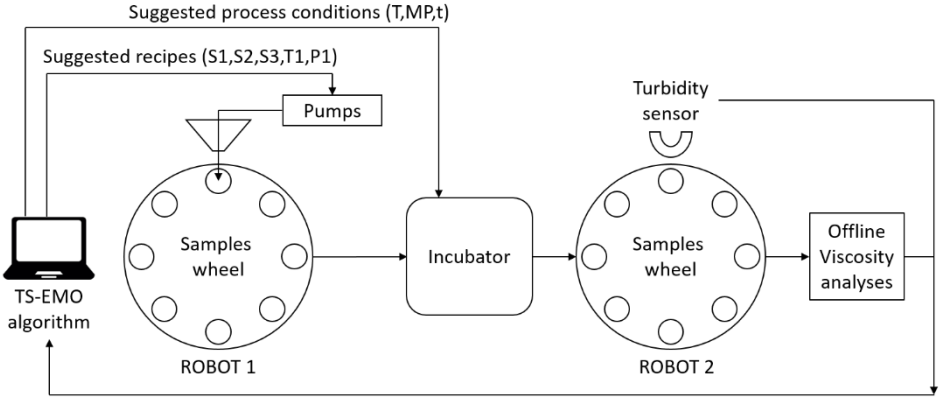

Figure 1. Scheme of the closed-loop optimization operations.

3. Results and Discussion

A batch of 224 experimental data at fixed process conditions (T = 50 °C; MP = 300 rpm; t = 2 h) was used to train the algorithm and start the iterative process. This data set was already available from a previous explorative experimental campaign devoted to optimise the formulation at fixed process conditions. The choice of using these previously collected data is justified to mimic a common situation in products development, in which a preliminary investigation provides an initial data set. Other 12 training data were collected at a fixed recipe (S1 = 5.62; S2 = 2.50; S3 = 6.88; P1 = 0.90; T = 2.00 g/L) at different process conditions. Hence, the overall training dataset consisted of 236 data points. 15 iterations of the closed-loop optimization (120 samples) were carried out in order to assess predictive performance of the obtained surrogate models and to evaluate the results of the optimization. Among the conditions suggested by the algorithm, 7 non-dominated solutions were found (Table 1) in the experimental Pareto front of the data set.

Table 1. Non-dominated solutions suggested by the TS-EMO algorithm.

S1 (g/L)	S2 (g/L)	S3 (g/L)	P1 (g/L)	T1 (g/L)	T (°C)	MP (rpm)	t (min)	Turbidity (NTU)	Viscosity (mPa·s)	Price ($/L)
2.80	3.20	9.00	0.40	1.46	35	137	77	152	2,409	1.81
1.09	2.45	11.45	1.20	1.92	54	211	118	157	3,424	1.79
0.00	0.52	14.48	0.40	1.33	30	220	42	28	197	1.51
0.00	2.01	12.99	0.01	1.24	51	180	73	31	409	1.45
5.10	5.89	4.01	0.00	1.97	49	230	70	24	3,681	2.05
5.10	5.65	4.25	0.76	1.91	49	230	83	25	3,071	2.14
0.93	5.63	8.44	0.94	1.94	52	206	115	30	2,337	1.74

All of the obtained formulations were clear, homogeneous samples, with no phase separation. 5 out of 7 non-dominated solutions satisfy the viscosity requirement to be in the range 2,000 – 4,000 mPa·s. The presence of two samples with a viscosity lower than 1,000 mPa·s is due to their relatively low price and turbidity, which is in agreement with the interpretation of the Pareto front as a trade-off between different conflicting objectives. Further criteria can be used to discriminate between the obtained best solutions. It is also worth noticing that all proposed solutions were obtained with a significant reduction of the required time and mixing power. The non-dominated solutions that passed the viscosity and turbidity criteria in the training set are reported in Table 2.

Table 2. Non-dominated experimental data in the training set.

S1 (g/L)	S2 (g/L)	S3 (g/L)	P1 (g/L)	T1 (g/L)	T (°C)	MP (rpm)	t (min)	Turbidity (NTU)	Viscosity (mPa·s)	Price ($/L)
3.97	3.16	7.87	0.84	1.60	50	300	120	11	2,678	2.00
4.61	2.62	7.76	1.24	1.04	50	300	120	28	3,574	2.06
8.40	3.18	3.43	0.48	1.80	50	300	120	18	2,948	2.43
2.79	2.93	9.28	1.72	0.88	50	300	120	26	2,632	1.92
10.94	3.94	0.12	1.8	1.36	50	300	120	28	2,992	2.80
4.02	3.09	7.89	0.99	1.34	50	300	120	15	2,824	2.00
3.01	0.64	11.35	0.53	1.75	50	300	120	50	2,789	1.87
3.06	1.96	9.95	0.31	1.42	50	300	120	23	3302	1.82

As one can see by comparing Tables 1 and 2, among the solutions that passed both criteria, those suggested during the optimization procedure have a lower average price of the ingredients, which together with the advantages in terms of low mixing power

and processing time, might have a significant effect on the overall economics and productivity. The predictive performances of the adopted models were evaluated comparing the predicted Pareto front of the GPs with the experimental non-dominated solutions, Figure 2.

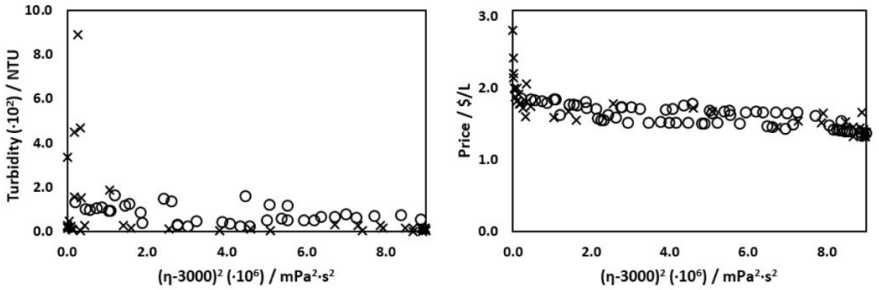

Figure 2. Two projections of the experimental (X) and predicted (O) Pareto front.

The satisfactory predictive performances can enable further improvements in formulations design, based on different *a posteriori* criteria that may be selected by human intuition and/or expertise.

4. Conclusions

In this paper, robotic experiments were used in combination with a machine learning algorithm to optimize both the recipe and the process conditions of a formulated product. The proposed methodology enabled to identify new formulations meeting the discriminating criteria. Moreover, the suggested sample were generally cheaper and required less mixing power and process time, which can generate considerable profits on scale. The overall optimization procedure was completed within 2 weeks, avoiding human bias and using automated operations, exploring a complex, multidimensional chemical space. As a result, the developed methodology can lay the groundwork for a faster and more efficient process development and a consequent early product release time, without requiring any extensive expertise of the human operators. GPs were confirmed to be suitable surrogate model to predict the complex relationships between the input variables and the target properties when no physical models are available.

Acknowledgements

LC is grateful to BASF for co-funding her PhD. This project was co-funded by the UKRI project “Combining Chemical Robotics and Statistical Methods to Discover Complex Functional Products” (EP/R009902/1), and National Research Foundation (NRF), Prime Minister’s Office, Singapore under its Campus for Research Excellence and Technological Enterprise (CREATE) program as a part of the Cambridge Centre for Advanced Research and Education in Singapore Ltd (CARES). The Authors are grateful to Prof. Lee Cronin, Dr. Abhishek Sharma, Mr. Daniel Salley, and Mr. Graham Keenan for providing designs, software and practical help in the assembly of the robotic platform.

References

Y. Amar, A.M. Schweidtmann, P. Deutsch, L. Cao, A. Lapkin, 2019, Machine learning and molecular descriptors enable rational solvent selection in asymmetric catalysis, Chem. Sci., 10, 27, 6697-6706.

J.A. Arrieta-Escobar, F.P. Bernardo, A. Orjuela, M. Camargo, L. Morel, 2017, An integrated methodology for emulsified cosmetic product formulation using integer programming with logical constraints, Comput. Aided Chem. En., 40, 985-990.
J.A. Arrieta-Escobar, F.P. Bernardo, A. Orjuela, M. Camargo, L. Morel, L. Wendling, 2019, Integration of consumer preferences and heuristic knowledge in the design of formulated products: application to a cosmetic emulsion, Comput. Aided Chem. En., 46, 433-438.
F.P. Bernardo, 2016, Chapter 12 – Integrated process and product design optimization, Comput. Aided Chem. En., 39, 347-372.
E. Bradford, A.M. Schweidtmann, A. Lapkin, 2018, Efficient multiobjective optimization employing Gaussian processes, spectral sampling and a genetic algorithm, J. Global Optim., 71, 2, 407-438.
N. Churi, L.E.K. Achenie, 1996, Novel mathematical programming model for computer aided molecular design, Ind. Eng. Chem. Res., 35, 10, 3788-3794.
E. Conte, R. Gani, Y.S. Cheng, K.M. Ng, 2012, Design of formulated products: experimental component, AIChE J., 58, 1, 173-189.
E.L. Cussler, G.D. Moggridge, 2011, Chemical product design, Cambridge University Press.
M.R. Eden, S.B. Jorgensen, R. Gani, M.M. El-Halwagi, 2004, Chem. Eng. Process.: Process Intensification, 43, 5, 595-608.
R. Gani, B. Nielsen, A. Fredenslund, 1991, A group contribution approach to computer-aided molecular design, AIChE J., 37, 9, 1318-1332.
R. Gani, C. Jimenez-Gonzalez, D.J.C. Constable, 2005, Method for selection of solvents for promotion of organic reactions, Comput. Chem. Eng., 29, 1661-1676
R. Gani, K.M. Ng, 2014, Product design – from molecules to formulations to devices, Comput. Aided Chem. En., 34, 108-123.
R. Gani, K.M. Ng, 2015, Product design – molecules, devices, functional products, and formulated products, Comput. Chem. Eng., 81, 70-79.
B.R. Goldsmith, J. Esterhuizen, J.X. Liu, C.J. Bartel, C. Sutton, 2018, Machine learning for heterogeneous catalyst design and discovery, AIChE J., 64, 7, 2311-2323.
I.E. Grossmann, 2004, Challenges in the new millenium: product discovery and design, enterprise and supply chain optimization, global life cycle assessment, Comput. Chem. Eng., 29, 29-39.
K.G. Joback, G. Stephanopoulos, 1989, Designing molecules possessing desider physical property values, Proceedings FOCAPD, 89, 363-387.
S. Kalakul, S. Cignitti, L. Zhang, R. Gani, 2016, Integrated computer-aided framework for sustainable chemical product design and evaluation, Comput. Aided Chem. En., 38, 2343-2348.
J.H. Lee, J. Shin, M.J. Realff, 2018, Machine learning: overview of the recent progresses and implications for the process systems engineering field, Compu. Chem. Eng., 114, 111-121.
M. Martin, A. Martinez, 2013, A methodology for simultaneous product and process design in the customer products industry: the case study of the laundry business, Comput. Aided Chem. En., 32, 715-720.
M. Martin, A. Martinez, 2016, Chapter 13 – Tools for formulated product design, Comput. Aided Chem. En., 39, 373-392.
A.J. Medford, M.R. Kunz, S.M. Ewing, T. Borders, R. Fushimi, 2018, Extracting knowledge from data through catalysis informatics, ACS Catal., 8, 8, 7403-7429.
K.M. Ng, R. Gani, K. Dam-Johansen, 2006, Chemical product design: towards a perspective through case studies, 23, Elsevier.
S. Macchietto, O. Odele, O. Omatsone, 1990, Design of optimal solvents for liwuid-liwuid extraction and gas absorption processes, Chem. Eng. Res. Des., 68, 429-433.
E.J. Pretel, P.A. Lopez, S.B. Bottini, E.A. Brignole, 1994, Computer-aided molecular design of solvents for separation processes, AIChE J., 40, 8, 1349-1360.
V. Venkatasubramanian, 2019, The promise of artifical intelligence in chemical engineering: is it here, finally?, AIChE J., 65, 2, 466-478.

Sauro Pierucci, Flavio Manenti, Giulia Bozzano, Davide Manca (Eds.)
Proceedings of the 30th European Symposium on Computer Aided Process Engineering (ESCAPE30), May 24-27, 2020, Milano, Italy.
http://dx.doi.org/10.1016/B978-0-12-823377-1.50300-1

A Novel Multi-stage Stochastic Formulation with Decision-dependent Probabilities for Condition-based Maintenance Optimization

Egidio Leo*, Sebastian Engell

Process Dynamics and Operations Group, Department of Biochemical and Chemical Engineering, Technische Universität Dortmund, EmilFigge-Str.70, 44221 Dortmund, Germany.

egidio.leo@tu-dortmund.de

Abstract

The challenge addressed in this work is the integrated production planning and condition-based maintenance optimization for a process plant. We take into account uncertain information of the predicted equipment degradation adopting a stochastic programming formulation. To adjust the likelihood of the failure scenarios, we embed a prognosis model, the Cox model, into the optimization problem. We propose here a novel endogenous uncertainty formulation where the decisions at one point in time have an impact on the probability of the uncertainty. We provide computational results implementing a custom branching within the global solver BARON and decomposing the problem via the Benders algorithm.

Keywords: Condition-based maintenance, Prognosis, Stochastic programming, Endogenous uncertainty, Cox model

1. Introduction

Condition-based maintenance (CBM) is a paradigm that is based on the idea of integrating production planning and maintenance scheduling via a degradation model that describes the health of the equipment. The goal of a CBM optimization is to find the best compromise between operating costs and maintenance costs. In fact, a high production rate might result into high production volumes but also high maintenance costs due to frequent maintenance activities because of high degradation rates. Most of the work in this direction assumes a perfectly known degradation model that is able to predict the degradation trajectory and the Remaining Useful Life (RUL) of the equipment according to the operating conditions (Leo and Engell, 2017). To the best of our knowledge, only two works perform a CBM optimization under uncertainty. In (Basciftci et al., 2018) the authors used a degradation model to create failure scenarios, which then were included into a chance-constraint programming approach. Since the degradation model is only used for the generation of the scenarios, the optimization does not take into account the effects of the selected operating strategy on the status of the equipment. This is taken into account in (Wiebe et al., 2018), where parametric uncertainty of the degradation model is considered by solving an adjustable robust optimization problem. To avoid uncertain time-varying parameters, which result in a very conservative solution, the authors assume a complete realization of the future degradation parameters after the first collection of measurements. In this work we propose a novel formulation that integrates CBM, prognosis and production planning, adopting the multi-stage stochastic programming framework with decision-dependent uncertainty (Hellemo et al.,2018).

2. Problem statement

We consider a continuous production plant with fixed and known product demand over the planning horizon. The goal is to minimize the difference between the plant costs, consisting of the feed purchasing cost, the resource consumption cost and the product purchasing cost, and the plant income, due to the produced products. The decisions variables are:

- the feeds to be purchased;
- the operating conditions of the plant and the resulting degradation trajectory;
- the amount of product to be purchased from other sources;
- the timing of the maintenance activities.

3. The proposed endogenous uncertainty MINLP formulation

3.1. Uncertainty modelling

The standard stochastic programming formulation models the uncertainty by discrete scenarios with fixed and known scenario probabilities and the decisions are made at different stages, which are defined by the realization of the uncertainty. In this work, the discrete scenarios represent possible realizations of the uncertain RUL of the equipment. The proposed endogenous uncertainty formulation computes the probabilities of the uncertain RULs according to the degradation trajectory that is defined by the plant operating conditions (e.g., a higher degradation, due to harder operating conditions, increases the failure probabilities by shorter RULs). The relation between the probabilities of the scenarios and the degradation trajectory is identified via the survival analysis equations and the Cox Model (Cox, 1972). The Cox model is a prognosis technique that is able to adjust the hazard function (and therefore the probability of an event) according to the influencing variables, in this work the degradation level and, therefore, the operating strategy. It is worth to highlight that even though the Cox model is a well-known standard prognosis model, in this work for the first time it is embedded into a stochastic programming optimization. Figure 1 shows the scenario tree of the proposed formulation. The first-stage decisions are the feed purchasing decisions, the maintenance timing decisions and the plant operating conditions before any RUL realizations. The recourse decisions are the plant operating conditions. We consider a time horizon of 40 days and the uncertain RULs belong to the set $F_s = \{30, \dots, 40\}$.

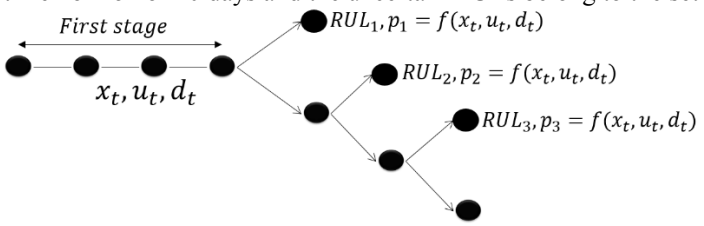

Figure 1 Scenario tree of the proposed formulation.

Indices *t: time, f: feed, i: input, p: product, j: state, s: scenario.*
Continuous variables: $y_{p,t,s}$: plant output, $x_{j,t,s}$: plant operating conditions, S_s: *survival function*, p_s: *scenario probability*, $purchase_{p,s}$: *purchased product*, $d_{t,c,s}$: *degradation trajectory*, $\mathrm{Pr}_{p,t,s}$: *cumulative production*, h_s: *hazard function*, $u_{i,t,s}$: plant inputs. **Binary variables** $x_{maintenance_t}$: 1 if maintenance is active in *t*, x_{feed_f}: 1 if feed *f* is purchased, $y_{feed_{f,t}}$: 1 if feed *f* is used at time *t*, $start_{feed_{f,t}}$: 1 if the utilization of feed *f* starts at time *t*.

3.2. Process constraints

Eqs. (1)-(2) represent the process constraints where $u_{i,t,s}$ indicates the resource consumption, $x_{j,t,s}$ the plant operating conditions and $y_{p,t,s}$ the plant production. The degradation level $d_{t,s}$ affects the plant production. Eqs. (3) - (4) set the upper and lower bounds of the plant inputs $u_{i,t,s}$. If the maintenance is active ($x_{maintenance_t} = 1$) the resource consumption is forced to be zero. Eq. (5) computes the cumulative production of product *p* at each time step *t*. The maximum production capacity is defined in Eq. (6). A demand satisfaction constraint (Eq. (7)) enforces that the product demand is covered by the production or by purchasing the product from external sources. The matrices $A_{j,i}, B_{p,j}$represent process parameters linking inputs, outputs and states of the plant.

$$x_{j,t,s} = \sum_i A_{j,i} * u_{i,t,s} \qquad \forall j \in J, s \in S, t \in T \quad (1)$$

$$y_{p,t,s} = \sum_j B_{p,j} * x_{j,t,s} - d_{t,s} * red_p \qquad \forall p \in P, s \in S, t \in T \quad (2)$$

$$u_{i,t,s} \leq UB_{i,s} * (1 - x_{maintenance_t}) \qquad \forall i \in I, s \in S, t \in T \quad (3)$$

$$u_{i,t,s} \geq LB_{i,s} * (1 - x_{maintenance_t}) \qquad \forall i \in I, s \in S, t \in T \quad (4)$$

$$\mathrm{Pr}_{p,t,s} = \sum_{t' \leq t} y_{p,t',s} \qquad \forall p \in P, s \in S, t \in T \quad (5)$$

$$y_{p,t,s} \leq yUB_{p,s} * (1 - x_{maintenance_t}) \qquad \forall p \in P, s \in S, t \in T \quad (6)$$

$$\mathrm{Pr}_{p,|T|,s} + purchase_{p,s} \geq D_p \qquad \forall p \in P, s \in S \quad (7)$$

3.3. Feed purchasing constraints

The following constraints define the feed purchasing strategy of the plant and the allocation of the feeds over the time horizon. The quality of the feed (indicated by the parameter IC_f) influences the degradation trajectory (see Eqs. (15) - (16)). Eq. (8) - (9) impose a minimum and maximum allocation of the purchased feeds. Eq. (10) ensures that no feed is used if the maintenance activities are performed. Eqs. (11) - (13) define the starting time of the feed utilization for each purchased feed.

$$\sum_t y_{feed_{f,t}} \geq Feed_{day_{min}} * x_{feed_f} \qquad \forall f \in F \quad (8)$$

$$\sum_t y_{feed_{f,t}} \leq Feed_{day_{max}} * x_{feed_f} \qquad \forall f \in F \quad (9)$$

$$\sum_f y_{feed_{f,t}} = 1 - x_{maintenance_t} \qquad \forall t \in T \quad (10)$$

$$start_{feed_{f,t}} \geq y_{feed_{f,t}} - y_{feed_{f,t-1}} \qquad \forall f \in F, t \in \{2, \dots, |T|\} \quad (11)$$

$$start_{feed_{f,t}} \leq x_{feed_f} \qquad \forall f \in F, t \in T \quad (12)$$

$$\sum_t start_{feed_{f,t}} \leq x_{feed_f} \qquad \forall f \in F \quad (13)$$

3.4. Degradation model

The following constraints compute the degradation trajectory. Eqs. (15) - (16) define the degradation model that depends on the feed quality IC_f, the operating conditions of the plant and the history of the degradation. Eq. (14) sets the threshold for the degradation.

$$d_{t,s} \leq d_{threshold_{s,t}} * (1 - x_{maintenance_t}) \qquad \forall t \in T, s \in S \quad (14)$$

$$d_{t,s} \geq d_{init} * (1 - x_{maintenance_t}) + \sum_f IC_f * y_{feed_{f,t}} + \sum_{t' \leq t,i} a_{1,i} * u_{i,t',s} + \sum_{t' \leq t,j} \alpha_{2,j} * x_{j,t',s} - M * x_{maintenance_t} \qquad \forall t \in T, s \in S \quad (15)$$

$$d_{t,s} \leq d_{init} * \left(1 - x_{maintenance_t}\right) + \sum_f IC_f * y_{feed_{f,t}} + \sum_{t' \leq t,i} a_{1,i} * u_{i,t',s} + \sum_{t' \leq t,j} \alpha_{2,j} * x_{j,t',s} + M * x_{maintenance_t} \qquad \forall t \in T, s \in S \quad (16)$$

3.5. Maintenance constraints

The maintenance constraints implement the maintenance policy. Eq. (17) ensures that the maintenance activities are started only once over the considered time horizon. Eqs. (18) - (19) forces the maintenance to be performed in a specific time window (between day 30 and 40). Eq. (20) defines the duration of the maintenance.

$$x_{maintenance_t} \geq x_{maintenance_{t-1}} \quad \forall t \in T, t \neq 1 \quad (17)$$
$$\sum_{t \in window} x_{maintenance\_t} \geq 1 \quad (18)$$
$$\sum_{t \notin window} x_{maintenance\_t} = 0 \quad (19)$$
$$\sum_t x_{maintenance\_t} \geq dur \quad (20)$$

3.6. Prognosis constraints

These constraints embed the prognosis model within the production planning optimization. This is achieved introducing as variables the probabilities of the scenarios (namely of the RUL estimations), the hazard function and the survival function (Eq. (21)) according to the Cox model. Eqs. (22) - (24) implement the relations among these variables. Eq. (25) sets to zero the probabilities of those scenarios with RULs that realize after the maintenance activities start. In other words, those scenarios do not realize. Eqs. (26) - (27) implement a linearized version of the Cox model ($h_s = h_s^0 * e^{\mu * d_{t,s}} \approx h_s^0 * \mu * d_{t,s}$). Eq. (26) determines the hazard function of the earliest uncertain RUL according to the degradation trajectory. The hazard functions of the remaining scenarios are adjusted linearly (Eq. (27)). The nominal hazard function (h_s^0) and the parameter μ must be estimated from plant data.

$$0 \leq h_s \leq 1, 0 \leq p_s \leq 1, 0 \leq S_s \leq 1 \quad \forall s \in S \quad (21)$$
$$p_s = h_s * S_s \quad \forall s \in S \quad (22)$$
$$S_s = \sum_{s'>s} p_{s'} \quad \forall s \in S \quad (23)$$
$$S_s - S_{s+1} = p_s \quad \forall s \in S \quad (24)$$
$$p_s \leq 1 - x_{maintenance_{F_S[s]-1}} \quad \forall s \in S \quad (25)$$
$$h_s = h_s^0 * \mu * d_{t,s} \quad s = 1 \quad (26)$$
$$h_s = h_{s1} + (1 - h_s)/(|S| - 1) * s \quad s \in S, s \neq 1 \quad (27)$$

3.7. Objective function

The following constraints compute the plant cost and the objective function Eq. (28). The plant cost (Eq. (29)) is the sum of the feed cost (Eq. (30)), the product purchasing cost (Eq. (31)), the resource consumption cost (Eq. (32)) minus the income of selling the products (Eq. (33)).

$$\min endo_{cost} = \sum_s p_s * cost_s \quad (28)$$
$$cost_s = feed_{cost} + purchasing_{cost_s} + R_{cost_s} + shutdown_{cost} - selling_s \quad (29)$$
$$feed_{cost} = \sum_f feed_{price_f} * x_{feed_f} \quad (30)$$
$$purchasing_{cost_s} = \sum_p price_p * purchase_{p,s} \quad (31)$$
$$R_{cost_s} = \sum_i \sum_t u_{i,t,s} * price_i \quad (32)$$
$$selling_s = \sum_{t,p} prices_{p,t} * y_{p,t,s} \quad (33)$$

4. The solution strategy

The proposed endogenous uncertainty formulation gives rise to a non-convex MINLP due to the bilinear terms in the survival equations and in the objective function (Eqs. (22) - (28)). We solved the deterministic equivalent with the global solver BARON (Kilinc and Sahinidis, 2018) implementing a custom branching strategy. We prioritize the variable influencing the probabilities of the scenarios (degradation variable) along the spatial branch-and-bound algorithm. Additionally, we implemented the Benders algorithm:

- the master problem corresponds to the first stage (all equations except of Eq.(7) for $t \in \{1, \ldots, 29\}$
- the sub-problem is the aggregation of the scenarios (equations (1) - (8), (17) - (19), (24) - (31) for $t \in \{30, \ldots, 40\}$).

After the solution of the master problem is passed to the sub-problem, the probabilities of the scenarios are fixed and therefore the sub-problem is a linear program whose solution provides also the dual variables to compute the optimality cuts in the Benders decomposition. However, in the case of bilinear terms, the Benders decomposition is not guaranteed to converge to the global optimum.

5. Results

5.1. Computational results

Table 1 presents the computational results obtained solving the deterministic equivalent problem with a custom branching and the Benders decomposition. The results show that the Benders decomposition clearly outperforms the global solver. The influence of the custom branching is very limited (the same results were obtained solving the deterministic equivalent without the custom branching). The reason might be the fact that even when the probabilities of the scenarios are branched, the problem remains an MINLP due to the nonlinear survival constraints (Eq. (22)).

Table 1 Computational results (time limit 3600 [s]) - UB is the best feasible solution found

	z^*	CPU [s]
DE with custom branching (BARON)	22423.2 (UB = 22423.2, LB = -4917.89)	3600
Benders Decomposition	17669.16 (UB=17669.16, LB= 17669.16)	383.6

5.2. Discussion

We compare the results obtained solving the proposed formulation with the Benders algorithm (upper and lower bounds shown in Figure 3) and the solution of the deterministic optimization problem where the degradation model is assumed to be perfectly known. The Value of the Stochastic Solution is equal 3031.43 (16.6%) (the objective value of the stochastic program is equal to 17669.16 and the objective value of the recourse problem is equal to 20700.6). The resulting cost items for the stochastic program and the recourse program (where the first stage variables are fixed to the solution of the deterministic problem) are shown in Figure 2. Figures 4 - 6 show the degradation trajectories, the timing of the maintenance activities, the feed purchasing strategies and the production levels. The stochastic approach proposes a different operating strategy compared to the deterministic optimization: the stochastic optimization anticipates the maintenance activities, increasing the production rates to reduce the product purchasing in all the scenarios. It is worth to highlight that the SP identifies also a different optimal feed purchasing strategy thereby reducing the feed cost. Figure 7 shows how the optimization shapes the probabilities of the scenarios via the prognosis variables (the survival and hazard functions).

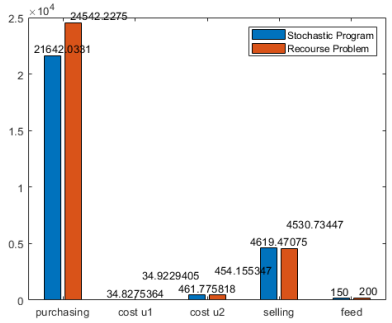

Figure 2 Cost items

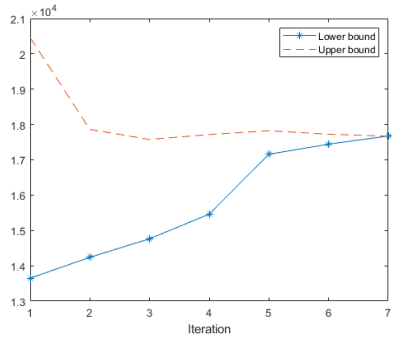

Figure 3 Bounds of the Benders decomposition

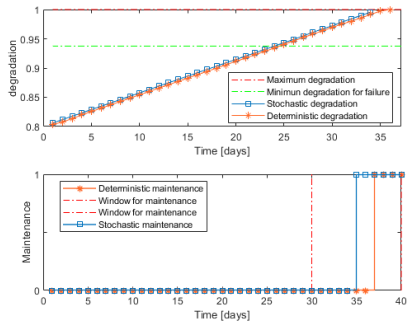

Figure 4 Degradation and maintenance profiles

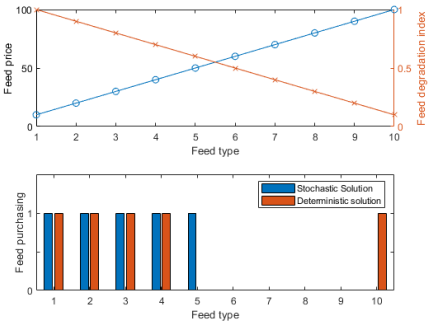

Figure 5 Feed purchasing strategy

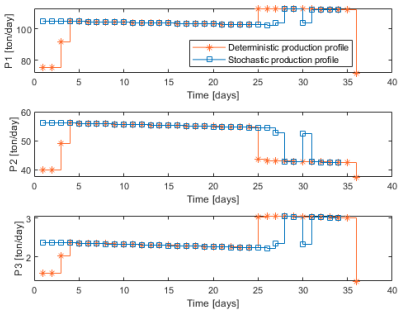

Figure 6 Production profiles

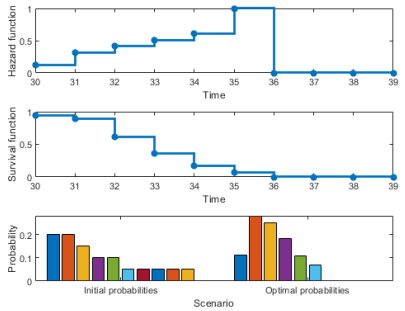

Figure 7 Prognosis variables

6. Conclusion

An endogenous uncertainty stochastic programming formulation is proposed to integrate condition-based maintenance, production planning and prognosis. The advantages of the proposed formulation and the benefit of the Benders decomposition are shown on a continuous plant. There are several open questions for this class of optimization problems from the algorithm design to find the global optimum to the integration of a risk measure.

Acknowledgements: Financial support is gratefully acknowledged from the EID-ITN project “PRONTO", Grant agreement No 675215.

References

E. Leo and S. Engell, Condition-based operational optimization of industrial combined heat and power plants under time-sensitive electricity prices. Proceedings of ESCAPE 27

B Basciftci, S Ahmed, N Gebraeel, M Yildirim, Stochastic Optimization of Maintenance and Operations Schedules under Unexpected Failures. IEEE Transactions on Power Systems, 2018

J. Wiebe, I. Cecílio and R. Misener, Data-Driven Optimization of Processes with Degrading Equipment, Ind. Eng. Chem. Res. 2018

L. Hellemo, P.I. Barton and A. Tomasgard, Decision-dependent probabilities in stochastic programs with recourse, Computational Management Scienc, 2018

Cox, David R (1972). Regression Models and Life-Tables. Journal of the Royal Statistical Society, Series B. 34 (2): 187–220. JSTOR 2985181

Kilinc, M. and N. V. Sahinidis, Exploiting integrality in the global optimization of mixed-integer nonlinear programming problems in BARON, Optimization Methods and Software, 540-62.

Sauro Pierucci, Flavio Manenti, Giulia Bozzano, Davide Manca (Eds.)
Proceedings of the 30th European Symposium on Computer Aided Process Engineering (ESCAPE30), May 24-27, 2020, Milano, Italy.
http://dx.doi.org/10.1016/B978-0-12-823377-1.50301-3

Efficient Evaluation of Vacuum Pressure-swing Cycle Performance using Surrogate-based, Multi-objective Optimization Algorithm

Héctor Octavio Rubiera Landa,[a] Yoshiaki Kawajiri,[b,a] Matthew J. Realff[a,*]

[a]*School of Chemical & Biomolecular Engineering, Georgia Institute of Technology, 311 Ferst Drive N. W., Atlanta, GA 30332-0100, U.S.A.*
[b]*Department of Materials Process Engineering, Nagoya University, Furo-cho 1, Engineering Building 1, Nagoya, 464-8603, Japan*
matthew.realff@chbe.gatech.edu

Abstract

The performance evaluation of vacuum pressure-swing adsorption (VPSA) cycles with detailed, full-order models (FOMs) is typically a time-consuming and resource-intensive task. Popular state-of-the-art approaches include e.g., dynamic optimization approaches—see e.g., Swartz and Kawajiri (2019); and application of evolutionary algorithms, i.e., genetic algorithms, see e.g., Fiandaca et al. (2009). In this work, we present a strategy that combines two techniques in order to improve the computational efficiency of VPSA process modeling. Firstly, we improve the convergence in the calculation of cyclic steady state (CSS), using the FOM, by treating the calculation task as a fixed-point iteration (FPI) problem. We apply the FPI acceleration method by Anderson (1965) to improve FPI computations. Secondly, we embed the accelerated CSS computation into algorithm 'Surrogate Optimization of Computationally Expensive Multiobjective Problems' (SOCEMO) created by Müller (2017), which specifically addresses multi-objective optimization of expensive-to-evaluate black-box functions. This combination of approaches improves computational performance for Pareto frontier estimation that requires evaluation of process metrics at CSS, without sacrificing high-fidelity of the full-order VPSA model, and thus constitutes an attractive alternative to evaluate cyclic adsorption processes.

Keywords: surrogate-based multi-objective optimization, periodic processes

1. Introduction

The dynamic character of periodic adsorption operations, as well as their required spatiotemporal description, continues to represent a challenge from the computational point of view. The lack of closed-form solutions to the mathematical models applied to represent these processes is traditionally addressed by numerical approximations, which oftentimes can become challenging to solve. Moreover, if the end goal is to conduct parametric investigations or optimization for conceptual process design using these models, we are confronted with a computationally-intensive task. The process optimization of periodic adsorption processes may become even more expensive if we include competitive adsorption equilibria principles with non-trivial adsorption isotherm courses, see e.g., Rubiera Landa et al. (2013), or more-detailed mass-transfer mechanisms meant to describe particle-level adsorption phenomena dynamically. Another potential source of complexity—not addressed herein—is related to multi-

column processes with column-interacting steps, e.g., pressure equalization. Therefore, there is an inherent need to develop computational tools & strategies to surmount these challenges.

Investigated vacuum pressure-swing adsorption cycle: The process that we consider in this work is a 4-step VPSA cycle with light-product pressurization (LPP) that targets heavy-product recovery at high purity. Figure 1 illustrates graphically this cycle and its operational steps. We have developed a full-order model (FOM) to describe the dynamic operation of this process applying a thermally-modulated structured fiber contactor in Rubiera Landa et al. (2020b). Interest in these types of adsorbents has grown in the last years driven by process intensification, as well as addressing difficult gas separations such as CO_2 capture by economically-viable routes—see e.g., Bui et al. (2018) and references therein. The applied mathematical model consists of a set of one-dimensional, time-dependent PDEs that represent the coupled, nonisothermal, non-isobaric, mass, energy & momentum balances, characterizing the dynamic behavior of a packed-bed adsorber. These equations describe the periodic features of the 4-step VPSA cycle by adscribing appropriate BCs and ICs. The model implementation includes competitive adsorption equilibria as expressed by the Ideal Adsorbed Solution Theory (IAST) developed by Myers and Prausnitz (1965), as well as other well-known explicit competitive equilibria equations. In order to represent thermal modulation, we consider microencapsulated PCM embedded in the fibers as demonstrated by DeWitt et al. (2019). A smooth-interface model, see e.g., Surana et al. (2015), is included in the energy balance equation to account for the phase-transition enthalpy and temperature-dependent physical properties of the PCM. Model details may be consulted in Rubiera Landa et al. (2020b).

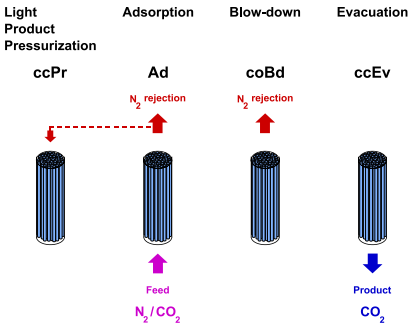

Figure 1: Illustration of investigated 4-step VPSA cycle with light-product pressurization (LPP), applying thermally-modulated fiber composite adsorbent—see DeWitt et al. (2019) & Rubiera Landa et al. (2020b).

2. Methods & algorithms

Numerical solution of model equations: We transform the PDEs that describe adsorber dynamics into a time-dependent ODE system by applying the method of lines with a cell-centered finite-volume spatial discretization (FVM). Cell averages of the state variables, $x = \left[\bar{y}_{1_j}, \bar{q}_{1_j}, \bar{y}_{2_j}, \bar{q}_{2_j}, \bar{p}_j, \bar{T}_j \right]^{\mathsf{T}}$, $j = 1, \ldots, J$, are integrated in time by adaptive step, multi-stepping, backward differentiation formulæ (BDF). This discretization warrants the necessary robustness to treat the adsorber model as a black-box function as required by the applied MOO algorithms.

Genetic algorithms for MOO of VPSA cycle: Several approaches exist to perform MOO of cyclic adsorption processes. If the process simulation is sufficiently robust,

then we can apply evolutionary optimization techniques—e.g., a genetic algorithm (GA). The FOM is hereby treated as a black-box function, without requiring its gradient information, which in turn may be difficult to generate for some adsorption process models. On the other hand, this aspect of evolutionary algorithms can be a drawback, because identifying non-dominated points that constitute the sought-after Pareto frontiers usually requires many function evaluations. Clearly, if these functions are expensive to evaluate, this becomes a computationally-intensive procedure. For the purpose of benchmarking our results, we applied a variant of the well-established NSGA-II algorithm by Deb et al. (2002) to our FOM.

Applied black-box function formulation: The function calls executed by the optimization algorithms entail the CSS simulation of the 4-step VPSA cycle for given values of the design variables and evaluating subsequently process performance metrics that define the objective space of the MOO tasks to solve. The selected design variables, u, include process conditions of the cycle or design parameters of the FOM; these are: 1.) high-pressure level, p_{high}; 2.) feed gas velocity, v_{feed}; 3.) adsorption step time, t_{Ad}; 4.) evacuation pressure level, p_{Ev}; & 5.) weight fraction of adsorbent in fiber composites, ω_{MOF}. The objective variables considered for the VPSA cycle are: 1.) product purity, $\Phi_{\text{Pu},i}(u)$; 2.) product recovery, $\Phi_{\text{Re},i}(u)$; 3.) productivity, $\Phi_{\text{Prod},i}(u)$; & 4.) specific energy consumption, $\Phi_{\text{En},i}(u)$.

Fixed-point iteration formulation of CSS calculation: Traditionally, calculation of CSS entails the dynamic simulation that the process would follow during transient operation, e.g., start-up. In essence, we simulate for a cycle ℓ, store the vector of state variables, x_ℓ, at a specified time of the cycle, e.g., at the end of the evacuation step, $t = t_{\text{Ev,end}}$, and then apply it as IC to obtain the next iterate, $x_{\ell+1}$. This is equivalent to the procedure expressed by Picard Iteration (PI)

$$x_{\ell+1} = g(x_\ell), \quad \ell = 0,1,2,\cdots, \textit{(until convergence)}, \tag{1}$$

where we simply substitute successively x_ℓ in map g to obtain $x_{\ell+1}$. In practice, we verify if CSS is attained by applying e.g., the ℓ_2-norm, $\| e \|_2 \leq \delta_{\text{tol.}}$, with $e := g(x_\ell) - x_{\ell+1}$, for a small, specified threshold, $\delta_{\text{tol.}}$. The simulation of the process is therefore formulated as a fixed-point iteration (FPI) task, which can be solved efficiently by applying methods for the acceleration of sequences, such as the vector extrapolation methods published by Sidi (2017).

Anderson Acceleration (AA): An interesting alternative that we investigate in Rubiera Landa et al. (2020a) consists of applying the algorithm developed by Anderson (1965) to accelerate the FPI calculation, Eq. (1), therefore reducing its computational cost. We implement AA as described by Walker and Ni (2011), employing their code. Application of this FPI acceleration technique helps to reduce the cost in terms of number of iterations required to fulfill the CSS condition by factors ranging from 1.3x

to 2x w.r.t. PI, with superlinear convergence rate, as documented in Rubiera Landa et al. (2020a).

Initialization of the fixed-point iteration: The CSS calculation may be initialized in two ways, depending on the IC applied at the start of the dynamic simulations: a) cold-start mode: the adsorber is either free of the more-adsorbed component or has been fully-regenerated; & b) warm-start mode: the adsorber has been partially loaded with adsorbates. Typically, a stored vector of state variables, $x = x(t,z)$, from a previous CSS calculation may be applied to perform warm-start initialization with the purpose of attaining CSS with a smaller number of iterations—this is the mode applied below.

Surrogate-based multi-objective optimization using accelerated black-box function evaluation: We apply the SOCEMO algorithm, a bound-constraint surrogate-based multi-objective optimization strategy created by Müller (2017) that has been designed to address expensive black-box problems with relatively large numbers of decision variables and objectives. In brief, this optimizer generates a radial-basis function (RBF) approximation for each objective constituting the specified multi-objective problem. A careful, well-thought-out algorithm that applies a GA plus adaptive sampling using the RBF surrogates' information aims at reducing the expensive black-box function evaluations—i.e., the accelerated FPI calculations—to a minimum, whilst simultaneously refining the quality of the RBF surrogates as the algorithm continues to identify the Pareto frontiers. This yields a powerful general-purpose MOO solver that can be applied easily to the periodic adsorption process at hand. We denominate the proposed combined solution strategy as 'SOCEMO+AA'.

Investigated MOO task: In order to assess the computational performance of this combination of techniques, we formulate a two-objective (bi-objective, BOO) task and solve it first with NSGA-II, applying the conventional PI and name this strategy 'NSGA-II+PI'. Afterwards, we solve identical tasks applying the 'SOCEMO+AA' strategy.

Table 1: Applied bounds for design variables of BOO Task.

Variable	p_{high}	v_{feed}	t_{Ad}	p_{Ev}	ω_{MOF}
Units	atm	m / s	S	atm	-
Lower bound	3.0	0.1	15	0.10	0.15
Upper bound	7.5	1.0	120	0.35	0.35

The optimization tasks explore the process performance of the aforementioned 4-step VPSA cycle w/ LPP for a typical dry flue gas stream, employing a thermally modulated fiber composite loaded with a metal-organic framework (MOF) and decision variables' bounds listed in Table 1:

- **BOO Task.** *Identify the Pareto frontier for recovery vs. purity* formulated as:

$$\text{maximize} \quad \{\Phi_{\text{Pu},CO_2}(u), \Phi_{\text{Re},CO_2}(u)\}, \text{s.t.} -\infty \le u^{lb} \le u \le u^{ub} \le \infty .$$

For 'NSGA-II+PI' we allow a maximum of 30 generations with a population size of 80 function evaluations. In the case of 'SOCEMO+AA' we set a total budget of 150 function evaluations.

3. Results & discussion

Figure 2 illustrates the Pareto frontiers obtained by applying 'NSGA-II+PI' as well as 'SOCEMO+AA' for cold-start and warm-start initialization modes. Table 2 summarizes the computational performance results of all runs. Both strategies allow us to identify non-dominated points accurately at the prescribed tolerances. A slightly worse result was obtained for the particular 'NSGA-II+PI' run executed with cold-start initialization mode. The two runs performed with 'SOCEMO+AA' yielded almost identical Pareto frontiers with good spread, while outperforming slightly the warm-start 'NSGA-II+PI' run in terms of the identified non-dominated points.

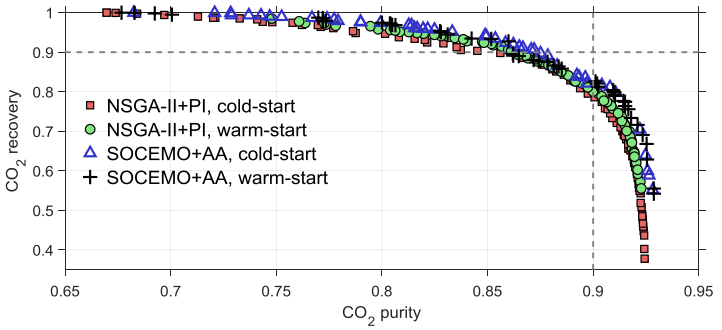

Figure 2: Computed Pareto frontiers for 4-step VPSA cycle w/ LPP applying a thermally-modulated contactor loaded with MOF UTSA-16 as reported by Xiang et al. (2012) and operating at 298 K. Design variables & bounds applied are listed in Table 1. AA parameters $(m = 4, \beta = 1)$ set in 'SOCEMO+AA' runs.

The two results obtained with 'NSGA-II+PI' would likely improve with tighter tolerances and increased function evaluations' budget, at the expense of an even higher computational cost, in order to match the obtained 'SOCEMO+AA' Pareto frontiers. The 'SOCEMO+AA' strategy applying warm-start initialization mode gave the most efficient result, requiring approximately 6 % of the time needed by 'NSGA-II+PI' with cold-start initialization mode. In other words, for this particular example, we achieved roughly a 17-fold reduction in computational cost. The effect of the initialization mode can be observed from the mean times required for computing a single CSS. Both warm-start runs required less time than their cold-start counterparts.

Table 2: Computational costs for solving BOO Task with 'NSGA-II+PI' & 'SOCEMO+AA'. Calculations were performed in MATLAB™ on a PC with i7-3770 CPU at 3.40 GHz & 8 GB RAM.

	NSGA-II+PI cold-start	NSGA-II+PI warm-start	SOCEMO+AA cold-start	SOCEMO+AA warm-start
No. generations (max. 30)	25	30	n/a	n/a
No. function evaluations	2000	2400	160	152
No. non-dominated points	80	80	47	47
Mean calculation time per CSS, s	46	37	84	36
Total calculation time, s	92815	88326	13440	5467

4. Conclusion

We have introduced a powerful and easy-to-implement strategy to perform multi-objective optimization of cyclic adsorption processes, exemplified by a 4-step VPSA

cycle designed for CO_2 capture. The strategy consists of applying AA to improve the convergence efficiency to CSS when evaluating expensive black-box function evaluations of FOMs for periodic adsorption processes. In combination with the MOO solver SOCEMO, we estimated the Pareto frontier of a typical VPSA process optimization task in a computationally efficient manner. An important feature of the proposed 'SOCEMO+AA' strategy is that no offline or *a priori* sampling phase needs to be carried out, as it is often required by other meta-modeling techniques, since SOCEMO constructs surrogates of objective functions and identifies non-dominated points *'on the fly'*, i.e., their calculation is embedded in the execution of the algorithm. We demonstrated that a reduction in computational cost of one order of magnitude, with only a fraction of the number of black-box function evaluations needed by a GA, can be achieved with the proposed strategy, preserving high-fidelity of the optimization results.

Acknowledgement: We thank the U.S. Department of Energy for support through grant DE-FE0026433. Any opinions, findings, conclusions or recommendations expressed herein are those of the authors and do not necessarily reflect the views of the DOE.

References

D. G. M. Anderson, 1965. Iterative Procedures for Nonlinear Integral Equations. Journal of the Association for Computing Machinery 12 (4), 547-560.

M. Bui, C. S. Adjiman, A. Bardow, E. J. Anthony, A. Boston, S. Brown, P. S. Fennell, S. Fuss, A. Galindo, L. A. Hackett, J. P. Hallett, H. J. Herzog, G. Jackson, J. Kemper, S. Krevor, G. C. Maitland, M. Matuszewski, I. S. Metcalfe, C. Petit, G. Puxty, J. Reimer, D. M. Reiner, E. S. Rubin, S. A. Scott, N. Shah, B. Smit, J. P. M. Trusler, P. Webley, J. Wilcox, N. M. Dowell, 2018. Carbon capture and storage (CCS): the way forward. Energy & Environmental Science 11 (5), 1062-1176.

K. Deb, A. Pratap, S. Agarwal, T. Meyarivan, 2002. A Fast and Elitist Multiobjective Genetic Algorithm: NSGA-II. IEEE Transactions on Evolutionary Computation 6 (2), 182-197.

S. J. A. DeWitt, H. O. Rubiera Landa, Y. Kawajiri, M. J. Realff, R. P. Lively, 2019. Development of Phase-Change-Based Thermally Modulated Fiber Sorbents. Industrial & Engineering Chemistry Research 58 (15), 5768-5776.

G. Fiandaca, E. S. Fraga, S. Brandani, 2009. A multi-objective genetic algorithm for the design of pressure swing adsorption. Engineering Optimization 41 (9), 833-854.

J. Müller, 2017. SOCEMO: Surrogate Optimization of Computationally Expensive Multiobjective Problems. INFORMS Journal on Computing 29 (4), 581-596.

A. L. Myers, J. M. Prausnitz, 1965. Thermodynamics of Mixed-Gas Adsorption. AIChE Journal 11 (1), 121-127.

H. O. Rubiera Landa, D. Flockerzi, A. Seidel-Morgenstern, 2013. A Method for Efficiently Solving the IAST Equations with an Application to Adsorber Dynamics. AIChE Journal 59 (4), 1263-1277.

H. O. Rubiera Landa, R. P. Lively, Y. Kawajiri, M. J. Realff, 2020a. Applying Anderson Acceleration to improve the simulation efficiency of periodic adsorption processes. (in preparation).

H. O. Rubiera Landa, R. P. Lively, Y. Kawajiri, M. J. Realff, 2020b. Theoretical investigation of vacuum pressure-swing adsorption process using thermally-modulated fiber composite adsorbents. (in preparation).

A. Sidi, 2017. Vector Extrapolation Methods with Applications. SIAM Series on Computational Science & Engineering. Society for Industrial and Applied Mathematics, ISBN 978-1-61197-495-9.

K. S. Surana, A. D. Joy, L. A. Quiros Fonseca, J. N. Reddy, 2015. Mathematical Models and Numerical Solutions of Liquid-Solid and Solid-Liquid Phase Change. Journal of Thermal Engineering 1 (2), 61-98.

C. L. E. Swartz, Y. Kawajiri, 2019. Design for dynamic operation – A review and new perspectives for an increasingly dynamic plant operating environment. Computers & Chemical Engineering 128, 329-339.

H. F. Walker, P. Ni, 2011. Anderson Acceleration for Fixed-Point Iterations. SIAM Journal on Numerical Analysis 49 (4), 1715-1735.

S. Xiang, Y. He, Z. Zhang, H.Wu,W. Zhou, R. Krishna, B. Chen, 2012. Microporous metal-organic framework with potential for carbon dioxide capture at ambient conditions. Nature Communications 3 (954), 1-9.

Sauro Pierucci, Flavio Manenti, Giulia Bozzano, Davide Manca (Eds.)
Proceedings of the 30th European Symposium on Computer Aided Process Engineering (ESCAPE30), May 24-27, 2020, Milano, Italy.
http://dx.doi.org/10.1016/B978-0-12-823377-1.50302-5

QMaC: A Quantum Mechanics/Machine Learning-based Computational Tool for Chemical Product Design

Qilei Liu, Kun Tang, Jinyuan Zhang, Yixuan Feng, Chenyang Xu, Linlin Liu, Jian Du, Lei Zhang*

Institute of Chemical Process Systems Engineering, School of Chemical Engineering, Dalian University of Technology, Dalian 116024, China
keleiz@dlut.edu.cn

Abstract

Chemical industry is focusing more on higher value-added materials compared to commodity chemicals. Chemical-based product design has now become a key topic in chemical engineering. A few computer-aided chemical product design platforms/tools have been developed to help design various chemical products. In this work, a Quantum mechanics/Machine learning-based Computational property prediction tool (QMaC) is developed for chemical product design, aiming to employ the Quantum Mechanics (QM) and Machine Learning (ML) techniques to better design organic solvents, inorganic materials, fertilizers and pesticides, polymers, catalysts and other chemical products for human needs. A case study is given to demonstrate the validity of the developed product design tool.

Keywords: product design, computer-aided molecular design, quantum mechanics, machine learning, surrogate model.

1. Introduction

Chemical-based product design is rapidly becoming a key topic in chemical engineering (Zhang et al., 2017). However, most of products are still designed based on trial-and-error methods, which need much manpower, material and financial resources. Therefore, it is desirable to develop a systematic method to design promising alternatives to satisfy sets of product attributes to serve as candidates for final experimental verification. Computer-Aided Molecular Design (CAMD) technique is a kind of such method (Zhang et al., 2016). It provides a systematic methodology where numerous molecules are assembled and evaluated through a set of predefined descriptors.

Up to now, many computer-aided chemical product design tools have been developed to assist in the chemical product design problems. Gani et al. (1997) developed the ICAS-Integrated Computer Aided System (www.pseforspeed.com/icas/), which combines computer-aided tools for property prediction, simulation, modelling, synthesis/design, analysis and control into a single integrated system. ProCAMD is a molecular product design toolbox based on a multi-level CAMD technique (Harper and Gani, 2000). Samudra and Sahinidis (2013) developed an Automated MOlecular DEsign using Optimization (AMODEO) toolbox to solve the CAMD problem in a non-gradient way. More recently, the VPPD-Lab has developed the chemical product simulator ProCAPD (Kalakul et al., 2017), which offers the options of single species product design, product evaluation, database search, modelling toolbox, multi-species product design templates,

and new product template design. Liu et al. (2019) developed an optimization-based framework for molecular and mixture product design, where associated models, solution algorithms and databases are implemented in a toolbox called "OptCAMD". However, even with these recently developed computer-aided tools, chemical product design is still problem specific due to the lack of product property parameters (e.g., binary interaction parameters in UNIFAC model) that obtained from experiments for modeling, and the difficulties in modeling some complex chemical products (e.g., catalysts). Therefore, a computer-aided tool based on quantum mechanics and machine learning techniques has been receiving increasing interest within the PSE community.
In this paper, a Quantum mechanics/Machine learning-based Computational property prediction tool (QMaC) for chemical product design is presented. In Section 2, the QMaC framework that consists of the QM-derived mechanism models and QM-based machine learning models is discussed in detail. In Section 3, a case study is given for highlighting the applications of QMaC tool in chemical product design.

2. QMaC framework

The QMaC framework and its relationships with the database and OptCAMD are shown in Figure 1.

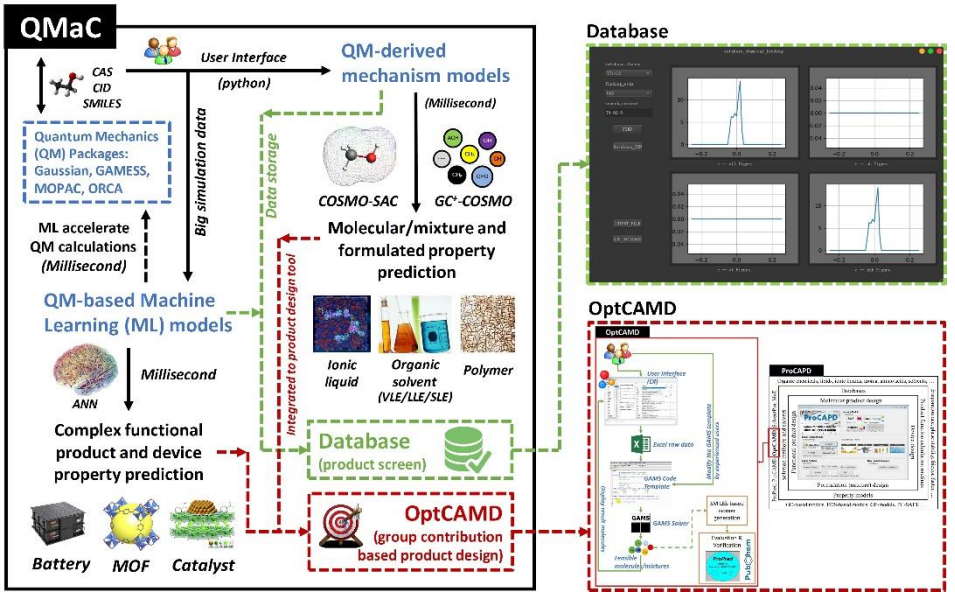

Figure 1. QMaC framework and its relationships with the database and OptCAMD. The input data of QMaC is a set of molecules represented with SMILES (Simplified Molecular Input Line Entry Specification), CAS number or CID number (in PubChem database). QM calculation packages, e.g., Gaussian (Ochterski, 2000), MOPAC (Stewart, 2016), GAMESS (Schmidt et al., 1993), etc., are incorporated into QMaC as the execution module for molecular simulations. The functions of the execution module include molecular structure optimization, single point energy calculation, Gibbs free energy calculation, HOMO-LUMO calculation and all other functions that QM packages provide. Users can select QM packages, execution module functions and functional method/basis set parameters in QMaC interface.

2.1. QM-derived mechanism models

The QM-derived mechanism models, e.g., the COSMO-SAC (COnduct-like Screening Model for Segment Activity Coefficient) model (Hsieh et al., 2010), have been developed using C++ and embedded in the QMaC tool. These models are able to predict molecular/mixture and formulated properties (e.g., activity coefficient, VLE/LLE/SLE) for organic solvents, ionic liquids, etc. Considering the computational cost, some shortcut methods are developed to make fast predictions (in milliseconds) for product properties, for example, the GC^+-COSMO method using group contribution-based methods to predict the σ-profiles. In the following we will take the COSMO-SAC model and GC^+-COSMO method as the examples for introduction.

2.1.1. COSMO-SAC model

In this paper, the state-of-the-art revised COSMO-SAC model (Hsieh et al., 2010) with its corresponding adjusted model parameters (Chen et al., 2016) is employed in our work. The procedure of the COSMO-SAC model can be divided into three steps.

Step (a). The COSMO calculation procedure starts from the Density Functional Theory (DFT) calculations (a variety of first principles methods in QM calculation), through which the structure of the molecule of interest is optimized and surrounded with a virtual conductor, inducing the screening charge density σ on the conductor surface. In this paper, a database of 1432 molecules (from Virginia Tech database (Mullins et al., 2006)) was established, and DFT calculations were performed by Gaussian 09W software (http://www.gaussian.com/) (Ochterski, 2000) using B3LYP/6-31g(d,p). The COSMO-SAC model parameters are adopted from Chen et al. (2016)'s work, which have been specially reparametrized for B3LYP/6-31g(d,p) functional method/basis set, since these parameters have great impacts on σ-profiles, activity coefficients γ and other activity coefficient related properties.

Step (b). With the screening charges obtained in Step (a), the surface of a molecule is dissected to segments. The segment σ distribution is projected into a two-dimensional discrete profile known as σ-profile.

Step (c). As σ-profiles provide qualitative information to identify isomers, complex molecular interactions, as well as quantitative information on both pure and solvent mixture properties, they are employed for the thermodynamic property calculations. More detailed information of the state-of-the-art revised COSMO-SAC model can be found in the literature (Hsieh et al., 2010; Chen et al., 2016).

2.1.2. GC^+-COSMO method

The time-consuming DFT calculations in the COSMO-SAC model have hindered the development of the COSMO-CAMD methodology for molecular design. A shortcut method should be developed to achieve the well-balanced compromise between accuracy and computation efficiency. Up to now, most COSMO-CAMD methodologies employed first-order group based GC-COSMO method to correlate σ-profile with functional groups (Mu et al., 2007). However, the GC-COSMO method has poor predictive powers in some cases when polarity effects exist among highly polar molecules and also has difficulties in identifying the isomers.

In this work, a GC^+-COSMO method is developed to solve the above problems, where a strategy of multi-order groups is adopted to introduce new group descriptors for the interactions between polar functional groups and allow the identification for the isomers. The multi-order groups consist of zero, first, second and third-order groups. The zero-order groups are defined as single molecules with small molecular weights (e.g., H_2O). Since the number of single molecules is limited and the GC methods have difficulties in describing small molecules, it is reasonable to define zero-order groups to

describe these molecules. The first-order and second-order (super-groups contain several first-order groups) groups are defined as MG (Marrero and Gani (2001)) groups in python scripts. As for the third-order groups, they are obtained from the Bemis/Murcko (BM)-type decomposition (Bemis and Murcko, 1996) method using the RDKit library (Landrum, 2006), which is able to transform the molecules to side chains and core circular skeletons. It should be noted that the QMaC tool has a set of options for GC-COSMO and GC^+-COSMO methods.

2.2. QM-based machine learning models

Besides, QMaC also provides abundant simulation data as the inputs or outputs for QM-based Machine Learning (ML) model constructions, which can further be used to predict complex functional product and device properties (e.g., cycling lifespan, selectivity) for battery, MOF, catalyst, etc. Machine learning has strong abilities in autonomously learning data characteristics and fitting nonlinear relationships between chemical product structures and properties, which is an opportunity to design complex chemical products since that the inherent mechanisms of these products are usually unclear and the traditional linear/nonlinear fitting methods often fail to capture the structure-property relationships. What's more, ML is also an efficient surrogate model with high-throughput calculation speed. When the simulation data are worked as the outputs for ML models, i.e., the simulation data are target properties to evaluate the product performances, easily accessible descriptors (e.g., a set of groups) need to be prepared as model inputs for QM-based ML model constructions (Zhang et al., 2018). If the simulation data are worked as the inputs for ML models (e.g., using σ-profiles to predict product properties), it suggested that some surrogate models (e.g., ML models) should be employed to correlate the molecular descriptors (e.g., molecular fingerprints) with the simulation data to ensure the inputs of QM-based ML model can be fast obtained, otherwise the product design efficiency will be limited to the bottleneck of DFT calculations.

2.3. The connection of QMaC to database and OptCAMD

All computation results will be stored in the database and users can make a fast product property screening through it. For example, users can choose 1432 commonly used solvents for COSMO-SAC model predictions. Experimental data can also be identified in this database for model (COSMO-SAC, ML, etc.) parameters fit or model prediction comparison. Besides, both QM-derived mechanism and QM-based ML models can be integrated to the OptCAMD tool to extrapolate their property prediction abilities for high-throughput chemical product design. Once the Quantitative Structure-Property Relationship (QSPR) models and their corresponding shortcut methods are given, the OptCAMD tool is able to design molecular structures within the constraints of molecular structure and product property to maximize/minimize objective functions based on the mathematical optimization-based approaches.

3. Case study

A case study of designing solvents for extracting phenol from wastewater (Liu et al., 2018) is performed through QMaC and OptCAMD tools using the COSMO-SAC model. The objective function is to design a solvent with a large distribution coefficient for phenol. The following groups are selected: CH_3, CH_2, CH, C, CH_2(cyc), CH(cyc), C=C, C=C(cyc), aCH, aC-CH_3, OH, CH_3CO, CH_2CO, CH_3COO, CH_3O, CH_2O, CH-O, COOH, COO, aC-OH. The lower and upper bonds for structure and property constraints and the best designed solvent are shown in Table 1.

A decomposition-based strategy (Karunanithi et al., 2006) was employed to solve the CAMD problem. 89 molecules were firstly obtained within the constraints of molecular structure and solvent properties (molecular weight Mw, melting point T_m, boiling point T_b, solubility parameter $Solp$, density ρ, viscosity η and toxicity LC_{50}), among which 3 molecules were further designed within the constraints of solvent loss Sl, solvent power Sp and selectivity β. Finally, the best designed solvent is listed in Table 1 for further experimental verification.

Table 1. The lower and upper bonds for structure and property constraints and the best designed solvent.

Properties	Lower bound	Upper bound	Properties	Prediction results	Experimental values
N_G	4	8	Molecule	$C_6H_{12}O$	-
N_S	-	7	Molecular structure		-
N_F	1	7			
Mw (g/mol)	74	170	Mw (g/mol)	100.2	100.2
T_m (K)	-	298	T_m (K)	219.6	189.2
T_b (K)	335	468	T_b (K)	377.1	389.6
$Solp$ ($MPa^{1/2}$)	16	22	$Solp$ ($MPa^{1/2}$)	16.1	-
ρ (g/cm^3)	-	0.95	ρ (g/cm^3)	0.763	0.800
η (cP)	-	10	η (cP)	0.494	-
$-\log(LC_{50})$ $(-\log(mol/L))$	-	5	$-\log(LC_{50})$ $(-\log(mol/L))$	2.098	-
Sl	-	0.005	Sl	0.0016	-
Sp	0.5	-	Sp	7.23	-
β	13	-	β	604	-

4. Conclusions

In this paper, a computer-aided property prediction tool (QMaC) for chemical product design is developed, where quantum mechanics and machine learning techniques are used. Database and OptCAMD tool are integrated with the QMaC tool for chemical product screen and design procedure. A case study of designing extraction solvents is performed, which demonstrates the effectiveness of the QMaC framework.

Acknowledgement

Thanks for the financial support of NSFC [21808025]; National College Students Innovation and Entrepreneurship Training Program [201910141010101010186].

References

Zhang, L., Mao, H., Liu, L., Du, J., & Gani, R. (2018). A machine learning based computer-aided molecular design/screening methodology for fragrance molecules. Computers & Chemical Engineering, 115, 295-308.

Zhang, L., Fung, K. Y., Zhang, X., Fung, H. K., & Ng, K. M. (2017). An integrated framework for designing formulated products. Computers & Chemical Engineering, 107, 61-76.

Zhang, L., Babi, D. K., & Gani, R. (2016). New vistas in chemical product and process design. Annual review of chemical and biomolecular engineering, 7, 557-582.

Schmidt, M. W., Baldridge, K. K., Boatz, J. A., Elbert, S. T., Gordon, M. S., Jensen, J. H., ... & Windus, T. L. (1993). General atomic and molecular electronic structure system. Journal of computational chemistry, 14(11), 1347-1363.

Samudra, A. P., & Sahinidis, N. V. (2013). Optimization‐based framework for computer‐aided molecular design. AIChE Journal, 59(10), 3686-3701.

Ochterski, J.W., 2000. Thermochemistry in gaussian. Gaussian Inc.

Mullins, E., Oldland, R., Liu, Y. A., Wang, S., Sandler, S. I., Chen, C. C., ... & Seavey, K. C. (2006). Sigma-profile database for using COSMO-based thermodynamic methods. Industrial & engineering chemistry research, 45(12), 4389-4415.

Mu, T., Rarey, J., & Gmehling, J. (2007). Group contribution prediction of surface charge density profiles for COSMO‐RS (Ol). AIChE journal, 53(12), 3231-3240.

MOPAC2016, James J. P. Stewart, Stewart Computational Chemistry, Colorado Springs, CO, USA, HTTP://OpenMOPAC.net (2016).

Marrero, J., & Gani, R. (2001). Group-contribution based estimation of pure component properties. Fluid Phase Equilibria, 183, 183-208.

Liu, X., Zhao, Y., Ning, P., Cao, H., & Wen, H. (2018). Modified structural constraints for candidate molecule generation in computer-aided molecular design. Industrial & Engineering Chemistry Research, 57(20), 6937-6946.

Liu, Q., Zhang, L., Liu, L., Du, J., Tula, A. K., Eden, M., & Gani, R. (2019). OptCAMD: An optimization-based framework and tool for molecular and mixture product design. Computers & Chemical Engineering, 124, 285-301.

Landrum, G. (2006). RDKit: Open-source cheminformatics.

Karunanithi, A. T., Achenie, L. E., & Gani, R. (2006). A computer-aided molecular design framework for crystallization solvent design. Chemical Engineering Science, 61(4), 1247-1260.

Kalakul, S., Eden, M. R., & Gani, R. (2017). The chemical product simulator–ProCAPD. In Computer Aided Chemical Engineering (Vol. 40, pp. 979-984). Elsevier.

Hsieh, C. M., Sandler, S. I., & Lin, S. T. (2010). Improvements of COSMO-SAC for vapor–liquid and liquid–liquid equilibrium predictions. Fluid Phase Equilibria, 297(1), 90-97.

Harper, P. M., & Gani, R. (2000). A multi-step and multi-level approach for computer aided molecular design. Computers & Chemical Engineering, 24(2-7), 677-683.

Gani, R., Hytoft, G., Jaksland, C., & Jensen, A. K. (1997). An integrated computer aided system for integrated design of chemical processes. Computers & Chemical Engineering, 21(10), 1135-1146.

Chen, W. L., Hsieh, C. M., Yang, L., Hsu, C. C., & Lin, S. T. (2016). A critical evaluation on the performance of COSMO-SAC models for vapor–liquid and liquid–liquid equilibrium predictions based on different quantum chemical calculations. Industrial & Engineering Chemistry Research, 55(34), 9312-9322.

Bemis, G. W., & Murcko, M. A. (1996). The properties of known drugs. 1. Molecular frameworks. Journal of medicinal chemistry, 39(15), 2887-2893.

Sauro Pierucci, Flavio Manenti, Giulia Bozzano, Davide Manca (Eds.)
Proceedings of the 30th European Symposium on Computer Aided Process Engineering
(ESCAPE30), May 24-27, 2020, Milano, Italy.
http://dx.doi.org/10.1016/B978-0-12-823377-1.50303-7

The Value of Direct Programming the PID Control Law in MATLAB®

Bartolomeo Cosenza, Michele Miccio

Dipartimento di Ingegneria Industriale, Università degli Studi di Salerno,
Via Giovanni Paolo II 132, 84084 Fisciano SA, Italy
mmiccio@unisa.it bartolomeocosenza@hotmail.it

Abstract

This work deals with Matlab® and the PID controller. Frequently, codes implementing PID-controlled case studies as tutorial sessions or examples for undergraduate students are available as programmed in Simulink®, the companion toolbox for block modeling, simulation and analysis of dynamic systems. Vice versa, the student, who has access to the source code and directly operates on it in Matlab®, better masters the underlying theoretical background, develops a greater skill related to coding and understands the computational results in a clearer way. This skill can be useful in any work context, especially where Simulink cannot be used.
In this article a particular didactic approach is suggested for "hands on" the PID controller and the feedback control system, a simple case study based on the classical continuous bioreactor is built together with and for the class students, both set-point tracking and disturbance rejection at closed loop are covered, the most important outcomes are discussed from a didactical viewpoint. The adopted teaching strategy and the various phases necessary to its effective implementation in Matlab® have been subjected to an assessment procedure during the class of "Modeling and control of process systems", with encouraging results.

Keywords: PID controller, Matlab®, bioreactor, feedback, set point tracking, disturbance rejection

1. Introduction

The PID control is known from about 1 century: huge numbers of scientific papers, textbooks and software (either commercial or open source) implementations cope with PID. It continues to be widely and successfully used even for complex and nonlinear processes, alone or integrated with other control strategies. As far as recent applications, a double Q-PID algorithm for mobile robot control was developed by Calucho et al. [2]; Urooj and Singh [3] developed a fractional-order PID control strategy for blood pressure control using sodium nitroprusside during surgical operation; Zhao et al. [4] proposed an adaptive PID control to improve the power tracking performance of solar photovoltaic air-conditioning systems, Miccio and Cosenza [5] developed the control of a distillation column by type-2 and type-1 fuzzy logic PID controllers and a graphical user interface for dynamics and feedback PID control of chemical reactors [6]; the control of a PWR nuclear reactor core power was realized by Mousakazemi [7] using scheduled PID with GA. In all these examples, ranging in all fields of control application, beyond the strategies used, the PID control action remains a simple and effective core of the control system. Matlab® is a well-known programming platform for engineers and scientists, with a lot

of free, user-developed codes in the File Exchange repository [1]. Its matrix-based language allows the most natural expression of computational mathematics [8]. To further simplify the study of dynamic systems, Matlab provides the Simulink® toolbox as an interactive, graphical environment for modeling, simulating, and analyzing dynamic systems. The great advantage of Simulink is a graphical user interface (GUI) for building models as block diagrams [9]. Predefined blocks, including the PID controller, are included in a library and can be easily used (drag-and-drop mouse operations) to construct graphical models of systems.

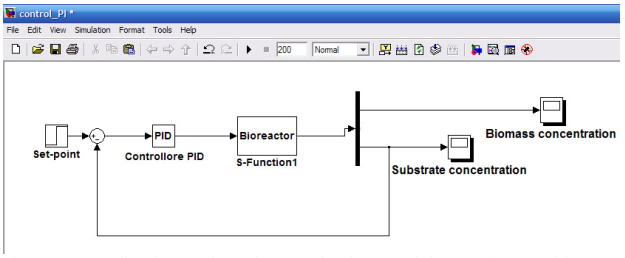

Figure 1. Feedback PID-based control scheme of the continuous bioreactor in a Simulink® worksheet

If it is true that a graphical block programming language in the school makes easy and immediate the student's job on the application of the PID control, it is also true that its excessive use promotes mechanical actions that lead to misunderstanding or even obscuring the content of each block. The greatest difficulty arises when switching from an easy and intuitive pre-packaged simulation environment to a real system whose automatic control, for example, requires non-block programming languages. For this reason it is important that students understand how to implement a PID control system from scratch, without needing pre-packaged blocks. Students must be aware of what they are doing, step by step, to develop computational thinking. This latter is essential not only in engineering, e.g., in computer programs (coding) for practical applications, but also in non-scientific disciplines, e.g., economics, social science, humanities, etc., to develop problem solving skills and tools [10].

In this work a teaching strategy is proposed and discussed to ensure that students implement, in a Matlab® code, the classical PID control algorithm applied to a continuous bioreactor.

2. A case study: bioreactor model and control

Biochemical reactors are usually produce a large number of intermediate and final products, including pharmaceuticals, food and beverages. The simplest bioreactor model needs only two "reacting" components: biomass and substrate. The biomass consists of cells that consume the substrate. The isothermal continuous bioreactor considered in this paper has constant volume V and constant physical-chemical properties. Its state-space dynamical model is given by the following mass balance eqs. [11]:

$$\frac{dX_b}{dt} = \mu(S)X_b - \frac{X_b F}{V} \tag{1}$$

$$\frac{dS}{dt} = -\frac{\mu(S)X_b}{Y} + \frac{(S_F - S)F}{V} \tag{2}$$

$$\mu(S) = \frac{\mu_{max} S}{K_m + S}$$

The considered model is a perfectly stirred continuous bioreactor; it is widely and successfully used for a large number of simplified nonlinear processes. The eqs.1 and 2

originate from the biomass, X_b, and the substrate, S, balance, respectively. Both are coupled through the nonlinear growth rate coefficient $\mu(S)$, in the form proposed by Monod, which is the main source of nonlinearity in the model. The model variables and parameters, together with their values, are reported in [11].
In a process control strategy of the bioreactor, the variation of the substrate feed concentration, S_F, represents a disturbance to the system. The variable to be controlled is the substrate concentration S. The dilution rate, F/V, represents the manipulation variable.

3. Implementation plan

3.1 Teaching strategy

It is well known that learning is effective when starts from a practical and problematic situation. The teacher's purpose is to show how programming skills can be used in many contexts. Some interface devices (for example Arduino® or National Instruments DAQ®) for the control of many real systems do not include the use of block language typical of Simulink®; vice versa, they lend themselves to be programmed by means of Matlab®, i.e., one of the most used programming environments in the educational field. There are many control methodologies of different type and complexity (e.g., Fuzzy, MPC, Feed-Forward, Neural Networks, etc.), but the PID controller, besides being widespread and widely used (as specified in the introduction), represents an excellent test bench for the development of programming skills. To carry out the control, for example that of a bioreactor, it is necessary for the student to acquire the skills to program (coding) a PID controller, ready to be applied to the control of a process variable (such as a tank temperature or, in the case of the bioreactor, the concentration of the substrate).
The present implementation plan is subdivided in sequential phases for the case study of closed loop control of a simple non-linear bioreactor. When possible, the direct Matlab coding is compared to its equivalent in the Simulink® environment.
To motivate the use of PID control, the teacher can focus on some of the recent and novel applications, as those listed in the Introduction. This is the first phase and is very important from a didactical viewpoint, because motivation and interest are the fuel of every learning process.
The following phases deal with actual programming.

3.2 Implementation of discrete time

The teacher must dwell on the fact that a simulation allows to see the behavior of a system (and therefore the trend of the state variables) over time. In Simulink® time is running in background and it is possible to change the start time and stop time for the simulation by entering new values in the “Start time” and “Stop time” fields. The same must be done in a corresponding Matlab® code. The teacher can then suggest the realization of a time interval (*deltat*) between a control action and the next one in a discrete time framework, the initial and final simulation time (*t0* and *tf*, respectively), a vector integration *time* and a count parameter *nstep* as follows:

```
deltat =1;          % interval between a control action and the next
                    % (since the PID always operates on a discrete system);
t0 = 0;             % initial simulation time;
tf = 200;           % final simulation time (200 hours);
time = [t0:deltat:tf];  % vector of integration times;
nstep = length(time);   % number of steps to consider;
```

3.3 PID controller guided implementation

In the phase 3, the teacher has to recall the PID control law, involving a proportional, integral and derivative action.
the teacher has first to declare the parameters of the controller (with their units) and its *bias*, and, second, to assign them a value:

```
Kc = 0.5;                 % controller gain;
tauI =5;                  % integral time constant;
tauD =0.5;                % derivative time constant;
ic0 = 0.3;                % bias, i.e., value of the control action at time t=0;
```

The simply proportional action is

```
ic = ic0 + Kc*(yysp-y(end,2));        % proportional controller;
```

where *ic* stands for the manipulation variable (the dilution rate, F/V, in the present case study); *y(end,2)* is the state variable to be controlled (the substrate concentration in the bioreactor) and *yysp* is the set-point.

Then, the teacher recalls that a proportional action only is not enough to guarantee the achievement of the set-point: integral action is necessary to avoid offset. At this point, the teacher has to points out that it is necessary to use a numerical method to implement an integral action in a simulation environment. Numerical integration methods can generally be described as combining algebraic evaluations of the integrand to get an approximation to the integral. The simplest numerical integration method is the "rectangle method", assuming that the function has a constant value within each little interval. Students are then invited to implement the integration algorithm in Matlab language as follows:

```
integral = integral + deltat*(yysp-y(end,2));
```

Then, the teacher recalls that reaching the set-point is sometimes not enough, but the derivative action is required to speed up or improve the quality of the control action.
Again, in a numerical simulation environment, the true derivative must be approximated by a numerical formula:

$$\frac{dy}{dx} \approx \frac{\Delta y}{\Delta x} = \frac{y_2 - y_1}{x_2 - x_1} \tag{3}$$

Here, the students are invited to adopt the simplest one by considering a unit time step (the true derivative is the limit to zero of the value of the difference quotient Δx). This becomes in Matlab:

```
derivative=(y(end,2)-y(end-1,2))/(t(end)-t(end-1));
```

Finally, the students add the above integral and derivative actions to the proportional action as follows:

```
ic = ic + (Kc/tauI)*integral + tauD*derivative;        % PID control action
```

Taking advantage of the previous code (the one concerning time and the simulation step)

the teacher invites the students to write the code of the control system for the set point tracking problem as follows:

```
ysp = 0.18*diag(eye(nstep-1));   % declaration of a row vector with nstep components
                                 % all  equal to 0.18 (initial set-point value);
for i = 60:100
ysp(i) = 0.20;                   %  starting at 60 (time, h) the set-point value
end                              %  is stepped from 0.18 to 0.20;
```

In a similar way (not addressed here for lack of space) the students can implement the control system for the disturbance rejection problem. With appropriate modifications, different time-variation laws of set-points and disturbances can be embodied within the Matlab simulation environment. Further, the effects of changing the PID parameters (tuning) can be investigated.

3.4 Implementation of the bioreactor model

This is perhaps the simplest phase of the whole work, because it is quite easy to write, in Matlab language, the mathematical model of the bioreactor. The teacher may advise to write the code in a different file, paying attention to the use of parentheses (a simple out-of-place parenthesis can compromise the whole simulation) as follows:

M.file (Bioreactor)

```
function yp = Bioreactor (t,y)   % y(1) and y(2) are state variables, respectively biomass
                                 % and substrate concentration. y(2) is the controlled
                                 % variable;
global Y km k1 mumax             % System parameters;
global ic yysp  ssf              % ic is the manipulation variable; yysp is the set-point
                                 % variable (included in ic) and ssf the disturbance;
yp = zeros(2,1);
yp(1) = y(1)*((mumax*y(2)/(km+y(2)))-ic);
yp(2) = ic*(ssf-y(2))-y(1)*(mumax*y(2)/(km+y(2)))/Y;
```

The teacher focuses on the mathematical model and on what it represents. It is therefore appropriate to briefly describe the characteristics of the bioreactor in question, focusing on the aspects related to the control (as highlighted in the section on bioreactor model and control). It is important for the students, before control the system, to know what the system is for, what its practical purpose is, what it produces, and what the reaction products are for. It would not make sense to ask for the control of something to be an end in itself, a mere speculative exercise without practical implications.

3.5 Simulation at closed loop

The next phase gets into the heart of the simulation. Within this 4th phase, the teacher introduces the students to a Matlab built-in ode system solver, for example ODE 45, and to a plotting command (not addressed here for lack of space).

Finally, the students get the plot of their simulated results. Just as a proving example, Fig. 2 reports the graph obtained from a simulation of the bioreactor control system that provides for set-point tracking and disturbance rejection.

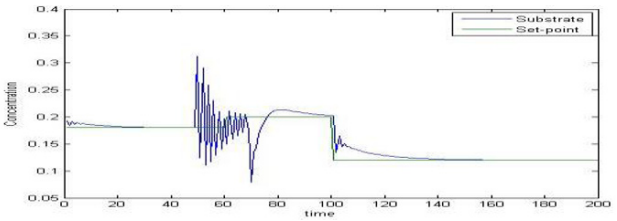

Figure 2. Time evolution of the substrate concentration after two step changes in the set-point: from 0.18 to 0.2 at time 60 h and from 0.20 to 0.12 at time 100 h; step disturbance in feed concentration from 4 to 5 at time 50 h and from 5 to 3 at time 70 h.

4. Evaluation results and conclusions

The simulation task on the control of a bioreactor was carried with 21 students in the class, who were asked to undergo an assessment test. Fig. 3 shows the marks obtained by the students (evaluation) and the grade that each student has attributed to the proposed teaching activity (auto-evaluation).

Both of the scores represent promising results. It is therefore concluded that the activity improved the sense of self-efficacy in each student and helped develop digital skills.

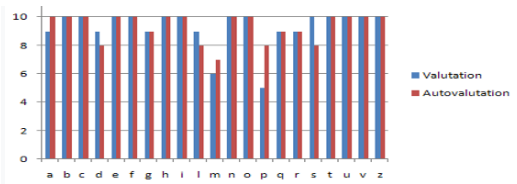

Figure 3. Evaluation and auto-evaluation for each student in the class.

References

[1] https://it.mathworks.com/matlabcentral/fileexchange, last visited on October 11, 2019

[2] I. Carlucho, M. De Paula, G. G. Acosta, 2019, Double Q-PID algorithm for mobile robot control Expert Systems with Applications, Vol. 137, Pages 292-307.

[3] S. Urooj, B. Singh, 2019, Fractional-order PID control for postoperative mean arterial blood pressure control scheme, Procedia Computer Science, Vol. 152, Pages 380-389.

[4] B.Y. Zhao, Z. G. Zhao, Y. Li, R. Z. Wang, R. A. Taylor, 2019, An adaptive PID control method to improve the power tracking performance of solar photovoltaic air-conditioning systems, Renewable and Sustainable Energy Reviews, Vol. 113.

[5] M. Miccio, B. Cosenza, 2014, Control of a distillation column by type-2 and type-1 fuzzy logic PID controllers, Journal of process control, Vol. 24, Pages 475–484.

[6] Cosenza B., Miccio M., 2017, A graphical user interface for dynamics and Feedback Control Studies: Focus On Chemical Reactors Proc. of the 5th Int. Conference on Advances In Civil, Structural and Environmental Engineering – ACSEE'17, Roma. Best paper certificate 5th ACSEE.

[7] S. Mohammad, H. Mousakazemi, 2019, Control of a PWR nuclear reactor core power using scheduled PID controller with GA, based on two-point kinetics model and adaptive disturbance rejection system, Annals of Nuclear Energy, Vol. 129, Pages 487-502.

[8] A. Stormy, Matlab – 5th Edition, 2018, A practical introduction to programming and problem solving, Butterworth-Heinemann.

[9] S.T. Karris, 2011, Introduction to Simulink: with engineering applications (third edition), Orchard Pubns.

[10] J. Krauss, K. Prottsman 2016, Computational Thinking {and Coding} for Every Student, Corwin.

[11] B.W. Bequette, 1998, Process dynamics: modeling, analysis and simulation. New Jersey: Prentice Hall, p. 534.

Sauro Pierucci, Flavio Manenti, Giulia Bozzano, Davide Manca (Eds.)
Proceedings of the 30th European Symposium on Computer Aided Process Engineering (ESCAPE30), May 24-27, 2020, Milano, Italy.
http://dx.doi.org/10.1016/B978-0-12-823377-1.50304-9

Treated Industrial Wastewater as a Water and Nutrients Source for Tomatoes Cultivation: an Optimisation Approach

Fatima-zahra Lahlou,[a] Sarah Namany,[a] Hamish R. Mackey,[a] Tareq Al-Ansari[a,b]

[a]*Division of Sustainable Development, College of Science and Engineering, Hamad Bin Khalifa University, Qatar Foundation, Qatar*
[b]*Division of Engineering Management and Decision Sciences, Hamad Bin Khalifa University, Qatar Foundation, Qatar*
talansari@hbku.edu.qa

Abstract

The need to meet growing demands for food products is heavily associated with intensive exploitation of energy and water resources to drive the operations for irrigation, production of fertilisers, transportation and machinery amongst other key operations, which result in the emissions of greenhouse gases (GHG). The reuse of treated industrial wastewater (TIW) represents a promising alternative for growing food products in water scarce regions, as it reduces the reliance on renewable water sources whilst remaining an important source of nutrients. In this work, the potential for using TIW to cultivate tomato is investigated through a mixed-integer linear program aimed at minimising the environmental impact represented by the global warming potential (GWP). The optimisation model developed determines the optimal configuration of industries generating TIW that satisfy the crop water requirement and nutrients intake. Transportation emission along with the offset of GHG generated from fertilisers production are used as criterions impacting the selection of the optimal sources of TIW generating industries. Outcomes suggest that for the practise to be carbon neutral, tomato water requirements should be obtained from various sources to meet water and nutrients whilst minimising the GWP emissions. To satisfy the potassium requirements, fruit and vegetable processing plants along with cement industries represent the most optimal TIW sources. As for the nitrogen intake, it should be fulfilled from TIW originating from meat and poultry slaughterhouses.

Keywords: industrial treated wastewater, nutrient recovery, fertigation, optimization, tomato.

1. Introduction

With the significant rise in the global population, the demand for food products is expecting a large increase that requires agricultural intensification and heavy cultivation activities. Irrigation is one of the major inputs for food production, which frequently is sourced from unsustainable sources, such as energy-intensive desalination processes or over-abstraction of groundwater. Both means contribute to resources depletion along with environmental emissions. Deploying sustainable water resources were proven efficient in reducing the environmental impact associated with conventional water systems such as groundwater (Namany et al., 2019). Treated industrial wastewater (TIW) represents a promising water substitute for crops irrigation. Agricultural irrigation requires high levels

of nutrients for optimal growth of crops. The use of TIW in agriculture can alleviate the burden resulting from the significant use of chemical fertilizers. In 2016, carbon emissions associated with agriculture were estimated at 49 Mt CO_2eq.year^{-1} (USEPA, 2019). One of the main contributors to these emissions is the use of commercial fertilisers, especially ammonia, which is produced through the natural gas intensive Haber-Bosch process. The main benefit of using TIW instead of raw wastewater (RW) resides in their diminished number of harmful contaminants whilst maintaining a large proportion of the original nutrients content. In contrast to RW, use of TIW for irrigation purposes does not; deteriorate soil characteristics, induce plant root diseases, and alter plant features such as height, length and leaf area (Neto et al., 2012). Rather, it was observed to have positive impacts on the soil fertility and plant growth. Foglia et al. (2019) examined the produced water from an anaerobic membrane bioreactor treatment process that requires low energy. The effluent constitutes high nitrogen (N) and phosphorus (P) levels, with 60 mg.L^{-1} and 6 mg.L^{-1} concentrations respectively, thus reducing the reliance on commercial fertilisers. Another study found that only 50% of gerberas flowers' water requirement need to come from nutrient solution, while the rest can be sourced from treated wastewater (Damasceno et al., 2010). Urbano et al. (2017) found that *Escherichia coli* levels were either undetectable or below the national threshold values established by the Spanish royal decree when irrigating lettuce with TIW. The same was observed with bacteria levels in pepper cultivation, which was not hindered during the legume's growth stages (Dagianta et al., 2014). In addition, wastewater produced from different industries contains diverse levels of contaminants, especially nutrients, due to the difference in the industrial processes for which the water is exposed to prior to treatment. For instance, wastewater produced from dairy processing industries contains high levels of phosphorus with values that can reach up to 700 mg.L^{-1} (Gil-Pulido et al., 2018). Alternatively, meat and poultry industries, contain phosphorus levels that do not exceed 300 mg.L^{-1}, although nitrogen concentrations can reach 6000 mg.L^{-1} (Martí-Herrero et al., 2018; Muhmood et al., 2019). For this reason, each industry uses different wastewater treatment processes to reach acceptable levels of discharge. In the light of the multiple advantages associated with the usage of TIW for irrigation systems, this paper investigates the benefits of using TIW as an alternative water and nutrients source for tomato crop cultivation, which represent an important segment in the agricultural sector, with the highest share in the area dedicated for vegetables cultivation (MDPS, 2017). It suggests an optimisation framework aiming to identify the set of TIW generating industries that minimise GWP emissions while satisfying the needs of the crop from nutrients and water.

2. Methods and methodology

2.1. Cultivation Area and Irrigation Standards

The farm chosen for this study is Wadi Al Araig. Situated in the south west of the State of Qatar, it is characterized with an area of 70 ha, and has a high average yield of tomato with 47.7 ton.ha^{-1} (Hashim, 2009). For this study, the contaminants considered in the irrigation water standards are the chemical oxygen demand (COD), biological oxygen demand (BOD), and total suspended solids (TSS), which need to be maintained at levels lower than 150, 30 and 50 mg.L^{-1} (Ras Laffan City, 2005).

2.2. Water and Nutrients Requirements

The potential evapotranspiration rates of tomato are computed using the Penman Monteith Equation (1) and the adjusted crop coefficient ($k_{c,adj}$) (Allen et al., 1998) for the

210 day cultivation period which is chosen to start in September to be able to have minimal crop water requirements.

$$ET_0 = \frac{0.408\,\Delta\,(R_n - G) + \gamma\,\frac{900}{T+273}u_2\,(e_s - e_a)}{\Delta + \gamma(1 + 0.34\,u_2)} \quad (1)$$

With Δ being the slope of the vapour pressure curve, $(R_n - G)$ is the difference between the net radiation measured at the crop surface and the heat flux density of the soil, γ is the psychometric constant, T is the temperature of the air, u_2 is the speed of the wind, $(e_s - e_a)$ is the deficit of the saturation vapour pressure.

The weather characteristics are retrieved from the closest meteorological station to the farm and from the literature. The irrigation technique used in Wadi Al Araig farm is the furrow method, which is found to have an irrigation efficiency of 60% (η) (Brouwer et al., 1989). The nutrients required for optimum growth of tomato are found from the literature. It is reported that for a yield approaching 50 ton.ha^{-1}, 290, 34 and 383 kg.ha^{-1} of N, P and K are required, respectively.

2.3. TIW source and quality

The industries chosen for this study are the ones that are important in the industrial sector, meaning that they generate significant amounts of wastewater (Sawe, 2018). The iron and steel, cement, meat and poultry, dairy processing and fruits and vegetables canning industries are the ones considered in this study. Table 1 shows the industries from the different sectors, their distances from the farm, and their N, P, K and contaminants concentrations. Due to lack of data regarding the effluent's nutrient and contaminant concentrations, the ones used in this study are retrieved from U.S.A based industries which adhere to the USEPA discharge guidelines. The industry retained from each sector is the closest one to the farm, in order to reduce the energy associated with water transportation.

Table 1: Distances from industries from six different sectors to Wadi Al Araig farm, and their nutrients and contaminants concentrations.

Name of the Industry	Distance (km)	Contaminants' concentration (mg.L^{-1})					
		N	P	K	TSS	COD	BOD
1- Iron and steel industry							
-Etihad Steel Factory	82	12	1.3	13	53	26	8.6
-Panorama Steel Aljaber Group	82						
-Qatar Steel	83						
2- Cement manufacturing							
-Qatar National Cement Co	68	3.9	0.6	235	77	41	6.7
-United Golf Cement Company	105						
-Al Jabor Cement Industries Company	105						
- Al Khalij Cement Company	84						
3- Meat and poultry production							
-Arab Qatari Company for Poultry Production	125	172	64	209	90	585	268
4- Petroleum refining							
Qatar Petroleum Oil Refinery	116	4.3	1.1	21	30	64	8.2
5- Canned fruits and vegetables processing							
Al Manal Food Factory	81	2.3	1.8	242	26	32	70
Gulf Food Production Factory	81						
Tasco Factory for Food Production	-						
6- Dairy processing							
Baladna	136	4.4	4.4	3.3	39	35	101

2.4. Optimization Model

A mixed integer linear optimization model was developed in Matlab®. The objective of the optimization was to minimize the carbon footprint (CF) associated with the fertigation using the TIW, as described in Equation (2), while meeting the water and ±5% of the nutrients demands of tomato, and while respecting the irrigation water standards.

$$CF = \sum_{i=1}^{6} 2.7 \frac{0.041\, x_i\, k_{c,adj}\, ET_0}{37.5\, \eta}\, d_i - \sum_{i=1}^{6}(19.13\, n_i + 4.28\, p_i + 3.37\, k_i)\, x_i \frac{k_{c,adj}\, ET_0}{1000\, \eta} \quad (2)$$

Where x_i is the decision variable and it designates the percentage of total water required that will come from industry i (%), d_i is the distance between the farm and industry i (km), $n_i, p_i, and\ k_i$ are the N, P and K concentration in the TIW originating from industry i (mg.L^{-1}). The reference evapotranspiration ET_0 (m^3.ha^{-1}) is multiplied by the crop coefficient of tomato ($k_{c,adj}$) to take into consideration the crop characteristics at the different growth stages.

The CF computation takes into consideration the energy required to transport in truck tankers the total water required for optimum tomato growth as well as the CF offset from relying on the TIW as a source of nutrients instead of energy intensive chemical fertilizers. The energy required for the TIW treatment is not considered as, in all cases, it needs to be treated to meet discharge quality. Truck tankers use 0.041 L of diesel per km, and have an average capacity of 37.5 m^3 (International Council on Clean Transportation, 2017). Each litre of diesel consumed is found to emit 2.7 kg-$CO_{2,eq}$ into the air (Australian Bureau of Statistics, 2007). The CF associated with the use of 1 kg of N, P and K when produced using natural gas is found to be equal to 10.9, 2.4, 1.9 kg-$CO_{2,eq}$, respectively (Gellings and Parmenter, 2004).

Equalities associated with the optimisation are:

$$\sum_{i=1}^{6} x_i = 1 \quad (3)$$

Inequalities associated with the optimisation are:

$$\forall\, x_i\ s.t.\ i \in (1-6), x_i \geq 0 \quad ; \quad 0.95\ N_R \leq \sum_{i=1}^{6} n_i \frac{x_i\, ET_c}{1000\, \eta} \leq 1.05\ N_R$$

$$0.95\ P_R \leq \sum_{i=1}^{6} p_i \frac{x_i\, ET_c}{1000\, \eta} \leq 1.05\ P_R \quad ; \quad 0.95\ K_R \leq \sum_{i=1}^{6} k_i \frac{x_i\, ET_c}{1000\, \eta} \leq 1.05\ K_R$$

$$\sum_{i=1}^{6} TSS_i\, x_i < 50 \quad ; \quad \sum_{i=1}^{6} COD_i\, x_i < 150 \quad ; \quad \sum_{i=1}^{6} BOD_i\, x_i < 30$$

3. Results and discussion

3.1. Tomato Water Requirements

The water requirements of tomato are found to be equal to 6580 m^3, with a maximum daily evapotranspiration rate equalling 6.7 mm. This rate was observed on the 12th of March and is mainly due to the high temperature and wind speed on that day which averaged 29 ºC and 8.1 m.s^{-1} and reached 38 ºC and 13.1 m.s^{-1}. The lowest rate recorded was witnessed on the 27th of December which was characterized with relatively low temperatures and wind speeds.

3.2. Optimization Model Results

No solution was found which meets the objective while satisfying all the constraints. In fact, the N requirement of tomato cannot be met with fertigation using TIW only. Therefore the model was changed into a multi-objective optimization one where the

constraint related to N was omitted, and where a new objective was added which is to maximize NT, the total N provided to the crop (Equation (3)).

$$NT = \sum_{i=1}^{6} n_i \frac{x_i \, k_{c,adj} \, ET_0}{1000 \, \eta} \quad (4)$$

The function used is "gamultiobj". The optimal pareto front of the multi-objective optimization is shown in Figure 1. All of the solutions result in more or less the same output. The average optimal solution supplies tomato with 125.7 kg-N.ha^{-1}, and offset as much as 2,116 kg-$CO_{2\text{-eq}}$. Table 2 shows the corresponding water allocation from the six industries. Most of the N and P will be supplied from the meat and poultry production industry's effluents, with almost 54% and 79% of the total requirements supplied from these two industries, respectively. 41.6% of total K required for tomato cultivation will come from canned fruits and vegetables processing industries. The BOD and TSS values happen to be equal to the irrigation limits, while the COD level supplied to the crop is lower than the maximum level allowed. This practise is environmentally friendly as it offsets the CF resulting from the transportation of the TIW. In addition, it can also offset the energy required for the remaining N needed. Even if the remaining 164.32 kg-N.ha^{-1} is provided through chemical fertilizers, for which carbon the footprint is computed to be equivalent to 1,775.28 kg-$CO_{2\text{-eq}}$, the practise will remain carbon neutral. Thereafter, each ton produced will offset more than 8 kg-$CO_{2\text{-eq}}$. Fertigation using TIW in the whole farm will result in a yearly CF offset of 27 ton-$CO_{2,eq}$.

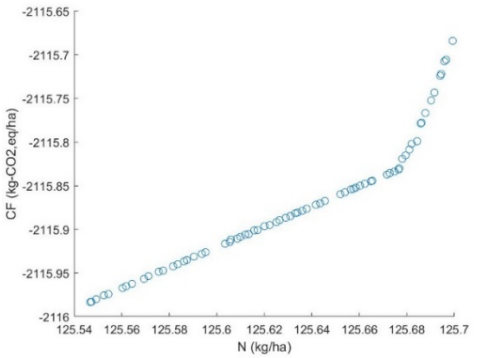

Figure 1: Optimal pareto front for the optimization model.

Table 2: Allocation of the water from the various industries, and the final contaminants concentration and nutrients supply. 1 – Iron and steel industry, 2 – Cement manufacturing, 3 – Meat and poultry, 4 – Petroleum refining, 5 – Canned fruit and vegetables processing, 6 – Dairy products processing.

Industry	%total water	TSS	COD	BOD	N	P	K
			(mg.L^{-1})			(kg)	
1	65.36%	34.80	17.32	5.61	50.92	5.55	57.76
2	3.27%	2.53	1.33	0.22	0.83	0.13	50.55
3	6.01%	5.41	35.20	16.14	67.96	25.30	82.99
4	15.82%	4.78	10.20	1.29	4.52	1.21	21.86
5	9.54%	2.48	3.03	6.73	1.44	1.13	151.86
6	0%	0	0	0	0	0	0
	Total	50.00	67.09	30.00	125.68	33.31	365.02

4. Conclusion

A water planning framework for tomato cultivation in a farm in the State of Qatar was developed. It was found that the TIW cannot supply all of the N demand of tomato which happens to be very high. Alternately, P and K demand were successfully satisfied, mainly from the meat and poultry industry and from the canned fruits and vegetables industry. This practice was found to be carbon neutral, which emphasizes on the sustainability of this fertigation technique. In future work, the study does not necessarily have to be limited to the biggest industries in Qatar. A better estimation of the fertilizers' embodied energy can be calculated depending on the country from which they are imported. Environmental burden can be evaluated using other parameters such as the water footprint.

References

R.G. Allen, L.S.Pereira, D. Raes, M. Smith, 1998, Guidelines for computing crop water requeriments, FAO Irrigation and drainage paper, https://doi.org/10.1016/j.eja.2010.12.001

Arabian Business, 2014, Qatar's top 30 companies [WWW Document]. URL:https://www.arabianbusiness.com/

Australian Bureau of Statistics, 2007, Survey of Motor Vehicle Use.

C. Brouwer, K. Prins, M. Heibloem, 1989, Irrigation Water Management: Irrigation Scheduling Training, Food and Agriculture Organization of the United Nations.

E. Dagianta, D. Goumas, T. Manios, N. Tzortzakis, 2014, The use of treated wastewater and fertigation in greenhouse pepper crop as affecting growth and fruit quality. Journal of Water Reuse and Desalination, 4(2), 92–99. https://doi.org/10.2166/wrd.2014.048

L. M. O. Damasceno, A. S. de Andrade Júnior, H. R. Gheyi, 2010, Cultivation of gerbera irrigated with treated domestic effluents. Revista Brasileira de Engenharia Agrícola e Ambiental, 14(6), 582–588. https://doi.org/10.1590/s1415-43662010000600003

G. Foglia, G. Cipolletta, N. Frison, S. Sabbatini, S. Gorbi, A. L. Eusebi, F. Fatone, 2019, Anaerobic membrane bioreactor for urban wastewater valorisation: Operative strategies and fertigation reuse. Chemical Engineering Transactions, 74(November 2018), 247–252. https://doi.org/10.3303/CET1974042

C. Gellings, K. Parmenter, 2004, Production and use, In Knowledge for Sustainable Development—An Insight into the Encyclopedia of Life Support Systems II, 419–450.

B. Gil-Pulido, E. Tarpey, E. L. Almeida. , W. Finnegan, X. Zhan, A.D.W. Dobson, N.O'Leary, 2018, Evaluation of dairy processing wastewater biotreatment in an IASBR system: Aeration rate impacts on performance and microbial ecology, Biotechnol, Reports 19, e00263.

M. A. Hashim, 2009,Water, Agriculture and Environment in Arid Lands: Water and Agricultural Vision by 2020 ,Friends of Environment Center.

International Council on Clean Transportation, 2017, Fuel Consumption Standards for Heavy - Duty Vehicles in India 1–9.

Ministry of Development Planning and Statistics, 2017, Agricultural Statistics.

S. Namany, R. Govindan, T. Al-Ansari, 2019, Optimisation of the energy, water, and food nexus for food security scenarios, Computers & Chemical Engineering, 129, 106513.

O. N. S. Neto, J. A. Filho, N. da S. Dias, J. R. L. Rebouças, F. R. A. de Oliveira, A. A. Diniz, 2012, Fertigação do algodoeiro utilizando efluente doméstico tratado. Revista Brasileira de Engenharia Agricola e Ambiental, 16(2), 200–208. https://doi.org/10.1590/S1415-43662012000200011

Ras Laffan City, 2005, Environmental Regulations for Ras Laffan Industrial City 30.

B.E. Sawe, 2018, What Are The Biggest Industries In Qatar? [WWW Document]. WorldAtlas. URL https://www.worldatlas.com

V. R. Urbano, T. G. Mendonça, R. G. Bastos, C. F. Souza, 2017, Effects of treated wastewater irrigation on soil properties and lettuce yield. Agricultural Water Management, 181, 108–115. https://doi.org/https://doi.org/10.1016/j.agwat.2016.12.001

USEPA, 2019, Inventory of U.S Greenhouse Gas Emissions and Sinks. 53(9), 1689–1699.

Sauro Pierucci, Flavio Manenti, Giulia Bozzano, Davide Manca (Eds.)
Proceedings of the 30th European Symposium on Computer Aided Process Engineering (ESCAPE30), May 24-27, 2020, Milano, Italy.
http://dx.doi.org/10.1016/B978-0-12-823377-1.50305-0

Uncovering the True Cost of Ionic Liquids using Monetization

Husain Baaqel,[a] Victor Tulus,[b,c] Benoit Chachuat,[a] Gonzalo Guillén-Gosálbez[b,*] Jason Hallett[a]

[a]*Department of Chemical Engineering, Centre for Process Systems Engineering, Imperial College London, London, United Kingdom*
[b]*Institute for Chemical and Bioengineering, Department of Chemistry and Applied Biosciences, ETH Zürich, Vladimir-Prelog-Weg 1, Zürich, Switzerland*
[c]*Departament d'Enginyeria Química, Universitat Rovira i Virgili, Av. Països Catalans 26, 43007 Tarragona, Spain*
gonzalo.guillen.gosalbez@chem.ethz.ch

Abstract

Due to their attractive properties, ionic liquids have found their way into many applications where they show high potential to replace existing chemicals. However, rising concerns over their ecological impacts, e.g., toxicity and biodegradability, and high cost have limited their use. Techno-economic and life cycle assessment studies were carried out to compare ionic liquids with existing solvents, yet the outcome of these analyses is often hard to interpret, as multiple metrics need to be considered simultaneously between which trade-offs exist. Here, for the first time the concept of monetization is coupled with process simulation and life cycle assessment to estimate the true cost of four lignocellulosic biomass pretreament solvents: triethylammonium hydrogen sulfate [TEA][HSO_4], 1-methylimidazolium hydrogen sulfate [HMIM][HSO_4], acetone from fossil sources and glycerol from renewable sources. The results show that monetized cost can be higher than or as high as the production cost. The real cost of production accounting for externalities can be more than 100% of direct costs estimated using conventional economic assessment methods. Our results show that [TEA][HSO_4] has the lowest cost, while glycerol has the highest cost. We expect this to be a starting point for future studies targeting the design of more sustainable ionic liquids.

Keywords: ionic liquids, techno-economic analysis, life cycle assessment, monetization.

1. Introduction

Some ionic liquids, such as protic ionic liquids, have shown high potential for commercialization due to their low production cost. Chen et al. (2014) conducted a technoeconomic assessment on the bulk production of protic ionic liquids, namely triethylammonium hydrogen sulfate [TEA][HSO_4] and 1-methylimidazolium hydrogen sulfate [HMIM][HSO_4]. Their results showed that the cost of ionic liquids could be as low as $1.24/kg, a value below the cost of some organic solvents such as acetone and ethyl acetate, which cost between $1.3-1.4/kg (Chen et al., 2014).

Conventional economic assessments of ionic liquids often disregard indirect costs due to environmental externalities, that is, impacts that occur along the product's life cycle and need to be mitigated *via* tailored actions that incur an additional cost, e.g., extra

expenditures in health care due to respiratory effects in humans. Hence, in order to calculate the "true" cost of a product, one needs to account for these "hidden" costs often omitted in any standard economic assessment.

Monetization or monetary valuation converts social and environmental impacts into monetary units. It has been used to determine the cost of non-market goods in a wide range of areas, e.g., in energy systems modeling to estimate the environmental cost of a specific energy mix, health care to quantify the value of informal care, and catastrophe insurance to predict the demand by homeowners, among others. It has also been used in the weighting phase of LCA to evaluate trade-offs (Fougerit et al., 2012; Lim et al., 2013; Nguyen et al., 2016).

Here we apply for the first time life cycle assessment and monetization to quantify the "true" cost of ionic liquids. To this end, we focus on two ionic liquids widely used for biomass treatment due to their lignin solvating power (Brandt et al., 2013), which were compared against acetone and glycerol regarded as the conventional business as usual alternatives (Huijgen et al., 2010; Liu et al., 2010). An environmental assessment of [TEA][HSO_4] and [HMIM][HSO_4] using LCA was first conducted to evaluate their environmental impact. The results, expressed in LCA units such as DALY and species.yr, were then converted into a single monetary unit via monetization, which was combined with the direct costs (CAPEX and OPEX calculations) to estimate the total economic cost. Finally, the results generated are analysed and conclusions are drawn.

2. Synthesis

In this study, we evaluate four different solvents, two produced at present industrially, i.e., acetone and glycerol, and two ionic liquids, i.e., [TEA][HSO_4] and [HMIM][HSO_4]. For the two ionic liquids we developed process models to scale-up experimental synthesis procedures. The synthesis of the two ionic liquids is described in the following subsections.

2.1. Ionic liquids

The ionic liquids in this work are synthesized through the transfer of a proton from a Brønsted acid to a Brønsted base (Greaves and Drummond, 2008). Since the reaction is highly exothermic, water is added to dilute the mixture and cool it down to avoid unwanted phase transition, thermal decomposition or undesired products. The product is then easily separated through a simple distillation, where the water can be recycled back to the process. The acid used is sulfuric acid, while the bases are triethylamine and 1-methylimidazole for [TEA][HSO4] and [HMIM][HSO4], respectively.

2.1.1. 1-methylimidazole

Imidazoles are prepared using the Debus-Radziszewski reaction (Ebel et al., 2012). This is a one pot synthesis, where glyoxal, formaldehyde, methylamine and ammonia react in equimolar molar ratios and condense to form water and 1-methylimidazole. The reaction takes place at 50-100°C in water with a yield between 60-85%.

3. Tools and Methods

Several tools and approaches were used to carry out the assessment. In essence, we combined process simulation models in Aspen-HYSYS with LCA, costing and monetization.

3.1. Process modeling and simulation

Aspen-HYSYS version 9 was used to model the production processes of the ionic liquids and their precursors for which no LCA or price data were available. Here, the synthesis of ionic liquids and 1-methylimidazole were modeled using a combination of experimental data, group contribution methods, literature data and heuristics.

3.1.1. Properties modeling

Data for some properties like density were obtained from experiments or from the literature ("Ionic Liquids Database - ILThermo," n.d.). Some unknown properties for the ionic liquids like critical properties, and normal boiling points were estimated using the group contribution method developed by Valderrama (2009). The missing properties for 1-methylimidazole were estimated from the molecular structure using the Property Constant Estimation System (PCES) built in Aspen-HYSYS V9.

3.2. Economic assessment

In order to estimate the cost of ionic liquids, both capital expenses (CAPEX) and operating expenses (OPEX) are calculated assuming a standard chemical plant that operates 330 days (equivalent to 7,920 hours) a year for 10 years with a production rate equivalent to 144,000 tons per year (Chen et al., 2014). The economic assessment methodology proposed by Towler and Sinnott (2012) is followed in this work. The prices of raw materials and utilities are obtained from ecoinvent 3.5, which reflect current market prices (Wernet et al., 2016). Size of equipment is determined from process simulation results using sizing guidelines by Towler and Sinnott.

3.3. Environmental assessment

A life cycle assessment following ISO 14040 principles was applied. The LCA modeling was performed using SimaPro® 9.0 software interfacing with ecoinvent 3.5.

3.3.1. Goal and scope

A cradle-to-gate scope is adopted that considers the impacts of extracting the raw materials up to the synthesis of the final product. In terms of geographic limits, it is assumed that the production takes place in Europe. The ionic liquids considered in this work are mainly used for biomass pre-treatment, where the efficiency of the ionic liquid is measured in terms of biomass loading defined as the weight ratio of biomass to ionic liquid. We neglect the use phase and set up one kilogram of IL/solvent as functional unit.

3.3.2. Inventory analysis

Data for the background processes were retrieved from ecoinvent 3.5 database (Wernet et al., 2016), which was combined with information of the foreground system, mainly mass and energy flows, obtained from the process simulation.

However, data like emissions and waste treatment are estimated using proxy data where data for similar processes or those with similar characteristics are adapted and used to bridge the gap.

3.3.3. Impact assessment

In this phase, the LCI entries are converted into impact using the ReCiPe 2016 method (Huijbregts et al., 2016), where the inventory entries are characterized and categorized

into 17 midpoints that are further aggregated into three endpoints or damage categories: resources, human health and ecosystems.

3.4. Monetization

There are several monetary valuation methods proposed in the literature (Pizzol et al., 2015). These methods usually measure individual's Willingness-to-Pay (WTP) to avoid the environmental impacts brought by the activity of concern. In this work, two methods are used for converting human health damage and ecosystem quality damage, respectively, into money (Weidema, 2009): (i) budget constraint and (ii) choice modelling. Budget constraint is a monetary valuation method where the value of one quality adjusted life year (QALY), a year-based biophysical unit for describing the human health quality, is derived from the potential economic production of the individual per year. Unlike other monetary valuation methods, budget constraint lowers the uncertainty by valuing directly the economic production, although it assumes that what is earned must be spent.

Choice modelling assigns a value to ecosystems based on the economic penalty that an individual is willing to accept for protecting certain areas such as the environment. Choice modeling is widely used in health state evaluations to monetize human well-being, and it can be applied on ecosystem quality.

Here the monetary values of 74k EUR2003/DALY (125.3k USD2019/DALY) and 9.5M EUR2003/species.yr (16M USD2019/species.yr) proposed by Weidema (Weidema, 2009) using the methods mentioned above are used to monetize human health and ecosystem quality, respectively, as illustrated in Equation 1.

$$Cost_{Monetized} = \sum_{i=1}^{e} MF_i EP_i \quad (1)$$

Where $\boldsymbol{e}$ refers to the end points to be monetized based on the characterization method used, MF_i is the monetization factor for endpoint i and EP_i is the damage in that endpoint.

4. Results and discussion

Figure 1 shows the total cost of production after combining the direct costs from the economic assessment and indirect costs from the monetization of environmental impacts. In terms of the direct costs, The results show that [HMIM][HSO_4] has the highest cost ($1.46/kg) while [TEA][$HSO_4$] shows the lowest ($0.78/kg). This is largely due to the relatively large number of processes involved in the production of [HMIM][HSO_4], i.e., around 11 steps, compared to the other solvents. Another factor that plays a key role is the raw materials cost. For example, [TEA][HSO_4] is produced from triethylamine with a cost of $1.4/kg, while [HMIM][$HSO_4$] is produced from 1-methylimidazole, with an estimated cost of $4.4/kg. The low cost of sulfuric acid ($0.05/kg) helps to reduce the overall cost of [TEA][HSO_4] below that of glycerol and acetone. The cost of glycerol is relatively higher than [TEA][HSO_4], since the former is produced from relatively more expensive starting materials like rapeseed and soybean oils (Quispe et al., 2013).

In terms of the indirect costs, glycerol has the highest monetized cost ($2.07/kg) while [TEA][$HSO_4$] shows the lowest ($1.09/kg). The low cost of [TEA][HSO_4] is mainly attributed to the fact that it is relatively simple to synthesize compared to other solvents and uses less fossil sources for processing. In contrast, glycerol's high monetized cost is

due to the significant impact on ecosystem quality, with land use being the major contributor. The latter is due to the large areas needed for planting and growing the necessary feedstock, mainly soybean and rapeseeds. The monetized cost of [HMIM][HSO_4] remains relatively high due to its complex synthesis and raw materials required, which affect both direct and indirect costs. Overall, the monetized costs are higher than the direct costs for all solvents. This finding shows that indirect costs, often omitted in conventional economic assessments, can be significant and thus need to be accounted for in the assessment.

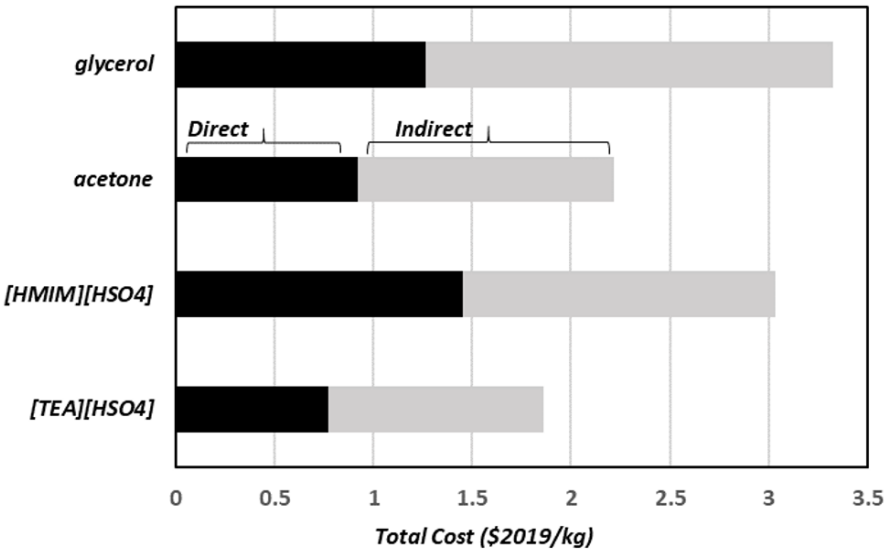

Figure 1. Total cost of production combining both direct and monetized costs.

5. Conclusion

A framework was developed to the assessment of ionic liquids combining process simulation, LCA and monetization to account for externalities. Monetized costs were added to direct costs to compare the total cost of two ionic liquids: [HMIM][HSO_4] and [TEA][HSO_4], a fossil-derived acetone and a bio-based glycerol. The results show that [HMIM][HSO_4] has the highest direct cost among all solvents due to the lengthy 1-methylimidazole production process. When externalities are considered, glycerol has the highest indirect cost, which is mainly due to its high impact on ecosystem quality linked to land use. The results also show that [TEA][HSO_4] is the cheapest option in both direct and indirect cost, since it is produced from relatively inexpensive materials and using simple synthesis procedure. When both costs, direct and indirect, are combined, glycerol's total cost is the highest followed by [HMIM][HSO_4], acetone and [TEA][HSO_4], respectively.

This shows that renewable solvents are not necessarily environmentally better than other solvents, including ionic liquids. Our results, therefore, challenge conventional wisdom that ionic liquids are costly and damaging to the environment. They also highlight the need to account for negative externalities in the comparison of solvents.

References

Brandt, A., Gräsvik, J., P. Hallett, J., Welton, T., 2013. Deconstruction of lignocellulosic biomass with ionic liquids. Green Chemistry 15, 550–583. https://doi.org/10.1039/C2GC36364J

Chen, L., Sharifzadeh, M., Mac Dowell, N., Welton, T., Shah, N., Hallett, J.P., 2014. Inexpensive ionic liquids: [HSO4]--based solvent production at bulk scale. Green Chemistry 16, 3098–3106. https://doi.org/10.1039/c4gc00016a

Ebel, K., Koehler, H., Gamer, A.O., Jäckh, R., 2012. Imidazole and Derivatives. Ullmann's Encyclopedia of Industrial Chemistry 610. https://doi.org/10.1002/14356007.a13_661

Fougerit, V., Auclair, P., Bonhoure, S., 2012. Monetary weighting of LCA results to integrate a two-stage management system in the decision process, in: Proceedings 2nd LCA Conference. p. 7.

Greaves, T.L., Drummond, C.J., 2008. Protic ionic liquids: properties and applications. Chem. Rev. 108, 206–237. https://doi.org/10.1021/cr068040u

Huijbregts, M.A.J., Steinmann, Z.J.N., Elshout, P.M.F., Stam, G., Verones, F., Vieira, M.D.M., Hollander, A., Zijp, M., Van Zelm, R., 2016. ReCiPe 2016: A harmonized life cycle impact assessment method at midpoint and endpoint level Report I: Characterization.

Huijgen, W.J.J., Reith, J.H., den Uil, H., 2010. Pretreatment and fractionation of wheat straw by an acetone-based organosolv process. Ind. Eng. Chem. Res. 49, 10132–10140. https://doi.org/10.1021/ie101247w

Ionic Liquids Database - ILThermo [WWW Document], n.d. URL https://ilthermo.boulder.nist.gov/ (accessed 5.28.19).

Lim, S.-R., Kim, Y.R., Woo, S.H., Park, D., Park, J.M., 2013. System optimization for eco-design by using monetization of environmental impacts: a strategy to convert bi-objective to single-objective problems. Journal of Cleaner Production 39, 303–311. https://doi.org/10.1016/j.jclepro.2012.07.040

Liu, J., Takada, R., Karita, S., Watanabe, Takahito, Honda, Y., Watanabe, Takashi, 2010. Microwave-assisted pretreatment of recalcitrant softwood in aqueous glycerol. Bioresource Technology 101, 9355–9360. https://doi.org/10.1016/j.biortech.2010.07.023

Nguyen, T.L.T., Laratte, B., Guillaume, B., Hua, A., 2016. Quantifying environmental externalities with a view to internalizing them in the price of products, using different monetization models. Resources, Conservation and Recycling 109, 13–23. https://doi.org/10.1016/j.resconrec.2016.01.018

Pizzol, M., Weidema, B., Brandão, M., Osset, P., 2015. Monetary valuation in life cycle assessment: a review. Journal of Cleaner Production 86, 170–179. https://doi.org/10.1016/j.jclepro.2014.08.007

Quispe, C.A.G., Coronado, C.J.R., Carvalho Jr., J.A., 2013. Glycerol: Production, consumption, prices, characterization and new trends in combustion. Renewable and Sustainable Energy Reviews 27, 475–493. https://doi.org/10.1016/j.rser.2013.06.017

Towler, G., Sinnott, R., 2012. Chemical Engineering Design: Principles, Practice and Economics of Plant and Process Design. Elsevier.

Valderrama, J.O., Rojas, R.E., 2009. Critical properties of ionic liquids. Revisited. Ind Eng Chem Res 48, 6890–6900.

Weidema, B.P., 2009. Using the budget constraint to monetarise impact assessment results. Ecological economics 68, 1591–1598.

Wernet, G., Bauer, C., Steubing, B., Reinhard, J., Moreno-Ruiz, E., Weidema, B., 2016. The ecoinvent database version 3 (part I): overview and methodology. Int J Life Cycle Assess 21, 1218–1230. https://doi.org/10.1007/s11367-016-1087-8

Sauro Pierucci, Flavio Manenti, Giulia Bozzano, Davide Manca (Eds.)
Proceedings of the 30th European Symposium on Computer Aided Process Engineering (ESCAPE30), May 24-27, 2020, Milano, Italy.
http://dx.doi.org/10.1016/B978-0-12-823377-1.50306-2

Multi-Objective Optimization of a Bioethanol Distillation considering Heat Exchanger Fouling and Sustainability Indicators

Fabian Zapf, Thomas Wallek

Graz University of Technology, Inffeldgasse 25C, 8010 Graz, Austria
fabian.zapf@tugraz.at

Abstract

A bio-ethanol column as part of an ETBE (ethyl-tert-butylether) plant is optimized in view of OPEX costs, CO_2 emissions as a sustainability indicator and the columns ethanol product stream. Therefore, three scalarization methods, i.e. the weighting approach, the ε-constraint method and a modified normal boundary intersection method, and a genetic algorithm (NSGA-II) are implemented and applied to two optimization cases. Additionally, a heat exchanger fouling model is incorporated to account for highly nonlinear maintenance interval effects in the reboiler of the column.

Keywords: Multi-objective optimization, Heat exchanger fouling, OPEX costs

1. Introduction

The use of a variety of commercial process simulators is state of the art, offering the possibility of calculating mass transfer phenomena, thermodynamics and reaction kinetics of single processes, individual production plants and entire production sites.
The final step in process simulation is the optimization of the design and/or operating parameters of the plant in view of economy, operational safety, environmental impacts and social aspects. As these aspects are often conflicting each other, this frequently implies a multi-objective optimization (MOO) problem, also called Pareto optimization, like optimizing investment costs vs. operational costs.
Beside these optimization issues, the aspect of process flexibility, such as load-shift and product-shift capability, is of increasing interest. Using MOO gives the possibility to investigate and optimize plants in view of varying production requirements.
Popular process simulators, like Aspen Plus®, Aspen HYSYS®, CHEMCAD® and gProms®, include optimization modules, which are capable of performing only single objective optimization (SOO). To overcome this drawback, introducing MOO in process simulators is commonly realized by coupling the process simulator with an external application which runs a stochastic optimization algorithm (Lopez et al., 2018). Stochastic optimization algorithms require only information about the dependent variables (objectives or output of the system) and the independent variables (process parameters to be optimized). Thus, they are suitable for optimizing black-box functions, such as process simulators running in sequential modular mode. Their main limitation is the relatively slow convergence, due to many evaluations of the objective functions in the course of evaluation runs of the process simulator (Rangajah, 2016).
In this work, several approaches for applying MOO in process simulation are compared among their effort for realization and their suitability for optimization in process engineering. They are implemented in the framework of Wolfram Mathematica®, which is coupled with KBC PetroSIM® as a process simulator via a COM Interface.

2. Methods

Multi-objective optimization can be divided in several classes. The top level divides them into generating methods, which do not require any preferences from the user, while preference-based methods do so and only generate one Pareto solution (Rangaiah, 2016). Thus, we are interested in generating methods, which provide sets of Pareto solutions, so called Pareto fronts. This class of methods can be split up into the class of scalarization methods and population-based methods.

Scalarization methods reduce the multi-objective optimization problem into several single-objective optimization problems, which then can be solved by one of the many available algorithms for single-objective optimization.

Population based methods, on the other hand, tackle the multi-objective optimization problem directly by storing the entire actual Pareto front and evolving the population in each iteration step.

2.1. Scalarization Methods

In this paper three different scalarization methods, which show a very different effort for implementation, are implemented, applied and compared. The single-objective optimization of the scalarized objectives is carried out with a simulated annealing algorithm, capable of finding global minima, which is essential when dealing with process simulators.

2.1.1. Weighting Approach

The weighting approach can be seen as the most primitive scalarization method. It bases on multiplying each objective function f_j with a weight w_j and optimizing the sum of them. Often the objective functions are of different orders of magnitude, thus it is necessary to rescale them, e.g. by linear transformation:

$$\bar{f}_j(x_i) = \frac{f_j(x_i) - f_j^{min}}{f_j^{max} - f_j^{min}} \tag{1}$$

Therefore, it is necessary to perform a single-objective optimization of each single objective function, thus the end points of the Pareto front (and by that, f_i^{min} and f_i^{max}) for rescaling can be obtained. The resulting objective function $u(x_i)$

$$u(x_i) = \sum_j w_j \cdot \bar{f}_j(x_i) \tag{2}$$

is the linear combination of the objective functions. By varying the weights whose sum has to be unity, several single objective optimization problems are generated which then can be minimized with the simulated annealing algorithm.

2.1.2. ε-constraint Method

The ε-constraint method is a very popular method, due to the fact that it is very simple to implement, while offering the possibility of producing very homogenously distributed Pareto points. This is done by setting only one of the objectives as the target function, e.g. the first objective $j=1$:

$$u(x_i) = f_1(x_i) \tag{3}$$

and converting all other objective function into inequality constraints, in the 2-dimensional case:

$$f_2(x_i) \leq \varepsilon \tag{4}$$

By optimizing the target function with a range of ε values a set of Pareto points can be obtained.
In this method, the realization of holding the constraint is an issue. Depending on which single-objective optimization algorithm is used, there are many methods available in literature. Due to the deterministic nature of the simulated annealing algorithm, which does not involve gradient information, a simple penalty function can be used (Yeniay, 2005). Incorporating this penalty function, the target function for the optimizer changes to:

$$u(x_i) = f_1(x_i) + p * Max(0, f_2(x_i) - \varepsilon) \quad (5)$$

where p denotes a factor for penalizing the violation of the constraint. It was found, that a value of 1000 works well for most applications.

2.1.3. Modified Normal Boundary Intersection Method

The modified normal boundary intersection from Lim et al. (2001) represents the most advanced scalarization method in this work. In general, this method obtains the end points of the Pareto front and normalizes the objective functions. By obtaining the middle point of the Pareto front, it gets possible to obtain an even more homogenous distribution of the Pareto points. This advantage is bought by using equality constraints, which are computationally expensive when using stochastic algorithms. These equality constraints are also enforced by using the penalty method.

2.2. Genetic Algorithm

The Nondominated Sorting Genetic Algorithm II (NSGA-II) from Deb et al. (2002) is part of the population based evolutionary genetic algorithms, which are known to be very robust and popular (Ramteke and Gupta, 2016). Especially in process simulation robustness of the algorithms plays a critical role, due to the fact that the results of process simulators are typically fluctuating because of numerical inaccuracy.
Genetic algorithms base on the decoding of the variables into genes (e.g. a bit), chromosomes (all bits of a variable) and chains of chromosomes (representing one individual with all its variables), e.g., binary coding, opening the possibility to perform simple and nature inspired operations on them. There are two main operators: the recombination operation between two chromosomes, which further improves the population, and the mutation operation, responsible for exploration of new areas of possible solutions.

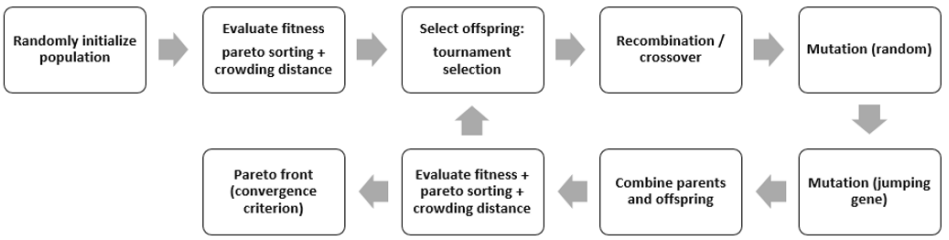

Figure 1: NSGA-II algorithm flowchart

A special aspect of the NSGA-II algorithm is its elitism preservation mechanism (prevents good solutions from random death), ensuring a fast convergence, and the crowding distance as a measure in selection, to ensure a broad Pareto front. This working principle of the algorithm is depicted in Figure 1.
In process simulation optima often lie directly on the bounds of the input variables, which can be hardly reached randomly by gene mutation or crossover. Thus, jumping

gene (JG) operators are introduced as a second type of mutation, facing these issues. These operators replace randomly larger parts of chromosomes, leading to larger fluctuations. There exist several types of JG operators in literature, in this work the five types from Ramteke and Gupta (2016) are implemented and tested.
All operators are always applied with a certain probability to each chromosome (crossover and JG) or gene (mutation). The parameters for the optimization are listed in Table 1.

Table 1: Genetic algorithm parameters

Population size	Generations	Chromosome length	Crossover probability	Mutation probability	Jumping gene probability
20	500	16	0.95	0.05	0.5

3. Example – Distillation Column

For demonstration, a distillation column for recycling bio-ethanol in an ETBE (ethyl-tert-butylether) process is selected. The reboiler is heated with an oil stream from a refinery, causing fouling inside the reboiler, which shows a highly nonlinear relationship to several parameters.
In general, the operation mode of the column can be widely varied, e.g., by changing reflux ratio and reboiler duty, and by that, product quantities and qualities are influenced. In daily business, columns are always operated at minimal energy costs and maximum product recovery. In this work, also economical aspects arising from maintenance caused by fouling in the reboiler are considered, which may lead to other optima.

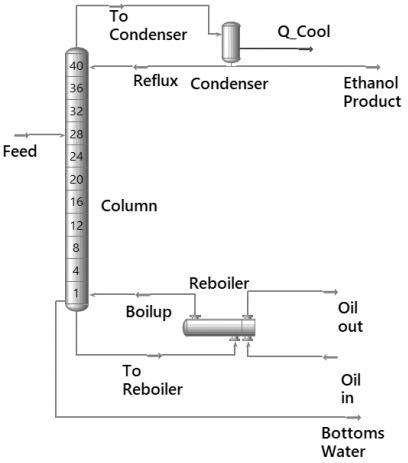

Figure 2: Column flowsheet

3.1. Column Model

The distillation column, which splits up ethanol and water, is simulated in KBC PetroSIM® as a process simulator, using NRTL with Poynting correction as a thermodynamic calculation method. This gives the capability of obtaining all stream data for further calculations, the column parameters are summarized in Table 2.

Table 2: Column parameters

Parameter	Value
Total Stages	40
Feed Stage	28
Condenser Pressure	1.7 bar abs.
Reboiler Pressure	2.1 bar abs.
Ethanol in Feed Stream	13 mol-%

Table 3: Fouling parameters (Costa et al., 2013)

Parameter	Value
α	277.8 m²K/J
γ	$4.17*10^{-13}$ m²K/J
E_a	48 kJ/mol
Pr (assumed)	25

3.2. Fouling Model

Heat exchanger fouling is commonly modeled as the change of fouling resistance R_f over time. The model used from Polley et al. (2002)

$$\frac{dR_f}{dt} = \alpha * Re^{-0.8} * Pr^{-0.33} * Exp\left(\frac{-E_a}{RT_f}\right) - \gamma * Re^{0.8} \quad (6)$$

depends on the Reynolds (*Re*) and Prandtl (*Pr*) number, the wall temperature T_f and the model parameters α, γ and E_a from Costa et al. (2013), which are listed in Table 3.

3.3. Economics

The operational expenditures (OPEX) in this work consider heat exchanger cleaning costs by relating the actual fouling rate to a base case (50,000 €/a), the make-up costs of the lost ethanol through the bottoms product (400 €/t) as well as energy costs of the reboiler (17.24 €/MWh).

3.4. Sustainability indicator

In this particular case, the energy taken from the oil stream for reboiling reduces the downstream district heat production, what is compensated by methane burners in the worst case. Thus, the reboiler duty can be expressed by a CO_2 emission per year. Assuming a boiler efficiency of 90%, this results in 1921 kg CO_2/a per kW reboiler duty.

4. Application and Results

The three scalarization methods and the NSGA-II algorithm are applied to two optimization cases: (i) optimization of CO_2 emissions vs. OPEX costs (both minimized), where the reflux ratio and ethanol recovery of the column are varied, and (ii) optimization of the ethanol product flow (maximized) vs. OPEX costs (minimized), by varying the feed stream, reflux ratio and ethanol recovery of the column. The number of calculated Pareto points is in each case 20.

Figure 3 shows the results for the first case. The dependency of both objectives shows a very linear relationship, even though highly nonlinear effects like heat exchanger fouling are incorporated. It gets clear, that the weighting approach fails to generate points between the ends points, while the NSGA-II algorithm generates a quite homogenous front, without travelling too much in the suboptimal region.

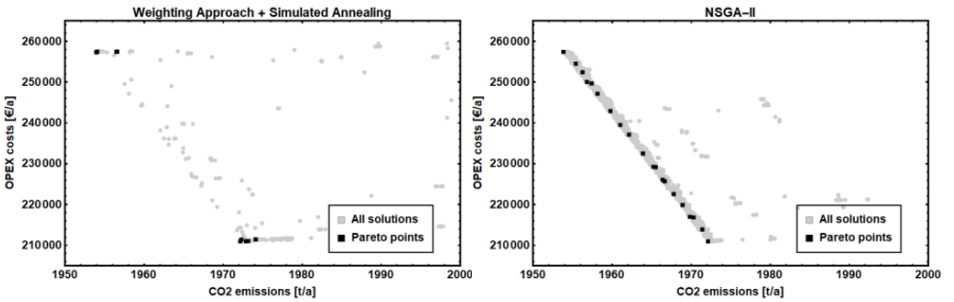

Figure 3: Results for the optimization of CO_2 emissions vs. OPEX costs

In Figure 4 the results for the second case are shown. Also in this case both objectives show a nearly linear relationship, the slope of the curve increases only slightly with increasing ethanol production. The ε-constraint method is capable of providing a very homogenously distributed Pareto front, while the modified boundary intersection

method randomly produces wrong points. This arises from the computationally expensive equality constraints, which need to be fulfilled and are obviously not met when running the single points with maximum 3000 iterations.

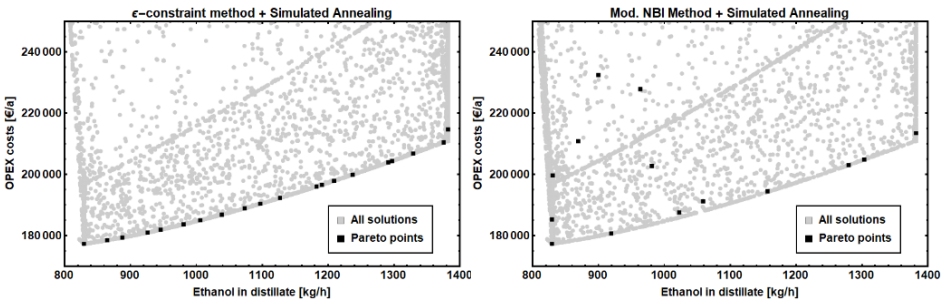

Figure 4: Results for the optimization of ethanol in distillate vs. OPEX costs

5. Conclusions

In process simulation multi-objective optimization can be a powerful tool for optimizing plants and processes in view of economic aspects as well as for evaluating them in view of process flexibility. Because multi-objective optimization is not part of commercial process simulators yet, scalarization methods provide an economic possibility to realize that. In this work it turns out, that the ε-constraint method is the fastest and most reliable beside the weighting approach and modified normal boundary intersection method. By implementing the NSGA-II algorithm with jumping gene adaptions, the convergence speed and stability of the optimization can be further improved significantly. The investigated bio-ethanol column was optimized in view of OPEX costs, CO_2 emissions as a sustainability indicator and the ethanol product, which showed linear relationship.

References

A.L.H. Costa, V.B.G. Tavares, J.L. Borges, E.M. Queiroz, F.L.P. Pessoa, F.d.S. Liporace, S.G.d. Oliveira, 2013, Parameter Estimation of Fouling Models in Crude Preheat Trains,: Heat Transfer Engineering, Vol. 34, No. 8-9, pp. 683-691

K. Deb, A. Pratap, S. Agrawal, T. Meyarivan, 2002, A fast and elitist multiobjective genetic algorithm: NSGA-II, IEEE Trans. Evol. Computat., Vol. 6 No. 2, pp. 182-197

Y.I. Lim, P. Floquet, Xavier Joulia, 2001, Efficient Implementation of the Normal Boundary Intersection (NBI) Method on Multiobjective Optimization Problems, Ind. Eng. Chem. Res., Vol. 40, pp. 648-655

C.A.M. Lopez, D. Telen, P. Nimmegeers, L. Cabianca, F. Logist, J. V. Impe, 2018, A process simulator interface for multiobjective optimization of chemical processes, Computers and Chemical Engineering, Vol. 109, pp. 119-137

R.T. Marler, J.S. Arora, 2004, Survey of multi-objective optimization methods for engineering, Structural and Multidisciplinary Optimization, Vol. 26, pp 369-395

G.T. Polley, D.I. Wilson, B.L. Yeap, S.J. Pugh, 2002, Evaluation of laboratory crude oil threshold fouling data for application to refinery pre-heat trains, Applied Thermal Engineering, Vol. 7, No. 22, pp. 777-788

M. Ramteke, S. K. Gupta, 2016, Multi-Objective Genetic Algorithm annd Simulated aAnnealing with the Jumping Gene Adaptions, Multi-Objective Optimization, Advances in process systems engineering, Vol. 5, pp 1-27

G.P. Rangajah, 2016, Introduction, Multi-Objective Optimization, Advances in process systems engineering, Vol. 5, pp 1-27

Ö. Yeniay, 2005, Penalty Function Methods for Constrainted Opimization with Genetic Algorithms, Mathematical and Computational Applications, Vol. 10., No. 1, pp. 45-56

Sauro Pierucci, Flavio Manenti, Giulia Bozzano, Davide Manca (Eds.)
Proceedings of the 30th European Symposium on Computer Aided Process Engineering (ESCAPE30), May 24-27, 2020, Milano, Italy.
http://dx.doi.org/10.1016/B978-0-12-823377-1.50307-4

Maximising Food Security through a Macronutrient Optimisation Approach Considering Energy and Water Constraints

Nayla Al-Thani[a], Tareq Al-Ansari[a,b*], Rajesh Govindan[b]

[a] *Division of Sustainable Development, College of Science and Engineering, Hamad Bin Khalifa University, Qatar Foundation. Doha, Qatar*
[b] *Division of Engineering Management and Decision Sciences, College of Science and Engineering, Hamad Bin Khalifa University, Qatar Foundation. Doha, Qatar*
talansari@hbku.edu.qa

Abstract

Considering the relationship between food security and malnutrition, a 'Decade of Action' was certified by the UN in 2016 promoting the need to end all types of malnutrition. In the context of nutrition, this study evaluates the possibility to maximise nutritional benefits through the optimal allocation of water and energy resources using a hypothetical case study in Qatar. Two complementary models were developed using goal programming and linear programming formulations, both of which were utilised to solve various scenarios. The multi-objective function of goal programming minimises the weighted negative deviation from the targeted food groups and nutrients. Meanwhile, the linear programming model was implemented to increase the self-sufficiency percentage of food groups and nutrients. For the case study analysed, the model results demonstrate clearly that the quantity of natural fresh water and energy utilisation is not sufficient to meet the targeted 40% self-sufficiency levels of either food groups or nutrients. In addition, the results indicate the dependency between increasing the self-sufficiency of different nutrients with the increased production of dates group, implying that dates can be considered a strategic crop for Qatar in terms of food security. Moreover, the results suggest an alternative production mix that will provide approximately 38% carbohydrates, 9% protein, and improves the fibres to about 3.5% from 0.5%, which offers more diversity in the diet and reduces the fat to about 8.5% from about 150% compared to the current production.

Keywords: Agriculture, Nutrients, Food Security, Optimisation, EWF Nexus.

1. Introduction

Agriculture is the main primary activity related to enhancing global food production, and thus it is fundamental for food security. As such, it involves the provision of nutrients required by mankind to lead a healthy and nutritious life (UNSDSN, 2013). According to the Food and Agriculture Organisation of the United Nations (FAO), since the 1960s, aggregate global food production has increased by 145%, resulting in a 5% more food per capita (Pretty, 2013). However, the effort was narrowly focused mass extensification of land to produce staples rich in calories, of which 12 species contributed to 80% of global dietary intake. Furthermore, intensification of agriculture production has demonstrated compounded effects on the environment, such as greenhouse gas (GHG) emissions contributing to climate change, resource depletion, and other environmental impacts. It

consumes 70% of global fresh water reserves, the single largest consumer (FAO, 2015), and contributes 17-32 % of global GHG emissions (Berntrup and Pallière, 2008). Thus, agriculture production requires a mobilisation of energy and water resources, and it is therefore considered important to derive maximum nutritional benefit within a sustainable development framework which promotes optimum resource consumption, minimal environmental impact, and maximum benefit to society. However, research into resource management and optimisation in the context of nutritional requirements is limited, and there is currently no appropriate methodology that exists linking the two.

The objective of this study is to develop such a framework that allows the optimisation of resources-use efficiency whilst maximising the nutritional benefit from agricultural output. The study adopts the energy, water and food (EWF) nexus approach which emphasises the interlinkages between EWF resource sectors (Hoff, 2011). The analysis of EWF Nexus systems forms an important aspect of modelling related to achieving food security targets (Al-Ansari *et al*., 2015), forming the basis of integrated nutrition and resource modelling. The tool presented in this study informs decisions pertaining to agriculture production and the optimum composition of production quantities that maximises the self-sufficiency ratio of food groups and nutrients. Essentially, the tool improves resources allocation whilst maximising the production of food groups. Furthermore, the study investigates the status of the water and energy allocation for agriculture in Qatar under macro nutrients constraints. As such, the contribution in this paper is two-fold: firstly, the introduction of two novel mathematical model formulations that aim to optimise agricultural benefits represented as the macro nutrients within food groups under different water and energy constraints; and secondly, the representation of food security in terms of the macro nutrients needs of a population.

2. Available Data

2.1. Nutrient guidelines

The report of the dietary guidelines for Qatar by the Ministry of Public Health listed six food groups that are recommended to be consumed for a healthy population (SCH, 2015). The food groups in the guideline are vegetables, fruit, cereals and starchy vegetables, legumes, milk and dairy products, and fish, poultry and meat. According to the MDPS (2016) legumes are not grown locally thus it is excluded from the analysis. In order to extract the nutrients content of each food group, an averaging approach is utilised by Gephart *et al*. (2016). The first step is to list all the crops produced locally along with their respective nutrient density (*i.e.* nutrient content per 100g) for each food group which is obtained from USDA (2018). Finally, the values are averaged to determine the nutritional content for each food group which are listed in Table 1.

Table 1. Quantity of nutrients n in different food groups per 100g.

Food Group	**Energy (kcal)**	**Carbohydrate (g)**	**Protein (g)**	**Fibre (g)**	**Fatty acids*** (g)**
Vegetables	23.5	5.4	1.3	1.9	0.1
Fruits	49.6	12.4	1.0	2.2	0.0
Dates	279.5	75.0	2.1	7.4	0.0
Cereals & Starchy Vegetables	213.0	44.9	7.3	6.2	0.2
Milk, Dairy Products	269.4	5.4	13.3	0.0	6.7
Fish, Poultry, Meat	280.2	0.2	17.3	0.0	10.1
Total amount required for the population per year (tonne)**	152869.8	143315.5	28663.09	6191.2	6191.2

2.2. Water and Energy resources

As for the life cycle energy and water requirements to produce different food groups, the data is estimated from Webber (2012) and is illustrated in Table 2.

Table 2. Unit amount of energy and water required to grow different food groups.

Food Group	The amount of energy required kWh/tonne	The amount of water utilised (m^3/tonne)
Vegetables (tonne)	7494.9	497.0
Fruits (tonne)	8657.9***	945.1
Dates (tonne)	8657.9***	866.7
Cereals & Starchy Vegetables (tonne)	3715.1	1934.0
Milk, Dairy Products (tonne)	10563.9	3920.8**
Fish, Poultry, Meat (tonne)	14537.5	10333.3**

**Average water requirement for combined fruits and dates.*

***(FAO, 2003).*

**** It is assumed that the energy required to grow one tonne of fruits and dates are identical.*

3. Methodology

The methodology utilised to fulfil the stated objectives of this study includes the development of complementary goal programming (GP) and linear programming (LP) model formulations. Table 3 lists the notations used in the mathematical formulations that follow.

Table 3. Nomenclature used in the formulations.

Notation	Description	
	Sets	
G	Set of food groups	
N	Set of nutrients	
g^*	number of food groups	
n^*	number of nutrients	
	Parameters	**Unit**
W_g	Unit amount of water needed by food group g, g=1,…, g^*	m^3/tonne
E_g	Unit amount of energy needed by food group g, g=1,…, g^*	kWh/tonne
E_w	Total amount of energy required for groundwater abstraction for agriculture	kWh
W_{max}	Maximum amount of water that is available for the agricultural sector	m^3
E_{max}	Maximum amount of energy that is available for the agricultural sector	kWh
N_{ng}	Fractional amount of nutrient n that is available in food group g, n=1,…, n^*, g=1,…, g^*	-
F_g	Target amount to be produced for food group g, g=1,…, g^*	Tonne
L_n	Target amount to be produced from nutrient n, n=1,…, n^*	Tonne
U_n	weight of nutrient n, n=1,…, n^*	Tonne
U_g	weight of food group g, g=1,…, g^*	Tonne

The GP model minimises the negative deviation (*i.e.* shortage) from the set target for the different food groups and selected macro nutrients, whereas the LP model maximises the self-sufficiency ratio of the food groups and nutrients. In effect, the models optimise the allocation of water and energy resources in order to increase the self-sufficiency of the

agriculture sector. The results of the two models were integrated, relating the model outputs through a self-sufficiency relationship. It is important to note that although both the production targets and food demand requirements are related, they are not necessarily satisfied simultaneously, and thus the need to have separate models to optimise and assess the solutions obtained therein.

3.1. GP model formulation

Minimise $\sum_{n\in N} U_n \frac{d_n^-}{L_n} + \sum_{g\in G} U_g \frac{t_g^-}{F_g}$

s.t.
$$\sum_{g=1}^{g} w_g x_g \le W_{max} \qquad \forall\, g \in G$$
$$\sum_{g=1}^{g} (E_g x_g + E_w W_{max}) \le E_{max} \qquad g \in G$$
$$\sum_{g=1}^{g} N_{ng} x_g = L_n - d_n^- + d_n^+ \qquad \forall\, n \in N$$
$$\sum_{g=1}^{g} x_g = F_g - t_g^- + t_g^+ \qquad \forall\, g \in G$$
$$x_g \ge 0 \qquad \forall\, g \in G$$

x_g: The amount to be produced locally from each food group that will optimally allocate the available water and energy for the agriculture sector.
t_g^-: The negative deviation from the set target of each food group g, g=1,…,g*
t_g^+: The positive deviation from the set target of each food group g, g=1,…,g*
d_n^-: The negative deviation from the set target of each nutrient n, n=1,…,n*
d_n^+: The positive deviation from the set target of each nutrient n, n=1,…,n*

3.2. LP model formulation

Maximise $\sum_{n\in N} U_n z_n + \sum_{g\in G} U_g y_g$

s.t.
$$\sum_{g=1}^{g} w_g x_g \le W_{max} \qquad \forall\, g \in G$$
$$\sum_{g=1}^{g} (E_g x_g + E_w W_{max}) \le E_{max} \qquad \forall\, g \in G$$
$$\sum_{g=1}^{g} N_{ng} x_g = z_n T_n \qquad \forall\, n \in N$$
$$\sum_{g=1}^{g} x_g = y_g F_g \qquad \forall\, g \in G$$
$$0 \le x_g, y_g \le 1 \quad \forall\, g \in G$$
$$0 \le z_n \le 1 \qquad \forall\, n \in N$$

F_g = Annual consumption of food group g, g=1,…, g*
T_n = Annual population requirements for nutrient n, n=1,…, n*
x_g = amount to be produced locally from food group g, g=1,…, g*
y_g = self-sufficiency ratio of food group g, g=1,…, g*
z_n = self-sufficiency ratio of nutrient n, n=1,…, n*,

4. Results and discussion

Both the GP and LP models are solved for multiple scenarios that are selected based on mainly two aspects: (a) it reflects the preferences of the policy makers; and (b) it is related to the water requirement for each food group. As such, weights are assigned that essentially reflect the dietary guidelines recommended for the state of Qatar that was developed by the Supreme Council of Health and the Nutrition Department in the WHO (SCH, 2015), according to which: (a) scenario 1 gives equal weightage to all food groups

and nutrients which represents the baseline scenario; (b) scenario 2 gives higher weightage to the vegetables, fruits and dates groups to reflect the recommendation developed by the Supreme Council of Health, in addition to the fact that it requires the least amount of water to be produced; (c) scenario 3 increases the weightage of some nutrients to study the impact on the optimal solution compared to scenario 2, and to test the sensitivity of the models; and (d) scenario 4 gives higher weightage to all nutrients to investigate which of the food groups will present a higher impact in satisfying the nutritional need.

Figures 1(a) and 1(b) illustrate the self-sufficiency levels achieved in different food groups when the desired target is set 40% of the total annual population requirements using the GP model, and for maximum achievable self-sufficiency level using the LP model, respectively. These results generally demonstrate that the production of fish, poultry, meat groups are not favourable in all the scenarios. This can be attributed to the large quantities of water required to produce one tonne in this food group. Meanwhile, the dates group satisfied with positive deviation implying that it exceeds target in all scenarios. This is due to the high nutritional content of the dates and the low water requirements. The respective self-sufficiency levels achieved for different nutritional requirements are illustrated in Figures 2(a) and 2(b).

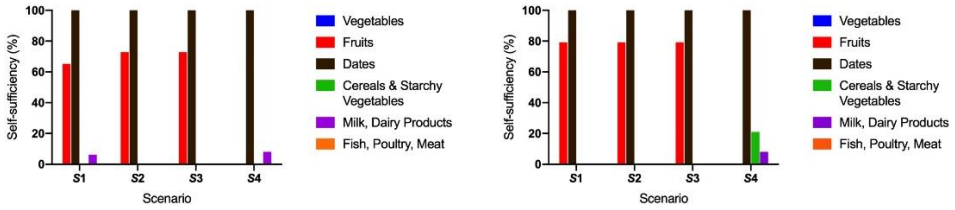

Figure 1. Self-sufficiency levels achieved for different food groups using: (a) goal programming; (b) linear programming

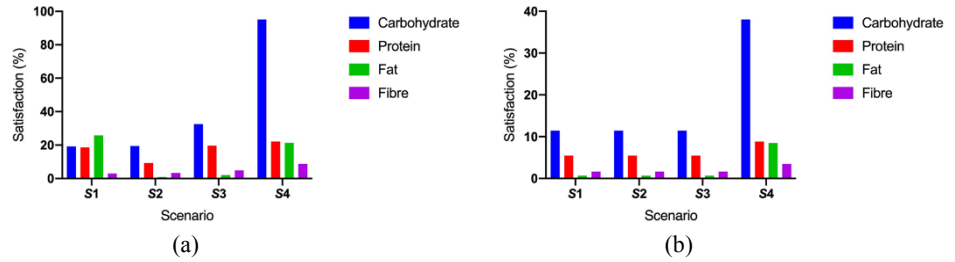

Figure 2. Self-sufficiency levels achieved for different nutritional requirements using: (a) goal programming; (b) linear programming

5. Conclusions

This study introduces a tool that can inform decision making with regards to maximising national food self-sufficiency. The methodology presented consists of two complementary mathematical formulation that optimises the status of the self-sufficiency ratios under given water and energy constraints for different cases and scenarios. The LP model aims to maximise the production of different food groups and nutritional content through examining different production quantities within pre-specified water and energy

resources. While the objective in the GP model is to minimise the undesired deviation from the set goals, *i.e.* the targets of different food groups and nutrients, which is essentially a sub-goal of the LP model. For the Qatar case study considered, the results demonstrate that the current quantity of utilised water and energy will not be sufficient to meet the target of the 40% self-sufficiency for all food groups or nutrients. Therefore, further investment in water and energy resources is required. The results demonstrate that dates are the most favourable group specific to Qatar, owing to the fact that it requires the least quantity of water and energy resources for production. The models developed as part of this study have not considered costs of production, land, environment and the climate condition of the area, which is considered a limitation, thus forming the basis of future work.

References

T. Al-Ansari, A. Korre, Z. Nie, N. Shah, 2015, Development of a life cycle assessment tool for the assessment of food production systems within the energy, water and food nexus, Sustainable Production and Consumption, 2, 52-66.

F. Berntrup, C. Pallière, 2008, GHG emissions and energy efficiency in European nitrogen fertilizer production and use, International Fertiliser Society Conference. UK.

FAO, 2003. Agriculture, Food and Water. Rome, Italy.

FAO, 2015, Towards A Water and Food Secure Future: Critical Perspectives for Policy-makers. Marseille.

J.A. Gephart, K.F. Davis, K.A. Emery, A.M. Leach, J.N. Galloway, M.L. Pace, 2016, The environmental cost of subsistence: Optimizing diets to minimize footprints, Science of The Total Environment, 553, 120-127.

J.A. Gephart, K.F. Davis, K.A. Emery, A.M. Leach, J.N. Galloway, M.L. Pace, 2016, The environmental cost of subsistence: Optimizing diets to minimize footprints, Science of The Total Environment, 553, 120-127.

J. Hoff, 2011, Understanding the nexus. In: Background Paper for the Bonn 2011 Conference: The Water, Energy and Food Security Nexus, Bonn, Germany. Stockholm Environment Institute, Stockholm, Sweden.

J. Pretty, 2013, The Consumption of a Finite Planet: Well-Being, Convergence, Divergence and the Nascent Green Economy, Environmental and Resource Economics, 55, 475-499.

MDPS, 2016, Economic Statistics : Agriculture Statistics. Ministry of Development Planning and Statistics, Qatar.

SCH, 2015, Qatar Dietary Guidelines, The Supreme Council of Health, Doha, Qatar.

UNSDSN, 2013, Solutions for Sustainable Agriculture and Food Systems- Technical Report for the Post-2015 Development Agenda. Sustainable Development Solutions Network: A Global Initiative for the United Nations.

USDA, 2018, USDA Food Composition Databases.

M.E. Webber, 2012, More Food, Less Energy: Changes in agriculture, policy and personal behaviors can reduce the energy a nation uses to feed itself and the greenhouse gases it emits, Scientific American, pp. 74-79.

Sauro Pierucci, Flavio Manenti, Giulia Bozzano, Davide Manca (Eds.)
Proceedings of the 30th European Symposium on Computer Aided Process Engineering (ESCAPE30), May 24-27, 2020, Milano, Italy.
http://dx.doi.org/10.1016/B978-0-12-823377-1.50308-6

Modelling Circular Structures in Reaction Networks: Petri Nets and Reaction Network Flux Analysis

Jana M. Weber,[a] Artur M. Schweidtmann,[b] Eduardo Nolasco,[a]
Alexei A. Lapkin [a,c*]

[a]*Department of Chemical Engineering and Biotechnology, University of Cambridge, West Cambridge Site, Philippa Fawcett Drive, Cambridge CB3 0AS, U.K.*
[b]*Process Systems Engineering (AVT.SVT), RWTH Aachen University, Aachen 52074, Germany*
[c]*Cambridge Centre for Advanced Research and Education in Singapore, CARES Ltd. 1 CREATE Way, CREATE Tower #05-05, 138602 Singapore*
aal35@cam.ac.uk

Abstract

Optimal reaction pathways for the conversion of renewable feedstocks are often examined by reaction network flux analysis. An alternative modelling approach for reaction networks is a Petri net. These explicitly take the reaction sequence into account. In the optimisation of a network, this can allow the implementation of constraints on circular reaction structures, which are common substructures in chemical reaction networks. In this study, we compare the performance of the models in an illustrative minimal working example of a circular reaction substructure. The reaction network flux analysis is shown to be a relaxation of the Petri net formulation. Most notable, this work contributes to well-reasoned model choices for reaction networks.

Keywords: Reaction network, Petri nets, Reaction network flux analysis

1. Introduction

By the year 2030, it is estimated that the chemical production will become the main driver of global oil consumption (Kätelhön et al., 2019), hence the transition towards sustainable chemistry (Jenck et al., 2004) and more explicitly the development of novel processes based on renewable feedstocks has gained major importance (Sheldon, 2014). However, identification of efficient process routes based on biological feedstocks remains a challenge, and suitable models for rapid evaluations of processes are highly desirable. Methods, such as reaction network flux analysis (RNFA), have recently received much attention, as they enable a system-wide study on the utilisation of feedstock components. Stochastic semantics, i.e. how many molecules go through each reaction, are used to describe such systems quantitatively (Bartocci and Lió, 2016). First introduced by Voll and Marquardt (2012b), the RNFA finds optimal reaction fluxes in a given set of reactions. The approach was applied for investigation of possible routes to biofuels (Ulonska et al., 2018, 2016; Voll and Marquardt, 2012a) and for biomass-derived polymer production (Zhang et al., 2017). It was shown that the RNFA is well-suited for optimal pathway identification within a set of alternative routes in networks of sizes of the order of 116 reactions and 80 substances (Voll and Marquardt, 2012b). Besides the size of a chemical reaction network, also its structure plays an important role. Networks of

chemical reactions naturally exhibit special architectures (Fialkowski et al., 2005; Grzybowski et al., 2009) and nodes with extreme connectivity patterns (Szymkuć et al., 2016; Weber et al., 2019). Furthermore, they include a multitude of local substructures (Feinberg and Horn, 1974; Van Der Schaft et al., 2016), such as bidirectionalities due to reversible reactions and circular structures due to e.g. chemical looping or molecules functioning as catalysts or protecting groups. In the manually assembled reaction networks, circular structures are seldom encountered. However, with the increasing availability of reaction data, there is a rapid advance in algorithmic assembling of reaction networks, which frequently contain circular substructures. In light of this, we present this work as a part of a much larger study. We investigate the influence of circular substructures on the RNFA and on an alternative approach, a Petri net optimisation (PNO) formalism. Petri nets have been used to model chemical and biological reaction networks (Chaouiya, 2007; Koch, 2010; Petri, 1962; Peterson, 1977), while the use of PNO in chemical engineering has to date mostly focused on batch scheduling (Gu et al., 2003; Yamalidou and Kantor, 1991).

In this work, we introduce PNO for chemical reaction sequences and show both models' behaviour regarding circular substructures. The remainder of this article is organised as follows. Section 2 describes the RNFA and PNO formalisms, Section 3 introduces an illustrative case study, and results are presented and discussed in Section 4. Lastly, Section 5 concludes the article and shows future perspectives.

2. Methods

The RNFA is formulated as a linear programming problem (LP) and the PNO as a mixed-integer linear programming problem (MILP). Both were implemented and solved using Python 3.6 with Pyomo modelling language and CPLEX 12.9 as a solver. (Implementation: https://github.com/Jana-Marie-Weber/Reaction_net_opt)

2.1. Reaction network flux analysis (RNFA) formalism

The RNFA originated from flux balance analysis of metabolic networks, where the overall metabolic supply chain is assumed to be at equilibrium (Orth et al., 2010). For this assumption to hold, the RNFA introduces both supply and removal pseudo-reactions. Due to the scope of this work, we do not show the formalism of RNFA, which we have adapted from Voll and Marquardt (2012b) and refer the reader to that reference.

2.2. Petri net optimisation (PNO) formalism

Petri nets, first introduced by Carl Adam Petri (Petri, 1962), are directed bipartite networks, where the two node types are *places*, represented by circles, and *transitions*, represented by bars (see Figure 1).

Reaction 1 (R1): $A + B \rightarrow C$
Reaction 2 (R2): $C + E \rightarrow B + D$

(a)

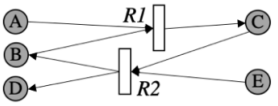

(b)

Figure 1. Sample reactions. (a) A reaction set with a circular substructure. (b) A graph representation of reactions in (a). Circles are *places* and bars *transitions* in Petri net notation.

The input and output relations between places and transitions are shown by connecting links, called *arcs* and an incidence matrix. The *state* of a Petri net is given by a marking of places with *tokens*. Tokens change from one place to another through firing of transitions. A transition is enabled, that is, it is able to fire and thus to move tokens, when its input places meet the incidence matrix' token demands (Ghaeli et al., 2005; Peterson,

1977). Firing a transition thereby leads to a change of state, introducing the order of events, a linear temporal logic (LTL) (Bartocci and Lió, 2016). The optimisation problem determines an optimal sequence of firing certain transitions. Extending the work of Yamalidou and Kantor (1991) we formulate the PNO as follows:

$$\min_{\substack{m_{p,k=K} \\ q_{t,k} \\ y_{t,k}}} J = -\sum_{p=1}^{P} c_p \cdot m_{p,k=K} + \sum_{t=1}^{T} \left(s_t \cdot \sum_{k=1}^{K} q_{t,k} \right) + \sum_{t=1}^{T} \left(b_t \cdot \sum_{k=1}^{K} y_{t,k} \right) \tag{1}$$

s.t.

$$m_{p,k=1} = a_p \qquad \forall p \in \{1,..,P\} \tag{2}$$

$$m_{p,k} \geq 0 \qquad \forall p \in \{1,..,P\}, \forall\, k \in \{2,..,K\} \tag{3}$$

$$m_{p,k+1} = m_{p,k} + \sum_{t=1}^{T} d_{p,t} \cdot q_{t,k} \qquad \forall p \in \{1,..,P\}\,, \forall k \in \{1,..,K-1\} \tag{4}$$

$$\sum_{t=1}^{T} y_{t,k} \leq 1 \qquad \forall k \in \{1,..,K-1\} \tag{5}$$

$$\sum_{t=1}^{T} y_{t,k+1} \leq \sum_{t=1}^{T} y_{t,k} \qquad \forall k \in \{1,..,K-2\} \tag{6}$$

$$y_{t,k}/M \leq q_{t,k} \leq y_{t,k} \cdot M \qquad \forall t \in \{1,..,T\}\,, \forall k \in \{1,..,K-1\} \tag{7}$$

where P is the number of places (molecules), K is the number of states (molar distributions after each reaction step), and T is the number of transitions (reactions) in the system. The elements $m_{p,k}$ represent the marking at molecule p, and reaction step k. Note that there are K mol distributions for $K-1$ reaction steps. The elements $q_{t,k}$ represent the amount of token (mol) passing reaction t, at reaction step k and the elements $y_{t,k}$ are binary variables with value one if the transition (reaction) is active and zero otherwise. We do not consider kinetics/reaction times; transitions fire without any associated time value. The binary variables offer the possibility to include throughput independent process costs, which is an important practical consideration in (bio-)chemical process development. The vector $\boldsymbol{c} \in \mathbb{R}^P$ is the revenue for selling molecule p, $\boldsymbol{s} \in \mathbb{R}^T$ is the cost associated with a reaction flux and $\boldsymbol{b} \in \mathbb{R}^T$ is a constant cost associated with a reaction. The objective function (Eq. (1)) minimises the total cost consisting of product revenue, flux related and non-flux related reaction costs. The parameters $d_{p,t}$ are the elements of the incident matrix (stoichiometric matrix) of the reaction system, where consumption and production of molecule p in reaction t is specified. The vector $\boldsymbol{a} \in \mathbb{R}^P$ represents the initial mol distribution. Similar to the RNFA (Voll and Marquardt, 2012b), the initial or the final state of the system need to be specified so that the MILP problem is bounded. We set the initial distribution in Eq. (2). The constraints in Eq. (4) describe the mol distribution over all molecules based on the previous distribution and the changes of the system due to a reaction step. In combination with Eq. (3), this guarantees that a reaction can only take place if the mol distribution of all incoming arcs is sufficient with regard to the stoichiometric matrix. Constraints in Eq. (5) allow only one reaction in every reaction step k, ensuring the LTL. The *big M* constraints in Eq. (7) couple the reaction fluxes $q_{t,k}$ to $y_{t,k}$, if and only if one is active the other can occur, and give a lower and upper bound for $q_{t,k}$. In case K is chosen too high, constraints in Eq. (6) guarantee that reaction steps

at the beginning are active while inactive reaction steps are at the end. This breaks a symmetry in the optimisation.
In general, we find that a PNO solution will always be a feasible solution of the RNFA, while the RNFA solution might be infeasible for the PNO due to the event dependencies. Thus, RNFA can be understood as a relaxation of the PNO problem.

3. An illustrative case study

The example chosen is a simplified circular substructure shown in Figure 1. *R1* is an irreversible bimolecular reaction producing intermediate C, whereas *R2* is an irreversible bimolecular reaction leading to the formation of product D and regeneration of species B. The chemical meaning of substance B could be for instance a homogeneous catalyst or a protecting group (PG). A and E are reactants. We introduce two scenarios. In Scenario I, 100 mol of each A, B, and E are given as the input; R1 and R2 have a reaction cost of five and product D has a selling price of 50 per mol. In Scenario II, no B, i.e. a catalyst or a PG, is initially available. Further parameters remain unchanged. Both scenarios are solved with both methods, allowing up to two reaction steps; $K = 3$ states for the PNO.

4. Results and Discussion

Hereafter, we outline and discuss the behaviour of both models with regard to a circular substructure. We also qualitatively compare the scalability of the two models. Note, that there are further important factors for model selection, e.g. the desired problem scenario, the actual size of a real-world problem, or the incorporation of evaluation metrics.
Comparing both methodologies for Scenario I, we find that either lead to the same molar distributions over reactions and substances and an identical objective value of -4,000 (see Table 1). Key differences are that the proposed PNO formalism provides information on the sequence of reactions but requires/allows defining the utmost number of the allowed reaction steps. If more steps than necessary are given, the problem size is larger than necessary, but the solution stays the same; there will be inactive steps.
Comparing both methodologies for Scenario II, we encounter differences in the optimal solution. Specifying the input of B as zero leads to no performed reactions in the PNO formalism as event dependencies prevent any reaction. The RNFA approach performs the same reactions as previously (objective value of -4,000), as the material balance for B is intrinsically fulfilled within the circular structure. One can imagine this circular structure as follows: assuming B is present (could be borrowed), we perform reaction *R1*. Then, *R2* takes place and reproduces B (it can be returned). This leads to the desired product D and is, based on the objective function, more desirable than not performing any reaction. Still, for conducting the actual set of reactions, B is needed at the start of the first reaction.

Table 1. Obj. value and molar flux distribution over reactions and outputs in both scenarios (Sc.I and Sc. II) and both approaches. For the PNO, * represents the first and $^{+}$ the second reaction step.

		Obj. value	Reaction flux		Final mol distribution				
			R1	R2	A	B	C	D	E
Sc. I	RNFA	-4,000	100	100		100		100	
	PNO	-4,000	100^{*}	100^{+}		100		100	
Sc. II	RNFA	-4,000	100	100				100	
	PNO	0			100				100

Comparing the model size, the RNFA is smaller (see Table 2) and scales linearly with the network size, i.e. number of reactions (T) and number of molecules (P). The PNO method further scales with the number of desired steps (K-1). This is often a constant parameter,

independent from the network size with K<<P and K<<T. Thus, the PNO also scales linearly with network size. According to the Leyffer-Linderoth-Luedtke measure of complexity, MILPs of approximately $2 \cdot 10^4$ variables (LPs of about $5 \cdot 10^7$) could be solved using state-of-the-art solvers in 2016. Thus, previous literature cases (Voll and Marquardt, 2012b) with about 116 reactions and 80 substances would also be solvable by the PNO. Regarding a network of all chemical knowledge contained in large databases, e.g. Reaxys® (>119M compounds and >46M reactions), problems most likely need to be broken down for both methods or heuristic solution strategies would be required.

Table 2. Model complexity of RNFA and PNO formalisms. * Variable bounds are not counted as constraints (PNO based on Eq. (4-7) and RNFA based on substance balances).

		RNFA	PNO
Problem size	No. of continuous variables	T+P	(P+T) · (K-1)
	No. of binary variables	0	T · (K-1)
	No. of constraints*	P	((P+T+ 1) · (K-1))+(K-2)

This illustrative experiment indicates firstly that network substructures play an important role in modelling. Secondly, if the aim is to build reaction sequences only on the currently available substances, PNO seems the more appropriate choice. If, on the other hand, the circular structures should be incorporated in the reaction sequences, e.g. through recycle streams and separation units, RNFA exhibits advantages. Thirdly, the event dependencies in the PNO lead to higher model complexity. Finally, a possible limit on the allowed number of reaction steps may be advantageous. Both methods are promising choices.

5. Conclusions

We compare RNFA and PNO for optimal decision making in a circular reaction substructure. The PNO accurately captures the possible assumption that only given feedstocks are utilised but shows higher model complexity, indicating potential problems when large networks are to be investigated. The RNFA can take advantage of intrinsic circular structures. Both approaches are valuable for the optimisation of reaction networks. The key contribution of this work is a better model understanding which will guide future works towards appropriate model choices, or possibly a model combining both approaches, for larger scales and more complex network optimisation problems.

Acknowledgments: J. M. Weber thanks Dr. W. Kähm for his support during the modelling process, Prof. Pietro Liò for advising the project, and the Department of Chemical Engineering for funding her studentship. This work was funded, in part, by the National Research Foundation (NRF), Prime Minister's Office, Singapore under its Campus for Research Excellence and Technological Enterprise (CREATE) program as a part of the Cambridge Centre for Advanced Research and Education in Singapore Ltd (CARES).

References

E. Bartocci, P. Lió, 2016, Computational modeling, formal analysis, and tools for systems biology, PLoS Computational Biology, 12, 1, 1–22.

C. Chaouiya, 2007, Petri net modelling of biological networks, Briefings in Bioinformatics, 8, 4, 210–219.

M. Feinberg, F. J. M. Horn, 1974, Dynamics of open chemical systems and the algebraic structure of the underlying reaction network, Chemical Engineering Science, 29, 3, 775–787.

M. Fialkowski, K. J. M. Bishop, V. A. Chubukov, C. J. Campbell, B. A. Grzybowski, 2005, Architecture and evolution of organic chemistry, Angewandte Chemie - International Edition, 44, 44, 7263–7269.

M. Ghaeli, P. A. Bahri, P. Lee, T. Gu, 2005, Petri-net based formulation and algorithm for short-term scheduling of batch plants, Computers & Chemical Engineering, 29, 2, 249–259.
B. A. Grzybowski, K. J. M. Bishop, B. Kowalczyk, C. E. Wilmer, 2009, The "wired" universe of organic chemistry, Nature Chemistry, 1, 1, 31–36.
T. Gu, P. A. Bahri, G. Cai, 2003, Timed Petri-net based formulation and an algorithm for the optimal scheduling of batch plants, International Journal of Applied Mathematics and Computer Sciences, 13, 4, 527–536.
J. F. Jenck, F. Agterberg, M. J. Droescher, 2004, Products and processes for a sustainable chemical industry: A review of achievements and prospects, Green Chemistry, 6, 11, 544–556.
A. Kätelhön, R. Meys, S. Deutz, S. Suh, A. Bardow, 2019, Climate change mitigation potential of carbon capture and utilization in the chemical industry, Proceedings of the National Academy of Sciences, 166, 23, 11187–11194.
I. Koch, 2010, Petri nets - A mathematical formalism to analyze chemical reaction networks, Molecular Informatics, 29, 12, 838–843.
J. D. Orth, I. Thiele, B. O Palsson, 2010, What is flux balance analysis?, Nature Biotechnology, 28, 3, 245-248.
J. L. Peterson, 1977, Petri nets, ACM Computing Surveys, 9, 3, 223–252.
C. A. Petri, 1962, Kommunikation mit Automaten. Ph.D. Thesis, Technische Universität Darmstadt, Darmstadt, Germany.
A. J. Van Der Schaft, S. Rao, B. Jayawardhana, 2016, A network dynamics approach to chemical reaction networks, International Journal of Control, 89, 4, 731–745.
R. A. Sheldon, 2014, Green and sustainable manufacture of chemicals from biomass: State of the art, Green Chemistry, 16, 3, 950–963.
S. Szymkuć, E. P. Gajewska, T. Klucznik, K. Molga, P. Dittwald, M. Startek, M. Bajczyk, B. A. Grzybowski, 2016, Computer-assisted synthetic planning: The end of the beginning, Angewandte Chemie - International Edition, 55, 20, 5904–5937.
K. Ulonska, A. König, M. Klatt, A. Mitsos, J. Viell, 2018, Optimization of multiproduct biorefinery processes under consideration of biomass supply chain management and market developments, Industrial and Engineering Chemistry Research, 57, 20, 6980–6991.
K. Ulonska, A. Voll, W. Marquardt, 2016, Screening pathways for the production of next generation biofuels, Energy and Fuels, 30, 1, 445–56.
A. Voll, W. Marquardt, 2012a, Benchmarking of next- generation biofuels from a process perspective, Biofuels, Bioproducts and Biorefining, 6, 3, 292–301.
A. Voll, W. Marquardt, 2012b, Reaction network flux analysis: Optimization-based evaluation of reaction pathways for biorenewables processing, AIChE Journal, 58, 6, 1788–1801.
J. M. Weber, P. Lió, A. A. Lapkin, 2019, Identification of strategic molecules for future circular supply chains using large reaction networks, Reaction Chemistry and Engineering, 4, 1969-1981.
E. C. Yamalidou, J. C. Kantor, 1991, Modeling and optimal control of discrete-event chemical processes using Petri Nets, Computers & Chemical Engineering, 15, 7, 503–519.
D. Zhang, E. A. del Rio-Chanona, N. Shah, 2017, Screening synthesis pathways for biomass-derived sustainable polymer production, ACS Sustainable Chemistry & Engineering, 5, 5, 4388–4398.

Sauro Pierucci, Flavio Manenti, Giulia Bozzano, Davide Manca (Eds.)
Proceedings of the 30th European Symposium on Computer Aided Process Engineering (ESCAPE30), May 24-27, 2020, Milano, Italy.
http://dx.doi.org/10.1016/B978-0-12-823377-1.50309-8

An Agent-based Model for Sustainable Power Generation using Optimal Biomass Utilisation

Sarah Namany, Ahmed AlNouss, Rajesh Govindan, Gordon Mckay, Tareq Al-Ansari *

Divison of Sustainable Development, College of Science and Engineering, Hamad Bin Khalifa University, Qatar Foundation, Doha, Qatar.
talansari@hbku.edu.qa

Abstract

Exponential growth in the global population induces larger dependencies on natural resources to meet the demands for products causing resource depletion and environmental degradation. As such, there is an impetus to transform current industrial systems into systems that operate based on inherent sustainable values. While most of the current energy systems are based on polluting fossil fuels, alternative sources have exhibited high performances both economically and environmentally. Biomass for instance, represents a potential source for energy utilisation. Understanding the functioning of biomass gasification strategies as part of the biorefinery system's operations is fundamental, yet, not sufficient to grant sustainable energy provision. The deployment of biomass technologies should also be assessed whilst considering the interaction with other energy sources. The purpose of this work is to design a dynamic and sustainable decision-making scheme that predicts the performance of the power generation system. The framework is developed as an agent-based model illustrating the several entities contributing to the shift towards a biomass-fuelled energy system. The power generation system and biomass feedstock producers are the main categories of agents interacting with one another following a set of rules restricting their behaviors with an ultimate aim to determine the optimal energy portfolio to meet energy demands whilst considering the contribution of existing natural-gas power plants and biomass blending. Rules of interactions impacting strategies adopted are imposed through two different scenarios representing the environmental and economic performances. Findings of this research demonstrate that under environmental restrictions, a diversified energy mix supporting the contribution of biomass is environmentally viable, as it contributes to a 34% reduction in emissions. However, it entails an economic expenditure amounting to 64% increase owing to the deployment of biomass technologies. The optimal biomass blending indicates the domination of manure feedstock over date pits, sludge and food waste in both scenarios, being the lowest in both economic and environmental costs.

Keywords: Power, Biomass, Agent-based Modelling, Sustainable decision-making

1. Introduction

In the light of the ever-increasing technological advancements, energy resources are experiencing significant pressures owing to the need to satisfy the growing demand. This upsurge will result in a major environmental degradation, especially with the contribution of fossil-fuel based power plants as a major supplier of energy, and which is the central cause of global CO_2 emissions. To offset the environmental burden engendered by conventional power sources, there is an incumbent need to invest in sustainable energy technologies. Biomass is considered a promising renewable energy source with a CO_2 neutrality that has the potential to support the worldwide energy demand with sustainable

power and fuels while contributing to an approximately 20% reduction in CO_2 emissions. The recent advancements in thermochemical conversion technologies of biomass demonstrates the excellence of the gasification technique in delivering a high-energy combustible gas. The biomass gasification process can positively result in a larger calorific value content through lowering the ratio of carbon to hydrogen in the effluent syngas. This high-energy syngas serves as an intermediate for the generation of clean fuels and power (AlNouss et al., 2020).

In a country like Qatar, where natural gas-based power plants are well established and are the largest suppliers of energy, deploying a new technology is challenging and requires a thorough decision-making process that considers the economic and environmental implications of each decision undertaken. In a gradually fluctuating environment, decision-making is a multifaceted process necessitating dynamic models. Agent-based modelling (ABM) is a powerful tool that enables the flexible and holistic representation of real-life problems through its modular characteristic allowing the dissection of complex problems into smaller sub-problems, which are analysed independently then aggregated to generate an integrated solution (Barbati et al., 2012). ABM is heavily used in problems involving several actors competing to either achieve conflicting or aligned goals. Marvuglia et al. (2017) assessed the economic and environmental performance of an agricultural system involving the simulation of crops' behaviour as a response to the farmers' decisions. Bieber et al. (2018) adopted an ABM approach to analyse the relationship between humans' socio-economic behaviours and the trend of water and energy demands. Generally, ABM has proven efficient in solving resources-related problems, especially, when it is combined with optimization, as both tools reveal a complimentary connection, such that optimisation models are embedded into an ABM scenarios to generate optimal results (Namany, 2019a). In this paper, ABM is used to forecast the future decisions of the power sector that is striving to satisfy monthly demands over a three-year time period using two sources of energy: natural gas and biomass. The model determines, in the form of an ABM behavioral rule, the optimal biomass feedstock blend that generates the maximum energy while minimising economic costs. This optimal feedstock blend is identified based on the results of economic and environmental performance according to Qatar's biomass feedstock availability and characteristics. Results of the model generate the percentage of contribution of each energy source in the satisfaction of the demand under cost and environmental constraints.

2. Model Development

The model developed as part of this study involves an ABM to perform sustainable planning within the energy sector in Qatar. The designed framework serves as a decision-making tool that enables the prediction of portfolio decisions for the power generation system, as a means to satisfy the local demand from energy. Benefits from deploying biomass energy systems as a sustainable alternative power source are also investigated through an economic and environmental scenario. The following section 2.1 describes the detailed formulation of the ABM along with the tool used to execute the simulation. Section 2.2 explains the proposed scenarios and the data sets available to run the model.

2.1. An ABM simulation for sustainable power generation

An agent is an independent unit characterized by a set of behaviors and attributes. It is governed by specific rules that regulate its interactions with other agents along with the environment where it exists (Lopez-Jimenez et al., 2018). In this study, two main categories of agents are interacting to satisfy the local demand from energy while abiding by economic and environmental constraints. The ABM model developed simulates the monthly decisions of the energy sector for a period of 3 years (n=36), where the main

agent, represented by the power generation system P, interacts with B_i, $i \in B$ such that B is the set of biomass feedstock producers. Both agents interact in an environment representing the local economy. Figure 1 and table 1 describe the different elements of the ABM studied along with their features.

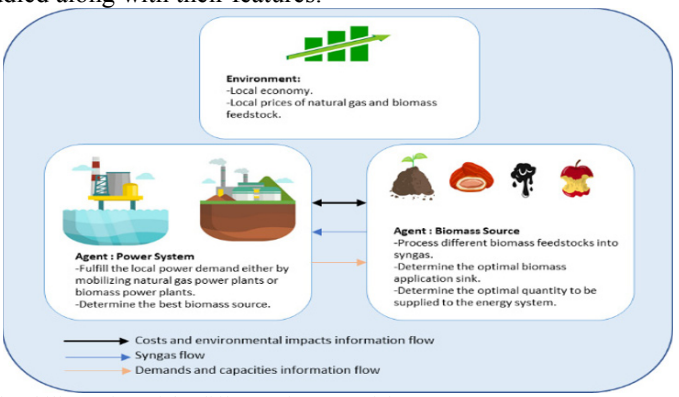

Figure 1: High-level illustration of the different elements of the ABM.

Table 1: Main characteristics of the participating agents.

Agent	Attributes	Behaviours
Power system (P)	- Total grid capacity C (kW) -Monthly demand for energy d_n (kWh) -Monthly energy supplied from natural gas plants Q_{ng} (kWh) -Monthly energy supplied from biomass Q_{bm}(kWh) -Global Warming Potential from generating power from natural gas or biomass (kg CO_{2eq}).	- Supply power from natural-gas plants (NG). - Supply power from biorefineries (BM).
Biomass producers (B_i)	-Monthly feedstock production capacities P_i (kg) -Monthly energy production capacities X_i (kWh)	-Determine the optimal biomass application sinks (S).

2.1.1 Agents

Agent: Power System

The power system P is the core element in the model as it is the agent that guarantees the satisfaction of monthly demands for power d. In order to achieve this aim, P represented by the power grid receives power from two sources: natural gas-based plants and biorefineries, such that the total grid capacity C is not exceeded. The choice of the source is formulated using two different strategies that can be individually or jointly selected: 1) supply the power from natural gas-based sources (NG) or 2) supply the power from biomass sources (BM). Each decision depends on economic and environmental factors elaborated in section 3, along with the operations and attributes associated with the biomass producers' agents B_i . Figure 2 describes the logic adopted by P to satisfy the monthly demand d_n.

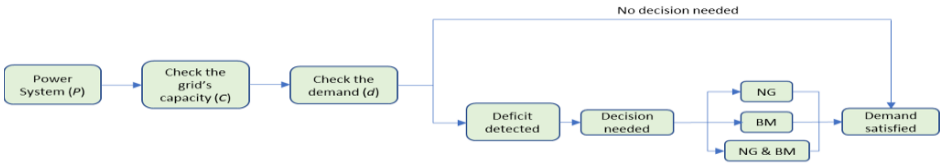

Figure 2. High-level representation of the power system's behaviors.

Agent: Biomass feedstock producers

In this study, four biomass feedstock producers are considered as agents B_i, counting producers of manure, date pits, sludge and food waste. These sources represent a promising sustainable and carbon neutral power supply when combusted. Gasification is

the utilisation strategy adopted to generate energy in this case. As part of their behavior, B_i first identify the optimal biomass blend to produce the syngas, which is used in power generation as an application sink. The quantities supplied to the grid from biorefineries depend on the production capacity of each feedstock P_i, the capacity of generation of energy from gasification X_i, along with the monthly demands for energy in the country d_n. Figure 3 describes the logic adopted by B_i to satisfy the monthly demand d_n.

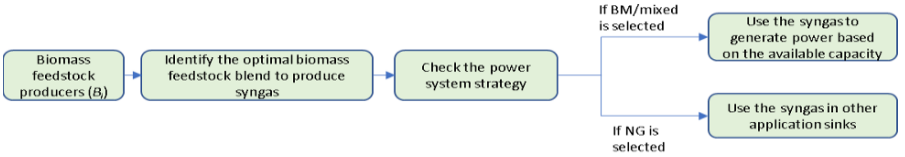

Figure 3. High-level representation of the biomass feedstock producers' behaviors.

To assess the performance of P, economic EC and environmental EI costs for each strategy are computed at each time step n using the following equations (1-4):

Strategy (NG):

$$EC = Q_{ng} \times p_{ng} \quad \text{eq.(1)}$$

$$EI = Q_{ng} \times e_{ng} \quad \text{eq.(2)}$$

such that Q_{ng} is the monthly amount of energy in kWh from natural gas-based plants represented by combined-cycle gas turbines (CCGT). p_{ng} is the unit cost of energy in \$/kWh estimated based on a previous study by Govindan et al. (2018). e_{ng} is the unit of environmental impact quantified as the global warming potential (GWP) associated with CCGT power generation calculated in previous study by Namany et al. (2019b).

Strategy (BM):

$$EC = Q_{bm} \times p_{bm} \quad \text{eq.(3)}$$

$$EI = Q_{bm} \times e_{bm} \quad \text{eq.(4)}$$

such that Q_{bm} is the monthly amount of energy supplied from biorefineries in kWh. p_{bm} is the total unit cost of producing energy from each biomass feedstock. It includes the cost of transforming it to syngas and the cost of transporting the syngas to the appropriate application sink, which is in this case power generation. e_{bm} is the GWP associated with the entire process of producing energy from biomass feedstock. Both p_{bm} and e_{bm} were estimated using Process Economic Analyzer and Energy Analyzer in Aspen Plus, as part of a previous study conducted by the authors (AlNouss, 2019).

3. Scenario formulation and results

Two scenarios were formulated to assess the viability of integrating biomass energy in Qatar's power production sector. The first scenario considers the economic costs associated with each energy technology as a decision-making criterion influencing the monthly strategies. The ABM model under this scenario allocates percentages of contribution for each technology to the energy mix giving the largest proportion to the cheapest one. The second scenario generates decisions based on the environmental performance of each energy source regardless of the cost of power generated. Although the economic and environmental components are the main selection criterion, the fluctuating monthly capacities along with varying demands have significant influence on the agents' behaviour.

To generate results, two softwares were used. First, Aspen Plus was applied to simulate the environmental and economic performances of biomass-based integrated oxygen gasification combined cycle (BIGCC) consisting of syngas production section from feedstock and power generation section from gas and steam turbines. This BIGCC model is simulated following the literature study in (AlNouss, 2019). Then, the results of this

simulation were used as data sets for the ABM that was formulated in Python using the MESA library (MESA, 2016).

Scenario 1: Economic restrictions

Under the economic scenario, the power generation system advises the adoption of a mixed strategy involving natural gas (NG) and biomass energy (BM) in order to satisfy the local demands. Yet, natural gas is assigned the largest share with a full 100% participation in some months (figure 4-5). This distribution is due to the low cost associated with producing power from natural gas. As for biomass, the manure and sludge are the dominating feedstock thanks to their high energy generation flowrates and their relatively cheap cost.

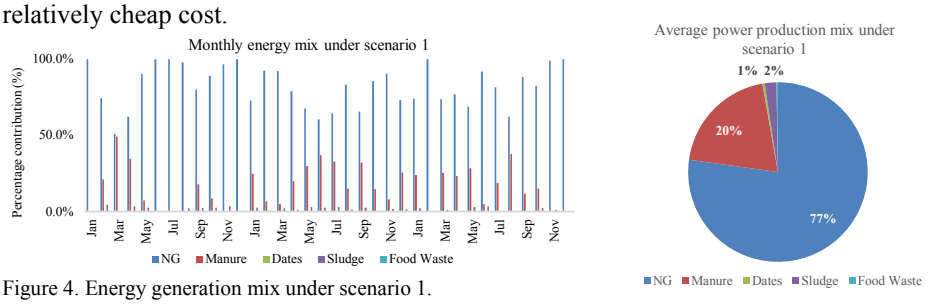

Figure 4. Energy generation mix under scenario 1.

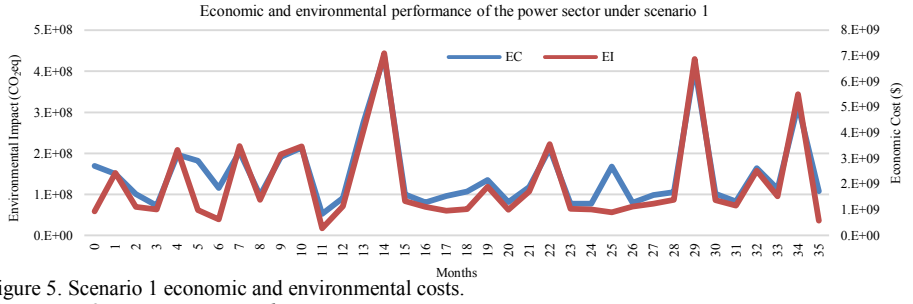

Figure 5. Scenario 1 economic and environmental costs.

Scenario 2: Environmental restrictions

Under environmental restrictions, the power generation system is still adopting a mixed strategy involving both natural gas and biomass with a major participation of natural gas (figure 6). However, the average share of fossil fuel is reduced by 12% in this scenario compared to the previous case (figure 7). This reduction is mainly associated with the high emissions it entails. Biomass share in this scenario is more diversified, allowing the date pits and food waste to contribute. However, manure and sludge are still dominating thanks to their cleaner thermal conversion to power. In comparison with the previous scenario, the environmental case proposes an interesting eco-friendly alternative that reduces the average GWP emissions by 34%. However, a 64% increase in costs is needed to deploy the cleaner biomass energy.

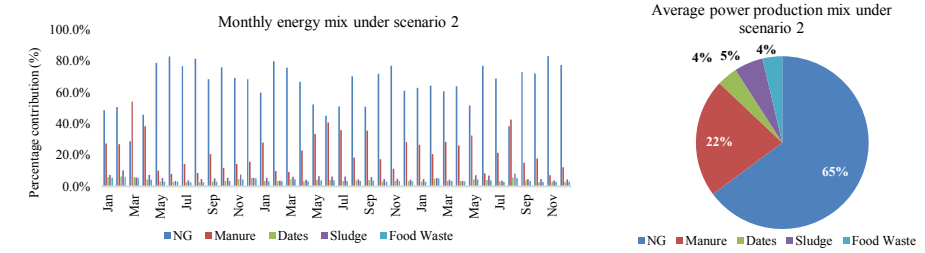

Figure 6. Energy generation mix under scenario 2.

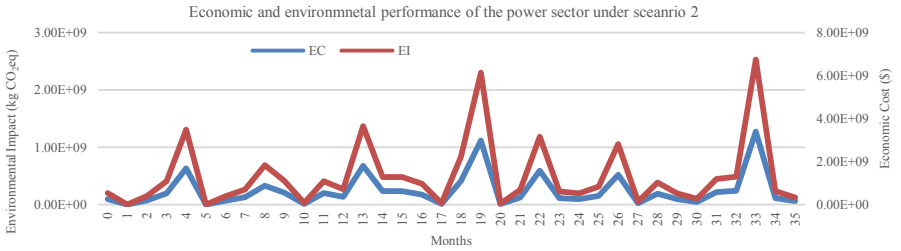

Figure 7. Scenario 2 economic and environmental costs.

4. Conclusion

In this work, an ABM was developed to predict the future behavior of the power generation sector under economic and environmental circumstances. The model also integrates the biomass energy as a sustainable alternative that reduces emissions while satisfying the local demand from power. Under the price-sensitive scenario, natural gas is dominant being the cheapest option, with a fewer contributions for biomass. Under the environmental-friendly case, the contribution of biomass energy, characterized by a large participation of manure and sludge as feedstock, is more significant. The results provide an insight to decision-makers in the power generation system about potential investment in the energy field.

References

A. AlNouss, G. McKay, and T. Al-Ansari, 2020, Production of syngas via gasification using optimum blends of biomass, Journal of Cleaner Production, 242, 118499.

A. AlNouss, G. McKay, T. Al-Ansari, 2019, A techno-economic-environmental study evaluating the potential of oxygen-steam biomass gasification for the generation of value-added products, Energy Conversion and Management, 196, 664–676.

M. Barbati, G. Bruno, A. Genovese, 2012, Applications of agent-based models for optimisation problems: A literature review, Expert Systems with Applications.

R. Govindan, T. Al-Ansari, A. Korre, N. Shah, 2018, Assessment of Technology Portfolios with Enhanced Economic and Environmental Performance for the Energy, Water and Food Nexus, Computer Aided Chemical Engineering, 43, 537-542.

J. Lopez-Jimenez, N. Quijano, A.V. Wouwer, 2018, On the Use of Agent-Based Modeling for Smart Farming, 22nd International Conference on System Theory, Control and Computing.

A. Marvuglia, S. Rege, T. Navarrete Gutiérrez, L. Vanni, D. Stilmant, E. Benetto, 2017, A return on experience from the application of agent-based simulations coupled with life cycle assessment to model agricultural processes, Journal of Cleaner Production, 142, 1539–1551.

Project Mesa Team, 2016, Mesa Overview.

S. Namany , T. Al-Ansari, R. Govindan, 2019a, Sustainable energy, water and food nexus systems: A focused review of decision-making tools for efficient resource management and governance, Journal of Cleaner Production, 225, 610-626.

S. Namany, R. Govindan, T. Al-Ansari, 2019b, Optimisation of the energy, water, and food nexus for food security scenarios, Computers & Chemical Engineering, 129, 106513

Sauro Pierucci, Flavio Manenti, Giulia Bozzano, Davide Manca (Eds.)
Proceedings of the 30th European Symposium on Computer Aided Process Engineering (ESCAPE30), May 24-27, 2020, Milano, Italy.
http://dx.doi.org/10.1016/B978-0-12-823377-1.50310-4

A New Lagrangian Relaxation Approach for Multistage Stochastic Programs under Endogenous Uncertainties

Zuo Zeng, Selen Cremaschi*

Department of Chemical Engineering, Auburn University, Auburn, AL 36849, USA
selen-cremaschi@auburn.edu

Abstract

Optimization problems with endogenous (decision-dependent) uncertainties are commonly observed in process industry. Most optimization problems with endogenous uncertainties, by nature, can be modelled as multi-period multi-stage stochastic programs (MSSPs), where possible future states of the system are modelled as scenarios by enumerating all possible outcomes of uncertain parameters. However, MSSPs rapidly grow and quickly become computationally intractable for real-world problems. This paper presents a new Lagrangian relaxation for obtaining valid dual bounds for MSSPs under endogenous uncertainties. By exploiting the structure of the MSSP, a tight dual problem is formulated, which reduces the total number of Lagrangian multipliers. The paper also introduces a modified multiplier-updating scheme. We applied the new Lagrangian relaxation to bound instances of artificial lift infrastructure planning (ALIP) problem under uncertain production rates and the clinical trial planning (CTP) problem under uncertain clinical trial outcomes. The computational results reveal that the proposed Lagrangian relaxation generates tight dual bounds compared to the original Lagrangian relaxation formulation and that the proposed multiplier-updating scheme reduces the zigzagging behavior of the Lagrangian dual solutions as iterations progress.

Keywords: multistage stochastic programming, Lagrangian relaxation, endogenous uncertainty, dual bound

1. Introduction

This paper considers multistage stochastic programs (MSSPs) under endogenous uncertainty, where the decisions determine the realization times of uncertain parameters e.g., R&D pipeline management (Colvin and Maravelias, 2008), synthesis of process networks with uncertain process yields (Apap and Grossmann, 2017), and artificial lift infrastructure planning (Zeng and Cremaschi, 2017). Uncertainty is incorporated using scenarios to MSSPs where scenarios represent the unique outcomes of uncertain parameters. Multistage stochastic programs have multiple stages where state decisions are made and recourse actions are taken. The decision variables are defined for each scenario and are constrained by non-anticipativity constraints (NAC) to avoid the state decisions from anticipating future realizations of uncertain parameters. The size of MSSPs, especially with endogenous uncertainty, grows exponentially with the increasing number of uncertain parameters and outcomes of uncertain parameters partially due to the increase in NACs. In general, the MSSPs are solved using heuristic or decomposition approaches, and it has been shown that moderate-size problems can be solved to optimality. Recent approaches include Lagrangian decomposition (Gupta and Grossmann, 2014), sequential scenario decomposition (Apap and Grossmann, 2017), a generalized

knapsack decomposition (Zeng et al., 2018), and absolute expected value solution (Zeng and Cremaschi, 2019).

This paper presents a new Lagrangian relaxation formulation for bounding MSSPs under endogenous uncertainties. Similar to the existing Lagrangian relaxation schemes (Gupta and Grossmann, 2014), the new Lagrangian relaxation regards the NACs as the complicating constraints, however it utilizes the special structure of the NACs to formulate a tighter dual problem, which also eliminates half of the Lagrangian multipliers. To obtain tight dual bounds using Lagrangian relaxation, the multipliers should be updated appropriately. The most widely used technique to update the multipliers is sub-gradient optimization method (Ardalan et al., 2016). We introduce an algorithm to be used in the sub-gradient optimization method to update multipliers. The algorithm dynamically updates the multipliers based on the ratio of the value of the dualized constraints in the objective function to the original objective function value. We applied the new Lagrangian relaxation to bound instances of ALIP problem (Zeng and Cremaschi, 2017) under uncertain production rates and the CTP problem (Colvin and Maravelias, 2008) under uncertain clinical trial outcomes. We describe an example MSSP formulation under endogenous uncertainty in §2. The original and new Lagrangian relaxation formulations and the modified multiplier updating schemes are presented in §3. The problem instances and the dual bounds obtained by Lagrangian relaxations are given and discussed in §4. Finally, we present the concluding remarks.

2. The MSSP formulation under endogenous uncertainty

A simple deterministic equivalent formulation of a MSSP with complete recourse under endogenous uncertainties is derived from Zeng et al. (2018). The uncertain source $i \in \boldsymbol{I}$ associated with its uncertain parameter (θ_i) has finite outcomes represented by a finite set $\{\theta_i^1, \theta_i^2, \dots, \theta_i^{R_i}\}$. The scenario set ($\boldsymbol{S}$) is constructed using the Cartesian product: $\boldsymbol{S} := \{\times_{i \in \boldsymbol{I}} \theta_i\}$. The planning horizon is discretized, $t \in \boldsymbol{T} = \{1, 2, 3, .., T\}$. The uncertain parameters are endogenous, and we define an endogenous scenario pair set $(s, s') \in S_E$ for scenarios s and s' that are indistinguishable in terms of the realization of the endogenous uncertain parameter i: $S_E := \{(i, s, s') : i \in I, \theta_i^s = \theta_i^{s'}\}$. The MSSP is defined by Eqns. (1)-(6):

$$OV = max \sum_s p_s \sum_i \sum_t G_{i,t,s}\left(\theta_i^s, b_{i,t}^s, \gamma_t^s\right) \tag{1}$$

$$h\left(b_{i,t}^s, \gamma_t^s, \theta_i^s\right) = 0 \quad \forall i \in \boldsymbol{I}, t \in \boldsymbol{T}, s \in \boldsymbol{S} \tag{2}$$

$$g\left(b_{i,t}^s, \gamma_t^s, \theta_i^s\right) \le 0 \quad \forall i \in \boldsymbol{I}, t \in \boldsymbol{T}, s \in \boldsymbol{S} \tag{3}$$

$$b_{i,1}^s = b_{i,1}^{s'} \qquad \forall i \in \boldsymbol{I}, \forall (s, s') \in \boldsymbol{S} \tag{4}$$

$$\begin{bmatrix} Z_t^{s,s'} \\ b_{i,t}^s = b_{i,t}^{s'} \end{bmatrix} \vee \left[\neg Z_t^{s,s'}\right] \qquad \forall (i, s, s') \in \boldsymbol{S_E}, \forall t \in \boldsymbol{T}, t > 1 \tag{5}$$

$$b_{i,1}^s, Z_t^{s,s'} \in \{0,1\}, \gamma_t^s \in \mathbb{R} \qquad \forall (i, s, s') \in \boldsymbol{S_E}, \forall t \in \boldsymbol{T}, \forall i \in \boldsymbol{I} \tag{6}$$

Binary variables $b_{i,t}^s$ represent state decisions made at the beginning of each time period, and variables γ_t^s represent recourse-action decisions that follow the state decisions. The state decisions $b_{i,t}^s$ are enforced to be identical until the differentiating event occurs either by initial or conditional NACs. The recourse variables γ_t^s are determined by scenario specific constraints. The optimum objective function value is defined by variable OV.

The objective function (Eqn. (1)) maximizes the expected value of the total profit/gain associated with state variables $b_{i,t}^s$ and recourse-action decision variables γ_t^s, where p_s is

the probability of scenario s and the function $G_{i,t,s}\left(V_{i,t}, \theta_i^s, b_{i,t}^s, y_{i,t}^s, \gamma_t^s\right)$ calculates the total profit/gain for specific scenario s. Scenario specific inequality and equality constraints are presented in Eqns. (2) and (3) that may or may not include the uncertain parameters (θ_i^s). Functions $G_{i,t,s}(\cdot)$, $h(\cdot)$, and $g(\cdot)$ in Eqns. (1), (2), and (3) can either be linear or nonlinear. Equation (4) is initial NACs, and Eqn. (5) is conditional NACs that are enforced depending on the value of the Boolean variable, $Z_t^{s,s'}$. This variable is equal to one if scenarios s and s' are indistinguishable at time period t, and zero otherwise.

3. A new Lagrangian relaxation formulation

3.1. Original Lagrangian relaxation problem (LR)

Lagrangian relaxation removes complicating constraints from the original problem and adds them to the objective function with a penalty term, which are called multipliers. The Lagrangian multipliers represent penalties for solutions not satisfying the particular constraints (Lin et al., 2011). In Lagrangian relaxation of a MSSP, the initial and conditional NACs are regarded as the complicating constraints. The conditional NACs in Eqn. (5) are reformulated as two inequalities, Eqns. (7) and (8):

$$b_{i,t}^s - b_{i,t}^{s'} \le 1 - Z_t^{s,s'} \quad \forall i \in \boldsymbol{I}, t \in \boldsymbol{T}, s, s' \in \boldsymbol{S} \tag{7}$$

$$b_{i,t}^s - b_{i,t}^{s'} \ge Z_t^{s,s'} - 1 \quad \forall i \in \boldsymbol{I}, t \in \boldsymbol{T}, s, s' \in \boldsymbol{S} \tag{8}$$

To construct Lagrangian relaxation of a MSSP, both initial (Eqn. 4) and reformulated conditional NACs (Eqns. (7) and (8)) are dualized in the objective function. The original Lagrangian relaxation of MSSP (LR) is given in Eqns. (9) – (12):

$$\begin{aligned} OV = max \sum_s p_s \sum_i \sum_t G_{i,t,s}\left(\theta_i^s, b_{i,t}^s, \gamma_t^s\right) \\ + \sum_{i,t,s,s'} \Big(\lambda 0_{i,s,s'}\left(b_{i,1}^s - b_{i,1}^{s'}\right) + \lambda 1_{i,t,s,s'}\left(1 - Z_t^{s,s'} - b_{i,t}^s + b_{i,t}^{s'}\right) \\ + \lambda 2_{i,t,s,s'}\left(1 - Z_t^{s,s'} + b_{i,t}^s - b_{i,t}^{s'}\right)\Big) \end{aligned} \tag{9}$$

$$h\left(b_{i,t}^s, \gamma_t^s, \theta_i^s\right) = 0 \quad \forall i \in \boldsymbol{I}, t \in \boldsymbol{T}, s \in \boldsymbol{S} \tag{10}$$

$$g\left(b_{i,t}^s, \gamma_t^s, \theta_i^s\right) \le 0 \quad \forall i \in \boldsymbol{I}, t \in \boldsymbol{T}, s \in \boldsymbol{S} \tag{11}$$

$$b_{i,1}^s, Z_t^{s,s'} \in \{0,1\}, \gamma_t^s \in \mathbb{R}, \lambda 0_{i,s,s'} \in \mathbb{R}, \lambda 1_{i,t,s,s'}, \lambda 2_{i,t,s,s'} \ge 0 \mathbb{R} \quad \forall (i,s,s') \in \boldsymbol{S_E}, \forall t \in \boldsymbol{T}, \forall i \in \boldsymbol{I} \tag{12}$$

The multipliers $\lambda 0_{i,s,s'}$ for initial NACs can either be positive or negative. The multipliers of conditional NACs, $\lambda 1_{i,t,s,s'}$ and $\lambda 2_{i,t,s,s'}$, can only take non-negative values, which enforces the dualized constraints to be great than or equal to zero. The solution of the relaxed problem LR yields a valid dual bound for the original MSSP.

3.2. A modified Lagrangian relaxation formulation (mLR)

In the original relaxation, Lagrangian multipliers penalize the violation of the dualized constraints (Eq. (9)). All possible values of the conditional NACs (Eqns. (7) and (8) in Eq. (9)) are given in Table 1.

Table 1. All possible values of dualized constraints (Eqns. (7) and (8) in Eq. (9))

$Z_t^{s,s'}$	$b_{i,t}^s$	$b_{i,t}^{s'}$	$1 - Z_t^{s,s'} - b_{i,t}^s + b_{i,t}^{s'}$	$1 - Z_t^{s,s'} + b_{i,t}^s - b_{i,t}^{s'}$	$Z_t^{s,s'}$	$b_{i,t}^s$	$b_{i,t}^{s'}$	$1 - Z_t^{s,s'} - b_{i,t}^s + b_{i,t}^{s'}$	$1 - Z_t^{s,s'} + b_{i,t}^s - b_{i,t}^{s'}$
0	0	0	1	1	1	0	0	0	0
0	0	1	2	0	1	0	1	1	-1
0	1	0	0	2	1	1	0	-1	1
0	1	1	1	1	1	1	1	0	0

As can be seen from Table 1, the conditional NACs are always satisfied when indicator variables ($Z_t^{s,s'}$) are equal to zero and can only be violated for indicator variable values equal to one. To tighten the dual bound (Eqn. (9)), we propose a modified relaxation that is shown in Eqns. (13) and (14), where the constraints ($b_{i,t}^{s} - b_{i,t}^{s'}$) are dualized only when indicator variable ($Z_t^{s,s'}$) values are equal to one.

$$OV = max \sum_s p_s \sum_i \sum_t G_{i,t,s}(\theta_i^s, b_{i,t}^s, \gamma_t^s) + \sum_{i,t,s,s'} \left(\lambda 0_{i,s,s'}(b_{i,1}^s - b_{i,1}^{s'}) + u_{i,t,s,s'}\right) \tag{13}$$

$$\begin{bmatrix} Z_t^{s,s'} \\ u_{i,t,s,s'} = \lambda_{i,t,s,s'}(b_{i,t}^s - b_{i,t}^{s'}) \end{bmatrix} \vee \begin{bmatrix} \neg Z_t^{s,s'} \\ u_{i,t,s,s'} = 0 \end{bmatrix} \quad \forall (i,s,s') \in \boldsymbol{S_E}, \forall t \in \boldsymbol{T}, t > 1 \tag{14}$$

The disjunction in Eq. (14) ensures that a conditional NAC is only dualized and added to the objective function (Eq. (13)) with a Lagrangian multiplier $\lambda_{i,t,s,s'} \in \mathbb{R}$ if its associated indicator variable ($Z_t^{s,s'}$) value is equal to one. If the value of the indicator variable is equal to zero, the dualized constraint variable $u_{i,t,s,s'}$ is set to zero. In this modified relaxation, the dualized constraint is equivalent to an equality constraint for indistinguishable scenarios (i.e., for $Z_t^{s,s'} = 1$) with assigned Lagrangian multipliers. The modified Lagrangian relaxation formulation has half of the Lagrangian multipliers compared to the original one ($\lambda_{i,t,s,s'}$ vs. $\lambda 1_{i,t,s,s'}, \lambda 2_{i,t,s,s'}$). Eqns. (13) and (14) can be reformulated as Eq. (15).

$$OV = max \sum_s p_s \sum_i \sum_t G_{i,t,s}(\theta_i^s, b_{i,t}^s, \gamma_t^s) + \sum_{i,t,s,s'} \left(\lambda 0_{i,s,s'}(b_{i,1}^s - b_{i,1}^{s'}) + \lambda_{i,t,s,s'} Z_t^{s,s'}(b_{i,t}^s - b_{i,t}^{s'})\right) \tag{15}$$

The modified Lagrangian relaxation formulation (mLR) is given by Eqns. (15), (10), (11), (12). Both LR and mLR have the same KKT conditions, and they are both dual bounds for the original MSSP.

3.3. A Lagrangian multiplier updating scheme for sub-gradient optimization method

To obtain tight dual bounds using Lagrangian relaxation, the multipliers should be updated appropriately. The most widely used technique to update the multipliers is sub-gradient optimization method (Gupta and Grossmann, 2014). Given an initial λ_n^0 ($n \in N$) (multipliers for a total of $|N|$ dualized constraints), the multipliers at the k^{th} iteration, λ_n^k, are calculated using Equation (16) (Fisher, 1981),

$$\lambda_n^{k+1} = max\{0,\ \lambda_n^k - \gamma^k (Ax_n^k - b)\} \tag{16}$$

where x_n^k is the solution of Lagrangian relaxation at iteration k. $Ax_n^k - b$ represents the dualized constraints in the objective function where A and b are parameters. The variable γ^k is the positive step size at iteration k, which is calculated by Equation (17),

$$\gamma^k = scale \frac{Z(\lambda_n^k) - Z^*}{\sum_n (Ax_n^k - b)^2} \tag{17}$$

where $Z(\lambda_n^k)$ is the dual bound from Lagrangian relaxation at the k^{th} iteration and Z^* is the best known primal bound. In Equation (17), the parameter $scale$ is a scalar satisfying $0 \leq scale \leq 2$. Often the value of $scale$ is set to two at the first iteration. If the dual bound fails to converge after a number of iterations, the value of $scale$ is decreased.

Here, we introduce an algorithm for dynamically updating the values of γ^k and $scale$ in the sub-gradient optimization method. This algorithm is summarized in Figure 1. The iteration counter (k) and multipliers are initialized as zero, and the scale is set to two at initialization. The first dual bound is obtained by solving the Lagrangian relaxation. The algorithm then determines the number of dualized constraints that were violated. The primal bound in Equation (17) is obtained by the generalized knapsack decomposition algorithm GKDA, $GKDA^*$ in Figure 1 (Zeng et al., 2018). The difference between the dual and the primal bounds are divided by the total number of violated dualized constraints. The step size variable γ^k is updated using the difference of the dual and the primal bounds, multiplying this difference with $scale$ and dividing it by the number of violated dualized constraints. From the second iteration, the algorithm dynamically updates the value of $scale$ based on the ratio of the sum of the dualized constraint values to the original objective function value to reduce the zigzagging behavior of the Lagrangian dual solutions as iterations progress. The stopping criteria are either reaching a predetermined maximum number of iterations or satisfying all dualized constraints.

$k, \lambda_n^k\ (n \epsilon N) \coloneqq 0, scale^k \coloneqq 2$
FOR $k = 1\ to\ K_{max}$
    $Z(\lambda_n^k) \coloneqq$ dual bound from Lagrangian relaxation with multipliers $\lambda_n^k\ (n \epsilon N)$
    $x^k \coloneqq$ solution of Lagrangian relaxation
    $N^v \coloneqq$ number of violated constraints of dualized constraints
    $GKDA^* \coloneqq$ primal bound from generalized knapsack decomposition algorithm
    IF $k \geq 2$ THEN
        IF $\frac{dualized\ constaints\ value}{Original\ objective\ function\ value} \geq 10\%$ THEN
            $scale^k = \frac{scale^{k-1}}{1.618}$
    $\gamma^k \coloneqq scale^k \frac{Z(\lambda_n^k) - GKDA^*}{N^v}$
    FOR $n = 1\ to\ N$
        Update λ_n^{k+1} with dualized constraints and γ^k
    IF no violated constraints THEN BREAK

Figure 1. Modified sub-gradient optimization method for updating Lagrangian multipliers

4. Case Study

We applied the original Lagrangian relaxation (RL) and modified Lagrangian relaxation (mLR) formulations to generate dual bounds for ALIP problem with a planning horizon of 12 months and CTP problem with three products and clinical trials, and a planning horizon of 12 periods. The complete parameters of the instances can be found in Zeng and Cremaschi (2017). The models and algorithms were implemented in Pyomo and solved using CPLEX 12.6.3 on a standard node of Auburn University Hopper Cluster. The maximum number of iterations was 100 for the sub-gradient optimization method.

The results are compiled in Figure 2, which plots how the relative gap (calculated using the optimum solution and the dual bound) changes with the number of iterations for standard (LR) and modified Lagrangian (mLR) dual problem formulations where the multipliers are updated using the standard and our proposed modified approaches. Figure 2 reveals that the modified algorithm, which dynamically updates the scale in the sub-gradient optimization method for estimating the multipliers, improves the quality of the dual bounds for both LR and mLR. It can also be seen that mLR yields tighter dual bounds compared to LR. The mLR obtains 0% percentage relative gap for ALIP instance. For the 3-product CTP problem, both LR and mLR cannot converge within 100 iterations, while LR (standard) and mLR (modified) yield 9.7% and 6.7% relative gaps, respectively.

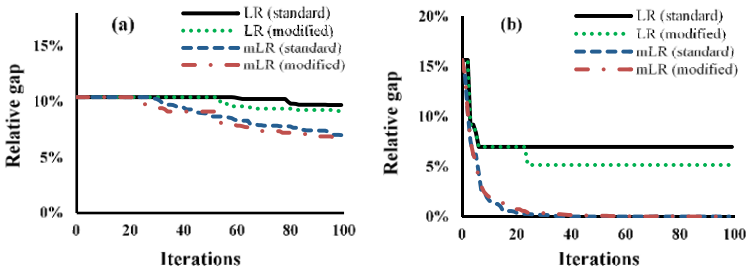

Figure 2. The change in relative gap with the number of iterations of multiplier updates using both LR and mLR dual problem formulations and standard (LR standard, mLR standard) and modified algorithms for sub-gradient optimization method (LR modified, mLR modified), (a) 3-product CTP problem; (b) 12-month planning horizon ALIP problem.

5. Conclusion

This paper contributes a new Lagrangian relaxation reformulation (mLR) and a modified scheme to dynamically update Lagrangian multipliers in sub-gradient optimization method for multistage stochastic programs under endogenous uncertainties. The modified Lagrangian relaxation utilizes a disjunctive structure to indicate which conditional NACs should be dualized to the objective function of the dual model. The mLR reduces the number of dualized constraints and of Lagrangian multipliers compared to the original Lagrangian relaxation formulation. We compare the bounds obtained by the original and the modified Lagrangian relaxation formulations for two planning problems. The results indicate that mLR generates tighter dual bounds in fewer iterations.

Acknowledgements

This work was financially supported RAPID Manufacturing Institute, the U.S.A and was completed in part with resources provided by the Auburn University Hopper Cluster.

References

Apap, R. M., & Grossmann, I. E. (2017). Models and computational strategies for multistage stochastic programming under endogenous and exogenous uncertainties. Comput. Chem. Eng, 103, 233-274.

Ardalan, Z., Karimi, S., Naderi, B., & Khamseh, A. A. (2016). Supply chain networks design with multi-mode demand satisfaction policy. Computers & Industrial Engineering, 96, 108-117.

Lin, Z., Liu, R., & Su, Z. (2011). Linearized alternating direction method with adaptive penalty for low-rank representation. In Advances in neural information processing systems (pp. 612-620).

Colvin, M., & Maravelias, C. T. (2008). A stochastic programming approach for clinical trial planning in new drug development. Comput. Chem. Eng, 32(11), 2626-2642.

Gupta, V., & Grossmann, I. E. (2014). A new decomposition algorithm for multistage stochastic programs with endogenous uncertainties. Comput. Chem. Eng, 62, 62-79.

Zeng, Z., & Cremaschi, S. (2017). Artificial lift infrastructure planning for shale gas producing horizontal wells. Proceedings of the FOCAPO/CPC, Tuscan, AZ, USA, 8-12.

Zeng, Z., Christian, B., & Cremaschi, S. (2018). A generalized knapsack-problem based decomposition heuristic for solving multistage stochastic programs with endogenous and/or exogenous uncertainties. Ind. Eng. Chem. Res., 2018, 57 (28), pp 9185–9199.

Zeng, Z., & Cremaschi, S. (2019). A general primal bounding framework for large-scale multistage stochastic programs under endogenous uncertainties. Chemical Engineering Research & Design, 141, 464-480.

Sauro Pierucci, Flavio Manenti, Giulia Bozzano, Davide Manca (Eds.)
Proceedings of the 30th European Symposium on Computer Aided Process Engineering (ESCAPE30), May 24-27, 2020, Milano, Italy.
http://dx.doi.org/10.1016/B978-0-12-823377-1.50311-6

A Hybrid Method for Integration of Heat Pump Assisted Distillation System with Intermediate Reboiler/condenser

Jiaxin Yang[a], Minbo Yang[a], Xiao Feng[a], Yufei Wang[b]

[a]*School of Chemical Engineering& Technology，Xi'an Jiaotong University，Xi'an 710049，China;*
[b]*State Key Laboratory of Heavy Oil Processing, China University of Petroleum, Beijing, 102249, China*
yangmb@xjtu.edu.cn.

Abstract

Setting an intermediate reboiler/condenser for heat transfer with the heat pump can reduce both requirements of hot and cold utilities and the temperature lift of the heat pump. This paper proposes a hybrid method that combines rigorous process simulation and mathematical programming for targeting the optimal heat pump placement in the presence of intermediate reboiler/condenser to minimize the overall energy consumption. First, the grand composite curve of distillation column is determined via rigorous process simulation. A simulation model for the vapor compression heat pump is also established. Next, the column grand composite curve is taken as constrains for formulating a simulation-based optimization model by data interaction between Aspen HYSYS and Matlab. The model is solved using the genetic algorithm toolbox to determine the optimal placement of the heat pump. A de-heavy fractionator in the isobutene unit is studied to illustrate the applicability of the proposed method.

Keywords: heat pump, distillation column, intermediate reboiler/condenser, minimum operating cost

1. Introduction

As well known, energy has become a hot issue around the world, and many countries are committed to developments of new energy and energy-saving technologies (Soave and Feliu, 2002). The chemical industry accounts for a large part of industrial energy consumption. As the most important and widely used separation operation, distillation is quite energy intensive and accounts for about 3% of the world energy consumption. Besides, it also suffers from very low thermodynamic efficiency of 5%-20% (Shahandeh et al., 2014). In order to improve energy efficiency and reduce operating costs, a large number of complex tower technologies, such as heat integration distillation columns, heat pump assisted distillation, and intermediate reboiler/condenser have been widely studied and applied.

In a conventional distillation column, heat is supplied at the bottom reboiler by a hot utility, while waste heat is discharged to a cold utility at the overhead condenser, thus causing a substantial energy degradation (Amiya K. Jana, 2014). An effective way to solve this problem is to couple the reboiler and condenser. The integration between a distillation column and a heat pump is well known as heat pump assisted distillation. Compared to conventional distillation, heat pump assisted distillation can separate the mixture with less energy consumption. The reasonable setting of a heat pump in a

distillation system can not only improve the utilization of low-grade heat, but also simultaneously reduce heating and cooling demands, which could achieve the purpose of energy saving. Amiya K. Jana (2014) portrayed heat pump assisted distillation as an energy-efficient separation technology, particularly vapor recompression column (VRC) and its hybrid configurations. Patrascu et al. (2018) proposed a novel hybrid separation process based on a heat pump assisted azeotropic dividing-wall column (A-DWC), which makes the energy requirement for butanol separation using heat integration and vapor recompression assisted A-DWC reduce a lot.

Traditional heat pump assisted distillation integrates the reboiler and condenser of a distillation column. Thus, it is only applicable to cases where the temperature difference between the reboiler and condenser is small. In a distillation column, the temperature gradually rises from the top to bottom. An alternative is the use of an intermediate reboiler whose temperature level is lower than the bottom reboiler. Thus, a lower-temperature, less expensive heat source can be used. Similarly, an intermediate condenser is able to save expensive cold utility. Based on the second law of thermodynamics, the addition of intermediate heat exchangers does not reduce the total energy demand, but it can reduce the irreversible energy loss and improve the thermodynamic efficiency of a distillation column (Bandyopadhyay et al.,1999). On this basis, Lynd and Grethlein (1986) presented the technique of IHOSR (intermediate heat pumps and optimal side stream return) distillation. The IHOSR distillation allows heat to be moved between points in a distillation column with greater efficiency than several other methods of heat addition and removal by stream removal, phase change, or optimal side stream return in a distillation column for distillation. An et al. (2008) presented a simulated annealing-based approach for the optimal synthesis of distillation column considering intermediate heat exchangers arrangements. The synthesis problem is formulated as a mixed integer nonlinear programming (MINLP) problem, which can then be solved with an improved simulated annealing algorithm. However, research on how to target the optimal setting location for a heat pump that connects the intermediate reboiler and condenser of a distillation column has not been reported.

The main objective of this paper is to address the optimal design of heat pump assisted distillation with intermediate reboiler/condenser based on simulation-based optimization. First, we simulate a distillation column in Aspen PLUS to obtain data of each stage and calculate the Column Grand Composite Curve (CGCC). Next, Aspen HYSYS is employed for rigorous process and thermodynamic modelling of the heat pump system. With help of the CGCC, the simulation-based optimization model is formulated and solved in the Matlab platform to minimize the operating cost, identifying the optimal setting position of the heat pump.

2. Model formulation

In this paper, a simulated-based optimization is established for heat pump assisted distillation with intermediate reboiler and condenser with the help of CGCC, which is a *T–H* curve at the practical near-minimum thermodynamic condition. The energy-saving potential for different column modifications like reflux reduction, feed conditioning, and scope for side reboiler/condenser can be addressed on such a *T–H* diagram (Bandyopadhyay et al., 1999). Therefore, the model includes the generation of CGCC, simulation of heat pump system, and the objective function.

2.1. The generation of CGCC

For a distillation column, Bandyopadhyay et al., (1999) put forward a method to obtain the CGCC through the Invariant Rectifying and Stripping (IRS) curve without extra enthalpy calculation as below.

For the rectifying section, the overall mass balance and component balance yield the minimum flows of liquid (L_{min}) and vapor (V_{min}), as Eqs. (1) and (2), respectively.

$$L_{min} = D(x_D - y^*) / (y^* - x^*) \tag{1}$$

$$V_{min} = D(x_D - x^*) / (y^* - x^*) \tag{2}$$

where D is the flow rate of top product, x_D is the mole fraction of the key component in the top product, y^* and x^* represent the gas and liquid molar fractions of the key component on the corresponding stage while gas-liquid equilibrium is reached.

The enthalpy balance for the envelope is used to evaluate the enthalpy surplus *(H_R)* as Eq. (3).

$$V_{min} H_V = L_{min} H_L + DH_D + H_R \tag{3}$$

where H_V、H_L、H_D indicate the enthalpy of gas, liquid, and top product on the corresponding stage, respectively.

For the stripping section, similarly, the overall mass balance and component balance yield the minimum flows for L_{min} and V_{min} as Eqs. (4) and (5), respectively.

$$L_{min} = B(y^* - x_B) / (y^* - x^*) \tag{4}$$

$$V_{min} = B(x^* - x_B) / (y^* - x^*) \tag{5}$$

where B signifies the flow rate of bottom product, x_B signifies the mole fraction of the key component in the bottom product.

The enthalpy balance for the envelope is used to evaluate the enthalpy deficit *(H_S)* as Eq. (6), where H_B indicates the enthalpy of the bottom product.

$$L_{min} H_L + H_S = V_{min} H_V + BH_B \tag{6}$$

The relationship between duties of condenser and reboiler (Q_c and Q_r) and H_{CGCC} is expressed as Eq. (7).

$$\begin{aligned} &H_{CGCC} = Q_c + H_{def} \\ &\text{Rectifying section}: H_{def} = -H_R \\ &\text{Stripping section}: H_{def} = -H_S + Q_r - Q_c \end{aligned} \tag{7}$$

2.2. Simulation of heat pump system

The vapor compression heat pump system consists of four major devices: evaporator, condenser, compressor, and throttle valve. The heat pump system connects the intermediate reboiler and condenser as shown in Figure 1(a). The working fluid is vaporized in the intermediate condenser of the distillation column and enters the compressor to be pressurized. It then releases heat and condenses in the intermediate reboiler. Afterwards, the working fluid passes through the throttle valve to reduce the pressure.

The heat transferred by a heat pump is constrained by the CGCC of a distillation column as shown in Figure 1(b). In the stripping section, the heat delivered to any stage should not exceed the corresponding heat deficit, namely $Q_1 \leqslant H_1$. Similarly, in the rectifying section, the heat taken from any stage cannot be greater than the heat surplus, namely $Q_2 \leqslant H_2$. In addition, the energy balance of a heat pump can be expressed as $Q_1=Q_2+W$.

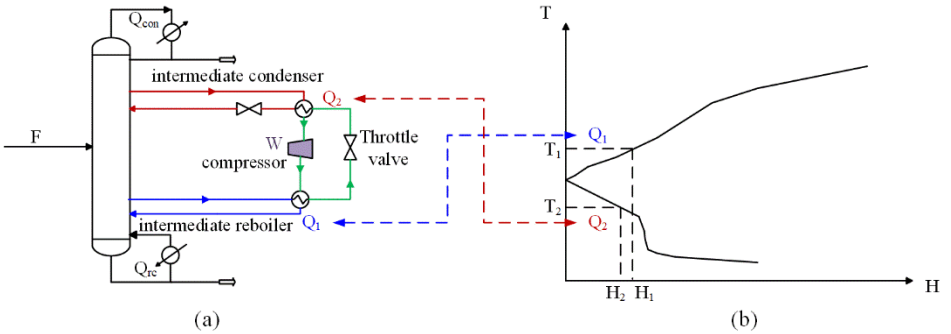

Figure 1 Integration of heat pump assisted distillation system with intermediate reboiler/ condenser: (a) illustrative process scheme; (b) analysis based on CGCC.

2.3. Objective function

The main purpose of setting heat pump is to minimize the operating cost of distillation. The total operating cost is composed of hot utility, cold utility, and power. The objective function is given as Eq. (8).

$$Obj = a \cdot Q_{\text{hot}} + b \cdot Q_{\text{cold}} + c \cdot W \tag{8}$$

where Q_{hot} and Q_{cold} represent the consumption of hot and cold utilities after setting the heat pump. a, b and c are prices of hot utility, cold utility, and power. a=￥0.29 $(\text{kW}\cdot\text{h})^{-1}$, b=￥0.04 $(\text{kW}\cdot\text{h})^{-1}$, and c=￥0.75 $(\text{kW}\cdot\text{h})^{-1}$.

A simulation-optimization model for a distillation column with intermediate condenser and reboiler is established by coupling the heat pump simulation model in Aspen HYSYS with the mathematical model of CGCC in Matlab. The use of CGCC can effectively avoid the convergence failure of column simulation that always stops the optimization. It also means that parameters except hot and cold duties are independent of the setting position of the heat pump. This model can be solved by genetic algorithm based on the data interaction between Aspen HYSYS and Matlab. It is a simulation-based mixed integer linear programming (MILP) problem, since the delivered and received temperature of the heat pump at every stage are discrete variables.

3. Case study

A methanol distillation column in an isobutylene production unit in a petrochemical plant is modelled using Aspen Plus V10. It has 20 stages (including condenser and reboiler) and the feed is introduced above the 10th stage. RadFrac is chosen for the distillation model with the SRK package. The simulation results are given in Table 1. The hot utility consumption is 580.56 kW, and the cold utility consumption is 308.33 kW. Taking methanol as the heavy key component, the temperature, molar flow rates and enthalpy of gas and liquid at each stage are extracted in order to calculate the H_{R}, H_{S}, and H_{CGCC}, according to Eqs. (1)-(7). The IRS curves and CGCC are illustrated in Figure 2.

Table 1. Feed and product specifications

	Feed	Top product	Bottom product
Molar flow (kmol·h^{-1})	181.53	19.68	161.85
Pressure (MpaG)	0.70	0.55	0.60
Temperature (℃)	63.10	52.40	119.61
More fractions			
MTBE	0.0068	5.08×10^{-7}	0.0076
i-butene	0.1144	0.9994	0.0068
Methanol	0.8768	0.0006	0.9833
Tert butyl alcohol	0.0020	3.62×10^{-11}	0.0022

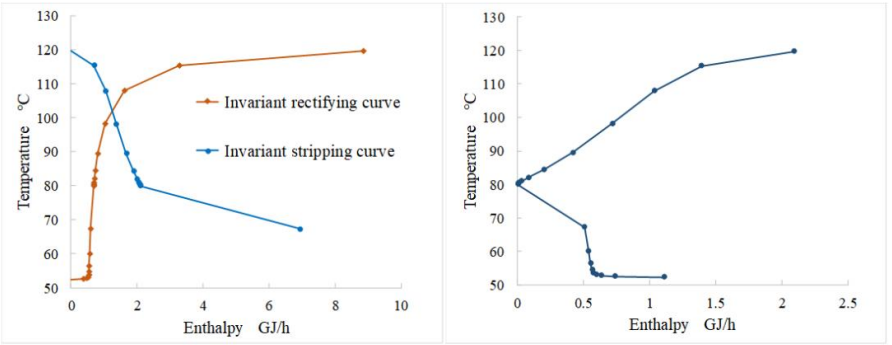

Figure 2 (a) Invariant rectifying-stripping (IRS) curves and (b) column grand composite curve

Table 2 The comparison of three conditions

Items	Distillation column	Traditional heat pump assisted distillation	The proposed model
Heat taken temperature (℃)	53.40	42.40	57.24
Heat delivery temperature (℃)	119.61	129.61	108.10
Temperature lift (℃)	-	86.21	50.86
Flow rate (kg·h^{-1})	-	531.0	229.0
Cold utilities (kW)	308.05	0	166.95
Hot utilities (kW)	580.53	116.23	404.53
Heat delivery (kW)	-	464.30	176.0
Heat taken (kW)	-	308.05	141.10
Power (kW)	-	156.25	34.85
COP	-	2.972	5.050
Operating cost (￥·yr^{-1})	1.426×10^{6}	1.205×10^{6}	1.189×10^{6}

A heat pump system is modelled in Aspen HYSYS V10. According to the temperature profile of the distillation column, R718 is chosen as the working fluid, because it can work at high temperature (Arpagaus et al., 2018). The Peng-Robinson package is selected for the heat pump system. The minimum temperature difference for heat exchange (ΔT_{min}) is taken as 10℃. By solving the model in Matlab R2018b, the optimal setting parameters of the heat pump is obtained as given in Table 2. The heat pump takes heat from the 9th stage and delivers heat to the 18th stage. For comprehensive comparison, traditional heat pump assisted distillation is modelled and results are presented as well. Compared with the distillation column without heat pump, the heat pump assisted distillation with

intermediate reboiler/condenser can save 35.7% of energy and reduce operating costs by 16.6%. Although traditional heat pump assisted distillation results in the most savings of hot and cold utilities, it leads to a notable higher temperature lift and a much lower COP than heat pump assisted distillation with intermediate reboiler/condenser. As a result, traditional heat pump assisted distillation shows a slightly higher operating cost by 1.3%. Such results indicate that heat pump assisted distillation with intermediate reboiler/condenser can increase the energy efficiency of the distillation column and improve the utilization of the heat pump.

4. Conclusions

In this paper, a simulated-based optimization method was presented to target the optimal placement of heat pump to assist distillation with intermediate reboiler/condenser, in order to minimize the operating cost. This model was formulated and solved by coupling the simulation model of heat pump in Aspen HYSYS with the mathematical model of CGCC in Matlab. The case study showed that the proposed method could reduce the annual operating cost by 16.6% compared with conventional distillation and by 1.3% compared with traditional heat pump assisted distillation. Besides, heat pump assisted distillation with intermediate reboiler/condenser resulted in a higher COP by 69.9% compared with heat pump assisted distillation. Therefore, the proposed method could extend the application of heat pumps. Furture work may take the investment of heat pump system into account.

Acknowledgments

This work was supported by the National Natural Science Foundation of China (No. 21736008) and the Fundamental Research Funds for the Central Universities (No. xzy012019031).

References

W. An, F. Yu, F. Dong, Y. Hu, 2008. Simulated annealing approach to the optimal synthesis of distillation column with intermediate heat exchangers. Chinese Journal of Chemical Engineering 16, 30-35.

C. Arpagaus, F. Bless, M. Uhlmann, J. Schiffmann, S.S. Bertsch, 2018. High temperature heat pumps: Market overview, state of the art, research status, refrigerants, and application potentials. Energy 152, 985-1010.

S. Bandyopadhyay, R.K. Malik, U.V. Shenoy, 1999. Invariant rectifying-stripping curves for targeting minimum energy and feed location in distillation. Computers & Chemical Engineering 23, 1109-1124.

A.K. Jana, 2014. Advances in heat pump assisted distillation column: A review. Energy Conversion and Management 77, 287-297.

L.R. Lynd, H.E. Grethlein, 1986. Distillation with intermediate heat-pumps and optimal sidestream return. AIChE Journal 32, 1347-1359.

I. Patrascu, C.S. Bildea, A.A. Kiss, 2018. Heat pump assisted azeotropic DWC for enhanced biobutanol separation, 28th European Symposium on Computer Aided Process Engineering. Elsevier Science Bv, Amsterdam, 791-796.

H. Shahandeh, J. Ivakpour, N. Kasiri, 2014. Internal and external HIDiCs (heat-integrated distillation columns) optimization by genetic algorithm. Energy 64, 875-886.

G. Soave, J.A. Feliu, 2002. Saving energy in distillation towers by feed splitting. Applied Thermal Engineering 22, 889-896.

Sauro Pierucci, Flavio Manenti, Giulia Bozzano, Davide Manca (Eds.)
Proceedings of the 30th European Symposium on Computer Aided Process Engineering (ESCAPE30), May 24-27, 2020, Milano, Italy.
http://dx.doi.org/10.1016/B978-0-12-823377-1.50312-8

Optimal Evacuation Route Prediction in Fpso Based on Deep Q-Network

Seokyoung Hong,[a] Kyojin Jang,[a] Jiheon Lee,[a] Hyungjoon Yoon,[a] Hyungtae Cho,[b] Il Moon[a*]

[a]*Department of Chemical and Biomolecular Engineering, Yonsei University, 50 Yonsei-ro, Seodaemun-gu, Seoul, 03722, Republic of Korea*
[b]*Green Materials & Processes Group, Korea Institute of Industrial Technology, 55 Jongga-ro, Jung-gu, Ulsan, 44413, Republic of Korea*
pselab@yonsei.ac.kr

Abstract

As a major production facility for oil and gas exploration, a dangerous working environment can cause serious accidents in FPSOs. The hull of the FPSO can be severely damaged or flooded, and in such cases, it is very difficult for workers to escape due to the large and complex structure of the FPSO. Even in an emergency situation, In an emergency situation, rational reasoning is blurred, and objective and prompt judgment cannot be made. It is necessary to provide quick and efficient evacuation guidance in case of emergency in order to prevent casualties. In this study, deep Q-network, a method of reinforcement learning, was applied to the optimal path prediction model to calculate the optimal evacuation route for workers in case of an accident. Deep Q-network can be applied to models with large and complex structure, and the environment of the model consists of 4 parts: deck, accommodation, backward, and frontward. The agent receives penalties for every move and is rewarded when it arrives at one of the four exits on the deck. As a result, the average number of movements is less than 30 when escaping from all locations in the environment consisting of 621 grids. This study contributes to provide an optimal escape route that is fast and safe in a changing environment. Through the analysis of the results of this study, it is expected that the safety inspection on the FPSO can be carried out and it will help the safe FPSO design.

Keywords: Deep Q-Network, Optimal Route Prediction, 3D Environment.

1. Introduction

Floating Production, Storage and Off-loading(FPSO) is a primary method of oil and gas processing and storage for deep-water fields. The number of FPSOs in operation or available for deployment has grown by 33% over the past 10 years. However, the FPSOs are still prone to accidents with a high probability of harsh working. Once serious accident occurs, FPSO may be seriously destroyed and even flooded. In these instances, it is very difficult for workers to evacuate out of the FPSO due to the large scale and complex structure of the FPSO. To avoid causalities, offering workers the effective escape route is essential.
Evacuation route analysis methods can be roughly divided into simulation and optimization. Optimization approaches in evacuation planning are adopted by numerous

previous researches. In mathematical modeling, linear programming and dynamic programming models are widely used. Network flow algorithm is utilized to model crowd movement with blocking effect(Luh et al., 2012). As a meta-heuristic approach, ant colony optimization algorithm is implemented to solve multi-objective evacuation routing problem(Fang et al., 2011) and has evolved into quantum ant colony algorithm(Liu et al., 2016). Genetic algorithm (GA) is also a popular heuristic solution method. Multi-criteria problem(Goerigk et al., 2014) and level of service design(Li et al., 2019) for efficient evacuation planning are solved by GA. Compared to mathematical modeling, using heuristic based algorithm reduces the computational cost but does not guarantee exact solution.

To solve this, Q-learning algorithm has been attempted to find a safe and short path(Su et al., 2011). Q-learning is very suitable for solving discrete motion sequence decision problem like path planning, but it is no longer able to approximate the value function as the number of states and actions increases. Most of maritime evacuation researches have been focused on passenger ship and little attention has been paid to the FPSO evacuation. In case of FPSO, different from ships or buildings, the structure of workspace is complex, passages are narrow, and the operating equipment are concentrated. There is a still lack of model to solve such a large-scale problem.

Thus, in this paper, we introduced deep Q-network(DQN)(Mnih et al., 2015) algorithm that combines deep learning with reinforcement learning to optimize the evacuation route in FPSO. We modeled the environment referring to the actual FPSO design (Figure 1). The agent is trained to find the shortest path without stepping back or passing the dangerous area. We compare the results of 2 scenarios and have a discussion about the evacuation system.

2. Problem statement and objective

Spill/release of chemicals occurs most frequently in the types of FPSO accidents. Since the accident may lead to the massive fire, operators who are working on the FPSO have to evacuate safely and quickly. When an accident happens, the operators are evacuated to the lifeboats which are located on both sides of the ship following the exit signs. Therefore, objective is to find an evacuation plan to get to the nearest destination of the four points from current position.

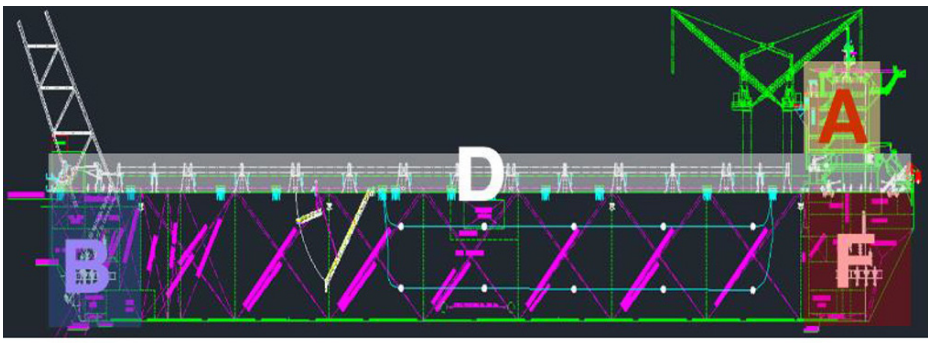

Figure 1. Structure of FPSO: ‘A’ for accommodation, ‘B’ for backward, ‘F’ for forward, ‘D’ for deck

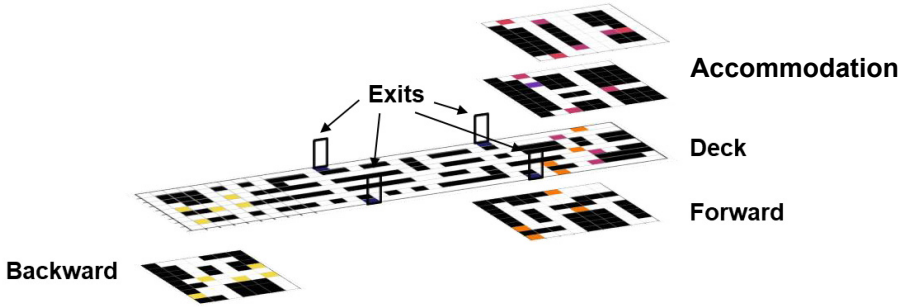

Figure 2. 3-D structure of FPSO environment.

However, as the accident progressed, the optimal route to the exits can be changed. Thus, we considered 2 possible evacuation scenarios under this situation. In the first scenario, an agent finds the nearest exit and chooses the shortest route in no accident, which is called 'normal situation'. The second scenario considered the case that one of the lifeboats reached the maximum capacity, which is called 'accident situation'. In this case, the exit is not available and a sign has to guide the route to another lifeboats before the agent goes in vain. The agent learns the optimal evacuation route and the evacuation time is calculated for each case.
The actual scheme is simplified and expressed as three-dimensional grids. It used to be multi-story structure, but each section is reduced into one or two floors. Therefore, the environment considered in this paper assumes 4 sections, total 621 states. The cells represent different area as the following:

1) Work space, room, or passage (white areas in Figure 2). Agent can move freely and safely.

2) Stair (pink, orange, yellow areas in Figure 2). Pink, orange, yellow respectively means that stairs link the deck to the accommodation, forward and backward section.

3) Blocked area (black areas in Figure 2). Agent cannot move to this kind of areas.

With this environment, the model should satisfy two requirements: 1) It should solve large size problem considering the scale and complexity of FPSO. 2) It should be fast in order to be used in real-time evacuation.

3. Reinforcement learning: Deep Q-Network

Reinforcement learning (RL) is one category of machine learning but it is different from supervised or unsupervised learning. It consists of an agent, an environment, states, actions, rewards and policies. The agent chooses a proper action at each state by trial-and-error and an optimal policy (or a series of actions) maximizing the reward back from the environment can be found. From the point of policy control method, the way to find the optimal policy, on-policy and off-policy learning are considered. A typical off-policy algorithm is Q-learning. In Q learning, a function $Q(s, a)$ is defined representing the expected discounted reward for action a at state s. Q-learning algorithm produces and updates a Q table to find the best action at a given state. However, this method is

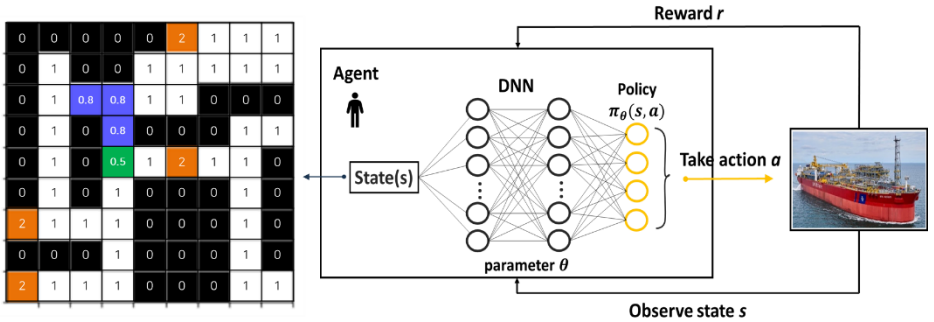

Figure 3. Training algorithm of DQN.

ineffective in large space environment since there are countless number of cases. To overcome the limit of Q-learning, deep Q network (DQN) algorithm was proposed. DQN algorithm uses neural network to approximate Q values instead of Q table. A neural network with weights θ is referred to as Q network. Q-network learns a state-action value function Q by minimizing loss function $L_i(\theta_i)$ Eq. (1):

$$L_i(\theta_i) = \frac{1}{2}[r + \gamma \max_{a'} Q(s', a'; \theta_{i-1}) - Q(s, a; \theta_i)]^2 \quad (1)$$

Also, the network is trained with a mini-batch from a replay memory which stores experience data collected during learning. This technique called experience replay makes the network more stable. (Target network) Therefore, the algorithm achieves stability by breaking temporal dependency and can obtain an optimal strategy.

In this paper the agent is assumed to be a worker on the FPSO. At each cell, according to the result of the neural network the agent decides an action between 4 directions - up, down, left and right. Also, agent can move up or down to the other floor by the stairs. The problem is how the agent finds the safe and fast route to the lifeboats. The agent gains the reward r_t for the selected action. The agent makes a decision sequentially to maximize the reward. Therefore, the reward represents the learning tendency and it also means objectives and constraints of the action. There are five different rewards according to the area types.

$$r_t = \begin{cases} r^{ga}, & if\ the\ agent\ reaches\ the\ goal \\ r^{ba}, & if\ the\ agent\ moves\ to\ the\ blocked\ cell \\ r^{va}, & if\ the\ agent\ moves\ to\ the\ visited\ cell \\ r^{sa}, & if\ the\ agent\ moves\ to\ the\ stair\ cell \\ r^{na}, & if\ the\ agent\ moves\ to\ the\ normal\ cell \end{cases}$$

and the reward value always satisfies $r^{ga} \gg r^{na} > r^{sa} > r^{va} > r^{ba}$. r^{ga} has a positive value to encourage the agent to find the goal and the others have negative values to find the optimal routes. Additionally, we restricted the minimum value of reward to prevent the agent wander endless.

At first, agent wanders the whole map without any information. Then sometimes the agent may reach the minimum reward we constrained and sometimes arrive at the destination by chance. Whether the agent succeed or not, the chosen action and reward the agent got at every discrete state he visited are used to update the neural network.

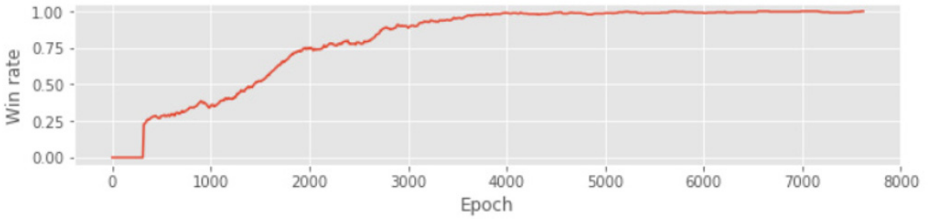

Figure 4. Result of win rate during the training

4. Result and discussion

The proposed DQN is trained with 20000 epochs. The policies and networks have been mentioned in previous section. To evaluate the performance of the model, success rate is recorded. Success rate is defined as the ratio of the number of episodes that successfully find the goal to the recent 300 episodes. Also, average number of moves is calculated in both normal and accident situation. The results are compared to verify whether the agent can find an alternative route properly.

In normal situation, all exits are available then the agent finds the nearest exit from the current position. When starting at 2nd floor of accommodation, the agent finds the shortest route to the exit via the 1st floor and deck and Figure 5 shows the result. The average moves of all starting points in each section are shown in Figure 6 and verify that the agent can evacuate safely regardless of where it starts.

In accident situation, one of four exits is not available due to the capacity of boats and the agent must detour by alternative route. Figure 6 shows how the agent bypasses when exit 3, which is available under normal situation, is closed. Seeing Figure 5, the closure of exit 3 affects escape from all sections except the backward. The reason the backward is not affected is that all escape routes in the backward are not involving exit 3. Although the agent bypasses the route by the effect of exit 3 closure, it finds an alternative route quickly and accurately.

5. Conclusion

A success rate at evacuation from FPSO consistently rises to 100% as training as the training progresses. Although it takes a lot of time to train the model at first, the model makes a quick caculation for every starting point once the train is completed.

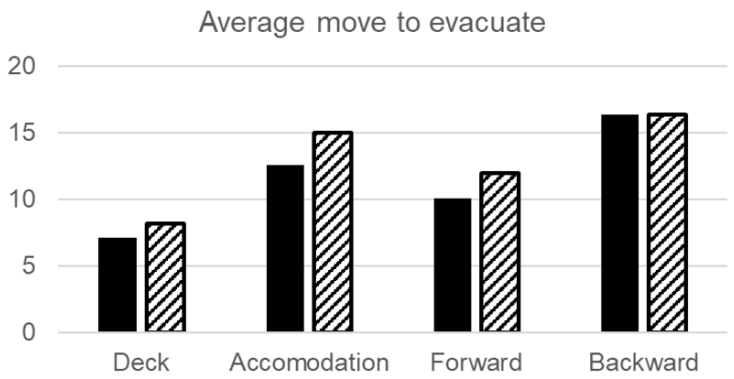

Figure 5. Result comparison of the number of moves between normal and accident situation.

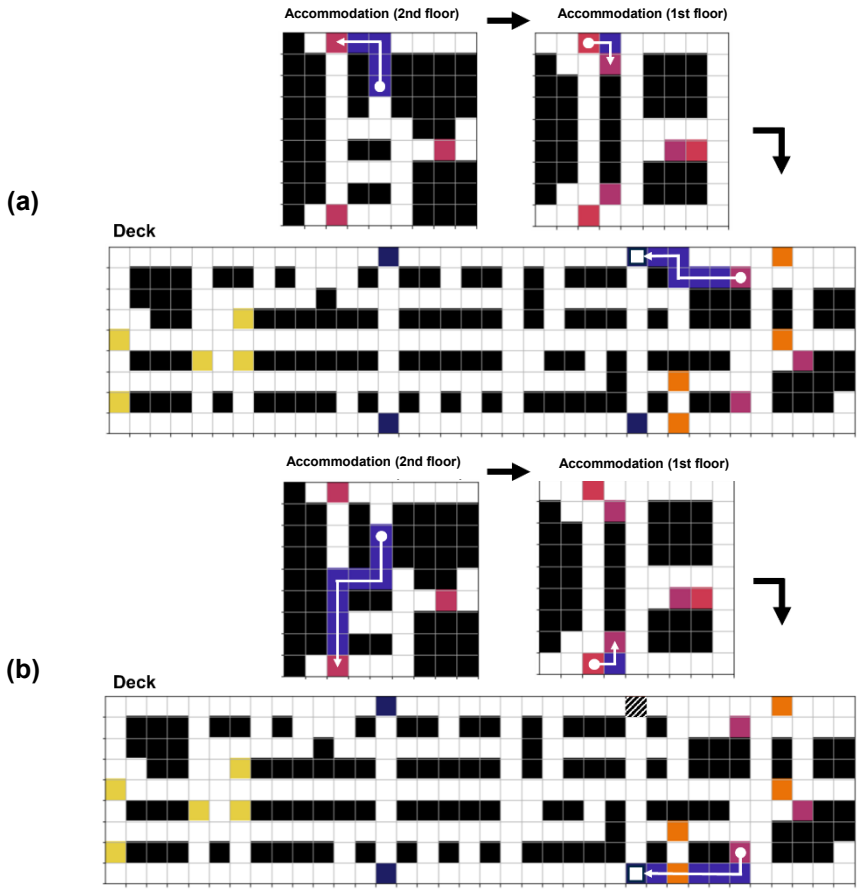

Figure 6. Evacuation test under normal situation (a) and accident situation (b)

Deep Q-Network model can find the shortest evacuation route in complex structure of FPSO. In addition, the route decision is flexible according to accidents and environmental changes. Used in actual marine rescue, it would be helpful to find the optimal evacuation route quickly and rationally in an emergency.

References

P. Luh, 2012, Modeling and Optimization of Building Emergency Evacuation Considering Blocking Effects on Crowd Movement, IEEE Transactions on Automation Science and Engineering, Volume 9, Issue 4, Pages 687-700.

Z. Fang, 2011, Hierarchical multi-objective evacuation routing in stadium using ant colony optimization approach, Journal of Transport Geography, Volume 19, Issue 3, Pages 443-451.

M. Liu, 2016, Evacuation path optimization based on quantum ant colony algorithm, Advanced Engineering Informatics, Volume 30, Issue 3, Pages 259-267.

M. Goerigk, 2014, A comprehensive evacuation planning model and genetic solution algorithm, Transportation Research Part E: Logistics and Transportation Review, Volume 71, Pages 82-97.

Z. Su, 2011, Path selection in disaster response management based on Q-learning, International Journal of Automation and Computing, Volume 8, Issue 1, pp 100–10.

Sauro Pierucci, Flavio Manenti, Giulia Bozzano, Davide Manca (Eds.)
Proceedings of the 30th European Symposium on Computer Aided Process Engineering (ESCAPE30), May 24-27, 2020, Milano, Italy.
http://dx.doi.org/10.1016/B978-0-12-823377-1.50313-X

A Methodology for Data Based Root-cause Analysis for Process Performance Deviations in Continuous Processes

Patrick D. Schiermoch,[a] Benedikt Beisheim,[a,b] Keivan Rahimi-Adli,[a,b] Sebastian Engell[b]

[a]*INEOS Manufacturing Deutschland GmbH, Alte Straße 201, 50739 Köln, Germany*
[b]*Technische Universität Dortmund, Department of Biochemical and Chemical Engineering, Process Dynamics and Operations Group, Emil-Figge-Str. 70, 44221 Dortmund, Germany*
patrick.schiermoch@ineos.com

Abstract

The surge of computational power and the increasing availability of data in the process industry result in a growing interest in data based methods for process modelling and control. In this contribution a concept is described that uses statistical methods to analyse the root-causes for deviations from baselines that are used for the monitoring of the resource efficiency of the production in dashboards. This is done by comparing historical data during resource efficient operation under similar process conditions with data during inefficient operation. Statistically significant deviations are identified, sorted by the likelihood of causing the performance deviation. The concept is applied to a reference model called Best Demonstrated Practice which is in use at INEOS in Cologne. It represents the most resource efficient process performance under given conditions. Deviations from efficient plant performance are analysed using the described concept and the results are given to the operators as a decision support tool, including reference values for the degrees of freedom under the control of the operators. This concept is already used in a root-cause analysis tool at INEOS in Cologne and detected energy savings of over 20% for specific cases.

Keywords: Data analysis, operator advisory, root-cause analysis, anomaly detection

1. Introduction

The European industrial landscape is faced with challenging changes in legal requirements and ambitious goals regarding emissions and the consumption of resources. Furthermore, the European market is driven by high pressure induced by the strong competition due to the imports from the Middle East and North America and a soft demand. To survive in a competitive market the industry is constantly developing methods to uncover improvement potentials and increase the cost and resource efficiency. However, due to high costs that are bound to retrofitting of mature processes or investments into new processes, the industry in Europe pursues alternative methods of process improvements.. One commonly used tool to improve the performance of processes is advanced process control (APC). However, APC solutions are usually bound to high investments. Another approach that is commonly found to improve processes is the development of first principle models. The development of these requires expert knowledge of the processes and is time intensive. A less cost intensive approach is the

use of resource monitoring and energy dashboards which have been reported by Sučić et al. (2015) for building complexes and by Rahimi-Adli et al. (2019) for chemical processes. They use historical data that is prevalent in the process industry to develop baseline models for resource efficient plant operation under the given circumstances. These models are incorporated into dashboards that indicate target values for the resource efficiency to the plant operators. However, the reasons for deviations of the current plant operation from these baseline values are not always straight-forward and the performance improvement depends on the experience and the training of the operators. In this paper a concept is developed that uses historical data and statistical methods to gain insight into the process and reasons for deviations from the baseline to facilitate the transition to more resource efficient process operation.

This concept is applied to an industrial case at INEOS in Cologne, where dashboards are used to monitor the resource efficiency of the production plants of the site. The approach is used as a decision support tool to return reference values for the degrees of freedom of a process that can be used by plant operators to increase the resource efficiency significantly.

2. Methodology

The models that are developed to predict the resource efficiency for the dashboards are data based. They have been developed using neural networks and adaptive neuro-fuzzy inference systems for buildings by Li et al. (2011) and by a set of predefined basis functions for chemical processes by Beisheim et al. (2019). The data based models according to Beisheim et al. (2019) can be described as input-output models shown in equation 1.

$$F(t) = I(t) \cdot M + C, \tag{1}$$

where $F(t)$ describes the predicted value and $I\ (t)$ is the input vector at specific time t, M and C are model parameter vectors and a constant term, both determined during the model development. For a time series $I\ (t)$ takes the form described in equation 2.

$$I(t) = \begin{pmatrix} I_{1,t_1} & \cdots & I_{n,t_1} \\ \vdots & \ddots & \vdots \\ I_{1,t_m} & \cdots & I_{n,t_m} \end{pmatrix}, n, m \in \mathbb{N}. \tag{2}$$

The index t indicates the time step that the input variables belong to, n describes the number of different input variables and m describes the number of time steps in the time series. Each value I can be a direct measurement or transformed into the form needed for the model by mathematical equations (e.g. squaring, exponential, etc.).

In this paper models that are used to calculate the energy or resource efficiency are called baseline models. In the remaining paper all sorts of energy or resources will be simply called resource.

This difference between the model prediction for the baseline and the actual current consumption is called ΔF and is calculated as:

$$\Delta F(t) = \hat{F}(t) - F(t), \tag{3}$$

where $\hat{F}(t)$ describes the measured resource efficiency at t. As previously discussed, reasons for deviations of measured resource efficiencies from the predicted values are usually not easily identified as the modelled system can be very complex. Expert knowledge is helpful to identify potential reasons for deviations, however, trial and error as well as intensive data analysis is usually required to be successful.

In order classify the resource efficiency into values that are within an acceptable range to the predicted baseline values and when the resource efficiency is not a maximal allowed deviation ΔF_{max} is introduced:.

$$\Delta F_{max}(t) = F(t) \cdot p_{allowed}. \tag{4}$$

$p_{allowed}$ describes a percentage of relative deviation from the model prediction that is considered to be acceptable and should be used as tuning factor. By introducing this classification a subspace of allowed data points can be defined that only contains data of efficient process operation. This concept is shown in **Errore. L'origine riferimento non è stata trovata.** for a model that is depending on the load of a plant.
However, comparing the measurement of an inefficient operation point $\hat{F}(t_{ineff})$ to the whole data set of efficient process data that is indicated as squares and circles in Figure 1 will most likely not result in insights into the root-causes for the deviation $\Delta F(t_{ineff})$. This is caused by data that is spread over the whole operational space of the process where it is assumed to contain multiple different operational states. Therefore, the data space that should be used for a comparison has to be further limited to only contain data that uses inputs that are similar to the inefficient operation point that is analyzed. In order to do that a neighborhood is defined that relies on the distance metric d_{I,t_j} defined in equation 5. This metric calculates the distance of the inputs $I(t)$ of each operating point to the inputs $I(t_{ineff})$ of the inefficient operation point. This value can be used to estimate the similarity of operating points in the efficient data set to the analyzed operation point.

$$d_{I,t_j} = \sqrt{\sum_i (I_{i,t_j} - I_{i,t_{ineff}})^2}\ , \forall\, j = 1,2, \dots m. \tag{5}$$

The index j describes the time step that is evaluated. It is assumed that operating points that result in a smaller value for d_{I,t_j} use similar inputs $I(t)$ to the inefficient operation point and are more suitable for a comparison. Due to the fact that the I_{i,t_j} for a model can vary greatly in size and range, a simple distance metric as used in equation 5 will strongly favor values with little variance to them. Therefore, it is necessary to standardize the size of the input space and equalize it. Mean centering and UV-scaling is used for data standardization as described in equation 6.

$$I_{i,t_j,\sigma} = \frac{I_{i,t_j} - \mu_{I_i}}{\sigma_{I_i}}, \tag{6}$$

where μ_{I_i} describes the mean and σ_{I_i} describes the standard deviation of the model input parameter i. After the standardization of the input space the distance metric described in equation 5 can be used in combination with $I_{i,t_j,\sigma}$ from equation 6 to obtain a standardized distance metric for the input space in equation 7.

$$d_{I,t_j,\sigma} = \sqrt{\sum_i (I_{i,t_j,\sigma} - I_{i,t_{ineff},\sigma})^2}\ , \forall\, j = 1,2, \dots m. \tag{7}$$

Due to the assumption that the operating points that result in small values for $d_{I,t_j,\sigma}$ are using similar input data for the models these should be used for a comparison.

Therefore, a neighborhood is defined that uses that metric. Due to the fact that the similarity of the data points is decreasing with increasing $d_{I,t_j,\sigma}$ the neighborhood has to be limited. In order to do guarantee enough data points to ensure a statistical sound comparison of the efficient data points the neighborhood should be defined large enough to hold a minimal amount of operating points. This has to be chosen based on the data density. If the data points are sparse in the input space of the inefficient operation point the neighborhood could become too big and the similarity of the data base will be lost. Therefore, a distance metric $d_{I,t_j,\sigma,max}$ is defined that is exactly the distance that includes the minimal number of operating points that was previously defined. All operating points that follow the inequalities in equation 9 and 10 are assumed to be efficient operating points in the neighborhood of the inefficient operation point that is analyzed and denoted here as "golden operating points" in the rest of this paper.

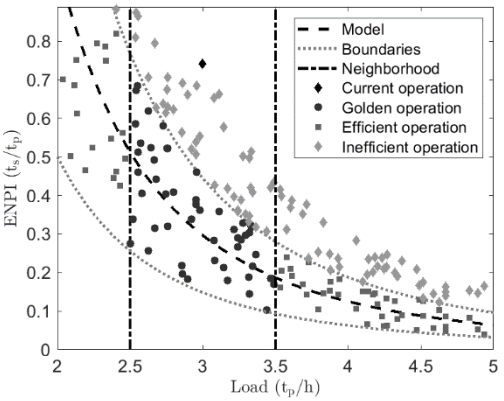

Figure 1: Schematic representation of the baseline model, allowed deviations (Boundaries), the neighborhood and the classification of the operating points

$$d_{I,t_j,\sigma} \leq d_{I,t_j,\sigma,max}, \tag{9}$$

$$F(t) - \Delta F_{max}(t) \leq \hat{F}(t) \leq F(t) + \Delta F_{max}(t) \tag{10}$$

This results in a clearly defined set of operating points as indicated in Figure 1, where the boundaries of the neighborhood are shown as vertical lines.

After the definition of the golden operating points these can be compared to the operation point that results in resource inefficiency. In order to do that all data that is suspected to have an influence on the resource efficiency (e.g. ambient temperature, pressure, etc) is collected for the same time as the golden operating points in the matrix D_{gol} which is described in equation 11, where k denotes the number of influences that is analyzed and s describes the number of golden operating points. The same data is collected for the current operation point in the vector D_{ineff} in equation 11.

$$D_{gol} = \begin{pmatrix} J_{1,t_{gol},1} & \cdots & J_{k,t_{gol},1} \\ \vdots & \ddots & \vdots \\ J_{1,t_{gol},s} & \cdots & J_{k,t_{gol},s} \end{pmatrix}, D_{ineff} = \begin{pmatrix} J_{1,t_{ineff}} & \cdots & J_{k,t_{ineff}} \end{pmatrix}, k, s \in \mathbb{N}. \tag{11}$$

As the data in D_{gol} is also subject to different variance, the data space has to be standardized. The mean value and standard deviation for D_{gol} is calculated resulting in the vectors μ_{gol} and σ_{gol}. These values are used in equation 12 to compute the standardized deviation $\Delta\sigma_{ineff}$ of each data point that was collected in D_{ineff}.

$$\Delta\sigma_{ineff} = \frac{D_{ineff} - \mu_{gol}}{\sigma_{gol}}, \tag{12}$$

which is a measure for the difference of that specific data to the golden operating points. It is assumed that a higher value of $\Delta\sigma_{ineff}$ for data makes it more likely to be the reason

for the deviations $\Delta F(t_{ineff})$. Therefore, $\Delta\sigma_{ineff}$ is sorted in a last step and shown to the operator in the order of magnitude as the potential reason for the inefficiency. To ensure that data is statistically considered anomalous when compared to the golden operating points, it is suggested to only consider values for $\Delta\sigma_{ineff}$ that surpass values of 2 because a standard deviation of 2 is considered to indicate a probability of 95% that the difference is significant as described by Czitrom et al. (1997).

3. Root-cause analysis at INEOS in Cologne

At INEOS in Cologne dashboards are used that indicate which resource consumption is efficient under the given operation conditions. Therefore baselines models are used that indicate how much resources were used in the same plant section when it was operated efficiently, given the specific operation mode. However, reaching the predicted resource efficiency is difficult and strongly depends on the experience and motivation of the plant operators to make the right adjustments to the process while maintaining a safe production.

The results of the root-cause analysis will be presented for a single plant section that was able to save significant amounts of energy using this concept. The investigated unit operation is an evaporator that is schematically shown in Figure 2. The analyzed operation point was prominent due to a highly inefficient operation that caused a resource consumption that was 25% higher than the baseline value. The unit operation consists of a feed stream that enters the evaporator on the side. Water is evaporated and leaves at the top where it is condensed using cooling water. The water is split into a part that leaves the evaporator and a part that is used as reflux flow into the evaporator to increase the purity of the water that leaves the unit operation on the top. The product stream leaves the evaporator at the bottom free of water. A reboiler is installed at the bottom of the evaporator to introduce heat into the system. $I(t)$ only contains the load of the evaporator which is defined as the process water stream leaving the unit operation on the top. The threshold of data that should be included in the golden operating points was set to 100 data points to ensure a sufficient data base for a comparison while maintaining a small neighborhood. All set-points for the controllers of the evaporator has been included in D_{gol} because they are the degrees of freedom a plant operator has. The calculation of $\Delta\sigma_{ineff}$ for the selected data resulted in high values for the set-points of the bottom temperature ($\Delta\sigma_{ineff,T_{bot}} \approx 3$) and for the reflux flow ($\sigma_{Reflux} \approx 2.5$). These results were discussed with plant personnel and it was determined that the deviation of these two set-points causes a high value of $\Delta F(t)$. The problem initially arose during the testing of a new operation mode. The reboiler temperature has been increased due to internal reasons. After a while the water contained increased amounts of organic compounds close to the product specifications. Instead of decreasing the bottom temperature the reflux stream has been increased resulting in a higher purity of the head product while also increasing the overall energy

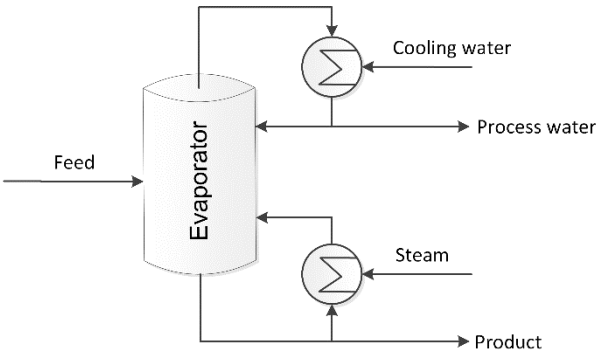

Figure 2: Schematic representation of the evaporator that is analyzed by the root cause analysis

consumption. The values for the controller set-points were adjusted to the mean value of the golden operating points μ_{gol}, resulting in a rapid decrease of the resource consumption by over 20%, resulting in an resource consumption approximately 5% above the baseline value. The root-cause analysis was used again after the adjustment and no other anomalies were detected.

4. Conclusions

In this paper a methodology has been presented that can be used to identify the root-causes for deviations of real process data from baseline values using statistical methods. This concept was implemented in resource efficiency dashboards at INEOS in Cologne that describe reference values for highly resource efficient process operation under similar operating conditions. The implementation of the root-cause analysis helps with the analysis of deviations in the dashboard and facilitates a more resource efficient operation of processes. The concept has been used on an evaporator and it is shown that the energy consumption for one process unit was reduced by over 20% by giving the plant operators set-points for controllers of process parameters. The use of the root-cause analysis facilitated the analysis of deviations from baseline values and gave the plant operators hints to increase the resource efficiency of the current production. This concept is expected to be universally applicable for dashboards that use baseline models for the process monitoring. This can have a contribution to increase the resource efficiency of different processes in the European industry which can lead to an improved position in the difficult market of the process industry.

Acknowledgment

The project leading to this publication has received funding from the European Union's Horizon 2020 research and innovation program under grant agreement No 723575 (CoPro) in the framework of the SPIRE PPP.

References

B. Beisheim, K. Rahimi-Adli, S. Krämer, & S. Engell, (2019). Energy performance analysis of continuous processes using surrogate models. Energy.

V.Czitrom, & P. D. Spagon, (1997). Statistical case studies for industrial process improvement, Siam, Vol. 1, p.486

K. Li, H. Su, & J. Chu, (2011). Forecasting building energy consumption using neural networks and hybrid neuro-fuzzy system: A comparative study. Energy and Buildings, Vol. 43(10), pp. 2893-2899.

K. Rahimi-Adli, P. D. Schiermoch, B. Beisheim, S. Wenzel, & S. Engell, (2019). A model identification approach for the evaluation of plant efficiency. In Computer Aided Chemical Engineering, Vol. 46, pp. 913-918

B. Sučić, A. S. Anđelković, & Z. Tomšić, (2015). The concept of an integrated performance monitoring system for promotion of energy awareness in buildings. Energy and Buildings, Vol. 98, pp. 82-91.

Sauro Pierucci, Flavio Manenti, Giulia Bozzano, Davide Manca (Eds.)
Proceedings of the 30th European Symposium on Computer Aided Process Engineering (ESCAPE30), May 24-27, 2020, Milano, Italy.
http://dx.doi.org/10.1016/B978-0-12-823377-1.50314-1

Reduced-order Modelling (ROM) Approach for Optimal Microclimate Control in Agricultural Greenhouses

Farhat Mahmood[a], Ikhlas Ghiat[a], Rajesh Govindan[b], Tareq Al-Ansari[a,b*]

[a]*Division of Sustainable Development, College of Science and Engineering, Hamad Bin Khalifa University, Qatar Foundation. Doha, Qatar*
[b]*Division of Engineering Management and Decision Sciences, College of Science and Engineering, Hamad Bin Khalifa University, Qatar Foundation. Doha, Qatar*
talansari@hbku.edu.qa

Abstract

Recent efforts to boost self-sufficiency for food through the intensification of domestic production has been considered imperative to insulate from the vagaries of the global food markets. The State of Qatar is an example where more local fresh food production is being promoted, including the current expansion of agricultural greenhouse facilities for domestic vegetables production across the country. However, the hyperarid regional climatic conditions and extreme weather volatilities locally has a direct impact on the greenhouse microclimate owing to the physical processes of energy transfer (radiation and heat) and mass balance (wind and humidity). This consequently results in unpredictability of requirements for: (a) energy for cooling and ventilation; and (b) water for irrigation. In view of these challenges, the objective of the research presented in this paper is to develop a simulation-based methodology for greenhouse microclimate control. A 2D computational fluid dynamics (CFD) model for indoor temperature distribution was used to implement low-dimensional reduced order models (ROM) based on the Proper Orthogonal Decomposition (POD) and Galerkin projection techniques. The results obtained demonstrate that ROM representations are computationally efficient for predictive greenhouse microclimate control systems, providing novel opportunities for timely mitigation of high temperature risks, thereby enhancing the resilience of greenhouses productivity.

Keywords: Food Security, Greenhouse Microclimate, Reduced Order Models.

1. Introduction

The global population is increasing exponentially and expected to grow up to 9.7 billion in 2050 (UN DESA, 2019). To meet the proportional increase in demand for food production, it is required to develop self-sustaining environment friendly solutions in terms of energy and water consumption. Agricultural greenhouses present a feasible solution as the yield production increases up to 10-20%, with a reduction in fuel consumption by 25-35% yearly (De Gelder *et al*., 2012). Greenhouses provide a closed and controlled environment for the plants to grow, thus optimising the yield conditions. As such, the greenhouse microclimate of a greenhouse can be controlled based on the region and type of crop being grown.

The greenhouse microclimate is constituted by a combination of variables, including temperature, humidity, wind and radiation to which the vegetation is directly exposed.

Besides external macroclimate conditions, the influence of factors inside the greenhouse, including vegetation type, soil conditions and irrigation, also play a major role in impacting its microclimate. As such, the temperature and photosynthetic day light integral (DLI) radiation are the main environmental factors that affect the growth and development of crops (Moccaldi and Runkle, 2007), whilst humidity can modify the final yield and quality of crops in varied ways.

The air temperature evolution inside the greenhouse is directly related to the heat flux from the radiation, conduction and convection with the air on the outside. Thus, greenhouses can be used to provide artificial cooling, especially during the summer season, providing optimally controlled temperature to ensure productivity throughout the year (Montero, 2006), particularly in the harsh climate of arid regions, such as that of the State of Qatar. Hemming *et al*. (2019) recently demonstrated that autonomous greenhouses equipped with sensor monitoring; actuators for screening, lighting, ventilation, fogging, CO_2 enrichment, irrigation and fertilisation; and predictive control using artificial intelligence performed better than manually controlled systems in terms of enhanced productivity, optimal land and water resource usage, and the overall efficient food production economics. Among various approaches, model predictive control (MPC) is an effective strategy that utilises prediction of disturbances to optimise future system behavior under certain constraints (Govindan and Al-Ansari, 2019).

Whilst data-driven algorithms have become indispensable for modern intelligent control problems, physical system models based on them are essentially “black boxes” that do not provide insights into the complex behavior of nonlinear dynamical systems, such as greenhouse microclimate, to better understand the potential development of emerging risks within them. Thus, the objective of the research presented in this paper is to develop physics-based models for greenhouse microclimate simulation and optimisation. Low-order representation, namely reduced order modelling (ROM), was used in this study to transform the complexities of the developed computational fluid dynamics (CFD) model of greenhouse microclimate, particularly for indoor temperatures, into computationally efficient surrogate models for predictive control and risk mitigation.

2. Data and model specifications

The model domain was setup using the COMSOL Multiphysics software. A 2D pitch roof greenhouse model was considered with silica glass as the covering material (Shklyar and Arbel, 2004; Al-Mahdouri *et al*., 2013). The properties of various materials considered were assumed from the built-in material library in the software, as indicated in Table 1.

Table 1. Physical and chemical properties of the materials used for the greenhouse model

Material	Thermal conductivity [W/(m*K)]	Density [kg/m^3]	Heat capacity at constant pressure[J/(kg*K)]
Silica glass	1.38	2203	703
Air	0.026	1.225	1420
Water	0.5918	1000	4185.5

The assumed model spans 6m in width and 5m in height (see Figure 1). The use of this model is justified due to the expectation of a high level of symmetry in the heat transfer within the greenhouse (Carlini *et al*., 2019), which further allows simplification for demonstrating the concept of model order reduction proposed in this study. The model domain is meshed using finite element method which allows flexibility for various boundary conditions whilst considering the governing the greenhouse microclimate. External factors, particularly impacting the temperature, namely the solar radiation and ambient air were applied at the model boundary in the form of a heat flux. The heat flux values were varied to determine the temperature distribution inside the greenhouse under different conditions throughout the year (Caponetto *et al.*, 2000). Furthermore, the cooling control is incorporated, in this case using five pipelines circulating cold water at the bottom of the greenhouse, as illustrated in Figure 1. Table 2 indicates other specifications assumed for the model.

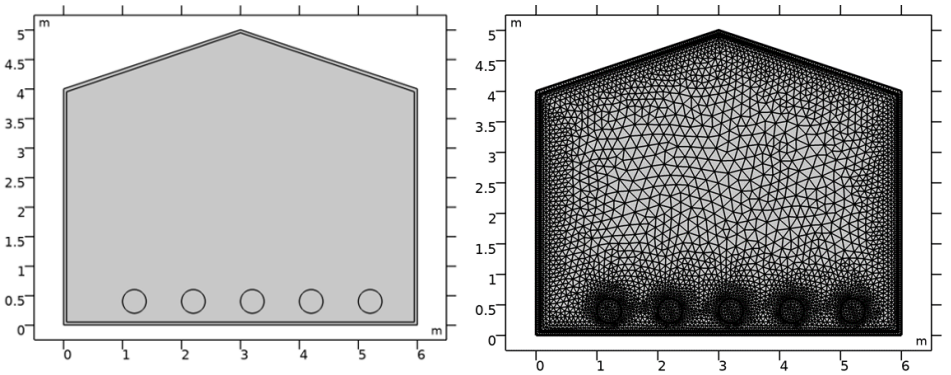

Figure 1. (a) 2D domain setup of greenhouse model; (b) Triangular meshing of the model domain

Table 2. Specifications of the greenhouse model setup

Parameter	Value	Definition
T_c	18^o C	Temperature of the cold water in the pipelines
R_p	100 cm	Radius of the pipeline carrying the cold water
L_{gh}	6 m	Length of the greenhouse
H_v	4 m	Height of the side wall
L_R	3.16m	Length of the inclined roof

Optimal control for temperature at various points inside the greenhouse is based on the data available for specific crops, namely tomato and lettuce (Table 3). As such, uneven temperature distribution inside the greenhouse poses a risk for these crops in terms of their development.

Table 3. Optimum temperature ranges for specific crop growth

Plant	Optimum Temperature[^{o}C]
Tomato	18 - 30
Lettuce	17 - 23

3. Methodology

3.1. Governing equations in the greenhouse model

The governing equation for convective heat transfer is a second order partial differential equation representing the energy conservation principle, which states that rate of change of total thermal energy equals the sum of: (a) the rate of exchange of heat flux (conduction); (b) the rate of change of energy due to convection and pressure variations (compression and expansion); and (c) the rate of change of energy due to viscous dissipation, expressed in terms of the variable temperature (T), as (Bird *et al*., 1966):

$$\rho C\left(\frac{\partial T}{\partial t}+\vec{v}\nabla T\right)-\kappa\nabla^2 T+T\alpha\nabla.\vec{v}+\boldsymbol{\tau}.\boldsymbol{\nabla}\vec{v}=0 \tag{1}$$

where, ρ is the air density; C is the specific heat; $\vec{v}$ is the 2D velocity vector; κ is the thermal conductivity; α is the coefficient of thermal expansion; and $\boldsymbol{\tau}$ is viscous stress tensor. Meanwhile, the governing equation for fluid flow, representing the conservation of momentum, based on the Naviér-Stokes equation, which states the rate of change of total linear momentum equals the sum of: (a) rate of change of momentum by convection; (b) pressure force and rate of change of momentum by viscous transfer; and (c) gravitational force, expressed as (Bird *et al*., 1966; White, 1999):

$$\rho\frac{\partial\vec{v}}{\partial t}+\rho\vec{v}(\nabla.\vec{v})+\vec{v}(\nabla.\rho\vec{v})+\nabla p+\nabla.\boldsymbol{\tau}-\rho\vec{g}=0 \tag{2}$$

where, p is the pressure force; and $\vec{g}$ is the gravitational force. The coupled heat transfer and fluid flow model aims to jointly solve for temperature, pressure and velocity vector, considering the conservation of mass principle, given by the flow continuity equation (Bird *et al*., 1966):

$$\frac{d\rho}{dt}+\nabla.\rho\vec{v}=0 \tag{3}$$

3.2. Reduction via Proper Orthogonal Decomposition (POD) and Galerkin projection

In the POD formulation, a new set of basis functions are constructed from the snapshots obtained from the solutions of equations (1), (2) and (3) that evolve through time. In this study, the snapshots of solutions obtained for the temperature variable is recorded for the simulation period of seven hours, with an interval of 30 minutes. A snapshots matrix $\mathcal{T} = [\mathcal{T}_1\ \mathcal{T}_2\ \ ...\ \mathcal{T}_{\mathcal{S}-1}\ \mathcal{T}_{\mathcal{S}}]$ is generated of size $\mathcal{N}\times\mathcal{S}$, where $\mathcal{N}$ denotes the number of mesh elements, and $\mathcal{S}$ denotes the number of snapshots. Taking the deviation from the mean ($\bar{\mathcal{T}}$) forms a modified snapshots matrix $\tilde{\mathcal{T}}$, given by:

$$\tilde{\mathcal{T}}_{\mathcal{S}}=\mathcal{T}_{\mathcal{S}}-\bar{\mathcal{T}} \tag{4}$$

$$\text{where, } \bar{\mathcal{T}}=\frac{1}{\mathcal{S}}\sum_{s=1}^{\mathcal{S}}\mathcal{T}_{\mathcal{S}} \tag{5}$$

Subsequently, the goal of POD is to find a set of orthogonal basis functions $\{\Phi_s\}$, s $\in$ $\{1, 2, ..., \mathcal{S}\}$. This was achieved by implementing Singular Value Decomposition (SVD) of the modified snapshots matrix $\tilde{\mathcal{T}}$, given by:

$$\tilde{\mathcal{T}}=\mathcal{T}_1\,\Sigma\,{\mathcal{T}_2}^T \tag{6}$$

leading to the orthogonal basis functions $\{\Phi_s\}$, such that:

$$\Phi_s = \left. \widetilde{\mathcal{T}}.\mathcal{T}_{2(:,s)} \right/ \sqrt{\lambda_s}, \text{ for s} \in \{1, 2, \ldots, \square\} \tag{7}$$

where, λ_s are the eigenvalues in the diagonal matrix Σ. Thus, in POD, the temperature variable for each snapshot was predicted using a subset of basis functions corresponding to the largest P eigenvetors (*i.e.* the first P columns of $\mathcal{T}$, and $P \ll \mathcal{S}$), expressed as:

$$\mathcal{T}_{\mathcal{S}}{}' = \bar{\mathcal{T}} + \sum_{j=1}^{P} \alpha_j \Phi_j \tag{8}$$

Finally, the POD coefficients α_j is solved in the ROM using the Galerkin projection in the model domain Ω, given by:

$$\frac{{\alpha_k}^t - {\alpha_k}^{t-1}}{\Delta t} = \langle\, F\left(\bar{\mathcal{T}} + \sum_{j=1}^{P} \alpha_j \Phi_j\right),\ \Phi_k \,\rangle_\Omega \tag{9}$$

such that, $F(\psi) = \frac{d\psi}{dt}$ (10)

4. Results and Discussion

The results of ROM prediction for the temperature distribution inside the greenhouse provides a high-fidelity representation comparable to the full CFD model simulation. Thus, the ROM model provides valuable predictive control information for the cooling system - the five pipelines circulating cold water - with enough load to maintain the desired temperature in the cultivation area of the greenhouse, and potentially mitigate the risk of increasing temperatures. Figure 2 illustrates example snapshots of temperature distribution during the simulation period, where the core temperature is roughly maintained in the optimal range of 17 - 27°C (see Table 3).

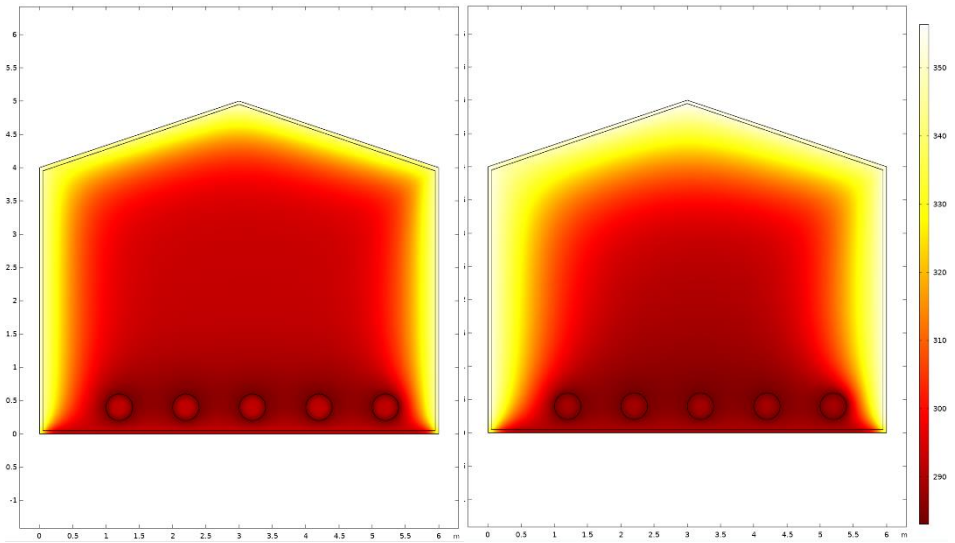

(a) (b)

Figure 2. ROM predictive control for temperature in the greenhouse after: (a) 3.5 hours; (b) 7 hours.

5. Conclusions

The study presented in this paper describes a computational physics-based approach for the development of prediction and optimal control of greenhouse microclimate parameters, particularly that of the evolution of indoor temperatures owing to impact of external climate conditions, including solar temperature, temperature and humidity. It is envisaged that the reduced order model (ROM) application for greenhouses provides the flexibility for rapid integration with "black box" data-driven approaches and artificial intelligence algorithms, so as to better understand the risks with low occurrence probability that can potentially arise within a greenhouse, and are not necessarily captured by historical data. One of the major limitations of the current study is, however, the lack of simultaneous prediction of multiple and non-linearly correlated microclimate variables, and coupling those with cooling and irrigation requirements, which is a subject of ongoing studies. Nevertheless, the model reduction approach presented in this paper is computationally efficient and expected to readily scale to larger number of predictors and model domains, that will also be considered in future investigations.

References

A. Al-Mahdouri, M. Baneshi, H. Gonome, J. Okajima, and S. Maruyama, 2013, Evaluation of optical properties and thermal performances of different greenhouse covering materials, Solar Energy, 96, 21–32.

R.B. Bird, W.E. Stewart and E.N. Lightfoot, Transport Phenomena, John Wiley & Sons, Inc., New York, 1966.

R. Caponetto, L. Fortuna, G. Nunnari, L. Occhipinti and M.G. Xibilia, 2000, Soft computing for greenhouse climate control, IEEE Transactions on Fuzzy Systems, 8, 6, 753–760.

M. Carlini, S. Castellucci, A. Mennuni, and S. Morelli, 2019, Numerical modeling and simulation of pitched and curved-roof solar greenhouses provided with internal heating systems for different ambient conditions, Energy Reports.

A. De Gelder, J.A. Dieleman, G.P.A Bot and L.F.M. Marcelis, 2012, An overview of climate and crop yield in closed greenhouses. Journal of Horticultural Science and Biotechnology, 87, 3, 193–202.

R. Govindan and T. Al-Ansari, 2019, Computational decision framework for enhancing resilience of the energy, water and food nexus in risky environments, Renewable and Sustainable Energy Reviews, 112, 653-668.

S. Hemming, F. de Zwart, A. Elings, I. Righini and A. Petropoulou, 2019, Remote Control of Greenhouse Vegetable Production with Artificial Intelligence - Greenhouse Climate, Irrigation, and Crop Production, Sensors, 19, 8, p.1807.

L.A. Moccaldi and E.S. Runkle, 2007, Modeling the effects of temperature and photosynthetic daily light integral on growth and flowering of Salvia splendens and Tagetes patula, Journal of the American Society for Horticultural Science, 132, 3, pp.283-288.

J.I. Montero, 2006, Evaporative cooling in greenhouses: Effect on microclimate, water use efficiency and plant respons, Acta Horticulturae, 719, 373–383.

A. Shklyar and A. Arbel, 2004, Numerical model of the three-dimensional isothermal flow patterns and mass fluxes in a pitched-roof greenhouse, Journal of Wind Engineering and Industrial Aerodynamics, 92, 12, 1039–1059.

UN DESA, 2019, World population prospects 2019. In United Nations, Department of Economic and Social Affairs, World Population Prospects 2019, Retrieved from http://www.ncbi.nlm.nih.gov/pubmed/12283219

F. M. White, Fluid Mechanics, McGraw-Hill, 1999

Sauro Pierucci, Flavio Manenti, Giulia Bozzano, Davide Manca (Eds.)
Proceedings of the 30th European Symposium on Computer Aided Process Engineering (ESCAPE30), May 24-27, 2020, Milano, Italy.
http://dx.doi.org/10.1016/B978-0-12-823377-1.50315-3

Network Optimization Model for a Sustainable Supply Network for Greenhouses

Ikhlas Ghiat,[a] Rajesh Govindan,[b] Sarah Namany,[a] Tareq Al-Ansari [a,b*]

[a]*Divison of Sustainable Development, College of Science and Engineering, Hamad Bin Khalifa University, Qatar Foundation, Doha, Qatar.*
[b]*Division of Engineering Management and Decision Sciences, College of Science and Engineering, Hamad Bin Khalifa University, Doha, Qatar.*
talansari@hbku.edu.qa

Abstract

Meeting the demand for food in arid and water-scarce regions can be economically and environmentally challenging. Uncertainties related to climate change and global warming exacerbates technical challenges for efficient food production. Protected agriculture in the form of greenhouses grow different types of crops in a controlled microclimate offering better conditions for healthy and profitable production. Moreover, CO_2 enrichment has also been proven to increase crop yields at low costs, and can be supplied from burning carbon-based resources and transferring the carbon recovered through pipeline networks or tanks. However, the sustenance of CO_2 supply to greenhouses requires compliance with the global sustainability standards, and as such there is a need for economically viable and environmentally-friendly networks for the supply of CO_2 required by the greenhouses. The objective of this study is to design an optimum supply chain network for a sustainable supply of CO_2 to greenhouses. The framework developed is based on an optimisation model solved using integer linear programing (ILP) aiming to minimise the economic cost associated with the operations of the entire supply chain network serving greenhouses. An environmental assessment is also conducted in quantifying the CO_2 offset related to the CO_2 utilisation in agricultural greenhouse applications. The proposed model was implemented for a case study based in Qatar, comprising of a set of hypothetical greenhouses placed at various locations; a source of CO_2 from a biomass based power plant, a distribution centre, and existing pipeline and roadway networks. GIS optimisation models previously developed for the Qatar case study provide locations for greenhouses, pipeline and road transportation routes for CO_2 fertilisation as inputs for the proposed supply chain model. The demand for resources, CO_2 transport networks, and the distances between the source and greenhouses were assumed to be the constraints impacting the design of the supply chain network. The results obtained indicate the optimal CO_2 supply quantities to the greenhouses following a proposed network of pipelines and road routes, with a minimum associated cost of transportation of approximately 0,09$/kg of CO_2.

Keywords: Sustainability, Agricultural, Greenhouse, Supply Chains, Network Optimisation.

1. Introduction

In view of the significant shift in the global world population, the food production is expecting an ever-increasing intensification to accommodate the growing demands. This

enlarged production entails the deployment of sophisticated agricultural technologies involving advanced machinery and developed processes (Al-Ansari et al., 2016). However, this change in the food system induces severe environmental degradation associated with energy-intensive water and fertilizers' production systems required for enhanced food production levels, such as high global warming potential (GWP) and water depletion (Namany et al., 2019). To offset the environmental impact caused by the food sector, novel techniques are implemented such that yields are enhanced while emissions are reduced. CO_2 fertilisation is a sustainable process that was proven effective in mitigating climate change by reducing CO_2 concentration in the atmosphere through using it in plants' cultivation (Islam, 2012). In fact, CO_2 enrichment improves the photosynthesis of crops leading to higher yields. It also reduces water consumption resulting in optimal water utilization for irrigation (Dion et al., 2011). Adopting CO_2 fertilisation as part of agricultural activities is a very promising approach to enhance crops behavior and increase productivity; applying this method is a challenging task that requires founded planning and significant investments. Current sources of CO_2 are still difficult to implement due to their relatively expensive costs including expenses associated with ways of processing and transportation from the source to greenhouses (Chau et al., 2009). Many efforts are conducted in literature to identify frameworks which might reduce economic and logistical complexities associated with using CO_2 enrichment in food production. Govindan and Al-Ansari (2019) proposed a novel model that analyses the potential of deploying CO_2 fertilisation in greenhouses with an aim to improve food security through increasing crops productivity. The framework determines, based on GIS, the optimal CO_2 fertilisation network comprised of power plants coupled with carbon capture technology, greenhouses and transportation means counting roadways and pipelines, that can satisfy the fulfillment rates. Similarly, this paper contributes to the efforts carried out to solve the supply chain issue associated with the implementation of this sustainable technique.

The objective of this study is to develop an optimisation model for a sustainable supply of CO_2 to agricultural greenhouses to enhance the productivity and reduce water usage. The model can be applied to a multi-echelon network with various complexities and interdependencies as shown in Figure 1. The study uses a hypothetical scenario of potential greenhouses for the supply of CO_2 captured from a potential biomass based power plant, and a potential distribution center all located in the State of Qatar. The aim is to supply the greenhouses with the required CO_2 concentrations to reduce the water use from the evapotranspiration of the plants by 25%. For this, an optimisation model is presented to sustainably supply CO_2 at a minimum cost and evaluate the overall CO_2 reduction in the atmosphere associated with CO_2 capture and utilisation.

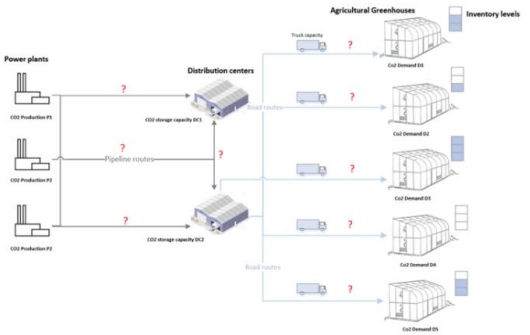

Figure 1: Multi-echelon network problem of CO_2 supply to greenhouses.

2. Available data and assumptions

Multimodal datasets specific to the State of Qatar are used to derive the information needed for this study based on spatially distributed data, mainly farming lands, weather data, and possible routes for CO_2 transport via pipeline and road. A previous study presented viable potential agricultural greenhouse locations in the State of Qatar based on balancing the energy used for CO_2 transport and the energy saved from water reduction by means of CO_2 enrichment (Al-Ansari et al., 2018). These locations were taken in this study for setting the greenhouse network model, along with a possible biomass based power plant, and a distribution center based on the available pipeline and road routes.

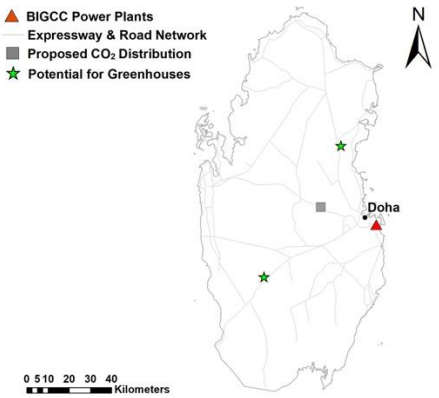

Figure 2: Potential locations for greenhouses, BIGCC plant, and a distribution center in the State of Qatar (Modified after Al-Ansari et al. (2018)).

Two greenhouses were selected, one located in Al-Khor area in the northern part, and one in Al-Kiranah area in the southern part of Qatar. Compressed CO_2 gas (~80 MPa) is assumed to be transported from the BIGCC to the distribution center via a 60 km pipeline following an existing pipeline road currently used for another application in Qatar. Once at the distribution center, the CO_2 follows further processing to get a low pressure liquid at a temperature below ambient, and is stored in 9kg capacity cylinders. This step is necessary for the next transportation of CO_2 from the distribution center to the two greenhouses via road by means of trucks. One truck is assumed to load a maximum number of 50 cylinders of CO_2. The distance between the distribution center and the greenhouses is 53 km for Al-khor and 69 km for Al-Kiranah.

The two greenhouses were assumed to have different crop profiles of producing tomatoes and cucumbers with a harvesting period of two months. Different crop profiles are studied particularly to showcase the importance of optimising a dynamic model that can depend on the owners' choice, or the market demand. Other assumptions are taken into consideration in this study related to source and sinks capacities, safety stocks, and distances between the different network nodes. In this study, a small scale BIGCC capturing 1 kt/year of CO_2 is considered. The storage capacities at each node are assumed; 84 tonnes/month for the distribution center, 180 kg/month for Al-Khorr greenhouse, 224 kg/month for Al-Kiranah greenhouse.

3. Methodology

3.1. CO_2 demand

The CO_2 demand corresponding to the crop profile of the two greenhouses was calculated to achieve a 25% reduction in water loss from the plants' evapotranspiration. The evapotranspiration equation takes into consideration monthly weather data of the particular greenhouse location, in addition to a CO_2 conductance factor as shown in equation (1) (Islam, 2012).

$$ET = k_c . \frac{0.408\,\Delta(R_n - G) + \gamma \frac{900}{T+273} u_2 (e_s - e_a)}{\Delta + \gamma\left(1 + \frac{0.34 u_2}{CO_2 factor}\right)} \quad (1)$$

The CO_2factor represents the stomatal conductance g_{CO2} at the unknown CO_2 level over the stomatal conductance a baseline CO2 level of 330 ppm as shown in equation (2) and (3).

$$CO_2 factor = \frac{g_{CO2=x}}{g_{CO2=330}} \quad (2)$$

$$g_{CO2} = 0.0485 - 7e^{-5}(CO_2) + 3.4e^{-8}(CO_2)^2 \quad (3)$$

where Δ represents the slope of the vapor pressure-temperature curve, R_n is the average solar radiation, G is the solar heat flux density, γ is the psychrometric constant, T is the average temperature, u_2 is the average wind speed, $(e_s - e_a)$ represents the vapor pressure deficit, and k_c is the crop coefficient.

An optimisation is conducted to find the optimal CO_2 levels needed to achieve 25% reduction in evapotranspiration for both tomatoes and cucumbers in both greenhouses and for every month. The CO_2 levels in ppm were then converted to a corresponding value in kg per month by multiplying the ppm levels with the volume of the greenhouses and an assumed CO_2 injection rate.

3.2. Network optimisation model

An integer linear programing model was developed for the optimisation of CO_2 supply network to greenhouses taking into consideration the varying evapotranspiration reduction levels between crop profiles and greenhouse locations. The objective of this optimisation is to minimize the operational cost associated with CO_2 transport, and storage at the level of the distribution center and greenhouses. The formulation of this optimisation problem is showcased below.

Variables:

-$C_{T,j}$: cost of transportation by truck to greenhouse j ($/cylinder)
-H_j: CO_2 holding cost in greenhouse j ($/kg of CO_2/month)
-H_{DC}: CO_2 holding cost in distribution center ($/kg of CO_2/month)
-cap_c: capacity of one cylinder (kg of CO_2/cylinder)
-S_j: safety stock needed for greenhouse j (kg of CO_2/month)
-$I_{i,j}$: initial CO_2 inventory in month i for greenhouse j (kg of CO_2/month)
-$D_{i,j}$: CO_2 demand in month i for greenhouse j (kg of CO_2/month)
-cap_j: CO_2 storage capacity in greenhouse j (kg of CO_2/month)
-cap_T: CO_2 capacity of a transport truck (cylinders)

Decision variables:

$Q_{i,j}$: number of CO_2 cylinders transported in month i to greenhouse j (cylinders)

Objective function:
Minimise:

$$\sum_{i=1}^{12}\sum_{j=1}^{2} Q_{i,j}C_{T,j} + cap_c \sum_{i=1}^{12}\sum_{j=1}^{2} H_j Q_{i,j} - cap_c\, H_{DC} \sum_{i=1}^{12}\sum_{j=1}^{2} Q_{i,j} \quad (4)$$

Constraints:

$S_j \le I_{i,j} + Q_{i,j}.cap_c - D_{i,j} \le cap_j$

$Q_{i,j} \le cap_T$

$Q_{i,j} \ge 0;\ integer$

where: $I_{i,j} = Q_{i-1,j}cap_c - D_{i-1,j} + I_{i-1,j}$; for $i = 1, 2, 3, \ldots, 12$ and $j = 1, 2$.

4. Results and discussion

The integer linear programing model was solved and the resulted minimised overall cost was retrieved to be around 0.09$/kg of CO_2. Figure 3) andFigure 4) represent the variation of the CO_2 transported with the changing demand and inventory levels. For example, for Al-Kiranah greenhouse in month 6, there is no demand for CO_2 because the crop profile for that greenhouse indicates that no production will take place in that month. Although, there will be no production, CO_2 is still being sent for that month to account for a safety stock. It is important to track the inventory levels at all echelons of the supply chain in order to minimise the holding and transportation costs while meeting the demand.

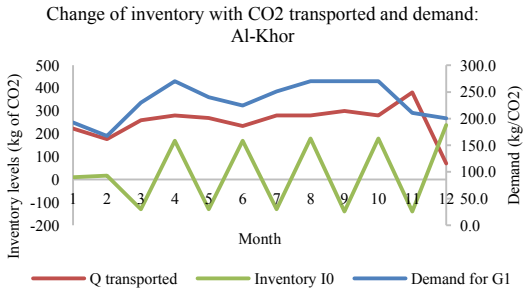

Figure 3: Change of CO_2 inventory levels with supply and demand: Al-Khor

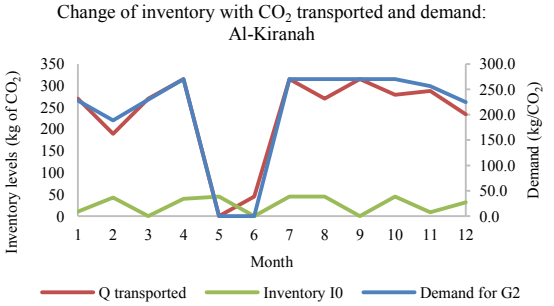

Figure 4: Change of CO_2 inventory levels with supply and demand: Al-Kiranah

The CO_2 offsetted by the two greenhouses during a year reaches 5,27 tonnes CO_2/year from direct CO_2 utilisation only, representing a small amount of CO_2 being produced from the BIGCC. Hence, more greenhouses can be added to this network to effectively use the CO_2 captured from the BIGCC, and efficiently use the pipeline and road transportation capacities suggested in this network model. Moreover, both greenhouses have been set to reduce their crop evapotranspiration by 25%, which represents an additional CO_2 reduction related to water production. Assuming the water source comes from reverse osmosis desalination, this model will reduce CO_2 emissions from virtual water by 1,2 tonnes CO_2/year as compared to the baseline case operating without CO_2 enrichment. Thus, the total abated CO_2 from this application adds to an amount of 6.47 tonnes CO_2/ year.

5. Conclusions

CO_2 enrichment in greenhouses has become a viable and proven solution to enhance crop productivity and reduce the water loss due to evapotranspiration of the plants. However, the CO_2 supply chain for agricultural greenhouse applications lacks research and more optimisation is needed to sustainably utilise this source. Thus, in this study an economic optimisation network model for CO_2 supply to greenhouses is presented. The model can be scaled up to include multiple CO_2 sources, distributions centres, and agricultural greenhouses having different crop profiles and CO_2 demands. For the hypothetical scenario chosen in this study, CO_2 supply to greenhouses can be possible at a cost of 0.09$/kg of CO_2, and a total amount of 6.47 tonnes of CO_2/year is offsetted from both CO_2 consumption and virtual water loss due to evapotranspiration.

References

T. Al-Ansari, A. Korre, Z. Nie, & N. Shah, 2016, Integration of Biomass Gasification and CO_2 Capture in the LCA Model for the Energy, Water and Food Nexus. 26th European Symposium on Computer Aided Process Engineering, 2085–2090.

S. Namany, R. Govindan, T. Al-Ansari, 2019, Optimisation of the energy, water, and food nexus for food security scenarios, Computers & Chemical Engineering, 129, 106513.

A. Islam, L. R. Ahuja, L. A. Garcia, L. Ma, A. S. Saseendran, 2012, Modeling the Effect of Elevated CO_2 and Climate Change on Reference Evapotranspiration in The Semi-Arid Central Great Plains, American Society of Agricultural and Biological Engineers ISSN 2151-0032.

L.-M. Dion, M. Lefsrud, & V. Orsat, 2011, Review of CO_2 recovery methods from the exhaust gas of biomass heating systems for safe enrichment in greenhouses, Biomass and Bioenergy, 35(8), 3422–3432.

J. Chau, J. Sowlati, S. Sokhansanj, F. Preto, S. Melin, X. Bi, 2009, Techno-economic analysis of wood biomass boilers for the greenhouse industry, Appl Energ, 86:364.

R. Govindan, & T. Al-Ansari, 2019, Simulation-based reinforcement learning for delivery fleet optimisation in CO_2 fertilisation networks to enhance food production systems. Computer Aided Chemical Engineering 29th European Symposium on Computer Aided Process Engineering, 1507–1512.

T. Al-Ansari, R. Govindan, A. Korre, Z. Nie, & N. Shah, 2018, An energy, water and food nexus approach aiming to enhance food production systems through CO_2 fertilization. 28th European Symposium on Computer Aided Process Engineering, 1487-1492.

Sauro Pierucci, Flavio Manenti, Giulia Bozzano, Davide Manca (Eds.)
Proceedings of the 30th European Symposium on Computer Aided Process Engineering (ESCAPE30), May 24-27, 2020, Milano, Italy.
http://dx.doi.org/10.1016/B978-0-12-823377-1.50316-5

Integration of Chemical Process Simulators with Algebraic Modeling Languages

R. Ruiz-Femenia[a], J. Javaloyes-Antón [a], R. Salcedo-Díaz [a], M. A. S. S. Ravagnani [b], J. A. Caballero[a]

[a]*Institute of Chemical Process Engineering, University of Alicante, Alicante, Spain.*
[b]*Chemical Engineering Department, State University of Maringá, Brazil*
ruben.ruiz@ua.es

Abstract

In this work, we use the external equations facility available in GAMS to incorporate in the optimization model the library packages of a commercial process simulator such as Aspen-Hysys, which provides an extensive component database and reliable physical property methods. To this end, we write a source code in the C programming language that connects with Matlab, which in turn uses the Microsoft Component Object Model (COM) interface to communicate with Aspen-Hysys. The methodology is illustrated with a case study of the reaction section of a methanol plant. The results show that a thermodynamic rigorous optimization can be performed without losing the high index capabilities, few verbose and simple syntax that an AML offers.

Keywords: GAMS, external equations, Aspen-Hysys, optimization.

1. Introduction

The relevant value of Algebraic Modeling Languages (AMLs) is widely accepted by their capability for solving real-world optimization problems. AMLs allow to define variables and write constraints with a concise mathematical representation, which is essential for large-scale problems that involve thousands or millions of variables and constraints. One of the main contributions for the development of AMLs came for the discipline of chemical engineering, under which is natural to view an understand the world and its behavior as a mathematical program (Kallrath, 2004). The General Algebraic Modeling System (GAMS) is one of the most widely used AMLs in universities and in the energy and chemical industries. One of its strengths is that provided access to more than 25 solvers, including the state-of-the-art commercial solvers. As other AMLs, GAMS distinguishes between abstract model and concrete problem instances, and also offers a file format (GDX) that allows to send data for a GAMS model and store the results from the same model to be post-processed in external software. An alternative strategy to AMLs for solving optimization problems is to use a high-level programming language to formulate optimization models, which are then solved with an optimizer written in low-level languages. This approach combines the flexibility of a high-level language to build the model with the efficiency of a low-level language for numerical computation. The most mature software that uses this approach is TOMLAB (Navarro-Amorós et al., 2014), which provides access to the commercial optimization solvers inside the Matlab environment. Like any other commercial AML, GAMS does not use this two-language approach, but GAMS does offer a customizable modeling component by the usage of the external equations facility, which permits to emulate the above-mentioned flexibility of a high-level programming language such as Matlab.

In this work, we use the external equations facility available in GAMS to incorporate in the optimization model the library packages of a commercial process simulator such as Aspen-Hysys, which provides an extensive component database and reliable physical property methods.

2. Methodology

2.1. Optimization with an embedded process simulator

When sequential modular process simulators are used as calculation engines in mixed-integer nonlinear programming (MINLP) optimization problems, it is convenient to define a partition of the vector of continuous variables x, into dependent and independent (or design) variables. The values of the dependent variables, x^{Sim}, are provided by the external equation. On the other hand, the design variables x^I, are the set of optimization variables and its dimension is equal to the degrees of freedom of the problem when the set of binary variables are fixed. By this partition, the resulting representation of the optimization problem, using the generalized disjunctive programming (GDP) formulation (Balas, 1979; Raman & Grossmann, 1994), is shown in Figure 1 (left problem). The common equality constraints $h(\cdot)$ can be solved for a given vector of independent variables. Then, the dependent variables are expressed as a function of decision variables $x^{Sim} = h^{Ext}(x^I)$. (see right problem in Figure 1). Similarly, in the disjunctions, for each equipment i assigned to a task k, the dependent variables associated with it can be expressed as functions of the decision variables $x^{Sim} = s_{ik}^{Ext}(x^I)$. In this work, dependent variables x^{Sim}, are not explicitly written in terms of decision variables, but they are externally calculated at the level of the process simulator, and then used at the optimization level to evaluate the objective function and the common and disjunctive constraints.

Note that in the reformulation of the GDP, as we introduce dependent variables in explicit equations (for example in $h(x^{Sim},x^I) = 0$ or in $g(x^{Sim}, x^I) \leq 0$, a sequential function evaluation is required). First, the implicit constraints are solved within the process simulator, and then, the explicit constraints written in GAMS are evaluated.

$$\min_{x,Y_{ik}} \; z = f(x) \longrightarrow \min_{x^{Sim},x^I,Y_{ik}} \; z = f(x^{Sim},x^I)$$

$$s.t. \quad h(x) = 0 \longrightarrow \begin{cases} x^{Sim} = h^{Ext}(x^I) \\ h(x^{Sim},x^I) = 0 \end{cases}$$

$$g(x) \leq 0 \longrightarrow g(x^{Sim},x^I) \leq 0$$

$$\bigvee_{i \in D_k} \begin{bmatrix} Y_{ik} \\ r_{ik}(x) \leq 0 \\ s_{ik}(x) = 0 \end{bmatrix} k \in K \longrightarrow \bigvee_{i \in D_k} \begin{bmatrix} Y_{ik} \\ r_{ik}(x^{Sim},x^I) \leq 0 \\ x^{Sim} = s_{ik}^{Ext}(x^I) \\ s_{ik}(x^{Sim},x^I) = 0 \end{bmatrix} k \in K$$

$$\Omega(Y) = True \quad x^{lo} \leq x \leq x^{up}, x \in \mathbb{R}^n \quad Y_{ik} \in \{True, False\} \longrightarrow \Omega(Y) = True \quad x^{I,lo} \leq x^I \leq x^{I,up}, x^I \in \mathbb{R}^{n_I} \quad x^{Sim,lo} \leq x^{Sim} \leq x^{Sim,up}, x^{Sim} \in \mathbb{R}^{n-n_I} \quad Y_{ik} \in \{True, False\}$$

Figure 1. Transformation of a general GDP formulation to embed a process simulator in the optimization model.

2.2. Connection between GAMS and process simulator

Figure 2 illustrates the main parts to establish a connection between the AML (GAMS) and the Hysys-Aspen simulator. The required inputs are the GAMS modeling file and the Aspen-Hysys flowsheet. Aside from the common GAMS declarations and definitions included in a GAMS file, it must be also defined each external equation by mapping its

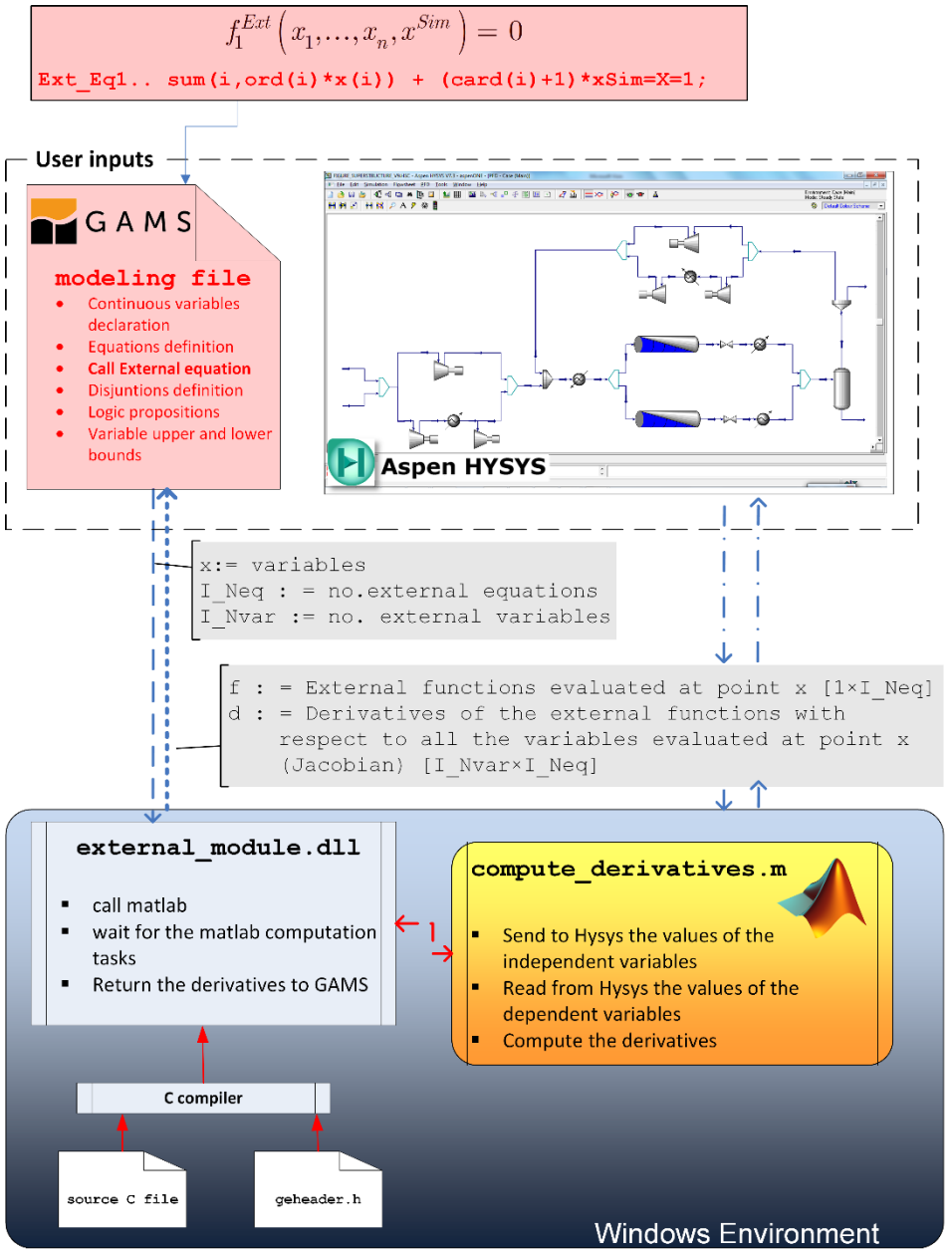

Figure 2. Scheme of the connection between GAMS and Aspen-Hysys through the external equations GAMS Facility.

variable names and its corresponding variables indices. The key component of this connection system is the external module, which is the responsible for the evaluation of the external equation and its Jacobian at a given point (these evaluations are not performed by the GAMS run-time system). The source code for this module is written in C, and as our methodology is developed under Windows environment, is built as a dynamically linked library (.dll). The final connection with Aspen-Hysys is performed through Matlab, which uses the Microsoft Component Object Model (COM) interface to send and receive information to and from the process simulator.

2.3. Solution strategy for a GDP model

The ongoing optimization problem is special since the evaluation of the black-box functions does not allow relaxed values for the binary variables. Such features automatically exclude some mixed-integer algorithms, such as, nonlinear branch and bound. To overcome this difficulty, we use the Logic-based Outer Approximation (OA) (Ruben Ruiz-Femenia et al., 2014; Türkay & Grossmann, 1996). The Logic-based OA shares the main idea of the traditional OA for MINLP (Mixed Integer NonLinear Programming), which is to solve iteratively a MILP master problem, which gives a lower bound of the solution, and an NLP subproblem, which provides an upper bound. The NLP subproblem is derived from the GDP representation of the problem by fixing the values of the Boolean variables (i.e., given a flowsheet configuration). The key difference of the logic approach versus the OA is that in the logic based OA algorithm only the constraints that belong to the selected equipment or stream are imposed. This leads to a substantial reduction in the size of the NLP subproblem compared to the direct application of the traditional OA method over the MINLP reformulation of the GDP problem.

2.4. Case study

We assess the performance of the proposed methodology using a simplified superstructure of the reaction section of the methanol process, where the synthesis gas reacts to produce methanol following this reaction system:

$$CO + 2H_2 \rightarrow CH_3OH$$
$$CO_2 + 3H_2 \rightarrow CH_3OH + H_2O$$
$$CO + H_2O \leftrightarrow CO_2 + H_2$$

These reactions are not independent, and then, only two of them are required for a complete description of the reaction system, which exhibits a trade-off between the conversion reached according to the thermodynamic equilibrium and the conversion governed by reaction kinetics and the residence time of particular a reactor.

The different flowsheet alternatives considered for this process are shown in Figure 3. A total of 64 feasible flowsheets topologies arise from the two types of the feed stream, the compression systems (located at the feed and recycle stream) that have one or two compressors and can operate at low and high pressure, and the two alternative rectors for the low and high operating pressure. These discrete decisions are modeled under the generalized disjunctive programming framework using 12 Boolean variables. A detailed description of this case study can be found in (Navarro-Amorós et al., 2014; Rubén Ruiz-Femenia et al., 2017).

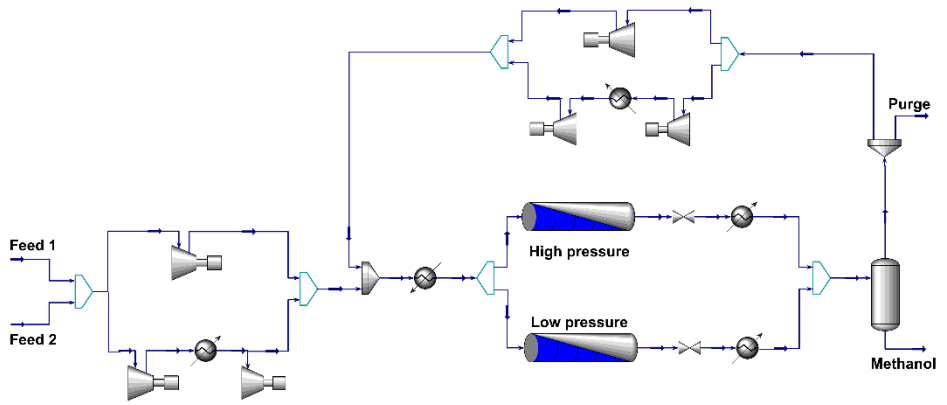

Figure 3. Superstructure for the reaction section of the methanol synthesis process.

The modelling framework above described provides the solution shown in Figure 4. Both, discrete (i.e. one stage compression and low pressure) and continuous decisions match the results obtained in the previous works (Navarro-Amorós et al., 2014; Rubén Ruiz-Femenia et al., 2017). This fact strengths the validation of our methodology.

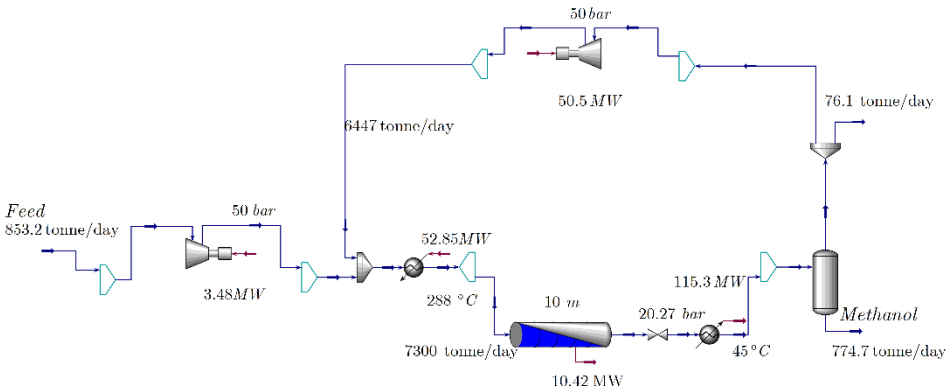

Figure 4. Optimal flowsheet for the reaction section of the methanol process.

3. Conclusions

The performance of the methodology to integrate process simulators with AMLs has been tested with a simplified case study of the reaction section of the methanol process. The results show that a thermodynamic rigorous optimization can be performed without losing the high index capabilities, few verbose and simple syntax that an AML offers.

An advantage of our approach, compared to similar ones, such as the optimization interface (OPTI) toolbox under Matlab environment, is that GAMS offers more NLP solvers, in particular the efficient and reliable solver CONOPT for the large-scale nonlinear optimization. Furthermore, the proposed approach allows to compute the submatrix of the total Jacobian only with respect the independent variables required to cover the degrees of freedom in the process simulator. An addition strength of the

proposed methodology is that the external equations, which could involve a large number of equations (e.g. rigorous thermodynamic relationships or detailed equipment design correlations) and variables, are solved at the level of the process simulator, taking advantage of reliable tailored methods implemented in the flowsheeting programs. Remark that these equations and variables do not contribute to enlarge the size of the optimization problem defined in the AML used, since they are hidden from the optimization solver.

A limitation of our approach is that solvers that need to analyze the algebraic structure of the model instance, such as global solver BARON (Tawarmalani & Sahinidis, 2005), cannot be used with external equations.

Further work involves extending this optimization tool to larger industrial case studies, and developing an approach to restore the optimization procedure from process simulator convergence failures.

Acknowledgements

The authors gratefully acknowledge financial support to the Spanish «Ministerio de Economía, Industria y Competitividad» under project CTQ2016-77968-C3-2-P (AEI/FEDER, UE).

References

Balas, E. (1979). Disjunctive Programming. Annals of Discrete Mathematics, 5, 3-51.

Kallrath, J. (2004). Modeling languages in mathematical optimization. Boston: Kluwer Academic Publishers.

Navarro-Amorós, M. A., Ruiz-Femenia, R., & Caballero, J. A. (2014). Integration of modular process simulators under the Generalized Disjunctive Programming framework for the structural flowsheet optimization. Computers and Chemical Engineering, 67, 13-25.

Raman, R., & Grossmann, I. E. (1994). Modelling and computational techniques for logic based integer programming. Computers and Chemical Engineering, 18, 563-578.

Ruiz-Femenia, R., Fernández-Torres, M. J., Salcedo-Díaz, R., Gómez-Rico, M. F., & Caballero, J. A. (2017). Systematic Tools for the Conceptual Design of Inherently Safer Chemical Processes. Industrial & Engineering Chemistry Research, 56, 7301-7313.

Ruiz-Femenia, R., Flores-Tlacuahuac, A., & Grossmann, I. E. (2014). Logic-Based Outer-Approximation Algorithm for Solving Discrete-Continuous Dynamic Optimization Problems. Industrial & Engineering Chemistry Research, 53, 5067-5080.

Tawarmalani, M., & Sahinidis, N. V. (2005). A polyhedral branch-and-cut approach to global optimization. Mathematical Programming, 103, 225-249.

Türkay, M., & Grossmann, I. E. (1996). Logic-based MINLP algorithms for the optimal synthesis of process networks. Computers and Chemical Engineering, 20, 959-978.

Sauro Pierucci, Flavio Manenti, Giulia Bozzano, Davide Manca (Eds.)
Proceedings of the 30th European Symposium on Computer Aided Process Engineering (ESCAPE30), May 24-27, 2020, Milano, Italy.
http://dx.doi.org/10.1016/B978-0-12-823377-1.50317-7

Prediction of Sustainability Related Properties: Data Science Methods with Incorporated Prior Knowledge

Gulnara Shavalieva[a], Pietro Postacchini[b,a], Stavros Papadokonstantakis[a]

[a]*Energy Technology, Chalmers University of Technology, Horsalsvagen 7B, Gothenburg 41296, Sweden*
[b]*AVT – Aachener Verfahrenstechnik, Process Systems Engineering, RWTH Aachen University, Aachen 52074, Germany*
gulnara.shavalieva@chalmers.se

Abstract

Many of the registered chemicals, newly synthesized or long existing, lack information on their hazard for the environment and human health. To perform the holistic safety assessment of chemicals, data on molecular properties, mostly obtained by test on living organisms, are collected. However, extensive experimentation is neither economically feasible nor ethical, and thus development of accurate prediction models is required. The recent advances in the area are associated with data science methods; however, there are certain limitations of these models with respect to their transparency, interpretability or even availability of well distributed training data to ensure robust generalization. Hybrid models combining machine learning with prior knowledge of the research field can potentially provide the solution to these limitations. The current study presents the first step of creating hybrid models, namely extraction of knowledge that can be utilized to create prior knowledge for future incorporation into hybrid models.

Keywords: prior knowledge, text mining, hybrid model

1. Introduction

There are currently over 157 million unique chemical substances registered with a Chemical Abstract Service (CAS) identifier and this number is constantly growing. Some of these chemicals enter our everyday life as food additives, ingredients of cosmetics, personal care products, cleaning agents, toys, clothes, electronics, pharmaceuticals, etc. (World Health Organization, 2016). Others are associated with industrial applications, such as solvents and separation agents for chemical and pharmaceutical industry, refrigerants, catalysts, ionic liquids, etc. The chemicals are constantly released to the environment as emissions during production and use. Despite the regular exposure of humans and environment to such chemicals, many of them lack information on their impact on human health and environment (ECHA,2019). Experimental hazard assessment of chemicals with respect to their impact on environment and human health is traditionally performed on living organisms, what is not feasible neither from economical nor ethical point of view. In fact, EU legislation promotes the use of alternative *in vitro* or *in silico* approaches to replace the cruel animal testing (European Commission, 2017). Furthermore, plethora of novel molecular structures need to be tested *in silico* during computer-aided molecular design approaches for innovative applications. Obviously, experimental testing is not a feasible option during thousands of iterations of the respective optimization approaches.

Various *in silico* approaches, including for instance structural alerts (Limban et al., 2018), read-across (Stanton and Kruszewski, 2016), and group contribution methods (Hukkerikar et al., 2012) have been developed over the years with the aim to predict molecular properties of chemicals required for safety assessment. Even though the approaches are widely used, recent models utilizing advanced methods of data science, mostly machine learning, reported to show improved accuracy of prediction (Zhang et al., 2018, Hartung, 2019). Despite the improvement of the prediction, the models obtained by means of machine learning are difficult to interpret (Zhang et al., 2018). Furthermore, it is challenging to create prediction models for some of molecular properties (e.g., permissible exposure levels, acute toxicity dermal, persistency, acidification potential, global warming) due to limited amount of experimental data. One of the ways to address these limitations is to incorporate to the model knowledge existing in the field (i.e., herein called prior knowledge). The prior knowledge can refer to data labelling, generic conclusions, functional trends between target and predictor variables, simplified input/output models for specific classes of chemicals, etc. The approach has been successfully applied in various fields, e.g., medicine (Craft et al., 2017), drug safety (Lysenko et al., 2018), materials (Chakraborty et al., 2017), image recognition (Bougie et al., 2018). However, to the best of our knowledge, the approach has not been systematically used for prediction of properties (e.g., acute aquatic toxicity, bioconcentration, persistency) required to perform holistic sustainability assessment of chemicals. One of the main reasons is that prior knowledge is not systematically extracted, classified and formulated in a way that can be effectively used for hybrid modelling.

The current work describes an approach for this first step of knowledge extraction for development of hybrid prediction models. The knowledge is extracted from research publications by means of natural language processing.

2. Method

The current method used for knowledge extraction is presented in Figure 1. It consists of two main steps: data collection and knowledge extraction. Each step is subdivided into procedures which can be either automated by machine learning approaches or require some form of human intervention.

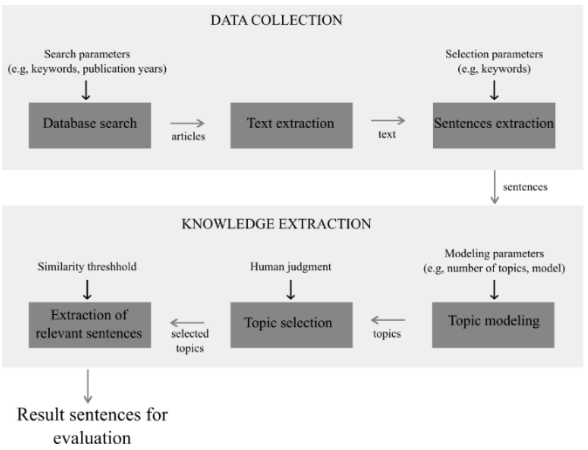

Figure 1. Schematic representation of method used for knowledge extraction

Aquatic toxicity molecular property is used for this study. The objective is, with the help of published work over the last 20 years research, to extract information that can be potentially used as prior knowledge in hybrid prediction model.

2.1. Data collection

Data collection involved the search of potentially relevant peer-reviewed research articles or review papers using a database of bibliographic information. Web of Science (WoS) was used as the main database for this study. The relevant papers were identified based on the following keywords search: "aquatic toxicity", which was selected to be as generic as possible for the investigated field. The timespan for publications was set to years from 1998 to 2018. The search resulted in 1780 papers. The distribution of the publications over the years is presented in Figure 2 together with the line showing the increase of the research works related to articles resulting from a search based on a the more generic keyword “environment”. Both lines show the same trend and as expected the sources related to the more generic topic (i.e., environment) are more smoothly increasing over the years. The outcome of the analysis of bibliometric information is presented in Figures 3a -3b. The results show that except three first articles and three authors, the results are very evenly distributed.

From the found works, 66 published in Elsevier were selected to perform text mining and illustrate the proposed approach. The current method seemed to perform better text extraction from the articles of the Elsevier format, however, the method is to be refined in the future to overcome this limitation.

Text extraction have been performed on the 66 selected papers with the help of Python packages PDFMiner (Shinyama, 2013) and Spacy (SpaCy, 2019). The collected text has been further processed to extract sentences that comply with selection criteria, which for this study comprised the words “toxicity, ‘LC50’ and ‘EC50’. LC50 and EC50 is the concentration of a chemical in water causing death or certain effect (e.g., growth reduction), respectively, in 50% of population of specific living organisms (e.g, daphnia magna, fish). The acute toxicity is a common parameter of various hazard assessment frameworks. Different selection criteria, e.g., certain structure of the sentence, indication to table, figure or equation can be added, depending on the scope of knowledge extraction and also considering the intended machine learning model hybridization approach.

At the end of this step, a significant text reduction is performed (i.e., 2-3 order of magnitudes in terms of counted words) and the available text is grouped into sentences or small paragraphs relevant to the selected keywords.

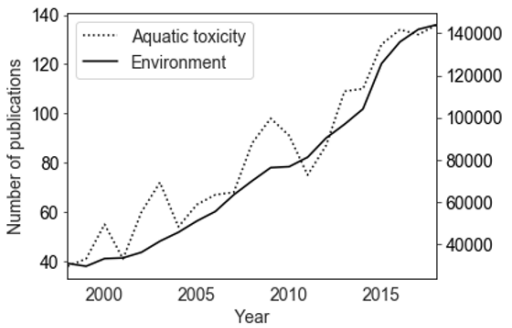

Figure 2. Number of articles published under two topics from year 1998 to 2018.

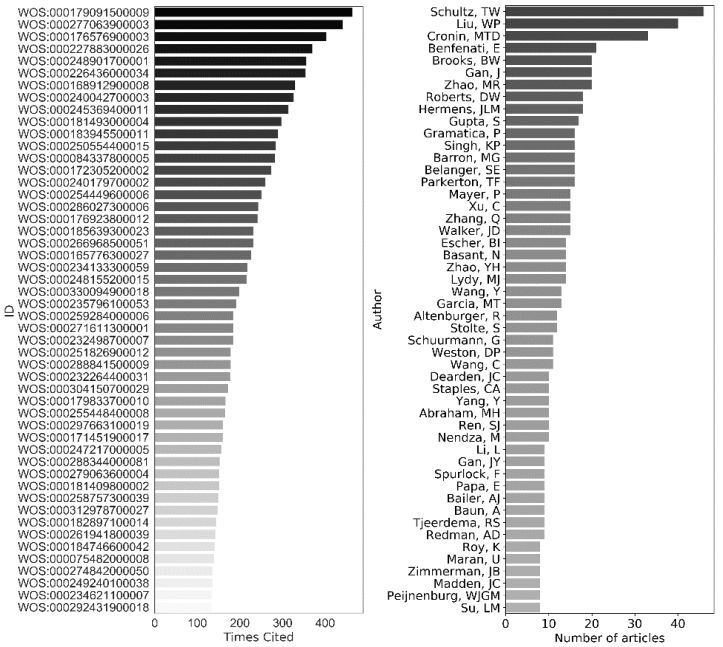

Figure 3. Fifty most cited articles (a) and fifty most common authors (b) for the found papers on WoS.

2.2. Knowledge extraction

The knowledge extraction starts with the topic modeling step that utilizes the sentences extracted from the articles during the data collection (See Figure 4). First, sentences go through a preprocessing step, consisting of the removal of stop words (e.g. articles), and lemmatization, which returns the base form of the words. The unique words found in the sentences are then numbered and collected to a list, called dictionary. The sentences are transformed into vectors containing the frequency of appearance of the unique words in the corresponding sentence. This results in a matrix (corpus) combining the corresponding of all the sentences. The corpus serves as basis for the actual topic modeling. Two different techniques have been tested for the topic modeling: Latent Semantic Indexing (LSI) and Latent Dirichlet Allocation (LDA). The techniques differ by the way they perform identification of topics. LSI performs truncated singular value decomposition to achieve dimensionality reduction based on the number of underlying topics and returns topics in form of vectors of words co-occurring together. LDA assumes that sentences, extracted from the articles, are set up by a probabilistic distribution of topics. Each topic, in turn, is probabilistic distribution of words. These distributions are obtained from the corpus matrix through variational Bayes approximations and Gibbs sampling (Williams and Betak, 2018).

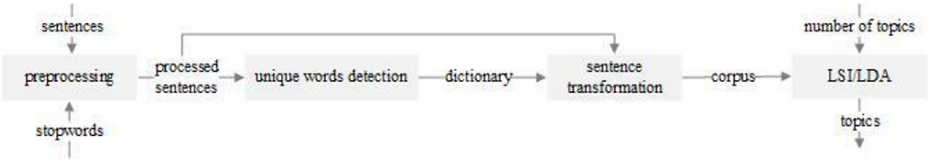

Figure 4. Topic modeling steps.

The optimal number of topics for LDA is taken based on a maximum value for a coherence score giving a measure of how good the topics generated by the model are. The maximum coherence score was obtained for a maximum number of topics equal to 50 for both models. From these 50 topics, five were selected as potentially relevant, based on human expertise. The selected five topics were used as a query to rank all the sentences extracted from the articles. The ranking used a cosine similarity score, which evaluates the similarity between the query and each of the sentence vectors. The closer the cosine similarity to one, the greater the match between the vectors. Thus, topic selection and threshold value for the cosine similarity score were used for information reduction to get a reasonable number of sentences. This kind of cut-off criteria are necessary to reduce the amount of information required to be processed by human.

3. Results

The results of two topic modelling models and various similarity scores are presented in Table 1. As can be seen, the LSI results are more sensitive to the similarity score threshold value than the LDA results both for the number of resulting sentences and for the number of potentially relevant sentences.

Table 1. Results for LSI and LDA models.

Similarity score	Number of resulting sentences		Number of potentially relevant sentences	
	LSI	LDA	LSI	LDA
0.3	1020	478	34	24
0.4	483	400	21	22
0.5	171	344	9	21

The potentially relevant sentences contain rules, correlations, indications to QSARs or read-across predictions of aquatic toxicity. For example, sentences like “Longer chain alcohols display a very strong structure-activity relationship to acute fish toxicity as a function of hydrophobicity”, “There is a linear relationship between both acute and chronic toxicities and $LogK_{ow}$, suggesting that with the increase of hydrophobicity the aquatic toxicity increases” might be obtained.

Additionally, the main parameters affecting the results of the study have been identified and considered for further improvement. More general keywords combination used for search of the articles (e.g. “aquatic toxicity” instead of “aquatic LC50”) result in more relevant sentences. More specific search (“aquatic LC50”) leads to identification of numerous sentences devoted to various experimental studies limited to certain test conditions difficult to be generalized as prior knowledge.

The identification of the potentially relevant topics generated by the models is not straightforward, is heavily based on human expertise and may have a significant impact on the results. The evaluation of the resulting sentences, in turn, revealed the necessity to back track the documents containing potentially useful information (e.g., extracting more context by the surrounding text of the identified sentences). Thus, the approach can serve as additional indication to promising articles to retrieve more data for generation of prior knowledge. However, it should be noted that this will require an

additional step of human intervention in the overall prior knowledge extraction procedure.

4. Conclusions

The presented procedure showed potential in extraction of relevant information to generate prior knowledge for hybrid data driven models. More general keyword combination for initial search of research papers and certain modelling parameters as topic selection criteria and cut-off score are the main factors affecting the results of the procedure. Including the various forms of extracted knowledge in machine learning approaches will further highlight which of these forms can be better utilised to develop hybrid models with advanced generalisation capabilities.

References

Bougie, N., Cheng, L.K., Ichise, R., 2018. Combining deep reinforcement learning with prior knowledge and reasoning. ACM SIGAPP Applied Computing Review 18, 33–45.

Chakraborty, S., Chattopadhyay, P.P., Ghosh, S.K., Datta, S., 2017. Incorporation of prior knowledge in neural network model for continuous cooling of steel using genetic algorithm. Applied Soft Computing Journal 58, 297–306.

Craft, D., Ferranti, D., Krane, D., 2017. The value of prior knowledge in machine learning of complex network systems. Bioinformatics 33, 3610–3618.

ECHA, 2019. REACH compliance - an Agency priority for 2019. Available at: https://newsletter.echa.europa.eu/home/-/newsletter/entry/reach-compliance-an-agency-priority-for-2019 (Accessed: 28 November 2019).

European Commission, 2017. Alternatives to animal testing and safety assessment of chemicals. Available at: https://ec.europa.eu/jrc/en/research-topic/alternatives-animal-testing-and-safety-assessment-chemicals (Accessed: 28 November 2019).

Hartung, T., 2019. Predicting toxicity of chemicals: software beats animal testing. EFSA Journal.

Hukkerikar, A.S., Kalakul, S., Sarup, B., Young, D.M., Sin, G., Gani, R., 2012. Estimation of environment-related properties of chemicals for design of sustainable processes: Development of group-contribution+ (GC +) property models and uncertainty analysis. Journal of Chemical Information and Modeling 52, 2823–2839.

Limban, C., Nuţă, D.C., Chiriţă, C., Negreş, S., Arsene, A.L., Goumenou, M., Karakitsios, S.P., Tsatsakis, A.M., Sarigiannis, D.A., 2018. The use of structural alerts to avoid the toxicity of pharmaceuticals. Toxicology Reports 5, 943–953.

Lysenko, A., Sharma, A., Boroevich, K.A., Tsunoda, T., 2018. An integrative machine learning approach for prediction of toxicity-related drug safety. Life Science Alliance 1, 1–14.

Shinyama,Y., 2013. PDFMiner. Available at: https://pdfminer-docs.readthedocs.io/pdfminer_index.html (Accessed: 28 November 2019).

SpaCy, 2019. Industrial - Strength Natural Language Processing. Available at: https://spacy.io/. (Accessed: 28 November 2019)

Stanton, K., Kruszewski, F.H., 2016. Quantifying the benefits of using read-across and in silico techniques to fulfill hazard data requirements for chemical categories. Regulatory Toxicology and Pharmacology 81, 250–259.

Williams, T., Betak, J., 2018. A Comparison of LSA and LDA for the Analysis of Railroad Accident Text. Procedia Computer Science 130, 98–102.

World Health Organization, 2016. Chemical safety and protection of human health: the Slovenian experience (2016) Available at: http://www.euro.who.int/en/countries/slovenia/publications/chemical-safety-and-protection-of-human-health-the-slovenian-experience-2016 (Accessed: 28 November 2019).

Zhang, L., Zhang, H., Ai, H., Hu, H., Li, S., Zhao, J., Liu, H., 2018. Applications of Machine Learning Methods in Drug Toxicity Prediction. Current Topics in Medicinal Chemistry 18, 987–997.

Sauro Pierucci, Flavio Manenti, Giulia Bozzano, Davide Manca (Eds.)
Proceedings of the 30th European Symposium on Computer Aided Process Engineering (ESCAPE30), May 24-27, 2020, Milano, Italy.
http://dx.doi.org/10.1016/B978-0-12-823377-1.50318-9

A Framework for Stochastic and Surrogate-Assisted Optimization using Sequential Modular Process Simulators

Alberto T. Penteado, Erik Esche, Joris Weigert, Jens-Uwe Repke

Group of Process Dynamics and Operations, Technische Universität Berlin, Sekretariat KWT 9, Straße des 17. Juni 135, 10623 Berlin, Germany
alberto.penteado@tu-berlin.de

Abstract

A Python framework is introduced enabling automated simulation and stochastic and surrogate-assisted optimization (SAO) using Aspen Plus flowsheets. A new modification to the Probability of Improvement method for SAO is proposed to handle non-converged simulations. Two chemical engineering optimization problems are solved using gradient-based, stochastic, and the new SAO algorithms.

Keywords: sequential optimization, black-box optimization, stochastic optimization, surrogate-assisted optimization, probability of improvement

1. Introduction

Process design and operation in both industry and academia rely heavily on simulation and optimization with Sequential Modular (SM) flowsheets. Gradient-based optimization with SM flowsheets is challenging because objective and constraints are only evaluated once and if flowsheet convergence is achieved and, most often, only numerical derivatives are available. Since the model structure and derivatives are unknown to the optimizer, this is often called a black-box problem. Further difficulties are imposed because objective and constraints may be numerically noisy, discontinuous, non-differentiable, and undefined at some points, which led the research community towards direct search (DS) methods (Martelli and Amaldi 2014). Surrogate-Assisted Optimization (SAO) has also been applied (Carpio et al. 2018). These normally require more simulations to converge, but additionally present important global search characteristics. This work presents a framework (Section 2) using Python and Aspen Plus for automated simulation and process optimization using DS methods and a new modified SAO algorithm (Section 3) to handle failed or non-converged simulations. Two chemical engineering problems are solved using different methods (Section 4).

2. The Framework

Most process simulators have built-in SQP algorithms. However, DS and SAO require connection to external software such as Matlab or Python. Several frameworks are reported in literature using Aspen Plus/HYSYS, ChemCad, Pro II, EMSO, among others, but programming code is seldom provided. Furthermore, this is often not supported by software developers. Aspen Tech only officially supports connection to Excel / VBA, so that essentially no documentation on other programming languages is available. This makes the development of such frameworks a tedious trial-and-error process and led to the idea of implementing and publishing the source code for the present framework.

$$PI(u,x) = \Phi\left(\frac{T - \hat{f}(u,x)}{s(u,x)}\right) \quad (1)$$

$$PC_c(u,x) = \Phi\left(\frac{0 - \hat{g}_c(u,x)}{s_c(u,x)}\right) \quad (2)$$

$$PI_c(u,x) = P_{conv} \cdot PI \cdot \prod_{c=1}^{constraints} PC_c \quad (3)$$

The framework for Black-Box Optimization of sequential modular flowsheets (Bbop) automates the connectivity and wraps the available functions/methods of the COM (Component Object Model) object exposed by Aspen Plus and is implemented in Python 2.7. The commented source code is provided in gitlab.tubit.tu-berlin.de/dbta/bbop.git along with an example containing the Aspen Plus model of example 4.1 and a Python script using Bbop to automate simulations and perform optimizations.

For the examples in Section 4, several optimization algorithms have been tested in an attempt to reach better results and to provide a comparison basis for the newly developed SAO algorithm. These are the built-in SQP algorithm from Aspen Plus, the gradient-based Sequential Least Squares Programming (SLSQP) algorithm by Kraft (1988), the stochastic Differential Evolution (DE) algorithm by Storn and Price (1997), and the Lipschitz optimization algorithm Simplicial Homology Global Optimization (SHGO) by Endres et al. (2018). DE and SHGO are chosen as readily available and robust global optimization methods and SLSQP is used to refine their solutions. The three methods are available in the SciPy optimization library (Jones et al. 2001).

3. The Enhanced Probability of Improvement Algorithm

The original Probability of Improvement (PI) method (Jones 2001) has recently been extended for constrained problems and applied to chemical engineering examples (Carpio et al. 2018). It attempts to use surrogate models in order to reduce the number of rigorous function evaluations, thus being suited for simulation-based optimization with expensive functions like SM process flowsheet.

To initialize the algorithm, a Design of Simulations (DoS) covering the entire design space is required. The PI method searches for the global minimum of an objective function $f(u,x)$ by repeatedly solving an auxiliary optimization problem as given in Figure 1. This consists in fitting a surrogate mode $\hat{f}(u,x)$ to the objective function using Gaussian Process Regression (GPR) and then maximizing the probability of achieving a target improvement *T* in the objective function as given by Eq. 1. *PI* is a multi-modal function with high values in points where the predicted objective function value is low and / or the predicted standard error *s* is high. In each iteration, the rigorous model (in this case the Aspen Plus simulation) is only sampled at the local maxima of the PI auxiliary function, thus very likely leading to improvements in the objective function value and / or in the surrogate model's prediction quality.

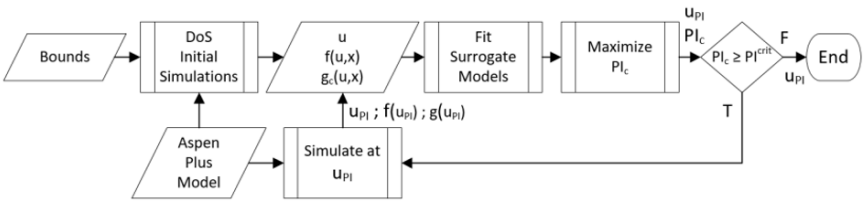

Figure 1 – Algorithm Flowchart for the enhanced PI method

For inequality constraints of the type $g(u,x) \leq 0$ an analogous approach has been proposed (Carpio et al. 2018). Surrogate models $\hat{g}(u,x)$ are fitted to each constraint c and the probability of fulfilling a constraint is then given by Eq. 2. The probability of improvement for a constrained problem is given by multiplying PI to the product of all PC_c leading to the two last product terms of Eq. 3. The toolbox scikit-learn has been used to fit all surrogate models using a squared-exponential kernel (Pedregosa et al. 2011).

In Eq. 1 and 2, PI is the probability of improvement for an unconstrained problem; u is the set of decision/control/optimization variables; x are the state-variables; Φ is the normal cumulative distribution function; T is the target improvement (e.g., a percentual improvement over the current best-known objective function value); $\hat{f}$ is the GPR surrogate model for the objective function; s is the standard error of the objective function predictions; PC_c is the probability of fulfilling constraint c; $\hat{g}_c$ is the GPR surrogate model for constraint c; s_c is the standard error of the constraint predictions.

One question that often arises when performing black-box optimization is what to do if a simulation fails. This issue is mentioned by Carpio et al. (2018), but no further discussion or solution is proposed. According to the authors, a large objective function value is returned to the optimizer if a simulation fails, creating an artificial peak in this area. This is a common and simple solution but has disadvantages. First, this has detrimental effects to the GPR surrogate model, which will incorporate the arbitrarily high value and falsely reduce standard error around it. Secondly, SM simulators often rely on previous solutions for initialization and, thus non-convergent areas may become convergent once more solutions become available in its neighbourhood. By completely avoiding non-convergent areas, the algorithm may oversee interesting points near them. This is critical if the simulation is difficult to converge near the optimum solution.

To overcome this issue, a k-Nearest Neighbour (kNN) binary classification method is applied using the algorithm available from scikit-learn (Pedregosa et al. 2011). In each iteration, all known simulation points are classified into non-converged (class=0) and converged (class=1). The probability of a new trial point belonging to the converged class (P_{conv}) is given by the distance-weighted average of the class values from its k known nearest neighbours. The failed simulations are left out of the construction of the surrogate models, so there is no need to assign arbitrarily high objective values to them. The term P_{conv} is introduced into the objective function of the auxiliary PI maximization problem, leading to Eq. 3. It acts as a dampener and reduces the probability of improvement (PI_c) near known failed simulations, thus reducing the chance of the optimizer moving in that direction on a probabilistic basis instead of an arbitrary basis. If later more simulations converge around the failed simulation, P_{conv} is increased and, if PI and PC_c are also high enough, this area may be revisited. This modified version of the algorithm has been implemented in Python 2.7 and applied for both optimization problems.

Table 1 - Optimization Results for the HDA Process

Method	Benzene Cost [$·t^{-1}]	Number of Simulations	Decision Variables	
			Purge Ratio	H_2 : Toluene Ratio
DE	86.3	831	0.049	0.913
PI	86.7	149	0.060	0.896
SHGO Sobol	86.8	1091	0.064	0.899

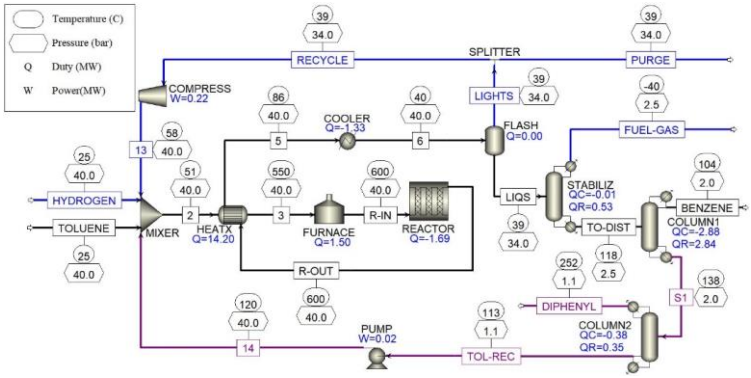

Figure 2 - Simulation Flowsheet of the HDA Process

4. Examples

4.1. Hydrodealkylation (HDA) Process

The HDA process for producing benzene from toluene and hydrogen has been implemented in Aspen Plus using property package PENG-ROB. The flowsheet containing two recycle streams is shown in Figure 2. The objective is minimizing the cost of benzene production given by the hydrogen (H_2) educt cost rate plus the total utility cost rate (electricity, gas-fired heat, steam, cooling water, and refrigeration) divided by the mass flow rate of produced benzene. The decision variables are (1) the hydrogen to toluene feed ratio (toluene feed is kept constant) and (2) the light gases purge ratio, which is set at the block SPLITTER.

This problem has been solved using PI, DE, and SHGO with Sobol sampling with the solutions being further polished by the SLSQP algorithm. Objective values, number of simulations, and decision variables are reported in Table 1. A high cost is assigned to the H_2 educt, so that the solution lies at very low H_2:Toluene and purge ratios, rendering simulation convergence challenging near the optimum. The SQP algorithm from Aspen Plus failed to converge, highlighting the importance of having other methods available.

The solution of this problem by the PI algorithm is shown in Figure 3. The initial design of simulations has been carried out using a low-discrepancy Hammersley set with 10 samples per input variable and the auxiliary PI maximization sub-problem is solved in every single iteration with the global SHGO algorithm. As it can be seen in the left-hand

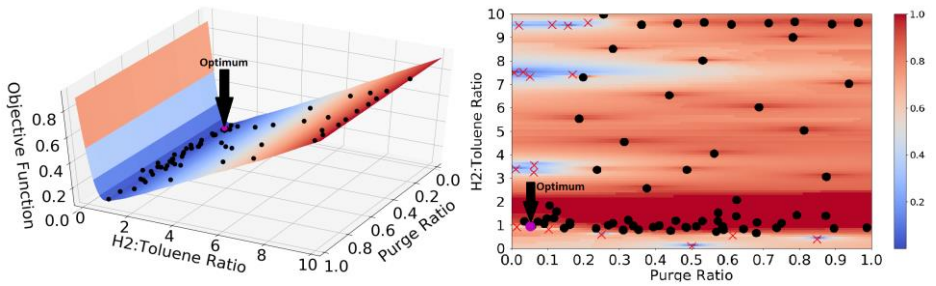

Figure 3 - HDA Process Optimization by the modified PI algorithm. Left: surrogate model predictions (surface) and rigorous model evaluations (dots). Right: Probability of convergence (colourmap), converged simulations (dots), failed simulations (crosses).

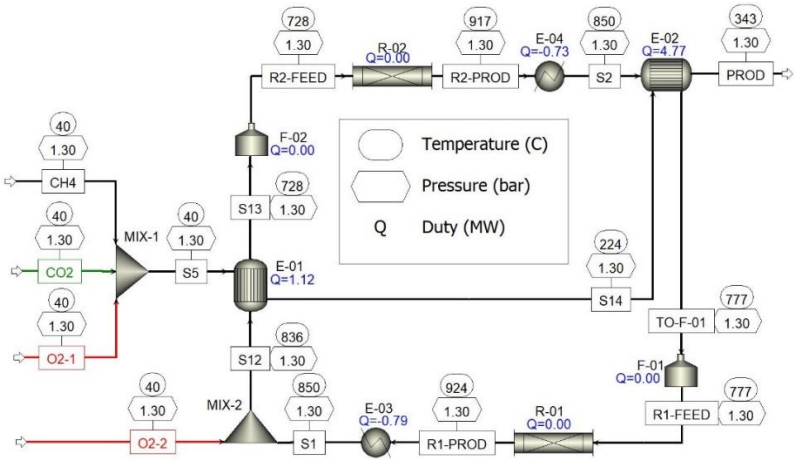

Figure 4 - Simulation Flowsheet of the OCM Process

plot of Figure 3, the convergence basin is quickly identified, and most new samples are placed therein. Yet, the global character of the PI method is also highlighted by the samples placed near the upper bounds of the decision variables, where objective value predictions were not particularly low, but the error was still high.

The right-hand plot in Figure 3 shows the probability of convergence (P_{conv}) for the HDA flowsheet computed by the kNN classifier with $k=3$ as a colour plot. This probability is high (darker colour) around converged simulations (dots) and lower (lighter colour) around failed ones (crosses). Simulations tend to diverge for hydrogen to toluene ratios below 1 and purge ratios lower than 0.1. Nevertheless, the solver is still able to move into this area, since the predicted objective values are low, and find the local optimum. In fact, the optimum lies very close to two failed simulations.

4.2. Oxidative Coupling of Methane (OCM) Process

The OCM reaction is the catalytic oxidation of methane into ethane and ethylene. The reaction section is modelled in Aspen Plus using two kinetic adiabatic Plug Flow Reactors (RPlug) (Penteado et al. 2018) as shown in Fig. 4. Biogas containing CH_4 and CO_2 can be used as renewable feedstock for this process. To model different types of biogas, CH_4 is mixed with a pure CO_2 stream, which serves as a diluent gas and helps to contain the reactions' exothermicity. The objective is to maximize the combined ethane and ethylene (C_2) yield, which is reported to be around 15% for industrial implementation (Siluria Technologies 2015). Methane feed is constant, and the seven decision variables are the feed temperatures, amounts of catalyst, and O_2 flowrates (limiting reactant) in each reactor, and the CO_2 flowrate. This is a very challenging problem because the objective function is incredibly stiff near the intended operating area of complete O_2 conversion.

Table 2 - Optimization Results for the OCM Process

Solver	C_2 Yield %	No. of Sim.	Decision Variables						
			°C		kmol·h^{-1}			kg	
			T_{feed}^{R-01}	T_{feed}^{R-02}	$\dot{F}^{CO2}$	$\dot{F}^{O2-1}$	$\dot{F}^{O2-2}$	w_{cat}^{R-01}	w_{cat}^{R-02}
DE	16.12	38,582	742	747	399	48	40	389	402
PI	15.96	4,869	760	776	402	46	38	134	196
SQP	15.12	1,457	755	756	392	36	39	337	246

The solution for the OCM process optimization is listed in Table 2. The highest yield is achieved with DE after 38,582 simulations. The PI algorithm achieved similar results with significantly fewer simulations. Nevertheless, optimization time is similar because (1) DE can be efficiently parallelized; (2) as the number of samples grow in the PI method, the surrogate model becomes more expensive to fit; and (3) for for higher dimensional problems, the PI maximization sub-problem becomes expensive and challenging to solve globally. Hence, the PI algorithm is better suited for time-consuming flowsheets with few decision variables. Both algorithms outperformed Aspen Plus' built-in SQP.
Higher CO_2 dilution (upper bound) is favourable to reaction performance. Optimal O_2 flow rates render CH_4:O_2 ratios of 8 and 10 for R-01 and R-02 respectively (stoichiometric is 2). Trade-offs are observed between feed temperature and amount of catalyst.

5. Conclusion

A framework for automated simulation, stochastic, and surrogate-assisted optimization of SM Aspen Plus flowsheets is implemented in Python and published as an open-source project. A new SAO algorithm is developed by modifying the PI method making it more suitable to handle failed simulations. The framework is successfully applied to solve two practical chemical engineering examples. Future work aims at minimizing the total annualized cost for the biogas-based OCM process, including the downstream CO_2 removal and distillation sections which have not been included herein.

Acknowledgements

Financial support from German Federal Ministry of Education and Research (BMBF 01DN1703/031B0608A) and CAPES/Brazil (11946/13-0) are gratefully acknowledged

References

R. R. Carpio, R. C.Giordano, A. R. Secchi, 2018, Enhanced surrogate assisted framework for constrained global optimization of expensive black-box functions, Computers & Chemical Engineering 118, 91–102

S. C. Endres, C. Sandrock,; W. W. Focke, 2018, A simplicial homology algorithm for Lipschitz optimisation, Journal of Global Optimization 72(2), 181–217

D. R. Jones, 2001, A Taxonomy of Global Optimization Methods Based on Response Surfaces, Journal of Global Optimization 21, 345–383

E. Jones, T. Oliphant, P. Peterson, others, 2001, SciPy: Open source scientific tools for Python. Available online at http://www.scipy.org/

D. A. Kraft, 1988, A software package for sequential quadratic programming, Cologne, Germany: DLR German Aerospace Center. Available online at Tech. Rep. DFVLR-FB 88-28.

E. Martelli, E. Amaldi, 2014, PGS-COM: A hybrid method for constrained non-smooth black-box optimization problems, Computers & Chemical Engineering 63, 108–139

F. Pedregosa, G. Varoquaux, A. Gramfort, V. Michel, B. Thirion, O. Grisel, M. Blondel, P. Prettenhofer, R. Weiss, V. Dubourg, J. Vanderplas, A. Passos, D. Cournapeau, M. Brucher, M. Perrot, E. Duchesnay, 2011, Scikit-learn: Machine Learning in Python, Journal of Machine Learning Research 12, 2825-2830

A. T. Penteado, M. Kim, H. R. Godini, E. Esche, J.-U. Repke, 2018, Techno-economic evaluation of a biogas-based oxidative coupling of methane process for ethylene production, Frontiers of Chemical Science and Engineering, 12(4), 598–618

Siluria Technologies, 2015, Oxidative Coupling of Methane Implementations for Olefin Production, Patent no. US 2015/0210610 A1

R. Storn, K. Price, 1997, Differential Evolution - A Simple and Efficient Heuristic for global Optimization over Continuous Spaces, Journal of Global Optimization, 11, 341–359.

Sauro Pierucci, Flavio Manenti, Giulia Bozzano, Davide Manca (Eds.)
Proceedings of the 30th European Symposium on Computer Aided Process Engineering (ESCAPE30), May 24-27, 2020, Milano, Italy.
http://dx.doi.org/10.1016/B978-0-12-823377-1.50319-0

Quantitative Risk Assessment and Management for CO_2 Utilisation Industrial Network

Ali Attiq Al-Yaeeshi[a], Rajesh Govindan[b], Tareq Al-Ansari[a,b]*

[a]*Divison of Sustainable Development, College of Science and Engineering, Hamad Bin Khalifa University, Qatar Foundation, Doha, Qatar*
[b]*Divison of Engineering Management and Decision Sciences, College of Science and Engineering, Hamad Bin Khalifa University, Qatar Foundation, Doha, Qatar*
talansari@hbku.edu.qa

Abstract

As a means to control CO_2 emissions, various technologies and processes related to carbon capture and utilisation have been studied with a view of creating large-scale industrial symbiosis for CO_2 recycling and re-use. Such industrial networks consequently provide new economic opportunities as value-added products can be produced from waste CO_2. However, investments in such networks at national or transnational scales entail technical, social and environmental risks that in turn affect the expected economic returns, with a further potential in devaluation of such investments. This study presents a hazard identification (HAZID) and quantitative risk assessment (QRA) methodology for large-scale carbon capture and utilisation networks based on existing sources and sinks in the State of Qatar, capturing technical viabilities at the process and systems levels, and compliance with local and international environment regulations. The QRA integrates hydrocarbon leakage and dispersion modelling simulation using data obtained from existing GIS databases into a single model. In assessing network failure scenarios, the model considers (a) CO_2 sources, such as from LNG plant and chemical process industries, such as Methanol, Urea and Gas-to-Liquid (GTL) fuels; (b) CO_2 transportation (pipeline) service corridors; and (c) CO_2 sinks that manufacture value added products. Stochastic variables used to assess network robustness are represented by pipeline layouts, material and composition, diameter, pressure, temperature, heat and mass balance, other equipment items, *e.g.* compression station, turbine and reactors. The results demonstrate that the CO_2 network should be located outside high population density area. The approach demonstrates CO_2 release from 20" pipeline rupture to nearby residential area is relatively very low 19.07 $\mu g/m^3$ (0.0191 ppm) that would no impact the population while the CO_2 concentration at 1,000 meter wide from the centerline, 4 $\mu g/m^3$.

Key words: CO_2 utilisation, Methanol, Urea, GTL, Quantitative Risk Assessment

Introduction

Carbon Capture and Storage (CCS) and Carbon Capture and Utilisation (CCU) technologies are considered effective methods to mitigate CO_2 emissions. Contrary to CCS, which depends on the storage of CO_2 in underground storage sites after capture, compression and transportation, CCU seeks to convert CO_2 into value-added products.

The Global CCS institute (2010) reported that there are 275 CCS projects globally, of which 213 were active, or still in the planning phase representing a growth in the industry. Transportation of CO_2 is a key component of the CCU network which largely depends on pipelines that can pass through densely populated areas resulting in costly routing challenges. The USA is the leading transporter of CO_2 pipeline worldwide with over 6000 km mainly dedicated to EOR projects, and a combined capacity from Australia, Europe, and Africa amounting to 500 km (Koornneef *et al*., 2010; Vianello *et al*., 2016). In anticipation of the growth of CO_2 pipeline capacity, it is important to devise safety and quantitative risk assessment (QRA) procedures that can inform routing challenges. In this regard, Nyborg *et al*. (2011) evaluated through the occurrence probabilities of pipeline leakages for different routes. The methodology combines the GIS-based risk analysis and social risk assessment to determine route selections in order to reduce costs and risks. Koornneef *et al*. (2010) presented a systematic assessment based on gaps and uncertainties of QRA results applied in different literature studies which include failure rate, pipeline pressure, temperature and the direction of release. The study demonstrated a significant difference in the risk results after applying dispersion and impact models that conclude the risk levels varies between 0 to 204 meter contours, extending to 7.2 kilometres. Woolley *et al*. (2014) demonstrated that to overcome the challenges to predict the equilibrium phase, thermodynamic and transport properties of the CO_2, the adequacy of control measures for CO_2 pipelines, along with practical guidelines and validated experiments shall be developed. Knoope *et al*. (2014) assessed the locational and societal risks of CO_2 transportation in dense area is cost effective attributed that to the additional risk mitigation measures. The study model used EFFECTS and RISKCURVES to estimate the dispersion and risk contour. The case study applied to meet regulations in the Netherlands, and conclude that the dense phase CO_2 transport can be routed in safe operation if system is well controlled. Vianello *et al*. (2016) elaborate some concerns in CO_2 release consequence as demonstrated in the QRA in CO_2 pipeline network in UK as one of the major consequences is the CO_2 phase when it releases from the pipeline where it will form gaseous, liquid and solid.

The objective of the study is to present a QRA for a CCU network in Qatar in order to assess the societal impact risk of pipeline rupture. This has an implication for making decisions on selecting the optimal route. The QRA considers failure risk type identification and quantification inventories for multiple stages of the network that are based on major hazards to the public and environment, such as pipeline layouts, and product properties. The QRA methodology is based on hydrocarbon leakage and dispersion modelling simulation, integrated with GIS mapping-based on the pipeline layout design and product properties.

Network data analysis for CCU system

The CO_2 pipeline network considered comprises of a single CO_2 source, namely Qatar Gas (QG), and five potential sinks that have been identified for the economic utilisation of CO_2, namely: Qatar Fertilizer Company (QAFCO); two plants in Qatar Fuel Additives Company (QAFAC), one utilising natural gas, whilst the other utilising hydrogen; Oryx GTL; and Pearl GTL, all located in the Mesaieed and Ras Laffan industrial zones. It is envisaged that the pipeline construction would be placed in accordance with a comprehensive risk analysis which includes the hazard scenarios and their impact on people, assets, environment and economics. Thus, the best practice

model would be applied to ensure the high level of safety for pipeline transmission and distribution along with risk mitigation measures by attempting to reduce the failure frequency and controlling the event consequences. The compression station is considered to be located at source section to meet the sinks pressure requirements. The pipeline length between Messaid and Ras Laffan industrial zones is 100 km, including the distribution network inside the industrial cities. The design is according to the API 5L X60 and diameter 20". The operating parameters are listed in Table 2. Locally, fuel and feed gas through a service corridor designed to comply with safety regulations and risk reduction by applying 120 km length and 800 m width (Al-Rasheed, 2014).

Methodology

The methodology developed in this study is an extension of previous studies by Al-Yaeeshi *et al*. (2018;2019) which set the basis of optimised allocation of CO_2 to sinks. The models considered a CO_2 pipelines from QG to QAFCO, QAFAC with NG, QAFAC with H_2, Oryx GTL and Pearl GTL. The objective of the research presented in this paper is to mitigate the risk of pipeline rupture potentially releasing CO_2 that can affect humans and the environment. Failure scenarios and their probability are varied from place to another due to the topographical features, construction guidelines, material selection and product properties. Based on the historical failure frequency per 1000 km /year of the pipelines, including different products based on the data from USA, UK and EU, are attributed to corrosion and weld defects.

3.1. Dispersion Model and consequences of a CO_2 release

In the assessment of CO_2 dispersion, an empirical Gaussian method is used to estimate the vertical and horizontal concentration of CO_2 that will reach the nearest residential area upon leakage (Sutton, 1932; Abdel-Rahman, 2008). The Gaussian dispersion model is applied to quantify CO_2 emissions and concentration levels in the atmosphere along with consequences scenario to measure the risk and to simulate hazard scenarios.

$$\mathrm{C(x,y,z;H)} = \mathrm{A1} * \mathrm{A2(A3+A4)}$$

$$= \frac{Q}{2\pi u \sigma_y \sigma_z}\left[Exp\left(-\frac{y^2}{2{\sigma_y}^2}\right)\right]\left[Exp\left(-\frac{(z-\mathrm{H})^2}{2{\sigma_z}^2}\right) + Exp\left(-\frac{(z+H)^2}{2{\sigma_z}^2}\right)\right]$$

C= Steady -state concentration at a point (x,y,z), μg/m^3
Q= mass emission rate, μg/m^3
X= downwind distance, m
y= horizontal distance from plume centerline, m
z= vertical distance from ground level, m
σ_y= Lateral dispersion coefficient function (m)
σ_z= vertical dispersion coefficient function (m)
u_s= average wind speed at stack height, m/s
H= stack height (H= h+Δh, where h= physical stack height and Δh= plume rise, m).

Coefficient function or Diffusion parameters are defined as the standard deviation and they are important to demonstrate the results. In this study, the McElroy-Pooler formula (for urban conditions) is used to estimate the coefficient functions σ_y and σ_z as indicated

in Table 1. Here, X is the downwind distance (X, m), and stability A is the worst case condition, classified as unstable scenario.

Table 1: Formulae McElroy-Pooler (Urban Condition).

Stability	σ_y	σ_z
A	$0.32X\ (1.0+0.0004\ X)^{-1/2}$	$0.24X\ (1.0+0.001\ X)^{1/2}$
B	$0.32X\ (1.0+0.0004\ X)^{-1/2}$	$0.24X\ (1.0+0.001\ X)^{1/2}$
C	$0.22X\ (1.0+0.0004\ X)^{-1/2}$	$0.20\ X$
D	$0.16X\ (1.0+0.0004\ X)^{-1/2}$	$0.14X\ (1.0+0.003\ X)^{-1/2}$
E	$0.11X\ (1.0+0.0004\ X)^{-1/2}$	$0.08X\ (1.0+0.015\ X)^{-1/2}$
F	$0.11X\ (1.0+0.0004\ X)^{-1/2}$	$0.08X\ (1.0+0.015\ X)^{-1/2}$

Discussion and Results

The CO_2 20" pipeline being proposed to lay above the ground on existing pipeline corridor from Ras Laffan to Mesaieed (north to south of State of Qatar), approximately 100 km length . The risk of pipeline rupture will release large volume of CO_2 gas in which it will affect to the human that living nearby the pipeline. The nearest populated area is at middle of the country, approximately 2.5 km away from the CO_2 pipeline. The empirical Gaussian method was thus used to estimate the vertical and horizontal concentration of CO_2 that will reach the nearest residential area. The following incident scenario, depicted in table 2, was considered in developing the CO_2 gas dispersion using Gaussian model:

Table 2: Data Input Gaussian model.

CO_2 Transmission Ton per year	6000000
CO_2 Transmission Ton per day	16438.3562
CO_2 Transmission kg/hr	684.931507
CO_2 Transmission g/s	190.26
CO_2 density at 30 deg c,kg/m^3	1.777
CO_2 flow rate, m^3/hr	385.442604
Operating Temperature, C	45
Operating Temperature, Kelvin	318.15
Ambient Temperature, C (Winter)	15
Ambient Temperature, K	288.15
Operating Pressure, barg	20
Pipe size, in	20
Pipe size, m	0.508
Velocity, m/s	1

The pipeline is considered to be on full transfer mode to customers in Mesaieed. It is assumed that the pipeline rupture occurs during night time, when most of the population are resting 2.5 km away from the pipeline. The wind speed is 5 m/s in the direction of the residential area. The residential area size is 1,000 m x 1,000 m and it is assumed the tallest building does not exceed 10 m. The weather condition is winter season, where the expected dispersion is generally low level. With the above scenario, outcomes of the Gaussian method calculated from the spread sheet are as follows:

- CO_2 concentration is high at the ground level, about 19.07 μg/m^3, refer figure 1.
- CO_2 concentration at 1,000 meter wide from the center line, 4 μg/m^3, refer figure 2.

Based on the HAZID Analysis and Risk Assessment, it can be suggested that:

1- CO_2 release from 20" pipeline rupture to nearby residential area about 2.5 km distance is relatively very low 19.07 µg/m^3 (0.0191 ppm) resulting in no impact to the population.
2- It is recommended to bury the CO_2 in a shared corridor with other gas pipelines, which will reduce the dispersion to the populated area in case of rupture. It should also consider future expansion of the residential area.
3- It is recommended for the asset holder to develop a pipeline inspection and maintenance program. A pigging facility should also be installed at Ras Laffan and Mesaieed to ensure the pipeline integrity and increase its lifecycle in addition mitigate the risk.
4- Leak detection system and emergency shut down valve system should be installed.
5- Proper access to the CO_2 pipeline should be provided for Maintenance.

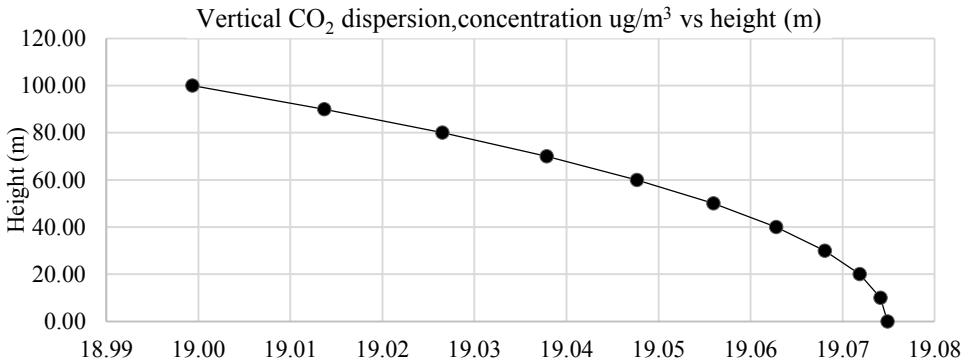

Figure 1: Vertical distribution of CO2 gas from source of leak, 2. 5 km away.

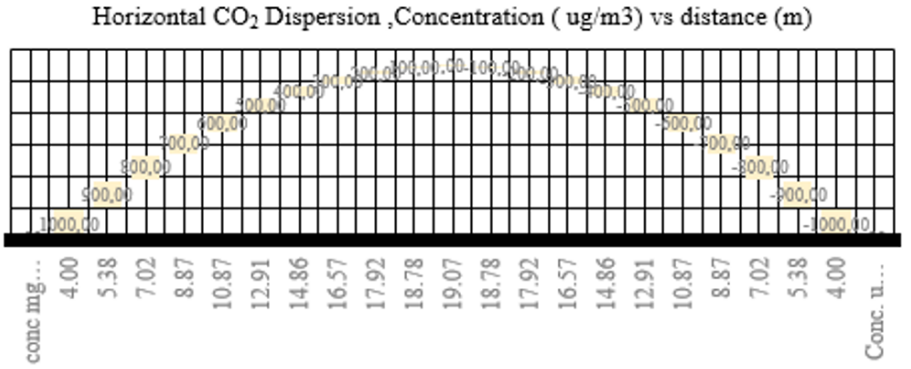

Figure 2: Horizontal distribution of CO2 gas from source of leak, 2.5 km away.

Conclusion

This study introduces a quantitative risk assessment (QRA) methodology for large-scale carbon capture and utilisation networks based on existing sources and sinks in the State of Qatar as a case study. The approach demonstrates CO_2 release from 20" pipeline

rupture to nearby residential area is very low 19.07 μg/m^3 (0.0191 ppm), and as a result there would be no impact on the population as the CO_2 concentration at a point 1,000 meter wide from the centerline is 4 μg/m^3. It is recommended to bury the CO_2 pipeline in a service corridor which includes many hydrocarbon pipelines and utilities in order to mitigate the risk of dispersion in the case of rupture. There should also be a consideration for urban development and expansion and how that may impact pipeline routing.

References

Abdel-Rahman, A.A., 2008, October. On the atmospheric dispersion and Gaussian plume model. In *Wwai'08: Proceedings of the 2nd International Conference on Waste Management, Water Pollution, Air Pollution, Indoor Climate* (pp. 31-39).

Al-Yaeeshi, A.A., Al-Ansari, T. and Govindan, R., 2018. The potential for carbon dioxide capture and utilisation within the State of Qatar. In Computer Aided Chemical Engineering (Vol. 43, pp. 1499-1504). Elsevier.

Al-Yaeeshi, A.A., Al-Ansari, T. and Govindan, R., 2019. A network model-based optimisation analysis for the utilisation of CO2 in Qatar's chemical industries. In Computer Aided Chemical Engineering (Vol. 46, pp. 295-300). Elsevier.

Al-Rasheed, A.E., 2014, January. The Hydrocarbon Pipeline Network and Development in Qatar. In IPTC 2014: International Petroleum Technology Conference.

GLOBAL CCS INSTITUTE, 2010, Strategic analysis of the global status of carbon capture and storage. Report 1: status of carbon capture and storage projects globally. Available from: https://hub.globalccsinstitute.com/publications/strategic-analysis-global-status-carbon-capture-storage-report-1/11-purpose [Accessed 7 December 2017].

Knoope, M.M.J., Raben, I.M.E., Ramírez, A., Spruijt, M.P.N. and Faaij, A.P.C., 2014. The influence of risk mitigation measures on the risks, costs and routing of CO2 pipelines. *International Journal of Greenhouse Gas Control*, *29*, pp.104-124.

Koornneef, J., Spruijt, M., Molag, M., Ramírez, A., Turkenburg, W. and Faaij, A., 2010. Quantitative risk assessment of CO_2 transport by pipelines, a review of uncertainties and their impacts. *Journal of hazardous materials*, *177*(1-3), pp.12-27.

Nyborg, M., Arvidsson, K., Johansson, J., Liljemark, S. and Olsson, L., 2011. Risk analysis methodology for CO2 transport including quantified risk calculation. *Energy Procedia*, *4*, pp.2816-2823.

Sutton, O.G., 1932. A theory of eddy diffusion in the atmosphere. Proceedings of the Royal Society of London. Series A, Containing Papers of a Mathematical and Physical Character, 135(826), pp.143-165.

Vianello, C., Mocellin, P., Macchietto, S. and Maschio, G., 2016. Risk assessment in a hypothetical network pipeline in UK transporting carbon dioxide. *Journal of Loss Prevention in the Process Industries*, *44*, pp.515-527.

Woolley, R.M., Fairweather, M., Wareing, C.J., Falle, S.A., Mahgerefteh, H., Martynov, S., Brown, S., Narasimhamurthy, V.D., Storvik, I.E., Sælen, L. and Skjold, T., 2014. CO2PipeHaz: quantitative hazard assessment for next generation CO2 pipelines. *Energy Procedia*, *63*, pp.2510-2529.

Sauro Pierucci, Flavio Manenti, Giulia Bozzano, Davide Manca (Eds.)
Proceedings of the 30th European Symposium on Computer Aided Process Engineering (ESCAPE30), May 24-27, 2020, Milano, Italy.
http://dx.doi.org/10.1016/B978-0-12-823377-1.50320-7

Assessing Thermodynamic Flexibility Boundaries via Residue Curve Maps

Alessandro Di Pretoro[a,b], Ludovic Montastruc[a]*, Flavio Manenti[b], Xavier Joulia[a]

[a]*Laboratoire de Génie Chimique, Université de Toulouse, CNRS/INP/UPS, Toulouse, France*
[b]*Politecnico di Milano, Dipartimento di Chimica, Materiali e Ingegneria Chimica "Giulio Natta", Piazza Leonardo da Vinci 32, 20133 Milano, Italia*
ludovic.montastruc@ensiacet.fr

Abstract

Residue curve maps (RCMs) are a widely exploited tool to assess whether a multicomponent mixture separation by distillation results to be feasible or not. They usually refer to a given feed composition and to the products purities as specifications; sometimes the whole distillation regions can be discussed in order to evaluate all the mixture possible splits (Petlyuk & Danilov (2001), Petlyuk (2004)).

All these considerations are nevertheless related to nominal operating conditions, that is for a given and constant feed composition. If feed perturbations are likely to occur (e.g. separation downstream a fermentation process) a flexibility analysis is required to assess the operation feasibility boundaries under uncertain conditions (Swaney & Grossmann (1985)). Moreover, product recovery is often a more appealing specification from an industrial point of view since it is directly related to the process productivity.

For all these reasons, this study deals with the use of RCMs to assess the thermodynamic flexibility limits of a simple distillation case study for a given bottom product recovery and purity under uncertain operating conditions. The starting binary mixture is water and n-butanol, a common and well-known mixture whose separation by simple distillation shows an heterogeneous azeotrope. One component at a time is then added up to obtain an ABE/W (acetone, butanol, ethanol and water) mixture.

Due to the high nonideality of the mixture, the addition of an organic component substantially affects the equilibria. A thermodynamic flexibility analysis methodology was outlined for both the binary and ternary cases as well as for the quaternary one. After that, the separation feasibility of the binary mixture was compared to the others (Di Pretoro et al. (2019)). Beside illustrating the procedure for thermodynamic flexibility assessment via RCMs, this analysis aims to show how to enhance the separation from a flexibility point of view taking advantage of the mixture nonideality.

Keywords: flexibility, residue curve maps, thermodynamics, distillation

1. Introduction

Residue Curve Maps (RCM) were first introduced by Ostwald in 1900 [1] to analyze phase equilibrium for three component azeotropic mixtures. They received poor attention until the second half of the 20th century thanks to Zharov and Serafimov (1967, 1968a, 1968b, 1969, 1975) who developed a generalized theory about these topological

objects aimed to classify multicomponent mixtures behaviors. However, it is only thanks to Petlyuk et al. (2001, 2004) that the scientific knowledge about residue curve maps was spread outside Russia. In particular he showed their useful application to the optimal design of distillation columns.
On the one hand then, this useful tool has a long history, on the other hand distillation column design under uncertain conditions is a younger research field. Thus this paper will couple them by mean of the procedure explained in the following chapter in order to provide the design engineer the physical feasibility boundaries of the process under perturbated operating conditions.

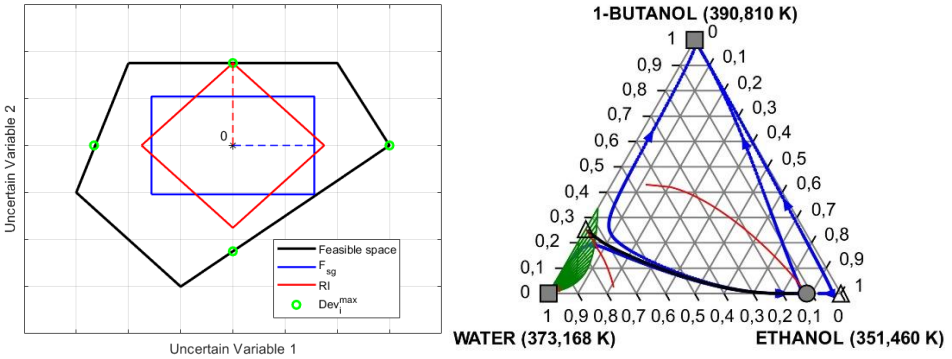

Figure 1 – Resilience Index Example (left); Residue Curve Maps Example (right)

2. Methodologies

2.1. A Measure for Flexibility

In order to quantify flexibility a corresponding flexibility index is required. Several flexibility indexes, both deterministic and stochastic, aimed to this purpose were proposed in literature.
In this paper the so called Resilience Index (Saboo et al. (1985)) is used since it is the most suitable for an easy understanding of the methodology. However, the outcome of the analysis does not qualitatively depend on the flexibility index that is used.
The Resilience Index (hereafter RI) is defined as the largest total disturbance load, independent of the direction of the disturbance, a system is able to withstand without becoming unfeasible. From a mathematical point of view it stands as:

$$RI = \min_i \{|l_i|\} \tag{1}$$

$$s.t.\{\max_j f_j(\theta) \leq 0, \forall l: \sum_i |l_i| \leq RI\} \tag{2}$$

From an operational point of view it corresponds to evaluating the largest possible polytope inscribed inside the feasible region defined by the inequalities here above. The RI is then equal to the distance between a vertex of the polytope and the nominal operating point 0 as shown in Figure 1 .

2.2. Residue Curve Maps

A Residue Curve (RC) is defined as the locus of compositions satisfying the equation:

$$\frac{dx_i}{d\xi} = x_i - y_i \tag{3}$$

The equation comes from the mass balance on the residue in an open distillation process where ξ indicates a temporal variable. The Residue Curve obtained by its integration describes the time evolution of the residue composition. The same expression can be found if the mass balances are performed on an infinite distillation column at infinite reflux; in that case the RC outlines the composition profile along the column equilibrium stages.

3. Case studies

Three distillation case studies about the ABE/W mixture are discussed. All of them aim to recover 96 % of the butanol present in the feed with 0.99 w/w purity by means of atmospheric distillation. Starting from the water-butanol binary mixture the ternary and quaternary case studies are built by adding namely Ethanol and Acetone one at a time. At the end a typical value of an ABE/W mixture feed composition upstream a separation section is obtained as shown in Table 1.

Table 1 - Feed components partial flowrates

Component	Partial flowrate (mol/s)
n-Butanol	61.328
Water	9.583
Ethanol	3.839
Acetone	12.030

The butanol recovery feasibility analysis is equivalent to the flexibility assessment of the first distillation column in the indirect configuration of a distillation train aimed to separate this multicomponent mixture.
The uncertain variables taken into account during the flexibility analysis are butanol and water partial flowrates since they are both the most critical parameters and the ones most likely to vary because of the floating nature of the feedstock and because of a possible underperformance of the upstream dewatering section.

4. Results

4.1. Binary Mixture

The first case study concerns the Water-Butanol binary distillation without decantation. This mixture was deeply studied in literature since it is the typical case of aqueous-organic mixture with liquid phase demixing and that shows an heterogeneous azeotrope (x_{water}=0.747 mol/mol). Given the feed composition and the distillation specifications discussed in the previous chapter, the corresponding equilibrium phase diagram is plotted in Figure 2.
As it can be noticed, in the binary case, the residue curve corresponds to the diagonal of the phase diagram. If the feed is located on the left of the azeotrope the stable and unstable nodes are namely pure butanol and the azeotrope. If the feed is located on the right of the azeotrope the stable and unstable node shifts to pure water and pure butanol cannot be obtained anymore by simple distillation.

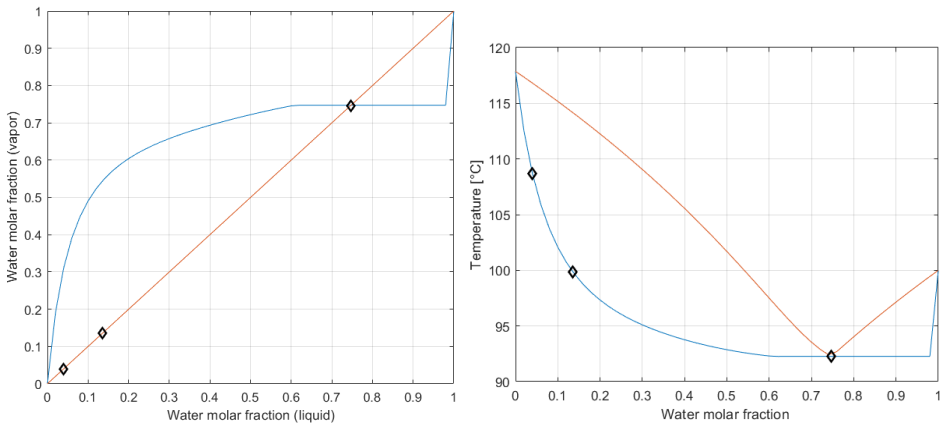

Figure 2 – Binary mixture phase diagram and characteristic points (y vs x and T vs xy)

Given the process specifications, the characteristic points related to the bottom product, feed and distillate respectively (from the left to the right) are represented in the phase diagram. Excepted particular cases, the necessary and sufficient condition to separate a multicomponent mixture by distillation is that the Residue Curve of the feed and the products lie in the same distillation region. As it can be noticed, under nominal operating conditions, the distillate characteristic point is close to the boundary defined by the azeotrope. This means that the operation is feasible under nominal operating conditions but as soon as an increase of the water content occurs the system is not able to obtain the desired products anymore, i.e. its flexibility index RI is equal to zero.

4.2. Ternary Mixture

Ethanol was then added to the previous components with the consequent introduction of the corresponding water-ethanol homogeneous azeotrope in the phase equilibrium diagram.

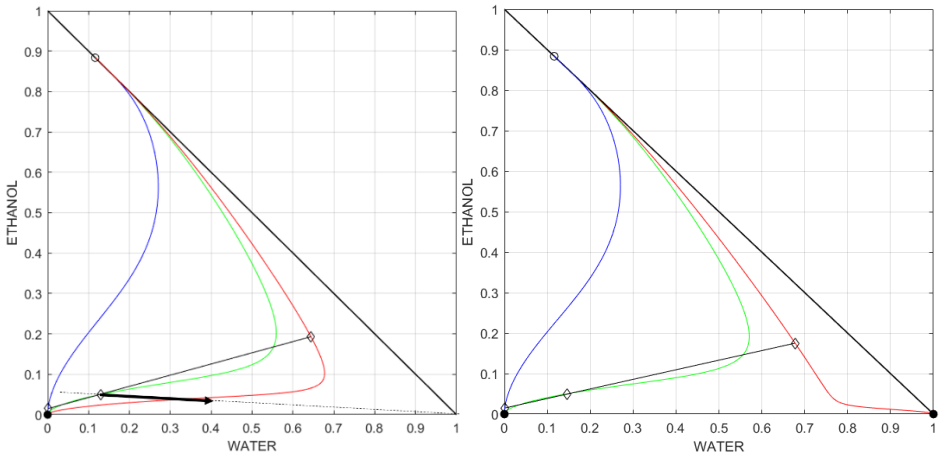

Figure 3 – Ternary mixture RCMs: nominal operating conditions (left); feasibility limit (right)

A new stable node is present in the phase diagram (i.e. the homogeneous azeotrope) while pure ethanol is a saddle point. Under nominal operating conditions separation by distillation results feasible (see Figure 3 left) since RCs corresponding to feed, bottom

and distillate fall into the same distillation region. The flexibility assessment can be then performed by perturbing butanol and water molar flowrates. The most constraining limit for each of them is 41.7 mol/s (-32%) and 10.55 mol/s (+10.1%) respectively. The Resilience Index for the ternary mixture is the most constraining among each single variable maximum load, i.e. RI=10.1 %. The RCMs for a water partial flowrate crossing the feasibility boundary is shown in Figure 3 (right).

4.3. Quaternary Mixture

Acetone is finally included in the analysis obtaining a feed composition equal to the feed stream composition of an ABE/W plant separation section after dewatering.

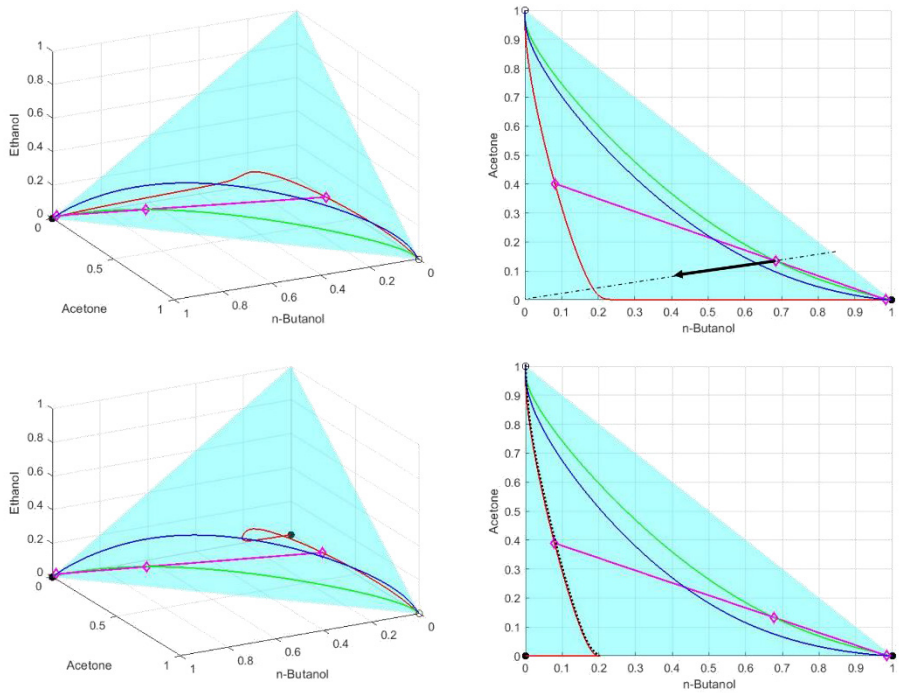

Figure 4 – RCM under nominal operating conditions (top); RCM out of the feasibility boundary (bottom) – Red: distillate, Green: feed, Blue: bottom.

While for binary and ternary mixtures process simulators are already able to provide 2D phase diagrams and RCMs, for the quaternary mixtures an interface between Matlab® and Simulis Thermodynamics® was coded in order to perform 3D Residue Curve Mapping. Results for nominal operating conditions are shown in Figure 4 (top).

Butanol and water partial flowrates are disturbed until unfeasible conditions are achieved. Water results once again the most constraining variable with a maximum flowrate in the feed equal to 13.3 mol/s. The RI for the quaternary mixture is then higher than the ternary one and equal to RI=39.1%. Due to the convexity of the distillation boundary (cf Figure 3 bottom) acetone addition enhances the separation showing an "entrainer-like" behavior.

On the other hand, if the separation process aims to recover water, i.e. a distillation column operating in the other distillation region, the feasibility boundary would show its concave side towards the operating line, that means the acetone addition would have a negative impact on the separation.

5. Conclusions

The thermodynamic flexibility assessment of a distillation process has been successfully performed by means of Residue Curve Mapping for binary, ternary and quaternary mixtures. The binary case study is barely feasible under nominal operating conditions, thus no flexibility could be detected.

The addition of ethanol, although introducing an additional azeotrope in the thermodynamic system, had a positive impact on the process shifting the maximum withstood water perturbation up to 10.1%. Finally, the presence of acetone strongly improves the separation performance under uncertain conditions with a corresponding RI value equal to 39.1 %.

Coupling the flexibility analysis with RCMs resulted to be an useful methodology to provide an "a priori" knowledge about the maximum flexibility of a distillation system likely to undergo disturbances. Moreover this paper shows how the presence of an additional component could positively (or negatively) affect the operation from a flexibility point of view.

The thermodynamic flexibility assessment is the very first step of a further detailed process design under uncertain conditions taking into account economic aspects as well and it represents the physical constraint of the design problem that cannot be violated whatever the investment that can be afforded.

References

Di Pretoro, A., Montastruc, L., Manenti, F., Joulia, X., 2019. Flexibility Assessment of a Distillation Train: Nominal vs Perturbated Conditions Optimal Design, Computer Aided Chemical Engineering, 29 European Symposium on Computer Aided Process Engineering, 46, pp. 667–672.

Ostwald, W. (1900). Dampfdrucke ternarer Gemische, Abhandlungen der Mathematisch-Physischen Classe derKonige Sachsischen. Gesellschaft derWissenschaften, 25, 413–53 (Germ.).

Petlyuk, F.B., Danilov, R.Yu., 2001. Theory of Distillation Trajectory Bundles and its Application to the Optimal Design of Separation Units: Distillation Trajectory Bundles at Finite Reflux. Chem. Eng. Res. Des., Distillation and Absorption 79, 733–746.

Petlyuk, F.B., 2004. Distillation Theory and its Application to Optimal Design of Separation Units. Cambridge University Press.

Saboo, A.K., Morari, M., Woodcock, D., 1985. Design of Resilient Processing Plants .8. a Resilience Index for Heat-Exchanger Networks. Chem. Eng. Sci. 40, 15531565. https://doi.org/10.1016/0009-2509(85)80097-X

Serafimov, L. A., 1969. The Azeotropic Rule and the Classification of Multicomponent Mixtures. 4. N-Component Mixtures. J. Phys. Chem., 43, 981–3 (Rus.).

Swaney, R.E., Grossmann, I.E., 1985. An index for operational flexibility in chemical process design. Part I: Formulation and theory. AIChE J. 31, 621–630.

Zharov, V. T., 1967. Free Evaporation of Homogeneous Multicomponent Solutions. J. Phys. Chem., 41, 1539–55 (Rus.).

Zharov, V. T., 1968a. Free Evaporation of Homogeneous Multicomponent. Solutions. 2. Four Component Systems. J. Phys. Chem., 42, 58–70 (Rus.).

Zharov, V. T., 1968b. Free Evaporation of Homogeneous Multicomponent Solutions. 3. Behavior of Distillation Lines Near Singular Points. J. Phys. Chem., 42, 195–211 (Rus.).

Zharov, V. T., & Serafimov, L. A., 1975. Physico-Chemical Foundations of Bath Open Distillation and Distillation. Leningrad: Khimiya (Rus.).K. M. Guthrie, 1969, 'Capital Cost Estimating', Chemical Engineering, 76.3, 114-142.

Sauro Pierucci, Flavio Manenti, Giulia Bozzano, Davide Manca (Eds.)
Proceedings of the 30th European Symposium on Computer Aided Process Engineering (ESCAPE30), May 24-27, 2020, Milano, Italy.
http://dx.doi.org/10.1016/B978-0-12-823377-1.50321-9

A Straightforward Optimization Approach for a Baseload Propane-Mixed Refrigerant Process

Mary Katebah, Mohamed Hussein, Easa I. Al-musleh*

Department of Chemical Engineering, Qatar University, P.O.Box 2713, Doha, Qatar
e.almusleh@qu.edu.qa

Abstract

As the energy markets adjust to the increasing demand on liquefied natural gas (LNG) and growing global warming concerns, a compelling need arises to operate existing LNG plants as efficiently as possible. Cryogenic systems, such as those used for natural gas (NG) liquefaction, are very complex. This makes optimizing their performance a frustrating task. In this paper, we propose a simple and systematic optimization approach for cryogenic processes characterized by large numbers of independent variables and sophisticated heat integration schemes. The method is composed of successive optimization levels that rely on shortcut thermodynamic techniques and sequential quadratic programming (SQP). In this paper, we are reporting the results of the proposed approach for optimizing an actual baseload propane mixed refrigerant (C3MR) process. Results showed a 6 % compression power reduction compared to the plant's current consumed power. The method is currently being tested for a more sophisticated LNG system employing C3MR cycles integrated with natural gas liquids (NGL) recovery, helium extraction, and nitrogen rejection processes.

Keywords: Natural gas liquefaction, C3MR LNG plant, Optimization, Aspen Plus™, Simulation

1. Introduction

Liquefied natural gas (LNG) plants are associated with large energy penalties, mainly compression power, that are costly and result in significant amounts of greenhouse gas emissions (Almeida-Trasvina and Smith, 2019). However, compared to other fossil fuels, LNG has gained popularity due to its abundance and high energy content per mole carbon (Bittante et al., 2015). As of November 2019, global nominal and proposed liquefaction capacity reached 393 and 843 million tonnes per year (tpy), respectively (IGU, 2019). A significant portion of the forecasted capacity is expected to be from Qatar's North Field Expansion (Energy Insights by McKinsey, 2019). Qatar's plans of increasing its production by 64 % in the 2020s solidifies its position as the global leader in terms of capacity and exports (John, 2019). Increased LNG demand and stringent environmental regulations place utmost importance on energy efficiency optimization. In addition to potentially higher production volumes and profit, LNG process optimization can reduce CO_2 emissions, thereby assisting with the global dual challenge of producing more energy with less carbon (BP, 2019).

Figure 1 illustrates the block flow diagram of a typical LNG plant. After the removal of condensate, carbon dioxide, and sulfur-containing compounds (H_2S, mercaptans, etc.), the NG is routed to the dehydration unit prior to entering the cold section. First, heavier hydrocarbons (NGLs) are removed from the NG, after which the gas gets liquefied and sent to the helium extraction and nitrogen removal units to produce in-spec LNG ready

to be stored and shipped to the consumers. Within the LNG processing plant, our LNG supply chain model showed that over 55 % of CO_2 emissions originate from the cold section (Katebah et al., 20XX). Furthermore, our chain exergy analysis indicated that within the cold section ~91 % of the losses occur in the propane pre-cooled mixed refrigerant (C3MR) liquefaction cycles and natural gas liquids (NGL) recovery unit (Bouabidi et al., 20XX). Therefore, this paper focuses on the energy efficiency optimization of an actual C3MR process in Qatar, the world's largest LNG capacity holder and exporter. While there are numerous studies in the literature on the optimization of LNG liquefaction cycles, most of them require linking standard simulators to sophisticated solvers and/or time intensive coding, resulting in complex and time-consuming calculations and convergence challenges (Austbø et al., 2014). For example, the work of Wang et al. focused on minimizing energy consumption of a C3MR plant by using LINDO Global solver in GAMS to solve the optimization problem. (Wang et al., 2012). Sun et al. utilized GA for the optimization of an AP-X process by reducing the process's power consumption (Sun et al., 2016). Aspelund et al. used a gradient free optimization-simulation method for a LNG process modeled using Aspen HYSYS®. Their approach was based on a Tabu Search and Nelder-Mead Downhill Simplex method (Aspelund et al., 2010). Almeida-Trasvina and Smith optimized a novel cascade refrigeration cycle and other commercial cycles by applying a stochastic search optimization (GA) routine and the best solution was used as an initial point for deterministic optimization (SQP) (Almeida-Trasvina and Smith, 2018) . In this work, we are proposing a simpler optimization approach that relies on system decomposition and thermodynamic considerations to simplify such optimization problems without compromising solution quality. In addition to reducing computational times and easing convergence, the simplicity of this approach caters to both experienced and inexperienced standard simulators users such as process engineers and students. Moreover, the methodology can result in meaningful process insights that are otherwise unseen in conventional approaches.

2. Methodology

Instead of optimizing the entire linked model at once, we suggest dividing the system into subcomponents for subsequent optimization in a step-wise approach, while using simplified black-box exergy models to predict the performance of the surrounding units. We also recommend shortlisting adjustable operating variables by conducting a degree of freedom (DOF) analysis. Furthermore, process constraints (such as design limits, products specification, etc.) need to be identified based on insights and discussions with plant operators. Variables and constraints that should be maintained at their limits (referred in this article as *active variables and constraints, respectively*) for enhanced performance should also be identified. In addition to prediction using exergy techniques, the method capitalizes on pairing designated variables with constraints that should be maintained active, thereby reducing the number of optimization variables and search space, and easing flowsheet convergence. We are currently validating methods, such as parametric analysis, that can be integrated with the proposed approach for validation and/or enhancing solution quality.

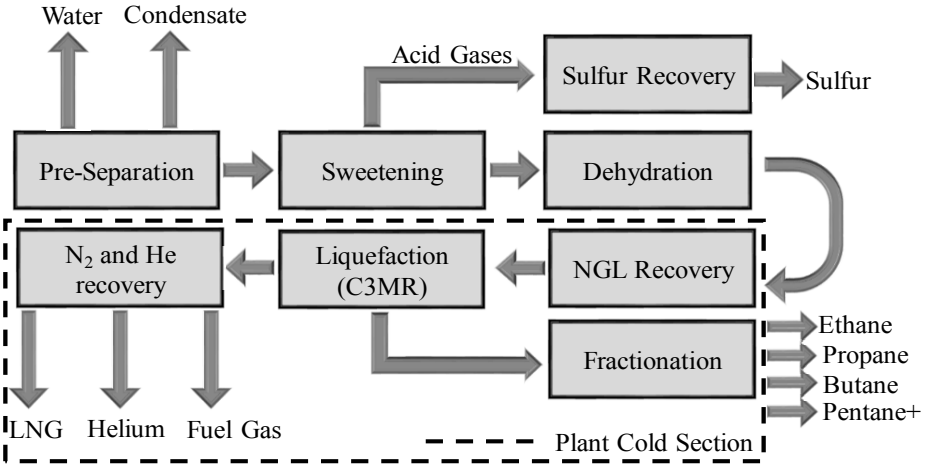

Figure 1: Block Flow Diagram of the LNG Plant

3. Process Description and Simulation

Figure 2 depicts a process flow diagram of the process at hand. We utilized actual plant data and AspenPlus™ software to build and validate a base-case model for the liquefaction section of a LNG plant with a 3.65 million tpy capacity. Sweet, dry, pre-treated NG enters the cold section of the LNG plant, where it gets pre-cooled by the C3 cycle from 21 to -27 ºC. NG is then throttled to 54.9 bar before entering the NGL recovery unit. GERG-2008 equation of state was used to model the NGL recovery as it was best suited to match model results with plant data. The process is essentially a distillation column (C-1) that uses part of the main cryogenic heat exchanger (MCHE, E-1) as the condenser. The liquid portion leaving the condenser at, -54ºC, re-enters the column as reflux, whereas the gas is routed to the MCHE for liquefaction and subcooling. This unit also produced approximately 9.9 KSbbl/day (at 15.6 °C and 1.01 bar) of extracted NGLs to be sent to the fractionation unit for further processing. The C3MR process comprises of two refrigeration cycles: a mixed refrigerant (MR) and C3 cycle. Peng-Robinson equation of state was used to simulate the cycles. C3 cycle pre-cools the NG and MR to about -31 ºC with four C3 evaporation pressures: high high pressure (HHP) at 7.8 bar, high pressure (HP) at 5.1 bar, medium pressure (MP) at 2.9 bar, and low pressure (LP) at 1.6 bar. Other streams cooled in the cycle include streams in the fractionation unit such as de-ethanizer overhead and liquefied petroleum gas (LPG). The evaporated C3's enter a 3-stage compressor (K-1) and gets compressed to 16.7 bar for subsequent condensation using sea water available at 33°C. At base-case conditions, the C3 cycle required ~ 44.3 MW of compression power. MR comprising of 2.1 % nitrogen (N_2), 43.8 % methane (C1), 40 % ethane (C2), and 13.8 % C3 passes through another 3-stage compressor (K-2), sea water intercooler, and pre-cooling exchangers in sequence. After reducing its temperature and pressure to -154 °C and 3.1 bar, respectively, the MR, in addition to a cold fuel gas stream from the helium extraction and nitrogen removal units, provide the cooling duty of the MCHE. LNG leaving the MCHE was subcooled to -144 ºC. The MR cycle required ~78.6 MW of compression energy. In total, the entire cycle necessitated 123 MW of compression power. When comparing simulation results with plant data, minimal discrepancy was observed.

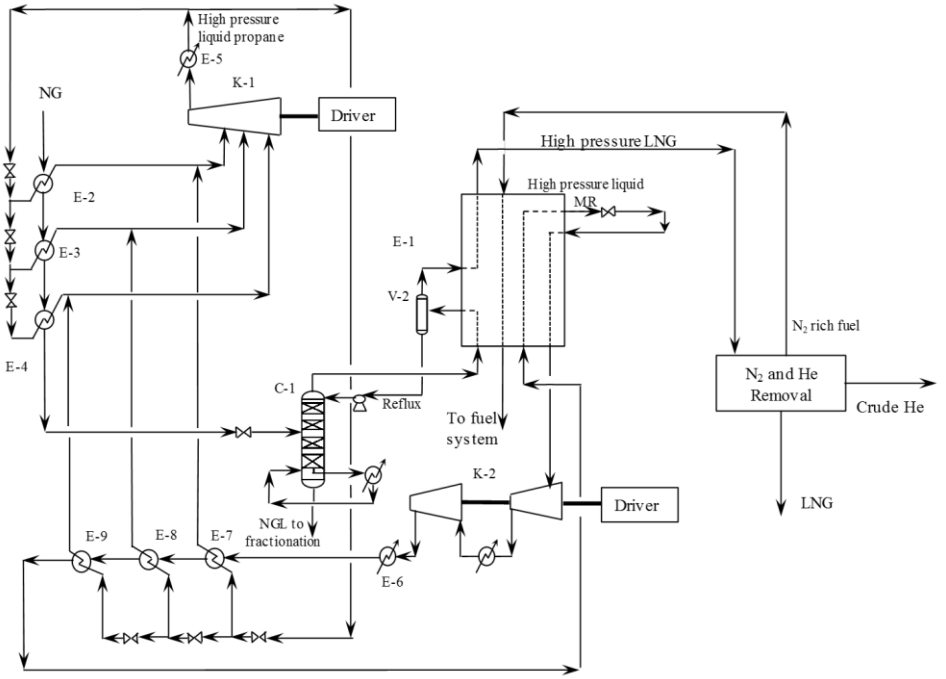

Figure 2: Process Flow Diagram of the integrated C3MR/ NGL recovery units. The de-ethanizer condenser and LPG cooling are not shown for clarity purposes

4. C3MR Optimization

For the C3MR process shown in Figure 1, the optimization approach consisted of two successive steps: first the MR cycle was rigorously optimized while predicting C3 cycle compression power. Next, the C3 cycle power was rigorously optimized at optimum MR cycle variables. DOF analysis showed that the process under consideration has 57 adjustable variables. After fixing active variables and devoting certain operating variables to maintain product specifications and active constraints (via for loop routines), variables available for optimization were reduced to 20. After further simplification, the adjustable variables decreased to 8.

4.1. MR Cycle

Optimization of the MR cycle was performed while modeling the C3 cycle as a black-box. The C3 cycle's power was predicted using exergy balances and C3 cycle base case efficiency, see Eq. (1) and Eq. (2). At base case conditions, the C3 cycle's efficiency was calculated to be 22%. The cycle's main constraints are the MCHE minimum temperature approach (MTA), NGL recovery/purities, and final LNG temperature. Pairing them with appropriate variables reduced the optimization variables from 57 to 13. Literature shows that the MR composition is one of the primary parameters in the cycle's optimization (Abdullah Alabdulkarema, Amir Mortazavi, 2011). Therefore, to simplify the problem, the effect of varying the composition (flowrates) was investigated while maintaining remaining adjustable variables at base values. Relative to the base-case, optimum MR composition was found to be 1.4, 39, 36.9 and 22.6 mol% N_2, C1, C2, and C3, respectively at a total MR and predicted C3 power of 105.5 MW (MR and C3 power of 87 and 18.5 MW, respectively). The system favored increasing the cooling load on the

MR, while decreasing the C3 load relative to the base case. This can be explained by the cycles' efficiencies, as the MR cycle (base-case efficiency of 37%) is almost twice as efficient as the C3 one. Since this method aims towards obtaining predictive independent variables values rather than actual power values, a final step of optimizing the C3 cycle at optimum MR was necessary to obtain actual powers that are operationally feasible.

$$W_{C3,\min} = Ex_{NG,in} + Ex_{MR,in} - Ex_{NG,out} - Ex_{MR,out} \quad (1)$$

$$W_{C3,predicted} = \frac{W_{C3,\min}}{\mu_{C3}} \quad (2)$$

Where:

- $W_{C3,\min}$ and $W_{C3,predicted}$ are the C3 cycle's minimum and predicted power, respectively.
- $Ex_{NG,in}$ and $Ex_{NG,out}$ are the exergy rates of the NG streams entering and leaving the C3 cycle, respectively.
- $Ex_{MR,in}$ and $Ex_{MR,out}$ are the exergy rates of the MR streams entering and leaving the C3 cycle, respectively.
- μ_{C3} is the C3 cycle efficiency at base-case conditions (22%).

4.2. C3 Cycle

In this final step, rigorous C3 cycle optimization was performed at optimum MR variables. C3 flowrates/ split fractions to evaporators and HHP/LP evaporation pressures were devoted towards maintaining base-case MTAs for all the chillers, in addition to propane degrees of superheat at the chillers' outlets. C3 was allowed to be slightly superheated to prevent the formation of liquid at the compressor suction. After variable pairing, the system was left with 2 adjustable variables available for optimization: HP and MP C3 evaporation pressures. Results showed that a C3 power of 28.5 MW was achievable at optimum operating variables. This gave a total actual C3MR power of 115.5 MW.

5. Conclusion

A simple and systematic method is proposed and tested for optimizing an actual C3MR liquefaction process. A base-case model was simulated using Aspen Plus™ software, and results were validated with plant data with minimal discrepancy. Detailed DOF analyses pinpointed the variables available and effective for optimization. Each unit was rigorously optimized while predicting the performance of its interlinked sections via an exergy model. Results showed that near 7 MW reduction of compression power can be achieved, which amounted to 6 % of current requirements. Advantages of this method compared to other approaches include its simplicity, lower computational time, and ability to produce trends/ insights. This approach is viable and can be extended to other highly integrated chemical processes. Currently we are testing the method for the rigorous optimization of a fully integrated system comprising of NGL recovery and helium/nitrogen extraction. Techniques to improve the quality of the solution are also under investigation and we expect to publish them soon.

Acknowledgements

This paper was made possible by NPRP grant No. NPRP8-964-2-408 from the Qatar National Research Fund (a member of Qatar Foundation). The authors would also like to acknowledge Dr. Hassan Alfadala for his contribution in this work. The statements made herein are solely the responsibility of the authors.

References

Abdullah Alabdulkarema, Amir Mortazavi, Y.H., 2011. Optimization of propane pre-cooled mixed refrigerant LNG plant. Appl. Therm. https://doi.org/10.1016/j.applthermaleng. 2010.12.003

Almeida-Trasvina, F., Smith, R., 2019. Novel refrigeration cycle configurations for performance improvements in LNG processes at small scale, in: Computer Aided Chemical Engineering. https://doi.org/10.1016/B978-0-12-818634-3.50071-0

Almeida-Trasvina, F., Smith, R., 2018. Design and Optimisation of Novel Cascade Refrigeration Cycles for LNG Production, in: Computer Aided Chemical Engineering. https://doi.org/10.1016/B978-0-444-64235-6.50111-X

Aspelund, A., Gundersen, T., Myklebust, J., Nowak, M.P., Tomasgard, A., 2010. An optimization-simulation model for a simple LNG process. Comput. Chem. Eng. 34, 1606–1617. https://doi.org/10.1016/j.compchemeng. 2009.10.018

Austbø, B., Løvseth, S.W., Gundersen, T., 2014. Annotated bibliography-Use of optimization in LNG process design and operation. Comput. Chem. Eng. 71, 391–414. https://doi.org/10.1016/j.compchemeng. 2014.09.010

Bittante, A., Jokinen, R., Pettersson, F., Saxén, H., 2015. Optimization of LNG Supply Chain, Computer Aided Chemical Engineering. Elsevier. https://doi.org/10.1016/B978-0-444-63578-5.50125-0

Bouabidi, Z., Katebah, M., Hussein, M., Shazed, A.R., Al-musleh, E.I., 20XX. Rigorous Thermodynamic Analysis for a Full-Scale Baseload LNG Supply Chain. In Preparation.

BP, 2019. BP Energy Outlook 2019 edition The Energy Outlook explores the forces shaping the global energy transition out to 2040 and the key uncertainties surrounding that. BP Energy Outlook 2019.

Energy Insights by McKinsey, 2019. Global gas & LNG outlook to 2035.

IGU, 2019. 2019 World LNG Report. World LNG Rep. 126.

John, P., 2019. LNG production increase a big boost for national economy: Al-Kaabi. Gulf Times.

Katebah, M., Hussein, M., Shazed, A.R., Bouabidi, Z., Al-musleh, E., 20XX. Simulation, Energy and Environmental Analysis of a baseload LNG Supply Chain. In Preparation.

Sun, H., He Ding, D., He, M., Shoujun Sun, S., 2016. Simulation and optimisation of AP-X process in a large-scale LNG plant. J. Nat. Gas Sci. Eng. 32, 380–389. https://doi.org/10.1016/j.jngse. 2016.04.039

Wang, M., Zhang, J., Xu, Q., 2012. Optimal design and operation of a C3MR refrigeration system for natural gas liquefaction. Comput. Chem. Eng. 39, 84–95. https://doi.org/10.1016/j.compchemeng. 2011.12.003

Sauro Pierucci, Flavio Manenti, Giulia Bozzano, Davide Manca (Eds.)
Proceedings of the 30th European Symposium on Computer Aided Process Engineering (ESCAPE30), May 24-27, 2020, Milano, Italy.
http://dx.doi.org/10.1016/B978-0-12-823377-1.50322-0

Market-like Distributed Coordination of Individually Constrained and Coupled Production Plants with Quadratic Approximation

Simon Wenzel*, Felix Riedl, Sebastian Engell

Process Dynamics and Operations Group, Department of Biochemical and Chemical Engineering, TU Dortmund, Emil-Figge Straße 70, 44227 Dortmund, Germany
simon.wenzel@tu-dortmund.de

Abstract

The optimal operation of large chemical or petrochemical production sites is challenging, because streams of shared resources such as steam or intermediates physically couple the individual production plants. For a feasible operation, it is essential to coordinate the production of the plants to balance the networks for the shared resources. Often, finding a central solution to this site-wide optimization problem is not possible due to various barriers such as the lack of models, too large complexity, or the management structure that hinders the exchange of relevant information. Market-like distributed optimization tackles some of these barriers, especially if only limited data exchange is possible between the constituent production plants. However, distributed optimization algorithms typically need many iterations, which hinders their practical application. In this contribution, we compare an algorithm for distributed market-like coordination that we formulated in previous work for individually constrained coupled systems with ADMM for a novel case study.

Keywords: Distributed optimization, Shared resource allocation, Quadratic approximation, Lagrangian relaxation, ADMM,

1. Introduction

In a more and more digitized, integrated, and connected production environment, the coordination of complex coupled systems of systems is essential to ensure a resource efficient and optimal operation. Large chemical or petrochemical production sites or industrial clusters are examples of such coupled systems of systems, where a large number of challenges exist in their coordination. One of the challenges is the physical coupling of the individual production plants via networks of shared resources. Figure 1 illustrates such a coupling of different production plants via three networks.

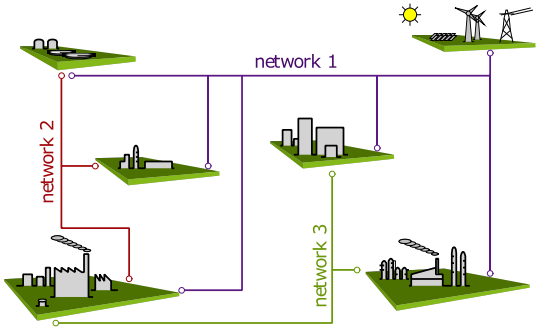

Figure 1 Visualization of shared resource networks at a production site.

Typical shared resources are steam on different pressure levels, intermediate products, waste treatment units or heating gas. Although the decision making on the operation of the individual production plants is usually done in a decentralized fashion, the overall balance of the shared resource networks has to be satisfied, which requires collaboration between the individual production plants either by communicating with the managers of the other production plants or with a central coordinator. If the individual production plants belong to different business units or to different companies in an industrial cluster, they can only share a restricted amount of data. In this situation, market-like distributed coordination methods can be used to establish an auction mechanism for shared resources within the system to coordinate the production and consumption of the subsystems and thus to balance the shared resource networks, i.e. to ensure that the consumed amount of shared resources meets the produced amount of shared resources. The limited data exchange in the auction mechanism ensures a high level of confidentiality between the subsystems. However, the drawback of these methods is that they typically require a large number of communication rounds between the production plants and the coordinator (auctioneer) to find the system-wide optimum. We recently proposed a hierarchical coordination algorithm that approximates the responses of the individual production plants by a quadratic function to find the optimal solution within fewer iterations. In this paper, we extend the evaluation of the performance of the algorithm from Wenzel et al. (2019) to a comparison with ADMM (Boyd 2010) for subsystems with individual constraints and coupling constraints.

The rest of the paper is structured as follows: First, the site-wide optimization problem is formulated as a general non-linear constrained mathematical optimization problem. Then market-like distributed coordination is introduced and ADMM as well as our novel algorithm are briefly introduced. Afterwards, the case study is explained, which is followed by the presentation of the computational results. Finally, we draw conclusions and indicate directions of future work.

2. Mathematical problem formulation

The coordination of the production of different production plants that are coupled by streams of material and energy can be formulated as a mathematical optimization problem:

$$\begin{aligned} \min_{\boldsymbol{u}_i, \forall i} \; & J(\boldsymbol{u}) = \sum_{i=1}^{N_S} J_i(\boldsymbol{u}_i) \\ \text{s.t.} \; & \forall i \in \mathcal{C}^{\boldsymbol{g}_i}: \boldsymbol{g}_i(\boldsymbol{u}_i) \leq \boldsymbol{0} \\ & \forall i \in \mathcal{C}^{\boldsymbol{h}_i}: \boldsymbol{h}_i(\boldsymbol{u}_i) = \boldsymbol{0} \\ & \mathcal{C}^{\boldsymbol{r}}: \sum_{i=1}^{N_S} \boldsymbol{r}_i(\boldsymbol{u}_i) = \boldsymbol{b}, \end{aligned} \tag{1}$$

where $J: \mathbb{R}^{n_{\boldsymbol{u}}} \rightarrow \mathbb{R}$ is the site-wide objective function, which can be split into N_s individual objective functions $J_i: \mathbb{R}^{n_{\boldsymbol{u}_i}} \rightarrow \mathbb{R}$ of the subsystems i (plants). Every subsystem has to satisfy a set of inequality constraints $\mathcal{C}^{\boldsymbol{g}_i}$ and a set of equality constraints $\mathcal{C}^{\boldsymbol{h}_i}$. The vector of manipulated variables of subsystem i is denoted by $\boldsymbol{u}_i \in \mathbb{R}^{n_{\boldsymbol{u}_i}}$. We assume that the only constraint that is not separable is the network balance of the shared resource networks $\mathcal{C}^{\boldsymbol{r}}$, which is also referred to as the complicating constraint. It is assumed that the individual resource utilization vectors $\boldsymbol{r}_i: \mathbb{R}^{n_{\boldsymbol{u}_i}} \rightarrow \mathbb{R}$ (i.e., the production or consumption of the resources) are affine in $\boldsymbol{u}_i$ and the cost functions J_i are convex (Boyd

2010). Streams that are fed into the networks are modelled as negative quantities; a positive sign denotes consumption. The right hand side of the complicating constraint $\boldsymbol{b}$ is a constant vector that, e.g., represents amounts of shared resources that enter or leave the balance space of the site. If it is zero, then all shared resource streams are consumed and produced at the site.

3. Market-like distributed coordination

The term market-like distributed coordination originates from the economic interpretation of distributed optimization algorithms based on Lagrangian relaxation of the complication constraint. At the optimal solution, the values of the Lagrange multipliers of the complicating constraint correspond to the equilibrium price in a Walrasian auction. At the equilibrium price, the demand and the supply of the traded goods match and thus the market clears. Applied to (1), this means that the amount of produced and consumed shared resources sums up to zero, i.e., the network is balanced. To find the equilibrium price, different strategies can be employed. These methods mainly differ in the way they find the equilibrium by iterating between a coordinator (auctioneers) and the subsystems. Depending on the method, more or less information on the individual optimization problems is communicated to the coordinator. We focus on methods that only exchange minimal information, i.e., the coordinator only receives information about the resource utilization of each subsystem, and the coordinator can only announce updated prices. In the case of ADMM, the coordinator in addition communicates reference values to the individual subsystems. In the following, we introduce the most intuitive and classic scheme of subgradient based price updates, ADMM (Boyd 2010), and our proposed algorithm QAC (Wenzel and Engell (2019), Wenzel et al. (2019)).

3.1. Subgradient updates

By relaxing the network constraint in (1), the Lagrangian of the optimization problem can be decomposed into N_s individual Lagrange functions

$$\mathcal{L}_i(\boldsymbol{u}_i, \boldsymbol{\lambda}) = J_i(\boldsymbol{u}_i) + \boldsymbol{\lambda}^T \boldsymbol{r}_i(\boldsymbol{u}_i), \tag{2}$$

where the vector of Lagrange multipliers $\boldsymbol{\lambda}$ represents the prices of the shared resources. Each individual subsystem solves the following optimization problem and computes its intended resource utilization $\boldsymbol{r}_i\left(\boldsymbol{u}_i^{k+1}\right)$ afterwards:

$$\begin{aligned} \forall i\ \boldsymbol{u}_i^{k+1} \coloneqq \arg\min_{\boldsymbol{u}_i}\ & \mathcal{L}_i(\boldsymbol{u}_i, \boldsymbol{\lambda}^k) \\ \text{s.t.}\quad & \mathcal{C}^{\boldsymbol{g}_i}\colon \boldsymbol{g}_i(\boldsymbol{u}_i) \le \boldsymbol{0} \\ & \mathcal{C}^{\boldsymbol{h}_i}\colon \boldsymbol{h}_i(\boldsymbol{u}_i) = \boldsymbol{0}. \end{aligned} \tag{3}$$

On the coordinator level, the resource utilization is aggregated and the following price update for the vector of Lagrange multipliers is performed:

$$\boldsymbol{\lambda}^{k+1} \coloneqq \boldsymbol{\lambda}^k + \alpha^k \left(\sum_{i=1}^{N_s} \boldsymbol{r}_i\left(\boldsymbol{u}_i^{k+1}\right) - \boldsymbol{b} \right), \tag{4}$$

where index k denotes the iteration index. For a sufficiently small α^k, convergence to the optimal solution is ensured for strictly convex problems (Bertsekas 1999). Choosing a very small value for α^k however results in many iterations, which can be a barrier for the implementation in practice (Wenzel and Engell (2019), Wenzel et al. (2019)).

3.2. The alternating direction method of multipliers (ADMM)

The alternating direction method of multipliers (ADMM, Gabay and Mercier (1976)) converges under milder assumptions on the optimization problem and gained a lot of popularity recently (Boyd 2010). The augmented Lagrangian term in ADMM is made separable by introducing auxiliary reference variables $\boldsymbol{z_i}$. Reformulating (1) results as

$$\begin{aligned} \min_{\boldsymbol{u}_i,\forall i} \; & \sum_{i=1}^{N_s} J_i(\boldsymbol{u}_i) \\ \text{s.t. } & \mathcal{C}^{\boldsymbol{r}_i}\colon \boldsymbol{r}_i(\boldsymbol{u}_i) - \boldsymbol{z}_i = \boldsymbol{0}, \forall i, \\ & \mathcal{C}^{\boldsymbol{z}}\colon \sum_{i=1}^{N_s} \boldsymbol{z}_i = -\boldsymbol{b}, \\ & \boldsymbol{u}_i \in \mathcal{C}^{\boldsymbol{g}_i} \cup \mathcal{C}^{\boldsymbol{h}_i}, \forall i, \end{aligned} \tag{5}$$

which has a separable augmented Lagrangian

$$\mathcal{L}_{\rho,i}(\boldsymbol{u}_i, \boldsymbol{\lambda}) = J_i(\boldsymbol{u}_i) + \boldsymbol{\lambda}^T(\boldsymbol{r}_i(\boldsymbol{u}_i) - \boldsymbol{z}_i) + \frac{\rho}{2}\|(\boldsymbol{r}(\boldsymbol{u}_i) - \boldsymbol{z}_i)\|_2^2 \tag{6}$$

with the penalty parameter ρ. The update steps can be written as

$$\forall i, \boldsymbol{u}_i^{k+1} \coloneqq \arg\min_{u_i \in \mathcal{C}^{\boldsymbol{g}_i} \cup \mathcal{C}^{\boldsymbol{h}_i}} J_i(\boldsymbol{u}_i) + \boldsymbol{\lambda}^T\left(\boldsymbol{r}_i(\boldsymbol{u}_i) - \boldsymbol{z}_i^k\right) + \frac{\rho}{2}\left\|\boldsymbol{r}(\boldsymbol{u}_i) - \boldsymbol{z}_i^k\right\|_2^2, \tag{7}$$

$$\forall i, \boldsymbol{z}_i^{k+1} \coloneqq \boldsymbol{r}_i\left(\boldsymbol{u}_i^{k+1}\right) - \bar{\boldsymbol{r}}(\boldsymbol{u}^{k+1}), \tag{8}$$

$$\boldsymbol{\lambda}^{k+1} \coloneqq \boldsymbol{\lambda}^k + \rho \cdot \bar{\boldsymbol{r}}(\boldsymbol{u}^{k+1}), \tag{9}$$

with $\bar{\boldsymbol{r}}$ as the mean of the network residuals.

3.3. Quadratic approximation coordination (QAC)

The quadratic approximation coordination (QAC) algorithm approximates the squared 2-norm of the network residual to compute the optimal Lagrange multipliers using less iterations compared to subgradient based price updates (Wenzel and Engell (2019), Wenzel et al. (2019)). In each iteration, the algorithm computes an updated quadratic approximation based on a selection of past points and performs a price update that is limited by a step size constraint:

$$\begin{aligned} \boldsymbol{\lambda}^{k+1} \coloneqq \arg\min_{\boldsymbol{\lambda}} \; & \phi\left(\boldsymbol{\lambda}, \boldsymbol{p}_\phi^k\right) \\ \text{s.t.} \quad & \boldsymbol{\lambda} \in \hat{\mathcal{E}}^k\left(\boldsymbol{\Lambda}_\phi\right). \end{aligned} \tag{10}$$

Here, $\boldsymbol{p}_\phi^k$ are the model parameters of the quadratic model and $\hat{\mathcal{E}}^k$ is the covariance based step size constraint. The constraint hinders the algorithm to perform too aggressive price updates. The individual subsystems compute their updated resource utilization in the same way as in classical subgradient based price updates (3). For a detailed description of the algorithm, the reader is referred to (Wenzel and Engell (2019), Wenzel et al. (2019)).

4. Case study

In order to compare the performance of the different algorithms, 1400 constrained quadratic problems were randomly generated. The 1400 problems were taken from Wenzel et al. (2019). They are of the following form, which is a special case of (1):

$$\begin{aligned} \min_{\boldsymbol{u}_i, \forall i} \; & \sum_{i=1}^{N_s} \frac{1}{2} \boldsymbol{u}_i^T \boldsymbol{Q}_i \boldsymbol{u}_i + \boldsymbol{q}_i^T \boldsymbol{u}_i \\ \text{s.t.} \; & \sum_{i=1}^{N_s} \boldsymbol{A}_i \boldsymbol{u}_i = \boldsymbol{0} \\ & \underline{\boldsymbol{u}} \leq \boldsymbol{u} \leq \overline{\boldsymbol{u}}. \end{aligned} \tag{11}$$

The optimization problems are strictly convex and the constraints are limited to the bounds on the decision variables with a lower bound $\underline{\boldsymbol{u}} = -10$ and an upper bound $\overline{\boldsymbol{u}} = \boldsymbol{10}$. We used a standard formulation of ADMM, where the penalty parameter ρ is updated dynamically as proposed by He et al. (2000). As convergence tolerance, we defined a threshold of $\varepsilon_p = 1 \times 10^{-2}$ for the primal residual, i.e., the 2-norm of the network balance $\|\boldsymbol{w}_p\|_2 = \sum_{i=1}^{N_s} \boldsymbol{A}_i \boldsymbol{u}_i$, and a maximum number of iteration of $k_{\max} = 500$.

5. Results

A graphical overview of the results for the constrained quadratic programs is shown in Figure 2, and Table 1 gives an overview about the mean of the 1400 test problems. In Figure 2 the results are illustrated as follows: On the horizontal axis the number of iterations upon convergence is shown and on the vertical axis the final primal residual is shown. With empty circles the results of the 1400 runs with subgradient based price updates upon termination of the coordination are shown, while the results for ADMM are shown with filled circles. The results of QAC are indicated with diamond symbols. The vertical black line marks the maximum number of iterations. Within the maximum number of iterations the subgradient based updates only solve overall 14% of the test problems, ADMM solves 89%, while QAC solves 76% (see Table 1). Many of the tested problems cannot be solved by subgradient based price updates at all within the maximum number of iterations, which is visible by the results on the black vertical bar. It can be seen that the average of the final primal residual of QAC is significantly smaller compared to subgradient based updates and to ADMM. For the converged instances, the subgradient based price updates require on average 370 iterations, ADMM requires on average 142 iterations, while QAC needs on average 129 iterations.

Table 1: Results for the coordination of constrained quadratic programs. The mean number of iterations including the runs that reached $k_{\max}$ is denoted as $\bar{k}$. The mean number of iteration of only the converged runs is denoted as $\overline{k_c}$. The percentage of the converged runs is listed under $\%_c$ and the mean final value of the primal residual of the converged runs is denoted with $\|\boldsymbol{w}_p\|_2$.

Algorithm	$\bar{k}$	$\overline{k_c}$	$\|\boldsymbol{w}_p\|_2$	$\%_c$
Subgradient based	479	370	9.87×10^{-3}	14
ADMM	161	142	6.74×10^{-3}	89
QAC	234	129	1.51×10^{-3}	76

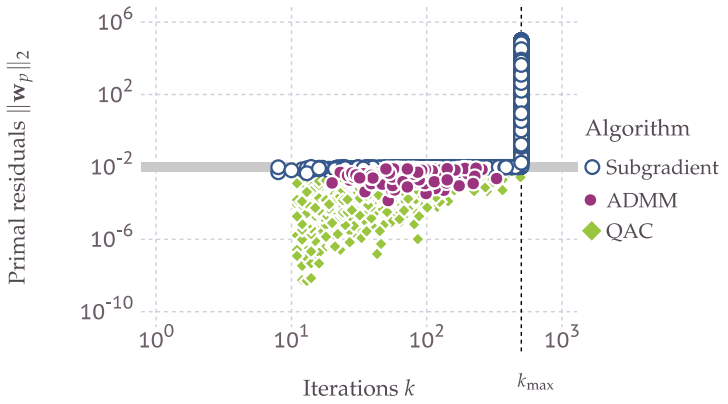

Figure 2: Results for the coordination of the constrained quadratic programs. The plots show the final values of the norm of the primal residual against the number of iterations. The vertical black line marks the maximum number of iterations; the horizontal gray bar marks the threshold for the primal residual ε_p.

6. Conclusions and future prospects

The number of iterations for QAC was reduced to approximately a third compared to subgradient based updates. QAC does not solve as many problems as ADMM. However, it has to be noticed that the exchanged data for QAC is more limited than for ADMM, which makes a fair comparison difficult. In addition, the mean final primal residual of QAC is far below the one of ADMM. Thus, for smaller thresholds of the primal residual, QAC is expected to also outperform ADMM w.r.t. the number of required iterations. Further research should be devoted to increasing the robustness of QAC and to a detailed investigation of the pitfalls that prohibit a convergence of the algorithm in certain cases.

Acknowledgement

The project leading to this publication has received funding from the European Union's Horizon 2020 research and innovation programme under grant agreement No 723575 (CoPro, spire2030.eu/copro) in the framework of the SPIRE PPP.

References

Bertsekas, D. P. Nonlinear Programming; Athena Scientific: Belmont, Massachusetts, 1999.

Boyd, S. Distributed Optimization and Statistical Learning via the Alternating Direction Method of Multipliers. *Found. Trends® Mach. Learn.* **2010**, *3* (1), 1–122. https://doi.org/10.1561/2200000016

Gabay, D.; Mercier, B. A Dual Algorithm for the Solution of Nonlinear Variational Problems via Finite Element Approximation. *Comput. Math. with Appl.* **1976**, 2 (1), 17–40. https://doi.org/10.1016/0898-1221(76)90003-1.

He, B. S.; Yang, H.; Wang, S. L. Alternating Direction Method with Self-Adaptive Penalty Parameters for Monotone Variational Inequalities. *J. Optim. Theory Appl.* **2000**, 106 (2), 337–356. https://doi.org/10.1023/A:1004603514434.

Wenzel, S.; Riedl, F.; Engell, S. An Efficient Hierarchical Market-like Coordination Algorithm for Coupled Production Systems Based on Quadratic Approximation. *Comput. Chem. Eng.* **2019**, *in rev.*

Wenzel, S.; Engell, S. Coordination of Coupled Systems of Systems with Quadratic Approximation. *IFAC-PapersOnLine* **2019**, 52 (3), 132–137. https://doi.org/10.1016/j.ifacol.2019.06.023

Sauro Pierucci, Flavio Manenti, Giulia Bozzano, Davide Manca (Eds.)
Proceedings of the 30th European Symposium on Computer Aided Process Engineering (ESCAPE30), May 24-27, 2020, Milano, Italy.
http://dx.doi.org/10.1016/B978-0-12-823377-1.50323-2

Synthesis and Assessment of Waste-to-resource Routes for Circular Economy

Adrián Pacheco-López[a], Ana Somoza-Tornos[a], Edrisi Muñoz[a], Elisabet Capón-García[b], Moisés Graells[a], Antonio Espuña[a]

[a]*Department of Chemical Engineering, Universitat Politècnica de Catalunya Escola d'Enginyeria de Barcelona Est, C/ Eduard Maristany 16, 08019 Barcelona, Spain*
[b]*ABB Switzerland Ltd., Segelhofstrasse 1K, 5405 Baden-Dättwil, Switzerland*
antonio.espuna@upc.edu

Abstract

The benefits of the circular economy paradigm have been proven during the past two decades, but its application poses some challenges that still need to be tackled. This contribution presents a systematic way to generate a list of potential waste-to-resource technologies based on the use of a semi-automatic ontological frameworks. The ontology is instantiated, giving the possibility to generate and assess a list of transformation processes alternatives, according to the potentially available waste streams and resource requirements in a specific area and/or sector. The resulting list is then analyzed and classified according to pre-established parameters, thus presenting which are the potentially best alternatives to close the material loops and recover chemical resources from available waste. The capabilities of the method to identify promising transformation technologies are assessed through an illustrative case study: the evaluation of different routes for the treatment of plastic waste materials, with the focus on chemical recycling.

Keywords: circular economy, product transformation, waste-to-resource, ontology, chemical recycling

1. Introduction

In the last years, there has been an increasing concern about the degradation of the environment due to the large amount of waste generated by the constantly growing world population. In this line, plastic waste deserves special attention, since it is one of the most abundant and lasting types of waste. Its manufacture entails a significant consumption of energy and resources considering its short average lifespan. Hence, there is a rising awareness on the need of not only treat waste, but also convert it into valuable feedstock for other processes, thus eliminating the problem of waste disposal and reducing the consumption of fresh raw materials.

Promising processes for chemical recycling have been proposed in the direction of closing the loop of materials, but most of them are still in development at lab scale. Hence, they are often disregarded, due to the lack of information on their cost, profitability and performance at industrial plant scale level. Furthermore, and opposed to traditional product-based processes, it is not always clear which is the best way to convert a specific waste stream into which added-value product(s), or even which specific waste streams will offer better economic or environmental potential to be reused or recycled.

Thus, systematic tools should be developed to address the generation of process alternatives that enhance resource upcycling. The aim of this work is to develop a method to synthesize and assess routes for waste-to-resource transformations.
The approach presented in this contribution is based on ontologies and knowledge modelling. An ontology is a formal, explicit specification of shared conceptualization (Studer R. et al, 1998). The extended use of ontologies has allowed the development of ontology-based engineering systems, providing a semantical environment and a knowledge management tool. Previous research has demonstrated the applicability of ontologies to circular economy and industrial symbiosis problems (Zhou et al., 2018, Cecelja et al., 2015, Rafaat et al., 2013).
In this work, a formal ontology that models the enterprise process engineering domain, so called Enterprise Ontology Project (EOP), has been used (Munoz et al, 2013). EOP model sets well-defined domain concepts encompassed by a taxonomic arrange, terminology, definitions and relations. The domain of this ontology is process system engineering including areas such as batch processes, control and automation, planning and scheduling, supply chain management and life cycle assessment. Thus, this ontology provides to process functionalities a consistent structure for explicit, shareable and reusable formal knowledge representation.

2. Problem statement

The problem addressed in this contribution can be stated in the following terms: ranging from a pre-defined ontology for the classification of waste-to-resource processes along with their specifications, and scientific documentation related to the domain of study. A list of tentative processes suitable to treat the considered waste with their specifications, such as operating conditions as well as economic and environmental data, should be determined.
Subsequently, given the previously obtained list, a set of characterized available wastes, potential products demand with quality requirements to meet, and data assessment criteria to analyze the adequacy of the process to the given waste, the objective is to determine a list of relevant technologies sorted by the criteria defined above.

3. Methodology

The methodology used in this work is described in Figure 1 and is divided into two main tasks; the first one consists of ontology selection and instantiation with information retrieved from scientific documentation, obtaining then a set of processes suitable for the domain of study. The second task consists of a reasoner that, starting from the potential transformation processes, would be able to obtain a list of processes and weight the best ones based on the assessment criteria mentioned below in section 3.2.

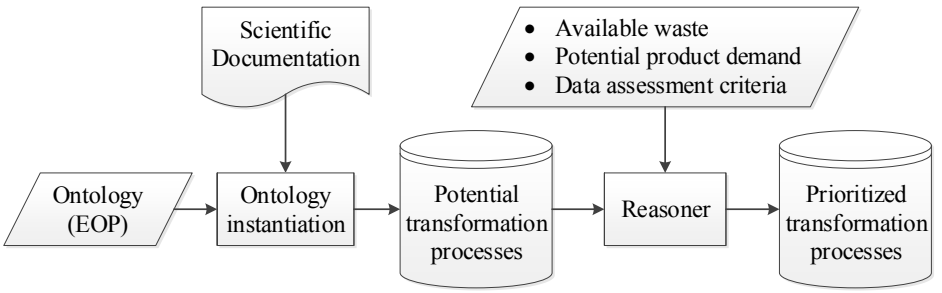

Figure 1. Methodology description

3.1. Ontological framework

An ontological framework is used to model resources, waste and potential transformation technologies considering their composition, characteristics and other specifications.

First, a set of transformation processes available in the domain of study are populated and implemented in the ontology framework mentioned above. These transformation processes have to be well defined and all the relevant parameters must be registered in the ontology.

In order to connect the available wastes with the final marketable products, an input-output matching method has to be applied, thus being able to generate different process paths (or routes) with their eventual outcomes and taking into consideration eventual intermediate products, which will enforce specific sequencing constraints.

Finally, end-of-life treatment processes for any non-marketable by-product, such as incineration for energy recovery or landfill, should be included in the proposed process network, if necessary.

3.2. Sorting and classification of instances (reasoner)

For each one of the transformation processes routes available in the ontology, a list is created and a ponderation is applied in order to sort them out, seeking the maximum economic and environmental profit, as well as promoting the use of simpler and more mature processes.

The process characteristics to be analyzed are sorted in three main categories: economical, environmental and matureness. Main economic aspects are: products selling price (including energy recovery benefits), waste purchase price, and processing cost. The environmental impacts of the feedstock, products and process are obtained (and eventually monetized) according to the life cycle impact model ReCiPe2016 (Huijbregts et al, 2016). And finally, the matureness of the technology is assessed with the Technology Readiness Level (TRL) as defined by the EU Horizon 2020 (European Commission, 2014).

Products prices are obtained from the Prodcom Annual Data 2018 (European Commision, 2018), waste prices and processes cost for the case study are taken from scientific literature review.

Then, the economic and environmental profits for every process path (the letter j is used to represent the set of processes to be studied) can be calculated as shown in Eq. (1) and Eq. (2).

$$P_{eco,j} = V_{products} - C_{waste} - C_{process} \tag{1}$$

$$P_{env,j} = EI_{products} - EI_{waste} - EI_{process} \tag{2}$$

Additionally, weighting factors are calculated in order to prioritize paths with higher economic and environmental profits against those with lower values, as shown in Eqs. (3, 4).

$$f_{eco,j} = \frac{P_{eco,j} - \min_j \left\{ P_{eco,j} \right\}}{\max_j \left\{ P_{eco,j} \right\} - \min_j \left\{ P_{eco,j} \right\}} \tag{3}$$

$$f_{env,j} = \frac{P_{env,j} - \min_j \{P_{env,j}\}}{\max_j \{P_{env,j}\} - \min_j \{P_{env,j}\}} \quad (4)$$

And another factor will be calculated from the TRL in order to promote the use of more mature technologies, as seen in Eq. (5):

$$f_{TRL,j} = \frac{TRL_j}{\max_j \{TRL_j\}} \quad (5)$$

Finally, an objective function can be calculated as shown in Eq. (6), which has to be maximized, that is to say, the routes with the greatest O.F. will be at the top of the list and the ones with lowest will be at the bottom.

$$OF_j = \left(P_{eco,j} + P_{env,j}\right) \cdot f_{eco,j} \cdot f_{env,j} \cdot f_{TRL,j} \quad (6)$$

4. Case study

With the purpose of illustrating the methodology, a case study has been proposed for the treatment of plastic waste, such as polyethylene waste (PEw). A list of tentative processes has been obtained from scientific literature and other public domain sources. Other alternatives have been added, such as, direct mechanical recycling, direct downcycling, landfilling and incineration for energy recovery. A list of processes suitable for PEw recycling has been obtained and schematized in Figure 2.

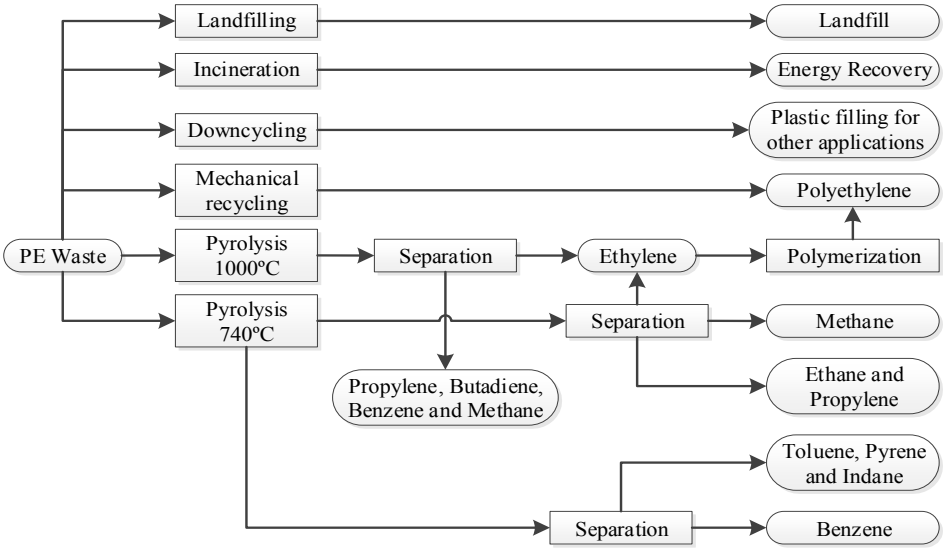

Figure 2. Possible alternatives for PE waste treatment.

According to the structure obtained in Figure 2, there are 7 different paths that can be followed for the conversion of waste into valuable products, each one of them leading to a different outcome. For simplicity purposes, the number of processes in the path generation has been limited to a maximum of 3. Tables 1 and 2 show the studied paths and their main specifications.

5. Results and discussion

Economic and environmental impacts of the processes are calculated in order to sort them out from the most profitable economically and environmentally to the less. The result is shown in Table 3, which is sorted by the objective function. Based on these results, the most profitable process would be PEw pyrolysis at 740ºC, followed by pyrolysis at 1000ºC, along with the separation of the resulting gas and oil fractions in each case; while landfilling is found to be the less profitable option.

Chemical recycling appears to be a very promising way of treating waste and closing the materials loop, thus obtaining raw materials that can potentially be used instead of fresh raw materials. Additionally, these processes are economically and environmentally far more profitable than the traditional way of treating this kind of waste, namely landfill or incineration.

Table 1. Economic specifications for the analyzed processes.

Process path	Total Cost (€/t)	Waste purchase price (€/t)	Products Value (€/t)	Economic Profit (€/t)
Pyrolysis 740ºC + Separation	216.61	307.98	698.47	173.88
Pyrolysis 1000ºC + Separation	215.15	307.98	695.63	172.50
Pyro. 1000ºC + Sep. + Polymerization	320.60	307.98	709.93	81.35
Direct Downcycling PE	0.00	307.98	307.98	0.00
Direct Recycling PE	106.66	307.98	528.03	113.39
Incineration	128.20	307.98	493.12	56.95
Landfill	97.53	307.98	0.00	-405.51

Table 2. Environmental impact (E.I.) specifications and TRL of the analyzed processes.

Process path	E.I. Process (€/t)	E.I. Feed (€/t)	E.I. Products (€/t)	E.I. Profit (€/t)	TRL
Pyrolysis 740ºC + Separation	79.27	13.23	292.13	199.63	7
Pyrolysis 1000ºC + Separation	105.27	13.23	185.47	66.97	6
Pyro. 1000ºC + Sep. + Poly.	141.37	13.23	221.57	66.97	7
Direct Downcycling PE	0.00	13.23	13.23	0.00	9
Direct Recycling PE	139.68	13.23	125.87	-27.04	8
Incineration	209.35	13.23	162.37	-60.21	9
Landfill	19.10	13.23	0.00	-32.33	9

Table 3. Results and weighting parameters for the different process paths

Process path	Economic factor	Environment. factor	TRL factor	O.F.	Global position
Pyrolysis 740ºC + Separation	0.98	1.00	0.78	1041.90	1
Pyrolysis 1000ºC + Separation	0.98	0.64	0.67	516.69	2
Pyro. 1000ºC + Sep. + Poly.	0.89	0.64	0.78	510.35	3
Direct Downcycling PE	0.82	0.46	1.00	376.03	4
Direct Recycling PE	0.92	0.39	0.89	344.85	5
Incineration	0.87	0.30	1.00	258.48	6
Landfill	0.44	0.37	1.00	92.88	7

6. Conclusions

This work presents a methodology for the systematic generation of a list of potential waste-to-resource technologies based on the use of ontologies. Thanks to this method, new technologies can be identified and compared to others that are well-established, and a manageable list of technologies can be obtained for further optimization and superstructure analysis, as well as a more profound development.

The growing application of circular economy principles entails the emergence of new waste-to-resource technologies, such as chemical recycling. A fair evaluation of the potential technologies has to consider its TRL, as its application is riskier than the one of well-established alternatives. Thus, the proposed objective function includes a factor to assess the maturity of the technology.

The framework also allows the generation of routes based on linking consecutive processes in a building-blocks approach. This method leads to flexible product compositions, aiding decision-makers to identify the most economically and environmentally beneficial solutions.

With the aim of ensuring that the list of alternatives includes the most up-to-date transformation technologies, future work will address the development of a procedure for the systematic search of waste-to-resource processes.

Acknowledgements

Financial support received from the Spanish Competitiveness, Industry and Economy Ministry and the European Regional Development Fund, both funding the research Projects AIMS (DPI2017-87435-R) is fully acknowledged. Adrian Pacheco-Lopez thankfully acknowledges financial support received from the Spanish Ministry Science, Innovation and Universities (grant ref. PRE2018-087135) and Ana Somoza-Tornos thankfully acknowledges financial support received from the Spanish Ministry of Education, Culture and Sport (grant ref. FPU15/02932).

References

Raafat, T., Trokanas, N., Cecelja, F., Bimi, X., 2013, An ontological approach towards enabling processing technologies participation in industrial symbiosis, Computers & Chemical Engineering 59, 33-46

Cecelja, F., Trokanas, N., Raafat, T., Yu, M., 2015, Semantic algorithm for Industrial Symbiosis network synthesis, Computers & Chemical Engineering 83, 248-266

Zhou, L., Zhang, C., Karimi, I.A., Kraft, M., 2018, An ontology framework towards decentralized information management for eco-industrial parks, Computers & Chemical Engineering 118, 49-63

Studer, R., Benjamins, V. R., Fensel, D., 1998, Knowledge engineering: principles and methods, data Knowledge engineering 25, 161-197.

Munoz E., Capon-Garcia E., Espuna A., Puigjaner L., 2013, Considering environmental assessment in an ontological framework for enterprise sustainability. Journal of Cleaner Production. Vol. 47, Pp. 149-164.

Huijbregts MAJ, Steinmann ZJN, Elshout PMF, Stam G, Verones F, Vieira MDM, Hollander A, Van Zelm R, 2016, ReCiPe2016: A harmonized life cycle impact assessment method at midpoint and endpoint level. RIVM Report 2016-0104. Bilthoven, The Netherlands.

European Commission Decision C (2014)4995 of 22 July 2014. Horizon 2020 Framework Programme 2014-2015 part 19. General Annexes, section G.

European Commission Eurostat, 2018, Statistical Classification of Economy Activity in the European Union (NACE 2). 2018 Annual detailed data by PRODCOM list

Sauro Pierucci, Flavio Manenti, Giulia Bozzano, Davide Manca (Eds.)
Proceedings of the 30th European Symposium on Computer Aided Process Engineering (ESCAPE30), May 24-27, 2020, Milano, Italy.
http://dx.doi.org/10.1016/B978-0-12-823377-1.50324-4

Shape Optimization of a Fixed-bed Reactor using Additive Manufacturing

Alexis Courtais[a,*], François Lesage[a], Yannick Privat[b], Cyril Pelaingre[c], Abderrazak M. Latifi[a]

[a]*Laboratoire Réactions et Génie des procédés, CNRS, Université de Lorraine, Nancy, France*
[b]*Institut de Recherche Mathématique Avancée, CNRS, Université de Strasbourg, France*
[c]*Centre Européen de Prototypage et Outillage Rapide, Saint-Dié des Vosges, France*
alexis.courtais@univ-lorraine.fr

Abstract

This paper deals with a geometric shape optimization of a fixed-bed reactor. The objective is to determine the shape of the packing that maximizes the reaction conversion rate subjected to the process model equations, operating constraints (iso-volume, energy dissipated by the fluid) and manufacturing constraints. The process model is described by the mass balance equations and Navier-Stokes equations. Incompressible fluid, a homogeneous first order reaction and steady-state conditions in the reactor are the main assumptions considered. The free software OpenFOAM is used as CFD solver. The optimization approach developed is based on the adjoint system method and the resulting algorithm is tested on a two-dimensional fixed-bed reactor in laminar flow regime. The results show a significant improvement of the conversion rate and the optimal shape obtained with the manufacturing constraints can be easily printed by means of an additive manufacturing technique.

Keywords: Shape optimization, CFD, Fixed-bed reactor, Additive manufacturing.

1. Introduction

The objective of shape optimization is to deform the outer boundary of an object in order to minimize or maximize a cost function, such as the performances of a process, while satisfying given constraints. Historically, the shape optimization methods have been used in cutting edge technologies mainly in advanced areas such as aerodynamics. However, they have recently been extended to other engineering areas where the shape greatly influences the performances. For example, in hydrodynamics, the shape of a pipe that minimizes the energy dissipated by the fluid due to viscous friction was analyzed (Henrot and Privat, 2010, Tonomura et al., 2010, Courtais et al., 2019).

In chemical engineering however where the shape of unit operations (e.g. reactors, tanks, stirrers, pipes…) is an important design parameter, the shape optimization has not been extensively investigated. This important issue deserves therefore to be addressed and will probably result in a paradigm shift in optimal design and operation of processes.

Basically, there are three types of shape optimization: parametric, geometric and topologic. In this paper, only geometric optimization is considered. The objective is to develop an optimization approach based on Hadamard method using the adjoint system equations. The case study is a 2D fixed-bed reactor with a laminar single phase liquid flow where a homogenous first order chemical reaction takes place. The objective is to determine the shape of the packing that maximizes the reactor conversion rate.

2. Fixed-bed reactor modelling

The optimization method developed in this work is based on the process model equations that describe the flow through the fixed-bed reactor. A two-dimensional model is therefore developed and involves mass and momentum balance equations. Figure 1 shows the schematic representation of the fixed-bed considered.

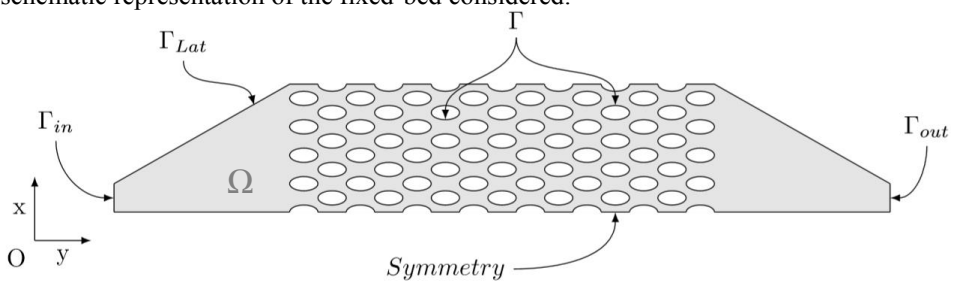

Figure 1: Schematic representation of the fixed-bed reactor

The studied domain consists of the free volume Ω and its boundaries given by the union of the inlet (Γ_{in}), outlet (Γ_{out}), lateral wall (Γ_{lat}) and free (Γ) limits.
The momentum transport is described by the following Navier-Stokes equations along with the associated boundary conditions:

$$\begin{cases} -\nu\,\Delta \boldsymbol{U} + \boldsymbol{U}\cdot\nabla\boldsymbol{U} + \nabla p = 0 & \text{in } \Omega \\ \nabla\cdot\boldsymbol{U} = 0 & \text{in } \Omega \\ \boldsymbol{U} = \boldsymbol{U_{in}} & \text{on } \Gamma_{in} \\ \boldsymbol{U} = 0 & \text{on } \Gamma_{lat}\cup\Gamma \\ \sigma(\boldsymbol{U}, p)\boldsymbol{n} = 0 & \text{on } \Gamma_{out} \end{cases} \tag{1}$$

where ν is the kinematic viscosity of the fluid, $\sigma(\boldsymbol{U}, p) = 2\nu\varepsilon(\boldsymbol{U}) - p\boldsymbol{I}$ the viscous stress tensor, p the fluid absolute pressure, $\boldsymbol{I}$ the identity matrix and $\varepsilon(\boldsymbol{U})$ the strain tensor.

The mass balance equations and their associated boundary conditions are given by Eqs. (2). It is important to point out that the reaction takes place only in the bulk of the reactor, i.e. in Ω and not on the walls Γ and Γ_{lat}.

$$\begin{cases} -D\Delta C + \boldsymbol{U}\cdot\nabla C + kC = 0 & \text{in } \Omega \\ C = C_{in} & \text{on } \Gamma_{in} \\ \dfrac{\partial C}{\partial n} = 0 & \text{on } \Gamma_{out}\cup\Gamma_{lat}\cup\Gamma \end{cases} \tag{2}$$

where C is the reactant concentration and D the constant diffusion coefficient of the reactant.

3. Optimization problem formulation

The formulation of the shape optimization problem requires the definition of a performance index, decisions variables and constraints. These ingredients are detailed below.

3.1. Performance index

The aim of this work is to determine the packing shape (i.e. the position and the shape of the free boundary Γ) of the fixed-bed reactor that maximizes the reaction conversion rate or minimizes the average outlet concentration of the reactant. The performance index is therefore defined by Eq. (3) as:

$$J(\Omega) = \int_{\Gamma_{out}} C d\sigma \tag{3}$$

3.2. Decision variable

The decision variable is defined by the free boundary Γ that will evolve with the iterations of the optimization algorithm. The other boundaries are fixed.

3.3. Equality and inequality constraints

The optimization problem is subjected to different constraints. The most obvious ones are given by the process model equations (Eqs.(1-2)). The other constraints consist of :

- An iso-volume constraint introduced in order to guarantee the same residence time between initial and optimized shapes (Eq.(4)).

- An inequality constraint on the energy dissipation by the fluid due to viscous friction and is given by Eq. and *(5)*. Such a constraint is relevant since the energy dissipation and the pressure drops are directly correlated.

$$C_1 = V(\Omega) - V(\Omega_0) = 0 \quad \text{and} \quad C_2 = 2\nu \int_{\Omega} |\varepsilon(U)|^2 \, dx - 2\nu \int_{\Omega_0} |\varepsilon(U)|^2 \, dx < 0 \tag{4) and (5)}$$

- Since the resulting optimal shape will be fabricated by means of a 3D printing technique, manufacturing constraints should be accounted for in the optimization problem. They are of inequality type and impose minimum values on the pores width (Ω domain) and on the packing thickness.

4. Optimization method

The shape optimization approach developed is a gradient-based method and uses the Hadamard's boundary variation method (Henrot and Pierre, 2006). The gradient, called shape gradient, is computed by means of adjoint system method. The shape gradient G is defined on the free boundary (Γ) and depends on the different state variables ($\boldsymbol{U}$,p and C) and their associated adjoint states introduced by the method ($\boldsymbol{U_a}$,p_a and C_a). The gradient will allow us to compute the mesh displacement vector $\boldsymbol{V}$ that decreases the Lagrangian of the constrained optimization problem given by (Eq.(6)).

$$L(\Omega) = \int_{\Gamma_{out}} C d\sigma + \lambda_V \left(V(\Omega) - V(\Omega_0) \right) + \lambda_E \left(2\nu \int_{\Omega} |\varepsilon(U)|^2 \, dx - 2\nu \int_{\Omega_0} |\varepsilon(U)|^2 \, dx \right) \tag{6}$$

The vector field $\boldsymbol{V}$ is the solution of Eqs. (7).

$$\begin{cases} -\Delta \boldsymbol{V} + \boldsymbol{V} = \boldsymbol{0} & \text{in } \Omega \\ \boldsymbol{V} = \boldsymbol{0} & \text{on } \Gamma_{\text{in}} \bigcup \Gamma_{\text{out}} \bigcup \Gamma_{lat} \\ \nabla \boldsymbol{V}\boldsymbol{n} = -G\boldsymbol{n} & \text{on } \Gamma \end{cases} \tag{7}$$

Once the vector field $\boldsymbol{V}$ is computed, the next step in the method is to move all meshpoints according to the following relation:

$$\Omega_{i+1} = (\boldsymbol{X} + t\boldsymbol{V})(\Omega_i) \tag{8}$$

where t is the method step and must be chosen small, $\boldsymbol{X}$ is the vector of each meshpoint coordinates. More details on the shape gradient calculations can be found in (Courtais et al., 2020).

5. Optimization algorithm

The optimization algorithm developed has been implemented using C++ language within the free and open source OpenFOAM software (Weller et al., 1998). The latter solves PDEs, i.e. Navier -Stokes, mass balance system and their adjoint system equations, using finite volume method. The python library "pyFoam" is used to link the iterations to each other using its utility *"pyFoamMeshUtilityRunner.py"*. The algorithm proceeds as follows:

1. Formulation of an initial shape and generation of the associated mesh using cfMesh and snappyHexMesh, two mesh utilities supplied by OpenFOAM.
2. Resolution of the four systems of PDEs. The pressure-velocity coupling equations are solved using SIMPLE (Semi-Implicit Method for Pressure-Linked Equations) algorithm.
3. Computation of the shape gradient G and the mesh displacement $\boldsymbol{V}$. The manufacturing constraints are considered at this stage. The pore constraint is considered using the OpenFOAM function "wallDist". This function computes the distance between the cells and boundaries. The thickness constraint is taken into account by computing the local distance between the obstacle and its skeleton. The skeleton of an obstacle is the set of equidistant points from the obstacle on each side (see (Feppon et al., 2018) for more details).
4. The Lagrange multipliers associated to the volume and energy constraints are updated by means of the following relation :

$$\lambda_{i+1}^{k} = \lambda_i^k + \varepsilon\, C_i^k \tag{9}$$

where ε is a parameter with a small value, k and i refer to the constraint and iteration respectively.

5. At the end of iterations, a test on the mesh quality is carried out through three criteria:
   i. the maximum value of the mesh aspect ratio which is defined as the ratio of the longer side to the shorter side of a mesh.
   ii. the mesh non-orthogonality defined by the angle between the vector linking two adjacent cell centers and the normal of the face connecting cells.
   iii. the face skewness defined by the distance between the face center and the intersection of the vector linking adjacent cells with their common face considered (see (Holzinger, 2015) for more details).

The upper bounds of these three criteria are 10, 65 and 3.8 respectively. If the mesh quality fails, remeshing process takes place.

6. A test on the convergence is done through the maximum displacement of the mesh. If the latter is higher than 10^{-5} m, then the algorithm goes back to step 2.

6. Results and discussion

Figure 2 presents the reactant concentration profiles in the initial configuration (a) of the fixed-bed reactor and in the optimized ones without (b) and with (c) the manufacturing constraints. It can be seen that in the initial configuration, a dead zone in the reactor inlet area (i.e. light zone on the figure) appears where the reaction conversion rate is very low, thus leading to lower reactor performances. In the optimized fixed-bed without manufacturing constraints, the dead zone has disappeared, but the reactor exhibits very narrow channels (pores) which are not easy to manufacture. In the optimized shape with constraints however, the dead zone is no longer there and all the channels can easily be printed. On the other hand, Figure 3 presents the residence time distribution (RTD) of initial and optimized (with manufacturing constraints) configurations and shows that the fluid flow is more homogeneous in the optimized configuration. Indeed, the standard deviation of the RTD is three times lower in the optimized reactor (i.e. 75 vs 25s). Finally, the disappearance of the dead zone and the better homogeneity of the flow the improvement of the conversion rate and therefore of the performance index by is about 10%.

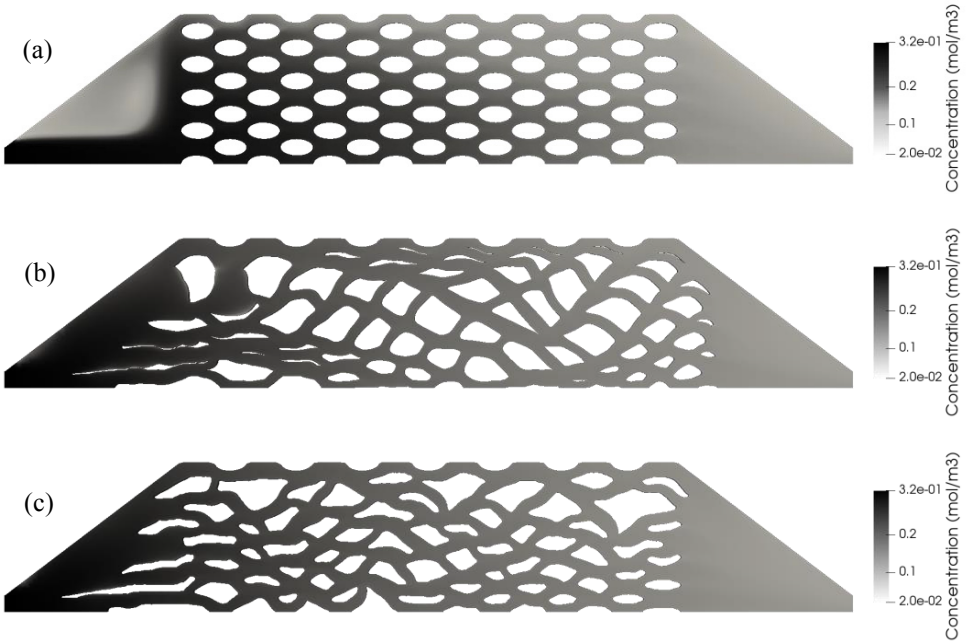

Figure 2: Initial configuration of the fixed-bed reactor (a), optimized shape without manufacturing constraint (b), optimized shape with manufacturing constraint (c)

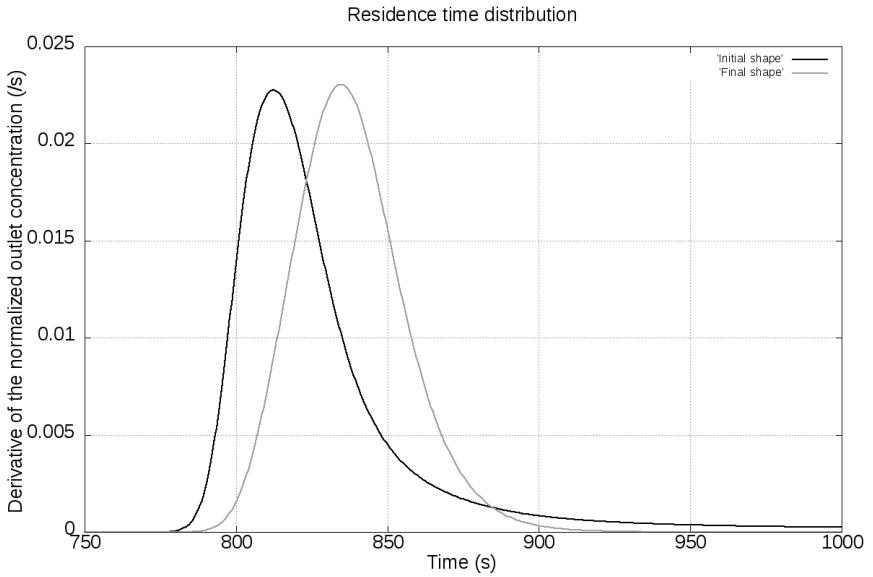

Figure 3: Residence time distribution of initial and optimized shapes

7. Conclusions

In this work, a geometrical shape optimization based on the adjoint system method has been developed, implemented within OpenFOAM and used in order to optimize the configuration of a fixed-bed reactor where a first order homogeneous reaction occurs. The objective was to determine the shape that minimizes the average concentration of the reactant at the reactor outlet. The optimization was subjected to volume, energy and manufacturing constraints and to momentum and mass balance equations. A significant decrease of the performance index is obtained which results in a substantial improvement of the reactor conversion rate.

References

C. Barlier , 1991, Procédé pour la création et la réalisation de pièces par CAO et pièces ainsi obtenues, Brevet français et brevet européen.

A. Courtais, F. Lesage, Y. Privat, P. Frey, A.M. Latifi , 2019, Adjoint system method in shape optimization of some typical fluid flow patterns. In Computer Aided Chemical Engineering, 46, 871-876. https://doi.org/10.1016/B978-0-12-818634-3.50146-6

A. Courtais, Y. Privat, F. Lesage, A.M. Latifi, 2020, Geometrical optimization of fixed-bed reactors in process engineering. *In preparation.*

F. Feppon, G. Allaire, C. Dapogny, 2018, A variational formulation for computing shape derivatives of geometric constraints along rays.

A. Henrot, M. Pierre, 2006, Variation et optimisation de formes: une analyse géométrique, 48, Springer Science & Business Media.

A. Henrot, Y. Privat, 2010. What is the optimal shape of a pipe?. Archive for rational mechanics and analysis, 196(1), 281-302. https://doi.org/10.1007/s00205-009-0243-8

G. Holzinger, 2015, Openfoam a little user-manual. CD-Laboratory-Particulate Flow Modelling Johannes Keplper University, Linz, Austria.

O. Tonomura, M. Kano, S. Hasebe, 2010, Shape optimization of microchannels using CFD and adjoint method. In Computer Aided Chemical Engineering, 28, 37-42.

H.G. Weller, G. Tabor, H. Jasak, C. Fureby, 1998. A tensorial approach to computational continuum mechanics using object-oriented techniques. Computers in physics, 12(6), 620-631.

Sauro Pierucci, Flavio Manenti, Giulia Bozzano, Davide Manca (Eds.)
Proceedings of the 30th European Symposium on Computer Aided Process Engineering (ESCAPE30), May 24-27, 2020, Milano, Italy.
http://dx.doi.org/10.1016/B978-0-12-823377-1.50325-6

Systematic Modelling of Flow and Pressure Distribution in a Complex Tank

Robert Pujan,[a,b] * Heinz A. Preisig[b]

[a]*DBFZ Deutsches Biomasseforschungszentrum gemeinnützige GmbH, Torgauer Straße 116, 04347 Leipzig, Germany*
[b]*NTNU Norwegian University of Science and Technology, Høgskoleringen 5, 7491 Trondheim, Norway*
robert.pujan@dbfz.de

Abstract

The presented study proposes a systematic modelling approach for both the flow and pressure distribution in dynamic plants. A generic example illustrates the method on a generic example, which describes the hydraulic behaviour of mixing and storage tanks as well as stirred tank reactors. First, the plant is abstracted as a topology, which in turn has a precise mathematical description. In order to depict the pressure distribution within a plant, the paper expands on the transformation of the dynamic topology into a pseudo-steady state one. The model is based on an ontology that includes the entirety of physical as well as geometrical concepts and definitions necessary for describing the plant's behaviour. The main advantage of this ontology-based approach is that most of common problems like typing errors are eliminated. Since the ontology is defined off-line, a centralisation of the crafted process models is feasible, thus allowing rapid assembly of new specific plant models.

Keywords: process modelling, ontology, topology, dynamics, model reduction

1. Motivation

The pressure distribution in a plant as well as this system's behaviour under dynamic conditions is essential information for process control, plant design and optimisation (Zhan et al., 2020), and hazard assessments (Labovská et al., 2014). Applying the modelling methods established by Preisig (2014b), this study proposes a systematic modelling approach for both the flow and pressure distribution in plants. The general workflow is 1) plant depiction in a network of directed graphs, 2) definition of the mathematical model ontology, 3) model reduction via time-scale assumptions, and 4) assembling of the reduced plant model. Step 1 specifies the model structure by subdividing the plant into a network of multiple, finite volumes (capacities) that are communicating with each other via fixed, directed arcs. This network is what we refer to as a topology. This abstraction as a graph enables the mathematical definition of complex processes within a plant. The mathematical characterisation is achieved in step 2 by an equation ontology. The term ontology encompasses the entirety of concepts, definitions, properties, and relations applied to the description of a plant's behaviour. Through step 3, the finite volumes captured in the graph are further detailed by defining their dynamic nature. For example, plug-flow reactors can be reduced to event-dynamic, distributed systems, whereas continuous stirred tank reactors can simplify to lumped volumes. Thanks to the ontology being centrally established, assembling the plant model in step 4 is easy. One merely combines the model assumptions and constraints

with the respective model equations. Each equation, even if used in several model units, has thus to be implemented only once. Combination of the ontology and an automatic code generator like the software *ProM*o (Elve and Preisig, 2019) essentially eliminates typing errors and eliminates code debugging, thus increases productivity.

Using the example of a gas-liquid tank with extensive piping, this paper illustrates the general procedure of ontology-based topology modelling, on the example a fundamental model for fluid-containing tanks.

2. The example – a fluid-containing tank

Figure 1 illustrates the tank *T* with a liquid feed *F* and a breathing pipe *B* at the top, a liquid bottom-outlet *O*, and a liquid outlet *W* at the tank's wall. The scope of this analysis is the hydraulic behaviour without considering heat transfer, phase transitions, and chemical reactions. The plant's structure is similar to the one studied in (Preisig, 2014a) but extended by valves and level control.

The liquid feed leaves its supply pipe *S* at the very top of the tank, thus forming a free jet *J* downwards to the surface of the tank's liquid phase *L*. In the beginning, the only liquid outflow occurs via the bottom outlet *O*, driven by the sum of hydrostatic pressure and the pressure of the gas phase *G* on top. As soon as the liquid is completely covering the opening of *W*, valve *V4* is opened to release a drain *D*, preventing the tank from flooding. If the liquid level rises even further, the level controller *LIC* intervenes by adjusting the feed via valve *V1*. This feed-controlled system is therefore suited for applications in which the feed can be altered but a certain product flow *P* has to be met. If an outflow-regulated level control is required, *LIC* would correspondingly be coupled with valve *V3*.

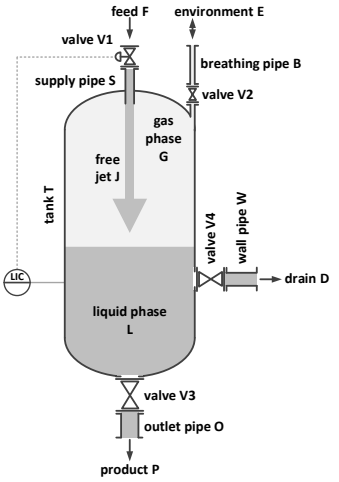

Figure 1: Sketch of the plant

While liquid accumulates, gas is squeezed out via *B*, thus equalising the tank's pressure with the pressure of the environment *E*. However, if the liquid level changes fast, the tank pressure can increase above the environmental pressure due to flow resistance in *B* and *V2*. Like any plant, the tank's dynamics are driven by the conditions at its boundaries. The boundaries are the ports of the system to its environment, namely *D*, *E*, *F,* and *P*. The pressures at these boundaries drive the convective mass flows in the established system.

3. Translation of the plant into a topology

The process modelling procedure by abstracting the plant as a topology represented as a graph with the nodes representing capacities of conserved quantities, and the arcs the flows of extensive quantities. The latter are driven by gradients of the intensive properties. For more details, Preisig (2014a) and (2014b) recommended. A possible first topology for the plant is shown in Figure 2 on the left. Mass flows are drawn as black arrows, volume work as dashed, grey arrows, and dynamic, distributed capacities as ellipses. In contrast to lumped systems, where the intensive properties are not a function of the position, they are so for distributed systems. The tank is assumed to be rigid as indicated by the dashed outlines of tank-internal volumes. Compared to the considered

dynamic system, the environment is modelled as infinitely large, a set of reservoirs that have constant properties. In the topology, reservoirs are represented as half circles. Black bars depict boundaries, which are event-dynamic surfaces that mark discrete changes between two coupled capacities.

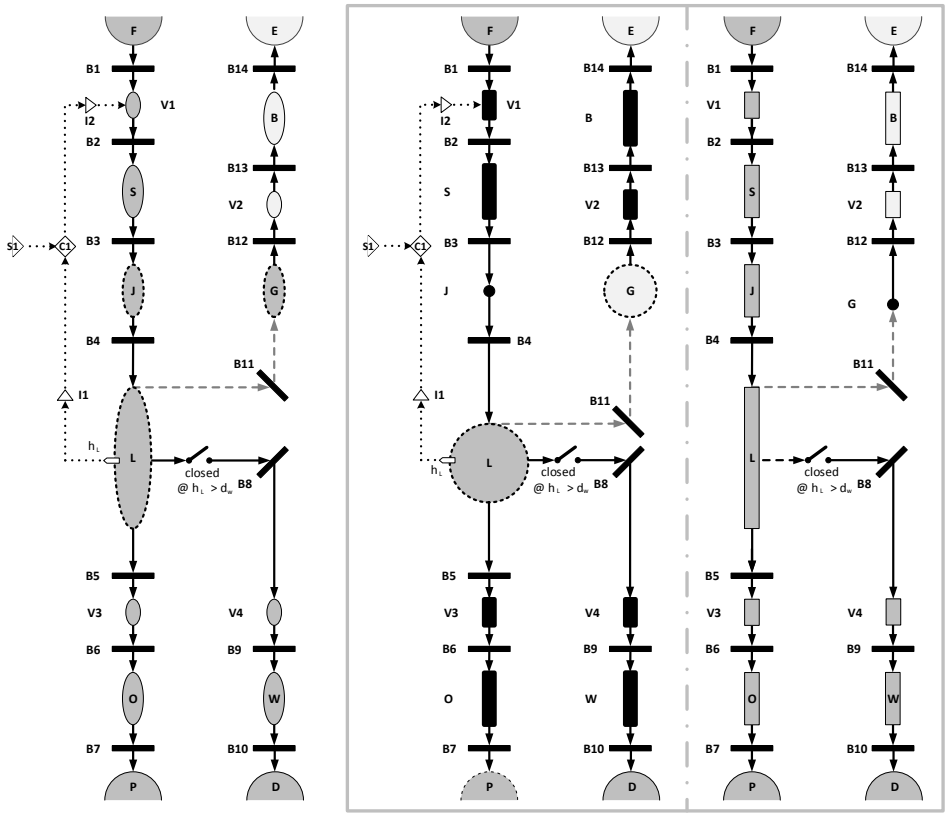

Figure 2: Topology representation of the plant with the initial structure on the far left and the time-scale model split in the box (left: dynamic, right: event-dynamic)

The described physical domain is augmented with a control domain, comprising the liquid level controller *C1* and a set-point *S1*, which defines the maximum liquid level. The controller collects information about the current liquid level in the tank and computes a control output $u(h_L)$, sent to valve *V1*. Dotted, black arrows represent information flow. The physical domain and the control domain are each self-contained networks. They communicate with each other through interfaces, which in the topology are represented as white triangles. The mathematical representation of these interfaces is outside the scope of this exposition and will be covered in another paper. The initial topology represents the choice of granularity. Therefore, it always contains maximum information. Model simplifications, which are fundamentally the neglect of structural parts of the model (Preisig, 2015), are possible in later stages but the addition of new structures is not. In order to represent the visible dynamics of mass distribution and the supposedly immediate pressure dissipation, the topology is split into two: One for the fast time scale, capturing the pressure distribution, and one for the slow time scale, representing the material and energy flow. The result is a dynamic domain for the mass and an event-dynamic one for the pressure. In the latter, the current state of the dynamic

mass distribution, the slow part in this relation, appears in pseudo-steady state. Mathematically, the split is the inner and the outer solution of a singular perturbation. As shown in the box of Figure 2, all pipes and valves are now reduced to a plug-flow. In the dynamic domain, they are drawn as black rectangles, indicating event-dynamic capacities without distributional effects, whereas in the event-dynamic domain they are depicted as coloured rectangles due to the pressure change within them. The tank volumes of gas and liquid are depicted as lumped systems in the dynamic domain (circles). In the event-dynamic domain, the capacity L is distributed due to the hydrostatic pressure. G is considered to hold the same pressure at any point, thus being a point capacity - a lumped, event-dynamic node (black circle). Since J is represented by a point capacity in the dynamic domain, its relatively small capacity is neglected and the mass transport from S to L instantaneous. Both are assumed to be negligible and of no impact to the mass-flow investigations.

4. Assembling the ontology

Each component in the topology is linked to a set of state-dynamic equations in the mathematical ontology. Table 1 shows the relevant equation ontology for the physical domain of example model. The structure of the directed graph of the topology enters as the incidence matrix $\underline{\underline{F}}$. Vectors are depicted as $\underline{x}$, where a dot decorator represents an accumulation and a hat a flow. In Eq. (12), $u(h_L)$ represents a controller output that adjusts the valve opening if required. Since flow through W is only enabled after reaching a specified h_L, Eq. (11) replaces Eq. (10) in W. The ontology is designed according to the assumptions that a) the tank is rotationally-symmetric with a rigid volume, b) all pipes and the free jet are cylindrical and straight with constant diameter, c) no reactions, heat exchange or thermal effects are considered, d) friction does not impact the internal energy U, e) liquid and gas phases are considered homogeneous, f) the liquid has constant density, and g) the friction factor of turbulent flows is taken from the Moody chart. Case-specific assumptions and constraints that are not universally valid are not part of the ontology but of the model reduction instead.

On closer inspection of Table 1, it becomes apparent that the vectors of velocity v and pressure p are not fully specified. In any mass transport, v and p are interdependent. Due to this correlation, the model's initiation has to provide appropriate initial values for at least one of these variables in every capacity to start the iterative process.

5. The reduced plant model

Assumptions reduce the initial model to a specific simulation case. Table 2 shows the assumptions and the resulting reduced model. The capacities' mass balances are either Eq. (3) with the accumulation term nullified (all pipes, valves, and J) or identical to Eq. (1) (L and G). Most of the assumptions eliminate particular terms. Implementing a constraint on the sum of the liquid and the gas volume to be constant, thus modelling a rigid tank, requires quite some effort. It leads to an overdetermined system, as the constraint introduces an algebraic link between the two accumulation terms. The constraint consequently replaces the volume workflow, thus Eq. (8) has to be eliminated from G to avoid over-determination.

All that is left at this point is the model initialisation with boundary conditions, parameters like density and molar mass, as well as basic geometrical dimensions of the plant.

Table 1: Equations ontology of the physical domain

Description	Equation	
Integrals		
Mass	$\underline{m} = \int_0^t \dot{\underline{m}}(\tau)d\tau + \underline{m}(0)$	(1)
Energy	$\underline{E} = \int_0^t \dot{\underline{E}}(\tau)d\tau + \underline{E}(0)$	(2)
Balances		
Mass conservation	$\dot{\underline{m}} = \underline{\underline{F}}\hat{\underline{m}}$	(3)
Energy conservation	$\dot{\underline{E}} = \underline{\underline{F}}\hat{\underline{U}} + \underline{\underline{F}}\hat{\underline{K}} + \underline{\underline{F}}\hat{\underline{P}} + \underline{\underline{F}}\hat{\underline{w}}^v + \underline{\underline{F}}\hat{\underline{w}}^f$	(4)
Flows		
Mass flow	$\hat{\underline{m}} = \underline{\rho}\hat{\underline{V}}$	(5)
Kinetic energy flow	$\hat{\underline{K}} = \frac{1}{2}\hat{\underline{m}}\underline{v}^2$	(6)
Potential energy flow	$\hat{\underline{P}} = \hat{\underline{m}}\underline{h}g$	(7)
Volume work flow	$\hat{\underline{w}}^v = \underline{p}\hat{\underline{V}}$	(8)
Friction work flow	$\hat{\underline{w}}^f = \Delta\underline{p}^f\hat{\underline{V}}$	(9)
Volume flow	$\hat{\underline{V}} = \underline{v}\underline{A}$	(10)
Volume flow (wall pipe)	$\hat{\underline{V}} = \mathrm{sgn}\left[1 + \mathrm{sgn}\left(\mathrm{sgn}\{h_L - d_W\} - \frac{1}{2}\right)\right]\underline{v}\underline{A}$	(11)
Material properties		
Cylindrical cross-section	$\underline{A} = \underline{u}(h_L)\pi\left[\underline{r}(l)\right]^2$	(12)
Liquid level	$h_L := root\left[\underline{\underline{F}}_L\underline{V} = \pi\int_0^{h_L}\left\{\underline{\underline{F}}_L\underline{r}(l)\right\}^2 dl\right]$	(13)
Mass density ideal gas	$\underline{\rho} = \underline{M}\underline{p}(R\underline{T})^{-1}$	(14)
Voluminous property	$\underline{V} = \underline{m}\underline{\rho}^{-1}$	(15)
Darcy-Weisbach model	$\Delta\underline{p}^f = \frac{1}{2}\underline{f}^i\underline{v}^2\underline{\rho}\underline{l}\left[2\underline{r}(l)\right]^{-1}$	(16)
Darcy friction factor	$f^i := f^{la}$ if $\mathrm{Re} \le 2{,}100$; $f^i := f^t$ if $\mathrm{Re} > 2{,}100$	(17)
Friction factor (laminar)	$f^{la} = 64\,\mathrm{Re}^{-1}$	(18)
Friction factor (turbulent)	$f^t = f(\mathrm{Re}, \in)$	(19)
Reynolds number	$\mathrm{Re} = 2\rho v r(l)\eta^{-1}$	(20)

6. Conclusions

As this paper shows, topologies are a fast and very handy method to discuss and define the structure of any model, while the implementation of ontologies minimises errors and time effort. For this reason, the modelling suite *ProMo is* currently in development at the NTNU (Elve and Preisig, 2019). Based on the user-imposed topology, the software automatically selects the required ontology equations and generates executable program

Table 2: Reduced plant model

Pipes	*s := B, O, S*	*Eq. (1-5, 7-10, 12, 16-20)*
Assumptions	$\underline{\underline{F}}_s \hat{\underline{U}} = 0\,;\ \ \underline{\underline{F}}_s \hat{\underline{K}} = 0$	
Pressure distribution	$0 = \underline{\underline{F}}_s \hat{\underline{P}} + \underline{\underline{F}}_s \hat{\underline{w}}^v + \underline{\underline{F}}_s \hat{\underline{w}}^f = \underline{\underline{F}}_s \left(\underline{\rho} \underline{h} g + \underline{p} + \Delta \underline{p}^f \right)$	
Wall pipe	*s := W*	*Eq. (1-5, 7-9, 11, 12, 16-20)*
Assumptions	$\underline{\underline{F}}_s \hat{\underline{U}} = 0\,;\ \ \underline{\underline{F}}_s \hat{\underline{K}} = 0$	
Pressure distribution	$0 = \underline{\underline{F}}_s \hat{\underline{P}} + \underline{\underline{F}}_s \hat{\underline{w}}^v + \underline{\underline{F}}_s \hat{\underline{w}}^f = \underline{\underline{F}}_s \left\lfloor \underline{\rho} \underline{h} g + \underline{p} + \Delta \underline{p}^f \left(\hat{V}(h_L) \right) \right\rfloor$	
Valves	*s := V1, V2, V3, V4*	*Eq. (1-8, 10, 12)*
Assumptions	$\underline{\underline{F}}_s \hat{\underline{U}} = 0\,;\ \ \underline{\underline{F}}_s \hat{\underline{w}}^f = 0$	
Pressure distribution	$0 = \underline{\underline{F}}_s \hat{\underline{K}} + \underline{\underline{F}}_s \hat{\underline{P}} + \underline{\underline{F}}_s \hat{\underline{w}}^v = \underline{\underline{F}}_s \left(\tfrac{1}{2} \underline{\rho} \underline{v}^2 + \underline{\rho} \underline{h} g + \underline{p} \right)$	
Free jet	*s := J*	*Eq. (1-5, 8, 10, 12)*
Assumptions	$\underline{\underline{F}}_s \hat{\underline{U}} = 0\,;\ \ \underline{\underline{F}}_s \hat{\underline{K}} = 0\,;\ \ \underline{\underline{F}}_s \hat{\underline{P}} = 0\,;\ \ \underline{\underline{F}}_s \hat{\underline{w}}^f = 0$	
Pressure distribution	$0 = \underline{\underline{F}}_s \hat{\underline{w}}^v = \underline{\underline{F}}_s \underline{p} \hat{\underline{m}} \underline{\rho}^{-1}$	
Liquid phase	*s := L*	*Eq. (1-5, 7, 8, 10, 12, 13, 15)*
Assumptions	$\underline{\underline{F}}_s \hat{\underline{U}} = 0\,;\ \ \underline{\underline{F}}_s \hat{\underline{K}} = 0\,;\ \ \underline{\underline{F}}_s \hat{\underline{w}}^f = 0$	
Pressure distribution	$0 = \underline{\underline{F}}_s \hat{\underline{P}} + \underline{\underline{F}}_s \hat{\underline{w}}^v = \underline{\underline{F}}_s \left(\underline{\rho} \underline{h} g + \underline{p} \right)$	
Gas phase	*s := G*	*Eq. (1-5, 10, 12, 14, 15)*
Assumptions	$\underline{\underline{F}}_s \hat{\underline{U}} = 0\,;\ \ \underline{\underline{F}}_s \hat{\underline{K}} = 0\,;\ \ \underline{\underline{F}}_s \hat{\underline{P}} = 0\,;\ \ \dot{V}_L + \frac{\partial}{\partial m_G} \frac{\partial}{\partial \rho_G} V_G = 0$	
Pressure distribution	$0 = \underline{\underline{F}}_s \hat{\underline{w}}^v = \underline{\underline{F}}_s \underline{p} + R \left(\underline{\underline{F}}_L \underline{\hat{m}} \underline{\rho} \right)^{-1} \underline{\underline{F}}_s \underline{\hat{m}} \underline{T} \underline{M}^{-1}$	

code, thus enabling rapid design of plant models. Current work focuses on the automatic realisation of the pressure distribution by the software as well.

Acknowledgments

As part of the research centre Bio4Fuels, this study has received funding from the Research Council of Norway (RCN) under the support code 257622 and is hosted by the Norwegian Centre for Environment-friendly Energy Research (FME).

References

A.T. Elve, H.A. Preisig, 2019, From ontology to executable program code, Comput. Chem. Eng., 122, 383-394

Z. Labovská, J. Labovský, Ľ. Jelemenský, J. Dudáš, J. Markoš, 2014, Model-based hazard identification in multiphase chemical reactors, J. Loss Prevent. Proc., 29, 155-162

H.A. Preisig, 2014a, A Graph Approach to Representing the Pressure Distribution in Complex Plants, Comput. Aided Chem. Eng., 33, 865-870

H.A. Preisig, 2014b, Visual Modelling, Comput. Aided Chem. Eng., 34, 729-734

H.A. Preisig, 2015, Model Reduction in Visual Modelling, Comput.Aided Chem.Eng, 37,629-634

Y. Zhang, S. Li, Y. Zheng, Y. Zou, 2020, Multi-model based pressure optimization for large-scale water distribution networks, Control Eng. Pract., 95, doi:10.1016/j.conengprac.2019.104232

Sauro Pierucci, Flavio Manenti, Giulia Bozzano, Davide Manca (Eds.)
Proceedings of the 30th European Symposium on Computer Aided Process Engineering (ESCAPE30), May 24-27, 2020, Milano, Italy.
http://dx.doi.org/10.1016/B978-0-12-823377-1.50326-8

A New Methodology to Design Optimal Exchanges Network for Facing Concrete Industrial Problems

Florent Mousqué, Marianne Boix*, Stéphane Négny, Ludovic Montastruc, Serge Domenech

Laboratoire de Génie Chimique, Université de Toulouse, CNRS, INPT, UPS, Toulouse, France

marianne.boix@toulouse-inp.fr

Abstract

Nowadays, industries are facing significant environmental and competitive stakes. An efficient way for companies to overcome these difficulties is to gather and collaborate in Eco-Industrial Parks (EIP). Nevertheless, establish an optimal eco-industrial exchange is a task that requires the development of methods. This article therefore proposes a method for Multi-Objective (MO) optimal design of EIP exchange networks that deals with net present cost and complexity of the network. A new network complexity indicator is defined that represents the topological feasibility but also the management of the designed network. An iterative resolution procedure is developed to solve large MILP problems. This procedure sets the minimum flow capacity threshold throughout the iterations, whereas in previous papers it was set arbitrarily. The developed method is assessed on a large EIP energy network. Results show that network complexity is considerably reduced using this MO approach in comparison to economic mono-objective solution.

Keywords: Industrial Ecology, Eco-Industrial Parks, Design, Multi-Objective Optimization, Mathematical Programming, Network complexity

1. Introduction

An EIP is a cluster of industries that aims at optimizing their economic gains while reducing their environmental impact through the synergistic benefits of cooperation (Chertow, 2000). This is being possible by mutualizing and sharing materials, energy, water and by-products. To achieve these objectives, optimization methods are required to design optimal exchange networks between companies.

A major challenge in optimization methods development is to deal with the network complexity of the solutions (Kastner et al., 2015), especially when a lot of interconnections are considered, as it is the case in EIP. Indeed, the so-called network complexity, previously defined as the number of interconnections (Aviso et al., 2011) is directly linked to the topological feasibility of the network, but also to its management complexity. Furthermore, (Boix et al., 2012) have shown that the cost and the complexity of networks, such as minimizing the number of interconnections are interesting criteria to address in a MO optimization approach because of their antagonism. Indeed, without these interconnections, there are no more synergetic economic benefits.
Classically in the literature, network complexity is optimized by minimizing the number of interconnections or managed by setting a minimum flow threshold for interconnections with an arbitrary value. For the latter constraint, it limits the number of interconnections by avoiding designing a network whose interconnection makes no sense on an industrial scale because the flow is smaller than the fixed value (Boix et al., 2012). This arbitrarily

fixed threshold constitutes a key parameter because it has a significant influence on the resulting network. Another issue in network design through mathematical programming is related to EIP large networks where many interconnected plants and processes must be involved. The developed optimization procedure has to be generic and able to handle these large complex problems.

The contribution of this paper is the development of a new methodology to perform MO optimization with concrete industrial challenges: the minimization of the net present cost, and the minimization of the network complexity. A new indicator is developed to assess the network complexity, based on two parameters: the number of interconnections to be minimized and the minimum flow capacity of interconnections to be maximized. The flow capacity represents the maximum flow rate of an interconnection over time. This method has been developed in an iterative way, in order to reduce computational difficulty and therefore to cope with the difficulty of solving such large mathematical problems. The main novelty of this work is the development of an iterative resolution procedure where the threshold of the flow capacity of interconnections evolves.
As a result, this method gives an optimal set of solutions, the final solution is determined with the TOPSIS Multi-Criteria Decision-Making (MCDM) tool. The procedure is assessed on a case study based on an EIP coupled energy network supplying heat and electricity that has been presented in a previous paper (Mousqué et al. 2019).

2. Methodology

This section discusses the methodology of resolution, the first part describes the new network complexity indicator, the issues and the principles of the method and then the last part details the general procedure.

2.1. Network Complexity Indicator definition

The defined network complexity indicator is based on the number of interconnections and the minimum flow capacity of interconnections in the network ($\mathrm{Min}_{\mathrm{Capacity}}^{\mathrm{Interc}}$).

- The number of interconnections is a classical criterion to be used during the design step (Boix et al., 2015). Indeed, interconnections cause maintenance operations, so it is important to minimize this objective function.
- The novelty of this method is the integration of $\mathrm{Min}_{\mathrm{Capacity}}^{\mathrm{Interc}}$ as a criterion: it measures the flow capacity of the smallest interconnection in the network. This criterion has to be maximized in order to foster larger flow interconnections rather than smaller ones that are not interesting at the industrial scale.

2.2. Computational challenges

As detailed hereafter, the two main challenges of the developed method are to solve large models as EIP exchanges network and to handle MO optimization with economic and network complexity criteria. With regard to the first issue, in models to design EIP networks, the number of binary variables used to select interconnections increases exponentially with the number of companies and processes. For this reason, these binaries classically become the super-variables, i.e. the bottleneck variables for the calculation time. The issue is that they are too many super-variables to be able to handle them separately. Hence, the principle of the procedure is to reduce the number of super-variables by designing with a limited number of interconnections. The selected interconnections are those of the mono-objective optimization with the economic criterion. This approach is intended to provide results close to the global optimum while ensuring shorter calculation time.

The second stake is to achieve a MO optimization having the value of the minimum flow capacity threshold of the interconnections ($\mathrm{Min}^{\mathrm{Interc}}_{\mathrm{Threshold}}$) that is no longer arbitrarily settled. For this purpose, the resolution procedure developed uses $\mathrm{Min}^{\mathrm{Interc}}_{\mathrm{Threshold}}$ as a parameter that varies throughout the iterative optimization procedure in order to select the optimal value for this threshold.
For the sake of clarification, $\mathrm{Min}^{\mathrm{Interc}}_{\mathrm{Threshold}}$ is the minimum threshold fixed as a parameter, while $\mathrm{Min}^{\mathrm{Interc}}_{\mathrm{Capacity}}$ is the minimum value measured on the solution obtained.

2.3. Resolution procedure

Resulting from these discussions, the complete resolution procedure shown in Figure 1 is described hereafter.

The first step consists of a mono-objective optimization to obtain the solution that minimizes the economic criterion. Then, from this initial solution, the limited list of interconnections used for the rest of the procedure is determined. This is done by setting the selection binary of the unused interconnection as a parameter that is equal to 0 (i.e. the interconnection is not selected). Afterwards, the procedure is iterative. At each iteration, the principle is to remove the minimum sized interconnection from the previous solution and to economically optimize the network with selected interconnections. Moreover, at each iteration, the minimum flow capacity threshold of interconnections in the network ($\mathrm{Min}^{\mathrm{Interc}}_{\mathrm{Threshold}}$) is constrained to be equal or greater to the minimum size of interconnection present in the network of the previous iteration. This $\mathrm{Min}^{\mathrm{Interc}}_{\mathrm{Threshold}}$ constraint, which increases throughout the resolution procedure, aims to avoid obtaining solutions with very low flow capacity interconnections ($\mathrm{Min}^{\mathrm{Interc}}_{\mathrm{Capacity}}$).
At the end of the method, when there are no more interconnections, a set of solutions is provided. In order to rank all the solutions obtained and to determine the selected one, TOPSIS MCDM tool is used during the post-treatment phase. To go further, TOPSIS (Technique for Order Preference by Similarity to Ideal Solution) is a well-known technique that consists in comparing the distance of each solution between the ideal one (having the best reachable value for each criterion) and its opposite, the negative-ideal one.

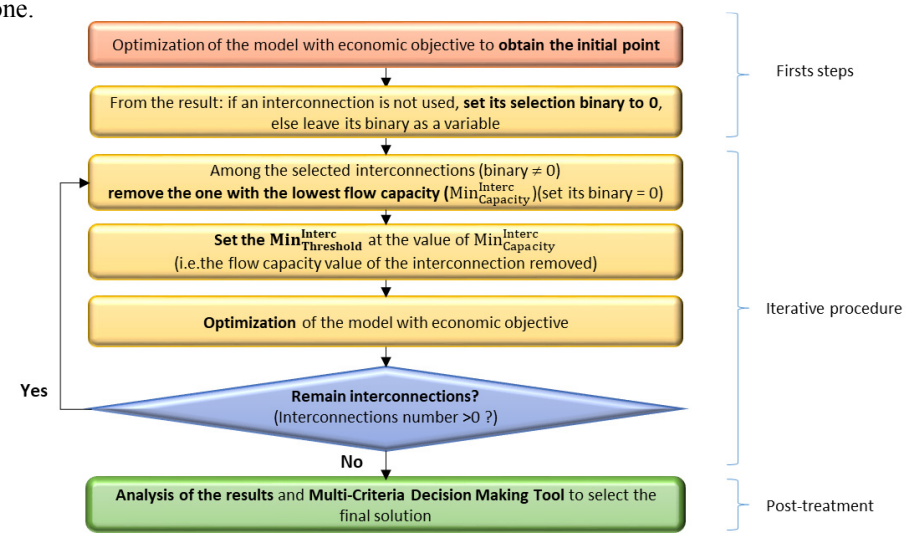

Figure 1: Iterative resolution procedure.

3. Case study

The developed method is then applied over the case study presented below. As mentioned before, the case study is based on a previous model developed by Mousqué et al. (2019). This case study is chosen for its specificity to represent a large EIP network because it couples heat and electricity energy networks with 15 industries and many interconnections possibilities.

The optimization model is formulated as a Mixed Integer Linear programming (MILP) to design an optimal energy network coupling the utility system supplying heat (i.e. steam) with the Hybrid Power System (HPS) producing electricity for an EIP.
The general superstructure of this model that represents design possibilities is presented in Figure 2. The utility system producing steam at four levels of pressures (j) works as a closed-loop in each industry, after production in the boilers (i), electricity production through the turbines (t) and process use, the condensed steam return to the water unit. The HPS can supply electricity thanks to solar panels, wind turbines or outsourced electricity purchased. The design is carried out using binary variables to select boiler and turbine technologies while the power for the HPS sources is sized thanks to continuous variables. Finally, the steam interconnections with other companies (e) are selected by means of binaries and sized thanks to a continuous variable, i.e. the flow-capacity of interconnections. Binaries are also used for the operating conditions of boilers, turbines and interconnections.

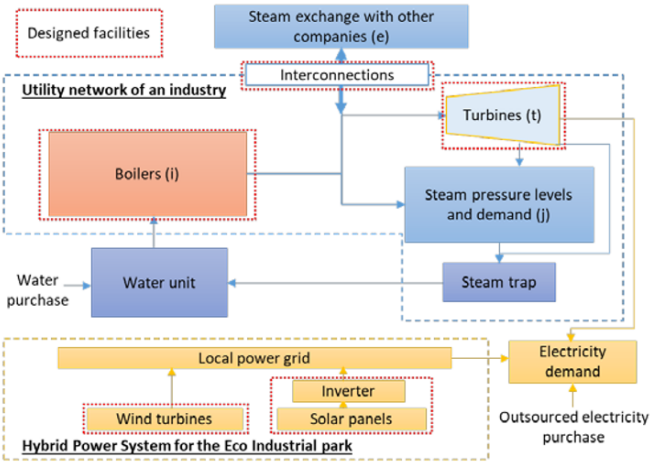

Figure 2: Superstructure of the coupled energy network of the EIP (from Mousqué et al., 2019).

4. Results and discussion

4.1. Resolution procedure assessment

A preliminary study was conducted to discuss the influence of the increase throughout the resolution process of the minimum flow capacity of interconnection threshold (i.e. $\mathrm{Min}^{\mathrm{Interc}}_{\mathrm{Threshold}}$). The procedure is then compared to the same method without the constraint to limit the minimum flow capacity of interconnection. The set of solutions obtained according to cost, number of interconnections and minimum flow capacity of interconnections is provided in Figure 3 (a) for the method with the increasing threshold and (b) for the method without threshold. On Figure 3 (a), the TOPSIS solution to be detailed hereafter is also represented.

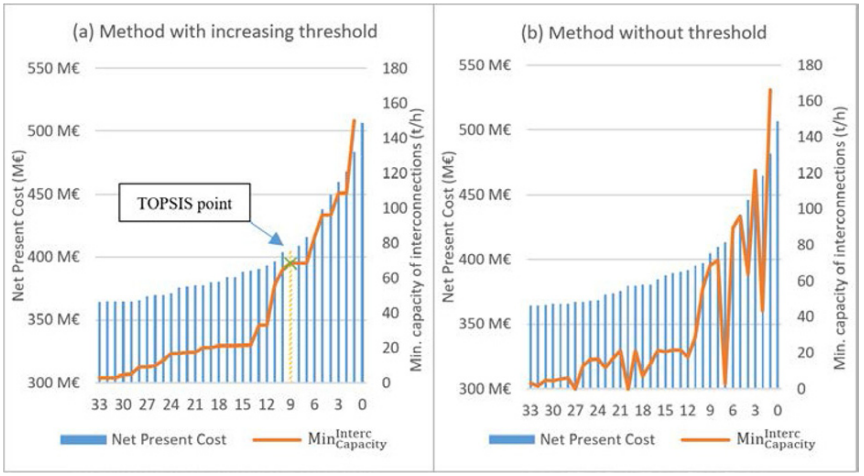

Figure 3: Results for the method with increasing threshold (a) and without threshold (b).

Thus, results are obtained starting from the mono-objective economic minimum (i.e 33 interconnections). The evolution profiles of the net present cost curves for both methods are similar, i.e. the cost increases with the decrease in the number of interconnections. Differences between both methods are observed at some points, interconnections number is similar while the cost is slightly different (+ or – 1.7 %). Then in relation to cost, results for both methods are close.

The other criterion highlighted in these figures is the minimum flow capacity of interconnections in the network, $\mathrm{Min}_{\mathrm{Capacity}}^{\mathrm{Interc}}$. Throughout the resolution process, when the number of interconnections decreases, the $\mathrm{Min}_{\mathrm{Capacity}}^{\mathrm{Interc}}$ increases for the method with constraint while it evolves in an irregular way and reaches very low levels at some points, for the method without constraint. It is then shown that the increasing threshold avoids nonsensical interconnections to be selected.

Finally, it is to be noticed, that the developed iterative procedure provides results with a significantly reduced calculation time compared to a one-step method consisting of constraining the number of interconnections. Indeed, the addition of a constraint on these super-variable binaries considerably increases the computation time.

In conclusion of this part, the developed resolution method, as proven to be able to solve large MILP network design problems. The procedure to set the key-parameter of $\mathrm{Min}_{\mathrm{Threshold}}^{\mathrm{Interc}}$ avoids interconnections with very low flow capacity without having a significant impact on the cost criterion. Then, in the following part, the final solution is selected, using MCDM tool.

4.2. TOPSIS optimal solution analysis

Henceforth, once the different solutions of the developed method have been obtained, these solutions are ranked using TOPSIS tool. The final solution selected by TOPSIS is indicated in Figure 3(a). For this case study, the same weight is assigned to economic and network complexity criteria.

The optimal solution selected using TOPSIS is the solution with a number of interconnections of 9 with a $\mathrm{Min}_{\mathrm{Capacity}}^{\mathrm{Interc}}$ of 68.4 t/h and a global cost of 405 M€. In comparison to the mono-objective optimization, the cost is increased by 11 % while

network complexity is significantly decreased, i.e. number of interconnections is decreased from 33 to 9, and $\mathrm{Min}^{\mathrm{Interc}}_{\mathrm{Capacity}}$ to be maximized goes from 3 t/h to 68.4 t/h.

Finally, these results lead to a conclusion on the general interest of the multi-objective method, namely that with complex systems such as EIP exchange networks, it is important and more realistic to consider several criteria.

5. Conclusions

In this paper, a method is provided for the optimal design of an EIP exchange network performing a MO optimization through economic (i.e. net present cost) and network complexity criteria. An iterative method for the optimization of the complexity and for solving large MILP problems has been developed. In previous industrial network design papers, the network complexity was managed with two criteria, the number of interconnections in the network and the threshold value for the minimum flow capacity of interconnections which was up to now set as an arbitrary value. Indeed, the minimum flow capacity threshold of interconnection is henceforth determined by the method as a threshold increasing during the procedure. As a result, the developed resolution procedure solves a large coupled energy network case study of 15 companies EIP. Results show that compared to mono-objective optimization on cost, a small cost increase allows getting a solution with significantly reduced complexity. Therefore, the selected interconnections are designed to be the most cost-effective, and their number is limited to reduce topological and management complexity of the network. Next improvements for this model are identified as integrating other criteria, particularly resilience and sustainability (i.e. environmental and social).

References

Aviso, Kathleen B., Raymond R. Tan, Alvin B. Culaba, and Jose B. Cruz. (2011). "Fuzzy Input-Output Model for Optimizing Eco-Industrial Supply Chains under Water Footprint Constraints." *Journal of Cleaner Production*. https://doi.org/10.1016/j.jclepro.2010.09.003.

Boix, Marianne, Ludovic Montastruc, Catherine Azzaro-Pantel, and Serge Domenech. (2015). "Optimization Methods Applied to the Design of Eco-Industrial Parks: A Literature Review." *Journal of Cleaner Production* 87 (1): 303–17. https://doi.org/10.1016/j.jclepro.2014.09.032.

Boix, Marianne, Ludovic Montastruc, Luc Pibouleau, Catherine Azzaro-Pantel, and Serge Domenech. (2012). "Industrial Water Management by Multiobjective Optimization: From Individual to Collective Solution through Eco-Industrial Parks." *Journal of Cleaner Production* 22 (1): 85–97. https://doi.org/10.1016/J.JCLEPRO.2011.09.011.

Chertow, Marian R. (2000). "Industrial Symbiosis: Literature and Taxonomy." *Annual Review of Energy and the Environment* 25: 313–37. https://doi.org/10.1146/annurev.energy.25.1.313.

Kastner, Catharine A., Raymond Lau, and Markus Kraft. (2015). "Quantitative Tools for Cultivating Symbiosis in Industrial Parks; a Literature Review." *Applied Energy*. Elsevier. https://doi.org/10.1016/j.apenergy.2015.05.037.

Mousqué, Florent, Marianne Boix, Stéphane Négny, Ludovic Montastruc, and Serge Domenech. (2019). "On-Grid Hybrid Power System and Utility Network Planning to Supply an Eco-Industrial Park with Dynamic Data." *Computer Aided Chemical Engineering*, 46:1717–22. https://doi.org/10.1016/B978-0-12-818634-3.50287-3.

Sauro Pierucci, Flavio Manenti, Giulia Bozzano, Davide Manca (Eds.)
Proceedings of the 30th European Symposium on Computer Aided Process Engineering (ESCAPE30), May 24-27, 2020, Milano, Italy.
http://dx.doi.org/10.1016/B978-0-12-823377-1.50327-X

Nested Sampling Strategy for Bayesian Design Space Characterization

Kennedy P. Kusumo[a], Lucian Gomoescu[a,b], Radoslav Paulen[c], Salvador García-Muñoz[d], Costas C. Pantelides[a,b], Nilay Shah[a], Benoit Chachuat[a,*]

[a] *Centre for Process Systems Engineering, Department of Chemical Engineering, Imperial College London, UK*
[b] *Process Systems Enterprise Ltd, London, UK*
[c] *Faculty of Chemical and Food Technology, Slovak University of Technology in Bratislava, Slovakia*
[d] *Small Molecule Design and Development, Eli Lilly & Company, Indianapolis, USA*
b.chachuat@imperial.ac.uk

Abstract

Design space is a key concept in pharmaceutical quality by design, providing better understanding of manufacturing processes and enhancing regulatory flexibility. It is of paramount importance to develop computational techniques for providing quantitative representations of a design space, in accordance with the ICH Q8 guideline. The focus is on Bayesian approaches to design space characterization, which rely on a process model to determine a feasibility probability that is used for measuring reliability and risk. The paper presents three improvements over an existing nested sampling method: two-phase strategy with the first phase using a cheap sorting function based on nominal model parameters; dynamic sampling strategy to refine the target design space; and vectorization to evaluate costly functions in parallel. These improvements are implemented as part of the python package DEUS and demonstrated on an industrial case study.

Keywords: pharmaceutical processes, quality-by-design, design space, nested sampling

1. Introduction

The quality-by-design (QbD) initiative, through the ICH Q8 guideline (Reklaitis et al., 2017), introduced the concept of design space (DS) to improve regulatory flexibility of processes in the pharmaceutical industry. Given a set of critical quality attributes (CQA), the DS represents a set of critical process parameters (CPP) that result in on-spec pharmaceutical production. Peterson (2008) defined the probabilistic DS in terms of feasibility probabilities, a concept akin to stochastic flexibility (Straub and Grossmann, 1990). As the use of mathematical models to support DS characterization is becoming more common in industrial practice (García-Muñoz et al., 2015), the uncertainty related to model parameters and structure needs to be considered and efficient computational tools are of great interest.

Existing computational approaches to probabilistic DS characterization differ in how they account for process model uncertainty and how they approximate the DS itself. Process model uncertainty may be represented as a sampled distribution (e.g. a joint posterior from Bayesian estimation) or a joint confidence region (e.g. a frequentist confidence ellipsoid). Sampling methods seek to produce a set of CPP values that belong to the DS at a desired reliability level, whereas optimization-based methods seek to inscribe a

simple shape (e.g. box or ellipsoid) within the DS. For instance, Laky et al. (2019) proposed two optimization-based strategies akin to the classic feasibility test and index formulations that exploit confidence ellipsoids for the model parameters. Monte Carlo and Bayesian techniques have also been used to propagate the uncertainty to the CQAs and estimate a feasibility probability (Peterson et al., 2017; Bano et al., 2018). These techniques have proven effective in practice, but they are computationally expensive and mainly tractable for low-dimensional DS at present.

Recently, Kusumo et al. (2019) presented a sampling strategy based on an adaptation of the nested sampling (NS) algorithm (Skilling, 2004). The algorithm maintains a given set of live points through regions with increasing probability feasibility until reaching a desired reliability level. It leverages efficient strategies from Bayesian statistics for generating replacement proposals during the search and is applicable to problems with disjoint DS or black-box models. This paper presents three ideas to further improve the computational performance of nested sampling for DS characterization. These improvements are demonstrated on a comparative study of the Suzuki coupling reaction.

2. Background

Consider a manufacturing process for a pharmaceutical product that has its quality defined by some CQAs, denoted by $\boldsymbol{s} \in \mathbb{R}^{n_s}$. Assume that a mathematical model of the process (either knowledge- or data-driven) is available that predicts the CQAs corresponding to the CPPs, denoted by $\boldsymbol{d} \in \mathrm{K}$ within the knowledge space $\mathrm{K} \subset \mathbb{R}^{n_d}$:

$$\boldsymbol{s} = \boldsymbol{f}(\boldsymbol{d}, \boldsymbol{\theta}) \tag{1}$$

The model parameters, $\boldsymbol{\theta} \in \mathbb{R}^{n_\theta}$ represent uncertain quantities e.g., physical constants, coefficients in a regression model, or disturbances that affect the CQAs. Feasibility of the process is defined by the CQA limits alongside other process constraints:

$$\boldsymbol{G}(\boldsymbol{d}, \boldsymbol{\theta}) := \boldsymbol{g}(\boldsymbol{d}, \boldsymbol{f}(\boldsymbol{d}, \boldsymbol{\theta})) \leq \boldsymbol{0} \tag{2}$$

The mappings $\boldsymbol{f}$ and $\boldsymbol{G}$ need not be given in closed-form but could be implicitly defined via a DAE model or a CFD simulation. Given a set of nominal model parameters $\boldsymbol{\theta}_{\text{nom}}$, the nominal DS is defined as:

$$\mathrm{D}_{\text{nom}} := \left\{ \boldsymbol{d} \in \mathrm{K} : \boldsymbol{G}(\boldsymbol{d}, \boldsymbol{\theta}_{\text{nom}}) \leq \boldsymbol{0} \right\}. \tag{3}$$

However, the value of $\boldsymbol{\theta}$ is inherently uncertain by nature of the modelling exercise. A Bayesian framework considers $\boldsymbol{\theta}$ as random variables with a joint distribution $p(\boldsymbol{\theta})$ that describes the belief on the value of $\boldsymbol{\theta}$. In this framework the model is used to predict the probability that the manufacturing process is feasible for a given $\boldsymbol{d} \in \mathrm{K}$:

$$\mathrm{P}\left[\boldsymbol{G}(\boldsymbol{d}, \cdot) \leq \boldsymbol{0} \mid p(\boldsymbol{\theta}) \right] := \int_{\{\boldsymbol{\theta} : \boldsymbol{G}(\boldsymbol{d}, \cdot) \leq \boldsymbol{0}\}} p(\boldsymbol{\theta}) \, \mathrm{d}\boldsymbol{\theta} \tag{4}$$

This paper focuses on characterizing the probabilistic DS given by:

$$\mathrm{D}_\alpha := \left\{ d \in \mathrm{K} : \mathrm{P}\left[\boldsymbol{G}(\boldsymbol{d}, \cdot) \leq \boldsymbol{0} \mid p(\boldsymbol{\theta}) \right] \geq \alpha \right\} \tag{5}$$

where $0 < \alpha \leq 1$ is the reliability value.

3. Improved nested sampling for design space characterization

The NS algorithm for DS characterization (Algorithm 1) starts with N_L *live points* $\boldsymbol{d}_i \in \mathrm{K}$, sampled uniformly within the knowledge space. These live points are sorted according to their estimated feasibility probabilities, evaluated as:

$$\hat{\mathrm{P}}\left[\boldsymbol{G}(\boldsymbol{d}_i,\boldsymbol{\theta}_j) \le \mathbf{0} \mid \mathrm{S}_\theta\right] := \sum_{(\boldsymbol{\theta}_j, w_j)\in \mathrm{S}_\theta} \mathbf{1}\left(G\left(d_i,\theta_j\right)\right) w_j, \quad \text{with } \mathbf{1}(\cdot) := \begin{cases} 1, & \text{if } g_k \le 0,\ \forall k \\ 0, & \text{otherwise,} \end{cases} \tag{6}$$

where S_θ is a set of model parameter scenarios θ_j and its weight w_j, sampled from $p(\boldsymbol{\theta})$. The feasibility probability of a point $\boldsymbol{d}_i \in \mathrm{K}$ is denoted by P_i below for brevity. Each iteration generates N_P *proposal points* $\boldsymbol{d}_k$, for instance by sampling within an enlarged ellipsoid enclosing the current live points (Mukherjee et al., 2006). Following the same order as per their generation, each proposal $\boldsymbol{d}_k$ will replace $\boldsymbol{d}_{min}$ – the live point with the lowest P – when $\mathrm{P}_{min} < \mathrm{P}_k$. The replaced point $\boldsymbol{d}_{min}$ – called a *dead point* – is recorded alongside its feasibility probability, while the point $\boldsymbol{d}_{min}$ and its feasibility probability P_{min} are updated. A stop criterion is checked after each iteration, for instance testing if all live points belong to design space with target reliability value α^*. Three improvement strategies over this basic algorithm are described next:

Strategy 1 – Two-phase nested sampling. A first phase, called *nominal*, is added to Algorithm 1 (lines 5-12), whereby the feasibility is only evaluated at $\boldsymbol{\theta}_{nom}$ - a much cheaper test than evaluating N_θ scenarios to estimate P (Eq. 6). This phase continues until all live points are in D_{nom} (Eq. 3). Though it is possible that D_{nom} may exclude parts of D_{α^*}, we observe that $\mathrm{D}_{\alpha^*} \subset \mathrm{D}_{nom}$ when the target reliability α^* is close to unity and $\boldsymbol{\theta}_{nom}$ is chosen as the maximum likelihood estimate or the mode or mean of the model parameter's posterior distribution. The second phase (lines 17-38), called *probabilistic*, is initialized with the live points from the first phase, after computing and sorting their feasibility probabilities (lines 13-16).

Strategy 2 – Dynamic live point population. The term *dynamic* is in reference to the strategy of increasing the number of live points N_L and proposals N_P over the course of the algorithm in order to generate a denser sample at the target reliability level (lines 27-34). N_L is increased every time the feasibility probability of the current nest, P_{min} gets larger than a predefined threshold, according to a user-specified top-up schedule S_T. The number of proposals N_P may also be adjusted when N_L is increased.

Strategy 3 – Vectorized function evaluations. Evaluations of the feasibility probability of the live points, replacement proposals, and top-up proposals are carried out in parallel using Python's multiprocessing to exploit multiple processors in modern computers.

An implementation of these algorithmic improvements is available in the Python package DEUS, which can be obtained from: https://github.com/omega-icl/deus. The input file for the case study below can also be retrieved from this link. In DEUS the candidate points are generated by sampling in a single ellipsoid enclosing the current live points (Mukherjee et al., 2006). In addition to setting the numbers of live points, replacement proposals, and the top-up schedule, other tuning parameters include the initial enlargement factor of the ellipsoid (default: 0.1), and the shrinking rate of that enlargement factor at each iteration (default: 0.3).

Algorithm 1 Nested sampling tailored to design space characterization

Inputs: $\mathrm{S}_\theta = \left\{\left(\boldsymbol{\theta}_j, w_j\right) \sim p(\boldsymbol{\theta}) : j = 1,\ldots,N_\theta\right\}$, $\mathrm{S}_\mathrm{T} = \left\{\left(\mathrm{P}_t^+, N_{\mathrm{L},t}^+, N_{\mathrm{P},t}^+\right) : t = 1,\ldots,N_\mathrm{T}\right\}$, K, α^*, $\boldsymbol{\theta}_\mathrm{nom}$, N_L, and N_P.

Initialization

$\mathrm{S}_\mathrm{L} \leftarrow \left\{\boldsymbol{d}_i \in \mathrm{K} : i = 1,\ldots,N_\mathrm{L}\right\}$
$\mathrm{DS} \leftarrow \varnothing$
$t \leftarrow 0$

Phase I: Nominal

while $\exists \boldsymbol{d}_\mathrm{i} \in \mathrm{S}_\mathrm{L} : \boldsymbol{G}(\boldsymbol{d}_\mathrm{i}, \boldsymbol{\theta}_\mathrm{nom})$ ' **0 do**
  $\mathrm{S}_\mathrm{P} \leftarrow \left\{d_\mathrm{k}^+ \in \mathrm{K} : k = 1,\ldots,N_\mathrm{P}\right\}$
  for all $\boldsymbol{d}_\mathrm{k}^+ \in \mathrm{S}_\mathrm{P}$ **do**
    if $\boldsymbol{G}\left(\boldsymbol{d}_\mathrm{k}^+, \boldsymbol{\theta}_\mathrm{nom}\right) \le \mathbf{0}$ **then**
      $\mathrm{S}_\mathrm{L} \leftarrow \mathrm{S}_\mathrm{L} \cup \left\{\boldsymbol{d}_\mathrm{k}^+\right\} \setminus \left\{\boldsymbol{d}_\mathrm{i}\right\}$
    end if
  end for
end while

Reinitialization

for all $\boldsymbol{d}_i \in \mathrm{S}_L$ **do**
  $\mathrm{DS} \leftarrow \mathrm{DS} \cup \left\{\left(\boldsymbol{d}_\mathrm{i}; \mathrm{P}\left[\boldsymbol{G}(\boldsymbol{d}_\mathrm{i}, \cdot) \le \mathbf{0} \mid \mathrm{S}_\theta\right]\right)\right\}$
end for

Phase II: Probabilistic

while $\exists \boldsymbol{d}_\mathrm{i} \in \mathrm{S}_\mathrm{L} : \mathrm{P}\left[\boldsymbol{G}(\boldsymbol{d}_\mathrm{i}, \cdot) \le \mathbf{0} \mid \mathrm{S}_\theta\right] \le \alpha^*$ **do**
  $\mathrm{S}_\mathrm{P} \leftarrow \left\{\boldsymbol{d}_\mathrm{k}^+ \in \mathrm{K} : k = 1,\ldots,N_\mathrm{P}\right\}$ ➢ propose replacements
  for all $\boldsymbol{d}_\mathrm{k}^+ \in \mathrm{S}_\mathrm{P}$ **do** ➢ decide accepted replacements
    $\mathrm{P}_\mathrm{min} \leftarrow \min\left\{\mathrm{P}\left[\boldsymbol{G}(\boldsymbol{d}_\mathrm{i}, \cdot) \le \mathbf{0} \mid \mathrm{S}_\theta\right] : \boldsymbol{d}_i \in \mathrm{S}_\mathrm{L}\right\}$
    $\boldsymbol{d}_\mathrm{min} \leftarrow \arg\min\left\{\mathrm{P}\left[\boldsymbol{G}(\boldsymbol{d}_\mathrm{i}, \cdot) \le \mathbf{0} \mid \mathrm{S}_\theta\right] : \boldsymbol{d}_i \in \mathrm{S}_\mathrm{L}\right\}$
    if $\mathrm{P}\left[\boldsymbol{G}\left(\boldsymbol{d}_k^+, \cdot\right) \le \mathbf{0} \mid \mathrm{S}_\theta\right] > \mathrm{P}_\mathrm{min}$ **then**
      $\mathrm{S}_\mathrm{L} \leftarrow \mathrm{S}_\mathrm{L} \cup \left\{\boldsymbol{d}_\mathrm{k}^+\right\} \setminus \left\{\boldsymbol{d}_\mathrm{min}\right\}$
      $\mathrm{DS} \leftarrow \mathrm{DS} \cup \left\{\left(\boldsymbol{d}_\mathrm{min}, \mathrm{P}_\mathrm{min}\right)\right\}$
    end if
  end for
  if $\mathrm{P}_\mathrm{min} \ge \mathrm{P}_{\mathrm{t+1}}^+$ **then** ➢ top-up live points if needed
    $t \leftarrow t + 1$
    while $N_\mathrm{L} < N_{\mathrm{L},t}^+$ **do**
      $N_\mathrm{L} \leftarrow N_\mathrm{L} + 1$
      $\mathrm{S}_\mathrm{L} \leftarrow \mathrm{S}_\mathrm{L} \cup \left\{\boldsymbol{d}_{N_\mathrm{L}} \in \mathrm{K} : \mathrm{P}\left[\boldsymbol{G}\left(\boldsymbol{d}_{N_L}, \cdot\right) \le \mathbf{0} \mid \mathrm{S}_\theta\right] > \mathrm{P}_\mathrm{min}\right\}$ ➢ top-up proposal
    end while
    $N_\mathrm{P} \leftarrow N_{\mathrm{P},t}^+$
  end if
end while
for all $\boldsymbol{d}_\mathrm{i} \in \mathrm{S}_\mathrm{L}$ **do** ➢ add current live points
  $\mathrm{DS} \leftarrow \mathrm{DS} \cup \left\{\left(\boldsymbol{d}_\mathrm{i}, \mathrm{P}\left[\boldsymbol{G}(\boldsymbol{d}_\mathrm{i}, \cdot) \le \mathbf{0} \mid \mathrm{S}_\theta\right]\right)\right\}$
end for
return DS

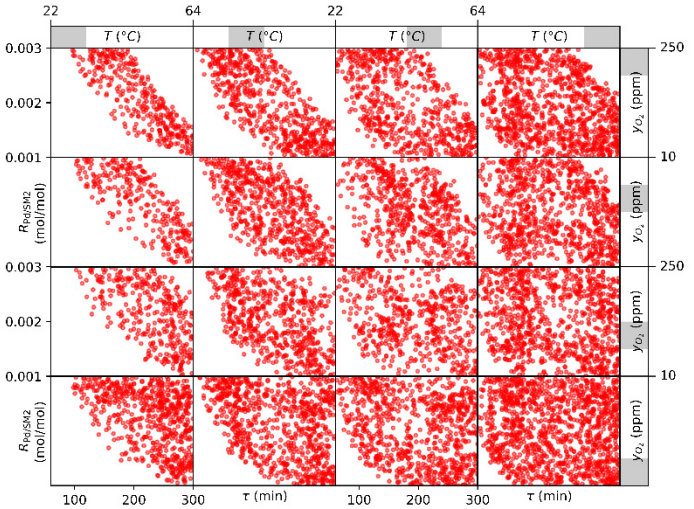

Figure 1: Probabilistic DS at a reliability $\alpha^* = 0.85$ for the Suzuki coupling reaction computed using Algorithm 1 with 1,000 uncertainty scenarios and 10,000 live points.

4. Case study: Suzuki coupling reaction

This case study investigates the Suzuki coupling reaction between a boronic ester (SM1) and an organohalide (SM2) to produce a desired pharmaceutical intermediate (P1) and a dimeric impurity (Imp1) related to SM1. The reaction is biphasic and conducted in batch mode. The gaseous phase is inert with traces of O_2 in vapor-liquid equilibrium with a liquid phase containing 17 chemical species dissolved in a mixture of water and THF. The active species participate in 12 reactions, 3 of which are reversible and 1 is considered instantaneous. The uncertain parameters are the 14 pre-exponential factors of the reactions. The DS is the set of (i) batch durations $\tau \in [75, 300]$ (min), (ii) catalyst equivalents $R_{\text{Pd|SM2}} \in [0.001, 0.003]$ (mol/mol), (iii) temperatures $T \in [22, 64]$ (°C), and (iv) O_2 molar fractions in the head space $y_{O_2} \in [10, 250]$ (ppm) such that the product has (i) unreacted SM2 less than 0.001 mol/mol, and (ii) Imp1 less than 0.0015 mol/mol. Full details about the case study can be found in Kusumo et al. (2019).

For comparison with Kusumo et al. (2019) we compute the probabilistic DS at a reliability $\alpha^* = 0.85$ using Algorithm 1 with and without parallelization, considering two cases: (i) $N_\theta = 200$ and $N_L = 5{,}000$; (ii) $N_\theta = 1{,}000$ and $N_L = 10{,}000$. Case (i) was initialized with $N_L = N_P = 100$ and schedule $S_T = \{(0.01, 1000, 200), (0.20, 2000, 200), (0.85, 5000, 500)\}$; case (ii) uses the same with double N_L and N_P. We opted for larger N_P to more efficiently parallelize proposal computations with Python's multiprocessing package. Computational statistics are presented in Table 1. Applying Strategies 1+2 decreases the number of evaluations by nearly 20% in both cases and saves 16 hours of computational time for case 2, but only minor savings for case 1. Parallelization results in approximately 4 to 5-fold reduction in CPU time. The returned 4-dimensional samples for case 2 are visualized with a trellis chart in Figure 1, where only the target DS at reliability $\alpha^* = 0.85$ is shown since the improvement strategies are designed to describe that set quicker. The comparison with Kusumo et al. (2019) confirms that no part of the target DS is missed.

Table 1: Computational statistics for Suzuki coupling reaction using Algorithm 1.

		Original		**With strategies 1–2**		
N_L	N_θ	# eval.[1]	Serial (hr.)[2]	# eval.[1]	Serial (hr.)	Parallel (hr.)[2]
5,000	200	1.45	9.6	1.18	9.3	2.3
10,000	1,000	14.54	112.4	11.80	96.5	21.8

[1] Number of model evaluations (in million).
[2] CPU times (in hours) obtained on AMD Ryzen 5 2600X processor with 6 cores.

5. Conclusions

To address the need for efficient tools for probabilistic DS characterization, Kusumo et al. (2019) proposed a tailored nested-sampling algorithm. We have presented three improvement strategies to the algorithm, namely a two-phase strategy to exploit information from nominal model parameters, a dynamic sampling strategy to delineate the target design space faster, and a vectorization strategy to evaluate costly functions in parallel. These improvements were demonstrated on an industrial case study, leading to a four-fold reduction in CPU time on a typical desktop computer.

Acknowledgements: This work is supported by Eli Lilly and Company through the Pharmaceutical Systems Engineering Lab (PharmaSEL) program. Radoslav Paulen gratefully acknowledges the contribution of the European Commission under grant 790017 (GuEst) and the contribution of the Slovak Research and Development Agency (project APVV 15-0007). The authors are grateful to Carla Vanesa Luciani for her assistance with the case study.

References

G. Bano, P. Facco, F. Bezzo, M. Barolo, 2018. Probabilistic design space determination in pharmaceutical product development: A Bayesian/latent variable approach. AIChE Journal 64 (7), 2438–2449.

S. García-Muñoz, C. V. Luciani, S. Vaidyaraman, K. D. Seibert, 2015. Definition of design spaces using mechanistic models and geometric projections of probability maps. Organic Process Research & Development 19 (8), 1012–1023.

K. P. Kusumo, L. Gomoescu, R. Paulen, S. García-Muñoz, C. C. Pantelides, N. Shah, B. Chachuat, 2019. Bayesian approach to probabilistic design space characterization: A nested sampling strategy. Industrial & Engineering Chemistry Research (in press, doi: 10.1021/acs.iecr.9b05006).

D. Laky, S. Xu, J. S. Rodriguez, S. Vaidyaraman, S. García Muñoz, C. Laird, 2019. An optimization-based framework to define the probabilistic design space of pharmaceutical processes with model uncertainty. Processes 7 (2), 96.

P. Mukherjee, D. Parkinson, A. R. Liddle, 2006. A nested sampling algorithm for cosmological model selection. The Astrophysical Journal Letters 638 (2), L51.

J. J. Peterson, 2008. A Bayesian approach to the ICH Q8 definition of design space. Journal of Biopharmaceutical Statistics 18 (5), 959–975.

J. J. Peterson, M. Yahyah, K. Lief, N. Hodnett, 2017. Predictive distributions for constructing the ICH Q8 design space. In: G. V. Reklaitis, C. Seymour, S. García-Muñoz (Eds.), Comprehensive Quality by Design for Pharmaceutical Product Development and Manufacture. Wiley & Sons, Ch. 4, pp. 55–70.

G. V. Reklaitis, C. Seymour, S. García-Muñoz (Eds.), 2017. Comprehensive Quality by Design for Pharmaceutical Product Development and Manufacture. Wiley & Sons.

J. Skilling, 2004. Nested sampling. AIP Conference Proceedings 735 (1), 395–405.

D. A. Straub, I. E. Grossmann, 1990. Integrated stochastic metric of flexibility for systems with discrete state and continuous parameter uncertainties. Computers & Chemical Engineering 14 (9), 967–985.

Sauro Pierucci, Flavio Manenti, Giulia Bozzano, Davide Manca (Eds.)
Proceedings of the 30th European Symposium on Computer Aided Process Engineering (ESCAPE30), May 24-27, 2020, Milano, Italy.
http://dx.doi.org/10.1016/B978-0-12-823377-1.50328-1

Neural Ordinary Differential Equations-based Explainable Deep Learning for Process Modeling

Michael R. Wartmann[a], B. Erik Ydstie[b]
[a]*Nouryon B.V., Digital Technology, Christian Neefestraat 2, 1077 WW Amsterdam, NL*
[b]*Carnegie Mellon University, 5000 Forbes Avenue, 15213 Pittsburgh, USA*
michael.wartmann@nouryon.com

Abstract

Most recent advances in the machine learning domain pose the challenge of how to naturally integrate new data-driven methods with classical process models and control. We propose a process modeling framework enabling integration of data-driven algorithms through consistent topological properties and conservation of extensive quantities. Interconnections among process network units are represented through connectivity matrices and network graphs. The basic requirement is that the flow conditions can be expressed in terms of conic sector (passivity) conditions. Our formalism allows integration of fundamental conservation properties from topology with learned dynamic relations from data through sparse deep neural networks.

We demonstrate in a practical example of a simple inventory control system how to integrate the basic topology of a process with a neural network ordinary differential equation model. The system specific constitutive equations are left undescribed and learned by the deep neural network using the adjoint method in combination with an adaptive ODE solver from synthetic time-series data. The resulting neural network forms a state space model for use in a model predictive control algorithm.

Keywords: neural ordinary differential equations, network theory, deep learning, process networks, process modelling

1. Introduction

Modeling process systems poses the challenge of deriving a meaningful mathematical representation capturing the fundamental laws of nature while representing the systems actual real-world behavior within its given system context. Intelligent use of data in the process of modeling complex systems provides the context while model structure and general behavior is derived from first principles knowledge of the system.

A typical challenge within the context of process systems is that available data of the process is limited for the particular case at hand (Venkatasubramanian 2018). Individual systems differ significantly from each other such that data of one system cannot be simply transferred or combined with data from similar other systems. As such, the need arises to model process systems in structurally consistent ways and take maximal advantage of the knowledge derived from first principles relationships (Ydstie 2002). While machine or deep learning algorithms are suitable to extract even very complex non-linear behavior, in the context of process systems, simple relationships such as fundamental mass, energy and component balances have to be learned ab initio, i.e., the data itself has to provide the context for those relationships. The available data should be used to provide information about the dynamics of the system beyond those fundamental relationships and be extracted through statistical methods or machine learning.

To provide the most optimal starting point for any machine learning based model in the context of process systems, the structure of the material and energy flow of the process system would need to be embedded in the model itself. In a deep learning context for example, the algorithm simply searches for the best possible fit of the given neural network structure to the input and output data provided. As a result, deep learning models have faced the challenge of explainability (Doran et al 2017), i.e., parameters and structure of the resulting neural network cannot be explained or related to the fundamental laws of nature.
A relevant component of using deep learning-based methods is therefore to understand how connections between the subunits of a process network lead to complex system behavior and how the connections can be built into a deep learning-based model, i.e., a neural network.
For the integration of data-driven methods, we provide an organizational framework for process systems using ideas from network theory in this paper.

2. Network theory and process systems

Process networks are written as a collection of interconnected sub-systems

$$\dot{x_I} = F(x_i) + \sum_{j=0, j\neq i}^{n} G(u_i, x_i, x_j), \qquad i = 0, \ldots, n \tag{1}$$

$$y_i = H(x_i) \tag{2}$$

x_i is the state of subsystem i and $x_i(0)$ is the initial condition. The function F describes the unforced motion of the system, the function G describes how the system is connected with other sub-systems, and the output function H relates the state of the system to the measurement functions y_i. The functions u_i represent the manipulated variables. The functions F, G, H are all differentiable at least once. The state of the entire network is given by the vector $x = (x_0^T, x_1^T, \ldots, x_n^T)^T$.
Subscript zero refers to the reference (exo-) system. Often, we are not interested in the dynamics of the exo-system, or more likely, it is too complex to model. The process system is modeled as the reduced system without the reference sub-system. Its state is given by the vector $x = (x_1^T, \ldots, x_n^T)^T$. The interactions with the exo-system are then established through the boundary conditions.
The network form, as illustrated in Figure 1 is convenient when we model systems with a graph structure.

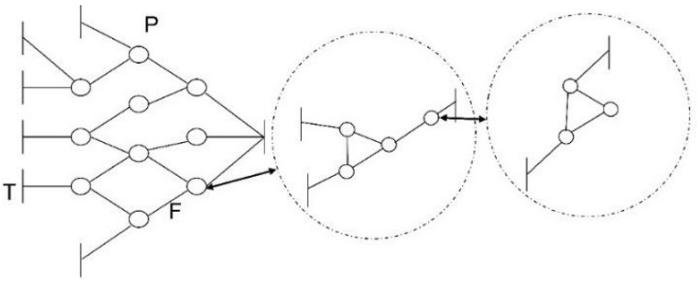

Figure 1: Graphical network representation: Topological structure of a network consisting of nodes, terminals, and flows. Nodes can contain subgraphs and give rise to a hierarchical multi-scale structure.

In such systems the interactions between the sub-systems depend on the state of the sub-system itself and the state of its immediate neighbors. Not all dynamical systems can be decomposed in this fashion. However, many large-scale systems have sparse interconnections and they can be modeled compactly as networks of sub-systems with interconnections. It is also easy to see that many physical systems, especially those that satisfy the principle of local action, can be decomposed in the manner shown in Eq. (1).

By a graph **G** we mean a finite set $\upsilon(\mathbf{G}) = (\upsilon_1, \ldots, \upsilon_{n_P})$, whose elements are called **nodes**, together with the set $\varepsilon(\mathbf{G})$ whose elements are called **branches**. A branch is therefore an ordered pair of distinct nodes.

Definition 1. A network of nodes P_i, $i = 1,\ldots,n_p,n_p+1,\ldots,n_v$ consisting of nodes and terminals interconnected through branches E_i, $i = 1,\ldots,n_f$ with topology defined by the graph set $\mathbf{G} = (E, P)$.

The system (1) is called a *process network* if its interconnection structure is described by a directed graph and we have

(1) **1st law:** There is an inventory E (the energy) satisfying the conservation property
(2) **2nd law:** There is an inventory S (the entropy) satisfying the Clausius-Planck property

Definition 2. The $n_t \times n_f$ matrix $\mathbf{A_a}$ is called incidence matrix for the matrix elements a_{ij} being

$$a_{ij} = \begin{cases} 1, \text{if flow } j \text{ leaves node } i \\ -1, \text{if flow } j \text{ enters node } i \\ 0, \text{if flow } j \text{ is not incident with node } i \end{cases}$$

One node of the network is set as reference or datum node P_0 representing the exo-system. The $(n_t - 1) \times n_f$ matrix **A**, where the row that contains the elements a_{0j} of the reference node P_0 is eliminated, is called reduced incidence matrix.

The connections between nodes through branches can be uniquely defined using the incident matrix **A**. The conservation laws of Eq. 1 can now be written

$$\mathbf{AF} = \mathbf{0} \tag{3}$$

for the node-to-branch incident matrix **A**, where $\mathbf{F}^T = (\frac{dZ_1}{dt}, \frac{dZ_2}{dt} \ldots, \frac{dZ_t}{dt}, f_{12}, f_{13}, .., f_{n_{t-1},n_t}, p_1, \ldots, p_t)$. The flows f_{ij} represent connections between two nodes i.e. f_{ij} connects node i to node j, p_i denotes sources or sinks. The direction of the flows is defined according to the directionality established in the graph. We now define a vector **W** so that

$$\mathbf{W} = \mathbf{A}^{\boldsymbol{T}}\mathbf{w} \tag{4}$$

where $W_{ij} = w_i - w_j$ are the potential differences across flow connections. The variables **w** are conjugate to **Z** if they are related via the Legendre transform of a convex potential like the entropy.

Eqs. 3 and 4 only reflect the topological properties of the process system. To complete a full dynamic model, we require functions relating the flow of extensive quantities **F** to the potential differences **W** and a relationship between the inventories **Z** and the potentials **w**. These relationships often contain non-linearities in classical process models, e.g.

kinetic relationships, pressure drop relations, thermodynamic models and chemicals potentials etc. (Wartmann and Ydstie 2009).

3. Neural Ordinary Differential Equations for Process Networks

A new family of deep neural network models have been introduced by Chen et al (2018). Instead of specifying a discrete sequence of hidden layers, in Chen et al. (2018) the derivative is parameterized using a neural network. The deep neural network models allow discretization of a dynamic system in time, in which each hidden layer of the neural network represents a particular state in time. These models are especially powerful, when used in the context of time-series correlated data and allow learning differential equations from data. For process systems, dynamic models for control can be derived by applying a deep neural network if trained from e.g. operational step testing data.

Chen et al. show that for training of continuous-depth neural networks, reverse mode differentiation or backpropagation can best be carried out through an ODE solver method. The well-known adjoint method is suitable to calculate the gradients of a scalar-valued loss function L for neural network weight training when combined with a gradient decent method for backpropagation. From a process network perspective, learning the dynamic behavior of a set of time-series data is essentially equivalent to modeling the right-hand side of a differential equation system as in Eq. 1 through a neural network representation. For a template of a neural network model with trainable weights, it would be ideal to have the process system's topology already represented in the neural networks layers such that the (non-linear) relations between flows **F** and inventories **Z** and the potentials **w** are learned from data while inventory balances and their structure are pre-imposed. As shown in Fig. 3, if potentials **w** of a network are measurable inputs, then continuity of the potentials allows relating them to differentials **W** and flow variables **F** through these relations (e.g. pressure differential drives convective flow). Further, flow variables **F** in the hidden layer relate to the inventory balance and allow calculation of the inventory differences $\Delta\mathbf{Z}$.

To represent the topology of a process network in a neural network model, some of the weights in the incident matrix **A** have to be set to zero resulting in a sparsely connected neural network where no physical connection is present. In the process of training the weights, these zero weights have to be pruned in training reducing the computational effort, preserving the process topology, and resulting in potentially explainable parameters for the remaining weights.

4. An inventory system modeled by a neural ODE

A small dynamic flow and storage example shows how process networks can be modelled using neural ODE's. The network consists of two connected pipelines where each pipeline flows through a cylindrical storage tank with volume open to the atmosphere, see Fig. 2. The resulting linear classical ODE can be derived from the balances around the nodes P_1 and P_2 for Z_1 and Z_2 i.e., $dZ_{1,2}/dt = F_{1,3}-F_{2,4}$, constant terminal potentials w_{T1} and w_{T2}, the flow constitutive equations $F_i=K_i W_i$ with i=1,..,4, the potential differences W = w1 – w2 as in Eq. (4), and $w_i = C_i Z_i$

$$\begin{aligned} C_1^{-1}\frac{dw_1}{dt} &= -(K_1 - K_3)w_1 + K_1 w_{T1} + K_3 w_{T2} \\ C_2^{-1}\frac{dw_1}{dt} &= -(K_2 - K_4)w_2 + K_2 w_{T1} + K_4 w_{T2} \end{aligned} \tag{5}$$

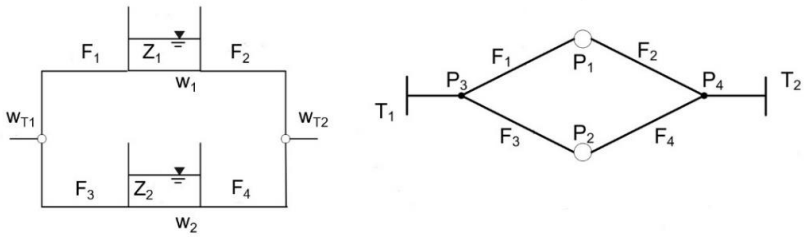

Figure 2: Graphical network representations: Problem specific representation on the left, a generalized graph representation on the right.

Discretization using the explicit Euler method for demonstration purposes and using ReLU's as activation functions leads to Eq. 6.

$$\boldsymbol{w^{t+1T}} = \boldsymbol{w^{tT}} + \Delta t\ \mathrm{ReLU}(\mathrm{ReLU}(\boldsymbol{w^{tT}}\mathbf{A_K})\mathbf{A_C}^T) \tag{6}$$

where the connectivity matrices $\mathbf{A_K}$ and $\mathbf{A_C}$ are given as in Fig 3.

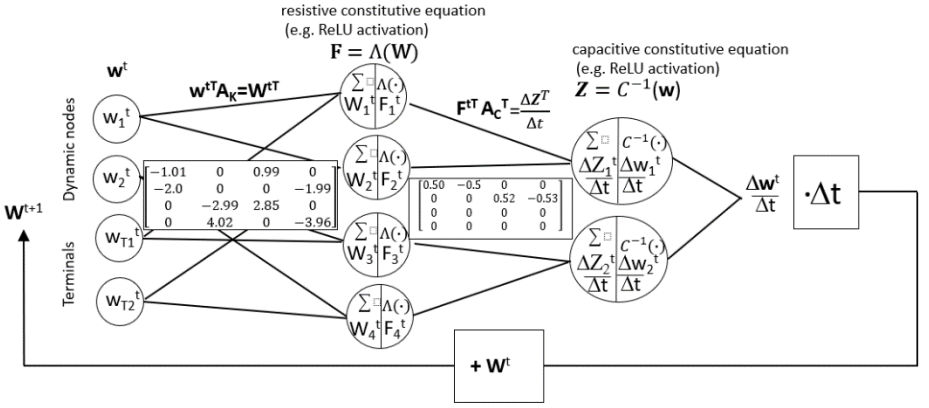

Figure 3: Neural network representation of the process network example, with potentials w in the input layer, flows F at the hidden layer, and potential differences per time step at the output layer. Final weights after training as given in the connectivity matrices are equivalent to the differential equation system from which synthetic data was derived.

The Neural ODE system was trained in Google Co-Lab using cloud GPU's based on synthetic dynamic data with added Gaussian noise (5%) from the corresponding ODE of Eqs. 5 with parameters K_1=1, K_2=2, K_3=3, K_4=4, C_1=C_2=2, and w_{T1}=4, w_{T2}=0. A Pytorch Python-based implementation was chosen with a time discretization using the explicit Euler method and time steps of Δt = 0.02 s. The process topology of the neural ODE was generated by pruning weights of non-incident edges, i.e., setting the corresponding weights to zero in every forward pass iteration during training. An adaptive deep learning stochastic gradient descent algorithm was applied for backpropagation to train the non-zero weights of the neural network. Training batches were selected through randomly choosing time periods within the synthetic data and 1000 training iterations carried out. The training run took T=17 sec and the neural network model matched the original data of the synthetic model where weights match with the original ODE (see Fig. 4) for the final w_1-w_2 time trajectory versus training data.

The resulting neural network simulates the dynamic system even if initial conditions are chosen differently from the original training data, i.e., extrapolates versus the dynamic trajectory of the original data.

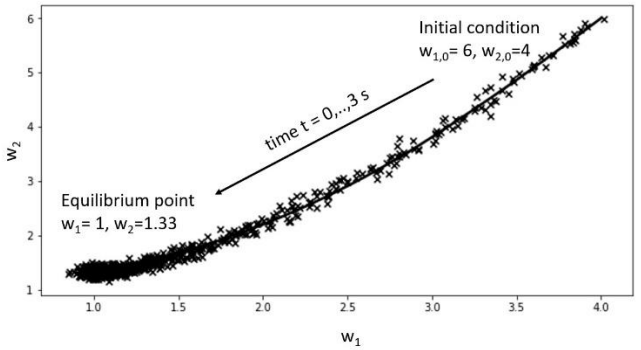

Figure 4: Time trajectory of dynamic potentials w1-w2 of inventory system after training the neural network. Synthetic time series data (marks) vs. neural network model (solid line).

5. Conclusions and Outlook

Using a graph theory based neural network representation for a process network allows using the topology of the system to be incorporated into the neural network through the incident matrices between edges and nodes. A sparsely connected neural network with meaningful topology allows preservation of e.g. inventory balances and a consistent potential field. Relationships between extensive quantities such as flows and inventories to intensive quantities, i.e., potentials are learned from data through training the remaining non-zero weights in the neural network through pruning. By applying classical ODE solvers and discretizing in time via e.g. the explicit Euler method in combination with adjoint equations allows determining gradients through backpropagation with a deep learning stochastic gradient descent method. Neural ODE models for process systems and networks have the potential to be used for model predictive control for which weight parameters are explainable and can be understood and updated when new data becomes available or the fundamental process structure is changed.

References

R.T.Q. Chen,Y. Rubanova, J. Bettencourt, and D. Duvenaud, 2018, Neural ordinary differential equations. *ArXiv 1806.07366*.

D. Doran, S. Schulz, and T. R. Besold. 2017, What does explainable AI really mean? a new conceptualization of perspectives. *ArXiv 1710.00794*.

M. R. Wartmann and B.E. Ydstie, 2009, Network-based analysis of stability, optimality of process networks. *Proceedings of ADCHEM*, 197–202.

B.E. Ydstie, 2002, New vistas for process control: Integrating physics and communication networks. *AICHE*, 48, 422–426.

V. Venkatasubramanian, 2019, The Promise of Artificial Intelligence in Chemical Engineering: Is It Here, Finally? *AICHE,* 65, 466-478.

Sauro Pierucci, Flavio Manenti, Giulia Bozzano, Davide Manca (Eds.)
Proceedings of the 30th European Symposium on Computer Aided Process Engineering
(ESCAPE30), May 24-27, 2020, Milano, Italy.
http://dx.doi.org/10.1016/B978-0-12-823377-1.50329-3

Global Optimization of Bilinear Programs by Elementary Functions Substitutions

Miloš Bogataj*, Zdravko Kravanja

Faculty of Chemistry and Chemical Engineering, University of Maribor, Smetanova ulica 17, SI-2000 Maribor, Slovenia
milos.bogataj@um.si

Abstract

In this paper, we present an approach to global optimization of bilinear programs based on a transformation of bilinear terms to elementary functions of single variables. The substitutions relocate bilinear terms to additional equality constraints. The complicating variables in these constraints are separated by logarithm operations. Finally, the log-linear constraints are relaxed by piecewise linear approximations and/or linearizations. The transformation produces a lower-bounding mixed-integer linear program, which is used in conjunction with the original bilinear program in a global optimization algorithm. The approach was tested by pooling problems from the literature. The global optimum was obtained in all the test problems; however, more elaborate algorithmic schemes would be needed to make the proposed approach computationally efficient.

Keywords: global optimization, bilinear programming, algorithm, elementary function, mixed-integer programming.

1. Introduction

Global optimization of bilinear programs is an ongoing endeavour in optimization. Its role is prominent in applications involving water networks and optimization of petroleum blending operations (Ahmetovic and Grossmann, 2010; Misener and Floudas 2009, Faria and Bagajewicz, 2012). The common approach to global optimization of bilinear problems is based on using convex envelopes (McCormick, 1976), coupled with spatial branch and bound search procedures. More efficient algorithms, which provide tighter convex relaxations, incorporate piecewise linear relaxation of bilinear terms (Karupiah and Grossmann 2006, Myer and Floudas 2006). Kolodziej et al. (2013) presented a derivation of the multiparametric disaggregation technique by Teles et al. (2001) for solving nonconvex bilinear programs. The relaxation derived by the authors scales more favourably than the relaxation that relies on piecewise McCormick envelopes. Finally, Misener et al. (2011) proposed a relaxation for modelling bilinear terms with piecewise McCormick envelopes, which ensures that the number of binary variables needed for the piecewise formulation scales logarithmically with the number of segments in the piecewise relaxation.

In this work, we focus on global optimization of bilinear problems in which the bilinear terms are the only source of nonlinearities and nonconvexities. As the main novelty, we present the formulation of a lower-bounding problem by convex envelopes of logarithmic functions of single variables. We propose a simple algorithm by which the gap is closed between the original nonconvex formulation, serving as an upper-bounding problem, and its lower-bounding counterpart. Finally, we present and discuss the results of numerical studies.

2. Bilinear problem

The bilinear problem considered in this work can be written as the nonconvex nonlinear programming problem (P). In (P), $a_{i,j}$, $b_{i,j,k}$, $b_{i,j,l}$ are scalars and $f_0(\boldsymbol{x})$, $f_l(\boldsymbol{x})$, $f_k(\boldsymbol{x})$ linear functions. The bilinear terms x_ix_j represent the nonlinear parts of the objective function and the constraints. We assume that the lower bounds on continuous variables $\boldsymbol{x}$ are zero and the upper bounds nonzero positive values $\boldsymbol{x}^{\mathrm{UP}}$. In addition, we assume that no quadratic terms (i.e. $i = j$) are present in (P), although the proposed approach is equally valid for those cases as well.

$$\begin{aligned} &\min Z = \sum_{i,j(i\neq j)} a_{i,j}x_ix_j + f_0(\boldsymbol{x}) \\ &\qquad s.t. \\ &h_k(\boldsymbol{x}) = \sum_{i,j(i\neq j)} b_{i,j,k}x_ix_j + f_k(\boldsymbol{x}) = 0 \\ &g_l(\boldsymbol{x}) = \sum_{i,j(i\neq j)} b_{i,j,l}x_ix_j + f_l(\boldsymbol{x}) \le 0 \\ &\boldsymbol{0} \le \boldsymbol{x} \le \boldsymbol{x}^{\mathrm{UP}},\ i \in I,\ j \in J,\ k \in K,\ l \in L \end{aligned} \tag{P}$$

3. Reformulation and relaxation of the bilinear problem

We reformulate (P) by substituting the bilinear terms x_ix_j with variables $w_{i,j}$ and introducing additional constraints $w_{i,j} = x_ix_j$. The variables in these constraints are separated by logarithm operation and the resulting logarithmic terms substituted by slack variables ($W_{i,j}$, X_i and X_j). The reformulation can be represented as a linear generalized disjunctive program (PL-GDP).

$$\begin{aligned} &\min Z = \sum_{i,j} a_{i,j}w_{i,j} + f_0(\boldsymbol{x}) \\ &\qquad s.t. \\ &h_k(\boldsymbol{x}) = \sum_{i,j(i\neq j)} b_{i,j,k}w_{i,j} + f_k(\boldsymbol{x}) = 0 \\ &g_l(\boldsymbol{x}) = \sum_{i,j(i\neq j)} b_{i,j,l}w_{i,j} + f_l(\boldsymbol{x}) \le 0 \\ &W_{i,j} = X_i + X_j \\ &\begin{bmatrix} Y_{W_{i,j}} \\ W_{i,j} \le \boldsymbol{f}^{\mathrm{O}}\left(\log\left(w_{i,j}\right)\right) \\ W_{i,j} \ge \boldsymbol{f}^{\mathrm{U}}\left(\log\left(w_{i,j}\right)\right) \\ \varepsilon_{x_i}\varepsilon_{x_j} \le w_{i,j} \le x_i^{UP}x_j^{UP} \end{bmatrix} \vee \begin{bmatrix} \neg Y_{W_{i,j}} \\ w_{i,j} = 0 \end{bmatrix}, \\ &\begin{bmatrix} Y_{X_i} \\ X_i \le \boldsymbol{f}^{\mathrm{O}}\left(\log\left(x_i\right)\right) \\ X_i \ge \boldsymbol{f}^{\mathrm{U}}\left(\log\left(x_i\right)\right) \\ \varepsilon_{x_i} \le x_i \le x_i^{UP} \end{bmatrix} \vee \begin{bmatrix} \neg Y_{X_i} \\ 0 \le x_i \le x_i^{UP} \end{bmatrix}, \begin{bmatrix} Y_{X_i} \\ X_j \le \boldsymbol{f}^{\mathrm{O}}\left(\log\left(x_j\right)\right) \\ X_j \ge \boldsymbol{f}^{\mathrm{U}}\left(\log\left(x_j\right)\right) \\ \varepsilon_{x_j} \le x_j \le x_j^{UP} \end{bmatrix} \vee \begin{bmatrix} \neg Y_{X_j} \\ 0 \le x_j \le x_j^{UP} \end{bmatrix} \\ &Y_{W_{ij}} \Rightarrow \boldsymbol{Y}_{X_i} \wedge Y_{X_i} \\ &0 < \varepsilon_{x_i}, \varepsilon_{x_j} \le 1 \\ &i \in I,\ j \in J,\ k \in K,\ l \in L \end{aligned} \tag{PL-GDP}$$

The disjunctions and the logical proposition encapsulate the generation of convex envelopes of the logarithmic terms. If all the Boolean variables in the disjunctions are *True*, the slack variables become bounded by linear over- and underestimators of logarithmic functions ($\boldsymbol{f}^{O}, \boldsymbol{f}^{U}$). Otherwise, the convex envelopes become redundant.
An important observation is that, if the Boolean variables are *True*, the continuous variables $w_{i,j}$, x_i and x_j become bounded by nonzero lower bounds. This is necessary because the logarithmic function is undefined at 0. In addition, to keep the feasible region of the original problem intact to the greatest extent, we set the lower bounds on variables $w_{i,j}$ to the product of the nonzero lower bounds on x_i and x_j (i.e. $w_{i,j} \geq \varepsilon_i \varepsilon_j$). Similarly, we set the upper bounds on $w_{i,j}$ to the product of the upper bounds on the x_i and x_j variables.

3.1. Lower bounding mixed-integer linear problem

We reformulate the (PL-GDP) to a mixed-integer linear program (PL) using the mixed-integer (MI) translation of variables. For comprehensive insight into the reformulation, the reader is referred to the works by Ropotar and Kravanja (2010) and Bogataj and Kravanja (2018, 2019). Here we offer a brief explanation for the two extreme cases.
In (PL), $w^{T}_{i,j}$, x^{T}_{i}, x^{T}_{j} and $w^{F}_{i,j}$, x^{F}_{i}, x^{F}_{j} are the disaggregated variables and $y_{i,j}$, y_i, y_j binary variables. First, we consider the case when $y_{i,j} = y_i = y_j = 1$. In this case, variables $w_{i,j}$, x_i and x_j become equal to $w^{T}_{i,j}$, x^{T}_{i} and x^{T}_{j}, which are bounded by nonzero lower bounds. $W_{i,j}$, X_i and X_j become bounded by the corresponding convex envelopes defined over the domains of $w^{T}_{i,j}$, x^{T}_{i} and x^{T}_{j}. In the case when $y_{i,j} = y_i = y_j = 0$, variables $w^{T}_{i,j}$, x^{T}_{i} and x^{T}_{j} are forced to their nonzero lower bounds ($\varepsilon_i \varepsilon_j$, ε_i, ε_j). Consequently, the variables $W_{i,j}$, X_i and X_j become fixed at their lower bounds ($\log(\varepsilon_i \varepsilon_j)$, $\log(\varepsilon_i)$, $\log(\varepsilon_j)$) too. The feasible region bounded by over- and underestimators thus becomes reduced to points ($[\varepsilon_i \varepsilon_j, \log(\varepsilon_i \varepsilon_j)]$, $[\varepsilon_i, \log(\varepsilon_i)]$ and $[\varepsilon_j, \log(\varepsilon_j)]$). On the other hand, variables $w_{i,j}$, x_i and x_j become equal to variables $w^{F}_{i,j}$, x^{F}_{i}, x^{F}_{j}, which are defined over the complete domain of variables $w_{i,j}$, x_i and x_j.

$$\min Z = \sum_{i,j} a_{i,j} w_{i,j} + f_0(\boldsymbol{x})$$

$$s.t.$$

$$h_k(\boldsymbol{x}) = \sum_{i,j(i \neq j)} b_{i,j,k} w_{i,j} + f_k(x) = 0$$

$$g_l(\boldsymbol{x}) = \sum_{i,j(i \neq j)} b_{i,j,l} w_{i,j} + f_l(x) \leq 0$$

$$W_{i,j} = X_i + X_j$$

$$\begin{aligned}
& w_{i,j} = w^{T}_{i,j} - (1 - y_{i,j})\varepsilon_i \varepsilon_j && x_i = x^{T}_{i} - (1 - y_i)\varepsilon + x^{F}_{i} && x_j = x^{T}_{j} - (1 - y_j)\varepsilon_j + x^{F}_{j} \\
& w^{T}_{i,j} \leq x^{UP}_{i} x^{UP}_{j} y_{i,j} + (1 - y_{i,j})\varepsilon_i \varepsilon_j && x^{T}_{i} \leq x^{UP}_{i} y_i + (1 - y_i)\varepsilon_i && x^{T}_{j} \leq x^{UP}_{j} y_j + (1 - y_j)\varepsilon_j \\
& w^{T}_{i,j} \geq \varepsilon_i \varepsilon_j && x^{T}_{i} \geq \varepsilon_i && x^{T}_{j} \geq \varepsilon_j \\
& && x^{F}_{i} \leq x^{UP}_{i}(1 - y_i) && x^{F}_{j} \leq x^{UP}_{j}(1 - y_j) \\
& && x^{F}_{i} \geq 0 && x^{F}_{j} \geq 0
\end{aligned} \qquad \text{(PL)}$$

$$y_{i,j} \leq y_i$$

$$y_{i,} \leq y_j$$

$$y_{i,j} \geq y_i + y_j - 1$$

$$\boldsymbol{f}^{\mathrm{U}}\left(\log\left(w_{i,j}^{\mathrm{T}}\right)\right) \le W_{i,j} \le \boldsymbol{f}^{\mathrm{O}}\left(\log\left(w_{i,j}^{\mathrm{T}}\right)\right)$$
$$\boldsymbol{f}^{\mathrm{U}}\left(\log\left(x_{i}^{\mathrm{T}}\right)\right) \le X_{i} \le \boldsymbol{f}^{\mathrm{O}}\left(\log\left(x_{i}^{\mathrm{T}}\right)\right)$$
$$\boldsymbol{f}^{\mathrm{U}}\left(\log\left(x_{j}^{\mathrm{T}}\right)\right) \le X_{j} \le \boldsymbol{f}^{\mathrm{O}}\left(\log\left(x_{j}^{\mathrm{T}}\right)\right)$$

The (PL) formulation encompasses two important facts. First, the linear over- and underestimators of logarithmic functions are defined over the domain of variables in interest even if the corresponding binary variables are set to 0. Second, the equivalency between the value of the bilinear terms when one or both of the variables x_i, x_j become 0 and the sum of slack variables is preserved (1).

$$x_i x_j = 0 \Leftrightarrow W_{i,j} - \left(X_i + X_j\right) = 0 \quad \begin{matrix} x_i=0 \\ \vee \\ x_j=0 \end{matrix} \quad \begin{matrix} x_i=0 \\ \vee \\ x_j=0 \end{matrix} \tag{1}$$

The relationship given by equation (1) is clearly true when both binaries (y_i, y_j) are 0 or 1. However, we should note that when only one of the two binaries becomes 1 (e.g. $y_i = 1$, $y_j = 0$), the corresponding constraints bounding the disaggregated variables ($\varepsilon_i \le x^{\mathrm{T}}{}_i \le x^{\mathrm{UP}}{}_i$) do not impose hard bounds on the original variables (x_i). If preferred by the direction of optimization, the binary variable y_i can become 0, thus keeping the domain of the original variable (x_i) intact and the equality constraint correlating the slack variables valid. The same is true in the opposite case.

3.2. Global optimization algorithm

The optimization algorithm used in this study is based on iterations between the upper-bounding problem (P) and the lower-bounding problem (PL). The relaxation gap is tightened by restricting the feasible region of (PL) through the addition of generated under- and overestimators. The algorithm is summarized as follows:

Step 1: Solve (P):
- i. Set $Z = Z^{\mathrm{UP}}$,
- ii. Generate a set of over- and underestimators (OUP) in the unique solutions of (P)
- iii. Add set (OUP) to (PL)

Step 2: Solve (PL):
- i. Set $Z = Z^{\mathrm{LO}}$
- ii. If: abs(Z^{UP}-Z^{LO}) $\le \varepsilon \rightarrow$STOP
- iii. Else: Generate a set of over- and underestimators (OUPL) in the unique solutions of (PL)
- iv. Add set (OUPL) to (PL)
- v. Return to step 1.

It should be noted that solving the upper bounding problem (P) in each iteration is not necessary. However, if the upper bound changes (improves) during the computation, it might help to tighten the relaxation gap.

4. Numerical studies

To demonstrate the proposed approach, we present the results of 5 numerical studies. The test problems were the following pooling problems in pq-formulation (Tawarmalani and

Sahinidis, 2002): Haverly1, Bental4, Foulds4 and Foulds5 and RT2. The results of the numerical experiments are summarized in Table 1.

The models were coded in GAMS. CONOPT was used as an NLP solver and CPLEX as the MILP solver. The overestimators in (PL) were modelled as tangents of logarithmic functions, while the underestimators were modelled as their piecewise linear approximations, using SOS2 variables. The lower bound on variables corresponding to x^{T}_{i} and x^{T}_{j} in (PL) was set to 0.0001. The convergence criterion (i.e. absolute tolerance) was set to 0.

Table 1: Results of numerical experiments.

Model	Haverly1	Bental4	Foulds4	Foulds5	RT2
			NLP		
No. of variables	11	14	673	673	35
No. of equations	24	29	767	767	69
Global optimum	–400.00	–450.00	–8.00	–8.00	–4,391.82
			MILP		
Initial lower bound[a]	–496.97	–549.23	–8.00	–8.00	-6,034.87
No. of iterations	31	33	1	1	25
No. of all variables[b]	253	336	4,468	4,468	803
No. of binary variables	8	11	672	672	30
No. of equations	215	294	7,031	7,031	981
t_{CPU}/s	5.6	9.6	0.8	1.2	>3,600
Final lower bound[b]	–400.00	–450.00	–8.00	–8.00	–4,391.82

[a]solution of first MILP
[b]total number of continuous variables incl. SOS2 variables
[c]solution of last MILP

The results presented in Table 1 indicate that the proposed approach identifies globally optimal solutions in all the cases studied. While the computational time is relatively short in the Haverly1 and Bental4 instances of the pooling problem, it is considerably longer in the RT2 instance, although the NLP sizes and the number of iterations to obtain the global optimum are within the same order of magnitude. On the other hand, the Foulds4 and Foulds5 instances, although the largest instances in terms of the problem size, are solved in a single iteration.

5. Conclusions

In this work, we presented an approach to the global optimization of bilinear problems that relies on transformation of bilinear terms to functions of single variables. A logarithm operation is used to separate the variables participating in bilinear terms. The reformulation to a lower-bounding MILP is then performed, using the mixed-integer translation of variables.

Although the proposed approach is presented as a method to solve bilinear problems to global optimality, it is apparent that its potential scope is greater. The approach can be applied in principle to any nonlinear problem whose nonlinearities can be transformed into elementary functions of single variables. The results presented in this study indicate that the proposed approach is feasible. However, to make it computationally more efficient, more elaborate algorithmic procedures should be adapted.

References

E. Ahmetović, I. E. Grossmann, 2010, Strategies for the Global Optimization of Integrated Process Water Networks. Computers and Chemical Engineering. 28, 901–906.
M. Bogataj, Z. Kravanja, 2018, Alternative Mixed-integer Reformulation of Generalized Disjunctive Programs, Computer Aided Chemical Engineering, 43, 549–554.
M. Bogataj, Z. Kravanja, 2019, On Robustness of Mixed-Integer Reformulations of Generalized Disjunctive Programs, Computer Aided Chemical Engineering, 46, 1117–1122.
D. Faria, M. Bagajewicz, 2012, A new approach for global optimization of a class of MINLP problems with applications to water management and pooling problems, AIChE Journal, 58, 2320–2335.
R. Karuppiah, I. E. Grossmann, 2006, Global optimization for the synthesis of integrated water systems in chemical processes, Computers and Chemical Engineering, 30, 650–673.
S. Kolodziej, P. M. Castro, I. E. Grossmann, 2013, Global optimization of bilinear programs with a multiparametric disaggregation technique, Journal of Global Optimization, 57: 1039, DOI 10.1007/s10898-012-0022-1.
G. P. McCormick, 1976, Computability of global solutions to factorable nonconvex programs: Part 1-convex underestimating problems. Mathematical Programming, 10, 147–175.
C. A. Meyer , C. A. Floudas, 2006, Global optimization of a combinatorially complex generalized pooling problem, AIChE Journal, 52, 1027–1037.
R. Misener, C. A. Floudas, 2009, Advances for the pooling problem: Modeling, global optimization, and computational studies Survey, Applied and Computational Mathematics, 8 (1), 3–22.
R. Misener , J. P. Thompson, C. A. Floudas, 2011, APOGEE: Global optimization of standard, generalized, and extended pooling problems via linear and logarithmic partitioning schemes, Computers and Chemical Engineering, 35, 876–892.
M. Ropotar, Z. Kravanja, 2009, Translation of Variables and Implementation of Efficient Logic-Based Techniques in the MINLP Process Synthesizer MIPSYN, AIChE Journal, 55 (11), 2896– 2913.
M. Tawarmalani, N. Sahinidis, 2002, Convexification and Global Optimization in Continuous and Mixed-Integer Nonlinear Programming - Theory, Algorithms, Software, and Applications, Springer Science+Business Media Dordrecht.
J. P. Teles, P. M. Castro, H. A. Matos, 2012, Global Optimization of Water Networks Design using Multiparametric Disaggregation, Computers and Chemical Engineering 40, 132–147.

Sauro Pierucci, Flavio Manenti, Giulia Bozzano, Davide Manca (Eds.)
Proceedings of the 30th European Symposium on Computer Aided Process Engineering (ESCAPE30), May 24-27, 2020, Milano, Italy.
http://dx.doi.org/10.1016/B978-0-12-823377-1.50330-X

Uncertainty Analysis and Model Reduction Based Global Optimisation of Distributed Large-scale Systems

Min Tao, Constantinos Theodoropoulos

Department of Chemical Engineering and Analytical Science, University of Manchester, Manchester M13 9PL, UK
k.theodoropoulos@manchester.ac.uk

Abstract

Uncertainty arises in many large-scale distributed industrial systems, needing efficient computational tools. Uncertainty propagation techniques have been developed and applied including power series expansions (PSE) and polynomial chaos expansions (PCE). However, such fast low-order approximate models generate errors and, in general, require prior knowledge about uncertainty distribution. In this work, the recursive projection method (RPM) was adopted to accelerate the computation of steady state solutions of complex large-scale dynamic systems. These accelerated models including uncertainty were subsequently utilised in an efficient Bayesian global optimisation framework. The performance of the proposed robust optimisation framework was demonstrated through an illustrative example: a tubular reactor where an exothermic reaction takes place.

Keywords: Uncertainty analysis, Distributed parameter systems, Recursive projection method, Bayesian global optimisation

1. Introduction

Complex distributed-parameter systems are common in industrial practice. Due to the inherent stochasticity and/or insufficient knowledge about processes, uncertainty arises (Eldred, 2009). In particular, parametric uncertainty in system models can greatly impact output performance. To robustly account for the impact of parametric uncertainties, uncertainty propagation techniques have been developed. Power series and polynomial chaos expansions methods have been used to address uncertainty through the application of low-order models, which worked efficiently for robust control (Nagy and Braatz, 2007). However, low-order approximate models may require prior knowledge about the distributions of parametric uncertainty (Kimaev and Richardez-Sandoval, 2018). For example, polynomial chaos expansion is implemented through “suitable” orthogonal polynomials corresponding to the uncertainty distribution (Xiu, 2010), which significantly affects computational accuracy. From the view of computational accuracy and generalised ability to handle uncertainty, directly using the original system model could be a better choice. To deal with intensive computational requirements of dynamic system models, the recursive projection method (Shroff and Keller, 1993) is used here. RPM has been multiply implemented as an effective model reduction technique for input/output systems for optimization and control purposes (Luna-Ortiz and Theodoropoulos, 2005; Bonis et al, 2013). RPM requires only a few utilisations of the (black-box) time integrator, to accelerate the computation of steady states through the calculation of low-order system Jacobians. Nevertheless, the

computation of low-order derivatives including uncertainty is costly. Kriging surrogate model and Bayesian optimisation strategies are efficient for the expensive black-box systems (Jones et al, 1998). In this work, uncertainty analysis and robust optimisation framework have been constructed for large-scale input/output systems. Firstly, a RPM-based methodology was proposed to propagate parametric uncertainty in an accelerated way. Subsequently, the accelerated model with uncertainty was used by kriging models and a Bayesian global optimisation procedure to produce a robust optimal solution.

2. Uncertainty Analysis

2.1. Large-scale distributed system with parametric uncertainty

This work deals with the optimization of large-scale spatially distributed processes, described by a set of nonlinear dissipative PDEs with uncertainty:

$$\frac{\partial X}{\partial t} = D\left\{\frac{\partial X}{\partial y}, \frac{\partial^2 X}{\partial y^2}, ..., \frac{\partial^n X}{\partial y^n}\right\} + E(X, P_1, P_2) \tag{1}$$

Where D is the dissipative spatial differential operator, $E(X, P_1, P_2)$ is the nonlinear function, X is the set of state variables, $P_1 \in R^{n1}$ are the design variables and $P_2 \in R^{n2}$ are the uncertain parameters.

2.2. Recursive projection method (RPM)

The dynamic systems in Eq. (1) are discretised and solved by a fixed-point procedure:

$$U^{n+1} = F(U^n, P_1, P_2; \tau) \tag{2}$$

Where $U \in R^N$ is the discretised unknown variable, n is the number of iteration steps, $F : R^N \times R^{n1} \times R^{n2} \to R^N$, τ is the reporting horizon of the black-box simulator.

The steady state solutions of the above fixed-point procedure are also the steady state solutions of the dynamic system:

$$X = f(X, P_1, P_2) \tag{3}$$

The recursive fixed-point procedure is time-consuming. To accelerate the computation, RPM is employed to decompose the solution space R^N into two subspaces: the low-dimensional P and its orthogonal complement Q:

$$R^N = P \oplus Q \tag{4}$$

The orthonormal basis Z of the slow subspace P can be efficiently computed by matrix-free algorithms, such as the Arnoldi method. Then:

$$I = Z^T Z, \quad P = ZZ^T \tag{5}$$

Where I is the identity matrix, $Z \in R^{N \times m}$ with m being the dimension of P.

The low dimensional Jacobians of subspace P can then be approximated by directional perturbations：

$$F_U Z = \frac{1}{2\varepsilon}(F(U + \varepsilon Z) - F(U - \varepsilon Z)) \tag{6}$$

Where ε is a small perturbation on the direction of Z.

Then the low-order Jacobian is given by:

$$H = Z^T F_U Z \tag{7}$$

Assuming the numerically stable time integration, the main RPM steps included the solution space decomposition (Eq. (8)), repeating Newton-Picard iterations (Eq. (9-10)) on the two subspaces and Picard iteration on the final sum to check the convergence $\|U(P_1,P_2)-F(U,P_1,P_2)\|$.

$$p^{(0)} = PU^{(0)}(P_1,P_2), \quad q^{(0)} = QU^{(0)}(P_1,P_2) \tag{8}$$

$$p^{(u+1)} = p^{(u)} + (I - ZHZ^T)^{-1} \times (PF(U^{(u)},P_1,P_2) - p^{(u)}) \tag{9}$$

$$q^{(u+1)} = QF(U^{(u)},P_1,P_2) \tag{10}$$

$$U^{(u+1)}(P_1,P_2) = p^{(u+1)} + q^{(u+1)} \tag{11}$$

Where u is the number of Newton-Picard iterations.

Here, the Monte Carlo (MC) sampling method was used to approximate the parametric uncertainty. Therefore, RPM coupled with MC sampling method together accelerate the computation of the parametric uncertainty at steady state. The computationally-accelerated model was subsequently applied in a Bayesian optimisation framework.

3. Bayesian optimisation

With the acceleration technique RPM, optimising the system model with uncertainty is still costly. In this work, Bayesian optimisation strategy was adopted through kriging model and expected improvement function, originating from efficient global optimisation (Jones et al, 1998).

3.1. Kriging model

Kriging model, a popular surrogate models, assumes that the random output variable $f(y)$ at any location point y with mean value μ and variance σ^2, and prior joint Gaussian distribution for the finite random variables:

$$f(Y) \sim N(\mu(Y), K(Y,Y)) \tag{12}$$

Where $f(Y) = \big(f(y_1), f(y_2) \dots f(y_N)\big)$, $\mu(Y) = \big(\mu(y_1), \mu(y_2) \dots \mu(y_N)\big)$ and $K_{ij} = k(y_i, y_j)$, $k(y_i, y_j)$ is the kernel function.

Here, Gaussian kernels are used:

$$k(y_i,y_j) = \sigma_f^2 \exp(-\frac{1}{2l^2}(y_i - y_j)^T(y_i - y_j)) \tag{13}$$

Where kernel parameters σ_f^2 and l are computed by a few initial observed samples.

The observed variables $f(Y)$ and unknown variables $f_*(Y_*)$ given new points Y_* satisfy a joint Gaussian distribution:

$$\begin{pmatrix} f(Y) \\ f_*(Y_*) \end{pmatrix} \sim N\left(\begin{pmatrix} \mu(Y) \\ \mu(Y_*) \end{pmatrix}, \begin{pmatrix} K & k(Y,Y_*) \\ k(Y_*,Y) & k(Y_*,Y_*) \end{pmatrix}\right) \tag{14}$$

The posterior predictive $f_*(Y_*)$ is still a Gaussian process:

$$f_* \big| (f(Y), Y, Y_*) \sim N(\mu_*, \sigma_*^2) \tag{15}$$

Where $\mu_* = \mu(Y_*) + k(Y_*, Y)K^{-1}(f(Y) - m(Y))$, $\sigma_*^2 = k(Y_*, Y_*) - k(Y_*, Y)K^{-1}k(Y, Y_*)$

3.2. Expected improvement (EI) function

In Bayesian global optimisation, acquisition functions decide the next sampling point. Here, EI function under kriging model is used to balance exploitation with exploration:

$$EI(y) = \begin{cases} (\mu(y) - f(y^+) - \varphi)\Phi(g) + \sigma(y)\phi(g) & \sigma(y) > 0 \\ 0 & \sigma(y) = 0 \end{cases} \tag{16}$$

Where $g = \begin{cases} \dfrac{\mu(y) - f(y^+) - \varphi}{\sigma(y)} & \sigma(y) > 0 \\ 0 & \sigma(y) = 0 \end{cases}$

Here $\mu(y)$ and $\sigma(y)$ are the mean and the standard deviation of the kriging model, respectively. Φ and ϕ are the CDF and PDF of the standard normal distribution, respectively. y^+ is the location of current best sample and φ is a parameter that determines the amount of exploration.

4. Application

The effectiveness of the proposed optimisation framework is illustrated using an exothermic tubular reactor (Tao et al, 2019). The mathematical formulation is as follows:

$$\begin{aligned} &\max_{Twi} a\mu(C_{exit}) - (1-a)\sigma(C_{exit}) \\ &s.t. \frac{\partial C}{\partial t} = \frac{1}{Pe_1}\frac{\partial^2 C}{\partial y^2} - \frac{\partial C}{\partial y} + Da(1-C)\exp(T/(1+T/\gamma)) \\ &\frac{\partial T}{\partial t} = \frac{1}{Pe_2}\frac{\partial^2 T}{\partial y^2} - \frac{\partial T}{\partial y} - \beta T + BDa(1-C)\exp(T/(1+T/\gamma)) + \beta T_w \\ &T_w(y) = \sum_{i=1}^{3}(H(y - y_{i-1}) - H(y) - y_i)T_{wi} \\ &Da \sim N(0.1, 0.01) \end{aligned} \tag{17}$$

Here C and T are the dimensionless concentration and temperature respectively, C_{exit} the dimensionless output concentration, $\mu(C_{exit})$ is the mean value of the uncertain output C_{exit}. $\sigma(C_{exit})$ is the standard variance value of C_{exit}. T_w is the adiabatic wall temperature at the three cooling zones. H is the Heaviside step function. The system parameters are $Pe_1 = 5, Pe_2 = 5, \beta = 1.5, \gamma = 10, B = 12.$ Da is the Damkohler number.

In this optimisation problem, the objective is to maximize the average value and minimize the variance of the output dimensionless product concentration, with uncertainty parameter Da and design variables T_w. a is the weight between the two terms, here set to be 0.6. The system model is given by a dynamic black-box simulator with inputs the design variables and the uncertain parameter and outputs the dimensionless concentration and temperature. The RPM algorithm was implemented in MATLAB R2019a and Bayesian optimisation in Python 3.7.3/PyCharm 2018.3.5 on a Desktop ((Intel Core(TM) i7-8700 CPU 3.2 GHz, 16 GB memory, 64-bit operating system, Windows 10).

4.1. Uncertainty analysis

To investigate the effect of parametric uncertainty on the output concentration, the uncertainty propagation was constructed. Firstly, the number of MC samples was decided to be 3000 by an independent numerical experiment. Then 3000 MC samples were generated to approximate the parameter distribution. To compare results of different uncertainty propagation methods, the same 3000 MC samples were utilized with the original dynamic solver, RPM using the dynamic solver, second-order PSE and second-order PCE. The report horizon was 0.01seconds the dimension of the dominant subspace was fixed to 10 for the RPM case. The perturbation, ε, was chosen to be 0.01 for PSE after numerical experiments with different perturbation sizes. 9 points of the original system were used for PCE. Table 1 shows that direct propagation uncertainty through the original dynamic solver is the most time-consuming. RPM significantly accelerated the computations with more than 87% saving and almost the same accuracy (also displayed in Figure 1). Although PSE took the least computational time, choosing the perturbation size increased the actual total cost to be 14.48 minutes. Compared with PSE, PCE produced more accurate mean value, low and upper bounds.Table 1 also shows the large variance of PSE and PCE because of missing a small spatial distribution as displayed in Figure 1.

Table 1. Uncertainty analysis (5% confidence level)

Models	**Low bound** C_{exit}	**Up bound** C_{exit}	**Mean** C_{exit}	**Standard variance** C_{exit}	**Computational time (minutes)**
Dynamic solver	**0.1204**	**0.3136**	**0.1963**	**0.0999**	**319.24**
RPM plus Dynamic solver	**0.1204**	**0.3136**	**0.1963**	**0.0999**	**40.49**
	Error : 0 %	**Error : 0 %**	**Error : 0 %**	**Error : 0 %**	
PSE	**0.1266**	**0.2856**	**0.1869**	**0.0418**	**4.29**
	Error: 5.15 %	**Error : -8.93 %**	**Error : -4.79 %**	**Error : -58.16 %**	
PCE	**0.1215**	**0.3018**	**0.1876**	**0.0478**	**8.71**
	Error: -0.91 %	**Error: -3.76 %**	**Error: -4.43 %**	**Error: -52.15 %**	

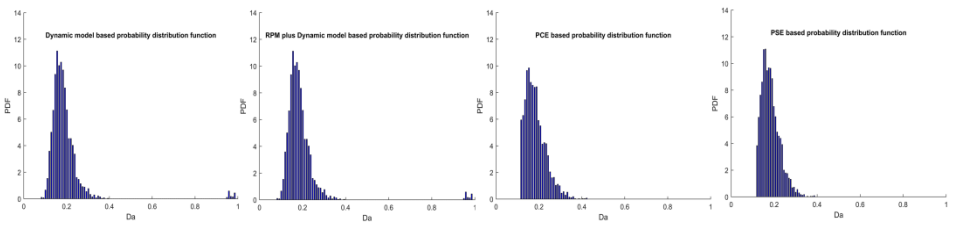

Figure 1. Probability density functions of the steady state output concentration

4.2. Bayesian optimisation

Using RPM with the black-box dynamic solver, Bayesian optimisation was constructed for the problem (Eq. (17)). Latin hypercube sampling method was utilised, taking 9.75

hours for the 8 initial samples. The optimisation process, as showed in Figure 2, converged to the optimum solution within 33 iterations and 30.91 hours.

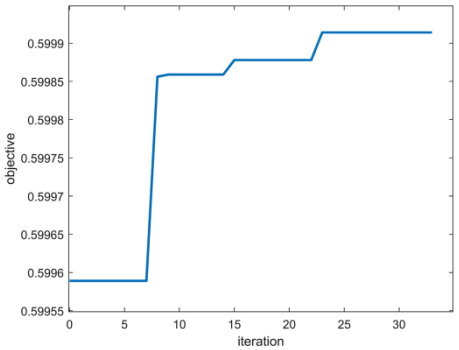

Figure 2. Bayesian optimisation of cooling process with parametric uncertainty

5. Conclusions

This paper presents a robust steady-state optimisation framework for large-scale dynamic systems with parametric uncertainty. RPM is employed to accelerate the dynamic systems to be steady state, resulting in significant cost reduction of uncertainty propagation. Furthermore, Bayesian optimisation with kriging model is utilised to find the optimum of the costly system within an acceptable number of iteration steps. The tubular reactor case study verifies the efficiency of our framework. In the future, the optimisation framework will be applied to scenarios of multivariate uncertainty and large-scale distributed stochastic systems.

References

M. Eldred, 2009, Recent advances in non-intrusive polynomial chaos and stochastic collocation methods for uncertainty analysis and design, In 50th AIAA/ASME/ASCE/AHS/ASC Structures, Structural Dynamics, and Materials Conference 17th AIAA/ASME/AHS Adaptive Structures Conference 11th AIAA No (p. 2274).

Z.K. Nagy, R.D. Braatz, 2007, Distributional uncertainty analysis using power series andlynomial chaos expansions, Journal of Process Control, 17(3), pp.229-240.

G. Kimaev, L.A. Ricardez-Sandoval, 2018, Multilevel Monte Carlo applied to chemical engineering systems subject to uncertainty. AIChE Journal, 64(5), pp.1651-1661.

G.M. Shroff, and H.B. Keller, 1993, Stabilization of unstable procedures: the recursive projection method, SIAM Journal on numerical analysis, 30(4), pp.1099-1120.

E. Luna-Ortiz, C. Theodoropoulos, 2005, An input/output model reduction-based optimization scheme for large-scale systems, Multiscale Modeling & Simulation, 4(2) pp. 691-708.

I. Bonis, W. Xie, C. Theodoropoulos, 2013, Multiple model predictive control of dissipative PDE systems, IEEE Transactions on Control Systems Technology, 22(3) pp. 1206-1214.

D.R. Jones , M. Schonlau, W.J. Welch, 1998, Efficient global optimization of expensive black-box functions, Journal of Global optimization, 13(4), pp.455-492.

M. Tao, J. Li, C. Theodoropoulos, 2019, Reduced model-based global optimisation of large-scale steady state nonlinear systems, In Computer Aided Chemical Engineering (Vol. 46, pp. 1039-1044). Elsevier.

Sauro Pierucci, Flavio Manenti, Giulia Bozzano, Davide Manca (Eds.)
Proceedings of the 30th European Symposium on Computer Aided Process Engineering
(ESCAPE30), May 24-27, 2020, Milano, Italy.
http://dx.doi.org/10.1016/B978-0-12-823377-1.50331-1

Global Optimization with Ensemble Machine Learning Models

Alexander Thebelt[a], Jan Kronqvist[a], Robert M. Lee[b], Nathan Sudermann-Merx[b]
Ruth Misener[a]

[a]*Imperial College London, Exhibition Road, London SW7 2AZ, United Kingdom*
[b]*BASF SE, Carl-Bosch-Straße 38, 67063 Ludwigshafen am Rhein, Germany*
alexander.thebelt18@imperial.ac.uk

Abstract

Gradient boosted trees and other regression tree models are known to perform well in a wide range of real-world, industrial applications. These tree models (i) offer insight into important prediction features, (ii) effectively manage sparse data, and (iii) have excellent prediction capabilities. We consider holistic decision-making problems where pre-trained tree models are part of larger optimization tasks. Our contributions include: (i) explicitly integrating model uncertainty considerations, (ii) solving the larger optimization problems that incorporate these uncertain tree models, (iii) proving that the resulting solutions are globally optimal, i.e., no better solution exists.

Keywords: Gradient Boosted Trees, Global Optimization, Machine Learning, Optimization under Uncertainty

1. Introduction

While machine learning and deep learning have become invaluable in fields like image recognition and automatic machine translation, the majority of traditional engineering disciplines, are still seeking to integrate these powerful tools into their routines. Such industrial applications are often subject to complex systems with high dimensional input feature spaces. Sophisticated data-driven frameworks offer an attractive solution, especially when complete models are too complex or unknown. While advances in sensor technology allow the collection of vast amounts of data, resulting datasets are subject to low variability as industrial processes are often kept close to a few well-defined operating states. On the other hand, experimental studies explore large regions of the input features but are often limited due to high expenses. These two settings result in either large datasets with low variability or small datasets with high variability, respectively. However, accurate data-driven models require large datasets with high variability, making model uncertainty considerations inevitable. Gradient Boosted Tree (GBT) models have been shown heuristically to work well in real-world industrial settings (Friedman, 2001). Moreover, GBT models can be easily embedded into decision-making problems by encoding them as a Mixed Integer Linear Program (MILP) (Mišic, 2017).
The algorithm presented here is partially based on the work of Mistry et al. (2018) and Mišic (2017), who investigate a similar optimization task. Generally, incorporating data-driven models as surrogate models into optimization problems is enjoying growing popular ity (Bhosekar and Ierapetritou, 2018), e.g., algebraic equations (Boukouvala and Floudas, 2017; Wilson and Sahinidis, 2017), artificial neural networks (Henao and Maravelias, 2011; Schweidtmann and Mitsos, 2019) and Gaussian processes (Palmer and Realff, 2002). We propose an algorithm that efficiently optimizes over pre-trained large-

scale tree models and that considers model uncertainty for arbitrarily distributed datasets. The algorithm derives mathematically proven global optimal solutions which is crucial in many industrial applications, e.g., production plants with high production margins, and safety critical settings.

2. Optimization over Ensemble Tree Models

Mistry et al. (2018) introduced the underlying Mixed Integer Nonlinear Program (MINLP) formulation:

$$\min_{v^L \le x \le v^U} \quad \text{GBT}(x) + \lambda\, \alpha_{Pen}(x), \tag{1}$$

$$s.t. \quad [\text{GBT MILP constraints}],$$

$$[\text{Variable linking constraints}],$$

$$[\text{Instance specific constraints}].$$

We seek to minimize the objective function (1) which consists of $\text{GBT}(x)$, referring to the GBT model prediction, and $\alpha_{Pen}(x)$, defining a penalty function that handles model uncertainty. Additional *GBT MILP* constraints ensure the correct model evaluation, i.e., all necessary splits per tree leading to a leaf value occur in the correct order and only one leaf per tree is included in the prediction value. The *Variable Linking* constraints relate the continuous variable $x \in [v^L, v^U]$ to the intervals that are defined by the tree splits of the GBT model. Both, *GBT MILP* and *Variable linking* constraints, are discussed in detail in Mistry et al. (2018). The penalty $\alpha_{Pen}(x)$ is weighted by a positive parameter λ, such that larger values move the optimal solution x^* closer into regions of high data density.

2.1. Cluster Distance as a Penalty Measure

According to Mistry et al. (2018), their convex quadratic penalty function $\alpha_{Pen(x)}$ can only be expected to work for data that is uniformly distributed in a reduced subspace that covers most of its variability. In order to handle arbitrarily distributed datasets, we present a novel approach that prioritizes optimal solutions close to the training data. Initially, the dataset is pre-processed by utilizing a clustering method of choice, e.g. k-means (Lloyd, 1982), to derive cluster center coordinates $x_k \forall k \in \mathcal{K}$, with defining the set of clusters. These cluster centers indicate distinct areas where training data is located and where the model prediction error is expected to be small. The new penalty includes the following equations to the problem defined in (1):

$$\|diag(\sigma)^{-1}(x-\mu) - x_k\|_2^2 \le \alpha_{Pen} + M(1-b_k) \qquad \forall k \in \mathcal{K}, \tag{2a}$$

$$\sum_{k \in \mathcal{K}} b_k = 1, \tag{2b}$$

$$\alpha_{Pen} \ge 0, \tag{2c}$$

$$b_k \in \{0,1\} \qquad \forall k \in \mathcal{K}. \qquad \text{(2d)}$$

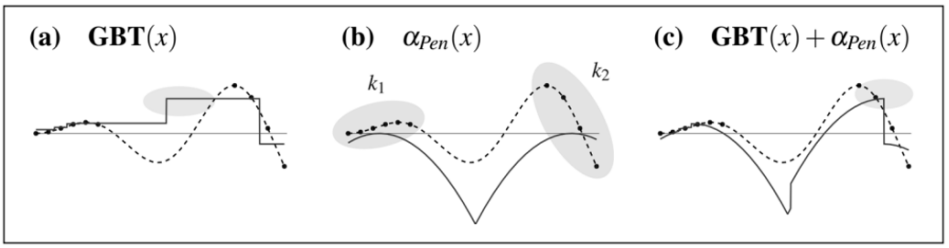

Figure 1: (a) Prediction of $f(x) = xsin(x)$ by GBT model; (b) Cluster distance penalty measure; (c) Summation of GBT model prediction and cluster distance penalty measure.

Equations (2) define α_{Pen} as the squared Euclidean distance of the optimal solution to the closest cluster center by introducing "Big-M" constraints. Applying k-means to the standardized dataset requires the standardization of x by using sample mean μ and sample standard deviation σ. The coefficient M can efficiently be calculated as the sum of the maximum Euclidean distance between two cluster centers and the maximum radius of all clusters. The variables $b_k \in \{0,1\}$ function as a binary switch: when $b_k = 0$, the constraint is inactivated as the large value of M makes them redundant and when $b_k = 1$, the large M coefficient is multiplied by 0 and effectively disappears. To ensure that the distance to only one cluster center is active, (2b) is included. The full optimization model given by (1) and (2) is then characterized as a convex MINLP (Kronqvist et al., 2019).

Example: We define the ground truth of a system of interest as $f(x) = xsin(x)$ and sample the function to create a dataset. Training a simple GBT model and maximizing it suggests a highly non-optimal point with respect to the ground truth due to large model prediction errors near a sample void in the middle of the function interval as shown in Figure 1 (a). Using the penalty definition introduced in Section 2.1 gives a function depicted in Figure 1 (b). Considering the sum of GBT model prediction and the penalty function as shown in Figure 1 (c) shifts the maximum to a more accurate solution with respect to the ground truth.

2.2. Main Algorithmic Elements

The main algorithm utilizes a deterministic branch-and-bound (B&B) approach that branches over the domain $[v^L, v^U]$, i.e., splits the domain into subdomains. Every domain is characterized by a lower bound on the best possible solution in the domain. B&B rejects individual domains in case of infeasible subproblems or when their lower bound exceeds the current best feasible solution, i.e., the upper bound. This way, the search space is constantly reduced, and B&B avoids the explicit enumeration of all possible solutions (Morrison et al., 2016). Mistry et al. (2018) propose strong branching to efficiently reduced the search domain. The new lower bound of objective function (1) is decomposed according to: $\hat{R}^S = b^{GBT,S} + b^{\alpha_{Pen},S}$, where $b^{GBT,S}$ and $b^{\alpha_{Pen},S}$ define lower bounds of GBT(x) and $\alpha_{Pen}(x)$ in domain S, respectively. Computing the tightest lower bound for GBT(x) in domain S is difficult to provide for large instances as it is NP-hard (Mišic (2017)). Therefore, an easier to compute weaker lower bound $b^{GBT,S}$ is derived by so-called partition refinement (Mistry et al., 2018). Due to the rapid growth of $\alpha_{Pen}(x)$ for regions distant from training data, deriving a weak bound for GBT(x) is often sufficient to reject domains as the "weak" lower bound already surpasses the current best feasible

solution. This is especially appealing if $b^{\alpha_{Pen},S}$ can be computed easily. For all domains that cannot immediately be rejected, $b^{GBT,S}$ is recomputed to derive tighter bounds for $\text{GBT}(x)$ in domain S. After every iteration the best feasible solution and the lowest lower bound move closer together and ultimately prove global optimality which in practice is subject to a pre-defined optimality gap.

2.3. Computational Enhancements

The convex MINLP penalty constraints in (2) are in general more difficult to solve than the convex quadratic constraints introduced by Mistry et al. (2018) and require advanced algorithmic enhancements to achieve faster convergence. Firstly, instead of calling an external solver to derive the lower bound $b^{\alpha_{Pen},S}$, enforced by Eq. (2), we project the cluster centers onto the box defined by S, to determine all cluster center distances explicitly. The smallest distance defines the lower bound $b^{\alpha_{Pen},S}$ and thereby avoids the time-consuming computational overhead of an external solver. Secondly, good feasible solutions are derived to warm-start the algorithm. This allows faster convergence, as the search space is constantly reduced by rejecting regions S for which $\hat{R}^S$ exceeds the current best feasible solution. Pre-defined cluster centers by definition have α_{Pen}=0 and a good initial feasible solution x_{feas} can therefore be derived by picking the coordinates x_k of the cluster center $k \in \mathcal{K}$ with the lowest value for $\text{GBT}(x_k)$.

3. Numerical Experiments

Here, we evaluate two case studies to show that the algorithm (i) derives optimal solutions with less model uncertainty for higher penalty parameter values and (ii) outperforms off-the-shelf global solvers for large instances. All numerical experiments are run on an Ubuntu 18.04.2 LTS system with 16GB RAM and an Intel Core i7-7700K @ 4.20Ghz CPU. For the modeling of the MINLP and interfacing with solvers we used Python 3.7.3 in combination with Pyomo 5.5.1 by Hart et al. (2017).

3.1. Penalty Parameter Study

A mechanistic model consisting of four differential and one algebraic equation Elqotbi et al. (2013) describes the product concentration C_P (output) of a fermentation process based on an oxygen mass transfer coefficient $k_L a$ (inputs) which is a control vector that determines how much oxygen is fed into the process at different time steps. The optimal control problem determines $k_L a$ to maximize C_P. The evaluation of the mechanistic model involves an integration procedure that is treated as a black-box. The mapping of input vector $k_L a$ onto the output C_P is given by: $C_P = Mech(k_L a)$. To imitate an industrial sample selection process, the input data is generated as blobs by using the scikit-learn library Pedregosa et al. (2011) and evaluated with the mechanistic model to create the dataset. The R package gbm Ridgeway (2007) is used to train a GBT model $GBT(x)$ which is then optimized for different penalty parameter values. The average relative model error $\bar{\epsilon}_{GBT}$ with respect to $Mech(k_L a)$ is computed based on 10 independent runs that each consider 10 different values for the penalty parameter. Directly optimizing the formulation with Gurobi 8.1.1. gives the results depicted in Figure 2. The results suggest that the penalty measure used can efficiently handle uncertainty in GBT models. A large penalty parameter value ($\lambda > 1$) resulted in average model errors $\bar{\epsilon}_{GBT} < 1\,\%$. On the other hand, low penalty parameter values identify regions where the average model error $\bar{\epsilon}_{GBT}$ is high but where good solutions with regard to optimality are predicted by the GBT model. Gathering more data in these regions could create an overall better performing GBT model and help to identify better solutions.

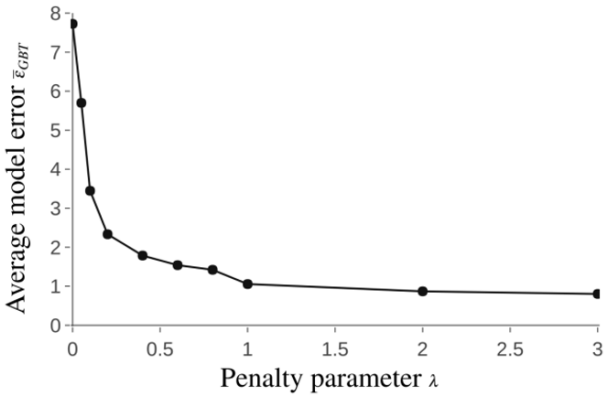

Figure 2: Average model error $\bar{\epsilon}_{GBT}$ for different penalty parameters λ.

3.2. Large-Scale Instance

Table 1: Results of the proposed algorithm and Gurobi 8.1.1 for a GBT model trained on the concrete mixture design dataset. Blank entries indicate premature solver termination.

	Proposed Algorithm			Gurobi 8.1.1		
[h]	ub	lb	gap	ub	lb	gap
2	-71.6	-105.7	48 %	-88.7	-138.8	56 %
4	-71.6	-103.0	44 %	-90.4	-127.5	41 %
6	-78.9	-102.0	29 %	-90.4	-116.9	29 %
8	-78.9	-100.8	28 %	-	-	-
40	-83.6	-94.7	13 %	-	-	-

To compare the overall performance of the proposed algorithm to the state-of-the-art solver Gurobi 8.1.1 we use the concrete strength dataset (Yeh (1998)) from the UCI machine learning repository (Dua and Graff (2017)). The dataset reports the compressive strength for different ingredient proportions. A GBT model is trained inside a caret framework Kuhn (2008) using cross-validation. The trained GBT model has 8 continuous variables describing different ingredient proportions of the concrete and maps onto its compressive strength. The resulting MINLP maximizes the compressive strength given a predefined time limit and has 8,481 binary variables $y_{i,j}$ and 280,107 constraints. With a penalty parameter $\lambda = 1$ and a solver time limit of 40 h, the results are summarized in Table 1. As shown in Table 1, the proposed algorithm reaches the same relative optimality gap as Gurobi 8.1.1 after 6 h of runtime, after which Gurobi 8.1.1 terminates prematurely due to memory exhaustion. While Gurobi 8.1.1 generates better upper bounds, the proposed algorithm derives stronger lower bounds which are needed to proof optimality and terminates due to the time limit of 40 h, reaching a significantly lower optimality gap of 13 %. Hence, the proposed algorithm outperforms off-the-shelf solvers, e.g. Gurobi, for large problem instances. Moreover, despite its more difficult to solve penalty function, the results compare well to Mistry et al. (2018), highlighting the efficiency of the proposed algorithm.

4. Conclusion

The proposed algorithm efficiently optimizes data-driven tree-based ensemble models to global optimality and outperforms state-of-the-art global solvers. Moreover, we introduce a novel penalty measure that allows model uncertainty consideration while optimizing and show its high effectiveness in numerical studies. Further improvements will focus on algorithmic, modeling and application related aspects. The results suggest that the proposed algorithm can also be useful in Design of Experiment applications and future research will include comparisons to other approaches in this field, e.g., Bayesian Optimization.

References

A. Bhosekar, M. Ierapetritou, 2018. Advances in surrogate based modeling, feasibility analysis, and optimization: A review. Computers & Chemical Engineering 108, 250 – 267.

F. Boukouvala, C. A. Floudas, Jun 2017. Argonaut: Algorithms for global optimization of constrained grey-box computational problems. Optimization Letters 11 (5), 895–913.

D. Dua, C. Graff, 2017. UCI Machine Learning Repository. M. Elqotbi, S. D. Vlaev, L. Montastruc, I. Nikov, 1 2013. CFD modelling of two-phase stirred bioreaction systems by segregated solution of the Euler-Euler model. Computers and Chemical Engineering 48, 113–120.

J. H. Friedman, 2001. Greedy function approximation: A gradient boosting machine. Annals of Statistics.

W. E. Hart, C. D. Laird, J.-P. Watson, D. L. Woodruff, G. A. Hackebeil, B. L. Nicholson, J. D. Siirola, 2017. Pyomo - Optimization Modeling in Python. Vol. 67 of Springer Optimization and Its Applications. Springer International Publishing.

C. A. Henao, C. T. Maravelias, 2011. Surrogate-based superstructure optimization framework. AIChE Journal 57 (5), 1216–1232.

J. Kronqvist, D. E. Bernal, A. Lundell, I. E. Grossmann, 6 2019. A review and comparison of solvers for convex MINLP. Optimization and Engineering 20 (2), 397–455.

M. Kuhn, 2008. Building Predictive Models in R Using the caret Package. Journal of Statistical Software 28 (5).

S. P. Lloyd, 1982. Least Squares Quantization in PCM. IEEE Transactions on Information Theory 28 (2), 129–137.

M. Mistry, D. Letsios, G. Krennrich, R. M. Lee, R. Misener, 2018. Mixed-integer convex nonlinear optimization with gradient-boosted trees embedded. arXiv 1803.00952.

V. V. Mišic, 2017. Optimization of tree ensembles. arXiv 1705.10883.

D. R. Morrison, S. H. Jacobson, J. J. Sauppe, E. C. Sewell, 2 2016. Branch-and-bound algorithms: A survey of recent advances in searching, branching, and pruning. Discrete Optimization 19, 79–102.

K. Palmer, M. Realff, 2002. Optimization and validation of steady-state flowsheet simulation metamodels. Chemical Engineering Research and Design 80 (7), 773 – 782.

F. Pedregosa, G. Varoquaux, A. Gramfort, V. Michel, B. Thirion, O. Grisel, M. Blondel, P. Prettenhofer,

R. Weiss, V. Dubourg, J. Vanderplas, A. Passos, D. Cournapeau, M. Brucher, M. Perrot, E. Duchesnay, 10 2011. Scikit-learn: Machine learning in Python. Journal of Machine Learning Research 12, 2825–2830.

G. Ridgeway, 2007. Generalized Boosted Models: A guide to the gbm package. Compute 1 (4), 1–12.

A. M. Schweidtmann, A. Mitsos, 2019. Deterministic Global Optimization with Artificial Neural Networks Embedded. Journal of Optimization Theory and Applications 180 (3), 925–948.

Z. T. Wilson, N. V. Sahinidis, 2017. The ALAMO approach to machine learning. Computers & Chemical Engineering 106, 785–795.

I. C. Yeh, 1998. Modeling of strength of high-performance concrete using artificial neural networks. Cement and Concrete Research 28 (12), 1797–1808.

Sauro Pierucci, Flavio Manenti, Giulia Bozzano, Davide Manca (Eds.)
Proceedings of the 30th European Symposium on Computer Aided Process Engineering (ESCAPE30), May 24-27, 2020, Milano, Italy.
http://dx.doi.org/10.1016/B978-0-12-823377-1.50332-3

ECO2DES: Python Framework for the Eco-Design of Industrial Processes

Miguel García Casas,[a,b] Javier Dufour Andía,[a,c] Jose Luis Galvez Martos[c]

[a]*Chemical and Environmental Engineering Group, Rey Juan Carlos University, Móstoles, 28933, Spain*
[b]*Contactica S.L., Madrid, 28021, Spain*
[c]*Systems Analysis Unit, IMDEA Energy, Móstoles, 28935, Spain*
m.garciacasa.2018@alumnos.urjc.es / miguel.garcia@contactica.es

Abstract

More than 80% of the costs and environmental impacts of a new process are defined in the design phase, often without being properly assessed. ***ECO2DES*** is a new methodological approach for the eco-design of industrial processes (chemical, petro-chemical, energetic, bio-based…), integrated in a Python framework. ***ECO2DES*** allows for maximising economic parameters such, as the net present value, and minimising environmental impacts by the integration and automation of modelling, process simulation, life cycle assessment (LCA), life cycle costing assessment (LCC) and multi-objective optimisation algorithms (MOOA). This new methodology does not only design the optimal process from and sustainable point of view, but also reduces the workload accelerating the time-to-market of research and innovative projects in the process industry. In order to illustrate the potential of the framework, the methanation process for energy storage will be evaluated. The outputs of the ***ECO2DES*** framework clearly mark the way for the detailed engineering in the development of this process.

Keywords: Eco-design, process simulation, life cycle assessment, life cycle costing, optimisation.

1. Introduction

During the development of new innovative processes, there are no industrial data that can support any life cycle assessment, LCA, or life cycle cost, LCC, study, which gives rise to numerous trial-and-error phases during technology upscaling, exorbitantly increasing time-to-market and costs. Predictive models and process simulations, however, are able to compute, through physicochemical relationships, the behaviour of that technology under development at industrial scale and formulate scenarios for environmental or cost optimisation. However, process simulation, LCA and LCC methodologies are well structured and there are many options of commercial software specialised in these areas. Nowadays, at the best of our knowledge, there is no current research combining them in a holistic way for their application in the economic and environmental optimisation of any industrial design of process under research and/or development. With this premise, the ***ECO2DES*** framework was born. It is an object-oriented Python framework for sustainability-oriented optimisation of industrial processes. The tool takes advantage of the full feature set of Python, such as its facilities for fast prototyping and the several available libraries for data processing, data analysis, scientific computing and data visualisation. ***ECO2DES*** is a descriptive tool, which documents life cycle inventories and characterises them through their environmental impact and associated costs. It is a

predictive tool, since it uses as inputs physicochemical models for process simulation in the research phase; and adaptive, since it automates process design selections based on multi-objective optimisation algorithms.

2. ECO2DES architecture

The architecture scheme of ***ECO2DES*** is illustrated in Fig. 1. It has an object-oriented design to make it flexible and expandable.

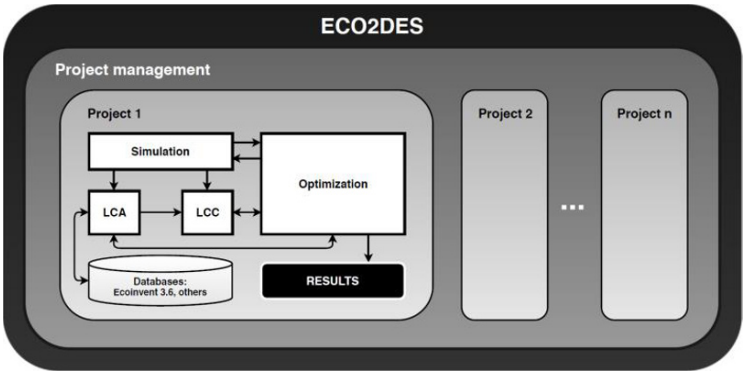

Figure 1. *ECO2DES* architecture scheme.

The core classes of ***ECO2DES*** are *projects, simulation, lca, lcc* and *optimization*. Class *projects* encapsulates the management tools, it offers several methods to create, delete, copy and assign projects. The initialisation of ***ECO2DES*** framework creates a folder inside the home directory in which all the projects are stored. Every project is linked to its own Ecoinvent 3.6 databases (Wernet et al., 2016), in order not to interfere with the changes made in another project. Class *simulation* allows to link with a model or simulation developed in Python, Excel or Aspen Plus, as well as defining the inputs and outputs of the simulation. Class *lca* inherits the most of its methods from *Brightway2*, (Mutel, 2017) an open-source framework for life cycle assessment. Some improvements regarding speedup calculation inside an optimisation loop, as well as several data visualisation tools were aggregated. Furthermore, this class allows the user to link the inputs and outputs defined in the class simulation with exchanges of an existing activity inside the database or a new one previously created. Class *lcc* was developed from scratch. It solves a financial life cycle costing of the product or products (from cradle to customer), but further implementations will be made to include a whole life cycle evaluation (from cradle to gate) and compute externalities costs derived from the environmental impacts assessed in the class *lca*. Finally, class *optimization* has methods to define the problem with variables from the classes *simulation*, *lca* and/or *lcc*; their boundaries, the problem constrains and the objectives from the three abovementioned classes. Class *optimization* has several algorithms for heuristic global optimisation and local optimisation, with a single or multiple objectives. These algorithms are inherited from *pygmo* (Biscani et al., 2010) and *scipy* (Virtanen et al., 2019), other libraries are under study to include their features, as well as own-developed implementations.

3. Case study: Sabatier for renewable energy storage in the natural gas grid

3.1. Background

Currently, conventional energy sources such as nuclear power or fossil fuels are being replaced by renewable ones such as wind or solar energy. However, most of the renewable sources cannot provide a base load electric power. To overcome this problem, storage systems have to be integrated in the power grid. For seasonal storage of the energy (charge / discharge period from 1 day to 1 year) in huge capacities, electrical energy can be converted into chemical energy by transferring it into fuels. The logical pathway is the conversion of electrical energy into hydrogen by water electrolysis, but nowadays there is no a hydrogen grid or a large enough storage system developed in any country. Until this requirement is satisfied, the highly developed natural gas grids can be used for the transport of excess energy (Bassano et al., 2019), using electrolysis to produce hydrogen to react with carbon dioxide in a methanation synthesis. So in addition to providing an energy carrier, the process consumes carbon dioxide, contributing to the reduction of GHGE. The methanation reactions of carbon monoxide and carbon dioxide were discovered at the beginning of the 20th century by Sabatier et al. (1902). The methanation of carbon dioxide is an exothermic catalytic reaction and is typically operated at temperatures between 200°C and 550°C depending on the used catalyst.

3.2. Sabatier process simulation

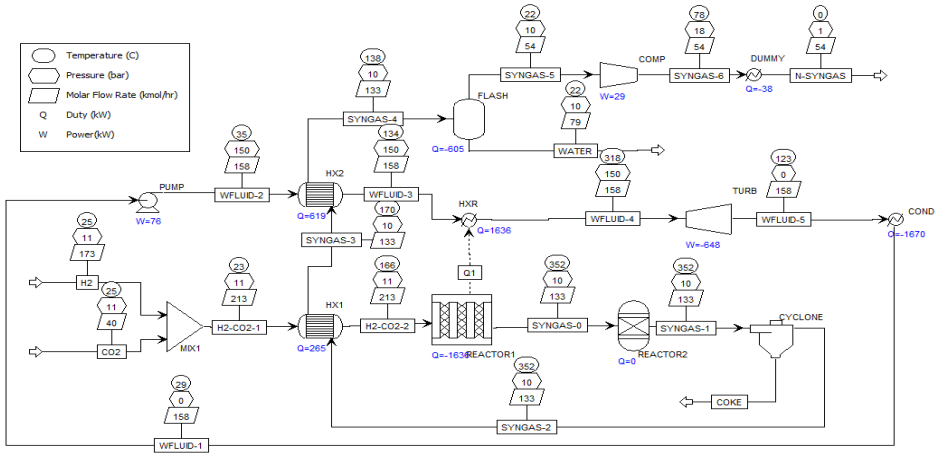

Figure 2. Aspen plus flowsheet of the Sabatier process simulation.

For the determination of the optimal reactor concept, the kinetic model 12 of Kopyscinski (2010) was used. The model parameters were implemented within a *RPLUG* reactor of Aspen Plus. Furthermore, the resulted gases are connected to a *RGIBSS* reactor to minimise the free energy of Gibbs following the Boudouard reaction (Gao et al., 2012). This way the potential formation of coke will be measured and taken into account for the deposition of solid over the catalysts, and, therefore, the economic model would take into account the regeneration and replacement cycles of the catalyst. The heat of the gas stream is recovered in the inlet current of the reactor as well as in the hybridisation with a Rankine cycle to generate electricity, which operates with water or cyclopentane as working fluid. Finally, the gas is dried and compressed to be injected into the grid. Then, if the hydrogen molar composition is higher than a 5 % a pressure swing adsorption, PSA, unit is needed, recovering 90 % of the hydrogen which is recirculated. Moreover, if

carbon dioxide molar composition is higher than a 2 % a monoethanolamine (MEA)-based capture is needed, recovering 97% of the dioxide of carbon which is then recirculated. Both of them modelled as black boxes. Fig. 2 illustrates the layout of the Aspen Plus simulation.

3.3. ECO2DES implementation

3.3.1. Project creation and simulation linking

After importing ***ECO2DES*** framework, the first step is setting a project by name (if the project does not exist, this method creates it) and link it to the Aspen Plus simulation:

```
import eco2des as e2d

e2d.projects.set_current('Sabatier_case_study')
e2d.simulation.link('Sabatier_k.bkp')
aspen = e2d.simulation.com
```

Once the *link* method of the class *simulation* is run, the com object of the Aspen Plus simulation is created as an attribute of the class (see line 6 of the above code). This com object could be used to get access to the whole simulation data (for further understanding, please visit the Aspen Plus user guide, ActiveX section (AspenTech, 2010)), and with the *define_input* and *define_output* methods the variables of interest could be built.

3.3.2. Life cycle assessment

When the simulation is linked and the inputs and outputs defined, the life cycle assessment of the process could be modelled. The following code illustrates as an example how a database is picked, how a new activity is created and how a technosphere exchange is added to it:

```
ei36 = e2d.lca.database('Ecoinvent 3.6 cutoff')
sabatier = ei36.create_activity(name = 'Sabatier for storage of renewable energy in the gas grid',
           location = 'ES', unit = 'cubic meter', ref_product = 'SNG', production_amount = 1.0)
wastewater = [act for act in ei36 if act['name'] == 'market for wastewater, from residence'
              and act['location'] == 'RoW'][0]
sabatier.new_exchange(amount= -1*e2d.outputs['waste water'] / e2d.outputs['SNG'],
                      input=wastewater, type="technosphere").save()
```

3.3.3. Life cycle costing assessment

When the simulation is linked and the inputs and outputs defined, the life cycle costing assessment of the process could be modelled. The following code illustrates as an example how the LCC object is instanced, how the reactor vessel is assigned to an ***ECO2DES*** correlation which calculates the cost based on the material needed computed based on the ASME BPVC, section VIII, division 1 (ASME, 1986). Finally, it shows how a William's correlation is used to compute the PSA cost.

```
lcc = e2d.lcc(local_factor = 0.89)
lcc.vessel(Q = e2d.outputs['Flow in'], rt = e2d.outputs['Residence time'], p=1e6,
           LD = e2d.inputs['LD ratio'], T = e2d.inputs['Reactor temperature'], phase = 'Fluids',
           kind = 'horizontal', material = 'Stainless 304', name = 'Sabatier reactor vessel')
lcc.william_equipment(name = 'PSA', cap = e2d.outputs['H2 recover']*0.09/1000*24, n = 0.7,
                      ref_cap = 155.24, ref_cost = 7.32e6, ref_CEPCI = 444.2, phase = 'Fluids')
```

3.3.4. Multi-objective optimisation

Finally, the following code shows how a multi-objective optimisation problem is defined in ***ECO2DES*** (line 2), the optimisation algorithm is picked in line 1, in this case the multi-objective evolutionary algorithm with decomposition (MOEA/D) is used. An initial population is randomly constructed in line 12 and evolved in line 13. The problem has some constrains marked, based on the regulations for the natural gas grid: hydrogen composition lower than a molar 5 %, monoxide of carbon and dioxide of carbon composition lower than a molar 2 %. In this case, the constrains are treated as penalties during the simulation outputs definition.

```
algorithm = e2d.optimization.moead(gen = 20)
problem = e2d.optimization.problem(
              variables =(e2d.inputs['H2/CO2'], e2d.inputs['Reactor temperature'],
                          e2d.inputs['Reactor length'], e2d.inputs['Reactor LD'],
                          e2d.inputs['Working fluid']),
              bounds = ([4, 250, 1, 1, 0], [5, 400, 20, 10, 1]),
              objectives = (-1*e2d.outputs['Storage efficiency'], e2d.outputs['Climate change'],
                            e2d.outputs['Levelized cost']))
population = e2d.optimization.population(problem, 190)
evolved_pop = algorithm.evolve(population)
```

3.4. Results

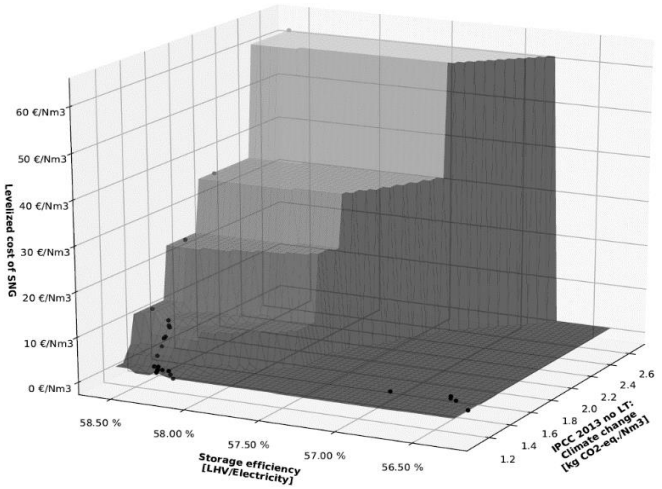

Figure 3. Methanation for energy storage using MOEA/D: Pareto front.

The storage efficiency is measured as the lower heating value (LHV) of the SNG divided by the electricity used (wind power for electrolysis minus the generated power). For LCA, the functional unit is 1 Nm^3 of SNG without considering the combustion and the limits of the system consider CO2 as free of environmental burdens, since it is a waste from the capture process. In this example, the climate change is assessed following the IPCC 2013 method without long term emissions for the characterization of the global warming potential. The levelised cost is calculated taking into account the capital expenditure (CAPEX) and operational expenditure (OPEX) assuming a loan of 60 % of CAPEX with a period for payment of 10 years and an interest of 4 %. A discount rate of 10 % is used during the 30 years of lifetime and a construction time of 1.5 years is assumed. The Pareto front for the three objectives optimisation problem is shown in Fig. 3. Moreover, two additional optimisation problems were solved using the non-dominated sorting genetic algorithm (NSGA-II): a two objectives problem with the storage efficiency and the levelised cost of SNG (see Fig. 4) and other with the climate change and the levelised cost of SNG which showed that these objectives are non-conflicting. The optimal solution of the methanation process, from the environmental and economic points of view, corresponds to the following conditions: hydrogen to carbon dioxide mole ratio of 4.44, a reactor temperature of 396 ºC, a reactor length of 2.64 m, a reactor length to diameter ratio of 5.72 and using water as working fluid in the Rankine cycle. The calculated levelized cost of SNG is 1.481 €/Nm3, the climate change impact is 1.088 kg CO2-eq./Nm3 and the storage efficiency is 57.95 %. With this configuration a hydrogen recovery system is required, but carbon dioxide conversion is 98.63 % which allows injection SNG to the grid without recovering it.

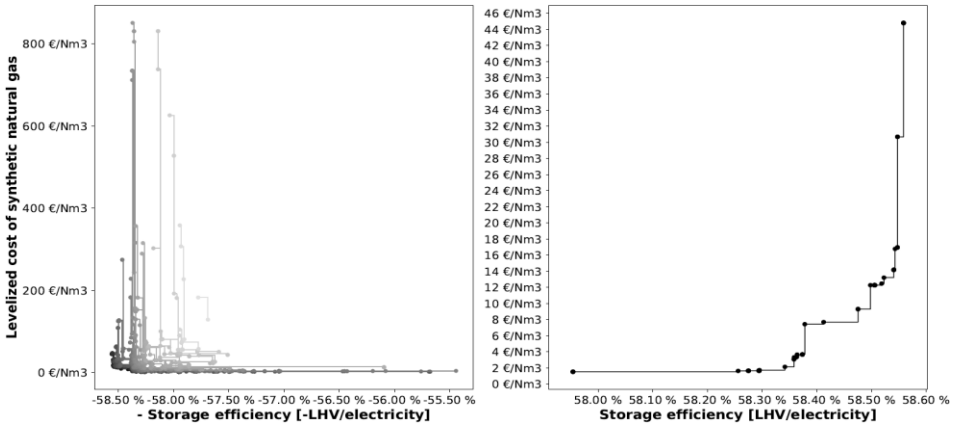

Figure 4. Methanation for energy storage using NSGA-II: Population evolution (left) and Pareto front (right).

4. Conclusions

ECO2DES, a Python-based framework for sustainability-based optimisation of industrial processes, has been presented in this paper. It provides support for accelerating the time-to-market of novel processes in different industries: automating the LCA and LCC, solving multi-objective and single-objective problems and performing upscaling studies. As an example, the methanation process has been analysed inside the framework. The results mark the way for the detailed engineering in the development of this process, showing that, on the one hand, environmental and economic objectives are non-conflicting. On the other hand, to improve storage efficiency will always compromise the environmental and economic performance of the process.

References

American Society of Mechanical Engineers (ASME), 1986. ASME Boiler and Pressure Vessel Code, Section VIII: Rules for Construction of Pressure Vessels, Division 1, pp. 382-383

AspenTech, 2010, Aspen Plus User Guide.

Bassano, C., Deiana, P., Lietti, L., Visconti, C. G., 2019. P2G movable modular plan operation on synthetic methane production from CO2 and hydrogen from renewables sources, Fuel, 253, pp.1071-1079.

Biscani, F., Izzo, D., Yam, C.H., 2010. A global optimisation toolbox for massively parallel engineering optimisation, preprint arXiv:1004.3824.

Gao, J., Wang, Y., Ping, Y., Hu, D., Xu, G., Gu, F., Su, F., 2012. A thermodynamic analysis of methanation reactions of carbon oxides for the production of synthetic natural gas, RSC Adv., 2(6), pp.2358-2368.

Kopyscinski, J., 2010. Production of synthetic natural gas in a fluidized bed reactor understanding the hydrodynamic, mass transfer, and kinetic effects, Doctoral Thesis.

Mutel, C. 2017. Brightway: An open source framework for Life Cycle Assessment. Journal of Open Source Software, , 2(12), pp.236.

Sabatier P., Senderens J.B., 1902. Direct hydrogenation of Oxides of Carbon in presence of various finely divided metals [in French]. C R Acad Sci, 134, pp.689–691.

Virtanen, P., Gommers, R., Oliphant, T., Haberland, M., Reddy, T., Cournapeau, D., et al., and SciPy 1.0 Contributors, 2019. SciPy 1.0–Fundamental Algorithms for Scientific Computing in Python, preprint arXiv:1907-10121.

Wernet, G., Bauer, C., Steubing, B., Reinhard, J., Moreno-Ruiz, E., and Weidema, B., 2016. The ecoinvent database version 3 (part I): overview and methodology. The International Journal of Life Cycle Assessment, 21(9), pp.1218–1230.

Sauro Pierucci, Flavio Manenti, Giulia Bozzano, Davide Manca (Eds.)
Proceedings of the 30th European Symposium on Computer Aided Process Engineering (ESCAPE30), May 24-27, 2020, Milano, Italy.
http://dx.doi.org/10.1016/B978-0-12-823377-1.50333-5

Operator Training for Non-Technical Skills in Process Industry

Hasan Mahbub Tusher[a], Steven Mallam[a], Gesa Praetorius[a,b], Zaili Yang[c], Salman Nazir[a*], Wilhelm Stock[d]

[a]*Training and Assessment Research Group (TARG), Department of Maritime Operations. Faculty of Technology, Natural Sciences & Maritime Sciences, University of South-Eastern Norway, Horten, 3184, Norway.*
[b]*Kalmar Maritime Academy, Linnaeus University, Sweden.*
[c]*Liverpool Logistics, Offshore and Marine Research Institute, Faculty of Engineering and Technology, Liverpool John Moores University, UK.*
[d]*RWE Power AG, Cologne, Germany.*

Salman.Nazir@usn.no

Abstract

The increasing levels of automation have redefined the nature of human-machine interactions in the process industry. The changing nature of work demands that Control-Room Operators and Field Operators are competent with the use of new and emerging methods and technologies in order to perform their tasks safely and effectively. A critical aspect of complex socio-technical systems is the requirement for humans to successfully interact with, and manage, both technical systems and team dynamics of human-to-human operations. Non-technical skills, such as communication, leadership, decision making, and teamwork are considered vital for safety in high-risk domains. Training has traditionally played a crucial role to instill the required technical and non-technical skills to the operators. Recurring training is also necessary for maintaining the knowledge and competencies required to face challenging operational environments. In this paper, four examples of non-technical skills training approaches used by an electric utility company for their operators are presented. This article reveals differing aspects of design and implementation of non-technical skills training in the process industry. It also demonstrates the necessity for research into the analysis of future training needs and assessment methods.

Keywords: process industry, training, safety, simulator, virtual reality

1. Introduction

Operators in the process industry are required to perform complex and safety-critical tasks with optimum efficiency. The complex nature of these tasks necessitates that operators manage adaptive automation, multilevel communication, and decision-making in dynamic work contexts. It is stated that approximately 90% of accidents in safety-critical industries are caused by human error (Leva, 2005). However, a wide range of issues from the organization, policies, equipment design, psychology, judgment and lack of competency are believed to contribute to underlying causes of what is eventually labelled "human error" (Whittingham, 2004; Manca et al., 2013). Both technical and non-

technical competencies are required by operators to ensure safe and efficient operation of a plant and its processes. Non-technical skills (NTS) are defined as "*the cognitive, social and personal resource skills and complement technical skills, and contribute to safe and efficient task performance*" (Flin and O'Connor, 2017).

The connection between human error and NTS first originated in the aviation domain. Outcomes stemming from different aviation accidents revealed that lack of pilot NTS contributed more to the accidents than a lack of technical knowledge or aircraft malfunctioning (Flin and Maran, 2004). Considering the complexity of modern workplaces and the safety-critical nature of operations, NTS training elements were originally developed in the late 1980s for aviation pilots through Crew Resource Management (CRM) courses. CRM courses and their learning objectives have since been adopted in many high-risk domains including the nuclear, maritime and healthcare industries (Kanki et al., 2019; Flin et al., 2015). Ironically, nuclear power plant operators and healthcare personnel follow similar CRM training methods as in aviation, even whilst the workplace dynamics and goals differ greatly. Thus, there is a need for improved precision and more standardization of training for specialized domains (O'Connor et al., 2008; O'Dea et al., 2014).

NTS training often comprises a mixture of classroom-based lectures and practical simulation-based exercises (Hayward, Lowe & Thomas, 2018). However, there is typically little guidance to know when, what and how to train operators in different domains on NTS, as technical skills are often the focus. This paper specifically focuses on how *communication,* as a NTS, is trained within the process industry. Since communication is identified as an important aspect of safety across different safety-critical domains, including transport (Huang et al., 2018), healthcare (Lyndon, 2019), maritime (Sætrevik et al., 2018) and aviation (Ford et al., 2018), we present an overview of NTS training methods utilized by an electric utility company. Additionally, we address how the adopted NTS training methods bears significance in terms of long-term training assessment and inter-domain transferability through improved applications.

2. Case Study: Communication Skills Training in an Electric Utilities Company

Although there is no universally adopted method for training operators in the process industry, they all undergo various forms of education and training programs. The contents of these programs are structured and governed by the companies themselves, the relevant regulatory authorities or a combination of the two. Most training frameworks focus on technical knowledge relating to different processes, control loops, operation and troubleshooting (Nazir et al., 2015). Process industries typically involve some level of task-engagement between CROPs and FOPs working in teams. An independent individual task can become an interdependent team task for normal operations in unexpected situations, and thus communication becomes an important factor for task efficiency among team members.

The rapid changes in the workplace environment have necessitated that the process industry diversifies its training tools and methods. For example, the shift in communication techniques due to the inception of automated processes have altered non-verbal communication, as it can now be performed electronically (Kaber et al., 2001). An electric utility company is used as a reference to better understand how they train their

CROPs and FOPs in accordance with the current workplace requirements. The company employs diverse team-training and communication exercises within the NTS skills training framework of CROPs and FOPs, as described in Figure 1.

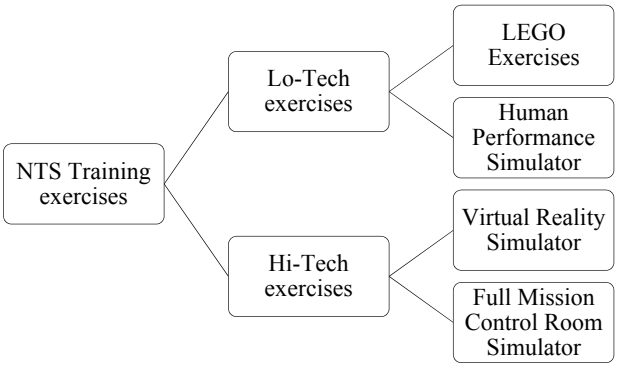

Figure 1: Differing methods of communication skill training.

2.1.1. Lo-Tech: LEGO Exercises

A lo-tech communication training exercise used in CROP training courses involves CROPs to interact with each other through the building of a LEGO toy (see Figure 2). For example, in one exercise, the pieces from a LEGO set (e.g., a 3-in-1 LEGO set which can form an aircraft, boat or car with the same combination of pieces) are presented to only one person without the build instructions, box or any reference to what the LEGO structure is. The step-by-step instructions for the LEGO sets are presented to another member of the team sitting across the room with their back to the person with the pieces. The individual with the instructions is tasked with describing the step-by-step procedures of building the desired structure (e.g. individual pieces to choose, sequence of construction, etc.) whilst under time pressure.

Figure 2: Examples of differing tools for NTS training (Lo-Tech)

Another example of a LEGO-based communication training exercise involves non-verbal communication. Members of a team are required to build a specific structure using LEGO pieces in the same configuration (one person with pieces, one person with instructions) but now physically facing each other. However, in this exercise, they are not allowed to communicate verbally.

In both exercises, the goal is to practice *communication skills* as a part of greater NTS training. The purpose of using LEGO as a medium to train is that it forces operators to use language and tasks that are not associated with their profession. These seemingly irrelevant tasks of LEGO building require operators to think, be creative, and communicate with their peers without falling into typical habits, shortcuts and nomenclature for which they are comfortable with and associated with their technical work and expertise. The second exercise has also been found to be useful for leadership training, as instructors' report that natural leaders emerge during these exercises. The subsequent debriefing sessions help establish "closed-loop communication" that

construct a joint picture and language for the task that was performed, providing a platform for self-assessment and reflection.

2.1.2. Lo-Tech: Human Performance Simulator

A portable system consisting of a combination of small valves on a simulated piping network in a simple vertically mounted structure is used to train NTS and communication skills amongst teams. A correct sequential action is required to be performed in operating the valves to start an intended process and requires inputs from multiple team members to be successful. The valves are positioned far from each other and the team members need to share a common mental model in order to perform the task successfully. The trainees don't need to be an expert of the system, but they are required to be efficient with communication and work as a team. The inherent characteristics of these types of exercises make the background of participants irrelevant, and thus people with expertise from different domains can be trained together.

2.1.3. Hi-Tech: Online and Virtual Reality Training Platforms

This company also utilizes e-learning and online knowledge-sharing platforms as part of their operator (and general employee) education and training. The online learning platform *Moodle* supports the company's social learning through virtual classrooms enabling synchronous online communication, media servers and plant simulators. For example, trainees can engage in virtual environments and scenarios to troubleshoot automated process control systems in power plants or open cast mining operations. 360-degree videos on VR headsets (see Figure 3) allow virtual tours of industrial environments and equipment in classroom training sessions or through the online learning portal. For operator training on bucket wheel excavators, Augmented Reality (AR) is deployed through Microsoft's HoloLens, providing training from complete virtual situations to on-site hybrid online support in the real working environment.

Figure 3: Virtual Reality Headset system used to train NTS in control room operations.

2.1.4. Hi-Tech: Full Mission Control Room Simulations

Within control room operator simulator courses, NTS training is typically embedded within the technical training content. Control room operators working for the company take periodic short-duration training courses (typically five days in duration) regularly throughout their career. Within one particular five-day course, two days are dedicated to communication and decision-making. During this time, short lectures on communication and decision-making are mixed with exercises and event-based simulation training (see Figure 4). The participants are exposed to differing process scenarios while being required to execute certain tasks. NTS performance indicators, including quality of communication, time to complete tasks, decision making and problem-solving, amongst other operational aspects are typically highlighted and discussed in the debriefing sessions. Furthermore, the training also contains leadership training, as participants are assigned different roles during the exercises, taking on the role of an assigned control room operator position (which may

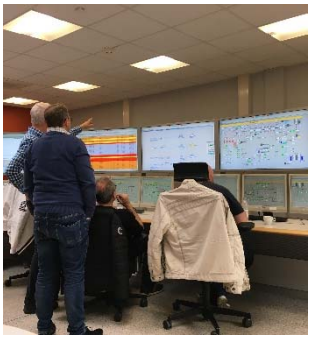

Figure 4: Team discussion in a full-mission central-control room simulator

not be their current professional position in real-world plant operations). Simulation scenarios can vary from emergency operations (e.g., plant blackout) to normal and planned operations (e.g., startup from a cold or warm plant, planned shutdown of a particular block). NTS skills are not assessed with objective, quantifiable metrics, but rather analyzed and discussed subjectively in post-simulation debriefing sessions. The assessment is based on peer-to-peer feedback and instructor-to-operator feedback. The instructors reported that they act more as facilitators to the discussion, rather than assessors of "good" and "bad" performance during a debriefing at the end of each exercise.

3. Discussion

The four examples of NTS training practices in the above-mentioned electric utility company includes both *lo-tech* and *hi-tech* methods. Traditionally, such training is limited and typically implemented in conjunction with technical training exercises. NTS can be viewed as a resource-intensive aspect of training. Thus, lo-tech options can be used to implement NTS training, which are considered to be an effective and practical solution for operator NTS competency development.

Differing industries choose NTS training methods in accordance with their operational requirements, both in the control room and in the field. Future research should focus on testing and validation of more streamlined training methods for specific operations. Furthermore, team dynamics in different levels of communication between the novice and experienced workers operating automated systems should also be addressed. Addressing the non-technical aspects of equipment and system operations along with appropriate training can help better prepare current and future operators for managing their work in a complex and highly automated work environment. The extended evaluation of the discussed training methods in the process domain could provide insight into the transferability of these methods in other safety-critical domains as well. It could also add new dimensions in training and assessment methods through extended NTS training needs analysis, identifying training postulates and training possibilities across emerging new systems.

4. Conclusion

It is crucial to understand and develop differing methods and tools to effectively and efficiently deliver NTS training for process operators. CROPs and FOPs working in teams within the process industry require NTS and NTS training in order to hold the competencies required for managing the complexity of safety-critical social-technical systems. Different types of lo-tech and hi-tech training tools, ranging from simple puzzle exercises to e-Learning platforms and immersive simulation technologies are effective in training current and future operators. Further study is required to map out NTS training methods and tools in order to establish a wider understanding of requirements for current and future systems.

Acknowledgements

This project has received funding from the European Union's Horizon 2020 research and innovation programme under the Marie Skłodowska-Curie grant agreement No 823904. The corresponding author also acknowledges the support of the project "Innovating Maritime Training Simulators using Virtual and Augmented Reality (InnoTraining)" funded by the Research Council of Norway, project number 269424.

References

Flin, R., & Martin, L. (2001). Behavioral markers for crew resource management: A review of current practice. *The International Journal of Aviation Psychology*, *11*(1), 95-118.

Flin, R., & Maran, N. (2004). Identifying and training non-technical skills for teams in acute medicine. *BMJ Quality & Safety*, *13*(suppl 1), i80-i84.

Flin, R., & O'Connor, P. (2017). Safety at the sharp end: a guide to non-technical skills. CRC Press.

Flin, R., Youngson, G. G., & Yule, S. (Eds.). (2015). Enhancing surgical performance: A primer in non-technical skills. CRC press.

Ford, J., Henderson, R., & O'Hare, D. (2013). Barriers to intra-aircraft communication and safety: The perspective of the flight attendants. *The International Journal of Aviation Psychology*, *23*(4), 368-387.

Hayward, B. J., Lowe, A. R., & Thomas, M. J. (2019). The migration of crew resource management training. In Crew resource management (pp. 421-447). Academic Press.

Huang, Y. H., Sinclair, R. R., Lee, J., McFadden, A. C., Cheung, J. H., & Murphy, L. A. (2018). Does talking the talk matter? Effects of supervisor safety communication and safety climate on long-haul truckers' safety performance. *Accident Analysis & Prevention*, *117*, 357-367.

Kaber, D. B., Riley, J. M., Tan, K. W., & Endsley, M. R. (2001). On the design of adaptive automation for complex systems. *International Journal of Cognitive Ergonomics*, *5*(1), 37-57.

Kanki, B. G., Anca, J., & Chidester, T. R. (Eds.). (2019). Crew resource management. Academic Press.

Leva, M. C. (2005). Human Errors Analysis and Safety Management Systems in Hazardous Activities.

Lyndon, A. U. D. R. E. Y. (2019). Failure to Rescue, Communication, and Safety Culture. *Clinical obstetrics and gynecology*.

Manca, D., Brambilla, S., & Colombo, S. (2013). Bridging between virtual reality and accident simulation for training of process-industry operators. *Advances in Engineering Software*, *55*, 1-9.

Mathieu, J. E., Heffner, T. S., Goodwin, G. F., Salas, E., & Cannon-Bowers, J. A. (2000). The influence of shared mental models on team process and performance. *Journal of applied psychology*, *85*(2), 273.

Nazir, S., Øvergård, K. I., & Yang, Z. (2015). Towards effective training for process and maritime industries. *Procedia Manufacturing*, *3*, 1519-1526.

O'Connor, P., O'Dea, A., Flin, R., & Belton, S. (2008). Identifying the team skills required by nuclear power plant operations personnel. *International Journal of Industrial Ergonomics*, *38*(11-12), 1028-1037.

O'Dea, A., O'Connor, P., & Keogh, I. (2014). A meta-analysis of the effectiveness of crew resource management training in acute care domains. *Postgraduate medical journal*, *90*(1070), 699-708.

Parasuraman, R. E., & Mouloua, M. E. (1996). *Automation and human performance: Theory and applications*. Lawrence Erlbaum Associates, Inc.

Sætrevik, B., Ghanonisaber, S., & Lunde, G. E. (2018). Power imbalance between supply vessels and offshore installations may impede the communication of safety issues. *Safety science*, *101*, 268-281.

Whittingham, R. (2004). *The blame machine: Why human error causes accidents*. Routledge.

Wiener, E. L., Chidester, T. R., Kanki, B. G., Palmer, E. A., Curry, R. E., & Gregorich, S. E. (1991). The impact of cockpit automation on crew coordination and communication. Volume 1: Overview, LOFT evaluations, error severity, and questionnaire data.

Sauro Pierucci, Flavio Manenti, Giulia Bozzano, Davide Manca (Eds.)
Proceedings of the 30th European Symposium on Computer Aided Process Engineering
(ESCAPE30), May 24-27, 2020, Milano, Italy.
http://dx.doi.org/10.1016/B978-0-12-823377-1.50334-7

A Deterministic Global Optimization Method Based on Legendre-Fenchel Transform

Karim Alloula[a*], Jean-Pierre Belaud[b]

[a] *Université de Toulouse, Toulouse INP-ENSIACET*
4, allée Emile Monso, CS 44362, 31030 Toulouse Cedex 4, France
[b] *CNRS, Laboratoire de Génie Chimique (UMR 5503)*
4, allée Emile Monso, CS 44362, 31030 Toulouse Cedex 4, France
Karim.Alloula@toulouse-inp.fr

Abstract

This paper introduces a deterministic global continuous optimization method. Given some properties of the criterion function –the first and second order derivatives satisfy Lipschitz conditions or the criterion function is analytic-, it takes full advantage of some theoretical results related to the local convergence analysis of the Gauss-Newton method to calculate points, which may be global minima. This method is original in two ways. First, using the Gauss-Newton method, we try to find least squares solutions to an overdetermined system of global optimality conditions. Second, instead of solving the initial formulation, we apply a uniform scaling to the criterion function and obtain an equivalent problem, where the local convergence of the Gauss-Newton method is improved. The modified overdetermined system is solved from several initial points belonging to a simplicial research domain. This simplicial domain is subdivided recursively into smaller simplices until each of the covering simplices either contains no global minimum (exclusion), or contains one and only one global minimum (inclusion)
Keywords: process simulation, symbolic numeric calculations, deterministic global optimization, Legendre-Fenchel transform.

1. Introduction

The process system engineering activity mainly consists in modeling, and then optimizing, process units or whole plants. For optimizing continuous models, the CAPE community usually tries to find the global minimum of a continuous criterion under a set of linear or non-linear constraints. When the global optimization problem is not convex, it may be hard to solve because the number of local minima may increase exponentially with the number of variables. Any method, either deterministic or heuristic, may stop its iterations nearby one local minima or the calculation complexity of the global optimization algorithms may lead to huge delays for producing some optimum.
This paper exhibits the main principles of a new global continuous optimization method, which tries to overcome, at least partially, some of the drawbacks of the other deterministic global continuous methods in the unconstrained case.

2. Main principles of the global continuous optimization method

(Stork et al., 2018) classify the today algorithms for continuous global optimization. As presented in (Ryoo and Sahinidis, 1995) the “deterministic approaches include branch-and-bound, cutting plane algorithms and decomposition schemes”. During the two last decades, when talking about the CAPE community only, the global continuous optimization research has mainly adopted branch-and-bound approaches. The original

paper by (Androulakis et al., 1995) introduced the αBB method which the main principle is to "underestimate nonconvex terms of generic structure" both in the objective function and in the constraints. This method has been refined but some drawbacks remain: the underestimation efficiency greatly depends on the type of the nonconvex terms; the upper bound calculations can drastically increase the complexity of the partitioning process. Consequently, we choose to base our deterministic optimization strategy, no longer on the objective function expression as in the αBB-like methods, but on a condition of global optimality, first presented by Jean-Pierre Dedieu, and then cited in (Hiriart-Urruty, 1986):

$$(x \text{ is a minimum of } f) \Leftrightarrow (Df(x) = 0 \text{ and } f^{**}(x) = f(x)) \quad (1)$$

where f^{**} is the Legendre-Fenchel bi-conjugate of f. A first paper by (Alloula et al., 2011) summarized the application of the discrete Legendre-Fenchel bi-conjugate of f as a means for estimating the global minimum value. The new algorithm takes full advantage of the condition of global optimality by calculating only points x for which $f^{**}(x) = f(x)$, that is to say points where the tangent plane to the representative surface of f is also a supporting hyperplane, and where $\nabla f(x) = \vec{\eta}$ with $\|\vec{\eta}\| \ll 1$. The smaller the value of $\|\vec{\eta}\|$, the closer to the condition of global optimality. In this paper, we try to solve the global optimality conditions for a fixed value of $\|\vec{\eta}\|$, where $0 < \|\vec{\eta}\| \ll 1$.

This paper is organized according to the following sequence. First, we translate the global optimality conditions into an overdetermined system of nonlinear equations. Then, we build an equivalent system, for which the local convergence properties of the Gauss-Newton method are better. Third, we illustrate the combination of Gauss-Newton sequences starting from different initial points with a subdivision strategy of the research domain. A conclusion summarizes the main benefits and drawbacks of this approach.

3. Global optimality conditions

Let us consider a twice differentiable function $f: \mathbb{R}^n \longmapsto \mathbb{R}$ and a compact set Σ of $\mathbb{R}^n$ such that $f_{|\Sigma}$ is bounded below. $f_{|\Sigma}$ has one or more global minima. Assuming that those global minima are interior points of Σ, we can prove the following:

$$\exists M_{\Sigma,f} \in \mathbb{R}^{+*}; \forall \vec{\eta} \in \mathbb{R}^n;\ \|\vec{\eta}\| \leq M_{\Sigma,f} \Rightarrow \exists x \in \Sigma; Df(x) = \vec{\eta} \quad (2)$$

Assertion (1) says that, provided that we choose a vector $\vec{\eta}$ in $\mathbb{R}^n$ which norm is small enough, we can find at least one point x in Σ for which $Df(x) = \vec{\eta}$.

Under the same assumptions, we have the following result:

$$\exists N_{\Sigma,f} \in \mathbb{R}^{+*}; \forall \vec{\eta} \in \mathbb{R}^n;\ \|\vec{\eta}\| \leq N_{\Sigma,f} \Rightarrow \exists x \in \Sigma; (Df(x) = \vec{\eta}) \text{ and } (f^{**}(x) = f(x)) \quad (3)$$

Eq. (3) means that, provided that we choose a vector $\vec{\eta}$ in $\mathbb{R}^n$ which norm is small enough, we can find at least one point x in Σ for which $Df(x) = \vec{\eta}$ and $(x, f(x))$ belongs to the representative surface of ${f_{|\Sigma}}^{**}$, the convex envelope of $f_{|\Sigma}$.

For any given vector $\vec{\eta}$ for which $\|\vec{\eta}\| \leq N_{\Sigma,f}$, we assume that we know $B = (b_1, b_2, \ldots, b_{n+1}) \in \mathbb{R}^{n+1}$ such that $\mathcal{H}(B, \vec{\eta})$, hyperplane defined by B and one normal vector $(\vec{\eta}, -1)$, is a hyperplane with no intersection with the hypograph of $f_{|\Sigma}$.

Let us consider now the function $F_{f,\vec{\eta},B}$ defined from $\Sigma \subset \mathbb{R}^n$ to $\mathbb{R}^{n+1}$ by:

$$F_{f,\vec{\eta},B}(x) = \begin{pmatrix} D_1 f(x) - \eta_1 \\ \vdots \\ D_n f(x) - \eta_n \\ \frac{[\sum_{i=1}^{n}(x_i - b_i)\eta_i] - (f(x) - b_{n+1})}{\|(\vec{\eta}, -1)\|} \end{pmatrix} \quad (4)$$

$\|\vec{\eta}\| \leq N_{\Sigma,\mathrm{f}}$ so, from Eq. (3), there exists at least one point x_* where the first n coordinate functions of $F_{f,\vec{\eta},B}$ are zero. For such a point, it is easy to show that we have:

$$DF_{f,\vec{\eta},B}(x_*)^t . F_{f,\vec{\eta},B}(x_*) = 0 \qquad (5)$$

In other words, provided that $\|\vec{\eta}\| \leq N_{\Sigma,\mathrm{f}}$, there exists at least one stationary point $x_* \in \Sigma$ of $F_{f,\vec{\eta},B}(x)^t . F_{f,\vec{\eta},B}(x) = \left\|F_{f,\vec{\eta},B}(x)\right\|^2$ for which the first n coordinate functions of $F_{f,\vec{\eta},B}$ are zero. Among all the stationary points x_* in Σ, for which the first n coordinate functions of $F_{f,\vec{\eta},B}$ are zero, at least one minimizes the last coordinate of $F_{f,\vec{\eta},B}(x)$, which is a strictly positive quantity: the distance between $(x, f(x))$ and $\mathcal{H}(B,\vec{\eta})$. Such a point is a solution of the nonlinear least squares problem:

$$\min_{x\in\Sigma} \left\|F_{f,\vec{\eta},B}(x)\right\|^2 \qquad (6)$$

The global optimization problem $\min_{x\in\Sigma} \left\|F_{f,\vec{0},B}(x)\right\|^2$ is an alternate formulation of the global optimality conditions (1). We choose to solve the minimization problem (6) for $\vec{\eta}$ such that $\|\vec{\eta}\| \leq N_{\Sigma,\mathrm{f}}$ in order to guarantee the existence of a solution. Assuming the minimum value $\min_{x\in\Sigma} \left\|F_{f,\vec{\eta},B}(x)\right\|^2$ is a continuous function of $\vec{\eta}$, the smaller the value of $\|\vec{\eta}\|$, the closer the solution of $\min_{x\in\Sigma} \left\|F_{f,\vec{\eta},B}(x)\right\|^2$ to the solution of $\min_{x\in\Sigma} \left\|F_{f,\vec{0},B}(x)\right\|^2$.

So, let us consider now that we try to solve $\min_{x\in\Sigma} \left\|F_{f,\vec{\eta},B}(x)\right\|^2$ with:

$$0 < \|\vec{\eta}\| \ll 1 \qquad (7)$$

The choice $0 < \|\vec{\eta}\|$ is justified later.

Figure 1 illustrates the geometrical meaning of Eq. (6). For a given function f, bounded below on a convex domain Σ, $\mathcal{H}(B,\vec{\eta})$ is a minorant hyperplane of the representative surface of $f_{|\Sigma}$. A solution of this optimization problem is a point x_* where the tangent hyperplane to the representative surface is normal to $(\vec{\eta}, -1)$ and for which the distance to $\mathcal{H}(B,\vec{\eta})$ is minimal. Provided that $\mathcal{H}(B,\vec{\eta})$ is horizontal enough, a solution exists.

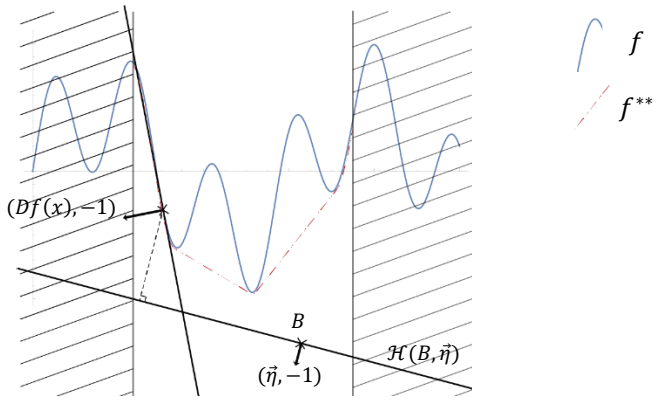

Figure 1: Trying to find a supporting hyperplane parallel to $\mathcal{H}(B,\vec{\eta})$.

As stated in (Ferreira et al., 2011), when the derivative of $\left\|F_{f,\vec{\eta},B}(x)\right\|^2$ is injective, finding stationary points of $\left\|F_{f,\vec{\eta},B}(x)\right\|^2$ "is equivalent to finding a least squares solution of the overdetermined nonlinear equation":

$$F_{f,\vec{\eta},B}(x) = 0 \quad (8)$$

The Gauss-Newton method can be applied to Eq. (8). If it converges to $x_* \in \Sigma$, x_* is a stationary point of $\left\|F_{f,\vec{\eta},B}(x)\right\|^2$, "but we cannot conclude that x_* is a solution of Eq. (6) or $F_{f,\vec{\eta},B}(x_*) = 0$". This paper takes full advantage of the local convergence analysis of the Gauss-Newton method detailed in (Ferreira et al., 2011) for identifying unicity balls around some stationary points x_* of $\left\|F_{f,\vec{\eta},B}(x)\right\|^2$ where $Df(x_*) = \vec{\eta}$. When the Gauss-Newton method, starting from an initial point, reaches such a stationary point x_*, we can quantify the radius r of a ball $B(x_*, r)$ containing only one stationary point of $\left\|F_{f,\vec{\eta},B}(x)\right\|^2$. Combining this inclusion approach with an exclusion approach –exclusion theorems, like in (Dedieu et al., 1996), state that within a given ball there is no candidate for solving some problem- one can build a subdivision method to minimize $f_{|\Sigma}$.
Theorem 18 from (Ferreira et al., 2011) gives quantitative values for the radii of the convergence balls and of the unicity balls including stationary points. More precisely:

Let $\Omega \subseteq \mathbb{X}$ be an open set, and let $F: \Omega \to \mathbb{Y}$ be a continuously differentiable function. Let $x_* \in \Omega$ and $c := \|F(x_*)\|$, $\beta := \|F'(x_*)^\dagger\|$, $\kappa := sup\{t \in [0, R): B(x_*, t) \subset \Omega\}$.
Suppose that $F'(x_*)^* F(x_*) = 0$, $F'(x_*)$ is injective, and that there exists a $K > 0$ such that $\sqrt{2}c\beta^2 K < 1$, $\|F'(x) - F'(y)\| \leq K\|x - y\|$, $\forall x, y \in B(x_*, \kappa)$.
Let $r := min\{\kappa, (2 - 2\sqrt{2}K\beta^2 c)/(3K\beta)\}$. Then, the Gauss–Newton method for solving (6), with initial point $x_0 \in B(x_*, r)/\{x_*\}$, $x_{k+1} = x_k - F'(x_k)^\dagger F(x_k)/k = 0,1, .../$ is well defined, the sequence generated $\{x_k\}$ is contained in $B(x_*, r)$, converges to x_*, and $\|x_{k+1} - x_*\| \leq \frac{\beta K}{2(1-\beta K\|x_0 - x_*\|)}\|x_k - x_*\|^2 + \frac{\sqrt{2}c\beta^2 K}{1-\beta K\|x_0 - x_*\|}\|x_k - x_*\|/k = 0,1, ... 1$
Moreover, if $(2 - 2\sqrt{2}K\beta^2 c)/(3K\beta) < \kappa$, then $r = (2 - 2\sqrt{2}K\beta^2 c)/(3K\beta)$ is the best possible convergence radius.
If, additionally, $2c\beta_0 K < 1$, then x_* is the unique stationary point of $F(x)^* F(x)$ in $B(x_*, (2 - 2c\beta_0 K)/(\beta K))$, where $\beta_0 := \|[F'(x_*)^* F'(x_*)]^{-1}\|$.

When this theorem is applied to the overdetermined system Eq. 8, and when only stationary points x_* such that $Df(x_*) = \vec{\eta}$ are considered, the quantities appearing in the radii expressions become:

$$c = \frac{\|[\sum_{i=1}^n (x_i - b_i)\eta_i] - (f(x) - b_{n+1})\|}{\|(\vec{\eta}, -1)\|}, \beta = \|D^2 f(x_*)^{-1}\|, \beta_0 = \|[D^2 f(x_*)^2]^{-1}\| \quad (9)$$

4. An overdetermined system suited for Gauss-Newton method

Assuming that a least squares solution is found to Eq. (8), Figure 1 can be updated to display the corresponding optimal point $(x_*, f(x_*))$ and the tangent hyperplane at this point. This updated figure can be scaled along the y axis by a scaling factor $\theta > 0$. The resulting figure represents a least squares solution x_* to Eq. (10):

$$F_{\theta f,\overrightarrow{\theta\eta},(b_1,b_2,...,\theta b_{n+1})}(x) = \begin{pmatrix} \theta.D_1 f(x) - \theta.\eta_1 \\ \vdots \\ \theta.D_n f(x) - \theta.\eta_n \\ \frac{[\sum_{i=1}^n (x_i - b_i)\theta.\eta_i] - (\theta.f(x) - \theta.b_{n+1})}{\|(\theta.\vec{\eta}, -1)\|} \end{pmatrix} = 0 \quad (10)$$

For any $\theta > 0$, the least squares solutions of Eq. (8) and Eq. (10) are identical. However, when θ very large, solving Eq. (10) may be easier than solving Eq. (8). The quantities appearing in the radii expressions become:

$$\begin{cases} c_\theta = \frac{[\sum_{i=1}^{n}(x_i - b_i)\theta.\eta_i] - (\theta.f(x) - \theta.b_{n+1})}{\|(\theta.\vec{\eta}, -1)\|} = \frac{\theta.\|(\vec{\eta}, -1)\|}{\|(\theta.\vec{\eta}, -1)\|}.c \\ \beta_\theta = \|D^2\theta.f(x_*)^{-1}\| = \frac{\beta}{\theta} \text{ and } \beta_{0_\theta} = \|[D^2\theta.f(x_*)^2]^{-1}\| = \frac{\beta_0}{\theta} \end{cases} \quad (11)$$

Assuming that both Df and D^2f are Lipschitzian over Σ and that $\theta \geq 1$, $F_{f,\vec{\eta},B}$ is K-Lipschitzian over Σ, $F_{\theta f,\overrightarrow{\theta\eta},(b_1,b_2,\ldots,\theta b_{n+1})}$ is K_θ-Lipschitzian over Σ and:

$$K_\theta \leq \theta.K \quad (12)$$

Consequently,

$$c_\theta.{\beta_\theta}^2.K_\theta \leq c.\beta^2.K.\frac{\|(\vec{\eta}, -1)\|}{\|(\theta.\vec{\eta}, -1)\|} \quad (13)$$

When $\vec{\eta} \neq \vec{0}$ and $\theta \gg 1$, Theorem 18 is modified in a nice manner:

$$\begin{cases} c_\theta.{\beta_\theta}^2.K_\theta \approx 0 \text{ and } c_\theta.\beta_{0_\theta}.K_\theta \approx 0 \\ r_\theta \approx \frac{2}{3K_\theta\beta_\theta} \text{ and } R_{\theta,unicity} \approx \frac{2}{K_\theta\beta_\theta} \approx 3.r_\theta \end{cases} \quad (14)$$

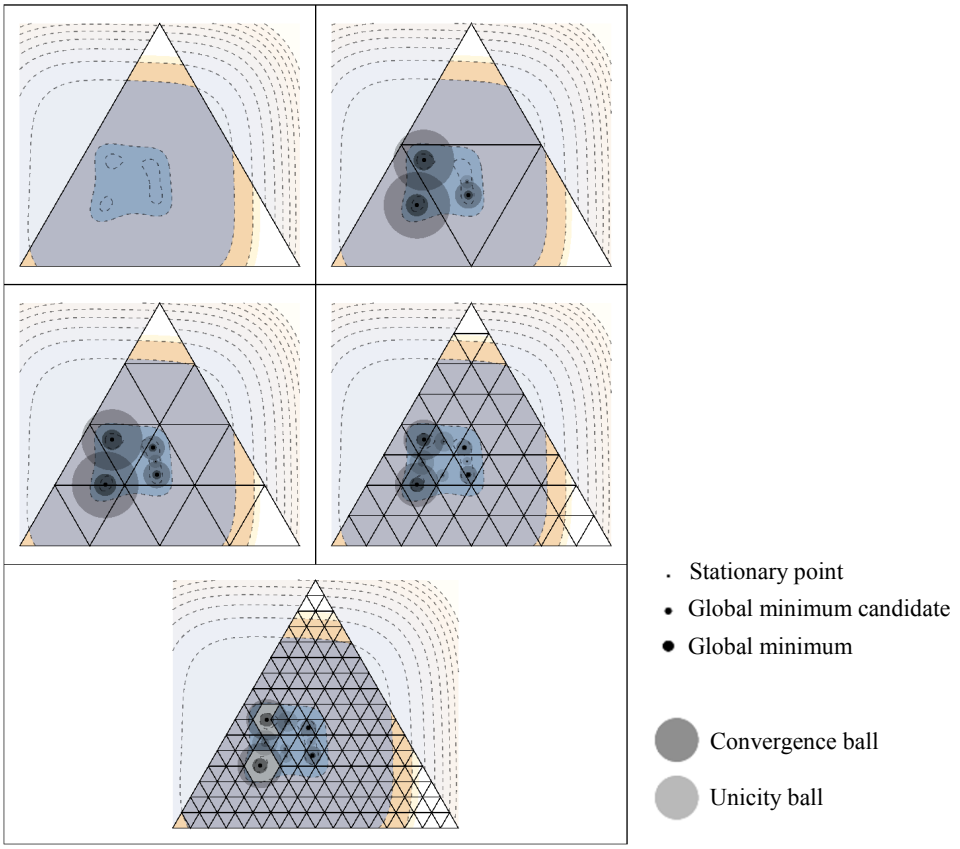

Figure 2: Locating the global minima of the Himmelblau function ($\|\vec{\eta}\| = 10^{-20}, \theta.\|\vec{\eta}\| = 10^{20}$)

From Eq. (14) we build a solving algorithm without information about the Lipschitz constants. We solve Eq. (10) by applying the Gauss-Newton method to a distributed set of initial points in Σ (Tóth et al., 2016). Whenever the sequence converges to a stationary point x_*, such that $Df(x_*) = \vec{\eta}$, we estimate numerically the convergence radius r_θ because it is also the quadratic convergence radius in this case. We get a ball centered on x_*, with radius $\mathrm{R}_{\theta,\mathrm{unicity}} \approx 3.\mathrm{r}_\theta$, containing only one stationary point: x_*. When several unicity balls are computed, the values of f at the stationary points are compared.

This global continuous optimization method is applied to the Himmelblau function $f(x) = (x^2 + y - 11)^2 + (x + y^2 - 7)^2$, which admits 4 global minima. In the top left image of Figure 2 we represent the level sets of the function and Σ, the research domain, a regular simplex containing the global minima. Step 1 (top right image), finds three global minima (not guaranteed at this time) and a local minimum. After step 2, the four global minima are located. Step three detects an inconsistency: K value estimated from the Gauss-Newton iterates is too small, so several unicity balls cover two stationary points. K value is increased according to the distances between the stationary points and the radii are reduced proportionally. At the end of step four, some singular simplices, covered by unicity balls, are removed from the research domain.

5. Conclusions

A global continuous optimization method has been introduced here. This deterministic approach is not certified, but is consistent with theoretical results related to the local convergence analysis of the Gauss-Newton method. By means of a criterion scaling, the radii of the unicity balls containing only one stationary point are enlarged. This allows us to build an inclusion-exclusion algorithm, which proved to be efficient on several usual test functions for optimization.

For the time being, this work suffers from two weak points. First, the radii of the unicity balls have been estimated under a Lipschitz condition. (Ferreira et al., 2011) gives another convergence result where the criterion is an analytical function. Its integration in our method is under progress. Second, usual exclusion theorems still have to be implemented in order to remove additional simplices, containing no global minima, from the research domain.

References

Androulakis I.P., Maranas C.D. and Floudas C.A., 1995, αBB: A global optimization method for general constrained nonconvex problems, Journal of Global Optimization, 7, Issue 4, 337-363.

Alloula K., Belaud J.-P. and Le Lann J.-M., 2011, An homotopy method for global optimization of continuous models, Chemical Engineering Transactions, 24, 325-330.

Dedieu J.-P., Gourdon J., Yakoubsohn J.-C., 1996, Computing the distance from a point to an algebraic hypersurface, Lectures in Applied Mathematics, 32, 285–293.

Ferreira O. P., Gonçalves M.L.N., Oliveira P.R., 2011, Local convergence analysis of the Gauss-Newton method using a majorant condition, Journal of Complexity, 27, 111-125.

Hiriart-Urruty J.-B., 1986, When is a point x satisfying $\nabla f(x) = 0$ a global minimum of f?, The American Mathematical Monthly, 93, Issue 7, 556-558.

Ryoo H.S. and Sahinidis N.V., 1995, Global optimization of nonconvex NLPs and MINLPs applications in process design, Computers & Chemical Engineering, 19, Issue 5, 551-566.

Stork J., Eiben A.E. and Bartz-Beielstein T., 2018, A new taxonomy of continuous global optimization algorithms, 2018arXiv180808818

Tóth B.G., Hendrix E.M.T., Casado L.G., 2016, On refinement of the unit simplex using regular simplices, Journal of Global Optimization, 64, 305-323.

Sauro Pierucci, Flavio Manenti, Giulia Bozzano, Davide Manca (Eds.)
Proceedings of the 30th European Symposium on Computer Aided Process Engineering (ESCAPE30), May 24-27, 2020, Milano, Italy.
http://dx.doi.org/10.1016/B978-0-12-823377-1.50335-9

A New Method for Food Production Analysis and Optimization Applied to Citrus Industry

Martina Raymo[a], Maria C. Rulli[b], Laura Piazza[c], Flavio Manenti[a], Giulia Bozzano[a]

[a]*Politecnico di Milano, Dept. DCMC, P.zza L. Da Vinci, 32, Milan, 20133, Italy*
[b]*Politecnico di Milano, Dept. DICA, P.zza L. Da Vinci, 32, Milan, 20133, Italy*
[c]*Università degli Studi di Milano, Department of Environmental Science and Policy (ESP), Via Celoria 2, Milan, 20133, Italy*
giulia.bozzano@polimi.it

Abstract

This work is aimed to present a method for analyzing and optimizing food production processes from the primary production until the final residue. The aim is to have a global view on the entire production chain in order to put in light, through a deep analysis, the strength and the weaknesses of the process and to propose solutions for its improvement and optimization. The solutions, of course, depend on which is the main objective of the involved production realities and consider also the location of the production. Here is reported the first case study, the citrus industry, which products are citrus juices and essential oils. In this case the authors individuated some solutions and started to develop some of them. The results will be here presented.

Keywords: Food Value Chain, Optimization, SWOT Analysis, Circular Economy

1. Introduction

This paper refers to the first steps of a project aimed to develop a methodology to perform the analyses and the optimization of any food value chain. The procedure has been structured using as a first case study the citrus industry.

In the literature, there are few other studies on the topic here dealt, and it appeared that none of the existing works considers the citrus production, and, in general, any food production from the cradle to the grave. Articles on treatments of secondary products (exhausted peel) (Negro et al., 2017, Zema et al., 2018) have been found as well as some on the water optimization for the transformation step (Beccali et al., 2010, Thevendiraraj et al., 2003). There are some books dealing with the processing of citrus fruits, providing details on the main production techniques, even better explained by the equipment producers themselves. Beside this, none of the works address both the primary production and the transformation.

The novelty brought by this article lies precisely in addressing both aspects, the primary production and the transformation, leaving out of the analysis only the logistics part. The reason why the study shall address both the aforementioned parts is related to the accuracy and completeness that a 360-degree analysis can provide. Another reason is the strong and unbreakable link that exists between these two worlds and that holds all the phases of the value chain together. The final quality of a food process depends on the technology used, but nothing can be done if the raw materials aren't excellent from the point of view of quality and environmental aspects related to the production. The data obtained from the entire production process have been analyzed by using a SWOT analysis enriched by

methods usually adopted by chemical engineering approach. This allowed to consider also the important aspects related to workers welfare and financial aspects related to the specific case study analyzed.

2. Objectives and Methodology

As aforementioned, the aim of the study is the definition of a method that thanks to a structured analysis allows to identify the existing gap of the value chain considered. The final goal of the citrus case is the presentation of innovative solutions to remove or reduce the detected issues. While structuring the study, defining each step and discovering the tools that best feted the needs, both the goals fixed for the "during construction" procedure and the citrus value chain have been accomplished.

The definition of all these needed steps has been done directly applying them to the case study. Some of the tools used are not typical of the engineering world (many of them are the results of talks with experts of other sectors: economics, design, mechanical and environmental engineering), giving to this work has an interdisciplinary face. Many of the information been collected during the visits to primary producers and the collaboration with the KOLs (Key Opinion Leaders) of both the sectors. The procedure adopted can be schematized as in Figure 1. It is a two-stage process, made of a theoretical and a practical part all of which is characterized by five sub-phases. To accomplish the theoretical stage the following tools have been adopted:

1. On site visits (three plantations and a plant), interview to the plantation holders, literature review. This helped in discovering what has been done in the field of multi-criteria optimization applied to food processes (Madoumier et al., 2019). Further, in the understanding of the value chain and in dividing it into macro-areas and sub-phases; it has further allowed to collect all the requested information to draw up the structured description.
2. SWOT (Strengths, Weaknesses, opportunities and Threats): it is a tool widely used in the world of strategic planning and is traditionally considered a form of brainstorming. It allows to investigate and at the same time identify and categorize in a 2x2 matrix the strengths and weaknesses (internal factors), opportunities and threats (external factors) typical of the area analyzed (Falcone et al., in press). The definition of the different points characterizing the matrix is often the result of qualitative considerations influenced by human subjectivity (Phadermrod et al., 2019). This make difficult to use the SWOT analysis as a single decision-making tool, since it is not only lacking in objectivity, but does not have an analytical method to prioritize the various activities identified for process optimization.

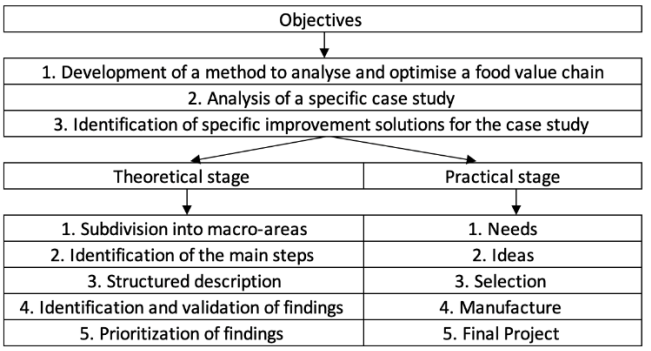

Figure 1- Objectives and Method

Here this technique is used to identify and validate the gap present in the citrus value chain and the critical issue aforementioned has been overcome using the tools and knowledge of the chemical engineering world.

3. Impact-Feasibility Map. It is a tool already seen and consolidated in areas such as Service Design, Enterprise Design Thinking and Project Management. It consists of a grid where the "impact" axis (y axis - on a low to high scale) expresses the importance and relevance that the proposal could have for users. The axis of "feasibility" (x-axis on a scale ranging from easy to difficult to realize) is instead connected to the feasibility of realization for the designer (information on how to realize it can be found in the IBM guide, "Design thinking field guide", (Johnson, 2016)). The aim of the amendments is to prioritize the result obtained from the SWOT analysis. This is the reason why the map just described has been modified, defining better the two parameters. The impact is quantified considering if the issues affect somehow the environment, the quality and yield, the selling price, the production speed and efficiency, the automation, the customer satisfaction and the worker safety. In the same time a note from high to low is given for the feasibility with respect to time, cost, resources needed to remove the gap.
4. For the realization of the practical phase the methodology used belongs to the Chemical Product Design (CPD) world. CPD is a branch of chemical engineering that deals with the development of new chemicals by acting as an interface between the world of consumers and industry, identifying customer needs and translating them into commercial products (Moggridge & Cussler, 2000). The typical steps of the CPD methodology are those shown here in bold and to apply them it appeared necessary to organize the analysis as follows:

Needs - Identification of the company's needs to answer the question: Which weak point characterizing the supply chain, the company must address? To answer the question the information used is the one collected during the field visits (farms and plantations), the writing of the structured description, the interviews with KOLs and the analysis of market trends.

Ideas - Presentation and characterization of improvement ideas. These possible solutions are for the sake of simplicity presented in a table in the form of a solution-criticality binomial.

Selections - Choosing the most appropriate solutions. This step can be made on the basis of the results obtained from the prioritization or following what has emerged from the needs identification steps. At this point, in order to support the decision making, heat and mass balances have been realized. This has made easier the decision-making procedure and has allowed to quantify the impact connected to the production (in terms of energy, water and wastes produced).

Manufacturing - Implementation of the selected solutions. To achieve these goals many tools have been used. For examples to quantify the amount of water needed for the plant (crop water requirement) a software called CROPWAT® has been used. It allows to quantify the amount of water needed for the cultivation of citrus fruits taking into account the climatic conditions and soil specific to the geographical area where the plantation is located. To accomplish the implementation of other solutions were helpful: Food Engineering-Unit Operations (Ibarz & Barbosa-Cánovas, 2002) and articles on filters, literature review (water legislation and filter technologies), interview and market analysis.

Figure 2- Relevant aspects of the analysis

Final project - Presentation of the results achieved. This might appear trivial, but due to the fact that the whole study has been structured on the idea of collaborating with the real world, it is also extremely relevant how the results are presented. This is the reason why for each solution implemented the results must refer to aspects reported in Figure 2.

3. Results and Discussion

The just introduced methodology has been followed to analyse the selected case study. The primary production of citrus value chain consists in the planting, cultivation and harvesting of lemons, oranges, tangerines, and bergamots from which during the transformation step the essential oil and the juice are obtained as main products and the exhausted peel as by-products. The production is characterised by both liquid and solid wastes that need to be treated and managed. While applying the first two steps of the method, it appeared that the production can be divided into four macro-areas each one characterised by its own subphases: 1)Primary production: planting, cultivation, harvesting; 2) Up-stream processes: unloading, visual inspection, washing; 3) Extraction: primary and secondary extraction; 4) Downstream processes: by-products, wastewater and solid wastes treatments, packaging and shipping.

The third step of the theoretical part allowed to acknowledge on the topic, collecting all the information needed for the next steps and understanding if there were any weak bond in the chain. The carried-out SWOT analysis putted on the light 18 findings and was used to both identify and validate them. Then a feasibility, impact map has been generated, (Table 1). Looking at Table 1 the number of crosses (from 1 to 8) gives the number related to process impact, the Low (L), Medium (M), High (H) have a corresponding number, respectively, 5,3 and 1 and are linearly organized in order to deduce the final feasibility. These critical issues have been so used, obtaining the map reported below (Figure 3). The findings present in the rectangle on the top right are the one that should be addressed immediately because with higher impact and feasibility: human error in visual inspection of fruits, visual inspection by a single operator, no recovery of washing and purified water, accumulation and dependence for fruits peelings treatment.

Once obtained the prioritised goals, the identification of the needs, ideas were sought to improve the chain, removing or reducing the weaknesses previously identified. Some of them were just mentioned and presented in the binomial form (criticality-ideas), others deeply investigated and presented in tables (here not reported for space reasons). Each table addressed the following points: hint, recourse needed, advantages, disadvantages,

how to carry it out. The ideas were then selected according to the needs and prioritized following the impact-feasibility map. At the end of the third step, the solutions that appeared to have all the wanted characteristic were three, therefore three were the weaknesses faced.

Table 1 – process impact and feasibility map

	Impact								Feasibility				
Critical issues	Environment	Quality & Yield price	Sell	Production rate	Production Efficiency	Safety	Automation	Customer satisfaction	Time	Costs	Resources	Resulting impact	Average feasibility
1.1. No recovery of irrigation water	X							X	H	M	L	2	3
1.2 Non efficient irrigation and fertilization	X	X		X				X	M	H	L	4	3
1.3 unquantified environmental impact	X		X					X	H	H	H	3	1
2.1 Manual handling of fruits and its consequences				X	X		X		M	H	L	3	3
2.2 use of trucks	X							X	H	M	L	3	3
2.3 randomly transport of fruits (no bins)		X					X		L	L	H	2	1
2.4 crushing of fruits in silos		X							M	H	M	1	2.5
2.5 human error in visual inspection of fruits		X	X		X		X		M	M	L	4	4
2.6 Visual inspection by a single operator		X	X	X	X	X			L	L	L	5	5
2.7 fruits with internal damages		X	X				X		L	H	L	3	3.5
2.8 No recovery of washing water	X		X					X	M	L	L	3	4.5
3.1 production standardisation		X	X	X	X			X	H	M	M	5	3
3.2 partial recovery of cooling water	X		X					X	H	H	M	3	1.5
3.3 energy from non-renewable resources	X		X					X	M	M	M	3	3
3.4 not optimized juice extractors		X	X					X	M	H	M	3	1.5
4.1 no recovery of purified water	X		X					X	L	M	L	3	4.5
4.2 waste water plant with no coverage	X					X			H	H	L	2	2
4.3 accumulation and dependence for fruits peelings (pastazzo) treatment	X		X		X			X	L	H	L	4	3.5

The implementation of the solutions allow the value chain to develop a sustainable agriculture, have a zero-wastewater production, move a first step in the direction of the circular economy. As a final result of the application of the method a ten years project has been obtained to improve the value chain. The goals to be achieved are fixed every two years and they regard different areas of the analyzed chain (water and energy optimization, anaerobic digestor, automatization of the lines). As an example (and for lacking of space) the two first years goal resulted in: cropwat analysis for all the company suppliers, water recycle system implemented into the fruit washing circuit, plantation irrigated with the purified water, two operators for the visual quality control of fruits, transportation of fruits by using bins.

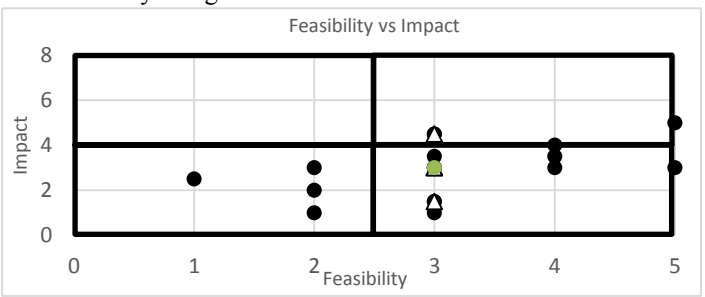

Figure 3- Feasibility vs Impact map

4. Conclusions

The method presented in this article appears to be a powerful tool to analyse and find solutions to optimise a food value chain. The first part of the theoretical stage allows to become experts of the sector investigated, while the second part, always of the theoretical stage, assures the identification of the strengths, the weaknesses, the opportunities and the threats of all the component areas of the chain. Besides, thanks to the prioritization process proposed the decision-making step is more objective and less dependent on whom is carrying out the analysis. Being interested in the optimization it is important to be able to easily select and define in which order addressing the critical issues.
The uniqueness of the approach is related to the possibility of finding solutions and therefore carry out projects to improve the chain having a global vision of the system.
It is the first time that the entire value chain has been studied within the same project allowing to find improvements for each of the two areas (primary production and transformation). The method gives the opportunity to work in line with the identified needs of the chain but at the same time it allows to detach from them by finding non inherent solutions. At the end of the analysis, together with the ten-years project also a has been obtained. The latest stress the importance of considering the workers, as a human being (soft skills) and as a member of a group (communication). A further results is the deduction of a way to improve the workspace, the security and safety of the workers, covering also the issue of plastic-free environment. Once again this underlines the ability of the method to take care of many different aspects. It comes up with a way to consider in the analysis also sustainability, that actually entails factoring in food production as well as processing.

References

Beccali M., M. Cellura, M. Ludicello, M. Mistretta, 2010, *Life cycle assesment of Italian Citrus-based products. Sensitive Analysis and imporvememtns scenario*, Journal of Environmental Management, 91(7), 1415-1428

Falcone P.M., A.Tani, V.E. Tartiu, C. Imbriani, 2020, *Towards a sustainable forest-based bioeconomy in Italy: Findings from a SWOT analysis*, Forest Policy and Economics, 110, 101910

Ibarz A., G.V. Barbosa-Cánovas, 2002, *Unit operations in food engineering*, Taylor & Francis Group, editor G.V. Barbosa-Cánovas

Johnson S., 2016, *Design Thinking Field Guide*, IBM, 1–46

Madoumier M., G. Trystram, O. Sèbastian, A. Colligan, 2019, *Towards a holistic approach for multi-objective optimization of food processes. A critical review*, Trends in Food Science and Technology, 86(feb), 1-15

Moggridge G. D, E.L. Cussler, 2000, *An introduction to chemical product design, Chemical Engineering Research and Design*, 78(1), 5–11

Negro V., B. Ruggeri, D. Fino, D. Tonini, 2017, *Life Cycle Assesment of orange peel waste management*, Resources, Conservation & Recycling. 127(September),148–158

Phadermrod B., R.M. Crowder, G.B. Wills, 2019, *Importance-Performance Analysis based SWOT analysis*, International Journal of Information Management, 44, 194–203

Thevendiraraj S., J. Klemeš, D. Paz, G. Aso, G.J. Cardenas, 2003, *Water and wastewater minimisation study of citrus plant*, Resource, Conservation and Recycling, 37(3), 227-250

Zema D. A., P.S. Calabrò, A. Folino, V. Tamburino, G. Zappia, S.M. Zimbone, 2018, *Valorisation of citrus processing waste: a review*, Waste Manag., 80, 252-273

Sauro Pierucci, Flavio Manenti, Giulia Bozzano, Davide Manca (Eds.)
Proceedings of the 30th European Symposium on Computer Aided Process Engineering (ESCAPE30), May 24-27, 2020, Milano, Italy.
http://dx.doi.org/10.1016/B978-0-12-823377-1.50336-0

Integration of Interactive CFD Simulations with AR and VR for Educational Use in CRE

Serkan Solmaz*, Tom Van Gerven
Department of Chemical Engineering, KU Leuven, Leuven 3001, Belgium
serkan.solmaz@kuleuven.be

Abstract
Engineering simulations have since long been considered an imperative design and analysis tool for chemical reaction engineering (CRE). Notably, reactor and process design are domains in which multiphysics computational fluid dynamics (CFD) simulations are applied to understand phenomena that are difficult, time-consuming or expensive to be explored with experiments. On the other hand, advanced post-processing methods and virtual reality can enable high-quality educational content with engineering simulations. Nevertheless, the utilization of these tools in education is still underdeveloped. This study explores the potential of integration of multiphysics CFD simulations with AR/VR and its educational use. By iterating on this potential we present a generic system architecture with inter-disciplinary consideration of two building stones: (1) Recent advancements in CFD & multiphysics simulations, and (2) Emerging immersive technologies. A case study is demonstrated applying the generic methodology in order to illustrate the integration. The study promotes a rich and engaging environment with engineering simulations where interactivity can be empowered to entertain learners with AR/VR. This will primarily assist enthusiasts to develop feasible complementary environments with simulations.

Keywords: Chemical reaction engineering, Computational fluid dynamics, Augmented reality, System architecture, Learning environment.

1. Introduction
Multiphysics CFD simulations, one of the most applied computer-assisted process engineering (CAPE) tools, have been a maturing method increasing comprehension of engineering design and analysis. However, the educational implementation of this tool is still directly made with engineering software which has a primitive educational context, thereby preventing students to understand challenging concepts. Augmented reality (AR) and virtual reality (VR) have been getting prevalent in society today including research and education (Suh and Prophet, 2018). The integration of interactive CFD simulations in AR/VR reveals supportive features such as advanced visualizations, interactivity, attractiveness of digital media and so forth. In that sense, a virtual environment with CFD simulations could yield remedies for this primitive context.
The interest in CRE and CFD on multiple scales has recently convinced researchers to consider AR/VR by promoting virtual process engineering (Li, 2015; Ge et al., 2019). Despite this, several ambiguities are still present concerning the integration of CFD simulations with AR/VR in terms of system architecture. The term system architecture has come to be used as a portrayal of the system that consists of software and hardware including their functionalities and interactions (Blach et al., 1998). The present study develops a methodology for a sustainable system architecture to integrate the desired digital simulation contents into AR/VR.

1.1. Interactive Multiphysics CFD Simulations in AR/VR

Multiphysics CFD simulations for CRE have received much interest in the past decade. To date, several commercial and open-source software packages have been developed providing miscellaneous options to design and analyze reactive flow phenomena (Tian et al., 2018). These result in a broad database in the literature illustrating and solving multiple spatio-temporal cases. Integrating CFD simulations with AR/VR recently received scholarly attention due to technical complexities related to system architecture. Berger et al. was among the first ones to develop a plausible workflow for implementing CFD simulation results in AR/VR using the Unity3D game engine. However, these early studies exhibit a manual integration of CFD and AR/VR with dedicated instruments, with no consideration given to system architecture (Berger and Cristie, 2015). Various approaches have since then been reported to deal with the hurdles encountered. Kim et al. proposed a cloud computing network to entertain users' interaction in VR with CFD simulations (Kim et al., 2018). More recently, Fukuda et al. examined system design parameters and network connections for visualization of CFD simulations at indoor environment with AR and mapped simulation results (Fukuda et al., 2019). Concerning data processing, Lin et al. developed a data format to reduce the data size of CFD dataset in a mobile device-based AR (Lin et al., 2019). A recent review by Li et. al on engineering simulations in AR found that systems were mostly developed for very unique elements due to the use of dedicated software, hardware, and platform. This eventually resulted in several constraints in terms of data- and workflow, thus the system architecture. It was also highlighted that most of the studies dismissed two-way coupling between CFD simulation and user-interaction, and merely focused on the visualization of simulation results (Li et al., 2017). Moreover, low-accuracy real-time CFD simulations with the Lattice-Boltzmann method were highlighted as an alternative to traditional CFD simulations. Harwood et al. claimed that interaction of real-time CFD simulations in VR generated with Unreal Engine 4 is applicable and can present a vivid advancement to simplify the system architecture. It was also mentioned that the integration of real-time CFD simulation with VR/AR brings its own hurdles for post-processing of CFD simulations (Harwood et al., 2018). Real-time CFD simulations are currently merely viable for oversimplified models, for instance, laminar external fluid flow. This raises many questions about whether real-time simulations could be applicable in the near future. An important downside of the above-mentioned studies is that they neglect a two-way coupling between CFD simulator and the end-user environment. Another major criticism is the need for dedicated software, hardware, data format, data processing method and thereby system architecture (Li et al., 2017). Every change or replacement of a building block in the system may affect the whole system architecture due to changes in the data- and workflow.

1.2. Utilization of CFD Simulations in Education

In spite of the friendly user-interfaces (UI), engineering simulation software is still lacking an educational approach. This can hence prevent lecturers to use these tools directly in education. Alternatively, a fully-integrated CFD simulation in VR might present a remedy to prevail over this uneasiness. Few studies have been published to support traditional learning methods with CFD simulations. Chemical process (Li, 2015), internal combustion engine (Tian and Abraham, 2014), biomedicine (Quam et al., 2015), and food engineering (Wong et al., 2010) were the recent application fields where CFD was promoted as a complementary asset. Glessmer et al. assessed the efficacy of low-accuracy real-time CFD simulations to teach the basics of fluid mechanics. Results showed that both students' interest and comprehension on the topic were increased with

using real-time CFD in an active learning environment (Glessmer and Janßen, 2017). The fundamental goal of the present research is to scrutinize the system design process of AV/VR with interactive multiphysics CFD simulations. Present study first proposes a methodology for a robust integration of CFD to AR/VR, then discusses a case study to illustrate the development of the digital environment, and finally dwells on the future direction of the proposed methodology.

2. Methodology

In our proposed methodology, integration of CFD simulations with AR/VR was demonstrated. To provide a sustainable integration, an approach was followed pinpointing each of the steps taken. This methodology presents a scaffold for a generic system architecture targeting two-way coupling.

2.1. Analysis of the system

To begin with, exploratory studies on integrating CFD simulation with AR/VR were performed using the methods available in the literature as reported in the introduction. CFD simulations from conventional to real-time and virtual environments from VR to AR were reviewed and evaluated in terms of the components of the system. Once a complete one-way integration was achieved, such as the visualization of streamlines in AR, steps taken throughout the integration were noted in the workflow and clustered with regards to the relevance of components. In this way, system components in the methodology were inclusively determined. This exploratory study indicated that software, hardware, bridging, add-in, networking and internet of things are the fundamentally required building blocks to develop a two-way coupled system architecture for interactive CFD simulations in AR/VR. In the second place, it was found that system architecture and end-user environment were also influenced by indirect components, namely academic content (Li et al., 2017) and learning analytics (Lai and Bower, 2019). Hamilton et al. reviewed an approach to design learning environments with relevant academic content and technological support. The study expressed the significant interference of indirect components to design a learning environment (Hamilton et al., 2016). In the present methodology only academic content was considered as an indirect component because of our focus on the system architecture.

2.2. Proposed methodology

A methodology was ultimately developed to establish a sustainable system architecture. A more generic, versatile integration was aimed at instead of using, for instance, a mere data format. The system architecture consists of components, requirements and indicators. Figure 1 outlines the proposed methodology integrating CFD simulation with AR/VR.

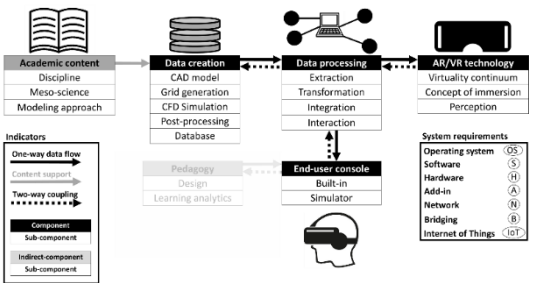

Figure 1. Proposed methodology for the system architecture to integrate process engineering simulation tools with AR/VR.

While components are the stages of workflow comprising dedicated tasks throughout the development of the end-user console, sub-components are the branches holding a responsibility to achieve devoted tasks. Indirect-components do not have any interference on the workflow, but may affect the requirements of components. System requirements are the

specified platforms utilizing a variety of options to execute the tasks attained for each component. A sub-component must also be designed by selecting at least one of the requirements. Lastly, indicators are illustrated as binders of the components to outline the data flow. We believe this method represents a viable alternative to the literature.

3. Case study

A case study was carried out to evaluate the proposed system architecture. For simplicity, a benchmark CFD study was selected where we evaluated the run-time of calculations and validation. Being a mature application in CRE, the mixing process inside a stirred tank was simulated and results were visualized with mobile marker-based AR. Requirements used for each component were selected intuitively based on functionality, license, and customer support. All of the softwares used in the following sections were either open-source or accessible with a free personal-developer license. Neither commercial utilization or broadcasting was aimed at.

3.1. CFD Simulations

Initially, 3D geometry was designed with FreeCAD v0.18.4. Grid generation, pre-processing and calculations were performed through the use of pimpledymfoam in OpenFOAM v3.0.1. Extraction of the simulation dataset was done with ParaView v5.6.0. Once data processing was performed, the dataset was stored in the internal hard disk. The hardware employed was a Dell Precision 5530 Notebook (processor Intel(R) Core (TM) i7-8850H CPU @ 2.60GHz, 2592 MHz, 6 Cores, 12 Logical processors) with both Linux Ubuntu 16.04 and Microsoft Windows 10 as operating systems.

3.2. Development of AR application

Due to the customer support, Unity 3D 2019 game engine was chosen to develop the AR application. Although several AR software are available on the market, Vuforia was applied which provides a plug-in to enable its functionalities in Unity. Hence, by using Unity with the Vuforia plug-in, the required software for the development of AR was limited to one single platform. Interaction between the AR application and the real environment was realized with marker-based detection as an easy-to-adapt feature. Any kind of marker can be implemented depending on the developers' preferences. A procedure before final use should be set up online via the website of Vuforia to optimize detection and stability of the selected marker. In the present study human-computer interaction (HCI) was implemented by applying virtual buttons with Vuforia. This feature allowed to increase user-immersion further. The same laptop was used for the development of the application.

3.3. Integration

In Table 1 the workflow used in the case study is shown. Direct import of CFD data to Unity was the bottleneck because these software were using non-identical data formats. Therefore it was evident that an intermediate software must be considered to make processing possible. Blender v2.8 was chosen due to its versatile features for modeling 3D datasets. By comparing import and export data formats of ParaView, Blender and Unity, data processing without any data loss was only attainable with a single method. Once CFD simulation was completed and saved as raw C++ document, the data was then processed with ParaView and extracted to '.x3d' format. Afterwards Blender was used to transform '.x3d' to '.fbx', thereby making the dataset usable in Unity without any data loss. Not surprisingly, a major hindrance was found in the post-processing of the CFD results. Generating an iso-surface from the streamline visualized in Unity was impractical. Both iso-surfaces and streamlines should separately be post-processed in ParaView prior to data processing. Despite this handicap, ParaView and Blender are both environments that are based on Python programming language. A bridge can, therefore, be applicable between ParaView and Unity to solve this issue

Table 1. Workflow of the case study developed based on the proposed methodology.

Component	Data creation					Data processing	
Sub-component	CAD	Grid	Simulation	Post-processing	Database	Extraction	Transformation
OS	Windows	Ubuntu	Ubuntu	Ubuntu	Ubuntu	Windows	Windows
Software	FreeCAD	OpenFOAM	OpenFOAM	ParaView	File-based	ParaView	Blender
Hadrware	laptop	laptop	laptop	laptop	laptop	laptop	laptop
Add-in							
Network							
Bridging	Python	C++	C++	Python		Python	Python
IoT							
Order of workflow	1	2	3	4	6	5	7

Table 1. Workflow of the case study developed based on the proposed methodology.

Data processing		AR/VR technology			End-user console	
Integration	Interaction	Virtuality continuum	Concept of immersion	Perception	Built-in	Simulator
Windows	Android	Windows	Android	Android	Windows	Android
Unity	Vuforia	Unity	Vuforia	Vuforia	Unity	Mobile application
laptop	smartphone	laptop	smartphone	smartphone	laptop	smartphone
Vuforia	Marker	Vuforia	Virtual button	Camera	smartphone	Marker
LAN & WLAN					USB	
C#	C#	C#	C#	C#	C#	C#
11	12	8	9	10	13	14

Applying system requirements for each sub-component gave a detailed workflow of the case study. It revealed that various softwares are available in the literature for tasks executed by each sub-component with different data formats. Nevertheless, direct integration was not possible without an intermediate data processing tool. A laptop and a smartphone were used to perform integration and to build the end-used application for mobile augmented reality, respectively. Interestingly, to give extra functions to both software and hardware, add-ins were found advantageous. This made workflow much more structured to express necessities clearly for each components. Another requirement that should not be dismissed was the network. It was experienced that the internet connection was needed to activate Vuforia plug-in inside Unity. The design of the marker for AR was also done through the website of Vuforia. To generate an AR application in a smartphone using Unity, a connection was realized between laptop and smartphone with a USB cable. The study also showed that communication between sub-components could be compatible with bridging different programming languages. Eventually, a two-way coupling might be developed between components. Further elaborations showed that the internet of things (IoT) could be an imperative asset to increase the level of communication and interaction among sub-components. The order of workflow presents a sequence for the particular case study. It can be readjusted in the other studies on purpose, for instance bridging.

3.4. End-user Console

A mobile application was generated with Unity 2019 to visualize the simulation results into mobile marker-based AR. Smartphone-based head-mounted display with Samsung A20e with Android Pie 9 was used to run the application for end-user interaction.

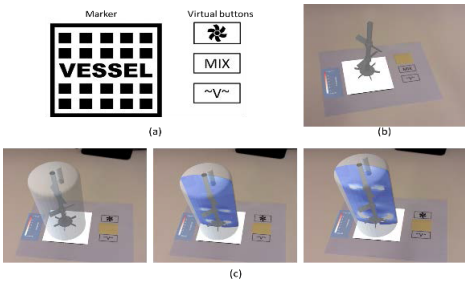

Figure 2. Mobile marker-based AR application; (a) marker and virtual buttons; (b) impeller; (c) visualization of transient CFD simulation.

Figure 2 illustrates the mobile AR application developed.

4. Conclusion

In this paper, we explored the integration of multiphysics CFD simulations with AR/VR. A methodology was presented to develop a sustainable system architecture. The results from this study indicate that the integration has significant potential to exploit multiphysics CFD simulation in AR/VR. This opens up new opportunities for developers dealing with engineering simulations to create desired digital content and integrate them with AR/VR. The research mainly stressed the importance of a sustainable system architecture by means of components, requirements, and indicators. A generic system architecture was proposed allowing alternative workflow and dataflow in the integration. Special attention should be paid by developers on dataflow to the integration of simulation data with AR/VR without the need of compromising on certain required datasets. This also underlines the importance of a database including a variety of complexities for CFD modeling from real-time to high accuracy. The present study only investigated a single way of dataflow. Therefore, future work will concentrate on accomplishing a two-way coupling. This will eventually deploy a sustainable integration.

Acknowledgements

This project has received funding from the European Union's EU Framework Programme for Research and Innovation Horizon 2020 under Grant Agreement 812716. This publication reflects only the author's view exempting the Community from any liability. Project website: https://charming-etn.eu/.

References

Berger, M., Cristie, V., 2015. CFD Post-processing in Unity3D. Procedia Computer Science 51, 2913–2922. https://doi.org/10.1016/j.procs.2015.05.476

Blach, R., Landauer, J., Rösch, A., Simon, A., 1998. A highly flexible virtual reality system. Future Generation Computer Systems 14, 167–178. https://doi.org/10.1016/S0167-739X(98)00019-3

Fukuda, T., Yokoi, K., Yabuki, N., Motamedi, A., 2019. An indoor thermal environment design system for renovation using augmented reality. Journal of Computational Design and Engineering 6, 179–188.

Ge, W., Guo, L., Liu, X., Meng, F., Xu, J., Huang, W.L., Li, J., 2019. Mesoscience-based virtual process engineering. Computers & Chemical Engineering 126, 68–82.

Glessmer, M., Janßen, C., 2017. Using an Interactive Lattice Boltzmann Solver in Fluid Mechanics Instruction. Computation 5, 35. https://doi.org/10.3390/computation5030035

Hamilton, E.R., Rosenberg, J.M., Akcaoglu, M., 2016. The Substitution Augmentation Modification Redefinition (SAMR) Model: a Critical Review and Suggestions for its Use. TechTrends 60, 433–441.

Harwood, A.R.G., Wenisch, P., Revell, A.J., 2018. A real-time modelling and simulation platform for virtual engineering design and analysis, in: Proceedings of 6th European Conference on Computational Mechanics (ECCM 6) and 7th European Conference on Computational FluidDynamics (ECFD 7). Glasgow, UK.

Kim, M., Yi, S., Jung, D., Park, S., Seo, D., 2018. Augmented-Reality Visualization of Aerodynamics Simulation in Sustainable Cloud Computing. Sustainability 10, 1362. https://doi.org/10.3390/su10051362

Lai, J.W.M., Bower, M., 2019. How is the use of technology in education evaluated? A systematic review. Computers & Education 133, 27–42. https://doi.org/10.1016/j.compedu.2019.01.010

Li, J., 2015. Approaching virtual process engineering with exploring mesoscience. Chemical Engineering Journal 278, 541–555. https://doi.org/10.1016/j.cej.2014.10.005

Li, W., Nee, A., Ong, S., 2017. A State-of-the-Art Review of Augmented Reality in Engineering Analysis and Simulation. Multimodal Technologies and Interaction 1, 17. https://doi.org/10.3390/mti1030017

Lin, J.-R., Cao, J., Zhang, J.-P., van Treeck, C., Frisch, J., 2019. Visualization of indoor thermal environment on mobile devices based on augmented reality and computational fluid dynamics. Automation in Construction 103, 26–40. https://doi.org/10.1016/j.autcon.2019.02.007

Quam, D.J., Gundert, T.J., Ellwein, L., Larkee, C.E., Hayden, P., Migrino, R.Q., Otake, H., LaDisa, J.F., 2015. Immersive Visualization for Enhanced Computational Fluid Dynamics Analysis. Journal of Biomechanical Engineering 137, 031004. https://doi.org/10.1115/1.4029017

Suh, A., Prophet, J., 2018. The state of immersive technology research: A literature analysis. Computers in Human Behavior 86, 77–90. https://doi.org/10.1016/j.chb.2018.04.019

Tian, Y., Demirel, S.E., Hasan, M.M.F., Pistikopoulos, E.N., 2018. An overview of process systems engineering approaches for process intensification: State of the art. Chemical Engineering and Processing - Process Intensification 133, 160–210. https://doi.org/10.1016/j.cep.2018.07.014

Tian, Z.F., Abraham, J., 2014. Application of Computational Fluid Dynamics (CFD) in Teaching Internal Combustion Engines. International Journal of Mechanical Engineering Education 42, 73–83.

Wong, S.Y., Connelly, R.K., Hartel, R.W., 2010. Enhancing Student Learning in Food Engineering Using Computational Fluid Dynamics Simulations. Journal of Food Science Education 9, 90–97.

Sauro Pierucci, Flavio Manenti, Giulia Bozzano, Davide Manca (Eds.)
Proceedings of the 30th European Symposium on Computer Aided Process Engineering
(ESCAPE30), May 24-27, 2020, Milano, Italy.
http://dx.doi.org/10.1016/B978-0-12-823377-1.50337-2

Motivational Active Learning in Chemical Engineering

Manuel Rodríguez, Emilio J. González, María González-Miquel, Ismael Díaz

Departamento de Ingeniería Industrial y del Medio Ambiente, ETSI Industriales, Universidad Politécnica de Madrid, Calle de José Gutiérrez Abascal, 2, 28006 Madrid

Manuel.rodriguezh@upm.es

Abstract

This paper presents how a new integrated innovative educational approach and shows how it helps students to improve their learning and understanding of the different concepts and thus to get better results in the subject and to achieve the desired outcomes. The approach is applied to core subjects taught in the Bachelor Degree in Chemical Engineering at the Technical University of Madrid. Different methodologies have been integrated and used as: flipped classroom, peer instruction, gamification, augmented reality, case-based learning, design thinking. In order to implement the mentioned methods, the following educational material has been developed: screencasts, concept tests, board games, augmented reality applications and simulations besides the traditional lecturing material (slides and text). Preliminary results show high student motivation, higher participation in class and better academic results.

Keywords: active learning, adaptive learning, flipped classroom, gamification, peer instruction

1. Introduction

Universities appeared more than 900 years ago, since the beginning lecturing has been, and still is in many places, the usual way of teaching. In the last 30 years new theories have appeared challenging the traditional approach. There is a change of paradigm as instruction now is seen as focused on learning and not on teaching and besides in this new paradigm an instructional method that engages students in the learning process seems fundamental. The importance of interest and motivation in education is not new, back in 1913 prof. John Dewey wrote an essay titled "Interest and effort in education" (Dewey,1913) where he indicated the influence of interest to achieve better results in education. The way our brain and cognitive processes work are still research subjects, everybody has experienced how differently we learn things depending on our interest in them (Renninger and Hidi, 2016, Harackiewicz et al., 2016, Shin et al., 2019). Active learning can be defined as "instructional activities involving students in doing things and thinking about what they are doing" (Bonwell,1991) or as "any instructional method that engages students in the learning process" (Prince, 2004). Previous approaches related to the implementation of active learning can be found in (Wilson and Jennings, 2000; Belcher, 2003; Beichner et al., 2007 or Nelson et al., 2019). The approach presented in this paper is closer to the format presented in Pirker et al. (2014).

2. Motivational Active Learning Integrated Approach

2.1. Motivation

Chemical Engineering is a Bachelor´s Degree that includes the design of industrial processes that turn raw materials into valuable products. Moreover, many of the processes within chemical engineering involve complex operations, which should be considered in order to formulate more adequate designs. It needs a thorough understanding of how the different unit operations are included in a chemical plant and what are the implications of changing operation variables in a process. All these concepts are difficult to grasp for many students and they stay in a quite passive attitude, so a different innovative approach has been implemented in order to increase students´ understanding, motivation and participation. The focus is on learning (instead of teaching) and motivating (or engaging) the students on the different subjects.

2.2. Objectives

The main objective is to foster a student-centred learning methodology. A motivating active learning integrated approach that allows a personalized evolution of the student. This objective is decomposed in the following subobjectives:

Implement a new student-centred learning methodology
Increase student motivation and participation in class
Increase the understanding of the more complex concepts by the students
Increase student results and the outcomes acquired
Increase student acquisition of transversal competences
Increase student awareness of the importance of sustainability
Increase student soft skills capabilities: creativity, leadership, communication and teamwork
Make the students aware of the importance of self-learning

The purpose of this work is to promote an active learning based on the joint use of several methodologies (flipped classroom, peer instruction, gamification, augmented reality, case-based learning, design thinking) in several subjects of the Chemical Engineering Degree at the Technical University of Madrid. Specifically, this approach has already been implemented in Process Control (4th course), Process and Product Design (4th course), Chemical Reactors (3rd course) and Chemical Engineering Lab III. Of course, not all the objectives are worked on with the same intensity in all the mentioned subjects.

2.3. Methodologies

Following the used methodologies are presented. Their use in the different subjects is commented on section 3.

2.3.1 Flipped Classroom

In this methodology educational material is provided to the students in advance of the lecture. The student has to learn by himself the contents of the topic that will be further discussed in class. The material developed has been mainly educational videos/screencasts. It has been complemented with traditional material such as slides or texts. One of the important benefits of this methodology is that it allows to spend more time in class for specific, more complex, parts of a topic. In order to decide what concepts are more difficult, flipped classroom must be combined with other methodologies like

peer instruction. In this way, the students are the ones who establish what is being harder to understand instead of the teacher

2.3.2 Adaptive learning & Peer Instructions

Adaptive learning and peer instruction are implemented using concepts tests. These tests are presented at the beginning of the class. Individual comprehension can be evaluated in this way. After the test, the students gather in small groups and think about the more difficult topics, then the tests are run again and finally the teacher explains the topic in detail.

2.3.3 Gamification

The purpose of gamification is to improve the classroom experience, it helps to motivate the students and what they learn is fixed more deeply (and thus more easily recalled afterwards). This is a very valuable methodology, but it has to be used carefully, as there is a risk that the students focus more on the "game" than on to the learning process.

2.3.4 Team work & peer learning

In peer learning the students explain things to each other without the teacher being involved. Student learn from their peers. This is implemented mainly dividing the class into small groups and then an activity is presented to them. It can be a problem that solved by each group or a laboratory practice. In some cases, the solution of the problem (or the results of the practice) is handed to other group which corrects and evaluates it.

2.3.5 Learning by doing

When using learning by doing (meaning that the students not only listen and watch), the student effectively does something that allows him to understand the theory or validate it. This methodology is very efficient as the students retain more easily what they learn.

2.3.6 Traditional teaching

In this methodology the approach is lecturing using slides to explain, usually, theory. In order to promote class participation and involvement, some blanks are in the presentation and some quizzes are also inserted where the students see the results in real time.

2.3.7 Case-based reasoning. Design thinking.

Open problems are presented to the students (mainly in the process & product design subject). These problems are very focused on sustainability and on working the SDGs (Sustainable Development Goals)

2.3.8 Augmented reality

Finally, the last methodology used is augmented reality. Different videos and guides have been prepared for the equipment used in the Laboratories. The students know how they work and besides they have access to the description of the task they have to follow. Auresma software has been used for Augmented reality.

It is important to stress that the main idea is to use several methodologies in a subject, in this way the student is more alert, motivated and keen to learn and fix what they learn. In order to implement the mentioned methods, the following material has been developed: screencasts, concept tests, trivia contest, simulations, augmented reality material and case-based studies besides the traditional lecturing material (slides and text). Fig.1 shows the methodologies used to motivate and engage the students.

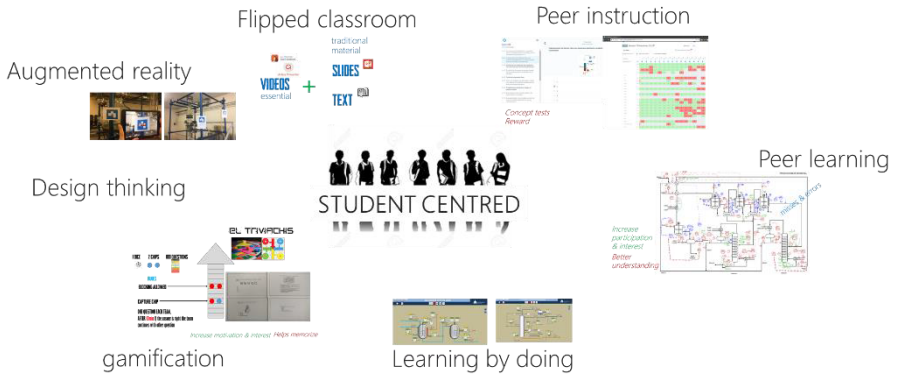

Figure 1. Integrated methodologies used to foster student motivation and learning.

3. Application to Chemical Engineering

3.1. Process Control

In this subject all the methodologies have been applied but case-based reasoning. This was the first subject where this integrated approach was implemented. The following material has been developed: more than 50 videos/screencasts (using ActivePresenter software), more than 300 questions for concept tests (using Classtime software), a board game (called Triviachis, a mix of a quiz game and a dice game) where the students divided in groups play between them in a tournament mode, augmented reality for use in the instrumentation lab and finally an Operator Training Simulator (implemented in Excel and using Aspen Dynamics) for learning by doing.

3.2. Process and Product Design

In this subject also many methodologies have been used and implemented. It is important to remark that this one has worked intensively the objective of sustainability. Fig. 2 shows how the different methodologies are related and have been approached in this subject. Educational material is comprised of more than 40 videos (mainly devoted to Aspen Plus), several Case-based reasoning scenarios focused more on creativity, communication and team work. The gamification has been implemented in a role-type game, where students play different roles (client, engineering company, contractors, etc).

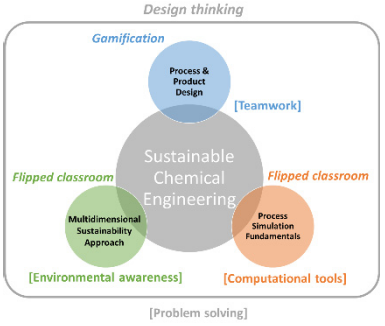

Figure 2. Methodologies and soft-skills applied in process and product design having sustainability as the leit motiv.

3.3. Chemical Reactors

This subject has also developed a lot of educational material related mainly to flipped classroom (using Active presenter), peer instruction with the creation of more than 150 tests (using Kahoot and Mentimeter software).

3.4. Chemical Engineering Lab III

Aurasma has been used to create real and virtual images and videos of the different equipment to be used in the Lab, like batch distillation, absorption or chemical reactors.

Table 1. Matrix showing the subjects and the methodologies applied.

Subject	flipped classroom	Adaptive learning & Peer Instructions	Gamification	Team work & peer learning	Learning by doing	Traditional teaching	Case-based reasoning, Design thinking	Augmented reality
Process control	X	X	X	X	X	X		X
Process & Product Design	X	X	X	X		X	X	
Chemical Reactors	X	X		X		X		
Chemical Eng. Lab				X	X	X		X

Table 1 summarizes the different techniques that have integrated in the subjects presented in this work.

4. Results

The implementation of this integrated approach in core subjects of Chemical Engineering is being very well accepted by the students. Although the application is very recent (3 years in process control, 2 years in the other subjects) there are some indicators to quantify in some manner the results achieved. Table 2 shows the academic results obtained in Process Control. The methodology was applied in 2017, the results (average and number of students that passed the subject) show a significant improvement, although more important than the marks are the students opinion about this new way of learning. In Chemical Reactors a survey was conducted (with Likert levels), the results obtained were:
Do you think that this methodology facilitates learning? 70% answered yes
Are you satisfied with this methodology? 75.1% are satisfied or very satisfied
Are you satisfied with the educational material (quality, contents, usefulness)? More than 90% said they were satisfied or very satisfied.

Table 2. Process control academic results since 2015

Year	Average grade (out of 10)	% Passed	# Students
2018	7.3	83	43
2017	7.4	91	54
2016	6.8	67	39
2015	5.6	72	43

The results are only of one-two years measurements so they have to be taken with caution but they seem quite promising and they show that this is the way to proceed.

5. Conclusions

New innovative education methodologies are not just a hype but a true improvement over traditional ones. Different methodologies have been presented in this work. All and every of them are valuable and can be used to improve the learning experience. But the main goal we seek is to engage our students in the learning process, to motivate them, and for that what best fits for a new way of teaching or more precisely a new way of learning is to integrate different methodologies (flipped classroom, peer instruction, gamification, augmented reality, case-based learning, design thinking). The main drawback is the amount of time and resources needed to develop all the material. Although this effort is compensated over time (as most of the material is reused) it would be more than desirable to have a shared platform in internet where teachers from over the world can share chunks of knowledge that others can reuse and take advantage of. To conclude, the use of motivational active learning will make the students more motivated, participative and more interested in what they are learning and thus enhancing their performance.

References

Beichner, R.J., Saul, J.M., Abbott, D.S., Morse, J.J., Deardorff, D., Allain, R.J., Bonham,S.W., Dancy, M.H., Risley, J.S., 2007. The student-centered activities for largeenrollment undergraduate programs (SCALE-UP) project. J. Res. Based Ref. Univ.Phys. 1 (1), 2–39.

Belcher, J.W., 2003. Improving Student Understandin with TEAL. MIT Fac. Newsl. 16(2), 7–11

Bonwell C.C, Eison J.A., 1991. Active Learning: Creating Excitemnet in the Classroom. ASHE-ERIC Higher Education Reports.

Dewey, J., 1913. Interest and Effort in Education. The Riverside Press, Cambridge.

Harackiewicz JM, Smith JL, Priniski SJ., 2016. Interest Matters: The Importance of Promoting Interest in Education. Policy Insights Behav Brain Sci.;3(2):220–227.

Nelson, Jill, et al., 2019. Improving STEM Teaching And Learning Through Active Learning. Innovations in Teaching & Learning Conference Proceedings. Vol. 11.

Pirker, Johanna, Riffnaller-Schiefer, Maria, Gütl, Christian, 2014. Motivational activelearning: engaging university students in computer science education. In: Pro-ceedings of the 2014 conference on Innovation & technology in computer scienceeducation (ITiCSE ’14), ACM, New York, NY, USA, pp. 297–302,

Prince, M., 2004. Does Active Learning Work? A Review of the Research. Journal of Engineering Education, 93, 223-231.

Renninger, K.A., Hidi, S.E., 2016. The Power of Interest for Motivation and Engage-ment. Routledge, New York and London

Shin, D., Lee, H., Lee, G., & Kim, S., 2019. The Role of Curiosity and Interest in Learning and Motivation. In The Cambridge Handbook of Motivation and Learning (Cambridge Handbooks in Psychology, pp. 443-464). Cambridge: Cambridge University

Wilson, J.M., Jennings, W.C., 2000. Studio courses: How information technology ischanging the way we teach, on campus a and off. Proc. IEEE 88 (1), 72–80.

Sauro Pierucci, Flavio Manenti, Giulia Bozzano, Davide Manca (Eds.)
Proceedings of the 30th European Symposium on Computer Aided Process Engineering (ESCAPE30), May 24-27, 2020, Milano, Italy.
http://dx.doi.org/10.1016/B978-0-12-823377-1.50338-4

An E-learning Bot for Bioprocess Systems Engineering

Simoneta Caño de las Heras, Mark Nicholas Jones, Krist V. Gernaey, Ulrich Krühne, Seyed Soheil Mansouri

Process and Systems Eng.Centre (PROSYS), Dept. of Chemical and Biochemical Eng., Technical University of Denmark, Søltofts Plads, 2800 Kgs. Lyngby, Denmark
seso@kt.dtu.dk

Abstract

Receiving an engineering education is not a smooth path and in the last years, several digital platforms have been developed with the aim to help the students in the field. Nonetheless, the initial efforts to use digital platforms have not yet been successful, partly due to the lack of support to the teachers, the lack of motivation strategies inside the platforms or the loss of the social interaction, which is key in a collaborative learning process. Collaborative learning integrates the interaction between the students and the teacher, or in the case of digital learning, with an educational software. However, it is difficult to provide such a frame of interaction between learners inside an educational software. Therefore, a chatbot is proposed with its own design and architecture which behaves like a "friend" or colleague in the education, here applied to bioprocesses. Along with the chatbot architecture, it is explained how it is integrated in the learning design through its database. This tailored database contains training example dialogs through questions raised by students from a course on Bioprocess Technology, while it also collects their common mistakes, etc. Moreover, this database contains a novel system of twin databases; one with correct information and another with small errors. Using this system, the chatbot provides a more accurate representation of a learner's peer and triggers critical thinking. Finally, the chatbot architecture is embedded inside a prototype open-source Educational Virtual Bioprocess Plant developed by the Department of Chemical and Biochemical Engineering of the Technical University of Denmark, called *FermProc*. **Keywords:** Knowledge transfer, Bioprocess, Chatbot, Process System Education.

1. Introduction

During the past two decades, our world has drastically changed due to the use of internet in our daily life and the democratization of personal smartphones and computers. It has affected our means of communication and added new societal dimensions with economic implications. In the case of education, the creation of massive open on-line courses (MOOC) (Conole, 2016), educational computer games (Zendesk, n.d.), or educational simulators (Dyrberg, et al., 2017; Ebner & Holzinger, 2007) has demonstrated a clear interest in using digital platforms in teaching. Moreover, in the case of higher and tertiary education, there has been a growing need for flexible training towards continuing education and professional training, endorsing a learning outside the classroom supported by digital tools. However, the success in the integration of digital platforms as learning tools has not been as expected with a dropout rate of about 96 per cent on average over five years (Reich & Ruipérez-Valiente, 2019) in on-line courses.

This could be explained by the need of support for the instructors to create and integrate on-line content, the lack of institutions offering on-line education (Brahimi & Sarirete, 2015), or the failure of simulators in engineering education in motivating the students (Kiili, 2005), amongst other factors. A reason behind unsuccessful integration of digital technology had been the loss of normal interaction that occurs in a real classroom or laboratory as the students are isolated from their peers and instructors (Balamuralithara & Woods, 2009). Therefore, students miss a collaborative learning experience, i.e. they miss the social and environmental elements in their traditional learning.
In this work, we intend to develop a collaborative e-learning for bioprocess systems engineering, which is integrated inside a computer-aided tool. Bioprocess development reaches from discovery to distribution of bio-products. Therefore, it is a necessity for engineering students to gain the ability to connect and use the knowledge and competences that those students acquire during their education. This is a challenge that can be tackled through a knowledge transfer computer-aided tool, in the form of a chatbot.

2. Collaborative e-learning

Collaborative e-learning (Figure 1) is a type of learning process. Here, a computer-aided media (acting as a teacher) provides the content, task and the assessment to the students. On the other side, a peer (the chatbot) communicates with the learner, who compares, argues and reflects with itself and the chatbot about ideas or practices. Although it is part of a natural learning process (Laurillard, 2009), it must be actively considered during the design of the learning experience.

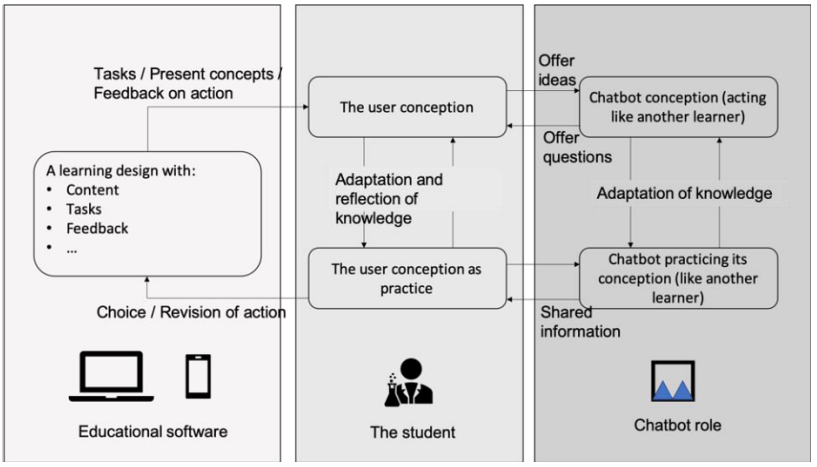

Figure 1. Collaborative e-learning scheme that provides a frame for the interactions between learners and their concepts and practice.

Collaborative e-learning has been investigated through the use of chats (Monahan, et al., 2008) and in fewer cases, chatbots (Kane, 2016). A chatbot is a computer program that works as a conversational agent and has huge potential as helper in education. A previous study had investigated the use of a chatbot for a negotiated learner model (Kerly, 2009), finding an improving accuracy in students' self-assessment. In another case, the co-development of a chatbot with students was tested, by incorporating their own questions, which increased their motivation and interest for the subject (Crown, et al., 2011). However, in those cases the chatbot is an independent tool, not supported by an

educational software that provides them with tasks, content…, and it lacks some of the characteristics of a peer, like the possibility of being wrong.
Mistakes are rather usual to make and critical thinking is an important tool in the education of process engineers. Therefore, collaborative e-learning provides a frame not only for the students to reflect upon and share ideas, but also to be critical, using their own knowledge while an external agent attempts to influence them.

3. Chatbot Architecture

The chatbot is acting as a peer inside the collaborative e-learning (Figure 1). The software architecture can be seen in Figure 2.
This chatbot is developed considering its objective as an educational tool for process engineering applied to bioprocesses. Based on its educational frame, the chatbot includes:

- *Engage the user.* It needs to be contextual and focused on the individual and on the objectives of the process (operational, economic and sustainability). For example, some enjoyable facts about the process and industrial information can be used to refer back to the main topic.
- *Learn.* Leverage machine learning to develop context and resolve issues in an automated fashion.
- *Communicate.* Create a comfortable and adapted mode of communication with the use of gifs, emojis or memes.
- *Promote curiosity.* By providing a possibility to connect one bioprocess concept to another.

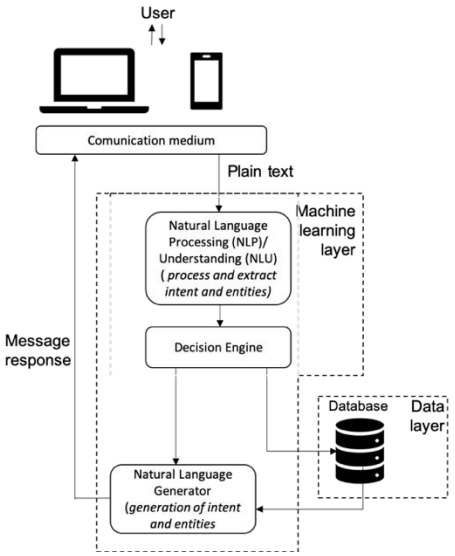

Figure 2. Chatbot architecture, in which is represented the transport of information and the different processes that form the chatbot.

The chatbot (Figure 2) is composed of a machine learning (data-driven) layer and a data layer. The machine learning layer contains the natural language processing (NLP), understanding (NLU) and generator (NLG) as well as the decision engine, and is programmed in Python and TensorFlow using predefined routines.
Meanwhile, the data layer is in charge of storing the information used in the training of the chatbot and therefore, it embeds the chatbots' specifications. Along other routine

dialogs, the chatbot database involves specific example dialogs for training purposes, information related to bioprocesses and information related to the pedagogically oriented software in which it is implemented. The training example dialogs are a collection of questions of the Bioprocess Technology course, a course shared by the Bachelor of Science study plans of Human Life Science Engineering, Biotechnology and Chemical Engineering at the Technical University of Denmark, along with other sources of information. In this course, undergraduate students learn to do systematic mass and energy balances, to analyse and predict fluid behavior, and to design basic equipment used in bioprocess engineering (DTU, 2019).
An example question from a student used in the training dialog database has been:

Student: "In pumps, I am seeing two equations for the Net Positive Suction Head (NPSH); one with all the common terms and another one that it is missing the velocity term. Why is that?"

In this action, the Natural Language Processing (NLP) and Natural Language Understanding (NLU) modules, that use machine learning in Python, extract entities such as *equation, NSPH, missing, velocity,* and intents, like *containNSPH* (the verb and the noun of the sentence). Then, it performs a comparison through the information collected from the database and the Natural Language Generator (NLG) will provide a reply:

Chatbot: "It is due to the calculation of the NPSH in a specific point in order to calculate the net positive suction head, not needing the velocity. To get more information, I like this one: http://www.pumpschool.com/applications/NPSH.pdf (explained the different between the NPSH available and required and the different terms)"

As it has been briefly mentioned, a novel feature of this chatbot is confronting misleading ideas or wrong understandings during the training process. As the chatbot is acting as a peer learner inside the collaborative learning (Figure 1), it is possible that a peer learner will give a false advise. Thereby, we hope to engage the students in the necessary critical thinking. In order to implement this feature, another database is developed (an evil twin database) that includes slightly wrong answers. This database can be activated by the students as a special feature. An example can be seen in Figure 3.

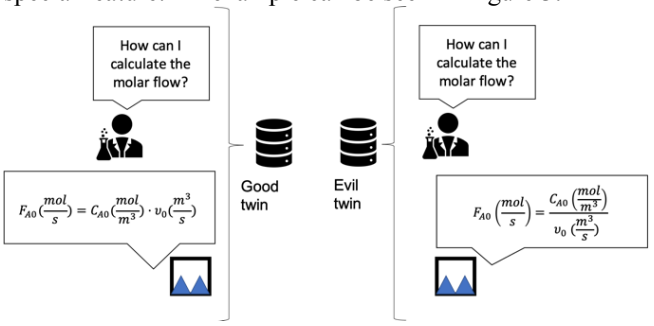

Figure 3. Example of the two databases

Furthermore, in the data layer, the two example dialog databases are connected together with a database developed for a pedagogically oriented software developed at the Department of Chemical and Biochemical Engineering of the Technical University of Denmark, called *FermProc*. The aim of *FermProc* is to be the educational software that presents the content and tasks to the students as well as feedback over the learning of

bioprocesses and a revision of the content and activities after the action of the student (Figure 1) in the collaborative e-learning.

4. Software integration

FermProc is based on a previously developed systematic methodology (de las Heras et al., 2018). This computer-aided tool has its prime pedagogical objectives in training people in the area of bioprocess operation. The interactive prototype includes understandably described and implemented mechanistic models, the possibility to modify them, learning-hints, questionnaires, mini-games, and the possibility to learn by failure. However, *FermProc* was not yet integrating the use of collaborative e-learning inside the platform and in the next development stage, the chatbot is added inside the software architecture.

FermProc is a three-layer software architecture. In its current state, the chatbot is a parallel feature in the software architecture of *FermProc*, connected through a shared data layer as well as the graphic user interface (Figure 4). However, in the future development, the chatbot will pass to be inside of the "special features" of the application layer of *FermProc,* together with the multimedia resources, or bioprocess mini-games implemented.

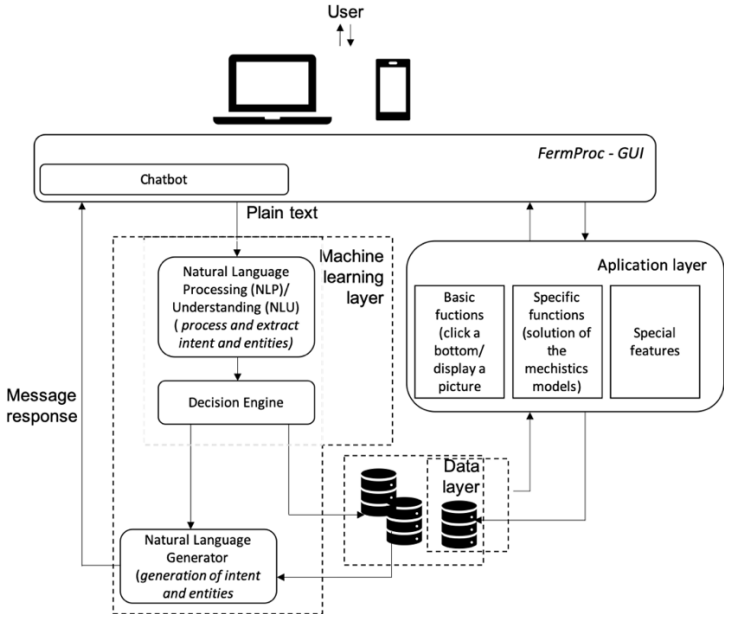

Figure 4. Integrated software architecture of the chatbot and *FermProc*. In this schema, the two combined architectures can be seen and the flux of information either from the chatbot or from *FermProc*.

5. Conclusions

Complexity is an intrinsic part of process systems and understanding such complexity requires the connection of different subjects and knowledge that undergraduate and graduate students acquire during their education. Although digital platforms could be excellent tools, they present some issues such as the lack of interaction between peers as well as the sharing and comparison of information. In this work, we proposed the use of a tailored chatbot. Through its data layer trained by actual questions from the students,

we hope to simplify the work of instructors and reduce the fear of students to ask questions. Furthermore, as peers are not always right, a novel system of twin databases is developed. This twin database system aims at enhancing the critical thinking of the students as the chatbot will not always provide the correct answer but the mechanisms to evaluate if the answer is wrong. Although the chatbot is specifically trained for the learning of bioprocess system engineering, its design is generic and it can be expanded to other fields and areas. Finally, the chatbot of this work has been implemented inside an educational bioprocess prototype software (*FermProc)* to provide a complete environment for a collaborative e-learning process.

References

Balamuralithara, B., & Woods, P. C. (2009). Virtual laboratories in engineering education: the simulation lab and remote lab. *Computer Applications in Engineering Education*. https://doi.org/10.1002/cae.20186

Brahimi, T., & Sarirete, A. (2015). Learning outside the classroom through MOOCs. *Computers in Human Behavior*, *51*, 604–609. https://doi.org/10.1016/j.chb.2015.03.013

Conole, G. (2016). MOOCs as disruptive technologies: strategies for enhancing the learner experience and quality of MOOCs. *Revista de Educación a Distancia (RED)*, (50), 1–18. https://doi.org/10.6018/red/50/2

Crown, S., Fuentes, A., Jones, R., Nambiar, R., & Crown, D. (2011). Anne G. Neering: Interactive chatbot to engage and motivate engineering students. *Computers in Education Journal*, *21*(2), 24–34. https://doi.org/10.1016/j.futures.2006.01.008

de Las Heras, S. C., Gutschmann, B., Gernaey, K. V., Krühne, U., & Mansouri, S. S. (2019). Facilitating learning by failure through a pedagogical model-based tool for bioprocesses. In *29th European Symposium on Computer Aided Process Engineering* (Vol. 46). https://doi.org/10.1016/b978-0-12-818634-3.50305-2

de las Heras, S. C., Mansouri, S. S., Cignitti, S., Uellendahl, H., Weitze, C. L., Gernaey, K. V., … Krühne, U. (2018). A Methodology for Development of a Pedagogical Simulation Tool used in Fermentation Applications. *Computer Aided Chemical Engineering*, *44*, 1621–1626. https://doi.org/10.1016/B978-0-444-64241-7.50265-2

DTU, C. (2019). Bio-Process Technology course description. Retrieved November 20, 2019, from https://kurser.dtu.dk/course/28025

Dyrberg, N. R., Treusch, A. H., & Wiegand, C. (2017). Virtual laboratories in science education: students' motivation and experiences in two tertiary biology courses. *Journal of Biological Education*, *51*(4), 358–374. https://doi.org/10.1080/00219266.2016.1257498

Ebner, M., & Holzinger, A. (2007). Successful implementation of user-centered game based learning in higher education: An example from civil engineering. *Computers and Education*, *49*(3), 873–890. https://doi.org/10.1016/j.compedu.2005.11.026

Kane, D. (2016). The role of chatbots in teaching and learning. *E-Learning and the Academic Library: Essays on Innovative Initiatives*, 131–147. https://doi.org/10.7280/D1P075

Kerly, A. (2009). *Negotiated Learner Modelling with a Conversational Agent*. (June).

Kiili, K. (2005). Digital game-based learning: Towards an experiential gaming model. *Internet and Higher Education*, *8*(1), 13–24. https://doi.org/10.1016/j.iheduc.2004.12.001

Laurillard, D. (2009). The pedagogical challenges to collaborative technologies. *International Journal of Computer-Supported Collaborative Learning*, *4*(1), 5–20. https://doi.org/10.1007/s11412-008-9056-2

Monahan, T., McArdle, G., & Bertolotto, M. (2008). Virtual reality for collaborative e-learning. *Computers and Education*, *50*(4), 1339–1353. https://doi.org/10.1016/j.compedu.2006.12.008

Reich, J., & Ruipérez-Valiente, J. A. (2019). The MOOC pivot. *Science*, *363*(6423), 130–131. https://doi.org/10.1126/science.aav7958

Zendesk. (n.d.). Prodigy. Retrieved November 19, 2019, from https://www.prodigygame.com

Sauro Pierucci, Flavio Manenti, Giulia Bozzano, Davide Manca (Eds.)
Proceedings of the 30th European Symposium on Computer Aided Process Engineering (ESCAPE30), May 24-27, 2020, Milano, Italy.
http://dx.doi.org/10.1016/B978-0-12-823377-1.50339-6

Knowledge Transfer, Experiences and Prospects from the Collaboration between an Energy Company and the University

Emilia M. Kondili[a*], Ioannis K. Kaldellis[b], Evangelos Demenagas[c], Athanasios Stefanakis[c]

[a] *Optimisation of Production Systems Laboratory, Dept. of Mechanical Engineering,*
[b]*Soft Energy Applications and Environmental Protection Laboratory,*
Dept. of Mechanical Engineering, University of West Attica, Campus 2, P. Ralli & Thivon Street, 12244, Egaleo, Greece
[c]*Hellenic Petroleum Grou of Companies, 17th km of Athens – Patras National Road*
ekondili@uniwa.gr

Abstract

The international trend towards cleaner fuels and carbon footprint minimisation puts a severe pressure on the prospects of the oil and gas companies worldwide. Commitment in knowledge development and innovation are required in today's severe conditions and call for collaboration with Universities and Research Centres. The objective of the present work is to describe the main parameters, the design and implementation issues and the future prospects of a successful collaboration between an energy industrial group and a University in an innovative Postgraduate MSc Course in Oil and Gas Process Systems Engineering.

Keywords: PSE, Oil and Gas, Energy transformation, Industrial collaboration

1. Introduction and Background of the work

Oil industry is one of the biggest and most important industries in the world with a crucial role in energy market in the future. The international trend towards cleaner fuels and carbon footprint minimisation puts a severe pressure on the prospects of the oil and gas companies worldwide. However, the continuous development of new products with better environmental behaviour, the important projects of oil and gas transportation, the excellent competitiveness of the refining units make this field interesting and attractive with very good research, development and innovation prospects.

The Mechanical Engineering Department of the University of West Attica, in collaboration with Hellenic Petroleum Group of Companies and Aspropyrgos Municipality have recently developed a Postgraduate Program in "MSc Oil and Gas Process Systems Engineering". The objective of the new Postgraduate Course is to provide students with a scientific background and extensive integrated and applied knowledge in hydrocarbons engineering and enable them to develop a successful career in the oil and gas process and supply chain management companies. Furthermore, the well-educated and trained professionals will be able to advance the communication of the local and regional authorities with these sectoral companies for the benefit of the society.

The postgraduate course leads to a Master of Science (MSc) degree and intends to educate professionals in the fields of oil and gas processing, storage, supply chain

management as well as in the new hydrocarbon fuel products and their applications in the light of the international pressure towards clean fuels and minimisation of the carbon footprint, the associated downstream processing technologies, operations and economics; process safety and operations integrity; and methods for the optimal design and operation of process systems. Furthermore, students will have learnt about the general economics of the energy sector, oil and gas production, transportation and logistics. In addition, advanced and practical knowledge related to the environmental behaviour of oil and gas processes, as well as special know-how on the novel transportation projects will also have been gained after the completion of the course.

2. The collaborating organisations

2.1. The University of West Attica

The University of West Attica - a newly developed University from the merging of two Technological Universities in the area of West Attica - has the vision to make collaborations with the organisations and industries in the area in order to support them with scientific knowledge and academic experience and, on the other hand, provide the University with the knowledge and experience of the real production world, interchange personnel and provide its students with a continuous contact with employment opportunities. The Department of Mechanical Engineering that participates in the Course development and implementation has a very successful track record in the design and operation of Postgraduate courses in the fields of energy and environmental technologies and business.

2.2. Hellenic Petroleum Group of Companies

Hellenic Petroleum is one of the leading energy groups in South East Europe with activities spanning across the energy value chain and presence in six countries. The Group's wide range of activities include: Supply, refining and trading of petroleum products both in Greece and abroad, Fuels marketing, Petrochemicals, chemicals production and trading, Oil and gas exploration and production, Power generation and natural gas, Renewable energy sources and Engineering services.

Hellenic Petroleum is one of the top 100 pioneer energy groups worldwide. The most significant vision of HELPE Group is the successful transition to a new competitive production model of sustainable development in the framework of Industry 4.0 and digitalisation critical changes. The main directions towards this new era are the 3Ds (HELPE, a): Decarbonisation, decentralization and digitalisation. Furthermore, HELPE adapts the model of the Knowledge Triangle (Figure 1, HELPE a) for the transition towards the Knowledge Society and – to that effect – encourages strategic alliances with Universities and Research Centers. The company is pioneer in the country in that respect also collaborating practically with most Universities and Research Centers.

2.3. Aspropyrgos Municipality

Aspropyrgos Municipality is very much interested in the development of this specific PG Course since Aspropyrgos is the area of Greece with the most significant hydrocarbons production plants and industries. Therefore, a number of employees are recruited from the area in these plants and there is a high interest for developing qualified scientists and engineers able to contribute to the optimal operation of these plants. Furthermore, the municipality communicates and cooperates in many respects with these companies; therefore, qualified human resources are required in various other relevant job positions that will be able to understand the complex issues for the mutual benefit of the companies and the local society.

3. Best Practices in Collaboration between Energy Companies and Universities

The need for continuous innovation and development of new knowledge and novel technologies in the oil and gas sector has been recognised from the largest companies worldwide. A great experience concerning the collaboration between Universities and oil and gas companies has been already recorded, leading to strategic alliances with world class quality measurable benefits for both sides.

As an example of the best practices worldwide, ExxonMobil cooperates with the best universities in USA in education and research. For example, in their cooperation with Princeton University they run five projects that focus on solar and battery technologies, plasma physics, Arctic sea-ice modeling, and the impact of carbon dioxide absorption on the world's oceans. ($5 million over five years to Princeton). They also announced a $15 million investment as a leading member of the University of Texas at Austin Energy Institute to pursue technologies to help meet growing energy demand while reducing environmental impacts and the risk of climate change. Research projects are expected to cover a range of emerging technologies and will take advantage of the university's capabilities in renewable energy, battery technologies and power grid modeling.

Scientists from ExxonMobil and the Georgia Institute of Technology have developed a potentially revolutionary new technology that could significantly reduce the amount of energy and emissions associated with manufacturing plastics. The University of Wisconsin-Madison and ExxonMobil continue to partner together to research the fundamental chemistry of converting biomass into transportation fuels. UW-Madison has long been known for its expertise in biomass conversion.

ExxonMobil is also a founding member of the Global Climate and Energy Project at Stanford University. In addition, the company is funding a broad portfolio of biofuels research programs including our ongoing efforts on algae as well as programs on converting alternative, non-food based biomass feedstocks, such as cellulosic biomass, to advanced biofuels.

4. Program Overview - Course Structure and Content

Expanding its collaboration with Greek Universities, Hellenic Petroleum has launched along with the Mechanical Engineering Department of the University of West Attica and Aspropyrgos Municipality a Postgraduate Program in "MSc Oil and Gas Process Systems Engineering". The objective of the new PG Course is to provide students with a scientific background and extensive integrated and applied knowledge in hydrocarbons engineering and enable them to develop a successful career in the oil and gas process and supply chain management companies. Furthermore, the well-educated and trained professionals will be able to advance the communication of the local and regional authorities with these sectoral companies for the benefit of the society.

In West Attica region, where the University of West Attica is located, the largest hydrocarbons processing production units are sited (Aspropyrgos and Elefsina Refineries of HELPE, Pachi - Megara installations, Aspropyrgos and Elefsina Docks, DEPA installations, Revythousa LNG Plant, EPA of Attica, DESFA etc.). In the context of the above discussion, the need of a new course is dictated by at least three reasons:

1. The geographical region of Attica as mentioned above.
2. The innovative characteristics of the program content that combines technologies, operations, economical and business issues.

3. The fact that participation of a local communities and societies and the most important sectoral companies in the design and organisation of the course.

The students of the PG Course will need to attend successfully eight taught Modules (Table 1) and carry out a research project (Dissertation) as well as a two months Practical Industrial Placement that will be organised for the students.

Table 1: Structure and Contents of Oil and Gas PSE Postgraduate Course

Structure and Contents of Oil and Gas PSE Postgraduate Course
1st Semester
Conventional and Renewable Energy Technologies
Basics of Refinery Processes
Process Safety in Hydrocarbons Processes-Risk Assessment
2nd Semester
Economics of Petroleum & Natural Gas/ Hydrocarbons Business – Evaluation of Investments
Advanced Process Control in Oil Refineries – Digital Transformation
Design and Operations of Refinery Processes
Attendance of two advanced seminars or Specialized Lectures or Conferences
3rd Semester
Supply Chain Management in Oil and Gas Industries
Selection of two between the following Modules
Environmental Technologies – Sustainable Development Applications
Optimisation and Decision Making in Oil and Gas Process Engineering
Strategic Management and Business Planning for the Oil Industries
Process Modelling and Simulation
Natural Gas Processing, Transportation and Distribution
4th Semester
Industrial Placement and Research Dissertation

Hellenic Petroleum as the partner in the course organisation has contributed substantially not only in the design and the development and the curriculum of the Course but also with the experienced high level employees has undertaken a very large percentage of the Modules implementation (Figure 2, CSR of HELPE, HELPE b).

5. The emerging technological and business needs and the PSE relevance of the PG Course

The oil and gas sector faces very serious and emerging issues, such as the digital transformation with special focus in the supply chain. Digital transformation can be used to refer to any element of technical progression within a company that utilises digital technology (Mahdi Asghari et al, 2013). There has been an active push for oil and gas companies to embrace the digital revolution, and as a result, the previously slow-to-adapt industry is now at the forefront of many types of emergent technology – including artificial intelligence, augmented reality, and the Industrial Internet of things.

As an asset-heavy industry, the oil and gas sector has been in immense need for digital operations for decades – but the cost and difficulty of properly implementing a strategy in such a hardware-intensive environment has slowed progress in the past. Digital transformation is no longer an option that some companies are choosing to pursue – it is rapidly becoming impossible to function without strategies in place.

Furthermore, there is an important issue that needs to be considered more carefully and this is the digital integration of the entire supply chain. Reviews for the optimisation of a digitalised successful supply chain may be found in Büyüközkan et al, 2018.

The course under consideration icludes Modules completely focused in the PSE implementation in oil and gas industry. More specifically, the following courses are completely relevant to PSE.

- Advanced Process Control in Oil Refineries – Digital Transformation
- Design and Operations of Refinery Processes
- Supply Chain Management in Oil and Gas Industries
- Optimisation and Decision Making in Oil and Gas Process Engineering
- Process Modelling and Simulation
- Natural Gas Processing, Transportation and Distribution

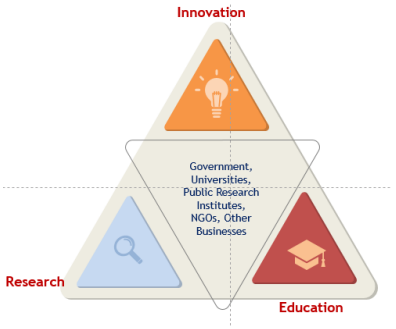

Figure 1: The Knowledge Triangle (HELPE, 2019, a)

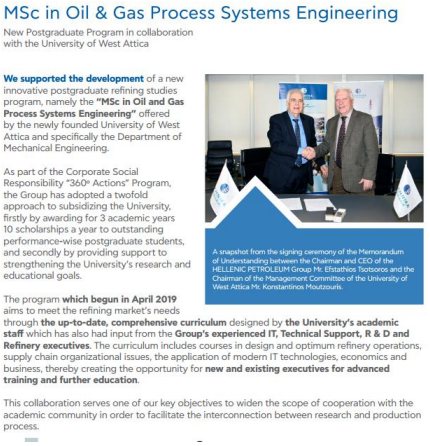
MSc in Oil & Gas Process Systems Engineering

New Postgraduate Program in collaboration with the University of West Attica

We supported the development of a new innovative postgraduate refining studies program, namely the **"MSc in Oil and Gas Process Systems Engineering"** offered by the newly founded University of West Attica and specifically the Department of Mechanical Engineering.

As part of the Corporate Social Responsibility "360º Actions" Program, the Group has adopted a twofold approach to subsidizing the University, firstly by awarding for 3 academic years 10 scholarships a year to outstanding performance-wise postgraduate students, and secondly by providing support to strengthening the University's research and educational goals.

A snapshot from the signing ceremony of the Memorandum of Understanding between the Chairman and CEO of the HELLENIC PETROLEUM Group Mr. Efstathios Tsotsoros and the Chairman of the Management Committee of the University of West Attica Mr. Konstantinos Moutzouris.

The program **which begun in April 2019** aims to meet the refining market's needs through **the up-to-date, comprehensive curriculum** designed by **the University's academic staff** which has also had input from the **Group's experienced IT, Technical Support, R & D and Refinery executives**. The curriculum includes courses in design and optimum refinery operations, supply chain organizational issues, the application of modern IT technologies, economics and business, thereby creating the opportunity for **new and existing executives for advanced training and further education**.

This collaboration serves one of our key objectives to widen the scope of cooperation with the academic community in order to facilitate the interconnection between research and production process.

Figure 2: CSR of HELPE referring to the PG Course (HELPE, 2019, b)

PSE methods and tools as well as the use of relevant software are included in the courses. In addition, specific and specialized themes of high added value will be included in the Module, either in the form of seminars, invited presentations or taught courses. Indicatively, the organisation of an advanced seminar concerning Oil Industry Digitalisation and one focused in the Supply Chain Optimisation in the digitalisation era are planned for spring 2020.

6. Future Steps – Strengthening of the Collaboration

The energy sector in Greece has very significant challenges to face in the future years. The ability to continuously innovate and be able to provide optimal technical, commercial and business solutions to the energy oil and gas industry is nowadays a necessity.

The Energy Plan of the country for the future years include 44 billion euros investments for the next decade, mainly in RES and power and Natural Gas transmission networks. To respond to the needs for continuous innovation in a very rapidly changing (in technological and business respect) environment, energy companies need to make strategic collaborations with universities.

There is not only the Postgraduate Course is only one of the collaboration fields that directs us towards the future. Within a global knowledge economy, there is more than ever a pressing need for strategic industry – academia partnerships that go much beyond the traditional funding of discrete programs. In that respect, the collaborating engineers of HELPE and UNIWA identify areas with the most scientific potential, particularly

ones that build on the university's existing strengths and interests in emerging energy technologies (conventional and RES) in order to develop an Energy Consortium to link energy companies with UNIWA in schemes like forums and partnerships.
The benefits of the companies joining an industry – university Consortium include:

- Continuous access to academics from many disciplinary areas and to well-trained energy/hydrocarbons focused MSc, PhD Students and Post-Doctoral Researchers.
- Opportunity to exploit research and development opportunities and guide research and development towards their own business needs.
- Collaboration offers possibilities for partnerships in research projects.
- Links to other UNIWA Departments and specialised accredited Laboratories.
- Opportunity to networking with other companies.
- Privileged access to excellent quality postgraduate courses and intensive innovative long life education programs focused in energy technologies and energy systems.

The key elements of a successful collaboration (Liew MS et al, 2015, adjusted) are shown in Table 2.

Table 2: Benefits of an Energy – University Consortium

Benefits to Academia	Benefits to Energy Companies
Access to the latest technologies and best practices	Access to excellent quality of seminars and postgraduate courses
Knowledge and experience transfer	Networking with other similar companies
Larger pool of professionals for attending of seminars and postgraduate courses	Access to new research ideas and R&D programs
Access to real projects and test beds for new research ideas	Access to specialised and very well educated personnel
Access to real technical/ business problems	Access to other Departments academics

7. Conclusions

A new successful collaboration in the development of a postgraduate course with very good prospects between the largest oil company of Greece and the University of West Attica has been described in the work. The Process Systems Engineering focus of the PG program with the continuous cooperation with a highly experienced and specialised PSE academic team in the University has provided the opportunity for further advancement of the already existing HELPE activities in the supply chain optimization, in the implementation of novel process modelling and simulation software as well as in the support of the company on their digitalization

References

www.helpe.gr Corporate Social Responsibility Panorama 2019, Issue 1. Hellenic Petroleum)
HELPE Group Edition,'Future Prospects of HELPE Group of Companies: The Knowledge Triange', Athens 2019, in Greek, HELPE edition
Collaborating with leading universities to meet global energy demand, Sept18, 2018, https://corporate.exxonmobil.com (site accessed Nov30, 2019)
Mahdi Asghari, Mohammad Ali Rakhshanikia, Technology transfer in oil industry, significance and challenges, PROCEDIA Procedia - Social and Behavioral Sciences 75 (2013) 264 – 271
Gülçin Büyüközkan, Fethullah Göçer, Digital Supply Chain: Literature review and a proposed framework for future research, Computers in Industry 97 (2018), 155-157
Liew MS, Eik LH, Zawawi NAWA Towards a sustainable collaboration between the oil and gas industry and university, http://dx.doi.org/10.5339/qproc.2015.elc2014.52

Sauro Pierucci, Flavio Manenti, Giulia Bozzano, Davide Manca (Eds.)
Proceedings of the 30th European Symposium on Computer Aided Process Engineering (ESCAPE30), May 24-27, 2020, Milano, Italy.
http://dx.doi.org/10.1016/B978-0-12-823377-1.50340-2

Industrial Software for Computer Aided Process Engineering (CAPE) Modeling and Programming Skills Development

Jeffrey D. Kelly,[a,*] Brenno C. Menezes,[b]

[a]*Industrial Algorithms Ltd., 15 St. Andrews Road, Toronto M1P 4C3, Canada*

[b]*Division of Engineering Management and Decision Sciences, College of Science and Engineering, Hamad Bin Khalifa University, Qatar Foundation, Doha, Qatar*

jdkelly@industrialgorithms.ca

Abstract

The Industrial Modeling and Programming Language (IMPL) software designed for the process system engineering (PSE) and operations research (OR) communities is architected to be a structural unit-operation-port-state superstructure (UOPSS) and a semantic quantity-logic-quality phenomena (QLQP) modeling language embedded into a computer programming language with the capability to model and solve industrial optimization, estimation or simulation problems (or sub-problems). In such computer aided process engineering (CAPE) systems, to evolve towards the requirements of advanced modeling and programming skills in a staged fashion, there is a mixture, blend or combination of IML (Industrial Modeling Language), IPL (Industrial Programming Language) and IMPC (Industrial Modeling and Programming Code) for convenience, expressiveness and expedience. IML is how the user may configure the problem using a flat file to fill specific fields or frames by configuring (without coding) the embedded sets (from the UOPSS and QLQP), parameters, variables, and constraints. IPL is how a user may code problems by using computer programming languages to manipulate IMPL using any of its receiving and retrieving routines and with and without using the IML facilities for configuration when required. IMPC is implemented into a machine-coded language (Intel Fortran) to allow IMPL's modeling facilities to be combined with a powerful general-purpose programming language to formulate any new type of set, parameter, variable and/or constraint. To summarize, IMPL may be considered as a confluence with the scientific disciplines of applied engineering, information and computing technologies, statistics, data analytics and decision sciences, that deliveries easy-to-handle and integrative capabilities for modeling and programming in a progressive-learning evolution and high-performance shareable work amongst PSE and OR teams.

Keywords: Modeling languages, Programming skills, Industrial Modeling and Programming Language, Computer programming languages, Exploitation of CAPE tools.

1. Introduction

To progress from a mere user of commercial software solutions supplied by vendors to the development of home-grown tools highly demanded in the process system engineering (PSE) and operations research (OR) communities in both academia and industry, there is a need for handy, integrative-method, progressive-learning and shared-work modeling and programming capabilities that are not difficult and costly to develop,

deploy and sustain. For this, a new generation of industrial modeling and programming language has been researched and developed, which is the *raison d'etre* of IMPL, and covers the computer aided process engineering (CAPE) needs among PSE and OR peers with the underlying concepts, constructs and configurations of its unit-operation-port-state superstructure (UOPSS) and its quantity-logic-quality phenomena (QLQP). IMPL models a super-problem, found in the batch- and continuous-process industries to solve design, planning, scheduling, coordination, real-time optimization, control, parameter estimation, data reconciliation and simulation problems and ultimately to capture significant economic, efficiency and environmental benefits. Toward advanced modeling and programming skills in a progressive pace, in IMPL there is a combination of configuration and codification modeling as well as mathematical and computer languages. They are: IML (Industrial Modeling Language), IPL (Industrial Programming Language) and IMPC (Industrial Modeling and Programming Code), as showed in Figure 1.

IML

```
&sUnit,&sOperation,@rSetup_Lower,@rSetup_Upper,@rBegin_Time,@rEnd_Time
BLACKBOX,,1,1,BEGIN,END
&sUnit,&sOperation,@rSetup_Lower,@rSetup_Upper,@rBegin_Time,@rEnd_Time
```

IPL

```
for ivv_NLP in range (0,iv):
    #for ispecs_NLP in range (0,specs):
    spec1 = str(ivSpecs[ivv_NLP][1])

    if spec1 == 'UOPScomponent':

       uname = c_char_p(str(ivSpecs[ivv_NLP][2]).encode("utf-8"))
       oname = c_char_p(str(ivSpecs[ivv_NLP][3]).encode("utf-8"))
       pname = c_char_p(str(ivSpecs[ivv_NLP][4]).encode("utf-8"))
       sname = c_char_p(str(ivSpecs[ivv_NLP][5]).encode("utf-8"))
       sname = c_char_p(b" ")
       cname = c_char_p(str(ivSpecs[ivv_NLP][6]).encode("utf-8"))
       value = c_double(value_lhs_x[nn_NLP+3][ivv_NLP+1])
       rtnstat = interacter.IMPLreceiveUOPScomponent(uname,oname,pname,sname,cname,value,value,c_double( ),IMPLkeep)
```

IMPC

```
         if (structure$ == SPARSIC$) then

c        25 - x1*x2*x3*x4 <= 0
           rtnstat = sdcreceive(rc1_f(1),25d+0 - sdvretrieve(rv1_x(1))*sdvretrieve(rv1_x(2))*
     &                                         sdvretrieve(rv1_x(3))*sdvretrieve(rv1_x(4)))
           if (succession$ == FIRSTSUCCESSION$) then
             rtnstat = sddratio(rc1_f(1),
     &                                  4,[rv1_x(1),rv1_x(2),rv1_x(3),rv1_x(4)])
             rtnstat = sdcretype(rc1_f(1),type=NONLINEAR_LE)
           end if

c        40 - x1^2 - x2^2 - x3^2 - x4^2 = 0
           rtnstat = sdcreceive(rc1_f(2),40d+0 - sdvretrieve(rv1_x(1))**2d+0 - sdvretrieve(rv1_x(2))**2d+0 -
```

Figure 1. IML configuration and IPL and IMPC codifications found in IMPL.

In IML the problem is configured in a flat file by filling specific fields into frames with keywords that call the embedded sets (from the UOPSS and QLQP), parameters, variables, and constraints. Currently, with the IML configuration, the user can invoke 621 set and parameter types, 196 variable types, and 309 constraint types. IPL is how a user may code problems by using computer programming languages as such as C, C++, C#, Fortran, Julia, Python, Visual Basic, Java, Matlab, R, etc., to manipulate IMPL using any of its receiving and retrieving routines by coding in the aforementioned computer programming languages, combined or not with the IML facilities for configuration. For a standalone and prototyping problem, IML is preferred since there is usually no need to retrieve its solution results to be used in further solving steps. However, IPL is necessary to program iterative problems such as decomposition heuristics and on-line solutions, whereby an algorithm to manage the retrieving of a solution to be fed (received) in another problem run must be codified to manipulate IMPL configurations and solutions externally in a computer programming language.

IMPC is the internal coding infrastructure of the problem's model and data in IMPL's specialized mathematical programming form by the IMPL Modeler library and is accessible via a developer user's, modeler's or analyst's Intel Fortran code. The fundamental essence of IMPC is to allow the developer user the capability to code and create any kind of discrete, nonlinear and dynamic (DND) formula, relation or constraint using sparse memory-resident arrays within Intel Fortran from one to eight dimensions (i.e., sparse vectors, matrices and tensors) with an omni-present ninth (9^{th}) dimension typically populated with time-period, time-series or trial-sampling data. This makes IMPL by using IMPC very suitable for the developer user to design, develop, deploy and distribute their own compiled and proprietary dynamic link libraries (DLL's) or shared objects (SO's) for third-party commercial use without having to share or expose their proprietary source code. Modeling and programming facilities found in the IML configuration and IPL codification integrated into the specialized mathematical programming form of the IMPC allows an effective and high-performance exploitation of CAPE tools among teams in manufacturing sites, R&D centers, headquarters and service teams (within the same company) integrated or not to third-part companies.

2. IMPL's facilities for IML configuration and IPL codification

The network in Figure 2 is constructed in the UOPSS network (Kelly, 2005) embedded in the open-source flowsheet software Gnome DIA. The main UOPSS palette for structures, shapes or objects are defined as: a) unit-operations for sources and sinks (◇), tanks or inventories (△), batch-processes (□) and continuous-processes (⊠) and b) the connectivity involving arrows (→), inlet-ports i (○) and outlet-ports j (⊗). Unit-operations and arrows have binary and continuous variables and the ports hold the states as process flows, yields and qualities.

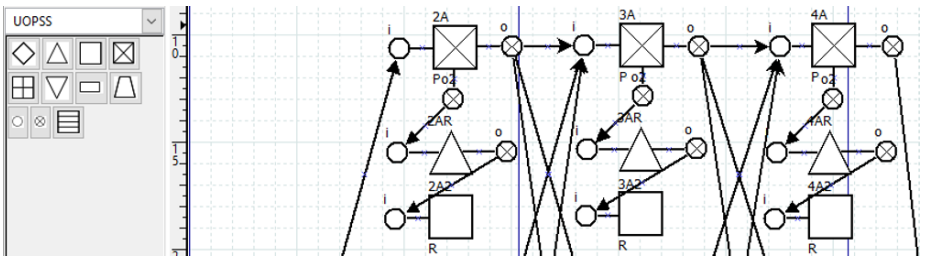

Figure 2. IMPL's drag and drop facilities for the UOPSS flowsheet network set.

IMPL modeling facilities in the UOPSS and QLPQ structures and relationships can be broken-down into several data categories or classes where these data categories are quantity (flows, holdups, yields), logic (discrete decisions such as setups, startups, shutdowns, etc.) and quality (densities, components, properties such as sulfur content, density, etc.). These are solved in linear (LP) or quantity, nonlinear (NLP) or quality and mixed-integer linear (MILP) or quantity-logic (or logistics) problems. Besides, these are categorized in static (non-time-varying) and dynamic (time-varying) cases suitable for optimization and estimation problems such as design, planning, scheduling, coordinating, control and data reconciliation and regression in either off- or on-line environments.

As a superset of the state-task network (STN) (Kondili et al., 1993; Shah et. al., 1993) and the resource-task network (RTN) (Pantelides, 1994) superstructures, the unit-operation-port-state superstructure (UOPSS) built into IMPL provides the arbitrary, ad

hoc or anywhere-to-anywhere connectivity generally referred to as a flowsheet, topology, mapping, routing or block-diagram in terms of its various shapes, objects or structures necessary to construct and configure it (Kelly and Menezes, 2019). UOPSS is more than a single network given that it is comprised of two networks we call the physical network (unit-port) and the procedural network (operation-state). The physical network involves the units and ports (equipment, structural) and the procedural network involves the operations (tasks) and states (activities, functional). Brunaud et al. (2020) showed the CPU or computer processing time reduction of large discrete optimization from hours to minutes and seconds by better modeling formulation of the quantity and logic flow networks in the UOPSS when compared to STN and RTN.

Moreover, in IMPL, multiple scenarios may be modeled and solved simultaneously into one problem where certain variables are linked or tied together to find essentially one solution to multiple sub-problems simultaneously, i.e., one solution to a family, group or collection of problems is known as scenario optimization or decision regression. This can be used in IML by configuring flags to access the results from one solution to be read in another solution, only for a single iteration. For several steps of iteration, this should be coded in a computer language to access IMPL's results using IPL and/or IMPC.

3. Industrial modeling and programming code (IMPC)

Also known as the internal mathematical programming code, IMPC is built upon Industrial Algorithms Limited's *Industrial Fortran Infrastructure* (I4I) that enables the developer user, modeler or analyst the capability to enhance, extend and encapsulate the standard or super-problem UOPSS-QLQP (structure-driven and semantic-driven) modeling in IMPL. This involves its own resource-entity roster-enumerators of sets, catalogs, lists, parameters, variables, constraints, derivatives, expressions and formulas (global / common data memory structures) which is machine-code protected via Intel Fortran. Essentially, the purpose of IMPC is to give the developer user complete accessibility and autonomy to the solvers through IMPC's imperative and declarative modeling framework where a model is defined as any collection of the resource-entities that models and solves a problem or sub-problem. This means that the developer user may both integrate and isolate to any degree the standard or super-problem IMPL modeling using IMPC where all of the data contained in IMPL are completely interoperable with IML, IPL and IMPC as these are all based on IMPL's global or common sparse memory data structures.

Programming with IMPC is useful when the developer user is required to model or sub-model with IMPL's *blackblank* unit-operation subtypes and/or when some amount of non-standard and non-supported (non-UOPSS and non-QLQP) custom modeling is necessary which can be combined and coordinated with any of the standard and super-problem UOPSS-QLQP modeling constructs involving multiple unit-operation constraints, etc. IMPC does not embed any third-party algebraic modeling language (AML) such as GAMS, AIMMS, AMPL, MPL, OPL (CPLEX), MOSEL (XPRESS), ZIMPL (SCIP), CMPL (COIN-OR), GMPL (GLPK), SolverStudio, etc., and is similar to other computer programming based AML add-ons, plug-ins or toolboxes such as Matlab's YALMIP and CVX, Python's OptLang, PuLP, Pyomo and PyOpt, Java's OptimJ (no longer supported), Julia's JuMP, APMonitor's GEKKO in Python and R's ROI though IMPC is function-based and not object-oriented. The major difference between IMPC and the others mentioned is that IMPC is implemented into a machine-

coded language (Intel Fortran), not an interpreted byte-coded language (e.g., C#, Java, Javascript, Matlab, Python, Julia and R) and is what we call an *arrayic* language due to its whole-array vector processing approach to modeling. Of notable mention is the open-source (COIN-OR) FLOPC++ / FLOPCPP ("Formulation of Linear Optimization Problems in C++") which compiles into C++ machine-code, although it is not suitable for nonlinear problems. However, FLOPC++'s principal strength, like IMPC, lies in the fact that its modeling facilities are combined with a powerful general-purpose programming language.

Programming with IMPC empowers the developer user to not only model problems of industrial scale, size and scope, but also to solve these problems using any of the commercial solvers in addition to allowing access to IMPL's proprietary SLPQPE (Successive Linear Programming and Quadratic Programming Engine) solver which is a very competitive alternative to other nonlinear solvers. One of the primary reasons IMPL's SLPQPE algorithm has a competitive advantage in terms of performance and reliability, is due to the fact that it embeds all commercial LP and QP algorithms such as GUROBI, CPLEX, XPRESS, OPTONOMY and LINDO. Other useful IMPL solvers, accessible via IMPC, are the Successive Equality-Constrained Quadratic Programming Engine (SECQPE) and the Supplemental Observability, Redundancy and Variability Estimator (SORVE) for nonlinear and dynamic data reconciliation and parameter estimation with diagnostics (observability, redundancy and variance). And finally, as IMPC is empowered and embedded in the machine-coded language Intel Fortran, the speed of generating any model of any industrial-scale problem will be faster than any byte-coded language especially suited to on-line real-time applications. Furthermore, the memory management of IMPL and IMPC is such that it can be tuned and tailored to any problem or sub-problem in order to minimize the memory requirements so as to enable multi-problem parallelism.

4. Modeling and programming skills for shared working process

Figure 4 shows a structure of a teamwork involving the manufacturing site's employees as the core modeler to validate the formulation and results of a development of a solution determined by its headquarters.

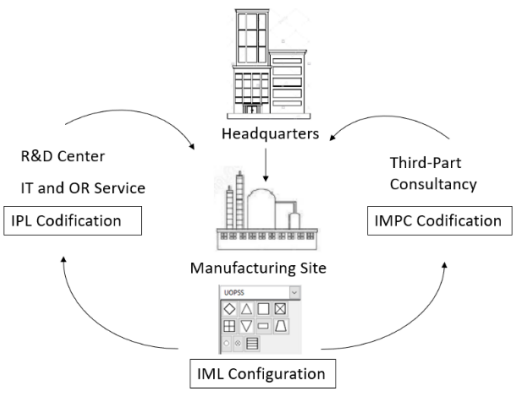

Figure 3. IMPL's modeling and programming steps within a company or organization.

This shared process-of-work considering the final user as the main actor can be achieved by using the IML configuration considering the vast number of parameters, variables and constraints and the UOPSS-QLQP elements found in IMPL. More complex requirements

for system integrations with database and application program interface (API) and specific libraries may be achieved in non-manufacturing centers using IPL and IMPL codifications. Therefore, the end-users will evolve from mere spectator of off-the-shelf software packages to high-skilled modelers capable to be involved in the development of solutions to be validated, operated and propagated by their own.

5. Conclusions

We present the concept for modeling and programming skills suitable for exploiting CAPE tools within a company among all segments to be involved in the development of a final solution. IMPL's feature to use IML configuration as well as IPL and IMPC codification allows the end-user to be involved as the main actor in the development of a system for its own future deployment. How the development and deployment (operational) teams work together and the perceptiveness of their accomplishments is a key factor for the involvement of the individuals and the success of the integrated groups with different skills and duties. IMPL is a highly comprehensive structure- and semantic-based language and has been successfully implemented in a broad range of industrial sectors such as oil and gas, petrochemicals, mining, pulp and paper, agriculture, among others. Its combination of configuration and codification modeling as well as mathematical and computer languages become the industrial modeling and programming language of IMPL the integrative system for development of industrial solutions to be demonstrated, deployed and disseminated in an organizational structure.

References

B. Brunaud, S. Amaran, S. Bury, J. Wassick, I.E. Grossmann, 2020, Batch Scheduling with Quality-Based Changeovers, Computer and Chemical Engineering, Computers and Chemical Engineering, 132, 106617.

J.D. Kelly, 2005, The Unit-Operation-Stock Superstructure (UOSS) and the Quantity-Logic-Quality Paradigm (QLQP) for Production Scheduling in The Process Industries, In Multidisciplinary International Scheduling Conference Proceedings: New York, United States, 327-333.

J.D. Kelly, B.C. Menezes, 2019, Industrial Modeling and Programming Language (IMPL) for Off- and On-Line Optimization and Estimation Applications. In: Fathi M., Khakifirooz M., Pardalos P. (eds) Optimization in Large Scale Problems. Springer Optimization and Its Applications, 152, 75-96.

E. Kondili, C.C. Pantelides, R.W.H. Sargent, 1993, A General Algorithm for Short-Term Scheduling Of Batch Operations – I MILP Formulation, Computers and Chemical Engineering, 17, 211-227.

B.C. Menezes, J.D Kelly, A.G. Leal, G.C. Le Roux, 2019, Predictive, Prescriptive and Detective Analytics for Smart Manufacturing in the Information Age, IFAC-PapersOnline, 52, 1, 568-573.

N. Shah, C.C. Pantelides, R.W.H. Sargent, 1993, A General Algorithm for Short-Term Scheduling of Batch Operations – II. Computational Issues. Computers and Chemical Engineering, 17, 229-244.

C.C. Pantelides. Unified Frameworks for the Optimal Process Planning and Scheduling. Proceedings on the Second Conference on Foundations of Computer Aided Operations. 1994, 253-274.

Sauro Pierucci, Flavio Manenti, Giulia Bozzano, Davide Manca (Eds.)
Proceedings of the 30th European Symposium on Computer Aided Process Engineering (ESCAPE30), May 24-27, 2020, Milano, Italy.
http://dx.doi.org/10.1016/B978-0-12-823377-1.50341-4

Studying Computational Fluid Dynamics in a New Dimension with Virtual Reality

Gregor D. Wehinger[a,b,*], Steffen Flaischlen[a,b]

[a]*Institute of Chemical and Electrochemical Process Engineering, Clausthal University of Technology, Leibnizstr. 17, 38678 Clausthal-Zellerfeld, Germany*
[b]*Research Center Energy Storage Technologies (EST), Clausthal University of Technology, Am Stollen 19A, 38640 Goslar, Germany*
wehinger@icvt.tu-clausthal

Abstract

Communication strategies for complex problems in the field of chemical and process engineering is becoming more and more important. Especially computational fluid dynamics (CFD) results require well-established spatial reasoning skills. In this contribution, we show how we implemented virtual reality (VR) into the Master course "CFD for process engineering" at Clausthal University of Technology. We discuss advantages and disadvantages of applying VR during the course. In addition, we show how VR can enable students to get a thorough understanding of the interplay between reactor design and performance.

Keywords: Virtual reality (VR), Computational fluid dynamics (CFD), higher education, chemical and process engineering

1. Introduction

A clear communication of scientific results is essential, especially nowadays where we are flooded by information. Similarly in education, communication is one key to success. In chemical engineering, transport phenomena play a paramount role and interact with local kinetics. Computational fluid dynamics (CFD) simulations in three dimensions, which are complex in terms of the underlying geometry and involve multi-phase and multi-physics phenomena, can help to identify potentials to improve existing designs or operating conditions. However, the presentation of these CFD results in two dimensions require high spatial reasoning skills. These skills are directly connected to good finale degrees in engineering programs (Sorby 2009). However, the same author highlights that 3D spatial skills are not given by birth but can be improved by training. The application of virtual reality (VR) can improve different learning concepts across many different fields, like material science, chemistry, medicine, and aerospace engineering (Caro et al. 2018, Merchant et al. 2012, Nicholson et al. 2006, Okutsu et al. 2013). A recent review states that especially head-mounted devices (HMD) in education are useful to improve cognitive skills related to remembering and understanding spatial and visual information and knowledge, as well as psychomotor skills related to head movement, such as visual scanning or observational skills (Jensen and Konradsen 2018). In light of these findings, VR could assist the students in deeper understanding of the complex interactions between reactor design and physics/chemistry in the field of chemical and process engineering. Exemplarily, Figure 1 shows a flow through a fixed-bed reactor in a 2D animated vector

scene (A) and in a virtual environment (B). The dimensions of the occurring eddy is much easier to realize in three dimensions.

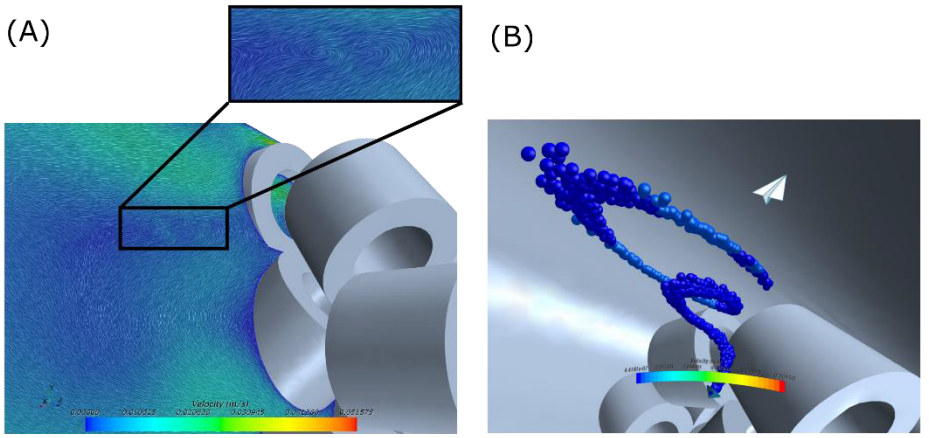

Figure 1: Flow through a fixed-bed reactor. (A) 2D vector scene. (B) 3D virtual environment.

In the Master's course "CFD for process engineering" at Clausthal University of Technology, small groups of students work on real-world problems from different areas of the chemical and process industry. First, the group learns the basics of CFD including governing equations, meshing and solving algorithms, as well as modeling techniques for multi-phase flows, etc. Second, the student groups work with customized input from the professor and CFD tutors on their specific problem. One fundamental part of the problem-solving process is the investigation of design variables in order to improve the process. Therefore, the group applies VR to explore their design proposition and its effect towards for example heat and mass transfer or conversion in the chemical reactor. Exemplarily, Figure 2 visualizes a "fly" through a fixed-bed reactor. Finally, VR supports the communication within the group and the understanding of the interplay between design and reactor performance.

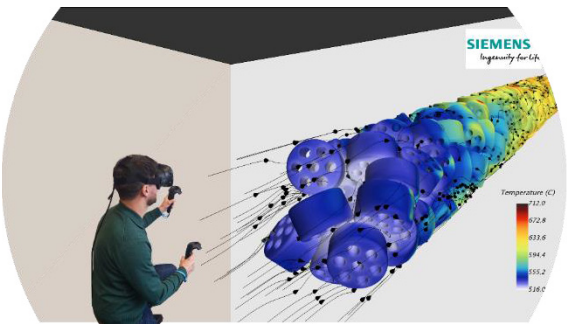

Figure 2: Virtual reality application of flow and heat transfer inside a fixed-bed reactor.

In this contribution, we show how we implemented VR into this Master's course at Clausthal University of Technology. We further discuss advantages and disadvantages of applying VR during the course. In addition, we show how VR can enable students to get a thorough understanding of the interplay between reactor design and performance.

2. Methods

2.1. Computational fluid dynamics and VR software

In computational fluid dynamics, the continuity, energy, and momentum conservation equations are solved numerically, in many cases with the Finite Volume Method. The CFD workflow consists of (i) pre-processing, (ii) solving, and (iii) post-processing. Hence, the typical CFD engineer needs a solid background in mathematics, fluid dynamics, heat transfer and computer programming. One type of CFD courses at universities focuses on the numerical methods part with only a few CFD applications. The other type of courses introduces a CFD software and let the students apply it to given problems. The inclusion of commercial CFD packages, such as ANSYS Fluent or STAR-CCM+ from Siemens PLM, guarantees a steep learning curve without having a strong theoretical background (Hu et al. 2008).

In this course, the commercial Computational Aided Engineering (CAE) solution package Simcenter STAR-CCM+ from Siemens PLM is used in order to teach the students the entire CFD workflow in one single integrated software environment. The software combines import and creation of geometries, mesh generation, solution of the governing equations, analysis of the results, and the connection to other CAE software. Figure 3 (A) shows the user interface with the appearing elements of the STAR-CCM+ software.

Over the last few years, the usage of VR for CFD post-processing has increased steadily in order to interpret the simulation results and communicate them to non-experts (Wu et al. 2010). Several software is capable to visualize the CFD results in three dimensions, e.g. ParaView, Unity3D, Ceetron 3D Viewer, and others. In this course, STAR-CCM+ VR is used which allows the students to explore CFD simulation results in a virtual environment. The running or already converged CFD solution can be loaded into STAR-CCM+ VR and the viewer can enter the virtual environment that the headset then displays. The viewer literally stands inside the CFD solution and examine the flow, temperature, and or concentration fields interacting with the digital prototype, see Figure 3 (B). In STAR-CCM+ VR, a floor below the model and a ceiling above appear. The floor in the scene corresponds to the real floor and the ceiling is set at a predefined position.

2.2. Hardware

STAR-CCM+ VR is designed to run with the head-mounted display "HTC Vive". This device applies a room-scale technology with two sensors to capture the movement in the room. Two wireless controllers mimicking hands allow haptic feedback in the virtual reality. In addition, the controllers provide several options for controlling view, movement, and other aspects of the scene. In order to guarantee a fluent meshing and solving with STAR-CCM+ and flying through the STAR-CCM+ VR scene, Siemens PLM suggests the following minimum requirements (Siemens PLM, 2019):

- Surface remesher: ~0.5 GB RAM per million faces
- Volume meshing: ~1 GB RAM per million cells for polyhedral cells
- Solving a single phase RANS model with the Segregated Solver: ~1 GB RAM per million polyhedral cells
- Using STAR-CCM+ VR: Windows 10 64-bit and NVIDIA Quadro P4000 or better and SteamVR software, which is installed as part of the HTC Vive setup

HTC recommends the following space for a fluent VR experience:

- Standing or sitting position: no minimum space requirements
- Room filling VR: minimum are of 2 m x 1.5 m required, maximum room size of 3.5 m x 3.5 m

From our experience, it is possible to use the VR environment in the standing or sitting position for testing and quick development of VR CFD scenes. Nevertheless, the room filling VR provides the full experience and leads to better understanding of e.g. geometric dimensions by a "real" walk through the scene. For this purpose, we have developed a VR lab, where the students have the chance to use 3 VR stations located on a full space of 120 m^2.

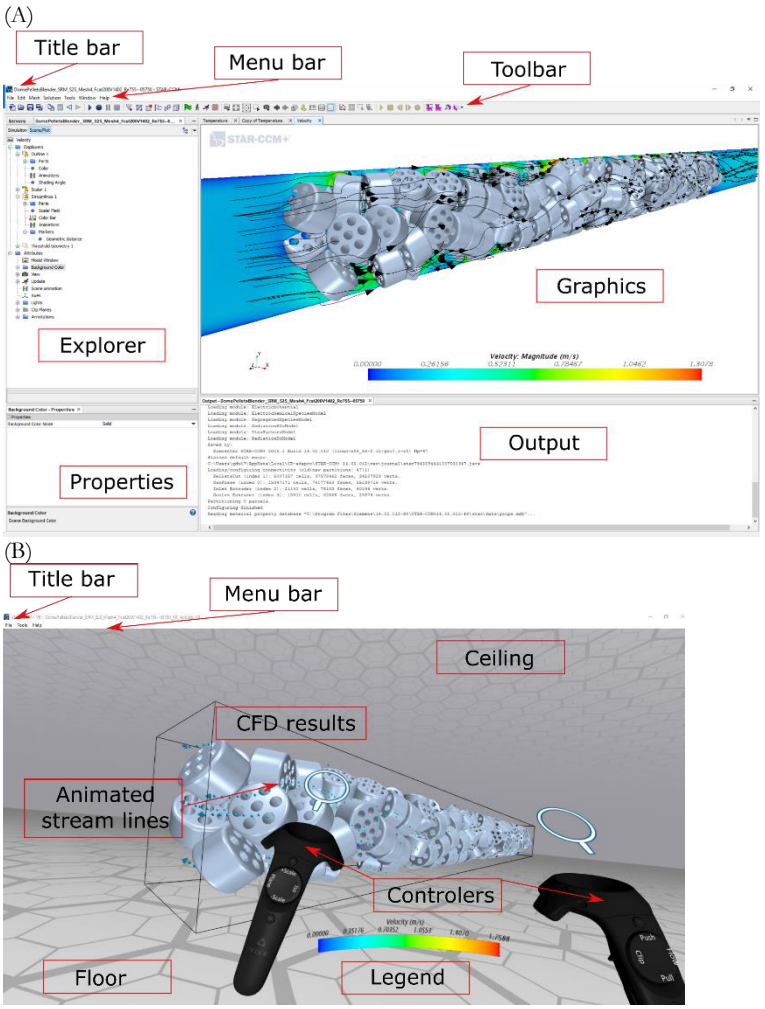

Figure 3: Graphical user interface of (A) Simcenter STAR-CCM+ and (B) STAR-CCM+ VR environment.

2.3. Online learning system

Moodle is used as an online learning management platform. It includes the weekly schedule, problems, documents, a chat forum, and the URL for all video tutorials. In addition, the students can participate in online tests and can hand in electronic documents, like posters and final reports. There are two types of video tutorials: CFD simulations and VR scenes. The video tutorials are basically records of the computer screen, on which the

tutors guide the viewer through different CFD simulation workflows or through the VR scenes and explains the steps to take.

3. Seminar contents

The seminar covers four ECTS credits and consists of four different phases: (i) a seminar for introducing CFD, (ii) hands-on training, (iii) students' projects, and (iv) the assessment. In five seminar sessions, the theoretical background of CFD is presented and discussed with the students. In this part of the course, an overview about recent CFD applications in industry is given, the concept of conservation equations is repeated, solving strategies are presented, different types of meshes and local mesh refinement approaches are discussed, and finally, special phenomena, like turbulence, multi-phase flows, and chemically reacting flows, are examined.

The four hands-on training sessions give the students the possibility to get in touch with the commercial software STAR-CCM+ and solve small problems individually at the computer. The students are personally assisted during the training by CFD tutors, which are Master students from higher semesters and PhD students. The problems to be solved are supported by short video tutorials, which are available on the Moodle webpage of this course. They give a short overview about geometry generation, meshing, solving, and post-processing in 2D and 3D Scenes in STAR-CCM+.

After the four hands-on training sessions, an individual test assesses the theoretical knowledge of CFD and the practical problem solving strategies within STAR-CCM+. With a positive result in the test, the students qualify for the group project phase. If students fail the test, they have the opportunity to repeat it one week later.

In the group project phase, groups of three students team up and work on a given CFD problem for at least 8 weeks. The problems typically consists of a validation case based on literature data. In a consecutive step, the students change certain geometrical features in the problem in order to obtain an improved process. During this phase, the students actively apply VR to explore their problem in three dimensions. This helps the students to identify quickly how the geometry/reactor/device interacts with the local flow field, temperature and/or concentration distribution. Consequently, the students are early enabled to judge on their geometrical feature modification. In addition, VR helps to communicate within the team, since more than one viewer can enter the VR scene.

After half of the project phase, the students communicate their preliminary results with posters and within the VR environment. The setting is similar to a classic poster session at a scientific conference, whereas PhD students and professors from the department act as conference participants. The basic principles of creating a well designed poster are taught earlier with each group individually. After the poster conference, the students received feedback from many experts such that they can proceed with the group project.

At the end of the semester, each group hands in a final report written as a scientific communication. In Moodle, evaluation criteria for the final report are given in order to keep the evaluation process as transparent as possible.

4. Discussion

Jensen and Konradsen (2018) give a comprehensive review about using VR HMDs in education and training. The authors recognized a number of situations where HMDs are useful for skills acquisition. Especially important for this CFD course are cognitive skills related to remembering and understanding spatial and visual information and knowledge as well as visual scanning or observational skills. We were able to observe this skills acquisition. Nevertheless, we have also witnessed cybersickness, especially where the

visual animation was not presented fluently. This was manly attributed to the technical limitation of the peripheral device. In order to not overcharge the students with new software and theoretical input, we decided to introduce the usage of VR in a stepwise approach. In the first third of the semester, the students use VR in prepared scenes. This guarantees a quick start into VR. At this time, the students should be familiar with the CFD workflow and developed a rough CFD problem solving strategy. After the first third of the semester, the students apply VR independently to investigate their CFD simulations.

5. Conclusion

In this contribution, we report on the integration of VR into a Master course for CFD simulations in the field of chemical and process engineering at Clausthal University of Technology. STAR-CCM+ is used as a user-friendly CFD software in order to guarantee learning success for students with a heterogeneous background in numerical mathematics, transport phenomena, and fluid mechanics. The CFD results obtained with STAR-CCM+ can be visualized with relatively small effort with the head-mounted display system HTC Vive and the STAR-CCM+ VR software. The total costs for an appropriate computer and the HMD is roughly 3,000 € plus enough space to walk inside the VR environment. During our CFD course, we have already observed a very positive attitude of the students towards using VR for immersing in the CFD results. The students projects guarantee a thorough examination with CFD and VR. In general, the entry threshold into VR is low, since many of the students are familiar with 3D gaming or even already use VR in their spare time. Still, we need the feedback of a larger number of students to make significant statements about the efficiency of including VR to this course.

References

V. Caro, B. Carter, S. Dagli, M. Schissler, J. Millunchick, 2018, Can Virtual Reality Enhance Learning: A Case Study in Materials Science, In 2018 IEEE Frontiers in Education Conference (FIE), 1-4

J. Hu, L. Zhang, X. Xiong, 2008, Teaching Computational Fluid Dynamics (CFD) to Design Engineers, ASEE

L. Jensen, F. Konradsen, 2018, A review of the use of virtual reality head-mounted displays in education and training, Education and Information Technologies, 23(4), 1515-1529

Z. Merchant, E.T. Goetz, W. Keeney-Kennicutt, O.M. Kwok, L. Cifuentes, T.J. Davis, 2012, The learner characteristics, features of desktop 3D virtual reality environments, and college chemistry instruction: A structural equation modeling analysis, Computers & Education, 59(2), 551-568

D.T. Nicholson, C. Chalk, W.R.J. Funnell, S.J. Daniel, 2006, Can virtual reality improve anatomy education? A randomised controlled study of a computer- generated three- dimensional anatomical ear model. Medical education, 40(11), 1081-1087

M. Okutsu, D. DeLaurentis, S. Brophy, J. Lambert, 2013, Teaching an aerospace engineering design course via virtual worlds: A comparative assessment of learning outcomes, Computers & Education, 60(1), 288-298

Siemens PLM, 2019, What are approximate RAM requirements for meshing and solving? The Steve Portal, https://thesteveportal.plm.automation.siemens.com

S.A. Sorby, 2009, Educational research in developing 3- D spatial skills for engineering students, International Journal of Science Education, 31(3), 459-480

B. Wu, G, Chen, J. Moreland, D. Huang, D. Zheng, C.Q. Zhou, 2010, Industrial application of CFD simulation and VR visualization. In ASME 2010 World Conference on Innovative Virtual Reality, 51-59, American Society of Mechanical Engineers.

Sauro Pierucci, Flavio Manenti, Giulia Bozzano, Davide Manca (Eds.)
Proceedings of the 30th European Symposium on Computer Aided Process Engineering (ESCAPE30), May 24-27, 2020, Milano, Italy.
http://dx.doi.org/10.1016/B978-0-12-823377-1.50342-6

Academic Education Involvement in Refinery Advanced Process Control

Cristian Pătrășcioiu*, Marian Popescu, Nicolae Paraschiv, Cristina R. Popa, Nicoleta Nicolae

Automatic Control, Computers and Electronics Department, Petroleum-Gas University of Ploiesti, Bd. Bucuresti, 39, Ploiesti 100680, Romania
cpatrascioiu@upg-ploiesti.ro

Abstract

The paper presents the achievements of Automatic Control, Computers and Electronics Department of Petroleum-Gas University of Ploiesti in the direction of developing the skills for the engineers' activity in the field of Refinery Advanced Process Control. In order to reach this objective, the teachers of the department have developed the specializations of Bachelor, Master and Doctorate in the field of Systems Engineering, a research area recognized in Romania. The paper is structured in four parts, each part presenting the organization of the education process and the obtained results.
Keywords: education, advanced process control, modelling, simulation, identification.

1. Curriculum of Advanced Control System Education

To increase the performance of chemical process control systems is necessary to develops components of Advanced Control Systems. Achieving this objective involves the following stages of study:

- Modelling and simulation of processes from refineries
- Dynamic identification of processes
- Design of advanced control algorithms

The final objective of the applied research is the design and testing of advanced automatic systems for refineries processes. From the point of view of the educational process carried out in Petroleum - Gas University of Ploiesti, Romania, the previously defined objective is achieved by going through the disciplines of the Master's degree specializations, presented in Table 1.

Table 1. Disciplines associated with Advanced Process Control Curriculum

Discipline	Study program
Advanced automation of chemical processes	Computer Aided Chemical Engineering in Refineries and Petrochemistry
Dynamic simulation of chemical processes	Computer Aided Chemical Engineering in Refineries and Petrochemistry
Advanced control systems for chemical processes	Advanced Technologies in Oil Processing
Advanced control algorithms	Advanced Automation
Distributed supervisory and control systems	Advanced Automation
Automatic control of chemical processes	Advanced Automation

All these disciplines contribute to the training of the specialists of chemical engineering and control engineering. The training of specialists in the field of Advanced Control Systems is continued in the doctoral studies. There is an average periodicity of 3 years in the completion of theses in the field of Advanced Process Control, a fact that attests the scientific and research concerns of the University but also the involvement of the industrial environment. Some examples of PhD theses in this field are: Research on the model-based control of fractionation processes, Contributions regarding the hierarchical control of the catalytic cracking process, Contributions regarding the development of a hierarchized distributed control system for fractionation processes, Contributions regarding the advanced control of the refining gas purification process.
All the elements listed above support the training of engineers from Petroleum - Gas University of Ploiesti in the field of Advanced Process Control.

2. Process modelling and simulation

From the automatic control point of view, the processes in the refineries can be approached are the following: tubular furnaces, distillation columns, absorption columns, catalytic cracking reactor. The modelling have been developed using analytical or simulation software way. The used software simulators have been HYSYS, Unisim Design and PRO II. Results of modelling and simulation refer to steady state model, process sensibility analysis, and process channels gains.
For tubular furnaces from refineries (e.g. furnaces in atmospheric distillation units), mathematical models for fuel combustion and heat transfer have been developed, in order to be used for optimal combustion control (Pătrăşcioiu and Marinoiu, 1997, 1998). Other research focused on modelling the tubular furnaces using Unisim FPH simulator, the aim being the validation of the developed analytical model (Pătrăşcioiu, 2016).
For the distillation columns, the research started from the distillation columns of binary mixtures (propylene-propane). The researches progressively followed several stages:

- Steady-state process modelling (Pătrăşcioiu et al., 2008, Pătrăşcioiu and Petre, 2017, Pătrăşcioiu and Cao, 2017);
- Dynamic process modelling and control systems modelling (Pătrăşcioiu et al., 2014, Popa and Pătrăşcioiu, 2010, Popa, 2013, Popa et al., 2015);
- Study of quality control systems (Mihaescu et al., 2013, Popescu, 2018, Pătrăşcioiu et al., 2015, Pătrăşcioiu and Florea, 2018).

Another research direction is the modelling of distillation columns equipped with heat pumps. The results highlighted the complexity of the process compared to the classic one and implicitly the difficulties of modelling the installation (Pătrăşcioiu and Cao, 2017). However, some progress has been made, with the prospect of designing, modelling and simulating a quality control system (Pătrăşcioiu and Cao, 2016).
Of the reactors existing in refineries, a special interest is represented by the reactor - regenerator block from the catalytic cracking plant, due to its special economic effect. An analytical mathematical model of the reactor and reaction block and subsequently a dynamic model (Popa, 2013) were developed.

3. Dynamic identification technique

Dynamic identification can be defined as a simple construction of the dynamic mathematical model, model determined on the basis of experimental data or on the basis of results obtained by simulation, test or normal operation.
The researchers used two software tools for systems identification. The first instrument was developed within the university and disseminated through publications (Pătrăşcioiu

and Mihaescu, 2011). The second instrument is the System Identification Toolbox – MATLAB (Pătrăşcioiu and Popa, 2014). This computer tool has some using particularities. Thus, the input and output data of the discrete function subjected to numerical processing are organized in the form (Δu_i, Δy_i), i=1,…,n. The time associated with the dynamics of the system is built internally, specifying the initial moment and the associated incremental value. Consequently, all sampling time intervals will be equal.
In the following are presented some of the transfer functions associated with the catalytic cracking process from a refinery, functions obtained using the System Identification Toolbox software tool.
The catalytic cracking process is a multivariable system, its dynamic characterization being extremely difficult. The decomposition of the multivariable system into monovariable subsystems is shown in Figure 1 (Popa, 2013).

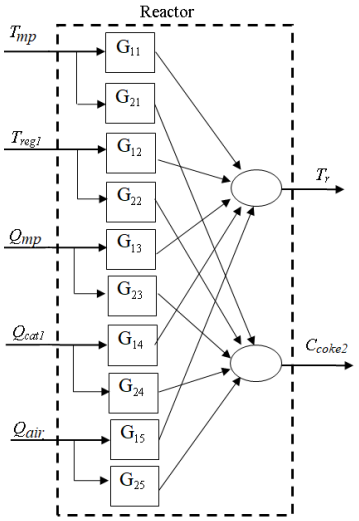

Figure 1. FCC reactor

Using the technique described above, the transfer functions of the sub-processes that characterize the catalytic cracking reactor were determined, Table 2.

Table 2. Identification of sub-processes from FCC

Input	Output	
	Riser output temperature	The amount of coke deposited on the catalyst from the cracking reaction
Temperature of raw material	$G_{11}(s)=\frac{0.17}{0.048s+1}$	$G_{21}(s)=\frac{2.2\cdot10^{-4}}{0.047s+1}$
Temperature of the regenerated catalyst	$G_{12}(s)=\frac{0.76}{0.048s+1}$	$G_{22}(s)=\frac{0.0013}{0.06s+1}$
Flowrate of raw material	$G_{13}(s)=\frac{-7.72\cdot10^{-4}}{0.052s+1}$	$G_{23}(s)=\frac{-9.5\cdot10^{-7}}{0.048s+1}$
Flowrate of the regenerated catalyst	$G_{14}(s)=\frac{1.751\cdot10^{-4}}{0.062s+1}$	$G_{25}(s)=\frac{2.6\cdot10^{-8}}{0.047s+1}$

4. Advanced control algorithms

The advanced control systems developed at Petroleum-Gas University of Ploiesti are based on the following advanced control algorithms:

- Feedforward control
- Model-based control
- Optimal control

In the following will be presented some results of the research regarding model-based control.

The two model based algorithms presented in the following are IMC (internal model control) and MPC (model predictive control). Both algorithms were used for the quality control of a butylene-butane distillation column.

The internal model control technique uses a representation of the process in the algorithm, based on the process parameters obtained using identification methods. Thus, such a model (Cîrtoaje and Băieşu, 2018) is

$$G_M(s) = \frac{K_M e^{-T_m s}}{(T_M s + 1)^2} \tag{1}$$

where K_M is the model gain (which usually is considered equal to process gain), T_M - model time constant (which depends on the process transient time), T_m – process dead time.

After tuning the two IMC controllers associated to the quality control of the separated products from the butylene-butane distillation column, the best system responses were obtained to set-point changes (Pătrăşcioiu and Popescu, 2018), Figure 2.

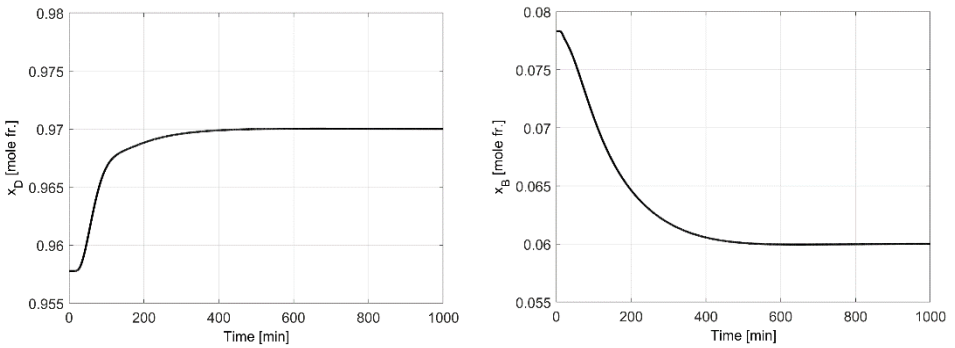

Figure 2. Concentrations evolutions to set-point changes when using IMC

Another model-based control algorithm used in the advanced control research is MPC. A control structure for the butylene-butane distillation column which involves MPC is presented in Figure 3. The multivariable MPC controller has a structure which uses the process transfer functions identified for the control agents – outputs channels and disturbances – outputs channels.

The MPC controller is tuned (by modifying sample time, prediction horizon and control horizon) so that the control system response to set-point changes (Figure 4) does not have overshoot or oscillations and the transient time is comparable to or smaller than the process transient time (Nicolae et al., 2019). Also, the system response to disturbances modifications is adequate, with the control system managing to bring back the controlled variable to the set-point value.

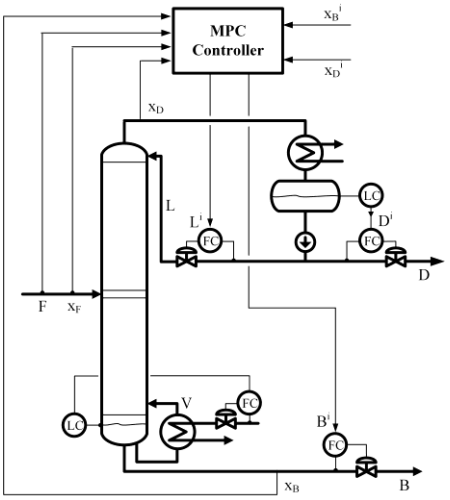

Figure 3. Control structure based on MPC controller

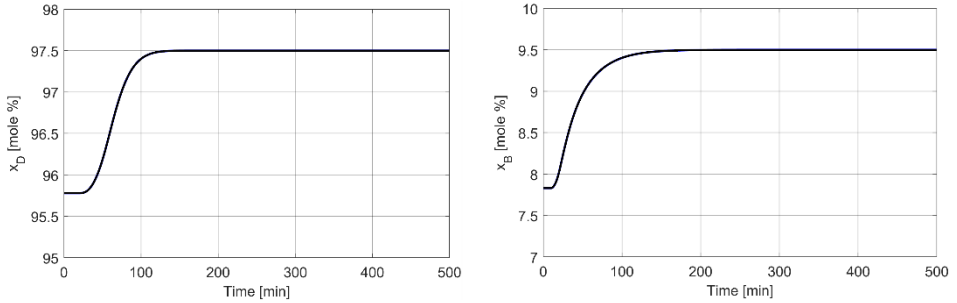

Figure 4. Concentrations evolutions to set-point changes when using MPC

5. Conclusions

At the Petroleum - Gas University of Ploiesti, the didactic structures aim to develop the skills for the engineers' activity in the field of Refinery Advanced Process Control. The didactic activity for engineers is carried out within the Master's specializations and in the doctoral courses. The activity was materialized by the elaboration of doctoral theses in the field of Refinery Advanced Process Control.

The components of scientific research developed within the doctoral theses refer to process modelling and simulation, dynamic identification techniques, advanced control algorithms. Each research direction is exemplified by results published in the academic literature.

All the elements presented in the article demonstrate the efficiency and performance of higher education within the University of Petroleum - Gases in Ploiesti.

References

V. Cîrtoaje, A. Băieşu, 2018, On a Model Based Practical Control Algorithm, Studies in Informatics and Control, vol. 27, No. 1, 83-96.

D. Mihaescu, N. Paraschiv, C. Pătrăşcioiu, A. Băieşu, 2013, Advanced Control System for a Refinery Hydrogen Sulphide Absorption Plant, REV. CHIM. (Bucharest), vol. 64, no. 9, 1028-1036.

N. Nicolae, M. Popescu, C. Pătrăşcioiu, 2019, Implementation of Advanced Process Control in Refineries, Proc. of the 23rd International Conference on System Theory, Control and Computing (ICSTCC), Sinaia, Romania, 95-100.
C. Popa, C. Pătrăşcioiu, 2010, New Approach in Modelling, Simulation and Hierarchical Control of the Fluid Catalytic Cracking Process I - Process modelling, REV. CHIM. (Bucharest), vol. 61, no. 4, 419-426.
C. Popa, 2013, Hierarchical control of the catalytic cracking process (in Romanian: Reglarea ierarhica a procesului de cracare catalitica), MatrixRom, Bucharest.
C. Popa, C. Pătrăşcioiu, O. Cangea, 2015, Performance Analysis of the Four Lump Kinetic Model of the Riser Catalytic Cracking, REV. CHIM. (Bucharest), vol. 66, no. 6, 883-885.
M. Popescu, 2018, Distillation column hierarchical control, REV. CHIM. (Bucharest), vol. 69, No. 9, 2585-2590.
C. Pătrăşcioiu, V. Marinoiu, 1997, Automatic control system for tubular furnaces from the atmospheric and vacuum distillation installation of crude oil I. Mathematical modelling of combustion and thermal transfer (In Romanian: Sistem automat evoluat pentru cuptoarele tubulare din instalatia de distilare atmosferica si in vid a titeiului I. Modelarea matematica a combustiei si transferului termic), REV. CHIM. (Bucharest), vol. 48, no. 4, 357-369.
C. Pătrăşcioiu, V. Marinoiu, 1998, Modelling and Optimal Control of an Industrial Furnace, Proceedings from the 5th IFAC Symposium, Corfu, Greece, 8 -10 June 1998, 477-482.
C. Pătrăşcioiu, M. Petre, I. Rabahi, 2008, Modeling, simulation and optimal control of the natural gas Jibissa plant, Proc. of the 8th conference on Simulation, modelling and optimization (SMO'08), 133-137.
C. Pătrăşcioiu D. Mihaescu, 2011, The Numerical Algorithms Used to the Identification of the First Order Dynamic Models. Case Study, Proceedings of the IASTED International Conference Modelling, Identification, and Control (MIC 2011), 167-173.
C. Pătrăşcioiu, C. Popa, 2014, System identification. System Identification Toolbox or properly algorithms?, Advances in Automatic Control - Proceedings of the 16th International Conference on Automatic Control, Modelling & Simulation (ACMOS '14), Brasov, Romania, 2014, 305-310.
C. Pătrăşcioiu, M. Popescu, N. Paraschiv, 2014, Specific Problems of Using Unisim Design in the Dynamic Simulation of the Propylene-Propane Distillation Column, REV. CHIM. (Bucharest), vol. 65, No. 9, 1086-1091.
C. Pătrăşcioiu, N. Paraschiv, M.A. Cao, M. Popescu, 2015, Robust Control of Industrial Propylene-Propane Fractionation Process, Computer Aided Chemical Engineering, Elsevier, Vol. 37, 1745-1750.
C. Pătrăşcioiu, 2016, The Modeling and Simulation of the Convection Section of the Atmospheric Distillation Plant Heaters, REV. CHIM. (Bucharest), vol. 67, no. 8, 1599-1606.
C. Pătrăşcioiu, M.A. Cao, 2016, Characterization and control of the distillation column with heat pump, Proc. of the 8th International Conference on Electronics, Computers and Artificial Intelligence (ECAI), Ploiesti, Romania, 1-8.
C. Pătrăşcioiu, M.V. Petre, 2017, Tubular furnaces performances study using UniSim FPH simulator, REV. CHIM. (Bucharest), vol. 68, no. 8, 1790-1795.
C. Pătrăşcioiu, M.A. Cao, 2017, A Comparative Study of the Modeling and Quality Control of the Propylene-Propane Classical Distillation and Distillation Column with Heat Pump, World Academy of Science, Engineering and Technology International Journal of Chemical and Molecular Engineering, Vol. 11, No. 5, 394-399.
C. Pătrăşcioiu, A. Florea, 2018, Simulation of benzene column distillation for quality control system design, Proc. of the 22nd International Conference on System Theory, Control and Computing (ICSTCC), Sinaia, Romania, 39-45.
C. Pătrăşcioiu, M. Popescu, 2018, Study of the control systems of a distillation process equipped with heat pump, REV. CHIM. (Bucharest), vol. 69, no. 9, 2535-2540.

Sauro Pierucci, Flavio Manenti, Giulia Bozzano, Davide Manca (Eds.)
Proceedings of the 30th European Symposium on Computer Aided Process Engineering
(ESCAPE30), May 24-27, 2020, Milano, Italy.
http://dx.doi.org/10.1016/B978-0-12-823377-1.50343-8

Aspen Hysys – Unity Interconnection. An Approach for Rigorous Computer- Based Chemical Engineering Training

Pedro Santos*, Tom Van Gerven

KU Leuven - CIT, Celestijnenlaan 300F, Leuven, Belgium
pedro.santosb@kuleuven.be

Abstract

Virtual educational simulations, ranging from realistic plant simulators for operators over internal visualizations of process units to virtual labs for students, are a focus of interest for chemical engineers in both industry and universities, as they can provide advantages of real life training without the costly requirements of real training setups. However, the application of these technologies is restricted by the fact that the design is complex, time demanding, and a task that most chemical engineers are not familiar with. One challenging aspect is the need to provide a simulation that behaves realistically, especially for complex systems: solutions such as hand-coding the behaviour of each element or directly coding a custom model of the system can often be exceedingly demanding, and are generally hard to reuse for new projects due to being highly targeted. Instead, a more favourable option is to use an available industry-standard flowsheet simulator (e.g. Aspen Plus, Aspen HYSYS, UniSim, CHEMCAD, DWSim), software with which most chemical engineers are familiar, and that can both guarantee rigorous behaviour and minimize design time. The main challenge with this option (beyond access to a license of the software) is connecting the model to the educational simulation, typically designed in a different software. In this work we study the interconnection between Aspen HYSYS and Unity (a game engine used to design interactive environments) using ActiveX, as opposed to some other popular methods such as OPC, and elaborate on both the technical aspects and the advantages and disadvantages of this methodology.

Keywords: Virtual educational simulations, Aspen HYSYS, Unity

1. Introduction

Virtual educational simulations (VESs) are popular educational tools, with research been done on the usefulness of this tools both in general (Aldrich, 2005) and for the process industry in particular, focusing generally on either virtual laboratories (see the bibliometric analysis by Heradio et al. (2016)) or operator training simulators (OTSs) (such as those developed by Manca et al. (2013), Ahmad et al. (2016), or Ouyang et al. (2017), among others). However, there is not much information on how to develop such tools from a technical point of view: while one can expect a multinational company to subcontract a targeted 3D VR environment for their operator training, it is probably overly ambitious to expect researchers, teachers, and even small companies, to have access to such resources. In these latter cases, any new VESs are often developed in-house, and complexity of design will be the main factor as to whether any solution is attempted or abandoned.

One of the challenges of designing a VES is providing a realistic behaviour to the underlying model. It is obvious that a simulation that behaves incorrectly will encourage the learning of wrong knowledge, as the user believes the behaviour to be correct. A first approach to provide rigorous behaviour is to directly code all interactions possible in the simulation and their effects. For this approach the complexity grows exponentially with the addition of new elements (that must implement the interactions with all previous elements), and so it is best practice to keep possible interactions limited: Nazir and Manca (2015), provide an example of an OTS where the user must select correctly which valves to open or close to prevent an accident, while Ouyang et al. (2017), implement a multiplayer simulation of a whole coking plant, but limit the possible interactions by users to a small set.

However, many scenarios cannot be properly reflected with such a limited set of options, and, for these, implementing a mathematical model of the simulated process can be a better choice. A first alternative is to implement the model directly, by coding it into whichever tool chosen to create the environment, but here the complexity of the dynamics of the system will play a large role in workload, making it often preferable to represent ideal behaviour with limited elements: for example, Mendes et al. (2010), implement a VES for ideal multicomponent distillation in this way, and Pavol et al. (2017) develop a laboratory for basic control in Matlab.

Modeling software is widely used in process engineering, and most engineers are at least familiar with the more widely known tools, such as Aspen Plus, Aspen HYSYS, UniSim, CHEMCAD, DWSim. Some of these tools provide their own VES software, but this is often expensive, rarely available in universities, and, more importantly in the eyes of the authors, in all cases oriented towards operator training, so that the functionalities and tools are heavily limited for any other purpose. Ahmad et al. (2016) provide an example of use for this technology for training of operators in biodiesel synthesis using Aspen OTS Framework.

When not using these specialized tools for VES design, one can instead benefit from some of the available general design tools, such as game engines, which are widely used for the design of a variety of virtual environments. Then the challenge of communicating between the simulation and the environment appears, that is, how to transfer information (such as the position of a valve or a temperature value) from the software where the chemical engineering models are being calculated, to the software which renders the environment that the user interacts with. The authors believe this challenge to constitute one of the major impediments for this approach, and in this work propose a methodology for implementing such a data exchange between Aspen HYSYS as simulator and Unity as virtual environment.

2. Choice of tools

2.1. Virtual environment designer

Unity 2019.2.19f1 has been chosen as the virtual environment design tool. Unity is a game engine, capable of creating both 3d and 2d environments, and designed in C++. It allows for the designer to include programmed behaviours in C#, implemented in Mono, an open-source platform-neutral implementation of the .NET standard, which eases the task of using ActiveX (see lower section).
Beyond lending itself naturally to the implementation of an ActiveX connection, Unity has been favoured as a choice because it is widely used, relatively easy to learn, and it

can develop environments to be implemented in all major formats (pc, phone, virtual reality glasses, etc). Previous works have already used the Unity engine for development of VESs in the process industry, such as the previously mentioned coking plant by Ouyang et al. (2017).

2.2. Process simulator

Aspen HYSYS V10 (AspenTech, 2011) has been chosen as the process simulator. HYSYS is one of the first process simulators developed, and has been widely used in research, industry and education, particularly for petrochemical processes. It was developed in C++, and the decision was made in an early stage to leave all program objects and functions open (AspenTech, 2011), which eases interconnection significantly, an attractive quality for the work proposed. It provides a variety of available thermodynamic and unit operation models, as well as vast thermodynamic libraries (generally the same included in Aspen Plus since V7).
The uses of this software in the process industry would be too many to elaborate, but particular interest is placed in the work of Santos et al. (2016), who used this same tool as a base process simulator for a VES of a petrochemical platform, developed as well in Unity.

2.3. Interconnection

ActiveX is used to communicate between Unity and Aspen HYSYS. Previous literature often uses OPC (OLE for process control) to enable a connection between environment and process simulator (e.g. Santos et al., 2016). This technology was developed for inter-software communication in the process industry, and has several advantages, such as parallel communication (two servers accessing the same client simultaneously), implementation in a network through tunnelling, and robustness. It is, however, lacking flexibility, as the variables that can be communicated must be determined during the setup of the server (so changes to the simulation like adding a new flow stream are not possible), and, while current process simulators often include tools to set up an OPC, the process is still complex, especially for engineers unfamiliar with OPC. An exception to this general OPC use are Manca et al. (2013), where an OTS is developed which mentions data exchange through OLE (former name of ActiveX) to both UniSim and an in-house accident simulator.
ActiveX has been used in previous work on interconnection, such as by Vaquerizo and Cocero (2018) where it is used as a part of data extraction from Aspen Plus to ANSYS Fluent, and it allows for a higher degree of control over the program, as well as more flexibility, since the variables and methods available are any that are enabled by the provider.

3. Technical implementation

The basics for interconnection with Aspen Hysys through ActiveX can be found in the automation manual provided by the supplier (AspenTech, 2011), which expands on basic functionalities, giving examples for Visual Basic for Applications (VBA). As indicated there, a necessary element of the process is the file Hysys.tlb, a type library that allows for the use of the interfaces and methods of Aspen HYSYS and that can be found in the installation directory of Aspen HYSYS.
Unity does not accept the type library extension. One possible approach to solve this problem is to convert the file to a dynamic library (dll) with the use of the Type Library Importer tool of Visual Studio. Once this is done, the dll file can be included into any

Unity project that requires this communication, where Unity will automatically recognize it and add it into the C# project. The explanations of the Aspen HYSYS automation manual (AspenTech, 2011) can be followed generally, with the peculiarity that the programming language is C# and the specific structure of the Unity Engine environment. C# scripting in the Unity engine works by adding new scripts into game objects, which by default include the class "MonoBehaviour": this class implements several default methods that execute during different events, such as Awake, that executes at the start of the environment, and Update, that executes each frame. Generally we propose to include an object for each simulation to be interconnected, so that each simulation can be started at the Awake method of its object, and can be stored as a public interface of the hysys.Simulation type within the object, accessible to other objects.

3.1. Technical challenges

The major limitation found in the study is a consistent error when interacting with vectors retrieved from HYSYS (concentrations, temperature profiles in a column, etc). Any of this variables cannot be returned to Unity, as an error will be displayed when trying to retrieve any value.

However, the problem can be fully solved by preparing the simulation so that all relevant values can be recovered as a scalar: e.g. in order to measure the concentrations in a stream, separating a stream into pure components and measuring the ratios by means of molar flows; in order to measure the temperature at a plate of the column, extracting a 0 flow outlet in the relevant column plate and measuring the temperature of that flow. Also, as the ActiveX connection allows for full flexibility and manipulation, it is possible to do these fixes dynamically when the value is needed, instead of previously for all possible wanted variables.

A second problem found is that executables built will not work: particularly, they will stop execution when trying to access the HYSYS simulation: this means that the VES can only be used within the Unity editor in play mode. However, since this software is free and any computer that can execute HYSYS can also execute the Unity editor, the authors did not find much problem with this. This issue would become significant when commercial releases are intended, or in hardware with very limited memory storage.

In any case, it should be noted that these technical issues are unexpected errors and not inherent to the technology. It is possible that some technical reworking or future releases will fix them entirely.

3.2. Resulting interconnection

Once the communication is achieved, and taking into account the limitation described in the previous subsection, all values from the simulation can be accessed from the training simulation. The experienced average time for both writing and reading values is 1.5 ms, with a maximum recorded delay of 2s (more than a thousand times the average). Measurements done in a DELL laptop XPS 15 9570 with Windows 10 Enterprise. The authors recommend using the multithreading capabilities of Unity to prevent the virtual environment from freezing due to spikes in communication delay by instead relegating this task to a background thread.

As many simulations as required can be connected, although the authors recommend restricting to a single simulation per scene to restrict complexity and troubleshooting. In some cases, however, use of many simultaneous simulations might be advisable: for example, virtual educational simulations designed to show learners the different behaviours of same systems under different inputs or thermodynamic packages simultaneously.

The hysys type library is comprehensive, and as far as the authors have been able to observe, any interaction that a user can perform though the user interface can be performed as well through the framework: creating new operations, flow streams, changing any connection, setting the properties package, etc., are all feasible. However, the authors discourage giving too much freedom to the user, since flowsheet simulators are well known to crash under badly calculated changes: designers should keep limitations in mind.

4. Demonstration example

For demonstration, a dynamic simulation of the esterification of acetic anhydride with methanol, using sulphuric acid as homogeneous catalyst in a CSTR is implemented in Aspen HYSYS (see Figure 1), using the data provided by Chiara et al. (2018). The reaction has the potential to produce a runaway in the reactor when incorrectly handled.

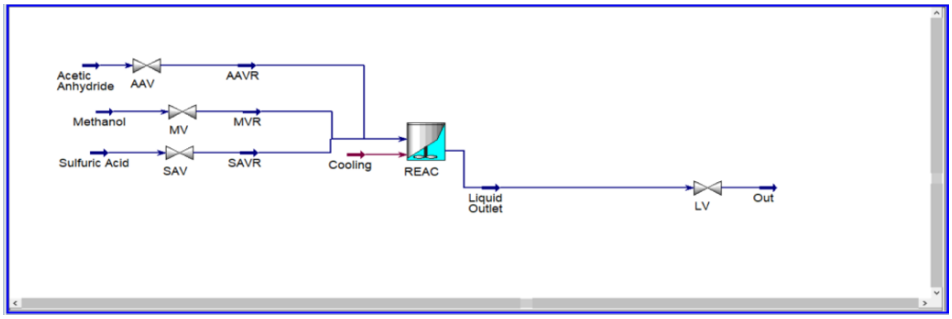

Figure 1: HYSYS Simulation of an esterification CSTR.

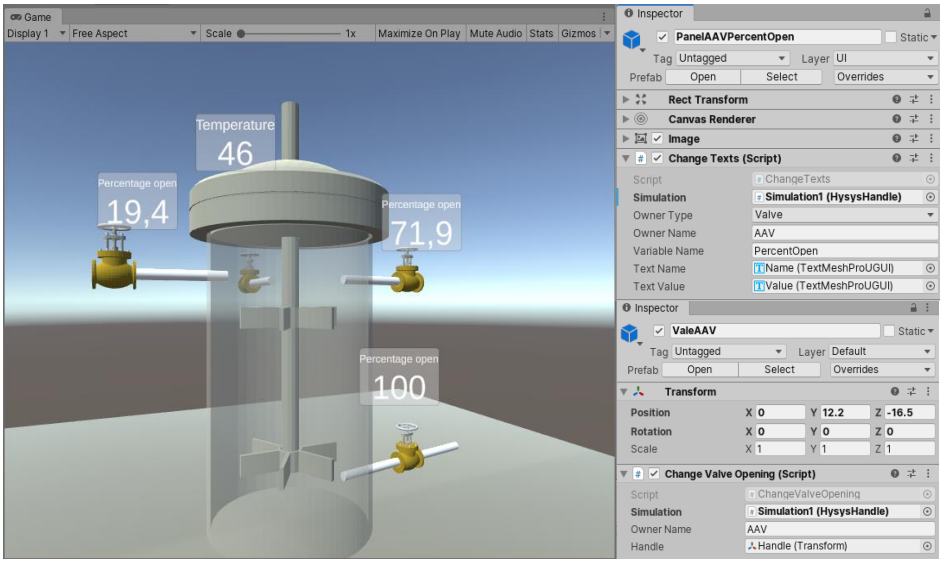

Figure 2: left: visual interface of Figure 1 in Unity. Right: objects interacting with HYSYS.

A VES is set up in Unity (see Figure 2 left, valve and reactor models thanks to GrabCAD (2019)), with a single "Simulation1" object that starts the simulation and stores it, and other objects that interact with the simulation: valves whose handle-rotation value will set the value of the valves in HYSYS, and texts that display the name and value of desired variables (Figure 2 right). It can be seen that once the connection is established, adding new linked objects in Unity requires no additional coding, as any variable from any object can be introduced just as text in the properties of the object, and all variables and elements are dynamically accessed. In the same way, adding new elements to the Aspen HYSYS simulation requires only saving the file.

5. Conclusion

A methodology was proposed for implementing the data exchange between Aspen HYSYS as simulator and Unity as virtual environment, through the use of ActiveX. The major limitation found was that vectors retrieved from HYSYS cannot be returned to Unity, which can be fully solved by preparing the simulation so that all relevant values can be recovered as a scalar. To demonstrate the methodology, a dynamic simulation was implemented of the esterification of acetic anhydride with methanol, using sulphuric acid as homogeneous catalyst in a CSTR.

Acknowledgements

This work has received funding from the European Union's EU Framework Programme for Research and Innovation Horizon 2020 under Grant Agreement 812716 as part of the CHARMING project (https://charming-etn.eu). This publication reflects only the author's view exempting the Community from any liability.

References

Ouyang, S. G., Wang, G., Yao, J. Y., Zhu, G. H. W., Liu, Z. Y., and Feng, C., 2018, A Unity3D-based interactive three-dimensional virtual practice platform for chemical engineering. Computer Applications in Engineering Education.

Ahmad, Z., Patle, D. S., and Rangaiah, G. P., 2016, Operator training simulator for biodiesel synthesis from waste cooking oil. Process Safety and Environmental Protection.

Heradio, R., De La Torre, L., Galan, D., Cabrerizo, F. J., Herrera-Viedma, E., and Dormido, S., 2016, Virtual and remote labs in education: A bibliometric analysis. Computers and Education.

Nazir, S., and Manca, D., 2015, How a plant simulator can improve industrial safety. Process Safety Progress.

Manca, D., Brambilla, S., and Colombo, S., 2013, Bridging between Virtual Reality and accident simulation for training of process-industry operators. Advances in Engineering Software.

Vaquerizo, L., and Cocero, M. J., 2018, CFD–Aspen Plus interconnection method. Improving thermodynamic modeling in computational fluid dynamic simulations. Computers and Chemical Engineering.

Mendes, D., Marangoni, C., Meneguelo, A. P., MacHado, R. A. F., and Bolzan, A., 2010, Educational simulator for multicomponent distillation research and teaching in chemical engineering, Computer Applications in Engineering Education.

Aldrich, C., 2005, Learning by Doing : A Comprehensive Guide to Simulations, Computer Games, and Pedagogy in e-Learning and Other Educational Experiences.

AspenTech, 2011, Aspen HYSYS: Customization Guide, Chapter 2: Automation.

GrabCAD, 2019, http://grabcad.com, Model authors: reactor: Edson M. J., valves: Yateesh P. A.

AUTHOR INDEX